Power Ultrasonics

Woodhead Publishing Series in Electronic and Optical Materials

Power Ultrasonics

Applications of High-Intensity Ultrasound

Second Edition

Edited by

Juan A. Gallego-Juárez
Higher Council for Scientific Research (CSIC), Madrid, Spain

Karl F. Graff
EWI, Columbus, OH, United States; The Ohio State University, Columbus, OH, United States

Margaret Lucas
James Watt School of Engineering, University of Glasgow, Glasgow, United Kingdom

WP
WOODHEAD PUBLISHING
ELSEVIER An imprint of Elsevier

Woodhead Publishing is an imprint of Elsevier
50 Hampshire Street, 5th Floor, Cambridge, MA 02139, United States
The Boulevard, Langford Lane, Kidlington, OX5 1GB, United Kingdom

Copyright © 2023 Elsevier Ltd. All rights reserved.

No part of this publication may be reproduced or transmitted in any form or by any means, electronic or mechanical, including photocopying, recording, or any information storage and retrieval system, without permission in writing from the publisher. Details on how to seek permission, further information about the Publisher's permissions policies and our arrangements with organizations such as the Copyright Clearance Center and the Copyright Licensing Agency, can be found at our website: www.elsevier.com/permissions.

This book and the individual contributions contained in it are protected under copyright by the Publisher (other than as may be noted herein).

Notices

Knowledge and best practice in this field are constantly changing. As new research and experience broaden our understanding, changes in research methods, professional practices, or medical treatment may become necessary.

Practitioners and researchers must always rely on their own experience and knowledge in evaluating and using any information, methods, compounds, or experiments described herein. In using such information or methods they should be mindful of their own safety and the safety of others, including parties for whom they have a professional responsibility.

To the fullest extent of the law, neither the Publisher nor the authors, contributors, or editors, assume any liability for any injury and/or damage to persons or property as a matter of products liability, negligence or otherwise, or from any use or operation of any methods, products, instructions, or ideas contained in the material herein.

ISBN: 978-0-12-820254-8 (print)
ISBN: 978-0-323-85144-2 (online)

For information on all Woodhead publications
visit our website at https://www.elsevier.com/books-and-journals

Publisher: Matthew Deans
Acquisitions Editor: Kayla Dos Santos
Editorial Project Manager: Zsereena Rose Mampusti
Production Project Manager: Prem Kumar Kaliamoorthi
Cover Designer: Miles Hitchen

Typeset by STRAIVE, India



Contributors

Numbers in parentheses indicate the pages on which the authors' contributions begin.

A. Alippi (53), La Sapienza Univefrsità di Roma, Rome, Italy

R.R. Andrés (109,743), Pusonics S.L., Pico Muihacén, Arganda del Rey, Madrid, Spain

M. Ashokkumar (701), University of Melbourne, Melbourne, VIC, Australia

F. Baillon (721), University of Toulouse, IMT Mines Albi, Research Centre in Particulate Solid Process Engineering, Energy and Environment (RAPSODEE UMR CNRS 5302), Albi CT, France

L. Barthe (665), Laboratoire de Génie Chimique, Toulouse, France

A. Benatar (205), The Ohio State University, Columbus, OH, United States

A.P. Bhat (639), Institute of Chemical Technology, Mumbai, India

J.A. Carcel (743), Universitat Politècnica de València, Valencia, Spain

A. Cardoni (109, 687), Independent Consultant, Madrid, Spain

F. Chemat (701), Université d'Avignon et des Pays du Vaucluse, Avignon, France

R. Cleary (539, 617, 665, 817, 887), James Watt School of Engineering, University of Glasgow, Glasgow, United Kingdom

R.O. Cleveland (599), Department of Engineering Science, University of Oxford, Oxford, United Kingdom

C. Cogné (721), University of Lyon, University Claude Bernard Lyon 1, Laboratory of Process Control and Chemical Engineering (LAGEPP UMR CNRS 5007), Villeurbanne, France

G. Cravotto (833), Department of Drug Science and Technology, University of Turin, Turin, Italy

Ch. Croënne (147), Univ Lille, CNRS, Ecole Centrale, Junia, Univ Valenciennes, IEMN, UMR, Lille Cedex, France

H. Delmas (665), Laboratoire de Génie Chimique, Toulouse, France

B. Dubus (147), Univ Lille, CNRS, Ecole Centrale, Junia, Univ Valenciennes, IEMN, UMR, Lille Cedex, France

N.P.K. Ellens (577), Acertara Acoustic Labs, Longmont, CO, United States

D.G. Eskin (473, 489), Brunel Centre for Advanced Solidification Technology, Brunel University London, Uxbridge, United Kingdom

F. Espitalier (721), University of Toulouse, IMT Mines Albi, Research Centre in Particulate Solid Process Engineering, Energy and Environment (RAPSODEE UMR CNRS 5302), Albi CT, France

R.J. Friel (227), Halmstad University, Halmstad, Sweden

F.J. Fuchs (455), Blackstone-NEY Ultrasonics (A Division of the Cleaning Technologies Group), Jamestown, NY, United States

L.F. Gaete-Garretón (509), Department of Physics, Universidad de Santiago de Chile, Santiago, Chile

J.A. Gallego-Juárez (1, 109, 687, 743, 861), Pusonics S.L., Pico Muihacén, Arganda del Rey, Madrid, Spain

J.V. García-Pérez (743), Universitat Politècnica de València, Valencia, Spain

A. Gedanken (431), Bar-Ilan University, Israel

P.R. Gogate (639, 773), Institute of Chemical Technology, Mumbai, India

I. González-Gómez (861), Consejo Superior de Investigaciones Científicas (CSIC), Madrid, Spain

K.F. Graff (1, 83, 163, 243, 277, 341), EWI, Columbus, OH, United States

P. Harkness (531), James Watt School of Engineering, University of Glasgow, United Kingdom

M. Hodnett (131), National Physical Laboratory, Teddington, United Kingdom

K. Hynynen (577), Sunnybrook Research Institute; University of Toronto, Toronto, ON, Canada

R.A. Khaire (773), Institute of Chemical Technology, Mumbai, India

J.D. Kramlick (455), Blackstone-NEY Ultrasonics (A Division of the Cleaning Technologies Group), Jamestown, NY, United States

S. Labouret (721), University of Lyon, University Claude Bernard Lyon 1, Laboratory of Process Control and Chemical Engineering (LAGEPP UMR CNRS 5007), Villeurbanne, France

W. Lauterborn (23), Third Physical Institute, Georg-August-University Göttingen, Göttingen, Germany

Xi. Li (531), State Key Laboratory of Mechanics and Control of Mechanical Structures, Nanjing University of Aeronautics and Astronautics, Nanjing, China

Xu. Li (531), James Watt School of Engineering, University of Glasgow, United Kingdom

L.R. Lindamood (163), EWI, Columbus, OH, United States

X. Liu (243, 277), The Ohio State University, Columbus, OH, United States

O. Louisnard (721), University of Toulouse, IMT Mines Albi, Research Centre in Particulate Solid Process Engineering, Energy and Environment (RAPSODEE UMR CNRS 5302), Albi CT, France

M. Lucas (1, 617), James Watt School of Engineering, University of Glasgow, Glasgow, United Kingdom

M. Marcus (205), EWI, Columbus, OH, United States

T.J. Mason (701), Coventry University, Coventry, United Kingdom

M.P. Matheny (163), EWI, Columbus, OH, United States

A. Mathieson (617), Thales Group UK, Reading, United Kingdom

R. Mettin (23), Third Physical Institute, Georg-August-University Göttingen, Göttingen, Germany

A. Mishra (599), Department of Engineering Science, University of Oxford, Oxford, United Kingdom

A. Moghaddas (341), EWI, Columbus, OH, United States

P. Mosbah (147), Univ Lille, CNRS, Ecole Centrale, Junia, Univ Valenciennes, IEMN, UMR, Lille Cedex, France

A. Mulet (743), Universitat Politècnica de València, Valencia, Spain

K. Nakamura (413), Institute of Innovative Research, Tokyo Institute of Technology, Tokyo, Japan

U. Neis (817), Ultrawaves GmbH, Hamburg, Germany

M. Norfolk (227), Fabrisonic LLC, Columbus, OH, United States

A.B. Pandit (639), Institute of Chemical Technology, Mumbai, India

L. Pardo (65), Instituto de Ciencia de Materiales de Madrid. Consejo Superior de Investigaciones Científicas (CSIC), c/ Sor Juana Inés de la Cruz, Cantoblanco, Madrid, Spain

R. Peczalski (721), University of Lyon, University Claude Bernard Lyon 1, Laboratory of Process Control and Chemical Engineering (LAGEPP UMR CNRS 5007), Villeurbanne, France

I. Perelshtein (431), Bar-Ilan University, Israel

N. Perkas (431), Bar-Ilan University, Israel

C. Pétrier (797), Université Joseph Fourier, Grenoble, France; King Abdulaziz University, Jeddah, Saudi Arabia

P. Prentice (131), Centre for Medical and Industrial Ultrasonics, University of Glasgow, Glasgow, United Kingdom

E. Riera (109, 687, 743, 861), Pusonics S.L., Pico Muihacén, Arganda del Rey; Consejo Superior de Investigaciones Científicas (CSIC), Madrid, Spain

G. Rodríguez (109, 687, 861), Pusonics S.L., Pico Muihacén, Arganda del Rey, Madrid, Spain

O.A. Sapozhnikov (7), Moscow State University, Moscow, Russia; University of Washington, Seattle, WA, United States

M.E. Schafer (539), Drexel University, Philadelphia, PA, United States

J.F. Sheehan (83), JFS Engineering, Ipswich, MA, United States

B.K. Tiwari (701), Teagasc Food Research Centre, Ashtown, Dublin, Ireland

I. Tzanakis (489), Faculty of Technology, Design and Environment, Oxford Brookes University, Oxford, United Kingdom

Y.P. Vargas-Hernández (509), Department of Physics, Universidad de Santiago de Chile, Santiago, Chile

A.R. Videla (509), School of Engineering, Mining Engineering Department, Pontificia Universidad Católica de Chile, Santiago, Chile

J. Virkutyte (887), Hammontree & Associates Ltd, North Canton, OH, United States

A.D. Walmsley (557), School of Dentistry, University of Birmingham, Birmingham, United Kingdom

Z. Wei (797), Centre for Water Technology (WATEC) & Department of Biological and Chemical Engineering, Aarhus University, Aarhus, Denmark

Z. Wu (833), Department of Drug Science and Technology, University of Turin, Turin, Italy

Ch. Zhao (531), State Key Laboratory of Mechanics and Control of Mechanical Structures, Nanjing University of Aeronautics and Astronautics, Nanjing, China

X. Zhu (701), Teagasc Food Research Centre, Ashtown; University College Dublin, Dublin, Ireland

About the editors

Juan A. Gallego-Juárez is Research Professor at the Spanish Higher Council for Scientific Research (CSIC), Madrid, Spain, where he founded the Ultrasound Laboratory in 1971 and was Director of the "Instituto de Acústica" for more than 12 years. He was also Director of the Center for Physics Technologies that integrated several research institutes. After his mandatory retirement in 2011, he continued for 7 years in the CSIC in the position "ad Honorem." Since 2018, he has been the president of Pusonics S.L., a company he founded in 2008. He was awarded the Rayleigh Medal 2017 by the Institute of Acoustics (United Kingdom).

Karl F. Graff is an international authority in the field of power ultrasonics, including transducers, applications, and systems. Graff led the efforts to found EWI and was the company's executive director from 1987 to 2000. He oversaw EWI's growth from a small startup to a world-leading organization in materials joining and allied manufacturing technologies. Since 2000, he has been researching in power ultrasonics in varied manufacturing processes and continues teaching and advising graduate students at the Ohio State University.

Margaret Lucas FREng FRSE holds the Regius Chair of Civil Engineering and Mechanics at the University of Glasgow, where she is also Professor of Ultrasonics and Director of the Centre for Medical & Industrial Ultrasonics in the James Watt School of Engineering. Her research is focussed on power ultrasonics across medical, manufacturing, space and terrestrial exploration applications, currently mainly working on ultrasonic surgical devices.

Chapter 1

Introduction to power ultrasonics

J.A. Gallego-Juárez[a], K.F. Graff[b], and M. Lucas[c]

[a]*Pusonics S.L., Pico Muihacén, Arganda del Rey, Madrid, Spain,* [b]*EWI, Columbus, OH, United States,* [c]*James Watt School of Engineering, University of Glasgow, Glasgow, United Kingdom*

1.1 Introduction

Power ultrasonics creates a broad range of phenomena that occur with the application of intense, inaudible acoustic waves to materials and processes. Even now, well into the twenty-first century, it is difficult to better express the fascination of our field than to quote the observation of Hubbard (1936) that "While it is a logical extension of well-known principles, its growth has been signalized by the discovery of phenomena peculiar to the new range of frequencies" (Graff, 1981). Our field, which now encompasses an already enormous range of phenomena and applications, continues to expand with each year revealing new inquiries and uses in scientific, engineering, industrial, chemical, medical, and biological applications. These chapters will continue the exploration of "phenomena peculiar" to these intense, high-frequency waves that defines *power ultrasonics*.

This 2nd edition will both build upon and extend the coverage of the 1st edition. It will build upon through retaining significant content from the previous edition, thus permitting the first-time reader to have at hand the extensive past developments without need for reference to the earlier work. However, in all cases, prior work has been extended with the most recent developments in the varied fields, these being augmented by new chapters on topics in engineering, medical, and materials applications.

1.2 The field of power ultrasonics

Power ultrasonics lies within the broad field of ultrasonics that is itself a branch of acoustics dealing with the generation and use of inaudible acoustic waves. While the audible upper limit of frequency in humans varies with age, occupation, and other factors, it is generally considered as 20 kHz. The science and technology of acoustics, which encompasses such diverse areas as speech, seismology, architecture, and music, touches every facet of human existence. Ultrasonics covers diverse topics such as underwater sound, medicine, electrical, chemical, and engineering applications. The field of ultrasonics may be divided into two broad areas:

- Low-intensity, high-frequency applications.
- High-intensity, low-frequency applications.

While it is difficult to fix the limit between low- and high-intensity waves, it can be approximately established for intensity values that, depending on the medium, vary between 0.1 and 1 W/cm^2 (Gallego-Juarez, 1999). In the case of low-intensity, high-frequency applications, some common examples are ultrasonic nondestructive testing; ultrasonic imaging, which is widely used in medicine; ultrasonic-range finders; and surface acoustic waves, used in electronics. In accordance with the low-intensity levels required, the power levels applied to the transducers are also typically low, often in the milliwatt range, while frequencies are high, typically in the megahertz and higher ranges (e.g., nondestructive testing typically operates at 2 MHz or higher). The general purpose of this field is the use of ultrasound as a means of exploration, detection, and information transfer (e.g., the location of a crack, the shape of a human form, the transmission of a signal). Every definition has exceptions; submarine sonar, for example, while used to convey information, may operate at high power levels. It is well known, of course, that the human use of high-frequency sound was long preceded by nature, for example, in bats and dolphins who use these frequencies for navigation and communication.

Power ultrasonics is the area of ultrasound devoted to the study of high-intensity applications. In this field, ultrasonics is used to *permanently change the physical, chemical, or biological properties of materials or systems to which it is applied*. Power levels for these uses may be in the range of 10s, 100s, or 1000s of watts, while frequencies may be low, in the order of 1000s of Hz. Typical operating frequencies for most power applications will range between 20 and 100 kHz, although some may be as low as 10 kHz and as high as 500 kHz. Some chemical and cleaning applications, for electronic components, may be in the megahertz range. The applications of power ultrasonics are generally

Power Ultrasonics. https://doi.org/10.1016/B978-0-12-820254-8.00039-7
Copyright © 2023 Elsevier Ltd. All rights reserved.

based on the effects of nonlinear phenomena created by high-intensity waves and include wave distortion, acoustic saturation, radiation pressure, streaming, cavitation in liquids, and formation and motion of dislocations in solids.

As a result of these nonlinear phenomena, a series of mechanisms may be activated by the ultrasonic energy. These include heat, agitation, diffusion, interface instabilities, friction, mechanical rupture, and chemical effects. These mechanisms can be employed to produce or enhance a wide range of processes that are dependent on the irradiated medium. A typical characteristic of high-intensity ultrasonic waves is their ability to produce different effects in different media to such an extent that they may appear to be opposites. For example, the application of power ultrasound to liquid suspensions produces particle dispersion, whereas its application to gas suspensions creates particle agglomeration. Such apparently opposing behaviors are due to the different mechanisms activated, which largely depend on the specific medium.

The many applications of power ultrasonics include the welding of metals and polymers, machining and metal forming in solids and fluids, cleaning, emulsification and dispersion, degassing, defoaming, particle agglomeration, drying, dewatering, and the enhancing of chemical reactions. Medical applications are another rapidly developing area in which high-intensity ultrasonic energy is used for noninvasive surgery, lithotripsy, and other therapeutic uses.

Although the demarcation between power ultrasonics and other areas of ultrasonics may be approximately indicated by the intensity levels, power densities, and/or frequency ranges, these boundaries are not always clear-cut. It should be kept in mind that the basic purpose of power ultrasonics is to permanently alter the characteristics of a material or system. It is this field of ultrasonics that is the subject of this book.

1.3 Historical notes

Although it is not known when humans first became aware of sounds beyond the limits of their hearing, the systematic study of these phenomena dates back to the early 1800s. The key developments from that era are significant in the field of power ultrasonics and include the discovery of the magnetostrictive effect by Joule, the piezoelectric effect by the Curie brothers, and the development of the ultrasonic whistle by Galton (Graff, 1981). Following the sinking of the Titanic in 1912, which resulted from a collision with an iceberg, many scientists rushed to develop acoustic methods for the detection of underwater obstacles. With the start of World War I, attention was focused on the detection of submarines. Work in this area came to fruition late in the war when the French scientist Langevin developed a powerful underwater sound projector based on quartz plates sandwiched between thick plates of steel.

The key development in power ultrasonics came when Professor Robert Wood, who had witnessed Langevin's experiments, showed that powerful ultrasonic waves gave rise to a number of unusual physical, chemical, and biological phenomena. Wood, in collaboration with Loomis (Wood and Loomis, 1927), demonstrated a range of effects, which included drilling, atomization, levitation, heating of tissue, flocculation, and crystallization. Since Wood and Loomis's landmark research, the field of power ultrasonics has broadened into many other applications, and advances have been made in understanding the science of many of the underlying phenomena. However, as will be evident in the pages that follow, accompanying these advances are challenging questions that remain on current and developing applications, not to mention new applications awaiting discovery.

1.4 Coverage of this book

The basic elements of a power ultrasonic system are shown in Figure 1.1 and consist of an electrical power source, having impedance matching and feedback control circuitry, driving a power ultrasonic transducer, which may be of piezoelectric or magnetostrictive construction. The acoustic output of the transducer is transmitted by a solid, liquid, or gaseous coupling medium into, interacting with and effecting a change in the material/process. This ultrasonic chain of events—generation, transmission, process/material interaction—provides the framework for a systematic coverage of power ultrasonics. This is reflected in the following overall contents of this book, which covers both the fundamentals and the state of art in this field.

In Part One: Fundamentals, Chapters 2 through 9, deal with the fundamental interactions of ultrasonic waves with materials, including fluids (Chapters 2 and 3); solids (Chapter 4, with selected coverage in Chapter 9); piezoelectric materials and transducers (Chapters 5–7, 9, with selected sections in Chapter 23); and methods of measuring ultrasonic processes (Chapter 8).

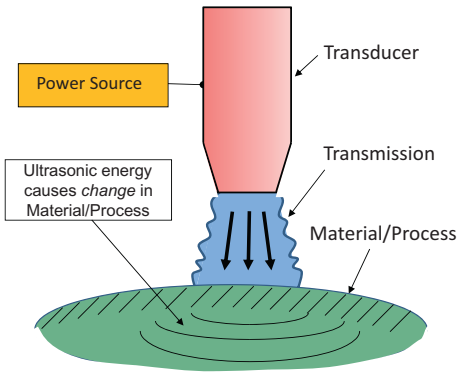


FIGURE 1.1 The power ultrasonic system. *(Source: EWI).*

In Part Two: Welding, metal forming, and machining applications, Chapters 10–15, cover the first of an array of power ultrasonic applications. Coverage is given to ultrasonic metal welding (Chapter 10); ultrasonic welding of plastics (Chapter 11); additive manufacturing (Chapter 12); and ultrasonic metal forming, including the effects of power ultrasound on the bulk and surface behavior of materials (Chapter 13), then on the wide range of forming processes (Chapter 14), and concluding with the application of ultrasonics to machine tool processes (Chapter 15).

In Part Three: Engineering applications, Chapters 16–22, diverse applications in these fields are explored, beginning with the field of ultrasonic motors (Chapter 16), followed by ultrasonic methods for the production of nanomaterials (Chapter 17); the long-standing field of ultrasonic cleaning, augmented by developments at high frequencies (Chapter 18); to the degassing of liquids (Chapter 19) is added new coverage on the solidification and casting of metals (Chapter 20); to the application of power ultrasound in mining (Chapter 21) is added a new chapter on a wide range of power ultrasonic measurement and exploration tools (Chapter 22).

Part Four: Medical applications, Chapters 23–27, cover varied surgical applications, including devices and procedures (Chapter 23), a new chapter on pulsed and shock wave surgeries (Chapter 26), and ultrasonic cutting in surgical applications (Chapter 27); another new chapter is added on ultrasonic dental instrumentation (Chapter 24) with new therapeutic developments being reviewed (Chapter 25).

Part Five: Food technology and pharmaceutical applications, Chapters 28–34. A diversity of applications is found in the food and pharmaceutical fields, beginning with the effects of cavitation in food processing (Chapter 28, supplementing cavitation coverage in Part One); homogenization and emulsification (Chapter 29); and defoaming and debubbling (Chapter 30). An overview of ultrasonic food processing, including the effects on food quality, is covered (Chapter 31), while the use of ultrasonics for freezing in the food and pharmaceutical industries (Chapter 32) and food drying (Chapter 33) is reviewed. Part Five concludes with the use of atomization in these industries (Chapter 34).

Part Six: Environmental and energy applications, Chapters 35–39. This concluding section of this book deals with the increasingly important field of environmental and energy applications. Application to water treatment (Chapter 35) is followed by uses for wastewater and biomass treatment (Chapter 36), the application to organic reactions in "green" chemistry (Chapter 37), and the agglomeration and conditioning of aerosols for environmental and other uses (Chapter 38). The section concludes with the use of power ultrasound in biofuel production and bioremediation (Chapter 39).

The reader is invited to learn, engage, and contribute to the continued growth of the field of power ultrasonics, which has been "signalized by the discovery of phenomena peculiar to the new range of frequencies."

References

Gallego-Juarez, J.A., 1999. High power ultrasound. In: Webster, J.G. (Ed.), Encyclopedia of Electrical and Electronics Engineering. vol. 9. John Wiley & Sons, Inc., New York, pp. 49–59.

Graff, K.F., 1981. A history of ultrasonics. In: Mason, W.P., Thurston, R.N. (Eds.), Physical Acoustics. Vol. 15. Academic Press, New York (Chapter 1).

Wood, R.W., Loomis, A.L., 1927. The physical and biological effects of high-frequency sound-waves of great intensity. Philos. Mag. 4 (22), 417.

Chapter 2

High-intensity ultrasonic waves in fluids: Nonlinear propagation and effects

O.A. Sapozhnikov[a,b]

[a]*Moscow State University, Moscow, Russia,* [b]*University of Washington, Seattle, WA, United States*

2.1 Introduction

Modern applications of power ultrasonics that encompass a wide variety of industrial processes and medical procedures are intrinsically associated with high levels of acoustic intensity. These high intensities lead to desired changes in the treated medium by initiation of one or more diverse mechanisms such as acoustic cavitation, heating, microfracture, or chemical reactions. Some applications do not involve ultrasound propagation effects; this is especially true when the wavelength is larger than the treated volume size, and thus, the ultrasonic excitation can be considered as a concentrated mechanical vibration. Other recent applications have been developed in which the wave nature of ultrasound plays a significant role. In the corresponding devices, the ultrasound wave propagates many wavelengths from the source before reaching the region where it initiates a particular interaction with the medium.

Intense ultrasound waves behave differently from low-intensity waves: they propagate nonlinearly and can change the medium parameters or, if intense enough, even destroy the medium. The branch of acoustics that deals with such waves is called *nonlinear acoustics*. Nowadays, it is a fairly well-developed field of science. Although the first theoretical studies on this subject were performed several centuries ago, the main progress was made relatively recently, in the second half of the 20th century. The basics of nonlinear acoustics can be found in several books on the subject written during that time (Beyer, 1997; Zarembo and Krasilnikov, 1966; Rudenko and Soluyan, 1977; Hamilton and Blackstock, 2008; Naugolnykh and Ostrovsky, 1998). A detailed description of the history of nonlinear acoustics appears in a book chapter by Blackstock (Hamilton and Blackstock, 2008). Advances in nonlinear acoustics in the second half of the last century were motivated by progress in the development of intense ultrasound sources. Soon after the first experimental studies on intense ultrasound, it became clear that powerful acoustic radiation can be used in practical applications to develop new technologies. In this regard, it is worth mentioning a series of books written in the 1960–70s under the editorship of Rosenberg (Rosenberg, 1971). In these books, the key concepts of power ultrasonics were described or introduced. Since then, the field of nonlinear acoustics has continued to develop along with related applications (e.g., in medicine).

This chapter does not attempt to describe the nonlinear acoustics of fluids in detail. Performing such a task would need much more space. The goal here is to review only those nonlinear acoustic phenomena that are fairly fundamental and thus underlie many current applications of intense ultrasound waves.

In the description below, acoustic waves are presumed to propagate in a classical thermoviscous fluid. In the framework of linear acoustics, sound waves in such a medium propagate with a constant speed and do not influence the fluid. The situation changes, sometimes dramatically, if the wave intensity is increased. First of all, for high-intensity waves, the superposition principle is no longer valid—that is, two intersecting ultrasound beams influence each other, or interact. Moreover, even a solitary wave starts to "feel" the nonlinearity—it interacts with itself by changing its own propagation speed; as a result, the initial wave can become severely distorted at some distance from the source. Another type of nonlinear acoustic effect is associated not with unusual changes in the acoustic field characteristics, but with the potential for a wave to influence the propagation medium itself: heat it, move it, and even destroy it. Understanding of the basic mechanisms of such nonlinear effects is very important in practical applications of intense acoustic waves.

2.2 Nonlinear phenomena

2.2.1 Basic equations. Acoustic, entropy, and vorticity modes

It may not always be obvious whether a considered process is linear or nonlinear. It is known that the classical wave equation follows from the basic hydrodynamics equations

Power Ultrasonics. https://doi.org/10.1016/B978-0-12-820254-8.00014-2
Copyright © 2023 Elsevier Ltd. All rights reserved.

after considering them in the linear approximation (linearization) (Pierce, 1994). To describe nonlinear waves, we have to go back to the initial set of hydrodynamics equations with the goal of finding a nonlinear wave equation that generalizes the linear theory of an acoustic field. The behavior of a classical thermoviscous fluid can be described based on the momentum and mass conservation equations as well as the entropy equation (Landau and Lifshits, 1987):

$$\rho\left[\frac{\partial \mathbf{v}}{\partial t}+(\mathbf{v}\cdot\nabla)\mathbf{v}\right]=-\nabla p+\eta\Delta\mathbf{v}+\left(\zeta+\frac{\eta}{3}\right)\nabla(\nabla\cdot\mathbf{v}), \tag{2.1}$$

$$\frac{\partial \rho}{\partial t}+\nabla\cdot(\rho\mathbf{v})=0, \tag{2.2}$$

$$\rho T\left[\frac{\partial s}{\partial t}+(\mathbf{v}\cdot\nabla)s\right]=\kappa\Delta T+\frac{\eta}{2}\left(\frac{\partial v_i}{\partial x_j}+\frac{\partial v_j}{\partial x_i}-\frac{2}{3}\delta_{ij}\nabla\cdot\mathbf{v}\right)^2+\zeta(\nabla\cdot\mathbf{v})^2. \tag{2.3}$$

Here ρ is density, $\mathbf{v}=(v_1,v_2,v_3)$ is particle velocity, p is pressure, T is temperature, s is entropy, η is the shear viscosity, ζ is the bulk viscosity, κ is the thermal conductivity coefficient, and δ_{ij} is the Kronecker delta. Eq. (2.1) is the well-known Navier-Stokes equation. The four thermodynamic variables p, ρ, s, and T are related by the following differential relations:

$$d\rho=dp/c^2-ds\cdot\alpha_V T\rho/c_p, \tag{2.4}$$

$$dT=dp\cdot\alpha_V T/(\rho c_p)+ds\cdot T/c_p. \tag{2.5}$$

Here $c=\sqrt{(\partial p/\partial\rho)_s}$, $\alpha_V=-\rho^{-1}(\partial\rho/\partial T)_p$, and $c_p=T(\partial s/\partial T)_p$ are the speed of sound, the volumetric coefficient of thermal expansion, and the specific heat. The relations mean that the corresponding temporal or spatial derivatives are related accordingly, e.g., $\nabla T=\nabla p\cdot\alpha_V T/(\rho c_p)+\nabla s\cdot T/c_p$. In Eqs. (2.1) and (2.3), it is assumed for simplicity that the viscosity coefficients η, ζ and the thermal conductivity coefficient κ are constants; for cases in which these coefficients vary in space and time, the equations should be written in a more general form (Zarembo and Krasilnikov, 1966).

Consider the linear approximation. Suppose that an undisturbed medium is not moving ($\mathbf{v}=0$) and is characterized by the thermodynamic variables p_0, ρ_0, s_0, and T_0. Then, the disturbed state is characterized by perturbations $\mathbf{v}$, $p'=p-p_0$, $\rho'=\rho-\rho_0$, $s'=s-s_0$, and $T'=T-T_0$. Density and temperature perturbations can be expressed through the perturbations of pressure and entropy using the mentioned thermodynamic relations, Eqs. (2.4) and (2.5): $\rho'=p'/c_0^2-s'\alpha_V T_0\rho_0/c_p$, $T'=p'\alpha_V T_0/(\rho c_p)+s'T_0/c_p$, i.e., it is enough to consider only $\mathbf{v}$, p', and s'. Here, c_0 is the speed of sound in the equilibrium state. In the linear approximation, Eqs. (2.1)–(2.3) give:

$$\frac{\partial \mathbf{v}}{\partial t}=\frac{\eta}{\rho_0}\Delta\mathbf{v}+\frac{\zeta+\frac{\eta}{3}}{\rho_0}\nabla(\nabla\cdot\mathbf{v})-\frac{1}{\rho_0}\nabla p', \tag{2.6}$$

$$\frac{\partial p'}{\partial t}=-\rho_0 c_0^2\nabla\cdot\mathbf{v}+\frac{c_0^2\kappa\alpha_V^2 T_0}{\rho_0 c_p^2}\Delta p'+\frac{c_0^2\kappa\alpha_V T_0}{c_p^2}\Delta s', \tag{2.7}$$

$$\frac{\partial s'}{\partial t}=\frac{\kappa\alpha_V}{\rho_0^2 c_p}\Delta p'+\frac{\kappa}{\rho_0 c_p}\Delta s'. \tag{2.8}$$

From these equations, it follows that an arbitrary perturbation can be decomposed into three independent modes, which can be described as vorticity, acoustic, and entropy modes: $\mathbf{v}=\mathbf{v}_{vor}+\mathbf{v}_{ac}+\mathbf{v}_{ent}$, $p'=p_{vor}+p_{ac}+p_{ent}$, and so on (Beyer, 1997; Chu and Kovasznay, 1958). Far from the boundaries, those modes do not interact (within the linear approximation). In this case, acoustic waves are described by linear equations, and in addition, they are independent of the two other modes.

Let us briefly describe those three modes.

The vorticity mode is associated with the behavior of the solenoidal part of velocity field. It is known that any vector field in three dimensions can be resolved into the sum of an irrotational (curl-free) vector field and a solenoidal (divergence-free) vector field; this is known as the Helmholtz decomposition $\mathbf{v}=\nabla\times\mathbf{A}+\nabla\varphi$, where $\mathbf{A}$ and φ are called vector and scalar potentials. The solenoidal velocity field $\mathbf{v}_{vor}=\nabla\times\mathbf{A}$ is described by the following diffusion-type equation:

$$\frac{\partial \mathbf{v}_{vor}}{\partial t}=\frac{\eta}{\rho_0}\Delta\mathbf{v}_{vor}. \tag{2.9}$$

Only velocity is disturbed for this mode, and the thermodynamic state variables remain in their equilibrium states: $p_{vor}=0$, $s_{vor}=0$, $\rho_{vor}=0$, and $T_{vor}=0$. Note that velocity divergence is also unperturbed: $\nabla\cdot\mathbf{v}_{vor}=0$.

The next mode is *the acoustic mode*. The corresponding velocity field is a potential, that is, $\nabla\times\mathbf{v}_{ac}=0$. When neglecting small terms proportional to κ^2 and $\kappa(\zeta+4\eta/3)$, acoustic pressure is governed by the following wave equation:

$$\frac{\partial^2 p_{ac}}{\partial t^2}-c_0^2\Delta p_{ac}\approx\delta\frac{\partial}{\partial t}\Delta p_{ac}. \tag{2.10}$$

Here, $\delta=[4\eta/3+\zeta+\kappa(c_v^{-1}-c_p^{-1})]/\rho_0$ is the effective dissipation coefficient (i.e., the diffusivity of sound). Not only pressure but all other thermodynamic parameters are perturbed when the acoustic mode is excited. These perturbations can be expressed through the acoustic pressure and particle velocity distributions as follows: $s_{ac}\approx-\alpha_V\kappa/(\rho_0 c_p)\nabla\cdot\mathbf{v}_{ac}$, $\rho_{ac}=c_0^{-2}p_{ac}+c_0^{-2}\kappa(c_v^{-1}-c_p^{-1})\nabla\cdot\mathbf{v}_{ac}$, and $T_{ac}=\alpha_V T_0/(\rho_0 c_p)\cdot(p_{ac}-\kappa c_p^{-1}\nabla\cdot\mathbf{v}_{ac})$. It is worth noting that the total entropy change (the volume integral of s_{ac})

equals zero, which follows from the divergence theorem for $s_{ac} \sim \nabla \cdot \mathbf{v}_{ac}$ in the assumption that the medium at infinity is undisturbed. Note also that in the absence of viscosity and thermal conductivity, Eq. (2.10) takes the form of the classical wave equation for waves propagating with the sound velocity c_0, the entropy perturbations are absent $s_{ac}=0$, and the density and temperature perturbations are expressed through p_{ac} by the adiabatic relations $\rho_{ac}=c_0^{-2}p_{ac}$ and $T_{ac}=\alpha_V T_0/(\rho_0 c_p)p_{ac}$. Therefore, the acoustic mode is associated with sound waves, which explains its name.

The last of the three modes is called *the entropy mode*. When neglecting small terms proportional to κ^2, $\kappa(\zeta+4\eta/3)$, and higher orders, the entropy perturbation is described by the following diffusion-type equation:

$$\frac{\partial s_{ent}}{\partial t} \approx \frac{\kappa}{\rho_0 c_p}\Delta s_{ent}\,. \tag{2.11}$$

The rest of thermodynamic parameters in this approximation are $p_{ent}\approx 0$, $T_{ent}=T_0/c_p \cdot s_{ent}$, and $\rho_{ent}=-\alpha_V T_0\rho_0/c_p \cdot s_{ent}=-\rho_0\alpha_V T_{ent}$. Thermal expansion of the medium results also in some potential flow $\mathbf{v}_{ent}\approx\kappa\alpha_V T_0/(\rho_0 c_p^2)\cdot\nabla s_{ent}$. The entropy mode describes heat transfer phenomena; this name accounts for the fact that entropy fluctuations are the most significant in this mode, whereas they are relatively small in the acoustic mode and absent in the vorticity mode.

2.2.2 Scope of nonlinear acoustics

For power ultrasonics, it is important to know what happens when the linear approximation is no longer valid, that is, the perturbations are not weak. The most obvious consequence is violation of the superposition principle, which means the medium behavior can no longer be described in the form of three independent modes. As a generalization of the linear approach, an arbitrary flow field can still be described using three basic modes of fluctuations that interact with one another and with themselves (Pierce, 2002). Among all possible interactions, the following three types are activated when the acoustic wave becomes intense: "sound-sound," "sound-vorticity," and "sound-entropy" interactions. The corresponding processes are the main subjects of study in nonlinear acoustics (see Figure 2.1).

What are these phenomena? First, nonlinear processes happen within the acoustic mode, e.g., waveform distortion, harmonic generation, and self-demodulation. Second, intense perturbations of the acoustic mode start to interact with the two other modes; the corresponding processes include acoustically induced heating and the generation of hydrodynamic flows.

Note that the two nonacoustic modes can also interact with each other, e.g., thermal convection is an example when heating of the medium gives rise to streaming; in turn, flow of a viscous fluid results in heating or cooling. The nonacoustic modes can also influence the acoustic mode, e.g., sound generation by irregular flow or by heating of the medium (as in laser acoustics (Gusev and Karabutov, 1993)). However, traditionally those processes are not attributed to nonlinear acoustics, because the driving cause for the interactions is not the acoustic intensity.

2.3 Nonlinear interactions within the acoustic mode

2.3.1 Simple waves

The simplest way of illustrating the effects of nonlinearity within the acoustic mode is to consider one-dimensional motion of an ideal fluid (no viscosity, no thermal conductivity). In this case, $\mathbf{v}=(u,0,0)$, all the variables depend only on x and t, and Eqs. (2.1) and (2.2) take the following form:

$$\rho\left(\frac{\partial u}{\partial t}+u\frac{\partial u}{\partial x}\right) = -\frac{\partial p}{\partial x}, \tag{2.12}$$

$$\frac{\partial \rho}{\partial t}+\frac{\partial}{\partial x}(\rho u)=0. \tag{2.13}$$

The system of equations is completed by the adiabatic equation of state in general form:

$$p=p(\rho). \tag{2.14}$$

One-dimensionality excludes the vorticity mode, and the absence of dissipation makes the process adiabatic to exclude the entropy mode as well. Therefore,

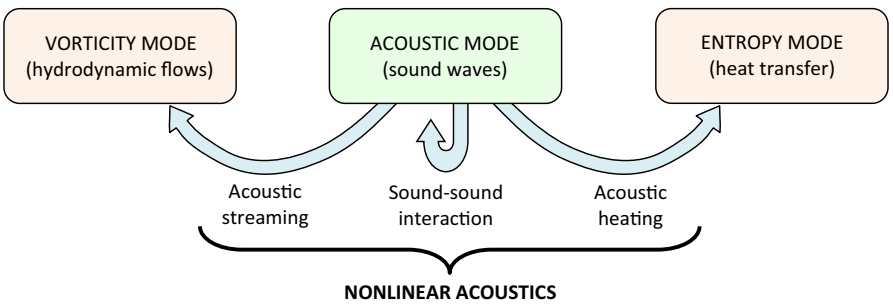


FIGURE 2.1 The subjects of study in nonlinear acoustics.

Eqs. (2.12)–(2.14) describe nonlinear behavior of the acoustic mode alone. Riemann showed a long time ago that these equations have an exact general solution in the form of waves. Because Riemann's approach elegantly introduces the concept of nonlinear acoustic waves, it is briefly presented here (a more detailed description can be found in most textbooks on nonlinear acoustics).

The derivation is based on an auxiliary function (Riemann's function)

$$\sigma = \int_{\rho_o}^{\rho} \frac{c(\tilde{\rho})}{\tilde{\rho}} d\tilde{\rho}, \tag{2.15}$$

where $c(\rho) = \sqrt{dp/d\rho}$ is sound velocity that corresponds to the density ρ. It can be easily shown that the system of Eqs. (2.12) and (2.13) can be written in the following form:

$$\frac{\partial J_+}{\partial t} + (u + c)\frac{\partial J_+}{\partial x} = 0, \tag{2.16}$$

$$\frac{\partial J_-}{\partial t} + (u - c)\frac{\partial J_-}{\partial x} = 0, \tag{2.17}$$

where $J_+ = (\sigma + u)/2$ and $J_- = (\sigma - u)/2$ are known functions of density (or pressure) and velocity. The system of Eqs. (2.15)–(2.17) is equivalent to the original system of Eqs. (2.12)–(2.14) but has a more convenient form that clearly shows that any possible motion of the medium is fully described by a superposition of two counter-propagating waves represented by the quantities $J_\pm$. Indeed, if an observer moves with the velocity $V_+ = u + c$, Eq. (2.16) provides $J_+ = \text{const}$, so that the quantity J_+ is an invariant in such a coordinate system. The same applies for J_- and $V_- = u - c$. The quantities J_+ and J_- are called *Riemann invariants* (Hamilton and Blackstock, 1998). The structure of the wave velocities $V_\pm$ has a clear physical sense: in the coordinate frame moving with the medium (i.e., with velocity u) the waves $J_\pm$ move with velocities $\pm c$, which should not be surprising as c is the local speed of sound. For an outside observer, the flow velocity u is added to the local wave velocity $\pm c$, which explains the expressions $V_\pm = u \pm c$.

Several important conclusions about nonlinear acoustic waves can be made from Eqs. (2.16) and (2.17). Note that u and c can be expressed through J_+ and J_-, and therefore, propagation velocities for those two waves depend on the invariants themselves: $V_\pm = V_\pm(J_+, J_-)$. That means the counter-propagating waves are interacting, but only "parametrically," through influencing each other's propagation velocities. In many practical cases, this interaction can be considered as negligible, which simplifies the analysis. For instance, intense standing waves in resonators can be considered as a superposition of noncoupled counter-propagating nonlinear waves (Kaner et al., 1977).

The very fact that the general solution of the nonlinear problem has a form of a superposition of two counter-propagating waves, similar to the linear case, is remarkable and not obvious. One of the consequences of this fact is the possibility of the existence of nonlinear waves propagating in only one direction, so-called simple waves. Such a solution corresponds to the case when one of the invariants is unperturbed, that is, equal to zero. Consider, for instance, a flow having an unperturbed backward Riemann invariant $J_- = 0$. Then, $\sigma = u$ and the forward invariant becomes $J_+ = u$. Eq. (2.16) transforms to the following:

$$\frac{\partial u}{\partial t} + (u + c)\frac{\partial u}{\partial x} = 0. \tag{2.18}$$

This equation is frequently named the *simple wave equation*; it governs a finite-amplitude acoustic wave propagating in the forward direction. A similar equation can be written for the wave propagating in the backward direction. The corresponding waves are "simple" in the sense that they are progressive, that is, propagate in only one direction, contrary to the general case when the flow is a superposition of counter-propagating waves.

Note that the relation $\sigma(\rho) = u$ means that, in the simple wave, the medium density ρ can be expressed through u, and thus, the same can be done for pressure: $\rho = \rho(u)$, $p = p(u)$; that is, among the three variables p, ρ, and u, only one is independent. A consequence of this result is the fact that the local speed of sound c also depends on the velocity u and so does the local wave propagation velocity: $V_+ = c(u) + u$. This fact means that the acoustic nonlinearity has a simple manifestation: it merely makes the propagation velocity of different parts of the waveform different. In the linear approximation, Eq. (2.18) transforms to $\partial u/\partial t + c_0 \partial u/\partial x = 0$, which has a general solution in the form a wave propagating without distortion with sound velocity c_0. Contrarily, in the nonlinear case, parts of the waveform with higher u propagate faster than those with lower u; accordingly, the initial waveform shape becomes distorted.

As mentioned, transition from the linear regime to a nonlinear one corresponds to the change $c_0 \to u + c$. From here, it is seen that there are two independent sources of the acoustic nonlinearity: (1) change of the wave speed due to the medium drift with velocity u and (2) change of the local sound velocity from c_0 to c. The first cause of nonlinearity can be called *convective nonlinearity,* and the second one is *material nonlinearity* (it is caused by the nonlinearity in the equation of state relating pressure and density, Eq. (2.14)).

In many practical cases, acoustic waves are radiated by vibrating sources, and therefore, one has to solve a boundary-value problem; for example, when the particle velocity $u(x,t)$ is given at $x = 0$: $u(0,t) = \Phi(t)$. For such a case, it is convenient to rewrite the simple wave equation as

$$\frac{\partial u}{\partial x} + \frac{1}{c + u}\frac{\partial u}{\partial t} = 0. \tag{2.19}$$

It has the following general solution

$$u = \Phi\left(t - \frac{x}{c + u}\right). \tag{2.20}$$

2.3.2 Quadratic approximation

In the majority of practical situations, the acoustic perturbations are small, and it is sufficient to describe nonlinear effects in the quadratic approximation. In this approximation, the adiabatic equation of state, Eq. (2.14), is usually written as

$$p = p_0 + A\frac{\rho - \rho_0}{\rho_0} + \frac{B}{2}\left(\frac{\rho - \rho_0}{\rho_0}\right)^2 + \ldots$$

Because this is simply a Taylor series, the constants used here are $A = \rho_0(dp/d\rho)_0 = \rho_0 c_0^2$ and $B = \rho_0^2(d^2p/d\rho^2)_0$. From here, it follows that

$$c = c_0\left(1 + \frac{B}{2A}\frac{\rho - \rho_0}{\rho_0} + \ldots\right),$$

$$u = \sigma = \frac{c_0}{\rho_0}(\rho - \rho_0) + \ldots,$$

and therefore, the corrected local speed of sound is expressed through particle velocity as

$$c = c_0 + \frac{B}{2A}u + \ldots$$

This allows the simple wave Eq. (2.18) to be written in the quadratic approximation:

$$\frac{\partial u}{\partial x} + \frac{1}{c_0}\frac{\partial u}{\partial t} = \frac{\beta}{c_0^2}u\frac{\partial u}{\partial t} \tag{2.21}$$

where the factor

$$\beta = 1 + \frac{B}{2A} \tag{2.22}$$

is called the *coefficient of acoustic nonlinearity*. Its value for most gases and liquids ranges from 1 to 10 (Hamilton and Blackstock, 2008). To account for the linear propagation time delay, it is convenient to introduce the retarded time variable $\tau = t - x/c_0$, thereby considering the waveform as a function of (x, τ) instead of (x, t). Then, the simple wave equation with the quadratic approximation of Eq. (2.21) has a shorter form:

$$\frac{\partial u}{\partial x} = \frac{\beta}{c_0^2}u\frac{\partial u}{\partial \tau} \tag{2.23}$$

Eq. (2.23) has the following exact solution:

$$u = \Phi\left(\tau + u\frac{\beta x}{c_0^2}\right) \tag{2.24}$$

Here, $\Phi(\tau) = u(0, \tau)$ describes the original waveform. It can be seen that the solution, Eq. (2.24), is a quadratic approximation of the exact solution, Eq. (2.20), of the original simple wave equation.

2.3.3 Nonlinear distortion and shock formation

Although solution (2.24) for a nonlinear wave has an implicit form, it allows an exact description of the nonlinear waveform distortion over some propagation distance x. In particular, Eq. (2.24) can be written as $u = \Phi[\tau - \Delta\tau(x, u)]$, where $\Delta\tau = -\beta x u/c_0^2$ expresses an additional time delay (or an advance, depending on the sign of u) for the arrival of a waveform part where the particle velocity equals u. It is seen that the delay $\Delta\tau_{nonl}$ is proportional to u and thus is different for different parts of the waveform. This inevitably causes waveform distortion. It is also important that $\Delta\tau_{nonl}$ is proportional to the travel distance x, which means such nonlinear distortion is initially small but accumulates. Nonlinear waveform distortion was discovered theoretically in the nineteenth century, and there are many excellent discussions on this subject in many textbooks.

One of the important consequences of nonlinear distortion is the formation of shocks (discontinuities) in the waveform. At a shock, all the quantities u, p, and ρ undergo an abrupt jump. Strictly speaking, the possibility of shock formation does not follow from the simple wave solution. Instead, solutions (2.20) or (2.24) predict the formation of nonphysical multivalued waveforms. Because Eq. (2.20) is an exact solution of the set of hydrodynamics Eqs. (2.12–2.14), the appearance of the multivalued waveforms indicates some serious flaw in the original mathematical formulation of the ideal fluid dynamics. This may sound mysterious because Eqs. (2.12) and (2.13) are nothing but the conservation of momentum and mass, and Eq. (2.14) is a general form of equation of state.

This multivalued waveform paradox was a major unsolved problem of fluid mechanics until the end of the nineteenth century. Its resolution came with the discovery and understanding of shock waves. It became clear that in the nonlinear case, the ideal fluid model cannot be applied to real media. When the waveform becomes steep due to nonlinear waveform distortion, the energy dissipation caused by viscosity and thermal conductivity becomes inevitable and cannot be neglected, even if the constants characterizing viscosity and thermal conductivity are very small. As a result, shocks are formed that prevent the multivalued waveforms. The analysis of acoustic perturbations containing shocks shows that the corresponding nonlinear wave cannot be one-directional, because such a wave partly reflects from its own shock front. Moreover, the equation of state cannot be adiabatic anymore, because the dissipation at the shock produces entropy, that is, excites the entropy mode. Fortunately (for theoreticians), those effects are negligible in the quadratic approximation, and for all practical cases, the nonlinear acoustic waves can still be considered as progressive.

As mentioned, nonlinear distortion accumulates gradually during finite-amplitude wave propagation. Therefore, shocks cannot appear immediately near a source if the radiated acoustic waveform is smooth. To learn whether a given ultrasound field contains shocks, it is important to compare the distance from the source with the theoretically predicted shock formation distance. The shock formation distance x_s corresponds to the first appearance of infinitely steep waveform regions ($\partial u/\partial\tau \to \infty$). This distance is easy to calculate in the case of plane waves in an ideal fluid. Eq. (2.24) provides

$$x_s = \frac{c_0^2}{\beta \max\left(\partial u/\partial\tau|_{x=0}\right)} = \frac{\rho_0 c_0^3}{\beta \max\left(\partial p/\partial\tau|_{x=0}\right)}. \quad (2.25)$$

Here, the linear relation $p = \rho_0 c_0 u$ between acoustic pressure and particle velocity has been used. The steeper is the initial waveform, the shorter is the shock formation distance. If P_0 is a characteristic pressure amplitude and τ_0 is a characteristic time scale of the initial waveform, then Eq. (2.25) means that $x_s \approx \rho_0 c_0^3 \tau_0/(\beta P_0)$. For the same initial waveform, the shock formation distance is therefore inversely proportional to the radiated wave amplitude, and so more intense waves are shocked at shorter distances. This explains why the first observations of nonlinear distortion and shock formation in ultrasound waves became possible only in the middle of the 20th century (when powerful piezoelectric sources became available), although the corresponding theory was completed a century earlier.

If the wave is far from being plane, Eq. (2.25) should be modified. For instance, if the wave diverges due to diffraction, the shock is formed at a longer distance as compared to that predicted by Eq. (2.25). On the other hand, if the wave is focused, then the waveform becomes shocked at shorter distances.

Some examples of measured shock wave profiles are shown in Figure 2.2, adapted from Sapozhnikov et al. (2019). Regardless of the propagation medium and the type of source, they are all seen to possess a universal form in which the shocks are connected by smooth transitions. The characteristic durations of the waveforms can vary over a wide range—from microseconds to fractions of seconds, but the duration of the shock itself can be extremely short, in fact so short that often it cannot be resolved by a microphone or hydrophone (see Section 2.3.4 below).

Nonlinear waveform distortion means that the wave spectrum also changes. For instance, when the initial waveform is sinusoidal, nonlinearity results in the generation of higher harmonics. The corresponding spectral broadening becomes especially pronounced when shocks are formed (the initial waveform transforms to a sawtooth shape). If the initial wave has the form of a modulated quasi-sinusoidal signal or a tone burst, then, in addition to generation of higher harmonics, nonlinear propagation results in the generation of a low-frequency signal. This effect is called *self-demodulation*. See more details elsewhere (Rudenko and Soluyan, 1977; Hamilton and Blackstock, 2008).

2.3.4 Shock structure

Nonlinear acoustic waves containing shocks are an interesting object not only because of the specific waveform structure, but also because they give rise to heating of the medium even if the viscosity and thermal conductivity constants are small. In the quadratic approximation, progressive acoustic waves are still possible, and the corresponding analysis of the hydrodynamics Eqs. (2.1)–(2.3) in the one-dimensional case gives the following generalization of the simple wave Eq. (2.23):

$$\frac{\partial u}{\partial x} = \frac{\beta}{c_0^2} u \frac{\partial u}{\partial \tau} + \frac{\delta}{2c_0^3} \frac{\partial^2 u}{\partial \tau^2} \quad (2.26)$$

where $\delta = [4\eta/3 + \varsigma + \kappa(c_v^{-1} - c_p^{-1})]/\rho_0$ is the effective diffusivity. Eq. (2.26) is called the *Burgers equation* and is one of the iconic model equations in the theory of nonlinear waves. Eq. (2.26) is useful for studying many interesting features of nonlinear waves in dissipative media. Similar to the simple wave equation, the Burgers equation has a general analytical solution (Whitham, 1974).

Here, only one solution will be considered to help analyze the shock region. In an ideal medium, shocks are introduced as discontinuities in the waveform. The Burgers equation reveals the fine shock structure. Consider a waveform with a step-like transition from a constant level $u = u_1$ to another constant level $u = u_2 > u_1$. The corresponding solution of the Burgers equation was obtained by Taylor (1910):

$$u = \bar{u} + \frac{\Delta u}{2} \tanh\left[\frac{\beta c_0 \Delta u}{2\delta}\left(\tau + \bar{u}\frac{\beta x}{c_0^2}\right)\right] \quad (2.27)$$

Here, $\bar{u} = (u_1 + u_2)/2$ is the mean value of the velocity levels before and after the shock front; $\Delta u = u_2 - u_1$ is the velocity jump.

Two important conclusions follow from Eq. (2.27). First, $u \sim \tanh(\tau/\Delta\tau + \text{const})$, where $\Delta\tau = 2\delta/(\beta c_0 \Delta u)$ is a characteristic shock transition time. Note that $\Delta\tau \sim \delta$, and therefore, this parameter tends to zero at the limit $\delta \to 0$, which confirms the fact that for an ideal medium the shock has a form of a waveform discontinuity. For real media, the shock duration is finite. Note also that $\Delta\tau \sim 1/\Delta u$, so the shock thickness decreases with an increase in the shock "amplitude" $\Delta u = u_2 - u_1$. In many modern applications of intense ultrasound, it is commonly true that when shocks are formed, their duration $\Delta\tau$ is so short that it cannot be resolved even with the best hydrophones or microphones.

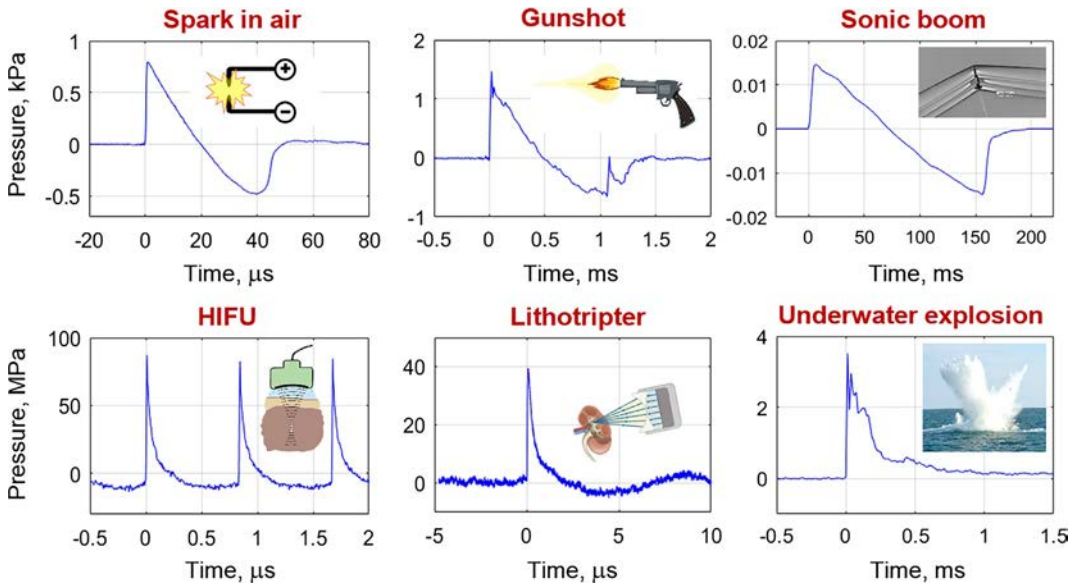


FIGURE 2.2 Pressure waveforms radiated by various powerful sources in air (top row) and water (bottom row). *(Reproduced with permission from Sapozhnikov et al. (2019). Copyright 2019, Acoustical Society of America.)*

Another feature of the shock described by solution (2.27) follows from the fact that the retarded time $\tau = t - x/c_0$ is present in combination with a shift $\overline{u}\beta x/c_0^2$. This means that a shock with $\overline{u} > 0$ propagates faster than low-amplitude sound; that is, it is supersonic. The shock wave with $\overline{u} < 0$ is slower than small signals. In practice, the shock frequently propagates in an undisturbed medium ($u_1 = 0$, $u_2 > 0$), so the shock front velocity exceeds the speed of sound c_0.

Everywhere in this chapter, it is supposed that the wave dissipation is caused by classical viscous absorption, which corresponds to a quadratic frequency law for ultrasound absorption: $\alpha(f) \sim f^2$. In many cases, the absorption law is different. A typical example is a medium with relaxation-type dissipation, when $\alpha(f)$ grows at low frequencies and is saturated at some level for higher frequencies (Landau and Lifshits, 1987; Pierce, 2002). In soft biological tissues, the absorption behaves as a power law $\alpha(f) \sim f^y$, where $y \approx 1$ (Duck, 2012). It can be shown that if the high-frequency asymptote of the absorption coefficient is $\alpha \sim f^y$ with $y > 1$, the absorption stabilizes nonlinear steepening and thus the shock has a finite thickness (Kashcheeva et al., 2000). In the case $y \leq 1$, the absorption is not sufficiently strong to prevent formation of multivalued waveforms; hence, some additional physical mechanism of energy dissipation must be present to stabilize the shock.

2.3.5 Intense acoustic fields radiated by finite-aperture sources

In the majority of modern applications of intense ultrasound, the aforementioned classical theory of nonlinear plane waves is not adequate to the real situation. The waves are never plane, because they are emitted by finite-size sources. In some cases, these sources are small in comparison with the wavelength (e.g., in the applications of low-frequency ultrasound (Rosenberg, 1971)). In other applications, ultrasound sources are large (e.g., in medical applications and in nondestructive testing). Real acoustic waves are far from behaving as a plane wave even if they are radiated by extended flat sources (Sapozhnikov et al., 2004). The plane wave theory is nevertheless useful, because nonlinear acoustic fields frequently behave locally as a plane wave. More importantly, the one-dimensional theory helps us to understand the physics underlying nonlinear acoustic phenomena.

To be useful in solving practical problems, nonlinear acoustics requires more appropriate theoretical formulations that involve two- or three-dimensional acoustic fields. The straightforward approach of direct numerical solution of the full system of fluid dynamics equations, Eqs. (2.1)–(2.3), can be used in some simplified situations, but it is fairly inefficient in most practical cases: simulation of nonlinear regimes, especially those with shocks, needs enormous computer resources. Contrary to the cases of the simple wave equation, the Burgers equation, or other equations of one-dimensional approximation, a theoretical approach based on analytical solutions also does not work here (for a simple reason: there are no such solutions). However, theoretical methods do exist in nonlinear acoustics that are fairly successful in describing nonlinear fields. This success relies on appropriate simplifications of the theory.

One of the effective approaches is based on the *Westervelt equation* (Hamilton and Blackstock, 2008). This equation follows from Eqs. (2.1)–(2.3) in the quadratic

approximation, with an additional assumption that cumulative nonlinear effects influence the waveform distortion much more strongly than noncumulative (local) nonlinear effects. Except for the situation of standing waves, the latter assumption is valid in most cases of practical interest. The Westervelt equation has the following form:

$$\Delta p' - \frac{1}{c_0^2}\frac{\partial^2 p'}{\partial t^2} = -\frac{\delta}{c_0^4}\frac{\partial^3 p'}{\partial t^3} - \frac{\beta}{\rho_0 c_0^4}\frac{\partial^2}{\partial t^2}\left(p'^2\right), \qquad (2.28)$$

where $\Delta = \partial^2/\partial x^2 + \partial^2/\partial y^2 + \partial^2/\partial z^2$ is the Laplacian. Eq. (2.28) has the form of the classical wave equation with additional terms (sources) on the right-hand side: the first term accounts for absorption caused by viscosity and thermal conductivity, the second term describes the effect of acoustic nonlinearity. Note that in the case of progressive plane waves, the Westervelt equation, which is limited to the second-order approximation, reduces to the Burgers equation. When nonlinear effects are weak, Eq. (2.28) can be efficiently solved following quasilinear theory, similar to the Born approximation in scattering theory. It consists of two steps: first, the linear wave equation with zero right-hand side is solved, and second, this linear solution is used in the right-hand side of Eq. (2.28) to calculate an additional pressure perturbation due to nonlinearity.

In the case of strong nonlinear effects, Eq. (2.28) has to be solved numerically. The numerical solution can be made simpler if calculations are made starting from the source plane, where the boundary condition is set, and marching along the x-axis that is directed outward from the source. To use this approach, it is convenient to rewrite the Westervelt equation in an evolution-like form by using the already mentioned retarded time $\tau = t - x/c_0$. In the coordinates x, y, z, τ, Eq. (2.28) transforms to the following:

$$\frac{\partial}{\partial \tau}\left[\frac{\partial p'}{\partial x} - \frac{\beta}{2\rho_0 c_0^3} p'\frac{\partial p'}{\partial \tau} - \frac{\delta}{2c_0^3}\frac{\partial^2 p'}{\partial \tau^2}\right] = \frac{c_0}{2}\Delta p'. \qquad (2.29)$$

In the numerical simulation, the Laplacian $\Delta p'$ can be calculated using the fairly realistic assumption that the angular spectrum of the field consists of components that describe plane waves propagating from the source. This is the so-called one-way approximation (Dagrau et al., 2011). Then, the Westervelt equation can be solved for many practical situations (Yuldashev and Khokhlova, 2011; Jing et al., 2011; Kreider et al., 2013).

When computer resources are limited, solution of the Westervelt equation becomes impossible even in the one-way approximation. In fact, numerical solution of the full Westervelt equation only became practical recently. For a less computationally intensive solution, an additional approximation can be made based on specific features of the presumed field. In many applications, acoustic fields are radiated from sources whose diameter is much larger than a wavelength. If the radiating surface is flat or only slightly curved, such sources emit directional beams, or quasi-plane waves. The traditional modeling for nonlinear directional beams is based on the Khokhlov-Zabolotskaya-Kuznetsov (KZK) equation, which accounts for diffraction in the parabolic approximation (Rudenko, 2010). The KZK equation directly follows from Eq. (2.29) if the full Laplacian is replaced by its transverse approximation $\Delta p \approx \Delta_\perp p$, where $\Delta_\perp = \partial^2/\partial y^2 + \partial^2/\partial z^2$:

$$\frac{\partial}{\partial \tau}\left[\frac{\partial p'}{\partial x} - \frac{\beta}{2\rho_0 c_0^3} p'\frac{\partial p'}{\partial \tau} - \frac{\delta}{2c_0^3}\frac{\partial^2 p'}{\partial \tau^2}\right] = \frac{c_0}{2}\Delta_\perp p'. \qquad (2.30)$$

This almost invisible replacement of Δp by $\Delta_\perp p$ changes the equation type, from second order in terms of the x-derivative to first order. As a result, the KZK equation is more amenable to both asymptotic and numerical analysis as compared to the Westervelt equation. The KZK equation has been very useful in studies of intense acoustic beams in underwater acoustics (Novikov et al., 1987), medical ultrasound research (Averkiou and Cleveland, 1999; Bailey et al., 2003), and studies of fundamental wave phenomena not directly related to a specific application. Although this approximation is fairly good for highly directional beams, it is not sufficient in the case of small sources or large but highly focused sources; in such cases, diffraction, scattering, or focusing/defocusing cause the acoustic field to effectively consist of waves propagating in very different directions. Nowadays, there are many applications in which such intense ultrasound fields are used, so the KZK equation should be replaced by a more appropriate model equation; for example, Eq. (2.28) or another "wide-angle" equation.

2.3.6 Formation of high-intensity ultrasound fields using focusing

One efficient way to make an ultrasound wave very intense is to use focusing. Focusing can be produced by different methods, e.g., by using an acoustic lens, reflecting a nonfocused wave from a curved surface, employing a source with a concave radiating surface, or by using a multielement array with proper phasing of the elements. Recently, there has been increasing interest in these problems mainly because of the development of new medical devices for extracorporeal destruction of tumors (high-intensity focused ultrasound therapy, HIFU) and for kidney stone comminution (shock wave lithotripsy, SWL) (Averkiou and Cleveland, 1999; Leighton and Cleveland, 2010). All of these and many other applications rely on the focusing of ultrasound waves.

An important parameter of any focused system is the amplitude focusing gain $G_p = p_F/p_0$, where p_F and p_0 are pressure amplitudes at the focus and the source,

respectively. Consider a source of diameter D and focal distance F. Let λ be a characteristic spatial scale of the acoustic field. For example, in the case of a continuous wave (CW) source operating at frequency f, this scale would be the wavelength c_0/f; in the case of a pulsed source, this scale would be $c_0\tau_0$, where τ_0 is the pulse duration. Linear acoustics gives the following estimate for the focusing gain $G_p \approx D^2/(\lambda F)$. For instance, if the ratio F/D (called F-number) is close to 1, then $G_p \approx D/\lambda$. The corresponding focusing gain for intensity in the linear case is $G_I \approx D^2/\lambda^2$. Therefore, noticeable intensity amplification can be achieved only if the source diameter is much larger than the wavelength. This is frequently the case for modern ultrasound sources used in medicine. For such systems, which typically operate at megahertz frequencies, the ratio D/λ ranges from 10 to 100. The corresponding intensity focusing gain is therefore enormous: $G_I \sim (10^2 - 10^4)$. For instance, typical peak pressures produced by lithotripters or focused ultrasound surgery systems are of the order of several tens of MPa, and the corresponding intensity levels in the focal area can reach 10,000–30,000 W/cm^2 (Wu et al., 2004). No surprise that ultrasound fields in such systems are frequently strongly nonlinear, and shock waves are common.

When acoustic nonlinearity plays a role, focusing effects cannot be calculated based on linear theory. It is difficult to tell beforehand whether the nonlinear effects will increase or decrease the focusing gain, because there are several competing mechanisms. On one hand, nonlinear waveform distortion results in generation of higher harmonics, which are better focused because of their smaller wavelengths. On the other hand, nonlinearity can reduce focal pressures, because it gives rise to shocks that significantly enhance ultrasound absorption. An additional decrease in the focusing gain may be caused by nonlinear refraction (self-defocusing) due to the fact that shock fronts propagate faster than small-amplitude signals (Rudenko and Sapozhnikov, 2004).

An important feature of nonlinear acoustic beams is asymmetric distortion of the waveform, which is a result of the combined action of nonlinearity and diffraction (Bakhvalov et al., 1987). Typically, the compressive parts of the pressure waveform become shorter and more intense as compared to the tensile parts. This peculiarity of the waveform distortion means that focusing gains for the positive and negative peak pressures, $G_p^{(+)}$ and $G_p^{(-)}$, are different (contrary to the linear situation). Moreover, the acoustic intensity focusing gain G_I is not anymore the square of the pressure gain; it is an independent parameter. Computer simulations based on the KZK equation have revealed characteristic behaviors of the aforementioned focusing gains as a function of the source amplitude p_0 (Bessonova et al., 2009). With increasing p_0, the negative pressure focusing $G_p^{(-)}$ always monotonically decreases. The focusing gains $G_p^{(+)}$ and G_I behave differently from $G_p^{(-)}$ but similar to one another. At lower source output levels, both gains grow with increasing p_0. For source output levels at which shocks develop in the focal region, the nonlinear enhancement reaches a maximum, so that further increase in p_0 result in a decrease in the focusing gains $G_p^{(+)}$ and G_I. With continuing increases in the source pressure p_0, the field parameters at the focus no longer depend on the source output (i.e., a saturation phenomenon occurs).

In early studies of focusing systems, approximate analytic models for estimating focal pressures and saturation levels were proposed for both continuous wave (CW) and pulsed nonlinear regimes. Although the nonlinear mechanisms of saturation are different in these two regimes (mainly nonlinear absorption for the CW case, and mainly nonlinear refraction in the pulsed regime), estimates for the pressure saturation level are expressed similarly:

$$p_{sat} = \Psi(G_p) \cdot \frac{D^2}{F^2} \cdot \frac{\rho_0 c_0^2}{2\beta}, \tag{2.31}$$

where the factor $\Psi(G_p)$ is some slow function of the linear focusing gain G_p having a value of order unity: $\Psi(G_p) \approx 0.4$ for pulses and $\Psi(G_p) = \pi/[4\ln(2G_p)]$ for continuous waves (Bacon, 1984; Musatov et al., 1992). The saturation phenomenon was studied numerically using the KZK equation for Gaussian sources over a wide range of source parameters (Karzova et al., 2012). The analytical Eq. (2.31) appears to be a reasonable estimate, especially for the pulsed regime. This approximation is less precise for the CW case, underestimating the values calculated numerically by several times.

Focusing gains represent only a part of the complex behaviors associated with ultrasound focusing. In a given application, it may be important to know more details about the pressure field. Nowadays, this task can be successfully solved numerically using the KZK or Westervelt equations, at least in a homogeneous medium (Jing et al., 2011; Bessonova and Wilkens, 2013).

2.4 Nonlinear interactions between the acoustic and entropy modes

2.4.1 General remarks

As mentioned at the beginning of this chapter, nonlinear phenomena are not limited to effects that happen within the acoustic mode. When the ultrasound intensity is not too low, the acoustic mode starts to excite the vorticity and entropy modes. A formal approach to study interactions between the fluid dynamics modes was described is several publications (Hamilton and Blackstock, 2008; Perelomova,

2003). Let us briefly outline this approach. The initial set of Eqs. (2.1)–(2.3) has the following form:

$$\partial \boldsymbol{\Psi}/\partial t + \hat{L}\boldsymbol{\Psi} = \mathbf{N}\{\boldsymbol{\Psi}\}, \tag{2.32}$$

where $\boldsymbol{\Psi}$ is a column-vector $\boldsymbol{\Psi} = (v_x, v_y, v_z, p', s')^T$ that consists of the particle velocity components $\mathbf{v} = (v_x, v_y, v_z)$ and perturbations of pressure and entropy, $\hat{L}$ is a linear operator represented by a five-by-five matrix, whose components are spatial derivation operators, and $\mathbf{N}\{\boldsymbol{\Psi}\}$ is a column-vector that consists of nonlinear terms. The matrix $\hat{L}$ can be easily extracted from the system of Eqs. (2.6)–(2.8), which has the form of Eq. (2.32) with zero nonlinear terms. The vector $\mathbf{N}\{\boldsymbol{\Psi}\}$ that accounts for the nonlinearity can be directly derived from Eqs. (2.1)–(2.3). As mentioned earlier, in the general case, three modes are excited: $\boldsymbol{\Psi} = \boldsymbol{\Psi}_{vor} + \boldsymbol{\Psi}_{ac} + \boldsymbol{\Psi}_{ent}$. To extract a specific mode from an arbitrary perturbation, suitable linear projector operators $\hat{P}_{vor}$, $\hat{P}_{ac}$, and $\hat{P}_{ent}$ can be defined, which are independent of time. Application of each operator to the vector $\boldsymbol{\Psi}$ provides the corresponding mode vector: $\hat{P}_{vor}\boldsymbol{\Psi} = \boldsymbol{\Psi}_{vor}$, $\hat{P}_{ac}\boldsymbol{\Psi} = \boldsymbol{\Psi}_{ac}$, $\hat{P}_{ent}\boldsymbol{\Psi} = \boldsymbol{\Psi}_{ent}$. These projection operators are required to satisfy the conditions that the three sum to the identity matrix, the product of two different operators is the null matrix, and multiplication of one operator by itself gives the same operator. Each operator also commutes with the operator $\hat{L}$. Once $\hat{P}_{vor}$, $\hat{P}_{ac}$, and $\hat{P}_{ent}$ are derived, nonlinear evolution equations for every mode can be obtained by applying the corresponding operator to Eq. (2.32). For instance, the vorticity mode in the nonlinear regime would be described by the following evolution equation: $\partial \boldsymbol{\Psi}_{vor}/\partial t + \hat{L}\boldsymbol{\Psi}_{vor} = \hat{P}_{vor}\mathbf{N}\{\boldsymbol{\Psi}\}$.

The mentioned formal approach may be fairly cumbersome. In most theoretical studies in nonlinear acoustics, interactions of the acoustic mode with the two nonacoustic modes are described by a simpler approach, which is based on a reasonable physical assumption that the characteristic time of the evolution of the nonacoustic modes is much longer than that of the acoustic mode (wave period). Indeed, this is a distinct specificity of the vorticity and entropy modes behavior when they are excited by the acoustic mode. Because vorticity and entropy are governed by diffusion-type equations, their perturbations do not leave the region where they are being excited and thus can grow in an accumulative manner. The nonacoustic modes then take the form of a combination of a slowly varying component and an oscillating component that follows the acoustic wave that excites them. The oscillating component is very weak even for extremely high acoustic amplitudes. For instance, single acoustic pulses used in lithotripsy that are shocked and have extremely high peak pressure (up to 100 MPa) result in very little heating (much less than 0.1 K). The slowly varying components of the nonacoustic modes, on the other hand, can grow significantly. In many practical situations, the acoustic streaming velocity can easily reach the value of acoustic particle velocity; similarly, ultrasound-induced heating can even result in boiling. Therefore, only slowly varying parts of the nonacoustic perturbations are of practical importance. This suggests an effective method of deriving the corresponding governing equations by averaging of the original equations over an acoustic wave period.

Excitation of the nonacoustic modes can be interpreted in terms of the conservation of wave energy and momentum. When an acoustic wave is attenuated in a dissipative fluid, it loses some amount of both of these quantities. The lost portion of the wave momentum is released in the fluid and results in the appearance of a volume force that gives rise to a vortical hydrodynamic flow—acoustic streaming. Therefore, the loss of momentum excites the vorticity mode. Similarly, the dissipated part of the acoustic wave energy is released and transformed into heat, which corresponds to excitation of the entropy mode.

2.4.2 Acoustic streaming and radiation force

Streaming generated by acoustic waves is often observed in fluids and has been extensively investigated by many researchers. It is used in medical applications to assess the state of biological liquids; for example, to differentiate between cystic and solid tumors (Nightingale et al., 1995) and to monitor thrombosis (Viola et al., 2004). Another promising application is in microfluidics for stirring and mixing liquids (Bruus, 2011). Acoustic streaming can be generated in a free space as well as near solid surfaces or vibrating boundaries.

The theory of acoustic streaming is considered in many papers. (Eckart, 1948; Westervelt, 1953; Rudenko and Soluyan, 1977; Hamilton and Blackstock, 2008) As mentioned in the previous section, the corresponding equations can be derived using temporal averaging over an acoustic wave period. The result of such a derivation can be presented in the form of classical hydrodynamic equations for an incompressible viscous flow in the presence of volume force:

$$\rho_0\left[\frac{\partial \mathbf{U}}{\partial t} + (\mathbf{U}\cdot\nabla)\mathbf{U}\right] = -\nabla P + \eta\Delta\mathbf{U} + \mathbf{F}, \tag{2.33}$$

$$\nabla\cdot\mathbf{U} = 0. \tag{2.34}$$

Here, several notations are used. First, the mass-transport velocity $\mathbf{U}$ is introduced for acoustic streaming in accordance with the nonacoustic situation where an incompressible fluid of constant density ρ_0 flows steadily with velocity $\mathbf{U}$; therefore, this velocity is defined from the condition that the averaged mass flux is $\rho_0\mathbf{U} = \langle\rho\mathbf{v}\rangle$, where $\langle . \rangle$ denotes temporal averaging over the high-frequency acoustic wave period. The quantity $\mathbf{F}$ in Eq. (2.33) is the mean force per unit volume due to acoustic wave absorption, and P is mean pressure. The force $\mathbf{F}$ is equal to the time-averaged rate of change of momentum of a unit

volume of fluid. Its components F_i can be expressed as a divergence of the Reynolds stress tensor $\langle \rho v_i v_j \rangle$: $F_i = -\partial \langle \rho v_i v_j \rangle / \partial x_j$ (Nyborg, 1965; Lighthill, 1978). In the second-order approximation,

$$\mathbf{F} = -\rho_0 \langle (\mathbf{v}_{ac} \cdot \nabla)\mathbf{v}_{ac} + \mathbf{v}_{ac}(\nabla \cdot \mathbf{v}_{ac}) \rangle. \tag{2.35}$$

Consider an important case of streaming excitation by an acoustic beam. In this case, acoustic quantities can be considered in the quasi-plane-wave approximation, and the force $\mathbf{F}$ is directed along the beam axis: $\mathbf{F} \approx (F, 0, 0)$. From Eq. (2.35),

$$F = -\frac{1}{c_0}\frac{\partial I}{\partial x}, \tag{2.36}$$

where $I = \rho_0 c_0 v_x^2$ is wave intensity. Because $-\partial I/\partial x$ is the acoustic energy released in a unit volume per unit time, Eq. (2.36) is in accordance with the known fact that the momentum carried by a plane wave is proportional to the wave energy with the coefficient of proportionality being the wave speed.

It can be shown that for a harmonic wave of arbitrary spatial structure, not limited to a progressive plane wave, expression (2.35) can be reduced to a form that may be more convenient for analysis (Prieur and Sapozhnikov, 2017):

$$\mathbf{F} = \frac{2\alpha}{c_0}\mathbf{I}, \tag{2.37}$$

where $\mathbf{I} = \langle p_{ac} \mathbf{v}_{ac} \rangle$ is the of acoustic intensity vector, and

$$\alpha = \frac{\delta \omega^2}{2c_0^3} \tag{2.38}$$

is the classical thermoviscous absorption coefficient at angular frequency and ω.

Acoustic streaming is associated with a constant component of the flow velocity in the steady state case ($\partial/\partial t = 0$) but is not easily defined when the acoustic field varies slowly in time. Indeed, nonlinear propagation of a quasi-CW acoustic wave with a modulated envelope results in the generation of a low-frequency acoustic signal (i.e., slowly varying in time)—the aforementioned self-demodulation phenomenon. As a result of such a nonlinear effect, the fluid slowly moves, but this movement is a purely potential flow that belongs to the acoustic mode, not to the vorticity one. A wave equation for the low-frequency pressure perturbations $p_{sd} = \langle p' \rangle$ can be derived by averaging the Westervelt equation, Eq. (2.28), over the high-frequency period:

$$\Delta p_{sd} - \frac{1}{c_0^2}\frac{\partial^2 p_{sd}}{\partial t^2} + \frac{\delta}{c_0^4}\frac{\partial^3 p_{sd}}{\partial t^3} = -\frac{\beta}{\rho_0 c_0^4}\frac{\partial^2}{\partial t^2}\left\langle p'^2 \right\rangle \tag{2.39}$$

This inhomogeneous wave equation can be formally obtained from the linearized system of initial hydrodynamic equations, Eqs. (2.6)–(2.8), if a volume force $\mathbf{F}_{sd}$ responsible for self-demodulation is added to the equation of motion, Eq. (2.6), so that divergence of this force is equal to the right-hand-side term of Eq. (2.39):

$$\nabla \cdot \mathbf{F}_{sd} = -\frac{\beta}{\rho_0 c_0^4}\frac{\partial^2}{\partial t^2}\left\langle p'^2 \right\rangle \tag{2.40}$$

In the case of progressive plane waves, $\partial/\partial t = c_0 \partial/\partial x$ and $\mathbf{F}_{sd} = (F, 0, 0)$, so Eq. (2.40) gives $\partial F/\partial x = -\beta c_0^{-1} \partial^2 I/\partial x^2$, where $I = \langle p'^2 \rangle / (\rho_0 c_0)$ is the high-frequency wave intensity. From here with the assumption that the force vanishes at $x \to \infty$, the following expression is obtained:

$$F_{sd} = -\frac{\beta}{c_0}\frac{\partial I}{\partial x} \tag{2.41}$$

It resembles Eq. (2.36) for the force term that describes acoustic streaming, with an important difference that Eq. (2.41) has an additional factor equal to the acoustic nonlinearity coefficient β.

This difference between Eqs. (2.36) and (2.41) has been (and still remains) a subject of discussion in relation with radiation pressure phenomena (Hamilton and Blackstock, 2008; Chu and Apfel, 1982, 1984). In our opinion, the source of possible confusion here is the fact that the time-averaging technique of deriving equations for slowly varying quantities does not separate acoustic waves from the vorticity-mode perturbations. Moreover, the expression for radiation force becomes different depending on the boundary conditions. For instance, if the fluid movement is constrained to be one-dimensional, for example, when an extended flat acoustic source radiates into a rigid-wall tube—then the vorticity mode cannot be excited at all, and the resulting flow is a potential flow; that is, it is nothing but a purely acoustic wave). The radiation force would then be described by Eq. (2.41). However, if the medium is not constrained, which is usually the case in practice, then the flow is not one-dimensional anymore, even if the acoustic source emits a highly directional beam. Under such unconstrained conditions, the low-frequency acoustic wave, which is excited in the region of the high-frequency field location, constantly escapes this region. In other words, the low-frequency pressure is released and thus remains very low. That is why the radiation force that appears due to absorption of the wave momentum in most practical situations is expressed by Eq. (2.36). Radiation force near the beam axis can be described by Eq. (2.41) only for a rather special case of a very broad acoustic beam with a not-too-low modulation frequency, so that the wavelength of the corresponding low-frequency acoustic wave is smaller than the beam diameter.

As mentioned, the force term $\mathbf{F}$ in Eq. (2.33) is equal to the time-averaged rate of change of momentum of a unit volume of fluid. This is a particular case of the more general situation in which a sound wave impinging on an object applies a steady force to the object. This force is called the *acoustic radiation force* and can be associated with a

(pseudo)momentum transfer from the wave to the object (McIntyre, 1981). In case of an inviscid fluid, the momentum conservation law can be written as $\partial(\rho v_i)/\partial t + \partial(p\delta_{ij} + \rho v_i v_j)/\partial x_j = 0$, which directly follows from Eqs. (2.1) and (2.2). From here, it is seen that $S_{ij} = -\langle p\rangle\delta_{ij} - \langle \rho v_i v_j\rangle$ is the mean mechanical stress resulting from the acoustic wave. This tensor S_{ij} is called the acoustic radiation stress tensor. The mean excess pressure $\langle p - p_0\rangle$ here involves terms of second-order smallness, since the first-order acoustic pressure vanishes when averaging. It can be shown, however, that in case of an acoustic beam in an open space the value of $\langle p - p_0\rangle$ can be tracked back to the acoustic quantities of the linear approximation and replaced by $\langle p - p_0\rangle = V - T$, where $V = \langle p'^2\rangle/(2\rho_0 c_0^2)$ is the mean potential acoustic energy density and $T = \rho_0\langle \mathbf{v}'^2\rangle/2$ is the mean kinetic energy density (Landau and Lifshits, 1987). In the quadratic approximation, the acoustic radiation stress tensor then becomes $S_{ij} = (T - V)\delta_{ij} - \rho_0\langle v_i' v_j'\rangle$. Note that the first term here may be of the same order as the second one and cannot be neglected in the general case. If acoustic streaming is generated by absorption of a quasi-plane wave, then $T \approx V$ and thus $S_{ij} \approx -\rho_0\langle v_i' v_j'\rangle$; therefore, the radiation stress tensor provides the volume force $F_i = \partial S_{ij}/\partial x_j$ in accordance with Eq. (2.35). The net acoustic radiation force on a finite-size target is given by the surface integral of the acoustic radiation stress tensor over a closed surface that surrounds the target: $\oiint S_{ij} n_j dA$, where n_j are components of the external unit normal vector for the surface element dA (King, 1933; Gor'kov, 1962). An example of the application of such an approach for calculating the radiation force on an elastic spherical scatterer is given in reference (Sapozhnikov and Bailey, 2013), where additional references can be also found.

The phenomenon of acoustic radiation force has numerous applications: It can be used for manipulation and levitation of small particles (Ueha et al., 2000; Laurell et al., 2007). In ultrasound metrology, the radiation force balance method is used to measure the total acoustic power of acoustic sources (Maruvada et al., 2007). In medical ultrasound, radiation force is a basis for new imaging modalities (Sarvazyan et al., 1998; Tanter et al., 2009). Another promising application is the ability to noninvasively expel stones from the kidney (Shah et al., 2010).

2.4.3 Medium heating due to absorption of acoustic waves

The aforementioned effect of acoustic streaming is usually described as a special subject in books on nonlinear acoustics because it is indeed a nonlinear acoustic phenomenon. To the contrary, heating of a medium by ultrasound (or other type of waves) is so obviously connected with acoustic energy loss that is frequently mentioned when absorption of linear waves is discussed; that is, usually heating is not thought of as a nonlinear effect. Confusion arises here because absorption is usually interpreted in terms of the acoustic mode. Absorption of small-amplitude waves is indeed a linear process, since a decrease in the amplitude of a wave over an infinitesimal propagation step is proportional to the amplitude itself. However, when interpreted in terms of the entropy mode, the response is found to be nonlinear because the increase in the temperature of the medium is proportional to the square of the wave amplitude. In particular, the temperature increase caused by the superposition of any two waves is not the sum of temperature increases caused by each of the waves separately, which is to say that the principle of superposition, a signature of linear systems, is clearly violated. Consideration of the temperature increase in a medium as a nonlinear process becomes more obvious when the absorption itself is nonlinear, that is, when the decrease in wave intensity with propagation distance is not proportional to the intensity. This feature is most pronounced when shocks form in the profile of a nonlinear wave.

For practical purposes, it is important to know the amount of heat Q produced per unit volume. This quantity can be found from an entropy balance equation that accounts for the heat transfer caused by convection and thermal conductivity:

$$\frac{\partial(\rho s)}{\partial t} + \nabla\cdot\left(\rho s\mathbf{v} + \frac{\mathbf{q}}{T}\right) = \frac{1}{T}\frac{\partial Q}{\partial t} \tag{2.42}$$

Here, ρs defines entropy per unit volume, $\rho s\mathbf{v} + \mathbf{q}/T$ is entropy flux in the forms of convection and thermal conductivity, $\mathbf{q} = -\kappa\nabla T$ is Fourier's law for the corresponding heat flux, and the right-hand side of Eq. (2.42) expresses the amount of entropy produced per unit volume and time by the heat source Q. An equation in the form of Eq. (2.42) directly follows from Eqs. (2.2) and (2.3) and provides the following expression for the heat produced in the fluid per unit volume and time:

$$\frac{\partial Q}{\partial t} = \frac{\kappa}{T}(\nabla T)^2 + \frac{\eta}{2}\left(\frac{\partial v_i}{\partial x_j} + \frac{\partial v_j}{\partial x_i} - \frac{2}{3}\delta_{ij}\nabla\cdot\mathbf{v}\right)^2 + \varsigma(\nabla\cdot\mathbf{v})^2 \tag{2.43}$$

From Eq. (2.43), it is seen that there are several physical mechanisms of heating during oscillatory fluid motion. The first one is energy dissipation caused by thermal conductivity between the regions of different temperatures that appear due to acoustically produced compressions and rarefactions. The second heat source comes from viscous shear stresses. The third mechanism is caused by relaxation processes, whose low-frequency action has a form of bulk viscosity. In the quadratic approximation, Eq. (2.43) can also be obtained by deriving the energy conservation law from the linearized system of Eqs. (2.6)–(2.8) (Pierce, 1994).

Similar to streaming, heating caused by absorption of an acoustic wave is usually studied by applying time-averaging to the original equations. If the heat is produced by acoustic waves, then $\mathbf{v}$ in Eq. (2.43) corresponds to particle velocity. Also, $(\nabla T)^2/T \approx (\nabla T')^2/T_0$ and $T' \approx p'\alpha_V T_0/(\rho_0 c_p)$, where T' is temperature fluctuation and p' is acoustic pressure. Therefore, in the quadratic approximation

$$\left\langle \frac{\partial Q}{\partial t} \right\rangle = \frac{\kappa\left(c_v^{-1} - c_p^{-1}\right)}{\rho_0^2 c_0^2} \left\langle (\nabla p')^2 \right\rangle + \frac{\eta}{2} \left\langle \left(\frac{\partial v_i}{\partial x_j} + \frac{\partial v_j}{\partial x_i} - \frac{2}{3}\delta_{ij} \nabla \cdot \mathbf{v} \right)^2 \right\rangle + \varsigma \left\langle (\nabla \cdot \mathbf{v})^2 \right\rangle. \tag{2.44}$$

Here, the thermodynamic identity $\alpha_V^2 T c^2/c_p = c_p/c_v - 1$ is accounted for.

Consider an important case when the fluid is heated by a one-dimensional acoustic field; then $\mathbf{v} = \{u(x,t), 0, 0\}$, and $p' = p'(x,t)$. Also, the continuity equation in the approximation of low dissipation can be written as follows: $\partial p'/\partial t + \rho_0 c_0^2 \partial u/\partial x \approx 0$. This results in the following formula:

$$\left\langle \frac{\partial Q}{\partial t} \right\rangle = \frac{\kappa\left(c_v^{-1} - c_p^{-1}\right)}{\rho_0^2 c_0^2} \left\langle \left(\frac{\partial p'}{\partial x} \right)^2 \right\rangle + \frac{\varsigma + \frac{4}{3}\eta}{\rho_0^2 c_0^4} \left\langle \left(\frac{\partial p'}{\partial t} \right)^2 \right\rangle \tag{2.45}$$

This expression is valid for both standing and propagating wave problems. When the wave is propagating in one direction, then $\partial p'/\partial x = \pm c_0^{-1} \partial p'/\partial t$, and thus, the energy dissipation per unit volume and time is

$$\left\langle \frac{\partial Q}{\partial t} \right\rangle_{\text{plane wave}} = \frac{\delta}{\rho_0 c_0^4} \left\langle \left(\frac{\partial p'}{\partial t} \right)^2 \right\rangle \tag{2.46}$$

where $\delta = [4\eta/3 + \varsigma + \kappa(c_v^{-1} - c_p^{-1})]/\rho_0$ is the diffusivity coefficient that was already mentioned earlier; for example, it enters the Burgers Eq. (2.26). For a particular case of a propagating harmonic wave of angular frequency ω, Eq. (2.46) takes a familiar form:

$$\left\langle \frac{\partial Q}{\partial t} \right\rangle_{\text{plane sine wave}} = 2\alpha I \tag{2.47}$$

Here, $I = \langle p'^2 \rangle/(\rho_0 c_0)$ is wave intensity, and α is the classical thermoviscous absorption coefficient defined by Eq. (2.38).

Note that Eq. (2.46) can be applied to any waveform, including nonlinearly distorted and even shocked profiles, if the shock structure is taken into account. However, this expression has been derived for a classical thermoviscous fluid. In many applications, the acoustic wave is attenuated differently from the quadratic law, Eq. (2.46). For example, in biological tissue, the corresponding frequency law is almost linear. Calculation of heating caused by a nonlinearly distorted wave for such media can be done in the frequency domain, using the fact that waves of different harmonics contribute to the heating independently, and therefore,

$$\left\langle \frac{\partial Q}{\partial t} \right\rangle_{\substack{\text{plane wave} \\ \text{of arbitrary} \\ \text{waveform}}} = 2\sum_{\omega} \alpha(\omega) I(\omega), \tag{2.48}$$

where $\alpha(\omega)$ and $I(\omega)$ are absorption coefficient and intensity of the corresponding harmonic. This approach is widely used in numerical studies of heating of biological tissue (Averkiou and Cleveland, 1999).

2.4.4 Heat release at a shock

One very important consequence of shock formation that is relevant to power ultrasonics is the possibility of intense heating of the medium. The mechanism of shock wave heating can be understood from an analysis of the discontinuities in pressure and other physical quantities that happen at the shock. The corresponding expressions are called the Rankine-Hugoniot relations (Landau and Lifshits, 1987). They are based on the general conservation laws and thus can be applied even to extremely strong shock waves such as those generated by explosions. In acoustics, even for very intense waves, the jumps are small: $|\Delta\rho| << \rho_0$, $|\Delta p| << \rho_0 c_0^2$, and so on. Accordingly, the corresponding shock waves are usually called *weak shocks*. For heating phenomena, the following consequence of the Rankine-Hugoniot relations in the weak-shock approximation is of interest (Courant and Friedrichs, 1948):

$$\Delta s = \frac{\beta}{6\rho_0^3 c_0^4 T_0} (\Delta p)^3 \tag{2.49}$$

where Δs and Δp are discontinuities of entropy and pressure. (Note that here and below the symbol Δ marks the corresponding jumps; that is, it is not the Laplacian as earlier.)

It is common in the nonlinear acoustics literature to interpret Eq. (2.49) as evidence of a negligible change in the entropy that occurs at the shocks. However, this statement may be misleading depending on whether the acoustic mode or entropy mode is considered. For the acoustic mode, the fact that $\Delta s \sim (\Delta p)^3$ means that the equation of state $\rho = \rho(p,s)$ in the second-order approximation does not depend on the entropy change; that is, the adiabatic equation of state can be used even if the nonlinear waves are shocked. For the entropy mode, the cubic relation (2.49) may have the opposite consequences, indicating the possibility of a significant increase in entropy production.

According to Eq. (2.49), heat deposition per unit volume is

$$Q_{\text{shock}} = \rho_0 T_0 \Delta s = \frac{\beta}{6\rho_0^2 c_0^4}(\Delta p)^3 \tag{2.50}$$

In the absence of thermal conductivity, the corresponding temperature jump (associated with the entropy mode) is $\Delta T_{ent} = Q_{\text{shock}}/(\rho_0 c_p)$. It is interesting to compare this increase with the temperature increase caused by adiabatic compression related to the acoustic mode: $\Delta T_{ac} = \alpha_V T_0/(\rho_0 c_p)\cdot\Delta p$. Consider, for instance, a shock wave in water at room temperature having a fairly strong pressure jump $\Delta p = 50$ MPa, which is typical for shock wave lithotripsy. Calculations result in $\Delta T_{ent} \approx 0.03$ K and $\Delta T_{ac} \approx 1.4$ K; so not only is the temperature jump ΔT_{ent} very small, but it is also much smaller than the corresponding acoustic temperature variation ΔT_{ac}.

The situation may change dramatically when an intense acoustic wave is radiated by a CW source. After shocks are formed, the initially sinusoidal waveform transforms to a sawtooth waveform, such that heat deposition occurs every cycle and accumulates with time. The amount of heat released per unit volume and time is then the one-cycle portion of heat defined by Eq. (2.50) divided by the wave period; that is, multiplied by the source frequency f_0:

$$\left\langle \frac{\partial Q}{\partial t} \right\rangle_{\substack{\text{sawtooth}\\ \text{wave}}} = \frac{\beta f_0}{6\rho_0^2 c_0^4}(\Delta p)^3. \tag{2.51}$$

Compare this heat deposition rate with the linear counterpart, Eq. (2.47): $\langle \partial Q/\partial t \rangle_{\text{sinewave}} = 2\alpha I$, where α is absorption coefficient at the source frequency, I is wave intensity. Consider for comparison a sinusoidal wave with the same amplitude $A = \Delta p/2$. Then, $I = A^2/(2\rho_0 c_0)$, and the ratio between the heat deposition rates becomes the following:

$$\frac{\langle \partial Q/\partial t \rangle_{\substack{\text{sawtooth}\\ \text{wave}}}}{\langle \partial Q/\partial t \rangle_{\text{sine wave}}} = \frac{2}{3}\frac{\beta f_0}{\alpha \rho_0 c_0^3}\Delta p \tag{2.52}$$

It is seen from here that for small-amplitude waves ($\Delta p \to 0$) absorption due to presence of shocks is indeed negligible as compared to classical absorption. But for finite-amplitude waves with sufficiently high amplitude, the situation may be different. Consider, for instance, an ultrasound wave of frequency $f_0 = 2$ MHz propagating in soft biological tissue of the following properties: $c_0 = 1500$ m/s, $\rho_0 = 1000$ kg/m^3, $\beta = 4$, and $\alpha = 0.5$ dB/cm/MHz. There are therapeutic applications in which acoustic intensity levels are fairly high. In histotripsy, for instance, focused ultrasound intensity may exceed 10 kW/cm^2 (Maxwell et al., 2012). In such regimes, Eq. (2.52) predicts that the heating efficiency of a sawtooth wave is more than 10 times higher than that of a harmonic wave of the same amplitude. Such rapid tissue heating can initiate tissue boiling in just several milliseconds (Canney et al., 2010). This indicates that using shock waves is beneficial to accelerate thermal effects.

2.5 Conclusion

The rapid development of the field of nonlinear acoustics during the last decades has resulted from a great interest of scientists and engineers in nonlinear phenomena and their promising applications. The current overall state of this branch of science and numerous specific results are presented in many journal publications on this subject. The recent progress in nonlinear acoustics can be also followed through proceedings of the International Symposia on Nonlinear Acoustics (ISNA) that are held typically every 3 years (Sapozhnikov et al., 2019; Hamilton and Blackstock, 1990; Hobaek, 1993; Wei, 1996; Lauterborn and Kurtz, 2000; Rudenko and Sapozhnikov, 2002; Atchley et al., 2006; Enflo et al., 2008; Kamakura and Sugimoto, 2012; Blanc-Benon et al., 2015; POMA, 2018). The scope of modern research in nonlinear acoustics includes a wide spectrum of various phenomena, from purely theoretical studies of mathematical features of nonlinear equations to applied research on the use of intense ultrasound in modern technologies. Although nonlinear acoustics has become an established discipline, there are still many interesting problems to solve, and various possibilities to broaden the use of nonlinear effects in modern applications.

Acknowledgments

I am grateful to Wayne Kreider, Michael Bailey, and Mark Hamilton for discussions and proofreading the text.

References

Atchley, A.A., Sparrow, V.W., Keolian, R.M., 2006. Innovations in Nonlinear Acoustics. American Institute of Physics, Melville.

Averkiou, M.A., Cleveland, R.O., 1999. Modeling of an electrohydraulic lithotripter with the KZK equation. J. Acoust. Soc. Am. 106, 102–112.

Bacon, D.R., 1984. Finite amplitude distortion of the pulsed fields used in diagnostic ultrasound. Ultrasound Med. Biol. 10 (2), 189–195.

Bailey, M.R., Khokhlova, V.A., Sapozhnikov, O.A., Kargl, S.G., Crum, L. A., 2003. Physical mechanisms of the therapeutic effect of ultrasound—a review. Acoust. Phys. 49, 369–388.

Bakhvalov, N.S., Zhileikin, Y.M., Zabolotskaya, E.A., 1987. Nonlinear Theory of Sound Beams. American Institute of Physics, Medville.

Bessonova, O.V., Wilkens, V., 2013. Membrane hydrophone measurement and numerical simulation of HIFU fields up to developed shock regimes. IEEE Trans. Ultrason. Ferroelectr. FrEquation Control 60 (2), 290–300.

Bessonova, O.V., Khokhlova, V.A., Bailey, M.R., Canney, M.S., Crum, L. A., 2009. Focusing of high power ultrasound beams and limiting values of shock wave parameters. Acoust. Phys. 55 (4–5), 463–473.

Beyer, R.T., 1997. Nonlinear Acoustics. Acoust. Soc. Am, Woodbury.

Blanc-Benon, P., Sparrow, V.W., Dragna, D., 2015. Recent developments in nonlinear acoustics. In: AIP Conf. Proc. vol. 1685. American Institute of Physics, Melville.

Bruus, H., 2011. Acoustofluidics 1: governing equations in microfluidics. Lab Chip 11, 3742–3751.

Canney, M., Khokhlova, V., Bessonova, O., Bailey, M., Crum, L., 2010. Shock-induced heating and millisecond boiling in gels and tissue due to high intensity focused ultrasound. Ultrasound Med. Biol. 36 (2), 250–267.

Chu, B.T., Apfel, R.E., 1982. Acoustic radiation pressure produced by a beam of sound. J. Acoust. Soc. Am. 72, 1673–1687.

Chu, B.T., Apfel, R.E., 1984. Response to the comments of Nyborg and Rooney (J. Acoust. Soc. Am. **75**, 263–264 (1984)). J. Acoust. Soc. Am 75, 1003–1004.

Chu, B.-T., Kovasznay, L.S.G., 1958. Non-linear interactions in a viscous heat-conducting compressible gas. J. Fluid Mech. 3, 494–514.

Courant, R., Friedrichs, K.O., 1948. Supersonic Flow and Shock Waves. Interscience, New York.

Dagrau, F., Renier, M., Marchiano, R., Coulouvrat, F., 2011. Acoustic shock wave propagation in a heterogeneous medium: a numerical simulation beyond the parabolic approximation. J. Acoust. Soc. Am. 130 (1), 20–32.

Duck, F.A., 2012. Physical Properties of Tissue: A Comprehensive Reference Book. Institution of Physics & Engineering in Medicine & Biology.

Eckart, C., 1948. Vortices and streams caused by sound waves. Phys. Rev. 73, 68–86.

Enflo, B.O., Hedberg, C.M., Kari, L. (Eds.), 2008. Nonlinear Acoustics—Fundamentals and Applications. American Institute of Physics, Melville.

Gor'kov, L.P., 1962. On the forces acting on a small particle in an acoustic field in an ideal fluid. Sov. Phys. Dokl. 6, 773–775.

Gusev, V.E., Karabutov, A.A., 1993. Laser Optoacoustics. American Institute of Physics, New York.

Hamilton, M.F., Blackstock, D.T. (Eds.), 1990. Frontiers of Nonlinear Acoustics. Elsevier Applied Science, London.

Hamilton, M.F., Blackstock, D.T. (Eds.), 1998. Nonlinear Acoustics. Academic Press, San Diego.

Hamilton, M.F., Blackstock, D.T. (Eds.), 2008. Nonlinear Acoustics. Acoustical Society of America, Melville, NY.

Hobaek, H. (Ed.), 1993. Advances in Nonlinear Acoustics. World Scientific, Singapore.

Jing, Y., Shen, D., Clement, G.T., 2011. Verification of the Westervelt equation for focused transducers. IEEE Trans. Ultrason. Ferroelectr. FrEquation Control 58 (5), 1097–1101.

Kamakura, T., Sugimoto, N., 2012. Nonlinear Acoustics State-of-the-Art and Perspectives. American Institute of Physics, Melville.

Kaner, V.V., Rudenko, O.V., Khokhlov, R.V., 1977. Theory of nonlinear oscillations in acoustic resonators. Sov. Phys. Acoust. 23, 432–437.

Karzova, M.M., Averiyanov, M.V., Sapozhnikov, O.A., Khokhlova, V.A., 2012. Mechanisms for saturation of nonlinear pulsed and periodic signals in focused acoustic beams. Acoust. Phys. 58 (1), 81–89.

Kashcheeva, S.S., Khokhlova, V.A., Sapozhnikov, O.A., Averkiou, M.A., Crum, L.A., 2000. Nonlinear distortion and attenuation of intense acoustic waves in lossy media obeying a frequency power law. Acoust. Phys. 46 (2), 170–177.

King, L.V., 1933. On the acoustic radiation pressure on spheres. Proc. R. Soc. London, Ser. A 147, 212–240.

Kreider, W., Yuldashev, P.V., Sapozhnikov, O.A., Farr, N., Partanen, A., Bailey, M.R., Khokhlova, V.A., 2013. Characterization of a multi-element clinical HIFU system using acoustic holography and nonlinear modeling. IEEE Trans. Ultrason. Ferroelectr. FrEquation Control 60 (8), 1683–1698.

Landau, L.D., Lifshits, E.M., 1987. Fluid Mechanics, second ed. Pergamon, New York.

Laurell, T., Petersson, F., Nilsson, A., 2007. Chip integrated strategies for acoustic separation and manipulation of cells and particles. Chem. Soc. Rev. 36, 492–506.

Lauterborn, W., Kurtz, T. (Eds.), 2000. Nonlinear Acoustics at the Turn of the Millenium. American Institute of Physics, Melville.

Leighton, T.G., Cleveland, R.O., 2010. Lithotripsy. Proc. Inst. Mech. Eng. H J. Eng. Med. 224 (2), 317–342.

Lighthill, J., 1978. Acoustic streaming. J. Sound Vib. 61, 391–418.

Maruvada, S., Harris, G.R., Herman, B.A., King, R.L., 2007. Acoustic power calibration of high-intensity focused ultrasound transducers using a radiation force technique. J. Acoust. Soc. Am. 121, 1434–1439.

Maxwell, A., Sapozhnikov, O., Bailey, M., Crum, L., Xu, Z., Fowlkes, B., Cain, C., Khokhlova, V., 2012. Disintegration of tissue using high intensity focused ultrasound: two approaches that utilize shock waves. Acoust. Today 8 (4), 24–36.

McIntyre, M.E., 1981. On the 'wave momentum' myth. J. Fluid Mech. 106, 331–347.

Musatov, A.G., Rudenko, O.V., Sapozhnikov, O.A., 1992. Nonlinear refraction and nonlinear absorption in the focusing of high-intensity pulses. Sov. Phys. Acoust. (USA) 38 (3), 274–279.

Naugolnykh, K., Ostrovsky, L., 1998. Nonlinear Wave Processes in Acoustics. Cambridge Univ. Press, Cambridge.

Nightingale, K.R., Kornguth, P.J., Walker, W.F., McDermott, B.A., Trahey, G.E., 1995. A novel ultrasonic technique for differentiating cysts from solid lesions: preliminary results in the breast. Ultrasound Med. Biol. 21, 745–751.

Novikov, B.K., Rudenko, O.V., Timoshenko, V.I., 1987. Nonlinear Underwater Acoustics. American Institute of Physics, New York.

Nyborg, W.L., 1965. Acoustic streaming. In: Mason, W.P. (Ed.), Physical Acoustics. Vol. 2. Academic Press, New York, NY, pp. 265–331. Pt B, Ch. 11.

Perelomova, A., 2003. Interaction of modes in nonlinear acoustics: theory and applications to pulse dynamics. Acta Acust. Acust. 89, 86–94.

Pierce, A.D., 1994. Acoustics: An Introduction to Its Physical Principles and Applications. Acoust. Soc. Am.

Pierce, A.D., 2002. Entropy, acoustic, and vorticity mode decomposition as an initial step in nonlinear acoustics formulations. In: Rudenko, O.V., Sapozhnikov, O.A. (Eds.), Nonlinear Acoustics at the Beginning of the 21st Century. vol. 1. Faculty of Physics, MSU, Moscow, pp. 11–19.

POMA, 2018. Proceedings of 21st International Symposium on Nonlinear Acoustics. Proc. Mtgs. Acoust. vol. 34.

Prieur, F., Sapozhnikov, O.A., 2017. Modeling of the acoustic radiation force in elastography. J. Acoust. Soc. Am. 142 (2), 947–961. https://doi.org/10.1121/1.4998585.

Rosenberg, L.D. (Ed.), 1971. High-Intensity Ultrasonic Fields. Plenum, New York.

Rudenko, O.V., 2010. The 40th anniversary of the Khokhlov-Zabolotskaya equation. Acoust. Phys. 56 (4), 452–462.

Rudenko, O.V., Sapozhnikov, O.A. (Eds.), 2002. Nonlinear Acoustics at the Beginning of the 21st Century. Faculty of Physics, Moscow State University, Moscow.

Rudenko, O.V., Sapozhnikov, O.A., 2004. Self-action effects for wave beams containing shock fronts. Phys. Usp. 47 (9), 907–922.

Rudenko, O.V., Soluyan, S.I., 1977. Theoretical Foundations of Nonlinear Acoustics. Consultants Bureau, London.

Sapozhnikov, O.A., Bailey, M.R., 2013. Radiation force of an arbitrary acoustic beam on an elastic sphere in a fluid. J. Acoust. Soc. Am. 133 (2), 661–676.

Sapozhnikov, O.A., Khokhlova, V.A., Cathignol, D., 2004. Nonlinear waveform distortion and shock formation in the near field of a continuous wave piston source. J. Acoust. Soc. Am. 115 (5, Pt 1), 1982–1987.

Sapozhnikov, O.A., Khokhlova, V.A., Cleveland, R.O., Blanc-Benon, P., Hamilton, M.F., 2019. Nonlinear acoustics today. Acoust. Today 15 (3), 55–64.

Sarvazyan, A.P., Rudenko, O.V., Swanson, S.D., Fowlkes, J.B., Emelianov, S.Y., 1998. Shear wave elasticity imaging: a new ultrasonic technology of medical diagnostics. Ultrasound Med. Biol. 24, 1419–1435.

Shah, A., Owen, N.R., Lu, W., Cunitz, B.W., Kaczkowski, P.J., Harper, J., Bailey, M.R., 2010. Novel ultrasound method to reposition kidney stones. Urol. Res. 38, 491–495.

Tanter, M., Touboul, D., Bercoff, J., Fink, M., 2009. High resolution quantitative imaging of cornea elasticity using supersonic shear imaging. IEEE Trans. Med. Imaging 28, 1881–1893.

Taylor, G.I., 1910. The conditions necessary for discontinuous motion. Proc. R. Soc. A 84, 371–377.

Ueha, S., Hashimoto, Y., Koike, Y., 2000. Non-contact transportation using near-field acoustic levitation. Ultrasonics 38, 26–32.

Viola, F., Kramer, M.D., Lawrence, M.B., Oberhauser, J.P., Walker, W.F., 2004. Sonorheometry: a noncontact method for the dynamic assessment of thrombosis. Ann. Biomed. Eng. 32, 696–705.

Wei, R.J. (Ed.), 1996. Nonlinear Acoustics in Perspective. Nanjing Univ. Press, Nanjing.

Westervelt, P.J., 1953. The theory of steady rotational flow generated by a sound field. J. Acoust. Soc. Am. 25, 60–67.

Whitham, G.B., 1974. Linear and Nonlinear Waves. Wiley, London.

Wu, F., Wang, Z.B., Chen, W.Z., Zou, J.Z., Bai, J., Zhu, H., Li, K.Q., Xie, F. L., Jin, C.B., Su, H.B., Gao, G.W., 2004. Extracorporeal focused ultrasound surgery for treatment of human solid carcinomas: early Chinese clinical experience. Ultrasound Med. Biol. 30 (2), 245–260.

Yuldashev, P.V., Khokhlova, V.A., 2011. Simulation of three-dimensional nonlinear fields of ultrasound therapeutic arrays. Acoust. Phys. 57 (3), 334–343.

Zarembo, L.K., Krasilnikov, V.A., 1966. Introduction into Nonlinear Acoustics. Nauka, Moscow (in Russian).

Chapter 3

Acoustic cavitation: Bubble dynamics in high-power ultrasonic fields

W. Lauterborn and R. Mettin

Third Physical Institute, Georg-August-University Göttingen, Göttingen, Germany

3.1 Introduction

Acoustic cavitation describes the phenomena associated with intense sound waves in liquids generating cavitation bubbles. The main physical phenomena connected with the dynamics of cavitation bubbles are broadband acoustic emissions (noise and shock waves), high-speed liquid jet formation, and generation of high temperatures inside the bubbles accompanied by plasma formation and light emission (sonoluminescence). The enormous energy density in the collapsing bubbles may be used in many applications, such as the cleaning of surfaces and the enhancement or initiation of chemical reactions (sonochemistry). There already exists a vast literature on the topic: acoustic cavitation was first reviewed by Flynn (1964) in his seminal work on the "Physics of acoustic cavitation," followed by further reviews (Neppiras, 1980; Apfel, 1981a) and a book (Rozenberg, 1971). Chapters on acoustic cavitation or bubble dynamics can also be found in more general books on cavitation and ultrasonics (Knapp et al., 1970; Lauterborn, 1980; Suslick, 1988; Young, 1989; Kuttruff, 1991; Brennen, 1995; Abramov, 1998). It was soon noticed that bubbles and their dynamics play an essential role in acoustic cavitation, and so bubble dynamics has become a topic of its own with reviews (Plesset and Prosperetti, 1977; Blake and Gibson, 1987; Feng and Leal, 1997; Lauterborn et al., 1999; Lauterborn and Kurz, 2010) and books (van Wijngaarden, 1982; Leighton, 1994; Blake et al., 1994; Doinikov, 2005).

Bubbles are at work in ultrasonic cleaning (as first shown by Olaf, 1957) and in sonochemistry (where they mediate chemical reactions; Suslick et al., 1999), and so, to serve as a foundation for understanding these and many other applications, the present knowledge of single and multibubble dynamics is summarized here. Starting from a discussion of the cavitation threshold, the oscillation behavior of single, spherical bubbles in sound fields is described according to various parameters (sound pressure amplitude, bubble radius, and acoustic frequency), illustrated with response curves and habitat diagrams. High-speed photographic observations of single bubbles and bubble ensembles are reported and discussed, as well as their acoustic and optic emissions. A multibubble model is presented, including simulations of bubble ensemble dynamics. The final sections discuss acoustic cavitation noise, sonoluminescence, and aspects of ultrasonic cleaning.

3.2 Cavitation thresholds

The susceptibility of a liquid to rupture when stretched is quantified by its cavitation threshold; that is, the tension (or negative pressure) needed to form an observable cavity in the liquid.

3.2.1 Static tension threshold

For a pure liquid, the cavitation threshold is determined by the strength of the bonds between its molecules. Theoretically, this can be thousands of bars, which must be overcome by a correspondingly strong tension. In the case of a pure (or homogeneous) liquid subjected to static tension, the cavitation threshold is also known as the homogeneous nucleation threshold. For pure water at 300 K, a tension value for homogeneous nucleation of -1320 atm (≈ -1340 bar, 1 atm = 1.01325 bar) was predicted by Fisher (1948). This is approximately the value measured by a constant liquid density (isochoric) cooling method using water inclusions in quartz. Zheng et al. (1991) report a minimum value of -140 MPa (-1400 bar) at 42°C from a set of different samples, while El Mekki Azouzi et al. (2013), performing statistical rupture measurements on a single sample, reach -120 MPa at 322.35 K. Measurements of this kind are done to explore the equation of state of liquids deep into the negative pressure region (Caupin, 2005; Herbert et al., 2006; Davitt et al., 2010a, b; Caupin et al., 2012).

The rupture of real liquids, however, does not require such large, negative pressures (Fisher, 1948; Briggs, 1950; Lauterborn 1969/1970; Strube and Lauterborn, 1970). In these cases, the cavitation threshold at static tension is called the heterogeneous (rather than

Power Ultrasonics. https://doi.org/10.1016/B978-0-12-820254-8.00005-1
Copyright © 2023 Elsevier Ltd. All rights reserved.

homogeneous) nucleation threshold, because it can be attributed to the almost ubiquitous heterogeneities present in real liquids. Heterogeneities may be impurities (suspended solid particles), tiny bubbles, ionizing particles, or just the walls of the container, when the adhesion of the liquid to the walls is less than the cohesion of the liquid itself. In the context of cavitation, such heterogeneities are called *cavitation nuclei* (see Mørch, 2007, for a review). The main candidates for cavitation nuclei are gas trapped in conical cracks or crevices on a hydrophobic solid surface (Apfel, 1970; Crum, 1979a; Atchley and Prosperetti, 1989) and microbubbles stabilized against dissolution by substances on their surface (organic skin) that prevent the transport of gas from the bubble interior to the liquid (Fox and Herzfeld, 1954; Crum, 1982).

More recently, nanometer-sized bubbles (nanobubbles) have been predicted to exist on solid surfaces (Parker et al., 1994). They could be photographed by total internal reflection fluorescence by Chan and Ohl (2012), whereby the nanobubbles are illuminated with the evanescent wave of the light from a laser. Nanobubbles on surfaces do not need cracks for longer persistence. Actually, they should quickly dissolve due to the higher pressure inside the bubble caused by surface tension. However, they do not seem to do so and may survive for hours or even weeks (Lohse and Zhang, 2015). A first theory resorted to strong contact line pinning leading to special dissolution properties (Petsev et al., 2013). Recently, the theory has been extended by addition of short-ranged attractive forces of the gas molecules at the solid surface for stabilizing surface nanobubbles (Tan et al., 2019; Tortora et al., 2020). Even bulk nanobubbles may exist (Tan et al., 2020). Thus, nanobubbles may act as an additional species of cavitation nuclei that limit the tensile strength of water and the cavitation threshold.

The limiting negative, static pressures that have been reached experimentally in larger water samples are in the range from only −20 bar at 1°C to −277 bar at 10°C, despite careful treatment to avoid cavitation nuclei by "scrupulous cleanliness" (Briggs, 1950). The tension in this case was generated by the centrifuge method with the water inside a spinning Pyrex glass capillary tube of diameter 0.6–0.8 mm. The value of −277 bar obtained by Briggs (1950) is still the highest negative pressure value measured in larger samples of water under static tension. With less careful treatment, any value can be obtained from the vapor pressure to this limiting value (see the precautions undertaken by Lauterborn (1969/1970) and Strube and Lauterborn (1970) with distillation, in experiments that still only obtained −175 bar as the limiting tensile strength for water). For many practical problems in flow applications concerned with hydrodynamic cavitation, like cavitation inception on ship propellers, the threshold is often assumed to be just the vapor pressure of the liquid. For acoustic cavitation in ultrasonic fields, however, this assumption does typically not work, as outlined in the following.

3.2.2 Acoustic cavitation threshold

Liquids do not rupture only under static tension. A second line of experimental investigation concerns the dynamic stretching of liquid by acoustic waves (Esche, 1952) or by converting pressure waves into tension waves upon reflection at a free surface (see Trevena, 1987). Trevena reported obtaining cavitation thresholds of −9 bar for ordinary tap water and −14.5 bar for boiled, deionized water by the pressure pulse reflection method. Recently, this method has been applied to very small volumes of liquid using laser-produced shock waves reflected at an air-liquid interface in a microchannel to minimize the influence of cavitation nuclei and thus approach the homogeneous case (Ando et al., 2012). A value of −60 MPa (−600 bar) has been reported for water at room temperature, the highest value obtained at present for dynamic loading.

The notion of an acoustic cavitation threshold should first be considered before proceeding further with cavitation thresholds (Atchley and Prosperetti, 1989). Because in acoustic cavitation, the pressure amplitude of the sound wave must be raised until it reaches the cavitation threshold, it is the positive threshold pressure amplitude that usually is taken as the cavitation threshold, although it is the negative pressure part of the sound wave that causes the rupture of the liquid. We will keep to this convention, as it is widely used in the cavitation literature and the literature on high-power ultrasound (e.g., Trevena, 1987; Kuttruff, 1991). Nevertheless, some care must be observed when comparing threshold values, because the literature from the early days of cavitation measurements gives "effective" pressures; that is, some mean value of the pressure amplitude in the sound wave (Esche, 1952). Also, when acoustic waves are used to probe the equation of state of a liquid in the negative pressure range, authors use the negative pressure values for consistency with the static tension case (e.g., Herbert et al., 2006; Caupin et al., 2012).

There is a long history of measuring acoustic cavitation thresholds with increasing sophistication (Esche, 1952; Galloway, 1954; Strasberg, 1959; Greenspan and Tschiegg, 1967; Crum, 1979a; Apfel, 1981b; Herbert et al., 2006). To avoid cavitation at the walls of the container, either the sound waves are focused into the interior of the liquid (Esche, 1952) or standing waves are used with the maximum sound pressure amplitude located in the interior of the container (Galloway, 1954; Greenspan and Tschiegg, 1967). However, the acoustic cavitation threshold depends not only on cavitation nuclei but also on parameters such as the frequency of the sound field, the static pressure, and the temperature of the liquid, as well as on the liquid itself.

The most thorough investigation of the dependence of the acoustic cavitation threshold for water on frequency is still that of Esche (1952). His results are shown in Figure 3.1, redrawn in the form of two limiting curves for the lowest and highest values of the threshold measured with water subject to different treatments, from tap water to distilled, filtered, and degassed water. The threshold range at a fixed frequency is a sign of the influence of cavitation nuclei. Up to about 15 kHz, the threshold is constant between ≈ 0.7 and 2.8 bar acoustic pressure amplitude, then strongly rises with higher frequency to a maximum of ≈ 420 bar at 3.3 MHz, the highest frequency investigated by Esche (1952). An extrapolation of the threshold curves to 1 GHz predicts a threshold of the order of 1 Mbar.

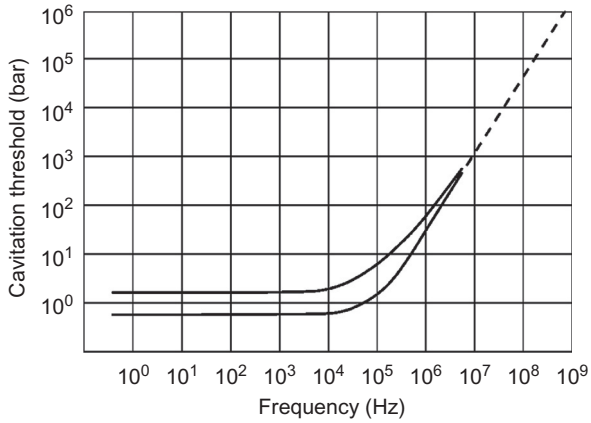


FIGURE 3.1 Acoustic cavitation threshold boundaries as a function of frequency for water. *(Adapted from Esche (1952).)*

The acoustic cavitation threshold is strongly dependent on the type and properties of the cavitation nuclei, which are usually unknown, and are therefore difficult to avoid or even to control in size, number, or form. For this reason, widely varying cavitation thresholds are measured with samples from different sources (tap water), following different treatments (distillation, filtration, degassing, and pressurization), and using different measurement methods (see Table I in the overview of Herbert et al., 2006). For practical purposes, once acoustic cavitation has set in, surface instabilities in the course of the oscillation and the collapse of the bubbles generated produce more bubbles. A basic example of this process is shown in Figure 3.2, which shows a bubble in a standing sound field of 25 kHz splitting repeatedly on collapse with proliferation of more bubbles (see the additional small bubble in the fifth and the following frames of the first row in Figure 3.2). These bubbles serve as further cavitation nuclei and facilitate the continuation of the cavitation process. Thus, in acoustic cavitation, bubbles play the essential role in all effects from acoustic cavitation noise via ultrasonic cleaning and erosion to sonoluminescence and sonochemistry.

3.3 Single-bubble dynamics

In acoustic cavitation, usually a large number of bubbles of different sizes oscillate and interact in complex ways to form clusters, filaments (streamers), and a wide variety of clouds (Mettin, 2005). However, a basic insight into many cavitation phenomena can be gained by considering just a

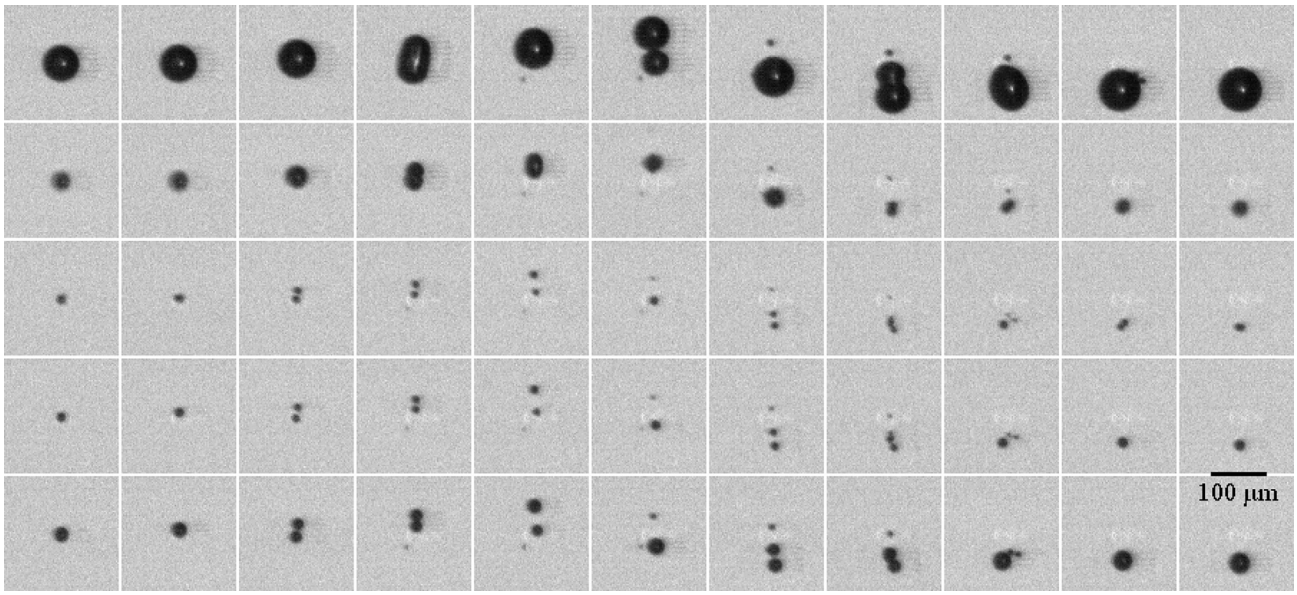


FIGURE 3.2 Bubble splitting by surface instabilities. Acoustic frequency = 25 kHz, 124,000 frames per second, exposure time = 1 µs. Picture series top to bottom and left to right. From column to column, the elapsed time is slightly more than one period of the sound field. *(Courtesy of J. Schneider and J. Eisener.)*

single bubble. A vast literature exists on single-bubble dynamics, much of which has been reviewed by Lauterborn and Kurz (2010).

3.3.1 Bubble models

The simplest model of a bubble is a spherical void (i.e., an empty bubble) of radius R in a liquid of density ρ at a static ambient pressure p_{stat}. This model was investigated by Rayleigh (1917) and takes the form of an ordinary differential equation of second order with the radius R of the bubble being a function of time:

$$\rho R\ddot{R} + \frac{3}{2}\rho\dot{R}^2 = -p_{\text{stat}}, \tag{3.1}$$

where an overdot signifies differentiation with respect to time t. When this differential equation is solved with the initial conditions $R(t=0)=R_{\text{max}}$ and $\dot{R}(t=0)=0$, the time T_c needed for the bubble to shrink from the radius R_{max} to zero is.

$$T_c = 0.915\, R_{\text{max}}\sqrt{\frac{\rho}{p_{\text{stat}}}}, \tag{3.2}$$

which is the Rayleigh collapse time for an empty bubble.

When the bubbles are very small (less than about 100 µm), the surface tension σ is no longer negligible in relation to the static pressure in Eq. (3.1) (Beeching, 1942; Plesset, 1949). For a spherical bubble of radius R, surface tension exerts the Laplace pressure p_σ, which grows in inverse proportion to R:

$$p_\sigma = \frac{2\sigma}{R}. \tag{3.3}$$

In reality, the bubble will contain gas and vapor, and this, as well as the viscosity of the liquid, will alter the dynamics of the bubble and therefore needs to be included in a more advanced model. For instance, when a constant saturation vapor pressure in the bubble is assumed (so that evaporation and condensation occur rapidly compared to the motion of the bubble wall), the Rayleigh collapse time changes to.

$$T_c = 0.915\, R_{\text{max}}\sqrt{\frac{\rho}{p_{\text{stat}}-p_v}}. \tag{3.4}$$

The validity of this relation has been tested with laser-induced single bubbles; for example, by Lauterborn (1974) for bubbles in the range of $R_{\text{max}}=1$–3.5 mm (Figure 3.3). The correction may become considerable for the high vapor pressures that occur with higher temperatures.

A now-standard bubble model, including surface tension, viscosity, and a constant saturation vapor pressure, is known as the Rayleigh-Plesset model, although many more scientists contributed to its formulation (Minnaert, 1933 (gas); Noltingk and Neppiras, 1950 (gas and acoustic driving); Poritsky, 1952 (viscosity)). Figure 3.4 shows the model parameters: internal pressure p_i and external pressure p_e, bubble radius at rest R_n, actual bubble radius R, polytropic exponent κ of the gas inside the bubble, density ρ and dynamic viscosity μ of the liquid, and surface tension σ between liquid and gas/vapor phases at the bubble wall. The Rayleigh-Plesset model then takes the form

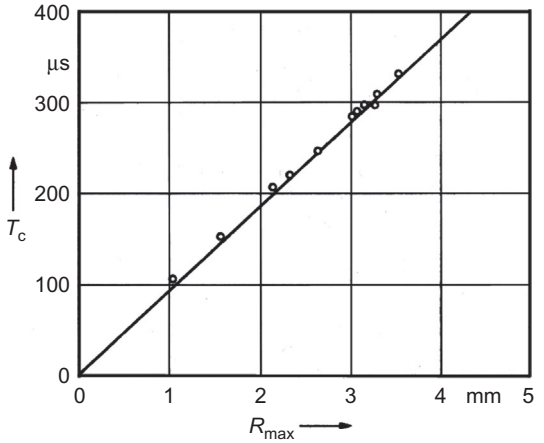


FIGURE 3.3 Rayleigh collapse time T_c versus the maximum bubble radius R_{max} in water. Open circles from laser-induced bubbles, solid line from theory (Equation 3.4).

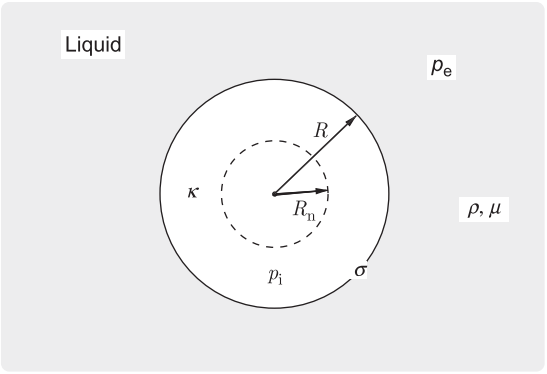


FIGURE 3.4 Bubble parameters.

$$\begin{aligned}\rho R\ddot{R}+\frac{3}{2}\rho\dot{R}^2 &= p_i - p_e \\ &= p_{gn}\left(\frac{R_n}{R}\right)^{3\kappa} + p_v - p_{\text{stat}} - \frac{2\sigma}{R} - \frac{4\mu}{R}\dot{R} - p(t)\end{aligned} \tag{3.5}$$

with.

$$p_{gn} = \frac{2\sigma}{R_n} + p_{\text{stat}} - p_v. \tag{3.6}$$

The additional parameters appearing in the equation are the gas pressure p_{gn} inside the bubble at rest, the (constant) vapor pressure p_v, and an additional external pressure $p(t)$ applied at the bubble wall. The time-dependent pressure $p(t)$ may be a shock wave compressing the bubble or the

pressure (and tension) from a sound wave; in the case of a single-frequency sound wave, it may be formulated as

$$p(t) = \pm p_a \ sin\,(2\pi v_a t) \tag{3.7}$$

with the sound pressure amplitude $p_a(>0)$ and the sound-field frequency v_a. When the equation takes the positive sign, it indicates that the bubble is initially compressed, starting from $t=0$; the negative sign indicates that the bubble is first expanded.

When considering strongly driven bubbles and their translational motion in sound fields, the eigenfrequency (linear resonance frequency) v_0 of a bubble is important, as bubbles in standing sound fields driven above their linear resonance frequency move to the sound-field pressure nodes, while those driven below move to the antinodes (provided they are not too strongly driven (Akhatov et al., 1997b; Matula et al., 1997)). When only a permanent gas (polytropic exponent κ) is present in a bubble of radius at rest R_{n0}, the linear resonance frequency (Minnaert, 1933) is given by

$$v_0 = \frac{1}{2\pi R_{n0}}\sqrt{\frac{3\kappa p_{stat}}{\rho}}, \tag{3.8}$$

where R_{n0} is the resonance radius with respect to a driving frequency $v_a = v_0$. For water under normal conditions and an air bubble that is not too small, this equation leads to the approximate relation

$$v_0 R_{n0} \approx 3\ \mathrm{ms}^{-1}. \tag{3.9}$$

With the inclusion of surface tension and a constant vapor pressure, the linear resonance frequency expands to

$$v_0 = \frac{1}{2\pi R_{n0}\sqrt{\rho}}\sqrt{3\kappa\left(p_{stat} + \frac{2\sigma}{R_{n0}} - p_v\right) - \frac{2\sigma}{R_{n0}}}. \tag{3.10}$$

Diagrams are often normalized to v/v_0 or R_n/R_{n0}.

The only damping in the Rayleigh-Plesset model is through viscosity. However, in reality, this is not the only damping mechanism and may not even be the strongest, at least for liquids with low viscosity such as water. That an oscillating bubble radiates sound is apparent when listening to the noise emitted from the thousands of bubbles in a cleaning bath. A bubble model that includes sound radiation from a (spherical) bubble was formulated by Gilmore (1952) and is given here in the form extended to include an incompressible volume of inert gas (Löfstedt et al., 1993), a constant vapor pressure inside the bubble, and a periodic driving sound field:

$$\left(1 - \frac{\dot R}{C}\right)R\ddot R + \frac{3}{2}\left(1 - \frac{\dot R}{3C}\right)\dot R^2 = \left(1 + \frac{\dot R}{C}\right)H + \frac{\dot R}{C}\left(1 - \frac{\dot R}{C}\right)R\frac{dH}{dR}, \tag{3.11}$$

where

$$H = \int_{p|_{r\to\infty}}^{p|_{r=R}} \frac{dp(\rho)}{\rho}, \tag{3.12}$$

$$p(\rho) = A\left(\frac{\rho}{\rho_0}\right)^{n_T} - B, \tag{3.13}$$

$$p|_{r=R} = \left(p_{stat} + \frac{2\sigma}{R_n} - p_v\right)\left(\frac{R_n^3 - bR_n^3}{R^3 - bR_n^3}\right)^{\kappa} + p_v - \frac{2\sigma}{R} - \frac{4\mu}{R}\dot R, \tag{3.14}$$

$$p|_{r\to\infty} = p_{stat} - p_a \ sin\,(2\pi v_a t), \tag{3.15}$$

$$C = \sqrt{c_0^2 + (n_T - 1)H}. \tag{3.16}$$

The new liquid parameters are the sound velocity C at the bubble wall, the sound velocity c_0 in the liquid under normal conditions, the enthalpy difference H between the pressure at infinity and at the bubble wall, and the parameters A, B, and n_T of the (isentropic) Tait equation for water. The new gas parameter is the van der Waals constant b, which describes the excluded volume of the noncondensable molecules inside the bubble; this becomes important in the case when the bubble contents are strongly compressed.

This equation is able to describe strongly collapsing bubbles, where the damping is mainly by sound radiation. An example is given in Figure 3.5, which shows a single, spherical bubble in a bubble trap driven at 21.4 kHz, photographed by sampling the bubble oscillation with a time shift of 500 ns between frames (Figure 3.5, upper diagram), and a comparison of the bubble radii obtained with the Gilmore model (Figure 3.5, lower diagram). The main parameter is the unknown bubble radius at rest, which is set to the (reasonable) value of $R_n = 8.1\,\mu$m, with the polytropic exponent $\kappa = 1.2$. Thus, the Gilmore model may serve as a good model for a deeper numerical investigation into the behavior of bubble dynamics in a sound field.

3.3.2 Response curves

There are numerous parameters in the Gilmore equation, the most important for acoustic cavitation being the sound-field frequency v_a, the sound-field pressure amplitude p_a, and the bubble radius R_n at rest. In other words, these are the parameters that determine how a bubble of radius R_n responds to a sound field at a given frequency and a given pressure amplitude. A huge catalogue of all the different types of possible bubble oscillations may be generated. There are infinitely many types of oscillation even considering only a single, spherical bubble in an infinitely extended liquid; nevertheless, some general categories can be found by looking for stationary solutions and their periodicity with respect to the driving sound field. Solutions that repeat with each cycle of the sound field are called harmonic

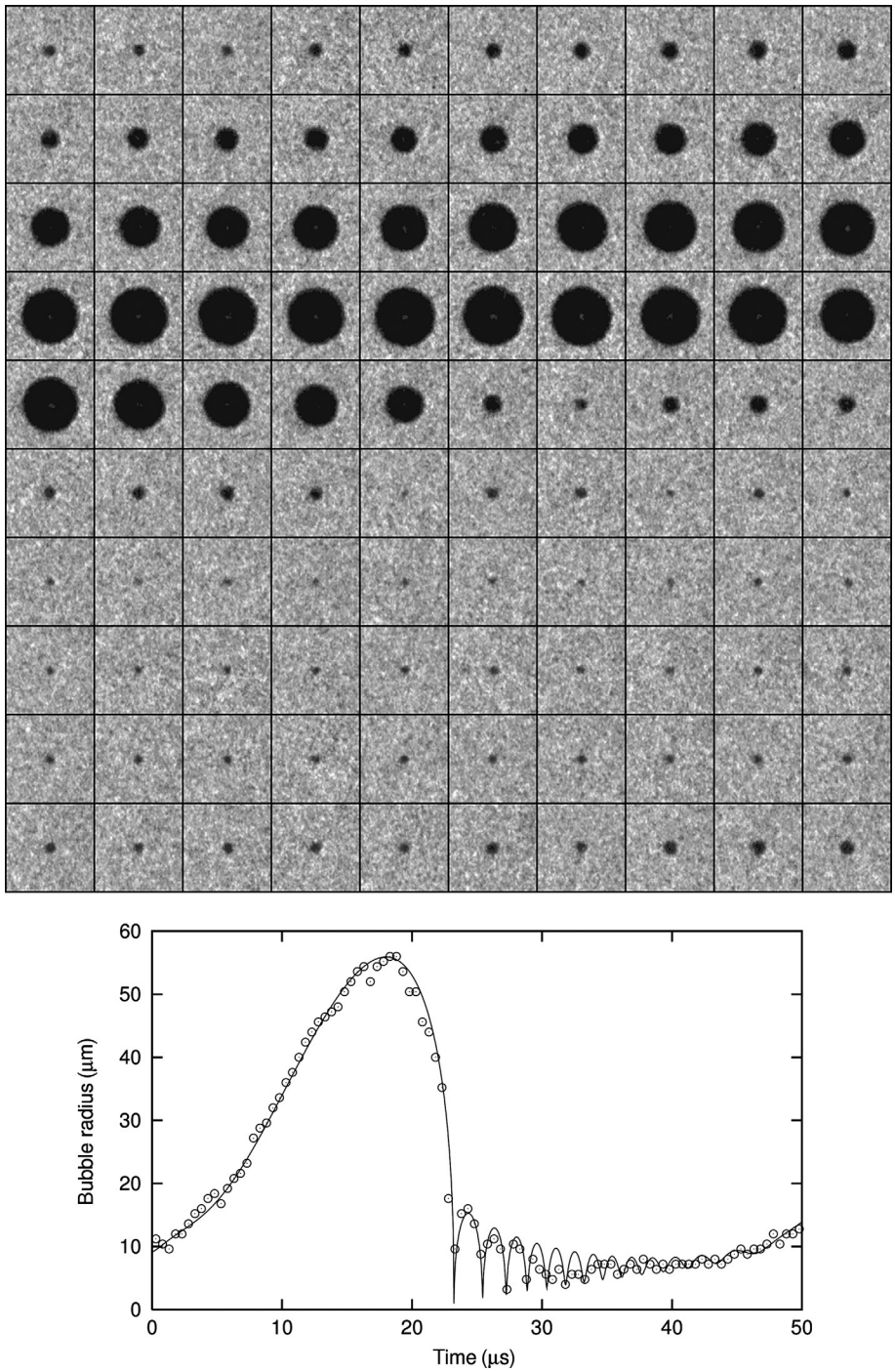


FIGURE 3.5 Upper diagram: photographic series of a single, spherical bubble driven at 21.4 kHz. One acoustic cycle is covered. Interframe time is 500 ns; frame size is 160 μm × 160 μm. Lower diagram: comparison with the Gilmore model (*solid line*). *(Courtesy of R. Geisler.)*

oscillations, although they are in general nonlinear and contain higher harmonics of the driving frequency in their oscillation spectrum and thus also in their acoustic radiation spectrum. There are also solutions that repeat their oscillations only after two, three, or more periods of the driving sound field. These are called *subharmonic oscillations*. One natural, distinguishing parameter between these types of oscillation will, therefore, be the number of cycles of the sound field after which the bubble oscillation repeats. This number is called the period number m, where $m = 1, 2, 3, \ldots$.

Each of these types of oscillation comes in an infinite variety but can be labeled by a second natural number, the torsion number n, where $n = 1, 2, 3, \ldots$ (Parlitz and

Lauterborn, 1986), which essentially describes the number of oscillations of the bubble before it repeats its cycle. More precisely, it describes the number of rotations or windings of neighboring trajectories in state space around the considered trajectory (the bubble oscillation in question). Even more complicated steady state solutions will be discussed later.

The oscillation types will be demonstrated via the different bubble resonances in a sound field. In the usual resonance curve of an oscillator, the amplitude of the oscillation is plotted against the driving frequency. Such frequency response curves showing many resonance peaks have been given by Lauterborn (1976) for the Rayleigh-Plesset model, and by Cramer (1980) and Cramer and Lauterborn (1981) for the Gilmore model. Here, the response of bubbles of different sizes, called *radius response curves*, is given for a fixed frequency of 20 kHz at selected sound pressure amplitudes for the Gilmore model (Lauterborn and Mettin, 1999). Radius response curves for the frequencies 7.208 and 23.56 kHz can be found in Cramer (1980) and Cramer and Lauterborn (1981).

3.3.2.1 Low driving

In Figure 3.6, the response of bubbles with radii from 10 to 500 µm is shown for four different sound pressure amplitudes of 10, 30, 50, and 70 kPa. The normalized maximum expansion of the bubble $(R_{max} - R_n)/R_n$, as a kind of oscillation amplitude, is shown against bubble radius at rest. Resonances (indicated by values of the radius at large excursions of the oscillation) are observed to follow a regular pattern. They are labeled by n/m, with n being the torsion number and m the period number, as introduced above. There is a main resonance near 200 µm labeled 1/1, which is the only resonance in a linear oscillator. The resonance leans over toward lower radii, because a bubble can be classified as a nonlinear oscillator with overall soft-spring behavior. The further peaks labeled 2/1, 3/1, and so on are harmonic resonances, as the denominator, indicating the period number, has value 1. They cease when the bubble radius at rest is smaller but grow with the sound pressure amplitude.

Three subharmonic resonances are present with period number 2, labeled 1/2, 3/2, and 5/2. They only appear after a threshold is reached in the sound pressure amplitude. Prosperetti (2013) gives a general derivation of the subharmonic threshold for the 1/2 resonance, which occurs at bubble radii at which bubbles in a free liquid would be driven to a pressure node in a standing sound field and where the (subharmonic) oscillations would thus cease because of low driving (unless fixed; e.g., in a soft gel or tissue). The other two subharmonic resonances appear at radii below the main resonance radius and are (positionally) stable in a standing sound field below a threshold of the driving pressure amplitude (Akhatov et al., 1997b; Matula et al., 1997). The numerator is the torsion number of the oscillation. Resonances with torsion numbers $n > 1$ at $m > 1$ are called *ultrasubharmonic resonances* or *ultraharmonic resonances*, when they occur in the region of harmonic resonances.

The dotted vertical lines in Figure 3.6 signify "jumps" in resonance behavior. They indicate the existence of hysteresis regions, where two or more types of oscillations (called *coexisting oscillations*) are stable for the same bubble radius at rest R_n, the different oscillations being reached from different initial conditions. This leads to further complexity in bubble resonance behavior. In Figure 3.7, for a sound pressure amplitude of 80 kPa, part of this complexity is resolved by taking two different initial conditions for each bubble radius at rest R_n, first stepwise increasing and then decreasing R_n, while preserving the state of the bubble from the previous calculation as the new initial condition. This identifies the regions of hysteresis for each harmonic resonance, but not for the ultrasubharmonic resonances in this range as they are located inside the hysteresis regions of the harmonic resonances and are

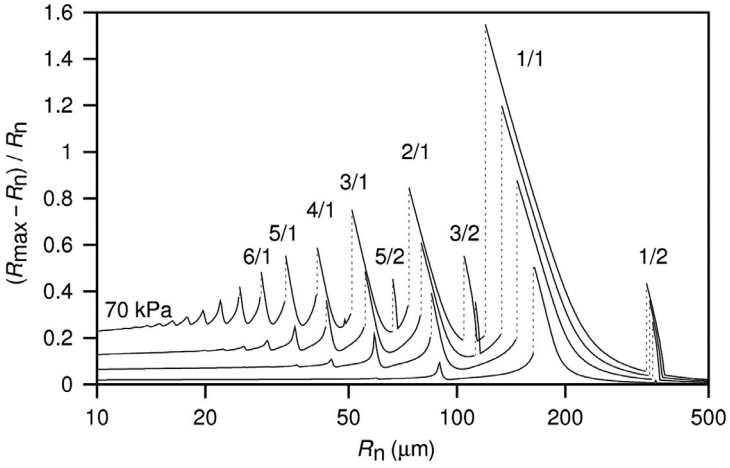


FIGURE 3.6 Radius response curves for bubbles of different sizes for a fixed sound-field frequency of 20 kHz. Driving amplitudes are 10 kPa (*lower curve*), 30, 50, and 70 kPa (*upper curve*). Initial conditions are the respective bubbles at rest.

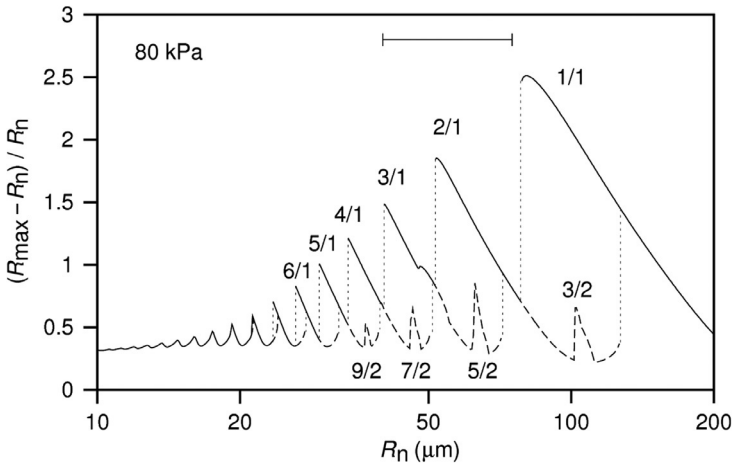


FIGURE 3.7 Radius response curves for bubbles of different sizes for a fixed sound-field frequency of 20 kHz. Driving amplitude is 80 kPa. The initial conditions are taken from the calculation at the previous radius at rest, when stepwise decreasing (*solid line*) and stepwise increasing (*dashed line*) the radius at rest. The two *dotted lines* belonging to each harmonic resonance encapsulate the hysteresis regions of the respective harmonic resonances.

thus accessible only from one direction (a stepwise increase in this case). The jumps occurring in the subharmonic resonances indicate further hysteresis regions; that is, more coexisting oscillations. For more details concerning these hysteresis regions, the reader is referred to the investigation by Lauterborn and Mettin (1999).

3.3.2.2 *High driving*

When the sound pressure amplitude is raised still further, new phenomena appear beyond harmonic and subharmonic resonances. One such phenomenon is bubble oscillations that double their period in geometric or near-geometric progression with alteration of a parameter, the period number not being related to a resonance. This progression may stop after a finite number of steps (or period doublings) or proceed to infinitely many steps. The bubble oscillations then no longer repeat with some finite period number; instead, similarly to noise, they do not repeat at all. Nevertheless, the oscillations are generated by a deterministic (periodic) sound field, not by some stochastic process.

Noise-like processes have been found to be a generic phenomenon in nonlinear dynamical systems and are known as deterministic chaos to distinguish them from stochastic processes. Oscillations with an infinite period number are accordingly termed *chaotic oscillations*. Special measures are required for the representation of chaotic oscillations in a resonance curve. Instead of the absolute maximum of the oscillation, a sufficiently large number of successive relative maxima are plotted from the infinitely many local maxima to indicate their amplitude range. Alternatively, one radius sample from the oscillation may be taken for each cycle of the sound field at a specified phase. This plotting mode has the advantage that oscillations with different period numbers m show up directly in the diagram with $m = 1, 2, 3$, and so on, number of points above the value of the radius at rest, R_n.

After an infinite period-doubling sequence a region of chaotic oscillations generally opens up, with windows of periodic oscillations. These periodic oscillations may again follow a period-doubling sequence into chaotic oscillations. Chaotic oscillations may also set in suddenly, upon the alteration of a parameter. In fact, chaotic oscillations may be classified intrinsically by a new number, the winding number; essentially, n/m, but remaining finite despite n and m both going to infinity. This complex oscillation behavior is described in more detail in Parlitz et al. (1990).

Figure 3.8 shows a response curve containing many chaotic oscillations and chaotic regions for a driving pressure amplitude of 130 kPa, together with the reference curve for 70 kPa from Figure 3.6. The chaotic regions are structured according to the harmonic resonances and cease toward lower rest radii. Simultaneously, the normalized "oscillation amplitude" grows to a maximum, being free of chaotic oscillations. This maximum is called the *giant response*, because it by far exceeds the main resonance, although it should be noted that the absolute maximum of the radius is about the same at 130 kPa throughout the given radius range after a sudden rise from small bubble radii at rest. Chaotic oscillations typically emerge from a period-doubling sequence upon alteration of a parameter. In Figure 3.8, one such sequence is seen for R_n between 40 and 50 μm on the right shoulder of the 2/1 resonance and similarly at the 3/1 resonance. More examples of bubble response behavior, including investigation of chaotic oscillations, can be found in the reviews by Lauterborn and Parlitz (1988), Lauterborn et al. (1999), and Lauterborn and Kurz (2010).

3.3.3 Parameter space diagrams

Many response curves would be needed to cover the full three-dimensional parameter space $\{R_n, p_a, \nu_a\}$. Only six of them (for six sound pressure amplitudes) have been given

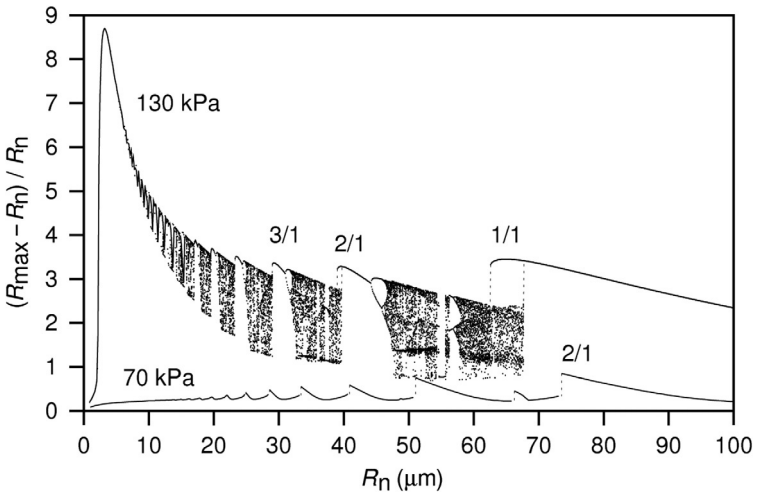


FIGURE 3.8 Radius response curves for bubbles of different sizes for a fixed sound-field frequency of 20 kHz at strong driving. Driving amplitudes are 70 kPa (*lower curve*) for reference and 130 kPa (*upper curve*).

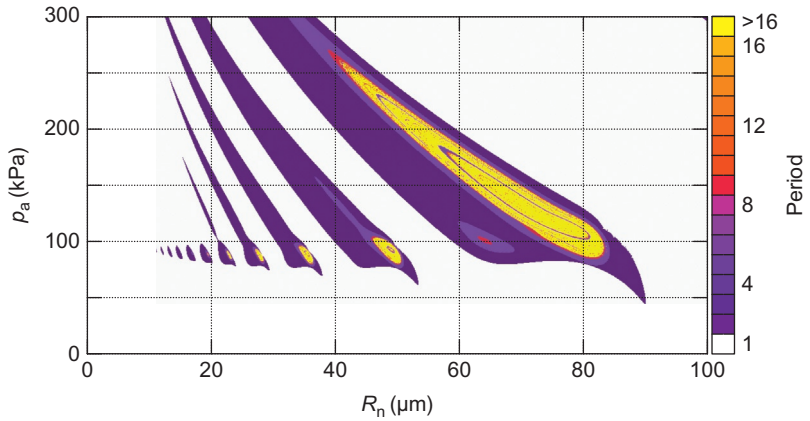


FIGURE 3.9 Period-number diagram in the parameter plane (R_n, p_a) for a driving frequency of 20 kHz in the harmonic response region. *(Courtesy of P. Koch, calculated for a slightly different bubble model than given in Equation (3.11).)*

here in Figures 3.6–3.8 for a sound field of 20 kHz, showing the dependence on the radius at rest. For a quicker overview, some property of bubble oscillation (e.g., period number) or just the change in some property (bifurcation) may be plotted in a parameter plane. This allows different regions of bubble behavior to be separated and viewed at a glance. Such plots are called *parameter space diagrams* or *phase diagrams* after the diagrams in thermodynamics for different phases of matter.

A parameter space diagram with the period number as the qualifying parameter (i.e., a period-number diagram) for 20 kHz is given in Figure 3.9 in the (R_n, p_a) parameter plane in the region of the harmonic resonances. The period is coded in color, white being period-1 oscillations. There is a repeating structure in the diagram, connected with the harmonic resonances; that is, with the torsion numbers. The largest structure is the main resonance with the (basic) torsion number 1 near its boundaries with the white area. At the boundary of the white and dark blue regions, the oscillation period doubles to 2, and then, proceeding to its interior, successively to 4, 8, and so on. In the inner (yellow) region, chaotic oscillations are found with complicated windows of finite period. The second largest structure at smaller bubble radii is the second harmonic resonance with the (basic) torsion number 2. It is very similar in structure to the main resonance, as are the next higher harmonic resonances. However, they shrink in size and lose ever more of their fine structure until they disappear completely at small bubble radii. More examples of phase diagrams can be found in the paper on bifurcation structures of bubble oscillators by Parlitz et al. (1990).

In view of emerging applications of power ultrasound that employ multifrequency driving, an interesting extension in bubble dynamics is the dual-frequency driving of a single, spherical bubble (Krefting et al., 2002). Then, six parameters are immediately apparent: the bubble radius R_n, the two frequencies ν_1 and ν_2, the two acoustic pressure amplitudes P_{A1} and P_{A2}, and the phase shift θ between the driving oscillations of the two frequencies at the start of the driving.

They form the six-dimensional parameter space $(R_n, v_1, v_2, P_{A1}, P_{A2}, \theta)$. The phase shift θ, however, seems to play a minor role and may be omitted from the studies. If so, already at a moderate resolution of 100 values per parameter, the calculation of 10^8 response curves for 100 bubble radii is necessary for an overview (different initial conditions for finding coexisting attractors not counted). Human perception would be overloaded in sighting a 100 million diagrams. Again, biparametric plots of a selected property are of great help in getting an understanding of bubble response to dual-frequency driving and its possible applications. Fig. 3.10 shows a biparametric period-number diagram with the two pressure amplitudes P_{A1} and P_{A2} as parameters and color coded bubble periods for a bubble radius at rest of $R_n = 10\,\mu m$ (Hegedűs et al., 2018). The two driving frequencies have a ratio of 2:3, i.e., $2 \times 340\,kHz$ and $3 \times 340\,kHz$. 4001×2501 points (P_{A1}, P_{A2}) were calculated for 25 initial conditions to find coexisting stable states. Altogether, about 250 million bubble oscillations were solved for their periodicity. Not to overload the diagram, only the highest period of the coexisting oscillations found is plotted. The notation PnBm, $n = 2, 3, 4$, $m = 2, 3$, means a period-n bubble oscillation which shows m branches. It is the three-branches structure that dominates the complex figure. On the P_{A1} axis, there are three such structures, a green one, a blue one, and a yellow one. In each of the three structures, two of the branches bow to the P_{A2} axis, the other one escapes to higher P_{A1} and P_{A2} pressures. Of course, this structure has to do with the 2:3 ratio of the driving frequencies. The application found is that a period-3 oscillation can be turned into a period-2 oscillation and vice versa by following the two green branches connecting the axes. Further examples can be found in Hegedűs et al. (2018, 2020a), also for other frequency relations, e.g., 3:4 and 3:5.

It is seen that a temporary addition of a second frequency can be used to switch between attractors of different periodicity. A more complete study of this technique, called attractor domain targeting, can be found in Hegedűs et al. (2020b). In particular, the transformation possibilities between different subharmonics are demonstrated and summarized in a table there.

So far, only the periodicity of the dual-frequency-driven bubble oscillation has been considered. But there is much more information hidden in the bubble oscillations, e.g., the maximum bubble radius R_{max} or the maximum absolute value of the bubble collapse velocity. These values are indicators for the strength of bubble collapses. Hegedűs et al. (2020c) have used the normalized maximum bubble radius $(R_{max} - R_n)/R_n$ as a quantity to define a dual-frequency cavitation threshold. Typically, the higher the value of this quantity, the stronger the bubble collapse. For $(R_{max} - R_n)/R_n = 2$, the following results are found for reaching this value with the minimum intensity of the dual-frequency sound field, called the active cavitation threshold. For bubble sizes below $R_n = 3\,\mu m$, the best choice is just a single, low frequency in the giant response region. For bubbles between $R_n = 3\,\mu m$ and $6\,\mu m$, a mixture of a low frequency in the giant response region and the main resonance frequency is the best choice, and for larger bubbles,

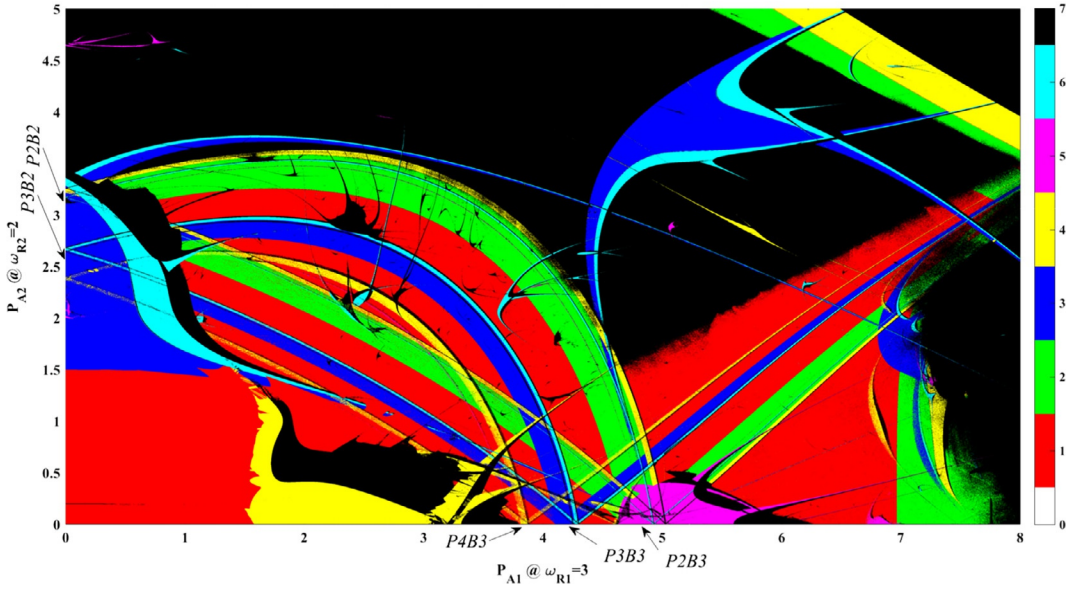


FIGURE 3.10 Period-number diagram with the two parameters P_{A1} and P_{A2}, the two acoustic pressure amplitudes of the driving for a bubble radius at rest of $R_n = 10\,\mu m$. The two driving frequencies have a ratio of 2:3, i.e., $2 \times 340\,kHz$ and $3 \times 340\,kHz$. The color bar gives the (highest) periodicity of the resulting bubble oscillation up to period 6 with periods 7 and higher (up to chaotic oscillations) being *black*. For further notations, see text. *(Figure 3 from Hegedűs et al. (2018) (CC BY 4.0).)*

the main resonance frequency dominates. Biparametric diagrams in the (v_1, v_2) parameter plane given in Hegedűs et al. (2020c) demonstrate these results.

All the parameter space diagrams given above do not address stability questions (e.g., the stability of the spherical shape), which is the topic of the next section in connection with the discussion of the habitat of single, spherical bubbles in a single-frequency sound field.

3.3.4 Bubble habitat

A bubble in a sound field is not only subject to the oscillating pressure force of the driving sound field, as considered so far, but also to other forces and influences. Pressure gradients are present that will give a bubble translational motion and thus may cause it to lose its positional stability in the pressure antinode of a standing sound field (Akhatov et al., 1997b; Matula et al., 1997). Moreover, a bubble will normally dissolve in a liquid because of surface tension creating a higher gas pressure inside the bubble than the partial pressure of the gas in the liquid would allow according to Henry's law. In a sound field, however, a bubble may grow through an effect called rectified diffusion (e.g., Crum, 1984; Brenner et al., 1996; Akhatov et al., 1997a). There are also limits to the spherical stability of a bubble, if its oscillation is too strong (Plesset, 1954; Eller and Crum, 1970; Strube, 1971).

The above issues can be combined in a bubble habitat diagram (Koch et al., 2011), where positional stability in the sound-field pressure antinode and shape stability are considered for nondissolving bubbles. Figure 3.11 is a bubble habitat diagram for a sound-field frequency of 20 kHz, and Figure 3.12 for 1 MHz, the habitat regions being colored green. In the lower white region, the bubble will dissolve unless it encounters the boundary of a green region. Above the lower white region and below the linear resonance radius, bubbles grow by rectified diffusion unless

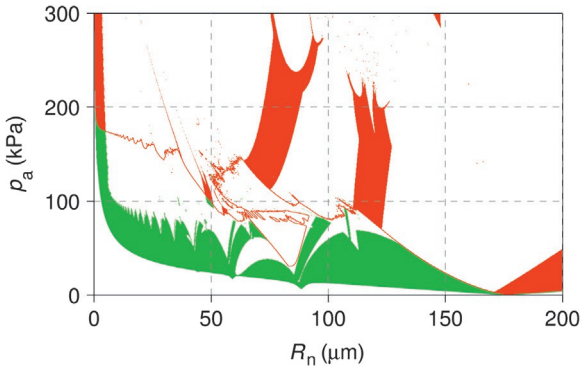


FIGURE 3.11 Bubble habitat diagram in the (R_n, p_a)-plane for bubbles in a standing sound field of 20 kHz in water at normal static pressure and gas saturation. *Green region*: positionally and shape stable bubble oscillations. *(Courtesy of P. Koch and T. Kurz, calculated for a slightly different bubble model than given in Equation (3.11).)*

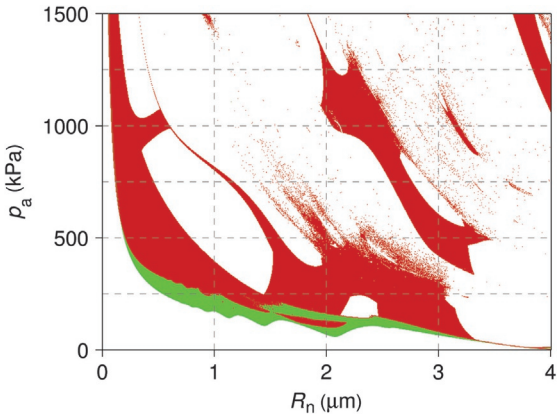


FIGURE 3.12 Bubble habitat diagram in the (R_n, p_a)-plane for bubbles in a standing sound field of 1 MHz in water at normal static pressure and gas saturation. *Green region*: positionally and shape stable bubble oscillations. *(Courtesy of P. Koch and T. Kurz, calculated for a slightly different bubble model than given in Equation (3.11).)*

they encounter a stability boundary. A special case is the very small sections of positive slope on the lower white boundary (the dissolution-rectified diffusion boundary). At these points, a bubble is stable in the sense of the three criteria considered (dissolution, shape, and position). In the upper white region, the bubble is unstable in shape and may split according to Figure 3.2. In the red region and the region above the thin red line running through the picture of Figure 3.11, the bubble is unstable in position; that is, it will not stay in the pressure antinode.

It can be seen that under conditions of normal static pressure and gas saturation, the circumstances, in which a spherical bubble will stay in place and neither grow nor shrink, are defined by only a very small part of the parameter plane (on the positive slope of the dissolution-rectified diffusion boundary; Krefting et al., 2003). When the gas content of the liquid is lowered, the positive slope of the dissolution-rectified diffusion boundary eventually shifts toward the giant resonance region at small bubble radii and higher driving pressures (Akhatov et al., 1997a). More habitat diagrams can be found in Koch et al. (2011), in particular for higher static pressures with their enlarged habitat areas.

The fate of a bubble cannot be predicted, especially at higher driving pressures. The usual behavior that may be concluded from habitat diagrams is that a bubble from the habitat region grows (equivalent to horizontal motion in the diagram) until it reaches the shape stability boundary (or positional stability boundary at high driving frequencies, Figure 3.12). There, it will develop shape oscillations (or be driven out of the pressure antinode). The shape oscillations may lead to bubble splitting with the resulting (two or more) smaller bubbles being reinjected into the habitat region or injected into the dissolution region. The dynamics of the now multiple bubbles, for instance, attraction or repulsion

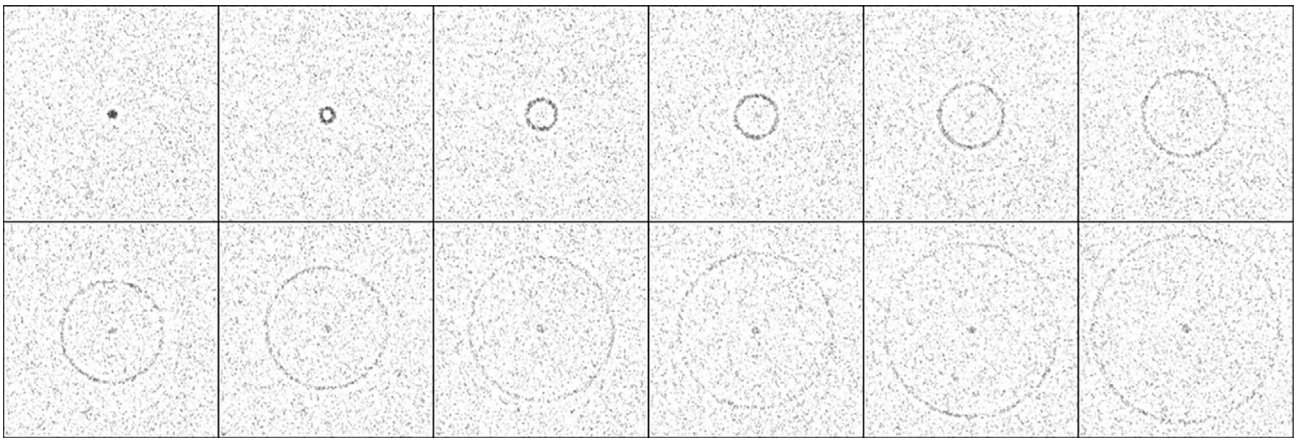


FIGURE 3.13 Spherical shock wave emitted by the bubble of Figure 3.5 in an acoustic trap. Interframe time is 30 ns, the frame size is 1.6 mm × 1.6 mm. *(Courtesy of R. Geisler.)*

of two bubbles oscillating in a sound field, are not included in the model. When the bubble encounters a positional stability boundary upon growth, it will be driven out of the pressure antinode; that is, it will follow a vertical track down the diagram, where it will grow further with a fate depending upon the geometry of the boundary and the specific dynamics of the situation.

3.3.5 Single-bubble dynamics: Examples

Although single bubbles are an exception in acoustic cavitation, they nevertheless constitute a basic unit, from which to build models of bubble ensembles to understand the complex bubble configurations that appear in reality. In this respect, more properties of a single bubble must be considered than merely their oscillation, and bubbles of other than spherical shape must be investigated. One property of an oscillating bubble (spherical or not) is sound radiation, including shock waves, as manifested in acoustic cavitation noise; another is its susceptibility to surface deformations that may lead to splitting. A third special property is jet formation in the presence of boundaries or disturbances of the perfect spherical geometry of the environment surrounding the bubble. These three properties of single bubbles will now be discussed.

3.3.5.1 Shock wave emission

An example of a stable, spherical bubble oscillation in a sound field has already been presented in Figure 3.5, which shows the expansion of the bubble, the collapse, and the subsequent rebounds. The rebound amplitudes point to a strong damping of the oscillation, caused mainly by emission of sound radiation into the liquid. This acoustic emission from oscillating bubbles is usually very faint and difficult to make visible. However, when a bubble is collapsing rapidly, a shock wave is radiated that is visible even in normal shadowgraphy, besides being audible as a click. Figure 3.13 shows the shock wave radiated by the bubble of Figure 3.5. It is a spherical shock wave that quickly detaches from the bubble. The bubble itself is seen only in the later frames, as a slowly expanding dot (on this time scale) in the center of the shock wave circle (in reality a sphere). The shock wave carries energy away from the bubble and is a strong source of damping and noise. The radiated shock waves can also be calculated numerically (Hickling and Plesset, 1964; Cramer, 1980; Cramer and Lauterborn, 1981; Koch et al., 2016).

3.3.5.2 Bubble splitting and merging

Single, spherical bubble oscillation is an exception in strong sound fields. Larger bubbles are unstable against surface oscillations, which may become so large as to destroy the bubble (Strube, 1971). The deformation and splitting of gas bubbles by surface instabilities are shown in Figure 3.14 (Hentschel, 1986). A gas bubble with a radius at rest of 510 µm has been inserted into a cylindrical piezoelectric transducer, with a horizontal axis of symmetry, driven at 7.055 kHz. The bubble has been holographed by high-speed holocinematography at 66700 holograms per second; that is, with an interframe time of 15 µs and nearly 10 frames per driving period. It can be seen that the bubble develops severe surface deformations, which lead to many tiny bubbles appearing on its surface and finally to the splitting of the bubble. These phenomena are to be expected in any application of acoustic cavitation. They are a continuous source of the smaller bubbles that sustain the cavitation process.

An example of bubble splitting, merging, and proliferation in a sound field has already been given in Figure 3.2 for 25 kHz. Informed by the habitat diagram (Figure 3.11), the fate of the bubble may be described as follows. The bubble oscillates spherically for some time

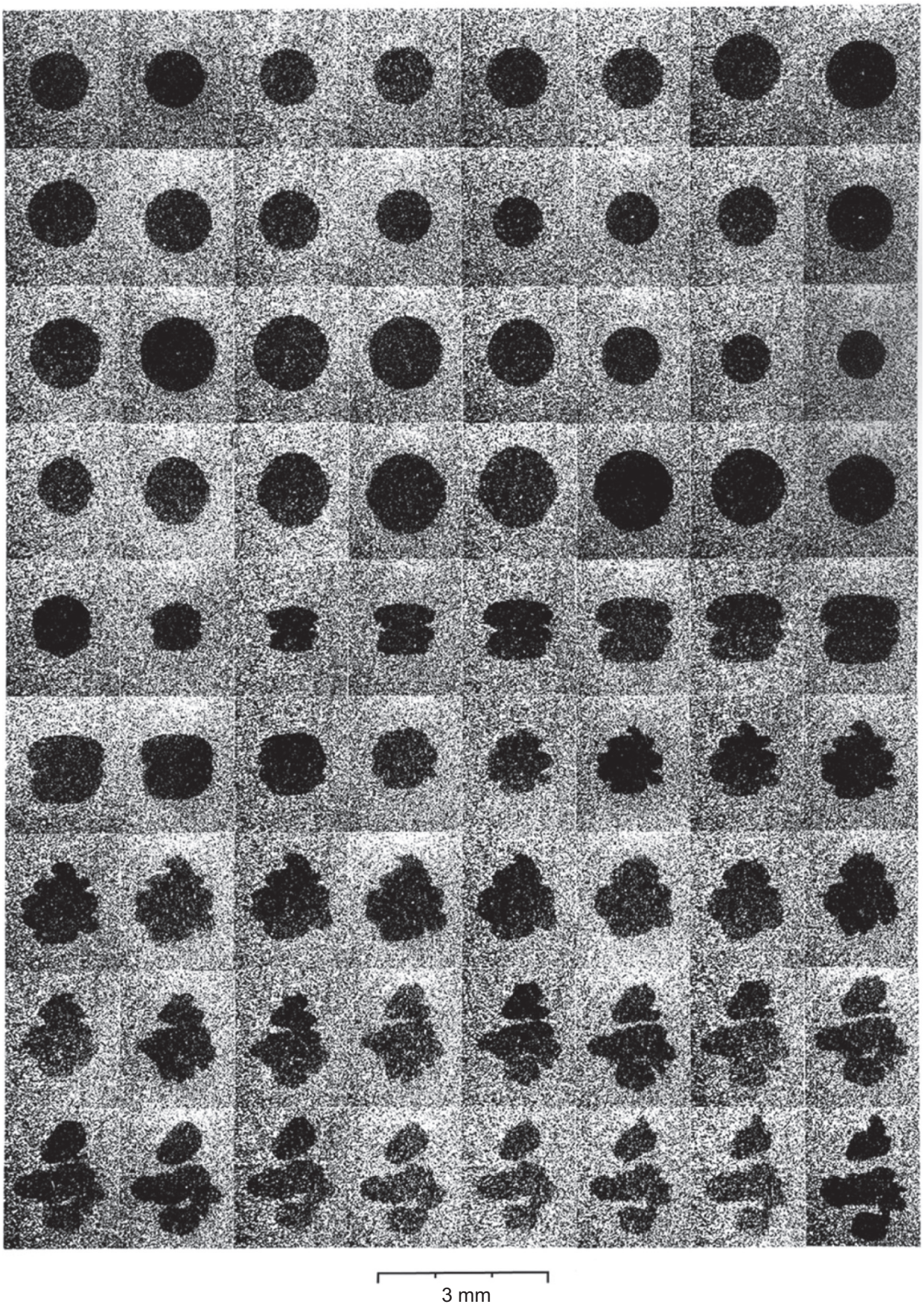


FIGURE 3.14 Gas bubble oscillating in a sound field of growing amplitude. Sound-field frequency = 7.055 kHz, bubble radius at rest = 510 μm, frame size = 2.4 mm × 2 mm. Reconstructed images from holograms taken at a holographic framing rate of 66.7 kHz. Time runs from left to right and from top to bottom. *(Courtesy of W. Hentschel.)*

and grows by rectified diffusion. It encounters the shape stability boundary and develops surface deformations that lead, upon collapse, to bubble splitting. These bubbles do not leave the habitat area, but go on to oscillate in the same pressure antinode region with recombination at maximum expansion due to their close contact. Obviously, they interact strongly and develop dynamics beyond simple spherical oscillation. A third tiny bubble appears in the course of these dynamics and seems to dissolve and/or be collected by the two other recombined bubbles, presumably with less gas content, as the main bubble resumes its spherical oscillation.

3.3.5.3 *Jet formation*

Besides the radiation of shock waves upon collapse and the splitting and merging of bubbles in acoustic cavitation, there is one more important phenomenon: jet formation. When the spherical symmetry of the surroundings of a bubble is disturbed by a boundary (solid wall, free surface, or another bubble) or by other means (gravity, bubble translation, or shock wave), the disturbance may lead to a jet of liquid passing into and through the bubble. In Figure 3.15, the phenomenon of jet formation is shown for a laser-induced bubble in front of a solid boundary. Laser-induced bubbles are a versatile tool for investigating jet formation and other properties of single bubbles in exceptionally clear settings (Lauterborn, 1979) that are also pertinent for acoustic cavitation problems (Crum, 1979b). The photographic series in Figure 3.15 was taken at 75,000 frames per second. The parallel beam of illuminating light comes from the back and deflects at the bubble wall to leave the image of the bubble black, except for the central part, where the light passes through undeflected. The jet that develops upon collapse shows up as the fine line in the central part of the bubble during the bubble rebound phase. The jet is directed toward the solid boundary. Depending on the distance of the bubble from the boundary, the jet may attain velocities reaching $100\,\mathrm{ms}^{-1}$ or more.

The shock waves radiated from the jet impact can be measured (Vogel and Lauterborn, 1988) and nowadays also calculated (Lechner et al., 2017).

There exists a vast literature on single laser-induced bubbles with jet formation, both experimentally and numerically, that may be accessed via Lechner et al. (2020). In the course of numerical studies, a new type of jet, an exceptionally fast jet in the range of $1000\,\mathrm{m\,s}^{-1}$, has been discovered for bubbles expanding and collapsing very close to a solid boundary (Lechner et al., 2019, 2020). An example of a fast jet, calculated in a full 3D-simulation (Koch et al., 2021), is shown in Figure 3.16. It is to be noted that the thin, fast jet seen in the inside of the bubble reaches the surface when the bubble is still comparably large. This is different from normal axial jet formation. A detailed study (Lechner et al., 2020) has revealed that the fast jet is formed by the self-impact of a converging annular inflow at the axis

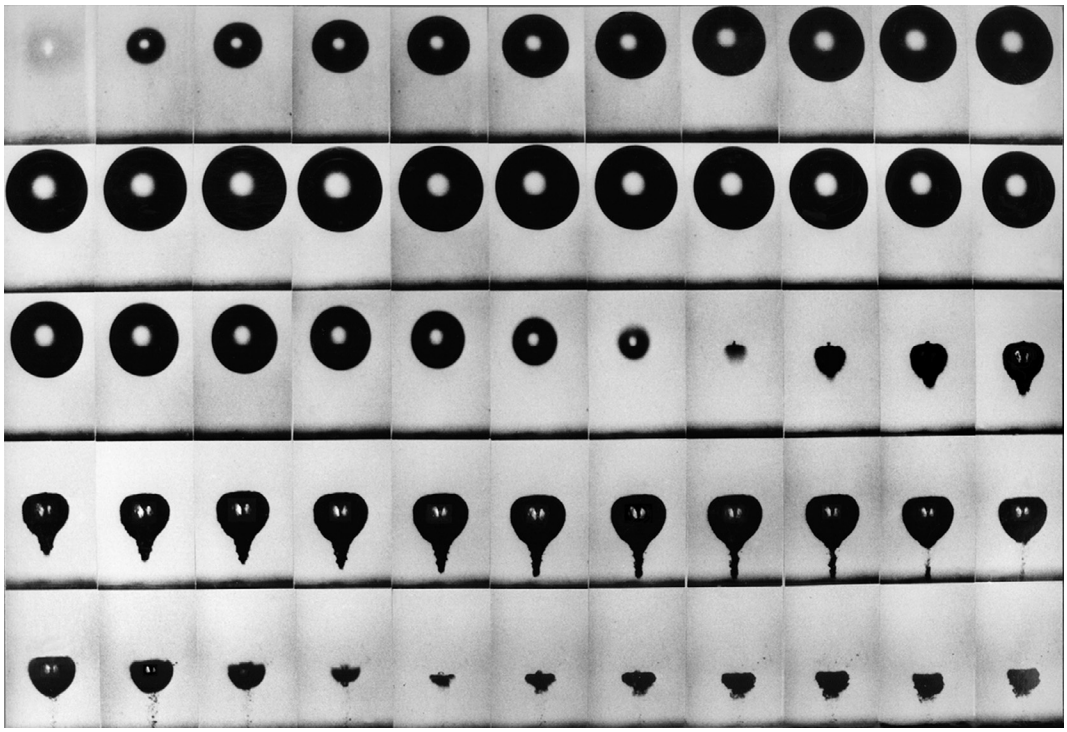


FIGURE 3.15 Jet formation toward a flat solid boundary (below in each frame) of a laser-induced bubble in water. Seventy-five thousand frames per second, frame size = 7.2 mm × 4.6 mm. Maximum bubble size = 2 mm, distance to the boundary = 4.9 mm.

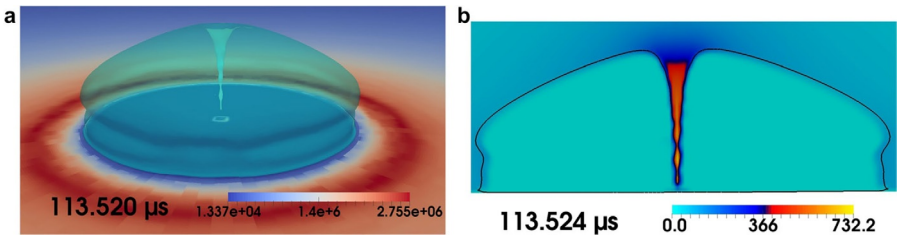


FIGURE 3.16 Frame from a full 3D-simulation of the formation of a fast jet of a bubble expanding and collapsing very close to a solid boundary. (a) A contour plot of the bubble is given together with the pressure in Pascal on the solid boundary. (b) Cross section through the bubble with the liquid velocity in ms^{-1}. *(Figure 17 from Koch et al. (2021) (CC BY 4.0).)*

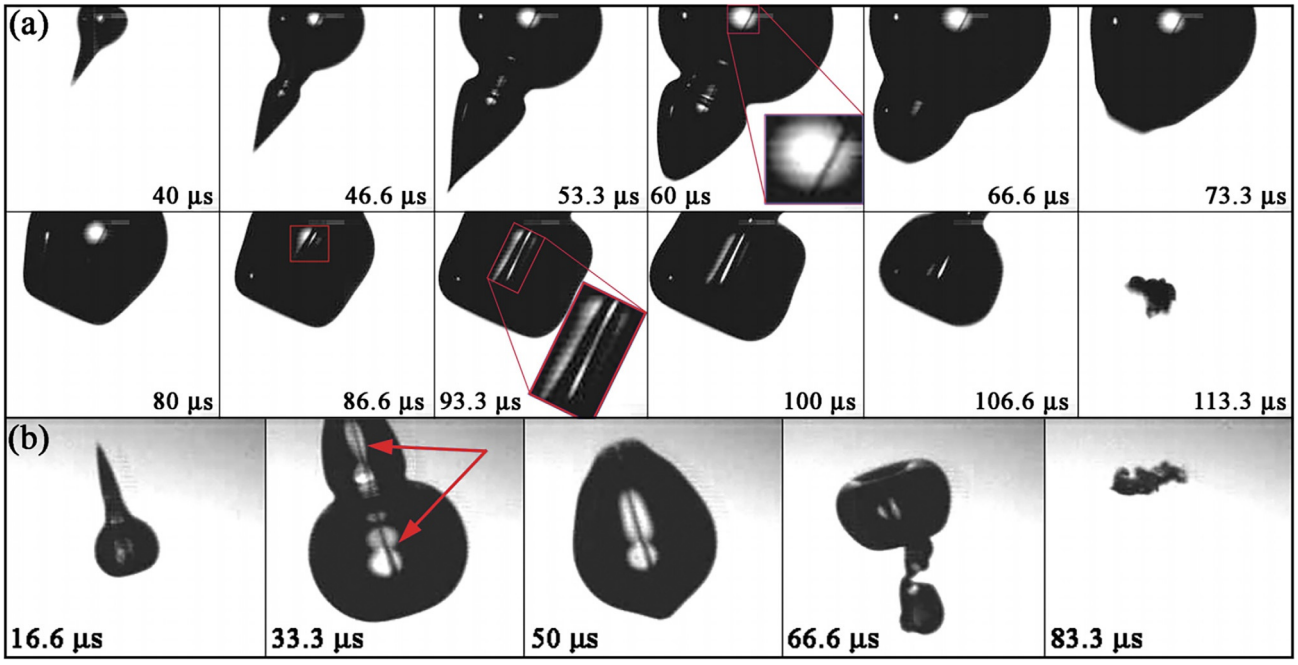


FIGURE 3.17 Two examples of jet and rebound-jet formation. The time scales refer to the bubble seeding time. (A) The first jet upon expansion of its gaseous hull develops a lancet-like shape. The rebound jet develops from the lancet tip into the opposite direction of the original jet. Frame width is 850 µm. (B) The rebound-jet involutes the upper part of the bubble (the bubble part of the first-jet impact), seen at 66.6 µs. Frame width is 1 mm. *(Figure 4 from Rosselló et al. (2018), reproduced with permission from American Institute of Physics.)*

of bubble symmetry. At self-impact, the liquid is squeezed out and redirected into the axial direction. The full 3D-calculations show that the fast jet is a robust phenomenon. Axial jet formation by annular inflow of liquid has also been documented experimentally (Lauterborn et al., 1999, figure 52). An experimental confirmation of the fast jet can be found in Koch et al. (2021). The experimental detection of the fast jet and the determination of its velocity is not an easy task. High resolution in space and time is needed, and even then, reliable results could only be achieved with heavy input of numerics, in particular digitization of the complete experimental arrangement with insertion of the numerical bubble simulations.

Bubble jet formation in acoustic fields is more difficult to study owing to the yet unpredictable appearance of bubbles in space and time. Here too, the seeding of a single bubble by laser light in a sound field (Ohl, 2000; Kurz et al., 2006; Rosselló et al., 2018) is of great help. It could be shown that bubbles in a standing sound field develop a jet in the direction of the pressure gradient (Rosselló et al., 2018). Complicated jetting phenomena may occur with one and the same bubble. Two examples are given in Figure 3.17 of bubbles seeded in phosphoric acid (PA75) in a standing sound field of 26.1 kHz. In Figure 3.17a, a usual jet is seen at 40 µs after bubble generation. The frames were composed from a series taken at 300,000 frames per second. The bubble surface stretched by the jet takes the form of a lancet during reexpansion of the bubble with the jet inside. The jet remains stable inside the bubble as seen in the frame at 60 µs. Upon collapse of the lancet head, a second jet in the opposite direction of the first jet forms, called rebound jet. The formation of the rebound jet is assisted by the changing pressure gradient direction of the sound field with time. In Figure 3.17b, the second jet

formation is clearly shown by the involution of the top of the bubble at 66.6 µs. Figure 3.17 demonstrates how complex the dynamics of just one bubble may be in a sound field.

3.4 Bubble ensemble dynamics

In applications, large numbers of bubbles do the work, be it for cleaning or for inducing or enhancing chemical reactions. Their interaction introduces new phenomena beyond the already complex oscillations of single bubbles and their disturbed motions (e.g., jet formation). One striking effect of the interaction of many bubbles is that a homogeneous distribution of (spherical) bubbles is not stable in a sound field (Akhatov et al., 1994). They form clusters, branched filaments (streamers), and very special stable or slowly varying patterns at higher driving (Thiemann et al., 2011) when bubbles are no longer positionally stable in the pressure antinode of a standing sound field (Akhatov et al., 1997b; Matula et al., 1997). The acoustic radiation forces of the applied sound field and the attractive and repulsive forces between oscillating bubbles lead to cooperative effects and self-organization. The following sections give some examples of bubble ensembles as a general overview (for more examples, see Mettin, 2005). A model will then be presented that covers the essential properties of bubble ensemble dynamics.

3.4.1 Bubble clusters

Bubble clusters appear in acoustic cavitation in a variety of forms, from those composed of only a few bubbles as in Figure 3.2 (the beginning of cluster formation by bubble splitting), to large and sometimes almost spherical clusters composed of many bubbles. In Figure 3.18, eight frames from successive periods of a 25 kHz sound field show a small bubble cluster in a pressure antinode. The cluster undergoes large variations from one frame to the next but reorganizes itself repeatedly with a varying number of bubbles, between three and eight in this case. The reason may be that small bubbles are driven to the pressure antinode (when the pressure amplitude is not too high) and merge there, having previously been split in a rapid collapse. It has been found by Krefting (2003) that small clusters are formed at sound pressure amplitudes between 190 and 300 kPa for frequencies in the 20 kHz range. More examples of bubble clusters can be found in the book edited by Rozenberg (1971, p. 310).

Crum and Nordling (1972), working with a cylindrical cavity operated at 55 kHz and a pressure amplitude of about 500 kPa, report on bubble clusters rapidly moving out of the high-pressure field at the center and retaining their identity over about 500 cycles until they disappear. This agrees with the experimental observation of Krefting (2003) that bubble clusters become unstable above 300 kPa and are either destroyed or move to the walls of the container, and also with theoretical considerations of the positional stability of oscillating bubbles in a sound field (Akhatov et al., 1997b; Matula et al., 1997; Doinikov, 2002).

Figure 3.19 gives an example of a larger bubble cluster that is obviously moving through a liquid as a distinct entity. It consists of two bigger bubbles in the center surrounded by a ring of smaller bubbles and with a tail of small bubbles. This cluster is a separate part of a larger, extended bubble ensemble in a cylindrical resonator driven at 23 kHz that has been imaged holographically to investigate its complex three-dimensional structure.

The motion of a large, spherical bubble cluster in a sound field is shown in Figure 3.20. The cluster has formed spontaneously in liquid insonated at 40 kHz in the course of experiments with bubbles near solid boundaries. Here, a glass plate has been placed in the liquid for cleaning experiments. It is seen that the glass plate (side view) attracts a large number of bubbles and also a bubble cluster that impinges on it. The cluster thereby alters its spherical shape

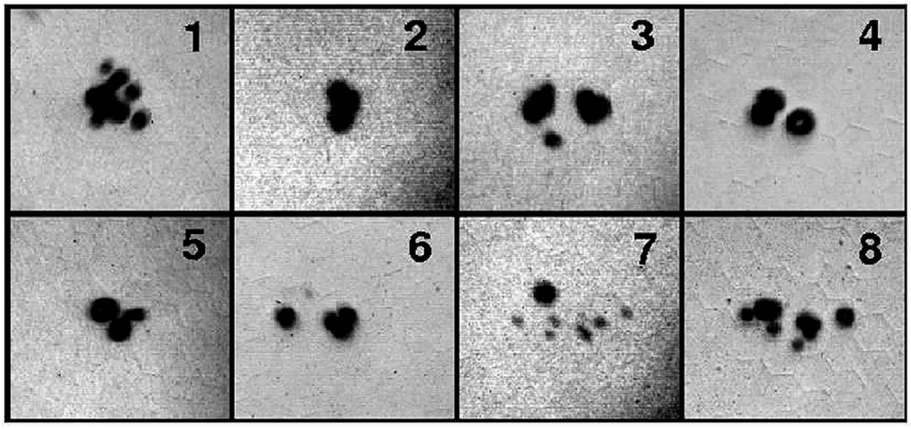


FIGURE 3.18 Small bubble-cluster dynamics and variability in a pressure antinode of a standing sound field of 25 kHz. Successive frames at the same phase of successive periods of the sound field. Frame size approximately 1 mm. *(Courtesy of D. Krefting.)*

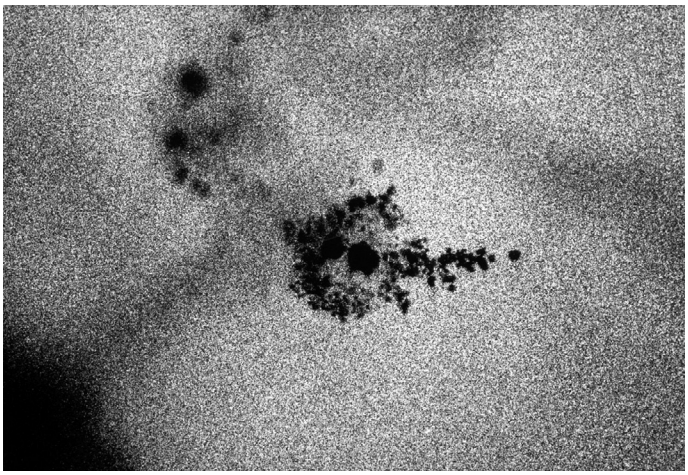


FIGURE 3.19 Big bubble cluster in a standing sound field of 23 kHz (cylindrical resonator). Two bubbles surrounded by a ring of bubbles and a bubble tail. Reconstructed image from a hologram.

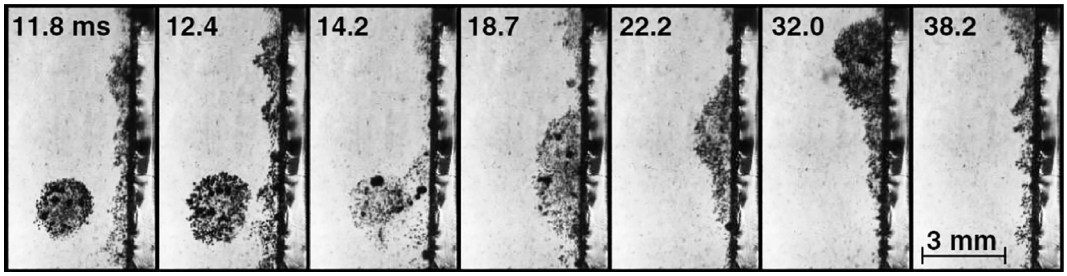


FIGURE 3.20 Big spherical bubble cluster in a sound field of 40 kHz moving toward a glass plate (side view) and deforming while attaching and spreading, and presumably do cleaning work. *(Courtesy of D. Krefting.)*

to that of a hemisphere and then to an ellipsoid until it flattens out along the surface with a bulge moving upward. Such clusters seem to play a role in ultrasonic cleaning (i.e., cleaning by bubbles; Olaf, 1957) in that their movement is perpendicular to the planes of a standing sound field (along pressure gradients), and thus, they can cover a substantial extent of the liquid volume (Krefting et al., 2004).

3.4.2 Bubble filaments

Besides the compact bubble cluster, more diffuse and extended bubble configurations are found in the form of branched filaments that also seem to act as distinct objects, remaining stable for many oscillations (see Lauterborn and Kurz, 2010; Figure 3.22). They are particularly extended in cylindrical sound-field geometries but also appear in rectangular configurations, which are preferred for cleaning baths. Figure 3.21 gives an example in which many branched filaments can be seen. The bubbles in these filaments move toward the branching points and the center of the bubble cloud and become quite separated as seen in a close-up view in Figure 3.22, taken with a short-exposure time of about 10 ns. Because of this streaming of bubbles along the same path, such filaments are known as *streamers*.

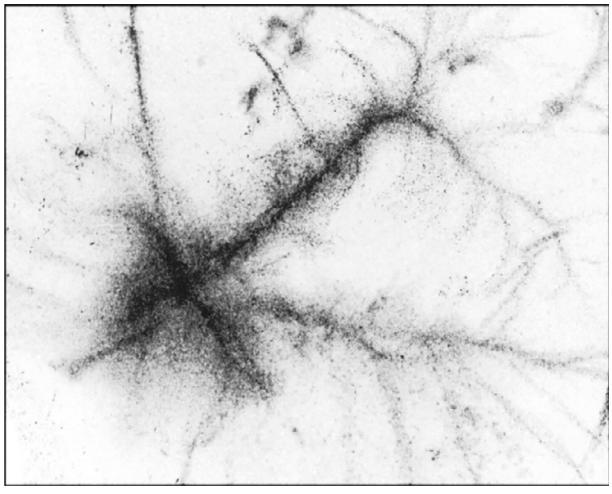


FIGURE 3.21 Filamentary bubble structure in a cylindrical resonator. *(Courtesy of A. Billo.)*

It is still an open question, how such a stream of bubbles is maintained, because there must be a continuous supply. One view is that invisibly small bubbles act as cavitation nuclei at the beginning of each branch. In the sound field, they oscillate with increasing amplitude on their way toward the center due to the increasing sound pressure amplitude, and the oscillation becomes so strong that the bubbles



FIGURE 3.22 Filamentary bubble structure in a cylindrical resonator. Extremely short exposure (about 10 ns) for not only stopping the translational motion but also the oscillatory motion of the bubble for an unblurred picture. *(Courtesy of A. Billo.)*

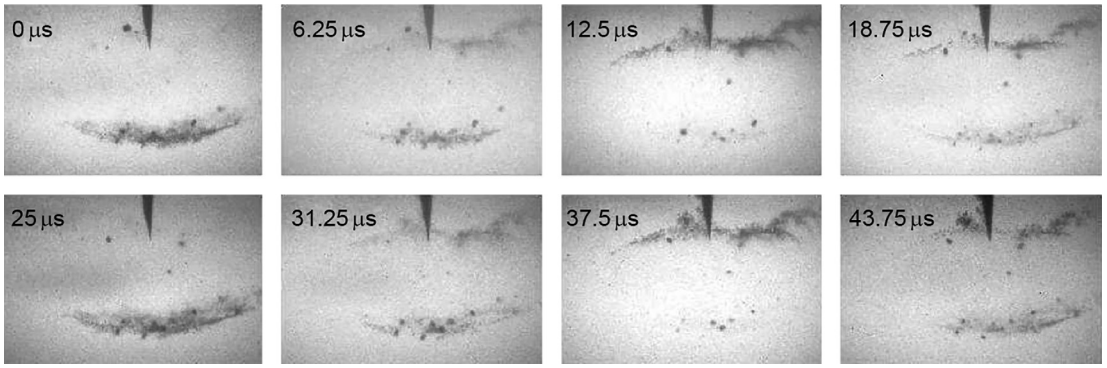


FIGURE 3.23 Bubble double layer in a rectangular resonator driven at 40 kHz (side view). Two periods of the driving sound field are covered. Frame width = 1 cm, exposure time = 1 μs.

themselves shed smaller bubbles and thus populate the filament. This interpretation is supported by the observation that larger bubbles are often followed along filaments by smaller bubbles, as seen in Figure 3.22, where three filaments are in focus and the center, toward which the bubbles are heading, is at the top of the picture. Other possibilities are source bubbles attached to walls or submerged objects. Such bubbles can shed a continuous stream of daughter bubbles and can be placed at walls artificially.

3.4.3 Bubble double layers

In cleaning baths, very special bubble configurations are observed that develop at higher intensities and show dynamic stability with the individual bubbles strongly oscillating, moving, and rearranging but not destroying the overall appearance of the configuration. One typical structure occurring in rectangular resonators is the double layer, which consists of two layers of bubbles that appear simultaneously on two sides of a pressure node in a standing sound field, as shown in Figure 3.23. Each layer has the filamentary appearance of the structure shown in Figure 3.21, when viewed from the direction that would be looking down from the top of Figure 3.23. These layers do not extend to the pressure antinode, which is largely depopulated of bubbles. Instead, they show a sharp, curved boundary in the direction of the pressure antinode. Obviously, the bubbles in the layers are not positionally stable in the pressure antinode but gather at some distance, thereby making visible contours of similar pressure and pressure gradient. The two layers oscillate in antiphase because they are located on adjacent, opposite sides of a standing sound field. This feature only shows up in time-resolved, short-exposure photographs as in Figure 3.23. When viewed with the human eye or when "long-exposure" (1 ms) photography is used, both layers seem to be present simultaneously. Double layers of bubbles have high potential for cleaning and erosion (Krefting et al., 2004).

A precursor to the double layer in large cubical resonators with many pressure antinodes seems to be the splitting of the filament center into two centers in small cubical resonators with just one pressure antinode, which is also observed to occur in cylindrical resonators along the symmetry axis. Figure 3.24 shows an example of a two-center bubble filament system in a small cubical resonator of 5 cm inner edge length, driven at 22.8 kHz and 132 kPa (Appel et al., 2004; Lauterborn et al., 2008). The three-dimensional bubble distribution has been composed from several frames of a stereoscopic high-speed digital videographic series taken at 2250 frames per second to give the visual appearance of simultaneity that human perception would generate. The bubbles are projected onto three perpendicular planes to make their three-dimensional bubble configuration apparent. In reality, the bubble ensemble is much more diluted and the individual bubbles can be followed by digital picture processing to give their velocities

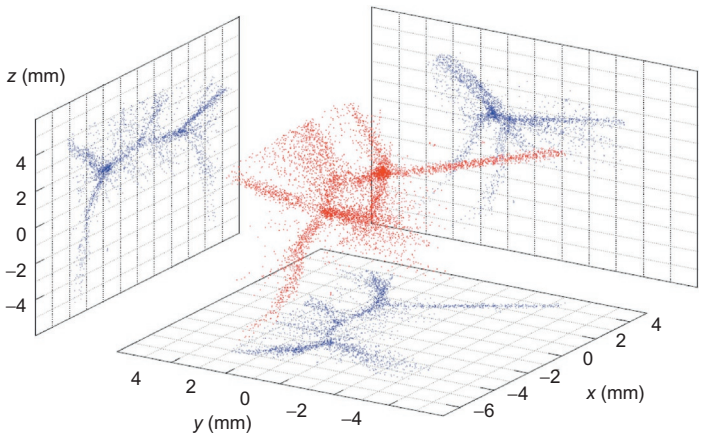


FIGURE 3.24 Double center in a rectangular resonator ($5 \times 5 \times 5\,cm^3$) driven at 22.8 kHz and 132 kPa. Bubble locations from several frames of a stereoscopic high-speed digital videographic series taken at 2250 frames per second. *(Courtesy of P. Koch.)*

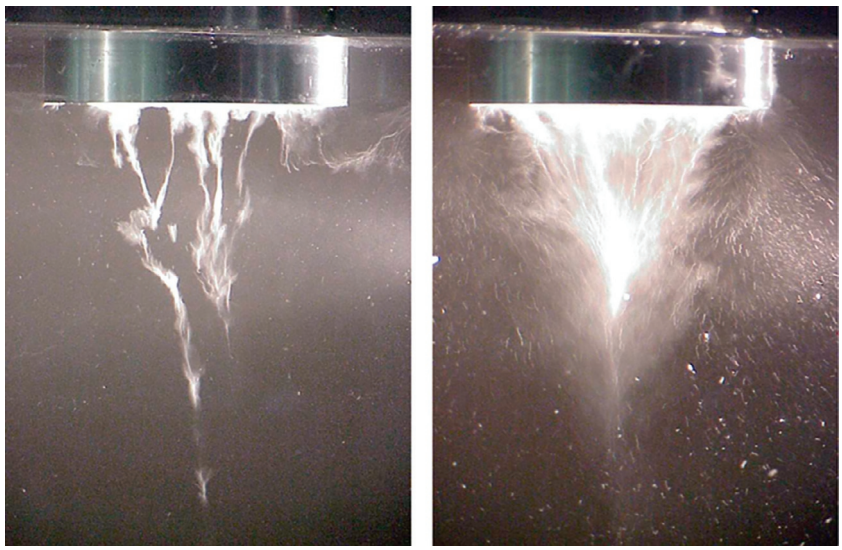


FIGURE 3.25 Bubble ensemble underneath a sonotrode of 120 mm diameter forming a conical shape (cone-like bubble structure). Sound-field frequency = 20.7 kHz. Acoustic intensities at the surface of the transducer are $1.8\,W\,cm^{-2}$ (left) and $7.0\,W\,cm^{-2}$ (right). *(Courtesy of B. Dubus and A. Moussatov.)*

(Luther et al., 2001). The velocity distribution exhibits a peak at $0.2\,ms^{-1}$.

3.4.4 Bubble cones

Rectangular resonators (cleaning baths) are usual for ultrasonic cleaning, but in sonochemistry, the sound field is often generated below sonotrodes, that is, cylindrical rods of various diameters and construction. They are dipped into the liquid to be irradiated and set into vibration at one end with the maximum amplitude occurring at the other end in the liquid. Again, beyond a cavitation threshold, bubbles are generated that appear in the liquid on and below the sonotrodes. Bubble structure beneath cylindrical sonotrodes has been investigated by Moussatov et al. (2003) for diameters of 20, 80, and 120 mm driven at 20.7 kHz and at high intensities. They found cone-like structures densely populated with bubbles and a focusing of the sound field under the sonotrode, with the phenomenon more pronounced for larger sonotrode diameters and higher intensities.

Figure 3.25 shows two examples of bubble ensembles below a sonotrode of 120 mm diameter driven at 20.7 kHz with low and high intensities. The bubble ensemble starts with a few bubbles on the surface of the sonotrode near the cavitation threshold (not shown). With increasing intensity, it develops a filamentary structure that extends far into the liquid and becomes more and more densely populated with bubbles (Figure 3.25, left). Finally, it attains the form of a cone-like structure with a focus below the sonotrode (Figure 3.25, right). Such structures should be taken into account, when discussing the yield of chemical reactions.

3.4.5 *N*-bubble model

Similar to the *n*-body problem in astrophysics, it is possible to formulate a theory of an *N*-bubble problem in acoustic

cavitation, when the bubbles are not too densely packed and can be considered as individual bubbles. However, the interaction forces are different from a simple gravitational attraction and much more involved. As with any motion, there is an inertial term, which opposes the setting of a bubble into translational motion (the added-mass force), and a frictional term, which opposes the motion of the bubble once it has begun (the drag force). For a discussion of these two forces, see Parlitz et al. (1999). Moreover, the bubbles experience an acoustic radiation force from the driving sound field (the primary Bjerknes force) and from each other (the secondary Bjerknes force), because their own oscillation also leads to radiated sound waves. As to the Bjerknes forces, see, e.g., Crum (1975), Matula et al. (1997), Akhatov et al. (1997b) and Mettin et al. (1997).

A many-bubble model incorporating a single-bubble oscillation model and these four forces has been formulated by Mettin et al. (1999a, b) and Parlitz et al. (1999). The equations of motion (without the equations for single, spherical bubble oscillation) for N bubbles are given by

$$\mathbf{F}^i_{\mathrm{M}} + \mathbf{F}^i_{\mathrm{B1}} + \mathbf{F}^i_{\mathrm{B2}} + \mathbf{F}^i_{\mathrm{D}} = 0,\ i = 1,\ldots,N \tag{3.17}$$

$$\mathbf{F}^i_{\mathrm{M}} = -\frac{\rho}{2}\langle V_i(t)\rangle_T \dot{\mathbf{v}}_i, \tag{3.18}$$

$$\mathbf{F}^i_{\mathrm{D}} = -12\pi\mu R_i \mathbf{v}_i, \tag{3.19}$$

$$\mathbf{F}^i_{\mathrm{B1}} = -\langle \nabla p_{\mathrm{a}}(\mathbf{x}_i; t) V_i(t)\rangle_T, \tag{3.20}$$

$$\mathbf{F}^i_{\mathrm{B2}} = \sum_{j\neq i} \frac{\rho}{4\pi}\left\langle \dot{V}_i(t)\dot{V}_j(t)\right\rangle_T \frac{\mathbf{d}_{ij}}{|\mathbf{d}_{ij}|^3}. \tag{3.21}$$

$\mathbf{F}^i_{\mathrm{M}}$ is the inertial force, $\mathbf{F}^i_{\mathrm{D}}$ is the drag force, $\mathbf{F}^i_{\mathrm{B1}}$ is the primary Bjerknes force, and $\mathbf{F}^i_{\mathrm{B2}}$ is the secondary Bjerknes force. The index i labels the bubbles according to their locations $\mathbf{x}_i$, velocities $\mathbf{v}_i$, accelerations $\dot{\mathbf{v}}_i$, radii R_i, and volumes V_i. The distance vector from bubble i to bubble j is denoted by $\mathbf{d}_{ij} = \mathbf{x}_j - \mathbf{x}_i$. The operation $(.)_T$ signifies an averaging over one period of the sound field, and ρ is the density of the liquid, μ the dynamic viscosity, and p_{a} the amplitude of the applied sound field. The averaging operation is valid for bubble oscillation solutions with period number 1, otherwise two or more periods of the sound field should be taken.

3.4.6 *N*-bubble simulation examples

A special experiment can be designed for a comparison of experiments with the N-bubble model. A wire ring is inserted into a cubical resonator for seeding and stabilizing the streamer structure in a plane. The resonator is driven at 23.65 kHz. The streamer structure is shown in Figure 3.26. It is not stable in time in its qualitative spatial form but oscillates between a form with the streamers running to a common center (the pressure antinode) and a form in which the center is depopulated of bubbles and the streamers stop and combine off the pressure antinode.

A simulation of the dynamics of filamentary streamers, for comparison with the experiment, is shown in Figure 3.27 for two sound pressure amplitudes. The frequency chosen is 20 kHz (a standard frequency for collecting numerical data for later comparison). Fifteen bubble sources have been placed along a ring, as observed in the experiment. Bubble starting-sizes chosen are 2 μm for all bubbles. The results from simulations with two pressure amplitudes of 150 kPa and 180 kPa are shown. The result is that the essential features of the experiment are reproduced: the merging of the filamentary streamers at the pressure antinode at low sound pressure amplitudes and the repulsion of bubbles from the pressure antinode at high sound pressure amplitudes.

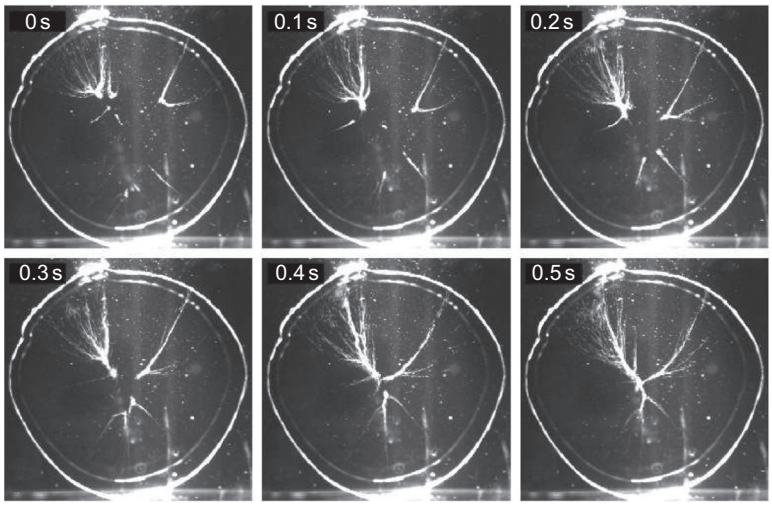


FIGURE 3.26 Dynamics of a filamentary streamer structure stabilized by a wire ring. Cubical resonator with one pressure antinode. Sound-field frequency = 23.65 kHz, frame width = 4 cm, exposure time = 16 ms (front illumination), interframe time = 100 ms. *(Courtesy of D. Krefting.)*

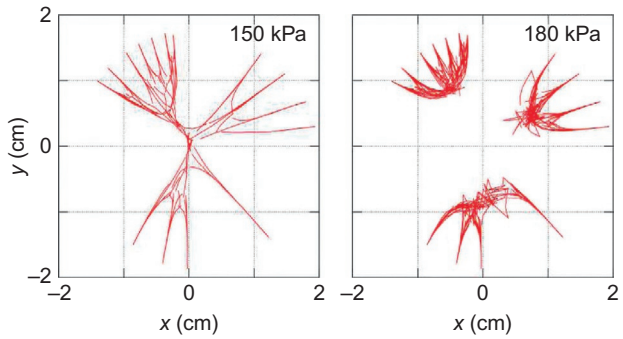


FIGURE 3.27 Simulation of the dynamics of a filamentary streamer structure. Sound-field frequency = 20 kHz, two different sound pressure amplitudes. *(Courtesy of P. Koch.)*

Further simulations have also reproduced the double-layer structure (Mettin, 2005) and qualitatively the cone-like bubble ensembles that are observed beneath sonotrodes (Koch et al., 2004). Advanced modeling tries to include the feedback from the bubble distribution on the sound field as well. This has been done by Mettin et al. (2006) by considering sound propagation in a bubbly liquid of low void fraction, linearizing the bubble oscillation in the pressure field equations for closure of the system and combining the sound-field propagation model with the *N*-bubble model (Eq. 3.17), now retaining full nonlinear bubble oscillation by using a Rayleigh-Plesset equation (for the equations and the full description, see Mettin et al., 2006). When this model is applied to the experimental situation in Figure 3.26, the autofluctuations between a populated and a depopulated center that show up in the experiments are reproduced.

Recent contributions to such modeling come from Louisnard (2012a, b) and Jamshidi and Brenner (2013), where sound propagation in bubbly (cavitating) liquids is modeled taking realistic damping terms into account. It turns out that strongly nonlinear bubble oscillations result in energy losses larger by orders of magnitude than those calculated by the previously used linear approximation, and the effects on the sound field can explain some additional aspects of the bubble structures observed beneath sonotrodes and in cleaning baths (Louisnard, 2012b). Further progress in modeling acoustic cavitation bubble ensembles can be expected due to the high level of interest in the applications (ultrasonic and megasonic cleaning, wastewater treatment, and sonochemical reactor development).

3.5 Acoustic cavitation noise

When acoustic cavitation sets in, a hissing sound is heard: this is acoustic cavitation noise. It radiates from the bubbles generated in the sound field and can be so intense that ear-protection is required in an acoustic cavitation environment. Therefore, the phenomenon has become the subject of much research.

3.5.1 Subharmonics and period doubling

The pressure-time curves of acoustic cavitation noise are not immediately informative, but their Fourier transforms or power spectra show interesting features. Esche (1952) investigated noise spectra for different sound-field frequencies between 3 kHz and 3.3 MHz and found a line spectrum superimposed on a broadband noise spectrum. The spectral lines ν_s consisted of the driving frequency $\nu_s = \nu_a$ and its harmonics $\nu_s = n\nu_a$, $n = 1, 2, \ldots$, and also lines at $\nu_s = 1/2\ \nu_a$ and its harmonics. Later, lines at 1/4 ν_a, 1/8 ν_a, and 1/16 ν_a were also found. The occurrence of subharmonic lines is a peculiar feature of acoustic cavitation noise and must therefore be traced back to the bubble oscillations in the sound field. Similarly, the broadband noise is a peculiar feature of the emission from the bubbles, as they are typically driven by a single frequency. The energy of a single frequency must somehow be transformed into the energy of many frequency components. Only nonlinear dynamical systems exhibit this feature. Subharmonics and even noise are common in these systems, their special type of noise being described as *deterministic chaos*.

Theoretically, one way to arrive at a broadband spectrum is through subharmonics and by successive period doubling that approaches chaos (or noise) when a parameter of the system is altered. It has been found that a single, spherical bubble can follow this route to chaos (Lauterborn and Parlitz, 1988) and is able to oscillate in a way that produces a broadband spectrum similar to those observed (Lauterborn and Suchla, 1984).

Period-doubling sequences have been found before in experiments involving a large number of bubbles, when the sound pressure amplitude is raised linearly at an appropriate rate, slow enough for the bubbles to approach the steady state and fast enough for the structure of the bubble ensemble not to alter significantly (Lauterborn and Cramer, 1981; Lauterborn, 1986; Lauterborn and Holzfuss, 1991). Figure 3.28 shows an example of an experimental period-doubling route to the final cavitation noise spectrum as encountered in a cylindrical resonator. The succession of four acoustic emission spectra at increasing sound pressure amplitude demonstrates the period-doubling property together with the appearance of broadband noise (bottom right). The connection of the noise with bubble oscillations has been confirmed by simultaneous high-speed optical, holographic, and acoustic measurements (Lauterborn and Koch, 1987; Lauterborn et al., 1999). The complete bubble ensemble shows period doubling. This has also been shown for double-layer bubble structures as well as filamentary bubble structures (Mettin, 2005).

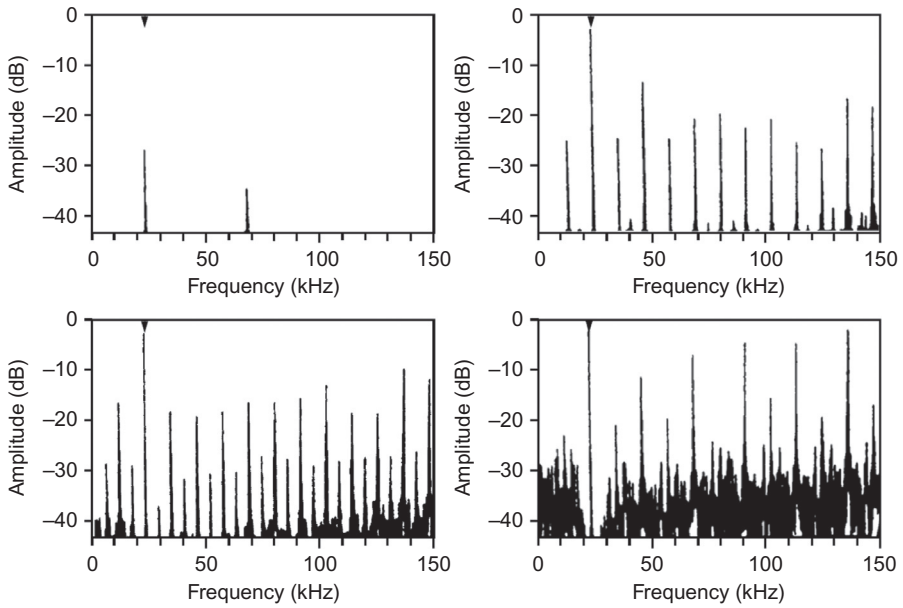


FIGURE 3.28 Power spectra of cavitation noise taken at a driving frequency of $\nu_a = 23$ kHz, marked in the figures by a small triangle. The driving pressure is increased from one graph to the next, giving first a periodic, anharmonic signal (top left), then a subharmonic motion with lines at multiples of $\nu_a/2$ (period-2 motion, top right), then period-4 motion with lines at multiples of $\nu_a/4$ (bottom left), and finally a broadband spectrum indicative of chaotic behavior (bottom right).

3.5.2 Synchronization

The synchronous oscillation of bubbles of different sizes in a large bubble ensemble is an astonishing fact that needs an explanation. It is known that when a large number of oscillators are coupled they tend to synchronize. Even two oscillators that are close in their resonant frequencies will phase lock to oscillate at the same frequency over an entire frequency range. This mechanism also works for larger oscillator ensembles. Phase synchronization of bubble oscillations has been investigated by Tervo et al. (2006) and Nasibullaeva and Akhatov (2013), following Nigmatulin et al. (2000), and exploring their bubble-cluster model of interacting bubbles more deeply.

Examples of phase synchronization are given in Figures 3.29 and 3.30. In Figure 3.29, two independent, monodisperse bubble clusters with 300 bubbles each have been subjected to a sound field with a frequency of 40 kHz and a pressure amplitude of 200 kPa. One cluster is composed of bubbles with a radius at rest of 15 µm (cluster 1); the other of bubbles with 20 µm radius at rest (cluster 2). Bubbles in cluster 1 oscillate with period number 1, bubbles in cluster 2 oscillate subharmonically with period number 2; moreover, their collapse takes place at different phases of the sound field. However, when both clusters are combined into one polydisperse cluster, bubbles from both species show subharmonic oscillations of period number 2 and both collapse at the same two phases of the sound field (Figure 3.30). Nevertheless, the two different bubble species have different maxima. Thus, the phase synchronization of interacting bubbles may be the explanation for period doubling to chaos

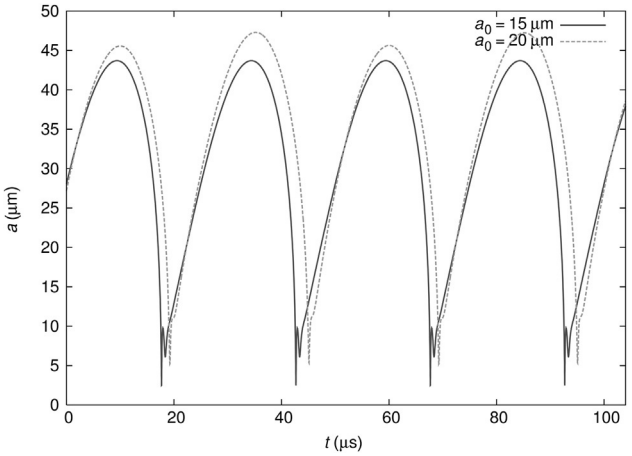


FIGURE 3.29 Oscillations of the bubbles in two separate monodisperse bubble clusters of cluster radius 1 mm, each containing 300 bubbles. *Solid line*: bubble radius 15 µm, *dashed line*: bubble radius 20 µm. Driving frequency = 40 kHz, pressure amplitude = 200 kPa.

in bubble ensembles with bubbles of different sizes and for the observation that at times no bubbles are seen in a cluster, a filament, or a double layer, because at that moment, all bubbles have collapsed at the same phase of the sound field.

3.5.3 Bubble splitting

While the preceding explanation is the only one that consistently can be given for subharmonic sound emission from bubbles, broadband noise may have additional components. Bohn (1957) pointed out that amplitude and phase

fluctuations in the oscillations of the bubbles can produce a noise background. Yasui et al. (2010) have developed the idea that a fluctuating number of bubbles will produce a noise background. This seems difficult to prove experimentally, but, by starting with the sound emission spectrum of a single bubble in a trap (a line spectrum), where from time to time the bubble becomes unstable (Figure 3.2) and splits into two or more bubbles, the idea can be tested.

In Figure 3.31, a spectral bifurcation diagram of the sound emission from a stable-unstable bubble oscillation is given. Whenever the bubble becomes unstable, the line spectrum changes, with additional noise at higher frequencies. It is conceivable that with more bubbles splitting, the noise component would be enhanced. This model of noise production is still deterministic. It invokes surface instabilities from growing bubbles that encounter a shape stability boundary and shed new bubbles as a source of sound emission. These new bubbles appear in the course of a violent collapse process (see Figure 3.2), presumably with the emission of a short sound-pulse, and will respond with nonlinear transient oscillations at the driving frequency and with the corresponding emission of many frequency components that appear as noise.

To calculate the noise spectrum, the number of splitting processes should be determined. Investigations into the behavior and stability of streamers have already shown that collision and coalescence (merging) of bubbles in streamers is the predominant phenomenon, whereas bubble splitting upon collapse is difficult to observe directly in a three-dimensional bubble configuration due to spatiotemporal resolution constraints (Luther et al., 2001). In a stationary cavitation bubble ensemble, the average number of bubbles can be considered a constant. Therefore, the number of splittings should equal the number of mergings. The average number of splittings can then be determined directly from the average number of (optically more accessible) mergings. However, there remains the problem of the phase of the splitting process with respect to the sound field. Here, acoustic measurements of the phase statistics of spikes in the time series of the acoustic cavitation noise may help.

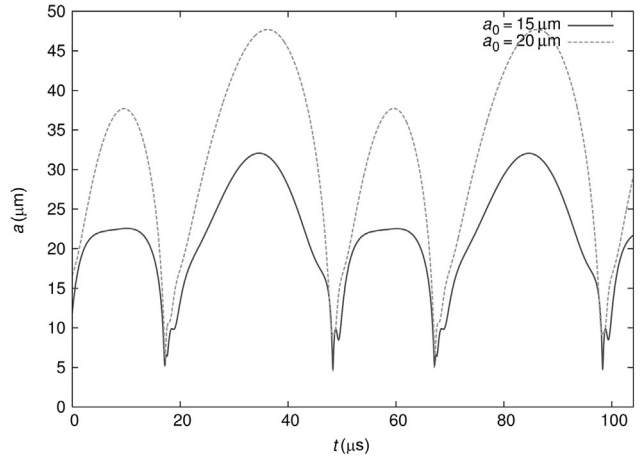


FIGURE 3.30 Oscillations of the bubbles in a polydisperse cluster of cluster radius 1 mm containing 300 bubbles of radius 15 µm (*solid line*) and 300 bubbles of radius 20 µm (*dashed line*). Driving frequency = 40 kHz, pressure amplitude = 200 kPa.

3.6 Sonoluminescence

Bubbles emit not only sound but also light. This topic is covered in several reviews (Walton and Reynolds, 1984; Verrall and Sehgal, 1988; Putterman and Weninger, 2000; Brenner et al., 2002; Suslick and Flannigan, 2008; Crum, 2015) and books (Crum et al., 1999; Young, 2005; Grieser et al., 2015). Several theories of light emission from bubbles have been proposed over the years. The explanation now generally accepted is the hot spot theory (Kuttruff,

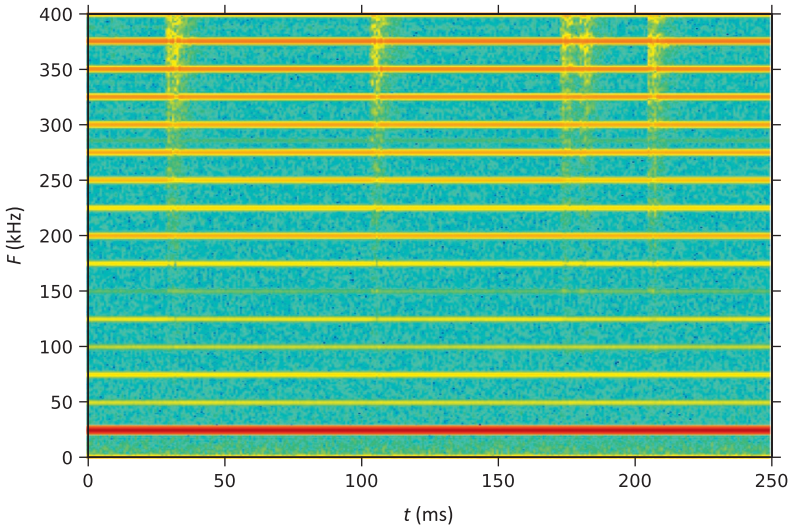


FIGURE 3.31 Spectral bifurcation diagram of the sound emission from a repeatedly splitting single, spherical bubble in a trap. Sound field frequency = 25 kHz. *(Courtesy of J. Schneider and J. Eisener.)*

1962): when a bubble collapses sufficiently fast, its contents are compressed so strongly that the adiabatic temperature rise leads to high enough temperatures for light emission. This implies that the light emitted upon collapse of the bubble is in the form of a short flash. The flash duration (and intensity) depends on the details of bubble collapse, which in turn depend on many parameters from sound-field frequency, sound pressure amplitude, and bubble size to the type of liquid and the gas inside the bubble. Flash durations are typically less than 1 ns.

In water, highly spherical, single bubbles in a bubble trap (single-bubble sonoluminescence) reach temperatures up to about 20,000 K, as measured from light-emission spectra, whereas in multibubble systems (multibubble sonoluminescence), temperatures no higher than 5000–6000 K (and sometimes even lower) are observed. It is suggested that these markedly different temperatures result from most bubbles in a multibubble ensemble not collapsing spherically, due to disturbance from other bubbles or translational motion leading to less compression, lower temperatures, and overall less light emission. Indeed, the effect of asphericity around the bubbles diminishing the light emission has been demonstrated by Ohl et al. (1998) with laser-induced bubbles near solid surfaces supporting this idea.

Interest in sonoluminescence stems from the potential usefulness for sonochemistry of the high temperatures that can be reached inside bubbles. The quest for ever-higher temperatures therefore began soon after the discovery of single-bubble sonoluminescence by Gaitan and Crum (see Gaitan et al., 1992) and is still ongoing. While measurements from the light spectrum peak around 20,000 K for water, when fitted to a blackbody spectrum, theory allows for the existence of a dense plasma at higher temperatures in the interior of an inhomogeneously heated bubble (Flannigan and Suslick, 2010; Kappus et al., 2011; Khalid et al., 2012). However, in water, the dissociation of water vapor in the bubble upon its collapse quenches the high temperatures (Toegel et al., 2000). Therefore, bubbles in low vapor pressure liquids such as sulfuric and phosphoric acids should give rise to higher temperatures. This, indeed, is suggested by experiments performed at 30.4 kHz (with addition of the second harmonic) in sulfuric acid (Rosselló et al., 2013), though not by measuring the light-emission spectrum. Instead, the maximum temperatures in the bubbles have been estimated by fitting the measured radius time curves to a bubble model. A temperature of 76,000 K is predicted from bubble oscillation curves obtained at 1.8 bar driving pressure.

In any case, the sonoluminescence observed from xenon or argon dissolved in concentrated sulfuric acid (or phosphoric acid) belongs to the brightest light emissions from collapsing bubbles achieved to date. It can be seen in daylight with the naked eye. These enormously bright flashes made it even possible to record high-speed movies of bubble dynamics and light emission at the same time in multibubble fields. To this end, a very dim background illumination is used. Examples are given in Figure 3.32, where still frames from movies are shown for various recording speeds and exposure times. The images have been taken from two different setups where concentrated phosphoric acid (sparged with xenon) was driven at 36.5 kHz in a rectangular cell, and at 23 kHz with a horn transducer, respectively. It can be observed that the bubbles in the multibubble environment indeed frequently appear deformed or jetting, but that light emission still can be possible.

When sonoluminescence is observed in the self-emitted light of the bubbles the filamentary and overall shape of the bubble structure is regained. Figure 3.33 shows an example from a bubble ensemble below a sonotrode, similar to the 23 kHz setup employed in Figure 3.32. The liquid is here sulfuric acid doped with xenon, and a bubble web is emitting light out of a strongly confined region below the sonotrode. More examples of sonoluminescence can be found in the review by Lauterborn and Kurz (2010), which includes illustrations of light emission from the standing wave pattern of a sound field, a split-center filamentary structure, and the dependence of light emission on the sound pressure amplitude and the phase of the sound field. The time- and space-resolved light-emission pictures indicate the phase and strength of bubble collapse (Lauterborn and Ohl, 1997; Ohl et al., 1999).

Of course, attempts have been made to find a theoretical description of the conditions inside the bubbles that lead to light emission. The bubble models presented here do not contain light-emission terms, which means that even more advanced models must be developed. One approach proceeds via a (continuum) fluid dynamics formulation for pressure and temperature fields (e.g., Moss et al., 1994). Another approach resorts to molecular dynamics (MD) calculations for the bubble interior (Schanz et al., 2012). The coupling to the external liquid is achieved via the interior pressure determined from the MD calculations inserted into a bubble dynamics equation in the Rayleigh-Plesset, Gilmore or other model.

One example is given here (Figure 3.34). A bubble with an equilibrium radius $R_n = 4.5\,\mu m$ filled with argon as a noncondensable gas and water vapor has been driven at 1.3 bar in a sound field of 26.5 kHz. The maximum temperature reached in this case is 16,450 K, as determined from the kinetic energy of the molecules. This compares well with spectroscopic measurements of single-bubble sonoluminescence. The temperature distribution inside the bubble is extremely inhomogeneous with a hot core, the maximum temperature being reached in the center. The density, by contrast, is nearly homogeneous in the bubble also in the collapse phase, and approaches the density of water (see Schanz et al., 2012, where more results on the interior

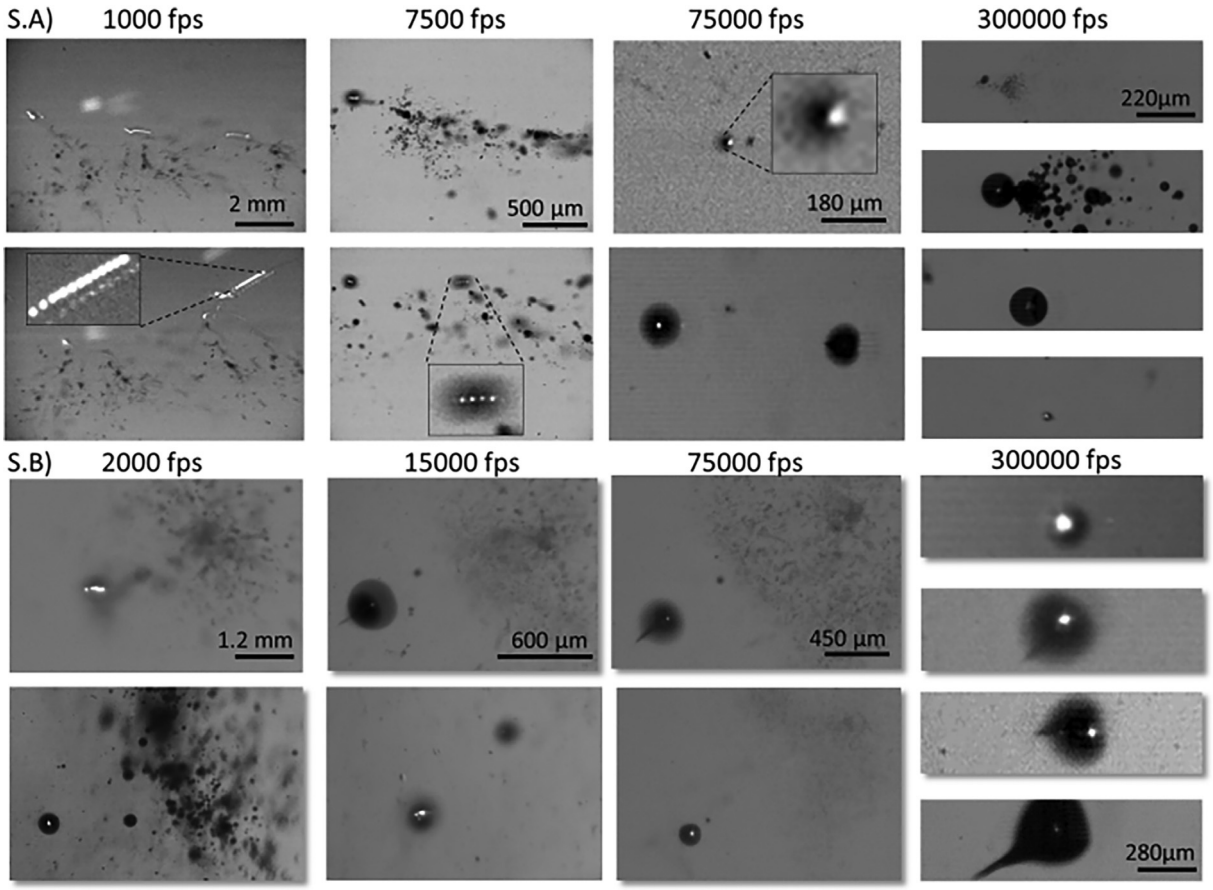


FIGURE 3.32 Simultaneous high-speed imaging of bubble dynamics (shape, motion) and sonoluminescence light flashes (frame rates and frame sizes indicated). Top: 36.5 kHz driving; large emitting bubbles run from right to left in a streamer, often followed by a "flock" of smaller bubbles. Bottom: 23 kHz driving; large emitting bubbles run partly back and forth in the vicinity of a dense bubble cloud closer to the ultrasound horn emitter. SL can occur together with pronounced jetting (indicated by an elongated bulge during bubble reexpansion). *(Reprinted figure with permission from Cairós and Mettin (2017). Copyright (2017) by the American Physical Society.)*

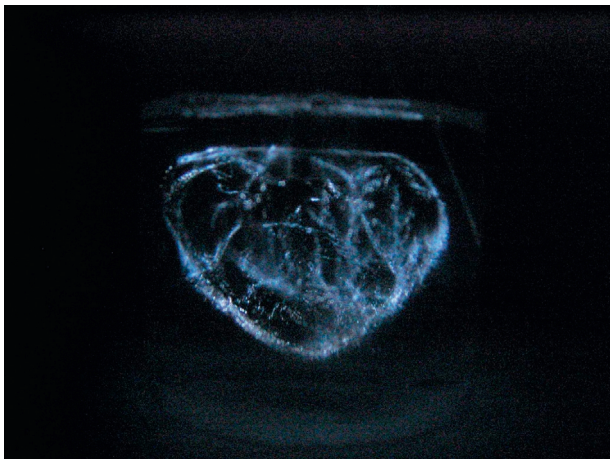


FIGURE 3.33 Sonoluminescence from the bubble structure below a sonotrode in sulfuric acid. Sound field frequency = 140 kHz. Picture size about a few millimeter. *(Courtesy T. Lepoint and R. Geisler.)*

dynamics of bubbles can be found, including water vapor chemistry). Smaller bubbles reach higher core temperatures when driven appropriately. However, investigations of temperature limits in water and other liquids are yet to be undertaken.

3.7 Ultrasonic cleaning

There always has been a close connection between basic phenomena of high-power ultrasound as reported in this chapter and practical applications. For instance, it has been shown in the seminal work of Olaf already in 1957 (Olaf, 1957) that ultrasonic cleaning is mediated by bubbles, i.e., acoustic cavitation. Since then, it is known that bubbles do the work of cleaning through their oscillations and that bubbles must be brought to the surfaces to be cleaned, not just the sound. This knowledge, among other insight, has led to the

investigations reported here. Thereby, it has been found out that a homogeneous distribution of bubbles, as desirable for cleaning, is unstable in a sound field (Akhatov et al., 1994). Instead, bubble clustering phenomena prevail (see Figures 3.18–3.27) that must be overcome—often by moving the objects in the ultrasonic cleaning bath up and down. Alternatively, one could invoke special bubble shifting mechanisms (acoustic or bubble brush) by controlling the ultrasonic wave field. Investigations of bubble motion in sound fields are helpful in this respect (Mettin et al., 2006; Xi et al., 2011, 2012). A survey of cleaning on a single-bubble level can be found in Reuter and Mettin (2016); Figure 3.35 from this work shows an example of particle removal caused by a bubble collapse at a glass plate. The detailed mechanism of loosening particles involves high shear forces in the boundary layer. These forces are caused by fast bubble wall and jet flows when the bubble comes into contact with the substrate, but also by vortex flows induced by more distant bubble collapses with jet.

Sticky particles are just one contamination on surfaces attackable by bubbles. In a further publication (Reuter et al., 2017b), the very action of a single cleaning bubble on the surface of a fouled filter membrane (for producing drinking water) could be demonstrated. In a movie of that work, the removal of a contamination layer (cake layer) along the path of the bubble is archived. The bubble even may creep under the cake layer to detach the contaminating cover from the filter membrane. Thus, besides the impact of shock waves, jet flows, and shear forces, layered material can also be loosened via bubble gas phase penetration into crevices.

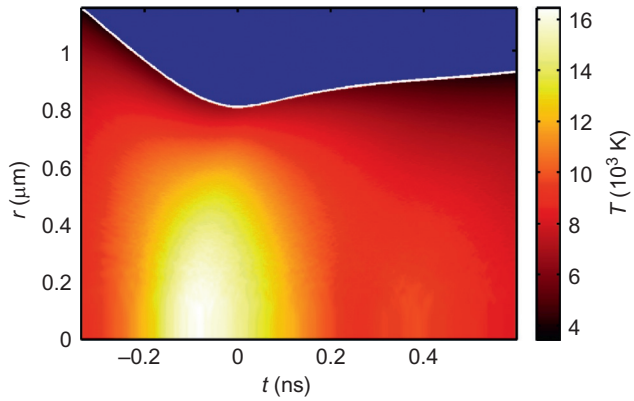


FIGURE 3.34 Space-time evolution of temperature during the final stages of collapse and the first stages of rebound of a bubble in water with an equilibrium radius of $R_n = 4.5\,\mu m$ driven at 26.5 kHz and 1.3 bar. The *white line* indicates the bubble wall. Ten million ensemble particles. *(Adapted from Schanz et al. (2012).)*

3.8 Conclusions

The fundamentals of acoustic cavitation, that is, bubble dynamics in sound-irradiated liquids, have been presented. The basic equations of bubble motion in a sound field have been given for single, spherical bubbles and extended to cases of many bubbles by consideration of bubble-bubble interactions. New results pertaining to acoustic cavitation noise (Figures 3.2 and 3.31), bubble structure formation in acoustic fields (Figures 3.26 and 3.27), and synchronization phenomena among bubble oscillations (Figures 3.29 and 3.30) have been discussed. The fascinating but involved phenomenon of sonoluminescence has been touched upon with a look into the latest developments coming from molecular dynamics.

While our knowledge of single-bubble dynamics is fairly well developed, the theoretical investigation of bubble ensemble dynamics in acoustic cavitation is still at its beginning. For the main applications of acoustic cavitation (ultrasonic cleaning and sonochemistry), bubble ensemble dynamics need to be investigated more deeply. Nonlinear bubble dynamics, translational bubble motion, bubble-bubble interaction, and the back-reaction of the bubble ensemble on the driving sound field, that is, the influence of bubbles on sound wave propagation and damping (sound-bubble-sound interactions), have yet to be combined into one large set of equations in which the boundary conditions play a major role. This would extend to the study of synchronization phenomena (on synchronization, see Pikovsky et al., 2001) and of self-organization problems for bubble ensembles in acoustic fields.

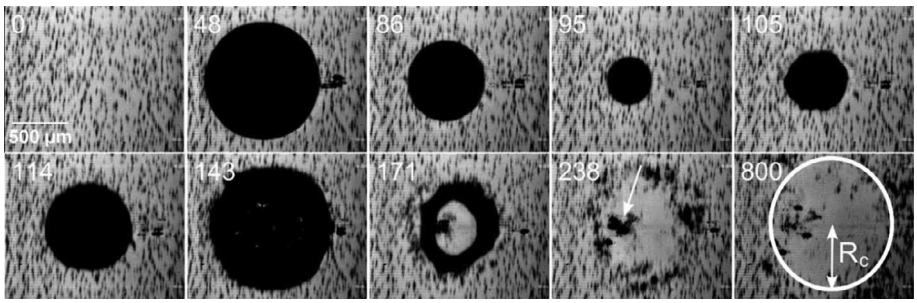


FIGURE 3.35 Particle removal by a bubble collapsing in vicinity to a glass boundary (view from bottom). The bubble was created by a focused laser pulse. Times indicated in µs after bubble creation, exposure time 2 µs, scale given in the first frame. The bubble reaches the maximum diameter of approximately 1 mm in the second frame. On the last frame, the resulting radius of cleaned area, R_c, is shown. *(Reprinted Figure 12 from Reuter and Mettin (2016), Copyright (2016), with permission from Elsevier.)*

However, there is still a gap remaining, which needs to be closed, between the basic phenomena now known and the needs of practical applications. The inclusion of additional phenomena, mainly from fluid flow, would drive further applications. Such phenomena are acoustic streaming, that is, the fluid flow induced by the damping and nonlinearity of acoustic waves (Eckart, 1948; Lighthill, 1978), the fluid flow induced by the motion of the bubbles (Reuter et al., 2017a), and externally introduced flows; for instance, the inflow of reactants with mixing in the cavitation zone and the outflow of chemical products. Research into acoustic cavitation with fluid flow is underway and will help to close the gap between fundamental research and the application of its results.

Acknowledgments

The authors thank their numerous coworkers who have contributed over the years to the results reported here, in particular U. Parlitz, T. Kurz, A. Vogel, I. Akhatov, C.-D. Ohl, R. Geisler, D. Krefting, P. Koch, K. Köhler, W. Hentschel, B. Dubus, A. Moussatov, T. Tervo, J. Schneider, A. Thiemann, T. Nowak, F. Reuter, C. Cairós, J. Eisener, M. Koch, C. Lechner, and F. Hegedűs. Special thanks go to R. Sobotta and C. Jung for the loan of equipment and for bringing the bubble double-layer structures to our attention. R. Mettin thanks the Austrian Federal Ministry of Economy, Family and Youth and the Austrian National Foundation for Research, Technology and Development, and the German Research Foundation (DFG) for financial support.

References

Abramov, O.V., 1998. High-Intensity Ultrasonics: Theory and Industrial Applications. Gordon and Breach, Amsterdam.

Akhatov, I., Parlitz, U., Lauterborn, W., 1994. Pattern formation in acoustic cavitation. J. Acoust. Soc. Am. 96, 3627–3635.

Akhatov, I., Gumerov, N., Ohl, C.D., Parlitz, U., Lauterborn, W., 1997a. The role of surface tension in stable single-bubble sonoluminescence. Phys. Rev. Lett. 78, 227–230.

Akhatov, I., Mettin, R., Ohl, C.D., Parlitz, U., Lauterborn, W., 1997b. Bjerknes force threshold for stable single bubble sonoluminescence. Phys. Rev. E 55, 3747–3750.

Ando, K., Liu, A.-Q., Ohl, C.-D., 2012. Homogeneous nucleation in water in microfluidic channels. Phys. Rev. Lett. 109, 044501 (5 pp.).

Apfel, R.E., 1970. The role of impurities in cavitation-threshold determination. J. Acoust. Soc. Am. 48, 1179–1186.

Apfel, R.E., 1981a. Acoustic cavitation. Methods Experiment. Phys. 19, 355–411.

Apfel, R.E., 1981b. Acoustic cavitation prediction. J. Acoust. Soc. Am. 69, 1624–1633.

Appel, J., Koch, P., Mettin, R., Krefting, D., Lauterborn, W., 2004. Stereoscopic high-speed recording of bubble filaments. Ultrason. Sonochem. 11, 39–42.

Atchley, A.A., Prosperetti, A., 1989. The crevice model of bubble nucleation. J. Acoust. Soc. Am. 86, 1065–1084.

Beeching, R., 1942. Resistance to cavitation erosion. Trans. Inst. Eng. Shipb. Scotland 85, 210–276.

Blake, J.R., Gibson, D.C., 1987. Cavitation bubbles near boundaries. Annu. Rev. Fluid Mech. 19, 99–123.

Blake, J.R., Boulton-Stone, J.M., Thomas, N.H. (Eds.), 1994. Bubble Dynamics and Interface Phenomena. Kluwer, Dordrecht.

Bohn, L., 1957. Schalldruckverlauf und Spektrum bei der Schwingungskavitation (pressure and spectra in acoustic cavitation). Acust. 7, 201–216.

Brennen, C.E., 1995. Cavitation and Bubble Dynamics. University Press, Oxford.

Brenner, M.P., Lohse, D., Oxtoby, D., Dupont, T.F., 1996. Mechanisms for stable single bubble sonoluminescence. Phys. Rev. Lett. 76, 1158–1161.

Brenner, M.P., Hilgenfeldt, S., Lohse, D., 2002. Single-bubble sonoluminescence. Rev. Mod. Phys. 74, 425–484.

Briggs, L.J., 1950. Limiting negative pressure in water. J. Appl. Phys. 21, 721–722.

Cairós, C., Mettin, R., 2017. Simultaneous high-speed recording of sonoluminescence and bubble dynamics in multibubble fields. Phys. Rev. Lett. 118, 064301 (5 pp.).

Caupin, F., 2005. Liquid–vapor interface, cavitation, and the phase diagram of water. Phys. Rev. E 71, 051605 (5 pp.).

Caupin, F., Arvengas, A., Davitt, K., El Mekki Azouzi, M., Shmulovich, K. I., Ramboz, C., Sessoms, D.A., Strook, A.D., 2012. Exploring water and other liquids at negative pressure. J. Phys. Condens. Matter 24, 284110 (7 pp.).

Chan, C.U., Ohl, C.-D., 2012. Total-internal-reflection-fluorescence microscopy for the study of nanobubble dynamics. Phys. Rev. Lett. 109, 174501. https://doi.org/10.1103/PhysRevLett.109.174501 (5 pp.).

Cramer, E., 1980. The dynamics and acoustic emission of bubbles driven by a sound field. In: Lauterborn, W. (Ed.), Cavitation and Inhomogeneities in Underwater Acoustics. Springer, Berlin, pp. 54–63.

Cramer, E., Lauterborn, W., 1981. Zur Dynamik und Schallabstrahlung kugelförmiger Kavitationsblasen in einem Schallfeld (on the dynamics and acoustic emissions of spherical cavitation bubbles in a sound field). Acustica 49, 226–238.

Crum, L.A., 1975. Bjerknes forces on bubbles in a stationary sound field. J. Acoust. Soc. Am. 57, 1363–1370.

Crum, L.A., 1979a. Tensile strength of water. Nature 278, 148–149.

Crum, L.A., 1979b. Surface oscillations and jet development in pulsating bubbles. J. Phys. Colloq. 40, C8-285–C8-288.

Crum, L.A., 1982. Nucleation and stabilization of microbubbles in liquids. Appl. Sci. Res. 38, 101–115.

Crum, L.A., 1984. Rectified diffusion. Ultrasonics 22, 215–223.

Crum, L.A., 2015. Resource paper: Sonoluminescence. J. Acoust. Soc. Am. 138, 2181–2205.

Crum, L.A., Nordling, D.A., 1972. Velocity of transient cavities in an acoustic stationary wave. J. Acoust. Soc. Am. 52, 294–301.

Crum, L.A., Mason, T.J., Reisse, J.L., Suslick, K.S. (Eds.), 1999. Sonochemistry and Sonoluminescence. Kluwer, Dordrecht.

Davitt, K., Arvengas, A., Caupin, F., 2010a. Water at the cavitation limit: density of the metastable liquid and size of the critical bubble. Europhys. Lett. 90, 16002 (6 pp.).

Davitt, K., Rolley, E., Caupin, F., Arvengas, A., Balibar, S., 2010b. Equation of state of water under negative pressure. J. Chem. Phys. 133, 174507 (8 pp.).

Doinikov, A.A., 2002. Translational motion of a spherical bubble in an acoustic standing wave field of high intensity. Phys. Fluids 14, 1420–1425.

Doinikov, A.A. (Ed.), 2005. Bubble and Particle Dynamics in Acoustic Fields: Modern Trends and Applications. Research Signpost, Kerala.

Eckart, C., 1948. Vortices and streams caused by sound waves. Phys. Rev. 73, 68–76.

El Mekki Azouzi, M., Ramboz, C., Lenain, J.F., Caupin, F., 2013. A coherent picture of water at extreme negative pressure. Nat. Phys. 9, 38–41.

Eller, A.I., Crum, L.A., 1970. Instability of the motion of a pulsating bubble in a sound field. J. Acoust. Soc. Am. 47, 762–767.

Esche, R., 1952. Untersuchung der Schwingungskavitation in Flüssigkeiten (investigation of acoustic cavitation in liquids). Acustica (Akustische Beihefte) 2, AB 208–AB 218.

Feng, Z.C., Leal, L.G., 1997. Nonlinear bubble dynamics. Annu. Rev. Fluid Mech. 29, 201–243.

Fisher, J.C., 1948. The fracture of liquids. J. Appl. Phys. 19, 1062–1067.

Flannigan, D.J., Suslick, K.S., 2010. Inertially confined plasma in an imploding bubble. Nat. Phys. 6, 598–601.

Flynn, H.G., 1964. Physics of acoustic cavitation. In: Mason, W.P. (Ed.), Physical Acoustics. Academic, New York, pp. 57–172.

Fox, E.F., Herzfeld, K.F., 1954. Gas bubbles with organic skin as cavitation nuclei. J. Acoust. Soc. Am. 26, 984–989.

Gaitan, D.F., Crum, L.A., Church, C.C., Roy, R.A., 1992. Sonoluminescence and bubble dynamics for a single, stable cavitation bubble. J. Acoust. Soc. Am. 91, 3166–3183.

Galloway, W.J., 1954. An experimental study of acoustically induced cavitation in liquids. J. Acoust. Soc. Am. 26, 849–857.

Gilmore, F.R., 1952. The Growth or Collapse of a Spherical Bubble in a Viscous Compressible Liquid. Report No. 26-4, Hydrodynamics Laboratory, California Institute of Technology, Pasadena, California, USA. http://authors.library.caltech.edu/561/.

Greenspan, M., Tschiegg, C.E., 1967. Radiation-induced acoustic cavitation; apparatus and some results. J. Res. Natl. Bur. Stand. 71C, 299–312.

Grieser, F., Choi, P.-K., Enomoto, N., Harada, H., Okitsu, K., Yasui, K. (Eds.), 2015. Sonochemistry and the Acoustic Bubble. Elsevier, Amsterdam.

Hegedűs, F., Lauterborn, W., Parlitz, U., Mettin, R., 2018. Non-feedback technique to directly control multistability in nonlinear oscillators by dual-frequency driving. GPU accelerated topological analysis of a bubble in water. Nonlinear Dyn. 94, 273–293.

Hegedűs, F., Krähling, P., Lauterborn, W., Mettin, R., Parlitz, U., 2020a. High-performance GPU computations in nonlinear dynamics: an efficient tool for new discoveries. Meccanica 55, 2493–2504.

Hegedűs, F., Krähling, P., Aron, M., Lauterborn, W., Mettin, R., Parlitz, U., 2020b. Feedforward attractor targeting for non-linear oscillators using a dual-frequency driving technique. Chaos 30, 073123 (13 pp.).

Hegedűs, F., Klapcsik, K., Lauterborn, W., Parlitz, U., Mettin, R., 2020c. GPU accelerated study of a dual-frequency driven single bubble in a 6-dimensional parameter space: the active cavitation threshold. Ultrason. Sonochem. 67, 105067 (10 pp.).

Hentschel, W., 1986. Zum Einschwingverhalten von Gasblasen in Wasser (on the transient response of gas bubbles in water). Acustica 60, 1–20.

Herbert, E., Balibar, S., Caupin, F., 2006. Cavitation pressure in water. Phys. Rev. E 74, 041603 (22 pp.).

Hickling, R., Plesset, M.S., 1964. Collapse and rebound of a spherical bubble in water. Phys. Fluids 7, 7–14.

Jamshidi, R., Brenner, G., 2013. Dissipation of ultrasonic wave propagation in bubbly liquids considering the effect of compressibility to the first order of acoustical Mach number. Ultrasonics 53, 842–848.

Kappus, B., Khalid, S., Chakravarty, A., Putterman, S., 2011. Phase transition to an opaque plasma in a sonoluminescing bubble. Phys. Rev. Lett. 106, 234302 (4 pp.).

Khalid, S., Kappus, B., Weninger, K., Putterman, S., 2012. Opacity and transport measurements reveal that dilute plasma models of sonoluminescence are not valid. Phys. Rev. Lett. 108, 104302 (5 pp.).

Knapp, R.T., Daily, J.D., Hammitt, F.G., 1970. Cavitation. McGraw-Hill, New York.

Koch, P., Mettin, R., Lauterborn, W., 2004. Simulation of cavitation bubbles in travelling acoustic waves. In: Cassereau, D. (Ed.), Proceedings of the Joint Congress CFA/DAGA'04. DEGA, Berlin, pp. 919–920.

Koch, P., Kurz, T., Parlitz, U., Lauterborn, W., 2011. Bubble dynamics in a standing sound field: the bubble habitat. J. Acoust. Soc. Am. 130, 3370–3378.

Koch, M., Lechner, C., Reuter, F., Köhler, K., Mettin, R., Lauterborn, W., 2016. Numerical modeling of laser generated cavitation bubbles with the finite volume and volume of fluid method, using OpenFOAM. Comput. Fluids 126, 71–90.

Koch, M., Rosselló, J.M., Lechner, C., Lauterborn, W., Eisener, J., Mettin, R., 2021. Theory-assisted optical ray tracing to extract cavitation-bubble shapes from experiment. Exp. Fluids 62 (3), 1–19.

Krefting, D., 2003. Untersuchung von Einzel- und Mehrblasensystemen in akustischen Resonatoren (Investigation of Single and Multi Bubble Systems in Acoustic Resonators) (dissertation). Universität Göttingen, Göttingen.

Krefting, D., Mettin, R., Lauterborn, W., 2002. Two-frequency driven single-bubble sonoluminescence. J. Acoust. Soc. Am. 112, 1918–1927.

Krefting, D., Mettin, R., Lauterborn, W., 2003. Single bubble sonoluminescence in air-saturated water. Phys. Rev. Lett. 91, 174301 (4 pp.).

Krefting, D., Mettin, R., Lauterborn, W., 2004. High-speed observation of acoustic cavitation erosion in multi-bubble systems. Ultrason. Sonochem. 11, 119–123.

Kurz, T., Kröninger, D., Geisler, R., Lauterborn, W., 2006. Optic cavitation in an ultrasonic field. Phys. Rev. E 74, 066307 (7 pp.).

Kuttruff, H., 1962. Über den Zusammenhang zwischen der Sonolumineszenz und der Schwingungskavitation in Flüssigkeiten (on the connection between sonoluminescence and acoustic cavitation in liquids). Acustica 12, 230–254.

Kuttruff, H., 1991. Ultrasonics—Fundamentals and Applications. Elsevier, London.

Lauterborn, W., 1969/1970. Fotografische Aufnahmen vom Aufreißen einer rotierenden Wassersäule und Zerreißfestigkeitsmessungen an Wasser nach der Zentrifugenmethode: Apparatur und erste Ergebnisse (photographic records of the tearing of a rotating water column and measurements of tensile strength in water by the centrifuge method). Acustica 22, 35–47.

Lauterborn, W., 1974. Kavitation durch Laserlicht (laser-induced cavitation). Acust. 31, 51–78.

Lauterborn, W., 1976. Numerical investigation of nonlinear oscillations of gas bubbles in liquids. J. Acoust. Soc. Am. 59, 283–293.

Lauterborn, W., 1979. Optic cavitation. J. Phys. Colloq. 40, C8-273–C8-278.

Lauterborn, W. (Ed.), 1980. Cavitation and Inhomogeneities in Underwater Acoustics. Springer, Berlin.

Lauterborn, W., 1986. Acoustic chaos. Phys. Today 39, S-4–S-5.

Lauterborn, W., Cramer, E., 1981. Subharmonic route to chaos observed in acoustics. Phys. Rev. Lett. 47, 1445–1448.

Lauterborn, W., Holzfuss, J., 1991. Acoustic chaos. Int. J. Bifurcation Chaos 1, 13–26.

Lauterborn, W., Koch, A., 1987. Holographic observation of period-doubled and chaotic bubble oscillations in acoustic cavitation. Phys. Rev. A 35, 1974–1976.

Lauterborn, W., Kurz, T., 2010. Physics of bubble oscillations. Rep. Prog. Phys. 73, 106501 (88 pp.).

Lauterborn, W., Mettin, R., 1999. Nonlinear bubble dynamics—response curves and more. In: Crum, L.A., Mason, T.J., Reisse, J.L., Suslick, K.S. (Eds.), Sonochemistry and Sonoluminescence. Kluwer, Dordrecht, pp. 63–72.

Lauterborn, W., Ohl, C.D., 1997. Cavitation bubble dynamics. Ultrason. Sonochem. 4, 65–75.

Lauterborn, W., Parlitz, U., 1988. Methods of chaos physics and their application to acoustics. J. Acoust. Soc. Am. 84, 1975–1993.

Lauterborn, W., Suchla, E., 1984. Bifurcation superstructure in a model of acoustic turbulence. Phys. Rev. Lett. 53, 2304–2307.

Lauterborn, W., Kurz, T., Mettin, R., Ohl, C.-D., 1999. Experimental and theoretical bubble dynamics. Adv. Chem. Phys. 110, 295–379.

Lauterborn, W., Kurz, T., Mettin, R., Koch, P., Kröninger, D., Schanz, D., 2008. Acoustic cavitation and bubble dynamics. Arch. Acoust. 33, 609–617.

Lechner, C., Koch, M., Lauterborn, W., Mettin, R., 2017. Pressure and tension waves from bubble collapse near a solid wall: a numerical approach. J. Acoust. Soc. Am. 142, 3649–3659.

Lechner, C., Lauterborn, W., Koch, M., Mettin, R., 2019. Fast, thin jets from bubbles expanding and collapsing in extreme vicinity to a solid boundary: a numerical study. Phys. Rev. Fluids 4, 021601(R) (7 pp.).

Lechner, C., Lauterborn, W., Koch, M., Mettin, R., 2020. Jet formation from bubbles near a solid boundary in a compressible liquid: numerical study on distance dependence. Phys. Rev. Fluids 5, 093604 (36 pp.).

Leighton, T.G., 1994. The Acoustic Bubble. Academic, London.

Lighthill, J., 1978. Acoustic streaming. J. Sound Vib. 61, 391–418.

Löfstedt, R., Barber, B.P., Putterman, S.J., 1993. Toward a hydrodynamic theory of sonoluminescence. Phys. Fluids A 5, 2911–2928.

Lohse, D., Zhang, X., 2015. Surface nanobubbles and nanodroplets. Rev. Mod. Phys. 87, 981–1035.

Louisnard, O., 2012a. A simple model of ultrasound propagation in a cavitating liquid. Part I: theory, nonlinear attenuation and traveling wave generation. Ultrason. Sonochem. 19, 56–65.

Louisnard, O., 2012b. A simple model of ultrasound propagation in a cavitating liquid. Part II: primary Bjerknes force and bubble structures. Ultrason. Sonochem. 19, 66–76.

Luther, S., Mettin, R., Koch, P., Lauterborn, W., 2001. Observation of acoustic cavitation bubbles at 2250 frames per second. Ultrason. Sonochem. 8, 159–162.

Matula, T.J., Cordry, A.M., Roy, R.A., Crum, L.A., 1997. Bjerknes force and bubble levitation under single-bubble sonoluminescence conditions. J. Acoust. Soc. Am. 102, 1522–1527.

Mettin, R., 2005. Bubble structures in acoustic cavitation. In: Doinikov, A. A. (Ed.), Bubble and Particle Dynamics in Acoustic Fields: Modern Trends and Applications. Research Signpost, Kerala, pp. 1–36.

Mettin, R., Akhatov, I., Parlitz, U., Ohl, C.D., Lauterborn, W., 1997. Bjerknes forces between small cavitation bubbles in a strong acoustic field. Phys. Rev. E 56, 2924–2931.

Mettin, R., Luther, S., Ohl, C.-D., Lauterborn, W., 1999a. Acoustic cavitation structures and simulations by a particle model. Ultrason. Sonochem. 6, 25–29.

Mettin, R., Ohl, C.-D., Lauterborn, W., 1999b. Particle approach to structure formation in acoustic cavitation. In: Crum, L.A., Mason, T. J., Reisse, J.L., Suslick, K.S. (Eds.), Sonochemistry and Sonoluminescence. Kluwer, Dordrecht, pp. 139–144.

Mettin, R., Koch, P., Lauterborn, W., Krefting, D., 2006. Modeling acoustic cavitation with bubble redistribution. In: Sixth International Symposium on Cavitation, CAV2006, Wageningen, The Netherlands. Paper No. 75.

Minnaert, M., 1933. On musical air bubbles and the sounds of running water. Philos. Mag. Ser. 7 (16), 235–248.

Mørch, K.A., 2007. Reflections on cavitation nuclei in water. Phys. Fluids 19, 072104 (7 pp.).

Moss, W.C., Clarke, D.B., White, J.W., Young, D.Y., 1994. Hydrodynamic simulation of bubble collapse and picoseconds sonoluminescence. Phys. Fluids 6, 2979–2985.

Moussatov, A., Granger, C., Dubus, B., 2003. Cone-like bubble formation in ultrasonic cavitation field. Ultrason. Sonochem. 10, 191–195.

Nasibullaeva, E.S., Akhatov, I.S., 2013. Bubble cluster dynamics in an acoustic field. J. Acoust. Soc. Am. 133, 3727–3738.

Neppiras, E.A., 1980. Acoustic cavitation. Phys. Rep. 61, 159–251.

Nigmatulin, R.I., Akhatov, I.S., Vakhitova, N.K., Nasibullayeva, E.S., 2000. Dynamics of bubble clusters. In: Lauterborn, W., Kurz, T. (Eds.), Nonlinear Acoustics at the Turn of the Millenium, ISNA 15. Vol. 524, pp. 455–458. In: AIP Conference Proceedings.

Noltingk, B.E., Neppiras, E.A., 1950. Cavitation produced by ultrasonics. Proc. Phys. Soc. Lond. B 63, 674–685.

Ohl, C., 2000. Luminescence from acoustic-driven laser-induced cavitation bubbles. Phys. Rev. E 61, 1497–1500.

Ohl, C.D., Lindau, O., Lauterborn, W., 1998. Luminescence from spherically and aspherically collapsing laser induced bubbles. Phys. Rev. Lett. 80, 393–396.

Ohl, C.D., Kurz, T., Geisler, R., Lindau, O., Lauterborn, W., 1999. Bubble dynamics, shock waves and sonoluminescence. Philos. Trans. R. Soc. Lond. A 357, 269–294.

Olaf, J., 1957. Oberflächenreinigung mit Ultraschall (surface cleaning with ultrasound). Acustica 7, 253–263.

Parker, J.L., Claesson, P.M., Attard, P., 1994. Bubbles, cavities, and the long-ranged attraction between hydrophobic surfaces. J. Phys. Chem. 98, 8468–8480. https://doi.org/10.1021/j100085a029.

Parlitz, U., Lauterborn, W., 1986. Resonances and torsion numbers of driven dissipative nonlinear oscillators. Z. Naturforsch. 41a, 605–614.

Parlitz, U., Englisch, V., Scheffczyk, C., Lauterborn, W., 1990. Bifurcation structure of bubble oscillators. J. Acoust. Soc. Am. 88, 1061–1077.

Parlitz, U., Mettin, R., Luther, S., Akhatov, I., Voss, M., Lauterborn, W., 1999. Spatio-temporal dynamics of acoustic cavitation bubble clouds. Philos. Trans. R. Soc. Lond. A 357, 313–334.

Petsev, N.D., Shell, M.S., Leal, L.G., 2013. Dynamic equilibrium explanation for nanobubbles' unusual temperature and saturation dependence. Phys. Rev. E 88, 010402(R). https://doi.org/10.1103/PhysRevE.88.010402 (5 pp.).

Pikovsky, A., Rosenblum, M., Kurths, J., 2001. Synchronization—A Universal Concept in Nonlinear Sciences. University Press, Cambridge.

Plesset, M.S., 1949. The dynamics of cavitation bubbles. J. Appl. Mech. 16, 277–282.

Plesset, M.S., 1954. On the stability of fluid flows with spherical symmetry. J. Appl. Phys. 25, 96–98.

Plesset, M.S., Prosperetti, A., 1977. Bubble dynamics and cavitation. Annu. Rev. Fluid Mech. 9, 145–185.

Poritsky, H., 1952. The collapse or growth of a spherical bubble or cavity in a viscous fluid. In: Sternberg, E. (Ed.), Proceedings of the First U.S. National Congress on Applied Mechanics. ASME, New York, pp. 813–821.

Prosperetti, A., 2013. A general derivation of the subharmonic threshold for non-linear bubble oscillations. J. Acoust. Soc. Am. 133, 3719–3726.

Putterman, S.J., Weninger, K.R., 2000. Sonoluminescence: how bubbles turn sound into light. Annu. Rev. Fluid Mech. 32, 445–476 (3 color plates).

Rayleigh, L., 1917. On the pressure developed in a liquid during the collapse of a spherical cavity. Philos. Mag. Ser. 6 (34), 94–98.

Reuter, F., Mettin, R., 2016. Mechanisms of single bubble cleaning. Ultrason. Sonochem. 29, 550–562.

Reuter, F., Gonzales-Avila, S.R., Mettin, R., Ohl, C.-D., 2017a. Flow fields and vortex dynamics of bubbles collapsing near a solid boundary. Phys. Rev. Fluids 2, 064202 (34 pp.).

Reuter, F., Lauterborn, S., Mettin, R., Lauterborn, W., 2017b. Membrane cleaning with ultrasonically driven bubbles. Ultrason. Sonochem. 37, 542–560.

Rosselló, J.M., Dellavale, D., Bonetto, F.J., 2013. Energy concentration and positional stability of sonoluminescent bubbles in sulfuric acid for different static pressures. Phys. Rev. E 88, 033026 (9 pp.).

Rosselló, J.M., Lauterborn, W., Koch, M., Wilken, T., Kurz, T., Mettin, R., 2018. Acoustically induced bubble jets. Phys. Fluids 30, 122004 (14 pp.).

Rozenberg, L.D. (Ed.), 1971. High-Intensity Ultrasonic Fields. Plenum, New York.

Schanz, D., Metten, B., Kurz, T., Lauterborn, W., 2012. Molecular dynamics simulations of cavitation bubble collapse and sonoluminescence. New J. Phys. 14, 113019 (35 pp.).

Strasberg, M., 1959. Onset of ultrasonic cavitation in tap water. J. Acoust. Soc. Am. 31, 163–176.

Strube, H.W., 1971. Numerische Untersuchungen zur Stabilität nichtsphärisch schwingender Blasen (numerical investigations on the stability of nonspherically oscillating bubbles). Acust. 25, 289–303.

Strube, H.W., Lauterborn, W., 1970. Untersuchung der Kavitationskeime an der Grenzfläche Quarzglas-Wasser nach der Zentrifugenmethode (investigation by the centrifuge method of cavitation nuclei at the interface between quartz glass and water). Z. Phys. 29, 349–357.

Suslick, K.S., 1988. Ultrasound. Its Chemical, Physical and Biological Effects. VCH Publishers, New York.

Suslick, K.S., Flannigan, D.J., 2008. Inside a collapsing bubble: sonoluminescence and the conditions during cavitation. Annu. Rev. Phys. Chem. 59, 659–683.

Suslick, K.S., Didenko, Y., Fang, M.M., Hyeon, T., Kolbeck, K.J., McNamara III, W.B., Mdleleni, M.M., Wong, M., 1999. Acoustic cavitation and its chemical consequences. Philos. Trans. R. Soc. Lond. A 357, 335–353.

Tan, B.H., An, H., Ohl, C.-D., 2019. Stability, dynamics, and tolerance to undersaturation of surface nanobubbles. Phys. Rev. Lett. 122, 134502 (5 pp.).

Tan, B.H., An, H., Ohl, C.-D., 2020. How bulk nanobubbles might survive. Phys. Rev. Lett. 124, 134503 (6 pp.).

Tervo, J.T., Mettin, R., Lauterborn, W., 2006. Bubble cluster dynamics in acoustic cavitation. Acustica 92, 178–180.

Thiemann, A., Nowak, T., Mettin, R., Holsteyns, F., Lippert, A., 2011. Characterization of an acoustic cavitation bubble structure at 230kHz. Ultrason. Sonochem. 18, 595–600.

Toegel, R., Gompf, B., Pecha, R., Lohse, D., 2000. Does water vapour prevent upscaling sonoluminescence? Phys. Rev. Lett. 85, 3165–3168.

Tortora, M., Meloni, S., Tan, B.H., Giacomello, A., Ohl, C.-D., Casciola, M., 2020. The interplay among gas, liquid and solid interaction determines the stability of surface nanobubbles. Nanoscale 12, 22698–22709.

Trevena, D.H., 1987. Cavitation and Tension in Liquids. Adam Hilger, Bristol.

van Wijngaarden, L. (Ed.), 1982. Mechanics and Physics of Bubbles in Liquids. Martinus Nijhoff Publishers, The Hague.

Verrall, R.E., Sehgal, C.M., 1988. Sonoluminescence. In: Suslick, K.S. (Ed.), Ultrasound. Its Chemical, Physical and Biological Effects. VCH Publishers, New York, pp. 227–286.

Vogel, A., Lauterborn, W., 1988. Acoustic transient generation by laser-produced cavitation bubbles near solid boundaries. J. Acoust. Soc. Am. 84, 719–731.

Walton, A.J., Reynolds, G.T., 1984. Sonoluminescence. Adv. Phys. 33, 595–660.

Xi, X., Cegla, F.B., Lowe, M., Thiemann, A., Nowak, T., Mettin, R., Holsteyns, F., Lippert, A., 2011. Study on the bubble transport mechanism in an acoustic standing wave field. Ultrasonics 51, 1014–1025.

Xi, X., Cegla, F.B., Mettin, R., Holsteyns, F., Lippert, A., 2012. Collective bubble dynamics near a surface in a weak acoustic standing wave field. J. Acoust. Soc. Am. 132, 37–47.

Yasui, K., Tuziuti, T., Lee, J., Kozuka, T., Towata, A., Iida, Y., 2010. Numerical simulations of acoustic cavitation noise with the temporal fluctuation in the number of bubbles. Ultrason. Sonochem. 17, 460–472.

Young, F.R., 1989. Cavitation. McGraw-Hill, London.

Young, F.R., 2005. Sonoluminescence. CRC Press, Boca Raton, FL.

Zheng, Q., Durben, D.J., Wolf, G.H., Angell, C.Q., 1991. Liquids at large negative pressures: water at the homogeneous nucleation limit. Nature 254, 829–832.

Chapter 4

High-intensity ultrasonic waves in solids: Nonlinear dynamics and effects

A. Alippi
La Sapienza Univefrsità di Roma, Rome, Italy

4.1 Introduction

The nonlinear dynamics of solids encompasses a very wide range of effects and conditions. Taken together with the additional considerations of field diffraction, energy dissipation, temperature dependent wave propagation, and even fluid behavior, which may also be paradoxically regarded as part of the subject matter, they present an overwhelming amount of information for consideration. The present author has therefore chosen to limit the treatment to general considerations in analytical form. This takes into account the typical anisotropic nature of a solid and provides evidence for the phenomenology of nonlinear wave propagation as it appears in solid media, harmonic generation, wavenumber modulation, frequency mixing, and finite media resonance. Each section is followed by suggestions on the appropriate application in technological developments. However, the specific details of such applications are explored in the following chapters as it is assumed that suggestions can be drawn from the analytical results when considering models for the development of these applications.

4.2 Fundamental nonlinear equations

4.2.1 Constitutive equations and equation of motion

The differential wave equation in a medium is derived from Newton's equation of motion. This is applied to the mass contained in an infinitesimal volume, combined with the constitutive equation that describes the deformation undergone by the volume under a system of forces applied to it. This may generally be written as

$$\mathbf{F}=\frac{d(\rho\mathbf{v})}{dt} \quad \text{and} \quad f(X_i)=0 \tag{4.1}$$

where $\mathbf{F}$ is the net force applied to the unit *v*olume; ρ, the medium mass density; $\mathbf{v}$, the velocity; X_i, the physical quantities describing the state of the medium; t, the time; and f is a specific function of the parameters X_i which define the state of the medium. The space coordinates will be taken as x_i, and correspond to the position of the particles of the medium when no forces are applied to it or when the medium is at rest (Lagrangian coordinates). They will be used throughout to describe the particle motion, as the density in this case is a constant function equal to ρ_o, even where the actual value changes under the relative motion of the different parts. By using primed coordinates x_i' for the current ones (Eulerian coordinates), the relationships with the unprimed coordinates and displacements u_i are given by (Landau and Lifchitz, 1967)

$$x_i' = x_i + u_i \tag{4.2}$$

whose differentials are bound through

$$dx_i' = dx_i + du_i \tag{4.3}$$

which permits the introduction of the strain tensor ε_{ij} through evaluation of the squared differential elements lengths dl^2 and dl'^2

$$dl'^2 = (dx_i + du_i)(dx_i + du_i) = dl^2 + 2\varepsilon_{ij}dx_i dx_j \tag{4.4}$$

with the strain ε_{ij} given by $\varepsilon_{ij}=\frac{1}{2}\left(\frac{\partial u_i}{\partial x_j}+\frac{\partial u_j}{\partial x_i}+\frac{\partial u_l}{\partial x_i}\frac{\partial u_l}{\partial x_j}\right)$, with the usual notation summing up the values of any index repeated within a term. The origin of the so-called geometrical nonlinearity term $(\partial u_l/\partial x_i)(\partial u_l/\partial x_j)$ is present as it has to be added to the linear definition of the strain tensor $\frac{1}{2}[(\partial u_i/\partial x_j)+(\partial u_j/\partial x_i)]$. This derives directly from consideration of the second order term in the differential displacement vector $\mathbf{u}$.

In order to write the wave equation in terms of the variable $\mathbf{u}$ alone, Newton's equation, written as

$$\mathbf{F}=\rho_o\frac{d^2\mathbf{u}}{dt^2} \tag{4.5}$$

should be combined with the constitutive equation, taking into account that $\mathbf{F}$ derives from the gradient of the stress tensor σ, which is bound to the strain tensor ε. The free

Power Ultrasonics. https://doi.org/10.1016/B978-0-12-820254-8.00004-X
Copyright © 2023 Elsevier Ltd. All rights reserved.

energy (or potential energy) of the medium per unit volume may be written as a series of power terms in the strain tensor components, as

$$W = \frac{1}{2!}C_{ijkl}\varepsilon_{ij}\varepsilon_{kl} + \frac{1}{3!}C_{ijklmn}\varepsilon_{ij}\varepsilon_{kl}\varepsilon_{mn} + \cdots \tag{4.6}$$

The strain/stress relation is therefore easily derived by taking the energy density as equal to the work done by the external stress on a unit volume or, alternatively, that the stress is the strain derivative of the energy density

$$\sigma_{ij} = \frac{\partial W}{\partial \varepsilon_{ij}} = C_{ijkl}\varepsilon_{kl} + C_{ijklmn}\varepsilon_{kl}\varepsilon_{mn} + \cdots \tag{4.7}$$

Any component of the wave equation may now be written in terms of the displacement vector alone; in particular,

$$\begin{aligned}\rho_o \frac{\partial u_i}{\partial t^2} = & C_{ijkd}\left(\frac{\partial^2 u_k}{\partial x_j \partial x_l} + \frac{\partial u_s}{\partial x_k}\frac{\partial^2 u_s}{\partial x_j \partial x_l}\right) \\ & + C_{ijklmn}\left[\frac{\partial u_m}{\partial x_n}\left(\frac{\partial^2 u_k}{\partial x_j \partial x_l} + \frac{\partial u_s}{\partial x_m}\frac{\partial^2 u_s}{\partial x_j \partial dx_l}\right)\right. \\ & \left. + \frac{\partial u_s}{\partial x_m}\frac{\partial u_s}{\partial x_n}\left(\frac{\partial^2 u_k}{\partial x_j \partial x_l} + \frac{\partial u_s}{\partial x_k}\frac{\partial^2 u_s}{\partial x_j \partial dx_l}\right) + \cdots\right]\end{aligned} \tag{4.8}$$

where no other forces are taken as acting on the mass elements. This last condition is demanding as internal friction is generally a determining factor in the behavior of solids. However, attenuation is ignored here, as the focus is on new evidence arising from nonlinearity. Eq. (4.8) may then be formally written in a shorter form, by using Thurston (1984) notation

$$\rho_o \frac{\partial^2 u_i}{\partial t^2} = \frac{\partial^2 u_k}{\partial x_j \partial x_l}\left(C_{ijkl} + M_{ijklmn}\frac{\partial u_m}{\partial x_n}\right) + \cdots \tag{4.9}$$

where

$$M_{ijklmn} = C_{ijklmn} + C_{ijkn}\delta_{km} \tag{4.10}$$

δ_{ij} being the Kronecker symbol, equal to 1 for $i = j$, and otherwise equal to 0. It should be noted that no symmetry rules hold for tensor M, such that $M_{ijklmn} \neq M_{jiklmn}$, although they hold for tensor C, in such a way that $C_{ijklmn} = C_{jiklmn}$ and $C_{ijklmn} = C_{klijmn} = C_{mnklij}$. (Lubarda, 1997; Cowin and Mehrabadi, 1955). The symmetry rules drastically reduce the independent elastic tensor components from $3^4 = 81$ to 21 for the linear second order elastic tensor C_{ijkl} and from $3^6 = 729$ to 56 for the third order one C_{ijklmn}. As may be seen from Eq. (4.9), the introduction of tensor M permits the generation of nonlinear effects to be confined to its components, while C_{ijkl} is bound to linear propagation.

As previously stated, no account has been taken of the internal viscoelastic dissipation in the propagation media, introduced by Landau and Lifchitz (1967), by considering a time-dependent force, bound to the strain time derivatives $\partial\varepsilon_{ij}/\partial t$. Nor has any thermal flux been considered, by implicitly assuming that solid particles undergo adiabatic transformations under elastic perturbation (Rienstra and Hirschberg, 2013). This assumption may easily be accepted where the frequencies are sufficiently high and no migration of heat is assumed to have taken place during a single wave period.

In cases where the acoustic propagation may be assumed to be linear, or if the acoustic strain is sufficiently low, in any spatial direction, there may propagate three independent plane waves, whose eigenvectors are mutually orthogonal and are called *quasi longitudinal* and *quasi transversal*. These fall into the longitudinal and transversal eigenvalues, respectively, where the propagation direction continuously changes from that selected to a crystallographic axis of symmetry (Morse and Ingard, 1986). No general rule can be stated in the nonlinear case, as pure modes do not exist where different acoustic waves couple one with the other throughout the propagation. The terms in Eq. (4.9), which are the product between two different components of the displacement vector, are responsible for the coupling between these components, or for the growth of one component resulting from the power drained from the other.

4.2.2 Approximate analytical solutions

No analytical solutions are available for the differential nonlinear Eq. (4.9), even where only those terms of the expansion which are specifically reported in the truncated expression are considered. Numerical approaches are therefore usually applied or simplifying approximations adopted. A description of the latter case is given here, and the former is left to a different chapter. A perturbation method is usually adopted, which is a good approximation in cases of weak nonlinearity, where the nonlinear terms are much lower than the linear ones (Ostrovsky and Gorshkov, 2000).

Eq. (4.9) may therefore be considered as being limited to the terms specifically reported there, with the assumption that the amplitude of the wave does not change greatly in respect of the ratio between the linear and nonlinear coefficients of the elastic tensors:

$$\frac{\partial u_m}{\partial x_n} << \frac{C_{ijkl}}{C_{ijklmn}} \tag{4.11}$$

and as a search for plane wave solutions of the equation. As described in the previous section, where the effects of nonlinearity may be ignored for any selected direction of propagation defined by the direction cosines θ_i or wavevector $\mathbf{k} \equiv (k_1, k_2, k_3)$, with $k_i = k\cos\theta_i$, three independent waves may propagate (sometimes erroneously called *modes*). These have normalized eigenvectors $\mathbf{a}^{\alpha}$, one quasi longitudinal, and two quasi transversal, identified by the index α.

Where only a low level of nonlinearity can be taken into account, it may be assumed that one of the modes (which should be properly identified with the α index, not reported here for sake of clarity in the subsequent notation) is propagating freely as

$$\mathbf{a}(\mathbf{r}, t) = \mathbf{A}\cos(\omega t - \mathbf{k}\cdot\mathbf{r}) \tag{4.12}$$

with $\mathbf{A}$ the amplitude vector of that mode, and generating three secondary waves $\mathbf{b}^{\beta}(r,t)$ ($\beta = 1, 2, 3$) along the direction of propagation of the wavevector $\mathbf{k}'^{\beta}$, whose amplitude B^{β} is a slowing and varying function of the propagation distance r:

$$\mathbf{b}^{\beta}(\mathbf{r}, t) = \mathbf{B}^{\beta}(r)\sin\left(\omega'^{\beta}t - \mathbf{k}'^{\beta}\cdot\mathbf{r} - \varphi^{\beta}\right) \tag{4.13}$$

with amplitude $B^{\beta} << A$ and phase φ^{β}; upper indexes β identify the mode of the generated wave. The solution of Eq. (4.9) should then be the sum of linear and nonlinear terms $\mathbf{a} + \mathbf{b}^{\beta}$. By introducing these into Eq. (4.9) and simplifying for the matching of terms that satisfy the linear equation, the following is obtained:

$$\rho_o\frac{\partial^2 b_i^{\beta}}{\partial t^2} - C_{ijkl}\frac{\partial^2 b_k^{\beta}}{\partial x_j \partial x_l} = \frac{1}{2}M_{ijklmn}k_j k_l k_n A_k A_m \sin 2(\omega t - \mathbf{k}\cdot\mathbf{r}) + \cdots \text{higher order terms} \tag{4.14}$$

A trial solution can be adopted for $\mathbf{B}^{\beta}$ equal to

$$\mathbf{B}^{\beta}(r, t) = f^{\beta}(r)\mathbf{D}^{\beta} \tag{4.15}$$

with $\mathbf{D}^{\beta}$ being the normalized amplitude vector and $f^{\beta}(r)$ a slowly varying function of the modulus of the displacement vector $\mathbf{r}$. This is evaluated by introducing the trial solution into Eq. (4.14):

$$\begin{aligned} &4f^{\beta}(r)\left(-\rho_o\omega^2 D_i^{\beta} + C_{ijkl}D_k^{\beta}k_j k_l\right)\sin\left(\omega' t - \mathbf{k}'^{\beta}\cdot\mathbf{r} - \phi^{\beta}\right) \\ &= C_{ijkl}D_k^{\beta}\left[-\frac{2}{r}\frac{\partial f^{\beta}}{\partial r}\left(x_j k_l + x_l k_j\right)\cos\left(\omega' t - \mathbf{k}'^{\beta}\cdot\mathbf{r} - \phi^{\beta}\right)\right. \\ &\quad \left. + \left(\frac{\partial^2 f^{\beta}}{\partial r^2} - \frac{1}{r}\frac{\partial f^{\beta}}{\partial r}\right)\frac{x_j x_l}{r^2}\sin\left(\omega' t - \mathbf{k}'^{\beta}\cdot\mathbf{r} - \phi^{\beta}\right)\right] \\ &\quad + \frac{1}{2}M_{ijklmn}k_j k_l k_n A_k A_m \sin 2(\omega t - \mathbf{k}\cdot\mathbf{r}) + \cdots \end{aligned} \tag{4.16}$$

Solutions of Eq. (4.16) are only possible if $\omega' = 2\omega$ and $\mathbf{k}'^{\beta} = 2\mathbf{k}$, since the identity should hold for any value of t and $\mathbf{r}$. The generated waves are second harmonic waves of the fundamental mode which should have the same velocity. Dispersion would prevent harmonic generation from being a cumulative effect along the propagation direction. This implies that the fundamental α mode can only generate β modes with wavenumbers equal to twice that of the fundamental, presumably the same α mode or a degenerate one. It may also be seen that terms within parentheses in the first component of Eq. (4.16) are equal to zero, as they correspond to the algebraic homogeneous system for the solution eigenvector of the linear equation. Therefore, the generated waves must correspond to the modes which are proper to the propagation direction of the fundamental: $\mathbf{D}^{\beta} \propto \mathbf{a}^{\beta}$. The second component should also be zero. As the second term within brackets can be assumed to be much smaller than the first for values of r greater than one wavelength, and where f^{β} is a slowly varying function of $\mathbf{r}$, it should give $\varphi^{\beta} = \pi/2$, so that the equation can be derived for function f^{β}

$$D_k^{\beta}C_{ijkl}\left(k_l\cos\vartheta_l + k_j\cos\vartheta_l\right)\frac{\partial f^{\beta}}{\partial r} \cong \frac{M_{ijklmn}}{4}k_j k_l k_n A_k A_m \tag{4.17}$$

Eqs. (4.17) for $i = 1, 2, 3$ is a system in the three unknown functions f^{β} which may be easily solved once the elastic coefficients are known for any direction of propagation for which the normalized eigenvectors $\mathbf{D}^{\beta}$ have been previously solved from the linear system. Solutions are given by

$$f^{\beta}(r) = \frac{\|Det'\|}{\|Det\|}r = \Gamma_{ijklmn}^{\beta}A_k A_m r \tag{4.18}$$

where $\|Det'\|$ and $\|Det\|$ are proper determinants of system (4.17), whose ratio equals $\Gamma_{ijklmn}^{\beta}A_k A_m$. The results clearly show that where dispersion effects may be ignored, a slight nonlinearity in the propagation of a harmonic wave in a solid medium generates second harmonic waves that grow along the propagation direction proportional to the propagation distance and to the square of the fundamental wave amplitude. This is a general effect and is well known in the case of fluids where only longitudinal modes can propagate. The difference in the case of solids relies on the possible coupling between different modes which are bound to the nonvanishing value of the correct nonlinear coefficients. It should be recalled that notation for the fundamental wave variables was previously adopted with no index α of the mode involved. By considering the specific α mode of the fundamental wave, it may be seen from Eq. (4.17) that each generated β mode is coupled to the fundamental through a selected set of coefficients Γ and depends upon the amplitude components of the fundamental. However, this condition depends on the matching of wavenumbers between generating and generated waves. In the case of a change between the generated and the generating modes, it may therefore be practically consistent only for coupling between degenerate transversal modes where there is no effective dispersion in the propagation medium. Quite a

different condition rises in the case of guided modes, as the Lamb waves produced in a plate, for instance. In such a case, there is an obvious dispersive effect rising between a generated mode and its second or higher harmonic. A various combination of cases is present, and the intensity of dispersion depends on the modes involved, particularly whether they are of the symmetric or the antisymmetric family (see, for instance, Chillara and Lissenden, 2016).

The general nonlinear Eq. (4.9) has thus far been solved through the so-called perturbative method which considers the linear solution as a first approximation and adds to it a small term to be determined successively. The solution may then be derived by limiting various terms in the equation to those of the first order. The method may be continued by considering the new solution as a better approximation and looking for a higher order term. The higher order terms in the equation are taken into account. It can therefore be qualitatively stated that each time a higher harmonic wave is involved at a low level of nonlinearity, it will grow along the propagation direction bound both to higher powers of the propagation distance and of the fundamental wave amplitude.

4.2.2.1 Applications

Second harmonic generation is probably the most commonly known effect of nonlinearity in wave propagation and is exploited in a variety of fields. It should be properly stressed that the theoretical approach previously presented is purposely limited to continuous homogeneous materials, while most of the applications of nonlinear effects rely on defect interaction with acoustic waves. That may sound as a strong limitation of the theory, unless one thinks the deviation of experimental results from theoretical predictions is a measure of the inhomogeneity or defect abundance of the materials. Of course, a preliminary evaluation of the sound/defect interaction is necessary for a correct definition of defect abundance and there a huge field of possibilities opens for each single case to be studied (see, for instance, Zheng et al., 2011). Generally speaking, it is difficult to use linear ultrasonic technique for detecting cracks whose faces close under compressive stress and do not easily scatter the impinging waves. The nonlinear technology has been developed to this aim, which is based on contact acoustic nonlinearity in order to overcome this issue (Maruyama and Touhei, 2016). In this case, an incident wave with large amplitude is used such that makes the closed cracks to vibrate and nonlinear ultrasonic waves which consist of higher and subharmonic components are generated. Most widely is the technique of nonlinearly generated acoustic waves from defects used in laminar structure, to test adhesive properties or delamination defects (Hong et al., 2018).

In the case of the nonlinear sounding of materials, as typically produced in medical echography, the second harmonic propagation permits the resolution in the imaging process to be doubled or acoustic microscopy where enhanced resolution is attained via the contemporary effect of π phase change in the focal point of a convergent beam.

Biological tissues are untypical materials which may be treated as liquids or lossy isotropic solids and are a highly nonlinear acoustic media due to their irregular structure. Harmonic growth is therefore easily produced along the propagation direction. Tissue harmonic imaging has now become a standard technique. The acoustic focalized beam from an array transducer has a narrower beam cross section in respect to the fundamental frequency beam and an even shorter beam waist zone, thus allowing a higher resolution in both the lateral and axial directions. Higher harmonic imaging is therefore produced to enhance these characteristics. Figure 4.1 is an example of such characteristics. Although the experiment was conducted in a water tank, the acoustic field of the beam from a transducer has been visualized at its fundamental frequency, second, third, and fourth harmonic, respectively. There is a visible decrease in the size of both the axial and the lateral focal region which corresponds to an increase of the imaging resolution (Bouakaz and de Jong, 2003). There are, however, some drawbacks. The bandwidth and attenuation increase correspondingly with the relative additional electronic demands and energy dissipation effects.

Figure 4.2 schematically represents the intensity of the fundamental wave and the second harmonic vs. the propagation distance inside of the body. While the fundamental wave constantly decreases because of attenuation, the harmonic initially increases due to the energy drain from the fundamental and then decreases when the energy dissipation is higher than the energy drain. This sets an optimum distance for the use of second harmonic imaging which is obviously dependent on the beam frequency. This effect is analogous to that which occurs in acoustic microscopy at much higher frequencies. A particular effect has been set into evidence which is bound to the focusing phenomena in wave propagation. The wave field undergoes a π phase change when crossing the focal point and produces an equal phase shift between the fundamental wave and the second harmonic due to the different relative wavelengths. Therefore, apart from any attenuation effect, the second harmonic increases up to the focal point because of the synchronous power draining from the fundamental wave. From that point onward, the phase shift between the two waves causes the draining to occur π out of phase from that generated prior to this point, so depleting the harmonic power which returns to zero. Despite the generation and detection of waves at a given frequency, the overall effect is that the sounding of the medium in the focal plane of a converging lens is performed via the second harmonic. An increased resolution then follows because of the reduced wavelength (evidence first given by Cunningham and Quate, 1972).

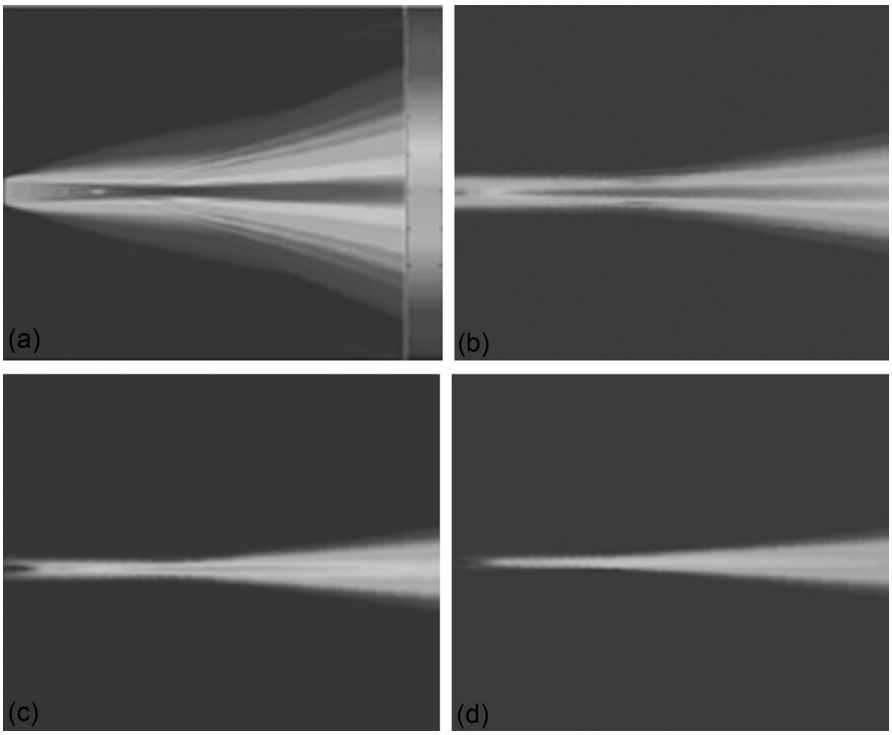


FIGURE 4.1 Imaging of an ultrasonic beam at the first four harmonic frequencies.

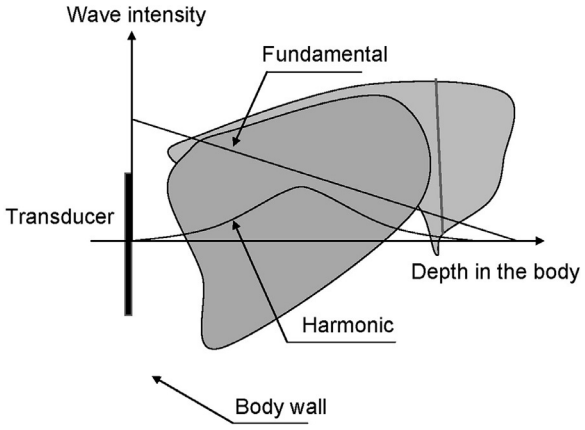


FIGURE 4.2 Schematic representation of the energy distribution versus distance of propagation for the fundamental wave and its first harmonic inside human body.

Similar effect affecting the phase relation between a fundamental progressive wave and its nonlinearly generated second harmonic may take place at the boundary between two media, where reflection and transmission take place for each component. The second harmonic wave flowing backward with respect to the incident one at the surface is really made of two parts: one from the reflected second harmonic wave and a second one from the newly generated one, the phase of the former being related to the phase of its incident counterpart and the phase of the latter to the fundamental wave. Being the two phases out of π, the growing of the latter component is going to destroy the overall harmonic, in a way similar to the focusing effect described earlier. This may be a relevant effect in pulse-echo devices that should be properly taken into consideration, particularly in linear phased-array transducers (Jeong et al., 2019).

General considerations should anyway be stated for all experimental devices that make use of nonlinear generated ultrasonic waves for material characterization that could be summarized in three points. High-amplitude fundamental mode has to be generated by the transducers in order to make higher harmonics measurable; proper bandwidth transducers should be used such that the tail of the frequency distribution does not produce higher harmonics; distortion should clearly avoided in the generation of the fundamental wave, so as to make the very low amplitude higher harmonics generated by the material more evident (Chillara and Lissenden, 2016).

4.2.3 Isotropic solids and wavenumber modulation

The general solution for the harmonic wave in solids is greatly simplified in isotropic solids where all directions in space are equivalent from the elastic standpoint. Therefore, the propagation direction may be considered as

the direction of the coordinate axis x, so obtaining the following equation of motion

$$\rho_o \frac{\partial^2 u}{\partial t^2} \cong \frac{\partial^2 u}{\partial x^2}\left[C_L + \frac{\partial u}{\partial x}(C_L + C_{NL})\right] \tag{4.19}$$

for any mode component u of the wave, where C_L is the linear elastic coefficient C_{1111} and C_{NL} the nonlinear one C_{111111}. For the second harmonic growing function $f(x)$,

$$f(x) \cong \frac{M}{4C_L} k^2 A^2 x \tag{4.20}$$

with $M = C_{NL} + C_L$ is obtained.

In the simplified case of an isotropic solid, it should be noted that the second harmonic generation obtained through the perturbation method is consistent with the model of propagation of a sinusoidal wave in a medium where the velocity, and thus, the wavevector is modulated by the perturbation induced by the wave itself. A solution of Eq. (4.19) in the form $a(x,t) = A\cos(\omega t - kx)$ may be assumed where a and A are the nonvanishing components of the displacement and of the displacement amplitude, respectively. The wave velocity c is then locally assumed to be given by

$$c = \sqrt{\frac{[C_L + Ak(C_L + C_{NL})\sin(\omega t - kx)]}{\rho_o}} \tag{4.21}$$

and the wavenumber to be correspondingly obtained, such that the final form of the wave is

$$a(x,t) \cong A\sin\left(\omega t - k_o\left[1 - Ak_o\frac{(C_L + C_{NL})}{2C_L}\sin(\omega t - k_o x)\right]x\right) \tag{4.22}$$

with k_o, the unperturbed wavenumber, or

$$a(x,t) \cong A\sin(\omega t - k_o x) + \frac{(C_L + C_{NL})}{4C_L}A^2 k_o^2 x \sin 2(\omega t - k_o x) \tag{4.23}$$

where use has been made of the Bessel function series for the development of the double sin-function. The solution is again obtained as the sum of a fundamental wave and a second harmonic whose amplitude grows linearly with the distance x, proportional to the square of both the amplitude and wavenumber of the fundamental, times the elastic parameter combination $(C_L + C_{NL})/(4C_L)$, as previously obtained through the solution of the unknown growing function in Eq. (4.20). The same procedure is currently used for fluids, where the equation of motion is formally the same (see, for instance, Blackstock et al. 1998).

4.2.3.1 Applications

The reduction of indices in isotropic solids in respect to anisotropic solids and the corresponding existence of pure modes in the propagation of waves in any direction of space limits the drain of power toward harmonic waves to a single component. The result is a simplification of the phase evaluation of the generated wave with respect to the fundamental. This is clearly seen from Eq. (4.23) and is partially responsible for the generation of shock waves, as in the case of fluids. The modulation of the wave velocity produced by the wave itself stands as a positive feedback effect of the energy aggregation in the wave profile which gradually increases to a saw-tooth shape and finally results in a shock (see Figure 4.3). This effect is exploited in clinical lithotripsy, which is the breaking up of stones anomalously grown within human organs, particularly the kidneys, saliva glands, or bladder. A high-intensity ultrasound pulse, a few microseconds long, is focused on the region of concern, where it may attain a positive pressure peak of about 50 MPa in a time that may be less than 5 ns. This is followed by a negative pressure peak around −10 MPa. The interaction of the highly nonlinear wave thus generated with the stone is complex, but the abrupt rise in the pressure value, followed by the negative waveform,

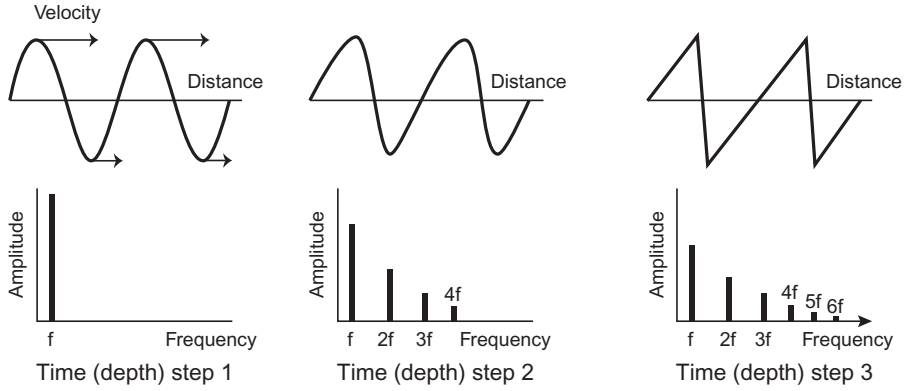


FIGURE 4.3 Deformation of wave profile and generation of harmonic components along the propagation direction.

induces a sequence of stresses inside the stone which breaks it into smaller pieces. These may be further subjected to the induction of stresses, or may be anatomically eliminated, depending upon their size. The effect of reflection from the stone surface has also to be taken into consideration, together with the corresponding change of pressure values at the interface between the medium of the organ and the stone.

Isotropic solids are usually treated in the same way as liquids with the parameter B/A standing as the nonlinear combination parameters $(C_L + C_{NL})/(4C_L)$ for the characterization of tissues in biomedicine or nondestructive evaluation in industrial applications. Granular materials, though highly anisotropic at smaller scales, usually present a statistical isotropy at larger scales. The presence of numerous discontinuity surfaces also makes them highly nonlinear from the elastic standpoint as the elastic response to compression differs greatly from that of dilation. The generation of harmonic waves is a common effect in acoustic propagation in granular media, as is the generation of harmonics from defects in homogeneous media.

4.3 Nonlinear effects in progressive and stationary waves

4.3.1 Harmonic balance in progressive waves: Dispersion and attenuation

The perturbation method described in the previous section assumes the nonlinear terms in the equation of motion to be an order of magnitude smaller than the linear one. The solution could be therefore be assumed to be the linear one slightly "perturbed" by the nonlinear contribution. This approach may be extended, as previously stated, with the third and higher harmonics deduced from those of the lower order. This also feeds back into the lower order harmonics, perturbing the previously obtained values in a never-ending process. This is the reason for the development of discontinuities in the generation of lower frequency waves, as may occur in the bistability phenomenon of the fundamental wave (Lyakov et al. 1995).

Where multiple coupling has to be taken into account, where energy flows from fundamental to higher harmonic waves and back again to the lower ones, a more general method can be adopted. This is termed "harmonic balance" and considers the solution of the equation to be given by a series of harmonic waves, each with its correct amplitude and phase.

$$\mathbf{u}^{\beta}(\mathbf{r},t) = \sum\nolimits_p \mathbf{B}_{\mathbf{p}}^{\beta}(r)\left[\sin\, p\left(\omega t - \mathbf{k}^{\beta}\cdot\mathbf{r}\right) - \varphi_p^{\beta}\right] \quad (4.24)$$

When such a solution is inserted into the truncated nonlinear wave equation (4.9),

$$\begin{aligned}
&\left(\rho_o\omega^2 - k_j^{\beta}k_l^{\beta}C_{ijkl}\right)\sum\nolimits_p B_{ip}^{\beta}p^2\sin\left[p\left(\omega t - \mathbf{k}^{\beta}\cdot\mathbf{r}\right) - \phi_p^{\beta}\right] \\
&\quad = -2k_j^{\beta}k_l^{\beta}k_n^{\beta}C_{ijkl}M_{ijklmn}\sum\nolimits_p\sum\nolimits_q B_{k(p+q)}^{\beta}B_{mq}^{\beta}(p \\
&\qquad + q)^2q^2\sin\left[p\left(\omega t - \mathbf{k}^{\beta}\cdot\mathbf{r}\right) - \phi_p^{\beta}\right] + \cdots
\end{aligned} \quad (4.25)$$

is obtained. This is only satisfied for each time t and position $\mathbf{r}$ if every harmonic term with index p identically satisfies the equation:

$$\left(G_p^{+}\right)^2 + \left(G_p^{-}\right)^2 = 0 \quad (4.26)$$

with

$$\begin{aligned}
G_p^{\pm} &= B_{i\,ip}^{\beta}p^2\left(\rho_o\omega^2 - k_j^{\beta}k_l^{\beta}C_{ijkl}\right)\left\langle\frac{\cos\,\phi_p^{\beta}}{\sin\,\phi_p^{\beta}}\right\rangle \\
&+ \frac{1}{2}k_j^{\beta}k_l^{\beta}k_n^{\beta}M_{ijklmn}\sum\nolimits_q\left(B_{k(p-q)}^{\beta}B_{mq}^{\beta}(p-q)^2q\left\langle\frac{\cos\left(\phi_{p-q}^{\beta}+\phi_q^{\beta}\right)}{\sin\left(\phi_{p-q}^{\beta}+\phi_q^{\beta}\right)}\right\rangle\right. \\
&\left. + B_{k(p-q)}^{\beta}B_{mq}^{\beta}(p+q)^2q\left\langle\frac{\cos\left(\phi_{p-q}^{\beta}-\phi_q^{\beta}\right)}{\sin\left(\phi_{p-q}^{\beta}+\phi_q^{\beta}\right)}\right\rangle\right) \\
&= 0
\end{aligned} \quad (4.27)$$

the double sign in the $G_p^{\pm}$ terms corresponds to the upper and lower expressions reported within the symbolic brackets and separated by the symbolic fraction sign $<->$.

This is an infinite set of nonlinear algebraic equations in the unknown coefficients B_i^{β}, defining the relative amplitudes of each harmonic wave and must be solved through numerical methods, by assuming that no strong nonlinearity is present in the phenomenon. In this case, a limited number of harmonic waves may be retained and summation of the trial function (4.24) limited to a finite value N. A set of correspondingly limited equations must be solved through the appropriate algorithms.

Obviously, the balancing of harmonics can only be performed if all the wavenumbers are multiples of the fundamental and are proportional to the corresponding circular frequency, i.e. if the propagation of the waves is not affected by dispersion. A small degree of dispersion would prevent the generation of harmonics increasing to their steady value, since the local generation of any harmonic wave from its coupling with others would take place out of phase with what had previously been generated.

4.3.2 Frequency mixing

The consideration of phase-matching leads us to the problem of the frequency mixing of waves. This occurs when two waves of different frequency give rise to a third,

with either a sum frequency value or a different frequency. As in the case of harmonic generation (see Eq. (4.12)), it may be assumed that two different frequency waves are propagating as

$$\mathbf{a}_1(\mathbf{r},t) = \mathbf{A_1}\cos(\omega_1 t - \mathbf{k_1}\cdot\mathbf{r}) \quad \text{and} \quad \mathbf{a}_2(\mathbf{r},t) = \mathbf{A}_2\cos(\omega_2 t - \mathbf{k_2}\cdot\mathbf{r}) \tag{4.28}$$

and that they generate waves

$$\mathbf{b}_{\pm}^{\beta}(\mathbf{r},t) = \mathbf{B}_{\pm}^{\beta}(r)\sin\omega'_{\pm}t - \mathbf{k'}_{\pm}^{\beta}\cdot\mathbf{r} - \varphi_{\pm}^{\beta} \tag{4.29}$$

with an obvious notation of the indexes and amplitudes $B^{\beta} << A_{1,2}$. The conditions of phase-matching and energy conservation require that $\mathbf{k}' = \mathbf{k}_1 \pm \mathbf{k}_2$ and $\omega' = \omega_1 \pm \omega_2$, where the upper sign corresponds to up-frequency and the lower one to down-frequency conversion. In the case of collinear propagation ($\mathbf{k}_1$ parallel to $\mathbf{k}_2$), it reduces to $k' = k_1 \pm k_2$ and $\omega' = \omega_1 \pm \omega_2$. When replicating what has been developed for harmonic generation, with consideration of slight nonlinear effects, the generation of cross product terms between the two interacting waves would be found (in addition to the case of second harmonic generation), whose growing functions $f_{\pm}^{\beta}$ have to satisfy the equation

$$D_k^{\beta}C_{ijkl}\left[(k_{1l}\pm k_{2l})\cos\vartheta_j + \left(k_{1j}\pm k_{2j}\right)\cos\vartheta_1\right]\frac{\partial f_{\pm}^{\beta}}{\partial r} \cong \frac{M_{ijklmn}}{4}\left(k_{1n}k_{2j}k_{2l}A_{1m}A_{2k} + k_{1j}k_{1l}k_{2n}A_{1k}A_{2m}\right) \tag{4.30}$$

where care has been taken in introducing a double sign for the function f, depending on whether it refers to the up-converted wave ($k_3 = k_1 + k_2$) or to the down-converted one ($k_3 = k_1 - k_2$).

As seen in the previous section, Eq. (4.30) greatly simplifies the case of isotropic solids where a single coordinate x can be taken in place of the general displacement vector $\mathbf{r}$. The solution would then reduce to

$$f_{\pm}^{\beta} \cong \frac{C_L + C_{NL}}{4C_L}k_1k_2A_1A_2x \tag{4.31}$$

Conservation of the linear momentum is satisfied in the dispersionless medium which has been assumed here, as both energy ($\hbar\omega$) and momentum ($\hbar\omega/c$) are linearly related in the particle description. A small degree of dispersion could easily be taken into consideration and would add an oscillating factor $\sin(\Delta kx)$ to the solution, with $\Delta k = k_3\text{-}(k_1 \pm k_2)$, responsible for the flowing back and forth of energy between the generating and the generated waves. (For the effect in surface acoustic waves (SAWs), see Adamou et al., 1979.) However, the phase-matching between harmonics may be seen from a different point of view when dealing with waves propagating into different directions. This is specific to solid state acoustics, where

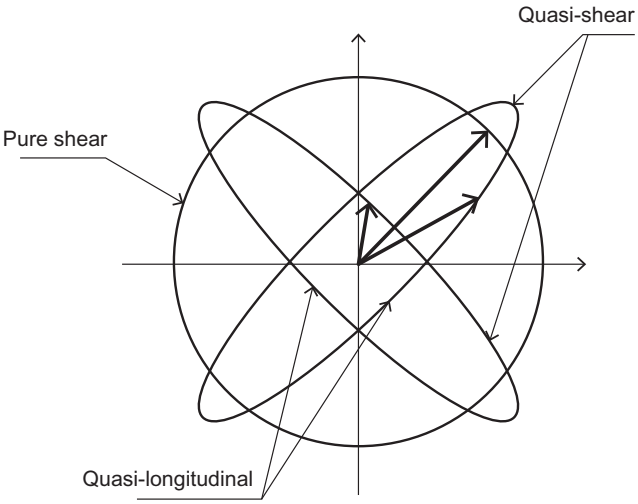


FIGURE 4.4 Slowness curves for the three acoustic modes propagating on the *XY* crystallographic plane of GaAs (cubic system) and wavevectors satisfying momentum ($\mathbf{k}_1 + \mathbf{k}_2 = \mathbf{k}_3$) and frequency ($\omega_1 + \omega_2 = \omega_3$, with $\omega_1 = \omega_2 = \omega_3/2$) matching conditions.

anisotropy and multiple modes may produce phase-matching conditions for waves propagating along different directions. In this case, phase-matching conditions can be achieved with different mode propagating waves, provided that two equations are contemporaneously satisfied (Figure 4.4):

$$\mathbf{k'}_{\pm}^{\gamma} = \mathbf{k}_1^{\alpha} \pm \mathbf{k}_2^{\beta} \quad \omega'^{\gamma}_{\pm} = \omega_1^{\alpha} \pm \omega_2^{\beta} \tag{4.32}$$

4.3.2.1 Applications

Frequency mixing is exploited in signal processing techniques and in underwater or soil exploration. The need for processing high-frequency signals was greater in the past when electronics largely relied on analogue hardware and SAW devices were in common usage. This was particularly the case where convolution/correlation, integrals, Fourier transformations, etc., were necessary for real-time signal-filtering processes, as in communicating through highly noisy environments or in image identification. The use of SAW on solid or crystal substrates, typically quartz or $LiNbO_3$, greatly improved the potential of devices because of the planar geometry of waves which limited undesired diffraction effects. The product between two signals was directly obtained through the nonlinear interaction of two waves propagating contra-directed, while integration was obtained either through acousto-optical interaction with light flashing on the interacting volume or through appropriate electrode distribution on the propagation surface.

Frequency mixing is also used for generating low-frequency waves for underwater or soil exploration. This utilizes transducers of limited size by means of down-conversion effect from the beating of two high-frequency

waves of close frequency. In this way, as pointed out in the pioneering work of Westervelt (1963), the directivity of the transducer is bound to the short wavelengths of the high-frequency emission, while the generation of the long wavelength taking place in the cylindrical volume of interaction limits the heavy diffraction effect of low-frequency waves. The low-frequency wave can then propagate with low attenuation to reach deeply submerged objects, although with partial loss of definition characteristics.

The harmonic balance method, on the other way, stimulated mathematical solutions to offer easier ways to attain the values of each single mode produced in the process. Grolet and Thouverez (2015) recently proposed a method based on the polynomial base of Groebner for computing the solutions in case that nonlinearity of the geometrical kind is present in a finite structure with no damping.

4.3.3 Stationary waves: Nonlinear sources

The excitation of elastic perturbations in a finite structure takes place according to a set of specific modes, i.e., to a stationary distribution of strains varying sinusoidally in time with a spectrum of well-defined frequencies. The specific mode that is set into resonance within the structure depends on the overlapping integral between the spatial distribution of strains and the spatial distribution of stresses in the exciting force in addition to the matching of the frequency values between the two distributions. A dissipative term causes the input energy acquired from the driving source to balance the loss of energy from the structure and to smooth out the response curve of the system at the resonance values of the frequency. The study of the spectral modes of a finite structure is facilitated by the assumption that there is no dissipation. This is achieved by considering a trial solution of the linear Eq. (4.9) with $M_{ijklmn} = 0$ and successively solving the space differential equation with the correct boundary conditions. As usual, the angular frequencies ω_n will stand as the eigenvalues of the equation of motion.

The insertion of nonlinear terms in the equation describing the elastic behavior of a finite structure subject to external driving forces will add the effect of coupling among different modes, thus exciting new modes in the structure which could not be directly excited by the driving force. In order to study the conditions for the onset of this effect, the equation must be written in its general form:

$$\rho_o \frac{\partial^2 u_i}{\partial t^2} = F_i(\mathbf{r}) \cos(\Omega t) + \left(C_{ijkl} + M_{ijklmn} \frac{\partial u_m}{\partial x_n} + \eta_{ijkl} \frac{\partial}{\partial t} \right) \frac{\partial^2 u_k}{\partial x_j \partial x_l} + \cdots \tag{4.33}$$

with $\mathbf{f}(\mathbf{r},t) = \mathbf{F}(\boldsymbol{r})\cos(\Omega t)$, the driving force per unit volume; and η, the shear viscosity coefficient (Landau and Lifchitz, 1967, p. 191). Transient solutions will eventually fail, while a stationary trial solution

$$\mathbf{u}(\mathbf{r}, t) = \mathbf{U}(\mathbf{r}) \cos(\Omega t + \psi) \tag{4.34}$$

can be inserted into Eq. (4.33) to give

$$\begin{aligned} &-\Omega^2 \rho_o U_i \cos(\Omega t + \psi) - \left[\left(C_{ijkl} + M_{ijklmn} \frac{\partial U_m}{\partial x_n} \right) \cos(\Omega t + \psi) \right. \\ &\left. - \eta_{ijkl} \Omega \sin(\Omega t + \psi) \right] \frac{\partial^2 U_k}{\partial x_j \partial x_l} \\ &= F_i(\mathbf{r}) \cos \Omega t \end{aligned} \tag{4.35}$$

The amplitude of displacement $\mathbf{U}(\mathbf{r})$ can be obtained by firstly separating, then squaring and adding, the $\sin\Omega t$ and $\cos\Omega t$ parts of the equation so as to be valid at any time t, giving

$$\begin{aligned} &\left[\Omega^2 \rho_o U_i + \left(C_{ijkl} + M_{ijklmn} \frac{\partial U_m}{\partial x_n} \right) \frac{\partial^2 U_k}{\partial x_j \partial x_l} \right]^2 \\ &+ \left(\eta_{ijkl} \Omega \frac{\partial^2 U_k}{\partial x_j \partial x_l} \right)^2 \\ &= F^2{}_i(\mathbf{r}) \end{aligned} \tag{4.36}$$

The phase can also be directly obtained through the separation of the $\sin\Omega t$ from the $\cos\Omega t$ parts and solving the $\sin\Omega t$ part which does not contain the forcing term $\mathbf{F}$:

$$\tan\psi = -\frac{\eta_{ijkl} \Omega \frac{\partial^2 U_k}{\partial x_j \partial x_l}}{\Omega^2 \rho_o U_i + \left(C_{ijkl} + M_{ijklmn} \frac{\partial U_m}{\partial x_n} \right) \frac{\partial^2 U_k}{\partial x_j \partial x_l}} \tag{4.37}$$

where the viscosity term may be correctly ignored ($\eta = 0$), the solution is greatly simplified, giving:

$$\begin{aligned} &\Omega^2 \rho_o U_i + \left(C_{ijkl} + M_{ijklmn} \frac{\partial U_m}{\partial x_n} \right) \frac{\partial^2 U_k}{\partial x_j \partial x_l} = \pm F_i \\ &\psi = 0 \end{aligned} \tag{4.38}$$

However, an external force with no dissipation would drive the system to an amplitude oscillation with an infinite value, so that the dissipationless case is better studied in the absence of external forces. If nonlinearity terms could also be ignored, the solution would further reduce to

$$\begin{aligned} &\omega_n^2 \rho_o U_i + C_{ijkl} \frac{\partial^2 U_k}{\partial x_j \partial x_l} \cong 0 \\ &\psi = 0 \end{aligned} \tag{4.39}$$

This case defines the eigenfrequencies ω_n of the structure and the corresponding modes $\hat{\mathbf{U}}_n(\mathbf{r})$. Prior to consideration of the nonlinearity terms, it should be remembered that the viscosity would smooth out the amplitude of any excited mode as

$$\mathbf{u}(\mathbf{r}, t) = \mathbf{U}(\mathbf{r}) \cos(\Omega t + \psi) \exp(-\alpha t) \tag{4.40}$$

with the α term depending on frequency. A driving force would then simply compensate for the loss of energy caused by the internal dissipation of the structure. The effects of a small degree of nonlinearity are better understood by considering a stationary condition in which one of the proper modes at ω_N remains at a constant amplitude U_N, depending on the excitation value of that single frequency. A small perturbation is produced which corresponds to the energy flowing out from that mode, so that a trial solution may be given as

$$\mathbf{u}(\mathbf{r}, t) = \mathbf{U}_N(\mathbf{r}) \cos \omega_N t + \varepsilon(\mathbf{r}, t) \tag{4.41}$$

with $\varepsilon << UN$. By inserting the solution into the nonlinear equation, taking into account that $\mathbf{U}N$ solves the linear equation and ignoring the higher order terms, the following is obtained:

$$-\rho_o \left(\frac{\partial^2 \varepsilon_i}{\partial t^2}\right) - C_{ijkl} \frac{\partial^2 \varepsilon_i}{\partial x_j \partial x_l} \cong M_{ijklmn} \frac{\partial^2 U_{Nk}}{\partial x_j \partial x_l} \frac{\partial U_{Nm}}{\partial x_n} \frac{1 + \cos(2\omega_N t)}{2} \tag{4.42}$$

which states that the perturbation term is drawing energy both from the dc term and from the time-second harmonic of the mode which are excited. If the perturbation term $\boldsymbol{\varepsilon}$ is developed into Fourier series, according to

$$\varepsilon(\mathbf{r}, t) = \sum\nolimits_s E_s(\mathbf{r}) \cos(s\omega_N t + \varphi_s) \tag{4.43}$$

and the harmonic balance is performed for the zero ($s = 0$) and second harmonic ($s = 2$) frequency, respectively, the following is obtained:

$$C_{ijkl} \frac{\partial^2 E_{oi}}{\partial x_j \partial x_l} = \frac{M_{ijklmn}}{2} \frac{\partial^2 U_{Nk}}{\partial x_j \partial x_l} \frac{\partial U_{Nm}}{\partial x_n} \tag{4.44a}$$

$$\left[\rho_o \omega_N^2 E_{2i} + C_{ijkl} \frac{\partial^2 E_{2i}}{\partial x_j \partial x_l}\right] \cong \frac{M_{ijklmn}}{2} \frac{\partial^2 U_{Nk}}{\partial x_j \partial x_l} \frac{\partial U_{Nm}}{\partial x_n} \tag{4.44b}$$

which shows how nonlinearity couples the principal mode to the others. Phase φ_o has been set equal to zero, with no loss of generality, since it simply modifies the value of the amplitude through the factor $\cos\varphi_o$. For reasons of simplicity, if the excited term is set as equal to the first order mode ($\omega_N = \omega_1$), the nonlinear coupling of the modes may draw energy from the fundamental mode back to the dc term as well as to the second harmonic, thus producing a feedback process on the driving mode that makes for bistability. Eqs. (4.44a), (4.44b) may be easily solved where mono-dimensional plane waves are set in an isotropic medium. By using the same notations already introduced in the case of progressive waves, they reduce to

$$C \frac{\partial^2 E_o}{\partial x^2} = \frac{M}{2} \frac{\partial^2 U_1}{\partial x^2} \frac{\partial U_1}{\partial x} \tag{4.45a}$$

$$\left[\rho_o \omega_2^2 E_2 + C \frac{\partial^2 E_2}{\partial x^2}\right] = \frac{M}{2} \frac{\partial^2 U_1}{\partial x^2} \frac{\partial U_1}{\partial x} \tag{4.45b}$$

Solutions of Eqs. (4.45a), (4.45b) which satisfy the correct boundary conditions set for the structure must then be found.

The possible growth of subharmonic waves in a finite structure from nonlinear interaction with the driven mode is of considerable interest. According to conservation laws, the rise of lower frequencies is only possible from the breaking down of one quantum state into two of lower frequency or, in terms of wave propagation, from the down conversion of one higher frequency wave into two lower ones. This is a typical threshold phenomenon which may only take place if the energy of the generating wave is sufficiently high to overcome a specific, or threshold, level. Where that is the case, any perturbation, however small, occurring at the correct frequency in the structure will be amplified by the draining of energy from the fundamental and will grow up to a defined level. Both the threshold value of the fundamental mode and the regime level of the subharmonic depend upon the value of the dissipation term. In the limiting case that the system is not dissipative, the threshold level decreases to zero as any quantity of energy introduced into the subharmonic frequency wave will accumulate without loss and may grow indefinitely in a manner similar to the indefinite growth of the fundamental in a dissipationless system.

The threshold effect may be evaluated in a manner parallel to that used for the growth of the harmonic waves. This is achieved by considering the general nonlinear Eq. (4.33) and supposing its solution to be given by a function $V(\mathbf{r},t)$, which is comprehensive of both the solution of the corresponding linear equation (M 0) and all the higher frequency terms (harmonics). It may be supposed that an infinitesimal perturbation $\varepsilon(\mathbf{r},t)$ at a frequency lower than that of the driving one—taken for example as one half of $\Omega/2$—is accidentally present in the system and added to the preexisting solution gives

$$W(\mathbf{r}, t) = V(\mathbf{r}, t) + \varepsilon(\mathbf{r}, t) \tag{4.46}$$

Such a perturbation is bound to be extinguished, because of the dissipation term η, unless the nonlinear coupling between the waves drains sufficient energy from the fundamental to overcome the dissipation loss. In order to verify this condition, solution (4.46) may be placed into Eq. (4.33) to give

$$\rho_o \frac{\partial^2 (V_i + \varepsilon_i)}{\partial t^2} = F_i(\mathbf{r}) \cos(\Omega t) + \left(C_{ijkl} + M_{ijklmn} \frac{\partial (V_m + \varepsilon_m)}{\partial x_n} + \eta_{ijkl} \frac{\partial}{\partial t} \right) \frac{\partial^2 (V_k + \varepsilon_k)}{\partial x_j \partial x_l} + \cdots \tag{4.47}$$

and subsequently

$$\rho_o \frac{\partial^2 \varepsilon_i}{\partial t^2} = \left(C_{ijkl} + \eta_{ijkl} \frac{\partial}{\partial t} \right) \frac{\partial^2 \varepsilon_k}{\partial x_j \partial x_l} + M_{ijklmn} \left(\frac{\partial \varepsilon_m}{\partial x_n} \frac{\partial^2 V_k}{\partial x_j \partial x_l} + \frac{\partial V_m}{\partial x_n} \frac{\partial^2 \varepsilon_k}{\partial x_j \partial x_l} \right) + \cdots \tag{4.48}$$

by retaining only the highest order terms and considering that $\boldsymbol{V}$ solves the nonlinear equation. As in the perturbative cases previously examined, the equation thus derived is linear for the perturbation term ε, with a driving force given by the cross products of first and second derivatives of ε and $\boldsymbol{V}$. These are periodical terms at frequencies Ω and $\Omega/2$, producing driving terms at the sum and difference frequencies, 3 $\Omega/2$ and $\Omega/2$. That means that a perturbation accidentally present in the system may produce a driving term which generates an oscillation at the same frequency with the same configuration as the initial one present in the system. If the generated wave amplitude is greater than the original, the perturbation may continuously increase its amplitude and attain a finite regime value much higher than the initial one. However, this condition is not easy to derive since the cross product generating the new oscillation is proportional to V and V is proportional to F and it could be qualitatively said that the threshold value of the driving amplitude Fth for the onset of the subharmonic wave is inversely proportional to the nonlinear parameter M.

Once a subharmonic oscillation at $\Omega/2$ is set up in a system where the driving term is greater than the threshold value, a successive subharmonic at $\Omega/4$ could be generated via the same process so that a new condition for a second threshold is satisfied and thus for subharmonic at $\Omega/8$ and $\Omega/16$, etc. When a subharmonic at $\Omega/4$ has been produced, nonlinearity can generate an oscillation at 3 $\Omega/4$, through the beating of the $\Omega/4$ frequency wave with that already generated at $\Omega/2$ and, analogously, oscillations at 3 $\Omega/8$ by the beating of $\Omega/8$ with $\Omega/4$. Successive values of the threshold amplitudes should be evaluated, but their values rapidly converge to a value Fch, where all possible subharmonic oscillations may increase suddenly and drive the system into a chaotic behavior.

4.3.3.1 Applications

Musical instruments provide the best examples of finite systems where elastic perturbations undergo nonlinear interactions. They are also the earliest known objects expressly made for producing sound, yet the approach to their study is usually presented in terms of linear theory, though musical "forte" conditions drive almost any instrument deep into nonlinear conditions. Schematically, nonlinearity may derive either from the nonlinear coupling of the driving device (the bow hair in the case of violins, the reed in case of clarinets, etc.) or from the resonant system emitting the sound (strings, tube, plates, and so on; see Fletcher et al., 1990). The focus here is on the second case which has been theoretically described in the previous section. It is sufficient to note, in regard to the first case, that it is mainly due to the onset of a positive resistance in the driving mechanism. At low amplitudes of oscillation in the linear regime, mono-dimensional structures such as strings or tubes present a spectral response of resonance frequencies, all of which are integral multiples of the lowest or fundamental frequency. At higher levels, the increased average time conditions of the stress usually increase the resonance frequencies and the harmonicity of the spectral response may be lost. The nonlinearity mechanism preserves the integral relation among the different mode frequencies through the coupling of different modes. In the case of string instruments for example, the coupling between the oscillations on the two possible planes makes the single point of the string to move in a "rosetta" type motion. The single component changes its oscillation period but the periodical motion from the inner and outer parts of the rosetta does not.

The conditions in multidimensional instruments such as cymbals and gongs are quite different as mode locking is prevented, and following percussion, energy flows from lower to higher harmonics, producing a variable pitch or "multiphonic" sound.

The results outlined above replicate at different bandwidths in the case of ultrasonic transducers, where nonlinearity drives the systems into motions which are rich in harmonic and subharmonic modes. These are usually difficult to analyze in detail. As the amplitude of the driving mode increases, a series of multiple harmonic modes appear at increasing intensities up to a point where the coupling between them cannot be easily followed. The appearance of subharmonic oscillations, mainly at half the fundamental frequency, is of great interest. When the corresponding threshold conditions are attained, successive period doubling will be present with the corresponding possible frequency coupling (3/4th, 3/8th, 5/8th of fundamental frequency, etc.; see Figure 4.5). As the chaotic state is attained, the frequency spectrum enriches to a level where it returns to an almost linear condition and continues for a short interval of amplitude before returning to chaos. This behavior is common to chaotic systems and could be successfully used in case of high power transducers where the chaotic conditions may damage transducers and affect the results of devices based on them (Cardoni et al., 2013).

4.4 Conclusions

The treatment of acoustic nonlinearities in solids presents a complex problem. The general anisotropy of materials combined with the various modes of propagation renders the formal approach a jungle of indices which must be carefully unraveled if the correct solution for individual cases is to be found. The general problem has been formulated here, and various phenomena were analyzed. These have been successively reduced to simplified forms (mainly to

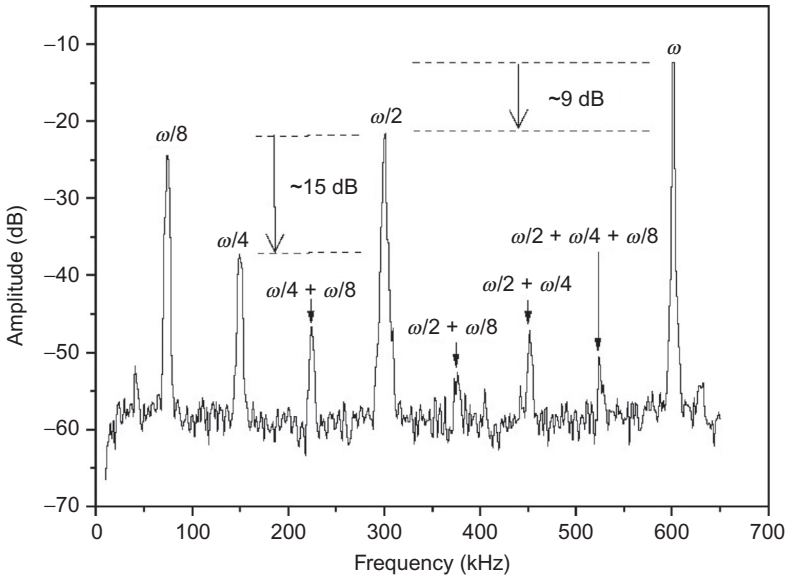


FIGURE 4.5 Spectrum of excited modes in a piezoelectric element, driven at fundamental frequency $f = 602.4$ kHz, with evidence of subharmonic fractional modes (Bettucci et al., 2008).

mono-dimensional cases for isotropic materials) to make clear the origin of the effects involved, while leaving the general form to further developments. The perturbation method has therefore been fully described where nonlinearity is considered as a recursive effect which slightly modifies the linear problem. This has been described in the case of progressive waves and stationary conditions. In the former, agreement with the model of self-modulation in the wavevector by the propagating wave itself has been described. Coupling between different modes and frequency mixing have also been discussed, together with the identification of the overall coupling coefficients and the feedback effect on the zero order mode.

References

Adamou, A., Alippi, A., Palma, A., Palmieri, L., Socino, G., 1979. Parametric mixing of surface acoustic waves. J. Appl. Phys. 40-C8, 262–265.

Bettucci, A., Biagioni, A., D'Orazio, A., Passeri, D., 2008. Periodic oscillations within the chaotic region in finite piezoelectric structures. In: Proceedings of the 18th International Symposium on Nonlinear Acoustics, Nonlinear Acoustics: Fundamentals and Applications, Stockholm, pp. 251–254.

Blackstock, D.T., Hamilton, M.F., Pierce, A.D., 1998. Progressive waves in lossless and lossy fluids. In: Hamilton, M.F., Blackstock, D.T. (Eds.), Nonlinear Acoustics. Academic Press, San Diego.

Bouakaz, A., de Jong, N., 2003. Native tissue imaging at superharmonic frequencies. IEEE Trans. Ultrason. Ferroelectr. Freq. Control 50 (5), 496–506.

Cardoni, A., Riera, E., Gallego-Juarez, J.A., 2013. Nonlinear response in airborne piezoelectric transducer for power ultrasonics. In: 2013 International Congress on Ultrasonics (ICU 2013), Singapore.

Chillara, V.K., Lissenden, C.J., 2016. Review of nonlinear ultrasonic guided wave nondestructive evaluation: theory, numerics, and experiments. Opt. Eng. 55 (1).

Cowin, S.C., Mehrabadi, M.M., 1955. Anisotropy symmetries of linear elasticity. Appl. Mech. Rev. 48, 247–285.

Cunningham, J.A., Quate, C.F., 1972. High-resolution, high-contrast acoustic imaging. J. Phys. Colloques 33 (C6), 42–47.

Fletcher, N.H., Perrin, R., Legge, K.A., 1990. Nonlinearity and chaos in acoustics. Acoust. Aust. 18 (1), 9–13.

Grolet, A., Thouverez, F., 2015. Computing multiple periodic solutions of nonlinear vibration problems using the harmonic balance method and Groebner bases. Mech. Syst. Signal Process. 52, 529–547.

Hong, X., Liu, Y., Lin, X., Luo, Z., He, Z., 2018. Nonlinear ultrasonic detection method for delamination damage of lined anti-corrosion pipes using PZT transducers. Appl. Sci. 8, 2240.

Jeong, H., Zhang, S.-Z., Li, X.-B., 2019. Second-harmonic generation in focused beam fields of phased-array transducers in a nonlinear solid with a stress-free boundary. Transp. Saf. Environ. 1 (2), 117–125.

Landau, L.D., Lifchitz, E.M., 1967. Theorie de l'élasticité. MIR, Moscow.

Lubarda, V.A., 1997. New estimates of the third-order elastic constants for isotropic aggregates of cubic crystals. J. Mech. Phys. Solids 45 (4), 471–490.

Lyakov, A., Proskuryakov, A.K., Shipilov, K.F., Umnova, O.V., 1995. Bistability and chaos in acoustic resonators. Ultrasonics 33 (1), 55–59.

Maruyama, T., Touhei, T., 2016. Steady-state analysis of nonlinear ultrasonic waves caused by crack face friction. In: 172nd Meeting of the Acoustical Society of America Honolulu, Physical Acoustics: Paper 4pPA10.

Morse, P.M., Ingard, K.U., 1986. Theoretical Acoustics. Princeton University Press, Princeton.

Ostrovsky, L., Gorshkov, K., 2000. Perturbation theories for nonlinear waves. In: Christiansen, P.L., Sørensen, M.P., Scott, A.C. (Eds.), Nonlinear Science at the Dawn of the 21st Century. Springer, Berlin.

Rienstra, S.W., Hirschberg, A., 2013. An Introduction to Acoustics. Eindhoven University Press, Eindhoven.

Thurston, R.N., 1984. Waves in solids. In: Truesdell, C. (Ed.), Mechanics of Solids. Vol. 4. Springer, Berlin, pp. 109–308.

Westervelt, J., 1963. Parametric acoustic array. J. Acoust. Soc. Am. 35, 535–537.

Zheng, Y., Maev, R.G., Sodolov, I., 2011. Review/sythèse nonlinear acoustic applications for material characterization: a review. Can. J. Phys. 77 (12), 927–967.

Chapter 5

Piezoelectric ceramic materials for power ultrasonic transducers

L. Pardo

Instituto de Ciencia de Materiales de Madrid. Consejo Superior de Investigaciones Científicas (CSIC), c/ Sor Juana Inés de la Cruz, Cantoblanco, Madrid, Spain

5.1 Introduction

This chapter outlines some fundamentals on the ferro-piezoelectric polycrystals also known as piezoceramics, which display complex behavior in frequency, time, and temperature that must be taken into consideration for proper device design. The modeling and design of piezoelectric devices using finite element methods relies on the accuracy of the dielectric, piezoelectric, and elastic coefficients of the active material used; commonly anisotropic ferro-piezoelectric polycrystals, which are the piezoelectric ceramics. The characterization by resonance methods, state of the art, and perspectives are also analyzed in this chapter. The focus of this chapter is power applications for piezoceramics and trends in the development and study of newly developed ceramics lacking lead in their compositions: the lead-free ceramics.

5.2 Fundamentals of ferro-piezoelectric ceramics

5.2.1 From the ferroelectric single crystal to the ceramic

The lack of a center of symmetry in the structure (Newnham, 1975) is the origin of the piezoelectric effect in single crystals. When a mechanical stress is applied to an ionic crystal in a direction that generates a separation of the center of positive and negative charges, an electric polarization (dipole) is generated. This is the direct piezoelectric effect. Conversely, the application of an electric field gives way to a mechanical strain. Piezoelectricity is an anisotropic effect that only takes place in some directions of the ionic crystal (Figure 5.1). This phenomenon was discovered by Jacques and Pierre Curie in 1880 (Pardo et al., 1999).

Figure 5.2 shows the subdivision of piezoelectric crystals (Nye, 1957) into pyroelectrics, in which there is a spontaneous polarization change with temperature. Pyroelectrics, in turn, are subdivided into ferroelectric crystals.

Ferroelectrics present a spontaneous polarization that can be reversed by an electric field. "La Rochelle" salt, the sodium potassium salt of tartaric acid with four molecules of water of crystallization, $NaKC_4H_4O_6{\cdot}4H_2O$ was the first ferroelectric known. It was studied by Joseph Valasek in his work "Piezoelectricity and Allied Phenomena in Rochelle Salt" in 1920 (Pardo et al., 1999). Valasek measured for the first time a ferroelectric hysteresis loop between the polarization and the applied electric field that results in a remnant polarization in absence of the field (Valasek, 1921). Ferroelectricity is a particular case of a more general phenomena, "ferroicity," presented by materials that show a nonlinear, hysteretic, relation between a material order parameter and a conjugated field (Fuentes-Cobas et al., 2011). Other examples of ferroic materials are the ferromagnetics, which show hysteresis cycles of magnetization versus magnetic field, and the ferroelastic, which show a strain vs. stress hysteresis.

Arthur R. Von Hippel studied the first ferroelectric refractory double oxide amenable to ceramic preparation, $BaTiO_3$ (BT), in 1950 (von Hippel, 1950). Between 1949 and 1959, around 100 new ferroelectric compounds were studied. Lead titanate, $PbTiO_3$ (PT), also studied in 1950, was one of the most promising from a theoretical and practical point of view (Pardo et al., 1999). It remained as the highest spontaneous polarization ($81\,\mu C/cm^2$) material until multiferroicity, the coexistence of two or more ferroic effects, was recently revisited and the polarization of $BiFeO_3$ (BFO) (Wang et al., 2003) along the pseudocubic 111 direction was found to have a magnitude of $90–95\,\mu C/cm^2$. At present, there are over 300 ferroelectric materials known and many others are under study (Landolt-Börstein, 1981).

Polycrystalline materials have randomly oriented grains (Figure 5.3). As processed, they are isotropic and centrosymmetric materials and, thus, nonpiezoelectric. Piezoelectric ceramics are built from ferroelectric crystallites

Power Ultrasonics. https://doi.org/10.1016/B978-0-12-820254-8.00013-0
Copyright © 2023 Elsevier Ltd. All rights reserved.

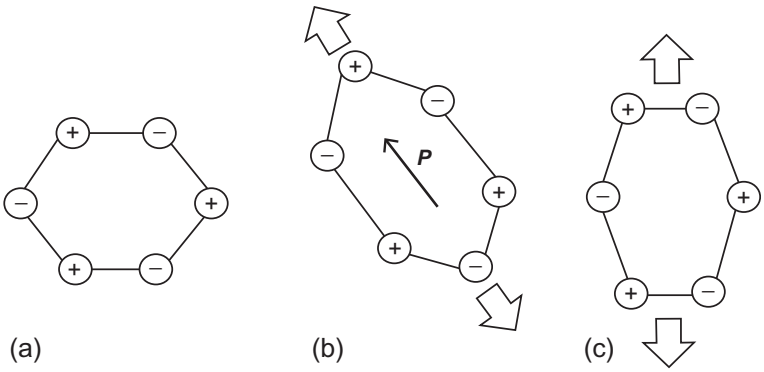


FIGURE 5.1 Arrangement of ions (a) unstressed, (b) under the action of an uniaxial mechanical stress in a direction that builds up a separation between the centers of positive and negative charges and, thus, an electric polarization (P), and (c) under the action of an stress which keeps the same position of the centers of charge and, thus, does not involves a piezoelectric effect. *(From Newnham (1975, Figure 33A–C, p. 83), with kind permission from Springer Science and Business Media.)*

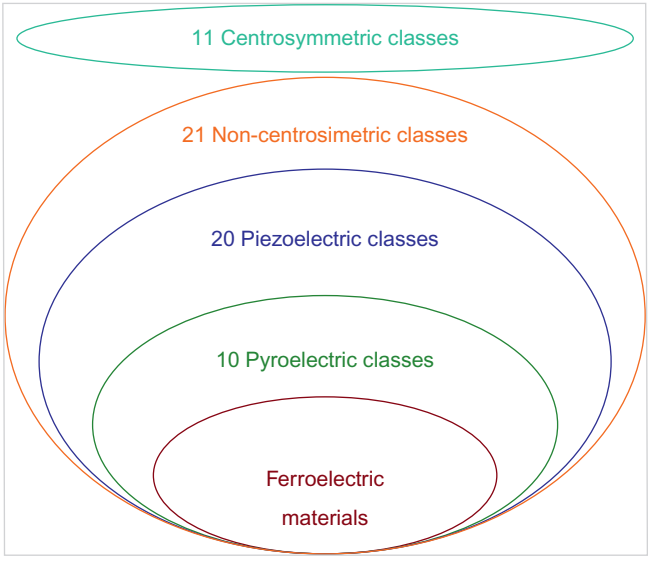


FIGURE 5.2 Classification of piezoelectric crystals on the basis of their crystal symmetry. *From Nye (1957).*

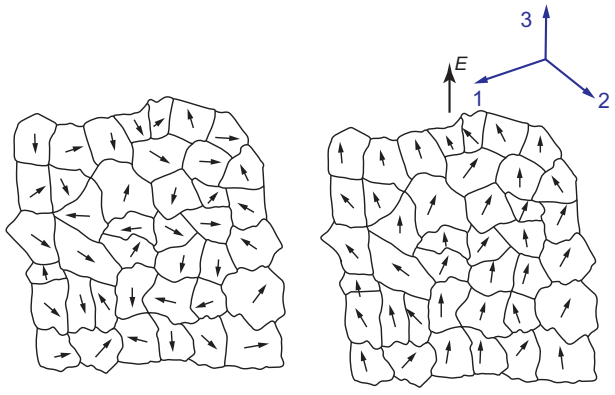


FIGURE 5.3 Schematic of the poling process of a ferro-piezoelectric ceramics.

and must be poled to show piezoelectric activity. Poling is a process in which a ceramic is subjected to an intense electric field at a certain temperature. Due to the ferroelectricity of the grains and orientation of the spontaneous polarization in parallel to the field direction, poling induces a cylindrical—noncentrosymmetric—symmetry in the ceramic with a preferential axis, commonly referred to as three axes (Figure 5.3). Poled ferroelectric ceramics became piezoelectric in this process. As an historical curiosity, poling was known before the ferroelectricity of $BaTiO_3$ was explained (Gray, 1949).

The four main ferroelectric families (Haertling, 1999) of crystal structures containing oxygen octahedra, to which all piezoelectric ceramic complex oxides compositions belong, are (1) perovskite-type, general formula ABO_3, which is a tridimensional network of oxygen octahedral (the structure of $BaTiO_3$, $PbTiO_3$, and $LiNbO_3$ among many other ferroelectrics); (2) tungsten-bronze, general formula $(A1)_4(A2)_2Nb_{10}O_{30}$, a

network of NbO_6 oxygen octahedra with three different type of cavities; (3) pyroclore-type, general formula $A_2B_2O_7$, which are of low technological interest due to a very small spontaneous polarization; and (4) Aurivillius-type structure, general formula $(Bi_2O_2)(A_{n-1} \cdot B_nO_{3n+1})$, which structure alternates layers of $[Bi_2O_2]^{2+}$ and pseudo-perovskite blocks with the thickness of n-layers of oxygen octahedral. These ferroelectrics possess the highest transition temperatures (>1400°C).

Most commercial ceramics are based on the perovskite-type structure in solid solution of $(1-x)PbTiO_3$-$xPbZrO_3$ or $Pb(Zr_xTi_{1-x})O_3$, also known as PZT (Haertling, 1999). These have either tetragonal (T) or rhombohedral (R) distorsions of the cubic perovskite-type structure along the 001 and 111 directions, respectively. Compositions close to the so-called morphotropic phase boundary (MPB), a temperature-independent composition-driven structural phase transition, with coexistence of the two symmetries of the crystal, for $x = 0.52–0.50$, are those achieving the maximum piezoelectric properties and currently used in transducers.

5.2.2 Ferroelectric hysteresis and domains

Ferroelectric single crystals are characterized by having two equilibrium states with the same value of spontaneous polarization (i.e., polarization in the absence of an electric field; Figure 5.4a or c). An external electric field favors the polarization state in the same direction (Figure 5.4b or d), giving rise to polarization reversal and the hysteresis cycle (Figure 5.4e).

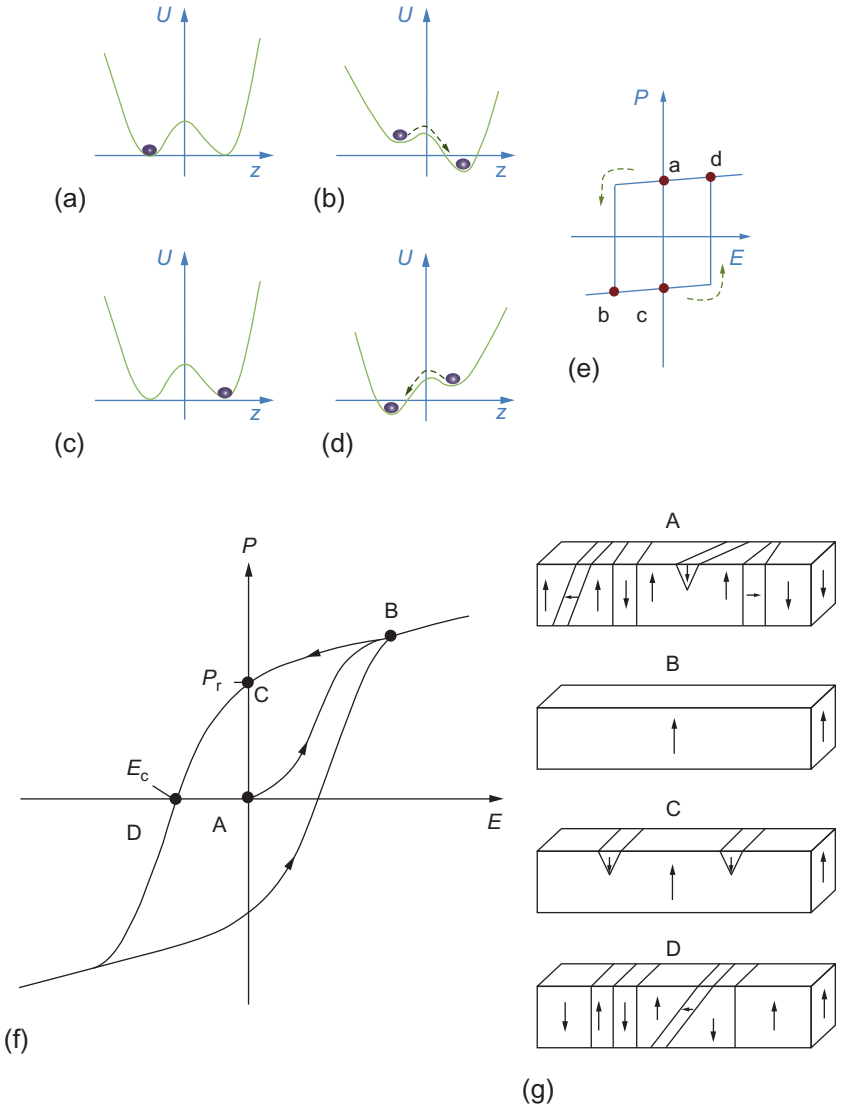


FIGURE 5.4 (a–e) Energy model of the hysteresis cycle for a single-domain single crystal. (f) Hysteresis cycle of a ferroelectric material and (g) examples of domain configurations that may correspond to the points (a–d) marked in the cycle, to illustrate the "switching" process (Pardo and Aragó, 2010).

Ferroelectric crystals present "domains," which are volumes of the material in which the long-range ordered spontaneous polarization of the crystal is oriented in a given, energetically favorable, direction. The hysteresis cycle of Figure 5.4f indicates the key parameters that characterize a ferroelectric material: the remanent polarization (Point *C*), P_r, that equals the spontaneous polarization, P_s, for a single-domain single crystal, and the coercive electric field (Point *D*), E_c, that is the minimum value that overcomes the energy barrier (Figure 5.4b or d) for polarization reversal. In a ferroelectric crystal, the polarization "switching" process results in the growth of domains aligned to the electric field at the expense of those that are not (Figure 5.4g). The remnant state of a ferroelectric crystal, or grains in a ceramic, has a strong dipolar order in the direction of the field (Figure 5.4c–g). As the temperature increases, thermal energy overcomes the energy needed to keep such a dipolar order and, at the same time, the crystal structure evolves so as to reduce the spontaneous polarization. Another characteristic of a ferroelectric material is that it undergoes a transition to a high-temperature nonpolar phase, known as a paraelectric phase, at the Curie temperature, T_C. In the proximity of this temperature, the material properties (thermal, elastic, optical) change and, in particular, the dielectric permittivity, $\varepsilon'(T)$, increases, in some cases by orders of magnitude in single crystals (lambda curve). Transitions between polar states of a ferroelectric, which are characterized by different crystal symmetry and spontaneous polarization, are also reflected in the thermal evolution of the dielectric permittivity (Figure 5.5).

5.2.3 The poling process

By the action of an intense dc electric field at a suitable temperature, which favors domain mobility, poling causes increasing orientation with the time of the ferroelectric domains until saturation is reached (Point B in Figure 5.4f). Upon removal of the field, a mechanical stress builds up in the material, which arises due to the connection between spontaneous polarization and unit cell strain. Some of the reoriented domains go back to their original orientations to minimize that stress and the material displays a remanent polarization, P_r (Point C in Figure 5.4f). Poling creates a macroscopic, noncentrosymmetric, 6 mm, ceramic symmetry that leads to piezoelectric activity (Figure 5.3).

The remnant polarization, P_r, in the field direction and, consequently, the piezoelectric performance in randomly oriented ferroelectric polycrystals, are limited by the symmetry of the crystal structure of the ferroelectric [tetragonal: $P_r^{max} = 0.83\, P_s$, with 6 $\langle 001 \rangle$ equivalent directions of the spontaneous polarization of the crystal, P_s; rhombohedral: $P_r^{max} = 0.87\, P_s$, with 8 allowed $\langle 111 \rangle$ equivalent directions; and orthorhombic: $P_r^{max} = 0.91\, P_s$, with 12 allowed $\langle 110 \rangle$ equivalent directions (Baerwald, 1957; Subbarao et al., 1957)]. Compositions near a MPB, where two crystal symmetries coexist, are often sought as they provide the maximum number of directions for polarization orientation and, thus, efficiency of poling.

Poling remains a major issue in the development of high-performance "lead-free" piezoceramics. The good piezoelectric behavior found in systems that are in a pseudocubic phase under zero electric field indicates that the search for lead-free alternatives should not exclude such systems. For some of these "lead-free" piezoelectrics, field-induced structural transitions to ferro-piezoelectrically active phases, which takes place prior to the process of domain orientation during poling, have been observed (Jo et al., 2009; Rubio-Marcos et al., 2010).

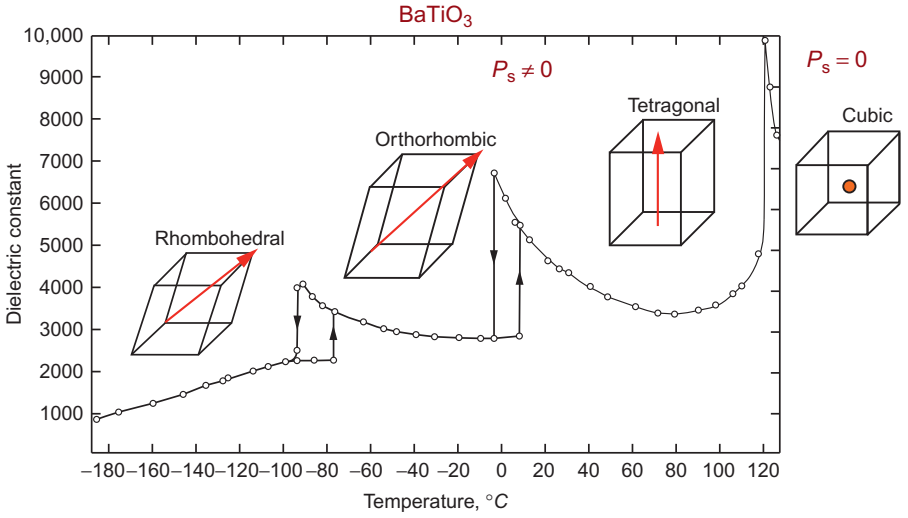


FIGURE 5.5 Thermal evolution of the dielectric permittivity of ferroelectric $BaTiO_3$ ceramics.

5.2.4 Multifunctional ferro-piezoelectric ceramics

Ferro-piezoelectric ceramics and thin films, due to their ferroelectricity, are also an important class of multifunctional materials whose properties have been exploited in a wide number of applications (Haertling, 1999). These include applications in ultrasonic transducers (e.g., ultrasonic medical imaging), sensors (e.g., accelerometers and energy harvesting), actuators (e.g., fuel injection and scanning systems), and IR detectors for sensors and imaging. Additionally, ferroelectrics have high dielectric permittivity and are thus used in capacitors as well as displaying the electro-optic effect, which can be applied for optical storage and optical switches. Polarization reversal allows establishment of two stable orientations under an electric field and thus use as computer memories (FERAMs).

Recently, trigged by the possibilities of new and enhanced applications in spintronics and data storage (Cheong and Mostovoy, 2007; Wang et al., 2003), there have been efforts toward the development of new materials that show coexistence and coupling of order parameters, the so-called multiferroics (Catalan and Scott, 2009; Ramesh, 2013).

The use of ferro-piezoelectrics and related materials in energy applications also constitutes a fast expanding field nowadays. Among these are the energy storage (Chauhan et al., 2015) and the electro-caloric or baro-caloric effects, used for solid state cooling technologies, by heat absorption from a source and storage near ferroic phase transitions and its liberation to a heat sink by an applied electric field or hydrostatic pressure, respectively (Mischenko et al., 2006; Prah et al., 2019; Stern-Taulats et al., 2016; Mikhaleva et al., 2020). Some ferroelectrics are also photovoltaics (Yin et al., 2019), potentially converting solar energy into electricity. The piezoelectric energy harvesting is also expanding as a clean and renewable energy source, amenable for integrated low-power sources, which generates electrical energy from low-frequency road traffic (Vázquez-Rodríguez et al., 2019) or human motions or from vibrations (Erturk and Inman, 2011; Patel et al., 2014).

5.3 Characterization methods of ceramics from piezoelectric resonances

The accurate description of piezoceramics involves the evaluation of the dielectric, piezoelectric, and mechanical losses accounting for the out of phase material response to the input signal. Losses in piezoceramics have undesired consequences for positioning actuator applications because they lead to hysteresis in the field-induced strain, and also for resonance applications, such ultrasonic motors, as they are the cause of heat generation. They are, however, suitable for application in force sensors and acoustic transducers, because they widen the frequency band for receiving signals.

The description of the material parameters by complex values ($P^* = P' - iP''$) is a convenient way to separately account for the dielectric, piezoelectric, and mechanical losses ($\tan\delta = P''/P'$). The origin of the losses in ferroelectric ceramics has been analyzed in numerous works (Haerdtl, 1982; Robert et al., 2001; Uchino and Hirose, 2001). While mechanical losses in piezoceramics arise from crystal lattice defects, microstructure (grain boundary, density, and porosity), and ferroelectric domain wall motions, the dielectric losses are related to the ionic and the ferroelectric nature of these compounds, and the piezoelectric ones are a consequence of coupling mechanisms.

Poled ferroelectric ceramics in the linear range show substantially linear relations between the stress (T_{ij}) and the strain (S_{ij}), which are tensor magnitudes, and between the electric field (E_i) and the dielectric displacement (D_i), which are vector magnitudes. These relationships can be expressed as follows:

$$\begin{aligned} S &= s^E T + d_t E \\ D &= dT + \varepsilon^T E \end{aligned} \tag{5.1}$$

where s^E is the matrix of elastic compliance, d the matrix of piezoelectric charge coefficients, d_t its transposed (changing rows by columns) matrix, and ε^T the dielectric permittivity matrix. Superindex E refers to constant (zero) field and superindex T to constant (zero) stress.

$$\begin{aligned} S &= s^D T + g_t D \\ E &= -gT + \beta^T D \end{aligned} \tag{5.2}$$

where g and g_t are the matrix of piezoelectric voltage coefficients and its transposed matrix and β^T is the dielectric impermittivity (also called impermeability) matrix. Superindex D refers to constant dielectric displacement.

$$\begin{aligned} T &= c^E S - e_t E \\ D &= eS + \varepsilon^S E \end{aligned} \tag{5.3}$$

where e and e_t are the matrix of piezoelectric coefficients and its transposed matrix and c^E is the elastic stiffness matrix. Superindex S refers to constant strain.

$$\begin{aligned} T &= c^D S - h_t D \\ E &= -hS + \beta^S D \end{aligned} \tag{5.4}$$

where h and h_t are the matrix of piezoelectric coefficients and its transposed matrix.

Eq. (5.1) of a poled ferro-piezoelectric ceramic having 6mm symmetry is shown in Figure 5.6. Such materials are characterized by five independent elastic constants (note that $s^E_{66} = 2(s^E_{11} - s^E_{12})$), three independent piezoelectric coefficients, and two independent dielectric coefficients.

$$\begin{pmatrix} S_1 \\ S_2 \\ S_3 \\ S_4 \\ S_5 \\ S_6 \\ D_1 \\ D_2 \\ D_3 \end{pmatrix} = \begin{pmatrix} s_{11}^E & s_{12}^E & s_{13}^E & 0 & 0 & 0 & 0 & 0 & d_{31} \\ s_{12}^E & s_{11}^E & s_{13}^E & 0 & 0 & 0 & 0 & 0 & d_{31} \\ s_{13}^E & s_{13}^E & s_{33}^E & 0 & 0 & 0 & 0 & 0 & d_{33} \\ 0 & 0 & 0 & s_{44}^E & 0 & 0 & 0 & d_{15} & 0 \\ 0 & 0 & 0 & 0 & s_{44}^E & 0 & d_{15} & 0 & 0 \\ 0 & 0 & 0 & 0 & 0 & s_{66}^E & 0 & 0 & 0 \\ 0 & 0 & 0 & 0 & d_{15} & 0 & \varepsilon_{11}^T & 0 & 0 \\ 0 & 0 & 0 & d_{15} & 0 & 0 & 0 & \varepsilon_{11}^T & 0 \\ d_{31} & d_{31} & d_{33} & 0 & 0 & 0 & 0 & 0 & \varepsilon_{33}^T \end{pmatrix} x \begin{pmatrix} T_1 \\ T_2 \\ T_3 \\ T_4 \\ T_5 \\ T_6 \\ E_1 \\ E_2 \\ E_3 \end{pmatrix}$$

FIGURE 5.6 The matrix of elastic, dielectric, and piezoelectric coefficients for the poled ferro-piezoelectric ceramic symmetry, 6mm.

Characterization methods for bulk piezoceramics from impedance measurements at the electromechanical resonances have been used since the 1960s. In the frequency range of an electromechanical resonance, the resonator of a given geometry has electrical impedance, Z, that depends on the frequency; the dimensions of the sample and its density; and a given set of dielectric, piezoelectric, and elastic material coefficients. For this reason, the values of the coefficients can be obtained from impedance measurements as a function of the frequency on a suitably shaped sample, provided that the analytical solution of the wave equation for the mode of motion of that sample is known and, thus, can be solved for the unknown coefficients.

5.3.1 IEEE and European standard methods

The first standard procedures of measurements on piezoceramics date from 1961 (IRE, 1961) and were issued by the North American "Institute of Radio Engineers (IRE)." The aim of this standard was to adapt previous definitions, relations, and measurement methods developed for piezoelectric single-crystal resonators in general to the characteristics of those new materials.

The electromechanical coupling factor, k, is defined as the square root of the energy transformed by the resonator divided by the total energy input and expresses the ability of the resonator to transform electric energy into mechanical energy, and vice versa. The resonator can be described by an LCR (inductance, capacitance, resistance) resonant circuit. As it is well known, the complex impedance of the resonator is $Z=R+iX$, where X is the reactance. The mechanical quality factor, Q_m, is defined as the expression of the internal mechanical damping of the resonator and by the ratio between the circuit reactance and resistance. The higher the mechanical quality factor, the lower the mechanical losses of the resonator.

The complex admittance of the resonator is defined as the reciprocal of the impedance and as $Y=G+iB$, where G is the conductance and B the susceptance. Standards define f_n and f_m as the frequencies of maximum and minimum impedance, respectively, in the neighborhood of the resonance and also define the procedures (the so-called transmission line, or transmission circuit method) to measure the resonator impedance in order to determine these frequencies. Coupling coefficients (k) and quality factors of the resonator are calculated from the difference between these two frequencies.

Standards also define other pairs of frequencies: f_s and f_p, the series and parallel frequencies, as the frequencies for maximum G and maximum R, respectively, and f_r and f_a, the resonance and antiresonance frequencies, as the frequencies of $B=0$ and $X=0$, respectively. The values of these frequencies are such that:

$$(f_n - f_m) > \left(f_p - f_s\right) > (f_a - f_r) \tag{5.5}$$

The main piezoceramic characteristics considered in the development of the 1961 standard were the high symmetry (6mm), leading to simpler relations than for most piezoelectric crystals, high electromechanical coupling constants, low mechanical quality factors, and noticeable dielectric loss factor ($\tan\delta=\varepsilon''/\varepsilon'$). If such conditions are fulfilled, the following approximations are valid (Figure 5.7):

$$(f_n - f_m) \approx \left(f_p - f_s\right) \approx (f_a - f_r) \tag{5.6}$$

This first standard was reviewed and updated several times, the most recent having been issued by the American National Standards Institute (ANSI) and the Institute of Electrical and Electronic Engineers (IEEE) in 1987 (Meeke, 1996). With a clear explanation of its limitations, the 1987 IEEE Standard is still based in the approximations given in Eq. (5.6). This standard is no longer supported by the IEEE Standard Association, and IEEE gave it the qualification of Withdrawn Standard; that is, "a Standard that is no longer maintained and which may contain significant obsolete or erroneous information" (Meeke, 1996).

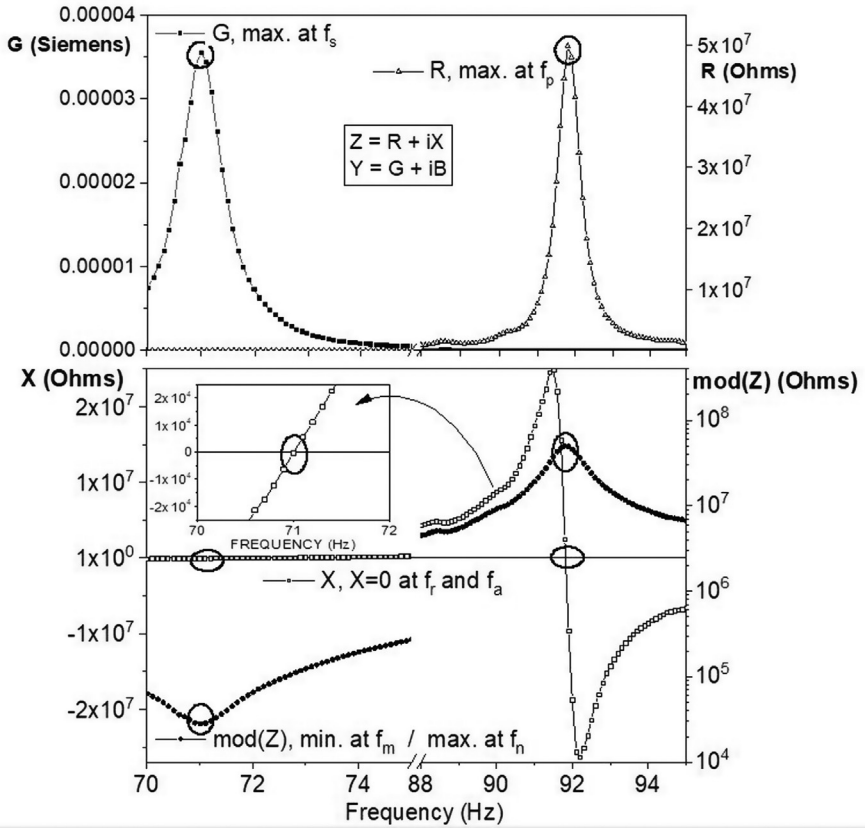


FIGURE 5.7 Impedance (modulus, $|Z|$, real, R, and imaginary, X, parts) and admittance (real part, G) dependence on frequency in the vicinity of an electromechanical resonance.

Nevertheless, the 1987 IEEE Standard is still widely used due to its validity for determination of parameters for many of the most widely used commercial piezoceramics based on lead titanate zirconate (PZT) compositions. These are high-Q_m, low loss, and high-coupling coefficients piezoelectric materials (Jaffe et al., 1971). The 1987 IEEE Standard is unsuitable for use with lossy materials like some lead-free piezoceramic materials, polymers, porous, and functionally graded piezoceramics.

The IEEE Standard was revised and re-edited by the European Committee for Electrotechnical Standardization (CENELEC). There are other international and Asiatic institutions that have also developed relevant standards (Cain and Stewart, 2014).

5.3.2 Alternative numerical methods, a review

One of the first attempts to treat losses in piezoceramics by considering complex coefficients was due to Holland (1967) and took place in 1967. Holland and EerNisse (1969) proposed a gain-bandwidth method for length extensional mode of thickness-poled bars that was valid for moderate losses and low electromechanical coupling coefficient materials. Since then, many papers on the topic have been published.

Smits (1976) published the first iterative procedure of analysis of the complex impedance curve for accurate determination of complex material coefficients. The major drawback of the method is that it requires a skilled user, as a judicious choice of the three frequencies for the measurement of Z is needed in order to avoid large errors. From such Z values, a system of nonlinear equations is established and solved by an iterative procedure.

The first extension to the complex parameters of the procedure proposed by Meitzler et al. (1973) adopted in the 1987 IEEE Standard for a piezoelectric resonator in the radial mode of a thin disk and was published by Sherrit et al. (1991). This is the most mathematically complex resonance mode. These authors also introduced a refinement of the IEEE Standard method by a polynomial fit that is easier to implement in terms of automatization and more accurate when compared to the linear interpolation used in the IEEE Standard for the data concerning Poisson's ratio, σ^P. These authors also proposed a noniterative evaluation method and applied it to thickness extensional plate resonators (Sherrit et al., 1992). This method implicitly assumes that the phase of the electromechanical coupling factor is only dependent

on the mechanical loss and is only applicable for materials with low dielectric and piezoelectric losses. Sherrit et al. accomplished the first complete material characterization in a complex form by the resonance method for a commercial ceramic (Sherrit et al., 1997a) and a composite (Sherrit et al., 1997b). They used four geometries and five resonance modes. For that purpose, they used their own method for the radial mode of a thickness-poled thin-disk resonator and the Smits method for the rest of the modes. No reliability criteria were considered for the material properties obtained in these works.

Kwok et al. (1997) published a comparative study applied to thickness extensional plate resonators. The methods compared were a nonlinear regression method proposed by the authors (the Gauss-Newton fitting method), a commercial software approach (the Piezoelectric Resonance Analysis Program based on the work of Smits and Sherrit et al.), the 1987 IEEE Standard method, the Smits method, and the Sherrit et al. method. Together with other moderate loss materials (copolymers, lead metaniobate ceramics, and composites), they characterized polyvinylidene fluoride (PVDF), a high-loss piezoelectric polymer. They confirmed the limitations of such methods. The authors' proposed nonlinear regression method had the drawback of being sensitive to the choice of the data segment used. Each calculated material parameter represents an average within the frequency range where data points are used. The narrower the fitting range, the closer are the calculated average values to the actual values of the parameters.

The most recent development in the characterization field, which exploits the large computing capabilities of modern central processor units (CPUs), is given by fitting methods of the experimental impedance curves at resonance (Tsurumi et al., 2002; Hong Du et al., 2003). Using finite element modeling for this, work on a given geometry and resonance to obtain a given set of parameters (Ebenezer, 2004) or, more relevant, fitting a wide spectra of a given sample namely a thin disk, including all resonances to obtain the full set of material parameters (Pérez et al., 2010), and, even more, all parameters as complex quantities, taking into account all the losses of the material (Pérez et al., 2014), has been published recently.

5.3.3 The iterative automatic method

Alemany et al. (Alemany et al., 1994, 1995; Algueró et al., 2004; Pardo et al., 2007b) developed an automatic iterative method to determine complex material coefficients. Based on Smits's approach, it overcomes the latter's main drawback by automatization of the choice of frequencies for the measurement of Z (or Y, depending on the resonance mode). This is the only numerical method that is applied to all resonator geometries and applications including the length resonance of a ring, thickness poled (Pardo et al., 2007c). Although the IEEE Standards require five geometries, we have demonstrated (Algueró et al., 2004) that the use of known relations among material parameters reduces the number of ceramic resonators required. The automatic iterative method has been applied to all four modes of three resonators needed for consistent complex characterization of a poled piezoelectric ceramic: (1) length extensional mode of thickness-poled bar (Alemany et al., 1994); (2) thickness extensional mode of thin plate or disk (Alemany et al., 1994); (3) radial mode of thin disks, thickness poled (Alemany et al., 1995); and (4) shear mode of thickness-poled, plate resonators (Pardo et al., 2007b, 2008, 2011a). In the trend of decreasing the number of resonators needed, the synergic use of the iterative method applied to the thickness-poled, thin disks and plates and the use of FEA and fitting methods of the full impedance spectra of the thin disk have allowed the complete characterization of a piezoceramic using only two resonators (Pérez et al., 2018).

The iterative method of analysis of the complex impedance curves also has been applied to the determination of the parameters from overtone resonances in the radial (Gonzalez and Alemany, 1996) and thickness (Gonzalez and Alemany, 1995) modes of thin disks, used, e.g., for determining the frequency dependence of the parameters. It is also possible to determine the frequency dependence of the shear parameters from the fundamental shear mode of thickness-poled plates (Reyes-Montero et al., 2019). The principles for the application of this method to the determination of the properties of self-standing films were developed and applied to PZT cantilevers (Pardo et al., 2010a).

5.4 Applications of the iterative automatic method in the characterization of ceramics

In this method, the coefficients are calculated via an automatic iterative numerical method for solution of a set of nonlinear equations with introduction of experimental impedance (or admittance) data. Such impedance or admittance data are taken at four automatically selected frequencies in the neighborhood of the resonance.

The dimensions and density of the resonator, together with the value of the complex admittance or impedance at each of the four frequencies around the resonance, are required to obtain the dielectric, elastic, and piezoelectric complex coefficients for each mode of resonance. In the radial mode of thin disks, the value of the first overtone, $f_{(2)s}$, is also required. In practice, an experimental data file of absolute values of admittance, $|Y|_i$, and its phase angle,

θ_i, at each frequency, f_i, is obtained in a frequency interval around the resonance. From these data, the corresponding values of conductance, $G_i = |Y|_i \cos\ \theta_i$, and resistance $R_i = \cos\ \theta_i |Y|_i^{-1}$ are obtained. Two of the four frequencies involved in the calculation, f_s and f_p, are determined by location of the maximum values of R_i and G_i in the measured interval, and the values of the complex impedance at these frequencies introduced into the system of nonlinear equations to be solved. The determination of the other two frequencies involved in the calculation of the central iteration, f_1 and f_2, constitutes a second iterative process, known as peripheral iteration, which is complete when the convergence of f_2 fulfills the criteria:/f_2(final) $-f_2$(initial)/ $<0.05\%$. Details concerning the two iterations of the Alemany et al. method are given in Alemany et al. (1994) and Alemany et al. (1995).

As a quality criteria of the results obtained by this method, both the G and the R profiles are reconstructed by insertion of the obtained complex coefficients in the analytical solution of the wave equation of the given resonance mode and by variation of the frequency (Figure 5.8). Typically, when the experimental results are free of spurious resonances, corresponding to a single resonator, the regression factor between the experimental and reconstructed values is higher than 0.99.

An analytical solution exists for all the four resonance modes (Table 5.1) needed for the determination of the complete set of parameters. The three resonators needed for full complex characterization of a poled piezoelectric ceramic are depicted in Figure 5.9, together with the relationships between dimensions discussed below.

5.4.1 Thin-disk resonator, thickness poled

Two resonances are considered for this resonator geometry. The impedance for the thickness resonance of a disk poled and excited along its thickness is given by the equation.

$$Z = R + \mathrm{i}X = -i\frac{t}{2\pi f S \varepsilon_{33}^{s}} + i\frac{h_{33}^2}{2\pi^2 S f^2 c_{33}^{D}\sqrt{\frac{\rho}{c_{33}^{D}}}}\tan\left(\pi f t\sqrt{\frac{\rho}{c_{33}^{D}}}\right), \quad (5.7)$$

where $S = \pi(D/2)^2$ (Figure 5.9a) is the electroded surface area and ρ is the ceramic density.

For the second resonance, the admittance is expressed by.

$$Y = G + \mathrm{i}B = i\frac{2\pi^2 f D^2}{4t}\left(\varepsilon_{33}^{T} + 2d_{31}^2\frac{c_{11}^{\mathrm{P}}}{\frac{1}{2-\Im\left[\pi f D\sqrt{\frac{\rho}{c_{11}^{\mathrm{P}}}}\right]} - \frac{1}{1+\sigma^{\mathrm{P}}}}\right) \quad (5.8)$$

where t is the thickness of the disk (Figure 5.9a), σ^{P} is the Poisson ratio, $\sigma^{\mathrm{P}} = -s_{12}^{E}/s_{11}^{E}$, c_{11}^{P} is a relationship among constants, $c_{11}^{\mathrm{P}} = s_{11}^{E}[(s_{11}^{E})^2, -, (s_{12}^{E})^2]^{-1}$, and $\Im$ is the one function defined as

$$\Im_1[z] = \frac{zJ_0(z)}{J_1(z)} \quad (5.9)$$

J_0 and J_1 are the Bessel functions of the first kind and of the zero and first orders, respectively.

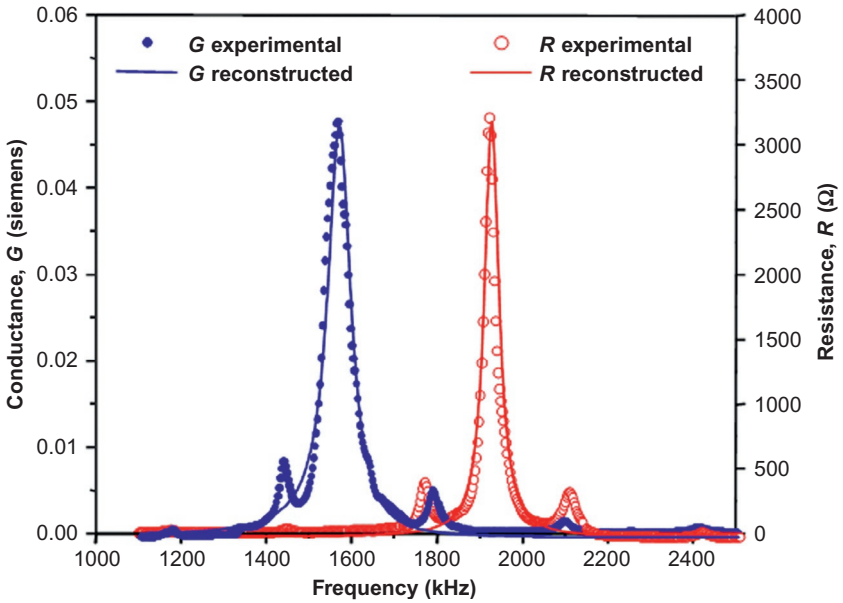


FIGURE 5.8 Plot of the resistance and conductance in the analysis of the complex impedance/admittance curve at resonance for the application of the automatic iterative method (shear mode of a commercial PZT plate). Experimental data and reconstructed curves after calculation of the coefficients are showed.

TABLE 5.1 Sample shapes which are needed for the determination of the full characteristic matrices of a poled ferroelectric ceramic according to the iterative automatic method described by Alemany et al. (Figure 5.9), required sample dimensional ratios, corresponding modes of resonance and directly obtained coefficients for each mode, and corresponding coupling coefficients (k_{ij}), are shown

Sample geometry	Resonance mode (standards)	Coefficients (standards)	Resonance mode (Alemany et al. method)	Directly obtained complex coefficients (Alemany et al. method)
Thin disks, thickness poled (diameter > 20 thickness)	Radial mode (RD)	d_{31}, ε_{33}^{T}, s_{11}^{E}, s_{12}^{E}, k_p	Radial mode	d_{31}, ε_{33}^{T}, s_{11}^{E}, s_{12}^{E}, k_p, k_{31}
	Thickness extensional mode (TE)	k_t, c_{33}^{D}	Thickness extensional mode of thin disks	h_{33}, ε_{33}^{S}, c_{33}^{D}, k_t
Long bars, length poled (length > 10 diameter)	Length extensional mode (LE)	d_{33}, ε_{33}^{T}, s_{33}^{E}, k_{33}	Length extensional mode	g_{33}, ε_{33}^{T}, s_{33}^{D}, k_{33}
Shear plates, thickness poled (length, width > 10 thickness)			Second thickness shear mode of thin plates	e_{15}, ε_{33}^{S}, s_{55}^{E}, k_{15}

The coefficients that are not displayed here are calculated using the relationships that exist among them and those here showed (Meeke, 1996; Pardo et al., 2007b, 2021).

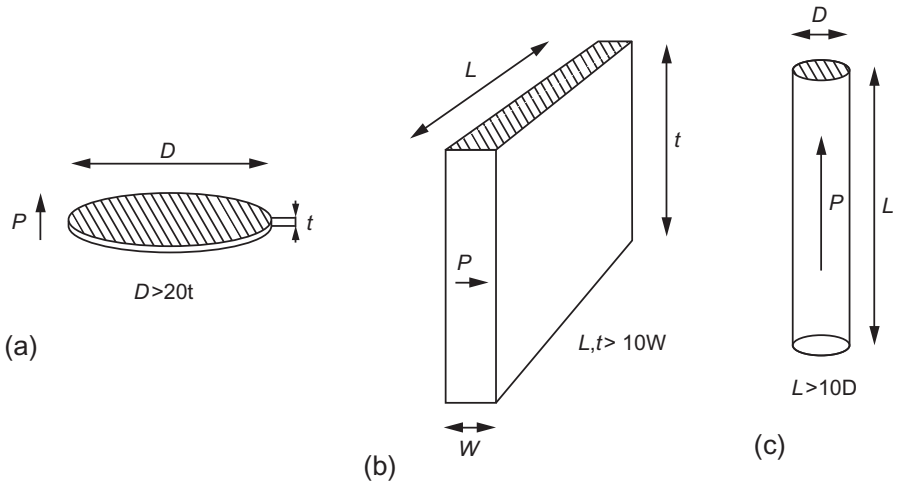


FIGURE 5.9 (a)–(c) Three resonator geometries needed to characterize a poled piezoelectric ceramic using the iterative automatic method.

5.4.2 Shear plate resonator, thickness poled

The impedance for the shear resonance of a plate poled across its thickness and excited along its length, for the condition of aspect ratio of the sample such as L, $t \gg w$, is.

$$Y = G + \mathrm{i}B = i\frac{2\pi f w L \varepsilon_{11}^{s}}{t} + i\frac{2we_{12}^{2}}{t}\sqrt{\frac{s_{55}^{E}}{\rho}}\tan\left(\pi f w\sqrt{\rho s_{55}^{E}}\right) \tag{5.10}$$

where $S = Lw$ (Figure 5.9d) is the electroded surface area. The resonator considered in the standards is the in-plane poled plate excited along its thickness, and the corresponding analytical expression and coefficients that can be obtained from it by the iterative method are h_{15}, ε_{11}^{S}, c_{55}^{D}, instead of e_{15}, ε_{11}^{S}, and s_{55}^{E}, which are directly obtained from the above. Analysis on how to get uncoupled resonances amenable for the proper use of the method for this specific resonance can be found in Pardo et al. (2007b, 2011a, 2020) and in Reyes-Montero et al. (2019).

5.4.3 Long bar resonator, length poled

The impedance for the length resonance of a bar poled and excited along its length is given by

$$Z = R + iX$$

$$= -i\frac{L}{2\pi fS}\left(\frac{1}{\varepsilon_{33}^{T}} + \frac{g_{33}^{2}}{s_{33}^{D}}\right)$$

$$+ i\frac{g_{33}^{2}}{2\pi Sf^{2}s_{33}^{D}\sqrt{\rho s_{33}^{D}}}\tan\left(\pi fL\sqrt{\rho s_{33}^{D}}\right) \qquad (5.11)$$

where $S = \pi(D/2)^2$ (Figure 5.9c) is the electroded surface area.

5.4.4 Using finite element analysis to check the validity of characterization

The above characterization of ceramics may also be modeled in 3D by finite element analysis (FEA). FEA modeling was performed using the ATILA software (ATILA, 1997). Originally developed for modeling sonar transducers, this program has the ability to model piezoelectric materials defined by a full data set of complex variables. The 3D harmonic analysis used yields the impedance values, modulus, and phase in a given interval of frequencies, which can be plotted as R and G peaks and compared with the experimental spectra (Figure 5.10).

It should be noted that this method is strictly valid only for uncoupled resonances. As the impedance spectra of the shear plates always show additional peaks, known as satellite resonances, around that of the main resonance (Figures 5.8 and 5.10), it is difficult to determine the characteristic frequencies of the resonance needed to determine the electromechanical coupling factor (k_{15}). These satellite resonances can also be found in the spectrum obtained by FEA modeling of the ideally homogeneous shear plate. This is observed for both the standard (Pardo et al., 2005, 2006) and the thickness-poled (Pardo et al., 2007a) shear resonators (Figure 5.10). This result indicates that the satellite resonances cannot be ascribed to material inhomogeneities but correspond to natural modes of vibration of plates, such as contour modes, associated with the shear geometry and aspect ratio being excited simultaneously to the shear mode.

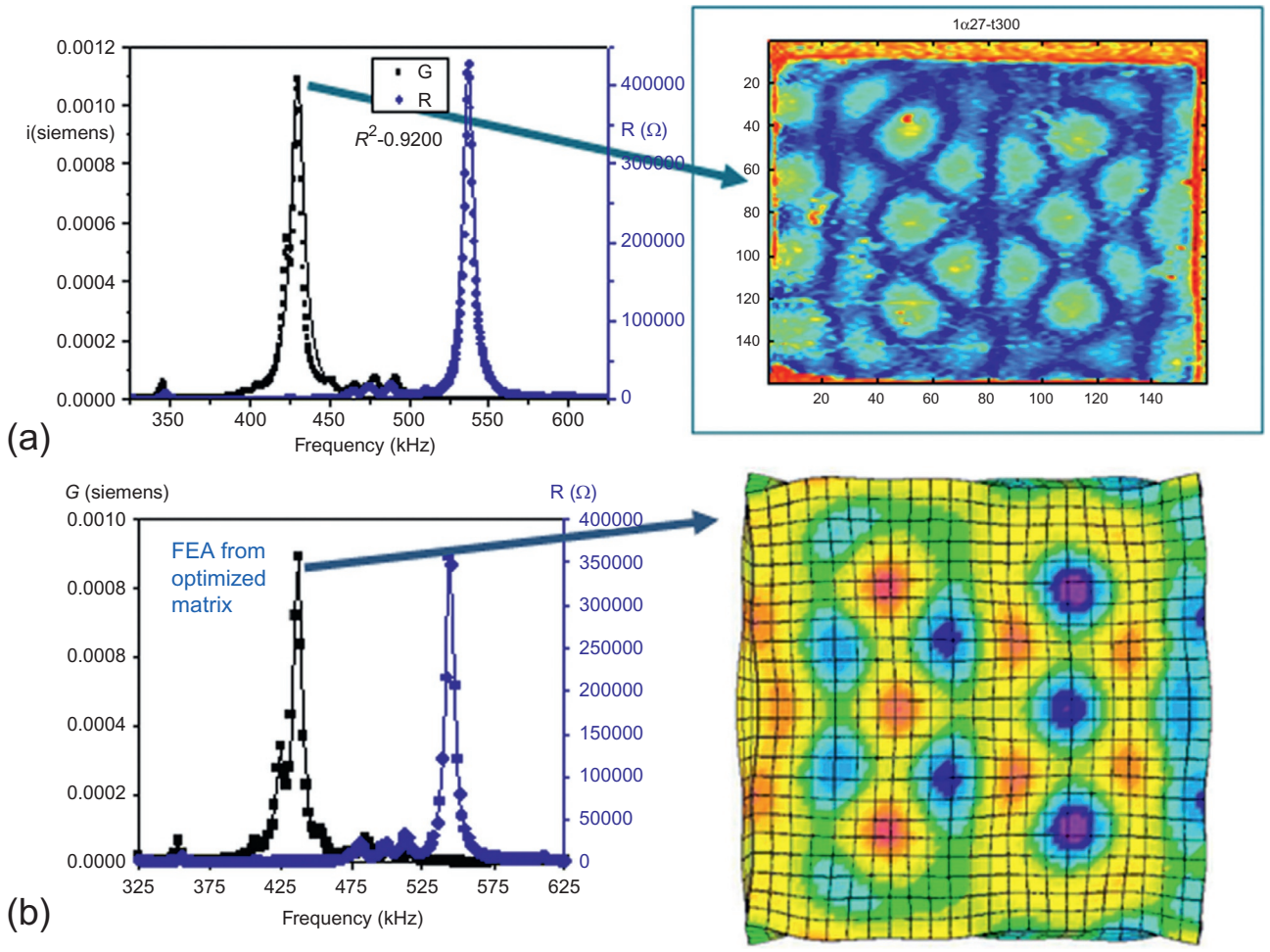


FIGURE 5.10 (a) Measured complex impedance (R and G plot) at the shear resonance, coupled with two standing plate wave, and pattern of vibration of this measured by laser interferometry of PZ27 ceramic plates of aspect ratio $L,t = 7.5$ w. (b) Results of the 3D computation by finite element analysis based on full PZ27 characterization by iterative automatic method and the use of the optimum thickness-poled shear plate.

Coupling of the shear resonance mode of piezoceramic plates is an unavoidable phenomenon (Pardo et al., 2011a) that can, however, be used to minimize the mode coupling in thickness-poled plates by fine-tuning of the aspect ratio L/w of the plate (Figure 5.9). This process leads to virtually uncoupled thickness-shear resonances for which the single resonator model used can be considered valid.

For the four periods studied as the aspect ratio, L/w, of a commercial PZT plate was varied via a change in L of 2.00–1.00 mm in steps of 0.02 mm, four optimum dimensional ratios were found for PZT shear plates in the study, all of which were below the value of $L/w = 20$ suggested in previous studies (Cao et al., 1998). Using the shear material parameters obtained from such optimum ratio resonators, 3D numerical computations were performed and successfully compared with the experimental measurements of impedance at resonance, and laser interferometric measurements (Pardo et al., 2011a) in a range between 325 kHz and 1.2 MHz. Figure 5.10 shows an example of such a comparison. Both the center frequencies and the magnitude of the R and G peaks, as well as those of the spurious resonances, can be accurately modeled. The close correspondence between experimental and theoretical results can be considered to be a validity criterion for the coefficients used.

5.5 Lead-free piezoceramics for environmental protection

European Union regulations arising in 2003 (EU-Directive 2002/95/EC, 2003; EU-Directive 2002/96/EC, 2003) on "Restriction of the Use of Certain Hazardous Substances in Electrical and Electronic Equipment (RoHS)" were among the first to require PZT piezoceramics to be substituted for more environmentally friendly alternatives. These regulations triggered the study of lead-free piezoelectric compositions (Ringgaard and Wurlitzer, 2005), a research field that from that time experienced a strong growth (Rödel et al., 2009; Takenaka, 2010). Exemption 7(c)-I, of this legislation concerns "lead in electronic ceramic parts (e.g., piezoelectronic devices)", has been recently reviewed and provides an exemption for lead in piezoelectronic devices until July 2021, with applications for further extension of this exemption due to the European commission by January 2020 (Rödel and Li, 2018). Whereas a direct lead-free alternative to PZT has not yet been developed, it is nowadays clear that the lead-free substitutes must also fulfill a number of required conditions, in addition to good piezoelectric performance (Koruza et al., 2018), among others, the low aging, the temperature endurance, and good mechanical properties.

There is a wide number of extensive works in the literature that analyze the optimal properties of commercial, lead-based, piezoelectric ceramics for use as high-power transducers (Uchino, 2010; Uchino et al., 2006). For that purpose, the so-called hard PZT doped compositions are used (Haertling, 1999). Materials to be used, for example, in ultrasonic motors, transformers, and high-intensity focused ultrasound requires, in addition to sufficiently high piezoelectric coefficients and low mechanical and dielectric losses, which prevents excessive heat generation at use. The "hardening" effect of PZT materials is obtained by modifying the composition using acceptor dopants such as Mn^{3+4+} and Fe^{3+}, due to the induced internal bias field, which pins the domain wall motion and stabilizes the domains, thus increasing the coercive field and decreasing the losses (Haertling, 1999).

Characterizations of the three most important families of lead-free ceramics for high-power applications are reviewed below.

5.5.1 Aurivillius-type structure ceramics

Development of bismuth-layered structure ferroelectrics (BLSF) or Aurivillius-type structure ceramics for piezoelectric use is a relatively recent development (Pardo et al., 2000). These types of ferroelectrics are characterized by the highest Curie temperatures of up to 1525°C (Yan et al., 2009). However, for applications requiring good sensitivity or high power, they cannot be used due to their very low sensitivity. For example, $d_{33} \sim 19$ pC/N is a typical value for a commercial composition for continuous use at 500°C (Pz46, Ferroperm™). Such a piezoelectric coefficient, although small, is stable until very high temperatures such as 800°C, when the Curie point is at 943°C (Yan et al., 2005). BLSF compositions with better piezoelectric properties are available; for example, with $K_t \sim 25\%$, which are stable up to 600°C (Gai et al., 2006). Some efforts were carried out over the last few years to obtain compositions with hard characteristics (Doshida et al., 2011; Noumura et al., 2011). In particular, it was found that with an increase in the vibration velocity, the rise in temperature for some ceramics was lower than that for PZT ceramics (Doshida et al., 2011).

5.5.2 Alkaline niobates

This is a promising and widely studied family of hard lead-free ceramics based on substitutions of the (K,Na) NbO_3 (KNN) solid solution system (Li et al., 2013; Shirane et al., 1954). Similar to PZT, the composition separates two polymorphs of the perovskite-type structure (polymorphic phase boundary, PPB), although this is temperature-dependent. Lithium and tantalum substituted KNN ceramics have been prepared by texturing ceramics (Saito et al., 2004) but also by simple pressureless solid-state sintering (Hollenstein et al., 2005) to reach high densities and improved piezoelectric properties. The piezoelectric properties are comparable to those in hard

PZT ceramics for the converse piezoelectric effect (strain-field) ($k_t = 52\%$ and d_{33}* over 300 pm/V).

One of the major drawbacks of this composition, however, is thermal stability relating to the onset of a phase transition (~200°C) between an orthorhombic and tetragonal polymorphs below its Curie temperature (~420°C), above which phase transition temperature, the piezoelectric properties deteriorate. Appropriated doping can, however, extend the thermal stability up to 250°C (Fu et al., 2009).

Research has also focused on the hardness characteristics of KNN-based materials, modified by $K_{5.4}Cu_{1.3}Ta_{10}O_{29}$, $K_4CuNb_8O_{23}$ (KCN), or CuO. These materials have piezoelectric coefficients of $d_{33} < 100$ pC/N but high mechanical quality factors. Compared with conventional hard PZT ceramics, these lead-free piezoceramics possess lower dielectric and piezoelectric properties but comparable values of mechanical Q (~1500), dielectric loss (0.6%), and coercive fields (~12 kV/cm) (Zhang et al., 2009). Many compositional modifications and fabrication procedures keep on being tested to gain high and ultrahigh piezoelectric d_{33} coefficients (≈700 pC/N) (Li et al., 2018) together with thermal stability. Simultaneous improvement of the mechanical Q has not been yet achieved, but the effect of humidity on Q was revealed (Zhen et al., 2017).

5.5.3 Bismuth-sodium titanates

The lead-free composition $Bi_{0.5}Na_{0.5}TiO_3$ (BNT) has been known to be ferroelectric since 1961 (Smolenskii et al., 1961). BNT presents a high conductivity associated with the loss of volatiles (Bi or ($Bi_{0.5}Na_{0.5}$)) at the sintering temperature (Hiruma et al., 2009) and a coercive field that causes incomplete poling, which prevents its use as piezoceramic. For these reasons, a large number of solid solution systems of increasing complexity have been tested and the improvement of their piezoelectric properties with respect to BNT demonstrated (Takenaka et al., 2009; Pardo et al., 2010b, 2011b).

In particular, the $(1-x)$ ($Bi_{0.5}Na_{0.5}$)TiO_3-$x$$BaTiO_3$ system of solid solutions has been studied and it was found that there is a MPB between the rhombohedral and tetragonal ferroelectric phases at room temperature (RT), for compositions close to $x = 0.06$ (BNBT6). BNBTs near the MPB are considered to be good candidates for lead-free piezoelectric ceramics due to the properties reported in the early 1990s (Takenaka et al., 1991), namely, an electromechanical coupling factor for thickness resonance of thin disks of $k_t = 52\%$ and a d_{33} piezoelectric coefficient of 125 pC/N for BNBT6 ceramics sintered at 1200°C for 2 h in air. BNBT ceramics also have been fully characterized (Lee et al., 2012), though not including all losses, and their possibilities as high-power ceramic analyzed (Doshida et al., 2011). To date, the main limitation of the use of these ceramics for high-power applications is the low depolarization temperature linked to a phase transition to a weakly polar phase at ~100°C (Pardo et al., 2012) and above which piezoelectricity vanishes.

5.5.4 Barium-calcium zirconate-titanates

Quite recently, a new family of high-performance lead-free ceramics ($d_{33} \sim 620$ pC/N) arising from the pseudobinary solid solution system $(1-x)Ba(Zr_yTi_{1-y})O_3$–$x(Ba_{1-z}Ca_z)TiO_3$ (BCZT) were reported (Liu and Ren, 2009). Further studies have shown that similar high piezoelectricity is also present in a generic class of BT-based materials, including Ba(*Sn*,*Ti*)O_3-(Ba,Ca)TiO_3 (BTS-BCT) and Ba(*Hf*,*Ti*)O_3-(Ba,Ca)TiO_3 (BHT-BCT) characterized by a multiphase coexisting point (MCP) instead of MPB (Gao et al., 2018). Their matrix characterization, not taking into account all losses, was carried out for a representative composition (Xue et al., 2011), although drawbacks of these materials are the low Curie temperature $T_C \sim 93$°C and the high synthesis (1300°C for 2 h) and ceramic sintering (1450°C for 3 h) temperatures. An increase in T_C (up to 114°C) has been demonstrated by changing the composition, but at the expenses of piezoelectric performance (down to 450 pC/N) and a high sintering temperature is still required (1450°C for 3 h) (Bao et al., 2010; Jiang et al., 2013). A recent approach for the reduction of the sintering temperature and simultaneous increase of the electromechanical strain response of BCZT piezoceramics is the aliovalent doping with Ce. The highest d_{33}* value of 1189 pm/V was reported for the sample with 0.05 mol% Ce, substituted on the A-site of the perovskite lattice (Hayati et al., 2019). Alternative processing methodologies by using reactive precursors are shown to be promising and high-sensitivity, dense, fine-grained materials can be obtained by sintering below 1300°C (Reyes et al., 2014). The results indicate a large potential of these materials for low temperature off-resonance piezoelectric applications.

5.6 Future trends

New processing techniques, as an alternative to the expensive crystal growth techniques, generate oriented growth of the ceramic grains (crystallites) that do not, however, eliminate the poling step in the fabrication of the piezoelectric ceramic. One of the most effective techniques is the reactive templated grain growth (RTGG) approach (Yilmaz et al., 2003), which makes use of crystallites with a plate-like growth habit and compatible composition with the one of the materials to be obtained (Figure 5.11). These are mixed with the ceramic powder to be molded and sintered to obtain a ceramic promoting an oriented crystal growth during the formation of the ceramic grains.

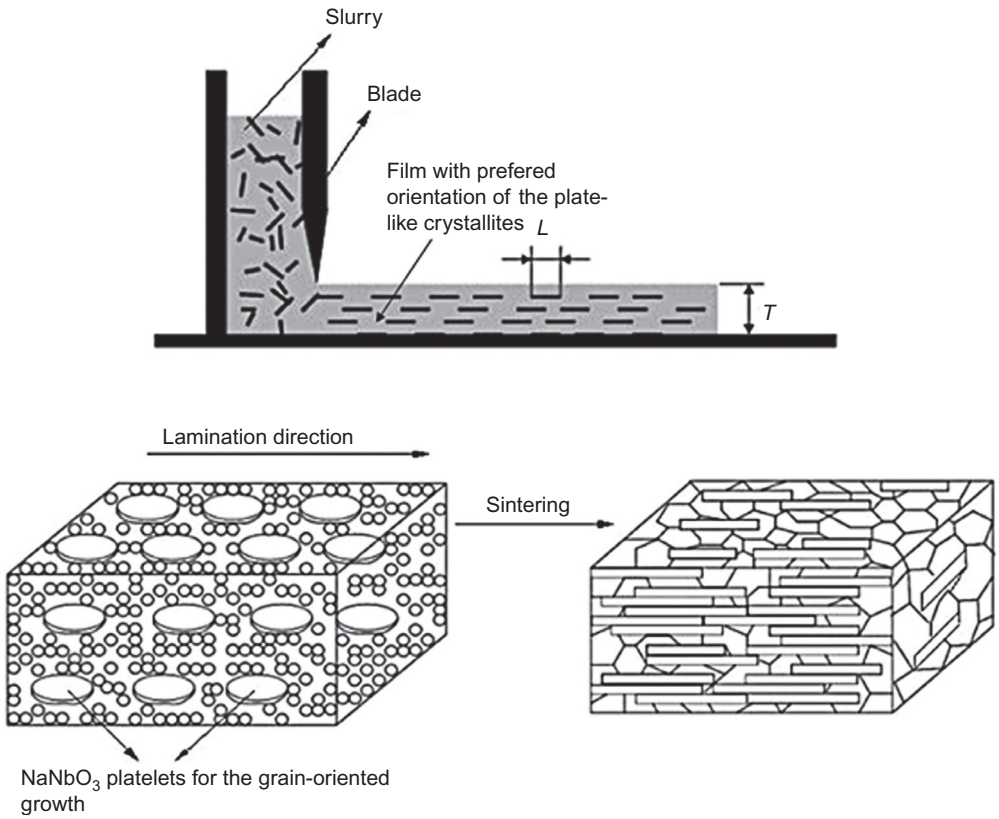


FIGURE 5.11 Upper row: Schematic of the process to obtain textured (K,Na)NbO_3-$LiTaO_3$-$LiSbO_3$ (LF) ceramics by reactive templated grain growth (RTGG). Lower row: Schematic of the microstructure of the laminated films before (left) and after (right) the thermal treatment of sintering.

Another technique to obtain textured ceramics is the growth of a seed crystal inside a ceramic precursor, the so-called solid-state single-crystal growth (SSSC) method, exploiting abnormal grain growth behavior of ceramic grains (Fisher et al., 2008).

As for new lead-free compositions explored nowadays, there is a great effort, on the one hand, in reduction of the drawbacks, including high leakage current, low resistivity, and the formation of impure phases, of $BiFeO_3$ (Rojac et al., 2014) by rare-earth doping (Tao et al., 2017), as this is a promising piezoelectric material for use at elevated temperatures due to the high Curie temperature (≈830°C). On the other hand, there is a strong trend to develop solid solution systems with MPB using $BiFeO_3$ and all other lead-free compositions mentioned here, aiming to increase the temperature of use of these.

There is not yet a lead-free system that can directly replace commercial PZT, which can be properly doped for enhancement of the properties required in each application. Instead, the current approach in the industry is the development of the most appropriate lead-free composition for each application. After more than two decades of research, and with much to be done still for the complete understanding of lead-free materials, the generalized commercial use of these novel eco-friendly piezoelectrics seems to be a reality in a close future.

References

Alemany, C., González, A.M., Pardo, L., Jiménez, B., Carmona, F., Mendiola, J., 1995. Automatic determination of complex constants of piezoelectric lossy materials in the radial mode. J. Phys. D Appl. Phys. 28 (5), 945.

Alemany, C., Pardo, L., Jiménez, B., Carmona, F., Mendiola, J., González, A.M., 1994. Automatic iterative evaluation of complex material constants in piezoelectric ceramics. J. Phys. D Appl. Phys. 27, 148.

Algueró, M., Alemany, C., Pardo, L., Gonzalez, A.M., 2004. Method for obtaining the full set of linear electric, mechanical and electromechanical coefficients and all related losses of a piezoelectric ceramic. J. Am. Ceram. Soc. 87 (2), 209.

ATILA User's Manual, 1997. Institut Superieur d'Electronique du Nord. Acoustics Laboratory.

Baerwald, H.G., 1957. Thermodynamic theory of ferroelectric ceramics. Phys. Rev. 105 (2), 480.

Bao, H., Zhou, C., Xue, D., Gao, J., Ren, X., 2010. A modified lead-free piezoelectric BZT-xBCT system with higher T_C. J. Phys. D Appl. Phys. 43, 465401.

Cain, M.G., Stewart, M., 2014. Standards for piezoelectric and ferroelectric ceramics. Chapter 12 in characterisation of ferroelectric bulk materials and thin films. In: Cain, M.G. (Ed.), Springer Series in Measurement Science and Technology. vol. 2. Springer, Dordrecht, Netherlands, https://doi.org/10.1007/978-1-4020-9311-1_12.

Cao, W., Zhu, S., Jiang, B., 1998. Analysis of the shear modes in a piezoelectric vibrator. J. Appl. Phys. 83, 4415.

Catalan, G., Scott, J.F., 2009. Physics and applications of bismuth ferrite. Adv. Mater. 21, 2463–2485.

Chauhan, A., Patel, S., Vaish, R., Bowen, C.R., 2015. Anti-ferroelectric ceramics for high energy density capacitors. Materials 8, 8009–8031. https://doi.org/10.3390/ma8125439.

Cheong, S.W., Mostovoy, M., 2007. Multiferroics: a magnetic twist for ferroelectricity. Nat. Mater. 6, 13.

Doshida, Y., Shimizu, H., Mizuno, Y., Itoh, K., Hirose, S., Tamura, H., 2011. Non-linear behavior and high-power properties of (Bi,Na,Ba)TiO_3 and $(Sr,Ca)_2NaNb_5O_{15}$ piezoelectric ceramics. Jpn. J. Appl. Phys. 50, 09ND06.

Ebenezer, D.D., 2004. Determination of complex coefficients of radially polarized piezoelectric ceramic cylindrical shells using thin shell theory. IEEE Trans. Ultrason. Ferroelectr. Freq. Control 51 (10), 1209.

Erturk, A., Inman, D.J., 2011. Piezoelectric Energy Harvesting. Jonh Wiley and Sons Ed, UK, Chichester.

EU-Directive 2002/95/EC, 2003. Restriction of the use of certain hazardous substances in electrical and electronic equipment (RoHS). Off. J. Eur. Union 46 (L37), 19–23.

EU-Directive 2002/96/EC, 2003. Waste electrical and electronic equipment (WEEE). Off. J. Eur. Union 46 (L37), 24–38. https://www.meggittferroperm.com/.

Fisher, J.G., BencĬan, A., Kosec, M., Vernay, S., Rytz, D., 2008. Growth of dense single crystals of potassium sodium niobate by a combination of solid-state crystal growth and hot pressing. J. Am. Ceram. Soc. 91 (5), 1503.

Fu, J., Zuo, R., Wang, X., Li, L., 2009. Polymorphic phase transition and enhanced piezoelectric properties of $LiTaO_3$-modified $(Na_{0.52}\ K_{0.48})(Nb_{0.93}\ Sb_{0.07})O_3$ lead-free ceramics. J. Phys. D Appl. Phys. 42, 012006.

Fuentes-Cobas, L.E., Matutes-Aquino, J.A., Fuentes-Montero, M.E., 2011. Magnetoelectricity. In: Buschow, K.H.J. (Ed.), Handbook of Magnetic Materials. vol. 19. Elsevier, Amsterdam (Chapter 3).

Gai, Z.G., Wang, J.F., Zhao, M.L., Wang, C.M., Zang, G.Z., Ming, B.Q., Qi, P., Zhang, S., Shrout, T.R., 2006. High temperature $(NaBi)_{0.48\text{-}0.04}Bi_2Nb_2O_9$-based piezoelectric ceramics. Appl. Phys. Lett. 89, 012907.

Gao, J., Ke, X., Acosta, M., Glaum, J., Ren, X., 2018. High piezoelectricity by multiphase coexisting point: barium titanate derivatives. MRS Bull. 43, 595. https://doi.org/10.1557/mrs.2018.155.

IRE, 1961. IRE standard on piezoelectric crystals: measurements of piezoelectric ceramics. Proc. IRE 49 (7), 1161–1169.

Gonzalez, A.M., Alemany, C., 1995. Estudio de los sobretonos del modo de vibración en espesor de resonadores piezoeléctricos con pérdidas. Bol. Soc. Esp. Ceram. Vidrio 34 (5,6), 368–371.

Gonzalez, A.M., Alemany, C., 1996. Determination of the frequency dependence of characteristic constants in lossy piezoelectric materials. J. Phys. D Appl. Phys. 29, 2476.

Gray, R.B., 1949. United States Patent Office No. 2,486,560 Transducer and Method of Making the Same. Application September 20, 1946, Serial No. 698,34.

Haerdtl, K.H., 1982. Electrical and mechanical losses in ferroelectric ceramics. Ceram. Int. 8, 121.

Haertling, G.H., 1999. Ferroelectric ceramics: history and technology. J. Am. Ceram. Soc. 82 (4), 797–818.

Hayati, R., Bahrevar, M.A., Ganjkhanlou, Y., Rojas, V., Koruza, J., 2019. Electromechanical properties of Ce-doped $(Ba_{0.85}Ca_{0.15})(Zr_{0.1}Ti_{0.9})O_3$ lead-free piezoceramics. J. Adv. Ceram. 8, 186. https://doi.org/10.1007/s40145-018-0304-2.

von Hippel, A., 1950. Ferroelectricity, domain structure, and phase transitions of barium titanate. Rev. Mod. Phys. 22 (3), 221.

Hiruma, Y., Nagata, H., Takenaka, T., 2009. Thermal depoling process and piezoelectric properties of bismuth sodium titanate ceramics. J. Appl. Phys. 105. 084112–084112.8.

Holland, R., 1967. Representation of dielectric, elastic and piezoelectric losses by complex coefficients. IEEE Trans. Son. Ultrason. SU-14 (1), 18.

Holland, R., EerNisse, E., 1969. Accurate measurement of coefficients in a ferroelectric ceramic. IEEE Trans. Son. Ultrason. SU-16 (4), 173.

Hollenstein, E., Davis, M., Damjanovic, D., Setter, N., 2005. Piezoelectric properties of Li- and Ta-modified $K_{0.5}Na_{0.5}NbO_3$ ceramics. Appl. Phys. Lett. 87, 182905.

Hong Du, X., Wang, Q.M., Uchino, K., 2003. Accurate determination of complex materials coefficients of piezoelectric resonators. IEEE Trans. Ultrason. Ferroelectr. Freq. Control 50 (3), 312.

Jaffe, B., Cook, W.R., Jaffe, H., 1971. Piezoelectric Ceramics. Academic Press, London.

Jiang, M., Lin, Q., Lin, D.M., Zheng, Q.J., Fan, X.M., Wu, X.C., Sun, H.L., Wan, Y., Wu, L., 2013. Effects of MnO_2 and sintering temperature on microstructure, ferroelectric, and piezoelectric properties of $Ba_{0.85}Ca_{0.15}Ti_{0.90}Zr_{0.10}O_3$ lead-free ceramics. J. Mater. Sci. 48, 1035–1041.

Jo, W., Granzow, T., Aulbach, E., Rodel, J., Damjanovic, D., 2009. Origin of the large strain response in $K_{0.5}Na_{0.5}NbO_3$ modified $Bi_{0.5}Na_{0.5}TiO_3$-$BaTiO_3$ lead-free piezoceramics. J. Appl. Phys. 105, 094102.

Koruza, J., Bell, A.J., Frömling, T., Webber, K.G., Wang, K., Rödel, J., 2018. Requirements for the transfer of lead-free piezoceramics into application. J. Mater. 4 (1), 13–26. https://doi.org/10.1016/j.jmat.2018.02.001.

Kwok, K.W., Chan, H.L.W., Choy, C.L., 1997. Evaluation of the material parameters of piezoelectric materials by various methods. IEEE Trans. Ultrason. Ferroelectr. Freq. Control 44 (4), 733.

Landolt-Börstein, R., 1981. New Series. Vol. III/16a.b Springer-Verlag, Berlin.

Lee, H.J., Ural, S.O., Chen, L., Uchino, K., Zhang, S., 2012. High power characteristics of lead-free piezoelectric ceramics. J. Am. Ceram. Soc. 95 (11), 3383–3386.

Li, J.F., Wang, K., Zhu, F.Y., Cheng, L.Q., Yao, F.Z., 2013. (K, Na)NbO_3-based lead-free piezoceramics: fundamental aspects, proc technologies, and remaining challenges. J. Am. Ceram. Soc. 96 (12), 3677–3696.

Li, P., Zhai, J., Shen, B., Zhang, S., Li, X., Zhu, F., Zhang, X., 2018. Ultrahigh piezoelectric properties in textured (K,Na)NbO_3-based lead-free ceramics. Adv. Mater. 1705171. https://doi.org/10.1002/adma.201705171.

Liu, W., Ren, X., 2009. Large piezoelectric effect in Pb-free ceramics. Phys. Rev. Lett. 103, 257602.

Meeke, T.R., 1996. Publication and proposed revision of ANSI/IEEE standard 176-1987. IEEE Trans. Ultrason. Ferroelectr. Freq. Control 43, 717–772. https://doi.org/10.1109/TUFFC.1996.535477.

Meitzler, A.H., ÓBryan Jr., H.M., Tiersten, H.F., 1973. Definitions and measurements of radial mode coupling factors in piezoelectric ceramic materials with large variations in Poisson's ratio. IEEE Trans. Son. Ultrason. SU-20 (3), 233.

Mikhaleva, E.A., Flerov, I.N., Gorev, M.V., Bondarev, V.S., Bogdanov, E. V., 2020. Features of the behavior of the Barocaloric effect near ferroelectric phase transition close to the tricritical point. Crystals 10, 51. https://doi.org/10.3390/cryst10010051.

Mischenko, A.S., Zhang, Q., Scott, J.F., Whatmore, R.W., Mathur, N.D., 2006. Giant electro-caloric effect in thin-film $PbZr_{0.95}Ti_{0.05}O_3$. Science 311 (5765), 1270–1271. https://doi.org/10.1126/science.1123811.

Newnham, R.E., 1975. Ferroelectrics and other ferroic materials. In: Structure-Property Relations. Springer-Verlag, Berlin, Heidelberg.

Noumura, Y., Hiruma, Y., Nagata, H., Takenaka, T., 2011. High-power piezoelectric characteristics at continuous driving of $Bi_4Ti_3O_{12}$-$SrBi_4Ti_4O_{15}$-based ferroelectric ceramics. Jpn. J. Appl. Phys. 50, 07HB06.

Nye, J.F., 1957. Physical Properties of Crystals. Oxford University Press, London.

Pardo, L., Aragó, C., 2010. Materiales ferroeléctricos: fundamentos, estado actual y tendencias. Rev. Esp. Fisiol. 24 (1), 57–62.

Pardo, L., Ricote, J., Algueró, M., Calzada, M.L., 1999. Ferroelectric materials based on lead titanate. In: Nalwa, H.S. (Ed.), Handbook of Low and High Dielectric Constant Materials and their Applications. Materials and Processing, vol. 1. Academic Press, San Diego, USA, pp. 457–499 (Chapter 10).

Pardo, L., Castro, A., Millán, P., Alemany, C., Jiménez, R., Jiménez, B., 2000. $(Bi_3TiNbO_9)_x$-$(SrBi_2Nb_2O_9)_{1-x}$ Aurivillius type structure piezoelectric ceramics obtained from mechano-chemically activated oxides. Acta Mater. 48 (9), 2421–2428.

Pardo, L., Algueró, M., Brebøl, K., 2005. Resonance modes in standard piezoceramic shear geometry: a discussion based on finite element analysis. J. Phys. IV France 128, 207–211.

Pardo, L., Algueró, M., Brebøl, K., 2006. Resonance modes in standard characterization of piezoceramics: a discussion based on finite element analysis. Ferroelectrics 336, 181–190.

Pardo, L., Montero de Espinosa, F., Brebøl, K., 2007a. Study by laser interferometry of the resonance modes of the shear plate used in the standards characterization of piezoceramics. J. Electroceram. 19, 437–442.

Pardo, L., Algueró, M., Brebøl, K., 2007b. A non-standard shear sample for the matrix characterization of piezoceramics and its validation study by finite element analysis. J. Phys. D Appl. Phys. 40, 2162–2169.

Pardo, L., García, A., Brebøl, K., 2007c. Finite element analysis study and automatic iterative method application to the non-standard, thickness poled, lossy piezoceramic ring (O1). In: Electrocerámica 2007 Aveiro, Portugal, June 24–26.

Pardo, L., Garcia, A., Montero De Espinosa, F., Brebøl, K., 2008. Choosing the best geometries for the linear characterization of lossy piezoceramics: study of the thickness poled shear plate. Appl. Phys. Lett. 92, 172907.

Pardo, L., Jiménez, R., García, A., Brebøl, K., Leighton, G., Huang, Z., 2010a. Impedance measurements for determination of the elastic and piezoelectric coefficients of films. Adv. Appl. Ceram. Struct. Funct. Bioceram. 109 (3), 156–161.

Pardo, L., Mercadelli, E., Brebøl, K., García, A., Galassi, C., 2010b. Piezoelectric properties of lead-free submicron structured $(Bi_{0.5}Na_{0.5})_{0.94}Ba_{0.06}TiO_3$ ceramics. Smart Mater. Struct. 19 (11), 11507.

Pardo, L., Garcia, A., Montero De Espinosa, F., Brebøl, K., 2011a. Shear resonance mode decoupling to determine the characteristic matrix of piezoceramics for 3-D modeling. IEEE Trans. Ultrason. Ferroelectr. Freq. Control 58 (3), 646–657.

Pardo, L., Mercadelli, E., García, A., Brebøl, K., Galassi, C., 2011b. Field-induced phase transition and relaxor character in submicron structured lead-free $(Bi_{0.5}Na_{0.5})_{0.94}Ba_{0.06}TiO_3$ piezoceramics at the morphotropic phase boundary. IEEE Trans. Ultrason. Ferroelectr. Freq. Control 58 (9), 1893–1904.

Pardo, L., García, Á., Brebøl, K., Mercadelli, E., Galassi, C., 2012. Anisotropy and dynamic thermal depolarization of $0.96(Bi_{0.5}Na_{0.5})TiO_3$-$0.04\ BaTiO_3$ lead-free piezoceramics. In: Proceedings of ISAF-ECAPD-PFM 2012, Aveiro. 2012, pp. 1–4, https://doi.org/10.1109/ISAF.2012.6297762.

Pardo, L., Reyes-Montero, A., García, A., Jacas-Rodríguez, A., Ochoa, P., González, A.M., Jiménez, F.J., Vázquez-Rodríguez, M., Villafuerte-Castrejón, M.E., 2020. A modified iterative automatic method for characterization at shear resonance: case study of $Ba_{0.85}Ca_{0.15}Ti_{0.90}Zr_{0.10}O_3$ - eco-piezoceramics. Materials 13 (7), 1666. https://doi.org/10.3390/ma13071666.

Pardo, L., García, A., Schubert, F., Kynast, A., Scholehwar, T., Jacas, A., Bartolomé, J.F., 2021. Determination of the PIC700 ceramic's complex piezo-dielectric and elastic matrices from manageable aspect ratio resonators. Materials 14 (15), 4076. https://doi.org/10.3390/ma14154076.

Patel, S., Chauhan, A., Vaish, R., 2014. A technique for giant mechanical energy harvesting using ferroelectric/antiferroelectric materials. J. Appl. Phys. 115, 084908. https://doi.org/10.1063/1.4866877.

Pérez, N., Andrade, M.A.B., Buiochi, F., Adamowski, J.C., 2010. Identification of elastic, dielectric, and piezoelectric constants in piezoceramic disks. Ultrason. Ferroelectr. Freq. Control IEEE Trans. 57 (12), 2772–2783.

Pérez, N., Carbonari, R.C., Andrade, M.A.B., Buiochi, F., Adamowski, J.C., 2014. A FEM- based method to determine the complex material properties of piezoelectric disks. Ultrasonics 54 (6), 1631–1641. https://doi.org/10.1016/j.ultras.2014.03.006.

Pérez, N., García, A., Riera, E., Pardo, L., 2018. Electromechanical anisotropy at the ferroelectric to Relaxor transition of $(Bi_{0.5}Na_{0.5})_{0.94}Ba_{0.06}TiO_3$ ceramics from the thermal evolution of resonance curves. Appl. Sci. 8 (1), 121. https://doi.org/10.3390/app8010121.

Prah, U., Rojac, T., Wencka, M., Dragomir, M., Bradesko, A., Bencan, A., Sherbondy, R., Brennecka, G., Kutnjak, Z., Malic, B., Ursic, H., 2019. Improving the multicaloric properties of $Pb(Fe_{0.5}Nb_{0.5})O_3$ by controlling the sintering conditions and doping with manganese. J. Eur. Ceram. Soc. 39 (14). https://doi.org/10.1016/j.jeurceramsoc.2019.05.062.

Ramesh, R., 2013. Complex functional oxide heterostructures. Curr. Sci. 105 (8), 1107–1114.

Reyes, A., Pardo, L., López, R., Gonzalez, A.M., Cruz, M.P., Villafuerte-Castrejón, M.E., 2014. Lead-free $Ba_{0.9}Ca_{0.1}Ti_{0.9}Zr_{0.1}O_3$ piezoelectric ceramics processed below 1300°C. J. Alloys Compd. 584, 28–33.

Reyes-Montero, A., Pardo, L., García, A., González, A.M., Villafuerte-Castrejón, M.E., 2019. $Ba_{1-x}Ca_xTi_{0.90}Zr_{0.10}O_3$ shear properties and their frequency dependence determined from ceramic plates by an effective method for resonance decoupling. J. Alloy Compd. 806, 428–438. https://doi.org/10.1016/j.jallcom.2019.07.210.

Ringgaard, E., Wurlitzer, T., 2005. Lead-free piezoceramics based on alkali niobates. J. Eur. Ceram. Soc. 25 (12), 2701–2706.

Robert, G., Damjanovic, D., Setter, N., 2001. Piezoelectric hysteresis analysis and loss separation. J. Appl. Phys. 90 (9), 4668.

Rödel, J., Li, J.F., 2018. Lead-free piezoceramics: Status and perspectives. MRS Bull. 43, 576. https://doi.org/10.1557/mrs.2018.181.

Rödel, J., Jo, W., Seifert, K.T.P., Anton, E.M., Granzow, T., Damjanovic, D., 2009. Perspective on the development of lead-free piezoceramics. J. Am. Ceram. Soc. 92, 1153.

Rojac, T., Bencan, A., Malic, B., Tutuncu, G., Jones, J.L., Daniels, J.E., Damjanovic, D., 2014. $BiFeO_3$ ceramics: processing, electrical, and

electromechanical properties. J. Am. Ceram. Soc. 97 (7), 1993–2011. https://doi.org/10.1111/jace.12982.

Rubio-Marcos, F., Romero, J.J., Ochoa, D.A., García, J.E., Perez, R., Fernandez, J.F., 2010. Effects of poling process on KNN-modified piezoceramic properties. J. Am. Ceram. Soc. 93 (2), 318.

Saito, Y., Takao, H., Tani, T., Nonoyama, T., Takatori, K., Homma, T., Nagaya, T., Nakamura, M., 2004. Lead-free piezoceramics. Nature 432, 84.

Sherrit, S., Wiederick, H.D., Mukherjee, B.K., 1997a. A complete characterization of the piezoelectric, dielectric and elastic properties of Motorola PZT3203HD including losses and dispersion. In: Medical Imaging 1997: Ultrasonic Transducer Engineering. SPIE Proceedings, vol. 3037, p. 158.

Sherrit, S., Gauthier, N., Wiederick, H.D., Mukherjee, B.K., 1991. Accurate evaluation of the real and imaginary material constants for a piezoelectric resonator in the radial mode. Ferroelectrics 119, 17.

Sherrit, S., Wiederick, H.D., Mukherjee, B.K., 1992. Non-iterative evaluation of the real and imaginary material constants of piezoelectric resonators. Ferroelectrics 134, 111.

Sherrit, S., Wiederick, H.D., Mukherjee, B.K., 1997b. The complete matrix of the piezoelectric, dielectric and elastic materials constants of 1–3 piezoelectric ceramic/polymer composites. In: Hariz, A., Varadan, V.K., Reinhold, O. (Eds.), Smart Materials, Structures, and Integrated Systems. SPIE Proceedings, vol. 3241, pp. 327–333.

Shirane, G., Newnham, R.E., Pepinsky, R., 1954. Dielectric properties and phase transitions of $NaNbO_3$ and (Na, K)NbO_3. Phys. Rev. 96 (1), 581.

Smits, J.G., 1976. Iterative method for accurate determination of the real and imaginary parts of the materials coefficients of piezoelectric ceramics. IEEE Trans. Son. Ultrason. SU-23 (6), 393–402.

Smolenskii, G.A., Isupov, V.A., Agranovskaya, A.I., Krainik, N.N., 1961. New ferroelectrics of complex composition IV. Sov. Phys. Solid State 2 (11), 2651–2654.

Stern-Taulats, E., Lloveras, P., Barrio, M., Defay, E., Egilmez, M., Planes, A., Tamarit, J.L., Manosa, L., Mathur, N.D., Moya, X., 2016. Inverse barocaloric effects in ferroelectric $BaTiO_3$ ceramics APL. Materials 4 (9), 091102. https://doi.org/10.1063/1.4961598.

Subbarao, E.C., McQuarrie, M.C., Buessem, W.R., 1957. Domain effects in polycrystalline barium titanate. J. Appl. Phys. 28 (10), 1194.

Takenaka, T., 2010. Lead-free piezo-ceramics. In: Uchino, K. (Ed.), Advanced Piezoelectric Materials. Science and Technology, Woodhead Publishing Ltd, Cambridge, UK (Chapter 4).

Takenaka, T., Maruyama, K., Sakata, K., 1991. (Bi1/2, Na1/2)TiO_3-$BaTiO_3$ system for lead-free piezoelectric ceramics. Jpn. J. Appl. Phys. 30 (9B), 2236–2239.

Takenaka, T., Nagata, H., Hiruma, Y., 2009. Phase transition temperatures and piezoelectric properties of (Bi1/2Na1/2)TiO_3- and (Bi1/2K1/2)TiO_3-based bismuth perovskite lead-free ferroelectric ceramics. IEEE Trans. Ultrason. Ferroelectr. Freq. Control 56 (8), 1595–1612.

Tao, H., Lv, J., Zhang, R., Xiang, R., Wu, J., 2017. Lead-free rare earth-modified $BiFeO_3$ ceramics: phase structure and electrical properties. Mater. Des. 120, 83. https://doi.org/10.1016/j.matdes.2017.01.083.

Tsurumi, T., Kil, Y.B., Nagatoh, K., Kakemoto, H., Wada, S., 2002. Intrinsic elastic, dielectric, and piezoelectric losses in lead zirconate titanate ceramics determined by an immittance-fitting method. J. Am. Ceram. Soc. 85 (8), 1993.

Uchino, K., 2010. High power piezoelectric materials. In: Uchino, K. (Ed.), Advanced Piezoelectric Materials. Science and Technology, Woodhead Publishing Ltd, Cambridge, UK (Chapter 16).

Uchino, K., Hirose, S., 2001. Loss mechanisms in piezoelectrics: how to measure different losses separately. IEEE Trans. Ultrason. Ferroelectr. Freq. Control 48, 307.

Uchino, K., Zheng, J.H., Chen, Y.H., Du, X.H., Ryu, J., Gao, Y., Ural, S., Priya, S., Hirose, S., 2006. Loss mechanisms and high power piezoelectrics. J. Mater. Sci. 41, 217–228. Frontier of ferroelectricity Special Issue.

Valasek, J., 1921. Piezo-electric and allied phenomena in Rochelle salt. Phys. Rev. 17, 475. https://doi.org/10.1103/PhysRev.17.475.

Vázquez-Rodríguez, M., Jiménez, F.J., Pardo, L., Ochoa, P., González, A. M., de Frutos, J., 2019. A new prospect in road traffic energy harvesting using lead-free piezoceramics. Materials 12 (22), 3725. https://doi.org/10.3390/ma12223725.

Wang, J., Neaton, J.B., Zheng, H., Nagarajan, V., Ogale, S.B., Liu, B., Viehland, D., Vaithyanathan, V., Schlom, D.G., Waghmare, U.V., Spaldin, N.A., Rabe, K.M., Wuttig, M., Ramesh, R., 2003. Epitaxial $BiFeO_3$ multiferroic thin film heterostructures. Science 299 (5613), 1719.

Xue, D., Zhou, Y., Bao, H., Zhou, C., Gao, J., Ren, X., 2011. Elastic, piezoelectric, and dielectric properties of $Ba(Zr0.2Ti0.8)O_3$-50 $(Ba0.7Ca0.3)TiO_3$ Pb-free ceramic at the morphotropic phase boundary. J. Appl. Phys. 109, 054110.

Yan, H., Zhang, H., Ubic, R., Reece, M.J., Liu, J., Shen, Z., Zhang, Z., 2005. A lead-free high-curie-point ferroelectric ceramic, CaBi2Nb 2O9. Adv. Mater. 17 (10), 1261–1265.

Yan, H., Ning, H., Kan, Y., Wang, P., Reece, M.J., 2009. Piezoelectric strontium niobate and calcium niobate ceramics with super-high curie points. J. Am. Ceram. Soc. 93 (5), 1409–1413. https://doi.org/10.1111/j.1551-2916.2009.03587.x.

Yilmaz, H., Trolier-Mckinstry, S., Messing, G.L., 2003. (Reactive) templated grain growth of textured sodium bismuth titanate (Na1/2 Bi1/2 TiO_3-$BaTiO_3$) ceramics—II dielectric and piezoelectric properties. J. Electroceram. 11, 217–226.

Yin, W.J., Weng, B.C., Ge, J., Sun, Q.D., Li, Z.Z., Yan, Y.F., 2019. Oxide perovskites, double perovskites and derivatives for electrocatalysis, photocatalysis, and photovoltaics. Energy Environ. Sci. 12, 442. https://doi.org/10.1039/c8ee01574k.

Zhang, S., Lim, J.B., Lee, H.J., Shrout, T.R., 2009. Characterization of hard piezoelectric lead-free ceramics. IEEE Trans. Ultrason. Ferroelectr. Freq. Control 56 (8), 1523.

Zhen, Y., Li, L., Lin, Y., Wang, K., Zhu, F., Jia, K., 2017. High Qm values and humidity effect on the electrical properties of (K, Na)NbO_3 lead-free piezoceramics doped with B_2O_3-CuO mixed oxides. J. Am. Ceram. Soc. 100 (4), 1561. https://doi.org/10.1111/jace.14586.

Chapter 6

Power ultrasonic transducers: Principles and design

K.F. Graff[a] and J.F. Sheehan[b]
[a]EWI, Columbus, OH, United States, [b]JFS Engineering, Ipswich, MA, United States

6.1 Introduction

As described in Chapter 1, a basic power ultrasonic process consists of an ultrasonic transducer, driven by an electronic power supply, with the transducer vibration output transmitted—by a gaseous, liquid, or solid coupling means—into a material or process (also known as the *load*) that is then changed by the ultrasonic energy. In this chain of components and media, the ultrasonic transducer is the essential starting point and will be the starting point of the many fascinating power ultrasonic applications described in this book. It is the purpose of this chapter to provide an introduction to the key features of this device that, while not the end, is always the means to the end of a given power ultrasonic application.

Any review of the field of power ultrasonics will show there are many different means for generating ultrasonic waves, such as whistles, sirens, and electrodynamic generators, most of which have receded into history. However, the magnetostrictive-based transducer has long played an important role in ultrasonic processes, especially before the advent of piezoelectric ceramics, and is still used in the field of cleaning and other selected areas. Nevertheless, with the introduction of barium titanate ceramics in the late 1940s, followed by the lead zirconate titanates, including their wide use in sonar systems, the field of power ultrasonic applications has been, and currently is, largely dominated by piezoelectric ceramics-based transducers. It is for this reason that coverage of this chapter is restricted to such devices.

The story of the discovery of the piezoelectric effect in quartz (and other materials) by the Curie brothers (1880) and the adaptation of this effect by Langevin/Chilowsky in 1918 to create powerful ultrasonic transducers of *sandwich construction* (a term in use to this day) to project underwater beams of sound is well known. The use of quartz generators by Wood and Loomis (1927) to create their spectacular range of breakthrough observations on the effects of "supersonic waves" is also well known, with these landmark tests followed by numerous extensions to other fields, all using, in those early years, crude, quartz-based systems that were limited by both the fragility and the size of available quartz (Graff 1981).

Following the first publications in 1947 on poled barium titanate ceramics, piezoelectric ceramics gained wide use in all areas of ultrasonics, enhanced by the introduction of lead zirconate titanates in the mid-1950s. Nearly all power ultrasonic transducers currently use formulations of lead zirconate titanate piezoceramics, although new formulations of piezo-active ceramics are under development, including some using lead-free materials (see Chapter 5 of this book for detailed coverage of piezoelectric ceramics).

This chapter will provide an introduction to the piezoelectric ceramic-based power ultrasonic transducer, and will cover the following:

- Ultrasonic vibrations of solids as they relate to power transducers.
- Basics of piezoelectric materials as immediately needed for an understanding of the power transducer (as noted, detailed coverage of piezoelectric materials is in Chapter 5).
- The ultrasonic power transducer—design, fabrication, and elements of modeling.
- Transducer characterization and control.
- Future trends in power transducers.

The general power ultrasonic system illustrated in Chapter 1 shows the generation of ultrasonic vibrations, transmission of ultrasonic vibrations, and interaction of ultrasonic vibrations with the "acoustic load." The obvious common theme in this process is "ultrasonic vibrations." Thus, in learning about power ultrasonics in general, and the power ultrasonic transducer in particular, an understanding of basic ultrasonic vibrations is a critical first step.

Power Ultrasonics. https://doi.org/10.1016/B978-0-12-820254-8.00018-X
Copyright © 2023 Elsevier Ltd. All rights reserved.

6.2 Ultrasonic vibrations: Mechanical oscillator

The simple, damped mechanical oscillator (i.e., a spring-mass-dashpot system) under forced vibration, shown in Figure 6.1, provides a general case for many of the important concepts of ultrasonic vibrations. Thus, the oscillator consists of the mass m, a spring of stiffness k, and a dashpot of resistance c, with the forcing function being given by $F_0 e^{i\omega t}$. By taking special cases of this general case, it is possible to illustrate many aspects of power ultrasonic vibrations.

6.2.1 Summary of vibration results

The key features describing the vibrations of a damped oscillator, which may be found in any introductory book on mechanical vibrations, are easily summarized. Thus, one starts with the equation of motion for the mass.

$$m\frac{d^2x}{dt^2} = -c\frac{dx}{dt} - kx + F_0 e^{i\omega t} \tag{6.1}$$

This may be expressed as.

$$\frac{d^2x}{dt^2} + 2\zeta\frac{dx}{dt} + \omega_n^2 x = \frac{F_0}{m} e^{i\omega t} \tag{6.2}$$

where

$$2\zeta = c/m, \quad \omega_n^2 = k/m \tag{6.3}$$

Several special cases follow from this.

6.2.1.1 *Free vibration of an undamped oscillator*

Let $F_0 = 0$, $c = 0$ in Eq. (6.1), which leads to the solution that may be expressed in the forms,

$$x = B\ \cos\omega_n t + C\ \sin\omega_n t = D\ \sin(\omega_n t + \varphi) \tag{6.4}$$

where

$$D = \left(B^2 + C^2\right)^{1/2},\ \tan\varphi = B/C \tag{6.5}$$

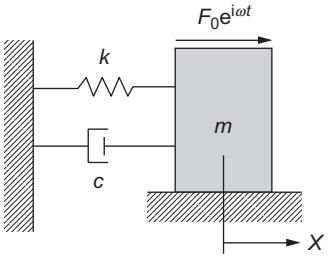


FIGURE 6.1 Damped mechanical oscillator under forced vibration. *(Source: EWI.)*

The latter form of the solution (6.4) brings out two foundation concepts of ultrasonic vibrations, namely that of a natural frequency of vibration, ω_n whose value is given by (6.3), with a period T, and a vibration amplitude D, both illustrated in Figure 6.2a; thus, we have:

- Natural frequency $\omega_n = (k/m)^{1/2} \sim$ (radians/unit time)
- Cyclic natural frequency $f_n = \omega_n/2\pi$
- Period of vibration at the natural frequency $T = 1/f_n$
- Amplitude of vibration D (from 0 to peak, 0–P)

It is worth emphasizing the 0–P measure of the vibration amplitude D. Most vibration instrumentation, such as a laser vibrometer, provides amplitude data in peak-to-peak (P-P). It is thus important to specify which amplitude is being reported in order to make meaningful comparisons between analytical and experimental results.

6.2.1.2 *Free vibration of a damped oscillator*

Let $F_0 = 0$ in Eq. (6.1), which leads to the solution that may be expressed in several forms, typically called the underdamped, critically damped, or overdamped cases, depending on the level of damping c. The underdamped case, which is most applicable to power ultrasonics and has the form shown in Figure 6.2b, can be expressed as

$$x = De^{-\zeta t}\sin(\Omega t + \varphi),\ \Omega = \left(\omega_n^2 - \zeta^2\right)^{1/2} \tag{6.6}$$

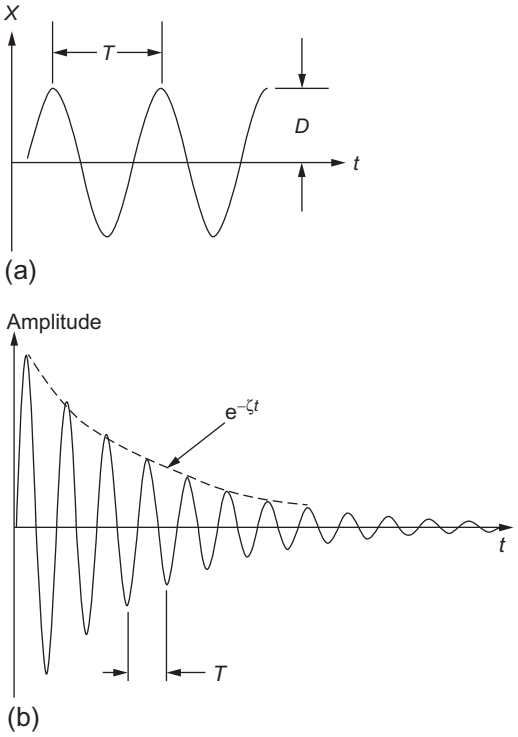


FIGURE 6.2 Free vibration of an oscillator: (a) undamped vibration; (b) damped vibration. *(Source: EWI.)*

This result brings out the expected decaying nature of the oscillation, governed by ζ (hence, c via the definition (6.3)), and the fact that damped natural frequency Ω differs from ω_n due to the damping effect. The period of oscillation, T, being given by $1/\Omega$, will also be affected by damping.

It is noted that a method of measuring system damping is contained within the solution (6.6). It may be shown that ratio between amplitudes one period, T apart is.

$$\frac{x(t)}{x(t+T)} = e^{\zeta T} \tag{6.7}$$

This leads to the logarithmic decrement Δ, given by

$$\Delta = \ln \frac{x(t)}{x(t+T)} = \zeta T \tag{6.8}$$

as a measure of damping. The fact that most ultrasonic oscillations are lightly damped, with successive vibration amplitude changes being small, makes practical use of this method difficult in ultrasonics.

6.2.1.3 Forced vibration of an undamped oscillator

Let $c = 0$ in Eq. (6.1). The transient part of the response will be ignored, with only a steady-state solution of the form.

$$x(t) = Ce^{i\omega t} \tag{6.9}$$

being considered. This leads to the steady-state vibration response.

$$x(t) = \frac{F_0}{k} \frac{e^{i\omega t}}{\left(1 - \frac{\omega^2}{\omega_n^2}\right)} \tag{6.10}$$

or, taking the real part $x_R(t)$,

$$x_R(t) = \frac{F_0}{k} \frac{\cos \omega t}{\left(1 - \frac{\omega^2}{\omega_n^2}\right)} \tag{6.11}$$

where it is seen from the basic spring equation, $F = k\Delta$, that F_0/k is simply the displacement of the spring–mass system under a static force F_0. The most noteworthy point in this solution is the response as $\omega \to \omega_n$, which is seen to become increasingly large; that is, $x \to \infty$. The absolute value of the amplitude response may be written as

$$\left|\frac{x}{\delta_{st}}\right| = \left|\frac{1}{1 - \omega^2/\omega_n}\right| \tag{6.12}$$

and is plotted in Figure 6.3a. This mathematically unbounded (i.e., infinite) response brings out the critical phenomenon of "resonance" as the driving frequency approaches the oscillator natural frequency ω_n. The concept of resonance, introduced with this simple example, will play a central role in all areas of power ultrasonic systems, however, complex they may be

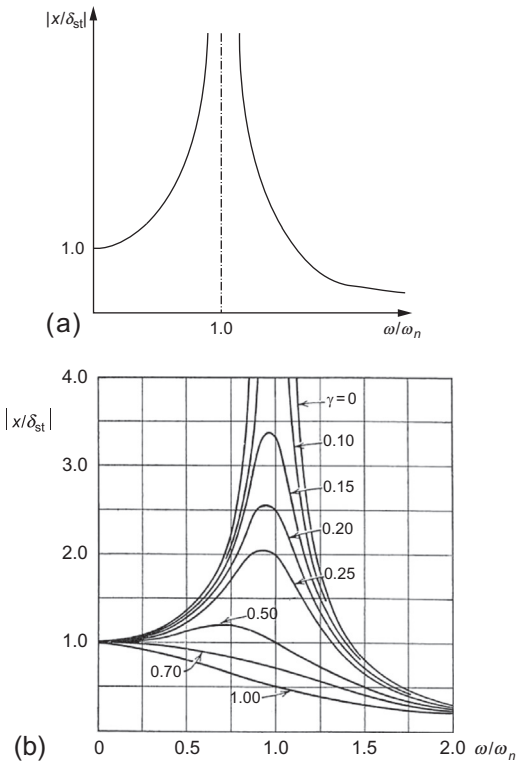


FIGURE 6.3 Forced vibration response of an oscillator: (a) undamped amplitude response; (b) damped amplitude response. *(Source: (a) EMI; (b) Timoshenko et al. (1974, Fig. 1.33). This material is reproduced with permission of John Wiley & Sons, Inc.)*

6.2.1.4 Forced vibration of a damped oscillator

This is the general case given by Eq. (6.1). As with the previous case, consider only the steady-state response, which is given by

$$x(t) = \frac{F_0}{k} \frac{e^{i\omega t}}{(\omega_n^2 - \omega^2) + 2i\zeta\omega} \tag{6.13}$$

The real part of the solution may be expressed as

$$x(t) = \frac{F_0}{kM^{1/2}} \sin(\omega t + \Phi),\ \Phi = \tan^{-1}\left[\frac{2\zeta\omega/\omega_n^2}{1 - (\omega^2/\omega_n)}\right] \tag{6.14}$$

where

$$M = \left(1 - \frac{\omega^2}{\omega_n^2}\right)^2 + 4\zeta^2 \frac{\omega^2}{\omega_n^2} \tag{6.15}$$

The behavior of the amplitude, expressed in terms of absolute value, is

$$|\text{Amp } x(t)| = \left|\frac{F_0}{k}\left[\left(1 - \frac{\omega^2}{\omega_n^2}\right)^2 + 4\zeta^2 \frac{\omega^2}{\omega_n^2}\right]^{1/2}\right| \tag{6.16}$$

and is plotted in Figure 6.3b for various values of the damping factor $\gamma = c/2m\omega_n$. This well-known result shows

that the amplitude response is strongly dependent on the amount of damping, so that for moderate levels of damping, for example, $\gamma = 0.25$–0.15, the amplitude response is broad in shape with an increasing sharp peak as damping becomes smaller (e.g., $\gamma = 0.15$). Further, the peaks of the damped response curves are close to, but not coincident with, the undamped natural frequency ω_n.

For smaller damping, for example, $\gamma = 0.10$, the curve becomes yet sharper in form, with a peak that is only slightly different than ω_n. The importance of this point, is that the behavior of most practical power ultrasonic systems exhibit the characteristics of light damping and are thus considered as "sharply tuned," exhibiting a narrow performance "bandwidth."

6.2.1.5 *A note on transient response*

In considering the forced vibration of the undamped and damped oscillator, only the steady-state solution has been considered, meaning that any system transients are assumed to have decayed away. However, to complete the vibration picture, the full solution to the forced vibration problem given by Eq. (6.1) will be presented in order to show the basis for such transient decay. From the theory of ordinary differential equations, it is known that the complete solution of Eq. (6.1) is given by.

$$x(t) = x_c(t) + x_p(t) \tag{6.17}$$

where $x_c(t)$ and $x_p(t)$ are the complementary and particular solutions, with a particular solution having already been obtained by the steady-state analysis result. Likewise, in solving the damped, free-vibration case, the complementary solution $x_c(t)$ has been found, given by Eq. (6.6). Thus, the complete solution (6.17) is given by

$$x(t) = e^{-\zeta t}\left(A_1 e^{i\cap t} + A_2 e^{-i\cap t}\right) + \frac{\frac{F_0}{k}}{\left(1 - \frac{\omega^2}{\omega_n^2}\right) + 2i\zeta\,\frac{\omega^2}{\omega_n^2}} e^{i\omega t} \tag{6.18}$$

where $x_c(t)$ comprises the transient part vibrating at the damped frequency Ω and that, due to the presence of the damping term $e^{-\zeta t}$, will decay with time, leaving the steady-state vibration at the driving frequency. This result provides the justification for considering the steady-state response for most power ultrasonic vibration analyses.

In most ultrasonic processes, which may last seconds, minutes, or hours, this transient period is of no consequence. Even for short-time cycle processes, such as ultrasonic plastic and metal welding, where the total cycle time may be 0.3–0.5 s, the transient portion may be neglected. However, as a result of increased sophistication of modern process controls, such as servo-controlled welders, efforts are being made to subdivide an already short-time cycle into several intervals for which the system transient response can approach the control intervals. Under such conditions, the transient response may be important and, if neglected, could affect the quality of system control.

6.2.2 Equivalent circuit, impedance

The equivalence between mechanical parameters and electrical parameters and, by extension, between mechanical systems and electrical circuits, is well known. In ordinary mechanical analysis, this equivalence might be of little more than academic interest; however, in ultrasonics, transducers are true electromechanical devices, because coupling exits between the electrical and mechanical parameters. Thus, an electrical representation of at least part of the system is necessary, with it being convenient to use electromechanical equivalences to then carry out a complete electrical representation of the system. While the more complicated aspects of this arise with respect to distributed mechanical systems, it is useful to first review the basic concepts for simple, lumped element systems.

Consider the damped mechanical oscillator and the simple series LRC circuit of Figure 6.4. The voltage drop equation for the circuit is

$$L\frac{dI}{dt} + RI + \frac{i}{C}\int Idt = V_0 e^{i\omega t} \tag{6.19}$$

The equation of motion for the mechanical system has been given by Eq. (6.1), which may be expressed in terms of the velocity, $v = dx/dt$ as

$$m\frac{dv}{dt} + cv + \int vdt = F_0 e^{i\omega t} \tag{6.20}$$

Comparing Eqs. (6.19), (6.20) leads to the following equivalences, and the concept of the series LRC circuit being equivalent to the force driven damped mechanical oscillator:

$$\begin{aligned} V &\sim F \\ I &\sim v \\ L &\sim m \\ R &\sim c \\ 1/C &\sim k \end{aligned} \tag{6.21}$$

The concept of impedance is widely used, both in electrical engineering and in mechanical vibrations and acoustics. The

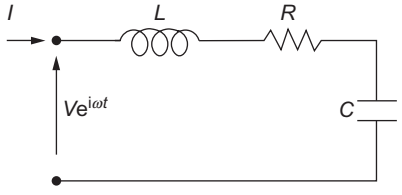


FIGURE 6.4 Simple series LRC circuit. *(Source: EWI.)*

definitions of the electrical impedance Z_e and mechanical impedance Z_m are

$$Z_e = V/I, \quad Z_m = F/v \tag{6.22}$$

The electrical impedances of the LRC elements are known to be

$$Z_L = i\omega L,\ Z_R = R,\ Z_C = \frac{1}{i\omega C} \tag{6.23}$$

Because series impedances are additive, this permits the impedance of the LRC circuit to be written by inspection as

$$Z_e = R + i\omega L + 1/i\omega c \tag{6.24}$$

Using the equivalences of Eq. (6.21), the mechanical impedance of the oscillator can be directly written as

$$Z_m = c + i\omega m + k/i\omega \tag{6.25}$$

(For those wishing to confirm this result by derivation, assume the steady-state solution $x(t) = Xe^{i\omega t}$ in Eq. (6.1) to obtain F_0/X, and then convert the result to velocity using the fact that $v = i\omega X$, which leads to Eq. (6.25).)

6.2.3 Displacement/velocity forcing, parallel equivalent circuit

There is an alternate way of applying a forcing function to the mass in the form of a prescribed displacement or velocity (vs. a prescribed force), as shown in Figure 6.5. The motivation for presenting this alternate approach, including its parallel circuit representation, lies in the later presentation of equivalent circuit models of the complete transducer, where both series and parallel circuit models will find application.

The equation of motion for this case is given by

$$m\frac{d^2x}{dt^2} = -c\left(\frac{dx}{dt} - \frac{du}{dt}\right) - k(x-u) \tag{6.26}$$

where $u(t) = u_0e^{i\omega t}$, and for a steady-state response, $u(t) = Xe^{i\omega t}$. This has the solution for X of

$$X = -\frac{(k + i\omega c)u_0}{m\left[\left(\omega^2 - \frac{k}{m}\right) + \frac{i\omega c}{m}\right]} \tag{6.27}$$

For simplicity in making a circuit comparison, neglect the damping so that $c = 0$ in the above, giving

$$X = \frac{u_0\omega_n^2}{\left(\omega^2 - \omega_n^2\right)} \tag{6.28}$$

where $\omega_n = (k/m)^{1/2}$ is the undamped frequency that arises for the forced vibration case, but now with a different behavior. Thus, the mechanical impedance of the system is given by $Z_m = F/v$, where F is the force on the mass, v is the velocity of the mass. For the simplified case at hand, this is found to be

$$Z_m = -\frac{i\omega k}{\left(\omega^2 - \omega_n^2\right)} \tag{6.29}$$

It is seen as $\omega \to \omega_n$, that $Z_m \to \infty$ (whereas, $Z_m \to 0$ for the forced vibration case).

For the parallel circuit of Figure 6.5b, the electrical impedance Z_e is found as

$$Z_e = \frac{1}{\frac{1}{R} - \frac{C\left(\omega^2 - \frac{1}{LC}\right)}{i\omega}} \tag{6.30}$$

As noted, for simplicity of comparison, consider the case without the resistance R, which corresponds to letting $R \to \infty$, that is, an open circuit in Eq. (6.30), thus reducing Z_e to

$$Z_e = \frac{i\omega}{C\left(\omega^2 - \frac{1}{LC}\right)} \tag{6.31}$$

where 1/LC is the frequency at which the parallel circuit impedance $Z_e \to \infty$. Comparing Eqs. (6.29)–(6.31) shows the equivalencies of $m = L$ and $k = 1/C$. It will be found this displacement/velocity forcing equivalency to the parallel circuit will find use in transducer circuit representations.

6.3 Ultrasonic vibrations: Longitudinal vibrations

The simple mechanical oscillator of Section 6.2.1 has permitted introduction of many of the concepts necessary to understand ultrasonic vibrations and transducers. However, the distributed nature of mass and shape must be accounted for in a more accurate representation of power transducers and will be covered in this section (for an expanded coverage of this subject, see Graff 1975).

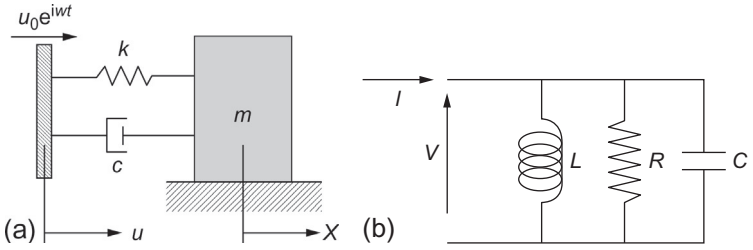


FIGURE 6.5 Displacement forcing of an oscillator with equivalent circuit: (a) displacement forcing function; (b) equivalent parallel LRC circuit. *(Source: EWI.)*

6.3.1 Governing theory, natural frequencies

The basic case for longitudinal vibrations of a rod is shown in Figure 6.6. The rod alternately expands and contracts about the central point of no vibration (i.e., the node). The opposite ends of the bar (the antinodes) go through cycles of maximum outward and inward displacement. The variation in amplitude along the bar is one-half of the total vibration wavelength, so that the length l is a half-wave, or $\lambda/2$. The key feature of this vibration is the longitudinal nature of the motion. This simply means that the particles of the bar move in the direction parallel to the axis of the bar, as shown by the small arrows in the figure. The expansions and contractions of the bar cause stress to be generated, with the distribution of stress along the bar also shown in Figure 6.6a.

While the analysis of ultrasonic vibrations of transducers and tooling is now routinely done by computer-based methods—as seen by examples later in this chapter and throughout this book—a fundamental understanding must still be based on the underlying solid mechanics governing theory. For the case of the longitudinal vibrations of a rod, this is given by considering a differential mass element, shown by the shaded segment of Figure 6.6a, and in detail in Figure 6.6b. The equation of motion of the element is given by

$$\rho A \mathrm{d}x \frac{\partial^2 u}{\partial t^2} = -\sigma A + \left(\sigma + \frac{\partial \sigma}{\partial x}\mathrm{d}x\right)A \tag{6.32}$$

where ρ is the mass density, A is the cross section area of the rod element, and σ and u being the stress and displacement at a location x along the rod. This reduces Eq. (6.32) to

$$\rho \frac{\partial^2 u}{\partial t^2} = \frac{\partial \sigma}{\partial x} \tag{6.33}$$

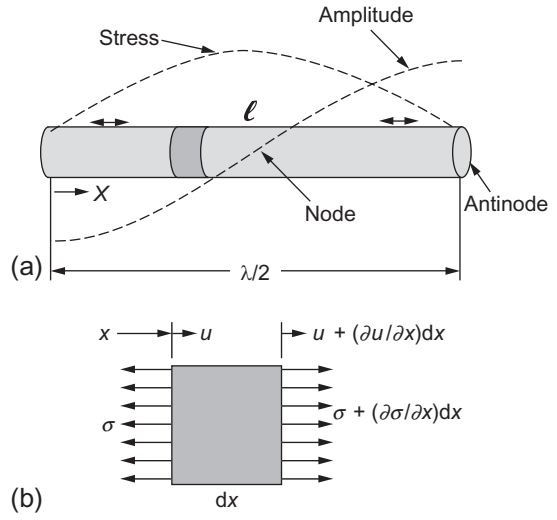


FIGURE 6.6 Longitudinal vibrations of a rod: (a) displacement, stress in a rod; (b) differential rod element. *(Source: EWI.)*

From the basic definition of strain, $\varepsilon = \Delta/L$, the strain in the element is given by

$$\varepsilon = \frac{\Delta u}{\Delta x} = \frac{du}{dx} = \frac{\partial u}{\partial x} \tag{6.34}$$

Then from Hooke's law $\sigma = E\varepsilon$, it follows that $\sigma = E(\partial u/\partial x)$, which when substituted in (6.33) gives

$$E\frac{\partial^2 u}{\partial t^2} = \rho \frac{\partial^2 u}{\partial t^2} \tag{6.35}$$

A final combination of terms yields the classical formula governing the thin rod, known as the *wave equation*; given that name for its basic governance for wave motion in the rod, and in many other physical systems, as

$$\frac{\partial^2 u}{\partial t^2} = \frac{1}{c_0^2}\frac{\partial^2 u}{\partial x^2} \tag{6.36}$$

where $c_0 = (E/\rho)^{1/2}$ is the wave velocity in a thin rod.

The solution for the case of steady-state vibrations is straightforward, where one lets $u(x, t)$ be expressed as

$$u(x, t) = U(x)\mathrm{e}^{\mathrm{i}\omega t} \tag{6.37}$$

which leads to the ordinary differential equation, identical in form to that seen for the oscillator,

$$\frac{\partial^2 U}{\partial x^2} + \beta^2 U = 0, \beta = \frac{\omega}{c_0} \tag{6.38}$$

which has the solution

$$U(x) = C\ \sin \beta x + D\ \cos \beta x \tag{6.39}$$

When the boundary conditions for the rod, which is considered free (i.e., stress-free) at each end, and

$$x = 0, l, \sigma = EA\frac{dU}{dx} = 0 \tag{6.40}$$

are applied, it results that $C = 0$, and the equation governing the natural frequencies of the rod emerges, namely.

$$\sin \beta l = 0, \quad \beta l = n\pi \rightarrow f_n = nc_0/2l, \quad n = 1,2,3,\ldots \tag{6.41}$$

For the first mode, that is, $n = 1$, one has the mode shape given by

$$U(x) = D\ \cos(\pi x/l) \tag{6.42}$$

which corresponds to the half-wave (i.e., $\lambda/2$) amplitude shape shown in Figure 6.6a. The stress is given from $\sigma = E(\partial u/\partial x)$ and is

$$\sigma(x) = -EA\beta D\ \sin \beta x \tag{6.43}$$

which corresponds to the stress distribution shown in Figure 6.6a. Of course, in these results, the amplitude D is indeterminate and needs to be specified or obtained from measurements.

This simple, but fundamental, solution to a fundamental equation has far-ranging application to ultrasonic vibrations, including power transducers. Thus, among the interpretive results, one has the following:

- Relation of frequency f, dimension l, and material c_0 is seen in the result (6.41).
- Relation of stress σ to the amplitude u, including how a measure of vibration amplitude permits a prediction of stress.
- Half-wave form of the rod vibration, with this being typically used as the basis for constructing ultrasonic transducers (as seen in Section 6.4) and for much of the tooling used in ultrasonic processes (e.g., for transmission lines, boosters, and welding tools).

6.3.2 Forced vibrations of a rod

Similar to the approach for the oscillator, the forced vibrations of a rod will be considered, looking at the two cases, the first being that of a prescribed force, $F_0 e^{i\omega t}$, shown in Figure 6.7.

Using the approach of the free vibrations case, one has

$$u(xt) = U(x)e^{i\omega t} \tag{6.44}$$

which leads to the previously shown solution (6.39). The boundary conditions for this problem are

$$\begin{aligned} &x = 0, A\sigma = EA\frac{\partial u}{\partial x} = EA\frac{dU}{dx}e^{i\omega t} = F_0 e^{i\omega t} \\ &x = l, A\sigma = EA\frac{dU}{dx}e^{i\omega t} = 0 \text{ (no stress on free end)} \end{aligned} \tag{6.45}$$

These two equations give

$$\begin{aligned} &EA\beta C\cos\beta x - D\sin\beta x_{x=0} = EA\beta C = F_0 \rightarrow C = F_0/EA\beta \\ &EA\beta C\cos\beta x - D\sin\beta x_{x=l} \\ &\quad = 0 \rightarrow D \\ &\quad = C\cos\beta l/\sin\beta l \\ &\quad = F_0/EA\beta\cos\beta l/\sin\beta l \end{aligned} \tag{6.46}$$

The solution for u is then

$$u(t) = \frac{F_0}{EA\beta}(\sin\beta x + \cot\beta l\ \cos\beta x)e^{i\omega t} \tag{6.47}$$

The key feature of the response is that when $\sin\beta l = 0$, at $\beta l = \pi, 2\pi, \ldots, n\pi$, then $u \rightarrow \infty$. In other words, using $\beta = \omega/c_0$ and the fact that $\omega = 2\pi f$, one has that at the frequencies.

$$f_n = nc_0/2l, \quad n = 1,2,3,\ldots \tag{6.48}$$

the amplitude grows to infinity, such as found for the case of a spring-mass system. These are the natural frequencies of a free-free rod, previously given by Eq. (6.41). The first mode has the appearance shown in Figure 6.7.

Now consider the second case, that of a prescribed displacement $u_0 e^{i\omega t}$, Figure 6.8 (left), this being the analog to the prescribed motion of a mass, Figure 6.5a. The solution (6.39) still holds, but the boundary condition on the left end is changed, the conditions now being

$$\begin{aligned} &x = 0,\ Ue^{i\omega t} = u_0 e^{i\omega t} \\ &x = 0, A\sigma = EA(dU/dx)e^{i\omega t} = 0 \text{ (no stress on free end)} \end{aligned} \tag{6.49}$$

These two equations give

$$\begin{aligned} &(C\sin\beta x + D\cos\beta x)|_{x=0} = D = u_0 \\ &EA\beta(C\cos\beta x - D\sin\beta x)|_{x=l} = 0 \rightarrow C = D \\ &\sin\beta l/\cos\beta l = u_0\sin\beta l/\cos\beta l \end{aligned} \tag{6.50}$$

The solution for u is then

$$u(x,t) = u_0(\tan\beta l\ \sin\beta x + \cos\beta x)e^{i\omega t} \tag{6.51}$$

The key feature of this response is that when $\cos\beta l = 0$, at $\beta l = \pi/2, 3\pi/2, \ldots, (2n-1)\pi/2$, then $u \rightarrow \infty$. In other words, using $\beta = \omega/c_0$ and the fact that $\omega = 2\pi f$, one has that at the frequencies.

$$f_n = (2n-1)c_0/4l, \quad n = 1,2,3,\ldots \tag{6.52}$$

the amplitude grows to infinity, such as found for the case of a displacement-driven oscillator. These are the natural frequencies of a rod fixed at the left end, free on the right end (fixed-free). The first mode has the appearance shown in Figure 6.8.

The basis for including these two approaches to forced motion of a rod is that they ultimately play a role in modeling transducer behavior, and in concepts relating to vibration control of transducers.

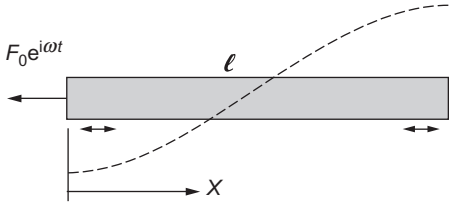


FIGURE 6.7 Prescribed force acting on a rod and first mode resonance. *(Source: EWI.)*

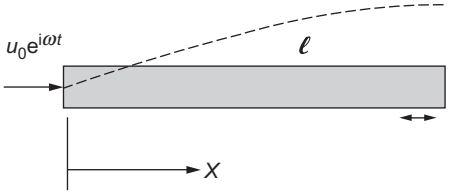


FIGURE 6.8 Prescribed displacement acting on a rod and first mode resonance. *(Source: EWI.)*

6.3.3 Three-dimensional effects

The preceding developments for the longitudinal vibrations of a rod are sufficiently accurate to describe many practical power ultrasonic vibration problems. However, in many instances, account must be made for higher-order vibration effects. Reference here is made to the effects of the natural lateral expansion and contraction of a rod that occurs under cyclic tension and compression of a rod element—known as the *Poisson effect*—as shown in Figure 6.9a. The effect on the vibration shape of a rod is shown in Figure 6.9b—upper, in exaggerated form. Thus, in deriving the wave equation, Hooke's law for elastic materials, $\sigma = E\varepsilon$, has been used.

The Poisson effect accounts for the fact that when a material is pulled (pushed), it will at the same time shrink (expand) in the lateral direction, as shown in Figure 6.9a and b. For an elastic material, the ratio of radial shrinkage (or expansion) to longitudinal extension (or compression) is governed by Poisson's ratio $v = \varepsilon_r/\varepsilon_l$, where ε_r and ε_l are the radial and lateral strains.

The lateral expansion and contraction, while always present, are generally of little consequence in low-frequency vibration problems. However, at the frequencies of power ultrasonics, these expansions/contractions can have an important role because of the vibrational energy associated with this motion, especially for rods of large diameter. This situation is brought out by Figure 6.9b—lower, which shows a section of rod and a small mass element of the rod. The element is shown undergoing longitudinal motion, u, along the axis of the rod, and, in addition, the cross section view shows the element undergoing lateral motion v and w. This is the motion associated with the Poisson expansion and contraction of the rod. There will be kinetic energy associated with both the longitudinal and lateral motion of the mass element. For rods of small cross section dimensions compared to their length, the lateral vibration energy is small compared to the longitudinal energy and has no appreciable effect on the longitudinal motion, so that the basic wave equation will describe the vibrations. However, if the lateral dimensions of a rod are continually increased, while keeping the overall length the same, it will first be found that the resonant frequency is no longer accurately predicted by the wave equation results—it being found to decrease below wave equation predictions. Second, it will be found that an increasing amount of the overall energy goes into lateral

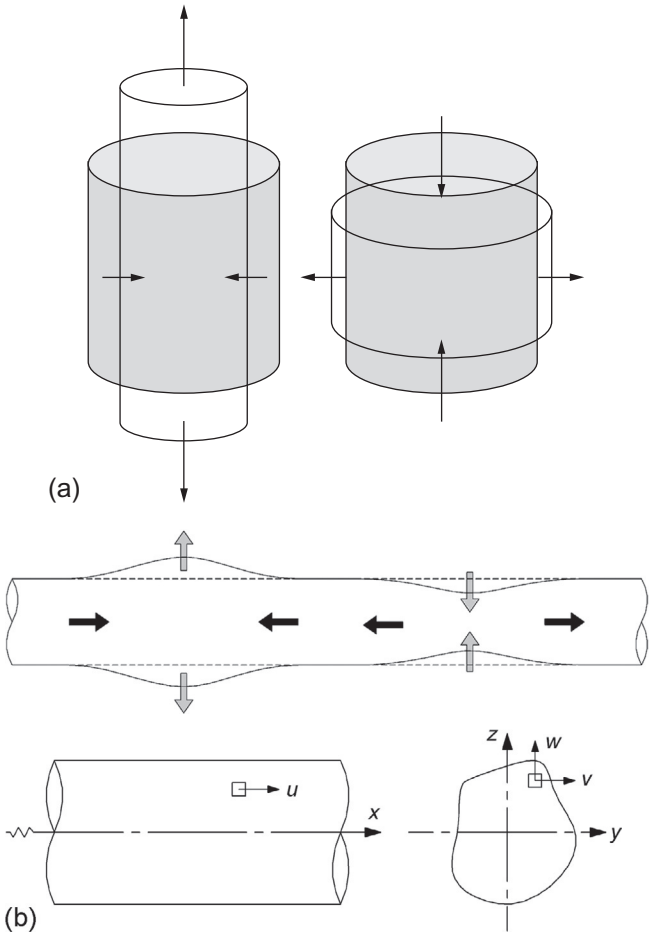


FIGURE 6.9 Poisson effect on vibrations: (a) Poisson effect; (b) lateral expansion, contraction due to the Poisson effect (upper) and motion of a mass element of the rod (lower). *(Source: EWI.)*

vibrations, so that the rod becomes less effective in transmitting longitudinal vibrations.

This somewhat complex effect of lateral vibrations is introduced because its consideration frequently arises in power ultrasonics. Thus, it is often desired to increase the size of transmission tools or welding horns in order to transfer more energy to larger work surfaces. Any effort to do this must contend with this basic principle of physics. Put another way, it tells us why we cannot build very large transducers and horns.

6.3.4 Ultrasonic horns

It is frequently desired, in power ultrasonics, to amplify and concentrate vibration energy to a small area or volume, such as in ultrasonic welding and drilling. Ultrasonic "horns" or "concentrators" of the general forms shown in Figure 6.10 are used for this purpose.

The figure shows the main features of most horns. The horn is a half-wavelength long, with a node located somewhere along the axis of the horn (location depending on horn shape). A low amplitude of vibration u_{large} at the large end is amplified to a larger vibration amplitude u_{small} at the small end. The amplification factor (or magnification factor) is given by.

$$M = u_{small}/u_{large} \tag{6.53}$$

The simplest case is that of a stepped horn, consisting of two cylindrical sections, of diameters D_1 and D_2, each one-quarter wavelength, as shown in Figure 6.10a. For this case, the amplification factor M is given by the ratio of the areas, $M = A_{large}/A_{small}$.

6.3.5 Equivalent circuit

It is also possible to represent the longitudinal vibrations of a rod with an equivalent circuit, as was done for the simple oscillator, with the LRC circuit shown in Figure 6.11 and seen to be identical to that of the oscillator. However, the development of the rod circuit is not simple, and there are significant restrictions on its range of validity.

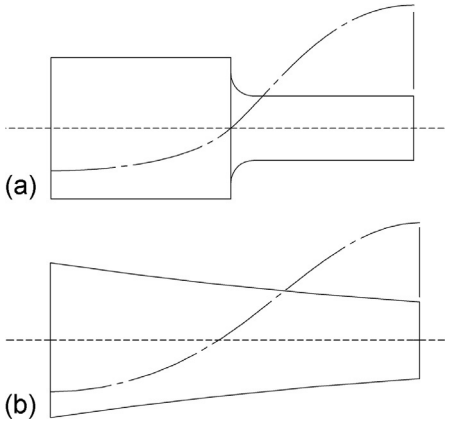


FIGURE 6.10 Ultrasonic horns: (a) stepped horn; (b) tapered horn. *(Source: EWI.)*

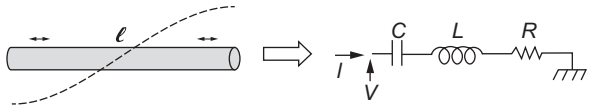


FIGURE 6.11 Equivalent circuit of a longitudinally vibrating rod. *(Source: EWI.)*

In brief, the technical approach is (1) to determine the driving point impedance of the rod; (2) to expand the result about the first mode resonant frequency; (3) to write the expression for the impedance of a series LC circuit; (4) to expand the result (3) about its resonant frequency; and (5) to compare (4) with (2), showing the equivalence of the circuit with the rod. The key point in the development, and the basis for a significant restriction, is that the result is only valid at or near the resonant frequency, and not over a broad band, as is the case for the simple oscillator. The results are

$$f_r = c/2l,\ 1/C = \pi^2 AE/2l, \quad L = \rho Al/2,$$
$$R = \text{Losses in rod} \tag{6.54}$$

where $c = (E/\rho)^{1/2}$, and E, ρ, A are the modulus, density, and cross section area of the rod.

For completeness, it will be further stated that the case of the free vibrations of a fixed-free rod, shown in Figure 6.12a (this case was noted in discussing the result (6.52)), has the parallel equivalent circuit shown in Figure 6.12b. Again, the value of these circuit representations arises in seeking to represent a complete piezoelectric ultrasonic transducer.

6.3.6 Summary of basic vibrations

In summary, while one hesitates to oversimplify what are often quite complex ultrasonic vibration issues, there is a great deal to be understood about the technology of ultrasonic transducers (and tooling) from the two simple cases of this section, that of the lumped parameter mechanical oscillator and the longitudinal vibrations of a rod.

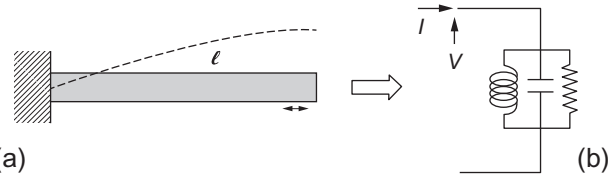


FIGURE 6.12 (a, b) Equivalent circuit of a longitudinally vibrating fixed-free rod. *(Source: EWI.)*

6.4 Piezoelectric materials

Power ultrasonic transducers are based on the ability of certain materials to transform (or "transduce") high-frequency electrical fields into mechanical vibrations. Magnetostrictive materials are one such class, able to transform magnetic fields into mechanical motion. Piezoelectric materials, able to transform electric fields into mechanical motion, are another such class. While magnetostrictive materials have historically played, and still do play, an important role in the power ultrasonic field (e.g., in ultrasonic cleaners), piezoelectric materials, especially in the form of piezoelectric ceramics, are now found in most power ultrasonic systems.

It was noted (Section 6.1) that the piezoelectric effect was discovered in the 1880s by the Curie brothers. The basic nature of the effect is illustrated in Figure 6.13, which shows that when a force is applied to a piezoelectric material, a voltage is produced. This is the "direct effect" (left). The "inverse effect" (right) occurs when a voltage is applied to the material, and a mechanical displacement occurs.

It is known that the piezoelectric effect is present in many natural crystals (e.g., quartz) and man-made crystals (ADP). In the late 1940s, it was discovered that a poled ceramic, barium titanate (BaTi), was piezoelectric. Other compositions of ceramics have since been developed, with lead zirconate titanate (PbZTi) now being widely used for power applications.

The basis for the piezoelectric effect is the fact that aligned electric dipoles exist within the material. These dipoles exist in a natural state for crystals such as quartz and tourmaline; for ceramics, this alignment is brought about artificially by firing a green ceramic in the presence of an electric field. The effect of the aligned dipoles is that application of a compressive stress decreases the dipole separation, producing a net charge on the faces of the ceramic and hence a voltage across the ceramic (a tensile stress will produce an opposite voltage).

The unique feature of a piezoelectric material is the combining, or "coupling," of mechanical and electrical properties in a single material. Thus, for a simple elastic solid, the relation between stress σ and strain ε is given by Hooke's law, $\sigma = E\varepsilon$, whereas before, E is Young's modulus.

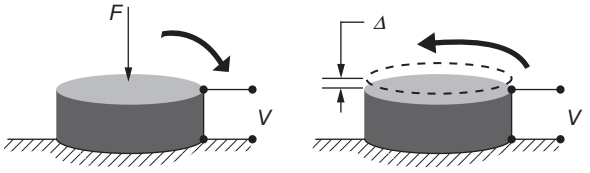


FIGURE 6.13 Piezoelectric effect: Direct (left) and inverse (right). *(Source: EWI.)*

A change of nomenclature is needed at this point, due to the potential confusion of Young's modulus with the standard definition of electrical field strength, E. Hooke's law is now expressed as

$$\sigma = c^{\mathrm{E}}\varepsilon \tag{6.55}$$

where σ is stress, ε is strain, and c^{E} is the elastic (Young's) modulus. The meaning of the superscript E on c^{E} is to define the electrical conditions under which the modulus is measured, in this case under constant electric field. In a similar fashion, the behavior of a simple capacitor can be described by

$$E = \beta D \tag{6.56}$$

where E is electric field, D the electric displacement, which is directly related to electric charge, and β is the dielectric coefficient.

The unique feature of a piezoelectric material is that these quantities are coupled, so that an application of force not only causes mechanical strain but also produces an electric charge. This behavior is exhibited in the following governing equations where a piezoelectric constant h couples, or ties, the mechanical and electrical responses together:

$$\begin{aligned} \sigma &= c^{\mathrm{D}}\varepsilon + hD \\ E &= -h\varepsilon + \beta D \end{aligned} \tag{6.57}$$

where the various quantities have been defined above, except that the modulus c_{D} indicates measurement under constant charge conditions. The form (6.57) is a basic one-dimensional representation of a piezoelectric material. However, as brought out in Chapter 5, a complete representation must account for, among other things, the (1) three-dimensional nature of the mechanical (i.e., stress, strain) and electrical (i.e., voltage, current) fields in a solid; (2) anisotropic nature of a piezoelectric material; and (3) conditions under which a material property is measured.

The material coefficients can number as high as 45 (21 elastic, 6 dielectric, and 18 piezoelectric). Fortunately, symmetries in the crystal structure of varied materials will greatly reduce this number; thus, a commonly used lead-zirconate-titanate-based ceramic will have 15 coefficients (10 elastic, 2 dielectric, and 3 piezoelectric). Finally, as noted, the conditions under which a property is measured must be noted. For example, it must be noted whether the elastic modulus is measured under "open circuit" or "closed circuit" conditions, because the material stiffness is altered by the electrical boundary conditions. This leads to the nomenclatures seen in the above, for example, c^{E}, c^{D}, which are in accord with IEEE Standards for this field (IEEE, 1987). In summary, this section has introduced the basic features of a simple piezoelectric material as a foundation

for understanding the power transducer, described in the next section.

6.5 The power ultrasonic transducer

6.5.1 Basic transducer

The fundamental construction of a power ultrasonic transducer is quite simple and is based on the previously described longitudinal vibrations of a rod and the properties of a piezoelectric disk, as described above. Thus, as shown in Figure 6.14, a piezoelectric ceramic disk is placed (also referred to as "sandwiched") between two metal end masses, with the length dimensions of the end masses and ceramic disk adjusted so that the entire unit is resonant at its half-wavelength mode at the desired operating frequency (e.g., 20 kHz). This basic construction, which can be traced back to the original discoveries of Langevin, is the driving engine of power ultrasonic systems and processes, and is variously known as the *transducer*, or *resonator*, or *converter*.

6.5.2 Practical design considerations

There are a number of practical considerations that arise in constructing a transducer that cause its appearance to differ markedly from the simple shape shown in Figure 6.14. These include the following:

- *Electrical safety*. The simple configuration of Figure 6.14 would result in one side of the transducer being at high voltage. Hence, the piezoelectric disks are used in oppositely poled pairs, thus minimizing the parts of the transducer at high voltage. Inserted between the disks are thin electrodes (typically steel, copper, or nickel) that connect the disks to the external power supply.
- *Ceramics are weak in tension*. It is necessary to add a compression bolt (or bolts) to the assembly to prestress the ceramics.
- *Vibration amplitude*. In order to increase the vibration amplitude of the front end of the transducer (variously called the "front mass" or "front driver") relative to the unloaded back portion ("back mass" or "back driver"), two means are commonly used:
  - A relatively low mass material (e.g., aluminum or titanium) is used in the front, with steel (or brass) used in the back to achieve a "mass" amplification.
  - The stepped horn concept, involving a smaller diameter front mass relative to the back mass, is used to achieve a "shape factor" amplification.
- *Assembly*. The practical requirements of assembling a bolted transducer will require flats or spanner holes in the front mass for purposes of torqueing the bolt.
- *Gripping/holding*. The vibrating transducer must be firmly held at some location (or locations) in order to force the transducer against a load. This is typically accomplished by providing a flange at the vibration node of the transducer.
- *Heating*. Heating will occur due to losses in the ceramics, metals, and at interfaces, with the resulting high temperatures able to cause damage to the ceramics and/or shifts in frequency due to dimensional changes. This heat must be removed by various cooling means.
- *Enclosure case*. This provides for electrical safety, mechanical protection, and as a means for providing cooling air to the transducer.

A representative transducer construction is shown, with external (Figure 6.15a) and internal (Figure 6.15b) views. Not shown in Figure 6.15b are inlet and exhaust ports for cooling air. The insulator shown is to separate the high voltage on the ceramic disks from the center bolt.

There are many variants of even this simple example. Thus, the compression bolt may be partially or fully recessed in the back mass, and the tool attachment thread may be continued to the compression bolt. The means for

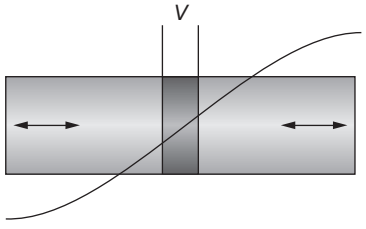


FIGURE 6.14 Basic power ultrasonic transducer. *(Source: EWI.)*

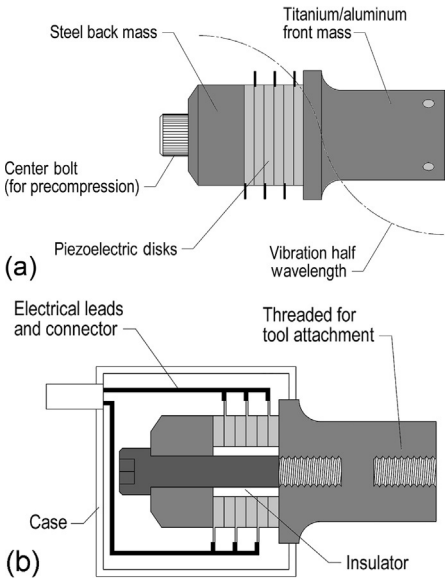


FIGURE 6.15 Representative power ultrasonic transducer: (a) external view; (b) internal view. *(Source: EWI.)*

attaching the case to the flange is not detailed in the figure, because there are many variants of attachment design.

An important characteristic of the transducer is that its operating frequency (e.g., 20 kHz) is sharply tuned to that specific frequency, with its vibration amplitude dropping off extremely rapidly just a few hundred hertz from its operating point. This behavior is the same that has been previously described for a lightly damped oscillator (see Figure 6.2), which means that just a slight shift from its resonant frequency results in a significant reduction in amplitude. The amplitude of vibration of the front end of the transducer is quite small, typically in the range of 10–30 μm, peak-to-peak, an amount invisible to the unaided eye.

6.5.3 Other configurations

While the design of Figure 6.15 is the most common form of the power transducer, other configurations are possible, as shown in Figure 6.16. Thus, Figure 6.16a shows a full-wave transducer where two sets of ceramics have been placed at the vibration nodes—the location of maximum stress where the piezoelectric effect will be most efficiently captured. The use of an exterior tension shell to achieve compression of the ceramic is shown in Figure 6.16b. The configuration of this latter figure is 1-1/2 wavelengths, a design developed by the Aeroprojects/Sonobond Corporation (Maropis 1969).

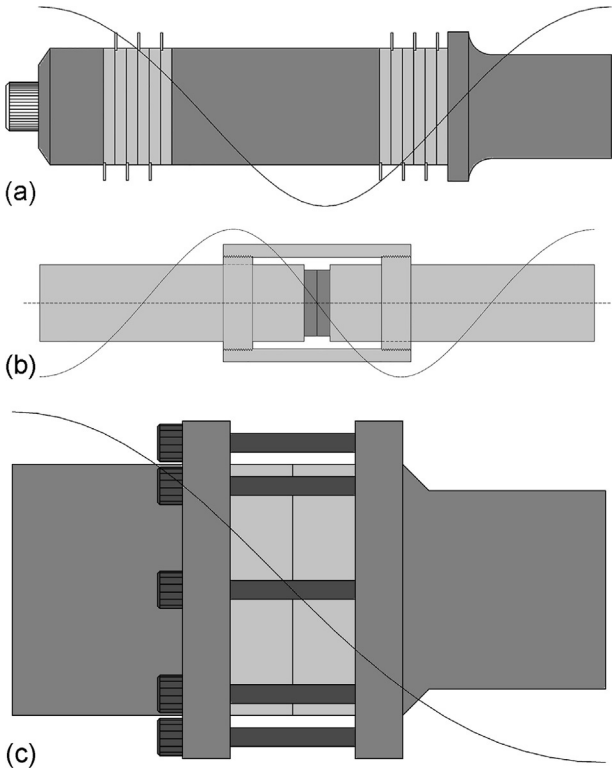


FIGURE 6.16 Various transducer designs: (a) full-wave transducer; (b) exterior tension shell; (c) external bolts. *(Source: (a and b) EWI.)*

Another means of applying compression is through a series of external bolts as shown in Figure 6.16c (not shown are insulating sleeves that would enclose each bolt). The Kulicke & Soffa Company has developed a microbonding transducer that has the transducer body machined from a single rectangular block (Safabakhsh et al., 1995), with the ceramics inserted in a central cavity and compressed by means of wedges. These design examples are simply representative of the variations of the basic transducer construction.

6.6 Transducer characterization and control

A number of means are employed to characterize the performance of a power transducer, several of which will be summarized in this section.

6.6.1 Transducer impedance: Equivalent circuit

Transducer impedance—the ratio of input voltage to current—as a function of frequency is a key measure of performance. For this purpose, the equivalent circuit representation of the transducer, Figure 6.17, serves as a starting point. Sometimes known as the "Mason equivalent circuit" after Warren P. Mason, who introduced it to wide use (Mason 1948), it has been described in many sources, of which one of the best remains that of Berlincourt et al. (1964). Shown in the figure is a basic resonator transducer and its equivalent circuit consisting of a capacitor in parallel with a series LRC circuit. The piezoelectric disk contributes to the parallel capacitor, while the longitudinally vibrating mechanical elements are captured by the LRC circuit (previously shown for a rod, Figure 6.12). Also, as previously noted for both the circuits of the ceramic disk alone and the rod alone, this circuit is an approximate representation valid at or near its resonant frequency.

The expression for the impedance of the transducer circuit is given by

$$Z = \frac{1}{i\omega C_0} \frac{\left(\omega^2 - \frac{1}{L_1 C_1}\right) - \frac{i\omega R_1}{L_1}}{\left(\omega^2 - \frac{C_0 + C_1}{L_1 C_0 C_1}\right) - i\omega \frac{R_1}{L_1}} \tag{6.58}$$

For ease of interpretation, ignore for the moment the resistor losses, so that $R_1 = 0$. The impedance reduces to

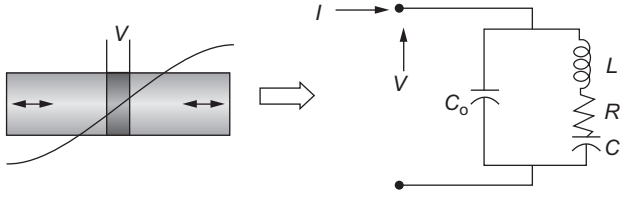


FIGURE 6.17 Power transducer equivalent circuit. *(Source: EWI.)*

$$Z = \frac{\left(\omega^2 - \frac{1}{L_1 C_1}\right)}{i\omega C_0 \left(\omega^2 - \frac{C_0 + C_1}{L_1 C_0 C_1}\right)} \tag{6.59}$$

Two frequencies of interest are immediately seen. Thus, one has

$$Z \to 0 \text{ at} \ldots \omega \to (1/L_1 C_1)^{1/2} = \omega_s \tag{6.60}$$

where ω_s is known (variously) as the "resonance" frequency, but also as the "series resonance" or as the "motional resonance," and corresponds to the resonance of the mechanical arm of the circuit. This would correspond to a short circuit in the L_1, C_1 arm. The second frequency of interest occurs at

$$Z \to \infty \text{ at} \ldots \omega \to [(C_0 + C_1)/L_1 C_0 C_1]^{1/2} \tag{6.61}$$

and represents an open-circuit condition of the equivalent circuit and is (variously) known as the "antiresonance" frequency, or as the "parallel resonance." This results in an impedance versus frequency curve, as in Figure 6.18. As noted, the curve is the absolute value of the impedance. The phase angle between voltage and current may also be measured, although it is not shown here.

The losses in the system can be from internal damping and from the effects of external loads. For the case of low losses, the effect is similar to that encountered for the lightly damped oscillator with very little shift in the series/parallel frequencies, but a rounding of the sharp valley and peak of the resonance curve. In more detailed circuit modeling of the transducer, losses in the ceramic are included in the form of a resistance in parallel with the C_0 capacitance.

Frequency response. The measurement of transducer amplitude versus frequency (i.e., the frequency response) is also an important characterization parameter.

6.6.2 Ultrasonic transducer systems

The end purpose of the power ultrasonic transducer is to transmit energy to a given application (i.e., to a process or load) via an ultrasonic system that can be shown in symbolic form, as in Figure 6.19. This figure brings out two key elements needed for a successful ultrasonic system, namely that of matching and feedback control. Thus, the transducer

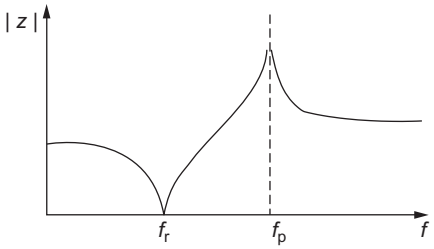


FIGURE 6.18 Equivalent circuit impedance curve. *(Source: EWI.)*

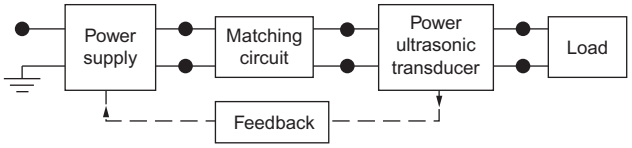


FIGURE 6.19 Power ultrasonic transducer system. *(Source: EWI.)*

is driven by the power supply. However, between the power supply and the transducer must typically be circuit components that serve to match the impedance of the combined transducer and load to that of the power supply. The transducer in turn transmits its energy to a load. In order to maintain the transducer at resonance under changing load and operating conditions (e.g., changing transducer temperature), a feedback control loop is required.

6.6.2.1 *Impedance matching*

Modern, transistor-based power supplies must typically work into a resistive load of comparatively low value (e.g., 50Ω). It is seen from the equivalent circuit representation of the transducer that a piezoelectric transducer will have a strong capacitance-driven reactance. Thus, the matching circuitry must incorporate an inductance to balance out the capacitance. A transformer is also typically needed to step the transducer/load resistance down to that required by the power supply. This sequence of matching is shown in Figure 6.20, from the transducer/load (left), to the addition of a series inductance (middle), to the addition of a transformer (right) to result in a low-impedance, resistive load that will match to the power supply. An alternate approach can begin with an inductance in series with the transducer. In modern power supplies, these matching components are typically compact in form, and are incorporated within the power supply.

6.6.2.2 *Frequency control*

The purpose of the feedback circuit in Figure 6.19 is to provide control of frequency and, for some systems, amplitude. The general basis for the need for such control is brought out in Figure 6.21. Thus, in operation, the resonance frequency of the transducer system may vary due to a number of factors, chief among them temperature effects and the effect of the acoustic load on the transducer resonance.

In the case of temperature, it is realized that losses in the transducer will cause it to heat during operation. The heating can cause some change in properties of the ceramic, but the main change is a thermal expansion of the metal components of the transducer. The net increase in transducer length will result in a decrease of the resonant frequency of the transducer, as shown by the leftward shift of the resonance curve in Figure 6.21. In the case of load, two general effects

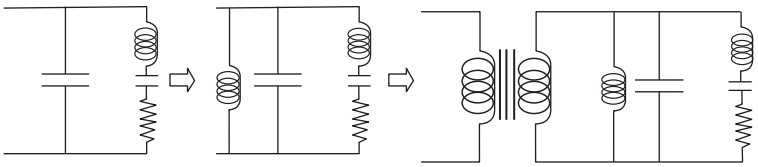


FIGURE 6.20 Sequence of matching a transducer (left) to the power supply via a balancing inductor (center) and transformer (right). *(Source: EWI.)*

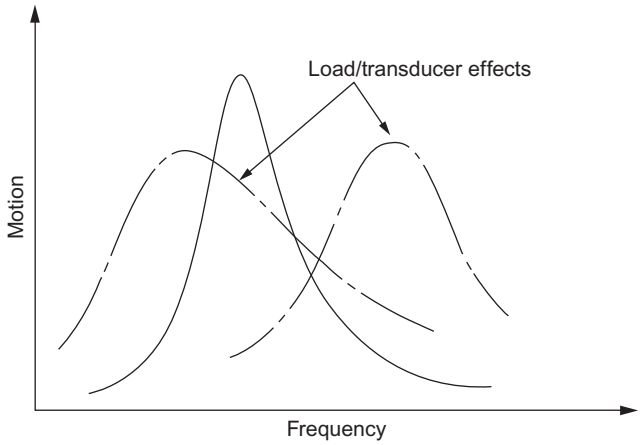


FIGURE 6.21 Shifts in resonant frequency due to load and transducer effects. *(Source: EWI.)*

can occur. Any additional energy-absorbing load will broaden the resonance curve; that is, the bandwidth of the system will be increased. At the same time, the added load may either increase or decrease the overall transducer/load stiffness. An increased stiffness will result in an upward shift of resonant frequency, while decreased stiffness will result in a downward shift in frequency. Likewise, the load may effectively add mass to the system, which would cause a downward frequency shift. The figure shows these possible shifts.

With these various frequency-varying effects in operation simultaneously, and possibly varying with time under time-varying temperature and load changes, it is essential that some type of frequency control be provided to keep the driving frequency tuned to the changing system resonance. One approach is to use phase-locked loop circuitry that drives the frequency to minimize the phase between input voltage and current, and to thus maintain resonance.

6.6.2.3 Amplitude control

While frequency control to keep an ultrasonic system at resonance is a near universal practice, the matter of amplitude control will vary among equipment suppliers, ranging from no amplitude control, to the ability to control to set amplitude under varying loads. The methods employed are typically seen as proprietary, but generally rely on principles involving equivalent circuit representations of the transducer system. One possible approach will be noted.

Again consider the equivalent circuit representation of the transducer in Figure 6.22 (left), where the currents flowing in the two arms, i_C and i_{mot}, have been noted, and recognize that the parallel LRC arm essentially represents the mechanical motion of the system. Hence, the current flowing in that arm, i_{mot}, can be seen as representing the vibration motion of the transducer. The total current will be $I = i_C + i_{mot}$. Per a preceding discussion on impedance matching, the capacitance is balanced out with a parallel inductance, Figure 6.22 (center), leaving only the motional arm, Figure 6.22 (right), and the total current now being $I = i_{mot}$. The basic control concept is to then control the drive voltage V to maintain a constant I, and hence a constant i_{mot}, thus maintaining a constant vibration motion (i.e., amplitude). The validity of this approach of course depends on the accuracy with which the equivalent circuit represents the actual transducer.

Another method that is used is based on the parallel circuit representation of the transducer (previously noted in Figure 6.12). The essence of this approach is that of holding constant voltage through variable current, because it is voltage that is found to correspond to transducer motion.

Numerous schemes for amplitude control have been put forth over the years, with a summary by Neppiras (1971) describing four approaches, with the classic reference in this area being that of van der Burgt (1963). Methods for using feedback of direct measures of motion (e.g., use of an accelerometer on the rear mass) have also been developed that, while suitable for laboratory use, are difficult for production situations.

6.6.3 Power

By its very definition, power ultrasonics is based on the capability of the transducer to deliver the necessary power to a process to affect a desired change (e.g., to create a weld). Hence, in developing a process, knowledge of the power capabilities of transducers is critical, and means of their measurement are necessary. The most widely accepted means to measure transducer power employs a setup, variously referred to as "motor-generator" or "back-to-back," as shown in Figure 6.23.

In Figure 6.23, the transducer being measured is on the left of (3), which is a transducer-transmission line-transducer combination, with the second transducer on the right being a twin of that on the left. The power supply (1) provides a measured input power, P_{in}, through the

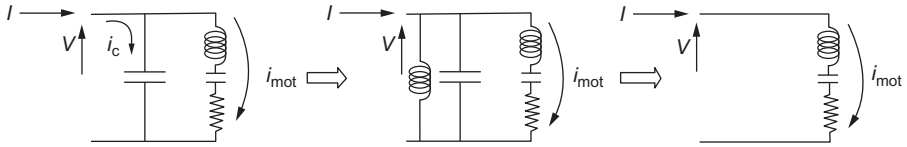


FIGURE 6.22 Concept for amplitude control based on constant current. *(Source: EWI.)*

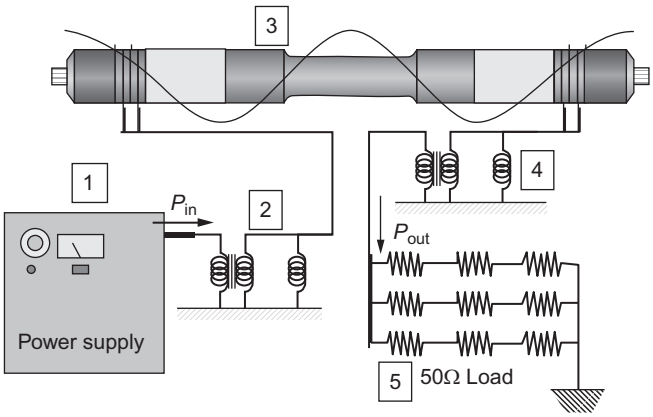


FIGURE 6.23 Transducer power measurement. *(Source: EWI.)*

matching network (2) to the test transducer (the "motor"), which transmits vibrations to the twin transducer (the "generator"), creating an electrical output at the transducer terminals. This output power, P_{out}, flows through the matching circuit (4) and is dissipated in the matched resistive load (5). The measure of P_{out} provides a power rating for the transducer, and the ratio of P_{out}/P_{in} gives the efficiency. This method will characterize a transducer's 100% duty cycle performance. Because many ultrasonic processes are transient in one form or another—plastic and metal welding operations being examples—transducers may be able to operate at higher power levels than their continuous duty rating under such circumstances.

The system shown in Figure 6.23 can be complex to set up and operate, leading to simpler tests that can serve practical needs. Thus, driving the transducer into a water load, measuring the temperature change of the water, can be an alternate test. To better match the transducer to the water load, a large block horn may be used.

6.7 Modeling transducer behavior

The modeling of power transducer performance—resonant/antiresonant (i.e., series and parallel) frequencies, amplitude, power output, stresses—has a long history of development, with much being traceable to developments of underwater sound systems (primarily sonar). The use of equivalent circuits for such modeling was the primary approach. Analysis based on classical mathematics and one-dimensional representations of the transducer components was common. These methods have now been long surpassed with use of FEA/FEM methods, as illustrated by the following development. Thus, modern transducer development generally requires advanced finite element (FE) modeling approaches, utilizing three-dimensional models of transducer designs. All electrical and mechanical transducer behavior can be modeled using modern high-end FE software packages such as ANSYS, ABAQUS, or COMSOL. Preparing the FE model inputs is similar between different software packages and is presented in a general manner here.

General transducer analysis results typically produce resonant frequencies, modal motion, amplitude output and distribution, strain distribution, stress distribution, ceramic electrical voltage distribution, total current output, and total impedance output. Obtaining these analysis results is achieved by considering the following FE model inputs and settings:

- Transducer geometry. It is usually imported from other model specialized software design packages and is typically 3D in nature but may be axisymmetric due to transducer symmetry.
- Material inputs. Mass and stiffness data are required for transducer and tooling components, while the piezoelectric materials require piezo, dielectric, and stiffness properties.
- Boundary conditions. The electrical boundary conditions (e.g., applied voltage) on the piezoelectric disks must be specified as well as the usual mechanical boundary conditions on the mechanical components.
- Analysis type. Common types of analysis for transducers are modal (sometimes called frequency) and harmonic (sometimes called dynamic).

- Analysis results. Result types are different depending on choice of analysis type.

The following sections describe these inputs and settings in more detail.

6.7.1 Transducer geometry input

Most modern transducer geometries utilize three-dimensional models of the transducer and related components imported from advance design packages such as solid works or CREO. Transducer symmetry may permit an axi-symmetric model form, thus speeding up analysis. The general setup is identical to the 3D format presented here.

The transducer geometry may be analyzed directly if the transducer design is in a half-wave or multiple half-wave format. If the transducer requires additional components to complete the half-wave design, those components will need to be added. Transducers may need to include an attachment stud or bolt, in which case a portion of the stud/bolt must be included in the model to ensure the transducer tunes properly. A cross section example of a typical transducer and half-stud design is shown in Figure 6.24.

Transducer components should be modeled in a line-to-line format, in which case FE packages will treat adjacent components as though they were bonded. As seen in Figure 6.24, the typical transducer uses a center bolt to exert a compressive preload on the ceramics, resulting in all components behaving in a bonded fashion. It should be noted that the preload will have a tendency to stiffen the structure and thus may raise the resonant frequencies over FE predictions, although this effect is usually quite small.

6.7.2 Materials inputs

Material data used in FE models fall into two categories, the general materials of transducer construction, including any added transmission or tooling components, and the piezoelectric materials. General materials may include titanium, aluminum, steel, nickel, brass, beryllium copper, as examples. These materials are modeled by providing a mass density, modulus of elasticity, and Poison's ratio. Accurate representations of these materials are critical to the analysis, since they make up the majority of the transducer structure. Whenever possible, direct measurement of these properties is recommended.

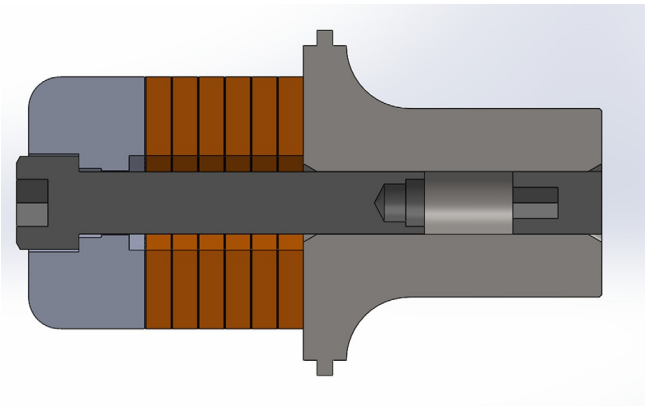


FIGURE 6.24 Half-wave transducer (cross section) and attachment stud. *(Source. James Sheehan.)*

The piezoelectric materials are at the core of the transducer analysis. Piezoelectric materials are incorporated into the transducer analysis using their geometric dimensions and their coupled field equations, shown in Eqs. (6.62)–(6.66):

$$\begin{aligned}\{T\} &= [c^E]\{S\} - [e]\{E\} \\ \{D\} &= [e]^T\{S\} + [\varepsilon^S]\{E\}\end{aligned} \tag{6.62}$$

or equivalently,

$$\begin{Bmatrix}\{T\} \\ \{D\}\end{Bmatrix} = \begin{bmatrix}[c^E] & [e] \\ [e]^T & -[\varepsilon^S]\end{bmatrix}\begin{Bmatrix}\{S\} \\ -\{E\}\end{Bmatrix} \tag{6.63}$$

where

$\{T\}$ = Stress vector
$\{D\}$ = Electric flux density vector
$\{S\}$ = Strain vector
$\{E\}$ = Electric field intensity
$[c^E]$ = Elasticity matrix—at constant electric field
$[e]$ = Piezoelectric matrix
$[\varepsilon^S]$ = Dielectric matrix—at constant mechanical strain

The piezoelectric properties matrices referenced above are as follows:

Elasticity matrix $[c]$:

$$[c] = \begin{bmatrix} c_{11} & c_{12} & c_{13} & c_{14} & c_{15} & c_{16} \\ & c_{22} & c_{23} & c_{24} & c_{25} & c_{26} \\ & & c_{33} & c_{34} & c_{35} & c_{36} \\ \text{Symmetric} & & & c_{44} & c_{45} & c_{46} \\ & & & & c_{55} & c_{56} \\ & & & & & c_{66} \end{bmatrix} \tag{6.64}$$

Piezoelectric matrix $[e]$:

$$[e] = \begin{bmatrix} e_{11} & e_{12} & e_{13} \\ e_{21} & e_{22} & e_{23} \\ e_{31} & e_{32} & e_{33} \\ e_{41} & e_{42} & e_{43} \\ e_{51} & e_{52} & e_{53} \\ e_{61} & e_{62} & e_{63} \end{bmatrix} \tag{6.65}$$

Dielectric matrix $[\varepsilon^S]$:

$$[\varepsilon^S] = \begin{bmatrix} \varepsilon_{11} & 0 & 0 \\ 0 & \varepsilon_{22} & 0 \\ 0 & 0 & \varepsilon_{33} \end{bmatrix} \tag{6.66}$$

Getting the above matrices into ANSYS often requires manipulation of the material properties units from the piezoelectric manufacturer's catalog into a form that is acceptable for FE packages. Acceptable inputs for FE packages in SI units are as follows:

Ceramic stiffness: c in N/m^2 in closed circuit format.

Piezoelectric constants: e in C/m^2.

Permittivity constants: ε in F/m.

Initially ceramic material properties are gathered from the manufacturer's catalog, with the following required:

- $s_{11}^E, s_{44}^E, s_{12}^E, s_{13}^E, s_{23}^E, s_{55}^E, s_{66}^E$—closed circuit compliances in m^2/N
- $d_{33}, d_{31}, d_{15}, d_{32}, d_{24}$—$d$ matrix in C/N
- $e_{11}^S, e_{22}^S, e_{33}^S$—permittivity constant strain values in F/m

Often manufacturers catalogs offer only a limited subset of the above values. However, several cross relations exist to permit obtaining other values. Thus:

$$d_{32} = d_{31}, d_{24} = d_{15}, s_{23}^E = s_{31}^E, s_{55}^E = s_{44}^E, s_{66}^E = 2\left(s_{11}^E - s_{13}^E\right) \tag{6.67}$$

Some manipulation is required to convert the catalog piezoelectric property values into a format suitable for input into the FE software. Example calculations are shown below.

The ceramic compliance is first assembled from catalog values (Table 6.1).

An inverse operation is performed on this matrix to create the stiffness matrix needed for input into the FE package, with the result (Table 6.2).

The d matrix is assembled from catalog values (Table 6.3).

This matrix is transposed to (Table 6.4):

It is then multiplied by the stiffness matrix to achieve the final form for input (Table 6.5):

$$[d]^*[c] = \text{Piezoelectric Matrix } \left(C/\text{m}^2\right) \tag{6.68}$$

The above final forms input can now be placed into the FE package piezoelectric material inputs.

TABLE 6.2 Stiffness matrix [c], N/m^2—closed circuit

1.282E+11	6.484E+10	6.441E+10	0	0	0
6.484E+10	1.282E+11	6.441E+10	0	0	0
6.441E+10	6.441E+10	1.125E+11	0	0	0
0	0	0	3.135E+10	0	0
0	0	0	0	3.135E+10	0
0	0	0	0	0	3.086E+10

6.7.3 Boundary conditions

In order to properly represent the transducer in a modal or harmonic type of analysis, the boundary conditions on the ceramics need to be set up with simulation electrodes. The ceramics each have a positive and negative electrode side. These individual surfaces in the model will need to be coupled together via electrodes on each of the ceramics. These individual ceramic electrodes will then be linked together across the ceramic stack according to how they are wired.

An example ceramic stack of six ceramics is shown in Figure 6.25a. The ceramic electrode polarities are also shown in the manner that a transducer is typically assembled. The ceramic polarity of each of the ceramics is shown as assembled. Each of the ceramics will need to have a local ceramic polarity coordinate system set up to match the figure.

The spaces between each ceramic are then filled by electrodes (not shown in the figure). In the FE model, the electrode material is not electrically conductive, and is modeled only through its density and stiffness. Since the electrodes

TABLE 6.1 Compliance matrix [s], m^2/N, closed circuit

1.208E−11	−3.700E−12	−4.800E−12	0	0	0
−3.700E−12	1.208E−11	−4.800E−12	0	0	0
−4.800E−12	−4.800E−12	1.439E−11	0	0	0
0	0	0	3.190E−11	0	0
0	0	0	0	3.190E−11	0
0	0	0	0	0	3.240E-11

TABLE 6.3 Piezoelectric matrix [*d*], C/N

0	0	0	0	3.80E−10	0
0	0	0	3.80E−10	0	0
−1.19E−10	−1.19E−10	3.09E−10	0	0	0

TABLE 6.4 Transposed piezoelectric matrix [*d*], C/N

0	0	−1.19E−10
0	0	−1.19E−10
0	0	3.09E−10
0	3.80E−10	0
3.80E−10	0	0
0	0	0

TABLE 6.5 Piezoelectric matrix

0	0	−3.02
0	0	−3.02
0	0	19.47
0	11.91	0
11.91	0	0
0	0	0

are not electrically conductive in the model, it is possible to set up the ceramic stack in a modeled format so that the individual ceramic coordinate systems are not required. An equivalent modeled format can be set up according to Figure 6.25b.

When the ceramic polarities are modeled in this format, it is possible to use a single coordinate system for the ceramics, or simply use the global coordinate system with the positive *Z*-axis set as the ceramic polarization axis. The boundary condition setup has been shown to be equivalent for both cases.

The modeling software can now be used to link together all the positive electrodes to a single controlling node. The negative electrodes can be set in a similar manner. When this setup is completed, the ceramic voltage boundary conditions can be set from just two voltage-controlled nodes—*Positive* and *Negative*.

6.7.4 Analysis type

To fully examine the characteristics of ultrasonic transducers, two analysis types are typically used—modal and harmonic (sometimes called dynamic). The specific boundary condition setup is dependent on the analysis type chosen, as described in the following.

Modal analysis is a type where only the natural frequencies of the transducer are obtained. The results of the modal analysis are essentially a list of natural frequencies and the associated amplitude or motion for each of these frequencies. The motion results are typically scaled to the mass matrix and are without units. The most significant input for the modal analysis is the transducer geometry and the corresponding mass and stiffness of the geometry. In addition, the boundary conditions of the positive and negative electrodes described in Section 6.7.3 are also a contributing factor. Material or external damping can also be added to the analysis, typically only affecting the motion but not the frequency solution.

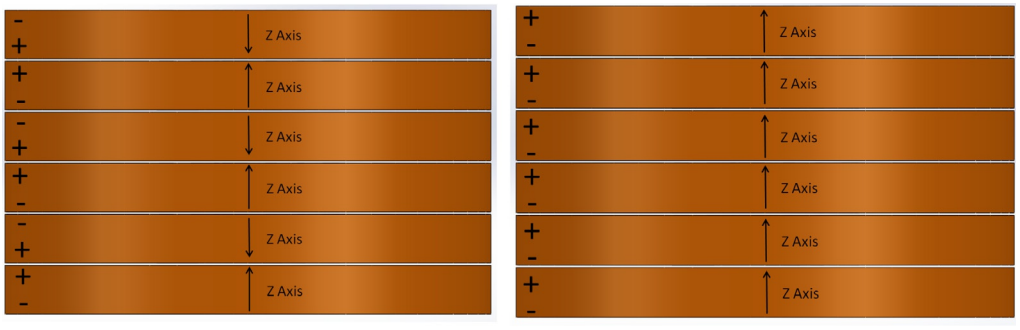


FIGURE 6.25 Ceramic stack: (a) typical stack with polarities shown; (b) modeled ceramic stack with polarities shown. *(Source: James Sheehan.)*

Modal piezoelectric negative and positive boundary conditions need to be defined according to the results intended. Thus, one needs to determine whether the parallel or series resonances are required. The parallel and series resonance conditions of the transducer are described analytically in Section 6.6.1. For parallel resonance, the electrodes will be set up for an open-circuit condition—that is, the negative electrode is set to 0, while the positive electrode is left open. For a series resonance, the electrodes will be set to a closed-circuit condition. Both the negative and positive electrodes are set to 0.

Harmonic analysis is the type where the transducer motion is solved for a specific frequency or multiple frequencies. As with the modal analysis, an important input is the transducer geometry and corresponding mass and stiffness. In addition, the driving voltage for the transducer electrodes is defined. Transducer motion results are now produced at a single frequency, or multiple frequencies, and are scaled to the voltage difference on the positive and negative electrodes. Ceramic current results are now also obtained. Typically, ceramic electrode input values are 0 at the negative electrode and a zero-to-peak value for the positive electrode.

6.7.5 Analysis example

An example of a transducer analysis will be now shown. For this example, a modal and Harmonic analysis for the transducer with a half-wave transmission line (or "horn") shown in Figure 6.26 will be done. The back and front mass components are steel and aluminum, and the horn is titanium. The bolt and attachment stud are both steel while the PZT-8 ceramics are 0.2 in. thick. The transducer-horn assembly is a full wavelength.

The piezoceramics were set up utilizing materials and techniques as detailed in Sections 6.7.2 and 6.7.3. Electrode nodes were set up as positive and negative for each of the electrode types. All other materials were modeled using typical handbook properties for aluminum, steel, titanium, and nickel (electrodes). All components will be considered as bonded together. ANSYS will be used for the analysis.

A modal analysis is first performed to determine the natural frequencies within the expected transducer tuned range of 20 kHz, that range being between 18,000 and 22,000 Hz. FE calculations are performed for both the parallel resonance condition (positive electrode set to open circuit, negative electrode set to 0) and the series resonant condition (positive and negative electrodes set to 0). Analysis yields the results for series f_s, and parallel f_p. resonances are shown in Table 6.6.

Modal analysis results within the frequency range reveal two different modes, a longitudinal mode and a flexural mode, shown in Figure 6.27. The axial mode shows a frequency difference between the series and parallel modes which essentially is a measure of what is known as the transducer coupling as calculated by the following:

$$K_{\text{eff}} = \left\{ \left[\left(f_p - f_s \right) / f_s \right]^2 \right\}^{1/2} \quad K_{\text{eff}} = 0.195 \qquad (6.69)$$

TABLE 6.6 Modal analysis results within 18,000–22,000 Hz

Mode	f_s	f_p	Description
1	19,400	20,138	Axial
2	21,285	21,285	Flexure
3	21,286	21,286	Flexure

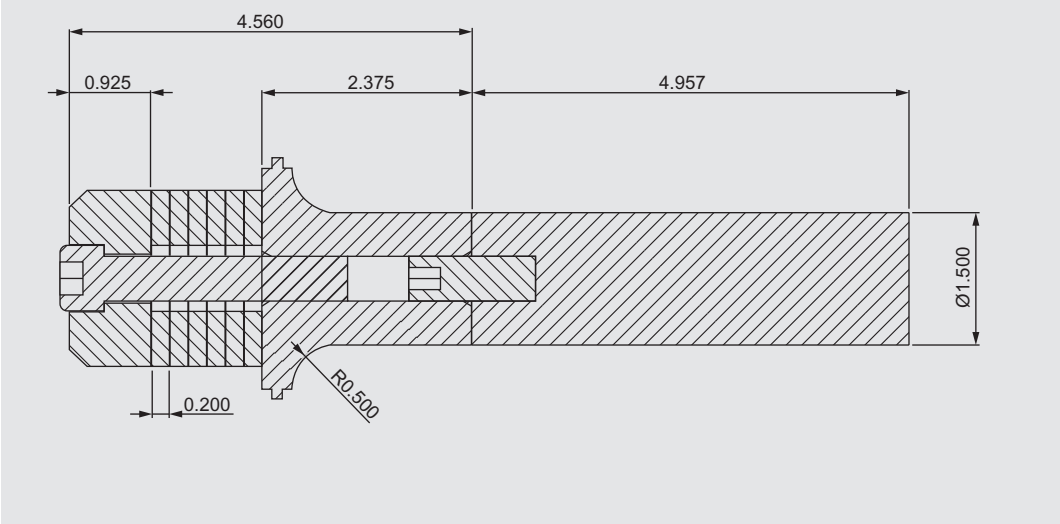
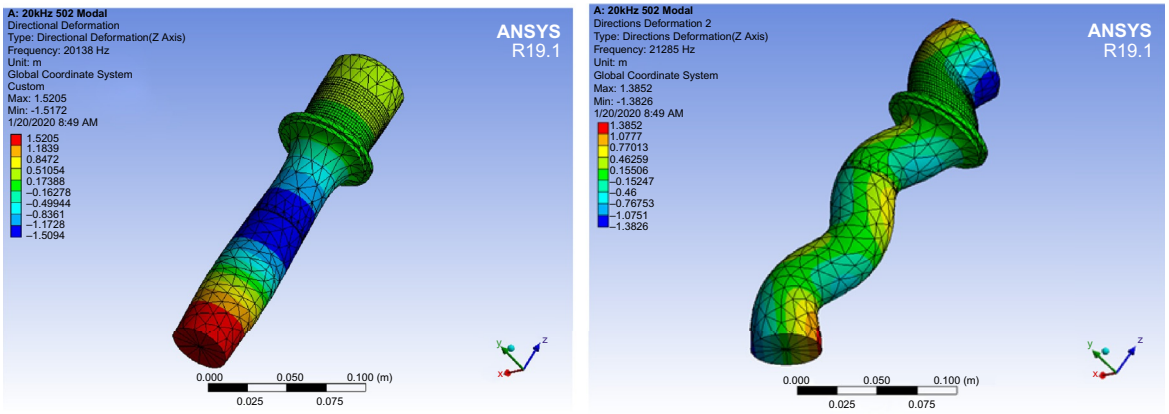


FIGURE 6.26 Full-wavelength transducer-horn system. *(Source. James Sheehan.)*



(a) **(b)**

FIGURE 6.27 Modal displacement results: (a) longitudinal mode, (b) flexural mode. *(Source. James Sheehan.)*

The flexure frequency shows up as a pair, flexing in each of the normal *X*- and *Y*-axes. This flexure frequency shows up in practice as a single frequency. Also noted is that there is no difference between the two flexure frequencies, indicating no coupling to the ceramics under ideal conditions. Modal plots of the total displacement are shown in Figure 6.27 for both the longitudinal frequency (parallel mode) and the flexure frequency.

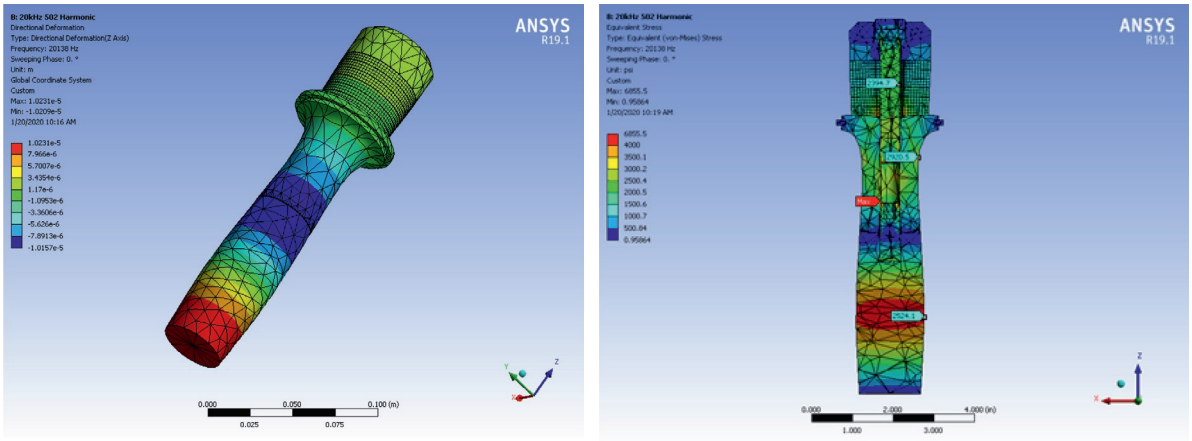
Once the modal frequencies are determined, a harmonic analysis can be performed at the parallel resonance of the longitudinal mode to determine the displacements and stresses for a given input voltage at the ceramics. For this analysis, the ceramic electrodes can be set to negative zero ("0") and positive of 1000 Vrms to represent a typical voltage drive at parallel resonance. For parallel resonance, the frequency will be set to the parallel resonance point of 20,138 Hz as determined by the prior modal analysis. Following computation, the results for transducer displacements and stresses are shown in Figure 6.28.

From the displacement plot, the transducer horn-tip output at 20138 Hz is 10.2 µm 0-P at 1000 Vrms. The von Mises stresses, shown in Figure 6.28b, at specific points are as follows: bolt—2400 psi, front mass radii—2900 psi, and horn node—2500 psi. Other plots, as examples, could show equivalent strain, directional stress, or strain.

As noted at the outset, modern transducer development generally requires advanced FE modeling approaches, utilizing three-dimensional models of transducer designs. This section has been intended to be illustrative of what are a wide range of computational approaches used in this field.

6.8 Transducer development

In the continued development of power transducers, it is necessary to deal with the factors that can limit, for example, achieving higher power levels. In broad terms, these are electrical, mechanical, and thermal limits. As examples, in the ceramics, dealing with heating due to dielectric losses



(a) **(b)**

FIGURE 6.28 Harmonic analysis results: (a) displacements, (b) stresses (von Mises). *(Source. James Sheehan.)*

and friction, as well as high-voltage arcing, is always a potential issue. In the metal components, dealing with design details to minimize risk of fatigue fracture is always important, as is minimizing three-dimensional vibration effects. Attention to the mechanical features for attachments to case, external supports, and power transmission components are critical.

Efforts to increase transducer power can face certain geometric limits. Keeping in mind that increase of power will basically be related to increasing the volume of piezoelectric ceramic, the two obvious ways to increase ceramic volume in the bolt-clamped transducer are to (1) increase the number of disks in the transducer and/or (2) increase the diameter of the disks. There is a limit to (1), because more disks will move ceramic away from the high-stress central region of the transducer, where electromechanical coupling is maximum. There is likewise a limit to (2), the greatest difficulty in increasing diameter is that of three-dimensional vibration effects, in the form of radial vibrations, which will reduce energy in the longitudinal mode. Other aspects can enter, such as achieving the desired compressive prestress on the ceramics. All of these are part of the challenges in achieving a successful power ultrasonic transducer design.

However, these very issues are the ones continually driving new developments that advance power transducer technology. Illustrative of such developments are the following examples. Thus, Zhang et al. (2016) have adapted the basic Langevin sandwich construction to achieve a bending-type transducer. The principle of construction is shown in Figure 6.29a where it is seen that a traditional sandwich construction is used, with the piezodisks being split with opposing polarizations on adjacent segments so that a bending action, versus purely longitudinal, is induced. It should be noted that this is not the first employment of this concept.

Figure 6.30 shows the frequency response (left) and modeling of the transducer bending mode (right). The positioning of the ceramics was optimized by maximizing the coupling coefficient. Comparison of experimental data with results from a refined transducer model was good, thus providing the basis for future successful application of the unit.

Lu et al. (2017) have also undertaken modification of the basic Langevin construction in, as they describe it, a "new topological structure" based on a unique shaping of the end masses. The resulting shape, set beside a conventional construction, is shown in Figure 6.31.

The unique features are the conically shaped end masses, each stiffened by plate-shaped side details and the large cooling fins located in the node area. The authors measured larger vibration velocities, lower part temperatures, and

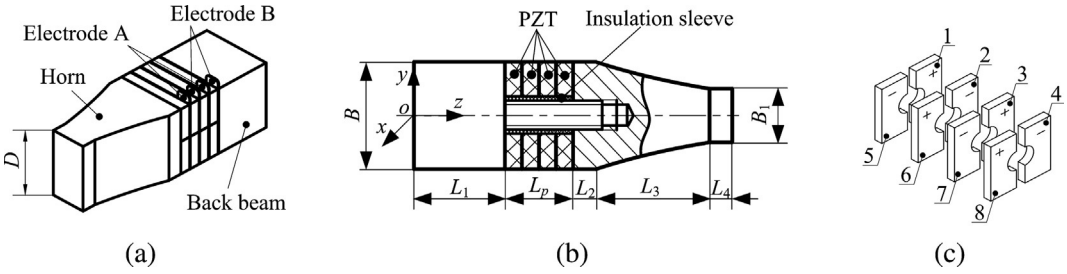


FIGURE 6.29 Structure of the transducer, (a) three-dimensional model, (b) structure parameters, (c) distribution of piezoelectric ceramics. *(Zhang et al. (2016), Fig. 1.)*

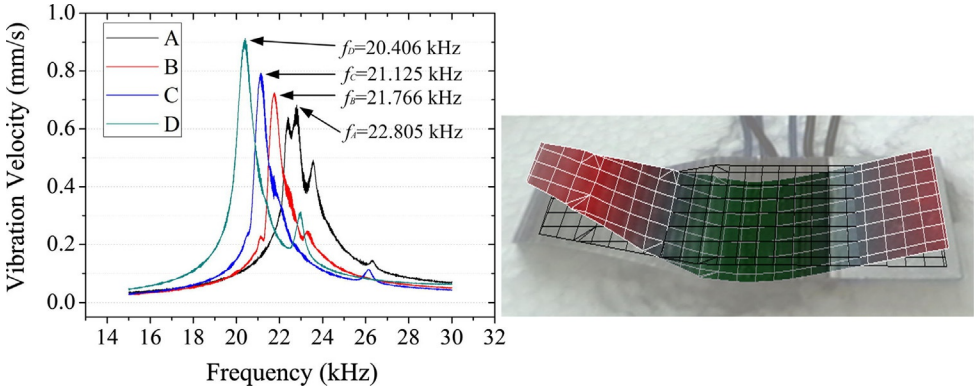


FIGURE 6.30 Resonance frequencies (left) and modeled vibration mode (right). *(Zhang et al. (2016), Fig. 9.)*

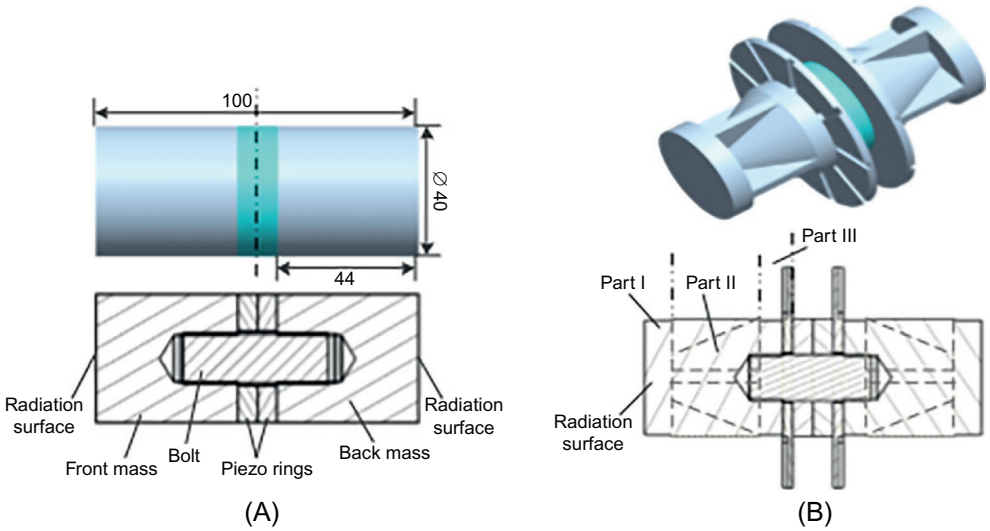


FIGURE 6.31 Configuration of (a) traditional Langevin transducer (TLT) and (b) mass optimized Langevin transducer (MOLT). *(Lu et al. (2017), Fig. 1.)*

higher efficiency than the conventional construction. The relative cooler temperature field of the new design compared to the conventional design, under the same operating voltage, is shown in Figure 6.32.

Xu (2015) have set forth a detailed development of a cup-shaped transducer that, while still based on the Langevin concept, provides a radiating horn useful for both solids—e.g., welding plastics—and liquids, for sonochemical applications. The basic transducer shape is shown in Figure 6.33 (it should be noted that cup-shaped horns have been previously developed), followed by FEA of the two key vibration modes, Figure 6.34.

In addition to the noted FEA results, the authors also derive the equivalent circuit for the cupped horn and show that it has a high vibration amplitude and is clear from nearby spurious frequencies.

The measurement of transducer vibrational characteristics is a subject of long-standing interest, as set forth in Chapters 8 and 10 of this book, but one example, due to its novelty, is nonetheless noted here. Thus, Saffar and Abdullah 2014 have described, in their words, a simple method for measuring vibration amplitude of high-power airborne transducers using a thermocouple technique. A typical transducer construction and its analytical model are shown in Figure 6.35.

The essence of the approach is to attach a balsa wood layer to the transducer radiating face, Figure 6.36, with a thermocouple at the radiating face/balsa interface. Balsa layers of various thicknesses are used, and the radiated sound intensity is correlated with the temperature changes at the interface and, through modeling, with the resulting vibration amplitudes.

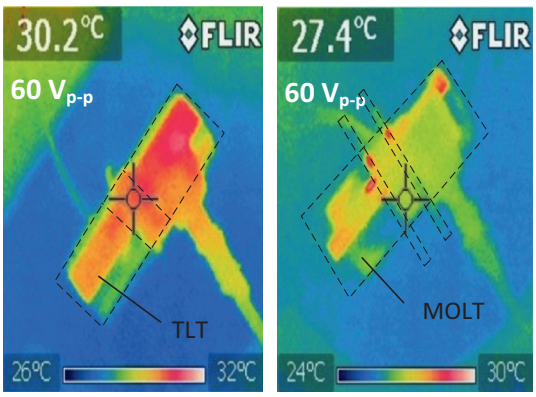


FIGURE 6.32 Measured temperature fields of two prototype transducers at same driving voltage, (a) TLT, (b) MOLT. *(Lu et al. (2017), Fig. 7.)*

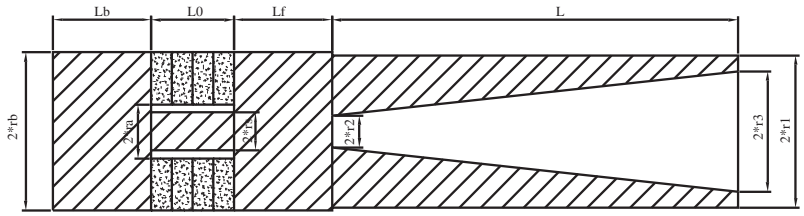


FIGURE 6.33 Schematic of the cup-shaped ultrasonic transducer. *(Xu (2015), Fig. 1.)*

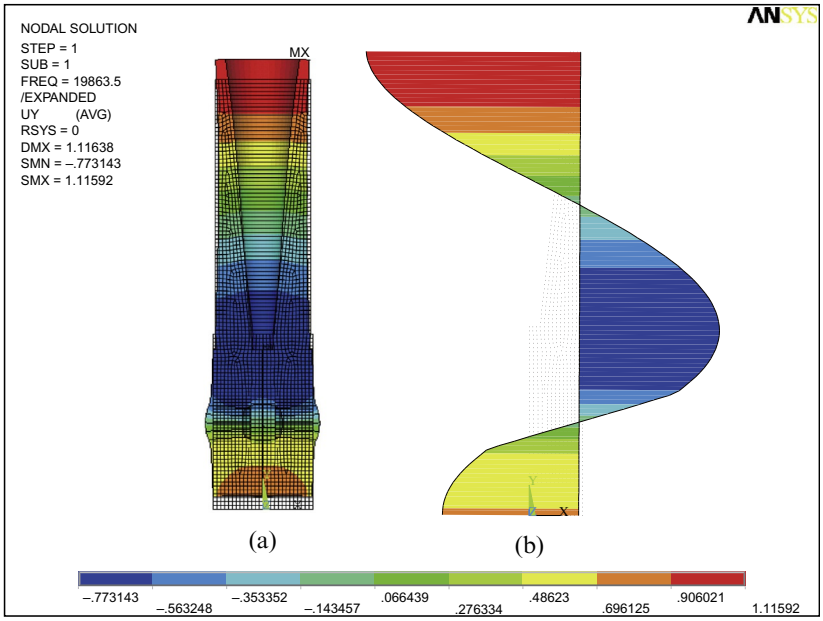


FIGURE 6.34 (a) Deformed shape and (b) corresponding longitudinal displacement distribution of the cup-shaped transducer at resonance. *(Xu (2015), Fig. 11.)*

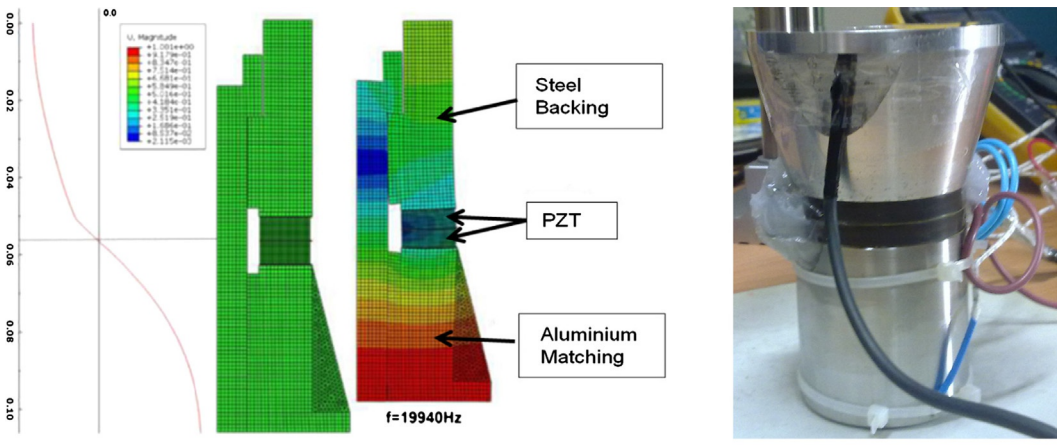


FIGURE 6.35 (a) Analytical model and (b) experimental transducer. *(Saffar and Abdullah (2014), Fig. 1.)*

The use of ultrasonic devices to create an atomized spray of liquid droplets is, of course, well known, but the development of a torsional transducer for this purpose, by Tsuyuki et al. (2015), is worthy of note. The objective was to achieve atomization over a wider range of flow rates and "Weber number" (a fluid mechanics number useful in characterizing multiphase fluid flows), with it being determined that achieving a torsional mode at the transducer tip could improve atomization performance. A Langevin-type design was used with a slotted radiating tip. Numerical

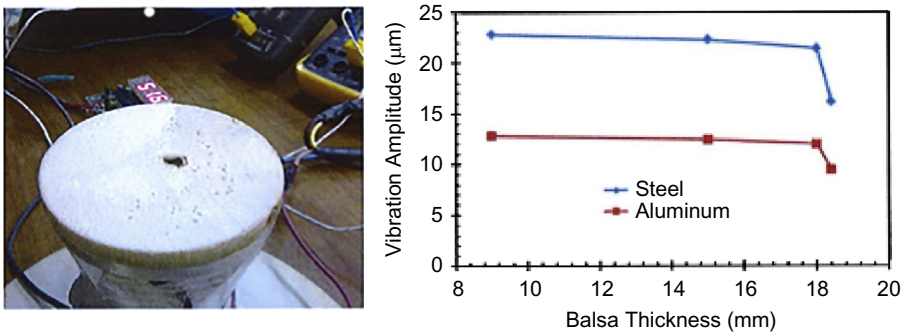


FIGURE 6.36 (a) Balsa layer on radiating face, with thermocouple attachments and (b) vibration amplitude at aluminum radiating face (blue line) for various balsa thicknesses. *(Saffar and Abdullah (2014), Figs. 8 and 7).*

analysis was used to predict the contour and vector details of the torsional mode as well as the longitudinal mode. The results showed the torsion mode more effective in atomizing at low flow rates, typically a more difficult condition for controlled atomization.

As noted in the introduction to this chapter, due to widespread use, the focus has been on piezoelectric devices. There have been for a number of years, however, developments in so-called giant magnetostrictive materials that demonstrated vibration amplitudes an order of magnitude (or more) over conventional magnetostrictive or piezoelectric materials. Despite their promise, they have not in general transitioned into the power ultrasonic field, possibly impeded by high loss issues. However, Zhou et al. (2020) have shown a recent design approach that may change this outlook. The "giant magnetostrictive ultrasonic transducer—GMUT" of Figure 6.37 consisted of Terfenol-D magnetostrictive material, a surrounding permanent magnet, a coil with the components held in place with a prestressing exterior shell. The output vibration is screw-attached to a stepped horn. System modeling was done by a lumped-parameter approach from which the importance of prestress in accurate modeling was brought. As shown in Figure 6.38, good agreement was achieved in prediction of vibration amplitude versus coil current at several resonant frequencies. Developments, such as this, could open the door to wider use of GMUTs in industrial processing applications.

Finally, again on the matter of transducer materials, the focus of this chapter has been on lead zirconate titanate (i.e., PZT) materials, these being currently and for many years the dominant driver of power transducers. Nevertheless, both the desire and the pressure to move to lead-free piezoelectrics continue. To this end, lithium niobate has emerged as a candidate replacement. However, other than laboratory reports, it does not yet appear to have been used in the traditional Langevin-type transducer. However, in the paper by Wang et al. (2015), the use of lithium niobate in a special transducer configuration for oil-field recovery technology, where an ultrasonic field is used to reduce the viscosity of heavy oil, is described. The purpose is to develop an immersed radiating unit consisting of a number of plate-like radiators, Figure 6.39. Each radiator would be a Li-Nb disk, of the general construction shown in the transducer of Figure 6.40. Tests of the prototype showed good results in viscosity reduction.

These examples of transducer development illustrate how the basic Langevin-type structure of PZT-based transducers continues, over a century from its original inception,

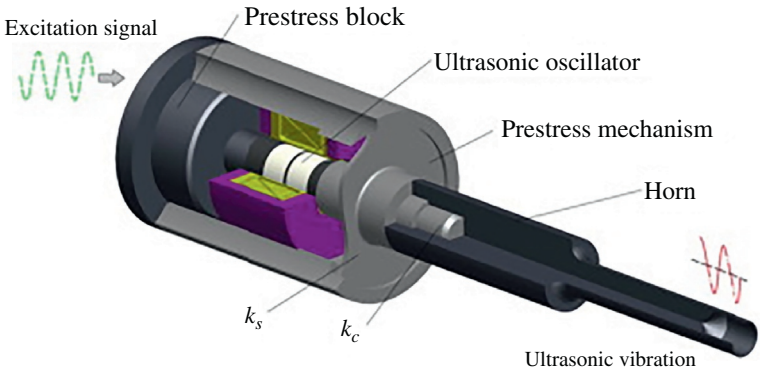


FIGURE 6.37 Structure of GMUT. *(Zhou et al. (2020), Fig. 1.)*

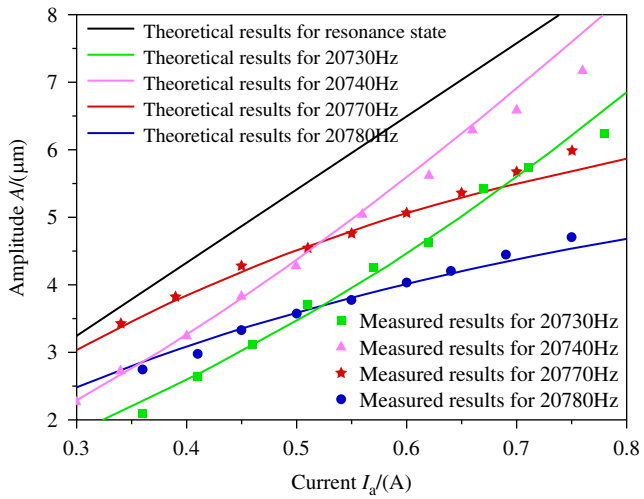


FIGURE 6.38 Amplitude-current response curves at different frequencies. *(Zhou et al. (2020), Fig. 13.)*

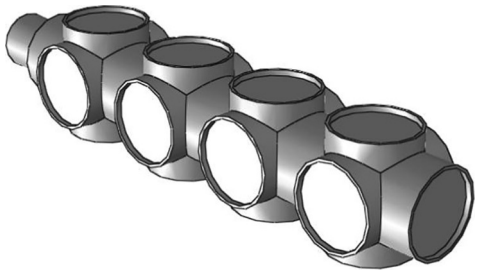


FIGURE 6.39 Three-dimensional model of lithium niobate transducer system. *(Wang et al. (2015), Fig. 5.)*

while new developments in both design and materials may yet possibly supplant a pioneer.

6.9 Future trends

It should be apparent that the basic construction of the piezoelectric power transducer, shown in Figure 6.15, and sometimes referred to as the "bolt-clamped Langevin sandwich construction," has changed very little over many years, so that any expectation of revolutionary future changes must be taken with some caution. Nevertheless, there are several trends that are leading or will lead to continued improvements in power transducers.

As one example, the evolution of sophisticated design and analysis tools has enabled continuous improvements in the accuracy of representations of transducer behavior to be achieved in recent years. Amplitude and frequency can be accurately modeled resulting in designs that can be adapted to almost any physical environment. Transducers can be designed to easily fit in hermetically sealed configurations for use in the food industry or in operating rooms. Often these designs can withstand the rigors of caustic solution wash downs or steam sterilizations. These advanced designs have focused attention to two areas for which improvements are still needed, namely that of amplitude control and thermal management.

Control of amplitude still relies on the circuit fundamentals described in Section 6.6.2.3 through control of V_{mot} or I_{mot} parameters. Often the aging and general variability characteristics of the piezoceramics make it difficult to predict transducer amplitude to better than ±10%. Improvement of this amplitude tolerance will require an understanding and acceleration of piezo-aging effects through the manufacturing process. Following application of preload in assembly, various manufacturing techniques that involve application of time, heat, and stress need to be formalized that reduce the d_{33} variation the transducer experiences in service. In addition, advanced calibration techniques utilizing custom-stored motional parameters within the transducer need to be applied. Programmable computerized chips located within the transducer that communicate real time with generators can be used for this purpose. Through these techniques, it should be possible to reduce transducer amplitude variability below the current accepted range of ±10%.

Future transducer design trends usually demand the need for equal or increased power output, often also requiring ever smaller designs. Essentially the future will demand higher-power densities of ultrasonic transducers. To achieve this advance, the current design and analysis tools can be used to generate designs that more effectively remove heat from transducers. FEA techniques should combine thermal analysis with the mechanical analysis. Thermal effects can be effectively modeled using heat generation rates linked

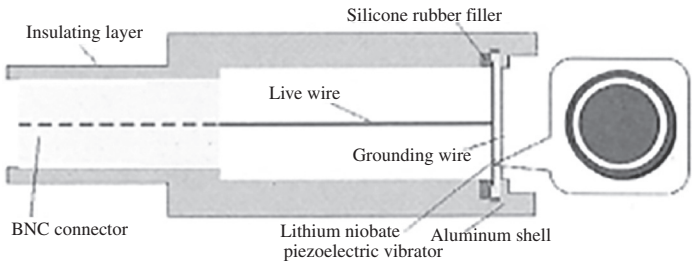


FIGURE 6.40 Cross section view of the lithium-niobate transducer. *(Wang et al. (2015), Fig. 3.)*

to tan δ losses of piezoceramics. Combining thermal and coupled field mechanical analysis can result in designs that incorporate heat sinks and other effective means to improve convection and conduction of heat away from ceramic components. Computational fluid dynamics can be used to optimize air and liquid cooling methods. Application of these advanced cooling methods can result in designs that are smaller yet have higher power densities than existing designs.

Insofar as needs for increased power levels, current maximum powers of transducers operating at 20 kHz are in the range of 6–7 kW and appear to be meeting most industrial applications. Although 10 kW would be within existing ceramics, materials, and modeling technology, neither the applications nor market conditions appear to be currently present for their adoption. Accompanying these considerations will be the fact that increasing environmental concerns have been accompanied by awareness that the lead content of the widely used lead zirconate ceramics should encourage the developments of alternate power ceramics.

This brief summary of future trends will be concluded with a question. Thus, while several variants of the power transducer have been discussed in this chapter, the fact remains that the basic design principles of the "bolt-clamped Langevin sandwich transducer" have remained the same for many years (estimated at three-quarters of a century). The question is raised—can a fundamentally new design, able to be applied to ultrasonic manufacturing processes (cleaning, welding, machining, forming, etc.), be created that is superior to this long-existing "standard"?

6.10 Sources of further information and advice

The technical literature on power ultrasonic transducers is extensive, as shown by a 2005 monograph by Graff (2005) that had a background of nearly 200 references on the topic. Highlights from that survey would note such classics as that of Cady (1964) on piezoelectricity, Neppiras (1973) on the prestressed piezoelectric sandwich transducer, and that of the van der Burgt chapter on "Composite prestressed high-intensity transducers" in van Randeraat and Setterington (1974 and later editions). More recent broad coverage of power transducers would include Gallego-Juarez (1991) and Dubus and Campos-Pozuelo (2000).

References

Berlincourt, D.A., Curran, D.R., Jaffee, H., 1964. Piezoelectric and piezomagnetic materials and their function in transducers. In: Mason, W.P. (Ed.), Physical Acoustics. vol. 1. Academic Press, New York. Part A, Chapter 3.

Cady, W.G., 1964. Piezoelectricity. vols. 1, 2 Dover Publications, New York. updated from original 1946 classic.

Dubus, B., Campos-Pozuelo, C., 2000. Numerical modeling of high-power ultrasonic systems: current status and future trends. Ultrasonics 38 (1–8), 337–344.

Gallego-Juarez, J.A., 1991. Transducer needs for macrosonics. In: Hamonic, B.F., Wilson, O.B., Decarpigny, J.N. (Eds.), Power Transducers for Sonics and Ultrasonics. Proceedings of the International Workshop held in Toulon, France, June 12–13, 1990. Spring-Verlag, Berlin, pp. 35–47.

Graff, K.F., 1975. Wave Motion in Elastic Solids. Oxford University Press and the Ohio State University Press, Columbus, Ohio (American Edition). Republished 1991 by Dover Publications, New York.

Graff, K.F., 1981. A history of ultrasonics. In: Mason, W.P., Thurston, R.N. (Eds.), Physical Acoustics. vol. 15. Academic Press, New York.

Graff, K.F., 2005. Power Limits of the Classical Design Ultrasonic Transducer. Part 1. January 5, 2005, EWI Project No. 48267GTH.

IEEE-SA-176-1987-IEEE, 1987. Standard on Piezoelectricity.

Lu, X., Hu, J., Peng, H., Wang, Y., 2017. A new topological structure for the Langevin-type ultrasonic transducer. Ultrasonics 75, 1–8.

Maropis, N., 1969. The design of high-power ceramic transducer assemblies. IEEE Trans. Son. Ultrason. SU-16 (3), 132–135.

Mason, W.P., 1948. Electromechanical Transducers and Wave Filters. D. Van Nostrand Company, Inc, New York.

Neppiras, E.A., 1971. Motional feed-back systems for ultrasonic transducers. In: Ultrasonics 56–58, 1971 Conference Papers.

Neppiras, E.A., 1973. The pre-stressed piezoelectric sandwich transducer. Proc. Ultrason. Int., 295–302.

Safabakhsh, A.R., (Assignee, Kulicke & Soffa Investments, Inc.), 1995. Unibody Ultrasonics Transducer. U.S. Patent 5469011.

Saffar, S., Abdullah, A., 2014. Simple method for measuring vibration amplitude of high power airborne ultrasonic transducer: using thermo-couple. Ultrasonics 54, 821–825.

Timoshenko, S., Young, D.H., Weaver Jr., W., 1974. Vibration Problems in Engineering, fourth ed. John Wiley & Sons, New York.

Tsuyuki, S., Kanda, T., Suzumori, K., Kawasaki, S., Ofuji, S., 2015. Low flow rate spraying using a torsional ultrasonic transducer. In: 2015 IEEE International Ultrasonics Symposium Proceedings. 4 pp.

van der Burgt, C.M., 1963. Motional positive feedback systems for ultrasonic power generators. IEEE Trans. Ultrason. Eng. UE-10 (1), 2–19.

van Randeraat, J., Setterington, R.E., 1963. Piezoelectric ceramics, Philips applications book. In: van Randeraat, J., Setterington, R.E. (Eds.), PXE High Intensity Transducers, first ed. Technical Publications Department, N.V. Philips Gloeilampenfabrieken, Eindhoven, The Netherlands. 2nd edition, 1974, with later editions available (Chapter 8).

Wang, Z., Xu, Y., Gu, Y., 2015. Lithium niobate ultrasonic transducer design for enhanced oil recovery. Ultrason. Sonochem. 27, 171–177.

Wood, R.W., Loomis, A.L., 1927. The physical and biological effects of high-frequency sound-waves of great intensity. Philos. Mag. 4, 417–436.

Xu, L., 2015. Investigation of a cup-shaped ultrasonic transducer operated in the full-wave vibrational mode. Ultrasonics 59, 109–118.

Zhang, Q., Shi, S., Chen, W., 2016. An electromechanical coupling model of a bending vibration type piezoelectric ultrasonic transducer. Ultrasonics 66, 18–26.

Zhou, H., Zhang, J., Feng, P., Yu, D., Wu, Z., 2020. An amplitude prediction model for a giant magnetostrictive ultrasonic transducer. Ultrasonics 108 (1–8), 106017.

Chapter 7

Power ultrasonic transducers with vibrating plate radiators

J.A. Gallego-Juárez[a], G. Rodríguez[a], E. Riera[a,b], R.R. Andrés[a], and A. Cardoni[c]

[a]*Pusonics S.L., Pico Muihacén, Arganda del Rey, Madrid, Spain,* [b]*Consejo Superior de Investigaciones Científicas (CSIC), Madrid, Spain,* [c]*Independent Consultant, Madrid, Spain*

7.1 Introduction

Until recently, the fields of application of power ultrasound have been mainly concerned with processes involving solid and liquid media, and, consequently, the great majority of the available transducer configurations have been designed taking only these media. Other propagation media, such as gases and multiphase media (i.e., gas with particles, bubbles, or drops in suspension), have thus been neglected, not least due to the difficulty of efficiently generating and propagating ultrasound through these media.

Development of suitable power transducers would represent a major step forward for the successful exploitation of high-intensity ultrasonic waves in processes involving gases and multiphase media. Requirements for these transducers include both robustness and scalability in order to provide adequate and practical technological solutions to real problems.

The recent development of a novel family of power piezoelectric transducers with extensive radiating surfaces represents a significant step forward in the implementation at laboratory, semi-industrial, and even industrial scale, of new power ultrasonic technologies applied to gases and multiphase media.

This chapter deals with the design and evaluation of the vibration characteristics of this innovative class of power ultrasonic piezoelectric transducers for gas and multiphase media, at both low and high power.

7.2 Structure of transducers: Basic design

The majority of existing high-power ultrasonic transducers are based on the classical piezoelectric sandwich transducer that was originally designed by Langevin (1920). Such devices, though improved over subsequent years (Neppiras, 1973), exhibit scale-up limitations that make them difficult to satisfy all industrial requirements. Sandwich transducers are typically limited in both power capacity and size, and in most applications, they are tuned to vibrate along their axis of symmetry in an extensional (or longitudinal) mode, to avoid coupling with radial vibration modes, and have a cross-sectional diameter smaller than ¼ of the wavelength of the tuned (extensional) mode. As a consequence, their use in industrial-scale production lines is both complex and expensive. Nonetheless, ultrasonic devices mounted along parallel lines are almost the sole commercial solution presently available to address large-scale industrial problems.

Another issue associated with existing power ultrasonic transducers regards the limited knowledge about the nonlinear behavior of such devices when they are operated under high driving voltages. Tuned systems, when excited at high power, exhibit a whole range of nonlinear phenomena, such as frequency shifts, modal interactions, and so on, which affect their performance (Nayfeh and Nayfeh, 1994). Guidelines are thus needed for eliminating or reducing nonlinear behavior at high power (Cardoni and Lucas, 2002).

In the case of the generation of ultrasonic energy in gas media, problems are even harder to overcome due to the additional difficulties posed by sound propagation through very-low-density media. As a result, the design strategy for the development of power ultrasonic transducers for the propagation of high-intensity waves in gases has been focused on the following: good impedance matching between the ultrasonic source and the medium for efficient energy transmission, highly directional or focused radiation for energy concentration, high-Q resonant transducers with mechanical amplification for obtaining large displacements, and a well-balanced distribution of stresses in the radiator for maximum power capacity. Moreover, specific mechanisms for avoiding or mitigating modal interactions and other undesirable nonlinear effects at high power operation are required.

Impedance matching between the transducer and the low-density medium can be obtained by increasing the

Power Ultrasonics. https://doi.org/10.1016/B978-0-12-820254-8.00011-7
Copyright © 2023 Elsevier Ltd. All rights reserved.

radiating surface of the transducer because the radiation impedance is proportional to the surface of the radiator. However, if the dimensions of the radiating surface are much larger than the wavelength, the radiator will not be able to vibrate in phase but will instead vibrate in one of its natural flexural modes. As a consequence, such a radiator would not generate a directional or focused acoustic field.

To overcome this problem, the radiating surface is designed with a stepped profile according to its vibration mode to compensate for the vibrating zones of the radiator in counter-phase on the two sides of nodal lines (or circles) of the excited flexural mode. The introduction of steps into the radiator profile allows modification of the radiation beam by shifting the initiation points of neighboring waves. In this way, it is possible to design extensive radiators for different acoustic field configurations.

To obtain large displacements, the transducer must contain a mechanical amplifier, and the different parts of the structure should be carefully designed to obtain a resonant assembly with a very-high-quality factor (Q). Further, for high power capacity, each of the electrical, mechanical, and thermal limits has to be considered. The most stringent thermal limitations will occur with the piezoelectric ceramics, as these can suffer depolarization due to excessive temperature rise. Under electrically limiting conditions, increasing the Q factor yields increased power, and the mechanical limitation for the radiated power is determined by the integral of the elastic strain energy density taken over the volume of the transducer structure. It is limited by factors such as material fatigue and elastic nonlinearities produced at high vibration amplitudes (Woollett, 1968), which should thus be minimized.

Given these requirements, the basic structure of the transducers has been designed as shown schematically in Figure 7.1. The transducers consist essentially of a piezoelectrically activated vibrator that drives an extensive radiator. The vibrator itself is constituted of a piezoelectric stack for transduction sandwiched between two metal ends, and a solid horn with a stepped or tapered profile that acts as a vibration amplifier. The extensional vibration generated by the piezoelectric element (PZT) and amplified by the mechanical amplifier drives the radiator into resonance in one of its flexural modes. The extensive surface area of the radiator increases the radiation resistance and offers the vibrating system good impedance matching with the medium. The radiator may be a circular or rectangular vibrating plate with a stepped profile, although alternative shapes may be required depending on the specific problems.

The reliable and safe operation of a stepped-plate power transducer in a fluid or gaseous medium requires the analysis and optimization of its structure, in particular the radiating plate, which has the largest influence in its efficiency, radiation field configuration, and power capacity. Therefore, the precise determination of the geometrical dimensions of the tuned components, the distribution and location of the stresses, along with studies of the nonlinear interactions between different vibration modes and of the fatigue limitations of component materials, all require special attention. Finite element modeling (FEM) constitutes a useful tool for such system design.

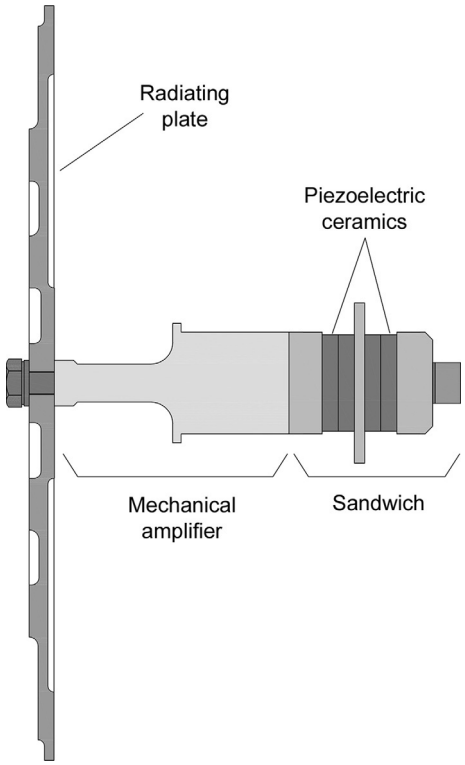


FIGURE 7.1 Basic structure of plate transducers.

7.3 Finite element modeling

The application of numerical methods in engineering and in particular in the design of piezoelectric transducers has great potential for the design, development, and optimization of new ultrasonic power generators. Plate transducer systems are designed to radiate in low-density fluids at both high efficiency (η) and quality factor (Q). This implies a very precise tuning of all components, which can be achieved by FEM provided it is performed with an accurate and proven methodology.

For the design, simulation, and dynamic analysis of the structure of new power transducers (Figure 7.1), the procedure is as follows: analytical transducer design, 3-D modeling and meshing of the geometry of the transducer, static analysis for the application of a defined prestress to the piezoelectric ceramic stacks, modal analysis to determine the natural frequencies of the system and operating mode, dynamic analysis with an applied harmonic load (harmonic analysis), and analysis of the acoustic–structure interaction in order to model the resulting acoustic field.

The initial calculation of the resonant frequency of the stepped plate is carried out by the Rayleigh–Ritz method,

or by applying the classical uniform plate solution to each zone of different thickness and establishing the continuity and boundary conditions between them (Barone and Gallego-Juárez, 1972; Gallego-Juárez, 1973; San Emeterio et al., 1987).

The analytical predesign of the piezoelectric sandwich and the mechanical amplifier is performed by calculating the length of each component so that it is resonant at one-half of the extensional wavelength propagated through it (Neppiras, 1973). This gives a first approximation for calculating the lengths of each of the components of the vibrator. The volume of ceramic in the sandwich is calculated based on the total power capacity required for the transducer to operate, taking into account the electrical, mechanical, and thermal limits of the piezoelectric material.

The 3-D geometry of the entire transducer structure is imported with the highest level of detail using computer-aided design (CAD) software. A tetrahedral mesh is typically created using a meshing algorithm that increases the mesh density (and therefore resolution) in the most critical areas where there is expected to be a high concentration of mechanical stress. It is important to perform a parametric study of convergence of the results with the density of meshing (Figure 7.2).

The mechanical properties of the linear elastic materials constituting the structure are defined and characterized by measuring the propagation velocities of the longitudinal and transverse ultrasonic waves generated in the components by conventional transmission and/or pulse-echo ultrasonic methods. This method defines the longitudinal elastic modulus, the shear modulus, and the Poisson ratio. The electromechanical properties of piezoelectric ceramics constituting the active part of the transducer are obtained directly from the manufacturer's catalog, and some of them are experimentally checked by impedance analyzer measurements.

A prestress of 25 MPa (Van Randeraat and Setterington, 1974) is applied on the ceramic stack through the central screw of the piezoelectric sandwich in order to increase the fatigue strength and to improve the coupling of the constitutive elements of the transducers at the interfaces, thus reducing mechanical losses and the electrical impedance. The piezoelectric boundary conditions are defined as open circuit by connecting one of the terminals or the electrode surfaces to a zero voltage of common ground and leaving the other without connection. As a result, the prestressed piezoelectric stack is electrically charged. This process determines the strains and stresses in the structure to be used for the subsequent dynamic analysis.

Modal analysis is performed to determine the modes of vibration of the structure. The frequency of the operating mode is calculated along with the modal parameters of nearby modes and harmonics of the tuned mode. The resonance is calculated under a short-circuit condition, where a constant voltage of zero is applied at all electrical contacts of the ceramic stacks, while the antiresonance is calculated under open-circuit conditions. The operating mode shape and location of the nodes in the driving vibrator are shown in Figure 7.3.

Once the resonance frequency of the operating vibration mode of the structure is determined through modal analysis,

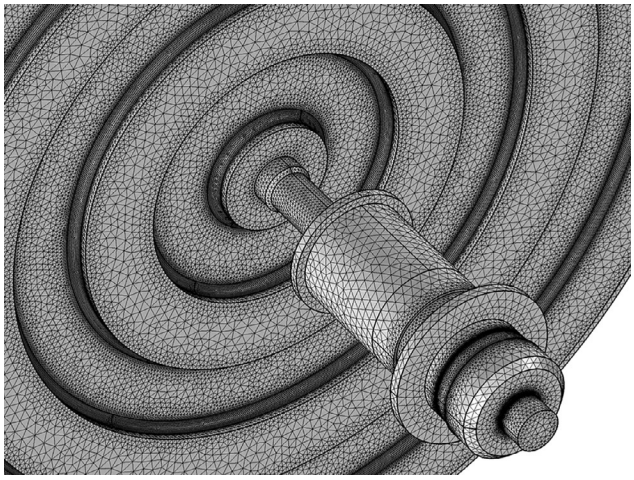


FIGURE 7.2 FE mesh of the plate transducer.

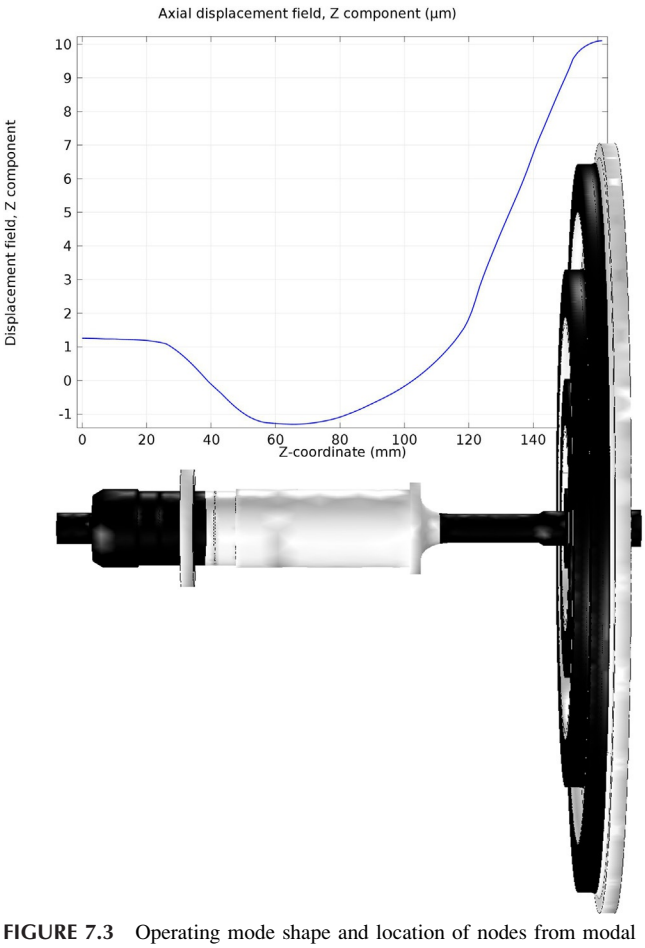


FIGURE 7.3 Operating mode shape and location of nodes from modal analysis.

harmonic analysis is performed by driving the transducer with an electric signal over a frequency span, inside which the resonant operating frequency is located. In this way, the influence of other nearby modes can be analyzed. The actual values of the displacements, deformations, and mechanical and electromechanical stresses are so quantified. The harmonic analysis determines the electromechanical response of the transducer structure when a sinusoidal electric signal is applied at the terminals of the ceramic stack. Dynamic stresses must not exceed certain limits, which depend on each material, in order to minimize nonlinear effects and to avoid fatigue failure problems of the components.

In the case of the flat-plate transducer with reflectors (Section7.6.4), the rectangular plates exhibit many eigenmodes at frequencies close to the tuned modal frequency, which could lead to modal coupling and loss of stability at high power. Therefore, a very precise numerical modal analysis must be carried out to identify the mode frequencies and shapes. The modal analysis is performed as a 3D FEM and under resonance (or "short circuit") conditions (Andrés et al., 2018).

Besides structural and piezoelectric analysis, a full model of the power ultrasonic transducer radiating in fluid media is required to model the acoustic–structure interaction and thus to simulate the generated acoustic field and the influence of the medium on the dynamic response of the transducer. FEM can be applied for bounded media, while other methods such as the boundary element method are applied for unbounded fluids (Campos-Pozuelo et al., 1998).

The fluid is considered to be ideal and homogeneous, and damping and scattering effects are neglected. The fluid is defined by the values of pressure P_0 and temperature T_0, which are independent in time. The fluid velocity is zero, and there is no convection. The variation of density $(\rho - \rho_0)$ is very small, and the compression of the fluid is thermodynamically reversible and adiabatic. The ultrasonic field is obtained by a multiphysics simulation in which the structural mechanics module simulates the vibration of the radiator, and the acoustics module simulates the ultrasonic field. The displacements that happen in the surface of the radiator excite the particles of the fluid creating an acoustic wave that propagates along the fluid domain.

FE models of the present versions of stepped-plate transducers and flat-plate transducers with reflectors have been developed by using the code COMSOL Multiphysics 4.2a (Acoustics Module, User's Guide COMSOL 4.2). The transducer is designed as a full vibrating structure, and there are some general basic requirements that must be taken into account. First, the operating frequency is basically imposed by the resonance frequency of the radiating plate in its selected flexural vibration mode. Second, the radiating plate is the most critical element to be computed, because, besides efficiency and radiation pattern, it determines the power capacity of the full transducer, which is fixed by the limiting strain of the plate material (see Section 7.5). In order to calculate the power capacity, the mechanical stresses to which the plate is subjected have to be analyzed using a very fine mesh (elements lower than 0.01 mm) in the critical areas. Such calculation implies a high computational cost to predict the potential fatigue failure zones. Third, nodal sections of the structure in which the housing devices have to be attached must be carefully adjusted to zero displacement to prevent overheating and vibration transmission. Finally, to avoid modal interactions, the untuned resonance modes should have no integer relationships with the tuned frequency or those in the vicinity of the operating tuned mode.

7.4 Controlling nonlinear vibration behavior

Plate transducers, as well as the most conventional power ultrasonic systems, exhibit a nonlinear behavior when they are driven at high power excitations. This occurrence may hamper their applicability to industrial problems.

A wide range of nonlinear phenomena, such as the presence of tuned frequency drops, multimodal responses, combination resonances, frequency and amplitude modulations, and hysteretic responses, have all been detected in tuned devices operated at high power.

Although basic design principles of simple power ultrasonic devices can be found in the literature, specific recommendations to eliminate/reduce their nonlinear behavior at high power are lacking. As a result, despite the fact that the number of companies developing power ultrasonic systems has increased over recent years, scaled-up applications of the technology remain limited. In order to progress in the design of system solutions that would enhance the widespread use of power ultrasound in industry, it is necessary to understand the dynamics of tuned devices at nominal excitation levels.

Tuned devices characterized by a complex geometry and resonating in a composite longitudinal-flexural vibration mode, such as the stepped-plate transducers, have good industrial potential, but are among those systems wherein nonlinear dynamic phenomena may occur (Cardoni et al., 2009, 2012). In order then to achieve an effective scale-up of this power ultrasonic technology, detecting, reducing, or controlling the nonlinear behavior of tuned systems is crucial.

In this section, two classes of nonlinear phenomena are investigated. The first class is associated with the inherent nonlinear behavior of ultrasonic transducers characterized by resonant frequency shifts and saturations of the tuned response during operation, which may result in bifurcations and chaotic behavior (Cardoni et al., 2009; Mathieson et al., 2013). The second category of nonlinearity investigated is due to the appearance of multimodal responses at well-separated frequencies when devices are driven at a single

modal frequency. This unwanted excitation of multimodal responses leads to poor device performance, noise, and potentially component fatigue failures. Strategies for the mitigation of these nonlinearities have been studied by the authors via a combination of FEM and experimental work (Cardoni et al., 2013; Mathieson et al., 2013).

7.4.1 Nonlinear piezoelectric responses

Tuned frequency variations and hysteretic responses similar to those of Duffing resonators are exhibited by power ultrasonic transducers. It has been shown, both theoretically and experimentally, that so-called softening response characteristics, corresponding to decreases in the driven resonant frequency and nonlinear dependence of the tuned modal response with power, occur when the devices are excited at increasing voltages (Blackburn and Cain, 2006; Mathieson et al., 2013). The incidence of this behavior leads to a difficulty in the control of the performance of ultrasonic systems, especially when sudden drops of the modal amplitude occur for small variations in frequency. It is generally believed that the inherent nonlinear behavior of the PZTs incorporated in the ultrasonic transducers is the main factor responsible for the occurrence of this softening response. Furthermore, experiments have proven that piezoelectric, dielectric, and elastic losses of piezoceramics are responsible for temperature increases at high power levels, which also cause a reduction in the value of the tuned frequency (Aurelle et al., 1996; Blackburn and Cain, 2006; Cardoni et al., 2009, 2013).

In order to distinguish between thermal and other loss contributions to the nonlinear response characteristics of piezoelectric transducers, Umeda et al. developed a bespoke burst excitation method (Umeda et al., 1999) by which an ultrasonic device was driven by a sinusoidal excitation step-swept over a frequency range centered in the tuned frequency. The excitation was generated through bursts of a fixed number of cycles at each frequency increment within the selected driving interval. The number of cycles was chosen to be large enough to allow measurement of the steady state responses of the excited devices, but short enough to limit heating of the PZTs, thus minimizing the influence of temperature on the frequency response measurements.

Other studies (Guyomar et al., 2011; Uchino et al., 2011) have shown that the dielectric and piezoelectric losses also have a prominent role in the occurrence of nonlinear phenomena. Specifically, Guyomar et al. introduced a scaling relation between the mechanical (i.e., stress and strain) and electrical (i.e., electric field and polarization) parameters in order to include all physical parameters (mechanical and electrical) in a unique differential equation that was solved by convolution. This model, which was able to account for the saturation behavior of polarization, was experimentally validated and determined that the dynamic nonlinearities of piezoceramics are largely due to dielectric losses.

The authors of this chapter have proposed a method to mitigate the nonlinear behavior of ultrasonic devices that relies on the reduction of the elastic nonlinear characteristic of the PZTs. Because in the proximity of the nominal mode, dynamic responses of ultrasonic transducers are influenced by the nonlinear compliance of piezoceramics, and elastic losses increase with the dynamic stresses generated in the material, alternative configurations of transducers have been investigated wherein piezoceramics undergo lower dynamic stress.

Four half-wavelength piezoelectric sandwich transducers were assembled as shown in Figure 7.4. Two of

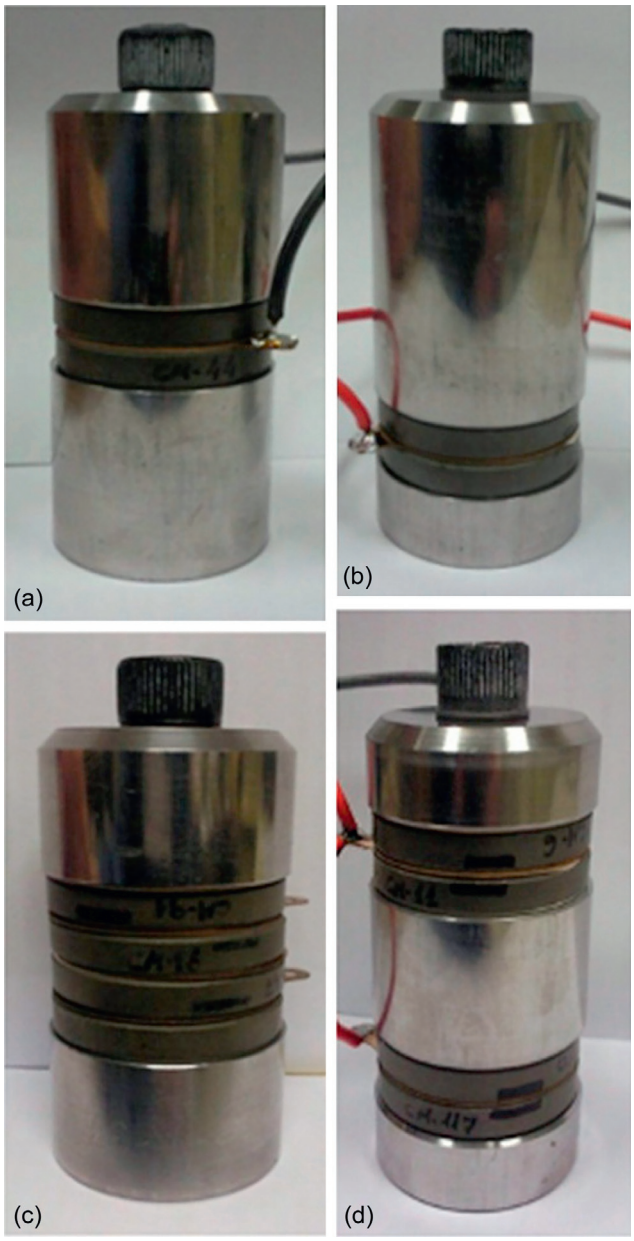


FIGURE 7.4 (a–d) Ultrasonic piezoelectric transducers under investigation.

the fabricated sandwich transducers were made from a pair of piezoceramic rings PZT-802 (manufactured by MTC Electroceramics) with two stainless steel cylinders as end-masses, while the remaining two transducer configurations incorporated four piezoceramic rings of the same type sandwiched between two (Figure 7.4c) and three (Figure 7.4d) stainless-steel masses, respectively. The assembled transducers were all tuned to vibrate in the first longitudinal mode at a frequency between 22 and 27 kHz. The configurations shown in Figure 7.4a and c placed the PZT stacks in the regions of highest stress, corresponding to the longitudinal node sections at the center of the transducers. In the configurations of Figure 7.4b and d, PZTs were located away from those regions. It should be noted that due to the repositioning of the PZT stack, the nodal section of the configuration shown in Figure 7.4b did not occur exactly at the center of the device.

A similar method to the one introduced by Umeda et al. (1999) was adopted by the authors to separate elastic and thermal losses while measuring the nonlinear (softening) response characteristics of the transducer configurations (Cardoni et al., 2009, 2013).

All transducer prototypes were driven near the resonant frequency of the first longitudinal mode at increasing voltage levels. The excitation frequency range was selected to be equal to 700 Hz, while bidirectional stepped sine sweeps of the burst excitation were performed at increasing voltages between 1 and 50 V, and at 10 V increments. In order to reduce the temperature increases of the PZT rings in proximity to the system resonance frequency, the driving signal was applied at each frequency in the excitation range for a fixed number of cycles. Velocity response curves excited through upward and downward step sweeps of the excitation frequency were measured at the output face of the transducer in the longitudinal direction using a laser vibrometer (Polytec, CLV-3D). The experimental setup used for the dynamic testing of the sandwich transducers is shown in Figure 7.5.

The results showed that by removing the PZT rings from the central region (the most stressed section) of longitudinally vibrating transducers, it was indeed possible to mitigate their nonlinear response characteristics. Figure 7.6 illustrates that under the same applied voltages, a higher vibration velocity was obtained in the transducer configurations with PZT stacks positioned away from the central section. This implies that for a fixed vibration velocity, a reduction in the shift of the tuned frequency of 75% and 45% could be achieved in the transducer configurations with two and four piezoelectric rings, respectively.

The design approach stemming from this study can be applied to the design of piezoelectric sandwich transducers used for industrial and medical applications (Cardoni et al., 2013; Mathieson et al., 2013). Algorithms for the control of nonlinear ultrasonic transducers are also under development (Perez-Alvarez et al., 2013).

7.4.2 Modal interactions

The response spectra of power ultrasonic systems operated in the tuned mode may be adversely affected by untuned modes giving rise to modal couplings. Multimodal responses due to the vicinity of one or more resonant frequencies to the tuned frequency (linear modal couplings) can be reduced/avoided through the application of design guidelines aimed at separating the frequencies of close modes from the operating frequency (Cardoni and Lucas, 2002; Gallego-Juárez et al., 2001, 2008). Such guidelines depend on the tuned system geometry and operating mode of vibration.

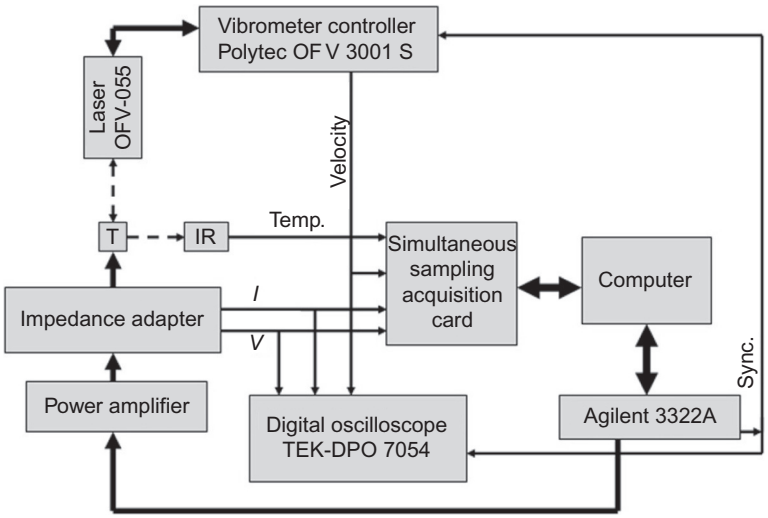


FIGURE 7.5 Diagram of the experimental rig for vibration testing of the ultrasonic transducer.

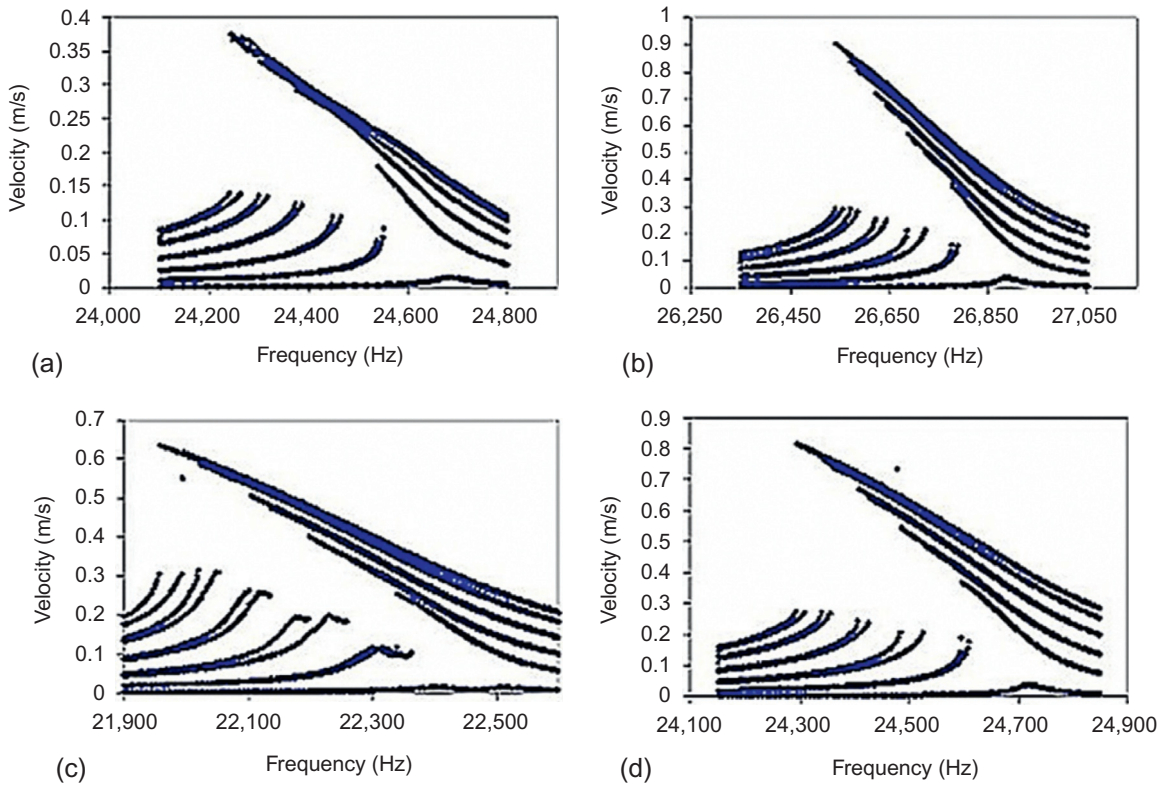


FIGURE 7.6 Measured nonlinear vibration response characteristics: (a) one stack made of two piezoelectric rings in the center of the transducer; (b) one stack of piezoelectric rings positioned asymmetrically respect to the transducer center; (c) one piezoelectric stack with four piezoelectric rings in the center of the transducer; (d) two piezoelectric stacks positioned symmetrically respect to the transducer center.

Even more problematic and difficult to predict at the design stage is the occurrence of untuned modes at frequencies far from the tuned frequency becoming excited above certain excitation thresholds, again resulting in nonlinear modal couplings (Cardoni et al., 2012, 2013; Lucas et al., 2003). Combination resonances can occur when there exist resonance conditions such as a modal frequency being almost half, or twice, the system tuned frequency, or the sum of two untuned natural frequencies almost equal to the operating frequency. The existence of a near-integer relationship between the tuned frequency and other resonances is a necessary, but not sufficient, condition for the excitation of multimodal responses in a system driven at a single frequency. The excitation must also exhibit a time-varying modification of a system parameter such as its stiffness (Cartmell, 1990). A type of excitation with this special characteristic is known as *parametric excitation*. A parametric excitation differs from a simple forced excitation because the action of the latter does not affect any system parameter.

A three-mode interaction typical of autoparametric systems has been detected and characterized in plate transducers for sound propagation through gas and multiphasic media. Autoparametric systems represent a special class of nonlinear systems wherein the parametric excitation is a result of the (external) excitation of a system near one of its modal frequencies. A redesign strategy to improve the dynamic behavior of the plate transducer through the elimination of unwanted modal contributions in the tuned response is outlined below.

An experimental study was conducted to investigate the vibration behavior of a circular stepped-plate transducer of the type shown in Figure 7.1 through increasing the applied driving voltage up to nominal conditions. In order to detect, characterize, and classify the dynamic characteristics of the device, its modal frequencies were initially identified over a wide frequency range at low power excitations. The plate transducer was designed to resonate in the tuned longitudinal-flexural composite mode at about 25.6 kHz. In this study, modal data were collected over a 1–80 kHz frequency range. The experimental setup was as illustrated in Figure 7.5.

Out-of-plane vibration velocity measurements were carried out by pointing the laser vibrometer normal to the radiating plate plane and close to its border. This location was chosen in order to detect the largest number of modal frequencies of the system, as the plate was vibrated under free boundary conditions. In this way, resonance conditions between the tuned frequency and one or more untuned modal frequencies could be detected.

Figure 7.7 shows the vibration velocity spectrum obtained applying a sinusoidal excitation of 10 V to the transducer. For the characterization of the nonlinear responses of the sandwich transducer, the vibration response of the plate transducer was investigated at increasing applied voltages. In this case, the maximum applied voltage was set equal to 300 V. Vibration velocity measurements were obtained over a 40-Hz interval, centered on the tuned frequency of the system via bidirectional frequency sweeps. Velocity responses were measured at increments of 0.5 Hz over the excitation frequency range.

Figure 7.8a shows the velocity response obtained at 10 V excitations, and the ones shown in Figure 7.8b are related to the response measured under a 300-V applied voltage. Comparing these figures, it can be observed that at high power, the vibration velocities detected through upward and downward sweeps differed.

Figure 7.9a reveals that the velocity response of the ultrasonic device exhibited a single spectral line near the tuned frequency when the system was excited at frequencies outside the V-shaped region shown in Figure 7.8b. At a driving frequency inside such an interval and high applied voltage, two lines around 11 and 14.5 kHz appeared, enriching the velocity spectrum of Figure 7.9b. The sum of these two frequencies was almost equal to the tuned frequency of the device, thus satisfying the relationship, $\omega_1 + \omega_2 \approx \omega_o$. Figure 7.7 indicates that the investigated ultrasonic device had two vibration modes at resonant frequencies close to ω_1 and ω_2, which are internally excited (or internal) modes. Figure 7.10 shows the normalized velocity response of one of the internal modes detected, while the plate transducer was excited in the 25.6–25.65 kHz range (i.e., inside the V-shape region highlighted in the spectrum response of Figure 7.8b at a 300-V excitation).

The V-shape region of Figure 7.8b suggests that a modal energy transfer, typical of autoparametric systems, may have occurred. To investigate this further, velocity spectra of the plate transducer driven at frequencies inside and outside the V-shape region were measured. For excitation frequencies within the V-shaped region of Figure 7.8b, the internal mode responded following the U-shaped curves shown in Figure 7.10a and b. For driving frequencies outside the V-shape region, the response of the internal mode was null. Hence, the measured response characteristics proved to be qualitatively similar to analytical models of primary and secondary responses obtained in simple autoparametric systems (Cartmell, 1990).

Given these conditions for the excitation of parametric resonances in dynamic systems, two approaches could potentially be adopted to prevent the occurrence of multimodal responses. The first strategy would consist of eliminating the parametric excitation acting on the plate transducer. Previous studies on the dynamics of simple plate structures have shown that the in-plane dynamic stresses arising in the vicinity of a resonant frequency of a flexurally vibrating plate may result in a time-varying modification of the radial stiffness, which may in turn result in a multimodal interaction. An alternative approach consists of avoiding untuned modal frequencies with near-integer relationships with the tuned frequency. For the plate transducer of the present investigation, it was decided to modify the geometry of the plate radiator in order to get rid of the combination resonance, $\omega_1 + \omega_2 \approx \omega_o$. Hence, the diameter of the radiating plate was reduced by less than 0.1% to increase the tuned frequency by approximately 300 Hz. No evidence of multimodal response was detected when the modified system was operated at the nominal power conditions, proving that the proposed redesign approach was valid. Further investigations regarding the mitigation of modal

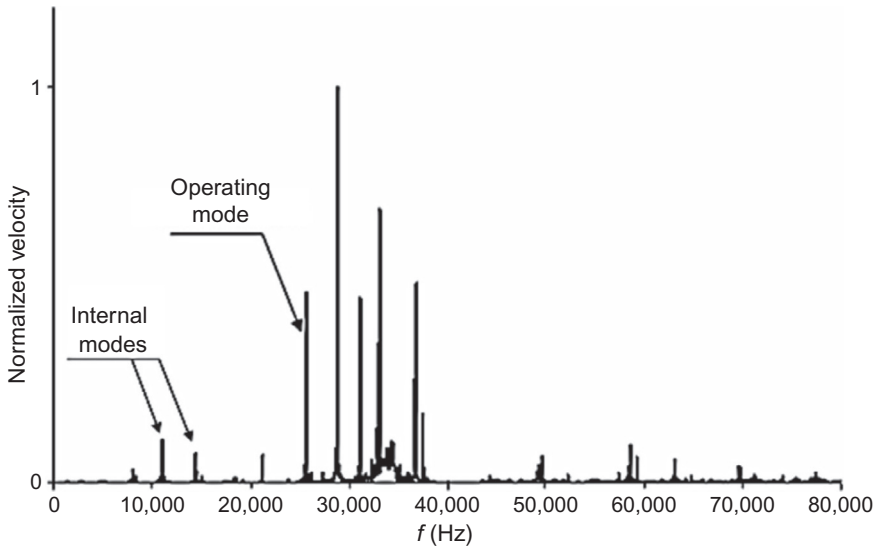


FIGURE 7.7 Vibration velocity response measured in the 1–80 kHz range under a 10-V excitation.

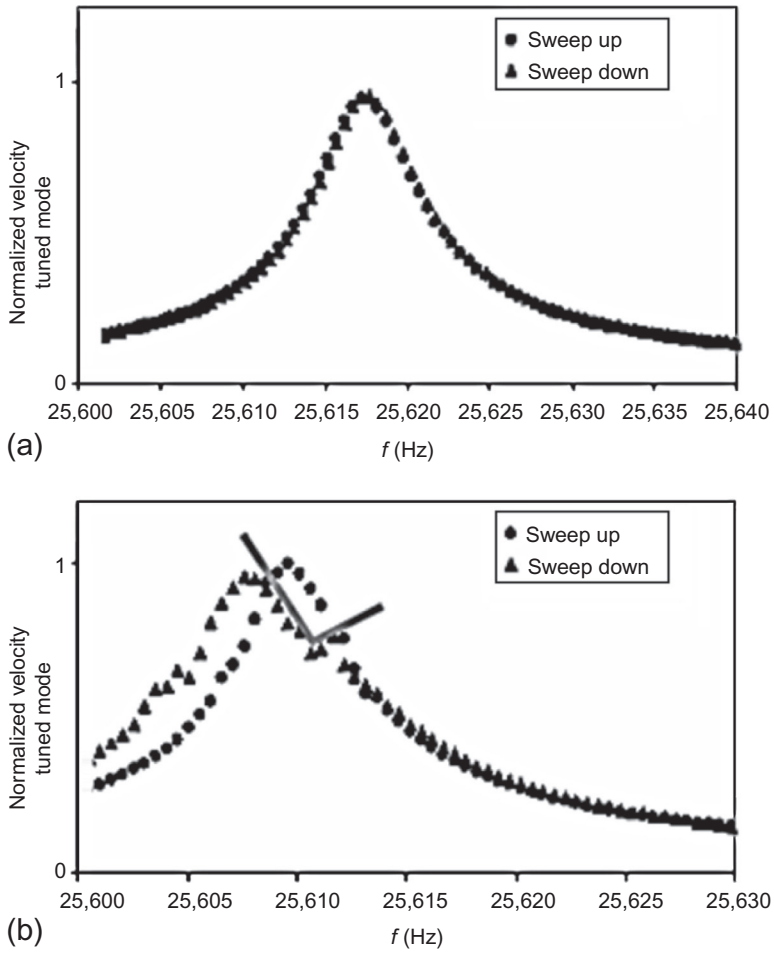


FIGURE 7.8 Normalized vibration velocity frequency responses obtained via upward and downward frequency sweeps around the tuned frequency: (a) applied voltage, 10 V; (b) applied voltage, 300 V.

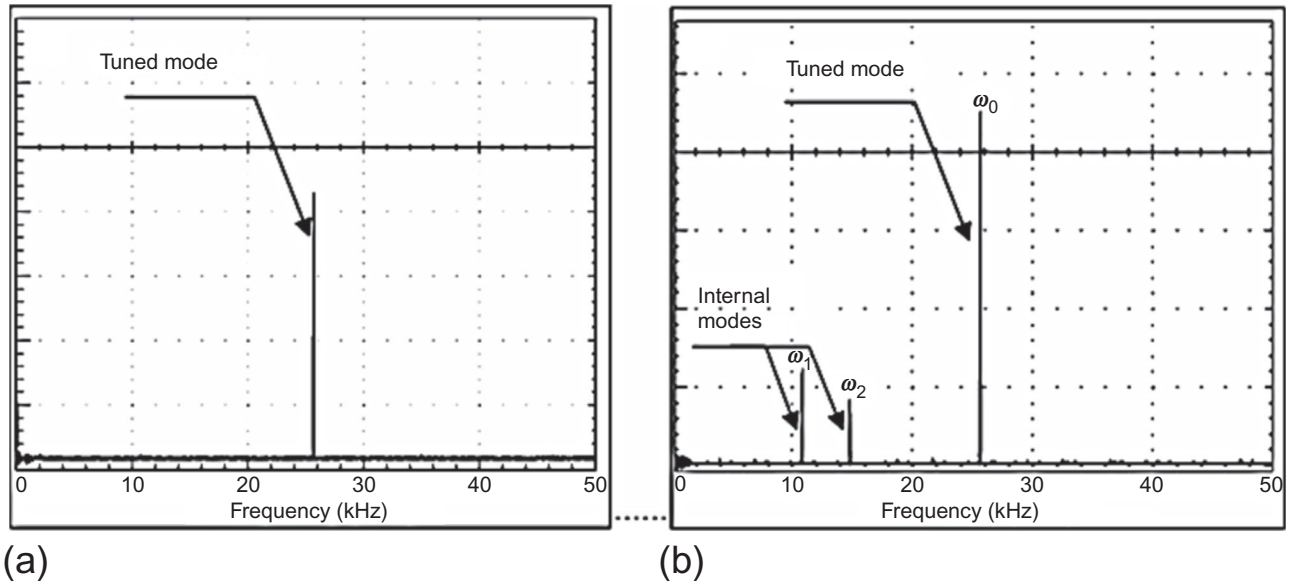


FIGURE 7.9 Vibration velocity spectra measured on the plate edge while the assembly was excited at 300 V: (a) excitation frequency outside the V-shaped region resulting in "single-mode" response, (b) excitation frequency inside the V-shaped region resulting in "multimodal" response.

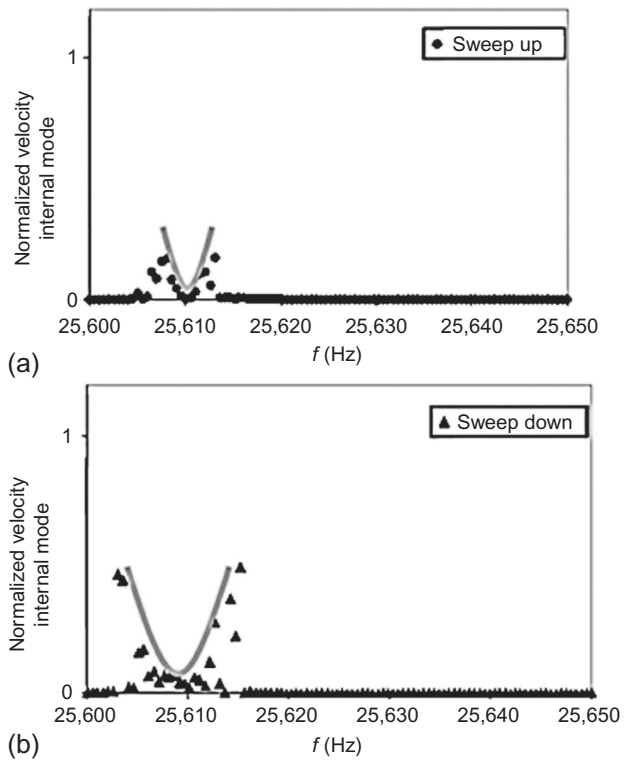


FIGURE 7.10 Normalized velocity (secondary) response of an internal mode of the plate transducer excited via frequency sweeps around the tuned frequency under a 300-V drive: (a) sweep up; (b) sweep down.

interactions in power ultrasonic systems are needed; geometrical modification of the tuned device may not be always effective in structures characterized by high modal densities. Under these circumstances, further experimental studies carried out by the authors showed that isolating the tuned modal frequency of the ultrasonic system from nearby modal frequencies via geometrical design helps to get rid of unwanted excitations of combination resonances between well-separated modes. This implies that the elimination of linear modal coupling between the tuned mode and closely spurious modes by opportune frequency separations may also help to restrict the occurrence of nonlinear modal couplings.

7.5 Fatigue limitations of transducers

There are two main factors limiting the maximum acoustic energy that a power ultrasonic transducer may deliver into a fluid medium: One is inherent to the propagation of high-intensity waves through gases and is associated with nonlinear attenuation, which leads to wave saturation and significant energy losses; and the other is related to the limited power capacity of the transducers, due to the fatigue limits below which tuned components must operate.

This section is devoted to the power capacity restrictions of power transducers imposed by component fatigue. Fatigue is a term that applies to changes in properties of materials subjected to alternated or repeated mechanical stresses or strains that lead to component cracking or failure. Fatigue failure may occur in many different forms. The most general form starts with the nucleation of permanent damage, followed by the creation of microcracks that gradually grow until they reach a critical size, at which the crack will propagate suddenly and the material will fracture. Dislocations play a major role in the initiation phase of a fatigue crack. After a high number of loading cycles, dislocations pile up and form structures called persistent slip bands (PSBs). There are many uncertainties in establishing fatigue reliability, particularly when the material is subjected to ultrasonic stresses.

For the development of power ultrasonic transducers, a new high-frequency fatigue testing procedure has been designed and implemented (Campos-Pozuelo and Gallego-Juárez, 1996). It mainly consists of measuring the internal losses in the component materials when subjected to different strain levels at ultrasonic frequencies. The internal losses are quantified through measurement of particle velocity in specially designed samples driven by a piezoelectric vibrator. For extensional vibration, cylindrical bar samples with thinned-out central sections were designed to achieve higher strain within this section, which is sized to resonate with the piezoelectric vibrator. All measurements are carried out by keeping the excitation of the driving vibrator within the linear regime, while the sample vibrates at high strain amplitude (nonlinear range) in the thinner central section.

A model of the assembly vibrator sample was developed to obtain the internal losses from the measurement of the particle velocity of the sample and the excitation voltage of the piezoelectric vibrator. Titanium and aluminum alloys commonly used in power transducer construction have been studied applying this procedure at frequencies around 23 kHz. The results have clearly shown that there exists a strain value beyond which the attenuation increases very rapidly and changes induced in the material can lead very quickly to fatigue failure. The maximum admissible stresses without danger of fatigue were approximately 200 MPa for the titanium alloy case.

For fatigue study of flexural vibrations, prismatic bars with a stepped profile have been designed (Campos-Pozuelo and Gallego-Juárez, 1995). In plate transducers, the flexural vibrating radiator (the plate) is the component of the tuned assembly that vibrates with maximum displacement, determining the maximum power capacity of the ultrasonic system. Numerical FE models are essential for the prediction of the plate zones where fatigue cracks can originate, and very fine meshes should be used in zones undergoing high dynamic stresses. Figure 7.11 shows the FE stress analysis of a critical zone in a plate radiator

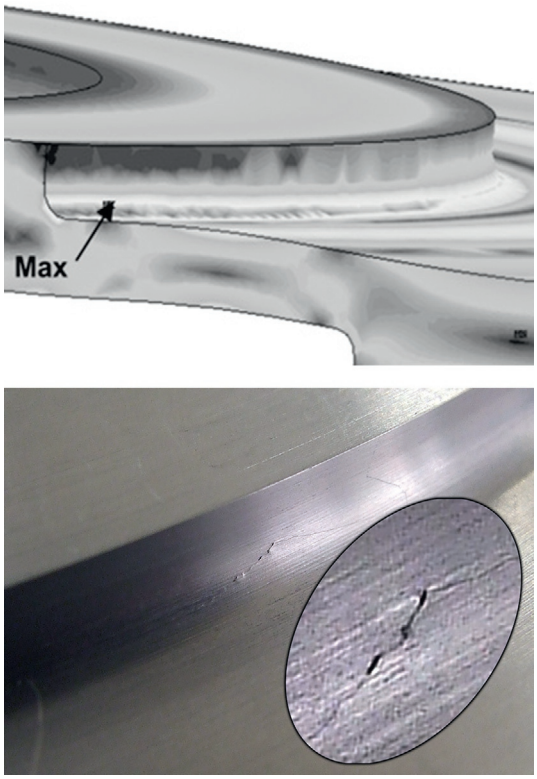


FIGURE 7.11 Stress analysis of a critical plate zone and actual crack there produced.

prototype, together with the fatigue crack generated in this zone when the stress limit is exceeded.

7.6 Characteristics of the different types of plate transducers

Following the design procedure outlined in Section 7.2, several types of power transducers have been designed and constructed for different applications. The main types of such transducers may be classified as stepped-plate, grooved-plate, stepped-grooved-plate, and flat-plate with reflectors (Gallego-Juárez et al., 2010b).

7.6.1 Stepped-plate transducers

The stepped-plate transducer has the basic structure described in Section 7.2 with a radiator that is in the form of an extensive circular or a rectangular plate with stepped profile, vibrating in one of their natural flexural modes. As previously stated, the stepped profile of the plate allows the acoustic radiation pattern to be tailored to requirements. Because a high concentration of energy is generally required, highly directional and focusing radiators have been designed and developed in order to produce high-intensity acoustic levels.

With a directional stepped profile, the objective of the design procedure is to place in phase the radiation across the entire beam. This requires that the surface elements vibrating in counter-phase on the two sides of each nodal lines or circles (depending on whether the plate radiator is rectangular or circular) should be shifted along the acoustic axis to one-half of the wavelength of sound in the propagation medium. As a result, the resulting stepped plate, even if excited in a flexural mode of vibration, will produce radiation in phase across the beam, as shown in Figure 7.12. This effect is clearly observed when comparing the measured acoustic pattern of a flat-plate radiator with the one of the stepped-plate radiators of the same diameter. Figure 7.13 shows flat- and stepped-plate radiators both vibrating at a resonant frequency of about 41 kHz in a flexural mode with three nodal circles. The acoustic field produced by the stepped plate is coincident with the one computed for a theoretical piston of the same diameter. In this way, piston-like radiators of any surface area and of any frequency may be designed.

Following a similar procedure, it is possible through adequate displacement of the different plate zones to achieve any acoustic field configuration. Figure 7.14 shows the procedure to follow for the design of focusing

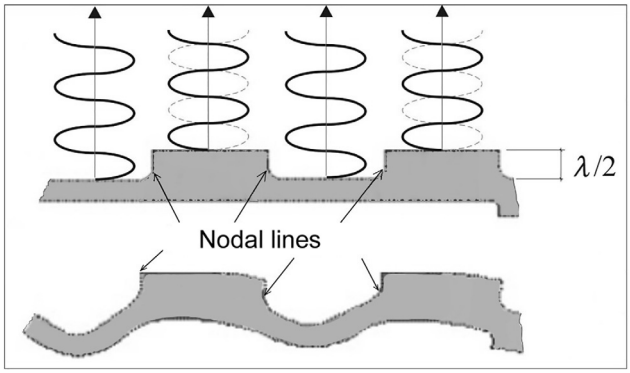


FIGURE 7.12 Phase coherent effect by the stepped-plate radiator.

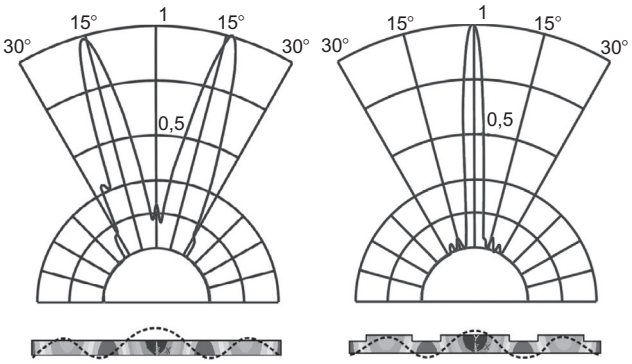


FIGURE 7.13 Directivity diagrams of flat-plate and stepped-plate radiators of the same diameter.

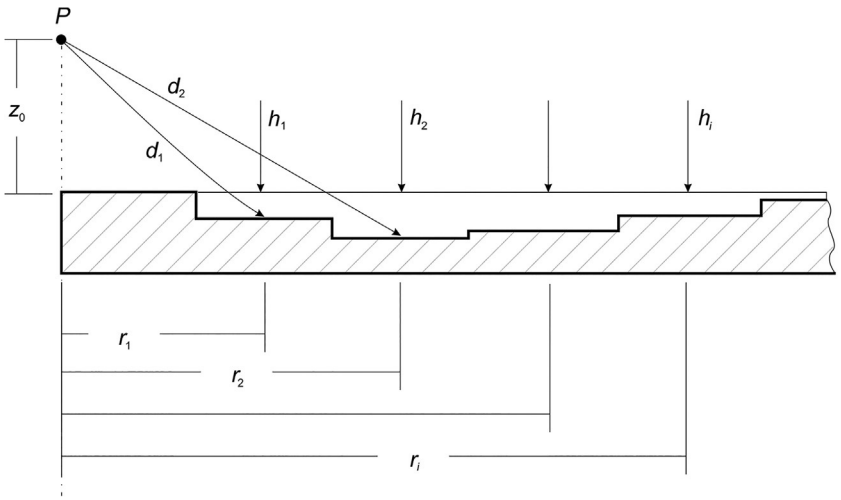


FIGURE 7.14 Scheme for the design of focusing radiators.

radiators. Given that the plate zones separated by a nodal line vibrate in counter-phase, the radiated energy may be focused around point P by modifying the profile of the plate in such a way that the plate zones comprised between two nodal lines are shifted with respect to a flat profile of height h_i, which is determined according to the following rule:

$$d_i = \left[(z_0 + h_i)^2 + r_i^2\right]^{\frac{1}{2}},$$

$$d_i - d_{i-1} = \frac{\lambda}{2},$$

where λ is the wavelength of the radiation in the medium, and the subscript $i = 1,2,3, \ldots,n$ indicates the different internodal zones.

In the circular stepped-plate transducer configuration, the plate radiator vibrates in an axisymmetric flexural mode when driven at its center by a length expander vibrator. Different prototypes of circular stepped-plate directional and focusing transducers have been developed for frequency ranges of between 10 and 40 kHz with power capacities up to approximately 1 kW (Figure 7.15). The design of these transducers, initially analytically constructed (Gallego-Juárez et al., 1978), has been further improved by applying the finite element approach. The main characteristics of the developed airborne directional circular stepped-plate transducers are summarized in Table 7.1. The directivity pattern of a stepped-plate transducer resonant at a frequency of about 20 kHz with a radiator of about 50 cm in diameter is shown in Figure 7.16.

Following the design scheme of Figure 7.14, focusing circular stepped-plate transducers have also been developed for frequencies in the range of 20–40 kHz. The efficiency and power capacity of these transducers is very similar to that of directional transducers of similar diameter. Figure 7.17 shows the acoustic field of a focusing circular plate transducer with a plate radiator of about 40 cm in diameter and an operating frequency of 25.8 kHz. The ultrasonic energy is concentrated in a focal volume of about 2 cm in diameter and 13 cm in length (dimensions taken at 3 dB of the maximum value) located at a distance of about 40 cm from the plate radiator. Intensities on the order of 170 dB can be obtained in the focus with an applied power of 200 W.

For specific industrial applications, stepped-plate transducers with a rectangular radiating surface may offer

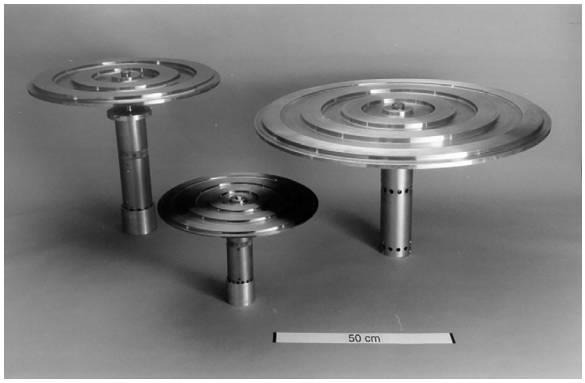


FIGURE 7.15 Circular stepped-plate directional transducers.

TABLE 7.1 Main characteristics of directional circular stepped-plate transducers.

Electroacoustic efficiency	**75%–80%**
Directivity (3-dB beam width)	<2°
Maximum power capacity	1 kW
Frequency range experimented	10–40 kHz
Maximum intensity levels	175 dB

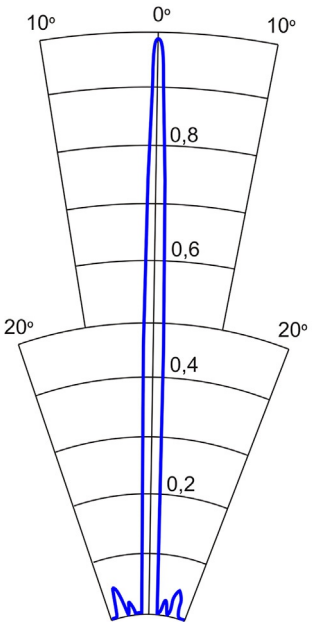


FIGURE 7.16 Directivity pattern of a circular stepped-plate transducer of 20 kHz.

technical and practical advantages over transducers with circular radiators. Rectangular-plate configurations allow a more uniform distribution of vibration displacements than circular plates. In fact, the distribution of displacements of axisymmetric circular plate vibrators, expressed by Bessel functions, presents high amplitudes in the inner area and much lower and decreasing amplitudes in the outer areas, while the deflection of rectangular plates, given by sine and cosine functions, shows more uniformity between the central and outer areas (Leissa, 1969; Timoshenko and Woinowsky-Krieger, 1959). Therefore, by using rectangular radiators, more homogenous acoustic fields may be reached. At the same time, the more uniform vibration distribution smoothes stresses, and, consequently, fatigue resistance improves and power capacity increases. This is a highly desirable feature for large-scale industrial applications in which powerful generators and homogeneous treatments are generally required. However, the complex structure of rectangular plate transducers, which combines the extensional vibration of the driving vibrator with the non-axisymmetric flexural mode of the plate radiator, together with the high modal density of rectangular vibrating plates, makes these transducers more prone to nonlinear response characteristics when driven at high power.

Rectangular radiators have been designed to operate in a resonant mode with 14 nodal lines parallel to the smaller side. Both faces of the radiator are stepped to obtain directional radiation from both faces. The purpose is to use the back radiation in the forward direction by means of adequate reflectors. Prototypes for 7 and 20 kHz frequencies have been developed with power capacities of up to 2.7 kW (Figure 7.18). The main characteristics measured in air are shown in Table 7.2. The acoustic patterns are shown in Figure 7.19.

7.6.2 Grooved-plate transducers

The development of large-scale industrial transducers depends on power capacity and behavior under high strain levels. The power limitations for the use of transducers are mainly related to the distribution and location of the stresses as well as the difficulties associated to reaching very high powers without generating nonlinear disturbances.

For reliable and safe power operation of plate transducers, the distribution and location of the stresses in the

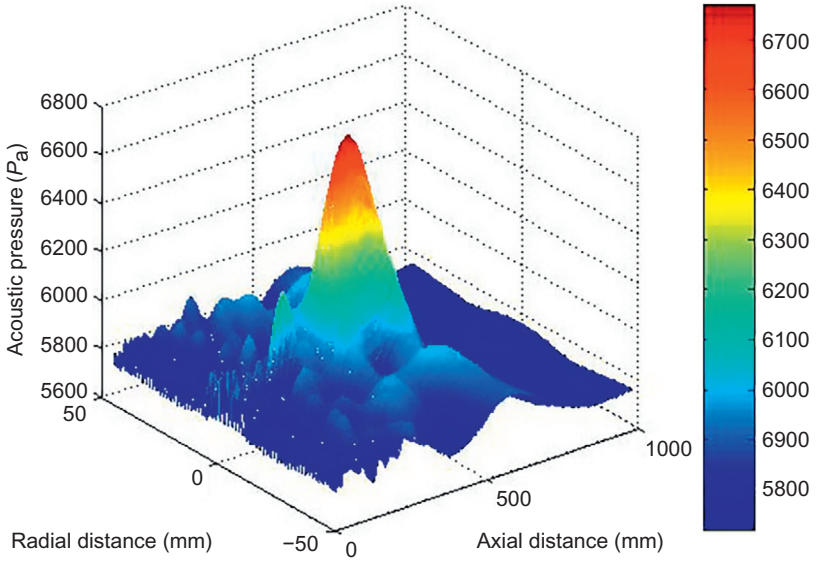


FIGURE 7.17 Acoustic field of a focusing circular stepped-plate transducer of 25.8 kHz.

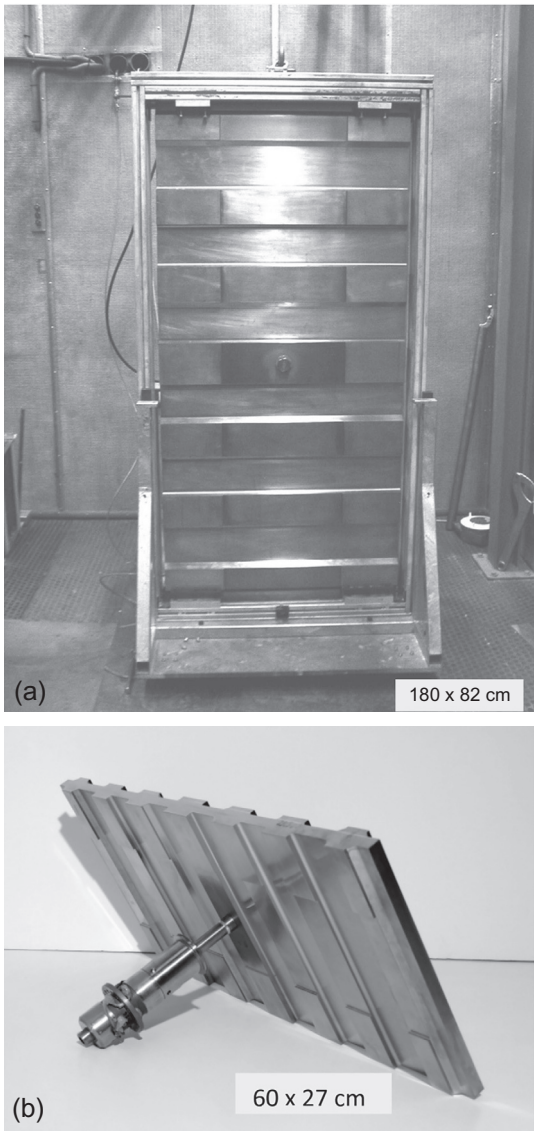


FIGURE 7.18 (a, b) Rectangular stepped-plate transducers (Figure 7.9 art US Sonochem).

plate radiator is a primary issue to take into account. The power capacity of the transducer depends directly on the maximum stress that the plate is able to withstand without material failure. Therefore, as a first condition, the plate must be made of a high fatigue resistance material, usually a titanium alloy. In addition, the stresses at the vibrating surface should be (as far as possible) uniformly distributed to avoid stress peaks. The objective is to reduce the stress differences in the flexural vibrating plate radiator. For this purpose, the profile of the back face of the plate can be modified by grooving, removing mass from different plate zones. Such modifications, guided by FEM, depend on the vibration mode of each plate radiator. It has been experimentally shown that the distribution of displacements in the grooved plate is very sensitive to the extracted mass even if the grooved area is very thin.

Nonlinear disturbances are frequently present with power ultrasonic transducers due to their inherent high-intensity vibration characteristics as a result of which, high-power operation of complex transducers designed to resonate in a tuned mode may be disturbed by the coupling or excitation of untuned modes, causing heating, noise, inadequate vibration amplitudes, low reliability, and even component failures (Cardoni and Lucas, 2002; Nayfeh and Nayfeh, 1994).

The complexity of the structure of plate transducers, which are high modal density systems that combine longitudinal and flexural vibrations at the required tuned frequency, makes modal interactions at high power operation difficult to avoid. Modal interactions cause the energy to be channeled from the excitation mode into other vibration modes, impeding power operation.

It has been determined that the mechanism causing the initiation of undesirable vibration modes, in addition to the mechanisms of parametric or autoparametric resonances, is the existence of an untuned mode too close to the operating driving frequency. The design strategy to mitigate such modal interactions is to separate the operating mode from undesired close modes by modifying the plate radiator. The methodology consists of finely adjusting the balance between the masses of the different zones of the plate radiator in order to magnify as much as possible the response of the operating tuned mode and, at the same time, to weaken and/or to move the closer undesired mode. The practical procedure is carried out by grooving the back face of the plate radiator in the appropriate zones. By following this procedure using FEM, it is possible to increase the separation between the closer modes. Such grooved-plate transducers can be operated at higher power excitation without the generation of unwanted modal interactions.

TABLE 7.2 Main characteristics of the directional rectangular stepped-plate transducers.

Radiating plate (m^2)	Frequency (kHz)	Bandwidth (Hz)	Directivity (3-dB beam width)		Efficiency (%)
			XZ plane	*YZ* plane	
1.8 × 0.8	7.6	1	About 2°		67
0.6 × 0.3	19.5	2.5	About 2º		75

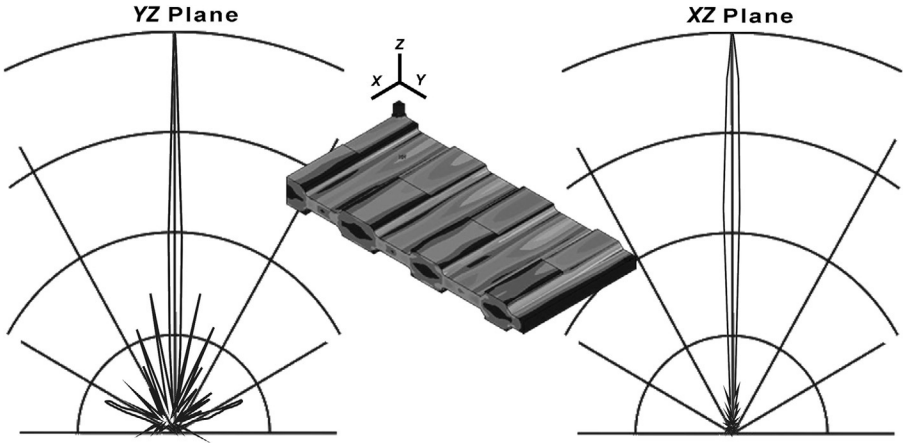


FIGURE 7.19 Directivity patterns of a rectangular stepped-plate transducer of 19.5 kHz.

7.6.3 Stepped-grooved plate transducers

As stated, the purpose of a stepped profile is to control and select the radiation pattern, while the grooved profile can be used to separate untuned vibrational and reduce modes the distribution of the amplitudes and stresses to increase the power capacity of the transducer. These two objectives are not mutually exclusive, as the radiating face of the plate may be stepped while the back face may be grooved. Transducers with stepped-grooved plate radiators have already been designed incorporating these two different profiles. In addition, it has been possible, with some approximations, to combine the grooved profile with the focusing design. In their practical realization, the stepped profiles have been slightly modified from the theoretical profiles to improve the behavior of the radiator with respect to modal interactions and stress distribution. Such transducers for frequencies of about 21 and 26 kHz and power capacities of 300 and 200 W, respectively, are already commercialized (Gallego-Juárez et al., 2010a, b). Figure 7.20 shows a picture of one of these transducers and its design using FEM.

7.6.4 Flat-plate transducers with reflectors

As stated, for the directional stepped-plate radiators, the height of the steps must be equal to one-half of the wavelength in the propagation medium. For ultrasonic radiation in air at about 20 kHz, this wavelength is shorter than 2 cm, but for radiation in water, the wavelength is five times higher, so that the use of directional stepped plates in the latter is impractical at low ultrasonic frequencies. A similar problem occurs in air when radiation is desired at sonic frequencies. Therefore, alternative solutions to obtain directional radiation in liquids or in air at sonic frequencies, without the use of steps, have also been studied. As a result, a new type of vibrating plate transducer has been designed and constructed to obtain highly directional radiation with a feasible and repeatable construction. This new type of transducer uses the radiation from both faces of the vibrating plate; thus, it has the ability to double the efficiency of the transducer.

The concept of this new design is again to put in phase the radiation that is emitted by plate zones vibrating in counter-phase. However, the use of the radiation from both plate faces implies that the emission from one specific plate sector is in counter-phase at both sides of the plate. The design consists of separating the radiation of each internodal sector by means of parallel walls that are perpendicular to the plate surface and exactly located in the nodal lines, without touching the plate. These walls form channels that are closed by a reflector at 45° with the radiating surface (Figure 7.21). The distance from the reflector to the surface of the radiating plate differs for the sectors vibrating in counter-phase by one-half of the wavelength ($\lambda/2$) of the radiation. Therefore, the acoustic field generated by the flexural vibrating plate and reflected by the reflectors placed alternatively at distances l and $l+\lambda/2$ will be formed by waves that are in phase on a plane perpendicular to the plate. It should be noted that the reflectors located on both sides of the same plate sector have to be placed at distances that differ from one another in $\lambda/2$ (Rodriguez-Corral et al., 2001).

Figure 7.22 shows a photograph of a transducer prototype constructed with a rectangular plate radiator for operation in air at a frequency of 9.7 kHz. The plate is driven at its center in a similar way to other plate transducers. The highly directional radiation obtained with the prototype (Figure 7.23) confirms its high performance.

This type of transducer has also been developed at ultrasonic frequencies for food-drying applications. In this case, the mechanical amplifier of the extensional driving vibrator is lengthened by $\lambda/2$ in the narrow section to avoid the interference of its whole structure with the radiation of the plate (Figure 7.24a). A picture of the transducer for a frequency of 21 kHz with a radiating plate of $570\times308\times34$ mm and an

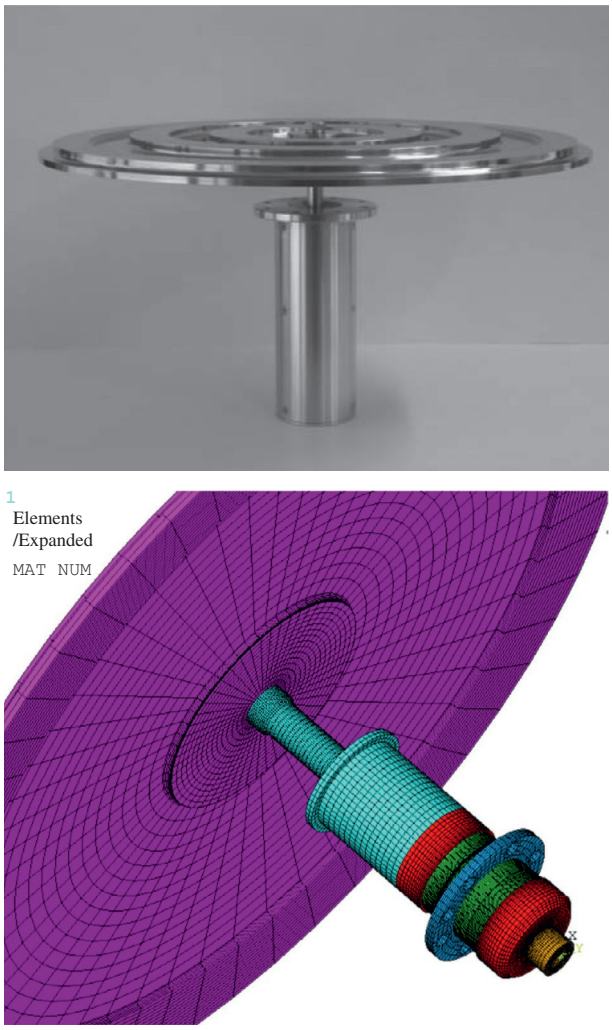


FIGURE 7.20 Circular stepped-grooved-plate transducer and FE simulation.

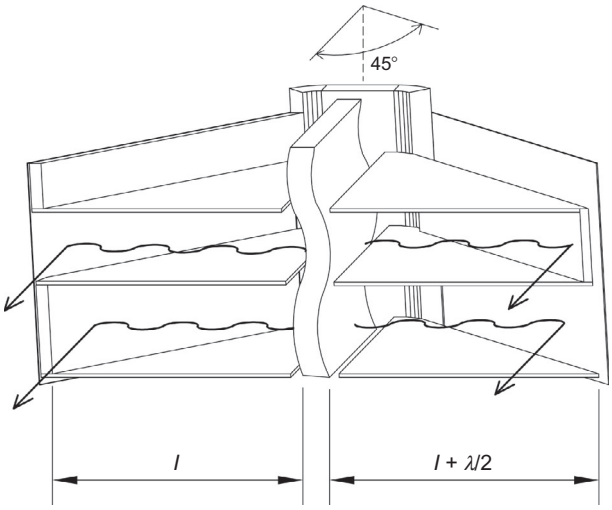


FIGURE 7.21 Scheme for the design of a flat-plate radiator with reflectors.

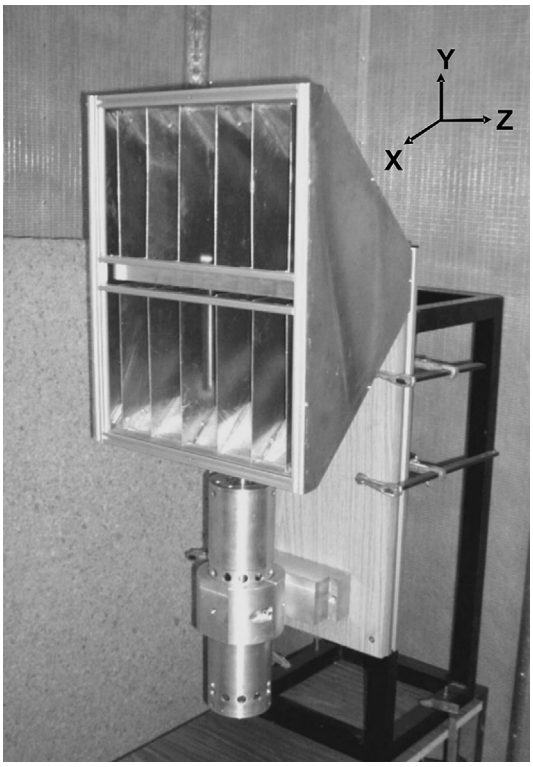


FIGURE 7.22 Flat-plate transducer with reflectors (Figure 7.15 art US Sonochem).

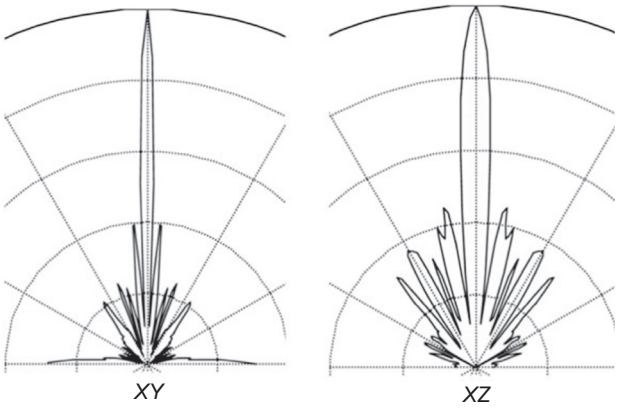


FIGURE 7.23 Directivity patterns of a flat-plate transducer with reflectors for operating in air at 9.7 kHz.

operational mode of 12 nodal lines (12|0) in the transversal direction ($m = 12$, $n = 0$) is shown in Figure 7.24b.

The acoustic fields of the transducer, without and with the reflectors, were numerically simulated by FEM and experimentally validated by measuring them in an anechoic chamber. Figs. 7.25 and 7.26 show, respectively, the measured radiated acoustic fields along the axial central

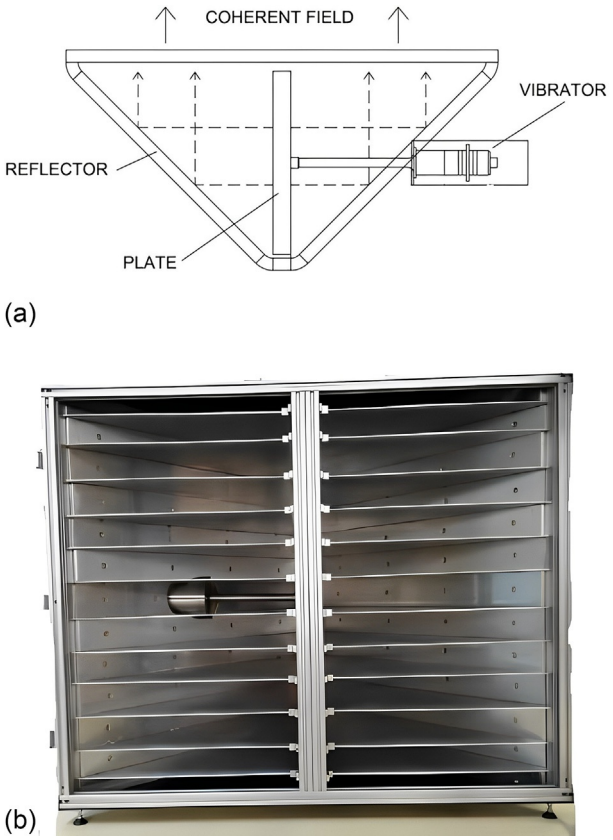


FIGURE 7.24 Scheme (a) and picture (b) of a flat-plate transducer with reflectors for 21 kHz.

plane XY and the corresponding directivity diagrams of the transducer with the radiating plate without reflectors and with reflectors.

As a conclusion, this type of plate transducer allows a very directional radiation to be obtained together with higher efficiency since energy from both sides of the radiating plate is used (Andrés et al., 2019, pp. 1–13).

7.7 Evaluating transducers in power operation: Electrical, vibrational, acoustic, and thermal characteristics

The development and application of power ultrasonic transducers requires an evaluation of their behavior under power operation. To study the different transducer behavior at low- and high-power conditions, a system was developed and tested (Riera et al., 2007) that is based on a combination of electrical excitation with electrical, vibrational, acoustic, and thermal measurements. Specific hardware and software were developed for excitation, control, signal recording, and processing in real time. In this section, two experimental configurations will be shown that allow the main parameters of the transducer to be controlled and monitored and that can also identify the resonance frequency.

The evaluation system allows the following parameters of the transducer to be controlled and monitored:

(a) voltage (V) and current (I) sampled on the out-port-side of the impedance-matching unit;
(b) vibration amplitude (ξ) and phase (φ) sampled by a laser scanning vibrometer;
(c) temperature (T) sampled by a thermocouple and infrared probes; and
(d) acoustic pressure (P_a) sampled by a microphone (M) or hydrophone (H) depending on the fluid media to be treated.

A block diagram of the driving and evaluation system is shown in Figure 7.27. This first version of the system consists of the following components: power ultrasonic transducer, impedance-matching unit, power generator, data acquisition unit, computer, and a set of probes. The ultrasonic devices to be tested are power piezoelectric transducers for use in fluids (air or water). They are generally driven by a power generator with frequency control and an impedance-matching unit to keep the transducer working at resonance and to maximize energy transfer between the electronic generator and the transducer. The impedance-matching unit provides a sample of the voltage and current of the driving signal of the transducer. Such sampled signals are also used to control the frequency and to monitor the system.

The electronic power generator includes a broadband power amplifier and a signal generator. The signal generator has two basic configurations:

(a) function/arbitrary waveform generator
(b) digital/analog output from the data acquisition unit

The first configuration is used to generate a signal according to the parameters provided by the computer. It allows frequency sweepings with different waveforms, high stability, accuracy, and frequency resolution at different amplitudes. Signal distortion may be controlled. The second configuration is used to compute and generate an arbitrary noise band. In this way, it is possible to find the frequency response of the different modes of the transducer. The frequency control unit drives the transducer at resonance by keeping the voltage (V) and the current (I) signals in phase throughout operations.

The second configuration is used to compute and generate an arbitrary frequency band. In this way, it is possible to find the frequency response of the different modes of the transducer. The data acquisition unit receives the signals and their corresponding phases from the set of probes, and digitizes them for processing. The computer is used for signal processing, data storage, and postprocessing of the data generated during the different tests. It is provided with a PCI-card A/D/A, and it also controls the function/

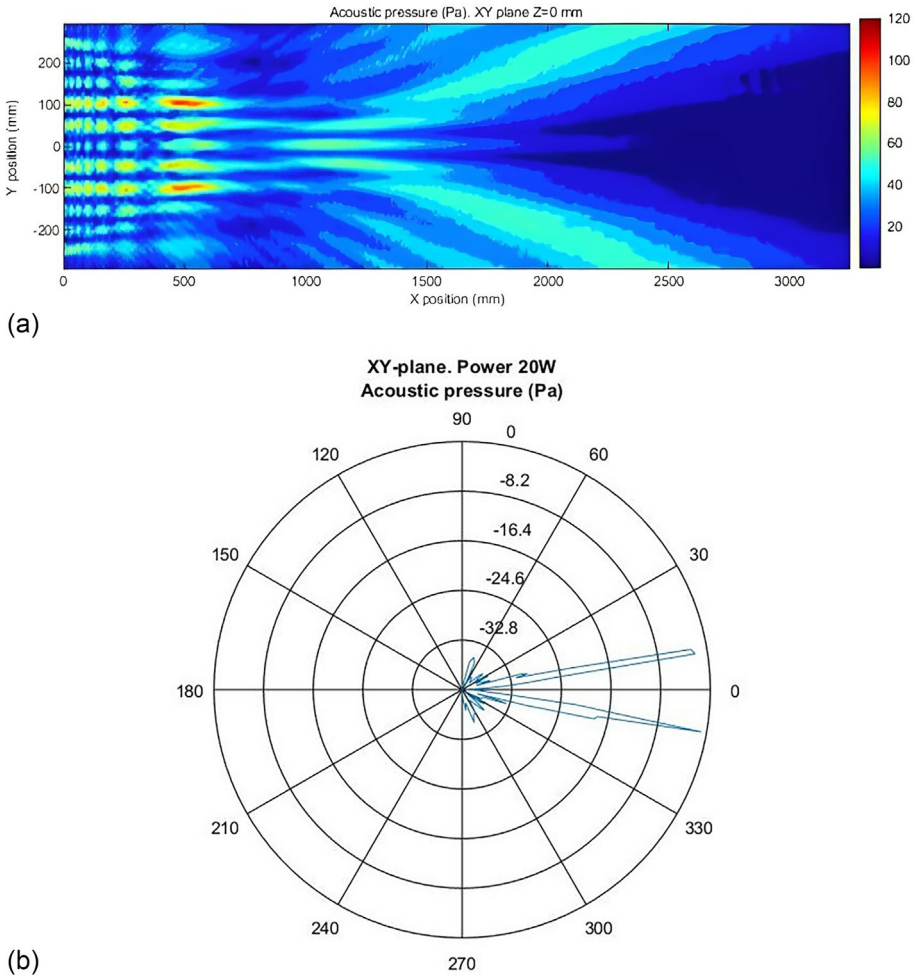


FIGURE 7.25 Acoustic field along the central plane XY of the plate transducer without reflectors (a) and the corresponding directivity diagram (b).

arbitrary signal generator and the resonance frequency control unit. Specific software based on the LabVIEW code was developed for driving and characterizing the transducer behavior at high power operation.

Signals from the excitation system (V, I) and from the probes (ξ, φ, P_a, T) are processed in both time and frequency domains, and may be analyzed in different ways. The first analysis for transducer characterization consists of a frequency sweep with measurement of the RMS values of the V and I signals. In such a way, the impedance or the admittance for any frequency may be obtained. The latter should be obtained under the following conditions: (i) single point, both frequency and voltage are fixed; (ii) linear-swept, constant voltage in a certain frequency range; and (iii) multiple-swept, both frequency and voltage are alternatively varied. In addition, the frequency sweep may be performed in two directions following increasing or decreasing frequencies in order to study the transducer hysteretic (nonlinear) behavior. In all cases, the excitation signals are applied at different amplitude levels.

In the time-domain analysis, two different configurations can be applied: function/arbitrary signal generator or resonance frequency control. Both are used to measure transducer performance and its time evolution. A waveform graphic page displays the signals (V, I, ξ, P_a, or T) in the time domain, together with their RMS values. A set of displays shows the ratio of the RMS values of the different signals to evaluate nonlinearity. Another set of tools have been developed to analyze the actual power, phase, impedance, and total harmonic distortion of the signals. The power applied to the transducer is always calculated by averaging a certain number of sampled values over the total acquisition time.

For the analysis in the frequency domain, three main forms of spectrum are used: FFT amplitude and phase, power spectrum (or power spectrum density), and time spectrum evolution. Actual, averaged, and cumulative spectra may be visualized, with the latter spectra useful for detection of transient events. The power spectrum is used for the evaluation of the energy content of the different

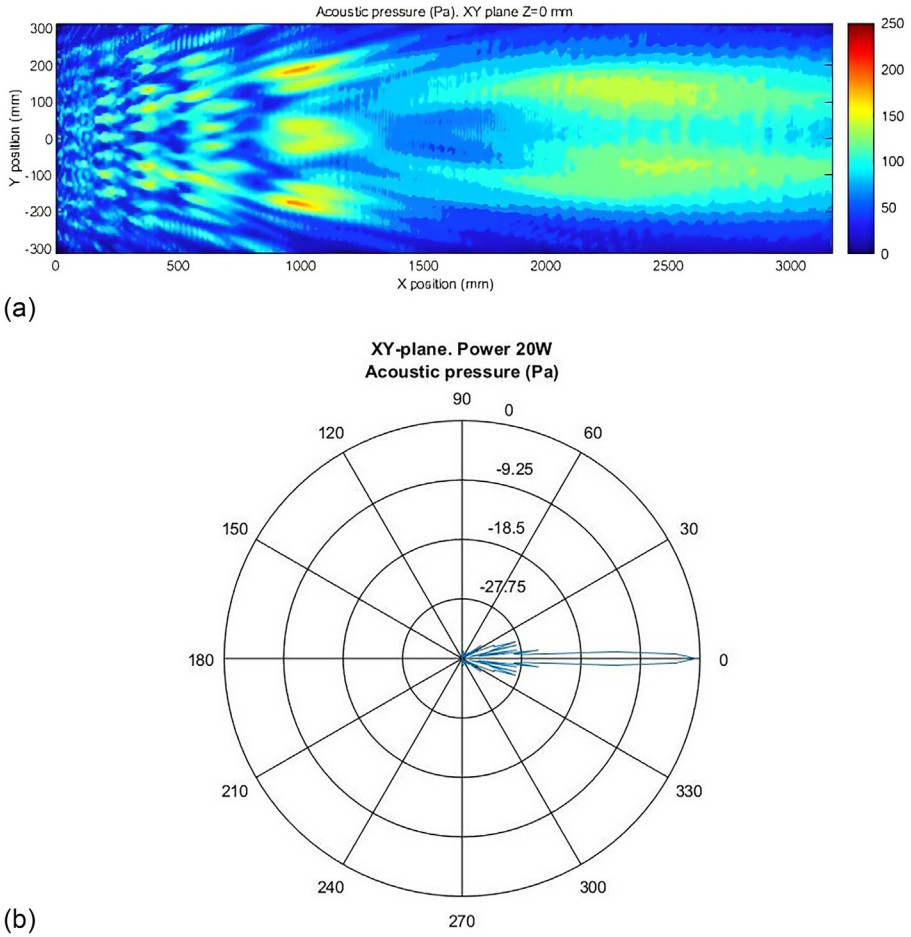


FIGURE 7.26 Acoustic field along the central plane XY of the plate transducer with reflectors (a) and the corresponding directivity diagram (b).

frequency modes. The time spectrum evolution allows observation of the evolution of the spectral content of the signals. Figure 7.28 summarizes these three tools.

An example application of the developed procedure is presented below. A roved rectangular plate transducer made of titanium was used and a rectangular plate radiator driven at its center by a piezoelectric vibrator. At low power, a HP-4194A Impedance Analyzer was used to analyze the admittance response of the transducer in the frequency range (20–22 kHz) around the operating frequency (20,281 Hz). Two vibration modes were detected, one at 20,281 Hz and the other at 21,431 Hz (see Figure 7.29). The first frequency corresponds to a vibration mode with eight nodal lines parallel to the shorter side of the plate (operating frequency), and the second one to a mode with four nodal lines parallel to the longer side of the plate. Both modes were detected at low- and high-excitation levels, and the difference in frequency between these modes at low and high excitation was almost constant and at about 1150 Hz. The transducer had an estimated power capacity of 200 W. In Figure 7.30, results of a multiple-sweep carried out in the 20–20.5 kHz frequency range at voltages from 10 up to 300 V are presented. It is apparent from the 2-D surface envelop that the transducer resonance frequency does not undergo a significant shift to lower frequencies when the excitation voltage increases, illustrating stable behavior at maximum power capacity.

A second and more advanced test rig was also developed (Riera et al., 2010) to separate elastic and thermal losses from piezoelectric transducers. In order to measure the vibration response characteristics of the targeted transducer, it was driven near the resonant frequency of the working mode at increasing voltage levels. Tests were carried out by applying a sinusoidal excitation signal to the piezoelectric stack and step-sweeping the driving frequency over a range centered in the tuned linear modal frequency of the transducer. The excitation signal was generated using a function generator (Agilent 3322A) and amplified via a QSC RMX 4050HD power amplifier. Current response curves were detected through upward and downward step sweeps of the excitation frequency at different applied voltages from 1 V up to hundreds of volts, depending on the transducer power capacity. In order to reduce temperature increases of the PZT rings in proximity of the system

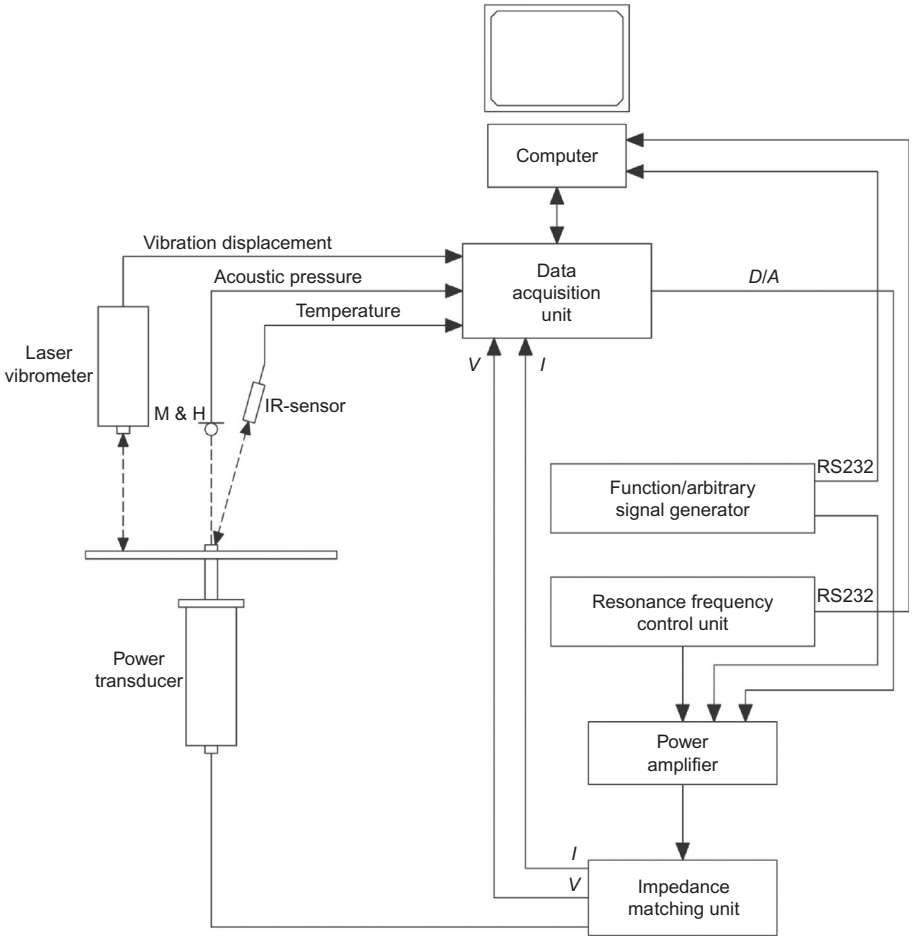


FIGURE 7.27 Scheme of the experimental setup for power evaluation of power transducers.

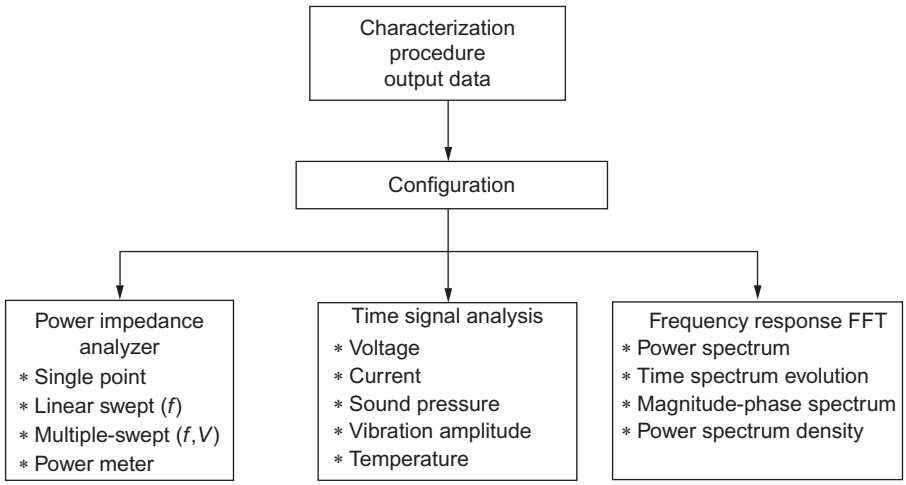


FIGURE 7.28 Developed tools for the power characterization procedure.

resonance frequency, a sine burst was applied at each frequency increment encompassing the upper and lower limits of the frequency sweeps. Hence, the driving signal was applied at each frequency for a fixed number of cycles. Bursts of 4000–10,000 cycles were chosen, as they proved to be sufficient for the generation of steady state responses of the transducer. Moreover, there was a time delay between successive bursts in order to reduce PZT thermal losses. Finally, the transducer response is measured with respect to vibration velocity and current. Vibration velocities are

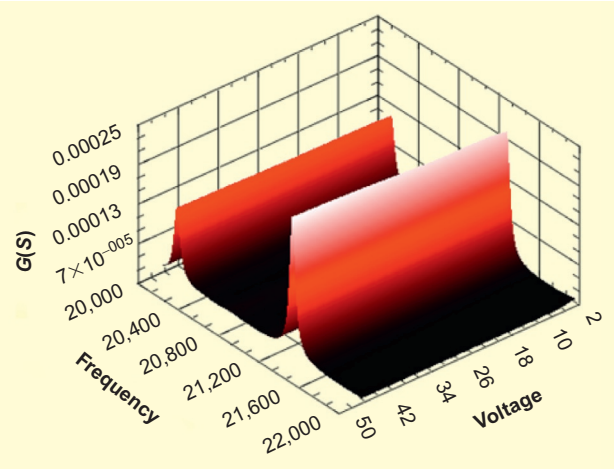


FIGURE 7.29 Conductance (G) of the transducer versus frequency (20–22 kHz) and excitation voltage (1–50 V).

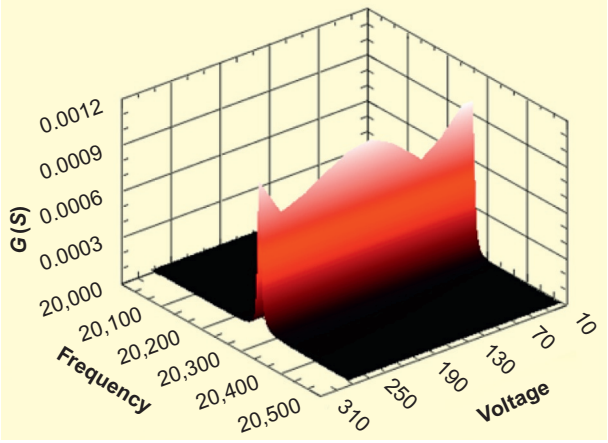


FIGURE 7.30 Conductance of the transducer versus frequency (20–20.5 kHz) and excitation voltage (10–300 V).

measured on different parts of the transducers to study the presence of longitudinal, radial, torsional, or flexural modes using a laser scanning vibrometer (Polytec PSV-100), and the PZT temperature was monitored by an infrared probe. Time and frequency domain representations of the measured current and velocity responses were viewed on a Tektronix oscilloscope (DPO 7054) screen.

7.8 Conclusions and future trends

The introduction of plate transducers represents an important advance in the field of airborne power ultrasonic transducers. Plate transducers have been designed for applications in fluids and multiphase media where they have achieved very high performance and have also opened applications of power ultrasonics to gaseous media. Their effectiveness and technological versatility have been demonstrated in various processes at laboratory, semi-industrial, and even industrial levels (Gallego-Juárez et al., 2010b). However, the industrial application generally requires significant increases in the amount of power delivered per transducer and/or adaptation of the technology to any specific problem. Therefore, the current commercial introduction of this technology is presenting important technological challenges (see www.pusonics.es). The increase of power implies an enlargement of the size of the plate radiator, and this means operation at higher vibration modes leading to an increase of modal interactions. On the other hand, high power capacity requires materials with high ultrasonic fatigue limit and low vibratory losses, as titanium alloys, and such materials are difficult to find for the dimensions of large radiators and are also very expensive. As a consequence, for full market penetration of these new transducers, several practical and technological issues remain to be overcome.

References

Andrés, R.R., Acosta, V.M., Lucas, M., Riera, E., 2018. Modal analysis and nonlinear characterization of an airborne power ultrasonic transducer with rectangular plate radiator. Ultrasonics 82, 345–356.

Andrés, R.R., Pinto, A., Martinez, I., Riera, E., 2019. Acoustic field generated by an innovative airborne power ultrasonic system with reflectors for coherent radiation. Ultrasonics 99, 105963 (1-13).

Aurelle, N., Guyomar, D., Richard, C., Gonnard, P., Eyraud, L., 1996. Nonlinear behavior of an ultrasonic transducer. Ultrasonics 34, 187–191.

Barone, A., Gallego-Juárez, J.A., 1972. Flexural vibrating free-edge plates with stepped thickness for generating high directional ultrasonic radiation. J. Acoust. Soc. Am. 51, 953–959.

Blackburn, J., Cain, M., 2006. Nonlinear piezoelectric resonance: a theoretically rigorous approach to constant IV measurements. J. Appl. Phys. 100, 114101–114110.

Campos-Pozuelo, C., Gallego-Juárez, J.A., 1995. Finite amplitude flexural vibrations at ultrasonic frequencies in metallic bars. J. Acoust. Soc. Am. 98, 1742–1750.

Campos-Pozuelo, C., Gallego-Juárez, J.A., 1996. Limiting strain of metals subjected to high-intensity ultrasound. Acta Acust. 82, 823–828.

Campos-Pozuelo, C., Lavie, A., Dubus, B., Gallego-Juárez, J.A., 1998. Numerical study of air-borne acoustic field of stepped-plate high-power ultrasonic transducers. Acta Acust. 84, 1042–1046.

Cardoni, A., Lucas, M., 2002. Enhanced vibration performance of ultrasonic block horns. Ultrasonics 40, 365–369.

Cardoni, A., Riera, E., Blanco-Blanco, A., Gallego-Juarez, J.A., Acosta-Aparicio, V.M., 2009. On the nonlinear dynamics of plate-transducers. In: IEEE International Ultrasonics Symposium, Rome, September.

Cardoni, A., Riera, E., Blanco, A., Acosta, V., Gallego-Juarez, J., 2012. Modal interactions in ultrasonic plate-transducers for industrial applications. Proc. Inst. Mech. Eng. C J. Mech. Eng. Sci. 226, 2044–2052.

Cardoni, A., Riera, E., Gallego-Juarez, J.A., 2013. Nonlinear response in airborne piezoelectric transducers for power ultrasonics. In: International Congress of Ultrasonics, Singapore, May.

Cartmell, M.P., 1990. Introduction to Linear Parametric and Non-Linear Vibrations. Chapman and Hall, London and New York.

Gallego-Juárez, J.A., 1973. Axisymmetric vibrations of circular plates with stepped thickness. J. Sound Vib. 26, 411–416.

Gallego-Juárez, J.A., Gaete-Garretón, L., Rodríguez-Corral, G., 1978. An ultrasonic transducer for high-power applications. Ultrasonics 16, 267–271.

Gallego-Juárez, J.A., Rodriguez-Corral, G., Riera, E., Vazquez-Martinez, F., Acosta-Aparicio, V.M., 2001. Development of industrial models of high-power stepped-plate sonic and ultrasonic transducers for use in fluids. In: IEEE Ultrasonics Symposium.

Gallego-Juárez, J.A., Riera, E., Acosta-Aparicio, V.M., 2008. Modal interactions in high-power ultrasonic processing transducers. In: Enflo, O., Hedberg, C.M., Kari, L. (Eds.), Nonlinear Acoustics Fundamentals and Applications. AIP Conference Proceedings, New York, pp. 595–604.

Gallego-Juárez, J.A., Rodríguez-Corral, G., Montoya-Vitini, F., Acosta-Aparicio, V.M., Riera, E., Blanco, A., 2010a. Macrosonic Generator for Industrial Defoaming of Liquids by Air-Borne Radiation. US Patent 7,719,924 B2, May 2010.

Gallego-Juárez, J.A., Rodriguez, G., Acosta, V.M., Riera, E., 2010b. Power ultrasonic transducers with extensive radiators for industrial processing. Ultrason. Sonochem. 17, 953–964.

Guyomar, D., Ducharne, B., Sebald, G., 2011. High nonlinearities in Langevin transducer: a comprehensive model. Ultrasonics 51, 1006–1013.

Langevin, P. 1920 French Patents Nr. 502913 (1920), Nr. 505703 (1920), Nr. 575435 (1924).

Leissa, A., 1969. Vibration of Plates. NASA SP-160, Washington, DC.

Lucas, M., Cardoni, A., Cartmell, M.P., Lim, F.C.N., 2003. Controlling the effects of modal interactions in ultrasonic cutting devices. In: Proceedings of the World Congress on Ultrasonics, Paris (France), pp. 49–56 (invited paper).

Mathieson, A., Cardoni, A., Cerisola, N., Lucas, M., 2013. The influence of Piezoceramic stack location on nonlinear behavior of Langevin transducers. IEEE Trans. Ultrason. Ferroelectr. Freq. Control 60 (6), 1126–1133.

Nayfeh, S.A., Nayfeh, A.H., 1994. Energy transfer from high to low frequency modes in a flexible structure via modulation. J. Vib. Acoust. 116, 203–207.

Neppiras, E.A., 1973. The prestressed piezoelectric sandwich transducer. In: Ultrasonics International Conference Proceedings, pp. 295–302.

Perez-Alvarez, N., Cardoni, A., Cerisola, N., Riera, E., Brizzotti, M.A., Adamowski, J.C., 2013. Nonlinear modeling of Langevin transducers using the Rayleigh law in the piezoelectric ceramics. In: Proceedings of the International Congress on Ultrasonics (ICU 2013), Singapore, pp. 197–202.

Riera, E., Gallego-Juárez, J.A., Blanco, A., Acosta-Aparicio, V.M., 2007. Power characterization of ultrasonic piezoelectric transducers. In: Proceedings of the International Congress on Ultrasonics, Viena, April 9–13. http://proceedings.icultrasonics.org/. (Paper ID 1435).

Riera, E., Cardoni, A., Blanco, A., Acosta-Aparicio, V.M., Gallego-Juárez, J.A., 2010. Characterizing the nonlinear dynamics of power ultrasonic systems. In: Proceedings 39th International Congress on Noise Control Engineering, Internoise 2010, 13–16 June Lisbon, Portugal.

Rodriguez-Corral, G., Gallego-Juárez, J.A., Vazquez, F., Campos, C., Riera, E., Acosta, V.M., 2001. Emisor ultrasónico de placa vibrante con reflectores y separadores para obtener radiación directiva en fluidos (Vibrating Plate Ultrasonic Emitter with Reflectors and Separators for Directive Radiation in fluids). Spanish Patent Application 200102610.

San Emeterio, J.L., Gallego-Juárez, J.A., Rodriguez, G., 1987. High axisymmetric modes of vibration of stepped circular plates. J. Sound Vib. 114, 495–505.

Timoshenko, S.P., Woinowsky-Krieger, S., 1959. Theory of Plates and Shells. McGraw- Hill, New York.

Uchino, K., Zhuang, Y., Ural, S.O., 2011. Loss determination methodology for a piezoelectric ceramic: new phenomenological theory and experimental proposals. J. Adv. Dielectr. 1 (1), 17–31.

Umeda, M., Nakamura, K., Ueha, U., 1999. Effects of vibration stress and temperature on the characteristics of piezoelectric ceramics under high vibration amplitude levels measured by electrical transient method. Jpn. J. Appl. Phys. 38 (9B), 5581–5585.

Van Randeraat, S., Setterington, R.E., 1974. Piezoelectric Ceramics. Philips Application Book. Mullard Ltd., London.

Woollett, S., 1968. Power limitations of sonic transducers. IEEE Trans. Sonics Ultrason. SU-15 (4), 218–229.

Further reading

Priya, S., Viehland, D., Vázquez Carazo, A., Ryu, J., Uchino, K., 2001. High-power resonant measurements of piezoelectric materials: importance of elastic nonlinearities. J. Appl. Phys. 90, 1469–1479.

Umeda, M., Nakamura, K., Takahashi, S., Ueha, S., 2000. An analysis of jumping and dropping phenomena of piezoelectric transducers using the electrical equivalent circuit constants at high vibration amplitude levels. Jpn. J. Appl. Phys. 39 (9B), 5623–5628.

Chapter 8

Measurement techniques in power ultrasonics

M. Hodnett[a] and P. Prentice[b,*]

[a]*National Physical Laboratory, Teddington, United Kingdom,* [b]*Centre for Medical and Industrial Ultrasonics, University of Glasgow, Glasgow, United Kingdom*

8.1 Introduction

The concept and need for measurement and standardization were perhaps first addressed in Magna Carta in 1215: "There is to be one measure of wine and ale and corn within the realm, namely the London quarter, and one breadth of cloth, and it is to be the same with weights." Today, we are all comfortable with standardized units of measure and devices that determine their values for basic quantities such as length and mass. Of course, beneath the simple reality of using a ruler or weighing balance lies an interlinked structure of standards, international collaborations and consensus, peer-reviewed literature, and underpinning science. These combine to define and disseminate a measurement unit traceable to some primary standard (which increasingly is moving away from a tangible artifact; http://www.nist.gov/pml/newsletter/siredef.cfm), which is then realized at various hierarchical levels of accuracy according to the user requirement.

When we consider the mechanical stimulation of a medium, that is, acoustics, and its subdivision of ultrasonics, the present standards infrastructure (International Electrotechnical Commission, 2020) broadly describes measurement parameters yielded by underwater microphones (hydrophones) in terms of acoustic pressure and intensities (loudness), frequency (pitch), power, energy, and ultrasound field dimensions. Yet, these are all applicable to the primary outcome of applying a vibrating surface to a medium—a sound wave—whereas in power ultrasonics applications, the stimulus of interest is very often cavitation, which is a secondary consequence of the sound wave. Measuring, characterizing, and describing this secondary effect (and, in turn, its tertiary effects) in a meaningful and transferable way present a series of challenges.

The drivers and motivation for making measurements of a power ultrasonic system are multifaceted and can be considered in terms of the interested audience, in a similar way to the stratified structure of traceability. Consider, for example, the case study of an automotive components manufacturer who has a novel production line containing an ultrasonic cleaning stage. The manufacturer's specific requirement is to ensure that the ultrasonic cleaning bath operates in a repeatable way such that each batch of components is suitably cleaned for the next manufacturing step, and ultimately meets the output specification. At this level, a simple global measurement of acoustic power, perhaps derived from calorimetry, compared to the previous day's result would seem to be fit for the purpose. However, if a reduction is seen in cleaning quality, though the calorimetric power value appears to be similar, a more refined type of measurement approach is needed, such as a hydrophone. This would provide an assessment of any significant change in the acoustic field distribution (which would also require a similar type of initial acceptance testing having been completed prior to the bath being put into service).

If the acoustic field also appears similar, then at the next level of detail, a measurement approach that provides information on the driving phenomenon behind ultrasonic cleaning—cavitation—is needed. As will be described later, there then exists many candidate techniques to describe the cavitation process, which are process-specific. Depending on the outcomes of the chosen method, it might then be determined that the spatial distribution of cavitation has changed. This may then necessitate the bath to be removed from service and returned to the manufacturer for further investigation, service, and repair, which might require detailed spatial measurements, electrical tests, and fluid composition analysis.

Within this simple example, the requirements for measuring power ultrasonic systems may be summarized as follows:

- marketplace competitiveness and advantage,
- manufacturing yield,

* Revised by

Power Ultrasonics. https://doi.org/10.1016/B978-0-12-820254-8.00008-7
Copyright © 2023 Elsevier Ltd. All rights reserved.

- acceptance testing,
- quality assurance,
- process safety,
- user-level fault investigation,
- service-level diagnosis, and
- system manufacturer fault-finding and repair.

Considering a second example of a novel laboratory application of high-power ultrasonics, the following can be added to this list:

- comparability with other researchers,
- supporting innovative science and engineering,
- understanding underpinning physics, and
- scaling up to industrial viability.

As illustrated before, each of these related aspects requires measurement techniques of different complexity and time investment, and in the later parts of this chapter, a range of approaches will be described in detail. As will be seen, there is significant measurement challenge posed by attempting to characterize (and ultimately, calibrate) a high-power ultrasonic system such that it remains a rapidly developing area of measurement, which often advances alongside the applications that are driving the need.

This chapter is structured predominantly around considering a conceptual source of power ultrasound, operating in a fluid medium (together, denoted as a *vessel*), and then describing and comparing myriad devices, methods, and protocols that the scientific and engineering community are using so as to characterize them in sufficient detail for their needs.

As such, the chapter comprises a brief commentary on the following:

- how to characterize the source itself, both outside and inside the propagation medium;
- how to measure the ultrasound field that is generated, using local and bulk measurement methods;
- how to characterize the resulting acoustic cavitation, comparing different techniques according to their end points and measurands; and
- how the suitability of particular approaches compares for the wide-ranging user requirements, and for standardization.

8.2 Characterizing the source

8.2.1 Electrically

Generating acoustic pressures at kilohertz frequencies in fluid media that are of sufficient magnitude to initiate and sustain cavitation generally requires a reasonably high-Q system. Once cavitation (defined in greater detail in Chapter 3) becomes established, the local medium conditions change due to the consequent void fraction induced by bubble formation, and this local change can influence the electrical performance characteristics of the transducer and drive system and, in turn, provide the opportunity for measurement. This is of particular interest in medical applications where cavitation occurs, in instances where focused transducers are used. Hence, the occurrence of cavitation can be monitored in terms of its consequence on the electrical drive signal, in particular the impedance or admittance of the transducer (McLaughlan et al., 2010; Campos-Pozuelo and Vanhille, 2012), and can be a sensitive threshold indicator. In industrial systems such as sonotrodes, devices operate on a "constant amplitude" basis, meaning that they are designed to draw more or less power depending on the acoustic impedance of the medium undergoing sonication, but maintaining the vibration amplitude of the excitation surface. Thus, if access is available to the transducer driving circuit, changes in voltage and current can also be used to monitor the load characteristics in the manner described in the reference.

8.2.2 Optically: Vibrometry and microscopy

High-frequency (scanning) laser vibrometry is a widely employed noninvasive tool for understanding both the vibration characteristics of an ultrasound source and, potentially, the acoustic field that results. Based on the Doppler shift of a laser beam, when a laser beam is reflected from a moving surface, devices such as those produced by Polytec are finding increasing utility. For example, in assessing medical applications such as dental descaling and bone cutting (Lea et al., 2006; Mathieson et al., 2013; Pecheva et al., 2016), three-dimensional optical scanning can provide detailed information on vibration modes, which can help system designers to overcome failure modes and also educate clinical practitioners on the best application. Advanced systems such as Polytec MSA-100-3D now facilitate the full-field characterization of 3D vibration measurements of MEMs and microsystems, including piezoceramic rings (Figure 8.1). Traveling microscopes can be used similarly to evaluate sonotrode tip motions, which can then be used to predict resulting field patterns.

There is a growing research area in harnessing the acousto-optic effect (Korpel, 1981) to measure acoustic fields noninvasively. Put simply, the propagation of an acoustic wave through a medium can be probed optically due to the differing local particle densities in the compressive and rarefaction regions; this serves to change the local refractive index such that an interrogating optical beam at right angles to the sound field can detect the sound beam through phase changes and diffraction (Harland et al., 2002). The method requires optically translucent media and would be adversely affected by significant cavitation through bubbles, causing optical scattering, but is a powerful and rapid investigation tool. A particular advantage

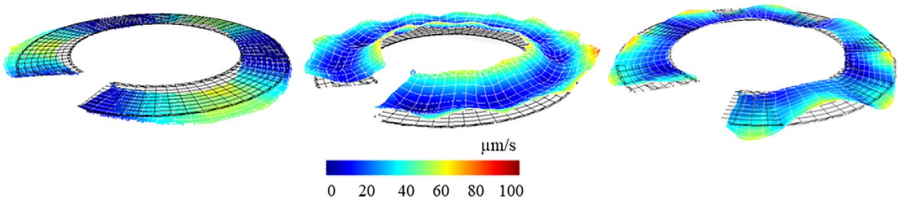


FIGURE 8.1 Full-field capture of the velocity across the face of a P181 ring, resonant vibrational modes modeled on a 2D wire-frame model. *(Courtesy of Dr Rebecca Cleary and Prof Margaret Lucas.)*

is in the spatial resolution, which is constrained only by optics, rather than by a physical device, and its noninvasiveness. The interrogating optical beam may in fact be deployed via a laser vibrometer (Buick et al., 2004) or an optical fiber (Pohl et al., 2013).

Optical scattering has also found utility in characterizing cavitation (Iida et al., 2009) in which an incident laser beam is scattered collectively, and potentially, individually, by oscillating bubbles, with broadband spectral analysis providing information on bubble behavior. This may be considered an analog of the acoustic emission approach described in Section 8.4.2. For research systems, in particular for studying single bubbles, Mie scattering (Marston, 1999; Weninger et al., 1997) has been used extensively; however, its applicability to more applied situations is rather more limited.

8.3 Characterizing the generated ultrasound field

High-power ultrasonic systems such as cleaning vessels are complex acoustic environments as at the frequencies of main interest (20–400 kHz), the sound fields generated within typical tanks are strongly reverberant, and the development of cavitating bubbles will reflect, scatter, and absorb the applied sound. Further, high applied powers—often generating inefficient transducer harmonics—result in heating and degassing of the liquid such that the driving field and the cavitation produced in the vessel under test are strongly time-dependent. All these factors increase the complexity in developing repeatable measurement methods. Measurement approaches that do not consider cavitation (Hodnett and Zeqiri, 1997) are essentially analogous to the techniques applied to characterizing sonar or medical ultrasound systems (International Electrotechnical Commission, 2020) and can be considered in terms of bulk assessment of acoustic power and local assessment of acoustic pressure and intensities.

8.3.1 Acoustic power: Bulk assessment

Measuring acoustic power is performed routinely in medical ultrasound systems, both high and low power, using radiation force balances (International Electrotechnical Commission, 2013), which employ absorbing or reflecting targets to intercept the transmitted plane wave field. Provided the target is sufficiently large with respect to the beam, there exists a simple proportional relationship between the measured radiation force and the acoustic power, and the method is well established. Such approaches are less applicable to low-frequency systems due to the spherically spreading nature of the fields and cavitation, which serves to scatter incident beams. However, at drive levels below or close to the cavitation threshold, radiation force balances for low-kilohertz systems that have been developed using waveguide approaches (to generate quasiplane waves) and employing strongly degassed water.

For a bulk assessment of system output, calorimetry is a useful approach (Contamine et al., 1995; Kimura et al., 1996), requiring temperature measurement and a thorough assessment, understanding, and minimization of the fluid and its thermal losses. Calorimetric techniques are frequently used to state the output characteristics of sonotrode systems (Son et al., 2012), where values for spatial average intensity are then estimated by calculating the ratio of the measured power to the vibratory area. Care should be taken in comparing such values, particularly when this approach is extended to vessel systems. It should be noted that neither acoustic power nor intensity should be used to state a "cavitation threshold" value; from a purely acoustic perspective, the parameter of interest is the peak negative acoustic pressure, which corresponds to the stress applied to the liquid.

8.3.2 Acoustic pressure and intensities: Local assessment

Determining acoustic pressure distributions in fluid media is carried out using underwater microphones or hydrophones, and a large range of commercially available devices exist (Reson, Precision Acoustics, Sonora, Onda, Brüel & Kjær, etc.) and have been used to characterize cavitating systems (Birkin et al., 2011; Torres-Sanchez and Corney, 2008). For typical high-power ultrasonic systems, acoustic wavelengths are in the range of a few centimeters, and at low drive levels, below the cavitation pressure threshold, the spatial distribution of the sound field may be mapped and related to simple geometric models yielding standing waves or structural modes (Memoli et al., 2012). As the drive level

is increased and cavitation begins to become established, the acoustic field becomes more complex, and phenomena such as acoustic shielding (Leighton, 1995; Ying et al., 2011) develop and can have a significant influence on the acoustic pressure distribution. Under cavitation conditions, void fractions of just a few percent can have a strong influence on the effective sound speed of the fluid, making measurements less meaningful. Cavitation itself is a random process, and this, in turn, affects the acoustic field, making a dynamically evolving environment.

Acoustic pressure values can be used to derive acoustic intensities, and using the general assumption that acoustic pressure and particle velocity are in phase, intensities are proportional to the square of the pressure. However, the underpinning assumptions are invalid in reverberant environments typical of cavitating systems, and so the concept of intensity (which, strictly, is a vector quantity) becomes less useful. As noted previously, a common misconception is to state the cavitation threshold of a fluid-filled vessel in terms of intensity (often, a figure of 1–2 W cm^2 is identified as a cavitation threshold value at around 20 kHz); however, whether cavitation occurs, as described later, is, in fact, a function of *acoustic pressure*. If the rarefactional half-cycle of the applied acoustic field is not of sufficient magnitude to exceed the tensile strength of the local fluid/impurity environment, then cavitation cannot occur, regardless of the power applied to the system. Bubble activity that is observed in such cases may be attributable to local boiling instead.

Several devices using thermal approaches have been developed (Marangopoulos et al., 1995; Pohlmann, 1971; Wilkens, 2010). Generally they employ some form of acoustic absorber, a thermal sensor (thermistor or thermocouple), and acquisition electronics. Using the linear relationship that exists between increases in temperature and time shortly after sound field activation, values for the local acoustic intensity can be derived. Such devices have the advantage of being inexpensive to build, comparatively small, and calibrated thermally, but they determine a sound field parameter that is not directly related to cavitation and, in the presence of cavitation, suffers from streaming, shielding, and erosion effects.

8.4 Characterizing the resultant acoustic cavitation

8.4.1 Scoping the challenge

A detailed description of the dynamics, mathematics, and classifications of acoustic cavitation can be found in Chapter 3 of this volume, but it is instructive to review briefly some of the key aspects and outcomes of the cavitation process as these not only manifest as desired or unwanted effects of cavitation but also afford the opportunity for detection, measurement, and characterization.

Whether cavitation occurs or not, and how much, is a function of the peak negative acoustic pressure and is strongly dependent on the fluid, specifically on the likelihood and origin of cavitation nucleation. In a typical water sample, nucleation sites (Apfel, 1997) may take the form of dissolved gas and also via small suspended dust particles—motes—and container imperfections, where pockets of air may be trapped. Hence, cavitation is a stochastic phenomenon, and so developing repeatable sources of cavitation against which measurement techniques may be tested is in itself a significant challenge (Hodnett and Zeqiri, 2008; Hodnett et al., 2007; Torres-Sanchez and Corney, 2008).

A nucleate-rich bubble-containing fluid, to which an ultrasound field of suitable peak negative acoustic pressure and frequency is applied, may then be said to be *cavitating* if the bubbles within the fluid oscillate, "breathe," and move in correspondence with the sound field. This is frequently termed *noninertial cavitation* in which the size changes of the bubble in each acoustic cycle are relatively small, and the bubble motion has a strong dependency on the forces attributable to its gaseous contents, such as compressibility. Depending on the medium characteristics and acoustic pressure amplitude, bubble motion and oscillation may increase in amplitude to a level where they may grow to more than twice their original size in one to two acoustic cycles. Here, the kinetic energy within the liquid dominates the bubble motion, and bubble motion features violent collapses, known as *inertial cavitation*.

It is estimated that the temperature inside a collapsing bubble may exceed 15,000 K (Flannigan and Suslick, 2005), with pressures in excess of 1000 atmosphere (Flannigan et al., 2006), and the microjets generated during asymmetric collapse at surfaces may exceed a speed of 200 m/s, impacting with pressures of over 400 MPa (Tzanakis et al., 2014). Shock waves are also generated (Birkin et al., 2005a; Yusuf et al., 2021) (Figure 8.2), and all these extraordinary effects drive the well-known processes of sonochemistry, light emission, free radical generation, and surface erosion (Marangopoulos et al., 1995; Ibanez et al., 2020), some or all of which may occur in real applications. These effects clearly represent measurement opportunities:

- Acoustic detection: oscillating and collapsing bubbles, and bubble clouds are secondary sources of sound.
- Chemical detection: strong shear forces around bubble walls, highly reactive free radicals generated within and around collapse events, and electrochemistry.
- Emitted radiation detection: light emission due to sonoluminescence, sonochemiluminescence, and thermal emissions.
- Mechanical detection: erosion of surfaces and material loss.

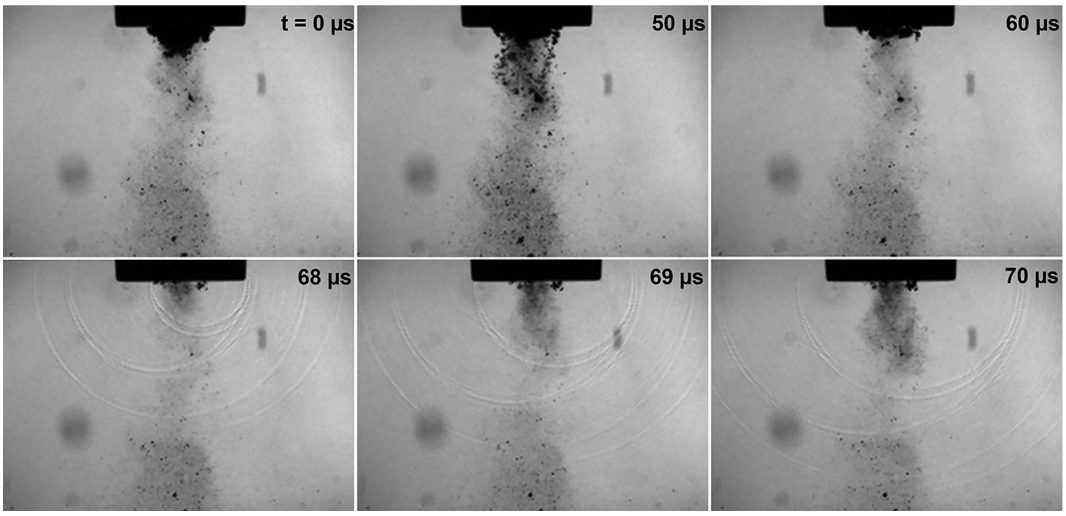


FIGURE 8.2 Shock wave emission from acoustic cavitation activity at the tip (6.4 mm in diameter) of a 20-kHz sonotrode, captured by high-speed shadowgraphic imaging. *(From Yusuf et al. (2021).)*

Each of these aspects will be considered briefly later; this section examines the methods and devices that can be used to describe cavitation occurring in a vessel in practical terms.

Whether a measurement method is useful and relevant is strongly dependent on the requirements of a given process or situation and, as such, can be used to compare the suitability of techniques. For example, acoustic, optical, and mechanical methods are perhaps the more versatile: they may be applied to characterize cavitation inception or threshold phenomena, whereas thermal and chemical methods find greater utility in activity or dosimetric measures, once cavitation is established.

8.4.2 Acoustic methods

Acoustic methods for detecting and characterizing cavitation are among the most widespread, accessible, and versatile, and detailed review articles exist on the topic (Leighton, 1998; Neppiras, 1980; Young, 1989). A cavitating fluid is a very noisy environment, and capturing the myriad acoustic signals provides a great deal of information on the process itself (International Electrotechnical Commission, 2019). Provided sensors of sufficient quality and performance are applied, data with high spatial and temporal resolution can be obtained, and sensors may be used for vessel development, research, and quality assurance. An example acoustic spectrum, obtained from a commercial ultrasonic cleaner using a Reson TC4035 hydrophone, is shown in Figure 8.3 (after Hodnett et al., 2004).

This shows the characteristic acoustic signals detected in a cleaning vessel, with components corresponding to the driving field (40 kHz) f_0, its harmonics nf_0, subharmonics f_0/m, ultraharmonics nf_0/m, and a continuum of signals over the full frequency band captured (white noise). The curved shape in the structure, with a local minimum at around 180 kHz, is a characteristic of the hydrophone response itself. Indeed, given the broadband nature of cavitation emissions, which for most applications of power ultrasonics will include bubble collapse shock wave content, the impulse response of any hydrophone used to measure them becomes an important consideration. Ideally, complex calibration over a representative bandwidth should be applied to deconvolve the detector response, for restoration of pressure data (International Electrotechnical Commission, 2019; Hurrell and Rajagapol, 2016; Johansen et al., 2017). The acoustic emission detected from a cavitating fluid is perhaps best described as a progression of emissions (Lauterborn and Cramer, 1981): with reference to Figure 8.3, as the acoustic pressures generated within the liquid increase (through greater input energy levels), subjecting more of the fluid to inertial cavitation, the white noise in the spectrum can "swamp" the harmonic emissions to form a continuum. The role of *periodic* shock waves in raising harmonic and subharmonic peaks, with the latter occurring with the onset of period-doubled cavitation behavior at sufficiently high driving amplitudes, in the spectrum of the emissions, has also been demonstrated (Song et al., 2016; Yusuf et al., 2021). The received signals are highly nonlinear in nature, as demonstrated by the complexity of the spectrum, and so the bandwidth of the receiver and electronics should be as wide as possible to enable data to be analyzed over as broad a frequency spectrum as possible.

Measurements made using broadband methods (Birkin et al., 2005a; Frohly et al., 2000; Zeqiri et al., 2003a) show that harmonics and broadband signals may extend up to

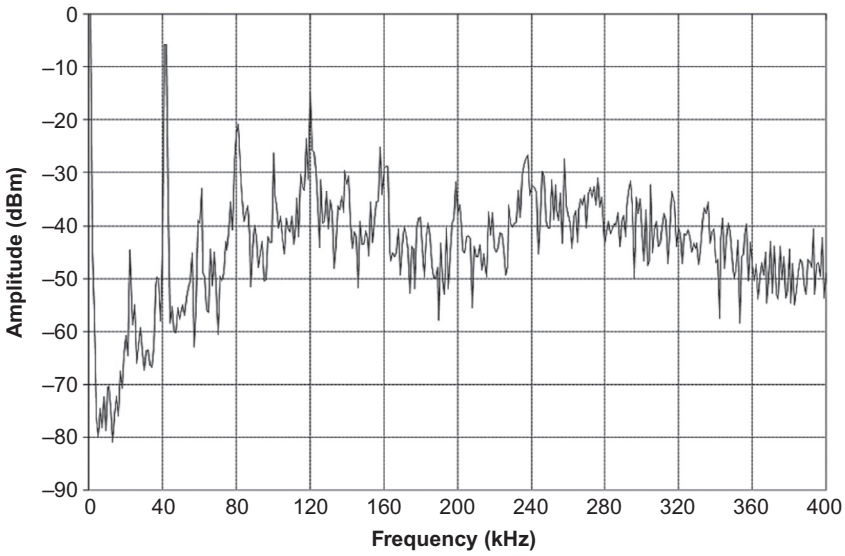


FIGURE 8.3 Hydrophone spectrum, measured in a 40-kHz commercial cleaner.

three orders of magnitude beyond the fundamental frequency, and this strongly demonstrates the nonlinear energy redistribution of the cavitation process (Lauterborn, 1996). The "swamping" effect noted previously is particularly seen when making measurements at megahertz frequencies (from kHz sources; Hodnett et al., 2004). Classically, various acoustic features have been linked with particular bubble phenomena (Leighton, 1994, 1998; Neppiras, 1980), and then to cavitation-mediated observables and processes. For example, correlations have been demonstrated between broadband acoustic emission and material surface damage when assessing an ultrasonic cleaner (see Zeqiri et al., 2006; Figure 8.5). Relationships have also been seen between acoustic emissions, surfactant characteristics, and optical spectra (Ashokkumar et al., 2007), and with dispersion of carbon nanotubes (Sesis et al., 2013). Acoustic emissions have also been used to examine dental descaler characteristics (Felver et al., 2009) and are commonly monitored during therapeutic applications of cavitation, for safety and efficacy purposes (Lipsman et al., 2018).

Capturing acoustic emissions from a cavitating fluid can be achieved by using sonar hydrophones of the type described earlier, in conjunction with a wideband oscilloscope or spectrum analyzer. While some research groups develop their own bespoke devices (Johansen et al., 2018), purpose-designed acoustic cavitation sensors are also commercially available, and some examples of these are compared in Table 8.1, alongside a popularly used sonar hydrophone.

Table 8.1 shows the breadth of designs available. Two key comparison aspects for users are in the performance of devices in terms of their ability to resolve cavitation in specific regions of the fluid and also the frequency range in which they operate due to the rich spectrum of sound produced by a cavitating liquid. A typical ultrasonic cleaning vessel may contain a series of standing wave nodes and antinodes, which may be separated by a few millimeters, and so it is important that if cavitation is to be detected and characterized, it should be done so in a spatially sensitive way. The significance of this is illustrated in Figure 8.4 (after Hodnett et al., 2007). These measurements were carried out in a 25-kHz cylindrical cavitation vessel and show comparisons between the acoustic pressure distribution as measured using a sonar-type hydrophone and that obtained using a spatially sensitive cavitation sensor, responding to high-frequency broadband acoustic emissions.

The graphs of Figure 8.4 show the significant difference in the measured peak negative acoustic pressure at 25 kHz and the resulting inertial cavitation (determined using the average RMS voltage in the frequency band 1.5–8 MHz), at two different excitation levels for the cylindrical vessel. At the lower driving levels, only the acoustic pressure amplitudes achieved at the focus of the vessel are of sufficient magnitude to cause cavitation to occur (the inset shows the sharpness of this); for higher excitation levels, a larger region of the vessel experiences acoustic pressures above the inertial cavitation threshold, and so the spatial variation of the cavitation shows a distribution with greater similarity to the driving field pressure. These plots first demonstrate that measuring the driving field pressure may not be representative of the acoustic cavitation and second that the spatial distribution of inertial cavitation has fine detail, which demands a sensor with spatial sensitivity and a broad bandwidth response.

The second example (after Zeqiri et al., 2006) in Figure 8.5 shows correlations between broadband high-frequency acoustic emissions and erosion, determined using the NPL Cavitation Sensor, produced by a 38-kHz commercial ultrasonic cleaner with four transducers attached to the base. This demonstrates correlations in the local spatial

TABLE 8.1 Comparison of some commercially available acoustic sensors for characterizing ultrasonic systems

Sensor details	Description	Active region dimensions (responding volume)	Operating frequency/ bandwidth	References to usage
Brüel & Kjær 8103	Cylindrical PZT sonar hydrophone	6.4 mm height and diameter	0.1 Hz to 180 kHz	Son et al. (2012), Datta et al. (2006)
Onda HCT-0310	PZT cleaning tank hydrophone	3 mm diameter	30–300 kHz	http://www.ondacorp.com/images/brochures/Onda_HCT_DataSheet.pdf
NPL CaviSensor	Combined PVDF hydrophone and cavitation sensor	34 mm diameter and height, internal 3 mm focus	20 kHz to 11 MHz	Hodnett et al. (2004), Leighton (1994), Zeqiri et al. (2003b)
Cavitometer ICH-3	PZT sensor with waveguide	5-mm-diameter tungsten tip	5–150 kHz	Komarov et al. (2013), Tzanakis et al. (2016)
PPB cleaning tank probe	Quartz/PZT cleaning tank hydrophone	6.4 mm diameter, 350 mm length	0–5 MHz	Azar (2011)

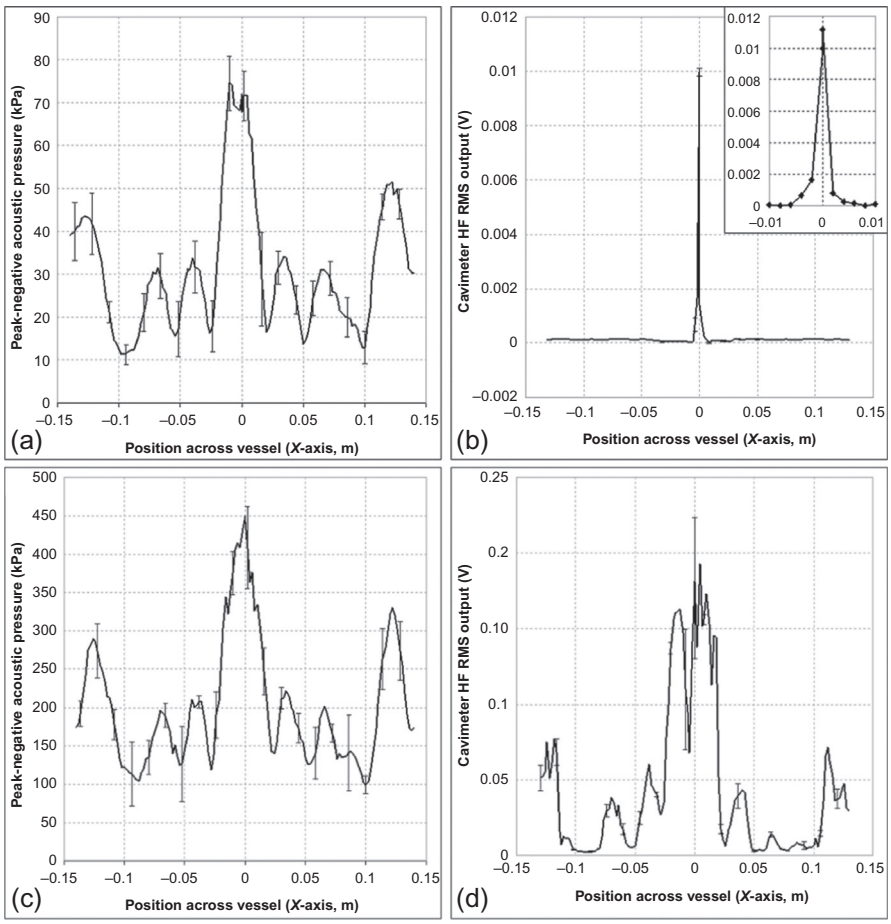


FIGURE 8.4 (a) Peak-negative acoustic pressure at 20 W excitation level; (b) resulting inertial cavitation activity at 20 W excitation level; (c) peak-negative acoustic pressure at 80 W excitation level; (d) resulting inertial cavitation activity at 80 W excitation level.

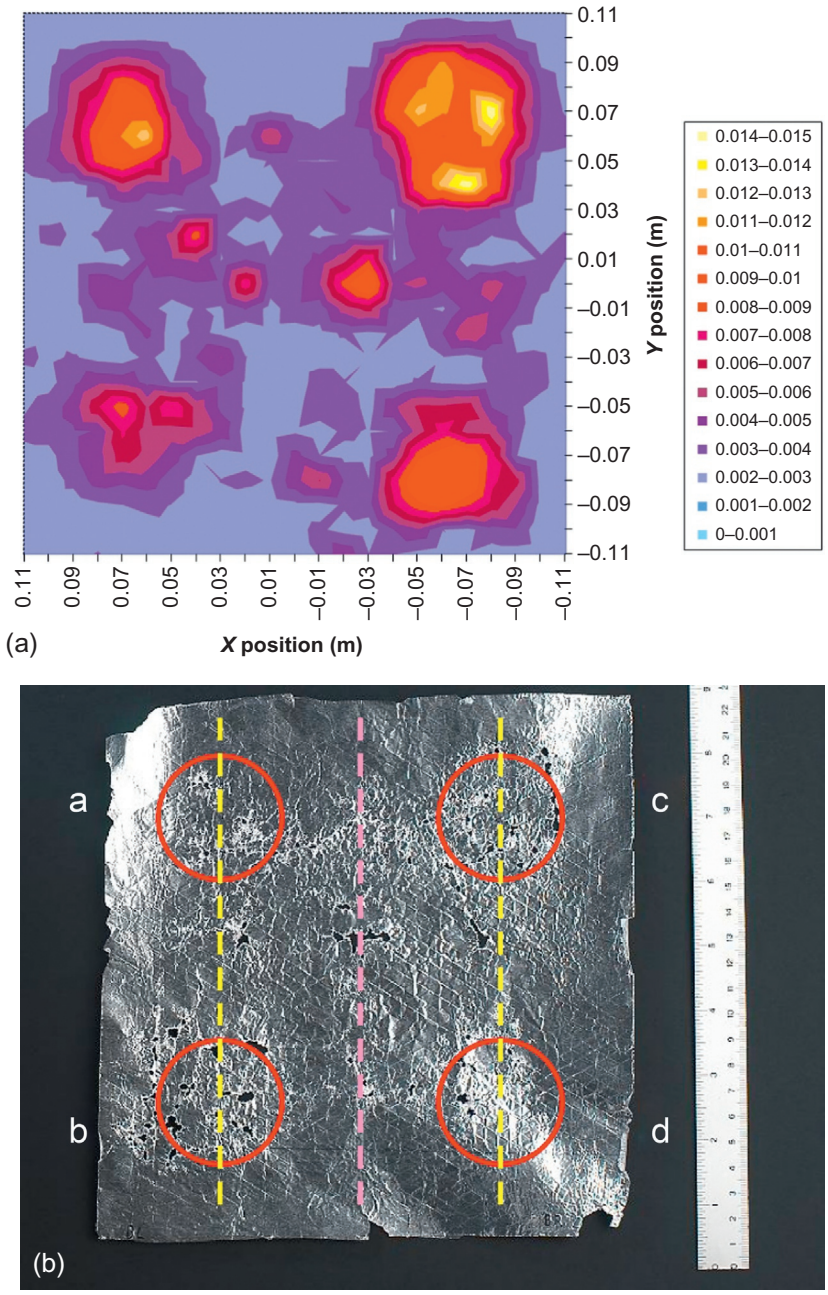


FIGURE 8.5 Inertial cavitation (a) and foil erosion (b), for a 38-kHz ultrasonic cleaner.

maxima of broadband acoustic emission and aluminum foil erosion. There is an important link between (acoustic) measurement in the fluid bulk and erosion at a surface.

8.4.3 Chemical methods

The term *sonochemistry* has been used somewhat ubiquitously to describe the general application of power ultrasound to fluid systems such that material changes occur (and that is described in detail in Part II of this book); more specifically, here, the chemical outcomes from cavitation occurring in fluids are considered as a means of measurement. Researchers have examined many reactions (Iida et al., 2005; Koda et al., 2003; Suslick et al., 1999a), and two examples are considered here.

The generation rate of $OH^{\bullet}$ radicals is the main mechanism responsible for what might be called sound-assisted chemistry; hence, free radical detection can be a versatile tool for characterizing cavitation systems and has evolved from similar approaches in radiation science. Weissler is

considered the first author to confirm the generation of free radicals as a consequence of cavitation (Weissler, 1959), through detecting the recombination production of H_2O_2. This work followed his earlier studies on the oxidation of I^- to I^{3-} in a solution of sonicated potassium iodide (Weissler et al., 1950). The Weissler reaction has since become something of a "standard" in homogeneous sonochemistry because of the ease of detection of I^{3-} using UV-vis spectrometry or electrochemistry (Birkin et al., 2002), and its temperature stability.

Using a similar approach, Fricke dosimetry (Azar, 2011; Mark et al., 1998) employs an acidified solution of Fe^{2+} that, when exposed to cavitation conditions, captures $OH^{\bullet}$ radicals to form Fe^{3+}, which is again readily detected using visible spectrometry methods. Fricke dosimetry initially found widespread use in ionizing radiation detection, and the two contrasting originating mechanisms have been usefully compared (Kratochvil and Mornstein, 2007). A further $OH^{\bullet}$ capture approach is to use fluorescence spectroscopy to examine the hydroxylation of terephthalate, which has been applied to assess the cavitation threshold and extent (Price and Lenz, 1993; Price et al., 1997). Salicylic acid has also been studied, over a broad range of excitation types (Milne et al., 2013).

Although attempts have been made to evolve sonochemistry measurement techniques toward a real-time measurement (Weissler et al., 1950) and to use a plurality of small vials to provide spatial maps, it is ostensibly an offline test that can be significantly perturbing to the sonicated volume under examination. However, the Weissler reaction remains the most accessible technique for detecting cavitation via free radical production.

8.4.4 Optical methods

The phenomenon of sonoluminescence has been the subject of significant research, commencing in the 1930s using cleaning vessels (Frenzel and Schultes, 1934), and following groundbreaking work was reinvigorated in the 1990s (Gaitan et al., 1992). Comprehensive reviews exist (Putterman and Weninger, 2000; Walton and Reynolds, 1984; Yasui et al., 2004), and so the method is only summarized here. The early research focused on light emitted from large numbers of bubbles in a cavitating volume (and so is termed multibubble sonoluminescence, MBSL), whereas much of the more recent research is on single-bubble sonoluminescence (SBSL). The latter requires specific experimental conditions to be set up, effectively isolating the gas bubble from its container and balancing acoustic and environmental forces such that its motion is repeatable about an approximately fixed position (Barber and Putterman, 1991). Such stability enables detailed academic study (Barber et al., 1997; Matula et al., 1998) but, in turn, distances it from a viable applied measurement method in real-world systems, which are all multibubble in nature. The two phenomena are clearly linked intrinsically, and comparison shows differences in the emitted spectra possibly due to shape instabilities (Matula et al., 1995; Posakony et al., 2006).

Much research has been carried out studying luminescence spectra in aqueous and nonaqueous media (Didenko et al., 1994; Suslick and Flint, 1987) and also investigating the effect of surfactants (Ashokkumar et al., 1997), with the main driver being to understand the physical conditions within the collapsing bubbles, such that reaction efficiencies and the fundamental physics of cavitation can be better understood. Slowly, consensus is being reached on the mechanism of MBSL, which, from optical emission studies, seems to correspond to luminescent chemical reactions of highly energetic species, which are themselves formed during bubble collapse (Suslick et al., 1999b). However, theories around corona discharge, bremsstrahlung radiation, proton tunneling, and other mechanisms are still discussed.

In terms of a measurement tool, the deployment of suitable optics, image intensifiers, and photomultipliers allows the emitted light to be measured in terms of photon counts and rates, thus enabling characterization of the cavitation process (Vian et al., 2010). With careful optical considerations, the regions of a vessel can be imaged, and hence, the photons counted associated with a specific region of fluid, providing spatial resolution. By using specific aqueous solutions and mixtures, the intensity of the emitted light may be enhanced significantly; the best known approach for this is to use luminol (Didenko et al., 1994; Price et al., 2010), which allows visualization of cavitation zones with the naked eye and conventional optics. Luminol enhancement could potentially provide a way to understand energy efficiency in cavitation processes, by critical control of reactants, and monitoring of emitted light levels as the chemical dopants are consumed. A recent report on high-speed observations in xenon-doped phosphoric acid demonstrated that sonoluminescence from individual bubbles within an MBSL-cavitating environment could be recorded, allowing the bubble dynamics to be tracked simultaneously (Cairós and Mettin, 2017).

8.4.5 Mechanical methods

Measurement of cavitation using mechanical techniques generally assumes that cavitation occurs at the surface, upon which the collapse phase generates a microjet, which can then modify the surface in some way, by mechanisms such as deformation, breakage, or removal. A simple but widespread example of this is to deploy a sheet of aluminum foil into the cavitating vessel, leave it for a period of around 30 s, and then examine the resulting perforations. Attempts were made to quantify this idea (Crawford, 1964), but it lacked repeatability and became swiftly nonlinear as cavitation

removed large areas of foil. Nonetheless, the method is a very useful visualization technique for estimating the activity zones in a typical vessel and, more recently, has been shown to correlate well with acoustic emission when mapping cleaning vessels (Jüschke and Koch, 2012; Koch and Jüschke, 2012; Leighton, 1994). A similar approach, favored by manufacturers of cleaning systems, is to apply soiled samples and inspect their progressive cleanliness as a function of dose (https://systems-shop.isopharm.co.uk/product/tosi-lumcheck-test-strips/; https://aseptium.com/products/veritest/).

A more sophisticated erosion-based approach has been developed, which characterizes the impact of cavitation on a metal surface by way of mass transfer and electrochemistry (Birkin et al., 1998, 2005b, 2011; Trabelsi et al., 1996). This is via the electrical current flow that occurs when the passivating oxide layer on an exposed electrode reforms following cavitation damage. Provided the metal surface is of a suitable surface finish and that the aqueous medium is suitably prepared, the technique is sensitive enough to detect individual cavitation events. A clear benefit of the approach is that it is more directly related to applications of cavitation such as cleaning (albeit under specific fluid conditions), in contrast to chemical and acoustic methods, which are more likely to operate in "free" fluid bulk. An early version of the erosion sensor was tested alongside acoustic emission and Weissler chemical dosimetry in the 25-kHz vessel described in Apfel (1997) and Hodnett et al. (2007), with the result shown in Figure 8.6, demonstrating a good quantitative correlation between spatially sensitive megahertz frequency acoustic emission (Zeqiri et al., 2003b) and electrode erosion.

Table 8.2 presents a semiquantitative comparison of the various approaches described so far in this section, in an attempt to provide the reader with some key points to consider before starting measurements.

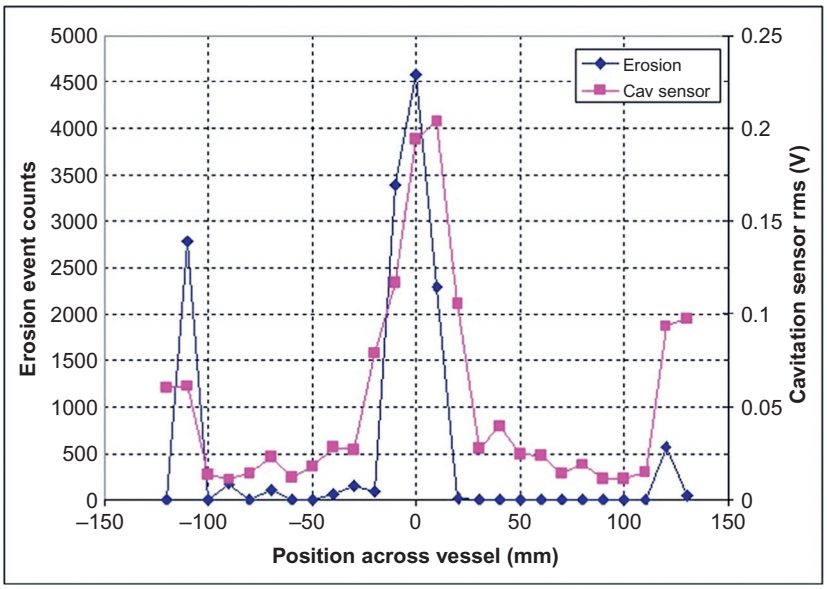


FIGURE 8.6 Direct comparison of megahertz acoustic emissions determined using a cavitation sensor and electrochemical erosion sensor output, across the diameter of a 25-kHz cylindrical vessel.

TABLE 8.2 Comparison of measurement methods

Method and operation	What it determines	Relative cost	Time required to yield useful data	Positives	Negatives
Hydrophone	Acoustic pressure amplitude, usually corresponding to direct field	£££	Fast	Quite robust; can be self-made using PZT and low-cost oscilloscope; can be repeatable and traceable	No direct information on cavitation; can perturb system under test
Broadband acoustic sensor	Acoustic emission corresponding to bubble oscillation and collapse	££££	Medium (fast if real-time filtering used)	Data can be available near real-time in situ; ease of use; useable in most media; portable	Detailed analysis needs postprocessing; perturbing to systems under test

TABLE 8.2 Comparison of measurement methods—cont'd

Method and operation	What it determines	Relative cost	Time required to yield useful data	Positives	Negatives
Chemical dosimetry	Free radicals generated by bubble collapse	£–£££££	Slow (fast for sealed vials)	Versatile, accessible; simplest (cheapest) method is via pH detection; can be made spatially sensitive	Vials can perturb system under test; unknown temperature dependence; mass spectrometry needed for full characterization
Optical emission	Radical generation and recombination	££–£££££	Medium	Can provide rapid visual maps of activity; noninvasive/ nonperturbing	Requires transparent media; quantification requires high-level equipment
Material erosion	Material removal or damage to a surface	£–£££££	Fast	Simplest method using thin foils; close link to actual mechanism of ultrasonic cleaning; refined designs can measure single cavitation events, or high precision mass loss	Perturbs system under test; variable performance due to surface finishes; contaminates fluid in system

8.5 Case studies: Characterizing two cavitating systems

In this penultimate section, two brief examples are described on measurements made at NPL to characterize cavitating systems. The first of these is a 20-kHz sonotrode device, typical of the type used in cell disruption and homogenization applications.

The objective of the measurements was to understand the optimum position at which the sonotrode tip should be immersed into a container of a given size such that the fluid volume undergoing cavitation was maximized. The vessel of interest was filled to a prescribed level with water at a controlled temperature, and using the NPL CaviSensor and Cavimeter (Hodnett et al., 2007), measurements of the spatial distribution of acoustic cavitation were made (defined as the averaged broadband emission in the range of 1.5–7 MHz), for a range of tip displacement amplitudes up to 44 µm (peak-to-peak), corresponding to operating powers from 5 to 60 W, and with the cavitation sensor located initially at 5 mm from the sonotrode tip and then at 40 mm. The experimental configuration is shown schematically in Figure 8.7 and the measurement results in Figure 8.8. It can be seen that at both distances, for lower drive levels, cavitation increases progressively with tip displacement amplitude. At 5 mm, the broadband cavitation increases up to a peak for a displacement of 30 µm, but for the 40-mm measurements, the peak is reached at around

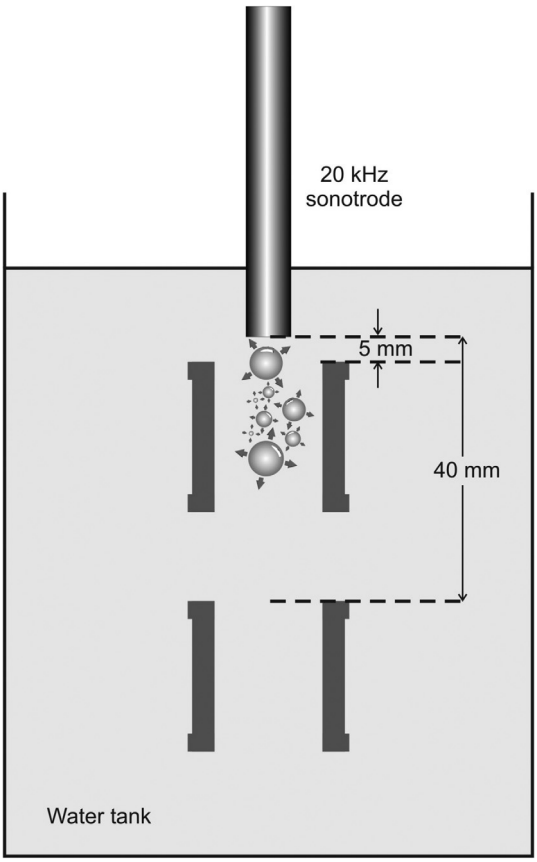


FIGURE 8.7 Schematic of experimental configuration.

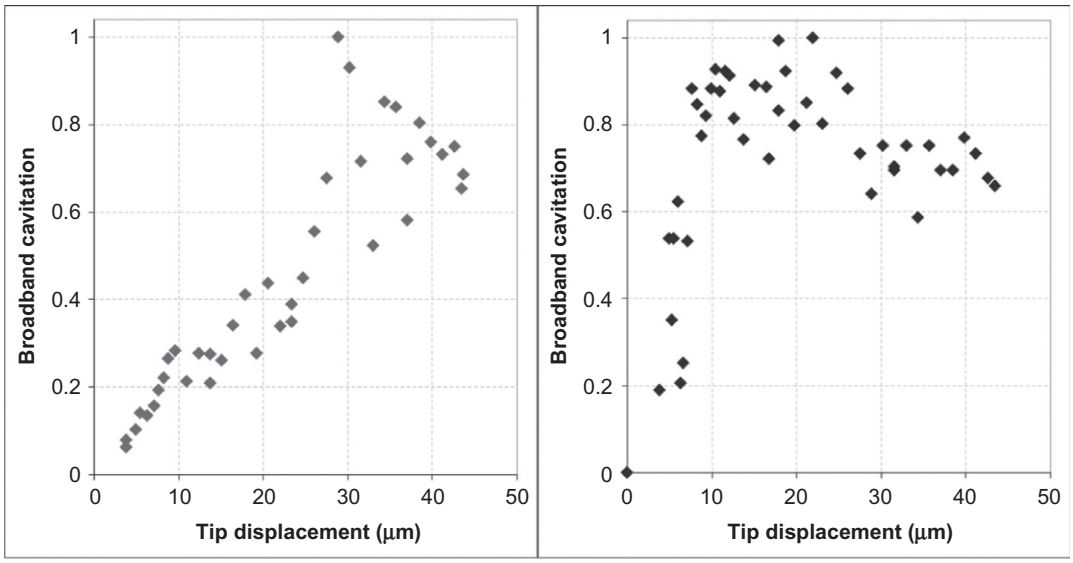


FIGURE 8.8 Comparison of broadband cavitation activity for a spatially sensitive sensor located at 5 mm from the sonotrode tip (left) and 40 mm from the sonotrode tip (right). "Broadband cavitation" is the integrated RMS voltage in the range 1.5–8 MHz, generated by bubbles and bubble clouds undergoing inertial cavitation.

10 μm. In each case, for higher excitation levels, the measured cavitation level decreases. This shows that the inertial cavitation generated by the sonotrode is not simply related to the output setting and that in some cases can actually reduce. For the sensor located at 40 mm, this is likely to demonstrate the phenomenon of cavitation shielding in which the sonotrode tip, at a particular amplitude, briefly decouples from the fluid immediately in front of it such that a large cloud of gas-filled bubbles forms there. These bubbles persist through buoyancy and scatter and absorb the subsequent acoustic waves generated by the sonotrode. Consequently, the acoustic pressures and resulting cavitation at deeper distances within the fluid (and at greater excitation levels) are reduced. This has important implications for the "active cavitation volume" within a given container and demonstrates that operating a sonotrode at its maximum output setting may not always provide the optimum sonication conditions, depending on the volume of fluid exposed.

The second system considered is a multitransducer cell operating in the frequency range of 20–140 kHz, which is a device being established at NPL as a reference source of cavitation (Wang et al., 2012). The cell is shown in Figure 8.9; it consists of three rows of seven transducers, each row being able to operate at two frequencies.

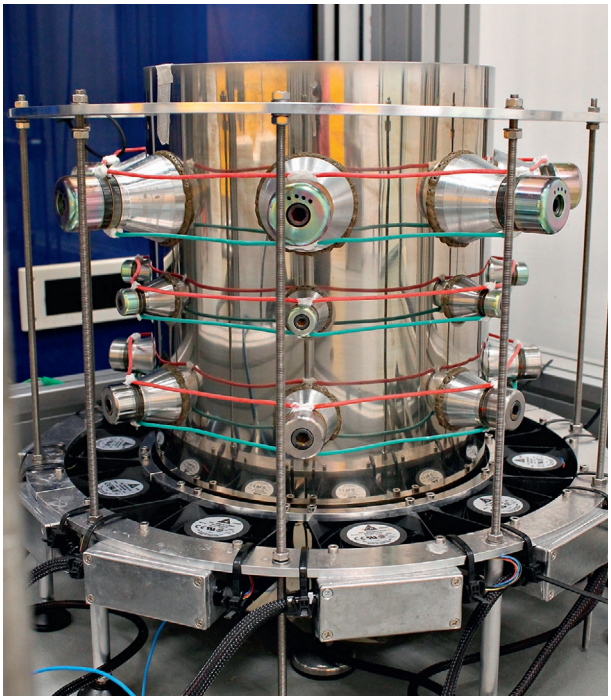


FIGURE 8.9 Multifrequency reference cavitation vessel at NPL. The three rows of transducers are clearly seen.

In this case, two characterization approaches are used: hydrophone measurements for ascertaining the acoustic pressure distribution and luminol-assisted sonoluminescence to identify the regions of local intense cavitation. Results are shown in Figure 8.10, for the same vessel excitation conditions. The upper plots are for operation at 21 kHz and the lower at 44 kHz; the left-hand plots show acoustic pressure over the central region of the 250-mm-diameter vessel, and the right-hand plots show the chemiluminescence recorded over the full vessel, captured using a conventional digital camera over a 60-s duration (Figure 8.10). The difference in the acoustic pressure amplitude and the cavitation activity at the two frequencies is clear and appears to correlate well: at 21 kHz, the central

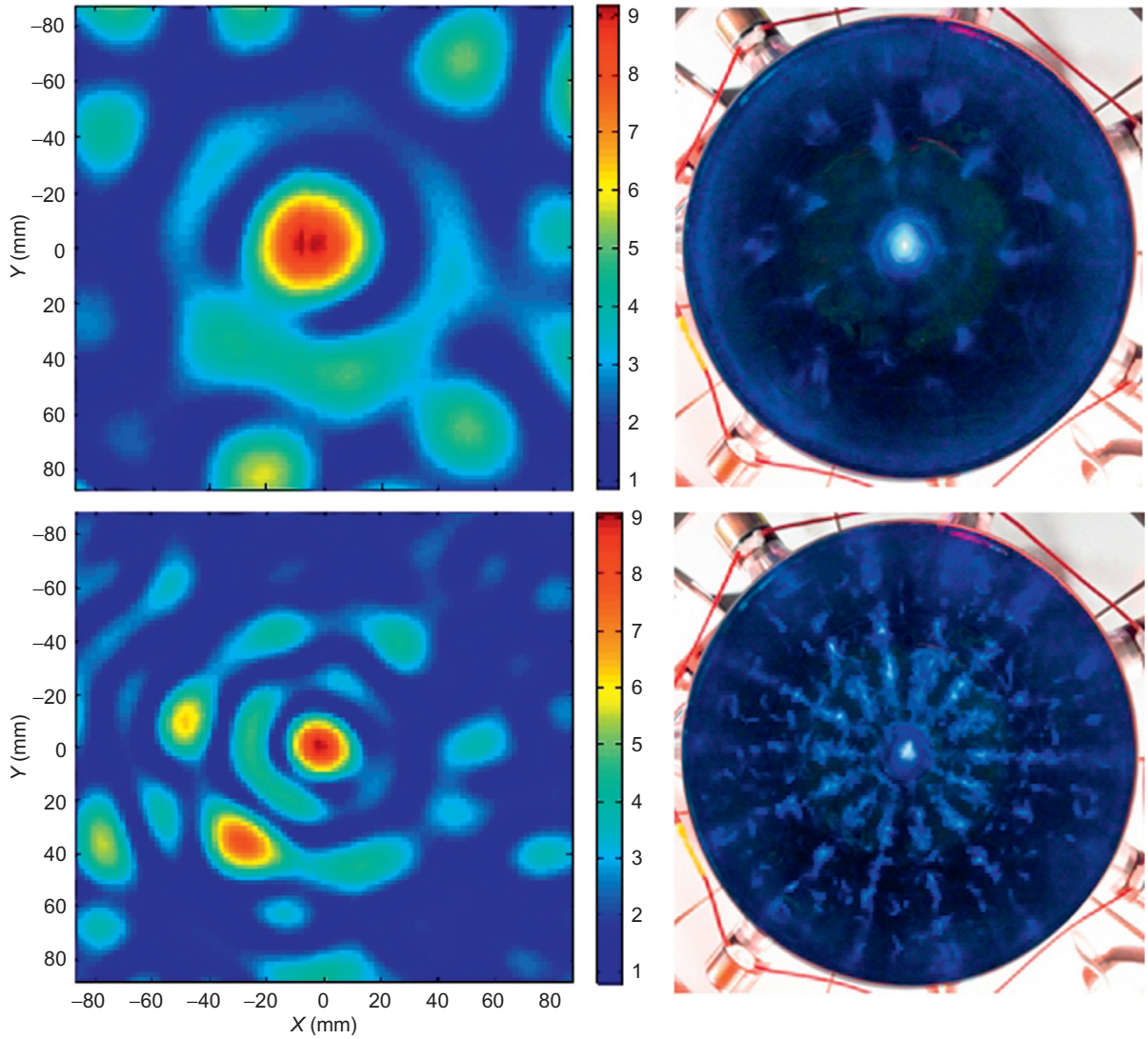


FIGURE 8.10 Comparison of acoustic pressure contour maps (left) and luminescence (right) for two operating frequencies (21 kHz upper; 44 kHz lower) within the cylindrical vessel.

region is broader and more prominent than the subsidiary peaks around it, whereas at 44 kHz, the central peak is narrower. There are clear features corresponding to the seven transducers at both frequencies; in fact, at 44 kHz, reflections generate data plots of both measurands, which are 14-sided.

8.6 Conclusions

This chapter has set out to describe the needs, benefits, and methods for characterizing and measuring high-power ultrasonic systems and has highlighted a broad range of techniques. The selection of a particular method is strongly dependent on the application, the desired effect/purpose, and the cavitation environment; not to mention cost, time, and expertise constraints. The diverse range of end points, environments, and driving phenomena that are employed by the measurement approaches detailed previously mean that their intercomparison is challenging and may even be misleading. Meaningful comparison requires testing all methods of interest against a repeatable cavitation source, and such an exercise was attempted during the 1990s in a collaboration between UK users carried out on a commercial cleaner, and this shows the correlations and differences that can be seen between different measurement approaches (Leighton et al., 2005) and also the difficulties in comparison.

Much of this difficulty stems from the fact that only the secondary effects of cavitation can be measured directly; as has been described before, these arise from different aspects of the cavitation process. For example, broadband acoustic emission originates from the acoustic shock waves generated shortly after bubbles have reached their minimum

size, and *periodic* shock waves (Song et al., 2016; Yusuf et al., 2021) may contribute to many of the other well-known spectral features (Lauterborn and Cramer, 1981); sonoluminescence is thought to occur at about minimum size, yet some chemical effects may arise from shear effects while the bubble wall is accelerating. By further contrast, erosion-based effects are specific to asymmetric bubble collapses at material surfaces, as opposed to within the fluid bulk, and the chemistry and physics in those two environments are likely to be significantly different. With this in mind, it is perhaps a pleasant surprise that correlations between cavitation measurements are seen at all. The secondary nature of characterizing cavitation means that users tend to pick a method that is most familiar and relevant to their field: this is often the best approach but may also mean that potentially useful detail is lost.

It is suggested that detecting, characterizing, and measuring acoustic cavitation form three interlinked aspects of a complex technical hierarchy. Within the measurement aspect comes calibration and standardization, in which published consensus documents specify devices suitable for use, and perhaps a greater challenge, parameters, and units are defined and agreed on that can be used to describe and intercompare acoustically cavitating systems. A cavitation measurement then becomes traceable to a primary standard, and this is the subject of ongoing research at laboratories and applied research centers globally. Such a traceability approach is structured by organizations such as the International Electrotechnical Commission (IEC), and Working Group 3 of IEC Technical Committee 87 is making progress in this area. Traceable acoustic measurement methods and devices would then enable the broadband acoustic emissions from cavitating systems to be described in terms of acoustic pressure amplitude (Pascals), and from this, detailed analyses would follow on aspects such as the energy effectiveness of the cavitation process, leading to meaningful comparison with other approaches used for producing changes in materials and fluids.

Significant technical progress has been made across the technical fields described in this chapter, and more besides, and the scientific community is making strong inroads toward prescribing standardizable measurement methods for cavitation. When achieved, these will provide the springboard for even greater achievements, innovation, and industrial-scale take-up in cavitation-mediated applications.

References

Apfel, R.E., 1997. Sonic effervescence: a tutorial on acoustic cavitation. J. Acoust. Soc. Am. 101, 1227.

Ashokkumar, M., Hall, R., Mulvaney, P., Grieser, F., 1997. Sonoluminescence from aqueous alcohol and surfactant solutions. J. Phys. Chem. B 101, 10845–10850.

Ashokkumar, M., Hodnett, M., Zeqiri, B., Grieser, F., Price, G.J., 2007. Acoustic emission spectra from 515 kHz cavitation in aqueous solutions containing surface-active solutes. J. Am. Chem. Soc. 129, 2250–2258.

Azar, L., 2011. Handbook for Critical Cleaning, second ed. CRC Press, Boca Raton, FL.

Barber, B.P., Putterman, S.J., 1991. Observation of synchronous picosecond sonoluminescence. Nature 352, 318–320.

Barber, B.P., Hiller, R.A., Löfstedt, R., Putterman, S.J., Weninger, K.R., 1997. Defining the unknowns of sonoluminescence. Phys. Rep. 281, 65–143.

Birkin, P.R., Delaplace, C.L., Bowen, C.R., 1998. Electrochemical and photographic detection of cavitation phenomena within a variable frequency acoustic field. J. Phys. Chem. B 102, 10885–10893.

Birkin, P.R., Power, J.F., Leighton, T.G., Vinçotte, A.M., 2002. Cathodic electrochemical detection of sonochemical radical products. Anal. Chem. 74 (11), 2584–2590.

Birkin, P.R., Offin, D.G., Joseph, P.F., Leighton, T.G., 2005a. Cavitation, shock waves and the invasive nature of sonoelectrochemistry. J. Phys. Chem. B 109 (35), 16997–17005.

Birkin, P.R., Offin, D.G., Leighton, T.G., 2005b. The study of surface processes under electrochemical control in the presence of inertial cavitation. Wear 258, 623–628.

Birkin, P.R., Offin, D.G., Vian, C.J.B., 2011. Multiple observations of cavitation cluster dynamics close to an ultrasonic horn tip. J. Acoust. Soc. Am. 130, 3379–3388.

Buick, J.M., Cosgrove, J.A., Douissard, P.-A., Greated, C.A., Gilabert, B., 2004. Application of the acousto-optic effect to pressure measurements in ultrasound fields in water using a laser vibrometer. Rev. Sci. Instrum. 75 (10), 3203–3207.

Cairós, C., Mettin, R., 2017. Simultaneous high-speed recording of sonoluminescence and bubble dynamics in multibubble fields. Phys. Rev. Lett. 118, 064301.

Campos-Pozuelo, C., Vanhille, C., 2012. Electrical detection of the ultrasonic cavitation onset. Ultrason. Sonochem. 19 (6), 1266–1270.

Contamine, R.F., Wilhelm, A.M., Berlan, J., Delmas, H., 1995. Power measurement in sonochemistry. Ultrason. Sonochem. 2 (1), S43–S47.

Crawford, A.E., 1964. The measurement of cavitation. Ultrasonics 2 (3), 120–123.

Datta, S., Coussios, C.C., McAdory, L.E., Tan, J., Porter, T., De Courten-Myers, G., Holland, C.K., 2006. Correlation of cavitation with ultrasound enhancement of thrombolysis. Ultrasound Med. Biol. 32 (8), 1257–1267.

Didenko, Y.T., Nastich, D.N., Pugach, S.P., Polovinka, Y.A., Kvochka, V.I., 1994. The effect of bulk solution temperature on the intensity and spectra of water sonoluminescence. Ultrasonics 32 (1), 71–76.

Felver, B., King, D.C., Lea, S.C., Price, G.J., Walmsley, A.D., 2009. Cavitation occurrence around ultrasonic dental scalers. Ultrason. Sonochem. 16 (5), 692–697.

Flannigan, D.J., Suslick, K., 2005. Plasma formation and temperature measurement during single-bubble cavitation. Nature 434, 52–55.

Flannigan, D.J., Hopkins, S.D., Camara, C.G., Putterman, S.J., Suslick, K.S., 2006. Measurement of pressure and density inside a single sonoluminescing bubble. Phys. Rev. Lett. 96, 204301-1–204301-4.

Frenzel, H., Schultes, H., 1934. Lumineszenz im ultraschallbeschickten wasser. Z. Phys. Chem. 27, 421–424.

Frohly, J., Labouret, S., Bruneel, C., Looten-Baquet, I., Torguet, R., 2000. Ultrasonic cavitation monitoring by acoustic noise power measurement. J. Acoust. Soc. Am. 108, 2012.

Gaitan, D.F., Crum, L.A., Roy, R.A., Church, C.C., 1992. Sonoluminescence and bubble dynamics from a single, stable, cavitation bubble. J. Acoust. Soc. Am. 91, 3166–3183.

Harland, A.R., Petzing, J.N., Tyrer, J.R., 2002. Non-invasive measurements of underwater pressure fields using laser Doppler velocimetry. J. Sound Vib. 252, 169.

Hodnett, M., Zeqiri, B., 1997. A strategy for the development and standardisation of measurement methods for high power/cavitating ultrasonic fields: review of high power field measurement techniques. Ultrason. Sonochem. 4 (4), 273–288.

Hodnett, M., Zeqiri, B., 2008. Towards a reference ultrasonic cavitation vessel. Part 2—investigating the spatial variation and acoustic pressure threshold of inertial cavitation in a 25 kHz ultrasound field. IEEE Trans. Ultrason. Ferroelectr. Freq. Control 55, 1809–1822.

Hodnett, M., Chow, R., Zeqiri, B., 2004. High frequency acoustic emissions generated by a 20 kHz sonochemical horn processor detected using a novel broadband acoustic sensor: a preliminary study. Ultrason. Sonochem. 11, 441–454.

Hodnett, M., Choi, M.J., Zeqiri, B., 2007. Towards a reference ultrasonic cavitation vessel. Part 1—preliminary investigation of the acoustic field distribution in a 25 kHz cylindrical cell. Ultrason. Sonochem. 14, 29–40.

Hurrell, A.M., Rajagapol, S., 2016. The practicalities of obtaining and using hydrophone calibration data to derive pressure waveforms. IEEE Trans. Ultrason. Ferroelectr. Freq. Control 64 (1), 126–140.

Ibanez, I., Zeqiri, B., Hodnett, M., Frota, M.N., 2020. Cavitation-erosion measurements on engineering materials. Eng. Sci. Technol. Int. J. 23 (6), 1486–1498.

Iida, Y., Yasui, K., Tuziuti, T., Sivakumar, M., 2005. Sonochemistry and its dosimetry. Microchem. J. 80 (2), 159–164.

Iida, Y., Lee, J., Kozuka, T., Yasui, K., Towata, A., Tuziuti, T., 2009. Optical cavitation probe using light scattering from bubble clouds. Ultrason. Sonochem. 16 (4), 519–524.

International Electrotechnical Commission, 2013. Ultrasonics—Power Measurement—Radiation Force Balances and Performance Requirements. IEC 61161, Geneva, Switzerland.

International Electrotechnical Commission, 2019. Ultrasonics—Measurements of Cavitation Noise in Ultrasonic Baths and Ultrasonic Reactors. IEC 63001, Geneva, Switzerland.

International Electrotechnical Commission, 2020. Ultrasonics—Hydrophones. Part 1: Measurement and Characterization of Medical Ultrasonic Fields up to 40 MHz. IEC 62127-1 Geneva, Switzerland.

Johansen, K., Song, J.H., Prentice, P., 2017. Deconvolution of acoustically detected bubble-collapse shock waves. Ultrasonics 73, 144–153.

Johansen, K., Song, J.H., Prentice, P., 2018. Performance characterisation of a passive cavitation detector optimised for subharmonic periodic shock waves from acoustic cavitation in MHz and sub-MHz ultrasound. Ultrason. Sonochem. 43, 146–155.

Jüschke, M., Koch, C., 2012. Model processes and cavitation indicators for a quantitative description of an ultrasonic cleaning vessel. Part I: experimental results. Ultrason. Sonochem. 19 (4), 787–795.

Kimura, T., Sakamoto, T., Leveque, J., Sohmiya, H., Fujita, M., Ikeda, S., Ando, T., 1996. Standardization of ultrasonic power for sonochemical reaction. Ultrason. Sonochem. 3 (3), S157–S161.

Koch, C., Jüschke, M., 2012. Model processes and cavitation indicators for a quantitative description of an ultrasonic cleaning vessel. Part II—multivariate data analysis. Ultrason. Sonochem. 19 (4), 796–802.

Koda, S., Kimura, T., Kondo, T., Mitome, H., 2003. A standard method to calibrate sonochemical efficiency of an individual reaction system. Ultrason. Sonochem. 10 (3), 149–156.

Komarov, S., Oda, K., Ishiwata, Y., Dezhkunov, N., 2013. Characterization of acoustic cavitation in water and molten aluminum alloy. Ultrason. Sonochem. 20 (2), 754–761.

Korpel, A., 1981. Acousto-optics—a review of fundamentals. Proc. IEEE 69, 1.

Kratochvil, B., Mornstein, V., 2007. Use of chemical dosimetry for comparison of ultrasound and ionizing radiation effects on cavitation. Physiol. Res. 56, 77–84.

Lauterborn, W., 1996. Nonlinear dynamics in acoustics. Acustica 82, S-46–S-55.

Lauterborn, W., Cramer, E., 1981. Subharmonic route to chaos observed in acoustics. Phys. Rev. Lett. 51, 1445.

Lea, S.C., Landini, G., Walmsley, A.D., 2006. The effect of wear on ultrasonic scaler tip displacement amplitude. J. Clin. Periodontol. 33 (1), 37–41.

Leighton, T.G., 1994. The Acoustic Bubble. Academic Press, New York.

Leighton, T.G., 1995. Bubble population phenomena in acoustic cavitation. Ultrason. Sonochem. 2 (2), S123–S136.

Leighton, T.G., 1998. A strategy for the development and standardisation of measurement methods for high power/cavitating ultrasonic fields: review of cavitation monitoring techniques. ISVR Technical Report No. 263.

Leighton, T.G., Birkin, P.R., Hodnett, M., Zeqiri, B., Power, J.F., Price, G.J., Mason, T.J., Plattes, M., Dezhkunov, N., Coleman, A.J., 2005. Characterisation of measures of reference acoustic cavitation (COMORAC): an experimental feasibility trial. In: Doinikov, A.A. (Ed.), Bubble and Particle Dynamics in Acoustic Fields: Modern Trends and Applications. Research Signpost, Kerala, pp. 37–94.

Lipsman, N., Meng, Y., Bethune, A.J., Huang, Y., Lam, B., Masellis, M., Herrman, N., Heyn, C., Aubert, I., Boutet, A., Smith, G.S., Hynynen, K., Black, S., 2018. Blood-brain barrier opening in Alzheimer's disease using MR-guided focused ultrasound. Nat. Commun. 9, 2336.

Marangopoulos, I.P., Martin, C.J., Hutchison, J.M.S., 1995. Measurement of field distributions in ultrasonic cleaning baths: implications for cleaning efficiency. Phys. Med. Biol. 40, 1897–1908.

Mark, G., Tauber, A., Laupert, R., Schuchmann, H.P., Schulz, D., Mues, A., von Sonntag, C., 1998. OH-radical formation by ultrasound in aqueous solution. Part II: terephthalate and Fricke dosimetry and the influence of various conditions on the sonolytic yield. Ultrason. Sonochem. 5 (2), 41–52.

Marston, P.L., 1999. Light scattering by bubbles in liquids and applications to physical acoustics. In: Crum, L.A., Mason, T.J., Reisse, J., Suslick, K.S. (Eds.), Sonochemistry and Sonoluminescence. Kluwer Publishers, Dordrecht, The Netherlands, pp. 73–86.

Mathieson, A., Cardoni, C., Cerisola, N., Lucas, M., 2013. The influence of piezoceramic stack location on nonlinear behavior of Langevin transducers. IEEE Trans. Ultrason. Ferroelectr. Freq. Control 60 (6), 1126–1133.

Matula, T.J., Roy, R.A., Mourad, P.D., McNamara, W.B., Suslick, K.S., 1995. Comparison of multibubble and single-bubble sonoluminescence spectra. Phys. Rev. Lett. 75, 2602–2605.

Matula, T.J., Hallaj, I.M., Cleveland, R.O., Crum, L.A., Moss, W.C., Roy, R.A., 1998. The acoustic emissions from single-bubble sonoluminescence. J. Acoust. Soc. Am. 103, 1377.

McLaughlan, J., Rivens, I., Leighton, T., Haar, G.T., 2010. A study of bubble activity generated in ex vivo tissue by high intensity focused ultrasound. Ultrasound Med. Biol. 36 (8), 1327–1344.

Memoli, G., Gélat, P.N., Hodnett, M., Zeqiri, B., 2012. Characterisation and improvement of a reference cylindrical sonoreactor. Ultrason. Sonochem. 19 (4), 939–952.

Milne, L., Stewart, I., Bremner, D.H., 2013. Comparison of hydroxyl radical formation in aqueous solutions at different ultrasound

frequencies and powers using the salicylic acid dosimeter. Ultrason. Sonochem. 20 (3), 984–989.
Neppiras, E.A., 1980. Acoustic cavitation. Phys. Rep. 61, 159.
Pecheva, E., Sammons, R.L., Walmsley, A.D., 2016. The performance characteristics of a piezoelectric ultrasonic dental scaler. Med. Eng. Phys. 38 (2), 199–203.
Pohl, A.A.P., Oliveira, R.A., Da Silva, R.E., Marques, C.A.F., de Tarso Neves, P., Cook, K., Canning, J., Nogueira, R.N., 2013. Advances and new applications using the acousto-optic effect in optical fibers. Photonic Sens. 3 (1), 1–25.
Pohlmann, R., 1971. Method and Apparatus for Energy Density Measurements in Standing Ultrasonic Wave Fields. US Patent 3593818A.
Posakony, G.J., Greenwood, L.R., Ahmed, S., 2006. Stable multibubble sonoluminescence bubble patterns. Ultrasonics 44 (Suppl. 22), e445–e449.
Price, G.J., Lenz, E.J., 1993. The use of dosimeters to measure radical production in aqueous sonochemical systems. Ultrasonics 31 (6), 451–456.
Price, G.J., Duck, F.A., Digby, M., Holland, W., Berryman, T., 1997. Measurement of radical production as a result of cavitation in medical ultrasound fields. Ultrason. Sonochem. 4 (2), 165–171.
Price, G.J., Harris, N.K., Stewart, A.J., 2010. Direct observation of cavitation fields at 23 and 515 kHz. Ultrason. Sonochem. 17 (1), 30–33.
Putterman, S.J., Weninger, K.R., 2000. Sonoluminescence: how bubbles turn sound into light. Annu. Rev. Fluid Mech. 32, 445–476.
Sesis, A., Hodnett, M., Memoli, G., Wain, A.J., Jurewicz, I., Dalton, A.B., Carey, J.D., Hinds, G., 2013. Influence of acoustic cavitation on the controlled ultrasonic dispersion of carbon nanotubes. J. Phys. Chem. B 117 (48), 15141–15150.
Son, Y., Lim, M., Khim, J., Kim, L.-H., Ashokkumar, M., 2012. Comparison of calorimetric energy and cavitation energy for the removal of bisphenol-A: the effects of frequency and liquid height. Chem. Eng. J. 83, 39–45.
Song, J.H., Johansen, K., Prentice, P., 2016. An analysis of the acoustic cavitation noise spectrum: the role of periodic shock waves. J. Acoust. Soc. Am. 140, 2494.
Suslick, K.S., Flint, E.B., 1987. Sonoluminescence of non-aqueous liquids. Nature 330, 553–555.
Suslick, K.S., Didenko, Y., Fang, M.M., Hyeon, T., Kolbeck, K.J., McNamara III, W.B., Mdleleni, M.M., Wong, M., 1999a. Acoustic cavitation and its chemical consequences. Phil. Trans. R. Soc. Lond. A 357 (1751), 335–353.
Suslick, K.S., McNamara III, W.B., Didenko, Y., 1999b. Hot spot conditions during multi-bubble cavitation. In: Crum, L.A., Mason, T.J., Reisse, J., Suslick, K.S. (Eds.), Sonochemistry and Sonoluminescence. Kluwer Publishers, Dordrecht, The Netherlands, pp. 191–204.
Torres-Sanchez, C., Corney, J.R., 2008. Effects of ultrasound on polymeric foam porosity. Ultrason. Sonochem. 15 (4), 408–415.
Trabelsi, F., Ait-Lyazidi, H., Berlan, J., Fabre, P.-L., Delmas, H., Wilhelm, A.M., 1996. Electrochemical determination of the active zones in a high-frequency ultrasonic reactor. Ultrason. Sonochem. 3 (2), S125–S130.
Tzanakis, I., Eskin, D.G., Georgoulas, A., Fytanidis, D.K., 2014. Incubation pit analysis and calculation of the hydrodynamic impact pressure from the implosion of an acoustic cavitation bubble. Ultrason. Sonochem. 21 (2), 866–878.
Tzanakis, I., Hodnett, M., Lebon, G.S.B., Dezhkunov, N., Eskin, D.G., 2016. Calibration and performance assessment of an innovative high-temperature cavitometer. Sens. Actuator A Phys. 240, 57–69.
Vian, C.J.B., Birkin, P.R., Leighton, T.G., 2010. Cluster collapse in a cylindrical cell: correlating multibubble sonoluminescence, acoustic pressure, and erosion. J. Phys. Chem. C 114 (39), 16416–16425.
Walton, A.J., Reynolds, G.T., 1984. Sonoluminescence. Adv. Phys. 33 (6), 595.
Wang, L., Memoli, G., Butterworth, I., Hodnett, M., Zeqiri, B., 2012. Characterisation of a multi-frequency cavitation vessel. IOP Conf. Ser. Mater. Sci. Eng. 42, 012–013.
Weissler, A., 1959. Formation of hydrogen peroxide by ultrasonic waves: free radicals. J. Am. Chem. Soc. 81 (5), 1077–1081.
Weissler, A., Cooper, H.W., Snyder, S., 1950. Chemical effect of ultrasonic waves: oxidation of potassium iodide solution by carbon tetrachloride. J. Am. Chem. Soc. 72, 1769–1775.
Weninger, K.R., Barber, B.P., Putterman, S., 1997. Pulsed Mie scattering measurements of the collapse of a sonoluminescing bubble. Phys. Rev. Lett. 78, 1799.
Wilkens, V., 2010. Thermal technique for local ultrasound intensity measurement. Part 1: sensor concept and prototype calibration. Meas. Sci. Technol. 21 (11), 115805-1–115805-8.
Yasui, K., Tuziuti, T., Sivakumar, M., Iida, Y., 2004. Sonoluminescence. Appl. Spectrosc. Rev. 39 (3), 399–436.
Ying, C., Bai, L., Li, C., Deng, J., 2011. Cavitation field from a horn—a new model. Sci. China Phys. Mech. Astron. 54 (1), 74–78.
Young, F.R., 1989. Cavitation. McGraw-Hill, Cambridge, UK.
Yusuf, L., Symes, M., Prentice, P., 2021. Characterising the cavitation activity generated by an ultrasonic horn at varying tip-vibration amplitudes. Ultrason. Sonochem. 70, 105273.
Zeqiri, B., Lee, N.D., Hodnett, M., Gélat, P.N., 2003a. A novel sensor for monitoring acoustic cavitation. Part II: prototype performance evaluation. IEEE Trans. Ultrason. Ferroelectr. Freq. Control 50, 1351–1362.
Zeqiri, B., Gélat, P.N., Hodnett, M., Lee, N.D., 2003b. A novel sensor for monitoring acoustic cavitation. Part I: concept, theory and prototype development. IEEE Trans. Ultrason. Ferroelectr. Freq. Control 50, 1342–1350.
Zeqiri, B., Hodnett, M., Carroll, A.J., 2006. Studies of a novel sensor for assessing the spatial distribution of cavitation activity within ultrasonic cleaning vessels. Ultrasonics 44, 73–82.

Chapter 9

Modeling of power ultrasonic transducers

B. Dubus, Ch. Croënne, and P. Mosbah

Univ Lille, CNRS, Ecole Centrale, Junia, Univ Valenciennes, IEMN, UMR, Lille Cedex, France

List of symbols

$[A]$, $[B]$	BEM matrices
c_f	sound speed of the fluid medium
c^E_{ijkl}	elastic stiffness tensor at constant electric field components
$[D]$	FEM matrix for acoustic dampers
D_i	electric displacement components
E_i	electric field components
e_{kij}	piezoelectric tensor components
f_i	surface force density vector components
F	FEM force vector
G	Green's function
g	3D free space Green's function
$[H]$	FEM fluid stiffness matrix
I	electric current
i, j, k, l	subscripts varying between 1 and 3
$[K_{uu}]$	FEM stiffness matrix
$[K_{u\varphi}]$	FEM piezoelectric matrix
$[K_{\varphi\varphi}]$	FEM dielectric matrix
$[L]$	FEM solid-fluid interface matrix
$[M]$	FEM solid mass matrix
$[M_f]$	FEM fluid mass matrix
n_i	surface normal vector components
P	FEM acoustic pressure vector
p	acoustic pressure
Q	electric charge
Q	FEM electric charge vector
t	time coordinates
S_{ij}	strain tensor components
T_{ij}	stress tensor components
U	FEM displacement vector
$\ddot{U}$	FEM acceleration vector
u_i	displacement components
$[X]$	DtN matrix
x_i	space coordinates
Z	electric impedance
Γ	surface of the piezoelectric domain
Γ_i	solid-fluid interface
Γ_∞	surface separating finite and infinite fluid domains
ε^S_{ij}	dielectric permittivity tensor at constant strain components
ρ_p	density of the piezoelectric medium
σ	surface charge density
Φ	FEM electric potential vector
φ	electric potential
Ψ	FEM vector of surface normal derivative of pressure
ψ	surface normal derivative of pressure
Ω_p	volume of the piezoelectric domain
Ω_s	volume of the fluid domain

9.1 Introduction

Ultrasonic systems are usually composed of three elements: a generator providing the electrical energy, an electromechanical transducer converting electrical energy into mechanical vibratory energy, and a propagation medium, fluid or solid, in which acoustic energy is radiated. These devices mainly utilize two mechanisms for energy conversion: an electromechanical transduction using the piezoelectric effect and, when necessary, a mechanoacoustic conversion through the fluid-structure coupling. When the external fluid cannot be considered as a light fluid, a strong interaction takes place between electrical, mechanical, and acoustic phenomena. To design such systems, models must take into account both transduction mechanisms for any geometry. Numerical methods are therefore an obvious choice.

In numerical models, the generator is often considered an ideal voltage (or current) generator delivering a sinusoidal electrical excitation at constant frequency. Detailed analysis of the electrical generator is generally not considered at the design stage. Hence, only the transducer, the propagation medium, and their interaction are considered in the model and are described by using the finite element method (FEM), which can be coupled with other methods to describe unbounded media: boundary element method (BEM), Dirichlet-to-Neuman (DtN) method, acoustic dampers, perfectly matched layers (PMLs), etc.

This chapter describes numerical methods utilized to model piezoelectric devices. It is divided into three parts, dedicated, respectively, to transduction phenomena and wave propagation in solids, acoustic wave propagation in

Power Ultrasonics. https://doi.org/10.1016/B978-0-12-820254-8.00034-8
Copyright © 2023 Elsevier Ltd. All rights reserved.

fluids, fluid-structure coupling, and acoustic radiation. The models are linear and rely upon the theory of elasticity, the constitutive equations of piezoelectricity, and the theory of linear acoustics. Application examples illustrate typical results and comparison with measurements.

9.2 Transduction and elastic wave propagation in solids

9.2.1 Physical equations and boundary conditions

Let us consider a piezoelectric domain Ω_p limited by a surface pointing outward Γ. Fundamental equations written using Einstein's notation are Newton's law,

$$\rho_p \frac{\partial^2 u_i}{\partial t^2} = \frac{\partial T_{ij}}{\partial x_j}, \tag{9.1}$$

and Gauss's law considering that the domain is free from macroscopic electric charges

$$\frac{\partial D_i}{\partial x_i} = 0. \tag{9.2}$$

Small strains and electrostatic theories are assumed, and therefore,

$$S_{ij} = \frac{1}{2}\left(\frac{\partial u_i}{\partial x_j} + \frac{\partial u_j}{\partial x_i}\right), \tag{9.3}$$

and

$$E_i = -\frac{\partial \varphi}{\partial x_i}. \tag{9.4}$$

Constitutive equations of piezoelectricity are written in choosing strain and electric field as independent variables (Wilson, 1988):

$$\begin{matrix} T_{ij} = c^E_{ijkl} S_{kl} - e_{kij} E_k \\ D_i = e_{ikl} S_{kl} + \varepsilon^S_{ij} E_j \end{matrix}. \tag{9.5}$$

Mechanical boundary conditions may correspond to a prescribed displacement $\boldsymbol{u}^0$ on the surface Γ_u (Dirichlet type):

$$u_i = u_i^0, \tag{9.6}$$

or a prescribed surface force density $\boldsymbol{f}^0$ on the surface Γ_f (Neumann type):

$$T_{ij} n_j = f_i^0. \tag{9.7}$$

Electrical boundary conditions correspond to a prescribed electrical potential φ^0 on the surface Γ_φ (Dirichlet type):

$$\varphi = \varphi^0, \tag{9.8}$$

or a prescribed surface charge density σ^0 on the surface Γ_σ (Neumann type):

$$-D_i n_i = \sigma^0 \tag{9.9}$$

The mechanical boundary condition (9.7) is used to describe a solid-vacuum interface by prescribing $f^0 = 0$. This condition is also a reasonable approximation to model the dynamic behavior of solid structures immersed in light fluids. The exact boundary condition for the fluid-structure interaction is discussed in Section 9.3.

A detailed examination is required to define the domain of application of the electrical boundary conditions (9.8) and (9.9):

- When the external surface is not covered by an electrode, the surface electrical charge density vanishes. Electrical boundary conditions imply the continuity of the normal component of the electrical displacement and the continuity of the tangential component of the electric field through the surface. If the dielectric permittivity of the piezoelectric medium is much larger than the dielectric permittivity of the external medium (e.g. PZT-air interface), the normal component of the electrical displacement tends to vanish at the surface, and Eq. (9.9) with $\sigma^0 = 0$ is a reasonable approximation. In the other cases (e.g., PVDF-air interface), the electrical boundary condition cannot be simplified, and the external medium must be considered in the frame of electrostatics.
- When an external surface of the piezoelectric medium is covered by an electrode, the boundary condition (9.8) is used if the electrical potential is known. In particular, $\varphi^0 = 0$ is used for a grounded electrode. If the electrical potential is unknown (floating electrode), the surface condition relates $\boldsymbol{D}$ to the total charge Q_{el} on the electrode surface Γ_{el}:

$$-\iint_{\Gamma_{el}} D_i n_i \mathrm{d}\Gamma = Q_{el}. \tag{9.10}$$

9.2.2 Finite element method

9.2.2.1 *Variational formulation*

The geometry of the surface Γ is assumed to be independent of time, but boundary conditions on Γ may be time-dependent. A generalized elementary displacement $\delta \boldsymbol{w}$ is considered:

$$\delta w = \begin{Bmatrix} \delta u \\ \delta \varphi \end{Bmatrix}. \tag{9.11}$$

Among all admissible generalized displacements satisfying spatial boundary conditions (9.6)–(9.9) and temporal boundary conditions $\delta w = 0$ at $t = t_1$ and $t = t_2$, the solution verifies (Washizu, 1975):

$$\int_{t_1}^{t_2}\left\{\iiint_{(\Omega_p)}\left[\rho_p\left(\frac{\partial u_i}{\partial t}\right)\delta\left(\frac{\partial u_i}{\partial t}\right)-\left(T_{ij}\delta S_{ij}+D_i\delta E_i\right)\right]d\Omega - \iint_{(\Gamma)}\left(\delta u_i T_{ij}n_j+\delta\varphi D_i n_i\right)d\Gamma\right\}dt=0. \tag{9.12}$$

The first integral corresponds to the variation of the Lagrangian defined as the kinetic energy density minus the electrical enthalpy. Surface integrals are associated with the work of external forces and the electrical energy exchanged with external generators, respectively. After integrating by parts with respect to time, and considering that $\delta u=0$ at $t=t_1$ and $t=t_2$, Eq. (9.12) becomes as follows:

$$\int_{t_1}^{t_2}\left\{\iiint_{(\Omega_p)}\left[\rho_p\delta u_i\frac{\partial^2 u_i}{\partial t^2}-\left(T_{ij}\delta S_{ij}+D_i\delta E_i\right)\right]d\Omega - \iint_{(\Gamma)}\left(\delta u_i T_{ij}n_j+\delta\varphi D_i n_i\right)d\Gamma\right\}dt=0. \tag{9.13}$$

As the choice of t_1 and t_2 is arbitrary, Eq. (9.13) may be written (Dubus et al., 1999) as follows:

$$\iiint_{(\Omega_p)}\left[\rho_p\delta u_i\frac{\partial^2 u_i}{\partial t^2}-\left(T_{ij}\delta S_{ij}+D_i\delta E_i\right)\right]d\Omega - \iint_{(\Gamma)}\left(\delta u_i T_{ij}n_j+\delta\varphi D_i n_i\right)d\Gamma=0. \tag{9.14}$$

9.2.2.2 Space discretization

Spatial discretization is obtained by meshing the piezoelectric domain Ω_p and the surface Γ into elements connected by nodes. Inside an element e, the displacement $\boldsymbol{u}^e$ (resp. acceleration $\ddot{\boldsymbol{u}}^e$) is related to the nodal values of displacement $\boldsymbol{U}^e$ (resp. acceleration $\ddot{\boldsymbol{U}}^e$) by (Dhatt and Touzot, 1981; Zienkiewicz and Taylor, 1989) the following equations:

$$u^e=\left[N_u^e\right]U^e, \tag{9.15}$$

$$\ddot{u}^e=\left[N_u^e\right]\ddot{U}^e, \tag{9.16}$$

where $[N_u^e]$ is a matrix containing interpolation functions. The condensed tensor of strains $\boldsymbol{S}^e$ is written as follows:

$$S^e=\left[B_u^e\right]U^e, \tag{9.17}$$

where $[B_u^e]$ is a matrix containing the spatial derivatives of the interpolation functions. Similarly, the electrical potential φ^e inside the element e is related to the nodal values of the electric potential $\boldsymbol{\Phi}^e$:

$$\varphi^e=\left[N_\varphi^e\right]\Phi^e, \tag{9.18}$$

where $[N_\varphi^e]$ is a matrix containing interpolation functions. The electric field is written as follows:

$$E^e=-\left[B_\varphi^e\right]\Phi^e, \tag{9.19}$$

where $[B_\varphi^e]$ is a matrix containing spatial derivatives of the interpolation functions. The generalized strain and stress vectors are, respectively, expressed inside the element e:

$$\Sigma^e=\begin{Bmatrix}S^e\\E^e\end{Bmatrix}=\begin{bmatrix}[B_u^e] & [0]\\ [0] & -[B_\varphi^e]\end{bmatrix}\begin{Bmatrix}U^e\\ \Phi^e\end{Bmatrix}, \tag{9.20}$$

$$\Theta^e=\begin{Bmatrix}T^e\\D^e\end{Bmatrix}=\begin{bmatrix}[c^E] & -[e]\\ [e] & [\varepsilon^S]\end{bmatrix}\begin{bmatrix}[B_u^e] & [0]\\ [0] & -[B_\varphi^e]\end{bmatrix}\begin{Bmatrix}U^e\\ \Phi^e\end{Bmatrix}. \tag{9.21}$$

Combining Eqs. (9.15)–(9.21) with (9.13) and introducing the vector of the nodal values of the second time derivative of the electrical potential Φ in order to simplify the notation, we get

$$\{\delta U^t,\delta\Phi^t\}\left(\begin{bmatrix}[K_{uu}] & [K_{u\varphi}]\\ [K_{u\varphi}]^t & [K_{\varphi\varphi}]\end{bmatrix}\begin{Bmatrix}U\\ \Phi\end{Bmatrix} + \begin{bmatrix}[M] & [0]\\ [0] & [0]\end{bmatrix}\begin{Bmatrix}\ddot{U}\\ \ddot{\Phi}\end{Bmatrix}-\begin{Bmatrix}F\\ -Q\end{Bmatrix}\right), \tag{9.22}$$

with

$$[K_{uu}]=\sum\nolimits_e\left[K_{uu}^e\right]=\sum\nolimits_e\iiint_{(\Omega_p^e)}\left[B_u^e\right]^t\left[c^E\right]\left[B_u^e\right]d\Omega^e, \tag{9.23}$$

$$\left[K_{u\varphi}\right]=\sum\nolimits_e\left[K_{u\varphi}^e\right]=\sum\nolimits_e\iiint_{(\Omega_p^e)}\left[B_u^e\right]^t[e]^t\left[B_\varphi^e\right]d\Omega^e, \tag{9.24}$$

$$\left[K_{\varphi\varphi}\right]=\sum\nolimits_e\left[K_{\varphi\varphi}^e\right]=\sum\nolimits_e\iiint_{(\Omega_p^e)}\left[B_\varphi^e\right][\varepsilon]^t\left[B_\varphi^e\right]d\Omega^e, \tag{9.25}$$

$$[M]=\sum\nolimits_e[M^e]=\sum\nolimits_e\iiint_{(\Omega_p^e)}\rho_p\left[N_u^e\right]^t\left[N_u^e\right]d\Omega^e, \tag{9.26}$$

$$F=\sum\nolimits_e F^e=\sum\nolimits_e\iint_{(\Gamma_f^e)}\left[N_u^e\right]^t f^0\mathrm{d}\Gamma^e+\sum\nolimits_e\iint_{(\Gamma_u^e)}\left[N_u^e\right]^t[T]\mathrm{nd}\Gamma^e, \tag{9.27}$$

$$Q=\sum\nolimits_e Q_e=\sum\nolimits_e\iint_{(\Gamma_\sigma^e)}\left[N_\varphi^e\right]^t\sigma^0\mathrm{d}\Gamma^e+\sum\nolimits_e\iint_{(\Gamma_\varphi^e)}\left[N_\varphi^e\right]^t Dnd\Gamma^e. \tag{9.28}$$

Eq. (9.22) is finally written as

$$\begin{bmatrix} [K_{uu}] & [K_{u\varphi}] \\ [K_{u\varphi}]^t & [K_{\varphi\varphi}] \end{bmatrix} \begin{Bmatrix} U \\ \Phi \end{Bmatrix} + \begin{bmatrix} [M] & [0] \\ [0] & [0] \end{bmatrix} \begin{Bmatrix} \ddot{U} \\ \ddot{\Phi} \end{Bmatrix} = \begin{Bmatrix} F \\ -Q \end{Bmatrix} \quad (9.29)$$

because generalized displacements are arbitrary.

9.2.2.3 Problem types

Three types of analyses are considered:

- The harmonic analysis is obtained considering that all the physical variables depend on time as $e^{+j\omega t}$. The resulting equation is as follows (Allik and Hughes, 1970; Decarpigny, 1984):

$$\begin{bmatrix} [K_{uu}]-\omega^2[M] & [K_{u\varphi}] \\ [K_{u\varphi}]^t & [K_{\varphi\varphi}] \end{bmatrix} \begin{Bmatrix} U \\ \Phi \end{Bmatrix} = \begin{Bmatrix} F \\ -Q \end{Bmatrix} \quad (9.30)$$

This analysis describes the response of the piezoelectric medium to an applied external load at constant angular frequency ω, that is, an external force or an electrical voltage applied to the electrodes. In the former case, the electrical impedance Z_i of the electrode i associated with the electrical potential Φ_i is

$$Z_i = \frac{\Phi_i}{I_i} = \frac{\Phi_i}{j\omega Q_i}, \quad (9.31)$$

where I_i is the electrical current entering the electrode. Mechanical, piezoelectric, or electrical losses associated with strain-stress, stress-electric field, and electrical displacement-electric field hysteresis, respectively, can be described using complex physical constants (Holland, 1967). The static analysis of a piezoelectric medium can be deduced from Eq. (9.30) by setting the angular frequency to zero.

- The modal analysis of the piezoelectric medium is obtained by the left-hand side terms of Eq. (9.30). The resulting equation is a classical eigenvalue problem for which eigenvalues and eigenvectors are associated with resonance angular frequencies and resonance modes, respectively. The motional (series) resonance angular frequency of the transducer ω_s is obtained when both $\boldsymbol{F}$ and the electrical potential Φ_i associated with the electrodes are set to zero. The parallel resonance angular frequency of the transducer ω_p is obtained when both $\boldsymbol{F}$ and the electrical charges on electrodes Q_i are set to zero. These results are used to calculate the coupling coefficient of the transducer k_c according to Meitzler definition (Meitzler et al., 1973):

$$k_c = \sqrt{\frac{\omega_p^2 - \omega_s^2}{\omega_p^2}}. \quad (9.32)$$

- The transient analysis corresponds to an arbitrary time dependency of the physical variables. Eq. (9.29) can be written as

$$\overline{[K]}W + \overline{[M]}\ddot{W} = \overline{F} \quad (9.33)$$

This equation is formally identical to the one obtained for a pure mechanical system (Zienkiewicz and Wood, 1987). The principle of time discretization derives from linear mechanics (Dhatt and Touzot, 1981; Zienkiewicz and Taylor, 1989). It may be noted that the $\overline{[M]}$ matrix cannot be inverted, and therefore, algorithms such as central difference cannot be used. An alternative system of equation is given by the condensation of the electrical degrees of freedom in Eq. (9.29):

$$\left([K_{uu}] - [K_{u\varphi}][K_{\varphi\varphi}]^{-1}[K_{u\varphi}]^t\right)U + [M]\ddot{U} = F - [K_{u\varphi}][K_{\varphi\varphi}]^{-1}Q. \quad (9.34)$$

Electrical potentials are then obtained by using the following expression:

$$\Phi = -[K_{\varphi\varphi}]^{-1}Q - [K_{\varphi\varphi}]^{-1}[K_{\varphi\varphi}]^T U. \quad (9.35)$$

Note that $\overline{[K]}$ and $\overline{[M]}$ are strongly sparse for large calculations, and the condensation of the electric degrees of freedom degrades their sparsity. Moreover, it requires to calculate $\{\Phi\}$ after having solved the system of equations. An alternative approach can use classical Newmark's integration scheme where U is expressed as follows: (Zienkiewicz et al., 2005):

$$\dot{U}_{n+1} = \dot{U}_n + \Delta t\ddot{U}_n + \alpha\Delta t\left(\ddot{U}_{n+1} - \ddot{U}_n\right). \quad (9.36)$$

$$U_{n+1} = U_n + \Delta t\dot{U}_n + \frac{\Delta t^2}{2}\ddot{U}_n + \beta\Delta t^2\left(\ddot{U}_{n+1} - \ddot{U}_n\right), \quad (9.37)$$

with α and β integration parameters. This leads to the system of equations to be solved at every integration step:

$$\begin{bmatrix} [K_{uu}] + \dfrac{1}{\beta\Delta t^2}[M] & [K_{u\varphi}] \\ [K_{\varphi u}]^t & [K_{\varphi\varphi}] \end{bmatrix} \begin{Bmatrix} U_{n+1} \\ \Phi_{n+1} \end{Bmatrix} = \begin{Bmatrix} F \\ Q \end{Bmatrix} - \begin{bmatrix} [M] & [0] \\ [0] & [0] \end{bmatrix} \begin{Bmatrix} \dfrac{U_n}{\beta\Delta t^2} + \dfrac{\dot{U}_n}{\beta\Delta t} + \left(\dfrac{1}{2\beta} - 1\right)\ddot{U}_n \\ 0 \end{Bmatrix}. \quad (9.38)$$

9.2.3 Illustrative examples

9.2.3.1 Length expander transducer

The aforementioned analyses can describe the mechanical prestress on ceramics, the evaluation of the resonance/antiresonance frequencies and coupling coefficients, and the determination of the transducer impedance as well as the

TABLE 9.1 Series resonance frequencies (f_s) parallel resonance frequencies (f_p) and coupling coefficients (k_c) of the length expander transducer.

	f_s (Hz)	f_p (Hz)	k_c (%)
Mode 1	5641	5646	4.2
	4920	*4924*	*3.9*
Mode 2	10327	10335	3.9
	10482	*10499*	*5.7*
Mode 3	20172	20219	6.8
	20583	*20607*	*4.8*

Roman characters, measurements; italics, computation.

vibrational amplitudes when coupled to light fluids. Typical results from finite element modeling of a length expander transducer are reproduced here (Dubus et al., 1991). Comparisons between computation and measurement results are provided for resonance/antiresonance frequencies and coupling coefficients (Table 9.1), displacement and strain fields (Figure 9.1), and electrical impedance (Figure 9.2). Differences between calculated and measured values are explained by the dispersion of physical constants of PZT ceramics or by the composed nature of the transducer (connections between parts are considered as perfect clamping in the model). Differences observed at the resonances in Figure 9.2 are typical from a lossless analysis. Absolute values at resonance are difficult to predict because they are mainly determined by energy dissipation (i.e., losses if radiation is not included). Most of energy dissipation occurs either in PZT ceramics or at the interfaces between pieces. The dielectric and mechanical loss angles of PZT ceramics are not accurately known because of both their dispersion and dependency with the excitation level and temperature. The interface losses are still more difficult to quantify.

9.2.3.2 *Ultrasonic motor*

Ultrasonic motors use the piezoelectric effect to deform a mechanical piece called stator. This strain produces the motion of another piece called a rotor by friction. Among these, circular motors are the most efficient and thus the most widely studied. They use a progressive wave having an elliptical displacement of the stator surface (Shashida, 1985). To create this progressive wave, segmented electrodes excite spatially phase-shifted resonances (Figure 9.3). The application of an electrical excitation having the adequate phase on each electrode generates the progressive wave that corresponds to the rotation of the mode around the symmetry axis. The considered stator is constituted by a PZT ring bonded on a bronze ring (Buchaillot and Bonnamy, 1998). The phase of the electrical excitation applied on each segment is given in Figure 9.3, the lower surface being grounded. The modal analysis is performed by setting the input A to ground and by successively applying to input B short-circuit and open-circuit conditions. The harmonic analysis is conducted by prescribing on each electrode a voltage having the adequate phase at the resonance frequency. The vibrating stator is

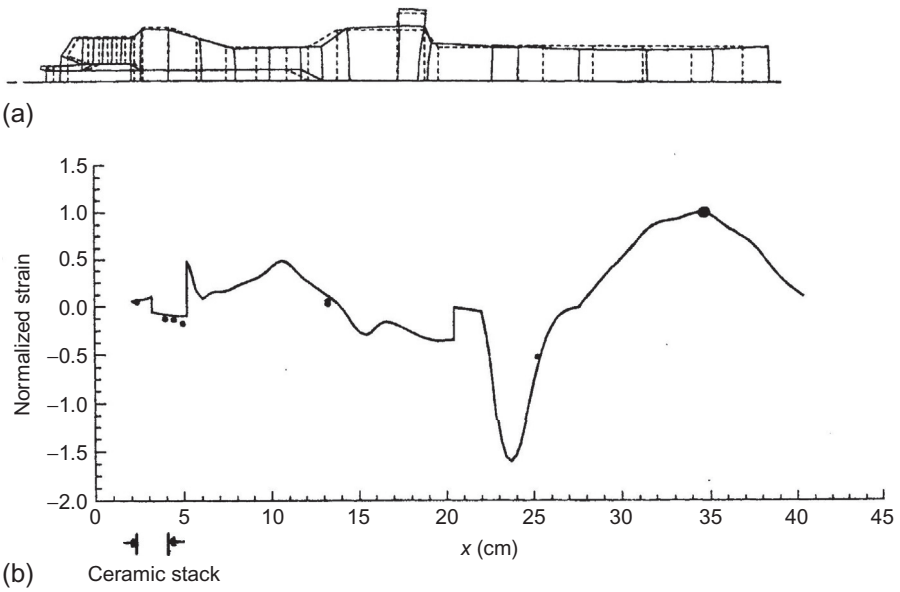


FIGURE 9.1 Length expander transducer, mode 3. (a) Computed displacement field; (b) normalized longitudinal (hoop for ceramics) strain on transducer surface. *Full line*, FEM computation; *dots*, measurement. *(From Dubus et al. (1991).)*

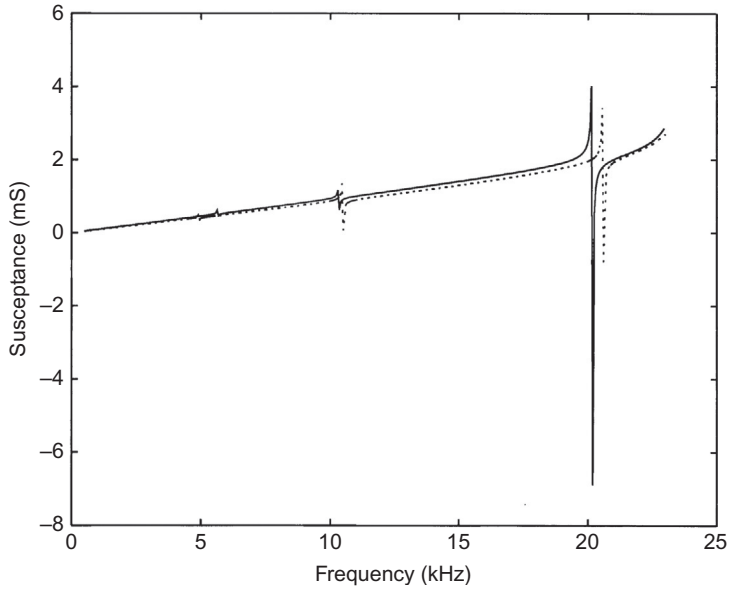


FIGURE 9.2 Susceptance of length expander transducer. *Full line*, FEM computation; *dashed line*, measurement. *(From Dubus and Campos-Pozuelo (2000).)*

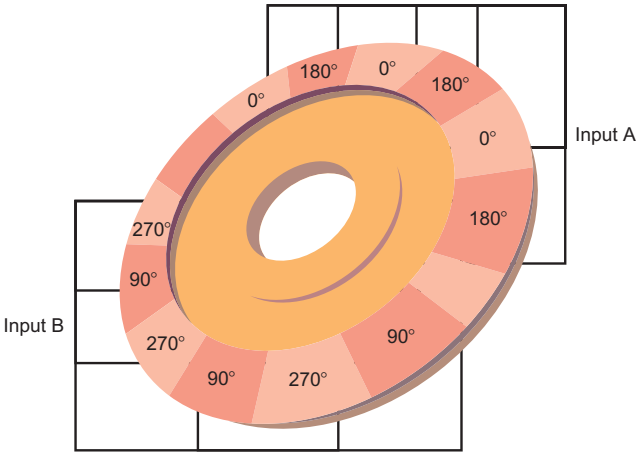


FIGURE 9.3 Geometry of the stator of the ultrasonic motor.

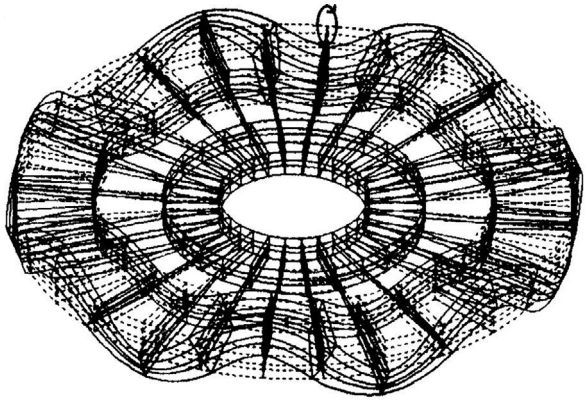


FIGURE 9.4 Stator excited by an electrical excitation with adequate phases. *Full line*, strained structure; *dashed line*, structure at rest. Elliptical displacement of surface is observed. *(From Buchaillot and Bonnamy (1998).)*

displayed in Figure 9.4, where the progressive wave (mode 7) and the elliptical displacement of the surface can be identified.

9.3 Acoustic waves in fluids and fluid-structure coupling

9.3.1 Physical equations and boundary conditions

Let us consider an ideal fluid medium Ω_f of finite limited by a surface Γ' pointing outward. According to the theory of linear acoustics, the pressure waves in the fluid verify Helmholtz's equation (Pierce, 1989):

$$\Delta p - \frac{1}{c_f^2}\frac{\partial^2 p}{\partial t^2} = 0. \tag{9.39}$$

Associated boundary conditions correspond to a prescribed pressure p^0 on the surface Γ_p (Dirichlet type):

$$p = p^0, \tag{9.40}$$

or a prescribed normal derivative of pressure ψ^0 on the surface Γ_ψ (Neumann type):

$$n_i \frac{\partial p}{\partial x_i} = \psi^0. \tag{9.41}$$

If the acoustic fluid Ω_f is in contact with a piezoelectric domain Ω_p, the dynamic and kinematic continuity

conditions must be prescribed at the solid-fluid interface Γ_i pointing toward the fluid:

$$T_{ij}n_j = -pn_i, \tag{9.42}$$

$$n_i \frac{\partial p}{\partial x_i} = -\rho_f n_i \frac{\partial^2 u_i}{\partial t^2}. \tag{9.43}$$

9.3.2 FEM formulation

The weighted residual method (Zienkiewicz and Taylor, 1989) is applied to Eq. (9.39), leading to the integral formulation:

$$\iiint_{\Omega_f} v\left(\Delta p - \frac{1}{c_f^2}\frac{\partial^2 p}{\partial t^2}\right) d\Omega = 0, \tag{9.44}$$

where v is an arbitrary scalar function. Using scalar and vector field properties and the Green-Ostrogradski theorem, Eq. (9.40) is modified as

$$\iiint_{\Omega_f}\left(\frac{\partial v}{\partial x_i}\frac{\partial p}{\partial x_i} + \mathrm{v}\frac{1}{c_f^2}\frac{\partial^2 p}{\partial t^2}\right) d\Omega - \iint_{\Gamma_p \cup \Gamma_\psi \cup \Gamma_i} v\psi d\Gamma = 0. \tag{9.45}$$

The spatial discretization is obtained by meshing the fluid domain Ω_f and the surfaces Γ_p, Γ_ψ, and Γ_i into elements connected by nodes. Inside an element e, the acoustic pressure p^e and its second time derivative are related to the nodal values of acoustic pressure and its second time derivative by the following equations:

$$p^e = \left[N_p^e\right] P^e, \tag{9.46}$$

$$\ddot{p}^e = \left[N_p^e\right] \ddot{P}^e, \tag{9.47}$$

where $[N_p^e]$ is a matrix containing interpolation functions. After combining Eqs. (9.40)-(9.43) and (9.45)-(9.47) and prescribing v to be equal to interpolation functions (Galerkin method) (Zienkiewicz and Taylor, 1989), we get

$$[H]P + \left[M_f\right]\ddot{P} = \rho_f c_f^2(\Psi + \Psi_i), \tag{9.48}$$

with

$$[H] = \sum\nolimits_e [H^e] = \sum\nolimits_e \iiint_{\Omega_f^e} \rho_f c_f^2 \left[B_p^e\right]^t \left[B_p^e\right] d\Omega^e, \tag{9.49}$$

$$\left[M_f\right] = \sum\nolimits_e \left[M_f^e\right] = \sum\nolimits_e \iiint_{\Omega_f^e} \rho_f \left[N_p^e\right]^t \left[N_p^e\right] d\Omega^e, \tag{9.50}$$

$$\Psi = \sum\nolimits_e \Psi^e = \sum\nolimits_e \iint_{\Gamma_p^e \cup \Gamma_\psi^e} \left[N_p^e\right]^t \psi \mathrm{d}\Gamma^e, \tag{9.51}$$

$$\Psi_i = \sum\nolimits_e \Psi_{i^e} = -\sum\nolimits_e \iint_{\Gamma_i^e} \rho_f \left[N_p^e\right]^t n_i \frac{\partial^2 u_i}{\partial t^2} d\Gamma^e, \tag{9.52}$$

where $[B_p^e]$ is the matrix containing a spatial derivative of interpolation functions. The vector $\boldsymbol{\Psi}_i$ on the solid-fluid interface Γ_i can be written (after inverting the sign to get the same surface orientation as in Section 9.2.1) as follows:

$$\Psi_i = \rho_f [L]\ddot{U}, \tag{9.53}$$

with

$$[L] = \sum\nolimits_e [L^e] = \sum\nolimits_e \iint_{\Gamma i}^{e} \left[N_p^e\right]^t n \left[N_p^e\right] \mathrm{d}\Gamma^e \tag{9.54}$$

The force vector associated with acoustic pressure on Γ_i acting on the solid is deduced from Eqs. (9.27), (9.54), and (9.7) with $f_i^0 = -p$:

$$F_i = -[L]P. \tag{9.55}$$

Finally, Eqs. (9.29), (9.48), (9.53), and (9.55) are combined to obtain the final set of equations for the solid-fluid coupled system:

$$\begin{bmatrix} [K_{uu}] & [K_{u\varphi}] & [L] \\ [K_{u\varphi}]^t & [K_{\varphi\varphi}] & [0] \\ [0] & [0] & [H] \end{bmatrix} \begin{Bmatrix} U \\ \Phi \\ P \end{Bmatrix} + \begin{bmatrix} [M] & [0] & [0] \\ [0] & [0] & [0] \\ -\rho_f^2 c_f^2 [L] & [0] & [M_f] \end{bmatrix} \begin{Bmatrix} \ddot{U} \\ \ddot{\Phi} \\ \ddot{P} \end{Bmatrix} = \begin{Bmatrix} F + F_i \\ -Q \\ \rho_f c_f^2 \Psi_i \end{Bmatrix}. \tag{9.56}$$

9.4 The unbounded problem: far-field radiation of acoustic waves

Finite element meshes are always bounded. In case of a problem involving unbounded media such as far-field acoustic radiation, specific conditions are needed at the domain boundaries to represent the unbounded part of the problem. Two types of methods are available: methods based on exact nonlocal boundary conditions (boundary element method, Dirichlet to Neuman method) and methods relying on approximate local boundary conditions (acoustic dampers, PMLs). This section discusses the case of unbounded acoustic fluids. Similarly, more complex methods may be used for the elastodynamic problem.

9.4.1 Methods based on exact nonlocal boundary conditions

9.4.1.1 *Exact nonlocal boundary conditions*

An unbounded acoustic fluid medium is considered. It is constituted by a finite fluid domain Ω_f and an unbounded fluid domain Ω_∞ separated by a boundary denoted Γ_∞. The exact boundary condition on Γ_∞ is the Helmholtz's

integral equation in the frequency domain (Morse and Feshbach, 1953; Pierce, 1989):

$$\frac{\alpha(r)}{4\pi}p(r)=\iint_{\Gamma\infty}\left(p(r')\frac{\partial G(\mathrm{r},\mathrm{r}')}{\partial \mathrm{n}'}-\psi(r')G(r,r')\right)\mathrm{d}\Gamma, \tag{9.57}$$

where $\boldsymbol{r}$ and $\boldsymbol{r}'$ denote points on Γ_∞, $G(r,r')$ is Green's function which describes for a given geometry, the influence of point $\boldsymbol{r}'$ on point $\boldsymbol{r}$, $\alpha(\boldsymbol{r})$ is the so-called solid angle at point $\boldsymbol{r}$ on Γ_∞, and $\partial G(r,r')/\partial n'$ and $\psi(\boldsymbol{r}')$ are the exterior normal derivatives of G and p at $\boldsymbol{r}'$. For an arbitrary geometry, $G(r,r')$, which is generally not known, is replaced by free space three-dimensional Green's function:

$$g(r,r')=\frac{1}{4\pi}\frac{e^{-jk|r-\mathrm{r}'|}}{|r,r'|}. \tag{9.58}$$

For time-domain problems, the boundary condition on Γ_∞ is given by the Helmholtz-Kirchhoff's equation, which is obtained from Eq. (9.57) (with $g(r,r')$ replacing $G(r,r')$) by means of Fourier transform:

$$\frac{\alpha(r)}{4\pi}p(rt)=-\frac{1}{4}\iint_{\Gamma\infty}\left[\frac{\psi(r'\tau)}{|r-r'|}-\frac{\mathrm{n}'.(r-\mathrm{r}')}{|r-r'|}\left(\frac{p(r't)}{|r-r'|^2}+\frac{1}{c_f|r-r'|}\frac{\partial p(r't)}{\partial\tau}\right)\right]\mathrm{d}\Gamma_\infty, \tag{9.59}$$

where the retarded time τ is defined as

$$\tau=t-\frac{|r-r'|}{c_f}. \tag{9.60}$$

9.4.1.2 Boundary element method (BEM)

The boundary element method relies upon the direct discretization of Eq. (9.57) in the frequency domain or Eq. (9.59) in the time domain, in which $g(r,r')$ replaces $G(r,r')$. The surface Γ_∞ is meshed using finite elements. Spatial discretization of p and ψ is performed using Eq. (9.42) and

$$\psi^e=\left[N_p^e\right]\Psi^e, \tag{9.61}$$

to get the linear set of equations (Lavie, 1989; Stupfel et al., 1988):

$$[A]P_{\Gamma_\infty}=[B]\Psi_{\Gamma_\infty}. \tag{9.62}$$

Here, $[A]$ and $[B]$ contain, respectively, the coefficients resulting from the integration of the Green function, and the normal derivative of the Green function on Γ_∞. To compute the radiation from a surface of known velocity distribution, Ψ_{Γ_∞} is prescribed, and P_{Γ_∞} is obtained by solving Eq. (9.62). The evaluation of the pressure field at different points in Ω_∞ is then directly obtained using a discretized version of Helmholtz integral equation, similar to Eq. (9.62) giving p in Ω_∞:

$$[A']P_{\Omega_\infty}=[B']\Psi_{\Gamma_\infty}. \tag{9.63}$$

Different methods are used to couple FEM and BEM depending upon the location of the surface Γ_∞. If Γ_∞ is a solid-fluid interface, FEM is used to model the structural part and BEM to model the unbounded fluid. In the case of an harmonic analysis, Eq. (9.62) is modified in order to introduce the nodal values of displacement U_{Γ_∞} on the interface:

$$[A]P_{\Gamma_\infty}=\rho_f\omega^2[B]U_{\Gamma_\infty}. \tag{9.64}$$

The force F_{Γ_∞} due to the fluid acting on the interface is obtained from Eqs. (9.55) and (9.64):

$$F_{\Gamma_\infty}=-[L]P_{\Gamma_\infty}=-\rho_f\omega^2[L][A]^{-1}[B]U_{\Gamma_\infty}. \tag{9.65}$$

Eqs. (9.30) and (9.65) are then combined to eliminate the pressure variable P_{Γ_∞} from the coupled system (structure variable coupling method) (Paulsen and Liu, 1992; Zienkiewicz et al., 1977; Dubus et al. 1997):

$$\begin{bmatrix}[K_{\mathrm{uu}}]-\omega^2[M]+\rho_f\omega^2[L][A]^{-1}[B] & [K_{\mathrm{u}\varphi}]\\ [K_{\mathrm{u}\varphi}]^t & [K_{\varphi\varphi}]\end{bmatrix}\begin{Bmatrix}U\\ \Phi\end{Bmatrix}=\begin{Bmatrix}F\\ -Q\end{Bmatrix}. \tag{9.66}$$

After solving Eq. (9.66), U_{Γ_∞} is extracted and used as input data to compute acoustic pressure in Ω_∞ using BEM.

If Γ_∞ is an interface between fluid domains, FEM is used to model the structure and the finite fluid domain, and BEM to model the remaining unbounded fluid domain (Dubus, 1994). Ψ_{Γ_∞} is identified from Eq. (9.62):

$$\Psi_{\Gamma_\infty}=[B]^{-1}[A]P_{\Gamma_\infty}, \tag{9.67}$$

and then inserted in Eq. (9.56) to give the coupled set of equations:

$$\begin{bmatrix}[K_{\mathrm{uu}}]-\omega^2[M] & [K_{\mathrm{u}\varphi}] & [L]\\ [K_{\mathrm{u}\varphi}]^t & [K_{\varphi\varphi}] & [0]\\ \rho_f^2c_f^2\omega^2[L] & [0] & [H]-\omega^2[M_f]-\rho_fc_f^2[B]^{-1}[A]\end{bmatrix}\begin{Bmatrix}U\\ \Phi\\ P\end{Bmatrix}=\begin{Bmatrix}F\\ -Q\\ \rho_fc_f^2\Psi\end{Bmatrix}. \tag{9.68}$$

The main difficulty of the BEM formulation is the existence of irregular frequencies, for which the solution is undetermined. Mathematically, this problem results from Fredholm's alternative, which applies to the second kind equation family and thus to (9.57). It can also be explained as the consequence of the use of $g(r,r')$, instead of $G(r,r')$, which does not verify boundary conditions on Γ_∞. Practically, for an irregular frequency, matrix $[A]$ cannot be

inverted. It can be demonstrated that irregular frequencies of the Neumann problem are the eigenfrequencies of the associated interior Dirichlet problem. Several methods were proposed to overcome this problem (Burton and Miller, 1971; Jones, 1973; Schenk, 1967). The most popular method is the CHIEF method, which was proposed initially by Schenk (1967). It relies on the overdetermination of Eq. (9.57) by adding the interior Helmholtz integral equation at some points $\boldsymbol{r}$ inside the volume limited by Γ_∞:

$$\iint_{\Gamma_\infty}\left(p(r')\frac{\partial G(r,r')}{\partial n'}-\psi(\mathrm{r}')G(r,r')\right)\mathrm{d}\Gamma_\infty=0. \quad (9.69)$$

Eq. (9.69) is discretized for each interior point and added to (9.62), resulting in a rectangular system of equations. A new square set of linear equations is then obtained by using the least squares method. The efficiency of the overdetermination is directly constrained to the choice of the interior points, which must avoid the nodal surfaces of the interior eigenmodes of the Dirichlet problem. As the frequency increases, the number of nodal surfaces also increases, and the choice of the interior points becomes difficult.

9.4.1.3 Dirichlet-to-Neumann (DtN) method

In the DtN method, the acoustic pressure and its normal derivative on Γ_∞ are related by a nonlocal linear operator M called the DtN map as follows (Keller and Givoli, 1989):

$$\frac{\partial p(r)}{\partial n'}=-Mp(r)=-\sum_{n=0}^{\infty}\iint_{\Gamma_\infty}m_n(r,r')p(\mathrm{r}')d\Gamma. \quad (9.70)$$

Assuming that Γ_∞ is a spherical surface of radius R_∞, the acoustic pressure in Ω_∞ is expended in a spherical harmonic series:

$$p(r,\theta,\varphi)=\frac{1}{2\pi R_\infty}\sqrt{\frac{r}{R_\infty}}\sum_{n=0}^{\infty}\sum_{j=0}^{n}\frac{(2n+1)(n-j)!}{(n+j)!}\frac{H^{(1)}_{n+1/2}(kr)}{H^{(1)}_{n+1/2}(kR_\infty)}\int P^j_n(cos\varphi)P^j_n(cos\varphi')cos(j(\theta-\theta'))u(r,\theta,\varphi)d\Gamma' \quad (9.71)$$

Eq. (9.71) is differentiated with respect to r and then set to $r=R_\infty$ to obtain $\partial p(R_\infty)/\partial n'$ and to identify

$$m_n(\theta,\varphi,\theta',\varphi')=\sum_{j=0}^{n}\frac{(2n+1)(n-j)!}{2\pi R^2_\infty(n+j)!}\frac{(\partial/\partial r)\left[r^{-1/2}H^{(1)}_{n+1/2}(kr)\right]_{r=R_\infty}}{R^{-1/2}_\infty H^{(1)}_{n+1/2}(kR_\infty)}P^j_n(cos\varphi)P^j_n(cos\varphi')\,cos\,(j(\theta-\theta')). \quad (9.72)$$

The spatial discretization of Eq. (9.70) is then performed at each node of Γ_∞ using the classical interpolation functions $[N^e_p]$. Thus, a discretized coupling matrix relating nodal acoustic pressure to nodal normal derivatives of pressure on Γ_∞ is obtained:

$$\Psi_{\Gamma_\infty}=[X]P_{\Gamma_\infty} \quad (9.73)$$

Eqs. (9.56) and (9.73) are finally combined to get the coupled system of equations.

9.4.2 Methods based on approximate boundary conditions

Other methods replace the integral Eq. (9.57) by an approximate boundary condition on Γ_∞ in order to improve computation efficiency. Two of these methods are described here: the acoustic dampers and the perfectly matched layers.

9.4.2.1 Acoustic dampers

At large distance r from the acoustic source, Sommerfeld's radiation conditions are written as follows (Pierce, 1989):

$$\lim_{r\to\infty} rp=\text{finite value}, \quad (9.74)$$

and

$$\lim_{r\to\infty} r\left(\frac{1}{c_f}\frac{\partial p}{\partial t}+\frac{\partial p}{\partial r}\right)=0, \quad (9.75)$$

If the boundary Γ_∞ is a spherical surface of radius R_∞ located in the far-field, the ratio of the outgoing acoustic pressure to the outgoing acoustic velocity is given in the frequency domain by the spherical wave impedance (Pierce, 1989):

$$\frac{\partial p}{\partial r}=\frac{-p}{r}-\frac{1}{c_f}\frac{\partial p}{\partial t}=-\left(\frac{1}{r}+\frac{j\omega}{c_f}\right)p, \quad (9.76)$$

which is discretized as (Bossut and Decarpigny, 1989)

$$\Psi_{\Gamma_\infty}=-\left(\frac{1}{R_\infty}+\frac{j\omega}{c_f}\right)[D]P_{\Gamma_\infty}, \quad (9.77)$$

with

$$[D]=-\sum_e\iint_{\Gamma^e_\infty}\left[N^e_p\right]^t\left[N^e_p\right]\mathrm{d}\Gamma^e. \quad (9.78)$$

The coupled set of equations is obtained by combining Eqs. (9.56) and (9.77); the finite element set of equations for an infinite acoustic fluid medium is then

$$\begin{bmatrix} [K_{uu}]-\omega^2[M] & [K_{u\varphi}] & [L] \\ [K_{u\varphi}]^t & [K_{\varphi\varphi}] & [0] \\ \rho_f^2 c_f^2 \omega^2 [L] & [0] & [H]-\omega^2[M_f]+\rho_f c_f^2\left(\frac{1}{R_\infty}+\frac{j\omega}{c_f}\right)[D] \end{bmatrix} \begin{Bmatrix} U \\ \Phi \\ P \end{Bmatrix} = \begin{Bmatrix} F \\ -Q \\ \rho_f c_f^2 \Psi \end{Bmatrix}. \tag{9.79}$$

9.4.2.2 Perfectly matched layers (PMLs)

The concept of PML (Bérenger, 1994) uses a layer of finite thickness, which is added outside Γ_∞. Properties of the layer are chosen in order to absorb the outgoing wave prior to reaching the outer boundary. Several approaches can be taken to design such a layer. In this section, we will follow a procedure inspired from transformation acoustics (Cummer, 2013) and apply it to a simple layer geometry.

Transformation acoustics designs start from the definition of a coordinate transformation. That is to say, one-to-one mapping of the real space to some virtual transformed space. For instance, to design acoustic cloaks, real space is mapped to a virtual space with one hole. Transformation acoustics equations then give the expressions of the material parameters in the virtual space as a function of those in the real space and the coordinate transforms. Due to the invariance properties of the fluid acoustics equations, two interpretations of the resulting parameters coexist:

(1) Topological interpretation: The new set of parameters describes the same material, but in the virtual transformed space.
(2) Material interpretation: It describes a different material in the same (real) space.

Interestingly, waves propagate exactly in the same manner for the two interpretations. As a consequence, transformation acoustics can be used as a tool to tailor wave propagation as needed. The basic procedure is to first find a space transform which would modify acoustic wave propagation in the desired fashion and then apply the transformation operations to find the corresponding material parameters.

In the context of PMLs, the idea is that incident plane waves should decay as they progress inside the layer. For this, a complex coordinate transform can be employed (see Teixeira and Chew (1999) for equivalent consideration in the context of electromagnetic waves). Indeed, if one considers a harmonic plane wave and complex notations since its space variations are dictated by a term of the form $e^{i\vec{k}.\vec{r}}$, it will decay either if the wavevector $\vec{k}$ is complex or if the position vector $\vec{r}$ is complex.

Since we will be dealing with two spaces, two sets of coordinates (x, y, z), and (x', y', z') will be used from now on. Similarly, two sets of fluid material parameters (ρ, κ) and (ρ', κ') are defined. Special care must be taken to the meaning of the primed notations. In the topological interpretation, the primed material parameters are the parameters in the virtual space (with primed coordinates), but in the material interpretation, they are precisely the parameters in the real space, *which in this case uses the primed coordinate system.*

At this point, the coordinate transforms can be chosen, in relation to the geometry of the PML to be designed. For the sake of simplicity, we consider here Cartesian coordinates. Note that the same procedures can be applied for any kind of curvilinear coordinate system by introducing the relevant scale factors in the transformations (see, for instance, Chen and Chan, 2010). If, for instance, we intend to design a layer that absorbs waves as they travel along $+x$ with Γ_∞ as a surface of constant x, one possible form would be as follows:

$$x = \left(1 + i\frac{F_{x'}(x')}{k}\right)_{\substack{y=y' \\ z=z'}} x', \tag{9.80}$$

with k as the wavenumber in the fluid medium (outside of the PML) and $F_{x'}(x')$ a continuous function equal to zero on Γ_∞. The normalization by k is chosen in order to adapt wave evanescence to the frequency of the incident plane wave. It should be noted that the virtual space is equivalent to the real space on the Γ_∞ boundary. This property is crucial since it ensures a "smooth" transition between the fluid medium and the PML and, consequently, no reflexion at the boundary.

In the general case, transformation acoustics relationships involve the full Jacobian of the coordinate transformation (i.e., all derivatives of the transformed coordinates with respect to the original ones, in the matrix form). Here, since each transformed coordinate depends only on one original coordinate, they reduce to (Chen and Chan, 2010)

$$[\rho'(x', y', z')]^{-1} = \frac{1}{\rho}\begin{pmatrix} \frac{Q_y Q_z}{Q_x} & 0 & 0 \\ 0 & \frac{Q_x Q_z}{Q_y} & 0 \\ 0 & 0 & \frac{Q_x Q_y}{Q_z} \end{pmatrix}, \tag{9.81}$$

$$\kappa'(x', y', z') = \frac{\kappa}{Q_x Q_y Q_z}, \tag{9.82}$$

with $Q_i = \frac{dx_i}{dx_i'}$ (and thus, in this case, $Qy = Qz = 1$). Several important observations can be made here regarding the material inside the PML:

– It necessarily exhibits spatial gradients that are to be correctly described by the interpolation functions inside the PML element.

– It is a (fictitious) anisotropic fluid, with a density in a matrix form. In such a material, force per unit volume is not necessarily aligned with particle acceleration. In the finite element formulation, Eqs. (9.49) and (9.50) expressing the stiffness and fluid mass matrices become in the PML domain Ω_{PML}.

$$[H'] = \sum_e [H'e] = \sum_e \iiint_{\Omega^e_{PML}} \kappa' \left[B^e_p\right]^t \left[B^e_p\right] d\Omega^e, \quad (9.83)$$

$$\left[M'_f\right] = \sum_e \left[M'^e_f\right] = \sum_e \iiint_{\Omega^e_{PML}} \left[N^e_p\right]^t [\rho']^t \left[N^e_p\right] d\Omega^e. \quad (9.84)$$

One advantage of the transformation acoustics point of view for PML is that it makes the usual shortcomings of PML remarkably straightforward. For instance,

– Their efficiency is relatively low for waves with a grazing incidence with respect to Γ_∞. This is expected since the transformation functions are typically chosen in order to introduce a continuously increasing evanescence as a function of *depth* inside the layer.
– By design, PMLs are particularly sensitive to the presence of evanescent fields at the Γ_∞ boundary. Indeed, if the complex virtual space attenuates incident waves with a real wavenumber, it will also propagate waves with a purely imaginary one, that is, evanescent waves. Those waves will then be reflected by the outer boundary of the simulation domain and ultimately affect the solution in the fluid domain. Various advanced PML models have been developed to limit this effect (see, for instance, Roden and Gedney, 2000). Nevertheless, it is generally advised to avoid placing PML domains in close proximity of regions where strong near-fields are expected to maximize their effectiveness.
– Depending on the transformation functions, the *metric* of the transformed space changes continuously inside the PML domain. This has important consequences on the meshing step. In practice, a mesh size suitable for the standard fluid domain at the operation frequency may not be suitable for the PML domain.

9.4.3 Illustrative example: Airborne stepped-plate transducer

The vibration and the acoustic radiation of a high-power stepped-plate transducer has been modeled using the FEM-BEM coupling (Campos-Pozuelo et al., 1998). It consists of a circular plate of stepped shape driven at its center by a piezoelectric Langevin-type transducer (Figure 9.5). The longitudinal vibration, generated by piezoelectric elements and amplified by the horn, drives the radiating plate vibrating in flexure. Thus, a good impedance matching is obtained for airborne applications. The stepped shape is designed in order to avoid the phase cancellation associated with flexural vibration and control acoustic radiation. Figure 9.6 compares measured and computed amplitude distributions on the surface of a stepped-plate directional transducer. The sound pressure plots along the transducer axis (Figure 9.7) and far-field directivity patterns (Figure 9.8) show the accuracy in the numerical calculation of the acoustic radiation both in near-field and far-field.

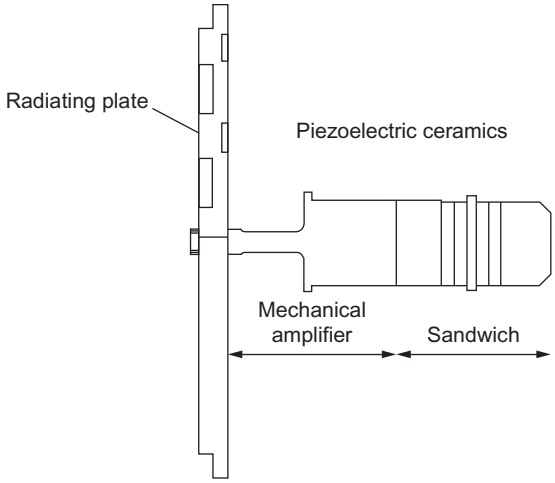


FIGURE 9.5 Typical geometry of stepped-plate airborne transducer.

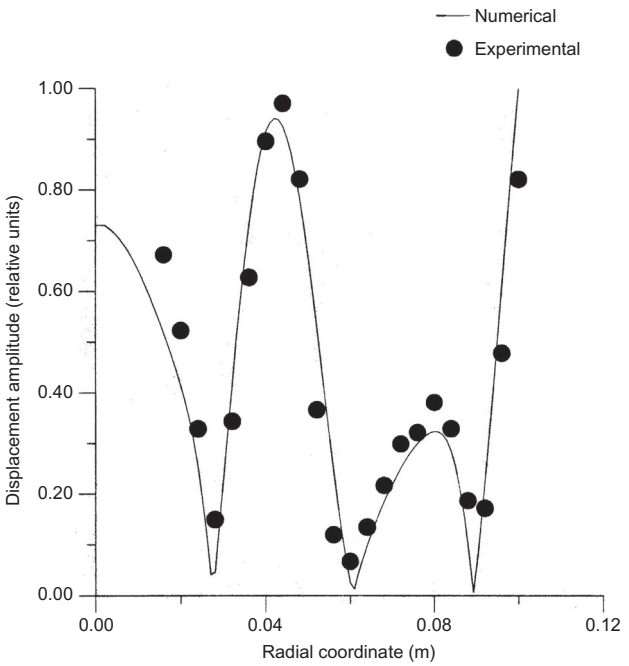


FIGURE 9.6 Distribution of displacement amplitude of stepped-plate transducer. *Full line*, FEM computation; *dots*, measurement. *(From Campos-Pozuelo et al. (1998).)*

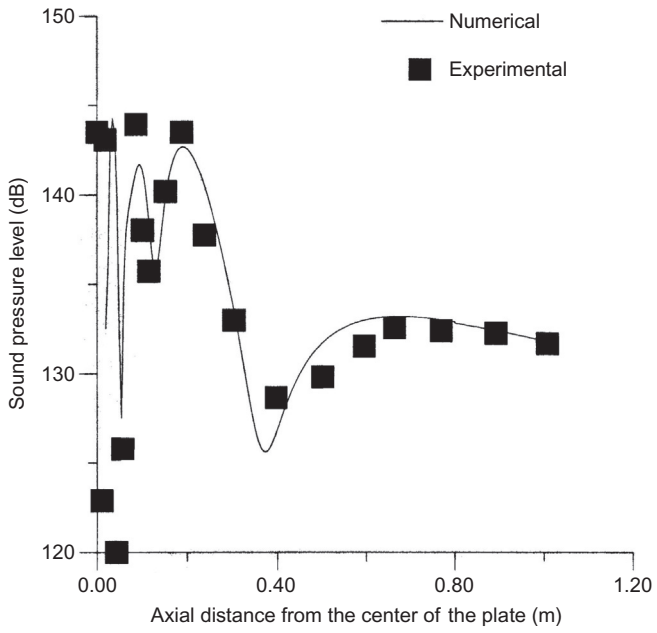


FIGURE 9.7 Sound pressure distribution along the acoustic axis of stepped-plate transducer. *Full line*, FEM computation; *squares*, measurements. *(From Campos-Pozuelo et al. (1998).)*

References

Allik, H., Hughes, T.J.R., 1970. Finite element method for piezoelectric vibration. Int. J. Num. Meth. Eng. 2, 151–157.

Bérenger, J.-P., 1994. A perfectly matched layer for the absorption of electromagnetic waves. J. Comp. Phys. 114, 185–200.

Bossut, R., Decarpigny, J.-N., 1989. Finite element modeling of radiating structures using dipolar damping elements. J. Acoust. Soc. Am. 86, 1234–1244.

Buchaillot, L., Bonnamy, A., 1998. Intégration d'un moteur piézoélectrique dans un équipement aéronautique. In: Actes du Congrès MAGELEC 98, ENSEEIHT, Toulouse, pp. 131–137 (in French).

Burton, A.J., Miller, G.F., 1971. The application of integral equation methods to the numerical solution of some exterior boundary value problems. Proc. R. London Ser. A323, 201–210.

Campos-Pozuelo, C., Lavie, A., Dubus, B., Rodriguez-Corral, G., Gallego-Juarez, J.A., 1998. Numerical and experimental study of airborne acoustic field of stepped plate high power ultrasonic transducers. Acust. Acta Acust. 84, 1042–1046.

Chen, H., Chan, C.T., 2010. Acoustic cloaking and transformation acoustics. J. Phys. D: Appl. Phys. 43, 113001.

Cummer, S.A., 2013. Transormation Acoustics. In: Craster, R.V., Guenneau, S. (Eds.), Acoustic Metamaterials. Springer, pp. 197–218.

Decarpigny, J.-N., 1984. Application de la méthode des éléments finis à l'analyse de transducteurs piézoélectriques. In: Doctoral thesis, Université des Sciences et Techniques de Lille (in French).

Dhatt, G., Touzot, G., 1981. Introduction à la méthode des éléments finis (in French). Les Presses de l'Université Laval, Maloine, Paris, Québec.

Dubus, B., 1994. Coupling finite element and boundary element methods on a mixed solid-fluid/fluid-fluid boundary for radiation or scattering problems. J. Acoust. Soc. Am. 96, 3792–3799.

Dubus, B., Campos-Pozuelo, C., 2000. Numerical modeling of high-power ultrasonic systems: current status and future trends. Ultrasonics 38, 337–344.

Dubus, B., Debus, J.C., Decarpigny, J.N., Boucher, D., 1991. Analysis of the mechanical limitations of high power piezoelectric transducers using the finite element modeling. Ultrasonics 29, 201–207.

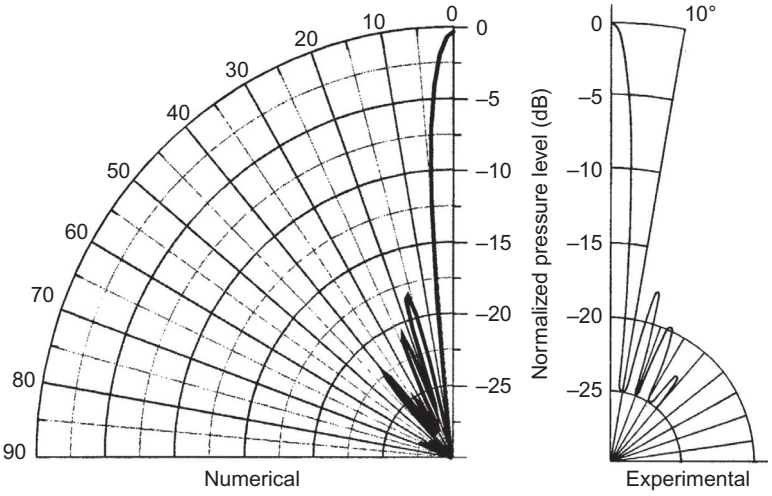


FIGURE 9.8 Stepped-plate transducer, directivity patterns of the far-field pressure. *(From Campos-Pozuelo et al. (1998).)*

Dubus, B., Lavie, A., Veksler, N.D., 1997. A frequency derivative approach for the identification of wave resonances on immersed elastic bodies. J. Acoust. Soc. Am. 102, 3523–3529.

Dubus, B., Debus, J.-C., Coutte, J., 1999. Modélisation par éléments finis de matériaux piézoélectriques et électrostrictifs. Rev. Euro. Eléments Finis 8, 580–606 (in French).

Holland, R., 1967. Representation of dielectric, elastic and piezoelectric losses by complex coefficients. IEEE Trans. Sonics Ultrason. 14, 18–20.

Jones, D.S., 1973. Integral equations for the exterior acoustic problem. Q. J. Mech. Appl. Math. XXVII, 129–142.

Keller, J.B., Givoli, D., 1989. Exact non-reflecting boundary conditions. J. Comput. Phys. 82, 172–192.

Lavie, A., 1989. Modélisation numérique du rayonnement et de la diffraction acoustiques par une méthode mixte équation intégrale-champ nul. PhD thesis, Université des Sciences et Techniques de Lille (in French).

Meitzler, A.H., O'Brian, H.M., Tiersten, H.F., 1973. Definition and measurement of radial mode coupling factors in piezoelectric ceramics with large variations in Poisson's ratio. IEEE Trans. Sonics Ultrason. 20, 233.

Morse, P.M., Feshbach, H., 1953. Methods of Theoretical Physics. Part I. - McGraw-Hill, New York.

Paulsen, K.D., Liu, W., 1992. Memory and operations count scaling of coupled finite-element and boundary-element system of equations. Int. J. Num. Meth. Eng. 33, 1289–1304.

Pierce, A.D., 1989. Acoustics, An Introduction to its Physical Principles and Aplications. Acoustical Society of America, New York.

Roden, J.A., Gedney, S.D., 2000. Convolutional PML (CPML): an efficient FDTD implementation of the CFS-PML for arbitrary media. Microw. Opt. Technol. Lett. 27, 334–338.

Schenk, H.A., 1967. Improved integral formulation for acoustic radiation problems. J. Acoust. Soc. Am. 44, 41–58.

Shashida, T., 1985. Motor Utilizing Ultrasonic Oscillation. U.S. Patent 4562374, pp. 12–31.

Stupfel, B., Lavie, A., Decarpigny, J.-N., 1988. Combined integral equation formulation and null-field method for the exterior acoustic problem. J. Acoust. Soc. Am. 183, 927–941.

Teixeira, F.L., Chew, W.C., 1999. Differential forms, metrics, and the reflectionless absorption of electromagnetic waves. J. Electromagn. Waves Appl. 13, 665–686.

Washizu, K., 1975. Variational Methods in Elasticity and Plasticity, second ed. Pergamon Press, Oxford.

Wilson, O.B., 1988. Introduction to Theory and Design of Sonar Transducers. Peninsula Publishing, Los Altos.

Zienkiewicz, O.C., Taylor, R.L., 1989. The Finite Element Method, fourth ed. McGraw-Hill, New York.

Zienkiewicz, O.C., Wood, W.L., 1987. Transient response analysis. In: Kardestuncer, H. (Ed.), Finite Element Handbook. McGraw-Hill, New York, pp. 2.275–2.314.

Zienkiewicz, O.C., Kelly, D., Bettess, P., 1977. The coupling of finite element and boundary solutions procedures. Int. J. Num. Meth. Eng. 11, 355–375.

Zienkiewicz, O.C., Taylor, R.L., Zhu, J.Z., 2005. The Finite Element Method, Its Basis & Fundamentals, sixth ed. Elsevier.

Chapter 10

Ultrasonic welding of metals☆

L.R. Lindamood, M.P. Matheny, and K.F. Graff
EWI, Columbus, OH, United States

10.1 Introduction

The application of ultrasonic vibrations to join materials dates back many years. The first used for grain refinement in molten metals in the 1930s, in the 1940s for soldering, as well as with resistance and arc welding, then for joining plastics in the 1950s; the ultrasonic metal welding process was first demonstrated in the early 1950s when it was found that ultrasonic vibrations were capable of welding metal parts without the need for melting the metals (Graff, 1981).

The process of ultrasonic metal welding is one in which ultrasonic vibrations create a friction-like relative motion between two surfaces that are held together under pressure. The motion deforms, shears, and flattens local surface asperities, dispersing interface oxides and contaminants, to bring metal-to-metal contact and bonding between the surfaces. The process is solid-state, occurring without melting of the base metals.

Applications of ultrasonic welding are extensive, finding uses in the electrical/electronic, automotive, aerospace, appliance, and medical products industries. Although nearly all metals can be ultrasonically welded, the widest current uses typically involve various alloys of copper, aluminum, magnesium, and related softer metal alloys, including gold and silver. A number of dissimilar metal combinations (e.g., copper-nickel) are readily welded with ultrasonics. It is used to produce joints between metal plates, sheets, foils, wires, ribbons, and opposing flat surfaces. Joining several stranded copper cables into a single junction, used in automotive wire "harnesses," is one common use, while the joining of multiple foils is finding wide uses in electric vehicle and other battery applications. Ultrasonic welding is finding increased uses for structural components in the automotive and aerospace industries. It is very useful for encapsulating temperature-sensitive chemical or pyrotechnic materials. The closely related process of ultrasonic microbonding is widely used in the semiconductor and microelectronics industries.

There are several variations in the welding process, the most common being that of ultrasonic spot welding, which uses two different equipment configurations known as *lateral drive* and *wedge-reed* welding systems. Ultrasonic seam welding, used to obtain continuous welds in thin gauge materials, and ultrasonic torsion welding, used for circular closure welds and stud welds, are variants of the ultrasonic process, as is the previously noted ultrasonic microbonding. A number of other laboratory or experimental configurations of ultrasonic welding systems have been developed, including a means of producing ultrasonic butt welds.

This overview of the ultrasonic metal welding process will

- outline the principles of ultrasonic metal welding;
- describe the features of several types of ultrasonic welding equipment;
- summarize information on the mechanics and metallurgy of the ultrasonic weld;
- review a number of applications of the process;
- summarize advantages and disadvantages of the process;
- examine future trends;
- provide sources of further information and references for further study.

10.2 Principles of ultrasonic metal welding

It was noted that ultrasonic welding uses high-frequency mechanical vibrations to create a friction-like relative motion between two surfaces, causing deformation and shearing of surface asperities that disperse oxides and contaminants, to bring metal-to-metal contact and bonding between the surfaces. The main features of the process may be illustrated by considering a lateral drive welding system as shown in Figure 10.1.

The key elements of the system are the transducer, booster, and sonotrode series of components, which produce and transmit the ultrasonic vibrations to the workpieces

☆ *Note:* This chapter is a revised and updated version of Chapter 9 "Ultrasonic metal welding" by K. Graff, originally published in *New Developments in Advanced Welding*, ed. N. Ahmed, Woodhead Publishing Limited, 2005, ISBN: 978-1-85573-970-3.

Power Ultrasonics. https://doi.org/10.1016/B978-0-12-820254-8.00012-9
Copyright © 2023 Elsevier Ltd. All rights reserved.

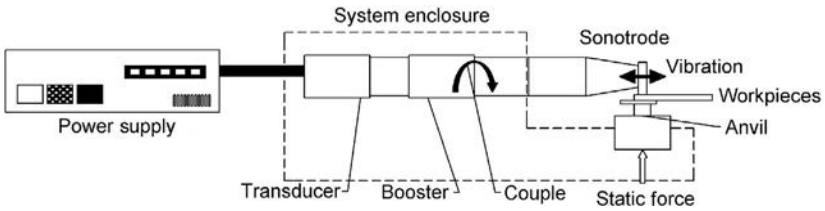


FIGURE 10.1 Lateral drive ultrasonic welding system. *(Source: EWI.)*

clamped between the sonotrode welding tip and a rigid anvil. The static force between the anvil and sonotrode tip may be produced in one of several ways, such as by a coupling moment created within the system enclosure by an arrangement of leveraged forces and pivots (details not shown in this simplified schematic). Other methods can include arrangements of the weld system mounted on a platform that moves on linear bearings with forces or motion applied by a pneumatic cylinder or a servo-controlled electric motor. The ultrasonic vibrations (e.g., 20 kHz) are produced in the transducer via a high-frequency input voltage from the electronic power supply. The main features of a typical piezoelectric ultrasonic transducer are shown in Figure 10.2 (see Chapters 6, 7, 9, and this chapter for more details on the power ultrasonic transducer).

Thus, from Figure 10.2, we see that the components of the transducer are a front driver (usually aluminum or titanium), several piezoelectric disks (in pairs of two, four, or six), and a rear driver (usually steel), with this assembly held together by a bolt to compress the ceramics. The piezoelectric properties of the disks result in conversion of the high-frequency electrical signal from the power supply to mechanical vibrations of the transducer. The transducer assembly vibrates in a longitudinal direction (i.e., along the axis of the transducer, as shown by the arrow) at a resonant frequency determined by the dimensions and material properties of the drivers and ceramics. The distribution of vibrations is shown by the curve labeled "vibration half wavelength," indicating that the maximum amplitude is at the front end of the transducer. There is a point of minimum vibration, known as the "node" that is usually designed to be located at the flange, where the transducer enclosure case is attached, as shown in the figure. The amplitude of vibration at the front end of the transducer is quite small, typically in the range of 10–40 μm, peak-to-peak; an amount invisible to the unaided eye. This combined with the fact that operating frequencies are typically above the audible limit results in little visible or audible action during a welding cycle. Finally, the transducer amplitude behavior with frequency is shown in Figure 10.2b, which emphasizes that it has a sharp peak at the resonant frequency f_r and drops off rapidly away from f_r. This feature is common to ultrasonic transducers and systems in general, leading to the need for precise frequency control.

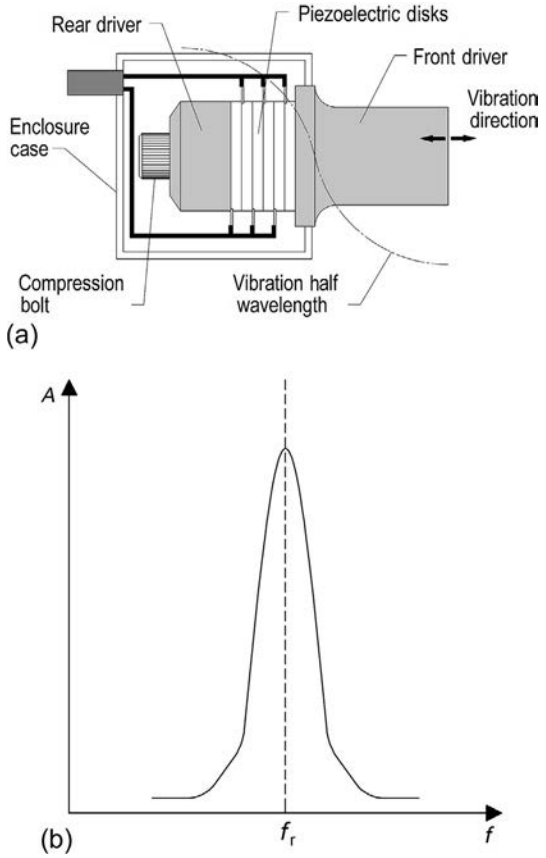


FIGURE 10.2 Ultrasonic transducer: (a) transducer assembly and (b) resonance behavior. *(Source: EWI.)*

The three components of transducer, booster, and sonotrode are shown assembled in Figure 10.3 (the assembly is by threaded fasteners at the component interfaces). While each differs in shape from the transducer, the booster and sonotrode are in longitudinal vibration, tuned to the same frequency as the transducer, and with a node in the middle region of each. Each is operating at a half acoustical wavelength with the result that the overall assembly is $3 \times ½ = 1½$ (1.5) wavelengths long. The exact value of the acoustic wavelength depends on the frequency, the materials of the different parts, and their geometric shapes. To an approximation, at 20 kHz, the acoustic half wavelength in several materials used in practical systems (e.g., steel, aluminum, titanium) is 12.5 cm, so that the length of the system shown in Figure 10.3 would be on the order of $1.5 \times 12.5\,\text{cm} \approx 18\text{–}19\,\text{cm}$. The booster and sonotrode are shaped to amplify the vibrations of the transducer, so that as one progresses down the length of the assembly, the amplitude is first increased by the booster and then again by the sonotrode. The result is that an amplitude at the

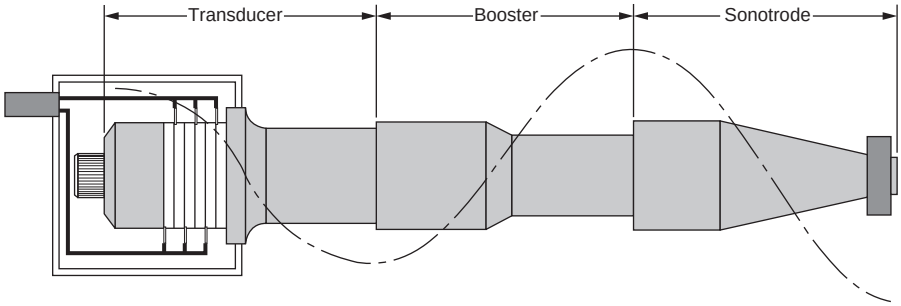


FIGURE 10.3 Transducer, booster, and sonotrode of the lateral drive welding system. *(Source: EWI.)*

transducer, possibly of 20 μm, may be increased to as high as 100 μm at the weld tip on the sonotrode (in some unusual circumstances, the booster/sonotrode combination may be designed for no net amplification, or even to de-amplify the vibration). The welding tip of the sonotrode may be detachable, held in place by a threaded connection, as suggested by Figure 10.3, or be machined as an integral part of a one-piece sonotrode.

The electronic power supply, shown in Figure 10.1, provides the driving power to the system, converting line frequency into the ultrasonic frequency required by the transducer. Depending on the power rating of the transducer and the application, the supply may need to provide power levels of 10s–1000s of watts. The power supply system also provides additional control and operation functions. The piezoelectric transducers typically have a high-level reactive (capacitance) electrical impedance of up to several 100 Ω that would be a poor match for modern electronic power supplies, which are designed for low-impedance (e.g., 50 Ω) resistive loads. Thus, impedance matching circuitry is typically built into the power supply.

Of equal importance is the fact that the sharply tuned resonant frequency of the transducer, booster, and sonotrode system will change during system operation, and from one welding application to another. As an example, continued operation of the system will cause heating of the various parts, resulting in a change in system dimensions due to thermal expansion, and hence in system frequency. The welding application serves to impose a mechanical impedance on the transducer system through the welding tip, with this also being capable of changing the system resonant frequency. These and other effects can result in shifts in the sharp resonance curve shown in Figure 10.2b away from the drive frequency and could greatly reduce vibration amplitude. However, all modern welding power supplies use frequency tracking circuitry to compensate for such shifts, so that the power supply frequency will stay tuned on the changing system resonant frequency. In addition to this, some welding power supplies control the vibration amplitude of the transducer during the weld cycle, with this typically being done using concepts based on equivalent circuit representation of the transducer.

A second type of widely used configuration for ultrasonic metal welding is known as a wedge-reed system. Although using different principles to impart ultrasonic vibrations to the workpieces, it ends up achieving the same effect of a frictional-like relative motion at the surfaces of the parts. A wedge-reed system is shown in Figure 10.4a. The key elements of this system are the transducer, wedge, and reed series of components, which produce and transmit the ultrasonic vibrations to the workpieces clamped between the sonotrode welding tip and an anvil. A static force is applied between the mass at the upper end of the reed and the anvil. As with the lateral drive, the high-frequency transducer vibrations are produced by a high-frequency input voltage from the electronic power supply.

The vibration behavior of the wedge-reed system is shown in Figure 10.4b. The transducer is of the same form as the lateral drive system. The wedge serves the same purpose as the booster in the lateral drive system, acting to increase transducer vibration amplitude. Thus, the longitudinal resonant vibration, as shown by the dashed wavelength pattern in the figure, produces vibrations in the direction of the arrow at the tip of the wedge. The wedge is solidly attached to the vertical reed by welding or brazing. The different feature of this system is that the wedge vibration drives the reed in a bending, or flexural, vibration mode. The general nature of the vibration pattern along the reed is shown by the solid line wave pattern. Being in bending vibrations means that the motion of the reed at any point is in a left-right (or transverse) direction, much like the vibrations of a string. This results in a transverse vibration of the welding tip against the workpieces, as shown in the figure. Thus, the wedge-reed produces the same vibration effect at the workpieces as the lateral drive (see Figure 10.1) but by a different means. Another variation of the lateral drive system is in the anvil, which also is in vibratory bending motion, as shown in the figure (although in some cases, a rigid anvil design may be used). Using a "contra-resonant" design, the anvil may vibrate out-of-phase with the reed, thus increasing the net transverse motion across the parts.

With this outline of the vibration principles that underlie ultrasonic welding, the weld, shown in Figure 10.5a, may now be more closely examined. It has been noted that both of the preceding welding systems end up applying the same

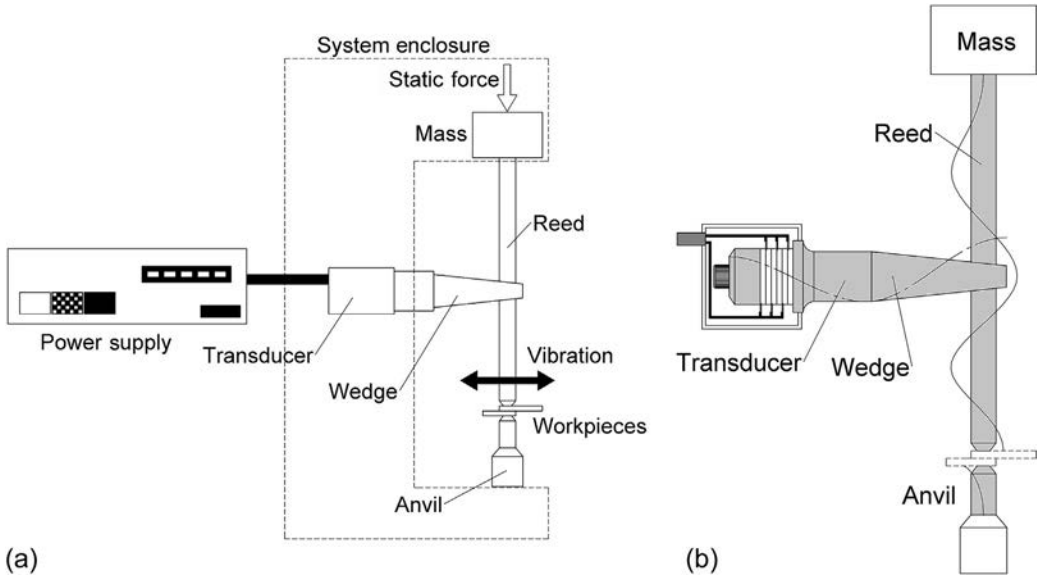


FIGURE 10.4 Wedge-reed ultrasonic welder: (a) overall system and (b) transducer, wedge, reed, and anvil. *(Source: EWI.)*

type of transverse vibration from the weld tip to the top surface of the workpiece, as shown in the figure. The top part moves in unison with the welding tip. This "anchoring" of the part to the tip is usually assisted by a roughened or knurled surface to the tip, to better engage with the surface. Similarly, the bottom part remains anchored to the anvil, also usually assisted by a patterned anvil surface. As a result, the motion of the welding tip produces a relative motion between the parts at the contact surfaces. It is this relative, transverse motion between the two opposing surfaces that creates the friction-like action, which causes shearing and plastic deformation between asperities of the opposing surfaces, bringing about increasing areas of metal-to-metal contact, and solid-state bonding between the parts. The actual bonding zone is suggested by the shaded region between the two parts. If the two parts are separated at the faying surfaces, as shown in Figure 10.5b, two types of force components will be seen acting at the interface. The first is the static clamping force, acting at right angles to the surfaces, and the second is a transverse shearing force, brought about by the friction-like transverse motion of the parts. These forces, and stresses, will be explored in more detail in Section 10.4.

While brought out in the preceding description, two unique features of ultrasonic metal welding are worth emphasis:

1. The nature of the motion between the parts during the metal welding process is one of the transverse oscillations, where the opposing surfaces move parallel to one another. This is in distinct contrast to the allied

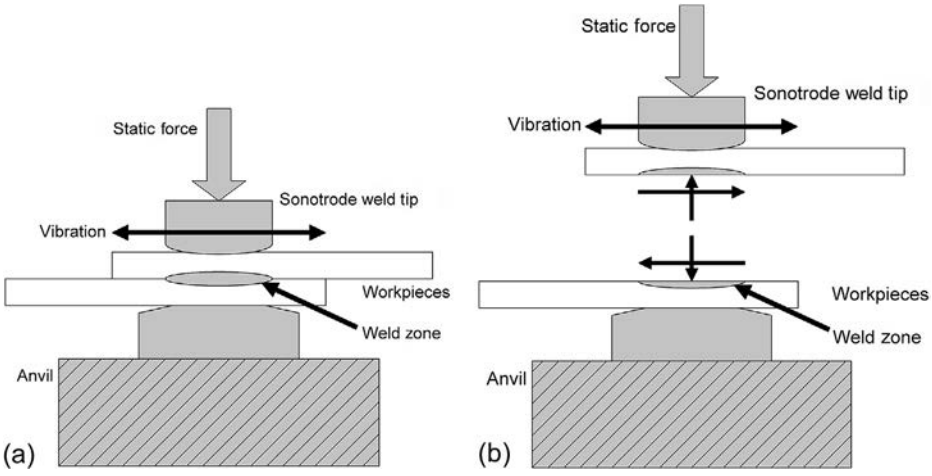


FIGURE 10.5 Ultrasonic metal weld: (a) transverse vibration imparted to workpieces and weld zone and (b) normal and shear forces acting at weld zone. *(Source: EWI.)*

process of ultrasonic plastic welding, where the opposing surfaces move at right angles to one another.
2. Although there is a local plastically deformed weld zone created between the parts, no melting of the metals occurs in this zone. The weld is via a solid-state bond, versus a fusion bond such as that occurs in the weld nugget of a resistance spot weld, or in other fusion-based processes such as arc or laser welding.

Additional features of the overall bonding mechanism of the ultrasonic metal weld will be brought out in Section 10.4.

From the illustrations of the lateral drive and wedge-reed welding systems, and of the weld zone, it is evident that a number of parameters can affect the welding process. The main ones can be summarized as follows:

- Ultrasonic frequency
- Vibration amplitude
- Static force
- Power
- Energy
- Time
- Materials (being welded)
- Part geometry
- Tooling

It will be found that not all of these are independent parameters. For example, the energy delivered to the welder is dependent on the power-time relationship, while the vibration amplitude may depend on the power level. These are all separately noted here because different welding systems may be set up to operate with differing sets of independent variables.

10.2.1 Ultrasonic frequency

It has been noted that ultrasonic welding transducers are designed and tuned to operate at a specific frequency, with these frequencies ranging, for different systems and applications, from 15 to 300 kHz. Most metal welding systems will operate at 20, 30, or 40 kHz, with the higher frequencies (e.g., 60 or 150 kHz) being used in microbonding work.

It is sometimes asked whether there might be "critical frequencies" from a fundamental metallurgical physics point of view (e.g., exciting dislocation fields) at which the welding process might be optimal. There is no evidence of such material behavior, at least in the frequency regimes of ultrasonic welding. Instead, welding frequency will be governed by such matters as welding power requirements, which will be governed by part dimensions and materials being welded, and the overall design of transducers and coupling components.

While reference has been made to the "single, specific operating frequency" of a transducer, and the nature of this sharply tuned resonant behavior illustrated in Figure 10.2b, in actual operation, there are several factors that act to shift the transducer resonant frequency. Small dimensional changes due to system heating during operation, varying static force, different tooling and changing tool conditions due to wear, and the changing effects of the welding load can all act to cause both long-term, as well as quite rapid, changes in the system resonant frequency.

However, while these shifting conditions of resonance can be complex, the key point from a practical user's standpoint is that, as will be noted in Section 10.3, modern power supplies employ feedback control circuitry that automatically compensates for these shifting conditions and track the driving frequency of the transducer to maintain the system on resonance.

10.2.2 Vibration amplitude

The vibration amplitude of the welding tip at the weld is one of the key parameters affecting welding. Thus, it directly ties to the energy delivered to the weld zone. It is again reminded that ultrasonic vibration amplitudes are quite small quantities, being of the order of 10–30–50 μm at the weld, and seldom exceeding 100 μm as a maximum. (A reminder that the diameter of a human hair is in the range of 75–100 μm.)

In some welding systems, the amplitude is a dependent variable, being related to the power applied to the system. In other systems, the amplitude is an independent variable, capable of being set and controlled at the power supply because of added features of the feedback control system. The selection of weld vibration amplitude will depend on the conditions of welding as governed by materials and tooling.

10.2.3 Static force

The static force is also a key parameter of ultrasonic welding. The force that is exerted on the workpieces via the welding tip and anvil, in pressing the parts firmly together, creates intimate contact between the opposing surfaces as a preparation for the ultrasonic vibrations in the weld zone. The magnitude of the force will be strongly dependent on the materials and thicknesses being welding, as well as the size of weld being produced, and may range from 10s to 1000s of newtons. For example, producing a weld of 40 mm^2 in 6000 series aluminums may use forces on the order of 1500 N, while 10 mm^2 welds in 0.5 mm thick, soft copper sheet may require only 400 N. In adjusting system parameters, an optimum range of static force is typically found, below which welds will be weak to nonexistent and above which excessive deformation of the parts may occur.

10.2.4 Power, energy, and time

While individually listed as separate weld parameters, these are most conveniently examined in a unified manner, because they are all tied closely together. When a weld is made, the voltage and current result in a time-varying electric power flow to the transducer over the weld cycle. A representative weld power curve is shown in Figure 10.6a and shows a peak power (P_P) and weld time (t_w). The area under the power curve is the weld energy (joules) or, more specifically, the electrical energy supplied to the transducer during the weld cycle. It is evident that not all three can be independent. Thus, in Figure 10.6a, one can set the peak power, with the welder running until that level is reached, with weld energy and time being dependent on reaching a certain level. Or, energy can be set, and the weld would run until such time as the set level is achieved, and so forth for other variations. In practice, the power-time curve can take many forms, depending on material types, dimensions, and surface finishes; ultrasonic parameters such as amplitude and static force; and the particular features of a given welding system. Figure 10.6b shows several variations that can be seen under different circumstances. Thus, curve 1 shows an early peak power as a tool engages the material, with this feature being frequently seen. Curve 2 shows a cutoff at a predetermined weld time, t_w, while both curves 2 and 3 show a general hardening of the weld. Curve 4 would be representative of a variable amplitude weld, where the welder vibration amplitude was increased about halfway through the weld. Curve 5 would show a continuous yielding, constant force weld. Many other variations occur in practice.

The power delivered to the transducer from the power supply is converted to ultrasonic power at the weld. However, between the electrical input and the weld, several conversions and transmission steps intervene. The actual power delivered to the weld zone is dependent on factors that can include (a) the efficiency of electromechanical conversion of the electrical input to mechanical output by the piezoelectric materials; (b) losses in the bulk materials and at interfaces of the transducer, booster, sonotrode system; and (c) power radiated from the weld into the workpieces and the anvil structure. The power setting may be indicated in terms of the high-frequency power input to the transducer, or the load power (the power dissipated by the transducer-sonotrode-workpiece assembly). Currently, estimates of actual power (and energy) to the weld itself are made by measuring input electrical power and subtracting the estimated system losses determined from no-load system measurements.

The weld time of ultrasonic metal welds, as noted, may be a dependent or independent variable, based on the type of welding system being used. By whatever means, however, metal welding times are quite short, typically being well under 1 s in duration; thus, 0.25–0.5 s are common. Longer welding times usually suggest the need to examine and/or modify system parameters.

10.2.5 Materials

The single category, "materials," in fact encompasses a wide range of issues and parameters relating to ultrasonic metal welding. First, of course, is the type of material. As will be noted in Section 10.4, claims have been made to ultrasonically weld nearly every metal in some fashion. The properties of the materials, including modulus, yield strength, hardness, and the underlying microstructure, are key considerations. Generally speaking, the softer alloy metals, such as aluminum, copper, nickel, magnesium, and gold/silver/platinum, are most easily welded ultrasonically. With increasing alloy hardness, ultrasonic welding increases in difficulty. The material surface characteristics come next, with these including finish, oxides, coatings, and contaminants. Given that the ultrasonic welding process by its very nature involves the transverse vibration of opposing surfaces, held together under pressure, it is evident that the conditions of these surfaces will play an important role.

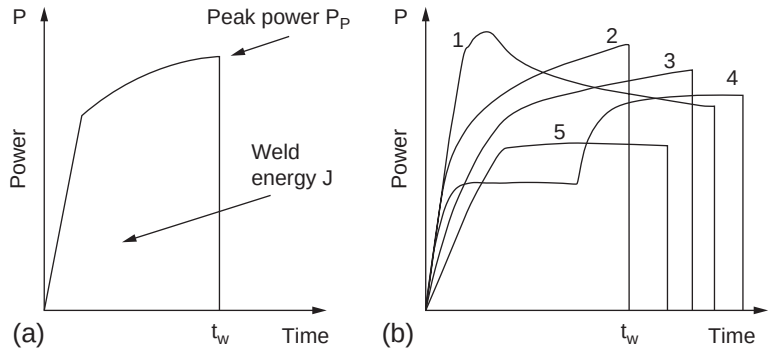


FIGURE 10.6 Weld power: (a) representative power curve and (b) examples of weld electrical power curves. *(Source: EWI.)*

10.2.6 Part geometry

The shape of the parts to be welded likewise plays an important role. The dominant feature here is that of part thicknesses. Simply put, the thinner the parts, of whatever material, the better the chances of achieving ultrasonic welds. Increasing part thickness, in particular that of the part in contact with the welding tip, requires larger welding tip areas, increased levels of static force, and generally increasing weld powers. Maximum thicknesses that can be achieved will obviously depend on the material being welded and the power levels available from a welder. For example, welding 1–2 mm 5XXX, 6XXX aluminum alloys is achievable with welding systems in the 2.5–3.5 kW ranges. Another part geometry factor, becoming increasingly appreciated in welding larger parts, is the overall lateral size (width, breadth) and shape of the parts. The very vibrations that create an ultrasonic weld can, when transmitted away from the weld and into the surrounding part, affect making of the weld itself, as well as affect previously made welds. Issues of part resonance, which may play little role for small parts, can become a factor in larger parts where dimensions may become on the order of ultrasonic vibration wavelengths. Typically, issues in this area can be accounted for by modifying part dimensions and stiffness, as well as the use of supplemental clamping points to dampen vibrations.

10.2.7 Tooling

The tooling consists of the sonotrode/welding tip that contacts the top surface of the top part and the anvil that contacts the bottom surface of the bottom part. The tooling serves as part support, and to transmit ultrasonic energy and the static force to the parts being welded. Detachable tool tips and replaceable anvils are used on some ultrasonic welders, while in other cases, the tool tip is machined as an integral part of a solid sonotrode. While the weld tip and anvil contact surfaces are usually flat, in some cases, the weld tip may be designed with a slight convex curvature in order to change the contact stress patterns. The tooling contact surfaces typically have machined knurled patterns of grooves and lands, or other surface roughening, to improve gripping of the workpieces. A wide range of tooling hardness, heat treatments, and coatings are employed to deal with the wide range of materials to be welded and the wear conditions that are encountered for varied applications.

10.3 Ultrasonic welding equipment

In reviewing the principles of ultrasonic metal welding, the basic features of two of the most widely used systems, the lateral drive and the wedge-reed, have been described and shown in Figures 10.1 and 10.4. Several systems used in production are shown in Figure 10.7. Thus, Figure 10.7a shows Sonobond's dual head welder that features two active welding heads, one on each side of the weldment and a 3.5 kW power supply. This system can weld wire bundles up to 100 mm^2 cross-sectional area. The Branson GMX-20DP, shown in Figure 10.7b, is based on the wedge-reed principle and a contra-resonant anvil, thus permitting low-amplitude, high forces to be applied that are advantageous for multifoil battery welds. The Tech-Sonic closed-loop servo-controlled lateral drive welder is shown in Figure 10.7c and d. Servo motors and load cells permit controlling force and amplitude during the weld. These types of systems produce spot welds whose areas will depend on the specifics of materials, thicknesses, and welder power capabilities. Thus, 2.5–3.0 kW, 20 kHz welders can produce spot sizes of the order of 40 mm^2 or larger.

Another type of weld that can be achieved with ultrasonics is a seam weld. The basic features of an ultrasonic seam welder are shown in Figure 10.8, where a continuously turning, lateral drive type of ultrasonic transducer vibrates a circular disk sonotrode that traverses the workpieces, producing a continuous weld. The details of fixturing and moving the rotating transducer system, including bearings and drivers, are not shown in this simplified diagram. The disk is machined as an integral part of the sonotrode, which requires turning the entire transducer-sonotrode assembly. A fixed anvil is shown in the figure, but in practice, the anvil may be moving in unison with the turning sonotrode disk. In some cases, the rotating ultrasonic transducer is fixed in space, or it may be traversed along the workpiece. As with spot welders, the transducer must be leveraged to apply a static force to the workpieces as it turns. Seam welders find extensive use in joining aluminum and copper foils.

Another means of achieving an ultrasonic weld is to impart a twisting, or torsional motion to specially designed horns and tooling, thus producing an ultrasonic torsion weld. The means of achieving this is shown in Figure 10.9, where two ultrasonic transducers, operating in longitudinal vibrations as previously shown in Figure 10.2, are attached (typically they are welded) to ultrasonic boosters and tooling to produce a push-pull, or torsional vibration to the booster system. The booster/tooling is specifically designed to be resonant in the torsional mode, versus the longitudinal mode, as used in the previous systems. The fact that torsional waves propagate at a different (slower) velocity than longitudinal waves means that torsion components are shorter than their longitudinal counterparts. The torsional resonance produces a circular vibration at the sonotrode and welding tip, which in turn creates a circular weld pattern on the workpiece. Although the vibration is of a circular nature, the motion of the tool surface is still parallel to the workpiece surface,

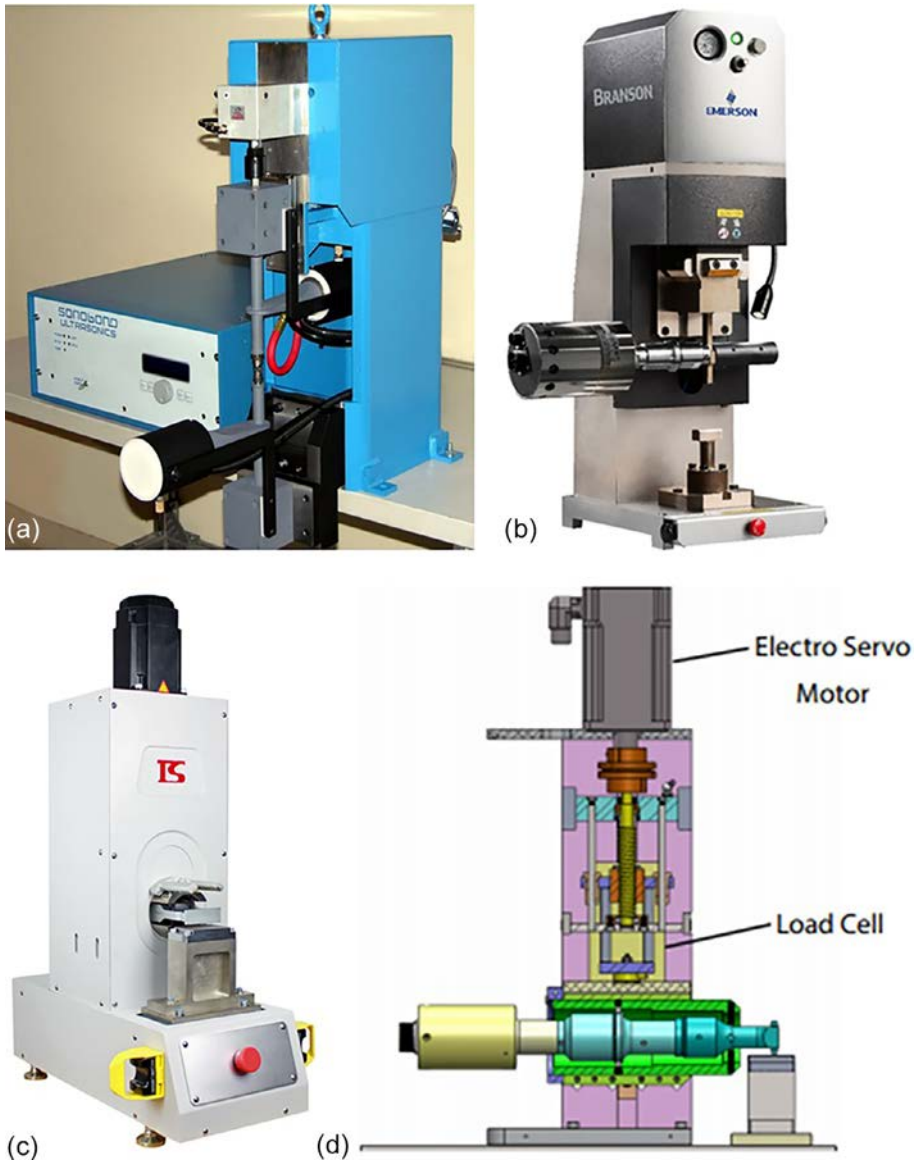


FIGURE 10.7 Ultrasonic metal welding systems: (a) Sonobond dual head wedge-reed welder. (b) Branson GMX-20DP with contra-resonant anvil. (c) Tech-Sonic closed-loop, servo-controlled lateral drive welding system. (d) Tech-Sonic system schematic. *(Sources: Sonobond—a, Branson—b, Tech-Sonic—c, d.)*

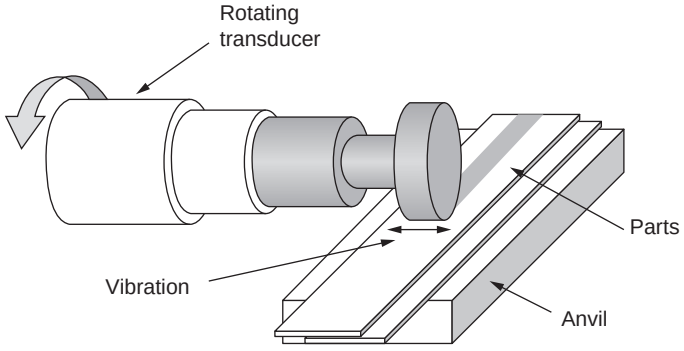


FIGURE 10.8 Ultrasonic seam welder. *(Source: EWI.)*

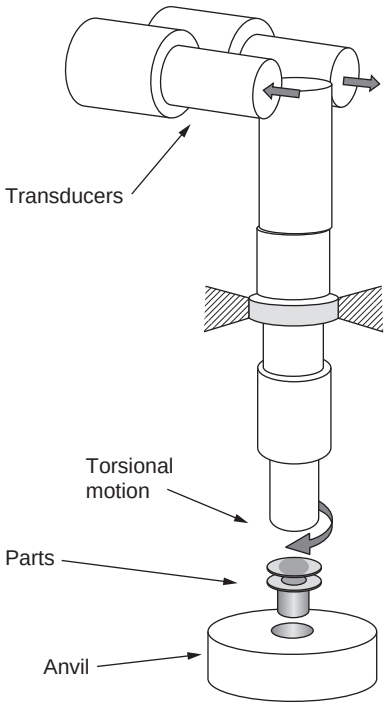


FIGURE 10.9 Ultrasonic torsion welder. *(Source: EWI.)*

as in the spot-welding action. Hence, the nature of the weld that is created is the same as that produced in spot and seam welding.

The concept of the torsion welder was illustrated for two transducers. Depending on power requirements, from one to four transducers may be used. A four-transducer torsion welder can produce up to 10 kW of power at 20 kHz.

10.4 Mechanics and metallurgy of the ultrasonic weld

In examining the mechanism of ultrasonic metal welding, it is helpful to start with the weld zone, as first depicted in Figure 10.5a, and separated, as shown in Figure 10.5b. This separation along the plane of the prewelding interface also shows the primary forces present in making an ultrasonic weld, namely, the shearing force, caused by the transverse ultrasonic vibration of the parts, and the normal force, caused by application of the static clamping force. The shear, normal force vectors are, of course, the resultant of a distribution of normal and shear stresses over the contacting surfaces of the two parts.

Now consider the condition of the two surfaces that will be in the zone of welding. Examined on a magnified scale, it is realized that the opposing surfaces consist of peaks and valleys whose profile depends on the surface finish of the materials. It is further realized that the surfaces, when pressed together, will initially be in contact only at intermittent asperities, or "high spots." While the number of contact points will depend on surface roughness and clamping force, the general nature of initial static contact between a small region of the surfaces within the weld zone is shown in Figure 10.10a. Further, it is realized that the surfaces have oxide coatings, as well as possible surface contaminants, such as finishing or forming lubricants and absorbed moisture, that generally prevents a pure metal-to-metal contact between the surfaces (although at some contact points, there may be penetration of oxides, and local microwelds might occur).

When the ultrasonic vibrations are started, the top piece moves relative to the bottom piece in a transverse, friction-like motion. Plastic deformation and shearing of the interfering asperities occur, cutting through surface contaminants and fracturing and dispersing surface oxides, resulting in bringing increased metal-to-metal contact across the surfaces and formation of weld zones (also called "microwelds"). Continued vibrations result in increased areas of contact, until complete, or nearly complete, contact and joining of the surfaces has occurred and a weld between the parts has developed, as shown by the final stage, Figure 10.10d, where some slight indications of the original interface may still be present.

The nature of the bond that is formed across the interface of the parts is in solid state; that is, it has been achieved without melting and fusion of the workpieces but instead brought about by direct metal-to-metal adhesion of the solid materials. Although the bond is in solid state, this does not suggest that temperature does not play a role in the process. The plastic deformation that occurs results in a noticeable temperature rise, with this rise varying with materials and welding conditions, but always below melting temperatures. However, the yield point of materials is temperature-sensitive, and it is found that ultrasonic welding temperature increases are sufficiently great to cause reduction in the local yield strength of materials in the weld zone. This reduction in turn enhances further plastic deformation and flow of the materials in the weld zone.

It should be noted that a number of studies have been done on the temperatures of the weld zone and at the weld interface, typically using thermocouple and infrared techniques. Temperatures were generally found to rise quickly in the initial welding stage, then to remain stable for the remainder of the cycle. Temperature rises varied greatly with the metals and metal combinations being welded. The heat generated by plastic deformation is quite localized at the interface and may be sufficient to cause recrystallization and diffusion. Studies of aluminum welds, for example, showed maximum temperatures reached to be on the order of 400°C. In general, the temperatures reached during welding will depend on the mechanical properties of the harder/stronger of the part materials. Thus, temperatures of a copper-Monel weld would be higher than a simple copper-copper weld.

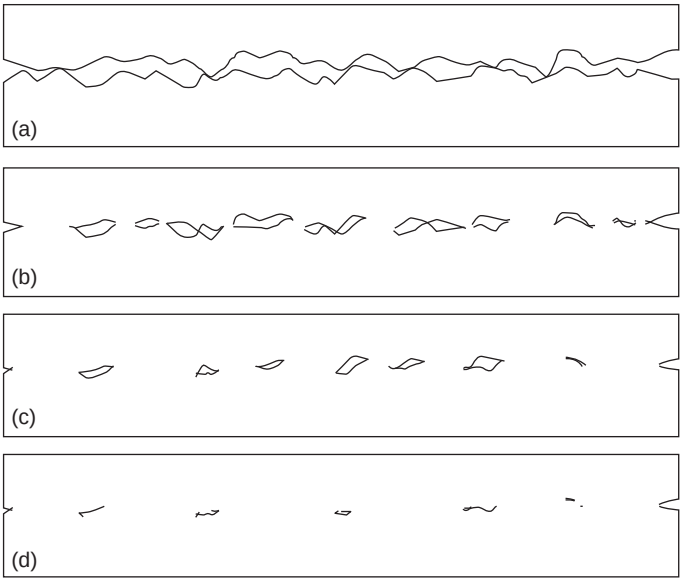


FIGURE 10.10 Development of contact surfaces in ultrasonic welding: (a) initial contact at asperities and (b–d) progression of shearing, deformation, and forming of weld zones as the weld develops. *(Source: EWI.)*

This general description of the weld process has been basically a mechanistic one, where local vibration, plastic deformation, and heating create the circumstances for a solid-state metallurgical bond to be achieved. Metallurgical examination of the weld zone shows local plastic deformation to be confined to a very small thickness, as brought out in Figure 10.11 showing a section of a weld in 6061T6 aluminum. The "saw-toothed" upper surface is a result of the weld tool imprint on the top weld part. The thickness of the actual weld zone of deformed material is quite small, approximately 50 μm for this particular case. This layer consists of fine grain structure resulting from heavy plastic deformation. After 0.1 s of weld time (i.e., approximately one-third of a 0.3-s weld cycle), one can see discrete deformation islands or microwelds separated by unbonded surface. At completion of a 0.3-s weld, one arrives at a continuous interface layer. The grain structure just a short distance from the weld is substantially undisturbed, while an irregular thin zone of fine or even amorphous structure exists in the zone. There is some undulation of the pattern, which is sometimes seen to transfer to near-turbulent patterns of mixing in some regions of the zone.

Special additional note should be made of recent contributions that expand the basic understanding of the ultrasonic metal-welding process. Thus, a driver of many developments in ultrasonic metal welding has been the needs of the automotive industry, where reduction of body weight has stimulated interest in the welding of aluminum or metal combinations involving aluminum. A far-reaching study in this area was reported by Hetrick et al. (2009) where the wedge-reed system was used to investigate issues affecting weld strength including weld microstructure, weld orientation, sheet rolling direction, residual stamping lubricants, and material aging. Among the findings were the effects of rolling direction relative to vibration direction and that relative orientation of rolling direction did not affect weld strength. Furthermore, weld strength was not strongly influenced by stamping lubricant, nor was material aging found to influence weld strength. These results showed the ultrasonic metal welding process to be robust for the intended applications.

Extending prior work by de Vries (2004) in modeling welding heat generation, Elangovan et al. (2009) applied FEA to computing the temperatures and stresses during

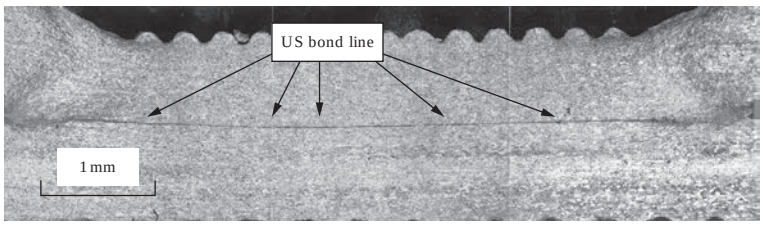


FIGURE 10.11 Ultrasonic weld metallography at interface. *(Source: de Vries (2004).)*

the weld process. Examining the setup shown in Figure 10.12a, the heat distribution for a 0.5 s weld is shown in Figure 10.12b. Their work also covered stresses in the weld joint and the influence of part thickness and friction on the process.

Another far-ranging study of ultrasonic welding by Watanabe et al. (2009) obtained temperature data from a near-weld thermocouple. Reported data included the effect of welding time and force on weld strength, hardness in the weld zone, temperature near the weld (a rise of 350°C in a 1.5 s weld was measured), and characterization of joint fracture surfaces. An interesting aspect of the work was to place a small amount of ethanol in the joint prior to welding, leading to strength increases of up to 50% due to its presence (this result substantiates what has long been a "trick of the trade" in the welding community of spraying a lubricant in the joint before welding to improve strength).

A new approach to measuring ultrasonic weld temperatures was taken by Cheng and Li (2007), as shown in Figure 10.13a, where an array of thin film sensors was directly fabricated on the Ni bottom workpiece near the weld interface. Modern thin film technology permitted practical fabrication of multiple samples for the weld tests. The approach was, using the multiple sensor outputs, to mathematically model the heat flow and essentially "back-calculate" to the heat generation (heat flux) at the weld interface. Figure 10.14 is a representative result for various welding sonotrode amplitudes.

Bakavos and Prangnell (2010) reported on an extensive investigation of the ultrasonic bonding mechanism in Al 6111 (with some tests also using 6082) alloys. Data on weld strength, weld microstructure as obtained by several microscopy techniques, by X-ray tomography, and weld flow were all reported. A dual wedge-reed system, Figure 10.15a, was used, which provided data on weld strength as a function of weld energy for various clamping loads (Figure 10.15b).

Although not pronounced, there is indication of optimum weld energy for maximum strength (e.g., for 40 MPa) often seen in such tests. Another set of results shows, through examination of the fracture interface, the progression of the bond with increasing weld energy. Weld temperatures immediately adjacent to the weld zone reached 400°C for a 1000 J weld.

Of special interest are the microstructure studies of Bakavos and Prangnell (2010). Thus, Figure 10.16 shows weld cross-sections at progressively higher weld energies (which result in increasing weld times). The increased material deformation and turbulence in the weld zone are to be noted. Extensive discussion is given to the material flow kinematics in the turbulent regions of the weld zone. It was noted that weld development first involves development of microwelds at contact surfaces, progressing from the outer edges inward, but with strong welds only produced when material softening through increased temperature occurred, with considerable plastic deformation and forging in the weld zone. The role of recrystallization in bond formation was questioned in favor of a recovered deformation mechanism. In an important follow-on paper, Bakavos et al. (2011) further discussed the existence of a heat-affected zone (HAZ) in ultrasonic metal welds, with this concept being at variance with most representations of the solid-state ultrasonic metal welding process. The formation and nature of a HAZ in ultrasonic spot welding of aluminum 6111-T4 automotive sheet were addressed by Chen et al. (2012).

Another commendable contribution to ultrasonic welding, in this case dealing with Al6022, was the work of Annoni and Carboni (2011a), where a lateral drive welding system was used to develop weld shear-strength data over a wide range of welding conditions, while questioning the presence of a HAZ (note preceding reference). While the Part 1 study does not break new ground as to the effects of welding parameters (amplitude, force, time) on weld performance, the extensively documented results are a useful addition to the field. In the companion Part 2 study (Annoni and Carboni, 2011b), emphasis was placed on the fatigue behavior of ultrasonic spot welded joints, including a comparison of the performance of mechanical fasteners to resistance spot welds, where ultrasonics was found to generally perform less well. Nevertheless, the advantages of the ultrasonic process for many applications were expected to lead to fatigue-improving developments that would make the process more competitive in this area.

Another emerging source of information on the ultrasonic metal welding process is that associated with the field of ultrasonic additive manufacturing (UAM) (see Chapter 13 of this book and Graff, 2011). The UAM process can be seen as a specialized adaption of the seam welding process shown in Figure 10.8, where seam widths of up to 25 mm are made under very high static forces and levels of ultrasonic power (currently) approaching 9 kW. The extensive literature that has developed in the UAM field has many useful contributions that can pertain to the ultrasonic metal welding field but cannot be reviewed within the scope of the present chapter.

Given this background information on the mechanism of ultrasonic welding, and some examples of metallurgical features, it is natural to inquire as to what metals are ultrasonically weldable. "Weldability," as defined by the American Welding Society, refers to the ease with which materials may be joined to meet the conditions of their intended service. Over the years, a large number of materials and material combinations have been investigated for their ultrasonic weldability. As a starting guideline, the chart shown in Figure 10.17 may be used (Graff et al., 2007, AWS). Thus, metals that have been shown, or claimed, to be weldable are listed along the top of the chart and range

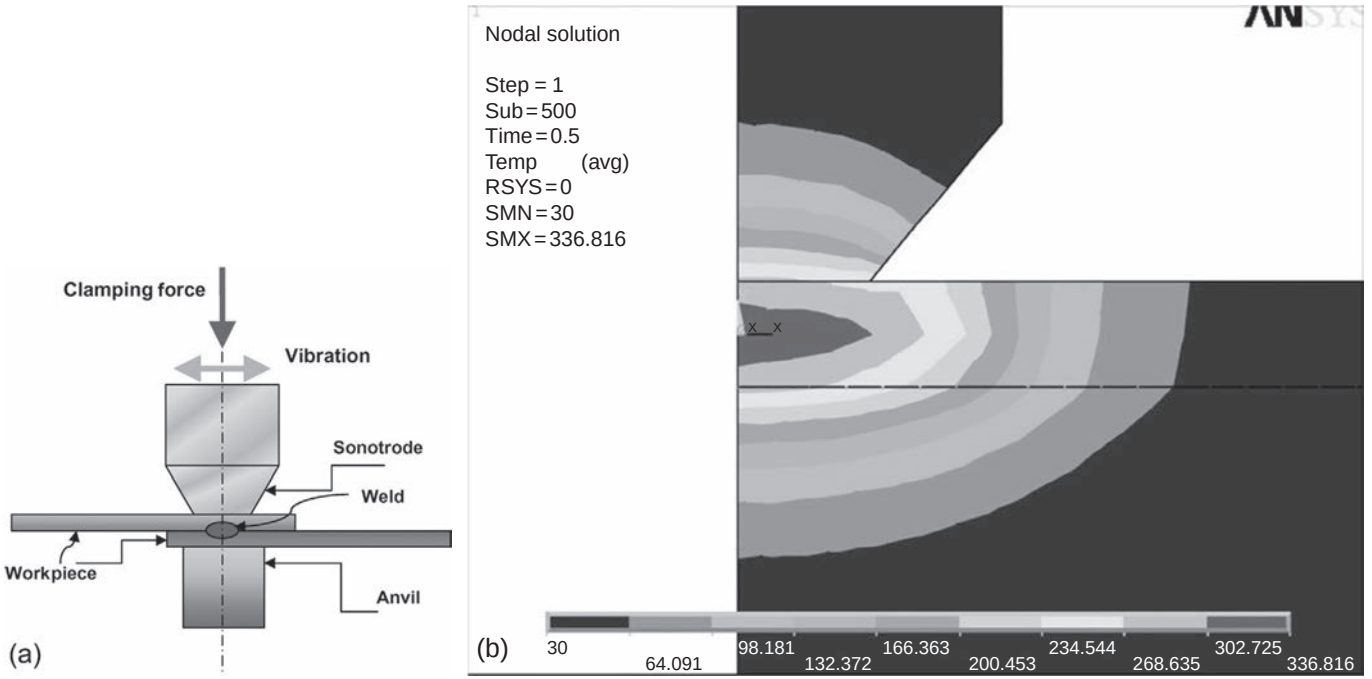


FIGURE 10.12 Temperature analysis in ultrasonic welding: (a) schematic of ultrasonic metal welding interface (Elangovan et al., 2009, Fig. 2) and (b) temperature distribution in workpiece at 1600 N force and 0.5 s weld time (Elangovan et al., 2009, Fig. 7).

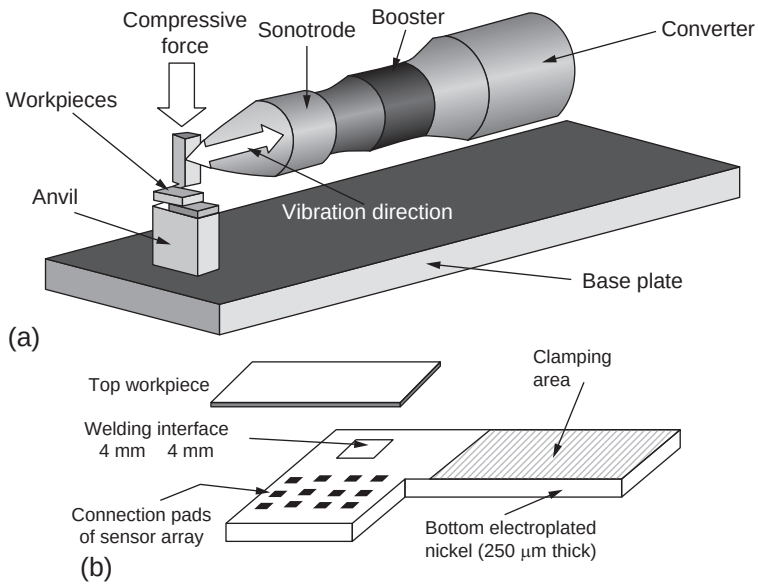


FIGURE 10.13 Setup for obtaining ultrasonic welding temperatures: (a) ultrasonic welding schematic (Cheng and Li, 2007, Fig. 1) and (b) illustration of L-shaped sensor unit (Cheng and Li, 2007, Fig. 2).

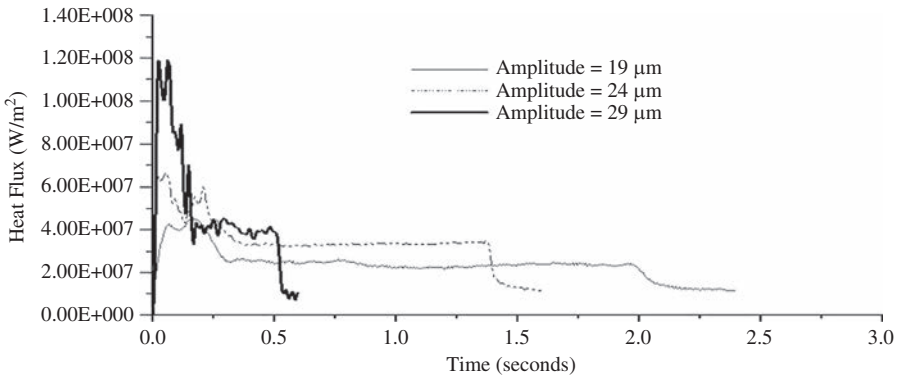


FIGURE 10.14 Results for back-calculated heat source at weld interface. *(Source: Cheng and Li (2007, Fig. 18).)*

from aluminum to zirconium. These same materials, or their alloys, are shown along the chart diagonal. Most materials can be joined to themselves or their alloys, that is, "monometal" welds. Exceptions to this are germanium and silicon. It is seen that aluminum is exceptionally weldable, having been joined to all the listed metals. Other easily welded materials include copper alloys and the precious metals (gold, silver, platinum). On the other hand, irons and steels, and refractory metals, such as molybdenum and tungsten, while weldable, can typically only be welded in thin gages (Bloss and Graff, 2009). Welding of softer alloys to these materials is more readily accomplished, however. In general, it is found that ease of weldability is tied to the ease of plastic deformation, so that material hardness and yield strength play important roles in ultrasonic welding, with higher strength and hardness materials being increasingly difficult to weld.

While attention here has been on metal weldability, it should be noted that ultrasonic welding has been used to achieve joints between metals and nonmetals; in particular, the joining of metals to ceramics and glass has been done. Typically, the metals are in the form of foils and are the more easily bonded metals (e.g., aluminum, copper). In most cases, a thin foil transition layer is used, or a thin metallization has been applied to the glass and/or ceramic substrates. The nature of the bond between the metal and glass and/or ceramic is believed to be one of mechanical bonding.

In addition to the limits imposed by materials on the scope of ultrasonic welding, there are limits imposed by the geometry and dimensions of the parts being welded, chief of which are thickness limitations. Thickness limits can be understood in terms of the contact stresses acting between the surfaces being welded, and their relationship to weld tip geometry and thickness of the top welded part.

Using Figure 10.5b as a starting point, the general case of a flat welding tip is illustrated in Figure 10.18a, where interface shear stresses and the vibration component of the weld tip have been omitted for simplification. Thus, the contact stresses between the flat weld tip and top surface are shown as approximately uniform. These contact stresses

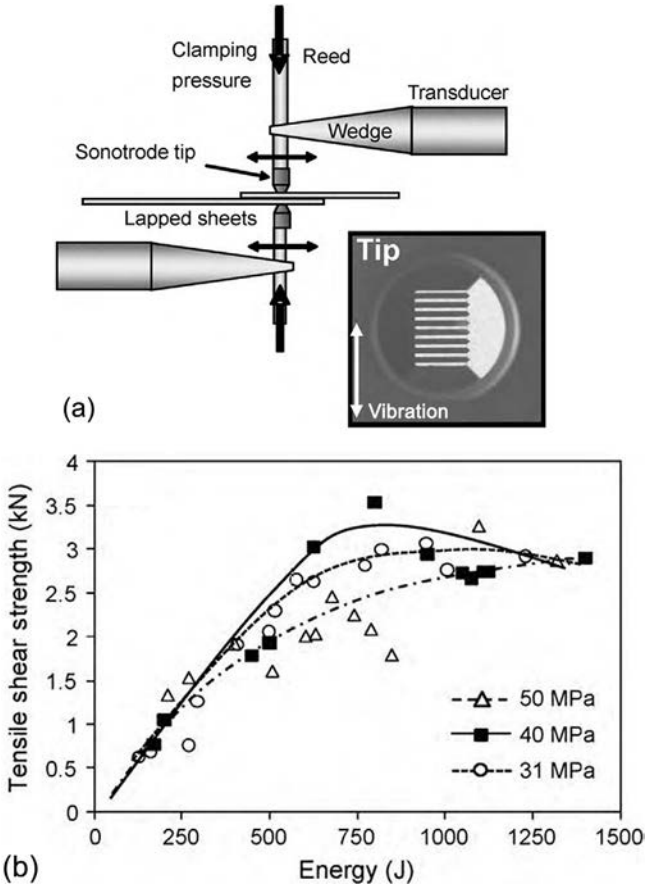


FIGURE 10.15 Weld strength using a dual wedge-reed system: (a) schematic of dual wedge-reed ultrasonic welder, with weld tool detail (Bakavos and Prangnell, 2010, Fig. 1). (b) Average shear strength versus weld energy, three clamping pressures (Bakavos and Prangnell, 2010, Fig. 2(a)).

are transmitted to the weld interface, spreading out somewhat to cover a wider contact area, with this resulting in a reduced contact stress amplitude and a smoothing out of the edges of the stress distribution.

If the top part is very thin, there will be very little reduction of contact stress between the tip and the interface, as brought out in Figure 10.18a, where just top part stresses are shown. On the other hand, if the top part is quite thick (with "thin" and "thick" being measured relative to the width of the weld tool), then the amplitude and shape of the contact stresses may be greatly changed. These situations are shown in Figure 10.18b, where the focus is reduced to just the top part. Thus, in the thin top part of Figure 10.18a, the contact stresses are little changed in transmission to the interface, with further spreading in Figure 10.18b. The case of a thick top part is shown in the lower part of Figure 10.18b, where the form and magnitude of the contact stresses are greatly changed at the interface.

Now, under ultrasonic vibration, the contact stresses directly influence the weld producing interface shearing stresses. If, for a given thickness, the total static clamping force is too small, the resulting contact stresses, and resultant shearing stresses, may be insufficient to create a weld. Obviously, an increase of static force will increase contact stresses, but if part thickness is too great, the amount of deformation at the top surface may be excessive, before conditions of welding are reached at the interface. The general relationship of part thickness, weld tip size, and contact stresses is important in understanding the basic factors influencing welding. Thus, increased part thickness requires an increased size of weld tip in order to maintain uniformity and level of stresses at the interface. Increased weld tip size in turn demands increased clamping forces to maintain stress levels for welding. This in turn demands greater power of the ultrasonic welding system in order to drive the welding tip, under high forces, at the vibration amplitudes needed to achieve the necessary shearing stresses and welding action at the interface. While this provides a general description of the issues of part thickness and welding, there are not currently formulas that relate these issues of tip size, part thickness, and materials to weldability.

Another issue of welding relates to overall lateral dimensions and shape of the parts being welded. It is evident that achieving an ultrasonic weld relies on vibrating the top piece relative to the bottom piece. Some motion is absorbed in the local plastic deformation at the weld zone, but there is also some net motion imparted to the top part. In many applications of ultrasonic welding, dimensions and mass of the top part are small; that is, dimensions are on the order

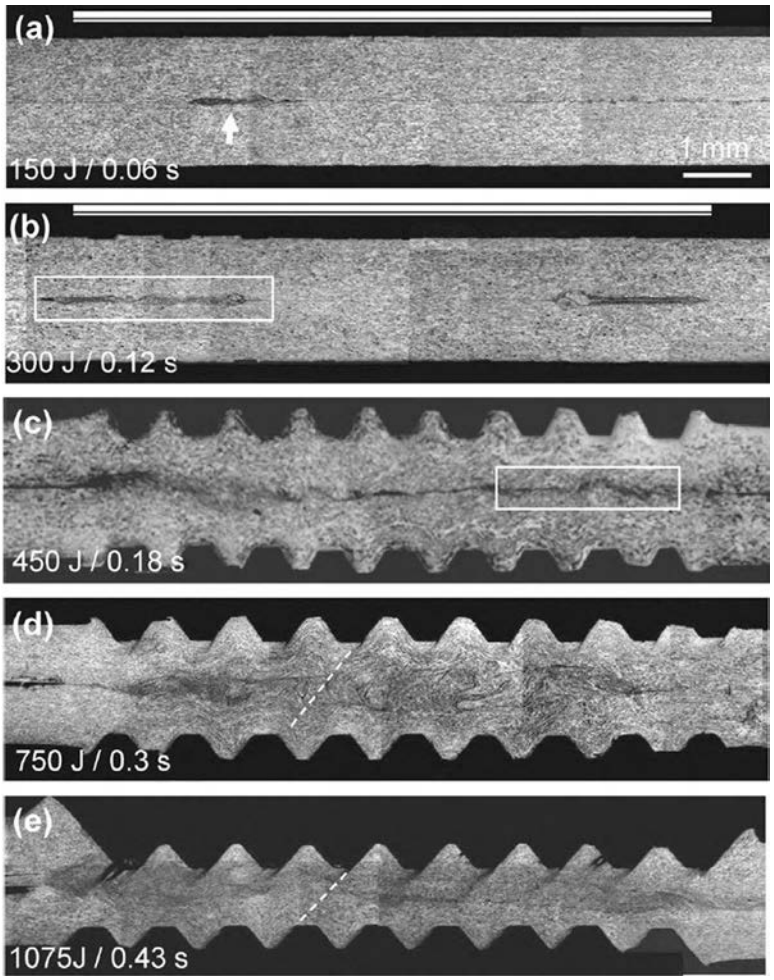


FIGURE 10.16 (a–e) Images of 6111 weld sections for increasing weld energies. *(Source: Bakavos and Prangnell (2010, Fig. 5).)*

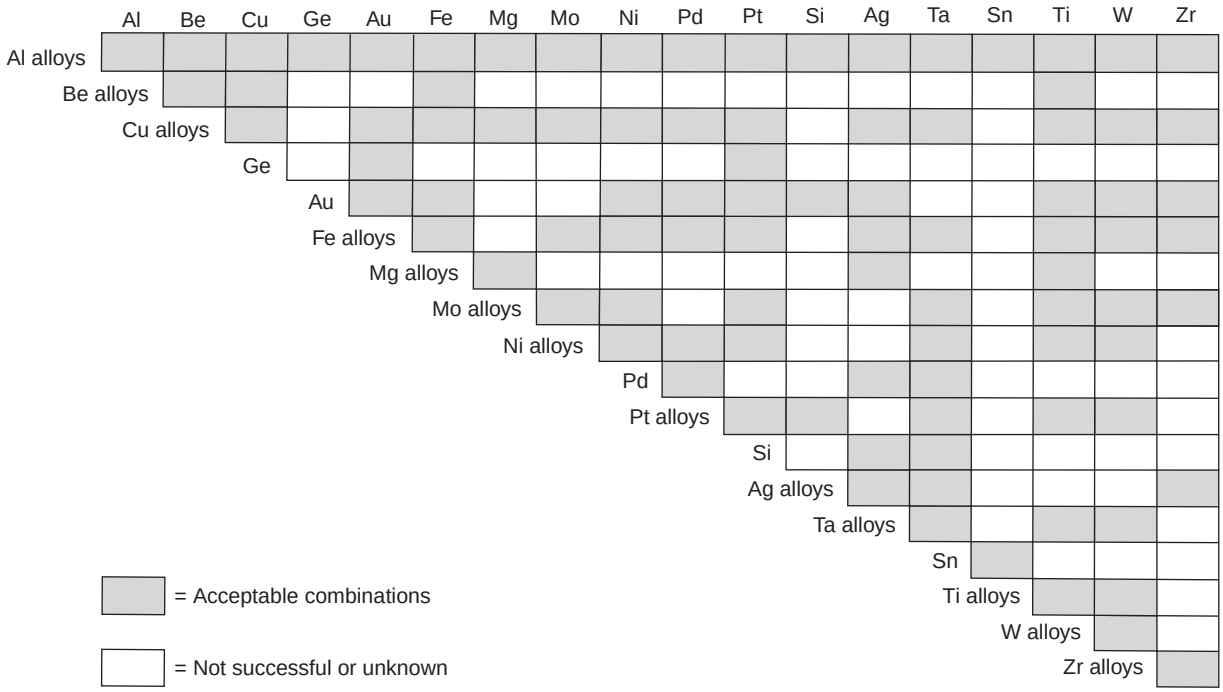


FIGURE 10.17 Ultrasonic material weldability. *(Source: Graff et al. (2007, Fig. 8.18).)*

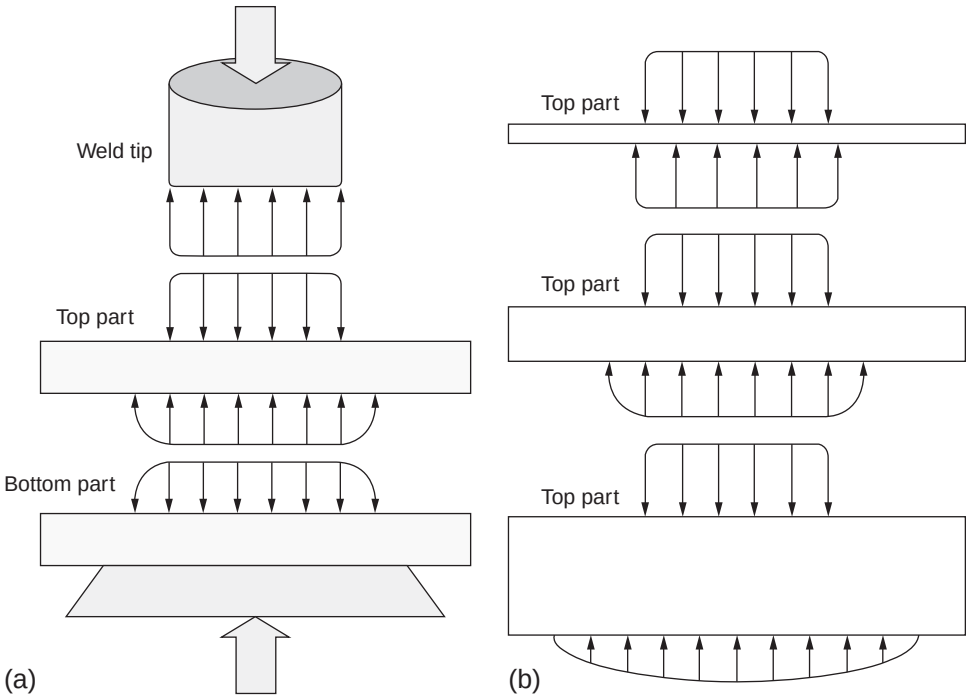


FIGURE 10.18 Contact stresses in weld zone: (a) stresses at weld tip, top, and bottom parts; (b) stresses on top part with increasing part thickness. *(Source: EWI.)*

of the welding tip (e.g., electrical contacts), or the mass of the part is uncoupled from the weld zone (e.g., as when welding flexible cables and wires), so that the impact of top part motion may be neglected. However, in applications where top part dimensions approach the longitudinal vibration wavelength in that material, the forces acting in the weld zone may be affected by top part mass and dimensions. In particular, the interface shearing forces may be impacted by these vibration phenomena, dropping dramatically and ceasing to create a weld. In general, when welding larger parts having dimensions on the order of acoustic wavelengths, attention must be paid to part vibrations as they may affect the weld being made, or welds previously made.

Another significant process issue is that of penetration of the ultrasonic tooling into the weld material. The depth of penetration of the sonotrode, known as "set-down," has been shown to directly contribute to plastic deformation and resulting weld strength. Optimum set-down of the sonotrode yields the maximum achievable weld strength. Too little set-down does not produce a full weld, and too much set-down forms a thicker layer of intermetallic compounds and cracking in the material. These studies have been conducted for both similar and dissimilar materials. Ultrasonic welding of magnesium, which plays a critical role in automotive light weighting, has been an ongoing investigation for Chen et al. (2019) and Huang et al. (2019). Through experimentation and modeling, bond formation as a function of temperature, vibration, and deformation by the sonotrode was all shown to play a critical role in proper bond formation. As temperature increases with increasing vibration amplitude, the sonotrode displaces material more easily. Aluminum and copper joints have been a primary focus as these materials are used extensively in vehicle electrification. Further, many authors have evaluated the composition of the weld to determine bonding mechanisms. Li (2019) observed that the displaced silicon from aluminum will eventually prevent further diffusion across the interface.

Macwan et al. (2016) also investigated mechanisms of ultrasonic welding of aluminum, including similar and dissimilar joints. In aluminum-to-aluminum welding, dynamic recrystallization was the driving mechanism at the interface. Conversely, interdiffusion was the most common mechanism for dissimilar welding. For example, it was found that aluminum-to-zinc-coated steel had less of a diffusion layer due to the zinc-aluminum eutectic and the interface appeared as braze. For aluminum to magnesium joints, longer weld times in addition to higher strain rates caused higher interfacial temperatures. This led to a thicker diffusion layer.

Bergmann et al. (2017) also reported the effects of temperature in bonding wires for vehicles, primarily analyzing nickel plating against nonplated copper-aluminum interfaces. By increasing the temperature, therefore decreasing activation energy, diffusion is promoted and intermetallic compounds are reduced. Modeling of the interfacial temperature and material displacement has allowed further

development in understanding the bonding mechanisms of ultrasonic welding. Ward et al. (2018) developed a model to predict the strength of an ultrasonic metal weld that can be used for both ultrasonic spot welding and ultrasonic additive manufacturing. This physics-based model of junction growth emphasizes that frictional heating dominates the softening mechanism and normal load is the only force acting on asperities. Real contact area at the interface is proportional to the normal load and surface asperities primarily respond to the normal load applied while shear loads are ignored. According to this model, acoustic softening and interfacial melting are not required for junction growth; however, melting can occur. Peak temperature can be minimized by using higher normal loads reducing requirements from thermal softening to collapse asperities. Satpathy and Sahoo (2017) has also investigated acoustic softening effects in ultrasonic welding of dissimilar material, developing a thermomechanical model to account for both thermal and acoustic softening effects. Results are claimed to clearly show the dominance of acoustic softening in the spot-welding process.

Friction of the interface is necessary for ultrasonic welding of metals to be achieved, and the effects are dependent on the amplitude, pressure, and energy of the system. Friction at the interface has been evaluated by monitoring the relative motion of the sonotrode as a function of energy. Chen et al. (2016) provides a visual to show both the movement of the material interface and the displacement of the materials relative to the sonotrode (Figure 10.19). The plastic deformation and material flow, as depicted in this figure, were qualified against energy input. For low energy inputs, some interfacial friction can be achieved. Increasing to moderate energy levels allows joint formation as large areas plastically deform. At high energy inputs, the saturation condition for plastic deformation and interfacial friction occurs and often results in cracking and a decrease in bond strength.

Chen et al. (2016) also showed the changing nature of the bonding with progression of the weld, as shown in Figure 10.20. Thus, at the start of the weld (leftmost curves of the figure), there is full motion of the sonotrode (black wave) across the upper plate, with just slight motion of that

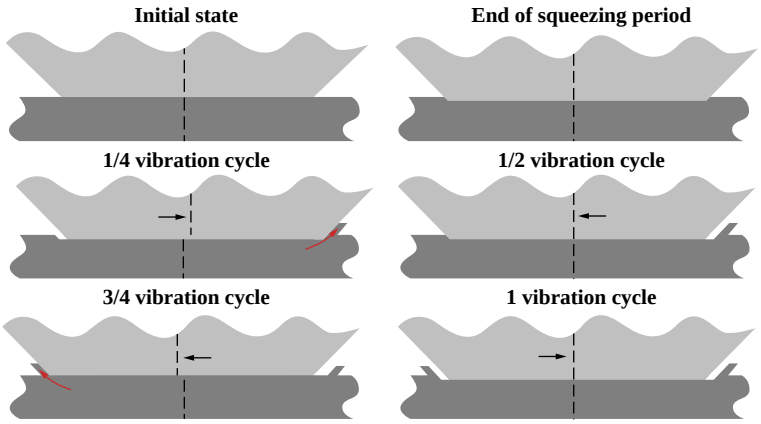


FIGURE 10.19 Schematic of material flow under sonotrode tips (Chen et al., 2016, Fig. 10).

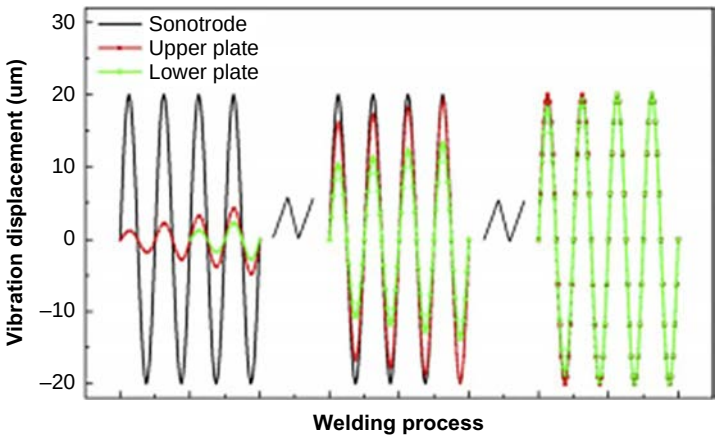


FIGURE 10.20 Illustration of relative movement between sonotrode, upper plate, and lower plate during the whole welding process (Chen et al., 2016, Fig. 11).

plate initiating (red wave) and a barely perceptible motion of the lower plate (green wave). As the weld progresses, increasing bonding between the plates occurs (middle waves) and the upper plate moves nearly at the amplitude of the sonotrode while the lower plate rapidly increases its amplitude as bonding with the upper plate increases. With complete bonding, the two plates move with the sonotrode (rightmost waves).

Time is another factor that plays a critical role in bond formation as temperature of the interface is dependent on time but will not increase linearly with increasing energy. The morphology of the joint has been shown to be largely affected by the duration of welding and therefore time at temperature. Specifically, dynamic recrystallization and grain growth have been experimentally observed and confirmed through modeling of the welding process. For short weld times, dynamic recrystallization can be achieved. Increasing the weld time, however, will lead to grain growth throughout the weld. Haddadi and Tsivoulas (2016) showed this transition in aluminum using EBSD. Shen et al. (2016) modeled the weld morphology at longer times for battery tab materials, aluminum and nickel-coated copper. Their model identifies three stages during long weld times (0.8 s or greater). In the first stage, the material exhibits severe plastic deformation from the sonotrode engagement. Second, dynamic recrystallization occurs as temperature increases. Finally, grain growth is observed while the material is held at temperature.

Beginning with the illustrations of the ultrasonic weld, shown in Figures 10.5 and 10.10, it is clear that the knowledge of the underlying mechanism(s) of the process has been dramatically advanced since its early 1950s discovery. Nonetheless, it is also clear from the review of this section that much remains to complete a full understanding of the process. A part of this is the inevitable result of a continued advancement in materials and applications. However, a remaining part is still associated with an incomplete understanding on the behavior of materials under the action of intense ultrasound, an issue that applies to other ultrasonic processes such as forming and machining. Advances in understanding in this critical area will advance both the reliability and scope of applications of ultrasonic metal welding and other processes.

10.5 Monitoring and control

Continued pressure to improve quality and productivity impacts ultrasonic metal welding (and all industrial processes). An important element of this is improvement of process monitoring and control methods. Thus, in the previous section, the work of Cheng and Li (2007) on weld temperature measurements was cited that could contribute to this area.

Identifying candidate monitoring tools and correlating these results to ultrasonic welding or models of ultrasonic welding is an ongoing challenge. Commercial ultrasonic welders typically contain some system monitoring capabilities. Power draw and data from displacement of the sonotrode can be collected by the user, but correlating these results with weld quality is not straightforward. They may, however, be used for detecting missing sheets or wires in a stack-up as displacement values will change, or excessive power draw may indicate a material or mechanical issue that could cause poor welding, but also may be difficult to identify (Lee et al., 2014).

Thermal monitoring, such as noted above and continued by Zhao et al. (2013), has been a dominant method for inspection due to the variety of sensors that can be employed. These have included thermocouples between sheets of material, thermography systems for noncontact viewing, and advanced microsensors embedded in parts to be welded (Kumar, 2018; Satpathy and Sahoo, 2017). Satpahty used thermocouples at the weld interface to show temperature variations dependent on the materials joined. For example, in Figure 10.21, weld times for aluminum to copper joints are longer but weld temperature is lower overall due to thermal conductivity of the materials removing heat from the weld joint. Further, the dependence of weld strength and temperature at the joint was correlated through modeling and experimental results by Kumar (2018). Their work showed the dependence of weld strength on temperature and demonstrated that reaching target temperatures at the joint may be one process control method to ensure quality and repeatable welds.

High-speed video is another noncontact method that has been investigated by monitoring sonotrode velocity (Chen et al., 2019; Huang et al., 2019). An example of the

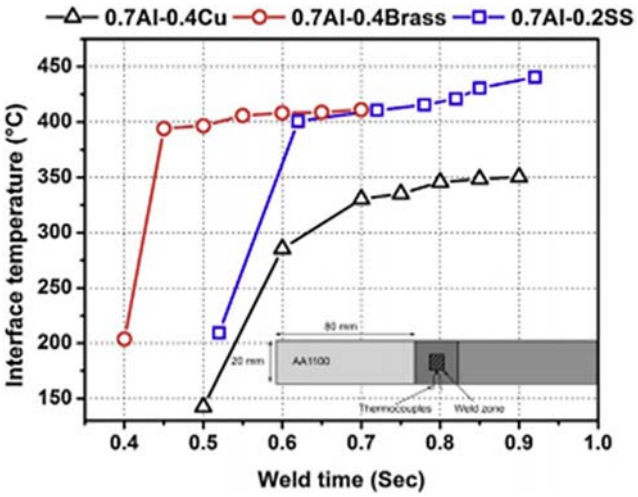


FIGURE 10.21 Comparison of interface temperature results for different weld coupons with position of thermocouple (Satpathy and Sahoo, 2017, Fig. 5).

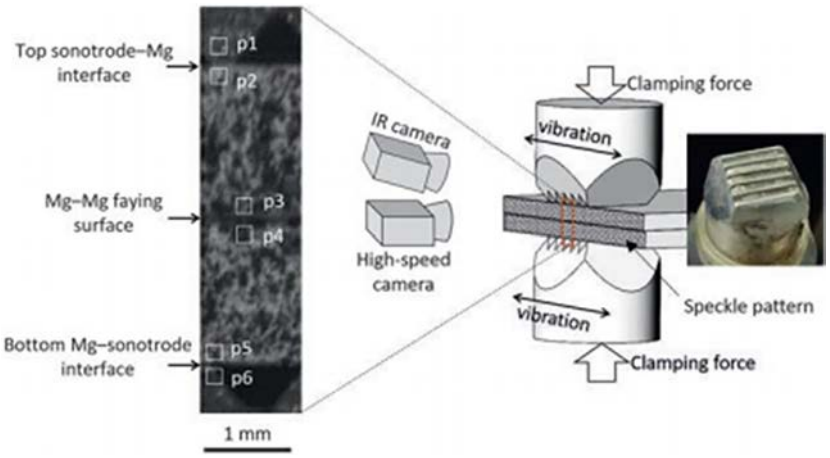


FIGURE 10.22 Schematic of experimental setup, (right) photograph of a sonotrode, and (left) a high-speed image frame showing part of the two AZ31B Mg sheets (coated with a speckle pattern) and the sonotrode teeth on the top and bottom of the Mg sheets (Chen et al., 2019, Fig. 1).

experimental setup is shown in Figure 10.22 for magnesium welds. Further, high-speed video results were correlated to postweld inspection using ultrasonic inspection by Chen et al. (2019). Six subsets of the image pixels within the small boxes in the image (p1–p6) were assigned to track the motion of sonotrodes and Mg sheets adjacent to three contact interfaces. These results showed that relative velocity was indicative of interfacial bonding as a function of weld time shown in the ultrasonic nondestructive evaluation C-scans in Figure 10.23. The NDE analyses suggest progressive joint formation with increasing welding time from 0.2 to 0.5 s.

Monitoring vibration in the weld component using piezo sensors has given insight into critical factors affecting frequency. An example of a piezoelectric sensor use for vibration monitoring is shown in Figure 10.24, where Mostafavi et al. (2019) used this method to monitor higher order harmonics of the ultrasonic transducer-operating frequency. Without restraining the weld components, detected amplitudes were observed to be lower as the component was free to move. Additionally, part geometry was shown to not affect the higher order harmonics, but that it did cause changes in natural frequencies and sideband frequencies. The amplitude of a given frequency was dependent on the hole position and diameter of the part shown in Figure 10.24. These conclusions lead one to consider identifying irregular components as well as tooling faults during production using advanced frequency monitoring methods.

Forces acting on the weld materials have also been monitored through piezo sensors. Shear force monitoring has been an ongoing effort at EWI (Lindamood, 2019) using the technique as reported by de Vries (2004). Shear forces are directly measured by installing a piezoelectric transducer in the anvil of the ultrasonic welder as shown in Figure 10.25, with representative shear force sensor data also shown in the figure.

In addition to this work, recent research has been conducted on shear forces at the weld interface using other collection methods (Ando et al., 2013; Takahashi et al., 2012; Huang et al., 2019). In this equipment, elastic vibrations are transferred laterally to a piezoelectric load cell. Vibration monitoring at the tool tip using a laser doppler vibrometry (LDV) was performed, confirming changes in the mechanical behavior of the system. Upon varying the power of the ultrasonic welding system, the signals for both shear forces and LDV showed variations consistent with the bonding and de-bonding of aluminum ribbons. Similar to the works cited in Section 10.3, welding was observed to occur throughout three distinct stages: (1) rapid increase of interfacial shear forces and high vibration amplitude;

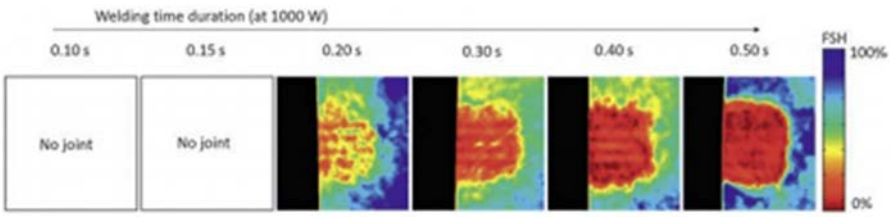


FIGURE 10.23 Ultrasonic nondestructive analysis of the weld samples (14 mm × 14 mm image area) as a function of welding time (Chen et al., 2019, Fig. 5).

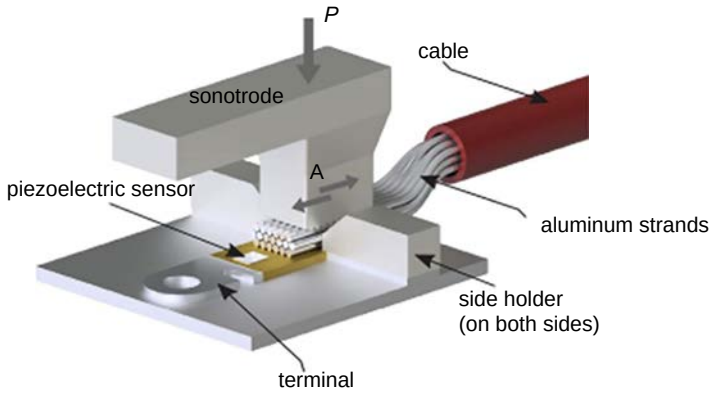


FIGURE 10.24 Schematic view of an aluminum cable and a brass terminal in the process of USMW. The terminal is constrained by side holders with a piezoelectric sensor for vibration monitoring (Mostafavi et al., 2019, Fig. 1).

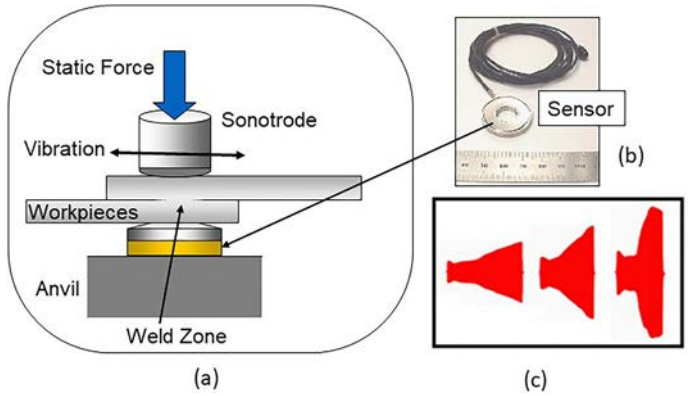


FIGURE 10.25 Ultrasonic metal welding shear force measurement: (a) ultrasonic weld zone with shear force sensor *(yellow)*; (b) piezo shear force sensor ring; (c) representative shear sensor signals (Lindamood, 2019). *(Source, EWI.)*

(2) slow increase of interfacial shear forces and suppression of vibration amplitude; (3) stabilized shear force and vibration amplitude.

Ongoing investigation of other monitoring tools is in progress (Lindamood, 2019), such as monitoring the IR signature at the point of ultrasonic metal welds, Figure 10.26, where the intensity of the IR signature, the weld input energy (Joules), and resulting weld strength are seen to directly correlate. The acoustic signature of the ultrasonic metal welding process is also of interest. Thus, it is becoming commonplace for machining operations to have integrated sensors for the detection of acoustic emission during manufacturing. These sensors give indications of operation consistencies through the sound generated by the equipment and machining process. This inspection method is expected to be useful for ultrasonic weld monitoring. Through strategic placement of microphones (contact or noncontact) as in Figure 10.27, weld-to-weld variations may be detected. These emission variations can include changes in mechanical behavior of the welder such as cracked or loose tooling, or changes in the interaction between the tooling and welded parts due to material condition, improper loading, or tool wear.

10.6 Applications of ultrasonic welding

The applications of ultrasonic metal welding are widespread, but with greatest use in all aspects of electrical and electronic connections as found in several industries in addition to electrical, including automotive, medical, aerospace, and consumer goods, with a number of these applications described in the following sections. A particular note will be taken on the increasing applications in the rapidly growing electric vehicle (EV) industry.

10.6.1 Electrical connections

Several examples of heavy-duty electrical connections are shown in Figure 10.28. Thus, wire splicing is shown in upper left; ring terminations are in upper middle; large cable terminations are in upper right; power electronic spot welds in lower left; lower middle—tube sealing; foil stack spot welding for electric vehicle batteries, lower right. Sensor terminations, contact assemblies, braided wire connections, and buss bar terminations are all examples of connections found in the automotive and trucking industries. Electric motors, field coils, transformers, and capacitors are other

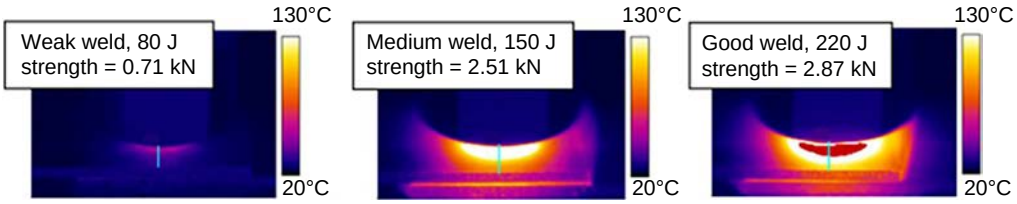


FIGURE 10.26 Infrared signature underneath welding sonotrode, showing correlation of weld strength to increasing IR intensity for increasing weld energy levels (Joules) (Lindamood, 2019). *(Source, EWI.)*

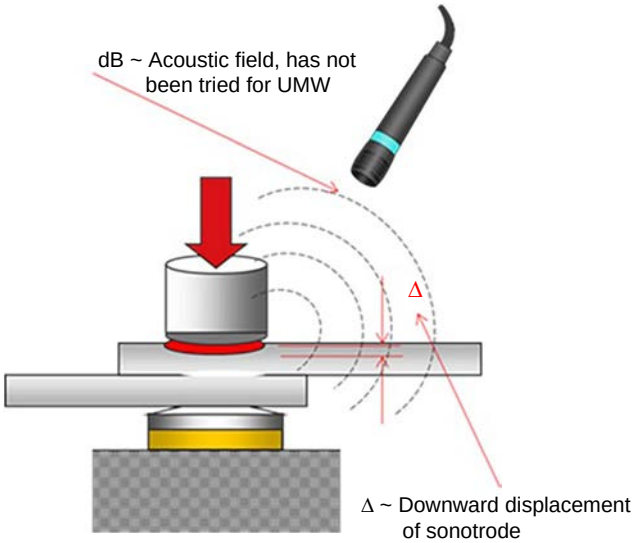


FIGURE 10.27 Detection of acoustic emissions from ultrasonic welding by high-fidelity microphone (Lindamood, 2019).

examples where ultrasonic welding is used in their assembly. The use of ultrasonic microbonding for microelectronic interconnections remains one of the most extensive uses of ultrasonic welding.

Battery and fuel cell manufacture uses ultrasonics to make various joints in these products, involving thin gauge copper, nickel, or aluminum tabs; foil layers; or metal meshes and foams. Thus, ultrasonic metal welding is well suited for the multilayer foil-to-tab joints found inside of a typical prismatic lithium-ion battery that is finding wide use in the electrical and hybrid vehicle market, as shown by Matheny (2012). The joint is usually made up of copper or aluminum foils joined to a similar material tab. The tabs may be nickel-plated for corrosion resistance and are between 100 and 250 μm thick depending on the application. The individual foils are under 25 μm in thickness and are stacked approximately 20 layers high, although extreme applications may have 100 or more layers. Figure 10.29a is a top view of a 25 × 50 mm aluminum foil stack and tab welded using the knurl tip of Figure 10.29b; the cross section, Figure 10.29c shows 20 foil layers with each layer being 18-μm thick welded to a 200 μm aluminum tab.

The ultrasonic metal welding process can be completed in a single step, which includes consolidation of the foils and joining of the consolidated foil stack to the tab. It should also be noted that the use of a sacrificial "buffer plate," which is often used with other joining processes to protect the top foil layers from ripping, is not needed. A key aspect to achieving repeatable foil-to-tab welds is the sonotrode knurl design. The knurl must provide localized force in the weld zone, which results in deformation of the foil stack; however, the knurl must not rip the delicate foil layers. In addition, the knurl height should be designed to bottom out on the top foil layers to prevent erratic motion, which leads to ripping of the foils.

Some of the previously mentioned benefits of using ultrasonic metal welding include single-step processing and the absence of a buffer plate. Another key benefit is the low heat input. This is important because the basic construction of a battery cell includes heat-sensitive components within a centimeter of the weld zone. Temperatures at 1 cm from the weld joint typically do not exceed 60°C.

Packaging applications are another wide field of use for ultrasonic welding using seam, torsion, or conventional spot-welding systems. For example, seam welding is widely used to hermetically seam foil food and cooking pouches and finds application for splicing foil rolls during their manufacture. Torsion welding is used to seal a wide variety of cylindrical containers, where the contents may be highly reactive or heat sensitive (e.g., airbag igniters), as well as making stud weld attachments. Other packaging uses include sealing of tubes in the refrigerant and air-conditioner industries.

A future trend in the use of ultrasonic welding will be in structural automotive and aerospace applications, joining thin gauge sheet aluminum and other lightweight metals. The feasibility of such uses has been demonstrated for closure panels in both helicopter and aircraft uses, while ongoing developments for automotive applications have been cited earlier.

10.6.2 Electric vehicles

The surge in development and commercialization of electric vehicles (EVs) is having far-reaching impacts in all areas of automotive manufacture, one of which is the field of

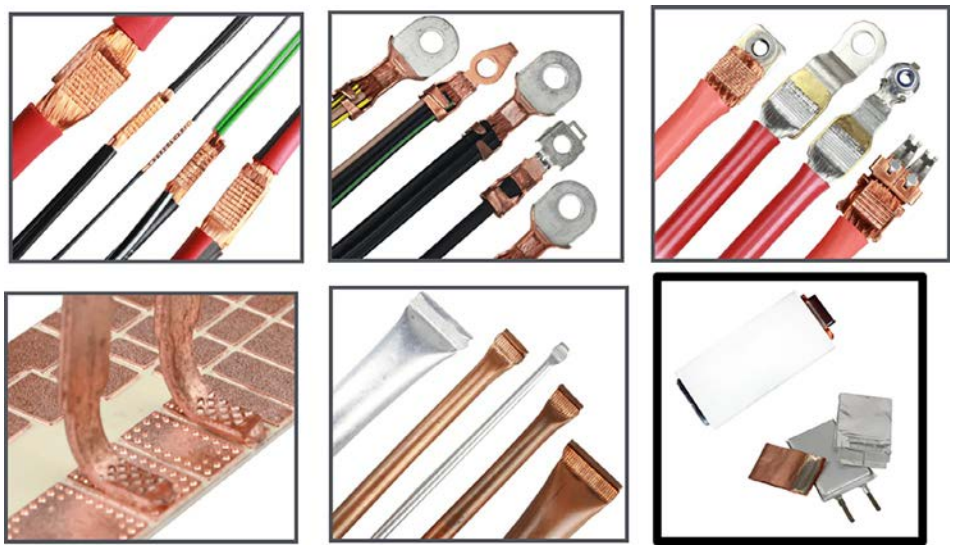


FIGURE 10.28 Ultrasonic welded applications; Upper left—wire splicing, upper middle—wire terminations, upper right—cable terminations, lower left—power electronic spot welds, lower middle—tube sealing, lower right—EV battery welding. *(Source: Tech-Sonic.)*

ultrasonic metal welding. In taking this view, it is recognized that the increased role of electronics in modern internal combustion engine vehicles (ICEVs) has already greatly expanded wiring and cable networks—generally termed "wire harnesses"—to systems of extensive lengths, number of interconnections, and significantly, total weight. EVs are placing unique additional demands on the electrical system through imposing the electric-based propulsion system on already complex electrical networks. The conductive materials of these networks, primarily copper, aluminum, and nickel, often of thin gauge, are particularly suited for ultrasonic metal welding, thus leading to its increasing use as a process of choice.

As noted, the electrical distribution systems in ICEVs consist of one or more wire harnesses. Paraphrasing a definition by Kawauchi et al. (2014), it may be said that "The wire harness is the set of wires used for supplying power and transmitting signals to electrical equipment by means of varied connectors, clamps and joints, with an ICEV having several independent wire harness systems."

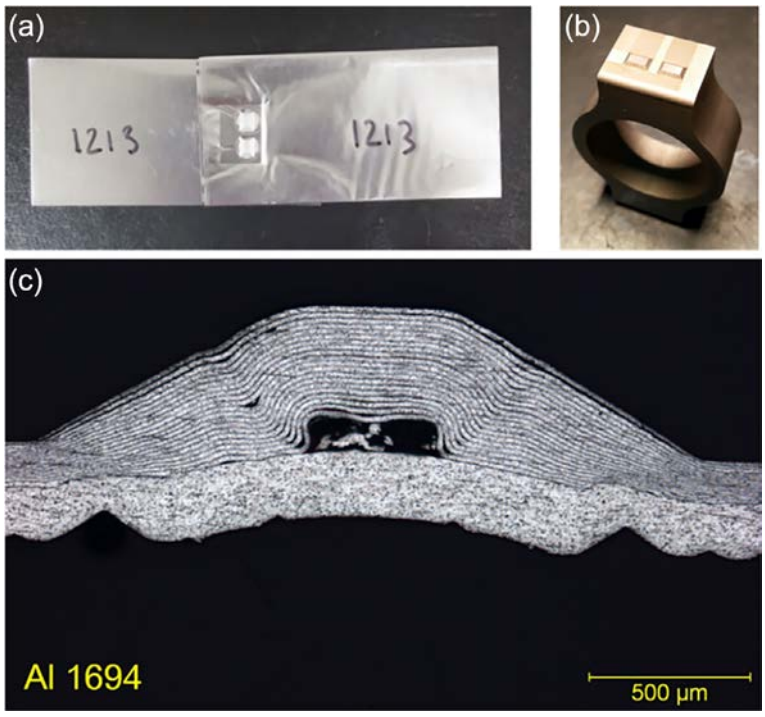


FIGURE 10.29 (a) Top view of a 25 × 50 mm aluminum foil stack and tab welded using the knurl tip (b); (c) The cross section shows 20 foil layers with each layer being 18-um thick welded to a 200 µm aluminum tab. *(Source: EWI.)*

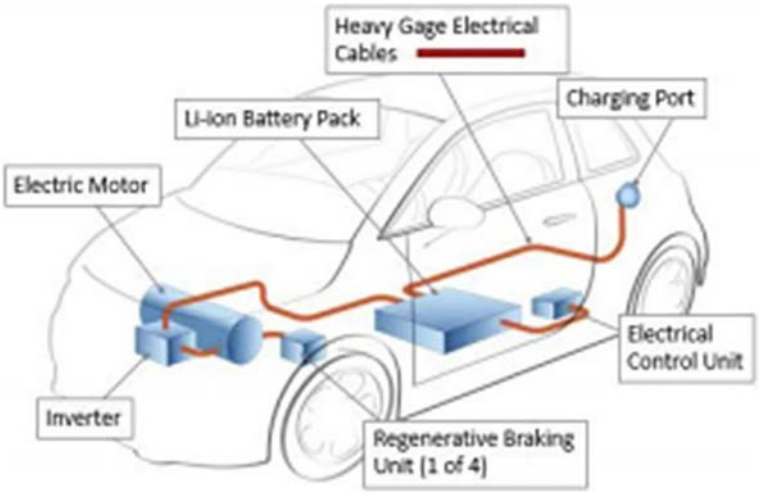


FIGURE 10.30 Main system components of an EV. *(Source, EWI.)*

EVs will impose their own additional wiring networks onto the already complex network of an ICEV, although some associated with the ICE will be supplanted. This can be illustrated by an example EV shown in Figure 10.30 where major system components of the EV—charging port, battery pack, control unit, motor, inverter, and regenerative braking, with heavy-gauge cabling—are emphasized. The example is simply illustrative since, obviously, with many models already in, and more entering, the marketplace, a single representation of the electrical system is not practical.

In Figure 10.30, the exterior charging port will be connected by heavy cabling to the BP—the heart of the EV system. The BP will have an electrical unit to monitor and control its varied functions, e.g., power to the motor and level of charge, with the interconnecting wiring being light gauge. Heavy duty cabling will connect the BP to the inverter and the inverter to the motor. There will be heavy duty cabling and control wiring to the regenerative brake units (only one of four units shown). A significant proportion of the connections in these systems is mechanical in crimp or plug form. However, there are connections for which a welding process is preferred, as reviewed in the following.

Despite the unique features of EV electrical systems compared to ICEVs, there are relatively few unique new types of welded connections, although with trends to continued higher powers, more robust connections will be required.

It is the BP, specifically the Li-ion BP that is a unique feature of most EVs and has unique welding requirements. A useful resource is the work of Cai et al. (2017) which will be drawn upon in the following. The discussions here apply to Li-ion BPs using flexible pouch cells.

The Li-ion BP, shown in simple block form in Figure 10.30b, is made up of an assembly of large numbers of individual, electrically connected Li-ion cells—where "large numbers" are dependent on the power levels of the pack and design details of the cells. Cai et al. (2017) notes the details of a pouch-type BP used in the GM Volt (Note: GM Volt was discontinued in 2020) (Figure 10.31), beginning with the progression of steps to create the pouch cell, the interconnections of cells to form a unit and the interconnection of units to form a module. Several modules are then connected to form the BP.

As noted by Cai et al. (2017) that a wide range of electrical connections are found within the overall EV electrical system, and within the BP, and that several welding processes may be used, such as resistance, laser, and arc welding. However, the commonly used materials of copper, aluminum and nickel, and joints involving thin gauge materials, all favor the ultrasonic metal welding process, which has found wide use.

This brief overview of the EV as related to the electrical system and connections, for which ultrasonic metal welding has been found highly applicable, can only be a "snapshot" of a rapidly, dramatically changing, advancing technical field, and should be accepted on that basis.

10.6.3 Microelectronics—Ultrasonic microbonding

The vast field of microelectronics, encompassing complex systems of ICs, interconnected transistors, LEDs, and power semiconductors, as examples, has as a central part of its functioning and manufacturing, an equally vast number of fine, wire interconnections for which the ultrasonic metal welding process, typically termed "microbonding" (but also "microwelding" and "microjoining"), has proved critical. Per Charles (2010), it is estimated that about 10 trillion wire bonds per year are—or were—made on the planet each year, with that number no doubt having grown proportionately

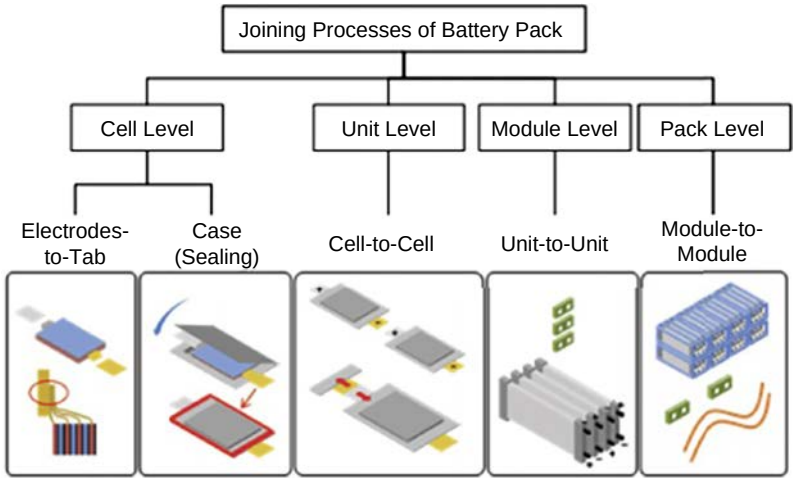


FIGURE 10.31 Joining processes of pouch-type cells (Cai et al., 2017, Fig. 1.2).

since the earlier accounting. Given the scope of ultrasonic metal welding, as set forth in the various sections of this chapter, there is little doubt that, purely from a numerical standpoint, its usage far exceeds all other applications, even if combined.

As noted in Graff et al. (2007), "The key difference between microwelding and other methods of ultrasonic welding is not in the principles of operation, which generally are the same as those of lateral-drive and wedge-reed welding machines, but in the frequency ranges and power levels used. Thus, microwelding machine frequencies tend to start at 60 kHz and range up to 150 kHz, with frequencies in experimental systems reported at 300 kHz. Power levels of microwelding equipment usually are in the range of 0.1 W to 50 W, whereas the higher power systems discussed in previous sections operate in the range of 10 W to 1000 W (or more)."

Given the scope of the ultrasonic microbonding field, it is evident that only an overview can be given here. "Wirebonding in Microelectronics" (Harman, 2010) has remained, through several editions, the excellent single source starting point, with an extensive supporting field of references and journals being available.

10.6.3.1 Ultrasonic microbonding system

The ultrasonic microbonding system must make large numbers of high-speed microbonds per minute (e.g., 1–5 bonds/s, depending on wire diameter and type) at high precision (e.g., $\pm 3\,\mu m$) under production conditions, so that its underlying mechanical and control technology must itself be complex, of which Figure 10.32a is a commercial example, with a close view of the wire bonding end effector tooling and motion structure shown in Figure 10.32b.

10.6.3.2 Ultrasonic wirebonder

The ultrasonic welding unit used for microbonding, shown in Figure 10.33b, is shown in detail in Figure 10.33a for a "wedge bonder" and consists of an ultrasonic transducer, on the left that drives a tapered horn having at its right end a vertical tool vibrating in a bending mode (Note: Figure 10.33a has been reversed from the original for



FIGURE 10.32 (a) Ultrasonic wire bonding system (Hesse Mechatronics Wire Bonder Bondjet BJ653). (b) Ball bond setup (Hesse Mechatronics). *(Photos courtesy of Hesse Mechatronics.)*

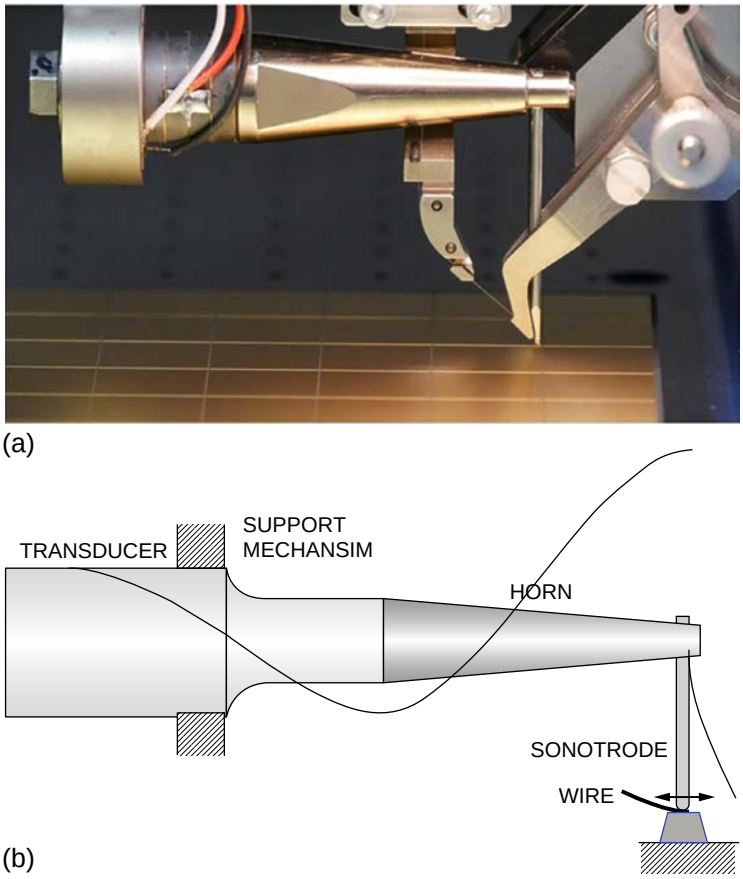


FIGURE 10.33 Ultrasonic wire bonding transducer and tooling. (a) Photo image—Note: this image reversed left/right from original to better align with (b). (b) Ultrasonic welding unit. *(Source: (a) Hesse Mechatronics, (b) EWI.)*

convenience of alignment with Figure 10.33b). Figure 10.33b is a schematic of this transducer-horn-tool setup. Thus, the transducer may be of standard, piezoelectric stack construction. Although transducer details are not shown in the figure, they are described in Section 6.5.2, with some details, e.g., the piezoelectric disks, being seen in Figure 10.33a. Other transducer-horn forms are possible, such as unibody design, noted by Harman (and also referenced in Chapter 6, Section 6.5.3).

The horn amplifies the transducer vibration, also described in Chapter 6. A full longitudinal wavelength transducer/horn design is shown—thus, the transducer is one-half wavelength, as is the horn. The welding sonotrode is attached to the horn tip and operates in a bending mode, directly engaging and bonding the wire, creating the ultrasonic solid-state bond that has been extensively described earlier in this chapter. It is similar to the behavior of the "wedge-reed" system described in Section 10.2.

The sonotrode is seen in Figure 10.33a and b as the vertical projection from the horn tip and is in direct contact with the bond surface. As noted, microbonding frequencies are high, relative to those described in earlier high-power applications, and can range from 60 to 150 kHz, or higher. The length dimensions of the unit will accordingly be small compared to earlier applications that have been described for 20 kHz. For example, a 60 kHz full wavelength unit will be on the order of 8–9 cm in length. The transducer is shown attached to an overall welding system support and actuating mechanism, thus enabling the movements, engagements, and clamping actions necessary to make high-speed, precision bonds to be achieved.

10.6.3.3 Types of wire bonds

As set forth in Harman (2010), and summarized by Charles (2010) and Graff et al. (2007), there are three major methods of wire bonding, thermocompression, wedge and thermosonic, of which the latter two are ultrasonic-based. The ultrasonic welds used in microelectronics applications are typically made with highly deformable materials such as aluminum, copper, and gold wires having diameters in the 25 to 50 μm range.

Ultrasonic wedge bonding

Figure 10.34a shows the details of wedge bonding at the wedge-wire interface, in which the wire is fed through the tip of the tool end (i.e., wedge) to the wire overlying the IC pad. The resulting transverse motion at the faying

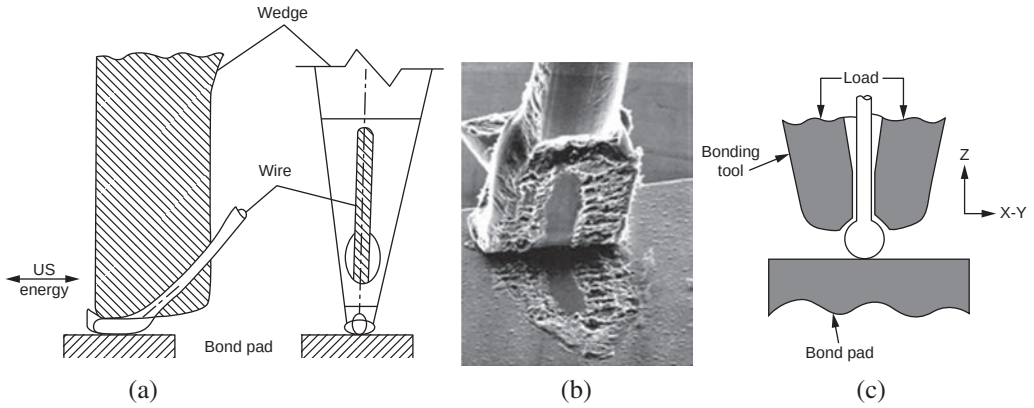


FIGURE 10.34 Ultrasonic wire bonding. (a) Wedge bonding—wire-wedge details at tool tip. (b) Partial peeled wedge bond interface. (c) Thermosonic bonding (Harman, 2010, Fig. 1-4, 2-14, 1-5, p5, p27, p5).

surface, resulting in the formation and growth of micro-welds, although on a small scale, will otherwise be similar to that described earlier for the mechanism of the welding process (e.g., Section 10.4). The bonded surface is shown in a partially peeled weld, Figure 10.34b.

The thermosonic bonding process, Figure 10.34c, shows a capillary welding tool tip with ball that has been formed by a spark discharge that melts the wire tip. The ball is pressed against a heated pad substrate, with ultrasonic vibration forming a bond in the manner previously described.

10.6.3.4 IC chip connections

The sophistication of IC chip designs, and ultimately, IC chip terminations, is both extensive and under continuous change. It is best, therefore, to simply consider a basic IC chip and its connections to other circuitry, as shown in Figure 10.35a. Thus, wire bonds are shown on the (green) IC pads that then loop to bonds on the exterior interconnection pads. These bonds may be either wedge or thermosonic bonds. An illustration of a series of ultrasonic wire bonds of Al wire is shown in Figure 10.35b. Gold and

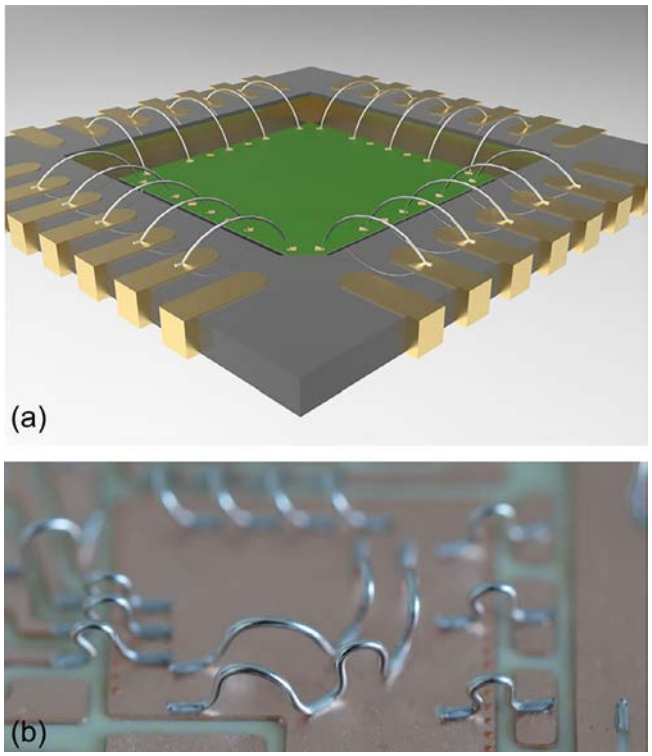


FIGURE 10.35 (a) IC chip wire bonds. (b) Wire bonds of 300 μm Al wire. *(Source: Hesse Mechatronics.)*

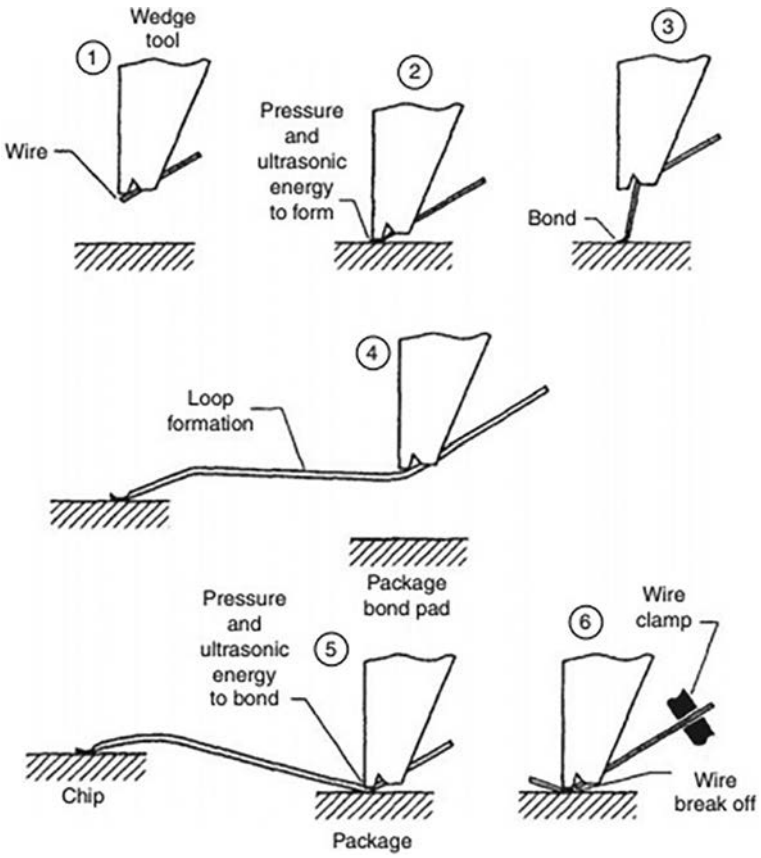


FIGURE 10.36 Wedge bonding sequence (Harman, 2010, Fig. 1-2).

aluminum are the most common interconnect materials but with significant competition from copper wires (Brökelmann et al., 2015).

As shown in Figure 10.35a, and also brought out in Figure 10.35b, an ultrasonic bond will typically consist of two junctions, one on the IC pad, with the wire then looping to a pad on the external circuit connection. Thus, a two-step sequence occurs, as brought out in Figure 10.36 for the case of wedge bonding.

Summarized from Harman, (1) wire located above the bond location; (2) tool lowered and presses wire against bond pad and welded; (3) tool raised; (4) tool moved to package bond pad, forming loop in process; (5) tool lowered and weld made to package bond pad; (6) wire is clamped and pulled to break wire. While obviously differing in some details, a similar sequence holds for the thermosonic process.

10.6.3.5 Wire bond examples

Given the enormity of microelectronics component configurations, there is no "representative" example, so that Figure 10.37 may merely be taken as "illustrative" of high-density IC chip, interconnection applications.

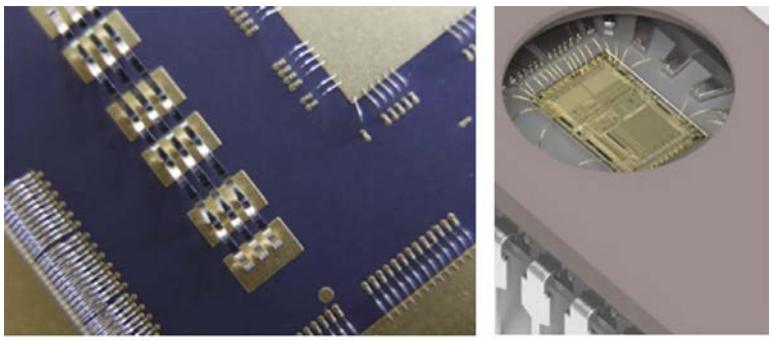


FIGURE 10.37 Illustrative example(s) of high-density IC chip interconnections. (a) Fine ribbon bonds and fine wedge-wedge bonds on ENIG plating on FR4 substrate. (b) Fine wedge-wedge bonds in a cavity in an integrated circuit. *(Source: Hesse Mechatronics.)*

In summary, as noted at the outset of this section, the enormous scope of ultrasonic microbonding is simply reflective of the enormous scope of microelectronics in nearly every product touching human activity and can only be "micro" summarized in this preceding section.

10.7 Ultrasonic metal welding—Process advantages and disadvantages

Having reviewed the principles, key features, and applications of ultrasonic metal welding, both the advantages and disadvantages of the process may be evident at this stage. Nevertheless, a summary of these features is in order:

Advantages

- A solid-state welding process; hence, low heat generation
- Excellent for Al, Cu, and other high thermal conductivity materials
- Able to join a wide range of dissimilar material combinations
- Can weld thin-thick combinations
- Welds through oxides and contaminants
- Fast, easily automated
- No filler metals; welding gases required
- Low energy requirements

Disadvantages

- Restricted to lap joints
- Limited joint thickness
- High-strength, high-hardness materials difficult to weld
- Material deformation may occur
- Noise from part resonance may occur
- Lack of familiarity with the process

These will be reviewed in more detail.

10.7.1 Solid-state welding process

Many of the advantages of ultrasonic metal welding stem from its basic solid-state nature. The weld zone, where joining of parts occurs, is a region of plastic deformation and flow, resulting in local mechanical deformation of grain structure, but with the absence of melting, fusion, or other evidences of high temperatures relative to melting. Little modification of grain structure is seen away from the deformation zone, which is itself thin, on the order of 10s of microns at most.

10.7.2 Aluminum, copper, other materials

The ultrasonic materials weldability matrix shows "in principle" that nearly every material and most material combinations can be welded. Nevertheless, the softer metal alloys such as aluminum and copper have shown to be the most weldable. Because of the high thermal conductivity of these alloys, they have often proved to be more difficult to weld by more traditional welding methods such as resistance spot welding. This benefit of welding high thermal conductivity materials is, of course, tied to the solid-state, nonthermal nature of the process.

10.7.3 Dissimilar materials

Note has been taken of the range of dissimilar metal combinations that are reported to have been welded, with this advantageous process feature again being due to its solid-state nature. A wide variation in welding conditions arises to achieve these joints, depending on materials. Thus, a weld readily achieved with 1.5 kW, 0.25 s, and 900 N of static force in 1 mm 6061T6 aluminum may require 2.5 kW, 0.5 s, and 1800 N for 2.5 mm, if the weld is achievable at all. In general, well-developed weld procedures for a wide range of materials and conditions do not currently exist (as they do, for example, for arc welding), so that each combination must be approached in an exploratory manner. In some cases, joints in widely dissimilar materials are assisted by thin foil transition layers or some intermediate material. Joints have also been made in metal-ceramic, metal-glass combinations, in some cases using transition layers or metallized coatings. Dissimilar metal combinations arising in efforts to reduce weight in automotive body frames (so-called light-weighting) have been of recent interest. Thus, reports on aluminum-coated steel (Haddadi et al., 2012; Prangnell et al., 2011), magnesium-steel (Patel et al., 2013), and aluminum-magnesium (Panteli et al., 2012) are among recent results.

10.7.4 Thin-thick combinations

Yet another advantage accruing from the solid-state nature of the process is the ability to join thin (e.g., thin sheet and foils in ranges of 0.025–0.250 mm) to thick parts. Making such joints, especially in high thermal conductivity materials, can be difficult due to the large heat sink of the thick material drawing heat from the weld zone. Such joints are readily made with ultrasonic welding, including joining of multiple foils to a thick substrate with a single weld.

10.7.5 Oxides and contaminants

By the very nature of the inherently friction-like ultrasonic welding action, oxides and contaminants are fractured, disrupted, and dispersed. For example, any oil-like surface residues are quickly vaporized in the early stages of the cycle, and some oxides will be dispersed to the weld periphery, or into the turbulent microvolumes of plastically deformed material at the interface. In summary, the ultrasonic welding process is somewhat tolerant to less than ideal surface

conditions. Nevertheless, there is sometimes the tendency to assume the process can achieve successful welds through *any* level of surface contamination or that control of surface conditions is unnecessary; both of which are unsound assumptions. As a minimum, varied conditions will yield variations in the process, such as variable weld times, and as a maximum, variation in a weld quality such as strength. While special cleaning methods may be needed only rarely, due consideration must be given to consistency of surface conditions.

10.7.6 Fast, easily automated

The typical ultrasonic weld cycle, from start to stop of the ultrasonic vibration, is a fraction of a second, with 0.2–0.5 s being common. Other time components of the weld-to-weld cycle are tied to details of the welder clamping force and retraction mechanism and are thus subject to being minimized by appropriate machine design and control. Any other aspects of weld-to-weld time are a function of the manufacturing system requirements of the specific application. No demands, such as cooling time or setting time, are placed on total cycle time by the weld process. The basic electromechanical nature of the process and simple mechanical features of the clamping action makes it ideal for automation and continued monitoring and control for production and quality assurance. For example, adaptation of ultrasonic welding systems to robotic systems for the auto industry has been demonstrated (Mariam et al., 2007).

10.7.7 Filler metals and gases

Neither filler metals nor shielding or consumable gases are needed in the usual ultrasonic welding processes. In some cases, in attempting difficult materials combinations, a thin foil transition layer has been placed between the parts. In cases of making welds under hazardous conditions (e.g., closure of explosive containers), an inert gas-filled enclosure can be used.

10.7.8 Low energy requirements

Typically, the ultrasonic welding process is selected based on one or more of the foregoing advantages, most being related to the solid-state nature of the process. If energy use is a factor, it is found that ultrasonic welding is a low energy user compared to other processes; thus, it uses about one-sixth of the energy of resistance spot welding for comparable welds, and even less if compared to arc processes.

In considering some of the process disadvantages, the following are to be noted:

10.7.9 Restricted to lap joints

The requirement to achieve a friction-like interface vibration, and the limits as to the amount of mass that can be moved with ultrasonic systems, logically requires the moving welding tool to be close to the interface, which results in the lap joint constraint of the process. Thus, butt, tee, and corner joints, easily done in fusion processes, are not yet routine with current ultrasonic systems.

10.7.10 Limited in joint thickness and material hardness

These items were covered in some detail and appear in both cases to be related to current restrictions on available ultrasonic power. In aluminum alloys of the 5XXX, 6XXX classes, 2 mm joints are close to the outer limits achievable with current 20 kHz systems and dropping to the order of 0.1 mm for titanium and harder alloys.

10.7.11 Material-part deformation

The ultrasonic weld tip will typically create some deformation of the top surface, in the softer alloys. This will be more or less pronounced depending on weld tip surface (whether flat, slightly hemispherical, and/or serrated or otherwise roughened or knurled) and welding conditions (forces and powers involved). Deformations depths of 5%–10% of part thickness may result. Anvil-side deformations can arise from the same circumstances but typically are less pronounced. Through special attention to tip design and parameters, it is usually possible to reduce, but seldom eliminate, some part deformation or marking.

10.7.12 Noise

Being an "ultrasonic" process, it would seem that audible sound would not be an issue in ultrasonic welding. Two aspects arise, however. The first and most common is that the 20 kHz (or higher) welding frequency may induce subharmonic vibrations in larger parts that are in the audible range. In such cases, it may be possible to dampen these modes by light clamping of the part at one or more locations. The second aspect is that for some higher-power welders, a driving frequency of 15–16 kHz may be used; frequencies that are in the high-audible range. For these cases, an acoustic enclosure is needed to shield the radiated sound.

10.7.13 Process unfamiliarity

The large majority of welding processes used in production are fusion based, using electric arcs, resistance heating, or high-energy laser or electron beams. Ultrasonic metal welding, being a solid-state process, and furthermore one that is based on high-frequency vibration mechanics, is not typically

encountered in the education and experience of manufacturing and welding engineers. Dealing with the unfamiliar is not typically a comfortable option, especially when faced with the pressures of modern manufacturing, and can be a disadvantage in considering the ultrasonic process.

10.8 Other ultrasonic metal welding processes

This chapter, as entitled, has been devoted to the application of power ultrasonics to the welding of metals. Despite the breadth of title, the focus has been on a single process, namely, configurations of ultrasonic components to create solid state spot or seam lap joints in thin gage materials. However, there are other metal joining processes toward which ultrasonics has been applied, including resistance spot welding, varied arc welding processes, and friction stir welding, for which brief summaries are given in the following.

10.8.1 Resistance spot welding/ultrasonics

Introducing electrical current during the ultrasonic welding operation has been investigated more recently since the historical inception of ultrasonic welding. Using the advantages of material disruption from the application of ultrasonic energy in conjunction with the thermal process of resistance welding, higher yield strength materials may be joined in either similar or dissimilar configurations. The polarity and series of applied energy events vary among recent investigators. Typically, for ultrasonic welding of metals, a transverse motion of the sonotrode is applied to weld coupons. This, as described in Section 10.2, breaks down asperities, distributes oxides and contaminates, and promotes metallic bonding. Additional heat to the joint will reduce the yield strength allowing these disruptions at the interface to happen more readily. One way to introduce heat is to use electrical current, such as a resistance welding power supply. This allows amperage to be delivered in a short amount of time to the contact interface of weld coupons (path of least resistance).

Concepts for hybrid welding have been used to observe effects on materials and improvement of weldability for materials not easily welded using ultrasonic methods. Lu et al. (2019b, 2020) used hybrid welding to join 1.0-mm thick aluminum 6061-T6 to 0.9-mm thick 1008 steel by first ultrasonically welding a 0.4-mm thick intermediate layer of aluminum 6061-T6 to the steel, as seen in Figure 10.38. Next, resistance welding electrodes are brought to the joint and weld the thicker aluminum to steel, taking advantage of the aluminum insert. The resulting weld shows the aluminum intermediate layer behaving as a braze with liquid aluminum forming a nugget on the aluminum side and wetting on the steel side forming a heat affected zone. From this work and others, the method has been shown to reduce intermetallic thickness and improve joint

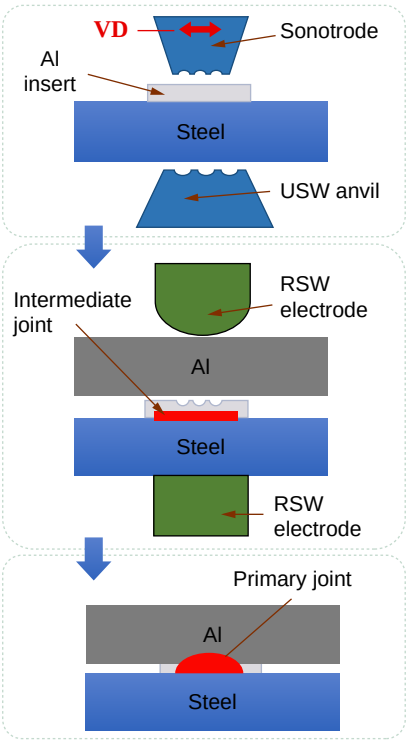


FIGURE 10.38 Hybrid ultrasonic and resistance welding system, first welding an intermediate aluminum with ultrasonics then welding larger aluminum sheet to steel. VD indicates ultrasonic vibration direction (Lu et al., 2019a, Fig. 1).

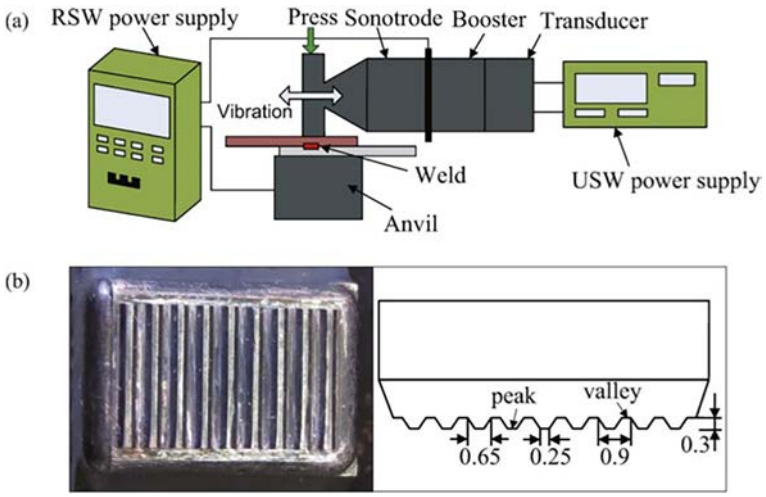


FIGURE 10.39 (a) Schematic of a hybrid ultrasonic and resistance welding system with current through the sonotrode. (b) Image of the tip geometry (mm) (Li et al., 2018, Fig. 1).

strength using a variety of aluminum intermediate layers when welding steel to aluminum (Lu et al., 2019a, 2019b, 2020).

Hybrid systems using the lateral metal welding equipment have also introduced electrical current either as separate electrodes attached to the weld coupons (Lindamood et al., 2018) or through the sonotrode (Yang and Cao, 2015). In both arrangements, electrical current is supplied during the ultrasonic welding process. This method keeps overall weld time relatively short and allows welding to occur in one step rather than two separate processes. The method reduces the yield strength of the material to maintain short ultrasonic weld times. While aluminum is easily welded using ultrasonics only, joint strength was shown to increase when resistive heating was used along with ultrasonic welding (Lindamood et al., 2018). Li et al. (2018) went further to model the weld joint resulting from this hybrid process showing a reduced intermetallic compound layer and reduced weld time (Figure 10.39).

In a more unconventional application of the ultrasonic and resistance hybrid method, a vertical ultrasonic welder commonly used for plastic welding, Figure 10.40, was demonstrated for aluminum 6061 to TRIP steel 780 joining (Shah and Liu, 2019a,b). Similar in concept to hybrid lateral welding, the purpose of the vertical hybrid welder was to reduce the yield strength of steel through this ultrasonic vibration while simultaneously applying electrical current through the sonotrodes. The method was successful in reducing cracking of the weld typical of using only resistance welding as well as forming a stronger weld joint.

As noted by Shah and Liu (2019a,b), "A 3-dimensional FEM model was successfully established to analyze the RUSW process. The model included the key ultrasonic and electrical current factors, such as patterns of sonotrode tip and anvil tip, ultrasonic softening, heat generation by friction, plastic deformation and electrical resistance. The experimental verifications based on the interface temperature, horn displacement and cross section patterns showed that the model results are in good agreement with the experimental results. The model can simulate the RUSW process well. The effects of resistance heat on USW process were simulated and analyzed. The resistance heat could significantly increase the body temperature, accelerate the penetration of the sonotrode teeth into the

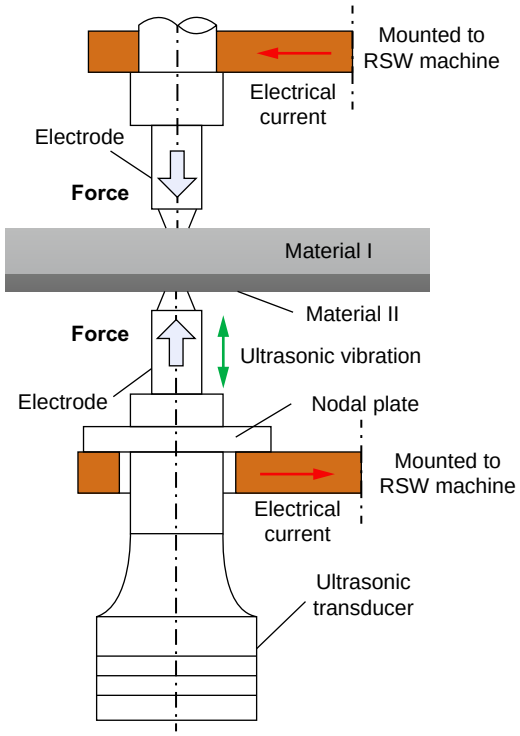


FIGURE 10.40 Schematic of a vertical ultrasonic welder with electrical current applied to the sonotrodes (Shah and Liu, 2019b, Fig. 1).

sheet and increase the plastic deformation in the materials. Assisted by a 3900A current, the interface temperature and plastic deformation in the RUSW process at welding time of 0.2s were similar to the corresponding values in conventional USW process at 0.4s, while a thinner IMC layer was obtained."

10.8.2 Arc processes/ultrasonics

Some of the earliest observations of power ultrasonics were its effects on solidifying molten materials, first simply being waxes and paraffins, but soon after on molten metals. As noted in Graff (1981), the earliest references to ultrasonics applied to welding were related to affecting the molten pool of an arc process. Kumar et al. (2017), in a far-ranging review of ultrasonics applied to welding and metal processing, notes a number of developments in ultrasonic/arc hybrid welding processes.

For example, Kumar takes note of the work of Sun et al. (2009) on ultrasonically vibrating the tungsten electrode in the gas-tungsten arc welding (GTAW, aka "TIG") process to cause the arc plasma field to transmit high-frequency vibrations into the molten pool, as shown in Figure 10.41. Improved weld pool depth and width were reported. Kumar also noted the work of Han et al. (2005) with the ultrasonic GTAW process, noting improved weld penetration for differing weld currents. The application of ultrasonic vibrations to the gas-metal arc welding (GMAW, or "MIG") process by Fan et al. (2012) was also noted by Kumar et al. (2017). In this case, it was the effects of the intense, ultrasonically generated acoustic field that affected the arc envelop and pool. It was found that droplets into the weld pool were smaller in size than without ultrasonics, leading to better arc stability and subsequent weld quality.

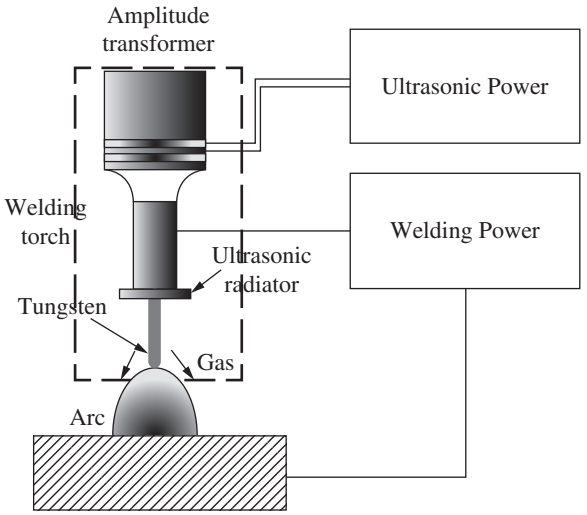


FIGURE 10.41 Schematic of ultrasonic assisted TIG welding process (Kumar et al., 2017, Fig. 13). *(From Sun et al. (2009).)*

Using a setup similar to that of Sun et al. (2009) shown in the previous figure, Wang et al. (2017) investigated the effects of intense acoustic waves on the GTAW process. Ultrasonics was introduced into the process in two ways, by continuous and by pulsations of the arc. It was found that the degree of arc contraction, weld pool oscillation, and weld penetration were significantly enhanced by the pulsed ultrasound. Likewise, joint tensile strength was improved.

Dai et al. (2015, 2016a,b,c) reported on several studies involving a hybrid arc-assisted ultrasonic seam welding process using a setup shown in Figure 10.42. Thus, Dai et al. (2015) reported on the welding of MgAZ31B and Al6061 alloy sheet, with the progression of the weld with increased current illustrated in Figure 10.43 (this progression, while appearing similar to that of conventional UMW, Figure 10.10, in fact shows regions of increased fusion bonding, versus increased solid-state bonding as in UMW). While increasing tensile shear strengths compared to conventional GTAW were obtained, there was a significant drop-off at higher welding currents. In Dai et al. (2016a), Mg to Al joints with an Sn interlayer were welded using the hybrid process, with it being found that the formation of intermetallic compounds was reduced. A progressive change in the interlayer with increasing weld current was noted.

In a continuation of the hybrid GTAW Sn interlayer work, Dai et al. (2016b) noted increase in joint strength as compared to welds without the interlayer and noted that joint failures occurred at the interface. The increasing strength and then sudden drop, with increasing weld current, previously noted, were observed, including an approximately 30% increase in strength of the hybrid over the conventional process. Finally, in Dai et al. (2016c), a composite Sn/Zn interlayer was tested, and yielded strength increases of 150% over conventional GTAW and well above those with just the Sn interlayer alone.

Voight and Vieira da Cunha (2018) applied the concept of ultrasonic arc excitation to the submerged arc welding (SAW) process. Different welding current levels and frequencies of 20, 50, and 80 kHz were used. However, results showed no significant changes in weld bead geometry or in

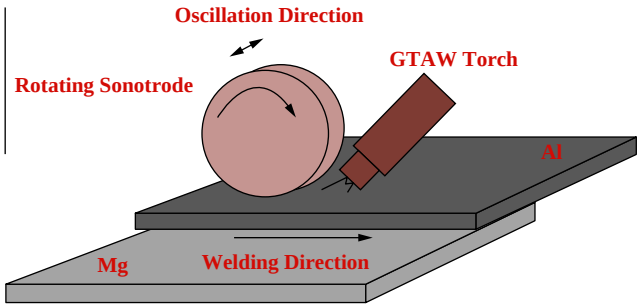


FIGURE 10.42 Schematic diagram of GTAW-assisted hybrid ultrasonic seam welding system (Dai et al., 2015, Fig. 1).

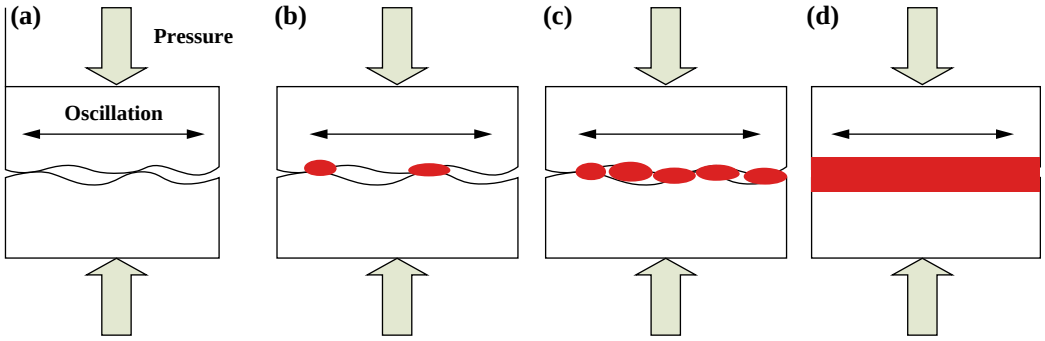


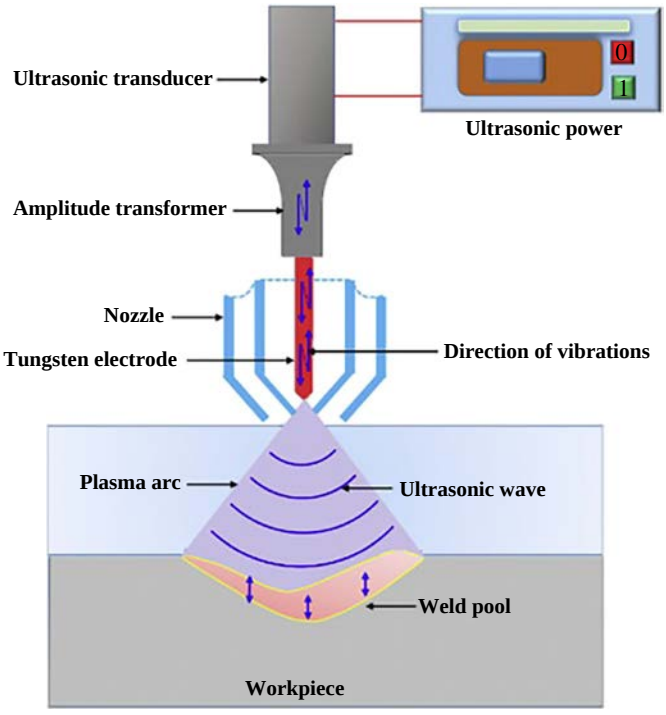
FIGURE 10.43 Weld formation model: (a) real contact, (b) micro-bond formation, (c) GTAW current of 20 A, (d) GTAW current of 30 A (Dai et al., 2016b, Fig. 13).

the HAZ that could be attributed to the ultrasonic effect. Thavamani et al. (2018) studied the effects of ultrasonic vibrations on hot cracking in Inconel 718 during GTAW. The test specimens were directly mechanically vibrated through mounting on an ultrasonic horn. It was found that the ultrasonic treatment during solidification decreased crack sensitivity, with dendritic fragmentation, grain refinement, and reduced solute segregation as being the main factors in mitigating hot-cracking.

Qiao et al. (2020) carried out both a numerical and experimental study of the key-holing effect when ultrasonics was applied to the plasma arc welding (PAW) process, using the setup shown in Figure 10.44 in which the vibrations of the tungsten electrode-induced pressure oscillations into the arc. For the U-PAW process, an example of the evolution of the keyhole up to an including breakthrough is shown in Figure 10.45 for 95 A arc and a travel speed of 115 mm/min. It was found that ultrasonics increased plasma arc pressure permitting an open keyhole to be established at lower welding currents and at higher welding speeds.

Xie, Fan, Chen and colleagues reported extensively on work involving intense ultrasonic acoustic fields on the shape and performance of the welding arc on the GMAW process. Thus, Xie et al. (2016) used equipment shown in Figure 10.46 (left) to create standing acoustic waves in the arc zone, as shown in Figure 10.46 (right). Modeling of the process included the influence of radiator shape on the plasma field. The effect on weld penetration is shown in Figure 10.47. Continuing this work, Fan et al. (2017) applied the ultrasonic acoustic field approach in GMAW and found the arc to be compressed, droplet size was

FIGURE 10.44 Schematic diagram of U-PAW process (Qiao et al. 2020, Fig. 1).



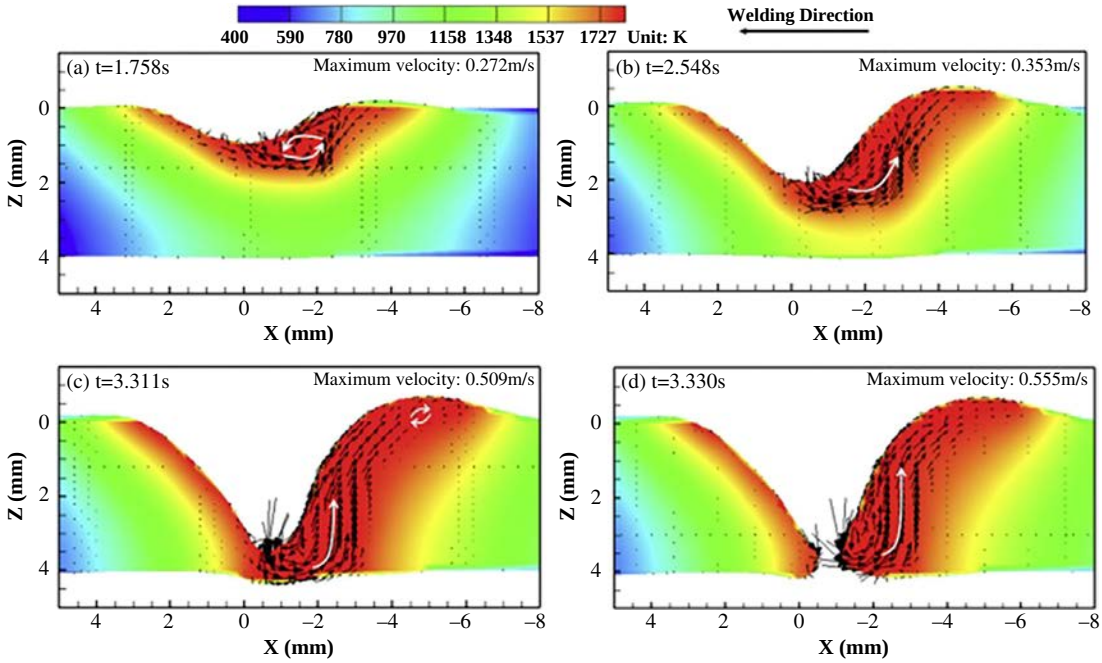


FIGURE 10.45 Evolution of temperature field, fluid flow in the weld pool, and keyhole surface over time for U-PAW at 95 Amp, 115 mm/min (Qiao et al., 2015, Fig. 14).

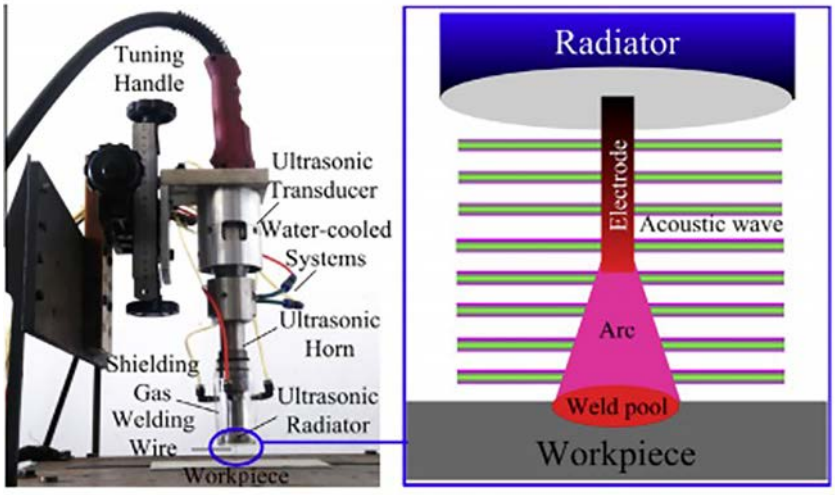


FIGURE 10.46 Device of ultrasonic wave-assisted arc welding (Xie et al., 2016, Fig. 1).

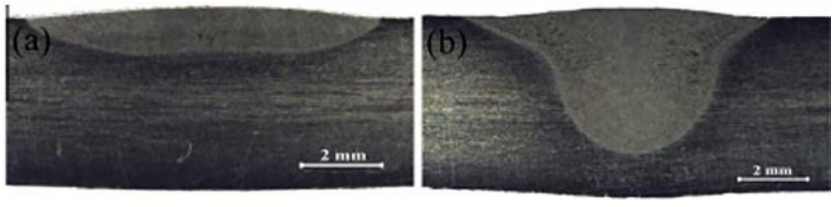


FIGURE 10.47 Weld penetration of (a) conventional arc welding and (b) ultrasonic wave-assisted arc welding (Xie et al., 2016, Fig. 3).

decreased, and droplet transfer frequency was increased. Other findings were increased stability of the GMAW arc.

Xie et al. (2018) reported further on the ultrasonic-assisted gas metal arc (U-GMAW) process, noting the pronounced effect of the ultrasonic radiator shape on droplet transfer stability. The nature of droplet transfer was examined for various conditions; thus, Figure 10.48 shows droplet transfer when welding in the flat or "down" position,

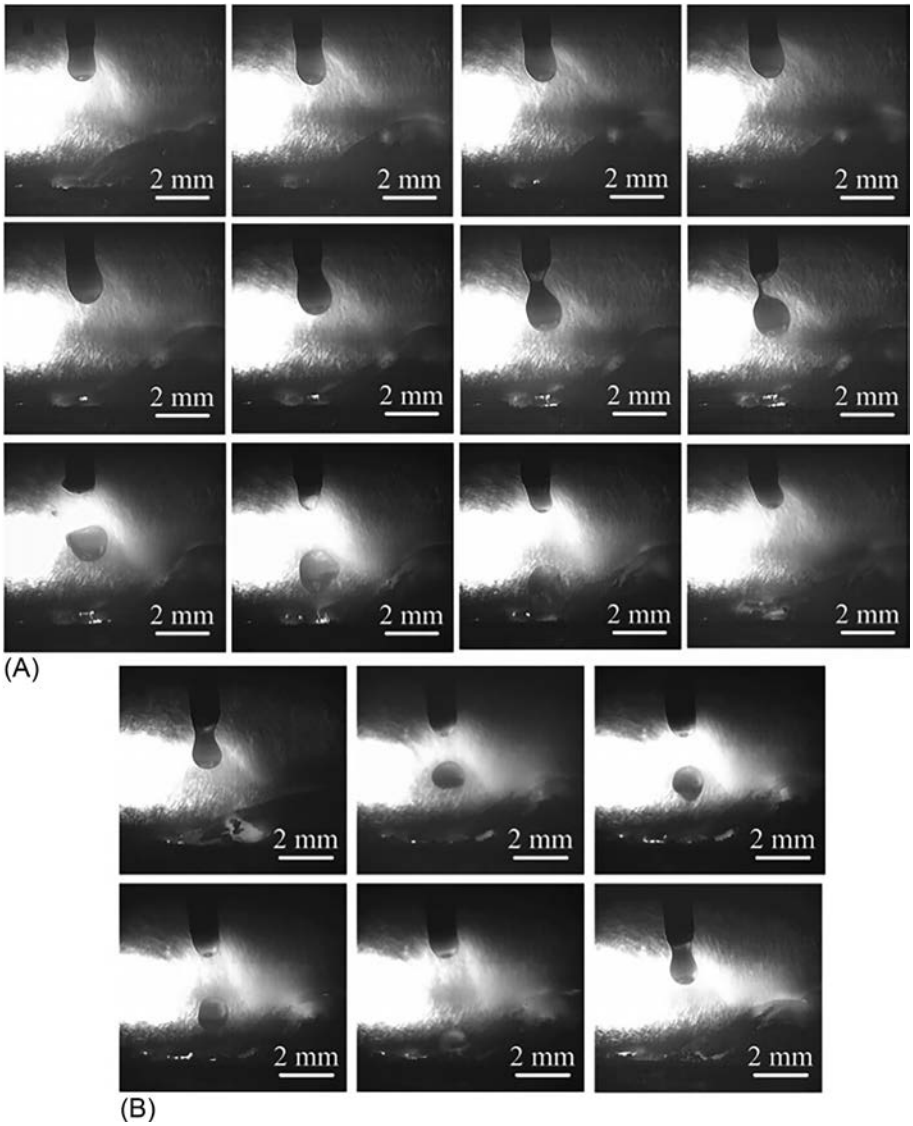


FIGURE 10.48 Typical droplet transfer in flat welding experiments. (a) Upper set—with ultrasonics. (b) Lower set—without ultrasonics. Interval between images is 1.998 ms (Xie et al., 2018, Fig. 6).

with favorable results also shown for—in welding nomenclature—the vertical up and overhead positions.

Chen et al. (2018) extended the acoustic field work to the tungsten inert gas (TIG, aka GTAW) process. Arc luminosity and arc shape were found to periodically differ (between so-called arc white bright and arc dark bright) zones. While the influence of the acoustic field on these effects was seen, the effects on weld shape or penetration were not reported. However, in a following report, Chen et al. (2020) reported on just these issues, comparing microstructure and mechanical properties of conventional GTAW and U-GTAW welding of Q235 joints as well as a further variation, pulsed ultrasonic, or PU-GTAW. The pulsed ultrasonic process was found more effective than continuous ultrasonics in improving joint properties. A comparison of the microstructure of the three processes, with two pulsing frequencies for PU-GTAW, is shown in Figure 10.49. It was found that the ultrasonic effect, whether continuous or pulsed, was to reduce microstructure compared to GTAW alone, as well as to increase hardness.

10.8.3 Friction stir welding

The application of ultrasonics to the friction stir welding (FSW) process is a third broad field of hybrid UMW development, as set forth by Kumar et al. (2017) in the following review.

As a solid-state welding process, FSW is advantageous in avoiding solidification defects, enabling joining of different materials and welding low temperature materials, e.g., aluminum alloys. During FSW, a nonconsumable tool containing pin and shoulder features rotates and plunges

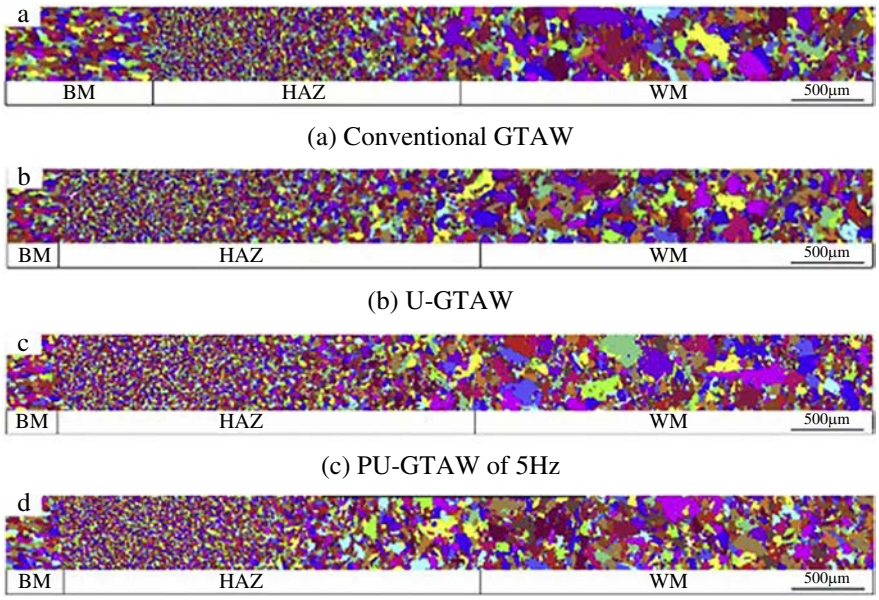


FIGURE 10.49 Grain distribution map of the cross-section of the welded joint (Chen et al., 2020, Fig. 3).

into the workpiece to a desired depth, then traverses along the weld line to the joint end. The heat from friction and plastic deformation softens and plasticizes the materials, which are intermixed under the stirring action of the pin and form the weld. Process disadvantages are known to be low welding speed and high welding force. Since materials are subject to severe plastic deformation at high strain rates and temperatures, possible benefits of superimposed ultrasonic vibrations have been explored both experimentally and numerically.

Different experimental approaches have been developed to introduce ultrasonic energy into FSW. Park (2009) applied a transverse ultrasonic vibration onto the FSW tool. Examination of the weld cross-section revealed that the wormhole defect was effectively removed under the ultrasonic assistance. Ji et al. (2016) applied a perpendicular ultrasonic vibration at the backing anvil during friction stir spot welding (FSSW) of AZ31 Mg alloy to 6061 Al alloy. Upward flow of the lower sheet material was enhanced and a better material mixing was achieved as was refinement of grain size.

Thomä et al. (2018) and Strass et al. (2014) applied a lateral ultrasonic vibration through the side of the workpiece into the weld interface, Figure 10.50. They performed

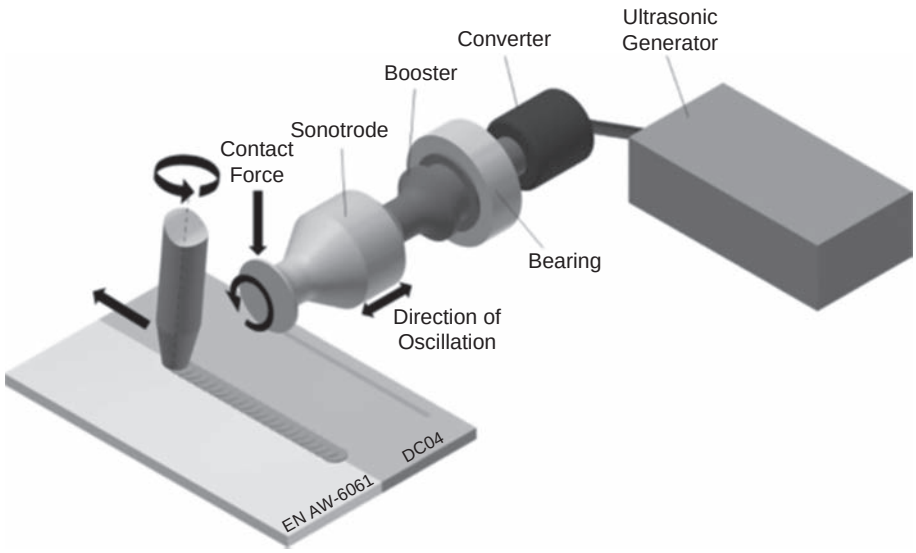


FIGURE 10.50 UA applied through the side of the workpiece during FSW (Thomä et al., 2018, Fig. 2).

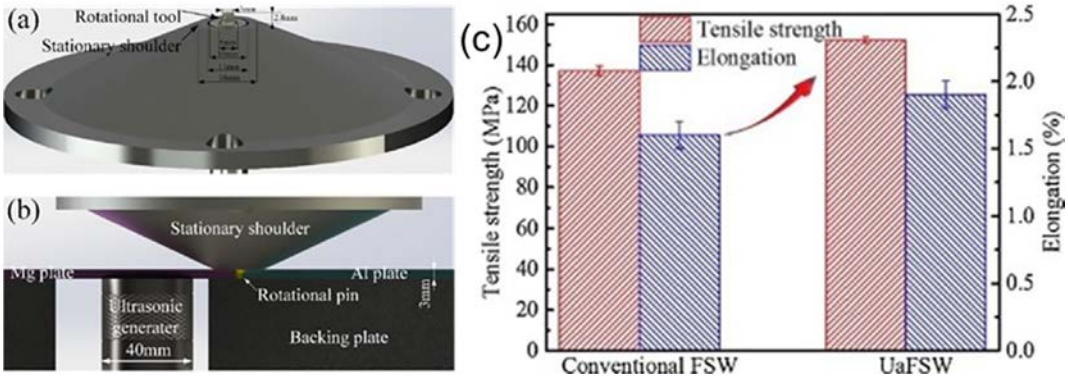


FIGURE 10.51 (a) FSW tool with stationary shoulder. (b) Ultrasonic vibration on the Mg plate. (c) Improved strength and ductility of UA FSW weld compared with conventional FSW weld between aluminum to magnesium alloy (Liu et al., 2018a, Figs. 1, 8).

ultrasonically assisted FSW of aluminum alloy to steel and showed a lesser amount of Al-Fe intermetallic particles with smaller sizes in the stirring zone. Alinaghian et al. (2018) designed an UA-FSW tool system which introduced ultrasonic vibrations in both longitudinal and bending modes. They performed UA FSW on Al alloy AA6061-T6 and observed a 24% reduction of longitudinal weld residual stress. Liu et al. (2018a,b) utilized a FSW tool with stationary shoulder and supplied UA at the bottom of the sheet away from the weld interface (Figure 10.51). Improved mechanical properties of the welds between AA6061-T6 and Mg alloy AZ31B and defect-free welds at low temperature were achieved.

The research group of Wu (Liu and Wu, 2015, 2016; Liu et al., 2015; Zhong et al., 2017) applied ultrasonic vibration on the workpiece in front of the FSW tool, as shown in Figure 10.52a and b as part of a comprehensive experimental analysis of the UA FSW process. The ultrasonic vibration reduced the welding force and torque, enlarged the volume of deformed material surrounding the pin, enhanced material flow, and increased the welding speed without generating wormhole defects. EBSD results from Padhy et al. (2016) showed more complete recrystallization and refined grains in UA FSW welds (Figure 10.53). They also reported that the ultrasonic contribution is maximum at the center of the stirring nugget and decays toward the outside layer of the nugget. Based on the same setup, Lv et al. (2017) performed UA FSW between aluminum AA6061-T4 and Mg alloy AZ31B-H24. The bi-layer Al-Mg intermetallic in conventional FSW welds is suppressed to a monolayer in UA FSW welds. With appropriate amount of ultrasonic energy, the intermetallic layer can be completely fragmented.

UA FSW models have also been developed to better understand the fundamental mechanisms of the hybrid process with regard to temperature, stress, and strain distribution. The computational fluid dynamics (CFD)-based model developed by Lai et al. (2014) applies ultrasonic vibration as an additional force boundary condition, which shows that the temperature is increased with ultrasonic vibration and the degree is more significant at a higher welding speed. Shi et al. (2015, 2016a,b) explicitly considered the ultrasonic softening effect on the material constitutive model with a softening coefficient in their CFD model. Their results show that UA enhances the plastic material flow in the vicinity of the tool and slightly increases the temperature profile. The calculated viscosity distribution indicates that a wider thermal mechanically affected zone (TMAZ) is in UA FSW, which agrees with the experimental results in Figure 10.54.

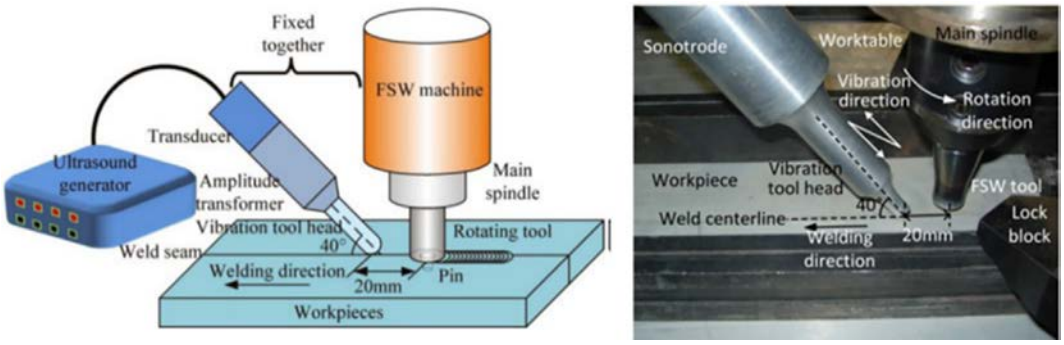


FIGURE 10.52 (a) Schematic of ultrasonic vibrations applied into the workpiece in front of the FSW tool. (b) Photo illustration of application of ultrasonic vibrations (Liu and Wu, 2015, Fig. 3).

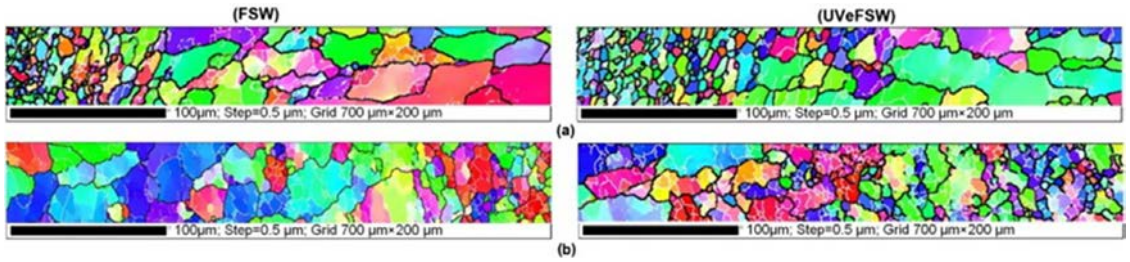


FIGURE 10.53 Grain microstructure comparison between conventional and UA FSW. (a) Advancing side: Stirring zone + TMAZ + HAZ. (b) Retreating side: HAZ + TMAZ + Stirring zone (Padhy et al., 2016, Fig. 8).

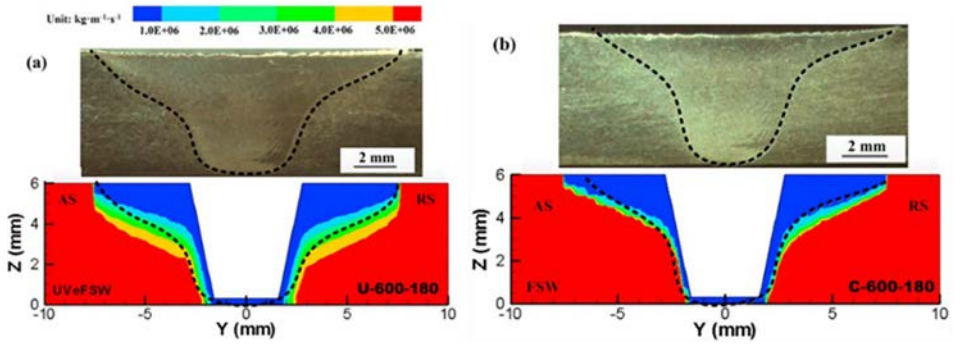


FIGURE 10.54 Optical microscopic images of the weld cross-section and CFD-simulated viscosity distribution in (a) UA FSW and (b) conventional FSW (Shi et al., 2015, Fig. 12).

In concluding this review of ultrasonics applied to FSW, reference is again made to the previously referenced work of Kumar et al. (2017) who has also discussed developments in this field.

10.9 Future trends

The future directions of ultrasonic metal welding are being driven by pushing back the current main boundaries of the process, which are (1) joint thicknesses, (2) weldable materials, and (3) joint types. The steps being taken in these directions, or that can be envisioned, are briefly summarized below.

10.9.1 System power and frequency

Most ultrasonic metal welders operate at 20 kHz and in the 2.5–3.5 kW range, with some now working in the 4–5 kW range. Such systems have been sufficient to achieve most of the results previously described, but also face limitations in joint thicknesses and materials that can be joined, as previously described. One area of future development will be the introduction of more powerful welding systems, with this being achieved by the development of more powerful transducers. Thus, 5–6 kW systems operating at 15 and 20 kHz are now becoming available on a select basis. This trend is expected to continue, with powers climbing to yet higher levels, potentially to 8–10 kW. An additional way of increasing the power of welders is to couple two or more additional transducers to the weld head, achieving an additive effect of the individual transducers. An example of this was shown for the case of the torsion welder, Figure 10.9, where two transducers were harnessed in a push-pull fashion. The design of coupling devices requires solution of a complex tool vibration problem but has been and is being done for special cases. Another example is the use of a two-transducer "push-pull" system for the UAM process (see Chapter 13). Yet another alternative being explored is to apply vibrations to both top and bottom of the workpieces, using two wedge-reed welding systems, with the Sonobond Corporation having shown such a system.

While increased power will meet some future needs, further development of higher frequency (i.e., greater than 20 kHz) systems will be needed to meet the increased array of small-scale applications such as in the electronics and medical fields. While 30–35–40 kHz welders are currently in use for such applications, moves to higher frequencies, already used in microbonding, will in no doubt continue.

10.9.2 Process controls and systems

Considerable attention is being given to in-process monitoring and controls and the mechanical aspects of the welding system, with this trend, being strongly driven by higher volume production needs for EV/HEV systems as well as increased light-weighting aluminum automotive

components, expected to continue. Improved controls are focused on measuring, recording, and reporting process conditions for purposes of quality control. Servomechanical (servo)-actuated systems are being increasingly used in place of pneumatic actuation of the weld head. This trend is leading to controlling force and motion within the weld cycle; in some cases breaking up the already short welding time (typically less than 1 s) into several programmed segments having different motion conditions. Finally, as noted in Section 10.3, movement of the weld head on linear bearings is now widely used.

10.9.3 Mechanism of ultrasonic welding

Over the years, as has been shown in some of the previous review, research has significantly advanced understanding of the ultrasonic metal welding process, both from a metallurgical and a mechanics perspective. Still, much remains to be done in several areas. Thus, the full range of the weldability of materials must be better understood, including specific procedure data on the various metallurgical combinations. This latter relates to development of benchmark welding procedures for some of the more common material combinations. An important development that is needed is providing a mechanics-based model of the welding process, with such a model relating welding and weld quality (e.g., weld strength) to measurable weld parameters, such as vibration amplitudes, forces, and power inputs. Some work has been accomplished here (e.g., de Vries, 2004; Gao and Doumanidis, 2002), but more remains to be done in order to provide methods of real-time monitoring and quality assurance.

10.9.4 Joint types

Some limited progress has occurred in this area, but progress may be slow in achieving welds in completely new joints. Achievement of butt welds has been reported, for example, by Tsujino et al. (1987), who has developed a means of creating a butt weld by clamping one part and creating a bending resonance in the second part, resulting in the friction-like vibration at the interfaces characteristic of the ultrasonic welding action. For small parts, butt welds have been made by attaching the small part to the vibrating weld tip. These developments notwithstanding, it is difficult to envision ultrasonic butt welds becoming a routine joint geometry. One may also inquire whether a concept of ultrasonic metal "far-field" welding might develop, such as is done in ultrasonic plastic welding, where vibrations are applied to a part at one location, and a weld created at a part interface some distance removed. If such were possible for metals, butt and tee joints would be feasible. However, no instances of such welds are known. It is believed that joint types for ultrasonic metal welding will largely remain restricted to lap-type configurations.

In summary, of the three areas of (1) joint thicknesses, (2) weldable materials, and (3) joint types, significant progress is expected in the first two, driven by more powerful welding systems and improved understanding of the ultrasonic welding mechanism, but with the process still having main application on lap-type joints.

10.9.5 Materials and tooling

The ultrasonic weldability of metallic materials has been reviewed in Section 10.4 and shown in the well-known chart of Figure 10.7. In that there are scant data to substantiate the varied entries of the chart, the chart, as noted, can at best serve simply as a beginning guideline as new applications and materials enter manufacturing. For example, the welding of plated metals, especially tin-plated materials, is particularly troublesome and more understanding is required for robust manufacturing processes. A systematic development of an ultrasonic metal welding database would greatly strengthen the use of this technology. Closely associated with any expansion in materials use will be the need for continued tooling design developments, specifically knurl patterns to impart stress to the components being welded, without cutting the metals or producing debris or particulates.

10.10 Sources of further information and advice

The numerous articles and books cited throughout this chapter are all potential sources of further information. Particular note should be made of chapters on ultrasonic metal welding that have appeared in previous handbooks, including the American Welding Society (Graff et al., 2007, AWS), ASM (Devine, 2011; Mitskevich, 1973). Of the several recent publications reviewed in Section 11.4, note is made to Hetrick et al. (2009), de Vries (2004), and the earlier edition of this chapter (Graff, 2005), which have excellent overviews of the technology, as well as extensive bibliographies that include many of the classical early references, and thus serve to expand on those cited here. Many equipment suppliers provide useful background on the process, with reference made to the websites of companies such as Branson Ultrasonics, Sonobond, Tech-Sonic, Stapla/Schunk, Telsonic, and Sonics and Materials.

References

Alinaghian, I., Honarpisheh, M., Amini, S., 2018. The influence of bending mode ultrasonic-assisted friction stir welding of Al-6061-T6 alloy on residual stress, welding force and macrostructure. Int. J. Adv. Manuf. Technol. 95 (5–8), 2757–2766.

Ando, M., Maeda, M., Takahashi, Y., 2013. Evolution of interfacial shear force during ultrasonic Al ribbon bonding. Mater. Trans. 54 (6), 911–915.

Annoni, M., Carboni, M., 2011a. Ultrasonic metal welding of AA 6022-T4 lap joints: part I—technological characterisation and static mechanical behaviour. Sci. Technol. Weld. Join. 16 (2), 107–115.

Annoni, M., Carboni, M., 2011b. Ultrasonic metal welding of AA 6022-T4 lap joints: part II—fatigue behaviour, failure analysis and modeling. Sci. Technol. Weld. Join. 16 (2), 116–125.

Bakavos, D., Prangnell, P.B., 2010. Mechanisms of joint and microstructure formation in high power ultrasonic spot welding 6111 aluminium automotive sheet. Mater. Sci. Eng. A A527, 6320–6334.

Bakavos, D., Chen, Y.-C., Prangnell, P.B., 2011. Mechanisms of joint formation in ultrasonic spot welding aluminium automotive sheet. In: Supplemental Proceedings: Materials Processing and Energy Materials. vol. 1. TMS (The Minerals, Metals & Materials Society), Warrendale, PA, pp. 735–742.

Bergmann, J.P., Regensburg, A., Schürer, R., Petzoldt, F., Herb, A., 2017. Effect of the interface characteristics on the joint properties and diffusion mechanisms during ultrasonic metal welding of Al/Cu. Weld. World 61, 499–506.

Bloss, M., Graff, K., 2009. Ultrasonic metal welding of advanced alloys: the weldability of stainless steel, titanium and nickel-based superalloys. In: David, S., et al. (Eds.), Trends in Welding Research, Proceedings of the 8th International Conference. ASM International, Metals Park, OH, pp. 348–353.

Brökelmann, M., Siepe, D., Hunstig, M., McKeown, M., Oftebro, K., 2015. Copper wire bonding ready for industrial mass production. In: IMAPS 2015 Orlando—48th Annual International Symposium on Microelectronics, October 26–29, 2015, pp. 000399–000405.

Cai, W.W., Kang, B., Hu, S.J., 2017. Ultrasonic Welding of Lithium-Ion Batteries. ASME Press.

Charles, H.K., 2010. The microelectronic wire bond: past, present, and future. In: IMAPS 2010—43rd International Symposium on Microelectronics, pp. 000462–000469.

Chen, Y.C., Bakavos, D., Gholinia, A., Prangnell, P.B., 2012. HAZ development and accelerated post-weld natural ageing in ultrasonic spot welding aluminium 6111-T4 automotive sheet. Acta Mater. 60, 2816–2828.

Chen, K.K., Zhang, Y.S., Wang, H.Z., 2016. Study of plastic deformation and interface friction process for ultrasonic welding. Sci. Technol. Weld. Join. 22 (3), 208–216.

Chen, C., Fan, C., Lin, S., Zhou, L., Yang, C., 2018. A new discovery of arc shape in pulsed ultrasonic wave assisted TIG welding. Phys. Plasmas 25, 080703.

Chen, J., Lim, Y.-C., Huang, H., Feng, Z., Sun, X., 2019. Ultrasonic welding of AZ31B magnesium alloy. MRS Bull. 44, 630–636.

Chen, C., Fan, C., Cai, X., Lin, S., Yang, C., Zhuo, Y., 2020. Microstructure and mechanical properties of Q235 steel welded joint in pulsed and unpulsed ultrasonic assisted gas tungsten arc welding. J. Mater. Process. Technol. 275, 116335.

Cheng, X., Li, X., 2007. Investigation of heat generation in ultrasonic metal welding using micro sensor arrays. J. Micromech. Microeng. 17, 273–282.

Dai, X., Zhang, H., Liu, J., Feng, J., 2015. Microstructure and properties of Mg/Al joint welded by gas tungsten arc welding-assisted hybrid ultrasonic seam welding. Mater. Des. 77, 65–71.

Dai, X., Zhang, H., Wang, B., Ji, A., Liu, J., Feng, J., 2016a. Improving weld strength of arc-assisted ultrasonic seam weld Mg/Al joint with Sn interlayer. Mater. Des. 98, 262–271.

Dai, X., Zhang, H., Zhang, J., Liu, J., Feng, J., 2016b. Arc assisted ultrasonic seam welding of Mg/Al joints with Zn interlayer. Mater. Sci. Technol. 12 (2), 164–172.

Dai, X., Zhang, H., Wang, B., Zhang, H., Liu, J., Feng, J., 2016c. Joining of magnesium and aluminum via arc-assisted ultrasonic seam welding with Sn/Zn composite interlayer. Mater. Lett. 176, 235–238.

de Vries, E., 2004. Mechanics and Mechanisms of Ultrasonic Metal Welding (Ph.D. dissertation). The Ohio State University, Columbus, OH.

Devine, J., 2011. Ultrasonic metal welding. In: Lienert, T., et al. (Eds.), ASM Handbook, vol. 6A: Welding Fundamentals and Processes. ASM International, Metals Park, OH.

Elangovan, S., Semeer, S., Prakasan, K., 2009. Temperature and stress distribution in ultrasonic metal welding—an FEA-based study. J. Mater. Process. Technol. 209, 1143–1150.

Fan, Y.Y., Yang, C.I., Lin, S.B., Fan, C.I., Wu, W.G., 2012. Ultrasonic wave assisted GTAW. Weld. J. 91, 91–99.

Fan, C., Xie, W., Yang, C., Lin, S., Fan, Y., 2017. Process stability of ultrasonic-wave-assisted gas metal arc welding. Metall. Mater. Trans. A 48A, 4615.

Gao, Y., Doumanidis, C., 2002. Mechanical analysis of ultrasonic bonding for rapid prototyping. J. Manuf. Sci. Eng. 124 (2), 426–434.

Graff, K.F., 1981. A history of ultrasonics. In: Mason, W.P., Thurston, R.N. (Eds.), Physical Acoustics. vol. 15. Academic Press, New York.

Graff, K.F., 2005. Ultrasonic metal welding. In: Ahmed, N. (Ed.), New Developments in Advanced Welding. Woodhead Publishing, Limited and CRC Press, New York.

Graff, K.F., 2011. Ultrasonic additive manufacturing. In: Lienert, T., et al. (Eds.), ASM Handbook, vol. 6A: Welding Fundamentals and Processes. ASM International, Metals Park, OH.

Graff, K.F., Devine, J.F., Keltos, J., Zhou, N.Y., 2007. Ultrasonic welding of metals. In: O'Brien, A.O. (Ed.), Welding Handbook, Welding Processes, Part 2, ninth ed. vol. 3. American Welding Society, Miami, FL, pp. 263–303.

Haddadi, F., Tsivoulas, D., 2016. Grain structure, texture and mechanical property evolution of automotive aluminium sheet during high power ultrasonic welding. Mater. Charact. 118, 340–351.

Haddadi, F., Strong, D., Prangnell, P.B., 2012. Effect of zinc coatings on joint properties and interfacial reactions in aluminum to steel ultrasonic spot welding. J. Mater. 64 (3), 407–413.

Han, Y., Li, K., Wang, J., Shu, D., Sun, B., 2005. Influence of high-frequency ultrasound on grain refinement performance of Al-5Ti-1B master alloy on aluminum. Mater. Sci. Eng. A 405, 306–312.

Harman, G., 2010. Wire Bonding in Microelectronics, third ed. McGraw-Hill.

Hetrick, E.T., Baer, J.R., Zhu, W., Reatherford, L.V., Grima, A.J., Scholl, D.E., Wilkosz, D.E., Fatima, S., Ward, S.M., 2009. Ultrasonic metal welding process robustness in aluminum automotive body construction applications. Weld. J. 88, 149s–158s.

Huang, H., Chen, J., Lim, Y.-C., Hu, X., Cheng, J., Feng, Z., Sun, X., 2019. Heat generation and deformation in ultrasonic welding of magnesium alloy AZ31. J. Mater. Process. Technol. 272, 125–136.

Ji, S., Li, Z., Ma, L., Yue, Y., Gao, S., 2016. Investigation of ultrasonic assisted friction stir spot welding of magnesium alloy to aluminum alloy. Strength Mater. 48 (1), 2–7.

Kawauchi, T., Onda, M., Matsuo, K., Kawamura, Y., Shiotani, Y., Sakai, N., 2014. The wire harness. In: Encyclopedia of Automotive Engineering. John Wiley & Sons, Ltd.

Kumar, J.P., 2018. Effect of temperature distribution in ultrasonically welded joints of copper wire and sheet used for electrical contacts. Materials 11 (1010), 1–13.

Kumar, S., Wu, C.S., Padhy, G.K., Ding, W., 2017. Application of ultrasonic vibrations in welding and metal processing: a status review. J. Manuf. Process. 26, 295–322.

Lai, R., Diqiu, H., Luocheng, L., Shaoyong, Y., Kunyu, Y., 2014. A study of the temperature field during ultrasonic-assisted friction-stir welding. Int. J. Adv. Manuf. Technol. 73 (1–4), 321–327.

Lee, S., Shao, C., Kim, T., Hu, S., Kannatey-Asibu, E., Cai, W., Spicer, J., Abell, J., 2014. Characterization of ultrasonic metal welding by correlating online sensor signals with weld attributes. J. Manuf. Sci. Eng. 136, 1–10.

Li, C., 2019. Effects of welding pressure on high-power ultrasonic spot welding of Cu/Al dissimilar metals. J. Manuf. Process. 46, 194–203.

Li, H., Cao, B., Yang, J.W., Liu, J., 2018. Modeling of resistance heat assisted ultrasonic welding of Cu-Al joint. J. Mater. Process. Technol. 256, 121–130.

Lindamood, L., 2019. Ultrasonic weld monitoring progress at EWI. In: EWI Technical Insights.

Lindamood, L., Workman, D., Gould, J., 2018. Development of a hybrid ultrasonic-resistance spot welding system for aluminum sheet. Mater. Sci. Technol., 844–851.

Liu, X., Wu, C., 2015. Material flow in ultrasonic vibration enhanced friction stir welding. J. Mater. Process. Technol. 225, 32–44.

Liu, X., Wu, C., 2016. Elimination of tunnel defect in ultrasonic vibration enhanced friction stir welding. Mater. Des. 90, 350–358.

Liu, X., Wu, C., Padhy, G.K., 2015. Characterization of plastic deformation and material flow in ultrasonic vibration enhanced friction stir welding. Scr. Mater. 102, 95–98.

Liu, Z., Meng, X., Ji, S., Li, Z., Wang, L., 2018a. Improving tensile properties of Al/Mg joint by smashing intermetallic compounds via ultrasonic-assisted stationary shoulder friction stir welding. J. Manuf. Process. 31, 552–559.

Liu, Z., Ji, S., Meng, X., 2018b. Joining of magnesium and aluminum alloys via ultrasonic assisted friction stir welding at low temperature. Int. J. Adv. Manuf. Technol. 97 (9–12), 4127–4136.

Lu, Y., Zhang, K., Tran, J., Mayton, E., Kimchi, M., Zhang, W., 2019a. Optimizing ultrasonic plus resistance spot welding for dissimilar metal joining. Weld. J. 98, 273–283.

Lu, Y., Mayton, E., Song, H., Kimchi, M., Zhang, W., 2019b. Dissimilar metal joining of aluminum to steel by ultrasonic plus resistance spot welding—microstructure and mechanical properties. Mater. Des. 165.

Lu, Y., Sage, D.D., Fink, C., Zhang, W., 2020. Dissimilar metal joining of aluminium to zinc-coated steel by ultrasonic plus resistance spot welding—microstructure and mechanical properties. Sci. Technol. Weld. Join. 25 (3), 218–227. https://doi.org/10.1080/13621718.2019.1667051.

Lv, X., Wu, C., Padhy, G., 2017. Diminishing intermetallic compound layer in ultrasonic vibration enhanced friction stir welding of aluminum alloy to magnesium alloy. Mater. Lett. 203, 81–84.

Macwan, A., Mirza, F.A., Bhole, S.D., Chen, D.L., 2016. Similar and dissimilar ultrasonic spot welding of 5754 aluminum alloy for automotive applications. Mater. Sci. Forum 877, 561–568.

Mariam, H., Baer, J.R., Scholl, D.J., Cooper, R.P., Wilkosz, D.E., Grima, A. J., Reatherford, L.V., 2007. Ultrasonic welding of aluminum 6111—reliability and maintainability study of robot mounted C-gun welding system. In: Proceedings of IMECE2007, ASME International Mechanical Engineering Congress and Exposition, November 11–15, 2007. ASME, New York, NY, pp. 689–697.

Matheny, M., 2012. Ultrasonic metal welding foils to tabs for lithium-ion battery cells. EWI Summary Report SR1301.

Mitskevich, A., 1973. Ultrasonic welding of metals. In: Rozenberg, L.D. (Ed.), Physical Principles of Ultrasonic Technology, Part 2. vol. 1. Plenum Press, New York.

Mostafavi, S., Hesser, D.F., Markert, B., 2019. Detection of terminal oscillation pattern in ultrasonic metal welding. J. Manuf. Process. 41, 159–167.

Padhy, G.K., Wu, C.S., Gao, S., Shi, L., 2016. Local microstructure evolution in Al 6061-T6 friction stir weld nugget enhanced by ultrasonic vibration. Mater. Des. 92, 710–723.

Panteli, A., Robson, J.D., Brough, I., Prangnell, P.B., 2012. The effect of high strain rate deformation on intermetallic reaction during ultrasonic welding aluminium to magnesium. Mater. Sci. Eng. A 556, 31–42.

Park, K., 2009. Development and Analysis of Ultrasonic Assisted Friction Stir Welding Process (Ph.D. diss.). Department of Mechanical Engineering, University of Michigan, Ann Arbor.

Patel, V.K., Bhole, S.D., Chen, D.L., 2013. Formation of zinc interlayer texture during dissimilar ultrasonic spot welding of magnesium and high strength low alloy steel. Mater. Des. 45, 236–240.

Prangnell, P., Haddadi, F., Chen, Y.C., 2011. Ultrasonic spot welding of aluminium to steel for automotive applications—microstructure and optimization. Mater. Sci. Technol. 27 (3), 617–624.

Qiao, J., Wu, C.S., Li, Y., 2020. Numerical and experimental investigation of keyholing process in ultrasonic vibration assisted plasma arc welding. J. Manuf. Process. 50, 603–613.

Satpathy, M.P., Sahoo, S.K., 2017. Mechanical performance and metallurgical characterization of ultrasonically welded dissimilar joints. J. Manuf. Process. 25, 443–451.

Shah, U.H., Liu, X., 2019a. Ultrasonic resistance welding of TRIP-780 steel. J. Mater. Process. Technol. 274, 116287.

Shah, U., Liu, X., 2019b. Effects of ultrasonic vibration on resistance spot welding of transformation induced plasticity steel 780 to aluminum alloy AA6061. Mater. Des. 182, 108053.

Shen, N., Samanta, A., Ding, H., Cai, W.W., 2016. Simulating microstructure evolution of battery tabs during ultrasonic welding. J. Manuf. Process. 23, 306–314.

Shi, L., Wu, C., Liu, X., 2015. Modeling the effects of ultrasonic vibration on friction stir welding. J. Mater. Process. Technol. 222, 91–102.

Shi, L., Wu, C., Gao, S., Padhy, G., 2016a. Modified constitutive equation for use in modeling the ultrasonic vibration enhanced friction stir welding process. Scr. Mater. 119, 21–26.

Shi, L., Wu, C., Padhy, G., Gao, S., 2016b. Numerical simulation of ultrasonic field and its acoustoplastic influence on friction stir welding. Mater. Des. 104, 102–115.

Strass, B., Wagner, G., Eifler, D., 2014. Realization of Al/Mg-hybrid-joints by ultrasound supported friction stir welding. Mater. Sci. Forum 783–786, 1814–1819.

Sun, Q.J., Lin, S.B., Yang, C.I., Zhao, G.Q., 2009. Penetration increase of AISI 304 using ultrasonic assisted tungsten inert gas welding. Sci. Technol. Weld. Join. 14, 765–767.

Takahashi, Y., Suzuki, S., Ohyama, Y., Maeda, M., 2012. Numerical analysis of interfacial deformation and temperature rise during ultrasonic Al ribbon bonding. J. Phys. Conf. Ser. 379, 1–12.

Thavamani, R., Balusamy, V., Nampoothiri, J., Subramanian, R., Ravi, K. R., 2018. Mitigation of hot cracking in Inconel 718 superalloy by ultrasonic vibration during gas tungsten arc welding. J. Alloys Compd. 740, 870–878.

Thomä, M., Wagner, G., Straß, B., Wolter, B., Benfer, S., Fürbeth, W., 2018. Ultrasound enhanced friction stir welding of aluminum and steel: process and properties of EN AW 6061/DC04-joints. J. Mater. Sci. Technol. 34 (1), 163–172.

Tsujino, J., Ueoka, T., Umemori, N., Fujisawa, H., Sugiyama, A., 1987. Ultrasonic butt welding of metal materials. In: Ultrasonic International 87 Conference Proceedings. Elsevier, The Netherlands, p. 315.

Voight, A.L., Vieira da Cunha, T., 2018. Effects of ultrasonic pulsation of the welding current on the geometry of the fusion zone and heat-affected zone in submerged arc welding. Weld. Int. 32 (3), 172–178.

Wang, J., Sun, Q., Liu, J., Wang, B., Feng, J., 2017. Effect of pulsed ultrasonic on arc acoustic bindging in pulsed ultrasonic wave assisted pulsed gas tungsten arc welding. Sci. Technol. Weld. Join. 22 (6), 465–471.

Ward, Zhang, Cordero, 2018. Junction growth in ultrasonic spot welding and ultrasonic additive manufacturing. Acta Mater. 158, 393–406.

Watanabe, T., Itoh, H., Yanagisawa, A., Hiraishi, M., 2009. Ultrasonic welding of heat-treatable aluminium alloy A6061 sheet. Weld. Int. 23 (9), 633–639.

Xie, W., Fan, C., Yang, C., Lin, S., 2016. Effect of acoustic field parameters on arc acoustic binding during ultrasonic wave-assisted arc welding. Ultrason. Sonochem. 29, 476–484.

Xie, W., Chenglei, F., Yang, C., Lin, S., 2018. Experimental investigation on acoustic control droplet transfer in ultrasonic-wave-assisted gas metal arc welding. Metall. Mater. Trans. B 49B, 274.

Yang, J., Cao, B., 2015. Investigation of resistance heat assisted ultrasonic welding of 6061 aluminum alloys to pure copper. Mater. Des. 74, 19–24.

Zhao, J., Li, H., Choi, H., Cai, W., Abell, J.A., Li, X., 2013. Insertable thin film thermocouples for in situ transient temperature monitoring in ultrasonic metal welding of battery tabs. J. Manuf. Process. 15, 136–140.

Zhong, Y., Wu, C., Padhy, G., 2017. Effect of ultrasonic vibration on welding load, temperature and material flow in friction stir welding. J. Mater. Process. Technol. 239, 273–283.

Chapter 11

Ultrasonic welding of plastics and polymeric composites

A. Benatar[a] and M. Marcus[b]
[a]*The Ohio State University, Columbus, OH, United States,* [b]*EWI, Columbus, OH, United States*

11.1 Introduction

Ultrasonic welding is popular for joining thermoplastics because it is fast (typical cycle time ranges from a fraction of a second to a few seconds), easily automated, and the equipment is relatively inexpensive. Typical operating frequencies range from 10 to 70 kHz, although 20 kHz is the most common, with amplitude of vibration ranging from 0.1 to 100 μm. Ultrasonic welding can be used to join amorphous and semi-crystalline thermoplastics as well as thermoplastic composites. While it is usually used in mass production, ultrasonic welding can also be used in small-lot production with flexible fixturing and interchangeable horns.

In ultrasonic welding of thermoplastics and thermoplastic composites, high-frequency and low-amplitude mechanical vibrations are used to generate heating, melting, and welding or fusion bonding of components. Once surfaces melt, squeeze flow occurs under the pressure producing intimate contact followed by intermolecular diffusion and entanglement of the polymer macromolecules. After the vibration is stopped, the joint cools under pressure until the melt solidifies resulting in a weld.

The typical plunge-style ultrasonic process can be considered to have seven stages, as described in Figure 11.1. No work is being done to the parts in stages I, II, and VII. During stage I, the parts are loaded into the fixture. The lower part is fixed in place, while the upper part is loosely rested on top. Once the parts are loaded in the welder, the start signal is activated, either by pushing manual buttons or activating a remote signal—such as for an automated process. During stage II, the horn travels downward to contact the parts. This is followed by stages III, IV, V, and VI, which make up the core of the welding process. Lastly, at the end of the programmed hold time, the horn retracts from the parts during stage VII.

Various types of work are being done to the plastic assembly during stages III, IV, V, and VI. Graphs detailing which type of work is performed during each stage are provided in Figure 11.2. These graphs have been split roughly to show relative timescale of each stage. It is important to note that stages III and IV have a much shorter time periods than the loading, melting, and hold stages. However, they are disproportionally wide on the timescale to provide clarity in the plastic welding process stages.

Stage III typically lasts 0.01–0.05 s. During this stage, an increasing load is applied to the plastic. This load is intended to be sufficient to ensure intimate contact but insufficient to deform the part. If using a pneumatic welder, a load cell is used to detect when the trigger force is reached, and then the program starts with initiating the ultrasonic vibration and counting toward the set weld time, or collapse distance, or energy—depending on the control mode selected. If using a servo welder, after the load cell detects part contact, as indicated by reaching the programmed trigger force, downward motion may be paused for the duration of stage IV.

Stage IV typically lasts 0.01–0.1 s. During this stage, ultrasonic vibrations and force are applied simultaneously. This stage ends once melting has been initiated, at which point the welding stage begins which involves displacement in the melt zone.

If using a pneumatic welder, the force continues to increase from the trigger force to the full set weld force while the ultrasonic energy is applied. As the material softens, or after it melts, this load becomes sufficient to squeeze the softened or melted material, with some of the melt being squeezed out of the weld region. For welding to occur, this displacement should begin once the polymer has melted. If the weld force is set high enough to allow deformation at higher viscosity (or closer to a solid state), insufficient melt will form to allow good intermolecular diffusion which may result in a weaker weld. This is especially a concern for amorphous materials where the transition between solid state and liquid state is more gradual.

If using a servowelder with constant force and/or displacement controls, the program can be set so that when

Power Ultrasonics. https://doi.org/10.1016/B978-0-12-820254-8.00006-3
Copyright © 2023 Elsevier Ltd. All rights reserved.

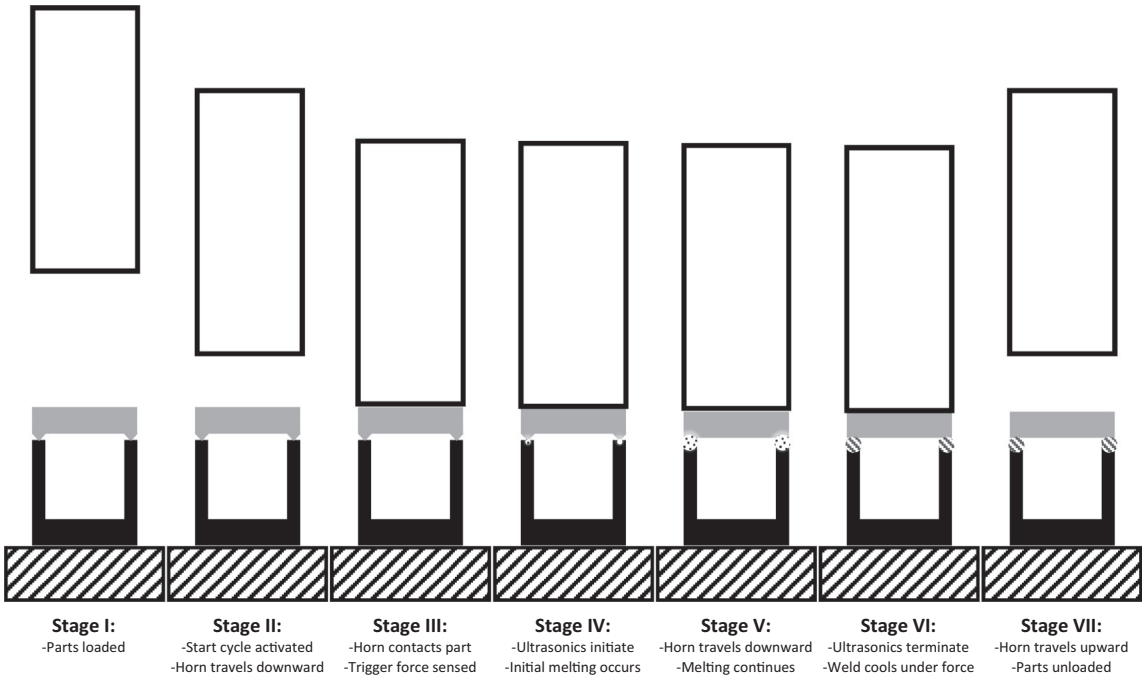


FIGURE 11.1 Stages for an ultrasonic plunge weld.

the trigger force is reached, the downward motion is stopped and the ultrasonic energy is initiated. During this time, the primary work acting on the plastic part is the ultrasonic vibration energy. By this way, when a drop in force is detected, it indicates that melting of the energy director started, and the weld head displacement can be controlled. This trigger force range is an area requiring further characterization, but it may be a less critical setting. The objective is to ensure enough force is used to displace the energy director gradually after it is fully melted to better control the flow.

Stage V typically lasts 0.5–2 s. During this stage, ultrasonic vibration and downward motion are applied simultaneously. If using a pneumatic welder, downward motion is applied via the constant set weld force.

If using a servowelder, downward motion is applied via a constant velocity or a preprogrammed velocity profile. Potentially, the speed could be programmed to be high enough to cause mechanical deformation. However, doing so will lead to a weaker weld.

Stage VI typically lasts 0.1–0.5 s. Once full programmed collapse (or weld time or energy) is reached, then the ultrasonics are deactivated. The hold time ensures there is enough force during cooling to prevent cracking or voids as the melt cools, which may occur in polymers where the material shrinks on solidification. Shrinking during cooling could cause some tensile force on the newly formed, and not fully cooled, weld.

If using a pneumatic welder, a hold force is applied, which can be the same or different from the weld force. Since most plastics shrink when cooled, it is expected that some additional collapse will occur. The force should be set high enough to support this collapse without mechanically deforming the parts or squeezing out all the melt.

If using a servo welder, there are additional options for hold time. Similar to using a pneumatic welder, some additional collapse of the part can be programmed to occur to a set distance with a set velocity. It may even be possible to calculate the hold settings to approximately match the solidification rate of the polymer and its associated shrink rate. Another option is to program the press to stay in a single location and not apply any downward motion for a set period. This simply delays the time before the part is handled without any additional compression.

11.2 History

As noted in Chapter 1 of this book, the field of ultrasonics can be traced back to the 1800s. The use of ultrasonics to weld plastics, however, is much more recent. In the early 1960s, ultrasonic welding of polymer films had already been established, but the technology was not applied to molded plastics until Bob Soloff accidentally touched an ultrasonic probe to a tape dispenser and noted that the plastic housing melted (Lupo, 2017). This observation led to the first ever paper on ultrasonic welding of molded plastic parts, which was published in Modern Plastics magazine in 1964 (Lupo) and provided some initial insight into the process (Figure 11.3).

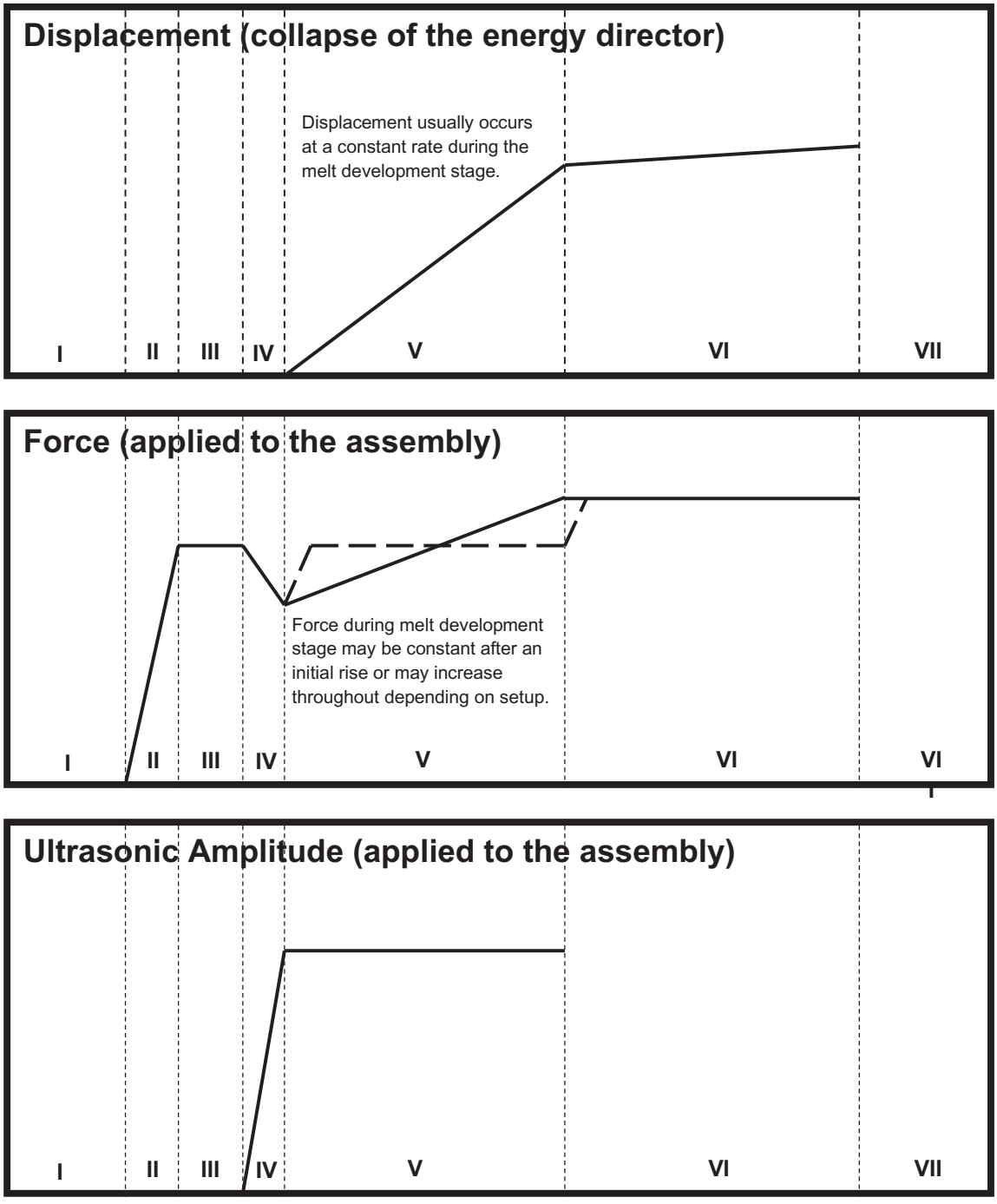


FIGURE 11.2 Typical time graphs for displacement, force, and vibration amplitude for an ultrasonic plunge weld.

The original caption of this early figure reads: *Idealized sketch shows how ultrasonic waves of energy travel through a transparent plastic box. Waves reaching the joint create vibrations which in turn create friction and subsequent conversion of mechanical energy into heat, welding the joint surfaces*. While it was initially hypothesized that the heating mechanism was due to frictional heating, it is now known that the primary heating mechanism for ultrasonic plastic welding is from internal losses due to inefficient transfer of vibrations through the viscoelastic polymer. The viscous portion of the polymeric materials absorbs part of the mechanical motions, and this lost mechanical energy is converted to heat.

Despite early misconceptions about the heating mechanism, early observations of the relative ease of welding different polymeric materials continue to hold true today.

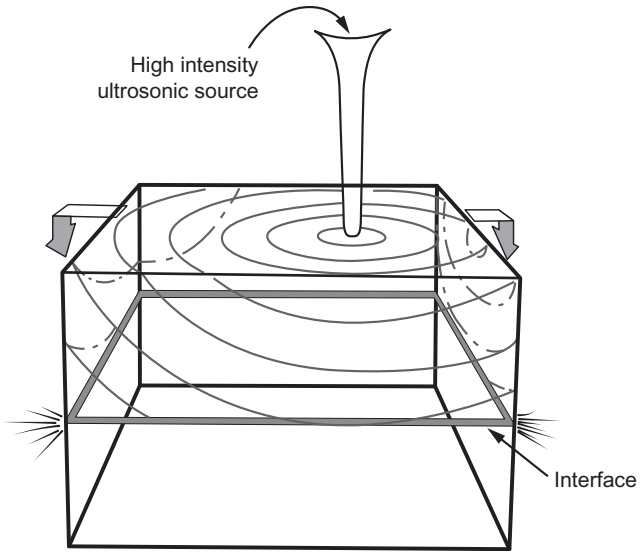


FIGURE 11.3 Initial insight into ultrasonic welding of plastics. *(Adapted from Lupo (1964)).*

Initial investigations showed that materials with a high modulus of elasticity and low melting temperature worked especially well with the ultrasonic heating process. Table 11.1 shows some relevant material properties along with a basic estimation of how easily that material is weldable with ultrasonics; data from the original 1964 Lupo paper.

In 1984, Potente showed how the transfer of the ultrasonic wave through a polymer rod was affected by the wavelength in the plastic. Figure 11.4 shows a fringe pattern that illustrates a standing wave in a plastic rod vibrated ultrasonically against a steel support. The locations marked are where the greatest strain amplitude of vibration occurs and would be where the polymer will melt, given sufficient amplitude or time. The first high strain amplitude zone appears at one-quarter wavelength, the second at three-quarters wavelength, and it can be extrapolated that high strain amplitude would occur at $(n/4)\bullet\lambda$, where λ is the wavelength of the ultrasonic wave in the plastic material, and n is the odd integer ($n = 1, 3, 5, 7$, etc.).

11.3 Theory of the ultrasonic welding process

Ultrasonic welding of thermoplastics and thermoplastic composites is a complex process where cyclical deformation results in localized heating and fusion bonding at the faying surfaces. Benatar and Gutowski (1989) described ultrasonic welding as consisting of six distinct but highly coupled sub-processes that include mechanics and vibrations of the parts, viscoelastic heating of the thermoplastic, heat transfer, squeeze flow and wetting, intermolecular diffusion and chain entanglement, and cooling and resolidification of the interface. While mechanics and vibrations of the parts and viscoelastic heating are somewhat unique to ultrasonic welding, the remaining sub-processes are common to all plastic welding methods (see Benatar, 2003).

11.3.1 Viscoelastic heating of polymers

For a linear viscous material (represented as a damper or dashpot), the force is linearly proportional to the velocity or stress is linearly proportional to the strain rate, as

TABLE 11.1 Weldability of polymers

Material	Modulus of elasticity (10^5 psi)	Melting temperature (°F)	Specific heat	Distance to joint	
				Near-field	Far-field
Polystyrene	4.0–5.0	325–600	0.32	E	E
Acrylonitrile butadiene styrene	1.0–4.1	350–600	0.33–0.40	E	E
Polycarbonate	3.2	525–600	0.30	E	E
Polypropylene	1.6–2.0	390–580	0.46	E	P
Polyethylene	0.6–1.5	300–600	0.55	E	P
Polyamide, 6/6	2.6–4.0	470–720	0.40	E	E
Polyvinyl chloride	3.5–6.0	300–400	0.20–0.28	E	E
Polymethyl methacrylate	4.5	325–500	0.35	G	P

E, excellent; *G*, good; *P*, poor.

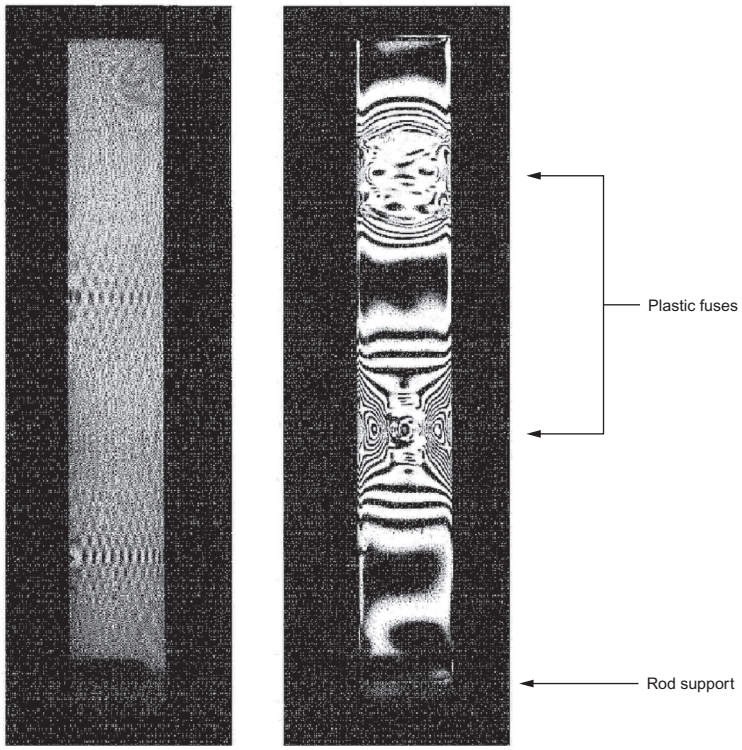


FIGURE 11.4 Fringe patterns of showing the standing wave and weld locations in a plastic rod. *Adapted from Potente (1984).*

described in Eq. (11.1). When a viscous material is subjected to cyclical loading, the force and velocity are in phase, while the force and displacement are 90 degrees out of phase. Therefore, all the power that is applied to a viscous material is dissipated in the form of heat.

$$F = bV \quad \text{or } \sigma = \eta\dot{\varepsilon} \tag{11.1}$$

where F is the force, b is the damping coefficient, V is the velocity, σ is the stress, η is the viscosity and $\dot{\varepsilon}$ is the strain rate.

For a linear elastic material (represented as a spring), the force is linearly proportional to displacement or stress is linearly proportional to strain, as described in Eq. (11.2). When an elastic material is subjected to cyclical loading, the force and velocity are 90 degrees out of phase, while the force and displacement are in phase. Therefore, for an ideal elastic material, the power that is applied during half of the cycle is stored and then recovered during the second half of the cycle resulting in no net power dissipation.

$$F = kx \quad \text{or } \sigma = E\varepsilon \tag{11.2}$$

where k is the spring constant, x is the displacement, E is the elastic modulus, and ε is the strain.

For small deformations, such as are present in ultrasonic welding, a linear viscoelastic model of the polymer behavior can be used. Linear viscoelastic materials can be represented as combinations of springs and dashpots (Ferry, 1980), since they exhibit behavior that is a combination of elastic and viscous materials. As shown in Figure 11.5, one of the simplest representations of a viscoelastic solid material is the Voigt-Kelvin model, with a spring and dashpot in parallel with each other. In this case, the relationship between stress and strain can be represented using a complex dynamic modulus, as shown in Eq. (11.3).

$$\sigma = E^{*}\varepsilon \tag{11.3}$$

where E^{*} is the complex modulus:

$$E^{*} = E' + iE'' \tag{11.4}$$

where E' is the storage modulus and E'' is the loss modulus.

The storage and loss moduli are related to the elastic modulus of the spring and viscosity of the dashpot in a Voigt-Kelvin solid using the following relations:

$$E = E' \tag{11.5}$$

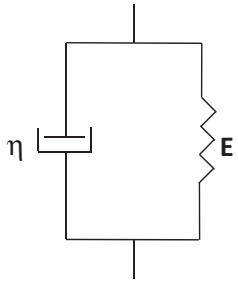


FIGURE 11.5 Voigt-Kelvin model of a viscoelastic material.

$$\eta = \frac{E''}{\omega} \tag{11.6}$$

where ω is the radial frequency.

In this case, the stress and strain would be out of phase by some angle that is smaller than 90 degrees depending on the magnitude of the storage and loss moduli, where the phase shift angle, δ, is determine from the loss tangent,

$$\tan\ \delta = \frac{E'}{E''} \tag{11.7}$$

Some portion of the ultrasonic vibrations will be transmitted or recovered through the elastic portion of the polymer, and some will be absorbed in the viscous portion. The absorbed energy is dissipated as heat. The storage modulus is related to the energy that is transmitted or recovered, and the loss modulus is related to the energy that is dissipated as heat.

Work is a measure of the energy input or output of a system. In the case of ultrasonic vibration of a polymer, the energy input into the joint of the plastic part is due to the mechanical deformations caused by the ultrasonic vibrations. Work is defined as

$$W = Fd \tag{11.8}$$

where F is the force applied, and d is the displacement over which the force is applied.

Stress is also defined as:

$$\sigma = F/a \tag{11.9}$$

where σ is the stress, F is the force being applied, and a is the area over which it acts.

Strain is defined as

$$\epsilon = \frac{\Delta x}{L} \tag{11.10}$$

where Δx is the change in length or displacement, and L is the length.

Eqs. (11.8)–(11.10) can be combined:

$$\frac{W}{aL} = \sigma * \varepsilon \tag{11.11}$$

where W is work, σ is the stress, and ε is the strain.

To find the work per volume per vibration cycle, the stress and strain are integrated over a single cycle, 0 to $2\pi/\omega$:

$$\frac{W}{V} = \int_0^{\frac{2\pi}{\omega}} \sigma\, d\varepsilon\, dt \tag{11.12}$$

where $V = aL$ is the volume.

As shown by Benatar and Gutowski (1989), for sinusoidal ultrasonic vibration, the work done in one cycle is

$$\frac{W}{V} = \pi E'' \varepsilon_0^2 \tag{11.13}$$

where ε_0 is the strain amplitude. To find the average power dissipated per unit volume or internal heat generation rate, the work done in one cycle is divided by the period of one cycle, giving,

$$\dot{Q} = \frac{P}{V} = \frac{\pi E'' \varepsilon_0^2}{\frac{2\pi}{\omega}} = \frac{\omega E'' \varepsilon_0^2}{2} \tag{11.14}$$

where $\dot{Q}$ is the internal heat generation rate and P is the power.

Assuming that most of the deformation occurs in the energy director, the strain amplitude generated during ultrasonic welding is typically approximated, per Eq. (11.10), as the amplitude of vibration (Δx) divided by the energy director height (L).

11.3.2 Wave propagation in polymers

As described above, because the polymer is viscoelastic, some of the vibration energy is dissipated as heat. While the heating is concentrated at the joint interface due to the high stress and strain experienced by the energy director, energy is being dissipated throughout the entire part. Therefore, not all the amplitude produced by the ultrasonic horn is transmitted to the weld interface. This loss in vibration amplitude is typically called attenuation.

For simplicity, consider the propagation of harmonic waves in a semi-infinite slender bar (extending from the origin in the positive x-direction) of a linear viscoelastic solid. Using the "correspondence principle," the 1-D wave equation for a linear viscoelastic bar is (Bland, 1980)

$$E^* \frac{\partial^2 u}{\partial x^2} = \rho \frac{\partial^2 u}{\partial t^2} \tag{11.15}$$

where u is the displacement in the x-direction and ρ is the density. For harmonic waves, the general solution to Eq. (11.15) is (Christensen, 1980)

$$u(x, t) = u_0 e^{-iw\left(\frac{x}{\sqrt{\rho/E^*}} - t\right)} \tag{11.16}$$

where u_0 is the input displacement amplitude at $x = 0$. Using Eq. (11.4) in Eq. (11.16) simplifies it to (Benatar and Cheng, 1989)

$$u(x, t) = u_0 e^{-\alpha x} e^{-i\omega\left(\frac{x}{V} - t\right)} \tag{11.17}$$

where $u(x,t)$ is the amplitude of the wave as a function of time, t, and distance, x, from the horn contact surface, u_0 is the amplitude at $x = 0$ (at the horn contact surface), ω is the frequency in radians ($2\pi f$), and α is the attenuation:

$$\alpha = \frac{\omega\sqrt{\rho} E''}{|E^*|} \tag{11.18}$$

and V is the phase velocity (m/s):

$$V = \frac{|E^*|}{\sqrt{\rho E^{III}}} \tag{11.19}$$

where ρ is the density, and E^{III} and E^{IV} are related to loss and storage modulus:

$$E^{III} - iE^{IV} = \sqrt{E' - iE''} \tag{11.20}$$

$$E^{III} = \sqrt{|E^*|}\cos\left(\frac{\delta}{2}\right) \tag{11.21}$$

$$E^{IV} = \sqrt{|E^*|}\sin\left(\frac{\delta}{2}\right) \tag{11.22}$$

As shown in the plot of Eq. (11.17) in Figure 11.6, the harmonic wave attenuates as it propagates along the viscoelastic bar due to the attenuation term in the first exponent on the right hand side, which depends on E^{IV} which is related to the loss modulus. Therefore, the length of slender viscoelastic bars that are excited by the ultrasonic horn at one end should be selected such that the other end with the energy director is at a displacement antinode. To maximize the amplitude of vibration experienced by the energy director, these bars should have lengths that are multiples of half a wavelength at the operating frequency (Menges and Potente, 1971; Sovetov et al., 1976). However, the longer these bars are or the larger the loss modulus then the smaller the amplitude will be at the energy director end due to viscoelastic attenuation in the bar.

For the purpose of predicting heat generation, only the maximum peak-to-peak amplitude is needed, so Eq. (11.17) can be simplified to disregard the cyclical oscillation portion. Considering this and applying Euler's relation to eliminate the imaginary component, the phase shift portion of the equation can be simplified:

$$e^{-i\omega\left(\frac{x}{V}-t\right)} = \cos\left(\frac{-\omega}{V}x\right) \tag{11.23}$$

where t is time, x is distance from the horn contact surface, ω is the frequency in radians ($2\pi f$), and V is the phase velocity.

By combining Eqs. (11.21)–(11.23), the following simplified equation is found that accounts for phase shift and attenuation over time in terms of the measured material properties of loss modulus, storage modulus, and density, along with the process parameters of frequency and amplitude and distance from the horn contact surface to the joint:

$$A(x) = A_0 \cos(Dx\cos\phi)e^{(Dx\sin\phi)} \tag{11.24}$$

where $A(x)$ is the maximum amplitude as a function of distance into the material, A_0 is the maximum amplitude at the horn contact surface, ϕ is the unitless phase shift factor:

$$\phi = \frac{\delta}{2} = \frac{1}{2}\tan^{-1}\frac{E''}{E'} \tag{11.25}$$

and D is the damping coefficient:

$$D = \frac{-\omega\sqrt{\rho}}{\sqrt{|E^*|}} \tag{11.26}$$

A graph of the attenuation for polycarbonate and polybutylene terephthalate, using Eq. (11.24) and previously measured material properties (Marcus et al., 2013), is shown in Figure 11.7.

An alternative method of calculating the loss in ultrasonic energy as the wave travels through an ultrasonic part is given by Sancaktar (1999):

$$T_r = \frac{F_t}{F_0} = \frac{\left[E^2 + (\eta\omega_f)^2\right]^{1/2}}{\left[(E - m\omega_f{}^2)^2 + (\eta\omega_f)^2\right]^{1/2}} \tag{11.27}$$

where T_r is transmissibility, F_t is transmitted force, F_0 is exciting force, E is the modulus, η is viscosity, ω_f is the forcing frequency, and m is the mass of the system.

For a constant cross section, T_r is also equal to the ratio of the transmitted stress to the exciting stress. And, because $\sigma = E\varepsilon$, T_r is also equal to the ratio of transmitted strain (amplitude at the joint) to exciting strain (amplitude delivered by the ultrasonic horn), within the same material.

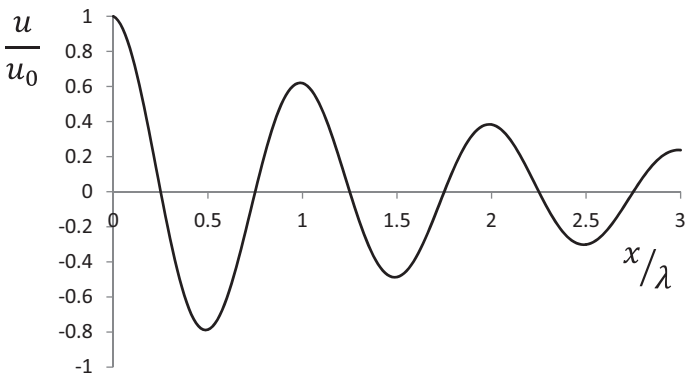


FIGURE 11.6 Normalized vibration amplitude for a wave propagating in a slender viscoelastic bar.

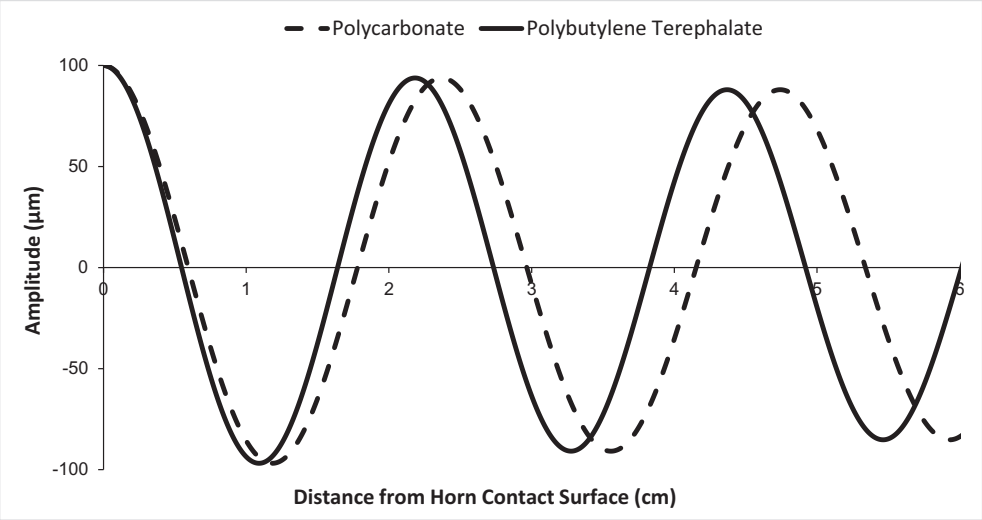


FIGURE 11.7 Ultrasonic attenuation in polycarbonate and polybutylene terephthalate.

In addition to the amplitude loss due to attenuation, Levy et al. (2014) found that there is a loss in the amplitude transmitted through the part due to a "hammering" effect, where the horn may not be in constant contact with the upper plastic part. To account for this, an additional variable, the empirical hammering correction factor (α_h) can be used, $\alpha_h = 1$ if the horn and the part are fully coupled (Levy et al., 2014).

$$Q = \frac{1}{2}\alpha_h{}^2 \omega E'' \varepsilon^2 \tag{11.28}$$

The hammering coefficient essentially describes the resultant actual amplitude of vibration of the plastic component due to the reduced period of contact, as shown in Figure 11.8 (Palardy et al., 2018).

The hammering coefficient is obtained by measuring the amplitude of vibration of the top surface of the plastic component and comparing that to a measurement of the amplitude on the face of the ultrasonic horn. It has been established that the hammering effect diminishes over time, resulting in improved transfer of vibrations, as shown in Figure 11.9 (Palardy et al., 2018). Additionally, it has been found that increasing the weld force or pressure will also reduce the effect.

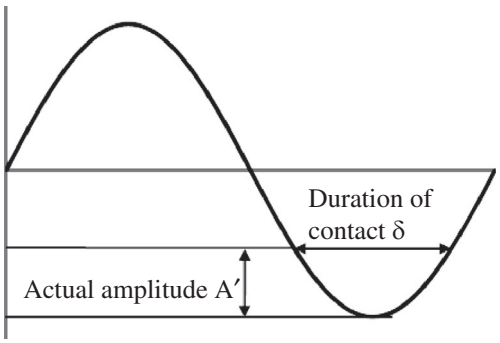


FIGURE 11.8 The effect of hammering by the ultrasonic horn on duration of contact and actual amplitude of vibration. *Adapted from Palardy et al. (2018).*

11.3.3 Diffusion

Intermolecular diffusion is the movement of polymer chains across boundaries, such as from melt generated from one side of the joint to melt generated by the other side of the joint, or into any solid polymer surface with which melt comes into contact. The depth that these polymer chains move into the other side of the boundary can be termed interpenetration depth.

In 1949, Voyutski proposed the basic equation for interpenetration depth, x:

$$X \propto e^{-E/2RT} t^{1/2} \tag{11.29}$$

where E is diffusion activation energy, R is molar gas constant, T is absolute temperature, and t is time.

A common approach to consider intermolecular diffusion of polymer chains is in terms of reptation, which considers the polymer chain to be completely enclosed in an imaginary tube representing the constraints imposed by adjacent chains. Over time, the ends of the polymer chain will exit the imaginary tube, then gradually more of the chain diffuses out until the entire chain has migrated from its original imaginary tube into a new imaginary tube. As polymer chain ends diffuse across the interface and get entangled with polymer chains for the other part, the interface strength gradually increases, which is referred to as healing. An interface where polymer chains diffuse

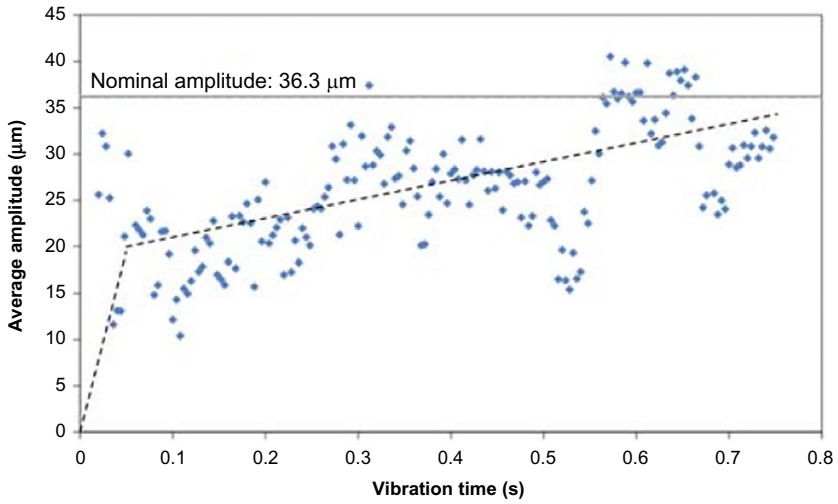


FIGURE 11.9 The average amplitude on the top surface of plastic part approaches the nominal horn amplitude with increasing vibration. *Adapted from Palardy et al. (2018).*

sufficiently to reach the equilibrium interpenetration distance thereby retaining full strength is considered fully healed.

An isothermal healing model considering intermolecular diffusion by reptation has been proposed by Bastien and Gillespie (1991):

$$D_h(t) = \frac{\sigma}{\sigma_\infty} = \sum_{t=0}^{t/\Delta t} \left[\frac{{t_{i+1}}^{1/4} - {t_i}^{1/4}}{{t_R^*}^{1/4}} \right] \tag{11.30}$$

where $D_h(t)$ is the degree of healing as a function of time, σ/σ_∞ is the ratio of weld strength versus ideal weld strength (complete healing), and t_R is reptation time for an entire polymer chain to diffuse out of its initial imaginary tube.

However, any welding process is non-isothermal. This limitation lead Yang and Pitchumani (2002) to develop a non-isothermal healing model of reptation:

$$D_h(t) = \left[\int_0^t \frac{1}{t_w(T)} dt \right]^{1/4} \tag{11.31}$$

where $D_h(t)$ is the degree of healing as a function of time (1, when fully healed), and $t_w(T)$ is welding time, defined as the time for an entire polymer chain to diffuse out of its initial tube.

The relationship of healing to the 1/4 power of time is referenced in other approaches to model the diffusion of polymer chains across a weld or knit line, and it has been experimentally verified many times and appears in several equations for degree of healing. For example, Grewell and Benatar (2008) proposed the following equation for degree of welding to jointly account for the effects of squeeze flow and intermolecular diffusion:

$$DW(T,t)_h = \sum_{t=0}^{t=t'} \Gamma e^{\frac{-A_0 e^{[k_a T]}}{kT}} t^{1/4} \tag{11.32}$$

where T is temperature, t is time, Γ is the squeeze flow and heating coefficient, A_0 is a material constant, and k_a is the temperature parameter $(1/k)$ that is the resultant of the activation energy divided by the Boltzmann constant (k), all parameters to be determined experimentally.

The welding time (i.e., in the Yang and Pitchumani equation) can be determined via a reptation model. The two most often used reptation models are the Doi-Edwards and the Rouse model. While the Rouse model was established first, the Doi-Edwards model is generally considered to better represent intermolecular diffusion. Bousmina et al. (1998) established that the Rouse model is effective for interfaces where there is an excess of chain ends. Whereas the Doi-Edwards model guided the behavior of melt interfaces where there is not an excess of chain ends. During welding of injection-molded parts, most chain ends will not be at the surface, so the Doi-Edwards model is more useful for plastic welding purposes.

Thus, the welding time, $t_w(T)$, can be approximated by the Doi and Edwards (1978) disentanglement time, or the time for a Gaussian chain to diffuse out of its imaginary tube, τ_d:

$$\tau_d = \frac{\zeta L^2}{\pi^2 K_B T} \tag{11.33}$$

where τ_d is diffusion time, ζ is the monomeric friction factor, L^2 is the characteristic length of the polymer chain, K_B is the Boltzmann constant, and T is the temperature.

The monomeric friction coefficient depends on viscosity per:

$$\zeta = \frac{36 M_0 \eta}{\rho N_A R^2} \tag{11.34}$$

where M_0 is the monomer molecular weight, η is the viscosity, ρ is the density, M is the molecular weight, N_A is

Avogadro's number, and R^2 is the characteristic length of the polymer chain.

Eqs. (11.32)–(11.34) can be combined to develop a single equation to predict the degree of healing as a function of common material properties, temperature, and viscosity during welding:

$$D_h(t) = \left[\frac{\pi^2 K_B N_A \rho}{36 M_0}\int_0^t \frac{T(t)}{\eta(t)}dt\right]^{1/4} \tag{11.35}$$

where K_B is the Boltzmann constant (m^2Kg/s^2K), N_A is Avogadro's number (1/mol), ρ is the density (Kg/m^3), M_0 is the monomer molecular weight (Kg/mol), $\eta(t)$ is the viscosity as a function of time (Kg/m s), and $T(t)$ is temperature as a function of time (K).

The following equation predicts the viscosity, η, of a polymer melt as a function of temperature and shear stress (Allara et al., 1986):

$$\eta = Ae^{\left(\frac{E_0 - k\omega t}{kt}\right)} \tag{11.36}$$

where A is a constant related to polymer structure, E_0 is the energy barrier, ω is the effective volume of the kinetic unit, t is time, and k is a parameter depending on shear stress (τ), $\tau \to 0$, $K = 0$; $\tau \to \infty$, $K = 1$.

11.4 Design for ultrasonic plastic welding

Due to the nature of heat generation in ultrasonic plastic welding, it is one of the most geometry restrictive plastic welding processes. However, with planning and thoughtful design, ultrasonic welding can be used for a wide range of applications. Care must be taken to avoid placing the joint too far from the horn contact surface, to avoid high stress regions in the part contacted by the horn, and to select an appropriate joint design.

11.4.1 Near-field and far-field ultrasonic welding

A common industry standard is to divide ultrasonic welding into near-field and far-field welding depending on the length of the top part (AWS, 2006). As shown in Figure 11.10, for near-field ultrasonic welding, the distance from the horn/part interface to the weld interface (L) is small compared to the wavelength (λ) in the part at the operating frequency. For far-field ultrasonic welding, the distance from the horn/part interface to the weld interface (L) is of the same order as the wavelength (λ) in the part. Therefore, during near-field ultrasonic welding, the amplitude of vibration experienced by the energy director at the weld interface is close to the amplitude of vibration applied at the horn face. For far-field welding, the amplitude of vibration at the weld interface depends on wave propagation in the parts.

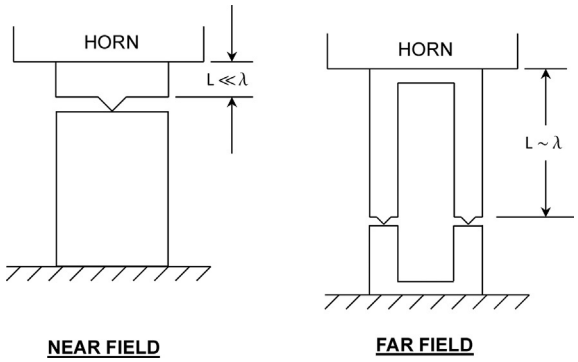


FIGURE 11.10 Industry accepted definition for near-field and far-field ultrasonic welding. *Adapted from Grewell et al. (2003).*

Current industry practice, which is based on 20 kHz ultrasonic welding where the wavelength in most plastics ranges from 6 to 13 cm, considers cases where $L \leq 6$ mm to be in near-field while cases where $L > 6$ mm to be in far-field. The mechanics and vibrations of the parts will differ for near-field and far-field ultrasonic welding, but the energy director will experience viscoelastic heating in both cases.

For near-field ultrasonic welding, the top part is thin enough so that the distance from the horn/part interface to the weld interface is small compared to the wavelength in the part at the operating frequency. Therefore, wave propagation in the top part can be neglected and it can be represented using lumped parameters (see Benatar et al., 1989). For simplicity, consider the case where the top and bottom parts are thin compared to the wavelength and a rectangular energy director is used, as shown in Figure 11.11. Each of the parts and the energy director can be represented using a lumped mass with a Voigt-Kelvin element, also shown in Figure 11.11. Doyle (1986) and Benatar et al. (1989) showed that the equations of motion for this case can be used to determine the deformation or strain amplitude in

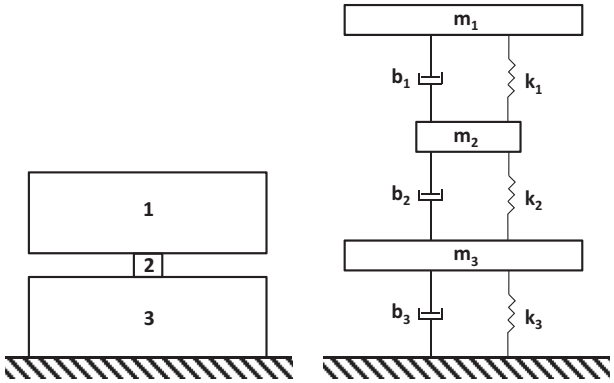


FIGURE 11.11 Lumped parameter model for parts with rectangular energy director.

each of the parts. The strain amplitude can then be used to determine the internal heat generation rate from Eq. (11.14), which together with a heat transfer model can be used to predict the temperature rise rate and temperature distribution. Benatar and Gutowski (1989) extended that approach to the case of triangular energy directors. They used that approach together with models for each of the ultrasonic welding sub-processes to develop a comprehensive model that improved understanding of the process.

For far-field ultrasonic welding, the distance from the horn/part interface to the weld interface is of the same order as the wavelength in the material at the operating frequency. Therefore, in this case, wave propagation through the part is important.

The location of the weld joint in relationship to the wavelength of the ultrasonic vibration can affect the amplitude available for welding at the weld interface. Since the complex modulus of polymers at ultrasonic frequencies is not readily available, one can approximate the wavelength by assuming that the polymer can be modeled as an elastic material using the published Young's modulus of elasticity. For long and slender bars with small cross-sections, the wavelength is approximated by Eq. (11.37), while for large cross-sections, it is approximated by Eq. (11.38).

$$\lambda = \frac{V_L}{f} = \frac{1}{f}\left[\frac{E}{\rho}\right]^{1/2} \tag{11.37}$$

$$\lambda = \frac{V_B}{f} = \frac{1}{f}\left[\frac{E}{\rho}\frac{(1-v)}{(1+v)(1-2v)}\right]^{1/2} \tag{11.38}$$

where λ is wavelength, V_L is the longitudinal velocity in slender bars, V_B is the longitudinal bulk velocity, f is frequency, E is Young's modulus, ρ is density, and v is Poisson's ratio.

If the distance from the horn contact surface to the joint is $\lambda/4$, then very little or no amplitude will be available at the weld interface, resulting in a weak, or no, weld. If the part has a complex geometry, computer modeling of the part would be more efficient to determine the approximate amplitude at weld interface.

11.4.2 General design considerations

The horn should contact the top part as close to the weld interface as possible and just above the weld area without requiring cyclical deflection of flanges or other sections to transmit the vibration to the weld interface. Whenever possible, sharp corners should be avoided, and large radii are preferred to reduce stress concentrations. Large unsupported walls, such as a lid, should be avoided to minimize resonant vibration and damage at the center due to overheating. Similarly, thin walls, fine features, and appendages that cannot be supported should be avoided or they may vibrate and break-off. Using higher operating frequencies with lower vibration amplitude can minimize damage to thin walls and fine features.

The horn contact surface should have as large a surface contact area as can be used to minimize damage to the part surface. Also, textures should be avoided where the ultrasonic horn will make contact. For parts which are contoured, the contour of the horn must match the part exactly to avoid surface damage. If a texture or contour must be used, placing a film between the part surface and the horn face may reduce surface damage.

11.4.3 Joint and part design

For ultrasonic welding, there are two primary joint designs, energy director and shear joints. Energy director joints usually include a triangular protrusion (although round, rectangular, or other geometries are also possible) that are molded at the weld interface of the top part. As shown in Figure 11.12, for a typical energy director joint, the base of the energy director is 1/4 of the wall width. For an energy director with an included angle of 90 degrees, the height of the energy director is then 1/8 of the wall width. A 90 degrees energy director is typically used for amorphous or softer polymers while a 60 degrees angle is used for semi-crystalline and harder polymers.

After welding, if the energy director fully fills the area between the parts then the final height would be 1/64 of the part width and a small amount of flash may be visible. Depending on the size of the components, the width of the

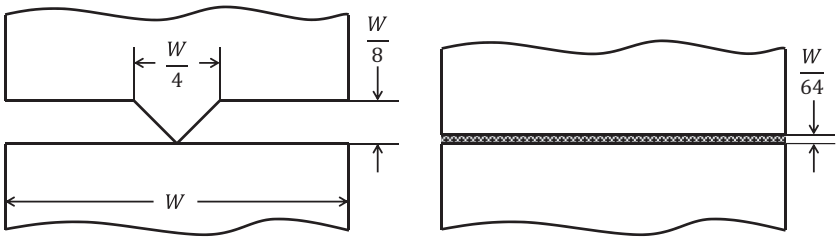


FIGURE 11.12 Basic energy director joint design.

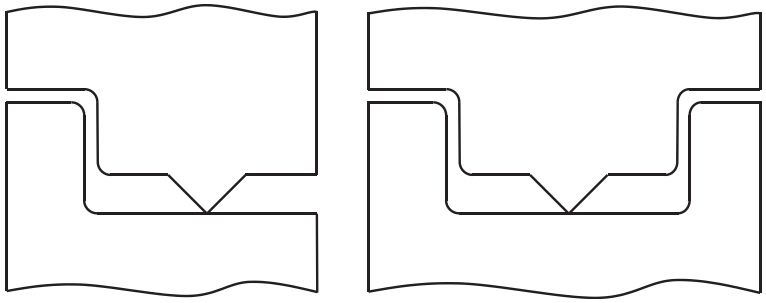


FIGURE 11.13 Step and tongue and groove energy director joint configurations.

energy director can typically range from about 0.12 mm for small parts to 1.5 mm for large parts.

If the joint area is wider than 6 mm, then multiple equally spaced energy directors may be used. As shown in Figure 11.13, to hide the flash on one side, a step joint may be used while a tongue and groove joint can hide the flash on both sides. A tongue and groove joint can also result in the extruded melt blocking potential leak paths to create a leak tight weld. For some applications, where minimal amplitude can be used because the part is large, or when using a difficult to weld material, a texture can be added to the joint surface opposing the energy director. This texture can be quite small, or it can be as large as the energy director itself, turned perpendicular and repeated along the joint length.

Shear joint designs are often preferred for applications that require hermetic seal, although they require a larger wall width to avoid deformation during welding. As shown in Figure 11.14, shear joints can be designed with a large weld depth to ensure that the weld is deep and strong through the perimeter of the part assuring a hermetic seal. The weld strength of shear joint, however, is typically more dependent on the interference width than the depth.

During ultrasonic welding of shear joints, it is important to use slow down speed to allow time for the material to heat and melt at the interface rather than simply press-fit the parts. If the interference width is small and the wall width is narrow, then there is a high chance for the walls to deform away from each other, rather than for melt to occur at the shear joint. This effect can sometimes be limited by using tooling that prevents outward movement of the wall. The interference and part tolerances are quite small with shear joints depending on the maximum part dimension. For small parts with maximum dimensions of 18 mm or less the interference per side is 0.2–0.3 mm $\pm$ 0.025 mm, increasing to 0.4–0.5 mm $\pm$ 0.075 mm for parts with maximum size of 35 mm or larger.

Part design for ultrasonic welding is also important to ensure that consistent and high-quality welds are produced without damage. For this reason, it is helpful to have small initial contact at the interface using an energy director or shear joint design to maximize local heating of the interface.

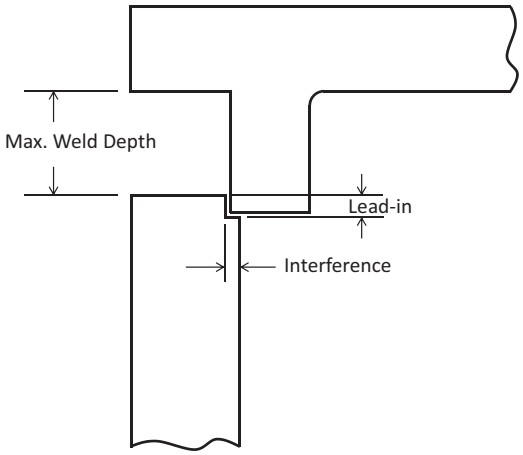


FIGURE 11.14 Typical shear joint design.

Features in the part design that enable easy or even self-alignment between the parts, as well as easy insertion and removal from the fixture, and proper alignment with the horn can be included.

11.5 Types of ultrasonic processing

Ultrasonic welding of thermoplastics and thermoplastic composites is often divided into two major categories, plunge and continuous welding. In plunge ultrasonic welding, parts are usually held in a fixture while the ultrasonic horn plunges down onto the top part applying pressure with superimposed amplitude of vibration. In continuous ultrasonic welding, the horn is pressed against the parts while either the parts are moved continuously under the horn or the horn is moved over the parts. In addition to welding, plastics are processed in many other ways using ultrasonics such as staking, swaging, spot welding, degating, and inserting.

11.5.1 Plunge welding

Plunge ultrasonic welding is usually used to join discrete parts that are held in a fixture while the welding cycle is executed. For a manual or semi-manual system, the welding cycle is initiated by an operator pressing on two palm

buttons, while for a fully automated system, a start signal would be transmitted to the ultrasonic welding controller. This will initiate the "down-stroke" where the ultrasonic horn moves downward until it contacts the top part. For pneumatic systems, the down speed is controlled through a combination of cylinder pressure and proportional valve. For electric cylinders, the down speed is determined by the lead-screw pitch and controlled through the rotation speed of the servomotor.

For some applications, the ultrasonic vibration will be triggered when the horn reaches a specified location during the down-stroke prior to reaching the part, which is known as pre-triggering; this is typically used in cases where the horn is large or has a high gain requiring high power to initiate the vibration. Otherwise, the ultrasonic vibration is triggered when the horn applies a preset force to the parts, known as the trigger force.

For time-controlled ultrasonic welding, the ultrasonic vibration will be applied for a preset time. If pre-triggering or a low trigger force is used, then the clamping force will continue to increase while ultrasonic vibration is applied until a preset welding force is reached. For time-controlled ultrasonic welding, after a preset time, the ultrasonic vibration is stopped, and the hold cycle begins. During the hold cycle, the parts are held for a preset hold time with a preset hold force that may or may not be the same as the weld force. At the end of the hold time, the horn is retracted beginning the "up-stroke." In some applications, at the start of the up-stroke, a short burst of ultrasonic vibration, which is often referred to as an "after-burst" or "post weld burst," may be applied to loosen the parts from the fixture, making them easier to remove.

As shown in Figure 11.15, sequential ultrasonic welding can be used to join large parts, where a section is ultrasonically plunge welded and then the part or welder are indexed, so that an adjacent section is welded until the whole interface is joined (Lu et al., 1991).

11.5.2 Continuous and scan welding

Continuous ultrasonic welding is most frequently used to join flexible thermoplastic films, woven and non-woven fabrics, and coated materials (Branson Ultrasonics Corporation, 2011). As shown in Figure 11.16, the material is usually placed between the horn and a rotary drum, where the welding pattern is usually applied to the rotary drum, and it is fed at a constant rate. The edges of the horn are usually slightly rounded to reduce the potential for snagging and to allow the clamping force to gradually increase and then decrease as the material passes under the horn. Usually the gap between the horn and drum is maintained constant, or for more advanced systems, it may be adjusted in real time based on variations in thickness of the materials. As the material passes between the horn and drum, it experiences pressures and vibrations that are similar to plunge ultrasonic welding but usually for a much shorter time. In some cases, the welded material may also be passed between the drum and a stationary roller to apply the hold pressure.

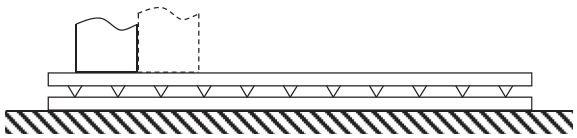


FIGURE 11.15 Sequential ultrasonic welding.

Scan ultrasonic welding can be used to join large sheets or plates (Benatar and Gutowski, 1986). As shown in Figure 11.17, one possible arrangement is where the parts are held stationary and the ultrasonic horn traverses or scans the parts. It is also possible to use a stationary ultrasonic welder with the parts fixed onto a motorized table that moves them under the horn as they are welded. As with continuous ultrasonic welding, the horn edges are usually rounded and the parts experience similar force and vibration amplitude to plunge ultrasonic welding. However, the scan speed is usually low allowing for longer ultrasonic vibration times than with continuous ultrasonic welding because the parts are usually thicker and often include energy directors. Here too, one may use a stationary roller to apply the hold pressure.

11.5.3 Staking and swaging

Staking and swaging are processes during which a formed plastic cylindrical protrusion is melted and reformed to retain a secondary part. This process can be performed using many different types of heating, including using ultrasonics. Several different geometries can be used in staking, three of the most common are shown in Figure 11.18. In dome style staking, the top of the post is tapered to a point to initiate melting, while in rosette style staking, the point is placed on the horn. For larger parts, a hollow boss style can prevent the formation of a sink mark on the opposite side of the part. This style of stake can also be removed and re-assembled using a screw.

Swaging is very similar to staking, except that instead of a plastic post through a hole in another part, the formed protrusion can be any shape and the part which it retains does not completely surround it. Often, the protrusion is rectangular and is formed to one side to hold in another part, like a frame.

11.5.4 Spot welding

Plunge ultrasonic welding can also be used for spot welding and sequential welding of large parts. Spot welding is usually used to join two thermoplastic sheets at one or more

FIGURE 11.16 Continuous ultrasonic welding of flexible materials.

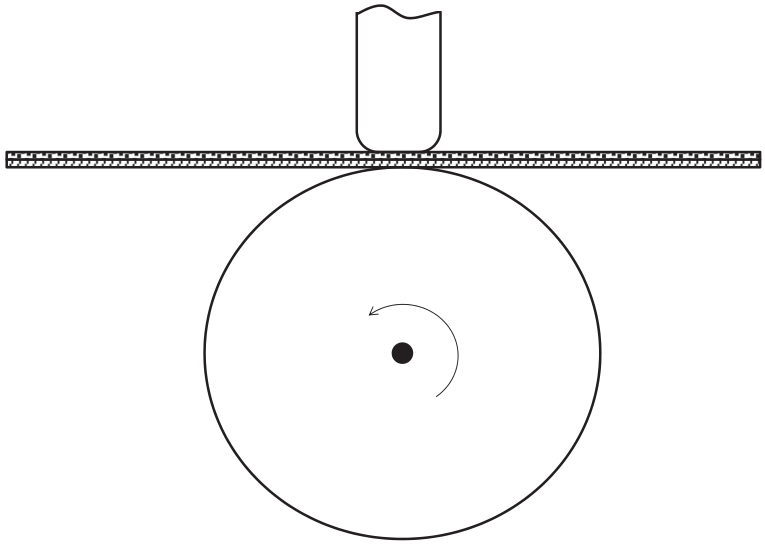


FIGURE 11.17 Scan ultrasonic welding of plates.

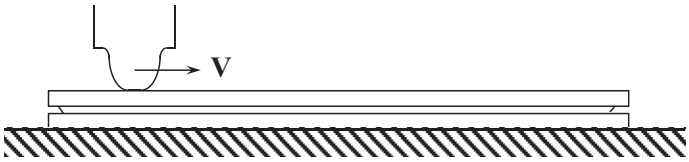
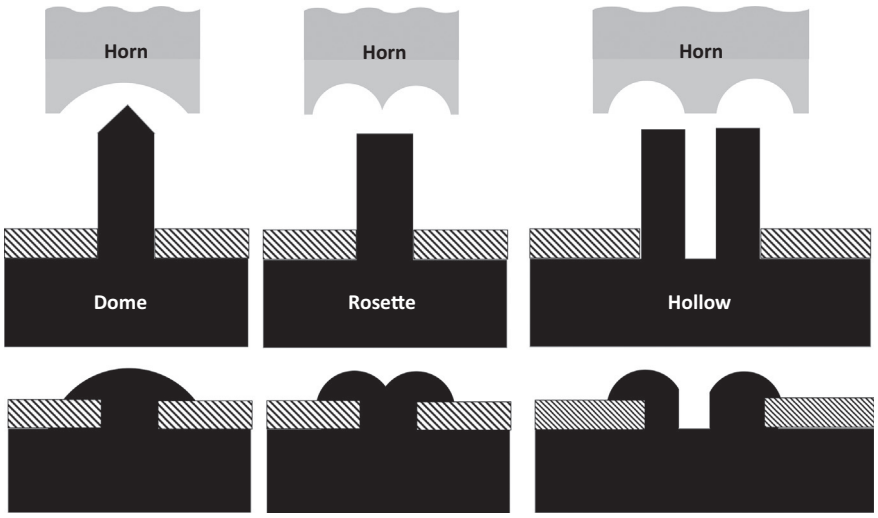


FIGURE 11.18 Common part and dome geometries for ultrasonic staking.



spots. As shown in Figure 11.19, the spot-welding tip penetrates through the top sheet resulting in a circular annulus around that hole where the two sheets are welded. For spot ultrasonic welding, a handheld transducer with attached horn that is manually plunged by an operator is frequently used.

11.5.5 De-gating

Ultrasonic de-gating arose from the early observation during ultrasonic welding that areas with a sharp radius or small cross-sectional area would melt or fracture during welding. While this is unfavorable during welding operations, de-gating of molded parts from the runner system

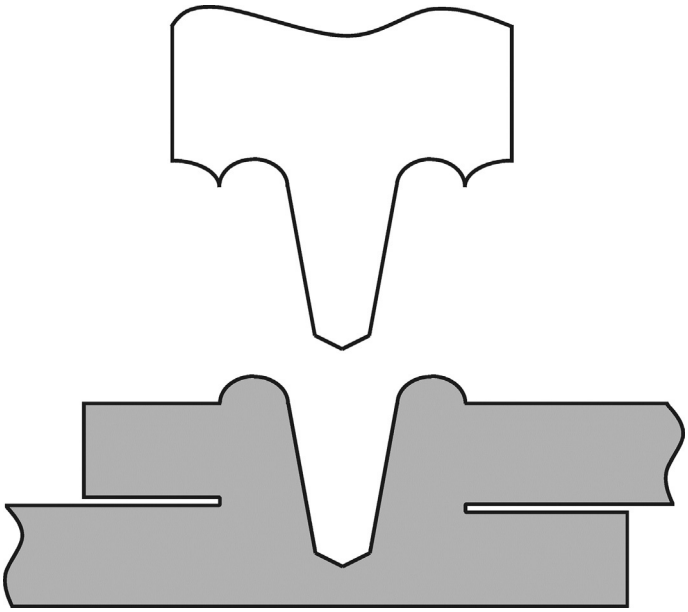


FIGURE 11.19 Spot welding of thermoplastic sheets.

was identified as a possible use for this phenomenon (Thomas, 1974). The process works by producing a standing ultrasonic wave in the runner that causes melting in the gate, and area of high stress concentration as shown in Figure 11.20.

11.5.6 Inserting

A typical screw cannot be directly threaded into a plastic hole because the plastic will loosen over time and the screw will lose strength. For this reason, brass inserts can be molded into the part or when that is not possible or expensive the insert can be pressed into a pre-molded or drilled hole in the plastic part. On the outer diameter of these inserts, special knurl patterns are used to improve the retentions strength of the insert in the plastic. On the interior diameter of the insert, a standard thread pattern is machined for a screw. While these inserts can be pressed into holes in plastic parts in many ways, including thermal staking and cold pressing, ultrasonic insertion is one of the most common processes used. Ultrasonics insertion is fast, can be done as a secondary process after molding, and allows the polymer to melt and flow into the insert knurls, improving strength over cold pressing methods.

11.6 Ultrasonic welding equipment

Ultrasonic welding equipment is composed of a power supply and controller, ultrasonic stack that includes the transducer/converter, booster and horn, actuation system and fixture or base. Since the stack operates at its vibrational resonance, each system is designed to operate at a fixed

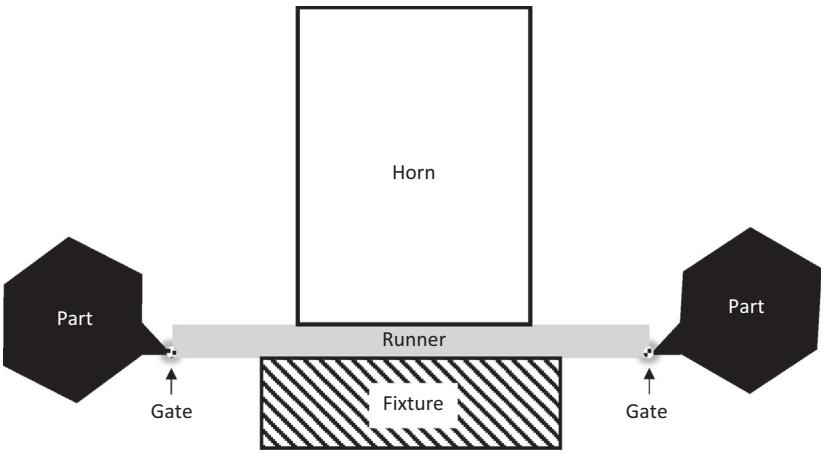


FIGURE 11.20 Typical configuration for ultrasonic de-gating.

frequency within a range between 10 and 70 kHz. As the frequency increases, the maximum power decreases from 6 kW at 10 kHz to 400 W at 75 kHz, and the amplitude of vibration for the transducer decreases from 40 μm at 10 kHz to 5 μm at 75 kHz. At lower frequencies, it is possible to join larger parts with greater joint areas, while at the higher frequencies, small parts can be joined without damaging small features due to the lower amplitude of vibration. Since the maximum audible range for people is slightly below 20 kHz, the equipment that operates at 10 and 15 kHz is placed in a sound enclosure. While using equipment that operates at 20 kHz and higher, it is recommended for the operators to wear hearing protection because of sub-harmonic vibrations that are produced within the parts and fixtures.

11.6.1 Power supply and controller

The main function of the power supply is to convert 100–240 V_{RMS} at 50–60 Hz line voltage to high voltage (typically 1500–2000 V_{RMS}) along with a tuning circuit to operate at the resonant frequency of the system. Older systems may require manual tuning while newer systems usually include an autotuning system that automatically tunes to, and it can track, the resonant frequency of the stack if it changes due to temperature changes. Newer systems also include amplitude regulation to ensure that the amplitude of vibration remains constant regardless of the power requirements up to the maximum rated power as well as self-protection overload shut-off circuit.

The controller is usually in the same housing as the power supply and includes a front panel with a built-in user interface, and advanced controllers can also link to a separate computer through a local area network or similar interface. While there is a wide range of controllers in the market, most of them include a microprocessor and they primarily differ in the number of control modes that they can utilize. The simplest and least expensive controllers include only time mode control with no interface to external sensors and they can usually use the least expensive actuator that does not include advanced sensors. At the other end of the spectrum, the controllers can interface with multiple sensors and use the whole array of control modes. They can usually monitor and record power, and interface with sensors in the actuator to monitor and record air pressure in the pneumatic cylinder, force, and displacement. Depending on the control mode, this data can be analyzed to determine energy, displacement, or position, as needed. With most controllers, the data as a function of time can also be exported in a variety of formats. Some controllers can vary the amplitude of vibration and clamping force during welding.



FIGURE 11.21 Ultrasonic stack with transducer, booster, and horn.

11.6.2 Ultrasonic stack

The ultrasonic stack is made up of the transducer or converter, booster, and horn, as shown in Figure 11.21. Each of these individual elements is usually a half wavelength long so that it resonates at the operating frequency and the ultrasonic vibration that is generated by the transducer propagates to the face of the horn. To minimize losses at the interface between these elements, a small amount of silicone grease may be used prior to tightening of the parts to each other.

The transducer or converter is used to convert electrical energy to mechanical vibration with typical output amplitude (0-peak) of 10–13 μm at 20 kHz. While it is possible to use magnetostrictive transducers, most commercial ultrasonic welding systems use piezoelectric transducers because of their high efficiency, which exceeds 90%. As shown in Figure 11.22, the transducer includes piezoelectric disks that are clamped using a center screw between the steel top and titanium bottom with metal washers in between the disks for electrical connections. As alternating high voltage is applied to the piezoelectric disks, they alternate between expanding and contracting to generate the vibration amplitude at the titanium face of the transducer. Since the transducer operates at resonance, its size decreases



FIGURE 11.22 Typical construction of 20 kHz piezoelectric transducer.

proportionally with increasing frequency. Internal losses within the transducer are dissipated as heat and most ultrasonic welding systems allow for cooling air to be used to cool it. As the frequency increases and the transducer size decreases, the volume and surface area decrease thereby decreasing the heat capacity of the transducer and the ability to cool it; this limits the maximum power that can be used. Therefore, as described earlier, the maximum power of ultrasonic welding systems decreases with increasing frequency.

The booster is used to mechanically amplify or reduce the amplitude of vibration from the transducer to the horn. As shown in Figure 11.23, there are a range of boosters with amplitude ratios ranging from 1:0.6 to 1:2.5. It is usually made of aluminum or titanium and it is also a half wavelength long at the operating frequency so that it operates at resonance. From conservation of momentum, for an amplitude reducing booster, the top half is smaller than the bottom half, while for amplification of the amplitude, the top half is larger than the bottom half. In the middle, at the displacement nodal point, there is a ring that is used to clamp the stack in the actuator. Although the clamping ring is at a nodal point, it usually includes a rubber O-ring to minimize transmission of the vibration from the stack to the actuator. It is possible to increase the clamping stiffness by using rubber O-rings with rectangular cross-section or to go to one-piece solid boosters that include the clamping ring.

The last component in the ultrasonic stack is the horn, which is used to apply the weld force with superimposed ultrasonic vibration to the top part, and it may also increase the amplitude of vibration (similar to the booster). Most horns are made of aluminum or titanium and they are also a half wavelength long at the operating frequency, so that they operate at resonance. The face of the horn needs to match the geometry of the top part. In some applications (e.g., spot welding), a replaceable insert that is mechanically fastened to the horn surface is used to accommodate new geometries or plate thicknesses. In cases where the horn surface may wear, such as with ultrasonic welding fiber filled composites, the surface of the horn may include brazed carbide or diamond inserts. The horn should also have uniform amplitude of vibration along the surface where it contacts the part, since, as was discussed earlier, heat generation is proportional to the amplitude squared. In addition, it is important to design the horn such that the stress distribution is as uniform and as low as possible to reduce the likelihood of premature failure. Finite element analysis can be used to model and simulate the behavior of ultrasonic horns allowing computer-based design iterations before the horn is manufactured, saving both time and money.

11.6.3 Actuator

The actuator holds the ultrasonic stack at the booster clamping ring, and during the down-stroke, it lowers the stack so that the horn contacts the top part for ultrasonic welding. Most actuators use pneumatic cylinders with proportional valves and solenoids to control the direction and speed of motion. In some cases, servomotors with electric cylinders are used to control the actuation of the stack. Simple actuators may include mechanical triggering mechanisms while more advanced actuators include force sensors to control the trigger force more precisely. Advanced actuators also usually include a linear encoder to determine the position of the stack at any time for distance-based control mode.

11.6.4 Fixture

The fixture is used to locate the parts and to secure them during ultrasonic welding while at the same time permitting easy and rapid manual or automated loading of the unwelded parts and unloading of the welded assembly. Usually the fixtures are manufactured from steel or aluminum, but for complex geometries, they may also include urethane or similar pouring and curing compounds for complex part geometries. The fixture may include moving parts to make it easier to load and clamp the unwelded parts and then to release and unload the welded assembly. For applications where high heat generation occurs, the fixtures are usually made from aluminum due to its high thermal

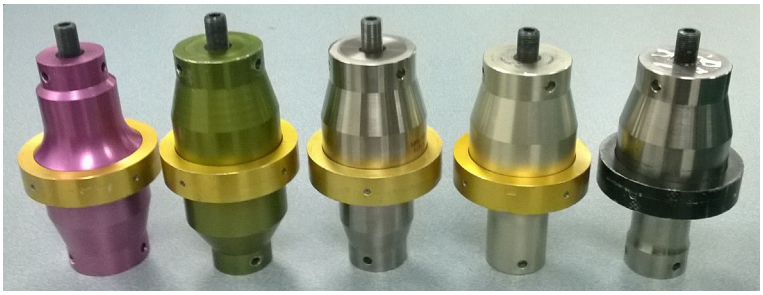


FIGURE 11.23 Boosters with various gains.

conductivity and may also include cooling channels to keep the fixture from overheating.

11.6.5 Automation

Ultrasonic welding is often incorporated into automated processes to take advantage of its fast cycle times. In these cases, air cooling of the ultrasonic transducer and/or horn may be necessary to prevent over-heating. If the horn heats excessively, the frequency may shift outside the range of the generator and cause equipment damage. If the transducer gets too hot, the ceramics may lose their piezoelectric properties.

Most ultrasonic equipment can be easily tied into automation, with options to allow external start signals and the ability to send out a signal when the weld is complete. Pick and place is commonly added to ultrasonic welding operations. In some cases, the ultrasonic stack can be removed from the press and fixed to a custom actuator, typically for parts too large to fit on a standard press.

11.7 Process variables

The three key variables that affect ultrasonic welding are amplitude, force, and duration. The amplitude applied ties directly into the heat generated in the part, per Eq. (11.14). Of course, the duration for which this amplitude is applied will significantly affect the total heat generation in the parts. Lastly, the force being applied can affect how well the amplitude is transferred into the weld joint. The amplitude in the system is a function of the maximum amplitude that the ultrasonic stack can apply. Also, most welding systems allow the input amplitude to be reduced electronically as a percentage of the total.

There are a variety of modes that can be used with plunge ultrasonic welding to control the weld duration including time, energy, distance, and peak power. Most basic systems include the time mode where the ultrasonic vibration is applied for a preset time. Variations in materials, part dimensions, factory voltage, and compressed air pressure can result in variations in weld quality and final dimensions of ultrasonically welded parts. Therefore, with the use of microprocessors and digital ultrasonic power supplies and controllers, other modes of closed loop control were developed to reduce the variations between welds. In addition, microprocessor-controlled ultrasonic welders can have built-in statistical process control (SPC) software, or it can communicate through a local area network with a computer that has SPC software. Critical process parameters would be monitored by the SPC software to observe trends over time and to warn of possible problems.

For energy control mode, when the ultrasonic vibration starts, the power dissipated in the ultrasonic transducer is measured and integrated over time until a desired energy level is achieved and then the ultrasonic vibration is stopped. It is assumed that the power dissipated in the transducer is directly proportional to the power dissipated at the weld interface. Together with energy control, operating windows or acceptable ranges in time and displacement can be set to further improve consistency. For example, if the time to reach the desired energy level is shorter than the minimum preset time or longer than the maximum preset time then it is assumed that there is a problem with that part and it can be rejected or undergo further inspection. Similarly, minimum and maximum displacements can be used to accept parts that have welding displacements within this range and reject ones that fall outside this range.

For distance control mode, linear encoders are usually used to determine the position of the horn at all times and use that information to control the duration of ultrasonic vibration. One way of using the distance control mode is to apply ultrasonic vibration until a preset amount of collapse occurs, to ensure for example melting and flow of the whole energy director. It is also possible to control the absolute final height of the parts, where the ultrasonic vibration is stopped when the horn reaches a final absolute position (fixed height from the base of the welder). The final height of the parts will be slightly smaller as some melt still squeezes out during the hold time. Here too, it is possible to set operating windows or ranges for time and energy.

The ultrasonic welding process simulation that was performed by Benatar and Gutowski (1989) showed that near the end of ultrasonic welding, when the energy director fully fills the gap between the parts, the impedance, and therefore, the power begins to rise rapidly. This led to the development of peak power control, where the power is monitored within a specific time or displacement window, and when it reaches a preset value, the ultrasonic vibration is stopped. He and Benatar (1996) used amplitude and pressure control together with peak power to improve the weld quality and consistency.

After the ultrasonic energy is discontinued, the parts continue to be pressed together for some amount of time or distance. This hold phase of the weld helps ensure that the polymer melt does not form voids or cracks as it cools. This is especially important for polymers which have a high shrinkage rate, or when there is internal pressure in the assembly that is opposing the weld—such as a sealing gasket or spring.

11.8 Material weldability

For thermoplastics and thermoplastic composites, the weldability may depend on several factors including the ability to transmit the vibrations to the weld interface, viscoelastic dissipation of energy to generate heating, and the intermolecular diffusion and chain entanglement for healing of the interface. Generally, for ultrasonic welding, the parts need

to be sufficiently rigid or the material needs to have a sufficiently high storage modulus to transmit the vibrations to the weld interface. Materials with low modulus, such as thermoplastic elastomers, easily deform and deflect without being able to transmit the vibrations to the weld interface. Therefore, only thin films of thermoplastic elastomers can be ultrasonically welded.

In addition to transmitting the vibration to the weld interface, it is important that the material can undergo viscoelastic heating to heat and melt the energy director or the material at the interference for shear joints. Therefore, the higher the loss modulus or loss tangent the faster the thermoplastic will heat at the interface.

The storage and loss moduli of the polymer are temperature- and frequency-dependent, and they can be measured using a variety of methods, as described by Read and Dean (1978). For example, Benatar and Gutowski (1989) used a rheovibron to measure these moduli at low frequencies and they used time-temperature superposition to extrapolate those values to 20 kHz. Benatar et al. (1989) used high-frequency (0.5–3.5 MHz) ultrasonic wave propagation and attenuation and extrapolated those results to estimate the room temperature 20 kHz storage and loss moduli. Aliosio et al. (1972), Tolunay et al. (1983), and Doyle (1986) found that initial temperature rise rates during ultrasonic welding were in good agreement with predictions using Eq. (11.14). Initial heating rates for the energy director can be on the order of a few thousands of degrees Celsius per second explaining the short cycle times that are possible with ultrasonic welding.

Many thermoplastics include mineral fillers (e.g., talc) and short glass or other fibers, which can adversely affect their ultrasonic weldability. Adding mineral or short fiber fillers to thermoplastics increases their stiffness or modulus enabling better transmission of the vibrations to the weld interface. It will usually also result in small increases in the loss modulus helping increase the heating rate for the energy director. However, even small amounts of filler can greatly increase the melt viscosity of the thermoplastics so that squeeze flow of the energy director occurs more slowly, and intermolecular diffusion and chain entanglement can also be adversely affected. In addition, as a result of the squeeze flow, there is a buildup of the filler at the interface, and for fiber-filled thermoplastics, there is also adverse fiber orientation at the interface, both of which can weaken the joint and reduce ultrasonic weldability of filled materials. Therefore, experimentation with actual materials is often required to confirm and try to mitigate these effects. Similar effects were also observed for advanced thermoplastic composites, and therefore, it is recommended to use thermoplastic only energy directors and thermoplastic-rich interfaces to enhance weldability of these materials (see Benatar and Gutowski, 1989).

11.8.1 Compatibility

Once the materials melt, the process of intermolecular diffusion and chain entanglement leading to healing of the interface can proceed. This is a complex process that depends on the molecular size of the polymer as well as the compatibility or miscibility between two polymers. Polymers with large molecules, like ultrahigh molecular weight polyethylene or high molecular weight polytetrafluoroethylene, are difficult to weld using most welding methods including ultrasonic welding. Figure 11.24 provides a qualitative ultrasonic weldability chart for many common thermoplastics including some dissimilar but compatible or miscible polymers.

The viscosity of a polymer melt, a critical factor in diffusion, changes with shear rate and temperature. While it can be generally said that viscosity decreases with increasing temperature, the change in viscosity with shear rate is less consistent. Polymers can be shear thinning or shear thickening, meaning that the viscosity may increase or decrease with increasing shear rate. A common industry recommendation is that the polymers melt flow index should be within 10% at the joining temperature in order to be welded.

11.8.2 Amorphous v. semi-crystalline polymers

There are two main types of thermoplastic polymers, amorphous and semi-crystalline. Amorphous polymers have disordered polymer chains and do not have a discrete melting temperature. Semi-crystalline polymers have disordered, amorphous regions, as well as ordered, crystalline regions. These polymers have a melting temperature which is the temperature at which the crystalline structure breaks down.

For plastic welding, this means that amorphous polymers can often be softened and displaced at lower temperatures, sometimes resulting in insufficient intermolecular diffusion. However, the temperature at which these polymers diffuse is typically lower than that for semi-crystalline materials, making them easier to weld. For both types of polymers, the critical flow temperature should be reached in the weld, which is the temperature at which the polymer shifts from behaving more like a solid to behaving more like a liquid. For amorphous polymers, this temperature is typically about 100°C above the glass transition temperature. For semi-crystalline polymers, this is the melting temperature, although aiming for 10–25°C higher is a good idea to ensure complete melting in the weld area.

11.8.3 Microstructure

For semi-crystalline polymers, the crystallinity of the weld will depend on the cooling rate, as well as the shear stresses

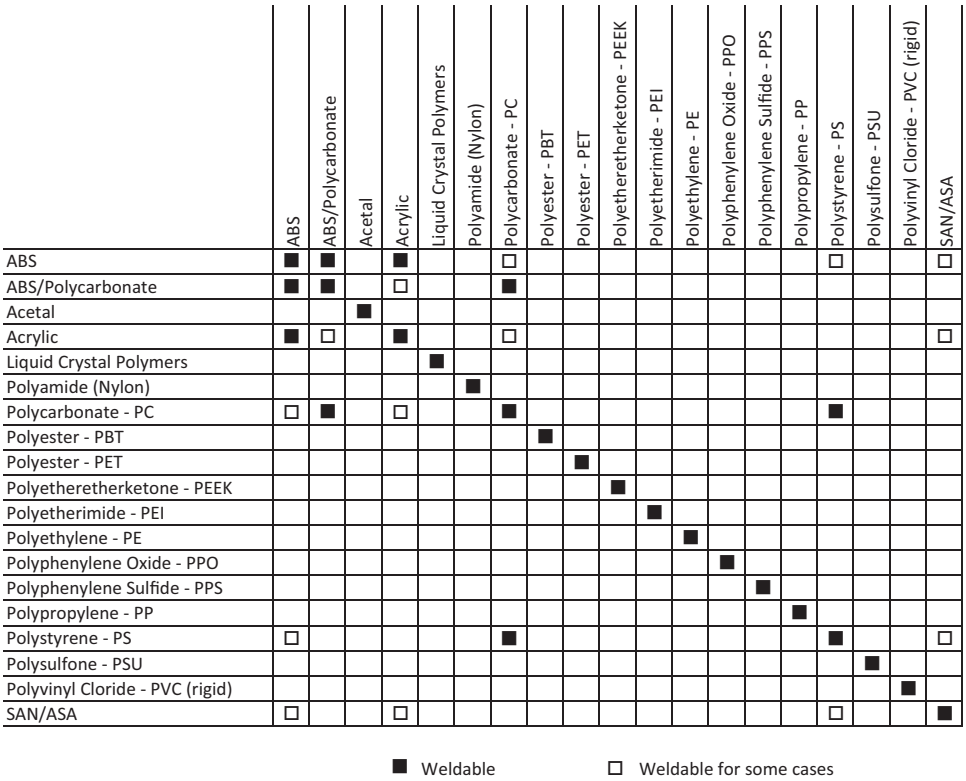


FIGURE 11.24 Ultrasonic weldability chart for common thermoplastics.

in the melt that are present when solidification begins. Both factors affect how well the polymer chains will organize and form crystallites as they solidify. In general, greater crystallinity leads to greater tensile strength and reduced ductility. For very large welds, the cooling rate is much slower and the crystallinity in the weld can be significantly different than in the bulk. Chung and Kamal (2008) found that slower cooling rates resulted in much larger spherulite formation. For these assemblies, heat treating after welding can help create uniform crystallinity throughout the parts.

In addition to the crystallinity in the weld, the orientation of polymer chains can significantly affect weld strength. Shieu et al. (1997) found that for highly oriented polymer chains in the weld, the weld strength was just 30% of the bulk, while for more randomly oriented polymer chains in the weld, the weld strength was 80% of the bulk.

References

Aliosio, C.J., Wahl, D.G., Whetsel, E.E., 1972. A simplified thermoviscoelastic analysis of ultrasonic bonding. Society of Plastics Engineers Technical Papers, pp. 445–451.

Allara, D.L., Fowkes, F.M., Noolandi, J., Rubloff, G.W., Tirrell, M.V., 1986. Chapter 5: Bonding and adhesion of polymer interfaces. Mater. Sci. Eng. 83, 213–226.

AWS, 2006. G1.1M/G1.1:2006, Guide to Ultrasonic Assembly of Thermoplastics. G1 Committee on Joining of Plastics and Composites, American Welding Society, Miami, Florida.

Bastien, L.J., Gillespie, J.W., 1991. A non-isothermal healing model for strength and toughness of fusion bonded joints of amorphous thermoplastics. J. Polym. Eng. Sci. 31, 1720–1730.

Benatar, A., 2003. Fundamental steps in plastics and composites welding. Chapter 2, In: Grewell, D.A., Benatar, A., Park, J.B. (Eds.), Plastics and Composites Welding Handbook. Hanser Publishers, Munich.

Benatar, A., Cheng, Z., 1989. Ultrasonic welding of thermoplastics in the far-field. Polym. Eng. Sci. 29, 1699–1704.

Benatar, A., Gutowski, T.G., 1986. Methods for fusion bonding thermoplastic composites. SAMPE Q. 18, 35–42.

Benatar, A., Gutowski, T.G., 1989. Ultrasonic welding of PEEK graphite APC-2 composites. Polym. Eng. Sci. 29, 1705–1721.

Benatar, A., Eswaran, R.V., Nayar, S.K., 1989. Ultrasonic welding of thermoplastics in the near-field. Polym. Eng. Sci. 29, 1689–1698.

Bland, D.R., 1980. Theory of Linear Viscoelasticity. Pergamon Press, New York.

Bousmina, M., Qiu, H., Grmela, M., Klemberg-Sapieha, J.E., 1998. Diffusion at polymer/polymer interfaces probed by rheological tools. Macromolecules 31, 8273–8280.

Branson Ultrasonics Corporation, 2011. Ultrasonic welding characteristics of textiles and films. PW-7 Technical Information, Danbury, CT.

Christensen, R.M., 1980. Theory of Viscoelasticity. John Wiley and Sons, New York.

Chung, Y.-M., Kamal, M.R., 2008. Morphology of PA-6 vibration welded joints and its effect on weld strength. Polym. Eng. Sci. 48, 240–248.

Doi, M., Edwards, S.F., 1978. Dynamics of concentrated polymer systems part 1—Brownian motion in the equilibrium state. J. Chem. Soc. 12, 1789–1801.

Doyle, J.L., 1986. Heating of Rectangular Energy Directors During Ultrasonic Welding. S.B. Thesis, Department of Mechanical Engineering, Massachusetts Institute of Technology, Cambridge, MA.

Ferry, J.D., 1980. Viscoelastic Properties of Polymers. John Wiley and Sons, New York.

Grewell, D., Benatar, A., 2008. Semi-empirical, squeeze flow, and intermolecular diffusion model. II. Model verification using laser microwelding. Polym. Eng. Sci., 1543–1549.

He, F.G., Benatar, A., 1996. Effect of amplitude and pressure control on the strength of ultrasonically welded thermoplastics. In: Society of Plastics Engineers Annual Technical Conference.

Levy, A., Le Corre, S., Villegas, I.F., 2014. Modeling of the heating phenomena in ultrasonic welding of thermoplastic composites with flat energy directors. J. Mater. Process. Technol. 214, 1361–1371.

Lu, H.M., Benatar, A., He, F.G., 1991. Sequential ultrasonic welding of PEEK/graphite composite plates. In: Society of Plastics Engineers Annual Technical Conference, pp. 2523–2526.

Lupo, J., 2017. Father of Ultrasonic Welding. Plastics Machinery.

Marcus, M., Anantharaman, S., Aldaz, B., 2013. Advantages of a servo-driven ultrasonic welder. In: ANTEC.

Menges, H., Potente, H., 1971. Studies on the weldability of thermoplastic materials by ultrasound. Weld. World 9, 47–58.

Palardy, G., Shi, H., Fernandez Villegas, I., Levy, A., LeCorre, S., 2018. Experimental investigation of amplitude transmission in ultrasonic welding of thermoplastic composites. In: ANTEC.

Read, B.E., Dean, G.D., 1978. The Determination of the Dynamic Properties of Polymers and Composites. John Wiley and Sons, New York.

Sancaktar, E., 1999. Polymer adhesion by ultrasonic welding. J. Adhes. Sci. Technol. 13 (2), 179–201.

Shieu, F.S., Wang, B.H., Wu, J.Y., 1997. Morphology and joint strength of polycarbonate-acrylonitrile/butadiene/styrene polymer blend. Plast. Rubber Compos. Process. Appl. 26 (5), 230–234.

Sovetov, A.N., Volkov, S.S., Orlov, Y.N., CHernyak, B.Y., 1976. Choice of the size of hard plastic parts for ultrasonic welding. Russ. Ultrason. 6, 137–143.

Thomas, R.H., 1974. Ultrasonics in Packaging and Plastics Fabrication. Cahners Books.

Tolunay, M.N., Dawson, P.R., Wang, K.K., 1983. Heating and bonding mechanisms in ultrasonic welding of thermoplastics. Polym. Eng. Sci. 23, 726–733.

Yang, F., Pitchumani, R., 2002. Healing of thermoplastic polymers at an interface under non-isothermal conditions. Macromolecules 35, 3213–3224.

Further reading

Benatar, A., Gillespie Jr., J., Kedward, K., 1997. Joining of polymer composites. Chapter 14, In: Gutowski, T.G. (Ed.), Advanced Composites Manufacturing. John Wiley and Sons, New York.

Grewell, D.A., Benatar, A., Park, J.B., 2003. Ultrasonic welding. Chapter 8, In: Grewell, D.A., Benatar, A., Park, J.B. (Eds.), Plastics and Composites Welding Handbook. Hanser Publishers, Munich.

Potente, H., 1988. Ultrasonic welding—principles and theory. In: Joining Plastics in Production. Maney Materials Science, pp. 62–82.

Soloff, B., 1984. New concepts in ultrasonic sealing. Mod. Plast. 5 (5), 228–234.

Chapter 12

Power ultrasonics for additive and hybrid manufacturing

R.J. Friel[a] and M. Norfolk[b]
[a]Halmstad University, Halmstad, Sweden, [b]Fabrisonic LLC, Columbus, OH, United States

12.1 Introduction

Ultrasonic additive manufacturing (UAM) is a process that combines the ultrasonic welding of metal, an additive process, with computer numerical control (CNC) machining, a subtractive process. This combination of additive and subtractive manufacturing techniques (often referred to as "hybrid manufacturing") allows UAM to use the greater freedom of form of additive manufacturing (AM) and couple this with the geometrical accuracy and surface finish of subtractive manufacturing.

AM is a form of production that sits alongside the other two more established categories of subtractive and formative manufacturing. In subtractive manufacturing (e.g., milling and turning), the process begins with an existing "block" of material that is then purposefully reduced in volume and geometry to attain a finished component (Figure 12.1a). During formative-type manufacturing (e.g., forging and casting), the process begins by having a predefined geometry (e.g., a die or mold) into/through which material is forced to take on that set volume and geometry (Figure 12.1b).

AM differs from these two more traditional manufacturing techniques in which material is selectively deposited, typically layer by layer, to create the 3D geometry of the finished component without the need for additional tooling and fixturing.

Hybrid manufacturing is the combination of both additive and subtractive manufacturing techniques within a single integrated system. The system deposits material in an additive fashion to create complex geometry directly from computer data. It then uses subtractive machining to attain part accuracies and surface finish beyond that of current additive techniques.

12.1.1 Steps necessary for moving from computer data to part via AM

There are many different AM processes; however, generic steps taken to move directly from a 3D computer-aided design (CAD) model to a finished manufactured component via AM are the same and detailed in Figure 12.2.

12.1.1.1 Step 1: CAD 3D model creation

The first step is the creation of the CAD model using software such as Solidworks, NX, and SketchUp. The software varies, but the creation of an electronic representation of the desired end design is required at this stage.

12.1.1.2 Step 2: .stl file conversion

Once a CAD file is complete, a file conversion process is necessary to allow the selected AM process to extract the Cartesian coordinates for tool path determination to manufacture each layer of the component. The most common file type is known as an .stl file. The conversion process is an automated software process that creates a "watertight" triangular facet mesh that approximates the original CAD geometry surface. The user can determine this mesh's accuracy by modifying tolerances used for the triangular facets. The higher the tolerance (smaller triangles), the better the approximation of the original CAD model. The .stl file type does not allow the full functionality of many AM systems to be utilized (e.g., color and variable material properties). Several parties have collaborated to provide superior alternatives to. stl formats; these alternatives are known as the 3D manufacturing format (3MF) and the additive manufacturing file format (AMF). However, at the current time, stl is still the de facto file format standard for AM.

12.1.1.3 Step 3: Build setup of specific AM machines

What is entailed in this step is dependent on the AM process being used. Each process will have a set of variable parameters (e.g., laser power, layer thickness, and build material), and these parameters can typically be altered for a specific build. The machine will normally have a software virtual machine environment, which allows the operator to

Power Ultrasonics. https://doi.org/10.1016/B978-0-12-820254-8.00009-9
Copyright © 2023 Elsevier Ltd. All rights reserved.

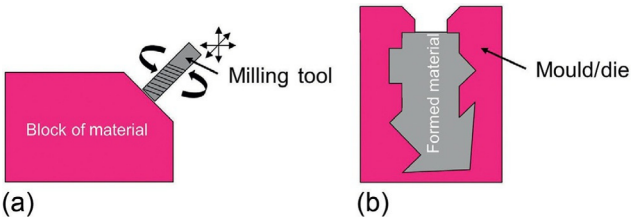


FIGURE 12.1 Schematic of subtractive (a) and formative (b) manufacturing categories.

orientate, place, scale, duplicate, and so forth the .stl files built during the building process. Once all .stl files and process parameters are set for the build, the individual layers or "slices" for the parts are extracted from the. stl data. The specific G-code for the particular equipment for these layers conveys to the machine the exact tool paths required for each layer via the use of interior and exterior boundary polylines. The layer number will be determined by the height of the build and the layer thickness being used by the AM process. Once the layers are calculated, they are loaded onto the AM machine. Before manufacturing begins, various AM machines have specific processes, such as preheating, calibration, and cleaning, that must be completed before proceeding.

12.1.1.4 Step 4: Manufacture of the component via the specific AM process

The loaded layer data from step 3 will be manufactured sequentially by the AM machine. The means by which the layers are manufactured and with what materials are specific to each AM process. The speed with which the manufacturing occurs depends on the AM process being utilized, as is the accuracy of the manufactured component. The manufacturing of the layers is a completely automated process, and no operator interference will be required during a normal build. Once manufacturing is complete, the AM equipment shuts down most functions (or begins some postprocessing tasks) and remains in a standby state awaiting manufactured part removal.

12.1.1.5 Step 5: Postprocessing of components

As with the manufacturing of the components, the postprocessing necessary is dependent on the specific AM process that was utilized. A myth pervades common understanding that AM techniques produce components in a fully finished state, but they rarely do. The effort and cost of postprocessing are AM process–specific but can include tasks such as excess powder removal, support scaffolding removal, further UV exposure, and heat treatment. Once postprocessing is complete, a final physical object of the original CAD file is obtained.

AM's ability to allow the creation of a physical part from a CAD file with four intermediate steps (.stl file creation, AM machine setup, component manufacture, and postprocessing) makes it extremely adept at creating prototype components, low-volume/high-value components, and customized components. The whole process of moving from electronic data to a finished manufactured component can be achieved in hours or days. In addition to these abilities, AM also offers a much greater degree of design freedom due to superior complexity being attainable when using a layer-by-layer (additive) manufacturing methodology, as opposed to a subtractive or formative methodology. Finally, AM has the potential to revolutionize manufacturing by allowing a direct link between the intricate complexities attainable with a CAD model (e.g., intricate internal lattice structures) and the manufactured end component. A user with sufficient CAD skills can produce designs of complexity that are unobtainable via subtractive and formative manufacturing and/or are beyond the manufacturing skills of the user.

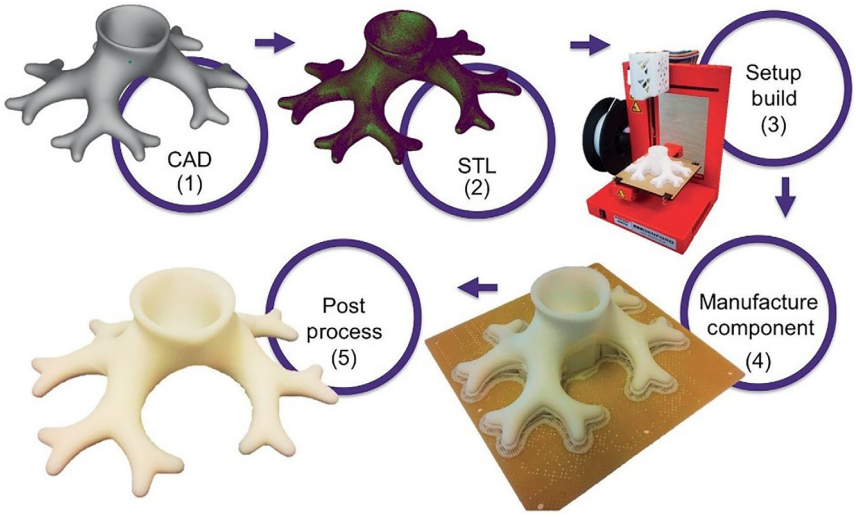


FIGURE 12.2 Steps required to move from CAD model to part via AM.

AM is a relatively new area of manufacturing (originally conceived in the mid-1980s) that is currently receiving much research, funding, and media attention globally; this, when coupled with the unique abilities stated before, helps explain why these technologies have been heralded by some as the next industrial revolution (Hopkinson et al., 2006).

Hybrid manufacturing is a new extension of AM and follows the same setup procedure as AM, with tool paths for the subtractive manufacturing processes also being created for each layer. The integration of the processes allows for some of the common disadvantages of AM (dimensional accuracy and surface finish) to be overcome while retaining the advantages of selectively depositing material and working in a layer-by-layer fashion.

12.1.2 AM process categories

As previously mentioned, AM is relatively new and, therefore, is often lacking in the level of standardization when compared with more mature processes. However, one area that has been standardized is the categorization and naming of the AM process families. AM is also known by many other names, the most common of which are 3D printing and rapid prototyping.

However, the American Society for Testing and Materials (ASTM) Committee F42 on Additive Manufacturing Technologies has standardized the terminology used, and this has now been formulated into an ISO standard (ISO/ASTM, 2015). This standard naming states that AM is the correct terminology for the technology area. The technology area was further broken down into seven process categories, namely, vat photopolymerization, powder bed fusion, material jetting, binder jetting, material extrusion, directed energy deposition, and sheet lamination.

Vat photopolymerization (VPP) is defined as the "process in which liquid photopolymer in a vat is selectively cured by light-activated polymerization" (ISO/ASTM, 2015). This process category contains the stereolithography process.

Powder bed fusion (PBF) is defined as the "process in which thermal energy selectively fuses regions of a powder bed." This process category contains the laser melting and laser sintering processes.

Material jetting (MJT) is defined as the "process in which droplets of feedstock material are selectively deposited." The object manufacturing process is an example process of this category.

Binder jetting (BJT) is defined as the "process in which a liquid bonding agent is selectively deposited to join powder materials." This category contains the ZCorp 3DP processes.

Material extrusion (MEX) is defined as the "process in which material is selectively dispensed through a nozzle or orifice." This category is the main driver for the small "desktop" 3D printer market.

Directed energy deposition (DED) is defined as the "process in which focused thermal energy is used to fuse materials by melting as they are being deposited." The laser engineered net shaping (LENS) is an example process in this category.

Sheet lamination (SHL) is defined as the "process in which sheets of material are bonded to form a part." UAM is an example process in this category where the sheets of material are bonded by ultrasonic welding, and CNC machining is used to define the internal and external material contours.

Not all AM processes are well suited or capable of producing solid metal components. The process categories that are most commonly utilized for metal components are PBF and DED. UAM also produces solid metal components, and the particular characteristics of each of these are compared in Figure 12.3.

12.2 Ultrasonic additive manufacturing

The UAM process (Figure 12.4) was invented and patented by Dr Dawn White (White, 2003) and is now commercially provided by Fabrisonic LLC, United States. UAM is a hybrid additive/subtractive manufacturing technology that combines ultrasonic welding (USW) with CNC machining by using an ultrasonic welder to join metal foils, layer by layer, and then periodic contour CNC milling to create a solid metal three-dimensional (3D) component (White, 2003a) that replicates the original 3D CAD model. This permits the production of a diverse array of net shape components.

During UAM, energy generated from an ultrasonic transducer is transferred to a metal workpiece through a roughened sonotrode in the form of ultrasonic oscillation. These oscillations, combined with a compressive normal force from the sonotrode, allow interlaminar metal flow with associated localized heating, which is much lower than the melting temperature of the metal (typically $<50\%$ of the melting temperature (Daniels, 1965; Jones and Powers, 1956; Joshi, 1971; Okada et al., 1963; de Vries, 2004), resulting in solid-state bonding at the consolidation interface.

UAM was originally patented as ultrasonic consolidation (UC)—a term by which it is still sometimes referred to. The initial commercialization of the UAM process was performed by Solidica Inc. (Ann Arbor, Michigan, United States) which was a company created by Dr White to commercialize the UAM technology. The first machines were sold under a brand name of Formation (Figure 12.5). The Formation systems consisted of a 3-axis CNC vertical mill with an integrated rolling USW assembly and an automatic metal tape feed. The Formation used a CAD system called RPCam

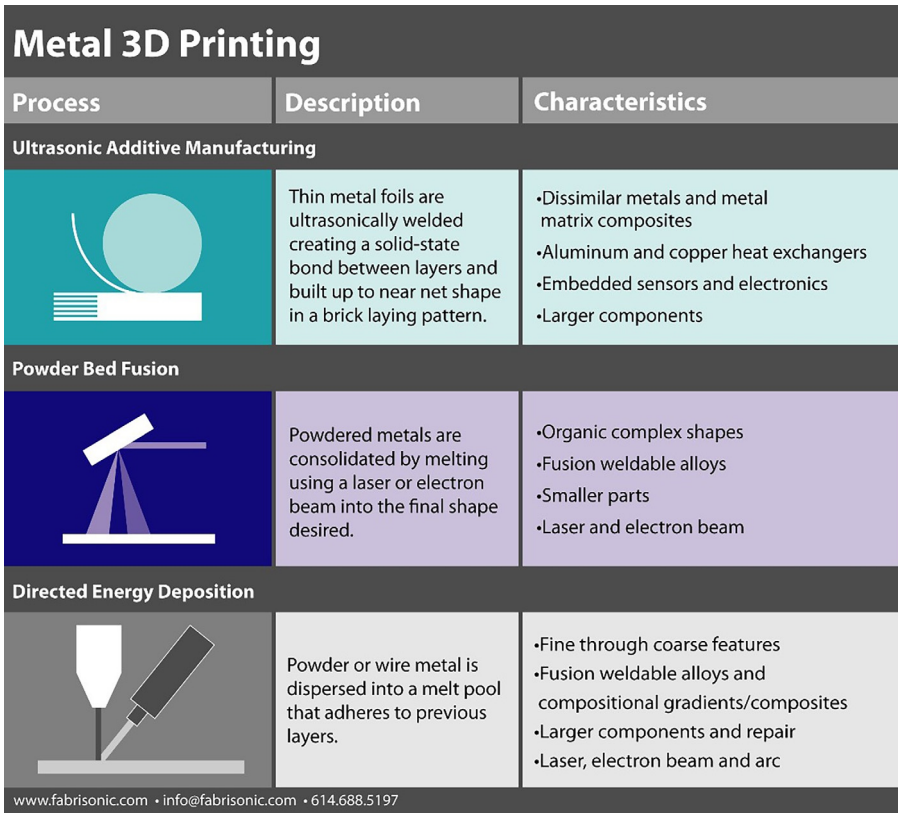


FIGURE 12.3 Comparison graphic for ultrasonic additive manufacturing (UAM) against powder bed fusion (PBF) and directed energy deposition (DED).

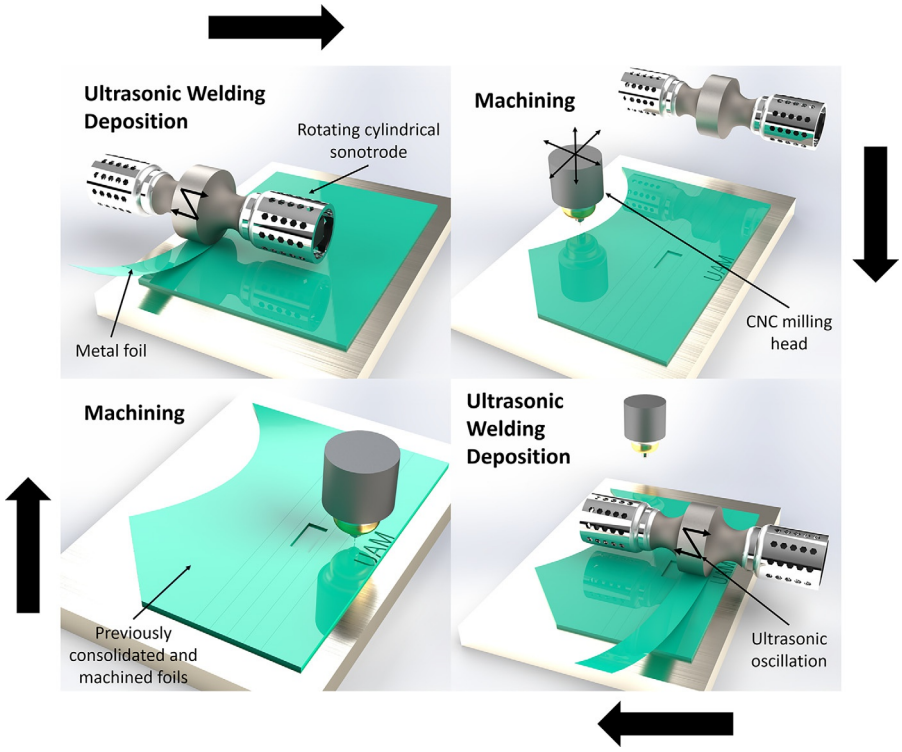


FIGURE 12.4 Schematic diagram of the ultrasonic additive manufacturing process. Beginning from top left, the process repeats the deposition machining cycle until the part is complete.



FIGURE 12.5 Solidica formation machine.

to create all the required machine codes for material deposition and CNC removal directly from a 3D CAD design.

More recently, the technology has become available through Fabrisonic LLC (Columbus, Ohio, United States). A new technology that used a dual transducer-booster setup allowed the UAM equipment to increase significantly in the energy input to the metal-to-metal bond interface. This setup relies on push-pull coordination between transducer elements, and the increased power allows for larger sonotrode amplitudes under higher loads. A greater range of materials are now possible with superior mechanical properties over the original system parts. The maximum power of the UAM systems has now increased from the initial 1 to 9 kW.

The original UAM systems (Formation) were based on a 1 kW seam welder that was a standard USW system. These systems allowed the processing of softer grades of aluminum alloys such as 3003 and 1050. These materials were suitable for creating rapid tooling, prototype metal components, and complex aluminum structures; however, they were limited in engineering applications due to the limits of the aluminum grades being used.

In 2008, Solidica Inc. partnered with the Edison Welding Institute (EWI) to research into and develop a higher power system that could be used for UAM. This was a significant technical challenge and resulted in the development of a patented weld head design that allows for higher powers as well as higher weld pressures. This new head (Figure 12.6)

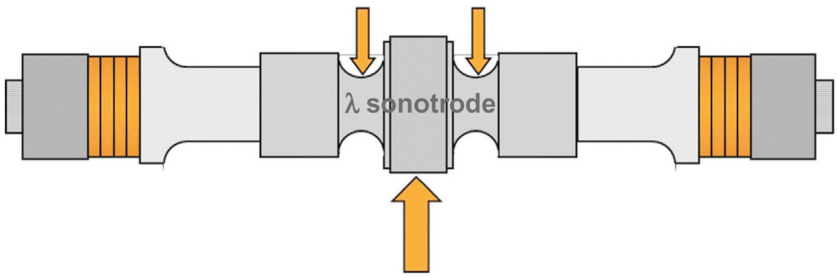


FIGURE 12.6 Push-pull sonotrode design that has allowed the move to higher power UAM systems. *(Image courtesy of the Edison Welding Institute.)*



FIGURE 12.7 Fabrisonic SonicLayer 4000.

design resulted in a ninefold increase in the USW power in the UAM system with the new state-of-the-art UAM machines, now boasting 9 kW power capabilities.

The result of the higher power UAM system has been a large-scale expansion in the metal materials that can be used. The material list now contains, but is not limited to, higher strength aluminum alloys (e.g., 2024, 7075), stainless steels (e.g., 316 L), coppers, and Inconel. In 2011, Solidica Inc. and EWI created a joint venture known as Fabrisonic LLC to manufacture, develop, and distribute this new phase of high-power UAM equipment.

Currently, there are three high-power UAM systems available from Fabrisonic: the SonicLayer R200, SonicLayer 4000 (Figure 12.7), and SonicLayer 7200. The main differences among the three systems are the build area available and the level of automation and CNC incorporation. Due to the lack of atmospheric control requirements, the UAM process is scalable and the 7200 has a build volume of 72 72 36″, which is very large for an AM process, and this scale would represent a very significant barrier to other metal-based AM processes such as selective laser melting and electron beam melting.

The development of the high-power UAM machine, referred to as very high-power ultrasonic additive manufacturing (VHP-UAM) was driven by the demand for higher amplitudes (de Vries, 2004) and normal forces to increase the plastic flow between bonds (Schick et al., 2011). For instance, the SonicLayer 7200 is able to apply oscillation amplitudes of up to 52 µm and normal forces of up to 15 kN (Sriraman et al., 2010).

12.2.1 System components

The "additive" component of the UAM process is USW, and as previously stated, this form of welding joins metal parts by transferring the energy of high-frequency oscillations to the bond interface area between the parts to be welded (Devine, 2011; Graff, 2007). Electrical energy is transformed into high-frequency mechanical vibration, and this mechanical vibration is transferred to the component material surfaces through the sonotrode. In UAM, the parts are oscillated together under a pressure of approx. 20,000 cycles per second, resulting in solid-state metal bonding (Graff, 2011). Figure 12.8 shows the components that make up the welding head in the UAM equipment.

12.2.1.1 *Power supply*

The power supply is used to convert the conventional mains electricity supply from 50/60 Hz to the high-frequency supply needed to operate the transducer at an ultrasonic frequency (typically 20–40 kHz). The power supply allows the amplitude of the ultrasonic oscillations of the sonotrode to be altered, which increases the energy supplied to the weld interface. The power supply also has built-in safety features to prevent the transducer from being damaged during the welding cycle by monitoring feedback from the transducer so as to stop the cycle if the resistance to welding/oscillation is too high.

12.2.1.2 *Transducer*

The transducer, also known as the converter, is part of the ultrasonic stack and is the component of the system that converts the high-frequency electrical signal into high-frequency mechanical oscillations. Within the transducer, there are multiple (most designs use two, four, or six) ceramic piezoelectric elements that, when subjected to an alternating voltage, will cyclically expand and contract at the frequency of the voltage alternation. The energy conversion by the transducer from electrical to mechanical energy is highly

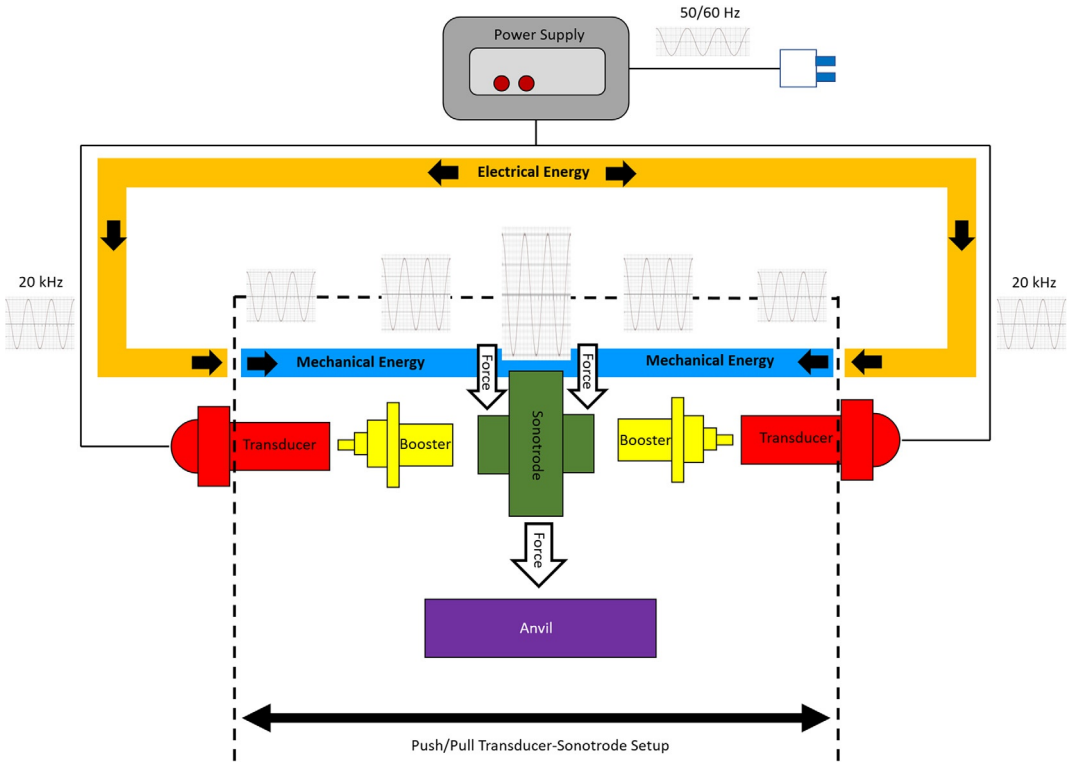


FIGURE 12.8 Schematic of the components of an ultrasonic welding system.

efficient (typically 90%). The modern UAM systems use two transducers on either side of the sonotrode that are synchronized to push and pull in unison to greatly increase the amplitude and underload performance.

12.2.1.3 Booster

The booster acts as a coupler between the transducer and the sonotrode and helps determine the amplitude of vibration produced at the tip of the sonotrode face. The booster is a resonant half-wave metal device that is typically made from titanium or aluminum (to help minimize mass and thus hysteresis of the system). A booster is specifically designed to resonate at the same frequency as the transducer that it is mechanically attached to. The booster is used as a rigid mounting point for the whole ultrasonic stack and acts as an amplifier to the transducer amplitude. The level of amplitude gain is specific to the booster. The modern UAM systems use a booster on either side of the sonotrode. A pneumatic actuator applies a downward force to the welding head via two points between the boosters and the sonotrode.

12.2.1.4 Sonotrode

The sonotrode (also known as the horn) is the "tool" of the ultrasonic welder. It is the component that comes into direct contact and supplies the energy to the metal materials to be welded. A sonotrode is specifically designed for its intended application and will typically be tuned to act as a half-wavelength resonant device that will uniformly supply pressure and vibration to the metal parts to be welded. The sonotrode is mechanically fixed to the boosters of the ultrasonic stack. The shape of the sonotrode determines the final amplitude that is experienced at the sonotrode face and, hence, the amplitude that will be used to weld two metal materials. To ensure adequate mechanical coupling and energy transmission between the sonotrode and the uppermost metal material to be welded, the sonotrode face is textured. Typical sonotrode materials are titanium, aluminum, and steel. Titanium materials are favored due to low loss of vibration and high strength; aluminum is often coated with chrome or nickel to reduce wear; and steel is generally used for low-amplitude applications for which hardness is required.

12.2.1.5 Anvil

The anvil is not attached to the ultrasonic stack but is essential to the operation of the UAM process. The anvil acts as the base for the metal materials to be bonded and provides the rigid platform to which the normal force, from the sonotrode, is applied. The anvil must be sufficiently strong and rigid to minimize deflection during the welding process. Material is not bonded directly to the anvil, instead a metal baseplate is placed upon and fixed to the anvil. It is onto the baseplate that the metal foils are bonded.

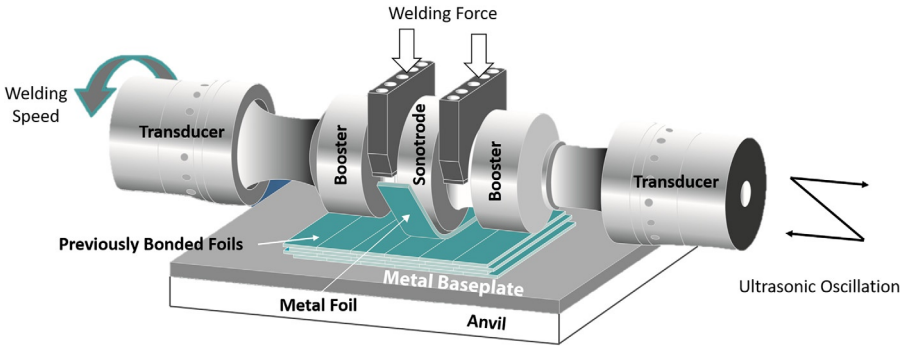


FIGURE 12.9 Schematic of ultrasonic additive manufacturing welding head and process parameters.

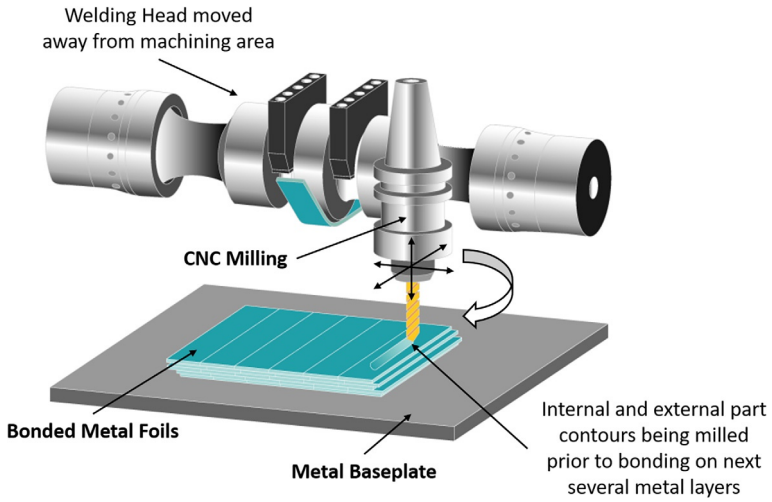


FIGURE 12.10 Schematic of the UAM machines integrated machining center.

12.2.2 Process operation

A schematic of the UAM system setup is shown in Figure 12.9. The second main component of the UAM machine is the integrated CNC system, which is used to create the geometry from the data supplied via the 3D CAD model (Figure 12.10).

As previously stated, the UAM process is both an additive and subtractive process—a hybrid manufacturing technology, if you will. The process deposits multiple foils over the build area to an area greater than the intended part. The CNC mill then removes the material to match the desired geometry. The desired geometry is determined via CADCAM software, which has "sliced" a 3D CAD geometry into layers to calculate each layer's deposition and machining requirements. By building up in a deposit-machine-deposit-machine method, UAM can create a full dimensionally accurate solid metal model of the original 3D CAD geometry directly from electronic data with no additional jigs, tooling, or fixturing required.

There are multiple process parameters that have been identified as significant in the quality and strength of the bonds that are formed between metal foils and the workpiece during UAM. The quality of this bonding is related to the coaction of the process variables (Yang et al., 2009) and the physical and chemical properties of the materials (Daniels, 1965; Joshi, 1971; de Vries, 2004). The most important known process variables are outlined in the following paragraphs.

12.2.2.1 Welding speed

The welding speed is a directly controlled (set via machine control) UAM machine parameter. This is the speed that the sonotrode traverses over the workpiece; the speed of the sonotrode rotation is matched to the speed of the welding head gantry to ensure the foil material is not stretched or crumpled. The welding speed directly influences the weld duration, which is the length of time that the area of material directly under the sonotrode will undergo compression and oscillation. Kong et al. (2003) stated that a decrease in the welding speed would increase the energy delivered to the workpiece at a given contact pressure and amplitude, which may result in higher levels of strain hardening. The converse of this effect is that too high weld speeds result in insufficient bonding (Kong et al., 2004b). Therefore, the welding speed must be correctly set for the given foil material to ensure that sufficient bonding takes place.

12.2.2.2 Sonotrode oscillation amplitude

The oscillation amplitude is a directly controlled UAM machine parameter that relates to the maximum lateral displacement of the sonotrode surface as it undergoes ultrasonic oscillations. This amplitude has been shown to dictate the density of the bonded area, the thickness of the interface area, and the size of the deformed area (Joshi, 1971). In addition to these bond characteristics, the oscillation of the amplitude also determines the amount of elastic/plastic deformation between the workpiece and the substrate (Jones and Powers, 1956). Typically, the greater the amplitude, the higher the energy input into the foil-to-part interface during UAM; higher energy input has been shown to result in superior bond strength and greater plastic flow during USW (Friel et al., 2010; Hopkins et al., 2011; Kong et al., 2004b; Li and Soar, 2009; Tuttle, 2007; Yang et al., 2009; Weare et al., 1960). The normal force applied to the sonotrode and work pieces can hinder the amplitude of oscillation for higher loads. Thus, higher loads with higher amplitudes require higher ultrasonic power, which is what the push-pull system in UAM provides.

12.2.2.3 Welding force

The welding force is a UAM machine process variable that ensures intimate contact between the build materials during processing and also aids plastic flow during the ultrasonic processing (Yang et al., 2009). The welding force is only effectual in combination with the ultrasonic oscillations, which are necessary for creating dynamic stresses at the bond interface that facilitate oxide layer disruption and plastic flow (Yang et al., 2009). Typically, the higher the welding force, the greater the bonding area and decrease in interface void volume (Friel and Harris, 2010). There is a material-dependent limit on the welding force as too high a value can produce large levels of deformation, which can distort the bonded materials and result in excessive stresses (Kong et al., 2005; Yang et al., 2007). Too low a welding force results in insufficient deformation and contact at the bond interface, which in turn leads to nonbonding or a weak bond.

12.2.2.4 Anvil temperature

The anvil temperature (and thus the metal build plate/part) can be increased from ambient. A higher temperature during UAM has been shown to create denser, stronger bonds (George and Stucker, 2006). Also, the anvil set temperature rise as a result of the ultrasonic oscillation has been theorized to reduce stresses and improve atomic diffusion and recrystallization at the foil-part interface (O'Brien, 1991). Any potential strain hardening may also be reduced due to elevated processing temperatures. The increased anvil temperature is far below the melt temperature of the metal being bonded, and the bonding process is a solid-state process. As the materials remain in the solid-state atmospheric control of the UAM process is unnecessary, the anvil, materials, welding, and machining process are all conducted in ambient atmosphere.

12.2.2.5 Sonotrode topology

The topology of the sonotrode on a UAM machine creates and directly influences a roughness on the surface of the bonded metal materials. Figure 12.11 shows two different sonotrodes with different textures, and the resultant

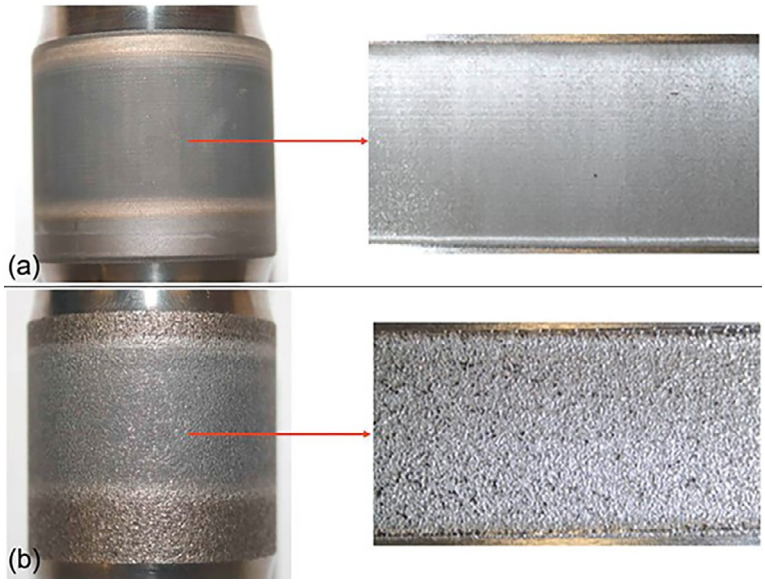


FIGURE 12.11 Different sonotrode topologies: (a) smooth topology (Sa 4.97 μm) and (b) rough topology (Sa 18.87 μm). *(Image reproduced courtesy of SAGE Publications (Johnson et al., 2011).)*

processed aluminum material to the right. The figure shows the level of topology transfer between the sonotrode and the workpiece during UAM.

The modified topology of the sonotrode is necessary to efficiently transfer kinetic energy to the bond interface during the oscillations and welding force transfer and to induce sufficient plastic flow for bonding (Friel et al., 2010; Johnson, 2008; Johnson et al., 2011; Li and Soar, 2009). The roughened surface creates a mechanical coupling and prevents energy loss through slippage (Weare et al., 1960). Although necessary, this topology transfer does result in a permanent change to the material surface (Friel et al., 2010; Kulakov and Rack, 2010), which can then adversely affect the bonding of subsequent metal layers (Edmonds, 2012), by increasing interlaminar defects at the bond interfaces.

During the UAM process operation, the sonotrode surface will wear, and thus, periodic resurfacing is needed for the sonotrode to maintain its efficiency in transferring the power supply power to the metal-to-metal bond interface.

The roughened surface and edge distortion that can occur due to the welding process do not affect the dimensional accuracy and finish of the end component in UAM as the component is manufactured at slightly larger than net shape and is then machined by the integrated UAM machining center to be final net shape.

12.2.2.6 CNC milling

The UAM system has an integrated CNC machining center that allows it to machine the external and internal contours of the UAM layers (see Figure 12.10). As with standard CNC systems, the choice of tool and cutting parameters (spindle speed, traverse speed, coolant on/off) can be varied and will result in differences to dimensional accuracy and surface finish. The integrated CNC milling ensures that UAM is capable of attaining metal components with greater dimensional accuracy and surface finish than PBF or DED metal components.

Figure 12.12 shows the bond development that occurs in UAM; this bond is affected by the specific processing parameters chosen for the machine and the specific metal materials being bonded.

In summary, the most important process variable parameters in UAM are welding speed, sonotrode oscillation amplitude, welding force, anvil temperature, sonotrode topology, and CNC milling.

12.3 Applications of UAM

12.3.1 Complicated geometry

By using UAM complex parts with unique features and attributes, which are not currently possible using traditional manufacturing techniques, can be and have been created. As with most other AM technologies, UAM can produce complex internal channels and voids that are impossible with traditional machining (Figure 12.13).

As the process builds layer by layer, it can be interrupted at any point in the z-height, and the integral CNC machining can be used to remove material from any point on the part. This allows the creation of voids that can subsequently be welded over, thus incorporating them into the structure. Because CNC machining can be performed on each individual layer of material deposited (if necessary), the size, shape, and orientation can be changed and produced in any axis.

This ability of UAM to create complex geometries out of solid metal components has been exploited for applications

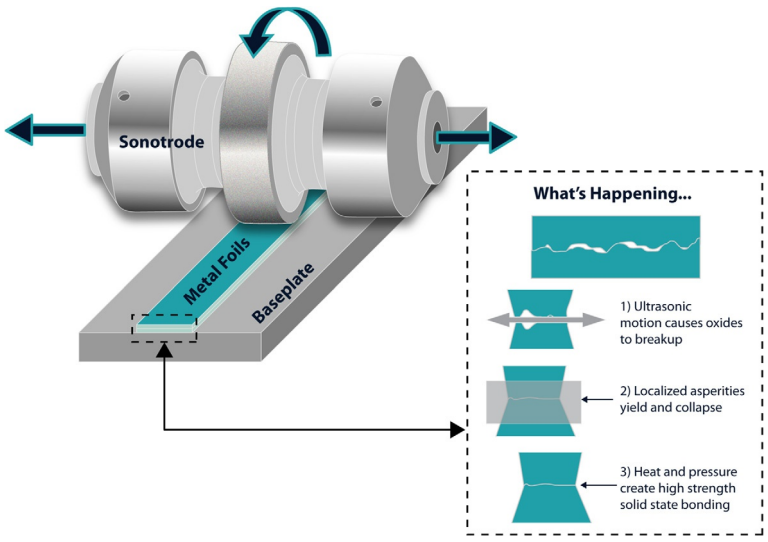


FIGURE 12.12 Schematic of the UAM bonding process.

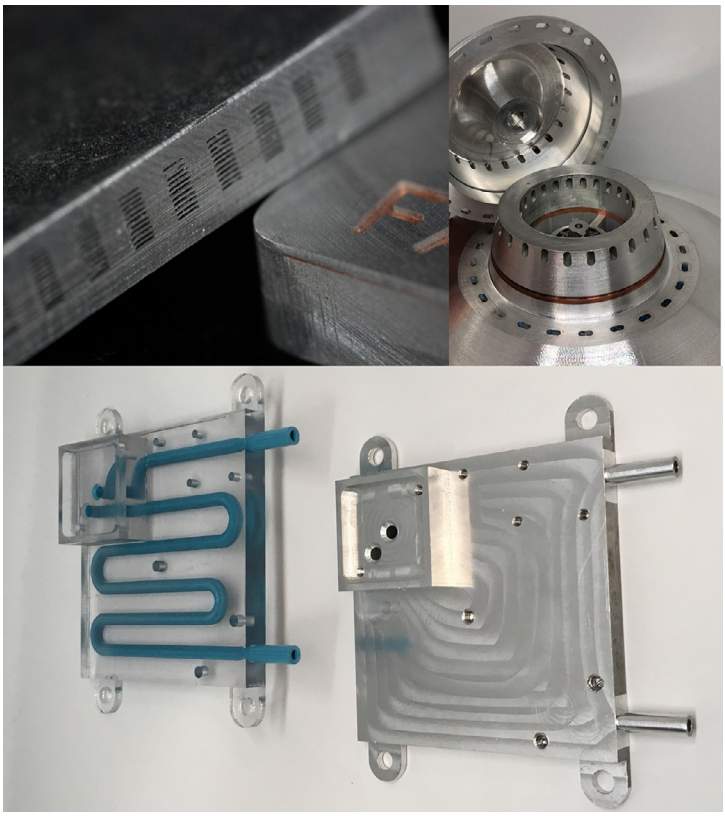


FIGURE 12.13 UAM complex geometry components. (Top left) Micron-scale channels throughout an aluminum component. (Top right) Integrated venting channels and machined coupling mechanism. (Bottom) Al 6061 metal heat exchanger and clear plastic demonstrator showing the internal piping present in the Al 6061 version.

such as creating complex three-dimensional channels for thermal management applications (i.e., microchannel cooling); integrated heat pipes; and conformal cooling channels for molds. Additionally, the ability to create complex internal geometry has been applied to radio frequency (RF) wave guides for antenna applications, light weighting of metallic components, and for cable runs that are completely internal to the structure.

12.3.2 Dissimilar material bonding

One of the key aspects of UAM that differentiate it from the vast majority of additive and traditional manufacturing techniques is that the metal joining is accomplished in the solid state; no bulk melting occurs during the process. This solid-state processing is beneficial in two ways. First, by avoiding material melting and staying below the transformation temperatures of most build metal materials, the inherent mechanical properties and metallurgical structure of the build metal are not adversely affected (e.g., aluminum alloys that have been precipitation-hardened do not reach and/or remain at a high enough temperature for long enough to result in any further precipitation reaction that would alter their desired properties). This has applications for materials such as high-strength aerospace aluminum alloys that are unable to be thermally welded without the loss or change of desired properties. The second benefit is that solid-state bonding allows for the creation of dissimilar metal structures. These structures avoid brittle intermetallics that can or would form with traditional thermal bonding processes and avoid the melt point mismatch that renders many metal combinations impossible.

There are many metal combinations that are possible with USW; however, not all combinations have been processed via UAM. Figure 12.14 depicts the known metal combinations available through ultrasonic metal welding and UAM. The advent of higher power UAM has expanded the dissimilar material possibilities.

The most straightforward application of the dissimilar material bonding via UAM is the cladding of one metal onto the surface of a component. In a traditional cladding operation, UAM is used to layer a more expensive or difficult material onto a bulk substrate of a cheaper or more workable material. Example applications of this have been, for instance, to weld titanium to aluminum so that the titanium acts as a heat- and wear-resistant layer on the outer edges of an aluminum component, thus prolonging the life of the base aluminum component. This cladding technique can

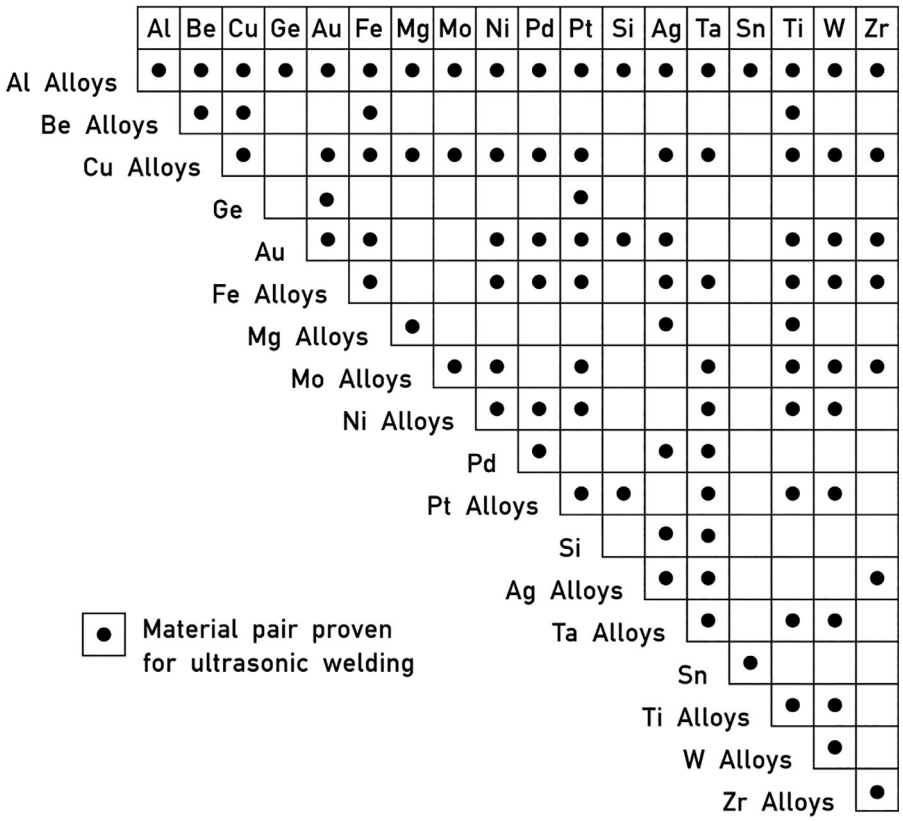


FIGURE 12.14 A chart depicting which materials are ultrasonically weldable and which have directly been used with the UAM process. *(Image courtesy of the American Welding Society (Johnson, 2009; O'Brien, 1991).)*

also be used to create transition joints between two dissimilar metal materials. For instance, UAM has been used to successfully manufacture steel-to-aluminum transition joints. The UAM process was utilized to create dissimilar transition parts that could then be integrated into larger structures through traditional welding technologies.

By using different materials in different layers during the UAM process, it becomes possible to create functionally graded metal laminates. Metal foils of alternating material types are welded into layered structures to create these laminates (Figure 12.15). By varying the ratio of one metal to another through thickness variations in the structures,

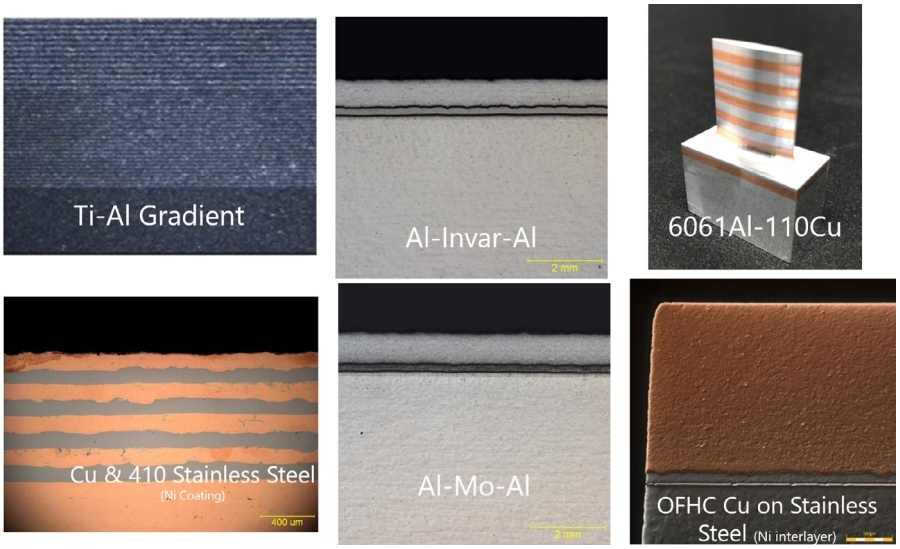


FIGURE 12.15 UAM manufactured functionally graded laminates using dissimilar metals bonded directly in the solid state.

material properties can be carefully controlled and engineered throughout the entire part.

12.3.3 Object embedment

In addition to dissimilar material bonding, a second unique key aspect of UAM is that a significant level of low temperature and high plastic flow can occur within the material during ultrasonic excitation, referred to as the "acoustoplastic effect" or "volume effect" in previous research (Kong, 2005; Sapozhnikov et al., 2000; Langenecker, 1966). This attribute can and has been exploited to allow the embedding of active (Kong, 2005; Kong et al., 2004a), passive (Yang et al., 2007), and optical fibers (Kong and Soar, 2005), as well as various other components (Kong, 2005; Mou et al., 2009), within an Al matrix (refer to Figure 12.16 for the embedding process and Figure 12.17 for an examples of embedded objects).

Metal foil material is bonded to a base plate by the sonotrode. Deposited foil fibers and/or other objects can be placed and secured onto this. A second metal foil is then placed on top of the objects, and the sonotrode then applies pressure and ultrasonic oscillations to the sample. The yield strength of the metal foil is reduced due to the acoustoplastic phenomena (Langenecker, 1966; Sapozhnikov et al., 2000), which, due to the pressure from the sonotrode, causes the foil to plastically deform around the objects between the foil layers. The metal foil then creates an intimate contact with the previously deposited foil and a solid-state bond is created. The "volume effect" takes place when the ultrasonic energy being inputted into the metal material increases the mobility of the dislocations between metal grains (Dawson et al., 1970; Hansson and Thölen, 1978; Langenecker, 1966). In plastic deformation, obstacles to dislocation movements, such as grain boundaries, result in the material, obtaining a higher strength and stiffness from a higher yield stress—work hardening. To overcome this effect and reduce the yield, stress energy input is required, which, in many other processing techniques, is provided in the form of heat. However, during UAM/USW, this energy is provided in the form of kinetic energy and allows the reduction of yield stress with little temperature increase. Experiments by Langenecker (1966) showed this phenomenon by obtaining stress-strain curves for static tensile tests in which samples were subject to ultrasonic excitation at 20 kHz (Figure 12.18). The graph on the right demonstrates the thermal requirements to obtain the same effect from ultrasonic excitation. The result of this phenomenon

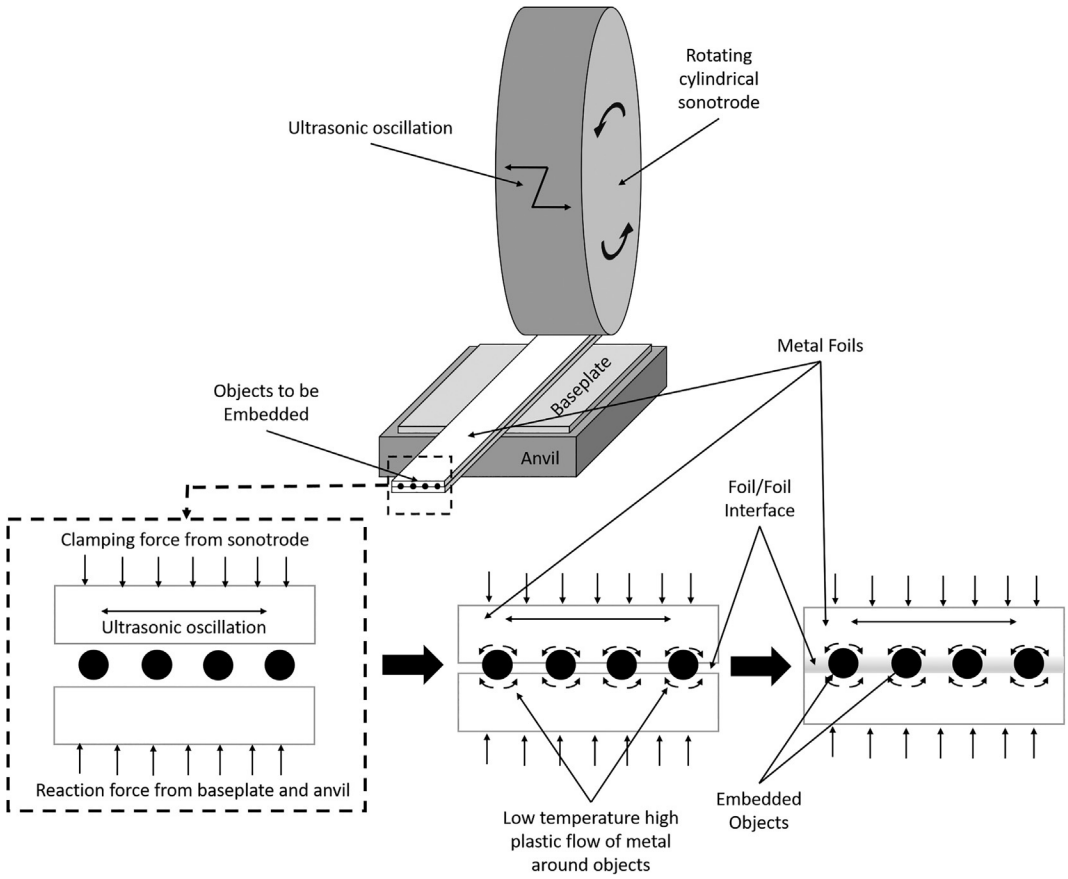


FIGURE 12.16 Schematic diagram of the ultrasonic additive manufacturing process for object embedment.

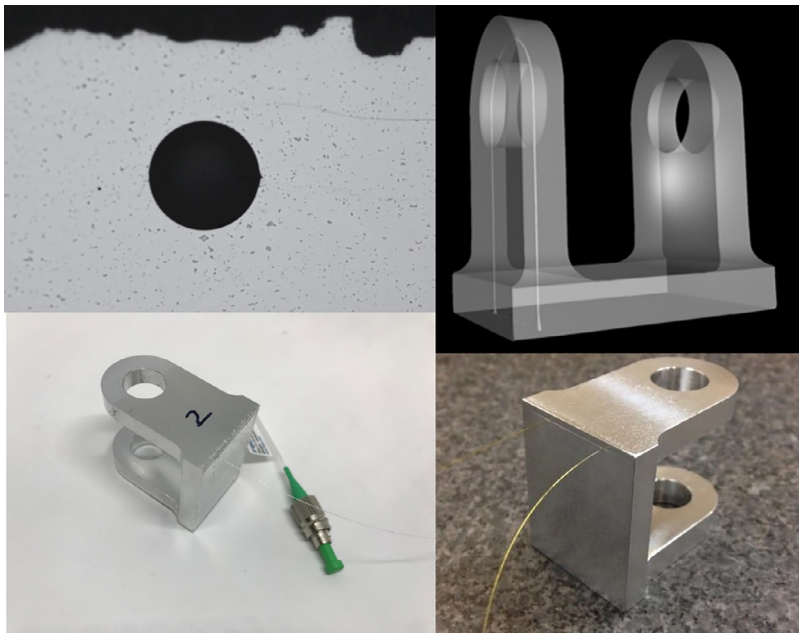


FIGURE 12.17 Example of embedded optical fibers in metal matrices via UAM. Clockwise: micrograph showing embedded optical fiber in Al 6061; CAD model of a bracket with an embed fiber optic strain sensor; UAM component with an embedded strain sensor; image showing the component and couplings for the fiber optic strain sensor.

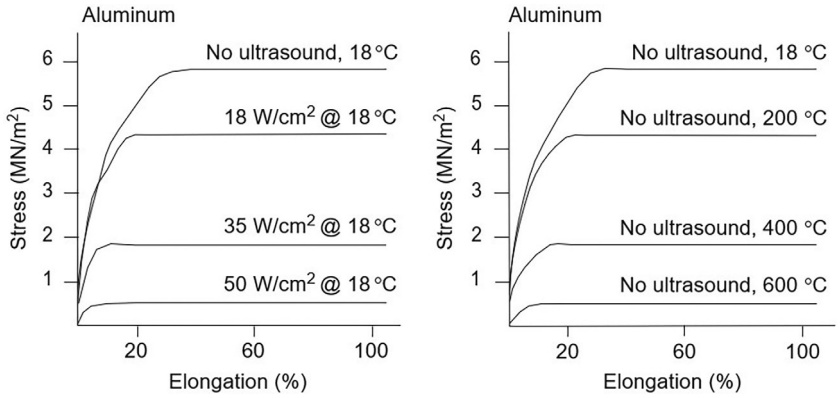


FIGURE 12.18 Comparison of the equivalent energy requirements for ultrasonic vs thermal energy. *(Image courtesy of the Institute of Electrical and Electronics Engineers (Langenecker, 1966).)*

is that plastic flow, due to reduced yield stress, during UAM/USW is sufficient to encapsulate objects that would otherwise require temperatures of over 50% of the metal matrix melt temperature.

There are multiple example applications of object embedment via UAM. Reconfigurable radio frequency antennas can be manufactured by laminating a shape memory alloy material to a spring steel to create a thin switch that can be easily embedded in a metal part. A small pocket is machined into a part, and UAM is used to embed the switch with subsequent layers of aluminum. By creating a predefined network of these switches, the narrow band limitations of existing antennae can be overcome to realize a multiband/broadband aperture, with a potential frequency bandwidth of 30:1 (100–3000 MHz). This particular application is of relevance to aerospace.

The expansion and contraction of engineered components when exposed to higher or lower temperatures (known as the coefficient of thermal expansion (CTE)) can often result in negative effects in many situations, such as causing fatigue, causing warping, and interfering with part tolerances. By embedding shape memory alloys into metal components via UAM, the CTE of the overall structure can be reduced.

This low CTE-engineered structure has applications for high-tolerance situations such as precision rotating parts within turbofan engines.

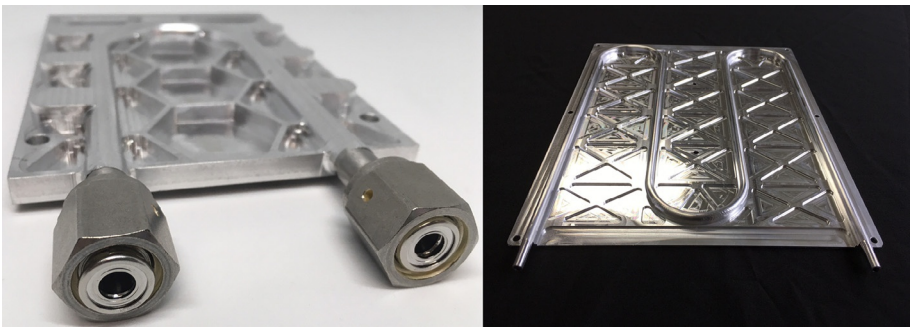


FIGURE 12.19 Examples of low-profile heat exchangers for high-pressure space applications.

UAM has been demonstrated to allow embedding of single-mode optical fibers into bulk metal for sensing applications (Figure 12.17). These optical fibers with the use of etched fiber Bragg gratings and broadband light sources can be used to function as strain and temperature sensors within solid metal components (Mou et al., 2009).

12.4 Future trends

With the new higher power UAM machines becoming de facto in the industry, new material combinations and never-before realized engineered structures are being developed via the exploitation of the unique combination of complicated geometry, dissimilar material bonding, and object embedding that UAM allows.

An increasing set of high-value applications have been benefitted by UAM such as bespoke heat exchanges, metal matrix composite structures, and RF waveguides (Figure 12.19).

Currently, UAM offers unique capabilities, and some future development is likely to continue into niche, high-value applications. In addition to this, reduction in machine size is being developed to make the process more suited to smaller components.

12.5 Conclusion

UAM takes well-established ultrasonic bonding techniques and moves them beyond simple planar welding into the realms of 3D AM. By building components from metal foils layer by layer, the UAM process is able to attain highly complex geometries that are only available from other metal-based AM processes. However, UAM is not limited by many of the issues surrounding metal powder–based AM processes, such as inert environment requirements, close temperature control requirements, powder handling requirements, and high-power laser requirements.

By exploiting two key properties of UAM, dissimilar solid-state metal bonding and object embedding, it is possible to manufacture components with embedded sensors, electronics, and strengthening components that are encapsulated within dissimilar metal matrices. These abilities of UAM are unique, and the direct exploitation of these abilities, coupled with the higher power UAM equipment now available, will likely lead to new possibilities in multiple engineering fields.

12.6 Sources of further information and advice

Other information on UAM may be found through the references used in this chapter. Two published book chapters on the area of UAM are as follows:

Gibson, Ian, Rosen, David W., Stucker, Brent (Eds.), 2010. Sheet lamination processes. In: Additive Manufacturing Technologies: Rapid Prototyping to Direct Digital Manufacturing. Springer, New York, ISBN: 1441911200 (Chapter 9).

Ultrasonic Additive Manufacturing. In: Lienert, T.J., Babu, S.S., Siewert, T.A., Acoff, V.L. (Eds.), 2011. Welding Fundamentals and Processes, AS M Handbook, vol. 6A. ASM International, Ohio, USA. ISBN: 1615031332.

The provider of the commercial UAM technology is Fabrisonic LLC. http://www.fabrisonic. com/.

References

Daniels, H.P.C., 1965. Ultrasonic welding. Ultrasonics 3 (4), 190–196.

Dawson, G.R., Winsper, C.E., Sansome, D.H., 1970. Application of high and low frequency oscillations to the plastic deformation of metals. Metal Form. 37 (2), 254–261.

de Vries, E., 2004. Mechanics and Mechanisms of Ultrasonic Metal Welding. PhD Thesis, Ohio State University, Ohio. ISBN: 9780496699346.

Devine, J., 2011. Ultrasonic welding. In: Babu, S.S., Siewert, T.A., Acoff, V.L., Lienert, T.J. (Eds.), Welding Fundamentals and Processes, ASM Handbook. vol. 6A. ASM International, Ohio, USA.

Edmonds, H., 2012. Interlaminar Bonding in Ultrasonic Consolidation. PhD Thesis, Wolfson School of Mechanical and Manufacturing Engineering, Loughborough University.

Friel, R.J., Harris, R.A., 2010. A nanometre-scale fibre-to-matrix interface characterization of an ultrasonically consolidated metal matrix composite. Proc. Inst. Mech. Eng. L J. Mater. Des. Appl. 224 (1), 31–40.

Friel, R.J., et al., 2010. The effect of interface topography for ultrasonic consolidation of aluminium. Mater. Sci. Eng. A 527 (16–17), 4474–4483.

George, J., Stucker, B., 2006. Fabrication of lightweight structural panels through ultrasonic consolidation. Virtual Phys. Prototyp. 4, 227–241.

Graff, K.F., 2007. Ultrasonic welding. In: O'Brien, A. (Ed.), AWS Welding Handbook. 3. The American Welding Society, USA, pp. 263–302 (Chapter 8).

Graff, K., 2011. Ultrasonic additive manufacturing. In: Lienert, T.J., et al. (Eds.), Welding Fundamentals and Processes, ASM Handbook. vol. 6A. ASM International, Ohio, USA.

Hansson, I., Thölen, A., 1978. Plasticity due to superimposed macrosonic and static strains. Ultrasonics 16 (2), 57–64.

Hopkins, C.D., Wolcott, P.J., Dapino, M.J., Truog, A.G., Babu, S.S., Fernandez, S.A., 2011. Optimizing ultrasonic additive manufactured Al 3003 properties with statistical modeling. ASME. J. Eng. Mater. Technol. 134 (1), 011004.

Hopkinson, N., Hague, R., Dickens, P., 2006. Rapid Manufacturing: An Industrial Revolution for the Digital Age. John Wiley & Sons, Ltd, Chichester, UK, ISBN: 9780470016138.

ISO/ASTM, 2015. INTERNATIONAL STANDARD ISO/ASTM 52900 Additive Manufacturing—General principles—Terminology. International Organization for Standardization, pp. 1–26, https://doi.org/10.1520/ISOASTM52900-15.

Johnson, K., 2008. Interlaminar Subgrain Refinement in Ultrasonic Consolidation. Doctoral Thesis, Loughborough University.

Johnson, K., 2009. Ultrasonic consolidation – a viable method of smart structure manufacture. In: Loughborough, 8th–9th July 2009, 4th International Conference on Rapid Manufacturing.

Johnson, K., Edmonds, H.C., Higginson, R.L., Harris, R.A., 2011. New discoveries in ultrasonic consolidation nano-structures using emerging analysis techniques. Proc. Inst. Mech. Eng. L J. Mater. Des. Appl. 225, 277–287.

Jones, J.B., Powers Jr., J.J., 1956. Ultrasonic welding. Weld. J. 35, 761–766.

Joshi, K.C., 1971. The formation of ultrasonic bonds between metals. Weld. J. 50 (12), 840–848.

Kong, C.Y., 2005. Investigation of Ultrasonic Consolidation for Embedding Active/Passive Fibres in Aluminum Matrices. PhD Thesis, Wolfson School of Mechanical and Manufacturing Engineering, Loughborough University, UK.

Kong, C.Y., Soar, R.C., 2005. Method for embedding optical fibers in an aluminum matrix by ultrasonic consolidation. Appl. Opt. 44 (30), 6325–6333.

Kong, C.Y., Soar, R.C., Dickens, P.M., 2003. Characterization of aluminum alloy 6061 for the ultrasonic consolidation process. Mater. Sci. Eng. A 363 (1), 99–106.

Kong, C.Y., Soar, R.C., Dickens, P.M., 2004a. Ultrasonic consolidation for embedding SMA fibres within aluminum matrices. Compos. Struct. 66 (1–4), 421–427.

Kong, C.Y., Soar, R.C., Dickens, P.M., 2004b. Optimum process parameters for ultrasonic consolidation of 3003 aluminum. J. Mater. Process. Technol. 146 (2), 181–187.

Kong, C.Y., Soar, R.C., Dickens, P.M., 2005. A model for weld strength in ultrasonically consolidated components. Proc. Inst. Mech. Eng. C J. Mech. Eng. Sci. 219 (1), 83–91.

Kulakov, M., Rack, H.J., 2010. Surface damage during ultrasonic consolidation of 3003-H18 aluminum. Rapid Prototyp. J. 16 (1), 12–19.

Langenecker, B., 1966. Effects of ultrasound on deformation characteristics of metals. IEEE Trans. Sonics Ultrason. 13, 1–8. https://doi.org/10.1109/T-SU.1966.29367.

Li, D., Soar, R., 2009. Influence of sonotrode texture on the performance of an ultrasonic consolidation machine and the interfacial bond strength. J. Mater. Process. Technol. 209 (4), 1627–1634.

Mou, C., et al., 2009. Smart structure sensors based on embedded fibre Bragg grating arrays in aluminium alloy matrix by ultrasonic consolidation. Meas. Sci. Technol. 20 (3), 034013.

O'Brien, R.L., 1991. Welding Handbook Eighth Edition, Vol. 2 – Welding Processes. American Welding Society, Miami, FL, ISBN: 0871713543, pp. 783–812.

Okada, M., et al., 1963. Joint mechanism of ultrasonic welding. Trans. Jpn. Inst. Metals 4 (1), 250–255.

Sapozhnikov, K., Golyandin, S., Kustov, S., Van Humbeeck, J., De Batist, R., 2000. Motion of dislocations and interfaces during deformation of martensitic Cu–Al–Ni crystals. Acta Mater. 48 (5), 1141–1151.

Schick, D., Babu, S.S., Foster, D.R., Dapino, M., Short, M., Lippold, J.C., 2011. Transient thermal response in ultrasonic additive manufacturing of aluminum 3003. Rapid Prototyp. J. 17 (5), 369–379.

Sriraman, M.R., Babu, S.S., Short, M., 2010. Bonding characteristics during very high power ultrasonic additive manufacturing of copper. Scr. Mater. 62 (8), 560–563.

Tuttle, R.B., 2007. Feasibility study of 316 L stainless steel for the ultrasonic consolidation process. J. Manuf. Process. 9 (2), 87–93.

Weare, N.E., Antonevich, J.N., Monroe, R.E., 1960. Fundamental studies of ultrasonic welding. Weld. J. 30, 331–338.

White, D., 2003a. Ultrasonic consolidation of aluminum tooling. Adv. Mater. Process. 161 (1), 64–65.

White, D., 2003. Ultrasonic object consolidation. U.S. Patent 6519500. Retrieved from https://patents.google.com/patent/US6519500B1/en.

Yang, Y., Janaki Ram, G.D., Stucker, B.E., 2007. An experimental determination of optimum processing parameters for Al/SiC metal matrix composites made using ultrasonic consolidation. J. Eng. Mater. Technol. 129 (4), 538–549.

Yang, Y., Janaki Ram, G.D., Stucker, B.E., 2009. Bond formation and fiber embedment during ultrasonic consolidation. J. Mater. Process. Technol. 209 (10), 4915–4924.

Chapter 13

Ultrasonic metal forming: Materials

X. Liu[a] and K.F. Graff[b]
[a]The Ohio State University, Columbus, OH, United States, [b]EWI, Columbus, OH, United States

13.1 Introduction

Metal forming is a primary manufacturing process whereby a material of a simple form emerging from a shaping operation (e.g. casting, melt extrusion, and die casting) is subjected to plastic deformation via processes such as forging, drawing, bending, extrusion, and rolling into a well-defined shape as an end product, or for subsequent processing through machining, metal treatment, and joining (Altan and Tekkaya, 2012; Altan et al., 1983). Ultrasonic metal forming is the application of ultrasonic vibrations to these varied processes for the purpose of enhancing performance, for example, achieving increased production speeds, less tool wear, reduced forming forces, and better surface finish.

While it had long been recognized that low-frequency vibrations could assist conventional metalworking (Sansome, 1986), the catalyzing event that initiated ultrasonic metal forming as a unique field was a brief note by Blaha and Langenecker (1955) that reported a significant reduction of yield stress with application of ultrasound. Variously identified as the "Blaha effect" or "acoustic softening," its potential importance to metal forming was quickly seen, resulting in lines of research and development that are active to the present day. It will be the purpose of this chapter to cover this field by examining the materials and the effects of power ultrasonics on metals as related to forming. Chapter 14 will then examine the forming processes to which ultrasonics have been applied.

While it is evident that the physical effects of ultrasound on materials will play a critical role in forming (as it does for machining, welding, and other processes), what is unusual in forming is the long attention this area has received since the earliest Blaha and Langenecker disclosure on yield strength reduction. This observation aroused both interest and controversy as to the underlying mechanism(s), the view being that ultrasonic metal forming could not be industrially developed without a better understanding of material behavior. For this reason, attention is first given to the materials area in this chapter, then the various forming processes are covered in Chapter 14.

Ultrasonic metal forming depends on the physical effects of vibrations on both the volume and surface of the metal being formed. The range of these effects is extensive and can include (Abramov, 1994, pp. 119–271) attenuation, generation of dislocations and plastic deformation, diffusion, heating, phase transformations, fatigue, and changes in surface friction. While subject to separate categorization, most are interdependent; thus, macroscopic levels of plastic deformation are tied at the microscopic level to dislocation behavior. In the following sections, the effects of ultrasound on metals will be reviewed in three categories: microstructure effects, macrostructure effects, and surface effects, with emphasis on the latter two as being critical to metal forming applications.

13.2 Microstructure effects

The effects of ultrasonic vibrations and waves on the microstructure of metals, or conversely, the effects of microstructure on vibrations and waves, is a field that is the source of an enormous number of studies, of which the collected papers in the 35-year landmark series "Physical Acoustics" (Mason et al., 1964–1999) are an example. While there may not be a single, all-inclusive source for such information, the work of Abramov (1994) may come closest to the needs of a chapter focused on ultrasonic metal deformation and will be closely followed in this brief overview.

First, considering energy losses under ultrasonic vibrations, there are numerous means by which the energy of ultrasonic waves and vibrations may be lost or attenuated. These can include scattering by defects in the crystal lattice and reflection from grain boundaries, where mode conversion can drive formation of complex wave structures, all subtracting energy from a propagating beam of sound. Thus, the result of wave interactions (reflection, transmission, mode conversion) at grain boundaries, phase changes, domain walls, or, in general, any type of inhomogeneity all can lead to loss of energy from the beam of sound. The strength of scattering from inhomogeneities, such as inclusions, is strongly dependent on the relation of the acoustic wavelength to the characteristic dimensions of the inclusion, becoming more pronounced as wavelengths approach the

Power Ultrasonics. https://doi.org/10.1016/B978-0-12-820254-8.00007-5
Copyright © 2023 Elsevier Ltd. All rights reserved.

object's dimensions. For power ultrasonics, where wavelengths may be on the order of 10^2 mm, scattering effects may be less pronounced than in physical acoustic regimes, where wavelengths can be 10^{-3} mm or shorter.

There are three absorption loss mechanisms, as summarized by Abramov, these being due to relaxation, hysteresis, and resonance. In many instances, studies in this field apply mainly at very high frequencies (e.g. >1 MHz). However, data have been developed that apply to the power ultrasonic range of frequencies, such as that for aluminum and copper, as shown by Figure 13.1, which accounts for heating observed under high-power vibrations.

Vibrations and waves in crystalline solids are also subject to losses due to dislocation movement. The incorporation of loss effects in the macroscopic modeling of material behavior may take the form of a complex modulus representation, such as $E^* = E(1+i\delta)$, where δ is the loss factor of Young's modulus of a material, or the use of Voigt-Kelvin model for viscoelastic materials.

Over many years, exhaustive studies have been conducted on the effects of power ultrasonics on the dislocation structure and formation of point defects in metals, as summarized by Abramov (Sec. 2.1) and in various sections of Puskar (1982). Data clearly show ultrasonic vibrations can increase dislocation density in metals, with the evolution of the dislocation structure leading to an increased concentration of point defects (Abramov, Sec. 2.2). Nearly every class of pure and engineering materials has, at one time or another, been examined under ultrasonic vibrations, with methods including examination of etch pits, SEM, and X-ray. The influence of ultrasonic frequency, amplitude, time, and temperature is among the parameters that have been studied. While there is extensive fundamental data on the effects of ultrasound on the metallurgical structure, as will be seen in a later section, the task remains of tying these data to accepted macroscopic engineering models of materials.

The effects of ultrasound on the diffusion of C and other elements (e.g. N, Cr, and Ni) into various alloy steels have also been extensively studied, with interest on the potential influence of high-temperature processes. Measurements of the diffusion coefficient have found there exist strain thresholds below which little effect is noted and, in some cases, maximum strain levels beyond which little additional effect is found. Limited results on the effect of frequency indicate a negligible frequency effect on diffusion. The basic mechanism affecting diffusion is directly related to the effects of ultrasonics on the dislocation structure of the material and is thus tied to effects described in the preceding section.

Studies conducted on the effects of ultrasonics on the structure of metal show that phase transformations can also be affected. Thus, the recrystallization rate of Cu was increased, with it being suggested as due to the activation of grain boundaries. Grain boundary migration in Al crystals was found to be increased, as was the rate of martensitic transformation in a bearing steel, if strain was beyond a critical threshold. Likewise, the rate of austenitic decomposition in steels was found to be increased.

Since the foregoing summary of Abramov, there have been a number of developments that have further advanced the understanding of ultrasound effects on the material microstructure, as described in the following text. Thus, ultrasonic effects on the microstructure evolution for different material systems have been performed in multiple length scales. Siu et al. (2011) performed ultrasonically assisted hardness indentation tests on FCC aluminum and observed enhanced subgrain formation, as shown in Figure 13.2. In their experimental setup, the ultrasonic vibration direction is transverse to the compression direction, whereas longitudinal vibrations aligned along the deformation direction are used in most ultrasonically assisted material tests. In a follow-up study by Siu and Ngan (2013) based on the same setup and procedures, ultrasonic effects on FCC copper and BCC molybdenum were studied. Similar to aluminum, enhanced subgrain formation

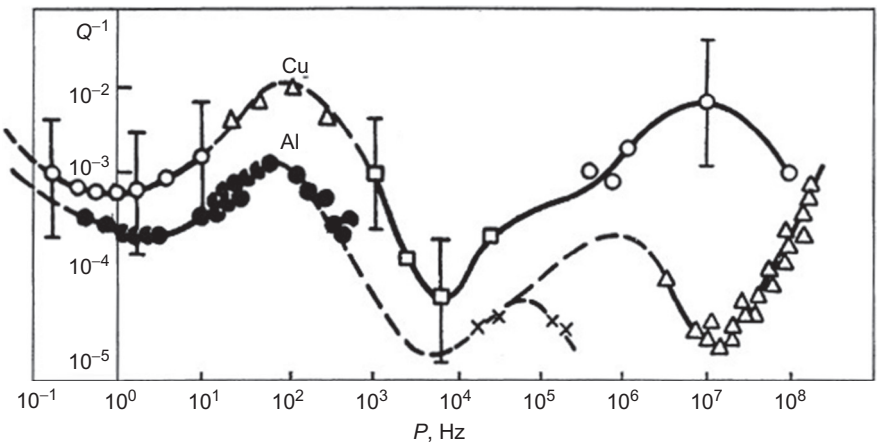


FIGURE 13.1 Losses in copper and aluminum in power ultrasonic range of frequencies (Abramov, 1994, Fig. 1.5).

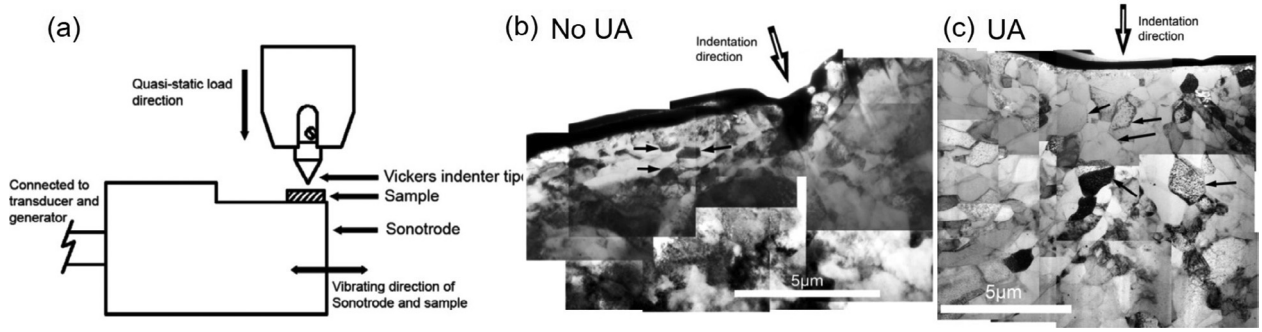


FIGURE 13.2 (a) Schematic of the ultrasonically assisted indentation test; (b) TEM images of the sample without ultrasonic (UA) vibration; (c) TEM images of the sample with UA, where enhanced subgrain formation is observed (Siu et al., 2011, Figs. 1, 6).

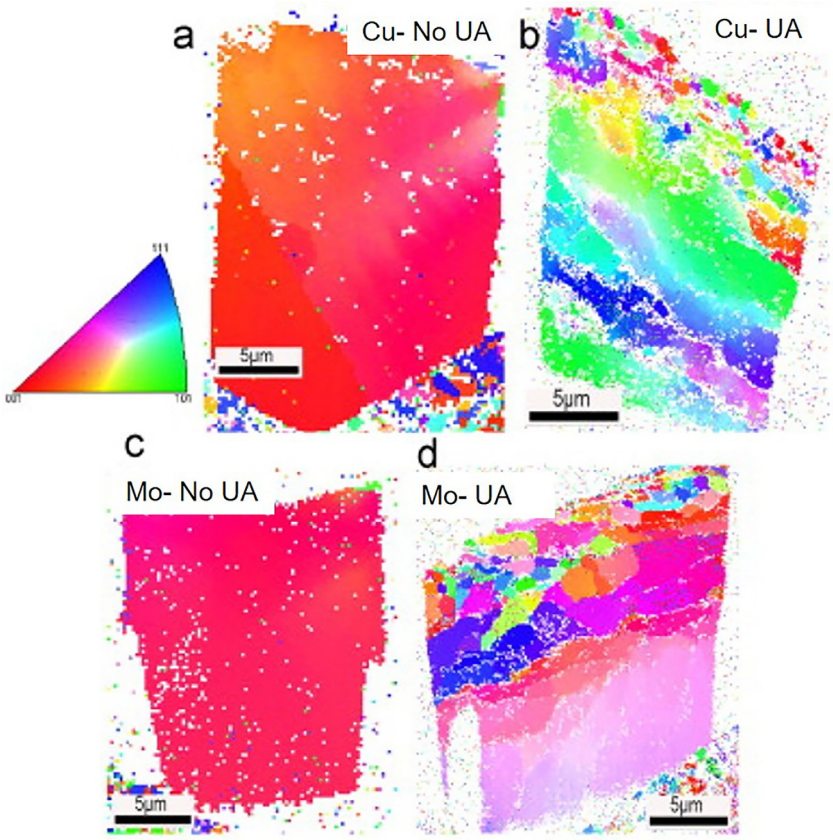


FIGURE 13.3 EBSD orientation map of samples with indentation tests: (a) copper without vibration, (b) copper with 2-μm ultrasonic vibration, (c) molybdenum without vibration, and (d) molybdenum with 2-μm ultrasonic vibration (Siu and Ngan, 2013, Fig. 2).

was also observed in those two material systems, as shown with the EBSD results in Figure 13.3. Sui et al. (2011) performed 2D dislocation dynamic simulations and attributed this microstructure evolution to enhanced dipole annihilation. Deshpande and Hsu (2018) applied transverse ultrasonic vibration during compression of pure aluminum and observed that dynamic recovery is enhanced, and the fraction of low-angle grain boundaries (LAGB) and grain size is increased with higher acoustic energy density. These are contrary to the findings of Hu et al. (2018a, b) who performed microcompression tests on pure aluminum with longitudinal vibrations and observed the ultrasonic dynamic impact generates a large amount of dislocations, which prohibits dynamic recovery. Zhou et al. (2018) also performed longitudinal ultrasonically assisted compression tests on aluminum and observed residual hardening effects, which are attributed to the grain refinement and crystallite rotation induced by ultrasonic vibration. Similar phenomena were also observed by Hung and Lin (2013) when they performed ultrasonically assisted upsetting on aluminum alloy AA6061-T6. Grain refinement occurred on the specimen surface.

Kang et al. (2020) studied ultrasonic softening effects from a new perspective based on ultrasonically assisted microtensile tests. In their experiments, the gauge length of the tensile specimen is one order of magnitude smaller than the ultrasonic wavelength. In addition to reduction of flow stress, the in situ digital image correlation (DIC) analysis shows that the ultrasonic vibration modifies the strain distribution on the pure copper specimen (Figs. 13.4 a-d). They also performed infrared thermal imaging during the tensile tests and found that the temperature increase is minimal with ultrasonic vibration. Their EBSD results showed ultrasonic vibration promotes preferential grain reorientation and reduces the misorientation within grains (Figs. 13.4 e–f), which can explain the residual softening effects on pure copper.

For BCC materials, Dutta et al. (2013) reported reduction of subgrain for a low-carbon steel with in situ ultrasonic treatment during tensile tests, as shown in Figure 13.5. The fraction of low-angle grain boundaries, the amount of misorientations, and the amount of geometrically necessary dislocations are significantly reduced by the superimposed ultrasonic vibration. This is opposite to the observations of Siu et al. (2011, 2013). The difference, on the one hand, can be related to the different slip systems and deformation mechanisms between FCC and BCC crystal structures. On the other hand, it is also related to the relative direction between the ultrasonic vibration and material deformation. The transverse vibration may induce additional shear stress, which leads to enhanced subgrain formation. Hoseini et al. (2019) performed a ultrasonically assisted tensile test on St52 steel and found that with the same amount of ultrasonic energy, the amount of yield strength reduction increases from 8%, 18% to 27% with the average grain size from 10, 35 to 60 μm. They explained this phenomenon based on the fact that in specimens with refined grains, the total length of the grain boundary is greater. Since the ultrasonic energy is distributed over the entire grain boundaries, the softening is less effective with a lower energy density per unit area. Similarly, Ahmadi et al. (2015) observed that during ultrasonically assisted tension tests of FCC pure aluminum, higher reduction of flow stress can be achieved in samples with larger grains under the same amount of ultrasonic energy input. In their samples, the grain structure is refined through the ECAP process. They hypothesized that the ultrasonically induced dislocation annihilation is more effective for larger grains. On the contrary, this trend is less significant in the results of Wang et al. (2016). They performed ultrasonically assisted tension tests on pure copper foils with different grain sizes from 1.3 to 8.6 μm. The length of their samples was 41 mm.

For the HCP materials, due to their limited slip systems in room temperature, twinning is a dominant plastic deformation mechanism. Zhou et al. (2018) observed ultrasonic vibration promotes saturation of deformation twinning,

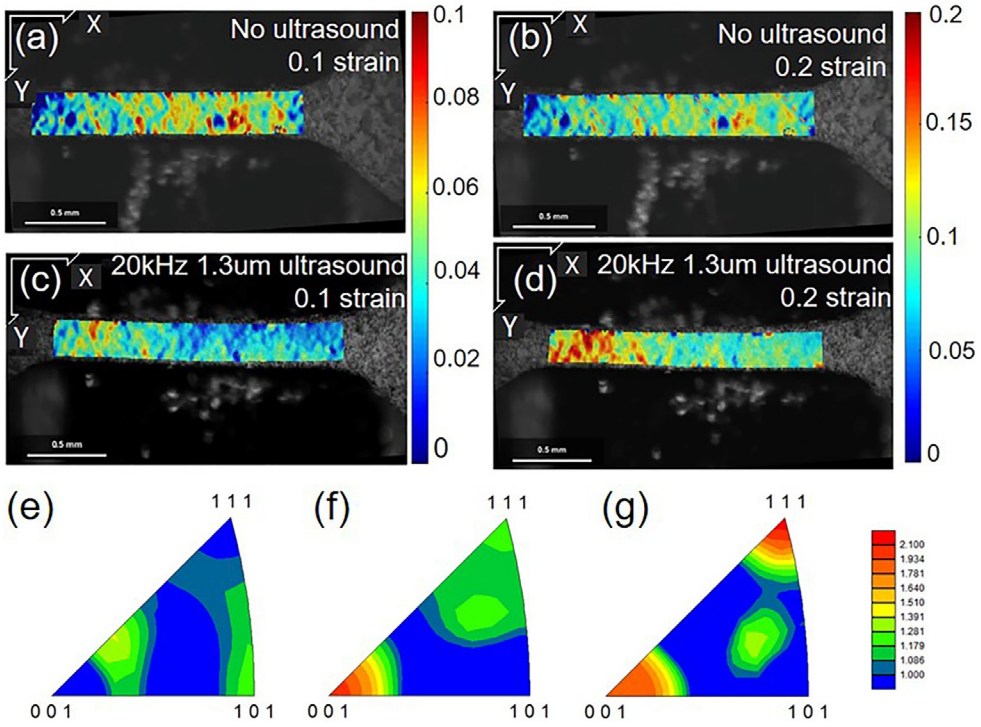


FIGURE 13.4 (a–d) DIC results of modified strain distribution under ultrasonic vibration, modified from original Figure 6 in Kang et al. (2020). (e–g) Inverse pole figure of tensile direction of undeformed sample; 20% strain; 20% strain with UA. *(Modified from original Fig. 11 in Kang et al. 2020).*

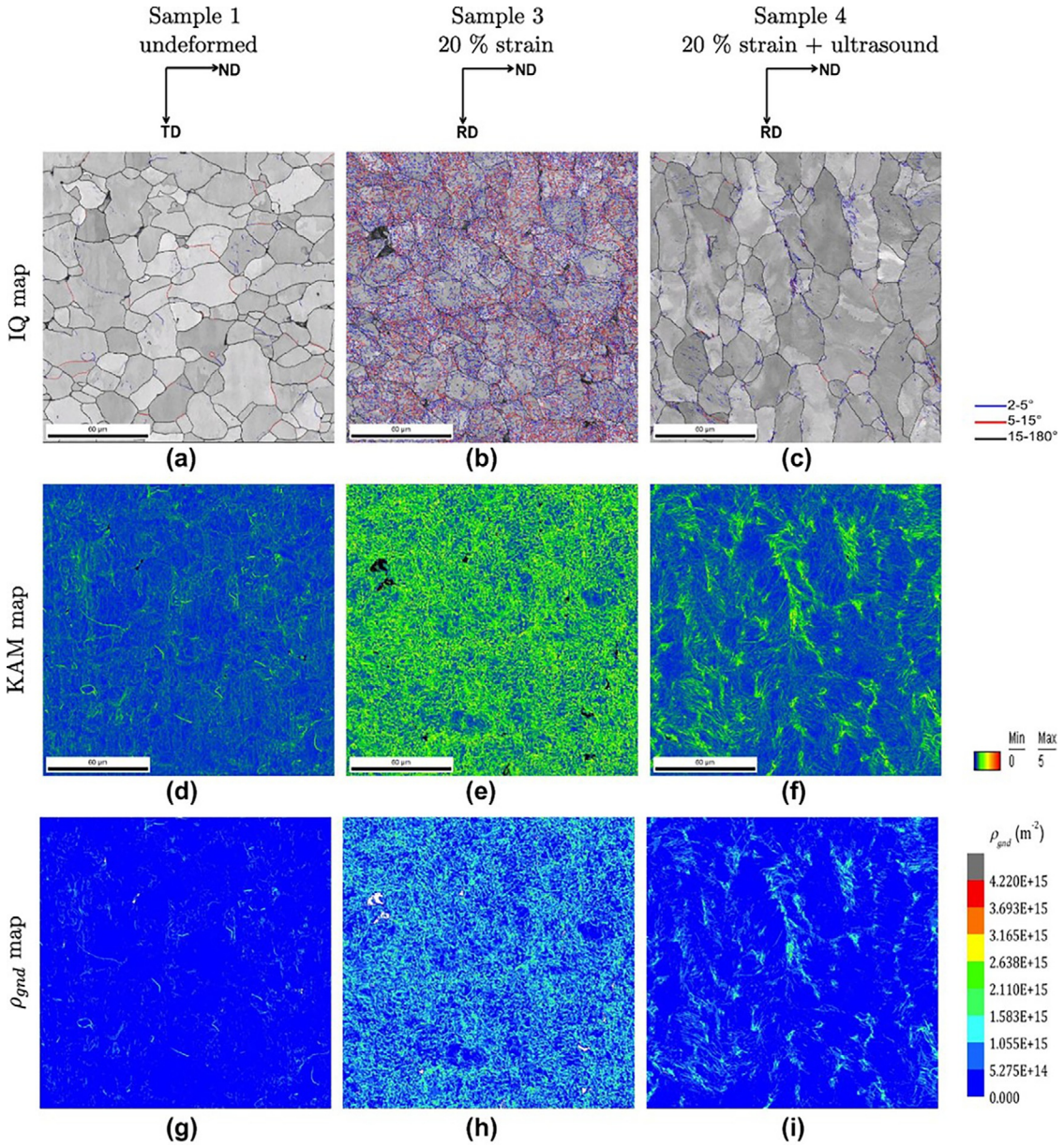


FIGURE 13.5 Microstructure comparison of low-carbon steel from regular and ultrasonically assisted tensile tests: (a–c) Image quality map showing high- and low-angle grain boundaries, (d–f) kernel average misorientation (KAM) map (unit: °), and (g–i) geometrically necessary dislocation density (ρ_{gnd}) maps (unit: m^{-2}) (Dutta et al., 2013, Fig. 6).

above which continuing deformation would reduce the number of twinning. Accordingly, residual softening is observed after the ultrasonically assisted compression test of pure titanium. Wen et al. (2011) performed ultrasonically assisted tensile tests of AZ31 magnesium alloy. They observed that lower ultrasonic energy results in the softening and better ductility, whereas high ultrasonic energy leads to the opposite behavior. In the microstructure, low ultrasonic energy would promote deformation twinning, while high ultrasonic energy suppresses twinning. A similar trend on the amount of twinning is also observed by Liu et al. (2017) with ultrasonically assisted compression of pure titanium. Ultrasonically assisted microblanking for titanium foil showed the softening effect from ultrasonic vibration is more remarkable for specimens with smaller grain size.

These modified microstructure features observed in ultrasonically treated materials further showed that ultrasonic softening is beyond pure stress superposition from the mechanics standpoint. The intrinsic material plastic deformation behavior can be permanently changed by the superimposed ultrasonic energy.

13.3 Macroscopic behavior

The macroscopic behavior of metals, in particular their plastic flow and deformation under the influence of power ultrasonics, has been a focus of interest since the landmark Blaha and Langenecker publication on a dramatic yield stress reduction under ultrasound. That report triggered numerous studies on the influence of ultrasonics on material properties and opened up the field of metal forming for development. Both of these areas, material science and engineering application, have continued to the present day. The field has not been without controversy as to the underlying mechanism(s), with some holding the view as to acoustic softening being responsible for observed effects, while others have supported the concept of stress superposition. Judged by continued publications to the present day, the issue is still not resolved. In the following text, an effort will be made to summarize the status of work, from early developments to recent contributions.

A note is in order on the subject of ultrasonic fatigue, an important part of the effect of ultrasonic vibrations on materials, and a field of extensive research over the years. However, the short periods of treatment of ultrasonic forming processes usually do not bring in fatigue effects. For this reason, this otherwise important part of ultrasonic material effects is not considered in this chapter.

13.3.1 Early developments

In one of the most well-known illustrations in power ultrasonics, the short note by Blaha and Langenecker (1955) showed (Figure 13.6a) force deformation for a zinc single crystal acted upon by ultrasound. Line A showed the abrupt 40% drop in force with the application of 800-kHz ultrasound pulses, while line B was the case of ultrasound being applied continuously to the crystal. While commenting that ultrasonic energy appeared to assist displacement and creep, no cause for the behavior was given in this first note, marking a 25-year period of contributions from the latter author.

Blaha and Langenecker (1958, 1959a,b) followed their groundbreaking note with further reports, the first of which discussed related work in plastic deformation, then extended their work to aluminum and cadmium, and tied the ultrasonic effect to an equivalence of an increase in temperature, as shown in Figure 13.6b, where (a) α, β, and γ are curves of increasing ultrasonic intensity at 18°C, while (b) shows curves of increasing temperature. In these, as well as other publications, it was proposed that the softening effect arose from the activation of previously blocked dislocations. In Blaha et al. (1960), the view on the mechanism was stated as follows: "As an explanation of these observations, it is assumed that dislocations which run up against barriers during deformation can be activated by an

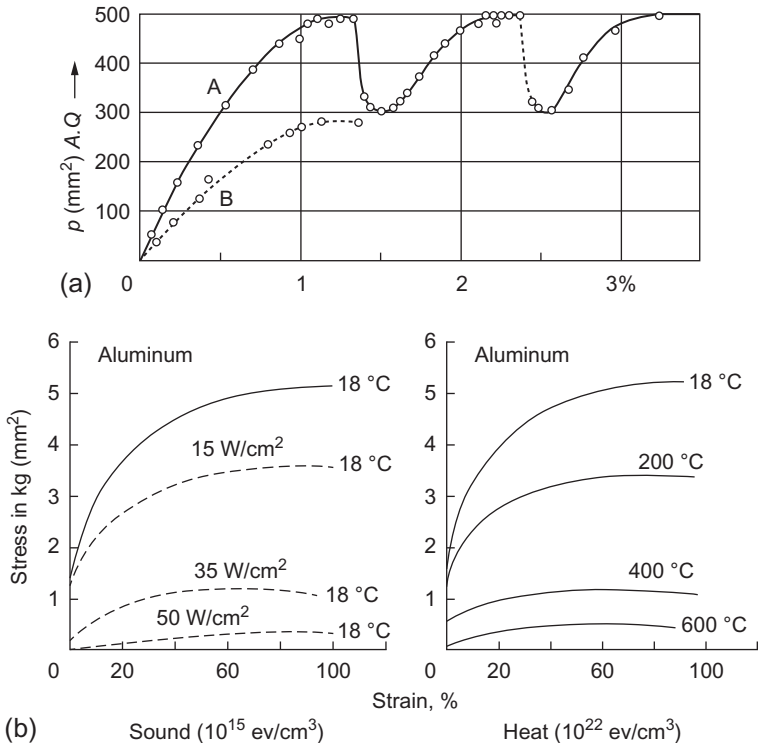


FIGURE 13.6 Results from early Langenecker work on ultrasound effects. (a) Effect of ultrasound on the force deformation of zinc (Blaha and Langenecker, 1955; Fig. 1); (b) equivalence of ultrasound treatment to increased temperature (Langenecker, 1963 based on Schmid and Boas, 1935; Fig. 4).

ultrasonic field, leading to the known decrease in stress. The dislocations are obviously more mobile with acoustic influence, and there is less obstruction at barriers."

The 1955 note created interest elsewhere, as seen by an extensive study by Spath (1956) on the effects of high-power ultrasound on creep of materials, followed by that of Siegel (1959), also on creep, with a specific note that the results were in agreement with those of Blaha and Langenecker. Most well known of the early studies were those of Neville and Brotzen (1957a, b) who reviewed and discarded both dislocation resonance and relaxation as well as hysteresis as causes of the force drops. Their paper concluded that "This phenomenon is attributed to a mechanism of superposition of steady and alternating stresses," thus setting forth the stress superposition view as accounting for the 1955 observations and in contrast to the dislocation activation model proposed by those authors. This early period should not be closed without noting the paper by Tanaka et al. (1952) that, using magnetostrictive apparatus similar to that used over a decade later by others, dealt with the effects of ultrasonics on the carburization of iron at elevated temperatures, showing the graphitization of cementite and the formation of nodular and lamellar graphite in the carburized microstructures.

The 1960s opened a remarkable period of study on the effects of power ultrasonics on deformation and flow of metals. Numerous papers were published by Langenecker and colleagues, of which Langenecker (1962) may be singled out. An improved, higher power test system was used, with further discussion of the dislocation mechanism underlying *work softening* (a term also used during this period). A new aspect was introduced when it was noted that repeated application of high-amplitude waves could result in a work-hardening effect on zinc. Thus, for repeated applications of ultrasound, there was an increase in yield stress up to a certain level, at which point it stabilized. This effect was also discussed in the context of dislocation action. Other contributions included Langenecker et al. (1962, 1963, 1970).

Other investigators on material effects included Balalaev (1960), who reported on heat generation; Chernenko and Cherkashin (1960), who tested "red copper" and found changes from a plastic to a brittle state; Kanavalau and Yafremau (1960, 1961), who reported on tests on brass giving results similar to those of Blaha and Langenecker (1959a, b). Davies and Yingling (1961) reported on 1100 aluminum noting that "In conclusion, we wish to state again that our test results indicate that the primary effect of ultrasonic vibration on aluminum is a superposition of an alternating load on a static load which causes the non-uniform deformation." Following earlier work on copper springs, Siegel (1962) tested creep of silver springs and noted that "The significant acceleration of deformation measured by Blaha and co-workers confirms that here a completely different mechanism in effect, as with creep."

Oelschlagel (1962, 1964) investigated the role of dislocations in explaining both the softening and hardening effects that had been reported. The reduction in the yield point was explained as the energy absorbed by dislocations in the sound field facilitated release of other dislocations and thus increased the mobility of the active dislocations, producing a reversible contribution to stress reduction. Schmid (1962) reviewed both nuclear and ultrasonic radiation effects on materials. For ultrasonics, the previous cited works of Langenecker, Neville-Bronston, Oelschlagel, and Siegel were reviewed, with the conclusion that "with regard to significance, one must accept the assumption that the sound activates anchored dislocations. If one also assumes that the ultrasonic waves are damped at lattice defects, then the sound acts to loosen the energy-absorbing dislocations," a viewpoint that supported the Blaha-Langenecker hypothesis.

The US Bureau of Naval Weapons sponsored a symposium on the application of ultrasonic energy to the deformation of metals (Rosenfeld, 1963). The meeting brought together a select group of researchers to assess developments since the Blaha-Langenecker paper, covering effects on metal properties and on several processes that included wire and tube drawing, rolling, forging, extrusion, and machining. Langenecker summarized results from his work since 1955, including the illustration of the apparent similarity of ultrasonic effects to thermal effects and a restatement of his views that the lowering of yield stress was not explainable by the acoustic stress alone (i.e. by stress superposition) but was caused by interaction between ultrasonic waves and dislocations.

Two lines of US Navy–sponsored research emerged in 1963, both tied to Langenecker, who was then at the US Navy China Lake Station. A line of fundamental research was started at the University of Vienna, while a second line of work, at China Lake, was started on ultrasonic wire drawing. Several publications by Langenecker et al. (1963, 1964), with these being representative but not inclusive, were to appear following the 1963 US Navy conference; these aimed at providing additional support to the softening/hardening behavior of ultrasonically treated materials. Of these, 1966 provided the most comprehensive summary of Langenecker's work, with discussions of the softening/hardening hypothesis, the experimental techniques to arrive at the results, and data on acoustic heating and microstructures of acoustically treated materials. In addition, early examples of metal forming, for example, wire drawing and deep drawing, were presented.

It was during this period that the results of a major US Air Force–sponsored project with the Cincinnati Machine Tool Company (later Cincinnati Milacron) became available (Kristoffy, 1969; Kristoffy et al., 1965). While mainly aimed at metal forming processes (cited in later sections), including machining, attention was also given to the material effects. Note was taken of the two major

viewpoints on ultrasonic deformation and concluded that "The flow stress of the material is not influenced (by ultrasound)" and that … "All observed phenomena can be explained by the laws of mechanics, stress and strain," this being the stress superposition concept.

(Note on the stress superposition hypothesis. Two hypotheses emerged in the early years to explain the ultrasonic effects on materials, acoustic softening and stress superposition. By either view, it was recognized that when ultrasonic stresses were added to static forces, a superposition of the two occurred. However, the essence of the stress superposition hypothesis was that the fundamental plastic behavior of materials was in no way changed by the ultrasound and that yielding was simply governed by the sum of the static and ultrasonic stresses.)

A steady stream of new research entered the field through the mid-1970s, of which only highlights can be noted. Severdenko and Klubovich (1964) looked at the properties of copper under ultrasonic compressive stresses, showing significant differences, with and without ultrasound, while Pogodina-Alekseeva et al. (1964) reported on tests on R18 steel. Improvements in hardness and heat resistance, and faster rates of property change were noted. The translated copy of this paper had an attached summary of 16 earlier publications, dating to 1958, showing this as a very active field of Soviet research.

Following the 1963 US Navy meeting, progress on ultrasonic metal forming was tracked in later US government reports. Thus, a materials advisory board (National Research Council, 1965) gave an extensive review of the field that, while noting the potential advantages to be gained in metal forming, was cautionary as to lack of understanding of the process mechanisms, as well as ultrasonic equipment able to meet industrial needs. This was followed by a report (Holden and Boulger, 1965) that summarized the main findings of the recently completed Kristoffy work, including the perspectives on stress superposition. A brief (National Research Council, 1967) report noted work in ultrasonic metal forming at the Aeroprojects company.

Reference should be made to the publications on ultrasonic forming that were to flow from Lewis Balamuth. His contributions to the area of ultrasonic machining during this period have been noted in Chapter 16. While his papers were generally not highly technical and often aimed at trade journals, they served to introduce ultrasonic metal forming to a wider audience than those reached by more scientific treatments. The first on forming was reported by Peacock (1961), noting dimpling of aluminum and titanium and the reduction of friction under ultrasonic action, followed by an overview of early forming work (Balamuth, 1963). Balamuth (1964) covered machining and welding processes, noted the work of Langenecker, and illustrated the flattening of wires by ultrasound. The concept of a giant sonic forging press, still of illustrative use to those with a sense of humor about the field, appeared (Balamuth, 1965), while Balamuth (1965a) provided an overview of Langenecker findings, as well as work by others on wire drawing, extrusion, and rolling and took note of the recent Kristoffy et al. (1965) work.

Numerous other works of greater depth appeared. Thus, Baker and Carpenter (1966), using 50-kHz equipment for tensile tests on copper, tantalum, and stainless steel, noted dips in the stress-strain curves, but called into question dislocation mobility interpretations, instead concluding that "in no case has a reduction of flow stress larger than the vibratory stress level been measured." A later publication (Baker and Carpenter, 1967) gave attention to the dislocation mechanics under ultrasonic vibration but did not further address differing views on the deformation mechanism. Cunningham (1966) gave an overview of four mechanisms that had been proposed for ultrasonic effects on metals but concluded "It is apparent from the above discussion that the volume effect is not completely understood and, until it is, no estimate of the magnitude of its effect on deformation processes can be made. It is this area of ultrasonically assisted metalworking that is most controversial and which requires further investigation." A review of developments in drawing and rolling concluded the article.

Izumi et al. (1966a, b) examined the properties of metals under ultrasonic vibration during compressive deformation using equipment, as shown in Figure 13.7a (Izumi et al., 1966a). Key system components include a magnetostrictive transducer and horn (1) and (2), amplitude pickup (4), optical microscope (6), and specimen location (10). Testing aluminum, copper, various brass alloys, magnesium, and steel, extensive data on load reduction under various amplitudes of vibration were obtained, as provided in Figure 13.7b (Izumi et al., 1966b) for steel. Data were reported on heat generation and on hardness distribution in test specimens. The results were interpreted in terms of a simple superposition formula, $\sigma = \sigma_0 - ku_0$. The adjustment constant k was seen as a variable sensitive to several material factors so that a clear picture of the underlying mechanisms of vibrations on properties still did not emerge from this otherwise most thorough study to have emerged till that time.

In the early part of a paper that addressed friction effects and wire drawing, Pohlman and Lehfeldt (1966) examined the yield force reductions that had been reported by earlier researchers. Using the equipment of Figure 13.8a, results such as Figure 13.8b were obtained for copper and seen to be of a similar form to those of Langenecker. The authors reviewed the several possible mechanisms for such results and concluded that "This result clearly indicates that the reduction of internal friction by ultrasound may be explained by the superposition of the induced acoustic stress on the static stress." In a later paper, Lehfeldt (1969) covered much of the same ground and restated the same conclusions.

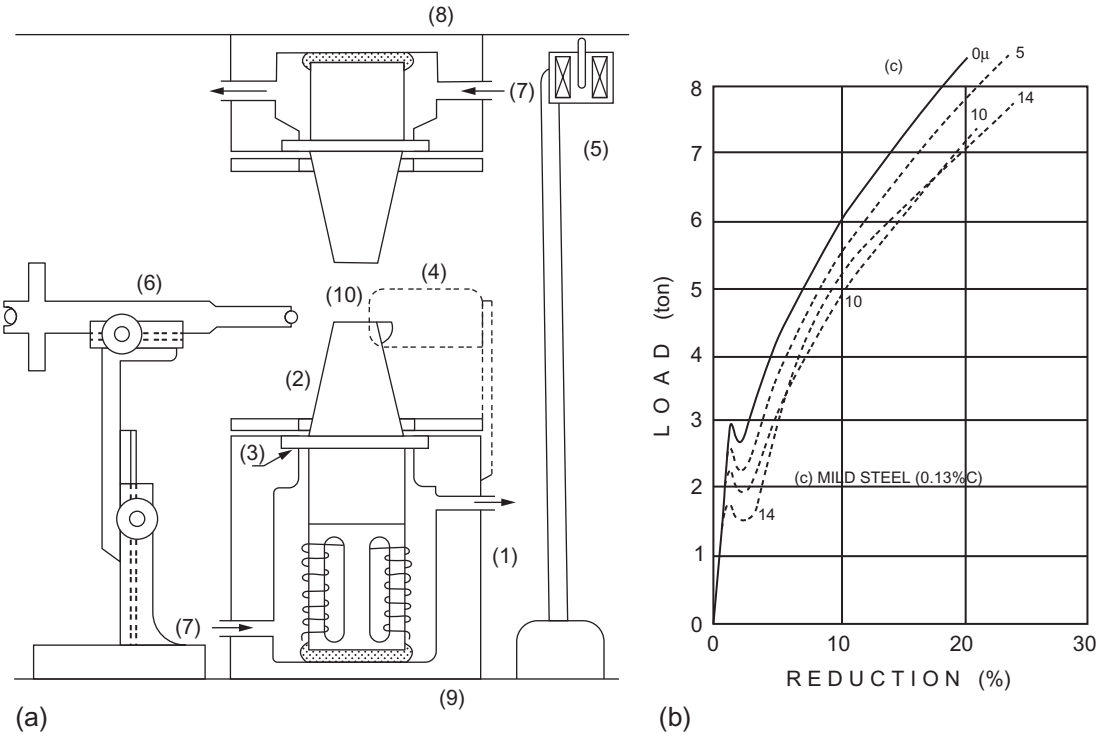


FIGURE 13.7 Results from Izumi et al. (1966a, b) on ultrasonic effects on metal deformation. (a) Experimental apparatus (Izumi et al., 1966a; Fig.1), see text for explanation; (b) load reduction under ultrasound for steel (Izumi et al., 1966b; Fig.1c).

In the first of numerous contributions to ultrasonic metal forming over the years by the D. H. Sansome-led group at the University of Aston at Birmingham, Winsper and Sansome (1967) reviewed the various theories of ultrasonic deformation of Langenecker, Kristoffy, and others. While not doubting the reductions in mean force that had been observed, the authors felt this was explained by (1) the simple superposition of vibration force on the static force, and/or (2) reduction in friction, and/or (3) generation of local heat. The numerous forming applications were also reviewed.

In the following years, the Sansome group was strongly identified with the stress superposition hypothesis, typically presenting the results of varied forming processes as being explained by the superposition mechanism, such as Winsper and Sansome (1969), Spiers et al. (1969), and Sansome (1970). The paper by Eaves et al. (1975) from this group presented the superposition hypothesis as a proven fact and conducted a review of the status of several forming processes, including a detailed critique of the numerous deficiencies of other researchers, and most forming results were explainable by stress superposition.

13.3.2 The 1970s through 1990s

As research on ultrasonic forming moved into the 1970s, Langenecker and colleagues provided several publications with additional data on acoustic softening/hardening and metal plasticity, for example, Langenecker (1970) where it was noted that "There is however no theory available as yet which could completely interpret the mechanisms of interaction of macrosonic waves and dislocation structures." Other papers addressed dislocation structures (Langenecker, 1970, 1972). In a three-paper series, Hansson and Tholen (1973, 1974, 1978) studied the interaction of power ultrasound with dislocation microstructures but did not reach conclusions as to a governing mechanism.

The work of Severdenko and colleagues on ultrasonic deformation continued with a monograph that gave a comprehensive survey of their own and others' work (Severdenko et al., 1972) on material effects, both volume and surface, and ultrasonic rolling and wire/tube drawing. In the materials section, an extensive review of their own and Langenecker's work was given. The conclusion reached was that although many different mechanisms influenced the decrease in yield point, "… it is obvious that the predominant mechanism is localized heating as a result of the adsorption of acoustic energy by defects in the crystalline structure of the metal."

In what was a then definitive review of work on power ultrasonic material effects, Green (1975) broke the field into acoustic softening, hardening, and friction effects. Although not endorsing a specific mechanism, the possibility of a more complex process than simple superposition was the general view, with a note that the role of friction needed to be better addressed. A model of test machine mechanics

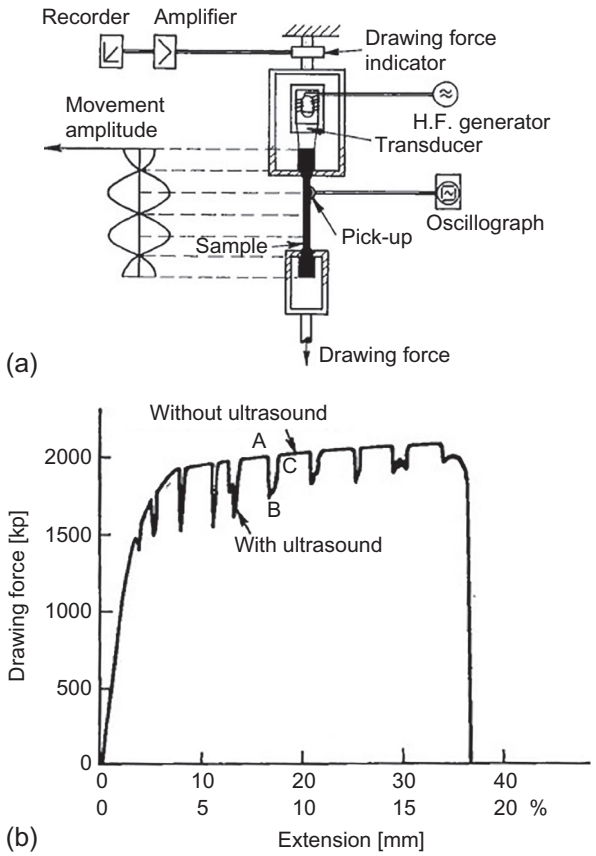


FIGURE 13.8 Study of Pohlman and Lehfeldt (1966) on effects of ultrasound on metals. (a) Experimental apparatus (Pohlman and Lehfeldt, 1966; Fig.1); (b) reduction in drawing force by ultrasound (Pohlman and Lehfeldt, 1966; Fig. 2).

and its impact on data interpretation was given. The final conclusion calling for more research did not resolve the question of the mechanism of ultrasonic effects on material plasticity.

A number of other contributions to materials effects of ultrasound completed the 1970s decade. Thus, Kulemin and Chernov (1975) and Grabchak and Kulemin (1976) investigated the effect of ultrasound on creep in copper and germanium, finding the acceleration in the creep rate to be attributable to the formation of vacancy-type point defects. Several studies aimed at ultrasonic fatigue also contributed to understanding general elastic-plastic material behavior under ultrasound, such as Bajons and Weiss (1975), where the distribution of plastic strain was investigated; Wielke and Stanzl (1976), which provided data on heat generation and distribution in test specimens; and Puskar (1976), which investigated heat generation, microhardness distribution, and dislocation density. Shaw and Kennedy (1977) developed a means of applying torsional vibrations to aluminum and titanium during a pull test, demonstrating previous observations on modulus reduction as well as adding the caution of potential degradation of fatigue properties during the process. Herbertz (1977) developed a nonlinear equation of state that was felt to better predict material behavior than the prevailing acoustic softening and superposition hypotheses. Endo et al. (1979) tested iron and iron alloys under ultrasonic compression, including the effects of "dislocation velocity stress exponents" to arrive at a modified stress superposition model. Mignogna and Green (1979) and Mignogna et al. (1981) reviewed the prevailing theories of ultrasonic effects and carried out thermal measurements during vibration, noting large-scale dislocation motion during testing.

Although the exact beginning of an "era" is at best inexact, perhaps entry into the 1980s marks that point because it brought in a new generation of researchers in ultrasonic forming, with new approaches to some of the old problems as well as dealing with the fundamentals needed to advance forming applications. For example, Bajons (1980), with the objective of improving ultrasonic fatigue testing, discussed an approach for better measurement of plastic deformation under ultrasonic vibrations, useful for both materials and fatigue studies. The book on power ultrasonics by Puskar (1982) covered several forming processes, while giving extensive coverage to the work of Langenecker and others who investigated the acoustic softening/hardening hypotheses.

Tsimbalistyj and Vlasenko (1983) examined creep and relaxation of aluminum, titanium, and iron alloys at 10-kHz and low-frequency vibrations, interpreting the results in terms of dislocation mechanics. Peslo (1984) studied ultrasonic hardening of aluminum alloys at 22 kHz, noting that the kinetics of the various stages of the precipitation hardening process were modified as shown by microstructure examinations. The work of Kirchner et al. (1984–1985) addressed the acoustic softening issue in aluminum alloys and noted the difficulty in determining the stress within a plastically deforming specimen at ultrasonic frequencies, leading to the use of low-frequency testing to also generate data. The stress dip at vibration initiation was attributed to a stress relaxation mechanism. The work of Ohgaku and Takeuchi (1987) on alkali halide and other crystals in reference to the Blaha effect noted the results could not be explained by stress superposition and concluded that dislocation activation was the underlying mechanism.

Kozlov and Selitser (1988, 1991) undertook mathematical modeling of the effect of ultrasonics on the deformation of materials, also making a helpful contribution to the field by referring to the "acoustoplastic effect" (APE), thus removing it from the "softening" and "superposition" vocabulary that had been in place for over 25 years. Their 1988 results permitted prediction of plastic deformation in an ultrasonic field as a function of vibration amplitude, frequency, and machine strain rate. In their 1991 work, the effect of test machine stiffness was included, as were effects of dislocation density. In a follow-on note, Kozlov (1994)

used testing of nonresonant specimen lengths to more accurately obtain the strengthening (i.e. work hardening) effects of ultrasound.

Efforts to mathematically model the Blaha effect by Tanibayashi (1991) reached a new level of sophistication with the inclusion of internal stresses, the prediction of a larger reduction of the static applied stress, and a better explanation of experimental results cited nearly 25 years earlier by Baker and Carpenter (1967). The reduction to practice of this complex formulation remains to be done. Vagapov et al. (1991) undertook modeling of the ultrasonic wire drawing process, incorporating a more advanced acoustoplastic model of material behavior to predict an observed draw force reduction for steel wire.

In a series of papers, Sapozhnikov and Kustlov (1995, 1996a,b,c, 1997) and Sapozhnikov et al. (1998), working with a range of single crystal materials (e.g. NaCl, aluminum, LiF, and Cu—Ni) at 100 kHz, the APE effect was examined under a range of conditions (e.g. temperature, impurities, and amplitude), and also noting that despite considerable research, the underlying mechanisms were still not resolved. Although concluding that the APE originated mainly from dislocation interactions, the overall picture of ultrasonic material deformation mechanisms that emerged from these studies was more complex than at their initiation.

13.3.3 Continued developments: 2000 onward

In a surge of renewed interest in the APE field, a large number of papers have appeared entering the 21st century and are continuing to appear. In the following continued review, note should be taken of the several papers dealing with modeling of macroscopic material behavior under ultrasound, which is the subject of the following Section 13.3.4. Thus, Malygin (2000) undertook a continuum mechanics modeling of the APE, thus having the potential of application to practical deformation problems and concluded that the effect was adequately described by the superposition mechanism when combined with thermally activated plastic deformation. However, the author recognized that inconsistencies remained regarding vibration amplitude effects and the nature of dislocation motion under ultrasonic vibrations, thus leaving the APE picture still unresolved. A note of appreciation is extended to Cai (2006), whose Ph.D. dissertation, while aimed at nonlinear elastic-plastic waves, contained an excellent overview of selected parts of the APE, including discussions of several of the preceding papers in more detail than could be included here.

The work of Huang et al. (2009, 2011) was illustrative of efforts to incorporate the effects of power ultrasonics on material deformation into modeling nonforming processes, and in this case, the effects of wire bonding. Noting the similarity in acoustic softening between copper and gold, it was noted that a residual softening remained after the ultrasonic bond. A dynamic annealing and dislocation mechanism was used to explain the effects. In the 2011 work, a nonlinear finite element analysis (FEA) model was used to study the deformation, with favorable comparisons made between theory and tests.

Lucas and colleagues at the University of Glasgow have been responsible for numerous papers in the APE field. First reporting on tests and modeling ultrasonic compression tests of aluminum, Daud et al. (2005, 2006) examined stress superposition and friction effects on force deformation, with favorable comparison of theory with experiment, although not all effects were fully explained. This was followed by Daud et al. (2007), where tests, while showing expected drops in flow stress with application of ultrasonics, did not behave in a manner supported by the generally accepted stress superposition theory. An FEA model was developed to better explain observations, with predicted deformations for tensile and compression tests.

There followed a wide-ranging paper by Lucas et al. (2009) that reviewed the status of the acoustoplasticity field as well as many forming applications. In the APE review, the authors concluded that "In the past half-century, a clear understanding of the APE has not been achieved," a statement similar to that found in many papers in this field. Citing procedures and results from Daud et al. (2007), it was noted for the case of a tensile test (Figure 13.9a) that the often seen drop in flow stress occurred with the application of ultrasound, with the dashed lines showing the excursion of the oscillatory stresses. Of importance is that the upper dashed line did not coincide with, or come close to, the static stress-strain curve, as it should according to the stress superposition APE theory. A similar result is seen in Figure 13.9b for a compression test. The authors conducted FEA modeling of the deformation process, using a material model that simulated the observed softening behavior, varying its properties to achieve a match to experimental deformation. The result of the test was the subsequent close agreement between calculated and measured stresses. The authors noted still existing limits on characterizing the APE and thus limits on ultrasonic metal forming technology.

These studies were followed by Aziz and Lucas (2010a,b, 2012) on the effects of ultrasonics during metal forming tests. In Aziz and Lucas (2010a,b), an experimental setup, as shown in Figure 13.10a, was used, with the transducer, booster, and die horn modeled and constructed, as shown in Figure 13.10b. Tests were run on aluminum Al 1050 and 7075-T73, die cast magnesium AC50, and 304 stainless steel.

Force drops with ultrasound were noted for A1050, magnesium, and stainless, although of a decreasing magnitude for increasing alloy hardness. In the case of Al 7075, there was no observable drop in force. The high-frequency oscillations of the piezoelectric load cell are shown in Figure 13.11a for soft aluminum and in Figure 13.11b for harder magnesium,

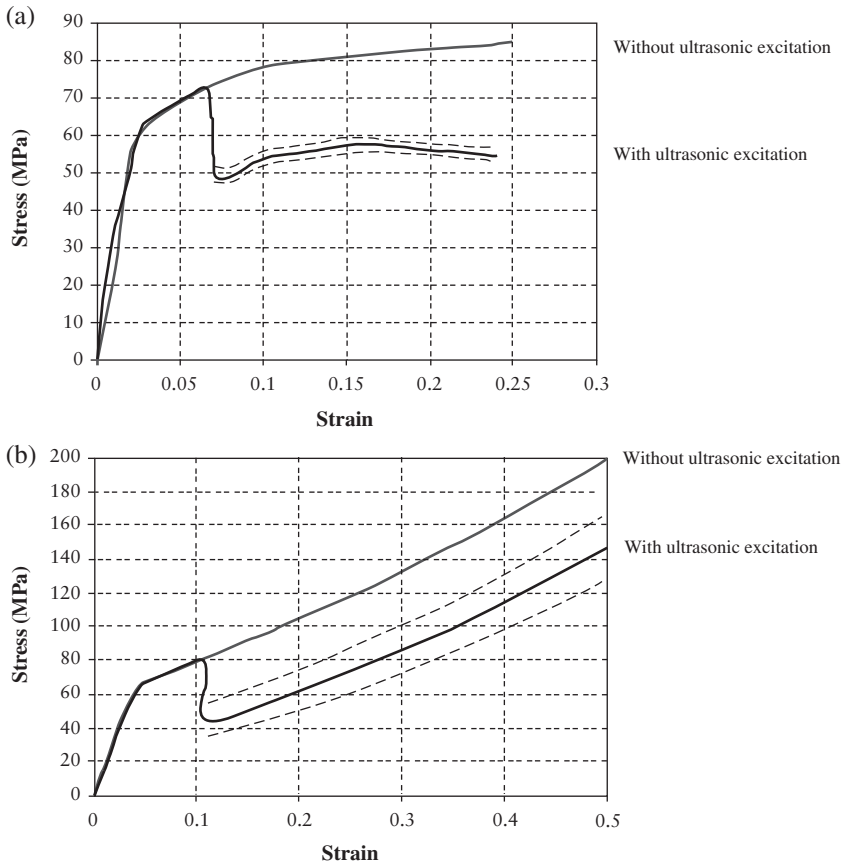


FIGURE 13.9 Static and ultrasonic tests of aluminum (Lucas et al., 2009). (a) Tensile tests (Lucas et al., 2009; Fig. 2a); (b) compression tests (Lucas et al., 2009; Fig. 2b).

where the wide gray bands show the bounds of stress oscillation, and the black line through the band is the stress mean value. Markedly different behavior is seen. For the aluminum, the mean stress is well below the static stress, as is the peak oscillatory stress. However, for magnesium, while the mean force is slightly below the static level, the peak oscillatory stress significantly exceeds the static level, showing that peak dynamic forming stresses exceed the static forming stresses. The cases of stainless steel and Al 7075 had even less drop in mean stress and higher stresses beyond the static stress. Aziz and Lucas (2012) provided further details of this work and noted that without improved methods of coupling ultrasonics to forming processes, the benefits in forming higher strength materials could be limited.

A research group at Iowa State University, interested in applying ultrasonics to microforming, has conducted some of the most recent ultrasonic material deformation studies. Thus, Witthauer et al. (2010) set forth various designs of ultrasonic microforming equipment. Follow-on work by Yao et al. (2010) noted early works on ultrasonic deformation mechanisms and reviewed more recent contributions that tied to the needs of microforming. Experiments used a Terfenol-D-based magnetostrictive transducer to drive the die, or the punch, with force reductions of the form first reported by Langenecker noted in both cases. The results were felt explainable by stress superposition, while noting the need for better understanding of friction effects.

Later, Yao et al. (2012a) showed an improved experimental system (Figure 13.12a) and measured barreling effects (a measure of friction) and surface roughness. The process was modeled using a classical plasticity power law, with results as shown in Figure 13.12b. Thus, the measured compression force is shown by the gray band, while the average stress value (solid line) is found to coincide with FEA analysis (that line not visible in the black and white figure). Lubrication effects were also examined. It was concluded that acoustic softening was the dominant mechanism. Then, Yao et al. (2012b) provided a 70-reference review of the development of ultrasonic deformation theory from Langenecker to the present. Noting that past single-cause process theories (e.g., superposition, or softening or heating) failed to predict the total response of the material, a new crystal plasticity model was developed that led to accurate predictions of the stress-strain curves for aluminum. Future application of these results to practical forming processes is awaited.

Research on applying advanced modeling methods to the APE continued with Siu and Ngan (2011) who, after

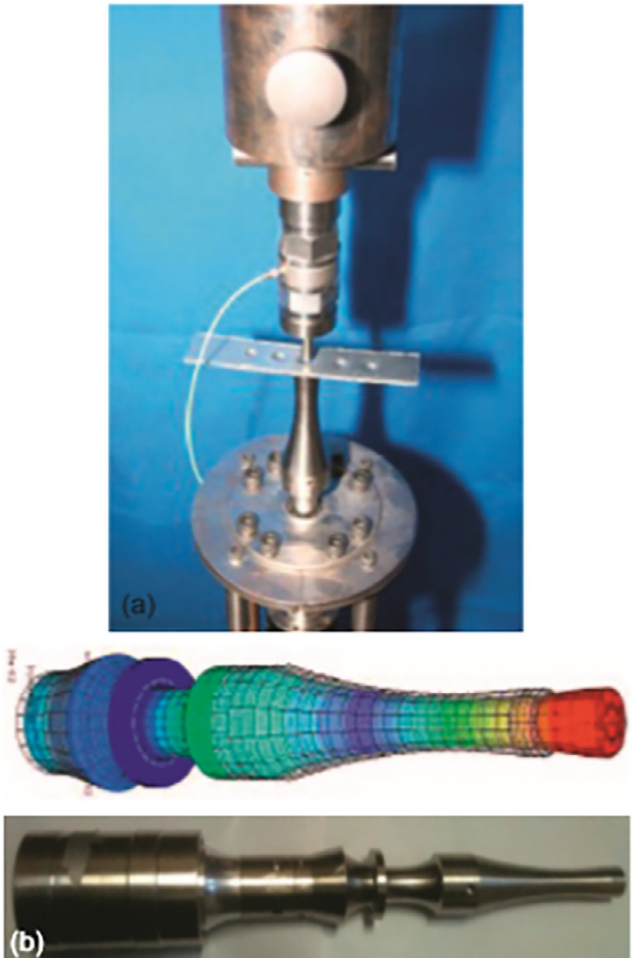


FIGURE 13.10 Ultrasonic test setup and tooling (Aziz and Lucas, 2010b). (a) Test setup (Aziz and Lucas, 2010b; Fig. 2); (b) FEA model of tooling, upper (Aziz and Lucas, 2010b; Fig. 1b) and transducer and tooling, lower (Aziz and Lucas, 2010b; Fig. 1a).

the usual review of historical and recent developments (the underlying mechanism is still not well understood), applied dislocation dynamic simulations, found dislocation annihilation to be enhanced, and accounted for a number of key features of the APE. Rusinko (2011) continued the contributions made to purely theoretical modeling of the process, introduced a new term *ultrasonic defect intensity*, and claimed a single constitutive equation that described both acoustic softening and hardening. Good agreement with experimental results reported by others was obtained. Siddiq and El Sayed (2011, 2012a, b) continued work in mathematical simulation of the APE, developed a micromechanics-based model to incorporate acoustic softening effects, and showed a qualitative comparison with other reported experimental results. In Siddiq and El Sayed (2012a, b), the model was then applied to simulations of sheet metal forming, upsetting, and wire drawing processes, showing friction and force reductions, with encouraging qualitative comparisons.

In contrast to the several theoretical treatments, Wen et al. (2011) undertook new experimental studies of ultrasonic deformation. Using a 15-kHz transducer and test specimen, as shown in Figure 13.13a, the behavior of AZ31 magnesium was investigated; examined the stress-strain curves under different vibration levels, the fracture surfaces, and the microstructure; and found both the softening and hardening effects to be present, depending on the vibration level. Thus, comparison of fractographs of static fracture (Figure 13.13b (left)) with those at high-amplitude vibrations (noted as 90%), as in Figure 13.13b (right), showed a transition from a cleavage fracture to a transgranular brittle fracture.

In an example of seeking practical use of ultrasonic plastic deformation, Li et al. (2012) looked at ultrasonic indentation tests as a means of generating data for ultrasonic spinning (a process for shaping seamless, dished parts through forces of rotation and pressure; Altan et al. (1983, p. 30). Key components included the transducer, amplitude transformer, and tool and test specimen. Indentation tests (termed *creasing*) were performed on Al 7050 and Hastelloy C-276. Increased penetration depth under ultrasonics was obtained, as well as increased indentation volume versus the static indenter force. While the general force deformation behavior was not new, given the history of work in this field, the effort by the authors to tie to a phonon-based mechanism was novel.

As may be noted from review of previous work, ultrasonic assisted (UA) material tests can be divided into two categories: large-scale tension and small-scale compression. The initial UA tensile system from Blaha and Langenecker (1955) has been adopted in several studies, for example, Mao et al. (2014), Mignogna and Green (1979), and Daud et al. (2007), where the longitudinal length of the tensile specimen is tuned at either single or multiple ultrasonic half-wavelengths in the corresponding material. The second group of UA tests have focused on small-scale compression, for example, Yao et al. (2012a, b) and Daud et al. (2006). However, during compression, the associated frictional effects cannot be decoupled from bulk acoustic softening since interfacial frictional heat can generate additional thermal softening (Liu et al., 2018). Zhuang et al. (2015) performed ultrasonic assisted compression tests on aluminum 1050 and reported reduced flow stress and improved surface topography. Together with the numerical simulation, they concluded stress reduction is a combined result of material softening, friction reduction, and stress superposition. In another ultrasonically assisted compression test by Hu et al. (2018a, b), the vibration amplitude was high enough to lift the compression punch from contact with the specimen. The resultant dynamic impacts additionally reduced the material deformation resistance. Different from these two types of setup, Siu et al. (2011) and Siu and Ngan (2013) developed an ultrasonically assisted

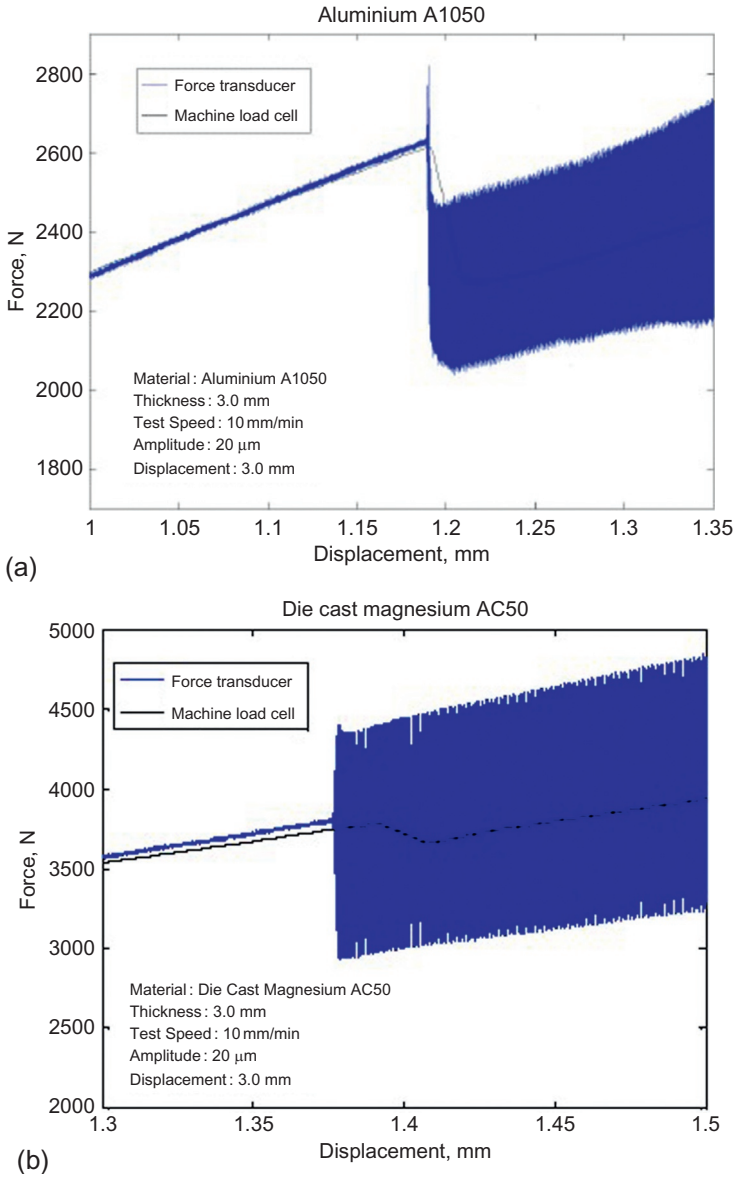


FIGURE 13.11 Forming tests showing oscillatory force (Aziz and Lucas, 2010b). (a) Aluminum (Aziz and Lucas, 2010b; Fig. 5a); (b) cast magnesium (Aziz and Lucas, 2010b; Fig. 5b).

indentation system, where a transverse vibration is applied perpendicular to the compression direction.

In material systems that are strengthened by different mechanisms, such as solution, precipitates, and multiple phase hardening, flow stress reduction under ultrasonic effects was consistently observed. With large-scale ultrasonically assisted tension tests, Mao et al. (2014, 2020) showed softening of aluminum alloy AA6061. Fartashvand et al. (2016) observed reduced flow stress and increased elongation for Ti-6Al-4V alloy. Hoseini et al. (2019) observed flow stress reduction on St52 steel, and Wen et al. (2011) observed softening of AZ31 magnesium alloy. Hung and Tsai (2013) performed ultrasonic assisted microupsetting on brass C2600 and reported that flow stress is also effectively reduced by ultrasonic energy.

Regarding the effects of different test parameters, the flow stress reduction is generally believed to be independent of ultrasonic frequency in the range of 15–80 kHz, as depicted by Siddiq and El Sayed (2011) and Siddiq and Ghassemieh (2008). A recent study by Zhou et al. (2018) involving ultrasonically assisted compression tests on HCP pure titanium, on the other hand, showed that above 40 kHZ that increasing the ultrasonic frequency reduced the softening effect. In addition to depending on the amplitude of ultrasonic vibration, there can be either residual softening or residual hardening, as shown in Figure 13.14a.

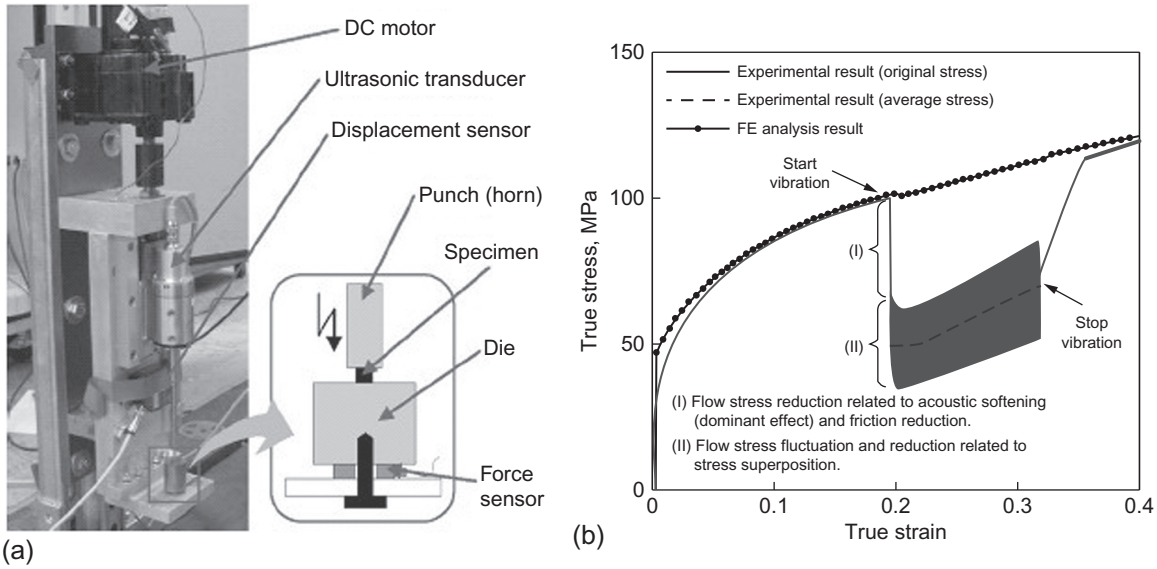


FIGURE 13.12 Experiments and analysis on ultrasonic deformation (Yao et al., 2012a). (a) Experimental setup (Yao et al., 2012a; Fig. 1); (b) comparison of stress-strain curves from experiment and analysis (Yao et al., 2012a; Fig. 10).

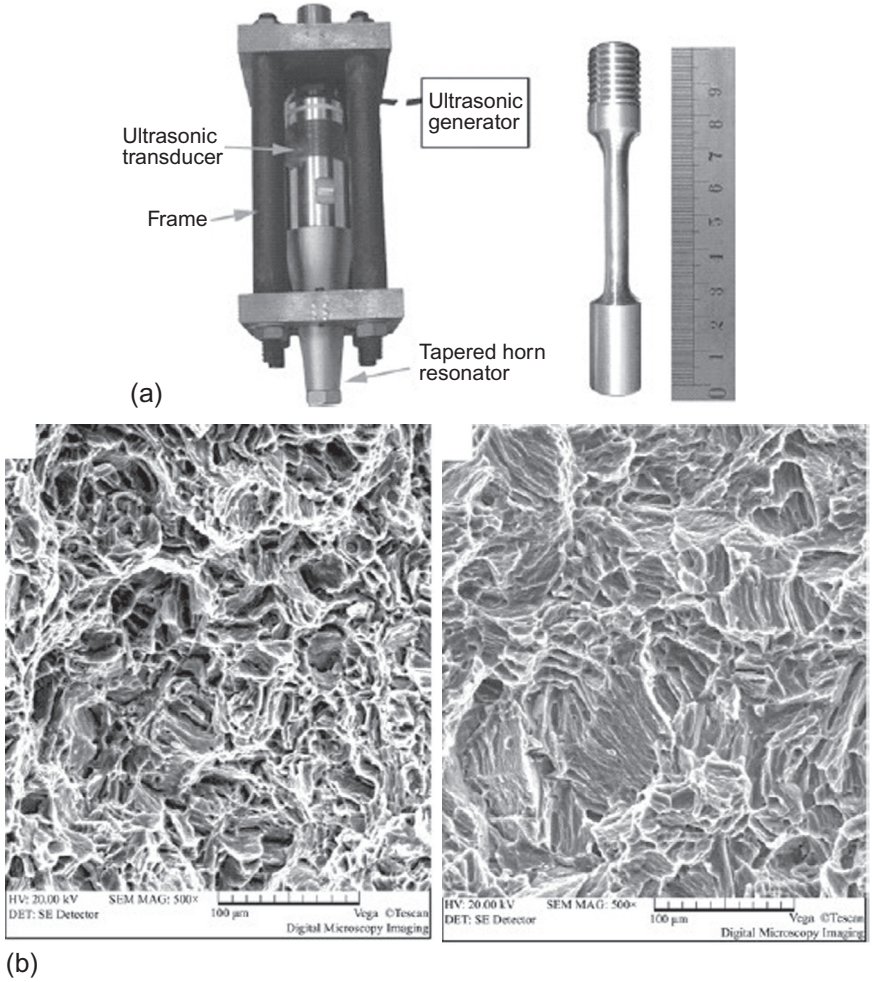


FIGURE 13.13 Ultrasonic tests of AZ31 by Wen et al. (2011). (a) Experimental setup (Wen et al., 2011; Fig. 1); (b) fractographs for static (left) and ultrasonic at 90% amplitude (right) (Wen et al., 2011; Fig. 5a, d).

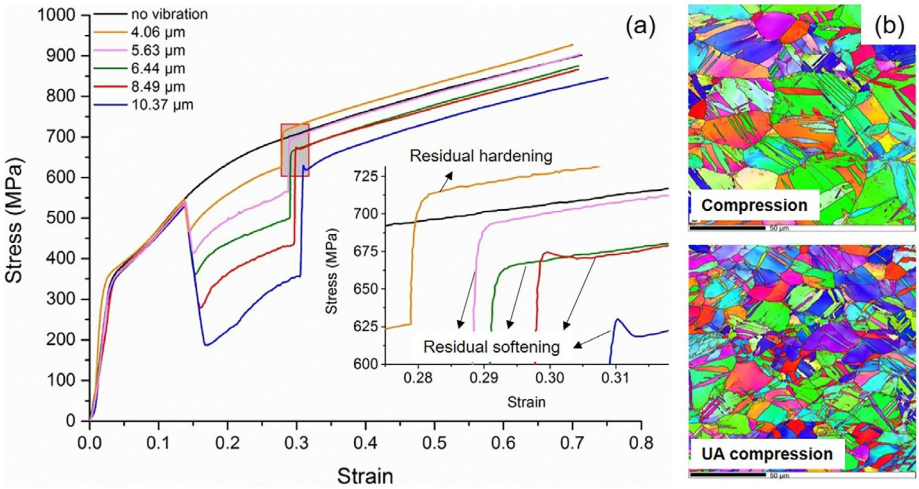


FIGURE 13.14 (a) Ultrasonically induced flow stress reduction and residual softening and hardening effect: 30-kHz UA compression test on titanium with different vibration amplitudes. (b) Refined grain size after UA compression (Zhou et al., 2018, Fig. 30).

A significant UA effect on grain size was also noted, as shown in Figure 13.14b. Regarding the dependence on strain rate, Hu et al. (2018a, b) showed a lower strain rate can lead to a higher degree of softening during the compression test of pure aluminum.

13.3.4 Modeling ultrasonically assisted material deformation

This section will focus on recent developments in the analytical modeling of ultrasonic material deformation. However, throughout the preceding review of ultrasonic macroscopic materials research, numerous references have been made to prior modeling efforts: Kozlov and Selitser (1988, 1991), Kozlov (1994), Tanibayashi (1991), Baker and Carpenter (1967), Vagapov et al. (1991), Malygin (2000), Cai (2006), Huang et al. (2009, 2011), Lucas et al. (2009), Daud et al. (2007), Siu and Ngan (2011), Rusinko (2011), and Siddiq and El Sayed (2011, 2012a, b).

The diversity of approaches to modeling has already been brought out in the foregoing. In considering recent developments, there is the stress superposition theory, which calculates the ultrasonically induced flow stress reduction by adding high-frequency alternating loads (Malygin, 2000; Neville and Brotzen, 1957a, b; Kirchner et al., 1984) or displacement boundary conditions (Zhuang et al., 2015). Beyond this, thus far, the modeling efforts to describe ultrasonically affected material constitutive behavior can be divided into two groups: empirically based and physically based models.

In the empirical models, the degree of material softening is quantified by regression fitting of the experimentally measured stress-strain curve. Flow stress reduction was shown to be proportional to acoustic energy intensity or density (Langenecker, 1966), both of which rely on the square of vibration amplitude (Frederick, 1965):

$$\text{Acoustic energy intensity } I_{acoustic} = 2\pi^2 f^2 A^2 \sqrt{E\rho}; \tag{13.1}$$

$$\text{Acoustic energy density } \xi_{acoustic} = 4\pi^2 f^2 A^2 \rho \tag{13.2}$$

where f is frequency, A is vibration amplitude, E is the material elastic modulus, and ρ is material density. On the other hand, stress reduction proportional to vibration amplitude was also reported (Yao et al., 2012a, b; Huang et al., 2009). Some more sophisticated empirical models incorporate additional material parameters. Thus, Sedaghat et al. (2019) treated ultrasonic vibration as an effective acoustic stress given as follows:

$$\sigma_{acoustic} = 2\pi\eta f A E/c = 2\pi\eta f A\sqrt{\rho E}, c = \sqrt{E/\rho} \tag{13.3}$$

where η is the efficiency factor and c is the ultrasonic wave velocity. Kelly et al. (2013) introduced an acoustic softening parameter ξ in front of the flow stress. This parameter is defined as a function of the dimensionless amplitude Λ (ratio between the vibration amplitude A and a workpiece critical dimension) and dimensionless stress P (ratio between the applied stress and yield strength of the material at room temperature), as follows:

$$\xi = 0.177 + \frac{1.74}{1 + \exp(0.109 + 171\Lambda - 47.0P)} \tag{13.4}$$

Daud et al. (2007) showed that the pure oscillatory stress superposition model does not satisfy the total stress reduction measured from experimental curves. Wang et al. (2016) developed a hybrid material model that includes both acoustic softening and stress superposition. Specifically, the total stress reduction is given as follows:

$$\Delta\sigma = \Delta\sigma_{so} + \Delta\sigma_{su} = -\beta M\hat{\tau}(\xi_{acoustic}/\hat{\tau})^m - K(\alpha_t A)^n \tag{13.5}$$

where the first term $\Delta\sigma_{so}$ corresponds to acoustic softening, β and m are material parameters, M is the Taylor factor, $\widehat{\tau}$ is the mechanical threshold of a given material determined from the critical resolved shear stress, and $\xi_{acoustic}$ is the acoustic energy density. The second term $\Delta\sigma_{su}$ describes the stress superposition from the oscillatory displacement field, where K is the material strengthening coefficient, n is the hardening exponent, A is the vibration amplitude, and α_t is the vibration transmission coefficient that accounts for the loss of acoustic energy during transmission from the ultrasonic horn to the experimental material. They verified their model with ultrasonically assisted tension tests on pure copper foils, as shown in Figure 13.15.

In a model developed by Siddiq and Ghassemieh (2008) for the ultrasonic additive manufacturing process, acoustic softening is considered phenomenologically by multiplying a coefficient in the isotropic R_{UA} and kinematic α_{UA} hardening terms in the material model, as follows:

$$R_{UA} = (1 - d \cdot E_{acoustic})^2 \left[Q\left(1 - e^{-b\bar{\varepsilon}^{pl}}\right)\left(1 - \left(\frac{\theta - \theta_{tran}}{\theta_{melt} - \theta_{tran}}\right)^m\right)\right] \tag{13.6}$$

$$\alpha_{UA} = (1 - d \cdot E_{acoustic})^2 \left[\left(\frac{C}{\gamma}\left(1 - e^{-\gamma\bar{\varepsilon}^{pl}}\right) + \alpha_1 e^{-\gamma\bar{\varepsilon}^{pl}}\right)\left(1 - \left(\frac{\theta - \theta_{tran}}{\theta_{melt} - \theta_{tran}}\right)^m\right)\right] \tag{13.7}$$

where Q, b, m, C, γ, and α_1 are material parameters; θ_{tran} is the transition temperature below which the yield stress is temperature-independent; $\bar{\varepsilon}^{pl}$ is the equivalent plastic strain; $E_{acoustic}$ is the acoustic energy density per unit time; and d is the ultrasonic related parameter that can be identified with inverse analysis from experimental results. This model describes acoustic softening in a wide range of temperatures and strains. In a similar effort to model the ultrasonic welding process, Chen et al. (2017) multiplied an acoustic softening coefficient into the Johnson-Cook constitutive material model as follows:

$$\sigma = \exp\left(n_2 \cdot \xi_{acoustic}\right)\left[A + B\left(\bar{\varepsilon}^{pl}\right)^n\right]$$

$$\left[\left(C \ln\left(1 + \frac{\varepsilon}{\varepsilon_0}\right) + 1\right)\left(1 - \left(\frac{\theta - \theta_{tran}}{\theta_{melt} - \theta_{tran}}\right)^m\right)\right] \tag{13.8}$$

where $\xi_{acoustic}$ is the acoustic energy density, $\bar{\varepsilon}^{pl}$ is the plastic strain, $\dot{\varepsilon}$ is the strain rate, and A, B, C, n_2, and n are material parameters.

The physically based ultrasonically affected material model is developed within the framework of crystal plasticity, which explicitly considers the deformation physics and microstructure evolution. Siddiq and El Sayed (2011, 2012a, b) multiplied a softening coefficient U_{soft} to the critical resolved shear stress in each slip system, as follows:

$$\dot{\gamma}^\alpha = \gamma^\alpha \operatorname{sgn}\left(\tau^\alpha\right)\left\{\left|\frac{\tau^\alpha}{g^\alpha \cdot U_{soft}}\right|\right\}^m \tag{13.9}$$

where $\dot{\gamma}^\alpha$ is the plastic strain rate of the slip system α, g^α is the strength of the slip system α, and m is a material parameter. The softening coefficient U_{soft} is a function of ultrasonic intensity $I_{acoustic}$ as follows:

$$U_{soft} = \left(1 - d_{ut} \cdot I_{acoustic}\right)^{e_{ut}} \tag{13.10}$$

where d_{ut} and e_{ut} are ultrasonic softening material parameters found from experiments. With this model, they simulated ultrasonically assisted deformation on single crystal aluminum at different orientations. Higher stress-strain response is obtained for orientations with slip systems of lower Schmidt factors. In addition, they also simulated effects of different levels of ultrasonic intensity on deformation of polycrystalline aluminum. A higher ultrasonic intensity leads to an increased amount of lattice rotation about all three axes, as shown in Figure 13.16. In other

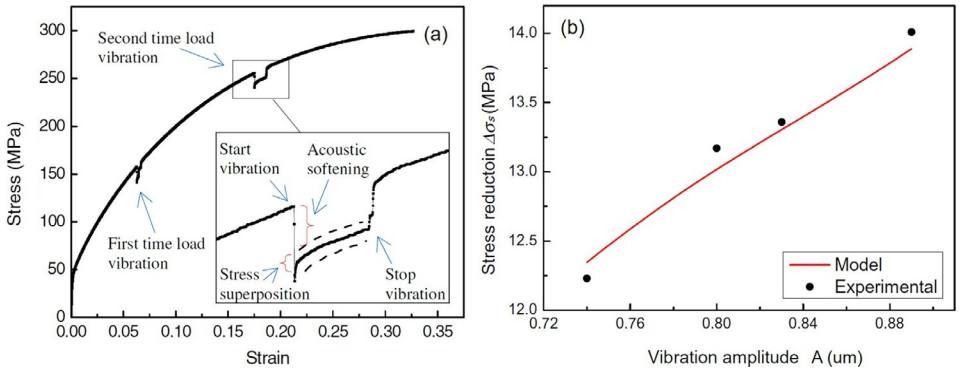


FIGURE 13.15 (a) Stress reduction from acoustic softening and stress superposition during ultrasonically assisted tensile test of copper; (b) stress reduction from model calculation and experimental measurements (Wang et al., 2016, Figs. 7, 13).

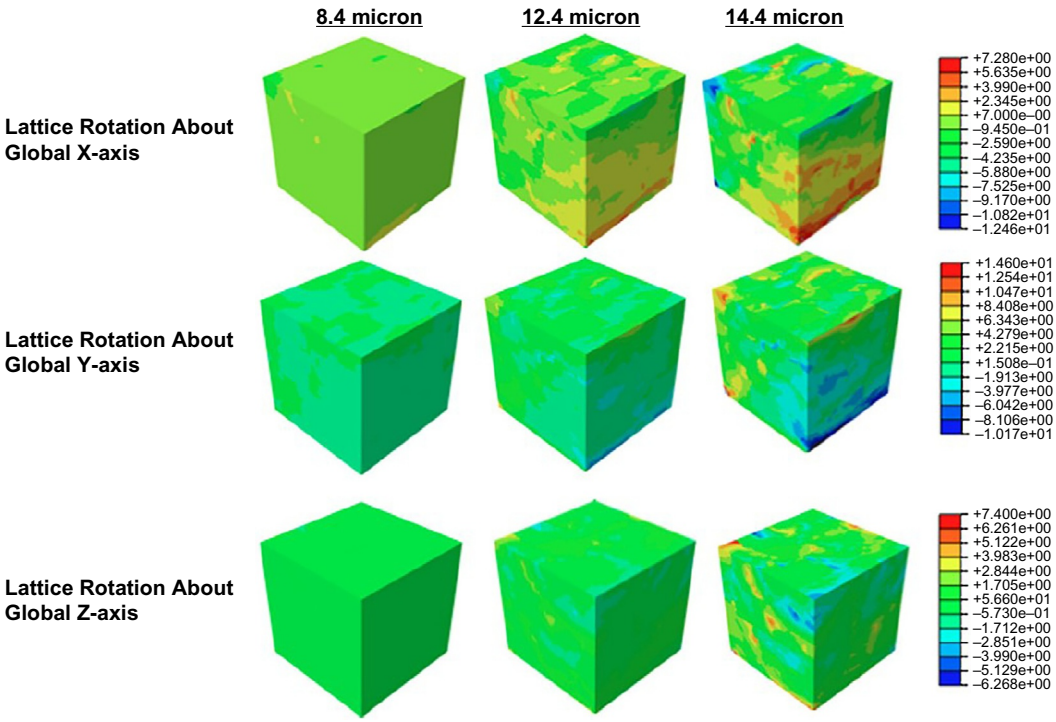


FIGURE 13.16 Lattice rotation about three axes at different ultrasonic vibration amplitudes, 8.4, 12.4, and 14.4 μm (Siddiq and Sayed, 2011, from Fig. 3).

words, ultrasonic energy can facilitate texture weakening through a higher degree of subgrain rotation.

Yao et al. (2012a, b) employed a dislocation density–based crystal plasticity model, where the ultrasonic density is incorporated into the stress reduction and dislocation evolution terms independently. Specifically, the stress reduction is expressed as a stress reduction ratio $\Delta\lambda$:

$$\Delta\lambda = \frac{\Delta\tau}{\widehat{\tau}} = -\beta(\xi_{acoustic}/\widehat{\tau})^m \tag{13.11}$$

where $\widehat{\tau}$ is the mechanical threshold, which is related to dislocation density ρ as follows:

$$\widehat{\tau} = \tau_0 + \mu\alpha b\sqrt{\rho} \tag{13.12}$$

where τ_0 and α are the material parameters, μ is the friction coefficient, and b is Burger's vector. Evolution of dislocation density can be determined as follows:

$$\frac{d\rho}{d\gamma} = k_1(1+\eta_{k1})\sqrt{\rho} - k_{20}\left(\frac{\dot{\varepsilon}}{\dot{\varepsilon}_0}\right)^{-1/n}(1+\eta_{k2})\rho \tag{13.13}$$

where γ is the shear plastic strain; k_{20}, $\dot{\varepsilon}_0$, and k_1 are the material-related parameters; and η_{k2} η_{k1} correspond to the additional dislocation multiplication and annihilation induced by ultrasonic energy, respectively, which can be expressed as follows:

$$\eta_{k1} = KP_0/\left[P_0 + (K-P_0)e^{\phi A}\right] \tag{13.14}$$

where A is the ultrasonic vibration amplitude, and K, P_0, and ϕ are material parameters. By modifying the coefficient on the dislocation density, this model can effectively capture both ultrasonically induced residual softening and hardening effects. A comparison of their model results and experimental measurements is provided in Figure 13.17. This model is also adopted by Bagherzadeh and Abrinia (2015) to quantify the softening and residual hardening during ultrasonically assisted compression tests of pure aluminum.

Prabhakar et al. (2017) also developed a dislocation density–based crystal plasticity model, where the ultrasonic energy is incorporated as a modification term on the activation energy, as follows:

$$\dot{\varepsilon} = \dot{\varepsilon}_0 \exp\left(-(\Delta Q + \Delta Q_v)/kT\right) \tag{13.15}$$

where ΔQ_v is the ultrasonically modified activation energy. Their model results matched well with the experimentally measured stress-strain curves at different ultrasonic vibration amplitudes, deformation strain rates, and different strains where ultrasonic vibration is applied intermittently.

Deshpande and Hsu (2018) adopted a modified Kocks-Mecking (KM) model to account for the ultrasonically induced dynamic recovery, where the activation energy for dislocation annihilation is reduced by a coefficient determined by acoustic energy density. Specifically, in the dynamic recovery term, the reduction of dislocation density is given as follows:

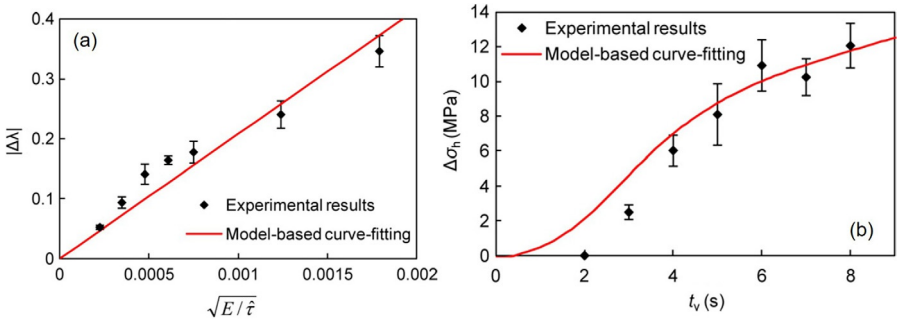


FIGURE 13.17 (a) Model and experimental results on relationship between the stress reduction ratio $\Delta\lambda$ and acoustic energy density $\xi_{acoustic}$. (b) Model and experimental results on stress increase $\Delta\sigma_n$ from acoustic residual hardening as a function of vibration duration t_v (Yao et al., 2012a, b, Figs. 6, 7).

$$\frac{d\rho}{d\gamma} = -k_{20}\left(\frac{\dot{\varepsilon}}{\dot{\varepsilon}_0^*}\right)^{-1/n}\rho \tag{13.16}$$

where under high temperature and ultrasonic vibration, $\dot{\varepsilon}_0^*$ is given by an ultrasonically modified Arrhenius equation:

$$\dot{\varepsilon}_0^* = \dot{\varepsilon}_{00}^* \exp\left(\frac{-\chi Q_d}{kT\xi_{acoustic}}\right) \tag{13.17}$$

where Q_d is the activation energy for self-diffusion, k is the Boltzmann constant, and T is the temperature. The ultrasonic effects are included with $\xi_{acoustic}$ as the acoustic energy density, and χ as an adjustable coefficient. Deshpande and Hsu (2018) verified this model with ultrasonically assisted compression tests on pure aluminum, where the vibration is transverse to the compression direction, as shown in Figure 13.18. This model can effectively capture the ultrasonically induced softening at different strain rates and ultrasonic energy densities.

There are both advantages and disadvantages for empirically based and physically based ultrasonically affected material constitutive models. In the mathematical expressions of empirical material models, the amount of flow stress reduction is explicitly quantified as a function of ultrasonic parameters. Accordingly, the computational efforts to implement these stress-strain relationships into manufacturing process models that utilize ultrasonic energy, such as ultrasonic welding, ultrasonically assisted forming, and machining, are relatively low. These process models can be further utilized for parameter optimization. However, empirical models can hardly capture the fundamental mechanisms of ultrasonic effects on material plastic deformation behavior. The physically based material model effectively describes the ultrasonic effects in multiple length scales in detail, starting from nanoscale dislocation movement, microscale grain deformation and rotation to the macroscale stress-strain functions. Material deformation mechanism and microstructure evolution under the superimposed ultrasonic energy can be directly revealed. On the other hand, these material models are computationally expensive to be incorporated in the manufacturing process models. In future studies, both empirically based and physically based models can be developed for advanced materials, such as the ultrahigh-strength steels and high-entropy alloys. Thus far, the majority of ultrasonically affected material models focus on the quasistatic deformation behavior at room temperature. Since many manufacturing processes involve material deformation at high temperature and strain rate, ultrasonically affected material models in this range are accordingly also desired.

13.4 Surface friction

It has been noted that the influence of power ultrasonics on material forming falls into two categories: volume effect, as reviewed in Section 13.3, and surface friction effect between the contacting surfaces of the formed material and the forming tooling. Surface friction effects will be reviewed in this section.

13.4.1 Early developments

The ability of ultrasonic vibrations to influence friction between contacting surfaces was recognized well before its importance in ultrasonic forming was understood. Thus, Mason (1958) used an ultrasonic apparatus, shown in Figure 13.19, to evaluate friction and wear in materials, while Weber (1954) studied the reduction of sliding friction from ultrasonics. Likewise, Fridman and Pascal (1959) at the Raytheon Company, an early developer of the ultrasonic drilling process, studied friction reduction due to ultrasonic vibrations as part of understanding its influence in drilling.

The importance of friction effects on ultrasonic deformation processes was recognized by all of the early workers but given differing levels of attention. The wire drawing work by Aeroprojects, cited in Rosenfeld (1963), took note of the just cited works on friction but did not report on any further measurements. Later papers from Aeroprojects (e.g., Jones, 1967) indicated a view as to friction being the dominant effect in wire and tube drawing but did not research the

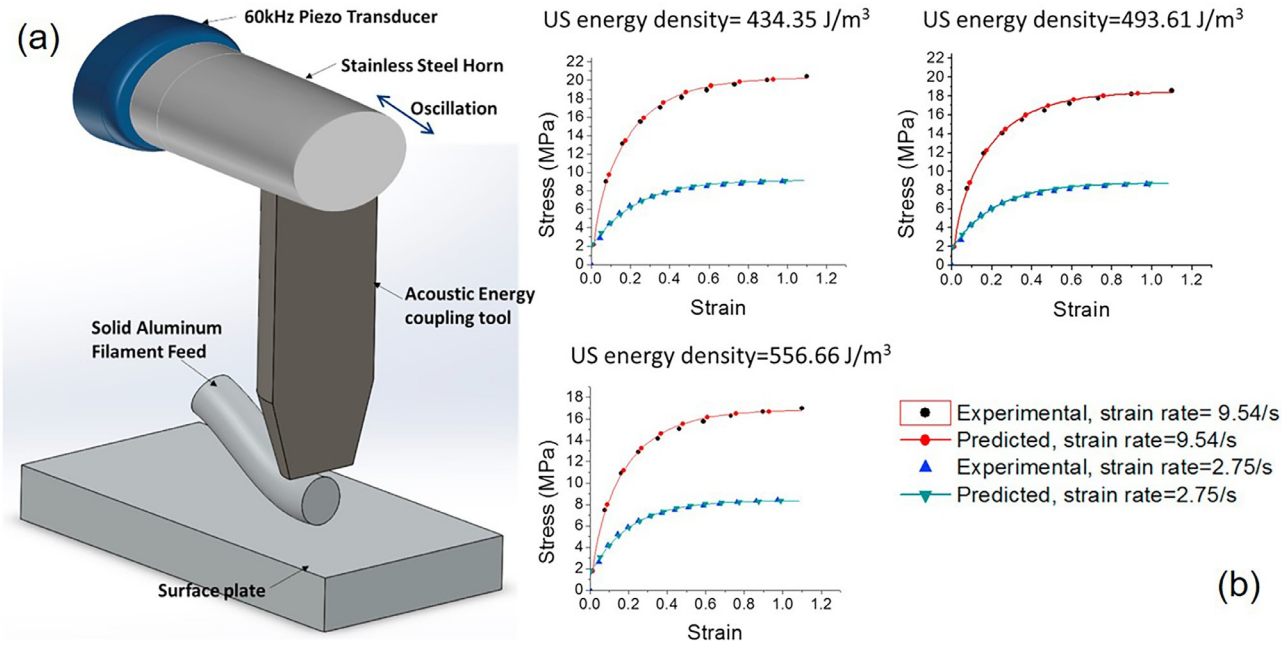


FIGURE 13.18 (a) Schematic illustration of ultrasonically assisted compression tests on pure aluminum. (b) Comparison of the experimentally measured and model predicted stress-strain curves at different strain rates and ultrasonic energy densities (Deshpande and Hsu, 2018, Figs. 1, 6).

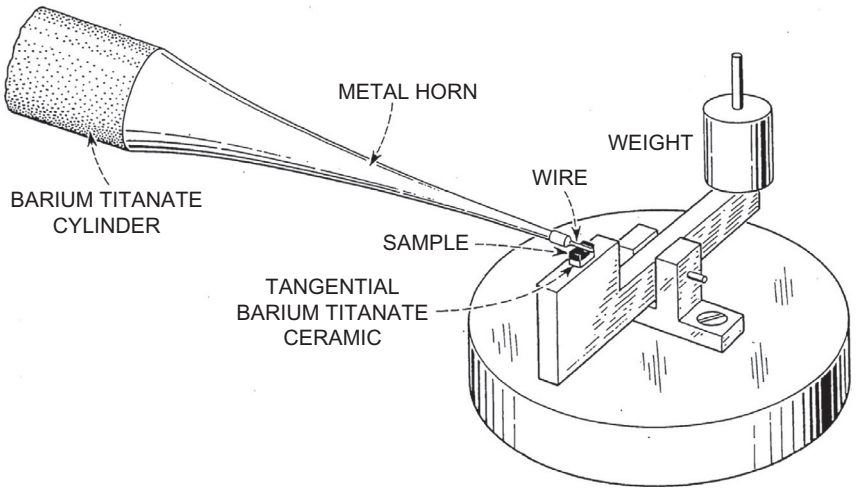


FIGURE 13.19 Equipment of Mason to study ultrasonic friction and wear (Mason, 1958; Fig. 6.6).

subject. A first note on friction effects relative to volume effects appears to be in Langenecker et al. (1964), but with little other mention in his numerous publications. On the other hand, Sansome and colleagues made note on friction effects in several of the works cited in the last section. Thus, the early paper by Winsper and Sansome (1967) suggested that friction reduction was associated with reduction in the yield point of contacting surface asperities, while in their wire drawing studies (Winsper and Sansome, 1969), the effects of friction reduction were seen as negligible. However, in Sansome (1970), it was noted that in some cases, oscillatory forces were reduced by amounts greater than predicted by superposition theory, and that friction effects possibly accounted for the difference. The greater effects of friction were noted in the deep drawing process (Biddell and Sansome, 1973), and the need to further evaluate the "friction vector" in tube drawing and other deformation was noted in Sansome (1973). In Eaves et al. (1975), it was recognized that frictional effects, as captured by the friction vector, played a critical role in load reduction in oscillatory metalworking processes.

Pohlman and Lehfeldt (1966), in one of the most frequently cited early studies, used several equipment configurations (Figure 13.20a) to measure ultrasonic friction reduction for varied orientations of vibration relative to contacting surfaces, with the contact speed relative to

the ultrasonic vibration speed able to be controlled. Key findings are summarized in the graph of Figure 13.20b, which shows for setups A, B, and C of Figure 13.20a that frictional forces were significantly reduced but that there was a clearly diminished effect as contact speed increased. In particular, as contact speed approached the local ultrasonic vibration velocity, friction reduction dropped off, leading to their conclusion that "It is very plain that the effect of the sound oscillations on the friction process can only be great whilst the contact speed remains small in comparison with the particle velocity $v = 2\pi fA$ …." The concept of a "critical velocity" put forth in this classical paper is found to be one that runs through many industrial applications of ultrasonics, whether in forming, machining, or others having high processing speeds.

Other contributors in this period included Mitskevich (1968), who studied the effects of friction on the motion of a body over a tangentially vibrating surface, developing a mathematical model for friction reduction, and Mikhenlman and Mashchinov (1969), who measured the change in force in drawing a weight along a longitudinally vibrating (at 20 kHz) waveguide, noting a reduction in the friction coefficient by a factor of four.

Rozner (1971) examined the effect of ultrasonics on friction reduction in strip drawing, using the setup shown in Figure 13.21a. Key system components included the test machine base (B), the die (C), die holder (D), the transducers (H), and the tension link (L). Results were obtained for Cu (Figure 13.21b) and steel strip. As is seen, there was significant friction reduction for Cu, 30% on average for various thickness reductions. For steel, the results were less, averaging about 25% for lower reductions and tapering to near zero at 30% reduction.

The previously noted monograph by Severdenko et al. (1972) had extensive discussion of friction effects. After reviewing the role and types of friction in conventional metalworking processes, the work of Pohlman and Lehfeldt (1966) was discussed, with questions raised on the results being affected by the test apparatus. A testing setup for examining friction reduction under various vibration modes (Figure 13.22a) was shown, leading to reductions of friction coefficient as a function of contact force, as shown in Figure 13.22b, where the letters in (b) coincide with the modes shown in (a). Extensive results were shown for various material pairs, vibration amplitudes, and sliding velocities. Analysis of the local vibration kinematics was given as was a review of the effects of lubricants on ultrasonic friction.

In the earlier cited article by Green (1975), the importance of contact friction reduction as part of the ultrasonic deformation process was noted, including the role of contact speed and vibration direction in friction results. The power ultrasonic books by Puskar (1982) and Abramov (1994, 1998), generally invaluable references on most metal applications, did not contain significant coverage of friction effects. Thus, while frequent reference to friction may be found in Puskar, there is little in the way of technical coverage, while the Abramov references cover work in the 1970s that may be found in Severdenko et al.

Goto et al. (1984, 1986), after noting that "… it is well known that … static and dynamic friction are reducing remarkably when one of sliding bodies is vibrated" and also noting the lack of prior work in this area, used equipment

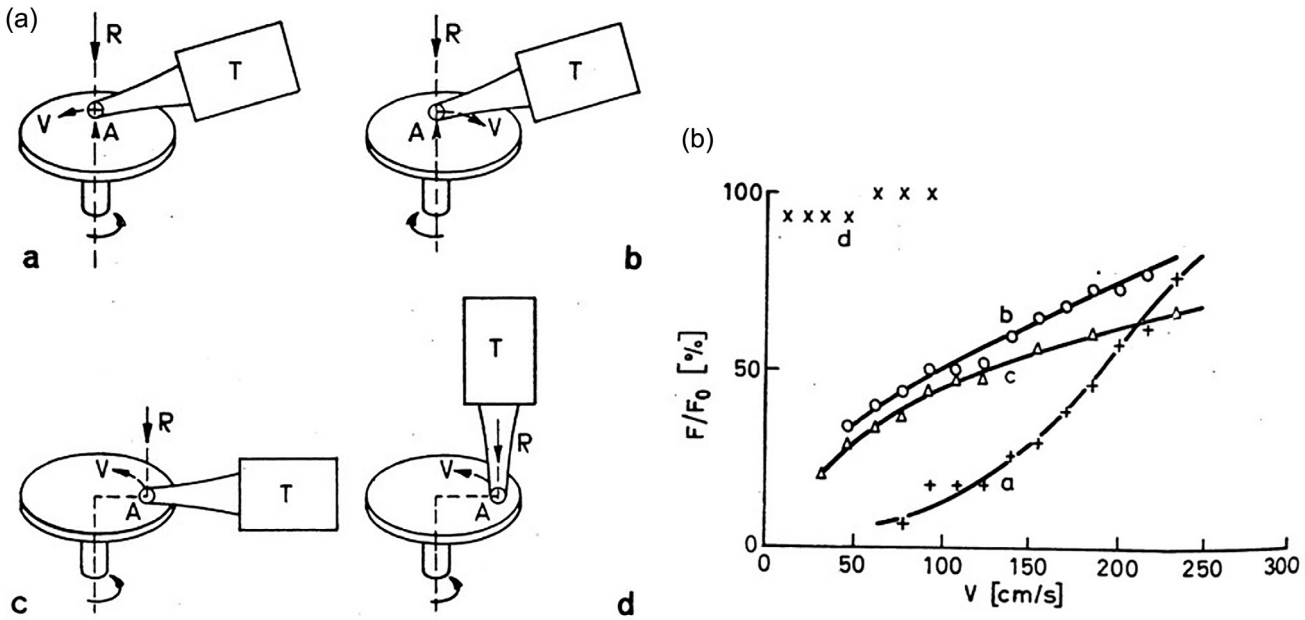


FIGURE 13.20 Effect of ultrasound on friction reduction (Pohlman and Lehfeldt, 1966). (a) Setups for measuring friction reduction (Pohlman and Lehfeldt, 1966; Fig. 5); (b) friction reduction in relation to contact speed for different vibration directions (Pohlman and Lehfeldt, 1966; Fig. 6).

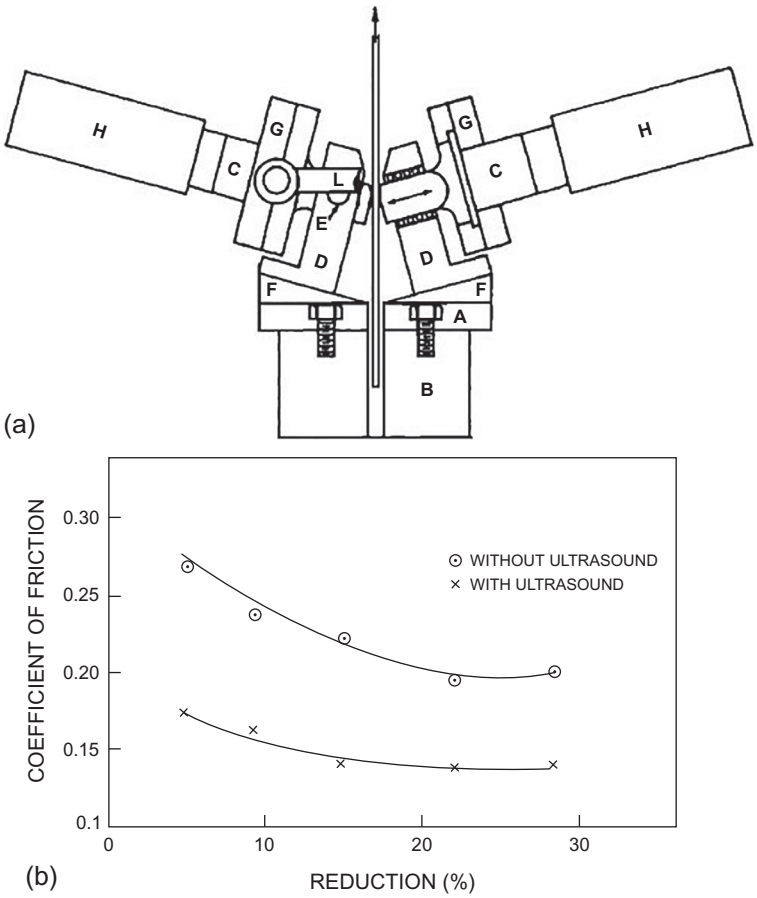


FIGURE 13.21 Study by Rozner (1971) on friction reduction. (a) Apparatus for friction measurements (Rozner, 1971; Fig. 1), see text for explanation; (b) coefficient of friction versus thickness reduction for copper (Rozner, 1971; Fig. 3).

seen to be similar to that of Pohlman and others. The effect of vibration amplitude and sliding velocity for steel was measured, and the ultrasonic wear process was modeled and compared favorably to experimental results. Unfortunately, the conditions for wear testing were not similar to those encountered in forming, which limits that applicability of the results.

13.4.2 Recent developments: 2000 onward

While possibly stretching the meaning of the word "recent", developments in ultrasonic surface friction from 2000 onward will be considered. Thus, after noting the range of ultrasonic industrial processes where dynamic friction effects can play a key role (e.g. turning, drilling, and wire drawing), Littmann et al. (2001a,b) undertook development of a theoretical model of the ultrasonic friction effect. A modification of Coulomb's friction law was developed and applied to the experimental situation, as shown in Figure 13.23a. The model predicted a major friction force reduction, that is, approaching zero, for low sliding velocities, but a diminishing effect with increased sliding velocity, finally with the friction reduction itself going to zero at sliding velocities equal to or greater than the vibration velocity, this being the "critical velocity" previously noted. Results are shown in Figure 13.23b, which shows friction reduction μ_i against the velocity ratio of vibration to sliding velocity, $\zeta = V_{vib}/V_{slid}$.

Siegert and Ulmer (2001), with the intent of achieving a better understanding of friction effects in ultrasonic forming processes, undertook studies using the system shown in Figure 13.24a to make friction measurements, while developing a friction law that accounted for normal forces, contact pressure, lubricant, and material parameters of the contact surfaces. Figure 13.24b shows the percentage of friction force reduction versus normal force and sliding velocity for three different vibration amplitudes. The highest reduction occurred with the highest vibration amplitude, as possibly expected, with a diminished reduction occurring with increasing sliding velocity, regardless of amplitude, this being yet another confirmation of the critical velocity concept.

Kumar and Hutchings (2004) examined the influence of 20-kHz ultrasonic vibrations on sliding friction, where the vibrations were both parallel and perpendicular to the

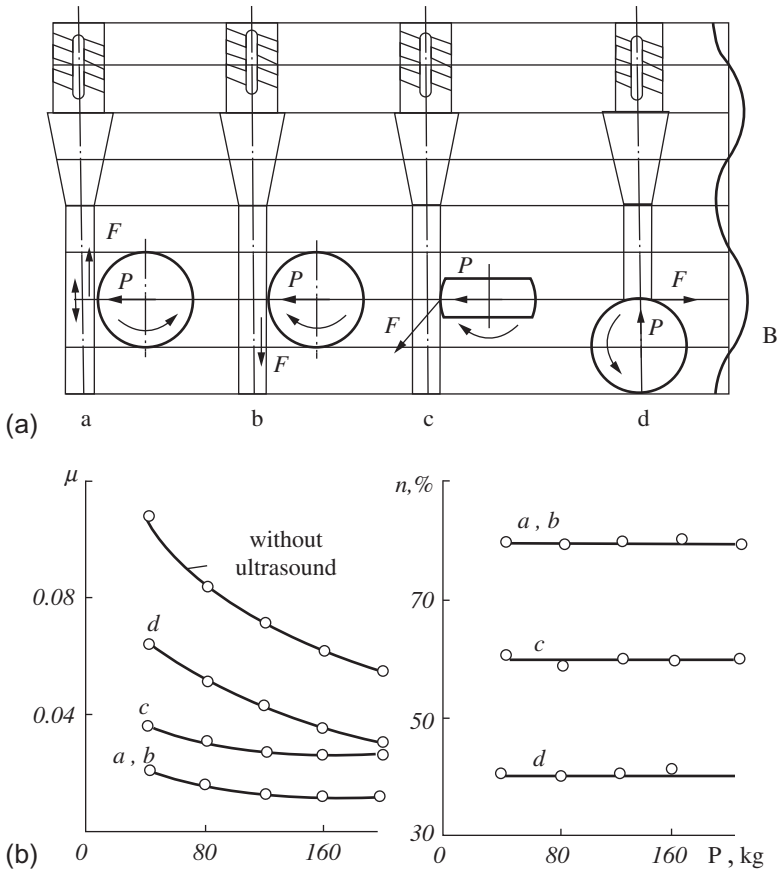


FIGURE 13.22 Ultrasonic friction reduction studies of Severdenko et al. (1972). (a) Different modes of ultrasonic friction reduction (Severdenko et al., 1972; Fig. 23); (b) coefficient of friction as a function of load (left) and percentage decrease (right) (Severdenko et al., 1972; Fig. 24).

sliding direction. The equipment was used to test aluminum, copper, brass, and stainless steel against a tool steel surface. The ultrasonic vibration interacted with the low-frequency table vibration, creating relative motion involving the table sliding velocity, V_s, and the ultrasonic oscillatory velocity, $V_u = a\omega \sin \omega t$. Both longitudinal and transverse vibration directions relative to table motion were considered. Mathematical models of the process were formulated, and comparisons with tests showed generally good agreement, with the results obtained for varying ultrasonic amplitudes for copper under longitudinal vibration. While friction force reductions were significant in both cases, longitudinal vibrations had the more pronounced effect. The effect of higher amplitudes, hence higher V_u relative to the sliding velocity V_s, was clear, an effect repeatedly seen in ultrasonic processes.

Popov et al. (2010), using a 40- to 70-kHz ultrasonic device (Figure 13.25a), having similarities to that of Littmann et al. (2001a) and the rotating disk approach (Figure 13.25b), first shown by Pohlman and Lehfeldt (1966), carried out dry friction studies between steel and materials that included steel, brass, copper, glass, rubber, and Teflon. The static friction coefficient as a function of vibration amplitude was found for the various materials. While some anomalies exist (e.g., upturns for some materials at high amplitudes, explained by equipment issues), the general downward trend in friction with increasing amplitude is similar to findings of others. Figure 13.25c shows the case of steel on steel for various vibration amplitudes, Δl, vs sliding velocity, V_s, again bearing the general trend seen by others, namely, a greater reduction as amplitude increases and a lesser reduction as velocity increases. Modeling of the friction process, introducing the concept of friction slip length, was done with general agreement with experiments being achieved. Teidelt et al. (2012) first showed the relevance of their friction studies to many of the past forming works and extended preceding work to look at two additional vibration directions relative to the sliding direction. Both macroscopic and microscopic models were used to interpret results. It was found that vibration amplitudes as low as 0.1 μm were sufficient to cause significant friction force reductions. When it is appreciated that most ultrasonic manufacturing processes involve amplitudes in the range of 10–100 μm, this was a very small number.

The concept of using the Poisson expansion of a solid driven by longitudinal vibrations as the friction-reducing

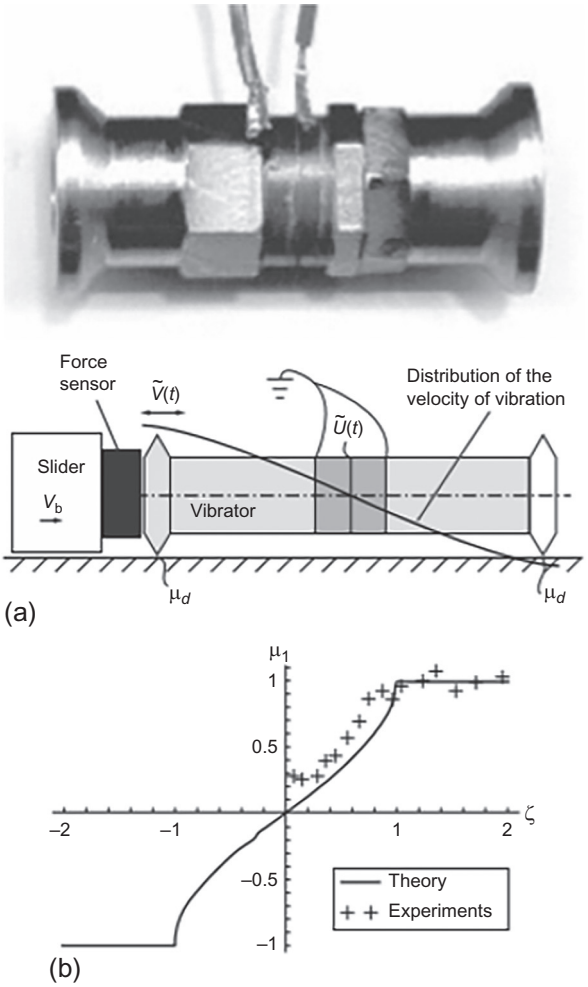


FIGURE 13.23 Friction reduction study of Littmann et al. (2001a). (a) Schematic and photo of the ultrasonic unit for friction tests (Littmann et al., 2001a; Fig. 5); (b) theory and experimental values for friction reduction (Littmann et al., 2001a; Fig. 7).

component was developed by Graff and Short (2009). Bharadwaj and Dapino (2013) and Dong and Dapino (2012, 2014) have researched the concept in-depth, developing a model of the "ultrasonic friction lubrication" process and using equipment, as shown in Figure 13.26a. An elastic-plastic cube model able to represent varied surface contact conditions and accounting for varied directions of ultrasonic vibrations across a surface was developed. Experiments examined friction reduction for different materials (aluminum, stainless steel, and their combinations) under normal loads that varied from 40 to 240 N, with tests showing up to 60% friction reduction and in general agreement with model simulations, of which Figure 13.26b is representative, with test 1 being Al-SS.

Popov (2017) analyzed the influence of ultrasonic vibration on both static and kinetic friction, where vibration is applied in the contact plane. The vibration direction can be either parallel or perpendicular to the sliding direction—each case was analyzed. They showed that for small oscillation amplitudes, the macroscopic Coulomb friction model was inaccurate. In another study by Teidelt et al. (2012) in the same group, both in-plane and out-of-plane ultrasonic vibrations are investigated. They found that a small vibration amplitude of 0.1 μm is sufficient to induce significant amount of friction force reduction and the force reduction is higher at lower sliding velocities. Experimental studies with in-plane ultrasonic vibration were also performed. In most materials, a higher reduction of friction coefficient was observed at larger vibration amplitude (except in aluminum and rubber). An overview of the typical experimental results regarding in-plane ultrasonic effects on kinetic friction was given.

In the experimental study performed by Milahin et al. (2015), the ultrasonic vibration was applied in the

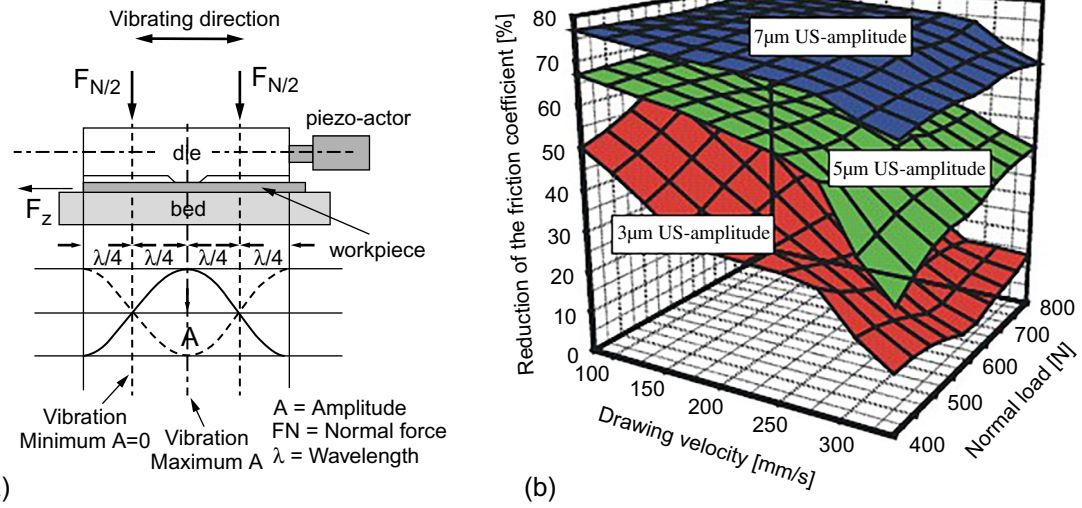


FIGURE 13.24 Results from Siegert and Ulmer (2001) on ultrasonic friction reduction. (a) Experimental setup for friction tests (Siegert and Ulmer, 2001; Fig. 1); (b) friction force reduction at various amplitudes, velocities, and forces (Siegert and Ulmer, 2001; Fig. 3).

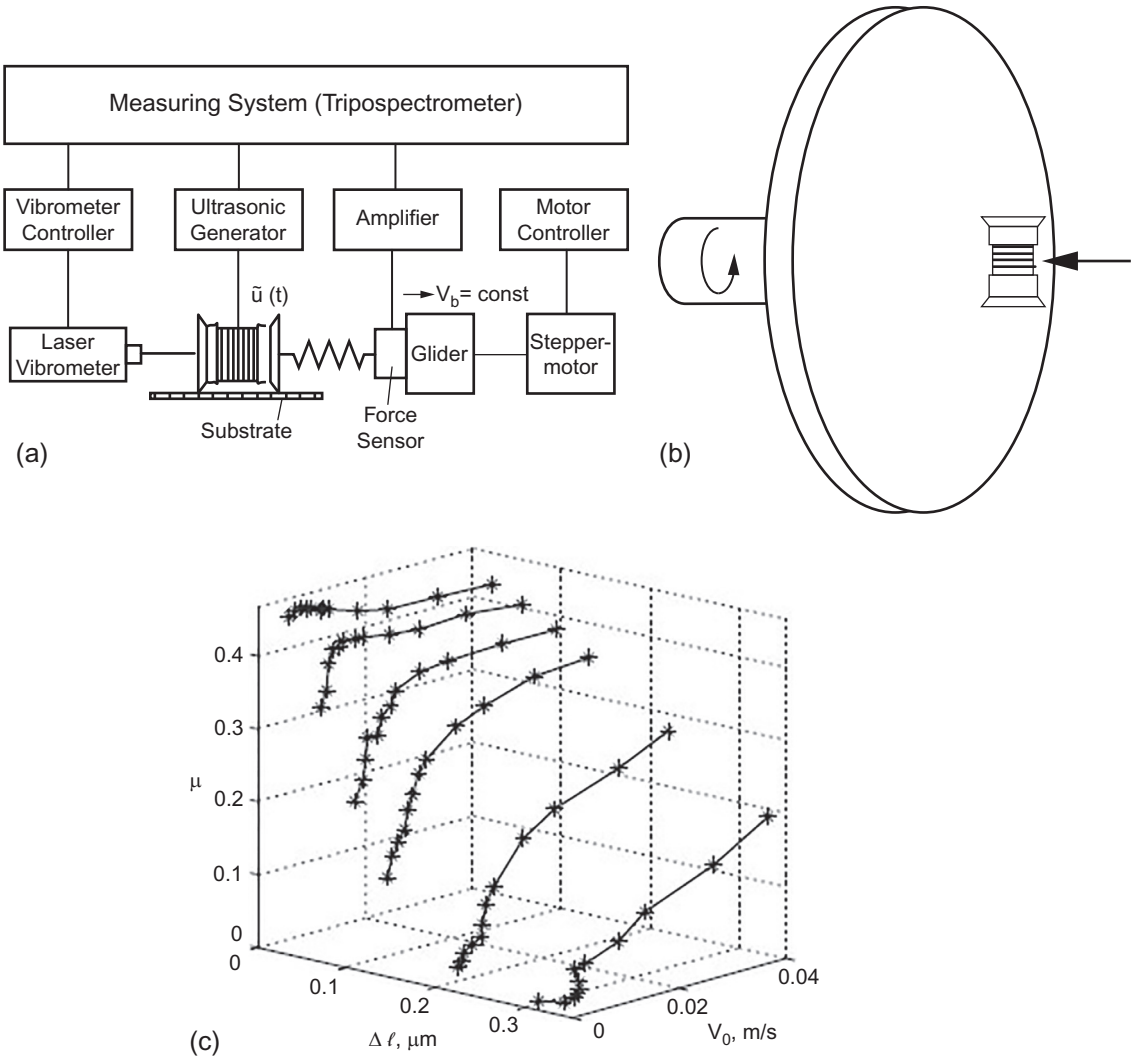


FIGURE 13.25 Sliding friction study of Popov et al. (2010). (a) Linear ultrasonic "tribometer" (Popov et al., 2010; Fig. 1); (b) rotating disk (Popov et al., 2010; Fig. 2); (c) sliding friction as a function of amplitude and sliding velocity (Popov et al., 2010; Fig. 9).

out-of-plane mode, that is, the vibration was perpendicular to the contact surface, as shown in Figure 13.27a. They proposed the ultrasonically affected friction coefficient is only a function of two dimensionless parameters, namely, dimensionless oscillation amplitude and dimensionless velocity, given as follows:

$$\Delta\widehat{u}_z = \Delta u_z / u_z^{(0)}; \widehat{v} = v / \left(\omega u_z^{(0)}\right) \tag{13.18}$$

where Δu_z is oscillation amplitude, $u_z^{(0)}$ is indentation depth, ω is frequency (radians/time), and v is the sliding speed. They also showed that the ultrasonic effect on friction reduction is less significant under a higher normal force, as in Figure 13.27b.

Dong and Dapino (2015) investigated ultrasonically affected friction behavior based on a modified pin-on-disc tribometer experimental system, as shown in Figure 13.28, where the vibration is applied in the out-of-surface mode. They observed that ultrasonically induced friction reduction is higher under lower linear velocity and higher electric power to the ultrasonic transducer, while it is insensitive to the normal stress, as shown in the contour plots in Figure 13.29a,b. They also proposed an efficiency coefficient parameter to quantify the relationship between the reduction of friction and the amount of electric power to the ultrasonic transducer. In another study from Milahin and Li (2016), which is also based on the pin-on-disc tribometer with out-of-plane vibration, wear rates of the spherical indenter after sliding tests were analyzed. They found that despite the reduced friction, the influence of ultrasonic oscillation on indenter wear was small.

Friesen et al. (2017) focused on utilizing ultrasonically modified friction to improve the haptic feeling (i.e., skin sensation) of touch screens. They developed an innovative finger friction test system in a vacuum chamber. An artificial finger was driven by a motor to rotate and pressed

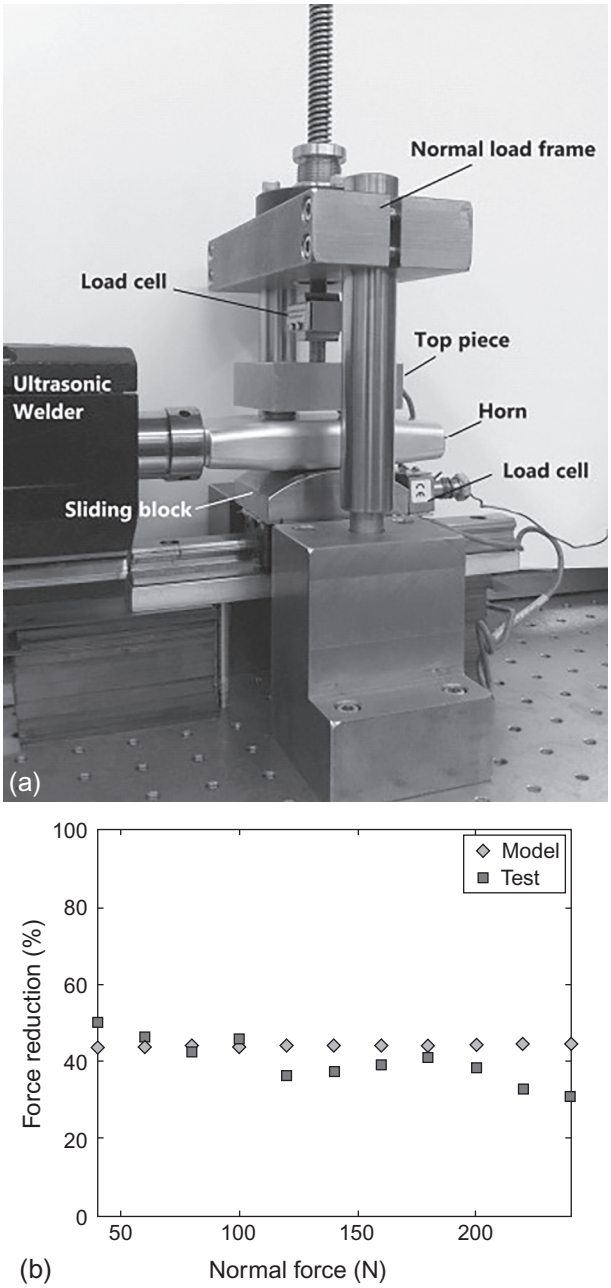


FIGURE 13.26 Friction reduction work of Dong and Dapino (2014). (a) Test apparatus (Dong and Dapino, 2014; Fig. 4); (b) force reduction for Al onto SS (Dong and Dapino, 2014; Fig. 11a).

against a Tactile Pattern Display glass plate, which vibrates at ultrasonic frequency. The motor current represents the amount of friction. By adjusting the air pressure in the vacuum chamber, the friction reduction from ultrasonic vibration was found markedly more significant in atmospheric than in vacuum conditions. These findings support the argument that squeeze film levitation is a major mechanism for ultrasonically induced friction reduction, as described by Friesen et al. (2016) in their earlier publication, which attributes the friction reduction to intermittent contact upon the vibrating surface.

Similarly, Vezzoli et al. (2017) and Sednaoui et al. (2017) performed comprehensive experimental and numerical analyses to understand the mechanisms of intermittent contact and squeeze film effects on ultrasonically induced friction reduction, which can then be adopted to improve touchscreen technology. They also developed a finger-ultrasonic vibrating plate system where the local velocity of fingerprint ridges was recorded based on a laser Doppler vibrometer. Finite element analysis (FEA) and a spring-Coulomb slider model were both developed, where the latter helped interpret the FEA model and identified a group of dimensionless parameters to calculate the friction coefficient. The numerical model accounted for the three most external layers of the skin, the stratum corneum, dermis, and subcutaneous tissues. They found that intermittent contact is the dominant mechanism for the reduction of friction coefficient under ultrasonic vibration. Stochastic adhesion and deocclusion mechanisms are determined to be relatively insignificant. Reduction of friction coefficient depends on the ultrasonic vibration frequency and amplitude, intrinsic friction coefficient of the device, and reciprocal of the exploration velocity. If the intermittent contact is sufficiently established, the reduction of the friction coefficient is independent of the shear and extensional elastic moduli of the finger skin.

Another application field of ultrasonically affected friction is in ultrasonic bearings, which serves as a promising alternative to traditional noncontact bearings. A typical structure of an ultrasonic bearing utilizes the near-field acoustic levitation phenomenon (Hu et al., 2003), where the high-frequency vibration of several objects can provide a suspension height of several micrometers. Li and Deng (2018) investigated the friction torque of an ultrasonic bearing at the start/stop, low- and high-speed stages. Running stability of the bearing at high speed closely depended on the load on the bearing and diameter clearance.

In the nanoscale and microscale, ultrasonic excitations also show the capability to reduce contact friction and suppress wear (Pedraz et al., 2015). This is promising in various applications, such as improving nanomanufacturing, increasing lifetime of atomic force microscope (AFM) probes, and enhancing functionality of nano/microelectromechanical systems (N-/MEMS). To understand the underlying principles of friction reduction under ultrasonic vibration in microscopic contact, Sharahi et al. (2018) compared conventional contact-AFM (C-AFM) and ultrasonic force microscopy (UFM). A schematic diagram of the setup is shown in Figure 13.30a, where the UFM was excited at 1.8 MHz. An example of the ultrasonic excitation signals and measured cantilever deflection curves are provided in Figure 13.30b. The results in Figure 13.30b shows

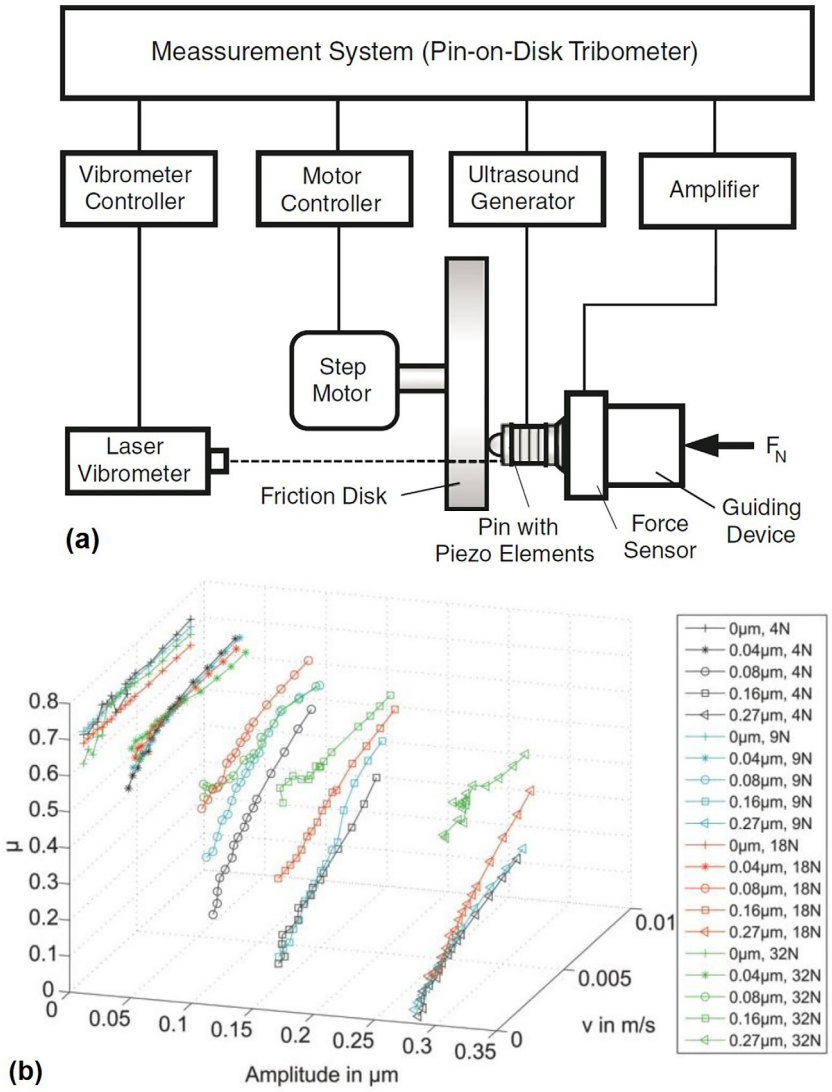


FIGURE 13.27 (a) Ultrasonically assisted pin-on-disc experimental setup (Teidelt et al., 2012, adapted from Fig. 6); (b) Reduction of sliding friction coefficient under different vibration amplitudes, sliding velocities, and normal loads. *(Milahin et al., 2015, adapted from Fig. 2).*

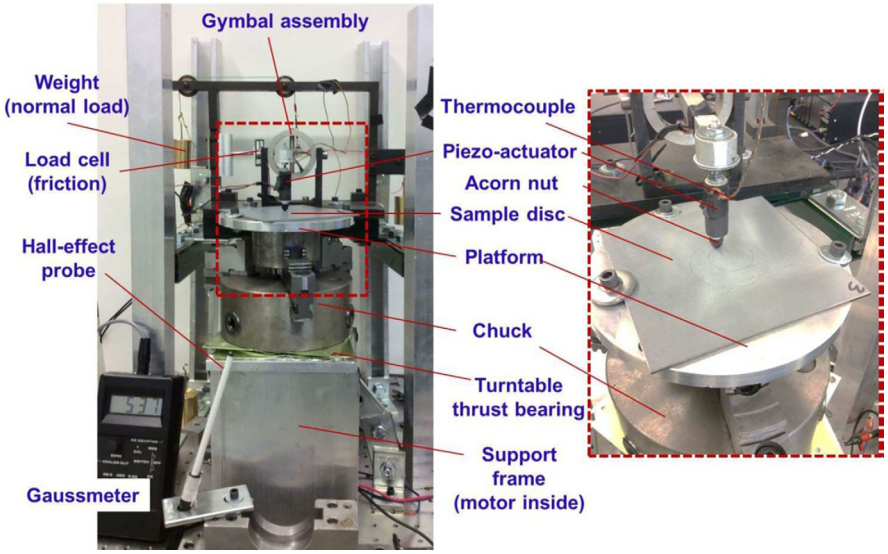


FIGURE 13.28 Ultrasonically assisted pin-on-disc experimental setup. *(Dong and Dapino (2015), adapted from Fig. 2).*

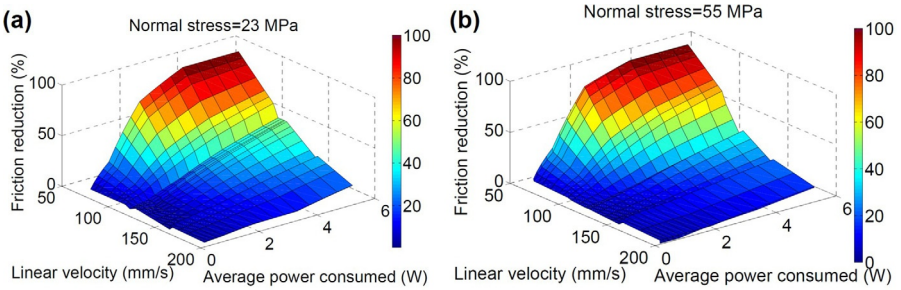


FIGURE 13.29 Contour plots of friction reduction under different parameters: (a) Lower normal stress of 23 MPa; (b) higher normal stress of 55 MPa. *(Dong and Dapino (2015), adapted from Fig. 8a, e).*

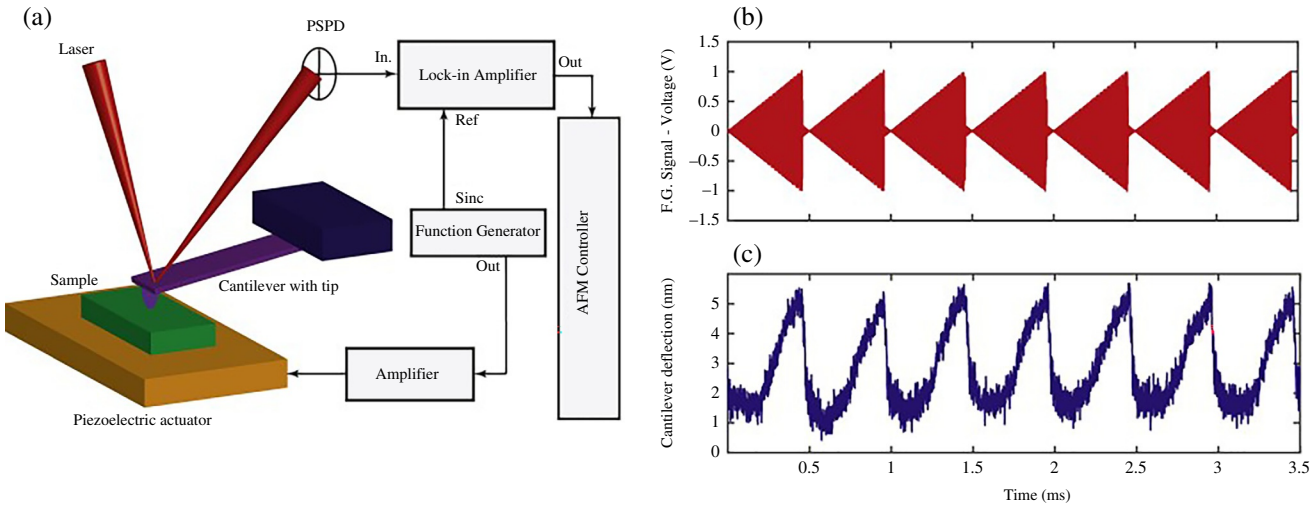


FIGURE 13.30 (a) Schematic illustration of the UFM system adapted from a commercial AFM system, where the sample is vibrated by the piezoelectric actuator underneath; (b) modulated ultrasonic excitation signals; (c) corresponding cantilever deflection response. *(Sharahi et al. (2018), modified from Fig. 1).*

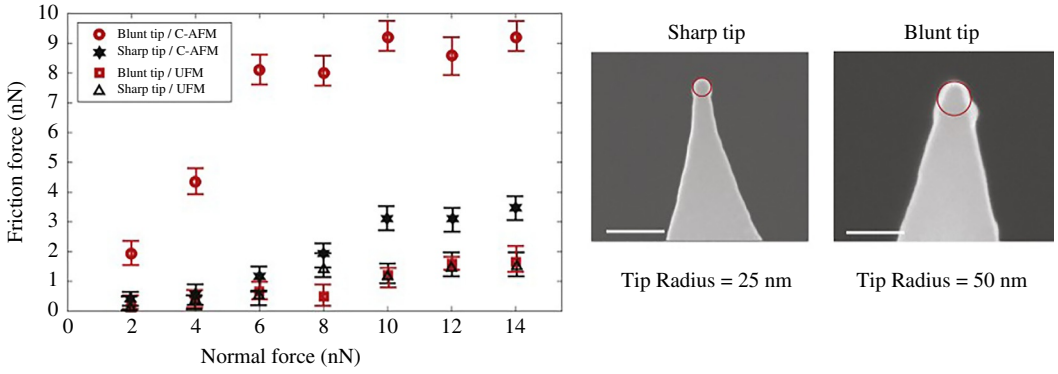


FIGURE 13.31 Comparison of UFM friction reduction on blunt and sharp tips. *(Sharahi et al., 2018, modified from Fig. 5).*

that a higher vibration amplitude leads to larger friction reduction and better topographic imaging. The ultrasonic excitation signal can also be clearly observed in the cantilever deflection, as shown in Figure 13.30b. It was found that in C-AFM, the friction force of a blunt tip is much higher than a sharp tip, whereas in UFM, the friction force is almost the same, as shown in Figure 13.31. For the blunt tip, the ultrasonic excitation is capable of reducing friction by almost one order of magnitude. Their analysis further revealed that the reduction of friction was mainly attributed to reduction in tip-sample adhesion and shear strength.

13.5 Future trends

In this chapter, the extensive coverage of the volumetric and surface effects of power ultrasonics on materials, while possibly being of justifiable interest on a purely scientific basis, has as its basic motivation the impact of this information on practical ultrasonic metal forming processes. Thus, how can—or will—advanced knowledge of bulk and surface effects assist in taking ultrasonic forming from the laboratory to the production floor?

Given the now eight decades plus that power ultrasonic studies of material effects have been in progress, one might believe that both a fundamental understanding of material effects and the application to practical processes would have been reached. However, as is evident by the continued activity in the materials side of forming, this is not yet the situation.

However, there are two trends evident in recent years that, if continued, could lead to the joint goals of fundamental understanding and practical application. Both are tied to modeling in one form or another, with the first being efforts to devise continuum mechanics models that incorporate more complex behaviors of materials. These models are being developed by a new generation of researchers not burdened by the controversies of the early years (acoustic softening, superposition, etc.), and if pursued with an end focus on their practical use, could have a major impact on the field.

The second trend, also modeling, relates to the use of increasingly sophisticated numerical (i.e. FEA) methods to model ultrasonic material behavior, both bulk and friction. Of course, this trend is ongoing in every area of materials and manufacturing analysis, so use in ultrasonics is to be expected. As noted in some of the developments discussed, these models have used existing material data or empirical adjustments to existing data to compute results. This approach may have an early impact on transitioning to practical production.

13.6 Sources of further information and advice

Information sources cited here are in many cases common to a number of chapters in this book. Thus, Abramov (1998) continues as an excellent reference to both the basics of power ultrasonics, as well as coverage of a number of manufacturing applications; as does Abramov (1994), which goes into greater depth on metallurgical processes. Attention is again drawn to Lucas et al. (2009) as it provides an excellent overview of the materials aspects of ultrasonic metal deformation. Numerous manufacturing and materials journals are cited throughout the chapter that can all be followed, time permitting. However, most significant developments in power ultrasonics will make some form of appearance, at one time or another, in the journals *Ultrasonics* or *Sonochemistry*.

References

Abramov, O.V., 1994. Ultrasound in Liquid and Solid Metals. CRC Press, New York.

Abramov, O.V., 1998. High-Intensity Ultrasonics: Theory and Industrial Applications. Gordon and Breach Science Publishers, Philadelphia.

Ahmadi, F., Farzin, M., Mandegari, M., 2015. Effect of grain size on ultrasonic softening of pure aluminum. Ultrasonics 63, 111–117.

Altan, T., Tekkaya, A.E. (Eds.), 2012. Sheet Metal Forming—Fundamentals. ASM International, Materials Park, Ohio.

Altan, T., Oh, S.-I., Gegel, H.L., 1983. Metal Forming—Fundamentals and Applications. American Society for Metals, Metals Park, Ohio.

Aziz, S.A., Lucas, M., 2010a. The effect of ultrasonic excitation in metal forming tests. Appl. Mech. Mater. 24–25, 311–316.

Aziz, S.A., Lucas, M., 2010b. A study of an ultrasonically assisted metal forming test. In: Chinesta, F., Chastel, Y., El Mansori, M. (Eds.), International Conference on Advances in Materials and Processing Technologies (AMPT2010b), pp. 733–738.

Aziz, S.A., Lucas, M., 2012. Characterising the acoustoplastic effect in an ultrasonically assisted metal forming process. In: International Symposium on Ultrasound in the Control of Industrial Processes (UCIP 2012). IOP Conference Series: Materials Science and Engineering, vol. 42. 4p.

Bagherzadeh, S., Abrinia, K., 2015. Effect of ultrasonic vibration on compression behavior and microstructural characteristics of commercially pure aluminum. J. Mater. Eng. Perform. 24 (11), 4364–4376.

Bajons, P., 1980. A new method for determining deformation amplitudes in ultrasonic fatigue systems. Ultrasonics 18, 61–66.

Bajons, P., Weiss, B., 1975. Determination of elastic and plastic strain of samples tested with the high frequency fatigue method. Ultrasonics 13, 248–250.

Baker, G.S., Carpenter, S.H., 1966. Deformation under combined static and vibratory stresses. Trans. Metall. Soc. AIME 236, 700–702.

Baker, G.S., Carpenter, S.H., 1967. Dislocation mobility and motion under combined stresses. J. Appl. Phys. 38 (4), 1586–1591.

Balalaev, Y.F., 1960. Structural changes and strength of steel under high-frequency cyclic loading. Metal Sci. Heat Treat. Metals 2 (4), 223–226.

Balamuth, L., 1963. Ultrasonic vibrations shape metals. SAE J. 71, 36–41.

Balamuth, L., 1964. Recent developments in ultrasonic metalworking processes. In: SAE/ ASME, Air Transport and Space Meeting, New York, April 27–30. 8pp.

Balamuth, L., 1965. Sonic press for forging, forming. American Machinist 1965, 118–119.

Balamuth, L., 1965a. Progress in ultrasonic metal forming. In: SAE International Automotive Engineering Congress, Detroit, MI, January 11–15. 10pp.

Bharadwaj, S., Dapino, M., 2013. Characterisation of friction reduction with tangential ultrasonic vibrations using a SDOF model. Int. J. Veh. Des. 63 (2/3), 291.

Biddell, D.C., Sansome, D.H., 1973. The deep-drawing of cans with ultrasonic radial oscillations applied to the die. In: Ultrasonics International 1973 Conference Proceedings, pp. 56–62.

Blaha, F., Langenecker, B., 1955. Dehung von zink-kristallen under ltraschalleinwirkung. Die Naturwissenschaften 42, 556.

Blaha, V.H., Langenecker, B., 1958. Untersuchungen zur Bearbeitungserholung (Verformungsentfestigung) von Metallkristallen ((investigation of mechanical recovery (deformation plasticization) of metal crystals)). Z. Met. 49, 357–360.

Blaha, F., Langenecker, B., 1959a. Plastizitatsuntersuchungen von metallkristallen in ultraschallfeld. Acta Metall. 7, 93–100.

Blaha, F., Langenecker, B., 1959b. Plastic behavior of metal crystals when exposed to sound waves. Bull. Natl. Inst. Sci. India, 14.

Blaha, F., Langenecker, B., Oelshlagel, D., 1960. The plastic behavior of metals under acoustic influence (Zum plastrschen Verhalten von Metallen unter Schalleinwirkung). Z. Met. 51, 636–638.

Cai, M., 2006. Acousto-Plastic Deformation of Metals by Nonlinear Stress Waves (Ph.D. dissertation). The Ohio State University. 2006.

Chen, K., Zhang, Y., Wang, H., 2017. Effect of acoustic softening on the thermal-mechanical process of ultrasonic welding. Ultrasonics 75, 9–21.

Chernenko, I.V., Cherkashin, V.S., 1960. The influence of ultrasound on the mechanical properties of copper. Primenenie Ul'traakustiki k Issledovanii Veshchestva 12, 141–145.

Cunningham, J.W., 1966. Effects of superimposed high-frequency vibrations on deformation processes. In: International Conference on Manufacturing Technology, pp. 973–981.

Daud, Y., Lucas, M., Huang, Z., 2005. Ultrasonic compression test on aluminum. Appl. Mech. Mater. 3–4, 99–104.

Daud, Y., Lucas, M., Huang, Z., 2006. Superimposed ultrasonic oscillation in compression tests of aluminum. Ultrasonics 44 (1), 511–515.

Daud, Y., Lucas, M., Huang, Z.H., 2007. Modelling the effects of superimposed ultrasonic vibrations on tension and compression tests of aluminium. J. Mater. Process. Technol. 186 (1–3), 179–190.

Davies, R.E., Yingling, G.B., 1961. Effects of High Frequency Vibrations on the Mechanical Properties of Aluminum Alloys. Internal correspondence, Alcoa Research Laboratories, July 28, 1961, 11 pp. and figures.

Deshpande, A., Hsu, K., 2018. Acoustic energy enabled dynamic recovery in aluminium and its effects on stress evolution and post-deformation microstructure. Mater. Sci. Eng. A 711, 62–68.

Dong, S., Dapino, M.J., 2012. Piezoelectrically-induced ultrasonic lubrication by way of Poisson effect. Proc. SPIE 8343. 11 p.

Dong, S., Dapino, M.J., 2014. Elastic-plastic cube model for ultrasonic friction reduction via Poisson effect. Ultrasonics 54, 343–350.

Dong, S., Dapino, M.J., 2015. Mapping of power consumption and friction reduction in piezoelectrically-assisted ultrasonic lubrication. In: Industrial and Commercial Applications of Smart Structures Technologies, International Society for Optics and Photonics.

Dutta, R., Petrov, R., Delhez, R., Hermans, M., Richardson, I., Böttger, A., 2013. The effect of tensile deformation by in situ ultrasonic treatment on the microstructure of low-carbon steel. Acta Mater. 61 (5), 1592–1602.

Eaves, A.E., Smith, A.W., Waterhouse, W.J., Sansome, D.H., 1975. Review of the application of ultrasonic vibrations to deforming metals. Ultrasonics 13, 162–170.

Endo, T., Kazuaki, S., Masayuki, I., 1979. Effects of superimposed ultrasonic oscillatory stress on the deformation of fe and Fe-3%Si alloy. Trans. JIM 20, 706–712.

Fartashvand, V., Abdullah, A., Vanini, S.S., 2016. Investigation of Ti-6Al-4V alloy acoustic softening. Ultrasonics (sonochemistry).

Frederick, J.R., 1965. Ultrasonic Engineering. Wiley.

Fridman, H.D., Pascal, L., 1959. Reduction of static friction by sonic vibrations. J. Appl. Phys. 30 (10), 1572–1575.

Friesen, R.F., Wiertlewski, M., Colgate, J.E., 2016. The role of damping in ultrasonic friction reduction. In: IEEE Haptics Symposium (HAPTICS), IEEE.

Friesen, R.F., Wiertlewski, M., Peshkin, M.A., Colgate, J.E., 2017. The contribution of air to ultrasonic friction reduction. In: 2017 IEEE World Haptics Conference (WHC), IEEE.

Goto, H., Ashida, M., Terauchi, Y., 1984. Effect of ultrasonic vibration on the wear characteristics of a carbon steel: analysis of the wear mechanism. Wear 94, 13–27.

Goto, H., Ashida, M., Terauchi, Y., 1986. Wear behaviour of a carbon steel subjected to an ultrasonic vibration effect superimposed on a static contact load. Wear 110, 169–181.

Grabchak, V.P., Kulemin, A.V., 1976. Influence of ultrasound on the diffusion of impurity atoms and the dislocation structure in germanium single crystals. Sov. Phys. Acoustics 22 (6), 475–478.

Graff, K.F., Short, M., 2009. Thermal stir welding ultrasonic friction reduction test bed. In: EWI Report on NASA/CR—2009–NNM09AB92P/52022GTH, December, 2009.

Green Jr., R.E., 1975. Non-linear effects of high-power ultrasonics in crystalline solids. Ultrasonics 13, 117–127.

Hansson, I., Tholen, A., 1973. Ultrasonic interaction with single dislocations as observed with the electron microscope. In: Proceedings of the Fifth International Conference on Internal Friction and Ultrasonic Attenuation in Crystalline Solids, August 27–30, 1973, Aachen, Germany. Vol. II, pp. 384–391.

Hansson, I., Tholen, A., 1974. Interaction between ultrasound and internal defects. In: Eighth International Congress on Electron Microscopy, Canberra, 1974, vol. I, pp. 590–591.

Hansson, I., Tholen, A., 1978. Plasticity due to superimposed macrosonic and static strains. Ultrasonics, 57–64.

Herbertz, J., 1977. The influence of mechanical vibrations on plastic deformation of metals. Ultrasonics Int. 77, 323–328.

Holden, F.C., Boulger, F.W., 1965. Fourth Status Report of the U.S. Government Metalworking Processes and Equipment Program, DMIC Report 221, Defense Metals, Information Center, BMI, Columbus, Ohio, December 7, 1965.

Hoseini, M., Shalvandi, M., Salimiasl, A., 2019. Experimental and theatrical evaluation of the effect of grain size of St52 on acoustic softening. Modares Mech. Eng. 18 (9), 40–45.

Hu, J., Nakamura, K., Ueha, S., 2003. Stability analysis of an acoustically levitated disk. IEEE Trans. Ultrason. Ferroelectr. Freq. Control 50 (2), 117–127.

Hu, J., Shimizu, T., Yang, M., 2018a. Investigation on ultrasonic volume effects: stress superposition, acoustic softening and dynamic impact. Ultrason. Sonochem. 48, 240–248.

Hu, J., Shimizu, T., Yoshino, T., Shiratori, T., Yang, M., 2018b. Ultrasonic dynamic impact effect on deformation of aluminum during microcompression tests. J. Mater. Process. Technol. 258, 144–154.

Huang, H., Pequegnat, A., Chang, B.H., Mayer, M., Du, D., Zhou, Y., 2009. Influence of superimposed ultrasound on deformability of Cu. J. Appl. Phys. 106, 6.

Huang, H., Chang, B.H., Du, D., 2011. Effect of superimposed ultrasound on mechanical properties of copper. Mater. Sci. Technol. 27 (7), 1117–1122.

Hung, J.-C., Lin, C.-C., 2013. Investigations on the material property changes of ultrasonic-vibration assisted aluminum alloy upsetting. Mater. Des. 45, 412–420.

Hung, J.-C., Tsai, Y.-C., 2013. Investigation of the effects of ultrasonic vibration-assisted micro-upsetting on brass. Mater. Sci. Eng. A 580, 125–132.

Izumi, O., Oyama, K., Suzuki, Y., 1966a. On the superimposing of ultrasonic vibration during compressive deformation of metals part 1. Trans. JIM 7, 158–162.

Izumi, O., Oyama, K., Suzuki, Y., 1966b. On the superimposing of ultrasonic vibration during compressive deformation of metals part 2. Trans. JIM 7, 162–167.

Jones, J.B., 1967. Ultrasonic metal deformation processing. In: Reprinted from Proceedings of the CIRP International Conference on Manufacturing Technology, American Society of Tool and Manufacturing Engineers (ASTME), September 25–28, 1967.

Kanavalau, Y.R., Yafremau, V.I., 1960. Effect of ultrasonic oscillations on endurance and plasticity of brass. In: Ukrainian Periodical, Vestsi An SSSR, Seriya Fizika-Technichnykh Navuk, Vol. 4, pp. 93–98.

Kanavalau, Y.R., Yafremau, V.I., 1961. Effect of ultrasound on the tenacity and plasticity of statically stressed brass. Izvestiya Akademii Nauk Belorusskoy SSR, Seriya Fiziko Tekhnicheskikh Nauk 1, 114–119.

Kang, J., Liu, X., Xu, M., 2020. Plastic deformation of pure copper in ultrasonic assisted micro-tensile test. Mater. Sci. Eng. A 785, 139364.

Kelly, G.S., Advani, S.G., Gillespie Jr., J.W., Bogetti, T.A., 2013. A model to characterize acoustic softening during ultrasonic consolidation. J. Mater. Process. Technol. 213 (11), 1835–1845.

Kirchner, H.O.K., Kromp, W.K., Prinz, F.B., Trimmel, P., 1984–1985. Plastic deformation under simultaneous cyclic and unidirectional loading at low and ultrasonic frequencies. Mater. Sci. Eng. 68, 197–206.

Kozlov, A.V., 1994. Peculiarities in strengthening of Nb and ta due to superimposed ultrasonic and plastic deformation. Ultrasonics 32 (3), 235–236.

Kozlov, A.V., Selitser, S.I., 1988. Peculiarities in the plastic deformation of crystals subjected to the acoustoplastic effect. Mater. Sci. Eng. A 102, 143–149.

Kozlov, A.V., Selitser, S.I., 1991. Kinetics of the acoustoplastic effect. Mater. Sci. Eng. A 131, 17–25.

Kristoffy, I., 1969. Metal forming with vibrated tools. J. Eng. Industry Trans. ASME 91, 1168–1174.

Kristoffy, I.I., Kegg, R.L., Weber, R.R., 1965. Influence of vibrational energy on metalworking processes. Final Technical Report on AFML-TR—65-211, Air Force Materials Laboratory, Wright-Patterson Air Force Base, Ohio, July, 1965.

Kulemin, A.V., Chernov, V.V., 1975. Creep in polycrystalline copper under the influence of ultrasound. Sov. Phys. Acoustics 20 (4), 346–349.

Kumar, V.C., Hutchings, I.M., 2004. Reduction of the sliding friction of metals by the application of longitudinal or transverse ultrasonic vibration. Tribol. Int. 37 (10), 833–840.

Langenecker, B., 1962. Work hardening of zinc crystals by high amplitude ultrasonic waves. Proc. Am. Soc. Test. Mater. 62, 602–609.

Langenecker, B., 1963. Effect of sonic and ultrasonic radiation on safety factors of rockets and missiles. AIAA J. 1 (1), 80–83.

Langenecker, B., 1966. Effects of ultrasound on deformation characteristics of metals. IEEE Trans. Sonics Ultrason. 13 (1), 1–8.

Langenecker, B., 1970. Dislocation damping in macrosonic fields. In: Proceedings of the 1st International Symposium on High Power Ultrasonics, pp. 32–35.

Langenecker, J.A.M., 1972. Dislocation structures in metal crystals grown in macrosonic fields. In: IEEE Trans. Sonics Ultrasonics, p. 396.

Langenecker, B., Colberg, S., Frandsen, W.H., 1962. Plastic deformation in zinc single crystals by sound waves. Bull. Am. Phys. Soc. 7, 362.

Langenecker, B., Frandsen, W.H., Colberg, S., 1963. Kinking in zinc crystalls by ultrasonic waves. Technical Note. J. Inst. Metals 91 (316–317), 1962–1963.

Langenecker, B., et al., 1964. Ultrasonics: an aid to metal forming. Metal Prog. 85, 97–101.

Langenecker, B., Jones, V.O., Illiewich, J., 1970. Metal plasticity in macrosonic fields. In: Proceedings of the 1st International Symposium on High-Power Ultrasonics, pp. 83–87.

Lehfeldt, V.E., 1969. Beeinflusssung der inneren Reibung durch Ultraschall bei der plastischen Verformung metallischer Werkstoffe (effect of internal friction through ultrasonics on plastic deformation of metallic materials). VDI-Zeitschrift 111, 359–363.

Li, H., Deng, Z., 2018. Experimental study on friction characteristics and running stability of a novel ultrasonic levitating bearing. IEEE Access 6, 21719–21730.

Li, X., Wang, Z., He, X., 2012. Influence principle of ultrasonic vibration on the rheological behavior of materials. Adv. Mater. Res. 538–541, 1393–1402.

Littmann, W., Storck, H., Wallaschek, J., 2001a. Reduction of friction using piezoelectrically excited ultrasonic vibrations. Proc. SPIE 4331, 302.

Littmann, W., Storck, H., Wallaschek, J., 2001b. Sliding friction in the presence of ultrasonic oscillations: superposition of longitudinal oscillations. Arch. Appl. Mech. 71 (8), 549–554.

Liu, Y., Wang, C., Guo, B., Shan, D., Zhang, M., 2017. Softening effect of ultrasonic vibration on micro-blanking deformation behaviour of titanium foil. Micro Nano Lett. 12 (10), 808–812.

Liu, T., Lin, J., Guan, Y., Xie, Z., Zhu, L., Zhai, J., 2018. Effects of ultrasonic vibration on the compression of pure titanium. Ultrasonics 89, 26–33.

Lucas, M., Gachagan, A., Cardoni, A., 2009. Research applications and opportunities in power ultrasonics. Proc. IMechE Part C: J. Mech. Eng. Sci. 223, 2949–2965.

Malygin, G.A., 2000. Acoustoplastic effect and the stress superposition mechanism. Phys. Solid State 42 (1), 72–78.

Mao, Q., Gibert, J.M., Fadel, G., 2014. Investigating ultrasound-induced acoustic softening of aluminum 6061. In: ASME 2014 International Design Engineering Technical Conferences and Computers and Information in Engineering Conference. American Society of Mechanical Engineers. pp. V008T011A100-V008T011A100.

Mao, Q., Coutris, N., Rack, H., Fadel, G., Gibert, J., 2020. Investigating ultrasound-induced acoustic softening in aluminum and its alloys. Ultrasonics 102, 106005.

Mason, W.P., 1958. Physical Acoustics and the Properties of Solids. D. Van Nostrand Company, Princeton, New Jersey.

Mason, W.P. (Ed.), 1964–1999. Physical Acoustics, Vols. 1–24. Academic Press, New York (and other editors over the series).

Mignogna, R.B., Green Jr., R.E., 1979. Changes in ultrasonic attenuation, velocity and other parameters resulting from high-power insonation of metals. In: Ultrasonics International 79 Conference Proceedings, pp. 215–220.

Mignogna, R.B., Green Jr., R.E., Duke Jr., J.C., Henneke II, E.G., Reifsnider, K.L., 1981. Thermographic investigation of high-power ultrasonic heating in materials. Ultrasonics 19, 159–163.

Mikhenlman, A.I., Mashchinov, A.N., 1969. Effect of ultrasonic vibrations on friction between solids. Russ. Eng. J. 49 (1), 42–43.

Milahin, N., Li, Q., 2016. Friction and wear of a spherical indenter under influence of out-of-plane ultrasonic oscillations. Phys. Mesomech. 19 (2), 149–153.

Milahin, N., Li, Q., Starcevic, J., 2015. Influence of the normal force on the sliding friction under ultrasonic oscillations. 13, 27–32.

Mitskevich, A.M., 1968. Motion of a body over a tangentially vibrating surface. Soviet Phys. Acoustics 13 (2), 348–351.

National Research Council, 1965. First Progress Report By The Ad Hoc Committee On Metalworking Processes and Equipment, Prepared For The National Academy of Sciences by the Materials Advisory Board. Subsection A. Vibrational Energy in Metalworking, March, 1965. pp. 5–11.

National Research Council, 1967. Minutes of the Eight Meeting of The Panel on Application of Deformation Theory to Practice of The Materials Advisory Board Committee on Metalworking Processes and Equipment, Materials Advisory Board, National Academy of Sciences, November 28–29, 1967. pp. 3–5.

Neville Jr., G.E., Brotzen, F.R., 1957a. Effect of vibrations on the yield strength of low-carbon steel, First Technical Report, AF Contract No. AF-49-(638)-78, April 15, 1957. 11 pp. and figures.

Neville Jr., G.E., Brotzen, F.R., 1957b. The effect of vibrations on the static yield strength of a low-carbon steel. In: American Society for Testing Materials, Proceedings. Vol. 57, pp. 751–758.

Oelschlagel, V.D., Verformung, D., von Zinkeinkristallen, b.U., 1962. The effect of ultrasonics on the deformation of zinc single crystals. Z. Met. 53 (6), 367–371.

Ohgaku, T., Takeuchi, N., 1987. The Blaha effect of alkali halide crystals. Phy. Stat. Sol. 102, 293–299.

Peacock, J., 1961. Forming goes ultrasonic. Am. Mach. 105, 83–85.

Pedraz, P., Wannemacher, R., Gnecco, E., 2015. Controlled suppression of wear on the nanoscale by ultrasonic vibrations. ACS Nano 9 (9), 8859–8868.

Peslo, A., 1984. Ultrasonic hardening of aluminum alloys. Ultrasonics 22 (1), 37–41.

Pogodina-Alekseeva, K.M., Bironf, V.S., Slavin, L.D., 1964. Effect of ultrasonic vibration on the mechanical properties of R18 steel. Metal Sci. Heat Treat. 6 (1), 35–38 (All-Union Correspondence Polytechnic Institute, Translated from Metallovendenie i Termicheska Obrabotka Metallov, No. 1, pp. 40–44).

Pohlman, R., Lehfeldt, E., 1966. Influence of ultrasonic vibration on metallic friction. Ultrasonics 4, 176–185.

Popov, V.L., 2017. Friction under the influence of ultrasonic vibrations. In: Contact Mechanics and Friction: Physical Principles and Applications. Springer Berlin Heidelberg, pp. 317–334.

Popov, V.L., Starcevic, J., Filippov, A.E., 2010. Influence of ultrasonic in-plane oscillations on static and sliding friction and intrinsic length scale of dry friction processes. Tribol. Lett. 39 (1), 25–30.

Prabhakar, A., Verma, G.C., Krishnasamy, H., Pandey, P.M., Lee, M.G., Suwas, S., 2017. Dislocation density based constitutive model for ultrasonic assisted deformation. Mech. Res. Commun. 85, 76–80.

Puskar, A., 1976. A new method of increasing the fatigue strength of metals. Ultrasonics 14 (3), 123–127.

Puskar, A., 1982. The Use of High-Intensity Ultrasonics. Elsevier Scientific Publishing Company, USA.

Rosenfeld, A.R. (Ed.), 1963. The application of ultrasonic energy in the deformation of metals. DMIC Report 187, Defense Metals Information Center, Battelle Memorial Institute, Columbus, Ohio, August 16, 1963.

Rozner, A.G., 1971. Effect of ultrasonic vibration on coefficient of friction during strip drawing. J. Acoustical Soc. Am. 49 (5 (Part 1)), 1368–1371.

Rusinko, A., 2011. Analytical description of ultrasonic hardening and softening. Ultrasonics 51 (6), 709–714.

Sansome, D.H., 1970. Oscillatory metal working research at the University of Aston in Birmingham. In: Proceedings of the 1st International Symposium on High Power Ultrasonics. 4pp.

Sansome, D.H., 1973. Recent developments in oscillatory metal working. Engineering 213 (4), 243–247.

Sansome, D.H., 1986. The drawing of metals. In: Blazynski, T.Z. (Ed.), Design of Tools for Deformation Processes. Elsevier Applied Science Publishers, USA, pp. 73–111 (chapter 3).

Sapozhnikov, K.V., Kustlov, S.B., 1995. Effect of temperature on the amplitude dependences of the internal friction during the deformation of crystals. Phys. Solid State 37 (9), 1554–1557.

Sapozhnikov, K.V., Kustlov, S.B., 1996a. Influence of temperature on the amplitude dependence of the acoustoplastic effect. Phys. Solid State 38 (1), 68–71.

Sapozhnikov, K.V., Kustlov, S.B., 1996b. Effect of impurity content on the amplitude of dependencies of the acoustoplastic effect and internal friction in the process of deforming LiF:Mg^{2+} single crystals. Phys. Solid State 38 (9), 1513–1517.

Sapozhnikov, K.V., Kustlov, S.B., 1996c. Acoustoplastic effect and amplitude-dependent internal friction during deformation of impure aluminum single crystals. J. Phys. IV. Coll. C8 (Suppl. J. Phys. III) 6, C8–293–C8–296.

Sapozhnikov, K.V., Kustlov, S.B., 1997. Acoustoplastic effect and internal friction of aluminum single crystals in various deformation stages. Phys. Solid State 39 (10), 1601–1606.

Sapozhnikov, K.V., Golyandin, S.N., Kustov, S.B., 1998. Influence of impurity content on the acoustoplastic effect, internal friction, and Yound's modulus defect during deformation of Cu—Ni single crystals. Philos. Mag. A 77 (1), 151–166.

Schmid, E., 1962. Effects of energy radiation on the plastic deformation of metals. Materialprufung 4 (8), 274–283.

Schmid, E., Boas, W., 1935. Kristallplastizitact. Spring-Verlag, Berlin, pp. 152–157.

Sedaghat, H., Xu, W., Zhang, L., 2019. Ultrasonic vibration-assisted metal forming: Constitutive modelling of acoustoplasticity and applications. J. Mater. Process. Technol. 265, 122–129.

Sednaoui, T., E., Vezzoli, B., Dzidek, B., Lemaire-Semail, B., Chappaz, C., Adams, M., 2017. Friction reduction through ultrasonic vibration Part 2: Experimental evaluation of intermittent contact and squeeze film levitation. IEEE Trans. Haptics 10 (2), 208–216.

Severdenko, V.P., Klubovich, V.V., 1964. Investigation of the Microstructure of Copper Deformed in an Ultrasonic Field. Academy of Sciences of the Belorussian SSR, Physical and Technological Institute. Collection of Scientific Papers (selected articles). Translation, 6pp.

Severdenko, V.P., Klubovich, V.V., Spepanenko, A.V., 1972. Ultrasonic Rolling and Drawing of Metals, Translated from 1970 Russian Publication. Consultants Bureau, New York.

Sharahi, H.J., Egberts, P., Kim, S., 2018. Mechanisms of friction reduction of nanoscale sliding contacts achieved through ultrasonic excitation. Nanotechnology 30 (7), 075502.

Shaw, H.W., Kennedy, L., 1977. A direct examination of volume effects when insonation is superimposed during mechanical deformation processes. In: Ultrasonics International 77 Conference Proceedings, pp. 329–337.

Siddiq, A., El Sayed, T., 2011. Acoustic softening in metals during ultrasonic assisted deformation via CP-FEM. Mater. Lett. 65 (2), 356–359.

Siddiq, A., El Sayed, T., 2012a. Ultrasonic-assisted manufacturing processes: variational model and numerical simulations. Ultrasonics 52, 521–529.

Siddiq, A., El Sayed, T., 2012b. A thermomechanical crystal plasticity constitutive model for ultrasonic consolidation. Comput. Mater. Sci. 51 (1), 241–251.

Siddiq, A., Ghassemieh, E., 2008. Thermomechanical analyses of ultrasonic welding process using thermal and acoustic softening effects. Mech. Mater. 40 (12), 982–1000.

Siegel, R., 1959. The effect of ultrasonics on the creep of copper springs (Der Einfluss von Ultraschall auf das Kriechen von Kupperfedern). Ann. Phys. 5, 107–112.

Siegel, R., 1962. Ultrasonic effect on the creep of silver springs. Acta Metall. 10, 169.

Siegert, K., Ulmer, J., 2001. Influencing the friction in metal forming processes by superimposing ultrasonic waves. CIRP Ann. Manuf. Technol. 50 (1), 195–200.

Siu, K.W., Ngan, A.H.W., 2011. Understanding acoustoplasticity through dislocation dynamics simulations. Philos. Mag. 91 (34), 4367–4387.

Siu, K.W., Ngan, A.H.W., 2013. Oscillation-induced softening in copper and molybdenum from nano- to micro-length scales. Mater. Sci. Eng. A 572, 56–64.

Siu, K.W., Ngan, A.H.W., Jones, I.P., 2011. New insight on acoustoplasticity – Ultrasonic irradiation enhances subgrain formation during deformation. Int. J. Plast. 27 (5), 788–800.

Spath, W., 1956. Creep phenomena in metals under load. Das Metall 10 (19–20), 910–915.

Spiers, R.M., Winsper, C.E., Sansome, D.H., 1969. Direct extrusion of metal with applied oscillatory energy. Metal Forming 35 (10), 271–277.

Tanaka, S., Yoshida, T., Takagi, K., 1952. Effect of ultrasound on behavior of [high purity] iron at elevated temperatures. Translated from, Tetsu Hagane 38 (11), 33–36.

Tanibayashi, M., 1991. A theory of the Blaha effect. Phy. Stat. Sol. 128. 83–94(a).

Teidelt, E., Starcevic, J., Popov, V.L., 2012. Influence of ultrasonic oscillation on static and sliding friction. Tribol. Lett. 48 (1), 51–62.

Tsimbalistyj, Y.I., Vlasenko, V.I., 1983. Studies of stress and creep relaxation under ultrasonic cyclic loading. In: Ultrasonics International 83 Conference Proceedings, pp. 507–512.

Vagapov, I.K., Zhydkevich, V.I., Klubovich, V.V., 1991. Examination of energy-force and physico-mechanical characteristics of steel in drawing with application of longitudinal ultrasonic oscillations. Phys. Chem. Mater. Treat. 25 (2), 205–209.

Vezzoli, E., Vidrih, Z., Giamundo, V., Lemaire-Semail, B., Giraud, F., Rodic, T., Peric, D., Adams, M., 2017. Friction reduction through ultrasonic vibration Part 1: Modelling intermittent contact. IEEE Trans. Haptics 10 (2), 196–207.

Wang, C., Liu, Y., Guo, B., Shan, D., Zhang, B., 2016. Acoustic softening and stress superposition in ultrasonic vibration assisted uniaxial tension of copper foil: experiments and modeling. Mater. Des. 112, 246–253.

Weber, W., 1954. Reduction in sliding friction by means of ultrasonics. Werkstatt Betrieb 84, 262.

Wen, T., Wei, L., Chen, X., Pei, C.-L., 2011. Effects of ultrasonic vibration on plastic deformation of AZ31 during the tensile process. Int. J. Minerals Metall. Mater. 18 (1), 70–76.

Wielke, B., Stanzl, S., 1976. The distribution of plastic deformation during 21 kHz fatigue of copper samples. Ultrasonics 14, 227–231.

Winsper, C.E., Sansome, D.H., 1967. A review of the application of oscillatory energy to metals deforming plastically. In: Advance 26 page draft of paper published in Proceedings of the Eighth International Machine Tool Design and Research Conference, Manchester, September, pp. 1359–1360.

Winsper, C.E., Sansome, D.H., 1969. Fundamentals of 'ultrasonic' wire drawing. J. Inst. Metals 97, 274–280.

Witthauer, A.T., Faidley, L.A., Kim, G.-Y., 2010. Bulk motion for ultrasonic-assisted microforming using Terfenol-D. In: Brett McMickell, M., Farinholt, K.M. (Eds.), Industrial and Commercial Applications of Smart Structures Technologies 2010. Proceedings of SPIE, p. Vol. 7645.

Yao, Z., Kim, G.-Y., Faidley, L.A., Zou, Q., Mei, D., Chen, Z., 2010. Micro-pin extrusion of metallic materials assisted by ultrasonic vibration. In: Proceeding of the ASME 2010 International Manufacturing Science and Engineering Conference, MSEC 2010, Erie, Pennsylvania, USA, October 12–15, 2010.

Yao, Z., Kim, G.Y., Faidley, L., Zou, Q., Mei, D., Chen, Z., 2012a. Effects of superimposed high frequency vibration on deformation of aluminum in micro/meso-scale upsetting. J. Mater. Process. Technol. 212, 640–646.

Yao, Z., Gap-Yong, K., Zhihua, W., LeAnn, F., Qingze, Z., Me, D., Zichen, C., 2012b. Acoustic softening and residual hardening in aluminum: modeling and experiments. Int. J. Plast. 39, 75–87.

Zhou, H., Cui, H., Qin, Q.H., 2018. Influence of ultrasonic vibration on the plasticity of metals during compression process. J. Mater. Process. Technol. 251, 146–159.

Zhuang, X.-C., Wang, J.-P., Zheng, H., Zhao, Z., 2015. Forming mechanism of ultrasonic vibration assisted compression. Trans. Nonferrous Met. Soc. China 25 (7), 2352–2360.

Chapter 14

Ultrasonic metal forming: Processing

X. Liu[a] and K.F. Graff[b]
[a]The Ohio State University, Columbus, OH, United States, [b]EWI, Columbus, OH, United States

14.1 Introduction

As noted in Chapter 13, the 1955 report by Blaha and Langecker on the phenomenon later termed acoustic softening triggered developments in the field of ultrasonic metal forming that continue to the present, with nearly every form of conventional forming, as well as forming methods unique to the use of ultrasonics, being the subject of past and present investigations. Figure 14.1 is illustrative of several forming processes, such as wiredrawing, deep drawing, forging, extrusion, and rolling, to which power ultrasonics has been applied, as suggested by the wavy "ultrasonic" lines of the figures. While a complete understanding of the effects of power ultrasound on the volume and surface of deforming metals is a work in progress, this has not prevented extensive developments in the practical application of ultrasound to forming processes. The purpose of this chapter is to review this extensive field of work.

A number of conventional metal forming processes would include rolling, forging, extruding, and deep drawing, among others. These processes can be grouped into two broad categories: bulk deformation and sheet forming processes. In bulk forming processes, the three-dimensional stressing of the material plays a key role. However, surface friction, acting between the bulk material and the process tooling, will also be important. Examples of bulk forming processes include wire and tube drawing, forging, extrusion, and rolling; all areas that have involved ultrasonic developments. In sheet forming processes, there is a high ratio of surface area to metal thickness, with deep drawing, bending, and punching as examples; these also being areas of ultrasonic development.

The major categories of ultrasonic metal forming that will be reviewed are wire and tube drawing, deep drawing and bending, forging and extrusion, and rolling. Other applications will include topics such as surface treatment, compaction, and microforming.

14.2 Wire and tube drawing

Wire or tube drawing is the process of reducing the cross-sectional area of a wire or tube by pulling through a die (Altan et al., 1983). Applying power ultrasonics to wire-drawing was the first application following the Blaha and Langenecker (1955) paper, with developments in this field becoming very active at that time and this activity continuing to the present day. Benefits being sought include increased draw speed, improved surface finish, reduced draw force, greater area reduction per draw, and longer tool life, with the emphasis varying, depending on end use.

14.2.1 Early developments

While early developments of ultrasonic wire and tube drawing were extensive, only an overview is provided here, with reference to Graff (2014) for more extended coverage of this period. Thus, a note has been made in Chapter 14 of the June 1963 U.S. Navy-sponsored symposium (Rosenfeld, 1963) that covered a wide range of ultrasonic effects on metal deformation, including early progress on wire and tube drawing, as shown by the patent drawing in Figure 14.2A, noting draw force reductions with ultrasound and evidence of decreased effects with increased draw speed. The first work at China Lake on wiredrawing was reported, showing up to 50% drops in draw force with the application of ultrasound (Figure 14.2B).

During the 1960s, numerous reports on wire and tube drawing appeared. Thus, Severdenko and Klubovich (1963) reported on force reductions in drawing copper wire and the need for a "vibration damping block" at a critical location along the exiting wire. Robinson (1964) reported on further progress at China Lake, drawing a 5200-grade aluminum wire, and also on the need for an "acoustic isolator" placed at a strategic location along the wire. Significant force reductions were noted. The Aeroprojects company, noted above, continued the development of tube drawing equipment, with a report by company founder Jones (1967) covering progress in tube, wire, and rod drawing. Throughout this period, trade journal articles appeared on the process of industrial trials at several companies with varying reviews. The Uniform Tubes Company adopted the technology for the production of waveguides and reported improved surface finish and dimensional

Power Ultrasonics. https://doi.org/10.1016/B978-0-12-820254-8.00021-X
Copyright © 2023 Elsevier Ltd. All rights reserved.

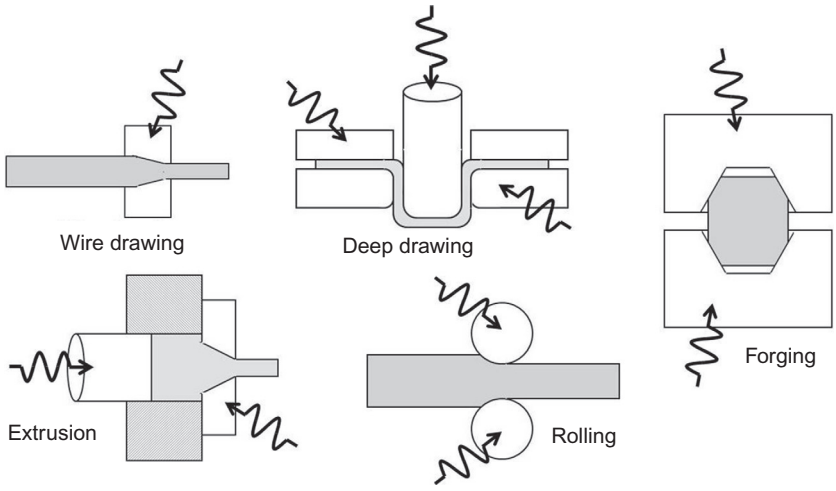
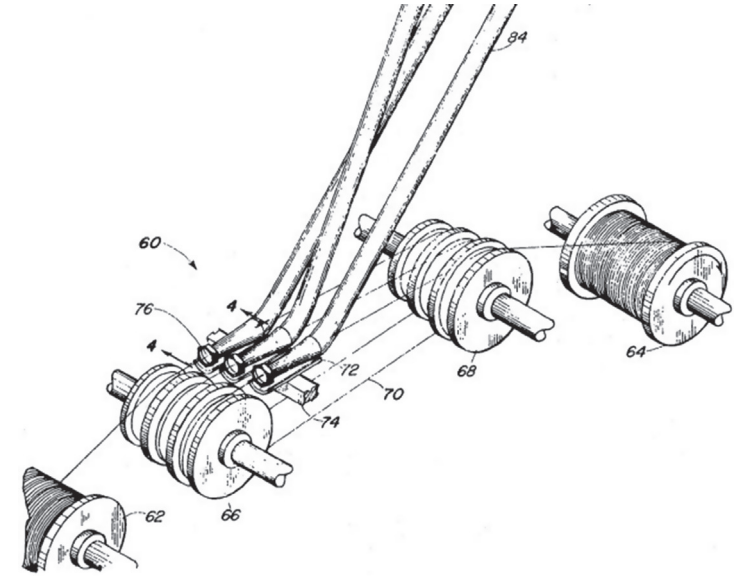
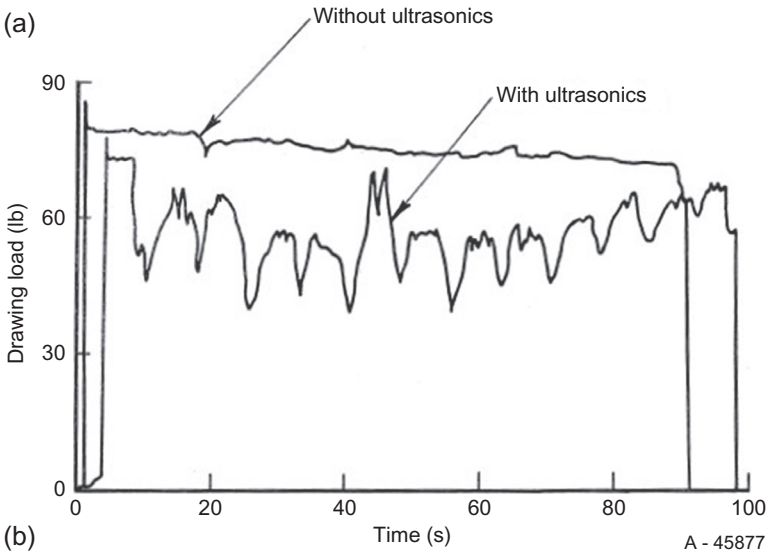


FIGURE 14.1 Ultrasonics applied to metal forming processes. *(Source: EWI.)*



(a)



(b)

FIGURE 14.2 Early work on ultrasonic forming processes. (a) Wiredrawing at Aeroprojects (Fig. 8, Aeroprojects patent illustration) and (b) China Lake work on wiredrawing showing force reductions (Fig. 7). *(Source: Rosenfeld (1963).)*

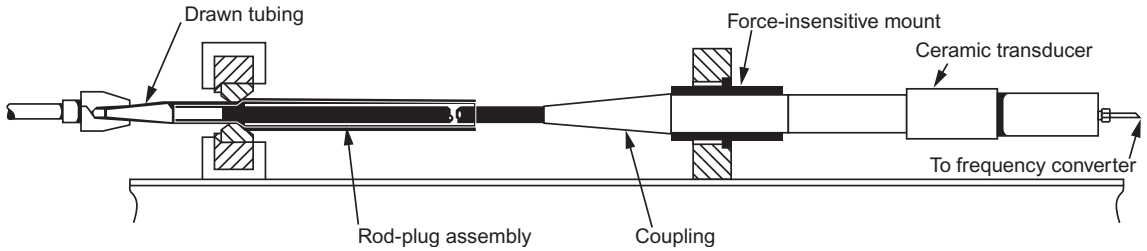


FIGURE 14.3 Ultrasonic tube drawing developed at Aeroprojects. *(Source: Buckley and Freeman (1970, Fig. 4).)*

accuracy in aluminum, steel, copper, and nickel tubes. Buckley and Freeman (1970) summarized several years of this development, illustrating the tube drawing process as shown in Figure 14.3. Reference should be made to the comprehensive Aeroprojects literature and patent survey of Meyer (1973) on ultrasonic manufacturing applications, in which over 50 papers and 20 patents in the wire and tube drawing area were identified and abstracted.

Langenecker's contribution to wiredrawing continued throughout the 1960s and into the 1970s. Thus, Langenecker (1964, 1965) and Langenecker et al. (1964) overviewed the familiar ground on several forming processes and restated views as to the governing mechanism being explainable by a preferred absorption of sound energy at lattice defects. In what was possibly the last of the contributions that originated in 1955, Langenecker and Vodep (1981) reviewed the progress in commercializing the wire drawing process.

In other work reflecting Langenecker's influence, Oelschlagel and Weiss (1965, 1966) introduced the idea of placing the wire die at the vibration antinode versus the usual nodal position and conducted comparative tests of the two methods. In their previously noted work on friction, Pohlman and Lehfeldt (1966) also conducted wiredrawing tests, using the apparatus of Figure 14.4a. An early observation was the influence of varying wire length between the draw die 1 and the vice (without the presence of die 2) leading to incorporating die 2 at a critical distance from the die to achieve a constant level of force reduction. Tests were run on several grades of steel wire, with force reductions (Figure 14.4b) being explained by the superposition effect. Lehfeldt and Pohlman (1968, 1969) carried their 1966 work further, describing several potential configurations of wire die placement and excitation, and looked in greater detail at surface effects and deformation.

Inoue and Mori (1968) reported on ultrasonic wiredrawing work in progress since 1963. They noted the critical distance between the die and drawing drum needed to be approximately an integer number of half wavelengths in the wire, with similar dimensions being needed when a back pull drum was used. Data on force reductions in copper, titanium, aluminum, and brass wire as affected by wire speed and vibration amplitude were presented.

Early wire drawing work by Severdenko was followed by Severdenko et al. (1971), where several draw configurations involving the direction of draw relative to the vibration direction and locations of the die (at nodes and antinodes) were explored. The results favored longitudinal drawing with the die at a stress antinode. Yet another arrangement was shown in Severdenko et al. (1973b), where the primary draw die was at the stress antinode, while other dies served to create a resonant length of the wire. Draw force reductions of 10%–50% were reported. In Severdenko et al. (1973b), the drawing of harder alloys, for example,

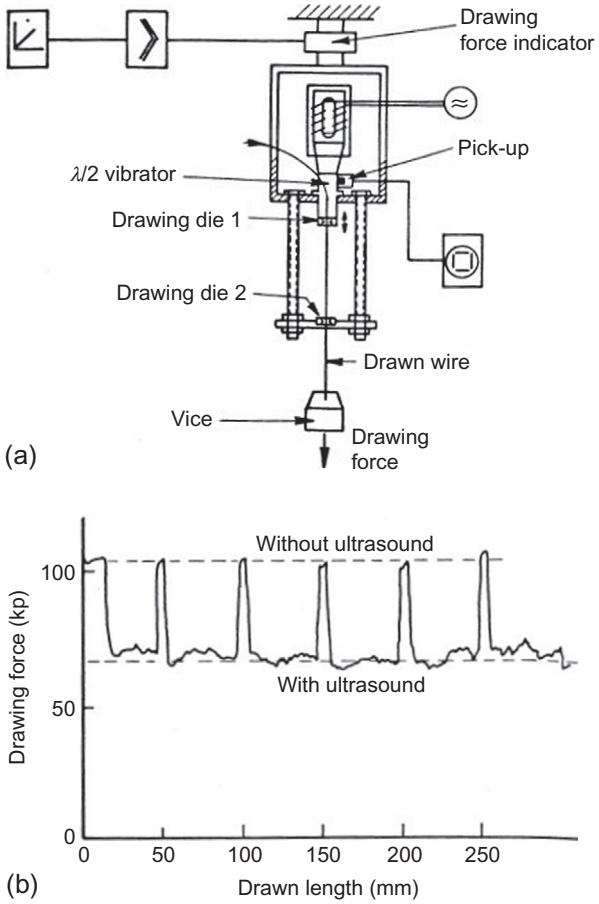


FIGURE 14.4 Wiredrawing work of Pohlman and Lehfeldt (1966). (a) Experimental wiredrawing setup (Fig. 7) and (b) draw force on copper wire with on-off ultrasound (Fig. 9).

nickel-manganese, molybdenum, tungsten, and X18H10T, was reported with high-percentage force reductions. Severdenko et al. (1972a, b) then produced their definitive monograph, already referenced in Chapter 13, on the subject of ultrasonic rolling and drawing of metals, providing a comprehensive review of the two fields to that date.

Turning to the work of others in this period, a unique tube drawing system was developed by Sugahara et al. (1970, 1971) where the radial oscillations of four disks were converted, via the Poisson effect, into longitudinal oscillations of the plug/mandrel. Much of Sugahara et al. (1970) was devoted to the acoustical design of this complex system. In Sugahara et al. (1971), results are reported for a carbon steel tube, covering various plug designs, area reductions, and effects of lubricants. Significant reductions in both plug and die forces were obtained, as well as the elimination of chattering.

The work of Sansome and colleagues on the effects of ultrasound on material properties has been noted. Around 1967, the first of numerous publications from this group appeared that, over a 20-year period, covered wire and tube drawing, deep drawing, strip drawing, and material effects. In the case of wire and tube drawing, Winsper and Sansome (1967) overviewed the work of others, citing some of their own low-frequency drawing works, while advancing the view that force reduction effects were attributable to the superposition concept. In a later report on the wire drawing process, Winsper and Sansome (1968–1969) again said that force reductions were explainable by stress superposition and noted decreased vibration effects with increasing draw speeds. An advanced treatment of the ultrasonic wire drawing process was provided by Winsper and Sansome (1969), utilizing the system as shown in Figure 14.5, which had provisions for measuring both die and wire vibration amplitude and draw force. The importance of proper spacing between the die and coiling drum was brought out. Wavelength analysis showed that maximum wire amplitude was achieved when die-drum spacing was a multiple of half-waves plus an "adjustment factor" that essentially placed the virtual wire vibration node just behind the die. Force reductions of 11%–16% were obtained on a steel wire, depending on the area reduction. No effects on wire finish and properties were found, and force reductions were seen as consistent with the stress superposition concept.

Applying ultrasonic vibrations to the plug drawing of the tube was the subject of Winsper and Sansome (1971). Improvement in outer and inner diameter surface finish was seen, and wavelength effects, seen in previous wire drawing work, were noted. Draw force reductions were obtained. A system for a floating plug tube drawing system, with the die driven in the radial vibration mode by 30 magnetostrictive transducers (Figure 14.6a) is one of the several processes reviewed by Sansome (1973), which included discussion of material and friction effects, swaging, and cup drawing. Both Biddell and Sansome (1974) and Eaves et al. (1975) were broad overviews of oscillatory metal forming technology, including the coverage of low-frequency work in wire drawing and other processes. Dawson (1975) applied radial vibrations to the die in the above-noted floating plug tube drawing process. The design of a tapered radial resonator of the form shown in Figure 14.6b was necessary in order to obtain the desired vibration amplitudes. The resulting disk had a 13-kHz resonance and was driven by magnetostrictive transducers spaced around the circumference. The results for drawing carbon steel tubing showed drops of draw force that varied with die vibration amplitude and the speed of draw. Thus, at the slowest draw speed (20 mm/s) and maximum die vibration amplitude (4 μm), a reduction of 18% was achieved. As the amplitude was decreased and/or draw speed was increased (to 50 or 150 mm/s), the amount of force reduction increased.

14.2.2 The 1970s and 1980s

From the mid-1970s, many new researchers entered the wire/tube drawing field. Thus, Atanasiu (1976) analyzed the wiredrawing processes, considering the axially vibrated wire die. Modeling incorporated viscoplastic and friction effects and predicted the drawing stress for various conditions of material, die angle, friction coefficient, and draw velocity, with good agreement with experimental data for aluminum wire. In Atanasiu (1980), the plug tube drawing process was considered. Again, using a viscoplastic material model, but allowing for a change in yield stress as a function of ultrasonic intensity, results showed a significant reduction in draw force for all die angles, with an optimum angle of 8°. The effects of area reduction on the draw force were presented with a greater effect noted for a smaller area reduction. Other results showed a decreased force reduction with increased draw velocity.

A U.S.-U.K. collaboration by Rees and Rippon (1983) evaluated the floating plug, axial die vibration system developed at Sonobond/Aeroprojects and the radial tube drawing system developed at Aston University. Conclusions were that reductions in draw force were seen with both systems, 15%–30% for the axial and 20% for the radial, and that tool wear and lubrication with ultrasound (both systems) were similar to conventional drawing. It was felt that the radial die provided an improvement in the surface finish over the conventional drawing.

Over 20 years after ultrasonic wire drawing work was first reported, Gebhardt and Funke (1983, 1984) provided a fresh look at the process; Gebhardt and Funke (1983) presented a review of the extensive past work with notes on the various means of introducing ultrasonics, force reductions, critical vibration-draw velocity effects, varied results on

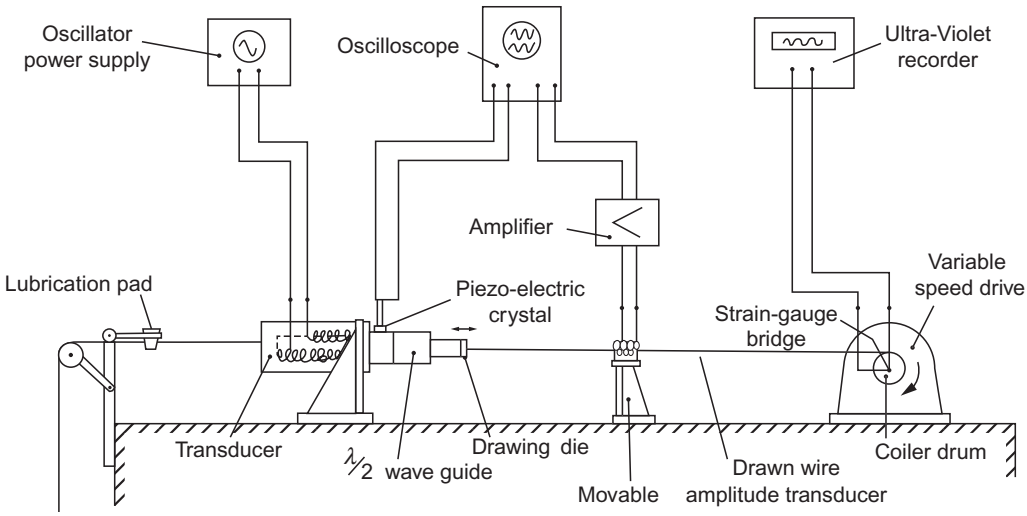


FIGURE 14.5 Details of Winsper and Sansome (1969) wiredrawing apparatus. *(Source: From Winsper and Sansome (1969, Fig. 1, www.maneyonline.com/mst).)*

surface finish, and overall process energy aspects. In Gebhardt and Funke (1984), ultrasonic wiredrawing equipment (Figure 14.7) was integrated into a commercial drawing machine. It is seen that the ultrasonic transducer (9) vibrating laterally to cross horn (12) is used to induce a longitudinal vibration at the die (2). A number of alloys (CuZn, Ni, AlMg, NiFe, NiCr, and CrAl) were studied with and without lubricants and at varied draw speeds, with results on force reductions, surface finish, and mechanical properties reported. The most important initial result was the draw force reduction with increased wire speeds, from a 34% drop to zero reduction at 1.5 m/s (for a 20-μm amplitude). Tensile, bending, and hardness tests showed no differences between wires drawn with and without ultrasonics, nor did roughness measurements show any conclusive differences. The authors felt that there was no

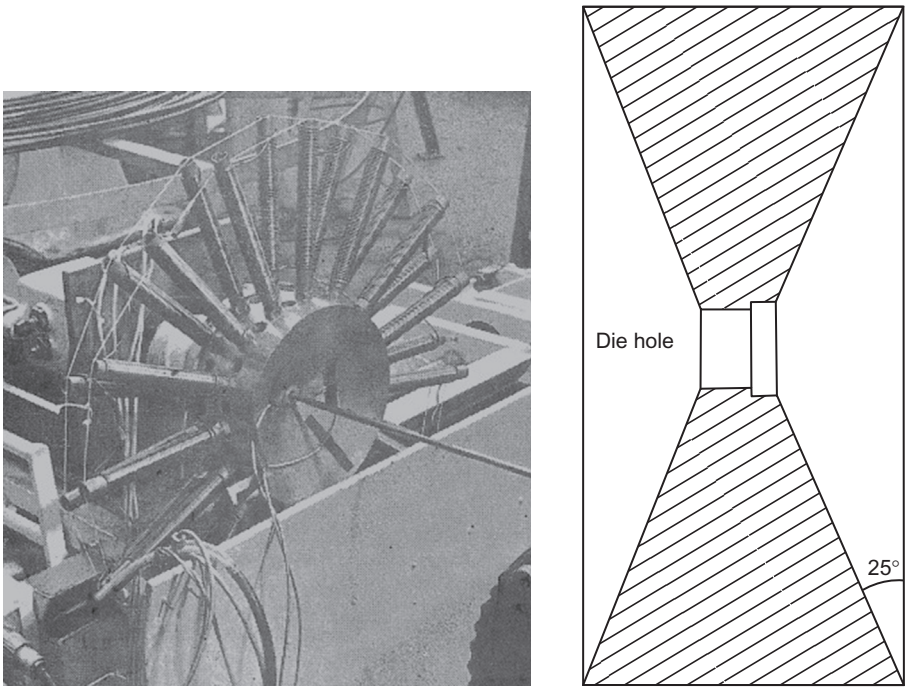
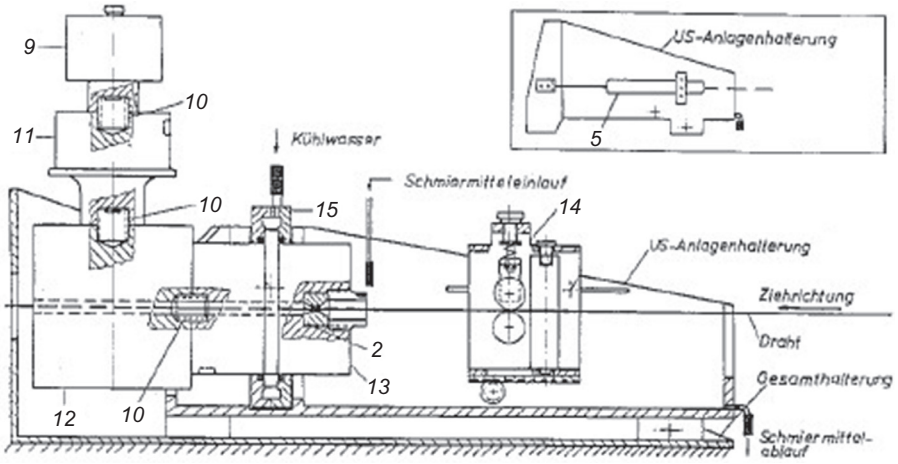


FIGURE 14.6 Tube drawing work from Sansome, University of Aston group. (a) Tube drawing equipment (Sansome, 1973, Fig. 1) and (b) design of radial resonator (Dawson, 1975, Fig. 2).



Schematic arrangement of ultrasonic system

2 Drawing die
5 Inductive transducer
9 US converter
10 Screw connection
11 Booster
12 Cross horn
13 Horn
14 Tuning rollers
15 Coolant coupling and System support

FIGURE 14.7 Schematic of ultrasonic wiredrawing system of Gebhardt and Funke (1984, Fig. 10).

evidence that draws that could not be made conventionally could be made with ultrasonics. It was felt, for the materials and conditions investigated, that there was little economic justification for adopting ultrasonics.

Petukhov et al. (1987) reported on wire and tube drawing of a number of high-alloy steels under industrial mill conditions, as well as process modeling and material studies in drawing an annealed iron. These latter studies showed that ultrasonic drawing could control wire ductility and lead to simplified manufacturing operations. Data were reported on the microstructure of drawn wires/tubes, indicating significant property changes under ultrasound. Although equipment details were lacking, this otherwise comprehensive work strongly supported the benefits of the ultrasonic wire/tube process. Likewise, Vagapov et al. (1991), as previously noted in Chapter 14, reported on an ideal elastoplastic model for draw force as a function of material, reduction, draw speed, and amplitude for a steel wire (30Kh13). Reductions in draw force were predicted and in good agreement with experiments.

A reminder of the continued availability of commercial tube drawing equipment from the Sonobond Company (the successor name of the Aeroprojects Corporation) was provided by Devine (1990), while Maropis (1991a, b, c) provided an overview of the many years of wire/tube drawing work at Aeroprojects/Sonobond.

In a progression of work dating from 1981, Petruzelka et al. (1984, 1996) conducted an analysis of the ultrasonic plug tube drawing process, indicated schematically in Figure 14.8a, where the ultrasonics was applied to the plug. The analysis examined various locations of the plug—at a node, antinode, or between. A typical result for the flow stress is shown in Figure 14.8b. The effect of placing the plug at the antinode had the maximum influence on friction reduction. However, it was found that placing the plug between the node/antinode positions gave optimum results in terms of uniformity of internal stresses in the wire and in friction reduction.

14.2.3 The 1990s onward

Siegert and Mock (1996) drew a stainless steel wire using a die mounted at the antinodal point of a longitudinal horn, with the transducer creating a longitudinal full wave resonance in the die system. Tests were also done on a half-wave die system, the die at the displacement node, with force reductions of 20%, better than obtained with the antinode approach, and with some improvement in surface finish.

Following an overview of prior work in ultrasonic wire and tube drawing, Siegert and Ulmer (2000) reviewed four methods of ultrasonically vibrating the wire die. Results for drawing a titanium wire with longitudinal die oscillations gave force reductions of 18% at draw speeds of 200 mm/s along with improved surface finish. As noted in other studies, as wire speeds were increased, force reductions diminished. In the same paper, tube drawing was covered, with several process arrangements as shown in Figure 14.9. Thus, in Figure 14.9a, longitudinal vibrations are applied to the mandrel (also called the "plug"); in Figure 14.9b, radial vibrations of the die are shown. In Figure 14.9c, radial vibrations of the die are created by three transducers (nozzles), while in Figure 15.4d, a combination

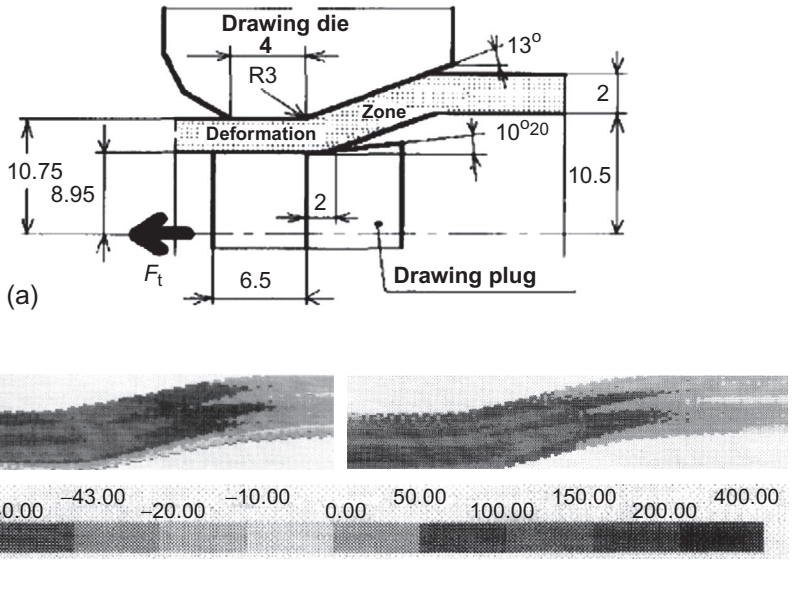


FIGURE 14.8 Tube drawing work of Petruzelka et al. (1996). (a) Ultrasonic tube drawing deformation zone (Figs. 2–5) and (b) axial stress in tube: top—without ultrasound; middle—with ultrasound, die between node and antinode (Fig. 3).

of Figure 14.9a and b is shown. Using the arrangement in Figure 14.9a, a number of benefits were reported in drawing Cu58, including improved surface finish and up to 33% reduction in draw force, with significant reductions in friction. These results were also extended and reported by Siegert and Ulmer (2001).

Jin et al. (1999) in a paper covered deep drawing and ironing, and coverage was also given to tube drawing using a setup where both radial oscillation of the die and longitudinal oscillation of the plug were created. Draw force reductions were reported, as were improved finish on both inner and outer surfaces of the Al 1100 tubing.

A report by Zust (2000) described applying torsional vibrations to wire drawing with significant improvements in surface finish being achieved. Studies by Murakawa and Jin (2001) and Hayashi et al. (2003) considered both longitudinal and radial die vibrations, of which the radially vibrated die unit is shown in Figure 14.10, with the process modeled by FEA methods in 2003. It was the finding that the radial vibration method yielded superior results in terms of force reductions and improved surface finish. An added result was the finding that a wider range of draw speeds was possible using the radial mode compared to the longitudinal mode. In a report by Mordyuke et al. (2004), a "bent waveguide" system was used to draw the tungsten wire—the waveguide permitting drawing of the wire without passing through the transducer. An improved microstructure was reported as was improved uniformity of wire diameter.

A theoretical analysis of the ultrasonic wiredrawing process was done by Susan et al. (2005), as applied to the steel ball-bearing wire. A determination of the draw force incorporated several factors, including Coulomb-type friction, the static flow behavior, and a material model based on the von Mises yield criterion. Experiments were conducted using equipment as shown in Figure 14.11a, where the wire is drawn through the body of the transducer–waveguide system (6–11). The vibration modes along the system are shown by waves B, C, and D. Of particular interest was that the longitudinal modes of the wire itself were accounted for, including the use of "reflectors" to keep the wire vibration in control within the draw region. The study focused on measuring the effects of die amplitude, $A = 5$, 15, and 20 μm (0–P) on the yield stress and tensile strength of the drawn wire as shown in Figure 14.11b. It is seen that with increasing vibration amplitude there was a progressive lowering of both yield stress and tensile strength compared to conventional wire drawing.

A study of the wiredrawing process done on industrial machinery was reported by Qi et al. (2008, 2009). A 50-kHz, 200-W wiredraw transducer was integrated into a multidie draw system. Data on the wire and dies were: wire, 0.3 mm brass, four dies at 0.26, 0.23, 0.23 (used for "float" adjustment), and 0.2 mm, with the vibrating die (at 15 μm) the last die. In the 2008 study, the draw force was measured and found to be reduced from 26 N, without ultrasonics, to around 21 N with ultrasonics. Wire breakage was virtually eliminated. In the 2009 study, more modest draw force reductions of 10% or less were reported. The effect of increasing transducer voltage on draw force showed, for three different draw speeds that in all cases, draw force decreased with increased voltage, which would correspond to greater transducer vibration amplitude. The slower the draw speed, the more pronounced the force reduction.

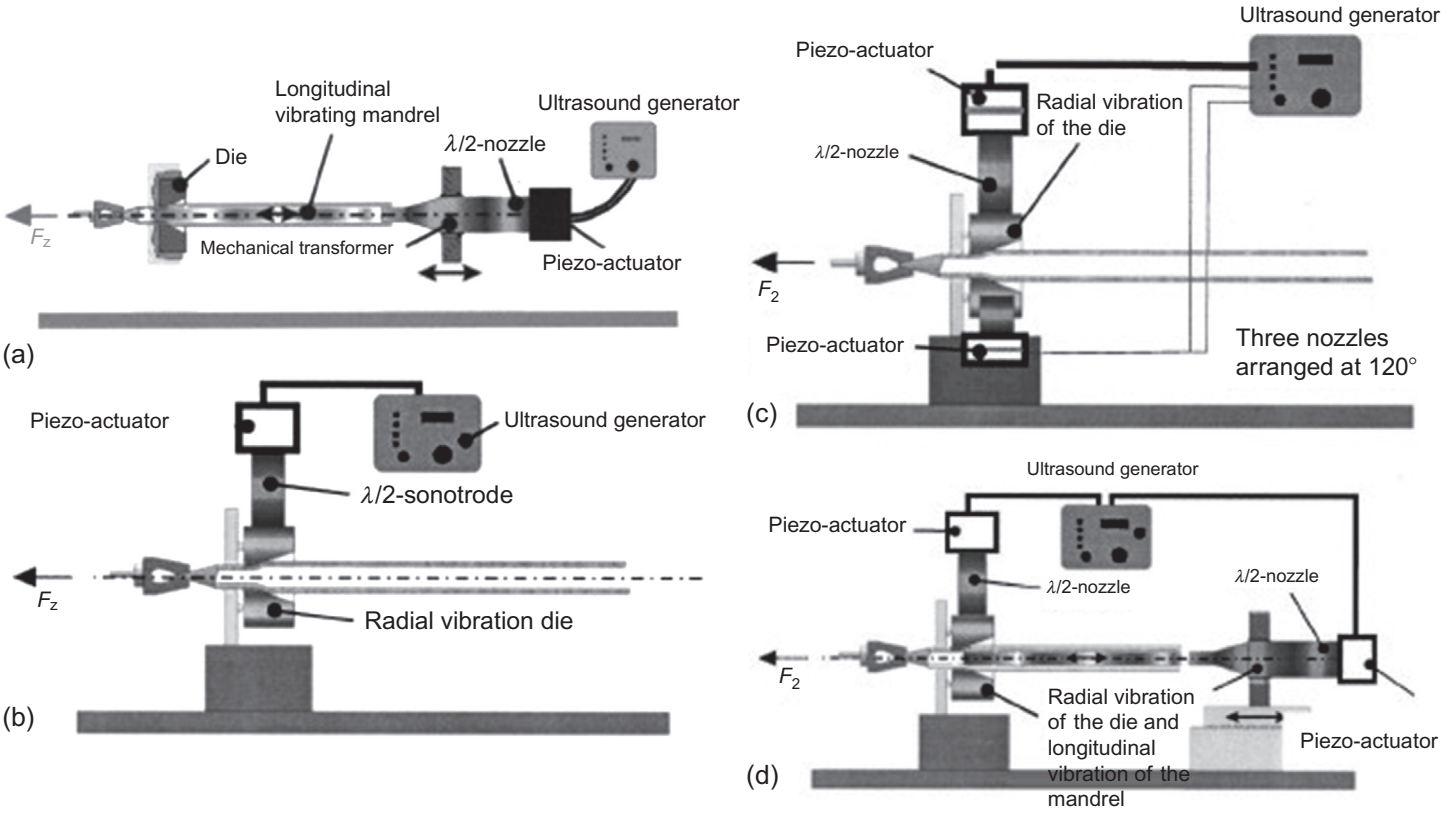


FIGURE 14.9 Methods of applying ultrasonics to tube drawing: (a) longitudinal to mandrel, (b) radial to die, (c) radial—three transducers, to die, and (d) combined longitudinal and radial. *(Source: Siegert and Ulmer, 2001, Fig. 9, originally published by ASME.)*

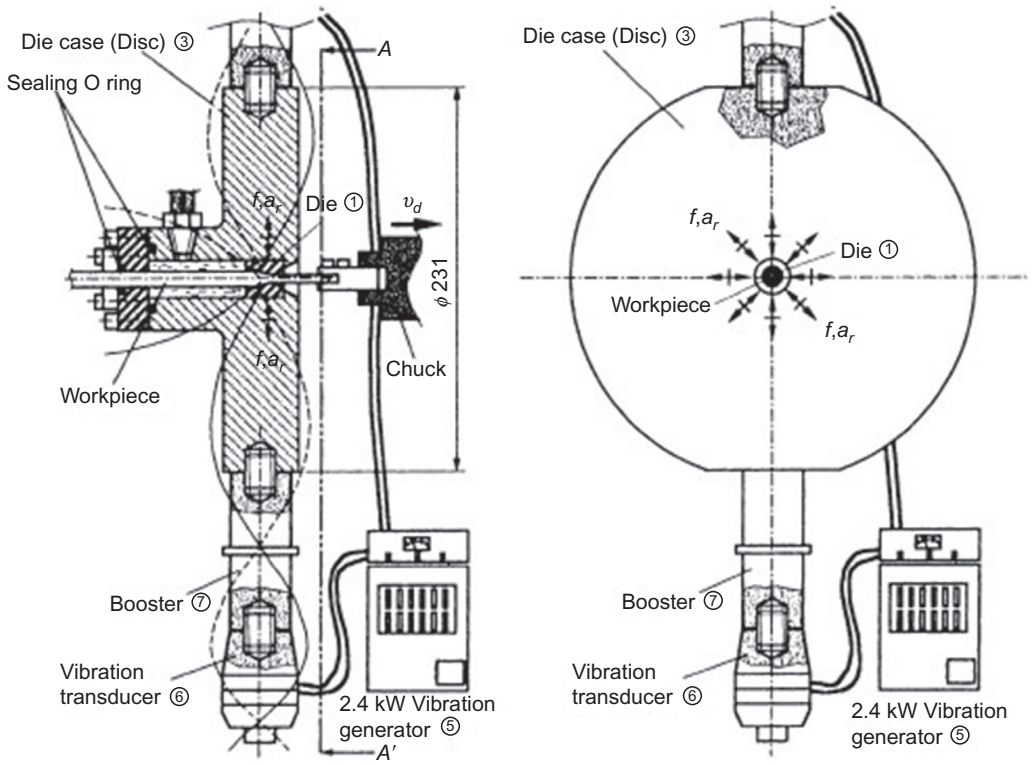


FIGURE 14.10 Radially vibrated ultrasonic tube drawing unit. *(Source: Murakawa and Jin (2001, Fig. 3).)*

To take the maximum effect case, for a voltage of 240 V at the slowest speed of 676 mm/s, the percent force reduction was about 7%. While vibration effects were evident, force reductions of these magnitudes would generally not be of great practical interest if force reduction alone is the only criterion. The matter of improved surface finish with ultrasonics was brought out in both the 2008 and 2009 studies.

To be noted is that Shan et al. (2012a) presented a new model of wiredrawing based on an antifriction effect. The wire/die was analyzed, showing the relationship between friction coefficient, drawing speed, and vibration amplitude in Figure 14.12. The ultrasonic antifriction effects on copper, stainless steel, and titanium wires were evaluated, with the latter showing the most pronounced effects. In further developments, Shan et al. (2012b, c) also reported on the development of a two-transducer, dual mode wiredrawing system where a horizontally oriented unit applied longitudinal vibrations along the length wire direction, while a vertical unit provided a radial vibration to the wire.

Nearly all ultrasonic wiredrawing involves longitudinal vibration of the die along the axis of the drawn wire. The concept of applying torsional vibrations to the wire was described by Zust (2000). Furthermore, Tsujino (1st edition references TBExxx) described how, by diagonal slits in the horn, to provide a mixed longitudinal/torsional vibration to the end of a horn, applying this concept to ultrasonic metal welding. The work by Yang et al. (2015) has applied the slit horn concept to achieving a longitudinal/torsional motion to the wiredrawing die, as shown in Figure 14.13. The criticality of the angle, number, and depths of the inclined grooves/slits is emphasized. In a follow-on, Yang et al. (2016) set forth a comprehensive modeling of the longitudinal/torsion process accompanied by experimental results. As shown in Figure 14.14, the effect of longitudinal vibration had a greater effect on stress reduction than torsional vibration, but the combined effect, when both were at maximum amplitude, was a predicted 53% reduction in draw stress as well as improvement in the plastic deformation of titanium wires.

Liu et al. (2016) set forth an alternate means of achieving mixed mode longitudinal-torsional vibrations for wiredrawing. Two longitudinal transducers, angled and offset, when coupled through the transformer block, created a mixed mode vibration at the die. In later work, Liu et al. (2018a) reported on a three-transducer unit that utilized the Poisson effect to create a powerful longitudinal vibration of the die, a concept also reported in early Tsujino work. They also showed the physical appearance of the skew-type vibration system. The influence of the two approaches to die vibration, compared to conventional drawing, for a 20% diameter reduction, was measured. The two systems gave about the same level of force reduction, approximately 5%. A somewhat improved surface finish was obtained with the ultrasonic systems

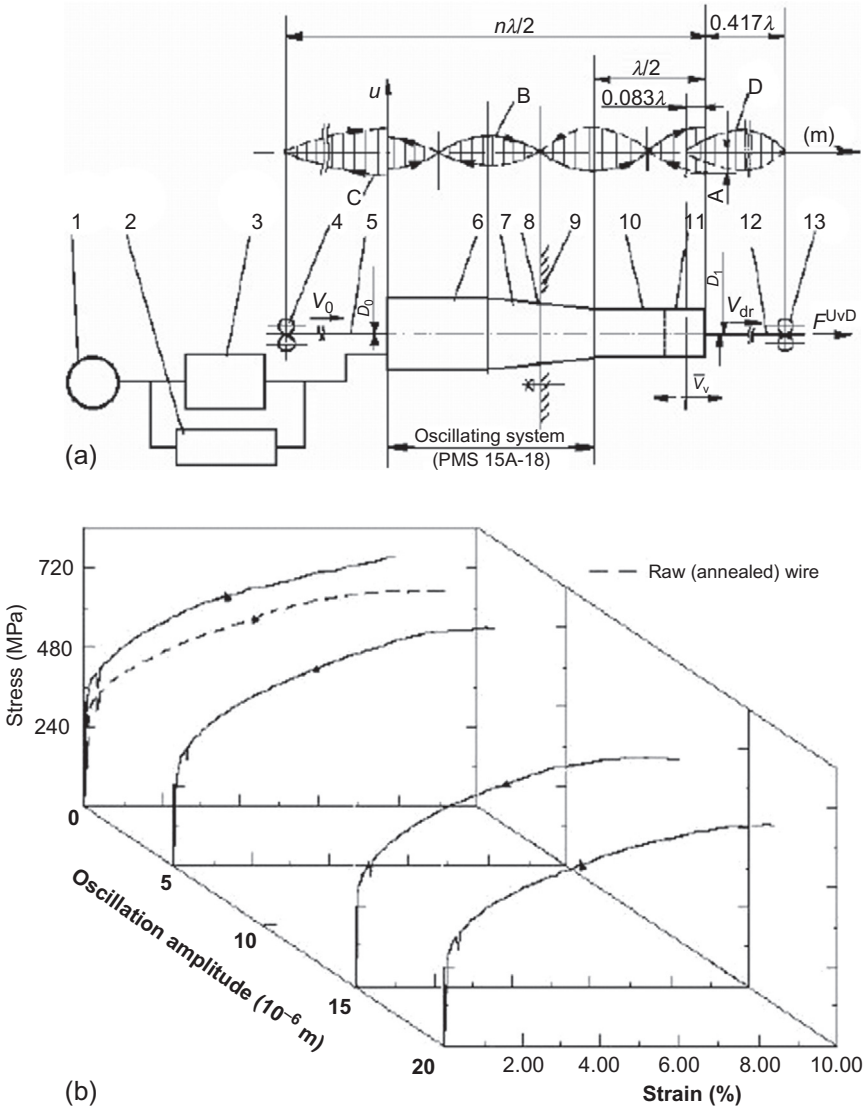


FIGURE 14.11 Ultrasonic wire drawing of Susan et al. (2005). (A) Experimental drawing setup (Fig. 3) and (B) effect of ultrasonics on mechanical properties at various amplitudes (Fig. 4).

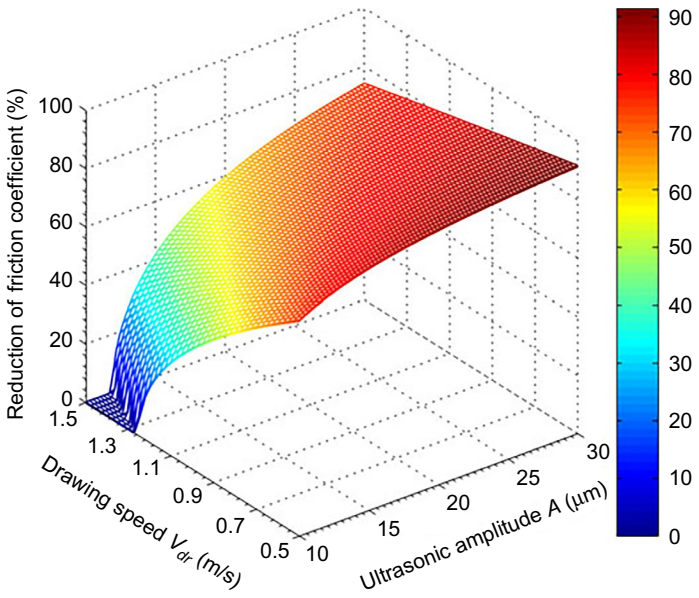


FIGURE 14.12 Nonlinear relationship of decrease in friction coefficient to ultrasonic amplitude and drawing speed (Shan et al., 2012a, Fig. 5).

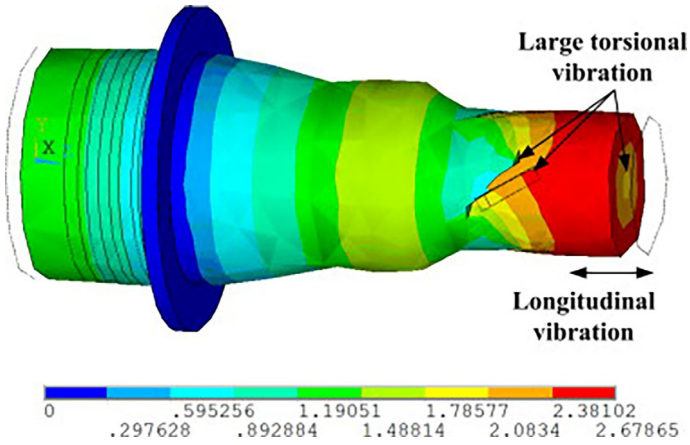


FIGURE 14.13 Stress contour of the vibrator with large L&T vibration (Yang et al., 2015, Fig. 7).

compared to the conventional drawing. Liu et al. (2018b) continued wiredrawing work with the development of a more traditional longitudinal mode system. While the overall design could be said to be "traditional," their paper set forth thorough, step-by-step design procedures for an ultrasonic system, and is to be recommended for review on that basis alone. After thoroughly characterizing system behavior, wiredraw tests on a titanium wire were performed, in which the wire was drawn through two draw transducer/die systems having slightly different horn designs for the two draw dies. The phase difference between the two systems was one of the control variables. The effect of die amplitude on the drawing force was determined for various wire velocities. In general, increased vibration amplitude caused a reduction in force, with the most pronounced effect at low velocity (99 mm/s) and somewhat less percentage reduction at higher velocities, an effect common to many ultrasonic processes where a "critical velocity" factor may enter. It was found in all cases that increased drawing speed improved the surface finish.

Liu participated with Cao et al. (2019) in the use of the equipment described in Liu et al. (2018a) for drawing a high-carbon steel wire. Experimental results showed ultrasonics reduced the draw force by approximately 17%. Through the use of the "wire circle" test, a reduction in residual stresses was shown. Liu et al. (2019b) continued reporting on wiredrawing research, with the focus of the work on drawing copper wire of various cross-sections—rectangular, pentagonal, and hexagon cross-sections. As with other wiredraw studies, the draw force was reduced with increasing die amplitude but increased with increased wire speed. It was also found that surface finish diminished with the application of ultrasound.

14.3 Deep drawing and bending

The deep drawing process consists of forcing a sheet metal blank into or through a die using a punch, with the blank being constrained by a peripheral hold-down pressure (the blank holder), to form a deep, recessed part having a wall thickness essentially the same as the blank (Altan et al., 1983). Frictional forces between the blank and punch and die and die holder play a critical role in the process, with the reduction of these forces through ultrasonic vibrations being the focus of many studies in this field. The allied process of ultrasonic bending will also be reviewed in this section as will the emerging process of incremental forming.

14.3.1 Deep drawing

14.3.1.1 Early years: 1960s and 1970s

Lewis Balamuth, already cited for contributions to the metal forming field, provided early examples of ultrasonics applied to "dimpling," a form of deep drawing (Peacock, 1961). A 14-kHz-activated punch was used to form shallow cavities in aluminum and titanium sheet that, when

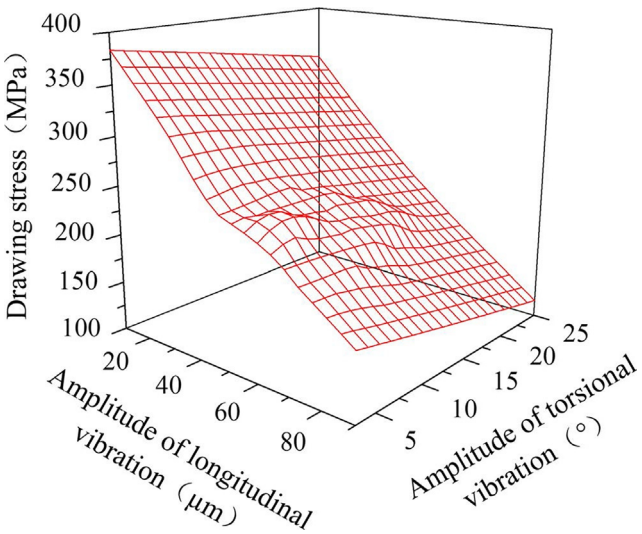


FIGURE 14.14 Drawing stress variation with longitudinal and torsional vibration amplitude (Yang et al., 2016, Fig. 13).

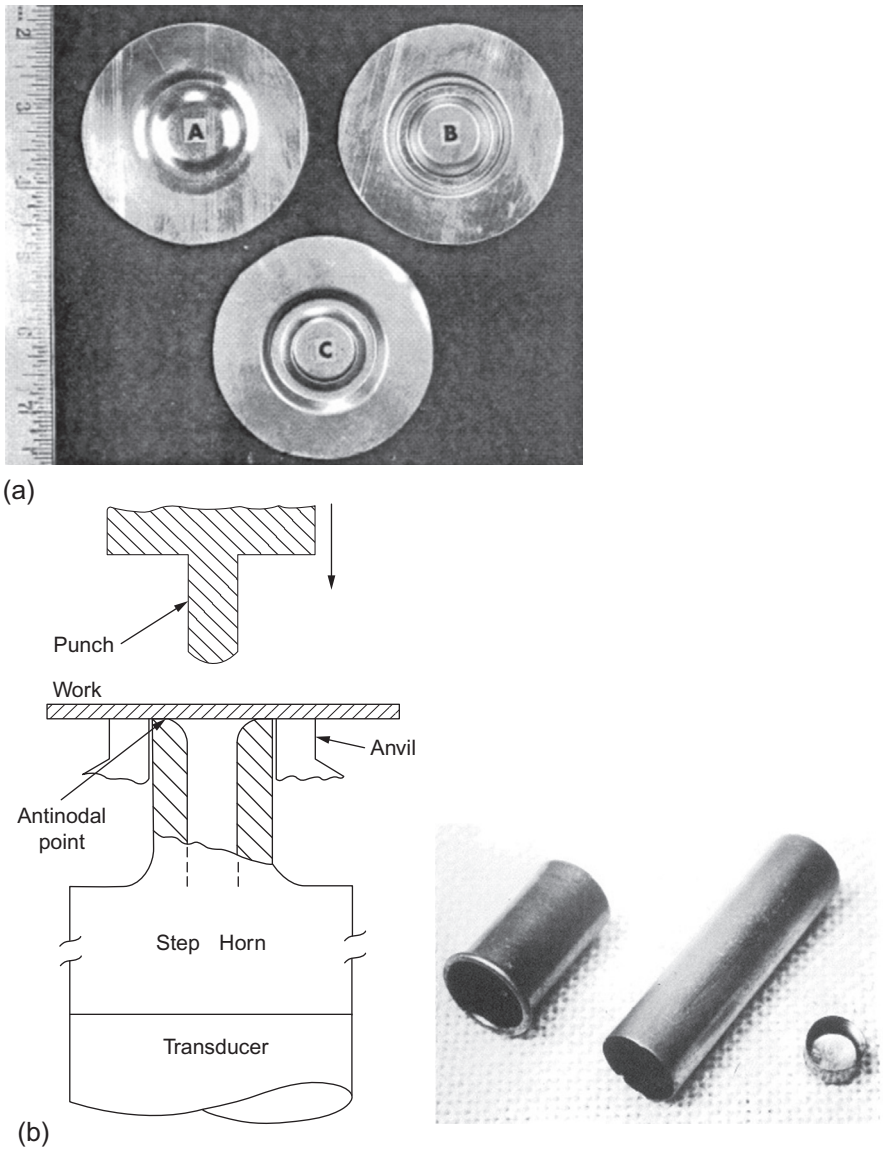


FIGURE 14.15 Early deep draw results. (a) Aeroprojects deep draw results (Rosenfeld, 1963, Fig. 23) and (b) Langenecker (1964) deep draw setup (left) and deep draw cups (Figs. 7 and 8).

compared to conventionally formed shapes, had sharper definition and less cracking. At the previously cited 1963 U.S. Navy-sponsored conference, Aeroprojects reported on deep drawing aluminum sheets (Figure 14.15a), indicating better shape definition, greater depth with less force, and elimination of tearing. Langenecker (1964) also contributed to deep drawing. Using the simple device of Figure 14.15b (left), copper cups, Figure 14.15b (right), were drawn to about twice the length as without ultrasound, and forces were reduced by 65%, while in a curling operation (leftmost cup of the figure), forces were reduced by 60%.

The most comprehensive early work on deep drawing was from Kristoffy et al. (1965) and Kristoffy (1969), previously cited in Chapter 14, where ultrasonic vibrations were applied, alone or in combination, axially to the punch and radially to the die as shown in Figure 14.16a. Thus, the transducers (9) are shown axially driving the punch (3) and radially driving the die. The effect of punch vibration in reducing the deep draw force is shown in Figure 14.16b, noting the "apparent force drop" under ultrasonic vibrations. By comparing forces measured by the load cell with direct measurement of forces at the punch using strain gages, the drop was shown to be a result of the low-frequency response of the load cell recording equipment and not a true drop in force.

Sansome contributed to the deep drawing area, such as in the Winsper and Sansome (1967) survey and in Sansome

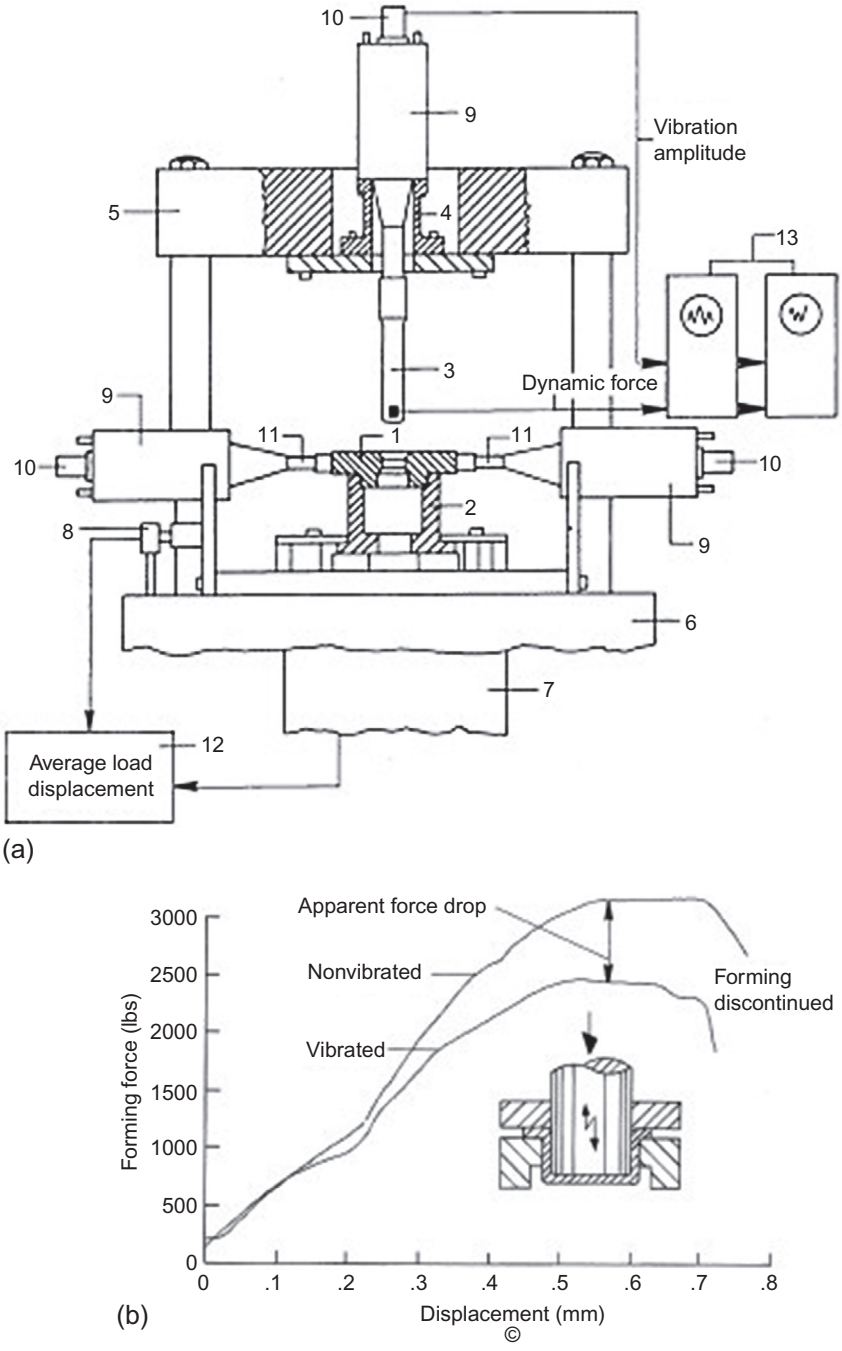


FIGURE 14.16 Work of Kristoffy (1969) on deep drawing. (a) Experimental setup (Fig. 3) and (b) influence of ultrasonics on the forming force (Fig. 6).

(1973), where reference is made to deep drawing work using an analog of the process and to work in drawing cups and cans. Biddell and Sansome (1973) and Sansome (1973) applied radial oscillations to the die, as shown by the equipment schematic and photograph of Figure 14.17a and b and obtained a 20% increase in the depth of the draw. Aluminum and brass blanks were drawn at varying speeds. It was found that punch load was decreased by about 7% at low-punch speeds with a diminishing effect at higher speeds. The depth of the draw was increased by 19%. Later, Smith and Sansome (1975) examined deep drawing using the processed analog involving two transducers driving opposed wedge-shaped dies and a strip being drawn through the dies. The punch load for the aluminum strip was decreased by 25% and the limiting draw ratio (LDR) was increased by 12%.

Biddell and Sansome (1974) then overviewed the field of oscillatory metalworking, noting early low-frequency

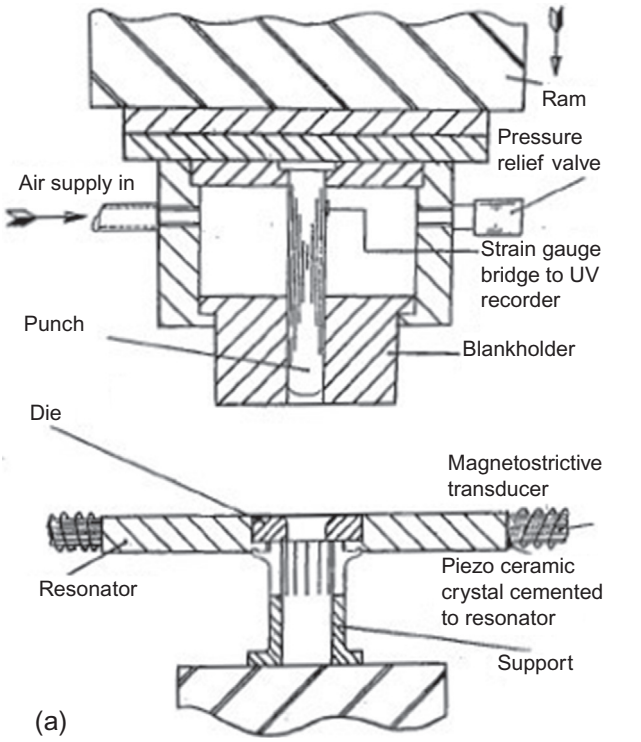


FIGURE 14.17 Ultrasonic deep drawing work reported by Biddell and Sansome. (a) Schematic of deep draw press and resonator (Biddell and Sansome, 1973, Fig. 2) and (b) experimental setup (from Sansome, 1973). *(Source: (A) Reprinted from Biddell and Sansome (1973).)*

deep drawing work by several investigators. Following an appraisal of the work of others, credit for ultrasonic deep drawing was directed to the work of Young et al. (1971) as detailed in their patent.

In a translation summary of Severdenko's work (Severdenko et al., 1975) that covers the 1960s through 1975, several versions of ultrasonic deep drawing equipment are shown where the die, or the punch, or the die/punch combination was vibrated. A wide range of alloys were tested, with the results showing draw force reductions, deeper draws, temperature increases during drawing, the effects of different lubricants, and galling under higher vibration amplitudes.

14.3.1.2 1980s onward

Following a gap in deep drawing work, Tisza (1983) developed equipment consisting of a radially vibrating die machined into the end of a longitudinally vibrating booster. A model of the drawing process was developed, accounting for ultrasonic effects, such as hardening, on the material. Aluminum, copper, and steel were tested, with increasingly deep draws achievable with an increased vibration amplitude and good agreement with theory. Okazaki and Kawaguchi (1990) developed radially vibrating die equipment along the same lines as Tizra, for deep drawing of aluminum foils. Increased draw ratios were obtained with a reduction or elimination of wrinkling and tearing and reductions in punch force.

Pasierb and Wojnar (1992) applied radial vibration to the die and found in the deep drawing of Al, Cu, zinc, and brass that there were significant draw force reductions (from 20% to 37%) and less thinning of the wall section, with the improvements attributed to friction reduction. The authors also reported on tube drawing tests using an ultrasonically activated plug.

Acoustic challenges in designing thick section-forming dies that maintain the desired resonant mode during forming were described by Lucas and Chapman (1993), where both numerical and experimental techniques were applied to the vibration of thick cylinders. This work was extended by Lucas (1996), as shown in Figure 14.18a, which shows the extensive number of modes near the desired die operating R0 mode at 20 kHz, including the very close R3 mode. It was shown how significant mode coupling could occur under load and cause loss of energy from the R0 mode and also shown thorough modification of the die structure that a separation of near modes could be achieved. In related work by Cheers (1995) on the deep drawing of cans, FEA resulted in a die-transducer system as shown in Figure 14.18b, with the die having a similar form to the die modification developed by Lucas.

Jimma et al. (1998) outlined several means of applying ultrasonics to the deep drawing process via longitudinal or radial oscillations of the die and/or blank holder and/or longitudinal oscillations of the punch. These included (1) applying axial vibrations to the blank holder and also axial vibrations to the die and axial vibrations to the punch. Alternate setups involve radial vibrations applied to the blank holder and die. The advantages and disadvantages of using either the first or second radial modes are discussed, concluding that the first radial mode was best. To acoustically isolate the die from the rest of the hardware, a "vibration-proof gum plate" was placed between the upper blank holder surface and the forming hardware. It was found

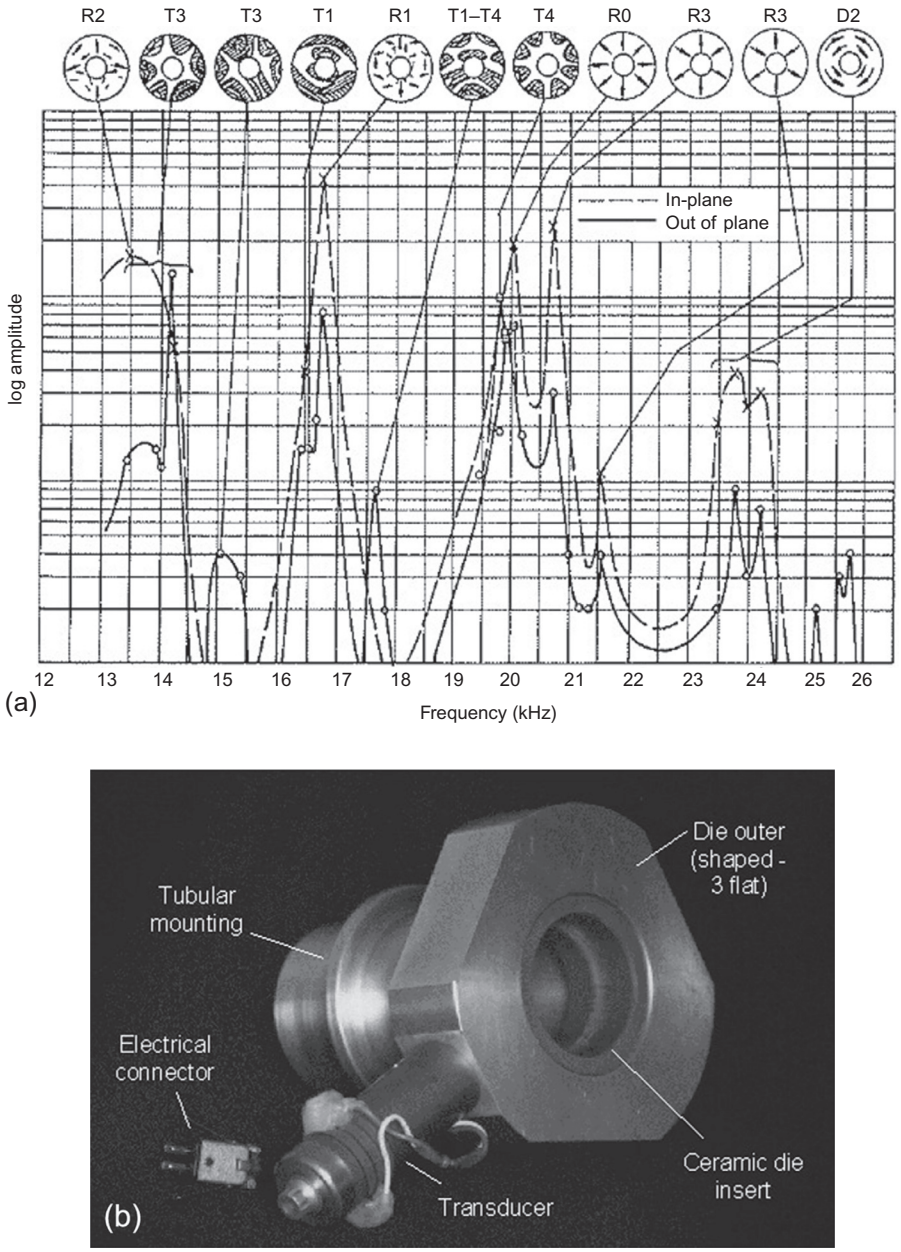


FIGURE 14.18 Design of ultrasonic deep drawing dies. (a) Experimental and analytical data on various die modes (Lucas, 1996, Fig. 6) and (b) ultrasonic transducer and die (Cheers, 1995, Fig. 1.13).

with ultrasound that the LDR was increased over that obtained by conventional means. Thus, for cold-rolled sheet steel, the LDR was increased from 2.58 (conventional) to 2.86 (blank holder vibration only) and to 2.94 (vibration of die and blank holder). For SS304, LDR increased from 2.38 to 2.77.

The work of Jin et al. (1999) on tube drawing was noted in Section 14.2, where attention was also given to ironing during the deep draw process. The equipment used (Figure 14.19a) was similar to that reported by some of the coauthors in wire and tube drawing work with the kinematics of the die/metal interaction (Figure 14.19b) for conventional ironing and ironing, with axial and radial die oscillations also being similar to those developed for wire and tube drawing. Qualitative results were reported, for example, "success of ironing, failure of ironing," for Al 1050 and cold-rolled steel in terms of reduction of wall thickness for various blank thicknesses and lubrication conditions. It was generally found that the application of ultrasonics increased the reduction in wall thickness for both materials under all lubrication conditions.

Ashida and Aoyama (2007) initially modeled the deep drawing process using a combination of classical analysis and FEA and then turned to the use of a commercial

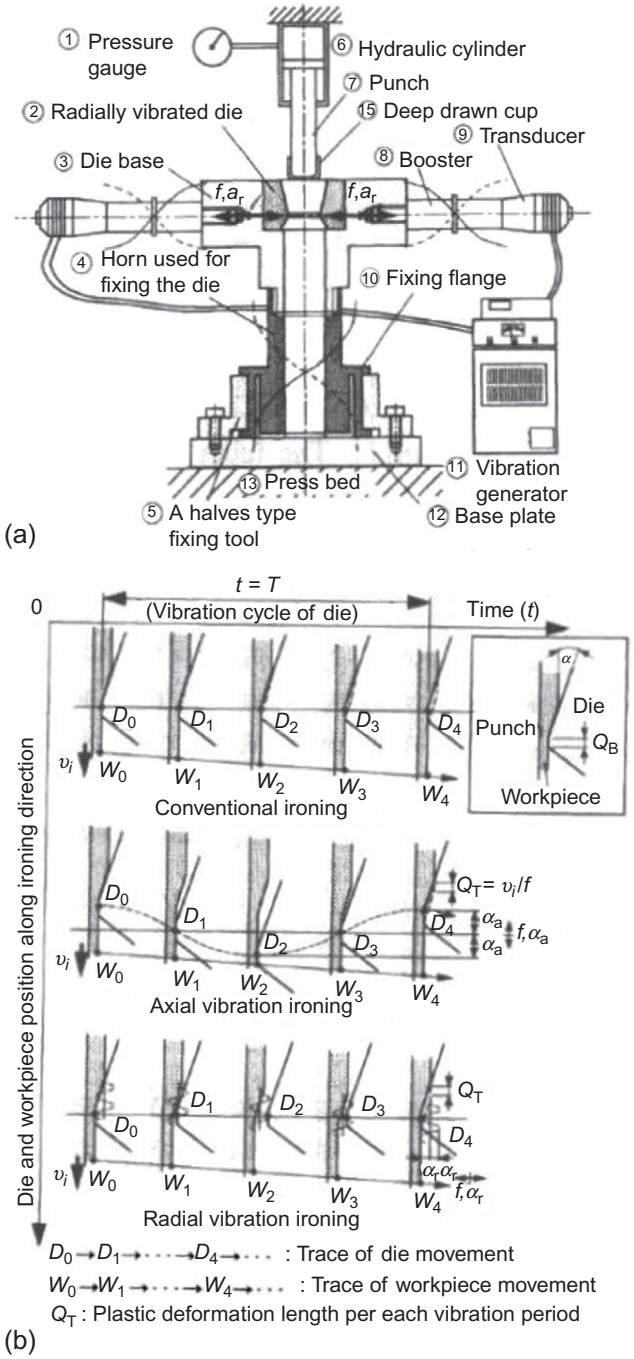


FIGURE 14.19 Ultrasonic deep drawing and ironing by Jin et al. (1999). (a) Experimental setup for ironing (Fig. 3) and (b) kinematics of conventional (top), axial (middle), and radial (bottom) vibration (Fig. 2).

press-forming software DYNAFORM. It was possible to vary the coefficient of friction at various locations on the punch, blank holder, die, and die shoulder, including the lubricant effects on the coefficient of friction. The simulations showed the potential of ultrasonics to reduce the fracture of drawn parts. Unfortunately, there was no tie between the initial ultrasonic vibration analysis and the forming analysis, leaving the value of the overall approach still to be determined. During this period, a brief summary of ultrasonic deep drawing was provided by Emmens (2011), citing the previous work of Jimma et al. (1998) and then drawing on low-frequency studies as to possible friction reduction mechanisms that could lead to process improvement.

The work of Aziz and Lucas (2010a, b) on the development of an ultrasonic-forming test having application to deep drawing was described in Chapter 13, Section 13.3. Additional notes on that work are that using the described equipment, the deformation behavior of 3-mm sheet Al 1050 and die-cast magnesium AC50 was evaluated. It was found that an amplitude-dependent reduction in forming force occurred for both Al and magnesium. For aluminum, the reductions ranged from 10% at the low amplitude of 5 μm up to 27% at 20 μm. For magnesium, the force reduction was less, ranging from 0.8% to 10% at 20 μm. Some reduction in breaking force was seen for magnesium. In later tests with a higher-power transducer, greater force reductions were achieved. Also of interest were tests that compared forces measured by the test machine load cell with a fast response piezoelectric force transducer and then related to FEA modeling results. The fact that the high-frequency load cell data showed a reduction in mean force, but increased oscillatory peak forces, was noted. These potential issues of reliable force measurement under ultrasonic conditions, first noted by Kristoffy (1969), and having potentially affected the interpretation of deformation studies since that time, indicated the importance of resolving these matters if reliable metal-forming studies were to be done.

FEA modeling of the deep draw process was reported by Daud et al. (2012), in which radial vibrations were applied to the die in a cylinder necking process, as shown in Figure 14.20a. The intent was to determine the influence of friction on the forming process, in comparison to conventional forming. The results showed a reduction in forming forces, as had been reported by other investigators. Can buckling results showed that it was necessary to achieve a friction coefficient of 0.07 in order to eliminate buckling, as shown in Figure 14.20b, where buckling occurred under conventional conditions but was eliminated with ultrasonics.

Chu et al. (2012) used a response surface method to study the effects of ram motion, amplitude, and draw speed on ram force and draw depth for ultrasonic deep drawing. The equipment (Figure 14.21a) featured a radially vibrated blank holder, with the drive frequency being variable—an unusual capability for ultrasonic equipment. Materials were CRS and Al 5052 with amplitudes of 19 and 30 μm with no lubricant. A servo-actuated press was operated in a two-step motion. Figure 14.21b is a representative of several response surface results relating to various parameters, in this case draw force as a function of vibration amplitude and drawing speed.

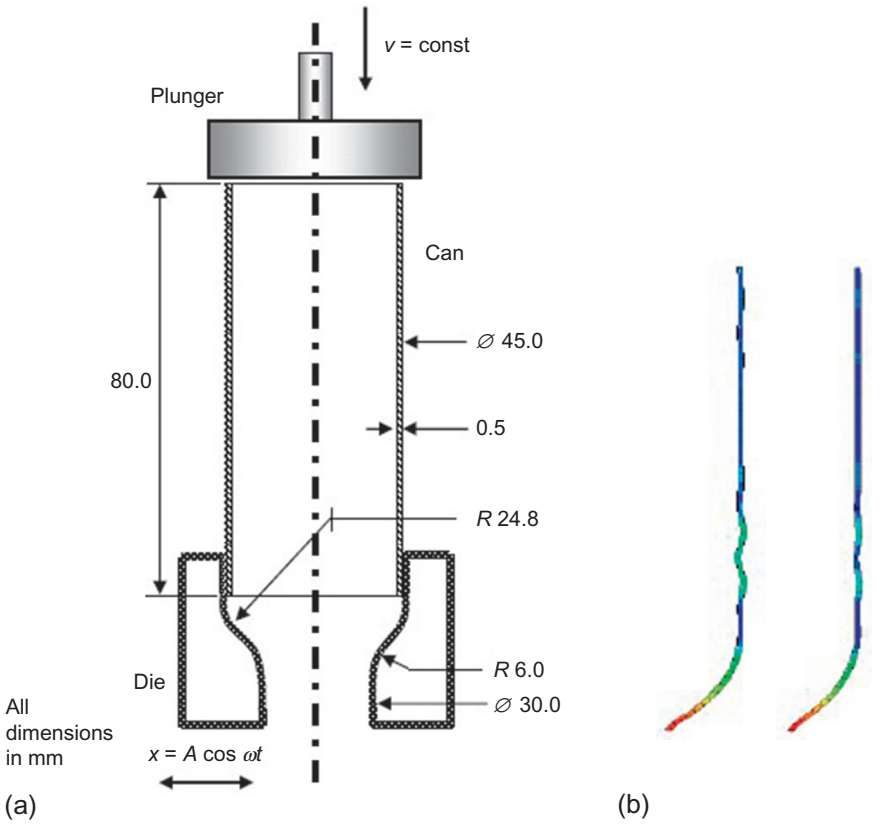


FIGURE 14.20 Sheet metal forming by Daud et al. (2012). (a) Thin cylinder ultrasonic die necking (Fig. 1) and (b) without (left) and with (right) ultrasonics, friction 0.03 (Fig. 4).

Chu et al. (2014) developed an ultrasonic deep draw system, Figure 14.22a, applying ultrasonic vibrations to the die (identified as the blank holder ring in Figure 14.22b), using a servo-controlled press to drive the ram. Deep draw force and depth were modeled with draw speed, ratio of ram motion, and die amplitude as variables for SPCC (cold rolled steel) and Al 5052. Figure 14.23 shows response surface results for the effects of drawing speed and range of ratio (at a fixed amplitude) for the two materials, noting a substantial difference in response for the two materials. Other results are presented for amplitude/speed combinations. The favorable results suggest that it is possible to greatly reduce the use of lubricants in the deep draw process.

While many ultrasonic deep draw systems seek to vibrate the die, or the punch, Kim and Lee (2014) applied vibrations to a thin plate resting on the surface of the die. As seen in Figure 14.24, little difference in appearance was noted in the first three draw ratios (DRs), whereas at DR 2.34 failure occurred without ultrasonics, while the draw was successful with ultrasonics. Slight reductions were noted in punch loads and friction coefficient under the influence of ultrasound.

Cao et al. (2017) combined solid granule forming with that of ultrasonic forming to that of ultrasonic granule medium forming (UGMF), using a setup as shown in Figure 14.25 (although illustrated, ultrasonics was not applied to the punch, just to die only). FEA was used to design the vibration components of the system. The effects of heating ($180 < T < 300^{o}$C) on limit-forming height were also examined. Test results showed varied microstructures in the drawn sample, depending on the location and vibration amplitude, and a substantial reduction in punch load under vibration. It was concluded that ultrasonics significantly influenced the friction/lubrication at the die/sheet interface (this is seen in other deep draw studies), with the unique effect of also enhancing the liquidity and transmission of the granular medium. Both volume and surface effects were said to be active in affecting sheet properties.

The application of ultrasonics to rubber die drawing was the subject of Sheykholslami et al. (2018). A numerical study was done for the case of circular sections with a rubber die, where ultrasonics at three different frequencies was applied to the punch. The basic effect of ultrasonics was shown to increase the deep drawing punch displacement limit from approximately 1.7 mm for conventional drawing to 2.7 mm with ultrasonics, including a reduction in force.

Cao et al. (2018) gave special attention to the analysis of surface friction effects in an ultrasonic deep drawing

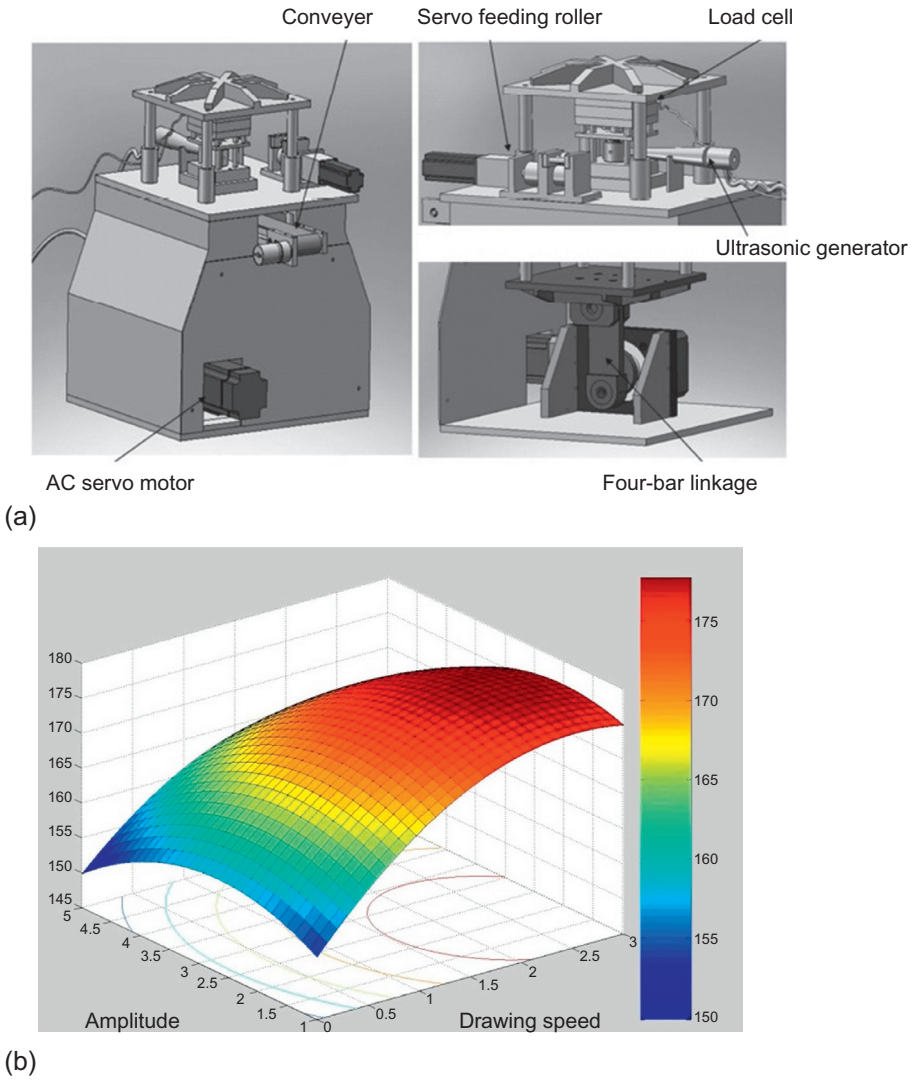


FIGURE 14.21 Ultrasonic deep drawing work of Chu et al. (2012). (a) The ultrasonic servo press system (Fig. 1) and (b) response surface of draw force versus amplitude and draw speed for an SPCC steel (Fig. 3c).

process as shown schematically in Figure 14.26a and in an operational form in Figure 14.26b. Their results showed an excellent comparison of theoretical and experimental values of friction effects with and without ultrasound, specifically noting a significant reduction of approximately 33% in the friction coefficient with ultrasonics. The surface topography of AZ31B sheets without and with ultrasonics is shown in Figure 14.27. While fretting wear was noted on the ultrasonic sheets, more serious deep scratches were noted on the nonultrasonic surface.

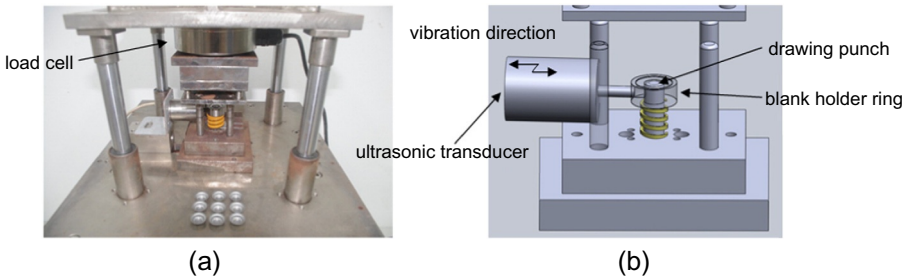


FIGURE 14.22 Schematic illustrations of tool set and servo press: (a) Close-up of tool set, (b) 3D model (Chu et al., 2014, Fig. 1).

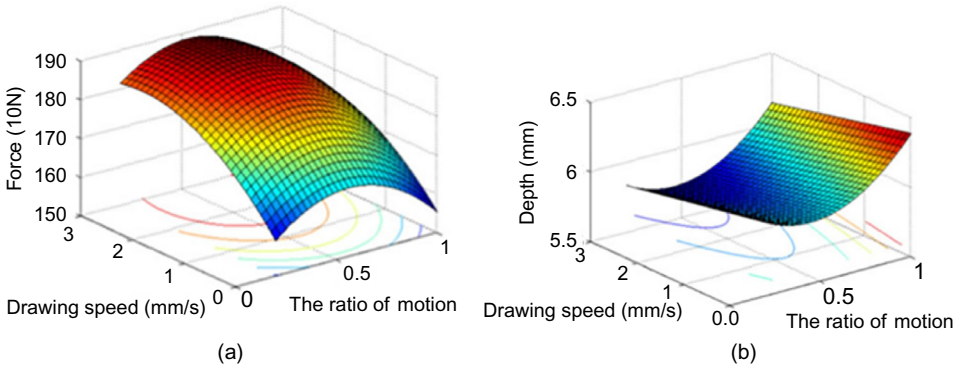


FIGURE 14.23 Response surfaces of force versus draw speed/ratio of motion at 3-micron amplitude: (a) SPCC, (b) Al 5052 (Chu et al., 2014, Figs. 3a and 4a).

While it is well known that the acoustic load imposed by the process can shift the system resonant frequency, e.g., lowering frequency if mass-dominated, raising frequency if stiffness-dominated, the details of this critical effect are seldom studied. However, Malekipour et al. (2020) focus exactly on these issues, both experimentally and analytically, in a study of the ultrasonic deep draw process. Following an extensive review of prior work, including the effects of acoustic softening and stress superposition on material response, the design of the deep draw system, based on ultrasonic activation of the die (versus punch or blank holder), is shown in Figure 14.28. An ABAQS-based analysis of the stepped horn vibrations and die components was carried out, as was a punch force analysis that included modeling of the die, blank holder, plate, and punch combination. Extensive results in the form of force-deformation curves are presented for various stages of loading and material effects, of which Figure 14.29 is merely representative. Thus, little effect is noted on force reduction until the 5-mm stroke, followed by cup failure at 8 mm for conventional drawing (CCD). If ultrasound is continued (red dashed line) but stopped at 10 mm, failure again occurs. Most importantly, continuous application of ultrasound permits completion of a full cup draw, otherwise unachievable without ultrasound. Decreased forming forces and increased draw ratios resulted from this ultrasonic deep draw system.

14.3.1.3 *Ultrasonically assisted incremental forming*

Incremental sheet forming (ISF) is a rapid prototyping technology for manufacturing complex sheet structures. During ISF, the sheet periphery is clamped in a blank holder. A generic tool, usually with a hemispherical end, is applied to locally deform the sheet with a predefined toolpath. The final desired geometry is achieved progressively. There are three main types of ISF—single-point incremental forming (SPIF), two-point incremental forming (TPIF), and double-sided incremental forming (DSIF) (Brosius, 2014). SPIF is performed with only one generic tool. In TPIF, a partial or full die is additionally needed. DSIF requires two generic tools, one of which will provide kinematic support at the bottom side of the sheet. The deformation is stabilized in the local region between the two tools (Malhotra et al., 2011).

Amini et al. (2017) and Vahdati et al. (2017) investigated ultrasonic effects on SPIF of annealed aluminum AA1050 through a single groove test, where a longitudinal ultrasonic vibration on the tool shows to reduce the forming



FIGURE 14.24 Drawn specimens for various DRs: (a) With and (b) without ultrasonic vibration (Kim and Lee, 2014, Fig. 2).

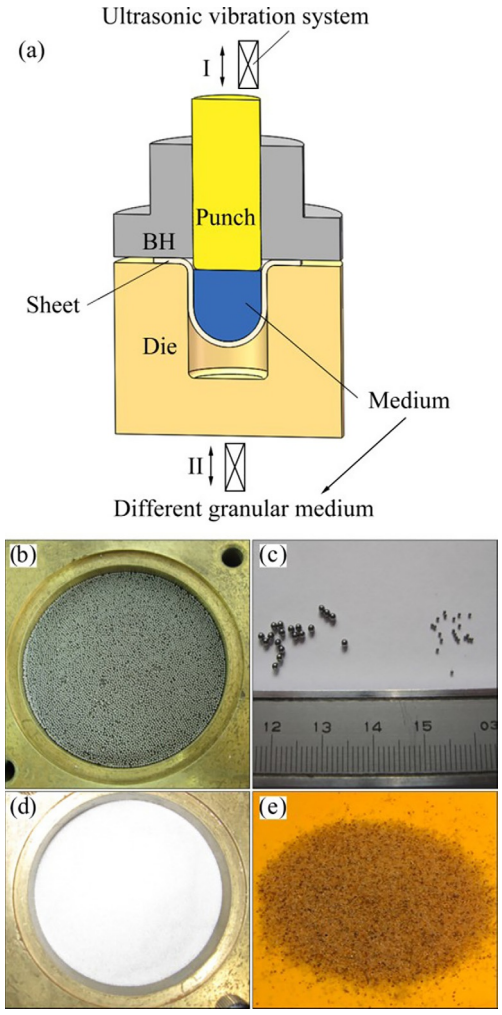


FIGURE 14.25 Schematic of UGMF technology (a) and different granular media: (b) metal granular, (c) metal granular with different sizes, (d) nonmetallic granular with high-temperature resistance, (e) nonmetallic of room temperature (Cao et al., 2017, Fig. 1).

force and increases the formability. Similarly, Li et al. (2020) performed ultrasonically assisted SPIF (UA-SPIF) of straight grooves on aluminum alloy AA1050-O. Forming force reduction was reduced in conditions of both ladder- and zigzag-type toolpaths. Furthermore, the ultrasonic assistance slightly increased the grain size and the fraction of low-angle grain boundaries. Yang et al. (2019) performed UA-SPIF on aluminum AA1060 and showed that the ultrasonic energy is beneficial to SPIF below a certain level. On the other hand, vibrations with amplitude larger than 6 μm made the sheets more susceptible to cracking and vibrations with a frequency higher than 25 kHz could lead to fatigue concerns. Su et al. (2018) performed UA-SPIF on magnesium alloy and showed that increasing the vibration amplitude could reduce the maximum shear stress. However, if the amplitude was higher than 0.16 mm, a large thinning rate was induced, and sheet fracture was more prone to occur. Obikawa and Hayashi (2017a, b) and Sekine and Obikawa (2010) applied an axial vibration to the forming tool during micro-SPIF of thin shell metallic foils. Ultrasonic vibration was shown to greatly improve the shape accuracy whereas the formability was only marginally increased.

In addition to experimental studies, several models have been developed to analyze the UA incremental forming process. Li et al. (2017a) performed a finite element model analysis with ABQUS software, where the influence of different frequencies and amplitudes of ultrasonic vibrations on SPIF of Q235 steel sheet were simulated by applying a vibration displacement boundary condition. Their results showed that below 40 kHz and 10 μm vibration amplitude, a greater drop in the forming force was observed. However, this trend was reversed if the ultrasonic parameters were above the noted frequency and amplitude levels, an effect attributed to potential sheet rebonding. Li et al. (2017b) employed LS-DYNA software to simulate ultrasonically

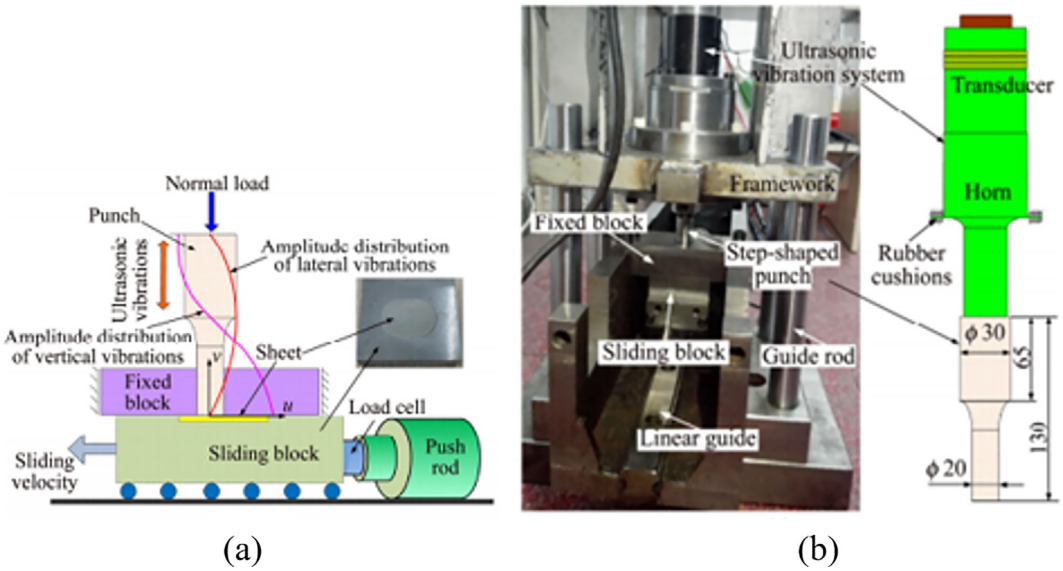


FIGURE 14.26 Friction test of sheets (unit: mm): (a) Test setup, (b) schematic diagram of friction test, (b) Test setup (Cao et al., 2018, Fig. 3).

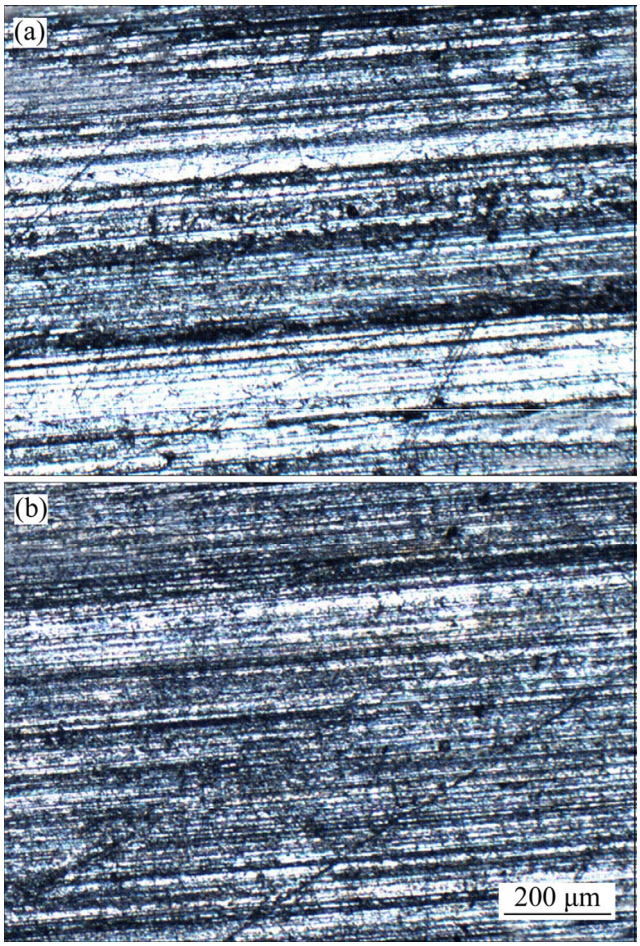


FIGURE 14.27 Comparison of AZ31B sheet surface topography: (a) Without ultrasonics. (b) With ultrasonic vibrations (Cao et al., 2018, Fig. 11).

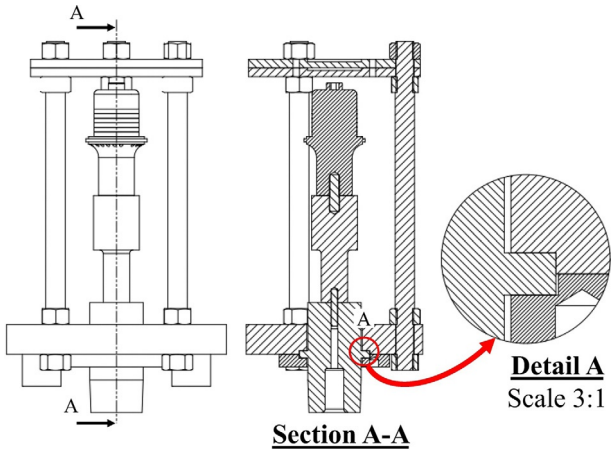


FIGURE 14.28 Drawing of the tuned vibrating set with die attachment detail A (Malekipour et al., 2020, Fig. 7).

assisted SPIF on aluminum alloys AA1050 and AA5052. According to their calculation, the force reduction would be higher for a material with higher yield strength and SPIF forming tool with a larger diameter. Similarly, Su et al. (2018) built a UA-SPIF model in LS-DYNA where an additional harmonic vibration boundary condition was applied to the forming tool. Effects of different forming parameters, including tool head size, friction coefficient, ultrasonic frequency, and amplitude, were studied in terms of the maximum shear stress and thinning rate. Bai et al. (2019) and Bai et al. (2018) developed both analytical and numerical models to calculate the forming force during ultrasonically assisted SPIF. The predicted force reduction was somewhat higher than their experiment measurements. It should be noted that in these modeling works, the ultrasonic vibration is defined as an additional displacement boundary condition rather than changing the material constitutive model. Sedaghat et al. (2019) built an acousto-plasticity constitutive material model that considered dislocation dynamics and acoustic energy transformations, which was implemented as a user-defined subroutine in ABAQUS for modeling different ultrasonically assisted forming processes. They could successfully calculate the force reduction in the UA-SPIF process. Li et al. (2020) developed both analytical and ABAQUS models for UA-SPIF of straight grooves, where the ultrasonic softening effect was explicitly considered in the material constitutive model. They showed that the material flow area was increased and the contact period was reduced with superimposed ultrasonic vibration.

Despite the experimental and modeling works on UA-SPIF, studies regarding ultrasonic effects on TPIF and DSIF are limited. Cheng et al. (2019) performed both UA-SPIF and UA-TPIF on tempered aluminum alloy AA7075 for different cone and funnel shapes. Their schematic and actual UA-SPIF setup are shown in Figure 14.30. In contrast to previous studies on UA-SPIF, the force reduction was found to be relatively insignificant. On the other hand, large spikes of force drop, particularly the axial forming force, were consistently observed at certain forming depths for various investigated shapes. This is potentially because the open forming area in their experiments was much larger than in other reported studies. As a result, the ultrasonic vibration was not only locally absorbed in the plastic deformation zone but also elastically absorbed by the entire sheet as a "drum" effect due to its structural compliance. During the forming process as the sheet was progressively deformed, the vibration mode and corresponding natural frequency of the deformed sheet were also continuously changing. When the natural frequency of the specific shape matched the applied ultrasonic frequency, the partially deformed sheet resonated constructively with the forming tool, which is reflected as a drastic reduction in the forming force curve.

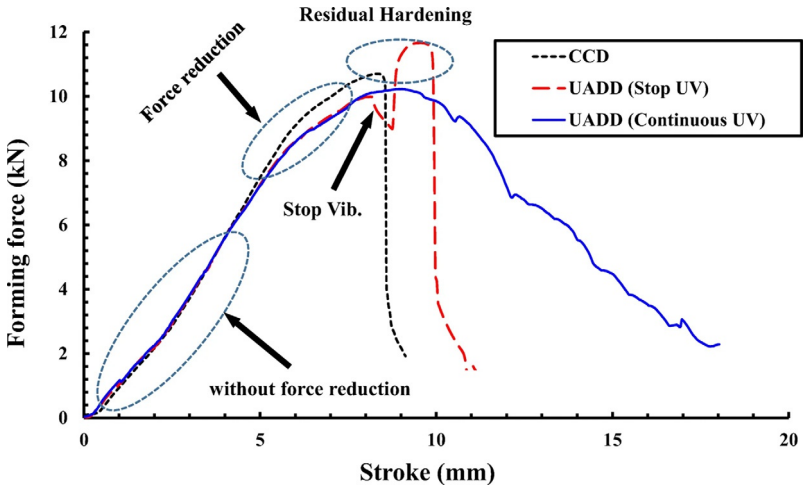


FIGURE 14.29 Forming force curve during conventional and UV-assisted deep drawing for a 39-mm blank (with 20 kHz frequency and 5-micron amplitude) (Malekipour et al., 2020, Fig. 10).

To effectively utilize ultrasonic energy and minimize the elastic drumming effect on the entire sheet, Cheng et al. (2019) investigated the effects of ultrasonic energy during TPIF. The supportive die allowed the ultrasonic energy to be absorbed in the local deformation zone. In their UA-TPIF experiments, ultrasonic vibration is applied intermittently and the forming force results are shown in Figure 14.31a–c. Figure 14.31a corresponds to a thinner sheet of 0.5 mm while Figure 14.31b and c are on thicker sheets of 1.5 mm. Overall, the amount of ultrasonically induced force reduction was more significant in UA-TPIF than UA-SPIF. Comparing Figure 14.31b and c, with a smaller step size, the force reduction was also higher. Surface finish of the formed part under the condition of Figure 14.31b is shown in Figure 14.31d. Modified surface roughness of the formed part can be observed in regions where ultrasonic vibration is superimposed.

14.3.2 Bending

Bending is a metal forming process involving "the straining of material, usually flat sheet or strip, by moving it around a straight axis…" with the metal flow taking place within the plastic range of the metal so that a permanent set is achieved after removal of the applied stress (Altan et al., 1983, p. 234). Although not all work on ultrasonic bending meets the formalism of this definition, several studies in this area have occurred, with generally encouraging results. Thus, Langenecker and Jones (1973) did early work in bending as shown in Figure 14.32a. Devine and Krause (1981) modified a wedge-reed ultrasonic welder to study the bending of Ti, stainless steel, and Ni. It was found that ultrasonic forming offered advantages over conventional forming of Ti, in that no preformed steps were required. No advantages were found in ultrasonic forming of Ni and stainless steel.

Ibrahim and Sansome (1983) examined the draw bending of tubes, with the intent to determine the role of friction in the process. A schematic of the apparatus is shown in Figure 14.32b, where a three-transducer array drives the coupling horn and mandrel, with the tube being pulled over the curved mandrel end to create the desired bending. Load cells permitted measurement of the bending torque and the axial mandrel force. Bending was done on mild steel tubing having different diameter-to-thickness

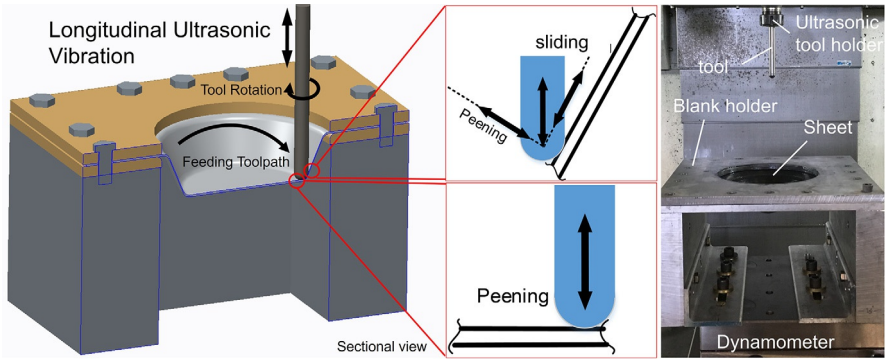


FIGURE 14.30 Schematic illustration and actual setup of the ultrasonic-assisted single-point incremental forming (SPIF) process. *(Modified from original Fig. 2 in Cheng et al., 2019.)*

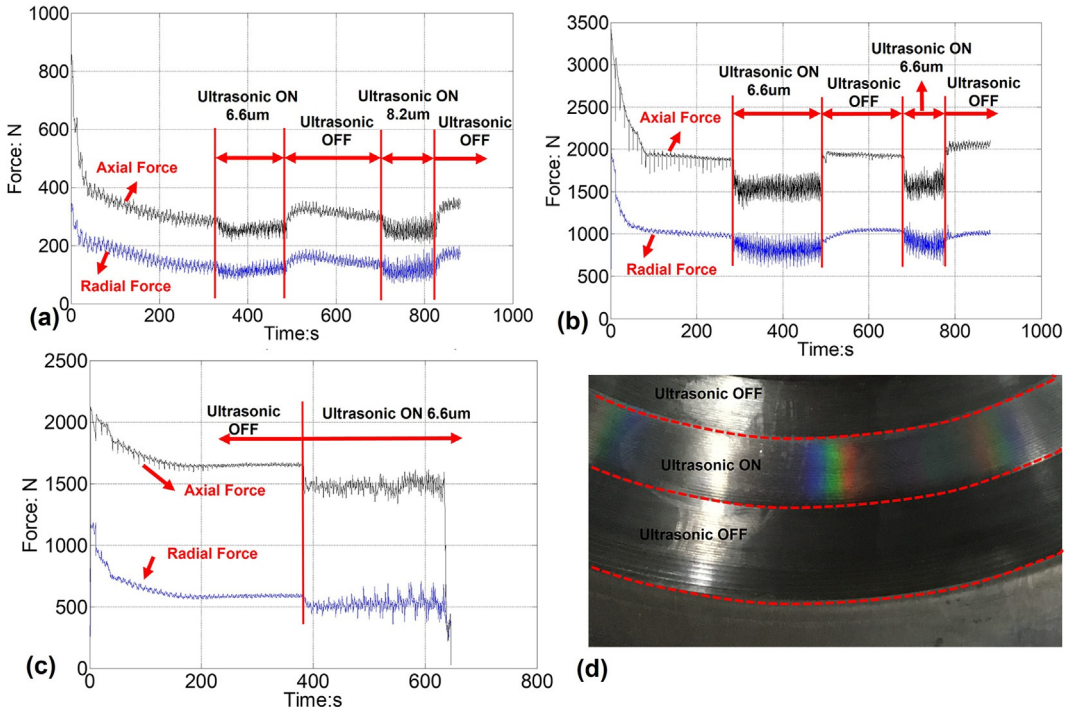


FIGURE 14.31 Forming forces during ultrasonically assisted TPIF for a 45° cone under different conditions: (a) Sheet: 0.5 mm Al2024; Squeeze factor: 30%; Step size: 0.25 mm; (b) Sheet: 1.6 mm Al7075; Squeeze factor: 40%; Step size: 0.25 mm; (c) Sheet: 1.6 mm Al7075; Squeeze factor: 40%; Step size: 0.5 mm; (d) Surface finish comparison corresponding to the forming condition in (b). *(Modified from original Figs. 9–11 Cheng et al., 2019.)*

ratios. The bending torque was reduced by up to 30%, for higher vibration amplitude, as were the outer surface strains.

Tsujino et al. (1991, 1993a, b) examined the effect of ultrasonics on the bending of 2- and 3-mm aluminum plates where both punch and die could be activated—the punch at 19 kHz and the die at 27 kHz—as shown in Figure 14.33a. A number of beneficial effects were found, reduced springback, as shown in Figure 14.33b, being one. The effects of ultrasonic punch alone, ultrasonic die alone, and combined punch and die showed the ability to decrease springback to zero. Other benefits were found to be an improvement in surface conditions, with decreased hardness and more uniform elongation along the bending surface.

The field of ultrasonic bending, of the type discussed in the foregoing section, has not been especially active in recent years (e.g., since the 1st edition), but will be briefly summarized in the following. A note will first be taken of an earlier work not covered in the 1st edition, that relates to the "classical" ultrasonic bending, as reviewed in the foregoing sections. Thus, Kosuge (2011) applied vibrations to bending of 50 and 100 μm stainless steel foils, using the setup and die/punch as shown in Figure 14.34. The approach is similar to that of Tsujino et al. (1993b) described above. However, Kosuge/Yang studied several vibration frequencies, 1570–9410 Hz (thus, not actual ultrasonic) at various amplitudes and durations. Results indicated that the springback ratio was reduced at the higher operating frequencies.

Yuhara et al. (2012) investigated the draw bending of tubes using an ultrasonically activated plug, as shown in Figure 14.35, where the plug is seen inserted into the bending location (left) and a bending torque then applied (right) to create a 90-degree bend. While the concept of an ultrasonically activated plug has been reported for use in tube drawing (e.g., Buckley and Freeman (1970), its use in tube bending appears new. The results for making two bends are as shown in Figure 14.36, where the plug load forces are seen to be significantly reduced, for both bends No. 1 and 2, under the effect of ultrasonics. Improvements in accuracy were also noted.

There has been a significant body of work by Zhang et al. (2018, 2019a, b, c, 2020) on the effects of ultrasonic surface treatment, referred to as "ultrasonic peening," on the bending behavior of thin sheet materials. However, a close review shows that the bending process is not itself ultrasonically driven but is conventional in nature, while the ultrasonics—through the surface treatment—is used to alter the material properties of the sheet metal to be processed. Thus, the technology is similar (if not identical) to that described in Chapter 14, Section 14.6.5. This is best illustrated by the recent result of Zhang et al. (2020), with this work being extensively backed up by the previously cited references.

The basic peening concept is that of conventional shot peening. The equipment of ultrasonic peening (UP) is

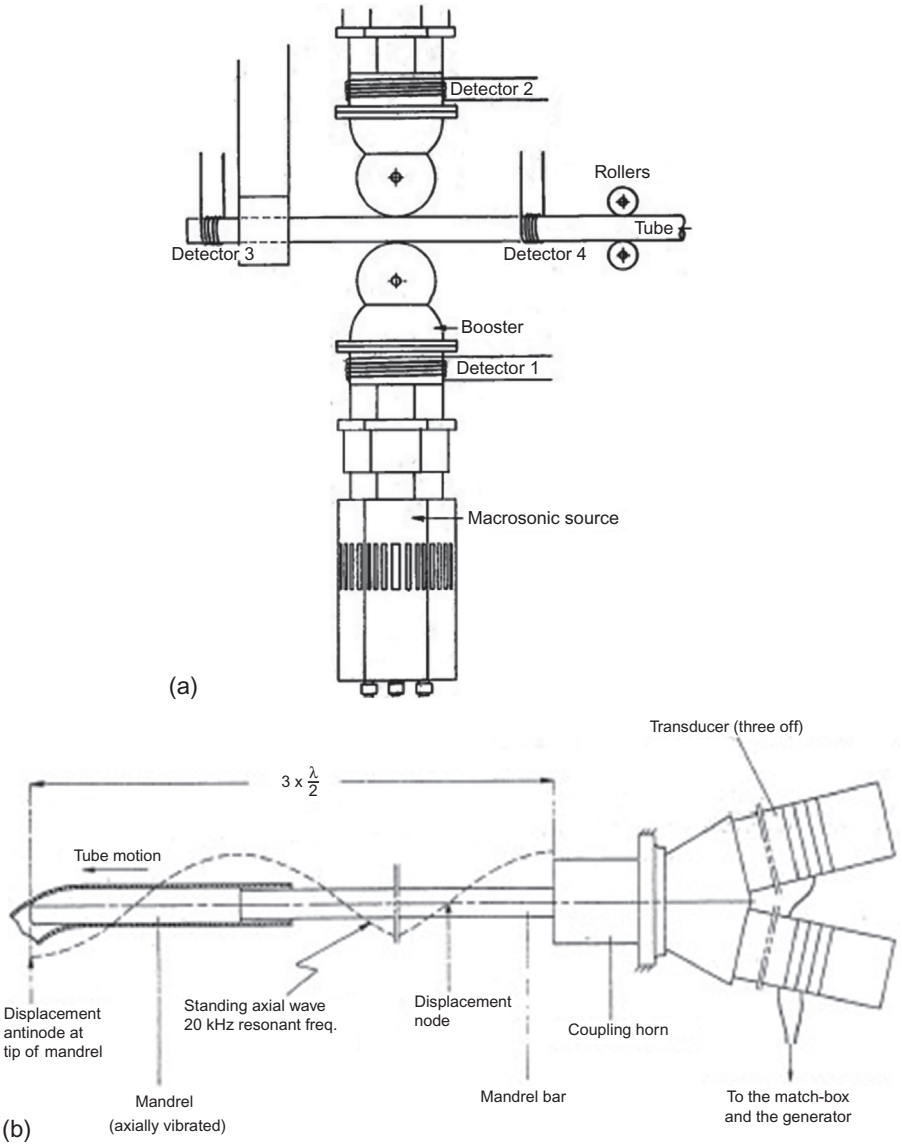
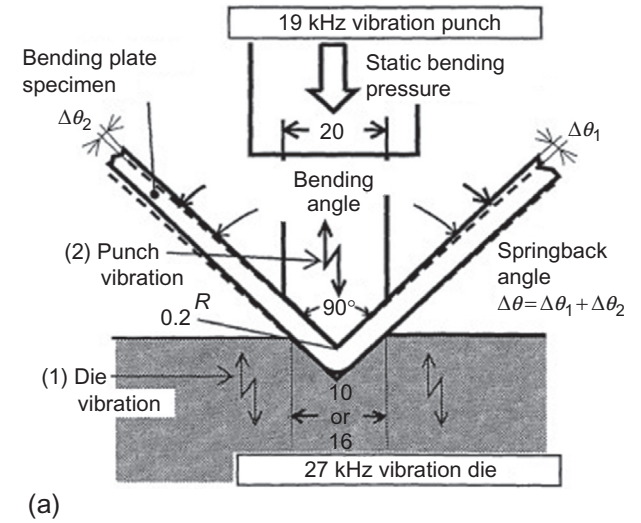


FIGURE 14.32 Ultrasonic bending. (a) Macroscopic tube bending system (Langenecker and Jones, 1973, Fig. 8) and (b) ultrasonic draw bending of tubes (Ibrahim and Sansome, 1983, Fig. 4).

shown in Figure 14.37, where the effect of the ultrasonic vibration of the tool is to cause the tool tip, referred to as the firing pin, to repeatedly impact the material surface (in a manner similar to that noted in Chapter 14, Section 14.6.5). Through control of vibration amplitude, varying tool tip impact velocities (referred to as firing pin velocity) are achievable. Stiffened 2024-T351 aluminum alloy plates, shown in Figure 14.38, were subject to UP treatment of various amplitudes and directions over the plate chord and span, including the plates being either freely supported or clamped. One, of many results, is shown in Figure 14.39 and illustrates the effect of UP on chord and span curvatures when subjected to chord- and spanwise peening directions. The critical effect of increasing ultrasonic amplitude (i.e., firing pin velocity) is clearly evident. The UP process also resulted in more uniform surface morphology and greater total depth of compressive residual stress.

14.4 Forging and extrusion

The forging process consists of deforming a volume of material by a punch in order to fill a cavity (closed die) or conform to the shape of a punch (open die), while extrusion consists of compression of a confined billet by a punch, forcing the billet material through a die opening (Altan et al., 1983). It will be found that most ultrasonic forging studies have looked at the upsetting of simple cylindrical shapes to better understand the materials' behavior (several such studies were referenced in Chapter 14) than



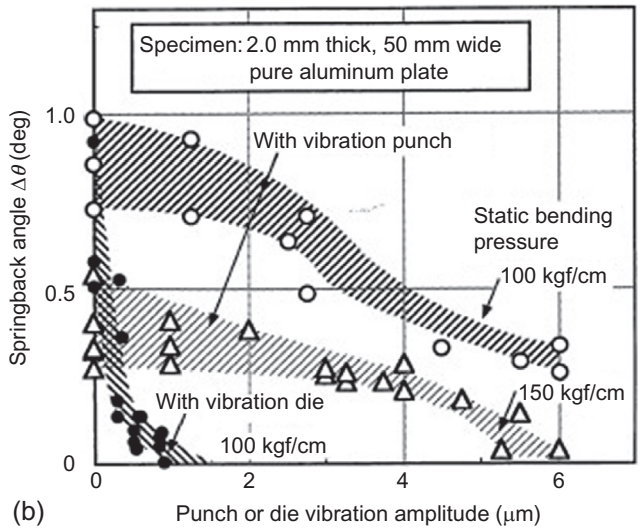
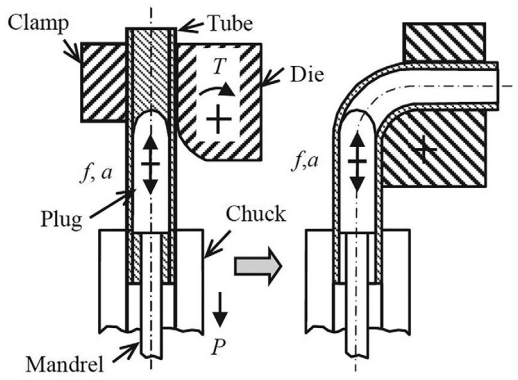


FIGURE 14.33 Ultrasonic bending work by Tsujino et al. (1993b). (a) Anvil and punch for a 90° bend (Fig. 1) and (b) relation of vibration amplitude to springback (Fig. 4).



f: frequency, a: amplitude, T: bending torque, P: plug axial load

FIGURE 14.35 Tube draw bending method with ultrasonic vibration plug (Yuhara et al., 2012, Fig. 2).

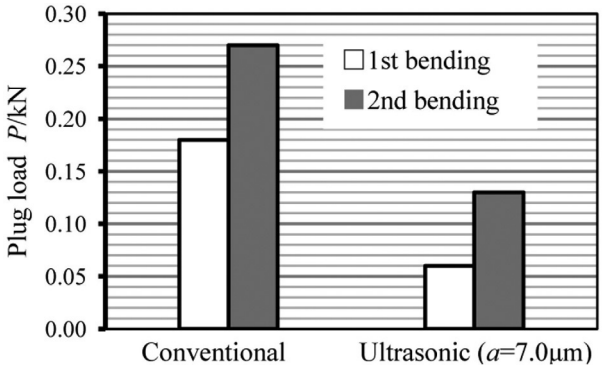
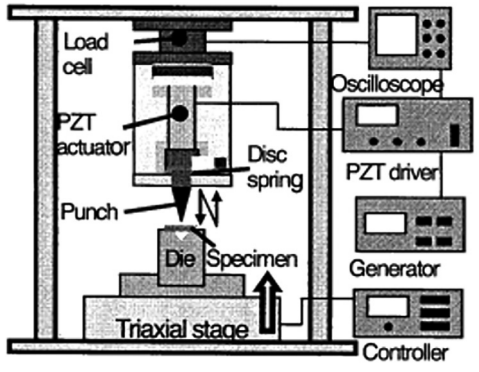


FIGURE 14.36 Comparison of conventional and ultrasonic axial loads, 1st and 2nd bends for carbon steel tube STKM11 ($a = 0$ to peak vibration amplitude) (Yuhara et al., 2012, Fig. 11a).



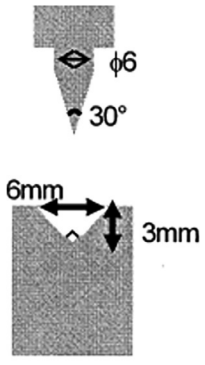


FIGURE 14.34 (a) Experimental ultrasonic bending setup. (b) Punch-die dimensions (Kosuge, 2011, Figs. 1 and 2).



FIGURE 14.37 (a) Ultrasonic peening (UP) system. (b) UP head and tool tip detail (Zhang et al., 2020, Fig. 4).

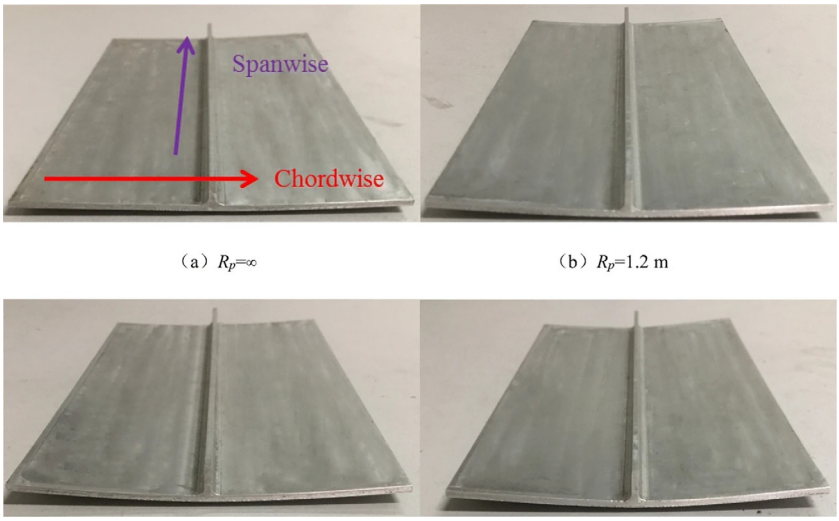


FIGURE 14.38 Stiffened 2024-T351 aluminum alloy plates under different prebending curvatures: (a) $R = 888$, (b) $R = 1.2$m, (c) $R = 0.8$m, (d) $R = 0.4$m (Zhang et al., 2020, Fig. 10).

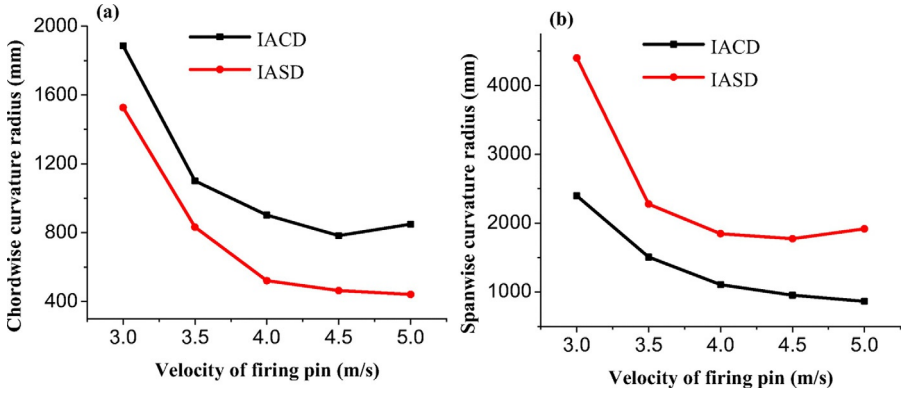


FIGURE 14.39 Effect of peening path on (a) chordwise curvature radius, (b) spanwise curvature radius (Zhang et al., 2020, Fig. 7).

for forging practical shapes. While such studies are important, they are generally not directly applicable to industrial forging processes.

14.4.1 Early developments

Forging and extrusion were among the topics at the previously cited 1963 U.S. Navy-sponsored symposium, where Aeroprojects reported on extruding lead and aluminum and extrusion cladding of aluminum onto steel tubing. The work of Kristoffy et al. (1965) and Kristoffy (1969), also cited on material properties and deep drawing work, carried out compression tests applicable to forging. Tests were on Al 1100 and involved upsetting cylindrical and tubular specimens, similar to that of Severdenko and Klubovich (1961) and Izumi et al. (1966a, b). It was observed that there were "apparent force reductions" with ultrasound, being noted that instrumentation frequency limitations were believed responsible for such apparent reductions. Balamuth, previously noted for his semitechnical articles, reported on forging applications (Balamuth, 1965a, b), including speculations on a "giant" sonic forging press that, along with a widely circulated trade magazine article, did not assist the credibility of the ultrasonic-forming field.

Severdenko and Klubovich (1965) then extended this work by measuring the deformation along the workpiece (copper and aluminum) during ultrasonic upsetting, using equipment as shown in Figure 14.40a, where the magnetostrictive transducer and transmission line (5, 4) drive the test specimen (1) via the flexible spring (2). The distribution of deformation along a Cu test piece is shown in Figure 14.40b, without (left) and with (right) ultrasound for differing degrees of deformation (noted by % notation; the "threads" are units of measure along the length). Deformation without

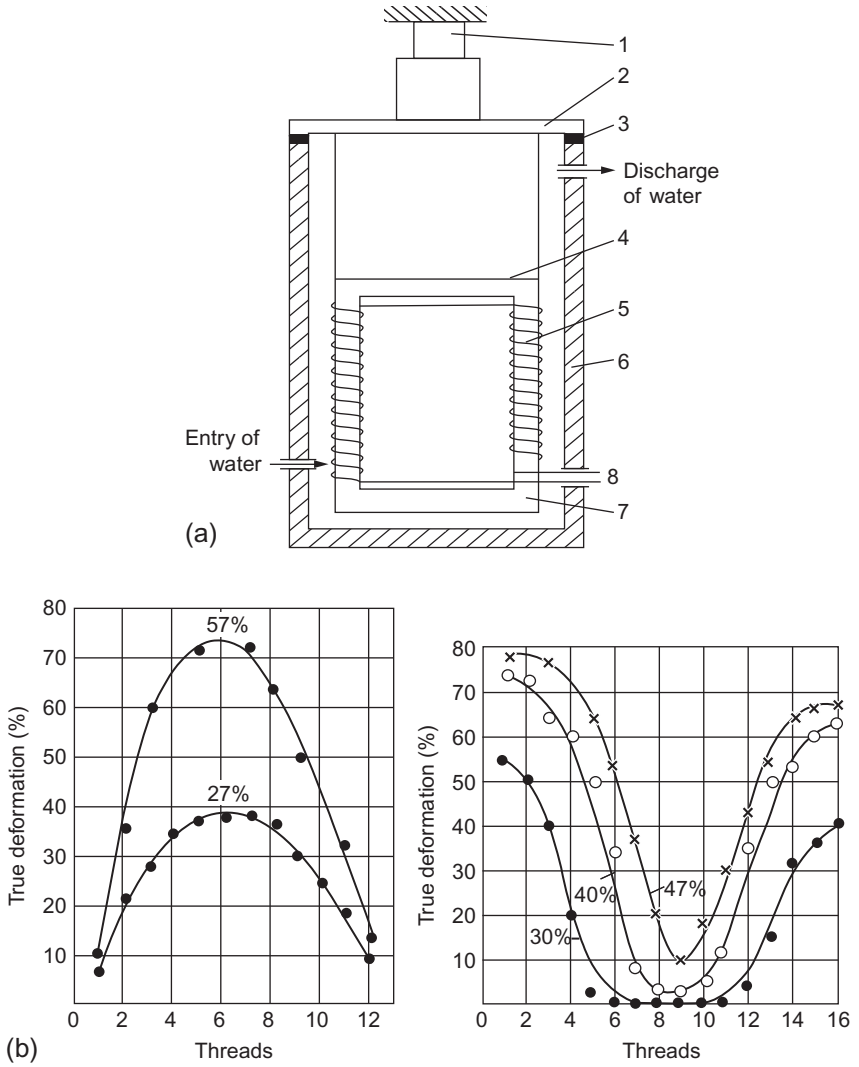


FIGURE 14.40 Ultrasonic upsetting by Severdenko and Klubovich (1965). (a) Experimental apparatus for upsetting specimen 1 (Fig. 1) and (b) distribution of deformation along the specimen without ultrasound (left) and with ultrasound (right) (Fig. 2).

ultrasound was quite uneven as was deformation with ultrasound, with the latter being the reverse of the no-ultrasound case. Likewise, the distribution of microhardness along the specimen reversed with ultrasonics, having a maximum at each end and reaching a minimum in the middle.

Zalesskii and Mishchenkov (1969) examined two configurations of an extrusion system, Figure 14.41a, that on the left (Figure 14.41a) where the die is at the displacement antinode, and on the right (Figure 14.41c) with the die at the node. The extrusion of lead permitted visualization of the flow field (Figure 14.41b), where Figure 14.41a is without ultrasound, Figure 14.41b using the antinode die location, and Figure 14.41c using the node location. Fracture occurred in Figure 14.41b while improved flow is evident in Figure 14.41c when compared without ultrasound. These benefits were attributed to friction reduction.

Again referring to the Meyer (1973) metal-forming process survey, 18 citations are found for forging, most having been noted in this chapter. Unique ones include Zhadan (1966) where from Meyer: "Experiments in upsetting heat-resistant steel specimens under 21-kHz vibrations showed reductions up to 15% in the deformation force. The effect was attributed to the superposition of dynamic force on the static force, which promoted the movement of dislocations and thus facilitated plastic deformation." Also, Abramov et al. (1971) on the use of ultrasound in metal forging: "A system was developed to deliver ultrasonic vibration to the punch, die, or container in direct forging of aluminum and to punch or reflector in reverse forging. Ultrasonic application reduced the overall compression force and increased homogeneity of the material, the effect becoming greater with increased

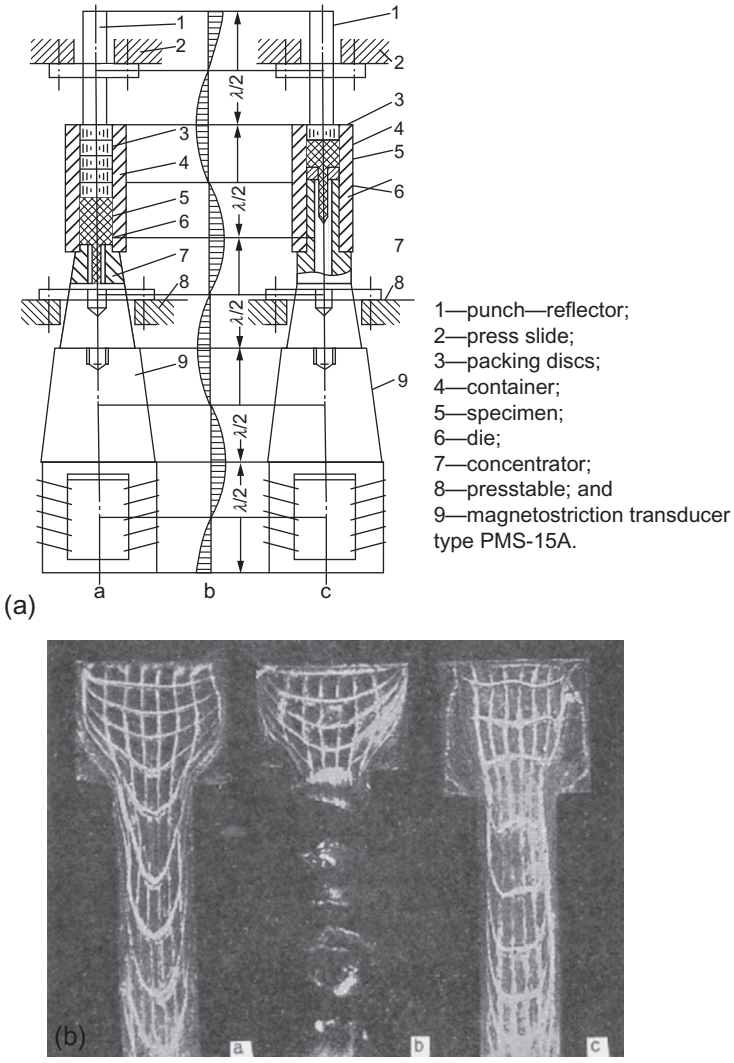
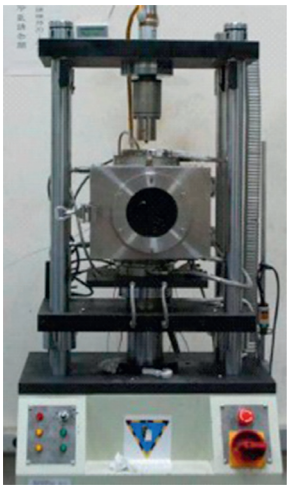


FIGURE 14.41 Ultrasonic extrusion work of Zalesskii and Mishchenkov (1969). (a) Extrusion with die at antinode (left) and node (right) (Fig. 1) and (b) extruded specimens without (left) ultrasound and with (right two) ultrasound, different die locations (Fig. 3).

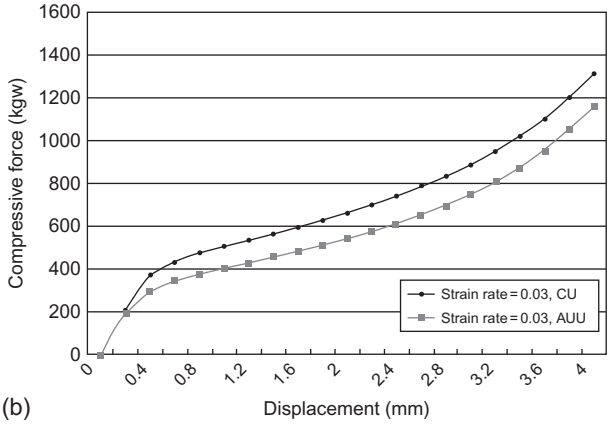
vibratory amplitude, with consequent lowering of surface friction forces. With reverse forging, activation of the punch was most effective."

14.4.2 Developments—2000 onward

Following a period of few forging/extrusion publications, several have appeared since 2000. Thus, in Hung and Hung (2005), ultrasonic hot upsetting of Al 6061 was examined at different temperature and strain rate conditions, comparing the extrusion force to that of conventional upsetting. Using the apparatus of Figure 14.42a, tests were run at different temperatures, with the axial ultrasonic vibration upsetting (AUU) compared with conventional upsetting (CU) results, of which Figure 14.42b for 200°C is a representative of the data. A force reduction of approximately 15% at maximum deformation is seen. The authors felt that the force reduction was not explained by frictional effects, stress superposition, or dislocation energy absorption, with further work required.



(a)



(b)

FIGURE 14.42 Ultrasonic hot upsetting work of Hung and Hung (2005). (a) Ultrasonic hot upsetting equipment (Fig. 1) and (b) load-displacement curves on Al 6061 at 200°C (Fig. 4).

In later work, Hung et al. (2007), using a ring compression test, examined friction effects on forging, with temperature measurements also being made. One result was the apparent increase of interface friction under ultrasonic vibrations. In a more extensive study of friction effects, Hung and Chiang (2009) applied ultrasonics to a new type of test, this being the double-cup extrusion tests (DCET) modified for ultrasonics, which was felt better suited to forging forces and deformations. Results showed that the ultrasonic DCET showed lower extrusion forces compared to the conventional test. The possibility of specimen heating under ultrasonic vibrations, thus changing material properties, was recognized as a possible cause. A later study by Hung and Huang (2012/2013) confirmed that ultrasonics resulted in increased friction for this type of test.

FEA methods were used by Akbari Mousavi and Feizi (2005) to study the ultrasonic extrusion process, comparing the results to the conventional extrusion of an annealed steel. As with many ultrasonic processes, the analysis showed the existence of a critical velocity, corresponding to the local ultrasonic velocity approaching the extrusion velocity. At low velocities, extrusion force reductions of 30% were possible but rapidly diminished at half the critical velocity or higher. If extrusion velocity was below the critical velocity, die separation would occur, resulting in a cyclic, impulse effect. Later, Akbari Mousavi et al. (2007) confirmed the importance of the critical velocity issue in reducing the extrusion force. The analysis also confirmed the importance of friction in the process. In an effort to apply advanced modeling techniques, in this case of artificial neural networks, Pazand and Feizi (2011) built on the preceding work to analyze ultrasonic extrusion. The method of validating the neural network results was to compare them to the previous FEA of the process.

Liu et al. (2012) modeled the wave propagation dynamics of a forging test, including variations in friction and the potential for die separation, with the latter leading to distinctly different deformations and stress distributions in the forged specimen, as shown in Figure 14.43. In later work, Liu et al. (2013) examined both theoretically and experimentally the ultrasonic upsetting of a cone-shaped copper indenter pressed against a hardened surface.

Rosochowska and Rosochowski (2007) did an FEA-based analysis of the ultrasonic extrusion process, using the model as shown in Figure 14.44a, with the ultrasonic vibrations applied to the Al sample in two ways: in Figure 14.44a (left), the punch applied a prescribed motion at the top of the sample, while the die moved at a prescribed velocity; in the model of Figure 14.44a (right), the punch was a component of the vibrating transmission line having a prescribed force applied to the top and mounted at the node with an elastic support, and with the total system vibrations being considered. The material was modeled with a Huber-Mises yield criterion.

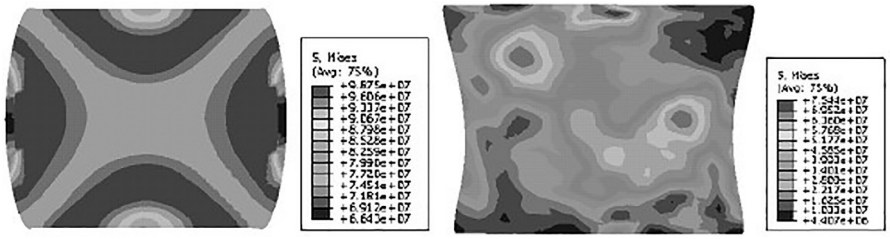


FIGURE 14.43 Differences in deformation and stress (gray patterns) of forged specimens: with (left) and without (right) ultrasound (Liu et al. 2012, Fig. 4C and D). *(Source: From Liu et al. (2012, C.E. Suarez, ed., p. 264, Fig. 4). The Minerals, Metals, & Materials Society. Reprinted with permission.)*

The results for the rigid vibrating punch for the case of a die (i.e., process) velocity of 100 mm/s showed the predicted extrusion force to drop on applying ultrasonics, with a large oscillation in a peak-to-peak amplitude. The greatest effect was seen to occur for low-die velocities, e.g., a 60% drop at $V = 20$ mm/s, tapering off to about 11% at $V = 500$ mm/s. The matter of ultrasonic velocities relative to process velocities, and "critical velocities," found in other ultrasonic processes, continued to apply. An evaluation of friction effects was done, which found that extrusion force reduction

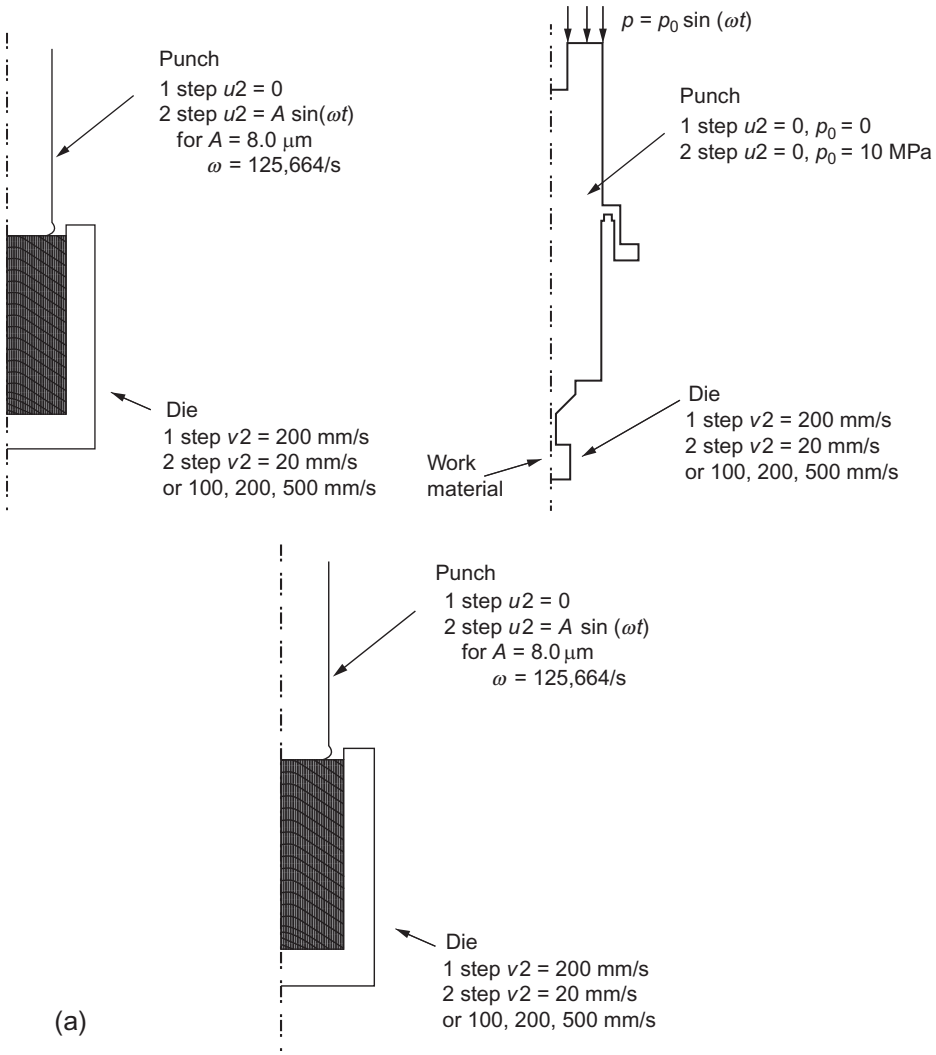


FIGURE 14.44 Ultrasonic extrusion analysis of Rosochowska and Rosochowski (2007). (a) FEA model for a rigid tool (left) and elastic punch (right) (Fig. 1).

diminished when friction was accounted for. A more elaborate analysis of the process, involving the total elastic vibrations of the transmission line including losses in the line, showed how the extrusion process loaded the vibrating system, causing an expected reduction of punch amplitude.

Building on earlier work on material properties of (see Chapter 13, Aziz and Lucas, 2010a, b; Daud et al., 2007), Lucas and Daud (2009) used FEA modeling of the extrusion process where the cases of longitudinal and radial vibrations of the die were considered. The case of force versus plunger displacement for radial die oscillation at a velocity below the critical velocity was obtained. Observations included confirmation of the importance of operating below the critical velocity for effective extrusion and ultrasonics does in fact lower the mean extrusion forces, although the peak forces are not changed. Further, a reduction in the coefficient of friction had a strong influence on ultrasonic effects, although friction changes alone may not explain measured data.

After reviewing the past work on ultrasonic deformation processes, Siddiq and El Sayed (2012) undertook the development of a "variational porous metal plasticity" model, modifying modeling efforts of others to account for ultrasonic material effects. Then, using ultrasonic material data reported by others, for example, Daud et al. (2006), the model was applied to sheet metal forming, using data of Ashida and Aoyama (2007); ultrasonic upsetting, using the data of Hung and Hung (2005); and ultrasonic wire-drawing, using the data of Murakawa and Jin (2001). The role of ultrasonics in reducing the forming forces and friction in each was demonstrated.

Note should be made to the work of several investigators, for example, Liu et al. (2012), Suh et al. (2007), and Zheng et al. (2011), that is labeled as forging, upsetting, or rolling, but that is actually a surface treatment technology that will be discussed in Section 14.7.

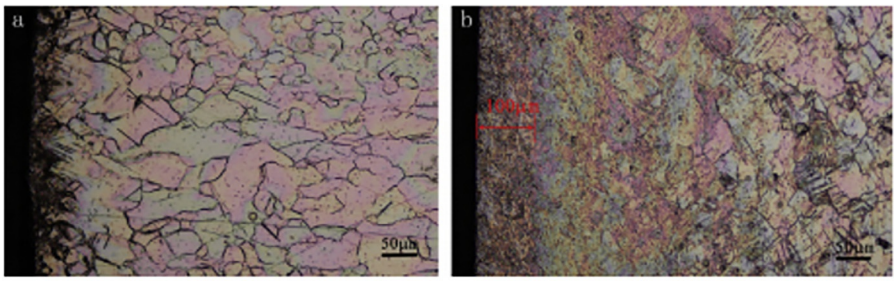
In recent years, there has been a transition in the terminology for the ultrasonic forging process, as described in the preceding, to that of "ultrasonic cold forging," which is fundamentally based on ultrasonic surface treatment as described in Section 15.7. Thus, the focus is on surface/subsurface property modification versus bulk deformation associated with "traditional" ultrasonic forging. With this awareness, the review of recent developments in ultrasonic (cold) forging will be continued.

Abbasi et al. (2016) summarize ultrasonic cold forging technology (UCFT) as a mechanical process used to improve material surface characteristics by the continual striking of the tool. A UCFT tool system was illustrated with an extensive description of system components being given, including the FEA-based design of the ultrasonic tooling, as well as modeling of the tool material deformation and stresses. The effect of UCFT on hardness profile showed an increase in surface hardness from 55 to 64 HRC but diminishing with depth such that at 150 μm or greater, there is little difference from the nontreated material. An improvement in surface smoothness was also measured.

Various additional aspects of the UCFT process have been reported. Thus, Chen et al. (2015) discussed the effect of UCFT on a calcium phosphate coating onto the AZ318 magnesium alloy by a micro-arc oxidation (MAO) process, noting the effect on the microstructure, as shown in Figure 14.45. Gu et al. (2016) used UCFT as a pretreatment to study the effect of surface nanostructure of Al 2024 on the corrosion performance of MAO coating. It was found that UCFT treatment decreased the surface roughness and refined the grain size of the surface layer. The pore size of the MAO coating was reduced and the density increased, as was the microhardness. The corrosion resistance of the UCFT-MAO samples was significantly increased, as shown in Figure 14.46, where the corrosion damage level of the uncoated sample, Figure 14.46a and b is much higher than that of the MAO-coated sample, Figure 14.46c and d.

Narkevich et al. (2016) studied the effects of UCFT (identified simply as "ultrasonic forging" in the paper) on the properties of a nitrogen austenitic steel and found a transformation of the structure to one with a high concentration of stacking faults. After treatment, the nitrided steel exhibited enhanced strength properties with a retained high plasticity.

With the intent of improving the properties of parts formed by additive manufacturing, Sun et al. (2019) applied



(a) (b)

FIGURE 14.45 Metallographic structure of (a) Untreated Mg alloy and (b) UCFT treated Mg alloy (Chen et al., 2015, Fig. 1).

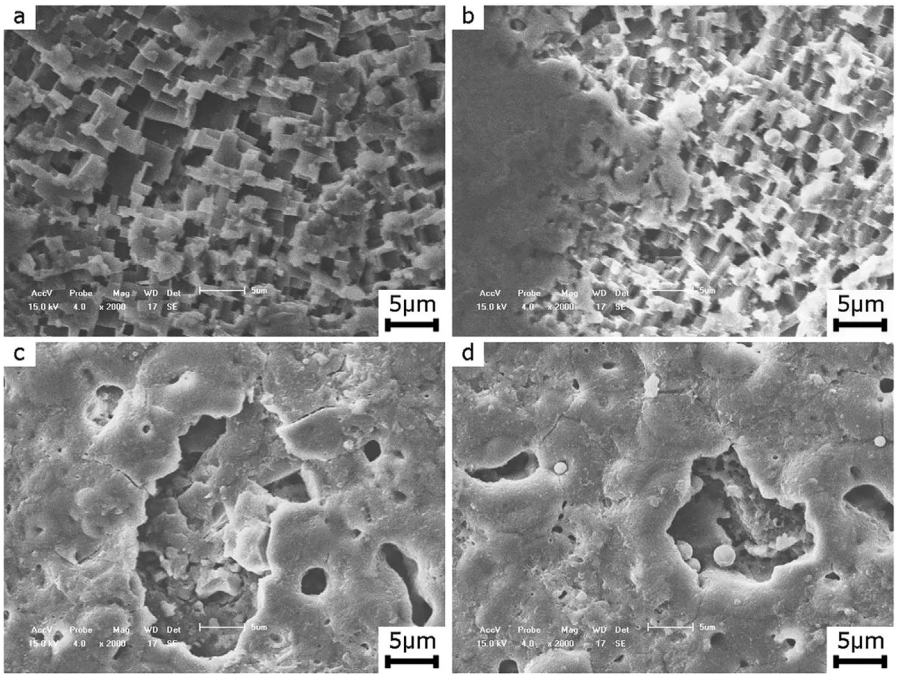


FIGURE 14.46 Postcorrosion SEM images of the samples: (a) Untreated, (b) UCFT only, (c) MAO only, and (d) UCFT-MAO (Gu et al., 2016, Fig. 10).

ultrasonic microforging to 304 stainless steel fabricated by the wire and arc additive manufacturing (WAAM) process. The microstructure of the WAAM material with and without ultrasonic microforging was compared for treatments of 1, 2, and 3 min. While only a slight effect was seen after 1 minute of treatment, progressive modifications to the microstructure were observed for longer treatment times. A 75% improvement in hardness was measured, with microforging effects reaching a depth of 1 mm.

Ye et al. (2020a, b) studied the combined effects of ultrasonic microforging technology (UMFT) with laser metal wire deposition (LMwD) on the mechanical properties of Ti-6Al-4V. An overall schematic of the experimental equipment is shown in Figure 14.47a, with a detailed UMFT/LMwD interaction zone as shown in Figure 14.47b. The effects of ultrasonic amplitude and forging force on surface roughness was studied with results shown in Figure 14.48 with a general reduction in surface roughness observed. The figure also shows modification in grain structure for the various levels of force/amplitude. It was found that force had a greater effect than amplitude as to depth of change in material properties while amplitude had a greater effect on grain refinement and hardness. While improvements in surface and microstructure were seen, some cases of pores or cracking were observed. Other researchers that have recently contributed to the microforging field include Sun et al. (2019), Zhai et al. (2019), and Presz (2020).

14.4.3 Further developments in ultrasonic extrusion

A note is made of the work of Adam and Stan (2013) on ultrasonic extrusion and injection molding. While focused on polymer processing, it reviews a wide body of work that

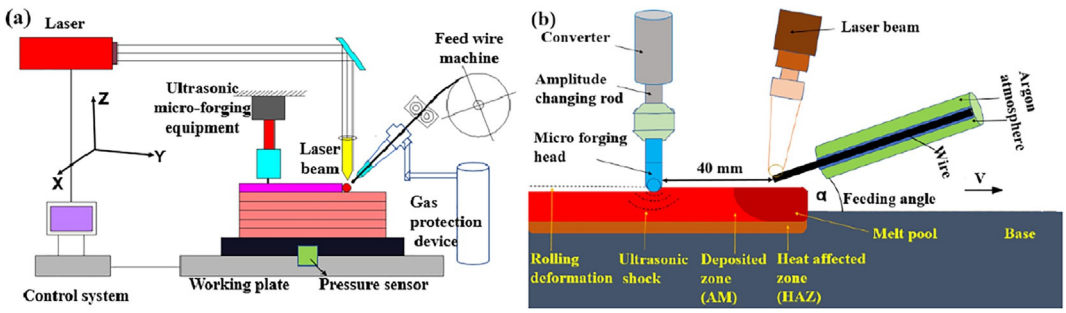


FIGURE 14.47 Equipment for the LMwD/UMFT process: (a) Overall schematic. (b) Detail of the LMwD/UMFT interaction zone (Ye et al., 2020a, b, Fig. 1).

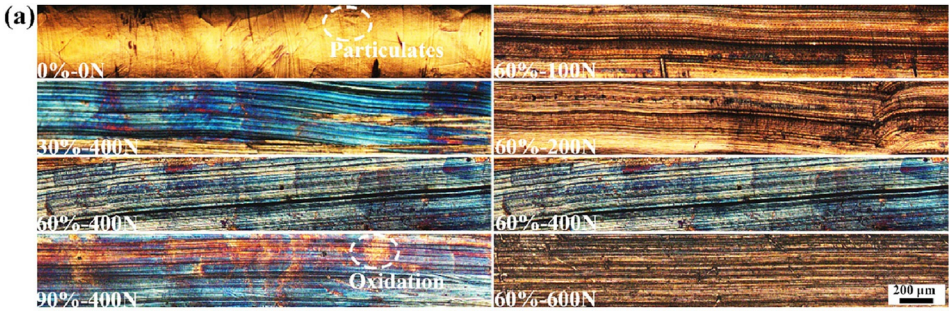


FIGURE 14.48 LMwD/UMFT bead surfaces for various UMFT ultrasonic powers (%) and forces (N) (Ye et al., 2020a, b, Fig. 4a).

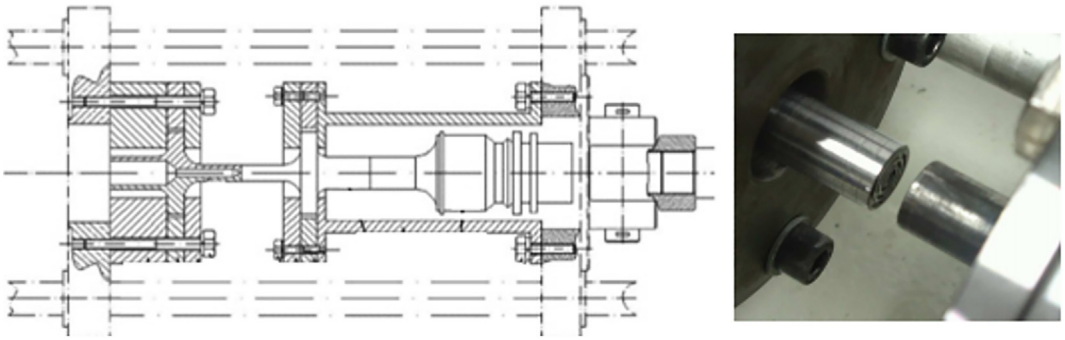


FIGURE 14.49 (a) Experimental system for ultrasonic extrusion and injection. (b) Spiral channel at the front of ultrasonic horn (Adam and Stan, 2013, Figs. 3 and 4).

has emerged in that field, including the author's earlier work that identified a "thermo-pellicular" effect relating to surface effects under ultrasonics. Using equipment as shown in Figure 14.49a, including a special extrusion port, Figure 14.49b, tests were conducted comparing the ultrasonic process with conventional extrusion for common polyolefins (LDPE, PP) with it being found that the ultrasonic process assisted in temperature and pressure reduction, although the effects were less pronounced under thin-wall injection and microinjection.

Hu et al. (2013) reported on the design of an "ultrasonic vibration extrusion system," Figure 14.50a. While an acoustic analysis of the ultrasonic unit is provided, Figure 14.50b, a careful review of the proposed process shows it to be basically one of the surface treatments, as has been reviewed in Section 15.7.

Bagherzadeh et al. (2016) applied ultrasonic vibrations to the conventional equal channel angular extrusion (CECAE) process, resulting in a hybrid process, ultrasonically assisted extrusion (UAE), as shown in two

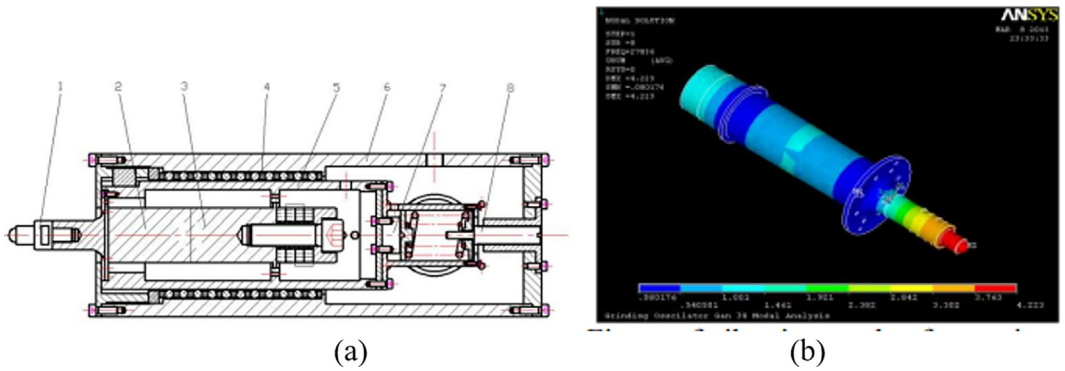


FIGURE 14.50 (a) Schematic of ultrasonic vibration extrusion system; 1-extrusion tool, 2-amplitude transformer, 3-piezoelectric transducer, 4-ball retainer, 5-inner sleeve, 6-outer sleeve, 7-pressure screw. (b) Vibration mode of extrusion vibrator (Hu et al., 2013, Figs. 1 and 7).

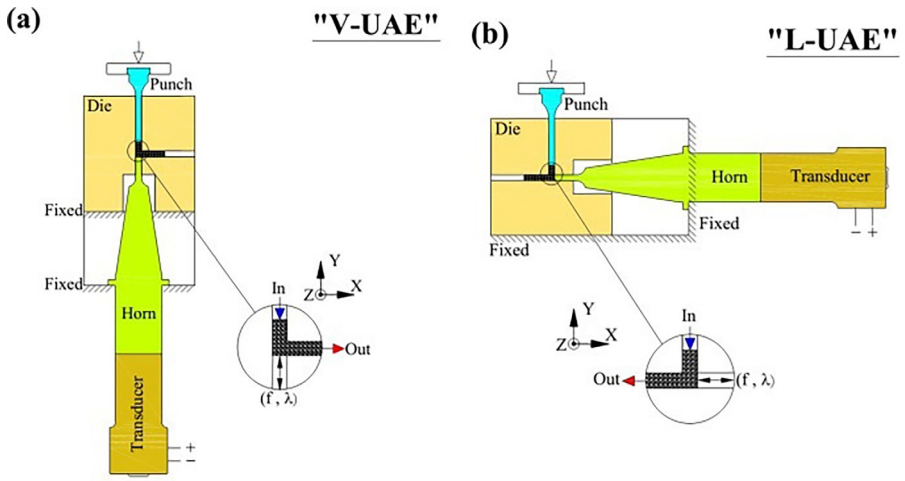


FIGURE 14.51 Schematic view of ultrasonic-assisted ECAE with: (a) Vertical vibration, V-UAE. (b) Lateral vibration, L-UAE (Bagherzadeh et al., 2016, Fig. 1).

configurations of Figure 14.51. The key to the process was to add a third channel to the usual two-channel CECAE process to permit the introduction of ultrasonic vibrations at the critical turning point of the die. This is shown in the green tooling of Figure 14.51 in a vertical (V-UAE) and lateral (L-UAE) configuration of the process.

The microstructure of samples after one pass of CECAE and UAE showed the formation of elongated grains. A lower angle of straining was seen in the UV direction, while a reverse was seen in the LU direction. In FE simulation of the process, Figure 14.52, it was found that the average values of equivalent plastic strain (PEEQ) for both VU @ 1.90, Figure 14.52c and LU @ 2.15, Figure 14.52b, were significantly higher than that of CE @ 1.14, Figure 14.52a. It was concluded that the UAE process resulted in finer grain structure and 30% lower loads as well as higher hardness values than CE.

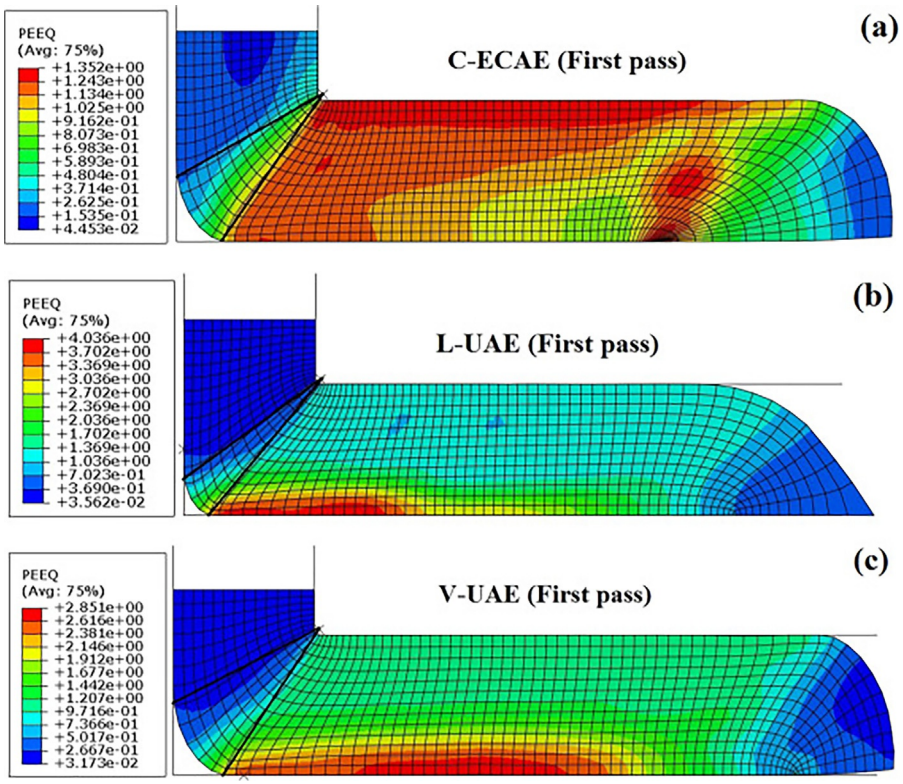


FIGURE 14.52 The distribution of PEEQ after one pass of: (a) CE, (b) L-UAE, (c) V-UAE simulations (Bagherzadeh et al., 2016, Fig. 3).

Razavi et al. (2017) applied ultrasonics to the equal channel angular extrusion (ECAE) process, whose severe plastic deformation is used to create micro- and nano-structure materials. While extrusion forces were found to be decreased with ultrasonics, there was little difference noted in stress and strain contours between the conventional- and ultrasonic-assisted processes as seen in Figure 14.53. This was attributed to equipment power limitations, it being either necessary to lower extrusion velocity, or to increase punch vibration amplitude.

Wang and Yu (2018a, b) reported on ultrasonic-assisted ECAE for marine applications. In 2018a, they described the experimental system, as shown schematically in Figure 14.54. Noting the ability of ECAE to achieve a refined microstructure, it was shown that UAECAE further improved microstructure, as shown in Figure 14.55. Thus, the microstructure without ECAE is shown in Figure 14.55a, while Figure 14.55b and c show, respectively, the effects of the ECAE process alone and the ultrasonically assisted process. Reduced extrusion forces were observed with the ultrasonic process. In a continuation of their work, Wang and Yu (2018b) looked at the effects of ultrasonically assisted ECAE-UAECAE, using the setup as shown in Figure 15.64, on the friction and wear characteristics of extruded materials. The results showed that UA ECAE also assisted by heat treatment contributed to improving the friction and wear behavior of 65 Mn.

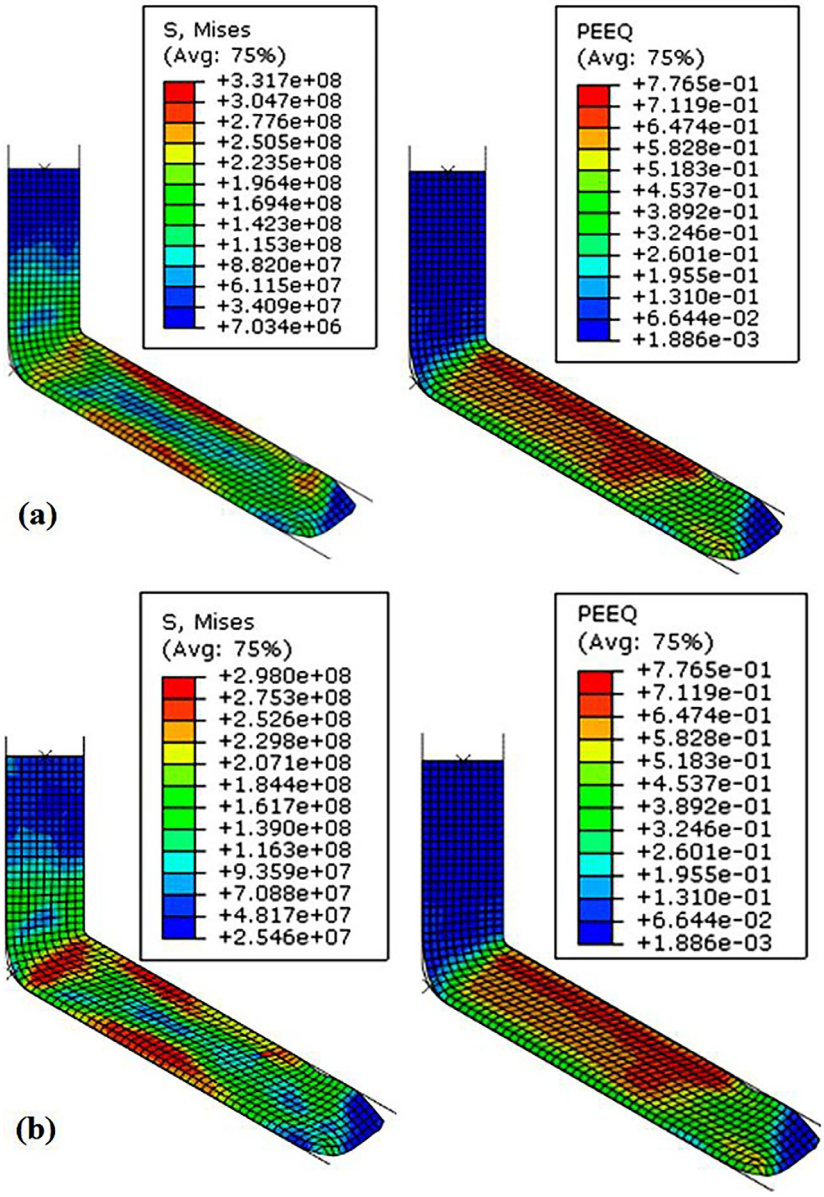


FIGURE 14.53 Stress and strain contours in (a) ECAE and (b) UAECAE (Razavi et al., 2017, Fig. 12).

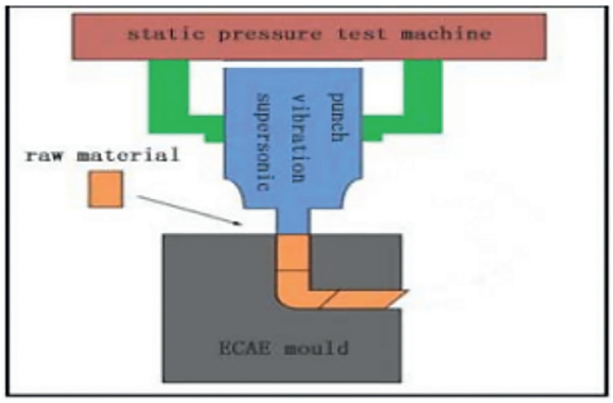


FIGURE 14.54 Schematic diagram of ultrasonic-assisted ECAE (Wang and Yu, 2018a, Fig. 1).

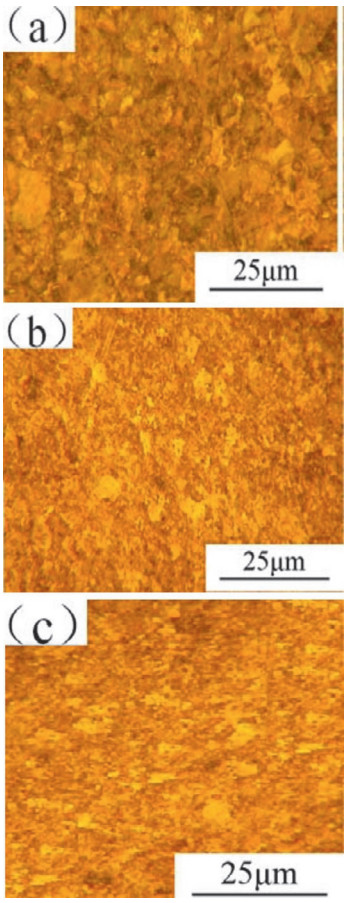


FIGURE 14.55 Microstructure of GCr15 steel: (a) Without ECAE, (b) with ECAE, and (c) with UAECAE (Wang and Yu, 2018a, Fig. 3).

14.5 Shearing and blanking

Shearing and blanking are cutting actions along a line or contour to separate a metal by two moving blades. It is typically an important component of sheet metal forming operations such as deep drawing and bending. The potential of applying ultrasonics to this process has been investigated

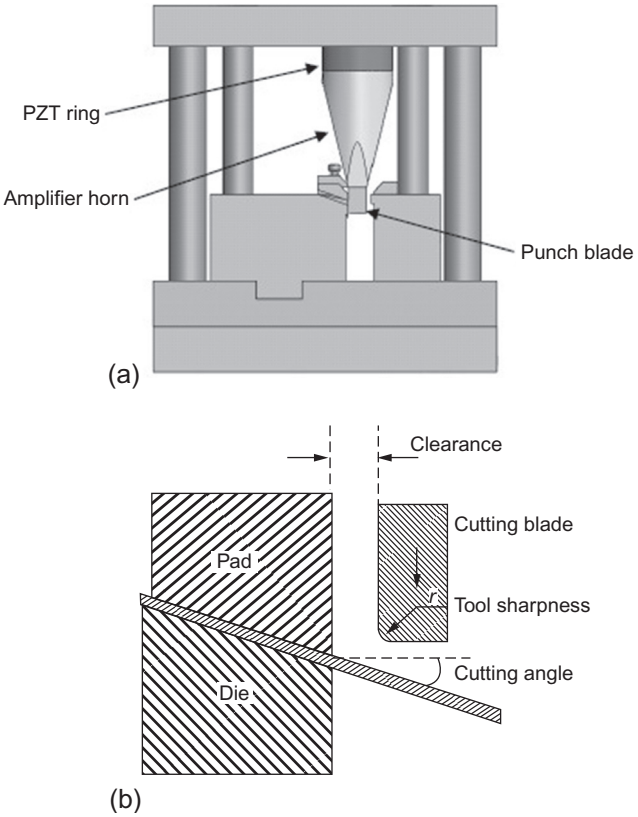


FIGURE 14.56 Ultrasonic blanking work of Yeh et al. (2011) and Yeh and Chu (2012). (a) Experimental blanking setup (Fig. 2a) and (B) blanking parameters (Fig. 2b).

by Yeh et al. (2011) and Yeh and Chu (2012), using the setup as shown in Figure 14.56a, with the local details of the interaction of the ultrasonically driven cutting blade with the sheet metal as shown in Figure 14.56b. The effects of ultrasonic vibration on the punch load, flow stress, and edge profile were studied, with the results compared to conventional blanking. The results showed ultrasonic vibrations reduced the punch load and improved the quality of the edge profile, with a particular note of reduction in burr height.

Liu et al. (2017a, b, c, d) applied ultrasonics to the fine blanking process that, while widely used in industry, can be degraded by edge rollover. The essential features of the process are shown in the shear zone, Figure 14.57a, where the ultrasonic activation is provided by the transducer/punch unit as shown in Figure 14.57b. The difference in rollover behavior between the conventional and ultrasonic processes is shown in Figure 14.58, showing an improvement in rollover with ultrasonics. Modeling of the process showed the difference in flow velocities between the conventional and ultrasonic processes at various times. Results showed the potential of ultrasonic vibrations to greatly reduce the rollover size.

Mita et al. (2018) developed the ultrasonic-assisted piercing system, shown in Figure14.59, to examine the

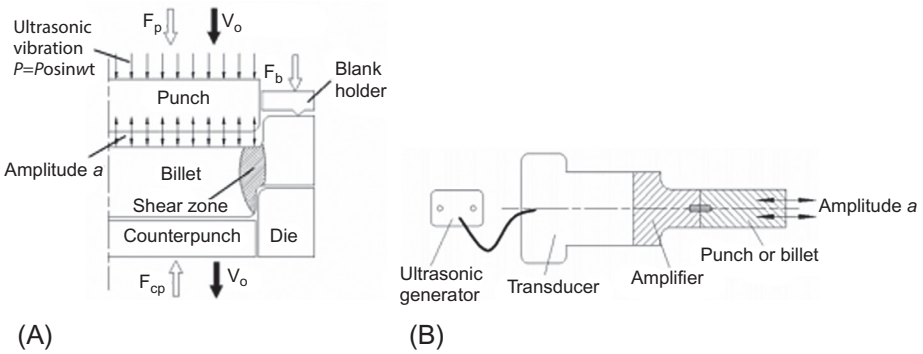


FIGURE 14.57 Ultrasonic-assisted fine blanking, (a) Shear zone of process. (b) Transducer-punch for system (Liu et al., 2017a, b, c, d, Figs. 1 and 2).

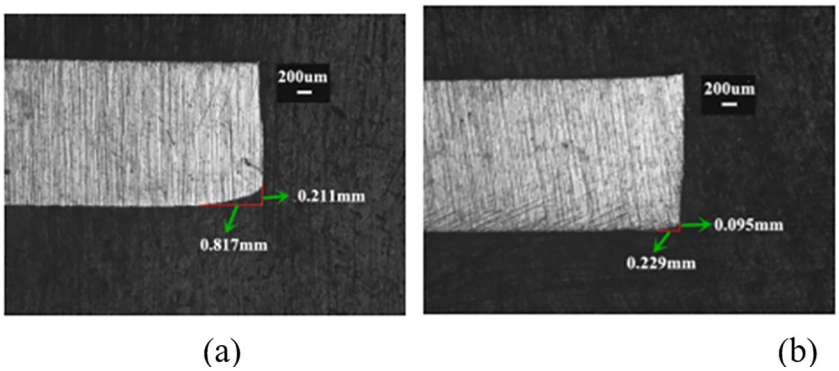


FIGURE 14.58 Roll-over size in: (a) Conventional fine blanking. (b) Ultrasonic-assisted fine blanking (Liu et al., 2017a, b, c, d, Fig. 14).

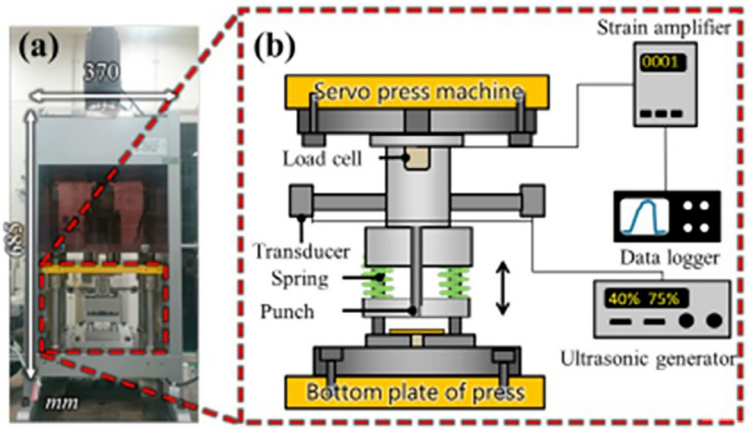


FIGURE 14.59 Configuration of ultrasonic-assisted piercing system: (a) Apparatus and (b) schematic (Mita et al., 2018, Fig. 2).

effects of varying ultrasonic amplitudes (0, 2.3, and 3.2 μm) on piercing SUS304 foils of two grain sizes, 9.0 and 1.5 μm. As shown in Figure 14.60a, there was little effect of ultrasonics on the shearing load for the large grain size, whereas the shear load was greatly reduced (approximately 60%) for the small grain size foil, Figure 14.60b. Cross sections of sheared foil edges of varied grain sizes and vibration amplitudes are shown in Figure 14.61 and showed increased burnished surface and reduced fracture surface with increasing vibration amplitude.

As with nearly every forming process considered in this chapter, there is a "microscale" component of the technology that has emerged as a nearly distinct part of the field, a situation that holds for shearling and blanking. Thus, works by Liu et al. (2017a, b) and Yang et al. (2019) fall in this category and are reviewed in Section 15.9.

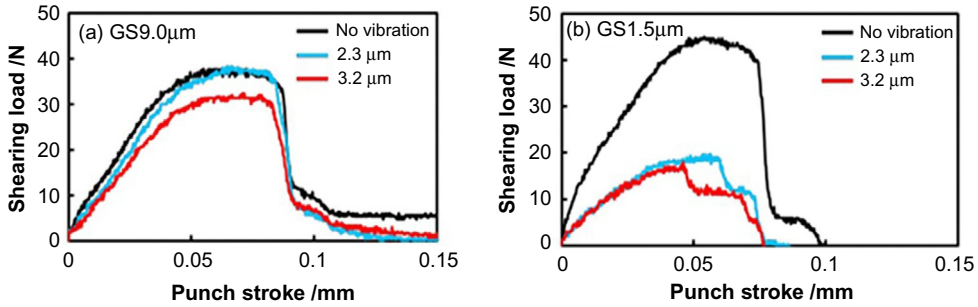


FIGURE 14.60 Load-stroke curves of specimens with different grain sizes: (a) Grain size 0.9 μm and (b) grain size 1.5 μm (Mita et al., 2018, Fig. 4).

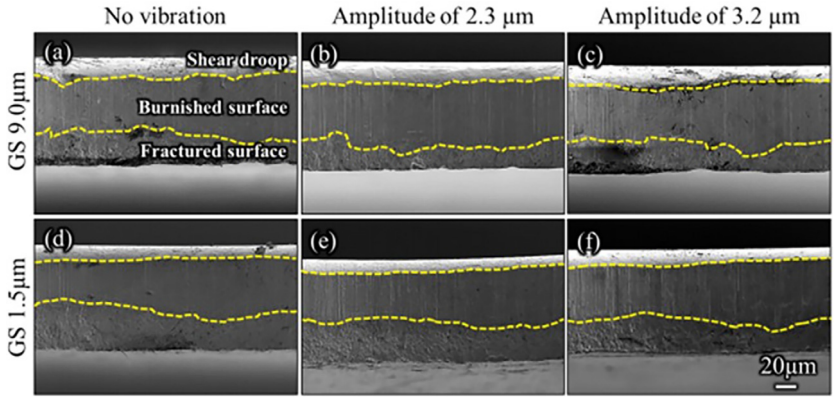


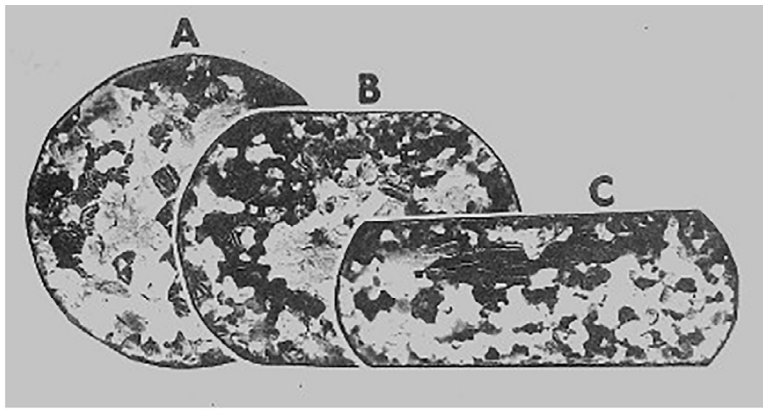
FIGURE 14.61 Cross sections of pierced specimens of different amplitudes and grain sizes (Mita et al., 2018, Fig. 6).

14.6 Ultrasonic rolling

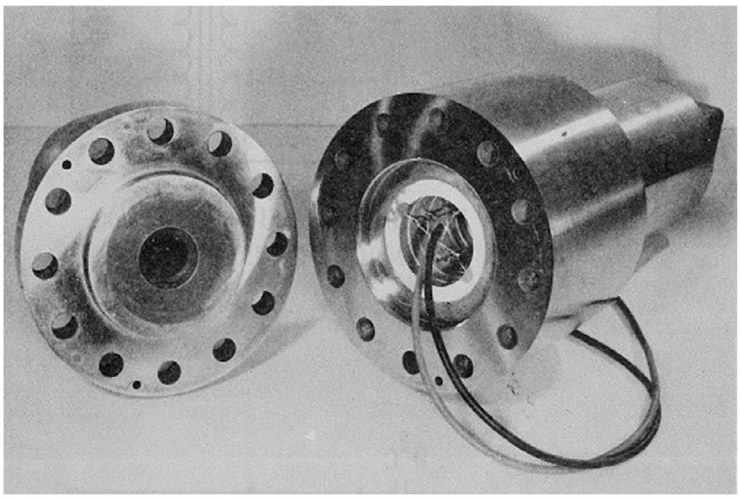
Rolling is a process for reducing the cross-sectional area of a sheet or plate by passing through rotating rolls (Altan et al., 1983). The application of ultrasonics to rolling received significant attention in the early years of ultrasonic metal forming, but with few recent developments. Early work at Aeroprojects was reported at the 1963 U.S. Navy conference with the microstructure deformation for various stages of rolling a 0.125 in. diameter zinc wire as shown in Figure 14.62a, where (B) is wire rolled without ultrasonics and (C) is with ultrasonics. Results were also reported on aluminum, copper, and steel.

The most significant early work was by Cunningham and Lanyi (1965) and Cunningham and Douglas (1966), who developed 8 in. (20.3 cm) diameter magnetostrictive and piezoelectric ultrasonic rollers, with tests showing the piezoelectric unit (Figure 14.62b) as superior. Rolling load reductions of greater than 50% were achieved on aluminum and lead at "light mill loads" but with reductions decreasing at higher loads. Load reductions became more pronounced on thinner gage materials, with this being interpreted as the effect of ultrasonics on reducing friction forces. In what is still the definitive work on ultrasonic rolling, Severdenko et al. (1972a, b) reviewed all aspects of the process. Various means of introducing ultrasonics into the rolled material were reviewed, concluding that oscillation of rolls is essential (versus vibrating the rolled material). Thus, various means of introducing torsional vibrations (Figure 14.63a) and a sliding contact (Figure 14.63b) are illustrative of many methods discussed. In Figure 14.63a, the torsional transducers (2) are (top diagram) supported at (4) with the maximum vibration amplitude at the antinode (3), where the rolled material is placed. In the middle diagram of the figure, the supports are at the antinode (4) with the two large-diameter rollers deforming the material (3). A highlight was the detailed illustrations of heavy-duty equipment for rolling, such as shown in Figure 14.64a. The complex system, involving two transducers, has the end result of forming the material at the vibration antinode (24). The scope of reported results is extensive, of which Figure 14.64b, showing the rolling of (a) steel, (b) copper, and (c) aluminum, is simply a representative. Thus, the data show the change in the rolling force (P, kg) for differing degrees of thickness reduction (ε_r, %), with 1—no ultrasound, 2—with ultrasound, and 3—n_p being the percentage reduction in rolling force.

In further articles, Severdenko et al. (1972b, 1973a, b, c) discussed the effect of roll velocity on the process Severdenko et al. (1972b) and phasing of torsional



(A)



(B)

FIGURE 14.62 Early work on ultrasonic rolling. (a) Rolling of 1/8 in. diameter zinc wire; A—before rolling, B—rolled with 1000 lb force, and C—rolled with 1000 lb force and ultrasonics (thickness 0.0625 in.) (Rosenfeld, 1963, Fig. 22) and (b) Piezoelectric rolling transducer by Cunningham and Douglas (1966, Fig. 21).

vibrations on rolling forces Severdenko et al. (1973a, b, c). Others include the rolling of dispersion-strengthened materials (Severdenko et al., 1974) and effects of ultrasonics on the steel rolling process (Severdenko et al., 1978). The previously cited comprehensive survey of ultrasonic manufacturing processes by Meyer carried 10 citations on rolling, most already noted in Severdenko or in the preceding references.

Following these early works, there appears to be little subsequent work in ultrasonic rolling. In recent years, a number of papers have appeared characterized as "ultrasonic rolling," but typically they do not involve rolling as defined above; instead, they are aimed at finishing a machined surface using ultrasonic excitation of a small-diameter short cylinder or ball, essentially ironing the asperities of a rough surface. These will be reviewed in the following Section 14.7.

14.7 Surface treatment, surface rolling

The use of ultrasonics to locally deform a metal surface for the purposes of smoothing, hardening, or shape modification has found several applications, reviewed in the following. As noted in Section 14.6, a surface treatment method known as "ultrasonic rolling" or "surface rolling" has emerged as an extensive field of development and will also be reviewed in the following.

14.7.1 Surface treatment

A leading ultrasonic treatment process is that of ultrasonic peening (UP) or also called ultrasonic impact treatment (UIT). The key elements of a UP/UIT system, as described by Graff (2009), are shown in Figure 14.65a. Thus, the basic system comprises a half-wavelength ultrasonic transducer,

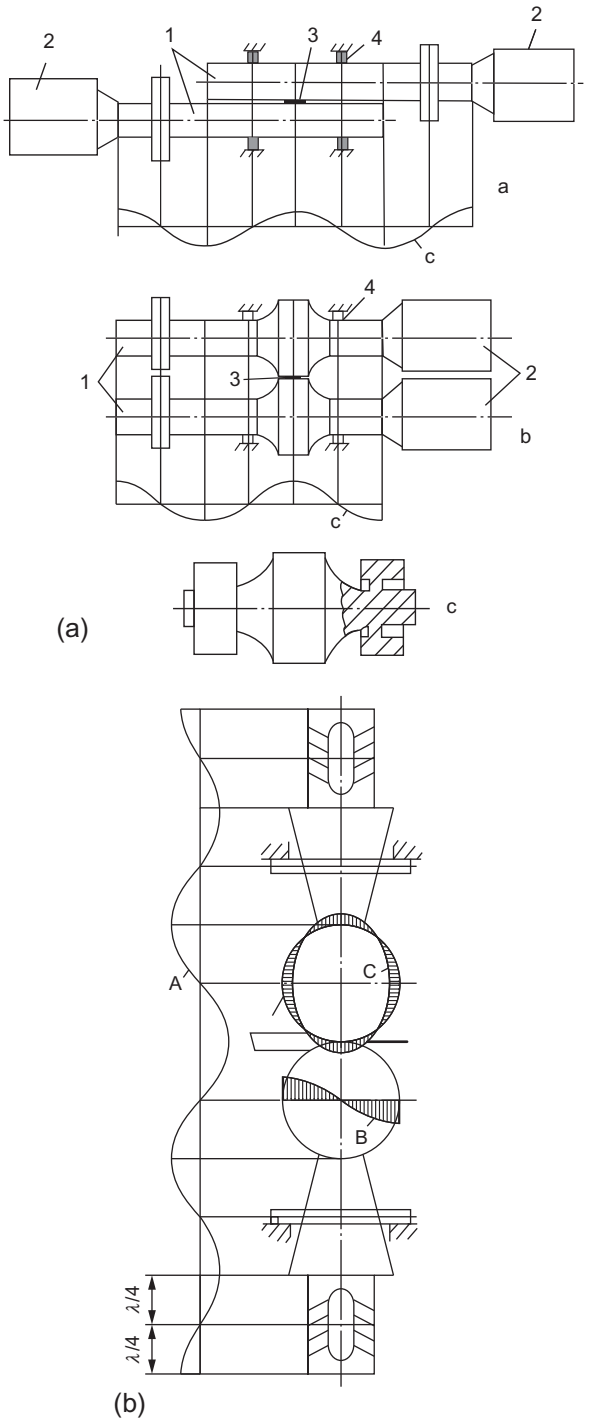


FIGURE 14.63 Illustrations of means of introducing ultrasound into the rollers (Severdenko et al., 1972a, b). (a) Exciting radial vibration modes through sliding contact (Fig. 36) and (b) rolling with torsional vibrations, "2" being torsion mode transducers (Fig. 38).

which in turn drives a half-wavelength horn. Impact pins are loosely placed (or "loosely coupled") at the end of the horn by a guide device, with the repeated impact of the horn tip against the pins that transmits stress pulses into the metal. The details of this interaction on a weld surface are shown in Figure 14.65b, where (upper figure) the horn tip impacts a pin that is in direct contact with the surface, transmitting a pulse through the pin (middle figure) and into the surface. The intensity of the pulse creates a local plastic zone of deformation (lower figure), which is the effect sought in the process. The details of equipment housings and attachment means are not shown in these simplified views. It is seen that the pin loose coupling and impact are the same principles as described in the previous section for impact riveting. This technology finds extensive use in the treatment of weldments to modify weld contours and residual stresses (Kudryavtsev et al., 2010) and is the subject of continued research.

A rapidly growing area of surface treatment involves the direct application of an ultrasonically vibrated tool to a metal surface to change the surface, near-surface microstructure, with several process variations in the development. Thus, a note should be made to the several works of Suh et al. (2006, 2007, 2010), of which 2007 is taken as an example, on a method of surface treatment referred to as ultrasonic cold forging (UCF), in which a small, hardened ball is ultrasonically impact-vibrated against a surface, thereby creating a localized plastic deformation zone, as shown in Figure 14.66a. The system for the process is shown in Figure 14.66b. Effects include reduced grain size along with increased hardness and fatigue life.

What appears to be a similar approach to surface modification is taken by Liu et al. (2011a, b), in what they designate as an ultrasonic surface rolling process (USRP) where an ultrasonically vibrated spherical indenter is pressed against a surface with a high static force. The treatment creates a nanostructured surface layer with improved mechanical properties. FEM results for residual stresses were in good agreement with measurements.

Other variants of ultrasonic surface treatment have appeared, such as ultrasonically rolled extrusion by Zheng et al. (2010, 2011), where a shaped curved surface tool is pressed and vibrated against a surface to improve microhardness and reduce surface roughness. Ding et al. (2010) and Mei et al. (2010) applied ultrasonic vibrations through a small roller, but otherwise with similar objectives to those previously described for improving surface quality, with the potential of replacing lapping and polishing. Chen et al. (2011) introduced yet another name, cylindrical ultrasonic rolling machine, for applying ultrasonics for increasing the surface hardness of components.

14.7.2 Ultrasonic surface rolling

Previous work under the general heading of "ultrasonic surface treatment" (USR) has been reviewed in the preceding section, and a note has been made, Section 14.xx, how the term "ultrasonic rolling" has transitioned in

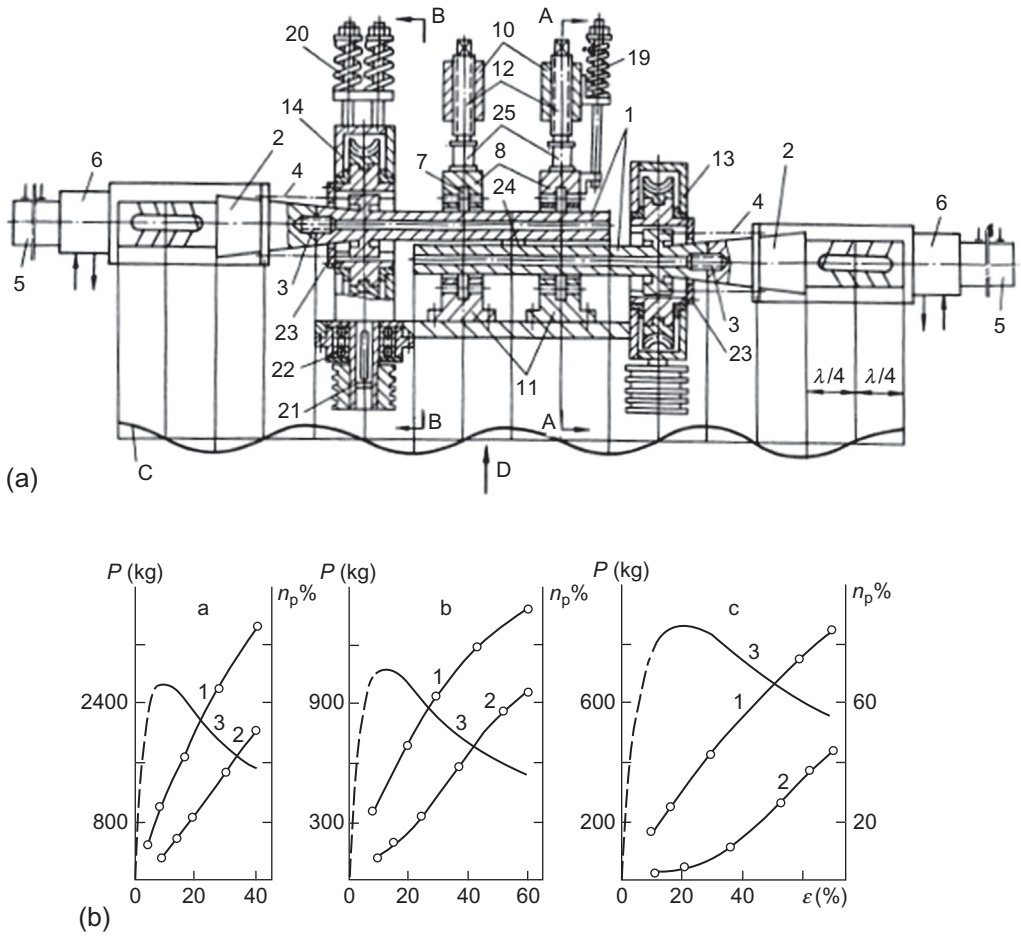


FIGURE 14.64 Rolling mill system and data (Severdenko et al., 1972a, b). (a) Design of a rolling mill using longitudinal oscillations of rolls (Fig. 48) and (b) change in rolling force with and without ultrasonics for steel (left), copper (middle), and aluminum (right) (Fig. 53).

meaning to apply to that of "ultrasonic surface rolling," discussed in the following.

The ultrasonic surface rolling process has been utilized to enhance surface integrity, create nanocrystalline surface layers, and improve various surface properties for different material systems, such as steel, titanium, and aluminum alloys. Zhang et al. (2017) performed ultrasonic surface rolling (USR) on 17-4 PH (precipitation hardened) stainless steel, which contains the body-centered tetragonal (BCT) martensite structure. During USR, the tool tip impacts the material surface at the ultrasonic vibration frequency under a certain amount of pressure. The ultrasonic vibration was found to improve the surface integrity in several aspects of the nanocrystalline structure, including reduced roughness, increased microhardness and residual compressive stress as well as enhanced wear and corrosion resistance. It was claimed that the ultrasonically induced grain refinements were the combined results of multiplication and rearrangement of dislocations as well as rotation of grain boundaries. USR of 17-4 PH stainless steel was also studied by Liu et al. (2018a, b, c). The surface nanocrystalline layer was comprehensively characterized—having a thickness of 650 μm, the layer comprised multiple sublayers including the thermomechanically coupled, elongated nanograins with the long axes parallel to the treated surface, elongated ultrafine grains, refined grains, and a low-strain matrix layer, as illustrated in Figure 14.67a. Near the surface, the dislocation density is less and the grain sizes are larger, potentially due to the coupled thermomechanical effects that induce mechanical recovery. As the depth increases, the dislocation density increases whereas the grain size is firstly reduced and then increases. Formation mechanisms of this gradient nanocrystalline layer are explained as shown in Figure 14.67b. Thus, during USR, elongated ultrafine grains are formed first, which were then refined by dislocation tangles, bands, and walls. Within the 10 μm depth of the surface, the formation of nanocrystallites was promoted by the interaction between dislocations and deformation twinning, as well as the dispersed ε-Cu precipitates, where the dislocation motion plays the most important role. The high compressive residual stress on the surface is an additively strengthening

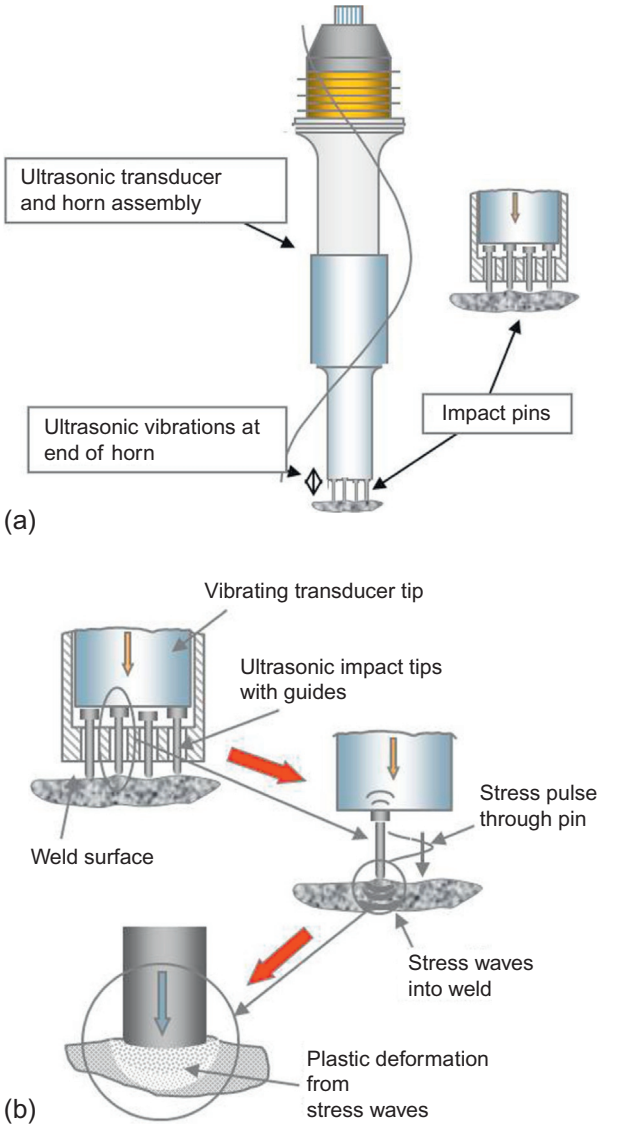


FIGURE 14.65 UP/UIT technology (Graff, 2009). (a) UP/UIT system and (b) Stress pulse transmission. *(Source: EWI.)*

result of dislocation density, grains, and precipitates. In addition to stainless steel, reduced surface roughness, introduced compressive residual stress, and improved fretting and corrosion fatigue performance were also achieved by USR on 300M ultra-high strength steel (Zhao et al. 2019). On the other hand, only a plastically deformed surface layer was reported in that study, and the nanocrystalline layer was not examined.

Several studies have been performed on different types and forms of titanium alloys. Liu et al. (2017a, b, c, d, 2019a, b, c) focused on the fretting fatigue (FF) behavior of Ti-6Al-4V alloy with USR treatment. They attributed the majority of the improvements of FF properties and suppressed FF crack initiation to the high compressive residual stress field induced by the USR process, whereas other factors, including surface work hardening, gradient nanostructured surface layer, and surface roughening played relatively minor roles, as schematically illustrated in Fig. 14.67. The compressive residual stress suppresses FF crack initiation and growth in the early stage. Ao et al. (2019) also studied USR on Ti-6Al-4V. Similar to the results on 17-4 PH stainless steel from Liu et al. (2018a, b, c), a gradient nanostructured surface layer is achieved on Ti-6Al-4V, which from the top surface to interior includes the equiaxed nanograin layer, elongated nanolamellar layer, and elongated ultrafine lamellar layer. This surface layer has a total thickness of more than 400 μm and is formed mainly through complex dislocation activities with supplementary contributions from phase transformation of HCP-Ti to BCC-Ti. During the USR process, the mechanisms of forming equiaxed nanograins are different between HCP and FCC Ti grains. For HCP-Ti, the grains were elongated into subgrain lamellae and then transformed into equiaxed nanograins through longitudinal splitting, transverse breakdown, and a certain degree of dynamic recovery. For FCC-Ti, deformation is dominated by twin-twin and twin-dislocation interactions, with longitudinal splitting and transverse breakdown as the secondary mechanism. Liu et al. (2019a, b, c) additionally showed, using the system and approach as shown in Figure 14.68, that the benefits of USRP on fatigue performance can be further enhanced with mechanical polishing.

Li et al. (2016, 2017a, b, c) investigated the effects of ultrasonic frequency and applied force on multipass ultrasonic surface rolling (MUSR) of Ti-6Al-4V alloy processed with hot isostatic pressing (HIP). Overall, the surface roughness, residual stress, microhardness, fretting friction, and wear properties of samples treated with MUSR were greatly improved. Dense dislocations and twins are generated on the surface layer. On the other hand, in the 40 kHz ultrasonic treatment, the high-impact energy leads to slight oxidation and adherence behavior on the material surface. USR of HIP'ed Ti-6Al-4V alloy at different temperatures of 25°C, 80°C, 120°C, and 160°C was also studied. The lowest surface roughness and highest compressive residual stress were achieved at 120°C. This was seen to be a result of certain levels of heating able to effectively improve material plastic deformation and facilitate healing of surface microdefects. However, overheated material has slight adhesion to the rolling wheel, which leads to undesirable plowing effects. The fretting friction and wear properties of USR samples processed at 120°C were lower than those at 25°C, which is potentially due to the effects of high temperature on the surface reducing the deformation strain energy and lowering surface microhardness.

Wang et al. (2017) performed USR on a selective laser-melted Ti-6AL-4V alloy. Selective laser melting (SLM) is

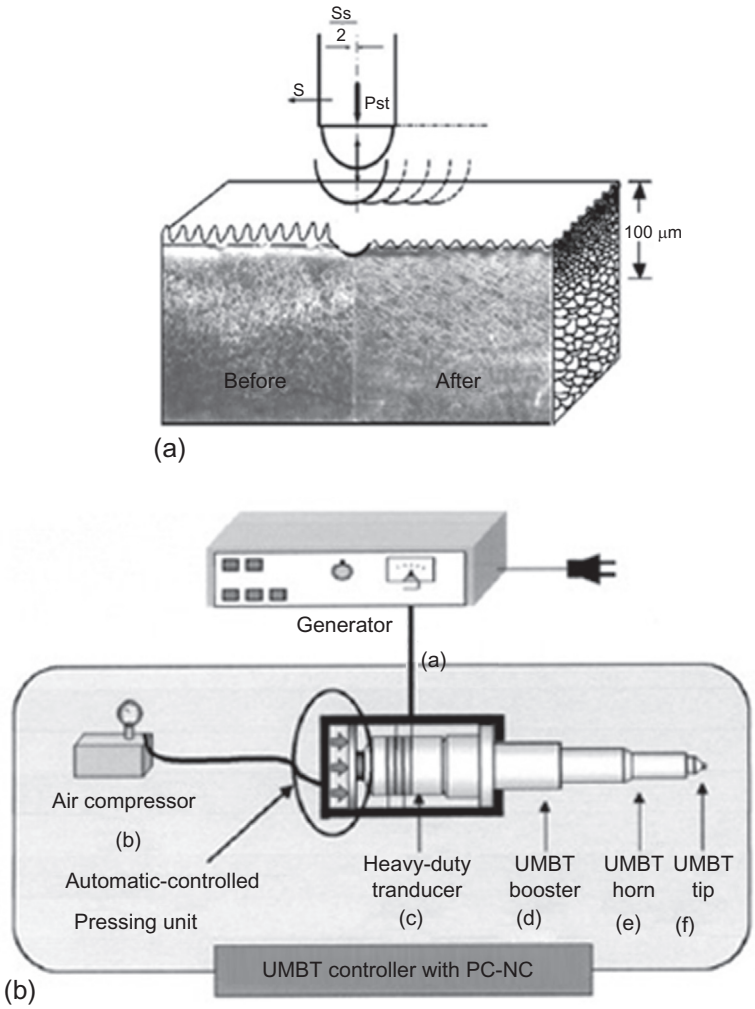


FIGURE 14.66 UCF technology by Suh et al. (2007). (a) Model of UCF (Fig. 1) and (b) configuration of the UCF system (Fig. 2).

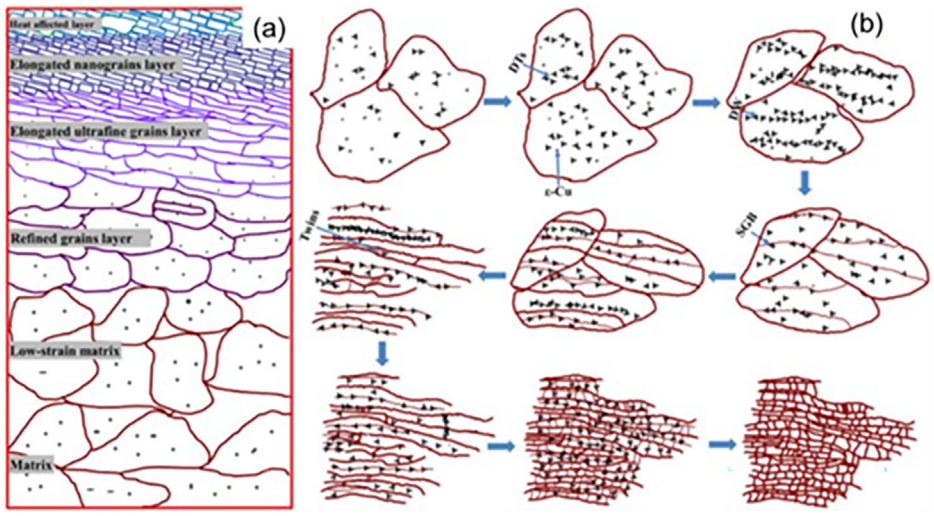


FIGURE 14.67 Schematic illustration of (a) Gradient surface structure on USR-processed 17-4PH steel. (b) Nanocrystallization mechanism (Liu et al., 2018a, b, c, Figs. 11 and 13).

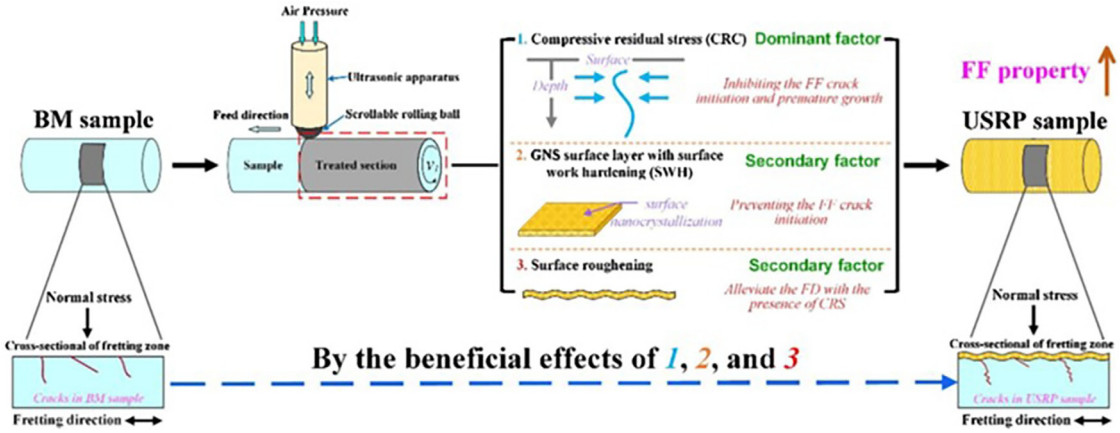


FIGURE 14.68 Schematic illustration of multiple factors induced by USR that contribute to the fretting fatigue (FF) behavior of Ti-6Al-4V (Liu et al., 2019a, b, c, Fig. 11).

one of the powder-based additive manufacturing technologies, which is advantageous in rapid prototyping and near-net-shape fabrication. However, because of the repeated melting and solidification, high tensile residual stress and microstructure defects, for example, porosity are generally associated with the products (Frazier, 2014). A comparison of untreated and USR-treated material is shown in Figure 14.69. After USR treatments, a pore-free surface layer can be achieved, as shown in Figure 14.69B. This densified layer shows severe work hardening characteristics with refined grains, dislocation walls, and deformation twins. Wear tests revealed that both the friction coefficient and wear volume were reduced in the USR-treated samples.

Lu et al. (2016) studied USR on surface characteristics of aluminum alloy AA7050-T7451. Similar to other material systems, the surface roughness, compressive residual stress, and microhardness were all increased. The trace lines of metal flow, fusion of surface grain boundary, and dissolution of impurity phases were evident. A nanocrystalline surface layer was not reported. Xu et al. (2019a, b) showed that both the surface integrity and

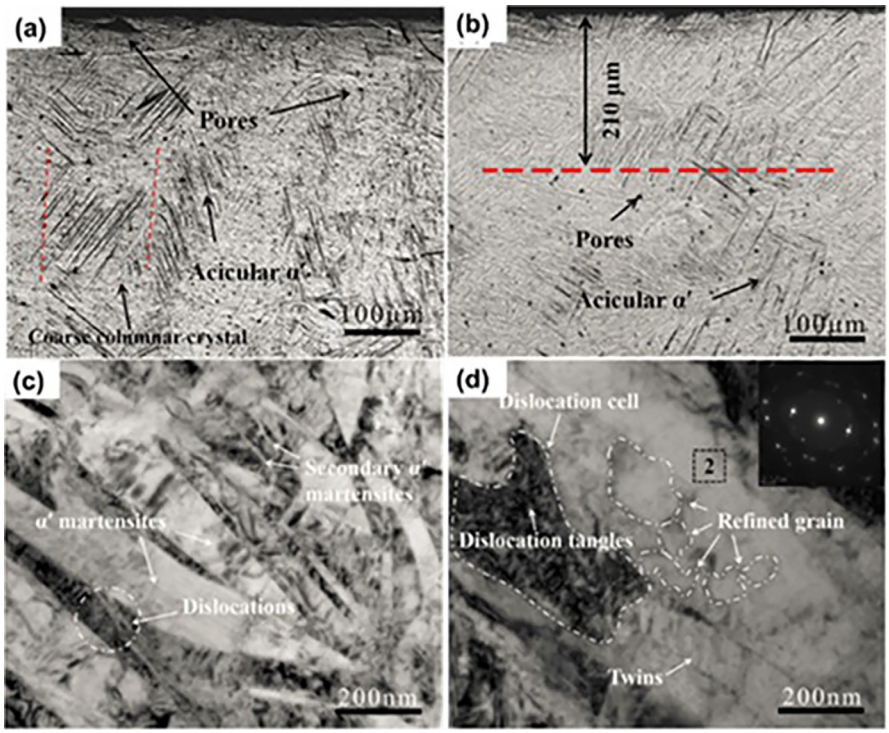


FIGURE 14.69 Optical images of longitudinal cross section of the sample (a) Without USR. (b) After 6 passes of USR; TEM images of the sample top surface. (c) Without USR. (d) After 6 passes of USR (Wang et al., 2017, Figs. 3 and 4).

corrosion fatigue behavior of aluminum alloy 7B50-T7751 are improved by multiple-pass USR treatment. The matrix precipitates (η′-MgZn2) and anodic grain boundary precipitates (η-MgZn2) were significantly reduced and subgrains were formed in the USR-treated sample surface. With more USR passes, the preferential sample texture gradually transitioned from (220) to (111). Hou et al. (2015) performed a parametric study of USR (referred to as ultrasonic deep rolling) on surface roughness reduction for aluminum alloy AA606-T6 based on a response surface method.

Xia et al. (2019) studied USR on the Cu-10Ni alloy and showed that a gradient nanocrystalline layer with an average grain size of 70 nm on the topmost surface is formed with the USR treatment, which increases the surface hardness by 80%. Furthermore, these nanograins increase the number of grain boundaries and promote the formation of a passive film on the surface, which effectively enhanced corrosion resistance.

Several variants of ultrasonic surface rolling have been studied. Cheng et al. (2016, 2019) analyzed the ultrasonic thread root rolling (TRR) process and showed that ultrasonic vibration plays a key role in successfully forming a nanocrystalline layer on the thread surface with grain size ranging from 15 to 20 nm, which remarkably improved the top surface hardness to 700 HV compared with the 580 HV from conventional TRR results. The fatigue life was also increased with the superimposed ultrasonic treatment. The experimental setup and TEM images of surface grain structures are shown in Figure 14.70. It was found that the relative motion distance is a more dominant factor in refining the grains than the dynamic force. The ultrasonic vibration also greatly increases the strain rate, which additionally facilitates the formation of the nanocrystals.

Wang et al. (2016) reported that the USR process can be further enhanced with the simultaneous passage of electrical current pulses during the process as shown in Figure 14.71a. The differences in surface layer microstructure between USR alone, Figure 14.71b and electropulse-assisted USR, Figure 14.71c are clearly seen. The benefits include facilitated surface crack healing and improved surface mechanical properties. For ASIS 304 stainless steel, the amount of the martensite phase is increased and the deformation twins are reduced on the surface layer. This is due to the coupling effects of ultrasonic impact and electropulsing, as the high strain rate associated with ultrasonic vibration increases the stacking fault energy, with both ultrasound and electropulsing increasing dislocation mobility. Ye et al. (2018) also studied the electropulsing-assisted USR process and focused on a pure titanium system. They found that the simultaneous electropulsing during the USR process is advantageous in promoting surface nanocrystallization by

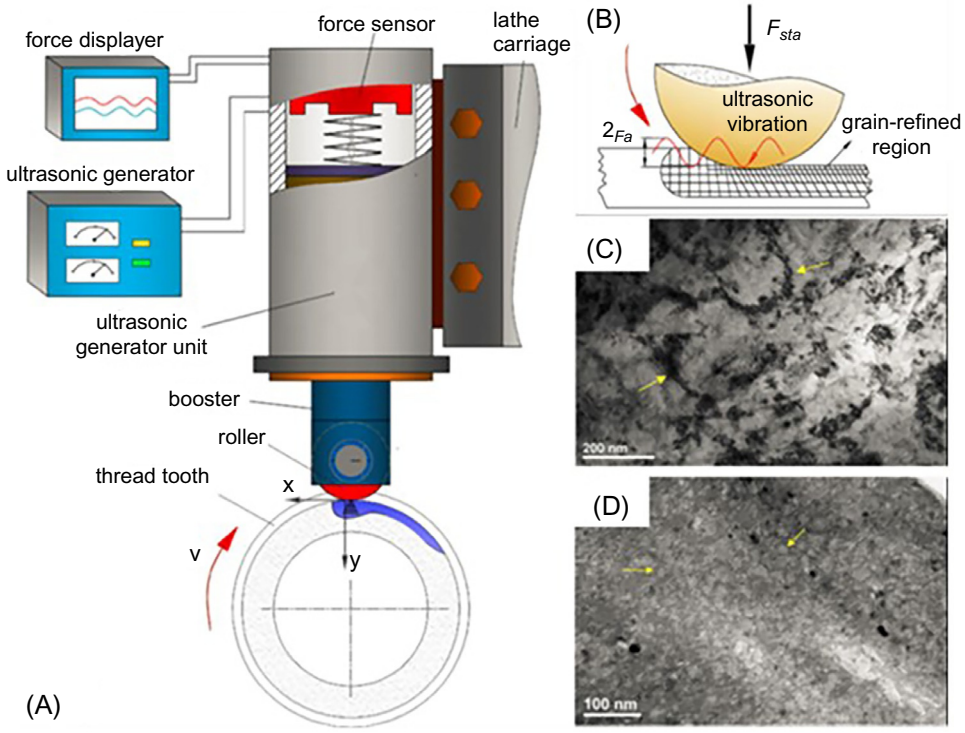


FIGURE 14.70 (a) Schematic illustration of the ultrasonic thread root rolling (TRR) process. (b) Ultrasonic vibration during the process. (c) TEM showing subgrain structure in the surface layer of conventional TRR sample. (d) TEM showing nanocrystals in the surface layer of ultrasonic TRR sample (Chen et al., 2015, Fig. 1).

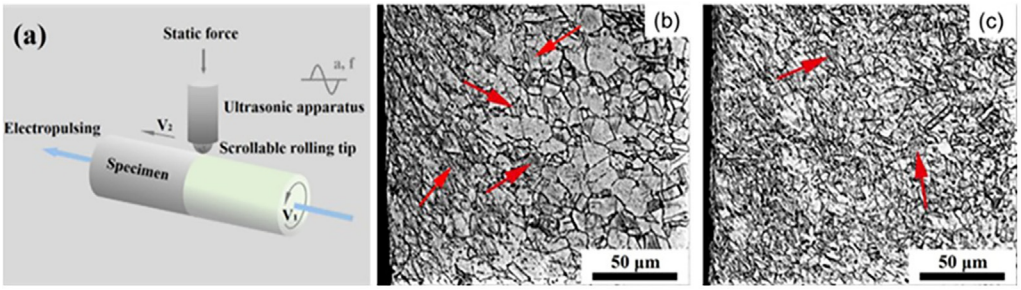


FIGURE 14.71 Illustration of the electropulsing-assisted USR process. (a) Surface layer microstructure of USR sample. (b) Surface layer microstructure of the electropulsing-assisted USR sample (c) (Wang et al., 2016, Figs. 1 and 8).

accelerating mobility of the immobile dislocations under the combined thermal and athermal effects of electropulsing as well as their coupling effects with the ultrasonic energy. It was found that at a depth of 15 μm below the surface, the USR sample still contains several dislocation bands, which are immobile and indicate incomplete recrystallization. As a comparison, more refined grains in equiaxed morphology were easily identifiable in the electropulsing-assisted sample.

14.8 Compaction

Compaction is a process in which metal powders are pressed, under high forces, into dies to achieve a part of desired shape and density able to be further processed by sintering to a final form. The purpose of applying ultrasonics to this process is to achieve higher density, better uniformity of density, and improved powder flow in the die cavity.

14.8.1 Early developments in compaction

The Aeroprojects/Sonobond Corporation, already noted for many contributions to power ultrasonics, carried out compaction studies beginning in 1958 (Anon, 1976) and as noted in Meyer (1973, pp. 148–152), where a work by a number of other investigators in this period was also summarized. An illustration of equipment used in the early Aeroprojects work is shown in Figure 14.72a, where the transducer and horn (B) and (D) drive the compaction die (E), with a static compaction force being applied by (F). Lehfeldt (1967) summarized several methods of achieving ultrasonic compaction, as shown in Figure 14.72b. It was reported that, for constant ram pressure, higher densities and increased dimensional stability were achievable with ultrasonics, while in hot pressing a given density could be achieved at lower working temperatures.

Tsujino and colleagues, beginning around 1977, were to make several contributions over many years to ultrasonic compaction, of which Tsujino et al. (1983) is an example. A complex compaction system (Figure 14.73a)

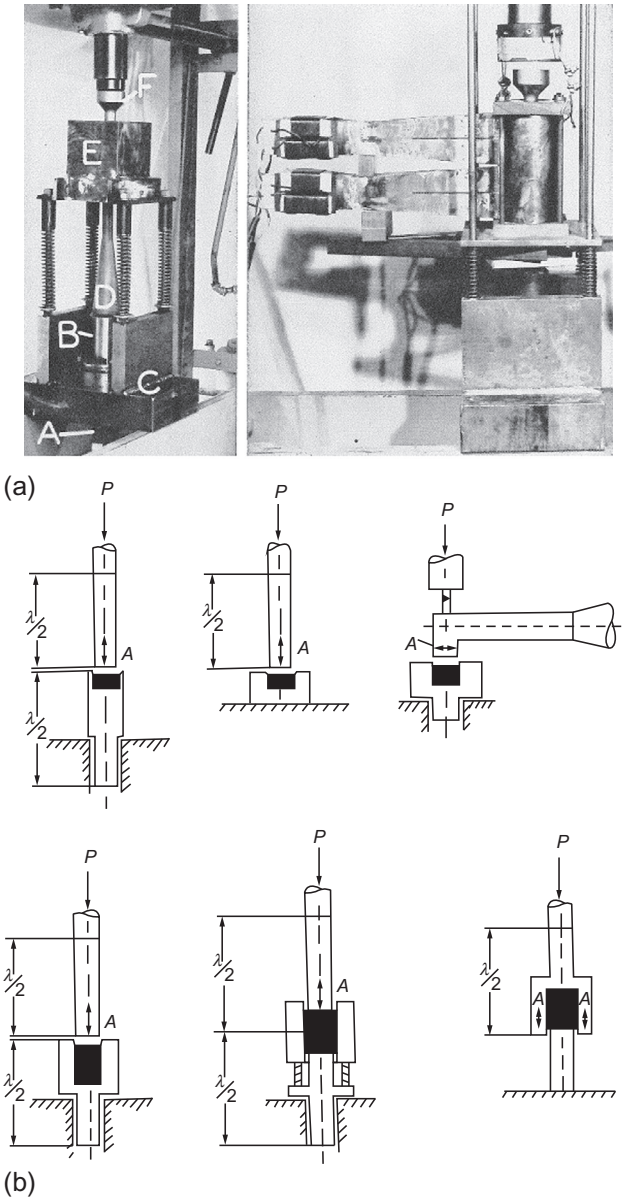


FIGURE 14.72 Ultrasonic compaction. (a) Aeroprojects compaction equipment (Anon, 1965) and (b) methods of ultrasonic compaction (Lehfeldt, 1967, Fig. 1).

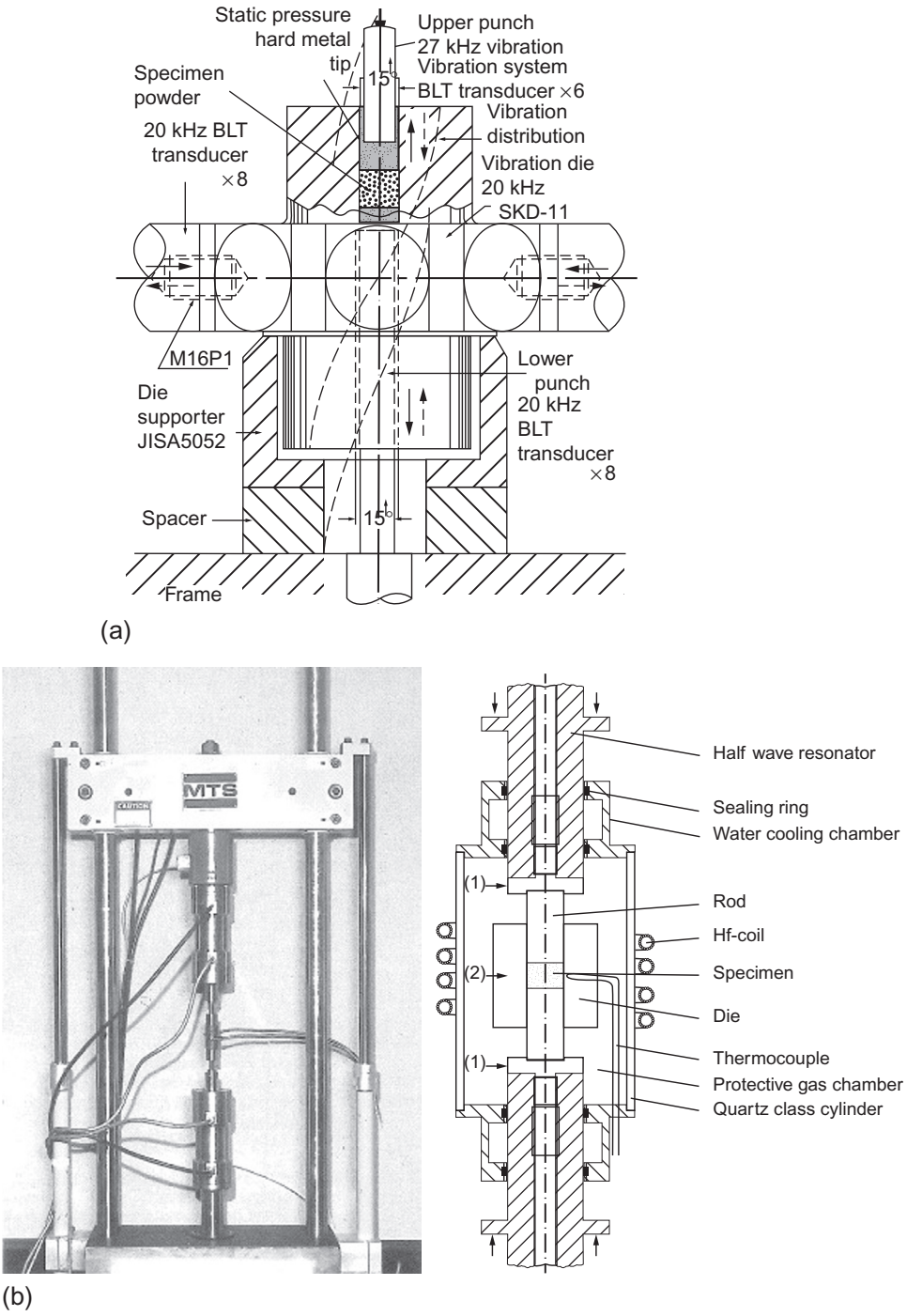


FIGURE 14.73 Ultrasonic compaction by Tsujino et al. (1983) and Kromp et al. (1985). (a) Multimode compaction press of Tsujino et al. (1983, Fig. 1) and (b) compaction setup of Kromp et al. (1985) (left—from Rosato et al. (1991, Fig. 12) and hot-pressing unit of Trimmel et al. (1979, Fig. 7)—right). *(Source: Part (b, left): From Rosato et al. (1991, Fig. 12). www.maneyonline.com/imr.)*

applied ultrasonic vibrations in three directions, via an upper punch operating at 27 kHz, a lower punch operating at 20 kHz, and radially to the die at a frequency of 20 kHz, where the latter causes, via the Poisson expansion of the die, an actual longitudinal die vibration. In an alternate arrangement (not shown here), the die is vibrated in the radial mode. Iron (200 and 350 mesh) and copper (200 mesh) powders were consolidated. It was found that both longitudinal and radial vibration of the die improved the compaction density over the cases of no vibration, or vibration of the punches, with the radial vibration being the most effective of various combinations. It was also noted

that friction forces with the die wall were decreased under longitudinal vibration but actually increased with radial vibration.

Likewise, Trimmel et al. (1979) and colleagues were to make several contributions to ultrasonic consolidation technology, of which the setup shown in Figure 14.73b (left) is a representative (Rosato et al., 1991). Two transducers are used to drive the upper and lower compaction punches, as shown in the detail of Figure 14.73b (right) for a hot-pressing unit, where the compact is placed at a vibration node. It was found that with ultrasonics, the force to achieve equivalent densities in a copper powder was significantly reduced from the no-ultrasonic case. Similar results were obtained for an aluminum powder by Kromp et al. (1985), where low-frequency (150 Hz) vibrations were also used but with ultrasonic vibrations gave superior results.

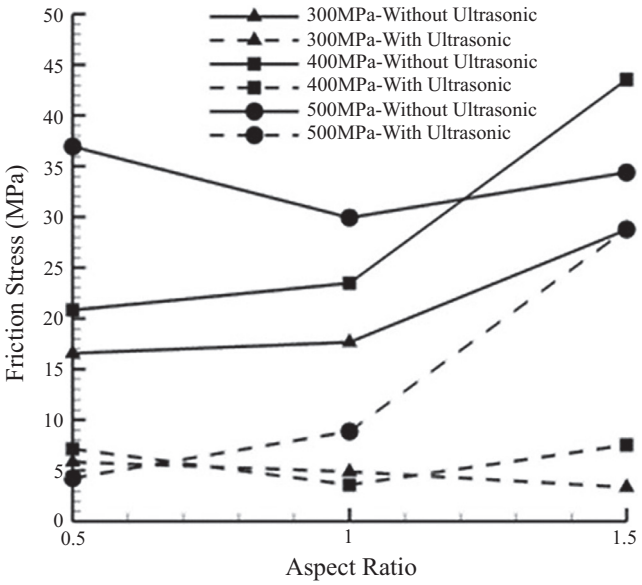


FIGURE 14.75 The effect of ultrasonic vibration on the friction pressure of <45 μm titanium (Fartashvand et al., 2017, Fig. 10).

14.8.2 Recent developments in ultrasonic compaction

A number of more recent developments have occurred in the field of ultrasonic compaction. Thus, Fartashvand et al. (2017) designed an ultrasonic press, Figure 14.74, to investigate the effects of powder size, compaction pressure, and powder compact thickness on density, with measurements made on density, friction force, ejection force, and springback. A three-wavelength acoustic punch system was designed with the compact at the center displacement node (stress antinode). Extensive results were presented, of which Figure 14.75 is representative, showing the effects of increasing compaction pressure on frictional forces for three-test compact aspect ratio—it being seen that ultrasonics causes a significant drop in friction. Among the conclusion was that powder size affected the compaction, increased densities were noted under some conditions and more uniform densities were achieved.

In a continuation of work at Amirkabir University, Abedini et al. (2017) investigated ultrasonic-assisted hot pressing of aluminum powder and found several benefits of the process. These included greater rates of densification, a greater effect of ultrasound on the finer powders, an increase in overall hardness, and a more consistent final compact. It was noted that ultrasound increased the

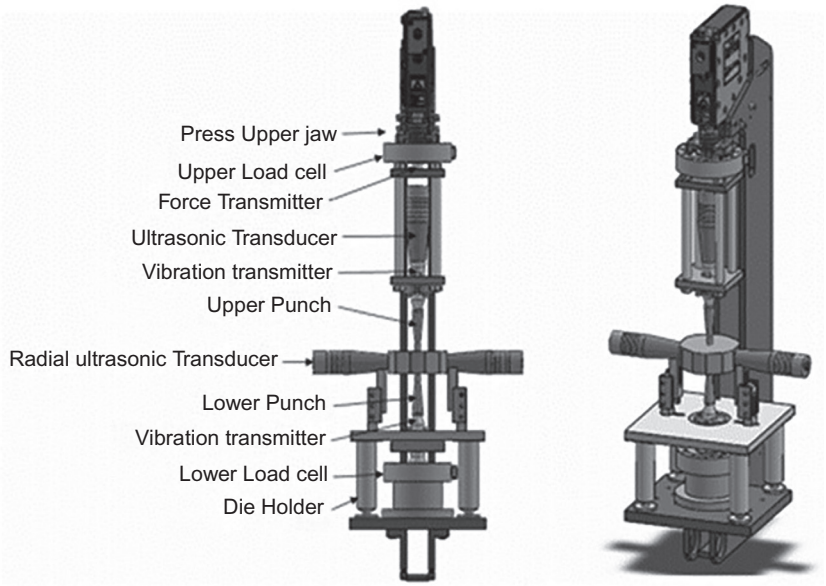


FIGURE 14.74 Schematic of ultrasonic-assisted powder compaction (Fartashvand et al., 2017, Fig. 2).

localized temperatures at the contact points of the powder particles, leading to local deformations that contributed to increased density. Trung et al. (2017) studied the compaction of Cu-CNT (carbon nanotube) composites using ultrasonic compaction, finding that both higher density and Brinell hardness were obtained for the ultrasonic-assisted process relative to conventional (thus 45.8 HB ultrasonic versus 49.2 HB). It was also noted that hardness decreased with increased CNT content.

The report by Hwang et al. (2019) deals with ultrasonic compaction of "soft magnetic materials" (SMCs), these being basically iron powders coated with thin electrically insulating layers that provide unique advantages for use in high-performance motors, as needed in the growing electric vehicle market. Reference is first made to the ultrasonic compaction system, as shown in Figure 14.76a, where it is seen to consist of a radial array (six in all) of transducers that achieve a radial compaction force through a resonant design of the compaction cavity. Upper and lower punches, Figure 14.76b, provide a static compression force. This concept, referenced by the authors, was first set forth by Tsujino (1983) (see Figure 14.73a). A schematic was presented, illustrating the barrier and particle friction forces present during compaction and also illustrating the well-accepted concept that ultrasonic vibrations of the barrier, i.e., cavity sidewall, reduces particle friction along that surface and transmits to the particles causing vibrations that reduces interface friction (it was noted that this was the main contributor to compaction force reduction), with the net result of enhanced compaction relative to static forces only. It was found that improved densities were achieved under ultrasonic compaction.

The effect of lubricant added to the SMC powder served to demonstrate the effect of ultrasound on the process, as shown in Figure 14.77. Thus, with a low percentage of lubricant, the ultrasonic effect dominated with higher densities, while with increased lubricant, the ultrasonic effect diminished, and the two techniques, with and without ultrasound, approached the same density limit. Finally, the marked difference in density microstructure was brought out in Figure 14.78, showing a dramatically lower void content with the ultrasonic sample.

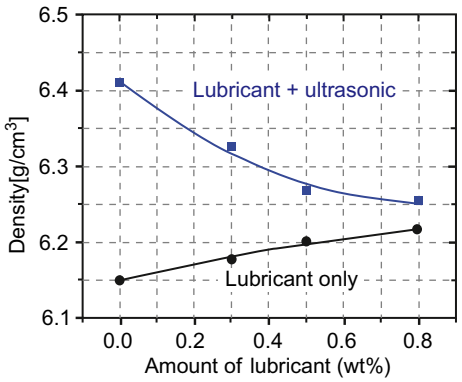


FIGURE 14.77 Density comparison between ultrasonic and nonultrasonic effects under different lubrication conditions (Hwang et al., 2019, Fig. 15).

14.9 Microforming

A growing field for ultrasonic forming is that of "microforming" that, while involving basically the same principles as the conventional forming processes such as drawing, forging, and extrusion, has been found to have unique challenges as a result of scaling down to the millimeter and submillimeter levels. Numerous publications have already appeared in this field, with notes taken here of works by Presz and Andersen (2007), Witthauer et al. (2010), Yao et al. (2010), and Bunget and Ngaile (2011). Thus, these varied authors note the wide range of applications for microforming, including medical devices, MEMS, electronics, computers, biotechnology, and optical devices. Examples can be pins for IC carriers, fasteners, sockets, and other connecting elements. Typically, such parts are machined, but net-shape and near-net-shape forming processes may have potential advantages. Examples of microextruded parts are shown in Figure 14.79a.

Early work in this field has involved applying both low- and high-frequency vibrations. Thus, Witthauer et al. (2010)

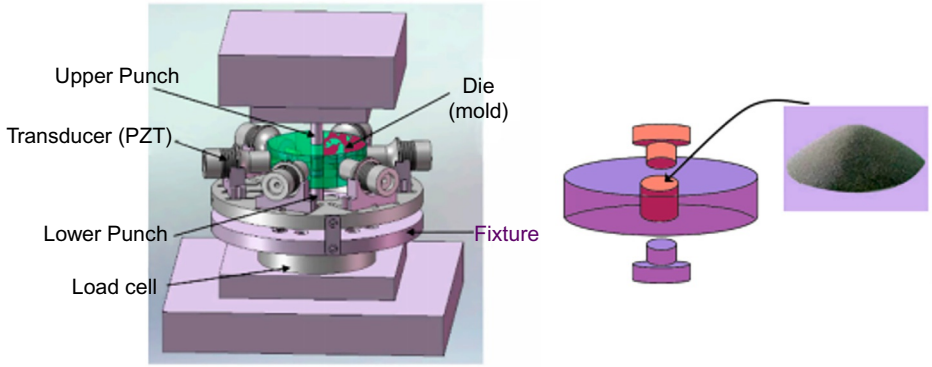


FIGURE 14.76 Ultrasonic vibration compaction system: (a) Compaction system schematic and (b) basic operating concept (Hwang et al., 2019, Fig. 6).

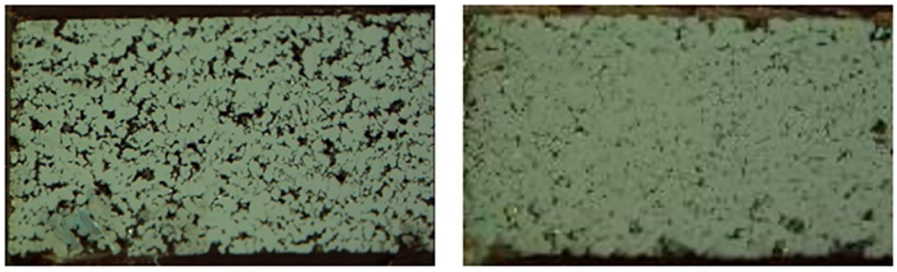


FIGURE 14.78 Optical microscopic observations of compacted material with and without ultrasonic vibration: (a) Conventional compaction. (b) Ultrasonic compaction (Hwang et al., 2019, Fig. 10).

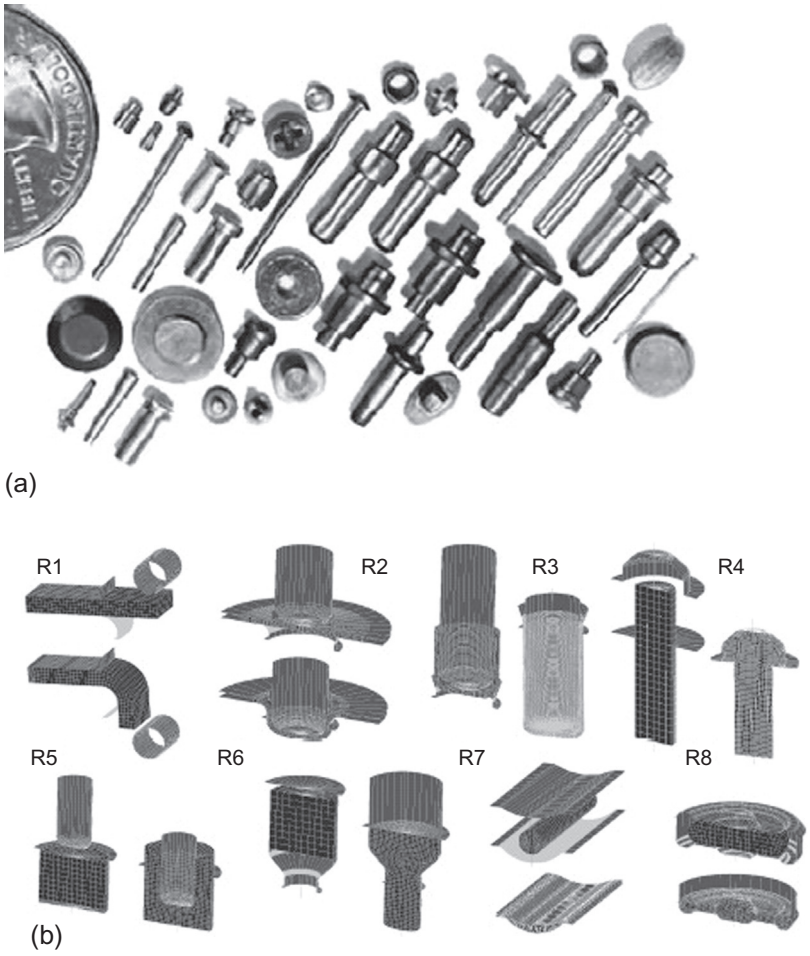


FIGURE 14.79 Ultrasonics applied to microforming. (a) Examples of microextruded parts (Bunget and Ngaile, 2011, Fig. 1, from Vollertsen et al., 2004) and (b) reference microparts (Presz and Andersen, 2007, Fig. 3).

describe several configurations of low frequency, Terfenol-D-based actuators to be used in microforming studies. Presz and Andersen (2007) review both high- and low-frequency aspects and elect the use of a variable frequency, low-frequency (less than 1 kHz) piezoelectric-based actuator for their work. They also provide a useful catalog of reference parts for vibration microforming, as shown in Figure 14.79b.

Challenges are encountered in this new forming field, specific to miniaturization itself. Scale-down to submillimeter levels can encounter material size effects, dimensional tolerances, surface finish, friction, repeatability, and tool wear; many, of course, not unlike those in conventional (macroscale) metal forming but having their own challenges due to small scales. For example, part dimensions may be on the order of metallurgical grain sizes,

resulting in greater anisotropy of properties, while different friction conditions may exist at the microscale level.

The scope of microforming processes closely parallels the scope of conventional forming processes, so that in a similar manner ultrasonic microforming processes follow those of the microforming field, there thus being ultrasonic microforging, extrusion, deep drawing, blanking/shearing, bending, and incremental forming, as examples. The very scope of the field prevents a detailed review within the present chapter, devoted as it is to the total field of ultrasonic forming, with emphasis on the large scale ("macroscale") processes. In the following, examples of several microprocesses are presented with reference to related works in each area.

Xu et al. (2019a, b) investigated two means of transferring ultrasonic vibrations into extrusion of T2 copper, via the tool/punch—which is the typical approach—and via workpiece or die. The key ultrasonic components of the system are shown in Figure 14.80, where it is seen that the vibrations are applied laterally to achieve a vertical vibration—this in itself is not unusual. The critical component labeled as a "porous" die acts to redirect the vibrations. The system is used in two ways, as shown in Figure 14.81; thus, Figure 14.81a is the tool vibration mode, while Figure 14.81b shows the workpiece vibration mode. The nature of the "porous die" is revealed in the vibration mode analysis as shown in Figure 14.82; thus, the so-called porosity is achieved by a series of parallel cylindrical cavities, which serve to greatly reduce the stiffness of the block. The effect of the two modes of vibration, at various power levels (and at zero power), on the stress-strain curves for a 147-m grain size was measured, with it being found that a slight stress reduction is achieved for die vibration. Extensive other results are presented, with it being

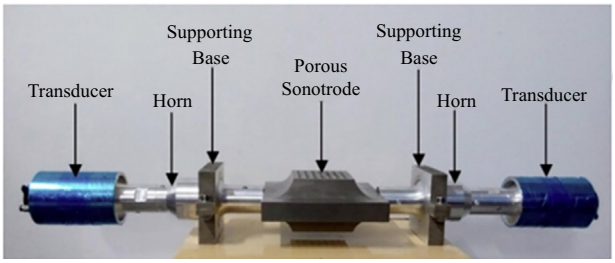


FIGURE 14.80 Ultrasonic system with porous sonotrode (Xu et al., 2019a, b, Fig. 1(b)).

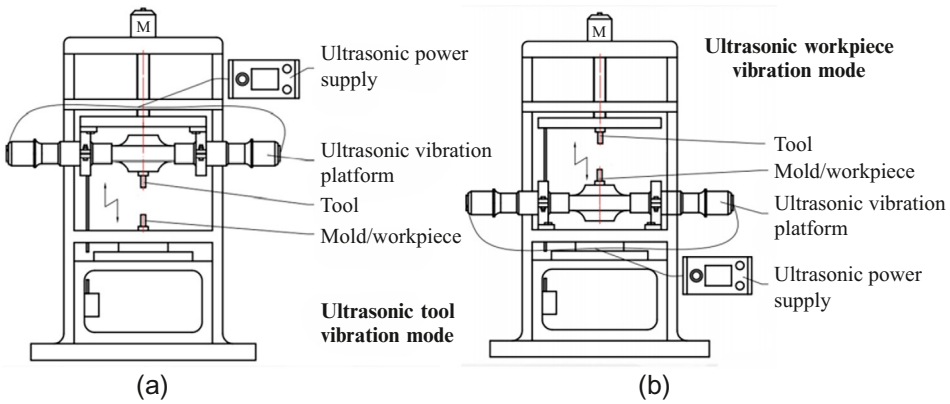


FIGURE 14.81 Schematic diagrams of extrusion press (a) tool vibration mode and (b) workpiece vibration mode (Xu et al., 2019a, b, Fig. 2).

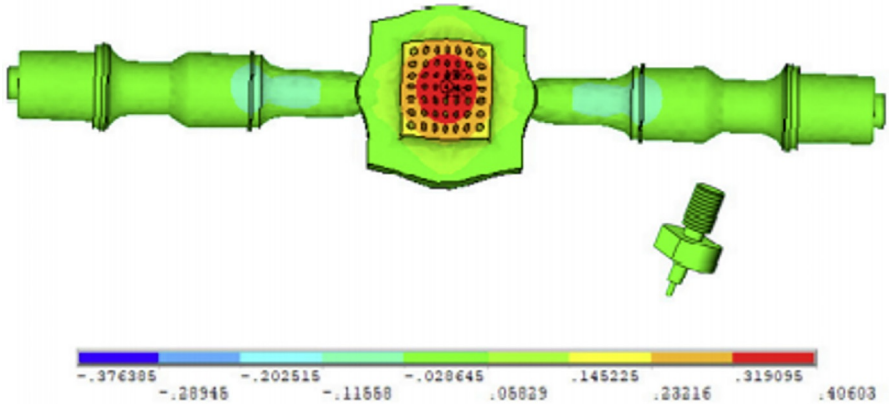


FIGURE 14.82 Structure of the microextrusion tool vibration mode, porous die in yellow (Xu et al., 2019a, b, Fig. 4(b)).

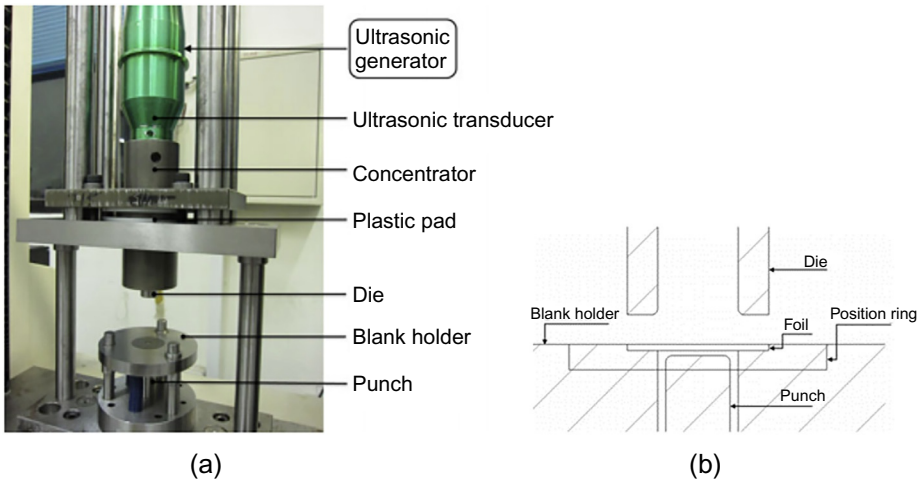
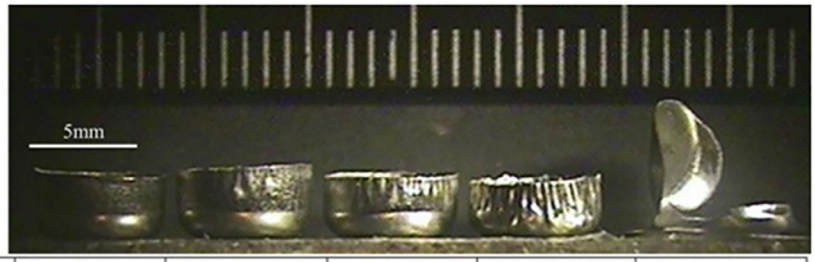


FIGURE 14.83 Ultrasonic micro-deep drawing, (a) System. (b) Schematic of die and tooling (Huang et al., 2014, Figs. 1 and 2).

concluded that the grain size was improved with ultrasonics, with the workpiece vibration mode providing better results.

Other recent contributions to ultrasonic microextrusion include those of Lou et al. (2018) and Lou and Liu (2019).

Illustrative of developments in ultrasonic micro-deep drawing is that of Huang et al. (2014) in a study of the effects of ultrasonic vibration on the micro-deep drawing of three 304 stainless steel foils using the apparatus as shown in Figure 14.83a, with a schematic of the tool region as shown in Figure 14.83b, where the die is ultrasonically activated. Typical wrinkling of cups drawn without ultrasonics is shown in Figure 14.84, while Figure 14.85 shows the absence of wrinkling in ultrasonically drawn cups. A significant reduction in draw force was noted with this being attributed to reduced friction between the die and blank.



	Cup without wrinkle (a)	Cup with small wrinkle (b)	Cup with large wrinkle (c)	Cup with serious wrinkle (d)	Fracture (e)
Diameter (mm)	10	10.5	10	10	10.5
Thickness (μm)	100	75	75	50	50

FIGURE 14.84 Wrinkling of deep-drawn cups without ultrasonics (Huang et al., 2014, Fig. 3).

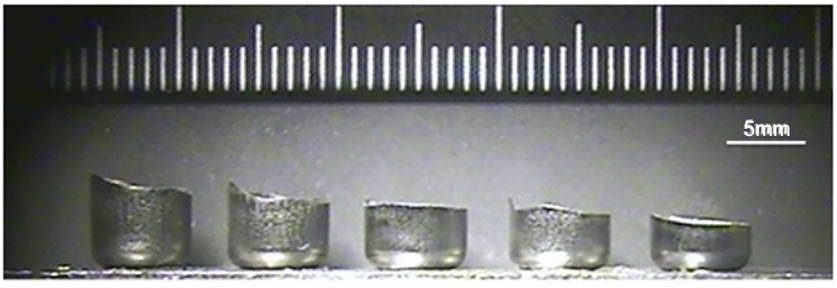


FIGURE 14.85 Ultrasonically drawn cups of 0.1 mm thickness at an amplitude of 4.1 m (Huang et al., 2014, Fig. 6).

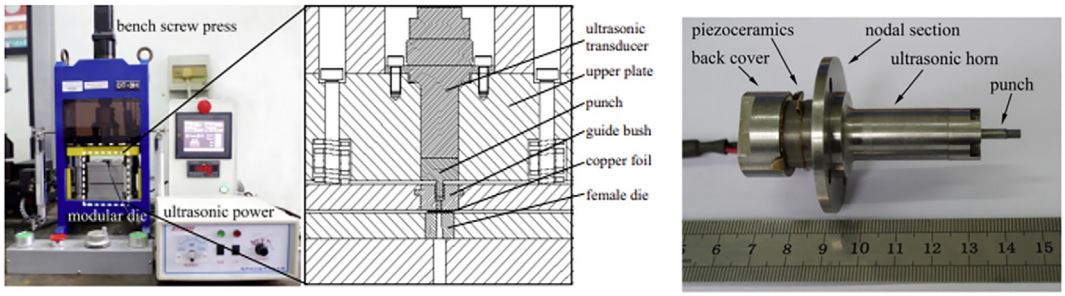


FIGURE 14.86 Ultrasonic microblanking (a) system, (b) system schematic, and (c) ultrasonic punch (Liu et al., 2017a, b, c, d, Figs. 1 and 2).

An increased depth of draw, characterized by increased limit draw ration (LDR), was obtained.

Other contributions to this field include Luo et al. (2015) and Zha and Chen (2019a, b).

Liu et al. (2017a, b, c, d) investigated microblanking of square holes in a T2 copper foil 0.2 mm thick using the system as shown in Figure 14.86a, with a photo of the ultrasonic punch (also shown schematically in (b)) as shown in Figure 14.86b. The punch operated at 36.1 kHz with a tip amplitude of 1.66 μm. Evolution of microstructure and grain size, crack initiation, and sheared surface quality was among the effects studied. Increased size of the critical "smooth" zone at the sheared surface was noted, as shown in Figure 14.87. The reduction in cracking was attributed to a softening effect of ultrasonic vibrations. Different stages of sheared surface, with and without ultrasonics, are shown in Figure 14.88, clearly indicating reduced deformation in the shear zone. Improvements in surface quality were also noted.

Other contributors to this area of microforming include Presz and Cacko (2017), Wang et al. (2019), and Liu et al. (2017a, b).

The preceding overviews have touched on the ultrasonic microforging, deep draw, extrusion, and shearing/blanking processes, including references to others that have contributed to these areas. Additional technologies could include those of microbending, microincremental forming, and micro-orbital forming. Tosello et al. (2019) have set forth methods for quality control in this field, as shown in outline form in Figure 14.89.

The effect of ultrasonic vibrations on the yield strength of metals has been noted at several points in the materials forming Chapters 13 and 14, as well as also affecting ultrasonic metal welding and machining processes. It is not

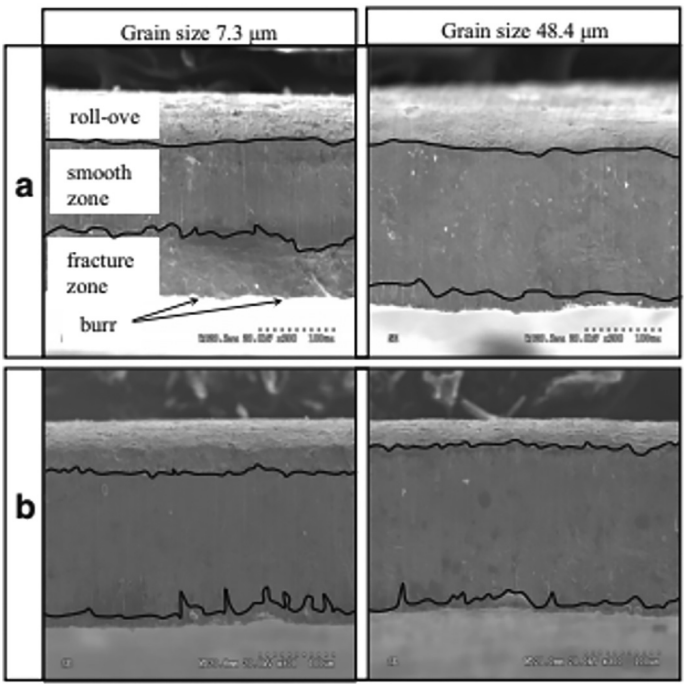


FIGURE 14.87 Shearing surfaces (a) Without ultrasonics. (b) With ultrasonics (Liu et al., 2017a, b, c, d, Fig. 4).

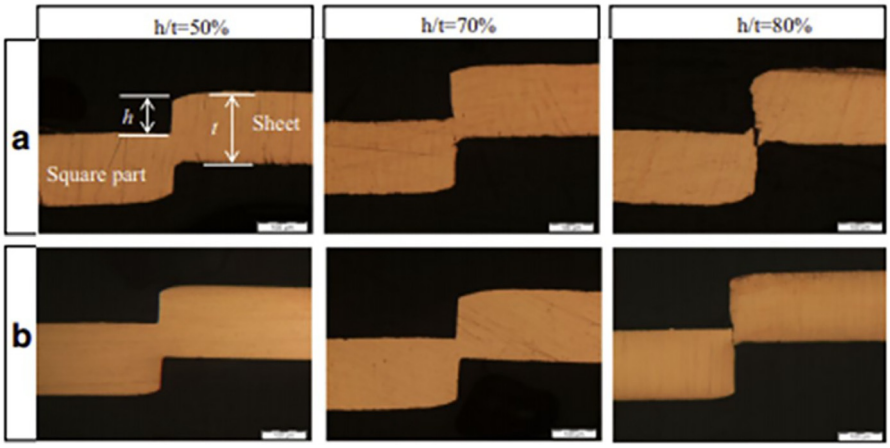


FIGURE 14.88 Cross sections of different blanking strokes (a) Without ultrasonics. (b) With ultrasonics (Liu et al., 2017a, b, c, d, Fig. 6).

surprising, therefore, to find the study of this effect in microforming processes, as extensively set forth by Hu et al. (2018).

As noted in this section's introduction, the field of ultrasonic microforming processes not only parallels that of large-scale macroprocesses but also brings in processes unique to the emerging field. It is hoped that this brief introduction to selected aspects of the field, including references to work not reviewed here, will serve as a basis for further review and research.

14.10 Other forming processes

While several major ultrasonic metal forming processes have now been reviewed, there remain a large number of other applications and processes that represent viable forming uses of power ultrasonics. In the following, a brief note will be made on several of these. In most cases, the technology does not appear to have advanced over that reported in the 1st edition. Tube expansion, wire flattening, and riveting will be summarized.

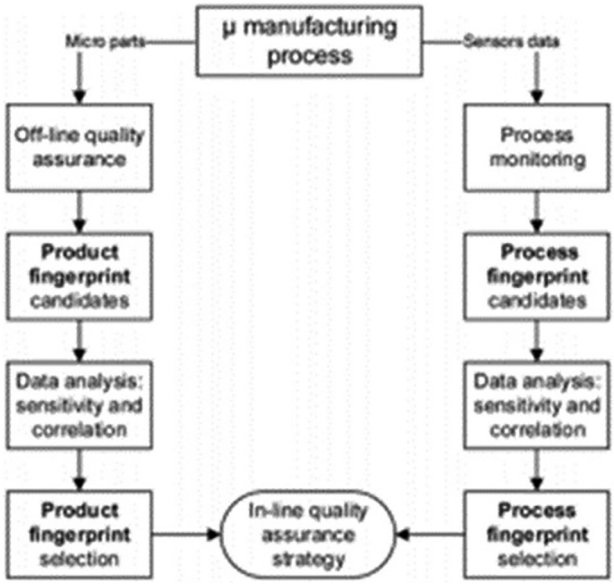


FIGURE 14.89 Flowchart representing the method to identify product and process fingerprints leading to the definition of an in-line quality assurance strategy (Tosello et al., 2019, Fig. 1).

The process of tube expansion consists of increasing the diameter of a tube by forcing a mandrel through the tube's inner diameter, causing plastic deformation of the tube wall to the desired final dimension. Nakagiri and Sansome (1977) applied ultrasonics to this process, using the two-transducer system as shown in Figure 14.90 (upper), with an example of an expansion tool shape as shown in Figure 14.90 (lower), able to be located at a node or antinode position. Tests were conducted on mild steel tubing. Results showed a reduction in axial expansion forces of up to 30% and identified optimum tool locations and die angles.

Several researchers have noted the use of ultrasound to flatten a wire, a process that is possibly close to that of forging. Thus, Balamuth (1964) showed such an operation, but with little additional details, while Konovalov and Ignashev (1972) described a similar arrangement for wire flattening and reported it being the best used on harder wires; that deformation by ultrasound was greater than what was achieved by longitudinal deformation or by rolling and was achievable without the use of lubricants. In the frequently cited 1972 Severdenko monograph, a summary of wire flattening work by Mori and Inoue (1968) was presented, where an ultrasonic welding system was modified to roll thin aluminum, copper, and steel wire and strip. It showed there was a reduction (ε in percent) of steel wire of two diameters as a function of rolling force, for varying vibration amplitudes. Increasing amplitude is seen to increase deformation; however, at high roll forces, the differences were seen to diminish.

Riveting, which is a forging type of process, has been accomplished using ultrasonics, as reported by McMaster

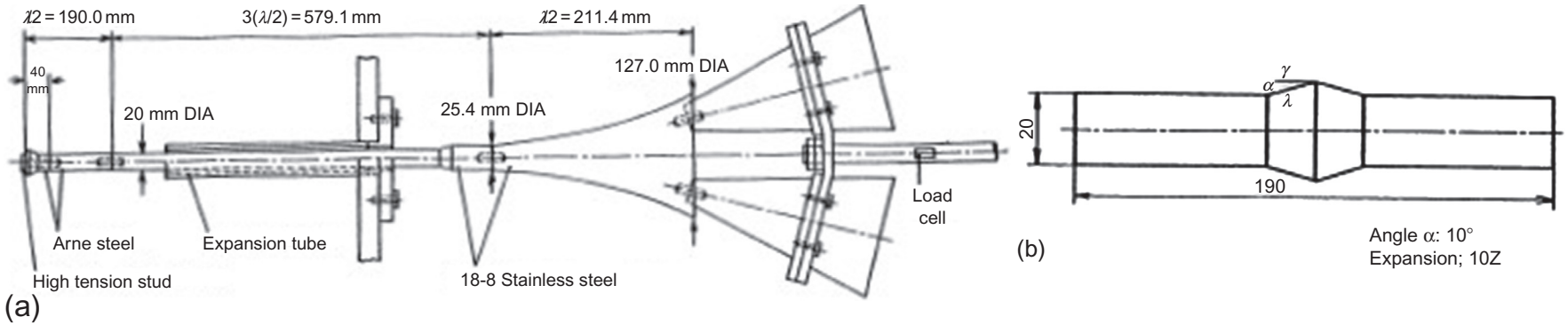


FIGURE 14.90 Tube expansion by Nakagiri and Sansome (1977). (a) Experimental setup (Fig. 2) and (b) tube expansion tools (Fig. 3).

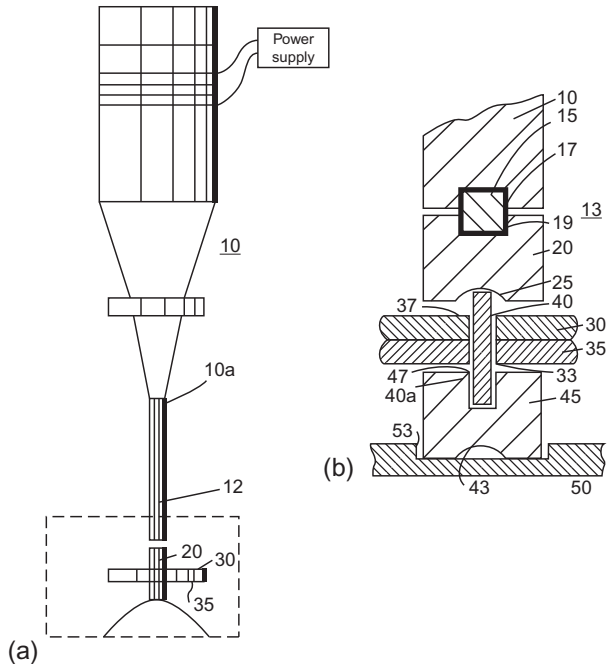


FIGURE 14.91 Ultrasonic transducer (a) and detailed view (b), by McMaster et al. (1967).

et al. (1967). A unique "impact coupling" method of energy transfer was used, as seen in Figure 14.91, which shows an ultrasonic transducer (labeled as "a") (the transducer actually operated at 10 kHz, thus being quite "sonic") vibrating against a rivet (40). In the detailed view (labeled as "b"), a loosely coupled impact tool (20) is placed between the end of the ultrasonic line (10) and the rivet (40). The harmonic vibrations of the line are thus transmitted into sharp impacts against the rivet, similar to that of a pneumatic hammer, without continuous coupling to the rivet. In this manner, the rivet was forged or "headed" into its final shape. This method of impact energy transfer was to find wide application in other fields of research, such as rock drilling, and was exploited by other researchers for surface modification and weld treatment.

14.11 Future trends

The 1st edition of this chapter concluded by noting:

> *"Given the extensive research and development that has occurred in the field of ultrasonic metal forming since the Blaha-Langenecker discovery of 1955, it may be somewhat surprising that some of the processes have not transitioned to wide use on the production floor."*

It is not clear, in the present 2nd edition, that the preceding situation has markedly changed. It should be clear, from the contents of this chapter, that there is continued widespread research and development in an equally widespread range of metal-forming processes. As is not uncommon, many of these studies have been in the research laboratory setting, generally several steps removed from production. Thus, as to future trends, one might inquire as to trends (or developments) that are needed if ultrasonic metal forming is to transition to large-scale industrial use. Some suggested developments can be noted.

- *Increased ultrasonic power*. A great many ultrasonic studies, often on a small scale but with promising early results, have utilized systems rated at 100s of watts. To go to many heavy-duty production uses, scale-up is needed, with increased transducer power often being a prerequisite development. Systems routinely operating at 10 kW or higher need to be developed.
- *Scale-up*. Many processes, of which deep drawing, rolling, and forging are examples, will need to scale-up to deal with part sizes found in major industries, such as automotive and aerospace. The size (both dimensions and mass) of tooling and dies typically found in these industries are beyond the capacity of present systems to ultrasonically vibrate at useful levels. While increasingly powerful transducers (noted above) will be a partial answer, just as important may be the development of innovative methods of selectively applying ultrasonics to critical areas of large tooling systems to achieve the desired benefits.
- *New fields of use*. While scale-up may be one area of future development, "scale-down" to microforming applications, noted in Section 15.6, appears to be a field of application especially suited to the current capabilities of ultrasonic systems and hopefully will be rapidly developed. The continued development of new materials and/or increased quality demands often challenge conventional forming methods. It is important to be vigilant for new opportunities arising because of changing circumstances in supposedly "established" applications, such as increased fatigue resistance in wires used in medical products.
- *Modeling*. Metal forming processes (and many other manufacturing processes) are being modeled using increasingly sophisticated computer techniques, permitting process improvements to be achieved with a minimum of hardware iterations. This trend must be carried over to various ultrasonic-forming processes, which add the complexity of superimposed vibrations to the already complex conventional forming materials and systems. Improved material modeling, noted later, will be important. However, advantages should be taken while incorporating available empirical data into process models that might permit workable, practical process models to be developed, while awaiting the results of more fundamental material studies.

- *Material behavior under ultrasonic vibrations*. The criticality of fully understanding the bulk and surface behavior of materials under ultrasonic-forming vibrations has been fully discussed in Chapter 14. Continued advancements in this area, including modeling of material behavior, will remain critical to the realization of wider industrial usage of ultrasonic forming.
- *New processes*. This section is concluded on a speculative note (or question) and is meant to be supplemental to the bullet points preceding. The foundation of ultrasonic-forming processes presently appears to rest solely on the quite extensive existing foundation of the so-called "conventional" forming processes. This leads logically it would seem, to a speculative question, as to whether there might be new ultrasonic processes that lie outside the conventional regimen, for which only the specific features of ultrasonics might make them a viable new entry to the existing litany of applications. An answer cannot be provided here, since, by their very definition, they do not yet exist (at least to public knowledge)—leading one to be hopeful of yet new and exciting future developments.

14.12 Sources of further information and advice

Recommendations for future information for this chapter are similar to those noted in Chapter 14, with slight modifications. Thus, information sources cited here are in many cases common to a number of chapters in this book. For example, Abramov (1998) continues as an excellent reference to both the basics of power ultrasonics, as well as coverage of a number of manufacturing applications; as does Abramov (1994), which goes into greater depth on metallurgical processes. To these should be added Puskar (1982), in which a wide range of manufacturing applications, including forming, are reviewed. Comprehensive references of Ensminger and Stulen (2009), Astashev and Babitsky (2007), and Ensminger and Bond (2012) are especially to be noted. Numerous manufacturing and material journals are cited throughout the chapter that can all be followed, time permitting. However, the most significant developments in power ultrasonics will make some form of appearance, at one time or another, in the journal *Ultrasonics*.

References

Abbasi, A., Amini, S., Emamikhah, A., 2016. Design and implementation of the ultrasonic cold forging technology process for improving surface mechanical properties of 6XB2C cold-worked alloy steel tool. Proc. Inst. Mech. Eng. Part B: J. Eng. Manuf. 230 (2), 267–278.

Abedini, R., Abdullah, A., Alizadeh, Y., 2017. Ultrasonic assisted hot metal powder compaction. Ultrason. Sonochem. 38, 704–710.

Abramov, O.V., 1994. Ultrasound in Liquid and Solid Metals. CRC Press, New York.

Abramov, O.V., 1998. High-Intensity Ultrasonics: Theory and Industrial Applications. Gordon and Breach Science Publishers, Philadelphia.

Abramov, O.V., Petukhov, V.I., Manegin, Y.V., 1971. The use of ultrasound in metal forging. Tsvetnye Metally 2, 64. Translated in Russian Ultrasonics, vol. 2, pp. 17–22 (January, 1972).

Adam, A., Stan, D., 2013. The influence of the processing parameters in the ultrasonic activated injection and extrusion. Appl. Mech. Mater. 420, 149–153.

Akbari Mousavi, A.A., Feizi, H., 2005. Simulation of ultrasonic vibration extrusion using the finite element method. In: VIII International Conference on Computational Plasticity, COMPLAS VIII. 5 pp.

Akbari Mousavi, S.A.A., Feizi, H., Madoliat, R., 2007. Investigations on the effects of ultrasonic vibrations in the extrusion process. J. Mater. Process. Technol. 187–188, 657–661.

Altan, T., Oh, S.-I., Gegel, H.L., 1983. Metal Forming—Fundamentals and Applications. American Society for Metals, Metals Park, OH.

Amini, S., Gollo, A.H., Paktinat, H., 2017. An investigation of conventional and ultrasonic-assisted incremental forming of annealed AA1050 sheet. Int. J. Adv. Manuf. Technol. 90 (5–8), 1569–1578.

Anon, 1965. Ultrasonic metal forming—inching toward full shop status. Steel 48 (17). 3 pp.

Anon, October, 1976. Ultrasonic Application to Powder Metallurgy and Ceramic Processing. Report. Sonobond Corporation, West Chester, PA.

Ao, N., Liu, D., Xu, X., Zhang, X., Liu, D., 2019. Gradient nanostructure evolution and phase transformation of α phase in Ti-6Al-4V alloy induced by ultrasonic surface rolling process. Mater. Sci. Eng. A 742, 820–834.

Ashida, Y., Aoyama, H., 2007. Press forming using ultrasonic vibration. J. Mater. Process. Technol. 187–188, 118–122.

Astashev, V.K., Babitsky, V.I., 2007. Ultrasonic Processes and Machines: Dynamics, Control and Applications. Springer-Verlag, Berlin Heidelberg.

Atanasiu, N., 1976. The wire drawing process with axial ultrasonic vibration of the die. Ultrasonics 14 (2), 69–72.

Atanasiu, N.E., 1980. Intensification of tube drawing by axial oscillation of the plug. Ultrasonics 18 (6), 255–260.

Aziz, S.A., Lucas, M., 2010a. The effect of ultrasonic excitation in metal forming tests. Appl. Mech. Mater. 24–25, 311–316.

Aziz, S.A., Lucas, M., 2010b. A study of an ultrasonically assisted metal forming test. In: Chinesta, F., Chastel, Y., El Mansori, M. (Eds.), International Conference on Advances in Materials and Processing Technologies (AMPT2010), pp. 733–738.

Bagherzadeh, S., Abrina, K., Han, Q., 2016. Ultrasonic assisted equal channel angular extrusion (UAE) as a novel hybrid method for continuous production of ultra-fine grained metals. Mater. Lett. 169, 90–94.

Bai, L., Li, Y., Yang, M., Yao, Z., Yao, Z., 2018. Influences of process parameters and vibration parameters on the forming force in the ultrasonic-assisted incremental forming process. Adv. Mater. Sci. Eng.

Bai, L., Li, Y., Yang, M., Lin, Y., Yuan, Q., Zhao, R., 2019. Modeling and analysis of single point incremental forming force with static pressure support and ultrasonic vibration. Materials 12 (12), 1899.

Balamuth, L., 1964. Recent developments in ultrasonic metalworking processes. In: SAE/ASME Air Transport and Space Meeting, New York, April 27–30. 8 pp.

Balamuth, L., 1965a. Progress in ultrasonic metal forming. In: SAE International Automotive Engineering Congress, Detroit, MI, January 11–15. 10 pp.

Balamuth, L., 1965b. Ultrasonics as applied to metal forming and assembly processes. In: SAE, National Aeronautic and Space Engineering Meeting, Los Angeles, October 4–8. 11 pp.

Biddell, D.C., Sansome, D.H., 1973. The deep-drawing of cans with ultrasonic radial oscillations applied to the die. In: Ultrasonics International 1973 Conference Proceedings, pp. 56–62.

Biddell, D.C., Sansome, D.H., 1974. The development of oscillatory metal-drawing equipment—an engineer's view. Ultrasonics 12 (5), 195–205.

Blaha, F., Langenecker, B., 1955. Dehung von zink-kristallen under ltraschalleinwirkung. Die Naturwissensch. 42, 556.

Brosius, A., 2014. Incremental forming. In: Laperrière, L., Reinhart, G. (Eds.), CIRP Encyclopedia of Production Engineering. Springer Berlin Heidelberg, Berlin, Heidelberg, pp. 689–692.

Buckley, J.J., Freeman, M.K., 1970. Ultrasonic tube drawing. Ultrasonics 8 (3), 152–158.

Bunget, C., Ngaile, G., 2011. Influence of ultrasonic vibration on micro-extrusion. Ultrasonics 51 (5), 606–616.

Cao, H., Shan, X., Liu, S., Shi, Y., Xie, T., 2019. Ultra-fine high carbon steel wire drawing with ultrasonic vibration. Model. Mech. Mater. 531, 012027.

Cao, M.-y., Li, J.-c., Yuan, Y.-n., Zhao, C.-c., 2017. Flexible die drawing of magnesium alloy sheet by superimposing ultrasonic vibration. Trans. Nonferrous Metals Soc. China 27, 163–171.

Cao, M.-y., Li, J.-c., Liu, Y.-y., Yuan, Y.-n., Zhao, C.-c., Dong, G.-j., 2018. Frictional characteristics of sheet metals with superimposed ultrasonic vibrations. J. Cent. South Univ. 25, 1879–1887.

Cheers, C.F., 1995. Design and Optimization of an Ultrasonic Die System for Forming Metal Cans (Ph.D. Dissertation). Loughborough University, Loughborough, UK.

Chen, L., Gu, Y., Liu, L., Liu, S., Hou, B., Liu, Q., Ding, H., 2015. Effect of ultrasonic cold forging technology as the pretreatment on the corrosion resistance of MAO Ca/P coating on AZ318 Mg alloy. J. Alloys Compd. 635 (278–288).

Chen, W., Ma, Y., Lou, Z., 2011. The research on cylindrical ultrasonic rolling machining used for strengthening metal surface. Adv. Mater. Res. 314–316, 28–32.

Cheng, M., Zhang, D., Chen, H., Qin, W., Li, J., 2016. Surface nanocrystallization and its effect on fatigue performance of high-strength materials treated by ultrasonic rolling process. Int. J. Adv. Manuf. Technol. 83 (1-4), 123–131.

Cheng, R.N.W., Short, M., Liu, X., Taub, A., 2019. Applying ultrasonic vibration during single-point and two-point incremental sheet forming. In: Proc. 47th SME North American Manufacturing Research Conference, NAMRC 47.

Chu, T., Fuh, K., Yeh, W., 2012. Experimental optimization of deep drawing using response surface methodology. Appl. Mech. Mater. 121–126, 1495–1499.

Chu, T.-H., Fuh, K.-H., Yeh, W.-C., 2014. Modeling and analysis of deep drawing with utilisation of vibrations and servo press using response surface methodology. Mater. Res. Innov. 18 (Suppl. 2), S2936–S2939.

Cunningham, J.W., Douglas, G.R., 1966. Investigation of the feasibility of applying ultrasonic energy to the rolling process for sheet metals. Final Report on Contract No. w65-0561-d, September, U.S. Naval Air Systems Command, by the Westinghouse Electric Corporation.

Cunningham, J.W., Lanyi, R.J., 1965. Study of the feasibility of applying ultrasonic energy to the rolling process for sheet metals (U). Final Report on Contract No. w64-0294-J, March 15, Bureau of Naval Weapons, by the Westinghouse Electric Corporation R&D Center.

Daud, Y., Lucas, M., Huang, Z., 2006. Superimposed ultrasonic oscillation in compression tests of aluminum. Ultrasonics 44 (1), 511–515.

Daud, Y., Lucas, M., Huang, Z.H., 2007. Modelling the effects of superimposed ultrasonic vibrations on tension and compression tests of aluminium. J. Mater. Process. Technol. 186 (1–3), 179–190.

Daud, Y., Lucas, M., Jamaludin, K.R., 2012. Finite element modeling in ultrasonic sheet metal forming. Adv. Mater. Res. 445, 3–8.

Dawson, G.R., 1975. Ultrasonic radial die oscillations in floating-plug tube drawing. In: Ultrasonics International 1975 Conference Proceedings, pp. 206–209.

Devine, J., 1990. Drawing tube with ultrasonics. TPQ 1 (1), 24–27.

Devine, J., Krause, P.C., 1981. Ultrasonic cold forming of aircraft sheet materials. AVRADCOM Report No. TR 81-F-3, 47 pp.

Ding, J., Shi, E., Zhang, K., Yu, F., 2010. The characterization and experiment research of ultrasonic rolling machining for column surface. Adv. Mater. Res. 102–104, 559–563.

Eaves, A.E., Smith, A.W., Waterhouse, W.J., Sansome, D.H., 1975. Review of the application of ultrasonic vibrations to deforming metals. Ultrasonics 13 (4), 162–170.

Emmens, W.C., 2011. Ultrasonic Forming. Formability, Springer Briefs in Applied Sciences and Technology. Springer Science & Business Media, New York, pp. 67–70 (Chapter 12).

Ensminger, D., Bond, L.J., 2012. Ultrasonics: Fundamentals, Technologies and Applications, third ed. CRC Press.

Ensminger, D., Stulen, F.B., 2009. Ultrasonics: Data, Equations, and Their Practical Uses. CRC Press.

Fartashvand, V., Abdullah, A., Vanini, S.A.S., 2017. Effects of high power ultrasonic vibration on the cold compaction of titanium. Ultrason. Sonochem. 36, 155–161.

Frazier, W.E., 2014. Metal additive manufacturing: a review. J. Mater. Eng. Perform. 23 (6), 1917–1928.

Gebhardt, J., Funke, P., 1983. Wire drawing with ultrasonic vibration—part 1. Wire 33 (6), 225–229.

Gebhardt, J., Funke, P., 1984. Wire drawing with ultrasonic vibration—part 2. Wire 34 (2), 47–51.

Graff, K.F., 2009. On the mechanics and mechanisms of the UP/UIT process. Appendices A, B, C. In: Mohr, W.C. (Ed.), Structural Performance Improvement Technologies: UIT Effect on Fatigue Life. EWI Report MR0904 on Project No. 51540GTO.

Graff, K.F., 2014. Ultrasonic metal forming—a review. EWI IRD Report 54226.

Gu, Y., Ma, H., Yue, W., Tian, B., Chen, L., Mao, D., 2016. Microstructure and corrosion model of MAO coating on nano-grained AA2024 pretreated by ultrasonic cold forging technology. J. Alloys Compd. 681, 120–127.

Hayashi, M., Jin, M., Thipprakmas, S., Murakawa, M., Hung, J.-C., Tsai, Y.-C., Hung, C.-H., 2003. Simulation of ultrasonic-vibration drawing using the finite element method (FEM). J. Mater. Process. Technol. 140, 30–35.

Hou, Y.L., Liu, C.S., Liu, S.Q., 2015. Effect of processing parameters on surface roughness in ultrasonic deep rolling 6061-T6 aluminum alloy with longitudinal-torsional vibration. Proc. Appl. Mech. Mater. Trans. Tech. Publ. 722, 60–63.

Hu, S.J., Chen, Y.R., Hou, J.B., Shu, Q., 2013. Study on the design of a preload adjustable ultrasonic vibration extrusion system. Appl. Mech. Mater. 341–342, 426–466.

Hu, J., Shimizu, T., Yang, M., 2018. Investigation on ultrasonic volume effects: stress superposition, acoustic softening and dynemic impact. Ultrason. Sonochem. 48, 240–248.

Huang, Y.M., Wu, Y.S., Huang, J.Y., 2014. The influence of ultrasonic vibration-assisted micro-deep drawing process. Int. J. Adv. Manuf. Technol. 71 (5–8), 1455–1461.

Hung, J.-C., Chiang, M.-C., 2009. The influence of ultrasonic-vibration on double backward-extrusion of aluminum alloy. In: Proceedings of the World Congress on Engineering 2009, vol. II, WCE 2009, July 1–3, London. U.K. Newswood Limited, pp. 1814–1819.

Hung, J.-C., Huang, C.-C., 2012/2013. Evaluation of friction in ultrasonic vibration-assisted press forging using double cup extrusion tests. Int. J. Precis. Eng. Manuf. 13 (12), 2103–2108.

Hung, J.-C., Hung, C., 2005. The influence of ultrasonic-vibration on hot upsetting of aluminum alloy. Ultrasonics 43, 692–698.

Hung, J.-C., Tsai, Y.-C., Hung, C., 2007. Frictional effect of ultrasonic-vibration on upsetting. Ultrasonics 46, 277–284.

Hwang, M.-H., Lee, H.-S., Han, J.-H., Kim, D.-H., Cha, H.-R., 2019. Densification mechanism of soft magnetic composites using ultrasonic compaction for motors in EV platforms. Materials 12, 824.

Ibrahim, I.N., Sansome, D.H., 1983. An experimental study of the mechanics of ultrasonic tube-bending. In: UI'83 Conference Proceedings, pp. 161–169.

Inoue, M., Mori, E., 1968. Ultrasonic metal wire drawing. In: The 6th International Congress on Acoustics, August 21–28, pp. K-105–K-108.

Izumi, O., Oyama, K., Suzuki, Y., 1966a. On the superimposing of ultrasonic vibration during compressive deformation of metals. Trans. JIM 7 (3), 158–161.

Izumi, O., Oyama, K., Suzuki, Y., 1966b. Effects of superimposed ultrasonic vibration on compressive deformation of metals. Trans. JIM 7 (3), 162–167.

Jimma, T., Kasuga, Y., Iwaki, N., Miyazawa, O., Mori, E., Ito, K., Htaano, H., 1998. An application of ultrasonic vibration to the deep drawing process. J. Mater. Process. Technol. 80–81, 406–412.

Jin, M., Kaewtatip, P., Murakawa, M., 1999. Utility of ultrasonic vibrations applied to metal-forming processes. In: Geiger, M. (Ed.), Advanced Technology of Plasticity, Proceedings of the 6th ICTP, September 19–24, vol. III. Springer-Verlag, Berlin, Germany, pp. 2193–2198.

Jones, J.B., 1967. Ultrasonic metal deformation processing. Reprinted from. In: Proceedings of the CIRP International Conference on Manufacturing Technology, September 25–28. American Society of Tool and Manufacturing Engineers (ASTME), pp. 983–1006.

Kim, S.-W., Lee, Y.-S., 2014. Investigations on the effect of ultrasonic vibration in cylindrical cup drawing processes. Key Eng. Mater. 622–623, 1152–1157.

Konovalov, E.G., Ignashev, E.P., 1972. Flattening round wire into microtape by ultrasonic oscillations. Russ. Ultrason. 2 (1), 49–54.

Kosuge, S., 2011. Evaluation of deformation characteristic in ultrasonic vibration assisted foil bending. In: Proc. 4th AWMFT.

Kristoffy, I., 1969. Metal forming with vibrated tools. J. Manuf. Sci. Eng. 91 (4), 1168–1174.

Kristoffy, I.I., Kegg, R.L., Weber, R.R., 1965. Influence of vibrational energy on metalworking processes. Final Technical Report on AFML-TR-65-211, Air Force Materials Laboratory, Wright-Patterson Air Force Base, Ohio.

Kromp, W., Trimmel, P., Prinz, F.B., Williams, J.C., 1985. Vibratory compaction of metal powders. In: Modern Developments in Powder Metallurgy. 15–17. Metal Powder Industries Federation, Princeton, NJ, pp. 131–141.

Kudryavtsev, Y., Kleiman, J., Lobanov, L., Knysh, V., Prokopenko, G., 2010. Fatigue Life Improvement of Welded Elements by Ultrasonic Peening. IIW Document XIII-2010-04.

Langenecker, B., 1964. Ultrasonic effects in metal processing. In: ASTME (American Society of Tool and Manufacturing Engineers) Technical Papers, SPE65-38 (TP64PUB143). Society of Manufacturing Engineers (SME), Dearborn, MI. 10 pp.

Langenecker, B., 1965. Metal deformation in macrosonic fields. In: Society of Automotive Engineers, National Aeronautic and Space Engineering and Manufacturing Meeting, Los Angeles, October 4–8. 17 pp.

Langenecker, B., Jones, V.O., 1973. Macrosonic wire drawing and tube bending. In: Proceedings of the 1st International Symposium on High-Power, Ultrasonics, pp. 157–160.

Langenecker, B., Vodep, O., 1981. Ultrasonic drawing of fine wires. Wire J. (September), 246–248.

Langenecker, B., et al., 1964. Effects of ultrasound on deformation characteristics of structural metals. NAVWEPS Report 8482 NOTS TP 3447, U.S. Naval Ordnance Test Station, China Lake, CA.

Lehfeldt, E., 1967. The effect of ultrasonic vibrations on the compacting of metal powders. Ultrasonics 5 (4), 219–223.

Lehfeldt, V.E., Pohlman, R., 1968. Drahtziehen mit uberlagerten Ultraschallschwingungen. Draht Fachzeitsch. Coburg 19 (10), 757–765.

Lehfeldt, E., Pohlman, R., 1969. Wire drawing with superimposed ultrasonic vibrations. Wire 102, 205–213.

Li, G., Qu, S., Pan, Y., Li, X., 2016. Effects of the different frequencies and loads of ultrasonic surface rolling on surface mechanical properties and fretting wear resistance of HIP Ti-6Al-4V alloy. Appl. Surf. Sci. 389, 324–334.

Li, G., Qu, S., Xie, M., Ren, Z., Li, X., 2017a. Effect of multi-pass ultrasonic surface rolling on the mechanical and fatigue properties of HIP Ti-6Al-4V alloy. Materials 10 (2), 133.

Li, P., He, J., Liu, Q., Yang, M., Wang, Q., Yuan, Q., Li, Y., 2017b. Evaluation of forming forces in ultrasonic incremental sheet metal forming. Aerosp. Sci. Technol. 63, 132–139.

Li, Y., Chen, X., Sun, J., Li, J., Zhao, G., 2017c. Effects of ultrasonic vibration on deformation mechanism of incremental point-forming process. Procedia Eng. 207, 777–782.

Li, Y., Zhai, W., Wang, Z., Li, X., Sun, L., Li, J., Zhao, G., 2020. Investigation on the material flow and deformation behavior during ultrasonic-assisted incremental forming of straight grooves. J. Mater. Res. Technol. 9 (1), 433–454.

Liu, C., Liu, D., Zhang, X., Yu, S., Zhao, W., 2017a. Effect of the ultrasonic surface rolling process on the fretting fatigue behavior of Ti-6Al-4V alloy. Materials 10 (7), 833.

Liu, C., Liu, D., Zhang, X., Ao, N., Xu, X., Liu, D., Yang, J., 2019a. Fretting fatigue characteristics of Ti-6Al-4V alloy with a gradient nanostructured surface layer induced by ultrasonic surface rolling process. Int. J. Fatigue 125, 249–260.

Liu, C., Liu, D., Zhang, X., Liu, D., Ma, A., Ao, N., Xu, X., 2019b. Improving fatigue performance of Ti-6Al-4V alloy via ultrasonic surface rolling process. J. Mater. Sci. Technol. 35 (8), 1555–1562.

Liu, D., Liu, D., Zhang, X., Liu, C., Ao, N., 2018a. Surface nanocrystallization of 17-4 precipitation-hardening stainless steel subjected to ultrasonic surface rolling process. Mater. Sci. Eng. A 726, 69–81.

Liu, S., Shan, X., Guo, K., Xie, T., 2016. Design and fabrication of a skew-type longitudinal-torsional composite ultrasonic vibrator for titanium wire drawing. IEEE Access.

Liu, S., Shan, X., Guo, K., Yang, Y., Xie, T., 2018b. Experimental study on titanium wire drawing with ultrasonic vibration. Ultrasonics 83, 60–67.

Liu, S., Yang, Yuancai (Student Member, IEEE), Xie, T., Shan, X., 2018c. Experimental study on fine titanium wire drawing with two ultrasonically oscillating dies. IEEE Access.

Liu, S., Xie, T., Cao, H.Q., Shan, X.B., 2019c. Simulation and experimental research on ultrasonic drawing of copper shaped wires. Model. Mech. Mater. 531, 012025.

Liu, Y., Wang, L., Wang, D., 2011a. Finite element modeling of ultrasonic surface rolling process. J. Mater. Process. Technol. 211, 2106–2113.

Liu, Y., Wang, L., Wang, D., 2011b. Study on ultrasonic surface rolling process using FEM analysis. Adv. Mater. Res. 189–193, 2112–2115.

Liu, Y., Han, Q., Hua, L., 2012. Finite element simulation analysis of the ultrasonic vibration forging of an aluminum cylinder workpiece. In: Light Metals 2012. TMS (The Minerals, Metals & Materials Society), Warrendale, PA, pp. 259–264.

Liu, Y., Han, Q., Hua, L., Xu, C., 2013. Numerical and experimental investigation of upsetting with ultrasonic vibration of pure copper cone tip. Ultrasonics 53, 803–807.

Liu, Y., Wang, C., Han, H., Shan, D., Guo, B., 2017c. Investigation on effect of ultrasonic vibration on micro-blanking process of copper foil. Int. J. Adv. Manuf. Technol. 93, 2243–2249.

Liu, Y., Wang, C., Guo, B., Shan, D., Zhang, M., 2017d. Softening effect of ultrasonic vibration on micro-blanking deformation behavior of titanium foil. Micro Nano Lett.

Liu, Y., Cheng, T., Hua, L., Mao, H., 2017b. Research on the effect of ultrasonic vibration on the roll-over during the fine blanking process. J. Mech. Sci. Technol. 31 (2), 835–843.

Lou, Y., Liu, X., He, J., Long, M., 2018. Ultrasonic-assisted extrusion of ZK60 Mg alloy micropins at room temperature. Ultrasonics 83, 194–202.

Lou, Y., Liu, X., 2019. Ultrasonic flexible microextrusion forming of ZK60 Mg alloy at room temperature. In: SAMPSE 2018, IOP Conf. Series: Materials Science and Engineering, p. 490.

Lu, L., Sun, J., Li, L., Xiong, Q., 2016. Study on surface characteristics of 7050-T7451 aluminum alloy by ultrasonic surface rolling process. Int. J. Adv. Manuf. Technol. 87 (9-12), 2533–2539.

Lucas, M., 1996. Vibration sensitivity in the design of ultrasonic forming dies. Ultrasonics 34, 35–41.

Lucas, M., Chapman, G., 1993. Design of ultrasonically assisted radial dies by validated finite element models. In: Ultrasonics International 93 Conference Proceedings, pp. 707–710.

Lucas, M., Daud, Y., 2009. A finite element model of ultrasonic extrusion. J. Phys. Conf. Ser. 181. 7th International Conference on Modern Practice in Stress and Vibration, Analysis.

Luo, F., Li, K.-h., Zhong, J.-m., Gong, F., Wu, X.-y., Ruan, S.-c., 2015. An ultrasonic microforming process for thin sheet metals and its replication abilities. J. Mater. Process. Technol. 216, 10–18.

Malekipour, E., Heidary, H., Majd, N.S., Mazdak, S., Sharifi, E., 2020. Effect of resonant frequency variation on the ultrasonically assisted deep drawing process: numerical and experimental study. Int. J. Adv. Manuf. Technol. 106, 2243–2264.

Malhotra, R., Cao, J., Ren, F., Kiridena, V., Cedric Xia, Z., Reddy, N.V., 2011. Improvement of geometric accuracy in incremental forming by using a squeezing toolpath strategy with two forming tools. J. Manuf. Sci. Eng. 133 (6), 061010–061019.

Maropis, N., 1991a. Ultrasonic energy applied to metal drawing—part I. Wire Ind. 58 (5), 251–253. 256.

Maropis, N., 1991b. Ultrasonic energy applied to metal drawing—part II. Wire Ind. 58 (6), 327–333.

Maropis, N., 1991c. Ultrasonic energy applied to metal drawing—part III. Wire Ind. 58 (7), 371–373.

McMaster, R.C., et al., 1967. Sonically assisted deformation of aluminum alloys. Interim Report Project EES291-X, June 14.

Mei, G., Zhang, K., Ding, J., 2010. Study on the effect of ultrasonic surface rolling processing parameters on the surface roughness of Q345 hydraulic prop. Adv. Mater. Res. 102–104, 591–594.

Meyer, F.R., 1973. Engineering feasibility study of ultrasonic applications for aircraft manufacture. Research Report 73-15, Contract DAAJ01-72-C-0737(P1G). Aeroprojects, Inc., West Chester, PA. Department of the Army, U.S. Army Aviation Systems Command, St. Louis, MO.

Mita, K., Hu, J., Shimizu, T., Yang, M., 2018. Shearing characteristics in ultrasonic vibration-assisted piercing of fine-grained stainless steel foils. Procedia Manufact. 15, 627–632.

Mordyuke, B.N., Mordyuk, V.S., Buryak, V.V., 2004. Ultrasonic drawing of tungsten wire for incandescent lamps production. Ultrasonics 42, 109–111.

Mori, E., Inoue, M., 1968. Nikhon Kindzoku and Gakkai Kaikho. Bull. Jpn. Ins. Met. 7 (1), 27–33. as summarized in Severdenko et al. (1972a,b).

Murakawa, M., Jin, M., 2001. The utility of radially and ultrasonically vibrated dies in the wire drawing process. J. Mater. Process. Technol. 113, 81–86.

Nakagiri, A., Sansome, D.H., 1977. Ultrasonic tube expansion. In: Proceedings Ultrasonics International. IPC Science and Technology Press, Ltd., Guildford, Surrey, UK, pp. 338–345.

Narkevich, N.A., Tolmachev, I.V., Surikova, N.S., 2016. Structure and mechanical properties of nitrogen austenitic steel after ultrasonic forging. Phys. Metals Metall. 117 (3), 288–294.

Obikawa, T., Hayashi, M., 2017a. Ultrasonic-assisted incremental microforming of thin shell pyramids of metallic foil. Micromachines 8, 142.

Obikawa, T., Hayashi, M., 2017b. Ultrasonic-assisted incremental microforming of thin shell pyramids of metallic foil. Micromachines 8 (5), 142.

Oelschlagel, D., Weiss, B., 1965. Ultrasonic facilitation of wire drawing. Acta Phys. Austrica 20 (1–4), 363–369 (translation of "Erleichterung des Drahtziehens durch Ultraschall").

Oelschlagel, D., Weiss, B., 1966. Improved efficiency in wire drawing with ultrasound. Trans. ASM 59, 685–693.

Okazaki, Y., Kawaguchi, K., 1990. Ultrasonic deep-drawing of aluminum foil. Adv. Technol. Plast. 3, 1333–1340.

Pasierb, A., Wojnar, A., 1992. An experimental investigation of deep drawing and drawing processes of thin-walled products with utilization of ultrasonic vibrations. J. Mater. Process. Technol. 34, 489–494.

Pazand, K., Feizi, H., 2011. Using artificial neural networks in investigations on the effects of ultrasonic vibrations on the extrusion process. Appl. Mech. Mater. 52–54, 103–108.

Peacock, J., 1961. Forming goes ultrasonic. Am. Mach. 105 (25), 83–85.

Petruzelka, J., Licka, S., Sarmanova, J., 1984. Analysis of a tube drawing process run on a mandrel vibrated at ultrasonic frequencies. Hutnik (Katowice) 4, 129–136.

Petruzelka, J., Sarmanova, J., Sarman, A., 1996. The effect of ultrasound on tube drawing. J. Mater. Process. Technol. 60 (1–4), 661–668.

Petukhov, V.I., Smirnov, O.M., Barantseva, Z.V., Borodkina, M.M., Alekseeva, L.E., Trakhimovich, I.M., 1987. The effect of alternating stresses at ultrasonic frequency on the structure and plasticity of metals. Izvest. Akad. Nauk SSSR, Metally 4, 110–117.

Pohlman, R., Lehfeldt, E., 1966. Influence of ultrasonic vibration on metallic friction. Ultrasonics 4 (4), 178–185.

Presz, W., Andersen, B., 2007. Flexible tooling for vibration-assisted microforming. J. Achiev. Mater. Manuf. Eng. 21 (2), 61–64.

Presz, W., Cacko, R., 2017. Ultrasonic assisted microforming. In: Metal 17, Proceedings of the 26th International Conference on Microforming, May 24th–26th, 2017. EU, Brno, Czech Republic.

Presz, W., 2020. Influence of experimental setup parameters on ultrasonic assisted micro-upsetting. Arch. Metall. Mater. 65 (1), 423–431.

Puskar, A., 1982. The Use of High-Intensity Ultrasonics. Elsevier Scientific Publishing Company, Amsterdam, the Netherlands, Oxford, UK, New York, USA.

Qi, H.-Q., Yuan, J.-B., Xie, T., 2008. Investigations on the effects of ultrasonic vibrations in the wire drawing. In: IEEE International Ultrasonics Symposium Proceedings, pp. 2134–2137.

Qi, H.-Q., Shan, X., Xie, T., 2009. Design and experiment of the high speed wire drawing with ultrasound. Chin. J. Mech. Eng. (Engl. Ed.) 22 (4), 580–586.

Razavi, H., Beni, Y.T., Baharvand, M., 2017. Ultrasonic assisted equal channel angular extrusion process (UAECAE). Int. J. Adv. Des. Manuf. Technol. 10 (1), 13–22.

Rees, T.W., Rippon, D.J., 1983. The application of ultrasonic vibrations in tube drawing. In: Proceedings of the International Conference on Developments in the Drawing of Metals, London, May 11–13. Metals Society, London, pp. 132–140.

Robinson, A.T., 1964. The application of ultrasonic energy to metal wire drawing. Wire Wire Prod. 39 (12), 1925–1931.

Rosato, A.D., Vreeland Jr., T., Prinz, F.B., 1991. Manufacture of power composites. Int. Mater. Rev. 36 (2), 45–61.

Rosenfeld, A.R. (Ed.), 1963. The application of ultrasonic energy in the deformation of metals. Defense Metals Information Center, Battelle Memorial Institute, Columbus, OH, DMIC Report 187, August 16.

Rosochowska, M., Rosochowski, A., 2007. FE simulation of ultrasonic back extrusion. In: Cueto, E., Chinesta, F. (Eds.), 10th ESAFORM Conference on Material Forming. American Institute of Physics, College Park, MD, pp. 564–569.

Sansome, D.H., 1973. Recent developments in oscillatory metal working. Engineering 213 (4), 243–247.

Sedaghat, H., Xu, W., Zhang, L., 2019. Ultrasonic vibration-assisted metal forming: constitutive modelling of acoustoplasticity and applications. J. Mater. Process. Technol. 265, 122–129.

Sekine, T., Obikawa, T., 2010. Single point micro incremental forming of miniature shell structures. J. Adv. Mech. Des. Syst. Manuf. 4 (2), 543–557.

Severdenko, V.P., Klubovich, V.V., 1961. Deformation of metal in an ultrasonic field. Dokl. Akad. Nauk BSSR 1, 15–16. Edited machine translation, USAF Foreign Technology Division.

Severdenko, V.P., Klubovich, V.V., 1963. Drawing of copper wire in an ultrasonic field. Dokl. Akad. Nauk BSSR 7 (2), 95–98.

Severdenko, V.P., Klubovich, V.V., 1965. Distribution of deformation along the height of the test piece when upsetting it under ultrasonic vibration. Izvest. VUZ Chern. Metall. 1 (January), 61–64.

Severdenko, V.P., et al., 1971. Ultrasonic metal-drawing programs. Russ. Ultrason. 1 (2), 92–95.

Severdenko, V.P., Klubovich, V.V., Spepanenko, A.V., 1972a. Ultrasonic Rolling and Drawing of Metals. Consultants Bureau, New York. Translated from 1970 Russian Publication.

Severdenko, V.P., Stepanenko, A.V., Zayash, I.V., 1972b. The effect of roll velocity on the efficiency of the ultrasonic oscillation technique. Russ. Ultrason. 2 (1), 33–36a.

Severdenko, V.P., Stepanenko, A.V., Kalenik, V.V., 1973a. Rolling with co-phased torsional ultrasonic oscillations in the rollers. Russ. Ultrason. 3 (3), 150–156.

Severdenko, V.P., et al., 1973b. Drawing of aluminium alloy tubes under ultrasound. Russ. Ultrason. 3 (3), 156–159.

Severdenko, V.P., et al., 1973c. The effect of ultrasonic vibrations on the force parameters for the drawing of wires made from hard metals and alloys. Russ. Ultrason. 3 (4), 216–220.

Severdenko, V.P., Lozhechnikov, E.B., Baek, M.A., Stepanenko, A.V., 1974. Rolling of dispersion-strengthened materials with the application of ultrasonic vibrations. Poroshkovaya Metall. 2 (134), 14–16.

Severdenko, V.P., et al., 1975. Deep Drawing of Sheet Metal with Ultrasonics. Nauka i Tekhnika, Minsk. 192 pp. (in Russian). Translated in "Effect of ultrasonic vibration on sheet metal drawing", in Metalworking Interfaces, pp. 8–13 (May–June, 1977).

Severdenko, V.P., Babchenko, A.M., Ofshtein, B.L., Burnos, V.A., Khodos, R.S., Tsirul'nikov, V.A., Shkurenko, A.A., 1978. Effect of ultrasonic vibrations on the steel-rolling process. Fiziko-Khimicheskaya Mekhanika Materialov 14 (2), 79–80.

Shan, X., Qi, H., Wang, L., Xie, T., 2012a. A new model of the antifriction effect on wiredrawing with ultrasound. Int. J. Adv. Manuf. Technol. 63, 1047–1056.

Shan, X., Qi, N., Wang, L., Xie, T., 2012b. A high efficient variable cross-section compound ultrasonic wiredrawing vibration system. Appl. Mech. Mater. 157–158, 1689–1694.

Shan, X., Qi, N., Wang, L., Xie, T., 2012c. Key factors affecting the amplitude of a composite ultrasonic wiredrawing vibration system. Appl. Mech. Mater. 157–158, 395–399.

Sheykholslami, M., Cinquemani, S., Mazdak, S., 2018. Numerical study of the ultrasonic vibration in deep drawing process of circular sections with rubber die. In: Proc. SPIE 10595, Active and Passive Smart Structures and Integrated Systems XII (15 March).

Siddiq, A., El Sayed, T., 2012. Ultrasonic-assisted manufacturing processes: variational model and numerical simulations. Ultrasonics 52, 521–529.

Siegert, K., Mock, A., 1996. Wire drawing with ultrasonically oscillating dies. J. Mater. Process. Technol. 60, 657–660.

Siegert, K., Ulmer, J., 2000. Superimposing ultrasonic waves on tube and wire drawing. SAE Technical Paper 2000-01-1283, 7 pp.

Siegert, K., Ulmer, J., 2001. Superimposing ultrasonic waves on the dies in tube and wire drawing. J. Eng. Mater. Technol. 123 (October), 517–523.

Smith, A.W., Sansome, D.H., 1975. An experimental investigation of the effect of blank-holder vibrations on an analogue of the deep-drawing process. In: Ultrasonics International 1975 Conference Proceedings, pp. 210–213.

Su, C.J., Xu, T.T., Zhang, K., Zhang, K., Lou, S.M., Wang, Q., 2018. Plastic deformation of magnesium alloy with different forming parameters during ultrasonic vibration-assisted single-point incremental forming. Rare Metals.

Sugahara, T., et al., 1970. Application of ultrasonic vibration to metal tube drawing process—1. Nippon Kokan Tech. Rep. Overseas, No. 11, December, 51–59.

Sugahara, T., et al., 1971. Application of ultrasonic vibration to metal tube drawing process—2. Nippon Kokan Tech. Rep. Overseas, June, pp. 27–36.

Suh, C.-M., Song, G.-H., Park, H.-D., Pyoun, Y.-S., 2006. A study of the mechanical characteristics of ultrasonic cold forged SKD61. Int. J. Mod. Phys. B 20 (25–27), 4541–4546.

Suh, C.-M., Song, G.-H., Suh, M.-S., Pyoun, Y.-S., 2007. Fatigue and mechanical characteristic of nano-structured tool steel by ultrasonic cold forging technology. Mater. Sci. Eng. A 443, 101–106.

Suh, C.-M., Lee, M.-H., Pyoun, Y.-S., 2010. Fatigue characteristics of SKD-61 by ultrasonic nanocrystal surface modification technology under static load variation. Int. J. Mod. Phys. B 24 (15–16), 2645–2650.

Sun, L., Jiang, F., Yuan, D., Sun, X., Su, Y., Guo, C., 2019. Effects of ultrasonic micro-forging on 304 stainless steel fabricated by WAAM. Miner. Metals Mater. Sci., 251–258.

Susan, M., Bujoreau, L.G., et al., 2005. On the drawing in ultrasonic field of metallic wires with high mechanical resistance. J. Optoelectron. Adv. Mater. 7 (2), 637–645.

Tisza, M., 1983. Deep drawing by superimposed ultrasonic vibration. BISE 23677, Banyasz, Kohasz, Lapok (Kohasz), from Hung 116 (3), pp. 104–109.

Tosello, G., et al., 2019. Micro product and process fingerprints for zero-defect net-shape micromanufacturing. In: Euspen's 19th International Conference & Exhibition, Bilbao, ES, June.

Trimmel, P., Kromp, W., Claussen, N., 1979. Ultrasonically aided hot-pressing of powder materials. In: Ultrasonics International 79 Conference Proceedings, pp. 562–571.

Trung, T.B., Phuong, D.D., Van Luan, N., Vasilievich, R.V., 2017. Effect of ultrasonic-assisted compaction on density and hardness of Cu-CNT nanocomposites sintered by capsule-free hot isostatic pressing. Acta Metall. Slovaca 23 (1), 30–36.

Tsujino, J., Ueoka, T., Atsumi, Y., Aoki, S., Yamamoto, J., 1983. Studies on the ultrasonic vibration press of powder with a vibration die. In: Ultrasonics International 83 Conference Proceedings, pp. 170–175.

Tsujino, J., Satoh, H., Takiguchi, K., 1991. Studies on ultrasonic vibration bending of thin metal plates. Jpn. J. Appl. Phys. 30 (30-1), 203–305.

Tsujino, J., Ueoka, T., Takiguchi, K., Takayama, Y., 1993a. Ultrasonic bending of thin metal plates using a vibration punch and a vibration die. In: Ultrasonics International 93 Conference Proceedings, pp. 691–694.

Tsujino, J., Ueoka, T., Takiguchi, K., Satoh, H., Takahashi, K., 1993b. Characteristics of bending parts of metal plates using ultrasonic bending systems with a vibration punch and a vibration die. Jpn. J. Appl. Phys. 32, 2447–2451 (Part 1, No. 5B).

Vagapov, I.K., Zhydkevich, V.I., Klubovich, V.V., 1991. Examination of energy-force and physico-mechanical characteristics of steel in drawing with application of longitudinal ultrasonic oscillations. Phys. Chem. Mater. Treat. 25 (2), 205–209.

Vahdati, M., Mahdavinejad, R., Amini, S., 2017. Investigation of the ultrasonic vibration effect in incremental sheet metal forming process. Proc. Inst. Mech. Eng. B J. Eng. Manuf. 231 (6), 971–982.

Vollertsen, F., Hu, Z., Schulze Niehoff, H., 2004. State of the art in micro forming and investigations into micro deep drawing. J. Mater. Process. Technol. 151, 70–79.

Wang, C., Liu, Y., Wan, S., Guo, B., Shan, D., Zhang, B., 2019. Effect of ultrasonic vibration on deformation in micro-blanking process with copper foil. J. Wuhan Univ. Technol. Mater. Sci. Ed. 34 (2), 404–409.

Wang, H., Song, G., Tang, G., 2016. Effect of electropulsing on surface mechanical properties and microstructure of AISI 304 stainless steel during ultrasonic surface rolling process. Mater. Sci. Eng. A 662, 456–467.

Wang, X., Yu, Y., 2018a. Experimental investigation on GCr15 steel for marine vessels treated by ultrasonic assisted equal channel angular extrusion. J. Coast. Res. 83 (Sp1), 548–551.

Wang, X., Yu, Y., 2018b. Effects of equal channel angular extrusion assisted by ultrasonic and subsequent heat treatment on tribological properties of 65Mn for marine vessels. J. Coast. Res. 83 (S1), 350–355.

Wang, Z., Xiao, Z., Huang, C., Wen, L., Zhang, W., 2017. Influence of ultrasonic surface rolling on microstructure and wear behavior of selective laser melted Ti-6Al-4V alloy. Materials 10 (10), 1203.

Winsper, C.E., Sansome, D.H., 1967. A review of the application of oscillatory energy to metals deforming plastically. In: Advance 26 Page Draft of Paper Published in Proceedings of the Eighth International Machine Tool Design and Research Conference, Manchester, September, pp. 1359–1360.

Winsper, C.E., Sansome, D.H., 1968–1969. The superposition of longitudinal sonic oscillations on the wire drawing process. Inst. Mech. Eng. Appl. Mech. Group, Proc. 183 (Part 1). 12 pp.

Winsper, C.E., Sansome, D.H., 1969. Fundamentals of "ultrasonic" wire drawing. J. Inst. Met. 97, 274–280.

Winsper, C.E., Sansome, D.H., 1971. Application of ultrasonic vibrations to the plug drawing of tube. Met. Form. 38 (3), 71–75.

Witthauer, A.T., Faidley, L.A., Kim, G.-Y., 2010. Bulk motion for ultrasonic-assisted microforming using Terfenol-D. In: McMickell, M.B., Farinholt, K.M. (Eds.), Industrial and Commercial Applications of Smart Structures Technologies. Proceedings of SPIE. vol. 7645. SPIE, Bellingham, WA.

Xia, T., Zeng, L., Zhang, X., Liu, J., Zhang, W., Liang, T., Yang, B., 2019. Enhanced corrosion resistance of a Cu10Ni alloy in a 3.5 wt% NaCl solution by means of ultrasonic surface rolling treatment. Surf. Coat. Technol. 363, 390–399.

Xu, L., Lei, Y., Zhang, H., Zhang, Z., Sheng, Y., Han, G., 2019a. Research on the micro-extrusion process of copper T2 with different ultrasonic vibration modes. Metals 9, 1209.

Xu, X., Liu, D., Zhang, X., Liu, C., Liu, D., Zhang, W., 2019b. Influence of ultrasonic rolling on surface integrity and corrosion fatigue behavior of 7B50-T7751 aluminum alloy. Int. J. Fatigue 125, 237–248.

Yang, C., Shan, X., Xie, T., 2015. A new piezoelectric ceramic longitudinal-torsional composite vibrator for wire drawing. Ceram. Int. 41, 5625–5630.

Yang, C., Shan, X., Xie, T., 2016. Titanium wire drawing with longitudinal-torsional composite ultrasonic vibration. Int. J. Adv. Manuf. Technol. 83, 645–655.

Yang, M., Bai, L., Li, Y., Yuan, Q., 2019. Influences of vibration parameters on formability of 1060 aluminum sheet processed by ultrasonic vibration-assisted single point incremental forming. Adv. Mater. Sci. Eng.

Yao, Z., Kim, G.-Y., Faidley, L.A., Zou, Q., Mei, D., Chen, Z., 2010. Micro pin extrusion of metallic materials assisted by ultrasonic vibration. In: Proceedings of the ASME 2010 International Manufacturing Science and Engineering Conference MSEC2010, October 12–15, pp. 247–251.

Yeh, W.-C., Chu, T.-H., 2012. The influence of blanking process by superimposing ultrasonic vibrations. Adv. Mater. Res. 579, 78–85.

Yeh, W., Chu, T., Wang, S., Fuh, K., Chen, K., 2011. Finite element analysis of blanking process by superimposing ultrasonic vibrations. Adv. Mater. Res. 201–203, 126–132.

Ye, H., Ye, K., Guo, B.-g., Le, F.-b., Wei, C., Sun, X., Wang, G.-y., Liu, Y., 2020a. Effects of combining ultrasonic micro-forging treatment with laser metal wire deposition on microstructural and mechanical properties in Ti-6Al-4V alloy. Mater. Charact. 162, 110187.

Ye, H., Ye, K., Guo, B.-g., Le, F.-b., Wei, C., Sun, X., Wang, G.-y., Liu, Y., 2020b. Effects of combining ultrasonic micro-forging treatment with

laser metal wire deposition on microstructural and mechanical properties in Ti-6Al-4V alloy. Mater. Charact. 162.

Ye, Y., Kure-Chu, S.-Z., Sun, Z., Li, X., Wang, H., Tang, G., 2018. Nanocrystallization and enhanced surface mechanical properties of commercial pure titanium by electropulsing-assisted ultrasonic surface rolling. Mater. Des. 149, 214–227.

Young, M.J.R., Biddell, D.C., Winsper, C.E., Sansome, D.H., 1971. Improvements in or relating to the forming of materials. NRDC UK Patent Application 8513/71, April 2.

Yuhara, M., Hoshino, M., Wada, O., 2012. Draw bending of tube using ultrasonic-vibration plug. J. Jpn. Soc. Technol. Plast. 53 (618), 646–650.

Zalesskii, V.I., Mishchenkov, Y.I., 1969. Selection of the vibration system for extrusion in an ultrasonic field. Izvest. VUZ Chern. Metall. 12 (1), 116–119.

Zha, C.-L., Chen, W., 2019a. Theories and experiments on effects of acoustic energy field in micro-square cup drawing. Int. J. Adv. Manuf. Technol. 104, 4791–4802.

Zha, C., Chen, W., 2019b. Experimental investigation into effects of acoustic energy field in micro-forming process. U.P.B. Sci. Bull. Ser. D 81, 3.

Zhadan, V.T., 1966. Influence of ultrasonics on the upsetting of steels that are difficult to work. Izvest. Vysshikh Uchebnykh Zavedenii, Chernaya Metallurgiya (Izvest. VUZ Chern. Met.) 11, 93–96.

Zhai, J., Guan, Y., Wang, W., Zhu, L., Xie, Z., Lin, J., 2019. Studies on ultrasonic vibration-assisted coining of micro-cylinder. Int. J. Adv. Manuf. Technol. 100, 2031–2044.

Zhang, Q., Hu, Z., Su, W., Zhou, H., Liu, C., Yang, Y., Qi, X., 2017. Microstructure and surface properties of 17-4PH stainless steel by ultrasonic surface rolling technology. Surf. Coat. Technol. 321, 64–73.

Zhang, T., Li, L., Lu, S.-h., Gong, H., 2018. Simulation of prestressed ultrasonic peen forming on bending deformation and residual stress distribution. Int. J. Adv. Manuf. Technol. 98, 385–393.

Zhang, T., Sha, H., Lu, S., Zhang, J., Zhou, Y., Gong, H., 2019a. Bending deformation and surface properties of stiffened plat during ultrasonic peen forming. Mech. Adv. Mater. Struct. 1537–1694.

Zhang, T., Sha, H., Lu, S., Li, L., Wang, Z., 2019b. Study of prestress ultrasonic peening on bending curvature and surface properties of stiffened plates. J. Brazil. Soc. Mech. Sci. Eng. 41, 409.

Zhang, T., Li, L., Lu, S.-h., Zhang, J.-b., Zhou, Z., Gong, H., 2019c. Effect of prestressed ultrasonic peen forming parameters on bending curvature and spherical deformation of plate. Trans. Nonferrous Met. Soc. China 29, 270–278.

Zhang, T., Zhang, S., Sha, H., Lu, S., Wang, Z., 2020. Effect of prebending curvature on bending strain and surface properties of stiffened plate during prestressed ultrasonic peening. Int. J. Adv. Manuf. Technol. 106, 2765–2777.

Zheng, J., Jiang, J., Liu, C., 2010. Experimental study on optimizing process parameters in two-dimensional ultrasonic rolled extrusion. Appl. Mech. Mater. 37–38, 435–438.

Zheng, J.X., Liu, C.S., Zhang, Y.M., 2011. Basic research on ultrasonic extrusion for 45 steel shaft. Key Eng. Mater. 455, 288–293.

Zhao, W., Liu, D., Zhang, X., Zhou, Y., Zhang, R., Zhang, H., Ye, C., 2019. Improving the fretting and corrosion fatigue performance of 300M ultra-high strength steel using the ultrasonic surface rolling process. Int. J. Fatigue 121, 30–38.

Zust, R., 2000. Wet and dry wire drawing with ultrasonic support. Wire Ind. (UK) 67 (796), 341–342.

Chapter 15

Using power ultrasonics in machine tools

A. Moghaddas and K.F. Graff
EWI, Columbus, OH, United States

15.1 Introduction

The application of power ultrasonics to machine tools falls within the broadly defined field of *ultrasonic machining* that dates back to the early 1950s and, due to both its longevity and diversity of developments, has accumulated a range of terminology that can be confusing as new developments appear on the scene.

In this chapter, ultrasonic machining will deal with the application of power ultrasonic vibrations to traditional machine tools and processes (e.g., drilling, milling, and single-point turning) to improve performance (e.g., faster drilling, improved finish, extended tool life, and challenging materials), as shown in concept by Figure 15.1 for several machining processes. The specific means by which ultrasonics (shown by the oscillating arrow) are coupled to these processes will be as varied as the processes themselves.

Most publications in this field have adopted terms involving variations of *ultrasonically assisted*, as in ultrasonically assisted turning (UAT), drilling (UAD), or milling (UAM). The term *vibration-assisted* will also be found. Whatever the variations, the intent remains that of ultrasonic vibration of traditional tooling.

Having defined what ultrasonic machining *is*, it is also important to emphasize what it *is not*. The technology often found in the literature as "ultrasonic machining" refers to a slurry-based process used to drill irregular-shaped holes in extremely hard materials (e.g., glass, ceramics, or quartz). While a somewhat special process, it finds valuable applications (e.g., in recent years to nanomachining) and may also be variously termed *ultrasonic impact machining*, *impact grinding*, or *ultrasonic drilling*.

From an historical perspective, the application of low-frequency vibrations to machining processes predates the use of ultrasonics. In his review of ultrasonics applied to machine tools, Markov (1962) states that Russian work on vibrating tooling can be dated back to 1910 and notes a number of other Russian developments on low-frequency machining in the late 1950s and early 1960s. It is uncertain as to the first application of ultrasonics to machine tools (excluding that of slurry drilling), but again, from Markov, note is made of 1957 work on applying ultrasonics to the grinding process, with numerous contributions to the literature from 1961 onward. These various early developments, through the 1980s, will be covered in the following, drawing from a review of the field by Graff (2007).

This chapter will address the application of ultrasonic vibrations to the major machining processes, thus turning, drilling, milling, reaming, honing, tapping, and grinding. Where possible, coverage will span from early development to the recent work in each of the fields.

15.2 Historical and technical review

The application of low-frequency vibrations to machining processes predates the use of ultrasonics. In his review of ultrasonics applied to machine tools, Markov (1962) states that Russian work on vibrating tooling can be dated back to 1910 and notes a number of other Russian developments on low-frequency machining in the late 1950s and early 1960s. It is uncertain as to the first application of ultrasonics to machine tools (excluding that of slurry drilling), but again, from Markov, note is made of 1957 work on applying ultrasonics to the grinding process, with numerous contributions to the literature from 1961 onward. Drawing from a review by Graff (2007), these various early developments through the 1980s will be covered in the present section and provide the foundation upon which recent developments, described in the later sections, are based.

15.2.1 Surface grinding

Voronin et al. (1961) applied ultrasonics to sharpening of cutters, using setups shown in Figure 15.2. The cutting tools being sharpened were ultrasonically vibrated and pressed against a standard grinding wheel, against the outer rim in Figure 15.2a, and against the side face in Figure 15.2b.

The work of Balamuth (Peacock, 1961; Peacock et al., 1962) on the application of ultrasonics to grinding wheels led to commercial equipment in the 1960s. In one approach, ultrasonics was applied through a fluid coupling to the top

Power Ultrasonics. https://doi.org/10.1016/B978-0-12-820254-8.00002-6
Copyright © 2023 Elsevier Ltd. All rights reserved.

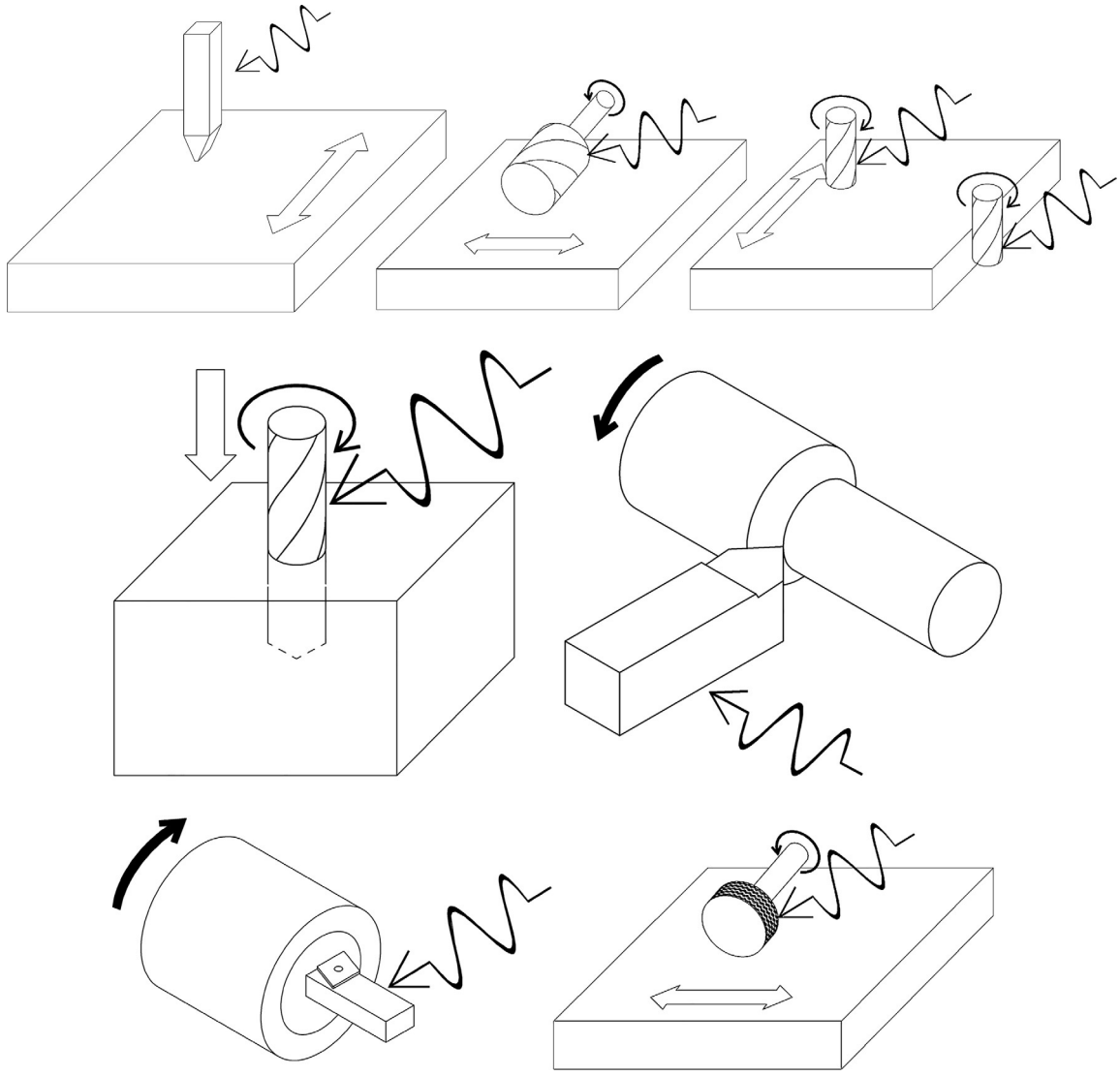


FIGURE 15.1 Addition of ultrasonic vibrations to machine tool processes. *(Source: EWI.)*

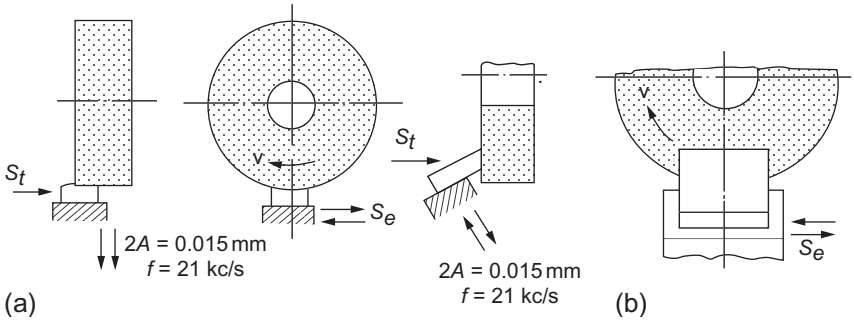


FIGURE 15.2 Setups for ultrasonic sharpening of cutting tools: grinding against the outer rim in (a) and against the side face in (b). Voronin (1961) as shown in Markov (1962), Fig. 137. *(Source: Markov (1962).)*

surface of the wheel, resulting in continuous ultrasonic cleaning of the wheel surface.

In a second Balamuth approach, the grinding wheel was designed to be radially resonant as shown in Figure 15.3a. This idea and related concepts for ultrasonic grinding were reported by the Sheffield Company (one of the pioneering companies in conventional ultrasonic machining) under U.S. Air Force sponsorship (Roney and Giardini, 1963). Balamuth (1964) also reported on tests of an ultrasonically vibrated single-point cutter as shown in Figure 15.3b.

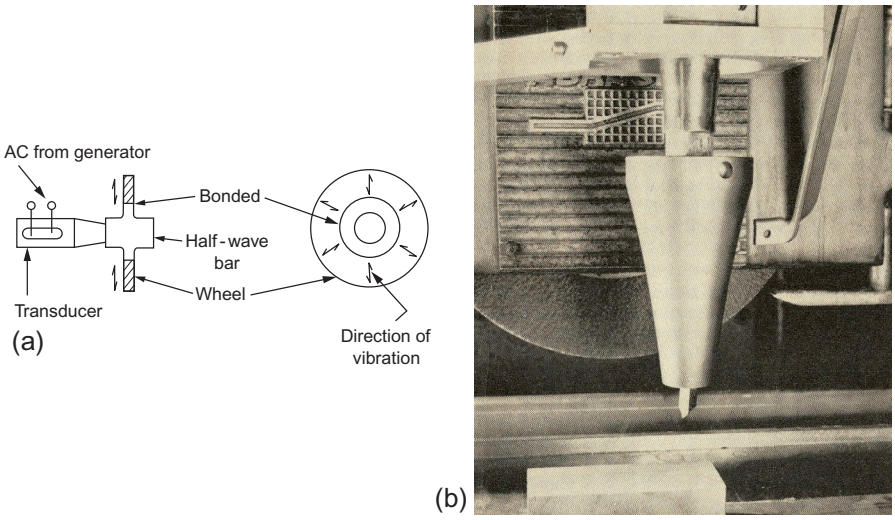


FIGURE 15.3 Machining developments by Balamuth: (a) ultrasonic grinding wheel (Peacock et al., 1962, Fig. 3, lower) and (b) single-point cutting system in Balamuth (1964, Fig. 1).

Without ultrasonics, considerable chatter was noted while with ultrasonics, a smooth cut was observed.

15.2.2 Turning

Markov (1962) also reviewed ultrasonics applied to turning operations, covering his own work and other Russian investigators. Thus, Figure 15.4a shows the turning system developed by Voronin and Markov, where the main components of the cutting tool (1), clamping (2), horn (3), and transducer (4) are within the housing (8). Data are presented on the influence of ultrasonics on tool life, surface profile, and friction. An ultrasonic machining head, consisting of the cutting tool (1), ultrasonic horn (2), and water-cooled transducer (4), developed by Isayev and Anokhin, is shown in Figure 15.4b and was used in cutting studies on steels.

Markov also describes an ultrasonic unit developed by Zhustarev et al. (1960) for use in thread-cutting, drilling, and milling. A review of the references in Markov shows ultrasonic machining to be an active research field in Russia in that period, with many publications in the early 1960s. Markov also notes Japanese work by Kamabe (1958) on ultrasonic cutting of aluminum, brass, and steel. Kumabe (1961a,b) describes work on ultrasonic turning.

A paper on ultrasonic turning by Dohmen (1966) covered effects on surface finish, including data on profiles for various materials. The acoustical design of the ultrasonic components was also noted. This work appears to be one of the more comprehensive studies to emerge from the early years of machining work. Figure 15.5a shows the experimental equipment, with Figure 15.5b showing results on chip formation.

Wang and Zhao (1987) reported on the effects of ultrasonic turning on surface roughness, with images showing the impact of varying turning conditions on surface finish, as well as results on surface micromorphology. Romanyuk (1988) applied ultrasonics to the honing process, including the use of contoured ultrasonic tooling. In the work of Takeyama and Kato (1991), the use of ultrasonics to reduce drilling burrs was studied. The approach was to apply ultrasonics to the workpiece, while otherwise using a conventional drilling system. The work by Cornier (1992) looked at both water jet and ultrasonic assistance in the turning process.

The Aeroprojects Corporation, formed in the late 1940s (and its successor Sonobond, Inc.), was a pioneering company in high-power ultrasonics, responsible for many innovations including invention of the ultrasonic metal welding process and was an early contributor to the machining field (Anon, 1964, 1965, 1971a). Figure 15.6a shows the ultrasonic unit mounted on a conventional lathe. The effect of ultrasonics on the part surface is shown in Figure 15.6b (left) by the alternating texture bands and a close view Figure 15.6b (right) of the transition from ultrasonic treatment (lower region) to no ultrasonics (upper region). Other developments in this period were reported by Devine (1978, 1979) and Devine and Krause (1980) on an advanced tool post design.

15.2.3 Reaming

Isayev and Anokhin (1962) reported on ultrasonic reaming and noting that the grooves in the tool were designed to create a torsional motion of the reamer. They noted the effect of ultrasonics in improving hole surface finish in working with two different grades of steel.

15.2.4 Milling

Balamuth (1964) introduced the application of ultrasonics to the milling operation, as shown in Figure 15.7. The overall

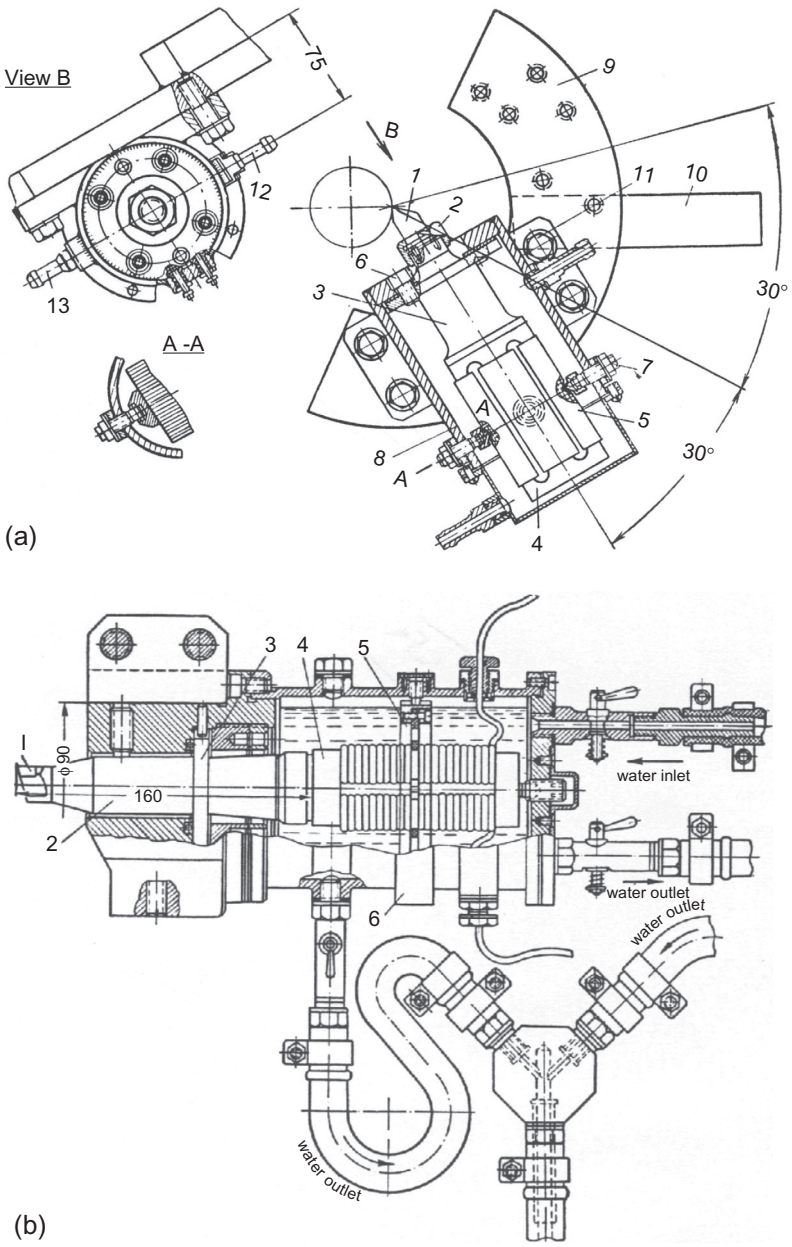


FIGURE 15.4 Ultrasonic turning systems: (a) system of Voronin and Markov (Markov, 1962, Fig. 144) and (b) system of Isayev and Anokhin (Markov, 1962, Fig. 151).

system of robust construction is shown in Figure 15.7a, while the details of the ultrasonic mill unit are shown in the upper part of Figure 15.7b. A ¼-in. deep milling cut on 4030 steel is shown in the lower part of the figure, with the left portion of the cut being with ultrasonic excitation, the right portion without.

15.2.5 Drilling

Aeroprojects (Anon, 1971b) reported on ultrasonic twist drilling, and the drilling system is shown in Figure 15.8. A separate, lathe bed mounted unit with an instrumented chuck permitted thrust force to be determined. Results included observations on reductions in drill force and chip formation. Thus, Figure 15.9a shows the chips from drilling at an accelerated rate, without ultrasound (left) and with 150 W of ultrasound (right). The chip material is not specified, although work was done on aluminum, steel, copper, and titanium. Figure 15.9b shows chips from titanium drilling, it being noted that "the chips were longer and thinner with a larger spiral diameter and exited freely around the drill."

Shoh (1970) reported on an ultrasonic drill attachment device having air-driven rotation, able to be used on a conventional drill stand. Other versions of this system were

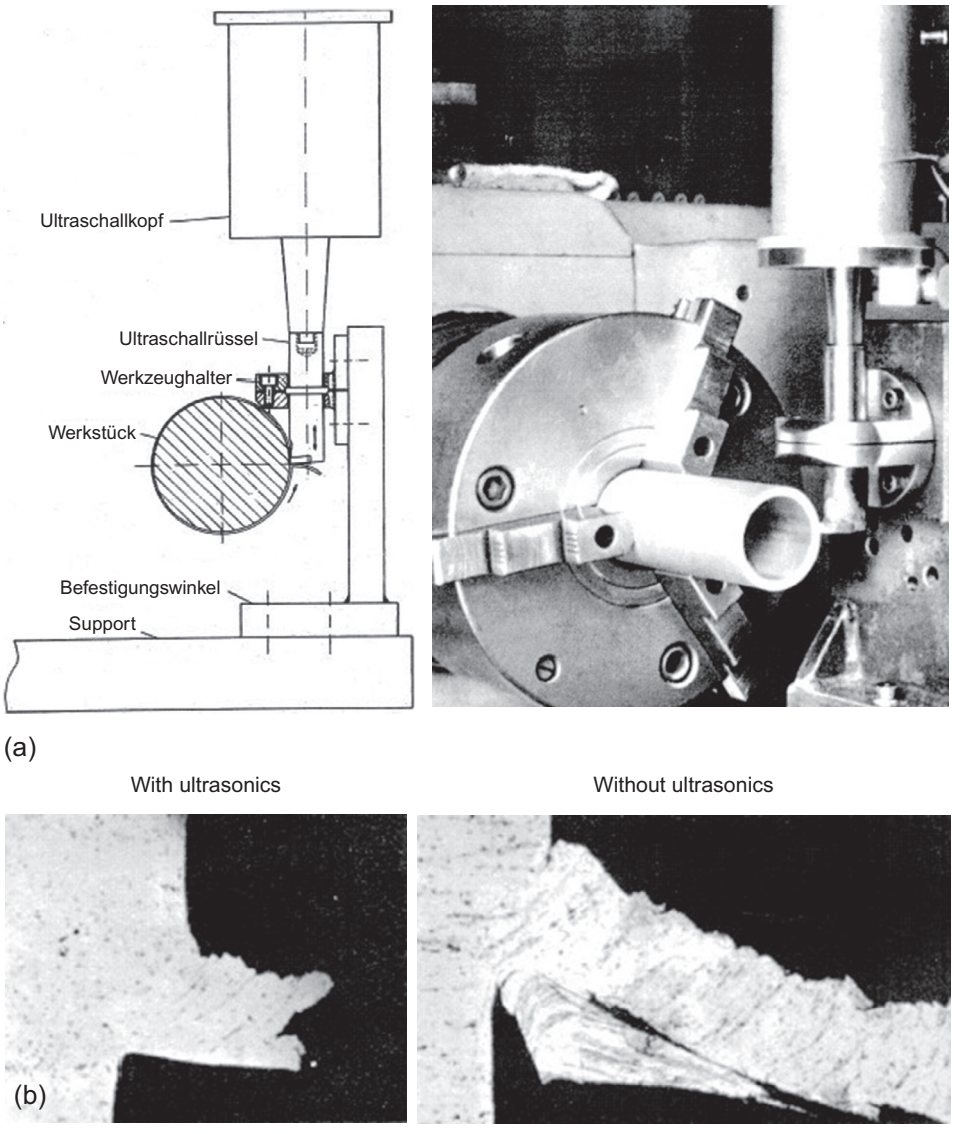


FIGURE 15.5 Ultrasonic turning work of Dohmen (1966): (a) experimental equipment (Dohmen, 1966, Fig. 9) and (b) chip formation (Dohmen, 1966, Fig. 18).

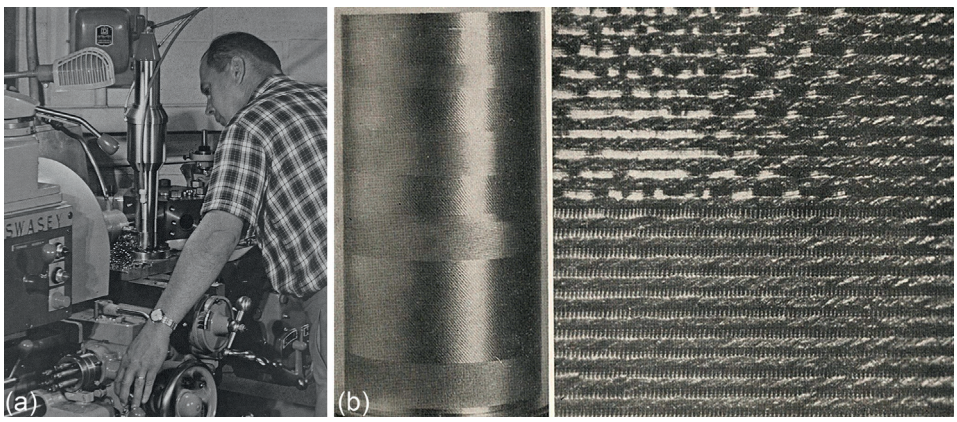


FIGURE 15.6 Aeroprojects ultrasonic turning: (a) ultrasonic tooling on lathe and (b) surface finish bands (left) with and without ultrasonics; close-up of transition region (right) (Anon, 1965).

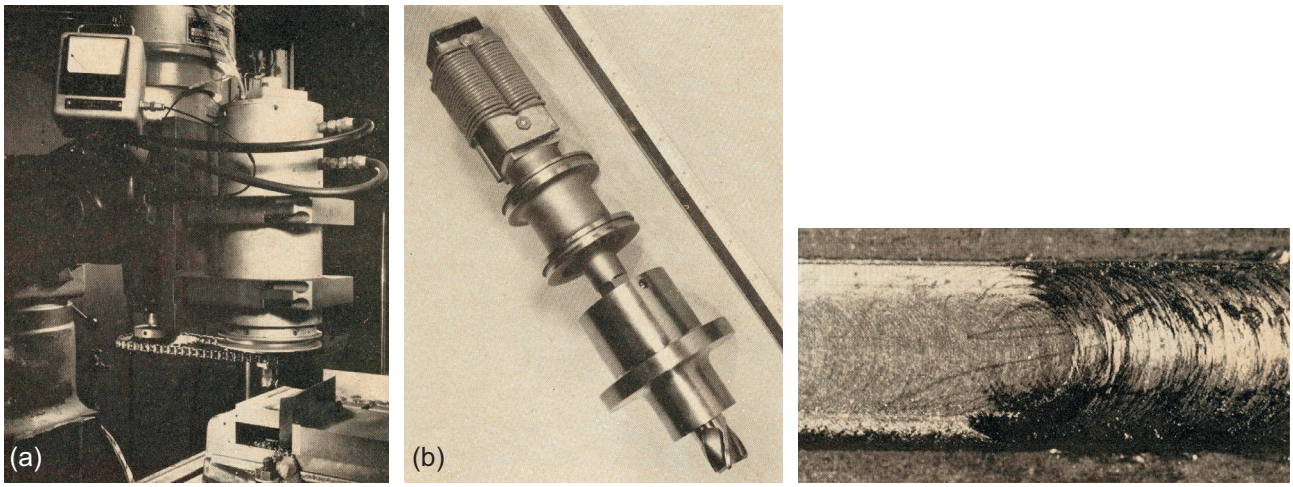


FIGURE 15.7 Ultrasonic milling system: (a) milling system, Fig. 4 and (b) ultrasonic milling unit, Fig. 3; milling cut with (left) and without (right) ultrasonics (Balamuth, 1964, Fig. 5).

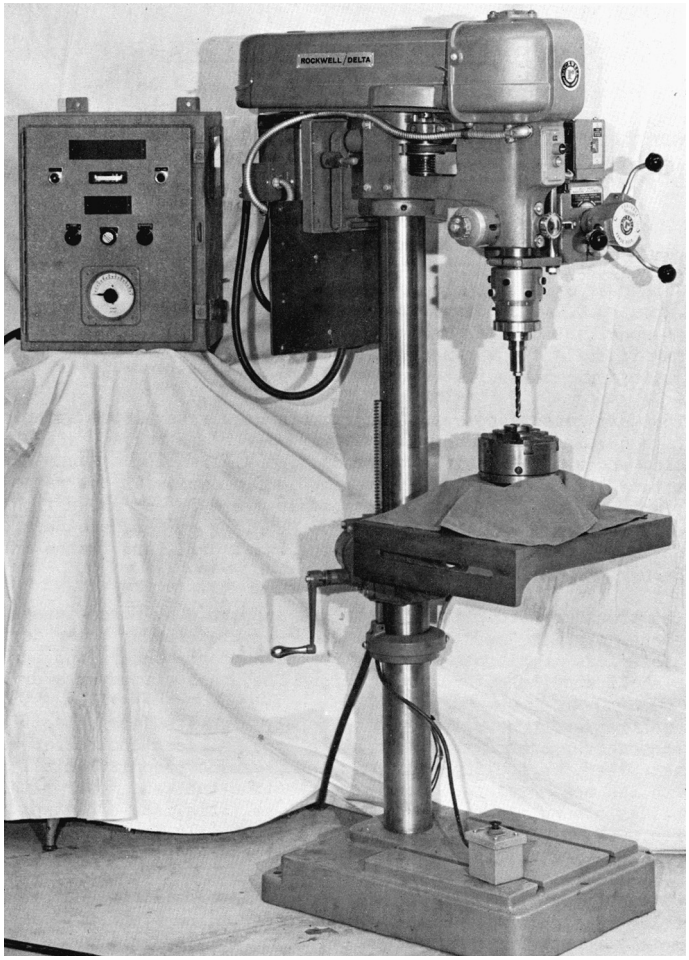


FIGURE 15.8 Aeroprojects twist drilling: drilling system, Fig. 1. See Figure 15.9.

studied in work reported by Grummann (Grauer, 1973) where drilling rates without and with ultrasonics were compared. Improvements in drilling rate of over 30% compared with conventional drilling were noted.

A variant of the drilling process is that of *gun drilling*, a boring process used in the manufacture of gun barrels and involves the turning of the workpiece against a stationary drill. It is used in drilling long holes and in many cases

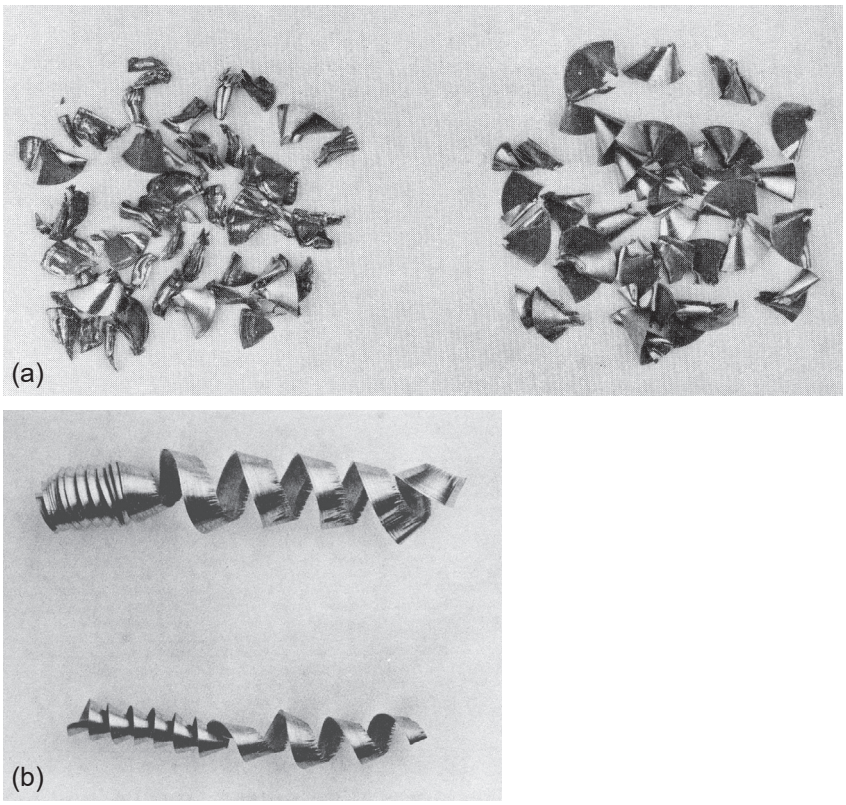


FIGURE 15.9 Aeroprojects twist drilling: (a) chip formation—without (left) and with ultrasonics (right) (Anon, 1971b, Fig. 11); (b) chip formation in titanium (Anon, 1971b, Fig. 12). *(Source: Aeroprojects.)*

permits elimination of a honing step required if twist drilling is used. Ultrasonics has been applied to this process (Kramer and Pizzola, 1982) using a setup similar to that of Isayev and Anokhin (1962) for ultrasonic reaming, with improved finishes reported.

15.2.6 Machining/forming

Possibly the most significant early work on ultrasonic machining done in the United States was that of Kristoffy et al. (1965), where both machining and forming were studied. Figure 15.10 shows the ultrasonic (magnetostrictive) transducer and tooling used in the turning study. The work covered low- and high-frequency vibrations, with the low-frequency work at 20 and 1000 Hz and the high-frequency work at 20 kHz.

The Kristoffy report surveyed the technical literature, noting that most work had been aimed at determining the influence of vibrations on the cutting forces, surface finish, and tool life. It was also noted that while prior studies found force reductions, these were average force measurements, not the dynamic forces (i.e., with instrumentation capable of measuring at high frequencies; an observation potentially applicable to many ultrasonic manufacturing studies, both past and present). A discussion of the effect of cutting tool motion on low-frequency cutting force was relevant to ultrasonic cutting and should be reexamined in present day work. The view put forth was that there were no net force reductions and that there were no conditions where a force drop occurred, as might be suggested by a critical "energy density" for optimum cutting.

15.2.7 Summary and future developments

This historical and technical review covering early developments in several machining technologies has laid the foundation upon which more recent advances, reviewed in the following sections, have been built. The ultrasonic machining technologies, and their order of review, will be as follows:

- Turning
- Drilling
- Milling
- Reaming/Honing/Tapping/Lapping/Threading
- Grinding
- Other processes

15.3 Ultrasonic turning

Since about 2000, there has been a resurgence of work in power ultrasonic machining, particularly in the field of

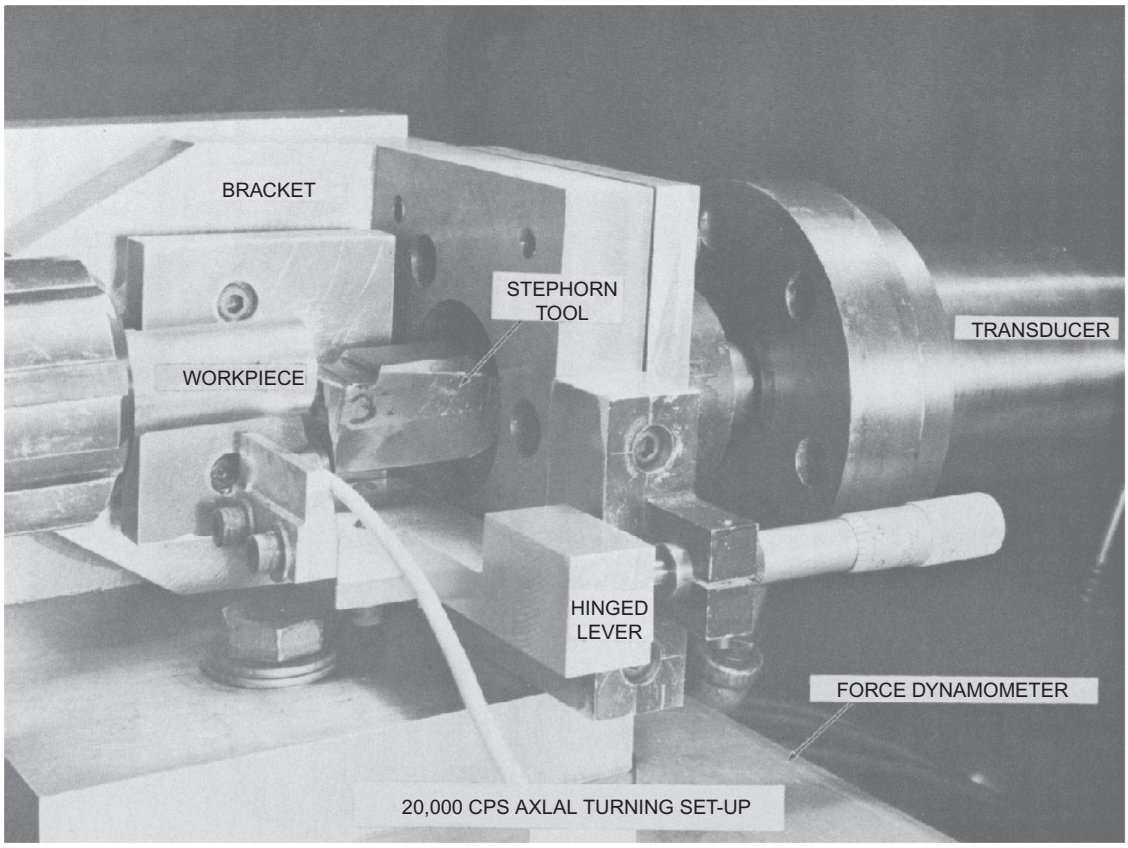


FIGURE 15.10 Ultrasonic setup for turning studies (Kristoffy et al., 1965, Figs. 4–16).

turning, with articles from several international sources, including contributions from the work of Babitsky and colleagues at Loughborough University. The drivers for this resurgence appear similar to those existing in the early years of the field; namely, machining hard, high-strength metal alloys, chiefly those used in the aerospace industry (e.g., titanium and nickel-based alloys). The new factors from an ultrasonic technology standpoint are that modern ultrasonic power supply and control technologies, essential for dealing with the time-varying loads of a machining process, are advanced over those of the past, and computer modeling of ultrasonic systems and the machining process itself have also advanced, thus permitting new approaches to the problem. This review of recent developments will start with the basic cutting modes.

15.3.1 Ultrasonic cutting modes

Any description of ultrasonic turning must identify the ultrasonic cutting direction relative to the surface of the part and its direction of turning. These are shown as three modes in Figure 15.11a relative to transverse turning—along the axis of the part and on the part end face (face cut) (Figure 15.11b) and defined as follows:

- Mode 1: Tangential. In transverse turning, Figure 15.11a, the vibration of the tool tip is at right angles to the part axis and tangent to the outer surface of the part. In face cutting, Figure 15.11b, the vibration is in the plane of the face and at right angles to the diameter through the tool tip.
- Mode 2: Radial. In transverse cutting, the vibration of the tool tip is at right angles to the part axis and to the outer surface. For face cutting, the vibration is at right angles to the face.
- Mode 3: Parallel (aka feed direction). For transverse cutting, the vibration of the tool tip is parallel to the tool feed direction. For face cutting, the vibration is in the plane of the face and along the diameter drawn through the tool tip.

15.3.2 Mechanism of ultrasonic turning

Although there are three different ultrasonic turning modes, most studies have been on Mode 1, where the tool vibrations

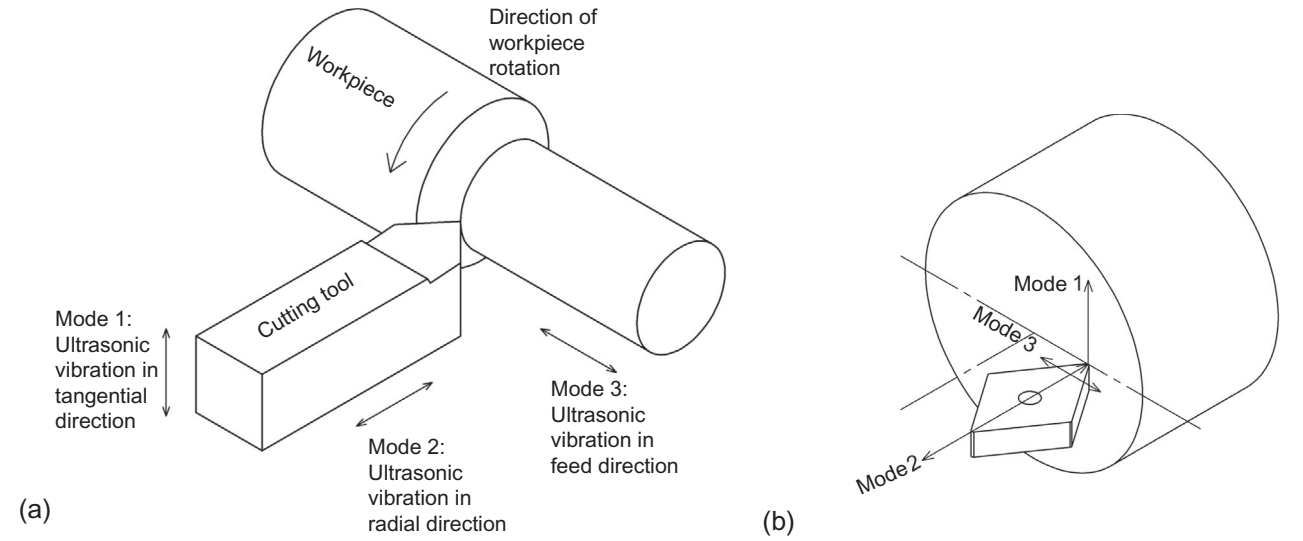


FIGURE 15.11 Modes of vibration of the ultrasonic turning tool: (a) transverse (along the axis) cutting modes and (b) face cutting modes. *(Source: EWI.)*

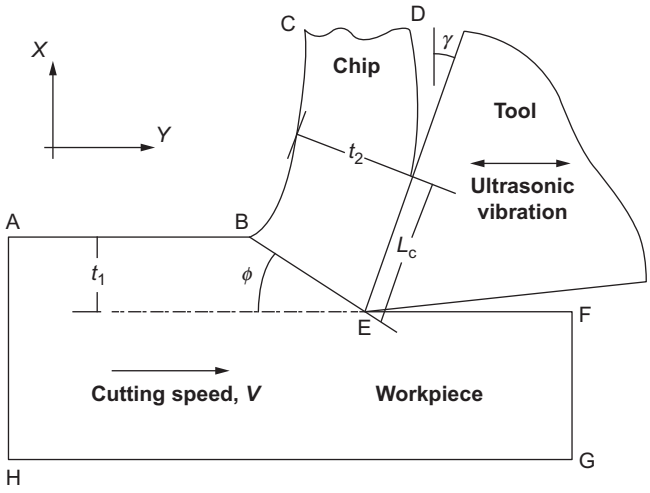


FIGURE 15.12 Relative movement of workpiece and cutting tool in orthogonal UAT (Mitrofanov et al., 2003, Fig. 3).

are tangent to the turning direction. The essential features of the process were first modeled by Mitrofanov et al. (2003). The starting point is the Mode 1 interaction (also known as orthogonal cutting) of the vibrating tool with the material turning at speed V at the point of cutting, as shown in Figure 15.12.

The ultrasonic vibration of the tool, u, is given by

$$u = a \cos \omega t \tag{15.1}$$

where a is the zero-to-peak (0–P) vibration amplitude and ω is the frequency (radians/unit time, related to the cyclic frequency f by $\omega = 2\pi f$). The vibration velocity v is given by

$$v = \frac{du}{dt} = -a\,\omega \sin \omega t = -2\pi fa \sin \omega t \tag{15.2}$$

with the maximum velocity being $v_m = 2\pi fa$. This will be the critical velocity of ultrasonic vibration that will govern whether tool separation with the workpiece can occur. The ultrasonic cutting mechanism is described as follows:

1. The ultrasonic tool velocity v is assumed greater than the turning velocity V, so that on each retraction cycle, there is separation of the tool from the cut face of the material.
2. With continuation of the vibration cycle, the tool returns to impact the cut surface at a velocity of $V + v$, thus dealing an impulse force at the cut.
3. The tool then separates from the cut face as described in (1) and the process is repeated at the vibration frequency, with a continued repetition of impulse forces.

This cyclic action, as modeled with FEA, is shown in Figure 15.13, although in a slightly different sequence than above. Thus:

- Figure 15.13a shows the tool in a fully separated position—(1) above—and on the return part of the cycle—(2) above—but before impact with the cut surface.
- Figure 15.13b shows the tool in cutting impact with the cut surface—(2) above.
- Figure 15.13c shows the tool in the separation phase of the cycle—(3) above.

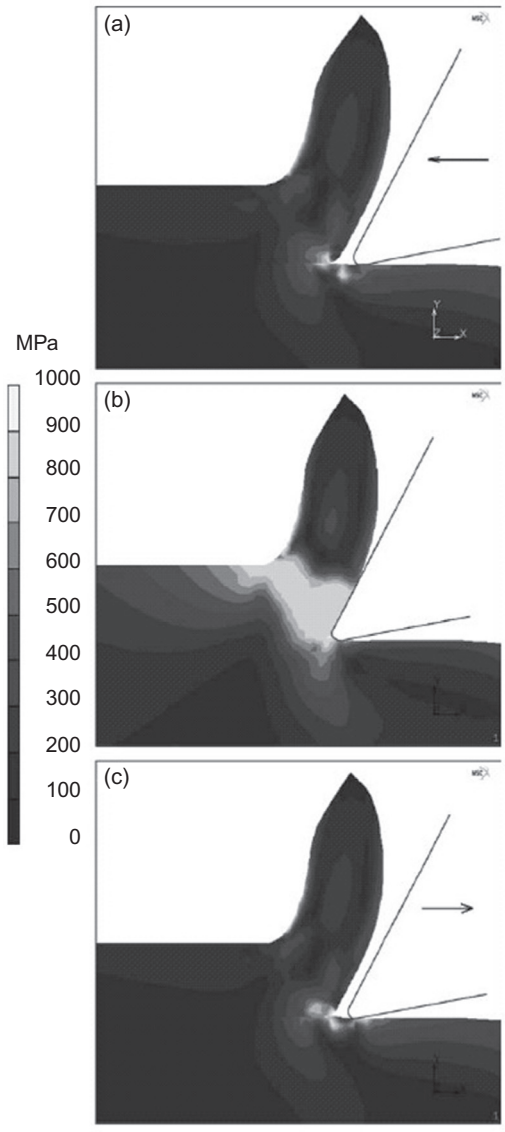


FIGURE 15.13 Distribution of (von Misis) stresses during ultrasonic turning: (a) tool approaching cut surface; (b) tool in full contact with cut surface and chip; and (c) tool moving away from cut surface (Mitrofanov et al., 2003, Fig. 6).

The FEA computed von Misis stresses created during cutting are shown by the gradations of gray at the cutter tip and in the chip.

This analysis identified the transient, impact nature of the ultrasonically assisted turning (UAT) process and was then extended by Babitsky et al. (2004a) with more complex modeling of the cutting process. Mitrofanov et al. (2005) then extended FEA to compute the impulse cutting forces, where a 3D model was used and the influence of friction on the forces was included. This was followed by Ahmed et al. (2007) in a work that brought all aspects of the analysis together and arrived at the full characterization of UAT. One result was a comparison of UAT forces with those of conventional turning (CT), as shown in Figure 15.14. While the peak UAT force exceeds the CT force, the average UAT force is substantially below that of CT. This is a significant differentiating feature and accounts for statements on force reductions in UAT. Another aspect is the effect of vibration amplitude on cutting forces is a reduction in the average cutting force.

Other results included the influence of different frequencies (10, 20, 30 kHz), finding that increasing frequency reduced the average cutting force. A result on feed rate effect indicated higher UAT forces at higher rates, with no change of pulse duration. This was followed by that of Ahmed et al. (2009) in which a full 3D FEA model was used. Amini et al. (2008) also accounted for the periodic nature of the cutting force, leading to stress distribution fields and forces similar to the preceding.

The work of Patten and Williams (2007) made use of commercial machining FEM software with adaptation to including the transient nature of *vibration-assisted machining* (another designation for UAT). Of interest is the analysis of below separation threshold cutting velocities; an area not addressed in other studies. The continuous, oscillatory nature of the cutting force under these conditions was noted with a slight "beating" action seen in the vibratory force levels.

15.3.3 Systems hardware

Given the number and diversity of ultrasonic turning studies, there is also a diversity of ultrasonic turning hardware, a review of which is beyond the scope of this chapter. Most systems are for laboratory use and not intended for the production floor although that of Koshimizu (2007) is worth noting because it is/was commercially available. That equipment was also used by Nath et al. (2007) and Nath and Rahman (2008). A feature is the vertical vibration created at the cutting tip by an innovative construction of the transducer that may be based on work reported by Mori et al. (1989).

Note should be made of the systems used in the several works of Babitsky and colleagues. In early reports on ultrasonic turning, Babitsky et al. (2004a) used feed direction (Mode 2 cutting), as shown in Figure 15.15a. In later publications, a change was made to a system using Mode 1 (vibration direction in the turning direction) as shown in Figure 15.15b, this being used in all later publications.

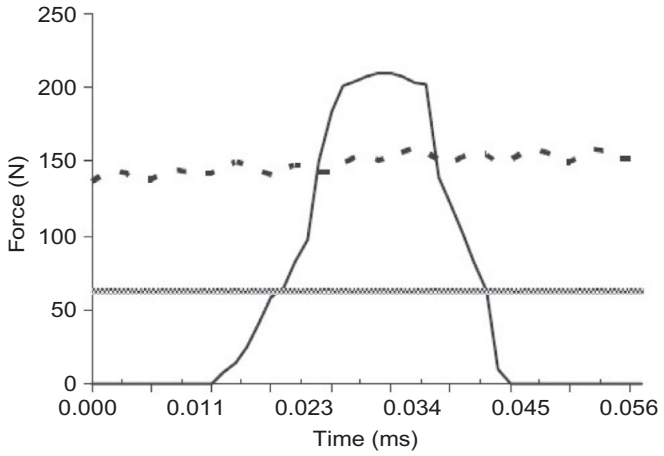


FIGURE 15.14 Comparison of forces on cutting tool in cutting direction for CT and UAT (amplitude = 15 μm, coefficient of friction = 0.5). *Dashed*, CT; *Solid black*, UAT; *Gray*, UAT average (Ahmed et al., 2007, Fig. 5).

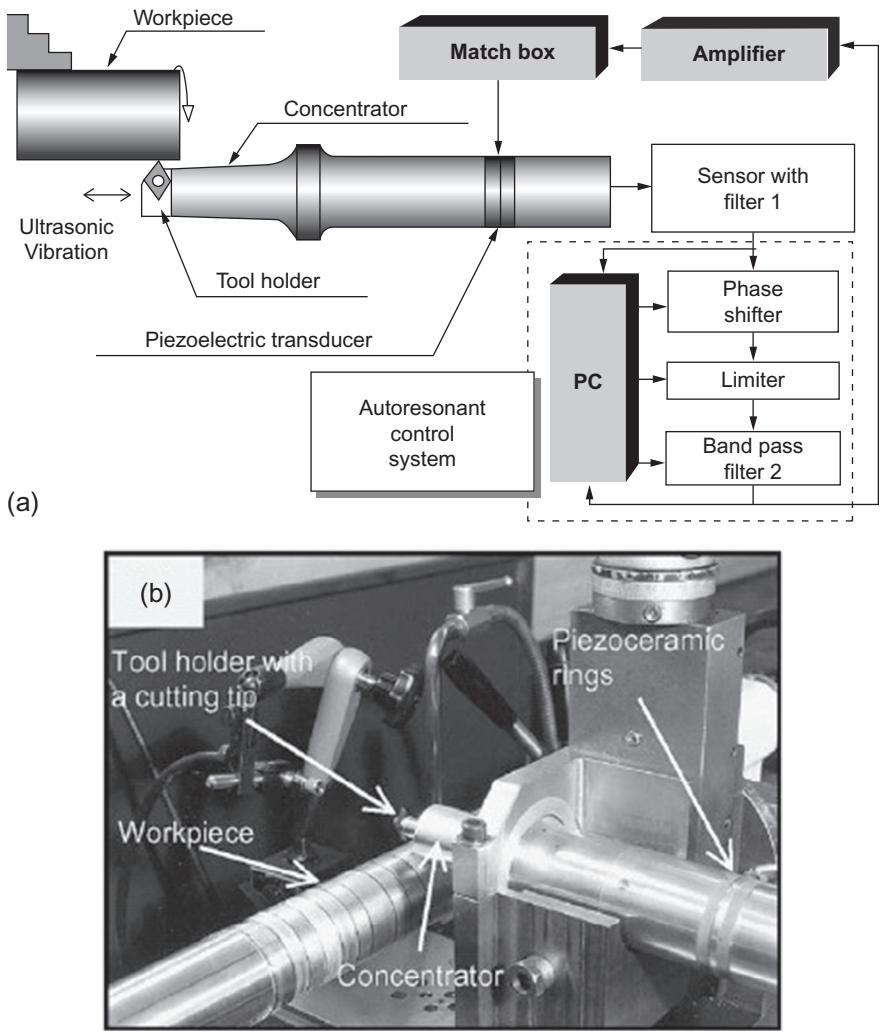


FIGURE 15.15 Ultrasonic turning systems: (a) system schematic of ultrasonic turning in feed direction (Babitsky et al., 2004a, Fig. 2) and (b) ultrasonic turning—tool vibration in turning direction (Babitsky et al., 2004b, Fig. 1(a)).

15.3.4 Ultrasonic turning data

Research in ultrasonic turning has generated extensive data for various materials that includes machining modes, turning speeds, depths of cut (DOCs), feed rate, insert configurations, coolants, surface characteristics, tool wear, chip morphology and forces, as well as ultrasonic parameters of frequency, amplitude, and power. Only a brief summary can be given here from an extensive review by Graff (2013). Materials results have been reported for Inconel 718, a range of mild steels (of varying terminologies), some high alloy steels (e.g., 4140), and stainless steels. Single results were reported on titanium (Ti 6-4) and on aluminum.

15.3.4.1 Turning speeds and machining practice

Turning speed is critical in production and in UAT, as it relates to critical velocity (previously discussed). A summary of a wide range of reported materials and conditions led to the comparison of ultrasonic and industrial speed ranges shown in Table 15.1.

For steels, the current values of ultrasonic turning speeds lie below those of industrial practice; thus, US at 90 m/min <IP at 104 m/min. In the case of Inconel 718, it appears that industrial practice far exceeds that of ultrasonics. In the case of Ti 6-4, it is seen that ultrasonics is comparable to but still slightly less than industrial practice.

15.3.4.2 Surface quality

An area noted in many publications has been the improvement in surface finish achieved by ultrasonic turning, with surface roughness data that substantiates such claims. Thus, Amini et al. (2009) provided extensive data on surface roughness, using the results of an 81-trial design of experiments, of which Figure 15.16a and b are representative.

Figure 15.16a shows that Ra is only slightly sensitive to variations in DOC and ultrasonic amplitude, whereas Figure 15.16b shows a strong effect of feed rate on Ra.

TABLE 15.1 Comparison of ultrasonic and industrial turning speeds (TS)

Material	Maximum US TS (m/min)	Minimum industrial TS (m/min)
Steels	90	104
Inconel 718	30	38
Ti 6-4	70	76

Photographs of surface finish show a clear difference in the two finishes.

The improved surface finish from ultrasonic turning of mild steel is also noted in Celaya et al. (2009). The work of Jiao et al. (2011a,b) also reports on improved surface finish. Surface images are seen in Figure 15.17, with those of ultrasonics being seen as continuous and regular in comparison with those of CT.

Others reporting on surface finish include Nath et al. (2007) and Nath and Rahman (2008), who included observations on improved surface finish, tool wear, chip formation, and cutting forces. Soleimanimehr et al. (2009) reported on improved surface finish, although the differences were not as pronounced as noted in the preceding citations. Babitsky et al. (2004b) provide both roughness and roundness data on UAT materials, comparing them to CT results.

15.3.4.3 DOC and feed rate

Results for DOC have ranged from shallow (e.g., 0.04/0.05 mm) up to 1 mm, with most work falling in the range $0.3^{\pm 0.1}$ mm. Feed rates have ranged from 0.04/0.05 up to 0.5 mm/rev, with most falling in the range of $0.3^{\pm 0.1}$ mm/rev.

15.3.4.4 Tool wear

Effects of UAT on the tool cutting tip—called the *insert*—including insert material, shape, dimensions, and angular orientation, are reported in a number of studies, reporting varying amounts of reduced wear. Thus, Koshimizu (2007) compared the cutting tip appearance with ultrasonic vibration with that of conventional cutting, with greater wear observed on the latter. Nath and Rahman (2008) compared tool wear for several cutting conditions, as shown in Figure 15.18. Likewise, Zhou et al. (2003) looked at the local wear conditions of a PCD (polycrystalline diamond) tool. See also the later reference to work by Koshimizu (2007), Figure 15.19, on the effects of coolants on tool wear.

15.3.4.5 Chip morphology

Several papers report on the shape of the chips from UAT. Thus, Koshimizu (2007) compares chips with and without ultrasonic vibration, Figure 15.19a, as do Nategh et al. (2009) in Figure 15.19b and Nath et al. (2007) in Figure 15.19c. Nath and Rahman (2008) and Zhou et al. (2003) provide high-magnification views of chip formation during the actual UAT process.

15.3.4.6 Coolants

It was found that most investigators did not use lubricants or coolants in their studies, running under dry conditions. Gao

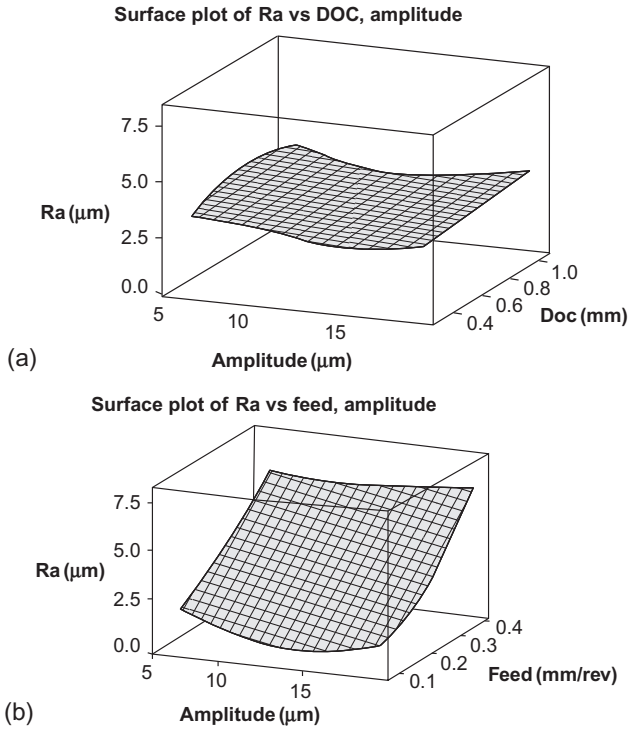


FIGURE 15.16 Effect of machining and ultrasonic parameters on Ra (Amini et al., 2009, Fig. 6): (a) Ra versus depth of cut (DOC) and US vibration amplitude and (b) Ra versus feed rate and US amplitude.

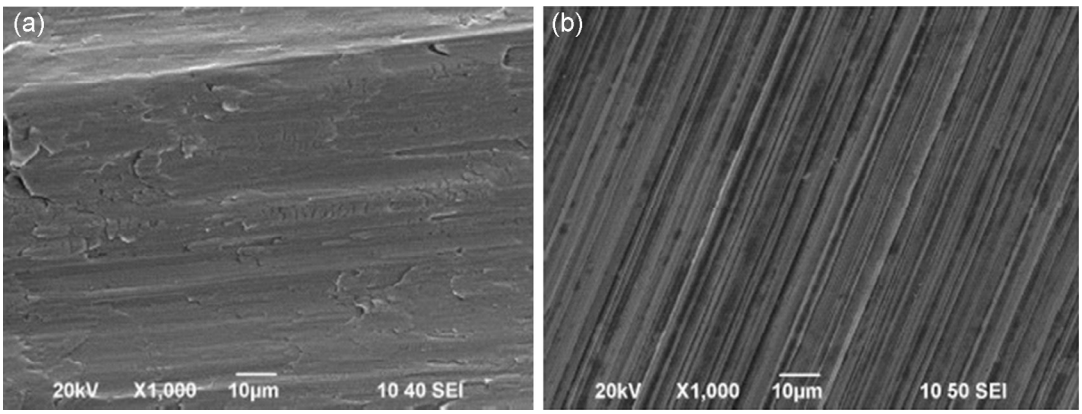


FIGURE 15.17 SEM photographs of machined surface of quenched steel ($n = 180$ r/min, feed = 0.103 mm/rev, DOC = 0.10 mm): (a) conventional turning (Jiao et al., 2011b, Fig. 5(a)) and (b) ultrasonic turning (Jiao et al., 2011b, Fig. 5(b)).

et al. (2002) reported on the effects of four coolant conditions on surface roughness, the conditions being oil-free (considered as dry), water, kerosene, and an emulsion. The oil-free condition had the worst results, and kerosene produced the best surface. Gao hypothesized that due to ultrasonic cavitation the coolant penetrated the cutting area more easily, increasing its effectiveness.

The effects of three conditions, dry, semidry, and wet, on surface roughness and tool wear were investigated by Koshimizu (2007). Vegetable oil was used in the semidry tests, and a water-soluble cutting fluid was used for the wet tests, with little roughness difference noted between semidry and dry tests and variable effects under wet conditions. The effects of coolants on tool wear were also reported, as shown in Figure 15.20. The greatest tool wear was seen for the wet cutting process, with the semidry process offering a slight improvement over dry cutting.

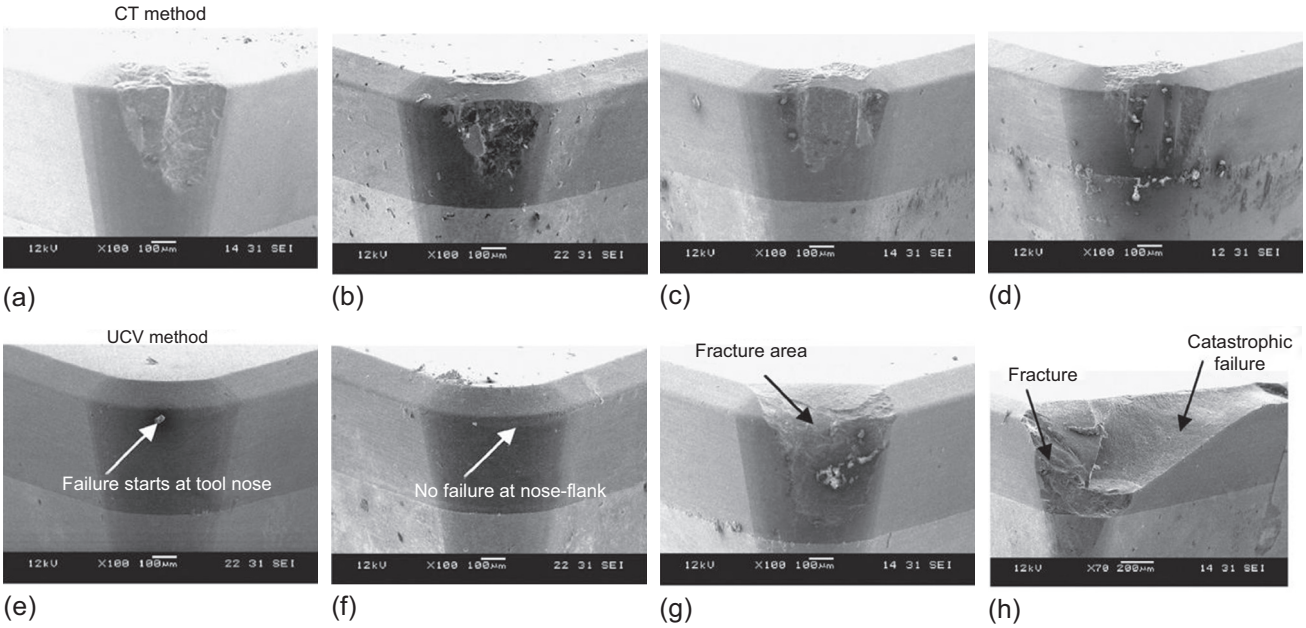


FIGURE 15.18 SEM photographs of tool wear at different cutting conditions. Conventional turning (CT)—(a) 10 m/min, 0.05 mm/rev; (b) 10 m/min, 0.1 mm/rev; (c) 15 m/min, 0.05 mm/rev; (d) 15 m/min, 0.1 mm/rev; ultrasonic vibration cutting (UVC); (e) 10 m/min, 0.05 mm/rev; (f) 10 m/min, 0.1 mm/rev; (g) 15 m/min, 0.05 mm/rev; (h) 15 m/min, 0.1 mm/rev (Nath and Rahman, 2008, Figure 8).

Other results included those of Wang and Zhao (1987) and Wang et al. (1987) where a 50–50 mix of oil and kerosene was used with no comparisons made to noncoolant conditions. Zhou et al. (2003) used an oil mist coolant, but no comparisons were made to noncoolant conditions. Zhou noted how ultrasonic vibrations might affect the process, hypothesizing that under ultrasonics, the cyclic separation between workpiece and tool promoted a dynamic lubrication that decreased the interface friction.

In the work of Ahmed et al. (2007), in addition to modeling, tests were also carried out using a commercial cutting fluid, looking at its influence on cutting force. The ratio of UAT to CT cutting force was measured, with ultrasonic cutting forces being as low as 25%–33% of conventional forces, for low feed rates and up to 63% for higher feed rates. Finally, several investigators indirectly examined the use of coolants/lubricants in modeling the UAT process, doing this by varying the coefficient of friction in the model. These included the just-referenced Ahmed et al. (2007, 2009) and Mitrofanov et al. (2003).

15.3.4.7 *Cutting forces*

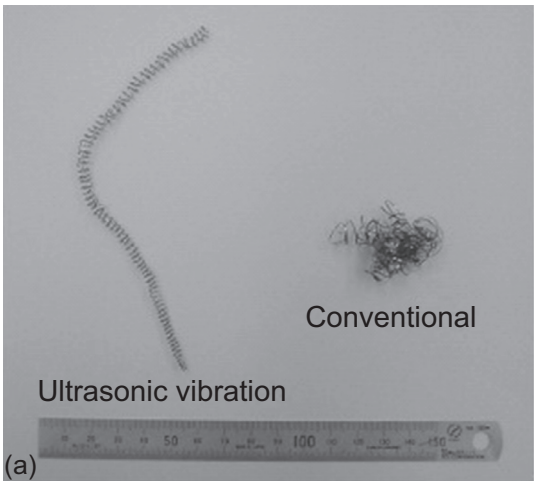
Cutting forces during UAT, which are covered in many of the publications, require a distinction be made as to two types:

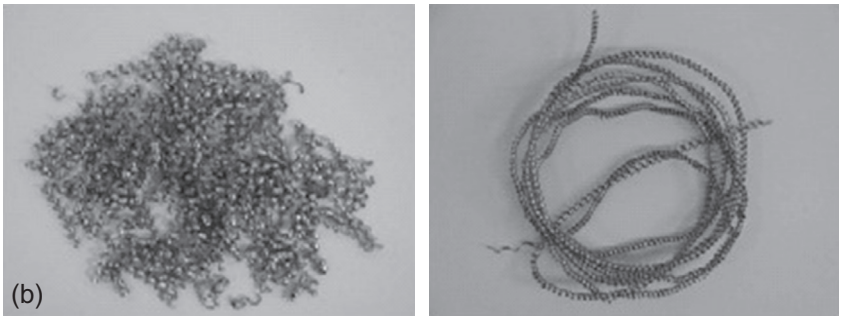
- Forces generated at the point of cutting between the tool and the workpiece.
- Forces transmitted from the point of cutting, through the tooling and fixtures, to a load cell mounted at a force isolation point in the system.

At the present time, no methods have been shown to measure forces directly at the point of cutting, so that these forces can only be predicted by modeling methods. Cutting forces discussed in the following will relate to those obtained by load cells.

In Amini et al. (2009), note is made of a dynamometer installed on a lathe for measuring the cutting force, although system details are not given nor is any data presented. However, Amini was part of the Nategh et al. (2009) team that reported more extensively on force measurements. The experimental setup used by Kim and Lee (1994) is shown in Figure 15.21, where the cutting force was measured using a dynamometer installed below the ultrasonic unit. An example of cutting force data is shown in Figure 15.22, where the ultrasonic forces are initially well below those of conventional cutting but rise to approximately the same levels at higher cutting speeds.

Nategh et al. (2009) noted that the (cutting) fixture was installed on a three-axis dynamometer and presented results on machining forces from full factorial experiments showing, for example, the influence of feed and amplitude. Numerous other results on cutting forces were presented by authors already cited in this section, including Koshimizu (2007) (UAT forces reported at one half to one third that of CT); Nath et al. (2007) and Nath and Rahman (2008) (three force components measured and showed significant reductions compared with CT); and Zhou et al. (2003), also reporting on use of a three-component dynamometer, but with force measurements that showed an increase in some components over CT forces. In the work of Ahmed et al. (2007), measurements of the cutting force were made with





Cutting speeds	CT	UVC
50 m/min		
70 m/min		
90 m/min		

(c)

FIGURE 15.19 Various chip morphologies: (a) chip comparison (TS = 20 m/min, DOC = 0.2 mm, feed = 0.1 mm/rev) (Koshimizu, 2007, Fig. 6); (b) shape of chip formations in UAT (upper) and CT (lower) (Nategh et al., 2009, Fig. 12); and (c) chips produced under CT and UVT for various cutting procedures (Nath et al., 2007, Fig. 7).

a dynamometer fixed to the cross slide of the lathe with the ultrasonic system mounted on its top. It was claimed that high rigidity of the system ensured measurements "practically without displacements—thus, the dynamometer does not noticeably affect the stiffness of the tool–workpiece system" and that the cutoff frequency of the system filter led to elimination of the high-frequency force components. It was concluded that the dynamometer force represented the mean value, which in the case of UAT was averaged over a large number of vibration cycles. This was one of the few publications where attention was given to system dynamics.

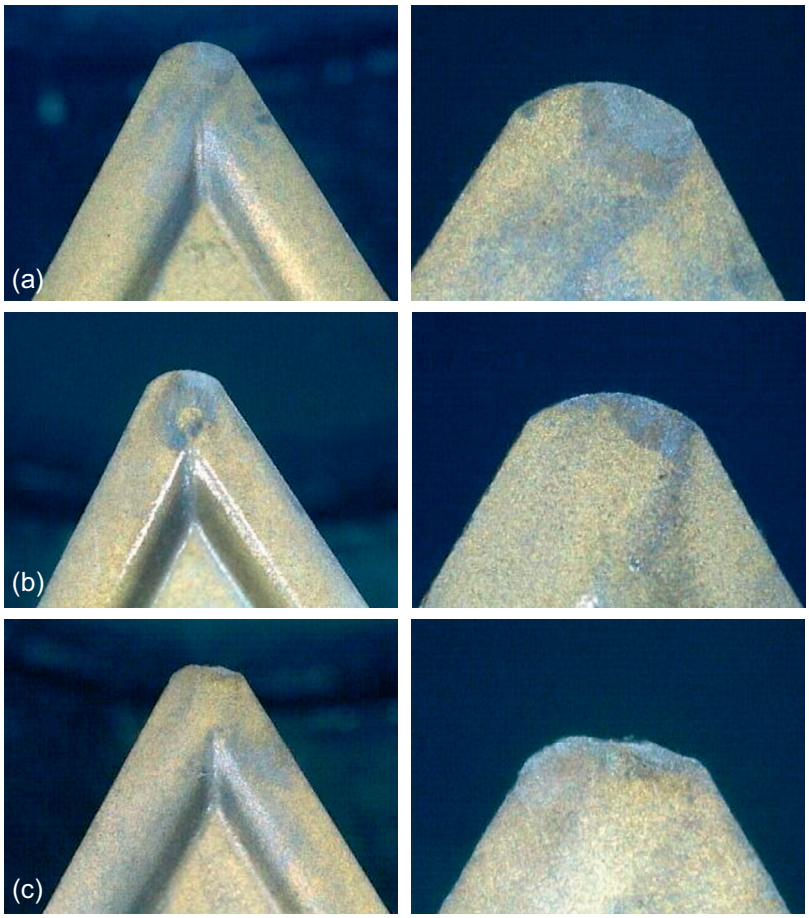


FIGURE 15.20 Tool tip images for various coolant cutting conditions, with ultrasonics: (a) dry; (b) semidry; and (c) wet (Koshimizu, 2007, Fig. 10).

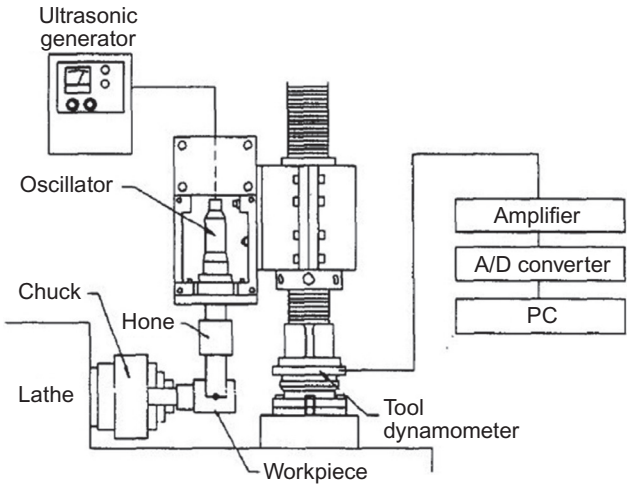


FIGURE 15.21 Experimental apparatus and data for UVC of composites: experimental apparatus, including dynamometer (Kim and Lee, 1994, Fig. 2).

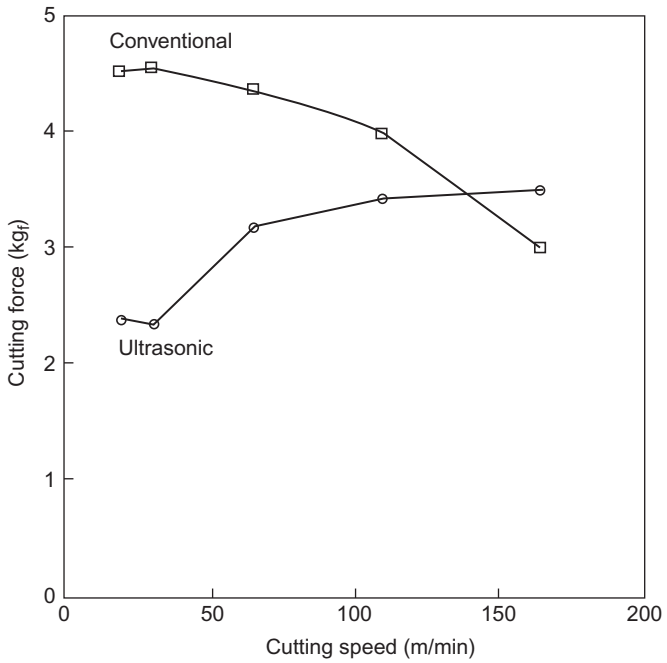


FIGURE 15.22 Experimental apparatus and data for UVC of composites: cutting force versus cutting speed (Kim and Lee, 1994, Fig. 9).

Caution should be exercised in the interpretation of cutting forces as measured by the various load cells referenced in this section. The basis for this caution is twofold: (1) the response of the dynamometer to high-frequency ultrasonic vibrations and (2) the response of the dynamometer to eccentric loading, that is, loadings having lever arms relative to the dynamometer load axes.

15.3.4.8 *Elliptical vibration cutting*

Thus far, three distinct modes of tool vibration have been considered in ultrasonic turning (Modes 1, 2, or 3, as shown in Figure 15.23). In recent years, an innovation has appeared known as *elliptical cutting*, which combines two of the modes to result in an elliptical tool path. The work of Ma et al. (2004) is an example, where the elliptical tool vibration pattern is achieved using a transducer operating in a bending mode, as shown in Figure 15.23a, thus creating a vibration of the cutting tool against a workpiece, as shown in Figure 15.23b. A model for the thrust force and cutting accuracy was developed and compared with measurements. Results for thrust force are shown in Figure 15.23c, where elliptical cutting is compared with conventional cutting and to conventional vibration cutting; that being cutting with a single mode of vibration. There is a major reduction in thrust force, both predicted and measured. Likewise, there is significant improvement in machining accuracy.

Li and Zhang (2006) also reported on elliptical vibration cutting. The tool configuration, consisting of a cutting tip mounted off center at the tool end, is shown in Figure 15.24a, with the expected cutting action shown in Figure 15.24b. The off-center tool mass results in an inevitable bending action in the cutting tool, with this predicted by FEA and confirmed by experimental measurements.

Measurements of cutting forces showed significant reductions in both thrust force (normal to the cutting tool face, N_r in Figure 15.25a) and transverse force (F_t in Figure 15.25a). Thus, at 12 µm a reduction of nearly 75% occurred in the thrust force with similar results noted for the transverse force. The surface appearance of an L12 workpiece machined at a 0.06-mm depth of cut is shown in Figure 15.25b, where an R_a of 0.08 µm was measured; better than achieved with conventional cutting.

Suzuki et al. (2007) extended the elliptical concept further by developing a transducer able to generate tool vibrations with three degrees of freedom and able to create a complex tool path to crate sculpted surfaces.

Although operating at low frequencies, the work of Brehl et al. (2007) and Brehl and Dow (2007) on elliptical cutting should be noted. A piezoelectric actuator, operating up to 4 kHz, created the elliptical cutting path, and a theoretical model for the elliptical vibration-assisted milling process was developed. Cutting forces and peak thrust forces were significantly reduced over conventional machining (e.g., 20%–50% reduction in cutting, 60%–75% in thrust), with good agreement between predictions and experimental results.

15.3.5 Recent developments in ultrasonic turning

In reviewing "recent developments in ultrasonic turning," attention will first be given to overview articles that might

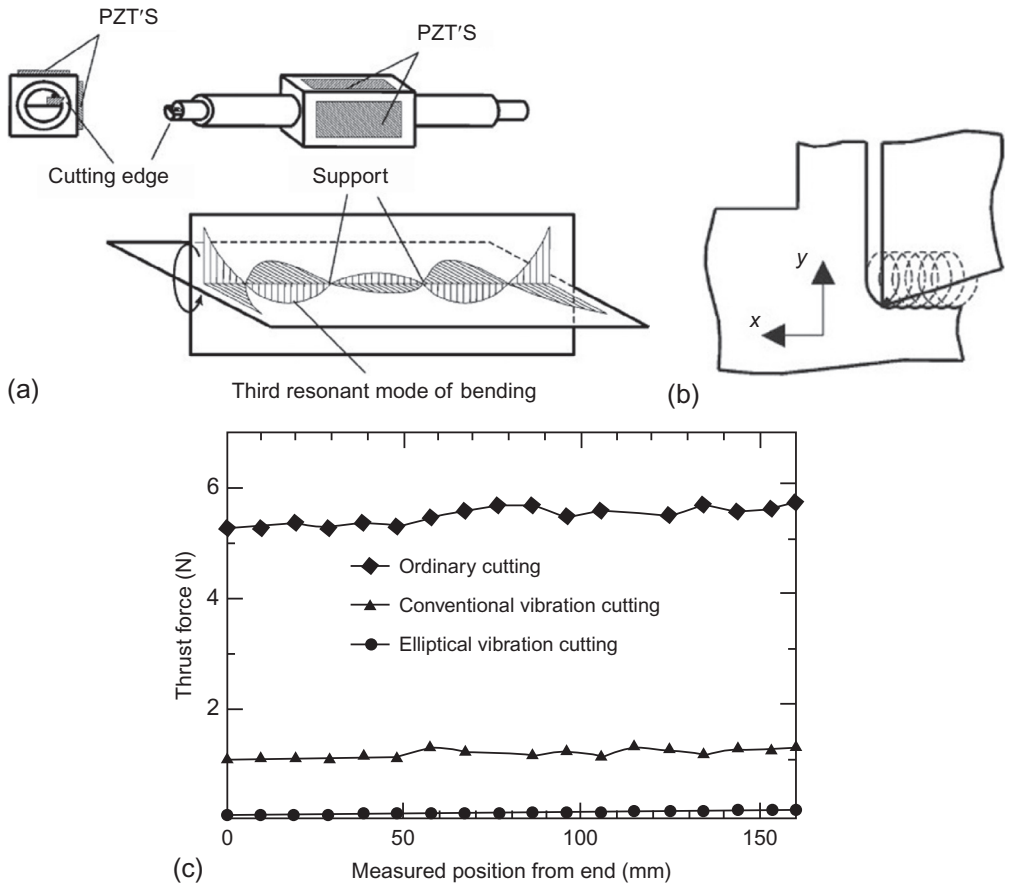


FIGURE 15.23 Elliptical vibration cutting: (a) ultrasonic elliptical vibrator, Fig. 5; (b) tool motion (Ma et al., 2004, Fig. 1b); and (c) cutting force measured by three methods (Ma et al., 2004, Fig. 8).

have recently appeared, and for this, special mention is made of Dixit et al. (2019). The review is broad in scope, giving attention to general principles of ultrasonic cutting, but having commentary on vibration effects, material behavior, system features and economic aspects. Informative summary charts are provided for the various technologies. Furthermore, other ultrasonic machining technologies are covered, including drilling, milling, grinding, and electrodischarge machining (EDM). Reference to these coverages will be made in the respective sections.

15.3.5.1 *Cutting forces and temperatures*

The work of Muhammad et al. (2018) focused on experimental and numerical investigation of cutting force and process zone temperature in conventional turning (CT), hot conventional turning (HCT), and hybrid turning (HT). The setup used in this work is shown in Figure 15.26a. As seen in Figure 15.26b, the level of temperature recorded from both experimental and FE simulation in HT was higher than that in HCT at the studied cutting conditions and was credited to the surplus energy imposed on the insert via vibration.

The FE results of the oblique model developed for HT shows that the cutting forces start to drop and eventually reached to zero at full retraction. The simulated peak force levels were lower in scale when compared with CT but were close to HCT. To check the formation of alpha precipitate (α-Ti), scanning electron microscopy (SEM) and backscatter analysis were used and the results showed no subsurface changes in the studied alloy.

Sharma and Pandey (2016) used response surface methodology (RSM) to develop a statistical model to study the effect of machining and vibration parameters on residual stress in UAT of Steel 4340. Their results showed that while the vibration amplitude, feed, and cutting velocity were the most significant parameters affecting residual stress, the depth of cut was not significant. This work concluded by finding the optimum values of machining parameters that minimize residual stress.

Llanos et al. (2018) used a 20-kHz UAT system and an experimental approach to evaluate the effect of amplitude, feed, cutting speed, and depth of cut on force reduction. A linear least squares fitting was used to develop an empirical model to calculate the reduction of the force components in UAT of titanium. While depth of cut had a

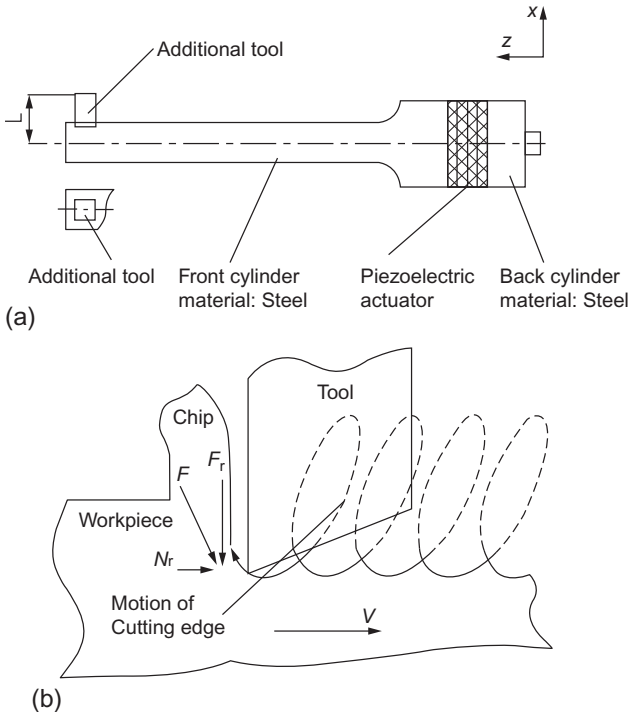


FIGURE 15.24 Elliptical cutting—additional results: (a) cutting transducer (Li and Zhang, 2006, Fig. 2) and (b) tool path (Li and Zhang, 2006, Fig. 1).

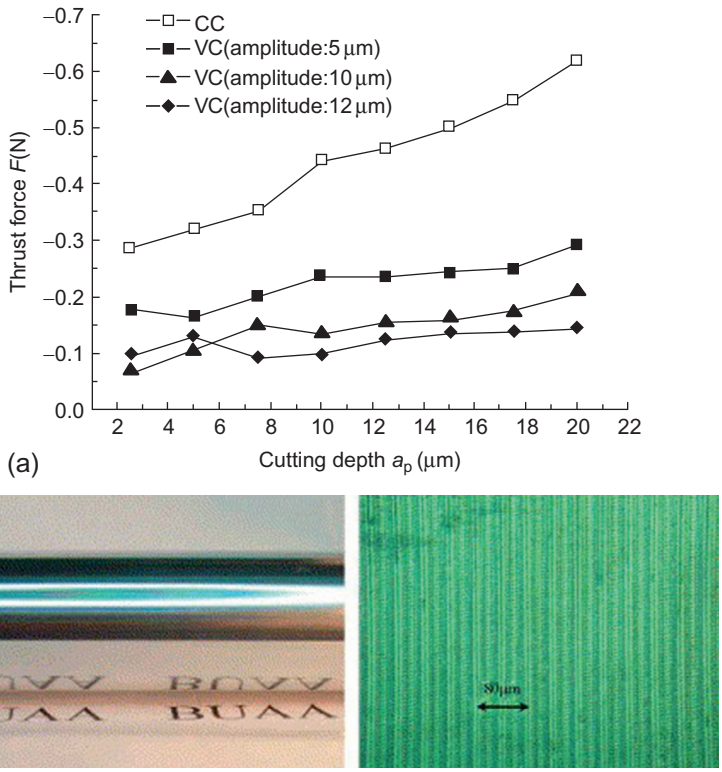


FIGURE 15.25 Force and finish results with elliptical cutting. (a) Force components (Li and Zhang, 2006, Fig. 9) and (b) workpiece surface finish (Li and Zhang, 2006, Fig. 11).

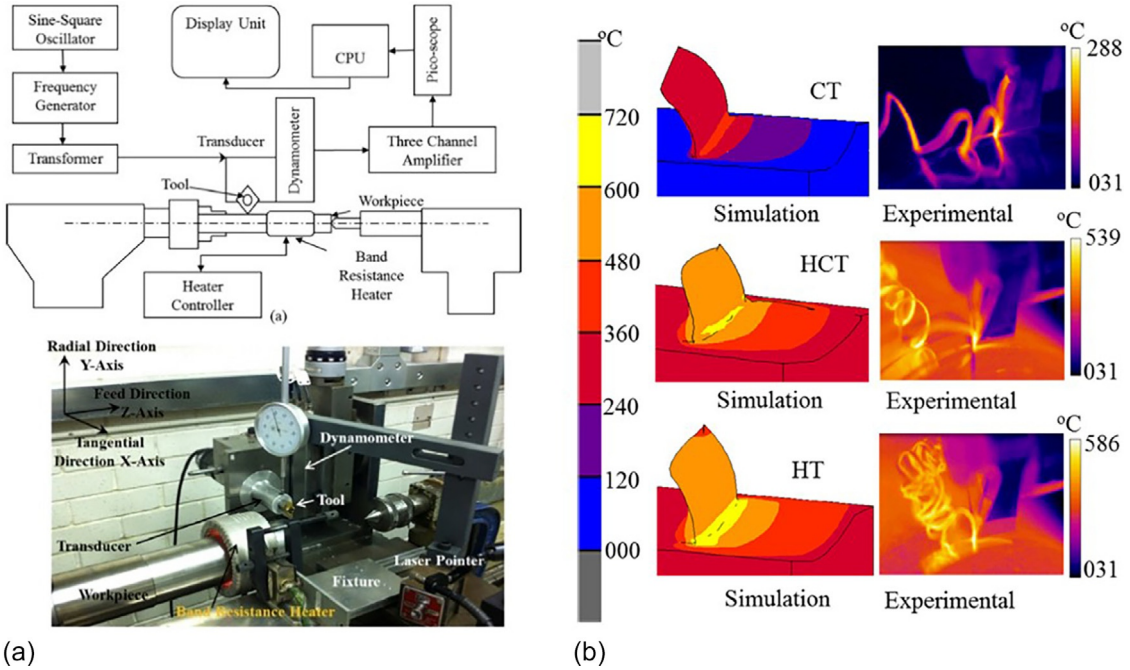


FIGURE 15.26 (a) The experimental setup and (b) temperature spreading in CT, HT, and HCT ($V = 10$ m/min; ap = 0.3 mm; fr = 0.1 mm/rev; $T = 300$°C) (Muhammad et al., 2018, Fig. 1, 23).

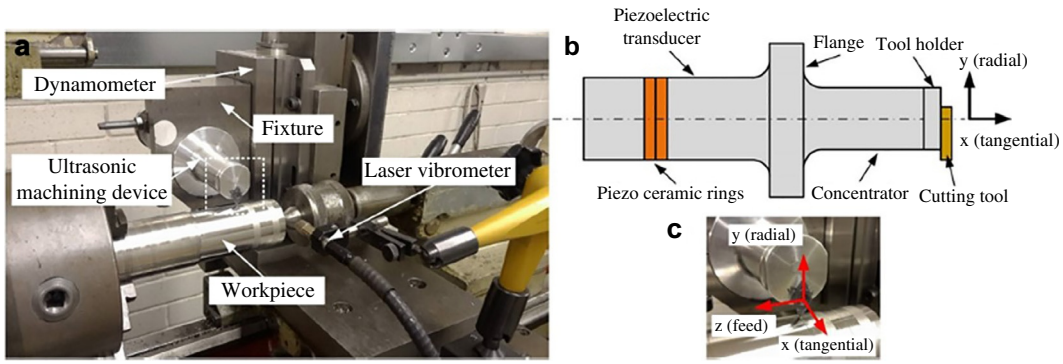


FIGURE 15.27 (a) Experimental setup; (b) ultrasonic cutting assembly; and (c) the main cutting directions (Bai et al., 2019a, Fig. 1).

negligible effect on force reduction, the parameters that affected tool-workpiece contact ratio (TWCR) (Nath and Rahman, 2008) were amplitude and cutting velocity, which had significant effects on force reduction. The effect of machining and vibration parameters on machinability and structural integrity in CT and UAT of two Inconel alloys were investigated by Bai et al. (2019a,b). The experimental setup is shown in Figure 15.27a, where the flange in the 18 kHz ultrasonic device that generates vibrations in tangential direction, Figure 15.27b, is connected to a dynamometer to measure the force components, Figure 15.27c. The results of this study showed that maximum force reduction was obtained at cutting speed less than the critical velocity at low levels of feed rate and depth of cut along with higher vibration amplitudes. As seen in Figure 15.28, UAT improved the surface roughness; however, the improvement decreased with an increase in the feed rate and amplitude. Finally, analysis of residual stress showed that UAT generated more compressive stresses, which helped reduce the net tensile stresses.

15.3.5.2 Surface roughness

The work of Sharma and Pandey (2018) presents an experimental investigation on surface roughness in UAT of steel 4340 using plane and textured (i.e., self-lubricating) cutting inserts. The results of this study showed up to 10% improvement in surface roughness in CT when a textured insert was used, and up to 28% improvement when ultrasonic vibrations was applied to the plane insert. However,

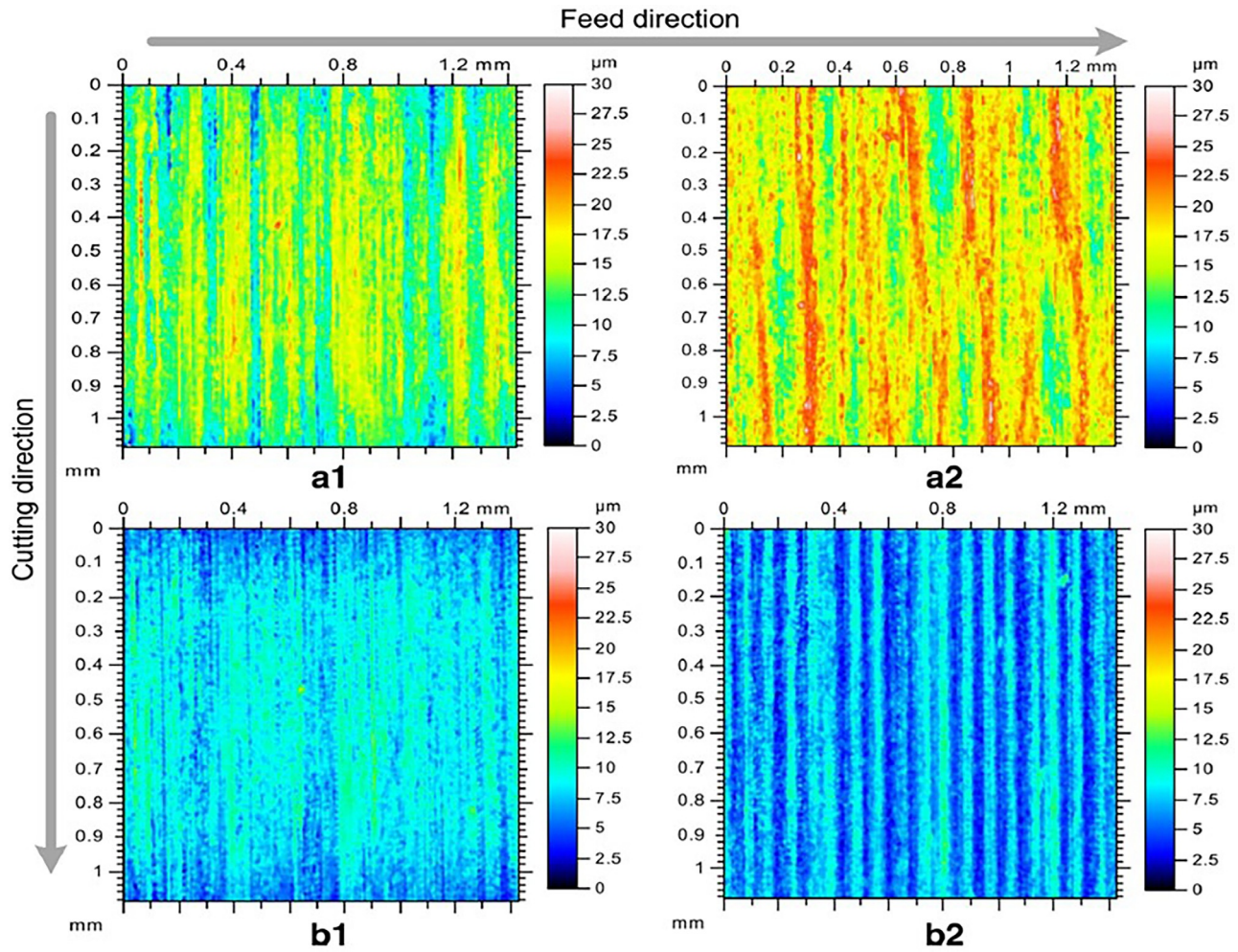


FIGURE 15.28 Surface topography: (a1) CT of Inconel 718; (a2) CT of Inconel 625; (b1) UAT of Inconel 718; (b2) UAT of Inconel 625 (Bai et al., 2019a, Fig. 5).

combining ultrasonic vibrations with a textured insert resulted in up to 35% improvement in surface roughness. An RSM-based statistical model was developed for surface roughness and ANOVA used to find the contribution of optimum machining parameters to generate 0.43 μm surface roughness. Xiangyu et al. (2018) studied surface quality and residual stress of high-speed UAT (i.e., cutting velocity of 200 m/min) of titanium alloys by applying 21 kHz vibration in the feed direction. Residual stress was measured using a prism electronic speckle pattern interferometry measurement apparatus. Results showed that as amplitude increased from 0 μm (i.e., CT) to 16 μm, the surface residual stress transferred from a tensile state to a compressive state. This is similar to that reported in Bai et al. (2019a,b). Surface roughness increased but was still less than 0.4 μm when vibrations were applied. Cutting-extrusion phenomena that occurred during high-speed UAT appeared to explain the observations.

Surface roughness and topography in CT and UAT of steel 4140 were investigated in the work of Lotfi et al. (2018). Figure 15.29a shows the experimental setup used in this work where a tungsten carbide insert was attached to a 20 kHz vibratory tool. Figure 15.29b shows the optical images of machined surfaces of CT and UAT samples, showing more than 50% improvement in UAT surface quality. Figure 15.30 shows 3D topography of machined surfaces in CT and UAT at two different feed rates where the negative effect of feed increment on surface roughness is lower in UAT compared with CT. The conclusion of this work was that radial force and tool-chip engagement time were two main factors affecting surface quality.

The work of Khanna et al. (2019) focused on finding optimized values of cutting speed, feed rate, depth of cut, and frequency to minimize surface roughness and power consumption in UAT of Nimonic-90 alloy. In UAT, up to 10% improvement was observed in surface roughness and

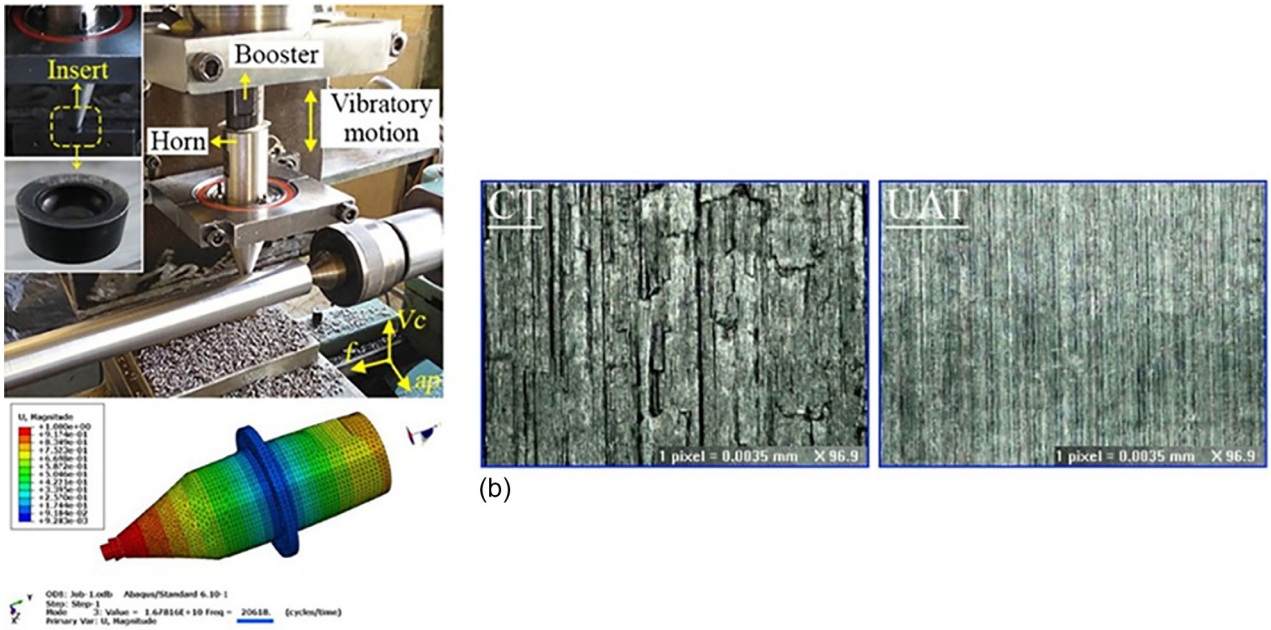


FIGURE 15.29 (a) Experimental setup; (b) microscopic images of machined surfaces of CT and UAT samples (Lotfi et al., 2018, Fig. 1, 3).

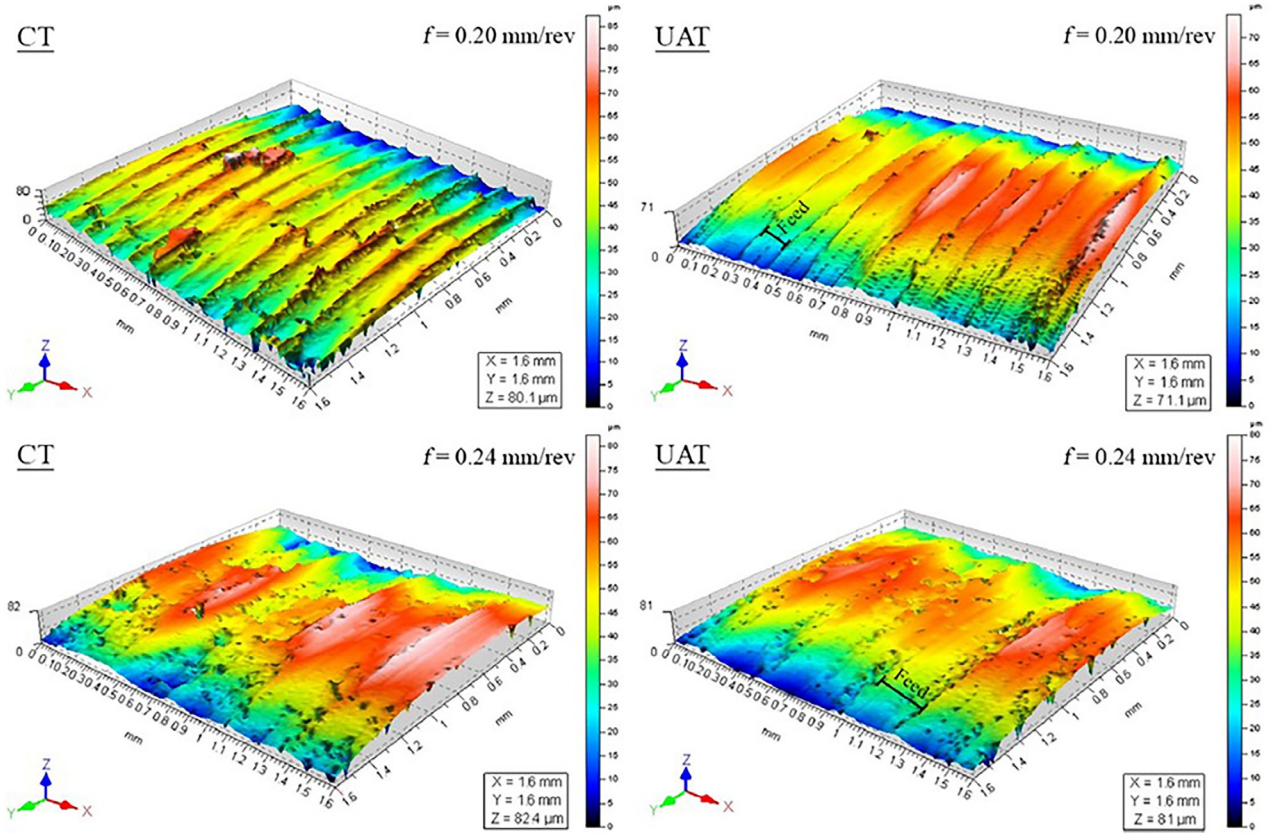


FIGURE 15.30 3D topography of samples machined with CT and UAT (Vc = 750 mm/s) (Lotfi et al., 2018, Fig. 6).

power consumption compared with CT, and this seen as due to microchipping that occurs in UAT. Optimization was performed using a standard particle swarm (PSO) and hybrid particle swarm with simplex methods (PSO-SM) where PSO-SM provided the most optimized results. The results of the statistical analysis showed that the feed rate and cutting speed were the most significant parameters affecting the surface roughness and power consumption, respectively. PSO was also used by Khanna et al. (2020) to identify the optimum cutting parameters in UAT of Inconel 718 to achieve minimum surface roughness and power consumption. Results showed that frequency and feed rate had the greatest impact on surface roughness and power consumption. The optimized parameters were then used to compare the surface roughness and chip morphology in cryogenic-ultrasonic-assisted turning (CUAT) with UAT and CT. Results showed that surface roughness of the CUAT samples were reduced by 14%–25% and 25%–33% compared with UAT and CT samples. CUAT resulted in discontinuous chips having smaller length compared with the UAT and the hardness of the machined surface of the CUAT samples increased by 4.7% as compared to UAT and CT samples.

15.3.5.3 Microstructure

Shi et al. (2016) focused on the microstructures in the primary and secondary shear zones of machining chips of Ti-15V-3Cr-3Al-3Sn produced by CT and UAT using electron backscatter diffraction (EBSD) and transmission electron microscopy (TEM). A 20 kHz system was used to generate vibration in tangential direction. Cutting was modeled into primary and secondary shear zones. To measure the shear strain in the primary shear zone, the chips were modeled as parallel plates. Optical micrographs of the chip produced by CD and UAT are shown in Figure 15.31. As indicated by squares A and B of Figure 15.31a, the primary zone (i.e., square A) consists of a homogeneous nano-microstructure and secondary shear zone (i.e., square B) is less homogeneous than that in the primary shear zone. As seen in Figure 15.31b, the secondary zones in the chip generated by UAT have similar thickness and cross-sectional microstructure to that of CT chips.

An SEM-EBSD orientation map of the cross-sectional microstructure of the UAT chip showed, due to reduced frictional force in UAT, that machined chips showed a larger shear plane angle and lower shear strain compared with CT machining chips. TEM micrographs of the secondary shear zone in the UAT chip indicated that ultrafine grains were also formed during UAT process and that due to the lower frictional force in UAT, the grain size was larger than for CT.

15.3.5.4 Tool wear

The work of Farahnakian et al. (2019) focused on tool wear in UAT of hardened alloy steel, which is due to the vibro-impact nature of UAT. To reduce the tool wear, a slight initial wear was applied to the cutting edge. A 27 kHz UAT system was used to apply 8 μm amplitude in the cutting direction.

Two sets of experiments were conducted; (1) CT and UAT using an ordinary tool; (2) CT and UAT using a modified tool. In the case of CT and UAT with the ordinary tool, results showed that while UAT provided a more stable process compared with CT, no improvements on flank wear were observed, microchipping of the sharp cutting edges occurred and the tool flank face was heavily scratched in some cases. However, when the cutting edges were modified, the tool flank wear was significantly reduced in UAD. However, improvement in tool flank wear decreased as cutting speed increased and the flank wear using the modified tool in UAT was about 20%, 25%, 40%, 50%, 55%, and 75% of the CT when cutting speed of 14, 18, 28, 34, 55, and 78 m/min were used.

Zou et al. (2017) experimentally investigated tool wear in UAT of die steels using single-crystal diamond tools. The diamond tool was attached to a 20 kHz UAT system that generated 16 μm amplitude perpendicular to the cutting direction. Diamond tool wear was measured by a scanning electron microscope (SEM), Raman spectral analysis, and energy-dispersive X-ray (EDX) analysis. The results

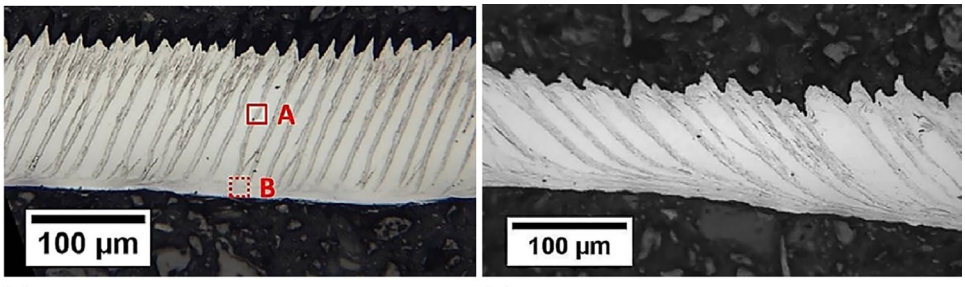


FIGURE 15.31 Optical micrograph of cross section of 15V-3Cr-3Al-3Sn chip produced by (a) CT; (b) UAT (Shi et al., 2016, Fig. 3, 9).

showed that tool wear mainly occurred on the flank face of the tool. In UAT of die steel, graphitization was one third of that in CT and diamond diffusion decreased by 58% in UAT. The improvement of tool wear in UAT was explained by the 84% reduction observed in friction force.

15.3.5.5 Composites

The study of Bai et al. (2019a,b) focused on the machinability and tool wear in CT and UAT of SiCp/Al metal matrix-composite (MMC) using cemented carbide (WC) and polycrystalline diamond (PCD) tools with and without using coolant. The results, using an 18.11 kHz system, showed that UAT reduced cutting force significantly while a slight increase in cutting temperature was observed. UAT also improved the quality of the machined surface and increased ductility of the workpiece material. Continuous and semicontinuous chips were obtained compared with the chips generated in CT. While applying minimum quantity lubricant (MQL) reduced cutting zone temperature and built-up edge (BUE), it had no major effect on cutting force or the quality of the machined surface. Finally, their tool wear studies suggested UAT with WC tools as a viable way for economic and sustainable machining of SiCp/Al MMC. Reduction in cutting force was also observed in the work of Kim et al. (2019), where the same setup was used to evaluate the suitability of using UAT in machining SiCp/Al MMCs with and without MQL. Results showed that dry machining of SiCp/Al MMCs was preferable with ultrasonic assistance.

15.3.5.6 Process modeling

Khajehzadeh and Razfar (2016) examined the theoretical and experimental characteristics of tool temperatures in machining aluminum 7075 using a 31 kHz UAT system. A mathematical model was developed to evaluate the effect of cutting speed, feed rate, and vibration amplitude on the average temperature distribution and verified their results with experimental data measured by thermocouples. Results showed that while increasing cutting velocity would increase tool temperature, applying high-frequency vibrations did not lower the cutting temperature. The effectiveness of UAT in lowering temperature was highly dependent on the value of machining and vibration parameters. It was noted that at low feed rate, where the coupling effect does not take place, UAT would decrease cutting temperature, while at high feed rate the effectiveness of UAT to lower the temperature was reduced.

Lotfi and Amini (2018) utilized DEFORM 2D to develop FE models to evaluate applying 20 kHz vibrations with 4 μm amplitude on machinability parameters in CT and linear and elliptical UAT of Inconel 718. The results of cutting force measurements, which were verified experimentally, showed that while the average value of cutting force was significantly lower in linear and elliptical UAT compared with CT, the maximum cutting force in linear UAT was very close to CT, but it was lower in elliptical UAT. Due to effect of shear angle on reduction in deformed chip thickness, which resulted in the decrease in tool-chip contact length and power consumption, shear angle of 45 degrees worked best. Study on the effect of the ultrasonic vibration on this parameter showed that elliptical UAT can increase shear angle to close to its ideal value and caused deformed chip thickness to be reduced.

There followed Lotfi et al. (2019) in which a theoretical model was developed to calculate sticking-sliding contact zone length in FEA, with experimental studies to evaluate the effect of ultrasonic vibrations on frictional behavior in the tool-chip contact zone in CT and UAT of stainless steel 304. Results showed that up to 15% reduction in friction coefficient was obtained when ultrasonic vibrations were added to CT. In UAT, the intermittent contact causes the total time of thermal conduction between tool and chip to be reduced which reduces the generated heat on tool rake face compared with CT. This condition decreases friction and sticky length in the tool-chip interface.

The concept of sticking-sliding contact zones and intermittent cutting mechanism was used by Sharma and Pandey (2019) to develop a mechanistic model to predict the components of cutting force in UAT with self-lubricating textured inserts. The predicted cutting force, which was verified by experimental data with 14% error, followed the same trend observed with rise in cutting speed.

Gholamzadeh and Soleimanimehr (2019) used ABAQUS in developing a 2D model to evaluate the effect of cutting speed, feed rate, and amplitude on tool tip temperature in dry UAT of aluminum 7075. The friction coefficient used in the model was obtained from experimental tests, and the Johnson-Cook plasticity model was used to express the material properties under large deformation. Figure 15.32 (upper image and lower image) shows tool tip temperature during engagement and disengagement of the tool where it increased while penetrating into the workpiece and decreased on separation. They observed a similar trend in cutting force. Their results also showed that by increasing vibration amplitude, the maximum cutting tool temperature increased but average temperatures, in some conditions, could decrease from CT. They concluded that to avoid increasing tool temperature in UAT, low amplitudes and high frequencies should be used.

A similar 2D FE model was developed by Zhang and Wang (2019) to evaluate the effects of ultrasonic vibration on forces, temperature, and stress in CT and UAT of Ti6Al4V. Their results showed that UAT can decrease cutting force, stress, and temperature of the cutting area.

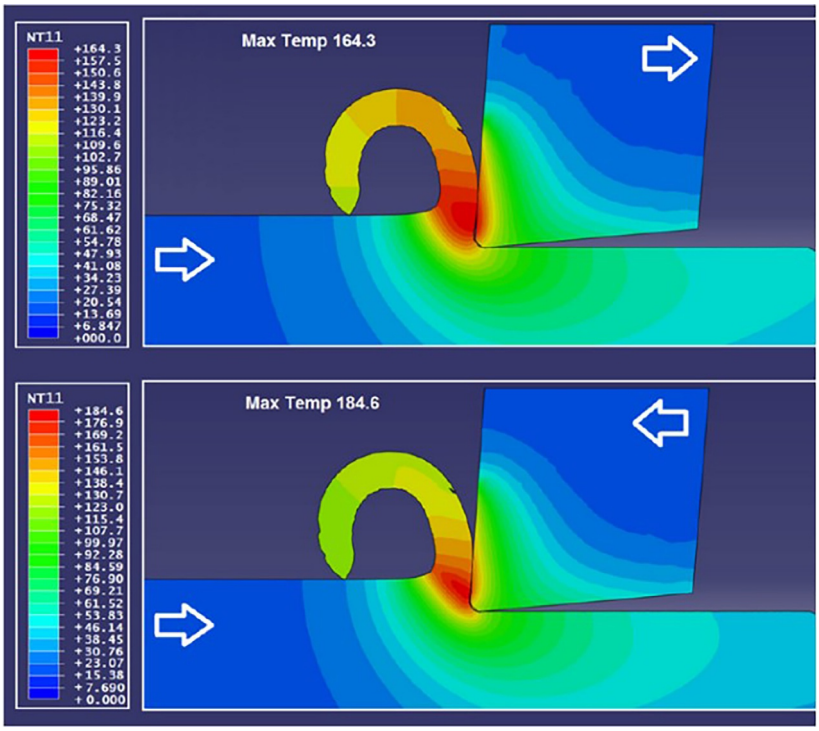


FIGURE 15.32 Contour temperature obtained from FEM tool disengagement (upper image) and engagement (lower image) (Carbide tool, Al7075-T6 workpieces; $f = 25\,\text{kHz}$, $a = 8\,\text{mm}$, $Vc = 20.420\,\text{m/min}$, $ac = 0.1\,\text{mm}$ (Gholamzadeh and Soleimanimehr, 2019, Fig. 9).

15.3.5.7 Modeling—Vibrations, tool stress

Amini et al. (2017) designed an 18 kHz UAT system that could generate elliptical vibrations (i.e., 2D UAT). In the tool, a set of ring-shaped and a set of half-ring-shaped piezoelectric stacks were used to excite the longitudinal and bending modes. To evaluate performance, preliminary machining tests were conducted on copper. The results were compared with CT and a 1D UAT and showed 85% and 81% reduction in force compared with CT and 1D UAT. A microhardness study of the chips showed them to be softened as a result of 2D UAT. The surface roughness improvement obtained in 1D UAT was more than that of 2D UAT.

The work of Sofuoğlu et al. (2018) focused on hot ultrasonic-assisted turning (HUAT) and used ANOVA to study the effect of cutting speed and tool overhang on machinability of a Nickel-based alloy. Test results, which combined the thermal softening effect of hot machining and intermitted cutting of UAT, showed improvement in surface roughness and stable cutting depth compared with UAT and CT. However, this method caused increasing maximum cutting temperatures, which could result in reduced tool life. Results of modal tests and analysis of the chatter vibrations conducted indicated that while chatter frequency was higher than natural frequency, both frequencies decreased with increasing overhang length.

Puga et al. (2019) used numerical and experimental approaches to investigate the effect of external loading (e.g., due to depth of cut and feed rate) on the resonant frequency shift in UAT using the setup of Figure 15.33.

The results showed that the increase in cutting load resulted in a deviation of resonant frequency and a decrease in vibration amplitude. Results also showed that in UAT of Al7050, depth of cut had a greater impact on the frequency shift and feed rate had a greater effect on surface roughness, and by adjusting frequency, surface roughness could be improved by 14%.

To overcome the challenges of generating two-dimensional ultrasonic vibrations, which includes using two sets of ultrasonic equipment to excite vibrations in different directions, FEA was used by Jinglin et al. (2019) to design a 35 kHz steel ultrasonic integrated turning tool (UITT). The resulting UITT was able to generate longitudinal-bending vibrations through excitation in one direction. The influence of tool geometrical parameters on the resonance frequency and longitudinal-bending ratio was studied with results showing that tip cutting edge angle and inclination had the greatest effect on resonance frequency.

15.3.5.8 Control

In UAT, due to the effect of load and temperature on system resonant frequency and amplitude, Ille and Twiefel (2015) used a digital resonance and current controller to guarantee constant vibration amplitude to achieve a stable, uniform

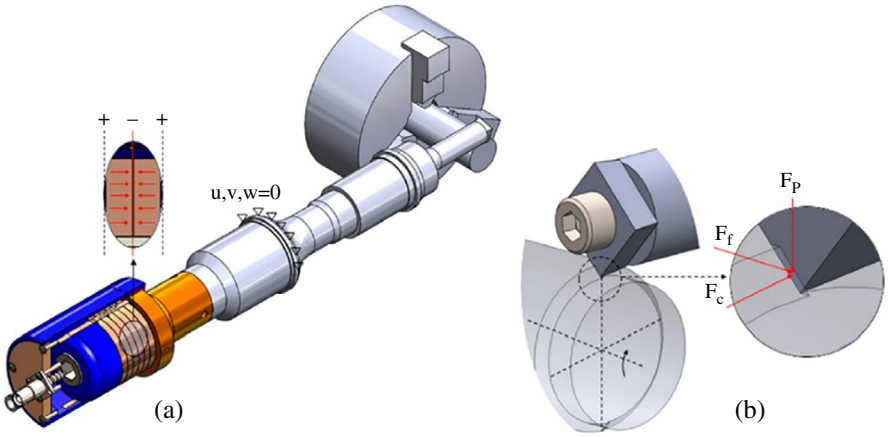


FIGURE 15.33 (a) Geometrical model and (b) schematic draw of the machining forces components (Puga et al., 2019, Fig. 1).

machining process. A model-based approach was developed to determine the parameters for the phase and amplitude. The approach was based on the work of Van der Pol (1927) and used phase sensitive demodulation (PSD) reported by Twiefel et al. (2008). Measurement of current amplitude, phase, voltage, and frequency in UAT of aluminum and steel showed a stable and fast behavior of the controller.

15.4 Ultrasonic drilling

Benefits sought in ultrasonic drilling are similar to those of turning and include increased feed rates, lower tool forces and torques, reduced tool wear, improved surface quality, and smaller chip sizes in comparison with conventional drilling. Early work in ultrasonic drilling was reviewed in Section 15.2. In continued developments, the study by Azarhoushang and Akban (2007) used a system consisting of a 21 kHz stationary 5 mm carbide drill and a rotating Inconel 738 workpiece, as shown in Figure 15.34. Tip vibration amplitude was up to 20 μm and workpiece RPM was varied at 250, 350, and 500. One result was that exit burrs were reduced with ultrasonics, as shown in Figure 15.35, for various RPM and feed rates f (mm/s). Data are presented on the effect of drill amplitude, RPM, and feed rate on hole circularity, cylindricity, and surface roughness, with improvements found with ultrasonics. A difference in chip morphology was noted, where ultrasonics produced small, discontinuous chips, while conventional drilling produced long continuous chips. Improvement were also seen in tool wear.

Deng et al. (1993) used a stationary magnetostrictive transducer in drilling stainless steel and noted that the ultrasonic vibrations of the drill also had a torsional component. A "sharpening mechanism" concept was put forth. Several studies have used a conventional rotating drill, introducing ultrasonic vibrations into the workpiece. Thus, in the experimental work of Chang and Bone (2009, see also 2005, 2010), excitation was provided by a variable frequency (4–12 kHz) actuator. A modeling approach was taken based on extending procedures for conventional drilling. Results were obtained for thrust force as a function of excitation frequency. Drilling in Al6061-T6 with a 4 mm drill operating at 4000 RPM, 0.006 mm/rev feed, and 2 μm amplitude, a good correlation between the model and measured forces was found. A continued decrease in force with increasing frequency was noted, with a minimum at 10 kHz, at which point force began to increase.

Also using a conventional, high-speed (30,000 RPM) precision drill (0.5 mm diameter), in conjunction with a vibrating workpiece (frequencies of 1000–10,000 Hz), Chern and Lee (2006) reported that (1) hole oversize and surface roughness were improved, (2) hole roundness was improved, but (3) there appeared to be a negative effect on drill life. In studying high-speed precision drilling, Lee et al. (2007) modeled the ultrasonic process, relating the kinematics of chip formation and chip thickness to machining parameters. The conditions for production of small segmented chips were obtained and observed in tests. Likewise, an improvement in hole surface finish was noted. Others conducting similar studies were Bijan and Reza (2011) and Pujana et al. (2009).

A number of investigators have directly applied ultrasonics to the rotating drill, thus more closely relating to practical applications. The work of Liao et al. (2007), while lacking detail on the means of vibrating the drill, provided comparisons of chip morphology (shorter chips observed with ultrasonics), noting thrust force reductions with ultrasonics and improvements in tool life under certain drilling conditions. Potthast et al. (2008) modeled the process and introduced a contactless, electromagnetic coupling means for vibrating the high-speed (25,500 RPM) ultrasonic drill, with results showing reduced tool wear, reduced torque,

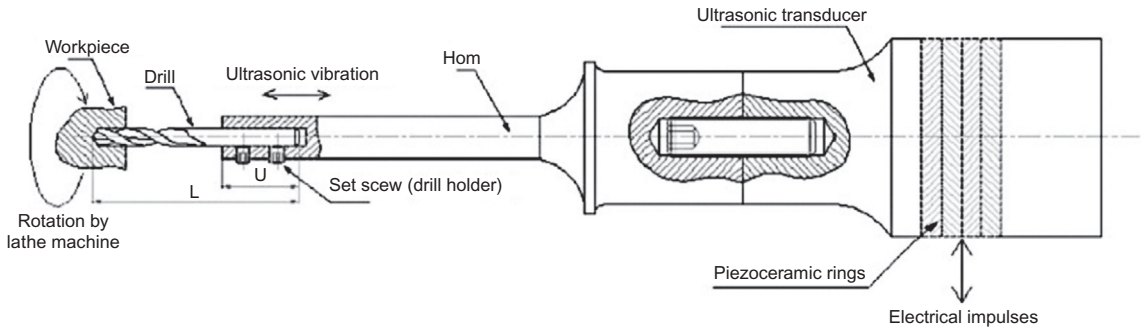


FIGURE 15.34 Ultrasonic drill (Azarhoushang and Akban, 2007, Fig. 1a).

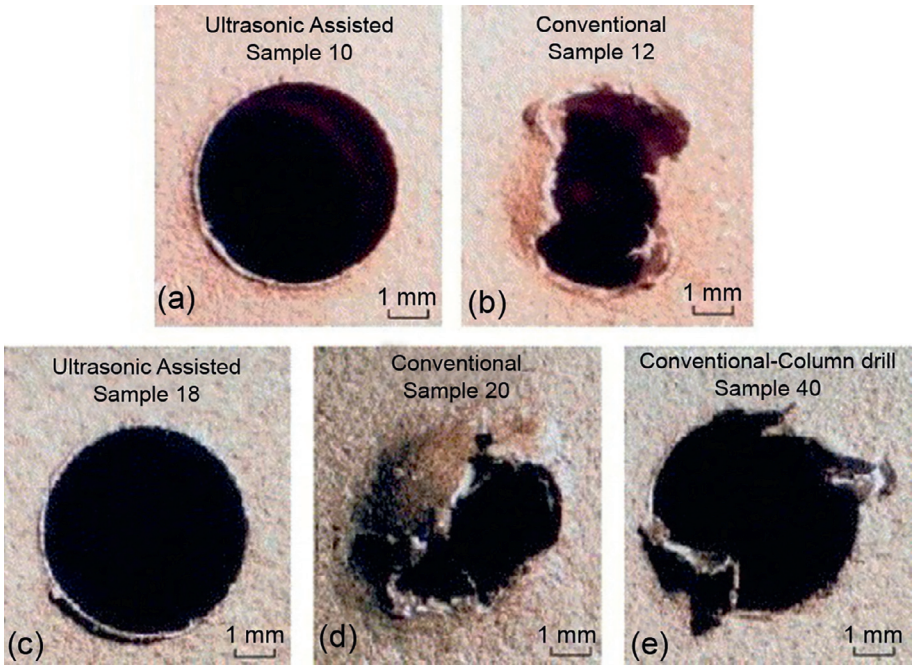


FIGURE 15.35 Drill exit burrs at 10 μm: (a) 250 RPM, $f = 0.8$ mm/s, (b) 250 RPM, $f = 0.8$ mm/s, (c) 350 RPM, $f = 0.5$ mm/s, (d, e) 350 RPM, $f = 0.5$ mm/s (Azarhoushang and Akban, 2007, Fig. 2).

and smaller chip sizes. Xu et al. (2009, 2011) applied ultrasonic vibrations to the drilling of composites and reported reduced forces and torques with ultrasonics as well as improved chip removal and reduced tool wear. The work of Yagishita (2007) introduced a torsional mode in drilling. Because of the natural twist of a drill, its longitudinal vibrations will induce an unavoidable torsion component of vibration, with some modes in which the torsion motion is the dominant vibration. It was reported that improved hole quality (improved finish, roundness, and reduced drill exit damage) as well as improved tool wear was obtained.

The work by Babitsky and colleagues, already cited in turning, was carried over to the drilling field (Babitsky et al., 2007). Thus, Figure 15.36 shows the drilling setup having a rotating transducer and drill. The system was modeled using the analytical impact dynamics methods set forth in Astashev and Babitsky (2007).

Experimental results, using a 3 mm drill at 125 RPM, included the influence of ultrasonics on rate of penetration, where the penetration rate was seen to nearly double when ultrasonics was applied, and on drill force where force was seen to drop by over 50% with the application of ultrasonics. A reduction in exit burrs was also seen. The authors also reported on the development of a torsion mode drill. Further results from the drill system were reported by Thomas and Babitsky (2007). The drill vibrations were modeled with FEA and then measured with a laser vibrometer. A pronounced dominance of a torsional component over the longitudinal component was noted at certain locations.

Zhang and Babitsky (2011) investigated high-speed ultrasonic microdrilling. Finite element modeling was applied to the transducer/drill system where several resonant frequencies, ranging from 6 to 37 kHz, were identified.

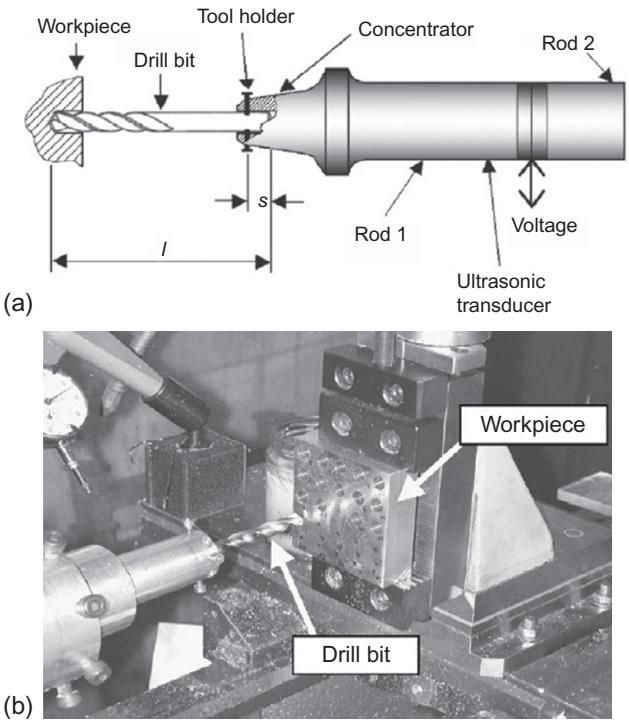


FIGURE 15.36 Ultrasonic drilling system: (a) schematic of ultrasonic drill (Babitsky et al., 2007, Fig. 1) and (b) experimental system (Babitsky et al., 2007, Fig. 2).

A 0.3 mm tungsten carbide drill was used, and rotational speeds ranged up to 100,000 RPM. An analytical approach based on a nonlinear force model of the process was developed. The experimental system used a dynamometer to measure thrust forces, under conventional drilling and with ultrasonic vibration, for various operating speeds. Some key results were that some force reduction occurred at all ultrasonic frequencies, with the most pronounced reductions, averaging 45% at 19.0 kHz, with a reduction of nearly 65% at 100,000 RPM.

The concept of elliptical tool motion, noted in the turning section, was applied by Ma et al. (2005) to drilling, with the small workpiece vibrated in an elliptical pattern pressed against a conventional rotating drill, as seen in Figure 15.37. Although details of the transducer were not given, it is believed similar to that shown for elliptical turning. The effects of elliptical vibration on the axial and radial drill force and chip thickness were compared with conventional drilling results. A 0.65 mm carbide drill at a feed rate of 0.025 mm/rev and at 100 RPM was used on aluminum 52S. The workpiece vibrated at 18.87 kHz and had a circular vibration locus. Results showed a reduction in axial force, as shown by Figure 15.37b (bottom), where a reduction of two-thirds of conventional forces is seen in the later stages of the drilling, with reductions of one half observed in the transverse forces acting on the drill. Likewise, chip thicknesses were reduced to about one half to one third of that of conventional drilling.

This section concludes by noting two review papers, the first by Neugebauer and Stoll (2004). In addition to reviewing various types of ultrasonic drilling, ongoing work at Fraunhofer IWU was highlighted. Only two references are provided, both to coauthored works by the lead author. The second paper by Yang and Lin (2010) provides an extensive overview of the field, including its historical developments. Although nearly all of the references deal with work from China and Japan, the extensive contributions from these sources make this necessary reading for workers in this field.

15.4.1 Recent developments in ultrasonic drilling, 2014 onward

Recent UAD literature to be reviewed in this section can be categorized into three groups: experimental, analytical, and finite element (FE) modeling. The focus of experimental literature is on data from UAD trials, while analytical literature focuses on vibrations and kinematics of UAD systems. FE literature covers design aspects of UAD systems and seeks to model the UAD.

Barani et al. (2014) designed and fabricated a UAD system with a 5-mm HSS twist drill held in a lathe chuck, Figure 15.38a. Tests were conducted on Al2024-T6 at feed rates of 130–436 mm/min and 460–1255 RPM, with UAD effects evaluated on the built-up edge (BUE), surface

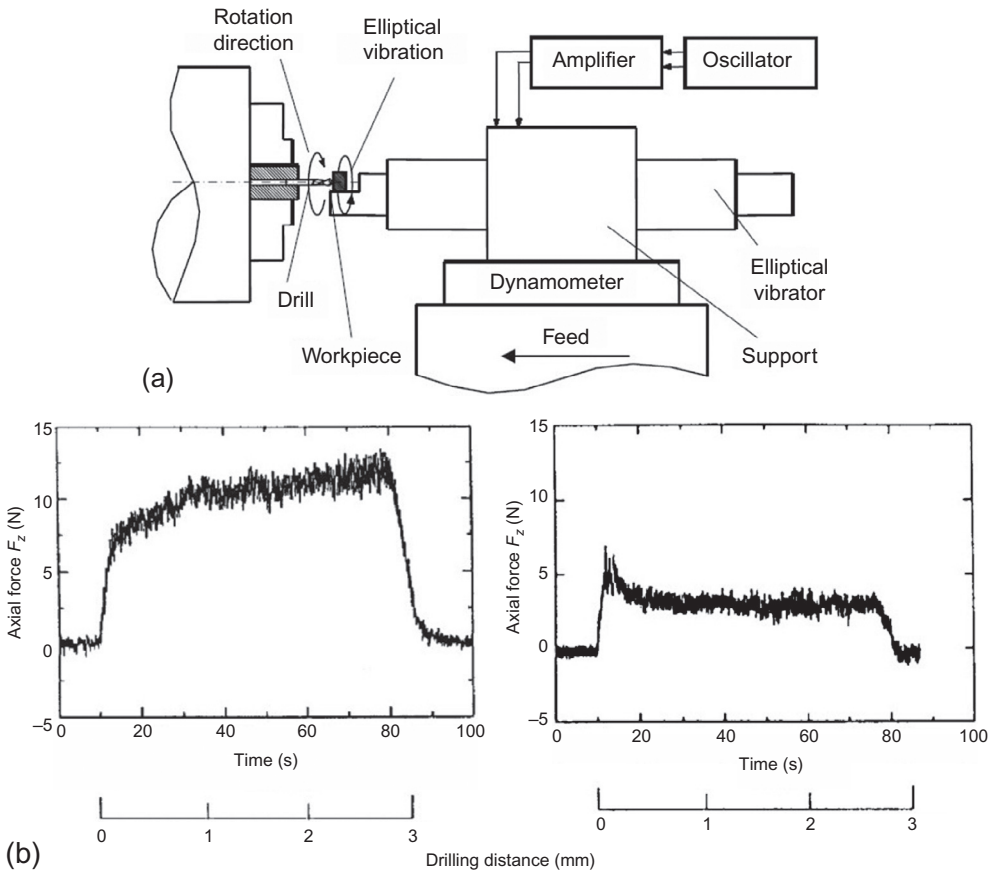


FIGURE 15.37 Elliptical vibration drilling: (a) experimental setup (Ma et al., 2005, Fig. 1) and (b) axial force for conventional drilling (left) (Ma et al., 2005, Fig. 4) and elliptical drilling (right) (Ma et al., 2005, Fig. 5).



FIGURE 15.38 (a) Experimental setup; (b) chip morphology with hole number. (1) First hole, 755 RPM, 0.104 mm/rev, $a = 0$. (2) Tenth hole, 755 RPM, 0.104 mm/rev, $a = 0$. (3) First hole, 755 RPM, 0.104 mm/rev, $a = 10\,\mu m$. (4) Tenth hole, 755 RPM, 0.104 mm/rev, $a = 10\,\mu m$ (Barani et al., 2014, Fig. 7, 30).

quality, chip morphology, and tool wear. They found that friction reduction due to ultrasonic tool vibrations could decrease the BUE and surface roughness and provide shorter chips compared with CD, Figure 15.38b.

Baghlani et al. (2013) applied high-frequency vibrations to a 5-mm tungsten carbide drill and drilled Inconel 738LC with a depth-to-diameter ratio of 10. Design of experiments (DOE) was used to determine the optimum values of cutting

and ultrasonic parameters to minimize thrust force and surface roughness. This was followed by Baghlani et al. (2016) that utilized DOE to evaluate the influence of vibration amplitude, spindle speed, and number of steps to drill each hole on machining force and surface roughness for three different drilling methods (CD, UAD, and electro-discharge drilling (EDD). Results confirmed that when compared to CD, UAD not only improved tool life significantly, but also reduced thrust force by 40%. The results also demonstrated that UAD reduced hole cylindricity and surface roughness by 50% and 52%, respectively.

The effects of applying coolant by flood and minimum quantity lubrication (MQL) methods were studied by Isobe and Hara (2014) for CD and UAD processes. A 40-kHz UAD system was used to drill 2-mm thickness Inconel 600 with a 0.3-mm drill. The results showed that the number of drilled holes increased by 4 and 15 times, in both CD and UAD, when the MQL method was used compared with the flood cooling method. It was also found that at 6 mm/min feed rate and 3000 RPM, when chip load was increased to 20 μm/rev, the number of holes increased by 10 times due to the reduction in the cutting force by 50%.

This was followed by that of Lotfi et al. (2017) where the MQL method was added to both CD and UAD of steel 1045 to evaluate its influence on drilling outputs. The results showed that the combination of MQL and UAD provided the maximum thrust force and surface roughness reduction as well as minimum BUE compared with CD, MQL-CD, and UAD. As seen in Figure 15.39, burr formation, which has a direct relationship with thrust force, was almost eliminated by using MQL method in UAD.

Li et al. (2016a,b) used a 30-kHz UAD system to study the effect of thrust force on the cutting lips and chisel edge in CD and UAD. Pilot holes with a 1.8-mm drill (i.e., the chisel edge diameter of a 6-mm drill) were used on 12-mm thickness aluminum 7075 to eliminate the thrust force of the chisel edge. Results showed the thrust force of the chisel edge would be affected more than the thrust force of the cutting lips. However, it was found that increasing spindle speed increased the thrust force of the cutting lips and had little influence on the thrust force of the chisel edge.

Chu et al. (2020) analyzed torque variations in CD and UAD of aluminum 6061 with high depth-to-diameter ratio (e.g., 13.3) by studying the components of cutting torque (T1), rubbing torque (T2), and stick-slip torque (T3). Their results showed that the reductions of both rubbing torque and stick-slip torque would be the main reason for the enhancement of machinability in deep drilling of UAD over CD.

Zhao et al. (2019a,b) used a dynamic model to study the effect of mechanical load and temperature on the amplitude and frequency in a 35-kHz UAD system, using the setup shown in Figure 15.40a to verify their theoretical analysis. The system attached to the dynamometer was able to adjust loads to the tool by pushing the squeeze head to the stationary tool for at least 10 min to increase the temperature of the system. The laser displacement sensor was used to measure the displacement of the tool. As seen Figure 15.40b and c, the results of tests showed that as load increased, the frequency and amplitude of the system increased, then decreased when system temperature increased. Results also showed good correlation between current and amplitude. Drilling tests were also done with two tools with different rigidity coefficients. It was found that the rigidity of the tool and the feed rate had significant effect on the system vibrational characteristics. It was concluded that the tool with a higher rigidity coefficient and a proper feed rate should be used for UAD. Zhao et al. (2020) conducted a similar investigation to evaluate the effect of load on resonant frequency and amplitude of an ultrasonic longitudinal-torsional composite drilling system (ULTCDS). Their results showed that detuning occurred when the frequency shift and the UAD current exceeded 350 Hz and 60%, respectively, thus reducing the positive effects of UAD.

The work of Li et al. (2017a,b) started with kinematic analysis of the UAD process, analyzing the velocity change that happens in UAD and used this concept to explain continuous and discontinuous chips in CD. The UAD system with a 5-mm 8-facet drill was held in the lathe three-jaw chuck, and tests were conducted on CD and UAD of Ti6Al4V at feed rates of 0.028 mm/rev and spindle speed of 800 RPM. Results showed that in UAD with 10-μm amplitude, the thrust force, torque, cutting temperature near

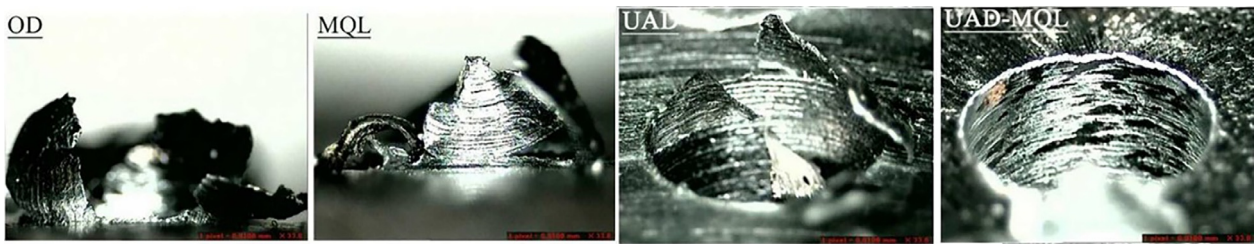
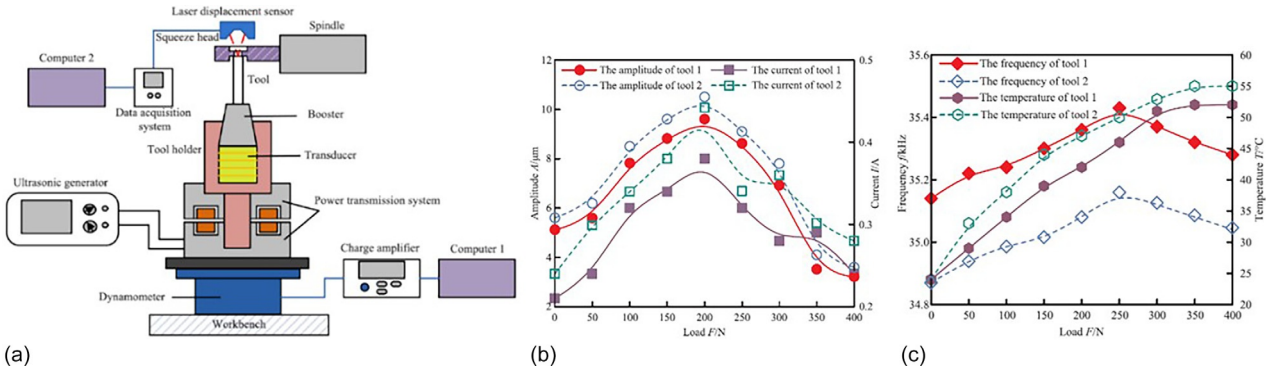
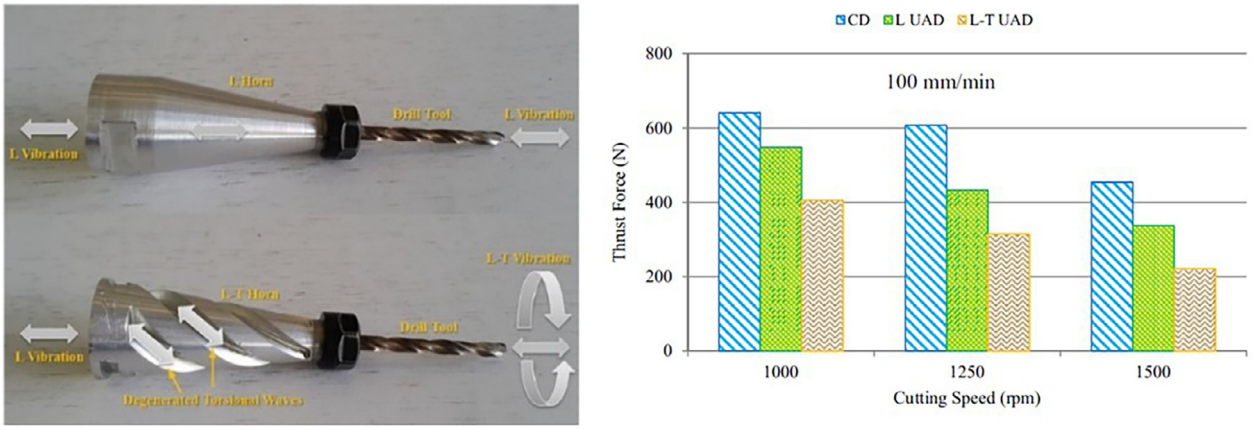


FIGURE 15.39 Burr formation during OD (Ordinary drilling or CD), MQL, UAD, and UAD-MQL processes ($N = 950$ RPM and $f = 165$ mm/min) (Lotfi et al., 2017, Fig. 7).



(a) (b) (c)

FIGURE 15.40 (a) Schematic of the experimental setup; (b) influence of load on amplitude and current of the vibration system; and (c) influence of load on the frequency and temperature of vibration system (Zhao et al., 2019b, Fig. 5, 9,11).



(a) (b)

FIGURE 15.41 (a) The longitudinal and longitudinal-torsional horns; (b) comparison of the measured thrust force in CD and UAD of steel 1045 using 5-mm drill with longitudinal and longitudinal-torsional horns (Paktinat and Amini, 2018b, upper image of Fig. 3, 13).

the hole exit, surface roughness, dimensional accuracy, and burr height could be reduced by up to 20.2%, 33.6%, 21.68%, 25.36%, 57.63%, and 89.18%, respectively. Results also showed that, in contrast to CD, UAD improved chip breaking and evacuation processes.

Chen et al. (2019) used a similar approach to that of Zhang and Wang (1998) to analyze chip breaking in CD and UAD. Results showed that while CD chip thickness was constant (half of the feed rate), UAD chip thickness had the form of a sine wave. Since chip breakage occurs as chip thickness approaches zero, phase displacement between two cutting edges should not be zero and that breakage happened when the following inequality was satisfied:

$$\frac{4A}{f_r} \geq \frac{1}{\sin\left[\pi\left(\frac{f}{2n} - K\right)\right]} \tag{15.3}$$

where A, f_r, f, and n are amplitude (mm), feed rate (mm/rev), frequency (Hz), and drilling speed (rev/s). K in this inequality is an integer. To verify the results, tests were done and the generated chips in CD and UAD of stainless steel using 20-kHz UAD with 6-mm drill were analyzed. The results showed that when the drilling and ultrasonic parameters satisfied inequality (15.3), smaller chips were generated. They used the chip breaking concept in UAD to explain the observed benefits.

Paktinat and Amini (2017-1, 2017-2) used modal analysis to develop a 20 kHz UAD system with a 5-mm drill and including a rotary mechanism installed into the spindle of a CNC milling machine. Results of tests on drilling Al7075 and FEM of UAD showed that ultrasonic vibrations reduced chip adhesion to the drill tool (i.e., BUE) and produced discontinuous chips. Results also showed up to 40% improvement in drill circularity, 40% reduction in burr height and 37% reduction in thrust force. This study was followed by Paktinat and Amini (2018a,b) where the experimental and FEA results of using two different UAD horns shown in Figure 15.41a were compared. As seen in Figure 15.41a, the horns could produce two types of vibrations, longitudinal (L) and longitudinal-torsional (L-T). The

measured thrust force of CD and UAD of steel 1045 using 5-mm drill is shown in Figure 15.41b.

As seen in Figure 15.41b, the measured thrust forces were less in UAD tests using longitudinal vibrations, with even smaller thrust forces obtained with L-T vibrations. These reductions were due to lower stresses which confirmed their FEA results.

The concept of a composite vibration mode was also explored by Zhao et al. (2019a,b) where theoretical, finite element and experimental studies were done to evaluate the effect of incident angle (angle α in Figure 15.42a) of the L-T horn on the ratio of torsional amplitude and longitudinal amplitude. In their studies, the incident angles that maximized ($\alpha = 47.6°$) and minimized ($\alpha = 62.2°$) this ratio were calculated. FEA was used to design two L-T horns using the calculated incident angles and resonant frequency and amplitude ratio were obtained. Figure 15.42b shows the longitudinal and torsional amplitude measured by laser displacement sensor for both horns.

From Figure 15.42b, it was concluded that the amplitude ratio in the horn with 47.6 degrees incident angle is approximately 4.9 times higher than the horn with 67.2 degrees incident angle. The results of UAD tests using both horns on Titanium showed that due to the higher amplitude ratio of the horn with an incident angle of 47.6 degrees, the average drilling force was reduced by 26% compared with the horn with an incident angle of 67.2 degrees. Moreover, higher amplitude ratios provided holes with less burr.

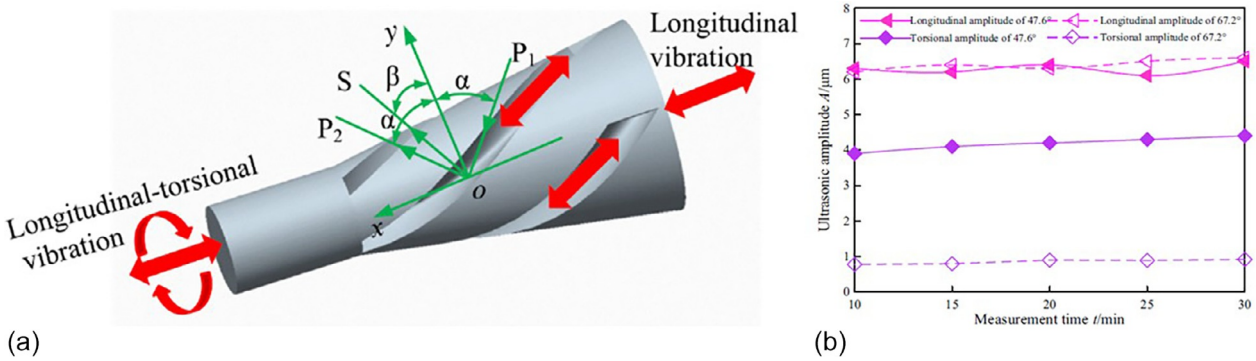
While most UAD systems were designed to apply vibrations in the axial direction, the work of Gao and Altintas (2019) used FEA to design a 3-degree of freedom ultrasonic vibration tool holder that could be used for both milling and drilling operations. X and Y piezoelectric rings delivered 17.5-kHz elliptical vibrations with 20-μm amplitude by resonating the third bending mode in the XY plane, and Z piezoelectric rings generate 16.5-kHz axial vibrations with 25-μm amplitude by exciting the first axial mode. The system was mounted to the CAT 40 spindle of a CNC machining center, with power transmitted to the system through four slip rings. The results of the preliminary test using this system showed 30% force reduction in milling and drilling of aluminum 7075 using an 8-mm tool with vibrations applied in the XY and Z directions, respectively.

Lotfi and Amini (2017) developed a 3D FE model of CD and UAD processes with a 5-mm diameter drill in DEFORM and evaluated the effects of ultrasonic vibrations on thrust force, chip morphology, heat generation, and built-up edge (BUE) in drilling 1045 steel. Using a similar experimental setup as Paktinat and Amini (2018a,b), thrust force, measured at different spindle speeds and feed rates by a dynamometer, verified the results of the model. Thus, the simulated CD and UAD thrust force profiles showed good agreement (10% error) with experimental results.

Study of the BUE formation based on the heat generated in the flank face and the chisel edge of the drill was also done in this research. It was found that heat generation on the flank face was less in UAD compared with CD due to the harmonic motion of drill.

Deform software was also used by Liang et al. (2019) for FEA evaluation of the effect of drill point angle on thrust force and generated heat in UAD and CD of Ti6Al4V. The results, verified by experimental analysis, showed that while thrust force and cutting heat was reduced in UAD compared with CD, an increase in drill point angle from 110 to 140 degrees would increase these parameters in both CD and UAD. The results showed that among point angle, feed rate, and spindle speed, drill point angle was the most significant factor that affected the surface roughness and the best surface roughness, exit burr and drill life was obtained using a drill with 130 degrees drill point angle.

In the work of Wei and Wang (2019), FEA was used to evaluate the effect of machining and ultrasonic parameters in drilling Ti6Al4V/Al2024-T351, Figure 15.43a. The results of this study showed that UAD can produce smaller chips, lower thrust force, and lower effective stress. However, the maximum temperature of the UAD titanium and aluminum layers were increased by 6.2% and 10.3%, respectively, compared with CD, Figure 15.43b.



(a) (b)

FIGURE 15.42 (a) Schematic of ultrasonic wave propagation in an L-T horn; (b) measured amplitude under different incident angles with tool (Zhao et al., 2019a, Fig. 1, 17).

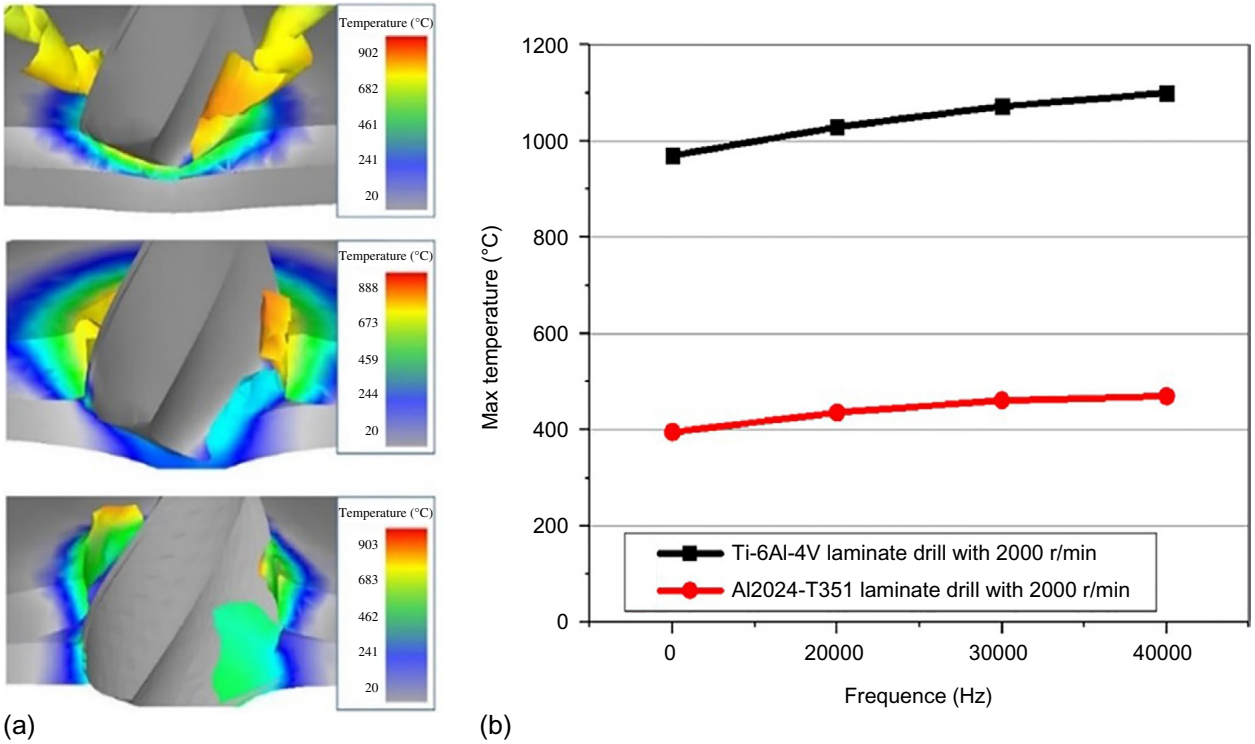


FIGURE 15.43 (a) Temperature in 3-stage of drilling process; (b) FE modeling of effect of vibration frequency on maximum temperature of laminated material (Wei and Wang, 2019, Fig. 11-a, 13).

Similar FE analysis using Deform-3D was done by Wei and Wang (2020) on Ti6Al4V/Al2024-T351 and also by Wang and Wang (2019) on Ti6Al4V using two different drill bits, with similar results obtained except that the temperatures were decreased in UAD compared with CD. In addition, improvements in chip thickness, tool life (Wang and Wang, 2019), burr height, and torque (Wei and Wang, 2020) were also reported when ultrasonics was applied to CD. Results of analysis of damage in a 2D model developed by Lotfi and Amini (2019) confirmed that vibration of the drill bit caused additional chip bending that increased the chip strain. The extra bending caused chip geometry changes from a continuous helical coil shape in CD to broken chips in UAD.

This section concludes by noting a review paper by Dixit et al. (2019). In this work, experimental and analytical studies in the field of ultrasonic-assisted machining (UAM), including 15 UAD papers were reviewed, covering research in this field from 2007 to 2014.

15.4.2 Amplitude, temperature, and force measurements in UAD

Ultrasonic-assisted drilling (UAD) is an active research field, a review of which shows both its extent and the advantages and limitations of the process. However, the laboratory nature of most studies limits extension to production systems. Thus, most studies are done under no-coolant conditions and do not account for the contribution of the torsion component present in any longitudinal drill vibration. Prior work is generally restricted to small drill sizes and RPM and feed rates well below typical production. There are only limited temperature measurements, and these mainly focused on UAD of composites and bone. The effect of ultrasonic vibration on drill life has also not been fully investigated. While serving as useful precursors to later production scale up or for specialized precision needs, such systems will not meet production demands.

This section describes the development of a robust UAD module compatible with computer numerical control (CNC) systems able to function in production conditions. Results of drilling aluminum, steel, stainless steel, and titanium will be presented. Techniques developed for measuring UAD temperatures will be evaluated, and a best technique will be used to evaluate the effect of UAD on heat generated in several materials. Finally, a technique developed to evaluate the effect of load on vibration amplitude will be described.

15.4.2.1 The UAD system

The design of the drilling module is shown in Figure 15.44a and consists of (1) a CAT 40 spindle, (2) the module case, (3) the front mass, (4) drill. The drill attaches to the front mass via an interference shrink fit.

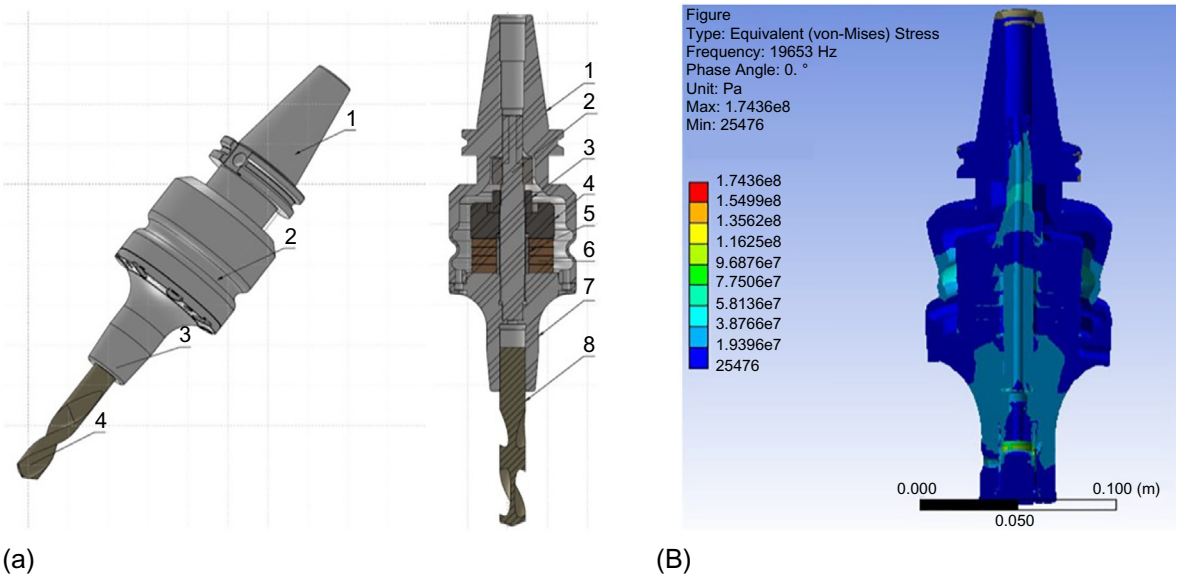


FIGURE 15.44 Ultrasonic drill module: (a) 3D and cross-sectional views, (b) finite element analysis of the module (Moghaddas et al., 2018, Fig. 1, 2b).

The transducer design is based on the well-known composite sandwich construction and consists of six parts including (2) compression stud, (3) nut, (4) back mass, (5) insulator, (6) piezoelectric ceramics, (7) front mass. Some distinguishing features of the unit include an all-steel construction, a minimum of amplification from the front mass, and allowance for the electrical connection in the back mass. The components housed inside the CAT 40 taper portion of the module are designed to transmit the signal from the ultrasonic power supply to the ceramic disks.

As seen in Fig. 15.44b, the UAD module was the result of an FEA-based modeling process, which includes modal and harmonic analyses. With the modal analysis, the free vibrations of the transducer are obtained under short and open circuit electrical boundary conditions to determine the series and parallel resonances. In the harmonic analysis, the transducer is driven with a given frequency and voltage to a resultant displacement and stress. The operating frequency of the module is 19,653 Hz, and the maximum von Mises stress is 174 MPa, a value lower than the fatigue strength of the steel used in the module.

Figure 15.45 shows the setup used for UAD tests of aluminum, steel, stainless steel, and titanium. Two scenarios were examined, and for each, the effect of ultrasonic vibration on thrust force, torque, surface roughness, dimensional accuracy, and microstructure was evaluated. In the first scenario, different amplitudes were imposed on the baseline parameters, while in the second scenario, at maximum amplitude, the feed rate was increased while the spindle speed was fixed until the thrust force reached that of the baseline parameters. In UAD of 4340 steel, it was found that UAD reduced the thrust force and torque by 42% and 24%, respectively, while the surface roughness was improved by 53%, as shown in Figure 15.46.

In UAD of aluminum 6061, it was found that as vibration amplitude increased, the average thrust force and torque decreased and that an 11-μm drill tip amplitude (at 100% power supply amplitude) produced a reduction of over 55% and 25%, respectively. In UAD of stainless steel 316, a reduction of over 33% in force and 12% in torque was obtained. Finally, UAD of Titanium (Ti-6Al-4V) reduced the thrust force by 37% and torque by 13%. For all materials, it was shown that while ultrasonics has no major effect on the dimensional accuracy of the holes, it improved the surface roughness of stainless steel 316 and Titanium (Ti-6Al-4V) by 8% and 30%. For aluminum 6061, stainless steel 316 and Titanium 6-4, productivity, based on the ratio of increased feed using ultrasonics—until the thrust force reached that of the baseline parameters—to the baseline feed rate, showed a significant increase.

As seen in Figure 15.47a, the results of microstructure analysis of the 4340 steel samples drilled with and without UAD showed that the area of the black and white regions, which are the martensitic and carbide structures, are the same for both cases. In Figure 15.47b, the hardness in the transverse direction is shown along the thickness of the sample. There is little difference in the hardness, with or without UAD.

15.4.2.2 *Evaluation of temperature measurement methods*

In UAD, measurement of drill tip temperature is important because of the significant effect of heat on drill life. In this section, the results of a study to evaluate five different techniques to measure drill tip temperature are in Moghaddas et al. (2019). As seen in Figure 15.48a,b, two test scenarios were used to evaluate the five temperature measurements techniques.

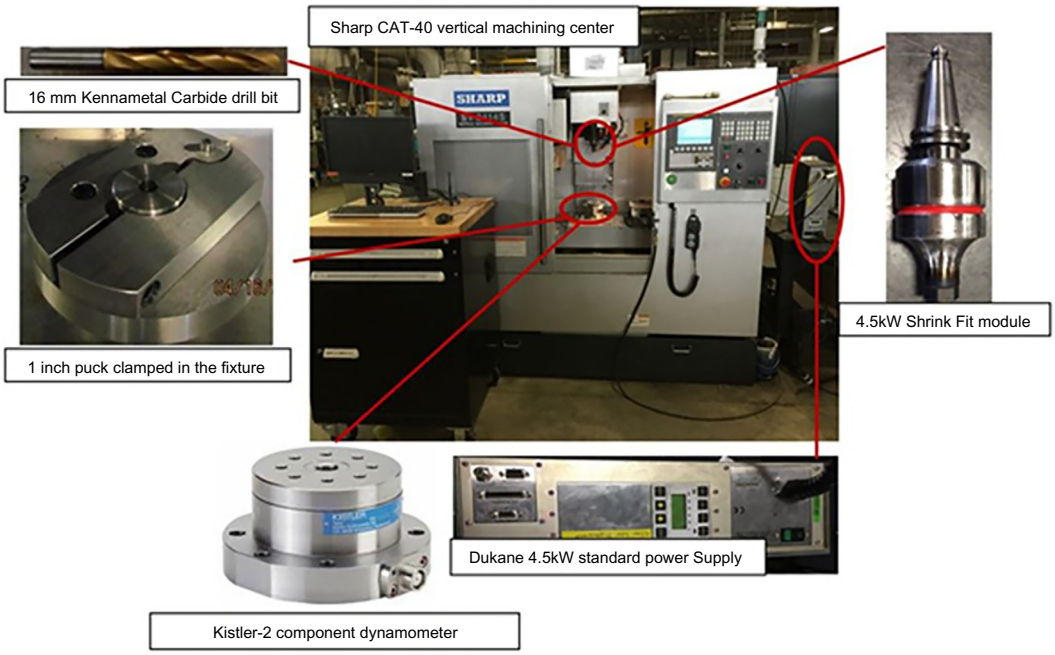


FIGURE 15.45 Experimental setup for UAD (Moghaddas et al., 2018, Fig. 1).

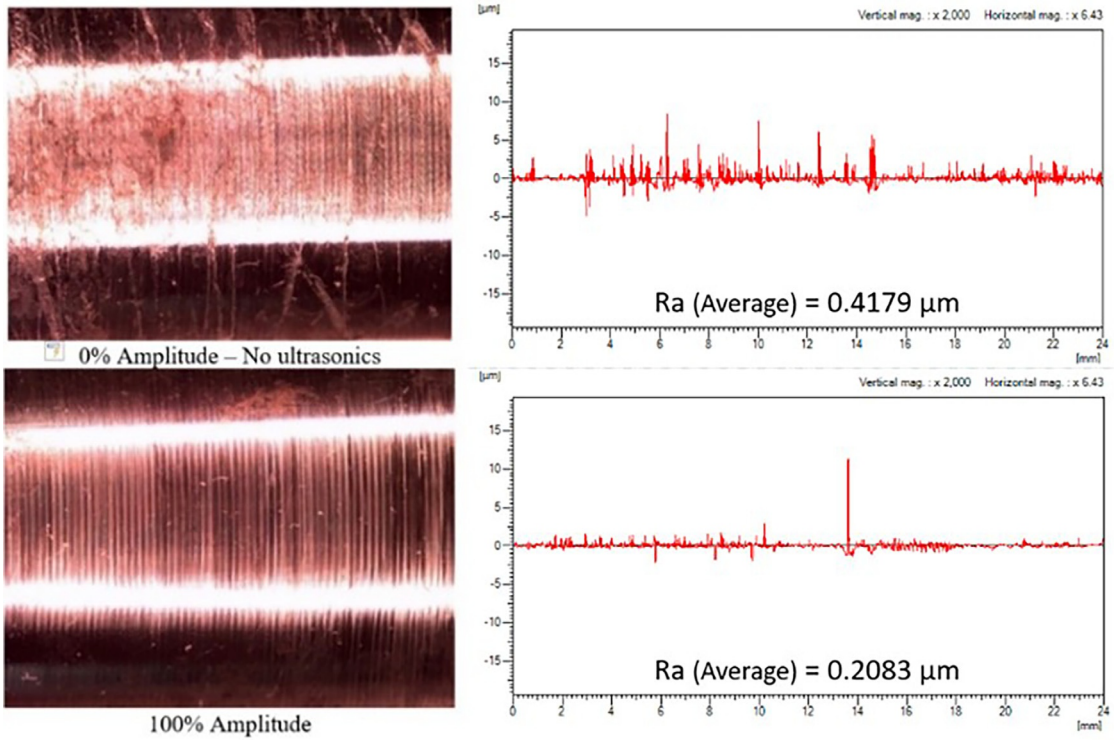


FIGURE 15.46 Improvement of surface roughness applying 100% amplitude to the baseline parameters in UAD of steel 4340. *(Source: EWI.)*

The temperature techniques evaluated in scenario 1 are, Figure 15.48a, (1) embedded thermocouples in the material, (2) infrared (IR) sensor, and (3) IR camera. The measurement techniques evaluated in scenario 2 are, Figure 15.48b, (4) embedding thermocouples in the drill cooling channels and (5) surface thermocouples. The experimental setup used for scenario 1 is shown in Figure 15.49a. Two thermocouples were embedded in 1.1 mm holes with a

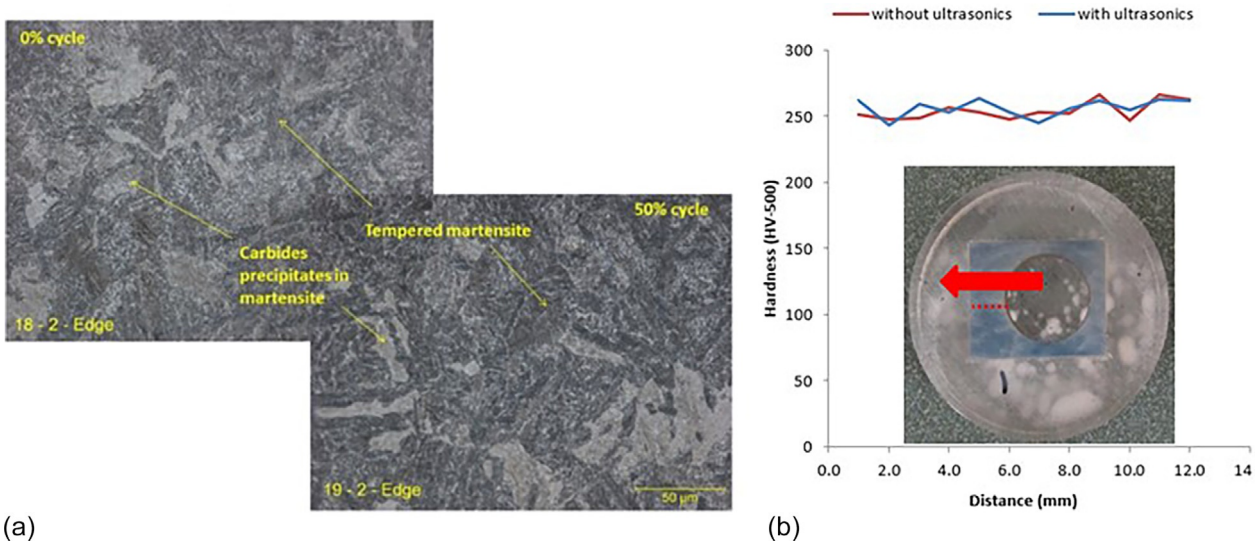


FIGURE 15.47 (a) The microstructure of the samples at the 4340 sample at 2161 RPM spindle speed, 5 IPM feed rate with and without ultrasonics; (b) the hardness of the 4340 steel samples drilled with and without ultrasonics (Moghaddas et al., 2018, Fig. 10, 9a).

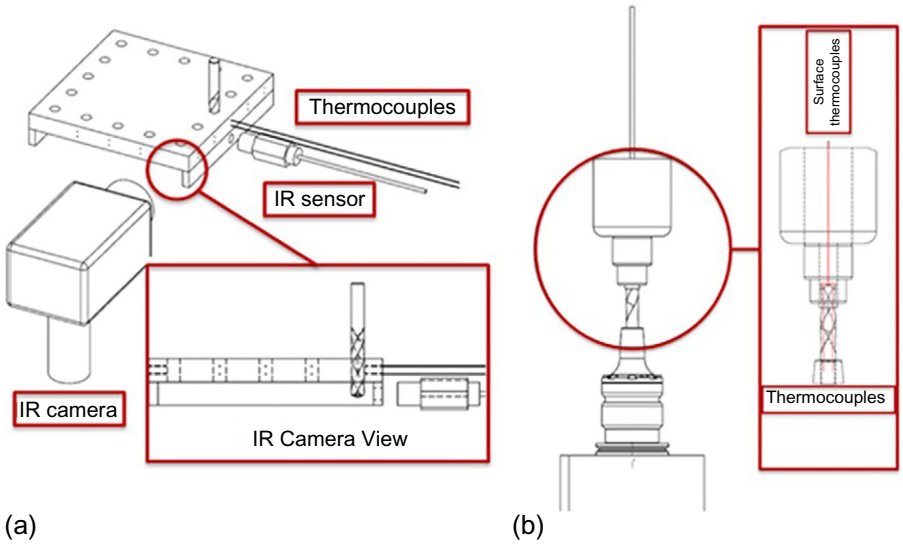


FIGURE 15.48 (a) Schematic view of scenario 1; (b) schematic view of scenario 2 (Moghaddas et al., 2019, Fig. 1).

1-mm gap maintained between the tip of the thermocouples and the wall of the drilled hole. In this scenario, an IR temperature sensor and an IR camera were used to measure the temperature of the drill tip as it exited the aluminum plate at the end of the drilling process. Figure 15.49b shows the IR thermal field of the drill tip as the drill exited the plate.

The experimental setup used for scenario 2 is shown in Figure 15.50a. Two thermocouples were inserted into the cooling channels of the drill to measure the temperature of the drill tip during the drilling process, Figure 15.50b. A thermocouple with a self-adhesive surface was attached to the back of the material to be drilled, Figure 15.50c. Using this setup, it was possible to measure the temperature of the drill tip at the end of drilling.

For both test scenarios, 14-mm carbide drills were used on aluminum 6061 using the 4.5-kW UAD module mounted in a Hwacheon vertical machining center.

Analysis of the results from each technique showed that the repeatability and reliability of embedding thermocouples into the cooling channels of a drill were better than the other techniques. Further, this method was simple to implement, no extra analysis was needed on the resulting data, the setup time was short, and it was possible to measure the temperature and thrust force on aluminum 6061 during the drilling process.

As seen in the figure, as the vibration amplitude increased, up to 33% reduction in thrust force and up to 22% increase in temperature were observed compared with CD.

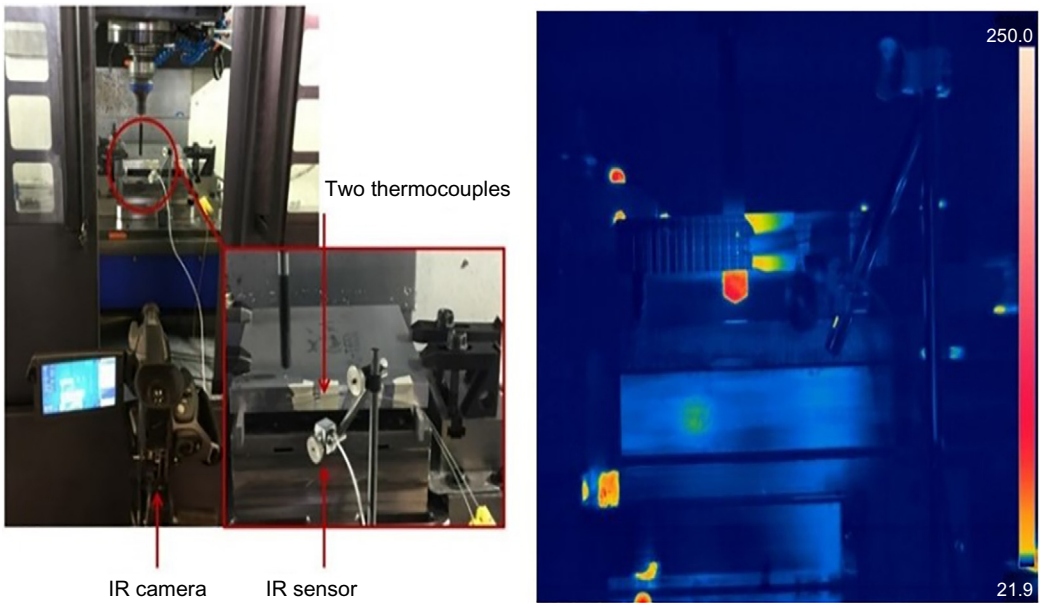


FIGURE 15.49 (a) Experimental setup for scenario 1; (b) thermogram of the drill at 1500 RPM, 15 IPM, using ultrasonic vibrations as the drill exited the material experimental setup for scenario 2 (Moghaddas et al., 2019, Fig. 2, 9).

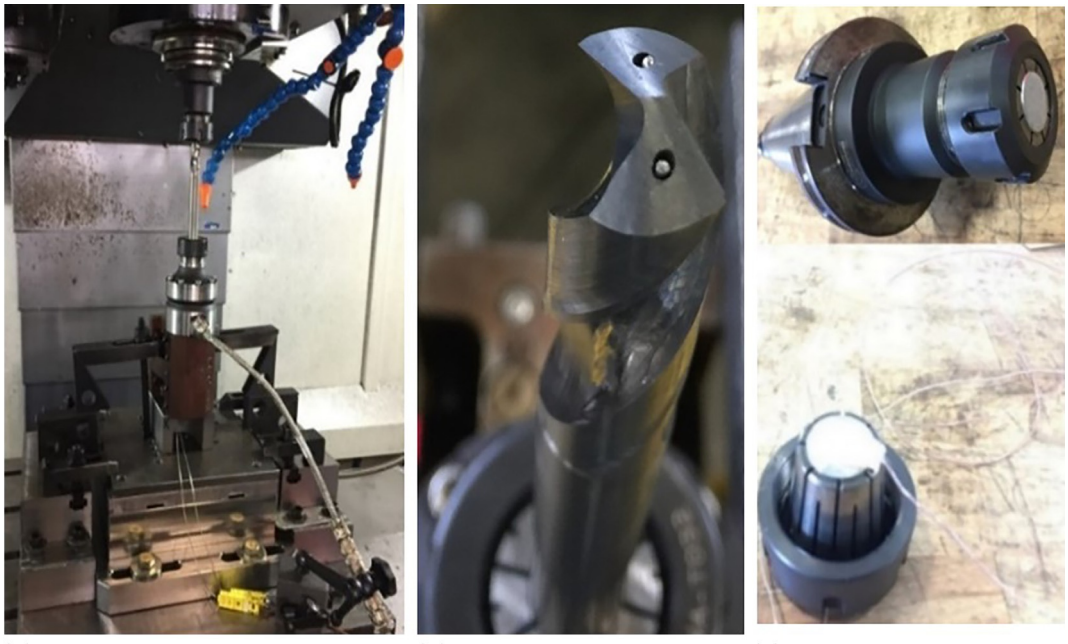
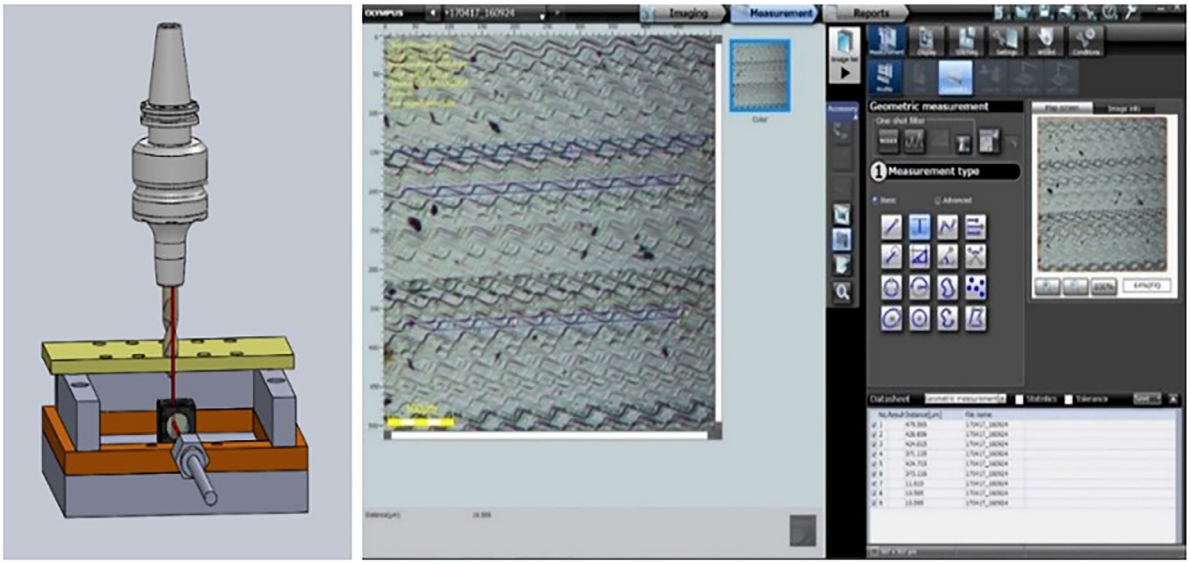


FIGURE 15.50 (a) Experimental setup for scenario 2; (b) installing thermocouples into the cooling channels of the drill (Photo was taken before applying epoxy); (c) thermocouple with self-adhesive surface attached to the back of an aluminum puck (Moghaddas et al., 2019, Fig. 11, 14).

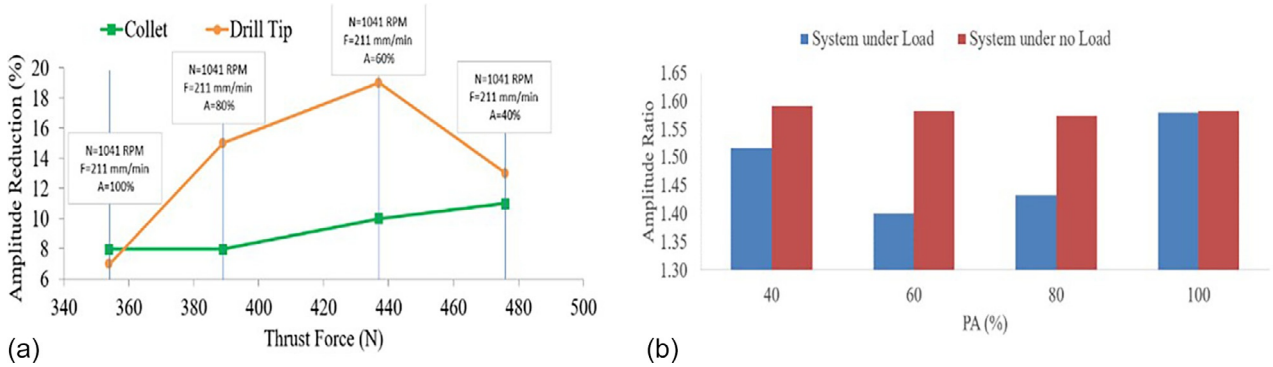
15.4.2.3 Measurement of load effects on vibration amplitude

While qualitatively the importance of drill vibration amplitude on UAD performance has seemed clear, quantitative data on amplitude effect have been lacking. This section reports on a method to measure "down the hole" drill tip amplitudes and the relationship with drilling forces (Moghaddas and Graff, 2020). The technique is based on examining the surface of the drilled hole where minute, oscillatory traces of the vibrating drill tip are found that



(a) (b)

FIGURE 15.51 (a) Setup for in situ UAD amplitude measurements; (b) image (left) taken by digital microscope (right) used to measure the peak-to-peak value of oscillatory traces of the vibrating drill tip (Moghaddas and Graff, 2020, Fig. 2, 4).



(a) (b)

FIGURE 15.52 (a) Amplitude reduction in scenario 1 (spindle speed = 1041 RPM, $F = 211$ mm/min and amplitude = 40%–100%) (Source: EWI); (b) amplitude ratio in test scenario 1 (Moghaddas and Graff, 2020, Fig. 15).

correspond to drill tip vibration amplitude, Figure 15.51a. These data, when coupled with in-process vibration measurements at the drill chuck, Figure 15.51b, as well as no-load amplitude measurements, permit the effects of vibration amplitude on load to be determined.

As shown in Figure 15.51a, for in situ measurement of amplitude, the drilling is done near the edge of the plate. This setup allows a prism to rotate the laser beam 90 degrees toward the reflective surface of the collet, from which the reflected beam returns to the prism and rotates 90 degrees toward the laser head to measure the peak-to-peak value of collet amplitude. Figure 15.51b shows the surface images (555X microscope magnification) of steel 4340 drilled with UAD with 10.5 μm amplitude. The harmonic striations seen in this figure that are used to measure the peak-to-peak value of the vibration amplitude of the drill tip.

Tests were conducted to evaluate the effect of UAD drilling loads on vibration amplitude in Brass C36000 using a 14-mm tungsten carbide drill. The drilling trials were conducted using the 4.5-kW module mounted in a Hwacheon vertical machining center. The test procedure began with measuring the amplitude of both collet and drill tip when the module was under no load. Then, the two test scenarios, previously noted, were carried out. The drill samples were sectioned, and the tip vibration amplitude measured from side wall scribe markings. In Figure 15.52a, the amplitude reduction data for test scenario 1 (1041 RPM, feed rate 211 mm/min) for increasing thrust force is shown. In Figure 15.52b, the behavior of amplitude ratio (i.e., the ratio of drill tip vibration to collet vibration) is shown for increasing power supply amplitude under load and no-load conditions.

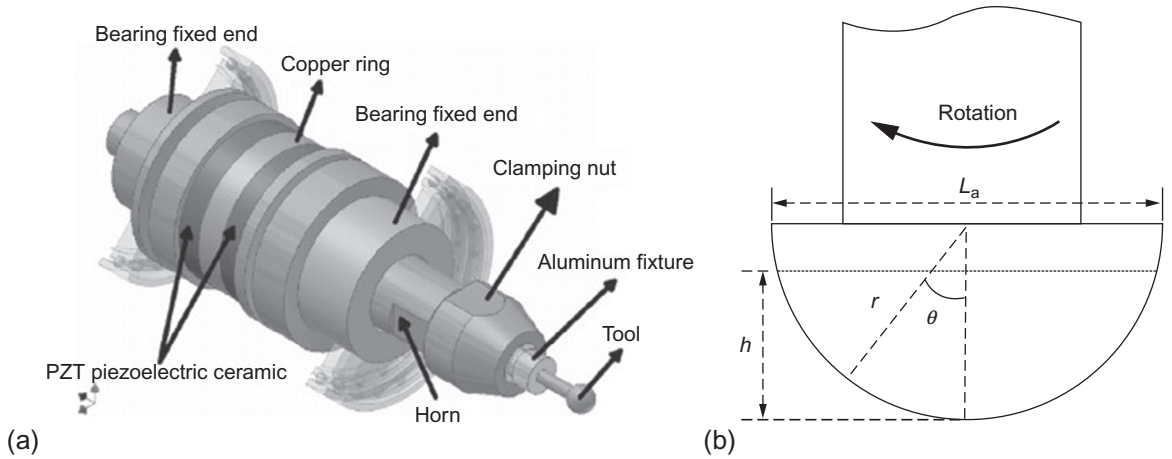


FIGURE 15.53 Ultrasonic milling system: (a) transducer with milling tool (Kuo, 2008a, Fig. 1) and (b) spherical milling tool (Kuo, 2008a, Fig. 2).

As seen in Figure 15.52a, the amplitude reduction at the drill tip is more than that of the collet and up to 19% reduction is seen when compared with the amplitude under no load. Evaluation of amplitude ratio data, Figure 15.52b, also showed that when the drill is under load, up to 11.5% reduction in drill tip amplitude compared to collet amplitude is obtained.

15.4.2.4 Summary and conclusion

An advanced UAD system compatible with CNC machining systems has been described with tests done on aluminum, steel, stainless steel, and titanium, using drill sizes, RPM and feed rates similar to production conditions. The study showed that, in all materials, a significant improvement in thrust force, torque, surface roughness, and productivity could be obtained compared to CD. These improvements were achieved while maintaining dimensional accuracy showing that the module kept its run-out accuracy under machining conditions. In UAD of steel 4340, the results showed no change in the microstructure and hardness of the drilled part. The system was then used to evaluate five techniques to measure temperature in UAD, followed by selecting the best technique and using that to evaluate the effect of ultrasonics on heat generated in UAD of aluminum 6061, 4340 steel, and stainless steel 316. The study showed, for all materials, an increase in temperature with an increase in vibration amplitude. Finally, a technique to measure the amplitude at the drill tip and module collet was described as were test procedures for examining the effect of drilling loads on vibration amplitude.

15.5 Ultrasonic milling

Although milling is its own branch of machining, there is similarity to drilling insofar as acoustic vibrations are concerned. The review of early work in ultrasonic machining touched on milling developments by Balamuth and others (Section 15.2), with more recent developments covered here.

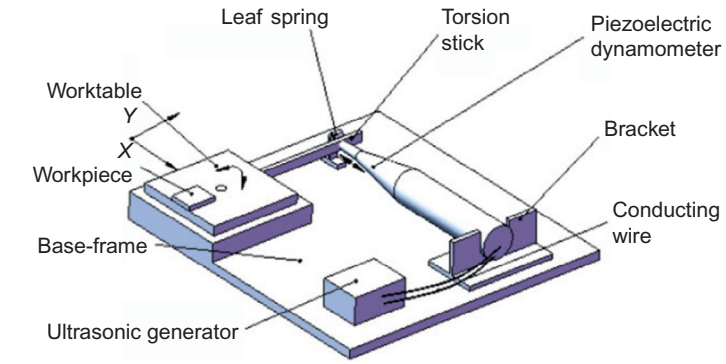
Analysis of the acoustic design requirements of an ultrasonic transducer, Figure 15.53a, and a spherically shaped ultrasonic milling tool, Figure 15.53b, was provided by Kuo (2008a,b,c). Test results on the use of this system were not reported at the time.

A leveraging arrangement, Figure 15.54a, was used by Hu et al. (2010) to create a torsional vibration of the workpiece undergoing high-speed milling with a conventional cutter. FEA modeling of the cutting was provided, with Figure 15.54b showing two stages in the process. Thus, Figure 15.54b (upper) shows cutting stresses during a transient period of tool engagement, while Figure 15.54b (lower) shows a moment when the vibrations cause a disengagement of the tool and the workpiece.

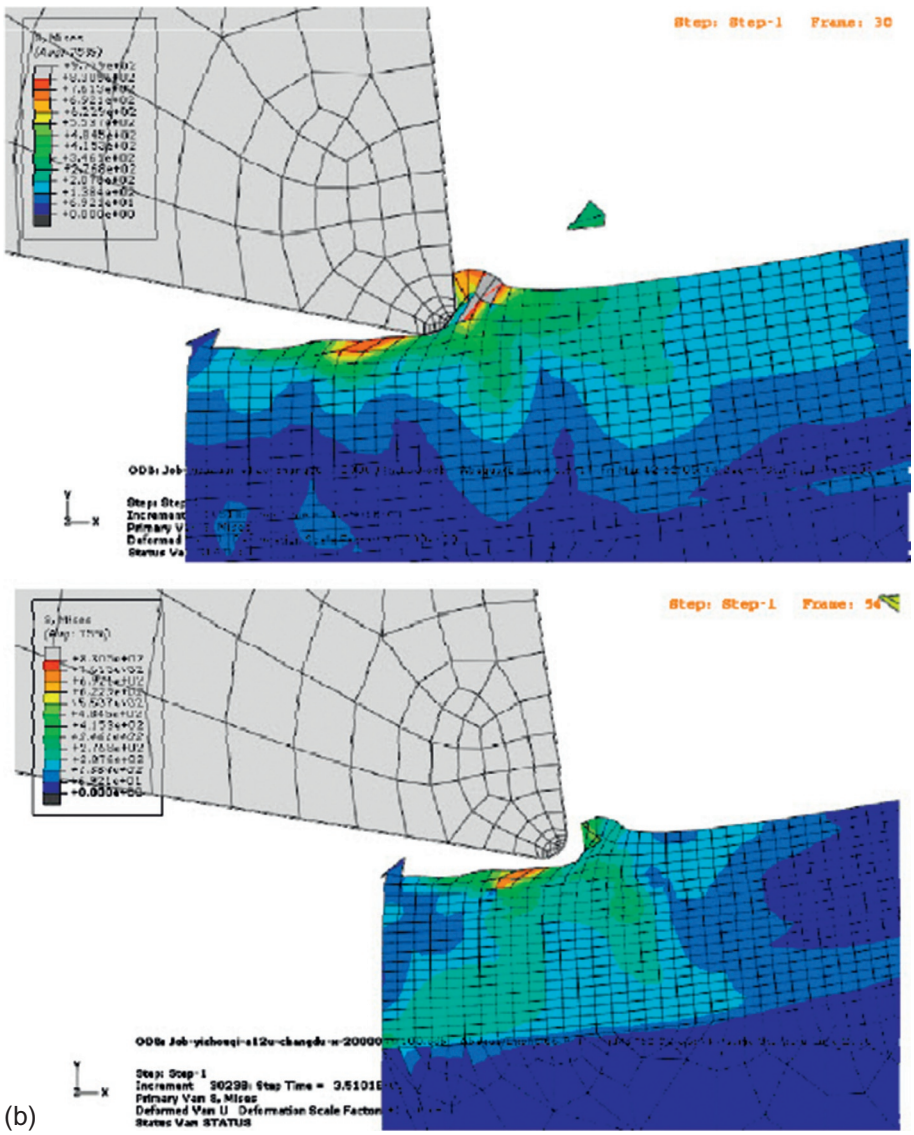
Measurements were conducted using a 1 mm tool at 25,000–45,000 RPM. While reductions in cutting forces for varying RPM and feed rates were noted, when compared to conventional milling, they did not appear pronounced. In a later study, Hu et al. (2011) reported a reduction of residual stresses in the ultrasonic milling process.

Razfar et al. (2011) applied ultrasonic vibrations through the workpiece (1020 steel), focusing on the influence of vibrations on surface roughness for varying feed rates, cutting depths, and RPM. There was in every case an improvement in surface roughness, although the improvements were not always large. A companion work by Abootorabi-Zarchi et al. (2012) looked at the effect of ultrasonic vibrations on cutting forces for various RPM, vibration amplitudes, and cutting speeds. In the former two cases, reductions in cutting forces were noted, while in the latter, force reductions were greatest for lower cutting speeds, an effect noted in turning studies as well.

Several publications by Shen et al. (2012a,b,c) examine ultrasonic milling of an aluminum alloy (2A12), using



(a)



(b)

FIGURE 15.54 Ultrasonic torsion-assisted milling: (a) torsion-assisted ultrasonic milling system (Hu et al., 2010, Fig. 1) and (b) stages in ultrasonic milling process (Hu et al., 2010, Fig. 4b,d).

vibration of the workpiece. Results were presented for both end cut and side wall surface finishes, with somewhat negative results for end cut finish, but with optimization of ultrasonic and cutting parameters, an improvement in side finish was obtained. The ultrasonic milling system developed by Xiang et al. (2011a) is shown in Figure 15.55a, with an innovative means of transmitting the high-frequency ultrasonic power to the 35 kHz transducer via magnetic coupling coils, creating an amplitude of 15 μm at the tool tip. The spindle was capable of up to 20,000 RPM with a PCD end mill of 6 mm diameter used to machine SiC metal matrix composites. The effect of increasing milling speed on the three components of milling force is shown in Figure 15.55b (z is in the direction of travel, y is vertical, and x is at right angles to the direction of travel). It is seen that y- and z-direction forces are little affected compared with conventional milling, while forces in the travel direction are noticeably reduced. Similar trends

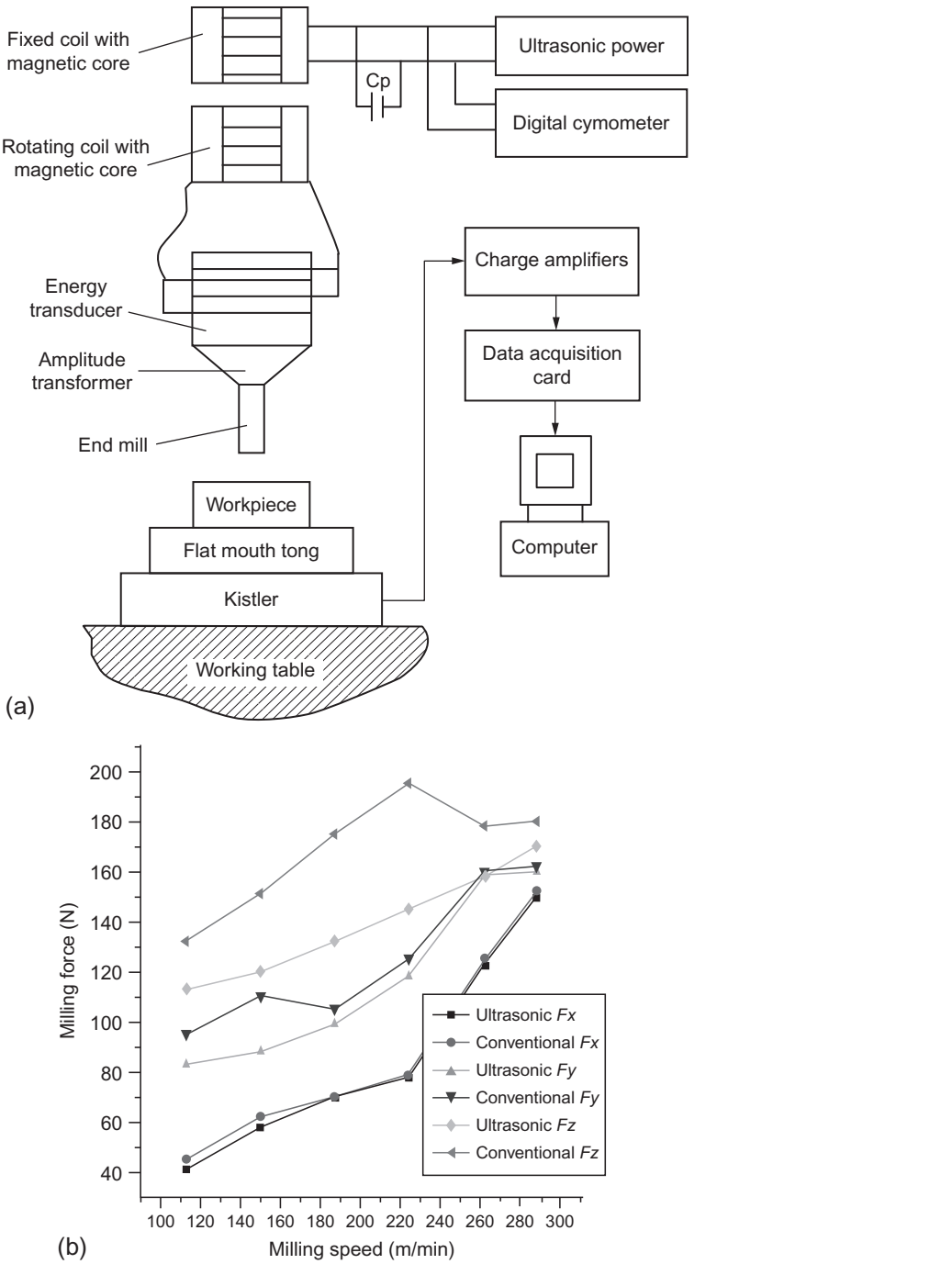


FIGURE 15.55 Ultrasonic milling -2: (a) ultrasonic milling apparatus (Xiang et al., 2011a, Fig. 1) and (b) effect of milling speed on force (Xiang et al., 2011a, Fig. 2).

were noticed for increasing feed rates and depth of cut. In all cases, at increased milling speed, feed, and depth of cut, the effects of ultrasonics compared with conventional milling decreased. Decreased tool wear was observed with ultrasonic milling. Similar results were reported in a companion paper (Xiang et al., 2011b).

Additional studies from Henan Polytechnic University were reported by Li et al. (2011), where an acoustic analysis of the ultrasonic milling system described in several Henan publications was presented, prior to conducting milling tests, and by Li et al. (2012). In the latter, results similar to those reviewed above were shown, but with the added comparison of dynamometer signals from conventional and ultrasonic milling, shown in Figure 15.56. Noting the difference in vertical scale, it is seen that the maximum forces do not greatly differ. However, the authors commented on the greater uniformity of the ultrasonic forces over the cutting period.

15.5.1 Recent development in ultrasonic-assisted milling

The review by Dixit et al. (2019) of other ultrasonic-assisted machining processes, also extended to ultrasonic milling, where beneficial results were also noted. Studies involving vibrations of the cutting tool and of the workpiece (in varied directions) were noted. Milling of varied metals, glass, and composites is noted, with reductions of residual stresses in metals reported. The importance of intermittent tool contact in reducing net average force, noted in turning, also was seen in milling. A discussion of varying textures of the machined surfaces is related to the varying vibration kinematics of the milling tool relative to surfaces. Some materials effects are attributed to acoustic softening. As with reports on other areas of machining, Dixit et al. cite numerous references to recent ultrasonic milling work.

15.5.1.1 *Experimental—Forces*

The analytical, numerical, and experimental studies of Elhami et al. (2015) focused on comparing cutting force in conventional milling (CM) of AISI 4140 with thermally enhanced milling (TEM), Figure 15.57a, ultrasonic-assisted milling (UAM), Figure 15.57b, and combination of the two techniques (i.e., thermally enhanced ultrasonic-assisted milling (TEUAM)).

The TEM process, where a plasma torch was used to apply up to 900°C to the workpiece, decreased cutting force by about 13%, while TEUAM, where 10 μm amplitude was applied to the workpiece in addition to heat, reduced the cutting force by 22%. The results also showed the effectiveness of ultrasonic vibrations was reduced when higher levels of feed were used. The results of their analytical model agreed with their numerical and experimental results, and it showed, in each cycle of vibration in TEUAM, the maximum value of cutting force was higher compared to CM, while the average value of cutting force was lower than CM. Experimental investigations were carried out by Verma et al. (2018) to develop statistical model to evaluate the effect of process parameters on average cutting force in machining aluminum 6063 using a 20 kHz system shown. The axial ultrasonic vibration reduced the average cutting force but increased its standard deviation. Results also

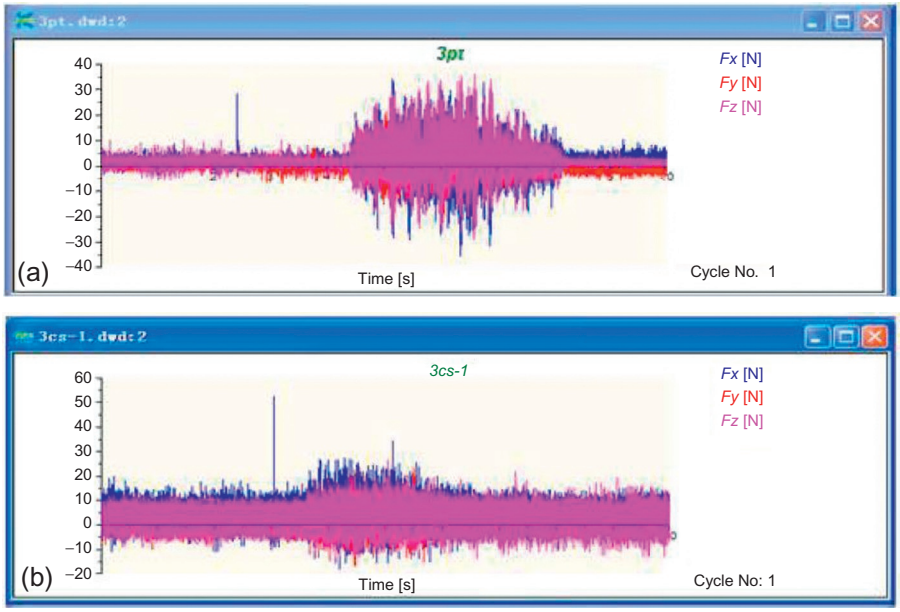


FIGURE 15.56 Milling force waveforms: (a) from conventional milling (Li et al., 2012, Fig. 2) and (b) from ultrasonic milling (Li et al., 2012, Fig. 1).

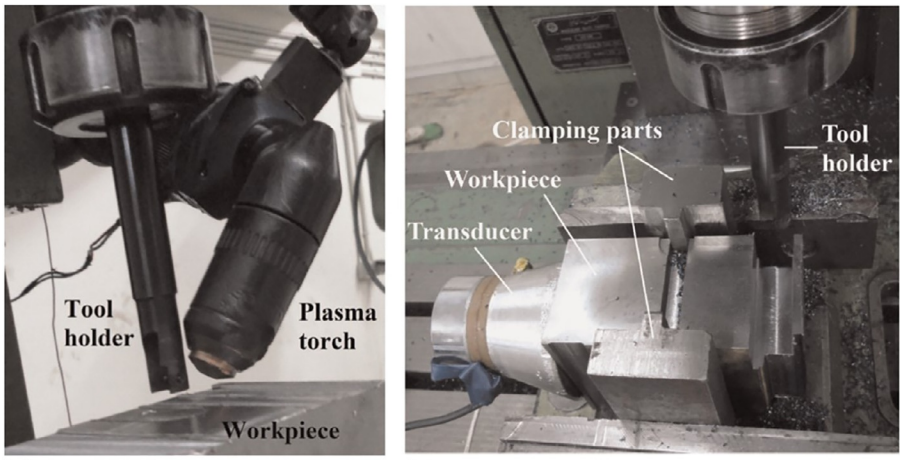


FIGURE 15.57 (a) TEM experimental setup with attached plasma torch, (b) UAM experimental setup (Elhami et al., 2015, Fig. 1, 2).

showed that feed rate had the most effect on the main cutting forces (i.e., Fx and Fy) followed by ultrasonic power (i.e., UP).

Abootorabi-Zarchi et al. (2012) developed an analytical model to study tool-workpiece engagement (i.e., cutting time) and separation (i.e., idle time) in each vibration cycle in UAM and found that contrary to UAT, cutting time in UAM is not constant in each vibration cycle. They also defined a parameter called engagement percent and found that cutting force reduction in UAM is due to the decrease in tool-workpiece engagement, which happens by imposing more amplitude or decreasing cutting speed.

Zhang et al. (2017) used velocity ratio as a criterion to define two types of systems (i.e., separated and unseparated) in UAM and applied a trajectory method to study the motion characteristics of these systems. They evaluated the effects of feed rate, spindle speed ultrasonic amplitude, and frequency on the system stability and found that the separated system was more sensitive to variations of processing parameters. The results also showed that while the feed rate and spindle speed have significant effect on system stability, the effect of amplitude on stability was minimal.

15.5.1.2 Experimental—Surface roughness

In the work of Chen et al. (2020a,b), the tool path in ultrasonic longitudinal-torsional assisted milling (ULTAM) was analyzed theoretically and surface morphology and tool wear studied in ULTAM of Titanium. Higher spindle speed produced a better surface micromorphology; however, when the critical cutting speed was exceeded, intermittent cutting was weakened and improvement in surface quality was reduced. The results showed that selecting proper vibration amplitudes was critical to reduce the formation of score marks and burrs and to improve surface micromorphology. The same conclusion was obtained by Chen et al. (2020a,b) where the effect of machining parameters on milling energy and temperature and their correlation with surface roughness was studied in UAM of Cf/SIC composites using PCD tooling. The results showed that surface roughness had a strong negative correlation with milling energy and at certain vibration amplitudes, macro brittle fracture could transform into micro brittle facture, which facilitated material removal and improved surface roughness. ULTAM of titanium was also investigated by Ying et al. (2017) by developing optimization models for milling parameters for surface roughness, residual stress, and surface hardness. For milling trials, the setup shown in Figure 15.58, which includes a 35-kHz ULTAM that could generate up to 6 μm amplitude, was used. The results of verification tests using optimized parameters showed good agreement with experimental results.

15.5.1.3 Experimental—Chip thickness

The work of Guo et al. (2018) focused on developing a numerical method to calculate instantaneous uncut chip thickness (IUCT) and tool path in UAM using cutter with non-uniform helix angle. The results showed a variation of IUCT in UAM compared with CM.

15.5.1.4 Experimental—Tool wear

Due to the serious tool wear in CM of Carbon fiber-reinforced silicon carbide matrix (C/SiC), Liu et al. (2020) studied the tool wear mechanism in CM and UAM of C/SiC using diamond-coated milling cutters. A 21 kHz UAM system was used that could generate up to 10 μm tool amplitude. Tool wear first decreased (e.g., to 6 μm amplitude), then increased with the increase in vibration amplitude (e.g., to 10 μm amplitude). Up to 28.06% and 33.12% reduction was obtained in the wear band width of the side edge and the bottom edge flank when 6 μm amplitude was used.

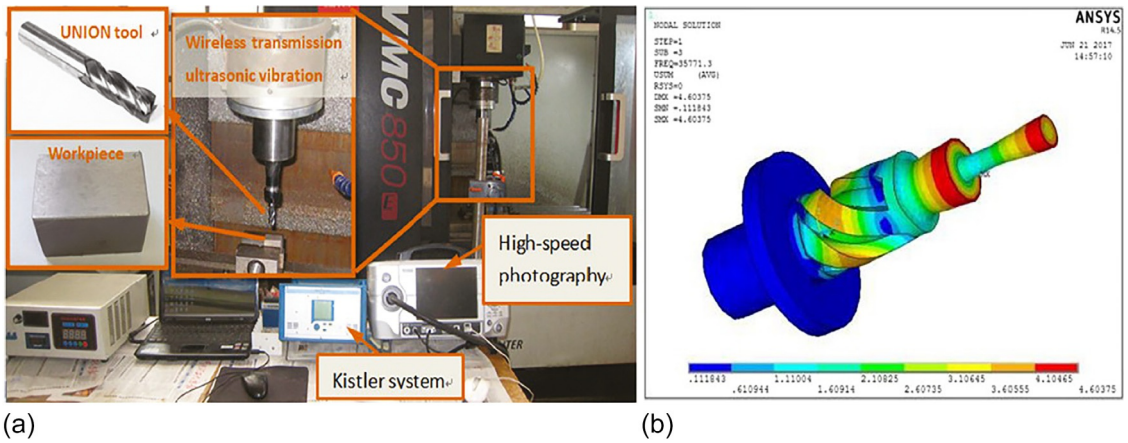


FIGURE 15.58 (a) Experimental setup, (b) vibration analysis of ULTAM tool (Ying et al., 2017, Fig. 1, 3).

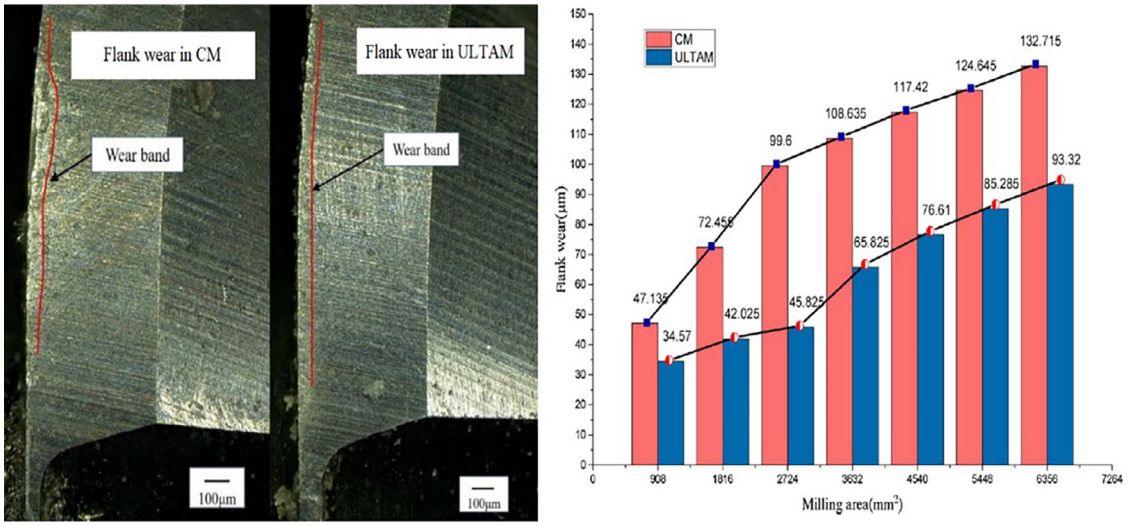


FIGURE 15.59 Flank wear resulting in CM and ULTAM (Chen et al., 2020a, Fig. 15, 16).

Tool wear was also analyzed in the work of Chen et al. (2020a,b) where a comparative study of CM and ULTAM of titanium using cemented carbide ball-end mill cutter was carried out. The flank wear value (VB) was measured at different removal areas obtained by changing the cutting parameters. As seen in Figure 15.59, the flank wear increased with an increase in the removal area for both CM and ULTAM. However, the flank wear in ULTAM was significantly less compared with CM.

15.5.1.5 Modeling

Several studies bearing on the modeling of milling processes and systems have appeared. Thus, in Zhang and Zhong (2014), a tapered ultrasonic cutting tool was designed, and a cutting tool separately analyzed and optimized with a multiobjective optimization method using ANSYS Six Sigma. A response surface approach was used to arrive at a combined optimum cutting tool design for future production milling applications.

The work of Ying et al. (2020) focused on analyzing cutting edge trajectory, Figure 15.60, and developing a 3D thermal-mechanical coupled FE model of UAM (i.e., longitudinal vibration only) of the ULTAM process, Figure 15.60b. In Figure 15.60a, it can be seen that, in contrast to CM (i.e., red line) in ULTAM (i.e., blue line), the tool separates from workpiece in point A and is in contact with workpiece in point B. The cutting force, cutting temperature, and residual stress were analyzed using the same setup shown in Figure 15.58a (i.e., Ying et al., 2017, Fig. 1). The simulation results showed good agreement with experimental results.

Verma et al. (2018) developed a physic-based numerical model to calculate cutting force in UAM of aluminum 6063. The developed model was able to evaluate the effect of ultrasonic vibrations on cutting kinematics and the material

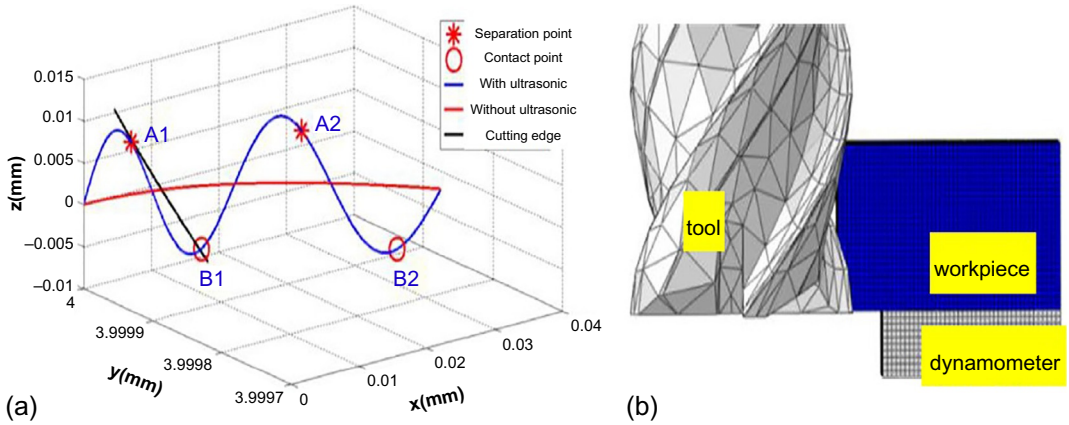


FIGURE 15.60 (a) Cutting edge trajectory model of LTUM and TM, (b) 3D finite element model of ultrasonic milling (Ying et al., 2020, Fig. 2, 4).

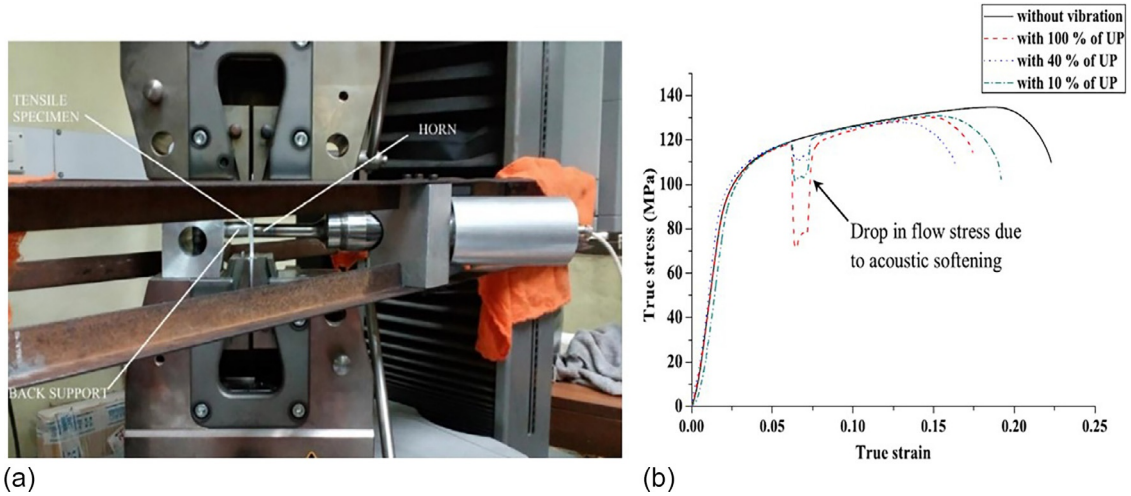


FIGURE 15.61 (a) Experimental setup for the tensile test with assistance of ultrasonic vibration, (b) stress-strain diagram with the assistance of transverse vibration at different ultrasonic power (Verma et al., 2018, Figure 2, 3).

flow stress (due to acoustic softening). ANSYS Workbench was used to study the kinematics of milling tool, which included analysis of the velocity at the cutting tip to evaluate tool-workpiece separation condition. To evaluate the simultaneous effect of ultrasonic softening and machining parameters, a modified version of J–C was used. The softening constants were evaluated by performing ultrasonic-assisted tensile tests at elevated temperature using the setup shown in Figure 15.61a to accommodate the effects of acoustic softening and softening due to temperature rise. The reduction of material flow stress at different percentages of ultrasonic power (UP) is shown in Figure 15.61b.

15.6 Ultrasonic grinding

Early work in applying ultrasonics to grinding has been cited in Section 15.2. More recent contributions include that of Mult et al. (1996), where ultrasonic vibrations of the workpiece and vibrations of the tool were investigated, with the setup for workpiece vibration shown in Figure 15.62a and that of tool vibration in Figure 15.62b.

The workpiece setup was used for grinding in the creep feed mode, where a conventional grinding wheel was brought in contact with the vibrating part. The tool vibration setup was used for face grinding, with water as a coolant. Grinding was done on silicon nitride and alumina. The effect of ultrasonics on machining forces showed a drop in the normal force is seen for both materials, whereas the already low tangential force was not changed. Some slight increase in wheel wear and surface roughness was observed. The face grinding approach, which was virtually the same as conventional ultrasonic grinding, but without a slurry, showed mixed results, with further developments anticipated.

Tawakoli et al. (2008, 2009) studied the effect of ultrasonically vibrating a steel workpiece underneath a conventional grinding wheel, shown in Figure 15.63, where the workpiece was supported on the lower side by bearings.

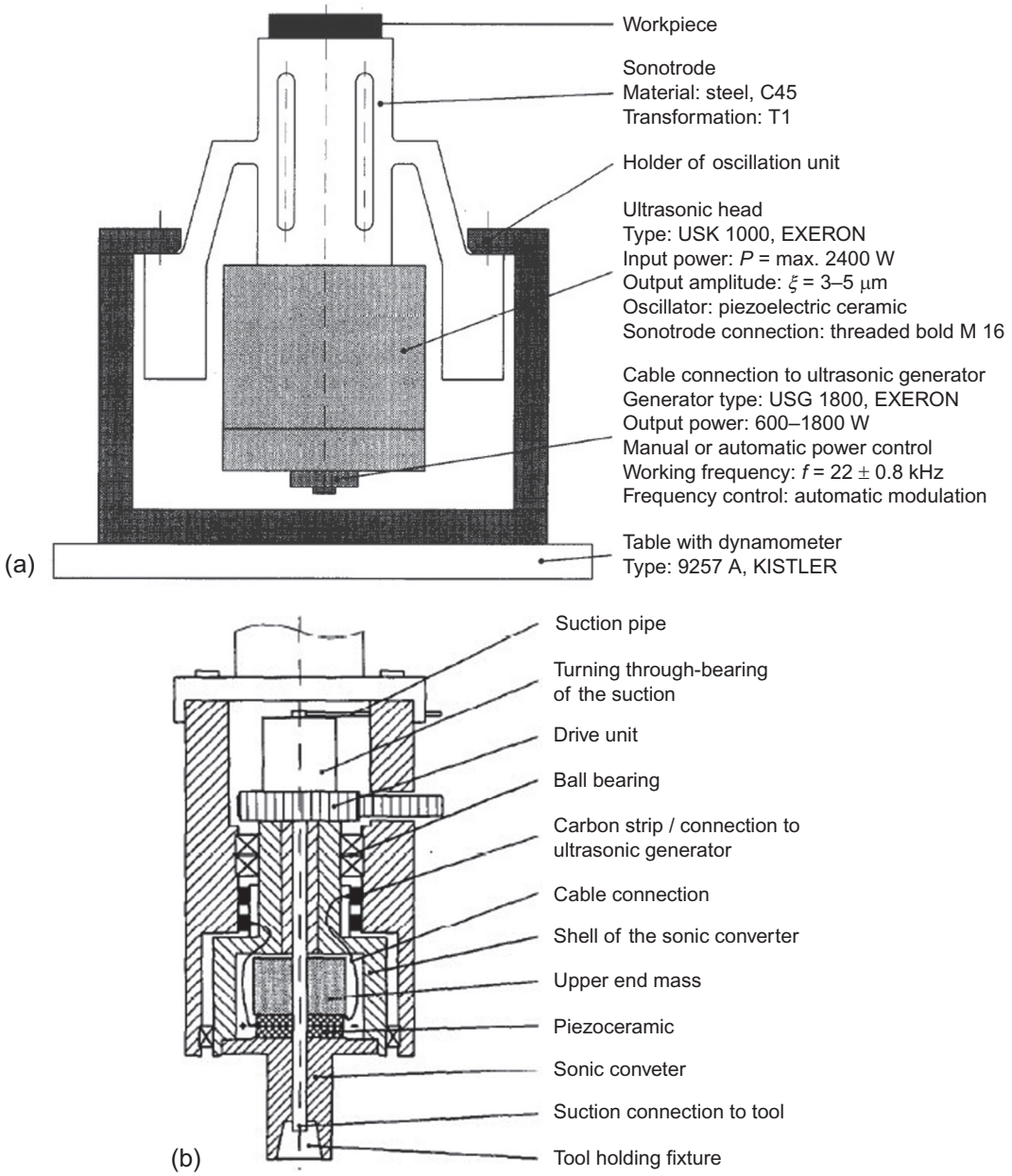


FIGURE 15.62 Applications of vibrations in ultrasonic-assisted grinding: (a) ultrasonic vibration of workpiece (Mult et al., 1996, Fig. 1) and (b) ultrasonic vibration of tool (Mult et al., 1996, Fig. 2).

Comparative tests, with and without ultrasonics, were conducted with results showing up to a 70% reduction in the normal grinding force and up to a 50% reduction in tangential force with ultrasonic vibrations. Improvements in surface roughness and reduction in tool wear were also reported. In a later investigation, using a setup similar to that of Figure 15.63 but with the grinding wheel now at right angles to the direction of vibration, Tawakoli et al. (2009) reported similar benefits when grinding a ball bearing grade chrome steel.

Zheng and Xu (2008) reported on a specialized application of ultrasonics to the grinding of complex ceramics impeller blade shapes. The process depended on vibration of the workpiece, as in Figure 15.64a, and the blade being of a geometry governed by "ruled surfaces." Initial results shown in Figure 15.64b provided sufficient encouragement for future work. The fundamental mechanics of the process were further developed by Zheng et al. (2009).

Other grinding work includes that of Zhang et al. (2007), where the workpiece was vibrated against a conventional grinding wheel using a magnetostrictive actuator that operated at low frequencies (1, 2 kHz) and variable amplitudes. Wheel loadings (loading being a measure of chip accumulation on the grinding wheel) were reduced up to

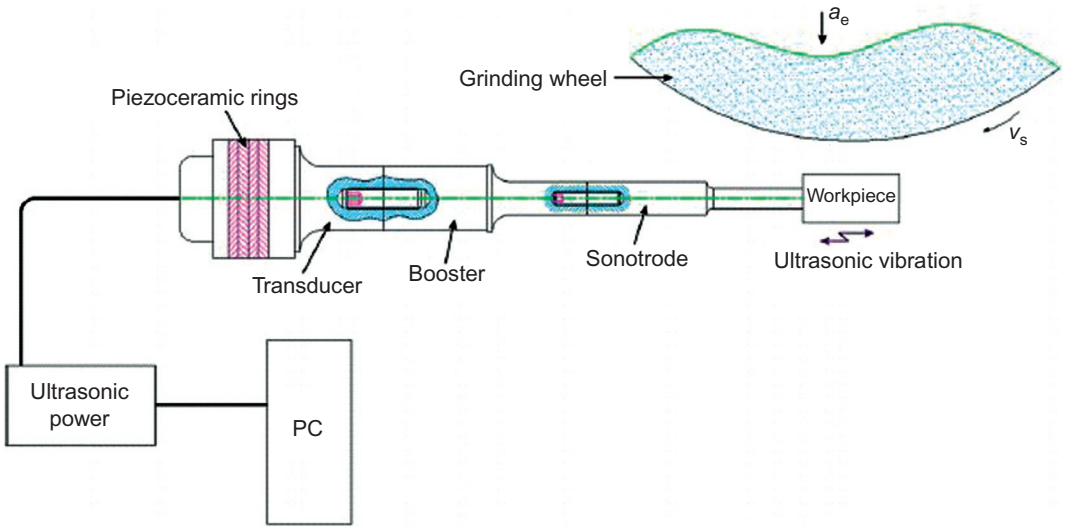


FIGURE 15.63 Ultrasonic grinding of a steel workpiece (Tawakoli et al., 2009, Fig. 1).

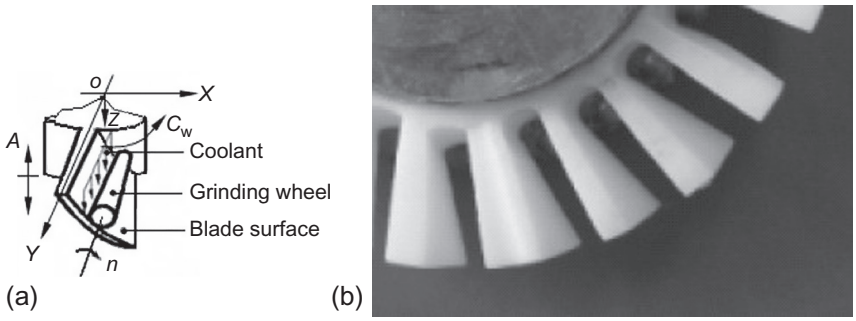


FIGURE 15.64 Ultrasonic grinding of ceramic blades: (a) relative motion between the grinding wheel and blade specimen (vibration along *z*-axis) (Zheng and Xu, 2008, Fig. 2) and (b) machined ceramic blades (Zheng and Xu, 2008, Fig. 7).

80%. Improved results were attributed to reduced surface temperatures under vibration conditions, as well as to smaller chip sizes that were produced. The work of Wu et al. (2009) is to be noted in that a new method, using electromagnetic excitation, of generating longitudinal ultrasonic vibrations in the grinding tool was used. The initial work covered the vibration analysis necessary to develop such a system, with evaluation of the grinding performance to follow.

Although operating below ultrasonic frequencies, the work of Zhang and Miller (2007) on reduction of wheel loading (wheel loading is defined above). Vibrations of 1 or 2 kHz are transmitted to the grinding wheel using the setup shown in Figure 15.65a (recall the early work of Balamuth, Figure 15.3, on reducing wheel loading). The unprocessed image of a segment of wheel surface is seen in Figure 15.65b (left), where chips are the dark areas. Figure 15.65b (right), shows the processed image of the chips in black. The effects of the two frequencies and tool amplitude on load reduction were examined, and it was found that wheel loading was reduced by nearly 80% at 2 kHz and at higher vibration amplitudes. Improved results were attributed to reduced surface temperatures under vibration conditions, as well as to the smaller chip sizes that were produced.

15.6.1 Recent developments in ultrasonic grinding

The overview paper of Dixit et al. (2019), which has been previously referenced in this chapter, also briefly examines ultrasonic-assisted grinding (UAG), noting that prior work has shown higher material removal rates, lower grinding forces, and better surface quality, including reduced thermal burns. Analytical studies of UAG were reported to show that both brittle fracture and material shear were involved in material removal. In Dixit's review, it is reported that effects of vibration direction have been evaluated, with vibration parallel to the surface improved quality and reduced temperatures, while vibrations perpendicular to the surface lowered forces, roughness and wear and to improved removal rates. Other reported results were on the benefits of two-dimensional tool motion on improved

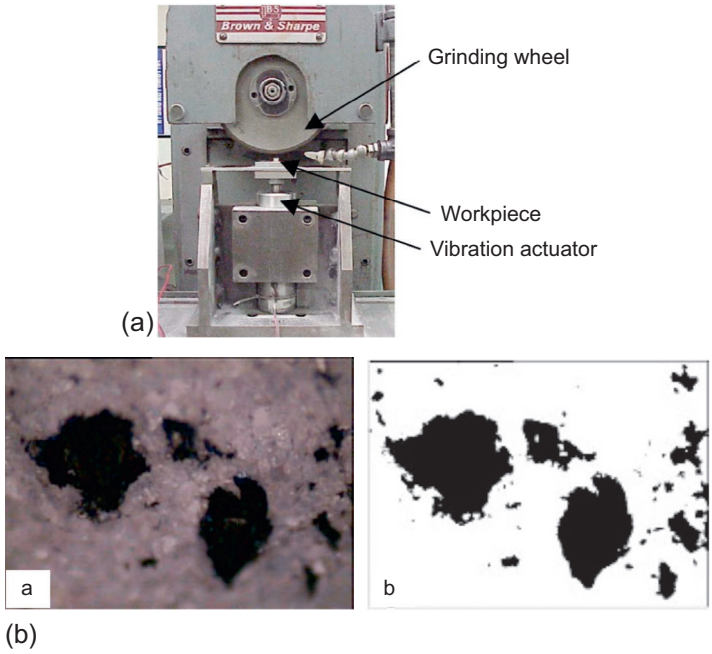


FIGURE 15.65 Ultrasonic reduction of grinding wheel loading: (a) experimental setup (Zhang and Miller, 2007, Fig. 2) and (b) raw image of wheel surface—left a, scanned image—right b (Zhang and Miller, 2007, Fig. 1).

removal rates and that ductile shearing deformation is important for brittle materials, yielding better surface finish.

Special attention is drawn to the review paper by Dambatta et al. (2017) that, although by title is focused on biomedical and aerospace applications and materials, is in fact comprehensive in nature (at 208 references) and provides information useful for anyone pursuing the UAG field. The effects of ultrasonic vibrations on material removal rates, grinding forces, energy, tool wear and surface/subsurface damages are reviewed. Comparisons are made between UAG and conventional grinding processes. Thus, results of studies showing that ultrasonics increases material removal rates, while reducing surface roughness, grinding forces and subsurface damages are reported. A self-sharpening effect in UAG is also reported, as are benefits of introducing biodegradable lubricants are also among the very extensive scope of this over 200 references review paper.

The review of recent ultrasonic grinding papers will organize into forces, etc., surface roughness, chips and hybrid processes.

15.6.1.1 *Forces, temperatures, wear, vibration*

A number of papers dealing with grinding forces, temperatures, wear, and vibration have appeared. Thus, Zhang and Zhong (2014) modeled forces on single abrasive grit, then obtaining average tangential and normal forces. It was found that the tangential grinding force under ultrasonic assistance (TUAG) was lower than under conventional conditions (TG), leading to a substantial reduction in grinding force ratio and improved machinability of the workpiece. Fujimoto et al. (2014) developed the techniques necessary to evaluate the surface topography of a small diameter ("mini") ultrasonically vibrated grinding wheel under varying grinding conditions, using three-dimensional scanning electron microscopy. Comparing surface images of UAG to those of conventional grinding is shown in Figure 15.66. In Figure 15.66a, the protrusion of grain cutting edges is observed on the wheel surface after UAG, the cutting edges are very sharp, whereas CG surfaces show greater wear, Figure 15.66b.

Fujimoto et al. (2015) extended this work to further investigate the wear behavior of the mini grinding wheel. They found that a good wheel surface was maintained during UAG due to a self-sharpening effect, as well as load reduction. As shown in Figure 15.67a and b, significant improvements in surface wear were observed in the UAG process compared with conventional grinding for the same material removal rates, with similar improvements noted of increase in cutting edges and cutting edge area compared with conventional grinding.

Given that ultrasonic processes are inherently vibration based, it is somewhat surprising that little attention has been given to the underlying vibrational phenomena—a situation that is well addressed by Wdowik et al. (2015) in their vibration measurements of ultrasonic grinding. An eddy current sensor system was used to measure the effects of different load parameters on vibration amplitude, and comparisons with laser vibrometer amplitude measurements were made. In continued work, Wdowik et al. (2016) presented results of measurements of surface texture that compared

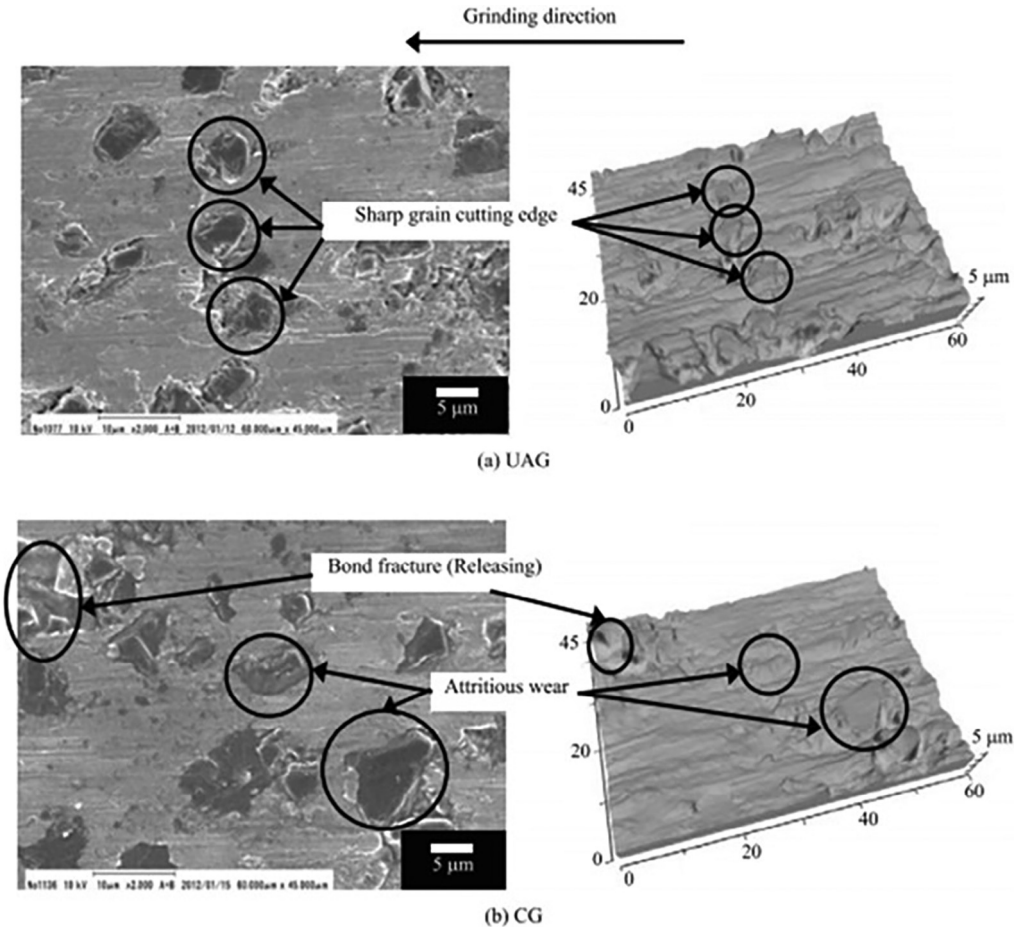


FIGURE 15.66 Typical 2D and 3D images of SEM observation of grinding wheel surface after UAG and CG processes at mesh size #1000 (Fujimoto et al., 2014, Figure 5).

UAG with conventional grinding (CG) of ceramic samples, using the system shown in Figure 15.68. Figure 15.69 is illustrative of results, where UAG (left) is compared to UG (right) for various grinding speeds and showed improved surface Ra for UAG.

Unyanin and Khusainov (2017) analyzed heat generation at the point of interaction of the grinding grain with the work surface using a finite element methods. Lowered workpiece temperatures by 10% and local temperatures in grain and chips by 30% were calculated. Based on the micro-removal mechanics of ultrasonic vibration-assisted grinding (UVAG), shown in the system Figure 15.70a and detail, Figure 15.70b, Li et al. (2019) developed a new process model for steel alloy grinding. Noting the abrasive grains go through two stages, plowing and chip formation, shown in Figure 15.71a, a force model was established. Grinding experiments were performed, with Figure 15.71b for the normal component of grinding force for increasing depths of cut at various amplitude, shown. Force reductions were observed with increasing amplitudes and were consistent with theoretical results.

15.6.1.2 *Surface roughness*

Fu et al. (2015) compared ultrasonic-assisted grinding (UAG) with conventional grinding (CG) of carbon fiber-reinforced silicon carbide matrix (C/SiC) composites, measuring machining quality, grinding force, and grinding energy of the two processes. Relative topographical features of the two processes are shown in Figure 15.72. It was found that normal and tangential grinding forces were reduced by 45% and 39%, respectively, by the UAG process. It was concluded that UAG significantly improved the grinding performance of C/SiC composites.

Following earlier work by Chen and Tang (2015) to establish a UAG surface roughness model, Chen and Tang (2016) evaluated the performance of UAG, compared with CG, using the Abbot-Firestone curve as the means of characterization. The latter, which permits more refined surface characterization than R_a, R_z alone (Salcedo et al. (2018)), showed that critical A-F parameters were lower for UAG compared with CG. The system shown in Figure 15.73a for tests, with the ultrasonic vibrations creating a surface cutting motion shown in Figure 15.73b—right,

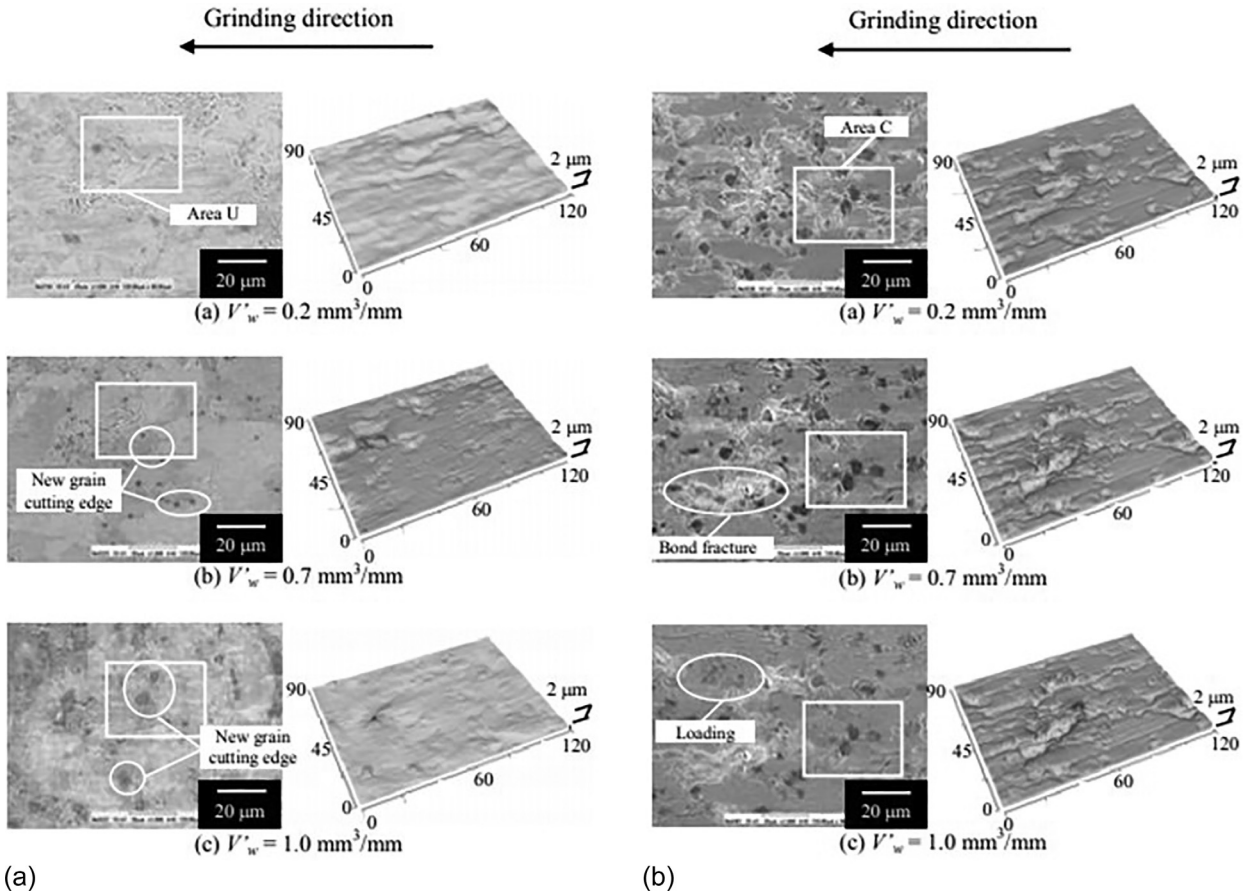


FIGURE 15.67 Changes in 2D and 3D images of the grinding wheel surface; (a) UAG process, (b) CG process (Fujimoto et al., 2015, Figures 3, 4).

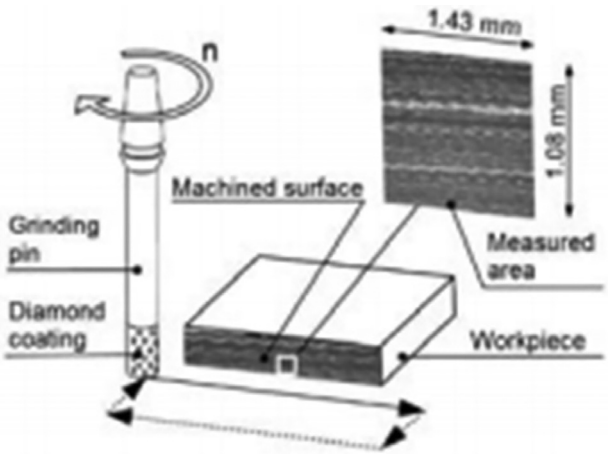


FIGURE 15.68 The UAG machining strategy (Wdowik et al., 2016, Figure 5).

compared with the straight path of CG, Figure 15.73b—left. A comparison of surface topography of CG versus UAG is seen in Figure 15.74. Some decrease in lubrication properties were noted for certain UAG condition, whereas a desired monotonically decrease in A-G parameters was seen for increasing vibration amplitude.

Wen et al. (2019), using the system shown in Figure 15.75a, which was similar to that reported previously for Li et al. (2019), used a rotating grinding wheel that better meta a production simulation, conducted a detailed analysis and modeling of grinding asperities for different grinding conditions. Emphasis was placed on roughness assessment as influenced by vibration amplitude, where it was found that R_a first decreased with increasing amplitude, then increased as shown in Figure 15.75b. A comparison was also made, Figure 15.76, between surface micromorphology of CD and UAG.

Chen et al. (2018a,b), using the equipment shown in Figure 15.73, reported on the effects of UAG on surface roughness, using the surface bearing index S_{bi} and core fluid retention index S_{ci} to assist in evaluation. It was found that the surface bearing index decreased with increasing grinding velocity and that the core fluid retention index increased with vibration amplitude, a general behavior noted in many ultrasonic processes as to velocity and amplitude. A comparison of surface profile, Figure 15.77, of UAG (top) to CG (bottom) shows the improved profile of UAG.

Continuing, Chen et al. (2018a,b) report on development of an "ordered" grinding wheel, modeling the kinematical

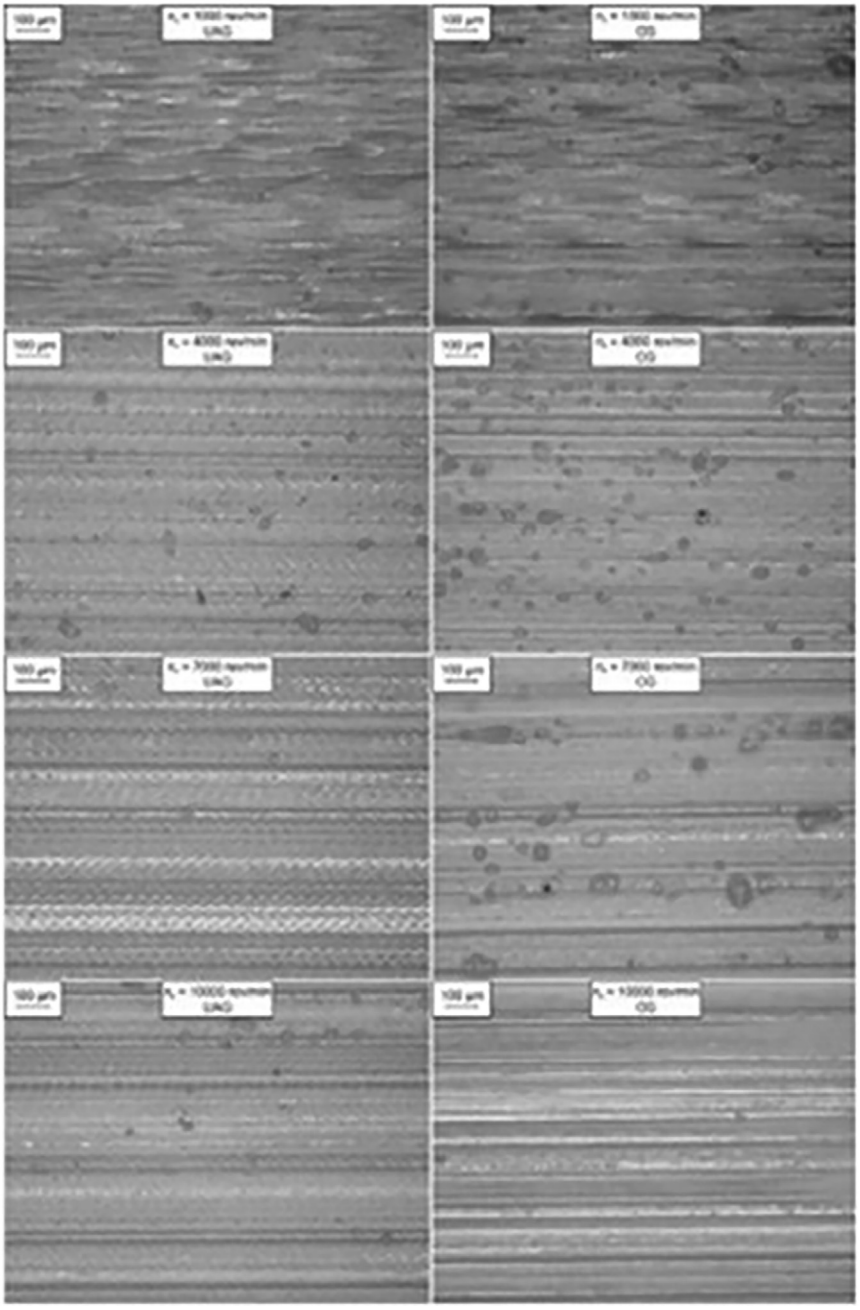


FIGURE 15.69 Comparison of machined surfaces of ZrO_2-based ceramic material by CG and UAG (Wdowik et al., 2016, Figure 2).

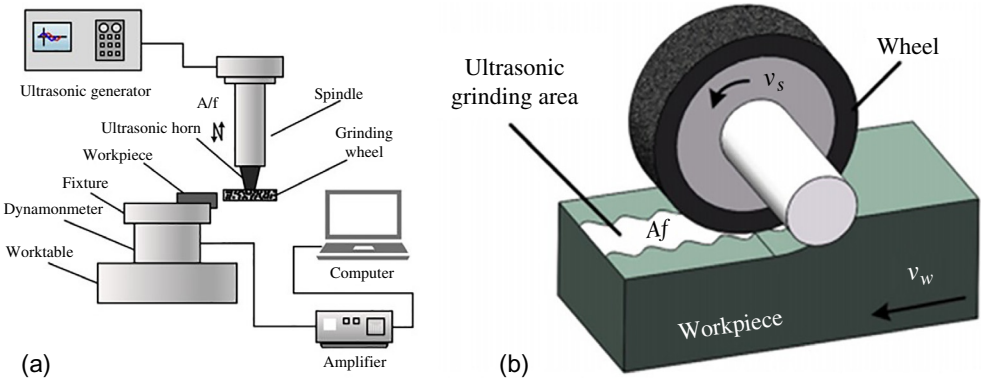


FIGURE 15.70 (a) Schematic of ultrasonic grinding system and (b) schematic of UVAG (Li et al., 2019, Figure 10, 1).

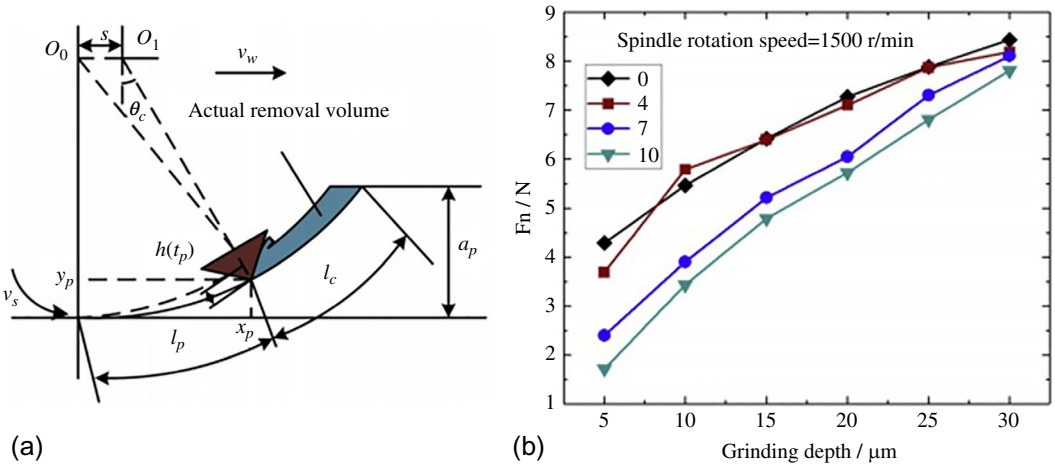
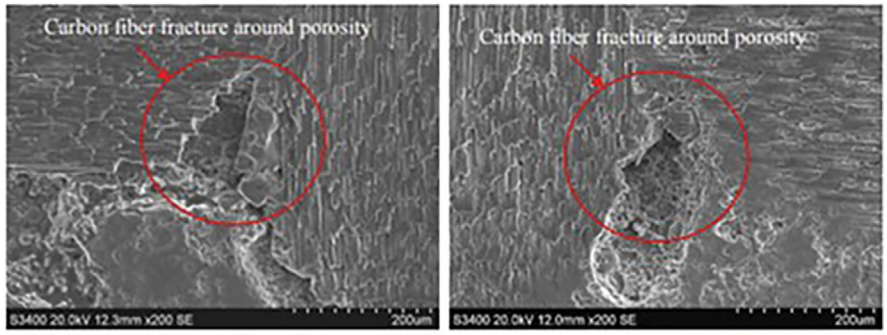
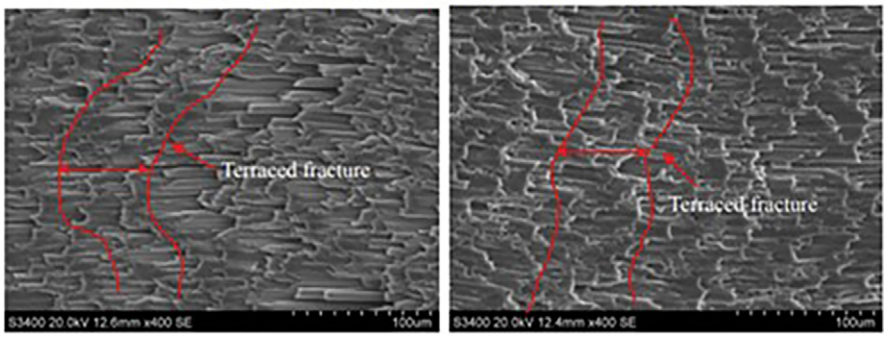


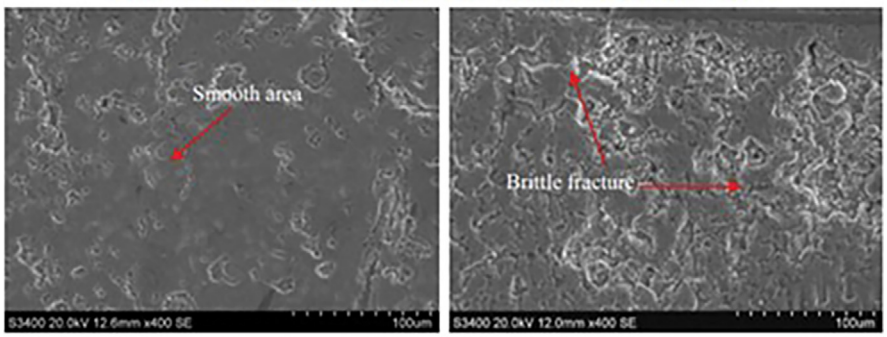
FIGURE 15.71 (a) Two stages of abrasive grain cutting for material removal; (b) relation between normal grinding force and grinding depth for different ultrasonic amplitudes (Li et al., 2019, Figure 6, 11).



(a) Micro topographies around porosities. (Left: CG, Right: UAG)



(b) Terraced fracture of carbon fiber. (Left: CG, Right: UAG)



(c) Micro topographies of SiC. (Left: CG, Right: UAG)

FIGURE 15.72 Ground surface topographies of C/SiC ($v_s = 12.6$ m/s, $v_w = 100$ mm/min, $a_p = 10$ μm) (Fu et al., 2015, Figure 3).

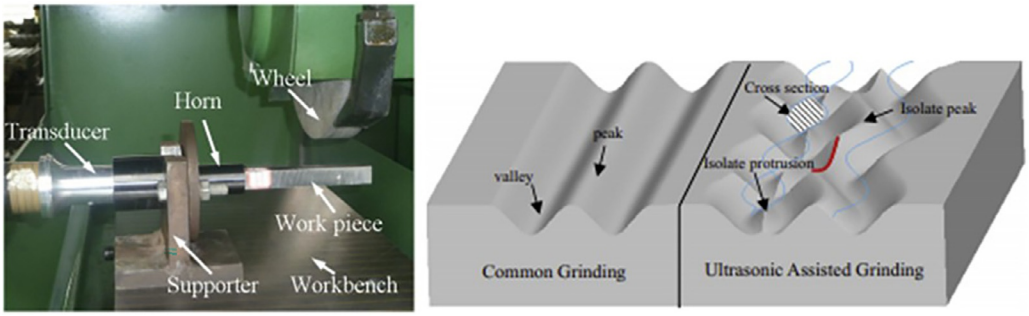


FIGURE 15.73 (a) Experimental setup for UAG; (b) schematic of motion on workpiece surface, CG-left, UAG-right (Chen and Tang, 2016, Figures 1, 7).

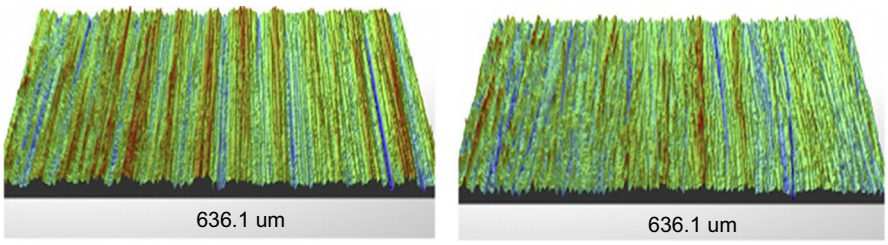


FIGURE 15.74 Comparison of surface topography of: (a) CG, (b) UAG (Chen and Tang, 2016, Figures 2, 3).

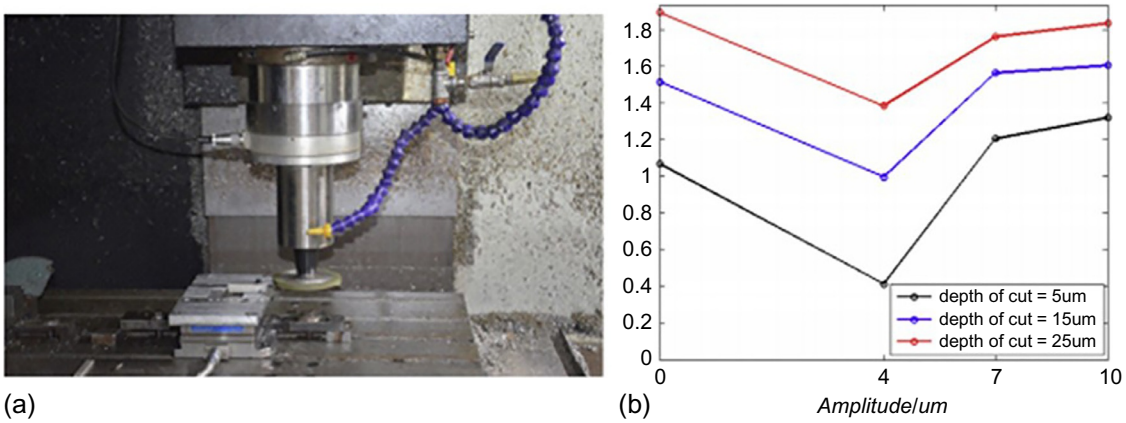


FIGURE 15.75 (a) Experimental equipment for ultrasonic grinding and (b) relationship between roughness and machining parameters (Wen et al., 2019, Figures 6, 9).

behavior of the grinding particulate trajectories with grinding wheel parameters, and predicting the crosshatch microstructure. Experimental work was done using the system shown in Figure 15.78. An illustration of the workpiece surface for a single pass is shown in Figure 15.79a. It is noted that the abrasive grains of most grinding wheels are randomly distributed, resulting in many useless grains, increasing costs, reducing chip capacity, and higher forces. An example of an ordered grinding wheel is shown in Figure 15.79b.

Using the same system reported by Chen and Tang (2016), Sun et al. (2019) reported further on the relationship of UAG parameters and workpiece surface roughness. The work of Zhou et al. (2020) on UAG grinding surface characterization can best be described as all encompassing, covering establishing a quantitative relationship between UAG parameters and their effect on surface microtopography (e.g., texture and roughness). A new parameter, "matching phase difference" (MPD) is developed and modeled to establish the desired relationship. The basic features of

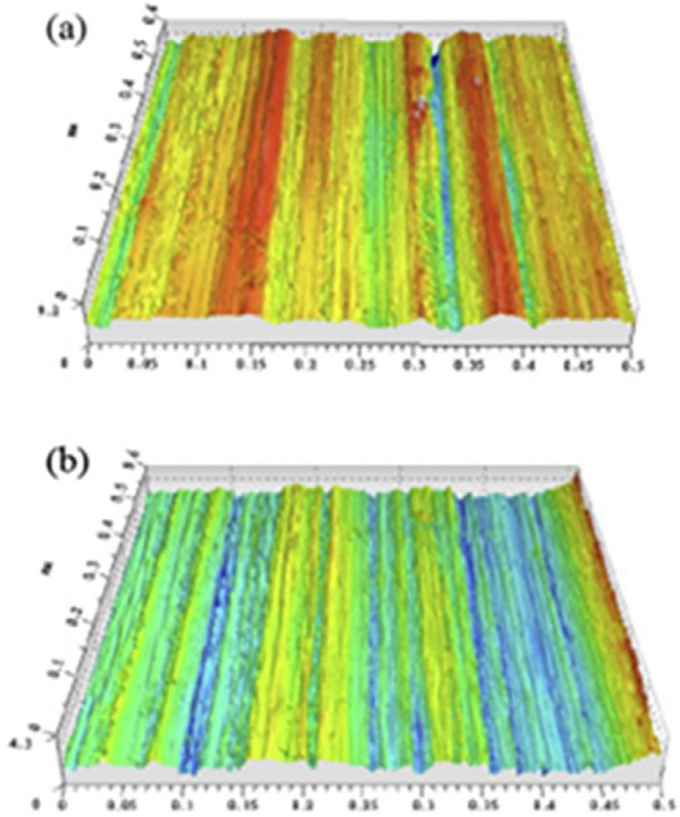


FIGURE 15.76 Surface morphology (a) common grinding and (b) ultrasonic-assisted grinding @ 4 μm amplitude (Wen et al., 2019, Figure 7).

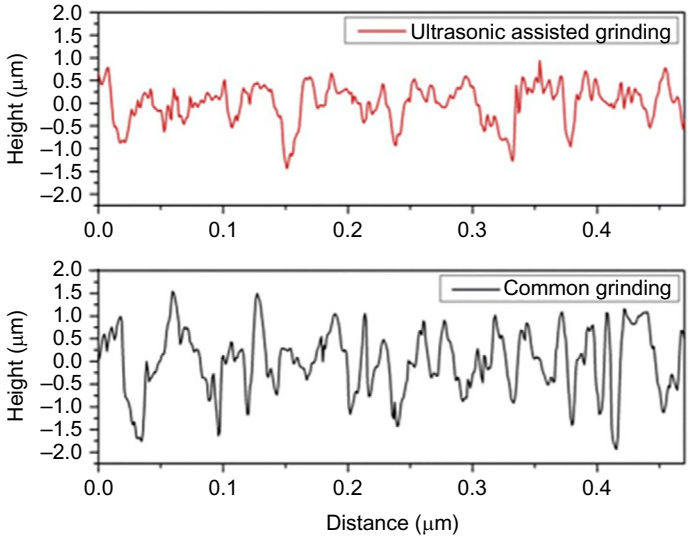


FIGURE 15.77 Surface profiles of the ground workpiece in UAG (top—grinding velocity 800 RPM, grinding depth 10 μm, feed—300 mm/min, ultrasonic amplitude—10 μm) and CG (bottom) (Chen et al., 2018b, Figure 4).

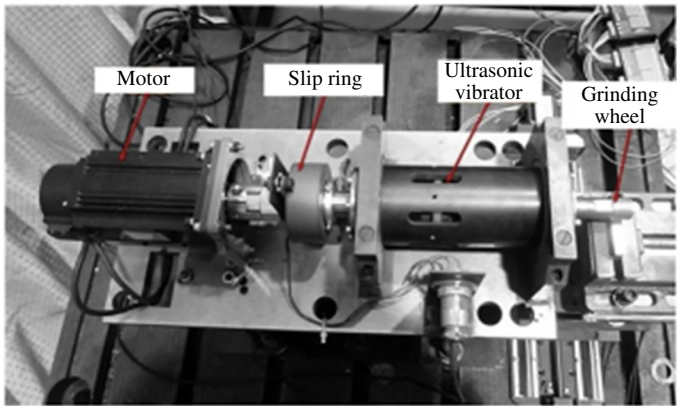


FIGURE 15.78 Experimental setup of UAG system (Chen et al., 2018b, Figure 14).

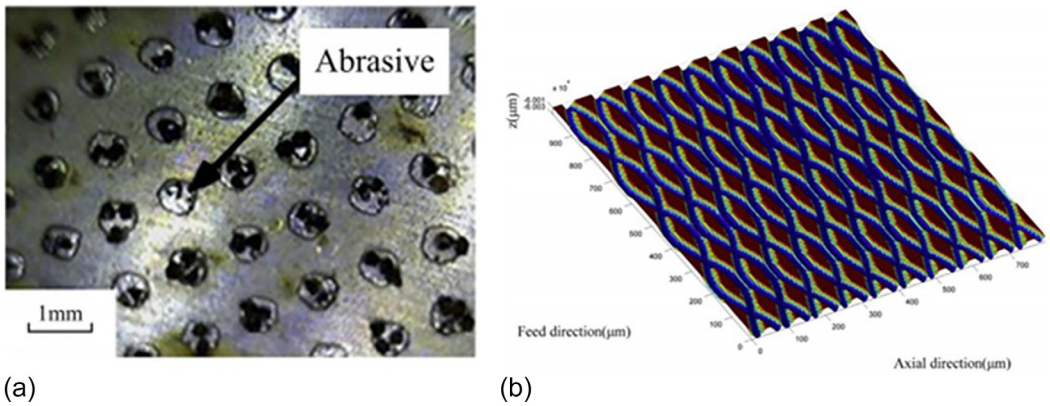


FIGURE 15.79 (a) Surface morphology of ordered grinding wheel and (b) simulated single pass grinding workpiece surface (Chen et al., 2018b, Figure 2, 10).

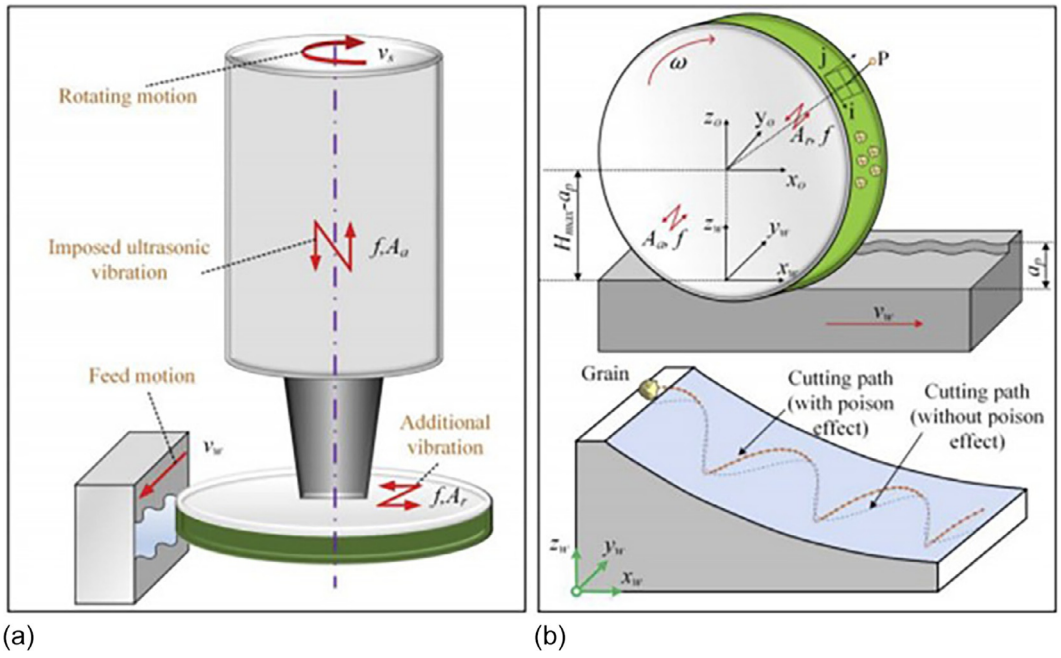


FIGURE 15.80 (a) Illustration of the UAG process and (b) motion kinematics on ground surface (Zhou et al., 2020, Figure 1).

the UAG process are shown, Figure 15.80a, and one step in representing the kinematics of a locus on the wheel surface, Figure 15.80b. A more complete depiction of the surface kinematics is shown in Figure 15.81a, while modeling of the grinding wheel surface is shown in Figure 15.81b. The interaction effect of adjacent wheel rotation cycles, under two different speeds, is illustrated in Figure 15.82. A flowchart of the MPD process is presented, and experimental verification of model predictions was carried. The results provide further insight on the material removal mechanism of UAG.

15.6.1.3 Chips

Li et al. (2016a,b) studied the effect of UAG grinding wheel vibration on Inconel 718 chip size and geometry. The basic UAG process, Figure 15.83a, was tested using the system shown in Figure 15.83b. Chip geometries were examined with 3D SEM and SEM, showing chip characteristics—cross-sectional area, length—were distinctly affected by UAG, Figure 15.84. Further, wheel speed was found to have less effect in UAG compared with CG, and an approximate reduction of 40% in grinding forces was observed at a 138.2 m/min. wheel peripheral speed, leading to varied chip CG/UAG chip formations, Figure 15.85. Specific grinding energy was less than in CG.

Dong et al. (2017) also characterized chip removal in UAG of difficult to machine SiCp/Al, using the system shown in Figure 15.86a. (As a side note, showing greater detail of the machining spindle, Figure 15.86b, using an induction-based drive means is to be commended, and

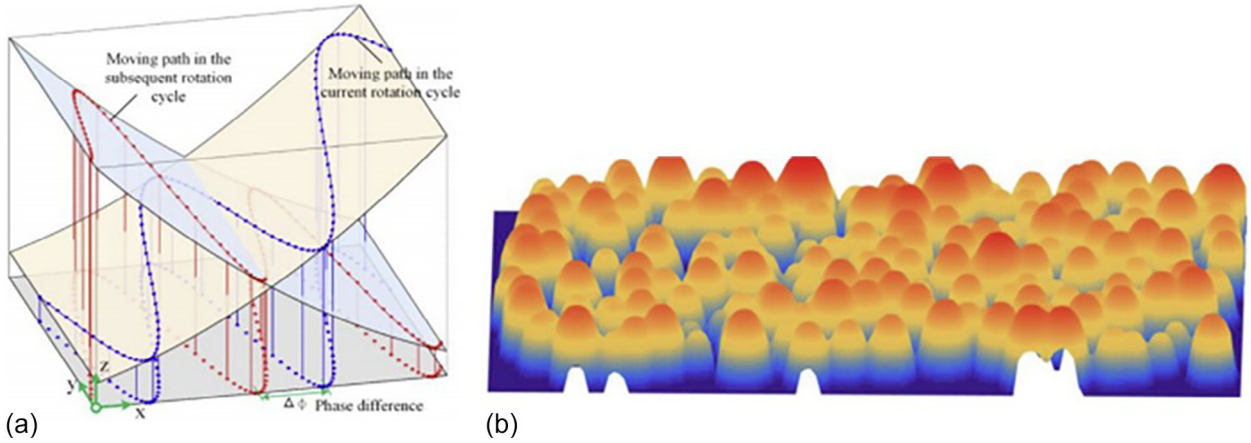


FIGURE 15.81 (a) Surface kinematics under UAG; (b) modeling process of grinding wheel (Zhou et al., 2020, Figure 2b, 4).

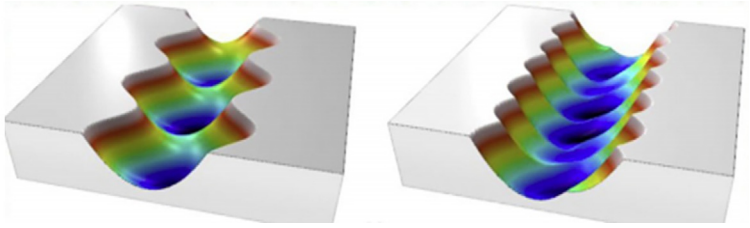


FIGURE 15.82 Interaction effects of adjacent wheel rotation cycles (Zhou et al., 2020, Figure 2c).

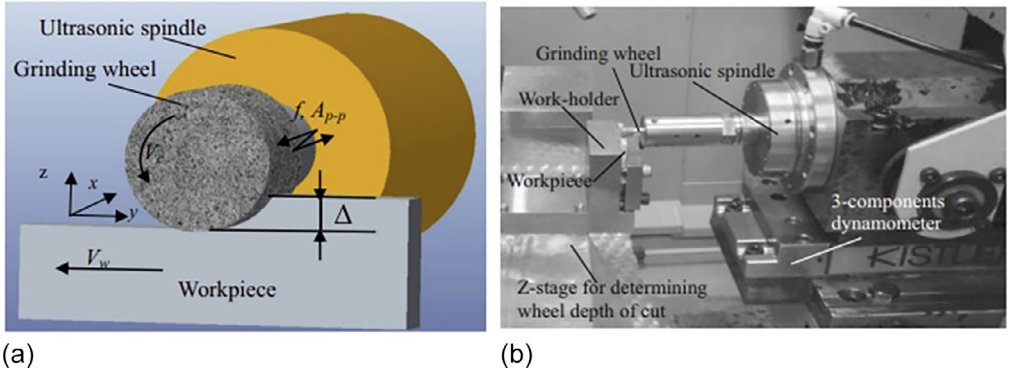


FIGURE 15.83 (a) Schematic of UAG processing principle and (b) UAG experimental setup (Li et al., 2016b, Fig. 1, 2).

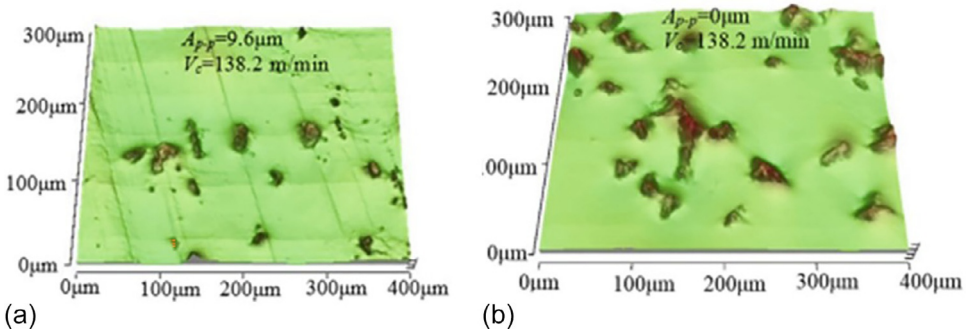


FIGURE 15.84 Effects of ultrasonic vibration amplitude and wheel speed on chip size; (a) 3D SEM of UAG chips, (b) 3D SEM of CG chips (Li et al., 2016b, Fig. 8a, 8b).

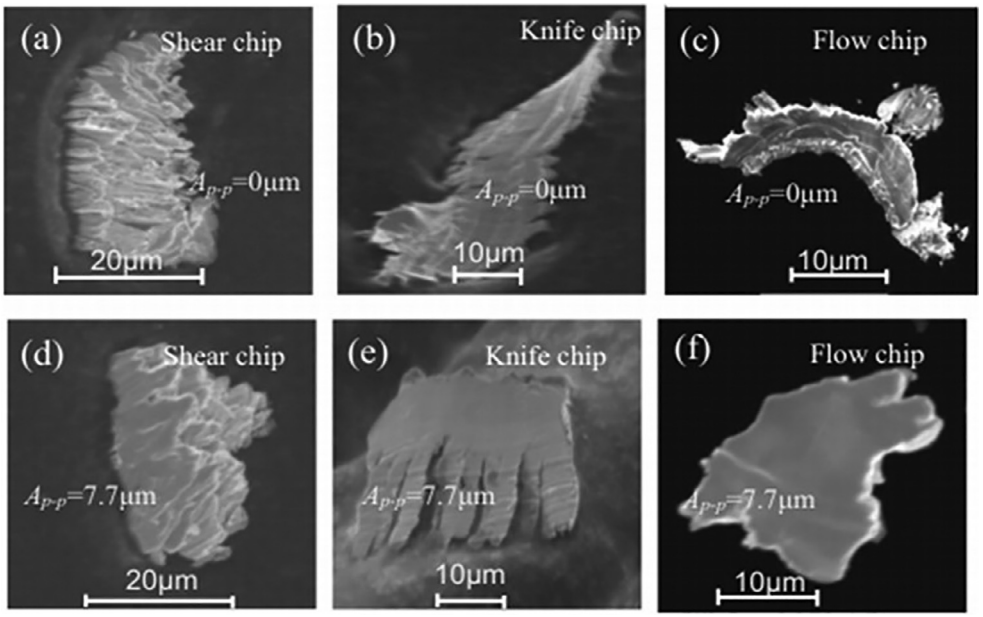


FIGURE 15.85 Types of chips at 138.2 m/min; (a, b, c) CG chips, (d, e, f) UAG chips at 7 μm amplitude (Li et al., 2016b, Figure 9).

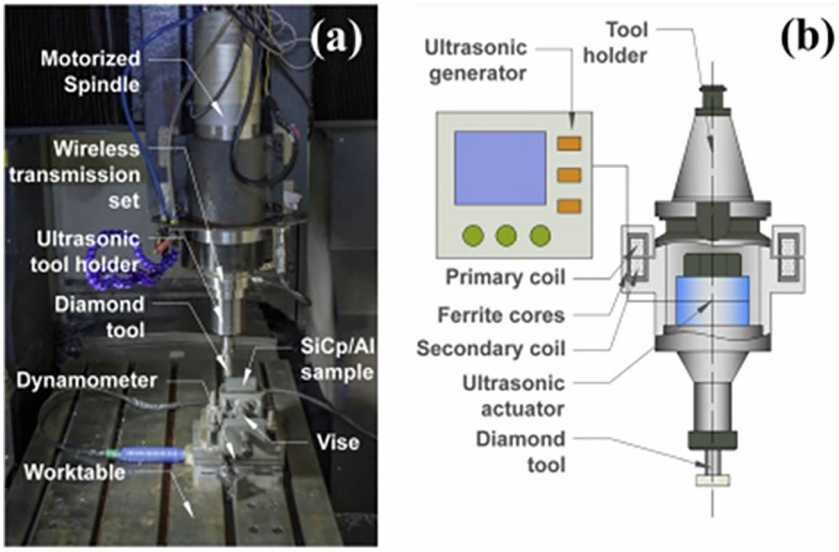


FIGURE 15.86 (a) Experimental setup for UAG study and (b) UAG machining module (Dong et al., 2017, Figure 2).

compared with the piezoelectric-based drive shown in Figure 15.44.) Results were obtained, comparing CG and UAG, on material removal mechanism, grinding forces, surface integrity, subsurface damage, and wheel wear. Thus, Figure 15.87 uses two different techniques to compare surface profiles of the CG and UAG processes. There was little differences between CG and UAG as to most surface characteristics. UAG did exhibit lower grinding forces of 35%–50%.

15.6.1.4 Hybrid processes

Li et al. (2017a, b) studied a hybrid ultrasonic-assisted plasma oxidation grinding (UAPOG) process applied to grinding Ti-6Al-4V. The system, used in the experimentally driven study, is shown in Figure 15.88. The means that the electrolytic solution is introduced into the grinding process is illustrated in Figure 15.89. Three conditions were investigated, CG, POG only, UAG only, and UAPOG hybrid. Figure 15.90 is illustrative of the varied work surface results. It was found that a lower, e.g., 100 V, plasma voltage was best, with it also being found that grinding forces were greatly reduced (normal by 60%, tangential by 70%) and decreased surface roughness by 46% compared with CG. It was concluded that the ultrasonic vibrations promoted the oxidation of the work surface, resulting in reduced surface hardness.

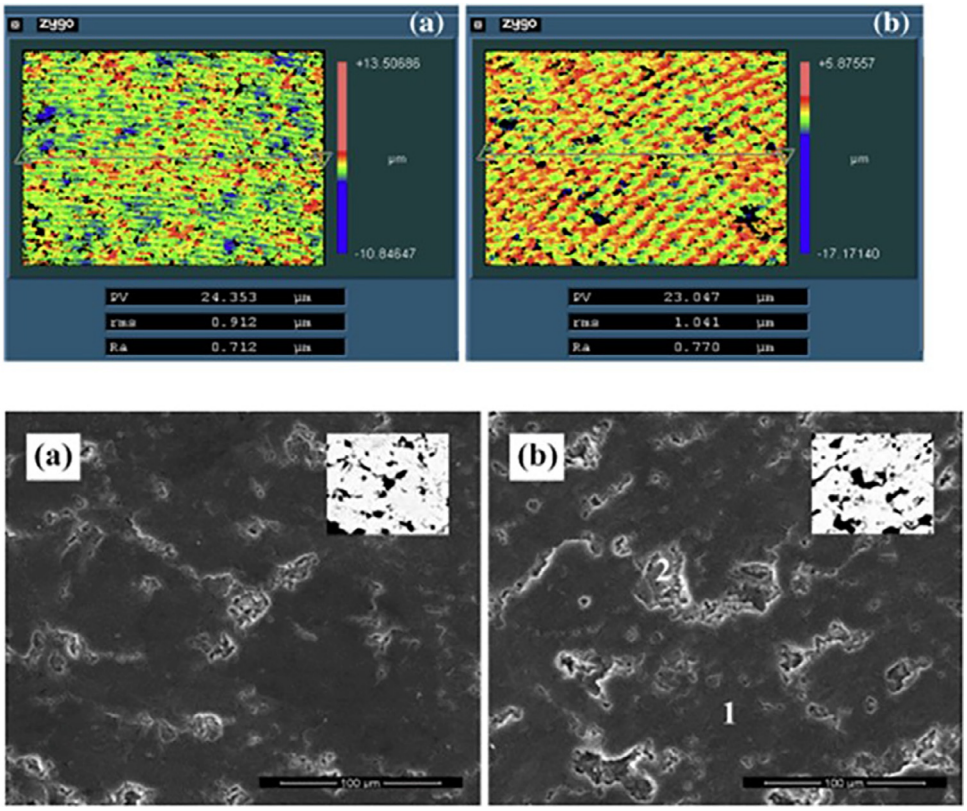
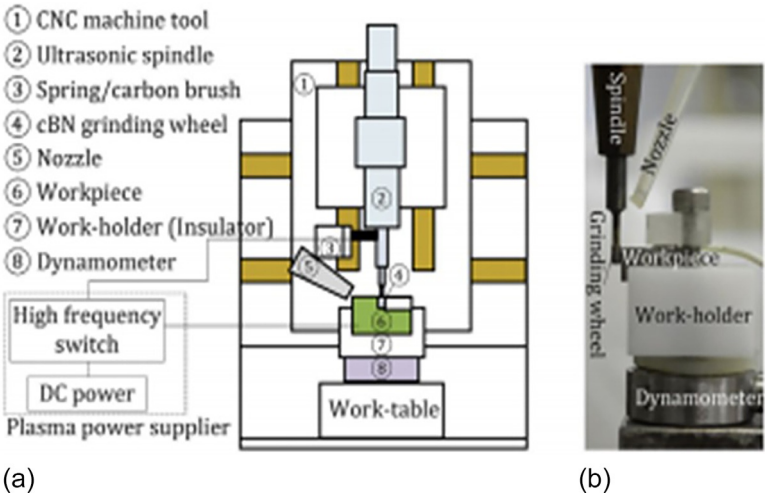


FIGURE 15.87 Top—surface profiler topographics of SiCp/Al (a) CG, (b) UAG; Bottom—surface SEM topographies, (a) CG, (b) UAG (Dong et al., 2017, Fig. 9, 10).

FIGURE 15.88 Experimental setup (a) schematic and (b) main components of setup (Li et al., 2017a, Fig. 2).



Li et al. (2018) continued reporting on the UAPOG process on Ti-6Al-4V, noting additional benefits of reduced wheel wear and that the formation of a titanium oxide (TiO_2) layer at the work surface by the electrochemical reaction led to a reduced Vickers microhardness. It was this latter effect to which the lower grinding forces were attributed.

15.7 Reaming, honing, lapping, tapping

While primary attention has been given to turning, drilling, milling, and grinding, the breadth of the machining field has resulted in ultrasonics being applied to a number of other cutting processes including reaming, broaching, lapping, honing, sawing, and tapping, some of which are reviewed here.

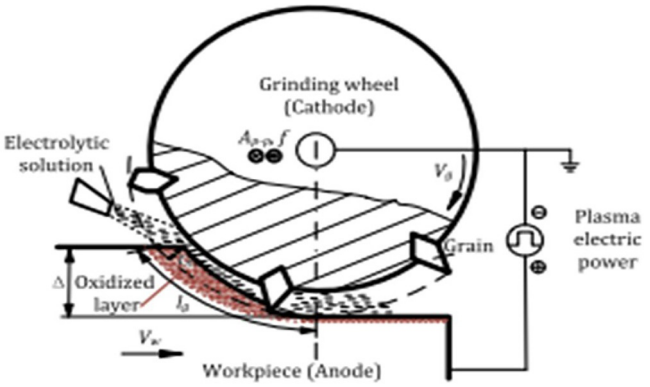


FIGURE 15.89 Illustration of processing principle of UAPOG (Li et al., 2017a, Figure 1).

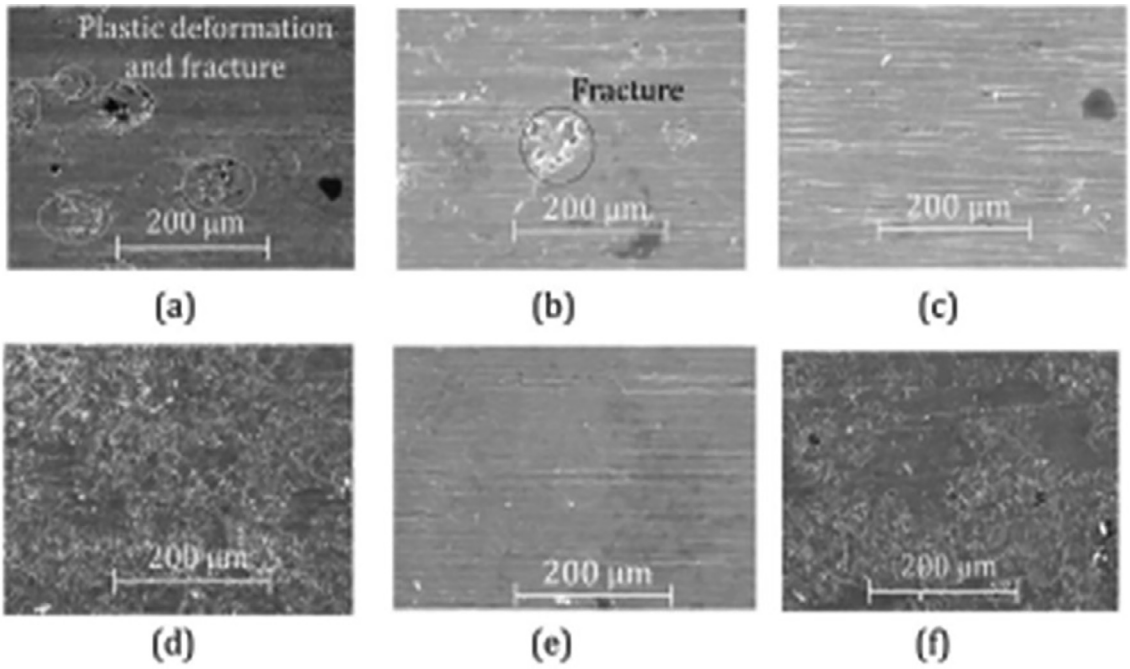


FIGURE 15.90 SEM work surface images for: (a) CG only, (b) UAG only, (c) POG at 100 V, (d) POG at 160 V, (e) UAPOG at 100 V, and (f) UAPOG at 160 V (Li et al., 2017a, Figure 4).

15.7.1 Reaming

Early work on reaming by Isayev and Anokhin (1962) was noted, while more recently, in the work of Zhang et al. (2012), ultrasonic vibrations were applied to the reamer shown in Figure 15.91a (it not being clear whether the workpiece or tool was rotated). Among the results were those for surface roughness as a function of cutting speed, Figure 15.91b, which were said to be equivalent to that achieved by grinding, but with a decreased ultrasonic effect at higher speeds. The existence of a critical cutting speed, similar to that in other ultrasonic processes, was noted. Other reaming work by Zhang et al. (2004) looked at dry reaming, with claims on improved precision and surface quality.

15.7.2 Honing

Zhu et al. (2002) developed an innovative ultrasonic system for delivering vibrations from a single transducer to two honing oilstones. Much of the paper is devoted to vibration analysis of the thin rod transmission lines. Experimental results were not reported. Zhang et al. (2007) also examined the acoustics of an ultrasonic honing system.

The desire to achieve a mixed mode, longitudinal-torsional vibration in an ultrasonic tool, has been of long standing in many applications but was fortunately solved many years ago by Tsujino et al. (1996a,b) through use of diagonal slits in a solid or hollow horn (a more recent description of the method has been provided by Ishii et al. (2013)). The work of Zhao and Shen (2014) uses

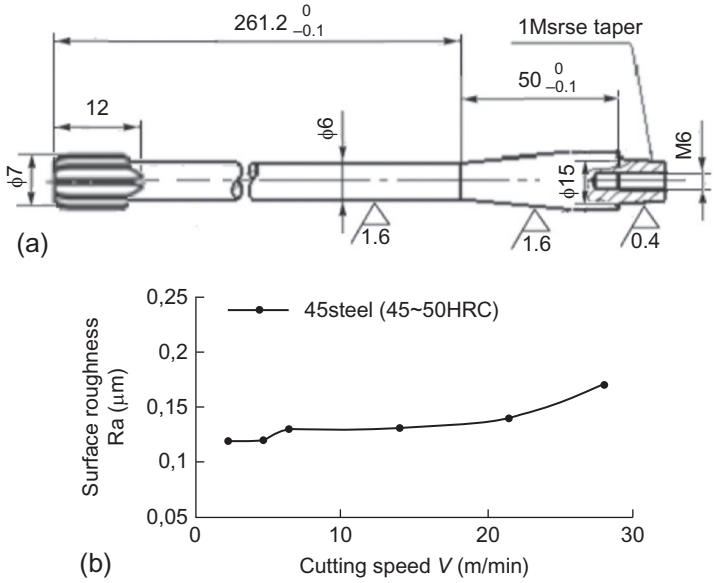


FIGURE 15.91 Ultrasonic reaming: (a) ultrasonic reaming tool (Zhang et al., 2012, Fig. 1), (b) surface roughness versus cutting speed (cut depth 0.1 mm, feed 0.07 mm/rev (Zhang et al., 2012, Fig. 2).

FEA to design a tool to apply longitudinal-torsional vibrations to the honing process. Shiying et al. (2014) used a control theory analysis to evaluate the influence of geometric parameters of a flexible-rod whetstone-seat vibration subsystem on the vibration behaviors of the ultrasonic honing system. Shiying et al. (2014) focused on developing a mathematical model for the ultrasonic-assisted honing of a gear. The components of the 20 kHz system are shown in Figure 15.92a, with the ANSYS-based modeling of the honing tool shown in Figure 15.92b. The results showed that the resonant frequency obtained by FEM was 23,504 Hz compared with the target resonant frequency of 20,000 Hz.

The gear was simplified to an annular plate and was analyzed for different design parameters. Both the simplified and actual gear were fabricated, Figure 15.93a, and used powder to check the first-order transverse vibration modes, where both systems showed a circular nodal line, as seen in Figure 15.93a and b.

The focus of Ye et al. (2018) was on cavitation phenomena that occurs in the grinding fluid during ultrasonic-assisted honing. The cavitation formation mechanism in the grinding zone was analyzed by considering the condensation and evaporation of kerosene steam and honing factors and established a model of a single cavitation bubble. MATLAB was used to analyze the influence of ultrasonic honing factors on the bubble radius, thus temperature, pressure, and the number of kerosene steam molecules inside the bubble were considered. The results showed that pressure is a significant parameter affecting bubble radius. Results also showed that the rotation speed of the honing head had a minor effect on the characteristic curves of the bubble.

Due to the small value of depth of cut in the honing process (e.g., 10 μm), the work of Linzheng and Xijing (2016) focused on developing an analytical model to evaluate the effect of honing depth and rotational speed on grinding force in UAH of structural steel. This study was done with and without considering the scale factor of the material, which reflects the influence of material geometry and microstructure on its mechanical behaviors. Results showed that by considering the scale factor, force values would be higher compared to the model without scale factor. Results also showed that when honing depth was less than 1.4 μm, normal and tangential grinding forces increased compared with the decreased values reported in a force model without scale factor. This was followed by another analytical study by Zhang et al. (2016), where the effect of machining parameters (i.e., amplitude, frequency, rotation speed) on workpiece temperature in ultrasonic-assisted honing was studied by modeling temperature based on a moving heat theory. The results showed that while frequency had no major effect on heat generation, the honing head rotation speed and ultrasonic amplitude had greater impact on temperature.

Ma et al. (2020) used the finite element method (FEM) to analyze and optimize a slotted block horn to improve the amplitude uniformity of the honing tool that was attached to the bottom of the vibrating horn in an experimental setup that measured the effects of processing parameters on surface roughness in conventional and ultrasonic-assisted honing of stainless steel 304.

The results indicated that while the absolute values of surface roughness of the samples honed with ultrasonic vibrations were larger (specially at higher amplitudes) than without vibrations (i.e., conventional honing), the application of ultrasonic vibration formed a dense punctiform morphology, Figure 15.94b) and reduced the defects compared with samples honed without ultrasonic vibrations,

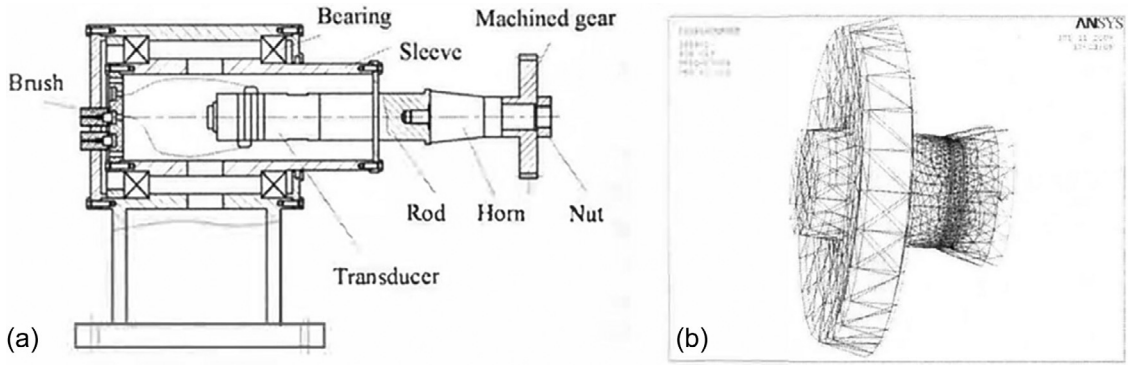


FIGURE 15.92 (a) The schematic of ultrasonic-assisted honing system for gear; (b) vibration analysis of ultrasonic honing gear system using ANSYS (Shiying et al., 2014, Figures 1, 6).

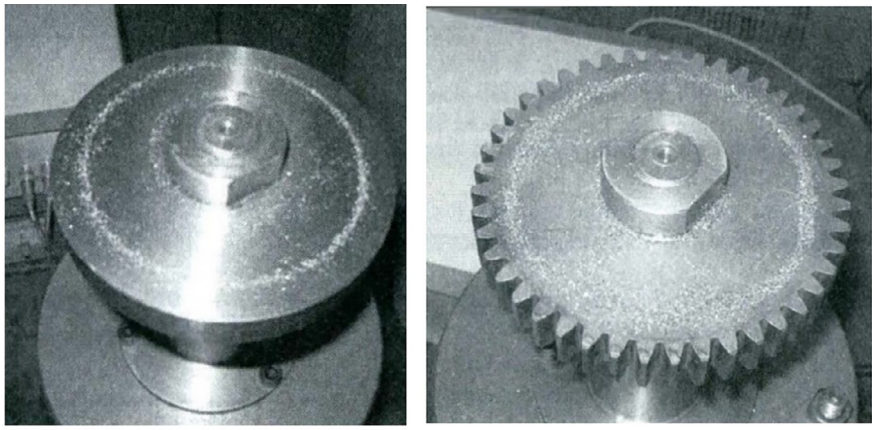


FIGURE 15.93 (a) Experimental testing of simplified system; (b) experimental testing of the system with real gear (Shiying et al., 2014, Figures 7, 8).

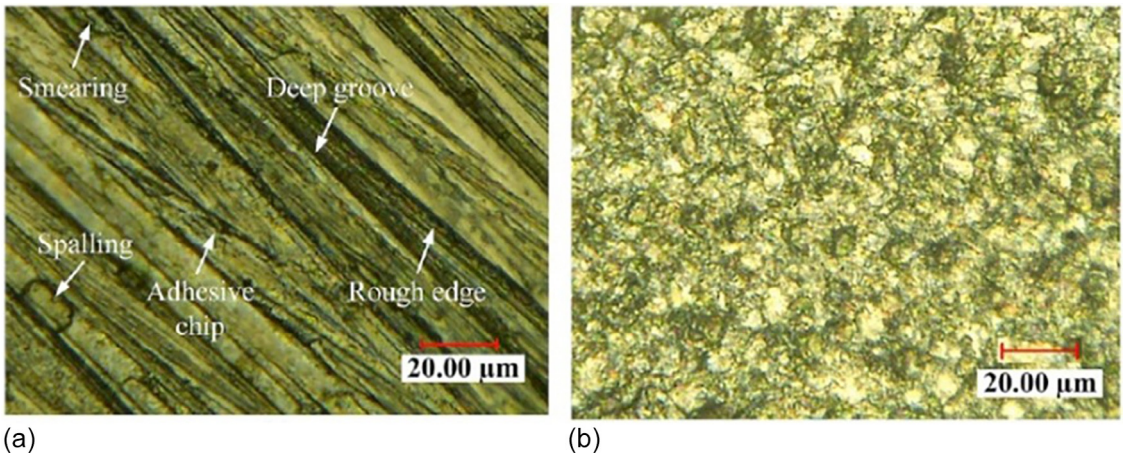


FIGURE 15.94 (a) Surface topographies of stainless steel in conventional honing; (b) surface topographies of stainless steel in ultrasonic-assisted honing (Ma et al., 2020, Figures 8, 9).

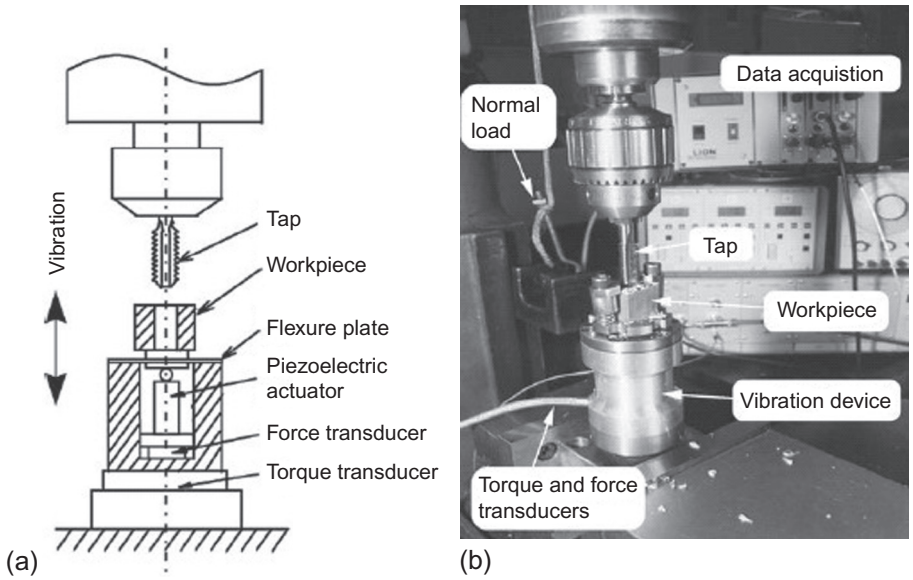


FIGURE 15.95 Vibration-assisted tapping system: (a) schematic view and (b) system photograph (Zhang et al., 2003, Fig. 6).

Figure 15.94a. It was concluded that the surface roughness could be improved by using a smaller amplitude, increasing the speed of revolution, and extending honing time.

15.7.3 Tapping

Applying vibrations to the tapping of screw threads has been studied by Zhang et al. (2003) where, using the system of Figure 15.95, a conventional tap was operated against a vibrated workpiece, with force and torque data being obtained. The process was modeled analytically, with friction, frequency, amplitude, and strain rate effects included in an effort to establish optimum conditions. Experimental work, in the frequency range of 50–1600 Hz, showed that a 35% reduction in torque with vibrations was obtained.

Kuo (2007) used a virtually identical setup as above but with an ultrasonically vibrated workpiece, with measurements of force and torque. The process was divided into six stages, with tests comparing conventional and ultrasonic tapping. No differences were found in the axial force, while torques were reduced by about one third in the early tapping stages. Variation of frequency was possible permitting an optimum frequency at 18.8 kHz to be found.

A similar setup, Figure 15.96, was used by Kuo (2008a, b,c) to evaluate the effect of machining and ultrasonic parameters on axial force and torque in ultrasonic-assisted tapping of Titanium using two different tap sizes (i.e., M3.5*0.5 and M3.5*0.6). The results which were obtained at three different spindle speeds, 50, 70, and 90 RPM, showed that the spindle speed was the most influential factor affecting axial force and torque. The results of their tests with and without use of ultrasonics showed that, in most cases, at lower spindle speeds the effect of ultrasonic vibration on reduction of axial force and torque was more than at higher speeds.



FIGURE 15.96 The apparatus for the ultrasonic-assisted tapping experiment (frequency: 18.8 kHz, max amplitude: 14 μm) (Kuo, 2008a, Figure 1).

Tsao and Kuo (2012) then considered two different scenarios, fixed frequency (FF) and limited tracing frequency (LTF) to apply 17 kHz vibrations during tapping Ti-6Al-4V. Taps having three different coatings (i.e., TiN, TiAlN

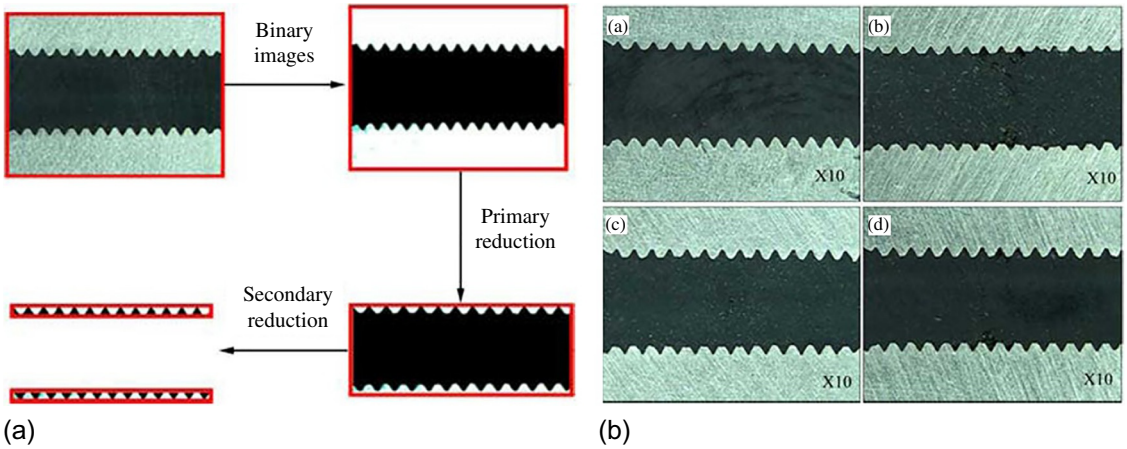


FIGURE 15.97 (a) Process for reduced binary image of tapped internal thread area; (b) comparison the thread profile of TT and LTF ultrasonic-assisted tapping of Ti6-Al-4V using taps with TiAlN Micran coating at different amplitude settings: (a) TT, 0 V; (b) LTF, A:1.37 μm; (c) LTF, A:2.35 μm; (d) LTF, A:3.14 μm (Tsao and Kuo, 2012, Figures 2, 8).

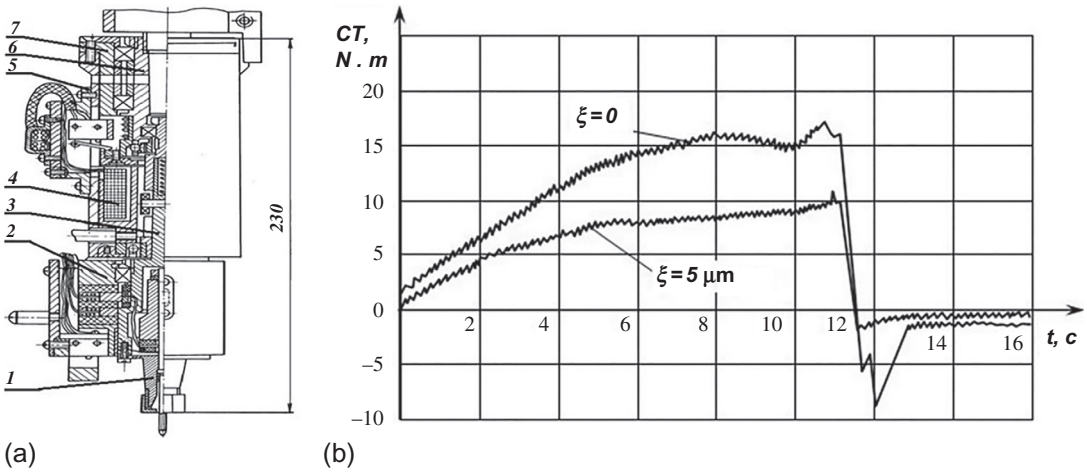


FIGURE 15.98 A schematic of (a) 20 kHz ultrasonic-assisted tapping system; (b) measured cutting torque during tapping (i.e., M8) of a titanium sample (Golovkin et al., 2018, Figures 1, 2).

Micran, and TiAlN+WC/C Hardlube) were used. Machine vision inspection was used to evaluate the quality of the internal threads by reducing the binary image of tapped internal thread area, Figure 15.97a, and calculating the number of pixels of the thread area. As shown in Figure 15.97b and c, comparing the results of traditional tapping (TT) with LTF ultrasonic-assisted tapping showed that applying 2.35 μm to the TiAlN Micran coated taps provided the maximum improvement (i.e., 30.2%) in thread quality.

In the work of Golovkin et al. (2018), a 20 kHz ultrasonic threading device was developed and used to apply ultrasonic vibrations with up to 6 μm amplitude to tap a titanium sample with an 8-mm diameter hole. A schematic of the ultrasonic-assisted tapping system is shown in Figure 15.98a. As seen in Figure 15.98b, the results showed that applying ultrasonic vibration with 5-μm amplitude can decrease the cutting torque by 40%.

This work was followed by that of Golovkin et al. (2020a,b) where the same experimental setup used in the preceding work was used to study the effect of cutting speed and amplitude on cutting torque. Taps with and without wear-resistant coating were used and the results showed a significant reduction in cutting torque, especially at higher amplitudes. The effect of amplitude on cutting torque was also studied using four different tap sizes (M5, M6, M8, and M10) and the results showed that, for tests with and without ultrasonics, the torque increased with same ratio as tap diameter increased.

Concluding this section, Golovkin et al. (2020a,b) examined the effect of ultrasonic vibrations on surface roughness, strain hardening, and residual stresses using tangential, axial, and radial ultrasonic vibrations. Similar to their previous works, the same experimental setup and material were used. It is unfortunately not clear how the system was able to generate tangential, axial, and radial

ultrasonic vibrations. The results of this study showed that when radial or axial ultrasonic vibrations were applied, up to 20% increase in surface hardness was obtained, and compressive residual stresses increased by 1.5–2 times.

15.8 Future trends

The future trends in this field should be marked by those developments that will transition ultrasonic machining (i.e., the application of power ultrasonics to machine tools) from one of laboratory research to that of factory production. For this to occur, the following trends will be important:

- Production designs need to emerge from the many laboratory systems, permitting field testing of the varied processes.
- Development of a more extensive database of ultrasonic machining "feeds and speeds" must occur so that direct comparisons with existing practices can be made.
- Continued research will still be needed on the fundamental mechanisms of the varied processes, permitting further advances in practical uses to be made.

To gain industry acceptance, these trends must answer the questions of the skeptical machinist, such as, "Is it commercially available? Can parts be made faster, better, and at lower cost? Can coolants be reduced? Can harder, tougher materials be machined?" While it is believed the answers to most of these questions may be positive, the answers must be obtained.

15.9 Sources of further information and advice

The general absence of a single source of information on ultrasonics applied to machine tools was, of course, a primary objective in preparing this chapter, with the hope being that that objective has in part been met. While most of Markov (1962) deals with traditional slurry-based machining, a small section deals with early machine tool developments in the former U.S.S.R. More recent is the review of Brehl and Dow (2008) on vibration-assisted machining. The best journal sources should be apparent from those frequently cited in this chapter and include the *Journal of Engineering Manufacture, International Journal of Materials and Product Technology, Advanced Materials Research, International Journal of Machine Tools and Manufacture, Journal of Materials Processing Technology, Key Engineering Materials,* and the *International Journal of Advanced Manufacturing Technology*. Of course, trade journals and trade shows are always standard sources and resources are increasingly available on the Internet.

References

Abootorabi-Zarchi, M.M., Razfar, M.R., Abdullah, A., 2012. Investigation of the effect of cutting speed and vibration amplitude on cutting forces in ultrasonic-assisted milling. Proc. Inst. Mech. Eng. B J. Eng. Manuf. 226 (7), 1185–1191.

Ahmed, N., Mitrofanov, A.V., Babitsky, V.I., Silberschmidt, V.V., 2007. Analysis of forces in ultrasonically assisted turning. J. Sound Vib. 308 (3–5), 845–854.

Ahmed, N., Mitrofanov, A.V., Babitsky, V.I., Silberschmidt, V., 2009. Enhanced finite element model of ultrasonically assisted turning. Int. J. Mach. Mach. Mater. 6 (1–2), 159–173.

Amini, S., Soleimanimehr, H., Nategh, M.J., Abudollah, A., Sadeghi, M.H., 2008. FEM analysis of ultrasonic-vibration-assisted turning and the vibratory tool. J. Mater. Process. Technol. 201 (1–3), 43–47.

Amini, S., Nategh, M.J., Soleimanimehr, H., 2009. Application of design of experiments for modeling surface roughness in ultrasonic vibration turning. Proc. Inst. Mech. Eng. B J. Eng. Manuf. 223, 641–652.

Amini, S., Khosrojerdi, M.R., Nosouhi, R., 2017. Elliptical ultrasonic-assisted turning tool with longitudinal and bending vibration modes. Proc. Inst. Mech. Eng. B J. Eng. Manuf. 231 (8), 1389–1395. https://doi.org/10.1177/0954405415592196.

Anon, 1964. Investigation of vibratory excitation of cutting tool during lathe turning. Aeroprojects Research Report, pp. 64–76.

Anon, 1965. Ultrasonic energy aids turning, grinding, machining. Steel 157, 58–60.

Anon, 1971a. Ultrasonically assisted gun drilling. Cutting Tool Engineering. pp. 24, 27.

Anon, 1971b. Ultrasonic Twist Drilling, Background and Potential. Aeroprojects Inc. Also (July 1971). 'Ultrasonic twist drilling', NAVMIRO Manufacturing Technology Bulletin No. 20, Naval Material Industrial Resources Office, Philadelphia.

Astashev, V.K., Babitsky, V.I., 2007. Ultrasonic Processes and Machines: Dynamics, Control and Applications. Springer, Berlin. ISBN: 978-3-540-72060-7.

Azarhoushang, B., Akban, J., 2007. Ultrasonically-assisted drilling of Inconel 738-LC. Int. J. Mach. Tools Manuf. 47, 1027–1033.

Babitsky, V.I., Kalashnikov, A.N., Molodtsov, F.V., 2004a. Autoresonant control of ultrasonically assisted cutting. Mechatronics 14 (1), 91–114.

Babitsky, V.I., Mitrofanov, A.V., Silberschmidt, V.V., 2004b. Ultrasonically assisted turning of aviation materials: simulations and experimental study. Ultrasonics 42, 81–86.

Babitsky, V.I., Astashev, V.K., Meadows, A., 2007. Vibration excitation and energy transfer during ultrasonically assisted drilling. J. Sound Vib. 308 (3–5), 805–814.

Baghlani, V., Mehbudi, P., Akbari, J., Sohrabi, M., 2013. Ultrasonic assisted deep drilling of Inconel 738lc superalloy. Procedia Cirp 6 (1), 571–576.

Baghlani, V., Mehbudi, P., Akbari, J., Nezhad, E.Z., Sarhan, A.A., Hamouda, A.M., 2016. An optimization technique on ultrasonic and cutting parameters for drilling and deep drilling of nickel-based high-strength Inconel 738lc superalloy with deeper and higher hole quality. Int. J. Adv. Manuf. Technol. 82, 877–888.

Bai, W., Bisht, A., Roy, A., Suwas, S., Sun, R., Silberschmidt, V.V., 2019a. Improvements of machinability of aerospace-grade Inconel alloys with ultrasonically assisted hybrid machining. Int. J. Adv. Manuf. Technol. 101 (5–8), 1143–1156. https://doi.org/10.1007/s00170-018-3012-8.

Bai, W., Roy, A., Sun, R., Silberschmidt, V.V., 2019b. Enhanced machinability of sic-reinforced metal-matrix composite with hybrid turning. J. Mater. Process. Technol. 268, 149–161. https://doi.org/10.1016/j.jmatprotec.2019.01.017.

Balamuth, L., 1964. Developments are coming fast in ultrasonic metalworking. Am. Mach./Metalworking Manuf. 108, 136–138.

Barani, A., Amini, S., Paktinat, H., Fadaei Tehrani, A., 2014. Built-up edge investigation in vibration drilling of Al2024-T6. Ultrasonics 54, 1300–1310.

Bijan, V.A., Reza, R.M., 2011. An experimental study on the effects of ultrasonic assisted drilling on chip characteristics and tool life. Adv. Mater. Res. 325, 351–356.

Brehl, D.E., Dow, T.A., 2007. 3-D microstructure creation using elliptical vibration-assisted machining. In: ASPE Proceedings, Vibration Assisted Machining Technology, Chapel Hill, NC.

Brehl, D.E., Dow, T.A., 2008. Review of vibration-assisted machining. Precis. Eng. 32 (3), 153–172.

Brehl, D.E., Cerniway, M.A., Dow, T.A., Negishi, N., 2007. Machining forces for elliptical vibration-assisted machining. In: ASPE Proceedings, Vibration Assisted Machining Technology, Chapel Hill, NC.

Celaya, A.L., de Campa, L.N.L., Javier, F., Aitzol, L., 2009. Ultrasonic assisted turning of mild steels. Int. J. Mater. Product Technol. 37 (1–2), 60–70.

Chang, S.S.F., Bone, G.M., 2005. Burr size reduction in drilling by ultrasonic assistance. Robot. Comput. Integr. Manuf. 21 (4–5), 442–450.

Chang, S.S.F., Bone, G.M., 2009. Thrust force model for vibration-assisted drilling of aluminum 6061-T6. Int. J. Mach. Tools Manuf. 49 (14), 1070–1076.

Chang, S.S.F., Bone, G.M., 2010. Burr height model for vibration assisted drilling of aluminum 6061–T6. Precis. Eng. 34 (3), 369–375.

Chen, H., Tang, J., 2015. A model for prediction of surface roughness in ultrasonic-assisted grinding. Int. J. Adv. Manuf. Tech. 77 (1–4), 643–651. https://doi.org/10.1007/s00170-014-6482-3.

Chen, H., Tang, J., 2016. Influence of ultrasonic assisted grinding on Abbott-Firestone curve. Int. J. Adv. Manuf. Technol. 86 (9–12), 2753–2757.

Chen, C.S., Tang, J., Chen, H.F., Zhao, B., 2018a. An active manufacturing method of surface micro structure based on ordered grinding wheel and ultrasonic-assisted grinding. Int. J. Adv. Manuf. Technol. 97 (5–8), 1627–1635.

Chen, H., Tang, J., Shao, W., Zhao, B., 2018b. An investigation on surface functional parameters in ultrasonic-assisted grinding of soft steel. Int. J. Adv. Manuf. Technol. 97 (5–8), 2697–2702.

Chen, S., Zou, P., Wu, H., Kang, D., Wang, W., 2019. Mechanism of chip formation in ultrasonic vibration drilling and experimental research. Proc. Inst. Mech. Eng. C J. Mech. Eng. Sci. 233 (15), 5214–5226. https://doi.org/10.1177/0954406219848464.

Chen, P., Tong, J., Zhao, J., Zhang, Z., Zhao, B., 2020a. A study of the surface microstructure and tool wear of titanium alloys after ultrasonic longitudinal-torsional milling. J. Manuf. Process. 53, 1–11. https://doi.org/10.1016/j.jmapro.2020.01.040.

Chen, J., Ming, W., An, Q., Chen, M., 2020b. Mechanism and feasibility of ultrasonic-assisted milling to improve the machined surface quality of 2d cf/sic composites. Ceram. Int. Part A 46 (10), 15122–15136. https://doi.org/10.1016/j.ceramint.2020.03.047.

Chern, G.-L., Lee, H.-J., 2006. Using workpiece vibration cutting for micro-drilling. Int. J. Adv. Manuf. Technol. 27 (7–8), 688–692.

Chu, N., Nguyen, V., Ngo, Q., 2020. Machinability enhancements of ultrasonic-assisted deep drilling of aluminum alloys. Mach. Sci. Technol. 24 (1), 112–135. https://doi.org/10.1080/10910344.2019.1636267.

Cornier, A., 1992. Turning assisted by non-conventional processes: ultrasonic assistance, high pressure water jet assistance: influence on productivity and workpiece quality. Bull. Cercle d'Etudes Metaux 16 (4). 5.1–5.16.

Dambatta, Y.S., Sarhan, A.A.D., Sayuti, M., Hamdi, M., 2017. Ultrasonic assisted grinding of advanced materials for biomedical and aerospace applications—a review. Int. J. Adv. Manuf. Tech. 92 (9–12), 3825–3858. https://doi.org/10.1007/s00170-017-0316-z.

Deng, G., Li, S., Wu, S., Yang, X., 1993. Ultrasonic vibration drilling of small-diameter deep holes of difficult-to-machine stainless steel: theoretical analysis and comparative experimental research. In: ASME Production Engineering Division Publications PED. vol. 64. ASME, New York, pp. 835–839.

Devine, J., 1978. Ultrasonically assisted metal removal. In: Materials Synergisms/Proceedings Conference, Kiamesha Lake, NY, USA, pp. 485–497.

Devine, J., 1979. Ultrasonically assisted metal removal. SAMPE Quart. 10 (3), 1–6.

Devine, J., Krause, P., 1980. Ultrasonically assisted machining of aircraft parts. Final Report, Cont. No. DAAG46–78-C-0059, Mantech Program, U.S. Army Aviation Research and Development Command.

Dixit, U., Pandey, P., Verma, G., 2019. Ultrasonic-assisted machining processes: a review. Int. J. Mechatron. Manuf. Syst. 12 (3–4), 227.

Dohmen, H.G., 1966. Machining research with ultrasonically excited turning tools. Ind.-Anz. 88, 115–122.

Dong, Z., Zheng, F., Zhu, X., Kang, R., Zhang, B., Liu, Z., 2017. Characterization of material removal in ultrasonically assisted grinding of SiCp/Al with high volume fraction. Int. J. Adv. Manuf. Technol. 93 (5–8), 2827–2839.

Elhami, S., Razfar, M.R., Farahnakian, M., 2015. Analytical, numerical and experimental study of cutting force during thermally enhanced ultrasonic assisted milling of hardened AISI 4140. Int. J. Mech. Sci. 103, 158–171. https://doi.org/10.1016/j.ijmecsci.2015.09.007.

Farahnakian, M., Keshavarz, M.E., Elhami, S., Razfar, M.R., 2019. Effect of cutting edge modification on the tool flank wear in ultrasonically assisted turning of hardened steel. Proc. Inst. Mech. Eng. B J. Eng. Manuf. 233 (5), 1472–1482. https://doi.org/10.1177/0954405416640416.

Fu, Y.C., Su, H.H., He, T., Ding, K., 2015. Experimental study on ultrasonic assisted grinding of C/SiC composites. In: ICCM International Conference on Composite Materials. vol. 2015.

Fujimoto, M., Wu, Y., Nomura, M., Kanai, H., Jin, M., 2014. Surface topography of mini-size diamond wheel in ultrasonic assisted grinding (UAG). Int. J. Autom. Technol. 8 (4), 569–575.

Fujimoto, M., Wu, Y., Nomura, M., Kanai, H., Jin, M., 2015. Wear behavior of grain cutting edge in ultrasonic assisted grinding using mini-size wheel. Int. J. Autom. Technol. 9 (4), 365–372.

Gao, J., Altintas, Y., 2019. Development of a three-degree-of-freedom ultrasonic vibration tool holder for milling and drilling. IEEE/ASME Trans. Mechatron. 24 (3), 1238–1247. https://doi.org/10.1109/TMECH.2019.2906904.

Gao, G.F., Zhao, B., Jiao, F., Liu, C.S., 2002. Research on the influence of the cutting conditions on the surface microstructure of ultra-thin wall parts in ultrasonic vibration cutting. J. Mater. Process. Technol. 129 (1–3), 66–70.

Gholamzadeh, B., Soleimanimehr, H., 2019. Finite element modeling of ultrasonic-assisted turning: cutting force and heat generation. Mach. Sci. Technol. 23 (6), 869–885. https://doi.org/10.1080/10910344.2019.1636266.

Golovkin, V., Batishcheva, O., Papshev, V., 2018. Enhance the efficiency of the internal threads cutting process with taps by applying ultrasonic vibrations. Matec Web Conf. 224. https://doi.org/10.1051/matecconf/201822401113.

Golovkin, V.V., Batishcheva, O.M., Papshev, V.A., 2020. Ultrasonic influence on the quality formation of surface layer when cutting thread. IOP Conf. Ser.: Mater. Sci. Eng. 709 (3). https://doi.org/10.1088/1757-899X/709/3/033043.

Golovkin, V.V., Batishcheva, O.M., Papshev, V.A., 2020a. Ultrasonic vibration-assisted thread cutting technology. Mater. Today Proc. https://doi.org/10.1016/j.matpr.2020.09.105.

Graff, K.F., 2007. A review of the literature on ultrasonic machining. EWI Project Report 50253GTH.

Graff, K.F., 2013. Review of the literature—ultrasonic turning. EWI Project No. 52794IRD.

Grauer, W., 1973. Ultrasonic machining. Grumman Aerospace Corporation, Technical Report AFML-TR-73-86. AF Materials Laboratory, AF Systems Command, WPAFB, Oh.

Guo, Q., Zhang, M.Y., Jiang, Y., Zhao, B., 2018. The determination of instantaneous uncut chip thickness for non-uniform helix angle tools with complex tool path in ultrasonic milling process. Int. J. Manuf. Res. 13 (2), 183–194. https://doi.org/10.1504/IJMR.2018.093262.

Hu, H.J., Sun, Y., Lu, Z., 2010. Simulation and experiment of cutting force in ultrasonic torsional vibration assisted micromilling. In: Proc. SPIE 7657. (poster).

Hu, H.J., Sun, Y.Z., Lu, Z.S., 2011. Simulation of residual stress in ultrasonic vibration assisted micro-milling. Adv. Mater. Res. 188, 381–384.

Ille, I., Twiefel, J., 2015. Model-based feedback control of an ultrasonic transducer for ultrasonic assisted turning using a novel digital controller. Phys. Procedia 70, 63–67. https://doi.org/10.1016/j.phpro.2015.08.043.

Isayev, A.I., Anokhin, V.S., 1962. Reaming with ultrasonically vibrated reamers. Mach. Tooling (USSR) 33, 27–29.

Ishii, T., Takada, M., Kubota, Y., Ohuchi, H., 2013. An ultrasonic motor using transmission line with oblique slits driven by a Langevin transducer. In: IEEE, 2013 Joint UFFC, EFTF and PFM Symposium, pp. 475–477.

Isobe, H., Hara, K., 2014. Improvement of drill life for nickel super alloy by ultrasonic vibration machining with minimum quantity lubrication. Key Eng. Mater. 625, 581–586. https://doi.org/10.4028/www.scientific.net/KEM.625.581.

Jiao, F., Jian, J., Liu, X., 2011a. Theoretical and experimental study on the surface roughness of quenched steel in ultrasonic turning with PCBN tool. Appl. Mech. Mater. 42, 1–4.

Jiao, F., Liu, X., Zhao, C.Y., Zhang, X., 2011b. Experimental study on the surface micro-geometrical characteristics of quenched steel in ultrasonic assisted turning. Adv. Mater. Res. 189–193, 4059–4063.

Jinglin, T., Peng, C., Junjin, M., Junshuai, Z., Zhiming, Z., 2019. Design and analysis of ultrasonic integrated turning tool. Int. J. Adv. Manuf. Technol. 103 (9–12), 4253–4263. https://doi.org/10.1007/s00170-019-03575-8.

Kamabe, M., 1958. A study of ultrasonic cutting. Trans. Soc. Mech. Eng. Jpn. 24 (138), 109–114.

Khajehzadeh, M., Razfar, M.R., 2016. Theoretical modeling of tool mean temperature during ultrasonically assisted turning. Proc. Inst. Mech. Eng. B J. Eng. Manuf. 230 (4), 675–693. https://doi.org/10.1177/0954405414556333.

Khanna, N., Airao, J., Gupta, M.K., Song, Q., Liu, Z., Mia, M., et al., 2019. Optimization of power consumption associated with surface roughness in ultrasonic assisted turning of nimonic-90 using hybrid particle swarm-simplex method. Materials (1996–1944) 12 (20).

Khanna, N., Shah, P., Agrawal, C., Pusavec, F., Hegab, H., 2020. Inconel 718 machining performance evaluation using indigenously developed hybrid machining facilities: experimental investigation and sustainability assessment. Int. J. Adv. Manuf. Technol. 106 (11/12), 4987–4999.

Kim, J.-D., Lee, E.-S., 1994. A study of the ultrasonic-vibration cutting of carbon-fiber reinforced plastics. J. Mater. Process. Technol. 43, 259–277.

Kim, J., Bai, W., Roy, A., Jones, L.C.R., Ayvar-Soberanis, S., Silberschmidt, V.V., 2019. Hybrid machining of metal-matrix composite. Procedia CIRP 82, 184–189. https://doi.org/10.1016/j.procir.2019.04.162.

Koshimizu, S., 2007. Ultrasonic vibration-assisted cutting of titanium alloy. In: ASPE Proceedings. Vibration Assisted Machining Technology, Chapel Hill, NC.

Kramer, R.F., Pizzola, R., 1982. Ultrasonically assisted gun drilling. Contractor Report, Cont. ARSCD-CR-81029, U.S. Army Aviation Research and Development Command.

Kristoffy, I.I., Kegg, R.L., Weber, R.R., 1965. Final Report on influence of vibrational energy on metalworking processes, Technical Report AFML-TR-65–211, preparedunder Contract AF33(657)–10821 by Cincinnati Milling and Grinding Machines, Inc., Cincinnati, OH. For Advanced Fabrication Techniques Branch, Manufacturing Technology Division, Air Force Materials Laboratory, Research and Technology Division, Air Force Systems Command, U.S. Air Force, Wright-Patterson Air Force Base, Ohio. MM Project Nr. 8–144.

Kumabe, J., 1961a. Study on ultrasonic internal grinding by using the longitudinally vibrated grinding wheel, 1st Report, Transverse ultrasonic cutting. Japanese Soc. Mech. Eng. Trans. 27, 1404–1411.

Kumabe, J., 1961b. Study on ultrasonic cutting, 3rd Report, An analysis of the mechanism of ultrasonic cutting. Japanese Soc. Mech. Eng Trans. 27, 1389–1396.

Kuo, K.-L., 2007. Experimental investigation of ultrasonic vibration-assisted tapping. J. Mater. Process. Technol. 192–193, 306–311.

Kuo, K.-L., 2008a. Design of rotary ultrasonic milling tool using FEM simulation. J. Mater. Process. Technol. 201 (1–3), 48–52.

Kuo, K.L., 2008b. A study on ultrasonic vibration assisted tapping of titanium. Adv. Mater. Res. 47–50, 218–221. https://doi.org/10.4028/www.scientific.net/AMR.47-50.218.

Kuo, K.-L., 2008c. A study on ultrasonic vibration assisted tapping of titanium. Adv. Mater. Res. 47–50 (Part 1), 218–221. Multi-functional Materials and Structures – International Conference on Multifunctional Materials and Structures Hong Kong, P.R., CHN 2008 07 28–2008 07 31.

Lee, S.K., Jang, S.H., Lee, S.W., Choi, H.Z., 2007. Geometric machining mechanism of the ultrasonic drilling. Key Eng. Mater. 339, 66–71.

Li, X., Zhang, D., 2006. Ultrasonic elliptical vibration transducer driven by single actuator and its application in precision cutting. J. Mater. Process. Technol. 180, 91–95.

Li, Z.D., Zhao, B., Ma, J., 2011. Experimental study on ultrasonic milling acoustic system. Appl. Mech. Mater. 42, 355–358.

Li, Z., Wang, X., Zhao, B., 2012. An experiment study on milling forces in the ultrasonic milling of CFRP. Adv. Mater. Res. 472–475, 1028–1031.

Li, X., Dong, Z., Kang, R., Wang, Y., Liu, J., Zhang, Y., 2016a. Comparison of thrust force in ultrasonic assisted drilling and conventional drilling of aluminum alloy. Mater. Sci. Forum 861, 38–43. https://doi.org/10.4028/www.scientific.net/MSF.861.38.

Li, S., Wu, Y., Nomura, M., 2016b. Effect of grinding wheel ultrasonic vibration on chip formation in surface grinding of Inconel 718. Int. J. Adv. Manuf. Technol. 86 (1–4), 1113–1125.

Li, Z., Zhang, D., Jiang, X., Qin, W., Geng, D., 2017a. Study on rotary ultrasonic-assisted drilling of titanium alloys (Ti6Al4V) using 8-facet drill under no cooling condition. Int. J. Adv. Manuf. Technol. 90 (9–12), 3249–3264. https://doi.org/10.1007/s00170-016-9593-1.

Li, S., Wu, Y., Yamamura, K., Nomura, M., Fuji, T., 2017b. Improving the grindability of titanium alloy Ti-6Al-4V with the assistance of ultrasonic vibration and plasma electrolytic oxidation. CIRP Ann. 66 (1), 345–348.

Li, S., Wu, Y., Nomura, M., Fuji, T., 2018. Fundamental machining characteristics of ultrasonically-assisted electrochemical grinding of Ti-6Al-4V. J. Manuf. Sci. Eng. Trans. ASME 140 (7), 071009–071017.

Li, D., Tang, J., Chen, H., Shao, W., 2019. Study on grinding force model in ultrasonic vibration-assisted grinding of alloy structural steel. Int. J. Adv. Manuf. Technol. 101 (5–8), 1467–1479.

Liang, W., Xu, J., Ren, W., Liu, Q., Wang, X., Yu, H., 2019. Study on the influence of tool point angle on ultrasonic vibration–assisted drilling of titanium alloy. Int. J. Adv. Manuf. Technol. 105 (1–4), 1069–1082. https://doi.org/10.1007/s00170-019-04231-x.

Liao, Y.S., Chen, Y.C., Lin, H.M., 2007. Feasibility study of the ultrasonic vibration assisted drilling of Inconel superalloy. Int. J. Mach. Tools Manuf. 47 (12–13), 1988–1996.

Linzheng, Y., Xijing, Z., 2016. Modeling and analysis of grinding force in ultrasonic honing considering the scale effect. Matec Web Conf. 45. https://doi.org/10.1051/matecconf/20164502004.

Liu, Y., Liu, Z., Wang, X., Huang, T., 2020. Experimental study on tool wear in ultrasonic vibration–assisted milling of c/sic composites. Int. J. Adv. Manuf. Technol. 107 (1–2), 425–436. https://doi.org/10.1007/s00170-020-05060-z.

Llanos, I., Campa, Á., Iturbe, A., Arrazola, P.J., Zelaieta, O., 2018. Experimental analysis of cutting force reduction during ultrasonic assisted turning of Ti6Al4V. Procedia CIRP 77, 86–89. https://doi.org/10.1016/j.procir.2018.08.227.

Lotfi, M., Amini, S., 2017. Experimental and numerical study of ultrasonically-assisted drilling. Ultrasonics 75, 185–193.

Lotfi, M., Amini, S., 2018. Fe simulation of linear and elliptical ultrasonic vibrations in turning of Inconel 718. Proc. Inst. Mech. Eng. E J. Process Mech. Eng. 232 (4), 438–448. https://doi.org/10.1177/0954408917715533.

Lotfi, M., Amini, S., 2019. Effect of longitudinally intermittent movement of cutting tool in drilling of AISI 1045 steel: a three-dimensional numerical simulation. Proc. Inst. Mech. Eng. C J. Mech. Eng. Sci. 233 (12), 4081–4090. https://doi.org/10.1177/0954406218786318.

Lotfi, M., Amini, S., Teimouri, R., Alinaghian, M., 2017. Built-up edge reduction in drilling of AISI 1045 steel. Mater. Manuf. Process. 32 (6), 623–630. https://doi.org/10.1080/10426914.2016.1221104.

Lotfi, M., Amini, S., Aghaei, M., 2018. 3d analysis of surface topography in vibratory turning. Int. J. Adv. Manuf. Technol. 95 (1–4), 197–204.

Lotfi, M., Amini, S., Ashrafi, H., 2019. Theoretical and numerical modeling of tool-chip friction in ultrasonic-assisted turning. Proc. Inst. Mech. Eng. E J. Process Mech. Eng. 233 (4), 824–838. https://doi.org/10.1177/0954408918812271.

Ma, C., Shamoto, E., Moriwaki, T., Wang, L., 2004. Study of machining accuracy in ultrasonic elliptical vibration cutting. Int. J. Mach. Tools Manuf. 44 (12–13), 1305–1310.

Ma, C.X., Shamoto, E., Moriwaki, T., 2005. Drilling assisted by ultrasonic elliptical vibration. Key Eng. Mater. 291–292, 443–446.

Ma, K., Zhu, X., Cui, X., Wang, J., Yu, R., Xiao, L., et al., 2020. Experimental investigation on surface quality in ultrasonic-assisted honing of 304 stainless steel. Precis. Eng. 63, 148–158. https://doi.org/10.1016/j.precisioneng.2020.02.006.

Markov, A.I., 1962. Ultrasonic Machining of Intractable Materials. Iliffe Books Ltd, London. 1966. Mashgiz, Moscow, Translation by Scripta Technica Ltd.

Mitrofanov, A.V., Babitsky, V.I., Silberschmidt, V.V., 2003. Finite element simulations of ultrasonically assisted turning. Comput. Mater. Sci. 28 (3–4), 645–653.

Mitrofanov, A.V., Ahmed, N., Babitsky, V.I., Silberschmidt, V.V., 2005. Effect of lubrication and cutting parameters on ultrasonically assisted turning of Inconel 718. J. Mater. Process. Technol. 162–163, 649–654.

Moghaddas, M.A., Graff, K.F., 2020. On the effect of load on vibration amplitude in ultrasonic-assisted drilling. Int. J. Adv. Manuf. Technol. 106 (7–8), 3081–3094.

Moghaddas, M.A., Short, M.A., Wiley, N.R., Yi, A.Y., Graff, K.F., 2018. Performance of an ultrasonic-assisted drilling module. Int. J. Adv. Manuf. Technol. 94 (9–12), 3019–3028.

Moghaddas, M.A., Yi, A., Graff, K.F., 2019. Temperature measurement in the ultrasonic-assisted drilling process. Int. J. Adv. Manuf. Technol. 103 (1–4), 187–199. https://doi.org/10.1007/s00170-019-03487-7.

Mori, E., Watanabe, Y., Tsuda, Y., Ohta, K., Yamamori, H., Mishiro, S., Hamada, H., 1989. New bolt clamped flexural mode ultrasonic high power transducer with one dimensional construction. In: Ultrasonics International 89 Conference Proceedings, p. 256.

Muhammad, R., Ahmed, N., Ullah, H., Roy, A., Silberschmidt, V.V., 2018. Hybrid machining process: experimental and numerical analysis of hot ultrasonically assisted turning. Int. J. Adv. Manuf. Technol. 97 (5–8), 2173–2192.

Mult, H.C., Spur, G., Holl, S.E., 1996. Ultrasonic assisted grinding of ceramics. J. Mater. Process. Technol. 62, 287–293.

Nategh, M.J., Amini, S., et al., 2009. A machining force model developed for ultrasonic vibration-assisted turning, through statistical analysis of influential parameters. Mech. Aerospace Eng. J. 4 (4), 83–91.

Nath, C., Rahman, M., 2008. Effect of machining parameters in ultrasonic vibration cutting. Int. J. Mach. Tools Manuf. 48 (9), 965–974.

Nath, C., Rahman, M., Andrew, S.S.K., 2007. A study on ultrasonic vibration cutting of low alloy steel. J. Mater. Proc. Technol. 192–193, 159–165 (The Seventh Asia Pacific Conference on Materials Processing (7th APCMP 2006)).

Neugebauer, R., Stoll, A., 2004. Ultrasonic application in drilling. J. Mater. Process. Technol. 149 (1–3), 633–639.

Paktinat, H., Amini, S., 2018a. Experiments and finite element simulation of ultrasonic assisted drilling. J. Manuf. Sci. Eng. Trans. ASME 140 (10). https://doi.org/10.1115/1.4040321.

Paktinat, H., Amini, S., 2018b. Numerical and experimental studies of longitudinal and longitudinal-torsional vibrations in drilling of AISI 1045. Int. J. Adv. Manuf. Technol. 94 (5–8), 2577–2592. https://doi.org/10.1007/s00170-017-0893-x.

Patten, J.A., Williams, A., 2007. Numerical simulations of vibrations assisted machining. In: ASPE Proceedings. Vibration Assisted Machining Technology, Chapel Hill, NC.

Peacock, J., 1961. Ultrasonics ups grinding efficiency. Am. Mach./Metalwork. Manuf. 105, 124–125.

Peacock, J., Kuris, A., Balamuth, L., 1962. Ultrasonics aids metal removal. Am. Mach./Metalwork Manuf. 106 (17), 85–88.

Potthast, C., Eisseler, R., Klotz, D., Wallaschek, J., Heisel, U., 2008. Piezoelectric actuator design for ultrasonically assisted deep hole drilling. J. Electroceram. 20 (3–4), 187–192.

Puga, H., Grilo, J., Oliveira, F.J., Silva, R.F., Girão, A.V., 2019. Influence of external loading on the resonant frequency shift of ultrasonic assisted turning: numerical and experimental analysis. Int. J. Adv. Manuf. Technol. 101 (9–12), 2487–2496. https://doi.org/10.1007/s00170-018-3122-3.

Pujana, J., Rivero, A., Celaya, A., de Lacalle, L.N.L., 2009. Analysis of ultrasonic-assisted drilling of Ti_6Al_4V. Int. J. Mach. Tools Manuf. 49 (6), 500–508.

Razfar, M.R., Sarvi, P., Abootorabi Zarchi, M.M., 2011. Experimental investigation of the surface roughness in ultrasonic assisted milling. Proc. Inst. Mech. Eng. B J. Eng. Manuf. 225 (9), 1615–1620.

Romanyuk, V.F., 1988. External honing with ultrasonic oscillation. Sov. Eng. Res. 8 (4), 124–125.

Roney, R.N., Giardini, D., 1963. Final Report on Imposed High Frequency Vibrations and Their Effect on Conventional Grinding of High Thermal Resistant Materials. Technical Documentary Report NR. ASD-TDR-63-203 (January, 1963). ASD Project NR 7-757. Fabrication Branch, Manufacturing Technology Laboratory, Aeronautical Systems Division, Air Force Systems Command, USAF, Wright-Patterson Air Force Base, Ohio.

Salcedo, M.C., Coral, I.B., Ochoa, G.V., 2018. Characterization of surface topography with Abbot Firestone Curve. Contemp. Eng. Sci. 11 (68), 3397–3407.

Sharma, V., Pandey, P.M., 2016. Optimization of machining and vibration parameters for residual stresses minimization in ultrasonic assisted turning of 4340 hardened steel. Ultrasonics 70, 172–182. https://doi.org/10.1016/j.ultras.2016.05.001.

Sharma, V., Pandey, P.M., 2018. Experimental investigations and statistical modeling of surface roughness during ultrasonic-assisted turning with self-lubricating cutting inserts. Proc. Inst. Mech. Eng., Part E: J. Proc. Mech. Eng. 232 (6), 709–722.

Sharma, V., Pandey, P.M., 2019. Mechanistic based cutting force model during ultrasonic assisted turning with self-lubricating cutting inserts. J. Adv. Manuf. Syst. 18 (01), 133.

Shen, X.H., Zhang, J.H., Li, H., Wang, J.J., 2012a. Study on surface roughness of ultrasonic vibration assisted milling. Adv. Mater. Res. 426, 309–312.

Shen, X.H., Zhang, J., Xing, D.X., Zhao, Y., 2012b. A study of surface roughness variation in ultrasonic-assisted milling. Int. J. Adv. Manuf. Technol. 58 (5–8), 553–561.

Shen, X.H., Zhang, J.H., Li, H., Wang, J.J., Wang, X.C., 2012c. Ultrasonic vibration-assisted milling of aluminum alloy. Int. J. Adv. Manuf. Technol. 63 (1–4), 41–49.

Shi, Q., Tse, Y.Y., Muhammad, R., Roy, A., Silberschmidt, V.V., Higginson, R.L., 2016. Effect of machining on shear-zone microstructure in Ti-15V-3Cr-3Al-3Sn: conventional and ultrasonically assisted turning. J. Mater. Eng. Perform. 25 (9), 3766–3773. https://doi.org/10.1007/s11665-016-2209-y.

Shiying, W., Ming, L., Gang, Y., Jiancheng, L., Guoxing, L., 2014. Theoretical and experimental research on design of non-resonant gear transformer. In: Proceedings ASME 2014 International Mechanical Engineering Congress and Exposition, November 14-20, 2014, Montreal, Quebec, Canada. Vibration, Acoustics and Wave Propagation, vol. 13. American Society of Mechanical Engineers, New York. https://doi.org/10.1115/IMECE2014.

Shoh, A., 1970. A new look at ultrasonic metal drilling. SAMPE Quart. 1, 11–16.

Sofuoğlu, M.A., Çakır, F.H., Gürgen, S., Orak, S., Kuşhan, M.C., 2018. Experimental investigation of machining characteristics and chatter stability for Hastelloy-x with ultrasonic and hot turning. Int. J. Adv. Manuf. Technol. 95 (1–4), 83–97. https://doi.org/10.1007/s00170-017-1153-9.

Soleimanimehr, H., Nategh, M.J., Amini, S., 2009. Modeling of surface roughness in vibration cutting by artificial neural network. World Acad. Sci. Eng. Technol. 52, 386–391.

Sun, S., Tang, J., Shao, W., Chen, C., Liu, Y., 2019. Research on the matching relationship between ultrasonic-assisted grinding parameters and workpiece roughness. Int. J. Adv. Manuf. Technol. 102 (1–4), 487–496.

Suzuki, N., Hino, R., Shamoto, E., 2007. Development of 3 DOF ultrasonic elliptical vibration system for elliptical vibration cutting. In: ASPE Proceedings. Vibration Assisted Machining Technology, Chapel Hill, NC.

Takeyama, H., Kato, S., 1991. Burrless drilling by means of ultrasonic vibration. CIRP Ann. (Switzerland) 40 (1), 83–86.

Tawakoli, T., Rasifard, A., Azarhoushang, B., 2008. Dressing of CBN grinding wheels with ultrasonic assistance. Int. J. Mech. Manuf. Syst. 1 (4/2008), 321–331.

Tawakoli, T., Azarhoushang, B., Rabiev, M., 2009. Ultrasonic assisted dry grinding of 42CrMo4. Int. J. Adv. Manuf. Technol. 42 (9–10), 883–891.

Thomas, P.N.H., Babitsky, V.I., 2007. Experiments and simulations on ultrasonically assisted drilling. J. Sound Vib. 308 (3–5), 815–830.

Tsao, C.-c., Kuo, K.-l., 2012. Ultrasonic-assisted vibration tapping using taps with different coatings. Trans. Nonferr. Metals Soc. China 22 (Suppl. 3), 768. https://doi.org/10.1016/S1003-6326(12)61801-9.

Tsujino, J., Suzuki, R., Takeuchi, M., 1996a. Load characteristics of ultrasonic rotary motor using a longitudinal-torsional vibration converter with diagonal slits: large torque ultrasonic motor. Ultrasonics 34 (2–5), 265–269. Proc. of Ultrasonics International 1995.

Tsujino, J., Suzuki, R., Yasojima, H., Takeuchi, M., 1996b. Load characteristics of ultrasonic rotary motor using a longitudinal-torsional vibration converter. In: Proc. of 1996 IEEE Ultrasonics Symposium. vol 1, pp. 377–382.

Twiefel, J., Klubal, M., Paiz, C., Mojrzisch, S., Krüger, H., 2008. Digital signal processing for an adaptive phase-locked loop controller. Proc. SPIE 6926. https://doi.org/10.1117/12.776091.

Unyanin, A., Khusainov, A., 2017. The ultrasonic grinding process temperature field study. MATEC Web Conf., 129. International Conference on Modern Trends in Manufacturing Technology and Equipment, ICMTMTE (2017).

Van der Pol, B., 1927. Forced oscillations in a circuit with non-linear resistance. Philosophical Magazine Series 7 3 (13), 65–80.

Verma, G.C., Pandey, P.M., Dixit, U.S., 2018. Modeling of static machining force in axial ultrasonic-vibration assisted milling considering acoustic softening. Int. J. Mech. Sci. 136, 1–16. https://doi.org/10.1016/j.ijmecsci.2017.11.048.

Voronin, A.A., Markov, A.I., Shcherbak, M.A., 1961. The effect on cutting of ultrasonic vibration in sharpening of tools. Mach. Tool. (USSR) 32, 15–17.

Wang, P., Wang, D., 2019. Study on ultrasonic-assisted drilling of Ti6Al4V using 3-flute drill in the finite element simulation. Proc. Inst. Mech. Eng. C J. Mech. Eng. Sci. https://doi.org/10.1177/0954406219893001.

Wang, L.-J., Zhao, J., 1987. Influence on surface roughness in turning with ultrasonic vibration tool. Int. J. Mach. Tools Manuf. 27 (2), 181–190.

Wang, L.-J., Zhao, J., Tan, Q.-C., 1987. Kinematics of ultrasonic vibration-cutting and a study of resulting surface quality. Acta Armamentarii 3, 24–31.

Wdowik, R., Nazarko, P., Porzycki, J., 2015. Application of eddy current sensor system and LDV device for ultrasonic vibrations measurements. In: Advances in Intelligent Systems and Computing. vol. 317, pp. 407–415.

Wdowik, R., Porzycki, J., Magdziak, M., 2016. Measurements of surface texture parameters after ultrasonic assisted and conventional grinding of ZrO_2 based ceramic material characterized by different states of sintering. Procedia CIRP 62, 293–298.

Wei, L., Wang, D., 2019. Comparative study on drilling effect between conventional drilling and ultrasonic-assisted drilling of Ti-6Al-4V/

Al2024-T351 laminated material. Int. J. Adv. Manuf. Technol. 103 (1–4), 141–152. https://doi.org/10.1007/s00170-019-03507-6.

Wei, L., Wang, D., 2020. Effect of ultrasound-assisted vibration on Ti-6Al-4V/Al2024-T351 laminated material processing with geometric tools. Int. J. Adv. Manuf. Technol. 106 (1–2), 219–232. https://doi.org/10.1007/s00170-019-04637-7.

Wen, Y., Tang, J., Zhou, W., Zhu, C., 2019. Study on contact performance of ultrasonic-assisted grinding surface. Ultrasonics 91, 193–200.

Wu, Y., Yokoyama, S., Sato, T., Lin, W., Tachibana, T., 2009. Development of a new rotary ultrasonic spindle for precision ultrasonically assisted grinding. Int. J. Mach. Tools Manuf. 12–13, 933–938.

Xiang, D., Zhi, X., Yue, G., Gao, G., Zhao, B., 2011a. Study on surface quality of Al/SiCp composites with ultrasonic vibration high speed milling. Appl. Mech. Mater. 42, 363–366.

Xiang, D.H., Yue, G.X., Zhi, X.T., Gao, G.F., Zhao, B., 2011b. Study on cutting force and tool wear of high volume SiC/Al MMCs with ultrasonic vibration high speed milling. Key Eng. Mater. 455, 264–268.

Xiangyu, Z., Zhenghui, L., He, S., Deyuan, Z., 2018. Surface quality and residual stress study of high-speed ultrasonic vibration turning Ti-6Al-4V alloys. Procedia CIRP 71, 79–82. https://doi.org/10.1016/j.procir.2018.05.075.

Xu, X., Mo, Y., Liu, C., Zhao, B., 2009. Drilling force of SiC particle reinforced aluminum-matrix composites with ultrasonic vibration. Key Eng. Mater. 416, 243–247.

Xu, X.X., Zhang, X.H., Liu, C.S., Zhao, B., 2011. Drilling characteristics of SiC particle reinforced aluminum-matrix composites with ultrasonic vibration. Key Eng. Mater. 455, 302–306.

Yagishita, H., 2007. Effect of ultrasonic torsional mode vibration cutting on drilling in CFRP laminates. In: ASPE Proceedings. Vibration Assisted Machining Technology, Chapel Hill, NC.

Yang, Y., Lin, B., 2010. Situations and development trends of ultrasonic machining tool and ultrasonic machining technology. Appl. Mech. Mater. 37–38, 1199–1205.

Ye, L., Zhu, X., Wang, L., Guo, C., 2018. Study on characteristics of single cavitation bubble considering condensation and evaporation of kerosene steam under ultrasonic vibration honing. Ultrason.– Sonochem. Part A 40, 988–994. https://doi.org/10.1016/j.ultsonch.2017.09.013.

Ying, N., Feng, J., Bo, Z., Dong, W., 2017. Multiobjective optimization of processing parameters in longitudinal-torsion ultrasonic assisted milling of Ti-6Al-4V. Int. J. Adv. Manuf. Technol. 93 (9–12), 4345–4356. https://doi.org/10.1007/s00170-017-0871-3.

Ying, N., Feng, J., Bo, Z., 2020. A novel 3d finite element simulation method for longitudinal-torsional ultrasonic-assisted milling. Int. J. Adv. Manuf. Technol. 106 (1–2), 385–400. https://doi.org/10.1007/s00170-019-04636-83.

Zhang, Z., Babitsky, V.I., 2011. Finite element modeling of micro-drill and experiments on high speed ultrasonically assisted micro-drilling. J. Sound Vib. 330 (10), 2124–2137.

Zhang, P., Miller, M., 2007. Wheel loading reduction with vibration assisted grinding. In: ASPE Proceedings. Vibration Assisted Machining Technology, Chapel Hill, NC.

Zhang, D., Wang, L., 1998. Investigation of chip in vibration drilling. Int. J. Mach. Tool Manu 38 (3), 165–176.

Zhang, J., Wang, D., 2019. Investigations of tangential ultrasonic vibration turning of Ti6Al4V using finite element method. Int. J. Mater. Form. 12 (2), 257–267. https://doi.org/10.1007/s12289-018-1402-y.

Zhang, B., Yang, F., Wang, J., 2003. Fundamental aspects in vibration-assisted tapping. J. Mater. Process. Technol. 132, 345–352.

Zhang, J., et al., 2004. Study on dry reaming technology with ultrasonic wave excitation (of the) reamer bit. Electromachining & Mould (4), 27–29.

Zhang, Y., Hu, H., Lin, J., 2007. Study of key technology for ultrasonic honing acoustics system. J. Vib. Eng. 20 (5), 538–542.

Zhang, J., Li, T., Zhang, Y., 2012. Study on reaming high-precision thin hole in hardened steel by ultrasonic vibration reamer. Adv. Mater. Res. 503–504, 396–399.

Zhang, Y.D., Zhong, Q.M., 2014. Selected, peer reviewed papers from the 2nd international conference on Machinery, Materials Science and Energy Engineering (ICMMSEE 2014), September 20-21, 2014, Changsha, China. In: The Study of Resonant Frequency of Horn and Circular Tool of Ultrasonic Milling System. Appl. Mech. Mat., vol. 86. Elsevier B.V. pp. 628–283.

Zhang, X., Zhu, X., Cheng, L., 2016. The influence study of ultrasonic honing parameters to workpiece surface temperature. Matec Web Conf. 45. https://doi.org/10.1051/matecconf/20164504008.

Zhang, Y., Zhao, B., Wang, Y., Chen, F., 2017. Effect of machining parameters on the stability of separated and unseparated ultrasonic vibration of feed direction assisted milling. J. Mech. Sci. Technol. 31 (2), 851–858. https://doi.org/10.1007/s12206-017-0137-x.

Zhao, H.B., Shen, X.H., 2014. Selected peer reviewed papers from the 4th international conference on advanced design and manufacturing engineering, ADME 2014, July 26-27, 2014, Hangzhou, China. In: The Dynamic Characteristic Analysis of Vibration System for Longitudinal and Torsional Ultrasonic Vibration Honing. Appl. Mech. Mat., vol. 633-634. TTP, Pfäffikon, Switzerland, pp. 1289–1293. https://doi.org/10.4028/www.scientific.net/AMM.633-634.1289.

Zhao, B., Bie, W., Wang, X., Chen, F., Chang, B., 2019a. Design and experimental investigation on longitudinal-torsional composite horn considering the incident angle of ultrasonic wave. Int. J. Adv. Manuf. Technol. 105, 1–17. https://doi.org/10.1007/s00170-019-04220-0.

Zhao, B., Bie, W., Wang, X., Chen, F., Wang, Y., Chang, B., 2019b. The effects of thermo-mechanical load on the vibrational characteristics of ultrasonic vibration system. Ultrasonics 98, 7–14. https://doi.org/10.1016/j.ultras.2019.05.005.

Zhao, B., Chang, B., Yuan, L., Li, P., 2020. Influence of force load on the stability of ultrasonic longitudinal-torsional composite drilling system. Int. J. Adv. Manuf. Technol. 106, 891–905.

Zheng, J., Xu, J., 2008. Basic experimental research on the NC-contour evolution ultrasonic assisted grinding ceramic blade surface. Key Eng. Mater. 359–360, 369–373.

Zheng, J., Xu, J., Liu, C., 2009. Studies on the grinding properties of ultrasonic assisted creep feed grinding using grinding wheel with small diameter. Key Eng. Mater. 416, 23–27.

Zhou, M., Eow, Y.T., Ngoi, B.K.A., Lim, E.N., 2003. Vibration-assisted precision machining of steel with PCD tools. Mater. Manuf. Process. 18 (5), 825–834.

Zhou, W., Tang, J., Shao, W., 2020. Modelling of surface texture and parameters matching considering the interaction of multiple rotation cycles in ultrasonic assisted grinding. Int. J. Mech. Sci. 166, 105246. https://doi.org/10.1016/j.ijmecsci.2019.105246.

Zhu, X.S., Xu, K.W., Zhao, B., Ma, D.Z., 2002. Experimental and theoretical research on 'local resonance' in an ultrasonic honing system. J. Mater. Proc. Technol. (Netherlands) 129 (1–3), 207–211.

Zhustarev, E.N., Zakharov, V.I., Matveyev, V.Y., Freydkin, M.Y., 1960. 'The cutting of metals with the application of ultrasonics,' in the collection. In: The Application of Ultrasonics in Engineering Technology, TsINTI, pp. 235–243.

Zou, L., Huang, Y., Zhou, M., Duan, L., 2017. Investigation on diamond tool wear in ultrasonic vibration-assisted turning die steels. Mater. Manuf. Process. 32 (13), 1505–1511. https://doi.org/10.1080/10426914.2017.1291958.

Chapter 16

Ultrasonic motors

K. Nakamura
Institute of Innovative Research, Tokyo Institute of Technology, Tokyo, Japan

16.1 Introduction

Actuators with a high power-to-weight ratio are necessary in robotics and other motion control systems. Fluidic devices such as air cylinder and oil pressure actuators have been widely used in various fields, although the pipe work and pressure generators increase the weight and volume of the total system. The performance of electromagnetic motors has improved greatly over the past decade because of the introduction of novel materials and numerical simulation techniques. The possibilities of new actuators have been explored by many researchers with a view toward further improving performance. Ultrasonic motors in which rotary or linear motion can be obtained from piezoelectric vibrations at ultrasonic frequency by means of friction have been found to be effective actuators because of their inherent high energy density. Historically, several concepts for actuators driven by piezoelectric vibrations were identified in the 1970s. However, practical proposals for the working principles that led to modern developments were largely made during the 1980s. Details of the history are reviewed in the book by Ueha and Tomikawa (1993) and other literature.

Ultrasonic motors have several unique features, such as high torque/thrust, quick response, position holding without use of an external brake, and very low emission of magnetic noise. Because piezoelectric ceramics generate a large force in relation to area, the output force from the motor is high. Low speed and high torque characteristics can therefore be realized in ultrasonic motors without the use of reduction gear. The elimination of gears enables quiet operation and high rigidity. The use of friction creates a holding force without an external braking system, thereby reducing energy consumption. These features make ultrasonic motors suitable as actuators in precise positioning systems. Low emission of electromagnetic flux may be an important advantage and is useful in applications that need to remain unaffected by a magnetic field.

Another vibration component is used to generate one-directional rotary or linear actuation via friction from vibratory motion. The two vibrations, which are essential in ultrasonic motors, should be orthogonal to each other both in time and space. This is usually explained by an elliptical motion as the fundamental principle of ultrasonic motors; this motion can be achieved by a combination of two standing waves or a traveling wave. The basic concepts of the standing-wave ultrasonic motor and the traveling-wave ultrasonic motor are explained in this chapter.

16.2 Traveling-wave ultrasonic motors

As described in the previous section, the production of surface elliptic motion is a common operating principle in ultrasonic motors. This section introduces a typical method of utilizing elliptic motion in a traveling-wave motor. If traveling waves of any kind of elastic vibration propagate along a straight bar or the circumference of a ring/disk, particle motion at the surface generally becomes elliptic. Techniques for constructing traveling-wave ultrasonic motors in both linear and rotary motion are presented below.

16.2.1 Principle of the traveling-wave linear ultrasonic motor

Traveling waves are excited along a bar to realize a linear motor. Figure 16.1 illustrates a basic setup for a flexural-wave linear motor (Kuribayashi et al., 1985). Two transducers of the same design are attached to ends of the bar at right angles: one is driven by an electrical source to excite flexural waves and the other is used to terminate the elastic waves. The absorbed mechanical energy is transformed to electrical energy through piezoelectricity and is consumed by a resister connected at the electrical terminal of the transducer. An inductor is often used in parallel to cancel the capacitance of the transducer. A Langevin-type transducer with a horn is used to obtain the necessary vibration amplitude and mechanical impedance matching the bar.

When a flexural traveling wave is propagated along the bar, each point on the surface displays elliptical motion, as illustrated in Figure 16.2. It should be noted that the shape of the surface deformation deviates from a pure sinusoidal curve because both vertical and horizontal components exist. The rotation direction of the elliptical motion is opposite the wave propagation in the case of flexural

Power Ultrasonics. https://doi.org/10.1016/B978-0-12-820254-8.00022-1
Copyright © 2023 Elsevier Ltd. All rights reserved.

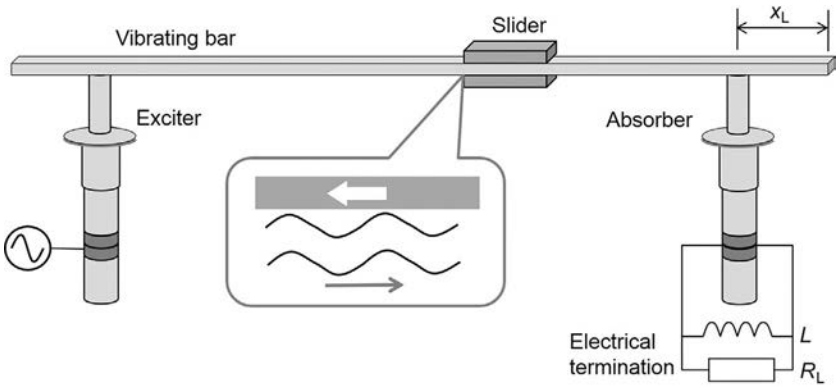


FIGURE 16.1 Traveling-wave linear motor.

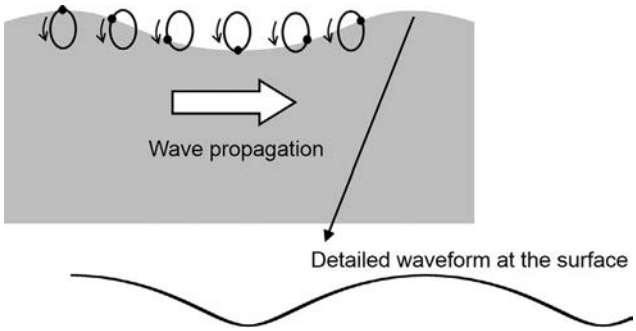


FIGURE 16.2 Particle motion on the surface of an elastic body transmitting traveling wave. The actual surface shape for a certain instance is not sinusoidal.

vibration. Thus, if an object is pressed to the vibrating surface, it experiences a thrust force from the elliptical motion by means of friction. The object moves from the sink of the wave to its source. The direction of the linear motion may be altered by exchanging the source and the sink. In designing a traveling-wave linear motor, the electrical load resistor R_L and the tail length x_L of the bar should be chosen to suppress standing waves. The excitation conditions of the traveling wave along a bar were discussed in detail by Kuribayashi et al. (1985).

A slider consists of two friction plates that sandwich the vibrating bar with the required pressure (preload), which is applied by the use of springs. The preload should be 5–10 times higher than the necessary thrust force because the friction coefficient ranges from 0.1 to 0.2 in ordinary friction materials. Experiments have shown that only 2.5% of the mechanical energy transmitted in the bar was obtained as the motor output, while the rest of the power injected into the source transducer was received by the sink transducer. The energy absorbed by the sink when driving the source should therefore be reused to obtain higher efficiency in this type of motor.

16.2.2 Variations of the traveling-wave linear ultrasonic motor

Although no traveling-wave linear motor has yet been put into commercial use, several promising trials are being carried out. Ridge mode vibration has been studied for smaller traveling-wave linear motors (Tominaga et al., 2005). Figure 16.3 shows a basic configuration of a prototype linear motor in which the ridge is formed by machining an aluminum block. Two Langevin transducers are attached at both ends of the ridge, as in the original traveling-wave linear motor. A ridge fabricated on a substrate works as a waveguide of elastic vibrations, where the vibration energy is confined in the ridge component. This type of configuration is therefore suitable for micro-linear motors integrated with other electronic and micromechanical components. Fundamental or higher mode of the ridge vibration may be applicable for motor operation.

A traveling-wave ultrasonic motor uses surface acoustic waves (SAWs) at very high frequency in tens of megahertz (Kurosawa et al., 1996), whereas the driving frequency of conventional ultrasonic motors using bulk vibrations ranges from 25 to 100 kHz. An interdigital transducer printed on a piezoelectric substrate is used to excite SAWs, as in filter devices used for communication. A special slider design is required because the vibration displacement of SAWs

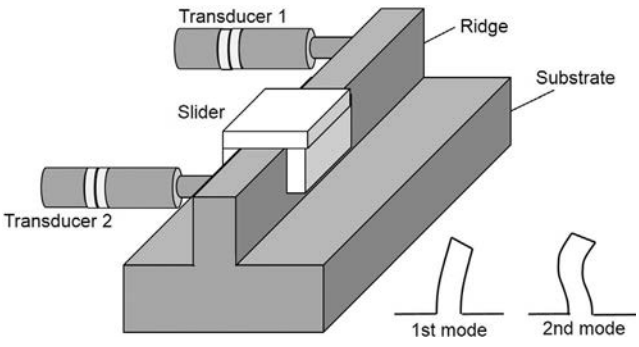


FIGURE 16.3 Ridge mode traveling-wave linear motor.

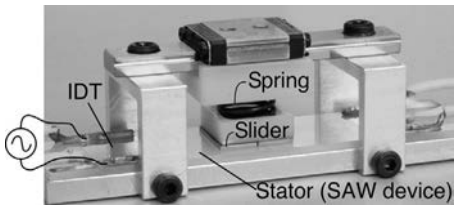


FIGURE 16.4 Setup of surface acoustic wave ultrasonic motor.

is very small because of the high frequency. A high power output has been successfully reported using a lithium nitrate substrate and a silicone slider with small dots on the surface. Figure 16.4 is a photo of the setup of a SAW motor.

16.2.3 Traveling-wave rotary motors: Ring or disk shape

The following case is presented for consideration. A standing wave of flexural vibration of the *n*th mode is excited along an elastic ring. The ring is usually composed of a metal body and a thin piezoelectric ceramic disk bonded to the bottom of the body, as shown in Figure 16.5. A rotor disk with an output shaft is attached to the vibrating body. The out-of-plane displacement of a standing wave can be expressed as

$$u_C(\theta,t) = A\ \cos\ n\theta\ \cos\ \omega t \tag{16.1}$$

Here, θ denotes the angular position, and ω is the angular frequency of the vibration. Integer number n shows the order of the vibration mode in the circumferential direction. Another standing wave of the same order but shifted by 90° both in space and time is written as

$$u_S(\theta,t) = A\ \sin\ n\theta\ \sin\ \omega t \tag{16.2}$$

The superposition of these two degenerated modes then produces a progressive wave in a circumferential direction, according to the mathematical formula:

$$\begin{aligned} u_Z(\theta,t) &= A\ \cos\ n\theta\ \cos\ \omega t + A\ \sin\ n\theta\ \sin\ \omega t \\ &= A\ \cos(n\theta - \omega t) \end{aligned} \tag{16.3}$$

The electrode on the outer surface of the piezoelectric ceramic ring is divided into an appropriate number of sections to excite the two standing waves, as illustrated in Figure 16.6. A two-phase electrical power source

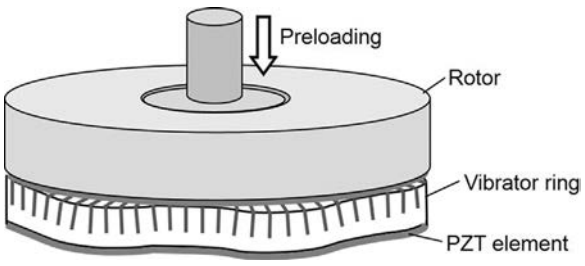


FIGURE 16.5 Basic configuration of traveling-wave rotary motor.

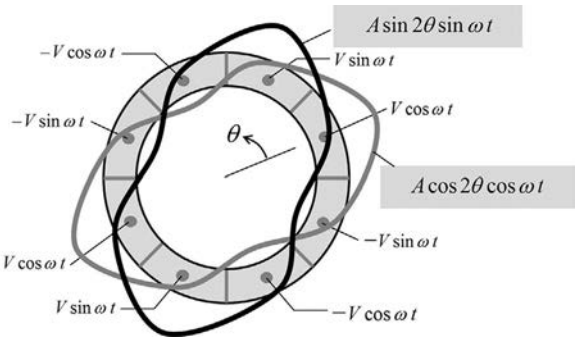


FIGURE 16.6 Voltage application for generating traveling waves along a ring vibrator.

($V\cos\omega t$, $V\sin\omega t$) or a four-phase source ($V\cos\omega t$, $V\sin\omega t$, $-V\cos\omega t$, $-V\sin\omega t$) is used as a driver. Figure 16.6 shows an example of the second-order ($n=2$) vibration and the four-phase balanced feeding. In the case of unbalanced two-phase excitation, a different electrode pattern with a ground port is adapted.

Considering the geometry shown in Figure 16.7, the in-plane (horizontal) vibration displacement $u_\theta(\theta, t)$ may be expressed by the gradient of the out-of-plane displacement $u_Z(\theta, t)$:

$$\begin{aligned} u_\theta(\theta,t) &= -\frac{b}{2}\frac{\mathrm{d}u_Z(\theta,t)}{\mathrm{d}x} - \frac{b}{2}\frac{1}{R}\frac{\mathrm{d}u_Z(\theta,t)}{\mathrm{d}\theta} \\ &= \frac{bnA}{2R}\sin(n\theta - \omega t) \end{aligned} \tag{16.4}$$

as a thin beam approximation for flexural waves. Here, the thickness of the body is b and the radius of the vibrator is R. It may be understood from the phase relation between Eqs. (16.3) and (16.4) that every point on the surface has elliptical motion. The rotational direction of the elliptical motion depends on the nature of the vibration mode. The shape of the elliptic motion and the ratio of the in-plane component to the out-of-plane component are determined by the thickness and radius of the body and the mode order. The rotational speed is proportional to the in-plane vibration component, whereas the contact between the vibrator surface and the rotor is controlled by the out-of-plane component. The design of the shape of the elliptical motion is

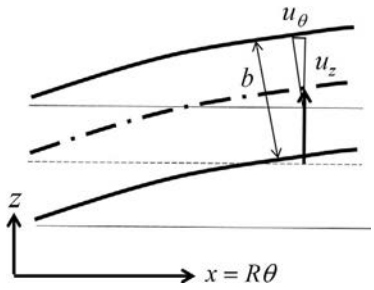


FIGURE 16.7 Out-of-plane and in-plane displacements in flexural vibration.

important in traveling-wave ultrasonic motors. The contacting surface of the metal body is toothed to amplify the in-plane vibration amplitude. This toothed structure also acts as a mechanical transformer for improved compatibility between the transducer and the motor load. Both the in-plane and out-of-plane displacement amplitudes are reduced together when the voltage is lowered for slow-speed operation. Such operation may become unstable or a dead region may appear near zero in this type of motor if the out-of-plane displacement is smaller than the roughness on the contacting interface.

An annular structure with space within the body is possible in this type of ultrasonic motor. It has attracted optical engineers and has been adapted for autofocusing mechanisms in commercial cameras. This structure is more difficult to create in conventional electromagnetic motors. A disk, rather than a ring-shaped vibrator, is used in a rotary motor. A flexural mode with a nodal circle provides firm support for the disk vibrator, and no clamping position can theoretically be found in the ring vibrator. In practical application, the ring vibrator is supported using soft material or springs. The supporting mechanism should ideally be rigid in the direction of rotation for the purpose of precise positioning, but it should also be sufficiently soft to prevent the vibrations from being blocked. Designing support mechanisms to meet these two contradictory requirements is one of the key factors in the practical application of ultrasonic motors.

16.2.4 Traveling-wave rotary motors: Bar shape

A bar-shaped configuration, shown in Figure 16.8, is constructed in a bolt-clamped Langevin structure (Kurosawa et al., 1989b). A rotor is attached to the end of the bar, or alternatively, two rotors may sandwich the bar. Two pairs of bending (lead zirconate titanate (PZT)) elements are installed in the transducer, and each pair is rotated 90° to excite the two orthogonal bending modes. The PZT disk is divided into two parts by the diameter. The two halves have opposite polarization to induce a bending moment in the bar. Alternatively, PZT disks with uniform polarization may be driven by four independent electrodes using a four-phase power source. This structure is also categorized as a traveling-wave motor. As shown in Figure 16.9, two orthogonal bending vibrations of the fundamental mode are driven with a phase difference of 90°, forming an elliptical motion at the end of the bar. The rotation is driven by the elliptical motion. A small motor with a diameter around 10 mm has been used in the automatic focusing system of some cameras.

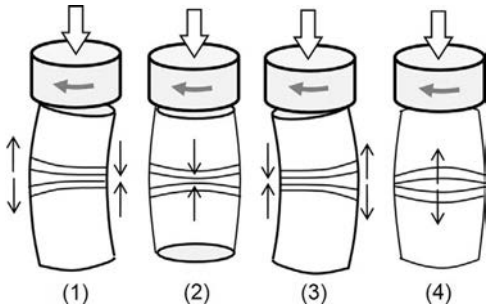


FIGURE 16.9 Operation principle of the bar-shaped rotary motor.

Much research into the manufacture of miniature or ultraminiature ultrasonic motors has been conducted based on the above principle. PZT plates are bonded on the side surface of a small rod, as illustrated in Figure 16.10a, instead of a bolt-clamped structure (Koc et al., 2002). A new deposition technique was applied to create a thin PZT film on a small metal pipe for a miniature rod-shaped motor, as shown in Figure 16.10b. The surface electrode is divided into four parts to excite two orthogonal bending vibrations (Morita et al., 1995). Micromotors with a diameter of 1–2 mm based on these structures have undergone trial demonstrations.

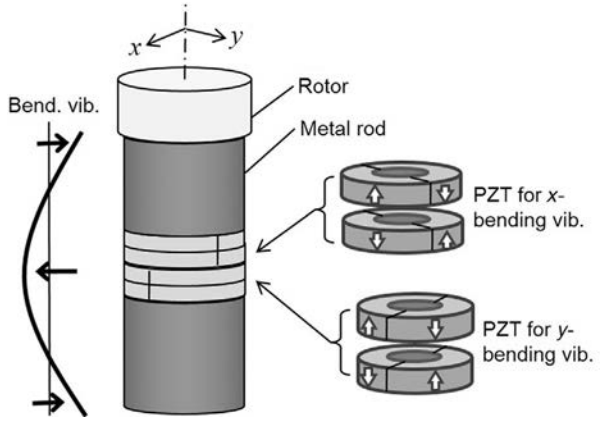


FIGURE 16.8 Configuration of the bar-shaped rotary motor based on Langevin structure.

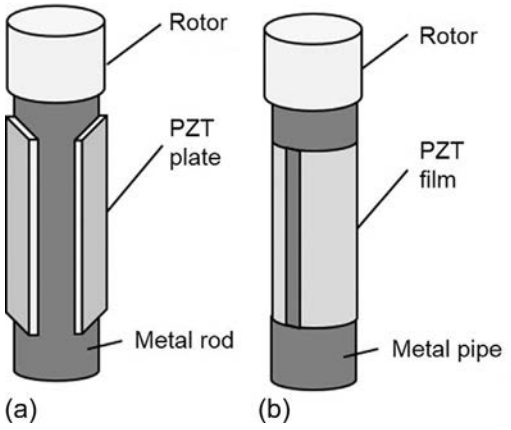


FIGURE 16.10 Miniature bar-shaped rotary motors. With bonded PZT plate (a) and thin PZT film (b).

16.3 Hybrid transducer ultrasonic motors

An alternative method of creating elliptical motion by combining two vibration modes is introduced in this section. This is referred to as the hybrid transducer ultrasonic motor. Two orthogonal vibrations with a 90° phase difference are obtained at the end of the hybrid transducer. Both linear and rotary motors can be realized using this method, and varying combinations of vibrations have been proposed. Several typical examples are introduced in the following sections.

16.3.1 Hybrid transducer linear motors

A model using multilayered piezoelectric elements is shown in Figure 16.11. A longitudinal Langevin transducer of half a wavelength is used to generate the thrust force, whereas two multilayered PZT elements are bonded to each end of the Langevin transducer to control the friction force (Kurosawa et al., 1989a). A pair of piezoelectric ceramic disks is sandwiched with a bolt between two aluminum cylinders to excite strong longitudinal vibrations. This motor is operated at the fundamental longitudinal resonance frequency of the Langevin transducer, which in this prototype is around 30 kHz. The multilayered PZT elements generate vibrations perpendicular to the longitudinal vibration of the Langevin transducer and provide sufficient friction control, even when driven at frequencies out of their resonance, which takes advantage of the multilayered structure. Voltages applied to the multilayered PZT elements are out of phase with the voltage to the Langevin transducer by −90° and 90°, respectively. Thus, the longitudinal vibration can be transformed to one-directional linear motion. When the longitudinal velocity at the end of the Langevin transducer is at its maximum, one of the multilayered elements extends to make a strong contact with the rail. At this moment, the multilayered element at the other end shrinks, thereby minimizing friction with the rail as the longitudinal vibration velocity is in the opposite direction. The moving direction is reversed by changing the phase relationship between the longitudinal vibration and the multilayered PZT elements by 180°. The maximum

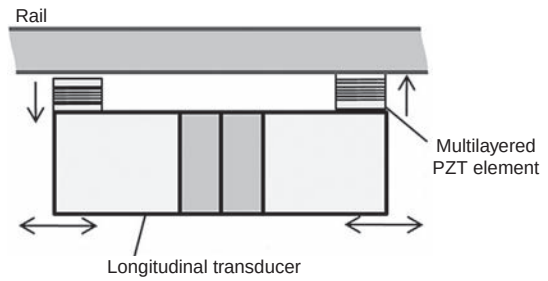


FIGURE 16.11 Linear motor working on the combination of longitudinal transducer and multilayered piezoelectric elements.

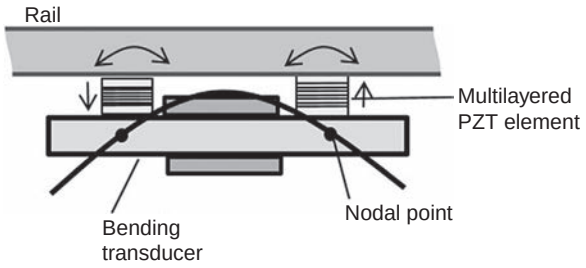


FIGURE 16.12 Linear motor using a bending vibrator and two multilayered piezoelectric elements.

thrust of 5 N and the no-load speed of 0.5 m/s were obtained using a prototype with a diameter of 20 mm.

A smaller version is illustrated in Figure 16.12; the longitudinal Langevin transducer is replaced by a bonded-type bending transducer (Kurosawa et al., 1991). Two PZT plates polarized in the thickness direction sandwich a rectangular aluminum bar. The polarization directions and the polarity of the applied voltages are chosen so that the top PZT plate extends in the lateral direction while the lower one shrinks, and vice versa. The fundamental bending vibration is excited in this way using the sandwich structure. Two multilayered piezoelectric elements are attached at the nodal points of the bending vibration on the metal bar where the rotational motion is generated. The top of the multilayered elements has horizontal vibration components because of the rotational motion at the bottom. The horizontal vibration is converted into linear motion with the help of the vertical vibration of the multilayered piezoelectric elements. The transducer should be pressed to the rail with an appropriate vertical force to create sufficient friction force at the contacting surfaces in both the motors shown in Figures 16.11 and 16.12. The transducers are held firmly at the nodal positions of the vibrations.

One of the most popular combinations of two vibrations for linear motion is the degenerated modes of the first longitudinal (L1) and the second bending (B2) vibrations. These modes are shown in a rectangular body in Figure 16.13. The ratio of the width to the length of the body is determined so that the resonance frequency of the longitudinal mode is close to that of the bending mode. The sound speed for the bending vibration is generally lower than for the longitudinal mode. It is therefore difficult to tune the resonance of the first bending mode B1 to the first longitudinal one L1. For this reason, the L1–B2 combination is often used for this type of motor. The longitudinal resonance frequency should be close to that of the bending frequency, as previously stated. However, an appropriate separation between the two resonance frequencies should be designed to avoid coupling between the two modes for the independent control of the two orthogonal vibration components. Particular care should be taken when designing the resonance frequencies of this type of motor.

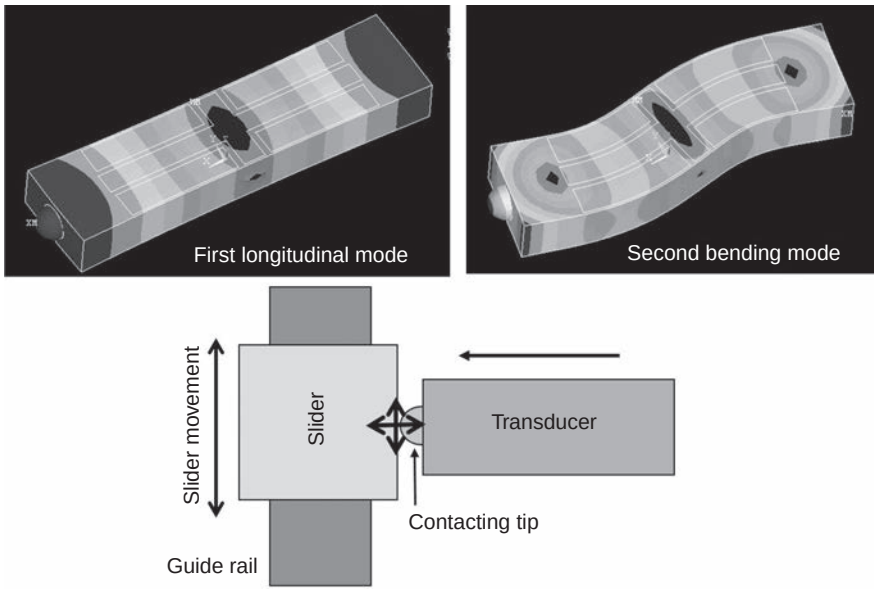


FIGURE 16.13 Linear motor using the L1–B2 mode of a rectangular PZT element.

The two vibrations can be excited in a single plate of piezoelectric material using special electrode design as proposed by Takano et al. (2011). A friction tip is attached at the end of the plate and is in contact with a rail or a slider. The bending vibration is in the horizontal direction to the rail, whereas the longitudinal vibration is in the vertical direction. The former works as the driving force and the latter modulates the preload to control the friction. Thus, an elliptical motion is formed at the contact point through the combination of the two orthogonal vibrations, which are out of phase by 90°. The amplitudes of the two vibrations should be controlled independently to regulate the motor speed. Only the vibration parallel to the moving direction should be reduced with the vertical vibration amplitude kept constant to reduce the motor speed to near zero. This is illustrated in Figure 16.14. If both vibrations are decreased simultaneously, the friction control using the vertical vibration is unable to work at the small-amplitude region because the contacting surface has finite roughness. This causes differences in controllability, as shown in Figure 16.15. The moving speed is plotted as a function of the voltages applied to the motor. The linearity is better in the case of independent control of the two vibration components, as indicated by curve 1. There also is a dead region if the two orthogonal components are changed simultaneously, as shown by curve 2. The control of ultrasonic motors is often perceived to be difficult because of the dead region in the speed-voltage characteristics. A special structure for independent control of the two components has been proposed (Takano et al., 2011), as shown in Figure 16.16.

A multilayered configuration is adapted for low-voltage operation, and two different electrode patterns are formed

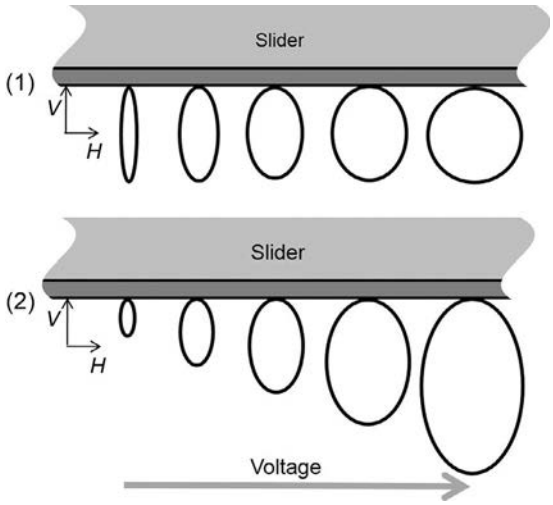


FIGURE 16.14 Control of the elliptical shape of vibration trajectory: (1) independent control of the vertical and the horizontal components; (2) simultaneous control of the out-of-plane and the in-plane components.

on each piezoelectric layer for independent excitation of the L1 and the B2 modes. One is designed for longitudinal vibration and the other for bending vibration. The shapes of the electrodes are optimized for higher efficiency of the transformation from input electrical power to the mechanical output power of the motor. The results using a 30-mm-long transducer presented in Figure 16.16 are demonstrated in Figure 16.17. A good linearity is achieved in the proposed operation method denoted above, although the slider movement is not obtained for the lower-voltage region around zero if the voltage for the longitudinal vibration is changed at the same time.

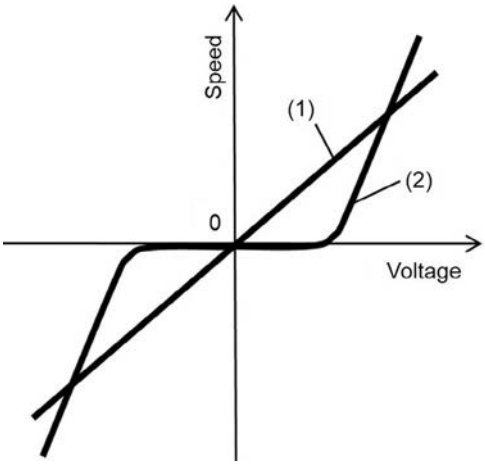


FIGURE 16.15 Motor speed as functions of the voltage: (1) independent excitation of the two modes; (2) simultaneous excitation of the two modes.

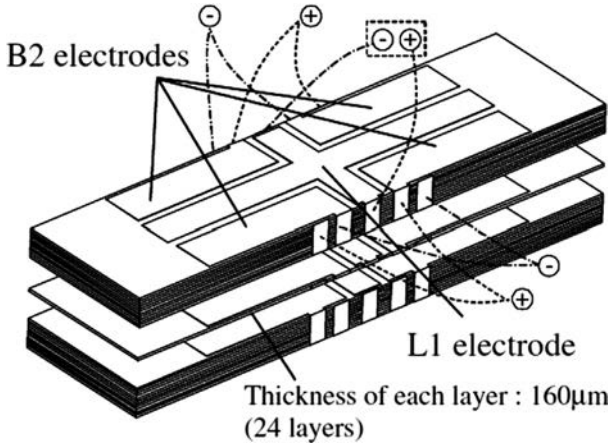


FIGURE 16.16 Electrode pattern for the 1st longitudinal and the 2nd bending modes.

A maximum thrust of 12 N and a no-load speed of 0.4 m/s were recorded with a 30-mm-long L1–B2 transducer with a resonance frequency of 52–54 kHz. The shape and materials of the contacting chip, which is bonded to the end of the transducer, are of practical importance. The material must possess good wear properties, and the contacting area should remain constant because it has a significant effect on the longitudinal resonance frequency and the preload between the transducer head and the rail. Nonlinear leaf springs are used in practical applications to maintain a constant preload over a long period of operation and abrasion of the friction material. The transducer is supported with four leaf springs, as illustrated in Figure 16.18. The springs are bonded onto the side surfaces of the transducer and connected to a rectangular frame. They exhibit nonlinear characteristics, as shown in Figure 16.19. The load-displacement curve changes with the arm length. At 0.8 mm, the generating load is unchanged at around 40 N for the displacement region from 0.6 to 0.8 mm. Because of the nonlinear characteristics of the spring, the preload remains stable over a long period.

16.3.2 High-power hybrid transducer linear motors

A more powerful linear motor may be obtained by using an all-bolt-clamped Langevin structure, as shown in Figure 16.20 (Yun et al., 2001). This motor is also based on the L1–B2 vibration modes. Two different types of PZT disks are sandwiched between aluminum blocks with a bolt. Uniformly polarized PZT disks are used for exciting the longitudinal vibration. Another set of PZT disks have a complex polarization. The disk is divided into two parts by the diameter. The polarities oppose each other, stimulating a bending force. One-half of the PZT disk extends into the thickness, while the other shrinks with the application of a uniform electric field. Using these PZT elements, the L1-mode and the B2-mode may be excited independently with a two-phase driver circuit. The longitudinal and bending modes are shown in Figure 16.21. Although the L1–B2 combination is again utilized, the roles of the longitudinal and bending modes differ from the state previously described. In this configuration, the longitudinal vibration is used as the driving force and the bending force as the friction control. The slider surface is covered with alumina

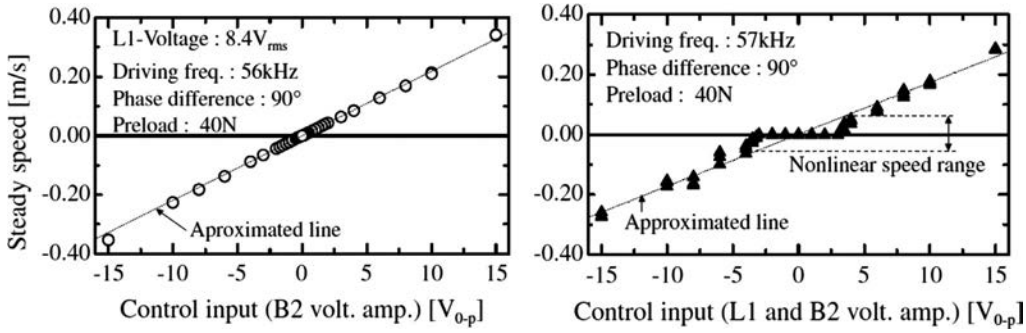


FIGURE 16.17 Slider speed: (left) only the voltage for the B2-mode is changed with that for the L1-mode constant; (right) the voltages for the L1-mode and the B2-mode are varied simultaneously.

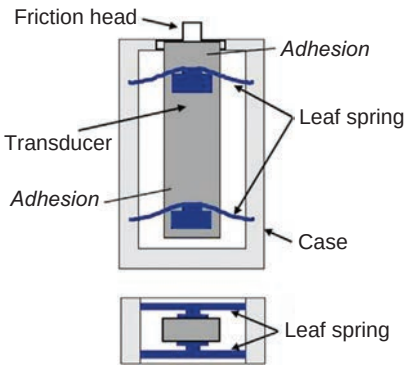


FIGURE 16.18 Holding mechanism of the L1–B2 transducer using nonlinear leaf springs.

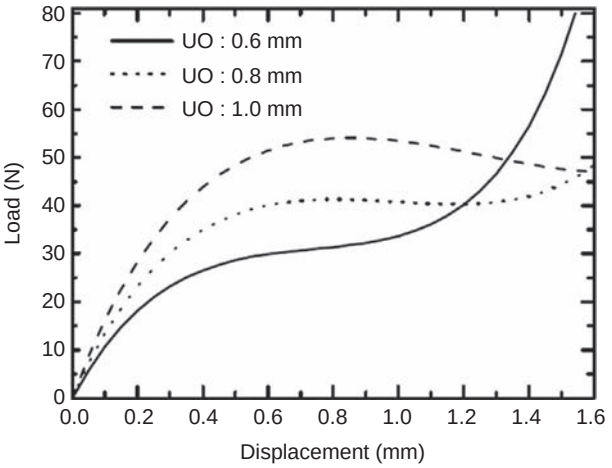


FIGURE 16.19 Load-displacement characteristics of the nonlinear leaf springs with different arm lengths UO.

ceramics as the friction material. The contacting chips attached to the both ends of the transducer are also made of alumina ceramics. The two vibrations with a phase difference of 90 or −90° result in a locus at the top of the contacting chips.

The elliptical vibrations generate driving thrust at the contact interface, as in other types of ultrasonic motors. The operation for one cycle over four phases is explained in Figure 16.22. For efficient operation, the resonance

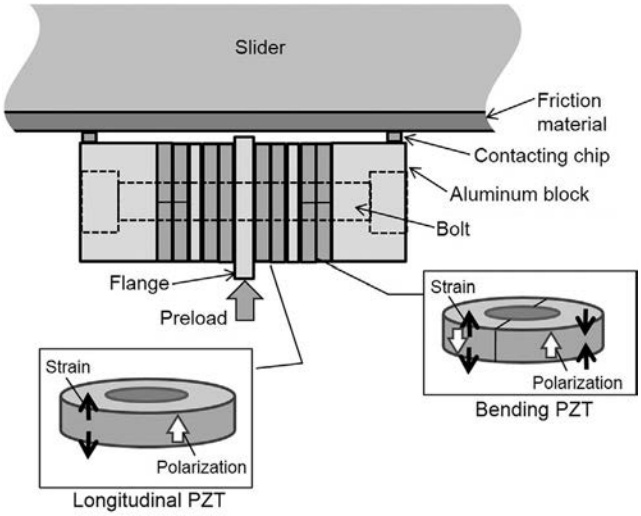


FIGURE 16.20 Configuration of the all-bolt-clamped linear motor for high output.

frequency of the L1-mode should be tuned to that of the B2-mode. Because the dependence of the longitudinal resonance frequency on the bolt length differs from that of the bending frequency, the two frequencies can be set close to each other if the appropriate bolt length is chosen, as demonstrated in Figure 16.23. In practice, the resonance frequencies were cut by shortening the bolt after assembling the transducer. The slider speed is plotted for a prototype motor as a function of the phase difference between the voltages applied for the longitudinal and bending PZT elements, as shown in Figure 16.24. As can be seen in the figure, the maximum speed is obtained at −110° and 80°, differing by 20° and 10° from the theoretically expected values of −90° and 90°, respectively, while the curve is distorted from a pure sinusoidal shape. The reason for this discrepancy can be attributed to the geometric structure of the contacting point. Although the role of the bending vibration is to generate the vertical component, it also produces the horizontal component, as shown in the displacement map in Figure 16.24. This is estimated through the numerical method; the contacting point is located away from the center line of the transducer. The horizontal component is found by

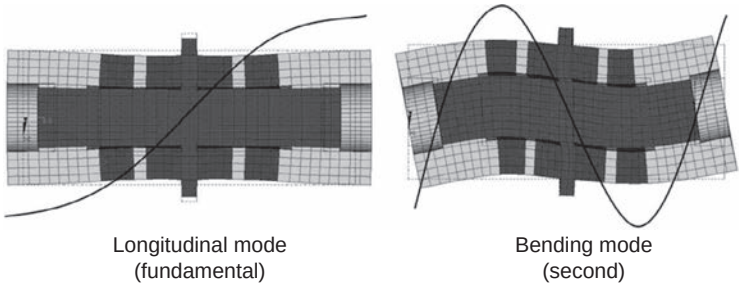


FIGURE 16.21 Vibration modes used in the linear motor of Figure 16.20.

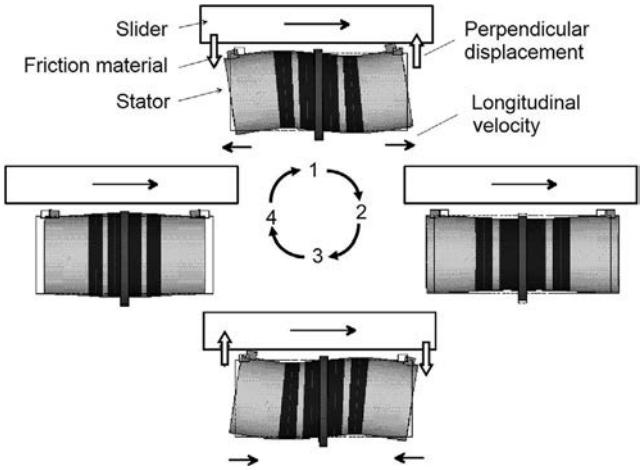


FIGURE 16.22 Operation principle of the high-power linear motor.

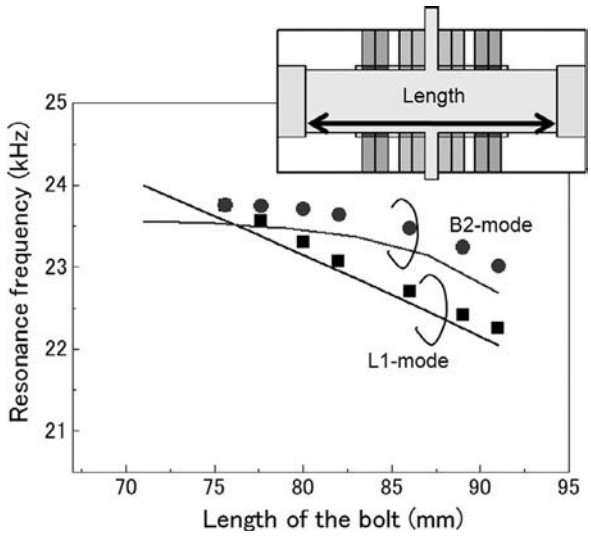


FIGURE 16.23 Adjustment of the resonance frequencies for the L1 and B2 modes by changing the bolt length. *Solid curves* indicate the numerical results while the *black circles* and *squares* represent the experimental ones.

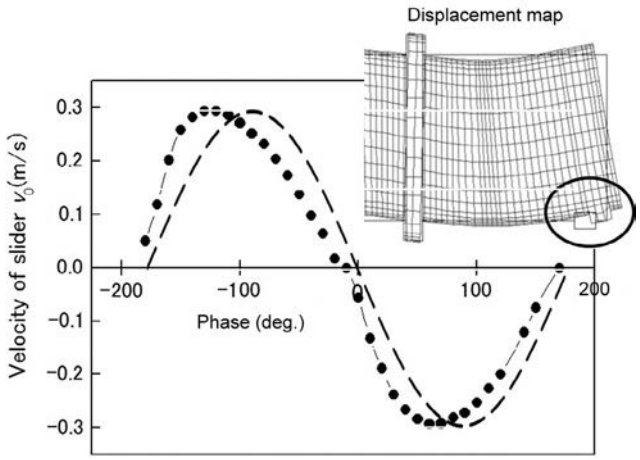


FIGURE 16.24 Slider speed as a function of the phase difference between the voltages for the longitudinal and bending electrodes. *Dotted line* represents the ideal case.

adding the longitudinal vibration and the bending vibration with a 90° phase difference. This phenomenon is similarly observed in the hybrid transducer linear motor, introduced in Section 16.3.1.

The slider speed is measured as a function of the mechanical load for different voltages applied to the longitudinal PZT elements. This is shown in Figure 16.25, where the voltage to the bending PZT elements and the preload is constant. The speed is linearly decreased with an increase in the mechanical load. The maximum friction force is calculated to be 36 N: the friction coefficient for the material used is 0.3 and the preload is 120 N. The maximum output force never exceeds the friction force given by the static preload, even when the voltage is increased to generate a larger vibratory force. This is the case in all types of friction-driven ultrasonic motors. Figure 16.26 shows the speed-load characteristics under higher preload and voltages. A maximum thrust of approximately 100 N and a no-load speed of 0.5 m/s have been assessed using a 40-mm-diameter prototype. The maximum efficiency was 20%, which is defined as the mechanical output power to the

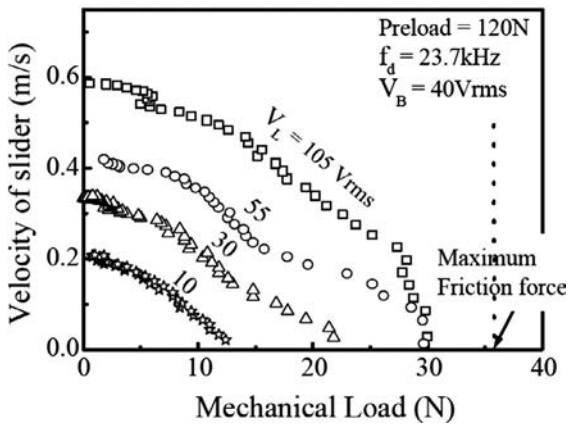


FIGURE 16.25 Speed-load characteristics for different voltages applied on the longitudinal PZT elements.

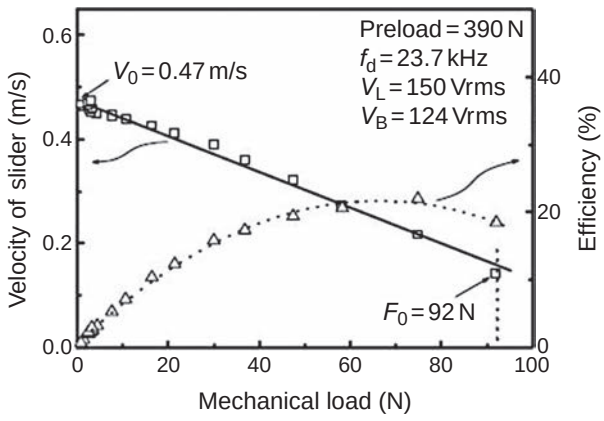


FIGURE 16.26 High-power performance of the motor.

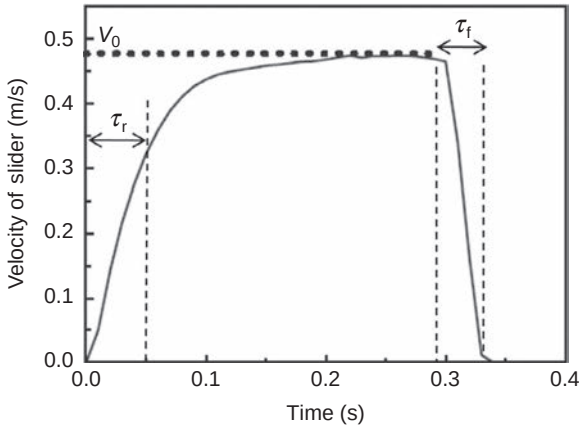


FIGURE 16.27 Start-stop transient responses of the velocity for a 10-kg slider.

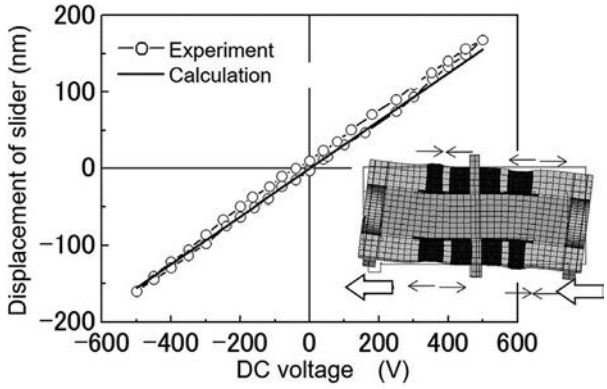


FIGURE 16.28 Fine positioning characteristics with static deformation.

electrical input power to the longitudinal PZT elements. A high static preload of around 400 N was needed to obtain a large friction force, and a greater bending vibration is needed for higher efficiency. The holding mechanism of the motor must be designed so that the transducer is firmly secured against the large external or inertial forces acting on the transducer during transient operation of the motor. Positioning performance also depends on the holding method. Figure 16.27 shows transient responses of the slider speed in the rise and fall states; the weight of the slider is 10 kg. The rise curve exhibits a first-order delay characteristic, where the time constant τ_r is simply determined by the maximum thrust F_0, the no-load speed V_0, and the weight of the slider M as:

$$\tau_r = M\frac{V_0}{F_0} \tag{16.5}$$

The fall state shows a constant negative acceleration due to the friction force. Consequently, the fall slope is simply calculated from the product of the friction coefficient μ and the static preload N divided by the slider mass:

$$\frac{V_0}{\tau_f} = \frac{\mu N}{M} \tag{16.6}$$

Here, τ_f is the fall time. These rise and fall characteristics can be used for measuring the maximum mechanical output F_0 and the friction coefficient (Nakamura et al., 1991). The settling time is short, with small residual vibrations. The excellent transient performance is effective in the high-speed control of a moving stage position. To achieve nanometer order positioning, static deformation is used by applying a high direct current (DC) voltage to the bending PZT elements in addition to the ultrasonic motor operation. Horizontal displacement of up to 200 nm is possible, as shown in Figure 16.28. After the slider has been roughly positioned through the motor operation, its position is adjusted by changing the DC voltage. A positioning error of less than 4 nm was achieved using a classical feedback control method. The error corresponded to the resolution of the linear position encoder used in the experiments.

16.3.3 Hybrid transducer rotary motors

Figure 16.29 illustrates a typical configuration for rotary motion based on the combination of longitudinal and torsional standing-wave vibrations (Kurosawa and Ueha, 1991). A set of torsional and longitudinal PZT elements are tightly clamped with a bolt between a metal head and the bottom blocks. The torsional and longitudinal vibrations can be excited independently because their respective piezoelectric units each have isolated electrodes. The torsional PZT disk is polarized in the circumferential direction to induce shearing strain with the piezoelectric constant of d_{15}, while the longitudinal disk is in the thickness direction to generate axial strain with the constant d_{33}, as shown in Figure 16.30. To obtain circular polarization, the torsional PZT disk is composed of small pieces of fan-shaped

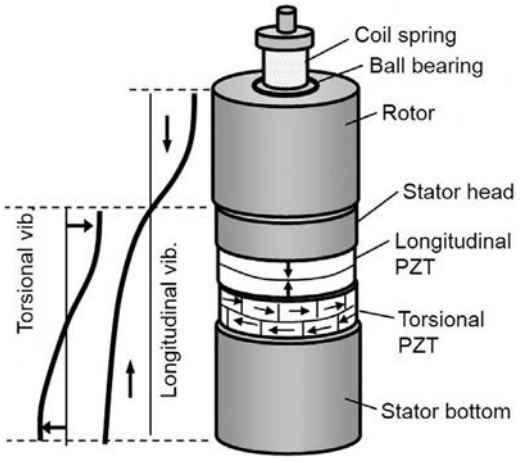


FIGURE 16.29 Structure of two-mode standing wave ultrasonic motor.

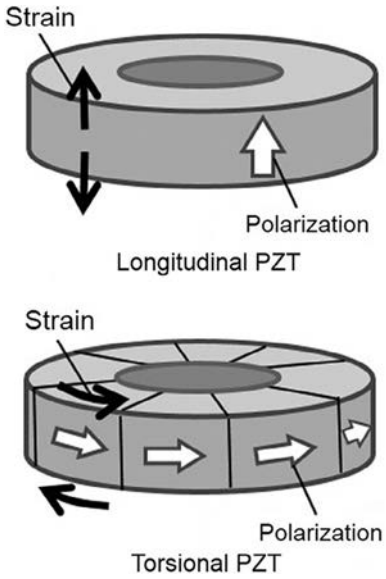


FIGURE 16.30 Piezoelectric elements used in the motor shown in Figure 16.29.

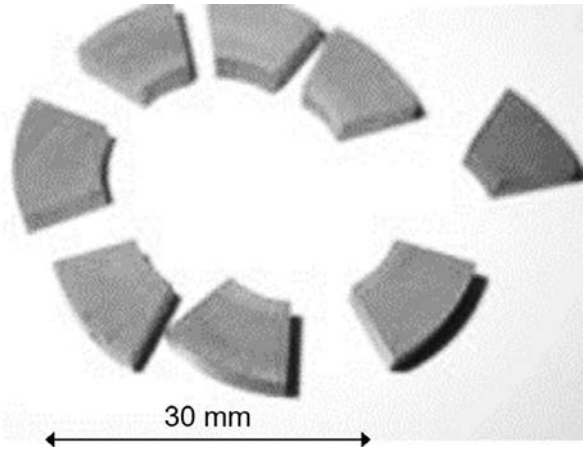


FIGURE 16.31 Photo of the fun-shaped pieces for the torsional PZT unit.

elements, a photograph of which is shown in Figure 16.31. Poling is processed to each fan-shaped element using a temporary electrode plated on both surfaces. These temporary electrodes are removed after the poling. The pieces then are bonded together into the original annular disk shape. This step makes the manufacture of a torsional PZT element more expensive than that of a longitudinal element. A rotor is held to the top surface of the transducer with a spring and a ball bearing to provide sufficient friction force and free rotation.

The operation principle is explained in Figure 16.32, where one cycle of vibrations is divided into four phases. The longitudinal and torsional vibrations are synchronized to extend the transducer in the axial direction to enable contact with the rotor when the torsional vibration velocity is at its maximum. The rotational force is transmitted to the rotor through friction force in this phase. When the torsional vibration velocity is in the direction opposite the rotation, the transducer shrinks and is removed from contact with the rotor. The torsional vibration is therefore transformed to the rotor motion. In other words, the longitudinal vibration modulates the friction force so that only a half cycle of the torsional vibration can be selectively transmitted to the rotor. If the phase relationship between the two vibrations is changed by 180°, the direction of the rotor is reversed. Rotational speed is almost proportional to the torsional vibration velocity.

A more precise consideration of the motor operation using Figure 16.33 is as follows. The waveform of the dynamic preload f_c acting vertically at the contacting surface between the transducer and the rotor is displayed at the top of the figure. The rotor is in contact with the transducer only for the angle ϕ_c. The time average of the dynamic preload should be equal to the static preload F_c applied to the rotor with the spring. The waveform shown here is conceptual; the actual waveform may be more complex in shape. The transmission of the torsional force is intermittent, but the torsional vibration waveform is almost sinusoidal because the motor is driven at the torsional resonance frequency of the transducer. The rotor speed is almost unchanged because of a large moment of inertia of the rotor. Instantaneous torque acting at the contact surface changes according to the sign of the difference in the angular velocities between the transducer, the rotor, and the friction force determined by the dynamic preload. The positive torque is generated for the period

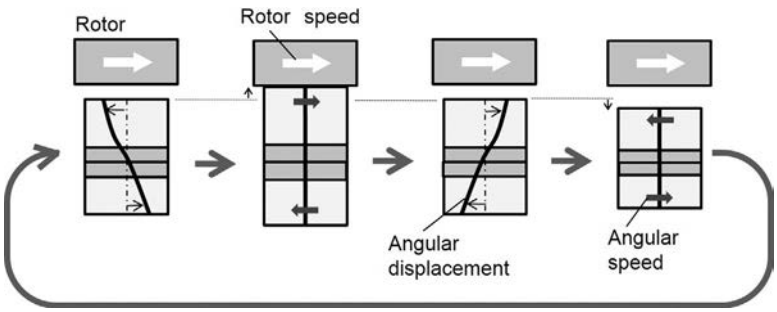


FIGURE 16.32 Operation principle of the hybrid transducer ultrasonic motor.

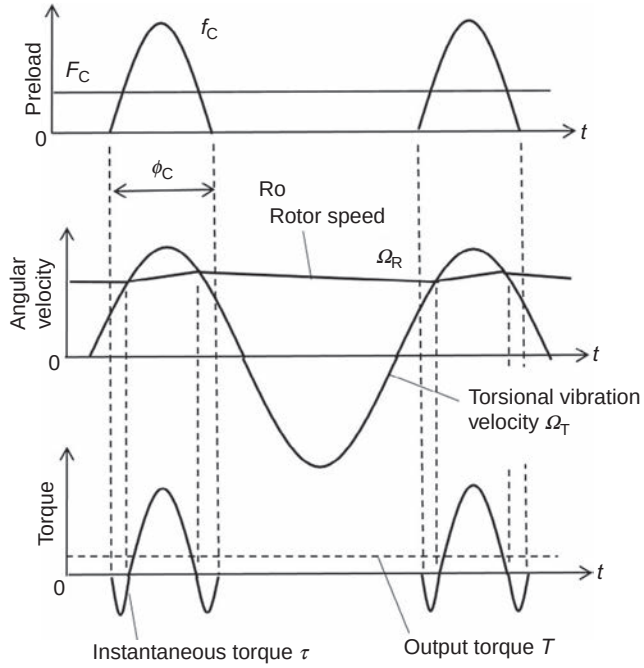


FIGURE 16.33 Waveforms for the preload, the angular velocities, and the torque.

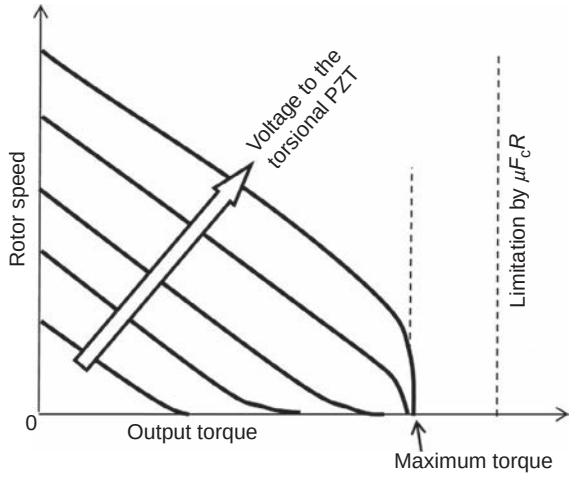


FIGURE 16.34 Typical speed-load characteristics of hybrid transducer motor.

during which the torsional vibration velocity is larger than the rotor speed, whereas negative torque is produced when the torsional vibration velocity is smaller than the rotor speed. The output torque may be obtained as an averaged value of the instantaneous torque over the period of the vibration. However, the contacting angle should ideally be less than 180° for higher efficiency. In many cases, it may be almost 360°, thus reducing efficiency to less than 50%.

The typical speed-load characteristics of the hybrid transducer ultrasonic motor are illustrated in Figure 16.34. If the voltage to the torsional PZT elements is increased with

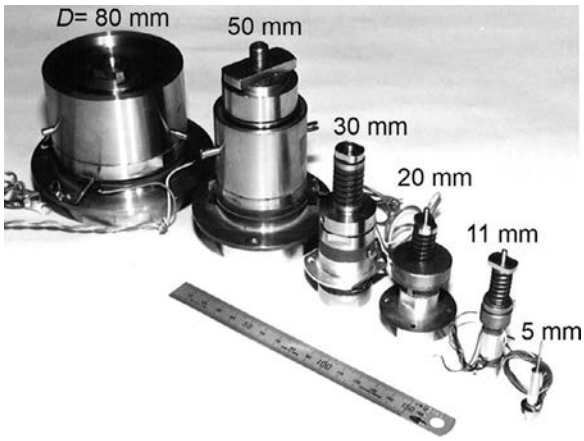


FIGURE 16.35 Lineup of hybrid transducer rotary motors from 5 to 80 mm in diameter.

constant voltage to the longitudinal PZT elements, the no-load speed increases almost linearly. The torque also increases but is saturated at a certain value. The maximum torque never exceeds the torque determined by the friction $\mu F_c R$, where μ is the friction coefficient and R is the average radius of the contacting surface. To increase the maximum torque, the static preload F_c should be increased. A stronger longitudinal vibration would also be required to balance to the larger static preload.

Figure 16.35 shows trial motors 5–80 mm in diameter; their output torques are plotted as functions of the diameter in Figure 16.36. The output torque obtained with other kinds of ultrasonic motors and electromagnetic motors is also plotted and is approximately proportional to the cube of the diameter. The hybrid transducer motor exhibits the largest torque. The bar-shaped ultrasonic traveling motor

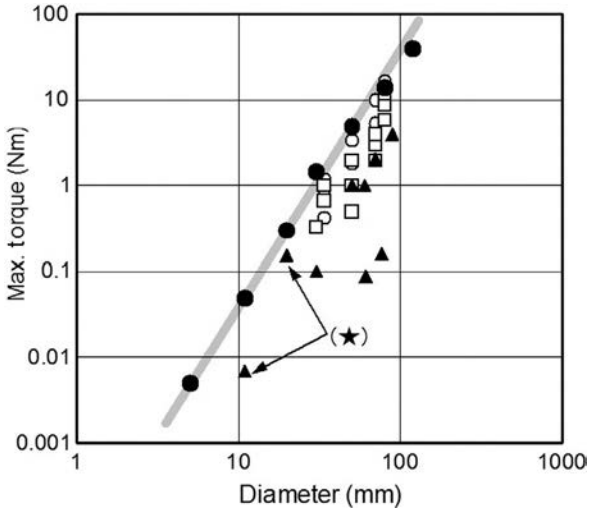


FIGURE 16.36 Maximum torque of various kinds of ultrasonic motors: *black circle*, hybrid transducer motor; *black triangle*, traveling-wave motor; *black star*, bar-shaped traveling-wave motor; *white circle*, DC servo motor; *white square*, AC servomotor.

also provides high torque with a small diameter. The torque of other traveling-wave ultrasonic motors appears to be lower than that of conventional electromagnetic motors with the same diameter because traveling-wave motors having a thin disk shape.

16.4 Performance of ultrasonic motors and driver circuits

Several trials have been conducted to simulate the operation of ultrasonic motors using electrical equivalent circuits. As an example, the transformation efficiency from the electrical input power in the torsional port of a hybrid transducer rotary motor to a mechanical output based on the electrical equivalent is demonstrated. The maximum output available with an ultrasonic motor also is discussed from the viewpoint of the potential ability of piezoelectric transducers. A basic introduction to driving electronics for ultrasonic motors is presented in the last part of this section.

16.4.1 Equivalent circuit modeling

Figure 16.37 shows an electrical equivalent circuit of a torsional transducer with the friction drive part of the rotor. The transducer is excited with a sinusoidal voltage V_T at the resonance frequency of the transducer. The dumped capacitance of the piezoelectric element is denoted by C_d, while its dielectric loss is expressed by R_d connected in parallel. The input current is branched into the piezoelectric port, which is referred to as the motional current i_m. The torsional angular vibration velocity Ω_T is proportional to the motional current with the coefficient of A_T:

$$i_m = A_T \Omega_T \tag{16.7}$$

The torque τ_0 induced in the transducer is proportional to the voltage:

$$\tau_0 = A_T V_T \tag{16.8}$$

using the same factor A_T, which is called the torque factor. Mechanical resonance is represented by the series of an inductor l_m and a capacitor c_m with a mechanical loss of r_m. The rotor is represented by a constant current source equal to the rotor angular velocity of Ω_R, which is the simplest model because the moment of inertia of the rotor is so large that the angular velocity may be almost constant. A special component representing the friction characteristics is connected with the mechanical output port parallel to the rotor. The relation between the slip and the instantaneous torque τ acting on the rotor is shown in Figure 16.38. The maximum available torque is determined by the friction force and temporally alternates in proportion to the instantaneous preload f_c. When the longitudinal vibration is strong enough, the rotor is in contact with the stator transducer for the limited duration of the phase angle ϕ_c. But if the longitudinal vibration is insufficient or the static preload is too high, the rotor will be in contact with the stator for whole period, and the preload will be modulated around the static preload, as illustrated in Figure 16.39. It is probable that the motor performance will be affected by the contact angle ϕ_c. The motor operation is simulated by numerically solving the circuit equations of the model. The waveform of the instantaneous torque is calculated for a given angular velocity of the rotor, and the output torque T is then obtained as a time average of the instantaneous torque:

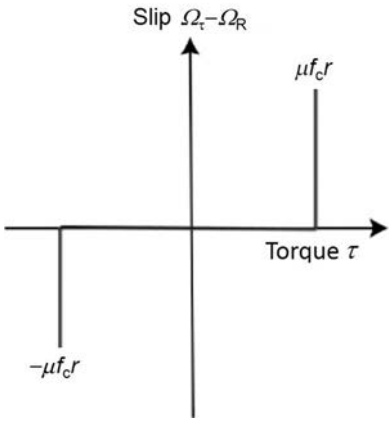


FIGURE 16.38 Friction characteristics.

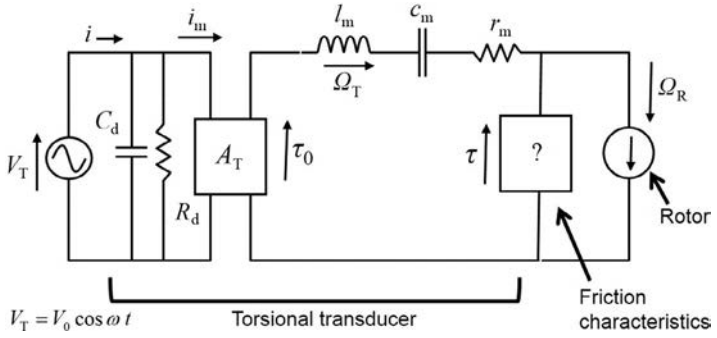


FIGURE 16.37 Equivalent circuit model of generation of the rotational motion from the torsional vibration.

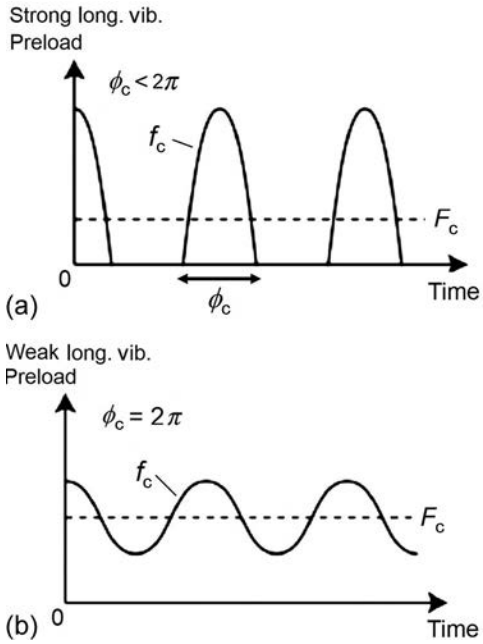


FIGURE 16.39 Dynamic preload (a) and static preload (b).

$$T = \frac{\omega}{2\pi}\int_0^{\frac{2\pi}{\omega}} \tau \, dt \tag{16.9}$$

By repeating the same calculation for the different rotation velocities, a load characteristic curve can be drawn. In the actual calculation, the friction component in the circuit can be simulated by a bidirectional Zener diode with a threshold voltage controlled by the instantaneous preload f_c. For more precise modeling, the rotor should be expressed by a large inductor representing its moment of inertia. The higher resonance should be taken into account when simulating more exact waveforms (Satonobu et al., 2002). The motor efficiency, which is defined as the ratio of the output mechanical power to the electrical input power to the torsional transducer, is summarized in Figure 16.40 as a function of the contact angle. If the contact angle is small,

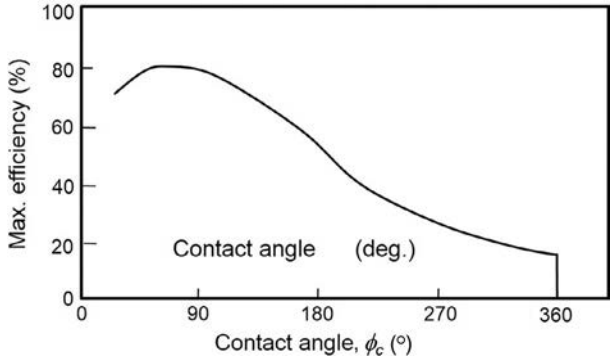


FIGURE 16.40 Maximum efficiency of the hybrid transducer ultrasonic motor as a function of the contact angle.

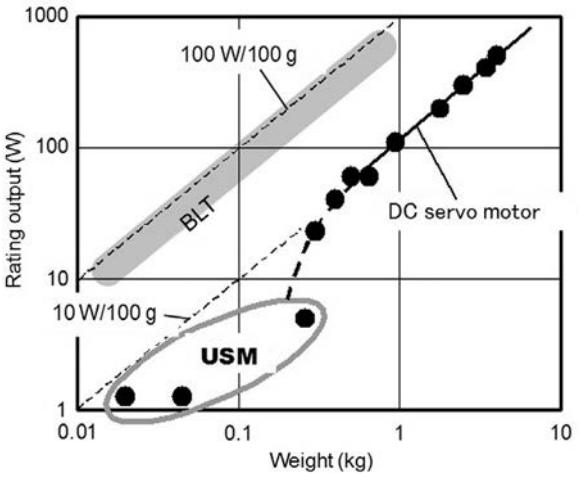


FIGURE 16.41 Mechanical output power and the weight.

the maximum efficiency may reach 80%. However, the efficiency decreases as the contact angle increases as the loss due to slip becomes higher. The maximum efficiency in prototypes of hybrid transducer rotary motors ranged from 20% to 40%. As a result, the contact angle in these prototypes was larger than 180°. If the power consumed in the longitudinal vibration is taken into account, the total efficiency becomes less. A design for efficient longitudinal systems is one of the key issues in designing hybrid transducer ultrasonic motors.

16.4.2 Discussion of motor performance

Mechanical output power plotted as a function of the weight for both commercialized traveling-wave rotary motors and DC servo motors is shown in Figure 16.41. The maximum possible input to bolt-clamped Langevin transducers is also indicated in Figure 16.17 (indicated by BLT), distributed around a line of 100 W/100 g. Output power per unit weight is constant at around 10 W/100 g for larger DC servo motors, although it decreases rapidly in smaller motors. The efficiency of conventional electromagnetic motors becomes too low for practical use when diameters are less than 10 mm. The output power and efficiency of ultrasonic motors remain moderate. This is one of the reasons why they are attractive as microactuators. However, the available power with BLT is much higher, and better performance may be expected from ultrasonic motors where sophisticated design transforms vibration to motor motion. The maximum torque is summarized against weight in Figure 16.42.

It is clear that ultrasonic motors provide higher torque than DC servo motors with the same weight. Because the working principle of the ultrasonic motor means that motor speed never exceeds vibration velocity, the vibration amplitude available with a transducer determines the

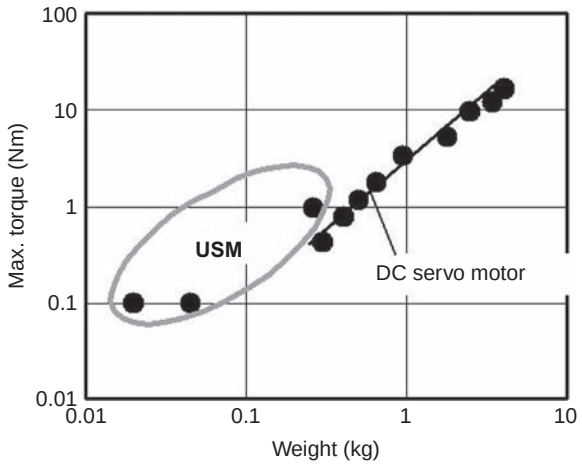


FIGURE 16.42 Maximum torque and the weight of motor.

maximum motor speed. Assuming the fatigue limit of piezoelectric ceramics to be 40 MPa under stress, a peak vibration velocity of 1.7 m/s is possible with a PZT ceramic plate transducer. However, the practical available vibration velocity is lower because of the heat generated through the mechanical and dielectric loss occurring at high-amplitude operation. The maximum speed of an ultrasonic motor is therefore limited to <1 m/s at best. The number of revolutions per second decreases in larger motors in reverse proportional to the diameter because the velocity at the circumference is subject to this limitation. It can therefore be seen that ultrasonic motors generally display low-speed and high-torque characteristics. It is necessary to develop a large transducer to obtain higher output power. However, if the diameter or width of the vibrator is increased, obtaining uniform vibration distribution over a wide output surface becomes difficult (Satonobu et al., 2000). To overcome this problem, the parallel operation of multiple transducers has been tested (Satonobu et al., 1997).

16.4.3 Driving circuits for ultrasonic motors

Rectangular-voltage waveform is used in the practical application of ultrasonic motors because the loss in the driver circuit is minimized in the switching operation. Metal oxide semiconductor field-effect transistors (MOS-FETs) are commonly used for the switching device (as shown in Figure 16.43) because of their high-speed on/off capability and low resistance in the on condition. Using this circuit, two voltage outputs with a 90° phase shift are fed to an ultrasonic motor. Inductors are connected in series at the output to minimize the steep rise and fall of current to the clamped capacitance of the PZT elements. If the inductance is correctly chosen, the voltage can be higher than the original source because of the electrical resonance of the inductor and the clamped capacitance. The output voltage is controlled by the source DC voltage applied to the MOS-FETs and is referred to as pulse amplitude modulation.

The motor speed can be changed through the pulse width control in the circuit shown in Figure 16.44. Transformers are used to step up the output voltage and create inverted outputs. The circuit can then be used as a four-phase driver for some traveling-wave rotary motors. The circuit should be designed so that the phase difference between the outputs may be maintained by varying the pulse width.

The vibration waveform remains sinusoidal in both circuits, though the voltages are rectangular, because the transducers are working at their resonance frequencies. The vibration amplitude can be altered smoothly with the pulse height or width. It should be noted that the vibration velocity is proportional to the current in the transducer; thus, the motor speed is related more to the current than to the voltage. If the load is increased, the current in the torsional transducer is reduced in proportion to the load. In a traveling-wave rotary motor, the current is not affected by the load in this way because the slip increases with the load. In several commercial ultrasonic motors, a frequency or

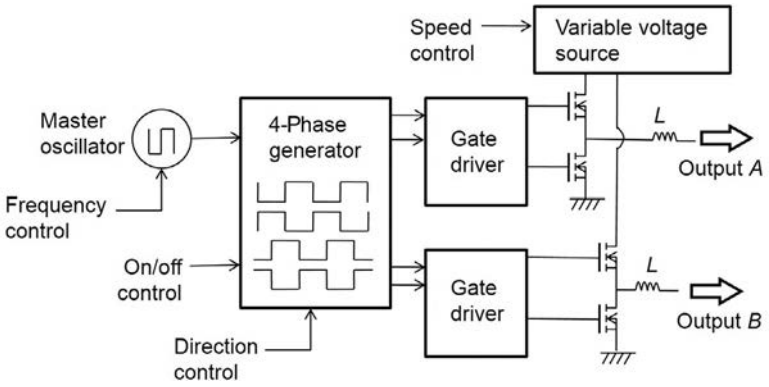


FIGURE 16.43 Two-phase driver circuit with pulse amplitude control.

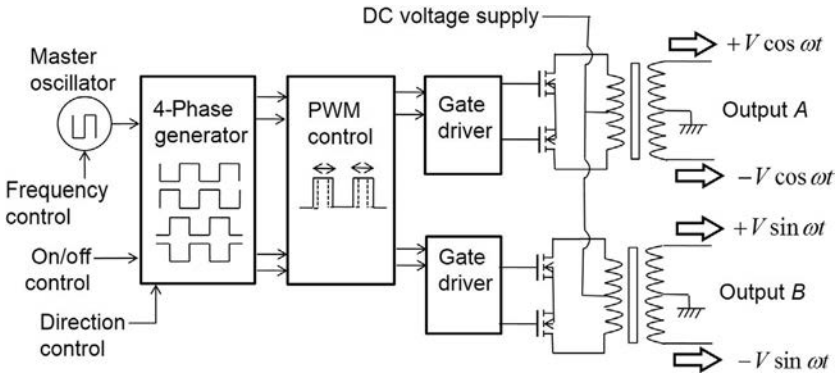


FIGURE 16.44 Four-phase driver circuit with pulse width control.

phase shift from the optimum position may be used to vary the motor speed while the voltages remain constant. The higher-side slope of the resonance curve is normally used to control the speed and to avoid the nonlinear jumping phenomenon exhibited in the vibration amplitude at the lower-side slope of the resonance peak. An external position encoder and a feedback system are used for precise speed and position control of the ultrasonic motor. Burst-wave operation is sometimes effective for very fine incremental positioning instead of closed-loop continuous control.

16.5 Conclusion and future trends

Several fundamental configurations for both linear and rotary ultrasonic motors are presented in this chapter. They may be generally categorized into traveling-wave and hybrid transducer types. In the hybrid transducer motors, various combinations of vibration modes of different shapes have been developed to create appropriate elliptical motions. Among these, small linear motors based on the L1–B2 mode have been successfully applied for positioning in optical components and cameras. Rotary motors with torsional and longitudinal modes, though small and powerful, are still in limited use because of the high cost of the torsional PZT element. Traveling-wave rotary motors have already established a consumer market in autofocusing applications for cameras. Linear traveling-wave motors have not yet found application because of their bulky structure and low efficiency. SAW motors are attracting interest in several fields. The high energy density of lithium nitrate crystal substrates provides high output in a motor with a compact structure. It will be necessary to incorporate energy circulation circuits in driving electronics toward a higher degree of overall efficiency.

The selection of friction materials is one of the most important issues to be considered in ultrasonic motors. The vibrator body of traveling-wave motors usually is made of aluminum alloy or brass. A thin sheet of engineering plastics or hard polymers is sometimes used as friction layer on the rotor surface. Plating or other special surface treatment is applied to the vibrating body and the rotor surface to strengthen the friction characteristics. In addition to metal and polymer, fine ceramics show potential as friction materials for ultrasonic motors. In some commercial ultrasonic motors, a life of 1000–5000 h has been achieved, and 10,000 h have been reported. However, this depends significantly on the operating conditions, including factors such as load, the number of start-stop actions, and the surrounding humidity. Wider research and detailed analysis of the contacting interface are required if the range of applications of ultrasonic motors is to be extended.

The output force/torque of ultrasonic motors is already superior to conventional motors of the same weight, although the efficiency of most commercially available versions is limited to around 50% or less. This value is lower than that of conventional motors, especially in larger machines. However, in practical usage, the total energy consumption of ultrasonic motors may become lower than that of electromagnetic motors because the required output torque can be obtained without reduction gears, and no extra energy is used to maintain positioning.

The potential energy density and efficiency of piezoelectric transducers in general are much higher than that so far exhibited by ultrasonic motors. This can be attributed to the friction loss generated in the contacting interface between the vibrator and the rotor/slider. Numeric simulations show that this loss can theoretically be reduced if the contact duration is shortened to a quarter period per wavelength of the ultrasonic vibrations. Some attempts have been done to improve the efficiency by introducing lubricant in the stator/rotor interface (Qiu et al., 2014). This idea was inspired by continuously variable transmission and exhibited good results to some extent in hybrid transducer ultrasonic motors.

Sophisticated designs to minimize the loss in driver circuit will be developed in the next generation of ultrasonic motors by taking advantage of recent progress in inverter technologies using MOS-FET.

References

Koc, B., Cagatay, S., Uchino, K., 2002. A piezoelectric motor using two orthogonal bending modes of a hollow cylinder. IEEE Trans. Ultrason. Ferroelectr. Freq. Control 49, 495–500. https://doi.org/10.1109/58.996568.

Kuribayashi, M., Ueha, S., Mori, E., 1985. Excitation conditions of flexural traveling waves for reversible ultrasonic linear motor. J. Acoust. Soc. Am. 77, 1431–1435. https://doi.org/10.1121/1.392037.

Kurosawa, M., Ueha, S., 1991. Hybrid transducer type ultrasonic motor. IEEE Trans. Ultrason. Ferroelectr. Freq. Control 38, 89–92. https://doi.org/10.1109/58.68464.

Kurosawa, M., Yamada, H., Ueha, S., 1989a. Hybrid transducer type ultrasonic linear motor. Jpn. J. Appl. Phys. 28, 158–160.

Kurosawa, M., Nakamura, K., Okamoto, K., Ueha, S., 1989b. An ultrasonic motor using bending vibration of a short cylinder. IEEE Trans. Ultrason. Ferroelectr. Freq. Control 36, 517–521. https://doi.org/10.1109/58.31795.

Kurosawa, M., Nishita, K., Koike, Y., Ueha, S., 1991. Hybrid transducer type ultrasonic linear motor using flexural vibrator. Jpn. J. Appl. Phys. 30, 209–211.

Kurosawa, M., Takahashi, M., Higuchi, T., 1996. Ultrasonic linear motor using surface acoustic wave. IEEE Trans. Ultrason. Ferroelectr. Freq. Control 43, 901–906. https://doi.org/10.1109/58.535493.

Morita, T., Kurosawa, M., Higuchi, T., 1995. An ultrasonic micro motor using a bending transducer based on PZT thin film. Sens. Actuators A 50, 75–80. https://doi.org/10.1016/0924-4247(96)80087-2.

Nakamura, K., Kurosawa, M., Kurebayashi, H., Ueha, S., 1991. An estimation of load characteristics of an ultrasonic motor by measuring transient responses. IEEE Trans. Ultrason. Ferroelectr. Freq. Control 38, 481–485. https://doi.org/10.1109/58.84293.

Qiu, W., Mizuno, Y., Tabaru, M., Nakamura, K., 2014. Can lubricant enhance the torque of ultrasonic motors? An experimental investigation. Appl. Phys. Lett. 105, 224102. https://doi.org/10.1063/1.4903238.

Satonobu, J., Magane, F., Koike, Y., Nakamura, K., Ueha, S., 1997. Development of the torque accumulation method for a torsional vibration system. IEEE Trans. Ultrason. Ferroelectr. Freq. Control 44, 1348–1354. https://doi.org/10.1109/58.656638.

Satonobu, J., Lee, D.K., Nakamura, K., Ueha, S., 2000. Improvement of the longitudinal vibration system for the hybrid transducer ultrasonic motor. IEEE Trans. Ultrason. Ferroelectr. Freq. Control 47, 216–221. https://doi.org/10.1109/58.818764.

Satonobu, J., Friend, J., Nakamura, K., Ueha, S., 2002. Numerical analysis of the hybrid transducer ultrasonic motor: comparison of characteristics calculated by transmission-line and lumped-element models. Ultrasonics 39, 559–565.

Takano, M., Takimoto, M., Nakamura, K., 2011. Electrode design of multilayered piezoelectric transducers for longitudinal-bending ultrasonic actuators. Acoust. Sci. Technol. 32, 100–108. https://doi.org/10.1250/ast.32.100.

Tominaga, M., Kaminaga, R., Friend, J., Nakamura, K., Ueha, S., 2005. An ultrasonic linear motor using ridge-mode traveling waves. IEEE Trans. Ultrason. Ferroelectr. Freq. Control 52, 1735–1742. https://doi.org/10.1109/TUFFC.2005.1561627.

Ueha, S., Tomikawa, Y., 1993. Ultrasonic Motors Theory and Applications. Oxford University Press, New York.

Yun, C., Ishii, T., Nakamura, K., Ueha, S., Akashi, K., 2001. A high power ultrasonic linear motor using a longitudinal and bending hybrid bolt-clamped Langevin type transducer. Jpn. J. Appl. Phys. 40, 3773–3776. https://doi.org/10.1143/JJAP.40.3773.

Chapter 17

Power ultrasound for the production of nanomaterials

A. Gedanken, I. Perelshtein, and N. Perkas
Bar-Ilan University, Israel

17.1 Introduction

The interest in nanomaterials has risen because their properties are different from those of the bulk properties of the same materials. New properties promise new applications, new devices, and a new horizon. Many synthetic methods have been developed over the years for the preparation of nanomaterials. They can be divided into gas phase process and solution methods.

In gas phase processes, vapor of the material fills the bubbles volume, the concentration of which in general is very low (Livage, 1981). It is therefore when the collapsing bubble contains the vapors of the solute (the solvent is usually not volatile), and the volume of the bubble is taken ranging from 1 to 10 μm, the number of molecules is small and therefore the size of the contracted bubble will form nanosized particles upon the collapse. When the solute is not volatile, the sonochemical reaction will occur in the liquid phase. A 200 nm ring around will maintain a high temperature, not as high as in the center of the collapsing bubble, and a few seeds of nanometer dimensions will be created upon the collapse of the cavity leading to the formation of nanoparticles. The collapse occurs in less than a nanosecond which not only prevents organization and crystallization but also avoids much interaction between the nanoparticles during the bubble's collapse, and if aggregation of the nanoparticles happens, it will occur only later in the bulk of the solution. It is therefore not surprising that the solid sonochemical product is in many cases is of nanometric size. In our previous review (Gedanken, 2007), we have outlined four properties that are unique to the use of ultrasonic waves to the fabrication of nanomaterials and are considered as the main advantage of sonochemicstry when compared to the many other methods used for the synthesis of nanomaterials. They are:

- Preparation of amorphous products. Although amorphous metals can be obtained by the cold quenching of bulk metals, when this is extended to metal oxides, the cooling rate required for many oxides is well beyond that which can be obtained using the cold quenching method. This is why glass-former materials are added to the mixture to form the amorphous products (Livage, 1981; Sugimoto, 1994). When sonochemistry is applied for the synthesis of amorphous metal oxides (or sulfides or other chacogenides), there is no need to add these glass formers, and as a bonus, the amorphous products are obtained in nanometer size.
- Insertion of nanomaterials into mesoporous materials. Ultrasonic waves are used for the insertion of amorphous nanosized catalysts into the mesopores (Landau et al., 2001; Perkas et al., 2001). A detailed study demonstrates that the nanoparticles are deposited as a smooth layer on the inner mesopores walls, without blocking them. When compared to the other methods such as impregnation or thermal spreading, sonochemistry shows better properties.
- Deposition of nanoparticles on ceramic and polymeric surfaces. Sonochemistry is used to deposit various nanomaterials (metals, metal oxides, semiconductors) on the surfaces of ceramic (Gedanken, 2004; Ramesh et al., 1997) and polymeric materials. A smooth homogeneous coating layer is formed on the surface. The nanoparticles are anchored to the surface by forming chemical bonds or chemical interactions with the substrate and cannot be removed by washing.
- The formation of proteinaceous micro- and nanospheres. We have demonstrated recently that any protein (e.g., polyglutamic acid) can be converted into a sphere upon sonication (Avivi Levi and Gedanken, 2002). We have also illustrated that we can encapsulate a drug, such as tetracycline, in the sphere (Suslick and Grinstaff, 1990). Our studies have shown that the spherical protein is biologically active, although its biological activity is reduced. The sonochemical spherization process takes only 3 min, which is shorter than any other similar process.

Power Ultrasonics. https://doi.org/10.1016/B978-0-12-820254-8.00017-8
Copyright © 2023 Elsevier Ltd. All rights reserved.

The review will emphasize the advantages of sonochemistry as a synthetic method when compared to the many other preparation techniques of nanomaterials. When discussing nanomaterials, the progress made in the control of size, the size distribution, and shape of the nanoproducts by varying sonochemical parameters will be highlighted. One section of this review will be devoted to the applications of ultrasonic waves for coating a large variety of surfaces by nanomaterials. We will stress the advantages of this deposition technique and its future possible applications. The current review will discuss the application of sonoelectrochemistry to the synthesis of nanomaterials but will not present results related to the use of ultrasonic spray pyrolysis for this goal.

The first edition of the review scanned the classes of nanomaterials that have been prepared sonochemically in the 2010–2012 years and later on updated with new works published on the same classes of materials till 2019 year. In listing these materials, we will follow the order of Bang and Suslick (2010), namely, metals, metal oxides, metal chalcogenides, and carbides, and will add the topic of the sonochemical synthesis of metal halides as well as sonochemistry related to graphene and graphene oxide. We will then refer to the work that has been done in 2010–2012 then updated till 2019 year in the applications of ultrasonic waves to the immobilization of nanomaterials on surfaces, and to the formation of proteinaceous microspheres as well as DNA, RNA, and other spheres using the technology that was developed by Suslick and Grinstaff (1990).

17.2 Ultrasound synthesis of metallic nanoparticles

A paper in Chinese language has described an ultrasonic assisted electrochemical method for the shape-controlled synthesis of Pt electrocatalysts at room temperature. The 3D Pt cubic sponge-like, branched, and spherical porous particles were prepared with or without shape controlling agents, such as polyvinylpyrrolidone (PVP) and cetyltrimethyl ammonium chloride (CTAC), respectively (Qingming Shen et al., 2010).

Sonoelectrochemistry was used for the synthesis of Fe–Cr alloy. The authors used a Ti sonotrode that was subjected to pulsed applied galvanic current and pulsed out-of-phase ultrasound (Zin and Dabala, 2010). The Fe–Cr alloy nanoparticles (NPs) were electrodeposited from a Cr (III) containing glycine to complex with metallic ions. As the Cr (III)–gly complex is formed, it is expected that this might affect the electrochemical reduction behavior of chromium in the bath, and as a result, codeposition of Fe and Cr can be realized by complex formation with glycine. The mean diameter of the NPs was determined by TEM and was found to be 8.03 nm with a standard deviation of 1.86 nm. The authors found that raising the temperature from 10°C to 60°C lowered the efficiency of the process from 21.3% to 2.2%. A second paper by this group reported the production of FeCo and FeCr alloy metal nanopowders by the pulsed sonoelectrochemical technique (Zin et al., 2010). The FeCo and FeCr NPs were synthesized at different bath's temperature, in order to study and evaluate the influence of this parameter on the process efficiency and nanoparticles' features.

The PdAg electrocatalyst of 12 nm particles in size was prepared using the sonochemical technique. In parallel, the authors also used borohydride reduction of the metallic ions crystalline PdAg particles with an average particle size of 10 nm. The electrocatalytic activity of PdAg, for the oxygen reduction reaction (ORR), was characterized using cyclic voltammetry (CV), rotating disk electrode (RDE), and electrochemical impedance spectroscopy (EIS) in 0.5 M H_2SO_4. EIS diagrams of PdAg electrocatalyst presented one or two time constants depending on the electrode potential, E. The E, at which the second time constant appears, depends on the method of catalyst preparation (Martinez-Casillas et al., 2010). The Pt-doped Pd nanoparticle catalysts (Pd_nPt, n is 12, 15, and 19) supported on carbon were synthesized by an ultrasound-assisted polyol method (Matin et al., 2012). The electrochemical activity of the electrocatalysts was investigated in terms of formic acid oxidation reaction, and $Pd_{19}Pt/C$ catalyst showed the highest catalytic activity compared to that of other catalysts. The Pt–Ni NPs for electrocatalysis were prepared sonochemically in a nonaqueous solvent to promote uniform alloying in the presence of a strong reducing agent (Guumlmeci et al., 2012). Metal NPs consistent with the Pt–3Ni stoichiometry were formed by sonication of a reaction mixture that contained a 3:1 mol ratio of Pt^{4+} and Ni^{2+} ions in tetrahydrofuran (THF). The sonochemically prepared Pt–Ni NPS showed a threefold enhancement in O_2 reduction kinetics compared with a commercial Pt catalyst.

Later on, the sonochemically prepared Pd nanoalloys were studied in different electrocatalytic reactions. The carbon-supported PtCo alloys of varying composition were synthesized using a sonochemical technique and their electrochemical properties were analyzed using cyclic voltammetry (CV) and linear sweep voltammetry (LSV). The electrochemical properties of the Pt_{83}–Co_{17}/C composition exhibited the best catalytic activity and the highest stability for the oxygen reduction reaction among all compositions synthesized in this study (Polagani et al., 2018). The similar sonochemically prepared PdCu nanoalloy supported on carbon nanotubes (PdCu/CNT) revealed the better activity and stability toward the electro-oxidation of methanol and ethylene glycol. The activity enhancement is due to its unique construction of zero-dimensional structured PdCu nanoalloy with one-dimensional CNTs and modified electronic effect of Pd on it (Arulmani et al., 2019).

Another type of bimetallic NPs with core-shell structure of Au@Pd was prepared sonochemically and successfully immobilized on a TiO_2 surface using ultrasonic waves as well (Mizukoshi et al., 2010). The immobilized bimetallic NPs with Au/Pd molar ratio of 25/75 on TiO_2 showed the highest activity for the photochemical H_2 evolution from an ethanol aqueous solution. Unique ultrasonic-assisted synthesis of Pd–Ni core–shell nanoalloys immobilized on magnetite was reported by Ghanbari (2017). The catalytic activity of the as-synthesized Pd-Ni/Fe_3O_4 core–shells was investigated in the Suzuki-Miyaura C–C coupling reaction and 4-nitrophenol reduction, and exhibited a high catalytic activity in both reactions.

In the first time, a sequential sonochemical synthesis was explored to achieve a core/shell structure of Pd@Pt/C nanoparticles (Zheng et al., 2019). The Pd core was firstly grown, and in the second step, the Pd^{2+} ion existing in the Pd core reduced simultaneously with Pt^{4+} ion in the solution as the first layer of PdPt alloy. Further, the Pt layer was formed subsequently. The Pd-based catalysts exhibited a superior ORR selective activity and exceptional methanol-tolerance property compared with the commercial Pt/C catalyst.

The sonochemical metallization of titania with Pt in propanol using as reduction agent for platinum ions resulted in synthesis of Pt/TiO_2. The as-prepared catalyst demonstrated pronounced increase of photocatalytic degradation of methyl orange (similar to 2 times), even with a deposition of small amounts of Pt (1.4 wt%) (Sivakumar et al., 2010).

Suslick and coworkers have synthesized highly fluorescent, stable, water-soluble Ag nanoclusters via a convenient sonochemical approach. They have used a simple polyelectrolyte, polymethylacrylic acid (PMAA), as a capping agent. The optical and fluorescence properties of the Ag nanoclusters can be easily controlled by varying the synthetic conditions, such as sonication time, stoichiometry of the carboxylate groups to Ag^+, and polymer molecular weight (Xu and Suslick, 2010). In Figure 17.1, a presentation of the absorption of the Ag NPs produced after different sonication times is depicted. The figure shows the emission spectrum as well and TEM images of the fabricated particles.

The effect of surfactant on the morphology and particles size of silver was also studied at ultrasound-assisted formation and deposition of Ag NPs on GaN (Dar et al., 2015). It was found that in the presence of PVP as surfactant, the smaller NPs were fabricated that which increased their surface-enhanced Raman scattering (SERS) intensity.

Mechanism of the sonochemical synthesis of Pt NPs nanoparticles in formic acid solutions under Ar and in pure water under Ar/CO atmosphere was investigated (Chave et al., 2012). It was shown that in pure water, sonochemical reduction of Pt(IV) occurs by hydrogen issued from homolytic water molecule split. The Pt(IV) ions reduction appears

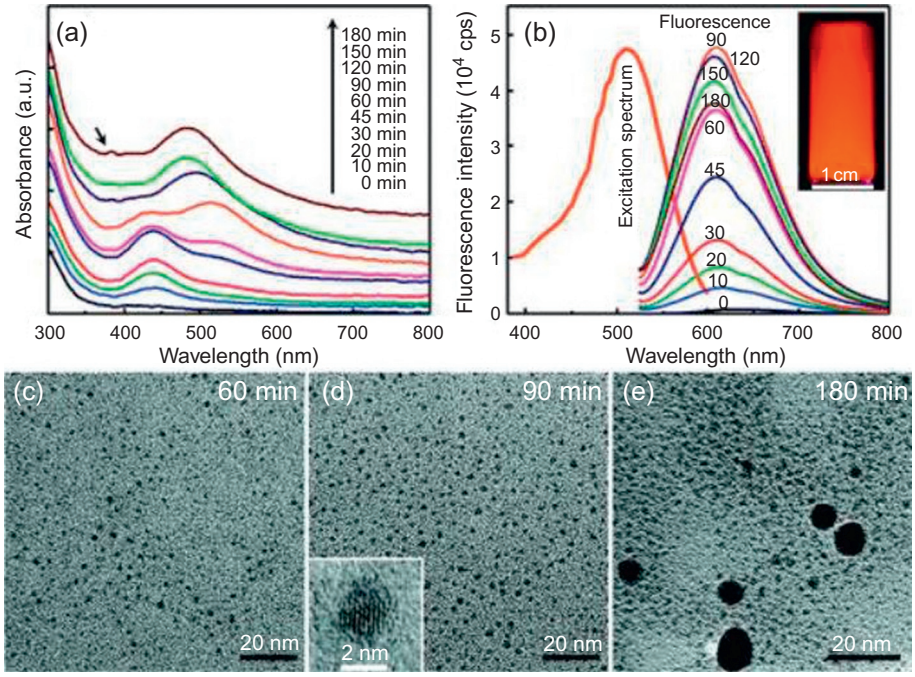


FIGURE 17.1 (a) UV–vis spectra and (b) fluorescence emission spectra of the solution containing PMAA and AgNO3 after increasing length of sonication time; the excitation spectrum shown in (b) corresponds to the 90 min sample with an emission wavelength of 610 nm (inset: solution of the Ag nanoclusters illuminated by a UV lamp with 365 nm excitation). TEM images of as-prepared Ag nanoclusters from different lengths of sonication: (c) 60 min, (d) 90 min (inset shows a single magnified Ag nanocluster), and (e) 180 min.

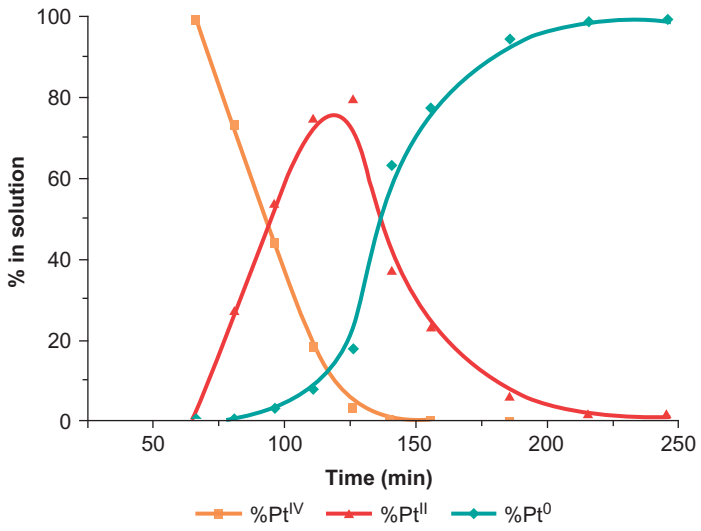


FIGURE 17.2 Evolution of the concentrations of platinum (IV) and (II) in solution and estimated percentage of metallic Pt(0) with hydrogen and CO2 emission curves.

to be a very slow process under argon atmosphere in pure water due to the formation of oxidizing species like OH radicals and H_2O_2 leading to reoxidation of intermediate Pt(II) ions. Sonochemical reduction is accelerated manifold in the presence of formic acid or Ar/CO gas mixture. Figure 17.2 demonstrates the evolution of the concentrations of Pt(IV) and Pt(II) in solution and estimated percentage of metallic Pt with hydrogen and CO_2 emission curves.

Raabe and Hessling reported on the synthesis of hollow metallic particles via ultrasonic treatment of a metal emulsion (Raabe and Hessling, 2010). The method is based on an ultrasound-assisted solidification route, where liquid metal droplets immersed in an emulsion are exposed to intense ultrasound radiation and solidify as micro- and nanoscaled spherical particles. This new technique does not directly use the extreme temperature or pressure of the collapsing cavities for driving chemical reactions. Instead, it exploits the stirring, jet, and Joule–Thomson effects to create metallic spheres of different morphology. It differs also from the previous work of Abramov (1994), in that the current work applies the ultrasonic waves to a water–metal emulsion rather than to bulk liquid metal. The metallic sample (Raabe and Hessling, 2010) was an eutectic solder consisting of 51 wt% In, 32.5 wt% Bi, and 16.5 wt% Sn (Field's metal, melting point 62°C). The paper lacks the elemental composition of the resulting particles.

A comprehensive review on the sonochemical synthesis of nanometals was published by Mohwald's group (Shchukin et al., 2010). They showed that control of cavitation requires control of interfaces at the microsecond timescale, and a diversity of phenomena is observed at the cavitation interface using different surfactants. Concrete examples showed that it is possible to prepare nonequilibrium mono- and multicomponent metallic nanostructures that possess properties considerably different from those of nanostructures prepared by conventional methods.

Composite electrode materials containing NPs of nearly amorphous CoSn and ultrathin layers of graphite were prepared while high-intensity ultrasonication was continuously applied (Gonzalez et al., 2011). For this purpose, Sn(II) and Co(II) ions in tetraethyleneglycol were reduced with $NaBH_4$ in the presence of ball-milled graphite under the sonic waves. The good electrochemical cycling behavior was connected to the small particle size of CoSn, the low crystallinity of the CoSn, and the dispersion of the CoSn particles in an optimized carbon matrix.

Binary Au–Ag nanostructures of preformed gold NPs (25 nm) in silver nitrate solutions were produced by a two-step sonication (20 kHz) (Radziuk et al., 2011a). Ultrasonic treatment of Au–Ag mixtures was carried out in the presence of sodium dodecyl sulfate in water or 2-propanol, and PVP in ethylene glycol solutions. The Au–Ag nano-worms, which consist of ripened gold particles connected by ultrasonically reduced silver, were formed after 1 h of sonication in sodium dodecyl sulfate aqueous solution.

Bimetal nanocatalysts with a narrow pore size distribution and high surface area were prepared using a fast, easy, and "green" method of ultrasound irradiation in water (Pazos-Perez et al., 2012). The concept was demonstrated for the case of Al–Au, Ag, or Pt but applicable to a large range of NPs. The application as effective nanocatalysts was shown. The authors formed functional nanostructures consisting of mesoporous aluminum frameworks with incorporated Au, Ag, or Pt NPs. The catalytic power of the synthesized materials was examined by monitoring the kinetic of the reduction of ferricyanide by thiosulfate. They authors followed the intensity of the hexacyanoferrate (III) absorption peak at 420 nm as a function of time via UV–Vis absorption spectroscopy.

In the last years, ultrasound-assisted "green" synthesis of nanoparticles was widely used. Eco-friendly synthesis of Ag

NPs of average size 33.8 nm was performed using weed plant *Lantana camara* L. leaf extract (Manjamadha and Muthukumar, 2016). The antioxidant activity of Ag NPs was assayed using 2,2-diphenyl-1-picrylhydrazyl (DPPH) test. The increase in the concentration of Ag NPs increased the DPPH scavenging activity. The Ag NPs revealed superior antibacterial activity against Gram-positive and Gram-negative organisms. Recently, the similarly prepared Ag NPs using *Mentha aquatica* leaf extract demonstrated enhanced antibacterial activity by lowering the minimum inhibitory concentration (MIC) against *P. aeruginosa*, *E. coli*, *B. cereus,* and *S. aureus* (Nouri et al., 2020). In addition, the as-synthesized ultrasound-assisted Ag NPs showed considerable catalytic activity for the reduction of different types of dyes as environmental pollutants. Ultrasonic approach reduced the time of the synthetic procedure and resulted in monodispersed and smaller Ag NPs compared with hydrothermal method.

Ultrasound-assisted synthesis of Au NPs in an eco-friendly manner using *Calothrix algae* was reported by Kumar et al. (2016). The production of the Au NPs in the reaction mixture was significantly accelerated by inducing ultrasound irradiation. Further, Au NPs showed significant catalytic efficiency (rate constant, $k = 0.0724752\,\text{min}^{-1}$) in reducing 4-nitrophenol to 4-aminophenol. One pot green synthesis of Au NPs was successfully achieved using palm oil leaves extracts as stabilizing agent and ultrasound radiation as reducing agent (Usman et al., 2019). The effect of concentration of palm oil leaves extracts was investigated. The functional groups such as OH^-, CO – stretch, NH – stretching, and other function groups were found to be responsible for stabilizing the Au NPs.

17.3 Ultrasound synthesis of metal oxide nanoparticles

Nanoparticles of metal oxides are the most popular nanomaterials and the number of papers reporting of their synthesis and application is the largest. This is true considering the various preparation methods including sonochemistry. Among the metal oxides, the synthesis and applications of transition metal oxides, and especially, TiO_2, ZnO, and Fe_3O_4 have attracted most of the interest.

Anatase TiO_2 nanocrystalline (6 nm) with BET specific surface area of 300 m^2/g and direct bandgap of 3.31 eV was prepared sonochemically (Gonzalez-Reyes et al., 2010) and was subjected to thermal treatment from 400°C to 900°C for 2 h, in order to produce variable anatase-rutile ratio. Three stages were considered in the samples thermally treated: (i) anatase grains coarsening as a result of heat treatment temperature increasing the structural homogeneity and crystallinity, and both phenomena produce a reduction in the specific surface area; (ii) coexistence of two phases (anatase and rutile) separated by a transition region, called an interface; and (iii) process where the rutile grains evolve into a new equilibrium shape without the presence of anatase phase, minimizing the total surface and the grain boundary energies, by mass transport diffusion. In this last stage, the rutile phase has the sole function of growth and densification. Titanium oxides with hierarchical structures were successfully replicated from biotemplate using a sonochemical method. The biotemplates, cedarwoods, were irradiated under ultrasonic waves in $TiCl_4$ solutions and then calcined at temperatures between 450°C and 600°C (Zhu et al., 2010). The photocatalytic activities were assessed by measuring the percentage degradation of methylene blue using UV–vis spectroscopy. The calcination temperature has a strong effect on the structural replication and photocatalytic activity of the replicas.

Epoxidation of styrene and cyclooctene by anhydrous tert-butyl hydroperoxide over sonochemically prepared Co_3O_4 and Mn_3O_4 nanocatalysts was investigated. The results of conversion activity were compared with bulk Co_3O_4 and Mn_3O_4. Under optimized reaction conditions, the nanocatalysts showed a superior catalytic performance as compared to the bulk catalysts (Askarinejad et al., 2010).

Nanoparticles of Mn_3O_4 were also prepared using a sonochemical method without requiring any pH adjustment (Baykal et al., 2010). The synthesized material was identified as tetragonal hausmannite crystal structure model of Mn_3O_4 from XRD analysis. Crystallite size was estimated from X-ray line profile fitting to be 17 ± 5 nm. Magnetic evaluation revealed a blocking temperature, T-B, of 40 K above which the material behaves paramagnetic. Asymmetric coercive field is attributed to the interaction between ferromagnetic Mn_3O_4 and antiferromagnetic Mn oxide at the surface of NPs.

Nanosized ZnO, NiO, and MnO were successfully synthesized by the sonochemical method in solutions at room temperature. The reactants used are $M(Ac)_2{\bullet}2H_2O$ and sodium hydroxide NaOH in H_2O/EtOH as a solvent with polyethylene glycol (PEG) as template. Some of the parameters such as effect concentration of NaOH solution, ultrasound power, and sonicating time in growth and morphology of the nanostructures were investigated (Aslani et al., 2010).

Single-phase ZnO NPs were prepared by solid-liquid reaction ball milling assisted by ultrasonic wave (Ding and Ting, 2010). It was found that ultrasonic wave was a key factor promoting the transformation from $Zn(OH)_2$ to ZnO. Based on hot-spot theory, the formation mechanism of the single-phase ZnO NPs under ultrasonic wave assistance is determined.

Hollow ZnO microspheres assembled by NPs were prepared by a sonochemical synthesis at room temperature using carbon spheres as template (Xiaohua et al., 2010). The diameter of the obtained hollow spheres is about

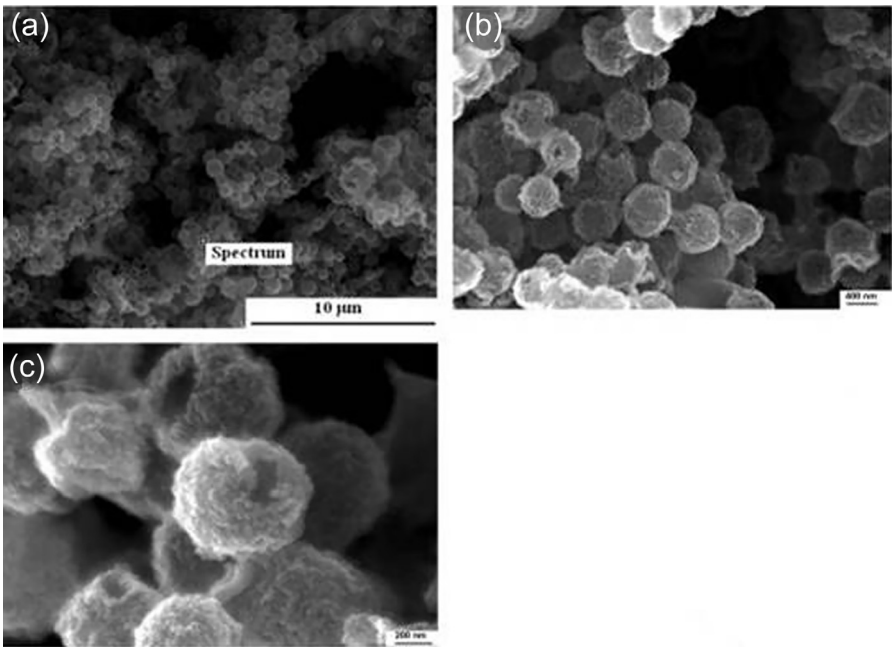


FIGURE 17.3 Low-magnification and high-magnification SEM image of the large-scale self-assembled ZnO hollow spheres dispersing harmoniously (a and b). (c) Nanoparticle-assembled surface image of ZnO hollow spheres.

500 nm, and the walls are composed of numerous ZnO aggregate nanocrystallines with diameters of 90 nm. A possible growth mechanism for the formation of ZnO microspheres has been proposed, in which carbon spheres play a crucial role in the formation of the wurtzite hollow ZnO microspheres. Figure 17.3 is a demonstration of the hollow ZnO spheres.

Hierarchical ZnO hollow spheres (400–500 nm in diameter) consisting of ZnO NPs with a diameter of approximately 15 nm were successfully prepared by a facile and rapid sonochemical process (He et al., 2010). The formation of hierarchical ZnO hollow spheres was attributed to the oriented attachment and subsequent Ostwald ripening process according to time-dependent experiments. The as-prepared ZnO hollow spheres were used as a photoanode in dye-sensitized solar cells and exhibit a highly efficient power conversion efficiency of 4.33%, with a short-circuit current density of 9.56 mA cm^{-2}, an open-circuit voltage of 730 mV, and a fill factor of 0.62 under AM 1.5 G one sun (1.00 mW cm^{-2}) illumination. Moreover, the photovoltaic performance (4.33%) using the hierarchical ZnO hollow spheres was 38.8% better than that of a ZnO NPs photoelectrode (3.12%), which is mainly attributed to the efficient light scattering for the former.

Nanoparticles of CuO were prepared by a sonochemical route from copper acetate and sodium hydroxide in the presence of polyethylene glycol (PEG), polypropylene glycol (PPG), and polyvinyl alcohol (PVA) (Ranjbar-Karimi et al., 2010). Variations of several parameters and their effects on the structural properties of NPs (particle size and morphology) were investigated. The 0.05 M solution of copper acetate in the presence of PEG gave the best results. The CuO and NiO NPs were also successfully prepared by means of solid liquid reaction ball milling assisted by ultrasonic wave at relative low temperature, using basic cupric carbonate (BCC) and basic nickel carbonate (BNC) as the raw materials (Chen et al., 2012b). By the comparison of the as-milled products with and without the help of ultrasonic wave, it was found that ultrasonic wave is a key factor in promoting the decomposition of BCC and BNC. Furthermore, the mechanism of the decomposition reaction assisted by ultrasonic wave was discussed.

Applerot attempted to understand the interaction of CuO NPs (prepared sonochemically) with bacteria and the possible permeation of the nanoparticles into bacterial cells (Applerot et al., 2012a). The potent antibacterial activity of CuO NPs was found to be due to ROS-generation by the nanoparticles attached to the bacterial cells, which in turn provoked an enhancement of the intracellular oxidative stress. This paradigm was confirmed by several assays such as lipid peroxidation and reporter strains of oxidative stress. Furthermore, electron microscopy indicated that the small NPs of CuO penetrated the cells. Collectively, the results reported may reconcile conflicting concepts in the literature concerning the antibacterial mechanism of CuO NPs as well as highlight the potential for developing sustainable CuO NPs-based devices for inhibiting bacterial infections.

The systematic study of CuO and ZnO NPs demonstrated that sonochemically prepared nanooxides are better antimicrobials than commercially available ones with the

same particle size range (Perelshtein et al., 2015). It was found that the crystallites, which have more defects and less organized structure, are more effective. The formation of reactive oxygen species (ROS) that are responsible on the antibacterial activity of the oxides was studied by electron spin resonance (ESR) measurements. A significant increase in the production ROS was found in the more defective, sonochemically prepared samples, as compared to the commercial NPs. The substantial enhancement of 10,000 times in the antimicrobial activity of the sonochemically prepared Zn–CuO nanocomposite ($Cu_{0.88}Zn_{0.12}O$) compared to the pure CuO and ZnO NPs was observed to the multidrug-resistant *E. coli* and *S. aureus* bacteria (Malka et al., 2013). The high antimicrobial activity is most likely associated with structural defects in the solid crystal that led to the formation of more ROS. Three types of ROS (Δ^1O_2, OH·, O_2-) were detected in the Zn–CuO nanocomposite by the ESR technique. These radicals were found to enhance the antibacterial effect relative to bear CuO or ZnO NPs.

The formation of uniform α-Fe_2O_3 NPs was reported, and their magnetic properties were investigated (Koo et al., 2010). The sonochemical synthesis and the subsequent take-off technique resulted in spherical-shaped α-Fe_2O_3 NPs with an average diameter of 60 nm. The temperature- and applied magnetic field-dependent magnetization of the α-Fe_2O_3 NPs was explained by the sum of two contributions, i.e., the Morin transition and superparamagnetism, because the critical size was within the size variation of the NPs.

A facile method has been developed to encapsulate Fe_3O_4 nanocrystals (NC) in morphology-tunable fibers (belt-like, solid, and tubal) by using a sonochemistry-driven synthesis and a subsequent reflux procedure (Yang et al., 2010). Supersonic treatment plays an important role to prevent the agglomeration of the Fe_3O_4 NCs in an alkaline condition. The Fe_3O_4 NCs mono-dispersed in fibers revealed superparamagnetic behavior. The binding of a semiessential amino acid, L-arginine, onto the surface of nanomagnetite Fe_3O_4 creating a stable aqueous suspension by an in situ one-step method using sonochemical synthesis was reported (Theerdhala et al., 2010). An ex situ two-step process was also attempted but was soon discarded owing to the relative short duration of the suspension attributed to increase in particle size and lower extent of binding. The initial concentration of the amino acid was found to play an important role in controlling the particle size. Lower concentrations of arginine were found to favor the formation of elongated tubular structures, while at higher concentrations, the elongated structures were less prominent and arginine was found to be adsorbed onto the surface of the magnetite.

The sonochemical preparation of magnetic fluorescent nanospheres (MFNs) was published by Wu et al. (2011). The first stage of the MFNs synthesis is the synthesis of Fe_3O_4 NPs by the coprecipitation method of Fe^{3+}:Fe^{2+} in the ratio of 3:2 under basic conditions in the presence of oleic acid and undecylenic acid as well as cyclohexane to form a ferrofluid. In the second stage, an aqueous solution of BSA was added to the ferrofluid. The emulsion was subjected to sonication to form Fe_3O_4/BSA nanospheres. To start fluorescent modification, Rhodamine solution was added and stirred for 4 h. The obtained water-soluble MFNs were collected with a magnet. The results indicate that the superparamagnetic nanospheres have a particle size of 160 nm, high-saturation magnetization of 54 emu/g, and significant fluorescence. MFNs possess potential in medical imaging, drug targeting, and catalysis. The possible formation mechanism of MFNs was discussed.

A combination of antibacterial and magnetic properties of iron oxides still attracted significant interest of many researches. Rapid and facile sonochemical methodology was applied for the synthesis of 12 nm Fe_3O_4 NPs functionalized with polysodium acrylate, trisodium citrate, branched polyethyleneimine, and sodium oleate (Neto et al., 2017). Mösbauer spectroscopy and magnetic resonance confirmed that the obtained NPs were transitioning to the superparamagnetic regime and possessed significant saturation values (59–77 emu/g). The product demonstrated excellent physicochemical properties for magnetic resonance imaging (MRI). Sonochemically prepared Fe_2O_3 and Fe_3O_4 were studied against bacterial pathogens with a minimal inhibitory concentration of 0.15 mg mL^{-1} for *Salmonella enterica, Staphylococcus aureus, Bacillus cereus, Pseudomonas aeruginosa,* and *E. coli* (Shin et al., 2019). The results emphasized the bioactive potency of synthesized iron nanooxides for future biomedical applications.

Niederberger has opened a new research field in conducting sol-gel synthesis in nonaqueous solvents (Niederberger et al., 2002). Ohayon has followed Niederberger's steps and conducted the same reaction in the same solvents but under the influence of ultrasonic waves (Ohayon and Gedanken, 2010). Highly crystalline metal oxide nanoparticles of TiO_2, WO_3, and V_2O_5 were synthesized in just a few minutes by reacting transition metal chloride with benzyl alcohol using ultrasonic irradiation under argon atmosphere at 363 K, in a nonaqueous solvent. The particles' size and shape reveal "quasi" zero-dimensional, spherical TiO_2 particles in the range of 3–7 nm. The V_2O_5 particles have a "quasi" one-dimensional ellipsoidal morphology, with lengths in the range of 150–200 nm and widths varying between 40 and 60 nm. The WO_3 particles were obtained as "quasi" two-dimensional platelets with square shapes having facets ranging from 30 to 50 nm. The thickness of these platelets was between 2 and 7 nm.

Sonochemistry was also employed to form three types of erbium oxide NPs in the presence of multiwalled carbon nanotubes (CNT) as a template material in water

(Radziuk et al., 2011b). The NPs are (i) erbium carboxyoxide NPs deposited on the external walls of multiwalled CNT and Er_2O_3 in the bulk with (ii) hexagonal and (iii) spherical geometries. Each type of ultrasonically formed nanoparticle reveals Er^{+3} photoluminescence from crystal lattice. The main advantage of the erbium carboxyoxide NPs on the CNT is the electromagnetic emission in the visible region, which is new and not examined previously. On the other hand, the photoluminescence of hexagonal erbium oxide NPs is long-lived and enables the higher energy transition $^4S3/2 \rightarrow {}^4I15/2$, which was not observed for spherical NPs. The source of erbium in these experiments was a solution of $ErCl_3$ in HCl.

Magnesium oxide NPs of average size between 35 and 120 nm were prepared by a sonochemical method (Ranjbar-Karimi et al., 2011). Polyhydroquinoline derivatives were prepared from dimedone, benzaldehyde, ethyl acetoacetate, and ammonium acetate under solvent-free conditions using MgO NPs as a catalyst. Easy handling, reusability, thermal stability, and nontoxicity of the catalyst make the present protocol as an eco-friendly and economically for the synthesis of these heterocycles.

The influence of ultrasound in the synthesis of nickel hydroxide from aqueous ammonia complexes was studied showing that ultrasound allows the fabrication of flower-like particles with sizes ranging in between 0.7 and 1.0 μm in contrast with the 6–8 μm particles obtained in the absence of ultrasound (Cabanas-Polo et al., 2011). The influence of gas flow, temperature of the process, and surfactants in the ultrasonically prepared powders was discussed in term of shape, size, and agglomeration of the particles. Adjusting the experimental condition, spherical, or platelet-like particles was obtained with sizes ranging from 1.31 μm to 200 nm.

The $BaTiO_3$ NPs were sonochemically synthesized in ethanol-water mixture solution at low temperature (Feng et al., 2011). Different growth mechanisms of the $BaTiO_3$ particles were identified in aqueous solution and ethanol-water solution under ultrasonication. Nanocrystals firstly formed and then oriented aggregated into large particles in aqueous solution under ultrasonic irradiation. Compared to the synthesis in aqueous solution, the $BaTiO_3$ NPs could be prepared at low temperature in ethanol-water solution. Furthermore, the oriented aggregation of $BaTiO_3$ nanocrystals was suppressed and the $BaTiO_3$ NPs grew up from the Ti-based precursor through a dissolution-precipitation process.

A new type of porous nano-MnO_2 for supercapacitors was synthesized for the first time by a facile sonochemistry route from a quick-redox reaction between $KMnO_4$ and D-glucose (Wang et al., 2011). The results show that the porous MnO_2 nanoparticles in the range 20–50 nm are interestingly composed of nanorods with diameters of about 2 nm and lengths of 4–8 nm. A possible growth mechanism of this nanostructure was identified based on the experimental results. The electrochemical properties of the porous MnO_2 were investigated in a symmetric capacitor cell using both 1 M Na_2SO_4 and 9 M KOH aqueous solutions. The results indicated that the MnO_2 electrodes have a good capacitive performance in both cases.

The only paper combining ultrasonic waves and microwave radiation was reported on the synthesis of carbonated hydroxyapatite (CHAp) nanopowders (Zhaoyong et al., 2012). Influences of microwave and ultrasonic irradiation on the crystallinity, morphology, yield, Ca/P molar ratio, specific surface area, and dispersibility were investigated and compared with the conventional precipitation method. The results showed that sonochemistry-assisted microwave process significantly increased the synthetic efficiency. The well-crystallized nanopowders could be obtained at high yield of 98.8% in ultrashort period of 5 min. In addition, the crystallization process was promoted with the increase of ultrasonic and microwave power and the reaction time during the sonochemistry-assisted microwave process. The sonochemistry assistance also remarkably increased the specific surface area and dispersibility of the as-obtained products.

Crystalline and nanostructures of two novel Pb(II) coordination polymers, $[Pb_2(2\text{-pyr})_4(MeOH)]_n$ (**1**), {2-Hpyr = 2-pyrazinecarboxylic acid} and $[Pb(2\text{-quc})_2]_n$ (**2**), {2-Hquc = 2-quinolinecarboxylic acid}, were synthesized via thermal gradient and sonochemical methods, respectively (Morsali and Panjehpour, 2012). The two coordination polymers were then heated to 600°C to produce PbO NPs with different morphology and size. Another lead (II) coordination polymer, $[PbBr_2(C_9H_{15}N_5O)]_n$ (1), where $C_9H_{15}N_5O$ is (2,4-diamino-6-piperidine-1-yl) pyrimidine N-oxide (minoxidil), was synthesized in methanol by combination of sonochemical and hydrothermal methods from lead(II) acetate, KBr, and the minoxidil ligand (Ranjbar et al., 2012). Microrods of PbO and nano-plates of PbOHBr were prepared by thermal decomposition of the nanostructured $[PbBr_2(C_9H_{15}N_5O)]_n$ as a precursor. The sonochemical method resulted in a significant reduction of reaction time, reaction temperature, and particle sizes of the products.

A sonochemistry-based synthesis method was used to produce nanocrystalline nickel oxide powder with 20 nm average crystallite diameter from $Ni(OH)_2$ precursor (Mohseni Meybodi et al., 2012). Dried precipitates were calcined at 320°C to form nanocrystalline NiO particles. Using sonochemical waves resulted in lowering of the size of the nickel oxide crystallites. Photoluminescence spectroscopy confirmed production of a wide band-gap structure.

The sonochemical approach was widely applied for synthesis of the multicomponent oxides. Well-crystallized manganese ferrite ($MnFe_2O_4$) NPs with mean size of

20 nm were synthesized at low temperature (≤100°C) by ultrasound wave-assisted solid-liquid reaction ball milling technique without subsequent calcination (Chen et al., 2012a). Analytical grade powders of MnO_2 and metallic Fe were used as starting materials. As a comparison, solid-liquid reaction ball milling without ultrasonic wave assistance and the effects of different milling balls were also investigated. The results showed that this technique is simple, environmentally friendly, and energy-saving for nanocrystal synthesis. The synthesis of manganese zinc ferrite ($Mn_{0.5}Zn_{0.5}Fe_2O_4$) nanoparticles with narrow size distribution using ultrasound-assisted emulsion (consisting of rapeseed oil as an oil phase and aqueous solution of Mn^{2+}, Zn^{2+}, and Fe^{2+} acetates) and evaporation processes were carried out by Sivakumar et al. (2012). In order to remove the small amount of oil present on the surface of the ferrite, it was subjected to heat treatment at 300°C for 3 h. As-prepared ferrite was nanocrystalline with particles size of 20 nm, whereas the heat-treated ferrite showed the size of 33 nm. In addition, the spontaneous magnetization (sigma (s)) of the heat-treated sample (24.1 emu/g) is significantly higher than that of the as-synthesized sample (1.81 emu/g).

Later on, the high specific capacity anode material Li- and Mn-rich layered $Li_{1.2}Ni_{0.13}Co_{0.13}Mn_{0.54}O_2$ cathode material was synthesized using sonochemical method followed by annealing at 700°C, 800°C, and 900°C for 10 h (Sivakumar et al., 2016). With the sample annealed at 900°C, an initial specific capacity of 240 mAh/g was obtained, which decreased to 215 mAh/g after 80 cycles, thus retaining about 90%of its initial capacity. The advantage of this synthesis, which includes a sonochemical stage, compared with a conventional coprecipitation synthesis, was confirmed.

Amorphous iron-chromium oxide $Fe_{2-x}Cr_xO_3$ ($x = 0$, 0.05, 0.10, 0.15, 0.20) NPs were synthesized by sonochemical method at 80°C (Dang et al., 2012). Crystallization process of the annealed samples showed a strong ferromagnetic behavior due to the existence of the maghemite phase. The effect of chromium replacing iron in the crystallization process of $Fe_{2-x}Cr_xO_3$ nanoparticles was systematically studied by adjusting initial concentration of Cr^{3+}. A second paper on a similar topic by the same group reported on the sonochemical preparation of amorphous Fe_2O_3 and $Fe_{1.9}Cr_{0.1}O_3$ materials (Phu et al., 2012). Upon heating, the sample prepared at 70°C presented a strong ferromagnetic behavior due to the presence of the magnetite phase coexisting with the hematite phase whereas the samples prepared at higher temperatures presented only the existence of the hematite phase. Thermal analyses of the sample prepared at 80°C revealed three exothermic peaks which were corresponding to the phase changes of dehydroxylation, crystallization of the maghemite phase, and maghemite-hematite transition, respectively. The activation energies of the phase changes deduced from the thermal analyses showed that the presence of Cr enhanced the activation energy which can slow down the ageing effect of the amorphous state when being used in practice.

The dissolution of ceria was studied through a catalytic reduction process involving Pt NPs in mild conditions at near ambient temperature (Virot et al., 2012). The deposition of Pt NPs was made by sonication, and further dissolution of ceria was studied as a function of different parameters such as stirring, sonication, dissolution media, and temperature. The quantitative dissolution of ceria can be performed in HNO_3-HCOOH-$[N_2H_5][NO_3]$, HNO_3-$[N_2H_5][NO_3]$ or H_2SO_4-HCOOH mixtures at 40°C. It was shown that the combined use of ultrasound with nitric media in the presence of Pt NPs can lead to passivating phenomena resulting in a decrease of the dissolution rate. In Figure 17.4, Nikitenko presented kinetic curves obtained

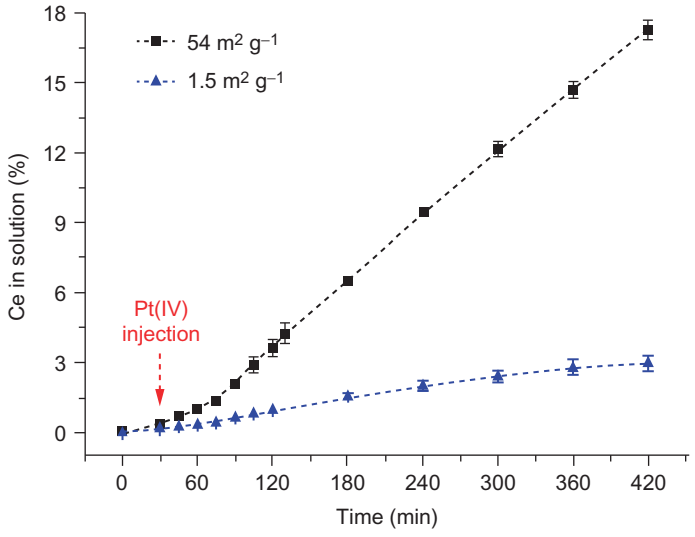


FIGURE 17.4 Kinetic curves obtained for the ultrasound-assisted catalytic dissolution of CeO2/Pt with different SBET in a 0.25 M HNO3–1.0 M HCOOH–0.2 M [N2H5][NO3] mixture at 40°C (I¼18 W cm_2, Ar, V¼50 mL).

for the ultrasound-assisted catalytic dissolution of CeO_2/Pt with different surface areas. Later on, Nikitenko et al. synthesized porous $(Ce_{0.5}Zr_{0.5})O_2$ solid solutions by thermolysis or sonolysis of Ce(III) and Zr(IV) acetylacetonates in oleylamine or hexadecylamine under argon followed by heat treatment of the precipitates obtained in air at 450°C (Cau et al., 2014). Pt NPs were deposited on the surface of the mixed oxides by sonochemical reduction of Pt(IV). It was found that the materials prepared by sonochemistry exhibit better resistance to dissolution during the deposition process of Pt. X-ray photoelectron spectroscopy analysis showed the presence of Pt(0) and Pt(II) on the surface of mixed oxides. The porous $(Ce_{0.5}Zr_{0.5})O_2$ mixed oxides loaded with 1.5%wt. Pt exhibit high activity in catalytic wet air oxidation of formic acid at 40°C.

17.4 Ultrasound synthesis of chalcogenide nanoparticles

ZnS NPs were prepared sonochemically by reacting zinc chloride and sodium sulfide in the presence of 3-mercaptopropionic acid (3-MPA) as a capping agent (Azizian-Kalandaragh and Khodayari, 2010). The average crystalline size of ZnS nanostructures was analyzed by X-ray diffraction pattern and estimated to be 4.7 nm. Optical measurements indicate a direct band gap of about 4.27 eV. The authors observed a blue shift of about 0.57 eV, in comparison to its bulk value due to quantum confinement effects of electrons and holes.

Drofenik and coworkers reported on the synthesis of CdS and CdSe NPs (Kristl et al., 2010). They used cadmium sulfate hydrate ($CdSO_4$•$8/3H_2O$), elemental S, and Se, as precursors. Aqueous solutions of NaOH, Na_2SO_3, and EDTA were used as the solvents. The average particle size was 4.5 nm for CdS, while the crystallite sizes for CdSe were 9.7 nm and 6.9 nm in two different synthetic methods. The sonocatalytic degradation of azo dyes, methyl orange (MO), and Rhodamine B (RhB) were studied catalyzed by cadmium selenide (CdSe)-graphene in dark ambiance (Ghosh et al., 2012). The CdSe-graphene composites were prepared by simple hydrothermal method.

A well-known solar cell material, CuInSe2 (CIS), was prepared by a combination of electrodeposition and the sonochemistry technique (Chraibi et al., 2011). The CIS NPs were obtained from an aqueous solution containing citrate as complexing agent. The size of the nanocrystallites was ranging between 6 and 30 nm.

A few papers reported on the sonochemical composite made of titania and metal chalcogenide. For example, ultrasound energy was successfully employed to synthesize CdSe/TiO_2 nanocatalysts for the photocatalytic degradation of phenol under solar light irradiation (Ghodrati et al., 2011). The composite nanocatalyst showed a shift in the absorption spectrum from the UV range to the visible range. The results of photocatalytic tests showed that the CdSe/TiO_2 nanocatalyst could remove phenol from waste water under solar light irradiation, while TiO_2 did not have enough activity in this process.

Colloidal cadmium telluride (CdTe) quantum dots and their NPs were synthesized by one pot sonochemical reactions (Hwang et al., 2011). $CdCl_2$ and tellurium powder with hexadecylamine and trioctylphosphine/trioctylphosphine-oxide (TOP/TOPO) as a dispersant were sonicated in toluene solvent for 5–40 min. at 60°C. The prepared CdTe QDs showed different colors from pale yellow to dark brown and corresponding photoluminescence properties due to mainly the quantum confinement effect. The CdTe NPs of about 20 nm in average were found to have a band gap of 1.53 eV, which is the most optimally matched band gap to solar spectrum. Drofenik and his group have applied the above-mentioned synthetic route (Gonzalez-Reyes et al., 2010) for the preparation of CdS and CdSe, to CdTe as well as (Ban et al., 2012). Changes of physical and chemical properties of the prepared CdTe NPs at increased temperature were studied.

CdTe NPs were also synthesized via a sonochemical method based on the reaction among cadmium acetate $Cd(OAC)_2$, $TeCl_4$, and potassium borohydride (KBH_4) in water, in the presence of various capping agents. The effects of preparation parameters such as the kind of capping agents, ultrasonic power, reducing agent, reaction time, and cadmium precursors were investigated. It was found that morphology, particle size, and phase of the products could be greatly affected by these parameters (Salavati-Niasari et al., 2015).

ZnS and CdS nanocrystals with a size of 5–10 nm were embedded in CdS/ZnS/In_2S_3 microspheres synthesized by a sonochemistry method at room temperature and normal pressure without the use of templates or surfactants (Zaoyu et al., 2012). The photocatalytic activity of CdS/ZnS/In_2S_3 for water splitting was investigated under visible-light irradiation ($\lambda > 400$ nm) and an especially high photocatalytic activity (apparent yield is 40.9% at 420 nm) was achieved in the absence of any cocatalysts.

Another group interested in photocatalysis was also involved with the sonochemical synthesis of CdS nanocrystals which were embedded in MoO_3 forming MoO_3-CdS core-shell nanospheres (Shen et al., 2012a). The reaction was conducted at room temperature and normal pressure without using any templates or surfactants. The unique core-shell nanostructures play a key role which results in a large increase in the photocatalytic activity for hydrogen production and photodegradation. In particular, the rate of MoO_3-CdS core-shell photocatalytic hydrogen yield reached 5.25 $mmol\,h^{-1}\,g^{-1}$ and exhibited a high apparent yield (28.86% at $\lambda = 420$ nm) of hydrogen production without noble metal cocatalysts. Moreover, the

MoO_3-CdS core-shell composites also showed a very high decomposition rate of Rhodamine B under the irradiation of visible light ($\lambda > 400$ nm).

Among other chalcogenides, Ni and Co sulfides are the promising materials in different cutting-edge research areas like solar cells, supercapacitors, catalysts, and electrode materials. Nickel and cobalt sulfides with various stoichiometries were synthesized sonochemically from nickel and cobalt acetates and different sulfur precursors using a direct immersion ultrasonic probe (Kristl et al., 2017). The following products have been obtained: NiS, Ni_3S_4, $CoS_{1.097}$, and Co_9S_8, with average crystallite sizes in the range of 7–30 nm. The optical band-gap energies in the range 3.3–3.8 eV were observed for the obtained NPs.

17.5 Ultrasound synthesis of metal halide nanoparticles

The common property of the metals, metal oxides, metal chacogenides, and many other nanomaterials that have been synthesized sonochemically or by any other method is that the synthesis was based on the fact that all the synthesized materials do not dissolve in water. While there are hundreds of papers reporting on the synthesis of CdS or ZnS, we are not aware of any report on the synthesis of Na_2S because the material is soluble in water. Section 17.5 will also present recent results in which NPs of NaCl, KI, and KBr, all soluble salts, were synthesized sonochemically. But this section will start with the water-insoluble metal halides.

17.5.1 Ultrasound synthesis of water-insoluble metal halides

The growth of AgCl NPs on silk yarn was achieved by sequential dipping steps in alternating bath of potassium chloride and silver nitrate under ultrasound irradiation (Abbasi and Morsali, 2010a). The effects of ultrasound irradiation, concentration, and sequential dipping steps in the growth of the AgCl NPs have been studied. Particle sizes and morphology of nanoparticle are depending on the power of ultrasound irradiation. Results show a decrease in the particles size as increasing power of ultrasound irradiation. Increase in concentration and sequential dipping steps result an increased particle size. The same author used the same technique for the growth of silver iodide nanoparticles on silk fiber (Abbasi and Morsali, 2010b). Morsali has repeated his sonochemical synthesis of AgCl NPs (Abbasi and Morsali, 2010a, b) for the deposition of the AgCl on ancient textile (Abbasi et al., 2011). The textile samples containing AgCl NPs were tested for their antibacterial efficacy against *Escherichia coli* and were found to possess significant antibacterial activity. Morsali continued this series of synthesizing metal halides by replacing the potassium chloride by potassium bromide preparing the NPs of silver bromide (Morsali and Panjehpour, 2012). These NPs were deposited on polyester fibers instead of on ancient textiles.

AgCl NPs became well known for their high photocatalytic activity and their plasmonic properties because of the metallic silver on their surface. Chen and coworkers reported on a novel one-step sonochemical approach to synthesize a plasmonic photocatalyst of AgCl nanocubes (ca. 115 nm in edge length) with a small amount of Ag metal species is presented (Chen et al., 2012c). The nanoscale Ag/AgCl hybrid photocatalysts with cubic morphology were readily formed under ambient ultrasonic conditions and neither external heat treatment nor reducing agents are required. The size of the Ag/AgCl photocatalysts could be controlled by changing the concentrations of $Ag+$ ions and PVP molecules in the precursor solutions. The compositions, microstructures, influencing factors, and possible growth mechanism of the Ag/AgCl hybrid nanocubes were systematically investigated. The Ag/AgCl photocatalysts show excellent photocatalytic performance for degradation of various dye molecules under visible light.

AgCl NPs were also produced sonochemically from NaCl, PVP, and $AgNO_3$, using a full 2^3 factorial design and three central points, resulting in 11 experiments (Andrade-Neto et al., 2017). The synthesis was carried out using ultrasonic tip at time intervals of 5, 20, and 35 min. The effect of the variables such as the time of synthesis, amount of surfactant, and reagent in the photocatalytic property of AgCl was investigated. The experimental design not only used variables present in the photocatalytic ability of the particles but also provided a mathematical model using the (ANOVA) analysis of variance. It has provided a response surface that characterizes the optimization zone of the photocatalytic activity of the AgCl particles to better visualize the information about its effects. The excellent photocatalytic properties also demonstrated a highly uniform 3D flower-like hierarchical AgCl microspheres (MCS) prepared by sonochemical method with the existence of β-dextrin (Maimaitizi et al., 2019). These Ag MCS exhibited photodegradation efficiency with degrading 98.17% of methylene blue and 88.50% of tetracycline within 40 min, which were both remarkably higher than those of irregular AgCl under visible light irradiation.

BaF_2 nanoparticles were synthesized via a mild sonochemical route from an aqueous solution of $Ba(NO_3)_2$ and NH_4F in the presence of EDTA as a complexing agent under ambient air (Guo et al., 2010). The as-prepared BaF_2 nanocrystals crystallize are in a cubic structure and have an average crystal size of 10 nm. The amount of EDTA plays an important role in controlling the shape and size of the product. Comparative experiments using CTAB as surfactant instead of complexing agent EDTA showed cubic-shaped product with diameter of 400–500 nm.

The substantiated isolation of the antimony subiodide Sb_3I was presented for the first time (Nowak et al., 2010). It was prepared using elemental Sb and I in ethanol under ultrasonic irradiation at 323 K. High-resolution transmission electron microscopy investigations exhibit that the samples are made up of large quantity of NP with diameters smaller than 20 nm and single crystalline in nature.

Fluorides are added to our tooth paste to avoid the formation of plaques (biofilm); it was thus natural that NPs MgF_2 an insoluble metal fluoride was probed for improving the antibiofilm properties (Lellouche et al., 2009). The NPs of MgF_2 were synthesized by microwave radiation using an expensive ionic liquid and its anion BF_4^{-1} as the fluorine source. A cheaper synthetic method using sonochemistry and an aqueous solution of $Mg(Ac)_2$ and HF was reported in 2012 (Lellouche et al., 2012a), affording crystalline well-shaped spherical MgF_2 NPs that showed much improved antibacterial properties against two common bacterial pathogens (*E. coli and S. aureus*). The authors were also able to demonstrate that the antimicrobial activity was dependent on the size of the NPs. In addition, using the described sonochemical process, glass surfaces were coated by the MgF_2 NPs and demonstrated inhibition of bacterial colonization for 7 days. Finally, the antimicrobial activity of MgF_2 NPs against established biofilms was also examined. To further prove that the antibiofilm activity is due to the fluoride ion and not to the cation a water-based synthesis of yttrium fluoride (YF_3) NPs was carried out using sonochemistry (Lellouche et al., 2012b). The sonochemical irradiation of an aqueous solution of yttrium (III) acetate tetrahydrate $Y(Ac)_3{\cdot}(H2O)_4$, containing acidic HF as the fluorine ion source, yielded nanocrystalline needle-shaped YF_3 particles. YF_3 NPs showed antibacterial properties against two common bacterial pathogens (*E. coli* and *S. aureus*) at a mu g/mL range. We were also able to demonstrate that antimicrobial activity was dependent on NPs size. In addition, catheters were surface-modified with YF_3 NPs using a one-step synthesis and coating process. The coating procedure yielded a homogeneous YF_3 NPs layer on the catheter, as analyzed by scanning electron microscopy and energy dispersive spectroscopy. These YF_3 NPs-modified catheters were investigated for their ability to restrict bacterial biofilm formation. The YF_3 -NP-coated catheters were able to significantly reduce bacterial colonization compared to the uncoated surface.

Later on, the group of Gedanken and Banin demonstrated that a combination of sonochemically prepared ZnO and MgF_2 NPs resulted in synergistic activity against both *S. pneumonia and S. aureus* pathogens considered the most common biofilm colonizers of cochlear implants (CI) (Natan et al., 2016). The biocompatibility studies demonstrated that coating with low concentrations of ZnO-MgF_2 resulted in no toxicity toward primary human fibroblasts from the auditory canal. Taken together, these findings underscore the potential of using NPs combinations such as the one presented here to efficiently inhibit bacterial colonization and growth on medical devices such as CIs.

17.5.2 Ultrasound synthesis of water-soluble metal halides

Gedanken and coworkers described a general method for the preparation of salt NPs made from an aqueous solution of ionic compounds (NaCl, KBr, CuSO4, and KI) (Kiel et al., 2012). These NPs were created by the application of ultrasonic waves to the aqueous solutions of these salts. The aqueous solution contained only the salt; no surfactant or any other material was added to the solution. To avoid the dissolution of the salts back into the water, the sonication was carried out in the presence of a glass microscope slide, a parylene-coated glass slide, or a silicon wafer. The ionic NPs were embedded in these substrates by a one-step, ultrasound-assisted procedure. Optimization of the coating process resulted in homogeneous distributions of nanocrystals, 30 nm in size, on the surfaces of the substrates. After 24 h of leaching into water, the NPs of the inorganic salts were still present on the slides, and complete leaching of NPs occurred only after 96 h. A mechanism of the ultrasound-assisted coating is proposed.

17.6 Using ultrasonic waves in the synthesis of graphene, graphene oxide, and other nanomaterials

Few-layered reduced graphene oxide-Pt composites were prepared using a combination of two ultrasound frequencies at 20 and 211 kHz (Vinodgopal et al., 2012). Such a unique dual frequency arrangement operating in tandem yields large exfoliated grapheme sheets with Pt NPs dispersed on them. The extent of reduction achieved by the use of this dual frequency sonication arrangement was evaluated by XPS, IR, and Raman spectroscopies. Transmission electron and atomic force microscopies confirmed the morphology of resulting assemblies to be bi- and single-layered sheets. These composites show good electrocatalytic activity toward methanol oxidation.

Graphene oxide (GO) was used as an effective oxidizing agent for the synthesis of aldehydes and ketones from various alcohols under ultrasonic irradiation (Mirza-Aghayan et al., 2012). Under optimized conditions, quantitative yields of the products were obtained. Compared to other reagents used for the same chemical transformation. GO displays several advantages, including low cost, ease of synthesis, and high stability to ambient conditions.

A facile sonochemical route for the synthesis of graphene nanosheets via reduction of graphene oxide (GO) was reported (Krishnamoorthy et al., 2012). The UV–vis

spectroscopy results showed that the absorption peak was red shifted due to the reduction of GO into graphene. Raman spectra confirmed the restoration of new sp2 carbon domains in graphene sheets after the reduction.

Suslick and coworkers have described a convenient sonochemical method for the preparation of polystyrene functionalized graphenes starting from graphite flakes and a reactive monomer, styrene (Xu and Suslick, 2011). Ultrasonic irradiation of graphite in styrene results in the mechanochemical exfoliation of graphite flakes to single-layer and few-layer grapheme sheets combined with functionalization of the grapheme with polystyrene chains. The polystyrene chains are formed from sonochemically initiated radical polymerization of styrene and can make up to similar to 18 wt% of the functionalized graphene, as determined by thermal gravimetric analysis. This one-step protocol can be generally applied to the functionalization of graphenes with other vinyl monomers for grapheme-based composite materials. TEM image of sonochemically prepared graphene is illustrated in Figure 17.5.

A simple, one-step method for preparing stabilized microspheres of graphene oxide (GO) by applying ultrasonic power to a biphasic system has been reported (Sametband et al., 2012). The microsphere's size was affected by the pH of the aqueous solution, ranging from a few mm to μ m. Further characterization indicated that the microsphere's inner content is composed mainly of organic solvents, though water and GO molecules may be also present at the microsphere's core. The microspheres were stable for several months without a significant conformation change. The authors proposed that the stability arises from hydrophobic and hydrophilic interactions between the GO sheets and the solvents. Changing the organic solvent resulted in changes in the microsphere's morphology.

A number of publications on ultrasound assisted synthesis of graphene and GO were summarized in the Review published in 2017 (Muthoosamy and Manickam, 2017). This review provides detailed fundamental concepts of ultrasonochemistry for the synthesis of graphene, its dispersion, exfoliation, and its functionalization. Necessary parameters of sonication such as frequency, power input, sonication time, type of sonicator, and temperature and dual-frequency sonication are discussed in great length to provide an overview of the resultant graphene products.

The sonochemical route was reported as a highly efficient and comfortable way to produce the copper sulfide (CuS-covellite) and sulfur-doped reduced graphene oxide (S-rGO) nanocomposite (Karikalan et al., 2017). As-synthesized CuS has an excellent electrocatalytic activity when compare to the bulk CuS. This S-rGO/CuS composite was further used for the determination of glucose and acquired good electrocatalytic performances. The S-rGO/CuS was exhibited a wide linear concentration range, 0.0001–3.88 mM and 3.88–20.17 mM, and a low-level detection limit of 32 nM. The practicability of the developed glucose sensor in real biological samples was validated.

In the last years, several new works reported on the sonochemical preparation of ultrasound-assisted synthesis of graphene and GO. Improved "green" method for synthesis of GO using graphite flakes, $KMnO_4$, a mixture of H_2SO_4/H_3PO_4, H_2O_2 and HCl was reported (Farazas et al., 2018). The use of ultrasound optimizes the effect of the reacting agents, decreasing the required amounts of used chemicals. This method produces graphene oxide highly oxidized with greater interlayer spacing over the Hummers' method without producing toxic gases. The results showed that this low-cost method is fully scalable without producing undesirable environmental effects.

An efficient route for graphene oxide (GO) and reduced GO (RGO) synthesis was developed by using an ultrasonic probe and bath alternatively (Sabbaghan et al., 2019). RGO was prepared in acidic and neutral conditions. Well-exfoliated and smooth sheets without crumples were observed in GO. The RGO synthesized in acidic media had fewer layers and smaller crystallite size than that derived from neutral condition. Electrochemical investigations

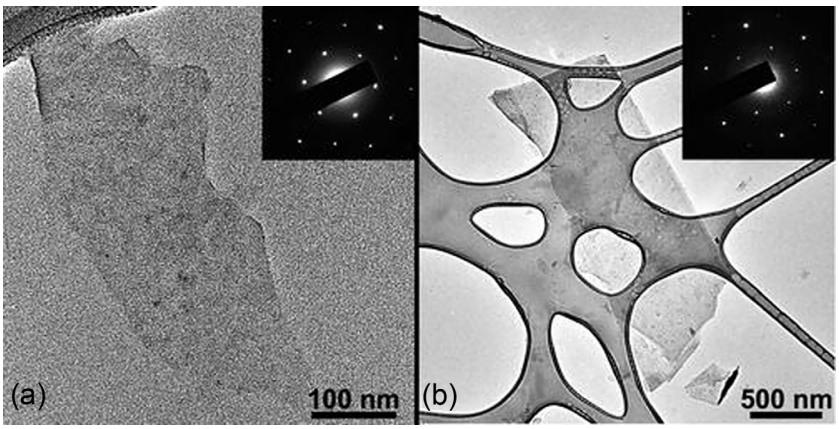


FIGURE 17.5 TEM images of (a) single-layer graphene and (b) trilayer graphene with SAED insets confirming single-layer and few-layer graphenes, respectively. Lacey carbon served as the support.

revealed higher effective surface area and better electrocatalytic activity for the RGO synthesized in acidic media (RGO1). Retained low disorders on the basal plane and high defect on the edge sites of the layers have provided high electrocatalytic activity for RGO1 that make it suitable for (bio)sensing applications.

17.6.1 Ultrasound synthesis of miscellaneous nanoparticles

In this chapter, we report on nanoparticles that do not belong to the various groups mentioned above that were synthesized by the sonochemical technique and we feel that they should be mentioned because they represent a unique class of materials.

The sonochemical synthesis of copper (I) hydride (CuH) by the ultrasonic irradiation of a copper (II) aqueous solution was conducted by Hasin and Wu (2012). A reaction mechanism based on the reduction of Cu(II) by the ultrasound-generated hydrogen atoms was discussed. According to the authors, this is the first time that a metal hydride has been synthesized through sonochemistry.

A report on the preparation of organic compounds made in nanometric size using ultrasonic waves was published recently (Elacqua et al., 2012). Organic nanocrystals of [2.2] paracyclophane (pCp) and tetrakis(4-pyridylcyclobutyl) [2.2] paracyclophane (tpcp) were synthesized. Both nanocrystals exhibit an enhanced fluorescence as compared to dilute solution, while the tpcp nanocrystals also demonstrate a red-shifted fluorescence.

17.7 The use of ultrasound for the deposition of nanoparticles on substrates

The sonochemical irradiation of a liquid causes two primary effects, namely, cavitation (bubble formation, growth, collapse) and heating. When the microscopic cavitation bubbles collapse near the surface of the solid substrate, they generate powerful shock waves and microjets that cause effective stirring/mixing of the adjusted layer of liquid. The after-effects of the cavitation are several hundred times greater in heterogeneous systems than in homogeneous systems (Suslick, 1989). This phenomenon can be applied for coating solid surfaces such as glasses, metals, paper, ceramic, textiles, etc., with active nanoparticles and imparting different properties to the product. In one-step sonochemical reaction, the ultrasonic waves promote the fast migration of the newly formed active nanoparticles to the surface. This fact might cause a local melting of the substrate at the contact sites, which may be the reason why the particles strongly adhere to the surface.

We have already mentioned the results of Sivakumar et al. (2010), which have shown the influences of parameters of ultrasonic power input, sonication time, sonication temperature, and the amount of propanol on the sonochemical reduction of Pt from its precursor hexachloroplatinic acid and then its deposition on rutile TiO_2 (platinization of rutile titania) catalysts. As mentioned above, Morsali (Abbasi and Morsali, 2010a) has shown the ultrasound-assisted coating of silk yarn with AgCl NPs.

An additional approach of the sonochemical deposition was shown by Dang et al. (2010). Magnetite NPs have been coated with silica through the hydrolysis and condensation of tetraethyl orthosilicate (TEOS) under ultrasonic irradiation. The ultrasonic irradiation was used to prevent the agglomeration of the magnetite particles and accelerate the hydrolysis and condensation of TEOS. The dispersibility of silica-coated magnetite particles in aqueous solution was improved significantly and the agglomerate particle size was decreased to 110 nm. It was found that the agglomerate particle size of silica-coated magnetite particles was mainly determined by the coating temperature and the pH value in the silica-coating process. The oxidation of magnetite particles in air was limited through the coated silica.

As mentioned by various examples above, the sonochemical deposition methods might include a one-step process in which the NPs are formed and subsequently deposited on substrates. However, in a case the required NPs cannot be synthesized by the sonochemical method, it is possible to use commercially available NPs and to apply ultrasound irradiation only for coating, so called "throwing stones" method. An example for such application has been shown by Gedanken (Perelshtein et al., 2010). Crystalline MgO and Al_2O_3 NPs have been purchased from Sigma-Aldrich and the ultrasonic waves were used only for the deposition of the commercial NPs on the textile surface. A very dense layer of NPs have been observed on the surface by SEM measurements. The metal oxides used in this research have intrinsic antibacterial properties, and by coating them on textiles, it is possible to impart antibacterial activity to the textiles.

The significant advantage of the sonochemical coating of textile is the stability of antibacterial coating to many washing cycles. This phenomenon was explained because of strong attachment of NPs throwing to the substrate by ultrasonic waves (Perelshtein et al., 2013). The last achievements in the sonochemical coating of various textiles with antibacterial NPs (Gedanken, 2008) were summarized in some reviews (Perelshtein et al., 2016; Perkas et al., 2018).

An additional example for functionalization of the surface was presented by Gedanken (Perkas et al., 2011). Parylene film-coated glass was coated with TiO_2 NPs by the sonochemical method, and its photocatalytic properties were investigated. The TiO_2 nanoparticles formed during the sonochemical hydrolysis of $Ti(i\text{-}OPr)_4$ were thrown to

the surface and strongly attached to the parylene substrate. The photocatalytic activity of the titania-modified parylene film in the photo discoloration of methylene blue was demonstrated. The experimental results revealed a correlation between the uniformity of the nanostructured anatase titania film and its photocatalytic properties.

The sonochemical method was used also for deposition of Ag NPs even on a hard surface such as stainless steel (Soloviev and Gedanken, 2011). The influence of the distance of the stainless steel plate from the sonicator tip was varied, and a homogeneous coating without agglomeration was achieved at a distance of 1 cm. By controlling the reaction conditions and the distance from the tip, a homogeneous monolayer coating of Ag NPs on the stainless steel surface was achieved.

Rodriguez-Gonzalez and coworkers showed the sonochemical method for the deposition of Ag-TiO_2 powder on commercial foamed waste-glass strips (Lee et al., 2011). In order to enhance Ag-TiO_2 deposition, different parameters such as the solvent effect and use of stabilizing agents were evaluated. The best deposition was obtained with an aqueous solution of polyvinyl alcohol (PVA) and an ultrasound irradiation source of 23.3 kHz.

The Ag NPs synthesized by sonochemical polyol reduction of silver ions with ethylene glycol and simultaneously deposited on different forms of TiO_2 powders (commercial Degussa P-25, synthetic anatase, and mesoporous titania) (Perkas et al., 2013). It was found that the sonochemical method provides a very fine homogeneous distribution and strong adherence of Ag NPs (2–3 nm in size) on the surface of the titania support. All prepared Ag–TiO_2 nanocomposites demonstrated a very high antibacterial activity against wide spectra of Gram-positive and Gram-negative bacteria under dark conditions regardless of the structure of the titania support. Biocidal properties of the studied Ag–TiO_2 composites were stable and did not change over more than a year.

We have already presented the work of Gedanken and coworkers that have prepared NPs of water-soluble salts (Kiel et al., 2012). These authors have described general sonochemical method for the preparation of salt NPs made from an aqueous solution of ionic compounds (NaCl, $CuSO_4$, and KI). The salt NPs were deposited on a glass microscope slide, a parylene-coated glass slide, or a silicon wafer, and the ionic NPs were embedded in these substrates by a one-step, ultrasound-assisted procedure. The leaching studies have revealed that after 24 h, no NPs of the inorganic salts were found in the washing solution.

The deposition of antibacterial and antibiofilm NPs on different substrates was shown by Gedanken. One of his works demonstrated the ability of sonochemical ZnO coating to inhibit *Streptococcus mutans* biofilm formation on teeth model as presented in Figure 17.6 (Eshed et al., 2012). Another work of this group demonstrated a novel water-based synthesis of MgF_2 NPs and their subsequent deposition on glass using sonochemistry. The antimicrobial activity and antibiofilm properties of MgF_2 were dependent on the size of the NPs. In addition, yttrium fluoride NPs were successfully deposited on catheter by sonochemical technique in one-step reaction (Lellouche et al., 2012b). The YF_3 NP-coated catheters were able to significantly reduce bacterial colonization compared to the uncoated surface. The ZnO-coated glass prepared by the same group (Applerot et al., 2012b) restricted the biofilm formation of common bacterial pathogens.

Later on the group of Gedanken and Banin studied antibiofilm properties and biocompatibility of urinary catheters coated with Zn-doped CuO ($Zn_{0.12}Cu_{0.88}O$) nanoparticles

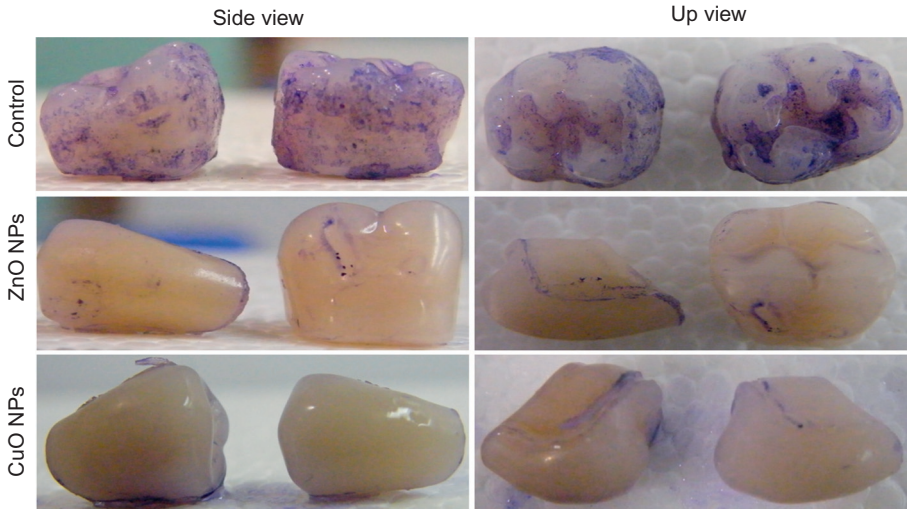


FIGURE 17.6 ZnO and CuO NP-coated teeth restrict *S. mutans* biofilm formation. Coated and uncoated teeth were incubated with *S. mutans* for 24 h. The biofilm biomass that developed was stained by a crystal-violet staining as described in the experimental section.

one-step sonochemical procedure (Shalom et al., 2017). The coated catheters displayed high antibiofilm activity and promising biocompatibility, as indicated by low in vitro cytotoxicity, negligible associated cytokine secretion, and absence of detectable irritation. The biocompatibility and ability of the Zn-doped CuO coating to inhibit biofilm formation were also evaluated in vivo using a rabbit model. The rabbits catheterized with uncoated catheters scored positive for CAUTI by day 4 of the experiment. In contrast, rabbits catheterized with Zn-doped CuO-coated catheters did not exhibit CAUTI until day 7 or remained completely uninfected for the whole duration of the 7-day experiment.

One of the advantages of the sonochemical coating of hollow tubes is the ability to coat the inner and outer walls of the tubes. The inner and the outer walls of hollow tubing with an inner diameter of 0.4–0.9 cm and an outer diameter of 0.6–1.3 cm were coated with Ag NPs by a one-step process using ultrasound irradiation (Friedman et al., 2012). The inner surface of the tubing was found to be coated with more silver than the outer surface. The coating was done on tubing made of rubber, PVC, Teflon, and polyethylene.

In order to inhibit the photocatalytic activity of ZnO, Siddiquey and coworkers have deposited silica layer on ZnO NPs by sonochemical method (Siddiquey et al., 2012). Ultrasonic irradiation of ZnO NPs dispersion in alkaline ethanol–water solutions of TEOS causes rapid coating of the ZnO core with uniform silica layer. The effect of ultrasound on the acceleration of TEOS alkaline hydrolysis is mainly due to the acoustic cavitation which includes three discrete stages: nucleation, bubble growth, and implosive collapse. Silica-coated ZnO NPs demonstrated a significant inhibition of photocatalytic activity against photodegradation of methylene blue dye in aqueous solution.

17.8 Ultrasound synthesis of micro-and nanospheres

In 1990, Suslick and coworkers developed a method using high-intensity ultrasound to make aqueous suspensions of proteinaceous microcapsules filled with water-insoluble liquids, and demonstrated the chemical mechanism of their formation (Suslick and Grinstaff, 1990). Suslick's paper opened up a new field that was extended in a few directions. On one hand, it was extended to include starch, chitosan, DNA, RNA, PEI (Polyethylene imine), PEG, and more. The second direction that Suslick discovery took is the encapsulation of drugs, dyes, magnetic materials, and others in various micro- and nanocapsules. The encapsulation process was a replica of Suslick synthesis, namely, it was done with a mixture of an aqueous solution containing the compound forming the shell of the capsule (various kinds of proteins) and an organic solvent. The ratio of the volumes of the aqueous solution to the organic solvent was also kept as in Suslick work, namely, protein:organic liquid 3:2, and the formation of the sphere was performed sonochemically. To encapsulate a material in the formed sphere, the desired material was added to the solution. In other words, the new mixture contained all the original components plus the encapsulated material. It was found that it is immaterial whether this encapsulated material dissolves in water or in the organic solvent, it was found at the end of the sonication inside the capsule.

Gedanken and coworkers have followed the research of Suslick and synthesized mixed proteinaceous microspheres (MPMs) by the sonochemical method (Angel et al., 2010a). The three proteins used in their experiments are bovine serum albumin (BSA), green fluorescent protein (GFP), and cyan fluorescent protein-glucose binding protein-yellow fluorescent fused protein (CFP-GBP-YFP). The two synthesized microspheres which were made of mixed proteins are BSA-GFP and BSA-(CFP-GBP-YFP). This research provides an estimate of the efficiency of the sonochemical process in converting the native proteins to microspheres. An additional work of this group has shown for the first time a fast and one-step process for the preparation of stable chitosan microspheres by a simple sonochemical method (Skirtenko et al., 2010). The encapsulation of different dyes into these microspheres was readily achieved with more than 75% efficacy by dissolving them into the organic phase before sonication. The chitosan microspheres demonstrated excellent stability toward acidic and basic conditions ranging from pH 4 to 9, thereby indicating their implementation as possible therapeutic and diagnostic agents.

The publication of Koseva (Vassileva and Koseva, 2010) aims to present the current state-of-the-art in the field of sonochemically produced protein micro- and nanocapsules, paying special attention to the proposed mechanisms for their formation, the factors that influence the capsules characteristics as well to the current applications of these particles. Current challenges in the field are also outlined as, for example, the ultrasound protein interaction and other possible aspects of the mechanism of their formation.

Sonochemical production of microspheres can be applied not only on proteins but also on inorganic compounds. Such an application has been presented by Fan (Jia et al., 2010) that shows the synthesis of hollow ZnO microspheres, using carbon spheres as template. A possible growth mechanism for the formation of ZnO microspheres has been proposed, in which carbon spheres play a crucial role in the formation of the wurtzite hollow ZnO microspheres. The specific structure of the hollow spheres may find applications in nanoelectronics, nanophotonics, and nanomedicine.

The unique way of sonochemical preparation of microspheres is also suitable for encapsulation of drugs inside the newly formed microspheres in one-step, simple reaction. A research, which was conducted by Gedanken's group, shows the preparation of starch microspheres loaded with insulin (Grinberg and Gedanken, 2010). A spectrophotometric analytical procedure was selected to evaluate the amount of loaded insulin in the starch microspheres and to perform the release studies. The product is organized in a double-layer structure (insulin layer covered by starch layer), and this composite may provide a new system for the administration of protein drugs. The microspherilization process involves the degradation of the starch to the smaller fragments due to the application of high-intensity ultrasound, and the organization of these fragments in a microsphere structure using the same type of bonds as in regular starch.

Li and coworkers have demonstrated a preparation of magnetic microspheres, based on BSA and Fe_3O_4 NPs (Wu et al., 2011). The nanospheres are modified with Rhodamine B through an electrostatic interaction. The results indicate that the superparamagnetic nanospheres have a particle size of 160 nm, high saturation magnetization of 54 emu/g, and significant fluorescence. MFNs possess potential in medical imaging, drug targeting, and catalysis. Rubira has also reported on the synthesis magnetic microspheres by ultrasound irradiation (Mauricio et al., 2012). Magnetite-nanostructured amylose (AMY) microspheres with well-defined outlines were developed through an ultrasound-induced hydroalcoholic emulsion in 30s. The formation of sphere-shaped polysaccharide particles occurred, upon ultrasound, via a complexation of iron ions from magnetite with carboxyl groups from carboxylated AMY at the interior of the benzyl alcohol-confined water droplets, within which the polysaccharide chains would have been fine-tuned. The introduction of magnetite into the microspheres under ultrasonic irradiation produced sub-1.78 μm size spheres and also rendered a narrower sphere size distribution. Spherical crystalline structures of magnetite with diameters ranging from 28 to 140 nm were observed in the AMY microspheres, indicating an excellent dispersion of the iron oxides if compared to its initial diameter. The author suggested that both the strong interactions resultant from complexation of iron ions with carboxyl groups and the ultrasound waves effectively contributed to disaggregate magnetic particles, dispersing them into smaller crystals. This work offers a self-healing, readily synthesized, friendly environmentally device that can be used in important fields of the health science and material technology.

Another application of sonochemically prepared microspheres as a drug delivery carrier was reported by Rahimipour (Richman et al., 2011). Serum albumin microspheres were synthesized by the sonochemical method, the surface of which is covalently decorated with a short recognition peptide to target amyloid-beta (A beta) as the main pathogenic protein in Alzheimer's disease. Fluorescence-activated cell-sorting analysis and Thioflavin-T binding assay demonstrated that the conjugated microspheres bind with high affinity and selectivity to A beta, sequester it from the medium, and reduce its aggregation.

The sonochemical technique was proven as a deposition method of active materials on various substrates (Angel et al., 2010b). Gedanken has reported on the sonochemical coating of cotton and polyester with drug-loaded proteinaceous microspheres made of BSA and casein proteins (Shimanovich et al., 2012a). It was done by a one-step reaction that lasts 3 min. The efficiency of the sonochemical process in converting the native proteins into microspheres, encapsulating the drug, and coating the fabric has also been studied. An additional work of this group on coating textiles with microspheres included encapsulation of dye in proteinaceous microspheres and their coating on textiles in the one-step reaction (Shimanovich et al., 2012b). The release of the dye was achieved by passing an electric current through the fabric. The conductivity of the polyester fibers resulted from nanosilver (Ag NPs) coated on the surface of these fibers. Both types of coatings (nanosilver coating and the coating of the proteinaceous microspheres) were performed using high-intensity ultrasonic waves. Two different types of dyes, hydrophilic RBBR (Remazol Brilliant Blue R) and hydrophobic ORO (Oil Red 0), were encapsulated inside the microspheres (attached to the surface of polyester) and then released by applying an electric current. The proteinaceous microsphere (PM)-coated conductive fabrics could be used in medicine for drug release. The encapsulated dye can be replaced with a drug that could be released from the surface of fabrics by applying a low voltage.

The same group has also reported on fragrance release profile from sonochemically prepared protein microsphere (Tzhayik et al., 2012). Protein microspheres have been prepared by sonicating a mixture of pure fragrant oil (amyl acetate (AA)) with an aqueous protein (BSA) solution. The prepared protein spheres are of nano- to micrometer sized with an encapsulation efficiency of approximately 97% for the AA present on the surface and inside the BSA capsule. Containers were found stable for more than 6 months when stored sealed at 4°C and 20°C. The evaporation rates were measured by continuously weighing the encapsulated microspheres. The release profiles at 15°C and 25°C display two different evaporation rates. The higher rate is the sum of a few evaporation rates, including water molecules, while the slower rate is due to the evaporation of pure AA. The changes in the evaporation rates occur upon the collapse of the container.

The mechanism of formation of protein microspheres in a biphasic system was reported by Cavaco-Paulo and coworkers (Silva et al., 2012a). Microspheres of BSA and

silk fibroin were produced by applying ultrasound in a biphasic system consisting of an aqueous protein solution and an organic solvent. The protein microspheres were dispersed in an aqueous media where the protein remains at the interface covering the organic solvent. This only occurs when high shear forces are applied that induce changes to force the protein to the interface. Fourier transform infrared results indicate a large increase in the content of the beta-sheet during the formation of silk fibroin microspheres. Molecular dynamics simulations show a clear adaption on the 3D structure of BSA when stabilized at the interface, without major changes in secondary structure. Further studies demonstrate that high water content, oil solvents, and larger peptides with separated and clear hydrophobic and hydrophilic areas lead to more stable and smaller spheres.

Protein microspheres of BSA and HSA for peroxicam release were synthesized sonochemically (Silva et al., 2012b). In order to get small particle size and higher stability, PVA was used during the reaction. These proteinaceous devices did not show cytotoxicity against human skin fibroblasts in vitro, for range concentrations below to 300 mg/L, greatly supporting their potential application in the treatment of inflammatory diseases.

Finally, inorganic microspheres of CdS/ZnS/In_2S_3 were prepared by sonochemical method and reported by Shen et al. (2012b). The photocatalytic properties of the synthesized material revealed an intense absorption band with a steep edge in the visible-light region, and the absorption edge shifts monotonically from 411 to 471 nm as the amount of CdS increases.

The sonochemical microspherization process was also applied to DNA, and nanospheres of 5 different DNA were prepared (Shimanovich et al., 2011a). The five DNAs were (1) genomic DNA extracted from cells, (2) genomic DNA extracted from leaves, (3) DNA plasmid, (4) linear DNA extracted from DNA plasmid, and (5) single-stranded DNA. Dodecane or soya oil was used as the organic solvents in the 3-min sonication process. The efficiency of the sonochemical method in converting native DNA to DNA nanospheres was analyzed by spectrophotometry. It was found that 73.6% of DNA was converted into nanospheres under air and 96% under argon. The stability of the DNA nanospheres was checked by the influence of elevated temperatures and acidity (pH) on DNA stability. Native DNA molecules are known to degrade at elevated temperatures and high pH values (pH > 11). The dsDNA nanospheres were found to be stable at elevated temperatures (from 50°C to 90°C) and over a wide pH range. The ssDNA spheres degraded between pH 13 and 14. Increasing the pH from 7 to 14 (by adding an aqueous solution of NaOH) caused almost no changes in the size of the dsDNA nanospheres or their electrical charge. In addition, the four kinds of dsDNA nanospheres remained spherical and unaffected after incubation with DNase solution. In addition, the genetic information that was encoded in the DNA nanospheres was successfully delivered to competent cells and to human U2OS cancer cells, and expressed in competent (*E. coli*) cells.

Unlike DNA, RNA is a more versatile molecule whose range in the cell is from 21 to thousands of nucleotides and is usually folded into stems and loop structures. For the first time, ultrasonic waves were shown to convert native RNA molecules to RNA nanospheres (Shimanovich et al., 2011b). Because gene expression analysis is becoming a clinical reality and there is a need to collect RNA in minute amounts from clinical samples, keeping the RNA intact is a growing challenge. The RNA samples are notoriously difficult to handle because of their highly labile nature and tendency to degrade even under controlled RNase-free conditions and maintenance in the cold. Silencing the RNA that induces the RNA interference is viewed as the next generation of therapeutics. The stabilization and delivery of RNA to cells are the major concerns in making siRNAs usable drugs. The creation of the nanobubbles was performed by a one-step reaction. Two kinds of RNA were used in this work, the total RNA extracted from cells and defined in-vitro-transcribed substrate. The RNA nanospheres were stable at room temperature for at least 1 month. Additionally, the nanospheres can be inserted into mammalian cancer cells (U2OS). Unlike the DNA, the RNA could be easily disintegrated back to the individual molecules. An investigation of whether the sonochemical radiation of an aqueous solution of RNA and dodecane leads to RNA degradation was performed. To this end, the integrity of RNA in the RNA spheres was stored for 1 week and 1 month. The RNs were destroyed by phenol/chloroform extraction and analyzed by the primer extension technique. The extracted RNA was compared with native (un-nanospherized) RNA. The results showed that sonochemical nanospherization did not lead to the degradation of the RNA during the formation of the sphere, since the size of the corresponding cDNA in the two samples was identical. The biological activity of the regenerated RNA was also explored by RNA kinases. The results suggest that the regenerated RNAs are recognized and labeled by the enzyme as the native RNA is. This research achieved (1) a solution to RNA storage and (2) a way to convert RNA molecules to RNA particles. RNA nanosphere formation is a reversible process, and by using denaturing conditions, the RNA can be refolded into intact molecules.

Shimanovich has also encapsulated RNA molecules in BSA microspheres using a one-step sonochemical process from a water-oil solvent biphasic system (Shimanovich et al., 2011c). For the encapsulation studies, a total RNA (t-RNA) was used as a prototype for siRNA delivery. Since both RNA and BSA form spheres, the question is whether the RNA is encapsulated in the BSA and not the reverse.

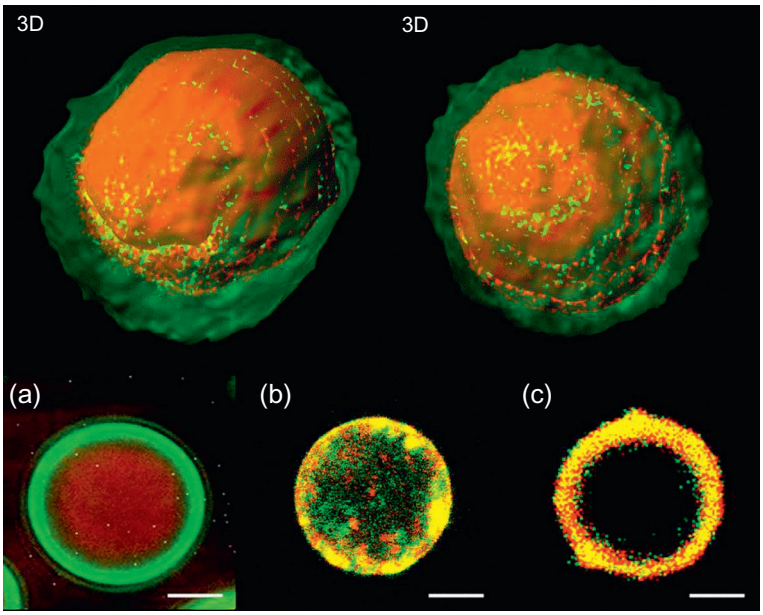


FIGURE 17.7 Confocal microscopy images of CY3-RNA (*red*) encapsulated within fitc-BSA (*green*). (a) *z*-stack confocal image of PMs where the red CY3-RNA was encapsulated inside green Fitc-BSA. (b) *z*-stack confocal image of PMs with CY3-RNA after 24–25 h (the encapsulated RNA, which was found previously to be spread inside the BSA sphere, is now delocalized close to the walls of the sphere). (c) *z*-stack confocal image of a mixed sphere (CY3-RNA and fitc-BSA construct the walls of PM). On the upper part of the image, the reconstruction of the 3D structure of PM with encapsulated CY3-RNA is presented. Left image, view from the side; right image, view from the front. The reconstruction was done from *z*-stack confocal images using "Imaris" image analysis sof.

To answer this question, the colored molecules for the experiment, i.e., fitc-BSA (green) and CY3-RNA (red), were used. The answer is demonstrated in Figure 17.7 below. Confocal microscopy and fluorescence-activated cell sorting indicate that a CY3-RNA (RNA labeled with red fluorescent indocarbocyanine Cy3 dye) sphere is encapsulated in the BSA outer sphere. The diameter of the sphere is 0.63 to 2.74 μm. The reason for this organization can be explained as follows: (1) Kinetically, the formation of RNA spheres is faster. (2) The ratio of BSA: RNA is so large that their interaction leads first to the formation of the BSA outer sphere carrying the RNA inside. A very broad size distribution characterizes the RNA spheres, and therefore, among the loaded BSA spheres, there were sufficiently small spheres to be successfully introduced into *Trypanosoma brucei* parasites and human osteosarcoma U2OS cancer cells.

Gene delivery is one of the steps necessary for gene therapy and for genetic modification. However, delivering DNA into cells is challenging due to its negative charge that leads to repulsion by the negative cell membrane. Gedanken et al. reported on the synthesis of DNA with a DNA encoding to a certain gene microspheres coated with bioavailable polymers polyethylene imine (PEI) and polycaprolactone (PCL) in a short, one-step sonochemical reaction (Reytblat et al., 2016). The polymers were used in order to neutralize the negative charge of the DNA. The study showed that the DNA microspheres not only managed to penetrate the cell without causing it any damage but also expressed the desired gene inside it. This sonochemically prepared DNA microspheres can be used for gene expression in living yeast cells.

The advances in synthesis investigation of polymer microspheres were summarized in the review of Teo (2016). The special emphasis on the sonochemical production of polymer nanocomposites and (bio)polymer microspheres and the biorelated applications of these microspheres was given.

In the review of Ashokkumar et al. (Zhou et al., 2016), specific focus was given to how various experimental conditions could be used to fine-tune the physical and functional properties of polymeric nano- and microspheres. It has been shown that their properties could be controlled by the power and frequency of ultrasound, the type of ultrasonic horn, and postsonication technique. The importance of thiol functional groups for enhancing the stability of shell was also highlighted.

To conclude, the sonochemical method for preparation of micro- and nanospheres has received great attention over the last years as it is evidenced by the increased number of papers and research groups involved in this topic. Great advantages are the one-step procedure, simple equipment required, and high yields gained when choosing the appropriate combination of parameters (ultrasound characteristics, irradiation time, components, temperature, pH, etc.). Moreover, it appears to be an efficient microencapsulation technique for producing core-shell vehicles of bioactive agents. The successful application of microbubbles in medical diagnostics encourages the design of protein-based microcapsules for drug targeting. The extension of the application area of sonochemistry as a tool for fabricating nanomaterials makes the method more universal and significantly increases its potential for practical implementation.

17.9 Conclusions and future trends

Scanning the literature for the work that has been done in relation to the application of ultrasonic waves to the synthesis of NPs and their application reveals a continuous growth. This arises from the many applications that the NPs fabricated sonochemically have. In the review, we have tried to bring to the attention of the reader a consisted list of these papers. Our goal was that a reader will have an opportunity to get an idea of what has been done in the period of 2010–2012 in this field, and it will enable him to quickly learn about the synthesis of certain NPs. In the second edition, we have extended the period of publications till 2019.

We have also emphasized the two unique properties of sonochemistry which are unparalleled, namely, coating NPs on surfaces, and the formation of microspheres and nanospheres of various compounds by ultrasonic emulsification. In the last years, the special attention was put on the ultrasound-assisted "green synthesis" of functional NPs with antibacterial, photocatalytic, and biosensoring properties.

Although it is difficult to predict in what direction sonochemistry is moving, we foresee that grapheme and graphene oxide in relation to ultrasonic waves will be a topic that will attract many researchers. Part of it is due to the decision of the European Community to choose graphene, one of the two flagships for the coming 10 years.

The application of sonochemical coating on various materials will also be a topic for scientific and technological developments. In the field of synthesis, much attention will be devoted to control over shape and size, because basically, scientists have already shown that all common chemical major materials can be prepared using ultrasonic waves, what will come now is the fine-tuning, namely, control over the mentioned parameters.

It is also predicted that a similar chapter that will be written in 5–10 years from now will have to address industries that are operating synthesizing nanoparticles using sonochemistry.

References

Abbasi, A.R., Morsali, A., 2010a. Ultrasound-assisted coating of silk yarn with silver chloride nanoparticles. Coll. Surf. A-Phys. Chem. Eng. Asp. 371, 113–118.

Abbasi, A.R., Morsali, A., 2010b. Formation of silver iodide nanoparticles on silk fiber by means of ultrasonic irradiation. Ultrason. Sonochem. 17, 704–710.

Abbasi, A.R., Bohloulzadeh, M., Morsali, A.J., 2011. Preparation of AgCl nanoparticles@ancient textile with antibacterial activity under ultrasound irradiation. J. Inorg. Organomet. Polym. Mater. 21, 504–510.

Abramov, O.V., 1994. Ultrasound in Liquid and Solid Metals. CRC Press, Boca Raton.

Andrade-Neto, N.F., Garcia, L.M.P., Longo, E., Li, M.S., Paskocimas, C. A., Bomio, M.R.D., Motta, F.V., 2017. Photoluminescence and photocatalytic properties of ag/AgCl synthesized by sonochemistry: statistical experimental design. J. Mater. Sci. Mater. Electron. 28, 12273–12281.

Angel, U., Matas, D., Michaeli, S., Cavaco-Paulo, A., Gedanken, A., 2010a. Microspheres of mixed proteins. Chem. A Eur. J. 16 (7), 2108–2114.

Angel, U., Silva, C.M., Cavaco-Paulo, A., Gedanken, A., 2010b. Attaching different kinds of proteinaceous nanospheres to a variety of fabrics using ultrasound radiation. Isr. J. Chem. 50, 524–529.

Applerot, G., Lellouche, J., Lipovsky, A., Nitzan, Y., Lubart, R., Gedanken, A., Banin, E., 2012a. Understanding the antibacterial mechanism of CuO nanoparticles: revealing the route of induced oxidative stress. Small 8, 3326–3337.

Applerot, G., Lellouche, J., Perkas, N., Nitzan, Y., Gedanken, A., Banin, E., 2012b. ZnO nanoparticle-coated surfaces inhibit bacterial biofilm formation and increase antibiotic susceptibility. RSC Adv. 2 (6), 2314–2321.

Arulmani, S., Kumar, P.V., Landi, G., Anandan, S., 2019. Palladium/copper nanoalloy supported on carbon nanotubes for the electrooxidation of methanol and ethylene glycol. Chem. Select. 2019 (4), 6130–6139.

Askarinejad, A., Bagherzadeh, M., Morsali, A., 2010. Catalytic performance of Mn_3O_4 and Co_3O_4 nanocrystals prepared by sonochemical method in epoxidation of styrene and cyclooctene. Appl. Surf. Sci. 256, 6678–6682.

Aslani, A., Bazmandegan-Shamili, A., Kaviani, K., 2010. Sonochemical synthesis, characterization and optical analysis of some metal oxide nanoparticles (MO-NP; M=Ni, Zn and Mn). Phys. B Cond. Matt. 405, 3972–3976.

Avivi Levi, S., Gedanken, A., 2002. S-S bonds are not required for the sonochemecial formation proteinaceous microspheres: the case of streptavidin. Biochem. J. 366, 705–707.

Azizian-Kalandaragh, Y., Khodayari, A., 2010. Aqueous synthesis and characterization of nearly monodispersed ZnS nanocrystals. Phys. Stat. Sol. (A) Appl. Mat. Sci. 207, 2144–2148.

Ban, I., Kristl, M., Danc, V., Danc, A., Drofenik, M., 2012. Preparation of cadmium telluride nanoparticles from aqueous solutions by sonochemical method. Mater. Lett. 67, 56–59.

Bang, J.H., Suslick, K.S., 2010. Applications of ultrasound to the synthesis of nanostructured materials. Adv. Mater. 22, 1039–1059.

Baykal, A., Kavas, H., Durmus, Z., Kazan, S., Topkaya, R., Toprak, M.S., 2010. Sonochemical synthesis and chracterization of Mn_3O_4 nanoparticles. Cent. Eur. J. Chem. 8, 633–638.

Cabanas-Polo, S., Suslick, K.S., Sanchez-Herencia, A.J., 2011. Effect of reaction conditions on size and morphology of ultrasonically prepared $Ni(OH)_2$ powders. Ultrason. Sonochem. 18, 901–906.

Cau, C., Guari, Y., Chave, T., Larionova, J., Nikitenko, S.I., 2014. Thermal and sonochemical synthesis of porous $(Ce,Zr)O_2$ mixed oxides from metal β-diketonate precursors and their catalytic activity in wet air oxidation process of formic acid. Ultrason. Sonochem. 21, 1366–1373.

Chave, T., Navarro, N.M., Nitsche, S., Nikitenko, S.I., 2012. Mechanism of Pt(IV) sonochemical reduction in formic acid media and pure water. Chem. A Eur. J. 18, 3879–3885.

Chen, D., Liu, H.Y., Li, L., 2012a. One-step synthesis of manganese ferrite nanoparticles by ultrasonic wave-assisted ball milling technology. Mater. Chem. Phys. 134, 921–924.

Chen, D., Liu, H.Y., Xia, S.R., 2012b. One-step decomposition of basic carbonates into single-phase crystalline metallic oxides nanoparticle by ultrasonic wave-assisted ball milling technology. Ceram. Int. 38, 821–825.

Chen, D.L., Yoo, S.H., Huang, Q.S., Ali, G., Cho, S.O., 2012c. Sonochemical synthesis of Ag/AgCl nanocubes and their efficient visible-light-driven photocatalytic performance. Chem. A Eur. J. 18, 5192–5200.

Chraibi, F., Fahoume, M., Loghmarti, M., Mzerd, A., Hassanain, N., Delplancke, J.L., 2011. Formation and characterization of $CuInSe_2$ nanoparticles. Sens. Lett. 9, 2364–2367.

Dang, F., Enomoto, N., Hojo, J., Enpuku, K., 2010. Sonochemical coating of magnetite nanoparticles with silica. Ultrason. Sonochem. 17 (1), 193–199.

Dang, P.N., Quoc, T.T., Xuan, S.T., Thanh, C.H., Hoang, N.N., Hoang, H. N., 2012. Crystallization and magnetic properties of amorphous iron-chromium oxide nanoparticles synthesized by sonochemistry. Adv. Nat. Sci.: Nanosci. Nanotechnol. 3, 015017.

Dar, N., Chen, K.Y., Nien, Y.T., Perkas, N., Gedanken, A., Che, I.G., 2015. Sonochemically synthesized Ag nanoparticles as a SERS active substrate and effect of surfactant. Appl. Surf. Sci. 331, 219–224.

Ding, C., Ting, X.A., 2010. One-step synthesis of Zn to single-phase nanocrystalline ZnO by solid-liquid reaction ball milling assisted by ultrasonic wave. J. Amer. Ceram. Soc. 93, 2675–2678.

Elacqua, E., Jurgens, P.T., Baltrusaitis, J., MacGillivray, L.R., 2012. Organic nanocrystals of [2.2] paracyclophanes achieved via sonochemistry: enhanced and red-shifted emission involving edge-to-face chromophores. CrystEngComm 14, 7567–7571.

Eshed, M., Lellouche, J., Matalon, S., Gedanken, A., Banin, E., 2012. Sonochemical coatings of ZnO and CuO nanoparticles inhibit streptococcus mutants biofilm formation on teeth model. Lang. Des. 28 (33), 12288–12295.

Farazas, A., Mavropoulos, A., Christofilos, D., Tsiaoussis, I., Tsipas, D., 2018. Ultrasound assisted green synthesis and characterization of graphene oxide. Int. J. Nanosci. Nanotechnol. 14, 11–17.

Feng, D., Kato, K., Imai, H., Wada, S., Haneda, H., Kuwabara, M., 2011. Growth of $BaTiO_3$ nanoparticles in ethanol-water mixture solvent under an ultrasound-assisted synthesis. Chem. Eng. J. 170, 333–337.

Friedman, A., Perkas, N., Koltypin, Y., Gedanken, A., 2012. Depositing nanoparticles inside millimeter-size hollow tubing. Appl. Surf. Sci. 258 (7), 2368–2372.

Gedanken, A., 2004. Using sonochemistry for the fabrication of nanomaterials. Ultrason. Sonochem. 11, 47–55.

Gedanken, A., 2007. Doping nanoparticles into polymers and ceramics using ultrasound radiation. Ultrason. Sonochem. 14, 418–430.

Gedanken, A., 2008. Preparation and properties of proteinaceous microspheres made sonochemically. Chem. A Eur. J. 14, 3840–3853.

Ghanbari, N., Hoseini, S.J., Bahrami, M., 2017. Ultrasonic assisted synthesis of palladium-nickel/iron oxide core–shell nanoalloys as effective catalyst for Suzuki-Miyaura and *p*-nitrophenol reduction reactions. Ultrason. Sonochem. 39, 467–477.

Ghodrati, M.S., Haghighi, M., Mohamdzadeh, J.S.S., Pourabas, B., Pipelzadeh, E., 2011. Phenol decomposition under sunlight using a sonochemically synthesized $CdSe/TiO_2$ nanocatalyst. React. Kinet. Mech. Catal. 104, 49–60.

Ghosh, T., Ullah, K., Nikam, V., Park, C.Y., Meng, Z.D., Oh, W.C., 2012. The characteristic study and sonocatalytic performance of CdSe–graphene as catalyst in the degradation of azo dyes in aqueous solution under dark conditions. Ultrason. Sonochem. 20, 768–776.

Gonzalez, J.R., Alcantara, R., Nacimiento, F., Tirado, J.L., 2011. CoSn-graphite electrode material prepared by using the polyol method and high-intensity ultrasonication. Electrochem. Acta 56, 9808–9817.

Gonzalez-Reyes, L., Hernandez-Perez, I., Arceo, L.D.B., Dorantes-Rosales, H., Arce-Estrada, E., Suarez-Parra, R., Cruz-Rivera, J.J., 2010. Temperature effects during Ostwald ripening on structural and bandgap properties of TiO_2 nanoparticles prepared by sonochemical synthesis. Mater. Sci. Eng., B 175, 9–13.

Grinberg, O., Gedanken, A., 2010. The development and characterization of starch microspheres prepared by a sonochemical method for the potential drug delivery of insulin. Macromol. Chem. Phys. 211 (8), 924–931.

Guo, Q., Geng, J., Jiang, L.P., Zhu, J.J., 2010. Sonochemical syntheses of BaF_2 nanoparticles and cubes. J. Inorg. Chem. 26, 2121.

Guumlmeci, C., Zhengrong, L., Casadonte, D.J., Korzeniewski, C., 2012. Pt-Ni nanoparticles for oxygen reduction prepared by a sonochemical method. J. Electrochem. Soc. 159, F35–F41.

Hasin, P., Wu, Y.Y., 2012. Sonochemical synthesis of copper hydride (CuH). Chem. Comm. 48, 1302–1304.

He, C.X., Lei, B.G.X., Wang, Y.F., Su, C.Y., Fang, Y.P., Kuang, D.B., 2010. Sonochemical preparation of hierarchical ZnO hollow spheres for efficient dye-sensitized solar cells. Chem. A Eur. J. 16, 8757–8761.

Hwang, C.H., Park, J., Song, M., Lee, J.H., Shim, I.W., 2011. Syntheses of CdTe quantum dots and nanoparticles through simple sonochemical method under multibubble sonoluminescence conditions. Bull. Korean Chem. Soc. 32, 2207–2211.

Jia, X.H., Fan, H.Q., Zhang, F.Q., Qin, L., 2010. Using sonochemistry for the fabrication of hollow ZnO microspheres. Ultrason. Sonochem. 17 (2), 284–287.

Karikalan, N., Karthik, R., Chen, S.M., Karuppiah, C., Elangovan, A., 2017. Sonochemical synthesis of sulfur doped reduced graphene oxide supported CuS nanoparticles for the non-enzymatic glucose sensor applications. Sci. Report. 7, art 2494.

Kiel, S., Grinberg, O., Perkas, N., Charmet, J., Keppner, H., Gedanken, A., 2012. Forming nanoparticles of water-soluble ionic molecules and embedding them into polymer and glass substrates. Beilstein J. Nanotechnol. 3, 267–276.

Koo, Y.S., Yun, B.K., Jung, J.H., 2010. Magnetic property of alpha-Fe_2O_3 nanoparticles prepared by sonochemistry and take-off technique. J. Magn. 15, 21–24.

Krishnamoorthy, K., Kim, G.S., Kim, S.J., 2012. Graphene nanosheets: ultrasound assisted synthesis and characterization. Ultrason. Sonochem. 20, 644–649.

Kristl, M., Ban, I., Danc, A., Danc, V., Drofenik, M., 2010. A sonochemical method for the preparation of cadmium sulfide and cadmium selenide nanoparticles in aqueous solutions. Ultrason. Sonochem. 17, 916–922.

Kristl, M., Dojer, B., Gyergyek, S., Kristl, J., 2017. Synthesis of nickel and cobalt sulfide nanoparticles using a low cost sonochemical method. Heliyon 3, e00273.

Kumar, B., Smita, K., Sánchez, E., Guerra, S., Cumbal, L., 2016. Eco-friendly ultrasound-assisted rapid synthesis of gold nanoparticles using *Calothrix* algae. Adv. Nat. Sci. Nanosci. Nanotechnol. 7, 02513.

Landau, M.V., Vradman, L., Herskowitz, M., Koltypin, Y., Gedanken, A., 2001. Ultrasonically controlled deposition-precipitation - co-MoHDS catalysts deposited on wide-pore MCM material. J. Catal. 201, 22–36.

Lee, S.W., Obregon-Alfaro, S., Rodriguez-Gonzalez, V., 2011. Photocatalytic coatings of silver-TiO_2 nanocomposites on foamed waste-glass prepared by sonochemical process. J. Photochem. Photobiol. A Chem. 221 (1), 71–76.

Lellouche, J., Kahana, E., Elias, S., Gedanken, A., Banin, E., 2009. Antibiofilm activity of nanosized magnesium fluoride. Biomaterials 30, 5969–5978.

Lellouche, J., Friedman, A., Lellouche, J.P., Gedanken, A., Banin, E., 2012a. Improved antibacterial and antibiofilm activity of magnesium fluoride nanoparticles obtained by water-based ultrasound chemistry. Nanomedicine 8, 702–711.

Lellouche, J., Friedman, A., Gedanken, A., Banin, E., 2012b. Antibacterial and antibiofilm properties of yttrium fluoride nanoparticles. Int. J. Nanomedicine 7, 5611–5624.

Livage, J., 1981. Amorphous transition – metal oxides. J. Phys. 42, 981–992.

Maimaitizi, H., Kadeer, K., Reheman, A., Talifu, D., Tursun, Y., Abulikemu Abulizi, A., 2019. One-pot sonochemical synthesis of 3D flower-like hierarchical AgCl microsphere with enhanced photocatalytic activity. Environ. Sci. Pollut. Res. 26, 26883–26892.

Malka, E., Perelshtein, I., Lipovsky, A., Shalom, Y., Naparstek, L., Perkas, N., Patick, T., Lubart, R., Nitzan, Y., Banin, E., Gedanken, A., 2013. Eradication of multi-drug resistant bacteria by a novel Zn-doped CuO nanocomposite. Small 9, 4069–4076.

Manjamadha, V.P., Muthukumar, K., 2016. Ultrasound assisted green synthesis of silver nanoparticles using weed plant. Bioprocess Biosyst. Eng. 39, 401–411.

Martinez-Casillas, D.C., Vazquez-Huerta, G., Perez-Robles, J.F., Solorza-Feria, O., 2010. Syntghesis and cheracterization of PdAg nanoparticles as oxygen electrocatalyst in acidic medium. J. New Mater. Electrochem. Syst. 13, 163–169.

Matin, M.A., Jang, J.A., Lee, E., Kwon, Y.U., 2012. Sonochemical synthesis of Pt-doped Pd nanoparticles with enhanced electrocatalytic activity for formic acid oxidation reaction. J. Appl. Electrochem. 42, 827–832.

Mauricio, M.R., Guilherme, M.R., Kunita, M.H., Muniz, E.C., Rubira, A. F., 2012. Designing nanostructured microspheres with well-defined outlines by mixing carboxyl-functionalized amylose and magnetite via ultrasound. Chem. Eng. J. 189, 456–463.

Mirza-Aghayan, M., Kashef-Azar, E., Boukherroub, R., 2012. Graphite oxide: an efficient reagent for oxidation of alcohols under sonication. Tetrahedron Lett. 53, 4962–4965.

Mizukoshi, Y., Sato, K., Konno, T.J., Masahashi, N., 2010. Dependence of photocatalytic activities upon the structures of Au/Pd bimetallic nanoparticles immobilized on TiO_2 surface. Appl. Catal. Environ. 94, 248–253.

Mohseni Meybodi, S., Hosseini, S.A., Rezaee, M., Sadrnezhaad, S.K., Mohammadyani, D., 2012. Synthesis of wide band gap nanocrystalline NiO powder via a sonochemical method. Ultrason. Sonochem. 19, 841–845.

Morsali, A., Panjehpour, A., 2012. Ultrasonic-assisted synthesis of nanostructured lead(II) coordination polymers as precursors for preparation of lead(II) oxide nanoparticles. Inorg. Chim. Acta 391, 210–217.

Muthoosamy, K., Manickam, S., 2017. State of the art and recent advances in the ultrasound-assisted synthesis, exfoliation and functionalization of graphene derivatives. Ultrason. Sonochem. 39, 478–493.

Natan, M., Edin, F., Perkas, N., Yacobi, G., Perelshtein, I., Segal, E., Homsy, A., Laux, E., Keppner, H., Rask-Andersen, H., Gedanken, A., Banin, E., 2016. Two are better than one: combining ZnO and MgF_2 nanoparticles reduces Streptococcus pneumonia and Staphylococcus aureus biofilm formation on cochlear implants. Adv. Funct. Mater. 26, 2473–2481.

Neto, D.M.A., Freire, R.M., Gallo, J., Freire, T.M., Queiroz, D.C., Ricardo, N.M.P.S., Vasconcelos, I.F.V., Mele, G., Carbone, L., Mazzetto, S.E., Bañobre-López, M., Fechine, P.B.A., 2017. Rapid sonochemical approach produces functionalized Fe_3O_4 nanoparticles with excellent magnetic, colloidal, and relaxivity properties for MRI application. J. Phys. Chem. C 121, 24206–24222.

Niederberger, M., Bard, M.H., Stucky, G.D., 2002. Benzyl alcohol and transition metal chlorides as a versatile reaction system for the nonaqueous and low-temperature synthesis of crystalline nano-objects with controlled dimensionality. J. Am. Chem. Soc. 124, 13642–13643.

Nouri, A., Yaraki, M.T., Lajevardi, A., Rezaei, Z., Ghorbanpour, M., Tanzifi, M., 2020. Ultrasonic-assisted green synthesis of silver nanoparticles using *Mentha aquatica* leaf extract for enhanced antibacterial properties and catalytic activity. Colloid. Interface Sci. Com. 35, 100252. https://doi.org/10.1016/j.colcom.2020.100252.

Nowak, M., Szperlich, P., Talik, E., Szala, J., Rzychon, T., Stroz, D., Nowrot, A., Solecka, B., 2010. Sonochemical preparation of antimony subiodide. Ultrason. Sonochem. 17, 219–227.

Ohayon, E., Gedanken, A., 2010. The application of ultrasound radiation to the synthesis of nanocrystalline metal oxide in a non-aqueous solvent. Ultrason. Sonochem. 17, 173–178.

Pazos-Perez, N., Schaferhans, J., Skorb, E.V., Fery, A., Andreeva, D.V., 2012. Ultrasound driven formation of metal-supported nanocatalysts. Microporous Mesoporous Mater. 154, 164–169.

Perelshtein, I., Applerot, G., Perkas, N., Grinblat, J., Hulla, E., Wehrschuetz-Sigl, E., Hasmann, A., Guebitz, G., Gedanken, A., 2010. Ultrasound radiation as a "throwing stones" technique for the production of antibacterial nanocomposite textiles. ACS Appl. Mater. Interfaces 2 (7), 1999–2004.

Perelshtein, I., Ruderman, Y., Perkas, N., Beddow, J., Singh, G., Vinatoru, M., Joyce, E., Mason, T.J., Blanes, M., Molla, K., Gedanken, A., 2013. The sonochemical coating of cotton withstands 65 washing cycles at hospital washing standards and retains its antibacterial properties. Cellulose 20, 1215–1221.

Perelshtein, I., Lipovsky, A., Perkas, N., Gedanken, A., Moschini, E., Mantecca, P., 2015. The influence of the crystalline nature of nano-metal oxides on their antibacterial and toxicity properties. Nano Res. 8, 695–707.

Perelshtein, I., Perkas, N., Gedanken, A., 2016. Ultrasonic coating of textiles by antibacterial and antibiofilm nanoparticles. In: Ashokkumar, M. (Ed.), Handbook of Ultrasonics and Sonochemistry. 2016. Springer, pp. 967–993.

Perkas, N., Wang, Y., Koltypin, Y., Gedanken, A., Chandrasekaran, S., 2001. Mesoporous iron-titania catalyst for cyclohexane oxidation. Chem. Comm., 988–989.

Perkas, N., Amirian, G., Girshevitz, O., Charmet, J., Laux, E., Guibert, G., Keppner, H., Gedanken, A., 2011. Modification of Parylene film-coated glass with TiO2 nanoparticles and its photocatalytic properties. Surf. Coat. Technol. 205 (10), 3190–3197.

Perkas, N., Lipovsky, A., Amirian, G., Nitzan, Y., Gedanken, A., 2013. Biocidal properties of TiO_2 powder modified with ag nanoparticles. J. Mater. Chem. B 1, 5309–5316.

Perkas, N., Perelshtein, I., Gedanken, A., 2018. Coating textiles with antibacterial nanoparticles using the sonochemical technique. J. Mach. Construct. Mainten. 111, 15–26.

Phu, N.D., Sy, T.X., Cao, H.T., Dinh, N.N., Thien, L.V., Hieu, N.M., Nam, N.H., Hai, N.H., 2012. Amorphous iron-chromium oxide nanoparticles prepared by sonochemistry. J. Non Cryst. Solids 358, 537–543.

Polagani, R.K., Suryawanshi, P.L., Gumfekar, S.P., Sonawane, S.H., Ashokkumar, M., 2018. Ultrasound-assisted synthesis of Pt–Co/C bimetallic alloys for oxygen reduction in PEM fuel cells. Sustain. Energy Fuels 2, 1491–1499.

Qingming Shen, Q.M., Min, Q., Shi, J., Jiang, L.P., Hou, W., Zhu, J.J., 2010. Ultrasonic assisted electrochemical synthesis of shape-controlled 3D platinum electrocatalysts. Acta Chim. Sin. 68, 1319–1324.

Raabe, D., Hessling, D., 2010. Synthesis of hollow metallic particles via ultrasonic treatment of a metal emulsion. Scr. Mater. 62, 690–692.

Radziuk, D.V., Shchukin, D.G., Mohwald, H., 2011a. Acoustic cavitation for engineering of gold sols in silver nitrate solutions. Ultrason. Sonochem. 18, 853–863.

Radziuk, D., Skirtach, A., Gessner, A., Kumke, M.U., Zhang, W., Mohwald, H., Shchukin, D., 2011b. Ultrasonic approach for formation of erbium oxide nanoparticles with variable geometries. Langmuir 27, 14472–14480.

Ramesh, S., Koltypin, Y., Prozorov, R., Gedanken, A., 1997. Sonochemical deposition and characterization of nanophasic amorphous nickel on silica microspheres. Chem. Mater. 9, 546–551.

Ranjbar, M., Celik, O., Najafi, S.H.M., Sheshmani, S., Mobarakeh, N.A., 2012. Synthesis of lead(II) minoxidil coordination polymer: A new precursor for lead(II) oxide and lead(II) hydroxyl bromide. J. Inorg. Organomet. Polym. Mater. 22, 837–844.

Ranjbar-Karimi, R., Bazmandegan-Shamili, A., Aslani, A., Kaviani, K., 2010. Sonochemical synthesis, characterization and thermal and optical analysis of CuO nanoparticles. Phys. B Condens. Matter 405, 3096–3100.

Ranjbar-Karimi, R., Hashemi-Uderji, S., Bazmandegan-Shamili, A., 2011. MgO nanoparticles as a recyclable heterogeneous catalyst for the synthesis of polyhydroquinoline derivatives under solvent free conditions. Chin. J. Chem. 29, 1624–1628.

Reytblat, I., Lipovsky, A., Gedanken, A., 2016. DNA microspheres coated with bioavailable polymer as an efficient gene expression agent in yeasts. J. Nanomater. art 5178029, 8 pp.

Richman, M., Wilk, S., Skirtenko, N., Perelman, A., Rahimipour, S., 2011. Surface-modified protein microspheres capture amyloid-beta and inhibit its aggregation and toxicity. Chem. A Eur. J. 17 (40), 11171–11177.

Sabbaghan, M., Charkhan, H., Ghalkhani, M., Beheshtian, J., 2019. Ultrasonic route of synthesis, characterization and electrochemical study of graphene oxide and reduced graphene oxide. Res. Chem. Intermed. 45, 487–505.

Salavati-Niasari, M., Bazarganipour, M., Ghasemi-Kooch, M., 2015. Facile sonochemical synthesis and characterization of CdTe nanoparticles. Synth. React. Inorg., Met.-Org., Nano-Met. Chem. 45, 1558–1564.

Sametband, M., Shimanovich, U., Gedanken, A., 2012. Graphene oxide microspheres prepared by a simple, one-step ultrasonication method *new*. J. Chem. 36, 36–39.

Shalom, Y., Perelshtein, I., Perkas, N., Gedanken, A., Banin, E., 2017. Catheters coated with Zn-doped CuO nanoparticles delay the onset of catheter-associated urinary tract infections. Nano Res. 10, 520–533.

Shchukin, D.G., Radziuk, D., Moehwald, H., 2010. Ultrasonic fabrication of metallic nanomaterial and nanoalloys. Ann. Rev. Mater. Res. 40, 345–362.

Shen, Z.Y., Chen, G., Yu, Y.G., Wang, Q., Zhou, C., Hao, L.X., Li, Y.X., He, L.M., Mu, R.D., 2012a. Sonochemistry synthesis of nanocrystals embedded in a MoO_3-CdS core-shell photocatalyst with enhanced hydrogen production and photodegradation. J. Mater. Chem. 22, 19646–19651.

Shen, Z., Chen, G., Wang, Q., Yu, Y., Zhou, C., Wang, Y., 2012b. Sonochemistry synthesis and enhanced photocatalytic H_2 production activity of nanocrystals embedded in CdS/ZnS/In_2S_3 microspheres. Nanoscale 4 (6), 2010–2017.

Shimanovich, U., Eliaz, D., Aizer, A., Vayman, I., Michaeli, S., Shav-Tal, Y., Gedanken, A., 2011a. Sonochemical synthesis of DNA nanospheres. Chem. Bio. Chem. 12, 1678–1681.

Shimanovich, U., Volkov, V., Eliaz, D., Aizer, A., Michaeli, S., Gedanken, A., 2011b. Stabilizing RNA by the sonochemical formation of RNA nanospheres. Small 7, 1068–1074.

Shimanovich, U., Tkacz, I.D., Eliaz, D., Cavaco-Paulo, A., Michaeli, S., Gedanken, A., 2011c. Encapsulation of RNA molecules in BSA microspheres and internalization into trypanosoma brucei parasites and human U_2OS cancer cells. Adv. Funct. Mater. 21 (19), 3659–3666.

Shimanovich, U., Cavaco-Paulo, A., Nitzan, Y., Gedanken, A., 2012a. Sonochemical coating of cotton and polyester fabrics with "antibacterial" BSA and casein spheres. Chem. A Eur. J. 18 (1), 365–369.

Shimanovich, U., Perelshtein, I., Cavaco-Paulo, A., Gedanken, A., 2012b. Releasing dye encapsulated in proteinaceous microspheres on conductive fabrics by electric current. ACS Appl. Mater. Interfaces 4 (6), 2926–2930.

Shin, N., Saravanakumar, K., Wang, M.H., 2019. Sonochemical mediated synthesis of iron oxide (Fe_3O_4 and Fe_2O_3) nanoparticles and their characterization, cytotoxicity and antibacterial properties. J. Clust. Sci. 30, 669–675.

Siddiquey, I.A., Furusawa, T., Sato, M., Bahadur, N.M., Alam, M.M., Suzuki, N., 2012. Sonochemical synthesis, photocatalytic activity and optical properties of silica coated ZnO nanoparticles. Ultrason. Sonochem. 19 (4), 750–755.

Silva, R., Ferreira, H., Azoia, N.G., Shimanovich, U., Freddi, G., Gedanken, A., Cavaco-Paulo, A., 2012a. Insights on the mechanism of formation of protein microspheres in a biphasic system. Mol. Pharm. 9 (11), 3079–3088.

Silva, R., Ferreira, H., Carvalho, A.C., Gomes, A.C., Cavaco-Paulo, A., 2012b. Protein microspheres as suitable devices for piroxicam release. Colloids Surf. B Biointerfaces 92, 277–285.

Sivakumar, M., Towata, A., Yasui, K., Tuziuti, T., Kozuka, T., Iida, Y., 2010. Dependence of sonochemical parameters on the platinization of rutile titania - an observation of a pronounced increase in photocatalytic efficiencies. Ultrason. Sonochem. 17, 621–627.

Sivakumar, M., Towata, A., Yasui, K., Tuziuti, T., Kozuka, T., Iida, Y., Maiorov, M.M., Blums, E., Bhattacharya, D., Sivakumar, N., Ashok, M., 2012. Ultrasonic cavitation induced water in vegetable oil emulsion droplets - A simple and easy technique to synthesize manganese zinc ferrite nanocrystals with improved magnetization. Ultrason. Sonochem. 19, 652–658.

Sivakumar, P., Nayak, P.N., Grinblat, J., Perkas, N., Markovsky, B., Aurbach, D., Gedanken, A., 2016. Effect of sonochemistry: Li- and Mn-rich layered high specific capacity cathode materials for Li-ion batteries. J. Solid State Electrochem. 20, 1683–1695.

Skirtenko, N., Tzanov, T., Gedanken, A., Rahimipour, S., 2010. One-step preparation of multifunctional chitosan microspheres by a simple sonochemical method. Chem. A Eur. J. 16 (2), 562–567.

Soloviev, M., Gedanken, A., 2011. Coating a stainless steel plate with silver nanoparticles by the sonochemical method. Ultrason. Sonochem. 18 (1), 356–362.

Sugimoto, M., 1994. Amorphous characteristics in spinel ferrites containing glassy oxides. J. Magn. Magn. Mater. 133, 460–462.
Suslick, K.S., 1989. The chemical effects of ultrasound. Sci. Am. 260 (2), 80–86.
Suslick, K.S., Grinstaff, M.W., 1990. Protein microencapsulation of nonaqueous liquids. J. Am. Chem. Soc. 112, 7807–7809.
Teo, B.M., 2016. Ultrasonic synthesis of polymer nanoparticles. In: Ashokkumar, M. (Ed.), Handbook of Ultrasonics and Sonochemistry. Springer, Singapore, pp. 365–393.
Theerdhala, S., Bahadur, D., Vitta, S., Perkas, N., Zhong, Z.Y., Gedanken, A., 2010. Sonochemical stabilization of ultrafine colloidal biocompatible magnetite nanoparticles using amino acid L-arginine, for possible bio applications. Ultrason. Sonochem. 17, 730–737.
Tzhayik, O., Cavaco-Paulo, A., Gedanken, A., 2012. Fragrance release profile from sonochemically prepared protein microsphere containers. Ultrason. Sonochem. 19 (4), 858–863.
Usman, A.I., Aziz, A.A., Noqta, O.A., 2019. Green sonochemical synthesis of gold nanoparticles using palm oil leaves extracts. Mater. Today 7, 803–807.
Vassileva, E.D., Koseva, N.S., 2010. Sonochemically born proteinaceous micro-and nanocapsules advances in protein chemistry and structural biology. Adv. Protein Chem. Struct. Biol. 80, 205–252.
Vinodgopal, K., Neppolian, B., Salleh, N., Lightcap, I.V., Grieser, F., Ashokkumar, M., Ding, T.T., Kamat, P.V., 2012. Dual-frequency ultrasound for designing two dimensional catalyst surface: reduced graphene oxide-Pt composite. Colloids Surf. A Physicochem. Eng. Asp. 409, 81–87.
Virot, M., Chave, T., Horlait, D., Clavier, N., Dacheux, N., Ravaux, J., Nikitenko, S.I., 2012. Catalytic dissolution of ceria under mild conditions. J. Mater. Chem. 22, 14734–14740.
Wang, H.Q., Yang, G.F., Li, Q.Y., Zhong, X.X., Wang, F.P., Li, Z.S., Li, Y. H., 2011. Porous nano-MnO_2: large scale synthesis via a facile quick-redox procedure and application in a supercapacitor. New J. Chem. 35, 469–475.
Wu, S.X., Jiang, W., Sun, Z.D., Dai, J.J., Liu, L., Li, F.S., 2011. Preparation of novel magnetic fluorescent nanospheres by sonochemical method. J. Magn. Magn. Mater. 323, 2170–2173.
Xiaohua, J., Huiqing, F., Faqiang, Z., Lei, Q., 2010. Using sonochemistry for the fabrication of hollow ZnO microspheres. Ultrason. Sonochem. 17, 284–287.
Xu, H.X., Suslick, K.S., 2010. Sonochemical synthesis of highly fluorescent ag nanoclusters. ACS Nano 4, 3209–3214.
Xu, H.X., Suslick, K.S., 2011. Sonochemical preparation of functionalized Graphenes. J. Am. Chem. Soc. 133, 9148–9151.
Yang, P., Zhang, A.Y., Cheng, X., Zhou, G.J., Lue, M.K., 2010. Morphology-tunable fibers with Fe_3O_4 nanocrystals fabricated through assembly. J. Colloid Interface Sci. 351, 77–82.
Zaoyu, S., Gang, C., Qun, W., Yaoguang, Y., Chao, Z., Yu, W., 2012. Sonochemistry synthesis and enhanced photocatalytic H_2 production activity of nanocrystals embedded in $CdS/ZnS/In_2S_3$ microspheres. Nanoscale 4, 2010–2017.
Zhaoyong, Z., Kaili, L., Lei, C., Jiang, C., 2012. Ultrafast synthesis and characterization of carbonated hydroxyapatite nanopowders via sonochemistry-assisted microwave process. Ultrason. Sonochem. 19, 1174–1179.
Zheng, H., Matseke, M.S., Munonde, T.S., 2019. The unique Pd@Pt/C core-shell nanoparticles as methanol-tolerant catalysts using sonochemical synthesis. Ultrason. Sonochem. 57, 166–171.
Zhou, M., Cavalieri, F., Ashokkumar, M., 2016. Ultrasonic synthesis and characterization of polymer-shelled microspheres. In: Ashokkumar, M. (Ed.), Handbook of Ultrasonics and Sonochemistry. Springer, Singapore, pp. 1021–1047.
Zhu, S.M., Zhang, D., Chen, Z.X., Zhou, G., Jiang, H.B., Li, J.L., 2010. Sonochemical fabrication of morpho-genetic TiO_2 with hierarchical structures for photocatalyst. J. Nanopart. Res. 12, 2445–2456.
Zin, V., Dabala, M., 2010. Iron-chromium alloy nanoparticles produced by pulsed sonoelectrochemistry: synthesis and characterization. Acta Mater. 58, 3311–3319.
Zin, V., Campadello, E., Zanella, A., Brunelli, K., Dabala, M., 2010. Synthesis and characterization of metal nanoparticles produced by sonoelectrochemistry. Metall. Ital. 1, 29–37.

Further reading

Avivi Levi, S., Nitzan, Y., Dror, R., Gedanken, A., 2003. An easy sonochemical route for the encapsulation of tetracycline in bovine serum albumin microspheres. J. Am. Chem. Soc. 125, 15712–15713.
Geng, J., Jiang, L.P., Zhu, J.J., 2012. Crystal formation and growth mechanism of inorganic nanomaterials in sonochemical syntheses. Sci. China Chem. 55, 2292–2310.
Islam, M.N., Phong, L.V., Jeong, J.R., Kim, C., 2011. A facile route to sonochemical synthesis of magnetic iron oxide (Fe_3O_4) nanoparticles. Thin Solid Film 519, 8277–8279.
Kharissova, O.V., Kharisov, B.I., Ruiz Valdes, J.J., Mendez, O.U., 2011. Ultrasound in nanochemistry: recent advances. Synth. React. Inorg., Met.-Org., Nano-Met. Chem. 41, 429–448.
Leonelli, C., Mason, T.J., 2010. Microwave and ultrasonic processing: now a realistic option for industry. Chem. Eng. Process. 49, 885–900.
Moosavi, R., Abbasi, A.R., Yousefi, M., Ramazani, A., Morsali, A., 2012. Ultrasound-assisted coating of polyester fiber with silver bromide nanoparticles. Ultrason. Sonochem. 19, 1221–1226.
Pol, V.G., Reisfeld, R., Gedanken, A., 2002. Sonochemical synthesis and optical properties of europium oxide nanolayer coated on titania. Chem. Mater. 14, 3920–3924.
Wang, X., Teng, X., 2010. Sonochemical synthesis of proteinaceous microspheres. Prog. Chem. 22, 1086–1093.
Wang, J.Z., Hu, T., Chen, Z.Y., 2003. Research on sonochemical preparation of nano-materials. Rare Met. Mater. Eng. 32, 585–590.
Zhang, K., Park, B.-J., Fang, F.F., Choi, H.J., 2009. Sonochemical preparation of polymer nanocomposites. Molecules 14, 2095–2110.
Zhu, J.J., Singh, V., 2005. Proceedings of the SPIE – 'The International Society for Optical Engineering. pp. 5929–5931.

Chapter 18

Ultrasonic cleaning

F.J. Fuchs[†] and J.D. Kramlick

Blackstone-NEY Ultrasonics (A Division of the Cleaning Technologies Group), Jamestown, NY, United States

18.1 Introduction

Ultrasonic cleaning utilizes high-frequency, high-intensity sound waves in a liquid to affect, facilitate, or enhance the removal of foreign contaminants from surfaces of objects immersed in the ultrasonically activated liquid. More recently, ultrasonic technology has been employed in a growing number of applications including chemical processes and surface conditioning which, although outside the classic definition of cleaning, utilizes basically the same mechanisms. Demands for increased cleanliness have driven the development of increasingly effective ultrasonic technology particularly within the last two decades. Today, it is possible to customize ultrasonic waves to optimize effects in a wide range of applications as described by Puskas and Piazza (2000).

18.2 Applications

18.2.1 Cleaning

The classic definition of cleaning is the removal of foreign contaminants from the surface of a substrate without creating a mechanical or chemical change to the substrate itself. In most cases, cleaning is employed for the purpose of either enhancing the performance or function of the object being cleaned or for cosmetic reasons. Contaminants are generally characterized as soluble, emulsifiable, or insoluble. Soluble contaminants include solids or liquids that can be directly dissolved by a liquid. An example of a soluble solid contaminant is common table salt. Salt can be directly dissolved by water. Oil is an example of a liquid contaminant that can be dissolved not only by solvents such as halogenated hydrocarbons but can also be emulsified using a mixture of water and cleaning agents specifically intended for the purpose. Insoluble contaminants include such things as glass particles and metal shavings. In some cases, insoluble solid contaminants are of the same composition as the substrate from which they are being removed. Removing loose graphite particles from a graphite substrate is an example. Although less common, there are also liquid contaminants, such as some silicone-based materials, which are difficult if not impossible to dissolve. It is not uncommon for contaminants to be comprised of a mixture of both soluble and insoluble components. Metal shavings adhered to a surface by a film of oil is an example of such a contaminant. Fingerprints are another example of a compound contamination containing organic oils and ionic compounds (salts).

18.2.2 Related applications

Although outside the definition of "cleaning" as defined above, there are a growing number of applications that utilize ultrasonic energy to enhance chemical processes. One example of such an application is passivation, a process in which an acid is utilized to remove acid-soluble components of a substrate and promote oxidation of key alloying elements. An example of this is the use of nitric acid in the removal of free iron and the oxidation of chromium during the passivation of stainless steels.

Although not yet fully developed as applications, there are a growing number of instances where ultrasonic energy is utilized to alter the surface configuration of a substrate to change properties including wettability and adhesion by altering the surface topography. This still poorly defined effect of ultrasonic energy in a liquid is difficult to distinguish from cleaning but may play a significant role in some applications including the modification of surfaces of electronics materials.

18.3 History

It is generally agreed that the roots of ultrasonic technology date back to the nineteenth century discoveries of Savart, Galton, Tyndal, and Rayleigh, among others. These were followed by discoveries of magnetostriction by Joule (1847) and piezoelectricity (1880) by Jacques and Pierre Curie (1880) and Graff (1981). The Curies discovered that some materials change dimension when an electrical voltage is applied, with an inverse effect of a voltage generated under application of force. The first piezoelectric materials were naturally occurring crystals such as quartz

[†]Deceased

Power Ultrasonics. https://doi.org/10.1016/B978-0-12-820254-8.00019-1
Copyright © 2023 Elsevier Ltd. All rights reserved.

and Rochelle Salts. With the early twentieth-century development of means of generating alternating electrical currents, it was found that these materials when cut, polished, and sized could be set into resonant vibration in electrical circuits to act as precise frequency generators. They were also used to generate ultrasonic sound waves. Paul Langevin and others utilized the piezoelectric effect as early as 1918 to develop early sonar devices intended to detect the presence of, and measure distances to, submarines during World War I (Graff, 1981; Katzir, 2012).

Observations of hydrodynamic and acoustic cavitation date to the nineteenth century. These include the first estimates of bubble collapse pressures by Rayleigh (1917). In the 1930s, researchers at RCA Corporation noticed the phenomenon as a cloudiness surrounding a crystal oscillator that was part of an electrical circuit being cooled by a fluorinated hydrocarbon liquid as described by Lamm (2003). The path from this recognition to the first practical use of ultrasonic energy to enhance cleaning in the early 1950s is not clear. What is known is that the first ultrasonic cleaning devices operated at frequencies up to several hundred kHz which is near the top of the ultrasonic frequency spectrum. Ultrasonic cleaners operating at such high frequencies found little initial practical application as high-frequency ultrasonic cleaning devices lacked the cavitation and implosion intensity required to remove significant amounts of contaminant as described later in this chapter. Once the mechanics of cavitation and implosion became better understood, lower ultrasonic frequencies providing higher implosion intensities were employed to improve the effectiveness of ultrasonic cleaning. There are (anecdotal) reports of early ultrasonic cleaners that operated at frequencies as low as 6–10 kHz. Although functional, their use was short-lived due to the unbearable noise they produced within the audible range for humans.

18.4 Ultrasonic cleaning hardware

An ultrasonic cleaning system is made up of two components: an ultrasonic transducer and a high-frequency power supply, commonly called an "ultrasonic generator." The ultrasonic transducer elements are attached to a diaphragm, sometimes called the "radiating surface," which is arranged to contact the liquid to be ultrasonically activated. This is accomplished either by physically attaching ultrasonic transducers to the outside of the cleaning vessel or through the use of a secondary housing with ultrasonic transducer elements attached to one or more of its faces from within which is immersed in the liquid. More recently, resonant tubular vibrators excited by driving elements mounted at the end(s) (generally called "push-pull" or "rod" transducers) have been employed in some applications. The vibration of the transducer is thereby introduced into the liquid. The ultrasonic generator is a source of high-frequency alternating electrical energy specifically designed to power the associated ultrasonic transducer array at one or more of its resonant frequencies.

18.4.1 Transducers

To avoid confusion, it should be noted that the term "transducer" is used in the industry to describe both the individual transducer driving elements as well as a collection of a number of these individual elements grouped together in an array and applied to a single vibrating diaphragm.

Early ultrasonic cleaning devices utilized slabs of piezoelectric material, often barium titanate, which were adhesively attached to the exterior of small metallic or glass vessels as a source of ultrasonic vibration. Partially due to a lack of understanding of the mechanics of the ultrasonic cleaning process and partially due to the limitations of design of early piezoelectric devices, most operated at relatively high frequencies up to several hundred kHz. Devices operating at such high frequencies were minimally effective and had limited use for reasons to be explained in more detail later in this chapter. As understanding of the technology increased, it was recognized that lower frequencies produced superior cleaning results. This discovery opened a wider range of applications for ultrasonic cleaning. Best results in early applications were commonly achieved at frequencies in the range of 20 kHz (just above the range of human audibility) where the implosion of cavitation voids releases the maximum amount of energy as will be discussed later. The early lower frequency devices were fragile and not very reliable due to the high internal stresses produced in both the adhesive bond and within the unconstrained piezoelectric material. Piezoelectric materials of the day were susceptible to fracturing and were sensitive to moisture which effectively limited their viability as a source of vibration. These piezoelectric materials also deteriorated with age and when used at high temperature as described by Wang et al. (1998).

In the late 1950s, magnetostrictive devices largely replaced early piezoelectric devices as a more robust and reliable source of vibration in ultrasonic cleaner applications. Magnetostrictive materials change dimension in response to the introduction of a magnetic field as observed by Joule (1847).

Magnetostrictive devices utilize a coil of wire surrounding a resonant "stack" comprised of strips of magnetostrictive material, often nickel, cut to a resonant length at the desired operating frequency. The benefit of this design was that the nickel strips could be metallurgically bonded to the cleaning vessel by means of silver brazing. This made them structurally superior to the quartz piezoelectric devices which could only be attached using the relatively

low-strength adhesive technology available at that time. The nickel strips, although somewhat susceptible to fatigue fracture at extremely high amplitude, are not sensitive to moisture and do not degrade with temperature or age. In some cases, magnetostrictive transducers were cooled by a recirculating bath of chilled water by either spraying or immersing the entire transducer assembly in chilled water.

With the advent of ceramic piezoelectric materials in the 1950s, the pendulum swung back toward piezoelectric devices as the source of vibration for ultrasonic cleaning. Ceramic piezoelectric materials were less susceptible to the effects of aging, moisture, and elevated temperature than were their crystal predecessors. Furthermore, when used in a sandwich (or composite) configuration developed by Langevin (Graff, 1981; Manbachi and Cobbold, 2011), these ceramics were kept in a constant state of compression which minimized the issue of fracturing although the ceramic piezoelectric materials were already far stronger than previous quartz piezoelectric materials.

Although there were early piezoelectric transducer designs that incorporated features that allowed transducer elements to be attached to radiating plates using metallurgical means such as silver brazing as patented by Antonevich (1968), adhesive technology had advanced by this time to allow reliable bonding using adhesives. This overcame the problem that the use of aluminum or an aluminum alloy is almost mandatory to provide the proper acoustic impedance match of the transducer to the radiating plate, usually stainless steel, and the contacting liquid beyond.

Today, most ultrasonic cleaning equipment utilizes piezoceramics in the Langevin "sandwich" configuration, as shown in Figure 18.1, in which the ceramic elements serve to excite a larger, resonant composite structure.

Although magnetostrictive transducers are still available from some suppliers of ultrasonic equipment, they suffer from low conversion efficiency as compared with that of piezoelectric devices. They also have a practical frequency limit of approximately 30 kHz due to geometric configuration limitations.

18.4.2 Generators

A high-frequency electrical power supply, commonly referred to as an ultrasonic generator, is required to power ultrasonic transducers. The continued development of new generator technology was nearly as important to the growth of ultrasonic technology as was the development of new transducer technology in the advancement of ultrasonics. Vacuum tube technology was used for ultrasonic generators up until the development of solid state devices in the late 1960s. Advances of solid-state technology up to the present have allowed the development of more sophisticated ultrasonic generators which can be made very powerful and can operate at a wide range of frequencies as well as produce custom-shaped waveforms. Customized waveforms are found beneficial in many applications.

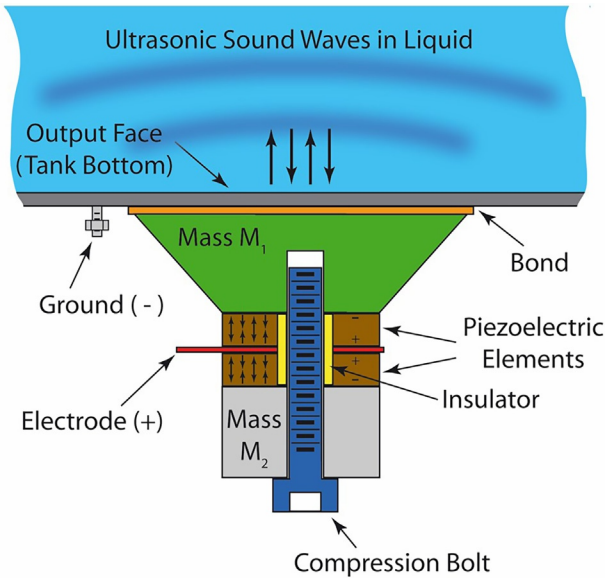


FIGURE 18.1 A piezoelectric transducer is comprised of one or more piezoelectric elements "sandwiched" between two masses. The entire assembly is resonant at the operating frequency. *(Source: Fuchs—Blackstone-NEY Ultrasonics.)*

18.4.3 Factors driving development

Ultrasonic cleaning technology advancements have been driven by both needs for new technology and to find new applications for evolving hardware technology. This mixture has resulted in a somewhat erratic path for the development of the technology which some will argue is, even today, more an "art" than a science. Major developments have often been closely held for competitive reasons by both the manufacturers of the hardware and those using the technology. The list of process variables is large and the range of their interaction is so complex that isolation of cause and effect is difficult even for those who have attempted to apply rigorous scientific methodology in their efforts. For the most part, advances in hardware technology have been spawned by the introduction of improved supporting technology including piezoelectric materials, adhesives, and electronic devices among others.

18.5 Mechanism of ultrasonic cleaning

Ultrasonic cleaning is normally performed at frequencies ranging from approximately 20 to 200 kHz. In this frequency range, high-intensity sound waves create cavitation voids, often referred to as bubbles, in liquids.

Author's note: The word "bubble" describes a pocket of gas surrounded by a thin liquid film and implies that the

bubble is supported by internal pressure and is buoyant. As this definition does not accurately describe the void produced during ultrasonic cavitation and since there appears to be no other word to apply to the phenomenon, we will use the terms void and cavitation void throughout the remainder of this chapter.

Sound waves above this frequency range are also beneficial in cleaning, but the cleaning mechanism is thought to be based on something other than cavitation as suggested by Pereira (2010). The use and effect of frequencies above several hundred kHz will be discussed later in this chapter.

18.5.1 Cavitation

When vibrations are introduced into a liquid, sound waves consisting of areas of alternating positive and negative pressure (as related to ambient) are created which radiate through a liquid from the source of vibration. The source of vibration is the ultrasonic transducer. The negative pressure area of a sound wave is called a rarefaction, while the positive pressure portion of the wave is called a compression. Any given point in an ultrasonically activated liquid will see alternating positive and negative pressures as sound waves pass through the liquid while the liquid remains essentially stationary. As the amplitude of vibration is increased, the pressure extremes in the rarefaction and compression portions of the traveling sound wave intensify accordingly. Liquids, although commonly thought of as noncompressible, are sufficiently compressible to support the travel of a sound wave. They will not, however, support negative pressures indefinitely as a liquid will vaporize under negative pressure conditions (Figure 18.2).

Many things can happen in a liquid under reduced pressure conditions. For one, a liquid subjected to a vacuum less than its vapor pressure will vaporize. Water, for example, will vaporize (boil) at lower temperatures in a vacuum than it will at atmospheric pressure. This phase transformation, however, requires a finite amount of time which varies with the physical properties of the liquid including temperature and the intensity of the localized vacuum created in rarefaction. The changes to a liquid under vacuum conditions are precipitated by and occur preferentially at locations where there are discontinuities in the liquid. Examples of discontinuities include small particles of solid material and microvoids or microbubbles present in the liquid.

Once the negative pressure in the rarefaction of the sound wave exceeds the tensile strength of the liquid, a void (cavitation bubble) is formed. A microbubble previously existing in the liquid, for example, may increase in size as it resonates, growing in size with each passing pressure cycle.

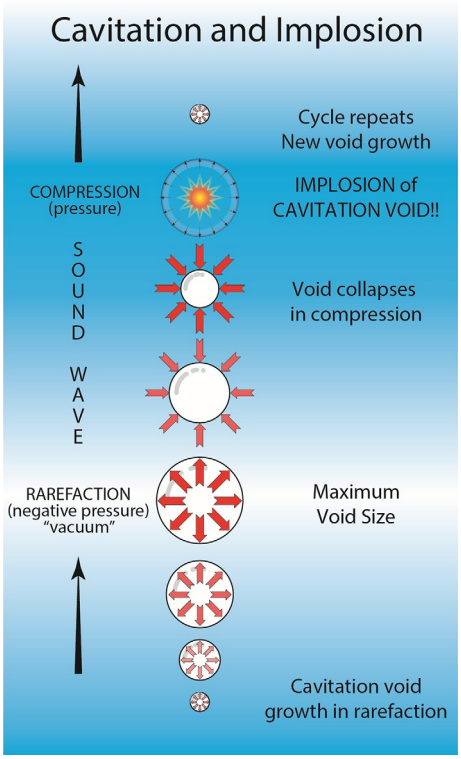


FIGURE 18.2 Cavitation voids form as a sound wave rarefaction passes. They may oscillate (stable cavitation) or implode (transient cavitation) as subsequent compressions, and rarefactions follow. Cavitation voids are often called "bubbles." *(Source: Fuchs—Blackstone-NEY Ultrasonics.)*

In the case of particles, a small void may form adjacent to the surface of the particle due to the relatively weak strength of the bond between the liquid and the surface of the particle. Over several compression-rarefaction cycles, voids thus formed grow to a size that exceeds that which can be supported by the recurring pressure cycles in the liquid.

This results in a catastrophic collapse of the cavitation void which may be precipitated or assisted by the passing of a subsequent area of compression. This catastrophic collapse is called an implosion. When a cavitation void implodes, it produces an intense wave or pressure which radiates from the point of implosion. It is these shock waves resulting from the implosions of myriads of cavitation voids that produce the beneficial effects of ultrasonics in cleaning. There is substantial evidence that pressures at the site of a cavitation void implosion may exceed 10,000 psi and that temperatures may reach 10,000°F. These numbers are based on calculation and, as yet, have not been directly measured—although spectroscopy has reportedly been used to verify the high temperatures. When a cavitation void implodes, the energy of the pressure wave created by the implosion is released preferentially in the direction of any nearby discontinuity. The junction between the liquid

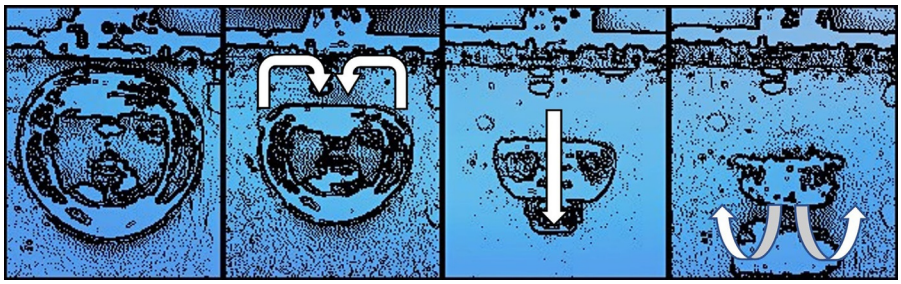


FIGURE 18.3 Once a cavitation void is created and grows sufficiently large, it collapses in implosion. Here (from left to right) is a sequence showing a void reaching critical size, the beginning of collapse and toroid formation, the micro-jetting effect and the subsequent shock waves emanating from the implosion. *(Source: Blackstone-NEY Ultrasonics.)*

and the surface of a part being cleaned as well as the contaminants to be removed create such discontinuities. The energy of the implosion of a cavitation void, therefore, is directed toward the surface being cleaned (Brennen, 1995) (Figure 18.3).

18.5.2 Cleaning

Removal of contaminants from the surfaces of parts being cleaned may be accomplished by dissolution or emulsification of the contaminant by a suitable liquid media. In the case of a nonsoluble contaminant, removal is accomplished by physically displacing particles to a distance sufficient to break the bonds holding them to the surface being cleaned. In the case of dissolution, the energy released by the implosions of cavitation voids serves to provide micro-agitation at the solvent/contaminant interface. This micro-agitation enhances the efficiency of interaction between the solvent and the contaminant being removed. It also serves to move liquid solvent with a high content of dissolved contaminant away from the site of interaction, thereby allowing less contaminated solvent to come into contact and interact with the remaining contaminant. In the case of insoluble contaminants, repeated cavitation implosions serve to physically break mechanical bonds. Once the contaminant is broken free from the surface, continuing implosions in the area serve to move it further from the part surface to prevent its re-attachment.

18.6 Benefits of ultrasonic cleaning

Ultrasonic cleaning is unique in its ability to remove contaminants that other technologies cannot remove and to effectively clean in areas that are not accessible using other techniques. Competing technologies include spray washing, turbulation, agitation, and brushing, among others. These technologies, in general, are line of sight in nature. There must be direct access to the contaminated surface for them to be effective. The physical energy in many of these cases is delivered indirectly. In a spray system, for example, the energy for the spray stream is imparted by a remote pump. Pressurized liquid is delivered to a nozzle which increases the stream's velocity and directs it growth the surface to be cleaned. Cleaning is achieved by the impact of the high-velocity stream with the surface being cleaned. Not only is energy lost in each step of the process, but only that energy in the portion of the stream that ultimately impacts the cleaning target provides benefit with the rest being lost. Sprays are not capable of reaching areas hidden from direct access of the spray nozzle to the part surface. Cleaning of blind holes with spray technology, for example, can only benefit from a flushing action as the spray creates a pressure differential across the hole opening to force liquid into and out of the hole.

Another technology, brushing, is similarly limited in that any surface the brush bristle is not able to reach will not be cleaned. In a world where surface geometry of many parts is measured in nanometers, brushes are unable to reach all surfaces of the part to be cleaned.

Ultrasonic cleaning technology, unlike those described above, can penetrate and clean any surface which can be reached by a sound-conducting liquid. This means that blind holes, thread roots, parts with complex geometry, minute surface contours, and many otherwise impossible cleaning tasks may be accomplished using ultrasonic cleaning technology.

The fact that ultrasonic energy can excite and pass through many solids (somewhat dependent on their thickness) makes it possible to effectively clean interior surfaces of hollow parts.

18.7 Ultrasonic cleaning process variables

Effective application of the ultrasonic cleaning process requires consideration of a number of process variables. Time, temperature, and chemistry remain important in ultrasonic cleaning as they are in other cleaning technologies. Other variables specific to the ultrasonic cleaning process must also be considered to maximize its effectiveness. As ultrasonic cleaning depends on the energetic implosion of cavitation voids, variables that affect the intensity and number of implosions of cavitation voids in the liquid must also be considered.

18.7.1 Size and number of cavitation voids

As one would expect, the amount of energy released in the implosion of a cavitation void is related to its size. Larger cavitation voids implode releasing more energy than smaller cavitation voids. The release of additional energy, in general, is beneficial to the ultrasonic cleaning process. Likewise, the ultrasonic cleaning process benefits as larger numbers of cavitation voids which result in implosions are formed. On the other hand, too much energy released by excessively sized cavitation voids or an overabundance of implosions due to cavitation void collapse can, in some cases, cause damage to parts susceptible to such damage as will be discussed later in this chapter. The intensity and number of implosions of cavitation voids are affected by many process variables as described by Brennen (1995).

18.7.2 The effect of temperature and chemistry on liquid properties

Temperature is one of the most significant variables to be considered in maximizing the energy released by imploding cavitation voids. This is because so many properties of a liquid are affected by changes in temperature. These include the viscosity of the liquid, the surface tension of the liquid, the solubility of gas in the liquid, the diffusion rate of dissolved gasses in the liquid, and the vapor pressure of the liquid, all of which will influence the energy and number of cavitation void implosions produced. In general, increasing the temperature of a cavitating liquid results in more effective ultrasonic cleaning. There are, however, diminishing benefits of increased temperature especially as the boiling temperature of the liquid is approached. At the boiling point, cavitation voids may form but are immediately filled with the vapor of the liquid which prevents their implosion (Brennen, 1995; Caupin and Hebert, 2006).

The effect of temperature may be amplified by the fact that increased temperature often improves the performance of a cleaning chemistry. It is often difficult to distinguish if the benefit of increasing temperature is due to enhanced ultrasonic performance or increased chemical activity.

Finally, increased temperature enhances the solubility of many contaminants. This is a factor that is often overlooked in the development of a cleaning process.

Many of the effects of temperature can also be achieved by other changes to the liquid including the addition of chemistry and the use of certain techniques to prepare a liquid for maximum ultrasonic cleaning effect.

18.7.3 Viscosity

The viscosity of most liquids is reduced as temperature is increased. Reduced liquid viscosity is beneficial to the ultrasonic cleaning process. Low liquid viscosity benefits the growth of cavitation voids. Viscous liquids are sluggish and cannot respond quickly enough to form cavitation voids which grow to a sufficient size to violently implode. Liquids such as motor oil and glycerin do not cavitate well, if at all, due to their high viscosity. The addition of chemical cleaning agents may also affect the viscosity of a liquid.

18.7.4 Surface tension

In general, the surface tension of a liquid is reduced by an increase in temperature. Reduced surface tension is beneficial to the ultrasonic cleaning process. Often the effect of temperature combines with that of a cleaning chemistry with surface tension reducing properties to enhance the beneficial effect of low surface tension in a liquid.

18.7.5 Dissolved gas and the diffusion rate of dissolved gas

For most effective cavitation void implosion, the cleaning liquid must contain as little dissolved gas as possible. Nearly all liquid at a temperature below its boiling point contains dissolved gas. Gas dissolved in the liquid may diffuse into a cavitation void in a process of "rectified diffusion" (see Chapter 2 for further information) during the void growth phase. Gas contained in the cavitation void effectively prevents its violent implosion as described by Rooze (2012).

During the negative pressure or rarefaction portion of the sound wave, cavitation voids begin to form. As negative pressure grows within the void, gasses dissolved in the cavitating liquid start to diffuse across the boundary into the void. Next, negative pressure is reduced due to the advancement of the high pressure or compression portion of the sound wave. Once atmospheric pressure is exceeded, the cavitation void starts to collapse due to increased pressure surrounding it and its own surface tension. During the compression portion of the sound wave, any gas which diffused into the void during rarefaction is compressed and finally starts to diffuse across the boundary again to re-enter the liquid. This process, however, is never complete if the void contains gas since the diffusion out of the void does not start until the void begins to be compressed. And once the void is compressed, the boundary surface available for diffusion is reduced. As a result, cavitation voids formed in liquids containing gas do not collapse in energetic implosion but rather result in a small pocket of compressed gas in the liquid which does not benefit the ultrasonic cleaning process as described by Crum (1984) referencing Rayleigh (1917).

As the temperature of a water-based liquid is increased, its ability to contain dissolved gas is decreased. Increased temperature also increases the diffusion rate of dissolved gas meaning that the liquid will more readily give up dissolved gas as temperature is increased. As this phenomenon

applies at all temperatures of a liquid up to its boiling point (all gas is liberated from the liquid at the boiling temperature), a liquid which is fully degassed at one temperature may again start liberating gas if the temperature is increased. Techniques for degassing liquids in preparation for ultrasonic cleaning will be discussed later in this chapter.

It should be noted that many nonaqueous liquids behave in the opposite manner as described by Battino (1984). In those liquids, at higher temperatures a greater capacity for dissolved gas exists. This fact negates the above and may contribute to the notorious difficulty found in attempts to create cavitation and implosion in nonaqueous liquids including hydrocarbons.

18.7.6 Vapor pressure

An increase in the temperature of a liquid increases its vapor pressure. The effect of moderate temperature changes is minimal but, as the boiling temperature is approached, the cavitation intensity is reduced as the liquid starts to boil at the cavitation sites. The presence of liquid vapor within the void prevents implosion in the same way described for liberated gas above.

The chart that follows summarizes the effect of liquid properties on cavitation and implosion (Figure 18.4).

18.7.7 Ultrasonic power

Cavitation intensity is directly related to ultrasonic power at the power levels generally used in ultrasonic cleaning systems but not over the entire frequency spectrum. Extremely low or high power may provide nonlinear effects as shown below (Figure 18.5).

At low power, the amplitude of vibration is not sufficient to create the pressure differentials within the liquid required to produce viable cavitation voids. As power is increased, more and more cavitation voids will form as the threshold level for various types of nucleation sites is achieved.

At extremely high power, cavitation intensity levels off as the cavitation effect is somewhat self-limiting. Existing cavitation voids prevent the effective transmission of sound waves required to produce additional cavitation voids. Increasing ultrasonic power even further may result in a decoupling effect at the radiating surface/liquid interface in what is known as surface cavitation. Surface cavitation may even reduce the intensity of cavitation in the rest of the liquid as vibrational energy is dissipated at this interface rather than being transmitted into the liquid. This effect may be overcome by the use of focusing techniques in which several transducers or reflectors reflecting the energy of a single transducer are arranged to provide synchronized ultrasonic energy from several directions on the same target area.

Many ultrasonic cleaning systems include the ability to vary ultrasonic power. This is accomplished in many ways. Most common is the use of a time-proportioning scheme in which the ultrasonic signal is interrupted for a portion of a time interval usually measured in milliseconds. Another scheme truncates the power at a certain level as the vibration intensity fluctuates with the alternating current power supply. Very few systems use true amplitude modulation to vary ultrasonic power. In cases of delicate parts which might be damaged if cleaned using the full available ultrasonic power, a duty cycle power control as described above may not prevent damage any more than would reducing the exposure time at full power in the author's opinion.

Effects of Liquid Properties on Ultrasonic Cavitation and Implosion

Liquid Property	Ease of Cavitation	Cavitation Void Size	Implosion Energy	Number of Cavitaton Voids
Lower Surface Tension	Makes Cavitation Easier	Results in Larger Cavitation Voids	Results in Reduced Implosion Energy	Results in More Cavitation Voids
Lower Tensile Strength	Makes Cavitation Easier	Results in More Caviation Voids	Results in Reduced Implosion Energy	Results in More Cavitation Voids
Lower Viscosity	Makes Cavitation Easier	Results in Larger Cavitation Voids	Results in Higher Implosion Energy	Results in More Cavitation Voids
Less Dissolved Gas	Makes Cavitation More Difficult	Results in Smaller Cavitation Voids	Results in Higher Implosion Energy	Results in Less Cavitation Voids
Lower Vapor Pressure	Makes Cavitation More Difficult	Results in Smaller Cavitation Voids	Results in Higher Implosion Energy	Results in Less Cavitation Voids
Lower Specific Gravity	Makes Cavitation Easier	Results in Larger Cavitation Voids	Results in Higher Implosion Energy	Results in More Cavitation Voids

FIGURE 18.4 Physical properties of a liquid affect the formation and implosion of cavitation voids. Note: The above shows general trends but, due to the complex interactions where one property has a significant effect that may counteract another, direct application may be difficult. This is especially true in the case of temperature which affects all of the above. *(Source: Fuchs—Blackstone-NEY Ultrasonics after Frederick, J.R., 1965. Ultrasonic Engineering. John Wiley & Sons, Inc. New York.)*

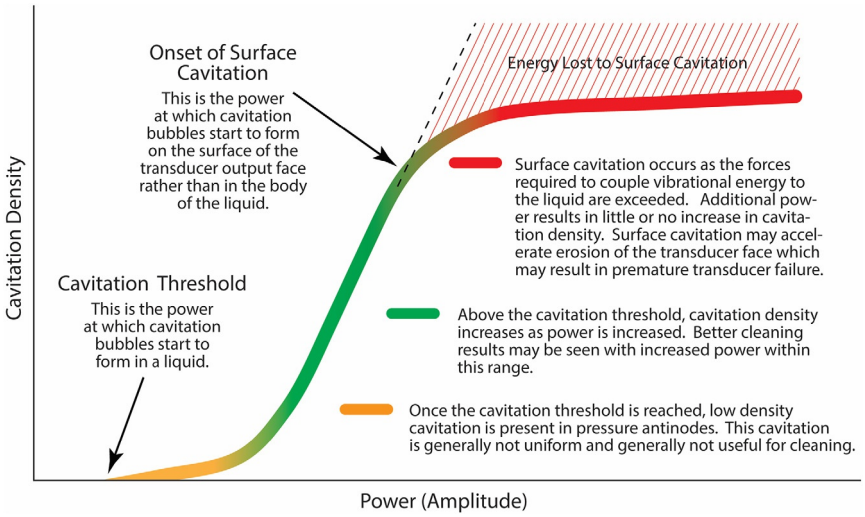


FIGURE 18.5 The relationship between power (vibration amplitude) and cavitation density is not linear. Extremely low power may result in no cavitation voids being formed while extremely high power may result in surface cavitation at the transducer output. *(Source: Blackstone-NEY Ultrasonics.)*

18.7.8 Ultrasonic frequency

Cavitation void size is inversely related to ultrasonic frequency. As ultrasonic frequency is increased, the size of cavitation voids produced becomes smaller due to the typically lower amplitude of vibration at higher frequency and the reduced time available for void growth between compressions and rarefactions. The energy released by each cavitation void implosion is reduced because the smaller size of the cavitation voids results in less violent implosions. However, due to the increased number of wavelengths passing through the liquid at a higher frequency, the number of cavitation voids forming and imploding is increased. Depending on the cleaning application, there may be benefit achieved by a smaller number of high-energy implosions or by a larger number of low-energy implosions. These effects will be discussed later in this chapter.

18.8 Ultrasonic cleaning chemistry

Although water is the most common media for ultrasonic cleaning, the process is seldom applied using water alone. Chemical additives enhance the cleaning process by enhancing the ability of water to remove soil. They also alter the properties of the resulting cleaning solution to enhance the cavitation and implosion process as shown in Figure 18.4. Cleaning chemical selection is extremely important to the overall success of the ultrasonic cleaning process. The selected chemical must be compatible with the substrate being cleaned and have the capability to remove the soils which are present. In the case of soluble contaminants, the chemistry must be able to dissolve or emulsify the contaminant. In the case of solid contaminants, the chemistry must have the ability to wet and surround the particles to be removed. In addition, the cleaning chemistry, either a solvent or a formulation of water and chemistry, must also support the formation and implosion of cavitation voids. Most cleaning chemistries can be used satisfactorily with ultrasonics. Some are formulated especially for use with ultrasonics. Notable examples of chemicals and formulations that may not support cavitation and implosion are some which are intended primarily for use in spray washing applications (which require a formulation that does not foam), solvent/water emulsions, aqueous formulations containing co-solvents, and many hydrocarbon solvents. In the case of nonfoaming formulations, it is thought that the same mechanisms that prevent foam formation interfere with the growth and collapse of cavitation voids. Emulsions and co-solvents are nonhomogeneous liquids which tend to disburse and absorb sound. Co-solvents increase vapor pressure when mixed with water. In the case of hydrocarbon solvents, the lack of cavitation implosions is thought to be due to the relatively high vapor pressure of solvents compared to water and the increasing solubility of gas in hydrocarbon liquids as temperature is increased (Battino et al., 1984).

18.8.1 Temperature

Temperature was mentioned earlier as being important to achieving maximum cavitation. The effectiveness of the cleaning chemical is also related to temperature. Although cavitation and implosion are maximized in a liquid at some particular temperature, optimum cleaning is often seen at a higher or lower temperature. This is because of the influence that temperature has on the effectiveness of the cleaning chemistry which may not coincide with the expected physical effects as noted earlier in this chapter. Aqueous cleaning

chemistries containing surfactants will have a characteristic cloud point, above which surfactants are no longer soluble and this will be a key driver for the recommended use temperature. As a general rule, each chemical will perform best at its recommended process temperature regardless of the temperature effect on the ultrasonics, but this is not always the case. In no case should cleaning chemistry be used above its recommended upper temperature limit or outside of the recommended concentration range.

18.9 Achieving optimum ultrasonic performance

18.9.1 Degassing

Degassing of cleaning solutions is important in achieving satisfactory cleaning results. Fresh solutions or solutions which have not been used for a considerable period of time must be degassed before proceeding with cleaning. As mentioned earlier in this chapter, liquids that are fully degassed at one temperature may not be fully degassed if the temperature is increased. This effect is somewhat dependent on the temperature cycling history of the liquid. There is little support for the notion that process procedures including pumping and spraying of a liquid have a significant effect on its dissolved gas content once the initial degassing process is complete. Degassing is speeded by the addition of cleaning chemistry, by heating of the liquid, and by intermittent application of ultrasonic energy which causes small gas voids (stable cavitation) which coalesce and, once sufficiently buoyant, rise to the surface. The time required for degassing varies considerably with the volume of liquid, the solution temperature, and the ultrasonic power and frequency. Degassing time may range from several minutes for a small, heated tank to an hour or more for a large, heated tank. A large unheated tank may require several hours to degas, especially if its temperature is also being increased during the degassing process. Unfortunately, there is no obvious indicator of the end point of the degassing process. Some say degassing is complete when small voids of gas cannot be seen rising to the surface of the liquid and a pattern of ripples can be seen on the surface of the liquid. Since it is not possible to "over-degas" a liquid, one can assume that this is one case where more is better.

18.9.2 Ultrasonic power

As stated earlier, there is some minimum amount of ultrasonic vibration magnitude required before cavitation voids will form and implode in a liquid. As power is increased above this threshold level, more and more cavitation voids are formed and implode. The ultrasonic power delivered to the cleaning tank must be adequate to produce cavitation void implosions throughout the entire volume of liquid with the workload in place. Watts per gallon is a unit of measure often used to express the level of ultrasonic power in a cleaning tank. As tank volume is increased, the number of watts per gallon required to achieve equivalent ultrasonic performance is reduced (Figure 18.6).

The graph shows a typical, empirical relationship between tank size and the power requirement per unit volume to produce an equivalent ultrasonic cleaning effect. This chart should, by no means, be used as an absolute reference as power requirements will vary widely depending on factors including the part and fixture load, temperature, chemistry, and others (Fuchs, 2013).

Cleaning parts that are very massive or that have a high ratio of surface area to mass (e.g., heat exchangers) may increase the ultrasonic power requirement in an ultrasonic cleaning system. Excessive power may cause cavitation

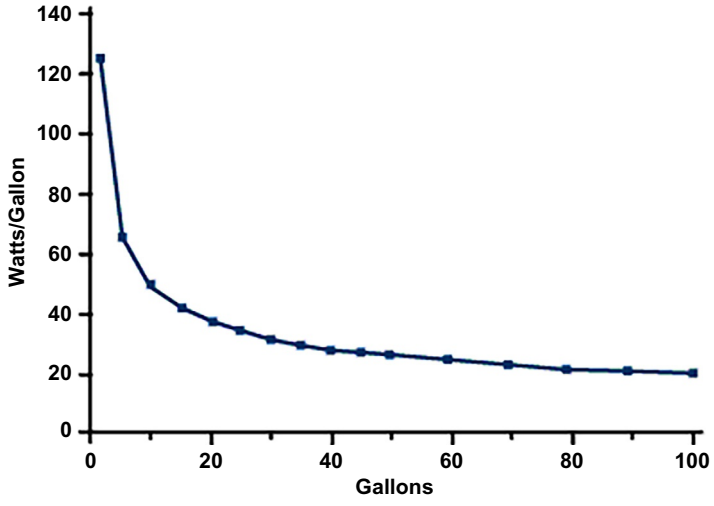


FIGURE 18.6 As ultrasonic tank size increases, the amount of ultrasonic power (watts) required to achieve an equivalent result diminishes. The above shows an empirical relationship which may be altered significantly by a number of factors as described in the text. *(Source: Blackstone-NEY Ultrasonics.)*

erosion or "burning" on the surfaces of soft metal parts including aluminum, brass, and copper. If parts of varying substrates are to be cleaned in a single cleaning system, an ultrasonic power control is recommended to allow the ultrasonic power to be adjusted as required for various cleaning needs as discussed by Puskas and Piazza (2000).

18.9.3 Part exposure

Exposure of surfaces being cleaned to both the cleaning chemical and ultrasonic energy is required for effective cleaning. Care must be taken to ensure that all areas of the parts being cleaned are flooded with the cleaning liquid. Parts baskets and fixtures must be designed to allow penetration of ultrasonic energy and position parts to assure that they are exposed to the ultrasonic energy. It is often necessary to individually rack parts in a specific orientation or rotate them during the cleaning process to thoroughly clean internal passages and blind holes. It should be noted that although not a "line-of-sight" technology, penetration of ultrasonic energy has some limitations, as described in Figure 18.7.

This is especially true of small holes in large parts. The requirement for part exposure also leads to concerns related to the baskets or fixtures used to hold parts during the cleaning process. Massive or very intricate baskets or fixtures may diminish the ultrasonic energy delivered to the parts being cleaned. Fixture and basket materials including rubber, plastic, plastisol coatings, and woven (unwelded) wire mesh can diminish the ultrasonic cleaning effect as they may absorb or dissipate ultrasonic energy.

18.9.4 Liquid movement "agitation"

As ultrasonic energy travels through a liquid, any discontinuity it encounters, such as the parts themselves or their containers, will reduce the efficiency of transmission.

For this reason, the use of liquid agitation produced by submerged propellers, underwater sprays, and other forms of turbulation are generally not recommended in ultrasonic cleaning and rinsing tanks. Instead, it is recommended that any source of liquid agitation including bubbling air, recirculated liquid, or filter pump returns be disabled during ultrasonic cleaning and used only alternately with ultrasonics if needed. Surprisingly, however, part agitation, as long as it is not at excessive speed is beneficial in removing loosened contaminants and does not disturb the ultrasonic field as does agitation of the liquid itself.

18.10 Evaluating ultrasonic performance

The quest for a means to measure the intensity of an ultrasonic cleaning field has been ongoing at least since the mid-1960s when the Ultrasonic Manufacturer's Association (now the Ultrasonic Industry Association) initiated an effort to develop standards for their industry. The goal of that effort was to establish a universal standard against which ultrasonic cleaners could be evaluated for performance. Several of the proposed methods of measuring ultrasonic performance are described below along with their limitations.

It is logical to assume that the effectiveness of the cleaning process is related to the intensity of the ultrasonic field and resulting implosions of cavitation voids. Cavitation intensity, therefore, is often identified as a parameter of interest to indicate cleaning effectiveness.

18.11 Measures of ultrasonic cleaning performance

Before proceeding, it is important to note that at ultrasonic frequencies below 300 kHz, it is believed that the existence of stable cavitation alone does relatively little to enhance cleaning. This may or may not be true at near-megasonic

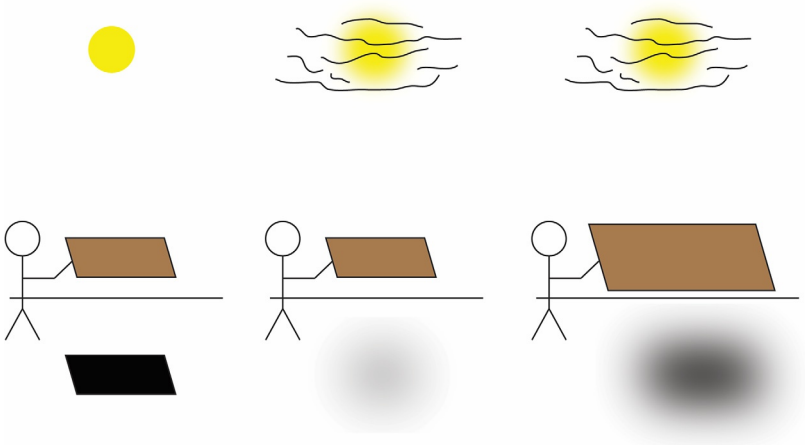


FIGURE 18.7 In an analogy to light, ultrasonic energy is diffused in an ultrasonic cleaning tank by reflections from the surface and side walls. On a sunny day, a shape will cast a defined shadow (line of sight), while on a cloudy day, the same shape will cast a poorly defined shadow. As the shape size increases, the shadow becomes darker but does not disappear. *(Source: www.ctgclean.com/tech-blog—John's Corner, Blackstone-NEY Ultrasonics.)*

frequencies of 300kHz and above as discussed later in this chapter. "Stable" cavitation voids which simply oscillate in size and do not implode with violent force can be created in a liquid due to the passage of sound waves. Any device intended to measure the cleaning ability of an ultrasonic cleaning system must detect and quantify the implosions of cavitation voids, not just their formation. The term "cavitation intensity" is typically used to characterize "transient" cavitation voids which result in implosions useful in enhancing the cleaning effect. Although the quest for a reliable and meaningful means to measure the performance of an ultrasonic cleaning system has been ongoing for decades, to date, no device or method has emerged as the definitive answer to this quest. As a result, users must often rely on an evaluation of part cleanliness to determine the effectiveness of an ultrasonic cleaning process.

The following reference summarizes techniques which have been advanced as measures of cavitation intensity and explanations of their shortcomings.

https://techblog.ctgclean.com/wp-content/uploads/Ultrasonic-Intensity-CleanTech-2002.pdf

While no test to date serves as a definitive measure of ultrasonic cleaning system performance, within limits, some of the schemes may be reasonably accurate indicators of relative cavitation intensity under repeatable and controlled conditions. It is troubling, however, that different testing schemes may give drastically differing results under virtually identical conditions.

18.11.1 New technology

Developments related to measuring cavitation intensity and other parameters relevant to high-power ultrasonic devices are ongoing. In 2019, the International Electrochemical Commission released IEC TS 63001: 2019 to provide a uniform standard for the measurement and evaluation of cavitation in ultrasonic baths. Any test method or devices used in the evaluation of ultrasonic system performance should consider the requirements and recommendations of this standard. Recent development in high speed, real time analysis of hydrophone derived signals is also showing major promise in this area (Frohly, 2000).

18.12 Advancements in ultrasonic cleaning technology

Over the past two decades, there have been significant developments in ultrasonic hardware technology. Although most developments occurred in response to a specific need, many simply reflect new equipment capability with speculated, but not always proven, benefits.

18.12.1 Ultrasonic transducers

Most recent developments have been in piezoelectric transducers. Magnetostrictive transducer technology appears to have reached a mature state with little development noted over the past three decades. Prior to the 1980s, piezoelectric transducers were, for the most part, single-frequency devices operating at their primary resonance frequency ranging, roughly, from 20 to 300 kHz. Most ultrasonic applications utilize a number of individual transducer elements to provide sufficient power to activate large volumes of liquid within a tank. Advances in the piezoelectric drivers used in the transducers and modifications to the basic transducer geometry have resulted in devices with both increased power output and more efficient transfer of ultrasonic energy into the activated liquid.

Changes to the classical transducer geometry now allow the ability to customize the ultrasonic waveforms generated within a liquid to enhance cleaning and, in some cases, prevent damaging effects due to the effects of cavitation on the parts being cleaned as described by Puskas and Piazza (2000).

Developments include the following:

(1) Q—The Q of a transducer defines the sharpness of its resonance. A high-Q transducer has a very sharp resonance which allows very high-peak ultrasonic power output to be achieved. Low-Q devices have a broader resonant range which allows them to perform at frequencies slightly above or below their primary resonant frequency without a significant loss of power output. This characteristic is beneficial in the application of sweep frequency technology which will be discussed in more detail in the section on application developments.

(2) Higher frequency—Transducers are now available which operate at ultrasonic frequencies exceeding 700 kHz. Higher frequencies are beneficial in removing submicron-sized particles from surfaces in critical cleaning applications.

(3) Multiple frequency—Transducers are now available which, with the aid of advanced generator technology, can operate effectively at a select group of distinct harmonic frequencies which reflect different modes of mechanical resonance of the transducer. Again, the benefits of this capability will be explored in more detail in the section on application developments.

18.12.2 Ultrasonic generators

In part, the advances in ultrasonic generator technology have been enabled by advances in electronic components capable of operating at higher frequencies and at higher power levels. The driving factors in development, in general, have been to enable exploitation of the advances in transducer design discussed above. In addition, however, the ability to precisely shape the output waveform of the generator has given rise to a number of ancillary developments enabled by the ability to change frequency and amplitude both individually and in combination. The

development of extremely high-power generators (10 kW or higher) for cleaning applications as speculated earlier has not come to pass.

Application developments

(1) Sweep frequency—Driving ultrasonic transducers at a single fixed frequency has some distinct disadvantages. Early rational for sweep frequency was that operation at a single frequency promotes the formation of standing waves in the liquid. Standing waves are the result of the ultrasonic waves reflecting within the tank (primarily from the liquid surface) to form areas of constructive and destructive interference. Parts cleaned in a single frequency unit may show what is called a "zebra effect" as different areas of the part are cleaned more or less effectively depending on their position relative to these standing waves. Another and possibly more significant effect of operation at a single fixed frequency is overall nonuniformity of the ultrasonic field due to effects other than the development of standing waves. These concepts are illustrated in Figure 18.8.

To understand this effect, it is necessary to understand that multiple transducer elements work in combination to power a single volume of liquid. Each of these transducer elements, despite the best possible control in manufacture, has a distinct and, likely, slightly different resonant frequency. The transducers operate in a parallel electrical configuration meaning that the characteristic impedance curve of the group will reflect their combined resonance which is the most efficient operating frequency for the group. In fact, however, each element will have a slightly different resonance. Using high-Q transducers, individual elements will operate more or less efficiently, depending on the deviation of the driving frequency (defined by the overall group) from the actual resonant frequency of each element. An ultrasonic generator operating in frequency sweep mode varies the driving frequency within a set deviation range over time. Common sweep rates are in the range of one to several hundred sweep cycles per second. The result is that each individual transducer element is excited by a signal at its precise resonant frequency at least twice during each sweep cycle. This provides a more uniform ultrasonic field. If each transducer element has a high Q, extremely high output power will occur each time a signal at the resonant frequency is delivered to a transducer element. With low-Q transducers, the power output of each transducer element is more uniform over the sweep cycle, thereby eliminating high power peaks which can be damaging to some parts being cleaned. In an extension of this technology, the sweeping rate may also be varied to eliminate the possibility of the repetitive sweep cycle exciting parts into resonance which may also cause part damage. This effect will be discussed in more detail in the section on damage mechanisms.

(2) Higher frequency—Increasing the ultrasonic frequency has several effects. First, the size of cavitation voids decreases with increased frequency, while their numbers are increased, as shown in Figure 18.9. The implosions of smaller cavitation voids can allow the penetration of smaller surface features. Secondly, the boundary stagnant or viscous layer which forms at the interface between the ultrasonically activated liquid and the part being cleaned is reduced in thickness.

The boundary layer is the region adjacent to the interface between a liquid and a stationary solid object that occurs as the result of the liquid molecules immediately adjacent to the solid object being essentially anchored to the solid

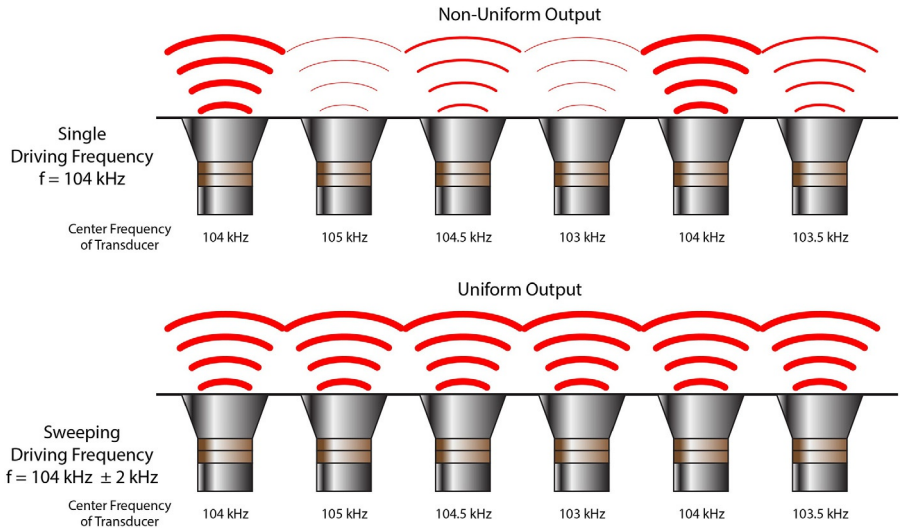


FIGURE 18.8 Sweeping ultrasonic frequency excites all transducers equally to improve uniformity of the sound field. *(Source: CTG www.ctgclean.com/tech-blog—John's Corner, Blackstone-NEY Ultrasonics.)*

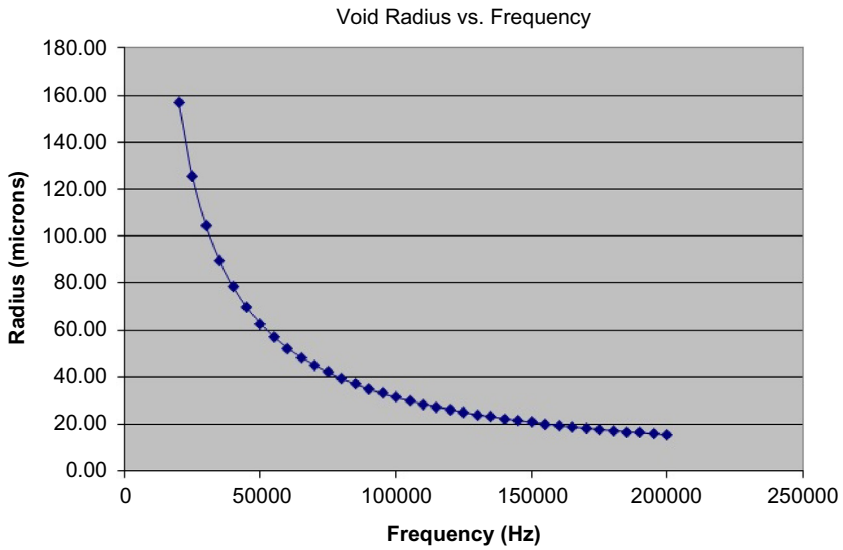


FIGURE 18.9 The radius of cavitation voids decreases with increased ultrasonic frequency. *(Source: CTG, Piazza, T., Puskas, W.L., 2003. The Ideal Ultrasonic Parameters for Delicate Part Cleaning Particulates on Surfaces: Detection, Adhesion and Removal, first ed., vol. 8. CRC Press.)*

by molecular bonding and held stationary relative to it, as shown in Figure 18.10. As the distance from the interface increases, the degree of freedom of motion of the molecules of the liquid increases as each layer of molecular bonding allows slightly more elastic movement of the molecules of the liquid. Liquid molecules in the "boundary layer" are sufficiently constrained to prevent the fluid mobility required to allow the formation and implosion of cavitation voids above a particular size. Smaller cavitation voids resulting from higher frequencies can occur closer to the substrate than larger voids resulting from lower frequencies. For example, a center frequency of 400kHz may be most effective at particle removal centered at 0.3um while a center frequency of 40kHz may be most effective at particle removal centered at 6um (CleanTech Proceedings, Lamm, 2000). The combined result of ultrasonic cleaning at both high and low frequencies is a higher cumulative particle removal, as shown in Figure 18.11.

Higher ultrasonic frequencies, due to the reduced energy released by each implosion of a cavitation void, have also enabled cleaning of parts which would otherwise be damaged by cavitation erosion or resonance effects at lower frequencies. The relationship between ultrasonic frequencies and their applications is described in Table 18.1.

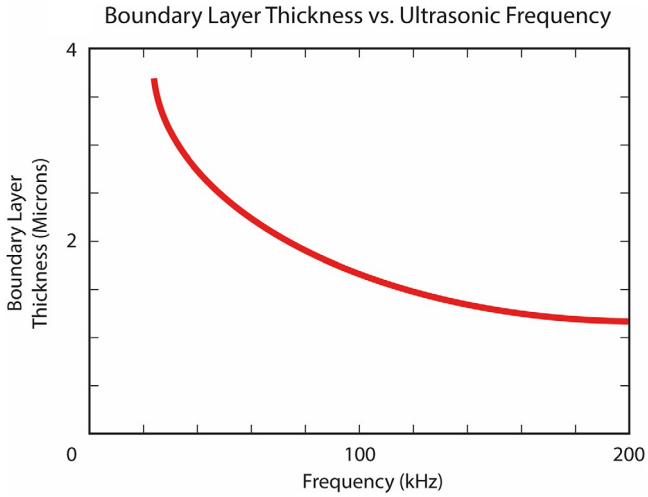


FIGURE 18.10 The thickness of the static boundary layer which prevents the formation of cavitation voids near a surface decreases as ultrasonic frequency is increased. *(Source: CTG, Piazza, T., Puskas, W.L., 2003. The Ideal Ultrasonic Parameters for Delicate Part Cleaning Particulates on Surfaces: Detection, Adhesion and Removal, first ed., vol. 8. CRC Press.)*

(3) While the use of higher ultrasonic frequency enhances the ability to remove smaller particles, it also reduces the capability to dislodge larger particles due to the reduced implosion intensity of the smaller voids produced. Removal of larger particles requires the higher intensity cavitation implosions delivered by lower frequencies. As a result, the use of two or more frequencies is often required to maximize the overall cleaning effect as described by Puskas and Piazza (2000). In the past, this has been accomplished using a sequence of baths each operating at a single frequency or by using a single tank populated with groups of transducer elements each operating at a distinct frequency powered by individual generators for each frequency group. Generators can often be activated either individually or in combination. One potential difficulty of this arrangement is that there is limited room for the placement of transducers in or on a given tank which limits the power available at each frequency. Transducers and generators are now available which allow the use of multiple frequencies in the same ultrasonic tank using a single generator and transducer array. Electronic switching of the generator from frequency

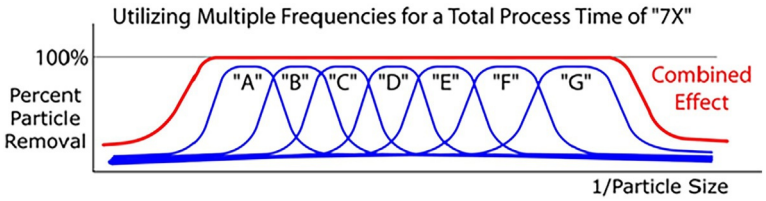


FIGURE 18.11 Higher ultrasonic frequency favors the removal of smaller particles from a surface. Each letter represents the cumulative particle cleaning affect at successively higher frequencies. *(Source: Blackstone-NEY Ultrasonics.)*

TABLE 18.1 Ultrasonic frequency application

Class	Industrial cleaning		Precision cleaning		Critical cleaning		Megasonic cleaning	
Particle size	20–400 µm		1–20 µm		0.2–1.0 µm		<0.2 µm	
Contaminants	Large metal chips, weld spatter, laser cutting scale, swarf		Metal flakes, fine chips, lapping compound		Handling residue, fingerprints, dust		Submicron-sized particles	
Industry	Hardware, plumbing, consumer products, automotive, aircraft		Precision automotive, medical, aerospace, pharmaceutical		Disk drive, optical, electronics		Chip fabrication, disk drive, precision optical	
Frequency	25 kHz	40 kHz	80 kHz	120 kHz	200 kHz	400 kHz	800 kHz	1–5 mHz

to frequency along with controlled power at each frequency allows the development of very complex recipes to produce the desired cleaning result.

18.13 Ultrasonic damage mechanisms

The powerful effect of cavitation void implosion along with other effects of ultrasonic activation of a liquid for cleaning opens the possibility for physical damage to parts being cleaned. These mechanisms range from cavitation "burning" in which the surface of the part being cleaned is attacked by implosions of cavitation voids to the fatigue fracture of parts excited by recurring events at or near their resonant frequency.

18.13.1 Cavitation erosion or "burning"

Cavitation erosion (often called "cavitation burning") occurs when the surface of a part being cleaned is attacked by the implosions of cavitation voids intended to remove contaminants from it. This effect, although mainly seen on relatively soft metals like aluminum and brass, can occur on nearly any substrate. The manifestation of cavitation erosion is more prevalent at lower frequencies with the effect being relatively unknown at frequencies over 100 kHz. Other factors including operating at elevated temperature and using certain chemistries such as strong bases and acids may also contribute to the rate of erosion. In a similar fashion, the erosion of transducer radiating surfaces is expected as operating time accumulates. This effect, too, diminishes as frequency is increased and can be affected by other operating variables as described above.

18.13.2 Mechanical resonance

Parts that are mechanically resonant at the ultrasonic frequency may be excited into resonant vibration by ultrasonic waves. Extreme motion due to mechanical resonance may cause fatigue fracture in delicate parts. This was dramatically illustrated when quartz crystals used in watches and resonant at a particular frequency were destroyed when they were being cleaned in an ultrasonic cleaner using a frequency that was the same as their resonant frequency. There may also be other recurring wave phenomenon that can excite parts into resonant vibration. For example, frequency sweep causes recurring peak intensity as the ultrasonic frequency sweeps through the resonant frequency of the transducer. These recurring pulses of high energy can also excite parts into mechanical resonance. Mechanical resonance and damage of delicate parts can be avoided by eliminating any recurring mechanical effect in the ultrasonic cleaner. Varying the rate of sweep, for example, can eliminate the secondary effects of resonance at this lower sweep frequency.

18.14 Megasonics

Megasonic technology is a relatively new addition to the field of ultrasonic cleaning. Although megasonic technology is a logical extension of existing ultrasonic technology, it is believed that the mechanism of cleaning

when using megasonic frequencies is somewhat different than that described above for ultrasonics. As discussed earlier, as the frequency of the input signal to the cleaning solution increases, the size of the cavitation voids produced decreases asymptotically. The implosion of smaller cavitation voids more efficiently removes smaller-sized particles. In this way, the target particle size can be tuned by choosing an appropriate frequency to remove particles within a target size range. As the frequency exceeds 350 kHz, however, the dominant mechanism of cleaning appears to change as the void size decreases to its ultimate limit in size. Typically, the range of frequencies at and above 350 kHz is known as the megasonic range.

Megasonic cleaning is primarily used in industries where the particle size of concern is submicron and the parts to be cleaned are prone to damage. One of the most common applications of megasonic technology is in the chemical surface preparation and cleaning of silicon wafers in semiconductor production. The critical feature size in modern integrated circuits can be less than ten nanometers, and so the removal of particles in the submicron range becomes critical between steps in masking, etching, metalization, oxidizing, and stripping. In these cases, the primary mechanism of particle removal is a combination of fluid behaviors known as acoustic streaming and microstreaming. Acoustic streaming is a time-independent bulk flow which results from high-frequency acoustic waves traveling through a fluid. This bulk fluid motion is driven by either the dissipation of the acoustic energy as the waves traverse the fluid medium or the development of a shear boundary layer. Microstreaming, on the other hand, is an intense though localized time-dependent flow resulting from the pulsation of voids in the fluid: the growing and shrinking of the cavitation bubbles with passing zones of compression and rarefaction.

Eckart's quartz wind (or Eckart streaming) is the name given to bulk fluid motion that results from the dissipation of the acoustic energy in the sound wave. Fluid is accelerated away from the sound source in the direction of decreasing acoustic energy as shown in Figure 18.12.

In the case where a standing wave is constrained by a solid boundary, acoustic streaming will be driven by the boundary layer at the solid surfaces. The resulting flow, known as Rayleigh streaming, will form cells outside the boundary layer which circulate within a quarter wavelength of the standing wave. Schlichting (1979), showed that an additional rotational flow inside the boundary layer is also present.

It has been measured that as the applied ultrasonic frequency in a bath increases above 200 kHz, transient cavitation gives way to stable cavitation. The higher density of cavitation events caused by the high-frequency sound field, coupled with the shorter wavelength, inhibits the ability of the population of cavitation voids to achieve

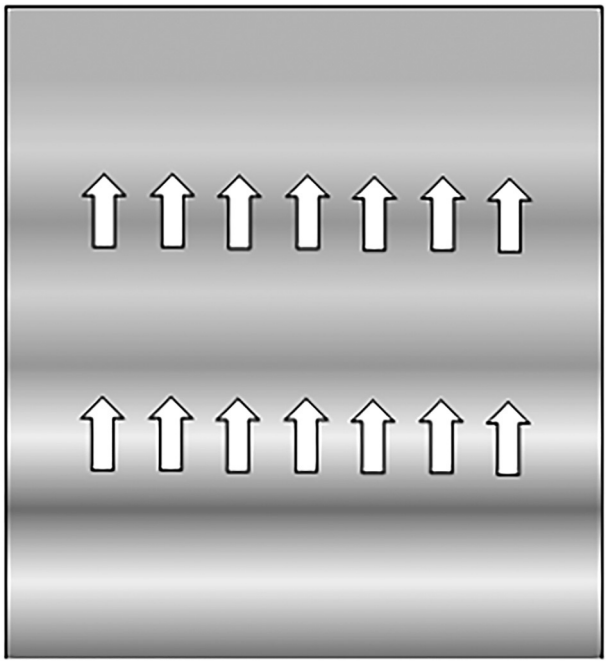


FIGURE 18.12 Bulk fluid motion due to dissipation of acoustic energy; Eckart streaming. *(Source: Blackstone-NEY Ultrasonics.)*

critical size for implosion. The resulting phenomenon is microstreaming. Microstreaming results from the pulsation of a void when the acoustic wave passes over it. Voids can comprise trapped gasses in the liquid, or they can form via cavitation. As these voids are subjected to the pressure oscillations of the acoustic wave, they will pulse. Pulsation of the voids at high frequency will cause the fluid in the vicinity of the voids to move rapidly and with significant force (Figure 18.13). These microstreams are narrow and focused with a high local velocity.

These phenomena all play a role in the removal of particles from a part. Microstreams aid in the removal of

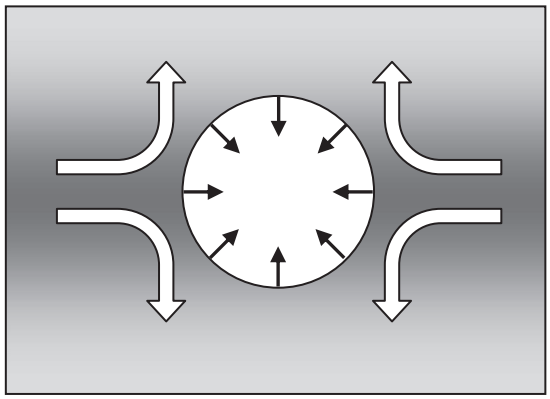


FIGURE 18.13 Fluid in the vicinity of the pulsing cavitation void moves at a speed proportional to frequency. *(Source: Blackstone-NEY Ultrasonics.)*

particles by focusing a strong jet at the particles to dislodge them. Once dislodged, the Schlichting stream inside the boundary layer will move the particle out into the general bulk flow where the particle is further moved away from the surface being cleaned.

18.14.1 Megasonic configurations

There are three common configurations of megasonic technology in cleaning applications, and those can be classified as follows:

(1) Megasonic tank: In a megasonic tank configuration, the energy is delivered to the cleaning fluid in a manner consistent with most ultrasonic cleaning configurations. The transducers are either bonded to a tank surface (metal, glass, or quartz) or to a metal plate which is mounted and sealed on its perimeter against the tank bottom. The parts are immersed in the tank in a preferred orientation that utilizes the streaming processes to pass over the part surfaces as uniformly as possible. Most commonly, the transducer face and bonding surface is perpendicular to the component surfaces. Typical frequencies for these applications range from 350 kHz to 1.4 MHz.

(2) Megasonic nearfield: In semiconductor applications, it is a common need to process single wafer surfaces to guarantee 100% surface exposure and achieve the target cleanliness. This is often accomplished via the use of a specially designed transducer which can be passed over the part surface at a controlled distance. The transducer face and the component surface are parallel in this configuration. The interface between the part and the transducer is maintained in flooded condition to provide a medium to convey the energy to the component surfaces. Frequencies commonly range from 1 to 3 MHz.

(3) Megasonic spray: Another type of system which utilizes megasonic energy in the cleaning of surfaces is a spray system. In a megasonic spray system, the imparted megasonic energy accelerates the cleaning fluid in the direction of the component surface without immersion. The fluid is directed over the oscillating face of a megasonic transducer and then into a nozzle configuration. These can be linear nozzles or a single point jet type. The mechanism of cleaning relies on the Eckart streaming principle and not on the microstreaming associated with cavitation. The frequencies employed in this application are commonly from 350 kHz to 3 MHz.

18.15 Future of ultrasonic cleaning

18.15.1 Higher frequency

The use of higher ultrasonic frequencies to expand the range of ultrasonic cleaning capabilities is likely approaching its end with the introduction of megasonic technology. Mechanical properties of liquids will, at some point, preclude the mechanisms of cavitation and implosion necessary for ultrasonic cleaning as we know it today. Future developments will probably involve the utilization of existing hardware with new applications technology. As the trend toward miniaturization of many mechanical and electronic devices continues, ultrasonic cleaning, applied using ongoing hardware advances, will continue to be a key component of many manufacturing processes.

18.15.2 Cost

The relative cost of ultrasonic hardware operating at the more conventional frequencies of 25 through 70 kHz has remained stable for the past several decades advancing only in proportion to other manufacturing commodities as related to manufacturing costs. The price of higher frequency and advanced controls technology reflects its greater worth in specialized applications and is higher than that of its lower frequency counterparts. Higher prices per unit of ultrasonic power support the higher cost of components and the cost of development of this advanced equipment.

18.15.3 Future applications

New applications for ultrasonic cleaning technology continue to emerge. For the most part, these new applications are developed behind closed doors and many are closely held as trade secrets by the developers. At this writing, there is no known institution devoted to the development of ultrasonic cleaning technology. Although perceived as a "mature" technology by many, the use of ultrasonic technology remains an "art" as its mechanisms have not been fully researched and understood. Ongoing development will likely include further defining these mechanisms so that they can be controlled to produce increasingly predictable and consistent results in critical applications.

There are many ultrasonic "cleaning" applications where the beneficial effect of ultrasonic cavitation and implosion may not be completely cleaning related. In some cases, benefit may be derived as a result of the surfaces being "cleaned" that is more related to surface texturing or some other mechanism as yet undiscovered or understood. Stabilizing surfaces to prevent particle shedding may be one such effect. Others likely exist which, if understood and exploited, could expand the use of ultrasonic cleaning or closely related technology.

The movement of ultrasonic cleaning into the household market, e.g., the washing of clothes and dishes, has long been thought a possibility but has not yet become a reality. In the case of clothes washing, the application of ultrasonic technology has been proven effective in removing contaminants from certain fabrics and weaves in high-tech applications. This benefit, however, exists only if the fabric is held relatively taught and is presented

in a way that assured that there were no more than a few intervening layers between a closely positioned transducer and the most remote layer of fabric to be processed. Thus far, these restrictions have ruled out its use in "bulk" application similar to today's domestic washing machines. However, there have been recent developments in the ultrasonic washing of textiles. In dishwashing, the use of ultrasonic technology is impeded by the fact that the items in order to be cleaned using ultrasonics must be immersed in liquid. Immersion, in general, requires considerably more washing solution than current domestic dish washers which pump liquid from a small reservoir at the bottom of the cleaning chamber through rotating spray nozzles. Additional cleaning solution requires more water and energy than conventional machines. While both of these applications, bulk washing to clothes and dishes, have not been previously found feasible due to the mechanical issues described above and/or for economic reasons due to the high relative cost of ultrasonic technology in a very cost-sensitive market, recent developments could change this situation. Small low-priced ultrasonic cleaners for home use are available commercially but find use today primarily in niche applications such as jewelry cleaning, dental and orthodontic devices and some hobby-related applications.

References

Antonevich, J.N., 1968. Ultrasonic Transducers. US Patent 3370186, Blackstone Corporation.

Battino, R., et al., 1984. The solubility of nitrogen and air in liquids. J. Phys. Chem. Ref. Data 13 (2), 1984.

Brennen, C.E., 1995. Chapter 3: Cavitation and bubble formation. Cavitation Voic Collapse. Oxford University Press.

Caupin, F., Hebert, E., 2006. Cavitation in water: a review. C. R. Phys. 7 (2006), 1000–1017. Available from: http://www.fast.u-psud.fr/~herbert/publis/Cavitation_review_2006.pdf. (Accessed 21 January 2014).

Crum, L.A., 1984. Rectified diffusion. Ultrasonics 22 (5), 215–223.

Curie, P.-J., Curie, P., 1880. "Développement par compression de l'électricité polaire dans les cristaux hémièdres à faces inclinées" (Development, via compression, of electric polarization in hemihedral crystals with inclined faces), *Bulletin de la Société minérologique de France*, vol. 3, pp. 90–93. Reprinted in: Jacques and Pierre Curie (1880) "Développement, par pression, de l'électricité polaire dans les cristaux hémièdres à faces inclinées," *Comptes rendus* …, vol. 91, pp. 294–295. See also: Jacques and Pierre Curie (1880) "Sur l'électricité polaire dans les cristaux hémièdres à faces inclinées" (On electric polarization in hemihedral crystals with inclined faces), *Comptes rendus* …, vol. 91, pp. 383–386.

Fuchs, F.J., 2013. Ultrasonics – Ultrasonic Power Density vs. Tank Size. www.ctgclean.com/tech-blog.

Graff, K.F., 1981. A history of ultrasonics. In: Mason, W.P., Thurston, R.N. (Eds.), Physical Acoustics. vol. 15. Academic Press. Chapter 1.

Joule, J.P., 1847. On the Effects of Magnetism upon the Dimensions of Iron and Steel Bars. The London, Edinburgh and Dublin philosophical magazine and journal of science (Taylor & Francis). 30, Third Series: 76–87, 225–241. Available from: http://books.google.com/books?id=VEgEAAAAYAAJ&lpg=PA76&dq=joule+annals+electricity+219+1842&pg=PA76&hl=en#v=onepage&q=joule%20annals%20electricity%20219%201842&f=false (Accessed 20 January 2014). Joule observed in this paper that he first reported the measurements in a "Conversazione" in Manchester, England, in (Sturgeon's) Annals of Electricity, Magnetism, and Chemistry 8, 219–224 (1842).

Katzir, S., 2012. Who knew piezoelectricity? Rutherford and Langevin on submarine detection and the invention of sonar, Notes & Records, The Royal Society Journal of the History of Science, Available from: http://rsnr.royalsocietypublishing.org/content/early/2012/03/06/rsnr.2011.0049.full.pdf+html (Accessed 20 January 2014).

Lamm, E., 2003. The Development of Ultrasonic Cleaning, Controlled Environments. Velted Associates, Inc. Available from: from:http://www.cemag.us/articles/2003/10/development-ultrasonic-cleaning (Accessed 20 January 2014).

Manbachi, A., Cobbold, R., 2011. Development and application of piezoelectric materials for ultrasound generation and detection. Ultrasound 19 (4), 187–196.

Pereira, A.H.A., 2010. Ultrasonic Cleaning: Overview and State of the Art. ATCP Physical Engineering, San Carlos, Brazil.

Puskas, W., Piazza, T., 2000. Designer waveforms. In: Proceedings, CleanTech 2000. Witter Publishing/Witter Expositions.

Rayleigh, 1917. On the pressure developed in a liquid during the collapse. Phil. Mag. 34.

Rooze, J., 2012. Cavitation in Gas-Saturated Liquids. Eindhoven University of Technology Library. ISBN: 978-90-386-3151-6. Available from: http://alexandria.tue.nl/extra2/732583.pdf. (Accessed 21 January 2014).

Schlichting, H., 1979. Boundary Layer Theory. McGraw-Hill.

Wang, D., Fotinich, Y., Carman, G.P., 1998. Influence of temperature on the electromechanical and fatigue behavior off piezoelectric ceramics. J. Appl. Phys. 83 (10). AIP Publishers. Available from: from:http://scitation.aip.org/content/aip/journal/jap/83/10/10.1063/1.367362 (Accessed 20 January 2014).

Chapter 19

Ultrasonic degassing of liquids

D.G. Eskin

Brunel Centre for Advanced Solidification Technology, Brunel University London, Uxbridge, United Kingdom

19.1 Introduction

Ultrasonic degassing is a phenomenon that has been studied since the 1920s and found some industrial- or pilot-scale applications. In this chapter, we will focus on fundamental and applied aspects of ultrasonic degassing with practical examples given for degassing of liquid aluminum alloys from hydrogen. The fundamental insights into the mechanisms and kinetics of ultrasonic degassing are also illustrated by experiments on water and by numerical modeling.

Boyle (1922) in one of the first studies on cavitation in liquids reported the possible use of ultrasound for the degassing of liquids. Sörensen (1936) quantitatively studied the degassing of water at frequencies from 190 to 950 kHz. Krüger (1938) was probably the first who applied the ultrasonic degassing to melts, especially to molten glass. He used low-power piezoceramic vibrators, and the main reported difficulty was the stable material for the sonotrode.

Ultrasonic degassing has been tried in many applications with demonstrated advantages, though it is not currently the mainstream degassing technology in any of them. As it is already mentioned, ultrasonic degassing of optical glass was one of the first successfully accomplished applications. To overcome the problem of sonotrode material selection for work in high-temperature and aggressive environment, Eckardt and Eden (1952) used high-frequency induction furnace with permanent magnets to induce contactless vibration in the melt. This approach is currently pursued by Pericleous and Bojarevics in design of a contactless ultrasonic cavitation device based on acoustic resonance (Bojarevics et al., 2015; Tonry et al., 2020). Degassing with the aid of ultrasound has been reported for extracting gases from hydrocarbons, oils, and resins in which case ultrasound application accelerates the process of degassing (Kapustina, 1970). Food industry is one of the potential niches for ultrasonic degassing with successful trials made on degassing of juices, beer, chocolate, vegetable oils. Removal of oxygen improves the quality and preservation (Kapustina, 1970), whereas removal of CO_2 accelerates fermentation (Patist and Bates, 2008). Purification of water from heavy metals (Hg ions) assisted by ultrasonic degassing was confirmed in laboratory experiments (Gill et al., 2008).

Acoustic degassing can find its application in materials production. For example, the quality of electrochemical plating can be substantially improved by removal of gas products of interfacial reactions with acoustic streaming accelerating the deposition (Kapustina, 1970). Liquid scintillators widely used in radiochemistry can benefit from hydrogen and oxygen removal without loss of radioactive components (Chleck and Ziegler, 1957; Danielsson and Greber, 1993). There are also some possible applications in medicine, e.g., ultrasonic degassing of dialysis solution may open the way to their miniaturization (Yang et al., 2002).

Yet the most widely studied and advanced field of ultrasonic degassing is degassing of liquid metals. As early as in the 1940s, Esmarch et al. (1940) studied the degassing of Al-Mg alloys by sonic vibrations induced by contactless electromagnetic stirring and vibrations in the crucible. Bradfield (1950) reported the works of Turner on degassing of molten aluminum and its alloys by direct introduction of ultrasonic oscillations into the melt at 15 and 26 kHz. In 1950, Eisenreich (1950) compared vacuum ultrasonic degassing with vacuum degassing, degassing with chlorine lancing, and sonic and ultrasonic degassing. He pointed out the potential of ultrasonic processing but also mentioned related practical difficulties. Sergeev (1952) noted that despite high potential of ultrasonic degassing, there was a challenge in transferring sufficient ultrasonic power to a large mass of liquid metal, which remains to this date one of the greatest challenges for large-scale application of ultrasonic degassing.

The nature of ultrasonic degassing was first revealed on water. Lindström (1955) investigated ultrasonic degassing and its relation to cavitation in water using oxidation of potassium iodide (so-called Weissler reaction) as an indicator of cavitation activity. He suggested that the ultrasonic degassing of water is due to the diffusion of dissolved oxygen into the cavitation bubbles, their oscillation and growth, and, finally, flotation to the surface. The roles of acoustic power (above cavitation threshold), gas concentration, and nature of the gas were reported to be not important. Kapustina (1970) gave a thorough analysis of ultrasonic degassing mechanisms in water and concluded

Power Ultrasonics. https://doi.org/10.1016/B978-0-12-820254-8.00023-3
Copyright © 2023 Elsevier Ltd. All rights reserved.

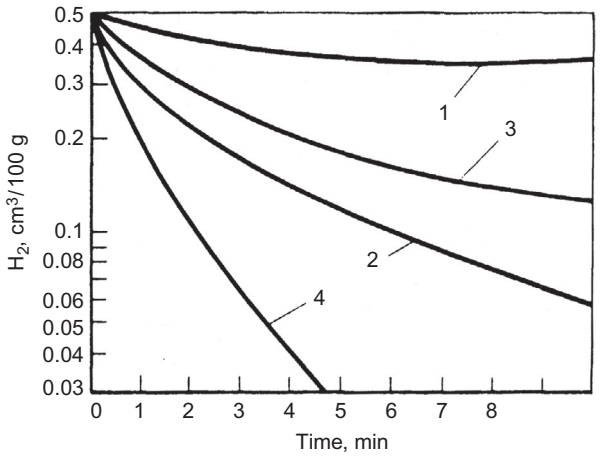


FIGURE 19.1 Kinetics of hydrogen removal from a 10-kg charge of an A356-type melt for different degassing methods: (1) with chlorine salts; (2) with ultrasound; (3) with vacuum; and (4) with ultrasound in vacuum. *(Courtesy G.I. Eskin.)*

that the most important role is played by the oscillations of the bubbles in the acoustic field, while ultrasonic cavitation takes the supportive role in intensification of the bubble formation and acceleration of bubble/liquid interfacial diffusion. Laugier et al. (2008) demonstrated that ultrasonic cavitation greatly enhanced liquid/gas mass transfer at the bubble interface in water saturated with nitrogen even at high pressure and temperature, and in the absence of artificially induced bubbles, with degassing being several times more efficient than re-gassing. Eskin (1965, 1995) argued that the cavitation was essential for ultrasonic degassing of metallic melts where the natural gas bubbles were not typically present, unlike those in water. Therefore, the formation and multiplication of bubbles (essential for degassing) can be only achieved by cavitation. Indeed, early investigations (Altman et al., 1958; Eskin, 1965) demonstrated that the removal of hydrogen from aluminum alloys depended greatly on the acoustic power transferred to the melt and on the development of cavitation. Figure 19.1 compares the degassing kinetics for hydrogen in an A356 melt treated with chlorine salts, ultrasound, vacuum, and ultrasound combined with vacuum. These results were recently reconfirmed, albeit in small-scale laboratory experiments (Xu et al., 2007, 2008; Puga et al., 2009a).

19.2 Fundamentals of ultrasonic degassing

19.2.1 General mechanisms

According to the theory of acoustic degassing suggested by Kapustina (1970) for liquids with existing vapor/gas bubbles, the degassing is controlled by the pulsating bubbles that accumulate dissolved gas due to its diffusion from the liquid in the rarefaction stage of bubble oscillation, and recombination to the molecular form inside the bubble. The bubbles then grow, coalesce, and eventually float to the surface. The role of cavitation according to Kapustina (1970) is in acceleration of the process due to multiplication of bubbles and more active diffusion of the dissolved gas into the small bubbles oscillating in nonlinear manner. In addition, intense cavitation produces acoustic flows and secondary convective flows that contribute to bubbles distribution and flotation. Water represents liquids where gas bubbles are readily present in the liquid volume. As a result, the degassing threshold for water (i.e., the sound intensity that leads to gas liberation from the liquid phase) is always lower than the cavitation threshold. This is not the case for liquid metals as will be discussed later in this chapter.

Let us now consider general mechanisms of ultrasonic degassing. The oscillation of a bubble in an acoustic field brings about a special type of convection that is called rectified diffusion. As a result, the gas transfer from the liquid phase into the bubble becomes possible even when the difference between the average gas concentration in the liquid C_0 and the gas concentration at the bubble/liquid interface C_g is not large. The gas concentration at the bubble interface can be written as (Kapustina, 1970):

$$C_g = C_p(1 + 2\sigma/(R_0P_0)) \tag{19.1}$$

where R_0 is the equilibrium bubble radius, P_0 is the hydrostatic pressure, σ is the surface tension, and C_p is the equilibrium gas concentration in the liquid phase.

When the bubble compresses, the gas concentration inside increases and the gas diffuses to the liquid. Upon bubble expansion, the opposite process takes place. As the bubble surface (hence, the interface available for diffusion) becomes larger upon expansion than that upon compression, the diffusion rate is higher in the rarefaction stage than in the compression stage of the oscillation. This results in gradual filling of the bubble with the gas dissolved in the liquid. In other words, the oscillating bubble acts as a pump extracting gas from the liquid phase. In addition to the rectified diffusion, microscopic acoustic streams generated in the viscous boundary layer around the bubble take their part in the mass transfer, bringing fresh liquid phase to the surface of the pulsating bubble.

The amount of gas M that is transferred to the bubble during several cycles N of ultrasonic wave oscillations can be estimated as (Boguslavsky, 1967):

$$M = \frac{16}{15}\sqrt{5\pi}\frac{z_0}{\rho_l}t^2C_0\sqrt{Dt}\sum_{n=1}^{N}\frac{1}{\sqrt{n}} \tag{19.2}$$

where z_0 is the tensile stress (or pressure) acting on the bubble, C_0 is the gas concentration in the liquid (g/cm^3), t is the time of bubble expansion during one period of sound, D is the gas diffusion coefficient, and ρ_l is the liquid density.

Zhang and Zhang (2019) analytically derived the threshold (in terms of the acoustic pressure) for the evaluation of the ultrasonic degassing effects in molten aluminum. For a given bubble size, the bubble will grow when the acoustic pressure is larger than the threshold, and dissolve otherwise. They demonstrated that the threshold for rectified diffusion is minimum near the resonance size of the cavitation bubble, and increases for nonresonance conditions. For oversaturation gas conditions, the threshold is lower, while for subsaturation conditions, the threshold is higher. For example, for an ultrasonic frequency of 18 kHz, the resonance bubble radius is about 150–170 μm and the threshold pressure is about 200 Pa. This pressure would be, however, about 0.1 MPa for bubbles 50 or 200 μm in radius. It is also shown that when the threshold is exceeded, the bubble growth occurs very quickly initially and then reaches a saturated value, followed by flotation of the bubble.

The actual gas solubility in the liquid phase under conditions of cavitation can be lower than the quasiequilibrium solubility. There exists a limit until which the gas can be extracted from the liquid phase by cavitating bubbles. This limit was estimated to be about 50% of the quasiequilibrium gas solubility under given environmental conditions. This was first established for degassing water from oxygen (Lindström, 1955) and then confirmed for degassing aluminum from hydrogen (Eskin, 1988, 1996; Eskin and Eskin, 2015). The actual value can be even smaller due to the hysteresis of gas diffusion (Lindström, 1955). This level can be called the cavitation quasiequilibrium level (see Figure 19.4a). Under conditions of cavitation, the instantaneous solubility can be described as:

$$C = \frac{C_0}{2} + \frac{1}{\pi}\left[\frac{C_0}{\sin\left(\frac{C_0}{C_A}\right)} - C_A + \sqrt{C_A^2 - C_0^2}\right] \qquad (19.3)$$

where C_0 and C_A are the gas solubilities at the atmospheric and acoustic pressure, respectively.

Kapustina (1970) reports that the quasiequilibrium concentration achieved under ultrasonic degassing depends on the acoustic pressure, time, and ultrasonic frequency.

19.2.2 Cavitation and degassing nuclei

Any gas (unless artificially introduced to the melt via lancing or blasting) is usually completely dissolved in the liquid metal, and no free bubbles exist in the liquid volume. Therefore, the theory of ultrasonic degassing well developed for water (Kapustina, 1970) is only applicable to the liquid metals after the cavitation starts to produce bubbles (Eskin, 1988, 1996). In other words, it is only possible to produce the bubbles if the external energy supplied to the melt by ultrasound creates conditions for heterogeneous nucleation of a bubble onto a not-wet solid nonmetallic inclusion.

Liquid metals and alloys always contain dispersed nonmetallic inclusions, e.g., oxides in liquid Al or Mg, that serve as hydrogen concentrators as well as the cavitation nuclei (Eskin, 1995, 1996; Eskin and Eskin, 2015). Experimental results (Arbuzova et al., 1971) show that alumina adsorbs hydrogen in considerable quantities that makes these particles efficient cavitation nuclei and decreases the cavitation threshold. Although free gas bubbles are not typical of metallic melts, gas can exist in capillaries on the surface of the inclusions. This model for cavitation nuclei in liquid metals has been suggested by Frenkel (1945).

Solidifying liquid melts without oxides will form supersaturated hydrogen solutions and would require large acoustic pressures to initiate cavitation. In real melts containing oxides or other insoluble particles, hydrogen will precipitate on poorly wetted insoluble inclusions forming configurations as shown in Figure 19.2 (Dobatkin et al., 1976; Makarov, 1983). Generally, the precipitation follows the basic rules of heterogeneous nucleation and growth as outlined by Kelton and Greer (2010).

Assume that an insoluble particle has the form of a flat disk with radius $r_d > r_{cr}$, where r_{cr} is the critical radius of a bubble under equilibrium conditions. Hydrogen will form a lens that progressively grows to form a sphere of radius r_{cr}, and then, this bubble will grow without further limitations as shown in Figure 19.2a. In this process, hydrogen lenses will remain on flat particles at almost any hydrogen

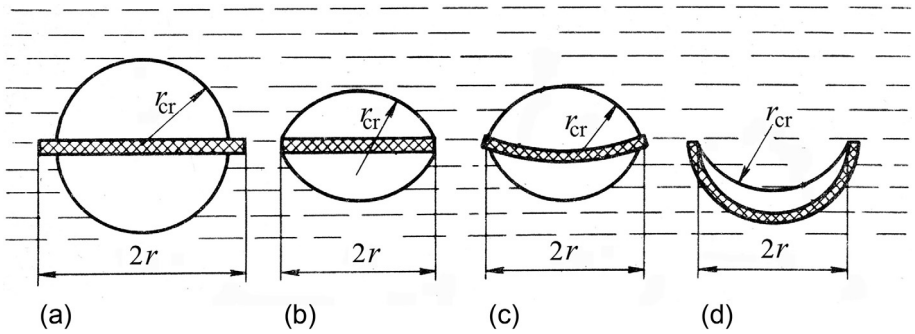


FIGURE 19.2 Possible connections between solid alumina inclusions and hydrogen in an aluminum melt. *(Courtesy G.S. Makarov.)*

concentration above the equilibrium solubility. If $r_d < r_{cr}$, the situation changes, and the bubble grows only until it is bound by a spherical segment of radius r_d (Figure 19.2b). The situation when the surface of the substrate particle is curved (Figure 19.2c) or has some concave segments such as fractures and slots is most common in reality. In this case, hydrogen forms lenses with negative curvature (Figure 19.2d) at hydrogen concentrations significantly below the equilibrium concentration. Calculations show that r_{cr} ranges from 15 to 30 μm in aluminum melts with typical hydrogen concentrations ($<0.5\,cm^3/100\,g$) (Dobatkin et al., 1976). As a result, the crevices and cracks that are smaller than 30 μm will be filled with hydrogen under normal pressure and concentration conditions.

It has been shown on many occasions that the cavitation threshold in liquid aluminum depends on the content of solid aluminum oxide inclusions (Eskin, 1988, 1996; Eskin and Eskin, 2015). It has been also reported that the increased amount of alumina in liquid aluminum slows down the degassing (Eskin, 1996; Eskin and Eskin, 2015). There is a seemingly contradictory situation: Contamination with solid inclusions lowers the cavitation threshold and, hence, facilitates the onset of the degassing, but it also slows down the process proper and decreases its efficiency. To understand this paradox, we need to take into account that the presence of small nonmetallic particles in the melt slows down the dissociation of supersaturated hydrogen solution in aluminum due to hydrogen adsorption by the particles (Kunin et al., 1971; Pimenov and Demenkov, 1972). On the other hand, the very same adsorption facilitates the formation of cavitation nuclei. The nonuniform hydrogen distribution near nonmetallic inclusions assists the transformation of cavities formed at the inclusion/melt interfaces into gas bubbles. This is due to the fact that near these particles, the melt is supersaturated with hydrogen, regardless of the type of hydrogen-particle bonds (Kapustina, 1970; Eskin and Eskin, 2015).

The volume of free hydrogen at typical alumina concentrations (0.005–0.01 wt%) in liquid aluminum is small and varies between 0.01 and 0.2 vol.% (at 700°C with the hydrogen concentration $0.25\,cm^3/100\,g$) (Makarov, 2011). Nevertheless, free hydrogen plays an important role in liquid aluminum as its amount is sufficient to maintain the suspension of small alumina inclusions in the melt volume, and because it provides cavitation and degassing nuclei.

Despite the strong relationship between the amount of nonmetallic inclusions and the amount of molecular hydrogen in the aluminum melt, the presence and concentration of alumina in the melt do not affect the solubility of hydrogen in the liquid aluminum proper (Makarov, 1983), only influencing the fraction of molecular hydrogen adsorbed on the surface of the inclusions.

In difference to water, vapor-gas bubbles do not usually exist in liquid metals and their formation requires cavitation of the liquid. In this case, the degassing and cavitation thresholds must coincide. The cavitation nuclei are of the same origin as the degassing nuclei and, as we have discussed above, are represented by gas adsorbed on the surface of poorly wetted inclusions. While the cavitation threshold determines the starting point of degassing, the degree of cavitation development controls the degassing in melts. In this process, the disruption of the dynamic equilibrium in the melt-oxide-hydrogen system by cavitation is strongly affected by the concentration of solid oxide inclusions.

Analyzing the family of curves in Figure 19.3a, one can conclude that (1) degassing is absent at ultrasonic intensities below $1.0\,W/cm^2$ and (2) degassing rate and intensity increase in proportion to the intensity at ultrasonic intensities above $2.5\,W/cm^2$. Redrawing the data as shown in Figure 19.3b shows three distinct regions, illustrating the generation and development of ultrasonic cavitation in liquid metal.

Region I: the region of precavitation treatment with ultrasonic degassing almost absent.

Region II: the region at the cavitation threshold, where the efficiency of degassing first increases rapidly and then gradually stabilizes.

Region III: the region of developed cavitation, where cavitation reaches a steady level and the efficiency of ultrasonic degassing increases in a linear manner with the ultrasonic intensity.

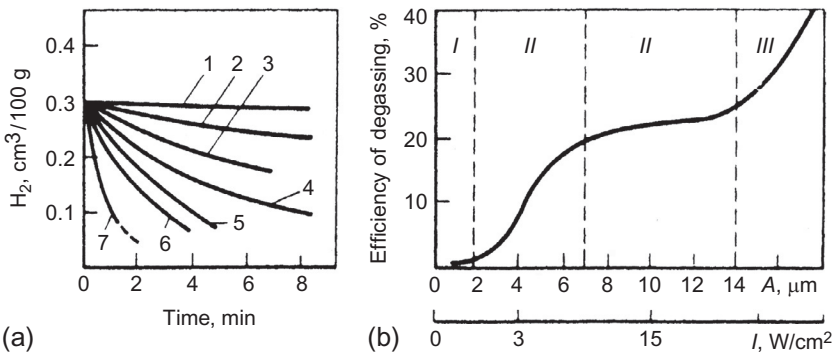


FIGURE 19.3 Effect of cavitation development on the kinetics of ultrasonic degassing of commercially pure aluminum AA1070: (a) different horn null–peak displacement amplitudes A equal to: (1) 2 μm, (2) 3 μm, (3) 5 μm, (4) 10 μm, (5) 15 μm, (6) 18 μm, and (7) 22 μm; and (b) effect of ultrasonic intensity on ultrasonic degassing: (I) pre-cavitation, (II) cavitation threshold, and (III) developed cavitation. *(Courtesy G.I. Eskin.)*

At even greater intensities of ultrasound introduced into the melt, there may be an additional region, where the efficiency of degassing is drastically reduced. In this case, the cavitation development is so great that the developed cavitation zone shields the rest of the melt from the propagation of acoustic pressure, with all energy consumed close to the sonotrode and cavitation events limited to the immediate vicinity of the ultrasonic source. This is a well-known phenomenon, and the practical solution to circumference it includes the reduced amplitude of vibrations and movement of the sonotrode in the melt.

19.3 Mechanism of ultrasonic degassing in melts

The degassing efficiency, irrespective of physical and technical means, is dependent on the concentration of dissolved gas in the liquid. Liquid aluminum and its alloys react actively with gases, either forming nonmetallic impurities or dissolving gas in the liquid phase. Oxygen in aluminum is an example of the former and hydrogen of the latter. Hydrogen finds the way to the liquid metal through the interface between the melt and the atmosphere. The main sources of hydrogen are the molecular hydrogen in air and water moisture or vapor in the atmosphere. The latter reacts with liquid aluminum at the surface of the melt and produces alumina and hydrogen through reaction (19.4). The resultant atomic hydrogen is dissolved in the liquid aluminum, and Al_2O_3 is deposited at the surface or dispersed in the liquid bulk. Hydrogen that is not dissolved or hydrogen that precipitates during degassing or solidification forms molecular hydrogen (reaction (19.5)). Water vapor can react with liquid Al producing molecular hydrogen as well; this will mostly vent back in the air (reaction (19.6)) (Dobatkin et al., 1976).

$$3H_2O + 2Al \rightarrow 6H + Al_2O_3 \quad (19.4)$$

$$H + H \rightarrow H_2 \quad (19.5)$$

$$3H_2O + 2Al \rightarrow Al_2O_3 + 3H_2 \quad (19.6)$$

It is important to understand that the solubility of hydrogen in liquid aluminum (indeed solubility of any gas in any liquid phase) is not a constant or a fixed number. The solubility depends on the temperature (according to the equilibrium phase diagram) but also on the conditions at the interface between the hydrogen-containing medium (atmosphere or bubble) and the liquid metal (surface or bulk). This latter quasiequilibrium solubility exists for each combination of the hydrogen concentration in the atmosphere (humidity), in the melt (dissolved hydrogen), and the pressure (air pressure and partial pressure of hydrogen).

The practical importance of dissolved hydrogen in liquid aluminum comes from the sharp decrease of its solubility with aluminum solidification: Dissolved hydrogen can be measured up to $0.65\,cm^3/100\,g$ in liquid aluminum just above the melting temperature, and just below, the solubility drops down to $0.034\,cm^3/100\,g$ (Campbell, 1993). During solidification, this difference forces the excess hydrogen to precipitate and, being trapped between solid dendrites, form porosity. Gas porosity combined with shrinkage porosity is detrimental to the mechanical properties of the final products, especially to the fracture toughness, fatigue endurance, and ductility (Eskin and Eskin, 2015). Moreover, hydrogen that has not had time to precipitate and formed a supersaturated solid solution with aluminum will precipitate during downstream processing, e.g., homogenization, extrusion, or hot rolling, forming delamination and secondary porosity, especially harmful in thin-gauge products or surface-critical applications.

In general, the hydrogen solubility in liquid aluminum is proportional to the concentration of atomic hydrogen in the atmosphere; however, its content in air is negligible (about 5×10^{-5} vol%), so the main source of hydrogen is the reaction (19.4) between liquid aluminum and water vapor. In the preparation of melts of aluminum and its alloys, the main sources of hydrogen are, therefore, water vapor in the furnace atmosphere and water adsorbed by charge components, fluxes, lining, etc. Carbohydrates present in the burning gas may also contribute to the hydrogen enrichment of melt in gas-heated furnaces.

Thermodynamic analysis of reaction (19.4) (Dobatkin et al., 1976; Makarov, 1983) shows that the partial pressure of hydrogen is extremely high even at low pressures of water vapor. At 727°C and a water vapor pressure of 1.33 kPa (typical atmospheric value), the equilibrium partial pressure of hydrogen at the liquid–gas interface reaches a huge value of 8.87×10^6 GPa, so the hydrogen content of the melt might be as high as $3.24 \times 10^5\,cm^3/100\,g$. This means that all available hydrogen can be dissolved in liquid aluminum and that relatively small atmospheric humidity may lead to high hydrogen concentration in the melt. One cubic meter of air contains about 10 g of water, which is equivalent to 1 g of hydrogen. This 1 g of hydrogen being dissolved in a ton of liquid aluminum may produce about 2%–3% porosity (Dobatkin et al., 1976).

However, not all hydrogen produced from water vapor and dissolved in liquid aluminum remains there. When its concentration reaches the concentration reflecting the equilibrium between liquid aluminum and molecular hydrogen at the current ambient pressure conditions, the dissolution stops and atomic hydrogen will have a driving force to recombine into molecules and leave the melt (natural degassing). As a result of these two processes, there will be a dynamic equilibrium between atomic hydrogen intake (re-gassing) and molecular hydrogen expulsion from the melt (degassing). This equilibrium can be shifted if the

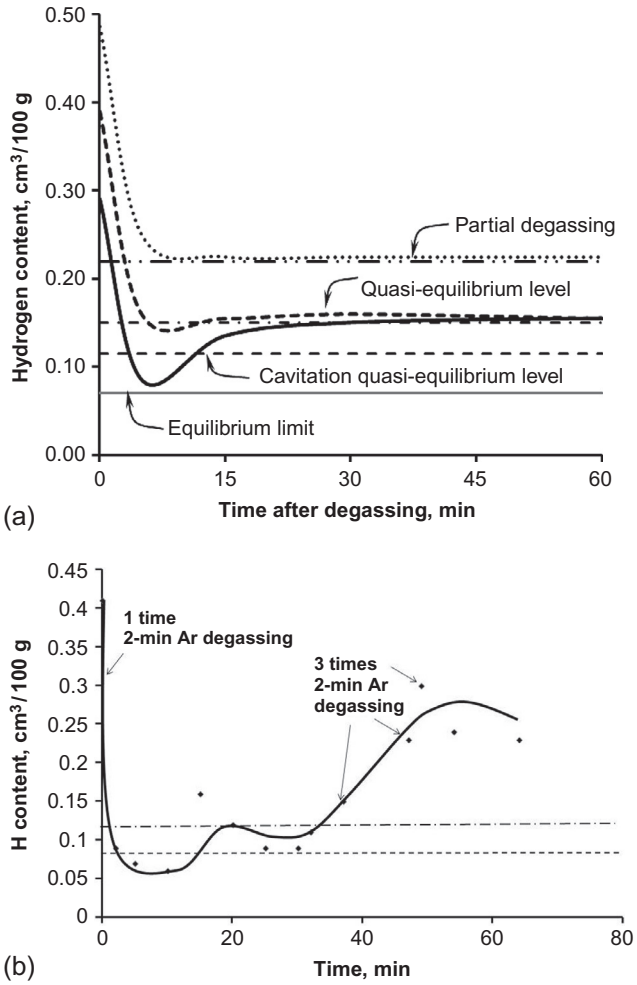


FIGURE 19.4 Kinetics of degassing and regassing: (a) different possible scenarios of variation in hydrogen content in liquid aluminum after degassing and (b) regassing after Ar rotary degassing of an aluminium alloy. *(Courtesy of T. Pabel.)*

pressure, temperature, humidity, or interface conditions change. The general possibilities for the variation of hydrogen content in liquid aluminum are illustrated in Figure 19.4a (Alba-Baena and Eskin, 2013). It is important to note that degassing process is usually faster than the re-gassing (Kapustina, 1970).

For a given charge of liquid aluminum, hydrogen content can be naturally reduced to 0.1–0.2 $cm^3/100\,g$ (degassing) giving time (up to 1 h) and typical conditions (750°C, 30% humidity) (Dobatkin, et al., 1976; Campbell, 1993).

The natural degassing takes long time and is impractical for industrial applications, so different methods have been proposed for accelerating this process. Two types of degassing methods are currently used for aluminum alloys: gas purging (rotary and lance systems) and vacuum degassing. Bubbles formed by purged gas create numerous interfaces that promote recombination of hydrogen to molecular form and evacuate this gaseous hydrogen from the melt. The number and size of the bubbles along with the forced convection seem to be the main parameters of the process (Dobatkin et al., 1976; Makarov, 1983; Waite, 1998). Vacuum degassing is based on the decreased pressure above the melt surface that should result in the decrease in the quasiequilibrium hydrogen solubility and facilitate degassing (Altman et al., 1970). Additionally, the decreased pressure helps in evacuating the bubbles from the melt, accelerating the process of natural degassing.

In most experiments and in the industrial practice, the degassing is performed until the desirable concentration of hydrogen (usually about 0.1 $cm^3/100\,g$) is achieved. After that, the melt is cast. It is known that in degassing large volumes, some time is required to finalize the process of degassing by allowing the bubbles to float to the surface. What is much less studied is the process of re-gassing, or what could happen to the degassed melt after the end of the degassing process. The re-gassing is seldom reported, but there are some data showing that it is not an unusual phenomenon. Experimentally re-gassing was observed after the end of rotary Ar-assisted degassing (see Figure 19.4b), with ambient humidity being reported responsible for that (Waite, 1998; Zhang, 1996).

Ultrasonic degassing has been suggested quite some time ago as an environment-friendly, robust, and efficient means of melt degassing (Eskin, 1965, 1988, 1995; Eskin and Eskin, 2015).

The ultrasonic degassing of any liquid is a process of three simultaneous stages (with the exception that cavitation is required for liquid metals) (Eisenreich, 1950; Eskin, 1965, 1968; Kapustina, 1970):

(1) gas bubbles form on cavitation nuclei and grow by rectified diffusion in the ultrasonic field (if the liquid already contains small bubbles, this stage consists only of their diffusion growth);
(2) separate bubbles coalesce under the action of the Bjerknes and Bernoulli forces; and
(3) bubbles float to the surface of the liquid and release gas into atmosphere.

We already considered the formation of degassing/cavitation nuclei in Section 19.2.2.

The analysis of numerical solutions of the dynamic cavity equations shows that cavitation is a necessary condition for liquid metal degassing (Eskin, 1996; Eskin and Eskin, 2015).

After the bubbles are created by cavitation and start to absorb gas dissolved in the liquid phase, they also start to interact with each other. Pulsating bubbles are either attracted (when oscillating in phase) or repulsed (when oscillating in antiphase). The forces of their interaction are called Bjerknes forces. It is important to note that the

bubbles with similar dimensions are usually attracted to each other whereas the bubbles with different sizes are repulsed. The calculations (Kapustina, 1970) show that the distance at which the bubbles are attracted to each other and then coalesce increases with the bubble diameter, sound pressure amplitude, and oscillation frequency. The time required for coalescence should be larger than the time within which the bubbles are passing each other at a distance when the attraction is possible. The maximum possibility of coalescence will be for the bubbles of the resonance size. The coalescence of bubbles is assisted by acoustic streaming and convective flows.

Bubbles that grow to a substantial size due to the gas intake and coalescence will float to the surface of the melt. The velocity of their rise to the surface depends on the size of the bubble, convective regime in the liquid volume, viscosity of the melt, and the surface tension. For liquid aluminum at 700°C, this velocity changes from 0.1 to 0.82 m/s for the bubbles with diameters from 0.4 to 3 mm, respectively, and does not change much with further increase in the bubble size (Makarov, 2011). The real residence time of such bubbles in the melt volumes used for degassing (depth up to 2 m) is therefore limited to a couple of seconds, which is not sufficient for reaching the full absorption capacity. Ultrasonic cavitation, on the one hand, intensifies the diffusion of hydrogen to the bubbles and, on the other hand, induces stirring of the melt volume that increases the residence time of smaller bubbles and accelerates the evacuation of larger bubbles.

19.4 Main process parameters in ultrasonic degassing

In principle, the effects of process parameters on degassing are similar in all liquids. Let us look at the main conditions of degassing process in liquid aluminum, as it was most studied. A series of such laboratory-scale experiments have been performed in Russia (USSR) (Eskin, 1965, 1968); United States (Meek et al., 2006; Xu et al., 2008); Switzerland and Portugal (Puga et al., 2009a, b); China and Japan (Li et al., 2008); and United Kingdom (Alba-Baena and Eskin, 2013; Eskin et al., 2015a). Figure 19.5 illustrates the influence of various process parameters on the degassing kinetics and efficiency. Let us look at these parameters in more detail.

19.4.1 Ultrasonic energy

Ultrasonic energy or the processing power can be estimated in different ways, e.g., input power of the generator (kW),

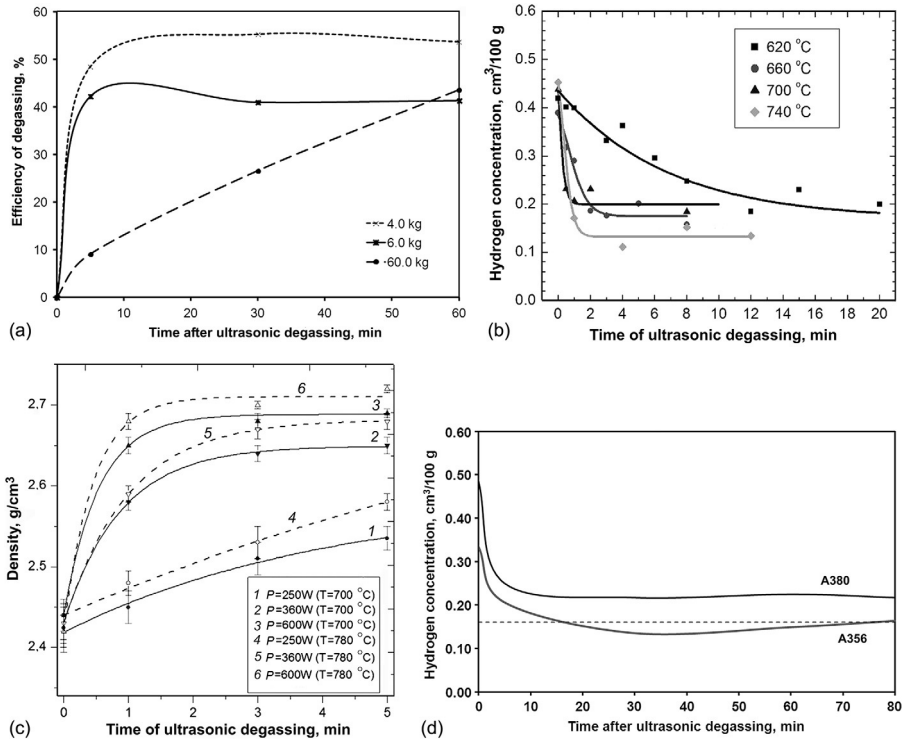


FIGURE 19.5 Effects of various process parameters on degassing of aluminum alloys: (a) effect of treated volume (A380, 2-min degassing); (b) effect of processing time and temperature (0.2 kg, A356); (c) effect of ultrasonic energy and melt temperature (4 kg, A380 type alloy); (d) effect of alloy type (4 kg, 2 min degassing). *(Panels (a and d) adapted from Alba-Baena, N., Eskin, D.G., 2013. In: Sadler, B. (Ed.), Light Metals 2013. TMS/Wiley, Warrendale, pp. 958–962; panel (b) adapted from Xu, H., Han, Q., Meek, T.T., 2008. Mater. Sci. Eng. A 473, 96–104; and (c) adapted from Puga, H., Barbosa, J., Gabriel, J., Seabra, E., Ribeiro, S., Prokic, M., 2011. J. Mater. Process. Technol. 211, 1026–1033.)*

amplitude of the sonotrode (μm) at a given frequency (kHz), input power to the liquid or power intensity (W or W/cm^2), and the level of acoustic pressure in the treated liquid (kPa). In any case, it is shown that the increase in the ultrasonic power results in the increased efficiency of degassing. The time of degassing for 10-kg A356 melt decreases from 25 to 10 min when the ultrasonic power intensity increases from 6 to 10 W/cm^2 (Eskin, 1965). A rule of thumb for the required input ultrasonic power is about 6–8 W/kg. Figures 19.3 and 19.5c illustrate the importance of ultrasonic power for the efficiency of degassing (Puga et al., 2011; Eskin and Eskin, 2015). At the same time, it is important to remember that the increased power results in a very strong cavitation confined to the tip of the sonotrode, shielding the rest of the volume from the sound waves and causing very strong attenuation of acoustic pressure in the melt bulk (Lebon et al., 2018). As degassing relies on the growth of oscillating bubbles, it is paramount that these gas bubbles are distributed in the melt bulk (not confined to the cavitation region) and oscillate (feeling the acoustic field farther from the source). One of the solutions is the decrease in the acoustic power, which may be counterintuitive. Another solution is the movement of the ultrasonic source or the generation of several cavitation zones in the treated liquid volume.

19.4.2 Melt temperature

Melt temperature affects the efficiency of degassing through hydrogen solubility, diffusivity, and melt viscosity. The recommended range of Al melt temperatures is from 700°C to 760°C, where the efficiency of the degassing increases with the melt temperature as the viscosity of the melt decreases and the diffusivity of hydrogen increases (Eskin, 1965; Xu et al., 2008; Puga et al., 2011). At lower temperatures, the viscosity increases and prevents efficient bubble removal and the diffusion of hydrogen from the melt to the bubbles slows down, while at temperatures higher than optimal, the intake of hydrogen due to its increased solubility in the liquid phase becomes comparable with the amount of hydrogen removed by degassing. Table 19.1 shows the duration of ultrasonic degassing of an A356 (Al-Si-Mg) alloy to the quasiequilibrium concentration versus temperature and viscosity. The optimum temperature for an A356 alloy would be around 730°C. Figure 19.5b and c further illustrate the importance of melt temperature for degassing of A356 and A380 (Al-Si-Cu) alloys.

19.4.3 Inclusions

The presence of insoluble inclusions (as we have already discussed above) provides interfaces for cavitation and gas bubble nucleation. As a result, the cavitation threshold is decreased and the degassing starts at a lower ultrasonic intensity. At the same time, the absorption of hydrogen at the inclusions retards the degassing and the earlier cavitation onset results in earlier reached dynamic equilibrium in the Al-oxide-hydrogen system. Therefore, the presence of inclusions may decrease the overall efficiency of degassing. However, as an added value, the absorption of hydrogen to the inclusions and the formation of an attached bubble may trigger flotation of small inclusions, effectively cleaning the melt of both inclusions and hydrogen (Eskin and Eskin, 2015).

TABLE 19.1 The effect of temperature on the duration of ultrasonic degassing of an A356 alloy

Temperature (°C)	Viscosity η (Pa s)	Hydrogen content (cm^3/100 g)		Duration (min)
		Initial	*Final*	
710	0.0089	0.36	0.1	10
730	0.0089	0.37	0.1	8
760	0.0082	0.34	0.1	10
790	0.0079	0.32	0.14	11

After Eskin, G.I., 1988. Ultrasonic Treatment of Molten Aluminum. Metallurgiya, Moscow 232 pp.

19.4.4 Alloy composition

Different physical properties of the liquids subjected to ultrasonic processing strongly affect the cavitation development, acoustic flows, and acoustic pressure distribution, therefore affecting the efficiency of ultrasonic processing (Tzanakis et al., 2017).

The alloy composition may affect the efficiency of degassing through the change of hydrogen solubility in liquid aluminum (increases with Mg, Zn, Li), change of viscosity (decreases with the amount of alloying elements), and surface tension (decreases with Li, Bi, Pb, Mg, Sb) (Korolkov, 1960). There are, however, not enough experimental data for making quantitative conclusions about the effects of specific alloying elements. Figure 19.5d shows that the presence of Mg in an A356 alloy makes a difference in the kinetics of melt degassing as compared to a Mg-free A380 alloy. In addition to affecting hydrogen solubility and physical properties of the melt, magnesium presence in aluminum alloys causes the change in the oxide composition, from alumina to spinel. The latter has a much more porous and weak structure that does not shield the melt surface from atmosphere as efficient as strong alumina film. As a result, the exchange of hydrogen through the surface is accelerated in both directions.

The experimental data on wrought alloys of 5XXX (Al-Mg), 2XXX (Al-Cu-Mg), and 7XXX (Al-Zn-Mg-Cu) systems show, however, that (at least for these alloy types) the efficiency of ultrasonic degassing depends much stronger on the intensity of ultrasound than on the alloy composition (Eskin and Eskin, 2015).

19.4.5 Treatment time and volume

Figure 19.5 illustrates the importance of the time and volume as important process parameters. In all cases, the degassing curve reaches the limit (plateau) when further treatment does not result in additional effect, which reflects the quasiequilibrium solubility of hydrogen under given processing conditions (see Figure 19.4a). Initially, the degassing efficiency is very high, but on increasing the time, the efficiency decreases. There is no readily available recipe to calculate the time and ultrasonic intensity required to degas a given volume. It is reported that the degassing of up to 10 kg of melt takes up to 10 min with most of degassing occurring in the first 2–5 min and can be done with a single sonotrode. Larger volumes will require much more time for the release of gas bubbles as shown in Figure 19.5a for 60 kg melt. When it comes to even larger volumes, flow management needs to be organized through application of several sonotrodes or other sources of cavitation, stirring of the melt, or a movement of the sonotrode.

19.5 Industrial implementation of ultrasonic degassing

Historically, the degassing was studied and implemented in stationary volumes, i.e., furnaces, ladles, crucibles. This is also a typical setting for laboratory experiments.

The degassing of a stationary volume by short sonication sessions with idle intervals between them proves to be a good option. Figure 19.6 illustrates this by ultrasonic degassing of a 2-kg charge of an A380 alloy by 2-min sessions. It is evident that each of the degassing sessions led to an additional decrease in hydrogen concentration, while the idle periods allowed for gas release from the melt through bubble flotation.

Table 19.2 shows how this approach works for larger melt volumes (Eskin and Eskin, 2015).

The ultrasonic degassing of aluminum has been implemented in the 1950–60s in foundries for precision investment, sand, gravity, low- and high-pressure die casting. Let us look at an example of sand casting. A special ultrasonic degassing system UZD-200 was developed in 1959 for degassing up to 250 kg of melt in a stationary volume (Figure 19.7). The installation (in stationary and mobile versions) consisted of a 10-kW generator that fed 4 magnetostrictive transducers that worked in a sequence with a time gap of 15–20 s. The frequency was 19.5 kHz and the total acoustic power 1.6 kW. The system was equipped with time relay that allowed for programmed degassing schedule. The waveguiding system was initially made of a steel extension and a Ti sonotrode. Later, Ti was substituted for a Nb alloy that proved to be much more stable in the melt under cavitation conditions (Eskin, 1988; Eskin and Eskin, 2015). Aluminum alloys were melted in a gas furnace of 3-t capacity, and then, 200-kg portions were taken by a ladle, where the melt was modified and refined using various degassing techniques, including ultrasonic degassing. The refined metal was then cast in sand molds to obtain 30-kg shape castings. Table 19.3 gives the comparison of degassing efficiency for different degassing techniques applied. It can be easily seen that ultrasonic degassing significantly increases the density of cast metal and makes it possible to obtain almost pore-free castings (rank 1 in the porosity scale).

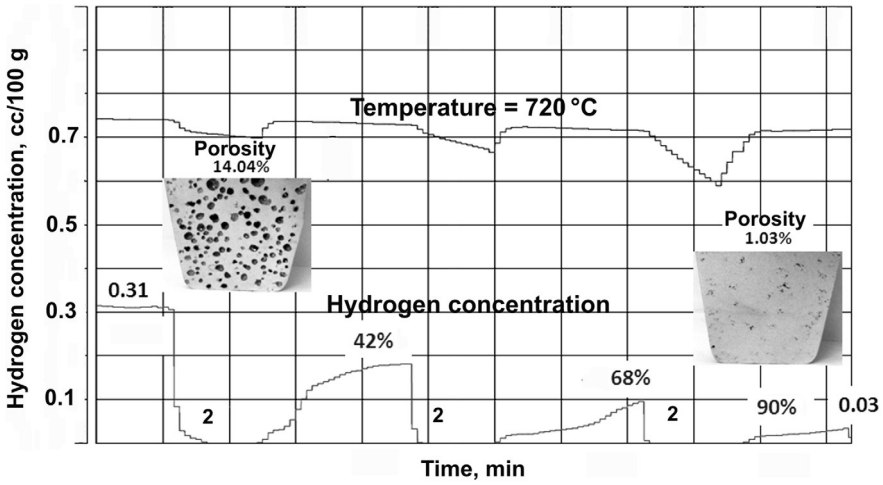


FIGURE 19.6 Kinetics of hydrogen removal from A380 melt (2 kg) as measured by Foseco Alpek-H detector.

TABLE 19.2 Duration (min) of ultrasonic degassing for various volumes of melts to achieve 50% degassing

	Mass (kg)							
US degassing (min)	**50**	**80**	**100**	**120**	**150**	**180**	**200**	**250**
First	6	4	5	6	8	10	10	14
Pause		5	5	6	5	5	5	5
Second		5	5	6	8	10	20	20

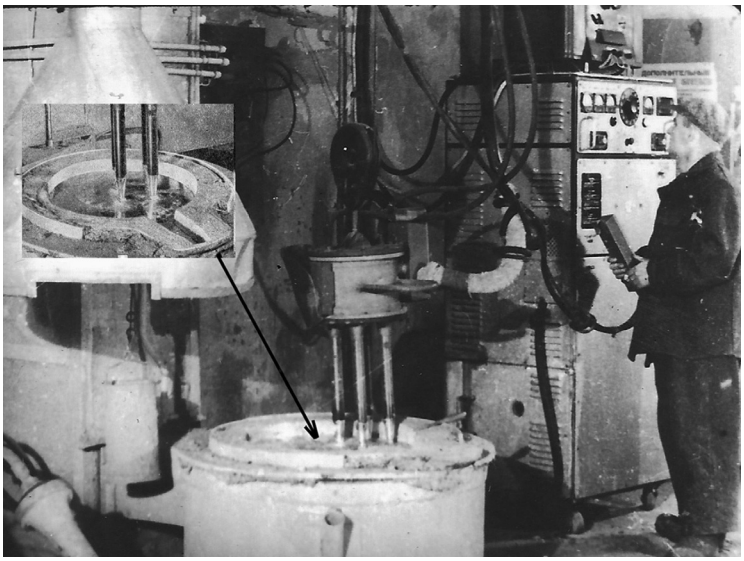


FIGURE 19.7 An industrial setup for batch ultrasonic degassing. *(Courtesy G.I. Eskin.)*

TABLE 19.3 Comparison of various degassing methods for an Al-Si-Mg alloy

				Tensile properties	
Degassing method	**H_2 content (cm^3/100 g)**	**Density (g/cm^3)**	**Porosity number**	***UTS (MPa)***	***El (%)***
Starting melt	0.35	2.660	4	200	3.8
Ultrasonic degassing	0.17	2.706	1–2	245	5.1
Vacuum treatment	0.2	2.681	1–2	228	4.2
Argon blasting	0.26	2.667	2–3	233	4.0

Adapted from Eskin, G.I., 1965. Ultrasonic Treatment of Molten Aluminum. Metallurgiya, Moscow 224 pp; Eskin, G.I., 1988. Ultrasonic Treatment of Molten Aluminum. Metallurgiya, Moscow 232 pp.

The main drawback of this approach is the necessity of using multiple sonotrodes/sources of ultrasonic cavitation with increasing the treated volume. A possible solution is implementing the movement of a single sonotrode that creates the cavitation bubbles in the unit volume and then moves to the next melt volume while the emitted acoustic waves facilitate oscillation and growth of the bubbles in the previous volume. In addition to this translational movement along the surface of the melt, the upward/downward movement of the sonotrode enables treatment of deeper liquid baths. Moreover, these movements also eliminate the shielding effect of the stationary cavitation zone. This concept has been implemented in a prototype installation capable of treating up to 500 kg melt in

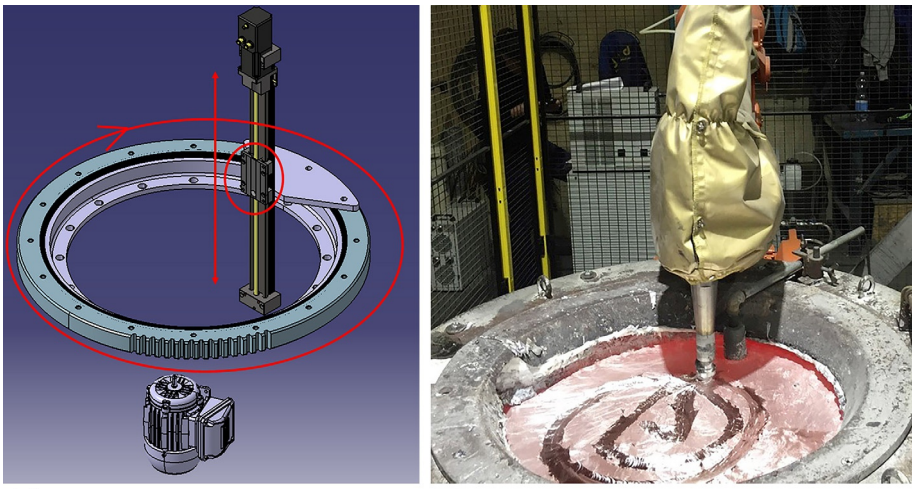


FIGURE 19.8 Pilot scale ultrasonic degassing machine: (a) principal scheme and (b) degassing machine in action. *(Courtesy of Doshormat consortium.)*

15 min with the same efficiency as the standard argon rotary degassing but with up to 5.5 times less dross produced (Da Silva et al., 2015). Figure 19.8 shows the concept and the prototype in action.

The requirement for processing large, industrial-scale volumes of melt, especially in large foundries and continuous casting plants, shows a limit for batch degassing operations. Another approach needs to be used, and the processing of the melt flow seems like a logical and viable possibility. In large melting/casting operations, it is more appropriate to relocate the cleaning of melts from gaseous and oxide inclusions from the melting or holding furnace to the zone of metal transfer, somewhere *en route* from the furnace to the mold. One of the examples of degassing in the melt flow is the combination with vacuum degassing during the melt transfer as shown in Figure 19.9a. Recently, there was a suggestion to combine the ultrasonic degassing with Ar lancing in a vessel through which the melt is constantly flowing (Han et al., 2010). Completely different approach is based on the use of a flat sonotrode that is positioned in the bottom of the launder (Eskin et al., 2015b). In this case, the flexural rather than longitudinal mode of oscillations is used, the amplitude becomes larger (from 11 to 12 to 18–25 μm null-to-peak) while the wavelength shorter (30–33 mm at a frequency of 17.15 kHz). It has been shown that efficient cavitation has been achieved in a prototype setup (Eskin et al., 2015a, b). As a result of the several points of cavitation excitation and the generation of cavitation bubbles at the bottom of a launder, which assists in their natural flotation to the surface, the efficiency of degassing was improved by at least 25% as compared to the degassing with a sonotrode. Figure 19.10 shows the concept and its practical implementation. Despite some reported technological schemes, ultrasonic degassing in melt flow has not yet found the way to foundries but it was successfully used in direct-chill (DC) casting.

First industrial trials on ultrasonic degassing in melt flow were performed in USSR in the early 1960s during DC casting of aluminum alloys using a setup similar to that described above for the batch ultrasonic degassing (UZD-200). The difference was in the arrangement of sonotrodes in line as shown in Figure 19.9b. Taking into account that DC casting involves high flow rates and relatively low melt temperatures, a principle of multiple sources of ultrasonic processing in the melt flow was used.

The launder was constructed in such a way that it contained a section of ultrasonic processing and a section of gas release. In the former, hydrogen bubbles were formed under cavitation conditions, and in the latter, the bubbles grew and float to the melt surface.

The industrial trials were performed for various aluminum alloys cast as flat ingots and round billets (Eskin, 1988; Eskin and Eskin, 2015). The melt flow varied between 70 and 100 kg/min. The amplitude of the sonotrodes was between 10 and 20 μm, and the number of sonotrodes varied between 5 and 11. The results demonstrated that the ultrasonic degassing in the melt flow allowed for 1.5–2 times decrease in hydrogen concentration in the melt, as illustrated in Table 19.4. The density measurement of the ingots and billets showed that the density was increased by 15% that corresponded to the 1.5–2 times decreased porosity. The amount of defects (porosity, nonmetallic inclusions) decreased by a factor of 5–8. The mechanical properties were also improved.

The efficiency of this process shows a distinct dependence on the metal flow rate and acoustic power (or the number of sources) conveyed to the melt (Eskin, 1988).

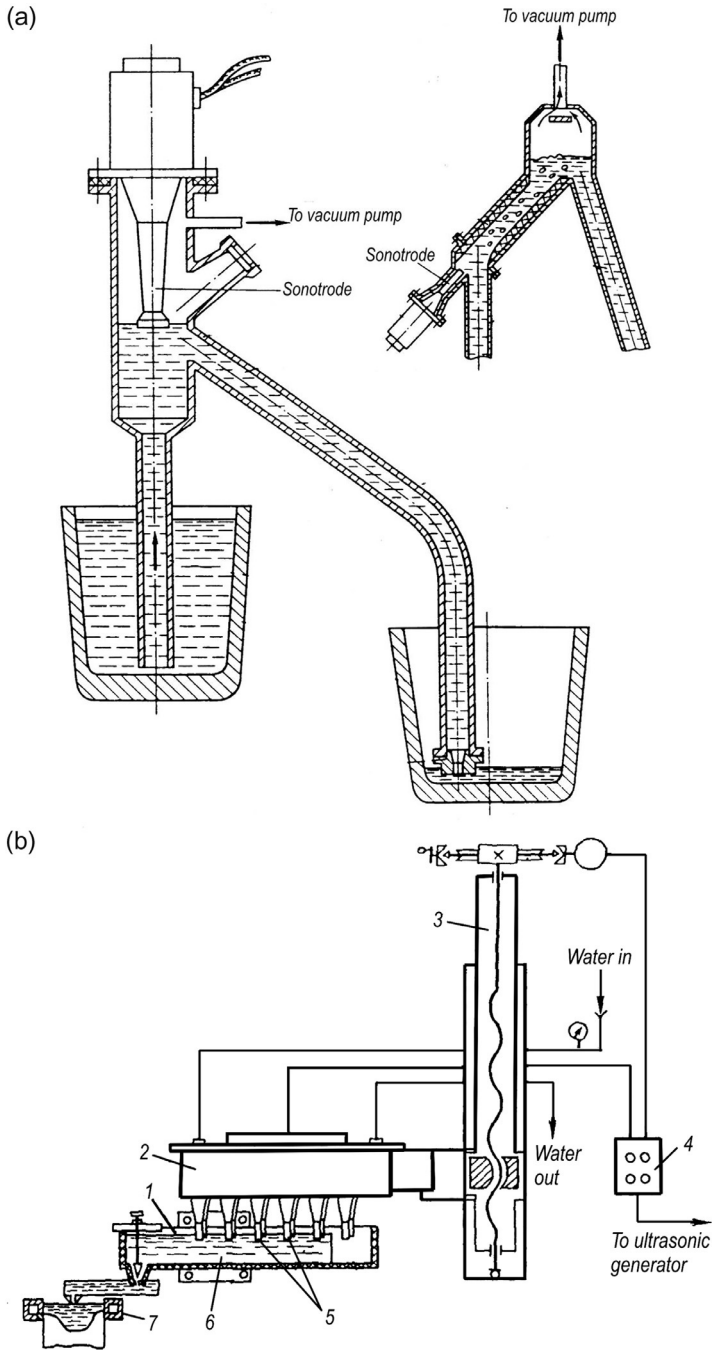


FIGURE 19.9 Suggested schemes for ultrasonic degassing in melt flow: (a) combined with vacuum degassing and (b) during DC casting. Arrangement of sonotrodes for melt processing en route from the furnace to the mould in DC casting: 1, degassing section; 2, assembly of ultrasonic transducers; 3, positioning arm; 4, terminal box; 5, sonotrodes; 6, melt; and 7, DC casting mould. *(Courtesy G.I. Eskin.)*

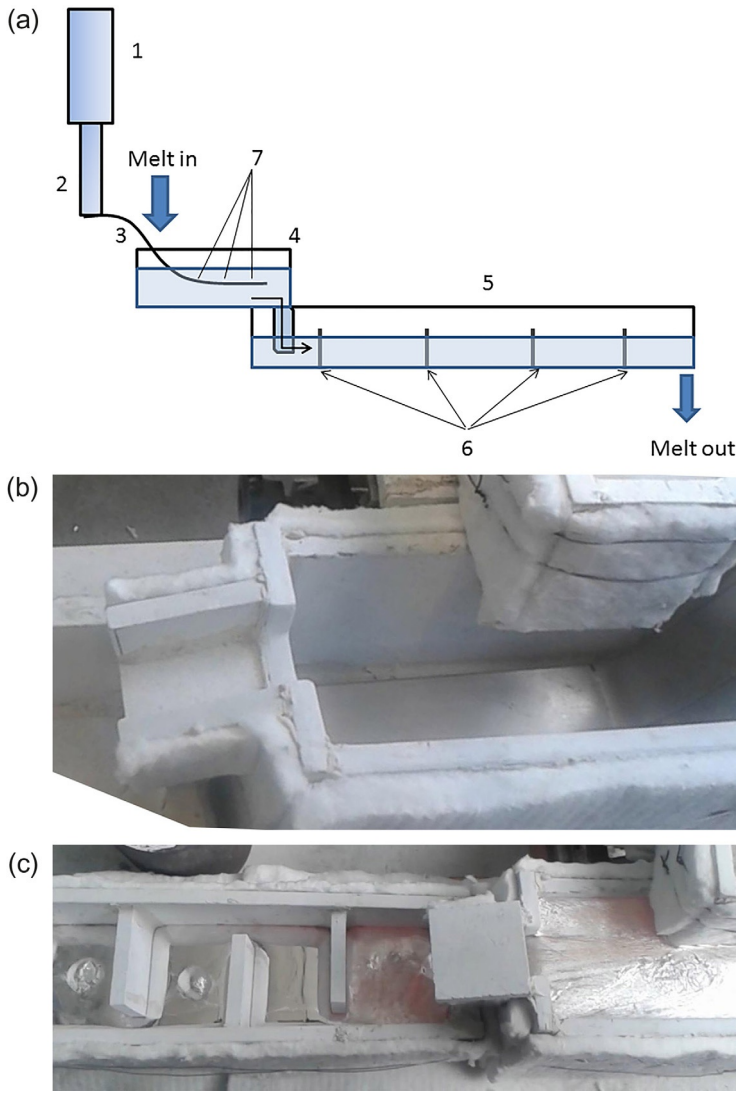


FIGURE 19.10 Innovative ultrasonic degassing scheme with a flat sonotrode: (a) schematic; (b) top view in a launder; and (c) ultrasonic degassing process in the aluminium melt flow.

TABLE 19.4 Concentration of hydrogen before and after ultrasonic degassing upon DC casting of aluminum alloys.

Alloy	Ingot/bullet size (mm)	Casting speed (mm/min)	Hydrogen concentration ($cm^3/100\,g$)	
			No degassing	*Ultrasonic degassing*
AD (AA1030)	1040 × 300	123	0.28	0.18
AD (AA1030)	1040 × 300	70	0.25	0.19
AA2024	1480 × 210	123	0.41	0.24
AMg6 (Al-6%Mg)	1700 × 300	80	0.56	0.29
AK6 (AA2038)	250 dia	70	0.33	0.18
AK6 (AA2117)	460 dia	35	0.4	0.21
AD1 (AA1070)	350 dia	44	0.2	0.10
AMg2 (AA5017)	350 dia	65	0.42	0.3

Adapted from Eskin, G.I., 1988. Ultrasonic Treatment of Molten Aluminum. Metallurgiya, Moscow 232 pp.

Despite these successful industrial applications, the further development and spreading of this experience were hindered by the bulkiness of the equipment and lack of optimization of melt flow. Current efforts are concentrated on understanding the interaction between the melt flow, cavitation field, and acoustic streaming via physical and numerical modeling (Subroto et al., 2020).

Acknowledgment

The author would like to thank Prof. G.I. Eskin for fruitful discussions and permission to use data and figures from his earlier work.

References

Alba-Baena, N., Eskin, D.G., 2013. In: Sadler, B. (Ed.), Light Metals 2013. TMS/Wiley, Warrendale, pp. 958–962.

Altman, M.B., Vinogradova, D.V., Slotin, V.I., Eskin, G.I., 1958. Izv. Akad. Nauk SSSR, Otd. Tekhn. Nauk. (9), 25–30.

Altman, M.B., Glotov, E.B., Ryabinina, R.M., Smirnova, T.I., 1970. Purification of Aluminum Alloys in Vacuum. Metallurgiya, Moscow. 158 pp.

Arbuzova, L.A., Slovetskaya, K.I., Rubinshtein, A.M., Kunin, L.L., Danilkin, V.A., 1971. Izv. Akad. Nauk. SSSR Khimiya (1), 169–170.

Boguslavsky, Y.Y., 1967. Akust. Zh. 13, 23–27.

Bojarevics, V., Djambazov, G., Pericleous, K.A., 2015. Metall. Mater. Trans. A 46A, 2884–2892.

Boyle, R.W., 1922. Trans. Royal Soc. Canada vol. 16, 157–162. 3rd Series.

Bradfield, G., 1950. Proc. Phys. Soc. B 63 (5), 305–321.

Campbell, J., 1993. Castings, second revised ed. Butterworth-Heinemann Ltd, Oxford, UK. 352 pp.

Chleck, D.J., Ziegler, C.A., 1957. Rev. Sci. Instrum. 28, 466–467.

Da Silva, M., Rebolledo, L., Pabel, T., Petkov, T., Planta, X., Tort, J., Eskin, D., 2015. Int. J. Cast Met. Res. 28 (4), 193–200.

Danielsson, M., Greber, H.-J., 1993. Nucl. Instr. Meth. Phys. Res. A 334, 339–340.

Dobatkin, V.I., Gabidullin, R.M., Kolachev, B.A., Makarov, G.S., 1976. Gases and Oxides in Wrought Aluminum Alloys. Metallurgiya, Moscow, pp. 65–90.

Eckardt, A., Eden, E., 1952. Class-Hochvakuumtechnik 1 (2), 15–19.

Eisenreich, H., 1950. Die Tech. 5, 310–315.

Eskin, D., Alba-Baena, N., Pabel, T., Da Silva, M., 2015a. Mater. Sci. Technol. 31, 79–84.

Eskin, D.G., Al-Helal, K., Tzanakis, I., 2015b. J. Mater. Process. Technol. 222, 148–154.

Eskin, G.I., 1965. Ultrasonic Treatment of Molten Aluminum. Metallurgiya, Moscow. 224 pp.

Eskin, G.I., 1968. Ultrasonic Degassing of Molten Metal. Mashinostronie, Moscow. 39 pp.

Eskin, G.I., 1988. Ultrasonic Treatment of Molten Aluminum. Metallurgiya, Moscow. 232 pp.

Eskin, G.I., 1995. Ultrason. Sonochem. 2, 137–141.

Eskin, G.I., 1996. Degassing, filtration, and grain refinement processes of light alloys in a field of acoustic cavitation. In: Mason, T. (Ed.), Advances in Sonochemistry. 4. JAI Press, pp. 101–159.

Eskin, G.I., Eskin, D.G., 2015. Ultrasonic Treatment of Light Alloy Melts, second ed. CRC Press, Boca Raton. 330 pp.

Esmarch, W., Rommel, T., Benther, K., 1940. Werkstof Sonderheft. W.V. Siemens Werke, Berlin, pp. 78–87.

Frenkel, Y.I., 1945. Kinetic Theory of Liquids. Izd. Akad Nauk SSSR, Moscow. 424 pp. (Translated in English by New York, Dover Publ., 1955).

Gill, S., Lavilla, I., Benicho, C., 2008. Ultrason. Sonochem. 15, 212–216.

Han, Q., Xu, H., Meek, T.T., 2010. Degassing of Molten Alloys with the Assistance of Ultrasonic Vibration. US Patent 7682556 B2, 23.03.2010.

Kapustina, O.A., 1970. Degassing of liquids. In: Rozenberg, L.D. (Ed.), Physical Principles of Ultrasonic Technology. Nauka, Moscow, pp. 253–336 (Translated by New York, Plenum, 1973).

Kelton, K.F., Greer, A.L., 2010. Nucleation in Condensed Matter. Application in Materials and Biology. Pergamon Press, Oxford, pp. 165–197.

Korolkov, A.M., 1960. Casting Properties of Metals and Alloys. Izd. Akademii Nauk SSSR, Moscow. 196 p.

Krüger, F., 1938. Glastech. Ber. (7), 233–236.

Kunin, L.L., Pimenov, Y.P., Arbuzova, L.A., Danilkin, V.A., 1971. Physical Chemistry of Surface Phenomena in Melts. Naukova Dumka, Kiev, pp. 99–103.

Laugier, F., Andriantsiferana, C., Wilhelm, A.M., Delmas, H., 2008. Ultrason. Sonochem. 15, 965–972.

Lebon, G.S.B., Tzanakis, I., Pericleous, K., Eskin, D., 2018. Ultrason. Sonochem. 42, 411–421.

Li, J., Momono, T., Tayu, Y., Fu, Y., 2008. Mater. Lett. 62, 4152–4154.

Lindström, O., 1955. J. Acoust. Soc. Am. 27, 654–671.

Makarov, G.S., 1983. Cleaning of Aluminum Alloys by Gases. Metallurgiya, Moscow. 119 p.

Makarov, G.S., 2011. Ingots of Aluminum Alloys with Magnesium for Extrusion. Intermet Engineering, Moscow. 526 p.

Meek, T.T., Han, Q., Xu, H., 2006. Degassing of Aluminum Alloys Using Ultrasonic Vibrations. Report ORNL/TM-2006/61, U.S. Department of Energy.

Patist, A., Bates, D., 2008. Innov. Food Sci. Emerg. Technol. 9, 147–154.

Pimenov, Y.P., Demenkov, A.I., 1972. Tekhnol. Legk. Spl. (6), 33–36.

Puga, H., Barbosa, J., Seabra, E., Ribeiro, S., Prokic, M., 2009a. Mater. Lett. 63, 806–808.

Puga, H.; Barbosa, J.; Seabra, E.; Ribeiro, S.; Prokic, M. (2009b) Fourth Intern. Conf. Advances and Trends in Engineering Materials and Their Applications, AES—ATEMA', Hamburg, Ottawa, AES—Advanced Engineering Solutions, 0-9780479.

Puga, H., Barbosa, J., Gabriel, J., Seabra, E., Ribeiro, S., Prokic, M., 2011. J. Mater. Process. Technol. 211, 1026–1033.

Sergeev, S.V., 1952. Physical and Chemical Properties of Liquid Metals. Oborongiz, Moscow. 172 pp.

Sörensen, C., 1936. Ann. Phys. 418, 121–137.

Subroto, T., Eskin, D.G., Beckwith, C., Tzanakis, I., Djambazov, G., Pericleous, K., 2020. In: Tomsett, A. (Ed.), Light Metals 2020. Springer/TMS, pp. 981–987.

Tonry, C.E.H., Djambazov, G., Dybalska, A., Griffiths, W.D., Beckwith, C., Bojarevics, V., Pericleous, K.A., 2020. Ultrason. Sonochem. 63, 104959.
Tzanakis, I., Lebon, G.S.B., Eskin, D.G., Pericleous, K.A., 2017. Ultrason. Sonochem. 34, 651–662.
Waite, P.D., 1998. In: Welch, B. (Ed.), Light Metals 1998. PA,TMS, Warrendale, pp. 791–796.
Xu, H., Meek, T.T., Han, Q., 2007. Mater. Lett. 61, 1246–1250.
Xu, H., Han, Q., Meek, T.T., 2008. Mater. Sci. Eng. A 473, 96–104.
Yang, Z., Matsumoto, S., Maeda, R., 2002. Sens. Actuators A 95, 274–280.
Zhang, L., 1996. A Kinetic Study of Hydrogen Absorption and Degassing Behaviour of DURALCAN Composites. MSc Thesis, University of Quebec at Chicoutimi.
Zhang, Y., Zhang, Y., 2019. Symmetry 11. paper 536.

Chapter 20

Applications to solidification and casting of metals

D.G. Eskin[a] and I. Tzanakis[b]

[a]*Brunel Centre for Advanced Solidification Technology, Brunel University London, Uxbridge, United Kingdom,* [b]*Faculty of Technology, Design and Environment, Oxford Brookes University, Oxford, United Kingdom*

20.1 Historical overview of ultrasonic cavitation science and applications

The ultrasonic processing of liquid and solidifying metals has been reviewed on numerous occasions, e.g., by Hiedemann (1954), Eskin (1961, 1965), Flynn (1964), von Seemann et al. (1967), Abramov and Teumin (1970), Kapustina (1970), Abramov (1972), Buxmann (1972), Campbell (1981), Abramov (1994), and more recently Eskin and Eskin (2015).

Extensive studies on solidification of various metals and alloys under ultrasonic fields of different frequencies and intensities were performed by (von Seemann (1936), von Seemann et al. (1967), von Seemann and Menzel (1947), Schmid and Ehret (1937), and Schmid and Roll (1939)). A significant refining of grain structure was achieved in these experiments, and crystal fragmentation was suggested to be responsible (Schmid and Roll, 1939). At the same time, a group of scientists advocated the cavitation-induced nucleation of the solid phase (Berlaga, 1939; Danilov et al., 1939, Altberg and Lavrov, 1939). Danilov and Teverovsky (1940) suggested cavitation-assisted heterogeneous nucleation through activation of insoluble impurities. Kapustin observed the formation of new crystallization centers under sonication of very pure liquids; hence, something different from activation of impurities might have happened (Abramov and Teumin, 1970). Hunt and Jackson (1966) demonstrated through calculations and dedicated experiments on water that the collapse of cavitation bubbles and the resultant surge of pressure might be responsible for the nucleation due to the local change of phase equilibria, increase of the melting point (by tens of degrees!), and the effective local undercooling.

The application of ultrasound to processing of commercial alloys started with the works of von Seemann and Menzel (1947) who demonstrated efficient refinement of the duralumin ingot grain structure and an improvement of its mechanical properties. This group also reported structure refinement of tin and zinc (von Seemann et al., 1967) as well as brass and steel (von Seemann et al., 1967; von Seemann and Wehner, 1973). Eskin (1965) applied ultrasonic cavitation treatment to a variety of model and commercial foundry Al alloys (hypo- and hypereutectic Al-Si alloys) and demonstrated that the grain structure, intermetallics, and primary crystals were refined under cavitation conditions. Later, ultrasonic processing was shown to be advantageous for receiving refined grain structure and improved mechanical properties of direct-chill (DC) cast wrought magnesium alloys (Ansyutina et al., 1970).

An important effect of ultrasonic vibrations and cavitation that attracted the interest of metallurgists was degassing of the melt, which is covered in Chapter 19 of this book.

Another important effect of ultrasound is atomization and dispersion of liquid and solid phases with obvious metallurgical applications in manufacturing composite materials as well as immiscible alloys. Schmid and Ehret (1937) and Becker (1941) described Al-Pb and Zn-Pb alloys produced with ultrasonic melt processing as stable suspensions.

Ultrasonic cavitation processing is widely used nowadays to effectively introduce nonmetallic and solid particles to form metal matrix composites, which also has a long tradition. Pogodin-Alekseev and Zaboleev-Zotov (1958) reported the introduction of particulate (from 2 to 20 μm) alumina, silicon carbide, and titanium nitride in liquid aluminum in quantities of 10–50 wt%. von Seemann and Staats (1968) summarized their earlier works on the dispersion of metallic (Ti, Fe) and ceramic (carbides, oxides) particles in molten aluminum using 20-kHz magnetostrictive transducer and an alumina sonotrode.

Herrmann (1958) described many pilot installations for ultrasonic treatment of molten metal. The versatility of the treatment was illustrated by examples with ultrasonic processing conducted in the furnace, melt flow, feeders of

Power Ultrasonics. https://doi.org/10.1016/B978-0-12-820254-8.00003-8
Copyright © 2023 Elsevier Ltd. All rights reserved.

castings, and in the molds with the aim to remove dissolved gases, refine structure, and improve casting properties.

One of the early pilot-scale trials of ultrasonic melt processing of aluminum alloys during aluminum semicontinuous casting was described by von Seemann and Menzel (1947). Commercial size (290 mm) billets from a duralumin (AA2024) were cast with ultrasonic processing of the melt in the sump of the billet. In these experiments, a powerful ultrasonic generator (up to 25 kW) excited four 2-kW magnetostrictive transducers at 40 kHz. The efficiency of the entire assembly was 14%, and it was able to deliver an intensity of 2.0 W/cm^2 to the cross-sectional area of the billet (660 cm^2), which was sufficient to achieve grain refinement, reduced porosity, and increased ultimate strength.

Later, multiple ultrasonic sources were used for ultrasonic processing in the sump of a billet or in the launder during DC casting of Al and Mg alloys (Eskin, 1988).

This brief historical overview shows that the ultrasonic melt processing (USP) has a long history. It originated from advances in physics that led to the design of modern equipment, followed by technological developments and trials that started in the 1930s and continued through the 1980s, leading to the first industrial implementations. This chapter follows the sequence of events as explained in the introduction section starting with the theoretical background and recent fundamental insights/discoveries in USP followed by the specific mechanisms (heterogeneous nucleation, fragmentation, activation of substrates, deagglomeration, dispersion, and emulsification) leading to structure refinement and closing by recent advances in continuous processing studies of cast alloys and metal matrix composites.

20.2 Brief theoretical introduction to ultrasonic cavitation processing

Commercial ultrasonic transducers are capable of generating power densities of about 10^5–10^6 W/m^2 at frequencies of 18–20 kHz, which is sufficient for treatment of liquid and solidifying melts. When a source of ultrasonic oscillations is introduced into the liquid pool, it induces an ultrasonic field whose characteristics depend on the oscillation parameters, cavitation activity, the properties of the treated medium as well on the geometrical features of the container.

The proper choice of the material for sonotrodes (horns, ultrasonic tips) needs to be treated with special care, and Nb-based alloys (Eskin, 1965) or Sialon-based materials (Komarov and Yamamoto, 2019) were recommended for use in molten aluminum, while Ti alloys can be used in liquid magnesium but dissolve rapidly in molten aluminum. Direct introduction of ultrasound to high-temperature melts is, however, almost impossible. Consumable steel horns were reported to be used to treat Fe-based alloys (Abramov, 1972). Indirect ways were tested including transmission of the oscillations via mold, through solid substrate upon ark vacuum remelting, or through the layer of molten slag upon electro-slag remelting (Benua et al., 1958; Lane et al., 1960). Most recently, a contactless excitation of cavitation in liquid aluminum through a combination of induction coils was developed (Tonry et al., 2019). Such indirect ways open the way to treat virtually all metals.

A very important parameter of the ultrasonic field affecting to a great extent the efficiency of processing is the ultrasonic intensity I, or power flux W_a normalized by area S. In the simplest case of a plane wave, the intensity [W/m^2] is given by

$$I = \frac{W_a}{S} = \frac{1}{2}\rho c v^2 = \frac{1}{2}\rho c (A_0\omega)^2 = \frac{1}{2}P_A v \qquad (20.1)$$

Here ρ is the liquid density, c is the sound velocity, P_A is the acoustic pressure, and v is the oscillation velocity. The acoustic intensity is, therefore, proportional to the squared amplitude (A_0) and angular frequency (ω), which determines the selection of processing equipment and regimes.

When cavitation develops in the melt, the temporal characteristics of force and velocity at the sonotrode radiating face and in the melt containing cavitation bubbles vary.

In the presence of cavitation, the acoustic impedance Z (resistance to the propagation of ultrasound waves into the melt) of the melt that is a function of oscillation amplitude or velocity with density ($Z = \rho \times c$) rapidly decreases. This is a result of a low density and a high acoustic absorption of the cavitating liquid phase, as the sound velocity and the pressure are controlled by bubbly cavitation clouds (mainly formed by gaseous H_2 in liquid aluminum), at difference from the noncavitating liquid that can be considered as a continuous medium. The intensity or transmitted power can still be considered proportional to the squared oscillation velocity, but with the acoustic impedance rapidly decreasing after the cavitation threshold has been reached.

Figure 20.1 shows the dimensionless parameter K, which is the ratio of acoustic impedance under cavitation to the acoustic impedance in the absence of cavitation, versus the oscillating amplitude of the sonotrode at 18 kHz for water (1) and aluminum melt (2) (Eskin, 1988). When the null-to-peak amplitude exceeds 0.5 μm for water at 20°C and 2–3 μm for an aluminum melt, the wave resistance decreases to values 10 times smaller than for sonication without cavitation. This phenomenon, called shielding, needs to be accounted for in the models of ultrasonic melt processing, which frequently is, unfortunately, not the case.

On the other hand, when acoustic cavitation kicks off, the acoustic power transferred to the fluid increases. Figure 20.2 gives the relation between the oscillation

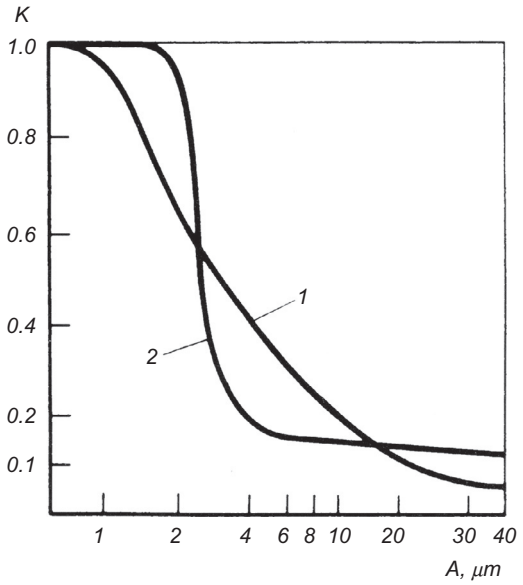


FIGURE 20.1 Relative acoustic impedance K versus the amplitude A of the sonotrode at 18 kHz. (1) Water and (2) aluminum melt. *(From Eskin (1988).)*

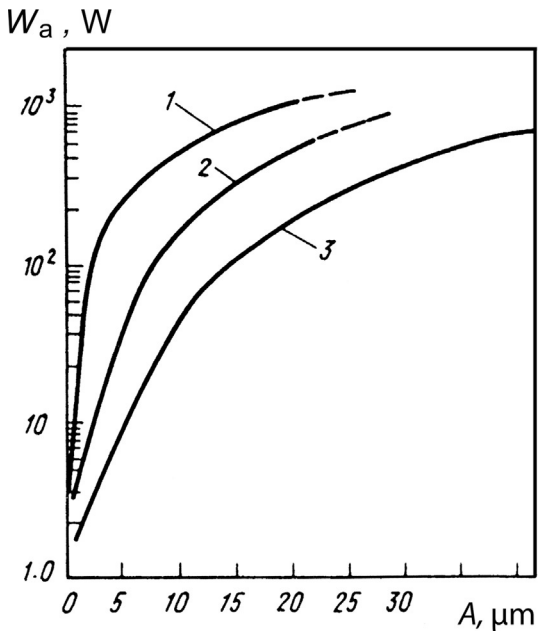


FIGURE 20.2 Power W_a transferred into the melt versus the amplitude A of the sonotrode at a resonance frequency of 18 kHz for three sonotrode diameters: (1) 65 mm, (2) 40 mm, and (3) 20 mm. *(From Eskin (1988).)*

amplitude and the acoustic power (measured by calorimetry) generated by standard ultrasonic equipment and transmitted into an aluminum melt of commercial purity at a resonance frequency of 18 kHz for different surface areas of the sonotrode radiating face. The combination of these two opposite effects (shielding and input energy) can profoundly affect the cavitating environment in a sonicated liquid as explained below.

The absorption of ultrasound in the liquid phase is related to the viscosity and thermal conductivity of the melt and changes with the ultrasound frequency. The attenuation factor depends on the squared frequency:

$$\alpha = \frac{\omega^2}{2\rho c^3}\left(\frac{4}{3}\mu + \mu' + a\left(\frac{1}{c_v} - \frac{1}{c_p}\right)\right) \tag{20.2}$$

where μ and μ' are the shear and volume viscosities, a is the thermal conductivity, and c_v and c_p are the specific heats at constant volume and pressure, respectively. This dependence demonstrates that very high ultrasonic frequencies would be impractical for melt processing because of their strong attenuation (even without taking into account the shielding effect of the developed cavitation region).

Thus, acoustic impedance and attenuation factor are decisive parameters for controlling acoustic pressures and the extent of the cavitation zone in a sonicated liquid environment.

Only recently dedicated instrumental facilities have been developed that allow the measurements of cavitation activity in liquid aluminum (Komarov et al., 2012; Tzanakis et al., 2016a,b) and a direct comparison with other low-temperature and transparent liquids. It is demonstrated that cavitation development in water closely resembles that of liquid aluminum; therefore, water can be used as a physical analogue for studying ultrasonic melt processing (Tzanakis et al., 2017). This finding gives the researchers a tool to experimentally investigate cavitation activity and evaluate acoustic streaming in water using advanced experimental equipment and techniques such as calibrated cavitometers and particle image velocimetry (PIV) and subsequently feed numerical models to replicate and validate the cavitation development in liquid aluminum (Lebon et al., 2017).

Experimental studies in water (as a transparent analogue for liquid aluminum) show that cavitation intensity initially increases with the increase of the input power (sonotrode amplitude), followed by a significant drop (i.e., at 10–15 μm p-p amplitude, reflecting the developed cavitation) and then a further increase at much higher powers, Figure 20.3.

This behavior suggests that shielding and scattering effects due to the formation of bubbly clouds can potentially reduce the emitted acoustic pressure levels traveling through the liquid media. Apparently, this is also true for liquid aluminum where it was demonstrated that apart from a significant drop, up to 10-fold, in the pressure levels with the initiation of cavitation (see Figure 20.1), there is an optimum power input where bubbly structures and vibration amplitude reach a physical balance and the cavitation intensity acquires maximum values (Tzanakis et al., 2016c). In line with

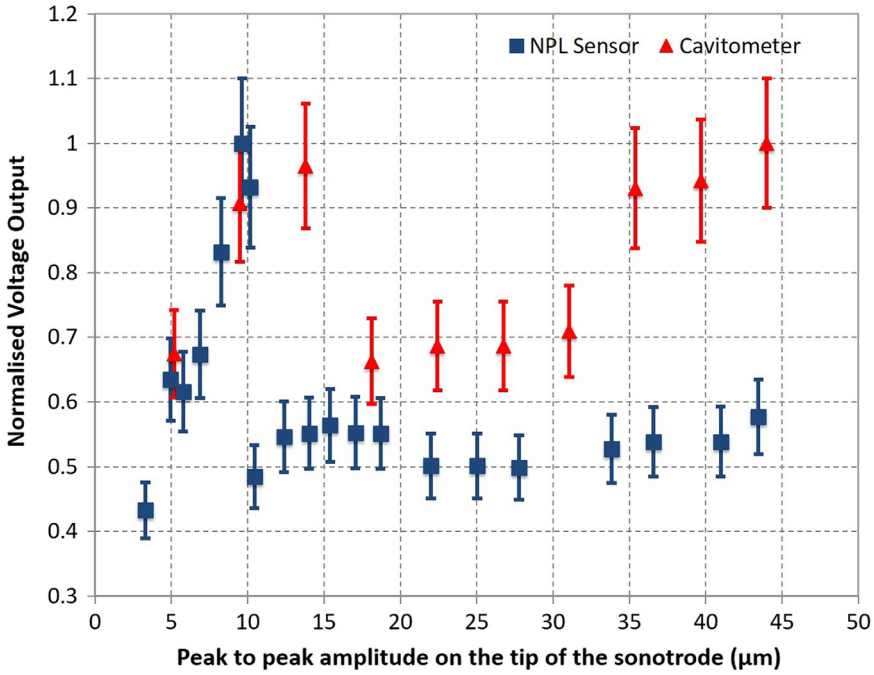


FIGURE 20.3 Comparison of the direct field (20 kHz) between two different sensor devices: a cavitometer and a CaviSensor. *(From Tzanakis et al. (2016a).)*

that, recent experimental and numerical studies in the aluminum melt (Tzanakis et al., 2016c; Lebon et al., 2017) show that the variation of the maximum pressure with distance from the sonotrode surface obeys a power law (Figure 20.4). The decay of pressure with distance is with an exponent of 1.28–1.45 per meter. This large decay is expected, as the efficiency in acoustic radiation is proportional to the ratio of the horn radius to the wavelength. The large wavelength in aluminum and a comparatively small sonotrode make the pressure decrease with distance more pronounced.

Figure 20.5 gives another illustration of direct measurements of acoustic pressure in the liquid aluminum using a calibrated cavitometer, showing significant shielding and acoustic dumping, more pronounced than those in water (Tzanakis et al., 2016b).

Apart from distance, which according to Tzanakis et al. (2016b) plays a predominant role (74% of contribution) in attenuating cavitation intensity and, hence, the efficiency of cavitation treatment in the melt alloy, the acoustic power and melt temperature also affect the cavitation development in the melt with corresponding contributions of 14% and 12%.

It should be noted that when we are dealing with alloys rather than pure metals such as in the previously mentioned aluminum studies, the interfaces between the liquid phase and suspended particles (nonmetallic inclusions and crystals) may also significantly affect absorption of the traveling acoustic waves (Bergmann, 1954). The attenuation factor increases with the amount of particles and with their fineness. Similar effect is produced by gas bubbles whose interfaces with the melt act as scattering sources (acoustic impedance increases). On the other hand, the very same interfaces of gaseous and solid inclusions act as cavitation nuclei and favor the development of cavitation, which absorbs additional ultrasonic energy.

According to well-adopted views on the cavitation threshold, the tensile stress-induced disruptions in liquids are not governed by molecular forces, but rather by the presence of cavitation nuclei such as vapor and gas bubbles, solid gas-adsorbing suspensions, and hydrophobic inclusions.

The cavitation strength is related to the surface tension at the liquid-gas interface and the initial bubble radius (the higher the surface tension, the lower the resonance size). The viscosity μ also markedly influences the cavitation response of the liquid, increasing the cavitation threshold and the critical resonance radius of a cavitation bubble (the higher the viscosity, the larger the resonance size) (Khismatullin, 2004). The cavitation threshold or critical pressure is directly proportional to the $\ln(\mu)$ (Briggs et al., 1947) or to μ (Connolly and Fox, 1954). It should be noted that the Minnaert equation frequently used for estimating the resonance size of cavitation bubbles does not take into account viscosity.

Chapter 3 discussed the behavior of cavitation bubbles in liquids. Figure 20.6 shows the simulated evolution of the bubbles in liquid aluminum in dependence on the acoustic pressure. If the sound pressure is below the cavitation threshold $P_C = 0.6\,\text{MPA}$ ($P_A < P_C$), the cavities pulsate and do not collapse. The pressure in gaseous bubbles varies very little. As the sound pressure P_A increases to values above 1 MPa and exceeds P_C, a significant fraction of cavities with $R_0 > R_{CR}$ behave like typical cavitation bubbles,

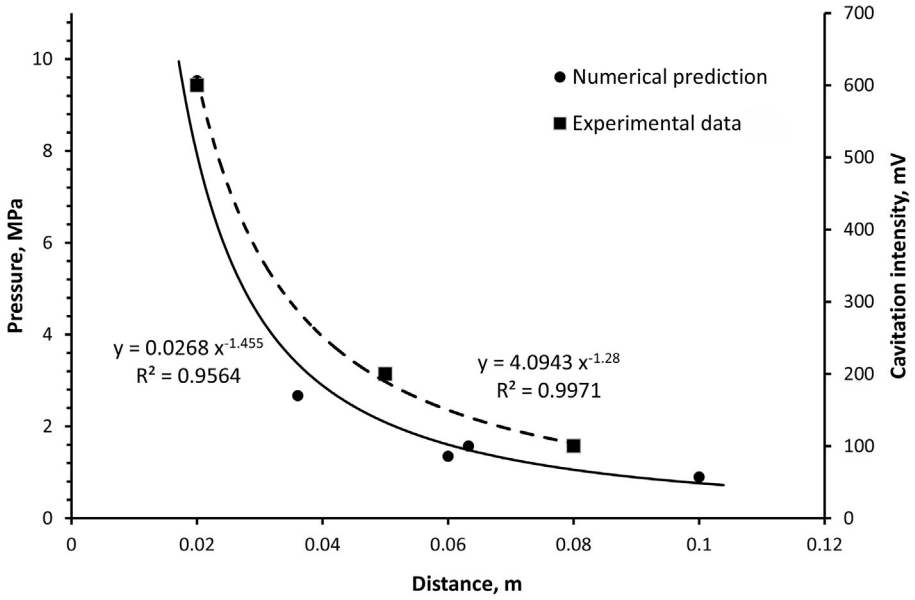


FIGURE 20.4 Attenuation of acoustic pressure (calculated numerically in MPa and experimentally measured as intensity in mV) in liquid aluminum with the distance from the sonotrode (ultrasonic frequency 17.7 kHz).

collapsing at the end of the first or second period of oscillations. With a further increase in sound pressure, i.e., for $P_A \gg P_C$, cavitation becomes developed and all cavities expand during one or two periods of the ultrasound wave and then catastrophically collapse (transient cavitation). The pressure inside the bubbles varies by several orders of magnitude.

This analysis is done with an assumption of spherical bubbles, which holds only for the first cycle of oscillations. In reality, the curved interface between the denser liquid and

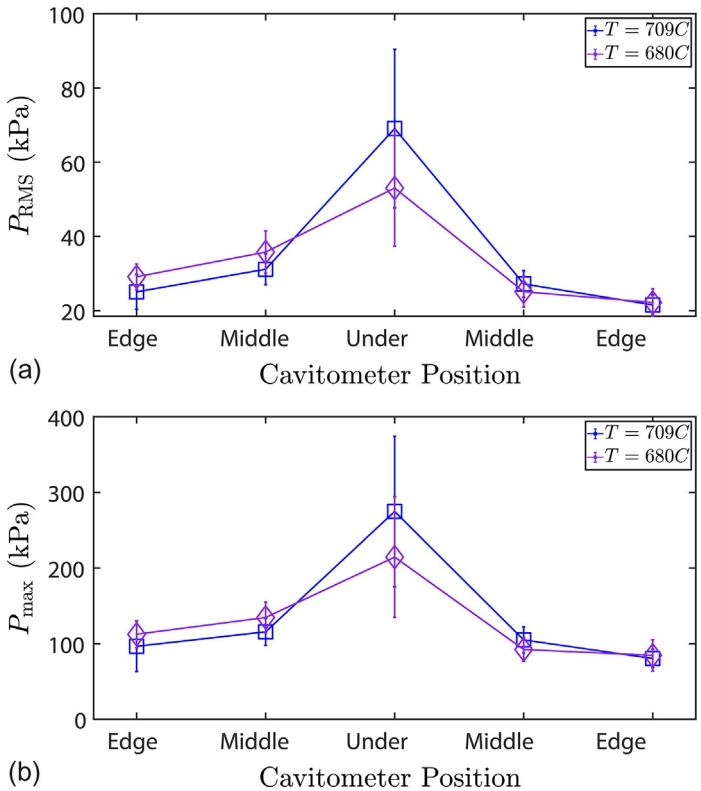


FIGURE 20.5 Variation of acoustic pressure (a: RMS, b: maximum) in liquid aluminum with respect to the position of the measuring point along the length of a rectangular vessel.

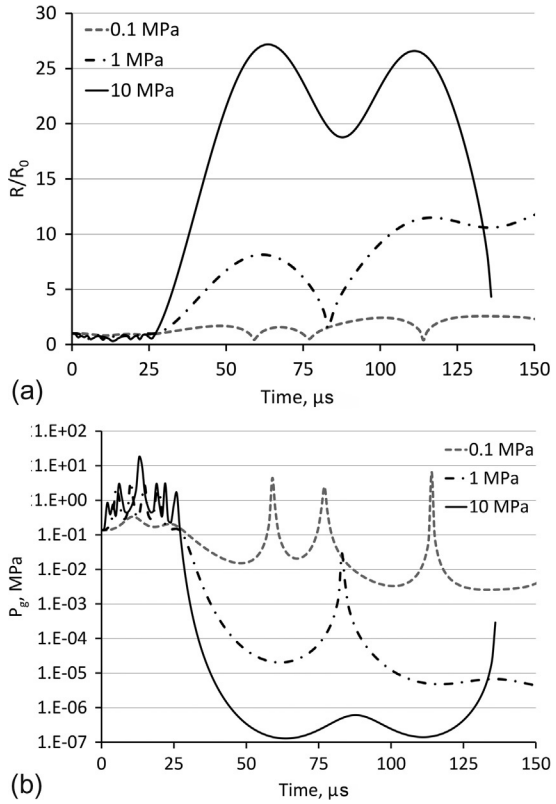


FIGURE 20.6 Evolution of cavities with initial radii $R_0 = 50\,\mu m$ in aluminum melt (a) and corresponding gas pressures (b) for acoustic pressures P_A: 0.1, 1.0, and 10.0 MPa. *(Courtesy of G.S.B. Lebon.)*

the less dense gas inside the bubble strongly accelerates inward, especially during last stages of collapse (Lauterborn et al., 1999). This results in the distortion of initially plane interface with the formation of kinks and folds. This phenomenon as well as the collapse of the bubbles resulting in the formation of a cloud of new, much smaller bubbles (satellites) can be observed experimentally as illustrated in Figure 20.7. The shape instability is counteracted by the smoothing effect of a higher surface tension and energy dissipation by a higher viscosity (Lauterborn et al., 1999).

The given results for bubble dynamics, though accounting for the gas contents inside the bubble, did not take into account the diffusion of gas dissolved in the liquid into and from the cavity. This rectified diffusion is considered in more detail in Chapter 19. Allowing for this diffusion would increase the survival chances of the bubble (Eskin, 1988). Details of numerical solutions can be found in a review by Plesset and Prosperetti (1977) and works of Fyrillas and Szeri (1994), Crum (1980), and Lebon et al. (2015).

The observation of bubbles 15 μm in size in liquid aluminum performed in a synchrotron study shows that the cavitation bubbles exhibit a nonlinear stable behavior surviving for prolonged periods of time in the melt, enhancing the broadband cavitation signal intensity and thus the cavitation treatment potential (Tzanakis et al., 2015a; Xu et al., 2016), Figure 20.8. This is also evident from recent findings where spectrum analysis (with an excitation frequency of 20 kHz) showed prominent peaks in the range of 300–350 kHz (Figure 20.9). This can be explained by the presence of a large number of bubbles with a natural frequency within this frequency range (oscillating at their resonance size) that give rise to those peaks. By using the classical Minnaert equation (size of oscillating bubbles is inversely related to the frequency of its volume oscillations), we can estimate the size of these resonating bubbles that interestingly fall within this measured range of 15 μm. This is also in agreement with Lebon et al. (2018) that shows that the majority of bubbles in liquid aluminum are indeed smaller in sizes than those of the theoretical linear resonance size at 20 kHz. Also, it should be noted that in water where bubbles' rate of survival is less, high-frequency pressure peaks are suppressed with the fundamental frequency being more prominent. This is the determinant that seems to regulate the difference in the extent of the cavitation zone between aluminum and water (however and in line with the previous remarks, the acoustic impedance and attenuation factor regulate the actual borders of the cavitation zone, and for aluminum, this is more pronounced than in water as shown in Tzanakis et al. (2016b)).

Another reason of these prominent high-frequency peaks can be related to high-energy stable cavitation (similar to that drives the sonoluminescence phenomenon). Experimental indication that cavitation bubbles are indeed collapsing in regular intervals (bubble collapses and rebounds for more than 2 s as shown in Figure 20.8) implies that those bubbles, even being far away from the cavitation zone (in this case about 0.5 cm away from the sonotrode tip of 1 mm in diameter, ratio 5/1), can emit acoustic pressures in the range of 0.2 MPa (Lebon et al., 2015), promoting cavitation for prolonged period of times and, therefore, favorable conditions for efficient localized treatment of the melt solution.

The geometry and size of the cavitation zone are important parameters detaining the efficiency of the USP in the bulk liquids. The empirical observations show that the cavitation originates on the interfaces (radiating face of the sonotrode, wall crevices, solid and gaseous inclusions) as well as inside the melt volume, forming a concentrated region close to the ultrasound source with complicated and changing in time spatial configurations at distance. These configurations gradually transform to streams, jets, and flows.

The rule of thumb says that the average dimensions of the cavitation zone are on the same scale as the diameter of the sonotrode. When cavitation is established, the cavitation region has a volume with the cross section ranging

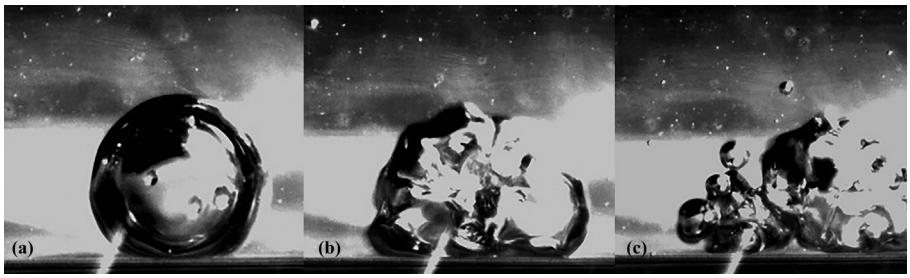


FIGURE 20.7 Evolution of a gas cavitation bubble in ethanol: (a) initial state, (b) shape distortion, and (c) implosion with generation of new bubbles.

approximately from $\lambda/4$ to $\lambda/2$. For example, this size is 20–40 mm for water and 50–100 mm for aluminum melts (that is also in a good agreement with the previous justification of the 5:1 ratio based on the active cavitation bubbles, i.e., for a sonotrode of 20 mm in diameter, the extended zone should be around 100 mm).

Sonication generates also directed hydrodynamic flows in melts. These steady-state flows are represented by (i) acoustic streams that originate from the pressure wave caused by high-frequency vibration of the sonotrode and pulsation of the cavitation region and (ii) secondary, forced convective flows. They occur both in the bulk of the liquid and near the walls, particles, and other objects within the volume subjected to the ultrasonic field. The velocity of acoustic streams increases with the ultrasonic intensity and the sound absorption. Typical velocities for acoustic streams in liquid aluminum are in the range of 0.05–0.5 m/s with their corresponding pressure field profile being affected by the bubble fraction ranging from 0.5 (lower bubble fractions) to 2 MPa (higher bubble fractions)

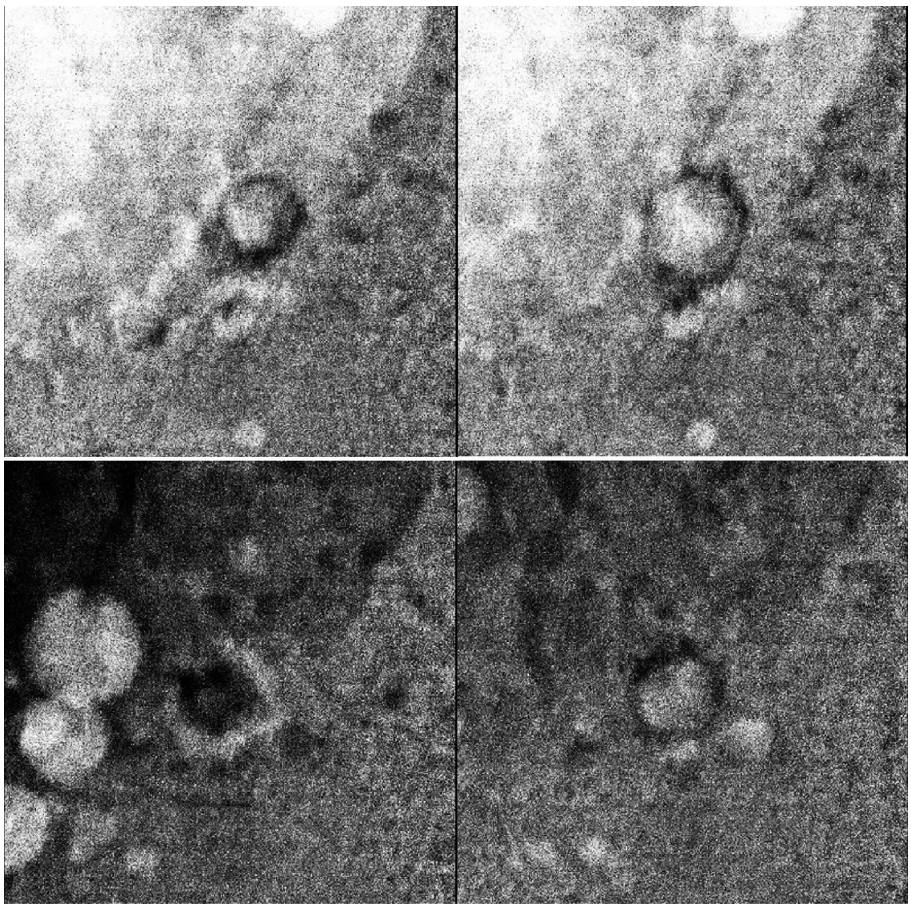


FIGURE 20.8 Pulsation and rebound of a cavitation bubble in a liquid aluminum alloy.

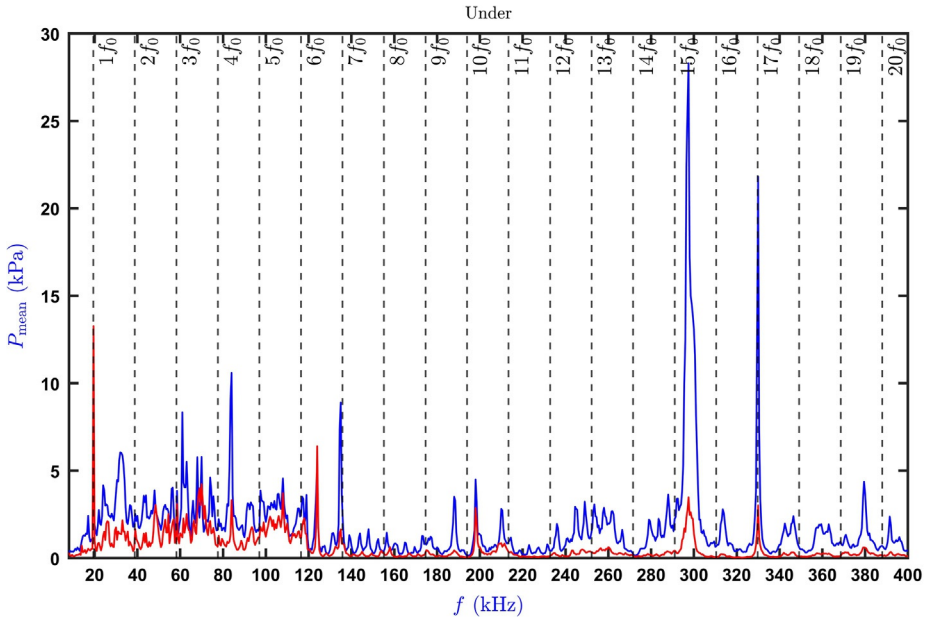


FIGURE 20.9 Typical acoustic spectra for water *(red)* and aluminum *(blue)* at 20 kHz excitation frequency acquired below the sonotrode tip with a calibrated cavitometer in the range of 8–400 kHz.

(Lebon et al., 2019a). In addition, it is demonstrated by experimental and numerical studies that the bubble volume fraction regulates the flow direction with streamers being upward for low bubble fractions and low input powers as illustrated in Figure 20.10. In a melt treatment situation, this may be attractive, extending the melt residence time in the cavitation zone and preserving the integrity on the free surface restricting the entrainment of oxides from the free surface.

20.3 Mechanisms of ultrasonic melt processing

20.3.1 Structure refinement

20.3.1.1 Cavitation-induced nucleation

The cavitation-induced nucleation can go along the two main mechanisms: (i) undercooling of the cavitation bubble surface during the expansion phase of oscillations and (ii) undercooling of the liquid phase resulting from the instantaneous increase of pressure during cavitation bubble collapse (according to the Clapeyron equation). The latter mechanism seems most probable as the decrease of bubble surface temperature during expansion does not exceed 1 K while the change of the melting point as a result of bubble collapse can reach tens of degrees and approach $0.2T_m$ (Hunt and Jackson, 1966). For example, if a pressure of 1 GPa is generated during bubble collapse as experimentally estimated by Tzanakis et al. (2014) and numerically resolved by Pishchalnikov et al. (2019), then the melting point of 99.99% pure aluminum will increase locally by about 60°C as shown in the table below:

P (MPa)	0.1	500	1000	2000	4000
t_0 (°C)	660.5	690.0	720.0	780.0	830.0

These mechanisms of cavitation-induced nucleation are, however, seldom realized as they consider homogeneous nucleation, which is not a common phenomenon in real metals.

20.3.1.2 Activation of nonmetallic inclusions

Solidification of real melts always occurs heterogeneously and on available substrates that are either naturally present (indigenous impurities) or deliberately added (exogenous, grain refiners) to the melt. In aluminum and magnesium alloys, the former are represented by oxides and carbides and the latter by borides, carbides, and primary phases. The term "activation" is usually applied to indigenous particles and includes the phenomena of wetting, formation of stable or metastable surface layers, deagglomeration, and nonequilibrium solidification.

Multiplication of solidification nuclei by activation of heterogeneous substrates was suggested in the 1930–1950 by Kazachkovsky (1948), Danilov and Neimark (1949), and Danilov (1956). In this case, the dynamic action upon solid/liquid interface facilitates wetting through improved access of the liquid phase to the solid, decreases surface tension, and promotes heterogeneous nucleation on the available insoluble substrates such as oxides and carbides,

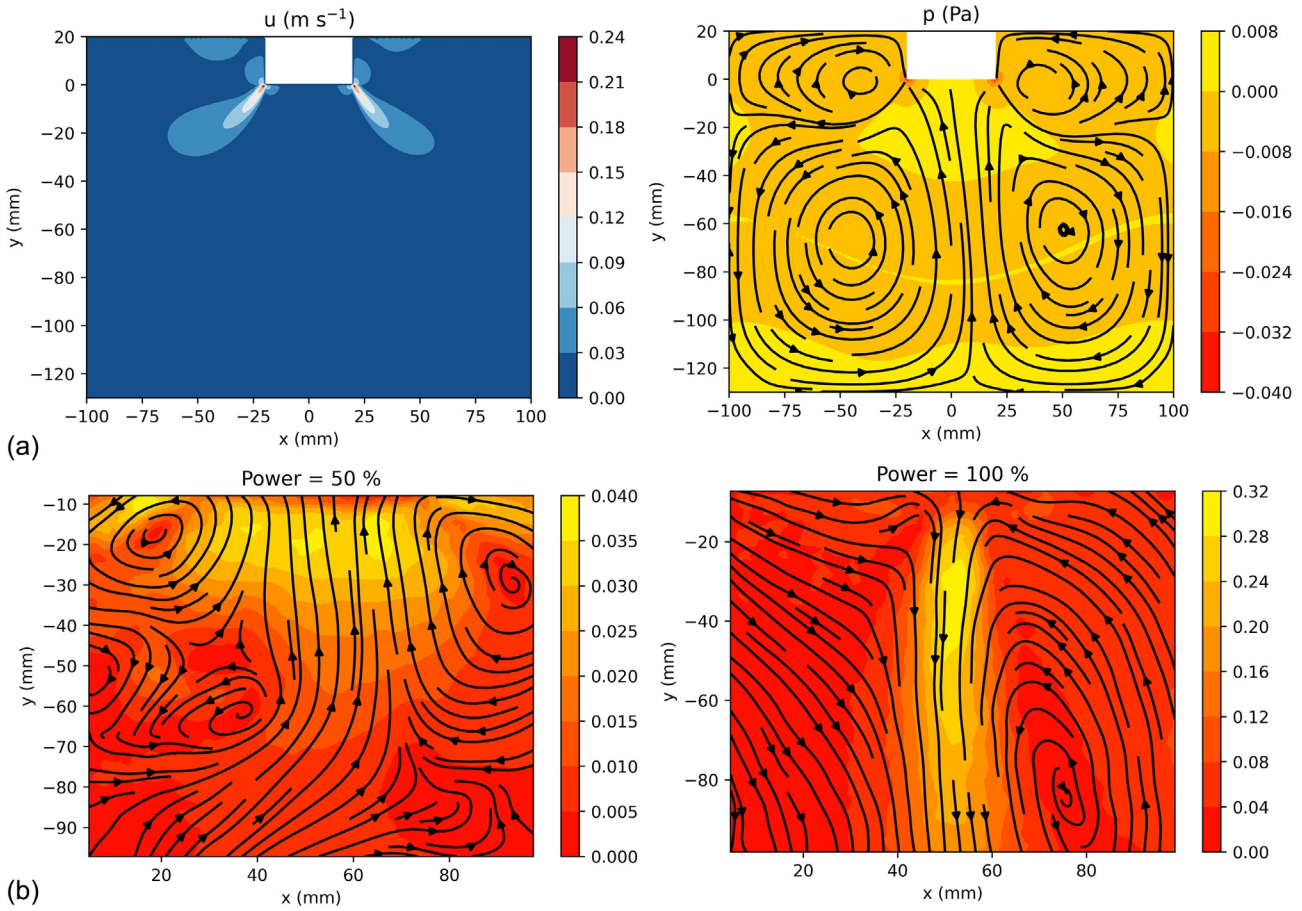


FIGURE 20.10 Acoustic streaming under a sonotrode 40 mm in diameter (20 kHz) is numerically simulated in liquid Al (50% power): (a, left) velocity contours, (a, right) pressure field with flow streamlines, and experimentally observed by PIV flow streamlines in water at (b, left) 50% power and (b, right) 100% power. Note the opposite directions of acoustic streaming in dependence on the transducer power.

being assisted by penetration of the liquid phase into discontinuities of the substrate surface and the formation of the adsorbed boundary layer at the substrate surface.

Cavitation treatment may turn particles into active solidification sites by the following mechanism (Eskin, 1988).

Any microscopic solid particle that has affinity to the solidifying phase has a potential to become an active solidification site. This affinity can be due to the match of crystal structures, or due to the presence of a special adsorbed layer resembling the structure and composition of the solid phase or even the matrix solid phase on its surface. In the latter cases, the stability of such a solidification site can be assured only when the adsorbed layer or the solid phase is thermally stable within some temperature range above the liquidus of the alloy. Such conditions can be met in discontinuities like microcracks where, due to the capillary effect, the melting temperature of the alloy is much higher than the equilibrium liquidus. The increase in the melting point under conditions of negative curvature (concave particle) is described by the Gibbs-Thompson equation (Dantzig and Rappaz, 2009):

$$T_{\mathrm{m}}^{\mathrm{r}} = T_{\mathrm{m}}^{\infty} - \frac{2\Gamma}{r} \tag{20.3}$$

where $T_{\mathrm{m}}^{\mathrm{r}}$ is the melting point of a concave particle inside a crevice, T_{m}^{∞} is the melting point of a particle with flat interface, r is the curvature (negative in the case of the concave particle), and Γ is the Gibbs-Thompson coefficient depending on the surface tension, density, and latent heat.

However, the presence of a gaseous phase at the surface and in the surface imperfections of nonmetallic particles hinders the access of the liquid phase to the inclusion, wetting, and filling of the imperfections with the melt. Therefore, the majority of the inclusions remain inert with regard to the solidification. During USP, the particle is stripped by cavitation jets of absorbed gas and other impurities and becomes accessible by the surrounding melt.

During ultrasonic treatment with the intensity higher than the cavitation threshold, a cavitation bubble is formed close to the capillary opening filled with gas. In this place, the cavitation strength of the melt is weakened by the presence of a gaseous phase as it cushions the traveling shock waves. Then,

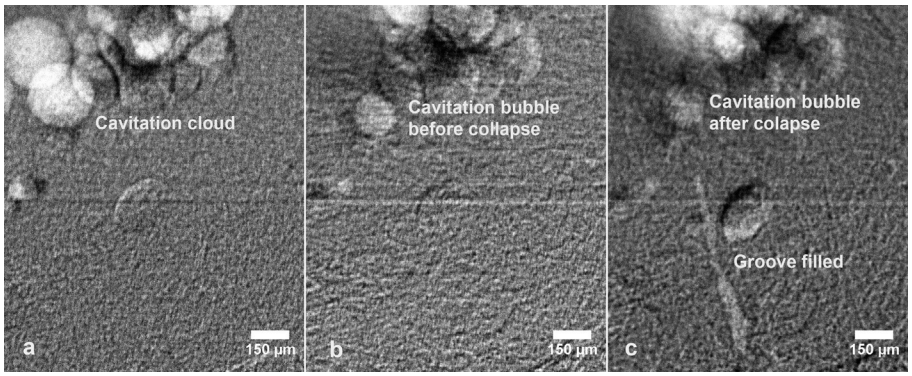


FIGURE 20.11 In situ synchrotron observation of the sonocapillary effect in a liquid aluminum alloy: (a) cavitation cloud at the entry to a groove in an alumina film (not visible), (b) cavitation bubble at the entry to the groove just before the collapse, and (c) the filled groove after the collapse of cavitation bubbles.

the sonocapillary effect takes over, filling the capillaries (cracks) of almost submicroscopic sizes. A comprehensive study using synchrotron radiography showed that a pressure up to 15 MPa exerted by the liquid micro-jet upon bubble implosion in the vicinity of the capillary opening is sufficient for filling tiny capillaries in the range of a few microns in size (Figure 20.11) (Tzanakis et al., 2015b).

As a result of this activation, the solidified alloy inside capillary openings of the particle stays solid at a temperature of the surrounding melt (Eq. 20.3) and acts as a perfect solidification site for the matrix melt. The same mechanism should be valid for any primary solidifying phase: solid solution, intermetallic, or silicon. Actually, the activation of nonmetallic impurities facilitates nucleation and refinement of any primary phase as reported by Wang et al. (2016a, 2017a, 2018a) and illustrated in Figure 20.12.

The activation of inclusions by ultrasonic cavitation and the corresponding refinement of the primary phase have been demonstrated for pure aluminum with mixed-in oxide surface film (Atamanenko et al., 2010) and for Mg-Al alloys with added carbon black nanoparticles (Bhingole and Chaudhari, 2012). Recently, an ultrasonic activation of spinel particles (potent substrates for aluminum) from an Al-1.3% Ti-1.8% $MgAl_2O_4$ master alloy added to an aluminum casting alloy has been demonstrated as shown in Figure 20.13 (Sreekumar et al., 2017).

Eskin and Eskin (2015) estimated that the number of active substrates increases by USP by 6, 4, and 3 orders of magnitude in small (65–74 mm), middle (270–285 mm), and large (830–845 mm) size DC cast billets from an AA7XXX (Al-Zn-Mg-Cu-Zr) alloy, respectively.

20.3.1.3 Fragmentation of primary intermetallics

The fragmentation of the solid phase under dynamic action is accepted by many as the main mechanism of structure refinement (Balandin, 1973; Abramov, 1972; Campbell, 1981). Chvorinov (1954) suggested that the dendrites growing in the two-phase transition region are separated from the solidification front by forced convection and the resultant crystals move to the bulk of the melt and act as nuclei for new grains, providing that they are not completely re-melted. Balandin (1973) further proposed that the insoluble inclusions deactivated by alloy melting with high superheat reactivate once the solid phase is formed around them. After separation from the two-phase zone by forced convection, a solid crystal containing this activated inclusion is transported to the liquid phase and the solid phase is melted away leaving behind an active insoluble substrate. These concepts have not, however, explained the mechanisms of dendrite (crystal) separation from two-phase zone or its fragmentation.

One of the earliest suggested mechanisms was the seemingly obvious fragmentation of dendrites by mechanical fracture caused by melt flow. This mechanical fracture assisted by bending deformation, formation of large-angle boundaries, and liquid metal embrittlement is still considered as one of the possibilities (Campbell, 1981; Vogel et al., 1979).

On the mesoscopic scale, and as previously discussed (Figure 20.10), forced melt flow can bring hot melt from the liquid pool into the undercooled two-phase zone and cause its partial re-melting with subsequent washing-out of loose solid crystals. On the microscopic scale and in the absence of cavitation, the most realistic mechanism of fragmentation is dendrite arm separation by root re-melting effects because of thermal, solute, or capillary effects. Solute accumulation at the solidification front causes the fluctuations in growth velocity that has direct effect on the kinetics of dendrite branches growth and coarsening (Jackson et al., 1966). The coarsening of dendrite branches results in their necking (Chernov, 1956; Kattamis et al., 1967) and accumulation of solute at their roots by both rejection from the solid phase and convection in the inter-dendritic space (Ruvalcaba et al., 2007). The local solute enrichment results in local superheating of the solid phase and its melting. Along with the local change of equilibrium, capillary effects cause dendrite roots to be more soluble than

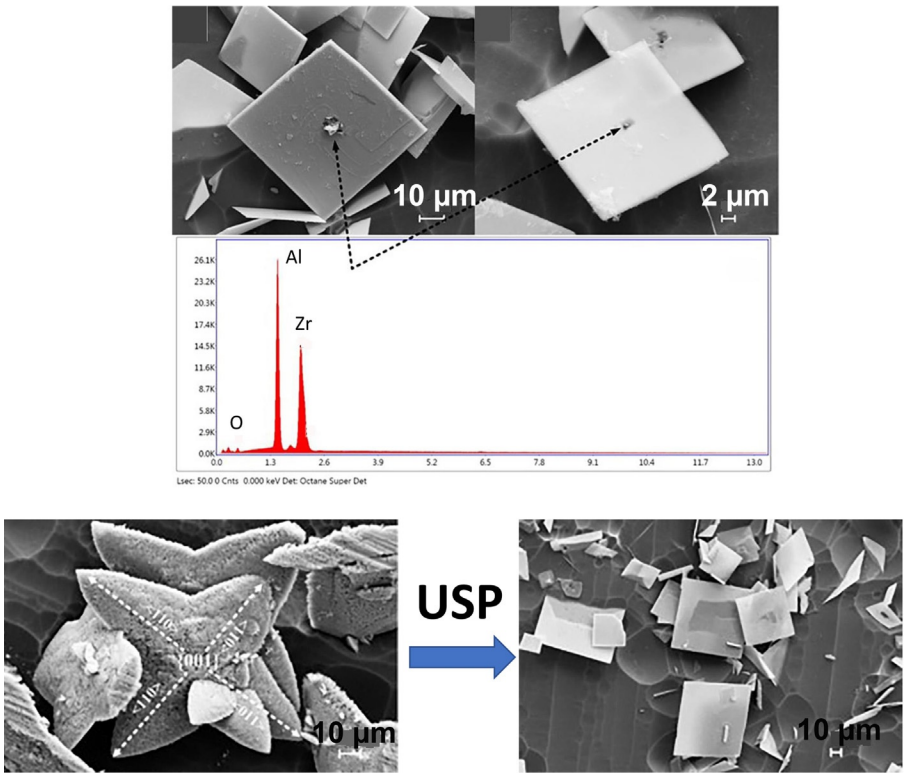


FIGURE 20.12 Nucleation of primary Al_3Zr intermetallics on oxide particles after ultrasonic processing and their respective refinement. *(Courtesy F. Wang.)*

other regions. The forced flow assists further by transporting the cavitation bubbles toward the dendrites to promote continuous fragmentation of the growing dendrites, and in transporting the fragments from the solidification front farther to the bulk of the melt. The fragmentation assisted by acoustic streaming is especially applicable to elongated crystals that are subjected to alternating flow, facilitating the root re-melting and fatigue-type fracture (Wang et al., 2017b).

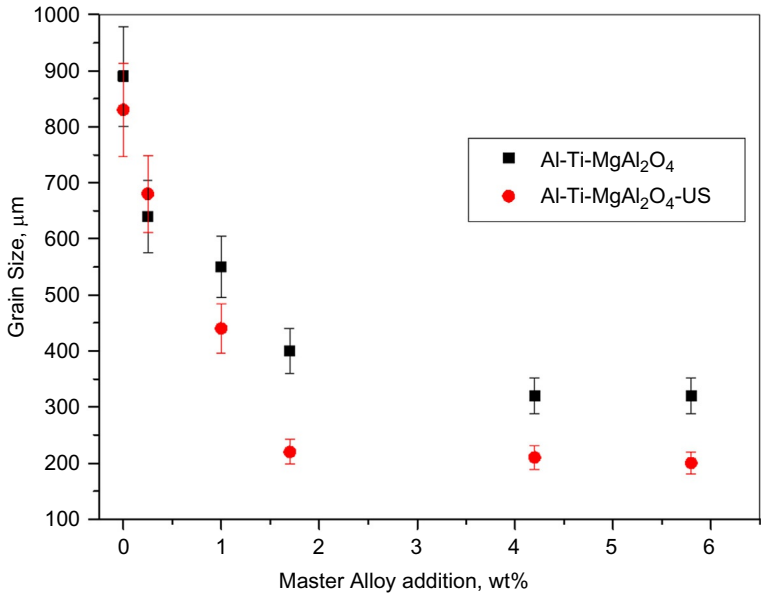


FIGURE 20.13 Relation between the grain size of an A357 alloy and the level of Al-Ti-$MgAl_2O_4$ master alloy addition with and without ultrasonic processing. *(Adapted from Sreekumar et al. (2017).)*

Another important mechanism of fragmentation is by cavitation itself. In the presence of cavitation accompanied by the implosion of bubbles, the fracture of dendrites has been demonstrated on transparent analogues (Swallowe et al., 1989; Shu et al., 2012) and recently on extracted intermetallic crystals subjected to cavitation in water (Wang et al., 2017c). The fragmentation of primary intermetallic particles by cavitation is one of the mechanisms for grain refinement of the main primary phase, e.g., aluminum dendrites. Fracture by oscillating and collapsing bubbles happens to the primary intermetallics in the temperature range of their formation, in addition to the enhanced nucleation of insoluble inclusions described earlier (Wang et al., 2016a, 2018a, 2018b). In this case, the alloy would be considered liquid from technological point of view as the formation of these particles as well as the ultrasonic processing occur well above the liquidus temperature of the matrix solid solution.

Figure 20.14 gives a sequence of frames capturing the fragmentation of extracted primary intermetallics by a single laser bubble (controlled cavitation) or a cloud of bubbles as a result of cavitation processing (Priyadarshi et al., 2021). The shock wave pressures generated by multiple collapsing events were found to be the governing fragmentation mechanism of intermetallics. Before fracture, propagating shock wave fronts continuously interfere with the nearby intermetallic crystals (with fracture toughness 1.1 MPa$\sqrt{m}$) causing a low cycle fatigue (around 100–200 shocks arriving at the sample surface in less than 10 ms with surges of acoustic pressures in the range 0.4–0.5 MPa) until the existing crack reaches its critical length and fragmentation occurs immediately afterward, via brittle fracture. Interestingly, repetitive subharmonic cloud collapses in the range of 0.1–0.5 MPa were found to be responsible for the bending modes of the fixed intermetallic crystals relevant to that of the growing dendrites at the solidification front as previously discussed.

The fragmentation of dendrites by ultrasound-induced streaming flow and powerful shock waves can result in spectacular structure refinement, when ultrasonic processing happens in the solidification range of the alloy. Despite very good grain-refining effect of fragmentation, the practical application of this mechanism is limited to small volumes. There might be a potential to use this mechanism in direct-chill casting or other continuous processes (e.g., arc re-melting) where the position of the solidification front is fixed in space and the cavitation can be applied throughout the process in the locations below the liquidus isotherm. The limitation in this case would be lateral spread of the effect, i.e., multiple cavitation sources would be required for processing of larger cross sections or a better flow management as will be discussed in Section 20.4.1.

The fragmentation of primary intermetallics, on the other hand, can offer more flexible technological options as the processing can be moved to a higher-temperature part of the casting mold, or even to the melt transport system. In aluminum alloys, titanium aluminide, scandium aluminide, or zirconium aluminide are well known to possess structural features required for powerful grain refinement effect; in magnesium alloys, zirconium forms a primary phase that is used in Al-free alloys for grain refinement.

It has been known since the 1960s that the addition of Zr in combination with ultrasonic treatment results in considerable grain refinement of aluminum alloys (Eskin, 1965).

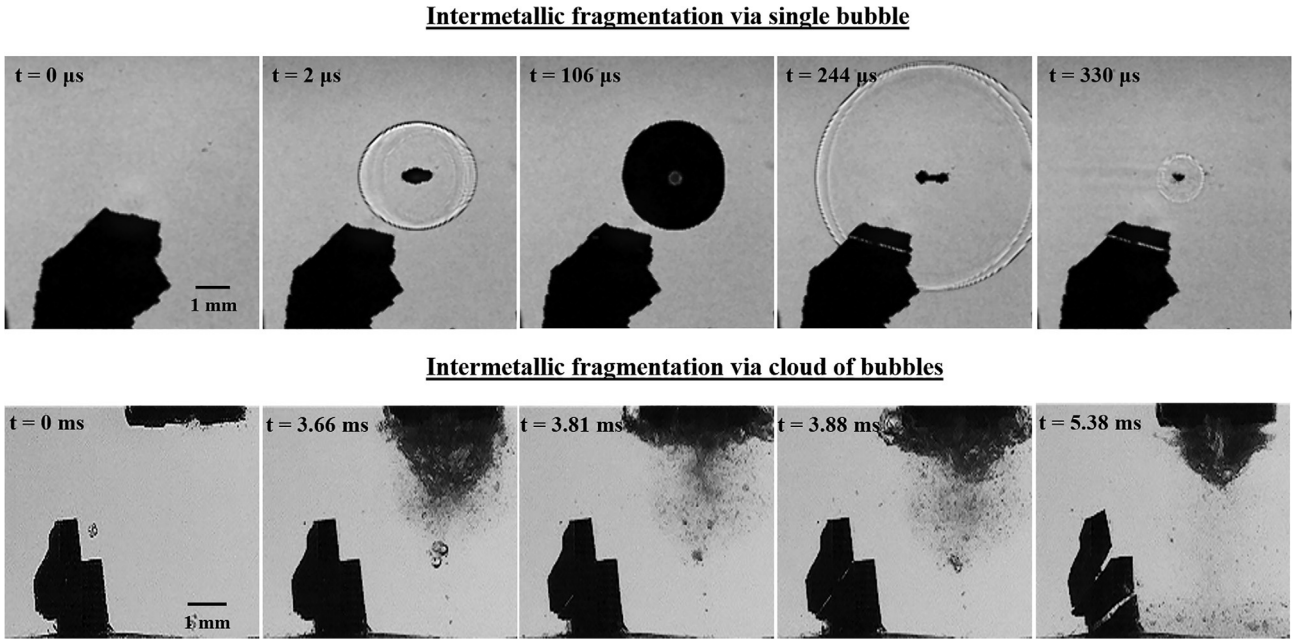


FIGURE 20.14 In situ observation of Al_3Zr particle fragmentation by single-bubble (upper row) or cloud (lower row) cavitation.

Later on, the essential role of small Ti additions has been demonstrated (Eskin, 1988) and the combined effect of Zr, Ti, and ultrasonic processing has been explained (Atamanenko et al., 2010, 2011). Recently, a role of USP and Ti in shifting the phase equilibrium in the Al-Zr system has been suggested (Eskin, 2020).

20.3.2 Deagglomeration and dispersion

De-agglomeration and dispersion of nucleating particles is another mechanism of grain refinement and also a base for the USP application in manufacturing of composite materials. The high-intensity ultrasonic oscillations create myriads of microscopic bubbles that are distributed within the treated volume by acoustic and secondary flows (as previously discussed). The bubbles preferentially form at the interfaces with gas pockets. Therefore, the agglomerates of the particles and particles themselves are the ideal nuclei for cavitation inception. The mechanisms of de-agglomeration can be represented as follows: The cavitation bubbles are formed at the interfaces particle/gas pocket/liquid. These bubbles pulsate intensely, implode, loosening the agglomerate and chipping off particles. Experiments on MgO and SiO_2 agglomerates showed that chaotic bubble oscillations deemed to be responsible for the deagglomeration and gradually chipping of particles. The forces that hold the agglomerates together are in the range of 1 MPa (capillary and adhesive forces) (Rumpf, 1962; Bochvar and Eskin, 2012), while the continuous pressure surges from the oscillating bubbles are in the order of 10^2 kPa (Kim and Kim, 2014) and the pressure generated by bubble implosion exceeds 150 MPa at 10 μm distance (Pishchalnikov et al., 2019), which is strong enough to break these bonds in due time and disperse particles in the bulk liquid with the assistance of the acoustic flows (similar to the dendritic fragments transportation).

Some practically important analytical calculations of capillarity and size of agglomerates show (though semi-quantitatively due to the assumptions) that the processing time decreases with the surplus of pressure at the capillary entry (difference between the capillary pressure and the pressure from cavitation) and the relative sizes of capillary channels (depth/radius) (Kudryashova and Vorozhtsov, 2016). There is also a requirement for the minimum acoustic intensity at the entry to the capillary that decreases with the ultrasonic frequency and the size of the particles in the agglomerate. It is important to make two notes: (i) the deagglomeration is not an instantaneous process but takes time and (ii) the ultrasonic frequency is preferable over sonic frequencies.

With regard to the structure refinement, the deagglomeration of TiB_2 particles added from master alloys to refine primary aluminum grains is an important example when USP can be used to improve the efficiency of these grain refiners. In manufacturing (nano)composites, the application of USP is in many cases indispensable for deagglomeration, wetting, and distribution of the reinforcing particles in the melt.

20.3.3 Emulsification (immiscible alloys)

The emulsification of immiscible liquids under the action of ultrasound is known since the 1920s and was demonstrated for water and oil and water and mercury (Wood and Loomis, 1927; Richards, 1929). The decisive role of cavitation in the process of emulsification was soon recognized (Bondy and Söllner, 1935). Some applications in food industry are covered in Chapter 29. Already in the 1930s, first successful experiments on using high-frequency sources (10 kHz) for the introduction of Pb in liquid Al and Cd in Al-Si melt were reported (Schmid and Ehret, 1937) and the possibility to produce emulsions of 7%–10% Pb in Al and Zn stable even upon re-melting was demonstrated (Becker, 1941).

The physics of ultrasonic emulsification is considered elsewhere (Neduzhy, 1961, 1964; Abismaïl et al., 1999, Behrend et al., 2000; Behrend and Schubert, 2001), and there were very little developments in that until recent works (Orthaber et al., 2020; Wu et al., 2021). In general, the basic factors controlling the process can be summarized as follows. The size of droplets in the emulsion decreases with the increasing ultrasonic frequency. At the same time, the higher frequency requires a greater sound intensity applied. With the increasing intensity and processing time, the emulsion concentration increases up to a certain value when saturation occurs. This saturation is a result of the equilibrium reached between the processes of emulsification (dispersion) and coagulation. A running sound wave is more efficient than a standing wave, with coagulation processes prevailing in the latter case. Precavitation sound processing results in de-emulsification. Therefore, cavitation is the important requirement of the process. A low viscosity and a lesser difference in viscosities between the components facilitate emulsification. Additions of surfactants (decreasing the surface tension at the interface) and stabilizers (coating of droplet surface) promote the stability of the emulsion and allow for higher concentrations. In general, it is believed that the emulsification occurs through local disturbances at the interface between two immiscible liquids with typically only one liquid undergoing dispersion while the other liquid acts as the source of cavitation bubbles. However, recent studies in ultrasonic emulsification show that both liquids can take part in the emulsification process contributing to the formation of cavitation bubbles with new insights involving the effect of liquid jets from the lighter liquid toward the interface (Orthaber et al., 2020) and chaotic oscillations (Wu et al., 2021) (similar to the de-agglomeration discussed previously).

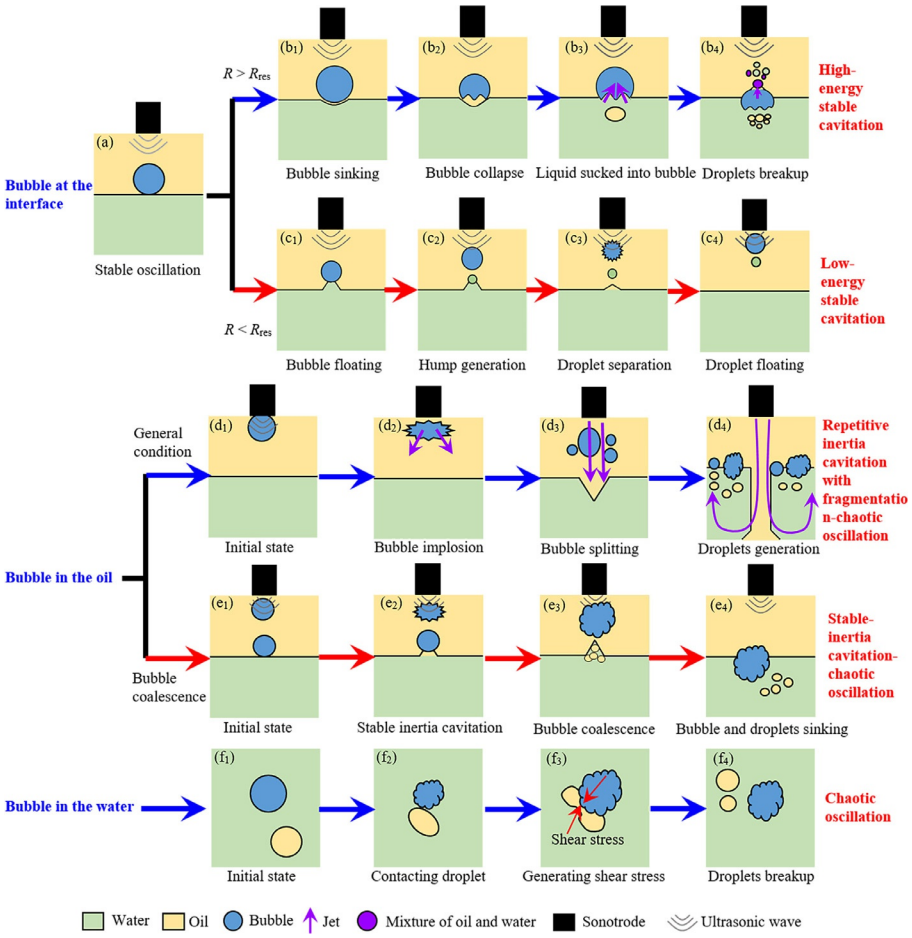


FIGURE 20.15 Variety of ultrasonic emulsification mechanisms observed by in situ experiments. *(Courtesy of W.H. Wu.)*

A complexity of emulsification phenomena and mechanisms occurring in an oil-water system are illustrated in Figure 20.15.

With respect to liquid metals and alloys, ultrasonic emulsification has practical value for manufacturing of free-machining and bearing alloys. These alloys contain additions of low-melting, soft elements such as Pb, Bi, and Sn that have either a miscibility gap with Al that causes stratification (Al-Pb, Al-Bi) or a very large solidification range that triggers gravity segregation (Al-Sn).

It was demonstrated that ultrasound-induced cavitation significantly decreases macrosegregation and promotes the uniformity of structure in an immiscible Al-Sn-Cu alloy. With a single ultrasonic source, the uniform distribution of monotectic Al-Sn-Al_2Cu cells was obtained close to the cavitation region, while nonuniformity triggered by gravity separation of Sn from Al remained in the areas farther from the ultrasonic source where only acoustic streaming was acting (Zhai et al., 2015). It was also observed that the monotectic cells nucleate on cavitation-affected substrates. An innovative scheme of ultrasonic processing with three orthogonal sources was developed and applied to the solidification of a similar immiscible alloy (Zhai et al., 2016). In this case, the homogeneous monotectic structure was obtained in the entire $30 \times 30 \times 100$ mm volume, due to the uniform cavitation field created in the melt.

20.4 Practical implementations of ultrasonic melt processing in solidification and casting

20.4.1 Structure refinement during casting

Direct-chill (DC) casting on the one hand simplifies the application of ultrasonic melt treatment as the melt containers (launder, mold, melt distribution systems) are simple and constant in shape with well-defined temperature profiles. On the other hand, DC casting requires processing of larger melt volumes in a continuous manner, which creates some challenges for the technology of ultrasonic processing. Extensive account of USP upon DC casting can be found elsewhere (Eskin, 1965, 1988; Eskin and Eskin, 2015).

It was demonstrated that aluminum grains can be refined substantially, especially in aluminum alloys containing Zr and Ti. In some cases, a uniform structure with nondendritic grains was obtained for billets 74–1200 mm in diameter. Depending on the size of the billets, one to ten transducers with sonotrodes placed into the sump of a billet were used in a single casting in order to achieve uniform nondendritic structure in the entire billet (Figure 20.16a,b). Fine equiaxed grains were also characterized by reduced microsegregation and finer nonequilibrium eutectic particles, which resulted in shorter homogenization times. The occurrence of hot and cold cracks was considerably reduced.

Ultrasonic melt processing and the formation of nondendritic structure in larger billets and ingots made it possible to meet the challenge and solve the problem of producing large-scale crack-free billets 960 mm (AA7055) and 1200 mm (AA2324) in diameter and ingots 450×1200 mm (AA2324) in cross section (Eskin, 1988; Eskin and Eskin, 2015).

When applied in the sump of a billet, USP induces significant changes in the melt flow and related temperature and concertation gradients, which affects solidification on the macroscopic level, in addition to the microscopic mechanisms that are related to cavitation proper. Figure 20.17 shows the changes in the flow patterns with USP (Lebon et al., 2019b). The flow pattern is reversed, the liquidus isotherm is depressed, the transition region becomes narrower, and the sump becomes shallower with USP.

The ultrasonic melt processing can be applied to the melt flow, during the transport of the melt from the holding furnace to the mold. This technological way is more versatile as the processed melt can be directed to several molds but also poses a number of challenges related to the treatment time-melt volume-acoustic power ratios. As the USP happens outside the solidification domain of a billet/ingot, only mechanisms of activating inclusions, fragmenting primary intermetallics, and deagglomerating grain-refining particles are acting. The grain refining achieved is demonstrated in Figure 20.16c,d with the inset in Figure 20.16d showing the refined Al_3Zr intermetallics that acted as solidification substrates. Current efforts are aimed at the optimization of the melt flow with the aim to improve the acoustic pressure distribution and the residence time (Subroto et al., 2019, 2020, 2022).

Application of USP upon solidification of different groups of alloys was shown to refine not only primary dendrites but also primary intermetallics in hyper-eutectic and hyper-peritectic alloys, e.g., primary Si (Eskin and Eskin, 2003; Komarov et al., 2015), Al_3Zr, Al_3Ti (Zhang et al., 2011; Wang et al., 2016b), and Al_3Ni, Al_3Fe (Chankitmunkong et al., 2020).

The application of ultrasonic cavitation to introduction of Al-Ti-B grain-refining master alloys is very promising.

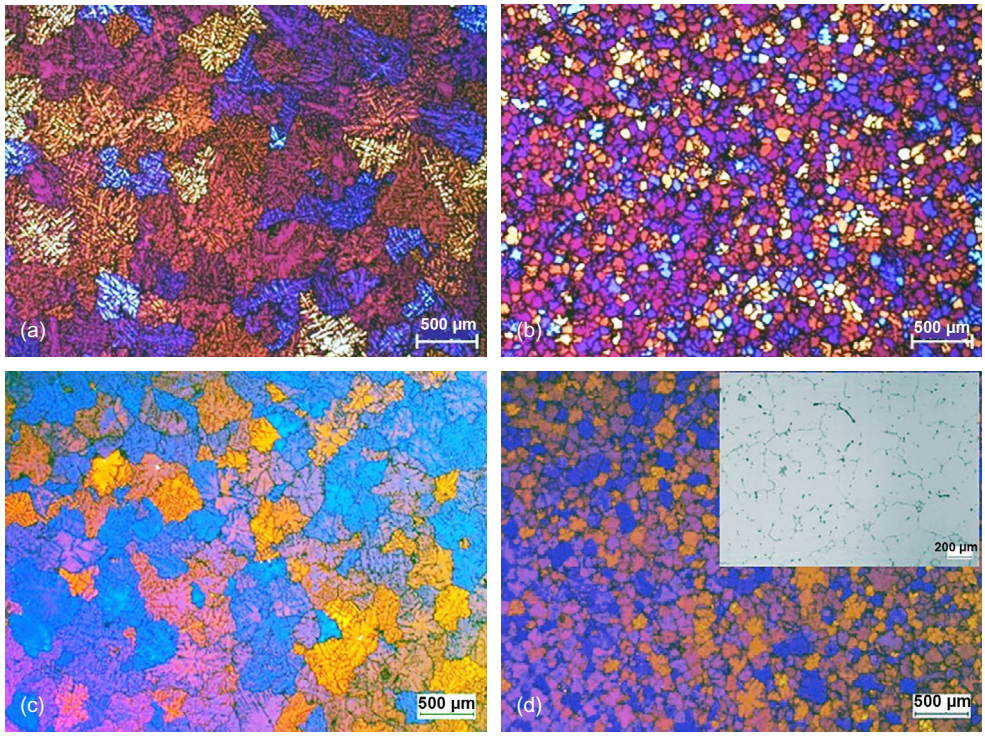


FIGURE 20.16 Effect of ultrasonic melt processing in the billet sump (a, b) and in the launder (c, d) on the grain structure of 150-mm billet from an AA6XXX (Al-Mg-Si) alloy with 0.2% Zr: no USP (a, c); with USP (b, d).

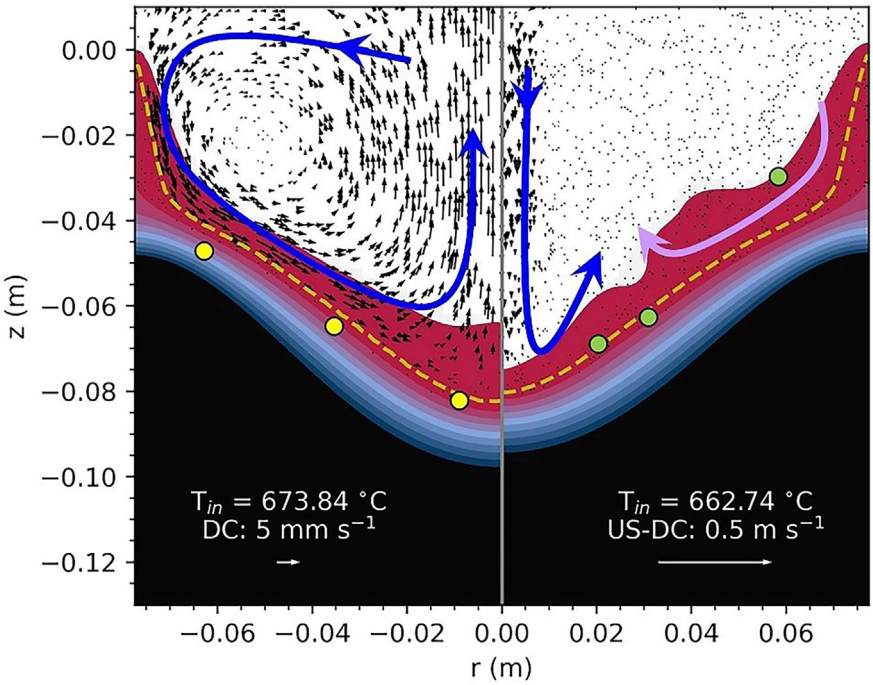


FIGURE 20.17 Effect of ultrasonic melt processing in the sump on the flow pattern and the shape of the sump during DC casting.

Despite being the main commercial technology of grain refinement, one of the deficiencies of grain-refining rod introduction is the agglomeration of TiB_2 particles, wide size distribution of these particles, and, as a consequence, low efficiency, i.e., only several percent of particles are acting as nucleation substrates. Ultrasonic melt processing improves the performance of standard AlTiB master alloys by dispersing agglomerates and activating substrates as has been confirmed by a number of studies (Eskin et al., 2008).

20.4.2 Composite materials and immiscible alloys

Ultrasonic cavitation and streaming are widely used for making metal-matrix composite materials through a liquid-metal route; for composites with nanoparticles, this is the main technique used nowadays (Eskin and Eskin, 2003; Cao et al., 2008; Choi et al., 2012; Vorozhtsov et al., 2015; Yang and Li, 2007). The previously discussed mechanisms of ultrasonic processing such as wetting, deagglomeration, and dispersion are used.

A combination of vortex created by an impeller and USP by a sonotrode is frequently used, the former assuring the introduction of the particles in the melt and the latter their dispersion. Particles are usually wrapped in a foil in a form of tubes for gradual introduction into the melt.

The next logical step would be to use a master alloy containing a metallic matrix with large concentration of particles, similar to grain-refining rods. The particles can be spatially distributed in such a composite master alloy and wetted by the matrix. The master alloy can be produced by a powder metallurgy route, using mechanical alloying for mixing and hot extrusion for consolidation and better particle distribution. Such a scheme was first suggested in the 1960s and implied the direct contact of a sintered aluminum powder (SAP) rod with the sonotrode (von Seemann and Staats, 1968). Later, this approach was tried in MMNC processing (Wang et al., 2012; Kandemir et al., 2014; Voroshtsov et al., 2015).

All these techniques are currently tried on the laboratory scale and, obviously, have advantages and disadvantages. The finer the particles, the more complicated their introduction to the melt is. In the case of microscopic (5–100 μm) particles, mechanical or electromagnetic mixing with subsequent or simultaneous ultrasonic processing is sufficient (Tsunekawa et al., 2001; Eskin and Eskin, 2003).

Most of the successful experiments are performed under conditions of developed cavitation with amplitudes 10–40 μm at frequencies 17–22 kHz. It seems that there is a consensus that cavitation is the basis of successful ultrasonic processing of composites, especially at the stage of wetting and deagglomeration. Physical modeling using transparent solutions and experiments on Mg melts with USP at variable ultrasonic parameters (17–40 kHz, 1.4–4 kW) demonstrated that a better distribution of particles in the volume could be achieved at a moderate frequency (20 kHz) and power (2.5 kW) (Shi Ying et al., 2009; Song et al., 2015). In this case, the re-agglomeration is prevented and particles are well distributed by acoustic flows in the volume.

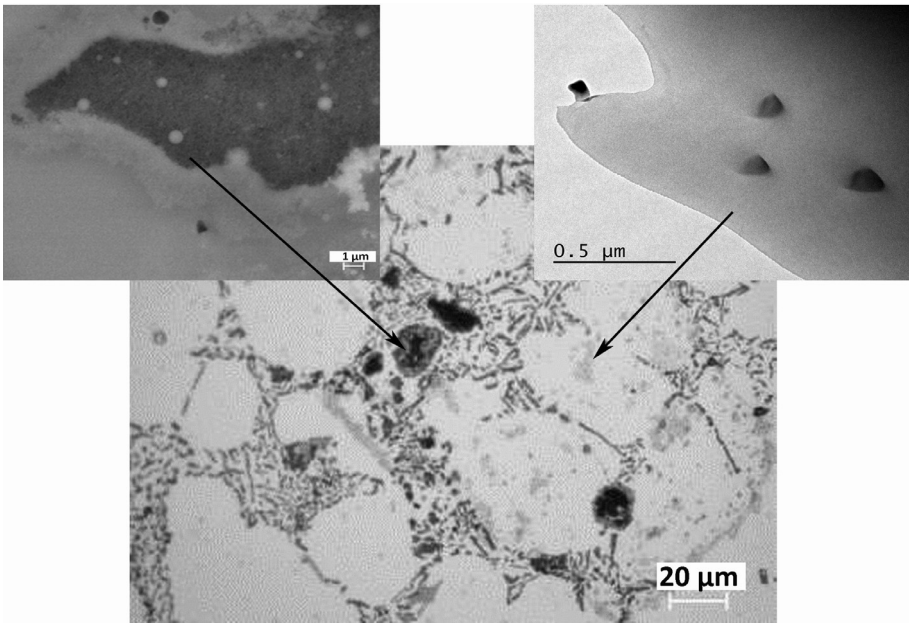


FIGURE 20.18 Distribution of Al_2O_3 nanoparticles (<100 nm) in the matrix of an Al alloy.

Figure 20.18 demonstrates reasonable distribution of alumina nanoparticles in an aluminum alloy. It has been confirmed by ultra-small-angle X-ray scattering that USP really results in deagglomeration of nanoparticle agglomerates.

Bearing alloys containing up to 10% Pb (additionally up to 10% Sn, up to 4% Sb) can be produced by the following route (Abramov, 2000). The melt is superheated to 1100–1200°C that allows for dissolution of 18%–30% Pb in liquid aluminum. The melt is then poured through a water-cooled ultrasonic funnel (magnetostrictive transducer arranged around the pouring channel). The ultrasonic processing then occurs simultaneously with melt cooling. This creates conditions for nucleation of Pb droplets under intensive mixing that prevents sedimentation. The process ends with DC casting of billets where high cooling rate helps to preserve the emulsion in the solid state. Lead particles 5–40 μm in size were uniformly distributed in the billet volume.

Another technological approach was suggested by Eskin (1988) and tested under laboratory conditions (casting of a 6XXX-series alloy in a metallic mold 95 mm in diameter, 300 mm in height, processed volume 5 kg). The idea was to avoid addition of the low-melting and immiscible components in the furnace, preventing contamination and necessity for high melt superheat. Relatively small (up to 6%) additions of Pb or Bi were done using a master alloy or pure-metal rod with ultrasonic processing in the launder. The same approach was used in DC casting of a 6XXX-series alloy with addition of Pb in the melt flow with simultaneous ultrasonic processing of the melt (Eskin and Eskin, 2015).

20.5 Concluding remarks

Beneficial effects of the cavitation melt treatment have been confirmed and well documented over the last few decades. However, it should be noted that for major industrial implementation, a controlled process optimization and well-defined and reproducible protocols should be developed. Currently, this is the biggest challenge that requires combined efforts from academia and industrial sector to effectively use cavitation melt treatment for large-scale processing and allow the widespread industrial application of this promising technology. Nevertheless, recent advances in the fundamental knowledge, process modeling, and technical implementation of a USP continuous process showed that the processing of large melt volumes with a single acoustic source is feasible, exploiting the optimum combination of acoustic flows and the required cavitation conditions. The future of casting would require the industry to adopt and adapt this easy-to-handle, environment-friendly, and cost-effective technology, along with the emerging contactless methods for ultrasonic treatment (that are on the edge of current technological progress) that will have a direct impact on manufacturing the advanced lightweight materials and composites.

References

Abismaïl, B., Canselier, J.P., Wilhelm, A.M., Delmas, H., Gourdon, C., 1999. Ultrason. Sonochem. 6, 75–83.

Abramov, O.V., 1972. Crystallization of Metals in an Ultrasonic Field. Metallurgiya, Moscow. 256 p.

Abramov, O.V., 1994. Ultrasound in Liquid and Solid Metals. CRC Press, Boca Raton. 512 p.
Abramov, O.V., 2000. Influence of Powerful Ultrasound on Liquid and Solid Metals. Nauka, Moscow, pp. 142–163.
Abramov, O.V., Teumin, I.I., 1970. Crystallization of metals. In: Rozenberg, L.D. (Ed.), Physical Principles of Ultrasonic Technology. Nauka, Moscow, pp. 427–514 (Translated by New York, Plenum, 1973).
Altberg, V.J., Lavrov, V., 1939. Acta Physicochem. USSR. 11, 287–290.
Ansyutina, A.E., Gur'ev, I.I., Eskin, G.I., 1970. Izv. Akad. Nauk SSSR, Met. (4), 76–81.
Atamanenko, T.V., Eskin, D.G., Sluiter, M., Katgerman, L., 2011. J. Alloys Compd. 509 (1), 57–60.
Atamanenko, T.V., Eskin, D.G., Zhang, L., Katgerman, L., 2010. Metall. Mater. Trans. A 41A, 2056–2066.
Balandin, G.F., 1973. Formation of Crystal Structure in Castings. Mashinostroenie, Moscow, pp. 192–261.
Becker, V., 1941. Novosti Teckhniki 10 (4), 25–26.
Behrend, O., Schubert, H., 2001. Ultrason. Sonochem. 8, 271–276.
Behrend, O., Ax, K., Schubert, H., 2000. Ultrason. Sonochem. 7, 77–85.
Benua, F.F., Vologdin, I.V., Katler, A.I., 1958. Svarochn. Proizvod. (5), 1–5.
Bergmann, L., 1954. Der Ultraschall und seine Anwendung in Wissenschaft und Technik, sixth ed. S. Hirzel Verlag, Zürich. 1114 p.
Berlaga, R.Y., 1939. Zh. Eksperim. Teor. Fiz. 9, 1397–1398.
Bhingole, P.P., Chaudhari, G.P., 2012. Mater. Sci. Eng. A 556, 954–961.
Bochvar, S.G., Eskin, G.I., 2012. Tekhnol. Legk. Spl. (1), 9–17.
Bondy, C., Söllner, K., 1935. Trans. Faraday Soc. 31, 835–842.
Briggs, H.B., Johnson, J.B., Mason, W.O., 1947. J. Acoust. Soc. Am. 19, 664–677.
Buxmann, K.Z., 1972. Metallkde 68, 516–521.
Campbell, J., 1981. Int. Met. Rev. (2), 71–108.
Cao, G., Konishi, H., Li, X., 2008. Mater. Sci. Eng. A 486, 357–362.
Chankitmunkong, S., Eskin, D.G., Limmaneevichitr, C., 2020. Mater. Sci. Eng. A 788. Paper 139567.
Chernov, A.A., 1956. Kristallografiya 1, 589–593.
Choi, H., Jones, M., Konishi, H., Li, X., 2012. Metall. Mater. Trans. A 43A, 738–746.
Chvorinov, N.I., 1954. Crystallization and Non-Homogeneity of Steel. Publishing House of Czechoslovak Academy of Sciences (NČSAV), Prague. 384 p.
Connolly, W., Fox, F.E., 1954. J. Acoust. Soc. Am. 26, 843–848.
Crum, L.A., 1980. J. Acoust. Soc. Am. 68, 203–211.
Danilov, V.I., 1956. Constitution and Crystallization of Liquids. Izd. Akad. Nauk SSSR, Kiev. 424 p.
Danilov, V.I., Neimark, V.E., 1949. Zh. Eksper. Teor. Fiz. 19, 235–241.
Danilov, V.I., Teverovsky, B.M., 1940. Zh. Experim. Teor. Fiz. 10, 1305–1310.
Danilov, V.I., Pluzhnik, E.E., Teverovsky, B.M., 1939. Zh. Experim. Teor. Fiz. 9, 66–71.
Dantzig, J.A., Rappaz, M., 2009. Solidification, Lausanne. EPFL, CRC Press, Boca Raton, pp. 51–56. 268–275.
Eskin, G.I., 1961. Ultrasound in Metallurgy. Metallurgizdat, Moscow. 47 p.
Eskin, G.I., 1965. Ultrasonic Treatment of Molten Aluminum. Metallurgiya, Moscow. 224 p.
Eskin, G.I., 1988. Ultrasonic Treatment of Molten Aluminum. Metallurgiya, Moscow. 232 p.
Eskin, D.G., 2020. Proc. ICAA17, MATEC Web of Conferences, 2020. vol. 326. 06002.
Eskin, G.I., Eskin, D.G., 2003. Ultrason. Sonochem. 10 (4–5), 297–301.
Eskin, G.I., Eskin, D.G., 2015. Ultrasonic Treatment of Light Alloy Melts, second ed. CRC Press, Boca Raton. 330 p.
Eskin, G.I., Rukhman, A.A., Bochvar, S.G., Yalfimov, V.I., Konovalov, D. V., 2008. Tsvetn. Met. (3), 105–110.
Flynn, H.G., 1964. Physics of acoustic cavitation in liquids. In: Mason, W. P. (Ed.), Physical Acoustics. vol. 1. Academic Press, New York, pp. 57–172. Part B.
Fyrillas, M.M., Szeri, A.J., 1994. J. Fluid. Mech. 277, 381–407. 1995, vol. 289, pp. 295–314.
Herrmann, E., 1958. Handbuch des Stranggiessens. Aluminium Verlag, Dusseldorf. 916 p.
Hiedemann, E.A., 1954. J. Acoust. Soc. Am. 26, 831–842.
Hunt, J.D., Jackson, K.A., 1966. J. Appl. Phys. 31, 254–257.
Jackson, K.A., Hunt, J.D., Uhlmann, D.R., Seward, T.P., 1966. Trans. Metall. Soc. AIME 236, 149–160.
Kandemir, S., Atkinson, H.V., Weston, D.P., Hainsworth, S.V., 2014. Metall. Mater. Trans. A 45A, 5782–5798.
Kapustina, O.A., 1970. Degassing of liquids. In: Rozenberg, L.D. (Ed.), Physical Principles of Ultrasonic Technology. Nauka, Moscow, pp. 253–336 (Translated by New York, Plenum, 1973).
Kattamis, T.Z., Coughlin, J.C., Flemings, M.C., 1967. Trans. Metall. Soc. AIME 239, 1504–1511.
Kazachkovsky, O.D., 1948. In: Danilov, V.I. (Ed.), Collective Papers of the Laboratory of Metals Physics. Izd. Akad. Nauk UkrSSR, Kiev, pp. 103–112.
Khismatullin, D.B., 2004. J. Acoust. Soc. Am. 116. Paper 1463.
Kim, T.H., Kim, H.Y., 2014. J. Fluid Mech. 750, 355–371.
Komarov, S., Yamamoto, T., 2019. In: Chesonis, C. (Ed.), Light Metals 2019. Springer, pp. 1597–1604.
Komarov, S., Oda, K., Ishiwata, Y., Dezhkunov, N., 2012. Ultrason. Sonochem. 20, 754–761.
Komarov, S., Ishiwata, Y., Mikhailov, I., 2015. Metall. Mater. Trans. A 46, 2876–2883.
Kudryashova, O.B., Vorozhtsov, S.A., 2016. JOM 68, 1307–1311.
Lane, D.H., Canningham, J.W., Tiller, W.A., 1960. Trans. Metal. Soc. AIME 218, 985–990.
Lauterborn, W., Kurz, T., Mettin, R., Ohl, C.D., 1999. Adv. Chem. Phys. 110, 295–380.
Lebon, G.S.B., Tzanakis, I., Pericleous, K., Eskin, D.G., 2015. Phys. Rev. E 92, 043004-1–043004-8.
Lebon, G.S.B., Tzanakis, I., Djambazov, G., Pericleous, K., Eskin, D.G., 2017. Ultrason. Sonochem. 37, 660–668.
Lebon, G.S.B., Tzanakis, I., Pericleous, K., Eskin, D., 2018. Ultrason. Sonochem. 42, 411–421.
Lebon, G.S.B., Tzanakis, I., Pericleous, K., Eskin, D., Grant, P.S., 2019a. Utrason. Sonochem. 55, 243–255.
Lebon, G.S.B., Salloum-Abou-Jaoude, G., Eskin, D., Tzanakis, I., Pericleous, K., Jarry, P., 2019b. Ultrason. Sonochem. 54, 171–182.
Neduzhy, S.A., 1961. Akust. Zh. 7, 275–294.
Neduzhy, S.A., 1964. Aksut. Zh. 10, 456–464.
Orthaber, U., Zevnik, J., Petkovšek, R., Dular, M., 2020. Ultrason. Sonochem. 68. Paper 105224.
Pishchalnikov, Y.A., Behnke-Parks, W.M., Schmidmayer, K., Maeda, K., Colonius, T., Kenny, T.W., Laser, D.J., 2019. J. Acoust. Soc. Am. 146. Paper 516.
Plesset, M.S., Prosperetti, A., 1977. Ann. Rev. Fluid Mech. 9, 145–185.
Pogodin-Alekseev, G.I., Zaboleev-Zotov, V.V., 1958. Litein. Proizvod. (7), 35–36.
Priyadarshi, A., Khavari, M., Subroto, T., Conte, M., Prentice, P., Pericleous, K., Eskin, D., Tzanakis, I., 2021. Ultrason. Sonochem. 70, 105260.

Richards, W.T., 1929. J. Am. Chem. Soc. 51, 1724–1729.
Rumpf, H., 1962. In: Knepper, W.A. (Ed.), Agglomeration. John Wiley, New York, NY, pp. 382–403.
Ruvalcaba, D., Mathiesen, R.H., Eskin, D.G., Arnberg, L., Katgerman, L., 2007. Acta Mater. 55, 4287–4292.
Schmid, G., Ehret, L., 1937. Z. Electrochem. 43, 869–874.
Schmid, G., Roll, A., 1939. Z. Electrochem. 45, 769–775.
Shi Ying, L., Fei Peng, G., Qiong Yuan, Z., Wen Zhen, L., 2009. Mater. Sci. Forum 618–619, 433–436.
Shu, D., Sun, B., Mi, J., Grant, P.S., 2012. Metall. Mater. Trans. A 43A, 3755–3766.
Song, S., Zhou, X., Li, L., Ma, W., 2015. Ultrason. Sonochem. 24, 43–54.
Sreekumar, V.M., Babu, N.H., Eskin, D.G., 2017. Metall. Mater. Trans. B 48B, 208–219.
Subroto, T., Eskin, D.G., Tzanakis, I., Lebon, G.S.B., Miranda, A., Pericleous, K., 2019. IOP Conf. Series: Mater. Sci. Eng. 529. Paper 012050.
Subroto, T., Eskin, D.G., Beckwith, C., Tzanakis, I., Djambazov, G., Pericleous, K., 2020. In: Tomsett, A. (Ed.), Light Metals 2020. TMS/Springer, Cham, pp. 981–987.
Subroto, T., Eskin, D.G., Beckwith, C., Roberts, D., Tzanakis, I., Pericleous, K., 2022. In: Eskin, D. (Ed.), Light Metals 2020. TMS/Springer, Cham, pp. 649–654.
Swallowe, G.M., Field, J.E., Rees, C.S., Duckworth, A., 1989. Acta Mater. 37, 961–967.
Tonry, C.E.H., Djambazov, G., Dybalska, A., Bojarevics, V., Griffiths, W. D., Pericleous, K.A., 2019. In: Chesonis, C. (Ed.), Light Metals 2019. Springer, pp. 1551–1559.
Tsunekawa, Y., Sizuki, H., Genma, Y., 2001. Mater. Design 22, 467–472.
Tzanakis, I., Eskin, D.G., Georgoulas, A., Fytanidis, D.K., 2014. Ultrason. Sonochem. 21, 866–878.
Tzanakis, I., Xu, W.W., Lebon, G.S.B., Eskin, D.G., Pericleous, K., Lee, P. D., 2015a. Phys. Procedia 70, 841–845.
Tzanakis, I., Xu, W.W., Eskin, D.G., Lee, P., Kotsovinos, N., 2015b. Ultrason. Sonochem. 27, 72–80.
Tzanakis, I., Hodnett, M., Lebon, G.S.B., Dezhkunov, N., Eskin, D.G., 2016a. Sensors Actuators A Phys. 240, 57–69.
Tzanakis, I., Lebon, G.S.B., Eskin, D.G., Pericleous, K., 2016b. J. Mater. Process. Technol. 229, 582–586.
Tzanakis, I., Lebon, G.S.B., Eskin, D.G., Pericleous, K., 2016c. Mater. Des. 90, 979–983.
Tzanakis, I., Lebon, G.S.B., Eskin, D.G., Pericleous, K.A., 2017. Ultrason. Sonochem. 34, 651–662.
Vogel, A., Doherty, R.D., Cantor, B., 1979. Solidification and Casting of Metals. 1979 TMS, London, pp. 518–525.
von Seemann, H.J., 1936. Metallwirtschaft 15, 1067–1069.
von Seemann, H.J., Menzel, H., 1947. Metall 1, 39–46.
von Seemann, H.J., Staats, H., 1968. Z. Metallde. 59, 347–356.
von Seemann, H.J., Wehner, F., 1973. Metallwissehschaft und Technik 27, 971–977.
von Seemann, H.J., Staats, H., Pretor, K.G., 1967. Arch. Eisenhüttenwesen 38, 257–265.
Vorozhtsov, S.A., Eskin, D.G., Tamayo, J., Vorozhtsov, A.B., Promakhov, V.V., Averin, A.A., Khrustalyov, A.P., 2015. Metall. Mater. Trans. A 46A, 2870–2875.
Wang, D., De Cicco, M.P., Li, X., 2012. Mater. Sci. Eng. A 532, 396–400.
Wang, F., Eskin, D., Mi, J., Connolley, T., Mounib, M., Lindsay, J., 2016a. Acta Mater. 116, 354–363.
Wang, F., Eskin, D., Connolley, T., Mi, J., 2016b. J. Cryst. Growth 435, 24–30.
Wang, F., Eskin, D., Connolley, T., Mi, J., 2017a. Trans. Nonferr. Met. Soc. China 27, 977–985.
Wang, F., Eskin, D., Mi, J., Wang, C., Koe, B., King, A., Reinhard, C., Connolley, T., 2017b. Acta Mater. 141, 142–153.
Wang, F., Eskin, D., Connolley, T., Wang, C., Koe, B., King, A., Reinhard, C., Mi, J., 2018a. Mater. Lett. 213, 303–305.
Wang, B., Tan, D., Lee, T.L., Khong, J.C., Wang, F., Eskin, D., Connolley, T., Fezzaa, K., Mi, J., 2018b. Acta Mater 144, 505–515.
Wang, F., Tzanakis, I., Eskin, D., Mi, J., Connolley, T., 2017c. Ultrason. Sonochem. 39, 66–76.
Wood, R.W., Loomis, A.L., 1927. Phil. Mag. 4, 417–425.
Wu, W.H., Eskin, D.G., Priyadarshi, A., Subroto, T., Tzanakis, I., Zhai, W., 2021. Ultrason. Sonochem. 73. Paper 105501.
Xu, W.W., Tzanakis, I., Srirangam, P., Mirihanage, W.U., Eskin, D.G., Bodey, A.J., Lee, P.D., 2016. Ultrason. Sonochem. 31, 355–361.
Yang, Y., Li, X., 2007. J. Manuf. Sci. Eng. 129, 497–501.
Zhai, W., Liu, H.M., Wei, B., 2015. Mater. Lett. 141, 221–224.
Zhai, W., Wang, B.J., Liu, H.M., Hu, L., Wei, B., 2016. Sci. Rep. 6. Paper 36718.
Zhang, L., Eskin, D.G., Katgerman, L., 2011. J. Mater. Sci. 46, 5252–5259.

Chapter 21

Applications of power ultrasound in mining

L.F. Gaete-Garretón[a], Y.P. Vargas-Hernández[a], and A.R. Videla[b]

[a]*Department of Physics, Universidad de Santiago de Chile, Santiago, Chile,* [b]*School of Engineering, Mining Engineering Department, Pontificia Universidad Católica de Chile, Santiago, Chile*

21.1 Introduction

This chapter describes the applications of power ultrasound in the mining industry. Mining activities are generally organized in three sequential stages: geological and rock characterization, extraction of minerals from the deposits, and process operations for separation and concentration. Before extraction, it is necessary to know the initial in-situ rock mass stress state that is going to be mined, mainly because the mine might have high stresses that can put personnel and facilities in active extraction areas at risk. With power ultrasonic transducers to generate relative intensity signals, it is possible to penetrate in situ into the rocks to determine their mass stress state. Once the mineral fragments have been extracted, separation and concentration processes are required to obtain the valuable product (ore). The waste material associated with the ore must be separated and discarded. Power ultrasound can play an important innovative role in rock size reduction, ore separation and concentration, and in the final solid-liquid separation for water recovery.

The topics covered in this chapter are as follows: an overview of mining operations, determining the rock mass stress state, application of power ultrasound in ore particle size reduction, application of power ultrasound in concentration, and application of power ultrasound in water recovery by sedimentation methods.

Measuring the mass stress state in rocks by propagating and detecting acoustic signals on site imposes significant challenges because of the large examination volume needed and the heterogeneity of the rock medium. This makes using the classical pulse-eco examination method impossible. This chapter presents the use of power transducers in a nontraditional way. It is based on transmission of intensity signals to detect the changes of the stress state in large areas of rock mass.

Mining processes require particle size reduction by crushing and grinding to prepare the material for further separation. Mineral crushing and grinding consume 60% of the total energy expended in the extraction process (Revnitsev, 1988). Moreover, the current conventional grinding systems wear out very quickly and waste a lot of material. Both aspects of the grinding process improve with the use of power ultrasound. Finally, laboratory studies will be presented showing the possible assistance of power ultrasound in the mineral concentration process and in the water recovery after flotation. Power ultrasound is useful in the recovery of fine and ultrafine particles that generally have very low recovery efficiency in conventional processes despite representing a significant percentage of the overall performance.

21.2 The mining process

Mining includes the complex process of extracting valuable minerals or other geological materials of interest. These materials can be found on the surface or in the form of veins, deposits, or layers of minerals that are exploited with underground mining methods.

Underground mining, to which we refer here, comprises activities to extract minerals from rocks. The extraction process requires digging tunnels or shafts into the soil to reach the underground deposits. Therefore, for transport and services, hard rock underground mining requires construction of long tunnels in the extraction area. Mining activities involve the removal of materials leaving pillars to support the roof of the spaces generated. These pillars are subject to extreme stress, sometimes resulting in dangerous phenomena such as rock explosion. Miners' work safety is one of the reasons why it is crucial to know the rock mass stress state.

As mining activities move deeper, rocks are subjected to stronger stresses than normal. Considering that average soil density has a value of about 2700 kg/m^3, the pressure that the weight of this mass generates, considering only the hydrostatic effect, is 0.027 MPa/m (Brown and Hoek, 1978). Additional stress can be produced by tectonic displacements, as was unexpectedly measured by one author of this chapter while working on the determination of rock stress tensors in underground mining in the Andes Mountains. These contributions interact in a very complex way with the vertical stress and have to be considered. Also,

Power Ultrasonics. https://doi.org/10.1016/B978-0-12-820254-8.00016-6
Copyright © 2023 Elsevier Ltd. All rights reserved.

when a rock mass is drilled for mining operations, the stress state is modified, making it necessary to control the variations of this parameter.

21.3 The rock mass stress state

This section deals with the important problem of the state of rock mass stress at a mine facility. Current methods to determine rock mass stress, including those using acoustic signals, are briefly described. The drawbacks of these methods have prompted research about the application of high intensity ultrasound to improve the control of this problem. The development of a new technique on this basis is presented here.

Civil mining engineering requires knowledge of the rock mass stress state to establish the stability of tunnels and excavations, planning and constructing the ventilation ducts, drilling the rocks for handling explosives, and designing pillar and support systems. In addition, this knowledge is necessary to plan the fracture processes, predicting microearthquakes and other events (Amadei and Stephansson, 1997).

There are several methods for measuring the stress state in rocks, some of which are designed to measure stress and strain conditions on site. These methods can be classified into two major groups: the first employs fluids to apply hydraulic pressure in the rock, and in the second, areas of rock mass are released to measure their deformation from which stress conditions are estimated (Jian-Hong and Wei-Pan, 2013; Sjöberg et al., 2003).

These methods have important drawbacks. First, the information they provide refers only to narrow areas but they do not allow a comprehensive representation of the mine's full stress-state conditions. Knowledge of the mechanical material properties is needed, but it is important to bear in mind that these may vary from point to point causing uncertainty in the determinations. Consequently, the determination of the stress state under these conditions is troublesome and does not allow real-time evaluation.

Currently, two types of conventional acoustic methods are used, acoustic emissions and nondestructive testing (NDT), both creating similar problems. Through acoustic emissions of rock mass, it is possible to estimate the stress state on site; the numbers of acoustic emissions per unit of time are counted and are related to the stress state of the rock (Villaescusa et al., 2002). However, when the rock is about to fail, the number of acoustic emissions per unit of time increases dramatically and chaotically (Majewska and Mortimer, 2001). In summary, by applying the NDT technique, it is not even possible to know the state of a single rock of significant size, even using low frequencies. Both methods are useful at the laboratory level, but this is not enough for reliable predictions and control.

To overcome this situation, power ultrasonic transducers have been used in mining facilities to transmit signals and detect changes of the stress state in rock mass in large areas.

21.3.1 Rock mass stress state measurements using power ultrasonic transducers

The speed of sound is a magnitude that is very sensitive to the rock mass stress state, as experimental work with rock sample materials has confirmed. Figure 21.1 shows a diagram of an experimental setup in which the rock samples are compressed by hydraulic press while measurements of the speed of sound are performed by applying the pulse transmission method. The system can measure the ultrasonic variables in both directions in which the stress is applied (Figure 21.1). The emitter and receiver labeled E(a) and R(a) refer to measuring the sound velocity in the stress direction. The emitter and receiver measuring the sound velocity perpendicular to the stress direction are labeled E(b) and R(b), respectively. This capacity is very important because, in practice, it is easier to measure the variations in the speed of sound produced by loads perpendicular to the direction of propagation. The curves in Figure 21.2 show a clear relation between the stress state of a rock and the speed of sound in the rock. The results for propagation velocity perpendicular to sound propagation velocity are similar. The attenuation is likewise a parameter of interest as it is notable in the process of rock fracturing.

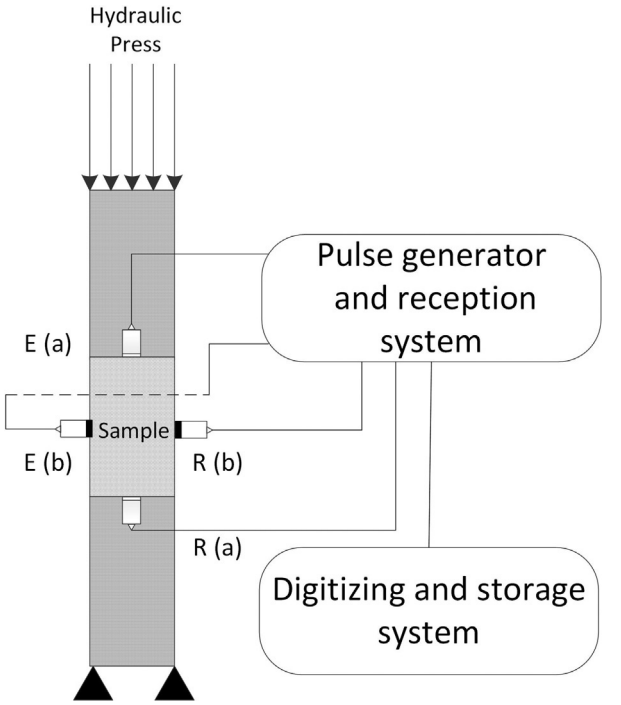


FIGURE 21.1 System to measure sound propagation velocity in rock samples under stress: E(a) and R(a) paralell to the applied stress, E(b) and R(b) perpendicular to applied stress.

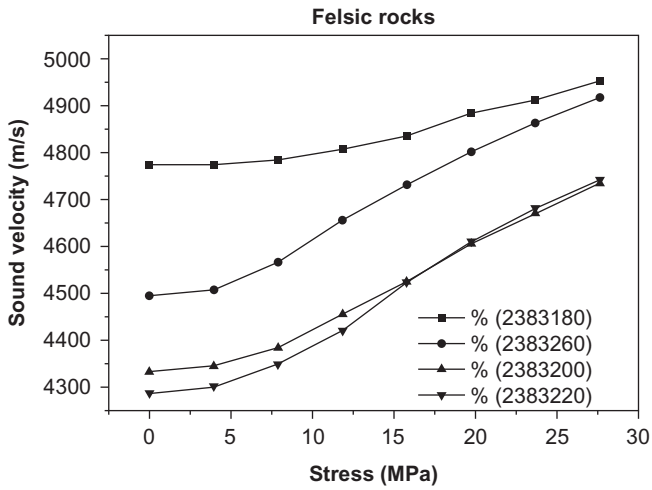


FIGURE 21.2 Sound velocity propagation in a felsic rock sample vs applied stress. Ultrasound frequency 1 MHz.

The laboratory study provides the basis for the development of an acoustic technology to determine the stress state of a rock mass.

An analysis of the characteristics of operation in an underground mining operation led to the conclusion that it is recommendable to measure the rock mass stress state in the supporting walls that separate two consecutive mining tunnels. These walls support the load weight of the material over the tunnel and may have a thickness of over 20 m. This measurement involves a great experimental challenge because it is almost impossible at that distance to propagate ultrasonic pulses of high and even low frequency, considering the characteristics of the propagation medium.

The experience here described refers to the study of rocks that are approximately 20 m thick. An analysis of the propagating conditions and the distances that need to be met with ultrasonic waves led us to conclude that using continuous waves of low ultrasonic frequencies and even sonic frequencies are the best options, rather than ultrasonic pulses, as usual under the NDT technique. A single frequency continuous wave emitted and received by devices tuned to the resonant frequency can be transmitted at a much greater distance than an ultrasonic pulse. For this reason, it was decided to use power ultrasonic transducers. The best performance is achieved using prestressed sandwich power transducers and (stepped horn) mechanical amplifiers tuned and built to operate as sending and receiving devices. The first transducers applied were designed to operate coupled in resonance at 20 kHz and can achieve signal paths of about 8 m. To increase the scanning distance, we used transmitting-receiving transducers tuned at 6.2 kHz, allowing us to reach rock depths of about 60 m. The transducers were designed following well-known classical analytical expressions (Neppiras, 1973), and the design was refined with a numerical finite element study. In Figure 21.3, a diagram shows the simulation results, also illustrating the displacement curve of the transducer at resonance frequency.

Rock mass exploration is performed by a continuous transmission signal transmitted as a very long tone burst to achieve, on the one hand, the desired penetration and on the other to produce a saving of recording media. The principle of this method is based on whether increased stress in the rock will increase the sound speed propagating inside it. This procedure involves constantly comparing the arrival phase of the waves with the phase emission. An increase of the sound propagation velocity in the rock is reflected as a positive phase shift. The system to perform these measurements consists of a pair of coupled transducers for emission-reception, the electronic setup for comparing signals, the power supply system for emission-detection, and systems ending with a computer for control and for signal

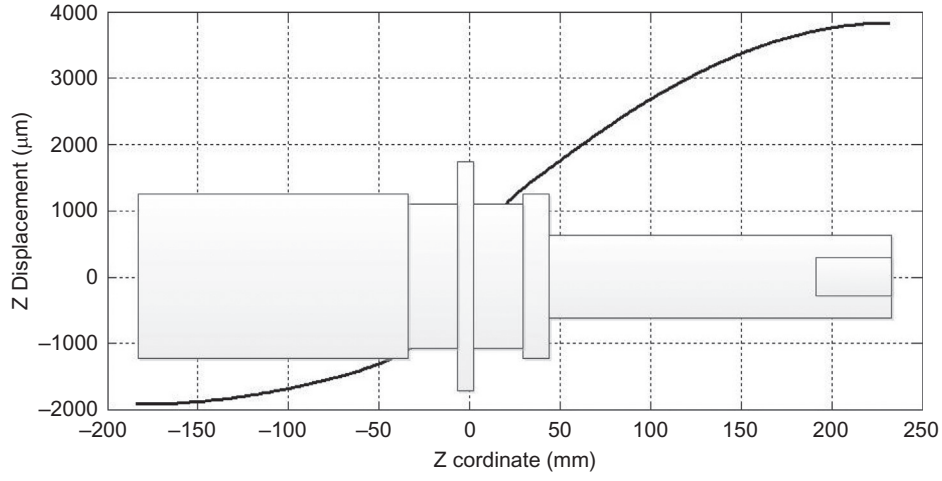


FIGURE 21.3 Schematic of power transducer and its finite element simulation (displacement curve).

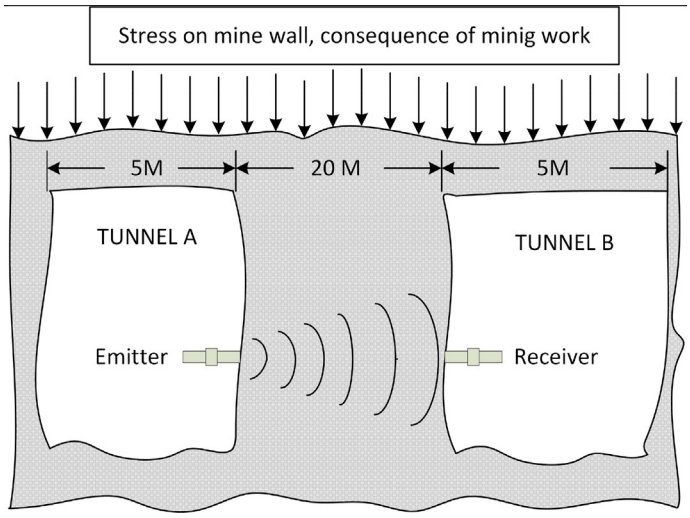


FIGURE 21.4 Schematic of relative position of transducers inside the mine; also, the stress direction is depicted.

processing. Figure 21.4 shows a schematic of the installation inside the mine with the relative position of the transducers, the distances, and the stress direction that supports the rock mass.

To achieve good acoustic signal transmission, a special installation protocol was developed to reach an excellent mechanical coupling of the transducers with the rock whose contact surface is very irregular. Cylindrical holes were drilled into the rock, large enough to hold the transducers, which were fixed to the rock with a bolt and attached using a strong adhesive. Figure 21.5 shows one of the ultrasonic transducers installed.

Measurements of the radiation impedance of the transducer rightly coupled confirmed the quality of the installation. In fact, the transducer impedance changed from about 100 Ω radiating in the air to about 1100 Ω coupled to the rock.

The measurements made with this system have shown that it is possible to transmit sound waves to rock depths of about 60 m. Crucially, it has not been necessary to apply more than a few Watts to the transducer for this distance. This way, significant nonlinear effects in the propagation signal are avoided. The phase changes of the ultrasonic signal were recorded on a computer and analyzed. The information was transmitted internally via computer so that the mining company's engineering department could identify changes in the stress state in the supporting walls. At present, there is a system installed that experimentally monitors the rock mass stress state in a major underground mine facility in the Andes mountains. Figure 21.6 shows a complete installation diagram (schematic).

Figure 21.7 shows the phase changes recorded during one observation period. Interesting to note are the phase changes resulting from seismic events of intensities marked by dots in red on the Richter scale.

The acquired data are under analysis, using big data techniques, searching for correlations between the phase register, attenuation, and seismic activity in the mine.

21.4 Application of power ultrasound in particle size reduction

Once the material is extracted from the mine, the pieces must be reduced in size before separation and concentration of the valuable ore. The first size reduction step is called crushing and is performed with dry material by high impact energy events that reduce the mineral pieces to a typical production size in the range of 5–7 in. This is carried out in huge jaw or gyratory crushers. Usually, the product is transported via conveyor belts toward a semiautogenous ball mill (SAG) to grind it through the tumbling action of steel balls. The resulting fragment obtained will be around 1–2 in. in size. Further particle size reduction is achieved in ball mills that, in a similar tumbling action as SAG mills, grind the ore particle down to product particle sizes between 50 and 150 mm. Conventional grinding consumes a lot of energy and it is estimated that only 40% of the applied energy is used for particle size reduction; the rest is lost to noise, heating, and steel deformation due to collisions. Particle breakage is a random process in which the interaction of the grinding media (usually steel balls) with the material being milled is subjected to shear and compression stress by collisions during the ball mill operation.

To improve the grinding milling process, researchers have explored the use of power ultrasound but have failed to bring to market a high performance ultrasonic grinding machine. Gärtner (1953) was the first to mill materials in suspensions by using ultrasound, although the results were modest and of little practical interest. Subsequently,



FIGURE 21.5 Ultrasonic transducer mounted in the mining wall.

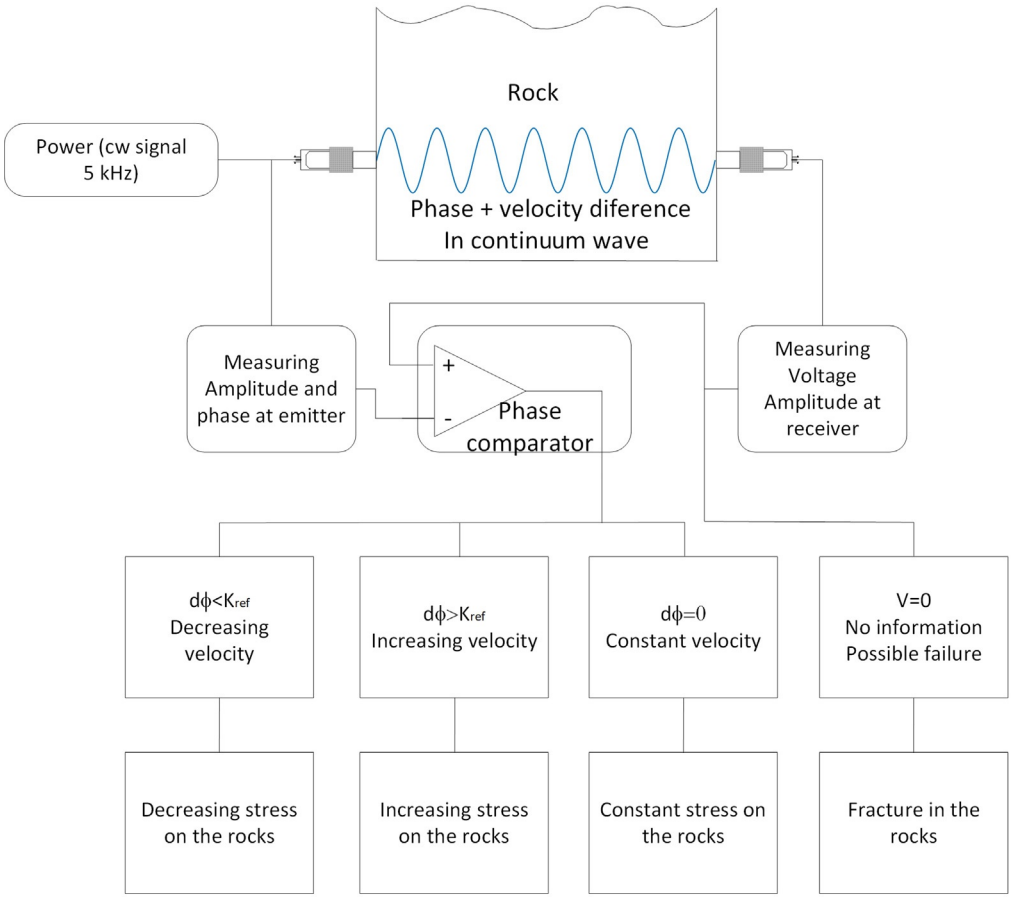


FIGURE 21.6 Full scheme of the stress state measuring system installed in the mine, including some operational details.

Fleischhauer and Kröger (1969) used ultrasonic power (600 W) to fragment coal minerals in a process of solvent extraction. The active area of the device consisted of a cone mantle driven by a high powered magnetostrictive ultrasonic transducer while the active cone faced another conical surface. Figure 21.8 shows a diagram of the Fleischhauer milling device. A high-intensity stationary field is established by cavitation between the conical surfaces that mill the particles in suspension. The grinding area must be cooled down with freshwater to facilitate the grinding

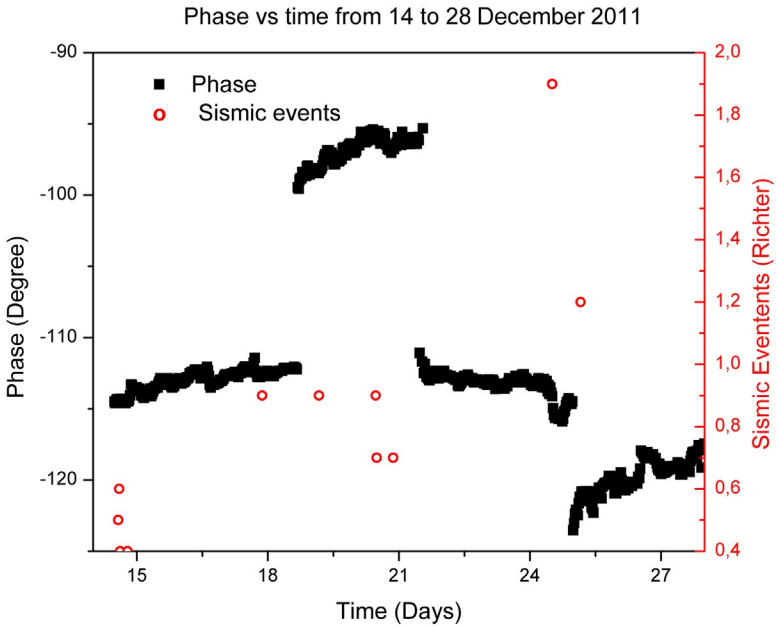


FIGURE 21.7 Record of the received wave phase that exhibits tension changes during mining work. *Dots in red* record seismic activity during operation time.

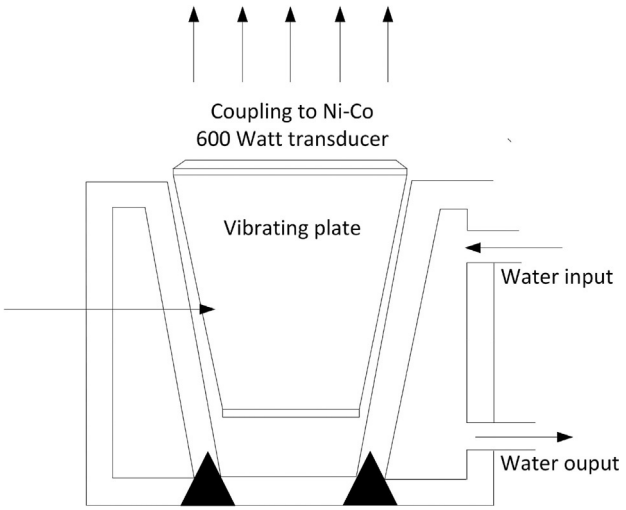


FIGURE 21.8 Schematic of Fleischhauer and Kröger grinding machine for suspensions.

process. Unfortunately, no details regarding the results were published.

Graff (1979) used a set of (prestressed sandwich type) ultrasonic transducers as part of a multistage stamp mill with which he reduced the sizes from a range of 50 to 65 mm to about 0.5 mm. There is no information on the energy consumption or the flow rate produced. However, in an experiment in one stage, Graff was able to get up to 40% material ground below 4.76 mm, 50% less, than 2.37 mm and with low percentage of fines. Projected energy consumption for this experiment was 15.6 kWh/ton. Leach and Rubin (1988) studied the ultrasonic fragmentation of cylindrical rock samples energized by a power transducer attached to one end, observing fractures in the nodes and better results in fragile materials. Tarpley et al. (1980) and Aber et al. (1985) studied the fine fragmentation of coal under ultrasonic fields. They designed and produced various devices for batch and continuum process. One of the most interesting is an Auger-type grinding machine. Its basic design is shown in Figure 21.9, comprising a cone mantle and a conical screw which forces the particles progressively into narrower portions of the system. For fine milling, the mantle is driven by a series of power transducers and the material to be milled is tightened between the solid core and the vibrating surface. The results were promising as a consumption of about 3 kWh/ton was achieved to produce 80% coal under 200 meshes. For context, a hammer mill would need about 20 kWh/ton to produce the same amount of equivalent material. Also, interesting results were achieved with this system for finer sizes.

Interestingly, Link and Killmeyer (1988) attempted to reproduce the results of Tarpley and Aber but without success. Lo and Kientzler (1992) recovered one of the original Tarpley and Moulder machines and then redesigned the ultrasonic generator applying it to a mineral milling system. While their results were similar to that of a ball mill, their research helped identify some weaknesses of the original design and proposed new designs. Yerkovic et al. (1993) conducted milling tests in a ball mill, comparing a standard mineral with one pretreated by ultrasound. The pretreated material exhibited a higher milling rate of around 32%, compared with the material

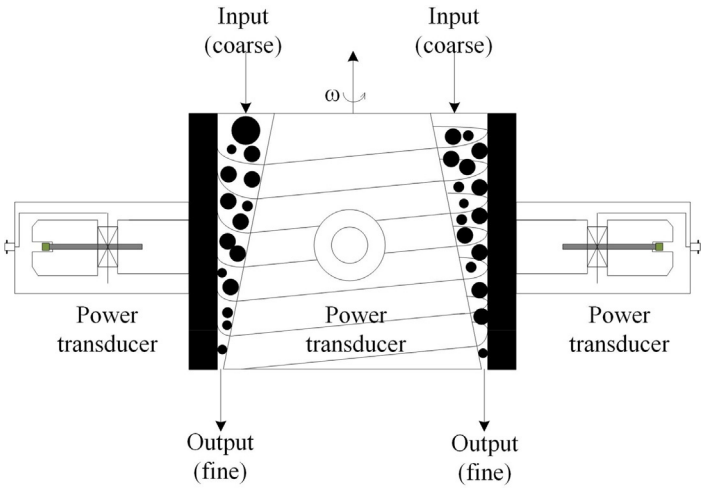


FIGURE 21.9 Schematic of Auger type mill. The coarse materials are fed in the upper inlet. The ground material comes out in the lower part.

without treatment, showing that ultrasound can effectively improve the grinding process.

The mechanisms and events leading to the results described are not yet fully explained and more information and research will be required. A key point that helps to understand the effect of ultrasound in materials is the experiment that was conducted by Blaha and Langenecker (1959) in which they studied the influence of ultrasound on the toughness of metallic crystals. The experiment consisted of subjecting metallic crystal samples to mechanical stress and checking how each time that ultrasonic vibrations were applied the stress that would be necessary to maintain the sample elongation fell notably. The decrease in mechanical resistance caused by the application of ultrasound was recovered each time the drive was cut off. These results showed that the effect of ultrasound in principle could be assumed as the propagation of microcracks present in the material.

21.4.1 Development of an ultrasonic-assisted high-pressure grinding roll

The high-pressure grinding roll (HPGR) developed by Schönert (1988) solves many of the abovementioned problems. This grinding technology comprises a pair of parallel rollers rotating in opposite directions, forcing the particles into the grinding area between both rolls. This allows the material to be crushed between the rollers, where all the particles are subjected to shearing and compression stresses, unlike processes in a ball mill where collisions are random. One of the rolls is in a fixed position while the other is controlled by a hydraulic pressure system which forces a motion toward or away from the fixed roll to control the grinding pressure. If excessively hard materials are fed between the rollers, pressure is released by increasing the gap between them, allowing the material to pass without grinding and save the grinding system from corresponding deterioration. The advantages of this technology have been established numerous times (Baum et al., 1996) but limitations for hard materials remain. In these cases, the HPGR's grinding action produces high wear rates on the surfaces of the rollers and premature fatigue in expensive components like bearings and shafts. A solution could be the application of power ultrasound. The new design addresses the milling problems by combining mechanical characteristics of a conventional machine with the action of ultrasound. As result, a high-pressure ultrasonic roller mill (HPURM) has been developed. This alternative can be a major contribution to improve performance in grinding processes of hard materials (Gaete-Garreton et al., 2000; Gaete-Garretón et al., 2003).

A high-pressure ultrasonic roller mill (HPURM) is composed of three parts. The first, called the active part of the mill, consists of a cylindrical ultrasonic vibrator driven by a sandwich type piezoelectric transducer. The second part is a passive roller whose purpose is to provide mechanical stress for the grinding. The third part is a frame that supports the two rollers and the system that allows one of the rollers to move with respect to the other, depending on the grinding stresses. The active roller vibrates extensionally in one of its modes driven at the proper frequency. In the prototype, the chosen frequency was 23.7 kHz. The vibration mode is selected so that the support, where the bearings are mounted, matches with the vibration nodes. To avoid shear vibrations, the active roller cross-section has a diameter smaller that ¼ of the wavelength. The power applied to the active roller can reach 400 W, but it generally operates with less power. The passive roller has a larger diameter with the only limitation that it must fit into the cavity of the active roller without structural mechanical difficulties. Figure 21.10 shows schematically the structure of the system.

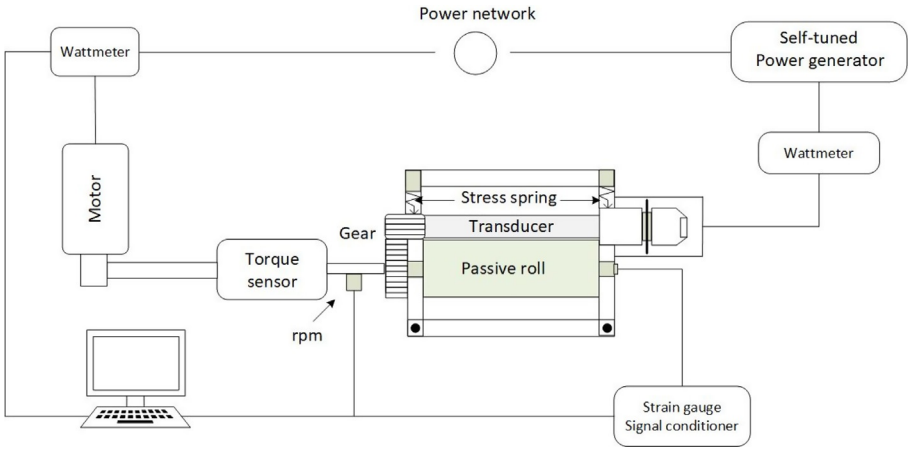


FIGURE 21.10 Schematic of experimental setup to test the HPURM.

The machine is equipped with a strain gauge to detect the relative displacement of one roller to the other. The HPURM tension is adjusted by springs and/or elastomeric devices, labeled "stress spring" in Figure 21.10. Milling occurs between the two rollers; tension is adjusted by springs and/or elastomeric devices between the two rollers, one (active) provides the elastic energy for milling and the other (passive) the grinding tension achieving optimum coupling to transmit the ultrasonic waves to the material during the process. Both rollers rotate in opposite directions but at the same speed. The material to be processed is introduced between the two rollers via a funnel. The active area of the prototype machine is 0.165 m long. The motor that drives the rollers has 2 HP and a variable angular speed driver ranging from 40 to 120 rpm.

The complete machine system occupies an area of approximately $1.6 \times 0.8\,\mathrm{m}^2$ and can treat about 10 tons of material (approximate material density of $2.7 \times 10^3\,\mathrm{kg/m}^3$) during a full working day (24 h).

To determine the benefits of using ultrasound, a comparative study was performed where the HPURM was run with and without activating the ultrasonic generator. Without applying ultrasound, the system works as a conventional HPGR. In the experimental tests, the status of all variables involved in the process such as rotational speed of the rollers, grinding pressure, ultrasonic energy applied, driving power, and torque was measured simultaneously. Hard and brittle materials such as quartz and igneous rock (Andesite) were used for these tests.

To evaluate machine performance, the "specific rate of breakage" (S_i^E) was determined. This parameter (Austin et al., 1984) is an estimate of the main characteristics of the efficiency of a particle size reduction machine and measures the velocity at which a particle size disappears per unit of energy used at each size class in a particle size distribution. The parameter representing the process is defined as

$$S_i^E = \frac{1}{E_{\text{specific}}} \ln\left(\frac{P_i\%}{F_i\%}\right) \tag{21.1}$$

where S_i^E is the specific rate of breakage, E_{specific} is the specific energy used in producing a unit mass of product (kWh/ton), $P_i\%$ is the mass cumulative percentage passing each particle size fraction i produced, and $F_i\%$ is the mass cumulative percentage passing each particle size fraction i in the feed.

The curves of the specific rate of breakage are shown in logarithmic scales and determine the efficiency of the grinding process. Below we show the results of tests conducted to characterize the HPURM.

21.4.2 Characterizing HPURM performance: Efficiency

The ultrasonically active parts are designed as resonant parts, so the conversion of electrical into acoustic energy is very efficient. The first parameter tested was the power requirement of the machine and its progress when the ultrasonic system is activated. Figure 21.11 shows the relationship between the power applied to the ultrasonic system and the total applied power in a typical quartz milling test. In the figure, it can be seen that the higher the acoustic power applied, the lower the total power required for grinding. This means that an overall economization of energy in the milling process can be expected. These predictions are confirmed by examining the curves of the specific rate of breakage indicating the relationship between energy consumption and the product obtained as a result of the grinding.

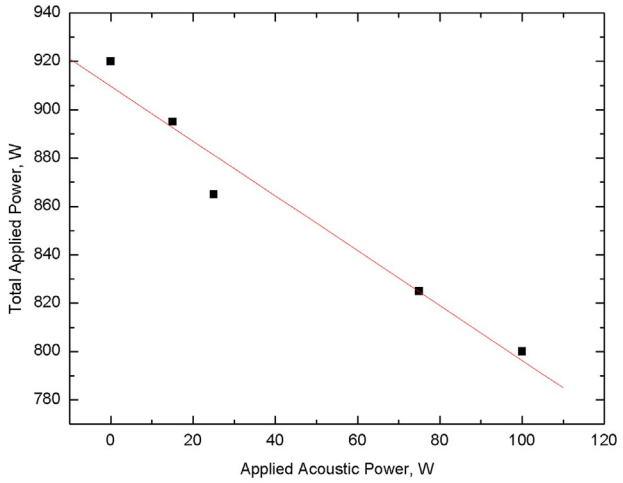


FIGURE 21.11 Influence of applied acoustic power on the total required power to grind.

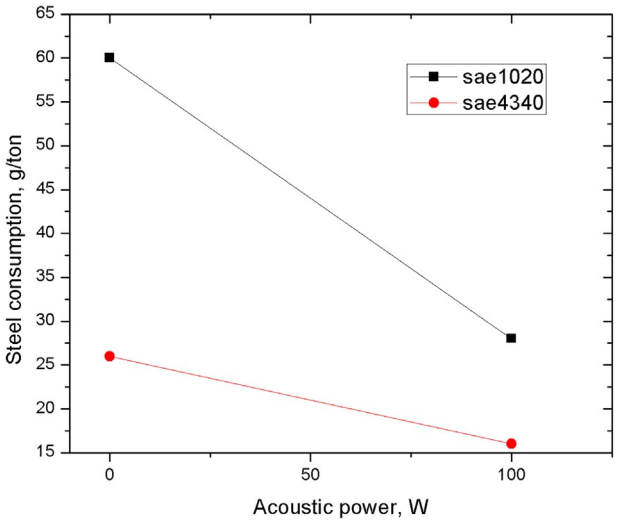


FIGURE 21.12 Curves of abrasive wear tests of HPURM with ultrasound at different power levels. Mineral from "Minera Pudahuel" 100%size-6# Tyler.

21.4.3 Characterizing the HPURM performance: Material wear testing

The technology assessment should also consider other aspects of the process. Thus, it becomes necessary to measure, for example, the wear rate of the equipment and components, an important parameter that complements the specific rate of breakage described previously (S_i^E).

The wear rate of the grinding rollers is very low because they are built with CA1220 hardened steel, so it is not possible to perform an experiment of wear on the milling machine in a reasonable period of time. To perform these tests in a shorter time, we have built rollers with softer or untempered material. The rollers were built with SAE1020 steel for structural use and with tool steel (SAE4340). After a 24-h test, we could evaluate the performance of the rollers with and without ultrasound. Figure 21.12 shows the decrease in the consumption of the material that occurs when ultrasound is applied at different power levels to the grinding rollers. The decrease in wear coincides with an appreciable reduction in working torque.

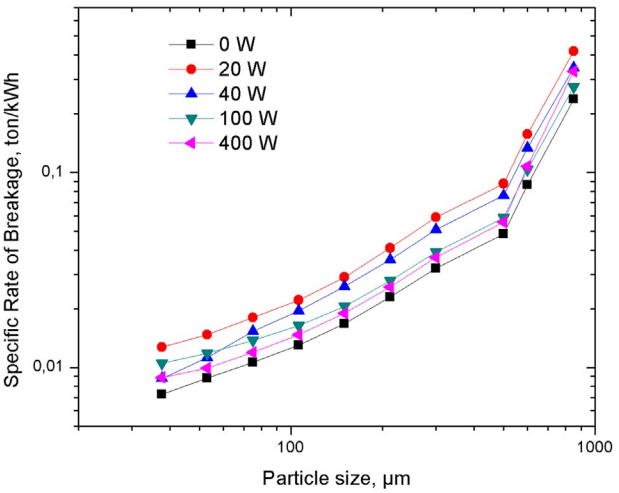


FIGURE 21.13 Specific rate of breakage curves copper mineral single size 10X14 mesh feed, Gap 200 μm 120 rpm.

21.4.4 Characterizing the HPURM performance: Rate of breakage tests

Figure 21.13 shows the HPURM performance of kinetic milling with andesite (copper ore). The machine was activated with different levels of power ultrasound, starting at 0 W, the power level at which it operates as a conventional high-pressure grinding roll (HPGR). Importantly, the best overall performance curve was obtained with an applied ultrasonic power of 20 W. By using a higher ultrasonic power, the overall fine production decreases, lowering the specific rate of breakage. This performance seems to occur as by increasing the vibrational displacements above a certain level, the capture of the particulate material can be hindered, decreasing the treated flow. This implies that for each type of particle and material, an optimal ultrasonic grinding power must be determined. These tests show that the ultrasonic vibration amplitudes that improved the grinding process performance are relatively small.

A second generation of HPURM was developed by activating the two rollers to solve the problems produced by the different sizes in the grinding rolls. The current version of this machine is shown in Figure 21.14. On the left of the figure, the two ultrasonic transducers that excite the grinding rollers at their resonant frequency can be observed.

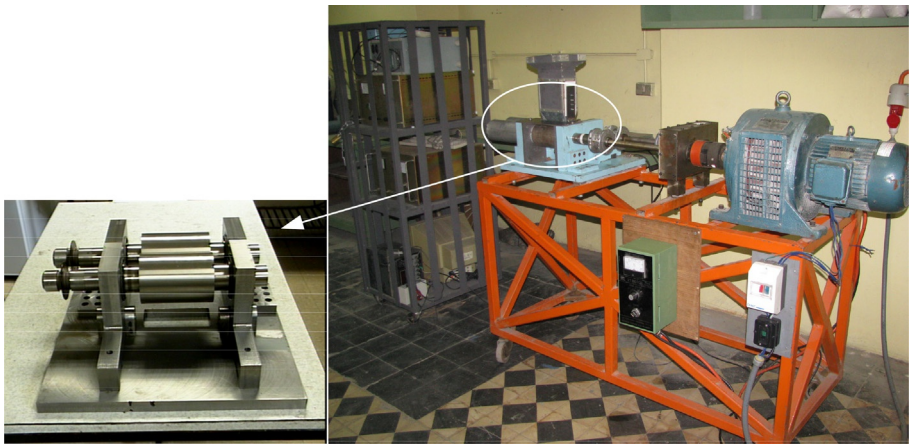


FIGURE 21.14 HPURM (2nd version), and a detail of the active zone of the mill.

The operating frequency of this second generation grinding system was 18 kHz. Figure 21.15 shows the ultrasonic displacement measured in the vibrating surfaces where the milling action has to be produced and the nodal zones where the bearings are held.

This machine can operate at a range of angular velocities substantially greater than that of the previous version: 100–1100 rpm compared to 40–120 rpm in the first version. Milling tests with the second version of HPURM have shown the beneficial effect of ultrasound with high-roller rotational speeds. This effect was also found in the previous version of the mill but in a less noticeable way. Tests were conducted at rotational speeds of 400 rpm to mill quartz and 700 rpm to mill corn, although it is possible to do testing at higher speeds. Figure 21.16 shows the specific rate of breakage grinding quartz at 400 rpm. The results were similar to those obtained from milling corn, because this material is soft and it has been ground at 700 rpm.

In summary, it has been established that the use of ultrasound in general grinding processes can produce significant benefits. For example, in the case of grinding corn, the energy savings reached more than 30%, regardless of the economy of materials whose wear is significantly decreased by the use of ultrasound.

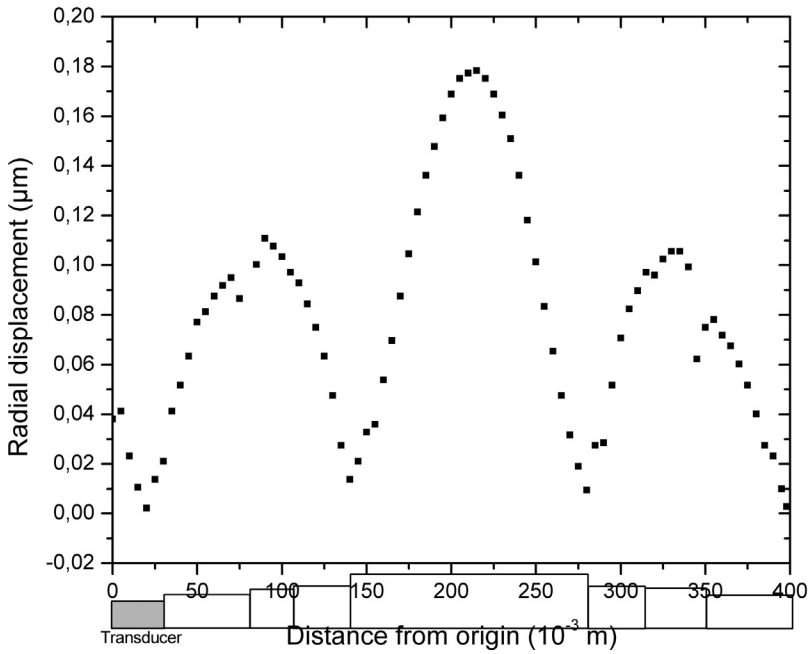


FIGURE 21.15 Displacement curve for active rollers in the HPURM, applied power 5 W.

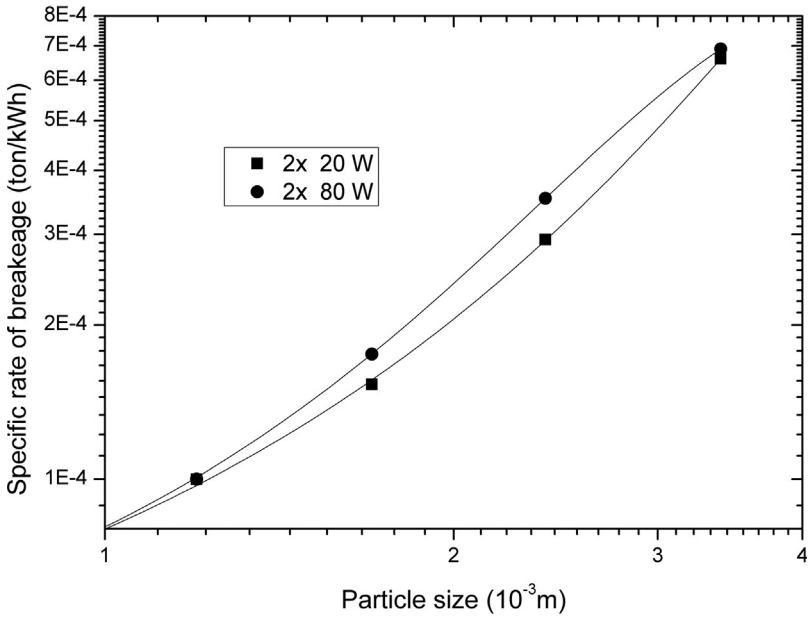


FIGURE 21.16 Specific rate of breakage for HPGR-US, version 2, quartz, 400 rpm.

21.5 Development of an ultrasonic-assisted flotation process for improving concentration of valuable minerals

This section covers an introduction to the flotation process, the use of power ultrasound in flotation, and recent developments of an ultrasonic-assisted flotation process.

21.5.1 The flotation process

Flotation is the most common mineral processing method to separate and concentrate valuable ores. To perform a flotation process, the ore is finely ground until achieving enough liberation of the valuable mineral from the nonvaluable mineral known as gangue. For instance, in copper sulfide treatment, a particle size liberation is achieved between 50 and 150 μm. The grounded mineral is mixed with water to form a suspension of around 30% solids known as slurry, a mixture of ore and water, which is later processed in a series of flotation cells for its selective separation, leading to a valuable concentrate and nonvaluable tailings. The separation inside the flotation cell is carried out in a multiphase system where water, solid particles, and injected bubbles are mixed, and bubbles are selectively attached to some solid particles. Flotation is a physicochemical process that takes advantage of the natural or induced differences in particle surfaces, with some of the particles having been wetted by water (hydrophilic) while others were not (hydrophobic). The flotation process is complex in nature and takes place in the solid/liquid, liquid/gas, and solid/gas interphases. The process involves attachment of the particle to air bubbles, transport of the particle-bubble cluster to the surface of the reactor by buoyancy, transport of the particle through the stable froth, and finally, discharge of the particles collected in the froth. The attachment between particle and bubble is determined by the hydrophobicity of the particle surface and is usually controlled by the addition of specific reactives known as collectors. The bubble-particle attachment will travel to the surface if there is enough buoyancy and if the bubble is stable enough to resist the agitation and turbulence inside the cell. The bubble and froth quality are usually controlled by addition of surfactants called frothers and by the injection of a correct air flow rate. Particles reaching the reactor surface are collected and recovered as a concentrate. The particles that do not adhere to the bubbles will remain in the pulp forming part of the mineral waste or tailings.

Given its complexity, the flotation process is governed by many variables that interact with each other, including surface and water chemical environment, circuit design, and flotation cell mechanisms. Hydrophobicity can be induced by addition of a proper selection of chemical reagents, which will act on the particle-water interface or the bubble-water interface. These reagents can be classified as frothers, collectors, activators, depressants, and pH modifiers. A flotation circuit usually involves several flotation stages with different objectives as shown schematically in Figure 21.17. The first stage in the flotation step is known as rougher flotation and its main goal is to recover as much as possible of the valuable ore. Along the

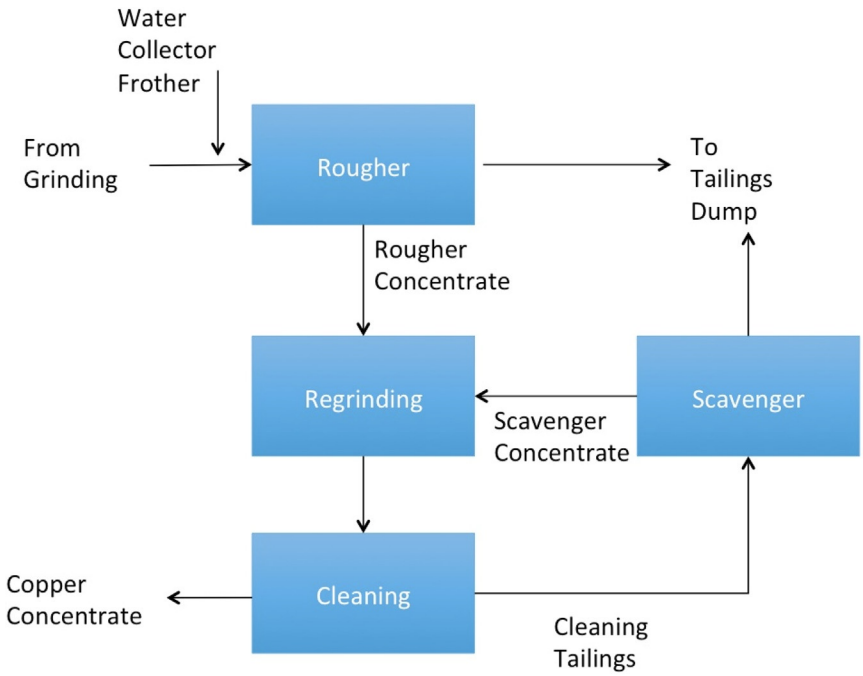


FIGURE 21.17 Schematic representation of simplified flotation process.

flotation steps, pH modifiers, collectors, frothers, and other reactives will be added to maximize recovery of valuable ore. Nearly 95% of the mass ends up in the rougher tailings, which are sent to tailing thickeners for water recovery and final disposal. A rougher concentrate will be obtained as a second product which does require a reprocessing step to achieve a commercial metal grade. In this regard, particles are ground again to achieve a higher degree of liberation and allow a better separation of particles in the cleaning step. The cleaning flotation is optimized for achieving a higher final concentrate grade than in the rougher concentrate. Cleaning tailings are usually rich in valuable metal and go to a final opportunity for recovery in a scavenger flotation step from where the concentrate scavenger is returned into the process while the final tailings are sent into the tailings dump for final disposal.

Although the flotation process has more than 100 years of application in mining, still there are significant challenges remaining. For instance, the presence of oxide precipitation on the particle surface interferes in the normal collector-solid surface adhesion process and therefore leads to a reduction in recovery performance or an increment in the consumption of reactive. In another side, fine and ultrafine particles require more kinetic energy and the presence of small bubbles to be attached with and transported. All these problems have been extensively tested with flotation assisted by ultrasound and slowly finding adapted industrial applications in cases where the benefits overcome the additional energy cost.

21.5.2 Power ultrasound in flotation

One of the biggest challenges facing the mining industry is the deterioration of mineral grades. This problem has made it necessary to improve operations to offset the steady decline of valuable ore grades. Such a decline of average saturation grade has led to, for example, in the case of copper mines, a fall of 1.0% Cu to 0.86% of global average mine grade during the last decade (Lagos et al., 2018), increasing the amount of energy and water consumption by more than 60% in the same period.

In this regard, various studies to optimize the flotation process by using ultrasound have been conducted (Feng and Aldrich, 1999; Ishak and Rowson, 2009; Kang et al., 2009; Özkan and Kuyumcu, 2007; Schlesinger and Muter, 1989; Vargas-Hernández et al., 2002). Özkan (2002) has shown that pretreatment of magnetite by ultrasound increases magnetite recovery. A cleaning effect was reported for the surface of the mineral that led to such improvement. Similarly, Kang et al. (2009) have shown that the application of ultrasonic radiation in coal flotation improves the efficiency of the process, reducing ash recovery. Feng and Aldrich (1999) observed an improvement in the ultimate recovery of sulfur from Africa's Merensky Reef, using ultrasound treatment, despite the negative effects of the concentration of solids, temperature, conditioning time, and gas flow. Vargas-Hernández et al. (2002) have found that conditioning by means of ultrasonic radiation could preserve the concentration of copper sulfides but increase the recovery of

impurities such as iron sulfides. Videla et al. (2016) have shown the potential to improve recovery of fine and ultrafine particles flotation by reprocessing copper tailings under ultrasound irradiation.

One of the most serious problems that occur in the rougher flotation stage relates to the recovery of fine and ultrafine particles. These particles generally do not have a sufficient kinetic energy level for attachment with a bubble within the flotation cell. They also have a relatively small surface area so the probability of collision with a bubble is very low. Application of power ultrasound in a flotation cell could increase the number of tiny bubbles and affect the particle motion due to the acoustic radiation force. An increment in the number of tiny bubbles increases the probability of collision with fine particles in the flotation zone. On the other hand, the probability of collision between particles and bubbles may be increased due to the dynamics followed by the bubbles and the particles due to radiation pressure and streaming. The bubbles have a very low density and follow acoustic fields much easier than particles whose density leads to slower responses to the acoustic field's stresses. Therefore, a bubble that is in the path of a particle when the acoustic field is perpendicular to the path would present a more dynamic effective cross section than if there were no acoustic field, increasing the probability of particle-bubble collisions. Moreover, if the acoustic field is directed in the same direction as the path of the particle-bubble system, effects such as the ortho-kinetic effect would give the bubble a supplementary kinetic energy for attachment to the particle.

Another potential improvement of applying an acoustic field is the particle surface cleaning effect due to cavitation, making them more sensitive to the adhesion of the collectors and activators on the particle surface. In fact, there are records of attempts to improve the performance of flotation cell processes by using mechanical vibrations and particle surface cleaning. Taplin (1937) registered a patent in the United States in which he describes flotation cells providing the ability to produce acoustic mechanical vibrations in the pulp. The frequency of mechanical excitation of the system was only 300 Hz but the author claimed that "supersonic" (ultrasonic) frequencies could also be used. Expanding on this work, Wohlert (1977) developed a process to assist the separation of carbon from carbon paper, pretreating the mixed ground carbon and water with power ultrasound, although this was not a conventional flotation cell like those used in mining nowadays. The process was, however, very similar and is of interest. Lecoffre (1980) registered a patent involving the use of vibrations to "chop" a liquid, producing cavitation bubbles that, because of their small size, would be particularly suited to capture small particles in a flotation cell. And Greenwald (1985) proposed the use of radiation to produce ultrasonic agitation in a carbon contaminated separation cell. He ensured that the power ultrasonic radiation assists in the separation of carbon contaminants besides weakening the chemical bonds between them with the surface of the carbon grains. St. Slaczka (1987) used ultrasound at 22 kHz and an intensity of 0.5 W/cm^2 to assist a barite flotation process, finding that an ultrasonic pretreatment of a barite-fluorite-quartz mineral improves the barite selective flotation process.

In a more recent development, Jordan (1991) patented an ingenious system for producing ultrasonic-assisted flotation in a continuous process as shown in Figure 21.18.

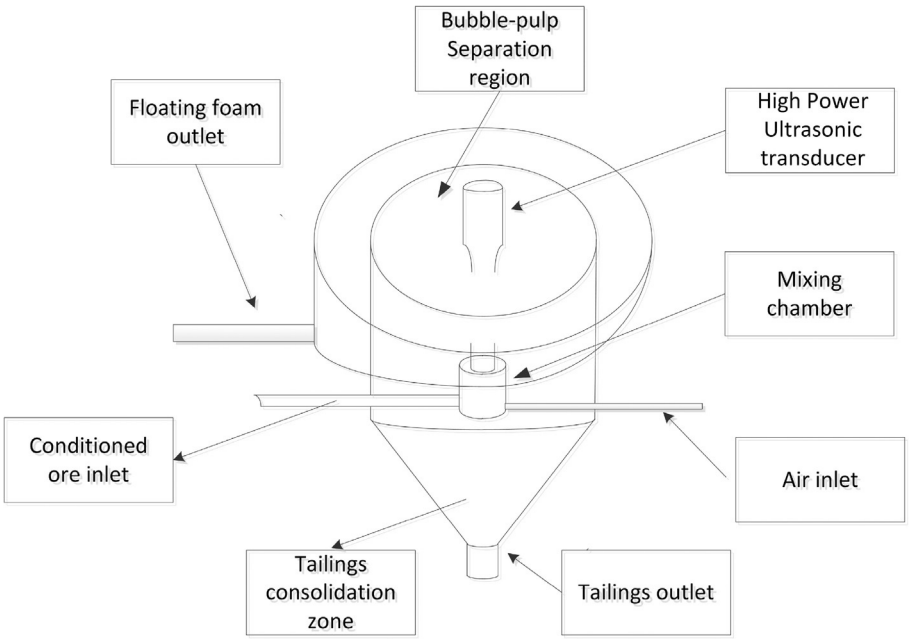


FIGURE 21.18 Schematic of Jordan's cell for continuous flotation process.

The system has two upper sections in the form of concentric rings; the inner ring has a small cylindrical chamber (mixer) where the particles and bubbles come together. The floating process starts as air is injected. Air bubbles are produced by the action of ultrasound, generated with a power transducer as shown in the top of the figure, and are mixed with particles in the mixing zone. The particles adhere to the bubbles and float toward the froth separation region. Finally, the froth overflows to a second outer cylindrical chamber wherein the foam concentrates while it is discharged through an overflow collector. Although interesting, there is no information on an industrial application of this design. However, the author claims a list of advantages of his system. The first advantage would be a superior flotation rate than in a conventional flotation cell. The second advantage would be that the small volume of the cell that is used to apply the ultrasonic radiation ensured a high level of energy that contributes to the performance of the particle-bubble mixture promoting the collision between them. Another advantage would include the improvement of the attachment between the particles and the bubbles. Finally, the small size of the cavitation bubbles would ensure the possibility that small particles float.

21.5.3 Recent developments in ultrasonic-assisted flotation process

More recently, an ultrasonic-assisted flotation cell has been built and used for particle flotation analysis (Vargas-Hernández et al., 2002; Videla et al., 2016). It consists of a Denver cell (Koh and Schwarz, 2006), equipped with ultrasonic capabilities for performing ultrasound-assisted flotation experiments. A Denver cell has a suspended mechanism that includes a stainless-steel air control valve, impellers, and air diffuser. The mechanism is supported on a spring-balanced movable arm that is raised or lowered on a column by a hand crank through rack and pinion gear and can be locked at any desired height. It uses a stainless-steel tank of a volume between 0.5 and 3 L where the ore and water are conditioned for conducting flotation tests with 250–2000 g of ore.

In Figure 21.19, a schematic of the Denver cell equipped with two power transducers is shown, operating at 20 kHz. In Figure 21.20a, a Denver cell is shown. More recently, another similar device has been built with an 8-L cell and nine transducers (Figure 21.20b).

The ultrasonic transducers are in acoustic contact with the body of the flotation cell but are not immersed in the slurry. The flotation chamber has a capacity of 2.7 L and is equipped with conventional systems to introduce air and mechanical agitation able to maintain the suspension of mineral pulp. In the upper part of the cell is an area in which the foam is recovered for further analysis via a process called "skimming." The transducers operate at 20 kHz and can handle up to 400 W. In the Denver cell, an acoustic probe, calibrated through a nonlinear system, which is capable of measuring high intensity acoustic fields, is placed (Gaete-Garretón et al., 1993, 1998). The probe is used to determine the different acoustic field intensities with a spatial scanning during the experiments. Figure 21.21 shows schematically the distribution of the ultrasonic field intensity in the flotation chamber.

Two different sets of experiments have shown good results in ultrasonic-assisted flotation for fine particles. As a first test, a sample of copper sulfide particles was floated at different levels of ultrasonic activation. A comparison can be done between the percentage of recovering for fine particles (under 45 μm) and the global recovering (for all particles under 147 μm). In Figure 21.22, the recovering of copper, molybdenum, and iron is shown. They are

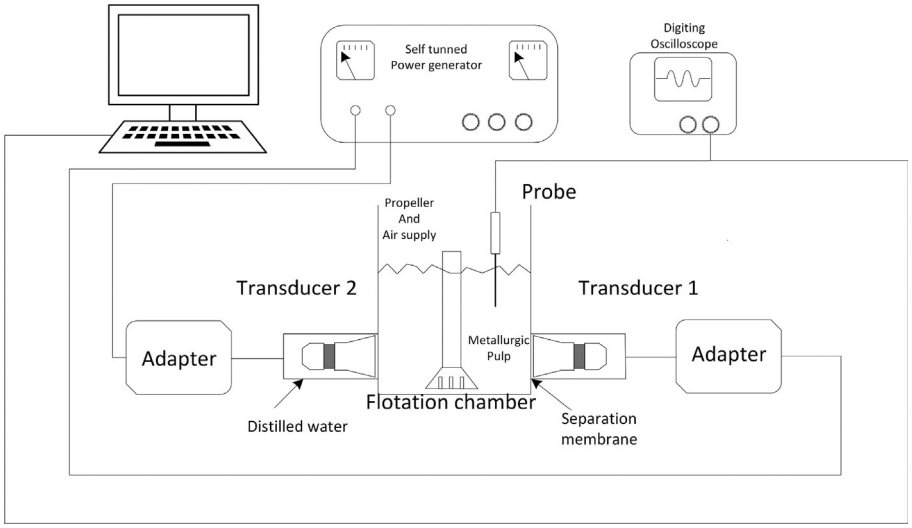


FIGURE 21.19 Schematic of Denver cell conditioned for ultrasonic-assisted flotation.

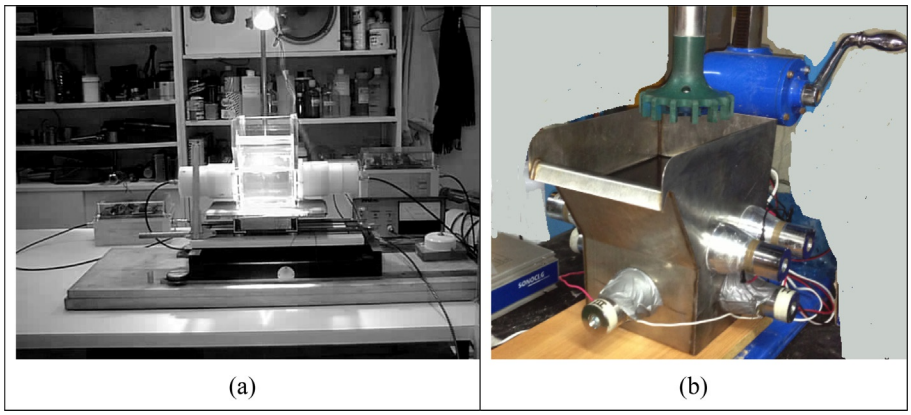


FIGURE 21.20 Ultrasonic-assisted Denver cell. (a) 2.7-L cell with two transducers; (b) 8-L cell with nine transducers.

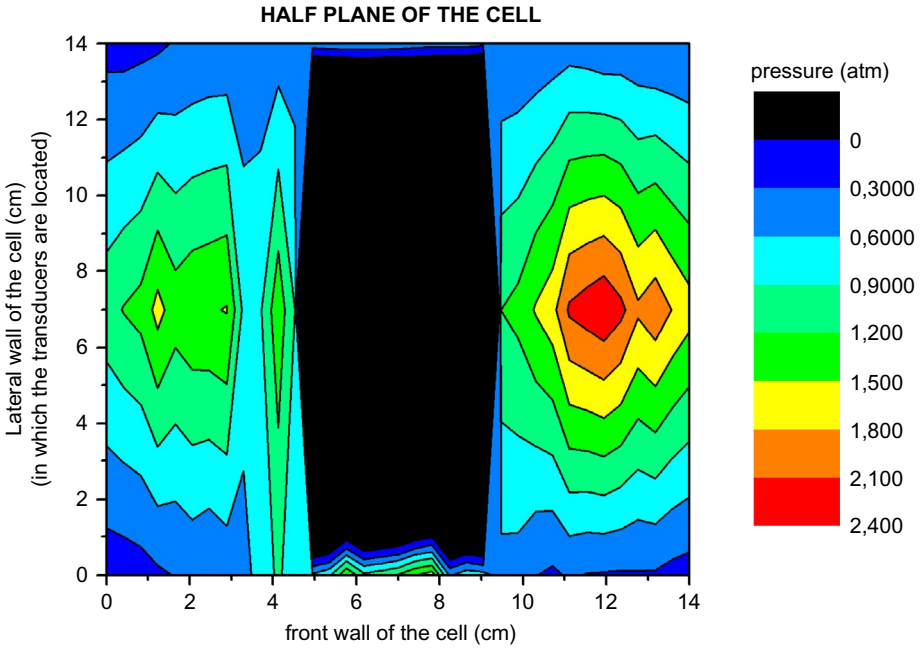


FIGURE 21.21 Acoustic field in the medium plane of ultrasonic-assisted Denver cell.

almost identical for fine and ultrafine particles at different power levels. The most interesting part of the flotation curves is the increment observed in the recovery of molybdenum with ultrasonic power. Molybdenum is a very valuable by-product. On the other hand, the increment in iron recovery may be detrimental because it reduces the copper concentrate grade.

Flotation tests in an 8-L Denver flotation cell were performed with copper tailings with an average particle size below 90 μm. Ultrasound was applied during conditioning (UC), flotation (UF), and during conditioning and flotation (FCU) for comparison. The results are shown in Figure 21.23 and a significant improvement was observed when ultrasonically assisted flotation was performed during conditioning and flotation. These experiments confirm the potential of power ultrasound in flotation.

Other works have been carried out to explore the benefits of ultrasound in flotation of different ore minerals. For instance, Özkan (2002) conducted experiments by preconditioning pulp with ultrasound during flotation. The objective was to evaluate floatability of magnesite slimes (particles smaller than 38 μm) with the help of ultrasound. Three types of experiments were carried out: conventional flotation, flotation with ultrasonic pretreatment, and flotation with simultaneous ultrasonic treatment. Ultrasonic pretreatment consisted of placing the sample in a beaker, slurried with water, and stirred with ultrasound. Then the content was transferred to a standard flotation cell. Simultaneous ultrasonic treatment was carried out by introducing the cell into an ultrasonic bath operating at 50 kHz. The results showed that under ultrasonic fields, the flotation foam bubbles are smaller, improving recovery rates for

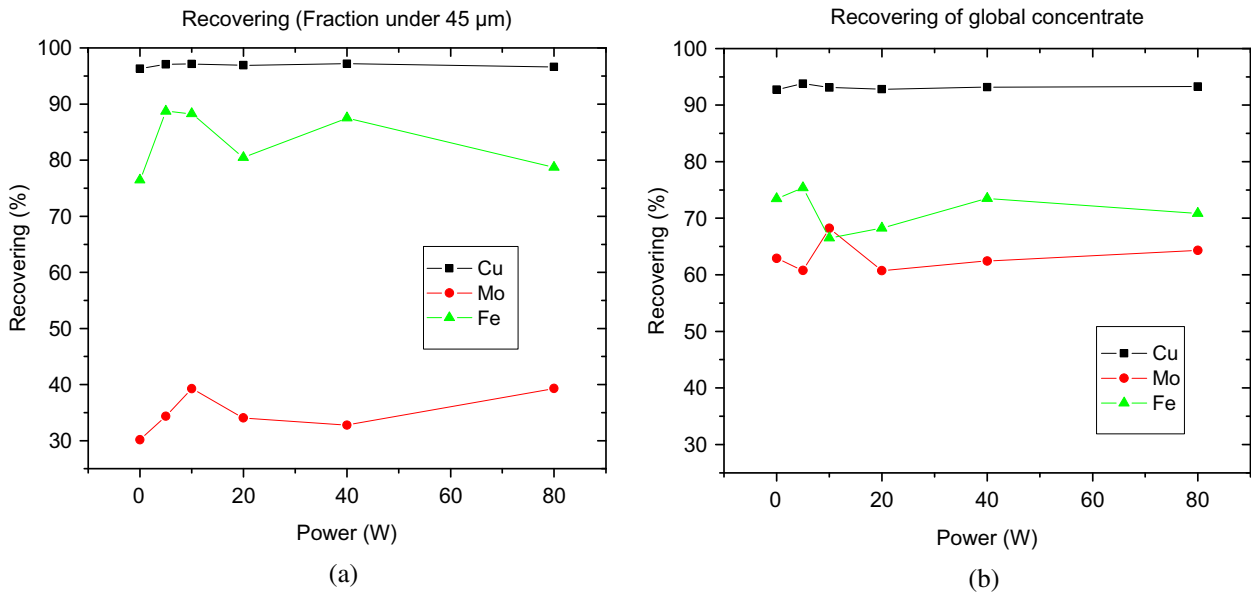


FIGURE 21.22 Comparison of recovering percentage with different applied power in ultrasonic-assisted flotation process in a Denver cell: (a) fine and ultrafine particles recovering (sizes under 45 μm) and (b) normal size particles recovering (under 147 μm).

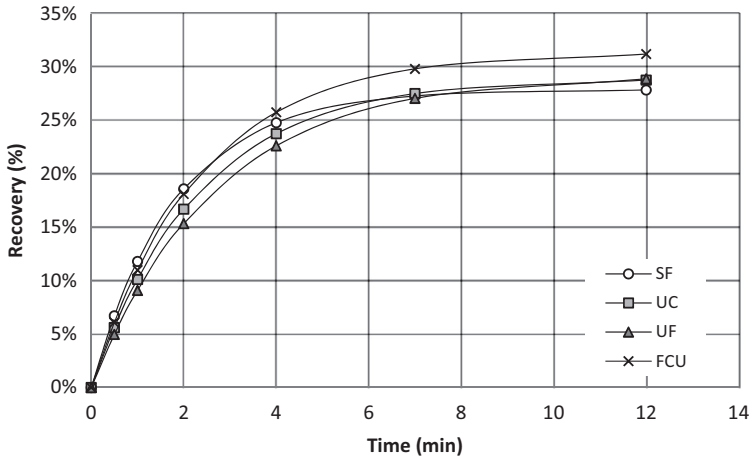


FIGURE 21.23 Flotation kinetic in ultrasonic-assisted flotation 8-L Denver cell.

magnesite. The beneficial effects of ultrasound were only manifested for mineral under ultrasonic preconditioning. The flotation performed under simultaneous ultrasonic field did not show improvement. This effect probably happens because power ultrasound improves the buoyancy of clay iron and this lowers the law of magnesite.

Kyllönen et al. (2004) employed power ultrasound (22 kHz, 100–500 W ultrasonic reactor) to remove metal compounds from soil particles to study the effect on float fractions in heavy medium separation processes, screen fraction, and mineral concentrates and tailings for flotation processes. They concluded that ultrasound improves the remediation results and the remediation process producing better float product (cleaned soil).

Özkan and Kuyumcu (2006) also investigated the action mechanisms of ultrasound under different flotation conditions. A cleaning effect on the floating particles was attributed to the ultrasonic energy, making them more reactive to the flotation reagents. Furthermore, because the cohesion of solid-liquid interface is weaker than the cohesive forces of the pulp liquids, solid-liquid interfaces are more favorable to the formation of cavitation bubbles. The unstable conditions of a cavitation environment can produce changes in the collectors and even lead to the formation of emulsions improving the flotation of fine particles. Ábrego-López (2006) studied a water recovery process of sludge from industrial plants. For this purpose, he employed a Denver flotation cell assisted by an

ultrasonic bath. In the first step, he made a flotation to recover heavy metals from the metallurgical pulp, obtaining a high level of recovery. In the second step, he added eucalyptus wood cones to the slurry to act like an adsorbent of copper, lead, nickel, iron, and aluminum. The author claimed that he obtained an excellent recovery of all elements to be extracted.

Özkan and Kuyumcu (2007) designed and constructed an experimental flotation cell equipped with power ultrasound transducers of different frequencies (25 and 40 kHz) and geometries to analyze the effects of the ultrasound on coal flotation at all stages of the process. Their results confirm the influence of the cavitation phenomenon and the main conclusion is that ultrasonic treatment positively affects the quality and quantity of the properties of floated coal at all stages of concentration.

Kang et al. (2008) intended to understand the mechanism that causes effects in ultrasonic flotation, analyzing the surface particles exposed to flotation, and an ultrasonic field by different techniques like X-ray diffraction, electron microscopy, and scanning electron microscopy techniques. A multifunction ultrasonic transmitter Model UGD was used in the tests. The total power of the ultrasonic transmitter was 200 W at a frequency of 20 kHz. Samples of 5 g of coal and pyrite were mixed with 70 mL of water and exposed for 3 mins to ultrasound. It was established that ultrasonic preconditioning may contribute to desulfurization and ash removal (deashing) in carbon minerals. Kang et al. (2009) used the same flotation and ultrasound system to study the effects of preconditioning of carbon mineral slurry by ultrasound with high sulfur content. They found that the oxygen generated by cavitation produces pyrite over oxidation lowering its hydrophobicity. The same effect happened with the change of pH induced by ultrasonic treatment. Additionally, ultrasound decreased the liquid gas interfacial tension by increasing the number of bubbles.

Finally, Özkan (2012) conducted flotation experiments with the presence of hard carbon sludge cavitation (slimes), encountering many of the effects that have been reported for the case of metallurgical pulp with ultrasound pretreatment. Flotation experiments were carried out using a Wemco flotation machine with an impeller speed of 1500 rpm. Stainless-steel flotation cells with 1.2 L of capacity and equipped with ultrasonic transducers were employed with a fixed 40 kHz frequency. Four transducers with 50 W power capacity were mounted on each side of the flotation cell and connected with cables to the ultrasonic generator. The total energy applied was calculated as 60 W/L. The results indicated an improvement in flotation, drastic reduction in reagent consumption, and the possible prevention of the oxidation of the carbon sludge surface. A decrease in the ash content in floating carbon was not detected. However, tailings do not seem to contain carbon particles. All these effects can be attributed to acoustic cavitation. However, according to the author, an examination is needed regarding the contribution of ultrasound to the probability of particle-bubble collision and the likelihood of getting the bubbles to connect to the particles. The latter effects have been proposed as causes of improvements in the flotation processes in many of the publications reviewed, but there is no systematic study of this aspect.

Recently, Chen et al. (2020) have attributed the positive effects of ultrasound-assisted flotation to three phenomena: the transient cavitation effect, the stable cavitation effect, and the acoustic radiation force effect. The transient cavitation effect usually happens at low frequencies (20–50 kHz) and leads to catastrophic collapse of bubbles resulting in surface cleaning, sonochemistry, and breaking effect. When frequencies are high (0.2–1.0 MHz), a stable cavitation effect is enhanced, and stable tiny bubbles are formed. The acoustic radiation force refers to the motion of particles and bubbles as exposed to a sound field. Most of the previous work mentioned has focused on the transient cavitation effect, neglecting the latter two effects.

In summary, the assistance of power ultrasound to the flotation processes shows promising results as a method of pulp conditioning before flotation, also as an assisting method in a continuous flotation process, and as a method to improve flotation recovery in conventional flotation cells. In particular, the result of ultrasonic-assisted flotation shows a significant impact and potential in the recovery and flotation selectivity of fine and ultrafine particles.

21.6 Ultrasonic-assisted sedimentation rate for increasing water-solid separation efficiency

21.6.1 Water-solid separation process

Flotation involves the use of substantial amounts of water to transport particles and perform the separation process. As result of flotation, a small amount of mass and water will be in the concentrate of the valuable ore and near 95% of the solid mass and water will end up in the tailings dump. In this regard, one of the biggest challenges facing the mining industry is the reduction of freshwater consumption. For instance, it is estimated that in Chile copper mines consume on average 0.44 m^3/ton ore treated (COCHILCO Comisión Chilena del Cobre, 2017) leading to a consumption of nearly 100,000 m^3 of freshwater per day in a standard mill plant operation. Therefore, any effort in improving water recovery is important.

Sedimentation is a gravity-driven water recovery method where the slurry is thickened by removing the bulk water from a solid suspension. The usual sedimentation equipment used is a thickener of a cylindrical form with a feeder at the central top point from where the solid

concentration in the suspension increases by gravitational sedimentation while a clear liquid is collected in the perimeter of the cylinder via overflow. Usually, the suspension mass percentage feed is 30%–40% solids, while at the discharge point, it reaches values of 55%–65% solids. The settling of particles is governed by Stoke's law and therefore will be affected by particle size and shape, solid percentage, fluid viscosity, and specific density of fluids and solids. As very small particles settle very slowly, particles are aggregated in particle clusters that resemble a bigger particle than the originals thus increasing the settling velocity. The aggregation or flocculation is generally driven by addition of a flocculant with a specific surface charge.

The rate of sedimentation in the thickeners is negatively affected by ultrafine particles like clays or overgrinded particles that sometimes appear in the concentration process. Such particles, sized less than 50 μm, reduce speed rate and throughput severely. This harmful effect must be compensated with a reduction in the feeding rate of the equipment, putting the entire upstream operation at risk. A solution to this problem has not yet been found. In this regard, ultrasonic-assisted sedimentation has captured recent attention as a promising alternative (Videla et al., 2020).

21.6.2 Power ultrasound in sedimentation

One of the first attempts to improve the separation of water from tailings in a metallurgic process was undertaken by Gallego-Juarez (1994), developing a successful technique to clean the rotatory filters used to deliquoring the cake in the production of TiO_2. Unfortunately, the company that commissioned the investigation abandoned the technique without explanation.

Some work has been done to evaluate the use of ultrasound in thickening and sedimentation (Locatelli et al., 2015; Pons et al., 2012; François et al., 2016; Onal et al., 2003; Hunter et al., 2011; Bekker et al., 1997; Riera-Franco de Sarabia et al., 2000; Zhang et al., 2012). Most of these studies show two potential improvements in the water recovery process by enhancing the flocculation process leading to a reduction of the flocculant consumption and/or by increasing the particle size and consequently the sedimentation rate. Gallego-Juarez et al. (2003) used power ultrasound to favor the separation process by exploiting the radiation pressure of the high-intensity ultrasonic radiation. Videla et al. (2020) extended these works by studying the effect of ultrasound in the sedimentation of copper tailings with transverse and longitudinal radiation at different excitation frequencies. Solid percentage, flocculant dosage, and emission direction configuration are evaluated.

21.6.3 Recent developments in ultrasonic-assisted sedimentation

An automatic sedimentation system was designed and built to homogenize a sample of up to 2000 mL of slurry in a borosilicate tube before starting the sedimentation process. The tube, 70 mm in diameter and 800 mm in length, was loaded with slurry before the test started. When appropriate, anionic flocculant was added in a defined dose and the slurry homogenized in the tube as it turned slowly, propelled by a 120 W rotational motor at around 10 rpm. Figure 21.24 shows the experimental setup for the sedimentation system, including the components that form part of the connection with the transducers. Preliminary tests determined that a suitable slurry homogenization time of 2 min was sufficient to guarantee the sedimentation results did not change significantly.

Ultrasound was applied in two different configurations: transverse radiation and longitudinal radiation. In transverse radiation, the wave was emitted on both sides of the tube, while in the longitudinal configuration, the wave was emitted in the upper part of the tube. At the end of the

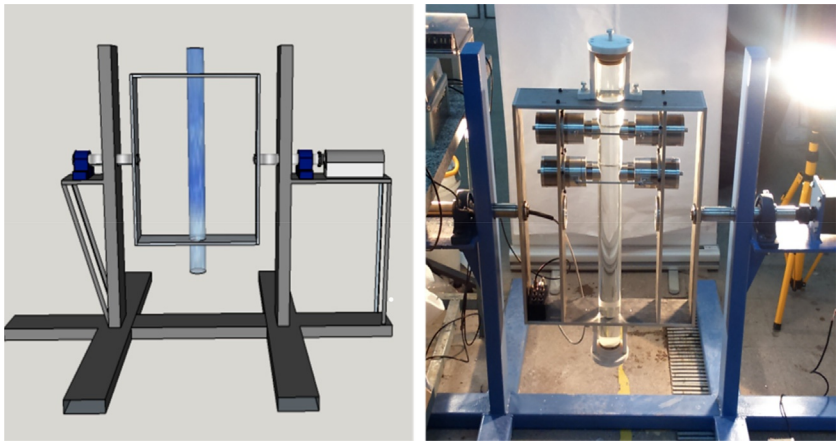


FIGURE 21.24 Experimental setup of the sedimentation.

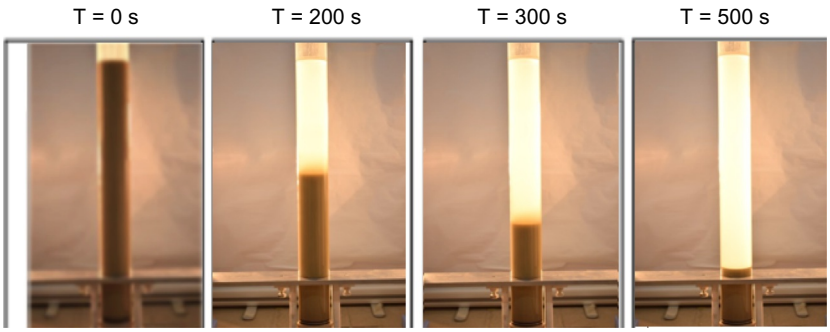


FIGURE 21.25 Trucking of the suspension to clarifier liquid in the sedimentation curve.

ultrasonic transducer, which was of "stepped horn" type, a disk with a diameter of 40 mm had been mounted and submerged in the slurry. The disk vibrated at its second flexural eigenmode at the working frequency. This way of operating the transducer considerably improved the overall performance of the system by facilitating the transmission of acoustic pressure to the slurry.

The results of the application of transversal and longitudinal ultrasound waves are shown in the sedimentation curves of tailings from copper mining. In this test, the interphase between the solid suspension and the clear supernatant liquid was followed in time as shown in Figure 21.25. In this way, the impact of ultrasound-assisted sedimentation can be compared to the reference test without ultrasound, thus establishing if the process can be accelerated.

Different sedimentation experiments were developed to evaluate the effect of the excitation frequency and the position of the transducers. For the configuration of transverse radiation, four transducers connected in parallel have been used, operating at a frequency of 20 kHz. For the longitudinal configuration only one transducer operating at 20 kHz was used. Figure 21.26 shows the results as obtained in a 20% solid slurry evaluated with different flocculants dosages and with and without ultrasonic application. The results show an improvement in sedimentation with the use of ultrasound in a transverse configuration for all the doses of flocculant evaluated. For a dosage of 10 g/ton, it was observed that after 500 s, the sedimentation front was at 54 cm height with ultrasound applied but reached only 59 cm without it. Similarly, for a dosage of 25 g/ton, it was observed that after 500 s, the sedimentation front was at 42 cm with ultrasound applied and about 38 cm without it.

Also, the influence of the modality of application of the ultrasounds used in their two configurations (transversal and longitudinal) was analyzed. Figure 21.27 shows a comparative study of the application of ultrasound in its transversal and longitudinal radiation versions. The curves in Figure 21.27 allow concluding that the longitudinal configuration clearly accelerates the sedimentation front with respect to the transverse application of ultrasound, reaching a height of 28 cm after 500 s.

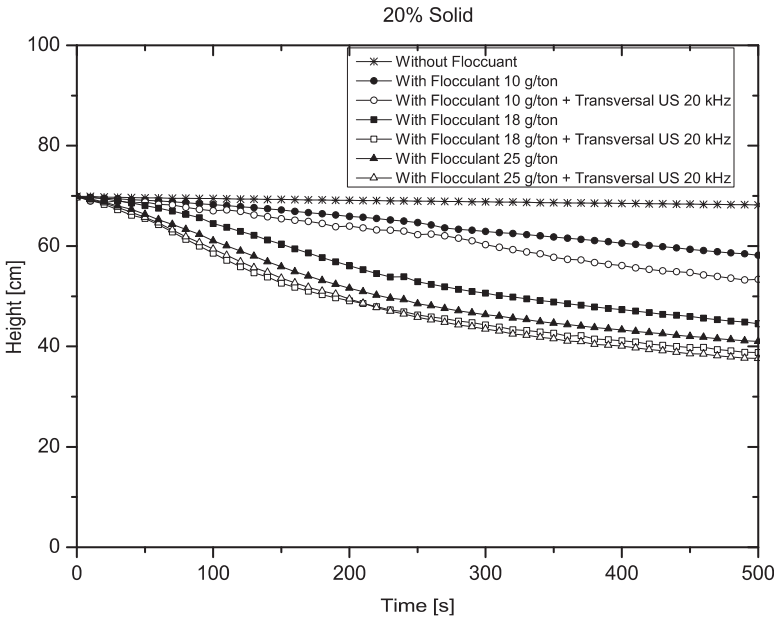


FIGURE 21.26 Sedimentation curves for a concentration of 20% solid at different flocculant dosages and compared with an ultrasonic-assisted sedimentation at 20 kHz.

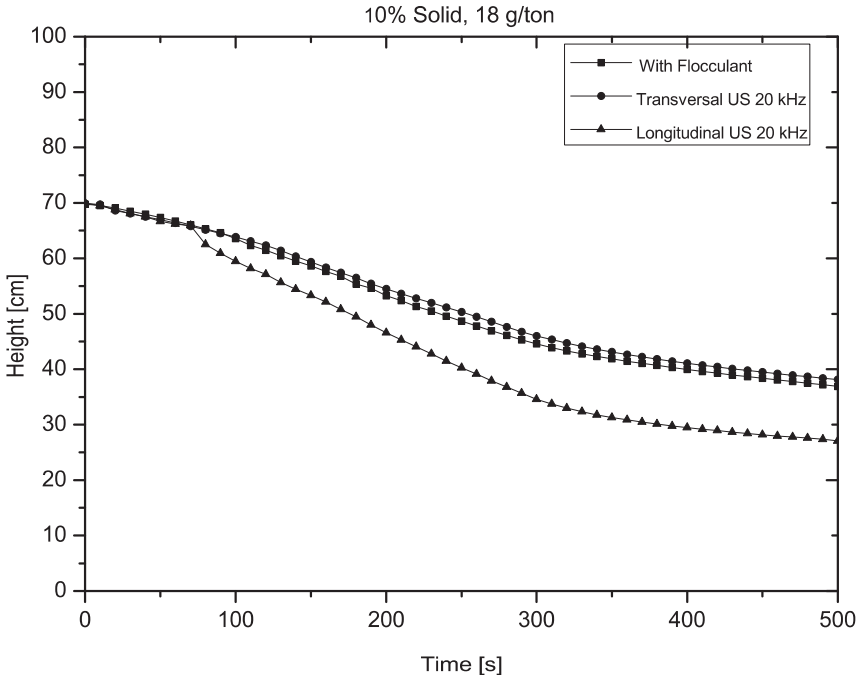


FIGURE 21.27 Sedimentation curves for a concentration of 10% solid and 18 g/ton flocculant assisted by transversal and longitudinal ultrasound at 20 kHz.

Applying ultrasound to a flocculation process appears as an attractive possibility to improve water recoveries in mining processes. It has been established that acoustic radiation favors the effects of flocculants increasing their performance, independently of slurry solid percentage and flocculant dosage. Acoustic longitudinal radiation emerged as better option than transverse radiation to improve the sedimentation rate at 10% solid and 18 g/ton flocculant dosage.

There is also a significant effect of the frequency of the acoustic wave as shown in Figure 21.28. The acoustic frequency that gives the best results to increase the sedimentation rate is the lowest evaluated, 7 kHz, probably due to its low attenuation as compared to 20 and 40 kHz. In the sedimentation experiment of 10% solids and 18 g/ton flocculant dosage, the sedimentation rate has been clearly accelerated by applying a 7 kHz longitudinal radiation as compared to slurry with only flocculant. In fact, the final settlement height at 500 s has been reduced by 40% by applying the 7 kHz longitudinal radiation.

21.7 Conclusions and future trends

Power ultrasonic systems have demonstrated their viability to be applied during different stages of mining operations to improve them.

The technique developed to determine in situ the state of stress in a rock mass has shown to be effective. The experimental system operating in a mine is presently providing significant data that are deeply analyzed to establish a reliable procedure correlated with the real status of the rock. The generalization of the process will require the laboratory study of the linear and nonlinear propagation of ultrasonic waves in many different representative mineral rocks.

Regarding grinding, the ultrasonically assisted procedure has shown its capacity to grind material at an effective energy consumption rate. The practical issues related to its upscaling have kept this technique still at laboratory level. Processes of about 1000 tons/day of material have to be reached and that requires a significant investment. Technically, higher power ultrasonic transducer systems, including proper electronics, can be developed even if their design and construction pose a great challenge.

Ultrasound flotation testing has shown significant improvements in different ore and applications. The cleaning effect, the production of tiny bubbles, and even the utilization of radiation force to control particle and bubble motion could find significant industrial applications in years to come. Additional work must be done to generate industrial designs that could balance capital investment, and operative costs and benefits to make the technology more attractive to the industry.

Finally, the new improvements in sedimentation rates by ultrasonic application make the technology very promising in particular in mining environments where water access is limited. There are specific factors related to particle size, flocculation dosage, solid percentage, and ultrasound frequency that need to be more deeply studied before moving to industrial scale. Particularly, the effect of optimum frequency and its relationship with particle size and shape must be explored further to develop a robust operational method for industrial control.

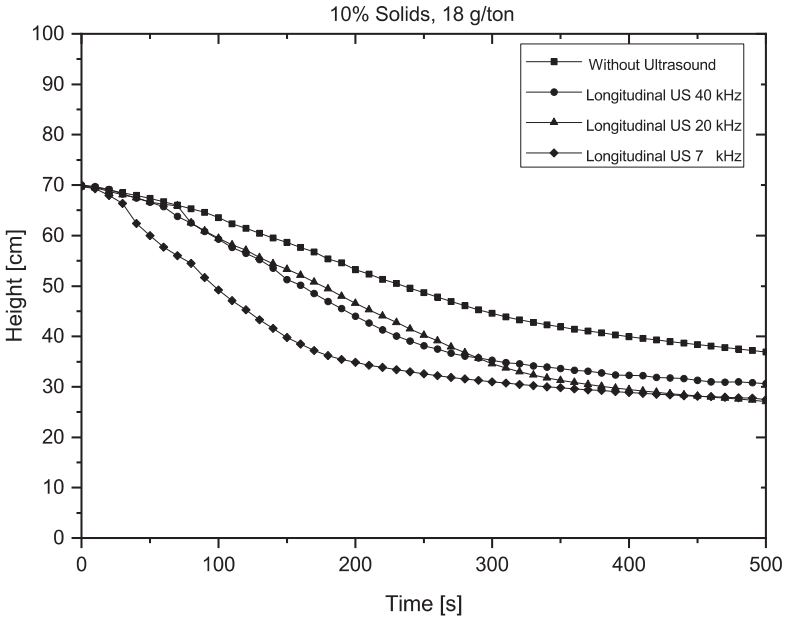


FIGURE 21.28 Sedimentation curves for a concentration of 10% solid and 18 g/ton flocculant assisted by longitudinal ultrasound at 40, 20, and 7 kHz.

References

Aber, R.C., Moulder, G., Tarpley, W.B., 1985. Ultrasonic comminution: scale-up and energetics. In: Presented at the Conference on Recent Development in Comminution, 8–13 December, Hawaii.

Ábrego-López, J., 2006. Process for separation heavy metals from industrial residues by using an ultrasound flotation and eucalyptus as sequestering agent. J. Appl. Sci. 6, 1886–1887.

Amadei, B., Stephansson, O., 1997. Rock Stress and Its Measurement. Springer-Science+Business Media, B.V.

Austin, L.G., Klimpel, R.R., Luckie, P.T., 1984. Process Engineering of Size Reduction: Ball Milling. Published by Society of Mining Engineers, New York.

Baum, W., Patzelt, N., Knecht, J., 1996. Metallurgical benefits of high pressure roll grinding for gold and copper. In: Comminution Practices Proceedings SME Symposium, pp. 111–116.

Bekker, M.C., Meyer, J.P., Pretorius, L., Van der Merwe, D.F., 1997. Separation of solid-liquid suspensions with ultrasonic acoustic energy. Water Res. 31, 2543–2549.

Blaha, F., Langenecker, B., 1959. Ultrasonic investigation of the plasticity of metal crystals. Acta Metallurg. 7, 93–100.

Brown, E.T., Hoek, E., 1978. Trends in relationships between measured rock in situ stresses and depth. Int. J. Rock Mech. Min. Sci. Geomech. Abstr. 15, 211–215.

Chen, Y., Truong, V.N.T., Bu, X., Xie, G., 2020. A review of the effects and applications of ultrasound in mineral flotation. Ultrason. Sonochem. 60, 104739.

COCHILCO Comisión Chilena del Cobre, 2017. Consumo de agua en la minería del Cobre. DEPP 04/ 2018, Ministerio de Minería, Gobierno de Chile. 2018, Ministerio de Minería, Gobierno de Chile.

Feng, D., Aldrich, C., 1999. Effect of particle size on flotation performance of complex sulphide ores. Miner. Eng. 12, 721–731.

Fleischhauer, W.J., Kröger, C., 1969. Versuche zur Zerkleireung und Extraktion von Khole duch Ultrashall. Forschungsberichte des Landes Nordrhein-Westfallen Nº 2081, pp. 1–24.

François, P., Locatelli, F., Laurent, J., Bekkour, K., 2016. Experimental study of activated sludge batch settling velocity profile. Flow Meas. Instrum. 48, 112–117.

Gaete-Garretón, L., Vargas-Hernández, Y., Pino-Dubreuil, S., Montoya-Vitini, F., 1993. Ultrasonic detectors for high intensity acoustic fields. Sens. Actuators A 37, 410–414.

Gaete-Garretón, L., Vargas-Hernández, Y., Pino-Dubreuil, S., Gallego-Juárez, J.A., 1998. A simple non-linear technique for secondary calibration of ultrasonic probes. Sens. Actuators A 69, 68–71.

Gaete-Garreton, L.F., Vargas-Hernández, Y.P., Velasquez-Lambert, C., 2000. Application of ultrasound in comminution. Ultrasonics 38, 345–352.

Gaete-Garretón, L., Vargas-Hernandez, Y., Chamayou, A., Dodds, J.A., Valderama-Reyes, W., Montoya-Vitini, F., 2003. Development of an ultrasonic high-pressure roller press. Chem. Eng. Sci. 58, 4317–4322.

Gallego-Juarez, J.A., 1994. New technologies in high-power ultrasonic industrial applications 3, 1343–1352.

Gallego-Juarez, J.A., Elvira-Segura, L., Rodriguez-Corral, G., 2003. A power ultrasonic technology for deliquoring. Ultrasonics 41, 255–259.

Gärtner, W., 1953. Über die Möglichkeit der zerkleinerung suspendierter stoffe durch ultrashall. Acustica 3, 124–128.

Graff, K.F., 1979. Ultrasonic comminution. In: Novák, Z., Bailey, S.L. (Eds.), Proceedings of Ultrasonics International Congress. IPC Science & Technology Press, Graz, Austria, pp. 171–175.

Greenwald, E.H., 1985. Process for Removing Sulfur and Ash From Coal. US Patent N° 4.537.599 Aug. 27.

Hunter, T.N., Peakall, J., Biggs, S.R., 2011. Ultrasonic velocimetry for the in situ characterization of particulate settling and sedimentation. Miner. Eng. 24, 416–423.

Ishak, W.M.F., Rowson, N.A., 2009. The effect of ultrasound pre-treatment onfroth flotation performance. World Acad. Sci. Eng. Technol. 30, 1529–1532.

Jian-Hong, W., Wei-Pan, Y., 2013. Three dimensional in situ stress evaluation using a new undercoring technique: the Tsen-Wen Reservoir Transbasin Water tunnel. Environ. Earth Sci. 68, 77–86.

Jordan, C.E., 1991. Ultrasonic Flotation System. US Patent N° 5.059.309 Oct. 22.

Kang, W.-Z., Xun, H.-X., Hu, J., 2008. Study of the effect of ultrasonic treatment on the surface composition and the flotation performance of high-sulfur coal. Fuel Process. Technol. 89, 1337–1344.

Kang, W.-Z., Xun, H.-X., Kong, X.-H., Li, M.-M., 2009. Effects from changes in pulp nature after ultrasonic conditioning on high-sulfur coal flotation. Min. Sci. Technol. 19, 0498–0502.

Koh, P.T.L., Schwarz, M.P., 2006. CFD model of a self-aerating flotation cell. In: Fifth International Conference on CFD in the Process Industries CSIRO, Melbourne, Australia, pp. 13–15.

Kyllönen, H., Pirkonen, P., Hintikka, V., Parvinen, P., Grönroos, A., Sekki, H., 2004. Ultrasonically aided mineral processing technique for remediation of soil contaminated by heavy metals. Ultrason. Sonochem. 11, 211–216.

Lagos, G., Peters, D., Videla, A., Jara, J.J., 2018. The effect of mine aging on the evolution of environmental footprint indicators in the Chilean copper mining industry 2001–2015. J. Clean. Prod. 174, 389–400.

Leach, M.F., Rubin, G.A., 1988. Fragmentation of rocks under ultrasonic loading. In: Proceedings of Ultrasonic Symposium of IEEE, Chicago. vol. 1, pp. 485–488.

Lecoffre, I., 1980. Method of Producing Microbubbles for Treating a Suspension. US Patent N°4.226.705, Oct.

Link, T., Killmeyer, R.P., 1988. Ultrasonic Comminution of Coal. PETC Coal Preparation Division Internal Report.

Lo, Y.C., Kientzler, P.J., 1992. Evaluation of the effectiveness of ultrasonic comminution. In: Kawatra, S.K. (Ed.), Proceedings of Comminution-Theory and Practice Symposium. SME Littleton, Co, pp. 645–659. Chapter 47.

Locatelli, F., François, P., Laurent, J., Lawniczak, F., Dufresne, M., Vazquez, J., Bekkour, K., 2015. Detailed velocity and concentration profiles measurement during activated sludge batch settling using an ultrasonic transducer. Sep. Sci. Technol. 50, 1059–1065.

Majewska, Z., Mortimer, Z., 2001. Chaotic behavior of acoustic emission generated in materials under stress. In: Rockburst and Seismicity in Mines RaSiM5. South African Institute of Mining and Metallurgy, pp. 181–190.

Neppiras, E.A., 1973. The pre-stressed piezoelectric sandwich transducer. In: Proceedings of Ultrasonic International Conference, pp. 295–301.

Onal, G., Ozer, M., Arslan, F., 2003. Sedimentation of clay in ultrasonic medium. Miner. Eng. 16, 129–134.

Özkan, S.G., 2002. Beneficiation of magnesite slimes with ultrasonic treatment. Miner. Eng. 15, 99–101.

Özkan, S.G., 2012. Effects of simultaneous ultrasonic treatment on flotation of hard coal slimes. Fuel 93, 576–580.

Özkan, S.G., Kuyumcu, H.Z., 2006. Investigation of mechanism of ultrasound on coal flotation. Int. J. Miner. Process. 81, 201–203.

Özkan, S.G., Kuyumcu, H.Z., 2007. Design of a flotation cell equipped with ultrasound transducers to enhance coal flotation. Ultrason. Sonochem. 14, 639–645.

Pons, M.N., France, X., Schmitt, P., Pallarés, A., 2012. Settling velocities: the ultrasound approach. In: Conference: IWA World Water Congress, Busan, Korea.

Revnitsev, V.I., 1988. We really need revolution in comminution. In: Forssberg, E. (Ed.), XVI Int. Mineral Processing Congress. Elsevier Sci. Publishers B. V., Amsterdam, pp. 93–116.

Riera-Franco de Sarabia, E., Gallego-Juárez, J.A., Rodríguez-Corral, G., Elvira-Segura, L., González-Gómez, I., 2000. Application of high-power ultrasound to enhance fluid solid particle separation processes. Ultrasonics 38, 642–646.

Schlesinger, L.M., Muter, R.B., 1989. The effect of ultrasonic conditioning on the froth flotation of Pittsburgh No. 8 coal. In: Proc. of 6th Annu. Int. Pittsburgh Coal Conf, pp. 1163–1172.

Schönert, K., 1988. A first survey of grinding with high-compression roller mills. Int. J. Miner. Process. 22, 401–412.

Sjöberg, J., Christiansson, R., Hudson, J.A., 2003. ISRM Suggested Methods for rock stress estimation-Part 2: overcoring methods. Int. J. Rock Mech. Min. Sci. 40, 999–1010.

St. Slaczka, A., 1987. Effect of an ultrasonic field on the flotation selectivity of barite from a barite-fluorite quartz ore. Int. J. Miner. Process. 20, 193–210.

Taplin, T.J., 1937. Froth Flotation Concentration Process. US Patent N° 2.093.898.

Tarpley Jr., W.B., Howard, P.L., Moulder, G.R., 1980. Efficient ultrasonic grinding: a new technology for micron-sized coal. Quarterly Technical Progress Report Nº2, Contract No.DE-AC02-79ER10466 for U. S. Department of Energy.

Vargas-Hernández, Y., Gaete-Garretón, L., Magne-Ortega, L., 2002. High power ultrasound to recover fine particles in flotation process. In: Proceedings of Forum Acoustics, Sevilla, Spain. ULT-02-001-IP.

Videla, A.R., Morales, R., Saint-Jean, T., Gaete, L., Vargas, Y., Miller, J.D., 2016. Ultrasound treatment on tailing to enhance copper flotation recovery. Miner. Eng. 99, 89–95.

Videla, A., Faúndez, D., Meneses, J., Gaete, L., Vargas, Y., 2020. Enhancement of the sedimentation rate of copper tailings by application of acoustic fields. Miner. Eng. 146, 106096.

Villaescusa, E., Seto, M., Baird, G., 2002. Stress measurements from oriented core. Int. J. Rock Mech. Min. Sci. 39, 603–615.

Wohlert, A.M., 1977. Carbon Paper Recicling System. US Patent N° 4.045.243.

Yerkovic, C., Menacho, J., Gaete-Garretón, L., 1993. Exploring the ultrasonic comminution of copper ores. Miner. Eng. 6, 607–617.

Zhang, P., Wan, T., Zhang, G., 2012. Enhancement of sludge gravitational thickening with weak ultrasound. Front. Environ. Sci. Eng. 6 (5), 753–760.

Chapter 22

Power ultrasonics: Exploration tools

Ch. Zhao[a], Xi. Li[a], Xu. Li[b], and P. Harkness[b]

[a]*State Key Laboratory of Mechanics and Control of Mechanical Structures, Nanjing University of Aeronautics and Astronautics, Nanjing, China,*

[b]*James Watt School of Engineering, University of Glasgow, United Kingdom*

22.1 Introduction

The use of high-frequency ultrasound (e.g., >1 MHz) for exploratory applications such as nondestructive evaluation and medical imaging is well known. Possibly less well known is that the lower frequency regimes of power ultrasonics also have numerous exploratory applications. This chapter will introduce those power ultrasonic and transduction devices which have already found direct applications in space, such as the ultrasonic motors and piezoelectric transducers that have flown to the Moon and on Mars.

Ultrasonic cleaning and testing techniques are widely used in the manufacture of components for the space industry. The highest possible levels of quality and cleanliness are vital to ensure, for example, that the intended containers for Mars sample return will not carry any appreciable terrestrial contamination. Some familiar ultrasonic sensors also fly in space: the International Space Station uses ultrasonic systems in a leak detection role, searching for the "hiss" signature of escaping gas, and piezoelectric MEMS systems are used to modulate the flow of propellant in some cold-gas propulsion systems. Research on new applications continues, and the key areas of activity in this domain will also be discussed.

22.2 Ultrasonic motors on the Moon

The Chinese Chang'e 3 probe was launched on December 2, 2013, and landed on the moon on December 14, 2013. It carried the YuTu lunar rover, with a visible and near-infrared imaging spectrometer (VNIS) for operations in the 0.45- to 2.4-μm spectral band (He et al., 2019) designed to inspect minerals close to the landing site. The calibration unit of the VNIS at the light entrance consisted of an ultrasonic motor (USM), harmonic reducer, framework, and an internal diffuser panel, as shown in Figure 22.1. The USM was designed by Prof. Chunsheng Zhao from the Nanjing University of Aeronautics and Astronautics (NUAA). The structure of USM is shown in Figure 22.2.

In its role as a driver of the VNIS, the TRUM-30A ultrasonic motor exhibits low mass (46 g), slow speed (100 r/min), a wide operating temperature range (−120°C to 180°C), and meets the torque, self-locking, and tribological requirements that can arise in almost all of the possible lunar environments (Zhao, 2011). Using the inverse piezoelectric effect, the metal stator can be excited such that a traveling wave touches the rotor at each peak. Each peak moves through an ellipse, realizing global mechanical motion through frictional contact. The mode shape of TRUM-30 is shown in Figure 22.3.

Chang'e 4, which landed on the far side of the moon on January 3, 2019, carried a similar ultrasonic motor to control the calibration board of the infrared imaging spectrometer. This motor is shown in Figure 22.4.

However, Chang'e 5, which landed on the moon on December 1, 2020, and subsequently returned samples to the Earth, had more stringent requirements on the accuracy of the ultrasonic motor. In this case, an ultrasonic motor (Figure 22.5) was used to control the direction and angle of the mirror surface of the spectrometer receiving the reflected spectrum.

22.3 Piezoelectric vibration techniques on Mars

Although the excitation frequency was below the ultrasonic band, the United States' Curiosity Mars rover used piezo actuators to homogenize samples such that crystallography might be conducted (Harkness and Lucas, 2012). There were 32 sample cells in the receiving wheel, with a transducer between each pair. Excitation caused the material inside the chamber to agitate, facilitating examination through the windows. The windows were made from different materials to help eliminate systemic errors and are approximately 8 mm across.

Power Ultrasonics. https://doi.org/10.1016/B978-0-12-820254-8.00035-X
Copyright © 2023 Elsevier Ltd. All rights reserved.

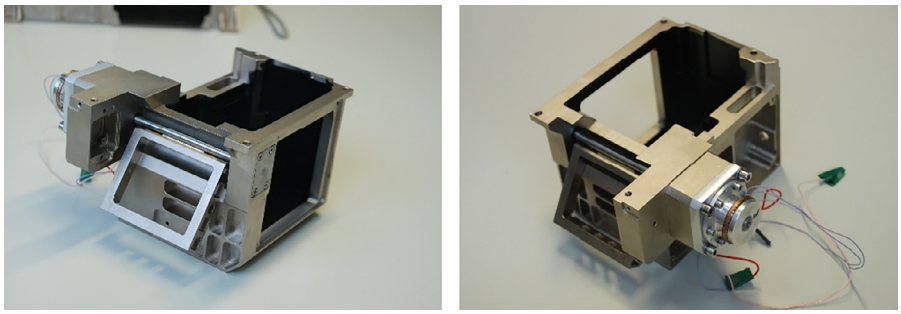


FIGURE 22.1 Visible and near-infrared imaging spectrometer, VNIS (NUAA).

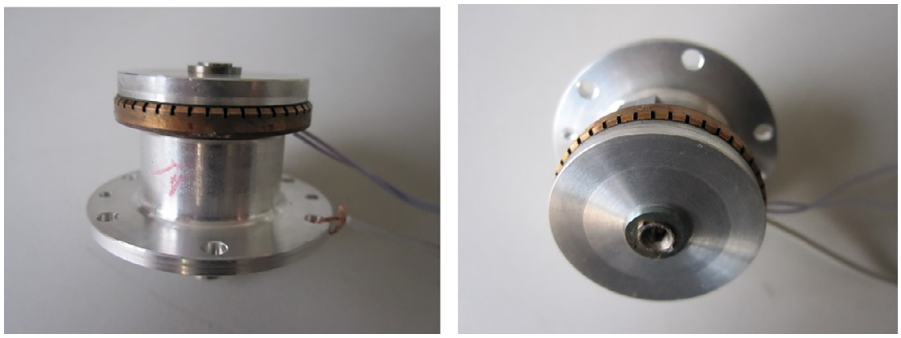


FIGURE 22.2 Ultrasonic motor (NUAA).

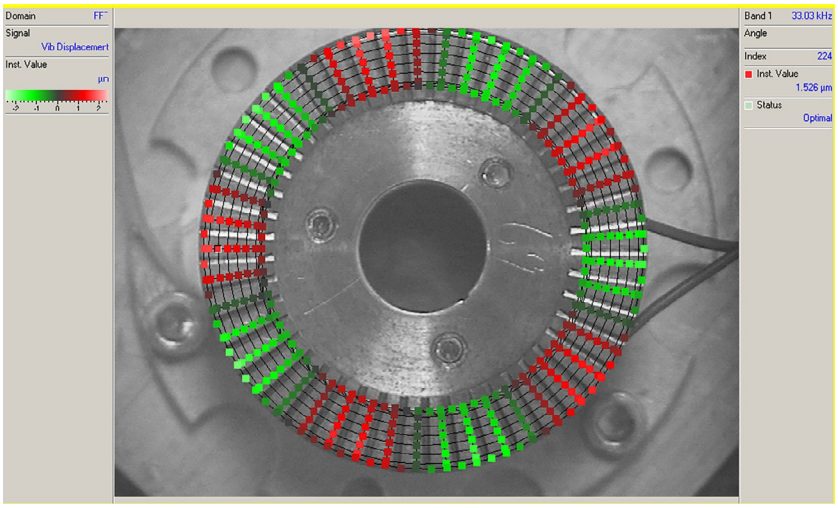


FIGURE 22.3 Mode nephogram of TRUM-30 (using a laser Doppler vibrometer, NUAA).

In addition to these 16 transducers, Curiosity carried additional transducers (Figure 22.6) to assist with the gravity-delivery of spoil into various instruments (Sherrit et al., 2009).

22.4 Ongoing research in power ultrasonics for space

Many of the research activities surrounding power ultrasonics and space are related to subsurface exploration. In this application, it is often vital to minimize power requirements as well as reacted torque and weight-on-bit. There are, broadly, three techniques involving granular materials, machining, and percussive techniques.

(1) Power ultrasonics in granular materials

Ultrasonic techniques have been proposed to fluidize granular materials, reducing power requirements under ideal circumstances (Firstbrook et al., 2017), as well as reducing both penetration forces (Firstbrook et al., 2017)



FIGURE 22.4 Ultrasonic motors used on Chang'e 3 and 4 detectors (NUAA).

and auger drag (Firstbrook et al., 2018a). Granular materials can be difficult to penetrate. A finger pressed into sand will meet impenetrable resistance after a few centimeters, and yet, the application of power ultrasonics (or lower-frequency vibration, provided that the relative acceleration is high enough) can make the same quasi-solid material behave like a quasi-liquid.

To consider mechanism underlying this change of state, we should note that granular materials already satisfy some informal criteria for "liquidity." They will fill a container but without true hydrostatic and distributed internal pressures. They can also maintain internal shear stresses and hence form enduring surface features. Like mayonnaise, they can appear solid at low stresses but as viscous fluids at higher stresses. The transition is more complex; however, because in mayonnaise (a Bingham plastic) transition occurs at an absolute yield stress, but in granular media, the breakdown (unjamming) is friction based (Reynolds, 1885) and influenced by pressure and particle shape (Staron et al., 2013).

If a granular material is fluidized, perhaps by applied vibration, it will remain unjammed at all times. The illusion of liquidity grows stronger because surface features collapse and flow structures appear, but nonstandard behaviors remain: for example, a shear rate applied at one location can affect the apparent viscosity at another (Woodcock and Mason, 1987). This is possible because, in quasi-solid scenarios, stable chains of relatively few contacting particles form dendritic patterns to transmit force into the far-field (Peters et al., 2005). With fluidization, the grains lose their permanent contacts (Vardoulakis, 2004) and the load-bearing mechanism breaks down. Experiments have shown that bodies in fluidized granular media float according to their relative density, which suggests that the yield stress is reduced to zero (Nichol and van Hecke, 2012) and that near-classical local viscosity can be recreated.

For penetration purposes, a viscous quasi-fluid is more attractive than a near-impenetrable quasi-solid, but ultrasonically-induced bulk fluidization is perhaps not practical in an exploration context. That said, sonicated penetrators and augers can create local fluidization in a thin boundary layer surrounding the device. This localized approach works, it is conjectured, by disrupting the dendritic force chains at the sonotrode interface.

However, if unjamming is affected by pressure and particle shape, we can also expect differing results in the local boundary layer case. So it proves: even under sonication, penetration forces are a strong function of the initial packing density, the material type, and the depth achieved (Firstbrook, 2017). While some of these effects are derived from the traditional understanding of unjamming, the extent to which the thin boundary layer can be understood using vibration-based granular viscosity tools, such as granular temperature (Seguin et al., 2011), remains a topic of exploratory research.

(2) Power ultrasonics in ultrasonically assisted drilling

Well-known ultrasonically assisted machining techniques have also been applied to ultrasonic drilling, creating ultrasonically-assisted drill bits that can penetrate rock at reduced weight-on-bit (Dassow et al., 2020). Ultrasonically assisted drilling is a technique by which a cutting bit is caused to vibrate at ultrasonic frequencies while in service, with or without a cutting fluid (Abdelkawy et al., 2016). The vibration used can be either longitudinal or longitudinal-torsional, superimposed on the rotation of the bit (Paktinat and Amini, 2018), and a key model of the technique holds that the vibration must be of sufficient intensity that the transition from conventional drilling (CD) to

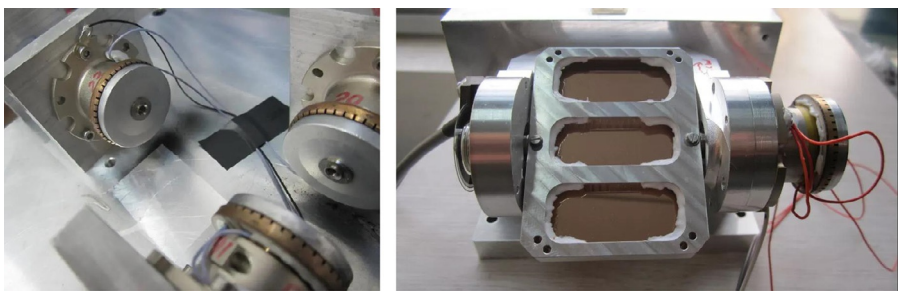


FIGURE 22.5 Ultrasonic motors used on Chang'e 5 detectors (NUAA).

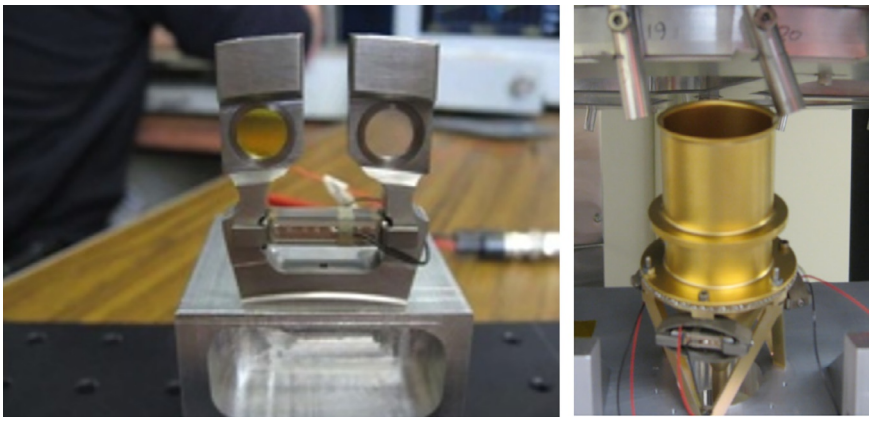


FIGURE 22.6 Curiosity rover. Piezoelectric transducer is used to agitate the contents of two circular sample cells (left) and a flextensional transducer is used to agitate a sample receiving funnel (right) (NASA, SPIE).

ultrasonically-assisted drilling (UAD) is made (Mikhailova et al., 2018). This transition is sometimes considered to occur at the point where the ultrasonic movement first permits the tool to disengage and reengage with each ultrasonic cycle.

The UAD technique can improve hole quality, reduce the mechanical demands, and lead to operations that have a lower specific power consumption (Firstbrook et al., 2018b). There is some evidence that UAD can result in a smoother drill campaign, so that features in the target are more strongly revealed in the feedback from the transducer (Dassow et al., 2020). This feedback can be of scientific value, as it can be used to detect salts inside the rock.

Finally, UAD has some potential in spoil extraction as well as in the cutting process itself. This is increasingly important at depth, where the energy expended in augering can exceed the energy expended in cutting. Spoil is often seen to be violently ejected from UAD holes at the near-surface, but at depth, the reduction in scroll friction will become especially significant. Given that the operating speed of an auger is a function of scroll friction (Zacny and Cooper, 2007), there is a possibility that the required speed may be reduced as well. This is an interesting area of research, given that maintaining auger speed under load is often a challenging requirement in exploration scenarios.

(3) Power ultrasonics and the ultrasonic-percussive technique

Finally, power ultrasonic behavior can be used to excite oscillatory behavior in another free-mass immediately below the sonotrode, concentrating the vibrational energy into fewer, but more intensive and more chaotic blows that are well-suited to drilling to shallow depths in a range of materials (Bar-Cohen et al., 2007). Depending on the mode shape selected, it is possible to induce rotation in the free-mass, which can be used to rotate the cutting surface and hence prevent imprintation of the tool into the rock (Sherrit et al., 2012). The impulse associated with the converted ultrasonic-percussive blows appears to cross mechanical interfaces relatively easily (Timoney, 2019), so ultrasonic-percussive devices can be combined with robotic systems that can assemble and disassemble drill-strings, and even cache samples of drilled materials in analogue environments (Worrall et al., 2018).

The ultrasonic-percussive technique uses ultrasonic vibration to excite chaotic behavior in a free-mass, which is then transferred to the cutting bit. Initially developed at the Jet Propulsion Laboratory, optimization efforts have improved the design of the device via modifications to the horn (with folded horns reducing length (Chang et al., 2005)), free-mass (with the insertion of keys to transfer rotation (Sherrit et al., 2012)), transducer (with mass-optimization for better dynamic performance (Li et al., 2018)), and supporting architecture (producing devices such as the Gopher (Bar-Cohen et al., 2018)). This technique is notably elegant, with the part count (or at least the assembly count) being driven down by the elimination of motors, moving or rotating parts, and even mechanical springs where replacement by magnets is possible.

The concept has shown penetration to a depth of 2 m in limestone (Bar-Cohen et al., 2012), and robotic operations have demonstrated that it is compatible with multi-bit robotic drillstring assembly and sample caching operations (Worrall et al., 2018). However, the applications can be wider-ranging: securing the steps of legged exploration vehicles (Badescu et al., 2005), or medical applications (Li et al., 2015), are among the use cases that have been considered.

22.5 Conclusion

Power ultrasonics, or its allied hardware, have already been deployed to the moon and Mars. Robust applications such as ultrasonic motoring have been exploited, as have interactions with granular materials. Research continues on how

power ultrasonics may be used for drilling applications, in harder materials, in the future.

References

Abdelkawy, A., Hossam, M., El-Hofy, H., 2016. Modelling of ultrasonic-assisted drilling: a review. In: The 2016 International Conference on Machining, Materials and Mechanical Technologies, Matsue, Japan.

Badescu, M., et al., 2005. Adapting the ultrasonic/sonic driller/corer for walking/climbing robotic applications. In: Proceedings of the SPIE Smart Structures Conference San Diego, CA. SPIE Vol. 5764-37.

Bar-Cohen, Y., Sherrit, S., Bao, X., Badescu, M., Aldrich, J., Chang, Z., 2007. Subsurface sampler and sensors platform – using the ultrasonic/sonic driller/corer (USDC). In: Paper #6529-18, Proceedings of the, SPIE Smart Structures and Materials Symposium, San Diego, USA.

Bar-Cohen, Y., et al., 2012. In: Deep drilling and sampling via the wireline Auto-Gopher driven by piezoelectric percussive actuator and EM rotary motor. Proceedings of the SPIE Smart Structures and Materials/NDE Symposium, San Diego, USA.

Bar-Cohen, Y., et al., 2018. Auto-Gopher-2—an autonomous wireline rotary piezo-percussive deep drilling mechanism. In: Earth and Space: Engineering for Extreme Environments, Cleveland, USA.

Chang, Z., Sherrit, S., Badescu, M., Bao, X., Bar-Cohen, Y., 2005. Design and analysis of ultrasonic actuator in consideration of length-reduction for a USDC (ultrasonic/sonic driller/corer). In: Proceedings of SPIE – The International Society for Optical Engineering., https://doi.org/10.1117/12.598851.

Dassow, J., Li, X., Lee, M.R., Young, M., Harkness, P., 2020. Ultrasonic drilling for the characterisation of building stones and salt induced decay. Ultrasonics 101, 106018.

Firstbrook, D., 2017. Ultrasonically Assisted Penetration Through Granular Materials for Planetary Exploration. PhD Thesis, University of Glasgow.

Firstbrook, D., Worrall, K., Timoney, R., Suñol, F., Gao, Y., Harkness, P., 2017. An experimental study of ultrasonic vibration and the penetration of granular material. Proc. Royal Soc. A 473 (2198). (PhD thesis) Available at: https://theses.gla.ac.uk/8256/1/2017FirstbrookPhD.pdf.

Firstbrook, D., Flessa, T., Worrall, K., McGookin, E., Harkness, P., Thomson, D., 2018a. Ultrasonic auger for narrow-gauge borehole drilling. In: IEEE International Ultrasonics Symposium (IUS 2018), Kobe, Japan.

Firstbrook, D., Harkness, P., Li, X., Timoney, R., Worrall, K., 2018b. Ultrasonically-assisted penetration of granular and cemented materials. In: Badescu, V., Zacny, K. (Eds.), Outer Solar System. Springer, Cham, https://doi.org/10.1007/978-3-319-73845-1_7.

Harkness, P., Lucas, M., 2012. A brief overview of space applications for ultrasonics. Ultrasonics 52, 975–979.

He, Z., Li, C., Xu, R., Lv, G., Yuan, L., Wang, J., 2019. Spectrometers based on acousto-optic tunable filters for in-situ lunar surface measurement. J. Appl. Remote. Sens. 13 (2), 027502.

Li, L., Mathieson, A., Lucas, M., 2015. A miniature surgical drill using ultrasonic/sonic frequency vibration. Phys. Procedia 70, 14–17.

Li, X., Lucas, M., Harkness, P., 2018. Full and half-wavelength ultrasonic percussive drills. IEEE Trans. Ultrason. Ferroelectr. Freq. Control 65 (11), 2150–2159.

Mikhailova, N., et al., 2018. Ultrasonically assisted drilling in marble. J. Sound Vib. 460, 114880.

Nichol, K., van Hecke, M., 2012. Flow induced agitations create a granular fluid: effective viscosity and fluctuations. Phys. Rev. E 85, 061309.

Paktinat, H., Amini, S., 2018. Numerical and experimental studies of longitudinal and longitudinal-torsional vibrations in drilling of AISI 1045. Int. J. Adv. Manuf. Technol. 94, 2577–2592.

Peters, J., et al., 2005. Characterization of force chains in granular material. Phys. Rev. E 72, 041307.

Reynolds, O., 1885. On the dilatancy of media composed of rigid particles in contact. Lond. Edinb. Dublin Philos. Mag. J. Sci. 20 (127), 469–481.

Seguin, A., et al., 2011. Dense granular flow around a penetrating object: experiment and hydrodynamic model. Phys. Rev. Lett. 107, 048001.

Sherrit, S., Frankovich, K., Bao, X., Tucker, C., 2009. Miniature piezoelectric shaker mechanism for autonomous distribution of unconsolidated sample to instrument cells. In: Proceedings of the SPIE 16th International Symposium on Smart Structures and Materials, San Diego, USA. Proceedings of SPIE 7290, 72900H.

Sherrit, S., Domm, L., Bao, X., Bar-Cohen, Y., Chang, Z., Badescu, M., 2012. Single piezo-actuator rotary-hammering (SPaRH) drill. In: Sensors and Smart Structures Technologies for Civil, Mechanical, and Aerospace Systems, Proceedings 8345, 83452B.

Staron, L., et al., 2013. Scaling laws for the slumping of a Bingham plastic fluid. J. Rheol. 57, 1265.

Timoney, R., 2019. Enabling Technologies for the Subsurface Exploration of the Solar System. University of Glasgow, p. 70. PhD Thesis.

Vardoulakis, I., 2004. Fluidisation in artesian flow conditions: hydromechanically stable granular media. Geotech 54 (2), 117–130.

Woodcock, C.R., Mason, J.S., 1987. Bulk Solids Handling. Springer.

Worrall, K., Timoney, R., Li, X., Harkness, P., Lucas, M., 2018. UPCD: field trial results and further work. In: Earth and Space: Engineering for Extreme Environments, Cleveland, USA.

Zacny, K., Cooper, G., 2007. Methods for cuttings removal from holes drilled on Mars. Mars 3, 42–56.

Zhao, C., 2011. Ultrasonic Motors: Technologies and Applications. Springer Science & Business Media.

Chapter 23

Ultrasonic surgical devices and procedures

M.E. Schafer[a] and R. Cleary[b,*]

[a]Drexel University, Philadelphia, PA, United States, [b]James Watt School of Engineering, University of Glasgow, Glasgow, United Kingdom

23.1 Introduction

Power ultrasound devices are ubiquitous in medicine and used in millions of surgical procedures a year. This chapter introduces the various applications of ultrasonic transducers and surgical devices for medical therapy. This topic involves a unique combination of the engineering requirements of power ultrasound system design, as well as biological aspects such as tissue types, mechanisms of action, and unwanted bioeffects. The goal is to provide sufficient information for a basic understanding and a springboard to further investigation and study.

The chapter begins with a discussion of the device requirements and goals, including brief review of the historical development of ultrasonic surgical devices and a discussion of the tissue types to be addressed and some of the requirements for devices used in surgery. Section 23.3 reviews the general characteristics of ultrasonic surgical devices, including topology, modes of operations, types of end effectors, and other notable features. The next section presents a summary of the various methods of action that have been identified, as well as intended and unwanted biological effects. Sections 23.5 and 23.6 review the various devices in common use today, and the latter section briefly presents high-intensity focused ultrasound (HIFU) systems. The next section gives an overview of the regulations that govern the development and use of ultrasonic surgical devices. Finally, Section 23.8 describes potential future developments within the field.

23.2 Surgical device requirements and goals

23.2.1 Historical overview

The roots of ultrasound surgical devices can be traced back to the mid-1950s with the development of ultrasound tools for dentistry (Balamuth, 1963). At that time, various power ultrasound devices had been developed for nonmedical applications such as welding, soldering, cleaning, and drilling (Frederick, 1965; Graff, 1981). Following a product development trajectory that would be repeated many times over, the first dental experiments used a commercial ultrasonic impact grinder to drill extracted teeth. While the initial goal was a new approach to drilling teeth, the more successful application was a dental descaler. The Dentsply-Cavitron descaler became a standard part of dental practice (Balamuth, 1963), and derivatives of the same basic system are still in use today. It was found that the combination of ultrasonic vibration of a small tip, with irrigation flow to cool the tip and flush away waste material, provided a simple effective treatment of dental calculus. The system reduced operator fatigue by eliminating the need for heavy scraping and improved the patient experience by reducing pain and bleeding. This pattern of exchanging ultrasonic vibration for operator effort, with improved patient outcomes, will be repeated again and again.

The next major step for ultrasonic surgical devices occurred in the late 1960s when Kelman (1967) adapted a Cavitron unit to the problem of breaking up, or emulsifying, the lens of an eye, now known as phacoemulsification. With the combination of ultrasound energy at the vibrating tip, irrigation to cool and flush the surgical field, and aspiration to remove lens fragments, the entire procedure was transformed (Kelman, 1973, 2004). Cataract surgery is one of the most widely performed surgical procedure in the United States, with over 5 million conducted in 2022 with this number expected to increase. It is predicted that improvements in surgical techniques will see phaco-aspiration replace phaco-emulisifaction, making surgery safer and faster (iOR, 2021).

Building on the success of phacoemulsification, the next major step was to apply the same principles to soft tissue removal, specifically for neurosurgery for tumor excision. In the late 1970s, the Cavitron Ultrasonic Surgical Aspirator (CUSA) was introduced and quickly became standard of care for open surgical dissection and removal of unwanted tissues (Epstein, 1983; Flamm et al., 1978; Horowitz and Rader, 2001; Henzi et al., 2019). The CUSA and competitive neurosurgical products are used in over 200,000 surgical procedures a year.

All of these devices were designed to minimize tissue heating, to reduce pain for the patient or damage to nearby

*Updated author for the second edition.

Power Ultrasonics. https://doi.org/10.1016/B978-0-12-820254-8.00010-5
Copyright © 2023 Elsevier Ltd. All rights reserved.

tissues. In the late 1980s and early 1990s, ultrasonic technology was redirected again, this time to the problem of tissue cutting and coagulation (O'Daly et al., 2008). In this case, the vibrating tip was specifically used as a controlled heating source, similar to electrosurgical devices then commercially available (Koch et al., 2003). Devices such as the Harmonic Scalpel from Ethicon were developed and are still in use for surgical procedures of all types, especially minimally invasive or so-called laparoscopic surgeries (Amaral, 1994; Harrell et al., 2004; McCarus, 1996). Ultrasonic scalpels are now the gold standard instrument for many minimally invasive laparoscopic surgeries.

Another more recent development is the application of ultrasound technology to body contouring, again starting in the late 1980s and early 1990s. With this technology, ultrasound energy is applied via a solid or hollow rod (or cannula) and is used to break up fat deposits under the skin (Zocchi, 1993). The "emulsified" fat is then more easily extracted and can, in some circumstances, be reimplanted elsewhere in the body (Schafer et al., 2013; Zocchi et al., 2020). The advantages of modern ultrasonically assisted liposuction over traditional liposuction and prior energy-based technologies are improved safety and efficiency, reduced physician fatigue, and minimized postoperative patient bruising, bleeding, and pain, thus allowing for faster recovery (Schafer, 2020).

Commercial devices for osteotomies first emerged in the 2000s and have since been widely accepted as a viable alternative to conventional powered devices (Vercellotti et al., 2001). Those procedures involve an ultrasonically vibrating surgical tip directly applied to hard tissue to cut selectively and precisely. The advantages of ultrasonic bone cutting devices include minimal risk of soft tissue damage, cavitational effects, and excellent visibility due to reduced bleeding (Pan et al., 2012; Bejarano et al., 2016).

Thus, the history of power ultrasonic devices for surgical applications shows the continued progress of the technology, each time exploiting some previously used method or device for a new use. Additional historical information can be found in several references (Ensminger, 1988; Ensminger and Stulen, 2008; O'Daly et al., 2008). The next few sections detail the goals and requirements of some other surgical devices.

23.2.2 Target tissues

One way to categorize the requirements of the ultrasound system is to specify the nature of the tissues that will be targeted. Depending on the tissue, different mechanisms of action can be used to effect treatment. It is important for the designer, developer, or user to be familiar with these tissue types and realize the concomitant advantages and limitations of ultrasound technology.

23.2.2.1 Soft tissues

Ultrasound aspiration devices have been used successfully on soft tissues such as skin, muscle, pathologic tissues (tumors), and fat. These devices generally rely on nonthermal mechanisms to disrupt tissue structures and do not affect connective tissues, nerves, and blood vessels. This has been exploited to great advantage in applications such as tumor removal, where the ultrasonic aspirator spares the surrounding nonpathologic tissues and structures. Similarly, ultrasonic fat removal devices can be "tissue-selective" in that nerves, blood vessels, and connective tissue are unaffected while the fat is loosened for removal. Wire-based ultrasound devices for dissolving clots have been found to be very effective in clearing clot burdens without damaging blood vessel walls. These effects can be traced to very specific mechanisms of interaction with tissue (see Section 23.4).

Ultrasound cutting/coagulating systems use thermal energy to cause tissue disruption and are used successfully for both cutting connective tissue and especially sealing and coagulating blood vessels. By the proper application of heat and pressure (i.e., between the vibrating tip and a clamping mechanism), blood vessels can be compressed and coagulated, forming an "autologous clip" for sealing off vessels during surgery (Krugman et al., 2011; Ogawa et al., 2011). The temperature of 60–80°C is considerably lower than electro-diathermy where temperatures can reach 350–450°C. Ultrasonic cutting therefore results in less thermal trauma and damage to surrounding tissue (Singhal et al., 2018). Further well-documented advantages include reduced operative time, reduced blood loss, and improved patient outcomes (Foreman et al., 2009; Cannizzaro et al., 2016).

23.2.2.2 Hard tissues

Hard tissues such as bone, calculi, and cataracts also have been successfully treated, although the mechanism of action is generally different. Ultrasonic bone drilling and shaping rely on repetitive impact mechanics, just as the nonultrasound approaches do (Labanca et al., 2008; Mathieson et al., 2016). Calculi (kidney and ureteric stones) are fragmented using shock waves, by shock wave lithotripsy (SWL), through either wire or rigid cannula approaches (Brannen and Bush, 1985; Farrell, 1986; Ghorbani et al., 2016), with a combination of cavitation and impact.

The ultrasound mechanism of action can be "tuned" to the properties of the target tissue. Those that are subject to cavitation erosion, such as soft tissue, are best treated with probes or end effectors with sufficient radiating area to permit cavitation; cataracts of the lens of the eye also fall in this category. More resilient tissues, such as blood vessels and connective tissue, are less affected by cavitation and better treated using frictional energy to create heat. More

brittle tissues, such as bone, are best addressed using direct impact or cavitation. These different tissue characteristics have been referred to as "impact toughness."

23.2.3 Surgical requirements

Many of the requirements for an ultrasonic surgical tool are common to any electrical device used in surgery, such as electrical safety, mechanical reliability, and the biocompatibility of parts that contact the patient, as documented in various international regulations and standards. Two specific requirements uniquely affect the design of ultrasound surgical equipment. First is the handpiece; the ability of the surgeon to manipulate the handpiece within the surgical field is often the key to the success of a product or surgical application. At the same time, the handpiece must generate enough vibrational energy to function effectively. This is a fundamental design trade-off. Some early handpieces were so heavy that an articulated support arm was required (Kelman, 2004). Handpieces have been designed in two styles: either a round cylinder or a gun style. The former is typical of phacoemulsification, tissue aspiration, and direct-contact ablation (tissue destruction), whereas the latter is more common for tissue coagulation, especially in laparoscopic instruments.

A second unique requirement for ultrasound surgical equipment is the need for sterilization. This typically involves pressurized steam autoclaves, with temperatures up to 250°C for 30 min or 270°C for 4–7 min for so-called flash sterilization. This puts constraints on material selection, especially for the piezoelectric ceramic elements, which can be affected by excessive temperatures. Other handpiece materials, such as plastics and metals, must also be chosen to survive the sterilization process. Some devices are designed with a presterilized, disposable tip element that is attached to a disinfected, but not sterile, main body. In this case, other forms of sterilization, such as electron beam, gamma radiation, or ethylene dioxide methods, can be used by the manufacturer. Other combinations of disposable and reusable components are possible depending on the exact design requirements.

23.3 General device design

23.3.1 Resonance as the fundamental design concept

A fundamental design requirement of ultrasonic surgical instruments is that they operate at or near a mechanical resonance. Resonance enables the device to have maximum possible excursion at the operative end while requiring the minimum external energy input. Thus, the entire structure is designed around the half-wave resonant condition. Careful design maximizes the desired resonant mode while minimizing the effects of any unwanted resonances.

Standing-wave resonance implies that there are both nodes (regions of maximum vibration excursion) and antinodes (regions of minimum vibration excursion) spaced at wavelength intervals along the entire active structure. The locations of minimum vibration excursion are also the locations of maximum stress, which are often the locations of mechanical failure caused by metal fatigue. The designer uses these locations strategically to, for instance, provide for gripping of or mounting the transmission rod or, alternatively, damping out unwanted vibrations (e.g., Davidson et al., 1994; Estabrook et al., 1994, 1999). The nodes and antinodes shift position as a function of sound speed in the material, which is typically temperature-dependent. Therefore, devices that operate under changing load or temperature require a control method to track the resonance frequency and stabilize the ultrasound system. Another factor that must be considered is the lot-to-lot variation in material properties; both piezoceramics and titanium are known to have such variations.

23.3.2 Key components: Generator, transducer, horn, probe, and wire

The key components of an ultrasonic surgical device are a generator of electrical energy; a transducer, which converts electrical energy into mechanical motion (typically includes piezoelectric material and metal back and front masses); a coupler or horn, which conveys or amplifies the mechanical motion; and a probe or wire, which conducts the mechanical motion to the tissue (Figure 23.1). There are, naturally, other

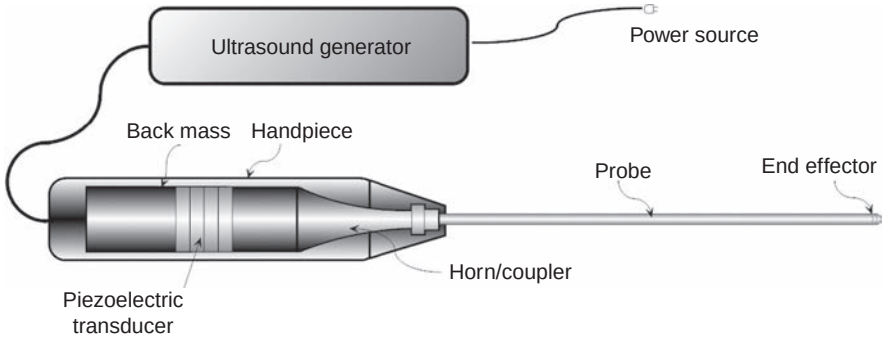


FIGURE 23.1 Components of an ultrasonic surgical system.

components, such as a control mechanism (foot pedal, hand switch, knobs, user interface) and a handpiece of some sort for the operator to grasp and manipulate the device.

23.3.2.1 Generator

The generator must supply sufficient power to operate the device, drive the transducer at or near its resonance frequency for optimal operation, track and maintain that optimal frequency as the transducer characteristics change (with changes in load or temperature, for instance, Chen Ying et al., 2006), and control either voltage or current to control the amplitude of the operating tip.

At its simplest, the generator can be a variable gain amplifier in which the transducer is the resonant element within a feedback loop, automatically setting the operating frequency to the resonant frequency of the transducer. At that frequency, the transducer has its minimum impedance and operates such that the current into the transducer is proportional to the amplitude of vibration. This operating condition is well described in the literature on ultrasonic resonators (Ensminger, 1988; Mason, 1948, 1958). Using a current sensor to control amplifier gain, it is then possible to create a constant current and thereby a constant amplitude system (Neppiras, 1971; Van der Burgt, 1963). This approach, while simple, has drawbacks in terms of the range of control it affords and the flexibility to operate different types of transducers. For instance, some transducer designs are best operated slightly off their minimum impedance frequency, which is not possible using this approach. Further, this approach takes some time to initially "lock" onto the resonant frequency, and therefore, it cannot be used to operate the transducer in a pulsatile manner with rapid on/off sequences.

Ultrasonic generators often employ a phase-locked loop (PLL) approach to maintain the desired operating frequency and stabilize the vibrational amplitude (Kuang et al., 2014). The PLL enables the generator to track any shifts in the resonance frequency and has a wide frequency range over which it can operate transducers. Modern PLL designs use direct digital frequency synthesis, allowing for more sophisticated drive schemes and offering flexibility for other applications.

23.3.2.2 Transducer

The transducer converts the electrical signal from the generator into mechanical motion and is the heart of the system. For a bolted Langevin transducer (BLT), a stack of ring-shaped piezoelectric ceramic elements is sandwiched between a rear loading mass and a front mass/coupler. The piezoelectric material is chosen to provide high electromechanical coupling and low loss (e.g., Berlincourt, 1971; Berlincourt et al., 1964). The "stack," as it is called, is held in compression using a bolt through the center of the ring elements. This precompression is required to avoid operating the piezoceramic elements in tension, which can lead to cracking and element failure (Brickman, 1962; Miller, 1963). Figure 23.2 shows an example of a typical transducer stack in a surgical device.



FIGURE 23.2 Typical transducer stack in a surgical device, including the back mass, piezoelectric elements, and coupler/horn, and transmission element. Note the support arrangement at the nodal position. A transmission rod screws on at the left.

23.3.2.3 Coupler/horn

This portion of the system is between the transducer and the end effector in contact with the tissue. In some instances, the coupler has a tapered diameter, creating an ultrasonic horn; this acts as a mechanical amplifier to increase the vibration amplitude from the transducer. There are a number of different possible tapers (linear, exponential, etc.), and the theory behind the horn design is well established (Ensminger, 1988; Frederick, 1965). In other cases, a coupler is used to convert, for instance, longitudinal vibration into torsional vibration (Tsujino et al., 2000; Al-Budairi et al., 2013) or into transverse motion (Stepanenko and Minchenya, 2010). The coupler often is designed to have a support at the vibration node, so that the entire assembly can be held in the handpiece shell in a way that does not transfer ultrasonic energy. In some cases, the coupler may include several cascaded amplification sections, called boosters, to achieve a desired level of excursion at the operative end of the device.

23.3.2.4 Transmission element/probe/wire

The transmission element, typically a rod-like structure, provides a conduit for the ultrasonic vibrations from the coupler to the end effector. It is often referred to as the probe (which can cause confusion because the same term is also applied to an ultrasonic imaging transducer). As an example, laparoscopic ultrasound surgical devices require lengthy transmission rods to keep the surgeon's hand well outside the immediate surgical area. The transmission rod can be solid or hollow, depending on the clinical requirements; in cataract removal, for example, the phaco needle serves as a hollow transmission element.

The diameter of the transmission rod is also an important design consideration. Obviously, in the case of phacoemulsification, the diameter of the phaco needle is a controlling factor in the size of the incision required. Smaller incisions are better for the patient, improving healing and recovery

time. There is a practical lower limit on phaco needle diameter because the cataract materials are aspirated through the needle, and too small an inner diameter leads to clogging. In devices intended for cutting tissue and sealing blood vessels, the transmission rod can be fairly substantial, with diameters of 3 mm or more. The diameter affects the column strength of the rod and thereby greatly influences whether unwanted vibration modes occur (see Section 23.3.3). Scaling down, wires have been used as transmission elements, allowing ultrasonic vibrational energy to be conducted down curving and even tortuous paths through the ureter or blood vessels.

The transmission element is typically made from a titanium alloy, specifically titanium with 6% aluminum and 4% vanadium, which can withstand the stresses caused by ultrasonic wave energy. Because the overall structure is designed to be mechanically resonant, the length of the transmission rod is an integer number of half wavelengths at the resonant frequency of operation ($n\lambda/2$). The transmission element is usually designed to attach to the coupler at an antinode location.

23.3.2.5 End effector

The end effector is designed to efficiently transfer the ultrasonic motion of the transducer/coupler/transmission element to the tissue. Depending on the desired clinical effect and the intended mechanism of action, the end effector can have a variety of shapes and sizes, ranging from simple flat or ball ends to hooks or curved cutting blades. The end effector requires careful design because any asymmetry (with respect to the longitudinal axis) will create unwanted lateral vibrations that must be either counterbalanced or damped. Without compensation, the concentration of stress from the induced lateral vibration often leads to premature failure and breakage. Some instruments for dental and bone-cutting applications exploit asymmetries to produce larger effective motions of the end effector.

In some applications, the intended effect is caused by the interaction of the end effector and a clamp arm, which closes on it, trapping tissue in-between them (see Figure 23.3). The relative motion of the end effector and the clamping surface then cause friction within the tissue, leading to heating and cutting. This type of device is among the most widely used of all ultrasonic surgical instruments because it allows for both cutting and effective coagulation of blood vessels, obviating the need for scalpels and suturing.

Wire-type devices have been designed both with and without end effectors, such as ball end tips. Tips can also provide a radiographic locator, allowing the end of the wire to be seen more easily on radiographic imaging. Of course, the effect of such a mass at the end of a vibrating wire must be accounted for in the design. Some simple devices have no separate end effector, and the end of the device is just the end of the transmission element, either a wire or a thin rod.



FIGURE 23.3 Typical clamp arm and end effector in the open and closed positions.

23.3.3 Modes of operation

23.3.3.1 Longitudinal

One of the most useful aspects of power ultrasound technology is that it can be applied in several different vibrational modes, which can be tailored to specific surgical needs. The most common vibrational mode is longitudinal, in which the probe moves in and out along its long axis. This approach is the oldest, is therefore well understood from a design perspective, and is used for most tissue coagulation and aspiration systems. Because the motion is simple, it has the advantage that a simplified mechanical model (Krimholtz et al., 1970; Mason, 1948, 1958) can be successfully used.

The typical range of motion at the tip of a longitudinally vibrating device is on the order of 50–200 μm, with operating frequencies between 21 and 65 kHz. Obviously, higher excursions require more energy input into the device. In addition, the maximum velocity of the tip (the product of the excursion and the frequency) is an indicator of the maximum stress within the transmission rod. Therefore, the higher-frequency systems typically have a lower maximum excursion. The tip velocity, multiplied by the area of the tip perpendicular to the direction of motion, is called the volume velocity. This, in turn, is the primary determinant of the acoustic source strength Q. The acoustic source strength is a reasonable first-order metric of comparison between systems operating at different frequencies,

velocities, and geometries. As will be discussed later in "Mechanisms of Action," source strength can be shown to relate to cavitation and ultimately to the cutting effectiveness of many styles of ultrasonic surgical devices.

The longitudinal mode of motion also is used as a springboard for other motions: by modifying the end effector to make it nonaxisymmetric, the tip can move in other directions. The most well-known of these modified tips is the Kelman phacoemulsification tip, which is essentially a bent needle probe. The bending amplifies the end motion, increasing the cutting effectiveness. Other modified tips include so-called curved blade ultrasonic scalpels (e.g., Estabrook et al., 1994) as well as the dental and bone-cutting devices mentioned earlier.

23.3.3.2 Torsional

The torsional mode of vibration involves motion that twists or "rolls" relative to the axis of the probe. One way to create this motion is by using a modified coupler between the transducer and the transmission element, as shown in Figure 23.4. Such tools achieve a combined longitudinal-torsional motion through mode degeneration, where geometric modifications (such as diagonal slits or helical cuts) of the front mass and/or horn manipulate the wave path (Al-Budairi et al., 2013; Cleary et al., 2022).

Torsional motion generally provides cutting utility only if the tip is bent or shaped to provide some surface perpendicular to the torsional motion. The cutting effectiveness of torsional systems is still controlled by the same fundamental principles of volume velocity (area multiplied by perpendicular velocity) as longitudinal systems, although there can be more flexibility in the design of the torsional end effectors. Care must be taken, however, to account for unwanted stress concentrations that can develop in torsional systems.



FIGURE 23.4 Transducer stack with torsional coupler element.

23.3.3.3 Lateral and ellipsoidal

By segmenting the piezoelectric stack elements and operating them out of phase, a side-to-side tip motion can be created. This mode can either be run singly or in combination with longitudinal motion to create an ellipsoidal tip motion. The advantage of this approach is that it combines the attributes of both longitudinal and lateral motions, increasing cutting aggressiveness. An ultrasonic aspirator for cartilage removal proposed by Zhang et al. (2021) generates an ellipsoidal vibration by coupling two bending vibrations perpendicular to the long axis.

23.3.3.4 Compound motions

Several devices use nominally longitudinal motion from the transducer and transmission means but, because of the shape of the end effector, produce compound motions. The motion can be amplified by a secondary mechanical resonance of the end effector. This approach is used in bone-cutting and dental devices (Sections 23.3.4 and 23.4.2).

23.3.3.5 Wire transverse

A unique device that exploits the tendency of an ultrasonically driven thin wire to "buckle" and creates a transverse mode was created. This approach was used in a device by Rabiner et al. (2003) (described later in Section 23.5.3). It was found that if the wire was properly tapered, the longitudinal vibration would excite a transverse mode in the wire at one-half the longitudinal resonance frequency. The transverse mode is much less susceptible to energy loss when the wire is bent; in addition, it creates an extended zone of mechanical action at the tip region.

23.3.3.6 Unwanted modes

While manipulation of tip motion can result in improved effectiveness, most often it is more important to focus on the suppression of unwanted modes. A good deal of effort has been undertaken to describe and prevent these modes (e.g., Estabrook et al., 1999; Mathieson et al., 2016), which generally lead to unwanted stress concentrations and heating and early failure, especially in slender horns and tips. The flexibility afforded by unique end effectors must be balanced (literally) by accounting for the impact of non-longitudinal vibration on the probe design.

23.3.4 End effectors

Because the end effector is the portion of the system in direct contact with tissue, a good deal of effort is focused on their design. The design process includes accounting for issues such as size, shape (symmetry), contact area, and intended mechanism of action.

23.3.4.1 Solid end effectors

The most common design is the most straightforward: a solid, rotationally symmetrical tip, which thus minimizes the creation of nonlongitudinal motion. This style encompasses bare tip designs adapted for tissue emulsification as well as solid elements used with clamps for tissue cutting and coagulation (Figure 23.3). This is also the style used for externally applied tissue disrupters (Section 23.5.1) as well as external noncontact devices (Section 23.5.5). The tips can be flat-faced, rounded, or bullet-nosed and can have circumferential ridges or rings at intervals from the end. Surgical devices that use clamps can have cross sections that are circular, square, rectangular, or some combination thereof (Davidson et al., 1994).

23.3.4.2 Hollow end effectors

When the goal is to aspirate tissue that has been ultrasonically disrupted, then the end effector (and the transmission element) is naturally hollow. One common form is an ultrasonically vibrated needle used for phacoemulsification, where, as noted earlier, the emulsified cataract material is aspirated from the eye once it is disrupted. General ultrasonic surgical aspiration systems use larger cannulas (Section 23.5.1).

It is also of interest to note that the central open channel of the end effector is generally continued back through the transmission element and then back through the transducer assembly. The back of the transducer assembly ends with a metal tube that is then connected to a vacuum source and tissue collection system. This approach complicates the design of the compression bolt assembly through the piezoceramic stack but produces a streamlined handpiece design. There are alternate approaches in which the aspiration tube is brought out to the side of the transmission element assembly (at a nodal location) and then back along the outside of the handpiece assembly.

In some cases, rather than being used for aspiration, the central opening of the cannula is used to infuse fluid that is nebulized or cavitated by ultrasonic motion of the tip. The fluid also is used to cool the device.

23.3.4.3 Wires

It is sometimes the case clinically where the tissue of interest is not directly accessible and must be reached via blood vessels or other duct(s) within the body. Examples include the destruction of blood clots within the veins or kidney stones within the renal system. In this case, the transmission element is a flexible wire or a thin, semiflexible rod (Gavin et al., 2007). As noted earlier, it can be difficult to transmit longitudinal ultrasonic energy down a wire that encounters curves and bends (as happens within veins and arteries). Bending causes the ultrasonic vibrational energy to couple out of the wire and into the surrounding tissue, which can lead to unwanted heating or other destructive effects. The wire can also operate in nonlongitudinal modes, further reducing the transmission of the desired longitudinal motion. Bends can also create an unwanted acoustical termination point along the wire, changing the resonant frequency and the damping conditions. This can affect the ability of the generator to maintain the proper frequency tracking, causing the entire system to drop out of a proper resonant condition. One technique to combat this issue is enclosing the wire in a tight-fitting plastic sheath that constricts its motion (Aliger, 1993; Vaitekunas et al., 2009).

23.3.4.4 Bends and shapes

The most interesting designs involve the various bent and shaped tips, each designed with a specific clinical purpose. They range from the simple bent tip of a dental descaler (one of the first ultrasonic surgical instruments) to intricate designs for bone cutting and sculpting (examples can be seen on various manufacturers' websites). One purpose of these bent shapes is to provide a final mechanical amplifier, converting limited longitudinal motion along the axis of the handpiece into a larger motion of the active tip. This is done by creating a second resonant system comprising the bent portion and the tip itself. The typical amplification factor is between 2 and 5.

Even simple tissue-cutting tools have slightly bent or formed shapes to enhance either ultrasonic or surgical performance. As noted earlier, if the end effector introduces asymmetries, it can introduce additional vibrational modes or characteristics that must be accounted for. These nonlongitudinal modes can be controlled by introducing "balancing asymmetries" elsewhere in the structure. Some end effectors are specifically designed to promote nonlongitudinal motion and thereby create some other desired surgical effect (e.g., Cimino, 2003). Above all, the potential for unwanted stress concentrations, which can lead to premature failure, must be fully determined as part of the design process.

23.3.5 Ancillary concerns

23.3.5.1 Irrigation and aspiration

Aspiration (vacuum-assisted movement of fluid or tissue) is clearly a necessity if the device is designed for the destruction and removal of tissue, and this is usually accomplished by suction applied via a central open channel through the end effector (and transmission element). Irrigation (introduction of fluid) is typically supplied via a flute or other concentric tube or catheter structure, depending on the exact application.

Nowhere is the issue of irrigation and aspiration during ultrasonic surgery more complicated than in phacoemulsification. With the surgical tip inserted into the eye via a

close-fitting wound, the eye becomes a closed fluid-filled chamber, and the relative inflow and outflow through the tip can either over- or underinflate the front portion of the eye where the cataract is located. During surgery, the phaco tip or aspiration tubing may be temporarily blocked with a lens fragment, and when the fragment finally is dislodged, there can be a sudden unwanted overaspiration (called "surge"). Note that this issue of fragments also is affected by the internal construction of the ultrasonic system. As the fragment passes through the vibrating needle, there are internal locations where vibration concentrations can cause cavitation, which erodes the fragment and helps reduce the incidence of clogging and surge.

23.3.5.2 Physician interaction

Ultimately, decisions regarding which ultrasonic surgical system to use and how it is to be applied rest with the surgeon. Careful design that takes into account human factors is important in terms of surgical effectiveness, operator fatigue, and ultimately, patient safety. The handpiece must be of a size and weight that allows for easy handling and manipulation. The irrigation and aspiration tubing must be simple to attach and must be "out-of-the-way." For clamp and cutter systems, the system must adapt to the laparoscopic approach being used, and the handle that closes the clamping mechanism must provide tactile feedback but must not be too difficult to close. Even the design of the control mechanism, which can be as simple as a trigger switch or as complicated as a multiposition foot pedal, with every foot motion creating a different device response, affects the ultimate acceptability of the final system.

23.4 Mechanisms of action

One of the most powerful aspects of ultrasound technology is that it can produce a wide range of clinical effects depending upon the choice of frequency, amplitude, mode of vibration, and end effector. The various mechanisms of action can be combined and/or tailored to meet specific clinical requirements.

23.4.1 Cavitation

Cavitation is the term given to the action of gas bubbles in fluids; the science of cavitation is the subject of entire books (e.g., Young, 1989; Franc and Michel, 2006; Brennan, 1995), so only a few highlights are given here. Cavitation is the key mechanism of action for many ultrasonic surgical devices, and evidence that cavitation is necessary for the efficient operation of phacoemulsification and similar devices has accumulated. Thus, understanding the different types of cavitation, and the circumstances under which ultrasound can create, sustain, and destroy bubbles, is fundamental to ultrasonic surgical instrument design.

23.4.1.1 Cavitation nuclei and rectified diffusion

At atmospheric pressure and temperature, water contains billions of microscopic air bubbles or cavitation nuclei. These are unavoidable because air diffuses into water until it reaches an equilibrium saturation point. This is also the case for any water-based fluid that has not been specifically degassed. Thus saline (salt water) solutions used during surgery contain dissolved gas (air) and cavitation nuclei. These microbubbles are in equilibrium with the gasses dissolved in the fluid, and gas continually diffuses into and out of the bubbles in equal amounts.

When cavitation nuclei are exposed to sinusoidal ultrasound waves of sufficient pressure amplitude, they naturally expand and contract with the rarefactional (negative) and compressional (positive) pressure cycles. When the bubbles are expanded, slightly more gas diffuses into them because of their larger surface area. However, when the bubbles are compressed, slightly less gas diffuses out because of the reduced surface area. With each pressure cycle, the bubbles grow in size; this process is called rectified diffusion (Crum, 1984; Crum and Hansen, 1982; Lewin and Bjørnø, 1981). Figure 23.5 illustrates this process.

Eventually, the bubbles reach a resonant size, which is determined by the physical properties of the fluid (surface tension, viscosity, and density) and the frequency of the applied ultrasound. For water-based fluids, the resonant bubble radius (in meters) is given by $R_r \approx 3.28/f_r$, where f_r is the ultrasound frequency (in Hertz) (Young, 1989, p. 49). At resonance, the bubble expands and contracts vigorously with the fluctuations in ultrasound pressure. At this point, there are two possible outcomes: either the bubble collapses violently or it breaks apart more gently. The former situation is called transient or inertial cavitation, and the latter is called stable cavitation.

23.4.1.2 Transient cavitation

In this case, the bubble collapses into a very small volume, creating extremely high focal pressures and temperatures exceeding 5000°C (Suslick, 1990). If there is nothing in the immediate vicinity of the bubble, the collapse is radially symmetric, and the bubble implosion creates a shock wave (Suslick and Flannigan, 2008). If there is a hard boundary within a few radii of the bubble during collapse, the collapse is asymmetric and causes a high-speed jet of fluid that has sufficient force to affect even metal surfaces (Brennan, 1995). The shock wave can destroy, or as a minimum erode, matter ranging from micro- and nanoparticles up to soft (cellular structure) and hard (bone, calculi) tissues and organs (Brujan and Vogel, 2006; Perra et al., 2021). This

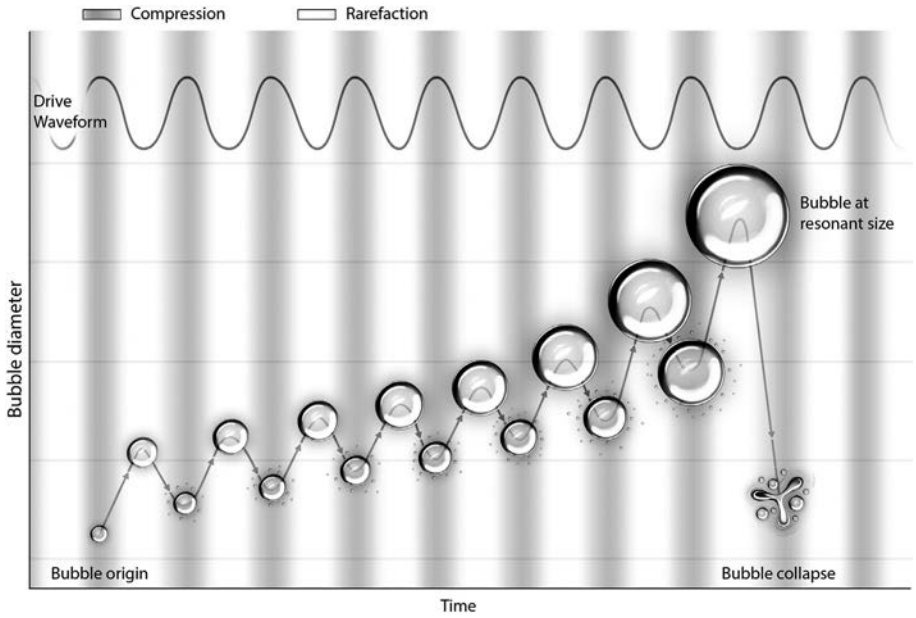


FIGURE 23.5 Illustration of the rectified diffusion process. *(Illustration by Travis Vermilye.)*

is the mechanism by which end effectors become eroded with use and the mechanism for efficient tissue emulsification. Experiments in which transient cavitation was suppressed (using high hydrostatic overpressure) have shown that cutting efficiency is directly related to transient cavitation. It should be noted that transient cavitation can also be created by exposure to very high levels of rarefactional pressure, such as those produced by extracorporeal shock wave lithotripsy systems and some cosmetic surgical devices (Brown et al., 2009; Zhong et al., 1999).

23.4.1.3 Stable cavitation

The other fate of resonantly vibrating bubbles is that they simply break apart before collapsing. In this case, the bubble fragments are then available to start the rectified diffusion process anew. One feature of stable cavitation is the large cyclic pulsations at resonance that cause large shear forces in the region around the bubble. These shear forces act on soft tissue as well and can either disrupt or merely dislodge cells from their tissue matrix. This is the approach of the tissue-preserving device discussed in Section 23.5.4. Another effect of the shear forces is to change the permeability of cell walls, allowing for increased cellular activity (see Section 23.4.4).

23.4.2 Direct impact

The most commonly quoted mechanism of action for many ultrasonic devices is so-called jackhammer effect, in which the end effector directly impacts the tissue. Upon closer examination, however, the analogy is not completely correct. In a true jackhammer, a sliding weight is propelled toward a chisel-type end effector, and the full kinetic energy of the weight (one-half mass multiplied by velocity squared) is transferred through the chisel to the target. However, the end effector of an ultrasonic surgical device, operating in longitudinal mode, vibrates with a sinusoidal motion. As such, at the exact moment of "impact" (when the tip is at its maximum forward displacement), the velocity is actually zero. This is not to say that there is no impact effect, just that one must be careful when ascribing analogies. The tip is at a maximal velocity when it is at the zero displacement, or midpoint, of its total excursion. These velocities can be quite high, on the order of several kilometers per hour, so considerable force can be exerted. The motion of an ultrasonically vibrating end effector also produces high shear forces in the fluid around the tip region, and these in and of themselves can be sufficient to disrupt tissue. The impact and shear forces are independent of the exact motion and can occur for not only longitudinal motion but also torsional and ellipsoidal.

Some devices also have cutting surfaces, most notably those for bone surgery (see Sections 23.3.4 and 23.5.1). The surfaces are disposed such that the ultrasonic vibration produces a sawing motion. The blade may be either serrated or flat, depending on the application.

23.4.3 Thermal

While in many instances thermal energy is to be avoided (such as in phacoemulsification), other devices are specifically designed to heat tissue to the point of denaturation (biochemical alteration or breakdown). The end effector

is typically designed to provide a laterally moving surface placed against tissue, which at ultrasonic frequencies and excursions provides a relative velocity on the order of several meters per second. This creates significant thermal energy. The other factors involved include the coefficient of friction, the force (normal to the vibration direction) applied between the tissue and the end effector, and the contact surface area. If the surgical device includes a clamping mechanism, then the force is controlled by the operator or the system design. The temperature of the tissue can increase quickly, and within a few seconds, the tissue is completely denatured and cut. For those instances where the goal is to cut and coagulate blood vessels, specific clamping pressures have been found to provide an optimal vessel seal (Houser and Noschang, 2012). Other devices for interstitial (within tissue) heating using ultrasound also have been described (Diederich et al., 1999).

23.4.4 Acoustic energy, acoustic streaming, and radiation force

The most easily quantified and measured source of energy, which has been well predicted by theory, is acoustic energy. Acoustic energy is caused by the vibrational movement right at the tip.

23.4.4.1 Acoustic pressure and power

The total acoustic power output can be expressed as a function of the vibrational frequency, the displacement (half of the total excursion), and the cross-sectional area of the tip. The acoustic power can be expressed as (International Electrotechnical Commission, 1998; Schafer and Broadwin, 1994)

$$P = \frac{\rho c k^2 Q_s^2}{8\pi}$$

where ρ is the density of the medium, c is the sound speed of the medium, k is the acoustic wavenumber ($2\pi/\lambda$ or $2\pi f/c$), and Q is the acoustic source strength (radiating area multiplied by the normal surface velocity). The normal surface velocity is expressed as $2\pi f\delta$, where δ is the tip displacement. Therefore, the source strength is $2\pi f\delta A$, where A is the radiating area. Substituting all terms into the above equation results in an expression for acoustic power strictly in terms of basic tip dimensions, the operating frequency, and the displacement at the tip:

$$P = \frac{2\pi^3 \rho f^4 A^2 \delta^2}{c}$$

As an example, assume a phacoemulsification system uses a 19-gage needle operating at 38 kHz, with a displacement of 25 μm. The calculations would look like

$\mathrm{OD} = 0.001067\,\mathrm{m}$
$\mathrm{ID} = 0.000914\,\mathrm{m}$
$\mathrm{Area} = 0.237 \times 10^6\,\mathrm{m}^2\ (\pi*[\{\mathrm{OD}\}^2 - \{\mathrm{ID}\}^2]/4)$
$\rho = 1000\,\mathrm{kg/m}^3$
$c = 1500\,\mathrm{m/s}$
$f = 38{,}000$
$\delta = 0.000025\,\mathrm{m}$

$$P = 2*\pi^3 1000*38{,}000^4*\left(0.237 \times 10^{-6}\right)^2*0.000025^2/1500$$
$$= 0.003\,\mathrm{W\ or\ 3\,mW}$$

23.4.4.2 Acoustic radiation force and streaming

A propagating ultrasonic wave creates a net force on the medium through which it travels, called the acoustic radiation force (Beyer, 1976; Chu and Apfel, 1982). This force can be used to calibrate the output of ultrasonic devices using a radiation force balance (International Electrotechnical Commission, 2013; Rooney, 1973), although this technique has limited utility at the frequencies used for ultrasonic surgery. In the tissue, the radiation force can exert an influence on cellular structures, and this has been used for diagnostic purposes (Nightingale et al., 1995) and was considered as a mechanism for cellular stimulation (Dyson, 1982). This force acting on fluids can produce a flow that is often called acoustic streaming, causing, for instance, fluid motion in a cyst (closed bladder-like sac within tissue) as an aid to diagnosis (Nightingale et al., 1995) or should be avoided during ultrasonic power measurements using radiation force techniques (International Electrotechnical Commission, 2013).

As noted earlier, the immediate volume around an ultrasonic source is subject to high shear forces. Some wire devices, as described below, also have a low-frequency whipping motion that is sometimes called "macromotion" because of its relative scale (millimeters rather than microns); this macromotion also causes shear effects. Similar shear-induced fluid flows can also occur around end effectors or transmission rods (Schafer, 2004). Confusingly, this flow also has been referred to as acoustic streaming. When a traveling ultrasonic wave interacts with a small particle or cell, it can create similar shear forces but on a much smaller scale (Lewin, 1982; Nyborg, 1965). This "micromotion" or "microshear" force can act on cells in the tissue through which the wave propagates (Starritt et al., 1989).

23.4.5 Nebulization

If sufficiently intense ultrasound energy is directed upward from within a liquid bath toward the air-liquid interface, acoustic atomization is created (Ensminger, 1988). This is the principle behind ultrasonic humidifiers and personal nebulizers. When a liquid, such as water or saline, is applied to an ultrasonically vibrating surface, the atomized liquid

sprays off as a mist (Parks, 1970). This is sometimes used as a means to indicate what parts of an ultrasonic system are vibrating, where the vibration antinodes are located, or where unwanted (e.g., transverse) vibrations are occurring. It often occurs during ultrasonic surgery when the vibrating element touches a pool of liquid in the surgical field. One product specifically uses nebulization to deliver a spray of saline to a tissue bed (see Section 23.5.5).

23.5 Device types

This section provides a brief review of some of the ultrasonic surgical devices that are currently (or recently) on the market. While not totally comprehensive, it does provide enough of a survey of the field to indicate the wide application of the technology and the resultant surgical benefits.

23.5.1 Aspiration devices: Open surgery

23.5.1.1 The CUSA and derivative devices

The CUSA (Epstein, 1983; Flamm et al., 1978; Jallo, 2001; Ulmer, 1993) is considered the original surgical device for tissue removal during open surgery. It has been used for countless surgeries since its initial introduction in 1977 as the NS100. Its important features include relatively large but powerful magnetostrictive handpieces and long end effectors (up to 30 cm) with large center bores for rapid tissue removal. It operates at both 23 and 36 kHz; the lower frequency is used for debulking, and the higher frequency is used for more delicate surgeries. Work by Schafer (Schafer and Broadwin, 1994) using the CUSA helped to establish standards for comparing devices of different frequencies and geometries (International Electrotechnical Commission, 1998). These devices are used for neurosurgery, gynecology, and other general surgery applications. There are now both a new generation of this product as well as several competitors. The CUSA EXcel with the same dual fixed vibrational frequencies can provide adjustable vibrational amplitude between 0 and 355 μm. This, alongside an electrocautery function, provides flexibility in multistage surgical procedures which require a combination of dissection, resection, and hemostasis maneuvers.

23.5.1.2 Contact debridement

A product type that is derived from the basic ultrasonic surgical aspirator uses a solid probe for contact debridement, which is the removal of foreign matter or dead tissue from open wound beds. A wound treatment solution is applied to the wound area, and the energized tip is brought into contact with the necrotic (dead tissue) margins. The ultrasonic energy (25–30 kHz) causes a contact emulsification process that is especially effective in removing dead tissue. The tip is typically either solid with a rounded front, or there can be a small central port through which additional fluid is introduced. It is reported that there is less patient discomfort from this treatment than standard mechanical or surgical debridement, perhaps because of some interaction between the ultrasound and the surrounding nervous tissues (Downs et al., 2018). Studies of contact ultrasonic wound debridement have found that wound healing is promoted by a significant reduction in bacterial load and suppression of bacterial growth (Novak et al., 2011; Lázaro-Martínez et al., 2018; Mori et al., 2019). Further studies into the treatment of chronic wounds through ultrasonic debridement are needed as the relevant literature remains sparse.

23.5.1.3 Phacoemulsification devices

As noted in the historical review, phaco devices are among the oldest examples of ultrasonic surgical instruments. There are several notable manufacturers, such as AMO, Alcon, and Bauch & Lomb, and while all share the same basic design, each system has different technological attributes such as "torsional" mode, "hyperpulse" (Kadziauskas et al., 2010), and various mechanisms for irrigation and aspiration control. The demonstrated key to efficient phacoemulsification is cavitation; experiments in which cavitation is suppressed (by using high static pressures in a hyperbaric chamber) showed reduced cutting effectiveness. Figure 23.6 shows the difference in cutting at atmospheric and at +6 atmospheres of overpressure. In another experiment, cutting effectiveness was measured as a function of tip geometry, excursion, and mode (linear vs torsional). The cutting force data were compared with acoustic measurements of the onset and extent of cavitation around the tip. The results showed that the cutting rate paralleled the amount of cavitation that occurred (see Figure 23.7). Other work (Arbisser, 2004; Schafer, 2004; Schafer and Arbisser, 2004) has shown that the acoustic output quantities can be used to quantify device characteristics, correlating well to clinical experience with different types of cataracts.

23.5.1.4 Bone cutting

Ultrasonic bone cutting devices achieve precise, safe, and selective cutting of mineralized tissue. The approach used for bone cutting was described earlier and involves modifying the end effector to have an amplified sawing or impacting motion. These devices are extensively used in maxillofacial, neural, spinal, and plastic surgeries with a wide range of tips available to suit the procedure. Other uses include drilling and cutting bone in orthopedics and removing bone cement from within the bone cavity when an artificial joint is replaced.

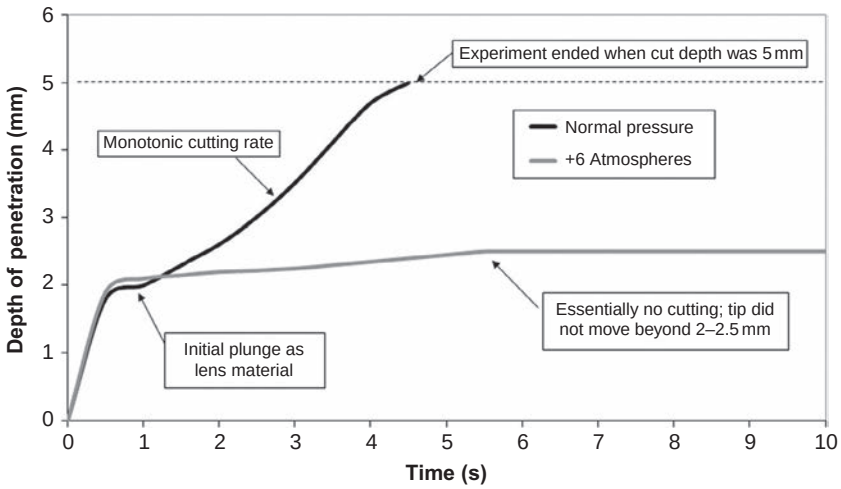


FIGURE 23.6 Results of cutting experiment conducted at atmospheric and +6 atmospheres. Note the lack of cutting/penetration when overpressure suppressed cavitation.

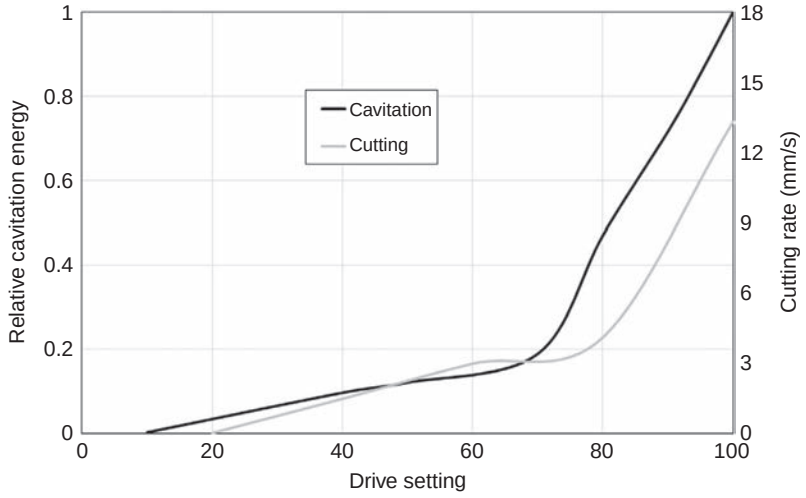


FIGURE 23.7 Comparison of cutting rate (right-hand scale) and relative cavitation activity (left-hand scale).

23.5.2 Cutting/coagulation devices: The harmonic scalpel and derivative devices

The harmonic scalpel and related products are currently used in more than 80% of laparoscopic surgeries involving tissue cutting and coagulation. The combination of heat (produced by friction with the vibrating end effector), pressure (from a tissue-clamping arm), and time (on the order of 5 s) can very effectively seal blood vessels (Houser and Noschang, 2012). This obviates the need for the traditional approach of clamping, cutting, and suturing or stapling, thus saving significant time during surgery (Krugman et al., 2011). The global market for this product class is predicted to grow, although adaption to more minimally invasive and robotic surgeries is required.

23.5.3 Remote disruptive devices

There are several devices where the "action" takes place quite remote from the transducer and generator using long transmission rods or wires. One notable example is the Cyberwand, which is used for the destruction of the kidney or bladder stones through a small incision (Kim et al., 2007). This particular technology uses a second free-floating, hollow shaft around the transmission rod, which creates a secondary jackhammer effect. The combination of the small excursion, ultrasonically driven inner shaft and the large excursion, low-frequency jackhammer shaft creates a very effective comminution effect (Pugh and Canales, 2010). Advances of this technology, such as the Uretron, offer enhanced control of the probe vibration and improved stone fragmenting and evacuation

of all types of stone from the urinary tract (Borofsky et al., 2015).

Another commercial device of this type uses a long wire to break up thrombi (blood clots) within the circulatory system. Originally released by Omnisonics, the system used a tapered titanium wire inserted into a vein and advanced to the point of the thrombus. The longitudinal ultrasound motion from the generator is converted into a controlled lateral motion (Rabiner et al., 2003), creating a combination of cavitation and strong shear forces in a region near the tip. Sonothrombolysis is an emerging modality gaining popularity in the past 10 years, particularly with the use of microbubbles. The microbubbles bind to the thrombus and when erupted cause more effective and localized fragmentation (Sitta and Howard, 2021).

23.5.4 Tissue-preserving devices

Many of the devices described in this section are designed to disrupt tissue for removal or to destroy it in place. The VASER, an ultrasonic-assisted liposuction (UAL) system, was designed to disrupt adipose (fat) tissue while specifically maintaining cellular viability during extraction (Schafer et al., 2013). Because of its relatively high frequency (36.6 kHz) and low excursion levels (<75 μm), the adipose tissue that is removed is viable and available for reimplantation elsewhere in the patient for reconstructive or cosmetic purposes (Fisher et al., 2013). There are other ultrasonic liposuction devices on the market, but they have been direct derivatives of more aggressive CUSA-type designs and therefore have not demonstrated the same level of cellular viability. The VASER system is the surviving UAL system in service today (Jewell, 2020), and is also used in combination with excisional body contouring procedures such as lipoabdominoplasties (Hoyos et al., 2018).

23.5.5 Externally applied devices

There are several devices that are applied externally for the purposes of wound debridement, such as those from Misonix (www.misonix.com) and Söring (www.soering.com). As described earlier, the cavitation that is generated at the end effector preferentially emulsifies necrotic (dead) tissue, and the ultrasound energy seems to suppress the patient's sensation of pain. Another device has been designed to not even touch the patient: the MIST Therapy System from Celleration (www.celleration.com) uses ultrasound to create a debriding fluid spray and to expose the tissue to ultrasound energy. It has been shown to accelerate wound healing (Bell and Cavorsi, 2008), even though the actual ultrasound levels present in the wound are quite low because of the impedance mismatch between air and tissue.

23.5.6 Focused ultrasound devices: High-intensity focused ultrasound

Although Chapter 25 deals specifically with HIFU devices (or high-intensity therapeutic ultrasound devices), it is appropriate to have some mention of them here because they do constitute an ultrasonic surgical application. By focusing ultrasound energy to a sufficiently high level of intensity, heat and cavitation action can occur to thermally denature and disrupt tissue.

The technology has been widely applied to cancers (Al-Bataineh et al., 2012; Gelet et al., 1996; Madersbacher et al., 1995), and other applications include benign prostatic hypertrophy (enlarged prostate) (Sanghvi et al., 1999), uterine fibroids (Hesley et al., 2013; Ji et al., 2017), and other conditions (e.g., Evans et al., 2007; Zimmer et al., 1995). Some experimental devices can completely cut through the liver tissue from outside the patient, allowing for a partial liver resection before the patient's skin is opened surgically (N'Djin et al., 2011).

Some of the devices are now available commercially from manufacturers such as Sonacare Medical (sonacaremedical.com), Hiafu (haifumedical.com), InSightec (www.insightec.com), and others. HIFU systems also are being used for cosmetic purposes: for brow lifts (ulthera.com) and fat disruption (liposonix.com and syneron-candela.com/int/product/ultrashape). HIFU treatment has also been enabled by precise targeting and follow-up techniques available due to advancements in modern diagnostic ultrasound scanning and magnetic resonance imaging (MRI).

23.5.7 Miniaturization of ultrasonic devices

Improved postoperative recovery and decreased length of hospital stay are two of many advantages offered by minimally invasive surgery. These advantages are driving adaptations and innovations of ultrasonic surgical technologies. Laparoscopic ultrasonic shears offer minimally invasive tissue cutting and vessel sealing; however, the long waveguide has restrictive mobility at the surgical site. There is an opportunity to integrate miniature ultrasonic devices with surgical robots to enable more minimally invasive surgeries to be carried out with ultrasonic surgical tips. However, miniaturization presents challenges in delivering the required ultrasonic vibrational modality of the surgical tip. The design of the device must balance trade-offs between the transducer size, volume of ceramic, resonance frequency, and the achievable displacement amplitude (Li et al., 2021a,b).

23.6 Medical device regulations

All devices intended to diagnose or treat humans are subject to regulations that ensure that the device is safe and effective

during use. In the United States, the Food and Drug Administration issues guideline documents for manufacturers seeking clearance or approval for each specific type of medical equipment. The Food and Drug Administration also recognizes both domestic and international "consensus" standards.

In Europe, the parallel system has been recently updated. The European Union Medical Device Regulations (EU MDR) has fully superseded its predecessor the Medical Device Directive. To commercialize medical devices in the European Union, a CE Mark certificate is needed which verifies that a device meets all regulatory requirements detailed in the MDR, implementing a Quality Management System (QMS) in accordance.

23.6.1 General requirements

The general requirements for medical devices include basic electrical, mechanical, electromagnetic, and thermal safety, and are encompassed in the IEC 60601 series of standards. The most basic standard, to which all medical devices must adhere, is the IEC 60601-1. There are also collateral standards covering areas such as electromagnetic compatibility, usability, alarms, and home healthcare, which may or may not apply to a given device.

23.6.2 IEC standards pertaining to ultrasonic surgical devices

For ultrasonic surgical instruments, there are several IEC particular safety standards, as well as supporting technical standards. One such technical standard is IEC 61847 (International Electrotechnical Commission, 1998), which describes methods for determining the vibration amplitude and acoustic output from aspirators and phacoemulsification devices. It thus provides a basis for comparison among systems in terms of radiated energy. This standard is currently under revision, principally to better address devices with nonlongitudinal motion (e.g., Section 23.3.3.3). One safety standard also specifically addresses phacoemulsification equipment (International Electrotechnical Commission, 2014). The IEC has numerous technical committees and working groups: Technical Committee 87 deals with ultrasonics and its Working Group 7 is specifically charged with standards for ultrasonic surgical and therapeutic instruments.

23.7 Future trends

Applications for ultrasonic surgical devices continue to expand, principally because of ultrasound's versatility as a tool for the manipulation of tissue. It is indeed fortunate that human tissue is amenable as a transmission medium; it is also fortunate that ultrasound has wavelengths (from centimeters down to millimeters) that correspond to tissues of interest, from whole organs down to cells. Finally, ultrasound's range of mechanisms of action provides a ready source for new applications. This section touches on only a few of the possibilities.

One unique opportunity with ultrasound is "theragnostics," or the combination of a diagnostic and a therapeutic application. Because ultrasound is well known as a diagnostic modality, combining this capability with a therapeutic purpose is only a matter of acoustic intensity or frequency. Systems that provide ultrasound imaging as a guidance tool for surgical applications will become available, for instance, using color Doppler to locate internal bleeding and then using HIFU capabilities to cauterize and stanch the bleeding. While this noninvasive approach is relatively straightforward, other more esoteric possibilities exist. For instance, the tip of an ultrasound surgical instrument may be used to determine tissue characteristics and then automatically adjust the vibration excursion to emulsify unwanted tumors while sparing adjacent healthy tissue.

Several areas that are now in the research phase show promise for entirely new treatment opportunities. For instance, sonoporation involves using ultrasound to change the permeability of cells or skin to allow for transdermal delivery of drugs that otherwise would be too big to pass through the dermis. The pores and intercellular spaces in the dermis are temporarily opened via cavitation and thermal effects (Deng et al., 2004; Postema and Gilja, 2007; Park et al., 2014). In addition, acoustic radiation force can be used to push drugs through skin. Combining these ultrasound effects improves the overall drug delivery capability (Smith, 2007). An emerging technology adjacent to this field is the application of noninvasive transcranial MR-guided focused ultrasound enabling a transient opening in the blood-brain barrier to access brain tumor and peritumoral tissue (Mainprize et al., 2019).

Ultrasound has recently been shown to have a neuromodulating effect, permitting remote excitation or suppression of neural signals with focused ultrasound (Bystritsky et al., 2011; Yoo et al., 2011; Schafer et al., 2021). Also, recent studies involving a nonhuman primate model of epilepsy demonstrated the use of low intensity pulsed ultrasound stimulation for treatment (Lin et al., 2020).

Surgical robots, such as the da Vinci Surgical System, represent a rapidly evolving technology for full or partial automation (Ng and Tam, 2014). Ultrasonic shears have been deployed in the da Vinci surgical robot, allowing robotically assisted laparoscopic ultrasonic surgery for soft tissue cutting and vessel sealing. The careful integration of the ultrasonic modalities described in this chapter with robotics could be transformative, offering high levels of precision, dexterity, and repeatability.

An alternative approach to the incorporation of ultrasonic surgical devices in surgical robots is via device miniaturization, so that the whole ultrasonic device and surgical tip can act as the end effector of the robot arm and can pass through the trocar. This requires a move away from

conventional Langevin configurations (Li et al., 2021a,b) and opens a new field of research in miniaturized ultrasonic surgical devices. Research has been reported, for example, which modifies the folded horn structure (Cleary et al., 2021). New designs are being proposed that are based on flextensional transducer configurations (Bejarano et al., 2016), and transducers incorporating piezoelectric tubes (Li et al., 2021a,b) and single crystal piezoelectric material (Fenu et al., 2020). The use of 3D printing of the transducer and surgical tip metal components is also being investigated as an enabler for miniaturizing ultrasonic surgical device configurations (Cleary et al., 2021).

23.8 Sources of further information and advice

There are a number of resources available that can provide the interested reader with further information and guidance. Several international organizations deal directly or partly with ultrasonic surgical systems, most notably the Ultrasonic Industry Association (www.ultrasonics.org), which holds a yearly symposium. Another relevant group is the Ultrasonics, Ferroelectrics and Frequency Control Society within the Institute of Electrical and Electronic Engineers (www.ieee-uffc.org), which also holds a yearly symposium on all aspects of ultrasonic technology and publishes a peer-reviewed journal. Other meetings of note are the Semi-annual International Congress on Ultrasonics (www.icultrasonics.org) as well as various medical meetings that have a significant surgical component that involves ultrasonic devices (cataract surgery, for instance). The major engineering journals involving ultrasonic surgical devices include the previously mentioned *IEEE Transactions on Ultrasonics, Ferroelectrics, and Frequency Control*, *Ultrasonics in Medicine and Biology*, as well as *Ultrasonics*.

There are several seminal books available, including those by Ensminger (1988) and Graff (1981). Because of the intense commercial competition in this area, one of the best sources of information is the patent literature. A search that starts with any of the patents cited in the reference section would quickly yield a wealth of background material as well as practical design information.

Acknowledgment

The author acknowledges Travis Vermilye for creating Figure 23.5 in this chapter and for granting permission to use it.

References

Al-Bataineh, O., Jenne, J., Huber, P., 2012. Clinical and future applications of high intensity focused ultrasound in cancer. Cancer Treat. Rev. 38 (5), 346–353.

Al-Budairi, H., Lucas, M., Harkness, P., 2013. A design approach for longitudinal–torsional ultrasonic transducers. Sensors Actuators A Phys. 198, 99–106.

Aliger, H., 1993. Ultrasonic Device Having Wire Sheath. US Patent 5,248,296 (Sonic Needle Corp).

Amaral, J., 1994. The experimental development of an ultrasonically activated scalpel for laparoscopic use. Surg. Laparosc. Endosc. 4 (2), 92–99.

Arbisser, L., 2004. A quantitative comparison of ultrasonic metrics required during cataract surgery. Clin. Surg. Ophthalmol. 22 (10), 300–302.

Balamuth, L., 1963. Ultrasonics and dentistry. Sound 2 (2), 15. https://doi.org/10.1121/1.2369595.

Bejarano, F., Feeney, A., Wallace, R., Simpson, H., Lucas, M., 2016. An ultrasonic orthopaedic surgical device based on a cymbal transducer. Ultrasonics 72, 24–33.

Bell, A., Cavorsi, J., 2008. Noncontact ultrasound therapy for adjunctive treatment of nonhealing wounds: retrospective analysis. Phys. Ther. 88, 1517–1528.

Berlincourt, D., 1971. Piezoelectric crystals and ceramics. In: Mattiat, O.E. (Ed.), Ultrasonic Transducer Materials. Plenum Press, New York (Chapter 2).

Berlincourt, D., Curran, D., Jaffe, H., 1964. Piezoelectric and piezomagnetic material and their function in transducers. In: Mason, W.P. (Ed.), Physical Acoustics—Principles and Methods. vol. 1-Part A. Academic Press, New York, pp. 169–270 (Chapter 3).

Beyer, R., 1976. Radiation pressure—the history of mislabeled tensor. J. Acoust. Soc. Am. 60, S21. https://doi.org/10.1121/1.2003222.

Borofsky, M., El Tayeb, M., Paonessa, J., Lingeman, J., 2015. Initial experience and comparative efficacy of the UreTron: a new intracorporeal ultrasonic lithotripter. Urology 85 (6), 1279–1283.

Brannen, G., Bush, W., 1985. Percutaneous ultrasonic versus surgical removal of kidney stones. Surg. Gynecol. Obstet. 161 (5), 473–478.

Brennan, C.E, 1995. Cavitation and Bubble Dynamics. Oxford University Press, New York.

Brickman, A., 1962. Preloading of acoustic transducer for high pressure operations. J. Acoust. Soc. Am. 34 (3), 305–311.

Brown, S., Greenbaum, L., Shtukmaster, S., Zadok, Y., Ben-Ezra, S., Kushkuley, L., 2009. Characterization of nonthermal focused ultrasound for noninvasive selective fat cell disruption (lysis): technical and preclinical assessment. Plast. Reconstr. Surg. 124 (1), 92–101.

Brujan, E.-A., Vogel, A., 2006. Stress wave emission and cavitation bubble dynamics by nanosecond optical breakdown in a tissue phantom. J. Fluid Mechan. 558, 281–308.

Bystritsky, A., Korb, A., Douglas, P., Cohen, M., Melega, W., Mulgaonkar, A., DeSalles, A., Min, B.-K., Yoo, S., 2011. A review of low-intensity focused ultrasound pulsation. Brain Stimul. 4 (3), 125–136.

Cannizzaro, M., Borzì, L., Lo Bianco, S., Okatyeva, V., Cavallaro, A., Buffone, A., 2016. Comparison between Focus Harmonic scalpel and other hemostatic techniques in open thyroidectomy: a systematic review and meta-analysis. Head Neck 38 (10), 1571–1578.

Chen Ying, C., Zhou Zhaoying, Z., Zhang Ganghua, Z., 2006. Effects of different tissue loads on high power ultrasonic surgery scalpel. Ultrasound Med. Biol. 32 (3), 415–420.

Chu, B., Apfel, R., 1982. Acoustic radiation pressure produced by a beam of sound. J. Acoust. Soc. Am. 72 (6), 1673–1687.

Cimino, W., 2003. Ultrasonic Cutting and Coagulation Knife Using Transverse Vibrations. US Patent 6,585,745, Sound Surgical Technologies.

Cleary, R., Li, X., Lucas, M., 2021. Incorporating direct metal laser sintered complex shaped Ti-6Al-4V components in ultrasonic surgical devices. J. Acoust. Soc. Am. 150 (3), 2163–2173.

Cleary, R., Wallace, R., Simpson, H., Kontorinis, G., Lucas, M.A., 2022. A longitudinal-torsional mode ultrasonic needle for deep penetration into bone. Ultrasonics 124, 106756.

Crum, L., 1984. Rectified diffusion. Ultrasonics 22 (5), 215–223.

Crum, L., Hansen, G., 1982. Growth of air bubbles in tissue by rectified diffusion. Phys. Med. Biol. 27 (3), 413–417.

Davidson, T., DiMatteo, S., Smith, P., Whipple, G., 1994. Clamp Coagulator/Cutting System for Ultrasonic Surgical Instruments. US Patent 5,322,055, Ultracision.

Deng, C.X., Sieling, F., Pan, H., Cui, J., 2004. Ultrasound-induced cell membrane porosity. Ultrasound Med. Biol. 30 (4), 519–526.

Diederich, C., Nau, W., Stauffer, P., 1999. Ultrasound applicators for interstitial thermal coagulation. IEEE Trans. Ultrason. Ferroelectr. Freq. Control 46 (5), 1218–1228.

Downs, M.E., Lee, S.A., Yang, G., Kim, S., Wang, Q., Konofagou, E.E., 2018. Non-invasive peripheral nerve stimulation via focused ultrasound in vivo. Phys. Med. Biol. 63 (3), 035011. https://doi.org/10.1088/1361-6560/aa9fc2 (Published 2018 Jan 26).

Dyson, M., 1982. Non-thermal cellular effects of ultrasound. Br. J. Cancer 45, 165–171.

Ensminger, D., 1988. Ultrasonics: Fundamentals, Technology, Application, second ed. Marcel Dekker, New York, ISBN: 0-8247-7659-3.

Ensminger, D., Stulen, F., 2008. Ultrasonics. CRC Press, Boca Raton, FL, ISBN: 0-8247-5830-7.

Epstein, F., 1983. The Cavitron ultrasonic aspirator in tumor surgery. Clin. Neurosurg. 31, 497–505.

Estabrook, B., DiMatteo, S., Motta, L., Wright, J., 1994. Laparoscopic Ultrasonic Surgical Instrument and Methods for Manufacturing the Instruments. US Patent 5,346,502, Ultrascision.

Estabrook, B., DiMatteo, S., Smith, P., 1999. Damping Ultrasonic Transmission Components. US Patent 5,989,275, Ethicon Endo-Surgery.

Evans, K.D., Weiss, B., Knopp, M., 2007. High-intensity focused ultrasound (HIFU) for specific therapeutic treatments: a literature review. J. Diagn. Med. Sonog. 23, 319–327.

Farrell, J., 1986. Percutaneous ultrasound procedures for the treatment of kidney stones. Int. J. Technol. Assess. Health Care 2 (1), 152–161.

Fenu, N.G., Giles-Donovan, N., Li, X., Liang, Z., Chibli, A.H., Luo, H., Stock, C., Zhang, S., Lucas, M., Cochran, S., 2020. Progress towards the miniaturization of an ultrasonic scalpel for robotic endoscopic surgery using Mn:PIN-PMN-PT high performance piezocrystals. In: IEEE International Ultrasonics Symposium (IUS 2020)., https://doi.org/10.1109/IUS46767.2020.9251823.

Fisher, C., Grahovac, T., Schafer, M., Shippert, R., Marra, K., Rubin, J., 2013. Comparison of harvest and processing techniques for fat grafting and adipose stem cell isolation. Plast. Reconstr. Surg. 132 (2), 351–361.

Flamm, E., Ransohoff, J., Wuchinich, D., Broadwin, A., 1978. Preliminary experience with ultrasonic aspiration in neurosurgery. Neurosurgery 2 (3), 240–245.

Foreman, E., Aspinall, S., Bliss, R., Lennard, T., 2009. The use of the harmonic scalpel in thyroidectomy: 'beyond the learning curve'. Ann. R. Coll. Surg. Engl. 91 (3), 214–216.

Franc, J.P., Michel, J.M., 2006. Fundamentals of Cavitation. vol. 76 Springer Science & Business Media.

Frederick, J., 1965. Ultrasonic Engineering. John Wiley & Sons, New York.

Gavin, G., McGuinness, G., Dolan, F., Hashmi, M., 2007. Performance characteristics of a therapeutic ultrasound wire waveguide apparatus. Int. J. Mech. Sci. 49 (3), 298–305.

Gelet, A., Chapelon, J.-Y., Bouvier, R., Souchon, R., Pangaud, C., Abdelrahim, A., Cathignol, D., Dubernard, J., 1996. Treatment of prostate cancer with transrectal focused ultrasound: early clinical experience. Eur. Urol. 29 (2), 174–183.

Ghorbani, M., Oral, O., Ekici, S., Gozuacik, D., Koşar, A., 2016. Review on lithotripsy and cavitation in urinary stone therapy. IEEE Rev. Biomed. Eng. 9, 264–283.

Graff, K.F., 1981. A history of ultrasonics. In: Mason, W.P., Thurston, R.N. (Eds.), Physical Acoustics. vol. XV. Academic Press, New York (Chapter 1).

Harrell, A., Kercher, K., Heniford, B., 2004. Energy sources in laparoscopy. Semin. Laparosc. Surg. 11, 201–209.

Henzi, S., Krayenbühl, N., Bozinov, O., Regli, L., Stienen, M.N., 2019. Ultrasonic aspiration in neurosurgery: comparative analysis of complications and outcome for three commonly used models. Acta Neurochir. 161 (10), 2073–2082.

Hesley, G., Gorny, K., Woodrum, D., 2013. MR-guided focused ultrasound for the treatment of uterine fibroids. Cardiovasc. Interv. Radiol. 36, 5.

Horowitz, N., Rader, J., 2001. Role of the ultrasonic surgical aspirator in gynecology. Obstet. Gynecol. Clin. N. Am. 28 (4), 775–790.

Houser, K., Noschang, S., 2012. Ultrasonic Surgical Shears and Method for Sealing a Blood Vessel Using Same. US Patent 8,182,501, Ethicon Endo-Surgery.

Hoyos, A., Perez, M., Guarin, D., Montenegro, A., 2018. A report of 736 high-definition lipoabdominoplasties performed in conjunction with circumferential VASER liposuction. Plast. Reconstr. Surg. 142 (3), 662–675.

International Electrotechnical Commission, 1998. Ultrasonics—Surgical Systems—Measurement and Declaration of the Basic Output Characteristics. IEC 61847, first ed. IEC, Geneva.

International Electrotechnical Commission, 2013. Ultrasonics—Power Measurement—Radiation Force Balances and Performance Requirements. IEC 61161, third ed. IEC, Geneva.

International Electrotechnical Commission, 2014. Medical Electrical Equipment—Particular Requirements for the Basic Safety and Essential Performance of Lens Removal Devices and Vitrectomy Devices for Ophthalmic Surgery. IEC 60601-2-58, first ed. IEC, Geneva.

iOR, 2021. The Future of Cataract Surgery by Richard Lindstrom. Available from: https://iorpartners.com/the-future-of-cataract-surgery/. (Accessed 26 April 2020).

Jallo, G., 2001. CUSA EXcel ultrasonic aspiration system. Neurosurgery 48 (3), 695–697.

Jewell, M.L., 2020. Ultrasonic-assisted liposuction: introduction and historic perspectives. In: Ultrasound-Assisted Liposuction. Springer, Cham, pp. 3–8.

Ji, Y., Hu, K., Zhang, Y., Gu, L., Zhu, J., Zhu, L., Zhu, Y., Zhao, H., 2017. High-intensity focused ultrasound (HIFU) treatment for uterine fibroids: a meta-analysis. Arch. Gynecol. Obstet. 296 (6), 1181–1188.

Kadziauskas, K., Rockley, P., Schafer, M., 2010. System and Method for Pulsed Ultrasonic Power Delivery Employing Cavitational Effects. US Patent 7,842,005, Abbott Medical Optics.

Kelman, C., 1967. Phacoemulsification and aspiration: a new technical of cataract removal. A preliminary report. Am. J. Ophthalmol. 64 (1), 23–35.

Kelman, C., 1973. Phaco-emulsification and aspiration: 500 cases. Am J. Ophthalmol. 75, 764–768.

Kelman, C., 2004. History of Phacoemulsification. CRC Press, pp. 97–107.

Kim, S.C., Matlaga, B.R., Tinmouth, W.W., Kuo, R.L., Evan, A.P., McAteer, J.A., et al., 2007. In vitro assessment of a novel dual probe ultrasonic intracorporeal lithotriptor. J. Urol. 177, 1363–1365.

Koch, C., Friedrich, T., Metternich, F., Tannapfel, A., Reimann, H., Eichfeld, U., 2003. Determination of temperature elevation in tissue during the application of the harmonic scalpel. Ultrasound Med. Biol. 29 (2), 301–309.

Krimholtz, R., Leedom, D., Matthaei, G., 1970. New equivalent circuit for elementary piezoelectric transducers. Electron. Lett. 6, 398–399.

Krugman, K., Martin, K., Cosgriff, N., Slakey, D., 2011. In search of the autologous clip: a case for experimental standardization. J. Laparoendosc. Adv. Surg. Tech. A 21 (8), 721–728.

Kuang, Y., Jin, Y., Cochran, S., Huang, Z., 2014. Resonance tracking and vibration stablilization for high power ultrasonic transducers. Ultrasonics 54 (1), 187–194.

Labanca, M., Azzola, F., Vinci, R., Rodella, L., 2008. Piezoelectric surgery: twenty years of use. Br. J. Oral Maxillofac. Surg. 46 (4), 265–269.

Lázaro-Martínez, J.L., Álvaro-Afonso, F.J., García-Álvarez, Y., Molines-Barroso, R.J., García-Morales, E., Sevillano-Fernández, D., 2018. Ultrasound-assisted debridement of neuroischaemic diabetic foot ulcers, clinical and microbiological effects: a case series. J. Wound Care 27 (5), 278–286.

Lewin, P., 1982. Acoustic microstreaming by pulsed radiators. In: IEEE Ultrason. Symp, pp. 757–760.

Lewin, P., Bjørnø, L., 1981. Acoustic pressure amplitude thresholds for rectified diffusion in gaseous microbubbles in biological tissue. J. Acoust. Soc. Am. 69, 846–852.

Li, X., Stritch, T., Manley, K., Lucas, M., 2021a. Limits and opportunities for miniaturizing ultrasonic surgical devices based on a Langevin transducer. IEEE Trans. Ultrason. Ferroelectr. Freq. Control 68 (7), 2543–2553.

Li, X., Fenu, N.G., Cochran, S., Lucas, M., 2021b. Ultrasonic surgical devices driven by piezoelectric tubes. In: IEEE International Ultrasonic Symposium (IUS 2021), September 2021., https://doi.org/10.1109/IUS52206.2021.9593462.

Lin, Z., Meng, L., Zou, J., Zhou, W., Huang, X., Xue, S., Bian, T., Yuan, T., Niu, L., Guo, Y., Zheng, H., 2020. Non-invasive ultrasonic neuromodulation of neuronal excitability for treatment of epilepsy. Theranostics 10 (12), 5514.

Madersbacher, S., Pedevilla, M., Vingers, L., Susani, M., Marberger, M., 1995. Effect of high intensity focused ultrasound on human prostate cancer in vivo. Cancer Res. 55 (15), 3346–3351.

Mainprize, T., Lipsman, N., Huang, Y., Meng, Y., Bethune, A., Ironside, S., Heyn, C., Alkins, R., Trudeau, M., Sahgal, A., Perry, J., 2019. Blood-brain barrier opening in primary brain tumors with non-invasive MR-guided focused ultrasound: a clinical safety and feasibility study. Sci. Rep. 9 (1), 1–7.

Mason, W., 1948. Electromechanical Transducers and Wave Filters. Van Nostrand Co., Princeton, NJ.

Mason, W., 1958. Physical Acoustics and the Properties of Solids. Van Nostrand Co., Princeton, NJ.

Mathieson, A., Wallace, R., Cleary, R., Li, L., Simpson, H., Lucas, M., 2016. Ultrasonic needles for bone biopsy. IEEE Trans. Ultrason. Ferroelectr. Freq. Control 64 (2), 433–440.

McCarus, S.D., 1996. Physiologic mechanism of the ultrasonically activated scalpel. J. Am. Assoc. Gynecol. Laparosc. 3 (4), 601–608.

Miller, H., 1963. Origin of mechanical bias for transducers. J. Acoust. Soc. Am. 35 (9), 1455.

Mori, Y., Nakagami, G., Kitamura, A., Minematsu, T., Kinoshita, M., Suga, H., Kurita, M., Hayashi, C., Kawasaki, A., Sanada, H., 2019. Effectiveness of biofilm-based wound care system on wound healing in chronic wounds. Wound Repair Regen. 27 (5), 540–547.

N'Djin, W., Melodelima, D., Schenone, F., Rivoire, M., Chapelon, J.Y., 2011. Assisted hepatic resection using a toroidal HIFU device: an in vivo comparative study in pig. Med. Phys. 38 (4), 1769–1978.

Neppiras, E., 1971. Motional feed-back system for ultrasonic transducers. In: Ultrason Conference Papers, Surrey, England. IPC Science and Technology Press, Guildford, UK, pp. 56–58.

Ng, A., Tam, P., 2014. Current status of robot-assisted surgery. Hong Kong Med. J. 20 (3), 241–250.

Nightingale, K., Kornguth, P., Walker, W., McDermott, B., Trahey, G., 1995. A novel ultrasonic technique for differentiating cysts from solid lesions: preliminary results in the breast. Ultrasound Med. Biol. 21, 745–751.

Novak, T., Schafer, M., Manna, R., 2011. Ultrasonic Wound Treatment Method and Apparatus. US Patent 8,025,672, Misonix.

Nyborg, W., 1965. Acoustic streaming. In: Mason, W.P. (Ed.), Physical Acoustics, IIB. Academic Press, New York, pp. 265–331.

O'Daly, B., Morris, E., Gavin, G., O'Byrne, J., McGuinness, G., 2008. High-power low- frequency ultrasound: a review of tissue dissection and ablation in medicine and surgery. J. Mater. Process. Technol. 1 (3), 38–58.

Ogawa, T., Hattori, R., Yamamoto, T., Gotoh, M., 2011. Safe use of ultrasonically activated devices based on current studies. Expert Rev. Med. Devices 8 (3), 319–324.

Pan, Z., Lucas, M., Ganilova, O., 2012. Study of an ultrasonic bone cutting blade for orthopaedic surgery. In: IEEE International Ultrasonics Symposium, pp. 1–4.

Park, D., Park, H., Seo, J., Lee, S., 2014. Sonophoresis in transdermal drug deliverys. Ultrasonics 54 (1), 56–65.

Parks, C., 1970. Mist therapy: rationale and practice. J. Pediatr. 76 (2), 305–313.

Perra, E., Lampsijärvi, E., Barreto, G., Arif, M., Puranen, T., Hæggström, E., Pritzker, K.P., Nieminen, H.J., 2021. Ultrasonic actuation of a fine-needle improves biopsy yield. Sci. Rep. 11 (1), 1–15.

Postema, M., Gilja, O., 2007. Ultrasound-directed drug delivery. Curr. Pharm. Biotechnol. 8 (6), 355–361.

Pugh, J., Canales, B., 2010. New instrumentation in percutaneous nephrolithotomy. Indian J. Urol. 26 (3), 389–394. https://doi.org/10.4103/0970-1591.70579.

Rabiner, R., Hare, B., Fischer, D., Levine, L., 2003. Ultrasonic Medical Device Operating in a Transverse Mode. US Patent 6,551,337, Omnisonics Medical Technologies.

Rooney, J., 1973. Acoustic radiation pressure and its use in power and intensity determinations. J. Acoust. Soc. Am. 53, 329.

Sanghvi, N., Foster, R., Bihrle, R., Casey, R., Uchida, T., Phillips, M., Syrus, J., Zaitsev, A., Marich, K., Fry, F., 1999. Noninvasive surgery of prostate tissue by high intensity focused ultrasound: an updated report. Eur. J. Ultrasound 9 (1), 19–29.

Schafer, M., 2004. Effect of pulse parameters on cavitation and acoustic streaming in ultrasonic surgical devices. In: Proc. 2004 IEEE Ultras. Symp, pp. 874–877.

Schafer, M., 2020. Basic science of ultrasound in body contouring. In: Ultrasound-Assisted Liposuction. Springer, Cham, pp. 9–21.

Schafer, M., Arbisser, L., 2004. Quantification of acoustic exposure during cataract surgery. In: Proc. 2004 IEEE Ultras. Symp, pp. 1824–1831.

Schafer, M., Broadwin, A., 1994. Acoustical characterization of ultrasonic surgical devices. In: Proc. 1994 IEEE Ultras. Symp, pp. 1903–1906.

Schafer, M., Hicok, K., Mills, D., Cohen, S., 2013. Acute adipocyte viability after third-generation ultrasound-assisted liposuction. Aesthet. Surg. J. 33 (5), 698–704.

Schafer, M.E., Spivak, N.M., Korb, A.S., Bystritsky, A., 2021. Design, development, and operation of a low-intensity focused ultrasound pulsation (LIFUP) system for clinical use. IEEE Trans. Ultrason. Ferroelectr. Freq. Control 68 (1), 54–64. https://doi.org/10.1109/TUFFC.2020.3006781.

Singhal, A., Baskota, D., Acharya, K., 2018. Ultrasonic cutting and coagulation device versus conventional diathermy dissection in thyroid surgery: prospective randomized trial. Int. J. Otorhinolaryngol. Head Neck Surg. 4, 335–338.

Sitta, J., Howard, C.M., 2021. Applications of ultrasound-mediated drug delivery and gene therapy. Int. J. Mol. Sci. 22 (21), 11491.

Smith, N., 2007. Perspectives on transdermal ultrasound mediated drug delivery. Int. J. Nanomedicine 2 (4), 585–594.

Starritt, H., Duck, F., Humphrey, V., 1989. An experimental investigation of streaming in pulsed diagnostic ultrasound beams. Ultrasound Med. Biol. 15, 363–371.

Stepanenko, D., Minchenya, V., 2010. Modeling of flexible waveguides for ultrasonic vibrations transmission: longitudinal and flexural vibrations of non-deformed waveguide. Ultrasonics 50 (3), 424–430.

Suslick, K.S., 1990. Sonochemistry. Science 247, 1439–1445.

Suslick, K.S., Flannigan, D.J., 2008. Inside a collapsing bubble, sonoluminescence and conditions during cavitation. Annu. Rev. Phys. Chem. 59, 659–683.

Tsujino, J., Ueoka, T., Otoda, K., Fujimi, A., 2000. One-dimensional longitudinal-torsional vibration converter with multiple diagonally slitted parts. Ultrasonics 38 (1), 72–76.

Ulmer, B., 1993. Ultrasonic surgical aspiration. An expanding method for patient treatment. AORN J. 57 (4), 865–869.

Vaitekunas, J.J., Lang, E., Schafer, M., 2009. Mechanisms of ultrasonic thrombolysis. In: 38th Ultras. Indust. Association, pp. 1–4.

Van der Burgt, C., 1963. Motional positive feedback systems for ultrasonic power generators. IEEE Trans. Ultrason. Eng. UE-10 (1), 2–19.

Vercellotti, S., De Paoli, S., Nevins, M., 2001. The piezoelectric bony window osteotomy and sinus membrane elevation: introduction of a new technique for simplification of the sinus augmentation procedure. Int. J. Periodontics Restorative Dent. 21 (6), 561–567.

Yoo, S., Bystritsky, A., Lee, J.-H., Zhang, Y., Fischer, K., Min, B.-K., McDannold, N., Pascual-Leone, A., Jolesz, F., 2011. Focused ultrasound modulates region-specific brain activity. NeuroImage 56 (3), 1267–1275.

Young, F.R., 1989. Cavitation. McGraw-Hill, London, ISBN: 0-07-707094-1.

Zhang, S., Guo, Y., Chen, Z., Li, G., Guo, Q., Wu, Y., Zeng, J., 2021. Proposal for a novel elliptical ultrasonic aspirator and its fundamental performance in cartilage removal. Ultrasonics 109, 106259.

Zhong, P., Xi, X., Zhu, S., Cocks, F., Preminger, G., 1999. Recent developments in SWL physics research. J. Endourol. 13 (9), 611–617. https://doi.org/10.1089/end.1999.13.611.

Zimmer, E., Hynynen, K., He, D., Marcus, F., 1995. The feasibility of using ultrasound for cardiac ablation. IEEE Trans. Biomed. Eng. 42 (9), 891–897.

Zocchi, M., 1993. Clinical aspects of ultrasonic liposculpture. Perspect. Plast. Surg. 7, 153–174.

Zocchi, M., Vindigni, V., Bassetto, F., 2020. 32 years of ultrasonic-assisted lipoplasty (UAL): from aesthetic to obesity. Aesthet. Plast. Surg. 44 (4), 1230–1240.

Further reading

Brujan, E.A., Ikeda, T., Matsumoto, Y., 2005. Jet formation and shock wave emission during collapse of ultrasound-induced cavitation bubbles and their role in the therapeutic applications of high-intensity focused ultrasound. Phys. Med. Biol. 50, 4797–4809.

Dhanraj, P., Vasanthan, K., 2020. Analytical study of advantages of harmonic scalpel in thyroid surgery. Int. J. Health Clin. Res. 3 (12), 96–103.

International Electrotechnical Commission, 2012. Medical Electrical Equipment—Part 1: General Requirements for Basic Safety and Essential Performance. IEC 60601-1, third ed. IEC, Geneva.

Mitsuyoshi, A., Inoguchi, K., Yokoyama, D., 2016. The Cavitron ultrasonic surgical aspirator with a low amplitude is a useful dissection device for surgical procedures: application to vascular detachment and lymph node dissection. Updat. Surg. 68 (2), 205–209.

Ngo, O., Niemann, E., Gunasekaran, V., Sankar, P., Putterman, M., Lafontant, A., Nadkarni, S., DiMaria-Ghalili, R.A., Neidrauer, M., Zubkov, L., Weingarten, M., 2018. Development of low frequency (20–100 kHz) clinically viable ultrasound applicator for chronic wound treatment. IEEE Trans. Ultrason. Ferroelectr. Freq. Control 66 (3), 572–580.

Chapter 24

Ultrasonic dental instrumentation

A.D. Walmsley
School of Dentistry, University of Birmingham, Birmingham, United Kingdom

24.1 Introduction

There has been a long history of the use of ultrasound in dentistry beginning in the 1950s when ultrasonic technology was applied to the drilling of teeth (Balamuth, 1952). It was not successful for this particular application but quickly found use to remove calcified deposits from the surfaces of the teeth. The ultrasonic scaler is now the instrument of choice to clean the surfaces of the teeth when you visit the dentist. The instrument has been redesigned to undertake several other procedures in dentistry including the first application that the instrument was first designed for which was the drilling of teeth. Dentistry brings together many disciplines due to the nature of the hard and soft tissues. Dental clinicians are comfortable working at the interdisciplinary interface and research collaborations with engineers, chemistry, and physical scientists are commonplace. The design and applications of dental power applications have arisen from these connections. The hard mineralized tissues of the teeth and the hostile environment of the mouth are unique and therefore require power applications such as ultrasound to solve particular clinical problems. It is an interdisciplinary subject ideally placed at the crossroads for different specialities to come together to solve clinical problems. The ultrasonic frequencies in dentistry are between 25 and 42 kHz and the range of applications varies from cleaning teeth to being used to cut the bone (Walmsley, 2015). The engineering principles described have not radically changed with refinements being in the choice of tip design required for the particular clinical job requested. Areas where there is particular interest are in the disruption of the bacterial biofilm and power applications of ultrasound to release antimicrobials to combat the disease process. In an era of antimicrobial resistance, dental ultrasonic instruments provide an avenue to ensure that both hard and soft tissues are free of bacterial contamination. This in turn will allow tissue resolution and repair to take place. In summary, there is agreement that the instruments are effective primarily due to the mechanical oscillation of the tip. During use, acoustic cavitation is produced in the cooling water supply as it passes over the oscillating tip. This leads to an increase in antimicrobial activity and helps to disrupt/eliminate the biofilm. The tip will also generate high temperatures especially if not efficiently water cooled and this in turn will damage the biofilm. These aspects of power ultrasonics provide direct benefit to patients by allowing them to keep their teeth in a healthy state. They also make many dental procedures more effective and allow dentists to provide a high level of clinical care (Figure 24.1).

24.2 Historical overview

In 1953, ultrasound technology was advancing rapidly, and ultrasonic drills offered a novel approach to cutting tooth enamel which is one of the hardest known materials in nature (Catuna, 1953). The engineering work behind this project was described by Balamuth (1963) who understood the interdisciplinary approach requiring the interaction of engineers and dentists. By being able to cut through the enamel, the ultrasonic drill would allow further treatment of the bacterial induced acid attack of the teeth termed dental caries. To remove the dental decay, enamel has to be removed allowing access to the underlying dentine. This allows the dentist to remove the soft decay that was caused by the bacteria attacking the structure of the tooth. Once the decay is removed, then it is possible to place a filling. The ultrasonic drill offered several advantages including the use of water cooling which reduced any heating produced during the drilling process. The internal soft tissues of the tooth known as the pulp are sensitive to heat and temperatures should not exceed 37°C; otherwise irreversible damage will occur with death of the tooth. These original instruments worked at 25 kHz and were based on a magnetostrictive design. The water flowed through the instrument to cool the working instrument and then passed out onto the tip of the device. There were several designs that were based on the shape of dental access cavities. The reports at the time showed that the drilling process worked well and caused minimal discomfort (Postle, 1958). The instrument was based on an industrial grinder and an abrasive slurry was incorporated in the water coolant. The instrument required high volume suction to remove remnants of the slurry (Postle, 1958; Balamuth, 1963). The procedure did not catch

Power Ultrasonics. https://doi.org/10.1016/B978-0-12-820254-8.00015-4
Copyright © 2023 Elsevier Ltd. All rights reserved.

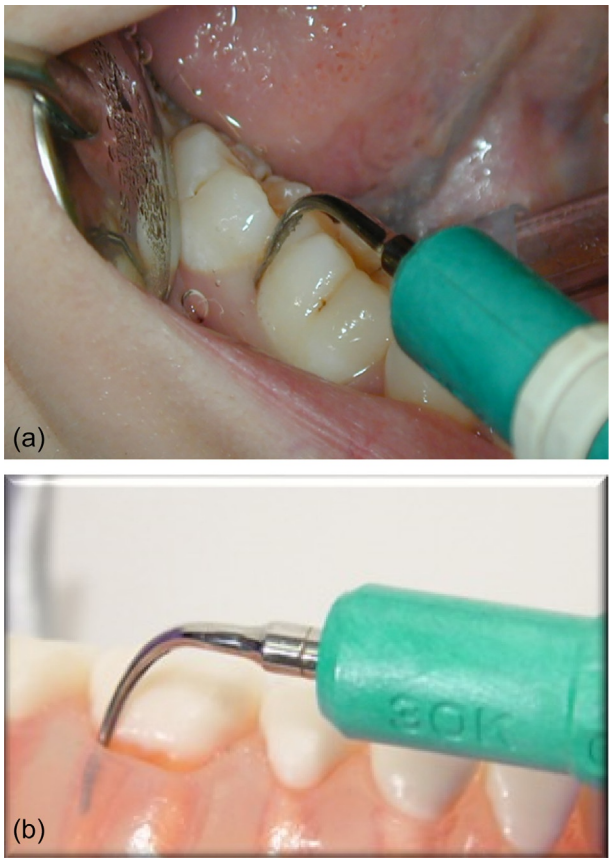


FIGURE 24.1 (a) and (b) Clinical use of ultrasonic scaler and a model showing the tip being used under the gumline (Walmsley, 2015).

on as it was unwieldly, slow, and was quickly superseded by the high-speed cutting technology which had also developed rapidly (Street, 1959; Dyson and Darvell, 1993). The high-speed drill working at revolutions above 100,000 was faster. Although it did produce heating, this was reduced to acceptable levels by an associated cooling water spray.

The ultrasonic drill was redundant and would have been consigned to history if the tips from the ultrasonic drill had not been redesigned to remove dental plaque and calculus from the teeth (Zinner, 1955). In the mouth, the teeth do not remain clean for long and very quickly saliva will stick to them. Following this, bacteria will colonize forming a biofilm which will allow the microorganisms to damage the hard tissues and inflame the soft tissues. Dental plaque will mineralize over time and this becomes tenaciously attached to the teeth. Such calcified deposits, known as calculus, are usually removed by sharp hand instrumentation. The ultrasonic instrument (now termed an ultrasonic scaler) was able to remove the deposits in a much quicker time period. The technology was taken up by various companies including the USA dental instrument company, Dentsply, United States, and ultrasonics became firmly established in dentistry. The first instruments made by Dentsply (now known as Dentsply-Sirona) were based on magnetostrictive technology and this was followed by others using piezoelectric generators (Piezon, EMS, Switzerland). There are now many different manufacturers of these instruments. Research on the ultrasonic scaler published in the next two decades broadly looked at the efficiency, the biological safety, and clinical usage. In the 80s and onward, major areas of development of the ultrasonic scaler took place in endodontics, biofilm removal by cavitation, bone cutting, and cleaning of dental implants. The instrument is even now used to cut into the teeth such as apical surgery where the tip of an infected tooth is removed (Waplington et al., 1995). The continued use of power ultrasonic applications in dentistry has led to an increased understanding of the capability of these instruments and how they should be used to maximize their efficiency. There is a continual supply of novel clinical applications using power ultrasonics.

24.3 Mechanisms of action

The back-and-forth vibrations of the ultrasonic scaler work in a chipping action to remove mineralized deposits from the teeth. The operating frequency of the instrument is between 25 and 40 kHz (Lea et al., 2002), and both magnetostrictive and piezoelectric designs are used to produce the vibrations. The chipping action produced by the rapid acceleration of the tip from the ultrasonic oscillation is central to the basic cleaning mechanism. The clinician has a range of tip shapes resembling hand instruments that are selected depending on the orientation to the tooth. Figure 24.2 shows a range of designs that are used which follow on from hand instrument designs. Unlike hand instruments which are sharpened, the ultrasonic scaler tip surface is smooth as it is the vibrations and the impact of the moving tip that break up and detach the deposits. Sharpening the tips may lead to excessive damage of the tooth and is not advocated. While the major removal mechanism is attributed to the chipping motion, research has indicated that cavitation and acoustic microstreaming in the water supply may lead to disruption of the bacterial biofilm that forms on the teeth (Vyas et al., 2020c; Walmsley et al., 1992). It is the disruption and removal of the biofilm that will allow the gum tissues (also known as the gingival and periodontal tissues) to resolve, thus reducing tissue inflammation.

24.3.1 Mechanical action of the ultrasonic scaler

Clinical ultrasonic scalers vibrate at around 20– 42 kHz. Understanding of the tip movement assists clinicians in how to obtain the maximum benefit of using their ultrasonic scalers. The movement of the tip has been described using scanning laser vibrometry, SLV (Lea et al., 2002). The SLV shows the main movement of the tip which is in the longitudinal direction and the tip is prone to damping by either the water flowing over it or when it is contacting the tooth

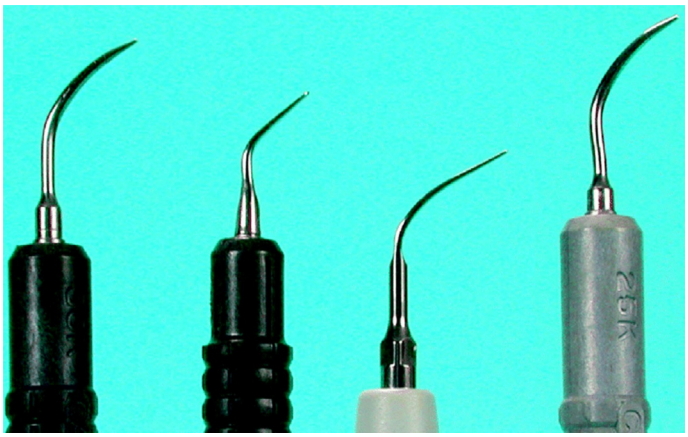


FIGURE 24.2 A selection of the commonly used ultrasonic scaler tip designs used in ultrasonic scaling ranging from left to right: Sickle-shaped for use in magnetostrictive (MS) 30 kHz units, flat-ended curved tip for (MS) 30 kHz units, a piezoelectric sickle shaped tip 30 kHz, and a sickle-shaped MS tip for 25 kHz (Lea et al., 2002).

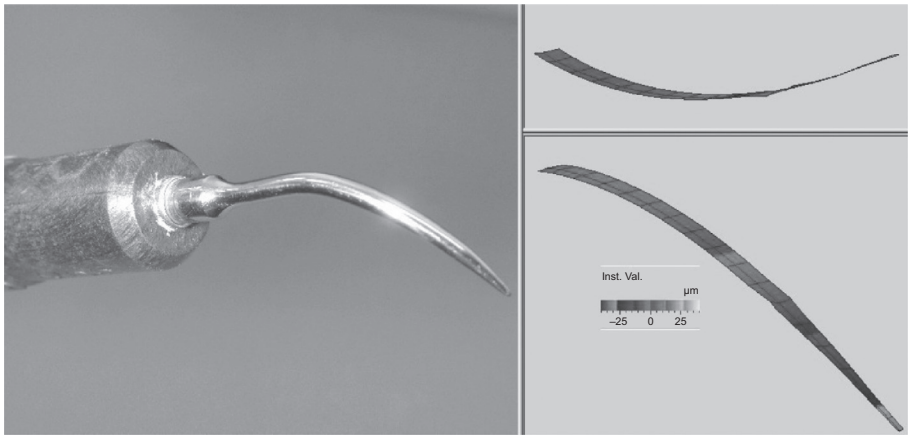


FIGURE 24.3 Oscillation of a sickle shaped tip using SLV showing the orientation of the animation. The animation has been frozen at the two points of maximum displacement from the resting position of the tip (Lea et al., 2002).

(Lea et al., 2003; Trenter et al., 2003). Stills of the animation are shown in Figure 24.3. The tip movement is not purely longitudinal and there is a 3D movement, i.e., elliptical envelope with both an upward and side-to-side movement superimposed on the longitudinal movement (Lea et al., 2009a). The longitudinal motion gives a displacement amplitude of around 50 µm equivalent to an amplitude of 100 µm. The ultrasonic tips powered by either a magnetostrictive or piezoelectric handpieces both display ellipsoidal patterns of movement. This finding is important as manufacturers of piezoelectric scalers cite the super efficiency of their machines due to the presence of a purely longitudinal motion which is not the case (Lea et al., 2009a). In turn, it is quoted as being kinder to the teeth during the removal process. This is not necessarily found with several studies in the literature. This is where clinicians require a better scientific understanding of an instrument that they use in everyday practice.

The amount of movement may be different between various ultrasonic scalers and it is the design of the ultrasonic tip that has the greater influence on the clinical result (Lea et al., 2009a; Lea and Landini, 2010). Ultrasonic tips are supplied in different lengths and widths. Also there are different shapes with curvature being the most common design encountered. The tips are modeled on hand instruments to provide clinicians with access to all places in the mouth. The curved tip shape is universally preferred, and clinicians asked for this design to be made thinner. This led to designs such as the Focussed Spray Slimline designs made by Dentsply Sirona (Dragoo, 1992). The many different designs that are available lead to a range of movement envelopes and displacement amplitudes. The load applied, tip design, and angle to the tooth will all influence the movement of the tip. It is likely that this may influence the clinical result and is an area where further understanding is required. It is rare to find studies where the settings of the

instrument are cited. It is even rarer to find discussion about the movement of the tip and which particular design was used including its orientation. Descriptions about the working parameters such as water flow and load applied are often missing. Most clinical studies leave it to the discretion of the operator on how the ultrasonic scaler is used. This makes it difficult to make meaningful comparisons on the efficacy of the action of the instrument. Other areas where clinical confusion may occur is that the oscillation of the tips will change over time as continual clinical use produces wear (Lea et al., 2006). Wear results in shortening of the tip leading to variations in its performance. Furthermore clinicians will seek to interchange tips between manufacturers (Lea and Walmsley, 2011). This is down to a cost-saving factor and favors the magnetostrictive design of scaler due to its popularity but again leads to unpredictable performances which will have a potential negative result on clinical performance.

The clinical relevance of this research is that on one level the ultrasonic scaler will remove deposits from the teeth. However, there are variations in tip design which in turn will influence the amount of movement that occurs. Having the knowledge of how the tips move allows the clinician to orientate the movement parallel to the surface of the teeth. This maximizes the amount of removal of the calculus from the tooth and will minimize any potential damage resulting from the metal probe impacting into the tooth structure. If the tip is orientated at a right angle to the tooth surface, the longitudinal vibrations have the capacity to cause damage. While damage from the oscillating tip does occur, clinical studies have shown that hand instruments may lead to more surface damage (Lea and Walmsley, 2009). As the clinician is not able to view the oscillating tip during clinical use, then there may be more unknown root surface damages. Currently, there is general agreement in the literature that hand instrumentation leads to more loss of the tooth substance especially on the root of the tooth.

24.3.2 Cavitation and acoustic microstreaming

The ultrasonic scaler was designed to chip and remove attached deposits from the teeth. To reduce frictional heating at the point of contact between the moving tip and the tooth, a flow of cooling water is directed over the area. The water will be subjected to the ultrasound vibrations. Some of this is thrown off as an aerosol but where it is allowed to pool around the tip then physical forces are generated and may prove useful in disruption of any bacterial biofilm that is present and bring about a microscrubbing of the tooth surface (Vyas et al., 2020b). These physical forces are potentially bactericidal. Acoustic cavitation will take place when ultrasonic energy passes through a liquid. In those areas where the pressure falls below the saturated vapor pressure, then bubbles will grow from small pockets of gas in the liquid. These bubbles will grow but will then be forced to shrink during the compression stage. In noninertial cavitation, repeated oscillation of the bubbles will occur. In the more disruptive form termed inertial, transient bubbles will collapse violently releasing energy. A range of bubble and fluid flow phenomena occurs, and it is usually a combination which takes place. High-pressure liquid jets may occur near a solid boundary producing large shear forces. Clouds of cavitating bubbles will produce disruption by the generation of shock waves and this includes the formation of high-pressure liquid jets. The cavitating microbubbles may also form ribbons termed microstreamers which strike the surface and also produce disruption. The inertial cavitation produced together with the acoustic microstreaming will release energy bursts around the tip of the ultrasonic scaler (Figure 24.4). These will break up clumps of bacteria and also break their cell walls, and therefore, ultrasonic scaling will reduce the pathogenic bacteria count.

Acoustic microstreaming is where shear forces are generated around the oscillating probe. These occur close to the tip of the scaler (around a few microns) but the forces still have the capacity to move fluid around and disrupt the bacterial biofilm at further distances away up to around 1 mm. The capacity for an acoustic turbulence to occur will disrupt the bacterial biofilm and also act to move the irrigant around (Vyas et al., 2020b).

Research *in vitro* and *in vivo* (Baehni et al., 1992) showed a reduction in bacteria activity after 10 s with a sizeable reduction after 60 s. Initially, there was little attention given to the presence of the ability of the cavitation to produce any effect during ultrasonic scaling. The main

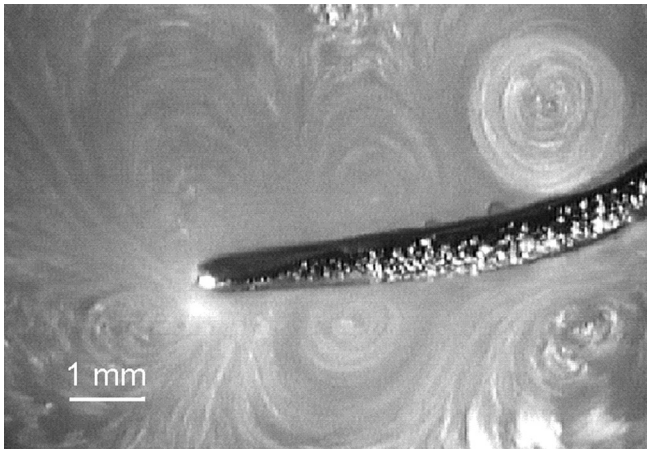


FIGURE 24.4 While the chipping action of the scaler is the predominant mechanism, both cavitation and streaming play a part as well as shown around the tip of a working instrument.

problem was the difficulty in both observing its presence and then measuring the effectiveness of the cavitation. Simple systems using *in vitro* model systems with particulate matter (Walmsley et al., 1984) and then the teeth (Walmsley et al., 1988) were developed to show its presence and how cavitation produced an effect at a distance from the tip. These early qualitative studies showed that the effectiveness was dependent on the type of tip that was used. Also how the tip was orientated to the surface influenced the amount of cavitation that occurred. Finally, the power setting used had a bearing on the removal process. A low setting allowed the water to pool around the tip, while at higher settings, there was a high level of water lost as an aerosol. Not only was cavitation seen as part of the cleaning process, but other forces such as acoustic microstreaming were cited (Laird and Walmsley, 1991).

The design of the probe will influence where the activity will take place. It is possible to visualize the occurrence of the cavitation and streaming at the end of a straight probe. However, in dentistry, the majority of clinical tip designs are curved. The handpiece moves longitudinally, and the water is passed out onto the curved tip. At the curve, there is predominantly longitudinal movement and this changes to a transverse oscillation at the tip. In order to visualize this, sonochemiluminescence (SCL) is used to determine where the most cavitation occurs. Cavitation will break water down into free radicals and their presence may be seen using a suitable chemical indicator. Luminol photography provides spatially resolved information on where the cavitation occurs. The interaction of the free radicals with the luminol provides a "glow" that can be picked up by long exposure photographic methods. The vibrational movement of the scaler was mapped against the occurrence of light produced when the tips oscillated in a solution of luminol (Figure 24.5). The greatest activity was seen at the antinodes which were at the curve and a smaller second area of activity at the end of the scaling tip. There were significant differences in the amount of cavitation found between various tip designs. However where the tip showed the greatest motion, only small amounts of cavitation were detected, and this was thought to be due to the thin design of the tip. It is hypothesized that the thin tip produced less turbulence and hence a smaller amount of cavitation.

Sonochemiluminescence does not show the cavitation in real time, and with a high-speed camera, the formation of the cavitation is identified especially around the working tip. A cloud of active cavitation with many observable bubble oscillations occurred around ultrasonic scalers working at 30 kHz (Vyas et al., 2016, 2020c). Both high-speed sequences and image analysis were used to track the bubble disruption of biofilm *in vitro*. Figure 24.6 shows contrast enhanced image stills from a high-speed video of different shaped ultrasonic tips (a, b, and c) operated at low-to-medium power settings. The images show cavitation occurring around the free end and at the bend of the tips. Green arrows indicate points of largest tip vibration and white arrows indicate the lowest movement. When the instrument is switched on, within a few seconds, a cloud of bubbles is generated on the surface and began to disrupt the biofilm (Vyas et al., 2016). Cleaning was seen to occur via microbubbles and fluid flow (Vyas et al., 2020c). This research showed that the closer the scaler tip is to the surface then the more effective the cavitation clouds will be. All this was done without the tip touching the tooth surface. It was also apparent that a distance of 0.5 mm from the surface is the ideal distance although effective cavitation clouds will build up at 2 mm from the tip. Although it was not possible to observe liquid jets, the remnants of their effect on the biofilm were seen.[1] Further work has shown that the amount of cavitation that occurs around an ultrasonic scaler can be increased if the fluid flowing over the tip is carbonated (Vyas et al., 2021). This may be a route to enhancing the cleaning ability of the ultrasonic scaler. An area where cavitation-based cleaning would provide enhanced benefit is for dental titanium implant surfaces. Early studies show that a nontouching approach with an ultrasonic scaler will clean the complex metal surfaces (Vyas et al., 2020a). Further studies have shown that carbonation of the water will increase the effectiveness of the cavitation. Figure 24.7 shows stills from high-speed videos recording the occurrence of cavitation in both still and carbonated water. Image (a) is the tip in still water. Images (b), (c), and (d) are taken when the ultrasonic tip is operated in low, medium, and high carbonation water levels, respectively. Image (e) shows the cavitation area around the tip over time at the different carbonation levels, calculated using image analysis from high-speed videos ($n = 5$). Finally, image (f) shows the total cavitation area around the tip at the different carbonation levels, calculated using image analysis from the high-speed videos (Vyas et al., 2020b). This is a promising area of further research in developing instrumentation that maximizes cavitation to remove biofilm from the surfaces of teeth.

24.3.3 Biofilm removal

Ultrasonic scaling not only removes the attached calculus but will also remove the bacterial biofilm. It is the later which is the causative agent in the inflammation process, and it is this removal which will lead to achieving health in the individual. However, it is easy to determine the mechanical ability of the scaler or the file to mechanically abrade the tooth or root canal. The ability to disrupt the

1. Vyas et al. (2020) contains video and other supplemental material which should be able to be viewed when accessed.

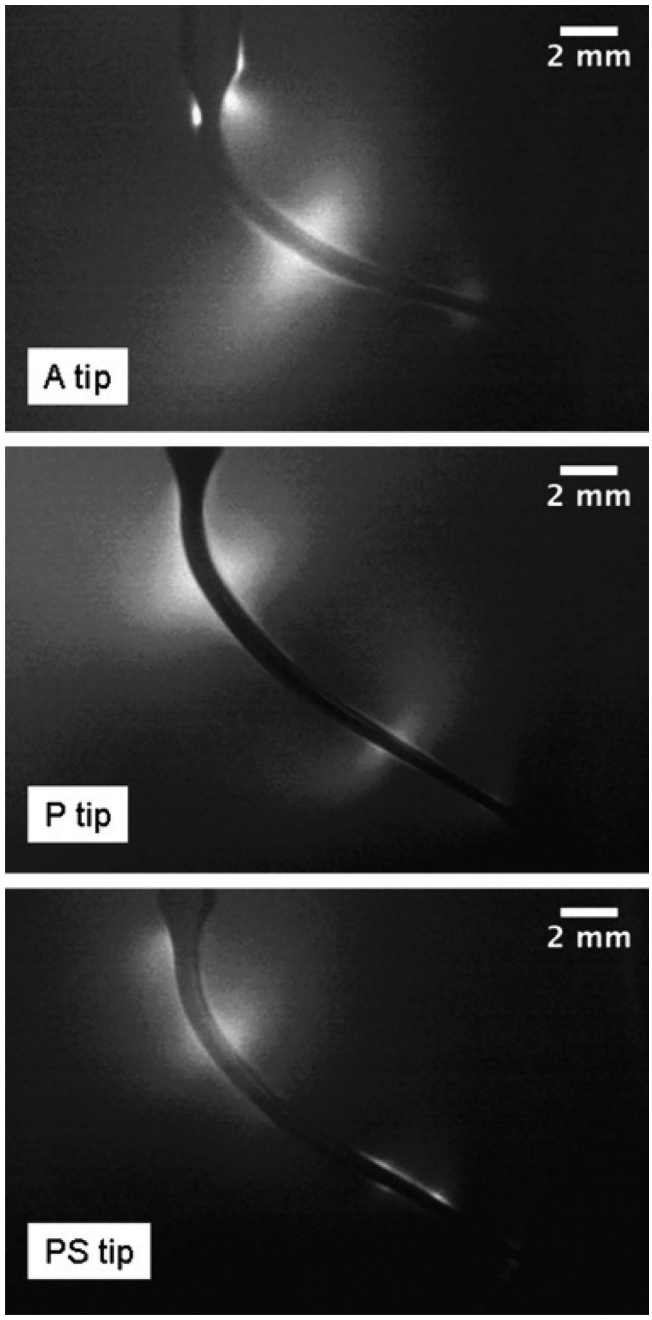


FIGURE 24.5 Luminol photography of various sickle tips at maximum power. *Light regions* indicate areas of high cavitation activity, with *dark regions* indicating little or no activity (Felver et al., 2009).

biofilm is more difficult to quantify. Biofilms are a concentrated mass of bacterial microorganisms that are attached to a surface (Vyas et al., 2019) and are recognized as being a major problem in many different areas of medicine and science. This can range from the bacterial plaques that build up on artificial heart valves to the fouling of the hull of ships by marine-based biofilms. In all cases, the aim is to remove the biofilm safely without damaging the underlying surface. The removal of biofilms from surfaces is becoming an important area of focus in clinical work. The biofilm is an efficient protective home to the microorganisms and the bacterial commune works synergistically offering protection and resisting removal. For instance, antimicrobials find it difficult to penetrate deeply into the biofilm which will hinder their effectiveness. However, a process that involves mechanical disruption will then allow antibacterial

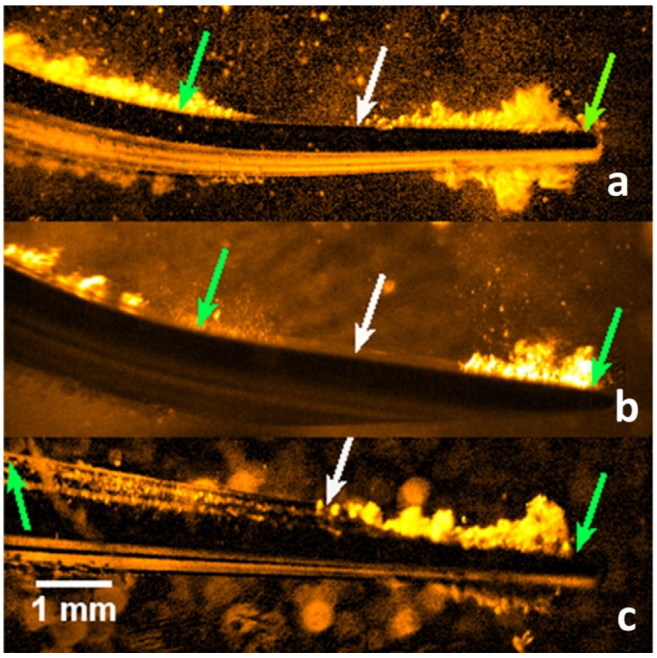


FIGURE 24.6 Contrast enhanced image stills from a high-speed video showing cavitation occurring around different ultrasonic tips (a, b, and c). *Green arrows* are where the largest tip vibration occurs and *white arrows* indicate the point of least displacement (Vyas et al., 2016).

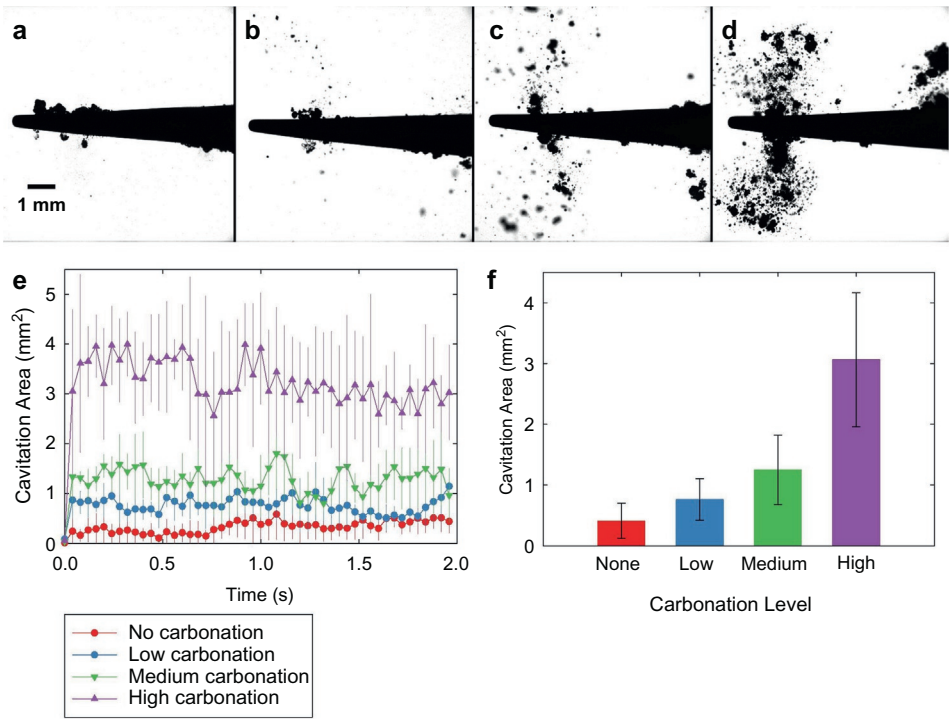


FIGURE 24.7 High-speed video stills showing cavitation around an ultrasonic scaler tip in both (a) still and (b, c, d) carbonated water. The cavitation area was calculated (e and f) using image analysis from high-speed videos ($n = 5$). See text for explanation. *(From Vyas et al. (2021)).*

agents to reach deeper into the biofilm. Acoustic cavitation is seen as one form of energy that will be useful in the battle against biofilms. A diagrammatic representation of the biofilm shows the interaction of the different forces involved in the removal process by ultrasound (Figure 24.8). The biofilm is removed by a combination of the acoustic streaming and microstreamers leading to shock waves, cavitation clouds, and microjets that contribute to the removal process. Microjets point away from the biofilm if it is soft (low elasticity), as illustrated in Figure 24.8, but point toward the biofilm if it is "stiff" (high elasticity) (e.g., mineralized biofilms).

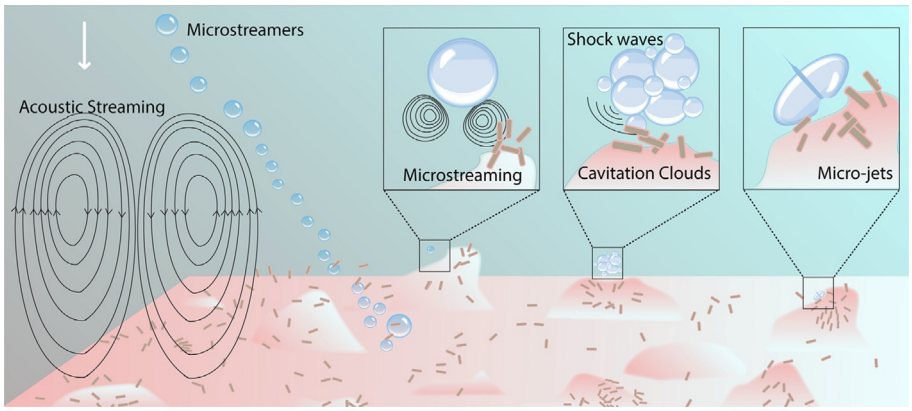


FIGURE 24.8 Schematic of the different methods in which cavitation can cause mechanical biofilm removal. The *white arrow* indicates the direction of ultrasound in sonification. *(From Vyas et al. (2019).)*

24.4 Clinical evaluation of ultrasonic scalers

Power ultrasonics in the form of dental ultrasonic scalers have been present since 1955, and the procedure of calculus removal has been done clinically to a satisfactory standard over the years. Dentistry like other branches of medicine must justify the use of any interventions, and clinical knowledge has advanced over time. With the establishment of evidence-based dentistry, researchers wish to quantify the effectiveness of an intervention and define clinical endpoints such as tissue health and retaining teeth, although other outcomes are used. Evidence-based dentistry is hierarchal with examples of poor evidence being the use of single-case studies where solitary procedures have been described in the literature to high levels of evidence where a clinical intervention has been assessed against a control. The latter are termed randomized clinical trials (RCT) where any bias that would influence the result is removed. Therefore, during the trial, the clinician is unaware of the procedure and/or the patient is also unaware, i.e., they are blind to the intervention and only after the study is completed is the protocol revealed. A meta-analysis is where several of these RCTs are compared and this provides a powerful overall conclusion. Evidence-based dentistry leads to important statements on the care of patients. However, in the field of clinical dental ultrasonics, there are few trials available to assess. The latest method of assessing clinical outcomes is the use of the GRADE scale (Guyatt et al., 2008) where the quality of evidence scale may be defined as

- High quality—Further research is very unlikely to change our confidence in the estimate of effect.
- Moderate quality—Further research is likely to have an important impact on our confidence in the estimate of effect and may change the estimate.
- Low quality—Further research is very likely to have an important impact on our confidence in the estimate of effect and is likely to change the estimate.
- Very low quality—Any estimate of effect is very uncertain.

Unfortunately, much of the clinical evidence for the effectiveness of the ultrasonic scaler is rated as low to very low quality. More clinical trials are needed to show with certainty the effectiveness of the ultrasonic scaler over hand instrumentation. The other questions include its effectiveness against other procedures such as the use of air powder abrasive systems, rotary polishing, or new technologies that are brought into clinical use that also remove biofilm and calculus.

There have been two systematic clinical reviews comparing the efficacy of ultrasonic instrumentation with hand instrumentation in the ability to clean tooth surfaces and resolve periodontal (gum) disease (Tunkel et al., 2002; Walmsley et al., 2008). The mechanical instrumentation included some forms of rotary instrumentation. The first review found 27 clinical articles suitable for inclusion while the second review found a further 14 articles. Both reviews found that power-driven instrumentation provides similar clinical outcomes compared with hand instrumentation although the evidence for this is at the low-to-moderate GRADE score. There was difficulty in pooling clinical studies, and this continues to hinder the drawing of definitive conclusions in the use of power ultrasonics in dentistry. The main problem is that the studies are not standardized or are comparing different aspects of the cleaning process. One conclusion that was common to many of the studies is that ultrasonic/sonic subgingival debridement (cleaning) requires less time than hand instrumentation. The studies highlighted the need for more research in several areas. These included how efficient the machine-driven debridement is on the multirooted teeth, the influence of complex tooth anatomy, and the difficulty of reaching the back of the mouth. All these will continue to challenge the designers of ultrasonic instruments. *In vitro* research has described different movements of the tips. The clinical relevance of this including the variation in the performance of different tip designs and generators remains unknown.

Traditionally clinical outcome variables have been orientated to the dental aspect and a call for clinical trials which have a tangible benefit to the patients treated should be run. There have been few clinical trials which have looked at these patient outcomes, but an interesting RCT looked at the effect of the temperature of the cooling water on patient comfort and acceptance (Daly et al., 2020). Patients who agreed to take part were given routine ultrasonic treatment. Ultrasonic scaling was performed on one side of the mouth with warm water (approx. 36°C) as opposed to the other side where the water used was set at room temperature (approx. 20°C). There was less pain and discomfort with patients experiencing reduced levels of noise and vibration when the ultrasonic scaler was used with warmed irrigant. There are several other studies that have looked at patient outcomes. The ultrasonic scaler is more comfortable than hand instrumentation (Derdilopoulou et al., 2007), and this confirms earlier studies as to which dental procedures are painful (Tripp et al., 1998). It is interesting that studies show that magnetostrictive devices are more comfortable than their piezoelectric counterparts (Ikeda et al., 2021). This may be down to a variety of factors and opens an interesting area for research. All these studies confirm that patient outcomes are an important consideration in the design and operations of ultrasonic instruments.

24.5 Endosonics

The ultrasonic scaler is a versatile instrument and clinicians have adapted it for use in other speciality areas of dentistry (Park, 2013). Endodontics is a branch of dentistry that treats the internal structure of the tooth which is known as the pulp. The pulp is composed of soft tissue but is surrounded by the hard layers of dentine and enamel. These soft tissues will become infected when dental decay breaks through the enamel and dentine and reaches the pulp. The main problem is once again bacteria which will lead to inflammation and infection of the soft tissues. The final result is a tooth abscess which may be painful, and the resulting infection may eventually lead to the tooth being removed. Root canal treatment aims to remove the infection and clean out the internal structure once the pulp is removed (Berman and Hargreaves, 2020). However, the anatomy of the tooth is complex (Figure 24.9) with many channels running through the tooth (Robinson et al., 2012). Dentists will use hand files to shape and clean the cavity and then follow this with a disinfectant such as sodium hypochlorite. Micro-CT imaging of the complex nature of the canal reveals the debris that is left when the canal is cleaned with files. The hypochlorite solution serves to dissolve the debris. While the disinfectant is effective, it is difficult to move it around and reach all branches of the internal structure of the root. Therefore, an adapted ultrasonic scaler was developed to both clean the root canal walls plus disinfect them effectively (Martin, 1976; Cunningham et al., 1982). The instrument is essentially an ultrasonic scaler generator with a facility for bolting a thin endodontic file onto the end. It operates at a higher frequency of 30 kHz and accepts files of different thicknesses and lengths. While the file oscillates in a transverse manner, a suitable disinfectant such as sodium hypochlorite is passed over the file. The theory is that the ultrasonically activated instrument mechanically cleans the walls of the canal, but it will also produce inertial cavitation and acoustic streaming in the closed space of the root canal (Walmsley, 1987). Further refinement of the system led to a specific procedure termed passive ultrasonic irrigation (PUI) technique (van der Sluis et al., 2005). The technique which had been popular in the late 80s and 90s (Walmsley, 1987) once again became the instrument of choice in the speciality of endodontics. The removal of the bacterial biofilm is key to the success of treating root canal of the pulp and power ultrasonics offer a solution to the problem of ensuring disinfection of the canal. A key factor is the motion of the ultrasonic file (Lea et al., 2010). The motion is along the file is a series of nodes and antinodes with the largest motion at the unconstrained end. The concept of PUI requires non touching of the canal wall as it relies on the generation of inertial cavitation and acoustic microstreaming to enhance the bactericidal activity of the chemical irrigant which is usually sodium hypochlorite. Using SCL and a scanning laser vibrometer, it was possible to show the occurrence of the cavitation. The file motion shows a series of nodes and antinodes, and inertial cavitation was observed around the nodes (Lea et al., 2004; Walmsley, 2015).

Passive ultrasonic irrigation of the root canal relies on the energy of inertial cavitation and acoustic microstreaming generated by the vibration of the endosonic file. In the confines of the root canal, it allows the irrigant to pass over the vibrating endosonic file leading to cavitation and acoustic microstreaming. The clinicians use files of similar length and thickness to those used for routine hand instrumentation. These are #10 and #30 (equivalent to 0.1 and 0.3 mm, respectively, at the tip) and lengths of 27 and 31 mm. These are common clinical designs, and the files are driven at a frequency of 30 kHz. The vibration characteristics of a #30 endosonic ultrasonic file at generator power settings 1–5 have been measured. It was found that there are no significant differences in the maximum file vibration displacement amplitudes (occurring at the free end of the file) at any of the generator powers tested (Figure 24.10). However, the oscillations along the rest of the file are reduced at powers 2–5, and this is likely caused by the transmission of energy from the transducer to the file (from Lea et al., 2010). Further research has demonstrated that there is good correlation with the mathematical calculations and the oscillations of the file (Verhaagen et al., 2012). Once again, these power ultrasonic instruments are based on hand instrument designs.

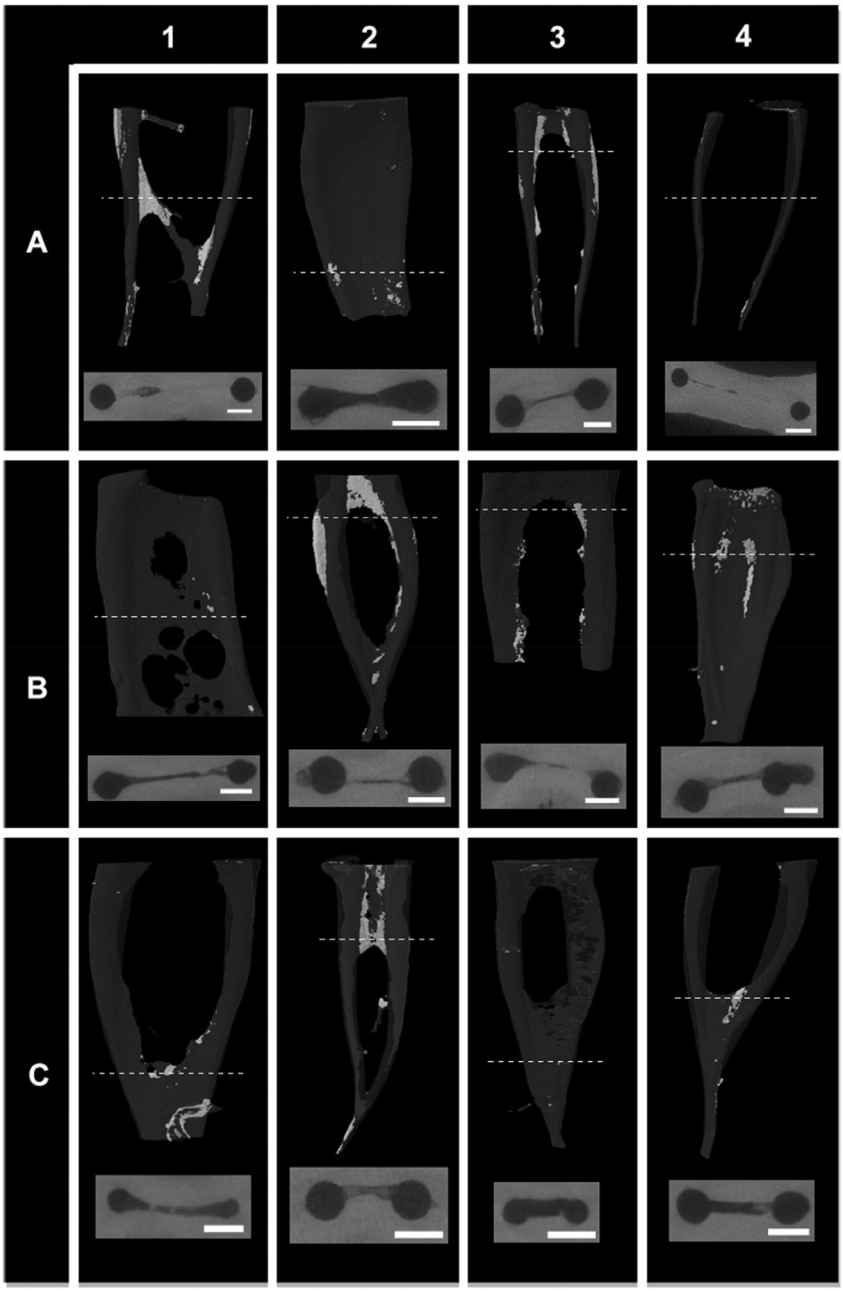


FIGURE 24.9 MicroCT reveals the complex nature of the internal structure of the tooth. Teeth instrumented with no irrigant (row A) have white debris, while chemical irrigants leave cleaner canals (B and C). Scale bars = 1000 µm. *(From Robinson et al. (2012).)*

It is by experimental trial and error that the lengths and thickness are derived. While the aim is to ensure there is no contact with the walls of the root canal, research shows that it is generally not possible for the vibrating files to remain passive in the canal. There is contact with the walls of the canal which does not lead to any detrimental effects to the overall technique. It may be better described as "Ultrasonically Activated Irrigation" (Boutsioukis et al., 2013). There was some dampening of the file and inertial cavitation was still detected.

One of the claimed advantages of ultrasonic activated irrigation is the ability to clean beyond the file and reach into lateral extensions of the main root canal. Researchers have observed the removal of a hydrogel (biofilm mimic) in the canal using an ultrasonic file. Both high-speed camera and particle imaging velocimetry showed that the hydrogel was removed from a simulated root canal in vitro up to 0.5 mm from the file. Figure 24.11 is a diagrammatic representation of the hydrogel removal from (a) a lateral canal and (b) an isthmus (Macedo et al., 2014). The color of the

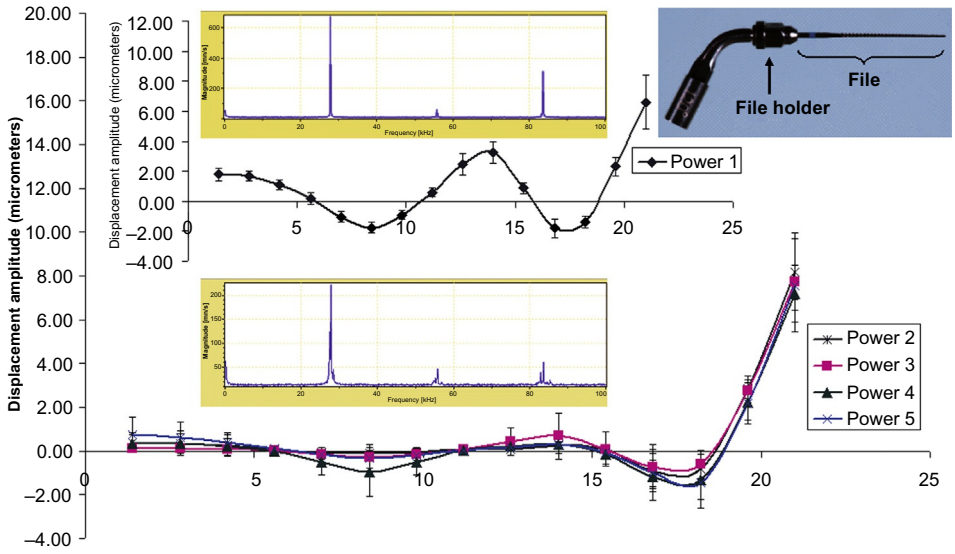


FIGURE 24.10 Vibration characteristics of a #30 endosonic ultrasonic file at generator power settings 1–5. *(From Lea et al. (2010).)*

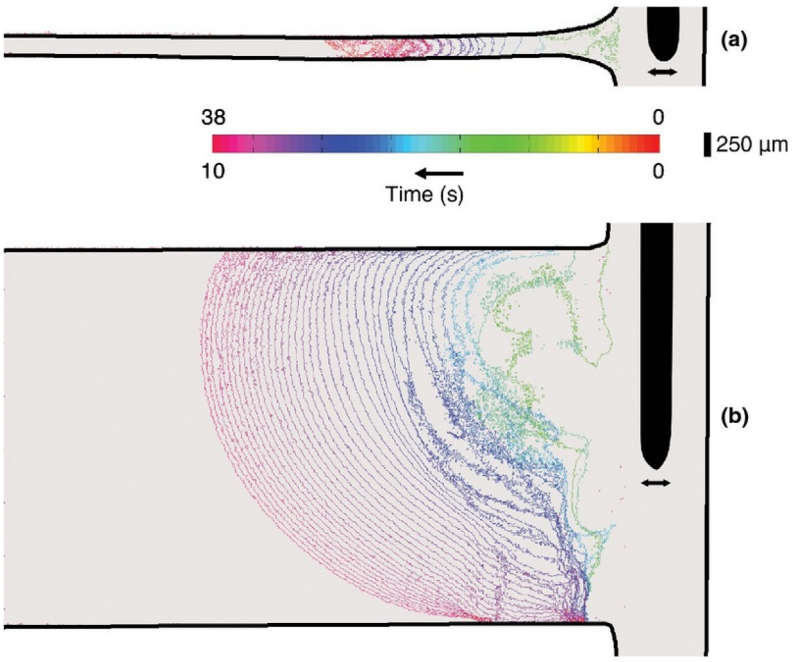


FIGURE 24.11 Hydrogel removal from a lateral canal (a) and isthmus (b). *(From Macedo et al. (2014).)*

lines represents the border at a specific time, with fixed time intervals (0.55 s for the lateral canal, 0.25 s for the isthmus) and a total time of 38 s for the lateral canal and 10 s for the isthmus. For the lateral canal, several lines overlap because there was no removal between those timepoints. For the isthmus, initial unsteady removal can be observed (green lines, followed by steady removal—purple lines). This work shows the success of the fluid flow in reaching into the complex anatomy of the root. It was found that sodium hypochlorite was a successful irrigant in these situations, and the cleaning was dependent upon the time of operation and the position of the file in the canal (Robinson et al., 2018).

While there have been many laboratory studies on the use of ultrasound in endodontics, there are a few clinical studies available. In summary, the use of ultrasound will influence the fluid dynamics and movement of the irrigant fluids in the root canal system. This has to be an advantage as it will allow the disinfecting irrigant to access the complex anatomy of the root which conventional or modern rotary instruments will not be able to reach. While there is poor evidence in the clinical research that has been undertaken so far, published results do suggest that the use of ultrasonic irrigation has a place in endodontics (George, 2019). Using the GRADE tool (Guyatt et al., 2008), clinical

studies have reported no evidence of effectiveness using the improvement on periapical healing as an indication of success. Bacterial disinfection is improved which supports the use of passive ultrasonic irrigation over nonactivated irrigation in clinical dental practice (Silva et al., 2019). However, the level of clinical evidence is low, so no strong clinical recommendations could be formulated (Căpută et al., 2019). Future studies should focus on the antimicrobial effect where there are conflicting results with studies reporting efficient cleaning of debris and microbial disinfection and others showing no difference. In another review, Susila and Minu (2019) reported that the risk of bias and quality of the clinical articles were moderate. Results showed that mechanically active irrigation reduces postoperative pain for patients. It improves debridement and the cleanliness of the canal/isthmus. It also improved delivery of the irrigant up to the working length of the root canal. The bacterial count was more with active irrigation, though this was not significant. However, there was a similar conclusion that there was no difference in ultrasonic technique compared to hand instrumentation as a clinical end point of tissue resolution, i.e., long-term periapical healing. The results are conflicting and more clinical trials are necessary to understand where any improvements occur when using power ultrasonics for cleaning root canals.

In summary, ultrasound remains a popular component of clinical treatment in the speciality of endodontics. It is used to enhance the cleaning of the root canals by increasing the effectiveness of the irrigant. Early clinical studies show it is as effective or may be more effective than hand instrumentation. Future clinical studies are required to demonstrate how much more effective endosonics is in cleaning the root canals of the teeth.

24.6 Cleaning of titanium implant surfaces

Teeth that are lost from the mouth may be replaced by dentures or crowns. A popular choice is to use a titanium dental implant as it is fixed in the bone (osseointegration) and may be seen as a permanent replacement. The provision of titanium metallic implants is a rapid growth area in dentistry. Market research reports that the global dental implants market was around $4 billion dollars in 2020 and expected to double by 2028. Dental implants are made from industrial pure titanium and are designed with specialized surface coatings for bonding to bone. These coatings may become exposed by gum disease. Normal methods of cleaning include using metal hand or ultrasonic instruments but the drawback is that this will lead to a roughened and potentially damaged surface (Mattheos et al., 2012; Mann et al., 2012) that provides an ideal surface for the growth of a bacterial biofilm, i.e., dental plaque (Quirynen et al., 1993). There is no system at present that removes the biofilm effectively (Schmage et al., 2014). Dental biofilm is a tenacious community of bacteria that sticks to the implant surfaces leading to gum disease. The mature biofilm may even calcify adding to its tenacity and makes its removal more difficult. Traditional methods include patient cleaning with modified toothbrushes or professional removal of the biofilm from the roughened implant surface, but all have met with limited success. Newer methods of cleaning such irregular surfaces are urgently needed, and it has become a major research focus in dentistry. One approach is to place a rubber sleeve onto the tip of the ultrasonic scaler and use this for cleaning, but research has shown that this is ineffective and leaves a residue of burnt rubber on the implant surface (Mann et al., 2012). Research has shown that inertial cavitation from the ultrasonic scaler is able to remove biofilm from the dental implant surface *in vivo* (Vyas et al., 2020a). The biofilm was removed at high power settings and scanning electron microscopy showed that cleaning had taken place on the implant surface especially in those areas where the cavitation was the most intense (Figure 24.12). The cleaning time was 2 s, and the metal scaler did not contact the implant as it was held in fixed noncontact position of 0.5 mm away. High-speed imaging of the biofilm removal shows removal takes place underneath the implant threads which may not be reached by traditional contact methods of removing the biofilm.

While this is an exciting way forward, it may remain impractical in its present form as the process needs to be much faster to be clinically acceptable. It took 2 s to clean one small area of the implant. Such timings need to be increased so that the implant cleaning occurs in an acceptable clinical time period.

24.7 Antimicrobial drug delivery

Enamel is a hard dense prismatic structure while dentine has a tubular configuration. The diameter of the tubular channels running through the dentine is between 2 and 4 μm, and there are generally around 60,000 per square millimeter. When dentinal tubules are exposed, they may act as a pathway to the pulp of the tooth. Bacteria involved in dental caries will take advantage of this once they have breached the hard outer enamel layer. Dentinal tubules are also linked to dentine hypersensitivity and allow the flow of fluids in these micro channels. This is turn will elicit pain from patients as it will cause stimulus to the pulp. Many treatments of tooth sensitivity are aimed at blocking the openings of the dentinal tubules. The use of antibacterial agents will assist in preventing bacteria from reaching the pulp of the tooth. Power ultrasonics delivered by dental instruments are able to deliver submicron particles with diameters of between 100 and

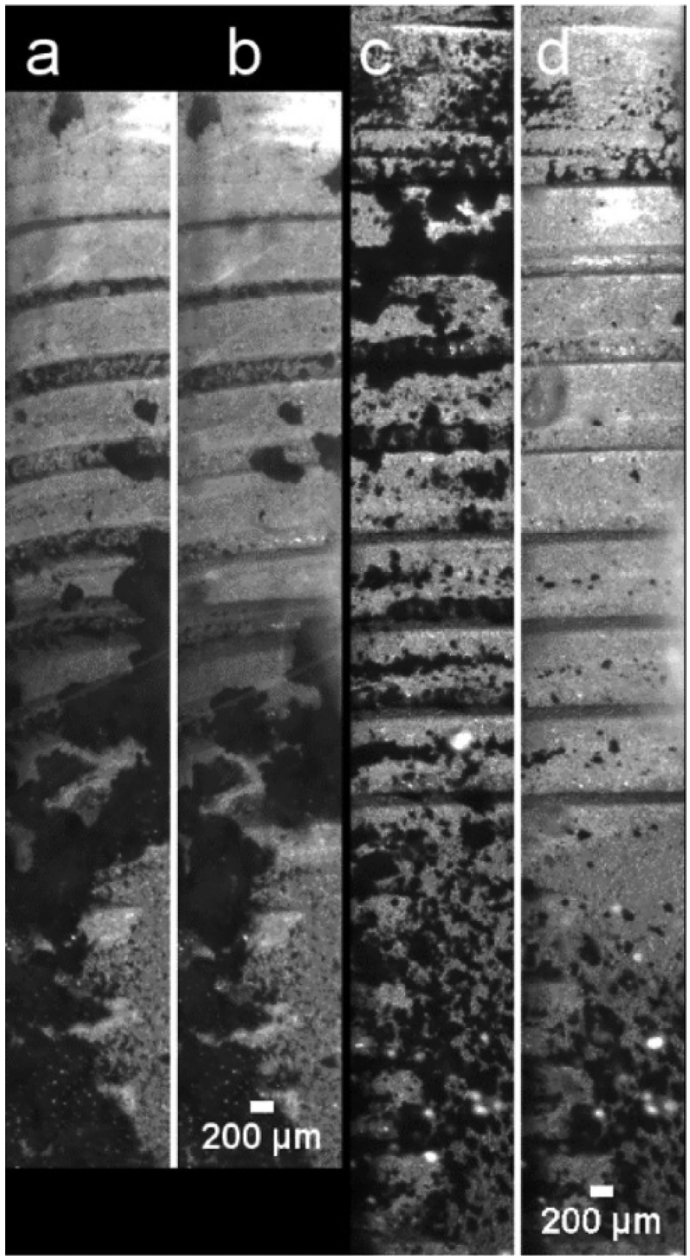


FIGURE 24.12 (a, b) Implant before and after cleaning at medium power for 2 s. (c, d) Implant after cleaning at high power for 2 s (Vyas et al., 2020a).

1000 nm into dentinal tubules (Vyas et al., 2017). The use of cavitation and acoustic streaming provides the mechanical energy to undertake this task. Research has shown that nanoparticles such as chitosan can be delivered into the tubules using cavitation (Ohl et al., 2010). Such delivery systems are of interest to the healthcare industry. Recent work with submicron silica particles has demonstrated that they may be pushed down into the dentinal tubules. Using the scanning electron microscope, it was possible to see tubule occlusion by the silica particles which penetrate inside the tubules up to 180 µm when there was cavitation delivered by the ultrasonic scaler (Vyas et al., 2017). Figure 24.13 shows electron micrographs of these silica particles. The particles are applied to the dentine surface and no cavitation is applied. Figure 24.13a shows the particles are in 50% acetone and in Figure 24.13b in water. Figure 24.13c and d shows how the particles are pushed down the tubules when ultrasound is applied. Scanning electron microscope images show the silica particles on the dentine prior to ultrasound exposure (Figure 24.13e). The comparison is when cavitation is applied in Figure 24.13f, the particles are moved into the tubules (from Vyas et al., 2017). Work is ongoing in this area to develop ultrasonic techniques to deliver antimicrobial particles in this unique manner.

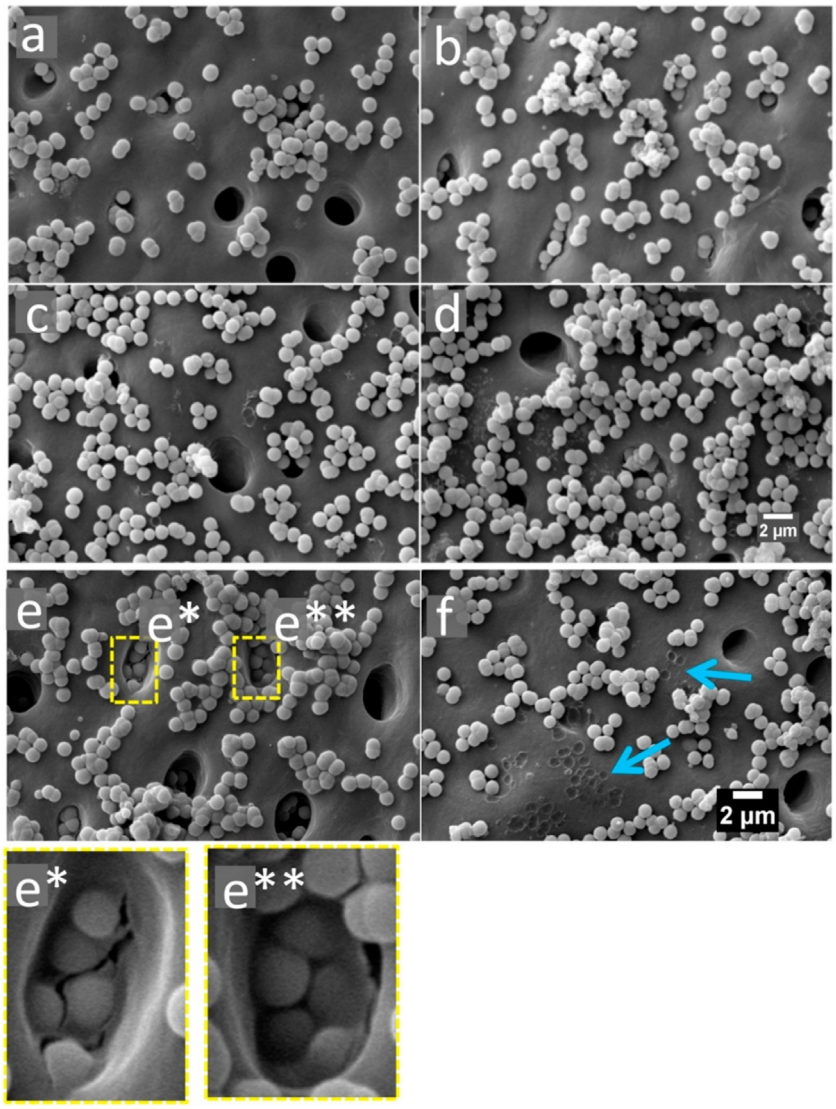


FIGURE 24.13 Electron micrographs of the silica particles on the dentine surface at ×11,000 magnification. Please see text for descriptions of the micrograhs (a–f) *(From Vyas et al. (2017).)*

24.8 Surgical applications

Ultrasonic cutting of bone around teeth has been used to remove teeth requiring extraction from the jaw bones but the process was slower compared to the rotary drill (Horton and Tarpley, 1981). The instrument is now routinely used in implant surgery and it is the precision that is preferred by dental surgeons. The placement of dental titanium implants in dentistry requires the use of more specialized cutting instruments. The rotary burs may be imprecise and lead to large removal of bone. The concept of piezoelectric surgery was introduced as an alternative to rotary cutting (Vercellotti, 2004). The instrument is similar to an ultrasonic scaler and employs specialized designs which resemble saws to cut the bone prior to implant placement. An ultrasonic scalpel has the advantage of being more precise (Cardoni, 2010) and incorporates many of the claims that are associated with ultrasonic cavitation. This includes the use of cavitation and acoustic streaming that allow for a cleaner operating field (Park, 2013). Reports of less bleeding around an ultrasonic drill are related to earlier research that show streaming forces will instigate blood clotting by disrupting platelets (Walmsley et al., 1987b). Following successful clinical studies, it has become integrated in the clinical care of patients requiring implants (Vercellotti et al., 2014). Such drills are adapted from ultrasonic scalers and their effectiveness is dependent on the load applied and the power setting of the instrument (Parmer et al., 2011; Claire et al., 2013). The structure of the bone influenced the rate of cut with the instrument cutting cancellous bone better than cortical bone (Claire et al., 2013). The clinical effectiveness of the instruments has been assessed by several clinical trials. Following GRADE classification, there is moderate to low evidence that there is less pain and other

discomfort following ultrasonic surgery after tooth extractions (Cicciù et al., 2021). Dental implants were more stable following piezoelectric surgery. It is a much longer procedure when using ultrasound (Strong Evidence). Finally, it is unclear if the use of the instruments has any real clinical advantage to the surgeon or patient (Bassi et al., 2020; Li et al., 2020). This is an area for further research.

Ultrasound is used in apical surgery (Waplington et al., 1995). Conventional endodontics is the common approach to treating the infected root canal (apical periodontitis) and access is gained through the crown of the tooth. If treatment is unsuccessful and it is not possible to retreat the tooth by this approach, then a surgical approach will be considered. A flap of tissue is raised, bone removed, and the tip of the root removed. A cavity is cut in the apex and then this is filled. This preparation is routinely done with an ultrasonic handpiece (Park, 2013). It allows improved access although care must be taken not to produce cracking of the tooth. The latest approach to surgery of the root end section is the use of targeted endodontics microsurgery (TEMS) which is a guided approach to surgery which incorporates ultrasonic preparation (Buniag et al., 2021). The resection of the root is done via a 3D printed surgical guide instead of a free surgical approach. These surgical approaches with guides may offer new ways for other aspects of surgery including the use of ultrasonic instruments in general.

24.8.1 Hazards: Damage to teeth

Power ultrasonics provide many advantages to clinical dental work. However, there are several potential hazards associated with its use. A side effect of the use of ultrasonic scaling instruments is that this cleaning process will invariably cause damage to the underlying tooth surface. The presence of a roughened tooth surface will become a new area for biofilm formation. Roughness will occur from the impact of the elliptical movement of either class of ultrasonic scaler generator, magnetostrictive, or piezoelectric. Ideally, this alteration of the root surface should be kept to a minimum; however, there is no consensus to which instrument causes the most damage to the tooth surface during ultrasonic scaling (Lea and Walmsley, 2009). Clinicians are taught during training to use a high-power setting with standard power tips for heavy calculus removal and then to use thinner tips for definitive debridement including light deposit removal and/or biofilm removal. The reason for the variability is once again the lack of standardization of the instruments without knowledge of the movement of the tip. Research has been clinician-driven where the instrument renders the surface clean to the satisfaction of the operator. This may be considered a subjective method and will vary between clinicians. There have been a series of studies where the cleaning is more controlled and the various operating variables such as load applied and contact angle are set as the variables. The two approaches differ, and it may be argued that the former is more clinically relevant. However, with such an approach, it is not possible to determine the influencing variables. The main advice from controlled studies is that the tips are kept as close to 0 degree (i.e., parallel) to the tooth surface and that both low loads and power settings are used (Flemmig et al., 1998a,b). There is no difference between the generator types, and if any occur, it is because magnetostrictive scaler tips oscillate with greater displacement amplitudes than piezoelectric probes. Both instruments produced similar defects. The dimensions of the defects were independent of the type of generator used. The shape of the scaler tip had a direct influence on the shape of the defect (Lea et al., 2009b).

24.8.2 Hazards: Aerosol production

As the cooling water flows over an oscillating ultrasonic scaler, a fine aerosol mist is produced. The envelope of this mist can extend to around 2 m, and while some of it will splatter on the patient and operator, other droplets may settle on the surrounding surgery (Figure 24.14). Saliva is a reservoir of microorganisms such as bacteria, and there will be small particles present in the air which will take up to 30 min to settle out. Such aerosols may transmit pathogenic microorganisms which will be hazardous to health (Trenter and Walmsley, 2003). It will also increase the risk of cross-infection between patients. This has been recognized since the introduction of ultrasonic scalers and the risk was considered low. It was recommended that any patients who may be at risk from infections should be treated with hand instruments. The use of well-ventilated surgeries to remove the aerosol and protection of dental personal has always been advocated. Properly fitted face masks with high filtration



FIGURE 24.14 The ultrasonic scaler tip working at full power setting with a water flow over the tip. The water leaves the tip as a jet but some is thrown off as an aerosol (Lea et al., 2002).

properties and large-bore high-volume evacuators to remove the aerosol are considered mandatory when using these instruments. Furthermore, preprocedural mouth rinse will reduce any bacterial hazard further.

The advent of the COVID-19 pandemic led to an immediate cessation of any aerosol producing instruments except in extenuating circumstances. While rotary burs were needed for tooth extractions, the cleaning of teeth could be undertaken with hand instruments. As the nature of the transmission of COVID19 has become better understood, there has been a slow return to the use of aerosol-generating procedures (AGP).

The ensuing pandemic meant that all protocols to minimize aerosol production have been revisited. When opening up dentistry to routine care, the threat of aerosol transmission must be minimized wherever possible (Chavis et al., 2021; Schwendicke, 2020). Therefore, mitigating the risk of transmitting the virus requires the highest standard of protection and high levels of barrier control such as facemasks and other protective clothing. There are several standard operating procedures that are produced in each country and these cover aerosol-generating procedures (AGPs) such as the ultrasonic scaler. These documents are constantly changing, and therefore, the reader needs to be aware of the most immediate information. The SARS-Cov-2 pandemic is a changing situation, and an area that engineering will play a part is the modification of power ultrasonic instruments to minimize aerosol production and any splatter that may occur during use.

24.8.3 Hazards: Hearing

The high frequencies of ultrasound used in clinical dentistry are above the limit of human hearing, but subharmonics and other noises associated with the ultrasonic scaler may be detrimental to the hearing of the operator and the patient being treated (Walmsley et al., 1987a; Trenter and Walmsley, 2003). The exposure may arise to the patient from bone conduction as the instrument is used on the teeth, especially the upper molars or to the operator by airborne conduction (Leighton, 2016). There is a very low research base behind many of the observations on hearing loss and several confounders are often not considered. Such examples include age-related hearing loss. It is interesting to note that the growth of personal music equipment with the ability to turn the volume up high is a potential hazard to doctors in training (Narahari et al., 2017). This should be considered when assessing the hearing loss in dental personnel. There are continuing reports in the literature where self-assessment reporting (Lazar et al., 2015) or audiometry based trials have reported hearing loss in dental personnel (Chopra et al., 2016). There has been little research on the hearing hazard posed to patients undergoing treatment.

24.8.4 Hazards: Cardiac pacemakers

A long-standing concern when using of either magnetostrictive or piezoelectric ultrasonic scalers is whether they will interfere with cardiac implantable electrical devices (CIEDs) during dental treatment (Trenter and Walmsley, 2003). Patients fitted with pacemakers as a result of cardiac bradycardia or severe heart failure are provided with instructions on how to avoid any interference to the systems. These include guidance on ultrasonic scalers, and manufacturers actively discourage patients from being exposed to such electric devices in the dental surgery (Conde-Mir et al., 2018). This has produced much concern over the years and dental operators have always been very careful to check the medical history of patients. The safest action has been to exclude those individuals with pacemakers from any treatment with the ultrasonic scaler. The main data to back up such recommendations were based on *in vitro* experimentation as there was hesitancy to undertake a clinical trial on the subject until recently. A clinical trial by Conde-Mir et al. (2018) recruited 66 patients fitted with cardiac pacemakers. To enter the trial, there was strict ethical considerations and patients all consented to dental treatment with an electrical device, one of which was a piezoelectric ultrasonic scaler. All the patients were nonpacemaker-dependent. No adverse reactions or changes were seen on the patients' electrograms and there was no alteration in the functioning of the pacemakers. The conclusion of this research is that ultrasonic scalers are compatible with current cardiac implantable electrical devices (CIEDs). There may be some debate as this work did not include magnetostrictive-designed scalers.

24.9 Future trends

Power ultrasonics are firmly established in dentistry and the ultrasonic scaler has been a versatile device since its introduction in the 1950s. This is demonstrated by its adaptation into many different specialties in dentistry. The instrument has undergone refinement over the years. Interestingly, there have been no major radical changes in its design. Both magnetostrictive and piezoelectric generators have changed little over those that were originally introduced into dentistry. The instruments have an inherent variability, but this has not prevented them being established for routine treatment. Clinical studies are generally directed at the ability to bring about tissue resolution and better understanding of the ultrasonic generation of the vibrations may lead to improved results. There is more work to be done on the role of cavitation in removing the biofilm and to improve the effectiveness of this action. This may require reassessment of the engineering of the generators and also more investigations in how tip design may influence the clinical performance. Following on from the COVID19

pandemic, the aerosol produced by the cooling water requires reduction and again this may require novel approaches to tip design. The increased use of dental implants in and around the jaws has indicated that ultrasonic surgery has an advantage. This may be a future growth area as the ultrasonic drill is used in preference to rotary burs.

24.10 Conclusions

Applications of power ultrasonics will continue to have a place in dentistry. The versatility of power ultrasonics has allowed several adaptations into different branches of dentistry. The continued success of ultrasound is dependent upon the interdisciplinary research where engineers and physical scientists interact with clinicians to develop innovative designs and applications that will ultimately benefit the patient and promote the health and longevity of hard and soft dental tissues.

Acknowledgments

Much of this work was made possible by a series of project grants from the Engineering and Physical Sciences Research Council (EPSRC) of the United Kingdom Research and Innovation (UKRI) from 1999 to 2023.

References

Baehni, P., Thilo, B., Chapuis, B., Pernet, D., 1992. Effects of ultrasonic and sonic scalers on dental plaque microflora in vitro and in vivo. J. Clin. Periodontol. 19, 455–459.

Balamuth, L., 1952. Method and Means for Removing Material From a Solid Body. U.S. Patent 2,580,716,.

Balamuth, L., 1963. Ultrasonics and dentistry. Sound 2, 15–19.

Bassi, F., Cicciù, M., Di Lenarda, R., Galindo Moreno, P., Galli, F., Herford, A.S., Jokstad, A., Lombardi, T., Nevins, M., Sennerby, L., Schierano, G., Testori, T., Troiano, G., Vercellotti, T., Stacchi, C., 2020. Piezoelectric bone surgery compared with conventional rotary instruments in oral surgery and implantology: summary and consensus statements of the International Piezoelectric Surgery Academy Consensus Conference 2019. Int. J. Oral Implantol. 13, 235–239.

Berman, L.H., Hargreaves, K.M., 2020. Cohen's Pathways of the Pulp. Elsevier.

Boutsioukis, C., Verhaagen, B., Walmsley, A.D., Versluis, M., van der Sluis, L.W., 2013. Measurement and visualization of file-to-wall contact during ultrasonically activated irrigation in simulated canals. Int. Endod. J. 46, 1046–1055.

Buniag, A.G., Pratt, A.M., Ray, J.J., 2021. Targeted endodontic microsurgery: a retrospective outcomes assessment of 24 cases. J. Endod. 47 (5), 762–769. https://doi.org/10.1016/j.joen.2021.01.007.

Căpută, P.E., Retsas, A., Kuijk, L., Chávez de Paz, L.E., Boutsioukis, C., 2019. Ultrasonic irrigant activation during root canal treatment: a systematic review. J. Endod. 45 (1), 31–44.e13. https://doi.org/10.1016/j.joen.2018.09.010.

Cardoni, A., 2010. Enhancing oral implantology with power ultrasonics. IEEE Trans. Ultrason. Ferroelectr. Freq. Control 57, 1936–1942.

Catuna, M.C., 1953. Sonic energy. A possible dental application. Preliminary report of an ultrasonic cutting method. Ann. Dent. 12, 256–260.

Chavis, S.E., Hines, S.E., Dyalram, D., Wilken, N.C., Dalby, R.N., 2021. Can extraoral suction units minimize droplet spatter during a simulated dental procedure? J. Am. Dent. Assoc. 152 (2), 157–165.

Chopra, A., Thomas, B.S., Mohan, K., Sivaraman, K., 2016. Auditory and nonauditory effects of ultrasonic scaler use and its role in the development of permanent hearing loss. Oral Health Prev. Dent. 14, 493–500.

Cicciù, M., Stacchi, C., Fiorillo, L., Cervino, G., Troiano, G., Vercellotti, T., Herford, A.S., Galindo-Moreno, P., Di Lenarda, R., 2021. Piezoelectric bone surgery for impacted lower third molar extraction compared with conventional rotary instruments: a systematic review, meta-analysis, and trial sequential analysis. Int. J. Oral Maxillofac. Surg. 50, 121–131.

Claire, S., Lea, S.C., Walmsley, A.D., 2013. Characterisation of bone following ultrasonic cutting. Clin. Oral Investig. 17 (3), 905–912.

Conde-Mir, I., Miranda-Rius, J., Trucco, E., Lahor-Soler, E., Brunet-Llobet, L., Domingo, R., Tolosana, J.M., Mont, L., 2018. In-vivo compatibility between pacemakers and dental equipment. Eur. J. Oral Sci. 126, 307–315.

Cunningham, W.T., Martin, H., Forrest, W.R., 1982. Evaluation of root canal débridement by the endosonic ultrasonic synergistic system. Oral Surg. Oral Med. Oral Pathol. 53 (4), 401–404.

Daly, S., Newcombe, R.G., Claydon, N.C.A., Seong, J., Davies, M., West, N.X., 2020. A randomised controlled trial to determine patient experience of a magnetostrictive stack scaler as compared to a piezoelectric scaler, in supportive periodontal therapy. J. Dent. 93, 103279.

Derdilopoulou, F.V., Nonhoff, J., Neumann, K., Kielbassa, A.M., 2007. Microbiological findings after periodontal therapy using curettes, Er: YAG laser, sonic, and ultrasonic scalers. J. Clin. Periodontol. 34, 588–598.

Dragoo, M.R., 1992. A clinical evaluation of hand instruments and ultrasonic instruments on subgingival debridement. I. With unmodified and modified ultrasonic inserts. Int. J. Periodontics Restorative Dent. 12, 310–323.

Dyson, J.E., Darvell, B.W., 1993. The development of the dental high-speed air turbine handpiece. Part 2. Aust. Dent. J. 38, 131–143.

Felver, B., King, D.C., Lea, S.C., Price, G.J., Walmsley, A.D., 2009. Cavitation occurrence around ultrasonic dental scalers. Ultrason. Sonochem. 16, 692–697.

Flemmig, T.F., Petersilka, G.J., Mehl, A., Hickel, R., Klaiber, B., 1998a. Working parameters of a magnetostrictive ultrasonic scaler influencing root substance removal in vitro. J. Periodontol. 69, 547–553.

Flemmig, T.F., Petersilka, G.J., Mehl, A., Hickel, R., Klaiber, B., 1998b. The effect of working parameters on root substance removal using a piezoelectric ultrasonic scaler in vitro. J. Clin. Periodontol. 25, 158–163.

George, R., 2019. Evaluation of the evidence of effectiveness of ultrasonic activated irrigation for root canal treatment. Evid Based Dent. 20, 83–84.

Guyatt, G.H., Oxman, A.D., Vist, G.E., Kunz, R., Falck-Ytter, Y., Alonso-Coello, P., et al., 2008. GRADE: an emerging consensus on rating quality of evidence and strength of recommendations. BMJ 336, 924.

Horton, J.E., Tarpley, T.M., 1981. Clinical applications of ultrasonic instrumentation the surgical removal of bone. Oral Surg. 51, 236–241.

Ikeda, Y., Kawada, A., Tanaka, D., Ikeda, E., Kobayashi, H., Iwata, T., 2021. A comparative questionnaire study of patient complaint levels between magnetostrictive ultrasonic scaler (Cavitron®) and piezoelectric ultrasonic scalers. Int. J. Dent. Hyg. 19 (3), 273–278. https://doi.org/10.1111/idh.12478.

Laird, W.R., Walmsley, A.D., 1991. Ultrasound in dentistry. Part 1—biophysical interactions. J. Dent. 19, 14–17.

Lazar, A., Kauer, R., Rowe, D., 2015. Hearing difficulties among experienced dental hygienists: a survey. J. Dent. Hyg. 89 (6), 378–383.

Lea, S.C., Walmsley, A.D., 2009. Mechano-physical and biophysical properties of power driven scalers—driving the future of powered instrument design and evaluation. Periodontology 2000 51, 63–78. https://doi.org/10.1111/j.1600-0757.2009.00300.x.

Lea, S.C., Landini, G., 2010. Reconstruction of dental ultrasonic scaler 3D vibration patterns from phase-related data. Med. Eng. Phys. 32 (6), 673–677.

Lea, S.C., Walmsley, A.D., 2011. Do ultrasonic scaler inserts and generators from the same manufacturer optimise performance? Ann. Clin. J. Dent. Health 1, 22–27.

Lea, S.C., Landini, G., Walmsley, A.D., 2002. Vibration characteristics of ultrasonic scalers assessed with scanning laser vibrometry. J. Dent. 30, 147–151.

Lea, S.C., Landini, G., Walmsley, A.D., 2003. Ultrasonic scaler tip performance under various load conditions. J. Clin. Periodontol. 30, 876–881.

Lea, S.C., Walmsley, A.D., Lumley, P.J., Landini, G., 2004. A new insight into the oscillation characteristics of endosonic files used in dentistry. Phys. Med. Biol. 49, 2095–2102.

Lea, S.C., Landini, G., Walmsley, A.D., 2006. The effect of wear on ultrasonic scaler tip displacement amplitude. J. Clin. Periodontol. 33, 37–41.

Lea, S.C., Felver, B., Landini, G., Walmsley, A.D., 2009a. Three-dimensional analyses of ultrasonic scaler oscillations. J. Clin. Periodontol. 36, 44–50.

Lea, S.C., Felver, B., Landini, G., Walmsley, A.D., 2009b. Ultrasonic scaler oscillations and tooth-surface defects. J. Dent. Res. 88, 229–234.

Lea, S.C., Walmsley, A.D., Lumley, P.J., 2010. Analyzing endosonic root canal file oscillations: an *in vitro* evaluation. J. Endod. 36, 880–883.

Leighton, T.G., 2016. Are some people suffering as a result of increasing mass exposure of the public to ultrasound in air? Proc. R. Soc. Math. Phys. Eng. Sci. 472 (2185), 20150624.

Li, X., Lin, X., Guo, J., Wang, Y., 2020. The stability and survival rate of dental implants after preparation of the site by piezosurgery vs conventional Drilling: a systematic review and meta-analysis. Int. J. Oral. Maxillofac. Implants 30 (3), e51–e56. https://doi.org/10.11607/jomi.5913.

Macedo, R.G., Robinson, J.P., Verhaagen, B., Walmsley, A.D., Versluis, M., Cooper, P.R., van der Sluis, L.W., 2014. A novel methodology providing insights into removal of biofilm-mimicking hydrogel from lateral morphological features of the root canal during irrigation procedures. Int. Endod. J. 47, 1040–1051.

Mann, M., Parmar, D., Walmsley, A.D., Lea, S.C., 2012. Effect of plastic-covered ultrasonic scalers on titanium implant surfaces. Clin. Oral Implants Res. 23, 76–82.

Martin, H., 1976. Ultrasonic disinfection of the root canal. Oral Surg. Oral Med. Oral Pathol. 42 (1), 92–99.

Mattheos, N., Collier, S., Walmsley, A.D., 2012. Specialists' management decisions and attitudes towards mucositis and peri-implantitis. Br. Dent. J. 212, E1.

Narahari, P.G., Bhat, J., Nambi, A., Arora, A., 2017. Impact of usage of personal music systems on oto-acoustic emissions among medical students. Noise Health 19, 222–226.

Ohl, S.W., Shrestha, A., Khoo, B.C., Kishen, A., 2010. Characterizing bubble dynamics created by high-intensity focused ultrasound for the delivery of antibacterial nanoparticles into a dental hard tissue. Proc. Inst. Mech. Eng. H 224, 1285–1296.

Park, E., 2013. Ultrasonics in endodontics. Endod. Top. 29, 125–159.

Parmer, D., Mann, M., Walmsley, A.D., 2011. Lea SC cutting characteristics of ultrasonic surgical instruments. Clin. Oral Implants Res. 22, 1385–1390. https://doi.org/10.1111/j.1600-0501.2010.02121.x.

Postle, H., 1958. Ultrasonic cavity preparation. J. Prosthet. Dent. 8, 153–160.

Quirynen, M., van der Mei, H.C., Bollen, C.M., Schotte, A., Marechal, M., Doornbusch, G.I., Naert, I., Busscher, H.J., van Steenberghe, D., 1993. An *in vivo* study of the influence of the surface roughness of implants on the microbiology of supra- and subgingival plaque. J. Dent. Res. 72, 1304–1309.

Robinson, J.P., Lumley, P.J., Claridge, E., Cooper, P.R., Grover, L.M., Williams, R.L., Walmsley, A.D., 2012. An analytical micro CT methodology for quantifying inorganic dentine debris following internal tooth preparation. J. Dent. 40, 999–1005.

Robinson, J.P., Macedo, R.G., Verhaagen, B., Versluis, M., Cooper, P.R., van der Sluis, L.W.M., Walmsley, A.D., 2018. Cleaning lateral morphological features of the root canal: the role of streaming and cavitation. Int. Endod. J. 51 (Suppl. 1), e55–e64.

Schmage, P., Kahili, F., Nergiz, I., Scorziello, T.M., Platzer, U., Pfeiffer, P., 2014. Cleaning effectiveness of implant prophylaxis instruments. Int. J. Oral Maxillofac. Implants 29, 331–337.

Schwendicke, F., 2020. Saliva is a potential source of Covid-19, and appropriate protection measures should be applied in dental practice. Evid. Based Dent. 21, 62.

Silva, E.J.N.L., Rover, G., Belladonna, F.G., Herrera, D.R., De-Deus, G., da Silva Fidalgo, T.K., 2019. Effectiveness of passive ultrasonic irrigation on periapical healing and root canal disinfection: a systematic review. Br. Dent. J. 227, 228–234.

Street, E.V., 1959. Critical evaluation of ultrasonics in dentistry. J. Prosthet. Dent. 9, 132–141.

Susila, A., Minu, J., 2019. Activated irrigation vs. conventional non-activated irrigation in endodontics – a systematic review. Eur. Endod. J. 4, 96–110.

Trenter, S.C., Walmsley, A.D., 2003. Ultrasonic dental scaler: associated hazards. J. Clin. Periodontol. 30, 95–101.

Trenter, S.C., Landini, G., Walmsley, A.D., 2003. Effect of loading on the vibration characteristics of thin magnetostrictive ultrasonic scaler inserts. J. Periodontol. 74 (9), 1308–1315.

Tripp, D.A., Neish, N.R., Sullivan, M.J., 1998. What hurts during dental hygiene treatment. J. Dent. Hyg. 72, 25–30.

Tunkel, J., Heinecke, A., Flemmig, T.F., 2002. A systematic review of efficacy of machine-driven and manual subgingival debridement in the treatment of chronic periodontitis. J. Clin. Periodontol. 29 (Suppl 3), 72–81. https://doi.org/10.1034/j.1600-051x.29.s3.4.x (discussion 90-1).

van der Sluis, L.W., Wu, M.K., Wesselink, P.R., 2005. The efficacy of ultrasonic irrigation to remove artificially placed dentine debris from human root canals prepared using instruments of varying taper. Int. Endod. J. 38, 764–768.

Vercellotti, T., 2004. Technological characteristics and clinical indications of piezoelectric bone surgery. Minerva Stomatol. 53, 207–214.

Vercellotti, T., Stacchi, C., Russo, C., Rebaudi, A., Vincenzi, G., Pratella, U., Baldi, D., Mozzati, M., Monagheddu, C., Sentineri, R., Cuneo, T., Di Alberti, L., Carossa, S., Schierano, G., 2014. Ultrasonic implant site preparation using piezosurgery: a multicenter case series study analyzing 3,579 implants with a 1- to 3-year follow-up. Int. J. Periodontics Restorative Dent. 34, 11–18.

Verhaagen, B., Lea, S.C., de Bruin, G.J., van der Sluis, L.W., Walmsley, A. D., Versluis, M., 2012. Oscillation characteristics of endodontic files: numerical model and its validation. IEEE Trans. Ultrason. Ferroelectr. Freq. Control 59, 2448–2459.

Vyas, N., Pecheva, E., Dehghani, H., Sammons, R.L., Wang, Q.X., Leppinen, D.M., Walmsley, A.D., 2016. High speed imaging of cavitation around dental ultrasonic scaler tips. PLoS One 11, e0149804.

Vyas, N., Sammons, R.L., Pikramenou, Z., Palin, W.M., Dehghani, H., Walmsley, A.D., 2017. Penetration of sub-micron particles into dentinal tubules using ultrasonic cavitation. J. Dent. 56, 112–120.

Vyas, N., Manmi, K., Wang, Q., Jadhav, A.J., Barigou, M., Sammons, R.L., Kuehne, S.A., Walmsley, A.D., 2019. Which parameters affect biofilm removal with acoustic cavitation? A review. Ultrasound Med. Biol. 45, 1044–1055.

Vyas, N., Grewal, M., Kuehne, S.A., Sammons, R.L., Walmsley, A.D., 2020a. High speed imaging of biofilm removal from a dental implant model using ultrasonic cavitation. Dent. Mater. 36, 733–743.

Vyas, N., Mahmud, M., Wang, Q.X., Walmsley, A.D., 2020b. Imaging and quantification of the area of fast-moving microbubbles using a high-speed camera and image analysis. J. Vis. Exp. 163. https://doi.org/10.3791/61509.

Vyas, N., Wang, Q.X., Manmi, K.A., Sammons, R.L., Kuehne, S.A., Walmsley, A.D., 2020c. How does ultrasonic cavitation remove dental bacterial biofilm? Ultrason. Sonochem. 67, 105112.

Vyas, N., Wang, Q.X., Walmsley, A.D., 2021. Improved biofilm removal using cavitation from a dental ultrasonic scaler vibrating in carbonated water. Ultrason. Sonochem. 70, 105338.

Walmsley, A.D., 1987. Ultrasound and root canal treatment: the need for scientific evaluation. Int. Endod. J. 20 (3), 105–111.

Walmsley, A.D., 2015. Ultrasonics in dentistry. Phys. Procedia 63, 201–207. https://doi.org/10.1016/j.phpro.2015.03.033.

Walmsley, A.D., Laird, W.R., Williams, A.R., 1984. A model system to demonstrate the role of cavitational activity in ultrasonic scaling. J. Dent. Res. 63, 1162–1165.

Walmsley, A.D., Hickson, F.S., Laird, W.R., Williams, A.R., 1987a. Investigation into patients' hearing following ultrasonic scaling. Br. Dent. J. 21 (162), 221–224.

Walmsley, A.D., Laird, W.R., Williams, A.R., 1987b. Intra-vascular thrombosis associated with dental ultrasound. J. Oral Pathol. 16, 256–259.

Walmsley, A.D., Laird, W.R., Williams, A.R., 1988. Dental plaque removal by cavitational activity during ultrasonic scaling. J. Clin. Periodontol. 15, 539–543.

Walmsley, A.D., Laird, W.R., Lumley, P.J., 1992. Ultrasound in dentistry. Part 2—periodontology and endodontics. J. Dent. 20, 11–17.

Walmsley, A.D., Lea, S.C., Landini, G., Moses, A.J., 2008. Advances in power driven pocket/root instrumentation. J. Clin. Periodontol. 35 (8 Suppl), 22–28.

Waplington, M., Lumley, P.J., Walmsley, A.D., Blunt, L., 1995. Cutting ability of an ultrasonic retrograde cavity preparation instrument. Endod. Dent. Traumatol. 11 (4), 177–180.

Zinner, D.D., 1955. Recent ultrasonic dental studies, including periodontia, without the use of an abrasive. J. Dent. Res. 34, 748–749.

Chapter 25

High-intensity focused ultrasound for medical therapy

N.P.K. Ellens[a] and K. Hynynen[b,c]

[a]*Acertara Acoustic Labs, Longmont, CO, United States,* [b]*Sunnybrook Research Institute, Toronto, ON, Canada,* [c]*University of Toronto, Toronto, ON, Canada*

25.1 Introduction

Ultrasound is a mechanical pressure wave propagating at a frequency above the range of human hearing (18–20 kHz). A diagram describing the propagation of ultrasound is shown in Figure 25.1. Ultrasound has been used for biomedical applications for decades and is among the most commonly used medical imaging modalities. Though many of its therapeutic applications have been known for as long or longer, its clinical adoption as a therapeutic modality has only begun in the past 20 years. As such, it is a technology in its infancy. This chapter provides an overview of the benefits and capabilities of therapeutic ultrasound, along with the challenges that currently limit clinical adoption.

Ultrasound therapies can be classified into two categories based on whether their effect is derived from mechanical or thermal mechanisms (Ter Haar, 2007). Mechanical mechanisms can be further subdivided as deriving their effect from cavitation or radiation forces (Dalecki, 2004). In the former, gas bubbles are either pulled out of tissue by the rarefaction region of a pressure wave of sufficient intensity or introduced to the system via an intravenous injection of synthetic, encapsulated bubbles. Ultrasound interacts with the bubbles to cause cavitation or with the tissue directly to produce a bioeffect. Conversely, thermal mechanisms rely on the absorption of ultrasound energy by the tissue, generating heat (Nyborg, 1981). Using focused ultrasound (FUS), it is possible to deposit energy such that tissue can be heated controllably and precisely, even deep in tissue, with minimal heating to the intervening tissue between the focus and the source transducer.

Unlike a linear accelerator for radiation therapy, there is no single ultrasound applicator that can treat a large range of clinical targets, primarily because it is very difficult for ultrasound to propagate through gas (the impedance difference between tissue and air is such that virtually all of the energy is reflected) and ultrasound is attenuated very quickly in bone, rendering access to many biological targets difficult (Fry and Barger, 1978). As such, ultrasound applicators are tailored to specific clinical targets. To accomplish this, external, endocavity, and interstitial devices have all been used to deliver ultrasound as required. In terms of patient care, however, this increased complexity might be worth the challenge for many diseases: FUS, unlike ionizing radiation, deposits no radiation dose and thus can be repeated as needed without residual risk to the patient. Moreover, FUS can be used to treat young patients for whom radiation dose is an especially large concern (Goske et al., 2014). FUS procedures also benefit patients' quality of life and can reduce the cost related to various conditions. Therapeutic ultrasound procedures can often replace invasive surgeries with noninvasive procedures—negating the danger of infection and reducing recovery times—and can replace fractionated radiation therapy treatment regimens with a single session, again without the need for any ionizing radiation. As such, there is much promise in therapeutic ultrasound to transform the treatment of many diseases and conditions. The following sections discuss therapeutic ultrasound devices, their methods of guidance and control, the bioeffects they cause, and the clinical outcomes that have been achieved with therapeutic ultrasound.

25.2 Ultrasound interaction with tissue

Ultrasound interacts differently with different tissues, depending on the frequency, acoustic pressure, or intensity and the amount of time the ultrasound is applied, be it in short bursts or as continuous-wave sonication. The interactions between ultrasound and tissue can be classified according to the primary mechanism: thermal or mechanical.

Power Ultrasonics. https://doi.org/10.1016/B978-0-12-820254-8.00038-5
Copyright © 2023 Elsevier Ltd. All rights reserved.

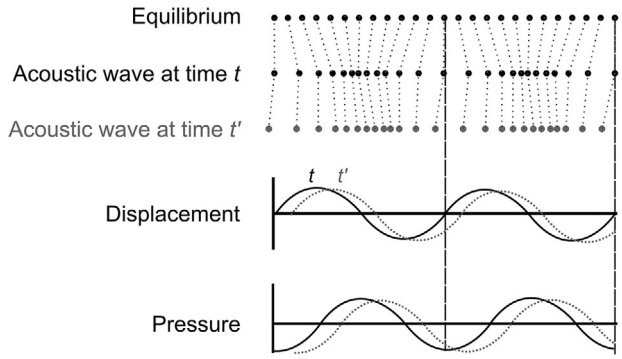


FIGURE 25.1 An ultrasound wave propagating from left to right, shown at time t and t', a short time later. Note that the pressure is 90 degrees out of phase with the displacement from equilibrium.

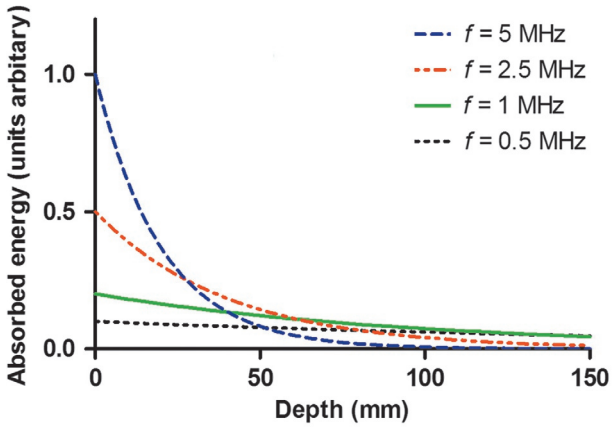


FIGURE 25.2 Absorbed energy as a function of depth for different frequencies. A tissue attenuation of 5 Nep/m/MHz was used to generate this figure. This figure shows the importance of frequency selection for different applications: higher frequencies produce concentrated absorbed energy but fall off quickly with depth. Lower frequencies, conversely, are not quickly absorbed and, thus, decay slowly with depth.

25.2.1 Thermal interaction

25.2.1.1 Energy absorption

Ultrasound is attenuated as it travels through tissue; the kinetic energy of the mechanical wave is converted into heat. This process involves both scattering and absorption, though it is dominated by the latter, and indeed, the scattered wave is subsequently absorbed. Unlike diagnostic ultrasound, therapeutic ultrasound is concerned with the deposition of energy and is less concerned about the profile of the scattered field. In short, scattering broadens the profile of deposited energy (Mahoney et al., 2001). Attenuation increases exponentially with frequency, though the power of this proportionality ranges from 1 to 2 for biological tissues (Duck, 1990). Attenuation varies greatly from tissue to tissue, a property that must be taken into account when delivering ultrasound for the purpose of thermal therapy.

Mechanically, absorption occurs when there is a phase difference between pressure and density: there is a lag between external and internal degrees of freedom in the constituent molecules as the acoustic wave passes (Wells, 1977). In an inviscid fluid, the pressure and density of an ultrasound wave are in phase and there is no attenuation. In biological media, however, this phase difference is present, caused by viscous friction and relaxation processes. As the wave passes, energy is redistributed into various forms, including molecular translation and lattice potential energy. This energy is returned to the wave in an oscillatory manner, but the speed is finite and the energy often is at least in partially out of phase, constituting a loss for the wave and an increase in kinetic energy for the tissue, macroscopically as heat. Given that this process relies on the finiteness of the speed of energy return, it is understandable that the effect is more pronounced at higher frequencies, which has been observed (Wells, 1977).

For an incident plane wave of intensity $I(0)$, the intensity at the depth of x in an attenuating medium is given as $I(x) = I(0)e^{-2ax}$. The absorbed energy q can be found by differentiating x, giving

$$q = -\frac{dI(x)}{dx} = 2aI(x)$$

The attenuation coefficient, α, is frequency dependent. In general, in soft tissue, it can be approximated as $\alpha = \alpha_0 f^n$ for n ranging from 1 to 2. As such, q becomes (Goss et al., 1980)

$$q = 2a_0 f^n I(0) e^{-2a_0 f^n x}$$

The absorbed energy as a function of depth at different frequencies is shown in Figure 25.2. Tissue, thus heated, experiences different bioeffects, depending on the extent and duration.

25.2.1.2 Thermal ablation

In 1927, it was observed that intense ultrasound at around 300 kHz caused rapid heating and eventually killed the various mice, frogs, fish, and paramecium that were subjected to this ultrasound application (Wood and Loomis, 1927). The authors acknowledged that the effects they observed were both thermal and mechanical in origin.

Since this early observation, thermal ablation with FUS has been examined in much greater detail. In the late 1950s and early 1960s, the Fry brothers performed clinical research with a stereotaxic therapeutic ultrasound system that produced thermal lesions in brain tissue through a craniotomy. They used their system to treat patients with Parkinson's disease and other tremors (Fry and Fry, 1960; Meyers et al., 1959). With their clinical system, they also performed many studies of cats and rodents in which they examined reversible and irreversible effects of ultrasound and derived relationships between damage thresholds (quantified by the degree of paralysis after sonicating the

spine), ultrasound intensity, and exposure time (Fry and Fry, 1960).

The mechanism at work in these procedures and, indeed, in most thermal therapies is thermal necrosis (in situ death of tissue caused exposure to excessive temperature). Necrosis is the result of severe cellular injury. It is thought that the loss of integrity of the cellular membrane is the decisive factor that ensures that the damage is irreversible. Whereas apoptosis (a type of cell death in which a programmed series of molecular steps that are triggered by exposure to excessive temperature in a cell lead to its death) is characterized by DNA lysed into short strings of 180–200 base pairs, necrosis results in intact DNA with random aberrations (Harmon et al., 1990). Over time, the difference becomes quite pronounced: apoptotic cells remain organized and undergo condensation of chromatin, whereas necrotic cells are left as random cellular debris and, eventually, there is an inflammatory response. At the peak temperatures of high-intensity FUS (HIFU; 60–70°C), the mechanism is almost exclusively necrotic at the center of the focus. These temperatures have been shown to create very well-defined lesions separated from viable cells by only a few cellular layers. Heating occurs much faster than diffusion, which can carry away the energy (Billard et al., 1990), and perfusion is stopped as the blood vessels are occluded (Damianou and Hynynen, 1994). It has been shown in uterine fibroid treatment that the extent of the nonperfused volume after treatment (as seen on contrast-enhanced magnetic resonance imaging (MRI)) is a good predictor of long-term treatment efficacy (Lenard et al., 2008).

The concept of thermal dose has been studied extensively in an attempt to predict what combination of temperature and duration will produce thermal necrosis (or, conversely, prevent the same). Moritz and Henriques (1947) studied the thermal effects of hot water and hot air on skin. Fry and Fry (1960) quantified thermal dose to some extent with their ultrasonic heating experiments, whereas Lele and Parker (1982b) discussed "heat dose" in the context of ultrasound-induced hyperthermia. Sapareto and Dewey (1984) formalized this discussion somewhat in 1984 for long treatments at relatively low temperatures (hyperthermia: 30–60 min at temperatures of 42–45°C) by introducing a unit of equivalent minutes at 43°C and a mathematical form for integrating temperature over time to determine its biological effect. This method has been widely adopted in the exploration of thermal ablation (Chung et al., 1999b).

25.2.1.3 Apoptosis

There has recently been increased interest in causing apoptosis rather than necrosis. At lower temperatures that induce necrosis, the cell can sustain sufficient damage that either signals transmitted through cell surface receptors trigger the binding of death stimuli to target receptors or the mitochondria release cytotoxic substances that, in turn, trigger downstream caspase activation. Caspases are a family of enzymes that degrade proteins and serve as primary effectors during apoptosis to break down proteins into smaller polypeptides or amino acids in order to dismantle most cellular structures. Both of these processes give rise to organized cell death that kills the cell without damaging those around it and minimizes or eliminates inflammation (Vykhodtseva et al., 2001). Temperature elevation results in many chemical changes in the cell and the microenvironment. It produces heat shock proteins, which generally have protective functions, such as chaperoning proteins, so that they refold without error and prevent the translocation of mitochondria-derived signaling proteins. High concentrations of heat shock proteins, however, can have the opposite effect and trigger apoptosis (Zylicz et al., 2001).

25.2.1.4 Hyperthermia

At lower ultrasound intensities than either thermal ablation or tissue disintegration, slight temperature elevations are achieved, and the treatment is classified as hyperthermia, characterized by tissue temperatures of 42–46°C, typically for periods of time from minutes to hours (Diederich and Hynynen, 1999). Hyperthermia can be used in various ways. Preclinically, hyperthermia has been used to trigger the release of a chemotherapy agent from a thermosensitive liposome in a selective and localized manner. For example, in a recent study (Santos et al., 2020), the chemotherapeutic agent pegylated lyso-thermosensitive liposomal doxorubicin (Thermodox, Celsion) was released from its encapsulated form in a region that had been repeatedly heated with FUS to a temperature of 43°C for a period of 30 s. The doxorubicin concentration was higher in the heated region than in the control and resulted in good tumor control, suggesting that hyperthermia-mediated chemotherapy could be more selective than traditional chemotherapy.

Hyperthermia has also been shown to sensitize tumors to radiotherapy and chemotherapy (Overgaard, 1989). In the 1980s, thermal distributions were mapped in tumors, near bones, and near blood vessels during ultrasound sonication (Lele and Parker, 1982a; Lele, 1980). It was shown that ultrasound transducers, properly steered and operating at the appropriate temperature, could heat regions to uniform and controllable levels to produce localized hyperthermia without the toxicity associated with whole-body hyperthermia. The body's first response to hyperthermia is the dilation of blood vessels and a corresponding increase of blood flow in that region (Shakil et al., 1999; Anhalt et al., 1995). Increased blood flow changes the level of oxygenation of the region, which can be exploited in

conjunction with other treatments. Increasing the oxygenation of tumors (typically hypoxic) can promote activity that in turn sensitizes the tumor to radiotherapy and some chemotherapeutic agents. In addition, cell sensitivity to hyperthermia is enhanced in hypoxic conditions. Thus, the elevated temperature is targeting the cells that are otherwise less sensitive to radiation or chemotherapy.

25.2.2 Cavitational interaction

25.2.2.1 Mechanism

Cavitation is the interaction between the ultrasound field and small gas volumes or bubbles. Small gas nuclei are naturally found in biological tissues, although when cavitational effects are desired, synthetic, encapsulated gas bubbles often are injected intravenously to enhance and standardize cavitational interactions (Goldberg et al., 1994; Averkiou et al., 2020).

When sonicated, bubbles expand and contract considerably due to the compressibility of gas, which is orders of magnitude higher than liquid. The amplitude is maximal when the bubble is sonicated at the resonant frequency, which depends on the size of the bubble: at 1 MHz, 3.5 μm is the resonant size in free fluid. Resonant size decreases with frequency. Through a process called rectified diffusion, bubbles grow while sonicated. Diffusion is proportional to the surface area of the bubble; thus, for a stably oscillating bubble, more air diffuses in during the rarefaction portion of the pressure wave, wherein the internal pressure of the bubble is low, then diffuses out during the compression portion of the wave, wherein the internal pressure is high; during rarefaction, the bubble is large and has a larger surface area than during compression (Leighton, 1994). A schematic of this is shown in Figure 25.3.

At moderate ultrasound intensities, a bubble oscillates stably in an acoustic field, absorbing and reradiating energy

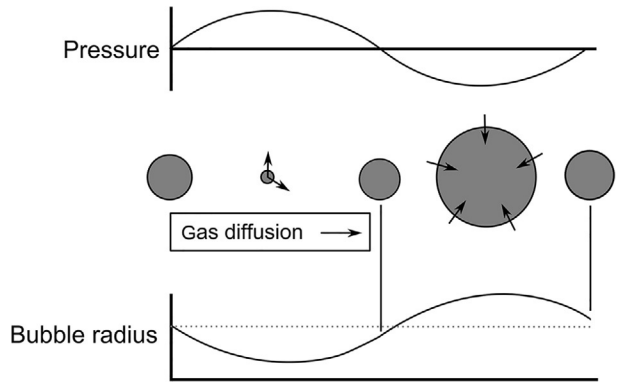


FIGURE 25.3 The equilibrium radius of a gas bubble grows in size through a process called rectified diffusion: more gas enters the bubble through its larger surface area during the rarefaction part of the wave than enters the bubble during the compression part of the wave.

to the surrounding tissue, greatly increasing the effective attenuation rate. At these intensities, the oscillation is typically stable over many oscillations, and the maximum radius rarely exceeds twice the equilibrium radius. This is called stable cavitation and gives rise to microstreaming of fluid near and around the bubble (Kooiman et al., 2020). Microstreaming, in turn, applies shear stress to the surrounding tissue. Ultrasound-generated shear stress can readily exceed the normal endothelial shear stress levels in blood vessels by three orders of magnitude under moderate, clinically diagnostic sonication pressures (Hosseinkhah et al., 2013; VanBavel, 2007). Elevated shear stress strongly affects endothelial cells: shear stress can modify gene expression and metabolism, result in vessel dilation, increase membrane permeability, and produce radicals (VanBavel, 2007). The signature emissions of stable cavitation from injected microbubbles can be used in diagnostic ultrasound to provide contrast to images. The oscillating microbubbles may also enhance energy absorption and may create local hot spots (Klotz et al., 2010).

When the acoustic intensity is sufficiently high, bubble oscillations become highly nonlinear and can give rise to violent collapse, known as inertial cavitation. Inertial cavitation induces microjets, shock waves, and highly local increases in temperature of thousands of degrees Kelvin (Apfel, 1982). These high temperatures can produce free radicals, which produce downstream bioeffects or cause mechanical tissue destruction, even liquefying tissue. The inertial cavitation threshold increases with frequency and decreases with burst length. For some therapeutic applications, inertial cavitation offers a means of concentrating the deposition of energy and generating specific, localized bioeffects such as lithotripsy (Leighton, 1994), soft-tissue vaporization (Smith and Hynynen, 1998), and mechanical tissue erosion called histotripsy (Xu et al., 2004; Khokhlova et al., 2015; Worlikar et al., 2022). For other applications, inertial cavitation is too violent and causes too many deleterious effects, such as bleeding (Hynynen et al., 1996); thus, it must be avoided through judicial selection of frequency and pulsing sequence.

Both stable and inertial cavitation substantially increase attenuation, which can be beneficial for thermal therapies (Holt and Roy, 2001; Hynynen, 1991), although this increase in heating efficiency sometimes occurs at the expense of control of the treatment extent. Because of this increase in attenuation, thermal lesions are formed closer to the transducer when bubbles are used than when they are not (Sokka et al., 2003).

25.2.2.2 Tissue disintegration and fragmentation

HIFU has long been used to break kidney stones into smaller pieces using large mechanical shocks (Chaussy et al., 1980).

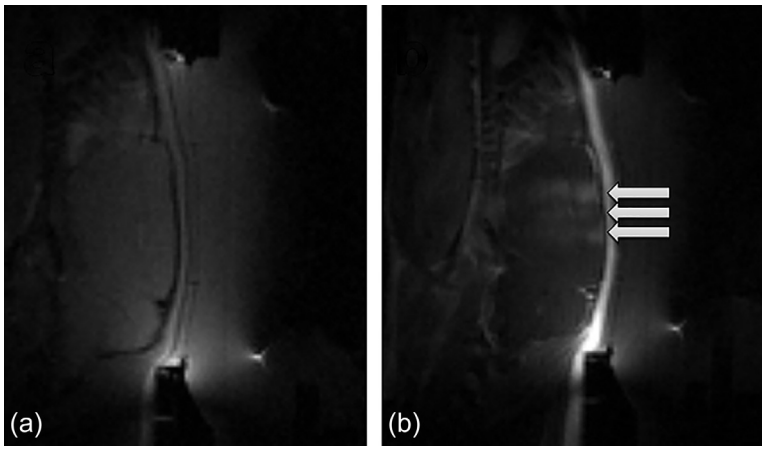


FIGURE 25.4 Sagittal T1-weighted MR images of a rat brain before (a) and after (b) MR-guided BBB disruption and the IV injection of gadolinium contrast agent. The *arrows* in (b) indicate the location of BBB disruption, and the direction of ultrasound propagation. Original data.

The use of HIFU for other forms of mechanical tissue destruction has been explored more recently. Mechanical tissue destruction in which the target volume is small is used, and it is desirable to highly localize the effect. With the intensities used, the ultrasound wave becomes highly nonlinear at and near the focus, which creates shock waves and violent pressure gradients. Cavitation is induced in bubbles that have been generated in situ (Lele, 1978). Cavitation is a highly efficient method of enhancing ultrasound attenuation; energy from the pressure wave causes the bubbles to oscillate violently and collapse, releasing energy into the immediately surrounding cells. This causes fragmentation and highly localized stress (VanBavel, 2007).

Using short bursts, vaporization that completely disintegrates tissue can be induced (Smith and Hynynen, 1998). Researchers at the University of Michigan have more recently investigated its uses for several medical conditions. For example, short pulses (20 μs) of very-high-intensity ultrasound (>20 kW/cm^2) at a frequency of 788 kHz can cause controlled erosion of tissue, generating neat punctures in pieces of porcine atrial wall (Xu et al., 2004, 2021). Based on their observations across different sonication parameters, these authors believe that tissue erosion (histotripsy) is most efficient when the pulses of ultrasound are separated by enough time that the induced bubble cloud has some time to begin to clear between pulses (to avoid acoustic shadowing, where the pulse is prevented from reaching the target) yet are close enough together so that the bubble cloud does not fully decay, such that subsequent pulses can use existing gas bubbles (Khokhlova et al., 2015). This method is now commercialized by HistoSonics for the treatment of benign prostatic hyperplasia and liver tumors (Xu et al., 2021) and by Cardiawave SA for calcified valve stenosis (Villemain et al., 2017). Tissue disintegration holds significant promise for the disintegration of blood clots (Maxwell et al., 2022; Wright et al., 2012; Zhang et al., 2017) and especially in the treatment of stroke (Burgess et al., 2012).

25.2.2.3 *Enhancement of drug treatments*

Targeted drug delivery can also be accomplished using mechanical means: sonoporation or ultrasound-mediated blood-brain barrier (BBB) permeability increase. Using high-speed photography in vitro, it has been shown convincingly that cavitation increases the cellular permeability of the surrounding cells following sonication (Ohl et al., 2006). This process could be used to selectively deposit higher concentrations of drug where sonicated. Ultrasound can also increase the permeability of the BBB, which is a specialized structure of endothelial cells in the wals of the blood vessels in the brain and form tight junctions. The BBB restricts the diffusion of all large molecules from the bloodstream and into the extracellular space. Although this is normally beneficial in preventing unwanted substances from entering the brain, it limits the desired entry of many therapeutic agents. The BBB can be modulated locally, safely, and reversibly by transcranially sonicating circulating synthetic microbubbles (Hynynen et al., 2001a). MRI of a rat brain before and after ultrasound exposure is shown in Figure 25.4. This technique is exceptionally promising and has been shown to enhance the delivery of many drugs (Kinoshita et al., 2006; McMahon et al., 2021) and even stem cells (Burgess et al., 2011; Zhu et al., 2022). Several studies have demonstrated that relatively low levels of ultrasound exposure can accelerate blood clot lysis in the presence of a thrombolytic agent (Kleven et al., 2021).

25.2.3 Radiation force

As ultrasound propagates through an attenuating medium such as tissue, there develops an energy gradient that produces a force on the medium in the direction of propagation, called radiation force (Beyer, 1950). All ultrasound fields produce radiation forces, but their effects are more

pronounced when undergoing highly nonlinear propagation or in the presence of microbubbles, which generate additional secondary radiation forces. Radiation forces have numerous bioeffects (Sarvazyan et al., 2010). Blood cells in circulation aggregate and align themselves into bands with half-wavelength separations when sonicated by an ultrasound standing wave (Dyson et al., 1974). With a traveling wave, ultrasound can be used to displace microbubbles in a vessel in vivo and push them up against the vessel wall farthest from the ultrasound source (Dayton et al., 1999; Acconcia et al., 2019). Intracellular organs and cells have been shown to spin under the effect of closely related radiation torque (Nyborg, 1982; Dyer and Nyborg, 1960). Radiation forces, especially from highly nonlinear ultrasound fields, can cause serious cellular damage. This damage can be used advantageously, however, when applied to enhance the penetration of thrombolytic agents such as recombinant tissue plasminogen activator into dense blood clots for the treatment of stroke (Bader et al., 2015).

25.3 Therapy devices

The utility of ultrasound stems largely from its good penetration through soft tissue at wavelengths that are short enough to allow precise focusing. The design of therapeutic ultrasound devices, then, reflects this ability to produce a therapeutic effect distant from the source transducer. As with diagnostic ultrasound, there are many types of applicators for therapeutic ultrasound that are tailored to the target and access point. In general, the deeper the target, the larger the aperture must be to spread the incident energy over a larger surface area and spare the near field from damage.

25.3.1 External devices

The first class of therapeutic ultrasound devices is the external class. External devices are those that perform a therapy purely noninvasively, at most requiring the removal of hair and the application of ultrasound coupling gel or water to provide a clear acoustic window between the applicator and the target.

The simplest external applicators are those that are used for localized hyperthermia. Although the heat can be applied in many ways, ultrasound is a desirable method because of its considerable penetration compared to optical or microwave radiation (Diederich and Hynynen, 1999). Even simple, planar, single-element transducers of varying frequencies and apertures were shown to be effective in enhancing radiation therapy with minimal side effects (Corry et al., 1982). Localized, unfocused transducers select for depth of penetration by the appropriate selection of frequency and otherwise localize the target by the form of the aperture. Although frequency adjustment offers some control of depth, these transducers are limited in their selectivity but are straightforward to use.

External FUS devices, instead, use various methods to focus the ultrasound beam deep in tissue. The most straightforward method is using a single-crystal, spherically curved radiator. By virtue of its shape, the compression wave generated by its oscillation focuses a short distance in front of the geometric focal point. The focus is ellipsoidal, with major and semi-major axes defined by the operating frequency and f-number, the ratio of the transducer's aperture to its focal length. Transducers with a lower f-number are more tightly focused. The pressure field generated by such a transducer is shown in Figure 25.5. This basic design is modified in several ways to allow versatility. To span a larger volume and thus treat a larger volume with either hyperthermia or ablation, the focus must be steered. The most basic method of accomplishing this is with physical translation (Lele and Parker, 1982b; Hynynen et al., 1987). A diagram illustrating this is shown in Figure 25.6a.

In the early 1990s, a device was developed to deliver "extracorporeal pyrotherapy" to patients. It utilized a focused transducer composed of multiple elements driven in phase with very short (0.015- to 1-s) bursts to create localized lesions. Using very high intensities, in situ temperatures reached up to 120°C (Vallancien et al., 1993). When the focus was scanned, small tumors could be treated, with mixed results (Vallancien et al., 1996).

Chongqing Haifu Technology has designed and built several systems that use spherically curved, single-element transducers that have been employed to treat breast (Wu et al., 2001b), liver, kidney and pancreatic cancer, bone metastases (Wu et al., 2004), and uterine fibroids (Zhang et al., 2010). These systems have used both ultrasound guidance and magnetic resonance (MR) guidance and monitoring.

At the cost of increased complexity and expense, the model of spherically curved, single-element transducers is improved through the use of phased-array transducers. Phased arrays use multiple transducer elements with electrical radiofrequency driving signals that can be controlled independently. A schematic of the function of a phased array is shown in Figure 25.7. For uniformly arranged transducer elements, grating lobes form if the elements are too large. Grating lobes are regions of off-focus constructive interference that form when many of the roughly hemispherical pressure waves transmitted from the different transducer elements intersect and combine constructively at different locations. To prevent the formation of grating lobes under all steering conditions, the interelement enter-to-center spacing must not exceed $\lambda/2$, a principle first described in the context of radiowave antennae arrays (Stone, 1927). Ultrasound at relevant frequencies has wavelengths of around 1–3 mm (1.5 MHz to 500 kHz) in soft

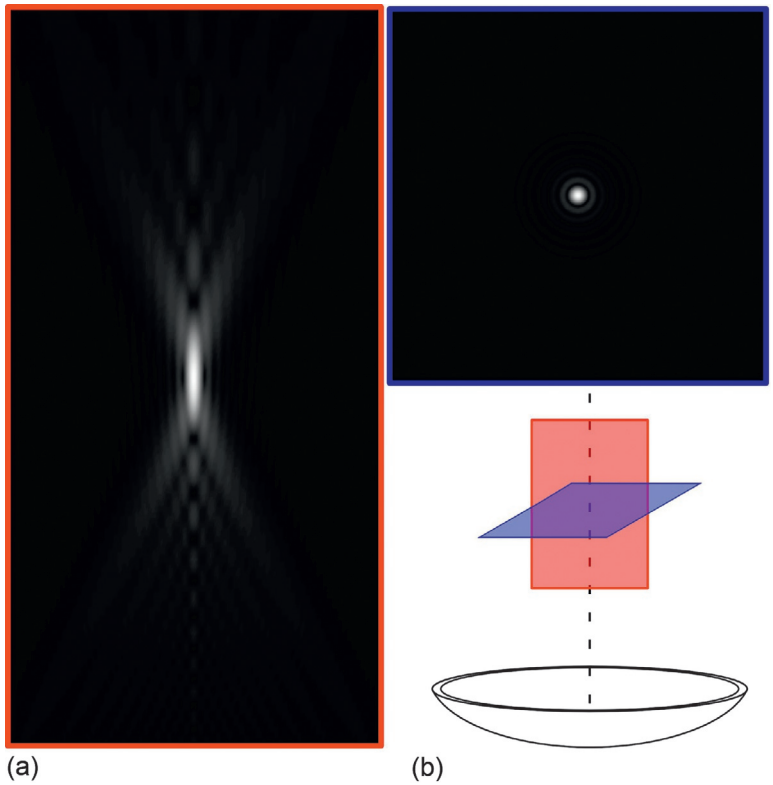
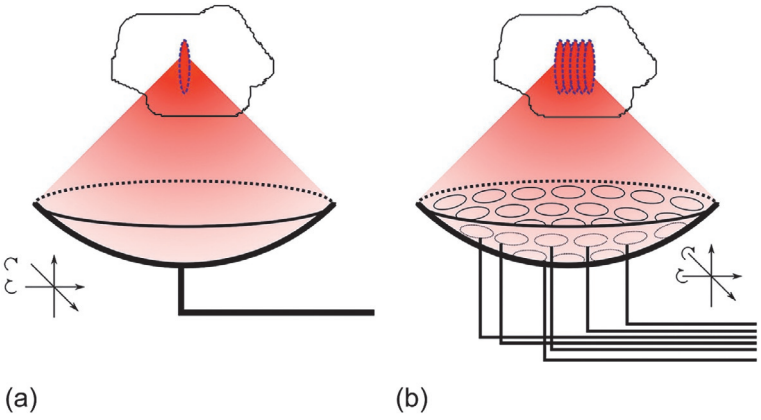


FIGURE 25.5 Simulated axial (a) and transverse (b) pressure field profiles from a 12 cm, *f*-number 1 transducer operating at 1 MHz.



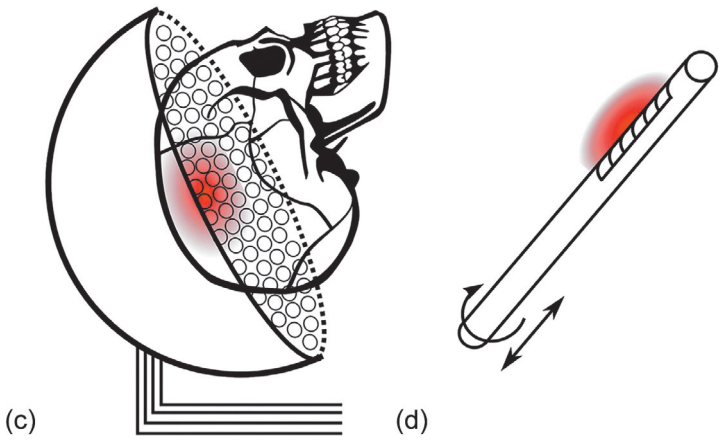


FIGURE 25.6 Illustration of different ultrasound transducer types: (a) single-element, spherically curved transducer that can be translated and tilted to span a target; (b) sparse phased-array transducer on a spherically curved shell that can be tilted and translated to span a target but can also be electronically steered to locations near to the geometric focus; (c) hemispherical phased-array transducer for trans-skull applications that can be steered electronically to locations within the skull and can be adjusted to account for skull inhomogeneities; (d) unfocused transducer array for interstitial or endocavity applications where the transducers are placed close to the target: localized rather than focused. *(The skull in (c) is modified from a graphic created by "Vectorportal": http://www.vecteezy.com/skulls-bones/36397-skull-profile-vector, licensed under Creative Commons 3.0 Unported.)*

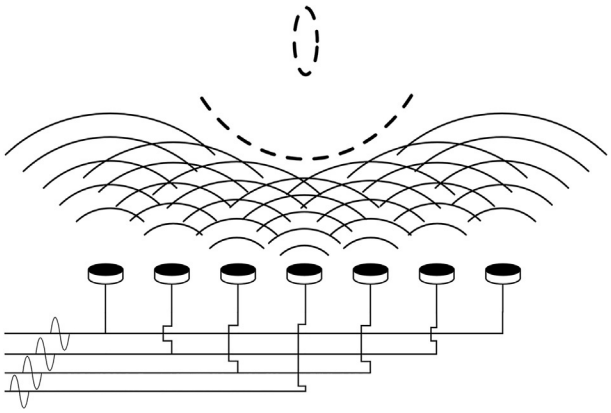


FIGURE 25.7 Phased-array schematic. To focus centrally, the elements on the outside are excited first such that all of the waves arrive in phase at the focus, indicated by the *dotted ellipse*. Similarly, by exciting the elements from left to right, the focus would shift right.

tissue, which imposes a rather stringent interelement spacing limit of 0.5–1.5 mm, requiring thousands or tens of thousands of individually driven and controlled elements to span across a transducer array of sufficient aperture.

The first proposed therapy devices of this type were described by Do-Huu and Hartemann (1981); they described a concentric ring array for focal depth control in hyperthermia treatments. In 1984, Cain et al. followed by describing methods that could allow electronic beam steering with an array driven with a reduced number of independent radiofrequency (RF) lines for producing mild hyperthermia (Ocheltree et al., 1984). Later, Cain and Umemura (1986) proposed two designs, again to take advantage of phased arrays with a reduced number of RF drivers, both with elements arranged on a spherically curved shell: in the first, the elements form concentric rings, whereas in the second, the elements form pie slice-like segments of the same spherically curved shell. The former allows electronic steering of the focal point in the axial direction, whereas the latter affords some degree of lateral focus steering. Combining both of these designs into a hybrid sector-vortex phased array allows for considerable freedom to generate focal regions of different sizes and forms. By selecting different excitation patterns or sonication modes, the focus splits from a single focus near the geometric focus to a series of foci spread around the geometric focus. This design has been shown to work well for thermal ablation to control the ablated tissue depth and volume (Fjield and Hynynen, 1997). The InSightec ExAblate 2000 uses this design with 208 transducer elements (Tempany et al., 2003). Ebbini et al. (1988) demonstrated the feasibility of using cylindrically or spherically curved arrays that allow larger than wavelength/2 element size with the trade-off of limiting the electronic beam steering but allowing advanced multifocal pattern optimization. This method was shown to be useful in increasing the ablated tissue volume (Fan and Hynynen, 1995; Daum and Hynynen, 1999) and thus the rate of ablation.

A second method of reducing the number of driving channels involves the use of a random sparse array. The half-λ criterion in element spacing is side-stepped by two techniques, the first of which is arranging the elements on a spherical surface with a geometric focus similar to that described above. This method functions well so long as the focus is not steered far from the geometric focus. Second, by using far fewer than this number of elements but placing them in a random arrangement, the limits of this criterion can be relaxed, a principle also first described in the development of radar arrays (Unz, 1960). Because of the randomness of the arrangement, only the desired focus sees full constructive interference from all of the elements. Small subsets of the elements produce pressure waves that combine constructively outside of the focus, albeit never with the coherence of the organized, uniformly spaced arrays, thus smearing the off-focus energy deposition and avoiding the formation of intense grating lobes. This design was first proposed in 1996 (Goss et al., 1996), further investigated by Gavrilov et al. (1997), Gavrilov and Hand (2000), and used in the Philips Sonalleve. In this system, 256 elements are placed on a 12- or 14-cm spherically curved shell and electronically steered to span treatment cells of up to 16 mm in diameter, centered about the acoustic axis (Kohler et al., 2009). The Sonalleve operating frequencies are between 1 and 1.5 MHz. The downside of the sparse arrays is that energy is lost and higher powers are needed to achieve the same peak intensity as with the fully populated arrays (Ellens et al., 2011). An example of this type of transducer array is illustrated in Figure 25.6b.

The final type of external applicator uses solely fixed transducer elements and electronic steering to perform the desired treatment. Philips developed a dedicated breast cancer ablation device that borrows heavily from their Sonalleve but replaces the mechanical translation of a vertically oriented, spherically curved transducer shell with the arrangement of 8 modules of 32 elements about a 270 degrees arc, all laterally oriented and directed into a pendant breast (Merckel et al., 2013). InSightec's ExAblate 4000 uses 1024 elements arranged in a hemisphere (f-number, 0.5) designed to encompass a human head (Hynynen and Clement, 2007). This design allows for external access to the brain. In addition to using the individual elements for beam steering, this phased array can compensate for the loss of focus caused by propagation through the heterogeneous skull (Clement and Hynynen, 2002). The ExAblate 4000's operating frequencies are 230 and 650 kHz. These frequencies are lower than the more commonly used therapeutic ultrasound frequencies. Although lower frequencies do not focus as tightly as higher frequencies, they are much less quickly attenuated and less distorted than higher frequencies, which, when focusing through the skull, is very

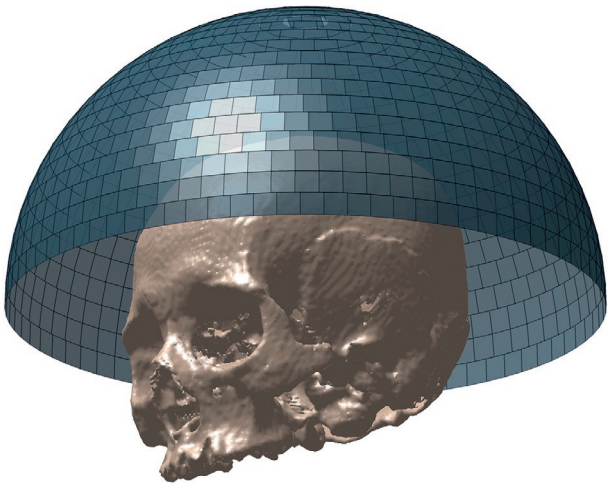


FIGURE 25.8 This image shows a conceptual arrangement of 1000 transducer elements in a hemisphere about a 3D model of a human skull. Such an array can target different areas within the skull using electronic steering exclusively. Moreover, different transducer excitation patterns can be employed to create anti-foci of intentionally low intensity near sensitive and vulnerable, off-focus structures. *(Image courtesy of Daniel Pajek.)*

important (Clement et al., 2000). Such a device with appropriate skull information allows for an unprecedented form of noninvasive neurosurgery. A conceptual model is shown in Figure 25.8, and a diagram is shown in Figure 25.6c.

25.3.2 Endocavity devices

Endocavity ultrasound applicators obtain their therapeutic effect by locating the source transducers near their targets by inserting them into body cavities in a minimally invasive approach. This method can be used to avoid sensitive structures or regions that do not support the propagation of ultrasound while still negating the need to make an incision in the patient, thus substantially reducing the risk of infection and recovery time. These devices have smaller apertures than external devices, limited by cavity size and access point. Because they are inserted near their targets, endocavity devices tend to operate at higher frequencies, such that a greater fraction of their energy is attenuated closer to the device.

The first endocavity devices developed for thermal ablation used the rectum to target the prostate. These devices are inserted into the rectum and use focused, mechanically moved transducers to target the prostate through the rectal wall. To cool the rectal wall, water is circulated in a water balloon that surrounds the devices and couples the ultrasound to the rectal wall. Sonocare's Sonablate 500 uses a two-element, concentric focused transducer; the outer ring delivers the therapy beam, and the inner element provides diagnostic ultrasound images for guidance purposes. The ultrasound images are obtained by rotating and axially scanning the transducer. The focal depth is controlled by increasing or decreasing the distance between the applicator and the rectal wall. The system operates at a frequency of 4 MHz (Sanghvi et al., 1999). EDAP TMS's Ablatherm is similar in design except that the therapy transducer is a concentric ring-shaped phased array that allows the depth of the focus to be controlled; the imaging transducer is positioned in front of the therapy transducer when imaging is performed but then is withdrawn in the applicator during therapy sonications. The therapy array operates at a lower frequency of 2.25 MHz (Chapelon et al., 1999). These devices have been used in routine clinical treatments of thousands of patients with good success, although randomized control studies assessing the true efficacy of the procedure are currently lacking (Crouzet et al., 2014). Alternatively, the feasibility of complete electronic steering with a transrectal probe was demonstrated (Hutchinson and Hynynen, 1998). InSightec has developed a 1000-element endorectal phased array that uses a frequency of approximately 2 MHz to electronically control the focal depth and focal size (Ghai et al., 2021). This system is now FDA approved for clinical use.

Profound Medical makes a device for transurethral prostate ablation. The device, about 6.4 mm in diameter, is inserted into the patient's urethra and advanced so that it rests within the prostate. Using a row of unfocused, planar ultrasound transducers and axial rotation, the prostate can be targeted. The treatment can be conformed to the geometry of the prostate by varying the power applied to each transducer element as well as selecting a frequency that is optimized for the desired depth of penetration. Because the targeted tissue is adjacent to the transducers, relatively high frequencies of 5–10 MHz are used (Burtnyk et al., 2010). Because the urethra lies within the prostate, energy is easily deposited in the target and has achieved good clinical results (Klotz et al., 2021). The guidance and efficacy of this transurethral device is discussed in Section 25.5.1. This device is now FDA approved for clinical use. A diagram illustrating this type of transducer is shown in Figure 25.6d.

Though not currently clinically approved, several systems have been proposed, built, and tested to some degree. Transesophageal arrays are designed to be inserted through the mouth and into the esophagus and used to perform cardiac ablations for the purpose of treating arrhythmia (Yin et al., 2006; Constanciel et al., 2013; Greillier et al., 2018). Unfocused arrays of multiple ultrasound transducers placed in the rectum have been used for the induction of hyperthermia treatments in the prostate (Fosmire et al., 1993; Hurwitz et al., 2001). These treatments were used for sensitizing the tumor tissue for radiation therapy.

25.3.3 Interstitial and intraoperative devices

Ultrasound can also be used interstitially. Ultrasound transducers mounted to intravenous catheters are currently used

for imaging, generally of arterial atherosclerotic plaques at very high frequencies (Nissen and Yock, 2001). Therapeutically, ultrasound is applied interstitially using several different dedicated applicators. After the first demonstration that adequate powers for tissue heating can be generated by small interstitial applicators (Hynynen, 1992), interstitial applicators for both the induction of hyperthermia and tissue ablation were developed (Hynynen, 1992; Diederich et al., 1996). In addition, ultrasound applicators mounted on catheters have been developed such that intravascular access can be used to access the inner wall of the heart, and ultrasound energy can be applied to thermally coagulate cardiac tissue for curing arrhythmias (Zimmer et al., 1995; Carias and Hynynen, 2016). More recent experiments have demonstrated that it is possible to use catheter-based phased arrays to focus the energy and also to image the tissue for targeting purposes (Joseph et al., 2022).

The Epicor Medical Ablation System is used as an alternative to the Cox maze procedure to treat atrial fibrillation. In this technique, a HIFU device is placed against the outside of the heart via a sternotomy or right anterolateral thoracotomy for invasive or minimally invasive access (Mitnovetski et al., 2009). A series of 10×15-mm transducers operating at frequencies from 3.8 to 6.4 MHz use varied powers (15–130 W) and sonication sequences to ablate the cardiac wall (from the most distal to the most proximal) in about 10 min (Ninet et al., 2005).

Therapy ultrasound transducers mounted on an endoscope have been developed for liver and bile duct tumor ablation (Lafon et al., 1998; Owen et al., 2010). Similarly, intraoperative applications of ultrasound have been tested for vascular stasis during liver resection and for thermal ablation of liver tumors (Chenot et al., 2010; Dupre et al., 2019).

25.4 Imaging guidance

25.4.1 Ultrasound

Ultrasound is among the most commonly performed diagnostic scans. It is rapid, portable, much cheaper than MRI and computed tomography (CT), and generally well tolerated by patients. For many ultrasound therapies, ultrasound guidance is also used. Ultrasound imaging is versatile, and as such, it can provide different types of information. First, conventional pulse-echo B-mode imaging is used for targeting solid tumors in systems like the Haifu/US system described previously (Wu et al., 2001a). Typically, an imaging transducer array is placed such that its imaging plane spans the focus of the therapeutic transducer. The hybrid therapy and imaging transducers can be physically translated before sonication, either by hand or using computer controllers, in order to target a tumor. Alternatively, if the therapeutic transducer is a phased array, the phases can be adjusted accordingly to target the desired depth.

Ultrasound can also monitor the extent of the treatment in real time. By exploiting the fact that tissue stiffens as it is ablated, thermal therapies can be monitored in real time. In practice, oscillatory localized harmonic motion is induced in the tissue by modulated radiation force from a HIFU transducer. An imaging transducer tracks this oscillatory motion and can detect the decrease in amplitude that occurs when a lesion is formed (Curiel et al., 2009; Carias and Hynynen, 2016; Han et al., 2017; Aslani et al., 2020). An example of these data is shown in Figure 25.9. Other radiation force-based elastic imaging methods have shown promise for detecting tissue coagulation (Bing et al., 2011).

Shear wave imaging can also detect changes in stiffness and may be used to monitor HIFU treatments (Sarvazyan et al., 1998). In this technique, longitudinal ultrasound is

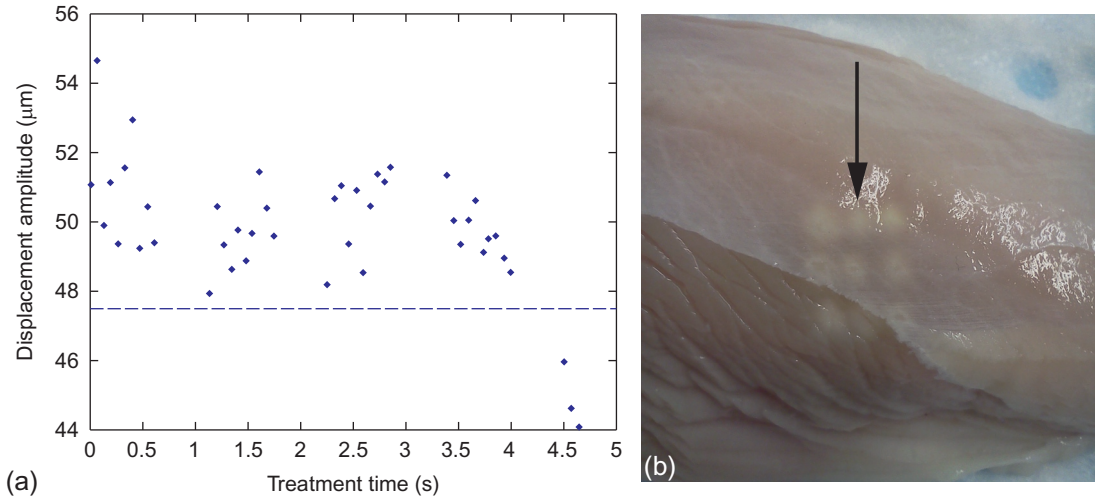


FIGURE 25.9 LHM amplitude (a) as a function of time for the top, center lesion shown in (b). An ex vivo turkey breast was sonicated at 1.5 MHz with a 75-Hz pulse rate, monitored at 825 kHz with a co-registered commercial diagnostic imaging probe. Once thermal necrosis was induced, the LHM amplitude dropped significantly, as evident after 4 s in (a).

focused into a cylinder in a quick, intense pulse. The accompanying radiation forces create a displacement, which in turn creates a cylindrical shear wave that moves out radially. When this propagating shear wave encounters a volume of different stiffness and elasticity, the shear wave speed changes and diffraction occurs. This change can be observed by longitudinal ultrasound imaging that observes the motion caused by the orthogonally propagating shear wave (Bercoff et al., 2004).

Elevations in temperature also affect the speed of sound, a property that has been proposed as a possible method of noninvasively monitoring temperature (Maas-Moreno et al., 1996). This technique is limited in its efficacy, however, by limitations in the temperature range over which the speed of sound changes consistently. This technique has been used in phantoms with good success but is limited in its application to heterogeneous targets such as in vivo tissue with volumes that contain different types of tissue with very different properties and temperature responses (Miller et al., 2002). Nevertheless, this technique holds some promise for treatment prescription where it is desirable to monitor small, subtherapeutic sonications (Casper et al., 2012; Ebbini et al., 2018).

25.4.2 Magnetic resonance imaging

MRI provides excellent soft-tissue contrast and is thus well suited for treatment planning. In addition, it can provide online temperature information. Several MR parameters are temperature sensitive: the apparent diffusion constant of water, the spin-lattice relaxation time, and the water proton resonance frequency (PRF). Diffusion increases with temperature, and even slight changes in temperature (compared with baseline) yield an appreciable change in apparent diffusion (Le Bihan et al., 1989). Spin-lattice relaxation decreases as temperature increases (Parker et al., 1983). This was one of the first temperature-dependent MR parameters examined but is the least applicable because its measurement is slow. Moreover, both of these techniques are very sensitive to the tissue composition of the volume imaged. Large temperature increases cause thermal necrosis, which irreversibly modifies the tissue parameters that both diffusion and spin-lattice relaxation measurements assume.

Conversely, PRF is applicable to a wide range of temperatures (Hindman, 1966; Ishihara et al., 1992) and is highly robust. It has been validated extensively and is used in many commercial FUS systems. PRF exploits the temperature sensitivity of the proton chemical shift of water, which is found in high concentrations in almost all soft tissues, with the exception of fat (Peters et al., 1998). The relationship between temperature and PRF is close to linear over a large range of temperatures (−15°C to 100°C) and is largely indifferent to tissue composition. Its major drawbacks are its lack of sensitivity in fat and bone and its sensitivity to motion. Although the dependence of PRF on temperature is small in tissues (approximately 0.01 ppm/° and the spectroscopic measurement of the PRF is slow with low spatial resolution) (Kuroda et al., 1995), this dependence on temperature can be exploited via its impact on the phase angle of the magnitude vector. Using fast gradient-echo imaging, rapid phase images can be acquired (Ishihara et al., 1995), and by subtracting each frame iteratively, accurate, real-time thermal maps can be acquired. By tracking the temperature in a voxel over time and applying thermal dose model (Sapareto and Dewey, 1984), the bioeffect of the thermal therapy can also be assessed in real time. Many studies have shown very good correlation between MR-derived thermal maps and subsequent effects, such as nonperfused volume in MRI or histological assessment of excised tissue (Chung et al., 1999a; Chopra et al., 2005; Huang et al., 2018; McDannold et al., 2000). An example of MR-derived thermal dose predictions and treatment results is shown in Figure 25.10.

25.4.3 Other imaging modalities

Although CT can provide temperature elevation maps (Fallone et al., 1982), it has not been used for online treatment monitoring because of its utilization of ionizing radiation. However, because of the high spatial resolution and the bone density information it provides, CT has been used in treatment planning for transcranial HIFU treatments (Clement and Hynynen, 2002). For this application, a computer algorithm processes high-resolution CT-derived density data and provides beam correction information by which to offset the phases of different ultrasound elements to produce a coherent focus through the skull of a patient.

Using single-photon emission computed tomography (SPECT), it is possible to obtain functional and molecular images with which to guide the FUS. This method offers the potential to increase efficacy in the treatment of hard-to-image diseases such as brain tumors (Meng et al., 2021b). Optoacoustic imaging may also offer potential for monitoring ultrasound therapy (Witte and Tamimi, 2022).

25.5 Clinical experience

25.5.1 Prostate

The Ablatherm and Sonablate ultrasound-guided transrectal prostate treatment devices have been under investigation in humans since 1993 and 1995, respectively. Both have received CE marks in Europe and the United States. The procedure was generally well tolerated, although many adverse responses have been noted (Fainberg et al., 2021; Chaussy and Thüroff, 2017; Warmuth et al., 2010). Depending on the study, problems with the urinary tract were noted in 1%–58% of patients, potency was an issue for 1%–77%,

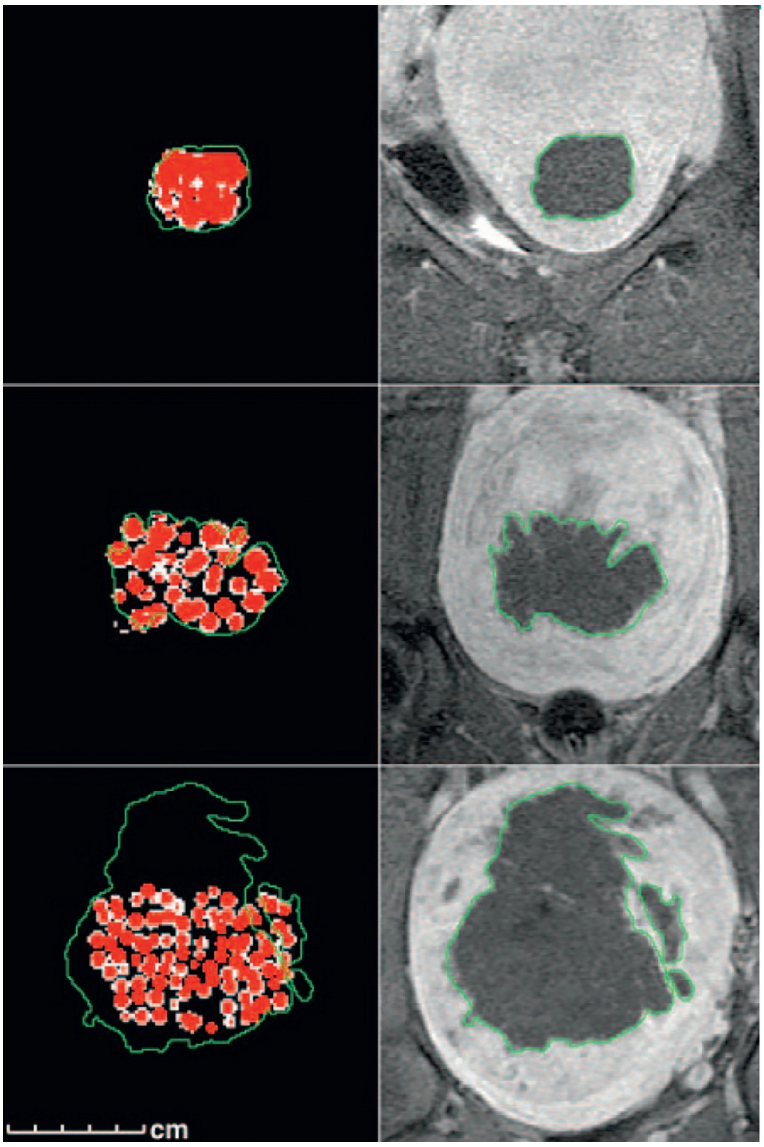


FIGURE 25.10 Predicted extent of MR-guided FUS treatment of uterine fibroids (left) and result (right). On the left, area with a dose over 240 TEM43 is indicated in *red*, while area with a dose over 18 TEM43 is indicated in white. The *green* contour marks the post-treatment nonperfused volume on the right. For comparison, this contour is also displayed on the left. In all three cases, the MR-thermometry-based predictions map closely with the result, with the exception of the third case where a significantly larger area was nonperfused after treatment, likely due to the occlusion of a blood vessel supplying that region. *(Image courtesy of McDannold et al. (2006).)*

complications with the rectum were noted in 1%–15%, and pain was experienced by 0%–6% (Warmuth et al., 2010). To date, there have been no randomized, controlled clinical studies. Most of the metrics used in retrospective analysis to assess the efficacy of these devices have proven. In conclusion, the devices seem to be safe to use, but their efficacy has not been demonstrated adequately.

Profound Medical's transurethral prostate ablation device is performed with on-line MR-thermometry control and has undergone clinical trials and is now FDA-approved. Temperature feedback was obtained by MRI and found to be adequate, and the MR-predicted extent of treatment corresponded very well to the histological analysis (Chopra et al., 2012). The clinical results are similar with other local therapies (Klotz et al., 2021).

InSightec's ExAblate 2100 prostate system has also been approved in America and Europe. The clinical results have indicated that the procedure is well tolerated and effective at causing persistent nonperfusion of the targeted tissue and elimination of clinically significant prostate cancer (Ghai et al., 2021).

25.5.2 Liver

Liver cancer has been a proposed target for FUS surgery for a long time, although it necessarily faces several key

challenges. First, acoustic access to the targets is obscured by the intervening rib cage, and second, the liver moves considerably during respiration, which poses a challenge for imaging in both guidance and monitoring treatment progression. Despite these challenges, several devices have undergone preliminary tests. The Pyrotech, a spherically curved extracorporeal device, was first used to perform ultrasound-guided FUS ablation on the liver in 1992 (Vallancien et al., 1992). Subsequently, several studies have used the ultrasound-guided JC HIFU system to ablate liver tumors, with favorable results, although these studies had small patient cohorts and no controls (Illing et al., 2005). Zhu et al. (2009) found that, with this system, better results were obtained by invasively resecting several ribs before treatment. The combination of these treatments with transcatheter arterial chemoembolization (TACE) in the treatment of primary liver cancer improved long-term efficacy and prognosis (Sun et al., 2021).

In a comparable study, a single patient was treated using the MR-guided ExAblate 2000. A 15-mm hepatic lesion was treated successfully under MR guidance, although the procedure took 2 h to complete. The procedure seemed to be safe, but this was only a very preliminary study. The ribs complicated the delivery of energy, necessitating significant targeting overlap (Okada et al., 2006). Both this MR-guided study and the previously discussed US-guided studies relied on breath holds during treatment to suppress liver motion (De Senneville et al., 2016).

Currently, clinical experience with liver ablation is quite limited, although there is much potential. Liver tumors are good candidates for thermal ablation, and such a treatment would be fully noninvasive and thus more desirable in this regard than comparable minimally invasive RF ablation. Nevertheless, no current system is able to efficiently overcome both key challenges of acoustic access and motion compensation. More device development is necessary if FUS ablation of liver tumors is to become an accepted, clinically feasible treatment (De Senneville et al., 2016).

25.5.3 Breast

Breast tumors were among the first targets for MR-guided FUS surgery. In many ways, they are excellent candidates: the tumors are readily acoustically accessible, breast tumors are highly prevalent, and there is considerable interest in preserving the cosmetic integrity of the breast. The challenges, however, are that the rib cage in the far field of the ultrasound beam is prone to heating and causing intolerable pain if the focus is placed too close, and PRF thermometry for treatment monitoring is less effective in fatty breast tissues. In 2001, breast fibroadenomas were treated in a clinical trial feasibility study with good success: treatment of 8 of the 11 lesions was partially or almost completely successful, despite a conservative treatment strategy (Hynynen et al., 2001b). Adenomas, benign tumors, were chosen initially for this feasibility study because it was not necessary to ablate the entire volume to provide a clinically relevant benefit to the patient.

Subsequently, there have been trials with the ExAblate (Gianfelice et al., 2003; Furusawa et al., 2006), Haifu JC (Wu et al., 2005), and Sonalleve devices targeting breast cancer (Peek and Wu, 2018). For this application, it is important to ablate all of the cancerous cells, which requires a more aggressive protocol and the ablation of a margin around the tumor. In general, the treatment has proved to be well tolerated, although some skin burns where an insufficient margin between the target and the skin was maintained have been reported (Peek and Wu, 2018).

There is certainly considerable promise in noninvasive FUS treatment of breast cancer. For it to be clinically accepted as an alternative to traditional surgery, it must be demonstrated to be as or more effective. It is difficult to see whether the whole tumor has been effectively targeted and sufficiently ablated. Because the current surgical gold standards for lumpectomies are quite effective, it is difficult to justify the long-term clinical trials necessary to demonstrate that FUS treatment is as good as the surgical alternatives. As such, there is certainly potential for FUS breast treatment, but more studies must be conducted if it is to become clinically accepted.

25.5.4 Uterine fibroids

MR-guided ablation of uterine fibroids has been performed in humans since 2001 beginning, with the ExAblate 2000 device (Tempany et al., 2003). Since then, many trials using this device, as well as the Sonalleve and Haifu systems, have been conducted. The procedure is very well tolerated and has been demonstrated to be safe. Pain and numbness are the most common adverse effects of the treatment, and these sensations usually resolve quickly (Fennessy et al., 2007). In some cases, minor skin burns have occurred and, in one case, a serious, full-thickness burn was caused by the procedure (Leon-Villapalos et al., 2005). Early on, the desire for future pregnancy was a contraindication for the procedure as a precaution. Given the overall success of unintended pregnancies in many woman who previously underwent the procedure (Anneveldt et al., 2021), this restriction has been lifted.

In terms of efficacy, MR-guided FUS ablation has been shown to provide significant symptomatic relief with relatively minor side effects (Napoli et al., 2021; Verpalen et al., 2019; Tsai et al., 2021). Clinically, the most comparable alternative to this procedure is uterine arterial embolization (UAE). While both methods are effective at treating fibroids, UAE has been shown retrospectively to provide greater improvements in quality of life (assessed

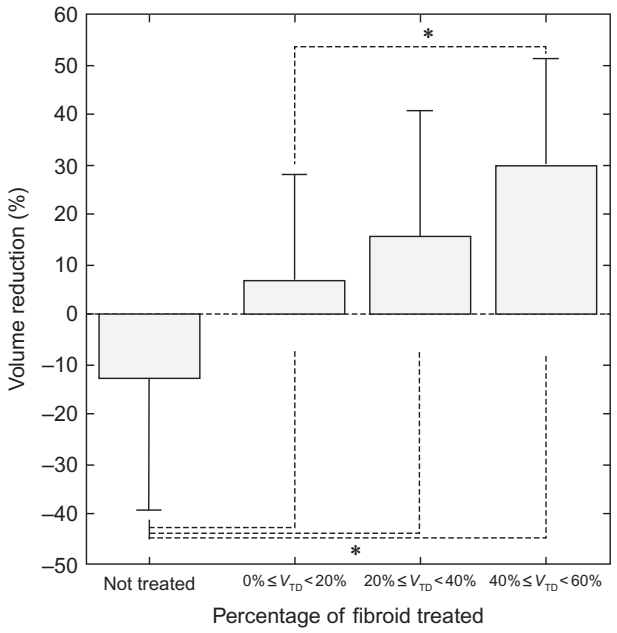


FIGURE 25.11 Fibroid shrinkage 6 months after MR-guided FUS as a function of the fibroid treated. Symptomatic response was also shown to correlate with the extent of the FUS treatment. *(Image courtesy of McDannold et al. (2006).)*

by questionnaires) and require fewer subsequent interventions (Jeng et al., 2020). However, the current clinical devices have limitations, and it is expected that the clinical outcomes will improve with new technology and treatment methods (Lozinski et al., 2018; Simon et al., 2022; Chen et al., 2018) entering in the clinical use. Figure 25.11 shows the increase in volume reduction of fibroids as the treated volume is increased. In terms of patient recovery time, FUS treatment is significantly better than all other treatment alternatives: patients usually return to normal activity within 24–48 h compared with 13.1 days with UAE (Stewart et al., 2007).

Clinically, uterine fibroid ablation with FUS has been very successful. The primary hurdles are in obtaining reimbursement for the procedure. Efforts to increase the efficiency of the treatment systems and sonications strategies are ongoing, with the goal of decreasing the cost of this procedure and rendering it a more commonly used treatment method (O'Sullivan et al., 2009).

25.5.5 Thyroid

Ultrasound is frequently used to image the thyroid gland. Through this same extracorporeal access, therapeutic ultrasound of the thyroid has been investigated. Although the majority of thyroid nodules are benign and require no treatment, even benign nodules can be a clinical concern if there are too many or they increase in size. For those with this condition, surgery is often required. FUS surgery has been proposed as a noninvasive treatment modality for this disease (Esnault et al., 2011) and for benign hyperparathyroidism (Kovatcheva et al., 2010). For the former, 25 patients scheduled for surgical removal of thyroid nodules were first treated with FUS. These patients went ahead with their thyroidectomies, and the excised glands were analyzed to assess the efficacy of ultrasound treatment. The procedure had no major complications, and 73% of the excised glands showed significant changes due to ultrasound, although the extent of destruction ranged from 2% to 80%. The later patients treated with greater energies showed greater effects (Esnault et al., 2011). FUS also was used to thermally ablate parathyroid tumors to treat hyperparathyroidism (Kovatcheva et al., 2010). Review of the clinical studies showed that the treatments were effective in reducing the nodules volume but not able to completely eliminate the nodules. Pain, edema, and skin changes were reported with some treatments. The only major complications were transient vocal cord paralysis and voice hoarseness (0.014%) and transient Horner syndrome (0.5%) (Cheong et al., 2022).

25.5.6 Bone

In late stages, cancer often metastasizes to the bone, which causes debilitating pain. Bone pain is the most common form of pain associated with cancer (Mundy, 2002). Current treatments involve analgesics, chemotherapy, radiation, and laser and RF ablation. Radiation is the most common treatment for patients with localized pain, although it requires many fractions, and 20%–30% do not experience pain relief (Selvaggi and Scagliotti, 2005). In this treatment landscape, noninvasive FUS therapy offers enormous potential. In other applications, the high ultrasound attenuation of bone (some 50 times greater than soft tissue) is a concern: bones block imaging beams and heat up quickly during ultrasound treatment. For bone metastases, however, this high attenuation is advantageous because it affords rapid and efficient ablation.

In an early multisite trial, 31 patients were treated using the ExAblate 2000 uterine fibroid ablation device under MR guidance and monitoring. The results were very promising. Of the 25 patients who underwent a full procedure and were available for follow-up, 72% had a significant reduction in pain, half of whom reported that their pain was gone altogether. No response was observed in 24% of patients, and 4% saw their pain worsen (Liberman et al., 2009). Similar results were obtained in a multi-institutional randomized trial where the response rate was 64% with FUS-treated patients and 20% with the placebo arm (Hurwitz et al., 2014). The response rate varied between sites and was found to correlate with higher energy density on the bone surface and the presence of post-procedural periosteal devascularization (Bitton et al., 2021). The pain reduction induced by

MR-guided HIFU in bone tumor patients, even in the presence of disseminated malignancy, was found to have a positive effect on physical functioning and quality of life of the patients (Harding et al., 2018). Similar results have been obtained in treating osteoid osteoma tumors (Napoli et al., 2017). In general, FUS surgery seems to be well suited for the treatment of bone tumors since it is as effective as current methods and is now FDA-approved. On the other hand, the need of an MRI scanner makes the treatments expensive, a problem that may potentially be addressed using diagnostic ultrasound to guide and quantify the exposures (Aslani et al., 2020).

25.5.7 Brain

One of the most exciting recent developments for FUS surgery is trans-skull ablation. Decades ago, FUS was used to treat patients with tremors caused by Parkinson's disease and nonpatterned muscle spasms. These treatments required that a piece of the skull be removed to afford the ultrasound acoustic access to the target (Fry et al., 1960; Meyers et al., 1959). Although these methods were somewhat successful, they necessitated an invasive surgery that brought with it extensive complexity and risk of complications.

With the development of large-aperture, multiple-element transducer arrays (Hynynen and Jolesz, 1998; Hynynen et al., 2004; Pernot et al., 2005), ultrasound could be focused through excised human skulls and intact animal skulls with appropriate phase and amplitude corrections. Based on preclinical findings, the ExAblate 4000 was developed for clinical use. This system consists of a hemispherical dome with 1024 active elements. Using CT-derived density information, appropriate phase offsets for each element are selected to form precise and localized volumes of high intensity within the brain (Clement and Hynynen, 2002). Clinically, the sharp focusing and feasibility of the method was first demonstrated in three patients with glioblastomas (McDannold et al., 2010). After system upgrades based on the first clinical experience, stage 1 clinical trials to treat patients with chronic neuropathic pain were conducted (Martin et al., 2009). The preliminary study involving nine patients saw pain relief of 30%–100%, with an average of 68%, 2 days following FUS thalamotomy treatment. This was accomplished with no major complications. In longer-term follow-up, the cohort that was followed showed a 42.3% and 40.7% decrease in pain after 3 months and 1 year, respectively (Jeanmonod et al., 2012).

For essential tremor, several clinical trials have been conducted where FUS was used to unilaterally ablate ventralis intermedius thalamic target, with very promising results (Lipsman et al., 2013; Elias et al., 2013). In a randomized multi-institutional phase 3 study, hand-tremor scores improved after FUS thalamotomy from 18.1 points at baseline to 9.6 at 3 months and after the sham procedure from 16.0 to 15.8 points. The adverse events observed in the FUS group included gait disturbance in 36% and paresthesias or numbness in 38% of the patients (Elias et al., 2016). The patients were observed to have mild degradation in some treatment metrics at 3-year follow-up; however, improvement from baseline remains significant (Halpern et al., 2019). Similar success was obtained by staged bilateral ablations (Iorio-Morin et al., 2021) and in the treatment of Parkinson's tremor (Bond et al., 2017). The device was FDA-approved for essential tremor and Parkinson's tremor treatments.

Transcranial FUS surgery is an exciting application that fills a substantial void. For the first time, it allows noninvasive surgical intervention in the brain, which has many possible applications.

Low-amplitude sonications with microbubbles for the modulation of the BBB are now investigated in clinical trials for the enhancement of drug delivery for brain tumors (Mainprize et al., 2019) and have been shown to be effective in enhancing drug delivery into the tumor (Meng et al., 2021b). These treatments can potentially revolutionize how brain diseases are treated in the future (Meng et al., 2021a).

25.5.8 Stroke

Diagnostic-level ultrasound can significantly improve the recanalization rate of clinical stroke patients when the sonication is performed during intravenous infusion of a thrombolytic agent (Alexandrov et al., 2004). This can be further enhanced by the presence of microbubbles, but this is associated with an increased risk of bleeding (Molina et al., 2006). There are several follow-up studies but the evidence about the utility of ultrasound-enhanced thrombolysis in patients with acute ischemic stroke is conflicting. Overall, the review literature indicates that sonothrombolysis is potentially effective treatment that increases recanalization while may or may not increase the rate of asymptomatic intracerebral hemorrhage in stroke patients (Li et al., 2020; Tsivgoulis et al., 2021).

25.6 Future trends

Although some of the therapeutic potentials of ultrasound have been known for over a half century, ultrasound is still not the dominant treatment of choice for any conditions. There are, however, several commercial products that have been used for the treatment of tens of thousands of patients in many centers around the world. The clinical experience is highly favorable, and it is expected that ultrasound treatments will gradually become more widely used. In addition, during the past decade, there here has been a great increase in potential new ways of using ultrasound for the treatment of disease, and it may be that these new treatments will

provide huge benefits to patients. However, current clinical devices are still not optimal, and there is a need for further commercial development to provide new methods that take advantage of modern technology to provide optimal treatment devices for clinicians.

References

Acconcia, C.N., Leung, B.Y.C., Winch, G., Wang, J., Hynynen, K., Goertz, D.E., 2019. Acoustic radiation force induced accumulation and dynamics of microbubbles on compliant surfaces. Phys. Med. Biol. 64. 135003-6560/ab2163.

Alexandrov, A.V., Molina, C.A., Grotta, J.C., Garami, Z., Ford, S.R., Alvarez-Sabin, J., Montaner, J., Saqqur, M., Demchuk, A.M., Moye, L.A., Hill, M. D., Wojner, A.W., 2004. Ultrasound-enhanced systemic thrombolysis for acute ischemic stroke. N. Engl. J. Med. 351, 2170–2178.

Anhalt, D.P., Hynynen, K., Roemer, R.B., 1995. Patterns of changes of tumor temperature during clinical hyperthermia: implications for treatment planning, evaluation and control. Int. J. Hyperth. 11, 425–436.

Anneveldt, K.J., Van't Oever, H.J., Nijholt, I.M., Dijkstra, J.R., Hehenkamp, W.J., Veersema, S., Huirne, J.A.F., Schutte, J.M., Boomsma, M.F., 2021. Systematic review of reproductive outcomes after High Intensity Focused Ultrasound treatment of uterine fibroids. Eur. J. Radiol. 141, 109801.

Apfel, R.E., 1982. Acoustic cavitation: a possible consequence of biomedical uses of ultrasound. Br. J. Cancer Suppl. 45, 140–146.

Aslani, P., Drost, L., Huang, Y., Lucht, B.B.C., Wong, E., Czarnota, G., Yee, C., Wan, B.A., Ganesh, V., Gunaseelan, S.T., David, E., Chow, E., Hynynen, K., 2020. Thermal therapy with a fully electronically steerable HIFU phased array using ultrasound guidance and local harmonic motion monitoring. IEEE Trans. Biomed. Eng. 67, 1854–1862.

Averkiou, M.A., Bruce, M.F., Powers, J.E., Sheeran, P.S., Burns, P.N., 2020. Imaging methods for ultrasound contrast agents. Ultrasound Med. Biol. 46, 498–517.

Bader, K.B., Gruber, M.J., Holland, C.K., 2015. Shaken and stirred: mechanisms of ultrasound-enhanced thrombolysis. Ultrasound Med. Biol. 41, 187–196.

Bercoff, J., Pernot, M., Tanter, M., Fink, M., 2004. Monitoring thermally-induced lesions with supersonic shear imaging. Ultrason. Imaging 26, 71–84.

Beyer, R.T., 1950. Radiation pressure in a sound wave. Am. J. Phys. 18, 25–29.

Billard, B.E., Hynynen, K., Roemer, R.B., 1990. Effects of physical parameters on high temperature ultrasound hyperthermia. Ultrasound Med. Biol. 16, 409–420.

Bing, K.F., Rouze, N.C., Palmeri, M.L., Rotemberg, V.M., Nightingale, K. R., 2011. Combined ultrasonic thermal ablation with interleaved ARFI image monitoring using a single diagnostic curvilinear array: a feasibility study. Ultrason. Imaging 33, 217–232.

Bitton, R.R., Rosenberg, J., Leblang, S., Napoli, A., Meyer, J., Butts Pauly, K., Hurwitz, M., Ghanouni, P., 2021. MRI-guided focused ultrasound of osseous metastases: treatment parameters associated with successful pain reduction. Investig. Radiol. 56, 141–146.

Bond, A.E., Shah, B.B., Huss, D.S., Dallapiazza, R.F., Warren, A., Harrison, M.B., Sperling, S.A., Wang, X.Q., Gwinn, R., Witt, J., Ro, S., Elias, W.J., 2017. Safety and efficacy of focused ultrasound thalamotomy for patients with medication-refractory, tremor-dominant Parkinson disease: a randomized clinical trial. JAMA Neurol. 74, 1412–1418.

Burgess, A., Yala-Grosso, C.A., Ganguly, M., Jordao, J.F., Aubert, I., Hynynen, K., 2011. Targeted delivery of neural stem cells to the brain using MRI-guided focused ultrasound to disrupt the blood-brain barrier. PLoS One 6, e27877.

Burgess, A., Huang, Y., Waspe, A.C., Ganguly, M., Goertz, D.E., Hynynen, K., 2012. High-intensity focused ultrasound (HIFU) for dissolution of clots in a rabbit model of embolic stroke. PLoS One 7 (8), e42311.

Burtnyk, M., N'Djin, W.A., Kobelevskiy, I., Bronskill, M., Chopra, R., 2010. 3D conformal MRI-controlled transurethral ultrasound prostate therapy: validation of numerical simulations and demonstration in tissue-mimicking gel phantoms. Phys. Med. Biol. 55 (22), 6817–6839.

Cain, C.A., Umemura, S.A., 1986. Concentric-ring and sector vortex phased array applicators for ultrasound hyperthermia therapy. IEEE Trans. Microwave Theory Tech. MTT-34, 542–551.

Carias, M., Hynynen, K., 2016. Combined therapeutic and monitoring ultrasonic catheter for cardiac ablation therapies. Ultrasound Med. Biol. 42, 196–207.

Casper, A., Liu, D., Ebbini, E.S., 2012. Realtime control of multiple-focus phased array heating patterns based on noninvasive ultrasound thermography. IEEE Trans. Biomed. Eng. 59, 95–105.

Chapelon, J.Y., Ribault, M., Vernier, F., Souchon, R., Gelet, A., 1999. Treatment of localised prostate cancer with transrectal high intensity focused ultrasound. Eur. J. Ultrasound 9, 31–38.

Chaussy, C.G., Thüroff, S., 2017. High-intensity focused ultrasound for the treatment of prostate cancer: a review. J. Endourol. 31, S30–S37.

Chaussy, C., Brendel, W., Schmiedt, E., 1980. Extracorporeally induced destruction of kidney stones by shock waves. Lancet 2, 1265–1268.

Chen, Y., Jiang, J., Zeng, Y., Tian, X., Zhang, M., Wu, H., Zhou, H., 2018. Effects of a microbubble ultrasound contrast agent on high-intensity focused ultrasound for uterine fibroids: a randomised controlled trial. Int. J. Hyperth. 34, 1311–1315.

Chenot, J., Melodelima, D., N'Djin, W.A., Souchon, R., Rivoire, M., Chapelon, J.Y., 2010. Intra-operative ultrasound hand-held strain imaging for the visualization of ablations produced in the liver with a toroidal HIFU transducer: first in vivo results. Phys. Med. Biol. 55, 3131–3144.

Cheong, C.W.S., Au, J.X.Y., Lim, M.Y., Fu, E.W., Li, H., Gan, J.Y., 2022. The efficacy and safety of high-intensity focused ultrasound in the treatment of benign thyroid nodules: a systematic review and meta-analysis from 1990 to 2021. Ann. Acad. Med. Singap. 51, 101–108.

Chopra, R., Burtnyk, M., Haider, M.A., Bronskill, M.J., 2005. Method for MRI-guided conformal thermal therapy of prostate with planar transurethral ultrasound heating applicators. Phys. Med. Biol. 50, 4957–4975.

Chopra, R., Colquhoun, A., Burtnyk, M., N'Djin, W.A., Kobelevskiy, I., Boyes, A., Siddiqui, K., Foster, H., Sugar, L., Haider, M.A., Bronskill, M., Klotz, L., 2012. MR imaging-controlled transurethral ultrasound therapy for conformal treatment of prostate tissue: initial feasibility in humans. Radiology 265, 303–313.

Chung, A., Jolesz, F.A., Hynynen, K., 1999a. Thermal dosimetry of a focused ultrasound beam in vivo by MRI. Med. Phys. 26, 2017–2026.

Chung, A.H., Jolesz, F.A., Hynynen, K., 1999b. Thermal dosimetry of a focused ultrasound beam in vivo by magnetic resonance imaging. Med. Phys. 26, 2017–2026.

Clement, G.T., Hynynen, K., 2002. A non-invasive method for focusing ultrasound through the human skull. Phys. Med. Biol. 47, 1219–1236.

Clement, G.T., Sun, J., Giesecke, T., Hynynen, K., 2000. A hemisphere array for non-invasive ultrasound brain therapy and surgery. Phys. Med. Biol. 45, 3707–3719.

Constanciel, E., N'Djin, W.A., Bessière, F., Chavrier, F., Grinberg, D., Vignot, A., Chevalier, P., Chapelon, J.Y., Lafon, C., 2013. Design and evaluation of a transesophageal HIFU probe for ultrasound-guided cardiac ablation: simulation of a HIFU mini-maze procedure and preliminary ex vivo trials. IEEE Trans. Ultrason. Ferroelectr. Freq. Control 60, 1868–1883.

Corry, P.M., Barlogie, B., Tilchen, E.J., Armour, E.P., 1982. Ultrasound-induced hyperthermia for the treatment of human superficial tumors. Int. J. Radiat. Oncol. Biol. Phys. 8, 1225–1229.

Crouzet, S., Chapelon, J.Y., Rouvière, O., Mege-Lechevallier, F., Colombel, M., Tonoli-Catez, H., Martin, X., Gelet, A., 2014. Whole-gland ablation of localized prostate cancer with high-intensity focused ultrasound: oncologic outcomes and morbidity in 1002 patients. Eur. Urol. 65, 907–914.

Curiel, L., Huang, Y., Vykhodtseva, N., Hynynen, K., 2009. Focused ultrasound treatment of VX2 tumors controlled by local harmonic motion. Phys. Med. Biol. 54, 3405–3419.

Dalecki, D., 2004. Mechanical bioeffects of ultrasound. Annu. Rev. Biomed. Eng. 6, 229–248.

Damianou, C., Hynynen, K., 1994. The effect of various physical parameters on the size and shape of necrosed tissue volume during ultrasound surgery. J. Acoust. Soc. Am. 95, 1641–1649.

Daum, D.R., Hynynen, K., 1999. A 256 element ultrasonic phased Array system for treatment of large volumes of deep seated tissue. IEEE Trans. Ultrason. Ferroelectr. Freq. Control 46, 1254–1268.

Dayton, P., Klibanov, A., Brandenburger, G., Ferrara, K., 1999. Acoustic radiation force in vivo: a mechanism to assist targeting of microbubbles. Ultrasound Med. Biol. 25, 1195–1201.

De Senneville, B.D., Moonen, C., Ries, M., 2016. MRI-guided HIFU methods for the ablation of liver and renal cancers. Adv. Exp. Med. Biol. 880, 43–63.

Diederich, C.J., Hynynen, K., 1999. Ultrasound technology for hyperthermia. Ultrasound Med. Biol. 25, 871–887.

Diederich, C.J., Khalil, I.S., Stauffer, P.R., Sneed, P.K., Phillips, T.L., 1996. Direct-coupled interstitial ultrasound applicators for simulataneus thermobrachytherapy: a feasibility study. Int. J. Hyperth. 12, 401–419.

Do-Huu, J.P., Hartemann, P., 1981. Annular array transducer for deep acoustic hyperthermia. In: IEEE Ultrasonics Symposium 81CH1689-9, pp. 705–710.

Duck, F.A., 1990. In: Duck, F. (Ed.), Physical Properties of Tissue. Academic Press, London.

Dupre, A., Melodelima, D., Perol, D., Chen, Y., Vincenot, J., Chapelon, J.Y., Rivoire, M., 2019. Evaluation of the feasibility, safety, and accuracy of an intraoperative high-intensity focused ultrasound device for treating liver metastases. J. Vis. Exp. 143. https://doi.org/10.3791/57964.

Dyer, H.J., Nyborg, W.L., 1960. Ultrasonically-induced movements in cells and cell models. IRE Trans. Med. Electron. Me-7, 163–165.

Dyson, M., Pond, J.B., Woodward, B., Broadbent, J., 1974. The production of blood cell stasis and endothelial damage in the blood vessels of chick embryos treated with ultrasound in a stationary wave field. Ultrasound Med. Biol. 1, 133–148.

Ebbini, E.S., Umemura, S.I., Ibbini, M.S., Cain, C.A., 1988. A cylindrical-section ultrasound phased-array applicator for hyperthermia cancer therapy. IEEE Trans. Ultrason. Ferroelectr. Freq. Control 35, 561.

Ebbini, E.S., Simon, C., Liu, D., 2018. Real-time ultrasound thermography and thermometry. IEEE Signal Process. Mag. 35, 166–174.

Elias, W.J., Huss, D., Voss, T., Loomba, J., Khaled, M., Zadicario, E., Frysinger, R.C., Sperling, S.A., Wylie, S., Monteith, S.J., Druzgal, J., Shah, B.B., Harrison, M., Wintermark, M., 2013. A pilot study of focused ultrasound thalamotomy for essential tremor. N. Engl. J. Med. 369, 640–648.

Elias, W.J., Lipsman, N., Ondo, W.G., Ghanouni, P., Kim, Y.G., Lee, W., Schwartz, M., Hynynen, K., Lozano, A.M., Shah, B.B., Huss, D., Dallapiazza, R.F., Gwinn, R., Witt, J., Ro, S., Eisenberg, H.M., Fishman, P.S., Gandhi, D., Halpern, C.H., Chuang, R., Butts, P.K., Tierney, T.S., Hayes, M.T., Cosgrove, G.R., Yamaguchi, T., Abe, K., Taira, T., Chang, J.W., 2016. A randomized trial of focused ultrasound thalamotomy for essential tremor. N. Engl. J. Med. 375, 730–739.

Ellens, N., Pulkkinen, A., Song, J., Hynynen, K., 2011. The utility of sparse 2D fully electronically steerable focused ultrasound phased arrays for thermal surgery: a simulation study. Phys. Med. Biol. 56, 4913–4932.

Esnault, O., Franc, B., Ménégaux, F., Rouxel, A., De Kerviler, E., Bourrier, P., Lacoste, F., Chapelon, J.Y., Leenhardt, L., 2011. High-intensity focused ultrasound ablation of thyroid nodules: first human feasibility study. Thyroid 21, 965–973.

Fainberg, J.S., Al Awamlh, B.A.H., Derosa, A.P., Chesnut, G.T., Coleman, J.A., Lee, T., Ehdaie, B., 2021. A systematic review of outcomes after thermal and nonthermal partial prostate ablation. Prostate Int. 9, 169–175.

Fallone, B.G., Moran, P.R., Podgorsak, E.B., 1982. Noninvasive thermometry with a clinical x-ray CT scanner. Med. Phys. 9, 715–721.

Fan, X., Hynynen, K., 1995. Control of the necrosed tissue volume during noninvasive ultrasound surgery using a 16 element phased array. Med. Phys. 22, 297–308.

Fennessy, F.M., Tempany, C.M., McDannold, N.J., So, M.J., Hesley, G., Gostout, B., Kim, H.S., Holland, G.A., Sarti, D.A., Hynynen, K., Jolesz, F.A., Stewart, E.A., 2007. Uterine leiomyomas: MR imaging-guided focused ultrasound surgery—results of different treatment protocols. Radiology 243, 885–893.

Fjield, T., Hynynen, K., 1997. The combined concentric-ring and sector-vortex phased array for MRI guided ultrasound surgery. IEEE Trans. Ultrason. Ferroelectr. Freq. Control 44, 1157–1167.

Fosmire, H., Hynynen, K., Drach, G.W., Stea, B., Swift, P., Cassady, J.R., 1993. Feasibility and toxicity of transrectal ultrasound hyperthermia in the treatment of locally-advanced adenocarcinoma of the prostate. Int. J. Radiat. Oncol. Biol. Phys. 26, 253–259.

Fry, F.J., Barger, J.E., 1978. Acoustic properties of the human skull. J. Acoust. Soc. Am. 63, 1576–1590.

Fry, W.J., Fry, F.J., 1960. Fundamental neurological research and human neurosurgery using intense ultrasound. IRE Trans. Med. Electron. ME-7, 166–181.

Fry, W.J., Fry, F.J., Meyers, R., Eggleton, R.C., 1960. The use of ultrasound in neurosurgery. In: Proceedings of the 3rd International Conference on Medical Electronics, London, England, pp. 453–458.

Furusawa, H., Namba, K., Thomsen, S., Akiyama, F., Bendet, A., Tanaka, C., Yasuda, Y., Nakahara, H., 2006. Magnetic resonance-guided focused ultrasound surgery of breast cancer: reliability and effectiveness. J. Am. Coll. Surg. 203, 54–63.

Gavrilov, L.R., Hand, J.W., 2000. A theoretical assessment of the relative performance of spherical phased arrays for ultrasound surgery. IEEE Trans. Ultrason. Ferroelectr. Freq. Control 47, 125–139.

Gavrilov, L.R., Hand, J.W., Abel, P., Cain, C.A., 1997. A method of reducing grating lobes associated with an ultrasound linear phased array intended for transrectal thermotherapy. IEEE Trans. Ultrason. Ferroelectr. Freq. Control 44, 1010–1017.

Ghai, S., Finelli, A., Corr, K., Chan, R., Jokhu, S., Li, X., McCluskey, S., Konukhova, A., Hlasny, E., Van Der Kwast, T.H., Incze, P.F., Zlotta,

A.R., Hamilton, R.J., Haider, M.A., Kucharczyk, W., Perlis, N., 2021. MRI-guided focused ultrasound ablation for localized intermediate-risk prostate cancer: early results of a phase II trial. Radiology 298, 695–703.

Gianfelice, D., Khiat, A., Amara, M., Belblidia, A., Boulanger, Y., 2003. MR imaging-guided focused US ablation of breast cancer: histopathologic assessment of effectiveness—initial experience. Radiology 227, 849–855.

Goldberg, B.B., Liu, J.B., Forsberg, F., 1994. Ultrasound contrast agents: a review. Ultrasound Med. Biol. 20, 319–333.

Goske, M.J., Frush, D.P., Brink, J.A., Kaste, S.C., Butler, P.F., Pandharipande, P.V., 2014. Curbing potential radiation-induced cancer risks in oncologic imaging: perspectives from the 'image gently' and 'image wisely' campaigns. Oncology (Williston Park) 28, 232–238. 243.

Goss, S.A., Johnson, R.L., Dunn, F., 1980. Compilation of empirical ultrasonic properties of mammalian tissues. II. J. Acoust. Soc. Am. 68, 93–108.

Goss, S.A., Frizzell, L.A., Kouzmanoff, J.T., Barich, J.M., Yang, J.M., 1996. Sparse random ultrasound phased arry for focal surgery. IEEE Trans. Ultrason. Ferroelectr. Freq. Control 43, 1111–1121.

Greillier, P., Ankou, B., Bour, P., Zorgani, A., Abell, E., Lacoste, R., Bessière, F., Pernot, M., Catheline, S., Quesson, B., Chevalier, P., Lafon, C., 2018. Myocardial thermal ablation with a transesophageal high-intensity focused ultrasound probe: experiments on beating heart models. Ultrasound Med. Biol. 44, 2625–2636.

Halpern, C.H., Santini, V., Lipsman, N., Lozano, A.M., Schwartz, M.L., Shah, B.B., Elias, W.J., Cosgrove, G.R., Hayes, M.T., Mcdannold, N., Aldrich, C., Eisenberg, H.M., Gandhi, D., Taira, T., Gwinn, R., Ro, S., Witt, J., Jung, N.Y., Chang, J.W., Rosenberg, J., Ghanouni, P., 2019. Three-year follow-up of prospective trial of focused ultrasound thalamotomy for essential tremor. Neurology 93, e2284–e2293.

Han, Y., Wang, S., Payen, T., Konofagou, E., 2017. Fast lesion mapping during HIFU treatment using harmonic motion imaging guided focused ultrasound (HMIgFUS) in vitro and in vivo. Phys. Med. Biol. 62, 3111–3123.

Harding, D., Giles, S.L., Brown, M.R.D., Ter Haar, G.R., Van Den Bosch, M., Bartels, L.W., Kim, Y.S., Deppe, M., Desouza, N.M., 2018. Evaluation of quality of life outcomes following palliative treatment of bone metastases with magnetic resonance-guided high intensity focused ultrasound: an international multicentre study. Clin. Oncol. 30, 233–242.

Harmon, B.V., Corder, A.M., Collins, R.J., Gobé, G.C., Allen, J., Allan, D. J., Kerr, J.F., 1990. Cell death induced in a murine mastocytoma by 42–47 degrees C heating in vitro: evidence that the form of death changes from apoptosis to necrosis above a critical heat load. Int. J. Radiat. Biol. 58, 845–858.

Hindman, J.C., 1966. Proton resonance shift of water in the gas and liquid states. J. Chem. Phys. 44, 4582–4592.

Holt, R.G., Roy, R.A., 2001. Measurements of bubble-enhanced heating from focused, mhz-frequency ultrasound in a tissue-mimicking material. Ultrasound Med. Biol. 27, 1399–1412.

Hosseinkhah, N., Chen, H., Matula, T.J., Burns, P.N., Hynynen, K., 2013. Mechanisms of microbubble-vessel interactions and induced stresses: a numerical study. J. Acoust. Soc. Am. 134, 1875–1885.

Huang, Y., Lipsman, N., Schwartz, M.L., Krishna, V., Sammartino, F., Lozano, A.M., Hynynen, K., 2018. Predicting lesion size by accumulated thermal dose in MR-guided focused ultrasound for essential tremor. Med. Phys. 45, 4704–4710.

Hurwitz, M.D., Kaplan, I.D., Svensson, G.K., Hynynen, K., Hansen, M.S., 2001. Feasibility and patient tolerance of a novel transrectal ultrasound hyperthermia system for treatment of prostate cancer. Int. J. Hyperth. 17, 31–37.

Hurwitz, M.D., Ghanouni, P., Kanaev, S.V., Iozeffi, D., Gianfelice, D., Fennessy, F.M., Kuten, A., Meyer, J.E., Leblang, S.D., Roberts, A., Choi, J., Larner, J.M., Napoli, A., Turkevich, V.G., Inbar, Y., Tempany, C.M., Pfeffer, R.M., 2014. Magnetic resonance-guided focused ultrasound for patients with painful bone metastases: phase III trial results. J. Natl. Cancer Inst. 106, dju082.

Hutchinson, E.B., Hynynen, K., 1998. Intracavitary ultrasound phased arrays for prostate thermal therapies: MRI compatibility and in vivo testing. Med. Phys. 25, 2392–2399.

Hynynen, K., 1991. The threshold for thermally significant cavitation in dog's thigh muscle in vivo. Ultrasound Med. Biol. 17, 157–169.

Hynynen, K., 1992. The feasibility of interstitial ultrasound hyperthermia. Med. Phys. 19, 979–987.

Hynynen, K., Clement, G., 2007. Clinical applications of focused ultrasound—the brain. Int. J. Hyperth. 23, 193–202.

Hynynen, K., Jolesz, F.A., 1998. Demonstration of potential noninvasive ultrasound brain therapy through intact skull. Ultrasound Med. Biol. 24, 275–283.

Hynynen, K., Roemer, R., Anhalt, D., Johnson, C., Xu, Z.X., Swindell, W., Cetas, T.C., 1987. A scanned focussed multiple transducer ultrasonic system for localized hyperthermia treatments. Int. J. Hyperth. 3, 21–35.

Hynynen, K., Colucci, V., Chung, A., Jolesz, F.A., 1996. Noninvasive arterial occlusion using MRI-guided focused ultrasound. Ultrasound Med. Biol. 22, 1071–1077.

Hynynen, K., Mcdannold, N., Vykhodtseva, N., Jolesz, F.A., 2001a. Noninvasive MR imaging-guided focal opening of the blood-brain barrier in rabbits. Radiology 220, 640–646.

Hynynen, K., Pomeroy, O., Smith, D.N., Huber, P.E., Mcdannold, N.J., Kettenbach, J., Baum, J., Singer, S., Jolesz, F.A., 2001b. MR imaging-guided focused ultrasound surgery of fibroadenomas in the breast: a feasibility study. Radiology 219, 176–185.

Hynynen, K., Clement, G.T., Mcdannold, N., Vykhodtseva, N., King, R., White, P.J., Vitek, S., Jolesz, F.A., 2004. 500-Element ultrasound phased array system for noninvasive focal surgery of the brain: a preliminary rabbit study with ex vivo human skulls. Magn. Reson. Med. 52, 100–107.

Illing, R.O., Kennedy, J.E., Wu, F., Ter Haar, G.R., Protheroe, A.S., Friend, P.J., Gleeson, F.V., Cranston, D.W., Phillips, R.R., Middleton, M.R., 2005. The safety and feasibility of extracorporeal high-intensity focused ultrasound (HIFU) for the treatment of liver and kidney tumours in a Western population. Br. J. Cancer 93, 890–895.

Iorio-Morin, C., Yamamoto, K., Sarica, C., Zemmar, A., Levesque, M., Brisebois, S., Germann, J., Loh, A., Boutet, A., Elias, G.J.B., Azevedo, P., Adam, E., Patel, U., Lenis, M., Kalia, S.K., Hodaie, M., Fasano, A., Lozano, A.M., 2021. Bilateral focused ultrasound thalamotomy for essential tremor (BEST-FUS phase 2 trial). Mov. Disord. 36, 2653–2662.

Ishihara, Y., Calderon, A., Watanabe, H., Mori, K., Okamoto, K., Suzuki, T., Sato, K., Kuroda, K., Nakagawa, N., Tsutsumi, S., 1992. A precise and fast temperature mapping using water proton chemical shift. In: Proc. SMRM, p. 4803.

Ishihara, Y., Calderon, A., Watanabe, H., Okamoto, K., Suzuki, Y., Kuroda, K., 1995. A precise and fast temperature mapping using water proton chemical shift. Magn. Reson. Med. 34, 814–823.

Jeanmonod, D., Werner, B., Morel, A., Michels, L., Zadicario, E., Schiff, G., Martin, E., 2012. Transcranial magnetic resonance imaging-guided focused ultrasound: noninvasive central lateral thalamotomy for chronic neuropathic pain. Neurosurg. Focus. 32, E1.

Jeng, C.J., Long, C.Y., Chuang, L.T., 2020. Comparison of magnetic resonance-guided high-intensity focused ultrasound with uterine artery embolization for the treatment of uterine myoma: a systematic literature review and meta-analysis. Taiwan. J. Obstet. Gynecol. 59, 691–697.

Joseph, J., Ma, B., Khuri-Yakub, B.T., 2022. Applications of capacitive micromachined ultrasonic transducers: a comprehensive review. IEEE Trans. Ultrason. Ferroelectr. Freq. Control 69, 456–467.

Khokhlova, V.A., Fowlkes, J.B., Roberts, W.W., Schade, G.R., Xu, Z., Khokhlova, T.D., Hall, T.L., Maxwell, A.D., Wang, Y.N., Cain, C. A., 2015. Histotripsy methods in mechanical disintegration of tissue: towards clinical applications. Int. J. Hyperth. 31, 145–162.

Kinoshita, M., Mcdannold, N., Jolesz, F.A., Hynynen, K., 2006. Targeted delivery of antibodies through the blood-brain barrier by MRI-guided focused ultrasound. Biochem. Biophys. Res. Commun. 340, 1085–1090.

Kleven, R.T., Karani, K.B., Hilvert, N., Ford, S.M., Mercado-Shekhar, K. P., Racadio, J.M., Rao, M.B., Abruzzo, T.A., Holland, C.K., 2021. Accelerated sonothrombolysis with Definity in a xenographic porcine cerebral thromboembolism model. Sci. Rep. 11, 3987.

Klotz, A.R., Lindvere, L., Stefanovic, B., Hynynen, K., 2010. Temperature change near microbubbles within a capillary network during focused ultrasound. Phys. Med. Biol. 55, 1549–1561.

Klotz, L., Pavlovich, C.P., Chin, J., Hatiboglu, G., Koch, M., Penson, D., Raman, S., Oto, A., Fütterer, J., Serrallach, M., Relle, J., Lotan, Y., Heidenreich, A., Bonekamp, D., Haider, M., Tirkes, T., Arora, S., Macura, K.J., Costa, D.N., Persigehl, T., Pantuck, A.J., Bomers, J., Burtnyk, M., Staruch, R., Eggener, S., 2021. Magnetic resonance imaging-guided transurethral ultrasound ablation of prostate cancer. J. Urol. 205, 769–779.

Kohler, M.O., Mougenot, C., Quesson, B., Enholm, J., Le, B.B., Laurent, C., Moonen, C.T., Ehnholm, G.J., 2009. Volumetric HIFU ablation under 3D guidance of rapid MRI thermometry. Med. Phys. 36, 3521–3535.

Kooiman, K., Roovers, S., Langeveld, S.A.G., Kleven, R.T., Dewitte, H., O'Reilly, M.A., Escoffre, J.M., Bouakaz, A., Verweij, M.D., Hynynen, K., Lentacker, I., Stride, E., Holland, C.K., 2020. Ultrasound-responsive cavitation nuclei for therapy and drug delivery. Ultrasound Med. Biol. 46, 1296–1325.

Kovatcheva, R.D., Vlahov, J.D., Shinkov, A.D., Borissova, A.M., Hwang, J.H., Arnaud, F., Hegedüs, L., 2010. High-intensity focused ultrasound to treat primary hyperparathyroidism: a feasibility study in four patients. AJR Am. J. Roentgenol. 195, 830–835.

Kuroda, K., Abe, K., Tsutsumi, S., Ishihara, Y., Suzuki, Y., Sato, K., 1995. Water proton magnetic resonance spectroscopic imaging. Biomed. Thermol. 13, 43–62.

Lafon, C., Chapelon, J.Y., Prat, F., Gorry, F., Margonari, J., Theillere, Y., Cathignol, D., 1998. Design and preliminary results of an ultrasound applicator for interstitial thermal coagulation. Ultrasound Med. Biol. 24, 113–122.

Le Bihan, D., Delannoy, J., Levin, R.L., 1989. Temperature mapping with MR imaging of molecular diffusion: application to hyperthermia. Radiology 171, 853–857.

Leighton, T.G., 1994. The Acoustic Bubble. Academic Press, London.

Lele, P.P., 1978. Cavitation and its effects on organized mammalian tissues. In: Ultrasound: Its Applications in Medicine and Biology. Part II. Elsevier, Amsterdam.

Lele, P.P., 1980. Induction of deep, local hyperthermia by ultrasound and electromagnetic fields: problems and choices. Radiat. Environ. Biophys. 17, 205–217.

Lele, P.P., Parker, K.J., 1982a. Temperature distributions in tissues during local hyperthermia by stationary or steered beams of unfocused or focused ultrasound. Br. J. Cancer Suppl. 45, 108–121.

Lele, P.P., Parker, K.J., 1982b. Temperature distributions in tissues during local hyperthermia by stationary or steered beams of unfocussed or focussed ultrasound. Br. J. Cancer 45, 108–121.

Lenard, Z.M., Mcdannold, N.J., Fennessy, F.M., Stewart, E.A., Jolesz, F. A., Hynynen, K., Tempany, C.M., 2008. Uterine leiomyomas: MR imaging-guided focused ultrasound surgery—imaging predictors of success. Radiology 249, 187–194.

Leon-Villapalos, J., Kaniorou-Larai, M., Dziewulski, P., 2005. Full thickness abdominal burn following magnetic resonance guided focused ultrasound therapy. Burns 31, 1054–1055.

Li, X., Du, H., Song, Z., Wang, H., Tan, Z., Xiao, M., Zhang, F., 2020. Efficacy and safety of sonothrombolysis in patients with acute ischemic stroke: a systematic review and meta-analysis. J. Neurol. Sci. 416, 116998.

Liberman, B., Gianfelice, D., Inbar, Y., Beck, A., Rabin, T., Shabshin, N., Chander, G., Hengst, S., Pfeffer, R., Chechick, A., Hanannel, A., Dogadkin, O., Catane, R., 2009. Pain palliation in patients with bone metastases using MR-guided focused ultrasound surgery: a multicenter study. Ann. Surg. Oncol. 16, 140–146.

Lipsman, N., Schwartz, M.L., Huang, Y., Lee, L., Sankar, T., Chapman, M., Hynynen, K., Lozano, A.M., 2013. MR-guided focused ultrasound thalamotomy for essential tremor: a proof-of-concept study. Lancet Neurol. 12, 462–468.

Lozinski, T., Filipowska, J., Krol, P., Kubaty, A., Wegrzyn, P., 2018. Oxytocin administration in high-intensity focused ultrasound treatment of myomata. Biomed. Res. Int. 2018, 7518026. https://doi.org/10.1155/2018/7518026 (eCollection;%2018., 7518026).

Maas-Moreno, R., Damianou, C.A., Sanghvi, N.T., 1996. Noninvasive temperature estimation in tissue via ultrasound echo-shifts. Part II. In vitro study. J. Acoust. Soc. Am. 100, 2522–2530.

Mahoney, K., Fjield, T., Mcdannold, N., Clement, G., Hynynen, K., 2001. Comparison of modelled and observed in vivo temperature elevations induced by focused ultrasound: implications for treatment planning. Phys. Med. Biol. 46, 1785–1798.

Mainprize, T., Lipsman, N., Huang, Y., Meng, Y., Bethune, A., Ironside, S., Heyn, C., Alkins, R., Trudeau, M., Sahgal, A., Perry, J., Hynynen, K., 2019. Blood-brain barrier opening in primary brain tumors with non-invasive MR-guided focused ultrasound: a clinical safety and feasibility study. Sci. Rep. 9. 321-36340.

Martin, E., Jeanmonod, D., Morel, A., Zadicario, E., Werner, B., 2009. High-intensity focused ultrasound for noninvasive functional neurosurgery. Ann. Neurol. 66, 858–861.

Maxwell, A.D., Haworth, K.J., Holland, C.K., Hendley, S.A., Kreider, W., Bader, K.B., 2022. Design and characterization of an ultrasound transducer for combined histotripsy-thrombolytic therapy. IEEE Trans. Ultrason. Ferroelectr. Freq. Control 69, 156–165.

McDannold, N.J., King, R.L., Jolesz, F.A., Hynynen, K.H., 2000. Usefulness of MR imaging-derived thermometry and dosimetry in determining the threshold for tissue damage induced by thermal surgery in rabbits. Radiology 216, 517–523.

Mcdannold, N., Clement, G.T., Black, P., Jolesz, F., Hynynen, K., 2010. Transcranial magnetic resonance imaging-guided focused ultrasound surgery of brain tumors: initial findings in 3 patients. Neurosurgery 66, 323–332.

McDannold, N., Tempany, C.M., Fennessy, F.M, So, M.J., Rybicki, F.J., Stewart, E.A., Jolesz, F.A., Hynynen, K., 2006. Uterine leiomyomas: MR imaging-based thermometry and thermal dosimetry during focused ultrasound thermal ablation. Radiology 240 (1), 263–272.

McMahon, D., O'Reilly, M.A., Hynynen, K., 2021. Therapeutic agent delivery across the blood-brain barrier using focused ultrasound. Annu. Rev. Biomed. Eng. 23, 89–113.

Meng, Y., Hynynen, K., Lipsman, N., 2021a. Applications of focused ultrasound in the brain: from thermoablation to drug delivery. Nat. Rev. Neurol. 17, 7–22.

Meng, Y., Reilly, R.M., Pezo, R.C., Trudeau, M., Sahgal, A., Singnurkar, A., Perry, J., Myrehaug, S., Pople, C.B., Davidson, B., Llinas, M., Hyen, C., Huang, Y., Hamani, C., Suppiah, S., Hynynen, K., Lipsman, N., 2021b. MR-guided focused ultrasound enhances delivery of trastuzumab to Her2-positive brain metastases. Sci. Transl. Med. 13, eabj4011.

Merckel, L.G., Bartels, L.W., Kohler, M.O., Van Den Bongard, H.J., Deckers, R., Mali, W.P., Binkert, C.A., Moonen, C.T., Gilhuijs, K. G., Van Den Bosch, M.A., 2013. MR-guided high-intensity focused ultrasound ablation of breast cancer with a dedicated breast platform. Cardiovasc. Intervent. Radiol. 36, 292–301.

Meyers, R., Fry, W.J., Fry, F.J., et al., 1959. Early experiences with ultrasonic irradiation of the pallidfugal and nigral complexes in hyperkinetic and hypertonic disorders. J. Neurosurg. 16, 32–54.

Miller, N.R., Bamber, J.C., Meaney, P.M., 2002. Fundamental limitations of noninvasive temperature imaging by means of ultrasound echo strain estimation. Ultrasound Med. Biol. 28, 1319–1333.

Mitnovetski, S., Almeida, A.A., Goldstein, J., Pick, A.W., Smith, J.A., 2009. Epicardial high-intensity focused ultrasound cardiac ablation for surgical treatment of atrial fibrillation. Heart Lung Circ. 18, 28–31.

Molina, C.A., Ribo, M., Rubiera, M., Montaner, J., Santamarina, E., Delgado-Mederos, R., Arenillas, J.F., Huertas, R., Purroy, F., Delgado, P., Alvarez-Sabin, J., 2006. Microbubble administration accelerates clot lysis during continuous 2-MHz ultrasound monitoring in stroke patients treated with intravenous tissue plasminogen activator. Stroke 37, 425–429.

Moritz, A.R., Henriques, F.C.J., 1947. Studies of thermal injury. II. The relative importance of time and surface temperature in the causation of cutaneous burns. Am. J. Pathol. 23, 695–720.

Mundy, G.R., 2002. Metastasis to bone: causes, consequences and therapeutic opportunities. Nat. Rev. Cancer 2, 584–593.

Napoli, A., Bazzocchi, A., Scipione, R., Anzidei, M., Saba, L., Ghanouni, P., Cozzi, D.A., Catalano, C., 2017. Noninvasive therapy for osteoid osteoma: a prospective developmental study with MR imaging-guided high-intensity focused ultrasound. Radiology 285, 186–196.

Napoli, A., Alfieri, G., Andrani, F., Scipione, R., Manganaro, L., Pecorini, F., Catalano, C., 2021. Uterine myomas: focused ultrasound surgery. Semin. Ultrasound CT MR 42, 25–36.

Ninet, J., Roques, X., Seitelberger, R., Deville, C., Pomar, J.L., Robin, J., Jegaden, O., Wellens, F., Wolner, E., Vedrinne, C., Gottardi, R., Orrit, J., Billes, M.A., Hoffmann, D.A., Cox, J.L., Champsaur, G.L., 2005. Surgical ablation of atrial fibrillation with off-pump, epicardial, high-intensity focused ultrasound: results of a multicenter trial. J. Thorac. Cardiovasc. Surg. 130, 803–809.

Nissen, S.E., Yock, P., 2001. Intravascular ultrasound: novel pathophysiological insights and current clinical applications. Circulation 103, 604–616.

Nyborg, W.L., 1981. Heat generation by ultrasound in a relaxing medium. J. Acoust. Soc. Am. 70, 310–312.

Nyborg, W.L., 1982. Ultrasonic microstreaming and related phenomena. Br. J. Cancer Suppl. 5, 156–160.

Ocheltree, K.B., Benkeser, P.J., Frizzell, L.A., Cain, C.A., 1984. An ultrasonic phased array applicator for hyperthermia. IEEE Trans. Sonics Ultrason. SU-31, 526–531.

Ohl, C.D., Arora, M., Ikink, R., De, J.N., Versluis, M., Delius, M., Lohse, D., 2006. Sonoporation from jetting cavitation bubbles. Biophys. J. 91, 4285–4295.

Okada, A., Murakami, T., Mikami, K., Onishi, H., Tanigawa, N., Marukawa, T., Nakamura, H., 2006. A case of hepatocellular carcinoma treated by MR-guided focused ultrasound ablation with respiratory gating. Magn. Reson. Med. Sci. 5, 167–171.

O'Sullivan, A.K., Thompson, D., Chu, P., Lee, D.W., Stewart, E.A., Weinstein, M.C., 2009. Cost-effectiveness of magnetic resonance guided focused ultrasound for the treatment of uterine fibroids. Int. J. Technol. Assess. Health Care 25, 14–25.

Overgaard, J., 1989. The current and potential role of hyperthermia in radiotherapy. Int. J. Radiat. Oncol. Biol. Phys. 16, 535–549.

Owen, N.R., Chapelon, J.Y., Bouchoux, G., Berriet, R., Fleury, G., Lafon, C., 2010. Dual-mode transducers for ultrasound imaging and thermal therapy. Ultrasonics 50, 216–220.

Parker, D.L., Smith, V., Sheldon, P., Crooks, L.E., Fussell, L., 1983. Temperature distribution measurements in two-dimensional NMR imaging. Med. Phys. 10, 321–325.

Peek, M.C.L., Wu, F., 2018. High-intensity focused ultrasound in the treatment of breast tumours. Ecancermedicalscience 12, 794.

Pernot, M., Aubry, J.F., Tanter, M., Boch, A.L., Kujas, M., Fink, M., 2005. Adaptive focusing for ultrasonic transcranial brain therapy: first in vivo investigation on 22 sheep. AIP Conf. Proc. 754, 174–177.

Peters, R.D., Hinks, R.S., Henkelman, R.M., 1998. Ex vivo tissue-type independence in proton-resonance frequency shift MR thermometry. Magn. Reson. Med. 40, 454–459.

Sanghvi, N.T., Foster, R.S., Bihrle, R., Casey, R., Uchida, T., Phillips, M. H., Syrus, J., Zaitsev, A.V., Marich, K.W., Fry, F.J., 1999. Noninvasive surgery of prostate tissue by high intensity focused ultrasound: an updated report. Eur. J. Ultrasound 9, 19–29.

Santos, M.A., Wu, S.K., Regenold, M., Allen, C., Goertz, D.E., Hynynen, K., 2020. Novel fractionated ultrashort thermal exposures with MRI-guided focused ultrasound for treating tumors with thermosensitive drugs. Sci. Adv. 6, eaba5684.

Sapareto, S.A., Dewey, W.C., 1984. Thermal dose determination in cancer therapy. Int. J. Radiat. Oncol. Biol. Phys. 10, 787–800.

Sarvazyan, A.P., Rudenko, O.V., Swanson, S.D., Fowlkes, J.B., Emelianov, S.Y., 1998. Shear wave elasticity imaging: a new ultrasonic technology of medical diagnostics. Ultrasound Med. Biol. 24, 1419–1435.

Sarvazyan, A.P., Rudenko, O.V., Nyborg, W.L., 2010. Biomedical applications of radiation force of ultrasound: historical roots and physical basis. Ultrasound Med. Biol. 36, 1379–1394.

Selvaggi, G., Scagliotti, G.V., 2005. Management of bone metastases in cancer: a review. Crit. Rev. Oncol. Hematol. 56, 365–378.

Shakil, A., Osborn, J.L., Song, C.W., 1999. Changes in oxygenation status and blood flow in a rat tumor model by mild temperature hyperthermia. Int. J. Radiat. Oncol. Biol. Phys. 43, 859–865.

Simon, A., Robinson, F., Anzivino, A., Boyer, M., Hendricks-Wenger, A., Guilliams, D., Casey, J., Grider, D., Valea, F., Vlaisavljevich, E., 2022.

Histotripsy for the treatment of uterine leiomyomas: a feasibility study in ex vivo uterine fibroids. Ultrasound Med. Biol. 48, 1652–1662.

Smith, N.B., Hynynen, K., 1998. The feasibility of using focused ultrasound for transmyocardial revascularization. Ultrasound Med. Biol. 24, 1045–1054.

Sokka, S.D., King, R., Hynynen, K., 2003. MRI-guided gas bubble enhanced ultrasound heating in in vivo rabbit thigh. Phys. Med. Biol. 48, 223–241.

Stewart, E.A., Gostout, B., Rabinovici, J., Kim, H.S., Regan, L., Tempany, C.M., 2007. Sustained relief of leiomyoma symptoms by using focused ultrasound surgery. Obstet. Gynecol. 110, 279–287.

Stone, J.S., 1927. Directive Antenna Array. United States Patent Application 1643323.

Sun, M., Shang, P., Bai, J., Li, S., Li, M., 2021. High-intensity focused ultrasound ablation combined with transcatheter arterial chemoembolization improves long-term efficacy and prognosis of primary liver cancer. J. Clin. Lab. Anal. 35, e23633.

Tempany, C.M., Stewart, E.A., Mcdannold, N., Quade, B.J., Jolesz, F.A., Hynynen, K., 2003. MR imaging-guided focused ultrasound surgery of uterine leiomyomas: a feasibility study. Radiology 226, 897–905.

Ter Haar, G., 2007. Therapeutic applications of ultrasound. Prog. Biophys. Mol. Biol. 93, 111–129.

Tsai, M.C., Chang, L.T., Tam, K.W., 2021. Comparison of high-intensity focused ultrasound and conventional surgery for patients with uterine myomas: a systematic review and meta-analysis. J. Minim. Invasive Gynecol. 28, 1712–1724.

Tsivgoulis, G., Katsanos, A.H., Eggers, J., Larrue, V., Thomassen, L., Grotta, J.C., Seitidis, G., Schellinger, P.D., Mavridis, D., Demchuk, A., Novotny, V., Molina, C.A., Veroniki, A.A., Köhrmann, M., Soinne, L., Khanevski, A.N., Barreto, A.D., Saqqur, M., Psaltopoulou, T., Muir, K.W., Fiebach, J.B., Rothlisberger, T., Kent, T.A., Mandava, P., Alexandrov, A.W., Alexandrov, A.V., 2021. Sonothrombolysis in patients with acute ischemic stroke with large vessel occlusion: an individual patient data meta-analysis. Stroke 52, 3786–3795.

Unz, H., 1960. Linear arrays with arbitrarily distributed elements. IRE Trans. Anntenas Propag. 8, 222–223.

Vallancien, G., Harouni, M., Veillon, B., Mombet, A., Prapotnich, D., Bisset, J.M., Bougaran, J., 1992. Focused extracorporeal pyrotherapy: feasibility study in man. J. Endourol. 6, 173–180.

Vallancien, G., Chartier-Kastler, E., Harouni, M., Chopin, D., Bougaran, J., 1993. Focused extracorporeal pyrotherapy: experimental study and feasibility in man. Semin. Urol. 11, 7–9.

Vallancien, G., Harouni, M., Guillonneau, B., Veillon, B., Bougaran, J., 1996. Ablation of superficial bladder tumors with focused extracorporeal pyrotherapy. Urology 47, 204–207.

VanBavel, E., 2007. Effects of shear stress on endothelial cells: possible relevance for ultrasound applications. Prog. Biophys. Mol. Biol. 93, 374–383.

Verpalen, I.M., Anneveldt, K.J., Nijholt, I.M., Schutte, J.M., Dijkstra, J.R., Franx, A., Bartels, L.W., Moonen, C.T.W., Edens, M.A., Boomsma, M.F., 2019. Magnetic resonance-high intensity focused ultrasound (MR-HIFU) therapy of symptomatic uterine fibroids with unrestrictive treatment protocols: a systematic review and meta-analysis. Eur. J. Radiol. 120, 108700.

Villemain, O., Robin, J., Bel, A., Kwiecinski, W., Bruneval, P., Arnal, B., Rémond, M., Tanter, M., Messas, E., Pernot, M., 2017. Pulsed cavitational ultrasound softening: a new non-invasive therapeutic approach of calcified bioprosthetic valve stenosis. JACC Basic Transl. Sci. 2, 372–383.

Vykhodtseva, N., Mcdannold, N., Martin, H., Bronson, R.T., Hynynen, K., 2001. Apoptosis in ultrasound-produced threshold lesions in the rabbit brain. Ultrasound Med. Biol. 27, 111–117.

Warmuth, M., Johansson, T., Mad, P., 2010. Systematic review of the efficacy and safety of high-intensity focussed ultrasound for the primary and salvage treatment of prostate cancer. Eur. Urol. 58, 803–815.

Wells, P.N.T., 1977. Biomedical Ultrasound. Academic Press, Boston.

Witte, R.S., Tamimi, E.A., 2022. Emerging photoacoustic and thermoacoustic imaging technologies for detecting primary and metastatic cancer and guiding therapy. Clin. Exp. Metastasis 39, 213–217.

Wood, R.W., Loomis, A.L., 1927. The physical and biological effects of high frequency sound waves of greater intensity. Lond. Edinb. Dublin Philos. Mag. J. Sci. 4, 417–436.

Worlikar, T., Zhang, M., Ganguly, A., Hall, T.L., Shi, J., Zhao, L., Lee, F. T., Mendiratta-Lala, M., Cho, C.S., Xu, Z., 2022. Impact of histotripsy on development of intrahepatic metastases in a rodent liver tumor model. Cancers (Basel) 14, 1612.

Wright, C., Hynynen, K., Goertz, D., 2012. In vitro and in vivo high-intensity focused ultrasound thrombolysis. Investig. Radiol. 47, 217–225.

Wu, F., Chen, W., Bai, J., Zou, J., Wang, Z., Zhu, H., 2001a. Pathological changes in human malignant carcinoma treated with high-intensity focused ultrasound. Ultrasound Med. Biol. 27, 1099–1106.

Wu, F., Chen, W.Z., Bai, J., Zou, J.Z., Wang, Z.L., Zhu, H., Wang, Z.B., 2001b. Pathological changes in human malignant carcinoma treated with high-intensity focused ultrasound. Ultrasound Med. Biol. 27, 1099–1106.

Wu, F., Wang, Z.B., Chen, W.Z., Zhu, H., Bai, J., Zou, J.Z., Li, K.Q., Jin, C. B., Xie, F.L., Su, H.B., 2004. Extracorporeal high intensity focused ultrasound ablation in the treatment of patients with large hepatocellular carcinoma. Ann. Surg. Oncol. 11, 1061–1069.

Wu, F., Wang, Z.B., Zhu, H., Chen, W.Z., Zou, J.Z., Bai, J., Li, K.Q., Jin, C. B., Xie, F.L., Su, H.B., 2005. Extracorporeal high intensity focused ultrasound treatment for patients with breast cancer. Breast Cancer Res. Treat. 92, 51–60.

Xu, Z., Ludomirsky, A., Eun, L.Y., Hall, T.L., Tran, B.C., Fowlkes, J.B., Cain, C.A., 2004. Controlled ultrasound tissue erosion. IEEE Trans. Ultrason. Ferroelectr. Freq. Control 51, 726–736.

Xu, Z., Hall, T.L., Vlaisavljevich, E., Lee Jr., F.T., 2021. Histotripsy: the first noninvasive, non-ionizing, non-thermal ablation technique based on ultrasound. Int. J. Hyperth. 38, 561–575.

Yin, X., Epstein, L.M., Hynynen, K., 2006. Noninvasive transesophageal cardiac thermal ablation using a 2-D focused, ultrasound phased array: a simulation study. IEEE Trans. Ultrason. Ferroelectr. Freq. Control 53, 1138–1149.

Zhang, L., Chen, W.Z., Liu, Y.J., Hu, X., Zhou, K., Chen, L., Peng, S., Zhu, H., Zou, H.L., Bai, J., Wang, Z.B., 2010. Feasibility of magnetic resonance imaging-guided high intensity focused ultrasound therapy for ablating uterine fibroids in patients with bowel lies anterior to uterus. Eur. J. Radiol. 73, 396–403.

Zhang, X., Macoskey, J.J., Ives, K., Owens, G.E., Gurm, H.S., Shi, J., Pizzuto, M., Cain, C.A., Xu, Z., 2017. Non-invasive thrombolysis using microtripsy in a porcine deep vein thrombosis model. Ultrasound Med. Biol. 43, 1378–1390.

Zhu, H., Zhou, K., Zhang, L., Jin, C., Peng, S., Yang, W., Li, K., Su, H., Chen, W., Bai, J., Wu, F., Wang, Z., 2009. High intensity focused ultrasound (HIFU) therapy for local treatment of hepatocellular carcinoma: role of partial rib resection. Eur. J. Radiol. 72, 160–166.

Zhu, Q., Xu, X., Chen, B., Liao, Y., Guan, X., He, Y., Cui, H., Rong, Y., Liu, Z., Xu, Y., 2022. Ultrasound-targeted microbubbles destruction assists dual delivery of beta-amyloid antibody and neural stem cells to restore neural function in transgenic mice of Alzheimer's disease. Med. Phys. 49, 1357–1367.

Zimmer, J.E., Hynynen, K., He, D.S., Marcus, F.I., 1995. The feasibility of using ultrasound for cardiac ablation. IEEE Trans. Biomed. Eng. 42, 891–897.

Zylicz, M., King, F.W., Wawrzynow, A., 2001. Hsp70 interactions with the p53 tumour suppressor protein. EMBO J. 20, 4634–4638.

Chapter 26

Pulsed waves for medical therapy

A. Mishra and R.O. Cleveland
Department of Engineering Science, University of Oxford, Oxford, United Kingdom

26.1 Introduction

The use of shock waves and pulsed acoustic waves for medical therapy was predominantly driven by the success of treating kidney stones with the first treatment with an extracorporeal device reported in 1980 (Holmes and Whitfield, 1991; Kerbl et al., 2002; Cleveland and McAteer, 2012). Shock wave lithotripsy (SWL) remains one of the first-line treatments for treating kidney stones today. After the success of SWL, the use of shock waves for a multitude of other indications has been explored including pain in the heel or foot, calcifications of the shoulder, pain of the elbow, bone fractures that do not heal, chronic wound repair, loss of blood supply to the heart tissue, and even brain disorders. For some of these applications, the use of "shock waves" was not considered critical and lower amplitude sources that generated pulsed waves have also been deployed. These sources are typically still branded as shock wave sources, although they do not satisfy the technical definition.

This chapter first covers the following: the different types of sources used for pulsed waves, the acoustic characterization of the pulses, and the mechanisms by which they can interact with tissue. It then reviews clinical outcomes for a number of indications for which shock waves have been employed: kidney stones, plantar fasciitis, bone fracture, wound repair, refractory angina pectoris, calcific tendinitis, and lateral epicondylitis. The chapter ends by reviewing the successes and challenges of using shock waves medically and discusses some future paths going forward.

26.2 Acoustic sources

There are four basic transduction mechanisms used for shock wave sources in medical therapy: electrohydraulic, electromagnetic, piezoelectric, and ballistic. In each case, the sources are optimized to generate a pulsed waveform, typically on the order of microseconds in duration and with amplitudes range from 100 kPa to in excess of 100 MPa. An example measured waveform is shown in Figure 26.1, with a leading positive pressure pulse followed by a negative tail. Every pulse will have both positive and negative pressure phases, because to a first approximation, the area under a pressure-time trace for an acoustic wave needs to integrate to zero. Figure 26.1b shows the spectra of the waveform showing a peak around 150 kHz but with energy present out to in excess of 10 MHz.

For low-amplitude waves, the propagation can be described by linear acoustics where every point on the wave travels at the same speed, the small-signal sound speed c_0 which is about 1500 m/s in water and in tissue. However, in reality, the local phase speed is dependent on the local pressure amplitude through the equation:

$$c = c_0 + \beta \frac{p}{\rho_0 c_0}$$

where p is the acoustic pressure, ρ_0 is the density of the medium (about 1000 kg/m^3 in water and tissue), and β is the coefficient of nonlinearity of the medium (about 3.5 in water and 5 in tissue). For an acoustic pressure wave with an amplitude of 100 kPa wave, the local sound speed is $c = 1500.3$ m/s and so nonlinear effects can normally be neglected over the distances relevant in the body. In comparison for a 100 MPa pressure wave, the local sound speed is $c = 1833$ m/s which results in nonlinear distortion of the pulse which steepens the rise time of the leading positive pulse. As the waveform steepens, then absorptive processes in the medium become important. A shock front forms when the nonlinear distortion and absorption processes are balanced. This depends on both the amplitude of the pressure and the distance propagated. The nonsymmetric waveform typically seen in a shock wave source, short-amplitude positive pressure followed by a longer low amplitude negative pressure, is due to an interaction of the nonlinearity with diffraction associated with focusing.

Acoustic waves in shock wave therapy are sometime characterized by their positive and negative peak pressures, $p+$ and $p-$, respectively. They are also characterized by their energy flux density which is given by

$$\mathrm{EFD} = \int \frac{p^2}{\rho_0 c_0}\, dt$$

Power Ultrasonics. https://doi.org/10.1016/B978-0-12-820254-8.00036-1
Copyright © 2023 Elsevier Ltd. All rights reserved.

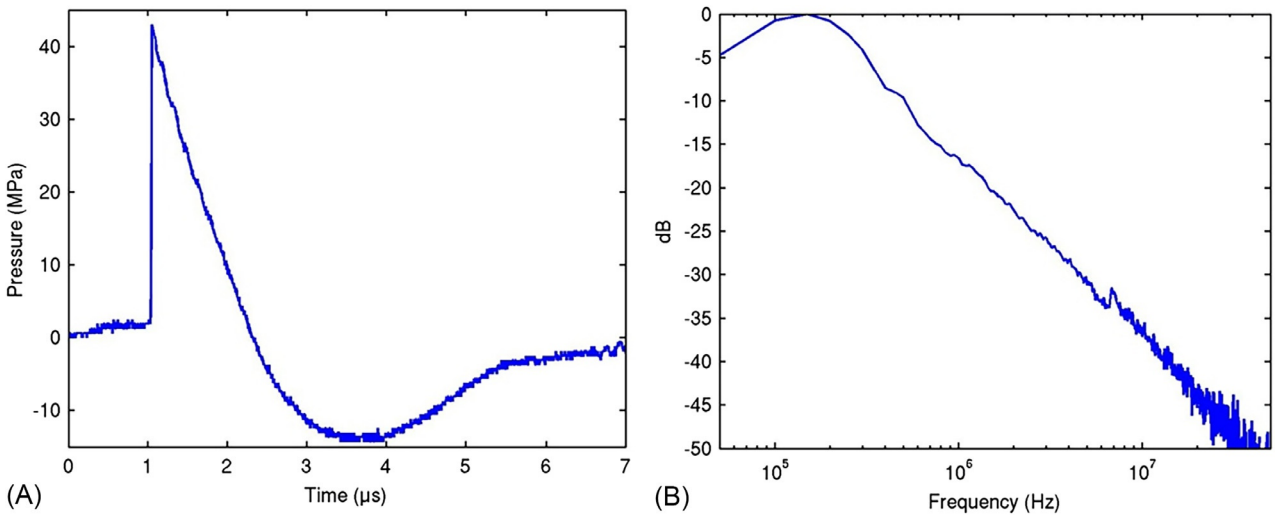


FIGURE 26.1 (a) A pressure waveform measured at the focus of an electrohydraulic lithotripter showing a positive leading phase followed by a negative tail. (b) The Fourier transform of the waveform in (a) showing a broad spectra with a peak around 150 kHz.

where the integration is done over the duration of the pulse. In many cases, it is difficult to reliably measure the negative pressure phase and so ED+, which is calculated only for the positive duration, is sometimes reported. For clinical studies, EFD is typically in the range of 0.02–0.64 mJ/mm^2.

26.2.1 Electrohydraulic source

In an electrohydraulic source, a high-voltage capacitor (10–30 kV) is discharged between two electrodes under water which leads to breakdown of water; the resulting expansion of a vapor cavity generates a spherically spreading shock wave. The electrodes are placed at the interior focus of ellipsoidal reflector which focusses the spherically spreading shock wave to the external focus of the ellipsoid (referred to as F2) (Figure 26.2). In this case, a shock wave is created by the source and remains present during the propagation path to the focal region. The electrohydraulic source requires regular replacement of the electrodes due to wear from the spark discharge.

26.2.2 Electromagnetic source

An electromagnetic source uses an electrical coil and a metal plate in close proximity. A high-voltage capacitor is discharged through the coil and the current produces a magnetic field which generates a repulsive force on the plate. The subsequent motion of the plate generates a pulsed acoustic wave. This wave can be focused either by means of lens, a parabolic reflector, or by forming the coil and plate on a spherical surface. In an electromagnetic source, the pulsed wave does not start off as a shock wave but if the amplitude is high enough as it propagates then due to nonlinear distortion it will produce a shock wave at the focus

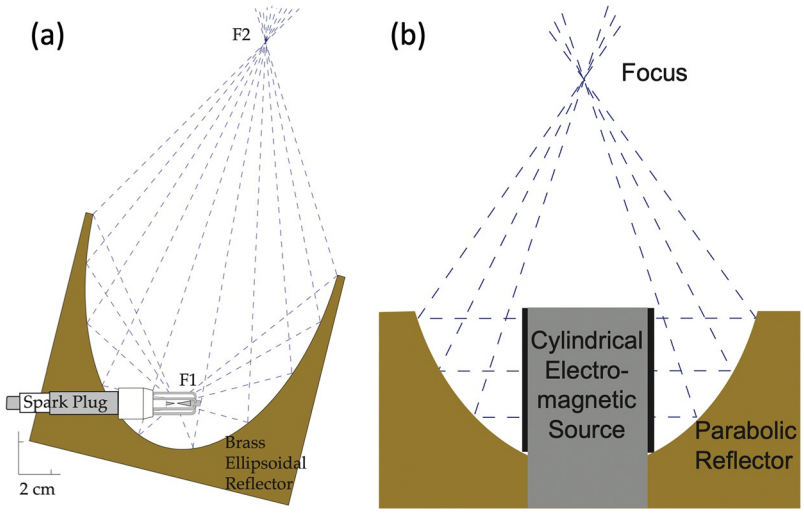


FIGURE 26.2 Two forms of focused shock source. (a) Electrohydraulic source: the spark plug places electrodes at the first focus of an ellipsoidal reflector. The *dotted lines* show the rays of the spherical wave that is reflected and focused to the second focus. (b) Electromagnetic source in which a cylindrical coil excites a membrane which generates an acoustic wave focused by a parabolic reflector. The *dashed lines* show the outgoing cylindrical wave that is focused by the parabolic reflector.

(Cleveland and McAteer, 2012). Depending on the energy setting of the source, the waveform can either be a pulsed waveform or it can have a shock wave.

26.2.3 Piezoelectric source

In a piezoelectric source, a large number of piezoelectric crystals are mounted on the inside surface of a sphere. When an electrical pulse is applied to the piezoelectric crystals, they undergo a mechanical deformation, predominantly a change in thickness, and the motion of the surface of the crystal produces a pressure wave. Focusing of the wave is achieved due to the geometric arrangement of the crystals on the spherical cap. The generation of shock waves only occurs when the amplitude is sufficiently high that nonlinear distortion effects produce a shock. Similar to an electromagnetic source, the source produces pressure pulses at low energy level settings and shock waves at higher energy levels.

26.2.4 Ballistic source

A ballistic source consists of a projectile that it is driven by compressed air (Figure 26.3a). The projectile strikes a metal applicator (therapy head) and the kinetic energy is transformed into a pressure wave which passes through the applicator and into the patient. A ballistic source is not focused but generates a pulse that diffracts and spreads as it propagates from the applicator. It is sometimes referred to as a radial wave due to the spreading effect. Clinical ballistic sources produce a pressure pulse (Figure 26.3b), and due to the lower pressure amplitudes and spreading effects, the nonlinear distortion is not high enough for them to produce a shock wave. The terminology for ballistic sources is not consistent with terms such as acoustic pulse therapy, extracorporeal pulse activation therapy, and radial extracorporeal shock wave therapy (rESWT), all being employed in the literature.

26.2.5 Coupling

The acoustic impedance of the body is very similar to water, and therefore, most shock waves are generated in water in order to impedance match to the body. In order to couple the shock source to the patient, it is important that there is no air in the interface. In the original lithotripters, the patient was immersed in a water bath which provides excellent coupling but is costly; a water treatment system is needed to ensure the water in the bath is degassed and clean, and it is inconvenient to have a patient in a water bath during treatment. Subsequent devices have placed the shock source in a therapy head which has a flexible membrane and water is pumped into the therapy head to expand the membrane until it is in contact with the patient. The membrane is then coupled to the patient using ultrasound coupling gel (Lingeman et al., 2009). This provides a much more convenient system but there is a cost in reduction of coupling performance as it is hard to avoid bubbles in the gel (Pishchalnikov et al., 2006). For ballistic sources, ultrasound coupling gel is usually deployed on the skin of the patient and the applicator pressed manually against the skin.

26.2.6 Mechanisms

There is no general agreement in the literature as to what mechanisms play the key role in shock wave treatment. The two mechanical processes that can play a role are direct stress and cavitation. It is unlikely that heating plays a role as the pulses are so short and the interpulse time is relatively long that temperature rises are expected to be less than 1°C.

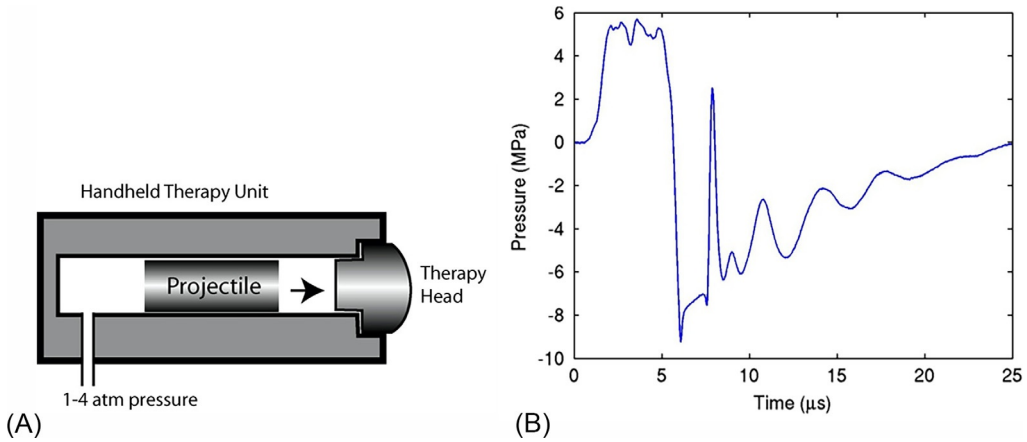


FIGURE 26.3 (a) A sketch of the components of a ballistic source. Pressurized gas drives a projectile that strikes a therapy head. The impact launches stress waves in the therapy head that then propagate into the patient. (b) A measured pressure waveform from a ballistic source with a leading positive pressure (amplitude less than 10 MPa and duration less than 5 μs) and a complex negative tail.

26.2.6.1 Direct stress

The acoustic waves result in stresses and strain to the tissue. The acoustic wave is a longitudinal wave and so the predominant strains will be compressive and tensile. Because tissue is almost incompressible (bulk modulus ~2.25 Gpa) even at high pressures (100 Mpa), the resulting strain is less than 1%. However, particular for musculoskeletal indications, the presence of bone will result in complex reflection phenomena which could result in local amplification of stress and also complex loading. In the presence of air pockets, the negative reflection coefficient could lead to high tensile strains. These strains could result in local microdamage of tissue that has the potential to initiate the natural repair processes of the body.

In addition, tissue is not a fluid but a viscoelastic solid, and therefore, there will be coupling into shear strain as well as the shock wave passes. The coupling will happen directly due to the response of the tissue to the acoustic deformation and the interaction with the bone. In addition, shear strain will also be produced due to the acoustic radiation force resulting from absorption of the acoustic energy. The coupling into shear waves is weak and it is unlikely that it generates enough shear strain to produce damage. However, it is possible that the shear waves can generate enough shear strain to induce a mechanical response in cells. For example, exciting or inhibiting nerve impulses (Wess, 2008) could therefore modulate pain response.

26.2.6.2 Cavitation

The negative pressure tail of the shock waves can be high enough amplitude to create cavitation, that is, the creation of cavities in fluid or fracture of tissue under a tensile strain. In the case of cavities, once formed, the subsequent tensile strain from the present SW, or subsequent ones, can result in violent growth and collapse cycles that can strain and damage surrounding tissue (Cleveland and McAteer, 2012; Coleman et al., 1987). The cavitation, like direct stress, could activate cells to impact signaling and/or result in microdamage that initiates the natural healing response. The action of cavitation in fluids near rigid surfaces results in violent jetting processes that will result in surface ablation and crack formation.

26.3 Clinical treatments

26.3.1 Kidney stones

Kidney stones are mineral deposits in the renal calyces and pelvis that are found free or attached to the renal papillae. They contain crystalline and organic components and are formed when urine becomes supersaturated with respect to a mineral, leading to crystal formation, growth, aggregation, and retention within the kidneys (Khan et al., 2016; Finlayson, 1978). SWL is a noninvasive procedure for treatment of kidney stones introduced in 1980, and at the time, it revolutionized the treatment of nephrolithiasis worldwide with more than 80% of stones being treated with shock waves by the 1990s (Holmes and Whitfield, 1991; Kerbl et al., 2002; Cleveland and McAteer, 2012). Shock waves fragment stones through a combination of direct stress, likely responsible for the initial fragmentation, and cavitation, likely responsible for reducing smaller fragments to sizes that can be passed (Cleveland and McAteer, 2012). The shock waves do results in some minor damage to kidneys with blood vessels and tubules in the vicinity of the focus being ruptured with most patients experiencing hematuria, blood in the urine after treatment (Cleveland and McAteer, 2012).

Since the initial success of SWL, there has been an advent of minimally invasive surgery, in particular, ureteroscopy (URS) where an endoscope is placed up the ureter to access the stone and a laser is usually used to fracture the stone, and percutaneous nephrolithotomy (PCNL) which involves keyhole surgery through a flank incisions through which a devise, often an ultrasonic probe, is used to fragment the stones. Table 26.1 shows a number of studies that compare SWL to other approaches in treating kidney stones. The stone-free rate for SWL varied from 48% to 92%, whereas for URS, it varied from 61% to 100%. Although URS shows better outcomes, it is a more invasive procedure that costs more and has higher incidence of side effects than SWL. Therefore, in the United Kingdom, NICE recommends SWL as the first line treatment for kidney stones in most patients with other procedures employed for stones that are resistant to shock waves.

26.3.2 Plantar fasciitis

Plantar fasciitis is a musculoskeletal disorder where the plantar fascia tendon attached to the heel bone becomes inflamed. Plantar fasciitis is one of the most common causes of heel pain, with a lifetime risk in the general population of approximately 11%–15% (Ozan et al., 2017; Liden et al., 2009) and a stronger association with athletes (Chew et al., 2013). Excessive foot pronation, running, obesity, and prolonged standing are the risk factors of plantar fascia (Chew et al., 2013; Irving et al., 2007; Riddle et al., 2003). Conventional treatments include stretching exercises, orthotics, splints, and pain medication while invasive strategies include corticosteroid injections and surgery to the fascia, percutaneous, endoscopic, or open fasciotomy. Shock wave therapy (SWT) has been used for treatment of plantar fasciitis since the early 1990s (Haake et al., 2003). The data on outcomes are quite variable with some

TABLE 26.1 Synopsis of shock wave settings and treatment outcomes for SWT of kidney stones compared to URS, PCNL, or no treatment

Study	Subjects	EFD (mJ/mm^2)	PRF	SW number per session	Treatments	Outcomes	Comments
Sener et al. (2015)	50 (SWL)	NA	NA	2500–3000	1–3 sessions	Success rate 92% after 3 months	Electrohydraulic shock source (focused ESWT) Postoperative analysis of stone was performed by CT-imaging Stone fragmentation less than 3 mm was considered successful
	50 (URS)					Success rate 92% after 3 months	
	50 (No treatment)					Success rate 2% after 3 months	
Sener et al. (2014)	70 (SWL)	NA	NA	2500–3000	Maximum of three sessions	Success rate 91.5% after 3 months	Electrohydraulic shock source (focused ESWT) Clinical evaluation was performed using plain X-ray and urinary ultrasound Stone fragmentation less than 3 mm was considered successful
	70 (URS)					Success rate 100% after 3 months	
Vilches et al. (2015)	31 (SWL)	NA	1	3000	Single session	Stone free rate 48.3%	Electromagnetic shock source (focused ESWT) Postoperative analysis of stone was performed by CT-imaging Stone fragmentation less than 3 mm was considered successful
	24 Retrograde Intrarenal Surgery (RIRS)					Stone free rate 70.8%	
Kumar et al. (2015)	42 (SWL)	NA	1.5	2500 (Maximum)	1–4 sessions	Re-treatment 63.4%	Electromagnetic shock source (focused ESWT) Assessed by ultrasound of the kidneys, ureter, and bladder after 3 weeks
	43 Retrograde Intrarenal Surgery (RIRS)					Re-treatment 2.1%	
	41 (PCNL)					Re-treatment 2.2%	
Fankhauser et al. (2021)	21 (SWL)	NA	NA	2500–4000	Single session	Stone free rate: 48% after 3 months	Electromagnetic shock source (focused ESWT) Abdominal CT was used to determine the stone free status 3 months after the treatment
	23 (URS)					Stone free rate: 61% after 3 months	

studies showing an improvement over control, some showing no difference, and some studies not having a control arm. It is challenging to compare across studies as there are differences in energy settings, shock wave number, number of treatments, how outcomes are assessed, and even the location to which shock waves are delivered. Table 26.2 shows a synopsis of a representative sample of papers in the literature, the shock wave parameters and the results for treatment of plantar fasciitis, and the control study if that was included in the work.

Figure 26.4 captures the outcomes from the reports as a function of total number of shock waves (over all sessions) and the EFD (energy flux density). It can be seen that the EFD does not appear to be a good predictor of outcomes in treating plantar fasciitis, but those studies with the highest number of shock waves do appear to have better outcomes.

26.3.3 Healing of nonunion/delayed union of bones

Failure of bone fractures to achieve cortical continuity on radiographic studies is known as nonunion. Procedures such as bone grafts and internal/external fixation for fracture stabilization are the most common treatments; however, there have been several concerns associated with them such as deep infections, persistent wound drainage, hematoma formation, sensory loss, persisting pain, and nonunions (Hak et al., 2014; Younger and Chapman, 1989; Warren and Brooker, 1992; Wang et al., 2001; Kertzman et al., 2017). ESWT (extracorporeal shockwave therapy) has emerged an alternative for nonunions where shock waves are applied to the site of the fracture (Kertzman et al., 2017). It is hypothesized that the shock waves disrupt scar tissue that

TABLE 26.2 Synopsis of shock wave settings and treatment outcomes for SWT of plantar fasciitis

Study	Subjects	EFD (mJ/mm^2)	PRF	SW number per session	Treatments	Outcomes	Comments
Chuckpaiwong et al. (2009)	225	0.36	NA	3500 + 300 graded	1 session	70.7% at 3 months	Electromagnetic source Clinical assessment: pain score
	No control						
Saber et al. (2012)	30	0.28	2	1000–1500	2 sessions	No statistically significant difference between the study groups	Electrohydraulic source Clinical assessment: pain score and functional status
	30	Ultrasound guided local steroid injection					
Eslamian et al. (2016)	20	0.2	2	2000	5 sessions, 3 day intervals	55% good or excellent	Ballistic source (radial ESWT) Clinical assessment: pain VAS and foot function index (FFI)
	20	Control: corticosteroid			Single injection	30% good or excellent	
Malliaropoulos et al. (2016)	68	NA	5 ± 0.2	2000	4–11 sessions (mean: 7 ± 1.6)	Success rate of 70% at 3 months	Ballistic source (radial ESWT) Clinical assessment: pain VAS
Ozan et al. (2017)	40	NA	15	2000	4 sessions	Improved outcomes in both groups at 3 and 6 months	Ballistic source (radial ESWT) Clinical assessment: pain scores
	16	Radiofrequency thermal lesioning	2 min impulses at 45 V and 2 min thermal RF at 80°C		1 session		

TABLE 26.2 Synopsis of shock wave settings and treatment outcomes for SWT of plantar fasciitis—cont'd

Study	Subjects	EFD (mJ/mm^2)	PRF	SW number per session	Treatments	Outcomes	Comments
Metzner et al. (2010)	63	0.35	2	1000–2000 (1st session) 2000–3500 (2nd session) 3000–4200 (3rd session)	1–3 sessions	81% success at 6-week followup	Electromagnetic lithotripter (focused ESWT) Clinical assessment: pain VAS
	No control						
Gollwitzer et al. (2007)	20	0.25	NA	2000	3 sessions	73.2% reduction in composite heel pain	Electromagnetic-focused ESWT Clinical assessment: pain VAS
	20	Sham treatment				40.5 reduction in composite heel pain	
Krishnan et al. (2012)	25	0.16	21	1000	5 sessions	92% reported moderate to high satisfaction with SWT	Ballistic source (radial ESWT) Clinical assessment: pain scores
	No control						
Lai et al. (2018)	47	0.07–0.29	1	1500	2 sessions	SWT had less pain. Thickness of plantar fascia increases in the first month followed by a gradual decrease to the baseline at third month	Focused ESWT Clinical assessment: pain VAS and thickness of plantar fascia by ultrasonography
	50	Control: corticosteroid (CSI)					

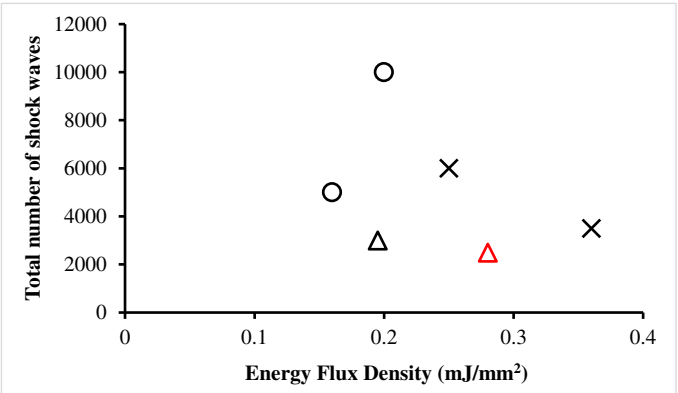


FIGURE 26.4 Outcomes of treating plantar fasciitis as a function of the total number of shock waves and EFD. The *symbols* represent the type of shock source employed Δ EH, X EM, and O Ballistic. The *red symbol* represents data from an unsuccessful treatment.

forms in the fracture of a nonunion and restarts the natural bone repair process, osteogenesis. It is thought that the SWs can trigger the process by which mesenchymal cells differentiate into cartilage, which then transforms to bone by ossification. Because the ostegenesis process is sensitive to mechanical loading, it is likely that the direct stress and cavitation of shock waves play a role in this process, with cavitation the most likely mechanism for disrupting the scar tissue that forms in the fracture.

Table 26.3 shows a synopsis of some of the studies that have used shock waves for the treatment of nonunions. It can be seen that the success rates vary from 56% to 81%. Figure 26.5 shows the outcome (bubble size) as a function of the total number of shock waves and the EFD. The range of energy levels is from about 0.2 to 0.5 mJ/mm^2 and the shock wave number ranges from 2000 to 18,000. It can be seen that the response does not appear to be strongly dependent on the shock parameters employed, although it does suggest that using high numbers of shock waves does not result in significant improvement in outcomes.

26.3.4 Chronic foot ulcers

Chronic foot ulcers are typically defined as ulcers that have not healed after 3 months. Diabetic ulcers form due to small vessel occlusion angiopathy followed by secondary infections. On the other hand, nondiabetic ulcers occur due to deep vein thrombosis or varicosity that predisposes to tissue edema, skin breakdown and secondary infection, and peripheral arterial diseases (Wang et al., 2014; Jeffcoate and Harding, 2003; Macfarlane and Jeffcoate, 1997). The management of chronic foot ulcers includes diabetic

TABLE 26.3 Synopsis of shock wave settings and treatment outcomes for SWT of bone nonunions

Study	Subjects	EFD (mJ/mm^2)	PRF	SWN per session	Treatments	Outcomes	Comments
Kertzman et al. (2017)	22	0.18	NA	3000	3 session; 1 week intervals	Success rate 73% at 6 months	Ballistic source (radial ESWT) Positive outcome defined by radiographic bone consolidation and function
	No control						
Haffner et al. (2016)	56	0.4	4	3000–4000	1–4 sessions	Success rate 88.5% at 6 months	Electrohydraulic source (focused ESWT) Endpoint was healing of the tibia nonunion
	No control						
Vulpiani et al. (2012)	143	0.25–0.84	NA	2500–3000	3–5 sessions	Complete healing: 55.9% Partial healing 28.7% No healing 15.4%	Electromagnetic source (focused ESWT) Lower energy protocols were used for short bones and higher energy for long or multiple bones or severe fractures
	No control						
Xu et al. (2009)	69	0.62 (Femur and Tibia)	NA	6000–10,000 (Femur and Tibia)	1 session	75.8% patients achieved bony union	Electrohydraulic source (focused ESWT) Nonunion was defined as a failed bone healing of more than 6 months after fracture or previous operation
		0.56 (Humerus)		4000 (Humerus)			
		0.56 (Radius and Ulna)		3000 (Radius and Ulna)			
	No control						

TABLE 26.3 Synopsis of shock wave settings and treatment outcomes for SWT of bone nonunions—cont'd

Study	Subjects	EFD (mJ/mm^2)	PRF	SWN per session	Treatments	Outcomes	Comments
Alvarez et al. (2011)	32	0.22–0.51	0.5–4	2000	Single session	Success rate of 89% at 6 months	Clinical evaluation was performed using VAS score, SF-36, and X-ray
	No control						
Furia (2010)	23	0.35	NA	2000–4000	Single session	Success rate of 87% at 3 months and 91% at 6 months	Electrohydraulic source (focused ESWT) Clinical evaluation based on antero-posterior and lateral radiographs
	20	Control: intramedullary screw fixation				Success rate 90% at 3 months	
Cacchio et al. (2009)	42 (Group I)	0.4 (Group I)	NA	4000	4 sessions	Success rate at 6 months: 70%	Electromagnetic source (focused ESWT) Healing of nonunion with a radiographic assessment at 6 months At 12 and 24 months, differences between all the groups were no longer significant
	42 (Group II)	0.7 (Group II)	NA	4000	4 sessions	Success rate at 6 months: 71%	
	42	Group III: surgical treatment				Success rate at 6 months: 73%	
Quadlbauer et al. (2019)	26	0.41	4	3000	1	Success rate: 81%	Electrohydraulic source (focused ESWT) Clinical evaluation: pain VAS and various functional tests
	16	9 patients were stabilized with headless compression screws and 7 with an angular stable scaphoid plate				Success rate: 75%	

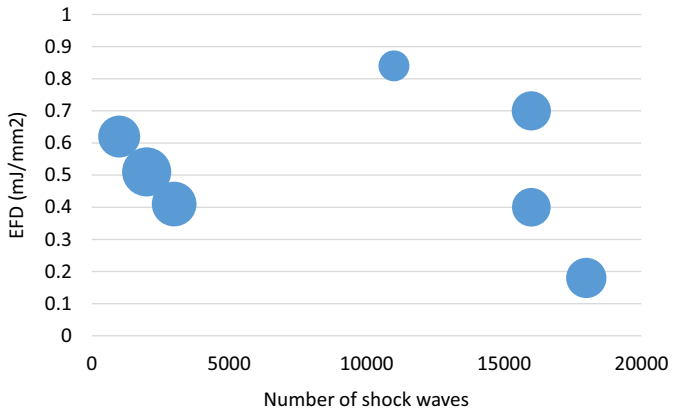


FIGURE 26.5 Success rates of treating bone nonunions with shock waves as a function of the total number of shock waves and EFD. The diameter of the bubble is proportional to the success rate of the shock wave treatment.

control, antibiotic, shoe wear, wound care, and surgery. However, many of these approaches which are both surgical and nonsurgical are inconsistent and yield unsatisfactory results (Schaper et al., 2003; Nomikos et al., 2006; Yager and Nwomeh, 1999).

Chronic foot ulcers are an indication in need of better treatment strategies particularly given they are likely to become more prevalent due to expected increase in issues with diabetes in the general population for the foreseeable future. Many adjunctive therapies have been developed such as hyperbaric oxygen therapy, ultrasound, recombinant human platelet-derived growth factor BB, vacuum-assisted wound closure, and acellular matrix, but they have achieved limited success and none of them have depicted universal results (Landau, 1998; Ruffieux et al., 1997; Abidia et al., 2003; Kalani et al., 2002; Kessler et al., 2003; Senior, 2000; Boykin, 2000; Faglia et al., 1996). ESWT is an emerging modality for the treatment of chronic foot ulcers as well as other indications such as skin flaps and burn wound healing (Meirer et al., 2005a,b; Kuo et al., 2009). It is hypothesized that shock waves help with blood flow to the site of the ulcer and that this accelerates the natural repair mechanisms that heal the wound. Table 26.4 shows some of the studies that have used shock waves for diabetic foot ulcers and other chronic wound repair. It can be seen that success varied from 34.5% to 70% when treated with

TABLE 26.4 Synopsis of shock wave settings and treatment outcomes for SWT of bone nonunions

Study	Subjects	EFD	PRF	SWN per session	Treatments	Outcomes	Comments
Omar et al. (2014)	19	0.11 mJ/cm^2	NA	100 pulse/cm^2	8 sessions (twice a week with 1-week interval)	Success rate: 54% at Week 20 Average healing time 64.5 days	Clinical evaluation was performed based on the wound surface area (WSA), and time to healing
	19	Control group				Success rate 28.5% at Week 20 Average healing time 81.2 days	
Wang et al. (2014)	38 (Diabetes mellitus group)	0.11 mJ/cm^2	4 Hz	>500	6 sessions, twice per week	Completely healed ulcers in 48% of group at 1 year	Electrohydraulic shock source Clinical evaluation included assessment of ulcer, local blood flow perfusion, and analysis of mortality and morbidity
	29 (Nondiabetes mellitus group)					Completely healed ulcers in 66% of group at 1 year	
Jeppesen et al. (2016)	11	0.2 mJ/mm^2	5	250 shocks/cm^2 + 500 (deep shocks)	6 sessions over 3 weeks	34.5% reduction in ulcer area at 7 weeks	Focused shock source Clinical evaluation: ulcer size, transcutaneous oxygen tension, and pain score
	12	Control group				5.6% reduction in ulcer area at 7 weeks	
Porso et al. (2017)	10	0.15 mJ/mm^2	4	300 (Standard) + 100 pulse/cm^2	3 sessions, 72 h interval	Healing of 7 out of 10 ulcers and complete pain relief in 9 out of 10 patients	Electromagnetic shock source (defocused ESWT) Clinical evaluation was based on the wound size and pain VAS
	No control						

shock waves with studies with control groups showing that SW-treated ulcers show a significant improvement in outcomes over the control groups.

26.3.5 Chronic refractory angina pectoris

Refractory angina pectoris (RAP) is defined as the occurrence of frequent angina attacks that cannot be controlled by pharmacological therapy and where the presence of coronary artery disease renders surgical intervention unsuitable. The chest discomfort suffered by the patients significantly impairs their quality of life; both physically, as it limits the activity that the patient is able to do, and also mentally as patients often have constant concern of an impending heart attack. Although there have been many advances in medical and invasive revascularization therapy, many patients have shown progression to end-stage ischemic coronary artery disease with chronic refractory angina symptoms and no further revascularization options (Manchanda et al., 2011; Vainer et al., 2016). Refractory angina patients with no revascularization option have low long-term mortality. Hence, therapeutic options for such patients must focus on reducing chest pain and improved quality of life (Henry et al., 2013). Novel therapeutic strategies have been developed for such "no-option patients" (DeJongste et al., 2004) in order to improve their quality of life and prognosis (Vainer et al., 2016). Some of these strategies include enhanced external counter-pulsation (Arora et al., 1999), spinal cord stimulation (Eddicks et al., 2007), therapeutic angiogenesis (van Ramshorst et al., 2009), coronary sinus intervention (Verheye et al., 2015), and newer drugs (Manchanda et al., 2011).

Shock wave therapy has been used to treat RAP. The proposed mechanism is that the shock waves induce angiogenesis in the heart muscle with a concomitant improvement of the local microcirculation (Vainer et al., 2016). Table 26.5 shows results from a number of studies used to treat RAP, shock wave parameters, and the results for treatment of refractory angina pectoris. All the studies claim that the patients had improved outcomes after treatment relative to baseline, but in the two studies with a control arm, one showed that shock waves resulted in no difference (Shkolnik et al., 2018) and one showed that the shock wave group did have better outcomes (Zhao et al., 2015).

26.3.6 Calcific tendinitis

Calcific tendinitis is defined as the deposition of calcium phosphate crystal in the rotator cuff tendons and is a common health problem typically occurring for people in their middle ages (Uhthoff and Sarkar, 1989; Ark et al., 1992; Wainner and Hasz, 1998; Cacchio et al., 2006). It affects a number of tendons in the shoulder area (Uhthoff, 1996) and reasons for the issue include hypo vascularization, and local degenerative and proliferative changes in tendinous tissue of the rotator cuff (Uhthoff and Sarkar, 1989; Gartner and Simons, 1990; Moseley, 1963).

Shock waves have been used to treated calcific tendinitis and Table 26.6 shows a synopsis of some studies in the literature. All these studies used ballistic sources and the energy levels, and the number of shock waves employed is not as variable as in other indications. All studies show an improvement over baseline but of the two studies with a control group, one shows an improvement over control and the other shows no statistical difference to the control group. Even in cases where the acoustic dose appears similar, the outcomes are not consistent. This captures the challenge associated with the indications that SWT attempts to address.

26.3.7 Lateral epicondylitis

The last indication that will be covered in this chapter is lateral epicondylitis (or tennis elbow), which is one of the most common orthopedic symptoms with a nonoperative management being initially effective in the patients. It is characterized by pain and tenderness around the elbow, and occurs most frequently as a result of minor, unrecognized trauma during sports activities, and occupation-related physical activities (Ozturan et al., 2010). Studies (Pettrone and McCall, 2005; Coonrad and Hooper, 1973; Nirschl and Pettrone, 1979) have shown that surgical intervention is necessary in 4%–11% of patients. Table 26.7 shows results from a few studies that have investigated the use of shock waves to treat of lateral epicondylitis. In all four studies, there was a control group, and in two studies, there was no difference between control and SWT, and in two studies, SWT was found to have better outcomes. As with other studies, this demonstrates the variability in results which could be due to the use of shock waves but is likely due to the complexity of the indication and the challenges in assessing outcome.

26.4 Conclusions and future directions

The introduction of shock waves for treating kidney stones revolutionized that treatment and SWL remain one of the major tools for treating kidney stones today. However, the success rates of SWL have not improved over time and newer minimally invasive technologies have been developed with better outcomes. One new approach using ultrasound is burst wave lithotripsy (BWL) (Maxwell et al., 2019) which uses burst of ultrasound to fragment stones. It is undergoing clinical trials and with a system that is compact enough that it could be employed in a doctor's office rather than in a hospital environment

TABLE 26.5 Synopsis of shock wave settings and treatment outcomes for SWT of refractory angina pectoris

Study	Subjects	EFD (mJ/mm^2)	PRF (Hz)	SWN per spot/ treatment zone per session	Treatments	Outcomes	Comments
Cassar et al. (2014)	15	0.09	NA	100 (per treatment zone) Five treatment zones	9 sessions	Statistically significant increase in exercise treadmill time	Electromagnetic shock source Clinical outcomes: treadmill test for exercise capacity
	No control						
Shkolnik et al. (2018)	37	0.09	NA	100 (per spot)	9 sessions	Total exercise duration was not significantly different in the SWT group	Electromagnetic shock source Clinical outcomes: treadmill test for exercise capacity
	35	Placebo group					
Zhao et al. (2015)	32 (Group A)	0.09	NA	200 shoots/ spot (9 spots)	9 sessions	Outcomes were improved in SWT group	Electromagnetic shock source Clinical assessment: myocardial function, ECG signals, and SPECT imaging
	30 (Group B)	0.09	NA	200 shoots/ spot (25 spots)	9 sessions		
	25	Control group (Group C)					
Vainer et al. (2016)	33	0.09	NA	100 impulses/ spot; 3–7 spots/ session	9 sessions	Heart function improved after SWT	Electromagnetic shock source Clinical assessment: exercise testing, echocardiography, and SPECT
	No control						

(Harper et al., 2021). The use of shock waves for other calculi has not been as successful. Initial efforts on treating gall stones did not result in compelling outcomes, likely because gall stones do not fracture in the same way and the ducts are not large enough to pass fragments (Paumgartner and Sauter, 2005). Shock waves have also been used in the treatment of salivary stones but it also has not gained traction (Capaccio et al., 2017).

The main areas in which research has been carried out are musculoskeletal indications where there are almost 30 years of studies, but the results are very variable. The indication with the most studies is plantar fasciitis. The hypothesis is that shock waves initiate the repair mechanism by inducing micro disruption of plantar fascia and achilles tendon (Chuckpaiwong et al., 2009; Ogden et al., 2001; Rompe et al., 1998; Chen et al., 2004; Maier et al., 2003; Martini et al., 2003; Wang et al., 2002, 2003). It was shown that there was significant variation in how shock waves are deployed, e.g., the number of shocks waves, energy, number of treatments, and the site of treatment. Measuring outcomes is challenging in plantar fasciitis as it relies on pain scores and there is a significant placebo effect ~40% when treating plantar fasciitis. Some studies show that SWs are better than control whereas some studies show SWs make no difference. SWT has also been used for bone healing where it is thought to create microfractures and bleeding (Vulpiani et al., 2012; Haupt et al., 1992; Kaulesar Sukul et al., 1993; Johannes et al., 1994; Forriol et al., 1994; Delius et al., 1995; Augat et al., 1995; Rompe et al., 1997; Vogel et al., 1997; Graff et al., 1989; Ikeda et al., 1999;

TABLE 26.6 Synopsis of shock wave settings and treatment outcomes for SWT of calcific tendinitis

Study	Subjects	EFD (mJ/mm^2)	PRF (Hz)	SW number per session	Treatments	Outcomes	Comments
Malliaropoulos et al. (2017)	67	NA	5 ± 0.3 (Mean)	2175 ± 266 (Mean)	7 ± 1.5 (Mean); 1-week interval	Success rate of 92% and recurrence rate of 7% at 1-year	Ballistic source (radial shock wave) Clinical evaluation was performed by pain VAS
	No control						
Duymaz and Sindel (2019)	40	0.03–0.28	2.5	1500	4 sessions; 1-week interval	SWT group had a statistically significant improvement	Ballistic source (radial shock wave) Clinical evaluation was performed by pain VAS and function scores
	40	Control group					
Kolk et al. (2013)	44	0.11	8	2000	3 sessions; 10–14 days interval	Significant improvement in both groups but SWT not better than control	Ballistic source (radial shock wave) Clinical evaluation was performed by pain VAS and function scores
	38	Control group					

Uslu et al., 1999). In most of the studies related to nonunions, success rates were defined as radiographic bone consolidation using X-ray and the absence of pain. Shock waves show similar outcomes to competing therapies, but although shock waves are noninvasive, the results have not been compelling enough to make an impact on clinical treatment. Two other applications described here were calcific tendinitis and lateral epicondylitis. Like plantar fasciitis, there are many studies that appear to show improvement in pain relief, range of motion, and muscular strength. However, there is such variation in treatment protocols and showing significant improvement relative to controls, where again there is a major placebo effect is challenging.

SWT has also been used for soft tissue repair. There is data to show that shock waves can induce angiogenesis in the wound tissue (Jeppesen et al., 2016), increased blood perfusion (Arnó et al., 2010; Wang et al., 2011), and improved vascularization (Stojadinovic et al., 2008). The present study showed data from two indications. For chronic foot ulcers, the success rates of ESWT have varied from 34.5% to 71% where the clinical evaluation was performed based on the blood flow perfusion, rate of healing, ulcer/wound size, and pain score. For treatment of cardiac muscle studies, how that shock wave therapy can improve refractory angina pectoris, where a treadmill test and SPECT analysis are used for clinical evaluation. These studies (Cassar et al., 2014; Vainer et al., 2016; Zhao et al., 2015) reported a significant reduction in myocardial ischemic segments and an increase in exercise treadmill time after the treatment.

In conclusion, after the initial promise of shock waves with the success in kidney stone treatment, shock waves have not managed to make an impact into many other areas of medical therapy. As captured in this chapter, there have been many studies which provide tantalizing evidence that shock waves can have an impact many indications. There are many other indications that have been treated with shock waves with one of the most recent and intriguing being applying shock waves to the brains of patients with Alzheimer (Beisteiner et al., 2020). But the variability in the outcomes of almost of studies makes drawing conclusions

TABLE 26.7 Synopsis of shock wave settings and treatment outcomes for SWT of lateral epicondylitis

Study	Subjects	EFD (mJ/mm^2)	PRF (Hz)	SWN per session	Treatments	Outcomes	Comments
Lee et al. (2012)	12	0.06–0.12	NA	2000	3 sessions, 1 week interval	Both groups showed improvement over baseline. No difference between SWT and steroid injection	Clinical assessment was based on pain scores
	10	Control: local steroid injection group					
Capan et al. (2016)	28	NA	10	2000	3 sessions	Both groups showed significant improvement in all outcome measures during follow-ups	Ballistic source (radial shock wave) Clinical evaluation was based on pain scores and a hand dynamometer for grip strength
	28	Sham rESWT					
Dedes et al. (2020)	117	NA	21 (initial) 15 (other sessions)	2000 (initial) 1500 (other sessions)	3–5 sessions	SWT is more effective than the ultrasound therapy which was more effective than control	Ballistic source (radial shock wave) Clinical evaluation was performed using questionnaire
	63	Ultrasound group • Ultrasonic waves at a frequency of 3 MHz and intensity 2 W/cm^2					
	18	Control group • Conservative therapy					
Vulpiani et al. (2015)	40	0.14–0.20		2400	3 sessions	SWT outcomes better than control at 6 and 12 months	Electromagnetic source (focused ESWT) Clinical evaluation was based on pain scores
	40	Control: cryo-ultrasound therapy group			12 sessions		

challenging. In some cases, this is because the delivery of shock wave energy has been too varied across many studies. But it should also be recognized that the biology and pathophysiology of many of the indications are poorly understood and that it is often very challenging to measure outcomes. The delivery of shock waves to the body though has been shown to induce responses that should be helpful in many of these indications, such as fragmenting calcifications, disrupting scar tissue, induce angiogenesis, and stimulating stress sensitive cells. However, it is not clear how any of these mechanisms work and what shock wave parameters are needed to enhance one mechanism over another. This is an area that is ripe for further studies, although it is acknowledged that the studies are not easy to conduct. But if progress can be made in better understanding the mechanisms by which shock waves can improve the outcomes of specific indications, then because there are so many years of clinical development, the manufacturers of shock wave devices are well poised to be able to make a big impact in medical therapy.

Acknowledgments

This work was supported in part the National Institutes of Health through NIDDK 43881.

References

Abidia, A., Laden, G., Kuhan, G., et al., 2003. The role of hyperbaric oxygen therapy in ischaemic diabetic lower extremity ulcers: a double-blind randomised-controlled trial. Eur. J. Vasc. Endovasc. Surg. 25, 513.

Alvarez, R.G., Cincere, B., Channappa, C., Langerman, R., Schulte, R., Jaakkola, J., Melancon, K., Shereff, M., Lee Cross III, G., 2011. Extracorporeal shock wave treatment of non-or delayed union of proximal metatarsal fractures. Foot Ankle Int. 32 (8), 746–754.

Ark, J.W., Flock, T.J., Flatow, E.L., Bigliani, L.U., 1992. Arthroscopic treatment of calcific tendinitis of the shoulder. Arthroscopy 8, 183–188.

Arnó, A., Garcia, O., Hernán, I., et al., 2010. Extracorporeal shock waves, a new non-surgical method to treat severe burns. Burns 36, 844–849.

Arora, R.R., Chou, T.M., Jain, D., et al., 1999. The multicenter study of enhanced external counterpulsation (MUST-EECP): effect of EECP on exercise-induced myocardial ischemia and anginal episodes. J. Am. Coll. Cardiol. 33, 1833–1840.

Augat, P., Claes, L., Suger, G., 1995. In vivo effect of shock-waves on the healing of fractured bone. Clin. Biomech. (Bristol, Avon) 10 (7), 374–378.

Beisteiner, R., Matt, E., Fan, C., et al., 2020. Focal brain therapy: transcranial pulse stimulation with ultrasound in Alzheimer's disease—a new navigated focal brain therapy. Adv. Sci. 7, 2070017.

Boykin Jr., J.V., 2000. The nitric oxide connection: hyperbaric oxygen therapy, becaplermin, and diabetic ulcer management. Adv. Skin Wound Care 13, 169.

Cacchio, A., Paoloni, M., Barile, A., Don, R., de Paulis, F., Calvisi, V., Ranavolo, A., Frascarelli, M., Santilli, V., Spacca, G., 2006. Effectiveness of radial shock-wave therapy for calcific tendinitis of the shoulder: single-blind, randomized clinical study. Phys. Ther. 86 (5), 672–682.

Cacchio, A., Giordano, L., Colafarina, O., Rompe, J.D., Tavernese, E., Ioppolo, F., Flamini, S., Spacca, G., Santilli, V., 2009. Extracorporeal shock-wave therapy compared with surgery for hypertrophic long-bone nonunions. JBJS 91 (11), 2589–2597.

Capaccio, P., Torretta, S., Pignataro, L., Koch, M., 2017. Salivary lithotripsy in the era of sialendoscopy. Acta Otorhinolaryngol. Ital. 37, 113–121.

Capan, N., Esmaeilzadeh, S., Oral, A., Basoglu, C., Karan, A., Sindel, D., 2016. Radial extracorporeal shock wave therapy is not more effective than placebo in the management of lateral epicondylitis: a double-blind, randomized, placebo-controlled trial. Am. J. Phys. Med. Rehabil. 95 (7), 495–506.

Cassar, A., Prasad, M., Rodriguez-Porcel, M., Reeder, G.S., Karia, D., DeMaria, A.N., Lerman, A., 2014. Safety and efficacy of extracorporeal shock wave myocardial revascularization therapy for refractory angina pectoris. Mayo Clin. Proc. 89 (3), 346–354. Elsevier.

Chen, Y.J., Wang, C.J., Kuender, D.Y., Yur-Ren, K., Huang, H.C., Huang, Y.C., Sun, Y.C., Wang, F.S., 2004. Extracorporeal shock waves promote healing of collagenase-induced Achilles tendonitis and increase TGF-B1 and IGF-I expression. J. Orthop. Res. 22, 854–861.

Chew, K.T.L., Leong, D., Lin, C.Y., Lim, K.K., Tan, B., 2013. Comparison of autologous conditioned plasma injection, extracorporeal shockwave therapy, and conventional treatment for plantar fasciitis: a randomized trial. PM R 5 (12), 1035–1043.

Chuckpaiwong, B., Berkson, E.M., Theodore, G.H., 2009. Extracorporeal shock wave for chronic proximal plantar fasciitis: 225 patients with results and outcome predictors. J. Foot Ankle Surg. 48, 148–155.

Cleveland, R.O., McAteer, J.A., 2012. The physics of shock wave lithotripsy. In: Smith's Textbook on Endourology, third ed. vol. 1. Wiley-Blackwell, pp. 527–558.

Coleman, A.J., Saunders, J.E., Crum, L.A., Dyson, M., 1987. Acoustic cavitation generated by an extracorporeal shockwave lithotripter. Ultrasound Med. Biol. 13 (2), 69–76.

Coonrad, R.W., Hooper, W.R., 1973. Tennis elbow: its course, natural history, conservative and surgical management. J. Bone Joint Surg. Am. 55, 1177–1182.

Dedes, V., Tzirogiannis, K., Polikandrioti, M., Dede, A.M., Mitseas, A., Panoutsopoulos, G.I., 2020. Comparison of radial extracorporeal shockwave therapy with ultrasound therapy in patients with lateral epicondylitis. J. Med. Ultrason. 47, 319–325.

DeJongste, M.J., Tio, R.A., Foreman, R.D., 2004. Chronic therapeutically refractory angina pectoris. Heart 90, 225–230.

Delius, M., Draenert, K., Al Diek, Y., et al., 1995. Biological effects of shock waves: in vivo effect of high energy pulses on rabbit bone. Ultrasound Med. Biol. 21 (9), 1219–1225.

Duymaz, T., Sindel, D., 2019. Comparison of radial extracorporeal shock wave therapy and traditional physiotherapy in rotator cuff calcific tendinitis treatment. Arch. Rheumatol. 34 (3), 281.

Eddicks, S., Maier-Hauff, K., Schenk, M., et al., 2007. Thoracic spinal cord stimulation improves functional status and relieves symptoms in patients with refractory angina pectoris: the first placebo-controlled randomised study. Heart 93, 585–590.

Eslamian, F., Shakouri, S.K., Jahanjoo, F., Hajialiloo, M., Notghi, F., 2016. Extra corporeal shock wave therapy versus local corticosteroid injection in the treatment of chronic plantar fasciitis, a single blinded randomized clinical trial. Pain Med. 17 (9), 1722–1731.

Faglia, E., Favales, F., Aldeghi, A., et al., 1996. Adjunctive systemic hyperbaric oxygen therapy in treatment of severe prevalently ischemic diabetic foot ulcer. A randomized study. Diabetes Care 19, 1338.

Fankhauser, C.D., Weber, D., Müntener, M., Poyet, C., Sulser, T., Hermanns, T., 2021. Effectiveness of flexible ureterorenoscopy versus extracorporeal shock wave lithotripsy for renal calculi of 5–15 mm: results of a randomized controlled trial. Eur. Urol. Open Sci. 25, 5–10.

Finlayson, B., 1978. Physicochemical aspects of urolithiasis. Kidney Int. 13, 344–360.

Forriol, F., Solchaga, L., Moreno, J.L., et al., 1994. The effect of shockwaves on mature and healing cortical bone. Int. Orthop. 18 (5), 325–329.

Furia, J.P., et al., 2010. Shock wave therapy compared with intramedullary screw fixation for nonunion of proximal fifth metatarsal metaphyseal-diaphyseal fractures. J. Bone Joint Surg. 92.

Gartner, J., Simons, B., 1990. Analysis of calcific deposits in calcifying tendinitis. Clin. Orthop. Relat. Res. 254, 111–120.

Gollwitzer, H., Diehl, P., von Korff, A., Rahlfs, V.W., Gerdesmeyer, L., 2007. Extracorporeal shock wave therapy for chronic painful heel syndrome: a prospective, double blind, randomized trial assessing the efficacy of a new electromagnetic shock wave device. J. Foot Ankle Surg. 46 (5), 348–357.

Graff, J., Pastor, J., Richter, K.D., 1989. Effect of high energy shock waves on bony tissue. Urolithiasis, 997–998.

Haake, M., Buch, M., Schoellner, C., Goebel, F., Vogel, M., Mueller, I., Hausdorf, J., Zamzow, K., Schade-Brittinger, C., Mueller, H.H., 2003. Extracorporeal shock wave therapy for plantar fasciitis: randomised controlled multicentre trial. BMJ 327 (7406), 75.

Haffner, N., Antonic, V., Smolen, D., Slezak, P., Schaden, W., Mittermayr, R., Stojadinovic, A., 2016. Extracorporeal shockwave therapy (ESWT)

ameliorates healing of tibial fracture non-union unresponsive to conventional therapy. Injury 47 (7), 1506–1513.
Hak, D.J., Fitzpatrick, D., Bishop, J.A., Marsh, J.L., Tilp, S., Schnettler, R., et al., 2014. Delayed union and nonunions: epidemiology, clinical issues, and financial aspects. Injury 45, S3–S7.
Harper, J.D., Metzler, I., Hall, M.K., Chen, T.T., Maxwell, A.D., Cunitz, B. W., Dunmire, B., Thiel, J., Williams, J.C., Bailey, M.R., Sorensen, M. D., 2021. First in-human burst wave lithotripsy for kidney stone comminution: initial two case studies. J. Endourol. 35, 506–511.
Haupt, G., Haupt, A., Ekkernkamp, A., et al., 1992. Influence of shock waves on fracture healing. Urology 39 (6), 529–532.
Henry, T.D., Satran, D., Hodges, J.S., et al., 2013. Long-term survival in patients with refractory angina. Eur. Heart J. 34, 2683–2688.
Holmes, S., Whitfield, H.N., 1991. The current status of lithotripsy. Br. J. Urol. 68, 337–344.
Ikeda, K., Tomita, K., Takayama, K., 1999. Application of extracorporeal shock wave on bone: preliminary report. J. Trauma 47 (5), 946–950.
Irving, D.B., Cook, J.L., Young, M.A., Menz, H.B., 2007. Obesity and pronated foot type may increase the risk of chronic plantar heel pain: a matched case-control study. BMC Musculoskelet. Disord. 8, 41.
Jeffcoate, W.J., Harding, K.G., 2003. Diabetic foot ulcers. Lancet 361, 1545.
Jeppesen, S.M., Yderstraede, K.B., Rasmussen, B.S.B., Hanna, M., Lund, L., 2016. Extracorporeal shockwave therapy in the treatment of chronic diabetic foot ulcers: a prospective randomised trial. J. Wound Care 25 (11), 641–649.
Johannes, E.J., Kaulesar Sukul, D.M., Matura, E., 1994. High-energy shock waves for the treatment of nonunions: an experiment on dogs. J. Surg. Res. 57 (2), 246–252.
Kalani, M., Jorneskog, G., Naderi, N., Lind, F., Brismar, K., 2002. Hyperbaric oxygen (HBO) therapy in treatment of diabetic foot ulcers. Long-term follow-up. J. Diabetes Complications 16, 153.
Kaulesar Sukul, D.M., Johannes, E.J., Pierik, E.G., et al., 1993. The effect of high energy shock waves focused on cortical bone: an in vitro study. J. Surg. Res. 54 (1), 46–51.
Kerbl, K., Rehman, J., Landman, J., et al., 2002. Current management of urolithisasis: progress or regress? J. Endourol. 16, 281–288.
Kertzman, P., Császár, N.B., Furia, J.P., Schmitz, C., 2017. Radial extracorporeal shock wave therapy is efficient and safe in the treatment of fracture nonunions of superficial bones: a retrospective case series. J. Orthop. Surg. Res. 12 (1), 164.
Kessler, L., Bilbault, P., Ortega, F., et al., 2003. Hyperbaric oxygen accelerates the healing rate of nonischemic chronic diabetic foot ulcers: a prospective randomized study. Diabetes Care 26, 2378.
Khan, S.R., Pearle, M.S., Robertson, W.G., Gambaro, G., Canales, B.K., Doizi, S., Traxer, O., Tiselius, H.G., 2016. Kidney stones. Nat. Rev. Dis. Primers. 2 (1), 1–23.
Kolk, A., Auw Yang, K.G., Tamminga, R., Van Der Hoeven, H., 2013. Radial extracorporeal shock-wave therapy in patients with chronic rotator cuff tendinitis: a prospective randomised double-blind placebo-controlled multicentre trial. Bone Joint J. 95 (11), 1521–1526.
Krishnan, A., Sharma, Y., Singh, S., 2012. Evaluation of therapeutic effects of extracorporeal shock wave therapy in resistant plantar fasciitis patients in a tertiary care setting. Med. J. Armed Forces India 68 (3), 236.
Kumar, A., Kumar, N., Vasudeva, P., Kumar Jha, S., Kumar, R., Singh, H., 2015. A prospective, randomized comparison of shock wave lithotripsy, retrograde intrarenal surgery and miniperc for treatment of 1 to 2 cm radiolucent lower calyceal renal calculi: a single center experience. J. Urol. 193 (1), 160–164.
Kuo, Y.R., Wang, C.T., Wang, F.S., Chiang, Y.C., Wang, C.J., 2009. Extracorporeal shockwave therapy enhanced wound healing via increasing topical blood perfusion and tissue regeneration in a rat model of STZ-induced diabetes. Wound Repair Regen. 17, 522.
Lai, T.W., Ma, H.L., Lee, M.S., Chen, P.M., Ku, M.C., 2018. Ultrasonography and clinical outcome comparison of extracorporeal shock wave therapy and corticosteroid injections for chronic plantar fasciitis: a randomized controlled trial. J. Musculoskelet. Neuronal Interact. 18 (1), 47.
Landau, Z., 1998. Topical hyperbaric oxygen and low energy laser for the treatment of diabetic foot ulcers. Arch. Orthop. Trauma Surg. 117, 156.
Lee, S.S., Kang, S., Park, N.K., Lee, C.W., Song, H.S., Sohn, M.K., Cho, K. H., Kim, J.H., 2012. Effectiveness of initial extracorporeal shock wave therapy on the newly diagnosed lateral or medial epicondylitis. Ann. Rehabil. Med. 36 (5), 681.
Liden, B., Simmons, M., Landsman, A., 2009. A retrospective analysis of 22 patients treated with percutaneous RF nerve ablation for prolonged moderate to severe heel pain associated with plantar fasciitis. J. Foot Ankle Surg. 48, 642–647.
Lingeman, J.E., McAteer, J.A., Gnessin, E., Evan, A.P., 2009. Shock wave lithotripsy: advances in technology and technique. Nat. Rev. Urol. 6 (12), 660–670.
Macfarlane, R.M., Jeffcoate, W.J., 1997. Factors contributing to presentation of diabetic foot ulcers. Diabet. Med. 14, 867.
Maier, M., Averbeck, B., Milz, S., Refior, H.J., Schimitz, C., 2003. Substance P and prostaglandin E2 release after shock wave application to the rabbit femur. Clin. Orthop. Relat. Res. 406, 237–245.
Malliaropoulos, N., Crate, G., Meke, M., Korakakis, V., Nauck, T., Lohrer, H., Padhiar, N., 2016. Success and recurrence rate after radial extracorporeal shock wave therapy for plantar fasciopathy: a retrospective study. Biomed. Res. Int. 2016, 1–8.
Malliaropoulos, N., Thompson, D., Meke, M., Pyne, D., Alaseirlis, D., Atkinson, H., Korakakis, V., Lohrer, H., 2017. Individualised radial extracorporeal shock wave therapy (rESWT) for symptomatic calcific shoulder tendinopathy: a retrospective clinical study. BMC Musculoskelet. Disord. 18 (1), 1–7.
Manchanda, A., Aggarwal, A., Aggarwal, N., et al., 2011. Management of refractory angina pectoris. Cardiol. J. 18, 343–351.
Martini, L., Giavaresi, G., Fini, M., Torricelli, P., Pretto, M., Schaden, W., Giardino, R., 2003. Effect of extracorporeal shock wave therapy on osteo-blastlike cells. Clin. Orthop. Relat. Res. 413, 269–280.
Maxwell, A.D., Wang, Y.N., Kreider, W., Cunitz, B.W., Starr, F., Lee, D., Nazari, Y., Williams Jr., J.C., Bailey, M.R., Sorensen, M.D., 2019. Evaluation of renal stone comminution and injury by burst wave lithotripsy in a pig model. J. Endourol. 33, 787–792.
Meirer, R., Kamelger, F.S., Piza-Katzer, H., 2005a. Shock wave therapy: an innovative treatment method for partial thickness burns. Burns 31, 921.
Meirer, R., Kamelger, R.S., Huemer, G.M., Wanner, S., PizaKatzer, H., 2005b. Extracorporeal shock wave may enhance skin flap survival in an animal model. Br. J. Plast. Surg. 58, 53.
Metzner, G., Dohnalek, C., Aigner, E., 2010. High-energy extracorporeal shock-wave therapy (ESWT) for the treatment of chronic plantar fasciitis. Foot Ankle Int. 31 (9), 790–796.
Moseley, H.F., 1963. The natural history and clinical syndromes produced by calcified deposits in the rotator cuff. Surg. Clin. North Am. 43, 1489–1493.

Nirschl, R.P., Pettrone, F.A., 1979. Tennis elbow. The surgical treatment of lateral epicondylitis. J. Bone Joint Surg. Am. 61, 832–839.

Nomikos, I.N., Malizos, C., Vamvakopoulos, N., 2006. Protective and damaging aspects of healing: a review. Wounds 18, 177.

Ogden, J.A., Alvarez, R.G., Levitt, R., Marlow, M., 2001. Shockwave therapy forchronic proximal plantar fasciitis. Clin. Orthop. Relat. Res. 387, 47–59.

Omar, M.T., Alghadir, A., Al-Wahhabi, K.K., Al-Askar, A.B., 2014. Efficacy of shock wave therapy on chronic diabetic foot ulcer: a single-blinded randomized controlled clinical trial. Diabetes Res. Clin. Pract. 106 (3), 548–554.

Ozan, F., Koyuncu, Ş., Gürbüz, K., Öncel, E.S., Altay, T., 2017. Radiofrequency thermal lesioning and extracorporeal shockwave therapy: a comparison of two methods in the treatment of plantar fasciitis. Foot Ankle Spec. 10 (3), 204–209.

Ozturan, K.E., Yucel, I., Cakici, H., Guven, M., Sungur, I., 2010. Autologous blood and corticosteroid injection and extracoporeal shock wave therapy in the treatment of lateral epicondylitis. Orthopedics 33 (2), 84–91.

Paumgartner, G., Sauter, G.H., 2005. Extracorporeal shock wave lithotripsy of gallstones: 20th anniversary of the first treatment. Eur. J. Gastroenterol. Hepatol. 17, 525–527.

Pettrone, F.A., McCall, B.R., 2005. Extracorporeal shock wave therapy without local anesthesia for chronic lateral epicondylitis. JBJS 87 (6), 1297–1304.

Pishchalnikov, Y.A., McAteer, J.A., Pishchalnikova, I.V., Beard, S., Williams Jr., J.C., Bailey, M.R., 2006. Bubbles trapped at the coupling surface of the treatment head significantly reduce acoustic energy delivered in shock wave lithotripsy. AIP Conf. Proc. 829 (1), 643–647. American Institute of Physics.

Porso, M., Loreti, S., Nusca, S.M., Luziatelli, S., Caccia, D., Taborri, G., Trischitta, D., Taurino, M., Padua, L., Saraceni, V.M., Vulpiani, M. C., 2017. Defocused shock wave therapy for chronic soft tissue wounds in the lower limbs: a pilot study. Ultrasound Med. Biol. 43 (1), 362–369.

Quadlbauer, S., Pezzei, C., Beer, T., Jurkowitsch, J., Keuchel, T., Schlintner, C., Schaden, W., Hausner, T., Leixnering, M., 2019. Treatment of scaphoid waist nonunion by one, two headless compression screws or plate with or without additional extracorporeal shockwave therapy. Arch. Orthop. Trauma Surg. 139 (2), 281–293.

Riddle, D.L., Pulisic, M., Pidcoe, P., Johnson, R.E., 2003. Risk factors for plantar fasciitis: a matched case-control study. J. Bone Joint Surg. Am. 85-A, 872–877.

Rompe, J.D., Kullmer, K., Vogel, J., et al., 1997. Extracorporeal shockwave therapy. experimental basis, clinical application. Orthopade 26 (3), 215–228.

Rompe, J.D., Kirkpatrick, C.J., Schwitalle, M., Krischek, O., 1998. Dose-related effects of shock waves on rabbit tendon Achilles: a sonographic and histologic study. J. Bone Joint Surg. Br. 80, 546–552.

Ruffieux, P., Hommel, L., Saurat, J.H., 1997. Long-term assessment of chronic leg ulcer treatment by autologous skin grafts. Dermatology 195, 77.

Saber, N., Diab, H., Nassar, W., Razaak, H.A., 2012. Ultrasound guided local steroid injection versus extracorporeal shockwave therapy in the treatment of plantar fasciitis. Alexandria J. Med. 48 (1), 35–42.

Schaper, N.C., Apelqvist, J., Bakker, K., 2003. The international consensus and practical guidelines on the management and prevention of the diabetic foot. Curr. Diab. Rep. 3, 475.

Sener, N.C., Imamoglu, M.A., Bas, O., Ozturk, U., Goktug, H.G., Tuygun, C., Bakirtas, H., 2014. Prospective randomized trial comparing shock wave lithotripsy and flexible ureterorenoscopy for lower pole stones smaller than 1 cm. Urolithiasis 42 (2), 127–131.

Sener, N.C., Bas, O., Sener, E., Zengin, K., Ozturk, U., Altunkol, A., Evliyaoglu, Y., 2015. Asymptomatic lower pole small renal stones: shock wave lithotripsy, flexible ureteroscopy, or observation? A prospective randomized trial. Urology 85 (1), 33–37.

Senior, C., 2000. Treatment of diabetic foot ulcers with hyperbaric oxygen. J. Wound Care 9, 193.

Shkolnik, E., Burneikaite, G., Jakutis, G., Scherbak, M., Zuoziene, G., Petrauskiene, B., Trush, E., Vasyuk, Y., Laucevicius, A., Celutkiene, J., 2018. A randomized, triple-blind trial of cardiac shock-wave therapy on exercise tolerance and symptoms in patients with stable angina pectoris. Coron. Artery Dis. 29 (7), 579–586.

Stojadinovic, A., Elster, E.A., Anam, K., et al., 2008. Angiogenic response to extracorporeal shock wave treatment in murine skin isografts. Angiogenesis 11, 369–380.

Uhthoff, H.K., 1996. Calcifying tendinitis. Ann. Chir. Gynaecol. 85, 111–115.

Uhthoff, H.K., Sarkar, K., 1989. Calcifiyng tendinitis. Baillière's Clin. Rheumatol. 3, 567–581.

Uslu, M.M., Bozdogan, O., Guney, S., et al., 1999. The effect of extracorporeal shock wave treatment (ESWT) on bone defects. An experimental study. Bull. Hosp. Jt. Dis. 58 (2), 114–118.

Vainer, J., Habets, J.H.M., Schalla, S., Lousberg, A.H.P., de Pont, C.D.J. M., Vöö, S.A., Brans, B.T., Hoorntje, J.C.A., Waltenberger, J., 2016. Cardiac shockwave therapy in patients with chronic refractory angina pectoris. Neth. Hear. J. 24 (5), 343–349.

van Ramshorst, J., Bax, J.J., Beeres, S.L., et al., 2009. Intramyocardial bone marrow cell injection for chronic myocardial ischemia: a randomized controlled trial. JAMA 301, 1997–2004.

Verheye, S., Jolicoeur, E.M., Behan, M.W., et al., 2015. Efficacy of a device to narrow the coronary sinus in refractory angina. N. Engl. J. Med. 372, 519–527.

Vilches, R.M., Aliaga, A., Reyes, D., Sepulveda, F., Mercado, A., Moya, F., Ledezma, R., Hidalgo, J.P., Olmedo, T., Marchant, F., 2015. Comparison between retrograde intrarenal surgery and extracorporeal shock wave lithotripsy in the treatment of lower pole kidney stones up to 15 mm. Prospective, randomized study. Actas Urol. Esp. 39 (4), 236–242.

Vogel, J., Rompe, J.D., Hopf, C., et al., 1997. High-energy extracorporeal shockwave therapy (ESWT) in the treatment of pseudarthrosis. Z. Orthop. Ihre Grenzgeb. 135 (2), 145–149.

Vulpiani, M.C., Vetrano, M., Conforti, F., Minutolo, L., Trischitta, D., Furia, J.P., Ferretti, A., 2012. Effects of extracorporeal shock wave therapy on fracture nonunions. Am. J. Orthop. (Belle Mead N.J.) 41 (9), E122–E127.

Vulpiani, M.C., Nusca, S.M., Vetrano, M., Ovidi, S., Baldini, R., Piermattei, C., Ferretti, A., Saraceni, V.M., 2015. Extracorporeal shock wave therapy vs cryoultrasound therapy in the treatment of chronic lateral epicondylitis. One year follow up study. Muscles Ligaments Tendons J. 5 (3), 167.

Wainner, R.S., Hasz, M., 1998. Management of acute calcific tendinitis of the shoulder. J. Orthop. Sports Phys. Ther. 27, 231–237.

Wang, C.J., Chen, H.S., Chen, C.E., Yang, K.D., 2001. Treatment of nonunions of long bone fractures with shock waves. Clin. Orthop. Relat. Res. 387, 95–101.

Wang, C.J., Huang, H.Y., Pai, C.H., 2002. Shock wave enhanced neovascularization at the tendon bone junction: an experiment in dogs. J. Foot Ankle Surg. 41 (1), 16–22.

Wang, C.J., Wang, F.S., Kuender, D.Y., Wang, L.H., Hsu, C.C., Huang, H. C., Yang, L.C., 2003. Shock wave therapy induces neovascularization at the tendon-bone junction: a study in rabbits. J. Orthop. Res. 21, 984–989. Volume 48, Number 2, March/April 2009155.

Wang, C.J., Wu, R.W., Yang, Y.J., 2011. Treatment of diabetic foot ulcers: a comparative study of extracorporeal shockwave therapy and hyperbaric oxygen therapy. Diabetes Res. Clin. Pract. 92, 187–193.

Wang, C.J., Wu, C.T., Yang, Y.J., Liu, R.T., Kuo, Y.R., 2014. Long-term outcomes of extracorporeal shockwave therapy for chronic foot ulcers. J. Surg. Res. 189 (2), 366–372.

Warren, S.B., Brooker Jr., A.F., 1992. Intramedullary nailing of tibial nonunions. Clin. Orthop. Relat. Res. 285, 236–243.

Wess, O.J., 2008. A neural model for chronic pain and pain relief by extracorporeal shock wave treatment. Urol. Res. 36 (6), 327–334.

Xu, Z.H., Jiang, Q., Chen, D.Y., Xiong, J., Shi, D.Q., Yuan, T., Zhu, X.L., 2009. Extracorporeal shock wave treatment in nonunions of long bone fractures. Int. Orthop. 33 (3), 789.

Yager, D., Nwomeh, B., 1999. The proteolytic environment of chronic wounds. Wound Repair Regen. 7, 433.

Younger, E.M., Chapman, M.W., 1989. Morbidity at bone graft donor sites. J. Orthop. Trauma 3, 192–195.

Zhao, L., Yang, P., Tang, Y., Li, R., Peng, Y., Wang, Y., Pu, L., Guo, T., 2015. Effect of cardiac shock wave therapy on the microvolt T wave alternans of patients with coronary artery disease. Int. J. Clin. Exp. Med. 8 (9), 16463.

Chapter 27

Ultrasonic cutting for surgical applications

M. Lucas[a], A. Mathieson[b], and R. Cleary[a]
[a]James Watt School of Engineering, University of Glasgow, Glasgow, United Kingdom, [b]Thales Group UK, Reading, United Kingdom

27.1 Introduction: The origins of ultrasonic cutting for surgical devices

During Paul Langevin's development of an ultrasonic echolocation system during the late 1910s, it was observed that the ultrasound field emitted could induce pain in humans and even kill small fish that attempted to swim through it. These observations were the first to highlight the destructive capability of ultrasound when applied to living organisms and did not go unnoticed by an American, Robert Wood, who had worked with Langevin during 1917 (Graff, 1977).

After returning to the United States, Wood's scientific interests lay away from ultrasound; however, after renewing an acquaintance with Alfred Loomis during the mid-1920s, the pair decided to investigate whether observations made during trials of the echolocation system offered further scope for research of interest to science and engineering.

Working from Loomis' independent research laboratory located at Tuxedo, New York, they investigated the influence and effect of high-power ultrasonics in a range of different topics, including pressure generated from acoustic radiation, the formation of emulsions and fogs, and the rate of chemical reactions; subsequently, publishing their findings in 1927. They also observed the biological effects of high-power ultrasound on animal and plant cells and the fatal effect it could have on fish, frogs, and mice, although some experiments had a more fortunate outcome: "Mice are less sensitive, a 20-min exposure not resulting in death, and though at the end of the treatment the animal was barely able to move, the recovery was fairly rapid" (Wood and Loomis, 1927). Significantly, with respect to ultrasonic cutting and tissue dissection, Wood and Loomis reported that a vibrating glass rod cemented to a quartz transducer had the capability to cut or etch wood and glass, but when held between fingers and thumb, it could induce blood blisters in the skin (Wood and Loomis, 1927).

From the late 1920s until the 1940s, much of the research in ultrasonics concentrated on sonar, ultrasonic nondestructive testing, and the effect of high-power ultrasound wave-fields in biological matter. The period between 1945 and 1955 saw the patenting (Balamuth, 1948, 1952) and commercialization of an ultrasonic impact grinder capable of machining hard and brittle materials such as tungsten carbide and glass (Cohan, 1951; Kelley, 1951). This device operated by impacting a vibrating tool against an abrasive slurry that gradually ground away the workpiece material.

An innovative application of the ultrasonic grinding device by Balamuth and Catuna, reported in 1953, cuts cavities in extracted teeth and introduced ultrasonics to dentistry and mineralized tissue cutting (Balamuth, 1963; Catuna, 1953). From these trials stemmed a miniaturized device designed for dentistry that operated on the same principles as its industrial counterpart. The ultrasonic dental unit, when compared to conventional mechanical or pneumatic-powered devices, promised several advantages: minimal tissue heating, reduced pressure applied to the operation site, and enhanced patient comfort (Balamuth, 1963; Catuna, 1953; Postle, 1958). Even though the ultrasonic dental device offered many benefits to both dentist and patient, it experienced only limited commercial success. A combination of factors contributed to this: the requirement for an abrasive paste that restricted the dentist's line of sight to the cutting site, the high cost of the device, and the eventual popularity of the competing technology, a high-speed miniature turbine handpiece, which had been developed during the same time frame (Cheery et al., 1974).

The limited commercial success of Balamuth and Catuna's dental device did slow the development of ultrasonic devices for a number of years, but by the early 1960s, an ultrasonic device capable of cutting the bone without the requirement of an abrasive paste had been used during bone-cutting trials (Mararow, 1960; McFall et al., 1961). Using an oscillatory motion to cut tissue directly was first filed for patent a few years earlier in 1955 by Vang (Vang, 1955). Vang's patent described a scalpel-like device that oscillated at frequencies between 6 and 12 kHz and claimed to be able to cut both hard and soft tissue. Two animal-based studies by Mararow (1960) and McFall et al. (1961) compared the performance of electric- and pneumatic-powered saws and burs to an ultrasonic scalpel device. Both studies reported that the ultrasonic device

Power Ultrasonics. https://doi.org/10.1016/B978-0-12-820254-8.00037-3
Copyright © 2023 Elsevier Ltd. All rights reserved.

had benefits to the surgeon similar to those of the original impact grinder: enhanced precision and accuracy during cutting and a reduction in soft-tissue damage. However, the studies also commented on the limitations of the ultrasonic device. Mararow reported that material removal rate and healing rate were both slower in sites operated on using the ultrasonic device, with McFall et al. confirming the slower healing rate. It also was reported that the introduction of saline solution to the cutting process reduced healing time, and all sites healed satisfactorily by the end of the study's trial period. These observations led to a conclusion that ultrasonic devices may be preferable in surgical procedures requiring high precision and accuracy, provided a saline solution was used to minimize heating at the surgical site.

The first recorded human osteotomies conducted with an ultrasonic device were reported by Volkov in 1974 after completing 311 clinical procedures during 1969 (Volkov and Shepeleva, 1974). Volkov's device operated in a longitudinal mode at frequencies between 25 and 30 kHz and incorporated a detachable exponential-shaped horn with a "chisel-like" cutting tip. The geometry of the device permitted Volkov to complete the osteotomies through smaller incisions than were possible with conventional devices, hence minimizing soft-tissue damage and simplifying the surgical procedure. Volkov also noted that highly precise cuts and normal regeneration rates of repair in bone were achieved during and after surgery, respectively. Subsequently, studies by Horton and Aro, published during the 1970s and 1980s, also reported highly precise and accurate cuts using ultrasonic devices and reduction of trauma to surrounding tissue compared with conventional devices and instruments (Aro et al., 1982; Horton et al., 1975, 1981). These studies also commented on the benefit of applying saline solution to the cutting site to control tissue temperatures and again confirmed the limitation of a slow cutting rate. Horton and Aro additionally commented on other disadvantages: the device was difficult to operate because of its size and shape, there were problems with the device overheating, and it was necessary to control manually the optimal operating frequency. Nevertheless, similar to Volkov, Horton and Aro noted that bone cuts using the ultrasonic device healed normally.

Regardless of the limited adoption in cavity preparation during the 1950s and mineralized tissue cutting during the following decades, ultrasonic devices continued to be developed and were commercially successful for other clinical applications, such as the periodontal treatment of oral prophylaxis (Zinner, 1955) and endodontic treatments during root canal procedures (Suppipat, 1974). Ultrasonic scaling and endodontic devices offered similar advantages over conventional scaling instruments, including reduced damage to surrounding soft tissue and reduced procedure time, as well as improved patient acceptance. The development of thinner scaling tips (Trenter et al., 2002) and the introduction of biocidal agents coupled with specialized endodontic tips in root canal treatments (Martin, 1976) during the 1970s and 1980s facilitated the routine adoption of ultrasonic devices for periodontal and endodontic procedures (Walmsley et al., 1992).

27.2 Developments in ultrasound for soft-tissue dissection

Although Vang had suggested that his oscillating device could be used to dissect soft tissues, it was not until 1965 when Kelman, an ophthalmologist, utilized an ultrasonic scaling device to fragment a cataract (a process that was later named phacoemulsification) that an ultrasonic device was first reported to cut or break up soft tissue (Kelman, 1967, 1994; Linebarger et al., 1999; Pandey et al., 2004). Kelman had spent the best part of the preceding 3 years searching for a novel method of removing cataract (the clouding of the lens of the eye) that could use a less invasive technique than intracapsular cataract extraction (ICCE), the most widely used method of cataract removal in the United States at the time. The ICCE technique freezes the cataractous lens before extracting it with its capsule intact through a 180 degrees incision made to the corneal limbus, the border of the cornea, and the sclera. Although the technique was regarded as safe and effective, the large incision required an average postprocedure hospitalization of 10 days followed by approximately 6 weeks of relatively inactive recuperation (Kelman, 1994).

Kelman's initial trials used the flexural motion of a dental scaler to emulsify cataract tissue while an irrigation fluid was used to keep the vibrating tip cool. Although the trials produced encouraging results, the scaling tip took several minutes to break up the cataract; forces induced in the eye by the oscillating scaling tip often resulted in iridodialysis, a localized separation of the iris from its attachment to the ciliary body. Nevertheless, by 1966, a prototype phacoemulsification device that attempted to address many of the initial limitations found with the scaling device had been developed, with a patent filed in 1967 (Banko and Kelman, 1971). Now utilizing a longitudinal motion and replacing the relatively large scaling tip with a sharp needle-like tip, damage to the tissue surrounding the cataract was reduced. The incorporation of an aspiration system ensured the cataract remained in contact with the oscillating tip, improving emulsification efficiency and reducing tip temperature by removing cataract debris that clogged the tip and interrupted the flow of irrigation fluid. Animal-based trials in 1967 led to the first phacoemulsification trial in a human patient during the same year, and although the patient had to have his eye removed at a later date (the eye had been scheduled for removal before the

phacoemulsification trial), the trial highlighted the need for further improvements. Similar to reports of ultrasonic devices for cutting mineralized tissue from the same decade, Kelman reported that the phacoemulsifier handpiece was bulky and heavy and required a sling support. Nevertheless, the design evolved, resulting in a smaller hand-piece, a change in operational frequency (from 20 to 40 kHz), and the incorporation of a peristaltic suction pump that matched the irrigation flow of the aspiration flow. This led to the first commercial Kelman-Cavitron phacoemulsification unit in 1970 (Kelman, 1994).

To access the cataract, the phacoemulsifier tool required a relatively small incision of 2–3 mm, which greatly reduced the patient's postprocedural stay in the hospital and often allowed patient discharge on the same or the following day. However, the radical change from the ICCE procedure resulted in significant opposition from a number of prominent ophthalmologists, who questioned the safety of phacoemulsification. Hostility climaxed during 1973 when Medicare, US social insurance, was successfully lobbied to block reimbursing phacoemulsification procedures on the grounds that it was an experimental technique. The ban was lifted by the end of the year, and many of the safety fears were found to be unfounded (Kelman, 1967, 1994; Linebarger et al., 1999; Pandey et al., 2004). Modern phacoemulsification devices now operate within the frequency range of 35–45 kHz (Packer et al., 2005) and, to enhance performance, can modulate between different excitation amplitudes and driving frequencies (Bethke, 2011). The surgeon also has the option of selecting a device that oscillates longitudinally, torsionally, or with a combination of longitudinal-torsional (L-T) motion (Bethke, 2011; Boukhny, 2000; Han and Miller, 2009; Packer et al., 2005). Recent studies indicate that phacoemulsification devices operating in a torsional mode possess advantages over longitudinal mode devices: smaller temperature increases provide enhanced thermal protection to the eye (Han and Miller, 2009; Jun et al., 2010).

The success of the Kelman-Cavitron phacoemulsification unit prompted the consideration of its use during neurosurgical procedures (Flamm et al., 1978). Although the original phacoemulsification unit was unable to fragment tissue encountered in intracranial tumors, a more powerful device, the ultrasonic aspirator, was developed. This device also operated in a longitudinal mode but at a lower frequency of 23 kHz and had the capability of a vibration amplitude up to 100 μm. Animal and human trials reported by Flamm et al. in 1978 successfully used an ultrasonic aspirator to fragment and aspirate tumor tissue. Although subsequent histological analysis of brain tissue of cats demonstrated hemorrhage and necrosis in the immediate area of the surgical site after exposure to ultrasonic aspiration, these were no greater than occurred with other techniques. However, applying the ultrasonic device at a surgical site close to the spinal cord was found to affect the animals; analysis showed extensive edema (accumulation of fluid) in the white matter (tissue containing sensory and motor neurons). Flamm et al. also reported 38 clinical cases in which the ultrasonic aspirator was successfully used to remove tumors located in the cranial cavity. The treatment of a meningioma (a slow-growing benign tumor) located between the optic nerve and carotid artery illustrated one of the benefits of the ultrasonic device, namely, high precision: the device was capable of removing the tumor while protecting the neighboring nerve and arterial structures. However, the study also mentioned some limitations of the ultrasonic aspirator. As with the phacoemulsifier, the handpiece was found to be awkward to use because of its size and weight, and the tuned needle-like tip was not able to access all surgical sites. It also was noted that, unlike conventional cautery and suction devices, it was difficult to achieve hemostasis with the vibration tip of the ultrasonic device (Flamm et al., 1978).

Over the past 35 years, ultrasonic aspirators have been used in open surgeries such as tumor debulking (removal of malignant tumors), neurosurgery, and liver surgery (Amaral, 1994; Bond and Cimino, 1996; Brock et al., 1984; Cimino and Bond, 1996; Flamm et al., 1978). However, it was not until the early 1990s in Europe and mid-to-late 1990s in North America that ultrasonic aspiration was used to remove fatty deposits during liposuction (Lawrence and Coleman, 1999; Zocchi, 1992). A review of different liposuction techniques (Berry and Davies, 2011) reported that even though ultrasonic aspiration has benefits of reduced blood loss and enhanced postoperative comfort, there are serious limitations in ultrasonic liposuction devices. It is proposed that their high cost, steep learning curve for the surgeon, risk of burns, and the capabilities of the competing technologies may have contributed to ultrasonic-assisted liposuction falling out-of-favor during the mid-2000s.

Laparoscopic surgery was first used for clinical diagnosis in 1901, and although it continued to be developed over the following 90 years, it was mostly used only as a diagnostic technique until the 1980s, when it was used in minimally invasive or key-hole surgery for the first time (Vecchio et al., 2000). It was not until 1991 that Wetter et al. (1992) reported the first (prototype) ultrasonic laparoscopic device and compared its surgical performance with that of conventional laparoscopic, electrosurgical, and laser devices. During a controlled trial of 73 patients undergoing laparoscopic cholecystectomy (surgical removal of the gallbladder), the ultrasonic aspirator was found to perform well during dissection of tissue, especially fatty tissues and tissue contained within the Calot's triangle (the anatomic area that is bordered by the common hepatic duct, the cystic duct, and the cystic artery). However, it also was reported that the ultrasonic device did not easily dissect fibrous gallbladders,

and another device or clips were required for coagulating the surgical sites. Later commercialized models of the ultrasonic laparoscopic aspirator included an electrosurgery feature that attempted to incorporate the benefits of ultrasonic aspiration and the coagulating capability of electrosurgery devices (Amaral, 1994).

Ultrasonic devices with the capability of cutting and coagulating soft tissues continued to be developed during the 1990s. By the mid-1990s, a number of "ultrasonic scalpel" architectures were available to surgeons. One configuration consisted of a hook-spatula tip with a sharp inside edge for cutting and an outside edge with a relativity large radius and surface area suitable for coagulating. Another device configuration contained a pair of jaws. The bottom jaw, tuned at 55.5 kHz, vibrated longitudinally, whereas the top articulated jaw clamps the tissue between the jaws, resulting in simultaneous tissue cutting and coagulation. Ultrasonic devices are currently used in both open and endoscopic operations ranging from general surgery to the treatment of obesity and gynecological, colorectal, and urological procedures.

27.3 Developments in ultrasound for bone cutting and other surgical applications

By the mid-1990s, ultrasonic cutting was routinely used in diverse industrial applications ranging from textile cutting to food cutting (Rawson, 1998), yet it still had limited use in bone surgery (Labanca et al., 2008). Trials continued to compare the performance of ultrasonic devices against conventional surgical devices through the 1990s. One in vitro study investigated the cutting force and cutting rate in bone-cutting experiments (Khambay and Walmsley, 2000a,b). As with previous studies, it was reported that the ultrasonic device resulted in higher precision and required a lower force to cut than bur and saw devices. However, it was also acknowledged that the cutting speed of the ultrasonic device was significantly slower. A novel technique was described by Vercellotti in 2000: an ultrasonic device was successfully used in oral surgery to perform osteotomies during sinus lift procedures (Labanca et al., 2008; Vercellotti, 2000). During these procedures, the Schneiderian membrane (membrane lining the maxillary sinus cavity) is at risk of perforation, requiring termination of the procedure. Vercellotti recognized that the vibrational motion of a scaling unit at maximum power would not perforate the membrane but could cut bone. Therefore, the scaling device was used to cut through the final layers of the bone tissue during an osteotomy on the maxilla, minimizing the risk to the membrane and other soft tissues. As with the first phacoemulsification device, a surgical device for bone cutting stemmed from a different technology application, in this case ultrasonic scaling device. This has since led to the routine application of ultrasonic cutting devices in oral and maxillofacial surgery, neurosurgery, and orthopedic surgical procedures (Beziat et al., 2007; Hoigne et al., 2006; Labanca et al., 2008; Pavlíková et al., 2011; Schaeren et al., 2008; Vercellotti, 2000; Vercellotti et al., 2001).

Since 2000, there have been many advances in ultrasonic bone-cutting devices, as well as developments in phacoemulsification devices, ultrasonic aspirators, and ultrasonic scalpels, demonstrating that many of the limitations of ultrasonic devices reported between the 1960s and 1980s have been addressed. In particular, finite element analysis (FEA) has enabled efficient and reliable devices to be designed and developed, allowing the designer to optimize the motion of the device through accurate prediction of the resonant frequencies, vibration response, and stress concentrations. Meanwhile, advances in manufacturing processes have realized the fabrication of more complex device geometries with higher precision and on a commercial scale and also have enabled miniaturization of devices for more delicate and less invasive procedures.

Since the mid-1990s, most ultrasonic surgical devices have incorporated piezoelectric transducers rather than magnetostrictive transducers, removing the need for the cooling system necessary for magnetostrictive stacks. This reduces device complexity and removes the potential for cross-contamination between sterile saline solutions directed to the surgical site and nonsterile stack cooling solutions. This also has reduced the risks of the device overheating during operation. However, the most significant technological advance is associated with the drive electronics, which now ensure that ultrasonic generators automatically track the resonant frequency and deliver the excitation signal at the optimal driving frequency. Furthermore, ultrasonic generators also have the capability to deliver a selectable excitation signal for cutting, fragmenting, or coagulating the specific tissue. This is achieved through the incorporation of amplitude bursts or the addition of a secondary excitation signal to the basal signal.

27.4 Cutting mechanisms in soft tissue

The process of cutting soft and hard tissues differs significantly; however, a number of factors must be considered for both techniques.

- Elevated temperatures: Increasing the temperature of tissue above a critical necrotic temperature for some critical duration causes the tissue to be damaged beyond repair. Because the presence of damaged tissue is known to be detrimental to healing and recovery times, it is important to consider both the average and maximum temperatures that tissue is exposed to and for how long.

- Blade-tissue interaction: The vibrational motion, size, and shape of the cutting blade can not only affect the performance of the ultrasonic device but also influence damage to surrounding tissues. It therefore is necessary for the interaction between the device, specifically the cutting tip, and the surrounding tissue to be understood.
- Debris removal: Efficient debris removal enhances the performance of an ultrasonic cutting device. Debris that remains at the surgical site can cause the cutting blade to become stuck, initially reducing device performance before causing it to stall. If not removed, debris is also capable of burning, resulting in damage to surrounding tissue.

Meanwhile, when comparing the performance of ultrasonic devices with that of conventional or competing techniques and technologies, especially during in vitro studies, it is crucial that not only cutting performance of specific devices is analyzed but also the cumulative surgical duration of the procedure is carefully considered.

The interaction between soft tissue and ultrasonic devices is complex. Tissue fragmentation can depend on the water and protein content of the tissue. Tissues with low water content but rich in proteins, such as vessels, nerves, and connective tissue, require considerably higher levels of energy to fragment than tissues with high water content and sparse protein, such as the liver, tumors, and the spleen. The excitation frequency, tip geometry, and vibrational amplitude of the ultrasonic device are all parameters that can also influence tissue fragmentation and coagulation.

Phacoemulsification and ultrasonic aspiration both rely on the fragmentation, emulsification, and then aspiration of tissue debris through the hollow center of the oscillating tip. However, the mechanism that instigates the breakup of the tissue in both phacoemulsification and ultrasonic aspiration has been the subject of debate in the literature since these procedures were first performed (Bond and Cimino, 1996; Brock et al., 1984; Cimino, 1999; Kelman, 1967, 1994; Packer et al., 2005). Nevertheless, the interactions between the oscillating tip and the tissue have been generally classified as thermal, cavitational and noncavitational, and mechanical (Amaral, 1994; Bond and Cimino, 1996; Cimino, 1999; Cimino and Bond, 1996). It is now almost universally accepted that mechanical contact between the vibrating tip and tissue (Packer et al., 2005; Zacharias, 2008, 2013), and not cavitational effects, is the primary source of tissue disruption.

Cimino and Bond (Bond and Cimino, 1996; Cimino and Bond, 1996) studied the physics of tissue fragmentation by ultrasonic aspirators during the mid-1990s, reporting that the two main parameters that influence tissue fragmentation are the vibrational amplitude of the device and suction levels. Observations from experimental work concluded that fragmentation of tissue was not a direct function of the water content of the tissue. Although cavitation was detected during tissue fragmentation procedures, it was observed only above a power threshold. If cavitation was critical to tissue fragmentation, it would be expected that below this threshold, tissue fragmentation would plateau. However, fragmentation was observed below this threshold, which led to the conclusion that the mechanical strength of the tissue is the overriding factor affecting tissue fragmentation.

The mechanism of dissection of tissue with high collagen and low water content with ultrasonic scalpels or shears relies on frictional heating in the tissue. The heating, which can exceed 100°C at the cutting interface, induces the tissue structure to chemically alter, primarily because of protein denaturation. Bleeding from the cutting interface is controlled via a process of coaptive coagulation, which is brought about by denatured proteins whose physical properties are more viscous and have increased adhesive properties (Amaral, 1994; Ebina et al., 2007; Hoenig et al., 1996; Koch et al., 2003). Ultrasonic shears can therefore provide hemostatic cutting by grasping tissue between a pair of jaws. Through the application of pressure from the jaws, cutting and coaptive coagulation occur simultaneously. Both the cutting and coagulation processes can be controlled by altering the vibrational amplitude of the oscillating tip. A lower amplitude of vibration results in slower cutting and a higher hemostasis rate, whereas a higher amplitude results in increased cutting speed and a lower hemostasis rate (Hoenig et al., 1996).

27.5 Ultrasonic dissection of mineralized tissue

Studies of the mechanisms at the blade-tissue interaction site during the ultrasonic cutting of mineralized tissue have not been extensively reported. A limited number of finite element (FE) studies (Lucas et al., 2006; Smith et al., 1996) based on simple fracture mechanics models relying on assumptions regarding specimen geometry and contact conditions at the blade-specimen cutting interface have been conducted (Lucas et al., 2006; Smith et al., 1996). FE models also have been used to investigate the effect that ultrasonic parameters (vibrational amplitude and frequency) stress, and cutting force (Alam et al., 2009).

More recent clinical studies have reported that surgical sites prepared with modern ultrasonic devices exhibit reduced tissue damage and enhanced recovery rates when compared with sites prepared by conventional devices. Enhanced levels of bone morphogenetic proteins (proteins that directly influence tissue formation), quantity of osteoblasts (premineralized bone tissue), and neo-osteogenesis (formation of young bone tissue) have all been reported

(Blus et al., 2010; Preti et al., 2007). Elevated temperatures and the duration of exposure to elevated temperatures, known as heat shock, can have an immediate necrotic response in bone cells or can induce longer apoptotic responses, although this is not well understood and can vary in the literature. However, it is known that if heat shock is maintained at or below a critical temperature of 47°C, necrotic and apoptotic responses can be avoided and irreparable damage can be minimized if temperatures are kept below 60°C (Dolan et al., 2012). Studies carried out since the mid-1900s have reported tissue temperatures at the surgical site ranging from 35°C (under in vitro conditions) to 160°C (Aro et al., 1982; Cardoni et al., 2006; Horton et al., 1975, 1981; Lucas et al., 2005; Volkov and Shepeleva, 1974). Although the duration of heating, the type of study (in vitro or in vivo conditions), and whether irrigation was supplied to the cutting site differed in each of the studies, it is clear that ultrasonic cutting—as with conventional cutting—has the potential to increase temperatures in tissue. For ultrasonic cutting of mineralized tissue, temperature increases stem from three main sources: the absorption of ultrasonic energy from the vibratory motion of the contacting cutting blade, frictional heating between the blade and the tissue, and burning of bone debris at the cut site. Tissue temperature can be controlled by delivering an irrigating solution to the cutting site. This helps to cool the oscillating blade and the cutting interface and assists in removing debris. The design of the device can also aid in debris removal and reduce frictional heating between the vibrating blade and surgical site; judicious control of the device can also influence heating in tissue (Blus et al., 2010; Dolan et al., 2012).

Ultrasonic devices designed for cutting mineralized tissue have been independently developed by various companies, and despite their differences, it is clear from Figure 27.1 that the ergonomics of the handpiece has changed very little from the device first patented in the 1950s. These devices are similar in that they all incorporate a signal generator and a handpiece, but the more modern devices incorporate a range of selectable cutting tips suited to specific surgical procedures. Modern devices also often use distinct modes of vibration or combine different modes, and they deliver an excitation signal that optimizes cutting efficiency.

A number of commercial ultrasonic devices are currently available for cutting mineralized tissue. The following summarizes the key capabilities and features of three of the devices currently used in surgery.

- Piezosurgery, Mectron S.p.A: The Piezosurgery device is used in dental, maxillofacial, spinal, ear, nose, thyroid, and neurosurgery, operating at a frequency between 24.7 and 29.5 kHz. The transducer operates in a longitudinal mode. However, when combined with a cutting tip, the device as a whole operates with a longitudinal-flexural (L-F) motion that enables the cutting tip to reach a cut depth of up to 20 mm. The tips are coated with titanium, with some additionally coated with diamond designed specifically for osteotomy, osteoplasty, drilling, and finishing procedures (cuts completed close to delicate anatomic features). The vibrational amplitude of the device, which ranges between 60 and 210 μm, is dependent on tip selection and power setting, whereas the excitation signal differs depending on bone density and bone type. To enhance cutting and minimize stalling, the excitation signal can feature a 10 ns, 50 kHz burst to the base frequency. In "boosted" mode, a digital modulation of this oscillation produces an alternation of high-frequency vibrations with pauses at a frequency of up to 30 kHz. A cooled irrigating solution, typically physiologic saline at 4°C, is delivered to the cutting tip via a channel that passes through the center of the handpiece. The flow is adjustable between 0 and 60 mL/min and is primarily used to remove detritus from the cutting area. The cutting device is designed such that the oscillatory motion of the tip selectively cuts only mineralized tissue and hence prevents or minimizes damage to surrounding soft tissue. The cutting head turns inactive as soon as it loses contact with the mineralized tissue, so that an accidental slipping of the device onto surrounding soft tissue does not cause any damage.
- BoneScapel, Misonix: The BoneScapel device operates at a nominal nonmodulated 22.5 kHz in a longitudinal mode and has the capability to cut both hard and soft tissues with a vibrational amplitude between 35 and 300 μm (Pakzaban, 2014). For cutting hard tissue, the device is used in orthopedic, plastic and reconstructive, and general surgical procedures. Under hard tissue dissection settings, it is also capable of minimizing soft-tissue damage. The controlled compression and splitting of rigid, crystalline structure are achieved, while soft elastic tissues are generally able to deform temporarily to maintain their integrity (Gilles et al., 2013). Operating with a range of different cutting tips, it can reach a maximum cutting depth of 20 mm. Irrigation, typically room temperature 0.9% saline solution, is delivered through an integrated peristaltic pump, variable from 15 to 90 mL/min via an outlet close to the cutting tip, to cool the blade and remove bone debris. Changing its settings (altering amplitude and irrigation settings), as well as incorporating a tip designed for soft-tissue dissection (sharp cutting tip compared with a relatively blunt tip for cutting hard-tissue), gives the device the capability to be used for wound care and thoracic procedures. The signal used to excite the device can be either continuous or pulsed. In addition, straight or angled telescopic waveguides, up to 145 mm long, allow the device to be used in minimally invasive procedures.

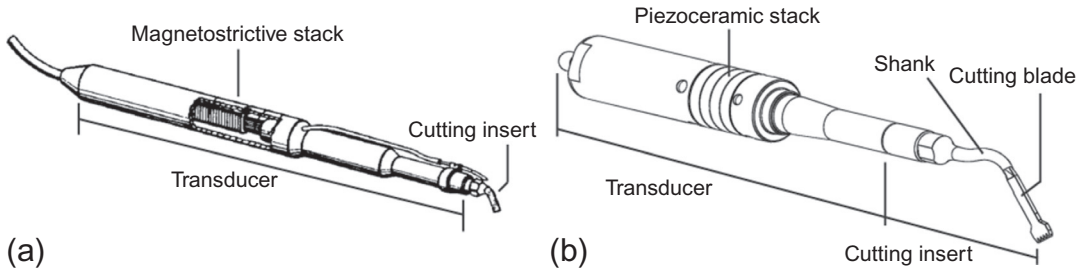


FIGURE 27.1 Ultrasonic handpieces. (a) Balamuth's magnetostrictive 1950s handpiece (Balamuth, 1963) and (b) a modern piezoelectric handpiece with cutting insert.

- Sonopet Ultrasonic Aspirator, Stryker: The Sonopet ultrasonic aspirator couples longitudinal and torsional motion at either 25 or 34 kHz, depending on the hand-piece used. Angled and straight models vibrating at 25 kHz operate with a longitudinal vibration amplitude varying from 120 to 365 µm, while the 34 kHz option operating at similar vibrational amplitudes offers greater precision for the surgical removal of soft tissue (Samy et al., 2007). Irrigation, typically at room temperature, is delivered to the surgical site via the hand-piece at an adjustable rate between 3 and 40 mL/min, whereas aspiration is through a central cannulated tip (Vrcek et al., 2015). The device is used in ear, nose, and throat, neurosurgical, and maxillofacial procedures (Ao et al., 2020) and is compatible with a broad range of cutting inserts. It is capable of dissecting hard tissue to a shallow depth, as well as fragmenting and aspirating soft tissue. The Sonopet's advantages include less trauma to soft tissues than conventional drills and less force required which allows for more control particularly when dealing with bone that is infiltrated or abnormal.

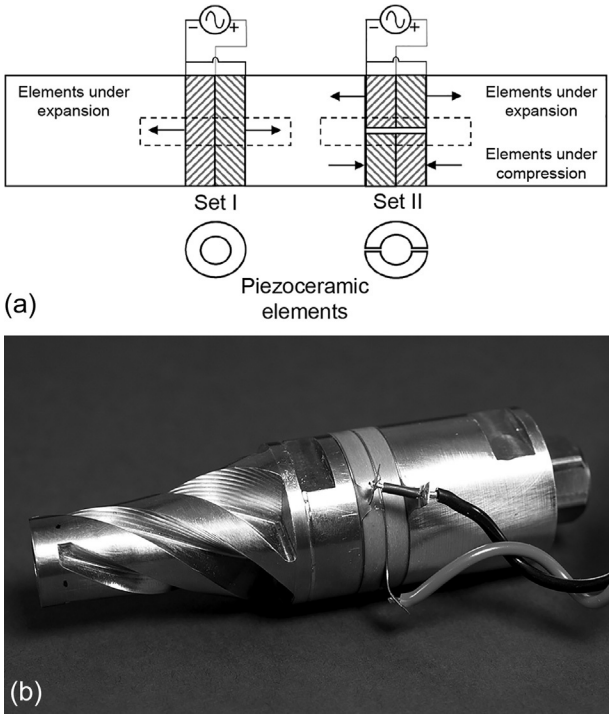


FIGURE 27.2 (a) Schematic of a transducer with multiple piezo stacks and (b) L-T Langevin transducer containing diagonal slots.

27.6 Factors affecting device performance

27.6.1 Multiple-mode devices

Coupling two or more modes of vibration, especially L-F modes or L-T modes, has enhanced the performance of devices used in both clinical and industrial applications and has facilitated the development of ultrasonic motors. Various design methodologies can be adopted to couple modes of vibration in ultrasonic devices. One method of generating a combined L-F mode is incorporating two piezoceramic stacks in a Langevin transducer (Figure 27.2A) and exciting them simultaneously. Set I, located at or close to the nodal plane, consists of complete, axially poled, piezoceramic rings to induce longitudinal vibration, whereas set II, located at a position that is optimal to induce flexural motion, contains two pairs of oppositely poled half-ring elements that oscillate 180 degrees out-of-phase with each other (Watanabe et al., 1993). A combined L-T mode of vibration can also be generated by a transducer configuration similar to that exhibited in Figure 27.2A, although the stack that generates the torsional motion would be poled transversely (Ohnishi et al., 1993; Watanabe et al., 1993).

The approach of using multiple piezoceramic stacks to generate combinational vibrational motions has the advantage that a high level of coupled motion can be generated at the output end of the device. In ultrasonic welding, a high weld strength is achieved with a planar vibration locus realized using a longitudinal-torsional vibration generated by incorporating one longitudinal and one torsional bolt-clamped Langevin transducer (Asami et al., 2017). In the development of an ultrasonic aspirator for cartilage removal, an elliptical vibration was generated by coupling two vertical bending vibrations through the design of the PZT ceramic stack polarity (Zhang et al., 2021).

An alternative method of generating combined L-F or L-T motion is to use a conventional Langevin transducer, exciting longitudinal motion, combined with an attached waveguide designed to degenerate part of the longitudinal motion into flexural or torsional motion. Ultrasonic scaling devices, used for periodontal cleaning, generally operate in a longitudinal mode; however, by incorporating a curved tip, a combined L-F motion can be excited in the scaling tool. The shape and motion of the tip permit dental clinicians to access (although to a limited extent) interproximal and other sites (Mathieson, 2012). Waveguide geometry can also be used to generate L-T motion in ultrasonic devices through the incorporation of helical or diagonal slots around an uncut core (Figure 27.2B). The longitudinal wave propagating through the uncut core will continue, while the slots deflect part of the wave to degenerate the longitudinal motion into torsional motion, resulting in combined L-T motion at the output end of the waveguide (Al-Budairi et al., 2013). An example is a prototype ultrasonic needle which vibrates with an L-T motion using this technique, which has been shown to penetrate deeper into bone and with less microdamage at the cut site than its L-mode counterpart (Cleary et al., 2022).

27.6.2 Nonlinear and undesirable behavior

Ultrasonic devices, as with all dynamic systems, are inherently nonlinear, but power ultrasonics devices are particularly prone to nonlinear behaviors because they are driven at high excitation levels. Linear dynamic systems are those where a change of state is proportional to the energy or load applied. Nonlinear systems do not conform to this rule of proportionality—even systems that initially exhibit linear behavior (Thomsen, 1997). Nonlinear behavior in power ultrasonic devices is well documented (Aurelle et al., 1996; Cardoni et al., 2002; Lucas et al., 2001; Mathieson, 2012; Rawson, 1998; Umeda et al., 1999, 2000), and the origin of these behaviors stems from a variety of sources. In power ultrasonic devices, these behaviors are known to originate from changes in material properties under conditions of elevated stress, strain, or temperature (Campos-Pozuelo and Gallego-Juárez, 1996; Puškár, 1982; Umeda et al., 1999, 2000), or are influenced by the geometric shape of the oscillating device (Cardoni et al., 2002; Lucas et al., 2001; Mathieson, 2012; Mathieson et al., 2013; Puškár, 1982; Rawson, 1998).

Phenomena such as Duffing-like behavior and autoparametric vibrations have been observed to manifest in ultrasonic devices, including surgical devices, and can have a detrimental effect on device performance and reliability. Duffing-like behavior is often characterized by resonant frequency shifts, jump phenomena, and hysteretic regions in an ultrasonic device. Figure 27.3A depicts the response of a dynamic system when excited through a frequency sweep close to resonance. The response of a linear system produces a symmetric curve; however, if the system exhibits a shift in resonant frequency (either an increase or a decrease), the response becomes asymmetric. The shift in resonant frequency stems from nonlinear relationships within the device. These can be the result of exposing the material that the device is manufactured from to high excitation levels or can arise from variations in device stiffness, such as a reduction in the torque in a threaded joint (Aurelle et al., 1996; Campos-Pozuelo and Gallego-Juárez, 1996; Cardoni et al., 2002; Lucas et al., 2001; Mathieson, 2012; Mathieson et al., 2013; Puškár, 1982; Thomsen, 1997; Umeda et al., 1999, 2000) or material interfaces within the device. This behavior is often referred to as stiffness hardening or stiffness softening, where the resonant frequency increases or decreases, respectively.

Consequences of stiffness hardening or softening behavior in Duffing-like systems can be the occurrence of the jump phenomenon and a hysteresis region, depicted in Figure 27.3B. The jump phenomenon is characterized by discontinuities in the response of a Duffing-like system and can be observed in the response to an upward frequency sweep between II and III and a downward sweep between V and VI. The upward and downward jumps enclose a hysteretic region, an area where multiple solutions (amplitudes of vibration) exist. Theoretically, three solutions exist: two

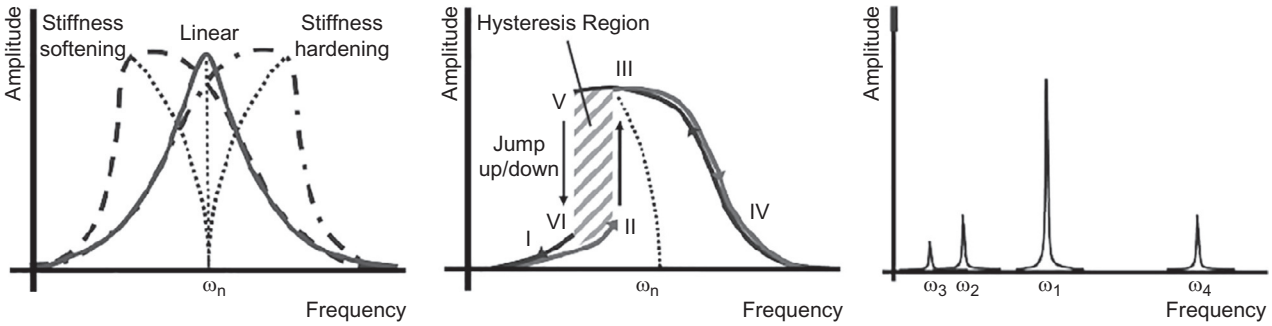


FIGURE 27.3 Depiction of (a) Duffing-like behavior, (b) the jump phenomenon and hysteretic regions, and (c) multiple modal responses.

stable solutions (if the amplitude response lies on the curve between VI and II or between V and III) and an unstable solution (if the response lies within the hysteresis region). Although the unstable solution is not observed experimentally, either of the stable solutions can exist, which provides the possibility for the system to alternate uncontrollably between these solutions (Thomsen, 1997).

Autoparametric vibration, depicted by Figure 27.3C, can occur when a dynamic system, such as a power ultrasonic device, is driven at a resonant frequency Ω and one or more modes are parametrically excited. For this behavior to manifest, the dynamic system must be excited above a vibration amplitude threshold, and one or more resonant modes are excited because of their simple integer (or near integer) frequency relationship. Examples of such relationships, shown in Figure 27.3C, are $\Omega \approx 2\omega_1$, $\Omega \approx \omega_1 + 2\omega_2$, and $\Omega \approx 1/2\omega_3$.

27.7 Device characterization

As an example of the characterization of devices used in bone cutting, the vibrational behavior of the commercial piezosurgery device is investigated. The device incorporates a cutting insert (called the OT7) that is used in a variety of surgical procedures and is shown in Figure 27.4. The cutting insert is attached to the transducer via a base unit (or base insert BI), which is common to the majority of piezosurgery devices. Two experimental characterization techniques are adopted: experimental modal analysis (EMA) and harmonic characterization. EMA is carried out under low excitation levels and is used to extract the modal parameters of the devices from frequency response measurements. Harmonic characterization measures the response at higher excitation levels in a small frequency range around resonance.

27.7.1 Modal analysis

Modal analysis is a computational or experimental process for predicting or measuring modal parameters. Resonant frequency, mode shape, and damping are all of the modal parameters. Commonly used during the initial design and design evolution stages during the development of ultrasonic devices, FEA enables designers to model an ultrasonic device before fabricating a prototype and to carry out numerical modal analysis.

To validate the results of FEA models or to verify the vibrational response of an ultrasonic device, EMA facilitates the characterization and visualization of the modal responses over a defined frequency range of interest in a linear excitation regime.

EMA involves the acquisition of vibration excitation and response signals from a grid of measurements points on the surface of a structure and the subsequent analysis of the measurement data to form a mathematical model that describes the vibrational behavior of the structure in terms of its resonance frequencies and mode shapes. The theoretical basis of EMA and the methodology necessary to carry out meaningful, accurate, and repeatable experiments have been thoroughly reported (Ewins, 2000). To carry out an EMA to characterize the modal parameters of an ultrasonic device, the following practical considerations are important.

- Experimental setup: The device should be mechanically supported as close to in situ conditions as possible, and it should be isolated from external sources of vibration.
- Measurement of vibrational responses: The excitation signal (random, swept-sine, or burst) should be controlled to excite responses in the device that are not significantly affected by heating in the piezoceramic stack and to minimize measurement errors as much as possible. The transducer used for measuring vibrational responses should not influence the behavior of the device. The most common (noncontact) approach is to measure the velocity response using a laser Doppler vibrometer. Measurements are taken over a grid of points that should have a mesh fine enough to capture the motion of the highest mode of interest.
- Analysis of measurements: The vibration response and input excitation measurement signals are processed to generate frequency response functions (FRFs). The FRFs contain frequency, amplitude, and phase data from which the modal parameters are extracted. This is achieved through a curve-fitting procedure to define a mathematical model that best fits the measurements.
- Extracting modal parameters and visualizing mode shapes: Modal parameters are extracted from the mathematical model obtained through curve-fitting of the



FIGURE 27.4 (a) OT7 insert and (b) base insert (BI).

FRFs, and the resulting data form a shape table. Geometry representing the structure of the device is generated from the measurement grid, and the modal data are applied to this grid. Animations then permit the modes of vibration to be visualized. Accurate modal data are important because the accuracy of the characterization of the off-resonance response can significantly influence the resulting animated mode shapes.

The curve-fitted FRF data in the frequency range of 0–80 kHz were measured using a three-dimensional laser Doppler vibrometer, and the results from the devices under investigation are presented in Figure 27.5. It can be observed that the FRF of the device operating in conjunction with an OT7 insert exhibits a larger number of resonant frequencies than the device only connected to the base insert. This shows that the presence of features such as a cutting blade, features that elongate the device, and geometries that are not symmetric in the longitudinal axis increase the spectral density of the FRF. Because there are an increased number of vibration modes, it is important to consider these during the design phase of the device to ensure that modal coupling—behavior where two or more modes of vibration are simultaneously excited because of their close modal frequencies—does not occur. Modal coupling can reduce the operating amplitude in the tuned mode of vibration and generate high stresses. High modal density also creates additional opportunities to excite autoparametric vibration.

Figure 27.6 demonstrates that good correlation between FEA and EMA is achieved in estimating the tuned resonant frequency and corresponding mode shape. Both the FE model predictions and EMA measurements show the transducer operating with axial vibrational motion and the cutting blade operating with L-F motion, with the flexural node located at the cutting blade.

27.7.2 Harmonic characterization

Harmonic characterization encompasses excitation and response measurement of an ultrasonic device via a bidirectional frequency sweep in a small frequency range through the resonant frequency. By increasing the excitation signal during subsequent sweeps, it is possible to determine the linear response threshold and characterize non-linear responses. It can then be possible to investigate strategies for mitigating these behaviors, identifying their source and understanding the effects on device performance. Different techniques can be used to carry out harmonic characterization, such as excitation under constant current or constant voltage conditions with either a continuous or a burst signal (Albareda et al., 2007).

Figure 27.7 shows a harmonic characterization of the surgical devices presented in Figure 27.4. Bidirectional frequency sweeps under constant voltage conditions were used to excite the surgical devices close to their tuned resonance frequency, corresponding to the first longitudinal mode.

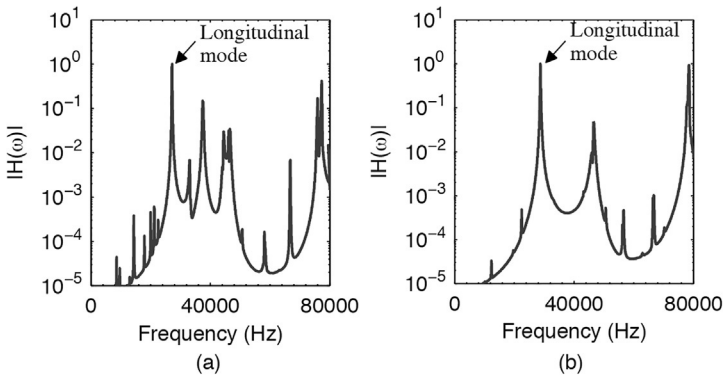


FIGURE 27.5 Curve fit FRF traces of (a) OT7 insert and (b) base insert.

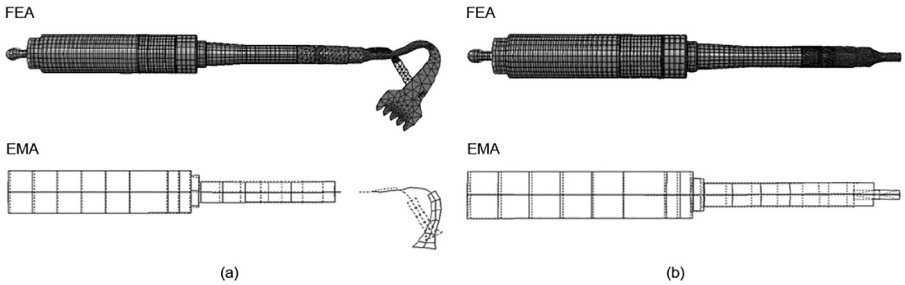


FIGURE 27.6 Tuned mode of vibration predicted through FEA and measured through EMA of the surgical device incorporating (a) OT7 insert and (b) base insert.

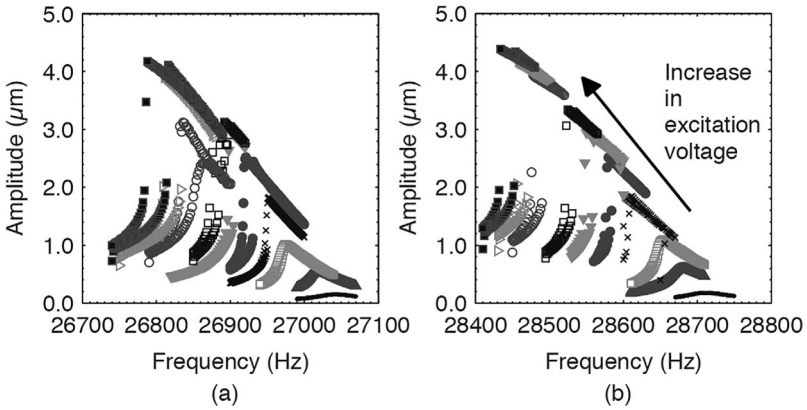


FIGURE 27.7 Response of surgical device close to resonance (a) OT7 insert and (b) base insert.

Heating of the piezoceramic stack of the transducer can alter the electromechanical properties of the piezoceramic elements, and the resulting frequency shift manifests as a pseudo-nonlinear response. It is therefore important to remove heating effects as much as possible to identify the influence of excitation level on the vibrational response. To minimize heating in the piezoceramic stack, the device was excited under constant voltage conditions with a burst-sine signal at each frequency increment in the bidirectional sweep. Each burst-sine signal was applied for a fixed number of 6000 cycles. This was long enough for steady-state vibration to be achieved but short enough to prevent any influence from a temperature increase in the stack. To ensure that any heat had been dissipated, a time delay between successive bursts was incorporated: 1 s for excitation levels in the range of 1–10 V_{rms} and 10 s for excitation levels in the range of 10–50 V_{rms}. To ensure capture of even small changes in the vibrational response, the frequency step between successive bursts was set at 1 Hz for excitation levels in the 1–10 V_{rms} range and 2 Hz for excitation levels in the 10–50 V_{rms} range.

It can be observed from Figure 27.7 that the device, both with and without the cutting tip attached, exhibits behavior typical of Duffing-like systems. Figure 27.8 shows that corresponding to the first longitudinal mode, heating of the piezoceramic stack of the transducer can alter the electromechanical properties of the piezoceramic elements, and the resulting frequency shift manifests as a pseudo-nonlinear response. It is therefore important to remove heating effects as much as possible to identify the influence of excitation level on the vibrational response. To minimize heating in the piezoceramic stack, the device was excited under constant voltage conditions with a burst-sine signal at each frequency increment in the bidirectional sweep. Each burst-sine signal was applied for a fixed number of 6000 cycles. This was long enough for steady-state vibration to be achieved but short enough to prevent any influence from a temperature increase in the stack. To ensure that any heat had been dissipated, a time delay between successive bursts was incorporated: 1 s for excitation levels in the range of 1–10 V_{rms} and 10 s for excitation levels in the range of 10–50 V_{rms}. To ensure capture of even small changes in the vibrational response, the frequency step between successive bursts was set at 1 Hz for excitation levels in the 1–10 V_{rms} range and 2 Hz for excitation levels in the 10–50 V_{rms} range.

Figure 27.9 shows power spectra of the ultrasonic device, in this case illustrating a significant difference with and without the cutting tip attached. Figure 27.9B is the power spectrum of the device without the cutting blade. The strongest response is at the excitation frequency Ω; two weaker responses, the first and second harmonics

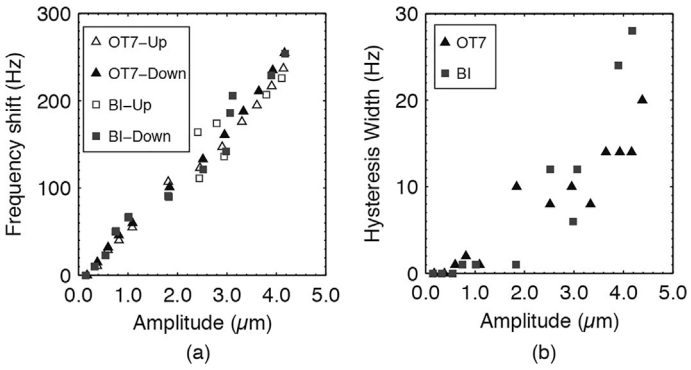


FIGURE 27.8 Nonlinear responses with respect to vibrational amplitude, (a) the shift in resonant frequency and (b) the width of the hysteresis region.

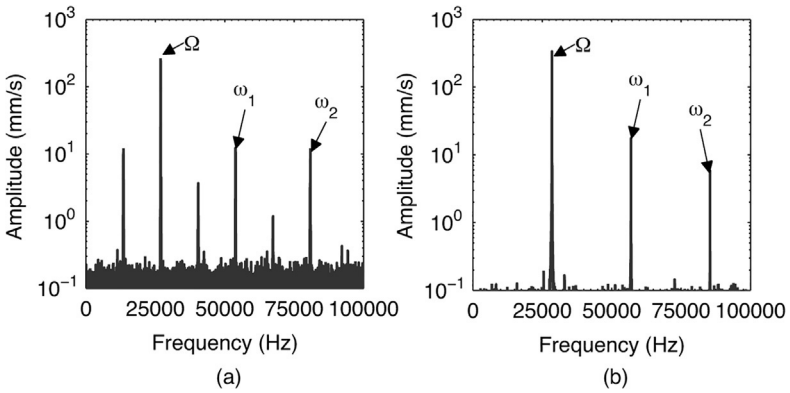


FIGURE 27.9 Power spectra of the surgical device excited close to resonance at 50 V_{rms} of (a) OT7 and (b) BI.

(ω_1 and ω_2) also are visible. However, Figure 27.9A exhibits responses other than those at Ω, ω_1, and ω_2. These responses, which have a frequency relationship of $\omega_k = k0.5\Omega$ (where k is the harmonic number), can be attributed to the flexural motion generated by the cutting tip, and the spectrum indicates a system exhibiting period-2 motion. This is the first step in the period-doubling route to chaotic behavior, which, if reached, results in unpredictable and uncontrollable behavior in devices (Thomsen, 1997). Although the response at this level of excitation remains relatively stable, the measured spectrum is an indication that this device could exhibit chaotic behavior at higher excitation levels.

27.8 Orthopedic, orthodontic, and maxillofacial procedures

27.8.1 Selective cutting

A documented limitation of power ultrasonic devices designed for orthopedic, orthodontic, and maxillofacial procedures is their slower cutting and material removal rates compared with conventional devices (Aro et al., 1982; Horton et al., 1975, 1981; Khambay and Walmsley, 2000a, b). It also has been widely reported that ultrasonic devices offer higher precision (Aro et al., 1982; Balamuth, 1963; Beziat et al., 2007; Catuna, 1953; Hoigne et al., 2006; Horton et al., 1975, 1981; Khambay and Walmsley, 2000a, b; Mararow, 1960; McFall et al., 1961; Pavlíková et al., 2011; Postle, 1958; Schaeren et al., 2008; Vang, 1955; Vercellotti, 2000; Vercellotti et al., 2001; Volkov and Shepeleva, 1974; Zacharias, 2008) and the capability of selectively cutting mineralized tissue while leaving surrounding soft-tissue intact (Beziat et al., 2007; Hoigne et al., 2006; Labanca et al., 2008; Pavlíková et al., 2011; Schaeren et al., 2008; Vercellotti, 2000; Vercellotti et al., 2001). This is a critical consideration for surgical procedures because the absence of damage to soft-tissue structures (such as nerves, vessels, and membranes) can result in a cumulatively shorter procedure and one that is less likely to be terminated and then postponed (Beziat et al., 2007; Blus et al., 2010; Hoigne et al., 2006; Pavlíková et al., 2011; Schaeren et al., 2008; Vercellotti, 2000; Vercellotti et al., 2001).

A study by Schaeren et al. reported a worst-case scenario of direct and prolonged exposure of delicate soft tissue (nerve tissue) to an ultrasonic surgical device. Although some structural and functional damage to the tissue did occur, the ultrasonic device did not dissect the tissue; within the control group, almost 90% of cases exhibited no long-term effects (Schaeren et al., 2008). Surgeons have highlighted this advantage for maxillofacial and craniofacial procedures. Vercellotti et al. reported that during bony window osteotomy and sinus membrane elevation, Schneiderian membrane perforation was absent in 20 of the 21 cases studied (Vercellotti et al., 2001), whereas during 140 palatal expansions, Beziat et al. reported an absence of palatal mucosal injury when using an ultrasonic device (Beziat et al., 2007).

Ramieri reported that using an ultrasonic device in neurocranial surgery allowed surgeons to save the periorbital tissue and reduce retraction on the brain tissue (Ramieri et al., 2015). In instances where the dura mater was accidentally touched, these injuries were superficial and did not require further repair. Patel and Mistry compared conventional surgical instruments, such as high-speed drills, with an ultrasonic bone scalpel for spinal decompressive surgeries, also reporting a reduction in the most unintended complication, dural tears (Patel and Mistry, 2019). This study also concluded that a lower mean operating duration and lower blood loss were achieved when operating with the ultrasonic device.

A review of the use of ultrasonic devices in otolaryngology, or head and neck surgery, Meller and Havas (2017) reported advantages, when compared with manual rotary instruments, including reduced tissue injury and necrosis, exemplified by reduced cellular damage without evidence of thermal coagulative necrosis. With relevance to otology, tissue selectively results in preservation of soft tissue where the lateral sinus, dura mater, and facial nerve exist encased in bone within a confined space.

27.8.2 A clinical procedure using ultrasonic devices

Commercial power ultrasonic surgical devices are capable of cutting mineralized tissues in a wide variety of procedures in dental, craniofacial, maxillofacial, reconstructive, spinal, and orthopedic surgery. The majority of these use an ultrasonic device for specific stages of the procedure, especially operating close to delicate soft-tissue structures. An example of a procedure that can be performed solely with an ultrasonic device is the bilateral sagittal split osteotomy (BSSO), a maxillofacial procedure. The BSSO is a procedure that corrects dentofacial deformities such as malocclusion, the misalignment of teeth, or an incorrect relationship between teeth and the dental arch due to congenital abnormal skeletal development or trauma-related sequelae. The mandible (lower jaw) or maxilla (upper jaw) can exhibit two conditions: prognathism (skeletal protrusion) or retrognathism (skeletal retrusion) (Figure 27.10). The BSSO corrects prognathism or retrognathism of the mandible through its mobilization and subsequent repositioning to achieve facial balance.

To mobilize the mandible through BSSO, the surgeon completes the following steps (Figure 27.11):

1. Osteotomy of the mandibular ramus: a cut parallel to the occlusal plane, partitioning it through the lingual cortex into the cancellous bone and terminating just posterior to the lingua.
2. Vertical osteotomy: commences from the osteotomy in step 1 and cuts vertically through the center of the ramus, passing through the cortex into the cancellous bone, and terminating at the second molar.
3. Mandibular body buccal osteotomy: commences at the lower border of the mandibular body and cuts to the termination point of the vertical osteotomy.
4. Sagittal split commencement: the cancellous bone is cut up to the neurovascular bundle.
5. Nerve protection: once the neurovascular nerve has been located, it is protected by a separator and a deeper cut is made into the cancellous bone of the lower border of the mandibular.
6. Sagittal split completion: the split is completed with an osteotome, allowing the mandibular body to be mobilized and its position corrected.

27.9 Current and future trends

27.9.1 Transduction materials

High-performance relaxor piezocrystals may herald the beginning of a new period in the development of transduction material, similar to that seen during the late 1940s and 1950s with the discovery of ferroelectric polycrystalline materials such as barium titanate and latterly lead zirconate titanate. Although relaxor crystals were first reported during the early 1960s, it was not until the late 1990s and early 2000s that first-generation crystals, PMN-PT (a solid solution of lead magnesium niobate-lead titanate), could be grown in sufficient sizes and volumes that permitted their commercial viability (Zhang and Li, 2012). Despite PMN-PT exhibiting ultrahigh piezoelectric coefficients and electromechanical coupling factors, their implementation in commercial power ultrasonic devices did not immediately ensue because of poor thermal stability, low phase transition temperatures ($T \sim 60$–$90°C$) and low Curie temperature ($T_c \sim 120$–$170°C$), as well as typically exhibiting high values for dielectric loss and low values for mechanical quality factor.

Second-generation relaxor crystals, PIN-PMN-PT (lead indium niobate-lead magnesium niobate-lead titanate), provided a combination of enhanced thermal stability with similar properties of first-generation crystals. However, their low mechanical quality factor restricted their use in power ultrasonics applications. Third-generation relaxor crystals consisting of PIN-PMN-PT with the addition of dopants, such as manganese, have now sufficiently increased the quality factor for incorporation into transducers for high-power ultrasonics applications; however, their moderate thermal stability suggests that they are likely best suited for applications with short duty cycles and drive amplitudes at the lower end of power ultrasonic applications. The next challenge will be growing third-generation doped piezocrystals in a commercially viable process to allow their

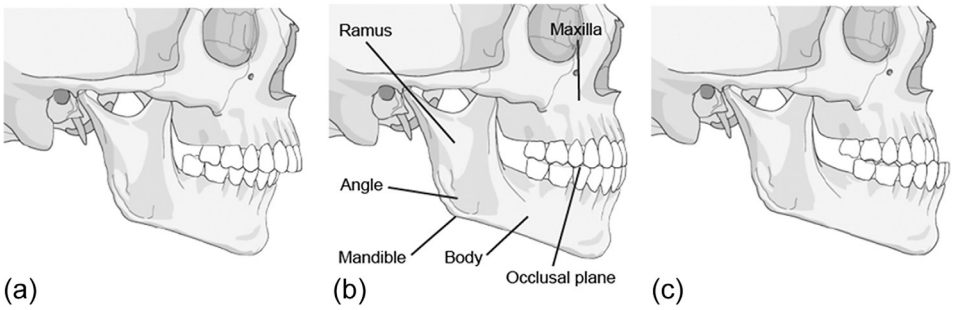


FIGURE 27.10 Diagram of the skull where the mandible (a) exhibits prognathism, (b) has a normal position, and (c) exhibits retrognathism.

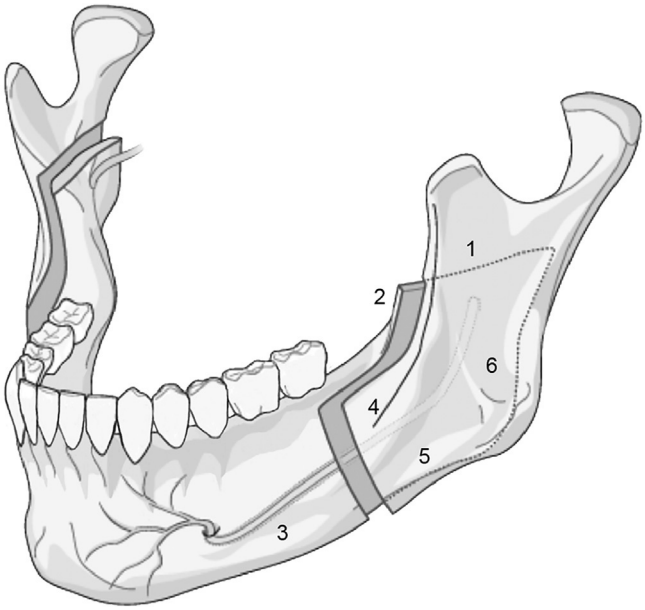


FIGURE 27.11 Osteotomies of the mandibular during the BSSO procedure.

adoption in commercial devices as well as further improving their thermal stability for high-power ultrasonic applications.

Textured piezoceramics are another class of piezoelectric materials which have been increasingly reported over the past two decades and which could offer an alternative to piezocrystals (Horn et al., 1999; Moriana and Zhang, 2018). Exhibiting a high piezoelectric response which is superior to conventional piezoceramics and comparable with piezocrystals, textured piezoceramics are fabricated using a combination of conventional piezoceramic powder and aligned piezocrystal template seeds. During sintering, a process all piezoceramics undergo during the manufacturing process, the piezoceramic particles grow in size and align to the template seeds forming "texturing." It is this alignment and subsequent enhanced polarization which enhances the piezoelectric performance.

The majority of investigations into textured piezoceramics have focused on enhancing the properties of soft piezoceramics to provide an alternative high-performance piezoelectric material to piezocrystals (Brosnan et al., 2009; Liu et al., 2020). Nevertheless, textured compositions based on PMN-PT (which have properties comparable to soft piezoceramic) have been demonstrated to perform well within Tonpilz sonar transducers in water. However, it has also been reported that when driven at an elevated drive level, even with a short duty cycle, these devices were susceptible to exhibiting nonlinear behavior which manifested in generating a Duffing-like stiffness softening response.

More recently, textured piezoceramics for power applications have been reported (Liu et al., 2020). It has been demonstrated that textured piezoceramic materials, based on compositions such as PMN-PZT or doped variants, exhibit piezoelectric properties which are typically associated with soft piezoceramic compositions, while exhibiting quality factors and dielectric loss more akin to hard piezoceramic (Liu et al., 2020; SolidStateCeramics.com). The relatively low cost of textured piezoceramics could make it an attractive alternative for high performance power ultrasonic devices. However, as with piezocrystals, an increase in maximum operating temperature may be required (maximum allowable temperatures are currently in the range of 120°C to 150°C), while there are also current limitations on the maximum thickness of piezoceramic elements that can be manufactured.

27.9.2 Transducer design

Power ultrasonic transducers have generally evolved from the Langevin stack transducer, operating axially to generate a longitudinal motion. The Langevin transducer configuration consists of an acoustically efficient front mass, a back mass that encourages the acoustic wave to propagate through the front mass, and a tension bolt for keeping the piezoelectric elements contained in the stack under a compressive preload. However, two other transducer types are currently being researched for use in surgical devices.

27.9.3 Additive manufacturing

Additive manufacturing (AM) encompasses a broad range of technologies which fabricate objects layer by layer until the desired shape has been achieved. AM has been heralded

as a distributive technology (Babu et al., 2015; Campbell et al., 2012) and is considered to be a key component of Industry 4.0 (Santos et al., 2017). The capability of AM to fabricate complex shapes, which conventional subtractive manufacturing processes are unable to generate, has been demonstrated within the field of acoustic meta-materials (Haberman and Guild, 2016; Laureti et al., 2020) and in the fabrication of piezoceramic actuators and arrays (Chen et al., 2016; Zhu et al., 2019; Cheng et al., 2019).

Metallic parts fabricated through additive manufacturing technologies, such as the powder bed fusion process, have already been demonstrated in power ultrasonic devices for surgical and sonar applications (Cleary and Lucas, 2020; Mathieson et al., 2019), providing confidence that AM could facilitate the design and manufacture of other power ultrasonic devices. Future advancements of AM could allow for control of material properties to optimize device performance. Exploitation of AM will enable the incorporation of nano- and micro-architectures in devices, to manipulate the propagation of the acoustic wave and excite tailored vibrational behaviors. For instance, power ultrasonic devices could integrate design features facilitated by AM that excite complex vibrational modes at the distill tip to facilitate surgical procedures, or that reduce the size of the device without increasing its resonance frequency, or that allow for suppression of nonlinear behaviors such as those discussed in Section 27.6.2.

27.9.4 Flextensional transducers

Flextensional transducers were first proposed during the late 1920s and 1930s and consist of an actuator, such as a piezoelectric material, that induces strain in a curved metal shell or plate to generate vibration. These transducers are categorized into classes I–V, and although they can be relatively large and bulky (Meyer et al., 2001; Rolt, 1990), miniaturized class V flextensional transducers with diameters of the order of 1 cm have recently been developed (Meyer et al., 2001). Class V configurations generally consist of two spherical end-cap shells bonded to a piezoceramic disc. Figure 27.12 depicts the "moonie," a miniaturized flextensional transducer developed during the late 1980s (Newnham et al., 1991). Because of the shape of the end-cap, the transducer exhibits a strain gradient, and hence a vibrational amplitude variation, across its output face. The "cymbal" configuration developed during the 1990s minimizes gradient strain and therefore produces more uniform vibrational amplitude across the output face (Meyer et al., 2001).

Although flextensional transducers have been primarily used in underwater and sonar applications, recent studies have shown that cymbal transducers can generate high vibrational amplitudes for comparatively low piezoceramic volume (Lucas and Bejarano, 2013). This has allowed them to be considered for power ultrasonics applications such as cutting while taking advantage of their small size to develop

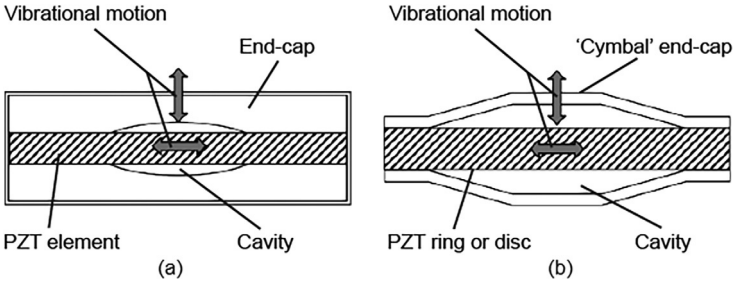


FIGURE 27.12 Schematic of (a) Moonie and (b) cymbal flextensional transducers.

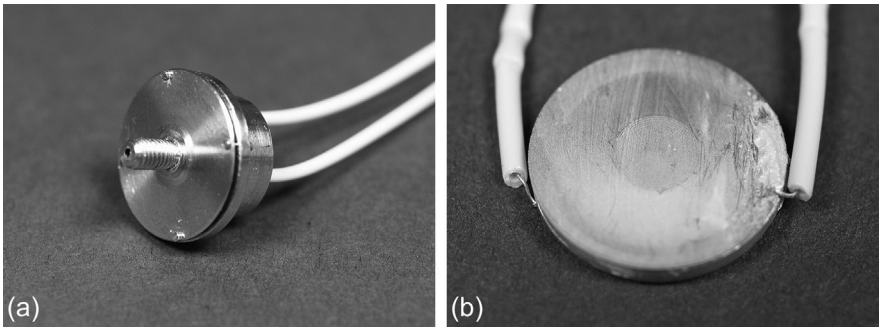


FIGURE 27.13 Prototype cymbal transducers with (a) brass end-caps and (b) SMA end-caps.

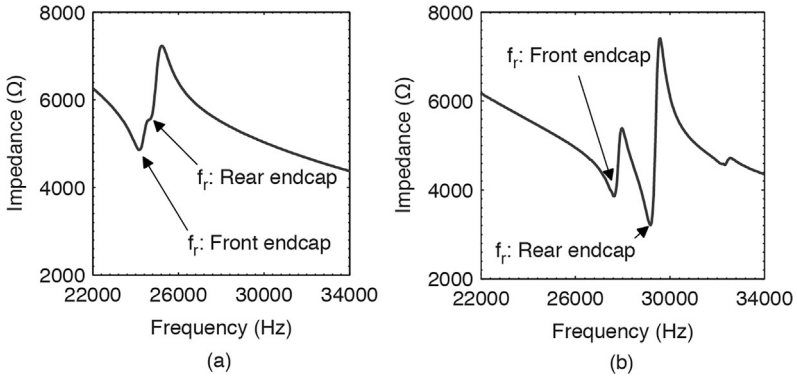


FIGURE 27.14 Impedance-frequency spectra for Nitinol (in superelastic condition) cymbal transducer in the (a) martensite phase and (b) austenite phase.

miniature devices (Figure 27.13). Relaxor piezocrystals have already been incorporated into cymbal configurations (Meyer et al., 2001); however, the incorporation of third-generation relaxor piezocrystals may provide further performance enhancements and new devices.

Recent research has reported the incorporation of shape memory alloys (SMAs), such as Nitinol in the superelastic condition, for end-caps in cymbal transducers. Because SMAs have the capability to change phase with applied stress and change in temperature, it is proposed that a cymbal transducer with SMA end-caps could operate at more than one selectable resonant frequency by altering the material phase. Figure 27.14 shows the temperature dependency of the resonant frequency and impedance of a cymbal transducer with Nitinol end-caps (Feeney and Lucas, 2013). At 10°C, the resonant frequency of the transducer is significantly lower than, while the impedance of the device is higher than the transducer at room temperature. This therefore creates an opportunity for cymbal transducers containing SMAs to be used in power ultrasonic applications such as cutting or ultrasonic cleaning, where multiple and selectable resonant frequencies are desirable.

References

Alam, K., Mitrofanov, A.V., Bäker, M., Silberschmidt, V.V., 2009. Stresses in ultrasonically assisted bone cutting. J. Phys. Conf. Ser. 181, 012014.

Albareda, A., Perez, R., Casals, J., Garcia, J., Ochoa, D., 2007. Optimization of elastic nonlinear behavior measurements of ceramic piezoelectric resonators with burst excitation. IEEE Trans. Ultrason. Ferroelectr. Freq. Control 54, 2175–2188.

Al-Budairi, H., Lucas, M., Harkness, P., 2013. A design approach for longitudinal-torsional ultrasonic transducers. Sens. Actuators A Phys. 198, 99–106.

Amaral, J., 1994. Ultrasonic dissection. Endosc. Surg. Allied Technol. 2, 181–185.

Ao, J., Juniat, V., Davis, G., Santoreneos, S., Abou-Hamden, A., Selva, D., 2020. Outcomes of surgical resection of sphenoid-orbital meningiomas with Sonopet ultrasonic aspirator. Orbit, 1–6.

Aro, H., Kallioniemi, H., Aho, A., Kellokumpu-Lehtinen, P., 1982. Ultrasonic device in bone cutting: a histological and scanning electron microscopical study. Acta Orthop. Scand. 52, 5–10.

Asami, T., Tamada, Y., Higuchi, Y., Miura, H., 2017. Ultrasonic metal welding with a vibration source using longitudinal and torsional vibration transducers. Jpn. J. Appl. Phys. 56 (7S1), 07JE02.

Aurelle, N., Guyomar, D., Richard, C., Gonnard, P., Eyraud, L., 1996. Nonlinear behavior of an ultrasonic transducer. Ultrasonics 34, 187–191.

Babu, S.S., Love, L., Dehoff, R., Peter, W., Watkins, T.R., Pannala, S., 2015. Additive manufacturing of materials: opportunities and challenges. MRS Bull. 40 (12), 1154–1161.

Balamuth, L., 1948. Improvements in or Relating to Cutting, Grinding, Polishing, Cleaning, Honing or the Like. British Patent 602801.

Balamuth, L., 1952. Method and Means for Removing Material from a Solid Body. US Patent 2580716.

Balamuth, L., 1963. Ultrasonics and dentistry. Soundings 2, 15–19.

Banko, A., Kelman, C.D., 1971. Material Removing Apparatus and Method Employing High Frequency Vibrations. US Patent 3589363.

Berry, M., Davies, D., 2011. Liposuction: a review of principles and techniques. J. Plast. Reconstr. Aesthet. Surg. 64, 985–992.

Bethke, W., 2011. Phaco: new tech, new techniques. Rev. Ophthalmol. 11, 33. Online Rev. Accessed 15 April 2011 http://www.revophth.com.

Beziat, J.-L., Bera, J.-C., Lavandier, B., Gleizal, A., 2007. Ultrasonic osteotomy as a new technique in craniomaxillofacial surgery. Int. J. Oral Maxillofac. Surg. 36, 493–500.

Blus, C., Szmukler-Moncler, S., Vozza, I., Rispoli, L., Polastri, C., 2010. Split-crest and immediate implant placement with ultrasonic bone surgery (piezosurgery): 3-year follow-up of 180 treated implant sites. Quintessence Int. 41, 463–469.

Bond, L., Cimino, W., 1996. Physics of ultrasonic surgery using tissue fragmentation: part II. Ultrasound Med. Biol. 22, 101–117.

Boukhny, M., 2000. Torsional Ultrasonic Handpiece. US Patent 6077285.

Brock, M., Ingwersen, I., Roggendorf, W., 1984. Ultrasonic aspiration in neurosurgery. Neurosurg. Rev. 7, 173–177.

Brosnan, K.H., Messing, G.L., Markley, D.C., Meyer, R.J., 2009. Comparison of the properties of tonpilz transducers fabricated with ⟨001⟩ fiber-textured lead magnesium niobate-lead titanate ceramic and single crystals. J. Acoust. Soc. Am. 126 (5), 2257–2265.

Campbell, I., Bourell, D., Gibson, I., 2012. Additive manufacturing: rapid prototyping comes of age. Rapid Prototyp. J. 18 (4), 255–258.

Campos-Pozuelo, C., Gallego-Juárez, J., 1996. Limiting strain of metals subjected to highintensity ultrasound. Acta Acust. United Acust. 82, 823–828.

Cardoni, A., Lim, F., Lucas, M., Cartmell, M., 2002. Characterising modal interactions in an ultrasonic cutting system. In: Forum Acusticum, 2002, ULT-02-003-IP, Seville, Spain.

Cardoni, A., MacBeath, A., Lucas, M., 2006. Methods for reducing cutting temperature in ultrasonic cutting of bone. Ultrasonics 44.

Catuna, M.C., 1953. Sonic energy: a possible dental application. Ann. Dent. 12, 100–101.

Cheery, C., Gibbons, M., Ronayne, J., 1974. The origins of the air-turbine dental handpiece. Br. Dent. J. 136, 469–472.

Chen, Z., Song, X., Lei, L., Chen, X., et al., 2016. 3D printing of piezoelectric element for energy focusing and ultrasonic sensing. Nano Energy 27, 78–86.

Cheng, J., Chen, Y., Wu, J.W., Ji, X.R., Wu, S.H., 2019. 3D printing of BaTiO3 piezoelectric ceramics for a focused ultrasonic array. Sensors 19, 4078.

Cimino, W., 1999. The physics of soft tissue fragmentation using ultrasonic frequency vibration of metal probes. Clin. Plast. Surg. 26, 447–461.

Cimino, W., Bond, L., 1996. Physics of ultrasonic surgery using tissue fragmentation: part I. Ultrasound Med. Biol. 22, 89–100.

Cleary, R., Lucas, M., 2020. Evaluation of direct laser sintered Ti6Al4V for a prototype power ultrasonic surgical device. In: IEEE IUS, Las Vegas, USA 6-11 Sept 2020.

Cleary, R., Wallace, R., Simpson, H., Kontorinis, G., Lucas, M., 2022. A longitudinal-torsional mode ultrasonic needle for deep penetration into bone. Ultrasonics, 106756.

Cohan, A., 1951. New method machines: sintered carbides, sintered borides, hardened tool steels. J. Met. 3, 217–219.

Dolan, E., Haugh, M., Tallon, D., Casey, C., McNamara, L., 2012. Heat-shock-induced cellular responses to temperature elevations occurring during orthopaedic cutting. J. R. Soc. Interface 9, 3503–3513.

Ebina, K., Hasegawa, H., Kanai, H., 2007. Investigation of frequency characteristics in cutting of soft tissue using prototype ultrasonic knives. Jpn. J. Appl. Phys. 46, 4793–4800.

Ewins, D.J., 2000. Modal Testing—Theory, Practice and Application, second ed. Research Studies Press Ltd, England.

Feeney, A., Lucas, M., 2013. An investigation of the vibration response of a superelastic nitonol cymbal transducer. In: Proceedings of the International Congress on Ultrasonics. vol. 2013, pp. 321–326.

Flamm, E.S., Ransohoff, J., Wuchinich, D., Broadwin, A., 1978. Preliminary experience with ultrasonic aspiration in neurosurgery. Neurosurgery 2, 240–245.

Gilles, R., Couvreur, T., Dammous, S., 2013. Ultrasonic orthognathic surgery: enhancements to established osteotomies. Int. J. Oral Maxillofac. Surg. 42 (8), 981–987.

Graff, K., 1977. Ultrasonics: historical aspects. In: Ultrasonics Symposium, 1977, pp. 1–10.

Haberman, M.R., Guild, M.D., 2016. Acoustic metamaterials. Phys. Today 69, 42–48.

Han, Y., Miller, K., 2009. Heat production: longitudinal versus torsional phacoemulsification. J Cataract Refract Surg 35, 1799–1805.

Hoenig, D.M., Chrostek, C.A., Amaral, J.F., 1996. Laparosonic coagulating shears: alternative method of hemostatic control of unsupported tissue. J. Endourol. 10, 431–433.

Hoigne, D., Stubinger, S., Kaenel, O.V., Shamdasani, S., Hasenboehler, P., 2006. Piezoelectric osteotomy in hand surgery: first experiences with a new technique. BMC Musculoskelet. Disord. 7, 36.

Horn, J.A., Zhang, S.C., Selvaraj, U., Messing, G.L., Trolier-McKinstry, S., 1999. Templated grain growth of textured bismuth titanate. J. Am. Ceram. Soc. 82 (4), 921–926.

Horton, J., Tarpley, T., Wood, L., 1975. The healing of surgical defects in alveolar bone produced with ultrasonic instrumentation, chisel, and rotary bur. Oral Surg. Oral Med. Oral Pathol. 39, 536–546.

Horton, J., Tarpley, T., Wood, L., 1981. Clinical applications of ultrasonic instrumentation in the surgical removal of bone. Oral Surg. Oral Med. Oral Pathol. 51, 236–242.

Jun, B., Berdahl, J.P., Kim, T., 2010. Thermal study of longitudinal and torsional ultrasound phacoemulsification: tracking the temperature of the corneal surface, incision, and handpiece. J Cataract Refract Surg 36, 832–837.

Kelley, S., 1951. Hard, brittle materials machined using ultrasonic vibrations. Mater. Methods 34, 92–94.

Kelman, C.D., 1967. Phaco-emulsification and aspiration: a new technique of cataract removal—a preliminary report. Am. J. Ophthalmol. 64 (1), 23–35.

Kelman, C.D., 1994. The history and development of phacoemulsification. Int. Ophthalmol. Clin. 34, 1–12.

Khambay, B.S., Walmsley, A.D., 2000a. Investigations into the use of an ultrasonic chisel to cut bone. Part 1: forces applied by clinicians. J. Dent. 28, 31–37.

Khambay, B.S., Walmsley, A.D., 2000b. Investigations into the use of an ultrasonic chisel to cut bone. Part 2: cutting ability. J. Dent. 28, 39–44.

Koch, C., Friedrich, T., Metternich, F., Tannapfel, A., Reimann, H.P., Eichfeld, U., 2003. Determination of temperature elevation in tissue during the application of the harmonic scalpel. Ultrasound Med. Biol. 29, 301–309.

Labanca, M., Azzola, F., Vinci, R., Rodella, L.F., 2008. Piezoelectric surgery: twenty years of use. Br. J. Oral Maxillofac. Surg. 46, 265–269.

Laureti, S., Hutchins, D.A., Astolfi, L., et al., 2020. Trapped air metamaterial concept for ultrasonic sub-wavelength imaging in water. Sci. Rep. 10, 10601.

Lawrence, N., Coleman, W.P., 1999. Ultrasonic-assisted liposuction: internal and external. Dermatol. Clin. 17, 761–771.

Linebarger, E.J., Hardten, D.R., Shah, G.K., Lindstrom, R.L., 1999. Phacoemulsification and modern cataract surgery. Surv. Ophthalmol. 44, 123–147.

Liu, H., Yan, Y., Leng, H., Heitmann, A., Blottman, J., Priya, S., 2020. High performance high power textured piezoceramics. Appl. Phys. Lett. 116 (25), 252901.

Lucas, M., Bejarano, F., 2013. An ultrasonic orthopedic surgical device based on a cymbal transducer. In: Proceedings of the International Congress on Ultrasonics, 2013, pp. 185–190.

Lucas, M., Petzing, J., Cardoni, A., Smith, L., McGeough, J., 2001. Design and characterisation of ultrasonic cutting tools. CIRP Ann. Manuf. Technol. 50 (1), 149–152.

Lucas, M., Cardoni, A., MacBeath, A., 2005. Temperature effects in ultrasonic cutting of natural materials. CIRP Ann. 54 (1), 195–198.

Lucas, M., MacBeath, A., McCulloch, E., Cardoni, A., 2006. A finite element model for ultrasonic cutting. Ultrasonics 44, e503–e509.

Mararow, H., 1960. Bone repair after experimentally produced defects. J. Oral Surg. Anesth. Hosp. Dent. Serv. 18, 107–114.

Martin, H., 1976. Ultrasonic disinfection of the root canal. Oral Surg. Oral Med. Oral Pathol. 42, 92–99.

Mathieson, A., 2012. Nonlinear Characterisation of Power Ultrasonic Devices used in Bone Surgery. PhD Thesis, School of Engineering, University of Glasgow.

Mathieson, A., Cardoni, A., Cerisola, N., Lucas, M., 2013. The influence of piezoceramic stack location on nonlinear behavior of langevin transducers. IEEE Trans. Ultrason. Ferroelectr. Freq. Control 60, 1126–1133.

Mathieson, A., Tyson, B., Bond, A., 2019. The demonstration of additive manufacture in power ultrasonic and sonar transducers. IEEE Trans. Ultrason. Ferroelectr. Freq. Control 67 (4), 817–824.

McFall, T., Yamane, G., Burnett, G., 1961. Comparison of the cutting effect on bone of an ultrasonic cutting device and rotary burs. J. Oral Surg. Anesth. Hosp. Dent. Serv. 19, 200–209.

Meller, C., Havas, T.E., 2017. Piezoelectric technology in otolaryngology, and head and neck surgery: a review. J. Laryngol. Otol. 131, S12–S18.

Meyer, R., Dogan, A., Yoon, C., Pilgrim, S., Newnham, R.E., 2001. Displacement amplification of electroactive materials using the cymbal flextensional transducer. Sens. Actuators A Phys. 87, 157–162.

Moriana, A.D., Zhang, S., 2018. Lead-free textured piezoceramics using tape casting: a review. J. Materiomics 4 (4), 277–303.

Newnham, R.E., Xu, Q.C., Yoshikawa, S., 1991. Transformed Stress Direction Acoustic Transducer. US Patent 4999819.

Ohnishi, O., Myohga, O., Uchikawa, T., Tamegai, M., Inoue, T., Takahashi, S., 1993. Piezoelectric ultrasonic motor using longitudinal-torsional composite resonance vibration. IEEE Trans. Ultrason. Ferroelectr. Freq. Control 40 (6), 687–693.

Packer, M., Fishkind, W.J., Fine, I.H., Seibel, B.S., Hoffman, R.S., 2005. The physics of phaco: a review. J Cataract Refract Surg 31, 424–431.

Pakzaban, P., 2014. BoneScalpel™ Ultrasonic Bone Dissector: Applications in Spine Surgery and Surgical Technique Guide. Misonix, Farmingdale, NY. https://igea.mx/wp-content/uploads/2017/06/BS-1302_BoneScalpel_Ultrasonic_Bone_Dissector_Applications_in_Spine_Surgery_by_Dr_Pakzaban1.pdf.

Pandey, S.K., Milverton, J., Maloof, A.J., 2004. History of ophthalmology: a tribute to Charles David Kelman MD: ophthalmologist, inventor and pioneer of phacoemulsification surgery. Clin. Experiment. Ophthalmol. 32, 529–533.

Patel, S., Mistry, M., 2019. A prospective study of results of laminectomy using ultrasonic bone scalpel vs. conventional methods. Int. J. Orthop. 5 (1), 421–423.

Pavlíková, G., Foltán, R., Horká, M., Hanzelka, T., Borunská, H., Šedý, J., 2011. Piezosurgery in oral and maxillofacial surgery. Int. J. Oral Maxillofac. Surg. 40, 451–457.

Postle, H., 1958. Ultrasonic cavity preparation. J. Prosthet. Dent. 8 (1), 153–160.

Preti, G., Martinasso, G., Peirone, B., Navone, R., Manzella, C., Muzio, G., Russo, C., Canuto, R., Schierano, G., 2007. Cytokines and growth factors involved in the osseointegration of oral titanium implants positioned using piezoelectric bone surgery versus a drill technique: a pilot study in minipigs. J. Periodontol. 78, 716–722.

Pušķár, A., 1982. Cyclic stress-strain curves and internal friction of steel at ultrasonic frequencies. Ultrasonics 3, 118–122.

Ramieri, V., Saponaro, G., Lenzi, J., Caporlingua, F., Polimeni, A., Silvestri, A., Pizzuti, A., et al., 2015. The use of piezosurgery in cranial surgery in children. J. Craniofac. Surg. 26 (3), 840–842.

Rawson, F.F., 1998. Chapter 14: An introduction to ultrasonic food cutting. In: Povey, M.J.W., Mason, T.J. (Eds.), Ultrasound in Food Processing. Blackie Academic & Professional, London, UK, pp. 254–269.

Rolt, K.D., 1990. History of the flextensional electroacoustic transducer. J. Acoust. Soc. Am. 87, 1340–1349.

Samy, R.N., Krishnamoorthy, K., Pensak, M.L., 2007. Use of a novel ultrasonic surgical system for decompression of the facial nerve. Laryngoscope 117 (5), 872–875.

Santos, C., Mehrsai, A., Barros, A.C., Araújo, M., Ares, E., 2017. Towards industry 4.0: an overview of European strategic roadmaps. Procedia Manuf. 13, 972–979.

Schaeren, S., Jaquiéry, C., Heberer, M., Tolnay, M., Vercellotti, T., Martin, I., 2008. Assessment of nerve damage using a novel ultrasonic device for bone cutting. J. Oral Maxillofac. Surg. 66, 593–596.

Smith, A., Nurse, A., Graham, G., Lucas, M., 1996. Ultrasonic cutting—a fracture mechanics model. Ultrasonics 34, 197–203.

Suppipat, N., 1974. Ultrasonics in periodontics. J. Clin. Periodontol. 1, 206–213.

Thomsen, J.J., 1997. Vibrations and Stability: Order and Chaos. McCraw-Hill, London.

Trenter, S., Walmsley, A., Landini, G., Shippen, J., 2002. Assessment of the ultrasonic dental scaler insert. Med. Eng. Phys. 24, 139–144.

Umeda, M., Nakamura, K., Ueha, S., 1999. Effects of vibration stress and temperature on the characteristics of piezoelectric ceramics under high vibration amplitude levels measured by electrical transient method. Jpn. J. Appl. Phys. 38, 5581–5585.

Umeda, M., Nakamura, K., Takahashi, S., Ueha, S., 2000. An analysis of jumping and dropping phenomena of piezoelectric transducers using the electrical equivalent circuit constants at high vibration amplitude levels. Jpn. J. Appl. Phys. 39, 5623–5628.

Vang, A., 1955. Vibratory Surgical Instruments. US Patent 2714890.

Vecchio, R., MacFayden, B., Palazzo, F., 2000. History of laparoscopic surgery. Panminerva Med. 42, 87–90.

Vercellotti, T., 2000. Piezoelectric surgery in implantology: a case report—a new piezoelectric ridge expansion technique. Int. J. Periodontics Restorative Dent. 20, 359–365.

Vercellotti, T., DePaoli, S., Nevins, M., 2001. The piezoelectric bony window osteotomy and sinus membrane elevation: introduction of a new technique for simplification of the sinus augmentation procedure. Int. J. Periodontics Restorative Dent. 21, 561–567.

Volkov, M., Shepeleva, I., 1974. The use of ultrasonic instrumentation for the transection and uniting of bone tissue in orthopaedic surgery. Reconstr. Surg. Traumatol. 14, 147–152.

Vrcek, I., Starks, V., Mancini, R., Gilliland, G., 2015. Use of an ultrasonic bone curette (Sonopet) in orbital and oculoplastic surgery. Proc. (Bayl. Univ. Med. Cent.) 28 (1), 91–93 (Taylor & Francis).

Walmsley, A., Laird, W., Lumley, P., 1992. Ultrasound in dentistry. Part 2—periodontology and endodontics. J. Dent. 20, 11–17.

Watanabe, Y., Tsuda, Y., Mori, E., 1993. A longitudinal-flexural complex-mode ultrasonic high-power transducer system with one-dimensional construction. Jpn. J. Appl. Phys. 32 (5B), 2430–2434.

Wetter, L., Payne, J., Kirshenbaum, G., Podoll, E., Bachinsky, T., Way, L., 1992. The ultrasonic dissector facilitates laparoscopic cholecystectomy. Arch. Surg. 127, 1195–1199.

Wood, R.W., Loomis, A.L., 1927. The physical and biological effects of high frequency soundwaves of great intensity. Lond. Edinb. Dublin Philos. Mag. J. Sci. 4 (22), 417–436.

Zacharias, J., 2008. Role of cavitation in the phacoemulsification process. J Cataract Refract Surg 34, 846–852.

Zacharias, J., 2013. Fluid dynamics, cavitation and tip-to-tissue interaction of longitudinal and torsional ultrasound modes during phacoemulsification. J Cataract Refract Surg 39, 611–616.

Zhang, S., Li, F., 2012. High performance ferroelectric relaxor-PbTiO3 single crystals: status and perspective. J. Appl. Phys. 111, 031301.

Zhang, S., Guo, Y., Chen, Z., Li, G., et al., 2021. Proposal for a novel elliptical ultrasonic aspirator and its fundamental performance in cartilage removal. Ultrasonics 109, 106259.

Zhu, B., Guerreiro, J., Zhang, Y., Tiller, B.P., Windmill, J., 2019. Additive manufacturing (AM) capacitive acoustic and ultrasonic transducers using a commercial direct light processing (DLP) printer. IEEE Sensors J. 20 (4), 1770–1777.

Zinner, D., 1955. Recent ultrasonic dental studies including periodontia, without the use of an abrasive. J. Dent. Res. 34, 748–749.

Zocchi, M., 1992. Ultrasonic liposculpturing. Aesthetic Plast. Surg. 16, 287–298. https://www.solidstateceramics.com/. Accessed 24 July 2020.

Further reading

Cleary, R., Lucas, M., 2019. Comparison of longitudinal-mode and longitudinal-torsional mode ultrasonic bone biopsy devices. In: IEEE IUS, Kobe, Japan, 22–25 Oct 2018.

Chapter 28

Design and scale-up of sonochemical reactors for food processing and other applications

P.R. Gogate, A.B. Pandit, and A.P. Bhat
Institute of Chemical Technology, Mumbai, India

28.1 Introduction

The passage of ultrasound through a liquid medium can create cavitating conditions, provided the intensity and frequency of irradiations are suitably adjusted. Cavitation is the phenomena where bubbles or cavities form, grow, and subsequently collapse very rapidly (typically in microseconds), releasing large amounts of energy locally in the reactor (Mason, 1992; Young, 1989). Cavitation occurs simultaneously at multiple locations in the reactor and generates very high temperatures and pressures locally while, most importantly, the overall operating conditions remain ambient (Leighton, 1994; Suslick, 1990). Cavitation also generates local turbulence and intense liquid circulation in the reactor. The type of cavitation generated using the passage of ultrasound over a frequency range of 16 kHz–2 MHz is known as acoustic cavitation, and the chemical changes occurring due to cavitation induced by the passage of sound waves are commonly known as sonochemistry. The reactors are described as sonochemical reactors.

Cavitation can be further classified as either transient or stable cavitation (Leighton, 1994) depending on

- the maximum radius reached (resonant size);
- lifetime of the cavity (which decides the extent of collapse) in the liquid; and
- the pattern of cavity collapse.

The type of cavitation generated (transient or stable) usually depends on the operating parameters and constitution of the liquid medium. The type of cavitation also dictates the energy requirements for the process; hence, it is important to identify the controlling intensification mechanism for the specific application in question so that the collapse conditions can be suitably tailored, maximizing the desired effects while minimizing energy consumption.

Transient cavitation is generally obtained in gaseous or vapor-filled cavities produced at an ultrasonic intensity over 10 W/cm^2 and involves larger and quicker variation in the bubble size (maximum size reached by the cavity can be a few hundred times the initial size) with much faster collapse. In contrast, stable cavitation involves the formation of smaller bubbles with nonlinear oscillations over many acoustic cycles, and the bubble formed contains gas (and a very small amount of vapor) at ultrasonic intensity over a range of 1–3 W/cm^2. Bubble dynamics analysis can be used to determine whether transient or stable cavitation can occur for a particular set of operating conditions.

In the case of sonochemical reactors, two aspects of cavity dynamics are of prime importance:

1. The maximum size reached by the cavity before a violent collapse
2. The cavity lifetime, which can decide the zone of influence in the reactor

The maximum size reached by the cavity determines the magnitude of the pressure/temperature pulse generated at the time of collapse. The life of the cavity determines the distance traveled by the cavity from the point where it is generated and is a measure of the active volume of the reactor. The aim of the equipment designer should be to maximize both these quantities by suitably adjusting the different operating and design parameters. It should be noted that despite extensive laboratory scale research, there is a lack of industrial scale operations that involve sonochemistry. Of course, some illustrations for food processing and biotechnology applications are indeed available. The rate and effectiveness of ultrasonication are highly dependent on the frequency, power, temperature, signal types, reactor geometry, transducer selection, and physiochemical properties of liquids.

Power Ultrasonics. https://doi.org/10.1016/B978-0-12-820254-8.00001-4
Copyright © 2023 Elsevier Ltd. All rights reserved.

28.2 Modeling of cavitational reactors

Modeling and understanding bubble dynamics and the pressure field distribution can be very helpful when designing large-scale reactors. Bubble dynamics analysis can be used to predict cavitational intensity, whereas understanding pressure field distributions can help in the development of proper designs with uniform cavitational activity distribution.

The simplest form of equation governing bubble behavior under fluctuating pressure fields driven by compression and rarefaction cycles of the incident sound waves is the Rayleigh-Plesset equation (Gogate and Pandit, 2000) given as follows:

$$R\left(\frac{\mathrm{d}^2R}{\mathrm{d}t^2}\right)+\frac{3}{2}\left(\frac{\mathrm{d}R}{\mathrm{d}t}\right)^2=\frac{1}{\rho_l}\left[p_i-\frac{4\mu}{R}\left(\frac{\mathrm{d}R}{\mathrm{d}t}\right)-\frac{2\sigma}{R}-p_\infty\right] \tag{28.1}$$

where R is the instantaneous radius of the cavity varying with respect to time t, μ is the viscosity of the liquid medium, ρ_l is the density of the medium, σ is the surface tension of the medium, p_i is the pressure inside the bubble, and p_∞ is the surrounding fluctuating pressure responsible for the various stages of the cavitation phenomena.

In the case of sonochemical reactors, the time-varying pressure, p_∞ (N/m^2) is expressed as

$$p_\infty=p_o-p_a\sin(2\pi ft) \tag{28.2}$$

where p_o is the ambient pressure and p_a is the amplitude of the driving pressure, which is given by the following equation:

$$p_a=\sqrt{2I\rho_l C} \tag{28.3}$$

where C is the velocity of sound in the liquid (in water $\cong$ 1500 m/s) and I is the intensity of ultrasound (W/m^2). The fluctuating pressure field is mainly decided by the operating frequency and intensity of ultrasonic irradiations.

The Rayleigh-Plesset equation has some inherent limitations because it assumes the incompressible nature of the cavitating medium and, therefore, underpredicts cavitational intensity in terms of collapse pressure/temperature for a given set of operating parameters. There are some other equations that explain bubble dynamics considering the compressibility of the liquid and time-dependent pressure fields inside the cavitating bubble, such as the equations by Tomita and Shima or the Gilmore model (Gogate and Pandit, 2004). Differential equations based on momentum and mass balance describing the various stages of the cavitation phenomena are also available; they differ in the following important aspects related to the growth and collapse of cavitating bubbles.

1. A cavity can be considered as a single cavity in isolation or a cluster where the dynamics of the cavity is affected by the surrounding cavities.
2. The bubble or cavity interior is composed of both vapor and gas, and the ratio is dependent on the operating conditions.
3. Many types of energy losses are involved in the damped oscillations of a cavity and the degree of attenuation during the transfer of energy into the reactor.
4. Considerations of liquid phase compressibility, heat conduction, viscous energy dissipation and surface tension, diffusion, and heat transfer effects.

Neppiras (1980) wrote an excellent review highlighting different aspects of bubble dynamics. The objectives behind cavitation modeling range from explaining the sonoluminescence of cavitating bubbles to explaining the effects caused by the collapse conditions in different chemical-processing applications. The cavitational intensity can be quantified in terms of the collapse pressure and temperatures generated (pyrolysis is the controlling mechanism for driving chemical reactions) and radical generation rates induced by cavitation where free radical attack is the controlling mechanism. Various models have been proposed to quantify the chemical transformations for specific reactors and explain the link between the bubble wall motion, cavitational intensity, and chemical kinetics. For example, Sivasankar and Moholkar (2009) reported physical insights into degradation of organics by studying the bubble dynamics. Similarly, Yasui et al. (2005) reported single-bubble dynamic modeling during cavitation. Very recently, Sarac et al. (2020) studied the bubble dynamics in submerged flow tube reactors. It is important to note that the acceptability of the model as well as the solution schemes strongly depends on the assumptions used in the model equations and the approximations used in the solution schemes.

Bubble dynamic equation solutions can help quantify cavitational intensity in terms of the magnitude of collapse pressures and temperatures, as well as the number of free radicals generated at the end of cavitation events and correlate them with levels of turbulence or liquid circulation. A detailed analysis of the bubble dynamics phenomena and predictions of collapse conditions are beyond the scope of this chapter. The work of Gogate and Pandit (2004) is recommended for a deeper understanding of these aspects.

28.3 Understanding cavitational activity

Cavitational activity distribution in the case of sonochemical reactors, especially in large-scale operations, is a very important issue, and if reactors are not designed

properly, there can be significant dead zones in the reactor, affecting its overall output. The objective of the efficient scale-up of sonochemical reactors is the reproducibility of cavitational activity in the large-scale design and associated improvement in the final product quality or attainment of the desired objectives from the reactor. It is necessary to characterize cavitational activity in sonochemical reactors to optimize the design parameters. The available methods can be classified based on the experimental techniques based on actual measurements (more suited to understanding the performance of existing reactors) and theoretical simulation-based techniques for predicting cavitational activity distribution (this can also be effectively applied in the design and optimization of new reactors).

Experimental techniques are based on the actual measurements of physical or chemical changes and can be further classified based on a quantification of the primary and secondary effects. The effects generated at the same time as the bubble collapse are called primary effects; these can be temperature/pressure pulse generated by the collapse, generation of free radicals (in the cavity), and microcirculation in the vicinity of bubble. Secondary effects are those generated as a result of the primary effects of the bubble collapse. Some examples include oxidation reactions, intensified mass transfer coefficients, and enhanced electrochemical effects.

28.3.1 Experimental techniques based on primary effects

1. Pressure intensity generated by cavitation in a liquid medium can be easily quantified using a hydrophone (Kanthale et al., 2003; Kumar et al., 2007). Hydrophones are electronic devices that measure the acoustic pressure intensity in the liquid medium with good spatial resolution, sensitivity, excellent directional characteristics (omnidirectional in both the axial and radial planes), and desired bandwidth. Different types of hydrophones available are piezoelectric and optical fiber-tip hydrophones. Some of the difficulties associated with the measurement of pressure intensity using hydrophones include disturbance induced by the external hydrophone; sluggish response; need for frequent recalibration, and measurement of total pressure intensity irrespective of the type of cavitation generated in the system.
2. The change in local temperature can be measured by using a thermocouple or thermistor at any position in the reactor with the objective of understanding the distribution. The change in local temperature is usually due to energy transfer by absorption of sound waves and/or energy transferred from the collapsing cavities in the medium. This energy transfer results in an increase in the local temperature of the liquid medium, which can also be used to provide quantitative information about the local cavitational activity. The anticipated difficulties in the use of temperature measurements for understanding local cavitational activity distribution include sensor damage caused by collapsing bubbles, low reproducibility and sensitivity, as well as the need for highly sensitive measuring instruments for discrete measurements.

28.3.2 Experimental techniques based on secondary effects

1. In the case of the KI oxidation method (Kanthale et al., 2003), when an aqueous solution of KI is irradiated, oxidation occurs and I^- ions are oxidized to give I_2^-. The excess I^- ions present in the solution react with I_2 to form I_3^-. The amounts of I_3^- ions can be quantified using an ultraviolet spectrophotometer at a wavelength in the range of 350–360 nm.
2. Fricke dosimetry (Feng et al., 2002) is based on the reaction of ferrous sulfate and most commonly, hydrogen peroxide. When sound waves pass through Fricke solution, Fe^{2+} ions in the solution are oxidized to Fe^{3+} ions and the amount of Fe^{3+} ions can be quantified using an ultraviolet spectrophotometer at a wavelength of 304 nm.
3. Salicylic acid dosimetry (Chakinala et al., 2007) can be a direct measurement of the rate of hydroxyl radical production. Dosimetry based on salicylic acid is very specific to cavitational effects; the reaction products are obtained exclusively by the hydroxyl radical oxidation reaction.
4. In another technique based on monitoring conductivity change caused by the formation of acids, ultrasound is passed through a known amount of water under a given set of operating conditions. Water contains dissolved N_2 and O_2 gas, which only under the drastic conditions of high temperature and pressure caused by cavitation react to ultimately form HNO_3 and HNO_2. The formation of acids results in a change in electrical conductivity of the water, which can be used to quantify the cavitational activity because the change in conductivity is dependent on the cavitational intensity.
5. When an aqueous solution of nonfluorescent terephthatic acid (TA) is subjected to ultrasonic irradiation, the reaction of generated hydroxyl radicals ($OH^•$) with TA gives highly fluorescent hydroxy-TA, which can be measured using a fluorescence spectrophotometer at excitation and emission wavelengths of 310 and 426 nm, respectively. It is also reported that IrC_6^- can be used as a potent oxidant to enhance the yield of hydroxy-TA (Feng et al., 2002).

6. The last chemical method is based on monitoring the intensity of sonochemiluminescence (SCL), which identifies the cavitationally active zone (Hu et al., 2008). Luminol (3-aminophthalhydrazide) is widely used as an SCL reagent, and the intensity of luminescence is proportional to the intensity of cavitation (number of collapses). When an aqueous solution of luminol is irradiated by ultrasound under alkaline conditions, it results in the emission of blue light. This property of luminol can be used to quantify cavitational activity. SCL images can be captured easily by a digital camera. The main problem associated with this chemical method is that cavitational activity is measured in terms of emissions due to the collapse of mainly transient cavitation bubbles and cavitational activity generated by oscillating bubbles is not considered, even though this can contribute to the overall effects depending on the specific application in question.
7. The physical methods typically work because of the mechanical or physical effects of cavitation in terms of turbulence, shear, and liquid microcirculation. A simple physical method can be based on the phenomena of aluminum foil erosion (Avvaru and Pandit, 2009). In this method, aluminum foil is typically kept parallel to the direction of the location of transducers, and the cavitational activity is measured qualitatively in terms of the erosion pattern obtained on the aluminum foil. A high-resolution digital camera can be used to capture the erosion patterns; this method is more suitable for low-frequency operations where physical effects are significant.
8. The measurement of the solid-liquid mass transfer coefficient (to or from an electrode) can also be an efficient approach for understanding cavitational activity. The use of redox agent $Fe(CN)_6^{-3}/Fe(CN)_6^{-4}$ results in an enhanced the mass transfer rate and can be used for greater sensitivity (Birkin et al., 2003).
9. Hallez et al. (2016) developed a specific sonoelectrochemical cell for the study of cavitational activity. Three electrode setups were used with ferrocene and tetramethylammonium tetrafluoroborate as the electrolytes. The use of ionic liquids leads to a nonvapor media, where cavitation can be controlled by gas pressure. This study demonstrated that it is possible to estimate individual contribution of cavitation activity and acoustic energy to mass transfer. The control and quantification of cavitation demonstrated by the study can be possibly used in various applications.
10. Particle image velocimetry (PIV) is a flow velocity measurement technique used extensively to study fluid dynamics. It is based on the assumption that the cavitation bubble can act as a tracer. The reactor media is seeded with fluorescent tracers (Kumar et al., 2007; Lanier et al., 2003). Boldo et al. (2004) reported the use of the PIV measurement approach to determine liquid circulation velocity and vibration amplitude using the time-averaging holography method. The results showed that maximum liquid velocity is observed near the irradiating surface, indicating that maximum cavitational effects are also obtained closer to the vibrating surface. The extent of liquid circulation and mixing time measurements can be used to explain the extent of uniformity in the cavitational activity in the reactor.
11. Another physical method for mapping cavitational activity is monitoring the acoustic emission spectra (Avvaru and Pandit, 2009; Hodnett et al., 2004) as the cavitating bubbles act as secondary acoustic sources whose emission spectra indicate the dynamics of the cavitation process. A typical spectrum consists of a fundamental frequency component produced by the direct driving frequency of the ultrasound device and a series of harmonics (integer multiples of the driving frequency) and subharmonics (fractional multiples of driving frequency) of the fundamental frequency component. In addition to the sensor, a spectrum analyzer is required to record the spectral content of the sensor output signals. The acoustic emission patterns can be monitored in real time over a specific fluid volume in the reactor; therefore, this method shows potential in optimizing, controlling, and scaling-up processes.
12. Tzanakis et al. (2016b) developed an advanced cavitometer for measuring acoustic emissions and pressure in liquid aluminum under irradiation. The cavitometer performs through a tungsten probe over a piezosensing element. The broadband signal (relating to the acoustic signals) collected by the cavitometer is displayed by appropriate instrumentation software. Advanced cavitometer has also been tested for its accuracy and reported to be quite successful in providing information on the cavitational activity distribution (Tzanakis et al., 2016a).

28.3.3 Theoretical techniques for cavitation prediction

After reviewing all the approaches based on experimental measurements, it is important to understand that determining variation in cavitational activity by experimental investigation is not always feasible or recommended on a larger scale because the experimental technique is usually quite expensive and time-consuming. Also, the medium is disturbed by the presence of external instruments such as thermocouples, hydrophones, aluminum foil, or test tubes. Therefore, a realistic picture of the cavitational activity distribution may not be obtained. Finally, the results may not

be reproducible because of the stochastic nature of cavitation phenomena.

Theoretical prediction of cavitational activity in terms of pressure fields provides an effective alternative to experimental mapping techniques. Theoretical predictions provide a particularly efficient way of achieving good reactor design with uniform activity (Klima et al., 2007; Yasui et al., 2007); a number of designs can be simulated with varying operating parameters. Simulations can be used to characterize the pressure field distribution based on the solutions of the wave propagation equations. This approach can help optimize maximum or uniform cavitational activity in the reactor. The modeling studies can also be extended to the quantification of other useful parameters such as temperature distribution, free radical concentrations, and mass transfer coefficients, which can be controlling parameters depending on the type of application.

1. The earliest works in the area of theoretical predictions of cavitational activity have been reported by Dahnke and Keil (1998) and Dahnke et al. (1999), investigating the variation in cavitational activity in different sonochemical reactors. The predictions were based on the solution of Helmholtz and Kirchhoff's integral equation with homogenous and inhomogeneous spatial bubble distribution. It was predicted that Cavitational activity is at its maximum closest to the transducer and decreases exponentially away from the transducer, which matches experimental results (Chivate and Pandit, 1995; Kanthale et al., 2003). Also, it was elucidated that the influence of the bubble fraction on the distribution of the pressure field can be neglected, and damping effects are more dominant for the homogenous distribution of bubbles compared with the inhomogeneous distribution, which is more realistically observed in actual practice.
2. Saez et al. (2005) used numerical simulations to characterize ultrasonic field propagation and obtain the spatial distribution of the mechanical effects. The model used in the work was based on the assumption of linear wave propagation in a homogeneous media, and the solution of the Helmholtz equation using a finite element method with an optimized mesh size was used for the predictions. Theoretical results matched the trends obtained using different experimental mapping techniques such as calorimetry, aluminum foil erosion, and the use of thermal probes.
3. Klima et al. (2007) used a similar approach for optimizing the geometry of a sonochemical reactor, and it was shown that appropriate selection of the reactor geometry in terms of its dimensions, liquid volume, and length of immersion of the ultrasonic horn in the reactor can result in much better uniform cavitational activity with intensification compared with the conventional approach. The intensification can possibly be attributed to multiple reflections of the incident sound waves from the reactor walls and liquid surface, leading to a resonance effect, that can be obtained based on using different positions of horn in the reactor.
4. Yasui et al. (2007) also used the solution of the wave equation based on the finite element method to characterize the acoustic field distribution, with contribution of the vibrations occurring because of the reactor wall. The effect of different types of reactor walls or the construction material of the sonochemical reactor has been evaluated. The work also contributes significantly to an understanding of the dependence of the attenuation coefficient as a result of the liquid medium on the contribution of the vibrations from the wall. As the attenuation coefficient increases, the influence of the acoustic emissions from the vibrating wall becomes smaller, and for very low attenuation coefficients, the acoustic field in the reactor is very complex because of the strong acoustic emission or reflection from the wall. The work clearly establishes the importance of selecting appropriate construction material for the reactor.
5. Sutkar et al. (2010) predicted cavitational activity in terms of pressure field distribution by solving the wave equation using Comsol multiphysics software in two different geometries of sonochemical reactors. It has been reported that cavitational activity in the case of the ultrasonic horn is concentrated near the transducer surface and is much less uniform compared with an ultrasonic bath reactor with a large longitudinally vibrating transducer. The work has clearly established an approach for predicting cavitational activity and analyzing the importance of the reactor geometry.
6. Louisnard derivatized a reduced mode that is based on nonlinear Caflish model that claims to open ways to more realistic simulations and calculation of cavitation dynamics (Louisnard, 2012). The report remodels the nonlinear Caflish equations into equations involving mechanical energy balances thereby quantifying the functions for bubble dynamics. The model calculates energy dissipation and further produces the harmonic components of acoustic field. The work also presented models on primary Bjerknes forces and 2D simulations for conventional cavitation configurations.
7. Recently, Louisnard also reported that acoustic streaming can be successfully predicted by standard turbulent flow calculations (Louisnard, 2017). With experiments combining acoustic streaming and forced flow in a duct, the report demonstrated a significant agreement of the experimental results with the reproduced modeled results on cavitation effects on the wall.

Overall, the magnitude of the cavitational intensity is not the only factor in deciding the efficacy of the reactors; the

cavitational activity distribution in the reactor is equally important. The final efficacy of the reactor is determined by the cumulative effects distributed throughout the reactor; consequently, it is very important to have a design that allows uniform cavitational activity above the minimum activation energies required for the specific application in question. Theoretical analysis can be a very effective tool when designing new reactors, but the trends should be well supported using experimental methodologies applied to existing reactors.

28.4 Types of reactors

For the success of large-scale configurations of sonochemical reactors, efficient reactor design is key, and the required information comes from diverse fields: Chemical engineering, Material science, and Acoustics. Different sonochemical reactor designs are discussed in this section, with some comments on their suitability for a specific scale of operation.

It is important to briefly understand the basic aspects of the transducer, a device used to transfer the supplied electrical energy into the liquid medium as mechanical energy in the form of vibrations finally occurring as sound energy. The sound energy dissipation into the medium creates the cavitation field, which, coupled with fluid-flow pattern existing in the reactor, determines the degree of expected effects. Transducers typically operate at a fixed frequency of irradiation but at variable power dissipation and area of irradiation. The three main types of transducers are liquid-driven, gas-driven, and electromechanical.

Liquid-driven transducers and gas-driven transducers do not have any significant chemical applications. Electromechanical transducers are the most versatile and widely used. The two main types of electromechanical transducers are the piezoelectric and the magnetostrictive transducers. Piezoelectric transducers are constructed using a piezoelectric material, which expands and contracts in an oscillating electric field, producing sound waves (pressure waves) from the electric signal. Magnetostrictive transducers are constructed from materials such as nickel alloys, which expand and contract in an alternating magnetic field.

28.4.1 Probe systems

Probe systems, also described as the ultrasonic horn, are most commonly used for characterization experiments at a laboratory-scale of operation. These are typically immersion-type reactors with the transducer directly in contact with the liquid medium. The important advantages and disadvantages of using a horn system are summarized below:

Advantages:

- Ability to deliver large amounts of power through a small transducer area to a small volume of reaction mixture in the vicinity of the probe. Very high intensities are generated close to the horn tip (Chivate and Pandit, 1995; Gogate et al., 2002).
- Irradiation intensities as high as several hundred Watts per square centimeter can easily be achieved using the probe systems.
- Acoustic streaming from the transducer may be powerful to provide efficient bulk mixing in a small volume. It is also important to note that in larger volumes, additional mixing in the form of mechanical agitation may be required.

Disadvantages:

- The scaling-up prospects for conventional horn-type systems are not expected to be very good because they cannot transmit the acoustic energy effectively into a large volume and contain significant dead zones. Typically the intensity decreases exponentially away from the horn and vanishes at a distance of as low as 2–5 cm restricting the zone of influence of ultrasonic horn.
- Also, it is important to note that continuous operation at high-power dissipation can lead to the erosion and pitting of the horn tip, which may contaminate the reaction medium.
- The design is not recommended for reaction mixtures with very high viscosity because this can cause the probe to stall.

28.4.2 Ultrasonic baths

Ultrasonic baths typically have cleaning tank-type configurations and have the transducers (single or multiple) attached to the bottom of the tank (Romdhane et al., 1995). The main features of ultrasonic bath in terms of the offered advantages and disadvantages are given as follows.

Advantages:

- In this type of equipment, the active zone is restricted to a plane just above the transducers and the use of multiple transducers allows a better distribution of cavitational activity in the reactor.
- In this case, to increase the active zones existing in the reactor, the position of the transducers can easily be modified so that the wave patterns generated by the individual transducers overlap, resulting in uniform and increased cavitational activity.

- The reaction vessel can be immersed in the coupling fluid contained in the bath (indirect sonication), or the bath itself can be used as the vessel. The use of coupling fluid allows better control of the activity in applications where there is a need to protect the materials, for example, in the case of enzymatic reactions, enzymes need to be protected.

Disadvantages:

- Using bath as the vessel may require additional mechanical agitation for uniform mixing because the liquid circulations induced by cavitating conditions cannot result in sufficient mixing.
- In the case of direct sonication, reactor walls would be exposed to the reaction mixture, making them susceptible to corrosion.
- Ultrasonic power dissipated into the system is low compared with other ultrasonic systems, such as a probe.
- The location of the reactant sample in the bath and the configuration of the reactor would be critical in determining the final effects because these play a major role in deciding the extent of attenuation.
- The coupling fluid surrounding the reaction vessel(s) will be heated because of the transfer of ultrasonic energy, making the maintenance of isothermal conditions difficult. Use of water as the coupling fluid limits the upper range for operating temperature below 100°C, but a change in the medium (high-boiling liquids to accommodate for higher temperatures) also decreases the transfer of energy from the transducer to the reaction vessel because of intensified attenuation attributed to differences in density or viscosity.

28.4.3 Flow systems

Flow systems can be based on either the use of many probes or the use of bath-type reactors operated in a sequential manner. The main features of the flow cell in terms of advantages and disadvantages include:

Advantages:

- A simple flow cell using an inbuilt probe system arranged in sequential manner is an excellent way to process relatively large volumes with a sufficient degree of cavitational intensity. One of the simplest approaches is to couple the probe transducer into a flow pipe using a T section (Nickel and Neis, 2007). A number of such transducers can be used to extend treatment times (Figure 28.1).
- For larger-scale operations and those involving and requiring high-intensity ultrasound, the sonic horn is best used as part of a flow loop outside of the main reactor. Temperature control can be provided through the circulating reaction mixture using an external heat exchanger.
- Flow cells offer advantage of continuous processing which is important for large-scale processing with lower capital costs.

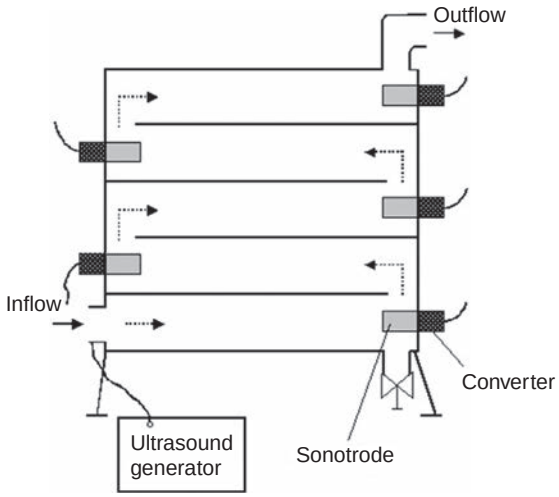


FIGURE 28.1 Schematic representation of flow systems based on ultrasonic horn (Nickel and Neis, 2007).

Disadvantages:

- The reactor, however, has the general disadvantage of the probe system. The configuration is not suitable for either very viscous reaction media or particulate systems due to the pumps used.
- Using T sections and use of several probes inserted through the walls of a pipe may suffer from problems associated with individual flow cells such as surface erosion or stalling of probes in highly viscous media but the system continues to function even if one or two probe units fail.
- A major disadvantage of such systems is that the sealing of the reactor or probe joints, particularly in high-pressure reactions, is a crucial factor because the small radial vibrations associated with the probe can lead to frequent leakages.

In the case of baths, the reacting liquids can be fed continuously into an ultrasonic tank with an overflow into the next process step, yielding a new configuration for the flow system. Such treatment can easily be intensified by connecting a number of such ultrasonic tanks in line, and the number of tanks depends on the irradiation time required for the application and the processing volumes.

Continuous systems with large numbers of transducers can easily be designed to give a uniform acoustic pattern above the required threshold throughout the working volume, based on different geometric configurations. There are various possible arrangements as follows:

- Tubular reactors with both ends provided with transducers or one end with a transducer and the other with a reflector (Gonze et al., 1998).
- Parallel plate reactors and flatbed reactors (Figure 28.2), with each plate irradiated with either the same or different frequencies (Gogate et al., 2001; Thoma et al., 1997).
- Transducers located on the sides of a hexagon/cylinder (Figure 28.3) to give uniform cavitational activity distribution (Gogate et al., 2003a).

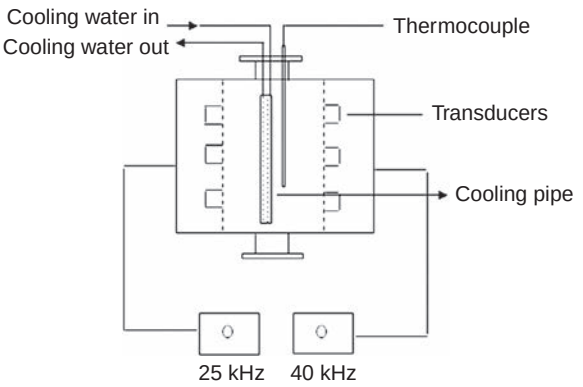


FIGURE 28.2 Schematic representation of a dual-frequency flow cell (parallel plate reactors) (Gogate et al., 2001).

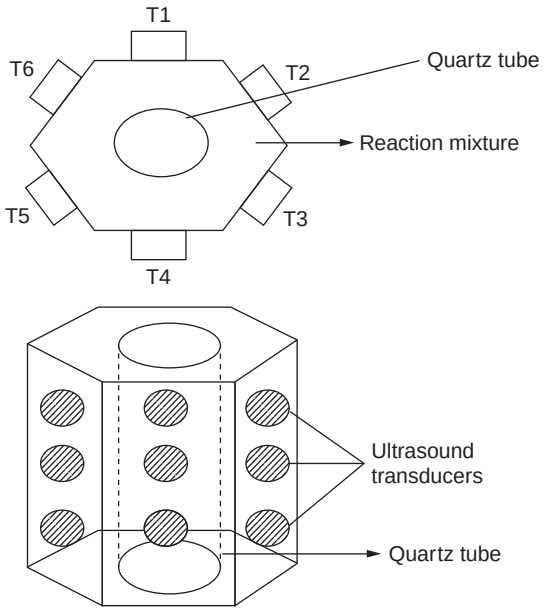


FIGURE 28.3 Schematic representation of triple-frequency hexagonal flow cell with a capacity of 7.5 L (Quartz tube for possible simultaneous UV irradiations) (Gogate et al., 2003a).

28.5 Developments in reactor design

We now present some of the novel combinations and modifications in the reactor configurations designed and successfully operated for intensified processing in Table 28.1. The table initially reports the data on the modified versions resulting from three basic types of ultrasonication systems. Further, the table reports published data on the batch processes that could also be operated in continuous manner, continuous industrially applicable processes, and very recently published novel rectors. The table also presents brief overview of the different studies highlighting the operating conditions and the main inferences from the reported study. From the table, it is evident that the use of multiple transducers enables uniform cavitational activity to be achieved with much larger active volumes as well as gives the flexibility to have multiple frequency irradiations. It is important to note here that the acoustic field distribution in the reactors, and hence, the overall cavitational activity distribution depends strongly on the geometric parameters, such as ratio of the diameter of the immersion transducer to reactor diameter, number of transducers, reactor geometry, liquid height, and position of the transducers, as well as on operating parameters such as frequency and intensity of the irradiation. Although not much data comparing the different reactors described earlier in terms of cavitational activity distribution using specific reactions are available, multiple transducer flow cells or reactors with large irradiation area typically yield excellent distribution of cavitational activity and are recommended for large-scale operations.

28.6 Selecting operating parameters

The intensification obtained for any physical or chemical processing application using sonochemical reactors depends strongly on the operating and geometric parameters of the equipment. The important parameters in the case of sonochemical reactors are the frequency and intensity of the irradiation, along with the temperature, signal type, geometrical arrangement of the transducers, the reactor geometry, and the physicochemical properties of the liquid phase. Before making actual recommendations for these parameters, it is important to highlight that the availability of transducers capable of performing efficiently at high-power dissipation is a significant problem that has restricted the application of sonochemical reactors on a commercial scale. The work of Gallego-Juárez et al. (2010) presents the difficulties in the effective use of piezoelectric transducers in large-scale operations, namely, lower power rating, limited dimensions, and altered performance due

TABLE 28.1 Development of novel reactor designs

Reactor	Operating conditions	Geometric/transducer details	Novelty/inferences	Reference
Batch reactors				
Modified conventional horn (Figure 28.4)	$f=20$ kHz; $P=1000$ W	Horn with cylindrical reactor	Temperature controlled below 40°C and continuous transducer usage. Possible non-uniformities in the cavitational activity distribution were eliminated by the mechanical rotation of the cylindrical reactor and linear oscillatory motion in a vertical direction.	Cravotto et al. (2005)
Barbell horn (Figure 28.5)	$f=20$ kHz; $P=1200$ W	Horn with larger tip of 12.7 mm	Barbell shape allows amplification at the output and an efficient scale-up for high-amplitude operations reducing the damage to horns.	Peshkovsky and Bystryak (2014)
Longitudinal horn	$f=36$ kHz; $P=150$ W	8 L working Volume, longitudinally vibrating horn (diameter of 3 cm and length of 24 cm)	66% energy efficiency as compared to typical 5%–20% for conventional horn (Table 28.2).	Bhirud et al. (2004)
Longitudinal horn (Figure 28.6)	$f=36$ kHz; $P=150$ W	8 L working Volume, longitudinally vibrating horn (diameter of 3 cm and length of 24 cm)	Quantification of cavitational activity revealed that cavitational activity is almost uniform in both directions, with a marginal variation in the range of 5%–20% compared with about 80%–400% variation in the conventional designs.	Kumar et al. (2007)
Reactors using reflection of waves (Figure 28.7)	–	Reactor with cylindrical circular geometry and aluminum cap at the top.	Effectively used the reflection and focusing of sound waves to enhance the reactors' performance. Proper reflection patterns were obtained in a circular geometry by allowing incident sound waves to enter sideways, whereas proper focusing was obtained in the cylindrical reactor by selecting an aluminum cap at the top of the reactor. Much higher cavitational activity as compared to conventional design.	Seymour et al. (1997)
Reactor with altered transducer location	$f=750$, 1000 kHz	Two transducers with diameter as 20 and 50 mm. One of the transducers was positioned at the bottom located eccentrically, while the other was located on the periphery of the reactor wall.	Good mixing characteristics. Because of the specific arrangement of transducers, acoustic streaming is generated both vertically and radially. The distance between the transducers can be optimized to significantly reduce the mixing time compared with the conventional approach. Suitable for large scale.	Suri et al. (2002)

Continued

TABLE 28.1 Development of novel reactor designs—cont'd

Reactor	Operating conditions	Geometric/transducer details	Novelty/inferences	Reference
Cavitation intensifying bags (CIB) (Figure 28.8)	$f = 37$, 80 kHz; 100% Amplitude	CIBs are plastic bags (11–15 mL) that contain indentations (pits) in their inner surfaces with a diameter of 100 to 500 μm and depth of 100–200 μm that trap gas bubbles and generate cavities in large quantities upon sonication	CIBs were 60 times more effective than conventional systems for making emulsions with low droplet size of up to 0.2 μm. For the scale-up, bags can be made bigger to accommodate more pits per unit area. More uniform cavitational activities were observed as compared to conventional horn system. It is important to note that pits cannot be increased indefinitely due to the negative effect of clustering of microbubbles.	van Zwieten et al. (2017)
Batch and continuous reactors				
Hexagonal flow cell (Figure 28.3)	f = 20 kHz, 30 kHz, 50 kHz, P = 900 W	7.5 L. 18 transducers (3 on each face of the hexagon), and 7 different frequency operating combinations (single-, dual-, and triple-frequency mode).	Higher cavitational yield and uniform distribution of cavitational activity in the bulk of the liquid are obtained with only a 10%–30% variation compared with 80%–400% in the conventional horn-type reactor configuration.	Gogate et al. (2003a)
Cylindrical flow reactor (Figure 28.9)	$f = 25$ kHz; $P = 600$ W	Cylindrical reactor of 6.5 L capacity. 30 piezoelectric transducers arranged on the outer cylindrical periphery.	Significant cavitational activity was reported up to a power of 500 W.	Hodnett et al. (2017)
Sonitube reactor (Figure 28.10)	$f = 20$ kHz; $P = 2000$ W	The geometrical configuration is a cylindrical stainless-steel tube.	The important feature of this reactor configuration is that it can be used in both continuous (by passing fluid through resonators) and batch (by submerging the emitter surface in the container) modes of operation. Uniform cavitational activity.	Faid et al. (1998)
Continuous reactors				
Sonitube reactor	$f = 35$ kHz	The configuration is a cylindrical stainless-steel tube with a 2-cm internal diameter and 26-cm length.	It has been reported that the tube-type configuration offers advantages such as uniform acoustic field and a higher cavitationally active volume. Comparison of the effectiveness of a similar configuration with a conventional horn and cup horn revealed much better homogeneity for the cavitational activity quantified in terms of the mass transfer coefficients.	Entezari et al. (2003)

TABLE 28.1 Development of novel reactor designs—cont'd

Reactor	Operating conditions	Geometric/transducer details	Novelty/inferences	Reference
3-Stage continuous flow reactor (Figure 28.11)	$f = 500$ kHz; $P = 100$ W	Cylindrical geometry was subdivided into three units, each interconnected by a polyvinyl chloride pipe, ensuring the desired direction to the fluid. Each unit was equipped with a piezoelectric disk (titanate-lead zirconate, 40-mm diameter).	The effect of flow rate, operating volume, and power dissipation on the conversion of pentachlorophenol in each unit has been quantified, and it has been observed that as the flow rate increases (reduction in the residence time) at a constant power dissipation rate, the extent of conversion decreases.	Gondrexon et al. (1999)
Ultrasonic airlift loop reactor (Figure 28.12)	$f = 40$ kHz; $P = 250$ W	Vertical cylindrical	A quantitative comparison of the degradation of dimethoate using combined ultrasound and ozone and both ozone and ultrasound individually indicated that 90% degradation was observed in the ultrasonically assisted airlift loop reactor compared with 21% and 14.5% for only ozone and ultrasound alone, respectively.	Liu et al. (2008)
Pilot-scale continuous reactor (Figure 28.1)	$f = 31$ kHz; $P = 3600$ W	The sonoreactor used in the work was a typical vessel with piezoceramic flat transducers fixed at each of the four sidewalls. The reactor volume was 1.3 L; acoustic intensities can be varied over a range of 5–18 W/cm^2.	Based on the lab findings, a full-scale design for sludge treatment applications has been successfully developed and operated. The total capacity of the full-scale reactor is 29 L, and it is equipped with five 20-kHz sonotrodes. Each sonotrode is supplied with a 2-kW generator. The intensity can be adjusted over a range from 25 to 50 W/cm^2.	Nickel and Neis (2007)
Cylindrical continuous sonoreactor	Two models with varying f over the range of 39–45 kHz; $P = 5$ kW or 50 kW	1 L treatment volume sonoreactor system (SR-31, 75 mm tube); 12 prismatic transducers; second model is SR-42, 100 mm tube suitable for large scale application	The new cylindrical sonoreactor design does not contaminate the processed liquids with erosion products because the cavitation zone is maintained away from the tube wall. The processing capacity of the largest models can be up to several tons per hour, depending on the cavitation energy per unit volume required to produce the desired process enhancement.	Dion (2009)
Large-scale rectangular sonoreactor (Figure 28.13)	$f = 35$, 72, 110, 170 kHz; $P = 400$ W	Dimensions of 1.2 m × 0.6 m × 0.4 m and a working volume of 250 L. The reactor was irradiated using a transducer module consisting of nine transducers located at the center of the sidewall.	The reactor's performance was evaluated by quantifying the variation in power dissipation, sonochemical efficiency, and damping factor for water and potassium iodide solution, and was reported to be better compared with conventional designs.	Son et al. (2009)

Continued

TABLE 28.1 Development of novel reactor designs—cont'd

Reactor	Operating conditions	Geometric/transducer details	Novelty/inferences	Reference
Large-scale rectangular sonoreactor (Figure 28.14)	$f = 500$ kHz; $P = 620$ W	Dimensions of 0.508 m × 0.508 m × 0.672 m and a maximum operating capacity of 112 L. The design is based on the use of 12 transducers (6 in each module). Liquid height varied for understanding the effect.	The analysis of variation in cavitational activity due to height indicated better results compared with conventional designs with lower reduction in cavitational intensity. Despite the ability to operate on a large scale, the efficacy of these reactors has not yet been checked for any industrially important transformations.	Asakura et al. (2008a,b)
Commercial sonochemical reactor	–	800 L as working volume.	Commercially applied.	Vinatoru (2001)
Commercial sonochemical reactor	$f = 20$ kHz; $P = 14$–160 W/cm^2	Concentrator horn. 4-ton capacity.	Commercially applied.	Horst et al. (1996)
Recently reported continuous reactors				
Rectangular continuous flow (Figure 28.15)	$f = 15$, 25, 35, 40 kHz; $P = 500$ W	US reactor with four individual ultrasonic reactors each, with different frequencies. Volume of 22 L.	The reactor was designed such that each of the transducer was at an eccentric distance equal to the radial distance of the next transducer. US propagation was supposed to be perpendicular to oil flow. The reactor was demonstrated to be effective and practical.	Zou and Chai (2017)
Novel ultrasonication system (Figure 28.16)	$f = 25$ kHz; $P = 2000$ W	The US tube length of 1250 mm was used. Both series and parallel systems were used.	The operation led to significant methane yield and COD reduction as compared to conventional systems. The entire system was low maintenance, but the power consumption was higher than other ultrasonic systems discussed.	Koch et al. (2017)
US flatbed reactor (Figure 28.17)	$f = 25$ kHz; $P = 300$ W	The reactor had a rectangular cross-section, length of 1000 mm, width of 80 mm, and height of 40 mm. It was installed with six US transducers mounted on top and bottom.	A recirculation loop with pump was used for continuous flow. The reactor performed well in low energy input conditions to yield a total energy positive operation for digestion of sludge. Demonstrates promise for scale-up and industrialization.	Lippert et al. (2018)
High-intensity US tubular reactor (HUTR) (Figure 28.18)	$f = 22$ kHz; $P = 100$–300 W	Transducers are located in the center of the rector for uniform ultrasonication.	Synthesized food-grade CNC-stabilized palm olein pickering emulsions stable for up to 30 days.	Low et al. (2019)
Multiprobe continuous reactor (Figure 28.19)	$f = 20$ kHz; $P = 400$ W	The reactor was cylindrical with ultrasonic horns of 20 kHz frequency and tip diameter as 12 mm.	The study aims at examining the effect of injection techniques, nozzle diameters and ultrasonic power, and the number of probes on the performance, thereby assisting in the scale-up of the process. CFD was also employed to understand the hydrodynamics of the reactor.	Rahimi et al. (2019)

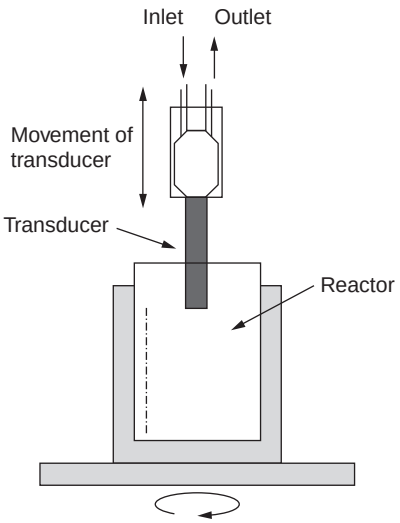


FIGURE 28.4 Modified sonochemical reactor with mechanical rotations (Cravotto et al., 2005).

to variations in the operating voltage. The aim of the equipment designer should be to maximize cavity life and the number of cavitation events as well as cavity size reached during the growth phase, which can essentially be achieved by adjusting the different operating/geometric parameters.

28.6.1 Selection of frequency of irradiation

The selection of irradiation frequency for any physicochemical transformation predominantly depends on the controlling mechanism (i.e., physical or chemical) because cavitation effects are strongly dependent on the operating frequency. Typically, lower frequency (in the range of 10–100 kHz) is recommended for applications where intense physical effects are required. Some examples of such applications are microbial cell disruption to release intracellular enzymes, textile processing, polymer degradation, and extraction of natural products. High-frequency operation (in the range of a few hundred kilohertz to 1 MHz) is recommended when chemical effects are principally required, such as for the degradation of various compounds in wastewater treatment and chemical synthesis. Disadvantages of high-frequency sonochemical irradiations include erosion of transducer surfaces and high-power requirement especially at larger scales of operation.

Multiple-frequency operation (combination of the same or different frequencies) also has been reported (Prabhu et al., 2004; Servant et al., 2003) to enhance the overall uniformity of distribution of cavitational activity and generating intensities suitable for chemical processing applications at higher energy efficiencies. More important, multiple frequency operations allow the use of lower frequency irradiations (e.g., a combination of 20, 30, and 50 kHz, as demonstrated in the work of Gogate et al., 2003a) even

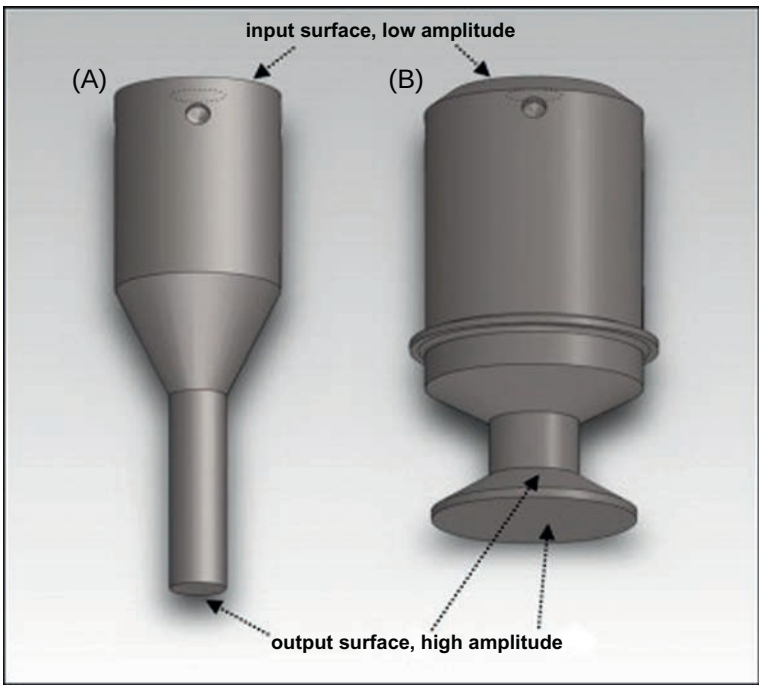


FIGURE 28.5 Barbell type horn as a modification of conventional horn (A) conventional horn (CH); (B) half-wave Barbell Horn (HBH). HBH gives similar amplitude amplification as CH, at the same time provides much higher cumulative output surface area based on two high-amplitude radiating zones (Peshkovsky and Bystryak, 2014).

TABLE 28.2 Cavitational yield obtained in different sonochemical reactors

S. no.	Reactor	Cavitational yield (mol/W)
1	Ultrasonic horn	0.0005
2	Ultrasonic bath	0.01
3	Dual-frequency flow cell	0.011
4	Triple-frequency flow cell	0.018
5	Radially vibrating reactor	0.077

Source: Bhirud et al. (2004).

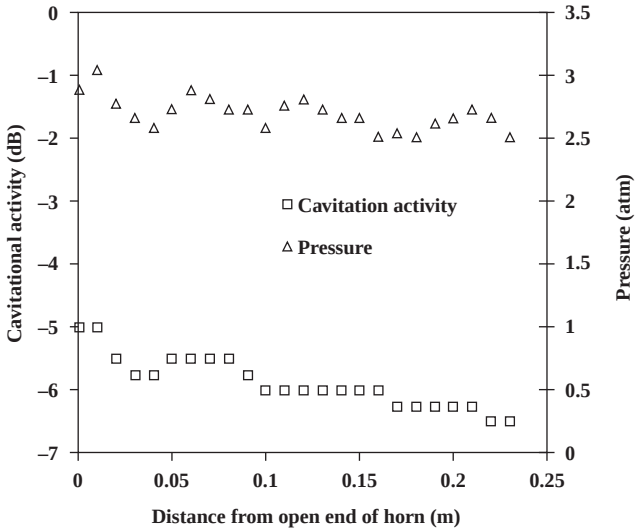


FIGURE 28.6 Variation in the cavitational activity and local pressure along the length of the horn (Kumar et al., 2007).

for chemical processing applications, avoiding the common disadvantages associated with higher frequency irradiations. Based on the results from multiple reports, it can be said that multiple-frequency operations generally lead to higher intensity of bubble collapse and cavitational intensity (Wood et al., 2017). Cavitational medium is greatly disturbed by combination of frequency leading to higher intensity collapse. Primary and secondary Bjerkens forces during combinational-frequency operation are responsible for stronger bubble-bubble and bubble-sound interactions in the liquid medium. Multiple frequency operation also leads to an increased sonoluminescence intensity that is not possible during single-frequency operation.

28.6.2 Selection of power dissipation levels

Other important operating factors affecting cavitational effects are the amount of energy entering the bulk of liquid as well as the area of transducers used for the said transfer of energy, which determines the irradiation intensity. Bubble dynamics studies indicate that the bubble size, number of bubbles, maximum lifetime, collapse pressure, and temperature rise are a complex function of the power dissipation rate, and hence, it is critically important to select the correct power dissipation levels. In the proper development of continuous sonochemical reactors, it is important to understand hydrodynamic behavior, including mixing time, which depends on the power density. Additionally, the rise in temperature is also a function of power dissipation which could lead to changes in gas solubility and vapor pressure, affecting the cavitational intensity and collapse of cavities. In addition to choosing the power rating for the equipment, it is also critically important to quantify the actual power dissipated in the bulk of liquid and thereby available to create cavitating conditions as compared to the supplied electric power to the bulk of liquid.

It is also important to optimize the power input by considering the effect of reaction volume or height of the liquid medium in the reactor and transducer area. Usually, acutal power dissipation has direct effect on the intensification obtained for specific application, though the extent of intensification can vary. For example, Auzay and Naffrechoux (2010) evaluated the performance of sonochemical reactors by comparing different chemical dosimetry techniques such as iodine, nitrite, and nitrate dosimetry. They also investigated the effects of temperature, power density, and reactor configuration. The results showed that sonochemical efficiency increases with acoustic power, regardless of the dosimetry; however, different rates confirm that the effect of acoustic power is also dependent on the end application.

It is also important to note that an optimum power dissipation would exist for obtaining maximum intensification benefits from the operation. The existence of optimum power dissipation levels also depends on the range of power dissipation levels in the reactor and the application in question. The optimum power dissipation can be attributed to the shielding effect and acoustic decoupling losses. Patil and Gogate (2018) studied the effect of power dissipation in synthesis of stable oil in milk emulsion and demonstrated the presence of optimum power over the range of powers used in the study as 85 to 145 W and reported 135 W as the optimum power dissipation. Bhangu et al. (2017) also reported that the yield of lipase catalyzed transesterification decreases sharply by an increase of power from 50 to 200 W during an operation with 20 kHz frequency, indicating that 50 W is the optimum power. Whillock and Harvey (1997) investigated the effect of power dissipation (maximum

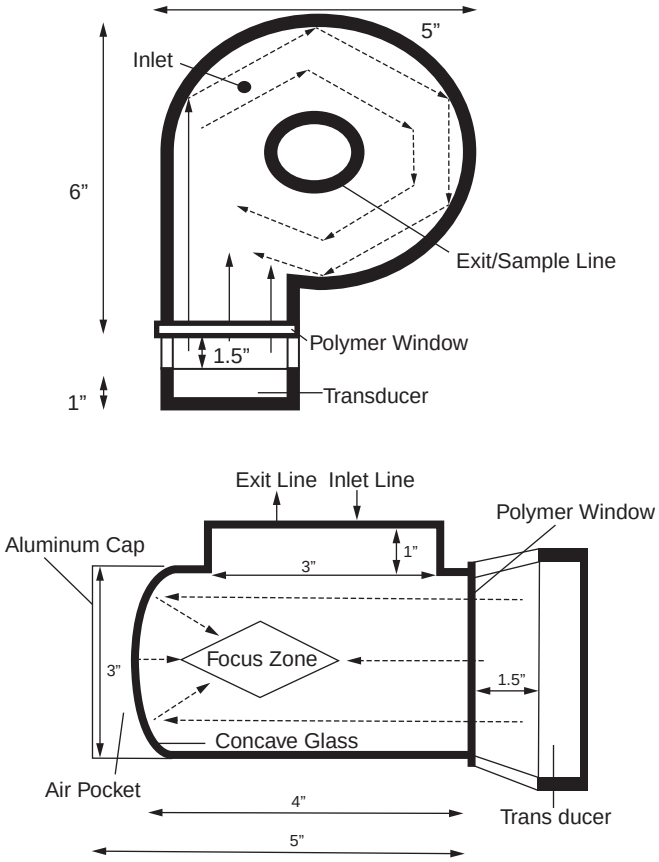


FIGURE 28.7 Modified sonochemical reactor accounting for reflections and focusing of sound waves (Seymour et al., 1997).

power of 100 W) on cavitational activity in terms of erosion of stainless steel in a horn-type reactor. The results showed that erosion rate (at a distance of 0.5 mm) at 40- and 60-kHz frequencies increases linearly, only initially giving optimum power of 40 W and 20 W, respectively. Overall, the optimum magnitude of power dissipation is a function of the desired application, reactor geometry, physicochemical properties of bulk liquid, location, and surface area of the irradiating element. Also, the presence of additional phases such as solid, gas, or immiscible liquids play a role in deciding the optimum levels. Choosing optimized operating power can increase the efficiency of the process thereby decreasing the operating cost of the operation. High-pressure amplitudes should be applied only to an extent that bubble structure and position presents a mechanism that leads to an optimum cavitational intensity (Wood et al., 2017).

In large-scale operations, it is extremely difficult to dissipate the entire power in the given reactor volume using a single transducer because of the limitations of the materials (vibrating piezoelectric crystal) and hence multiple transducers are required. Also, because the active zones with required cavitational activity are concentrated very near to the irradiating surface (within 2–3 cm), more than one irradiating surface is required to reduce the decoupling losses. The exact number of transducers depends on the operating volume, dimensions of each transducer, and power requirement for the given application. Thus, the efficient design of any sonochemical reactor should optimize both key parameters, that is, the total irradiating surface area and actual power dissipation levels. The total area of transducers should be distributed using multiple transducers, which makes the location of the transducers an additional design optimization parameter.

28.6.3 Selection of signal type or duty cycle

Pulsed mode, sweeping mode, or bi-modal signals are generally preferred over continuous sonication signals. Duty cycle of an ultrasonic operation is selected by setting the ON/OFF time of the irradiation during one cycle. Time of exposure of irradiation directly impacts the efficiency of the operation(Henglein and Gutierrez, 1990). Generally, it would be expected that more the ON exposure time, better would be the operation or efficiency of generating cavitating bubbles; but increasing the exposure time too much can also have negative effects on the operation, like transducer wear and tear and a higher increase in temperature. Damage to the transducers due to excessive heating during



FIGURE 28.8 Novel ultrasound bath with cavitation inducing surface indented bags (van Zwieten et al., 2017).

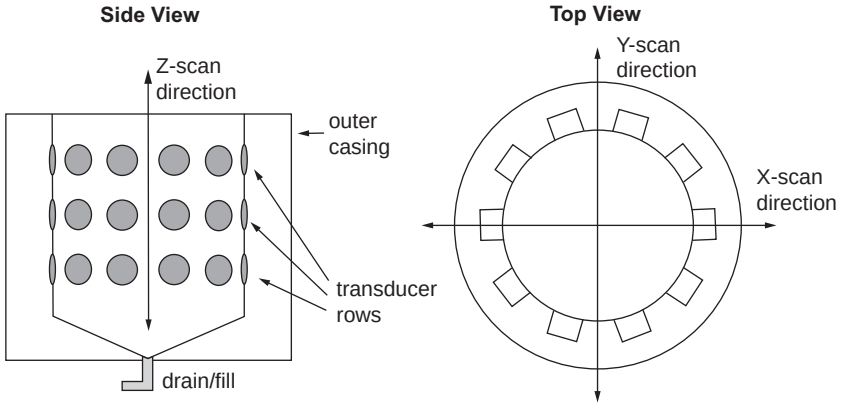


FIGURE 28.9 Cylindrical ultrasonic reactor with multiple transducers on the periphery (Hodnett et al., 2017).

continuous irradiation can be significant. Continuous mode also leads to limited spatial distribution of cavities and bubble growth beyond the region of active cavitation (Tuziuti et al., 2008). Pulse mode of operation is generally recommended by researchers and manufacturers due to decrease in local temperature rise and better life time of transducer. Excessive cavity formation also leads to cloud formation and cushioning effects and its associated cavitational effect can be detrimental to the operation. For example, excessive cavity formation during enzymatic

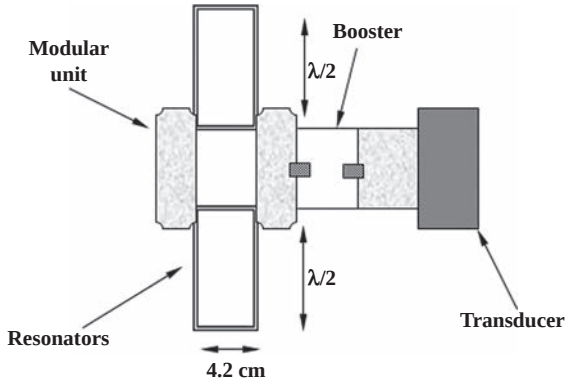


FIGURE 28.10 Schematic representation of sonitube (Faid et al., 1998).

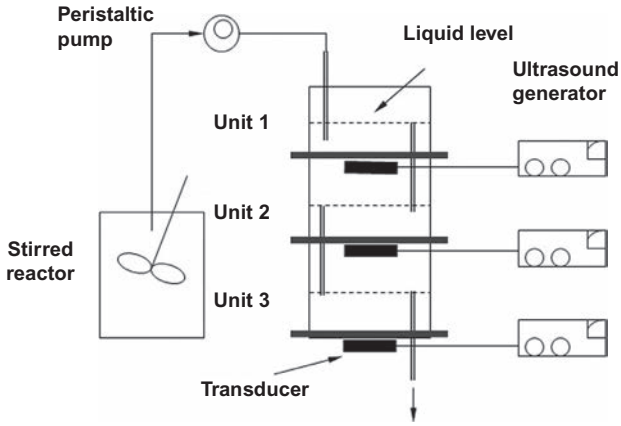


FIGURE 28.11 A novel continuous-scale sonochemical reactor with three stages (Gondrexon et al., 1999).

operations can lead to rise in temperature and deactivation of enzymes. At the same time, a very small ON time will lead to disappearance of all cavities before the next duty cycle is ON, leading to lower activation of bubbles. Reports have shown that three- to fivefold increase in efficiency can be obtained using an optimum duty cycle for pulsed input (Tuziuti et al., 2008).

The optimum duty cycle may be also provided in the manufacturer recommendations, and using ON times more than the recommended manufacturer value will damage the transducer equipment. The optimum duty cycle obtained from experimentation may be less than the recommended value. The optimum value will depend on the reactor configuration in terms of geometry, location and the number

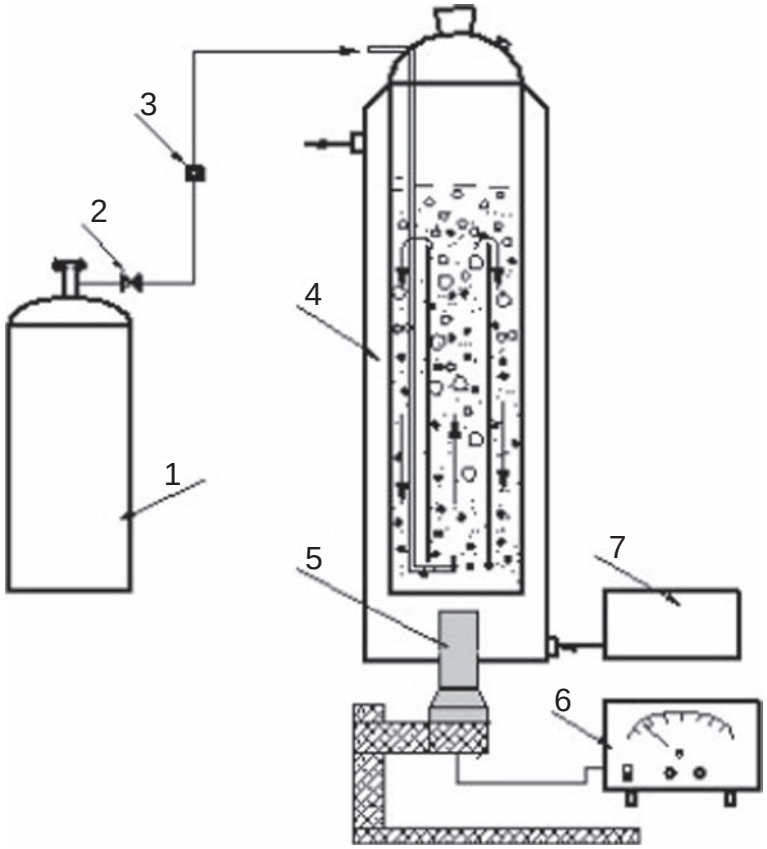


FIGURE 28.12 Ultrasound-assisted air loop reactor. (1) Gas cylinder, (2) stopvalve, (3) flowmeter, (4) airlift loop reactor, (5) ultrasonic probe, (6) ultrasonic generator, and (7) thermostatic bath (Liu et al., 2008).

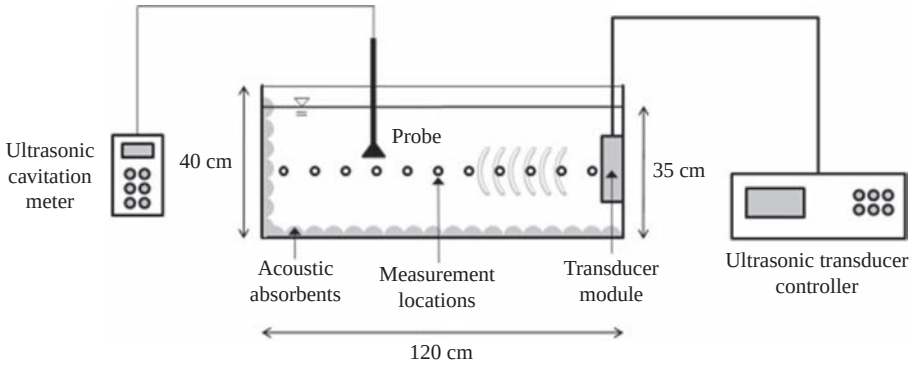


FIGURE 28.13 Schematic of large-scale sonochemical reactor and measurement locations for mapping of cavitational activity (Son et al., 2009).

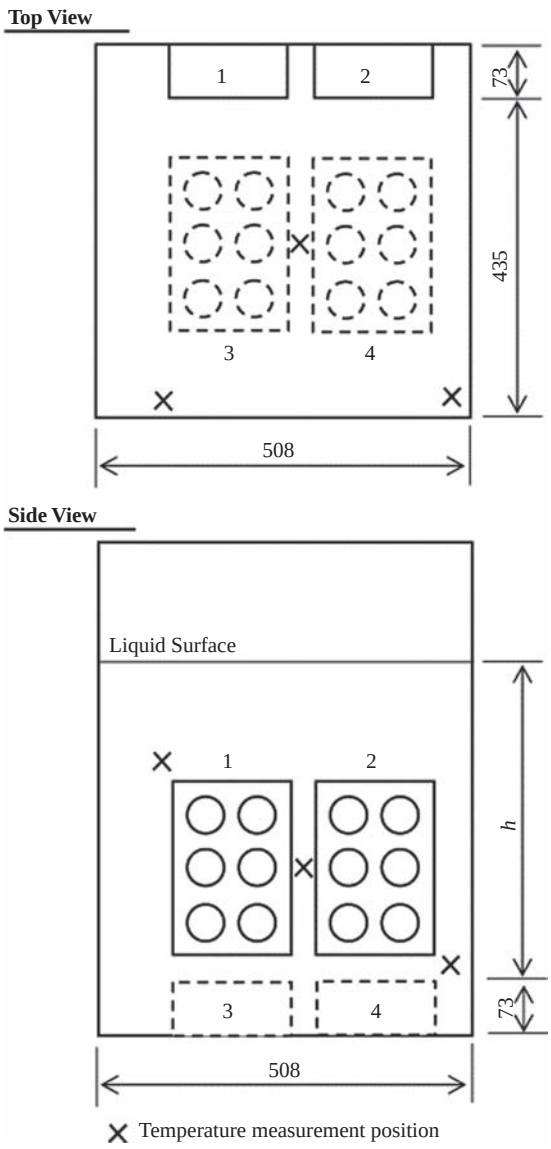


FIGURE 28.14 Schematic representation of the experimental apparatus for a large-scale sonochemical reactor (Asakura et al. (2008a,b)).

of transducers, as well as the chemical or biochemical transformations taking place.

Frequency sweeping and mixing signals have not been reported widely, although can lead to both negative and positive effects. A recent report on sweeping frequency. both upward and downward, showed that negative sweeps increased the cavitational yield for the process (Hallez et al., 2016).

28.6.4 Selection of temperature

An optimum temperature might exist based on the counteracting effects. While temperature increase might lead to enhanced chemical effects, cavitational intensity and bubble collapse are negatively influenced at higher temperatures due to less violent collapse and cushioning effect (Sancheti and Gogate, 2017). Most studies have reported an optimum temperature of operation, mostly dependent on the specific process and kinetic effects. Studies like Shirsath et al. (2017) report an increase in efficiency with a rise in temperature due to enhanced kinetics, but this typically depends on the range of temperature investigated. The actual optimum temperature value is strongly affected by the governing mechanisms. For example, an increase in temperature can lead to enzymatic deactivation in enzyme-based processes, and hence, the value of optimum can be still lower compared to the chemical systems, where no such strong deactivating effect is expected. Another important point is that at maintained temperatures lower and higher than room temperatures, the use of temperature control baths (for batch processes), and heat exchangers (for continuous processes) is required, which will add to the power and utility consumption in the processes, ultimately contributing to the cost of operation. The trade-off between additional cost of operation and increased efficiency of the process should be taken into consideration while choosing an optimum temperature for the operation.

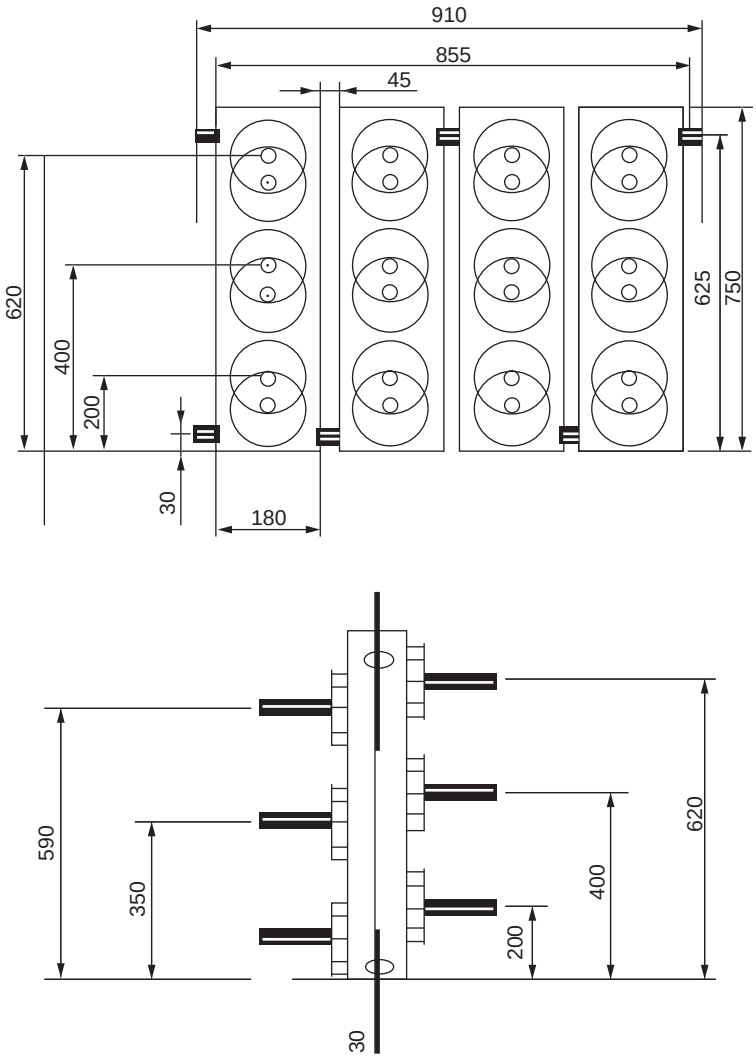


FIGURE 28.15 Continuous flow rectangular ultrasonic reactor with four individual subreactors (Zou and Chai, 2017).

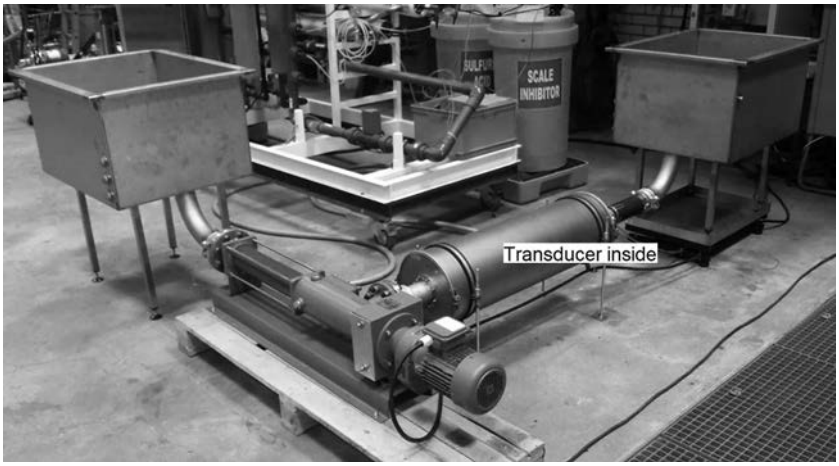


FIGURE 28.16 Continuous flow novel tube ultrasonic reactor (Koch et al., 2017).

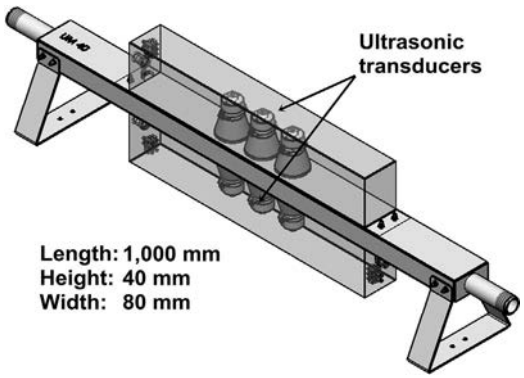


FIGURE 28.17 Novel ultrasonic flatbed reactor with six transducer configurations (Lippert et al., 2018).

28.6.5 Liquid phase physicochemical properties

The most important liquid phase physicochemical properties that affect the cavitation phenomena in terms of inception of cavitation and size of initial nuclei include vapor pressure, viscosity, and surface tension. These properties have a significant effect on the extent of the cavitation for the given application and need to be properly selected (Gogate et al., 2003b).

Lower liquid vapor pressure is usually preferred because the vapor content of the cavity increases with an increase in vapor pressure, resulting in cushioned collapse, thereby decreasing the energy released during the collapse. Thus,

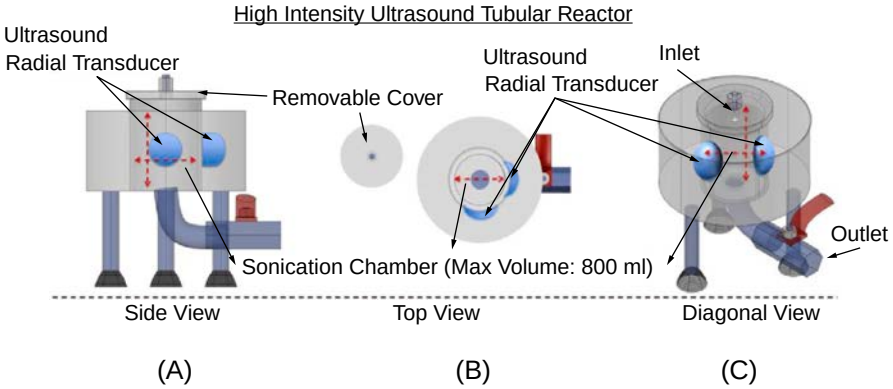


FIGURE 28.18 High-intensity ultrasonic tubular reactor (HUTR) with centrally located transducer (Low et al., 2019).

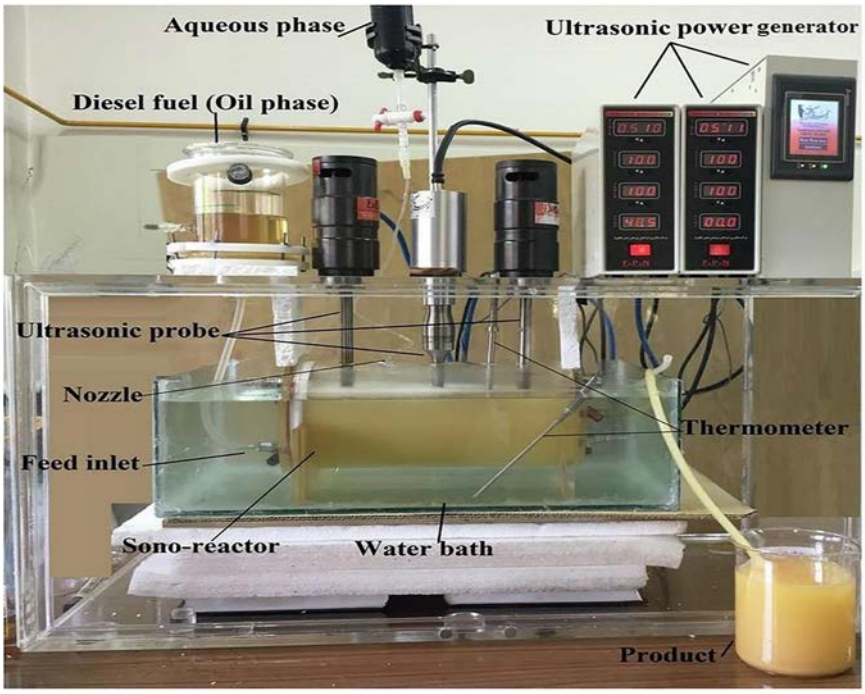


FIGURE 28.19 Continuous flow multiprobe ultrasonic cylindrical reactor with three horns (Rahimi et al., 2019).

the net cavitational effects are lower for liquids with higher vapor pressure.

For cavitation to occur in a liquid, it must overcome the natural cohesive forces present. Any increase in these forces tends to increase the threshold pressure and, therefore, the energy required to generate cavitation. In highly viscous liquids, severe attenuation of the sound intensity occurs and the active cavitating zone is substantially reduced. Consequently, using liquids with lower viscosity is recommended. In some cases of low viscosity, bubble coalescence could be high leading to a decrease in cavitational intensity. An increase in viscosity of the bulk brought about by a change in temperature could reduce coalescence in such cases. Increasing the viscosity, however, could lead to change in chemical reactions by attenuation of sound waves. Also, electrolytes can be used to reduce coalescence between bubbles due to uneven concentration at bubble surfaces (Wood et al., 2017). In general, the effect of viscosity on cavitational intensity and on coalescence cannot be easily established and need to be specifically investigated for the system under consideration.

Liquids with higher surface tension, such as water, generally result in higher cavitational intensity. Theoretical studies have indicated that aqueous liquids and organic liquids, such as glycerol, show a higher cavitating effect compared to acetone, ethanol, and formamide. The presence of surfactants in the system as additives can further enhance the cavitational activity.

28.6.6 Geometrical design of the reactor

The reactor design in terms of the ratio of the diameter of the transducers to the diameter of the reactor, liquid height, and arrangement of the transducers plays an important role in deciding the final efficacy of sonochemical reactors. The following important guidelines can be applied (Sutkar and Gogate, 2009).

- In the case of immersion reactors, an increase in the diameter of the immersion transducer relative to the reactor diameter increases the cavitational activity until an optimum ratio, which is usually dependent on the application. The ratio mainly affects the level of turbulent dissipation of energy and the intensity of the acoustic streaming and so would be more important in applications where physical effects are controlling. Nanzai et al. (2009) reported that the efficiency of operation increased as the reaction vessel diameter increased (up to 90 mm) and then decreased for diameters in excess of 90 mm, establishing that an optimum diameter exists.
- The depth of the ultrasonic horn in the liquid or the total liquid height in the reactor, affecting the extent of reflection of the incident sound waves from the liquid surface as well as the reactor walls, also has an optimum value, which means that significantly increasing the depth of the ultrasonic horn does not give the desired result. A typical depth of the horn into the liquid is about 2–5 mm, whereas the recommended maximum liquid depth for ultrasonic horn-type reactors is about 15 times the wavelength. The heights should be adjusted to avoid any induction of gases, which can completely alter the hydrodynamics and the cavitational activity distribution. A report also states that the height of an odd multiple of one-fourth of the wavelength can be suitable for increase in cavitational intensity. By choosing an optimum height, efficiencies similar to that of higher frequencies can be obtained with significantly lower frequencies (Asakura et al., 2008a). The position of the transducers in the reactors based on multiple transducers should be selected in such a way that maximum and uniform cavitational activity is obtained. Theoretical analysis of pressure field distribution can give guidelines for the optimum location of the transducers. The work of Saez et al. (2005) and Klima et al. (2007) is recommended to gain a greater understanding of theoretical pressure field distributions. Typically, the use of multiple transducers in a large-scale reactor is recommended so that uniform cavitational activity distribution can be achieved, avoiding the problems associated with decoupling losses. The use of multiple transducers allows lower power dissipation per unit area of dissipation while maintaining the required power dissipation levels in the reactor.
- Size and the shape of the reactor including the position of transducers affect the cavitational activity within the bulk significantly (Wood et al., 2017). Larger vessels need larger power dissipation and may not always lead to better sonochemical activity. Increasing volumes create dead zones if the transducers are placed at suboptimal distances. Vessel diameter-transducer diameter ratio has been reported to be somewhere close to 1.5 to 1.45 for significant sonochemical efficiency (Nanzai et al., 2009; Thangavadivel et al., 2013).
- Some reports also suggest the use of reflective plates to stabilize and reinforce the standing wave component to ultrasonic waves that could increase the amplitude and increase the sonochemical activity (Murdoch and Leng, 1971; Zhou et al., 2013). This phenomenon is highly dependent on the frequency of operation. The region of activation also changes with the position of reflective plates. Best sonochemical activity can be obtained when the reflective plate is positioned exactly at the liquid surface. Theoretical and practical studies on this phenomenon are lacking and can form a useful scope for future work.

- Typically, flow cell arrangements are more suitable for large-scale operations because they provide flexibility in terms of continuous operation and also give an option of arranging the transducers on opposite walls of the reactor so that standing wave patterns can be generated. Hexagonal or rectangular cross-sections should give excellent distribution of cavitational activity and are recommended for large-scale operations. The number and location of the transducers also affect the hydrodynamic behavior and mixing characteristics in the reactor, which can be of prime importance, especially for physical processing applications. While maintaining geometric similarity in the design of large-scale reactors, it is also important to maintain similar conditions of hydrodynamics and mixing characteristics in the reactor so that the desired objectives are achieved.

28.7 Reactor choice, scale-up, and optimization

When deciding on the type of reactor (ultrasound based, simple mechanical agitation based, or a combination, including combinations with microwave and hydrodynamic cavitation) required for a particular chemical or physical transformation, an important question that needs to be addressed is whether the cavitation enhancement is only a result of an improved mechanical process due to enhanced mixing. If this is the case, then cavitation pretreatment of a slurry may be all that is required before the system is subjected to a conventional type of transformation scheme, and the scale-up of the pretreatment vessel would be a simpler task. However, if the effect is truly based on cavitation chemistry, then cavitation must be provided during the transformation (Mason, 2003). Development of design correlations to predict the cavitational yield as a function of different operating parameters can be an important indication of such information. These design equations should help in selecting the operating parameters to achieve the desired level of transformations. The work of Gogate and Pandit (2000) and Gogate et al. (2003b) is recommended to gain greater insight into the development of design equations and other design aspects of sonochemical reactors. The work of Zhang et al. (2006) is recommended to get more insights into the design modifications required for efficiently combining the use of gases and sonochemical reactors as a means to achieve process intensification.

For an efficient design, the first step is understanding the mechanisms of interaction from the observed phenomena so that the desired cavitation field can be created on a larger scale to promote similar interactions. The important scale-up consideration is to establish the optimum conditions for the transformation in terms of the operating or design variables that influence the cavitation phenomena (Mason, 2000). In this analysis, the nature of the transformation also has an impact on the suitability of the given cavitational reactor.

The physicochemical properties of the reaction medium dictate the required level of cavitation power. Highly viscous media with low vapor pressure require higher energy to generate cavitation. The presence of entrained or evolved gases and the presence or generation of solid particles facilitate cavitation.

An efficient coupling of acoustic energy to the material that will provide the transmission path for the ultrasonic energy is also very important. Although a detailed discussion related to these issues is beyond the scope of this chapter, the important factors that need to be analyzed are listed below.

- Mechanisms of cavitation and their interaction with the reactor material
- Wave propagation in structures
- Acoustic coupling and mode of excitation
- Transducers and power generator technology
- Integration of ultrasonics into the process system
- Combination of ultrasonics with other physicochemical transformation methods

28.8 Future trends

It is important to describe some future trends for efficient reactor design in terms of suitability for large-scale operations. Efficient reactor design for large-scale operations must try to achieve uniform cavitational activity distribution in the reactor so that maximum utilization of the cavitational intensities can be achieved, giving desired process intensification effects. One of the recommended ways to achieve this uniformity is to use a number of transducers in the reactor design and preferably flow cell-type designs with transducers attached on opposite walls of the reactor. Another important requirement for the design is operation under continuous or recirculation mode, especially for large-scale applications, although for specialty chemicals, batch operation might also be desirable. Depending on the application, a single large transducer can also be inserted in the flow loop, but the possible contamination of the surface by erosion needs to be considered, especially for pharmaceutical applications.

At this stage of development, a generalized design cannot be recommended for all applications because the intensity requirements vary depending on the expected mechanism of intensification. For example, for applications where mostly physical effects are required, required intensification can easily be achieved at a lower frequency (typically 20–100 kHz) and lower power dissipation levels. In contrast, for chemical processing applications, more intense cavitation is recommended, and this can be achieved using

high-frequency or multiple-frequency operation with higher power dissipation levels.

Mass transfer limitations and mixing times are also important factors affecting the operation, and it is recommended that more investigation should be carried out on studying the hydrodynamic behavior and mixing in sonochemical reactor for effective scale-up of the operation.

More investigation can be done on trade-offs between increased the cost of operation and increased efficiency. Detailed life cycle assessment and technoeconomic analysis also need to be performed for various designs of sonochemical reactors.

Further, it is recommended that more studies should be done on controlling bubble coalescence. It is recommended that methods for localizing bubbles to regions within the bulk will be highly advantageous. Surface modifications by changing viscosity or addition of electrolytes and surfactants may lead to a decrease in coalescence.

Finally, it is recommended that the controlling mechanisms are established on a laboratory-scale and then, based on those experimental results, coupled with a theoretical understanding of bubble dynamics, proper scale-up procedures should be adapted. The guidelines provided in this chapter are useful for this process.

28.9 Conclusions

In terms of generated high temperature and pressure conditions along with the quantum of active radicals, cavitational intensity can be easily manipulated by adjusting the operating and geometric parameters, depending on the desired intensity of cavitation phenomena appropriate for a particular transformation or application. Such optimization minimizes processing costs and enhances the acceptability of sonochemical reactors in commercial practice. Bubble dynamics models can be used effectively to predict the optimized conditions needed to maximize the physical or chemical effects, depending on the specific application. The distribution of cavitational events throughout the reactor volume is an important parameter determined by the reactor geometry and the arrangement of the transducers.

In sonochemical reactors, the selection of suitable operating parameters, such as the intensity and frequency of ultrasound, duty cycle, temperature, and the physicochemical properties of the medium, along with the geometry of the reactor, is very important because the bubble behavior and the yields of sonochemical transformation are significantly affected by these parameters. It is necessary that frequency and intensity of irradiation along with temperature and cycle time should not be increased beyond an optimum value, and the liquid phase physicochemical properties should be adjusted in such a way that the generation of cavitation events is eased, giving a large number of smaller-sized cavities.

The use of multiple transducers and multiple frequencies with the possibility of variable power dissipation is recommended. Theoretical analysis for predicting cavitational activity distribution is recommended to optimize the reactor geometry, including the transducer arrangements.

Overall, sonochemical reactors offer a novel means for process intensification of a variety of physical and chemical transformations, including chemical synthesis, biotechnology, food processing, pharmaceutical processing, and polymer engineering, and the proper design of these reactors following the guidelines given in this chapter should lead to achieving their application on a commercial-scale.

References

Asakura, Y., Nishida, T., Matsuoka, T., Koda, S., 2008a. Effects of ultrasonic frequency and liquid height on sonochemical efficiency of large-scale sonochemical reactors. Ultrason. Sonochem. 15, 244–250.

Asakura, Y., Yasuda, K., Kato, D., Kojima, Y., Koda, S., 2008b. Development of a large sonochemical reactor at a high frequency. Chem. Eng. J. 139, 339–343.

Auzay, S.R., Naffrechoux, J.B.E., 2010. Comparison of characterization methods in high frequency sonochemical reactors of differing configurations. Ultrason. Sonochem. 17, 547–554.

Avvaru, B., Pandit, A.B., 2009. Oscillating bubble concentration and its size distribution using acoustic emission spectra. Ultrason. Sonochem. 16, 105–115.

Bhangu, S.K., Gupta, S., Ashokkumar, M., 2017. Ultrasonic enhancement of lipase-catalysed transesterification for biodiesel synthesis. Ultrason. Sonochem. 34, 305–309.

Bhirud, U.S., Gogate, P.R., Wilhelm, A.M., Pandit, A.B., 2004. Ultrasonic bath with longitudinal vibrations: a novel configuration for efficient wastewater treatment. Ultrason. Sonochem. 11, 143–147.

Birkin, P., Power, J.F., Abdelsalam, M.E., Leighton, T.G., 2003. Electrochemical, luminescent and photographic characterisation of cavitation. Ultrason. Sonochem. 10, 203–208.

Boldo, P., Renaudin, V., Gondrexon, N., Chouvellon, M., 2004. Enhancement of the knowledge on the ultrasonic reactor behavior by an interdisciplinary approach. Ultrason. Sonochem. 11, 27–32.

Chakinala, A.G., Gogate, P.R., Burgess, A.E., Bremner, D.H., 2007. Intensification of hydroxyl radical production in sonochemical reactors. Ultrason. Sonochem. 14, 509–514.

Chivate, M.M., Pandit, A.B., 1995. Quantification of cavitation intensity in fluid bulk. Ultrason. Sonochem. 2, S19–S25.

Cravotto, G., Omiccioli, G., Stevanato, L., 2005. An improved sonochemical reactor. Ultrason. Sonochem. 12, 213–217.

Dahnke, S., Keil, F., 1998. Modeling of three dimension linear pressure field in sonochemical reactors with homogenous and inhomogenous density distribution of cavity bubbles. Ind. Eng. Chem. Res. 37, 848–864.

Dahnke, S., Swamy, K., Keil, F., 1999. Modeling of three-dimensional pressure fields in sonochemical reactors with an inhomogeneous density distribution of cavitation bubbles. Comparison of theoretical and experimental results. Ultrason. Sonochem. 6, 31–41.

Dion, J.-L., 2009. Contamination-free high capacity converging waves sonoreactors for the chemical industry. Ultrason. Sonochem. 16, 212–220.

Entezari, M.H., Petrier, C., Devidal, P., 2003. Sonochemical degradation of phenol in water: a comparison of classical equipment with a new cylindrical reactor. Ultrason. Sonochem. 10, 103–108.

Faid, F., Contamine, R., Wilhelm, A.M., Delmas, H., 1998. Comparison of ultrasound effects in different reactors at 20kHz. Ultrason. Sonochem. 5, 119–124.

Feng, R., Zhao, Y., Zhu, C., Mason, T.J., 2002. Enhancement of ultrasonic cavitation yield by multi-frequency sonication. Ultrason. Sonochem. 9, 231–236.

Gallego-Juárez, J.A., Rodriguez, G., Acosta, V., Riera, E., 2010. Power ultrasonic transducers with extensive radiators for industrial processing. Ultrason. Sonochem. 17, 953–964.

Gogate, P.R., Pandit, A.B., 2000. Engineering design methods for cavitation reactors I: sonochemical reactors. AICHE J. 46, 372–379.

Gogate, P.R., Pandit, A.B., 2004. Sonochemical reactors: scale up aspects. Ultrason. Sonochem. 11, 105–117.

Gogate, P.R., Shirgaonkar, I.Z., Sivakumar, M., Senthilkumar, P., Vichare, N.P., Pandit, A.B., 2001. Cavitation reactors: efficiency analysis using a model reaction. AICHE J. 47, 2526–2538.

Gogate, P.R., Tatake, P.A., Kanthale, P.M., Pandit, A.B., 2002. Mapping of sonochemical reactors: review, analysis and experimental verification. AICHE J. 48, 1542–1560.

Gogate, P.R., Mujumdar, S., Pandit, A.B., 2003a. Large scale sonochemical reactors for process intensification: design and experimental validation. J. Chem. Technol. Biotechnol. 78, 685–693.

Gogate, P.R., Wilhelm, A.M., Pandit, A.B., 2003b. Some aspects of the design of sonochemical reactors. Ultrason. Sonochem. 10, 325–330.

Gondrexon, N., Renaudin, V., Petrier, C., Boldo, P., Bernis, A., Gonthier, Y., 1999. Degradation of pentachlorophenol aqueous solutions using a continuous flow ultrasonic reactor: experimental performance and modelling. Ultrason. Sonochem. 5, 125–131.

Gonze, E., Gonthier, Y., Boldo, P., Bernis, A., 1998. Standing waves in a high frequency sonoreactor: visualisation and effects. Chem. Eng. Sci. 53, 523–532.

Hallez, L., Lee, J., Touyeras, F., Nevers, A., Ashokkumar, M., Hihn, J.-Y., 2016. Enhancement and quenching of high-intensity focused ultrasound cavitation activity via short frequency sweep gaps. Ultrason. Sonochem. 29, 194–197.

Henglein, A., Gutierrez, M.J., 1990. Chemical effects of continuous and pulsed ultrasound: a comparative study of polymer and iodide oxidation. J. Phys. Chem. 94, 5169–5172.

Hodnett, M., Chow, R., Zeqiri, B., 2004. High-frequency acoustic emissions generated by a 20kHz sonochemical horn processor detected using a novel broadband acoustic sensor: a preliminary study. Ultrason. Sonochem. 12, 441–454.

Hodnett, M., Choi, M.J., Zeqiri, B., 2017. Towards a reference ultrasonic cavitation vessel. Part 1: preliminary investigation of the acoustic field distribution in a 25 kHz cylindrical cell. Ultrason. Sonochem. 14, 29–40.

Horst, C., Chen, Y.-S., Kunz, U., Hoffmann, U., 1996. Design, modelling and performance of a novel sonochemical reactor for heterogeneous reactions. Chem. Eng. Sci. 51, 1837–1846.

Hu, Y., Zhang, Z., Yang, C., 2008. Measurement of hydroxyl radical production in ultrasonic aqueous solutions by a novel chemiluminescence method. Ultrason. Sonochem. 15, 665–672.

Kanthale, P.M., Gogate, P.R., Pandit, A.B., Wilhelm, A.M., 2003. Mapping of ultrasonic horn: link primary and secondary effects of ultrasound. Ultrason. Sonochem. 10, 331–335.

Klima, J., Frias-Ferrer, A., Gonzalez-Garcý, J., Ludvýk, J., Saez, V., Iniesta, J., 2007. Optimisation of 20kHz sonoreactor geometry on the basis of numerical simulation of local ultrasonic intensity and qualitative comparison with experimental results. Ultrason. Sonochem. 14, 19–28.

Koch, K., Lippert, T., Sabadini, N.H., Drewes, J.E., 2017. Tube reactors as a novel ultrasonication system for trouble-free treatment of sludges. Ultrason. Sonochem. 37, 464–470.

Kumar, A., Gogate, P.R., Pandit, A.B., 2007. Mapping the efficacy of new designs for large scale sonochemical reactors. Ultrason. Sonochem. 14, 538–544.

Lanier, N., Barnes, C.W., Perea, R., Steckle, W., 2003. Feasibility of fluorescence-based imaging of high-energy-density hydrodynamic experiments. Rev. Sci. Instrum. 74, 2169–2173.

Leighton, T.G., 1994. The Acoustic Bubble. Academic Press, London, UK.

Lippert, T., Bandelin, J., Musch, A., Drewes, J.E., Koch, K., 2018. Energy-positive sewage sludge pre-treatment with a novel ultrasonic flatbed reactor at low energy input. Biores. Tech. 264, 298–305.

Liu, Y.N., Jin, D., Lu, X.P., Han, P.F., 2008. Study on degradation of dimethoate solution in ultrasonic airlift loop reactor. Ultrason. Sonochem. 15, 755–760.

Louisnard, O., 2012. A simple model of ultrasound propagation in a cavitating liquid. Part I: theory, nonlinear attenuation and traveling wave generation. Ultrason. Sonochem. 19, 56–65.

Louisnard, O., 2017. A viable method to predict acoustic streaming in presence of cavitation. Ultrason. Sonochem. 35, 518–524.

Low, L.E., Wong, S.K., Tang, S.Y., Chew, C.L., de Silva, H.A., Lee, J.M. V., Hoo, C.H., Kenrick, K., 2019. Production of highly uniform Pickering emulsions by novel high-intensity ultrasonic tubular reactor (HUTR). Ultrason. Sonochem. 54, 121–128.

Mason, T.J., 1992. Practical Sonochemistry: Users Guide in Chemistry and Chemical Engineering. Series in Organic Chemistry, Ellis Horwood Ltd. Chichester, UK.

Mason, T.J., 2000. Large scale sonochemical processing: aspiration and actuality. Ultrason. Sonochem. 7, 145–149.

Mason, T.J., 2003. Sonochemistry and sonoprocessing: the link, the trends and (probably) the future. Ultrason. Sonochem. 10, 175–179.

Murdoch, P.G., Leng, D.E., 1971. The mathematical formulation of hydrodynamic film thinning and its application to colliding drops suspended in a second liquid-II. Chem. Eng. Sci. 26, 1881–1892.

Nanzai, B., Okitsu, K., Takenaka, N., Bandow, H., Tajima, N., Maeda, Y., 2009. Effect of reaction vessel diameter on sonochemical efficiency and cavitation dynamics. Ultrason. Sonochem. 16, 163–168.

Neppiras, E.A., 1980. Acoustic cavitation. Phys. Rep. 61, 159–251.

Nickel, K., Neis, U., 2007. Ultrasonic disintegration of biosolids for improved biodegradation. Ultrason. Sonochem. 14, 450–455.

Patil, L., Gogate, P.R., 2018. Ultrasound assisted synthesis of stable oil in milk emulsion: study of operating parameters and scale-up aspects. Ultrason. Sonochem. 40, 135–146.

Peshkovsky, A.S., Bystryak, S., 2014. Continuous-flow production of a pharmaceutical nanoemulsion by high-amplitude ultrasound: process scale-up. Chem. Eng. Proc. 82, 132–136.

Prabhu, A., Gogate, P.R., Pandit, A.B., 2004. Optimization of multiple frequency sonochemical reactors. Chem. Eng. Sci. 59, 4991–4998.

Rahimi, M., Shahhosseini, S., Sobati, M.A., Movahedirad, S., Khodaei, B., Hassanzadeh, H., 2019. A novel multi-probe continuous flow ultrasound assisted oxidative desulfurization reactor; experimental investigation and simulation. Ultrason. Sonochem. 56, 264–273.

Romdhane, M., Gourdon, C., Casamatta, G., 1995. Local investigation of some ultrasonic devices by means of a thermal sensor. Ultrasonics 33, 221–227.

Saez, V., Frýas-Ferrer, A., Iniesta, J., Gonzalez-Garcý, J., Aldaz, A., Riera, E., 2005. Characterization of a 20kHz sonoreactor. Part I: analysis of mechanical effects by classical and numerical methods. Ultrason. Sonochem. 12, 59–65.

Sancheti, S.V., Gogate, P.R., 2017. A review of engineering aspects of intensification of chemical synthesis using ultrasound. Ultrason. Sonochem. 36, 527–543.

Sarac, B.E., Stephens, D.S., Eisener, J., Rosselló, J.M., Mettin, R., 2020. Cavitation bubble dynamics and sonochemiluminescence activity inside sonicated submerged flow tubes. Chem. Eng. Process. Process Intensif. 150, 107872.

Servant, G., Laborde, J.L., Hita, A., Caltagirone, J.P., Gerard, A., 2003. On the interaction between ultrasound waves and bubble clouds in mono- and dual-frequency sonoreactors. Ultrason. Sonochem. 10, 347–355.

Seymour, J.D., Wallace, H.C., Gupta, R.B., 1997. Sonochemical reactions at 640kHz using an efficient reactor: oxidation of potassium iodide. Ultrason. Sonochem. 4, 289–293.

Shirsath, S.R., Sable, S.S., Gaikwad, S.G., Sonawane, S.H., Saini, D.R., Gogate, P.R., 2017. Intensification of extraction of curcumin from Curcuma amada using ultrasound assisted approach: effect of different operating parameters. Ultrason. Sonochem. 38, 437–445.

Sivasankar, T., Moholkar, V.S., 2009. Physical insights into the sonochemical degradation of recalcitrant organic pollutants with cavitation bubble dynamics. Ultrason. Sonochem. 16, 769–781.

Son, Y., Lim, M., Khim, J., 2009. Investigation of acoustic cavitation energy in a large- scale sonoreactor. Ultrason. Sonochem. 16, 552–556.

Suri, C., Takenaka, K., Yanagida, H., Kojima, Y., Koyama, K., 2002. Chaotic mixing generated by acoustic streaming. Ultrasonics 40, 393–396.

Suslick, K.S., 1990. Sonochemistry. Science 247, 1439–1445.

Sutkar, V.S., Gogate, P.R., 2009. Design aspects of sonochemical reactors: techniques for understanding cavitational activity distribution and effect of operating parameters. Chem. Eng. J. 155, 26–36.

Sutkar, V.S., Gogate, P.R., Csoka, L., 2010. Theoretical prediction of cavitational activity distribution in sonochemical reactors. Chem. Eng. J. 158, 290–295.

Thangavadivel, K., Okitsu, K., Owens, G., Lesniewski, P.J., Nishimura, R., 2013. Influence of sonochemical reactor diameter and liquid height on methyl orange degradation under 200kHz indirect sonication. J. Environ. Chem. Eng. 1, 275–280.

Thoma, G., Swofford, J., Popov, V., Som, M., 1997. Sonochemical destruction of dichloromethane and o-dichlorobenzene in aqueous solution using a nearfield acoustic processor. Adv. Environ. Res. 1, 178–193.

Tuziuti, T., Yasui, K., Lee, J., Kozuka, T., Towata, A., Iida, Y., 2008. Mechanism of enhancement of sonochemical-reaction efficiency by pulsed ultrasound. J. Phys. Chem. A 112, 4875–4878.

Tzanakis, I., Hodnett, M., Lebon, G.S.B., Dezhkunov, N., Eskin, D.G., 2016a. Calibration and performance assessment of an innovative high-temperature cavitometer. Sensors Actuators A Phys. 240, 57–69.

Tzanakis, I., Lebon, G.S.B., Eskin, D.G., Pericleous, K.A., 2016b. Characterisation of the ultrasonic acoustic spectrum and pressure field in aluminium melt with an advanced cavitometer. J. Mater. Process. Technol. 229, 582–586.

van Zwieten, R., Verhaagen, B., Schroën, K., Rivas, D.F., 2017. Emulsification in novel ultrasonic cavitation intensifying bag reactors. Ultrason. Sonochem. 36, 446–453.

Vinatoru, M., 2001. An overview of the ultrasonically assisted extraction of bioactive principles from herbs. Ultrason. Sonochem. 8, 303–313.

Whillock, G.O.H., Harvey, B.F., 1997. Ultrasonically enhanced corrosion of 304L stainless steel II: the effect of frequency, acoustic power and horn to specimen distance. Ultrason. Sonochem. 4, 33–38.

Wood, R.J., Lee, J., Bussemaker, M.J., 2017. A parametric review of sonochemistry: control and augmentation of sonochemical activity in aqueous solutions. Ultrason. Sonochem. 38, 351–370.

Yasui, K., Tuziuti, T., Sivakumar, M., Iida, Y., 2005. Theoretical study of single-bubble sonochemistry. J. Chem. Phys. 122, 224706.

Yasui, K., Kozuka, T., Tuziuti, T., Towata, A., Iida, Y., King, J., Macey, P., 2007. FEM calculation of an acoustic field in a sonochemical reactor. Ultrason. Sonochem. 14, 605–614.

Young, F.R., 1989. Cavitation. McGraw Hill, London, UK.

Zhang, P., Yang, M., Lu, X., Han, P., 2006. The preparation of ε-caprolactone in airlift loop sonochemical reactor. Chem. Eng. J. 121, 59–63.

Zhou, M., Yusof, N.S.M., Ashokkumar, M., 2013. Correlation between sonochemistry and sonoluminescence at various frequencies. RSC Adv. 3, 9319–9324.

Zou, H.S., Chai, J., 2017. A novel ultrasonic reactor for continuous production of biodiesel from waste acid oil. Korean J. Chem. Eng. 34, 353–359. https://doi.org/10.1007/s11814-016-0280-6.

Chapter 29

Ultrasonic mixing, homogenization, and emulsification in food processing and other applications

H. Delmas[a], L. Barthe[a] and R. Cleary[b,*]
[a]Laboratoire de Génie Chimique, Toulouse, France, [b]James Watt School of Engineering, University of Glasgow, Glasgow, United Kingdom

29.1 Introduction

The use of power ultrasound (US) to intensify physicochemical processes is now a large area of research. The most famous application of high-power US is cleaning, but many other processes may be dramatically enhanced or qualitatively improved by ultrasonic irradiation. Various industrial fields are concerned as materials ([nano]materials, polymers, surface coatings, and electrochemistry), the environment (especially water, sludge, and soil treatments), and cosmetic and food engineering (mainly through extraction of natural products from plants, dissolution, homogenization, and emulsification processes). Among these various applications of power US, the main unit operations most often involve multiphase media for either production and/or dispersion of a solid phase in a liquid through precipitation, crystallization, or simple deaggregation or disruption and/or dissolution of particles, floc, curd, and cells. These operations may be highly improved by power US.

This chapter analyzes the effects of power US on such physical operations, excluding any reactive process. First, it has to be emphasized that hydrodynamics connected with power US does control its mechanical effects through acoustic cavitation, a key phenomenon, and through acoustic streaming, albeit to a much lesser extent. Thus, a brief survey of cavitation and acoustic streaming gives the minimum information necessary to understand the local and global US-induced hydrodynamics. As a direct consequence of acoustic cavitation and streaming, US mixing—both at a reactor scale (macromixing) and a molecular scale (micromixing)—is presented, with reference to the engineering approach linking cavitation and acoustic streaming phenomena to micro- and macromixing, respectively.

Concerning specific US applications for solid-liquid suspensions, dispersion, or deagglomeration, the process of separating and suspending tiny particles that are initially naturally aggregated by attraction forces is reviewed first. Then particle size reduction, achieved either by mechanical erosion/disruption or by dissolution, is detailed, including the combination of simultaneous disruption and dissolution. Rather similar applications concerning cells disruption and the dissolution of their organic content, especially for sludge treatment, are detailed. Finally, two main applications of the general principles of homogenization and emulsification are developed. Homogenization is an important unit operation in food engineering to reduce the size of particles and globules in milk, fruit juice, tomato products, and sauces. Here only US milk homogenization, the main case by far, is detailed. US emulsification is then specifically emphasized. It consists of intimately mixing two liquid phases (at least) to achieve a stable concentrated suspension of droplets. This operation has important applications in the food and cosmetic industry by creating new complex media with specific end-use properties.

29.2 Cavitation and acoustic streaming

29.2.1 Acoustic cavitation

It is now clearly stated that most of the US outstanding effects are due to transient acoustic cavitation. Transient acoustic cavitation is a very complex highly nonlinear phenomenon which occurs at given acoustic pressure conditions (needing rather high US intensity—about 1 W/cm^2 in water at room conditions). Microbubbles are generated from nuclei—favored by dissolved gas, wall defects, and liquid impurities—during the low-pressure half periods (bubble expansion). They may oscillate for a few periods, undergoing slow average growth through the so-called rectified diffusion process (up to several micrometers), and having reached a critical size, they suddenly dramatically grow during the low-pressure half period and collapse violently

*Updated author for the second edition.

Power Ultrasonics. https://doi.org/10.1016/B978-0-12-820254-8.00020-8
Copyright © 2023 Elsevier Ltd. All rights reserved.

in a very short fraction of the high-pressure half period. Most often the bubble breaks up after collapse, reproducing the same scenario for smaller bubbles: oscillatory growth driven by rectified diffusion and then sudden collapse. Because such fast collapse is nearly adiabatic, it gives rise to extreme conditions inside and around the collapsing bubble: up to 5000 K at the bubble center, 1000 bar, a high radial velocity up to sound speed and then shock waves as the bubble rebounds (according to single-phase models or high-velocity video recordings). These cavitation characteristics have different impacts on the sonicated media: high temperature peaks produce very active free radicals (mainly $OH^{\bullet}$ in aqueous media), giving way to intense radical chemistry either inside or at the interface of the cavitation bubble, depending on the volatility of the dissolved target molecules. High-pressure, high-velocity gradients, and shock waves have mainly physical effects through very strong microturbulence and intense local mixing, increasing heat and mass transfer. These physical effects are even more efficient in multiphase systems and especially on solid surfaces because of asymmetrical collapse, with the projection of a fast jet toward the solid close to the cavitation bubbles. This is the main mode of action in ultrasonic cleaning and in most ultrasonic solid processing.

The main parameters affecting cavitation are either related to US emission (US power or, more likely, power intensity—in W/cm^2—or acoustic pressure and US frequency, generally from 20 to 1000 kHz), to pressure and temperature, and to physicochemical properties of the irradiated medium, such as compressibility, vapor pressure, surface tension, viscosity, nature of gas above the liquid, and multiphase characteristics (fraction of gas, immiscible liquid, dispersed solid).

It has been known for 25 years—and has recently been more precisely quantified—that the two main effects of acoustic cavitation are inversely dependent on US frequency: high frequency is better for chemical activation because free radicals are faster in contact with the reacting molecules because of much smaller cavitation bubbles; low frequency, however, gives rise to much larger bubbles, which collapse more violently and involve greater physical effects.

The main direct measurement of cavitation intensity is performed by a hydrophone, which records and analyzes noise spectra (Brotchie et al., 2010; Guo et al., 2007; Komarov et al., 2013; Moholkar et al., 2000; Son et al., 2012; Verhaagena and Rivas, 2016). Such measurements are not simple to read; the hydrophone interacts with the acoustic field and gives an integrated response because of its large size compared to cavitation bubbles. Other direct approaches aim to utilize the chemical or physical effect after the collapse such as monitoring the erosion rate of a metal plate or the erosion behavior of applied coating/paint materials (Triawan et al., 2019). Piezoelectric sensors have also been proposed that measure of the onset of cavitation can be characterized by an increase in the first subharmonic of the ultrasonic driving frequency (Verhaagena and Rivas, 2016) and the impact force of the collapsing cavitation bubble through the use of a PVDF sensor (Wang et al., 2006).

More information on cavitation properties is given by the characteristics of acoustic cavitation bubbles. Ashokkumar (2011) comprehensively reviewed this topic. Bubble size and velocity in nonstanding wave cavitation were first attempted by Burdin et al. (1999) and Tsochatzidis et al. (2001) using laser light diffraction and a phase Doppler granulovelocimeter. The two techniques gave roughly consistent information: along the axis of a 13-mm ultrasonic horn, the mean bubble velocity clearly decreased from 1.5 m/s to a few centimeters per second at maximum US intensity (180 W), and the mean bubble diameter slightly decreasing with US power (from 40 μm at 40 W to about 10 μm at 180 W). The bubble void fraction seems rather difficult to quantify. Near the horn at maximum bubble concentration, the void fraction was as low as 5×10^{-4} with light diffraction and 5×10^{-3} with phase Doppler, whereas magnetic resonance imaging measurements (Mastikhin et al., 2012) proposed 8×10^{-3} for the same conditions. Recent studies have applied high-speed imaging to characterize cavitation including the radius distribution of the bubble structures and resultant shockwave (Reuter and Kaiser, 2019; Yusuf et al., 2021).

29.2.2 Acoustic streaming

The emission of ultrasonic waves gives rise to a forward motion of the fluid. The liquid jet formed on the axis of the emitter (when cylindrical) includes the more concentrated population of acoustic cavitation bubbles because this region is the most irradiated. Velocity was measured with laser Doppler anemometry and particle image velocimetry and showed coherent results: the velocity depends mainly on US density and on liquid or slurry viscosity. In water velocity between 0.1 and 0.3 m/s (Hihn et al., 2011) when the jet impacts a solid surface and up to 1.5 m/s (Kumar et al., 2007) at 70 W on a 13-mm horn, and even up to 2 m/s (Tsochatzidis et al., 2001) near the emitter surface of a large volume at a much higher intensity (180 W on a 13-mm horn) has generally been reported. Some saturation due to bubble accumulation at the surface often has been mentioned (Hihn et al., 2011), leading to a smaller increase in velocity when increasing too much the power. Concerning the whole velocity field, because of acoustic streaming, like a usual jet, the velocity exhibits a sharp radial profile near the emitting surface and a strong decrease along the axis (Kumar et al., 2007). Acoustic streaming has been found to be an effective means of realizing microfluidic applications such as fluid mixing (Zhang et al., 2019),

pumping (Huang et al., 2014), and particle manipulation (Feng et al., 2019).

29.2.3 Conclusion

Power US in a liquid or a multiphase mixture with a continuous liquid phase may generate two distinct hydrodynamic phenomena: acoustic cavitation and acoustic streaming. Only acoustic cavitation at high acoustic pressure may have a significant effect on the sonicated medium because of the violent collapse of microbubbles, giving rise to hot spots in the gas phase and intense turbulence and shear stresses at the micron scale in the liquid phase. The attraction of the collapsing bubble toward solid surfaces and the possible excess of nuclei near the interface make acoustic cavitation extremely performing in multiphase processes, whereas acoustic streaming may sometimes be used to optimize the overall flow in the sonicated volume; most often, however, it may be ignored in large-scale US processes.

29.3 Mixing

When trying to explain the outstanding performances of some US-assisted processes, improved mixing is often cited. Nevertheless, this claim is generally connected with visual observations (Guo et al., 2007; Parvizian et al., 2011; Yusaf and Buttsworth, 2007), although rather few works have been devoted to the quantification of mixing under US using conventional engineering criteria. Indeed, mixing should characterize the degree of homogeneity of either a single phase or a multiphase medium and may be quantified either at the overall apparatus scale (as a mixing time in a batch condition or a dispersion of the residence time distribution [RTD] in continuous operation)—referred to as macromixing—or at much lower scale (e.g., particles or droplets) and referred as micromixing. The quality of micromixing has a major effect on many phenomena occurring at the submicronic scale: precipitation, emulsification, mass transfer at interfaces, reaction rate, and selectivity.

29.3.1 Macromixing

Depending on whether the process is batch or continuous, macromixing is characterized by a mixing time (time to obtain a quasi-homogeneous concentration from mixing) or by the variance of the RTD. The dimensionless variance of RTD, σ^2, ranging from 0 for perfectly unmixed flow (plug flow) to 1 in perfectly mixed flow often is used to obtain either the number N of equivalent perfectly stirred tanks in a series ($N = 1/\sigma^2$) or the Péclet number, based on the axial dispersion model.

$$Pe = \frac{Lv}{D_A} \approx \frac{2}{\sigma^2} \tag{29.1}$$

where L is defined as the reactor length (m), v is the average fluid velocity (m/s), and D_A is the axial dispersion (m^2/s). Both criteria (mixing time or σ^2) are obtained through tracer experiments. In batch operation, the mixing time is the time needed to reach a quasi-uniform concentration (e.g., 90% or 95% of the average final concentration) after tracer injection. Of course, this mixing time may depend on the location of both the tracer injection and the tracer detection. Mixing time is the most important criterion concerning homogeneity at the apparatus scale, but it does not reflect the quality of mixing at the molecular scale (micromixing), which may govern the reaction rate and selectivity, as mentioned earlier. To simplify, it may be assumed that macromixing results from the velocity field in the reactor, which is mainly governed by stirring or pumping and, in small-scale US equipment, by acoustic streaming, especially with a small horn and high US intensity. Few works have been devoted to macromixing under US (Murugan and Nagarajan, 2008; Vichare et al., 2001; Yusaf and Buttsworth, 2007), probably because of a rather poor US effect.

US does not significantly improve macromixing because the acoustic streaming velocity is generally one order of magnitude lower than the velocity achieved by mechanical devices (stirrer or pump) in large US reactors. Conversely, it is important to get a good mixing in any US apparatus when acoustic energy is not homogenously distributed, which is most often the case (Kojima et al., 2010). However, in a recent study, Patil and Gogate (2018) demonstrated superior droplet size distribution and energy requirements established by an ultrasonic bath reactor with a manual mixer over similar technologies when obtaining stable emulsion of turmeric oil in skimmed milk. Good mixing forces the fluid or mixture being treated to pass regularly through the best irradiated zones and therefore improves the overall effectiveness of US. Alternatively, premixing with conventional equipment could be dramatically helpful, as in emulsification (see Section 29.7).

29.3.2 Micromixing

Micromixing is linked to small-scale turbulence and velocity gradients, and compared with macromixing, it is dramatically affected by intense cavitation when using power US (Yusaf and Buttsworth, 2007). Contrary to macroscopic hydrodynamics, micromixing cannot be measured directly because of microsensor limitations. Experiments are based on chemical selectivity when carrying out either consecutive competing reactions ($A + B \rightarrow R$ and $R + B \rightarrow S$) or parallel competing reactions ($A + B \rightarrow R$ and $C + B \rightarrow S$). In the two schemes, the first reaction is

extremely fast, whereas the second is moderately fast. With an excess of A, and in perfectly mixed conditions, all B should be consumed by the first reaction and no S should be formed. From C_s (the experimental final concentration of S), a micromixing or segregation index $X_s \sim C_s$ may be calculated and linked to turbulence theory with the convenient model of engulfment-deformation-diffusion (Baldyga and Bourne, 1984). This model links X_s and the micromixing time t_m. The first works on US micromixing (Monnier et al., 1999a,b) and later ones (Parvizian et al., 2011, 2012) were conducted with a competing scheme: the so-called Dushman reaction. Other works used precipitation reactions (Pohl et al., 2012a,b).

Micromixing in jets or stirred tanks results from the transmission of kinetic energy from the large eddies to the smaller ones, down to the Kolmogorov scale, defined as $\eta = (\nu^3/\varepsilon)^{1/4}$, where ε is the dissipated power per unit mass (in W/kg) and ν is the kinematic viscosity. Viscosity dominates at the Kolmogorov scale, and the turbulent kinetic energy is dissipated into heat. Under this scale, molecular diffusion completes the homogenization. The transmission of energy in acoustic cavitation occurs differently: acoustic bubble collapses directly concentrate very high amounts of energy at the micron scale. Nevertheless, the engulfment-deformation-diffusion model conveniently represents the evolution of micromixing time in both situations (Monnier et al., 1999a).

It was clearly demonstrated that power US strongly enhances micromixing by dramatically reducing the segregation index, especially at low frequencies (20 kHz), whereas frequencies of 514 and 1000 kHz were much less efficient. Figure 29.1 shows the effect of energy dissipation on mixing time for three reactor volumes. Interestingly, at the same energy dissipation (then the same energy density), better micromixing was achieved in larger volumes. When

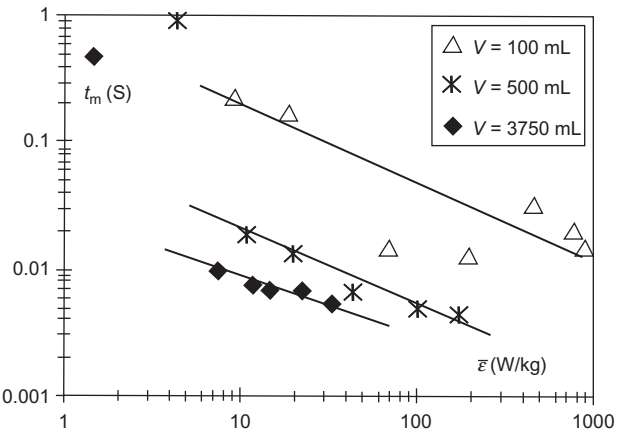


FIGURE 29.1 Characteristic micromixing time t_m versus global energy dissipation rate for three volumes (probe-horn, $f = 20$ kHz, $T = 273$ K), according to Monnier et al. (1999b).

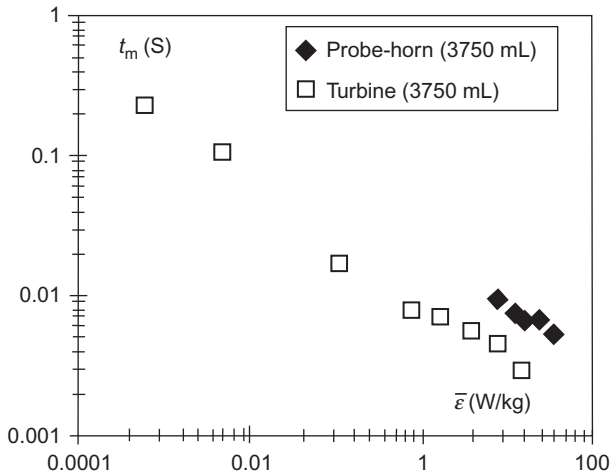


FIGURE 29.2 Micromixing time t_m versus global rate of dissipated energy both probe-horn (20 kHz) and mechanical stirring (Rushton turbine), according to Monnier et al. (1999b).

compared to classical stirring with a Rushton turbine, US was not competitive at the highest volume tested because it needed about two to three times more energy to reach the same micromixing quality (Figure 29.2). In a more recent study, the Villermaux-Dushman reaction, another widely used technique used to study micromixing efficiencies, was employed by Jordens et al. (2016). This work showed that the effect of ultrasound on the segregation indices could be strongly correlated with the energy dissipation ratio and the frequency.

By extrapolating Figure 29.1 toward higher volumes, it might be supposed that US could become more attractive than usual stirring because of its focused energy dissipation near the injection (and reaction zone); stirring spreads more turbulent energy throughout the whole reactor volume. Another interesting use of US to improve fast reaction selectivity is to develop a small continuous reactor (Figure 29.3) in which high US energy may be confined and added to natural mixing through the two reactor feds. The quality of micromixing in conventional flow reactors depending mainly on flow rates and the size of injectors was clearly improved by US, especially at low flow rates and even at low input power. As often observed in many applications, too much power may have a negative effect. It also was shown that in such US reactors, the negative effects of viscosity on micromixing could be significantly reduced (Monnier et al., 2000).

29.4 Particle and aggregate dispersion and disruption

US has been extensively used for chemical effects, but physical and mechanical effects, including particle and aggregate dispersion and disruption, have more recently

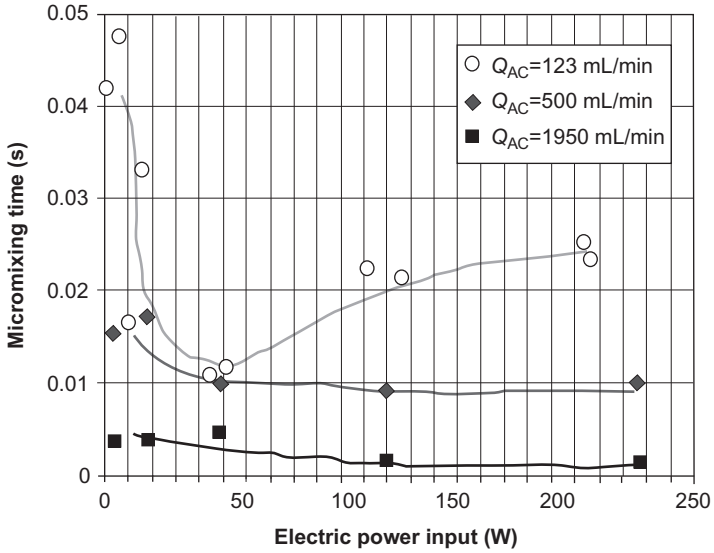


FIGURE 29.3 Influence of the input electric power versus the micromixing time for three flow rates $Q_{AC} = 123$, 500, and 1950 mL/min ($a = 10$ mm, $d = 13$ mm, $f = 20$ kHz), according to Monnier et al. (2000).

been investigated. These two phenomena are controlled by the same main mechanisms involving shocks and particle separation or breakup: on the one hand, vibration and implosion of the cavitation bubbles and, on the other hand, collisions between suspended particles.

29.4.1 Dispersion or deagglomeration

Nanomaterials such as nanoparticles are increasingly used because of interesting properties such as a large specific area. Therefore, it is imperative to produce and keep them individually avoiding agglomeration; US may be convenient for both. Before discussing US effect for dispersion or deagglomeration, it is interesting to point out that sonication can play an important role in the preparation step. US physical effects can improve considerably this stage. Indeed, acoustic cavitation permits chemical reactions under extreme conditions of temperature and pressure, as reported in Section 29.2. In addition, mass transfer is enhanced by acoustic streaming. Numerous reviews deal with the sonochemical preparation of nanomaterials (Bang and Suslick, 2010; Gedanken, 2004; Suslick and Price, 1999; Suslick et al., 1996; Xu et al., 2013). Sonication is chosen for the preparation of nanostructured metals, alloys, oxides, carbides and sulfides, colloids, and catalysts, among others, and this area is expanding quickly. In particular, sonication is well known to be advantageous in sonocrystallization because US reduces the induction time of nucleation, ensuring the formation of many small crystals and preventing their agglomeration. Moreover, the cooling rate in the liquid at the bubble surface is very high (10^8 K/s), and collapse occurs in about a nanosecond. This could play a significant part in increasing supersaturation (De Castro and Riego-Capote, 2007; Ruecroft et al., 2005).

The dispersion or deagglomeration of (nano)particles into liquids such as aqueous solutions is required for a variety of applications: catalysis, pharmaceutics, cosmetics, and paints, to name a few. However, the attracting electrostatic forces (e.g., van der Waals forces) get stronger as the particles size decreases, so nanoparticles tend to form agglomerates. Mechanical stirrers are conventionally used for the dispersion of particles into liquids. This includes high-pressure homogenizers, stirred bead mills, and rotor-stator mixers. Nevertheless, they are not sufficient in the case of nanoparticles. Sonication at a low frequency is an interesting alternative to these techniques (Guo et al., 2007). In this case, as explained previously in Section 29.2, acoustic cavitation creates micron-sized cavitation bubbles, which collapse violently. These shear forces break particle agglomerates into single dispersed particles. Even if US succeeds in disrupting the agglomerates, the use of stabilizers seems necessary to avoid re-agglomeration. Indeed, to maintain a stable suspension, salts are used for electrostatic stabilization and surfactants or dispersants for steric stabilization to maintain good dispersion (Fasaki et al., 2012). However, it is assumed that interparticle bonding is not the same for initial agglomerates and for agglomerates formed during sonication. In the second case, the dispersant is sufficient to break them.

One parameter that is particularly important during cavitation and of special influence for deagglomeration and dispersion is the gas content in the liquid. This dissolved or dispersed gas facilitates cavitation through the availability of gas nuclei. These nuclei provide the basis for bubble formation and growth and so decrease the cavitation threshold.

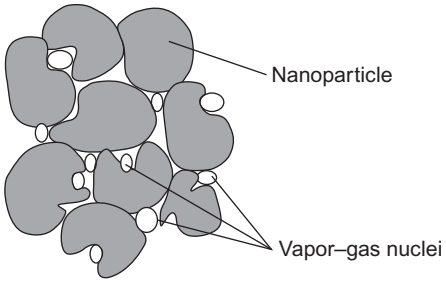


FIGURE 29.4 Vapor-gas nuclei trapped in crevices and recesses of nanoparticle agglomerates, according to Mason and Lorimer (2002).

TABLE 29.1 Specific energy and final mean diameter obtained under ultrasonic conditions for different kind of particles

Particle nature	Power (W)	Time (min)	E_v (J/L)	Final mean diameter (μm)
Aluminum oxide	360	2	4.3×10^4	0.90
Titanium dioxide	300	30	5.4×10^5	0.12

Moreover, the nanoparticle agglomerates contain crevices and recesses that can trap the vapor-gas nuclei (see Figure 29.4). The acoustic cavitation can start inside or around the agglomerates (Mason and Lorimer, 2002). This results in more efficient deagglomeration.

Another key phenomenon is shock waves accelerating solid particles suspended in the liquid. Interparticle collisions are very violent and can reach a high velocity (200 m/s). This results in the separation of the agglomerates and modification of particle morphology and surface composition. It is important to note that in particular cases, this phenomenon can cause the opposite effect. Indeed, metal microparticles hitting each other at such a high speed can induce local melting at the collision point and generate agglomeration. However, it can only happen in the case of metals with a low melting point (<700 K) such as zinc and tin and a specific particle size (a few microns). These collisions under US were carefully investigated (Doktycz and Suslick, 1990; Prozorov et al., 2004). It is noteworthy that the collapses are more violent at a high external pressure, which can be an interesting operation parameter (Sauter et al., 2008).

US can be used to deagglomerate and disperse different kinds of particles in suspension, for example, metallic oxide (Pohl et al., 2004), ceramic (Chartier et al., 1991), soil (Hereter et al., 2002; Roscoe et al., 2000), and carbon nanotubes (Cheng et al., 2010; Krause et al., 2010). For the latter, it is important to note that US should be used carefully because it can induce damage to the carbon nanotubes (defects and even scission).

To quantify the energy input required for deagglomeration, most authors selected the specific energy, E_v, to link to the final mean diameter (Table 29.1). E_v is defined as

$$E_v = \frac{E}{V} = \frac{Pt}{V} \tag{29.2}$$

E_v (J/L) takes into account the energy provided E (power of US multiplied by the sonication time) and the sonicated volume V. However, it is important to note that it would be better to consider the solid content rather than the suspension volume (Le et al., 2013b).

29.4.2 Disruption and breakage

In addition to particle separation (deagglomeration and dispersion), US can also lead to particle disruption and breakage. Some analogy with mechanical effects in ultrasonic cleaning may be pointed out. Despite its widespread use, the associated physical phenomena have not been conveniently analyzed. Nevertheless, it is recognized that the main observed phenomenon under low-frequency US is erosion (Mason et al., 2011). The microjets emanating from the asymmetric collapse of the transient cavitation bubbles achieve particle surface erosion, leading to fines production. However, particle breaking can occur as a distinct mechanism. Violent interparticle collisions when the shock occurs at a particle defect may propagate a crack and lead to particle breakage.

An experimental and theoretical US investigation of an alumina suspension (Raman et al., 2011) provided a kinetic model of breakage based on a Kapur function approach and determined the main mechanism. Numerical modeling of grinding was developed to predict the evolution of particle size distributions using population balance. The R_i function is defined as the cumulative oversize fraction above size x_i at time t from m_i, which is the mass fraction of particles sized x_i at time t. R_i is linked to two functions, as shown in Eq. (29.3): the breakage function $B_{i,j}$, which represents the particle size distribution resulting from the breakdown of fraction of size x_j, and the selection function S_i, that is, the probability of this size x_i to be fragmented.

$$\frac{dR_i}{dt} = -S_i R_i(t) + \sum_{j=1}^{i-1} R_j(t)\left[S_{j+1}B_{ij+1} - S_j B_{ij}\right] \tag{29.3}$$

This equation is normally solved using the similar solutions presented by Kapur (Eq. 29.4), adopting simplified expressions for B and S.

$$R(x,t) = R(x,0)\exp\left[\sum_{k=1}^{p} K^{(k)}(x)\frac{t^k}{k!}\right] \tag{29.4}$$

The term set in brackets includes what is known as the Kapur functions, from which $B_{i,j}$ and S_i can be derived.

For short grinding times, a residual ratio, representing the fraction of particles not yet broken, can be defined as Eq. (29.5):

$$f(x,t) = \frac{R(x,t)}{R(x,0)} = \exp\left(K^{(1)}(x)t\right) \tag{29.5}$$

By plotting $\log\left[\frac{R(x,t)}{R(x,0)}\right]$ versus time t, it is possible to obtain the first Kapur function $K^{(1)}$ and thereby S^i and $B^{i,j}$ from Eqs. (29.6) and (29.7).

$$S_i = -K_i^{(1)} \tag{29.6}$$

$$B_{i,j} = \frac{K_i^{(1)}}{K_j^{(1)}} \tag{29.7}$$

By plotting the curve $B_{i,j} = f\left(\frac{x_i}{x_j}\right)$, it is possible to determine the main mechanism of breakage and compare its positions on the two extreme curves (abrasion and breakage curves) (Figure 29.5). The experimental curve is expected to lie between the two extreme curves, indicating a combination of abrasion and breakage. Under sonication, the experimental curve $B_{i,j}$ is nearer to the abrasion curve, which would suggest that the dominant breakage mechanism is abrasion. However, it is important to note that it is only a qualitative analysis.

So the Kapur function takes into account the particle size. But Raman et al. (2011) proposed to include in Eq. (29.8) an ultrasonic parameter a, the function of the amplitude ratio:

$$K^{(1)}(x) = -a(1 - \exp(-bx)) \tag{29.8}$$

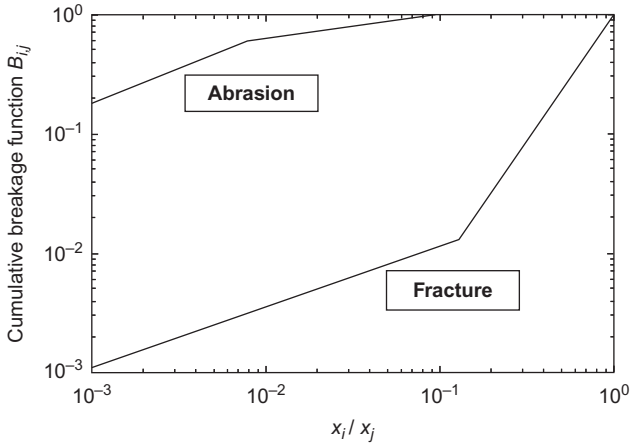


FIGURE 29.5 Cumulative breakage function representation $B_{i,j}$ versus x_i/x_j obtained for different grinding mechanisms according to Raman et al. (2011).

a is connected to the amplitude ratio:

$$a = a_0 + a_1 \frac{\varepsilon}{\varepsilon_{\max}} \tag{29.9}$$

where $\frac{\varepsilon}{\varepsilon_{\max}}$ is the amplitude ratio (equivalent to the relative input power); a_0, a_1, and b are parameters. Referring to calorimetric measurements, the amplitude ratio variation with the specific input ultrasonic power (W/kg) was linear at a given temperature.

Monitoring patterns of population could be achieved correctly, taking into account not only particle size but also operation parameters such as temperature and US power input. It shows that even if particle abrasion is the main mechanism, fracture can occur in specific cases. Note that this model is valid only for short sonication times (10 min). Because of breakage, the number of particles increases. So, cavitation areas might be reduced because of possible damping of the acoustic intensity, even under the cavitation threshold.

US can also disrupt different types of cells. In this particular case, the objective is not to reduce the size of the element but to break the membrane in order to destroy the cell (e.g., for sterilization) or to recover products inside. Bacteria cells, for example, can be broken or lysed to recover protein. The energy liberated during bubble collapse is dissipated in eddies which, depending on their size compared to the cells, result in cell membrane deformation and erosion or in cell motion (Doulah, 1977, 1978). Kinetics of bacteria cell disruption (*Lactobacillus acidophilus*, *Acetobacter peroxydans*) based on the theory of local isotropic turbulence was proposed (Choonia and Lele, 2011; Kapucu et al., 2000). The model takes into account the sonication power. Fn, the cumulative fraction of the cells disrupted at a given acoustic power, was a function of the sonication time t:

$$\mathrm{Fn} = 1 - \exp\left[-\left(\frac{t}{\alpha}\right)^{\beta}\right] \tag{29.10}$$

where α gives the characteristic lifetime of the equipment being tested (it is a sequential process; for example, the generator used by Kapucu et al. (2000) permits control of the wave duty cycle, which was a 4-s cycle: 2.5 s with the generator acting and 1.5 s of rest). β determines the pattern of failure: $\beta < 1$ indicates early life failure, $\beta = 1$ gives a constant failure, and $\beta > 1$ implies the failure results from wear effects. β values decreased when the acoustic power increased and so the disruption efficiency. Cell disruption was shown as directly proportional to the acoustic power. The same work carried out on *Escherichia coli* proved US to be 22 times faster than enzymatic methods in terms of protein release (Ho et al., 2006). Gerde et al. (2012) also conducted work on breakage of heterotrophic (*Schizochytrium limacinum*) and autotrophic (*Chlamydomonas reinhardtii*) microalgae cells, further confirming the correlation between energy input and

TABLE 29.2 Order of magnitude of required time for the disruption according to ultrasonic energy and cell nature

Particle nature	Power	Time (s)	E_v (J/L)	Lysed cells (%)
Spores	10 W/cm^2	60	–	100
Vegetative cells	0.9 W/cm^2	10	–	82
Polymer micelles	40 W	600	4.8×10^6	100

maximal cell disruption while warning that excessive time produces free radicals.

Of course, the efficiency of the cell disruption process is not only dependent on the acoustic power of the sound waves but also on the physical strength of the cell wall of the microorganisms (Sauer et al., 1989). Particular attention should be paid to the control of temperature, especially close to the probe. Indeed, most of the ultrasonic energy is dissipated into the medium, and the subsequent increase in temperature can also cause the degradation of proteins. Another parameter to take into account is the size and the shape of the cell. The smaller and rounder the cell, the more difficult it is to disrupt (Alliger, 1978).

Other examples of particle disruption exist, such as polymer micelles for medical applications (Xuan et al., 2011) and spores (Chandler et al., 2001). Recent experiments show that US can induce leakage from lipid vesicles. The mechanism is not so clear: cavitation bubbles would induce transient structural deformation, resulting in the formation of transient mesopores (Marmottant et al., 2008; Wrenn et al., 2013). The few results indicating the order of magnitude of time required for the disruption according to the ultrasonic energy and the nature of the cell are reported in Table 29.2.

29.5 Solid and liquid dissolution

When no chemical reaction is involved, dissolution is usually controlled by mass transfer from the solid surface to the liquid bulk. In this case, mass transfer depends on the concentration gradient (difference between equilibrium concentration at the solid surface and bulk concentration), the liquid-solid interfacial area, and the liquid-solid mass transfer coefficient. In well-mixed batch dissolution, the solid-liquid mass transfer process can be modeled by Eq. (29.11):

$$\frac{dC}{dt} = k_c \left(\frac{S}{V}\right)\left(C^* - C\right) \tag{29.11}$$

where C is the concentration of solute in solution (mol/m^3), t is the time (s), k_c is the intrinsic mass transfer coefficient (m/s), S is the surface area (m^2), V is the volume of solvent (m^3), and C^* is the solubility, the saturation concentration of the solute (mol/m^3).

Dissolution is usually performed by suspending the solid in the solvent under stirring, and this process may be rather slow for sparingly soluble solids. In the case of suspension, the mass transfer coefficient k_c is nearly independent of the stirring speed as long as total particle suspension has been achieved. This important feature, often ignored, may be explained by the fact that (i) k_c is connected to the relative velocity between the particles and the stirred liquid (nearly equal to the terminal velocity) and (ii) increasing turbulence by increasing stirring speed results in two opposite effects: reduced terminal velocity but increased mass transfer coefficient at a given velocity. Then very intensive stirring does not improve dissolution in suspension unless the particles break up.

High-power US may provide an efficient alternative to usual dissolution in a stirred reactor, where energy is dissipated in the whole liquid bulk. With US in cavitation conditions, because of the specific interaction between cavitation bubbles and solid particles, a much higher fraction of the energy is dissipated in the close vicinity of the particle surface. The bubble collapse near the suspended particles provides intense microstreaming and efficient renewal of the liquid in the boundary layer, leading to a much faster mass transfer coefficient. In addition, some authors have claimed that solubility C^* could also be improved under sonication, but it seems to be more likely to be an effect of the temperature increase caused by US energy input in uncontrolled temperature experiments (Sandilya and Keenan, 2012).

In Eq. (29.11), the surface area S/V also will be increased if the ultrasonic break up of solid particles occurs (see Section 29.4) which can significantly enhance the whole dissolution process. Of course, the addition of these two additive effects of low-frequency power US—enhanced mass transfer coefficient and enhanced solid-liquid surface because of particle break up—will provide the best US efficiency, well above that of usual stirring.

Work dedicated to liquid solid mass transfer in suspension during sonication is uncommon. However, Stoian et al. (2019) found success in the use of sonification for process intensification of agitated slurry vessels where the rate and degree were higher in the desorption system (phenolpolymeric resin) systems but were ineffective using an ion-exchange (NaOH-cation) resin system.

It is rather difficult to find examples of dissolution under US without resizing (breaking) the particles. More often, erosion or break-up takes place simultaneously and modifies the particle size distribution, generating fine particles that are rapidly dissolved. One example of noneroded

particles is the dissolution in water of crystallized salts in the pore network of stones (granite and sandstone) (Inigo et al., 2001). In this case, dissolution takes place only for one of the components present in the solid. The standard method is carried out under stirring for 3 days at a temperature of 60°C. Using sonication, it was possible to achieve a comparable dissolution in only 45 min. However, the role of US inside the solid matrix was not explained.

Research involving the effect of US on simultaneous size reduction and dissolution of particles is scarce. Dissolution and particle size reduction of alumina and silica have been described in the context of contaminated sediment treatment (Lu et al., 2002). Sonication permits improvements in the dissolution of aluminum and silicon compared with classic mechanical stirrers (concentration after sonication is 7–20 times that of only mixing). The average particle size decreases and a new population of small particles appear. Therefore, this phenomenon cannot be explained only by dissolution. Scanning electron microscopy observations show that the solid surfaces become smoothed as a result of sonication, confirming erosion. The two phenomena were observed but not quantified.

Interesting studies of the breakage and dissolution of sparingly soluble benzoic acid dispersed in aqueous glycerol solutions were recently performed. A smart chemical engineering approach is followed to separate break-up and mass transfer effects (Sandilya and Keenan, 2012). To delineate the effects of particle breakage from solid dissolution, additional experiments without mass transfer limitation (by presaturating the solvents with benzoic acid) were carried out. Empirical correlations were developed to describe the evolution of the surface area according to the ultrasonic energy. So, it is possible to estimate the specific area and decouple the effect of sonication on the mass transfer coefficient and on surface area. A Sherwood number correlation is proposed to estimate US influence on intrinsic mass transfer coefficient k_{US}, taking into account the variation of the De Brouckere particle mean diameter (d_{43}). The Sherwood number is classically defined according to Eq. (29.12):

$$Sh_{US} = \frac{k_{US} d_{43}}{D_{AB}} \tag{29.12}$$

where k_{US} is the intrinsic mass transfer coefficient under sonication, d_{43} is the De Brouckere particle mean diameter (the equivalent diameter of a sphere of same volume), and D_{AB} is the mass diffusivity. A Sherwood number correlation is proposed:

$$Sh_{US} = 0.6732 (Re_{US})^{0.4360} (Sc)^{0.3366} \tag{29.13}$$

This correlation is based on a usual Schmidt number Sc, defined as the ratio of kinematic viscosity v (m^2/s) and mass diffusivity D (m^2/s) and a specific US Reynolds number. Re_{US} is based on the energy dissipation ε (dissipated power per unit weight [W/kg or m^2/s^3]) and kinematic viscosity v (m^2/s), as is often used in modeling turbulent mass transfer (Kawase and Mooyoung, 1987).

$$Re_{US} = \frac{d_{43}^{4/3} \varepsilon^{1/3}}{v} \tag{29.14}$$

This unique correlation could be used in any dissolution case, even when the solid is strong enough not to undergo breakage or erosion.

Another type of transfer enhancement by sonication was suggested by cellulose-improved dissolution in ionic liquids under US (Lan et al., 2011). The operating time was reduced from 190 to 20 min. In this case, US was supposed to provide a greater penetration of the ionic liquid into cellulose and increase the mass transfer. However, the conditions of dissolution might be better because of the temperature increase.

In addition to the two fundamental effects of power US on solid dissolution (mass transfer increase and particle breakage, leading to a larger solid surface), a third positive effect of US may be found in more complex situations, including reactions where the dissolution of some species may give rise to the formation of another solid that tends to coat the solid particles and then stop dissolution. In this case, US-induced continuous erosion of the particles erodes this passivation layer and allows the dissolution process to continue.

One example in the case of zinc extraction is direct oxidative leaching of sphalerite concentrates (zinc sulfide concentrates) with ferric iron (Grenman et al., 2007). Zinc is dissolved and at the same time ferric iron is reduced to ferrous iron in a sulfuric acid solution. Using a low US frequency (30 kHz), it was assumed that no US radical chemistry was performed. Indeed, experiments carried out under strong mechanical agitation but with silent conditions gave the same results: no increase in the reaction rate. One interesting point is that under some conditions, another undesired reaction can occur and form a layer of sulfur on the particle surface, hindering the dissolution reaction. However, their experimental data could be better fitted by a model that does not take into account the diffusion in this sulfur layer. This could suggest that the possible layer is continuously removed or not formed because of the sonication. Similar behaviors were observed by other researchers (Park and Fan, 2004; Trofimov et al., 2001). So, it may be concluded that US-enhanced dissolution of chemicals is often the result of several beneficial effects: enhancement of the mass transfer coefficient, of the solid-liquid surface area through particle breakage, and regeneration of the active surface through intense cleaning and erosion.

The dissolution phenomenon is also concerned by the very important application of US in activated sludge

treatment. Reduction and valorization of sewage sludge is a serious environmental and economic issue for which power US has become an industrial application. It is a well-studied area that has resulted in interesting reviews (Khanal et al., 2007; Le et al., 2013b; Yagci and Akpinar, 2011; Yin et al., 2004; Raheem et al., 2018). Since 2000, full-scale application of this treatment in Germany has shown that US disintegration offers a reliable and cost-effective means for treating wastewater treatment sludge, resulting in a decrease in sludge quantity (volume and mass) and an increase in the biogas yield. It also results in a larger output of dry solids and a lower requirement for polymer/additives in the dewatering process.

The first step is floc breakage by sonication. A floc will be broken if the stress applied at its surface is larger than the bonding strength. Therefore, there exists a critical ultrasonic power above which the floc structure can be disintegrated. As for a solid particle, two phenomena previously described in Section 29.4 can take place: surface erosion and large-scale fragmentation. Ultrasonic sludge treatment can be divided into two stages: first, porous flocs (100 μm) are disrupted into small microfloc aggregates or floccule with a diameter of 10–20 μm. Then, floccules are slightly reduced to a diameter < 10 μm (primary particle about 2 μm), bacteria and coliform are lysed, and the intracellular organic substances are released. The two stages are not entirely separated because sludge is not homogeneous. Short periods of intense sonication are sufficient to quickly reach a stable small particle size (micron). However, if the bacteria must not be damaged, a low level of ultrasonic energy over a long time is preferred.

In addition to disintegrating cells and flocs, US also helps to dissolve organic compounds, generally quantified in terms of chemical oxygen demand (COD), during or before anaerobic digestion, which is particularly interesting for methanization. Sludge COD is the quantity of oxygen needed to fully oxidize the organic material (mineralization) contained in the sludge (both in cells and in the various solid materials). It must be transferred from the cell content (disruption) and solid materials (solubilization) into the external liquid phase of sludge and then transformed by the anaerobic methanization process. COD and rate of nitrogen solubilization gradually increase during the sonication, as did supplied ultrasonic energy (Bougrier et al., 2005; Chang et al., 2011). However, at same specific ultrasonic energy, it is better to use high power for a short time (Figure 29.6) (Le et al., 2013b). The influence of some parameters on COD dissolution has been studied by Le et al. One parameter is temperature (Le et al., 2013a). US under adiabatic conditions permits an increase in temperature, which is beneficial to the COD solubilization. The external pressure also plays an interesting role, increasing cavitation, and an optimum exists (Figure 29.7). The effect of frequency also was studied, showing an acceleration of COD dissolution at 12 kHz compared with 20 kHz. However, it was shown that the kinetics of particle size reduction was much faster and not directly correlated to COD solubilization. Reduction of mean particle size during sonication is, then, a first step to dissolve COD.

Other research concerning dissolution assumes that US could increase solubility. Although remarkable results were observed, this hypothesis is very controversial and has no scientific basis: contrary to a gas-liquid system, a change of solubility in liquid-liquid or liquid-solid systems would involve some chemical change or some change in thermodynamic conditions, such as temperature. One example is whey protein. It could be solubilized more under sonication (Jambrak et al., 2008), but experiments were carried out

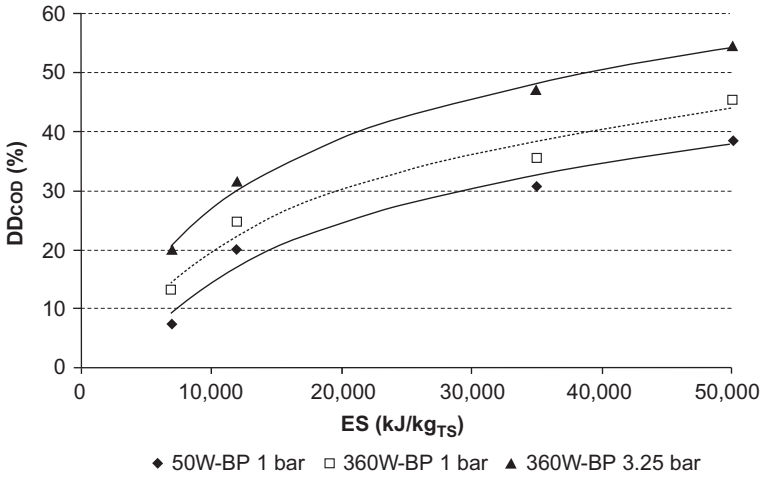


FIGURE 29.6 Effect of specific energy ES on COD dissolution (DD_{COD}) according to power input and external pressure according to Le et al. (2013a).

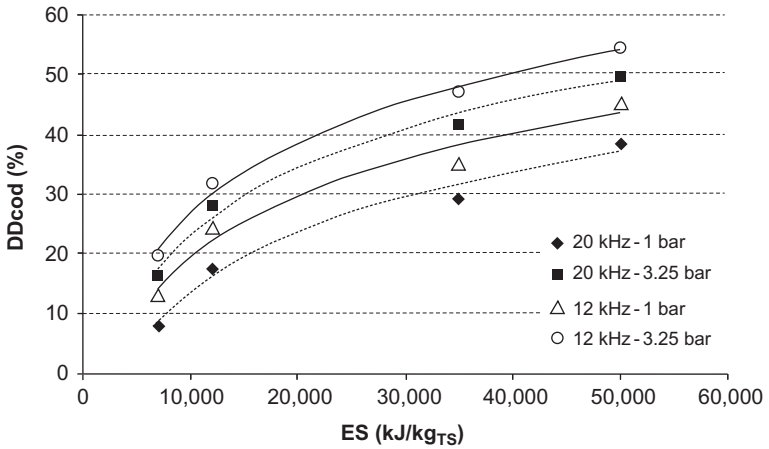


FIGURE 29.7 Effect of specific energy ES on COD dissolution (DD_{COD}) according to external pressure and frequency according to Le et al. (2013b).

under adiabatic conditions, so the resulting increase of temperature did contribute to enhancing the protein solubility. Moreover, sonication induced the lysis of the globular protein, which results in changes in the three-dimensional structure. This caused an increased number of charged groups (NH_4^+,COO^-), leading to better protein-water interaction. Again, it seems more probable that this solubility improvement under sonication is simply caused by changing the operating conditions (higher temperature) and/or modifying the nature of the product to be dissolved. In the same way, conclusions were drawn from results of dissolution of glycyrrhizic acid from glycyrrhiza uralensis in water (Yang et al., 2012). US was able to change the structure of glycyrrhiza uralensis, so a new equilibrium was reached. Another work clearly demonstrated that US does not affect the solubility of docosane in heptane (Alves et al., 2001).

To a lesser extent, examples of liquid dissolution can be found. The dissolution and reaction modeling for hydrolysis of tetraethoxysilane in a heterogeneous tetraethoxysilane-water-hydrogen chloride mixture under US stimulation was investigated (Donatti et al., 2002). US was claimed to maintain a quantity of water under a virtual state of dissolution. Sonication could induce a thermodynamic modification and create a new equilibrium. As previously explained, it is true that US generates locally a hot spot with a high temperature and pressure. So, it could change the equilibrium. But in the liquid phase, this increase in temperature is not so large (about 12 degrees) and concerns only a small part of its volume. Under sonication, alcohol was no longer needed to promote the reaction. The explanation of the enhancement is more likely faster mixing due to cavitation. It was considered equivalent to an increase of contact area between the two phases (alkoxide and water). In the same way, US is highly recommended for producing biodiesel, and a commercial US reactor is available (Hielscher). Over the past decade, Kumar et al. (2012) have investigated transesterification with sonication improving the oil-ethanol mass transfer while also allowing faster operation (7 min instead of the 4 h necessary for conventional techniques) under mild conditions (no high temperature and/or pressure). Furthering this work in a recent study into continuous methanolysis of *Jatropha curcas* oils yielded purity and conversion of biodiesel at over 98% completed within 1.09 min (Kumar et al., 2017).

29.6 Homogenization

In a chemical engineering approach, homogenization generally means "to obtain a homogeneous concentration," that is, a uniform concentration everywhere in the reactor, and most often, "mixing" is preferred to homogenization. In food engineering, it has a much more specific meaning: homogenization is the important process of decreasing the particle size in fluids such as milk, fruit juice, tomato products, and sauces. Classically, in the case of fat globules, the final size to reach is about 1–5 µm, whereas for solid food, it is about 1–3 µm. The goal of this size reduction is to prevent the settling, agglomeration, and segregation of particles during storage to keep a good dispersion as long as possible. This provides improved product stability, shelf life, digestion, and taste. Indeed, according to the density of the dispersed phase, agglomeration leads to a higher concentration at the top (fat globules) or at the bottom (fruit pulp). Milk homogenization is essential to avoid obtaining various levels of flavor and fat concentrations. Homogenization increases viscosity and the feel of the final product in the mouth. Milk homogenization is by far the most important industrial application, and the most investigated, and this section focuses on it.

Homogenization can be performed using a high-speed blender, but a high-pressure homogenizer (100–200 bar) is

conventionally used. Initial suspended particles with sizes ranging typically from 5 to 20 μm enter the homogenizer. The pressurized suspension enters through the homogenization head and is abruptly forced to change direction (angle of 90 degrees) and pass through a smaller section. Then acceleration causes a large increase in kinetic energy, resulting in particle size reduction. The proposed mechanisms to explain this phenomenon are shear, microturbulence, and hydrodynamic cavitation. Indeed, fluid velocity dramatically increases. Because of energy conservation, the pressure decreases and can become lower than liquid vapor pressure, leading to the formation of cavitation microbubbles, which later collapse in higher-pressure zones where the fluid decelerates.

Therefore, it is logical to use US to benefit of the acoustic cavitation effects (Herceg et al., 2009; Mohammadi et al., 2014; Carrillo-Lopez et al., 2021). The disruption of fat globules is still caused by pressure differences due to collapsing bubbles (shockwaves and microjets). This breakage is not spectacular because the mean particle size is not decreased much. In general, the average size has to be reduced from 10 to <1 μm under sonication. The objective is principally to break large particles to obtain a very narrow final size distribution and to form a homogeneous suspension. Homogenization can be controlled through the variance of the particle size distribution generally fitted by a log normal law. In addition to the particle size reduction, the location of fat is also determined after 2 days in a refrigerator: fat contents of the sample from the upper part, that one-tenth (a), and from the bottom nine-tenths (b). Therefore, the homogenization efficiency is defined as shown in Eq. (29.15):

$$H_e = \frac{a-b}{a} \times 100 \tag{29.15}$$

A lower H_e indicates better homogenization. A diameter around 0.8 μm seems to be convenient for avoiding a creaming effect during storage.

The mean globule size and H_e decrease rather quickly with the sonication time (diameter around ≤1 μm within ≤15 min). This process is even faster at high US power, as shown in Table 29.3 (Ertugay and Sengul, 2004), which compares fat globule diameters obtained in conventional and ultrasonic homogenization treating an equivalent quantity of milk. Sonication for 10 min at 180 W obtains smaller-diameter fat globules than conventional homogenization at 200 bar.

US also has a very good effect on homogenization compared with conventional homogenizers but only at high power levels (>180 W during 5 min to treat 250 mL of milk). It should be noted that for the same energy, the best results are obtained at the highest power and the shortest time. Such results also were found by Le et al. for sludge disintegration (see Section 29.4).

The breakage mechanism is not clear because milk is a complex fluid. Milk fat globules are quite spherical although delimited with a membrane. US waves disrupt and crack this membrane by releasing triacylglycerols. Indeed, electronic microscope observations of raw milk fat globules show very circular particles with a smooth surface. After sonication, the globules are very small (diameter of <1 μm), are no longer spherical, and have orifices visible on their surface. Moreover, this surface is completely roughened and granular. This can be caused by the interaction between the disrupted milk fat globule membrane and some casein micelles existing in the milk. These micelles coat the fat globule surface. So the suspension homogenization is more stable during the time. Consequently, sonication also modifies milk's composition and thus its physical properties such as viscosity and pH (Michalski and Januel, 2006; Shanmugam et al., 2012).

Much research in the field of homogenization of milk of different origins (animal, vegetable, and sometimes human; skim or not) resulted in the same US efficiency even if the fat content (0.6%–4%) and globule size of these milks differ slightly (Bosiljkov et al., 2009, 2011; Ertugay and Sengul, 2004; Silva et al., 2011; Wu et al., 2000). Some examples of homogenization conditions are presented in Table 29.4.

An interesting operation is thermosonication; milk can be pasteurized and homogenized in a single step, providing

TABLE 29.3 Fat globule diameters obtained in conventional and ultrasonic homogenization

Treatment	Raw milk	Conventional homogenization	Ultrasonic homogenization Power (W) Time (min)							
		(Alfa Laval homogenizer 200 bar)	90	90	180	180	360	360	450	450
			5	10	5	10	5	10	5	10
Mean fat globules size (μm)	5.5	2.63	3.88	3.5	3.38	2.38	2.13	1.25	1.13	0.72

TABLE 29.4 Times classically required to homogenize different types of milk

Milk origin	Time (min)	Fat globule diameter (μm)	Power input (W)	Volume (mL)
Cow	10	1.25	360	250
Soybean	10	1.5	100	150

important cost savings (Bermudez-Aguirre et al., 2008; Czank et al., 2010; Carrillo-Lopez et al., 2021). A synergy could be observed. Indeed, as described in Section 29.4, US can disrupt biological structures and cause cell death. Moreover, operation under adiabatic conditions leads to an increase in temperature due to high power dissipation. From a nutritional point of view, the combination of US and heat is a food preservation technique that retains higher quantities of bioactive components compared with common thermal pasteurization practices (Earnshaw et al., 1995; Miles et al., 1990). One proposal could be to use sonication alone to both homogenize and pasteurize. However, research seems to indicate that sonication alone is not sufficient as a nonthermal alternative to pasteurization. US was found to eliminate spoilage and reduce potential pathogens to zero or to acceptable levels, but it is ineffective in deactivating some enzymes such as alkaline phosphatase and lactoperoxidase (Cameron et al., 2009).

Others research on homogenization of other food suspensions such as fruit juice, tomato products, and sauces also was carried out. Texture is a critical quality attribute in consumer acceptability (Cao et al., 2010; Luisina Gomez et al., 2011). The objective of ultrasonic treatment in this case is to significantly enhance the total solid content; viscosity is more the key parameter (Anese et al., 2013; Vercet et al., 2002; Wu et al., 2008). In some cases, the particle size distribution is followed by chord length distribution as a function of US intensity. Pulsed US with a short on/off sequence (5 s), for a total sonication time of few minutes, was preferred (Keenan et al., 2012). As another example, Wu et al. studied the sonification of tomato juice (200 mL) for 8 min at different power inputs (Wu et al., 2008). The resulting mean diameters are presented in Table 29.5. A recent area of research has focused on the effect of the ultrasound treatment on the functional and physiochemical properties of starch-based sauce where it has been reported to reduce retrogradation and improve intrinsic viscosity and textural properties (Okonkwo et al., 2021).

TABLE 29.5 Particle diameters obtained in 200 mL tomato juice after 8 min under sonication versus the input power

Sonication power (W)	0	60	90	120
Particle size (μm)	423	371	70	58

Source: Wu et al. (2008).

One last point is that the use of US has a slight limitation because of equipment. The risk of metal contamination because of probe erosion is an important drawback of these applications. Such metal contamination is totally prohibited in the food industry, which is very controlled. A possible design would be to use many transducers of rather low power dispatched around the US homogenizer diameter to focus US in the central zone, where cavitation would take place, and to avoid it at the emitter surfaces (Dion, 2009).

29.7 Emulsification

An emulsion is a heterogeneous system consisting of at least one immiscible liquid intimately dispersed in another in the form of droplets, whose diameters, in general, exceed 0.1 μm; recently, however, growing interest was focused on nanoemulsions down to 20 nm (Leong et al., 2009). Such systems are of great importance as final products in the food, pharmaceutical, and cosmetic industries and as reaction media in emulsion polymerization or for extraction purposes. They may be stabilized by surface-active agents.

The type of simple emulsion (water-in-oil or oil-in-water, commonly abbreviated as w/o or o/w) is chosen mainly by the volume ratio of the two liquids, their order of addition, and the nature of the emulsifier. Nevertheless, using US favors the phase undergoing first cavitation (it has the lower cavitation threshold) to be the continuous phase. O/w emulsions are more easily prepared and most often investigated. Note that three-phase o/w/o emulsions also were prepared by ultrasonic vibration (Lin and Chen, 2008).

Emulsions may remain practically unchanged to the naked eye for several months but eventually return to their stable state, that is, a phase-separated system. In emulsion breaking, two kinds of phenomena can be discriminated: those that are generally reversible and involve particle aggregation and migration (by Stoke's law), and those that are irreversible and related to particle size modification (through Ostwald ripening and coalescence). Briefly, emulsion stability depends on (i) droplet size, (ii) difference in the density of the dispersed and continuous phases, (iii) viscosity of the continuous phase, and above all (iv) the electrostatic and/or steric repulsion between droplets (in which the surfactant plays a major role).

Except in special cases where spontaneous emulsification can occur, energy must be supplied to produce such metastable mixtures. A much larger amount of energy, with respect to the thermodynamic part ($\Delta G = \gamma \Delta A$), is required; the excess energy is dissipated as heat. Energy may be provided through various means, namely, mechanical agitation (stirrer, colloid mill, mixer, valve homogenizer) and US.

Emulsification is one of the oldest applications of high-power US (Wood and Loomis, 1927), and the first patent was granted in 1944 in Switzerland. US emulsification is thus an already known phenomenon, has been reviewed by Canselier et al. (2002), and is still largely investigated (Cucheval and Chow, 2008; Freitas et al., 2005, 2006; Gaikwad and Pandit, 2008; Jafari et al., 2006, 2007; Leong et al., 2009; Lin and Chen, 2008; Mosavian and Hassani, 2010; O'Sullivan et al., 2015; Taha et al., 2020).

29.7.1 Specific aspects of US emulsification

Most of the main features and main parameters of emulsification are still expected in US emulsification: role of the surfactant, the energy supply, the physicochemical properties of the two phases (mainly density, viscosity, and surface tension), and the volume fraction of the dispersed phase. Recall that, as for previous operations described in this chapter, the energy cost should be estimated as $P_{US} \cdot t$ per volume or weight of emulsion, and the quality is mainly related to droplet size (mean diameter and distribution), and finally, stability, which is reported much less often. Note that sonoemulsification without any surfactant, although used by Reddy and Fogler (1980) in a special emulsion system at a very low oil fraction, has not been confirmed in general.

US emulsification results from a two-step mechanism (Li and Fogler, 1978a,b). First, some drops form in the continuous phase because of Rayleigh-Taylor instability. Second, these drops progressively break into tiny droplets because of shock waves involved by transient cavitation near the interface. The first step in creating a coarse emulsion (preemulsification) is the most critical concerning US efficiency (Canselier et al., 2002) because it is very dependent on geometry (Cucheval and Chow, 2008). Intense acoustic streaming performed by a small horn at a very high acoustic intensity and located near the interface (a few millimeters) in the phase to be dispersed conveniently achieves this first step. Alternatively, for example, in a large-scale operation, a gentle preemulsification with usual stirred or motionless equipment is needed (Abismail et al., 1999). Note that because of the limited macromixing achieved by US alone, a double emulsion may be generated simultaneously with w/o at the top of the beaker and o/w at the bottom (Gaikwad and Pandit, 2008).

Most often, surfactants have the desired property of being located at the cavitation bubble interface. As seen in Section 29.2, they are in contact with free radicals produced during transient collapse and might be chemically modified or even degraded (Alegria et al., 1989). Nevertheless, at a low frequency and short sonication time, this chemical degradation is not noticeable (Canselier et al., 2002; Leong et al., 2009).

A possible drawback of US emulsification, especially for food or pharmaceutical applications, is possible contamination by very small metal particles through probe erosion. Several improvements have been proposed to avoid this contamination. Freitas et al. (2006) designed a new US continuous emulsifier where US is first emitted to a steel tube containing pressurized water, which transmits the US energy to an inner glass tube where the preemulsified liquid-liquid mixture is flowing. This equipment is well suited for aseptic continuous processing, but because of US losses through the coupling of pressurized water and two tubes, it probably is less efficient than the multiple emitter reactor, which focuses US around its axis and avoids cavitation on emitter surfaces (Dion, 2009).

The effect of pressure was noticed in very old works (Bondy and Sollner, 1935) and was especially detailed for a nanoemulsion preparation (Leong et al., 2009) for which an optimum pressure of four bar was obtained; no more

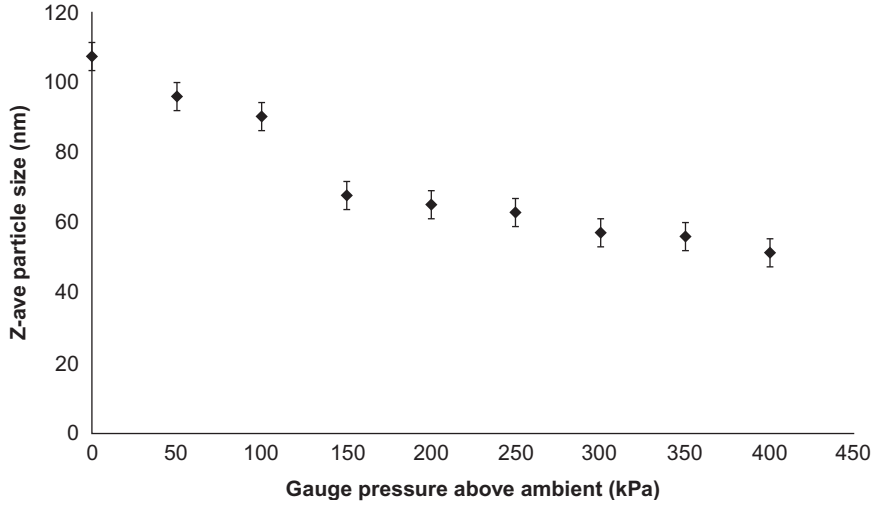


FIGURE 29.8 Effect of increasing overpressure in the continuous flow-through cell on emulsion particle size, according to Leong et al. (2009).

emulsification occurred at higher pressures, where the transient cavitation threshold was probably not reached (Figure 29.8).

Very different results were found in some previous work (Behrend and Schubert, 2001), but it should be emphasized that the effect of pressure depends on many other conditions controlling cavitation. Cavitation intensity is connected with pressure in a rather complex way, leading to an optimum pressure, which is a function of liquid properties and gas content and acoustic density; such complex dependence should be expected for US emulsification. Thus, this optimum pressure depends on temperature, the nature of the dissolved gases, the boiling point of the continuous phase, and probably, the selected surfactant.

29.7.2 Main features of US emulsification

In addition to general physicochemical parameters (surfactant nature and concentration, viscosity and density of the two phases), the main operation parameter concerns energy consumption. According to turbulence theory, the maximum particle size in turbulent flow is proportional to $P_v^{-0.4}$ (where P_v is the power density). This corresponds to a final stage, and in any emulsification processes, the operation time (here sonication time t_e) has to be accounted for, and the energy density ($E_v = P_v \cdot t_e$ in kJ/m^3) is the key parameter to estimate the efficiency of a given emulsion formula. Most recent works use this parameter instead of separate irradiated time and US power. Nevertheless, note that previous works related to similar US applications (cell disruption, sludge disintegration) showed a slight improvement when using higher power during a shorter time at the same E_v (Le et al., 2013b). Importantly, that US emulsification does not occur at all under the transient cavitation threshold means that US is not convenient for performing coarse emulsion at low energy consumption. Above this minimum energy, most results agreed with the $P_v^{-0.4}$ dependence on mean particle diameter, whatever the US equipment, but when operating at a higher pressure, a better effect of dissipated power ($P_v^{-0.6}$) was found, showing trends very similar to those of high-pressure homogenizers (micronizer) (Leong et al., 2009) (Figure 29.9).

A rather complete comparison of US and Ultra Turrax emulsification (operating according to the principle of a turbine, the dispersion head draws liquid upward then rejects the product laterally through the slots of the stator) on a simple three-component model system (water/kerosene/polyethoxylated [20 EO] sorbitan monostearate) (Abismail et al., 1999) is summarized in Figures 29.10–29.13. It affords several interesting results in favor of the US technique: (i) much smaller average drop sizes d_{32} were obtained at the same energy consumption (down to 0.3 μm) (Figure 29.10) with less polydispersion (Figure 29.11) at any dispersed volume fraction (Figure 29.12); (ii) for a given desired diameter, the surfactant amount required was reduced (about five times less; Figure 29.13); and (iii) as expected with the previous improvements, stability was greatly improved, as quantified using a Turbiscan MA 2000, an optical analyzer that is able to detect the phenomena of migration of the particles in the medium: creaming, sedimentation, clarification, and coalescence at the beginning. The need for much less surfactant could be linked to the intense foaming that occurred when using the Ultra Turrax and captured a large amount of surfactant. Most of these findings have been confirmed by other works (Cucheval and Chow, 2008; Freitas et al., 2005; Gaikwad and Pandit, 2008; Jafari et al., 2006, 2007; Mosavian and Hassani, 2010). Interestingly, continuous US emulsification proved to be as efficient as batch operation (Abismail et al., 2000; Freitas et al., 2006; Leong et al., 2009; O'Sullivan et al., 2015) with the same performance at the same energy

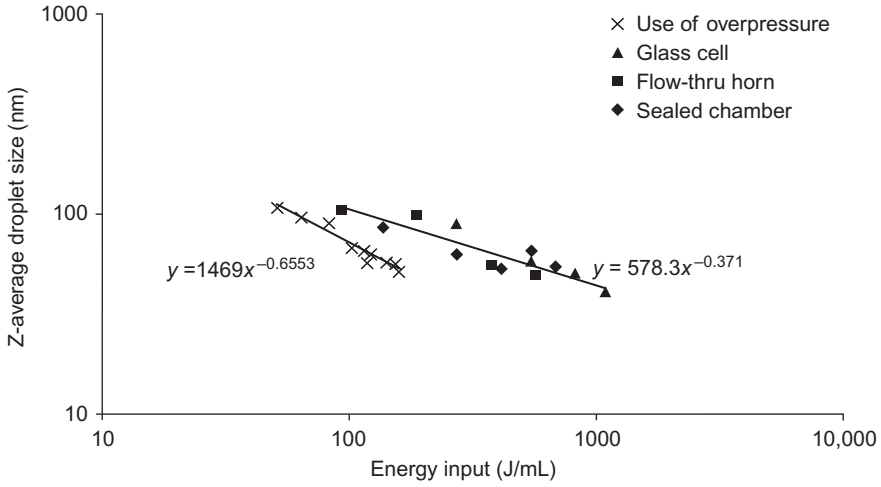


FIGURE 29.9 Relationship between the specific energy input and droplet size according to Leong et al. (2009).

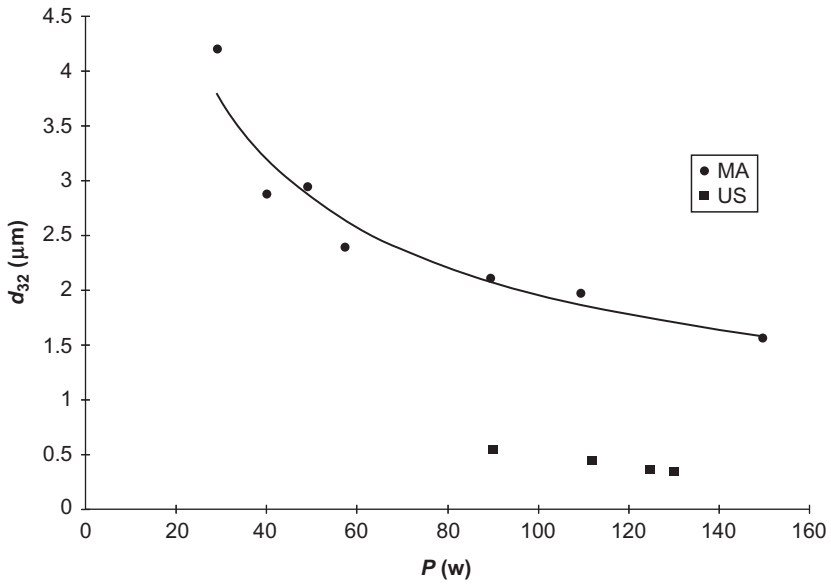


FIGURE 29.10 Variations of d_{32} versus power (*MA*, mechanical agitation; *US*, power ultrasound, $t = 30$ s, $c = 10$ g/L, $\varphi = 0.25$), according to Abismail et al. (1999).

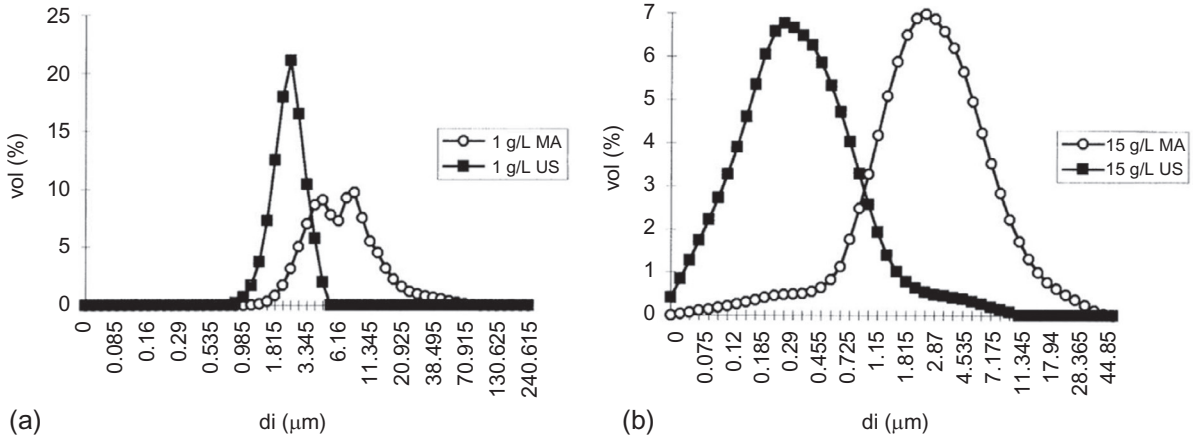


FIGURE 29.11 Volume drop size distribution: (A) low surfactant concentration, (B) high surfactant concentration (*MA*, mechanical agitation; *US*, power ultrasound), according to Abismail et al. (1999).

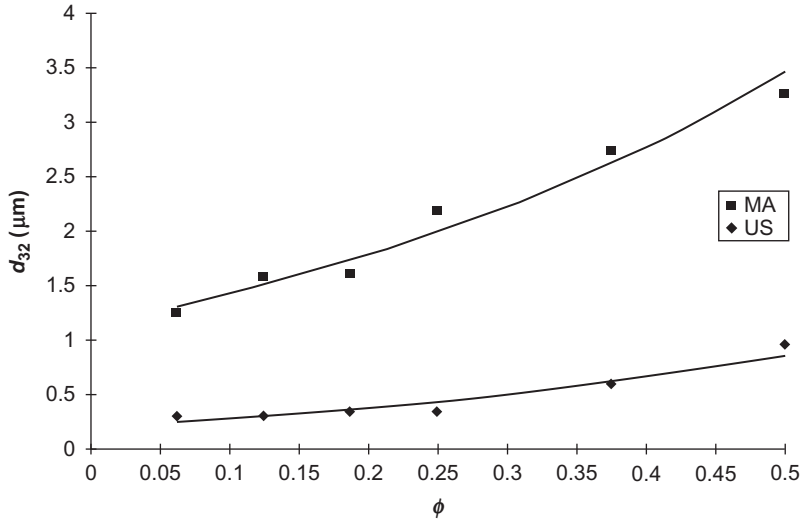


FIGURE 29.12 Variation of d_{32} versus oil fraction ($t = 30$ s, $c = 10$ g/L, PMA = 170 W, PUS = 130 W) (*MA*, mechanical agitation; *US*, power ultrasound), according to Abismail et al. (1999).

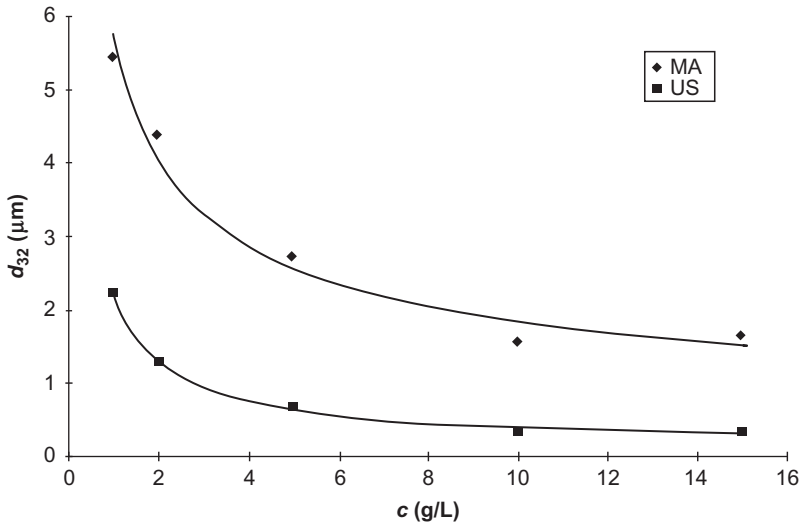


FIGURE 29.13 Variations of d_{32} versus surfactant concentration (*MA*, mechanical agitation; *US*, power ultrasound) ($t = 30$ s, $\varphi = 0.25$, PMA = 170 W, PUS = 130 W), according to Abismail et al. (1999).

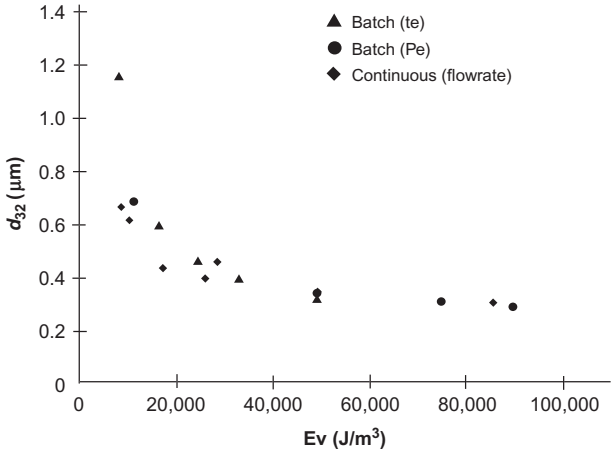


FIGURE 29.14 Variation of d_{32} versus energy density (varying emulsification time ($P = 130$ W), varying power ($t = 30$ s); varying flowrate ($P = 170$ W)), according to Canselier et al. (2002).

density, as shown in Figure 29.14. This important result confirms that the main operation parameter is the energy density, which should be kept constant in any scale-up procedure, as for other emulsification techniques, while keeping in mind to largely overpass the transient cavitation threshold.

29.8 Conclusions and future trends

This chapter reviews how US can improve mixing, disruption, dissolution, homogenization, and emulsification through transient cavitation and the high concentration of energy provided by bubble collapses. Despite convenient micromixing performance, because of microeddies on the same scale as cavitation bubbles, it should be emphasized that US mixing of a single liquid phase is clearly less attractive than other applications involving a multiphase system, such as solid-liquid or liquid-liquid suspensions. Indeed, the great advantage of acoustic cavitation when compared with other means of providing energy to a multiphase system is the preferential action of collapsing bubbles near interfaces (which may be caused by easier nucleation) and their attraction toward the interface during asymmetrical collapse, achieving much better local mass and momentum transfers, which lead to faster dissolution, erosion, or breakage.

Among the future possible improvements of US applications in solid and liquid suspensions, the use of higher static pressure conditions (up to a few bar) and of ultralow US frequency (well below 20 kHz) seems very promising, according to detailed comparisons on sludge break-up and organic dissolution (Le et al., 2013b).

From a more fundamental point of view, there is still a large gap between fundamental knowledge of single-bubble cavitation and the actual complex hydrodynamics of acoustic bubble clouds in suspensions. Simulations based on the well-known Rayleigh-Plesset equation (Rayleigh, 1917; Plesset, 1949) give excellent predictions for the nonlinear oscillations of single, isolated bubbles, subject to lower amplitude acoustic driving. At higher amplitudes, however, bubbles collapse inertially and tend to fragment into closely packed bubble clusters within a few ultrasonic cycles (Leighton, 1995; Johnston et al., 2014), which is beyond current modeling capabilities. Moreover, cavitation bubbles rarely occur in isolation, such that a full understanding of a real cavitating environment is extremely challenging. Although some progress has been made on characterizing the cavitation activity around the tip of a sonotrode/ultrasonic horn, and the dependence of tip-vibration amplitude (Yusuf et al., 2021), for example, there is still much that remains to be understood.

For any US application in processing, in a cavitating medium, the bubble population dynamics are extremely complex because of the bubble interactions in clouds (Tervo et al., 2006) and high acoustic damping in cavitation; the acoustic field is highly disturbed by cavitation (Dahnke et al., 1999). In addition, it is noteworthy that acoustic multibubble measurements in high cavitation conditions always show smaller diameters than expected by single-bubble dynamics at the strongest collapse conditions (Tsochatzidis et al., 2001). Using complex cavitation equipment, the main measurement of cavitation was performed with hydrophones (Harris, 1996) to record and analyze noise spectra, but the link with turbulence characteristics and resulting mass and momentum transfers has not been identified. In addition, specific features of cavitation in suspensions have not been conveniently investigated. This difficult task, which is very useful for a rational approach to any particle, drop, and cell process, should attract more sonochemical engineers.

References

Abismail, B., Canselier, J.P., Wilhelm, A.M., Delmas, H., Gourdon, C., 1999. Emulsification by ultrasound: drop size distribution and stability. Ultrason. Sonochem. 6, 75–83.

Abismail, B., Canselier, J.P., Wilhelm, A.M., Delmas, H., Gourdon, C., 2000. Emulsification processes: on-line study by multiple light scattering measurements. Ultrason. Sonochem. 7, 187–192.

Alegria, A.E., Lion, Y., Kondo, T., Riesz, P., 1989. Sonolysis of aqueous surfactant solutions—probing the interfacial region of cavitation bubbles by spin trapping. J. Phys. Chem. 93, 4908–4913.

Alliger, H., 1978. New methods in ultrasonic processing. Am. Lab. 10, 81–87.

Alves, K.C.M., Condotta, R., Giulietti, M., 2001. Solubility of docosane in heptane. J. Chem. Eng. Data 46, 1516–1519.

Anese, M., Mirolo, G., Beraldo, P., Lippe, G., 2013. Effect of ultrasound treatments of tomato pulp on microstructure and lycopene in vitro bioaccessibility. Food Chem. 136, 458–463.

Ashokkumar, M., 2011. The characterization of acoustic cavitation bubbles—an overview. Ultrason. Sonochem. 18, 864–872.

Baldyga, J., Bourne, J.R., 1984. A fluid mechanical approach to turbulent mixing and chemical reaction part ii micromixing in the light of turbulence theory. Chem. Eng. Commun. 28, 243–258.

Bang, J.H., Suslick, K.S., 2010. Applications of ultrasound to the synthesis of nanostructured materials. Adv. Mater. 22, 1039–1059.

Behrend, O., Schubert, H., 2001. Influence of hydrostatic pressure and gas content on continuous ultrasound emulsification. Ultrason. Sonochem. 8, 271–276.

Bermudez-Aguirre, D., Mawson, R., Barbosa-Canovas, G.V., 2008. Microstructure of fat globules in whole milk after thermosonication treatment. J. Food Sci. 73, E325–E332.

Bondy, C., Sollner, K., 1935. On the mechanism of emulsification by ultrasonic waves. Trans. Faraday Soc. 31, 835–843.

Bosiljkov, T., Brncic, M., Tripalo, B., Karlovic, S., Ukrainczyk, M., Jezek, D., Brncic, S.R., 2009. Impact of ultrasound-enhanced homogenization on physical properties of soybean milk. In: Pierucci, S. (Ed.), Icheap-9: 9th International Conference on Chemical and Process Engineering, pp. 1–3.

Bosiljkov, T., Tripalo, B., Brncic, M., Jezek, D., Karlovic, S., Jagust, I., 2011. Influence of high intensity ultrasound with different probe diameter on the degree of homogenization (variance) and physical properties of cow milk. Afr. J. Biotechnol. 10, 34–41.

Bougrier, C., Carrere, H., Delgenes, J.P., 2005. Solubilisation of waste-activated sludge by ultrasonic treatment. Chem. Eng. J. 106, 163–169.

Brotchie, A., Grieser, F., Ashokkumar, M., 2010. Characterization of acoustic cavitation bubbles in different sound fields. J. Phys. Chem. B 114, 11010–11016.

Burdin, F., Tsochatzidis, N.A., Guiraud, P., Wilhelm, A.M., Delmas, H., 1999. Characterisation of the acoustic cavitation cloud by two laser techniques. Ultrason. Sonochem. 6, 43–51.

Cameron, M., Mcmaster, L.D., Britz, T.J., 2009. Impact of ultrasound on dairy spoilage microbes and milk components. Dairy Sci. Technol. 89, 83–98.

Canselier, J.R., Delmas, H., Wilhelm, A.M., Abismail, B., 2002. Ultrasound emulsification—an overview. J. Dispers. Sci. Technol. 23, 333–349.

Cao, S., Hu, Z., Pang, B., Wang, H., Xie, H., Wu, F., 2010. Effect of ultrasound treatment on fruit decay and quality maintenance in strawberry after harvest. Food Control 21, 529–532.

Carrillo-Lopez, L.M., Garcia-Galicia, I.A., Tirado-Gallegos, J.M., Sanchez-Vega, R., Huerta-Jimenez, M., Ashokkumar, M., Alarcon-Rojo, A.D., 2021. Recent advances in the application of ultrasound in dairy products: effect on functional, physical, chemical, microbiological and sensory properties. Ultrason. Sonochem. 73, 105467.

Chandler, D.P., Brown, J., Bruckner-Lea, C.J., Olson, L., Posakony, G.J., Stults, J.R., Valentine, N.B., Bond, L.J., 2001. Continuous spore disruption using radially focused, high-frequency ultrasound. Anal. Chem. 73, 3784–3789.

Chang, T.-C., You, S.-J., Damodar, R.A., Chen, Y.-Y., 2011. Ultrasound pre-treatment step for performance enhancement in an aerobic sludge digestion process. J. Taiwan Inst. Chem. Eng. 42, 801–808.

Chartier, T., Jorge, E., Boch, P., 1991. Ultrasonic deagglomeration of Al_2O_3 and $BaTiO_3$ for tape casting. J. Phys. III 1, 689–695.

Cheng, Q., Debnath, S., Gregan, E., Byrne, H.J., 2010. Ultrasound-assisted SWNTs dispersion: effects of sonication parameters and solvent properties. J. Phys. Chem. C 114, 8821–8827.

Choonia, H.S., Lele, S.S., 2011. Beta-galactosidase release kinetics during ultrasonic disruption of *Lactobacillus acidophilus* isolated from fermented *Eleusine coracana*. Food Bioprod. Process. 89, 288–293.

Cucheval, A., Chow, R.C.Y., 2008. A study on the emulsification of oil by power ultrasound. Ultrason. Sonochem. 15, 916–920.

Czank, C., Simmer, K., Hartmann, P.E., 2010. Simultaneous pasteurization and homogenization of human milk by combining heat and ultrasound: effect on milk quality. J. Dairy Res. 77, 183–189.

Dahnke, S., Swamy, K.M., Keil, F.J., 1999. Modeling of three-dimensional pressure fields in sonochemical reactors with an inhomogeneous density distribution of cavitation bubbles. Comparison of theoretical and experimental results. Ultrason. Sonochem. 6, 31–41.

De Castro, M.D.L., Riego-Capote, F., 2007. Ultrasound-assisted crystallization (sonocrystallization). Ultrason. Sonochem. 14, 717–724.

Dion, J.-L., 2009. Contamination-free high capacity converging waves sonoreactors for the chemical industry. Ultrason. Sonochem. 16, 212–220.

Doktycz, S.J., Suslick, K.S., 1990. Interparticle collisions driven by ultrasound. Science 247, 1067–1069.

Donatti, D.A., Ruiz, A.I., Vollet, D.R., 2002. A dissolution and reaction modeling for hydrolysis of TEOS in heterogeneous TEOS-water-HCl mixtures under ultrasound stimulation. Ultrason. Sonochem. 9, 133–138.

Doulah, M.S., 1977. Mechanism of disintegration of biological cells in ultrasonic cavitation. Biotechnol. Bioeng. 19, 649–660.

Doulah, M.S., 1978. Application of statistical-theory of reliability to yeast-cell disintegration in ultrasonic cavitation. Biotechnol. Bioeng. 20, 1287–1289.

Earnshaw, R.G., Appleyard, J., Hurst, R.M., 1995. Understanding physical inactivation processes: combined preservation opportunities using heat, ultrasound and pressure. Int. J. Food Microbiol. 28, 197–219.

Ertugay, M.F., Sengul, M., 2004. Effect of ultrasound treatment on milk homogenisation and particle size distribution of fat. Turk. J. Vet. Anim. Sci. 28, 303–308.

Fasaki, I., Siamos, K., Arin, M., Lommens, P., Van Driessche, I., Hopkins, S.C., Glowacki, B.A., Arabatzis, I., 2012. Ultrasound assisted preparation of stable water- based nanocrystalline TiO_2 suspensions for photocatalytic applications of inkjet- printed films. Appl. Catal. A Gen. 411, 60–69.

Feng, L., Song, B., Chen, Y., Liang, S., Dai, Y., Zhou, Q., Chen, D., Bai, X., Feng, Y., Jiang, Y., Zhang, D., 2019. On-chip rotational manipulation of microbeads and oocytes using acoustic microstreaming generated by oscillating asymmetrical microstructures. Biomicrofluidics 13, 064103.

Freitas, S., Rudolf, B., Merkle, H.P., Gander, B., 2005. Flow-through ultrasonic emulsification combined with static micromixing for aseptic production of microspheres by solvent extraction. Eur. J. Pharm. Biopharm. 61, 181–187.

Freitas, S., Hielscher, G., Merkle, H.P., Gander, B., 2006. Continuous contact- and contamination-free ultrasonic emulsification—a useful tool for pharmaceutical development and production. Ultrason. Sonochem. 13, 76–85.

Gaikwad, S.G., Pandit, A.B., 2008. Ultrasound emulsification: effects of ultrasonic and physicochemical properties on dispersed phase volume and droplet size. Ultrason. Sonochem. 15, 554–563.

Gedanken, A., 2004. Using sonochemistry for the fabrication of nanomaterials. Ultrason. Sonochem. 11, 47–55.

Gerde, J.A., Montalbo-Lomboy, M., Yao, L., Grewell, D., Wang, T., 2012. Evaluation of microalgae cell disruption by ultrasonic treatment. Bioresour. Technol. 125, 175–181.

Grenman, H., Murzina, E., Ronnholm, M., Eranen, K., Mikkola, J.P., Lahtinen, M., Salmi, T., Murzin, D.Y., 2007. Enhancement of solid dissolution by ultrasound. Chem. Eng. Process. 46, 862–869.

Guo, Z., Jones, A.G., Li, N., Germana, S., 2007. High-speed observation of the effects of ultrasound on liquid mixing and agglomerated crystal breakage processes. Powder Technol. 171, 146–153.

Harris, G.R., 1996. Are current hydrophone low frequency response standards acceptable for measuring mechanical/cavitation indices? Ultrasonics 34, 649–654.

Herceg, Z., Brncic, M., Jambrak, A.R., Brncic, S.R., Badanjak, M., Sokolic, I., 2009. Possibility of application high intensity ultrasound in milk industry. Mljekarstvo 59, 65–69.

Hereter, A., Josa, R., Candela, X., 2002. Changes in particle-size distribution influenced by organic matter and mechanical or ultrasonic dispersion techniques. Commun. Soil Sci. Plant Anal. 33, 1351–1362.

Hihn, J.Y., Doche, M.L., Mandroyan, A., Hallez, L., Pollet, B.G., 2011. Respective contribution of cavitation and convective flow to local stirring in sonoreactors. Ultrason. Sonochem. 18, 881–887.

Ho, C.W., Chew, T.K., Ling, T.C., Kamaruddin, S., Tan, W.S., Tey, B.T., 2006. Efficient mechanical cell disruption of *Escherichia coli* by an ultrasonicator and recovery of intracellular hepatitis B core antigen. Process Biochem. 41, 1829–1834.

Huang, P.H., Nama, N., Mao, Z., Li, P., Rufo, J., Chen, Y., Xie, Y., Wei, C. H., Wang, L., Huang, T.J., 2014. A reliable and programmable acoustofluidic pump powered by oscillating sharp-edge structures. Lab Chip 14 (22), 4319–4323.

Inigo, A.C., Alonso, R., Vicente-Tavera, S., 2001. Dissolution of salts crystallised in building materials using ultrasound: an alternative to NORMAL (1983) standard methodology. Ultrason. Sonochem. 8, 127–130.

Jafari, S.M., He, Y.H., Bhandari, B., 2006. Nano-emulsion production by sonication and microfluidization—a comparison. Int. J. Food Prop. 9, 475–485.

Jafari, S.M., He, Y., Bhandari, B., 2007. Production of sub-micron emulsions by ultrasound and microfluidization techniques. J. Food Eng. 82, 478–488.

Jambrak, A.R., Mason, T.J., Lelas, V., Herceg, Z., Herceg, I.L., 2008. Effect of ultrasound treatment on solubility and foaming properties of whey protein suspensions. J. Food Eng. 86, 281–287.

Johnston, K., Tapia-Siles, C., Gerold, B., Postema, M., Cochran, S., Cuschieri, A., Prentice, P., 2014. Periodic shock-emission from acoustically driven cavitation clouds: a source of the subharmonic signal. Ultrasonics 54 (8), 2151–2158.

Jordens, J., Bamps, B., Gielen, B., Braeken, L., Van Gerven, T., 2016. The effects of ultrasound on micromixing. Ultrason. Sonochem. 32, 68–78.

Kapucu, H., Gulsoy, N., Mehmetoglu, U., 2000. Disruption and protein release kinetics by ultrasonication of *Acetobacter peroxydans* cells. Biochem. Eng. J. 5, 57–62.

Kawase, Y., Mooyoung, M., 1987. Solid turbulent fluid heat and mass-transfer—a unified model based on the energy-dissipation rate concept. Chem. Eng. J. Biochem. Eng. J. 36, 31–40.

Keenan, D.F., Tiwari, B.K., Patras, A., Gormley, R., Butler, F., Brunton, N. P., 2012. Effect of sonication on the bioactive, quality and rheological characteristics of fruit smoothies. Int. J. Food Sci. Technol. 47, 827–836.

Khanal, S.K., Grewell, D., Sung, S., Van Leeuwen, J., 2007. Ultrasound applications in wastewater sludge pretreatment: a review. Crit. Rev. Environ. Sci. Technol. 37, 277–313.

Kojima, Y., Asakura, Y., Sugiyama, G., Koda, S., 2010. The effects of acoustic flow and mechanical flow on the sonochemical efficiency in a rectangular sonochemical reactor. Ultrason. Sonochem. 17, 978–984.

Komarov, S., Oda, K., Ishiwata, Y., Dezhkunov, N., 2013. Characterization of acoustic cavitation in water and molten aluminum alloy. Ultrason. Sonochem. 20, 754–761.

Krause, B., Mende, M., Poetschke, P., Petzold, G., 2010. Dispersability and particle size distribution of CNTs in an aqueous surfactant dispersion as a function of ultrasonic treatment time. Carbon 48, 2746–2754.

Kumar, A., Gogate, P.R., Pandit, A.B., 2007. Mapping of acoustic streaming in sonochemical reactors. Ind. Eng. Chem. Res. 46, 4368–4373.

Kumar, D., Kumar, G., Johari, R., Kumar, P., 2012. Fast, easy ethanomethanolysis of *Jatropha curcus* oil for biodiesel production due to the better solubility of oil with ethanol in reaction mixture assisted by ultrasonication. Ultrason. Sonochem. 19, 816–822.

Kumar, G., Singh, V., Kumar, D., 2017. Ultrasonic-assisted continuous methanolysis of Jatropha curcas oil in the appearance of biodiesel used as an intermediate solvent. Ultrason. Sonochem. 39, 384–391.

Lan, W., Liu, C.-F., Yue, F.-X., Sun, R.-C., Kennedy, J.F., 2011. Ultrasound-assisted dissolution of cellulose in ionic liquid. Carbohydr. Polym. 86, 672–677.

Le, N.T., Julcour, C., Ratsimba, B., Delmas, H., 2013a. Improving sewage sludge ultrasonic pretreatment under pressure by changing initial pH. J. Environ. Manag. 128, 548–554.

Le, N.T., Julcour-Lebigue, C., Delmas, H., 2013b. Ultrasonic sludge pretreatment under pressure. Ultrason. Sonochem. 20, 1203–1210.

Leighton, T.G., 1995. Bubble population phenomena in acoustic cavitation. Ultrason. Sonochem. 2 (2), S123–S136.

Leong, T.S.H., Wooster, T.J., Kentish, S.E., Ashokkumar, M., 2009. Minimising oil droplet size using ultrasonic emulsification. Ultrason. Sonochem. 16, 721–727.

Li, M.K., Fogler, H.S., 1978a. Acoustic emulsification. 1. Instability of oil-water interface to form initial droplets. J. Fluid Mech. 88, 499–511.

Li, M.K., Fogler, H.S., 1978b. Acoustic emulsification. 2. Breakup of large primary oil droplets in a water medium. J. Fluid Mech. 88, 513–528.

Lin, C.-Y., Chen, L.-W., 2008. Comparison of fuel properties and emission characteristics of two- and three-phase emulsions prepared by ultrasonically vibrating and mechanically homogenizing emulsification methods. Fuel 87, 2154–2161.

Lu, Y.F., Riyanto, N., Weavers, L.K., 2002. Sonolysis of synthetic sediment particles: particle characteristics affecting particle dissolution and size reduction. Ultrason. Sonochem. 9, 181–188.

Luisina Gomez, P., Welti-Chanes, J., Maris Alzamora, S., 2011. Hurdle technology in fruit processing. Annu. Rev. Food Sci. Technol. 2 (2), 447–465.

Marmottant, P., Biben, T., Hilgenfeldt, S., 2008. Deformation and rupture of lipid vesicles in the strong shear flow generated by ultrasound-driven microbubbles. Proc. R. Soc. A Math. Phys. Eng. Sci. 464, 1781–1800.

Mason, T.J., Lorimer, J.P., 2002. Applied Sonochemistry: The Uses of Power Ultrasound in Chemistry and Processing. Wiley-VCH, Weinheim.

Mason, T.J., Cobley, A.J., Graves, J.E., Morgan, D., 2011. New evidence for the inverse dependence of mechanical and chemical effects on the frequency of ultrasound. Ultrason. Sonochem. 18, 226–230.

Mastikhin, I.V., Arbabi, A., Newling, B., Hamza, A., Adair, A., 2012. Magnetic resonance imaging of velocity fields, the void fraction and gas dynamics in a cavitating liquid. Exp. Fluids 52, 95–104.

Michalski, M.-C., Januel, C., 2006. Does homogenization affect the human health properties of cow's milk? Trends Food Sci. Technol. 17, 423–437.

Miles, C.A., Shore, D., Langley, K.R., 1990. Attenuation of ultrasound in milks and creams. Ultrasonics 28, 394–400.

Mohammadi, V., Ghasemi-Varnamkhasti, M., Ebrahimi, R., Abbasvali, M., 2014. Ultrasonic techniques for the milk production industry. Measurement 58, 93–102.

Moholkar, V.S., Sable, S.P., Pandit, A.B., 2000. Mapping the cavitation intensity in an ultrasonic bath using the acoustic emission. AICHE J. 46, 684–694.

Monnier, H., Wilhelm, A.M., Delmas, H., 1999a. Influence of ultrasound on mixing on the molecular scale for water and viscous liquids. Ultrason. Sonochem. 6, 67–74.

Monnier, H., Wilhelm, A.M., Delmas, H., 1999b. The influence of ultrasound on micromixing in a semi-batch reactor. Chem. Eng. Sci. 54, 2953–2961.

Monnier, H., Wilhelm, A.M., Delmas, H., 2000. Effects of ultrasound on micromixing in flow cell. Chem. Eng. Sci. 55, 4009–4020.

Mosavian, M.T.H., Hassani, A., 2010. Making oil-in-water emulsions by ultrasound and stability evaluation using Taguchi method. J. Dispers. Sci. Technol. 31, 293–298.

Murugan, R.V., Nagarajan, R., 2008. Pulsed ultrasonic mixing: an experimental study. Chem. Eng. Res. Des. 86, 454–460.

O'Sullivan, J., Murray, B., Flynn, C., Norton, I., 2015. Comparison of batch and continuous ultrasonic emulsification processes. J. Food Eng. 167, 114–121.

Okonkwo, V.C., Kwofie, E.M., Mba, O.I., Ngadi, M.O., 2021. Impact of thermo-sonication on quality indices of starch-based sauces. Ultrason. Sonochem. 73, 105473.

Park, A.H.A., Fan, L.S., 2004. CO_2 mineral sequestration: physically activated dissolution of serpentine and pH swing process. Chem. Eng. Sci. 59, 5241–5247.

Parvizian, F., Rahimi, M., Faryadi, M., 2011. Macro- and micromixing in a novel sonochemical reactor using high frequency ultrasound. Chem. Eng. Process. 50, 732–740.

Parvizian, F., Rahimi, M., Azimi, N., 2012. Macro- and micromixing studies on a high frequency continuous tubular sonoreactor. Chem. Eng. Process. 57–58, 8–15.

Patil, L., Gogate, P.R., 2018. Large scale emulsification of turmeric oil in skimmed milk using different cavitational reactors: a comparative analysis. Chem. Eng. Process. 126, 90–99.

Plesset, M.S., 1949. The dynamics of cavitation bubbles. J. Appl. Mech. 16 (3), 277–282.

Pohl, M., Hogekamp, S., Hoffmann, N.Q., Schuchmann, H.P., 2004. Dispersion and deagglomeration of nanoparticles with ultrasound. Chem. Ing. Tech. 76, 392–396.

Pohl, B., Jamshidi, R., Brenner, G., Peuker, U.A., 2012a. Characterization of the mixing and precipitation of sonochemical flow reactors under special consideration of the reactor geometry. Chem. Ing. Tech. 84, 70–80.

Pohl, B., Jamshidi, R., Brenner, G., Peuker, U.A., 2012b. Experimental study of continuous ultrasonic reactors for mixing and precipitation of nanoparticles. Chem. Eng. Sci. 69, 365–372.

Prozorov, T., Prozorov, R., Suslick, K.S., 2004. High velocity interparticle collisions driven by ultrasound. J. Am. Chem. Soc. 126, 13890–13891.

Raheem, A., Sikarwar, V.S., He, J., Dastyar, W., Dionysiou, D.D., Wang, W., Zhao, M., 2018. Opportunities and challenges in sustainable treatment and resource reuse of sewage sludge: a review. Chem. Eng. J. 337, 616–641.

Raman, V., Abbas, A., Zhu, W., 2011. Particle grinding by high-intensity ultrasound: kinetic modeling and identification of breakage mechanisms. AICHE J. 57, 2025–2035.

Rayleigh, L., 1917. VIII. On the pressure developed in a liquid during the collapse of a spherical cavity. Lond. Edin. Dub. Philosop. Mag. J. Sci. 34 (200), 94–98.

Reddy, S.R., Fogler, H.S., 1980. Emulsion stability of acoustically formed emulsions. J. Phys. Chem. 84, 1570–1575.

Reuter, F., Kaiser, S.A., 2019. High-speed film-thickness measurements between a collapsing cavitation bubble and a solid surface with total internal reflection shadowmetry. Phys. Fluids 31, 097108.

Roscoe, R., Buurman, P., Velthorst, E.J., 2000. Disruption of soil aggregates by varied amounts of ultrasonic energy in fractionation of organic matter of a clay Latosol: carbon, nitrogen and delta C-13 distribution in particle-size fractions. Eur. J. Soil Sci. 51, 445–454.

Ruecroft, G., Hipkiss, D., Ly, T., Maxted, N., Cains, P.W., 2005. Sonocrystallization: the use of ultrasound for improved industrial crystallization. Org. Process. Res. Dev. 9, 923–932.

Sandilya, K.D., Keenan, A., 2012. Quantification of surface area and intrinsic mass transfer coefficient for ultrasound-assisted dissolution process of a sparingly soluble solid dispersed in aqueous solutions. Ultrason. Sonochem. 19, 509–521.

Sauer, T., Robinson, C.W., Glick, B.R., 1989. Disruption of native and recombinant *Escherichia-coli* in a high-pressure homogenizer. Biotechnol. Bioeng. 33, 1330–1342.

Sauter, C., Emin, M.A., Schuchmann, H.P., Tavman, S., 2008. Influence of hydrostatic pressure and sound amplitude on the ultrasound induced dispersion and de-agglomeration of nanoparticles. Ultrason. Sonochem. 15, 517–523.

Shanmugam, A., Chandrapala, J., Ashokkumar, M., 2012. The effect of ultrasound on the physical and functional properties of skim milk. Innov. Food Sci. Emerg. Technol. 16, 251–258.

Silva, A.C., Gonzalez-Mira, E., Garcia, M.L., Egea, M.A., Fonseca, J., Silva, R., Santos, D., Souto, E.B., Ferreira, D., 2011. Preparation, characterization and biocompatibility studies on risperidone-loaded solid lipid nanoparticles (SLN): high pressure homogenization versus ultrasound. Colloids Surf. B Biointerfaces 86, 158–165.

Son, Y., Lim, M., Khim, J., Ashokkumar, M., 2012. Acoustic emission spectra and sonochemical activity in a 36 kHz sonoreactor. Ultrason. Sonochem. 19, 16–21.

Stoian, D., Eshtiaghi, N., Wu, J., Parthasarathy, R., 2019. Solid-liquid mass transfer in sonicated agitated vessels with high concentration slurries. Heat Mass Transf. 55, 1327–1335.

Suslick, K.S., Price, G.J., 1999. Applications of ultrasound to materials chemistry. Annu. Rev. Mater. Sci. 29, 295–326.

Suslick, K.S., Hyeon, T.W., Fang, M.M., 1996. Nanostructured materials generated by high-intensity ultrasound: sonochemical synthesis and catalytic studies. Chem. Mater. 8, 2172–2179.

Taha, A., Ahmed, E., Ismaiel, A., Ashokkumar, M., Xu, X., Pan, S., Hu, H., 2020. Ultrasonic emulsification: an overview on the preparation of different emulsifiers-stabilized emulsions. Trends Food Sci. Technol. 105, 363–377.

Tervo, J.T., Mettin, R., Lauterborn, W., 2006. Bubble cluster dynamics in acoustic cavitation. Acta Acust. Acust. 92, 178–180.

Triawan, F., Budiman, B.A, Nurprasetio, I.P., Sunnardianto, G.K., 2019. Direct and indirect measurement techniques of cavitation intensity: a brief review. J. Phys. Conf. Ser. 1402, 044048.

Trofimov, T.I., Samsonov, M.D., Lee, S.C., Smart, N.G., Wai, C.M., 2001. Ultrasound enhancement of dissolution kinetics of uranium oxides in supercritical carbon dioxide. J. Chem. Technol. Biotechnol. 76, 1223–1226.

Tsochatzidis, N.A., Guiraud, P., Wilhelm, A.M., Delmas, H., 2001. Determination of velocity, size and concentration of ultrasonic cavitation bubbles by the phase-Doppler technique. Chem. Eng. Sci. 56, 1831–1840.

Vercet, A., Sanchez, C., Burgos, J., Montanes, L., Buesa, P.L., 2002. The effects of manothermosonication on tomato pectic enzymes and tomato paste rheological properties. J. Food Eng. 53, 273–278.

Verhaagena, B., Rivas, D.F., 2016. Measuring cavitation and its cleaning effect. Ultrason. Sonochem. 29, 619–628.

Vichare, N.P., Gogate, P.R., Dindore, V.Y., Pandit, A.B., 2001. Mixing time analysis of a sonochemical reactor. Ultrason. Sonochem. 8, 23–33.

Wang, Y.C., Huang, C.H., Lee, Y.C., Tsai, H.H., 2006. Development of a PVDF sensor array for measurement of the impulsive pressure generated by cavitation bubble collapse. Exp. Fluids 41 (3), 365–373.

Wood, R.W., Loomis, A.L., 1927. XXXVIII. The physical and biological effects of high- frequency sound-waves of great intensity. Philos. Mag. 7 (4), 417–436.

Wrenn, S.P., Small, E., Dan, N., 2013. Bubble nucleation in lipid bilayers: a mechanism for low frequency ultrasound disruption. Biochim. Biophys. Acta 1828, 1192–1197.

Wu, H., Hulbert, G.J., Mount, J.R., 2000. Effects of ultrasound on milk homogenization and fermentation with yogurt starter. Innov. Food Sci. Emerg. Technol. 1, 211–218.

Wu, J., Gamage, T.V., Vilkhu, K.S., Simons, L.K., Mawson, R., 2008. Effect of thermosonication on quality improvement of tomato juice. Innov. Food Sci. Emerg. Technol. 9, 186–195.

Xu, H., Zeiger, B.W., Suslick, K.S., 2013. Sonochemical synthesis of nanomaterials. Chem. Soc. Rev. 42, 2555–2567.

Xuan, J., Pelletier, M., Xia, H., Zhao, Y., 2011. Ultrasound-induced disruption of amphiphilic block copolymer micelles. Macromol. Chem. Phys. 212, 498–506.

Yagci, N., Akpinar, I., 2011. The investigation and assessment of characteristics of waste activated sludge after ultrasound pretreatment. Environ. Technol. 32, 221–230.

Yang, X., Dong, H., Yue, G., Lv, Y., Tang, J., Liu, W., 2012. Ultrasound changes solid- liquid leaching equilibrium of glycyrrhizic acid from glycyrrhiza uralensis in water. Future Mater. Res. Indus. Appl. 455–456, 721–725. Pts 1 and 2.

Yin, X., Han, P.F., Lu, X.P., Wang, Y.R., 2004. A review on the dewaterability of bio- sludge and ultrasound pretreatment. Ultrason. Sonochem. 11, 337–348.

Yusaf, T.F., Buttsworth, D.R., 2007. Characterisation of mixing rate due to high power ultrasound. Ultrason. Sonochem. 14, 266–274.

Yusuf, L., Symes, M.D., Prentice, P., 2021. Characterising the cavitation activity generated by an ultrasonic horn at varying tip-vibration amplitudes. Ultrason. Sonochem. 70, 105273.

Zhang, C., Guo, X., Brunet, P., Costalonga, M., Royon, L., 2019. Acoustic streaming near a sharp structure and its mixing performance characterization. Microfluid. Nanofluid. 23, 104.

Further reading

Chiu, Y.C., Chang, C.N., Lin, J.G., Huang, S.J., 1997. Alkaline and ultrasonic pretreatment of sludge before anaerobic digestion. Water Sci. Technol. 36, 155–162.

Leighton, T., 2012. The Acoustic Bubble. Academic press.

Mason, T.J., Paniwnyk, L., Lorimer, J.P., 1996. The uses of ultrasound in food technology. Ultrason. Sonochem. 3, S253–S260.

Villamiel, M., De Jong, P., 2000. Influence of high-intensity ultrasound and heat treatment in continuous flow on fat, proteins, and native enzymes of milk. J. Agric. Food Chem. 48, 472–478.

Chapter 30

Ultrasonic defoaming and debubbling in food processing and other applications

J.A. Gallego-Juárez[a], G. Rodríguez[a], E. Riera[a,b], and A. Cardoni[c]

[a]*Pusonics S.L., Pico Muihacén, Arganda del Rey, Madrid, Spain,* [b]*Consejo Superior de Investigaciones Científicas (CSIC), Madrid, Spain,* [c]*Independent Consultant, Madrid, Spain*

30.1 Introduction

Liquid foam, commonly referred as "foam," is a dispersion of a gas within a liquid that is formed by gas bubbles separated from each other by thin liquid films. There is also the so-called solid foam, in which gas bubbles are separated by solid films. This chapter deals exclusively with liquid foam. In a liquid foam medium, the volume ratio of gas to liquid is very high, and therefore, the bulk density approaches that of the gas.

Foam may be generated by the aeration and agitation of liquids if a gas is already dissolved in the liquid, by the vaporization of the liquid phase, and also by means of microbiological or chemical reactions that release gases. Stability is one of the most important features of foam because it determines the difficulty of its destruction. In a typical foam structure, bubbles in the lower part are spherical and of smaller size than those at the top. When liquid drains from the upper to the lower layers, the bubbles at the top distort to form polyhedra, consisting of plane-parallel films joined by channels. This type of honeycombed structure of gas bubbles separated by thin liquid walls is very common in almost all foams. As the films at the top become thinner, they are more susceptible to breakage by external stress. However, this process is opposed by the capillary pressure gradient along the height of the foam column, which prevents the liquid from running out. This means that there is a critical height of foam at which the drain processes and capillary pressure are balanced. Other relevant factors affecting the stability of foams are surface tension, viscosity, pH, molecular surface electrical charge, and temperature. In general, solutions may not produce stable foams if the surface tension gradients are not sufficiently high enough to enable the bubble film to withstand stress (Garret, 1993).

In spite of their tendency to collapse, foams can be constituted in such a way that they persist long term or have a long lifetime because of factors such as high viscosity of the liquid and/or of the surface and the adsorption of ionic and nonionic surfactants. Another important characteristic of foam is the use of foaminess as a measure of the foaming capacity, which is mainly dependent on the ingredients incorporated in the liquid medium and their relative concentrations.

Foam is generally an unwanted by-product in industrial processes because it causes difficulties in process control and in equipment handling. In the fermentation industry, for example, foam is a significant problem and can result in the loss of culture fluid and cells, the contamination of the environment, the formation of a barrier to oxygen transfer, and the promotion of cell lysis. For these reasons, there is a great interest in the prevention, destruction, and/or control of foams. Several methods are used to prevent the formation of foam (antifoaming), and/or to break it once, it is formed (defoaming). Antifoamers are foam inhibitors added to the liquid phase to prevent foam formation. Defoamers are foam breakers developed to eliminate the existing foam.

Defoaming methods may use chemical or physical effects. Chemical defoaming is based on the use of antifoam agents, which can produce a surface tension gradient acting as a shear force. They are generally very effective but can cause adverse effects such as contamination of the process (Pugh, 1996). Physical methods try to rupture bubbles via thermal, electrical, or mechanical effects (Ghildyal et al., 1988). The thermal methods are based on the application of thermal stresses to rupture the bubbles. The foam is then heated or cooled in some way, which generally is difficult and expensive. Electrical methods depend upon the generation of an electric current passing through the foam in order to destroy it. The activity may be based on the fact that the forces created by the current act differently in liquid and gas. Nevertheless, these methods are still not well known and have been rarely used in experiments. Mechanical methods are more widely used, mainly to avoid the contamination problems related to the use of antifoam agents. The collapse of bubbles is produced by any kind of mechanical

Power Ultrasonics. https://doi.org/10.1016/B978-0-12-820254-8.00032-4
Copyright © 2023 Elsevier Ltd. All rights reserved.

shock (rapid pressure changes, shear force, compressive force, impact force, suction, and centrifugal forces). In general, mechanical methods are effective, particularly for coarse foams.

The use of the ultrasonic energy can be considered a mechanical method based on irradiation of the foam with high-intensity ultrasonic waves. It represents a clean means of breaking foams without contacting the liquid. The potential use of ultrasound for breaking foam was first introduced during the 1950s and the 1960s by using various types of acoustic defoamers. The majority of them were based on aerodynamic acoustic sources of various types, such as whistles and sirens (Boucher and Weiner, 1963). The major drawbacks of these systems are related to noise (they usually operated in the hearing frequency range), the need for high air generation capacity, the control and sterilization of the air flow, and the high energy consumption. A new type of ultrasonic defoamer based on a new kind of powerful and efficient airborne ultrasonic generators has been recently introduced in the market (www.pusonics.es) (Gallego-Juárez et al., 2005). Through this novel device, the use of ultrasonic energy for defoaming processes has been given a renewed impetus.

30.2 Foams

30.2.1 Types and characteristics

A foam is a nonpermanent form of matter wherein bubbles are separated by thin films of liquid and interconnected by channels known as plateau borders, which contain most of the liquid (Figure 30.1). The foams generated in detergents, beers, or fermentation processes are examples of common multiphase media with specific properties and characteristics.

There are several classifications of foams based on stability, structure, composition, and liquid content. We already mentioned the significance of stability. With this factor in mind, foams are classified into various categories, such as unstable, metastable, transient, or persistent. In unstable foams, the equilibrium state is continuously approached but not achieved. Instead, the foam collapses as a result of overwhelming effects of surface tension and gravitational forces. Metastable foams may persist for a long time, although their progress to the equilibrium state is arrested. Persistent foams have a lifetime of hours or days if left undisturbed, whereas transient foams have a lifetime of only seconds (Ghildyal et al., 1988). Stability depends on the composition and structure of the foam.

A broad classification of foams could be that of dry and wet foams. Dry foams are those with a low liquid content and, consequently, are very "rigid." On the other hand, wet foams contain much liquid and therefore are very "fluid" (Gaden and Kevorkian, 1956). Because foams are not a permanent form of matter, they undergo changes as a result of processes that remove liquid from wet foam, transforming it into dry foam. In general, the bubble film loses liquid by drainage between bubbles, which depends on the foam structure, viscosity, and density of the liquid. Because dry foam is more "rigid," it may be more easily destroyed by mechanical vibrations.

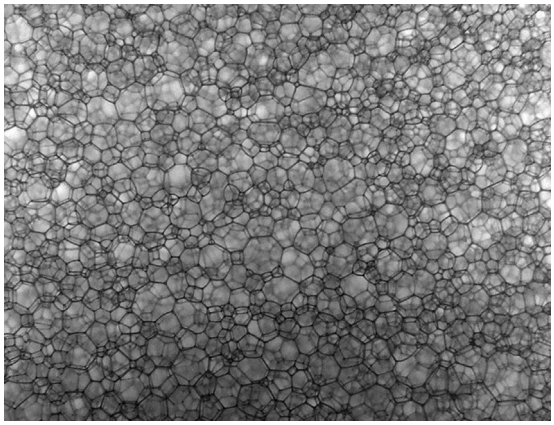


FIGURE 30.1 Foam structure.

30.2.2 Effects of foam in processes

As a dispersion of a gas within a liquid, foam can be formed and introduced into a system in different ways. The simplest way is by aerating and/or agitating liquids, but liquids do not foam unless some impurities are already present in them. Foam may be also produced when a gas is dissolved in the liquid, or even from the vaporization of the liquid phase. Chemical or biochemical reaction is another form of foam generation that may release a gas as a result. Therefore, there are many industrial processes whereby foams are produced, such as in reaction vessels, stirred tanks, canning/bottling lines, boilers, distillation columns, and particularly fermenters, where foam is one of the major problems. Chemical, pharmaceutical, and food industries are the sectors most directly affected by the production of excess foam.

Whenever it occurs, foam leads to a reduction in process/product efficiency. General adverse effects of foam are reduction in working capacity, overflows, product loss and changes in the relative proportion of components, and a slowing of the process speed. In the specific case of fermentation processes, additional effects are the loss of culture fluid and cells, inhomogeneity, contamination, action as a barrier to oxygen transfer, and the deposition of cells in the upper part of the broth (Allen et al., 1993; Gaden and Kevorkian, 1956; Ghildyal et al., 1988).

30.3 Conventional methods for foam control

As previously mentioned, foam can be controlled by chemical and physical methods. Chemical methods are based on the use of antifoam products that are usually surface-active agents formulated to disrupt the surface around the gas bubbles, destabilizing bubble walls so that a bubble can break and release the trapped gas. The number of chemical antifoam agents is very large and includes natural compounds such as sunflower oil, oleic acid, sperm whale oil, soapstock from plant oil, as well as synthetic compounds such as silicone, polypropylenes, and synthetic fatty acids (Gutschick et al., 1982). The foam destruction mechanisms exploited by a chemical antifoaming agent depend on the nature of the agent, the substances causing the formation of foam, and the type of foam. The most general mechanisms to be cited are the reduction in surface elasticity, the local reduction in surface tensions, the promotion of drainage, and the lowering of viscosity. The selection of suitable antifoam agents has to be evaluated according to the process in the foaming medium. In general, antifoam agents, if selected correctly, are effective for defoaming but may cause serious adverse effects, particularly by contaminating the product. Such an occurrence results in the need for extra operations to separate and remove the agent from the product to diminish its influence. Therefore, it seems much more convenient to use physical methods whenever possible.

Conventional physical methods for defoaming include thermal, electrical, and mechanical foam breakers. Thermal methods consist of heating and cooling the foam, producing the expansion and compression of the bubbles that result in their destruction. The application of thermal methods in industrial plants, however, has been very limited because of the practical difficulties, the energy consumption, and the effects of high temperatures on the product. Electrical methods are based on the different action of the forces created by an electric current on liquid and gas when they pass through foam. However, the exact mechanism of this action is not well known. In addition, this method has hardly been used in practice.

Mechanical methods have a greater and a more widespread use. There are a large number of mechanical systems for foam-breaking designed according to specific requirements. Mechanical foam breakers collapse the foam bubbles by mechanical shocks produced by centrifugal, compressive, impact or shear forces, suction, or pressure changes. The most widely used mechanical systems include rotary devices, cyclones, jetstreams of liquid or air, and vacuum chambers. However, only a limited number of mechanical systems are used in industrial plants, apparently because they do not always offer economic advantages, particularly when compared with chemical defoamers, and they may also be a potential source of contamination, depending on their feasibility under sterile conditions. In addition, the design and manufacture of the systems are costly and complicated, and for larger units, significant scaling-up problems frequently arise. In general, mechanical systems are effective for coarse foams (Deshpande and Barigou, 2000; Viesturs et al., 1982).

30.4 Ultrasonic defoaming

The use of the ultrasonic energy for defoaming is based on the irradiation of foam by high-intensity ultrasonic waves. It can be considered a special type of mechanical method and represents a clean means of breaking foams without contacting with them. Therefore, ultrasonic radiation offers a potential alternative to conventional chemical and mechanical techniques.

The possibility of destroying foam using ultrasonic waves has been explored for several decades, and a certain number of experimental studies have been carried out to investigate the effect of ultrasound on foam. However, only few defoaming systems have been developed at the commercial stage. This may result from the difficulty in efficiently generating high-intensity ultrasound in air, as well as the lack of a thorough understanding of the mechanisms of ultrasonic defoaming.

The potential use of ultrasound for defoaming was suggested as early as 1944 by Ross and McBain (1944), and the first extended research on this problem was carried out by Sun (1951), who used a high-frequency rotary siren of the type described by Allen and Rudnick (1947) to generate sound and ultrasound waves in the range of 3–34 kHz. A highly mineralized foam was treated at different frequencies, and the sequence of the foam's collapse was studied by a motion picture camera at a speed of 16 frames per second. The best results were obtained at frequencies in the range of 6–11 kHz and at 147- to 148-dB sound levels. The main conclusion of this initial study was the confirmation of the potential of acoustic waves to break foams, provided that frequencies and sound pressure levels are appropriate. However, from a practical point of view, the experimental process in the laboratory setup proved very inefficient because it required an extremely high air flow at the sound source (202 cfm at 11 psi) to control only 0.017 cfm of growing foam.

Dorsey (1959), using a Hartman whistle, applied ultrasonic waves at three different frequencies (26, 29, and 34 kHz) for foam control during fermentation process. The Hartman whistle, an air-driven ultrasonic generator, had no moving parts and was easily sterilized; hence it was suitable for incorporation in fermenters. The whistle was fed with filtered compressed air at a minimum pressure of 40 psi and an air flow rate of 2–4 cfm. The cylindrical fermenter was 24 in. high and 12 in. in diameter; the

fermentation medium was a casein acid digest with *Serratia marcescens* organisms. Foam breakage was effective in controlling a growing rate of foam of 0.9 cfm; also, there was a noticeable improvement in efficiency at the highest frequency (34 kHz) than at the lower frequencies. Another positive result was that no harmful effects of the ultrasonic radiation on culture cells were observed. This positive result was attributed to the small fraction of the ultrasonic energy that enters the liquid during sound radiation because of the great impedance discontinuity at the air-water interface.

Further studies on foam destruction were carried out in the same period by using steamjet acoustic generators. Boucher and Weiner (1963) evaluated the potential of sonic defoaming at an industrial scale and concluded that within a wide frequency range (0.7–29 kHz), high-amplitude airborne sound waves are effective in controlling medium viscosity foams. However, this technique did not always seem attractive from an economic standpoint because the best air jet generator can only handle 0.3 cfm of foam per cubic foot per minute of free air supplied to the sound source (Boucher and Weiner, 1963). They also established that a minimum intensity level of about 145–148 dB was needed to efficiently control the foam. These authors also studied a new aerodynamic technique to produce defoaming energy, which was based on the deflection of an air stream by a plain resonator and the creation of a negative pressure underneath the resonator resulting from velocity differentials.

Despite the uncertain results obtained during the first phase of exploration of the defoaming process, using pneumatic sources for the generation of sonic and ultrasonic waves, the interest in gaining a deeper understanding in the potential applicability of this technique has been maintained throughout the years, although discontinuously. Sandor and Stein (1993) studied foam destruction via airborne ultrasonic vibrations produced at 20 kHz by using piezoelectrically-driven Sonifier probes with very small horn tips (diameters of 3.3 and 12.8 mm). This research was more focused on understanding the mechanisms of the process rather than investigating any possible extension into practical applications.

In the late 1990s and early 2000s, a group at the School of Chemical Engineering at the University of Birmingham devoted significant experimental research to ultrasonic defoaming and its mechanisms (Barigou, 2001; Morey et al., 1999). Again, the experimental tests were performed only at the laboratory level using an ultrasonic sonicator of 20 kHz with a horn tip with a 12.7-mm cross-sectional diameter for controlling a 15-mm-diameter foam column. The sonicator could vary its vibration amplitude at the radiating tip to a maximum of 123 μm. Static and dynamic tests were performed with the tip of the vibrator radiating in air at a distance of 20 mm from the foam and also in contact with it. Ultrasonic defoaming results were compared with mechanical defoaming tests carried out with low-frequency vibrations (0–40 Hz). The authors concluded that ultrasonic vibration is efficient for static and dynamic defoaming of Newtonian and non-Newtonian liquids, whereas mechanical vibration would be most useful for persistent static foam beds. Other aspects of this research concerned specific defoaming mechanisms which will be discussed in the next section.

The studies of foam destruction by ultrasound continued during the decade from 2000 to 2010. The work carried out by Dedhia et al. (2004) at the University of Mumbai in India also must be mentioned. Once again, their experiments were carried out at a very small scale, using as a source of ultrasound an ultrasonic horn operating at 20 kHz. A 32-mm-diameter foam column was generated with 60 mL of surfactant solution and an air sparger that formed 1- to 2-mm-diameter bubbles. The results confirmed the efficiency of the use of ultrasonic energy for defoaming. In this work, the mechanisms of ultrasonic defoaming were also discussed, as is referred to in the next section.

Despite the studies and experimental work conducted during over half of a century and the generally quite supportive results obtained in the reported investigations, it appears that ultrasonic defoaming devices that could be efficiently used at industrial stage were not developed. As previously mentioned, one of the main problems that hampered the industrial applicability of the technology has been the lack of powerful ultrasonic generators capable of efficiently transmitting sound pressure waves through air. The air jets required by the acoustic sources (whistles and sirens) used in the 1950s and the 1960s showed many practical inconveniences, such as low efficiency, high energy consumption, a need for high air generation capacity, and control and sterilization of the air flow, as well as the difficulty in operating the devices at ultrasonic frequencies.

Therefore, the first and main goal for the advancement of this technique lies in the development of suitable acoustic sources. Rodriguez et al. (1985) proposed a new concept of high-intensity ultrasonic defoamers based on a first prototype of a novel family of stepped-plate power ultrasonic transducers for airborne applications (Gallego-Juárez et al., 1978). The first laboratory-scale system was successfully tested controlling the foam produced in filling operation of bottles and cans. Through the efforts made in the following years, the system could be scaled up for its use at industrial scale. Hence, a patent associated to such development was filed (Gallego-Juárez et al., 2005) and transferred to the company Pusonics, S.L. (www.pusonics.es) with the aim of pursuing industrial and commercial exploration of the new system. This novel type of ultrasonic defoamer and its performance will be described next.

30.5 Mechanisms of ultrasonic defoaming

As we have already seen, the idea of using high-intensity ultrasonic waves to destroy foam bubbles is not new. However, a basic understanding of the mechanisms of the process is still lacking at present. In fact, it is surprising that the great majority of the studies performed so far did not manage to establish detailed correlations between ultrasonic parameters (frequency, intensity, and time) and foam parameters (viscosity and density of the liquid, size and distribution of the bubbles, thickness of the foam walls, and compressibility). The preliminary studies carried out by Sun (1951) attributed the mechanism of acoustic defoaming to the resonant vibration of the bubbles induced by the acoustic waves. In addition, the effects of the radiation pressure against any obstacle, as well as the acoustic streaming causing the collision and coalescence of the bubbles, which, in turn, broke the bubble walls, were highlighted.

Similar assumptions were proposed by Boucher and Weiner (1963), who attributed foam destruction by means of high-amplitude acoustic waves to acoustic pressure, unidirectional radiation pressure, and induced resonant vibration in the bubbles and turbulence produced by acoustic streaming. Acoustic pressure is the major source of external positive or negative pressure. Because the pressure inside each spherical bubble is higher than the ambient pressure by a quantity of $2T/R$ if the bubble is in a liquid or $4T/R$ if it is in a gas (where T is the surface tension and R is the radius of the bubble) to destroy the bubbles, it is first necessary to overcome the excess of internal pressure by an external applied pressure (Hueter and Bolt, 1955). In addition to the acoustic pressure, the effect of the so-called radiation pressure, a steady radiation force exerted by the high-intensity acoustic waves on obstacles and interphases as a consequence of the change of the momentum also has to be considered. Radiation pressure is a second-order effect that only plays a determinant role in bubbles exploding at very high intensities. As a general rule, the effects of radiation pressure are negligible below 143 dB and only become important above 150 dB. Another important factor in the mechanisms of acoustic defoaming to bear in mind is the natural resonance frequency of the bubbles. The natural resonance frequency of a bubble in a foam according to the bubble-in-cell model (McDaniel et al., 2002) is determined from the relation:

$$f_b = \frac{f}{\sqrt{(1-\alpha_g)^{1/3}}}, \tag{30.1}$$

where α_g is the initial gas volume fraction of the cell and f is the natural resonance frequency of a single bubble in an infinite liquid:

$$f = \frac{1}{2\pi R}\sqrt{\frac{3\gamma\left(P+\frac{2T}{R}\right)}{\rho}}, \tag{30.2}$$

where R is the radius of the bubble, P is the hydrostatic pressure, $\gamma = c_p/c_v$ is the specific heat ratio, and ρ is the density of the liquid. For bubbles with a radius longer than 0.002 cm, the influence of surface tension on the pressure may be neglected, and the previous expression can be simplified as

$$f \cong \frac{1}{2\pi R}\left(\frac{3\gamma P}{\rho}\right)^{1/2}. \tag{30.3}$$

For air bubbles in water,

$$fR = 0.328 \text{ kHz cm}.$$

The bubbles of most industrial foams range from 0.5 to 10 mm in size; therefore, the resonance frequencies obtained by substituting these radius values in the above expressions are in the very low audible range. This could partly explain the good results observed in the referenced experiments performed at low-frequency sound radiations. The resonance of the bubbles increases interstitial frictions and may weaken the bubble walls. However, such a resonance effect would not have much influence at ultrasonic frequencies. In fact, Sandor and Stein (1993) have proposed as the main action of the ultrasonic radiation the enhancement of the foam film drainage causing to attain its critical thickness faster, hence increasing the foam collapse rate. They claim that their experimental results confirm such theoretical predictions. Other authors (Barigou, 2001; Morey et al., 1999) confirmed the effect of ultrasonic vibrations on foam drainage and collapse, and their experimental results also suggested that the ultrasonic mechanism of destabilization of foam is different from that of mechanical vibration at a very low frequency (0–40 Hz). Chendke and Fogler (1974) confirmed that the waves generated in the interfaces of foam films are of the "squeezing"-type and are responsible for accelerating thin film thinning, but they also added that other phenomena, such as cavitation, atomization, and high-shear convective streaming currents, are assumed to play a key role. Based on the above-mentioned mechanisms, it is possible to assume that the alternating pressure exerted on the foam surface can excite capillary waves, leading to a fast rupture of the film (Komarov et al., 2000).

Other physical phenomenon to be considered is the acoustic streaming, a kind of fluid flow induced by the high-intensity acoustic waves as a result of the radiation forces set up by the viscous losses in the transmission medium. Again, this is a second-order effect relevant only at very high intensities. The acoustic streaming generates turbulence above the foam interface that may help to destroy the upper layer of bubbles.

In conclusion, it could be considered that, from a practical point of view, there are two main mechanisms resulting in foam destruction: one at high sonic and ultrasonic frequencies and high acoustic intensity levels, in which radiation forces are predominant to accelerate film drainage leading to foam collapse; and the other at low sonic frequencies and high acoustic intensities, in which sound pressure and natural bubble resonance frequency play a major role. However, the conclusion about the mechanisms discussed here is to be taken in a qualitative form because practically no authors have been able to quantify their single effects on the whole process. Foams are very complex media and unfortunately until now there are no reliable simple techniques to measure them (Ben Salem et al., 2013).

Therefore, to summarize, breaking and destroying foams using ultrasonic energy can be seen as an effect caused for a combination of the following acoustic mechanisms: the creation of a partial vacuum on the foam bubble surface produced by high acoustic pressure; impingement of radiation pressure on the bubble surface; vibration of the foam bubbles, which creates interstitial friction and causes bubble coalescence, cavitation, and atomization of the liquid film surface; and acoustic streaming.

Although all authors agree that the defoaming process depends on the main acoustic parameters (intensity and frequency) and, of course, on the foam structure, no studies quantifying the separate influence of intensity and treatment time had been carried out. Experimental studies of the incidence of these parameters on the process have recently been conducted for the first time (Rodriguez et al., 2009). Two different types of soap foam were studied: one with moderate water content (ratio of liquid to foam volume of 0.02, bubble size in the range of 0.2–2 mm) and other very dry (ratio of liquid to foam volume of 0.005, bubble size in the range of 0.2–10 mm). The experimental setup developed for this study is shown in Figure 30.2. It was designed to check the dynamic defoaming effect occurring when the foam is subjected to the action of an ultrasonic beam applied to it in different time periods. The purpose was to control the acoustic intensity and the treatment time required for efficient defoaming, according to the actual industrial operation needs. The ultrasonic generator applied was a focusing stepped-plate radiator with a power capacity of 200 W and a resonance frequency of 25.8 kHz. The acoustic energy needed to produce a specific defoaming volume within the product was measured under static conditions as a function of the applied acoustic power and treatment time. Different treatment times were explored by interrupting at different times the ultrasonic radiation by means of a simple mechanical apparatus consisting of a rotating disc driven by a variable-speed motor. The radiating disc incorporated a hole that let the ultrasonic energy passing and reaching the foam below at any time that the axis of the radiation beam coincided with the hole axis. In addition to a clear effect that after a certain liquid drainage, foam more easily collapses, the results showed that, even when the applied energy is the same, the defoaming effect may be different, depending on each one of the single parameters involved, acoustic intensity, and treatment time. The conclusion is that specific time and intensity thresholds have to be achieved to trigger the defoaming effects. Therefore, it does not seem very accurate to identify a defoaming threshold only associated with the amount of acoustic energy applied, as some authors do.

30.6 Ultrasonic defoamers

In spite of the lack of a basic knowledge about the mechanisms of ultrasonic defoaming, the interest for the industrial application of this process has been considerable since the very beginning. As early as 1961, the company Teknika Inc. presented at the Chemical Industries Exposition in New York a "revolutionary modern system to destroy foam by using sonic energy." The system schematically consisted of a cylindrical chamber wherein an acoustic resonance was set up by using a whistle located at the top of the chamber (Figure 30.3). The whistle was operated by compressed air, steam, nitrogen, carbon dioxide, and other gases. The excess foam produced during the corresponding industrial process (detergent manufacture, filling machines, and fermenters) was diverted to the treatment chamber, where it was apparently destroyed in less than 1 s. We do not know the specific characteristics and capacities of this commercial system and therefore cannot provide any further information about its practical performance. What is known is that the Teknika trademark expired in 1988. To the knowledge of the authors, no other commercial equipment was launched into the market between the 1960s and the 1990s. However, a number of patents have been registered over the years, mainly from companies interested in commercializing this process. A brief review of these patents is provided below, along with various experimental procedures used in the exploration of ultrasonic defoaming applications.

As previously stated, the first ultrasonic defoamers were based on the use of aerodynamic acoustic generators, specifically whistle and sirens. The early experimental work of Sun (1951) was carried out using the siren developed by Allen and Rudnick (1947) as an acoustic generator, and so a specific arrangement of this generator for industrial defoaming was proposed (Figure 30.4). As referred by Boucher and Weiner (1963), in 1952–1953, the US Air Force sponsored a project for suppressing fuel foaming in jet aircraft fuel during rapid altitude climbs. An air-driven Hartmann whistle (Figure 30.5) operating at 27.5 kHz was successfully used in suppressing fuel foaming. In the Hartmann whistle, a jet of gas is directed into a cavity, hence, the impact of the gas stream at the bottom of the cavity and the interaction with its counterflow produces

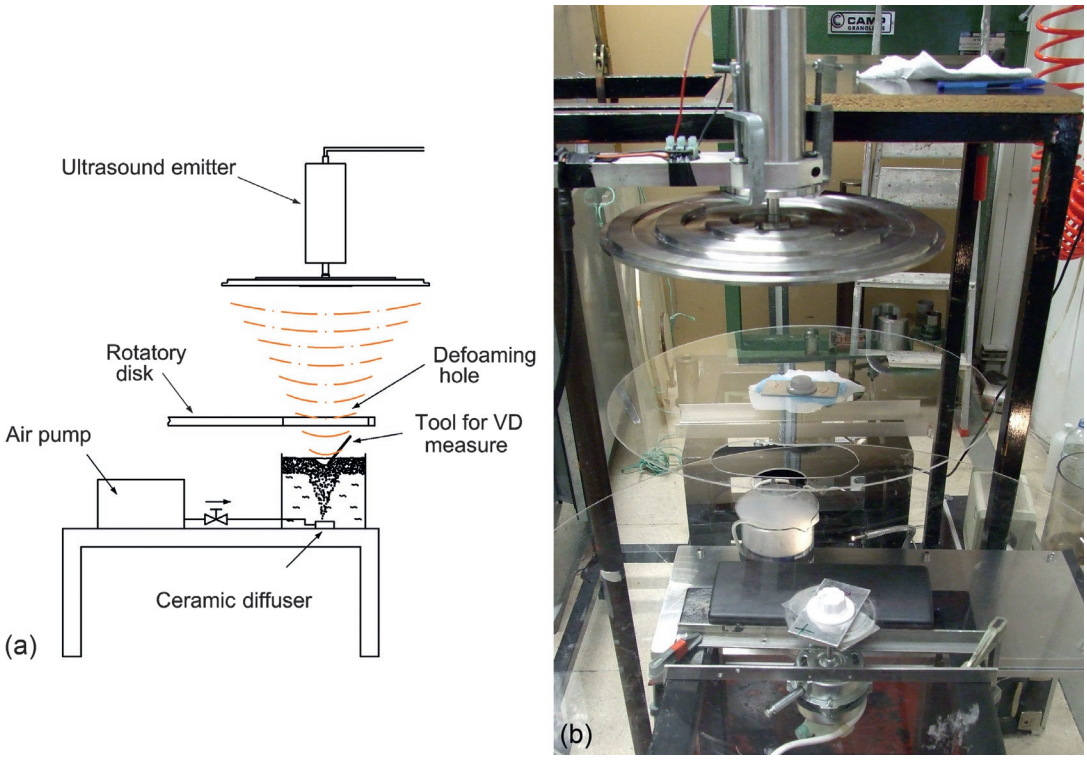


FIGURE 30.2 Scheme (a) and picture (b) of the experimental setup to quantify the defoaming effect.

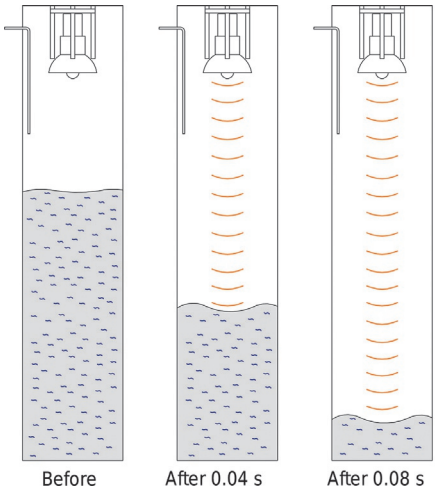


FIGURE 30.3 Scheme of the ultrasonic defoamer developed by Teknika Inc.

increases and rarefactions of the acoustic pressure within the resonant cavity. The modified Hartmann whistle, proposed by Brun and Boucher (1957), incorporates a reflector and some other small improvements, resulting in an efficiency of 14% instead of the 5% of the original whistle design. Despite design improvements, the efficiency of air jet generators remained very low; this, together with the problems posed by the introduction of an air jet, were crucial factors that halted the industrial use of such acoustic devices.

A possible solution to overcoming efficiency problems consisted of establishing resonant conditions in the foam vessel. Still, such an approach was difficult to pursue in most cases. The alternative, as proposed in the system commercialized by Teknika, was to separate the foam in an auxiliary resonant chamber, where this could be treated (Hay and Shapland, 1970). This proposed solution to overcome foam problems caused additional inconveniences during the operation of the industrial process.

To summarize, the main disadvantages of aerodynamic systems are related to noise problems (they are generally operated in the human-hearing frequency range), the need for high air generation capacity, the control and sterilization of the air flow, and the high energy consumption. Hence, it seems that none of the acoustic defoamers reported in the literature until the 1970s could be successfully implemented in industrial plants.

The main basic difficulty hindering the introduction of the defoaming process at the industrial level was clearly the lack of adequate airborne power ultrasonic generators. As a consequence, successive developers tried to find solutions to this problem, looking for new types of ultrasonic generators. One of the few solutions found was proposed by the German company Jagenberg-Werke A.G. that patented a method and apparatus for removing froth based on the use of an array of sonotrodes (Matzner, 1980). This invention tried to overcome the drawbacks of previous foam elimination methods, particularly of those used in the

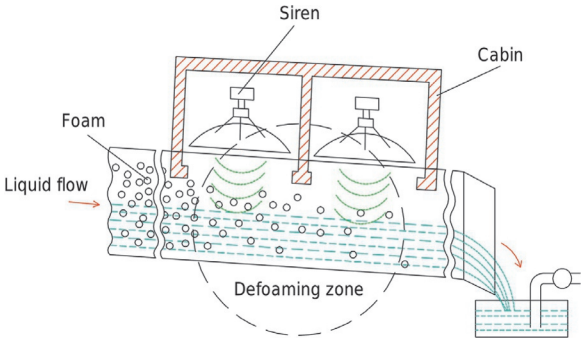


FIGURE 30.4 Scheme of the ultrasonic defoamer proposed by Sun.

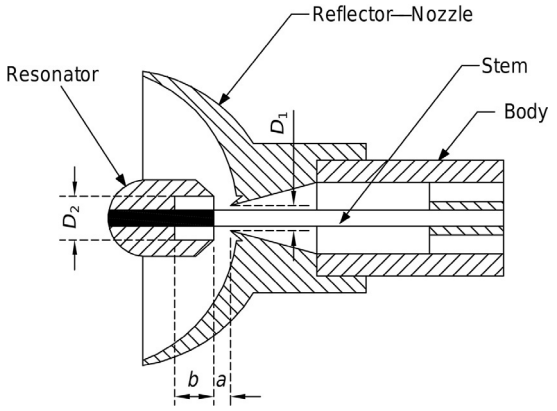


FIGURE 30.5 Scheme of the Hartman whistle.

packaging lines of beverages. Foam generated during packaging could be suppressed by applying multiple overlapping ultrasonic wave fields at frequencies of about 20 kHz by means of horns, or sonotrodes, located above the foam layer and not immersed in the foam structure. In this way, it was possible to destroy the foam while maintaining aseptic conditions in the process (Figure 30.6). As can be seen in Figure 30.6, multiple sonotrodes are required to fully treat the foam layer overlaying the liquid.

As is widely known, a horn, or sonotrode, is a length expander typically tuned to resonate in a longitudinal mode of vibration. Normally, horns are tapered half-wavelength-long resonators whose piezoelectrically activated vibratory movement is maximal at their smaller output (working) section (Ensminger, 2009). It seems evident that this invention represented an advance in comparison with the first commercial system developed by Teknika. However, a number of limitations still characterized this device. First, because of their structure, the sonotrodes have a very small radiation surface, which implies a very small radiation resistance in air and, consequently, a very low electroacoustic efficiency (<10%). Furthermore, the small radiation surface of the sonotrodes, which is of the order of 2 cm^2 for a frequency of 20 kHz, makes it necessary to use a large number of units to cover any surface, even a small one. In summary, these longitudinal horn-type devices can only be considered potentially useful in bottling or canning processes of foamy liquids, where the foaming surface is very small and the filling speed is relatively slow (<300 bottles per minute), according to the performance indicated by the inventors, all this in line with their limited efficiency.

To expand the radiation zone over the opening of bottles or cans, a transducer consisting of a sonotrode driving a rectangular plate vibrating in the strip mode was proposed by Nakamura et al. (1966) in Japan. These researches built a transducer with a plate radiator with a 585×93-mm^2 surface tuned in a vibration mode with several nodal lines parallel to the smaller side (Figure 30.7). To concentrate the radiation over the mouth of the bottles or cans, they use parabolic reflectors and a kind of waveguide to put in phase different sectors of the vibrating plate. In this way, they claimed to obtain radiating sound pressure levels between 155 and 160 dB. In addition, they mentioned that

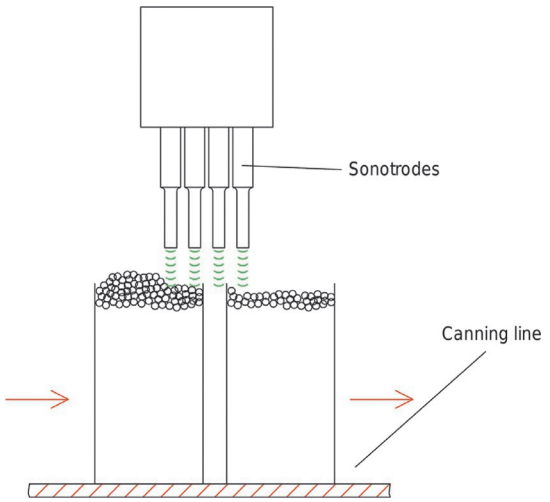


FIGURE 30.6 Scheme of the defoamer patented by Jagenberg-Werke A.G.

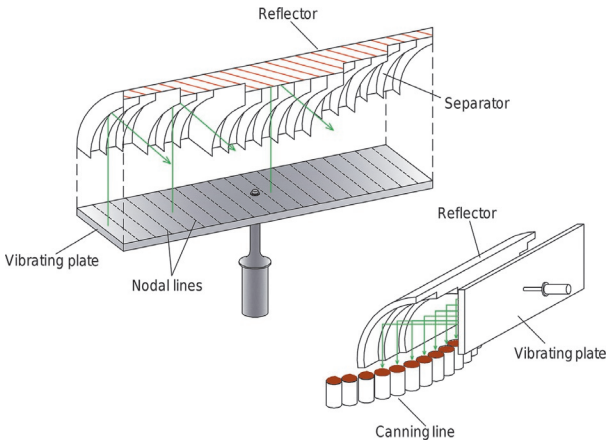


FIGURE 30.7 Scheme of the defoamer developed by Nakamura et al.

the defoaming system was tested in bottling lines of carbonic beverages but did not indicate the speed of the filling lines.

The nature of foaming problems in industry varies; in general, they are associated with high-volume and/or high-speed production processes. Foaming issues in bottling and canning lines of carbonated beverages and other foamy liquids have to be tackled at very high speeds (i.e., >900 bottles or cans per minute). Moreover, the major problem of foam excess occurs in large reactors with surfaces that may be many square meters. Therefore, from a practical perspective, it is necessary to find a solution for these real situations.

Currently, the only device capable of generating the high-intensity ultrasonic fields required to eliminate foams produced in various practical situations is the new type of stepped-plate transducers (Gallego-Juárez et al., 2005) marketed by Pusonics, S.L. (www.pusonics.es). Such a commercial ultrasonic defoaming system (UDS) is constituted by one or several piezoelectric power transducers driving specially designed plate radiators by means of a finely tuned electronic generation and control system (Figure 30.8). These airborne ultrasonic devices are capable of focusing high ultrasonic intensities through the flexural vibration of circular stepped-grooved radiators driven by piezoelectric vibrators (Figure 30.9). In a 26 kHz airborne transducer, the ultrasonic energy is concentrated in a focal volume about 2 cm in diameter and 13 cm in length (these dimensions define the air volume within which the generated acoustic pressure varies <3 dB from the maximum value). The maximum acoustic pressure is located at a distance of about 40 cm from the plate radiator (Figure 30.10).



FIGURE 30.8 Photograph of the ultrasonic defoaming system developed by Pusonics.

Intensities of the order of 170 dB are obtained in the focal volume with a power of 200 W applied to the transducer. The power electronic system generates, controls, and supervises the electric excitation provided to the transducers by continuously adjusting the driving frequency and maintaining a constant level of acoustic energy transmitted to the medium, thus ensuring that the correct dose of sound pressure is provided at all time. The control algorithm and preconfigured parameters recorded in the nonvolatile memory provide a fully automatic operation at all times. Different UDS units are manufactured to operate at frequencies of 21 and 26 kHz. These UDS units produce highly focused radiation and are powerful and compact devices that do not interfere adversely in the processes wherein they are applied; these tuned systems can be easily sterilized in order to fulfill industrial requirements. This type of transducer can be static or mounted on a rotary device. A static UDS (Figure 30.11) may be used in the control of excess foam in high-speed bottling and canning lines of carbonated beverages. Industrial trials have shown that lines filling 1200 cans per minute may be successfully defoamed at an ultrasonic frequency of 21 kHz and at an applied power of about 300 W.

Rotary UDS systems (Figure 30.12) are used for the dissipation of foam in reactors. Rotational movement is achieved by an electronically controlled motor that rotates a horizontal shaft. Each ultrasonic transducer is attached at the end of such a shaft via an offset connection. Because the ultrasonic transducers are rotated at variable speeds, device movements with different tilting angles with respect to the axis of rotation are also produced thus forming complex trajectories that allow the treatment of large areas of foam.

Defoaming rates achieved through a single-plate transducer operated at an applied power in the range of 200–300 W vary between 10 and 40 m^3/h in reactors with diameters from 6 to 12 m. This means an energy consumption less than 30 W h/m^3. Presently, UDSs constitute a clean, fast, safe, and efficient approach for the control of excess foam produced in fermenting vessels and in other type of reactors, as well as in high-speed canning and bottling lines during filling operations (Figure 30.13).

30.7 Using ultrasound to remove bubbles in coating layers

As discussed in the previous section, high-intensity airborne ultrasound technology represents an adequate contactless tool to break up the bubbles formed in foam layers. However, not all the bubbles are in the form of foams; in practice, there are situations wherein bubbles submerged or partially submerged in a liquid need to be removed. A common procedure to remove bubbles completely

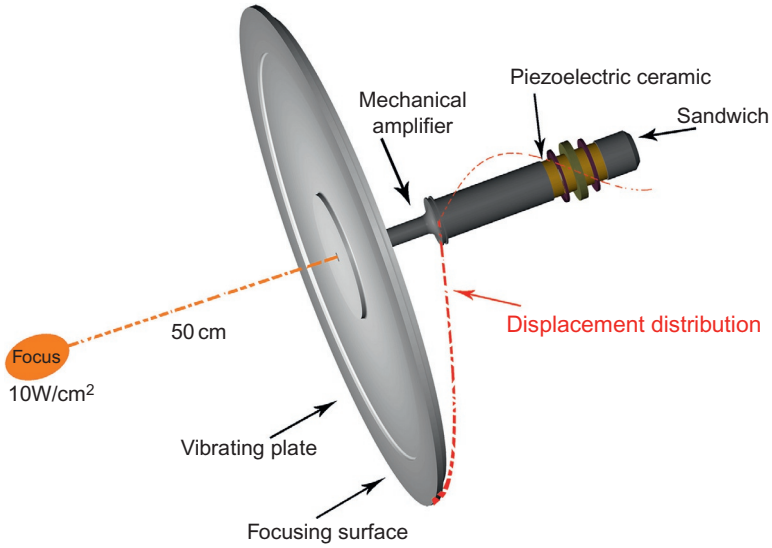


FIGURE 30.9 Scheme of the stepped-plate focusing transducer.

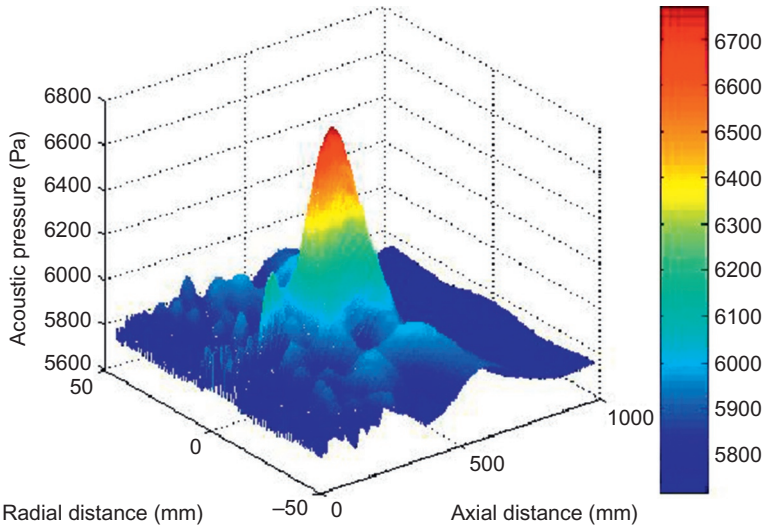


FIGURE 30.10 Acoustic field of the stepped-plate focusing transducer.

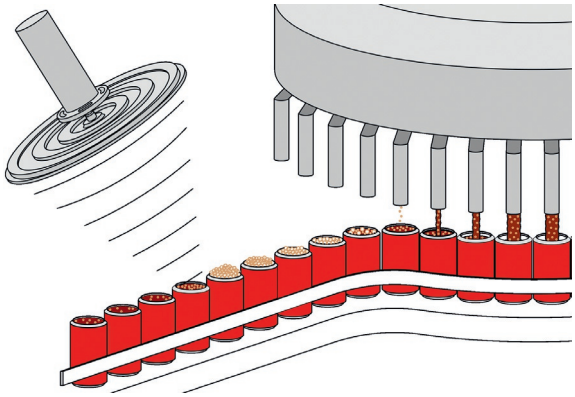


FIGURE 30.11 Scheme of the static stepped-plate ultrasonic defoamer working in a canning line with a single transducer.

submerged in liquids using ultrasound is known as the ultrasonic degassing method. Chapter 19 is specifically devoted to this application. There also exist cases where the bubbles are only partially submerged in the liquid phase and that require rapid elimination. For example, this is often the case of air-entrapped bubbles that are generated during industrial coating processes performed at high speeds. These bubbles result in the formation of permanent surface defects after drying. The majority of existing processes used to alleviate this problem rely on the de-aeration of the liquid used in the coatings before the coating process takes place. Therefore, either chemical antifoaming agents or ultrasonic degassing is the common method applied (Yasuo et al., 1998). However, chemical antifoaming agents are not completely effective because the used additives are difficult to dose. Moreover, many of the entrapped bubbles are produced

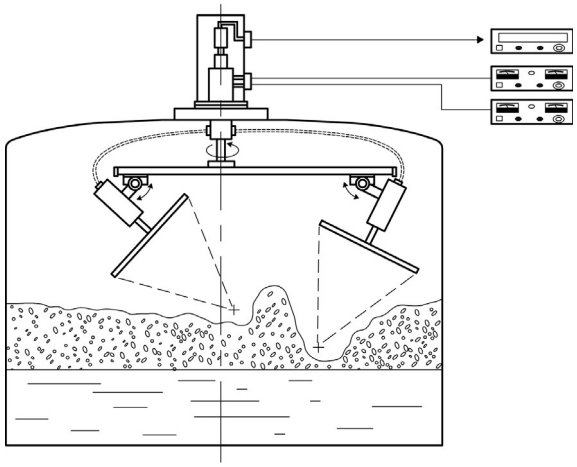


FIGURE 30.12 Scheme of the rotary ultrasonic defoaming system working in a reactor with two transducers.

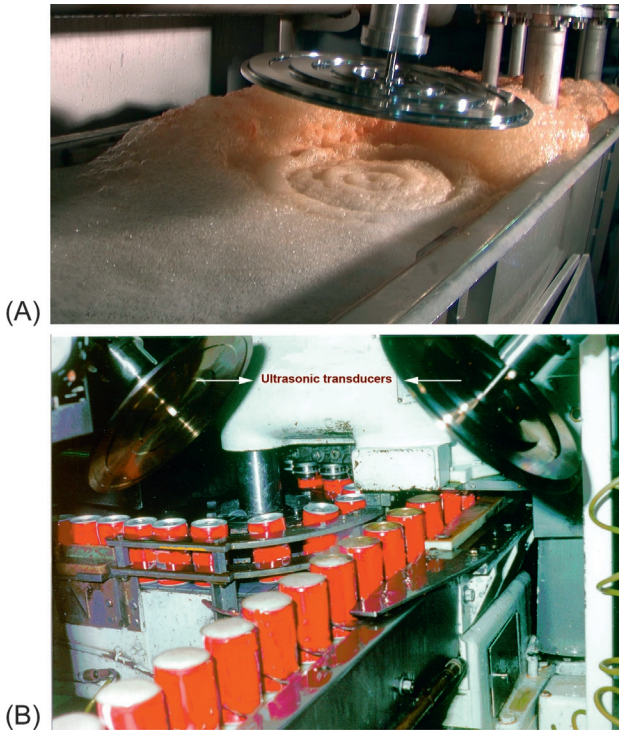


FIGURE 30.13 Photographs of the stepped-plate ultrasonic defoamer working in (a) a sea food processing reactor and in (b) a canning line.

during the application of the coatings. Therefore, a more effective way of removing such bubbles by breaking them directly in the coating layer is necessary. High-intensity airborne ultrasound may be a suitable method to achieve this aim. The application of airborne ultrasonic fields is a novel method that has been shown to be effective in this type of process (Gallego-Juárez et al., 2006), and it is briefly described here.

High-intensity coherent ultrasonic fields have been generated by an airborne plate-transducer operated at 21 kHz and spread over the surface of coating layers immediately after being deposited on the substrate. Tests carried out at laboratory and semi-industrial stages in an attempt to validate this new application of ultrasonic energy have shown promising results. A high-intensity ultrasonic field was generated by a highly directional stepped-plate transducer driven by an electronic generator with a feedback loop control system. The radiator of the ultrasonic generator was placed parallel to the treated layer at a distance of about 30 cm, obtaining an acoustic sound pressure level of about 153 dB (González et al., 2006). Experimental tests used substrates of wood materials (pine, oak, and sapelly) and coating layers of water- and solvent-based varnishes. The coating layers were applied manually and also by means of a pilot industrial coating curtain machine, in both cases obtaining bubbles of different sizes (between 100 and 500 μm in diameter) formed within the layer that were ultrasonically irradiated (Figure 30.14). A remarkable debubbling efficiency was achieved for all bubbles of different sizes entrapped within water-based coating layers (Figure 30.15). The effect, on the other hand, proved more selective with solvent-based coatings. In this case, a significant influence of bubble size on debubbling was observed. Specifically, debubbling of 80%–90% of the bubbles in the range of 100 μm and of 40%–60% of those with a diameter near 250 μm were achieved. Such different effects can be mainly attributed to the diverse viscosity of the two coating media (118 cP for water-based coatings and 198 cP for solvent-based solutions), which in the solvent-based case required higher acoustic intensities for breaking the partially submerged bubbles via a combination of radiation pressure and bubble resonance.

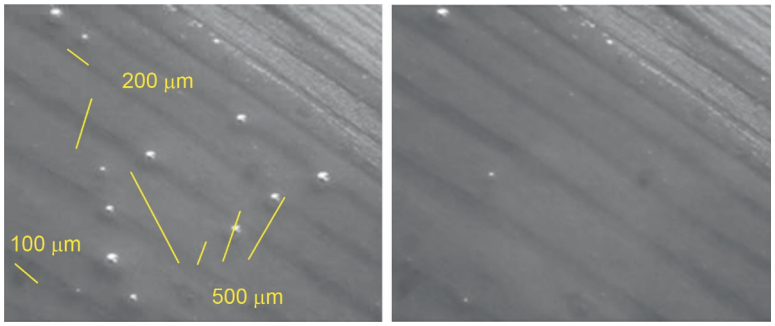


FIGURE 30.14 Semi-submerged bubbles within a coating layer before and after ultrasonic irradiation.

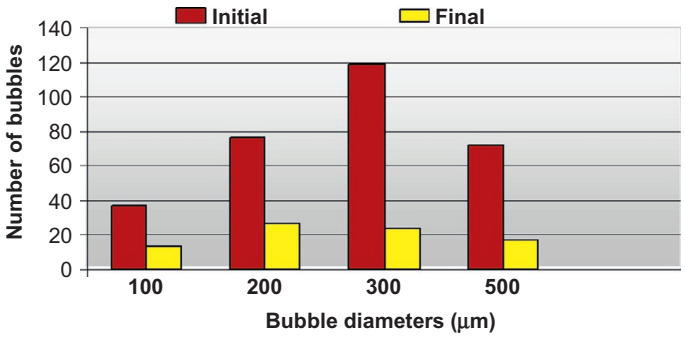


FIGURE 30.15 Bubble population in water-based coating layer before and after ultrasonic irradiation.

30.8 Conclusions and future trends

Airborne ultrasonic defoaming is an attractive technique that could potentially revolutionize the way foam issues at industrial level are currently dealt. There is therefore a need to work toward the enhancement of this application of ultrasound, given the practical advantages that it offers over other defoaming methods, especially from the point of view of the cleanliness of the ultrasonic tools and their ability to perform an effective no-contact operation. This last capability is crucial in most industrial areas where an excess of foam may take place, such as in the food, chemical, and pharmaceutical sectors. However, further industrial development of this technology needed to be performed to investigate its adaptability to the wide range of applications presently existing in the market. In fact, the industrial extension of ultrasonic defoaming requires the technical and economical adaptation of ultrasonic devices to the specific commercial requirements. To this purpose, it would be necessary to deepen the knowledge about defoaming mechanisms associated with the targeted processes. As a result, ultrasonic parameters used in defoaming should be adjusted to the specific requirements. For instance, a wider range of operating frequencies and powers might be needed in order to make the ultrasonic technology an even more versatile solution to industrial defoaming. In conclusion, future diffusion of this technology will depend on pursuing basic and applied research studies focused on the mechanisms of ultrasonic defoaming and in the corresponding adaptation of airborne ultrasonic systems to specific requirements. These are no simple issues due to the heterogeneity and complexity of the foam media and the wide variety of industrial problems. Nevertheless, the great advantages of this technology push to overcome difficulties.

Ultrasonic debubbling that extends to a more restricted area of application relies on the correct combination of the parameters involved in the process that will stem from the collaboration between industrial end users and manufacturers of the ultrasonic technology.

References

Allen, C.H., Rudnick, I., 1947. A powerful high frequency siren. J. Acoust. Soc. Am. 19 (5), 857–865.

Allen, S.L., Allen, L.H., Flaherty, T.H., 1993. Defoaming in pulp and paper industry. In: Garret, P.R. (Ed.), Defoaming, Theory and Industrial Applications. Taylor & Francis, Boca Raton, pp. 151–175.

Barigou, M., 2001. Foam rupture by mechanical and vibrational method. Chem. Eng. Tehcnol. 24, 659–663.

Ben Salem, I., Guillermic, R.-M., Sample, C., Leroy, V., Saint-James, A., Dollet, B., 2013. Propagation of ultrasound in aqueous foams: buble size dependence and resonant effects. Soft Matter 9, 1194–1202.

Boucher, R.M.G., Weiner, A.L., 1963. Foam control by acoustic and aerodynamic means. Br. Chem. Eng. 8 (12), 808–812.

Brun, E., Boucher, R.M.G., 1957. Research on the acoustic-jet generator: a new development. J. Acoust. Soc. Am. 29, 573–583.

Chendke, P.K., Fogler, H.S., 1974. Second order sonochemical phenomena-extensions of previous works and applications in industrial processing. Chem. Eng. J. 8, 165–178.

Dedhia, A.C., et al., 2004. Static foam destruction: role of ultrasound. Ultrason. Sonochem. 11 (2), 67–75.

Deshpande, N.S., Barigou, M., 2000. Mechanical suppression of the dynamic foam head in bubble column reactors. Chem. Eng. Process. 39, 207–217.

Dorsey, A.E., 1959. Control of foam during fermentation by application of ultrasonic energy. J. Biochem. Microbiol. Technol. Eng. 1 (3), 289–295.

Ensminger, D., 2009. Ultrasonic horn couplers and tools. In: Ensminger, D., Stulen, F.B. (Eds.), Ultrasonics: Data, Equations and Their Practical Uses. CRC Press, Boca Raton, pp. 27–128.

Gaden, E.L., Kevorkian, V., 1956. Foams in chemical technology. Chem. Eng. 63, 173–184.

Gallego-Juárez, J.A., Rodriguez-Corral, G., Gaete-Garretón, L., 1978. An ultrasonic transducer for high power applications in gases. Ultrasonics 16 (6), 267–271.

Gallego-Juárez, J.A., Rodriguez-Corral, G., Montoya Vitini, F., Acosta Aparicio, V.M., Riera, E., Blanco Blanco, A., 2005. Macrosonic Generator for the Air-Based Industrial Defoaming of Liquids. CSIC. International patent application PCT/ES2005/070113, July 27, 2005.

Gallego-Juárez, J.A., González Gómez, I., Rodriguez Corral, G., Riera, E., Garmendia Barrena, M.I., 2006. Procedimiento y dispositivo ultrasónico para la eliminación de burbujas ocluidas en recubrimiento

con pinturas y/o barnices aplicados a alta velocidad. CSIC. Spanish patent application 200600619, 2006-mar-10.

Garret, P.R., 1993. Recent development in the understanding of foam generation and stability. Chem. Eng. Sci. 48 (2), 367–392.

Ghildyal, N.P., Lonsane, B.K., Karanth, N.G., 1988. Foam control in submerged fermentation state of the Art. Adv. Appl. Microbiol. 33, 173–222.

González, I., Rodriguez, J., Garmendia, I., Gallego-Juárez, J.A., 2006. Application of high- intensity air-borne ultrasound for debbubling liquid coating layers. Ultrasonics 44 (S1), e529–e532.

Gutschick, V.P., Harder, A., Humphrey, A., Kristapsons, M.Z., Levitans, E. S., Roels, J.A., Rolz, C., Viesturs, U.E., 1982. Foam in microbiological processes. In: Fiechter, A. (Ed.), Microbes and Engineering Aspects. Advances in Biochemical Engineering/Biotechnology, Springer-Verlag, Berlin, pp. 169–224.

Hay, B., Shapland, D.G., 1970. Improvements in or Relating to Destruction of Foam. GB Patent application 1354678 A, 18 August, 1970.

Hueter, T.F., Bolt, R.H., 1955. Sonics. John Wiley & Sons, Inc, New York, London.

Komarov, S.V., Kuwabara, M., Sano, M., 2000. Supression of slag foaming by a sound wave. Ultrason. Sonochem. 7, 193–199.

Matzner, E., 1980. Method and Apparatus for Removing Froth on a Liquid. Jagenberg-Werke A.G., Germany. UK Patent Application 2051754 A.

McDaniel, J.G., Akhatov, I., Holt, R.G., 2002. Inviscid dynamics of a wet foam drop with monodisperse bubble size distribution. Phys. Fluids 14, 1886–1894.

Morey, M.D., Deshpande, N.S., Barigou, M., 1999. Foam destabilization by mechanical and ultrasonic vibrations. J. Colloid Interface Sci. 219 (1), 90–98.

Nakamura, S., Abe, S., Iwata, H., Itoh, Y., 1966. Development of foam breaking system in ultrasonics. Tech. Bull. Mitsubishi Heavy Ind. 33 (5), 374–377 (1996–1999).

Pugh, R.J., 1996. Foaming, foam films, antifoaming and defoaming. Adv. Colloid Interface Sci. 64, 67–142.

Rodriguez, G., Gallego-Juárez, J.A., Ramos, A., Andres, E., San Emeterio, J.L., Montoya, F., 1985. High power ultrasonic equipment for industrial defoaming. In: Conference Proceeding of Ultrasonics International 1985, pp. 506–511.

Rodriguez, G., Gallego-Juárez, J.A., Riera, E., Acosta, V.M., Blanco-Blanco, A., 2009. Experimental study of defoaming by air-borne power ultrasonic technology. Phys. Procedia 3 (1), 135–139. https://doi.org/10.1016/j.phpro.2010.01.019.

Ross, S., McBain, J.W., 1944. Inhibition of foaming in solvents containing known foamers. Ind. Eng. Chem. 36 (6), 570–573.

Sandor, N., Stein, H.N., 1993. Foam destruction by ultrasonic vibrations. J. Colloid Interface Sci. 161, 265–267.

Sun, S.C., 1951. Destruction of flotation froth with intense high frequency sound. Trans. AIME 190, 865–867.

Viesturs, U.E., et al., 1982. Foam in microbiological processes. In: Fiechter, A. (Ed.), Advances in Biomedical Engineering. Springer-Verlag, Berlin, pp. 169–224.

Yasuo, N., et al., 1998. Method and Device for Debubbling a Liquid Using Ultrasonic Waves. European patent application EP0885641.

Chapter 31

Power ultrasonics for food processing

X. Zhu[a,b,*], T.J. Mason[c], F. Chemat[d], M. Ashokkumar[e], and B.K. Tiwari[a,*]

[a]Teagasc Food Research Centre, Ashtown, Dublin, Ireland, [b]University College Dublin, Dublin, Ireland, [c]Coventry University, Coventry, United Kingdom, [d]Université d'Avignon et des Pays du Vaucluse, Avignon, France, [e]University of Melbourne, Melbourne, VIC, Australia

31.1 Introduction

Long-standing applications of ultrasound in the food industry can be divided into two categories: low-power ultrasound (low energy, high frequency) in the megahertz range, used for nondestructive testing, and high-power ultrasound (high intensity, low frequency) in the kilohertz range, used for cutting and processing (Povey and Mason, 1998a). In this chapter, we are concerned only with the latter. The earliest reference to the use of power ultrasound in processing was in 1927, when a paper entitled *The Chemical Effects of High Frequency Sound Waves: A Preliminary Survey*, which described the development of power ultrasound and included its uses in a range of applications including emulsification and surface cleaning, was published (Richards and Loomis, 1927) The physical and biological effects of ultrasound were reported in the same year (Wood and Loomis, 1927), and the importance of this technology in food industry was identified in the 1930s (Szent-Györgyi, 1933). This work found that ultrasound was able to modify the properties of proteins through the observation that the sonication of egg albumin made it turbid, as the albumin was precipitated out in fine shreds (Wu and Liu, 1931). One of the oldest applications of ultrasound in food processing is emulsification, and the development of the "Pohlmann whistle" or jet edge transducer proved to be an important new technology for efficient emulsification (Janowsky and Pohlmann, 1948). In 1960, a series of experiments were undertaken to compare four methods then in common usage for the emulsification of mineral oil, peanut oil, and safflower oil (Singiser and Beal, 1960). The results proved that a homogenizer that operated via a liquid whistle was superior to three other types of apparatus, namely a colloidal mill and two types of piezoelectric sonicator. In 1959, ultrasound was also investigated in terms of improving defrosting (Brody and Antonevich, 1959), and the origins of ultrasonically assisted drying were suggested in the same year (Boucher, 1959).

In the 1990s, ultrasonic processing became more accepted in food technology and a number of relevant review articles, books, and book chapters were published (Mason, 1999; Mason et al., 1996; Povey and Mason, 1998a). It is now a quickly developing research area because of its potential benefits in the food industry, as evidenced by an increasing number of books and review articles in recent years (Chandrapala et al., 2012, 2013; Chemat and Khan, 2011; Feng et al., 2011).

Power ultrasound produces its effects in liquid media through the phenomenon of acoustic cavitation (Figure 31.1a). Like any sound wave, ultrasound is transmitted via waves that alternately compress and stretch the molecular structure of the medium through which they pass. During each "stretching" phase (rarefaction), provided that the negative pressure is strong enough to overcome intermolecular binding forces, a fluid medium can be literally torn apart, producing tiny cavities (microbubbles). In succeeding cycles, these cavities can collapse violently, releasing large amounts of energy in the immediate vicinity of the microbubbles. Temperatures of up to several thousand Kelvin and pressures of several hundred atmospheres are estimated to be produced during this collapse (Figure 31.1b). The mechanical and chemical effects of the collapsing bubble are felt in two distinct regions: (i) within the bubble itself, which can be thought of as a high-pressure and high-temperature microreactor and (ii) in the immediate vicinity of the bubble, where the shock wave produced upon collapse creates enormous shear forces. The microbubble (or cavitation bubble) formed in the rarefaction cycle does not enclose a vacuum; it contains vapor from the solvent or any volatile reagent present so that, upon collapse, these vapors are subjected to the enormous increases in both temperature and pressure referred previously. Under such extremes, the solvent and/or reagent suffers fragmentation, generating reactive free radical species. In food processing, the normal solvent is water, and the extreme conditions generated upon collapse of the cavitation bubbles are sufficient to cause rupture of the O-H bond itself, forming hydrogen and hydroxyl radicals; one of the end products of the recombination of such radicals is hydrogen peroxide.

*Updated author for the second edition.

Power Ultrasonics. https://doi.org/10.1016/B978-0-12-820254-8.00030-0
Copyright © 2023 Elsevier Ltd. All rights reserved.

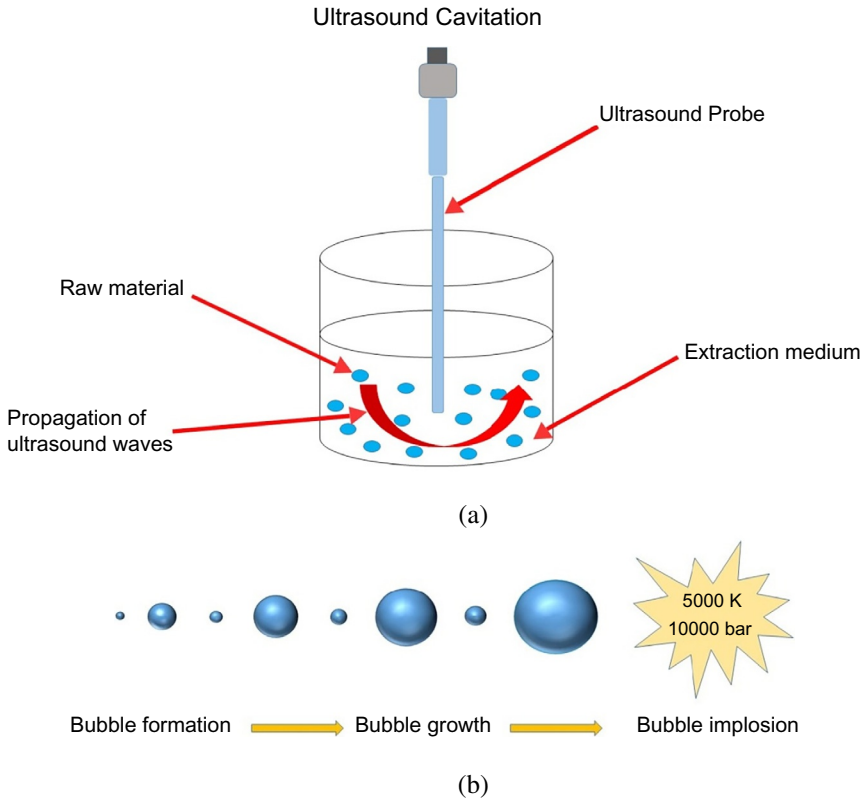


FIGURE 31.1 Ultrasound cavitation and its mechanism. (a) Ultrasound cavitation. (b) Cavitation mechanism. *(Modified from Medina-Torres et al. (2017).*

Power ultrasound also produces its effects in fluids (gases and liquids) and in multiphase media (fluids with bubbles and/or particles in suspension and porous solids with fluids inside) through other nonlinear phenomena such as wave distortion, acoustic streaming, and radiation pressure. These phenomena may activate a series of mechanisms such as heat, agitation, diffusion, interface instabilities, friction, and mechanical rupture.

The collapse of bubbles near a surface is asymmetric in that the inrush of liquid is hampered from the surface side and the majority of the inflow during collapse is from the bulk liquid side. A jet of solvent is generated and impinges on the surface when a cavitation bubble collapses close to it. Such a jet can cause physical and chemical effects as follows: (i) The mass transfer rate is increased and the penetration of the solvent into the cell is enhanced since the temperature and pressure generated during the bubble collapse events cause membrane thinning and cell rupture. (ii) The diffusion is enhanced by microscopic-level turbulence, strong collisions between particles, and the agitation of matrix microporous particles due to the implosion of cavitation bubbles. (iii) The diffusion of the solvent into the matrix is enhanced due to the hydration and swelling of the matrix and the expansion of pores. (iv) The surface area of matrix is increased due to the decomposition of shock waves and microjets. (v) Highly reactive free radicals is generated and cell disruption is driven by the associated radical (Panda and Manickam, 2019).

31.2 Ultrasonically assisted extraction (UAE)

Food products are complex mixtures of proteins, lipids, aromas-antioxidants, and other organic and mineral compounds. Before such substances can be used as food additives or supplements, they have to be extracted from the food matrix. Different methods can be used for this purpose, for example, Soxhlet extraction, maceration, elution, steam distillation, cold pressing, and simultaneous distillation–extraction. Many food ingredients, however, are known to be thermally sensitive and vulnerable to chemical changes during processing. In conventional extraction, there is always loss of targeted compounds because of low extraction efficiency, prolonged heating and stirring in boiling solvent, and the use of large volumes of solvents, which subsequently require concentration.

Ultrasound has been identified as a key technology for process intensification and is particularly effective in achieving sustainable "green" chemistry (Mason, 1990). In the chemical and food industry, ultrasound has a significant effect on the rate of various processes. Ultrasound can

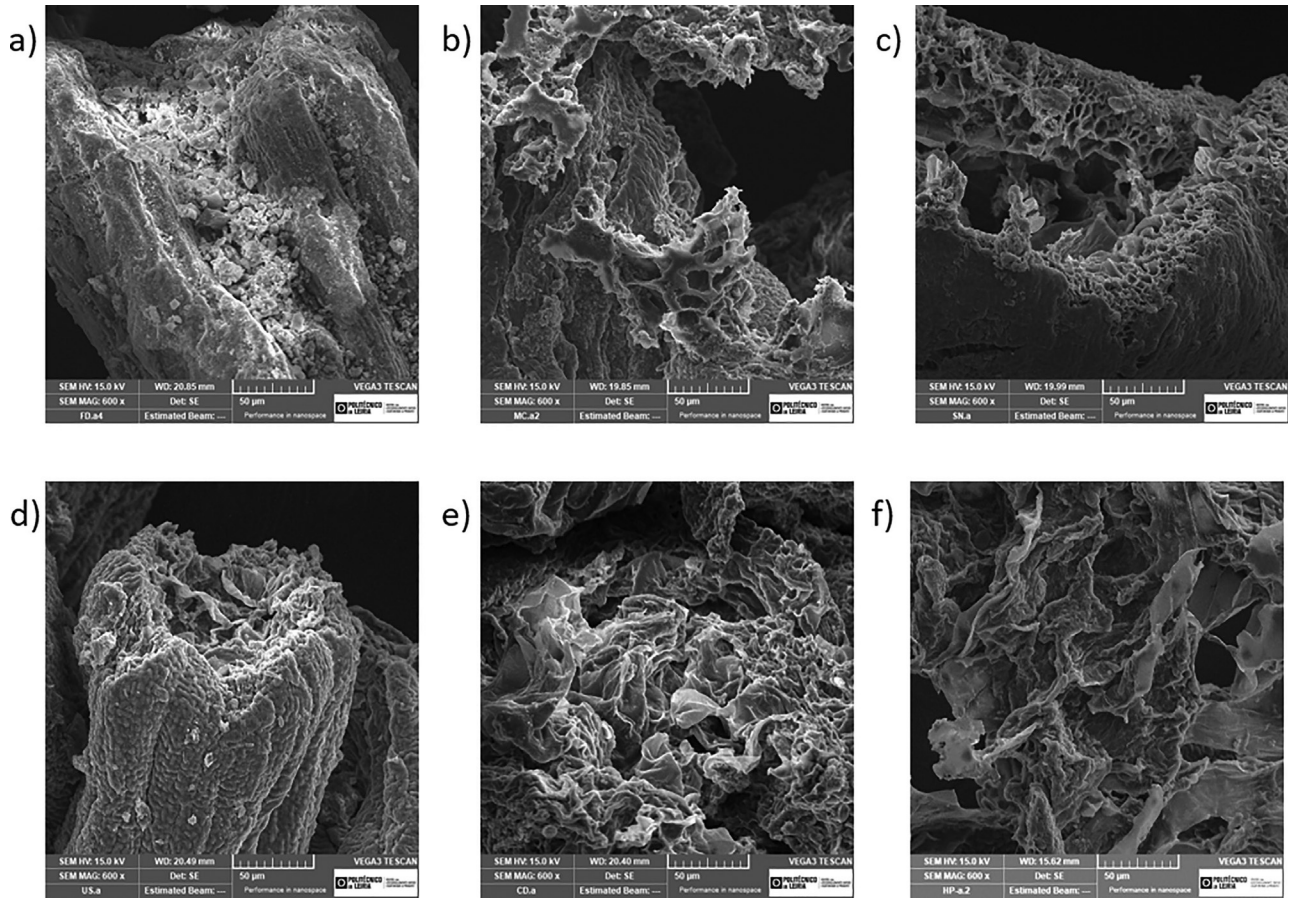


FIGURE 31.2 SEM images of the *Gracilaria gracilis* biomass cells (a) before and (b–f) after the extraction treatments (b—maceration, c—ultrasonic probe, d—ultrasonic bath, e—freeze–thaw, f—high-pressure-assisted extraction) at a magnification of 600×. *(Adapted from Pereira et al. (2020).)*

be employed in both the pretreatment process and extraction process in the form of ultrasound bath, ultrasound probe, or noncontact ultrasound system. Figure 31.2 shows SEM images of *Gracilaria gracilis* treated using different extraction technologies. Figure 31.2c illustrates that ultrasound probe treatment (50–60 kHz, 200 W) for different periods of time (10 s–10 min), on and off cycles (30 s and 20 s), increases cell rupture over other methods such as freeze–thaw, maceration, high-pressure-assisted, and ultrasound bath extraction and releases the chlorophyll *a*nd phycobiliprotein from *G. gracilis* (Pereira et al., 2020). Less sulfate was observed in agar extracted using a combination of sonication and ultrasound. Ultrasound as a pretreatment enhances the greenness by having the following advantages: significantly reducing the process time required for extraction, digestion etc.; reduces energy consumption; facilitates use of low concentration and quantities of solvents; may be carried out at room temperature and atmospheric pressure; reduces analyte loss and contamination risks; and increases productivity (Bendicho et al., 2012).

Several types of food components such as proteins, aromas, lipids, antioxidants, and bioactive compounds have been extracted and analyzed efficiently from a variety of matrices (mainly animal tissues, food, and plant materials). In the following sections, we present an overview of current knowledge about ultrasonically assisted extraction (UAE) in food processing.

31.2.1 Proteins

Because of the rapid increase in the demand for protein caused by the rising population, plant-based protein is getting more and more attention and can be used as a sustainable substitute for animal protein. A nontoxic prokaryotic cyanobacterium, spirulina contains high value-added compounds such as protein (50%–70% of its dry weight) (Matos et al., 2017) and is approved by the FDA (Food Drug Administration) as a food or food supplement. Manothermosonication (MTS) assisted by ultrasound and conventional way was used to extract protein from dry *Arthrospira platensis* (spirulina) cyanobacteria. Results shown that compared to conventional way without ultrasound, MTS could effectively produce 229% more protein (28.42 ± 1.15 g/100 g DW). Also, microscopic observations indicated that acoustic cavitation had influence on spirulina filaments by fragmentation, sonoporation, and detexturation (Vernès et al., 2019).

Li et al. (2017b) applied counter-current ultrasound-assisted alkali for the extraction of rice dreg protein (RDP) from rice dreg flour (RDF). Ultrasond treatment was considered as an effective method in extraction yield of RDP, which could reach to 88.44% at 0.08 mol/L alkali concentrate. The high yield of RDP could be related to the changes of RDF and RDP microstructure by ultrasound. Peanut is always used to make oil products; however, it could be a potential product of plant-based protein because of its high protein contents (26% to 29%) and excellent amino acid profile. Ochoa-Rivas et al. (2017) reported the extraction of protein from peanut flour under alkaline conditions by using ultrasound. Compared to a control treatment, an increase of 100% in protein extraction yield was obtained under ultrasound-assisted treatments (100% amplitude and 15 min). Soy protein is drawing the current interest of research due to its complete set of essential amino acids and cholesterol-lowering attributes. Some reports indicated that traditional aqueous extraction is not satisfactory for protein extraction rate and yield from soy milk and okara. Ultrasound had been implemented on milled soybean slurry and okara samples with a lab-scale probe system (20 kHz, 400 W) for 0, 0.5, 1, 5, and 15 min. Results showed that after 1 min treatment, protein yield had increased up to 10%, which may be attributed to improved solubility and elevated separation efficiency by ultrasound (Preece et al., 2017b). Also, high-pressure homogenization (HPH) was reported to able to enhance the protein yield of soy slurry up to 82% at 100 MPa with a single pass (Preece et al., 2017a), which could be a result of availability of protein and separation efficiency due to cavitation effects.

31.2.2 Oils and aromas

Some plants or plant seeds are rich in oil, which can not only be used to produce paint, linoleum, varnish, ink, and cosmetics but also may play an important role in functional foods due to their nutritional and medicinal value. Currently, some traditional methods, such as pressing and solvent extraction, are used to extract oil from plants. However, due to some of the shortcomings by these conventional methods, including increased energy consumption, extended extraction time, environmentally unfriendly organic solvents, and degradation of thermally unstable substances, these have prompted some novel extraction methods to be studied, such as UAE. The oil from flaxseed was extracted by UAE, which was reported to have a positive effect on reducing many diseases, such as hyperlipidemia, colon tumors, breast cancer, and atherosclerosis (Zhang et al., 2008). Gas chromatography showed that the fatty acid composition of the oil extracted by ultrasonic and conventional methods was not significantly different, while UAE required shorter extraction time and less solvent consumption compared to the conventional methods. Similarly, Li et al. (2004) combined 20 kHz high-intensity ultrasound with different solvents, including hexane, isopropanol, and a 3:2 hexane–isopropanol mixture, to extract the oil from two varieties of soybeans (TN 96-58 and N 98-4573). Reduced extraction time and enhanced oil yield from both two varieties of soybeans can be obtained via high-intensity ultrasound, which was attributed to the mechanical action caused by ultrasound-induced cavatation to increase the permeability of plant tissues. In addtion, ultrasound-assisted dynamic extraction (UADE), which allowed the solvent to circulate back and forth in the sample under ultrasound, was applied for the extracton of chickpea oil (Lou et al., 2010). UADE could obtain a higher extraction rate (incerased 10.45% and 2.06%, respectively) at a lower cost in only 20 min as compared to 4 h with traditional solvent extraction and 30 min with UAE. The Jalili et al. (2018) used Soxhlet extraction and UAE with hexane and hexane–isopropanol mixture for canola oil extraction and compared their extraction efficiency. Under the optimal conditions, when the processing time were 30 min and 90 min, the extraction efficiency of oil using UAE solvent extraction could be increased by 10% and 15%, respectively, compared with Soxhlet only extraction. Papaya seed oil is rich in monounsaturated fatty acids and contains functional compounds. The UAE extraction of oil from papaya seed recovered a relatively high oil yield (73%), and a very reliable antioxidant activity ($88.1 \pm 0.8\%$) of extracted oil was obtained using low solvent/sample ratio at high temperature via DPPH free radical scavenging activity assay (Samaram et al., 2015).

UAE also has been developed for essential oils from aromatic plants such as lemon balm and peppermint leaves (Zlabur et al., 2016), artemisia (Bahmani et al., 2018), and lavender (Chen et al., 2019) or from other vegetal matrices such as clove (Tekin et al., 2015), citrus flowers, and caraway seeds (Chemat et al., 2004). Except for the work on citrus flowers, these authors compared UAE with different procedures for essential oil extraction, for example, hydrodistillation, microwave-assisted extraction, and supercritical carbon dioxide. UAE produced increased yields of essential oil in all cases (Table 31.1). Moreover, UAE proved to be faster and ran at lower temperatures so that the final product generally showed less thermal degradation than traditional or microwave-assisted methods. This is especially important in the case of extracts used in food or cosmetics because in these two fields, essential oils must be of high quality and good flavor.

31.2.3 Lipids

UAE can be used as an effective method for lipid recovery, which involves destroying cells to release lipids present in the cytoplasm. Araujo et al. (2013) researched the extraction of lipids from *Chlorella vulgaris* by applying five extraction

TABLE 31.1 Ultrasound-assisted extraction of essential oils and aromas

Plant source	Components isolated	Operating conditions and remarks	Reference
Caraway seeds	Carvone and limonene	US bath, 20 kHz, 150 W, 20–55°C, *n*-hexane, 60 min Increased yield by US compared with Soxhlet extraction	Chemat et al. (2004)
Citrus flowers and honey	Linalool	US bath, 25°C, 5 g fresh flowers in 30 mL n-pentane:diethylether (1:2), extraction time 10 min More than 80% of compounds detected are linalool derivatives	Alissandrakis et al. (2003)
Clove	Eugenol	US bath, 53 kHz, 32–52°C, clove with ethanol for 30–60 min Higher extraction efficiency with US	Tekin et al. (2015)
Greek saffron	Safranal	US bath, 35 kHz, 25°C, 5 g saffron in 100 mL water/diethyl ether (1:1), sonication 5 × 10 min US increases the amount of safranal	Kanakis et al. (2004)

US, ultrasound.

methods: Bligh and Dyer, Chen, Folch, Hara and Radin, and Soxhlet. The higher contents of lipid from *C. vulgaris* (52.5% w/w) were obtained by the Bligh and Dyer method assisted by ultrasound as compared to others. Solvent-free UAE was reported by Adam et al. (Adam et al., 2012) for lipid recovery from fresh *Nannochloropsis oculata* biomass, which resulted in the high lipid content, showing an innovative and effective extraction method suitable for the recovery of microalgae lipid. Keris-Sen et al. (2014) combined ultrasound with two different solvents, n-hexane and chloroform/methanol mixture, for lipid extraction from the mixed microalgae. At 0.4 kWh L^{-1}, UAE was reported to increase lipid production by 1.5- to 2.0-fold in the presence of solvent. Some microorganisms can also serve as an important source of lipids, such as the production of polyunsaturated fatty acids (PUFA), which play an important role in the function of the brain system, cardiovascular system, and certain types of cancer. The oleaginous fungus *Mortierella isabellina* was studied for the optimization of lipid extraction with UAE. Under optimal conditions (ultrasound intensity of 75.11 W cm^{-2} and pulse cycle of 0.93), 14.47 w.t.% oil with ethanol and 19.49 w.t.% oil with mixture of solvents (chloroform:methanol:water) were obtained, respectively, which indicated UAE had higher extraction efficiency and yield compared to the conventional methods (Sallet et al., 2019). Meullemiestre et al. (2016) also reported the efficiency of lipid recovery from *Yarrowia lipolytica* yeast in terms of lipid extraction yield and lipid composition analysis via UAE as well as other various modern techniques of extraction. The lipid extraction rate through UAE and microwave-assisted methods showed a slight increase, but there were differences in lipid profiles partly due to the degradation of diacylglycerol (DAG) to free fatty acids (FFA), as compared to other conventional methods.

31.2.4 Antioxidants

The term antioxidant originally referred to a chemical that prevented the consumption of oxygen. In the late nineteenth and early twentieth centuries, chemists extensively studied the uses of antioxidants for industrial processes, which range from prolonging food storage to vulcanizing rubber, but it was the identification of vitamins A, C, and E as antioxidants that led to the realization of the importance of antioxidants in the biochemistry of living organisms. Later, explanations for the effects of antioxidants on cancer susceptibility and overall health expanded rapidly with research into mechanisms, molecular targets, and molecular interactions.

The presence of antioxidants is essential not only for the better human health but also for the quality, retention, and safety of foods. In current years, intensive research on natural antioxidants has received considerable attention because synthetic antioxidants, such as butylated hydroxyanisole and butylated hydroxytoluene, have been proven to cause various health effects because they have a degree of toxicity and are responsible for carcinogenesis and liver damage.

Antioxidants are able to scavenge free radicals and thereby inhibit deleterious oxidative processes (such as lipid peroxidation) that are responsible for food deterioration. Fruits and vegetables are well known for being rich in these antioxidants, and thus, they have become targets both as food preservatives and as food because of their nutritional value. A new trend in the food industry is to make use of constituents in waste materials and by-products generated during processes such as juice production. Waste fruit skin and pips usually have good proportions of antioxidants that are valuable after being extracted from the plant matrix. Thus, UAE is an interesting tool for antioxidant isolation (Table 31.2).

TABLE 31.2 Ultrasonically assisted extraction of antioxidant

Plant source	Components isolated	Operating conditions and remarks	Reference
Grape and grape seeds	Tartaric and malic acids	US probe, 24 kHz, 200 W, 70°C, 1 g of freeze-dried sample in water, extraction time 30 min US was more efficient	Palma and Barroso (2002)
Pepper	Capsaicinoids	US bath, 360 W, 50°C, 1 g cayenne pepper, extraction in 25 mL methanol for 10 min	Barbero et al. (2008)
Raspberries	Anthocyanins	US horn, 22 kHz, 650 W, < 40°C, 60 g frozen raspberries in 240 mL 1.5 M HCl-95% EtOH (15:85) Same yield was achieved after 3.3 min (200 s) by US-assisted extraction compared with 53 min with conventional extraction	Chen et al. (2007)
Strawberries	Phenolic compounds	US probe, 20 kHz, 100 W, 5 g of strawberries, extraction in 10 mL aqueous 0.4 M HCl for 2 min at 60°C Same efficiency was achieved in 2 min compared with 20 h by conventional extraction	Herrera and De Castro (2005)
Tomatoes	Lycopene	US bath, 40 kHz, 300 W, 1 g of tomato in 8 mL of ethyl acetate, sonicated for 29 min at 86°C 90% of total lycopene extracted in 29 min by US	Lianfu and Zelong (2008)

Wide varieties of fruits and vegetables have been studied using UAE because antioxidants are present in different amounts in different varieties of plants, and these antioxidants come from different families. One of the most common antioxidants is the lycopene extracted from tomatoes (Lianfu and Zelong, 2008; Herrera and De Castro, 2005) worked not only on UAE but also on coupling ultrasounds with microwaves, which extracts large amounts of lycopene in only 6 min. They showed that similar amounts of phenolic compounds could be extracted from strawberries in 2 min, whereas it took 20 h with a conventional method and 3 h using supercritical fluid extraction. Another example is the extraction of anthocyanins from raspberries, a process developed by Chen et al. (2007). In this study, the same yields of anthocyanins were reached in 3 min when using UAE compared with 53 min with a conventional extraction system. A fast UAE of capsaicinoids from pepper was reported by Barbero et al. (2008) who developed a reproducible ultrasonic extraction method using methanol as a solvent. The difference between ultrasounds and conventional methodology is to some extent dependent on the part of the plant studied. This has been highlighted in the case of grape and grape seeds (Palma and Barroso, 2002). These authors found that the advantages of using ultrasound instead of maceration were more significant when working on seeds than on whole fruit. Ultrasound facilitates the diffusion of the solvent into the seeds, which allows better extraction of malic and tartaric acids.

31.2.5 Other bioactive compounds and current industrial applications

Apart from the aforementioned compounds, UAE was also studied and proved to be a promising extraction for polyphenols and pigments. Table 31.3 collated various valuable components that were extracted by ultrasound-assisted extraction technologies in recent years. A good example of industrial-scale applications is to be found from the Italian company Giotti (www.giotti.it). For more than 20 years, they have used ultrasound for the extraction of plant materials to produce alcoholic drinks, food, and nutraceutical additives. As a company, Giotti supplies flavors, extracts, semifinished products, and concentrated juices. They claim that extraction with ultrasound is rapid, clean, and efficient (Table 31.4). Giotti uses ultrasound technology in 500-L batch reactors (Figure 31.3).

31.2.6 Power ultrasound to intensify extractions

Supercritical fluid extraction (SFE) is a separation process based on the contact of a substance containing the extractable compound with a solvent under supercritical conditions. One of the main problems in SFE is the slow kinetics of the process due to the difficulties in the mass transfer. A typical way to accelerate mass transfer processes is by mechanical agitation. In the case of SFE, the characteristics of the equipment do not easily allow the use of mechanical stirrers. The application of high-intensity

TABLE 31.3 Ultrasound-assisted extraction of plant components

Technology	Category	Components	Matrix	Conditions	Yield	References
UAE	Protein	Protein	Partially defatted peanut flour	F(kHz): 24; ET(min): 15; A(μm):100	65%	Ochoa-Rivas et al. (2017)
		Protein	Sesame bran	F(kHz): 35; P(W): 528; T (°C):40; ET(min):65; S/L (*w/v*):1:10	39.8%	Görgüç et al. (2019)
		Protein	Hexane-defatted soy flakes	F(kHz): 20; P(kW): 2.2; ET(s):120; A(μm):84; T (°C):4; S/L (*w/v*):1:5	40%	Karki et al. (2010)
	Polyphenol	Naringin and hesperidin	Orange (*Citrus sinensis* L.) peel	F(kHz): 25; P(W): 150; T (°C):40; ET(min):60	70.3 mg of naringin and 205.2 mg of hesperidin/100 g fresh weight	Khan et al. (2010)
		Total flavonoids	*Thymus serpyllum* L. herb	F(kHz): 20; P(W): 750; A(μm):80; T (°C):25; S/L (w/v):1:30	16.7 mg of catechin equivalents (CE) per liter of extract	Jovanović et al. (2017)
		Total polyphenols	Grape (*Vitis vinifera* L.) seeds	F(kHz): 20; P(W): 150; ET(min):30; T (°C):30; S/L (w/v):1:8	105.20 mg GAE/g flour	Da Porto et al. (2013)
	Oil	Oil	Almond seeds	F(kHz): 40; P(W): 150; ET(min):55; T (°C):51; S/L (w/v):1:19	81.89 ± 0.23%	Zhang et al. (2009)
		Oil	Full fact rice bran	F(kHz): 60; ET(min):70; T (°C):25; pH: 12	–	Khoei and Chekin (2016)
		Oil	*Moringa oleifera* seeds	F(kHz): 40; P(W): 200; ET(min):15; T (°C): 30 ; S/L (w/v):1:8	35.80%	Zhong et al. (2018)
	Lipid	Microbial lipid	Inoculums of *Trichosporon* sp.	F(kHz): 520; P(W): 40; ET(min):20; T (°C): 35	37 ± 0.38%	Jeevan Kumar and Banerjee (2019)
		Oleaginous yeast lipid	The oleaginous yeast *Naganishia liquefaciens* NITTS2 biomass	concentration of yeast biomass (g/L): 80; power density (W/mL): 0.5; ET(min):30; T (°C):32	78 ± 1.5%	Selvakumar and Sivashanmugam (2019)
		Microalgal lipid	Green algae *Dunaliella tertiolecta*	P(W): 370; ET(min): 5; S/L (w/v):1:125	45.94%	Qv et al. (2014)
	Dyes and pigments	Dyes	Madder (*Rubia tinctorum*) roots	F(kHz): 25; P(W): 150; ET(min):18; T (°C): 36 ; S/L (w/v):1:25	64.3%	Cuoco et al. (2009)
		Betacyanin and betaxanthin	*Bougainvillea glabra* flowers	P(W): 88; ET(min):37; T (°C): 55; S/L (w/v):1:17	Betacyanin of 1.72 ± 0.001 and betaxanthin of 5.78 ± 0.23 mg/g	Maran et al. (2015)
		Natural pigments	Annatto seeds	F(kHz): 20; P(W): 200; ET(min):7.25; T (°C): 72.7; S/L (w/v):7:50	6.35%	Yolmeh et al. (2014)
		Anthocyanin pigments	*Ficus carica* L. peel	P(W): 310; ET(min):21; T (°C): 30–35	3.82 mg cyanidin 3-rutinoside/g residue	Backes et al. (2018)

Note: A: amplitude, P: power, F: frequency, ET: extraction time, T: temperature, L/S: liquid to solid ratio, CN: cavitation number.

TABLE 31.4 Products obtained by ultrasound-assisted extraction by Giotti, Italy (http://www.giotti.it)

Product	Composition
Emulsions for soft drinks	Orange, lemon, tangerine, tropical, grapefruit, strawberry, raspberry
Natural flavors	Orange, lemon, cola, mango, pineapple, blueberries, apples, peaches, tea, coffee, energy drink
Alcoholic beverages	Amaretto, orange, bitter alkermes, Florence coffee, curacao, strawberry, limoncello, maraschinno, fishing, rum, sambuca, mandarin, vanilla
Flavored waters	Orange, lemon, mint, strawberry, peach, tangerine, lime



FIGURE 31.3 Batch ultrasound extraction reactors (2×500 L). *(With permission of REUS, 06390 Contes—France.)*

ultrasonic waves may be an interesting alternative for this purpose. Such process has been experimentally studied and applied to several products with good results. Supercritical CO_2 extraction of almond oil by applying a power ultrasonic transducer with a frequency of about 20 kHz and a power of 50 W was for the first time installed inside of a high-pressure extractor (289 bar) of 5 L capacity. The results showed that the kinetic of the process improved over 30% and the extraction yield in about 20% in a process lasting about 8.5 h (Riera et al., 2005, 2004). This pioneer process has further been studied and successfully applied for extraction of essential oils and other products from different vegetable substrates (Balachandran et al., 2006; Hu et al., 2007; Macías-Sánchez et al., 2009; Riera et al., 2010).

Enzymatic extraction (EE) is a straightforward, safe, and specific extraction method that depends on the characteristic property of enzymes with accurate specificity, region selectivity, and their ability to conduct reactions under mild conditions with the retention of their biological potencies of bioactive compounds (Puri et al., 2011). However, conventional enzymatic extraction has setbacks like relatively low efficiency and high cost, which can be overcome with the aid of innovative and green techniques (Bruno et al., 2019). Ultrasound technique, which is broadly known to be cheap, eco-friendly, with lower energy consumption, has been proved to speed up the enzymatic extraction (Chen et al., 2019; Cheng et al., 2017). Wu et al. (2015) investigated ultrasound-assisted enzymatic extraction for extracting phenolics from broccoli inflorescences with water instead of organic solvents. A cocktail of enzymes including cellulase, pectinase, and papain coupled with a low-frequency sonotrode (20 kHz) was investigated and optimized for maximum extraction yield with significant free radical scavenging and total antioxidant activity. Li et al. (2017a) also applied ultrasound-assisted enzymatic extraction to obtain the highest yield of phenolic content, antioxidant, and antitumor activities and to optimize the extraction conditions of Trapa quadrispinosa Roxb. residues. Ultrasound-assisted enzymatic extraction not only suits plants but animals. Liao et al. (2015) employed UAEE for extraction of polysaccharides from Asian clams (*Corbicula flu*min*ea*). They reported a significantly higher extraction yield of ultrasound-assisted enzymatic extraction in 32 min compared to enzyme-assisted extraction over 4 h. They also claimed that the polysaccharide extracted by the hybrid method had lower molecular weight, higher sulfate content, and higher superoxide radical scavenging activity compared to the polysaccharide extracted by enzyme extraction alone.

Another industrial example involving extraction is provided by Cavitus (www.cavitus.com), an Australian company that developed a range of applications in high-power ultrasound. One interesting application in the area of wine making is the extraction of grape must be designated to fermentation to produce wine. The company noticed an approximately 30% increase in color without degrading the final aroma and taste. The process involves a continuous ultrasound reactor similar to the ultrasound reactor presented in Figure 31.4.

31.3 Emulsification

Most manufactured foods, as well as natural foods, are dispersed systems (Figure 31.5). They may have a simpler



FIGURE 31.4 Continuous ultrasound extraction reactor. *(With permission of Hielscher—D14513 Teltow, Germany.)*

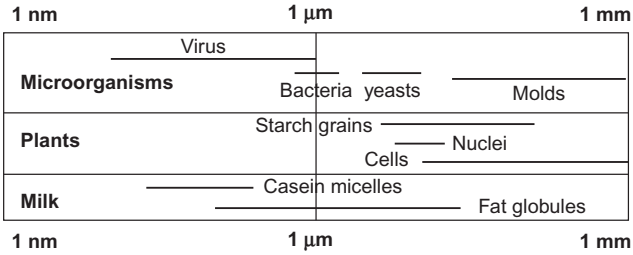


FIGURE 31.5 Approximate size of some structural elements in foods.

structure (e.g., milk is a solution containing fat droplets and protein aggregates); other manufactured foods, however, are structurally complicated in that they contain different structural elements of widely varying size and state of aggregation (such as mayonnaise, margarine, butter, and sauces) (Fennema and Tannenbaum, 1996).

Emulsification is an important means of delivering hydrophobic bioactive compounds into a range of food products. Acoustic emulsification produced stable particles in the submicron range with an extremely narrow particle size distribution using a smaller emulsifier ratio and lower energy. In the food industry, ultrasonic emulsification is attracting interest for in-line treatment of products such as fruit juices, mayonnaise, and tomato ketchup, in the homogenization of milk, and in aroma encapsulation (Chemat and Khan, 2011). It is comparable to microfluidization in terms of generating submicron dispersions, but there are indications that the emulsification of edible oils might lead to some deterioration in quality (Pingret et al., 2013).

One example is the production of mayonnaise by sonoemulsification of sunflower oil in water using polyoxyethylene sorbitan monooleate (Twin). With an oil/water volume fraction of 0.35 and power supply of 150-W ultrasound and mechanical agitation (MA), the variations of drop size distribution as a function of surfactant concentration and the emulsification mode are presented in Figure 31.4. In both cases (ultrasound and MA), volume drop size distributions flatten with higher surfactant concentrations. In the case of ultrasound, a peaked distribution was observed at low surfactant concentrations but a flattened distribution at higher surfactant concentration. The same tendency is observed in the case of MA. A typical photomicrograph of insonated food emulsion is shown in Figure 31.6. If the two techniques are

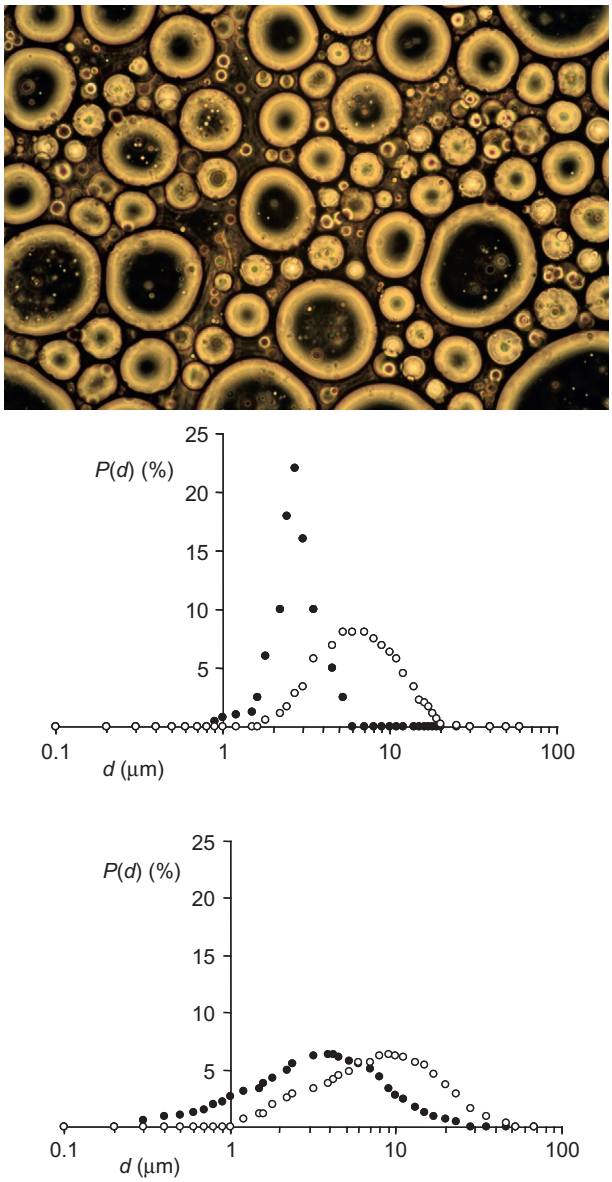


FIGURE 31.6 Drop size distribution at low (1 g/L) and high (10 g/L) surfactant concentration (power ultrasound (•) mechanical agitation (○)).

compared, UAE reduces the diameter of oil droplets compared with MA. The average drop size for classical and ultrasound emulsifications are 1–10 and 0.5–1 μm, respectively.

Comparison between ultrasound and MA emulsification techniques in the case of energy consumption reveals that MA always creates complete emulsification after few minutes, whatever the power involved. In contrast, with an ultrasonic device, a minimum power of 90 W is necessary to emulsify the mixture completely. Emulsification is a successive disintegration process consisting of two stages. The first stage is the incipient instability of the oil–water interface to produce large oil drops with a diameter of approximately 70 μm. The second stage involves the breakup of these larger droplets by shock waves produced by cavitating bubbles. That means that the sole ultrasound energy does not allow the bulk oil phase to break efficiently into primary large drops. This is likely because of insufficient acoustic streaming under the ultrasound horn. If more than 90 W of power ultrasound is used, droplet size is about five times smaller. Comparison of the stability of emulsions obtained by both techniques indicate a much higher stability of insonated emulsions. This phenomenon is due to the droplet size differences between MA and ultrasound. A higher interfacial area in the case of insonated emulsions implies a higher amount of adsorbed surfactant and therefore a lower amount of micellized surfactant, which could enhance emulsion stability.

31.4 Viscosity modification

The physical forces generated during acoustic cavitation have been used to modify the viscosity of polymeric solutions. This area of research was of great interest to polymer scientists in that the viscosity reduction was attributed to the fragmentation of polymer chains (Weissler, 1950). With the resurgence of sonochemistry in the 1990s, more detailed investigations were reported (Kim et al., 2006; Koda et al., 1994). In terms of applications of ultrasonic modification of the viscosity of food ingredients, starch systems have been extensively studied and were reported as early as 1933 (Szent-Györgyi, 1933). Starch is used as a thickener and gelling agent to alter the viscosity of many final food products. Hence, modification of the viscosity of starch systems is an important issue in the food industry, and systematic and quantitative studies have been performed (Sujka and Jamroz, 2013; Luo et al., 2008; Huang et al., 2007; Chung et al., 2002).

In most of these studies, high-power (100–500 W), low-frequency (20 kHz) ultrasound was used. In the work of Azhar and Hamdy, 1979, potato starch powder and a slurry of freeze-dried sweet potato were sonicated at 20 kHz and 300 W in an aqueous medium. The degradation of starch was monitored by relative viscosity measurements. A decrease in viscosity with an increase in sonication time was observed. The viscosity change was suggested to be caused by the breakdown of the starch powder rather than the depolymerization of the individual polymer molecules; this conclusion was made based on the analysis of reducing sugars. The absence of reducing sugars after sonication indicated that the starch polymer molecules were not degraded by the physical forces generated during sonication.

Iida et al. (2008) sonicated 5%–10% waxy maize starch solutions after gelatinization and found a substantial decrease in the viscosity of the solution after 30 min of sonication at 20 kHz and 120 W: the viscosity of a 10% starch solution decreased from 2000 to 20 mPa/s. They monitored the degree of granule disintegration and the degree of solubilization of starch. Under normal conditions, starch granules swell by absorbing water molecules and grow in size. However, under sonication conditions, the swelling process was reduced because of the disintegration of the granules by the physical forces generated during acoustic cavitation. In the meantime, they also noticed the solubilization of the starch to generate polysaccharides.

Recent work by Zuo et al. (2009), Zuo (2011) reported the effect of sonication on the viscosity of various starch systems. Of particular interest is the dependence of the sonication effect on the nature of the starch. Figure 31.7 shows the viscosity changes observed when a 5% normal rice suspension was sonicated at 211 kHz (acoustic intensity, 0.18 W/cm^2) and 77°C.

The pasting behavior in Figure 31.7 exhibits three regions: an initial slight decrease in viscosity, a second stage of steep increase in viscosity, and a third region where the viscosity decreases followed by a second increase. This is a typical pasting behavior for starch suspensions. The initial decrease in viscosity is caused by an increase in the solution temperature. The steep increase in viscosity is caused by the swelling of starch granules. The decrease observed in the third stage is caused by granule breakup, and the final increase in viscosity is caused by aggregation of free starch and the decrease in solution temperature. The interesting aspect is the sonication for up to an hour did not significantly affect the pasting behavior and the viscosity profile. In contrast, the pasting behavior observed with waxy rice starch under similar sonication conditions is completely different, as shown in Figure 31.8.

The sonicated samples show significantly lower viscosities compared with the nonsonicated samples, in particular at longer sonication times. The sonication effects may be due to the solubilization of the starch aggregates by sonication. The difference between normal and waxy rice starch behavior is likely because of the difference in amylose content. It is expected that the presence of amylose in normal rice starch results in a stronger binding between starch molecules (likely in the form of swollen granules). Hence, in the case of normal rice starch, sonication intensity higher than that used in this study may be necessary to fully

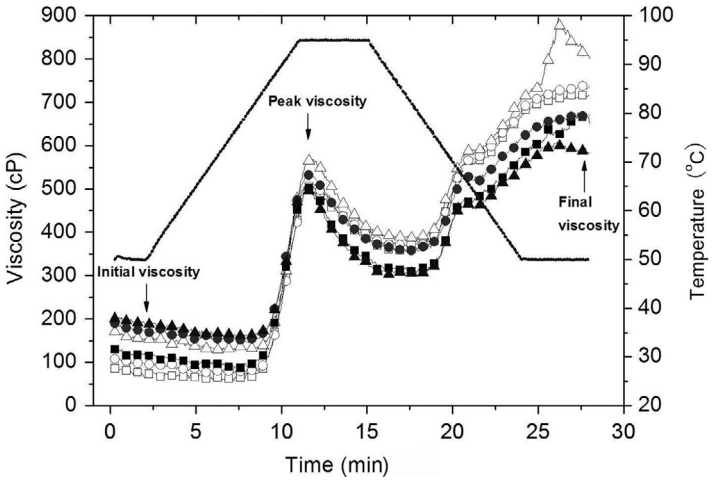


FIGURE 31.7 Viscosity as function of pasting time for nonsonicated (*open symbols*) and sonicated (*solid symbols*) normal rice starch dispersions. Suspensions (5 wt% in 60 mL water) were sonicated at 77°C, with $I = 0.18\,W/cm^2$ and a frequency of 211 kHz. Time: (□,▪) 15 min; (○,•) 30 min, and (△,▲) 60 min. *Dashed line* is the heating profile. *(Adapted from Zuo et al. (2009), Zuo (2011).)*

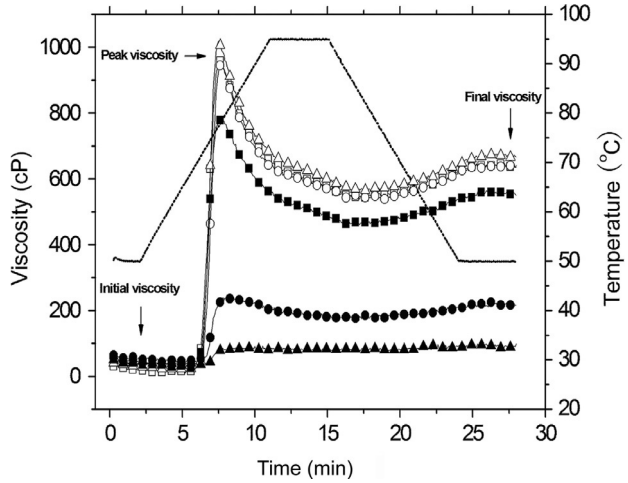


FIGURE 31.8 RVA viscosity as function of pasting time for nonsonicated (*open symbols*) and sonicated (*solid symbols*) waxy rice starch dispersions. Suspensions (5 wt% in 60 mL water) were sonicated at 63°C, with power intensity of $0.18\,W/cm^2$ and a frequency of 211 kHz. Time: (□,▪) 15 min; (○,•) 30 min and (△,▲) 60 min. *Dashed line* is the heating profile. *(Adapted from Zuo et al. (2009), Zuo (2011).)*

solubilize starch aggregates. It has been noted that the observed viscosity changes are caused by the physical effects of ultrasound; however, the involvement of free radicals generated during acoustic cavitation cannot be completely overruled.

31.5 Defoaming

Foam formation is a common problem encountered in food processing operations including, for example, fermentation and mixing. Foam formation can lead to product loss, prevent efficient filling of containers, reduce pump capacity, and in some cases facilitate microbial growth. Foams are composed of thousands of microscopic bubbles generated within a liquid. Foam formation occurs if these bubbles rise and agglomerate at the surface of the food matrix more rapidly than they decay (Atri, 2010). Conventional methods employed to destroy foams include thermal (heating or cooling process which lead to the rupture of the bubbles), chemical (defoaming agents which decrease the surface tension), electrical, and mechanical methods. Airborne ultrasound is an alternative method which can be employed as a noncontact physical technique to suppress foam (Figure 31.9). Ultrasonic waves induce effects such as high acoustic pressures, radiation pressure, cavitation and acoustic streaming, and resonance of the foam bubbles that can lead to foam destruction (Riera et al., 2006). The use of high-intensity ultrasound in foam destruction has been reported in various studies. Rodríguez et al. employed an airborne ultrasonic plate transducer as a defoaming tool (Rodríguez et al., 2010). Defoaming efficiency was found to increase with an increase in the ultrasonic intensity (reaching $5\,cm^3$ at $10\,W/cm^2$) and treatment time at comparable foam concentrations. Furthermore, the authors compared the efficiency of ultrasound application on two different types of foam: a stable foam made with 2.85 g/L of surfactant concentration, with the bubble size between 0.2 and 2.0 mm, and a dry and light foam made with 0.71 g/L concentration, with the bubble size in the range of 0.2–10.0 mm. The ratio of the liquid volume to foam volume was 0.02 and 0.005, respectively. An ultrasonic treatment of 98 ms allowed a defoaming volume of $5\,cm^3$ for the foam at 2.85 g/L, compared to $13\,cm^3$ for the foam at 0.71 g/L. This work demonstrated that the ultrasound effect is more efficient on bubbles with a larger diameter (Rodríguez et al., 2010).

31.6 Sonocrystallization

Ultrasound has been used to beneficially alter the crystallization behavior of materials. The first work on sonocrystallization was reported as early as 1927 (Wood and Loomis,

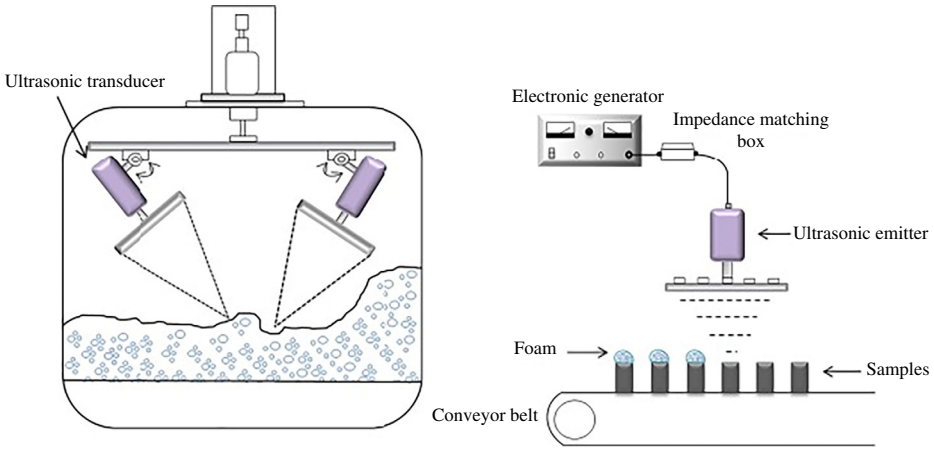


FIGURE 31.9 Defoaming setup in reactors (left) and canning line (right). *(Adapted from Gallego-Juárez et al. (2015) (left) and Povey and Mason (1998b) (right).)*

1927) and has continued to be of interest because crystallization as a unit operation is widely practiced throughout the chemical process industries (Price, 1997; Ruecroft et al., 2005).

Improvements in food preservation by freezing using ultrasound has been the subject of considerable research. Its use in freezing has two benefits: (i) through a reduction in the "dwell time" incurred while the material remains at a steady low temperature, while the whole mass freezes before the temperature reduces further (due to latent heat considerations) and (ii) a reduction in ice crystal size due to ultrasonic seeding of crystallization, a benefit when freezing soft fruit because smaller crystals reduce problems of cell wall damage. A patent for ultrasonic freezing was secured (Acton and Morris, 1992). Subsequent research into ice crystal formation is of relevance to food freezing and has attracted attention (Chow et al., 2005; Kiani et al., 2012; Saclier et al., 2010). The applications of ultrasound in crystallizing relating to food freezing has been less extensively studied, but two recent reviews summarize the key features of sonocrystallization in food processing (Deora et al., 2013; Zheng and Sun, 2006). A detailed literature review of early reports of sonocrystallization in food systems is provided in a PhD thesis by Chow-McGarva (2004). These studies showed that sonocrystallization can influence the primary and secondary nucleation processes. The effect on the primary nucleation process in turn decreases the nucleation time and overall yield, whereas the effect on secondary nucleation is found to affect the size, size distribution, and shape of the crystals.

To explore the possible mechanism involved in sonocrystallization, Chow-McGarva (2004) recorded images of ice crystals produced during sonication of a 15% sucrose solution at 20 kHz (Figure 31.10). It can be observed that the ice crystals are generated from the active cavitation zone just below the horn. The ice crystals (primary nuclei) move away from the horn because of the liquid's movement. This is followed by the formation of ice dendrites from the nuclei. Based on these observations, the author suggested that crystallization is induced by the cavitation process.

In an early work by Ohsaka and Trinh (1998) using a single bubble system, strong evidence for the involvement of cavitation bubbles in the nucleation process was provided. Chow-McGarva (2004) supported these findings using a better imaging system. As shown in Figure 31.11, a single bubble is trapped at the pressure antinode (frequency ~27 kHz) in water at −3.2°C. When the bubble was driven below the cavitation threshold at a low pressure (<0.69 bar), no nucleation can be observed. When the pressure increased above the cavitation threshold (about 1 bar), nucleation of ice crystals can be observed.

Patrick et al. (2004) later showed that the physical properties of palm oil fat crystals could be controlled by varying acoustic power levels below and above the cavitation threshold. The study investigated the texture, structure, and size of fat crystals produced when palm oil was sonicated in a custom-made cell attached with ring transducers operating at a resonance frequency of 20 kHz. A mixture of large and small spherulitic crystals was obtained when no ultrasound was applied during the crystallization process. When ultrasound was applied at power levels below the cavitation threshold (30–35 dB), more uniform crystals with a very high viscosity were obtained (Figure 31.12). The physical properties of the crystals seemed to vary depending on the location of the crystals within the cell. The crystals above the cavitation threshold (>35 dB) seemed to be more amorphous (cotton wool–type) in nature. While the exact mechanism involved in the generation of different crystal structures was not discussed in this report, it is possible that inhomogeneous standing wave patterns existed below the cavitation threshold that led to the growth of the crystals. The shear forces and shock waves generated above the

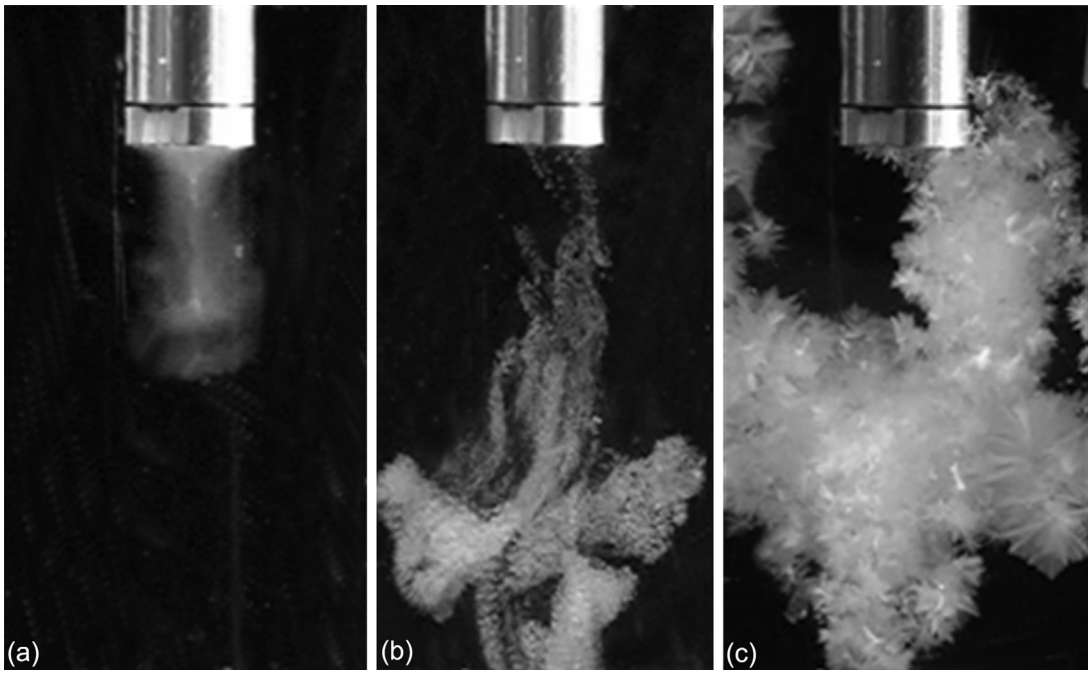


FIGURE 31.10 Ice nucleation observed in a 15 wt% sucrose solution at −3.8°C following a single pulse at ultrasonic output level 4 (10% duty cycle): (a) $t = 0.03$ s, (b) $t = 0.18$ s, (c) $t = 5.0$ s. *(Adapted from Chow-Mcgarva (2004).)*

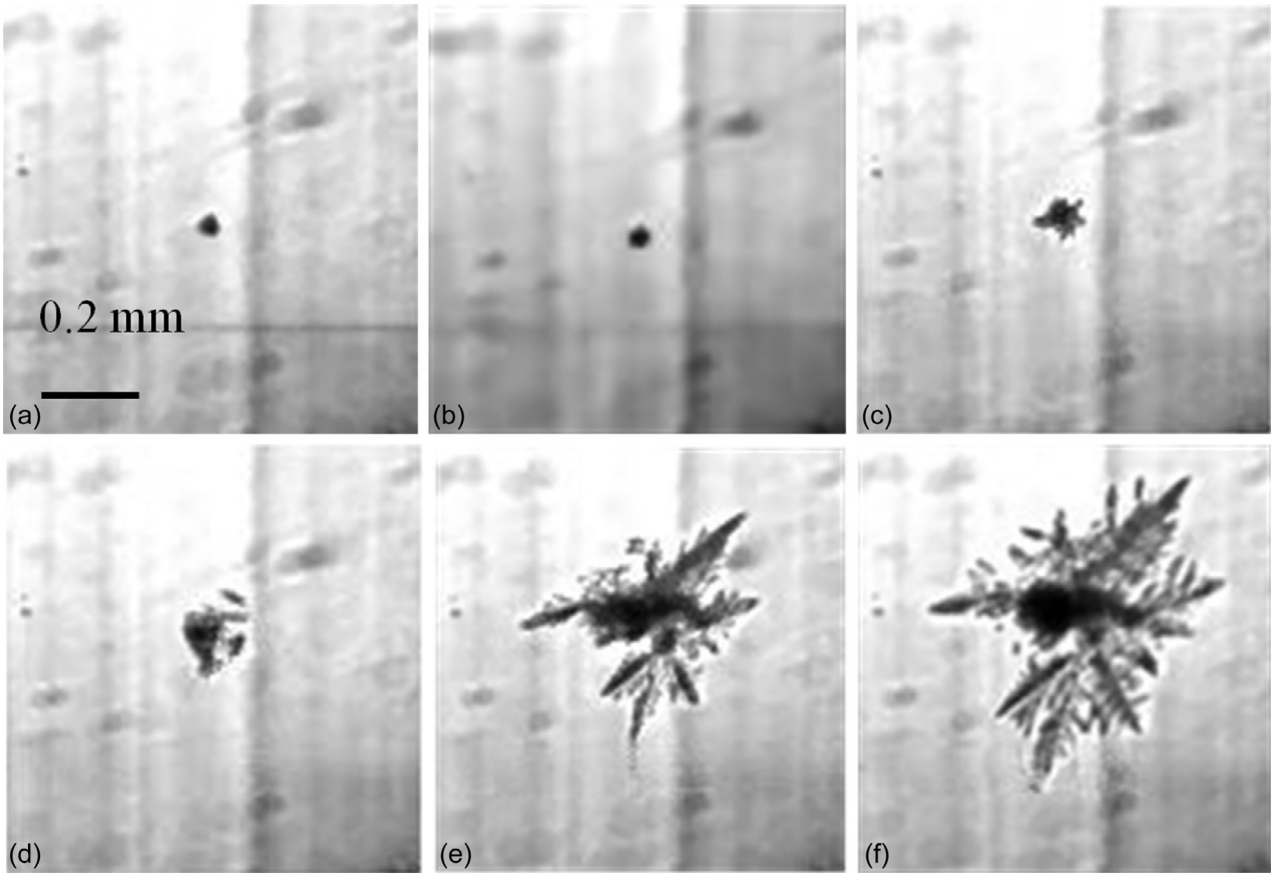


FIGURE 31.11 High-speed photography of the nucleation of ice from a single acoustic bubble at −3.26°C. Prior to nucleation, the pressure was increased from 0.69 to 0.98 bar (27.34 kHz): (a) $t = 0$ s, (b) $t = 0.023$ s, (c) $t = 0.050$ s, (d) $t = 0.100$ s, (e) $t = 0.235$ s, (f) $t = 0.3$ s. *(Adapted from Chow et al. (2005).)*

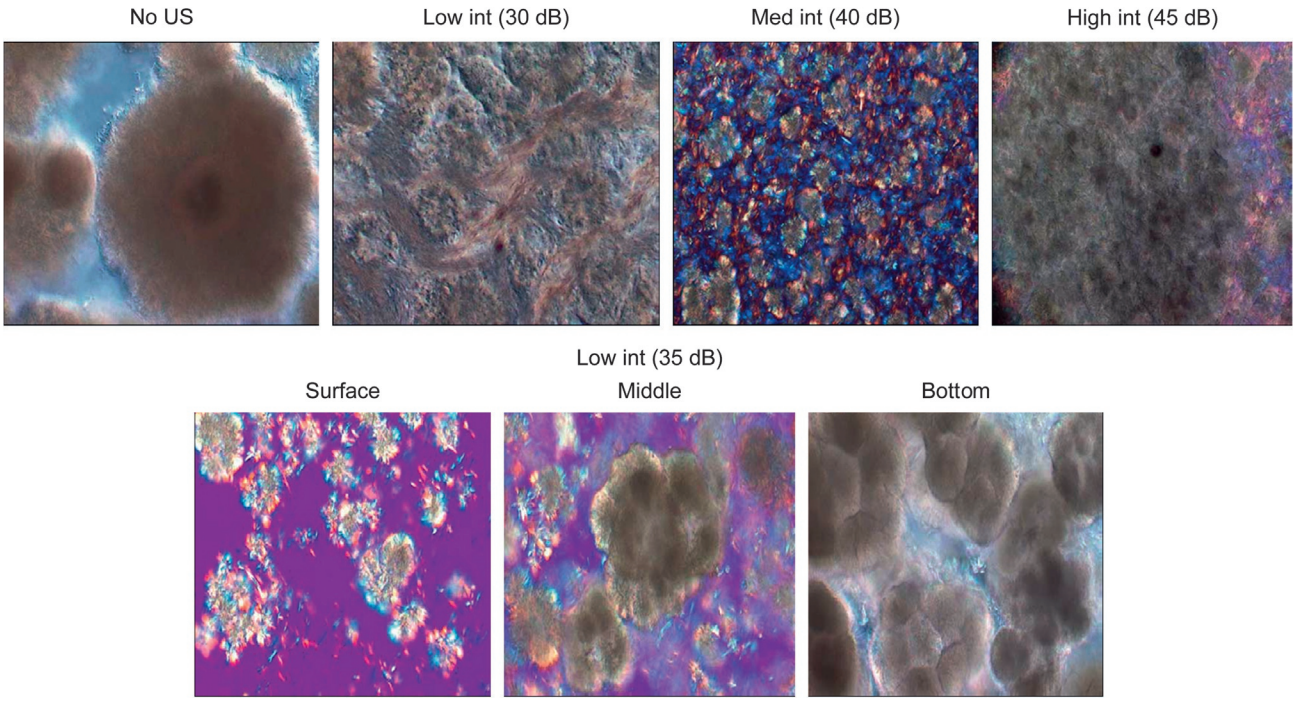


FIGURE 31.12 Top: The images show the effect of sonication power on the nature of the fat crystals produced. Bottom: The images show the nature of fat crystals obtained at different parts of the reactor.

cavitation threshold may be responsible for the amorphous nature of the crystals because these forces can be expected to prevent the formation of larger crystals.

31.7 Fat separation

The application of standing waves to separation technologies in food science is a relatively new development. The origins lie in the work of Sollner and Bondy (Söllner and Bondy, 1936) at University College, London; they showed that quartz particles (density, 2.66) in water collect at pressure antinodes, whereas toluene (density, 0.87) in water moves to pressure nodes. There was a gap of many years in research publications in the field until Dyson et al. (1971) at Guys' Hospital Medical School published a letter in Nature concerning the way ultrasound could stop the flow of red blood cells; this letter stimulated much interest and activity. Many advances in the development of standing wave separations in liquids were made, and these were reviewed by Schram (1991). A systematic study involving a standing wave pattern for the separation of fat globules from dairy systems is reported by Juliano et al. (2011). Using high-frequency ultrasound to establish a standing wave pattern is a useful technique in specific applications. For example, ultrasonic degassing of processing liquids can be achieved by migrating gas bubbles to pressure nodes within a standing wave, where they coalesce to generate larger bubbles that can exit the liquid by buoyancy. Figure 31.13 shows the existence of a standing wave pattern; the bright bands represent antinodes, showing active cavitation bubbles (picture shows sonochemiluminescence) (Ashokkumar et al., 2010), and the dark bands represent nodes where "inactive" bubbles can accumulate.

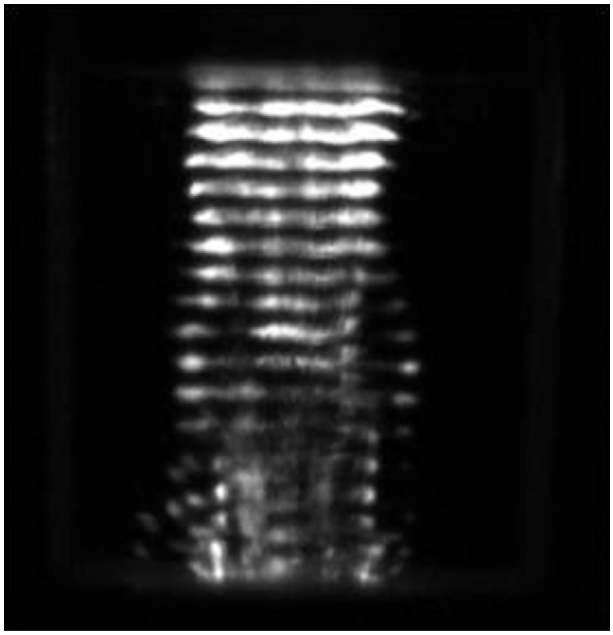


FIGURE 31.13 Image showing a standing wave pattern. The bright stripes are antinodes where active cavitation bubbles generate sonochemiluminescence and the dark stripes are nodes where inactive bubbles accumulate. The image was taken using a reactor operating at 170 kHz and 30 W. *(From Ashokkumar et al. (2010).)*

The use of such standing wave patterns in fat separation from dairy systems was recently reported by Juliano et al. (2011). They studied the effect of ultrasound on the creaming of fat globules in dairy systems. Acoustic standing waves were established at 400 kHz and 1.6 MHz. Two different reactor configurations with a single plate transducer located at the bottom of the vessel and two sandwich transducers located parallel to each other along vertical axis were used in this study. When dyed, reconstituted milk emulsions systems containing fat were sonicated at 400 kHz in cylindrical containers, the accumulation and coalescence of fat globules in the standing waves could be clearly seen (Figure 31.14). Fat aggregation occurs during sonication, and the aggregated fat globules then migrate to the liquid surface after the ultrasonic field is switched off. Juliano et al. (Söllner and Bondy, 1936) showed that the sandwich-type sonicator is more efficient in fat separation because of the establishment of a better and stronger standing wave field, which might be due to the homogeneous distribution of the acoustic field in the sandwich type ultrasonic reactor.

31.8 Other applications: Sterilization, pasteurization, brining, and marinating

Thermal methods for pasteurization and sterilization are the most common techniques in current use for the inactivation of microorganisms in food products. The effectiveness of these techniques is dependent on the



FIGURE 31.14 Dyed coarse emulsion. Left: Under sonication (400 kHz) in an open vessel where distinct bands can clearly be observed; middle: in an open vessel after switching off the ultrasound field; the formed floccules start to rise immediately; right: after sonication in the sandwich two-transducer geometry. *(Adapted from Juliano et al. (2011).)*

treatment temperature and time; unfortunately, increased temperatures and extended processing times can both lead to nutrient loss, undesirable flavors, and the deterioration of functional properties of food products. Power ultrasound provides a method of improving thermal processing in terms of both temperature and time through acoustic cavitation. At sufficiently high acoustic power inputs, ultrasound alone can rupture cells, but a cell can be inactivated at a substantially lower intensity in combination with a biocide or heat treatment (Mason and Joyce, 2008; Mason et al., 2005; Piyasena et al., 2003). The effect on a common bacterium such as *Escherichia coli* also has been shown to be dependent on factors such as temperature and pH (Salleh-Mack and Roberts, 2007). The effects of acoustic cavitation on microbial killing is a combination of radical attack and shear forces induced during bubble collapse, leading to cell wall weakening and the thinning of cell membranes; both effects make the cells more susceptible to heat treatment. Therefore, ultrasound can accelerate the rate of sterilization of foods (thermosonication) and lessen both the duration and intensity of thermal treatment and the resultant damage. The advantages of ultrasound over heat pasteurization include minimizing flavor loss, greater homogeneity of treatment, and significant energy savings. In addition, the treatment can be intensified with the application of pressure manothermosonication (Vercet et al., 2001; Cameron et al., 2009). In addition to microbial killing, sonication can also be used to inactivate enzymes, which is of importance for both fruit juice and dairy products (O'Donnell et al., 2010).

There are some problems associated with current brining and marinating processes: (i) a high sodium chloride content is required for brining, and this often requires a "desalting" process before it can be released and (ii) any marinating process requires a long period of soaking, which can lead to enzymatic softening, structural damage, and bloating. The advantage of using ultrasound in such processes is that it can reduce processing time, which is particularly important for foods that have a crisp texture (Kingsley and Farkas, 1990), but it also has reduced the brining and marinating time for a range of raw meat foodstuffs (Hatloe, 1995). Brining is a common operation in meat processing and involves two mass transfer processes: water migration from the meat to the brine and solute migration from the brine to the meat. The influence of ultrasound on the brining of pork loin slices has been studied (Cárcel et al., 2007). The effect of ultrasound on mass transfer during cheese brining has been investigated as well (Sánchez et al., 1999). The rate of water removal and sodium chloride gain increased when ultrasound was applied, suggesting that ultrasound improves both external and internal mass transfer.

31.9 Hazard analysis critical control point (HACCP) for ultrasound in food processing operations

The hazard analysis critical control point (HACCP) system is a process that identifies and assesses the hazards and risks associated with the manufacture, storage, and distribution of foods and implements the appropriate controls, aiming at the elimination or reduction of these hazards at specific points of the production line. The common terms of HACCP are defined below:

- Hazard: Any biological, chemical, or physical factor that can lead to an unacceptable risk for consumer safety or product quality.
- Critical control point (CCP): Any place, personnel, operation, or protocol where inadequate control would result in the appearance of some danger associated with food.

A hazard becomes a CCP when an unacceptable risk for the product quality can occur if this step is not monitored. In any food processing operation involving ultrasound, the parameters that affect CCP and thus require monitoring in terms of final food quality are temperature, physical properties of the product, treatment time, frequency and power of the ultrasound, and the type of ultrasonic transducer used. When each of these CCPs is identified, their values and range limits can be set. Then, a checking system must be set up so that the limits of the CCPs are not exceeded. This system gathers together all of the control procedures and the general hygiene measures that need to be applied. If the checking procedures show that a CCP's limit is exceeded, corrective measures are undertaken to meet the requirements, and the effectiveness of these actions must be monitored again (Mortimore and Wallace, 2013).

For each part of any food process that includes ultrasonic processing, an evaluation and classification of hazards must be performed. In this way, a grade is given to each hazard that has been identified, according to its importance, risk of occurrence, and ability to detect it. For each hazard, preventive measures are set up with procedures that indicate who will do it, how, when, and where. Preventive measures aim primarily at avoiding the occurrence of the hazard. For example, a good maintenance plan decreases the risk of metal contamination from any erosion from the tip of an ultrasonic horn.

The effectiveness of ultrasound in food processing depends on the quality of the ultrasound equipment, the parameters used, and the initial rate of microorganism growth in the product. The main causes of contamination by microorganisms are (i) poor hygiene of the personnel caused by bad work habits (known as handling

contamination), (ii) inadequate or lack of attention to cleaning procedures, (iii) cross-contamination, and (iv) abnormal growth of microorganisms due to bad storage conditions of the raw materials and/or lack of care by the purveyor. Thus, to optimize preservation operations, several preventive measures must be set up:

1. Control of raw material supply
2. Identification of purveyor requirements
3. Control of the effectiveness of cleaning
4. Control of possible chemical danger during the cleaning stages
5. Verification of the efficiency of the ultrasonic system and the parameters used

31.10 Conclusions and future trends

It is perhaps interesting to reflect on the progress of ultrasound in food processing over the past 25 years. In a paper published in 1996, Mason et al. concluded that "The use of ultrasound in processing creates novel and interesting methodologies which are often complementary to classical techniques. It has proved particularly useful in sterilization, extraction, freezing and filtration providing reduced processing times and increased efficiency. There is wide scope for further research into the use of ultrasound in food processing both from an industrial and academic viewpoint." This remains generally correct, although there have been many advances in the technology since that time. Perhaps a more apposite conclusion for today is that reached by Chemat and Khan (2011), indicating that "Many traditional food processing techniques are reaching their optimum performance while consumers demand's stretch and food and environmental regulations tighten.'' However, a survey and market study of the possible future applications of new process technologies (like microwaves and ultrasound) in the food industry has revealed that many companies were reluctant to apply these new technologies. The lack of expertise, awareness, and inability to give up the conventional procedures prevent ultrasound from being adopted and commercialized at industrial levels.

Now it is becoming clear that the drivers for new technology are increasing in strength so that ultrasound may well become a technology of choice when its advantages in areas that contribute to the efficiency of processing in the food industry are recognized and become more acceptable to the public in terms of environmental and ethical aspects. In particular, four elements of food technology will incorporate power ultrasound in the future:

- Extended shelf life: New methodologies are required for the rapid sterilization of liquid foods without affecting flavor, for the disinfection of the surfaces of solid foodstuffs, and for more efficient freezing technology.
- Development of hybrid technologies in food industry: Ultrasound technique has demonstrated its potential for extraction and processing in the food industry. It has many benefits over other preexisting technologies and, which when combined with them, helps to resolve their own limitations. The combination of ultrasound with different food processing technologies can improve process efficiency and product qualities as well as reduce the time required for various processing operations and improvement in the overall rate of extraction and yield.
- Food functionality and health issues: As a result of legislation and consumer pressure, there will be an increasing emphasis on the manufacture of more healthy food products. New processing technologies will be required to solve problems incurred by reductions of salt or fat in food. Specific additions, preferably natural, will be used to improve nutrition.
- Sustainability in food manufacturing: The knowledge that ultrasound technology can be combined with other existing and novel technologies will create awareness for commercial application of this technology and help in the development of environmentally friendly technologies for food industry. This will involve reductions in waste or the recycling and reuse of materials. This will become particularly relevant for the valorization of lower quality food products.

References

Acton, E., Morris, G., 1992. Method and Apparatus for the Control of Solidification in Liquids. Worldwide Patent WO, 92, 20420.

Adam, F., Abert-Vian, M., Peltier, G., Chemat, F., 2012. "Solvent-free" ultrasound-assisted extraction of lipids from fresh microalgae cells: a green, clean and scalable process. Bioresour. Technol. 114, 457–465.

Alissandrakis, E., Daferera, D., Tarantilis, P., Polissiou, M., Harizanis, P., 2003. Ultrasound-assisted extraction of volatile compounds from citrus flowers and citrus honey. Food Chem. 82, 575–582.

Araujo, G.S., Matos, L.J.B.L., Fernandes, J.O., Cartaxo, S.J.M., Gonçalves, L.R.B., Fernandes, F.A.N., Farias, W.R.L., 2013. Extraction of lipids from microalgae by ultrasound application: prospection of the optimal extraction method. Ultrason. Sonochem. 20, 95–98.

Ashokkumar, M., Lee, J., Iida, Y., Yasui, K., Kozuka, T., Tuziuti, T., Towata, A., 2010. Spatial distribution of acoustic cavitation bubbles at different ultrasound frequencies. ChemPhysChem 11, 1680–1684.

Atri, M.R., 2010. The importance of foams and antifoaming in bioprocesses. Pak. J. Biotechnol. 7, 19–39.

Azhar, A., Hamdy, M., 1979. Sonication effect on potato starch and sweet potato powder. J. Food Sci. 44, 801–804.

Backes, E., Pereira, C., Barros, L., Prieto, M.A., Genena, A.K., Barreiro, M. F., Ferreira, I.C.F.R., 2018. Recovery of bioactive anthocyanin

pigments from Ficus carica L. peel by heat, microwave, and ultrasound based extraction techniques. Food Res. Int. 113, 197–209.
Bahmani, L., Aboonajmi, M., Arabhosseini, A., Mirsaeedghazi, H., 2018. Effects of ultrasound pre-treatment on quantity and quality of essential oil of tarragon (Artemisia dracunculus L.) leaves. J. Appl. Res. Med. Aromat. Plants 8, 47–52.
Balachandran, S., Kentish, S.E., Mawson, R., Ashokkumar, M., 2006. Ultrasonic enhancement of the supercritical extraction from ginger. Ultrason. Sonochem. 13, 471–479.
Barbero, G., Liazid, A., Palma, M., Barroso, C., 2008. Ultrasound-assisted extraction of capsaicinoids from peppers. Talanta 75, 1332–1337.
Bendicho, C., De La Calle, I., Pena, F., Costas, M., Cabaleiro, N., Lavilla, I., 2012. Ultrasound-assisted pretreatment of solid samples in the context of green analytical chemistry. TrAC Trends Anal. Chem. 31, 50–60.
Boucher, R., 1959. Drying by airborne ultrasonics. Ultrason. News 3, 8–9.
Brody, A., Antonevich, J., 1959. Ultrasonic defrosting of frozen foods. Food Technol. 13, 109–112.
Bruno, S.F., Kudre, T.G., Bhaskar, N., 2019. Impact of pretreatment-assisted enzymatic extraction on recovery, physico-chemical and rheological properties of oil from *Labeo rohita* head., p. 42. Available from: https://go.exlibris.link/YcDpsKXM.
Cameron, M., McMaster, L.D., Britz, T.J., 2009. Impact of ultrasound on dairy spoilage microbes and milk components. Dairy Sci. Technol. 89, 83–98.
Cárcel, J.A., Benedito, J., Bon, J., Mulet, A., 2007. High intensity ultrasound effects on meat brining. Meat Sci. 76 (4), 611–619.
Chandrapala, J., Oliver, C., Kentish, S., Ashokkumar, M., 2012. Ultrasonics in food processing–food quality assurance and food safety. Trends Food Sci. Technol. 26, 88–98.
Chandrapala, J., Oliver, C.M., Kentish, S., Ashokkumar, M., 2013. Use of power ultrasound to improve extraction and modify phase transitions in food processing. Food Rev. Int. 29, 67–91.
Chemat, F., Khan, M.K., 2011. Applications of ultrasound in food technology: processing, preservation and extraction. Ultrason. Sonochem. 18, 813–835.
Chemat, S., Lagha, A., Aitamar, H., Bartels, P.V., Chemat, F., 2004. Comparison of conventional and ultrasound-assisted extraction of carvone and limonene from caraway seeds. Flavour Fragr. J. 19, 188–195.
Chen, F., Sun, Y., Zhao, G., Liao, X., Hu, X., Wu, J., Wang, Z., 2007. Optimization of ultrasound-assisted extraction of anthocyanins in red raspberries and identification of anthocyanins in extract using high-performance liquid chromatography–mass spectrometry. Ultrason. Sonochem. 14, 767–778.
Chen, P., Liu, B., Liu, X., Fu, J., 2019. Ultrasound-assisted extraction and dispersive liquid–liquid microextraction coupled with gas chromatography-mass spectrometry for the sensitive determination of essential oil components in lavender. Anal. Methods 11, 1541–1550.
Cheng, Y., Liu, Y., Wu, J., Ofori Donkor, P., Li, T., Ma, H., 2017. Improving the enzymolysis efficiency of potato protein by simultaneous dual-frequency energy-gathered ultrasound pretreatment: thermodynamics and kinetics. Ultrason. Sonochem. 37, 351–359.
Chow, R., Blindt, R., Chivers, R., Povey, M., 2005. A study on the primary and secondary nucleation of ice by power ultrasound. Ultrasonics 43, 227–230.
Chow-Mcgarva, R.C.-Y., 2004. A Study on the Sonocrystallisation of Ice. University of Leeds.
Chung, K.M., Moon, T.W., Kim, H., Chun, J.K., 2002. Physicochemical properties of sonicated mung bean, potato, and rice starches. Cereal Chem. 79, 631–633.
Cuoco, G., Mathe, C., Archier, P., Chemat, F., Vieillescazes, C., 2009. A multivariate study of the performance of an ultrasound-assisted madder dyes extraction and characterization by liquid chromatography-photodiode array detection. Ultrason. Sonochem. 16, 75–82.
Da Porto, C., Porretto, E., Decorti, D., 2013. Comparison of ultrasound-assisted extraction with conventional extraction methods of oil and polyphenols from grape (Vitis vinifera L.) seeds. Ultrason. Sonochem. 20, 1076–1080.
Deora, N., Misra, N., Deswal, A., Mishra, H., Cullen, P., Tiwari, B., 2013. Ultrasound for improved crystallisation in food processing. Food Eng. Rev. 5, 36–44.
Dyson, M., Woodward, B., Pond, J., 1971. Flow of red blood cells stopped by ultrasound. Nature 232, 572–573.
Feng, H., Barbosa-Cánovas, G.V., Weiss, J., 2011. Ultrasound Technologies for Food and Bioprocessing. Springer.
Fennema, O.R., Tannenbaum, S.R., 1996. Introduction to food chemistry. In: Food Science And Technology. Marcel Dekker, New York, pp. 1–16.
Gallego-Juárez, J.A., Rodríguez, G., Riera, E., Cardoni, A., 2015. Ultrasonic defoaming and debubbling in food processing and other applications. In: Power Ultrasonics: Applications of High-Intensity Ultrasound. Elsevier.
Görgüç, A., Bircan, C., Yılmaz, F.M., 2019. Sesame bran as an unexploited by-product: effect of enzyme and ultrasound-assisted extraction on the recovery of protein and antioxidant compounds. Food Chem. 283, 637–645.
Hatloe, J., 1995. Methods for Pickling and/or Marinating Non-vegetable Foodstuff Raw Material. Int. Pat. WO, 9518537.
Herrera, M., De Castro, M.L., 2005. Ultrasound-assisted extraction of phenolic compounds from strawberries prior to liquid chromatographic separation and photodiode array ultraviolet detection. J. Chromatogr. A 1100, 1–7.
Hu, A.-J., Zhao, S., Liang, H., Qiu, T.-Q., Chen, G., 2007. Ultrasound assisted supercritical fluid extraction of oil and coixenolide from adlay seed. Ultrason. Sonochem. 14, 219–224.
Huang, Q., Li, L., Fu, X., 2007. Ultrasound effects on the structure and chemical reactivity of cornstarch granules. Starch-Starke 59, 371–378.
Iida, Y., Tuziuti, T., Yasui, K., Towata, A., Kozuka, T., 2008. Control of viscosity in starch and polysaccharide solutions with ultrasound after gelatinization. Innovative Food Sci. Emerg. Technol. 9, 140–146.
Jalili, F., Jafari, S.M., Emam-Djomeh, Z., Malekjani, N., Farzaneh, V., 2018. Optimization of ultrasound-assisted extraction of oil from canola seeds with the use of response surface methodology. Food Anal. Methods 11, 598–612.
Janowsky, W., Pohlmann, R., 1948. Sonic and ultrasonic generation in liquids for industrial purposes. Z. Angew. Phys. 222.
Jeevan Kumar, S.P., Banerjee, R., 2019. Enhanced lipid extraction from oleaginous yeast biomass using ultrasound assisted extraction: a greener and scalable process. Ultrason. Sonochem. 52, 25–32.
Jovanović, A.A., Đorđević, V.B., Zdunić, G.M., Pljevljakušić, D.S., Šavikin, K.P., Gođevac, D.M., Bugarski, B.M., 2017. Optimization of the extraction process of polyphenols from Thymus serpyllum L. herb using maceration, heat- and ultrasound-assisted techniques. Sep. Purif. Technol. 179, 369–380.
Juliano, P., Kutter, A., Cheng, L.J., Swiergon, P., Mawson, R., Augustin, M., 2011. Enhanced creaming of milk fat globules in milk emulsions by the application of ultrasound and detection by means of optical methods. Ultrason. Sonochem. 18, 963–973.

Kanakis, C.D., Daferera, D.J., Tarantilis, P.A., Polissiou, M.G., 2004. Qualitative determination of volatile compounds and quantitative evaluation of safranal and 4-hydroxy-2, 6, 6-trimethyl-1-cyclohexene-1-carboxaldehyde (HTCC) in Greek saffron. J. Agric. Food Chem. 52, 4515–4521.

Karki, B., Lamsal, B.P., Jung, S., Van Leeuwen, J., Pometto, A.L., Grewell, D., Khanal, S.K., 2010. Enhancing protein and sugar release from defatted soy flakes using ultrasound technology. J. Food Eng. 96, 270–278.

Keris-Sen, U.D., Sen, U., Soydemir, G., Gurol, M.D., 2014. An investigation of ultrasound effect on microalgal cell integrity and lipid extraction efficiency. Bioresour. Technol. 152, 407–413.

Khan, M.K., Abert-Vian, M., Fabiano-Tixier, A.-S., Dangles, O., Chemat, F., 2010. Ultrasound-assisted extraction of polyphenols (flavanone glycosides) from orange (*Citrus sinensis* L.) peel. Food Chem. 119, 851–858.

Khoei, M., Chekin, F., 2016. The ultrasound-assisted aqueous extraction of rice bran oil. Food Chem. 194, 503–507.

Kiani, H., Sun, D.-W., Delgado, A., Zhang, Z., 2012. Investigation of the effect of power ultrasound on the nucleation of water during freezing of agar gel samples in tubing vials. Ultrason. Sonochem. 19, 576–581.

Kim, K., Nam, G., Lee, S., Lee, J., 2006. Rheological properties of polypropylene modified by high-intensity ultrasonic waves. J. Appl. Polym. Sci. 99, 2132–2137.

Kingsley, I., Farkas, P., 1990. Pickling Process and Product. Int. Pat. WO, 5458. 1990.

Koda, S., Mori, H., Matsumoto, K., Nomura, H., 1994. Ultrasonic degradation of water-soluble polymers. Polymer 35, 30–33.

Li, H., Pordesimo, L., Weiss, J., 2004. High intensity ultrasound-assisted extraction of oil from soybeans. Food Res. Int. 37, 731–738.

Li, F., Mao, Y.-D., Wang, Y.-F., Raza, A., Qiu, L.-P., Xu, X.-Q., 2017a. Optimization of ultrasonic-assisted enzymatic extraction conditions for improving total phenolic content, antioxidant and antitumor activities in vitro from Trapa quadrispinosa Roxb. residues. Molecules 22, 396.

Li, K., Ma, H., Li, S., Zhang, C., Dai, C., 2017b. Effect of ultrasound on alkali extraction protein from rice dreg flour. J. Food Process Eng. 40, e12377.

Lianfu, Z., Zelong, L., 2008. Optimization and comparison of ultrasound/microwave assisted extraction (UMAE) and ultrasonic assisted extraction (Uae) of lycopene from tomatoes. Ultrason. Sonochem. 15, 731–737.

Liao, N., Zhong, J., Ye, X., Lu, S., Wang, W., Zhang, R., Xu, J., Chen, S., Liu, D., 2015. Ultrasonic-assisted enzymatic extraction of polysaccharide from Corbicula fluminea: characterization and antioxidant activity. Food Sci. Technol. 60, 1113–1121.

Lou, Z., Wang, H., Zhang, M., Wang, Z., 2010. Improved extraction of oil from chickpea under ultrasound in a dynamic system. J. Food Eng. 98, 13–18.

Luo, Z., Fu, X., He, X., Luo, F., Gao, Q., Yu, S., 2008. Effect of ultrasonic treatment on the physicochemical properties of maize starches differing in amylose content. Starch-Starke 60, 646–653.

Macías-Sánchez, M.D., Mantell, C., Rodríguez, M., Martínez De La Ossa, E., Lubián, L.M., Montero, O., 2009. Comparison of supercritical fluid and ultrasound-assisted extraction of carotenoids and chlorophyll a from Dunaliella salina. Talanta 77, 948–952.

Maran, J.P., Priya, B., Nivetha, C.V., 2015. Optimization of ultrasound-assisted extraction of natural pigments from Bougainvillea glabra flowers. Ind. Crop. Prod. 63, 182–189.

Mason, T.J., 1990. Sonochemistry. Royal Society of Chemistry.

Mason, T.J., 1999. Sonochemistry: current uses and future prospects in the chemical and processing industries. Philos. Trans. R. Soc. London, Ser. A 357, 355–369.

Mason, T.J., Joyce, E., 2008. Sonication used as a biocide. A review: ultrasound a greener alternative to chemical biocides? Chem. Today 26.

Mason, T.J., Paniwnyk, L., Lorimer, J., 1996. The uses of ultrasound in food technology. Ultrason. Sonochem. 3, S253–S260.

Mason, T.J., Riera, E., Vercet, A., Lopez-Buesa, P., 2005. Application of Ultrasound. Emerging technologies for food processing. Elsevier.

Matos, J., Cardoso, C., Bandarra, N., Afonso, C., 2017. Microalgae as healthy ingredients for functional food: a review. Food Funct. 8, 2672–2685.

Medina-Torres, N., Ayora-Talavera, T., Espinosa-Andrews, H., Sánchez-Contreras, A., Pacheco, N., 2017. Ultrasound assisted extraction for the recovery of phenolic compounds from vegetable sources. Agronomy 7, 47.

Meullemiestre, A., Breil, C., Abert-Vian, M., Chemat, F., 2016. Microwave, ultrasound, thermal treatments, and bead milling as intensification techniques for extraction of lipids from oleaginous Yarrowia lipolytica yeast for a biojetfuel application. Bioresour. Technol. 211, 190–199.

Mortimore, S., Wallace, C., 2013. HACCP: A practical approach. Springer Science & Business Media.

O'Donnell, C., Tiwari, B., Bourke, P., Cullen, P., 2010. Effect of ultrasonic processing on food enzymes of industrial importance. Trends Food Sci. Technol. 21, 358–367.

Ochoa-Rivas, A., Nava-Valdez, Y., Serna-Saldívar, S.O., Chuck-Hernández, C., 2017. Microwave and ultrasound to enhance protein extraction from peanut flour under alkaline conditions: effects in yield and functional properties of protein isolates. Food Bioprocess Technol. 10, 543–555.

Ohsaka, K., Trinh, E.H., 1998. Dynamic nucleation of ice induced by a single stable cavitation bubble. Appl. Phys. Lett. 73, 129–131.

Palma, M., Barroso, C.G., 2002. Ultrasound-assisted extraction and determination of tartaric and malic acids from grapes and winemaking byproducts. Anal. Chim. Acta 458, 119–130.

Panda, D., Manickam, S., 2019. Cavitation technology—the future of greener extraction method: a review on the extraction of natural products and process intensification mechanism and perspectives. Appl. Sci. 9, 766.

Patrick, M., Blindt, R., Janssen, J., 2004. The effect of ultrasonic intensity on the crystal structure of palm oil. Ultrason. Sonochem. 11, 251–255.

Pereira, T., Barroso, S., Mendes, S., Amaral, R.A., Dias, J.R., Baptista, T., Saraiva, J.A., Alves, N.M., Gil, M.M., 2020. Optimization of phycobiliprotein pigments extraction from red algae Gracilaria gracilis for substitution of synthetic food colorants. Food Chem. 321, 126688.

Pingret, D., Fabiano-Tixier, A.-S., Chemat, F., 2013. Degradation during application of ultrasound in food processing: a review. Food Control 31, 593–606.

Piyasena, P., Mohareb, E., McKellar, R., 2003. Inactivation of microbes using ultrasound: a review. Int. J. Food Microbiol. 87, 207–216.

Povey, M.J., Mason, T.J., 1998a. Ultrasound in Food Processing. Springer Science & Business Media.

Povey, M.J.W., Mason, T.J., 1998b. Ultrasound in Food Processing. Blackie Academic & Professional, London.

Preece, K., Hooshyar, N., Krijgsman, A., Fryer, P., Zuidam, N., 2017a. Intensification of protein extraction from soybean processing materials

using hydrodynamic cavitation. Innovative Food Sci. Emerg. Technol. 41, 47–55.
Preece, K.E., Hooshyar, N., Krijgsman, A., Fryer, P.J., Zuidam, N.J., 2017b. Intensified soy protein extraction by ultrasound. Chem. Eng. Process. Process Intensif. 113, 94–101.
Price, C.J., 1997. Take some solid steps to improve crystallization. Chem. Eng. Prog. 93 (9).
Puri, M., Sharma, D., Barrow, C.J., 2011. Enzyme-assisted extraction of bioactives from plants. Trends Biotechnol. 30, 37–44.
Qv, X.Y., Zhou, Q.F., Jiang, J.G., 2014. Ultrasound-enhanced and microwave-assisted extraction of lipid from *Dunaliella tertiolecta* and fatty acid profile analysis. J. Sep. Sci. 37, 2991–2999.
Richards, W.T., Loomis, A.L., 1927. The chemical effects of high frequency sound waves I. a preliminary survey. J. Am. Chem. Soc. 49, 3086–3100.
Riera, E., Golás, Y., Blanco, A., Gallego, J.A., Blasco, M., Mulet, A., 2004. Mass transfer enhancement in supercritical fluids extraction by means of power ultrasound. Ultrason. Sonochem. 11, 241–244.
Riera, E., Juárez, J.A.G., Vitini, F.M., Blanco, A.B., Pons, A.M., Fort, J.J. B., Cervero, R.P., Sánchez, Y.G., Prats, Á.B., Huerta, S.S., Piquer, M. B., Reverter, J.G., 2005. Separation or Extraction Method Using Supercritical Fluids Assisted by High-Intensity Ultrasound.
Riera, E., Gallego-Juárez, J.A., Mason, T.J., 2006. Airborne ultrasound for the precipitation of smokes and powders and the destruction of foams. Ultrason. Sonochem. 13, 107–116.
Riera, E., Blanco, A., García, J., Benedito, J., Mulet, A., Gallego-Juárez, J. A., Blasco, M., 2010. High-power ultrasonic system for the enhancement of mass transfer in supercritical CO2 extraction processes. Ultrasonics 50, 306–309.
Rodríguez, G., Riera, E., Gallego-Juárez, J.A., Acosta, V.M., Pinto, A., Martínez, I., Blanco, A., 2010. Experimental study of defoaming by air-borne power ultrasonic technology. Phys. Procedia 3, 135–139.
Ruecroft, G., Hipkiss, D., Ly, T., Maxted, N., Cains, P.W., 2005. Sonocrystallization: the use of ultrasound for improved industrial crystallization. Org. Process. Res. Dev. 9, 923–932.
Saclier, M., Peczalski, R., Andrieu, J., 2010. Effect of ultrasonically induced nucleation on ice crystals' size and shape during freezing in vials. Chem. Eng. Sci. 65, 3064–3071.
Salleh-Mack, S., Roberts, J., 2007. Ultrasound pasteurization: the effects of temperature, soluble solids, organic acids and pH on the inactivation of Escherichia coli ATCC 25922. Ultrason. Sonochem. 14, 323–329.
Sallet, D., Souza, P.O., Fischer, L.T., Ugalde, G., Zabot, G.L., Mazutti, M. A., Kuhn, R.C., 2019. Ultrasound-assisted extraction of lipids from Mortierella isabellina. J. Food Eng. 242, 1–7.
Samaram, S., Mirhosseini, H., Tan, C.P., Ghazali, H.M., Bordbar, S., Serjouie, A., 2015. Optimisation of ultrasound-assisted extraction of oil from papaya seed by response surface methodology: oil recovery, radical scavenging antioxidant activity, and oxidation stability. Food Chem. 172, 7–17.
Sánchez, E.S., Simal, S., Femenia, A., Benedito, J., Rosselló, C., 1999. Influence of ultrasound on mass transport during cheese brining. Eur. Food Res. Technol. 209, 215–219.
Schram, C., 1991. Manipulation of particles in an acoustic field. Adv. Sonochem. 2, 293–322.
Selvakumar, P., Sivashanmugam, P., 2019. Ultrasound assisted oleaginous yeast lipid extraction and garbage lipase catalyzed transesterification for enhanced biodiesel production. Energy Convers. Manag. 179, 141–151.
Singiser, R.E., Beal, H.M., 1960. Emulsification with ultrasonic waves II: evaluation of three ultrasonic generators and a colloid mill. J. Am. Pharm. Assoc. 49, 482–487.
Söllner, K., Bondy, C., 1936. The mechanism of coagulation by ultrasonic waves. Trans. Faraday Soc. 32, 616–623.
Sujka, M., Jamroz, J., 2013. Ultrasound-treated starch: SEM and TEM imaging, and functional behaviour. Food Hydrocoll. 31, 413–419.
Szent-Györgyi, A., 1933. Chemical and biological effects of ultra-sonic radiation. Nature 131, 278.
Tekin, K., Akalın, M.K., Şeker, M.G., 2015. Ultrasound bath-assisted extraction of essential oils from clove using central composite design. Ind. Crop. Prod. 77, 954–960.
Vercet, A., Burgos, J., López-Buesa, P., 2001. Manothermosonication of foods and food-resembling systems: effect on nutrient content and nonenzymatic browning. J. Agric. Food Chem. 49, 483–489.
Vernès, L., Abert-Vian, M., El Maâtaoui, M., Tao, Y., Bornard, I., Chemat, F., 2019. Application of ultrasound for green extraction of proteins from spirulina. Mechanism, optimization, modeling, and industrial prospects. Ultrason. Sonochem. 54, 48–60.
Weissler, A., 1950. Depolymerization by ultrasonic irradiation: the role of cavitation. J. Appl. Phys. 21, 171–173.
Wood, R.W., Loomis, A.L., 1927. XXXVIII. The physical and biological effects of high-frequency sound-waves of great intensity. Lond. Edinb. Dublin Philos. Mag. J. Sci. 4, 417–436.
Wu, H., Liu, S.-C., 1931. Coagulation of egg albumin by supersonic waves. Proc. Soc. Exp. Biol. Med. 28, 782–784.
Wu, H., Zhu, J., Yang, L., Wang, R., Wang, C., 2015. Ultrasonic-assisted enzymatic extraction of phenolics from broccoli (Brassica oleracea L. var. italica) inflorescences and evaluation of antioxidant activity in vitro. Food Sci. Technol. Int. 21, 306–319.
Yolmeh, M., Habibi Najafi, M.B., Farhoosh, R., 2014. Optimisation of ultrasound-assisted extraction of natural pigment from annatto seeds by response surface methodology (RSM). Food Chem. 155, 319–324.
Zhang, Z.-S., Wang, L.-J., Li, D., Jiao, S.-S., Chen, X.D., Mao, Z.-H., 2008. Ultrasound-assisted extraction of oil from flaxseed. Sep. Purif. Technol. 62, 192–198.
Zhang, Q.-A., Zhang, Z.-Q., Yue, X.-F., Fan, X.-H., Li, T., Chen, S.-F., 2009. Response surface optimization of ultrasound-assisted oil extraction from autoclaved almond powder. Food Chem. 116, 513–518.
Zheng, L., Sun, D.-W., 2006. Innovative applications of power ultrasound during food freezing processes—a review. Trends Food Sci. Technol. 17, 16–23.
Zhong, J., Wang, Y., Yang, R., Liu, X., Yang, Q., Qin, X., 2018. The application of ultrasound and microwave to increase oil extraction from Moringa oleifera seeds. Ind. Crop. Prod. 120, 1–10.
Zlabur, J.S., Voca, S., Dobricevic, N., Pliestic, S., Galic, A., Boricevic, A., Boric, N., 2016. Ultrasound-assisted extraction of bioactive compounds from lemon balm and peppermint leaves. Int. Agrophys. 30, 95–104.
Zuo, Y.Y.J., 2011. Effect of Sonication Treatment on the Physico-Chemical Properties of Starch-Based Suspensions.
Zuo, J.Y., Knoerzer, K., Mawson, R., Kentish, S., Ashokkumar, M., 2009. The pasting properties of sonicated waxy rice starch suspensions. Ultrason. Sonochem. 16, 462–468.

Chapter 32

Crystallization and freezing processes assisted by power ultrasound

F. Baillon[a], F. Espitalier[a], C. Cogné[b], S. Labouret[b], R. Peczalski[b], and O. Louisnard[a]

[a]*University of Toulouse, IMT Mines Albi, Research Centre in Particulate Solid Process Engineering, Energy and Environment (RAPSODEE UMR CNRS 5302), Albi CT, France,* [b]*University of Lyon, University Claude Bernard Lyon 1, Laboratory of Process Control and Chemical Engineering (LAGEPP UMR CNRS 5007), Villeurbanne, France*

32.1 Introduction

During a crystallization operation, it is important to control the purity, the yield, the crystalline structure, and the size distribution of crystals, as well as the crystal morphology. Depending on the type of solid and its applications (chemical, pharmaceutical, food, minerals, etc.), some of these may be critical objectives. For instance, a narrow size distribution may be sought. The final mean size will depend on the future application of the solid. Deep insight into the elementary nucleation and growth mechanisms is needed for the control of the crystallization processes in order to produce crystals with the required properties such as size distribution, purity, or crystalline structure and shape. For two decades, ultrasound has been more and more frequently used for enhancing crystallization processes. According to the literature, ultrasound is generally reported to accelerate nucleation and growth, decrease the crystal size, and narrow the size distribution. Thus, the application of ultrasound appears to be a very promising tool for controlling the crystal properties, enhancing the process yield, or replacing seeding of metastable solutions. However, much of the pioneering work dates from the 1960s. The ultrasound effect is generally attributed to the presence of cavitation bubbles, but the precise mechanism at the bubble scale has not been clarified, and few works discuss the fundamental aspects.

This chapter is structured as follows. First, the theoretical bases of crystallization are presented to explain the elements of the thermodynamics and kinetics of crystallization. Then, the second part reviews different applications of ultrasound for crystallization in solutions and melts (in multi-bubble or single-bubble configuration) over the last 20 years. The third part concerns the fundamental physical mechanisms underlying the sonocrystallization process described on the basis of both the literature and the authors' own studies.

32.2 Fundamentals of crystallization

Crystallization mechanisms have been studied and described extensively in the literature. This part will present only the elements of the thermodynamics and kinetics of crystallization needed to understand the results presented. For more detail, the reader may refer to the references (Mullin 2001; Mersmann 2001; Söhnel and Garside, 1992; Kashchiev 2000).

In this chapter, mainly works on crystallization in solution will be treated. For melted media, only ice will be studied.

32.2.1 Saturation and supersaturation in solutions and melts

32.2.1.1 Saturation

Figure 32.1 presents the isobar phase diagram of an A-H_2O system with an eutectic (E) (coexistence point of two solid phases and one liquid phase). This point corresponds to the minimal temperature that the liquid phase can exist. For mixture presenting an eutectic, one component (A or H_2O) precipitates in a pure state on each side of the eutectic point in one theoretical separation step (Mersmann, 2001). In practice, eutectic systems are most common (Mullin, 2001). In the example, the components (A and water) do not combine to form a chemical compound or hydrate. The liquidus curves represent the temperature above which mixtures of these two components are completely liquid. For a temperature below the horizontal line, the two components are completely solid.

From an aqueous solution (water + component A) presenting this type of phase diagram, it is possible to crystallize component A, or ice independently. For a solution with a composition of A higher than the composition of the eutectic (E) and for a temperature ranged between the

Power Ultrasonics. https://doi.org/10.1016/B978-0-12-820254-8.00025-7
Copyright © 2023 Elsevier Ltd. All rights reserved.

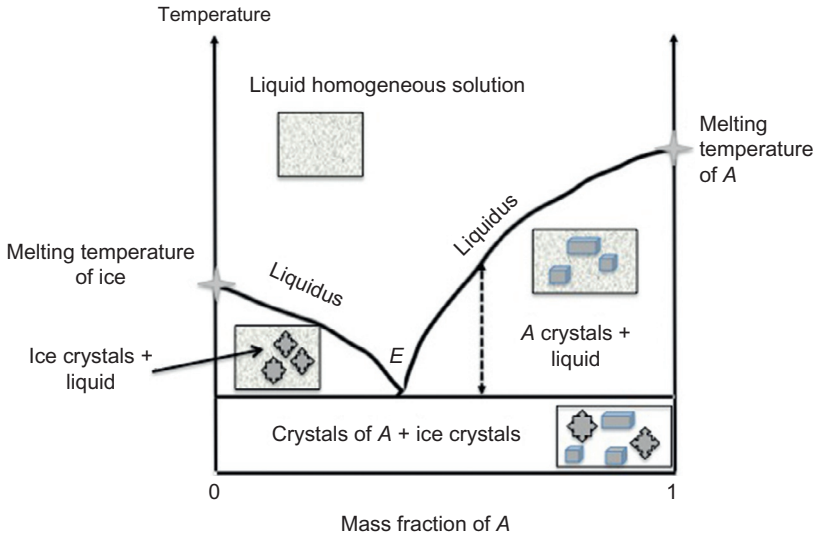


FIGURE 32.1 Isobar phase diagram for a system A–H_2O.

temperature of the eutectic and the liquidus temperature, component A can crystallize (zone "A crystals + liquid"). At the equilibrium, an aqueous solution and the solid A are in balance.

For a solution with a composition of A smaller than the composition of the eutectic and for a temperature ranged between the temperature of the eutectic (E) and the liquidus temperature, ice crystals are formed (zone "ice crystals + liquid"). At the equilibrium, the solution and ice crystals are in balance. These two cases will be examined (Nakagawa et al., 2006; Hottot et al., 2008). The crystallization of ice will be called freezing.

It is routine to present only a part of the phase diagram, depending on the product the operator wants to crystallize. For instance, if the chosen solid is A, the focus will be on the concentration higher than the concentration of the eutectic mixture and the temperature higher than the eutectic temperature. Figure 32.2 gives this representation: the liquidus curve, also called the solubility curve, as a function of temperature. The solution is stable below this curve and supersaturated above it.

To crystallize a solid, the experiment must be carried out in the metastable zone. From a liquid phase (an undersaturated or saturated solution), cooling, evaporation of solvent(s), addition of an anti-solvent, or creation of a chemical reaction may all be used for crystallization purposes. These different operations can be combined. In Figure 32.2, two operations are represented: cooling and evaporation.

32.2.1.2 *Supersaturation*

Supersaturation represents the deviation from the equilibrium at a given temperature and pressure for a component i. It is the thermodynamic driving force for crystallization $\Delta\mu_i$. $\Delta\mu_i$ is the difference between the chemical potential of the

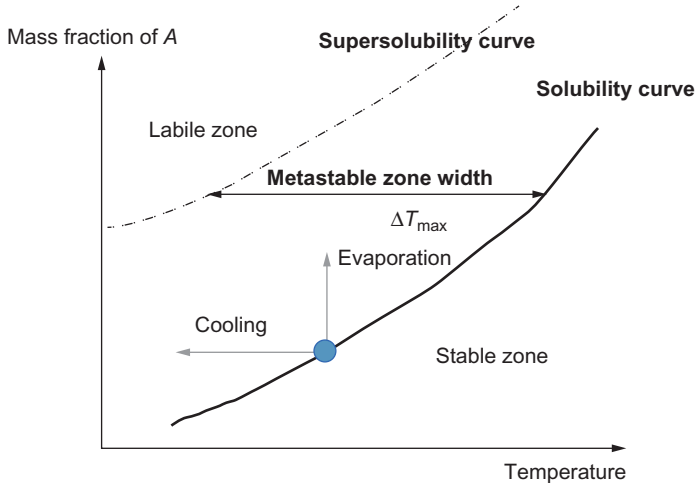


FIGURE 32.2 Crystallization techniques.

crystallizing compound i in a supersaturated solution and in the crystal or solid. The chemical potential of a component i in a mixture, μ_i (T,P,x_i), is the partial free energy of this component. It is defined by:

$$\mu_i(T,P,x_i) = \left(\frac{\partial G}{\partial N_i}\right)_{T,P,N_{j,j\neq i}} \tag{32.1}$$

where G is the free enthalpy of the system (J), N_i the mole number of component i, T the temperature (K), P the pressure (Pa), j the other components, and x_i the molar fraction of i in the mixture. It quantifies the global effect of microscopic interactions on component i with its environment. Higher is the chemical potential of a component, more the component will tend to transfer to another phase where its chemical potential will be lower or to disappear by chemical reaction.

In a spontaneous crystallizing system, the solution is supersaturated ($\Delta\mu_i > 0$). For a non-ionic species, this can be quantified by the expression as a function of temperature T and pressure P (Virone et al., 2006):

$$\begin{aligned}\Delta\mu_i &= \mu_i(T,P) - \mu_i^*(T,P)\\ &= RT\ln\left(\frac{a_i^L(T,P)}{a_i^{*,L}(T,P_0)}\right)\\ &\quad + \int_{P_0}^{P} (\bar{v}_{i,solute}(T,P) - v_{i,\text{solid}}(T,P))dP\end{aligned} \tag{32.2}$$

where P_0 is the ambient pressure, μ_i the chemical potential of the equilibrium of i at T and P, $a_i^L(T,P)$ the activity of compound i in the liquid phase at T and P, $\bar{v}_{i,\text{solute}}(T,P)$ the partial molar volume of the solute, and $v_{i,\text{solid}}(T,P)$ the molar volume of the crystalline or solid species. The symbol * represents the liquid–solid equilibrium state. The first term represents the driving force at ambient pressure P_0 and the second term the variation of this driving force due to the pressure.

The activity of component i in the phase k, a_i^k, is a non-dimensional value which the value is linked to the choice of the reference state. The temperature and the pressure of this reference state are respectively equal to the temperature and the pressure of the solution. The activity of a component i can be expressed on different bases of concentration (mass fraction, molar fraction, molar concentration, etc.). It is related to the activity coefficient γ_i. For instance, the activity expressed in mass ratio is written:

$$a_i^L = \gamma_i \frac{C_i^L}{C_i^{0,L}} \tag{32.3}$$

C_i^L is the mass ratio of solute in solvent (g of solute/g of solvent) and $C_i^{0,L}$ is a reference equal to 1 g of solute/g of solvent. The activity coefficient γ_i is a corrective coefficient permitting to describe the behavior of the component i in the mixture. At the reference state, this coefficient is equal to 1.

From the Eq. (32.2), if the term $\int_{P_0}^{P} (\bar{v}_{\text{solute}}(T,P) - v_{\text{solid}}(T,P))dP$ is positive, then a pressure increase causes $\Delta\mu_i(T,P)$ to increase, while a negative value leads to a decrease in $\Delta\mu_i(T,P)$. This pressure term is generally neglected for moderate pressure since the pre-factor $(\bar{v}_{\text{solute}}(T,P) - v_{\text{solid}}(T,P))$ is rather small (typically $0.01\,\text{nm}^3$ either positive or negative):

$$\begin{aligned}\Delta\mu_i(T,P) &= \mu_{i,\text{solute}}(T,P) - \mu_{i,\text{solute}}^*(T,P)\\ &= RT\ln\left(\frac{a_i(T,P_0)}{a_i^*(T,P_0)}\right)\end{aligned} \tag{32.4}$$

The ratio of activity is called supersaturation ratio S:

$$S_i = \left(\frac{a_i(T,P_0)}{a_i^*(T,P_0)}\right) \tag{32.5}$$

In the case of low supersaturation, $\frac{\gamma_i}{\gamma_i^*}$ tends towards 1 and the supersaturation ratio can be written:

$$S_i = \left(\frac{C_i(T,P_0)}{C_i^*(T,P_0)}\right) \tag{32.6}$$

It is common practice to speak about an absolute supersaturation ΔC_i. Its expression is:

$$\Delta C_i = C_i - C_i^* \tag{32.7}$$

In the case of melt crystallization by cooling ($T < T_{\text{melting}}$) (Kashchiev, 2000):

$$\Delta\mu_i(T,P) = \frac{\Delta h_{\text{crytallization}}}{T_{\text{melting}}}\left(T_{\text{melting}} - T\right) \tag{32.8}$$

where T_{melting} (K) and $\Delta h_{\text{crystallization}}$ (J/mol) are respectively the melting temperature and the latent heat of crystallization of the pure crystallizing component. This equation is valid when the undercooling conditions satisfy the condition $\Delta T << 2\Delta h_{\text{crytallization}}/\Delta c_{p,e}$. $\Delta c_{p,e}$ can be approximated by $c_{p,\text{melt}}(T_{\text{melting}}) - c_{\text{p,crystal}}(T_{\text{melting}})$. $c_{p,\text{melt}}(T_{\text{melting}})$ and $c_{p,\text{crystal}}(T_{\text{melting}})$ are respectively the heat capacity of the melt and the heat capacity of the crystal at melting temperature T_{melting}.

32.2.2 Nucleation

In a supersaturated solution ($\Delta\mu_i > 0$), **primary nucleation** occurs in the absence of solid particles of the crystallized substance. For homogeneous primary nucleation, no additional solid substrate is required, while **heterogeneous primary nucleation** is catalytically initiated by any foreign surface, such as the reactor wall, the stirring rod, or solid impurities.

Secondary nucleation takes place when crystals are already present in the supersaturated solution. Different mechanisms are proposed for secondary nucleation (Mullin, 2001; Mersmann, 2001). These are not described here.

32.2.2.1 Primary nucleation

Nucleus formation is based on the condensation of a vapor to a liquid, and this treatment has been extended to crystallization from melts and solutions (Mullin, 2001). It is based on the idea that molecules (or atoms or ions) in the vapor phase combine to form aggregates (embryos) according to the following reaction scheme:

$$\begin{aligned} &A_1 + A_1 \Leftrightarrow A_2 \\ &A_1 + A_2 \Leftrightarrow A_3 \\ &\ldots A_1 + A_j \Leftrightarrow A_{j+1} \ldots \\ &\ldots A_1 + A_{M-1} \Leftrightarrow A_M \ldots \end{aligned} \tag{32.9}$$

where A_1 represents the monomer (molecule, atom, or ion) and A_2, A_i … A_M the molecular aggregates composed of 2, … i … M monomers. M represents the maximal degree of aggregation. This scheme represents the successive addition of units A with another unit A or with an aggregate A_i to form a thermodynamically stable crystal.

The reactions of the type:

$$A_j + A_k \Leftrightarrow A_{j+k}, \text{where } k \text{ and } j \geq 2 \tag{32.10}$$

are not considered due to their low probability (low concentration of A_j and A_k aggregates). It has been shown that in supersaturated solutions, the molecules or ions constituting the solute are structured (Myerson and Lo, 1990; Larson and Garside, 1986). However, aggregates are mainly in the form of dimers and trimers, although there are a few with up to 100 molecules.

At constant pressure and temperature, the reversible work to form an aggregate is the sum of two free enthalpies, the free enthalpy proportional to the volume and the free enthalpy proportional to the surface:

$$\Delta G = \gamma_{sL} \Delta\Omega + \sum_k \mu_i^k \Delta n_i^k \tag{32.11}$$

where ΔG represents the free enthalpy variation during the creation of an aggregate with a size d_p, $\Delta\Omega$ the variation of surface of cluster that is proportional to the surface of cluster ($\sim d_p^2$), Δn_i^k the variation of moles number of crystallizing solid i in the phase k (liquid and solid phases) that is proportional to the volume of cluster ($\sim d_p^3$), and γ_{sL} the surface energy crystal/solution (J/m^2).

A thermodynamically stable nucleus exists when the free enthalpy variation does not vary when a monomer added or removed from the cluster. Mathematically, this corresponds to

$$\left.\frac{\partial \Delta G}{\partial d_p}\right|_{d_p \to d_p^*} = 0 \tag{32.12}$$

The diameter of this nucleus, d_p^*, and its mole number, n_i^*, are respectively given for a spherical cluster by:

$$d_p^* = \frac{4\gamma_{sL} v_{i,\text{solid}}}{\Delta\mu_i} \tag{32.13}$$

$$n_i^* = \frac{32\pi\gamma_{sL}^3 v_{i,\text{solid}}^2}{3\Delta\mu_i^3} \tag{32.14}$$

where $v_{i,\text{solid}}$ is the molar volume of solid (m^3/mol) and $\Delta\mu_i$ the driving force (J/mol).

The critical nucleus n^* could be a miniature crystal that is nearly perfect in form (Mullin, 2001).

The primary nucleation rate is defined as the number of nuclei generated per unit of volume and per unit of time. The nucleation rate represents the frequency of appearance at time t of supernuclei per unit of volume. The general definition is (Kashchiev, 2000):

$$J_{PN}(t) = \frac{d\zeta_i(t)}{dt} \tag{32.15}$$

where $\zeta_i(t)$ is the concentration of supernuclei or aggregates with a size higher than n_i^*+1 (number/m^3/s).

The steady-state homogeneous primary nucleation rate, J_{PN}^{stat}, is generally expressed with the following classical relation for spherical nuclei (Mullin, 2001):

$$J_{PN}^{stat} = K \exp\left[-\frac{16}{3}\frac{\gamma_{SL}^3 v_{i,\text{solid}}^2}{RT\Delta\mu_i^2}\right] \tag{32.16}$$

An expression of kinetic constant K is given by (Kashchiev, 2000):

$$K = zf^* C_0 \tag{32.17}$$

K depends on z called the Zeldovich factor, on f^* the frequency of monomer attachment to the nucleus, and C_0 the concentration of sites nucleation.

At constant supersaturation, stationary nucleation means that the aggregate size distribution is time independent. The time to approach this steady state is a few hundred nanoseconds.

For the primary nucleation rate, there are also more empirical equations of the form, function of the absolute supersaturation ΔC_i:

$$J_{PN}^{stat} = k_n \Delta C_i^n \tag{32.18}$$

32.2.3 Growth

Once established, the crystal grows, thus reducing the concentration in the solution.

Put simply, the crystal growth can be divided into two steps: the diffusion of the solute from the solution to the surface of the crystal and the reaction consisting of the integration of growth units to the face. The slower of these steps determines the crystal growth rate.

The overall linear growth rate G can be expressed as a function of the absolute supersaturation ΔC_i:

$$G = \frac{dL}{dt} = k_g \Delta C_i^g \tag{32.19}$$

G refers to any characteristic length L of the 3D crystal. The value of L depends on the technical measurement (sieving, laser granulometry, image analysis, etc.). This rate is linked to the mass flux density (Mersmann, 2001). k_g is the growth rate constant and g the order of the growth rate.

32.2.4 Induction time and metastable zone width

In order to characterize the primary nucleation, we can measure the induction period, which is defined as the time elapsed between the creation of supersaturation and the appearance of crystals. Kashchiev et al., (1991) and Kashchiev and van Rosmalen (2003) proposed a general expression of induction time valid for all nuclei that are born and grow in a saturated solution:

$$t_{\text{ind}} = \frac{1}{VJ_{\text{PN}}} + \left[\frac{\alpha_o}{a_p J_{\text{PN}} G^{p-1}}\right] \tag{32.20}$$

where V is the volume of solution, α_o the detectable mass fraction of formed solid, J_{PN} and G respectively the stationary primary nucleation and growth rate, and a_p p are two parameters depending on the shape of crystal and on the growth rate mechanism.

Assumptions can be made to simplify the expression of the induction time (Kashchiev et al., 1991).

Three cases are possible:

- Nucleation time $\left(t_n = \frac{1}{VJ_{\text{PN}}}\right)$ is much higher than growth time $\left(t_g = \left[\frac{\alpha_o}{a_p J_{\text{PN}} G^{p-1}}\right]\right)$: nucleation is predominant.
- t_n is much smaller than t_g: the growth mechanism of the nucleus to a detectable size is predominant.
- t_n is of the same order of magnitude as t_g: nucleation and growth act upon the induction time.

The metastable zone width represents the maximum undercooling $\Delta T_{\max}$ where the solid formation is spontaneous and uncontrolled (Figure 32.2). The position of this supersolubility curve is not well defined and depends on operating conditions, including the rate at which supersaturation is created and whether crystals are present in the medium (Mullin, 2001).

32.3 Impact of ultrasound on solute crystallization

This part will review the principal studies that have been carried out on crystallization assisted by ultrasound in solutions and melts (multi-bubble or single-bubble configuration). The influence of the ultrasound conditions on the crystal properties and on the process will be discussed. A specific paragraph will be devoted to ice crystallization in super-cooled aqueous solutions.

Typically, the experimental results show that the crystals formed in the presence of ultrasound are smaller than those obtained without ultrasound. Their mean size decreases with an increased dissipated power. The yield and the crystallinity increase. Some examples are given below to illustrate these effects.

32.3.1 Induction time

Different studies present the induction time or metastable zone width obtained with ultrasound at different scales from ml to L (Lyczko et al., 2002; Li et al., 2003, 2006; Guo et al., 2006a,b; Virone et al., 2006; Kordylla et al., 2008; Harzali et al., 2011; Gürbüz et al., 2012; Kiani et al., 2012, Nikolaev et al., 2018, Majal Belca et al., 2019, Devos et al., 2021). To summarize standard results observed for induction time, we have chosen to present the study on potassium sulfate (Lyczko et al., 2002). Induction time measurements were carried out for cooling crystallization using a thermostated vessel of 0.2 L stirred with a magnetic rod. The induction time is defined as the time interval between the formation of an appreciable amount of the solid phase and the initial moment of supersaturating the solution. The solution was rapidly cooled from the saturation temperature plus 5°C to a final temperature of about 15 ± 0.4°C. Ultrasound (20 kHz) was applied at the top of the vessel by a titanium probe. Two dissipated ultrasonic power levels were measured by calorimetry: 0.05 and 0.12 W/g solution, respectively. Ultrasound was applied at the end of the cooling phase. Figure 32.3 presents the results of the induction time vs the absolute supersaturation. The same shapes of curves are obtained with and without ultrasound. The induction time decreases when the absolute supersaturation increases. These curves agree with standard induction time curves obtained for crystallization processes (Mullin, 2001). Ultrasound has a significant effect on the induction time, especially for low supersaturation ($\Delta C < 0.016$ g K_2SO_4/g water or $S < 1.100$). For lower supersaturations ($\Delta C < 0.012$ g K_2SO_4/g water or $S < 1.077$), a dissipated power of a magnitude of 0.12 W/g solution seems to be more efficient than a dissipated power of 0.04 W/g solution. In the case of a glycine aqueous solution, the cyclical application of ultrasound revealed that induction time decreases when the cyclical ratio ($\text{time}_{\text{US, on}}/\text{time}_{\text{US, off}}$) increases (between

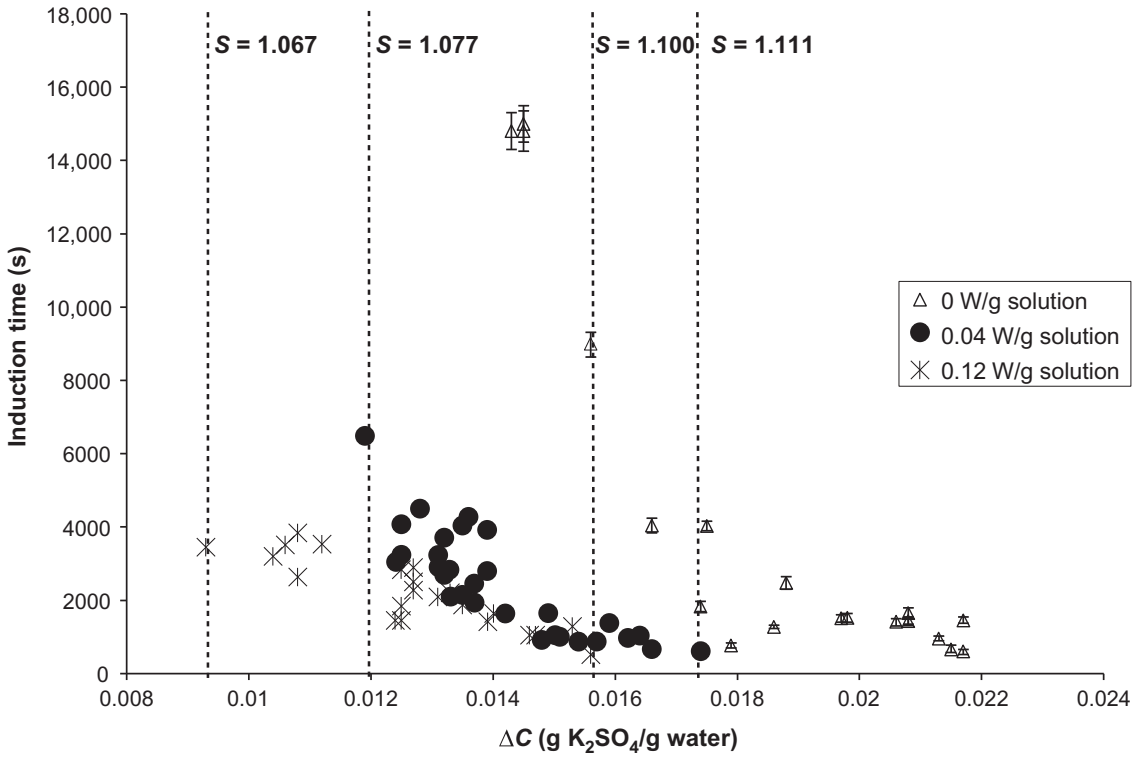


FIGURE 32.3 Induction times as function of absolute supersaturations and ultrasonic powers.

3 and 10). Moreover, for a given cyclical ratio, the induction time seems to be the same or lower than induction times measured in continuous mode (Louisnard and Espitalier, 2007).

Kordylla et al. (2008) measured the metastable zone width of dodecanedioic acid in three solvents. This zone is reduced in the presence of ultrasound. Furthermore, in the presence of ultrasound, the metastable zone width is not influenced by the solvent properties (vapor pressure and surface tension). They tested different frequencies ranged between 40 and 1050 kHz. The optimal frequency was found to be 355 kHz.

Devos et al. (2021) measured the induction time of paracetamol in the aqueous phase at the mL scale at 30 kHz and 45 W. They compared the induction time for different nucleation mechanisms (primary and secondary) with and without ultrasound. Ultrasound are applied continuously or periodically. They observed that ultrasound decreases the induction time of paracetamol whatever the type of nucleation.

32.3.2 Polymorphism and crystallinity

A study on calcium carbonate, formed by reaction between calcium chloride and ammonium carbonate, showed that the formation of vaterite is favored by the application of ultrasound (40 kHz, 800 W et 20 kHz 400 W) (Kojima et al., 2010). Without ultrasound, the tendency is for calcite to be created. The particles are smaller and the specific area increases with the ultrasonic wave amplitude. In parallel, a work on the same product showed that ultrasound affects the deposition of calcium carbonate on a surface (Al Nasser et al., 2013). The authors note two effects: a decrease in the deposition rate of calcium carbonate by heterogeneous primary nucleation and an increase of the primary nucleation rate in solution.

In the case of titanium dioxide precipitation by thermal hydrolysis (sulfuric process) for strong supersaturation, the application of ultrasound (20 kHz) orients the precipitation markedly towards the rutile form. Rutile and anatase are the two most common and widely used polymorphs of TiO_2. Deconvolution of the peak obtained by XRD leads to an estimation of 60% for the mass fraction of rutile in the final powder. The facies and the size distributions of crystals are unchanged (Dodds et al., 2007). Other authors (Ghows and Entezari, 2010) studied the synthesis of titanium dioxide at low temperature (75°C) by hydrolysis of titanium tetraisopropoxide $Ti(OC_3H_7)_4$. Under these conditions, the particles are usually amorphous, but in the presence of ultrasound (500 kHz), they obtained well-crystallized anatase nanoparticles.

A study was carried out on the crystallization of glycine by cooling from aqueous solutions with ultrasound (Louhi-kultanen et al., 2006). Glycine presents three polymorphs,

β, γ, and α. The formation of any particular polymorph depends on pH and seeding. The ultrasonic power ranged between 24 and 122 W/kg. The quantification of polymorphs was obtained from XRPD patterns by assuming a linear combination of the intensity of the different polymorph forms. Under certain operating conditions, ultrasound seems to allow the purest α-polymorph to be obtained. Another study on the crystallization of L-glutamic acid showed that the use of ultrasound produces a pure polymorph (α-polymorph), whereas without ultrasound and seeding, a mixture of two polymorphs is obtained (Hatakka et al., 2010). Similar results were found in the case of mannitol crystallization by cooling (Hottot et al., 2008), of vanillin by evaporative crystallization (Parimaladevi et al., 2018), and of ticagrelor by cooling in methanol–water medium (Majal Belca et al., 2019). For instance, mannitol is a polyol which leads to three crystalline systems α-polymorph, β-polymorph, and δ-polymorph. In this study, the authors showed that it is possible to control the form of the polymorph with ultrasound. The increase in the dissipated power increased the crystallinity and made it possible to obtain the metastable δ-polymorph, regardless of the temperature. In case of vanillin, pulsed ultrasound can be used to control the polymorph of vanillin and relatively medium powers appeared to favor the formation of the metastable polymorph. In the case of cooling crystallization of α-lactose, in a continuous device, in solutions containing low levels of whey protein, ultrasound reduces the formation of amorphous solid at low power (<0.5 W/g) (Sánchez-García et al., 2018).

During the sonochemical synthesis of a zeolite, ultrasound allowed a more rapid production of crystals with a better crystallinity (measured by XRD) (Kim et al., 2010; Aldahri et al., 2016). Belviso and co-authors (Belviso et al., 2013, 2011) showed that the synthesis of zeolite from fly ash with seawater is more rapid when a pre-treatment is made with ultrasound and that this synthesis becomes possible at low temperature. The syntheses were made in an ultrasonic bath at 240 W and 35 kHz. Ultrasound was applied for 1 h. In the same way, Aldahri et al., 2016 have shown that a treatment under ultrasound (125 W, 20 kHz, 100°C, 1–3 h), during the synthesis of zeolite nanoparticles after a first phase of conventional hydrothermal heating, allows a drastic reduction of the crystallization time (factor 6). This process, faster and with lower energy demands, allows to improve the crystallinity of the particles obtained in less time and at lower temperatures (100°C instead of 200°C) but also to strongly increase the surface area (x1.8).

In a review, Jordens et al., 2019 conclude that the probability of formation of the less stable polymorph increases with ultrasound. Ultrasound power and pulse frequency also affect the selectivity of polymorphs in a crystallization process in some cases. The use of pulsed or low-power ultrasound avoids the practical problem of increased temperature which could affect supersaturation and hence the polymorph. The kinetically controlled polymorph can be favored over the thermodynamically stable polymorph by the application of ultrasound (Kaur Bhangu et al., 2016). Thus, according to Kaur Bhangu et al. (2016), it is possible to produce a polymorphic metastable form by increasing the frequency (up to 98 kHz) or the acoustic power. This increase in this polymorph was attributed to the decrease in induction time, caused by the acoustic cavitation activity.

32.3.3 Morphology and size distribution

In the presence of ultrasound, the size distribution is narrower. Moreover, the shapes of crystals are modified: potash alum crystals are octahedric without ultrasound and decahedric with ultrasound (10, 30, and 100 W in 500 mL) (Amara et al., 2001). The change in the crystal shape is assigned to the modification in the growth rate of the faces of the crystal.

Nikolaev et al. (2018) studied the impact of ultrasound in non-cavitation and cavitation modes during the synthesis of hydroxyapatite by high supersaturation precipitation. They found that using the non-cavitation regime at low intensity leads to smaller particles than using high intensity in the cavitation regime. They explain this result by the formation of smaller vortices at high frequencies of the non-cavitation ultrasound regime, which leads to smaller particles formed by agglomeration of nuclei at the surface of these vortices.

The use of pulsed ultrasound (80 W, 20 s on/2 s off in 120 mL) leads to the creation of fine particles of magnetite with a different morphology from those obtained without ultrasound. The crystallinity of magnetite is also improved (Cheng et al., 2011).

Ultrasound leads to crystals with a reduced size in comparison to those produced without ultrasound (8 to 60 W at 20 kHz for Sayan et al., 2011; Dodds et al., 2007) and increases the specific surface of particles. Usually, the specific surface increases with the acoustic wave amplitude or dissipated power (Kojima et al., 2010; Zou et al., 2012).

The characterization of potassium sulfate crystals by SEM highlights cavities at the surface of crystals for crystals generated with ultrasound. Without ultrasound, crystals do not have cavities (Lyczko et al. 2002). These intra-particle cavities create porosity. The porosity increases when the dissipated power increases (5% at 50 W/kg solution and 13% at 120 W/kg solution) for experiments conducted in a vessel of 200 mL. The mean diameter of the cavities is constant regardless of the dissipated power and is around 4–5 μm.

32.3.4 Nucleation and growth rates

Some authors have attempted to identify the nucleation and growth rates during their experiments.

Boels et al. (2010) measured the growth rate of calcite. Dry seed crystals were added to a solution of calcium carbonate obtained by the mixing of sodium bicarbonate and calcium chloride. The pH and the ionic strength were maintained constant during the crystallization. They conducted some experiments with an inhibitor (methylene phosphonic acid). Ultrasound was applied 30 min after the seeding and for a duration of 45 min. A frequency of 42.15 kHz and a dissipated power of 17 W/L (measured by calorimetry) were used. Results showed that the precipitation rate was enhanced by the use of ultrasound (+46%). In the presence of an inhibitor in solution, they noted a strong decrease in the crystal growth rate when ultrasound was not used. A reduction of the inhibition period after ultrasonic irradiation was observed.

Dodds et al. (2007) and Sayan et al. (2011) carried out their experiments in a MSMPR crystallizer (Mixed Suspension Mixed Product Removal) and studied the cooling crystallization of sucrose (1.5 L) and potassium dihydrogen phosphate (0.5 L). With this type of crystallizer, in a steady-state regime, it is possible to determine an analytical expression of the population density of crystals as function of the residence time and the kinetic parameters of the nucleation and growth rates. In both cases, the growth rate, G, is size dependent. Agglomeration and attrition are neglected. In the case of sucrose, the calculated growth rate of 10 μm crystals (between 30 and 70 W) was comparable to that obtained by other authors without ultrasound in the same range of supersaturation. However, the nucleation rate increased with the applied acoustic power. It is interesting to note that, without ultrasound, no crystals are created for a residence time of 10 min. For two experiments at 25 and 70 W, ultrasound was stopped after the steady-state regime was attained. The sucrose concentration stayed constant. It seems that ultrasound initiates the crystallization, but after this initiation, ultrasound can be stopped or applied alternatively, without affecting the result. In the case of potassium dihydrogen phosphate, ultrasound modifies nucleation and growth rates.

Sayan et al. (2011) showed that ultrasound had an influence on the crystallization rate and that there was an optimal level of dissipated power. For a dissipated power ranged between 0 and 8 W in 500 mL, the average particle size decreased. It remained constant, however, for a higher ultrasound power. The nucleation rate decreased with residence time. For dissipated power higher than 20 W, the crystals present some defects.

According to Gürbüz et al. (2012), the nucleation and growth rates increase when ultrasound is applied during the synthesis of silicalite-1 (TPAOH:SiO_2:H_2O). The growth rate increases with the ultrasound power.

Kordylla et al. (2009) proposed a model to simulate a batch cooling crystallization of dodecanedioic acid with ultrasound (355.5 kHz and a nominal power of 200 W). They added a specific term of nucleation. This term replaced the classic terms of nucleation (primary and secondary) and was valid only during the application of ultrasound (30 s). The growth rate was assumed to be size-independent. They solved the population and mass balances in order to calculate the concentration profile and the size distributions of the crystals. The simulation results showed a qualitative agreement with the experimental observations. Optimal ultrasonic condition during crystallization for achieving a narrow CSD turned out to depend strongly on the supersaturation ratio at which the ultrasound was applied.

Pawar et al. (2018) studied the antisolvent semibatch crystallization of alpha-lactose monohydrate using ethanol as an antisolvent. The kinetic parameters of growth and nucleation were estimated by fitting an estimation model to the experimental data. The mathematical modeling of this process is formulated including a population balance equation and a material balance. The application of ultrasound (20 and 40 kHz) leads to the formation of smaller crystals, due to order-of-magnitude higher nucleation rates as estimated by fitting. The fitted parameters suggest that the growth kinetics and mechanisms do not change under sonic conditions (change in k_n but the parameters k_g, n, and g remain constant ($B = k_n\,\Delta C^n$ and Eq. 32.18)). From induction time measurement in microvials, Devos et al. (2021) determined the kinetic and thermodynamic nucleation rate by assuming that nucleation is a Poisson process. They showed that ultrasound had a large influence on kinetic parameter K (Eq. 32.16).

32.3.5 Agglomeration

A study on the precipitation of hydroxyapatite conducted in a micro-channel equipped with piezoelectric actuators showed that ultrasound either prevents the formation of agglomerates or breaks up agglomerates, preventing the channel from plugging. The particles obtained with ultrasound are smaller (Castro et al., 2013). Ramirez Mendoza et al. (2020) apply ultrasound during the first hour of zeolite synthesis, during the crystal growth stage. They observe a deagglomerating effect, leading to smaller sizes of the final agglomerates.

32.4 Impact of ultrasound on ice crystallization (freezing)

According to the reviews of Zheng and Sun (2006) and Kiani and Sun (2011), power ultrasound could have

promising applications in the freezing of food and pharmaceutical products, for instance:

- enhancing the process rate for immersion freezing of fresh foodstuffs;
- controlling ice crystal size in final products for freeze-concentration, freeze-drying, and ice-slurry production;
- preventing incrustation on freezing surfaces for partial freezing of ice cream inside a scraped surface freezer.

Although the mechanism of sononucleation has not yet been definitively elucidated (see next paragraph), there is clear evidence that the application of ultrasound has a notable and quantifiable effect on ice nucleation (Zhang et al., 2001, 2003; Hozumi et al., 2002; Chow et al., 2003, 2005). An ultrasound intensity threshold is needed for the formation of these bubbles and subsequent nucleation. A quite short (10 ms) acoustic impulsion, in the frequency range from 20 to 40 kHz and at a power higher than 2 W/L, was suggested in a patent application (Acton and Morris, 1992).

Inada et al. (2001) and Zhang et al. (2001) studied the potential application of ultrasonic waves to produce ice slurries. They found out that applying ultrasound greatly increased the probability of phase change from super-cooled water to ice at a given initial water temperature. The probability of phase change was calculated as the ratio of the number of successful freezing tests to the total number of tests in given conditions. The occurrence of phase change induced by ultrasound increased with the total number of gas bubble nuclei in super-cooled water, independently of other experimental conditions. Comparing their experimental results with a theoretical estimation, they concluded that the nucleation triggering is mainly due to the onset of inertial acoustic cavitation.

Chow and co-authors (Chow et al., 2003, 2005) evaluated the effect of ultrasounds on the primary and secondary nucleation of water in sucrose solutions (Figure 32.4). They showed the results of direct optical observations of crystals formed around an immersed sonication probe, around a single levitating and cavitating bubble, and in a special ultrasonic cold stage. They pointed out that the primary nucleation of ice in sucrose solutions can be achieved at higher nucleation temperatures in the presence of ultrasound. It was also shown that the nucleation temperatures of ice increase with increasing ultrasonic power. It was observed that pre-existing ice crystals could be fragmented by ultrasound, which modifies the size distribution and generates nucleation sites. This fragmentation may be caused by inertially collapsing bubbles or by high shear flow in the vicinity of stably oscillating bubbles.

Nakagawa et al. (2006) and Hottot et al. (2008) carried out freezing and freeze-drying experiments with an aqueous solution of mannitol in a small glass tube. Ice crystals were

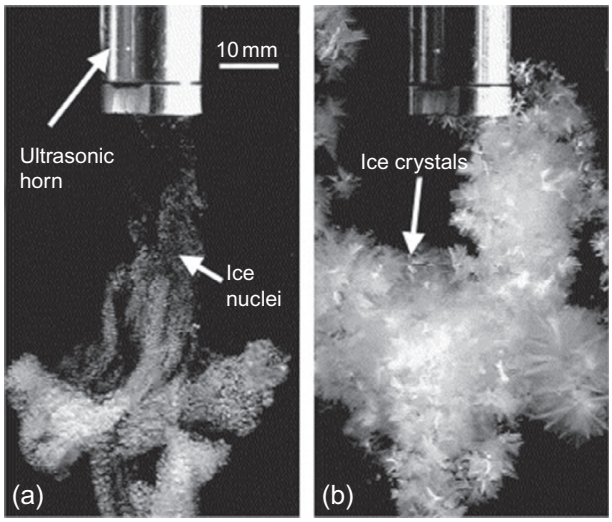


FIGURE 32.4 Photographs of ice crystals nucleated in a 15 wt% sucrose solution at 3.4 _C by a commercial ultrasonic device: (a) ice nuclei just after an ultrasonic pulse, (b) ice crystals 5 s later (Chow et al., 2005).

observed using reflected light optical microscopy over frozen samples in transversal and longitudinal sections in a cold chamber. It was found that the number of crystals decreases significantly (or their size increases) when ultrasound is applied at low super-cooling levels where spontaneous nucleation is not likely to occur (Figure 32.5). It was also shown that the nucleation could be readily triggered at selected sample temperature values below the equilibrium freezing temperature and that small and numerous ice crystals are obtained at lower nucleation temperature (higher super cooling degree), while large and directional ice crystals (dendrite type) are obtained at a higher nucleation temperature (lower super-cooling degree). The ice-crystal distribution in the frozen sample directly affects the vapor permeability of the freeze-dried cake, and consequently, the measured freeze-drying rate increases considerably with the nucleation temperature.

Saclier et al. (2010) continued the work on mannitol solution sono-freezing in vials. Using the same apparatus and methodology, they confirmed the above qualitative results but further adopted a second-order experimental design and quantitatively assessed the effect of both the nucleation temperature and the acoustic power on the final crystal size and shape. The ice crystal size was found to decrease with both the degree of super-cooling and the acoustic power level, whereas their circularity was found to increase with these parameters (see Figure 32.6). Empirical correlations for crystal size and circularity prediction were proposed.

Kiani et al. (2011) studied ultrasound-assisted nucleation of pure water, sucrose solution, and agar gel samples inserted in tubing vials. Ultrasound was applied continuously for different durations and at different sample

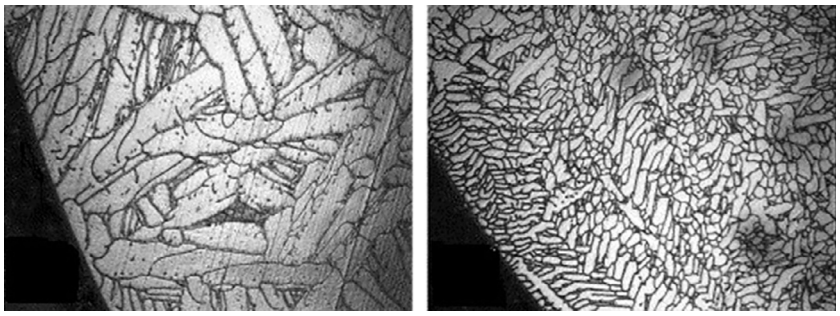


FIGURE 32.5 Photographs of ice crystals in axial sections of frozen samples (10% mannitol solution), on the left side: nucleated at _2 _C, at the right side: nucleated at _8 _C (Nakagawa et al., 2006).

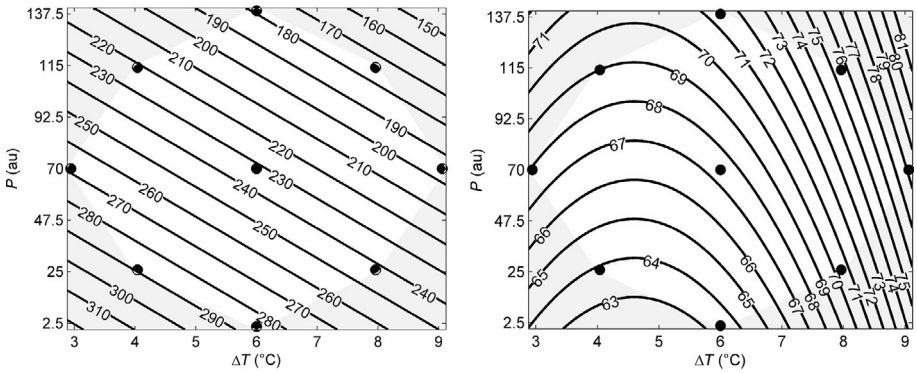


FIGURE 32.6 Ice crystals' measured mean size (μm, left side) and crystals' mean circularity (%, right side) vs supercooling (ΔT) and acoustic power (P) in transversal sections of frozen mannitol solution (Saclier et al., 2010).

temperatures in the range up to 5°C below the freezing point. They observed that ultrasound can trigger ice nucleation with high repeatability at the targeted temperatures and hence can be used to control the onset of nucleation. Ultrasound was able to induce nucleation in the fluid samples more efficiently than in the solid samples. In a continuation of this study (Kiani et al., 2012), the effect of ultrasound intensity on the nucleation of ice in agar gel samples was additionally studied. It was observed once again that ultrasound irradiation was able to initiate nucleation at different super-cooling levels in agar gel if optimum intensity and duration of ultrasound application were chosen. Higher intensities of ultrasound were found to be effective when a shorter time of sonication was used, while lower intensities resulted in nucleation only when a longer sonication time was applied.

Several studies (Inada et al., 2001; Zhang et al., 2001 among others) pointed out that a high content of dissolved air in the super-cooled liquid favors inertial cavitation intensity and ice nucleation rate. The direct link between the initial air concentration in the liquid and the number and size of the ice crystals was established by Jabbari-Hichri et al. (2014). In the context of this study, samples of mannitol aqueous solution at various contents of dissolved oxygen were frozen using ultrasound and the ice-crystal size distributions were measured by optical microscopy. Increasing the content in oxygen led to a fairly significant decrease in the average crystal size and an increase in the homogeneity of the size of crystals within the sample. The average size was simply inversely proportional to the oxygen content in the initial liquid solution. On this basis, the dissolved air concentration appeared as an additional and essential parameter for the control of crystal sizes in freezing processes assisted by ultrasound.

32.5 Solute nucleation mechanisms induced by ultrasound

This part will concern the different fundamental physical mechanisms underlying the sonocrystallization process described on the basis of the literature but also of the authors' own studies. It will investigate how an acoustically driven gas bubble may induce crystallization in the surrounding liquid. A special paragraph will be devoted to ice crystallization in super-cooled aqueous solutions.

The ultrasound induces various physical effects in the receiving liquid medium. Among them, the cavitation phenomenon is the most significant, as it may lead to the generation and collapse of gas bubbles but also to the occurrence of micro-streamings or collisions. The former can promote solid nucleation, while the latters are able to enhance interfacial heat and mass transfer processes (Suslick and Zieger, 2011). Moreover, already formed crystals may fracture when subjected to alternating acoustic

shock wave. All these phenomena affect crystal size distribution and crystal morphology in the final product.

When an ultrasonic wave propagates in a liquid, a phenomenon called acoustic cavitation may be observed. Acoustic cavitation corresponds to the formation, growth, and implosive collapse of bubbles in the liquid during expansion and compression phases. The results of simulation of the acoustic inertial cavitation of an air bubble (initial radius of 4 μm) are shown in Figure 32.7 (Harzali et al., 2012). This figure presents, respectively, during one oscillation period (a) the evolution of the bubble diameter, (b) the acceleration at the vicinity of the bubble, and (c) and (d) the temperature and the pressure in the center of the bubble. One may observe, around 27 μs (the moment of collapse), a very high temperature (at the collapse) and very low temperature of around 200 K (just after collapse) in the bubble as well as a very high pressure (at the collapse) in the bubble of around 1 GPa, with violent accelerations in the surrounding liquid after the collapse (Louisnard, 2008).

The ultrasound effect on nucleation is generally attributed to the presence of cavitation bubbles, but the precise mechanism at the bubble scale has not been yet assessed experimentally. Different theoretical qualitative or semi-quantitative mechanisms at the bubble-scale have been considered:

- the pressure effect: fast local liquid pressurization when the bubble collapses (see Figure 32.7d) (Virone et al., 2006; Grossier et al., 2007), creating a very high supersaturation, in the case where the solute solubility decreases with pressure;
- the diffusive effect: increase in the apparent solute diffusion coefficient (Guo et al., 2006a; Li et al., 2006) due to liquid micro-streaming induced by the bubble collapse (Suslick et al., 1990);
- the segregation effect: inertial segregation of solute and crystal precursors by the liquid acceleration during a very short period of time after the collapse, modifying the nucleation kinetics (Grossier et al., 2007);
- the chemical effect: formation of radicals in the bubbles and hot spots in the solution (Suslick et al., 1990);

The first two phenomena act on the thermodynamics of the process by modifying the supersaturation (or the supercooling in melts). The two other phenomena act on the kinetics of the process and affect the aggregation mechanism of molecules or ions involved in the formation of the solid phase.

We shall examine these different issues: thermodynamic, kinetic, and chemical effects.

32.5.1 Thermodynamic (temperature and pressure) effect

Pressure and temperature are the driving force of crystallization, as is shown by Eq. (32.2).

A pressure variation in the liquid at the bubble interface can have an effect on supersaturation. For instance, in the

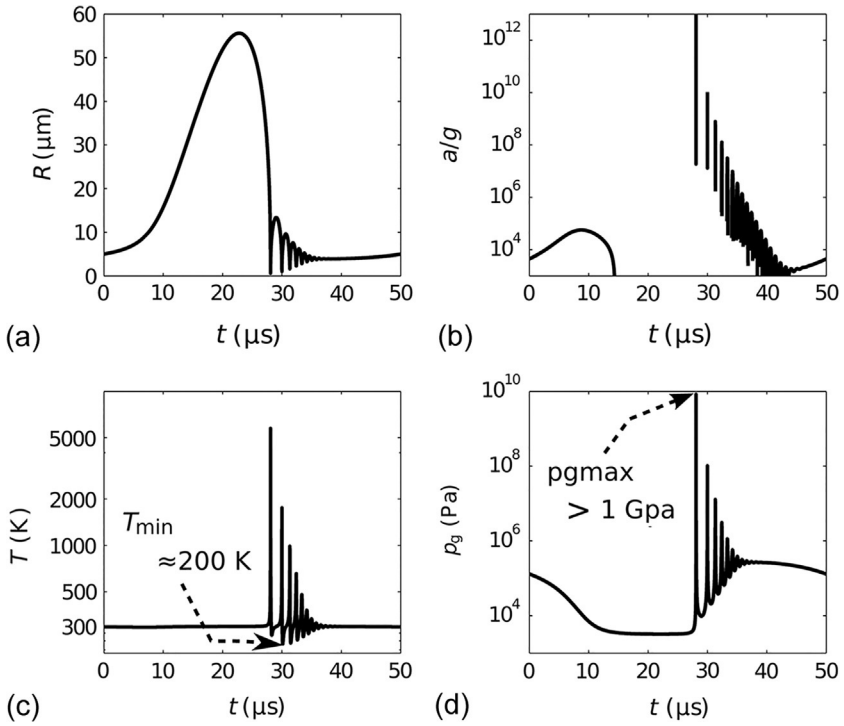


FIGURE 32.7 Simulation of an inertial cavitation air bubble for a field amplitude of 130 kPa, R0¼4 μm, and frequency of 20 kHz: radius of bubble on one acoustic period (a), acceleration (b), and temperature (c) and pressure (d) in the liquid at the bubble interface.

case of ammonium sulfate, the pressure effect could favor nucleation because the term $\overline{v}_{\text{solute}}(P) - v_{\text{solid}}(P)$ is positive (Virone et al., 2006). These authors attempted to calculate the nucleation rate using the above theory, assuming that homogeneous nucleation occurs, and using an estimate of the collapse pressure of the cavitating bubbles. They compared the calculated induction times to the values measured in a specially designed cavitator. They found poor agreement between the experimental and calculated induction times. In other studies, a strong reduction in induction times has been observed for different crystals under ultrasound: potassium sulfate (Lyczko et al., 2002) and glycine (Louisnard and Espitalier, 2007) which oppositely are less dense in the solid phase than in solute form ($\overline{v}_{\text{solute}}(P) - v_{\text{solid}}(P) < 0$), and zinc sulfate heptahydrate, whose molecular volumes of solute and solid are very close ($\overline{v}_{\text{solute}}(P) - v_{\text{solid}}(P) = 0$) (Harzali et al., 2012). In these cases, the high increase in the pressure at the bubble wall during the collapse cannot explain the decrease in induction time found in the case of potassium sulfate. The lower induction time observed experimentally with such crystals demonstrates that the pressure effect alone cannot explain all experimental results.

The same reasoning can be applied to temperature. Indeed, if the temperature decreases for a solid whose solubility increases with temperature, the supersaturation ratio increases. The severe reduction of temperature observed in the bubble just after the collapse could lead to a decrease of a few degrees in the liquid at the vicinity of the bubble. A small decrease in temperature could induce an increase in the nucleation rate. In order to verify this assumption, it is necessary to test the application of ultrasound in the case of a solid whose solubility is constant or decreases when the temperature increases. To date, no results have been found in the literature.

32.5.2 Kinetic effect

32.5.2.1 Effect on diffusion coefficient

Some authors suggest that diffusion acceleration is the main reason for the reduction of the induction time. The increases in the apparent diffusion coefficient may be due to the micro-mixing induced by the collapse of the bubbles (Suslick et al., 1990).

In the papers of , Guo et al. (2006a, 2006b), the ultrasonic effect on homogeneous nucleation was analyzed during the precipitation of barium sulfate obtained from a reaction between barium chloride and sodium sulfate. The induction time of $BaSO_4$ was measured. They found that nucleation is predominantly homogeneous and they assumed that nucleation is the limiting phenomenon, eg: $t_n >> t_g$. In this case (from Eq. (32.19)), the induction time is written:

$$t_{\text{ind}} = \frac{N_c}{J_{\text{PN}}} \tag{32.21}$$

Combining the Eq. (32.20) and the Eq. (32.16), and the Eq. (32.4) and the Eq. (32.6) ($\Delta\mu_i = RT\ln(S_i)$) for the primary homogeneous mechanism and taking the logarithm, the expression of the induction time becomes:

$$\ln(t_{\text{ind}}) = \ln\left(\frac{N_c}{K}\right) + \frac{16}{3}\frac{\gamma_{sL}^3 v_{i,\text{solid}}^2}{R^3T^3}\frac{1}{\ln^2 S_i} \tag{32.22}$$

This equation shows that the plot of the induction time as function of $1/(T^3\ln^2 S)$ is a straight line with a slope equal to $\frac{16}{3}\frac{\gamma_{sL}^3 v_{i,\text{solid}}^2}{R^3}$ and the intercept is proportional to the frequency K depending on the diffusion coefficient of the monomer and of the solute aggregates.

For a supersaturation ratio, S, higher than 30 (homogeneous nucleation), by plotting $\ln(t_{\text{ind}})$ as a function of $1/\ln^2(S)$ (T is constant), within the experimental error, the authors showed that the straight lines corresponding to different acoustic energy inputs are parallel to each other, but the intercepts of the lines are different. The slope of the straight lines is proportional to the interfacial tension of the crystal solution (Eq. 32.21). So this value remains constant or changes only slightly regardless of the ultrasound energy input. The intercept is proportional to the frequency factor (K) depending on the diffusion coefficient of the monomer and of the clusters of solute. The authors estimated the diffusion coefficient from the intercept with and without ultrasound and compared them. They found that when the power was 8.622 W in 500 mL, the diffusion coefficient was increased by a factor ranging between 1.9 and 6.5 (Guo et al., 2006a). This factor was a function of the dissipated power. The authors proposed a modification of the law of Stokes-Einstein for the calculation of the diffusion coefficient (Guo et al., 2006b). The new relationship was consistent with the results of their experiments.

Guo et al. (2006a, 2006b) also demonstrated that although the number of monomers in dominating clusters is 3 for different powers, the concentrations of larger clusters seem to increase slowly with the increase in energy input. The same observation was made by Dalvi and Dave (2010) during the study of the crystallization of four active pharmaceutical drugs by anti-solvent effect (75 W, 20 kHz).

32.5.2.2 Segregation

Some authors have examined the segregation of clusters around bubbles. An inertial bubble is theoretically able to segregate large molecules or nanoparticles from a host liquid. A species denser than the liquid should be depleted, on average, near the bubble wall during the bubble expansion and strongly over-concentrated during a very short time at the end of the bubble collapse (Louisnard et al., 2007; Grossier et al., 2007). In the case where the species is a solute in a metastable state, segregation may enhance the attachment of solute molecules to form clusters, and therefore increase the nucleation kinetics, as commonly

observed in sonocrystallization. The existence of segregation is evidenced for instance by the observation of gradients of cluster concentration in a quiescent column of supersaturated solutions (Larson and Garside, 1986).

This segregation effect around a cavitation bubble has been quantified analytically by the mathematical perturbation method (Louisnard et al., 2007). This model allows for calculating the spatiotemporal variations in the concentration of any species of known density and diffusion coefficient (or hydrodynamic radius), once the bubble radial dynamics is known. To verify the theory of segregation, this model was applied to evaluate the concentration of clusters resulting from segregation by the bubble motion in the conditions of the crystallization experiments. For four driving amplitudes, the concentration of clusters with sizes ranging between 1 and $3n^*$, near a typical inertial cavitation bubble, was calculated for zinc sulfate heptahydrate crystallized by cooling (Harzali et al., 2011). The over-concentration of clusters increased when the driving acoustic amplitude increased (Figure 32.8). In this figure, the steady-state dynamics of the bubble is calculated using the model of Toegel et al. (2000). An air bubble of ambient radius $R_0 = 4\,\mu m$ in water is assumed. The bubble is driven by a far sound field of the form $p_0 = (1\text{-}\ p_a\ \sin(2\ \pi\ f\ t))$, where p_0 is the ambient static pressure, $f = 20\,kHz$ the frequency, and p_a the dimensionless driving amplitude. It was found that segregation over-concentrates all the clusters, especially in a region below the critical cluster ($n^* = 117$), up to more than 20 times for an acoustic pressure of 1.5 bar (upper curve). In the classical nucleation theory, it is assumed that, in supersaturated solution, the clusters change their size as a result of addition or loss of single molecules, because the concentration of clusters of size higher than one is very low (Kashchiev, 2000). At the vicinity of the bubble, the concentrations of n-sized clusters are different, due to segregation, so all aggregations $A_n + A_m \Leftrightarrow A_{n+m}$ become possible. In this case, it is not possible to describe the nucleation rate as stationary. On the basis of Eq. (32.15), which relates the non-stationary nucleation rate to the change in the over-concentration of supernuclei, the non-stationary nucleation rate must increase in the case of segregation. This theory is applicable for zinc sulfate heptahydrate, ammonium sulfate, glycine, and potassium sulfate.

To date, and to the authors' knowledge, no new experimental or numerical studies have invalidated the segregation theory (see review by Jordens et al., 2019). The segregation theory still remains semi-quantitative, even if modeling experimental data showed the over-concentration of clusters around the critical nucleus of collapsing bubbles (Nalesso et al., 2019a).

These authors (Nalesso et al., 2019a) rightly note that if most of the time it is possible to consider being in a homogeneous situation at the macroscopic scale, during sonocrystallization, this is not the case at the bubble scale. Micro-inhomogeneities are then responsible for the US-induced nucleation, which makes the homogeneous theory for nucleation fragile. The nucleation law is probably still valid, but the micro-inhomogeneities must modify the pre-factor K (Eq. 32.16).

32.5.3 Chemical effect

Some authors suggest hypotheses on the effect of OH radicals, though without experimental evidence. Ghows and Entezari (2010) explain the effect of ultrasound on nucleation of titanium dioxide by arguing that localized hot spots in the vicinity of collapsing bubble promote polycondensation of Ti-OH, and the nucleation of TiO_2 is thus accelerated. The observed effects of the initial temperature and solvent (ethanol added) support this hypothesis. A similar effect was observed by Dodds et al. (2007), who studied the precipitation by thermo-hydrolysis of TiO_2 from titanyl sulfate. In this study, the effects of dissolved gases were examined. It turns out that the dissolved gas has an effect

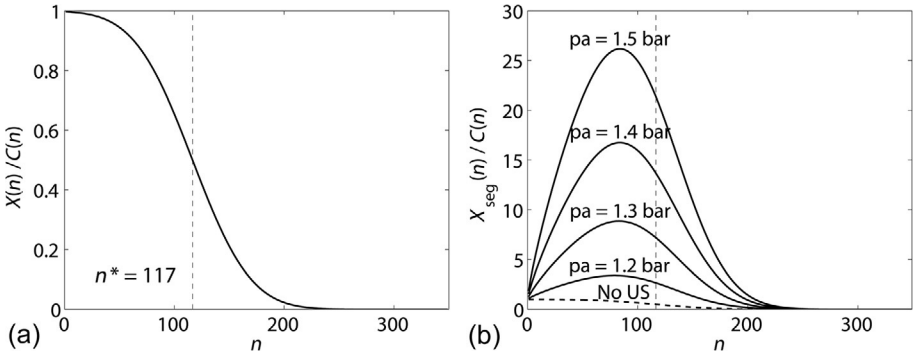


FIGURE 32.8 $X(n)$ is the stationary cluster size distribution and $C(n)$ the equilibrium cluster size distribution (a) without ultrasound*, (b) with ultrasound as function of the acoustic pressure. Case of zinc sulfate heptahydrate, S¼1.222 and n^*¼117 (Harzali et al., 2011).

on the resulting crystalline form (anatase or rutile). The hot spots and the production of OH radicals during the collapse would then explain the different polymer-like structures.

The formation of magnetite nanoparticles appeared to be accelerated by the oxidation of $Fe(OH)_2$ by hydrogen peroxide created during the collapse by the decomposition of water into hydrogen atoms and hydroxyl radicals (Cheng et al., 2011).

32.5.4 Heterogeneous nucleation

Kordylla et al. (2008) and Kordylla et al. (2009) adopted a different approach towards nucleation. They assumed that the generated cavitation bubbles act as foreign particles, and nucleation is probably caused by a heterogeneous nucleation mechanism. They proposed to use this assumption to model and simulate their batch experiment for one solvent (Kordylla et al., 2009). In addition, Wohlgemuth et al. (2009) studied the effect of gas bubbles on nucleation. They concluded that bubbles act like foreign entities and favor heterogeneous nucleation.

32.6 Growth and breakage mechanisms

In comparison with nucleation, few studies present the effect of ultrasound on crystal growth. No tendency in particle size distribution has been highlighted. Different assumptions can be proposed: modification of the diffusion step or modification of the integration step or chemical effects.

The effects observed by Boels et al. (2010) on the growth rate of calcite crystals were attributed to physical damage on seed crystals. Seeds crystals were broken, and thus, some of their fragments appeared in the solution. These fragments induced an increase in the available surface resulting in an increase in the precipitation rate. Boels et al. (2011) studied the growth of calcite crystals in the presence of growth inhibitor (methylene phosphonic acid). In the presence of this inhibitor, the damage caused by ultrasound creates a fresh surface. A chemical explanation is given for the degradation of methylene phosphonic acid. Several breakdown products detected by mass spectroscopy were identified. They showed that ultrasound caused the progressive loss of phosphonate groups from inhibitor at the particle surface, probably by means of physico-chemically generated free radicals and/or pyrolysis in the hot bubble–bulk interface.

Bubble collapse near a solid can induce a fast-moving stream of liquid with velocities of 100 m/s (Suslick, 1989). This liquid stream can modify the integration of growth units in the network. Two cases are presented in Figure 32.9. In the case of barium sulfate (Figure 32.9a and b), crystals are growing in the presence of ultrasound. Ultrasound induces a massive nucleation by secondary contact nucleation (Gatumel et al., 1998). Moreover, jets of liquid during the bubble collapse make it difficult for growth units to integrate the face of the crystal and modify its facies. In the case of potassium sulfate, crystals are generated under ultrasound and their growth occurs in the absence of ultrasound. The cavities observed on crystal faces (Figure 32.9d) may be created by these violent jets, preventing the integration of growth units and so creating defects on the face of the crystals. When the crystals grow later in silent conditions, the faces conserve these defects.

Guo et al. (2007) also took an interest in breakage processes. They investigated the dispersion of inert particles of different sizes in ethanol, comparing mixing by stirring and by ultrasound. In their experiments, the larger particles were more sensitive to ultrasound. The authors showed that the breakage of agglomerated crystals was due to both collisions between crystals and the vibration and implosion of cavitation bubbles.

32.7 Ice nucleation mechanisms induced by ultrasound

32.7.1 A general survey

Although ultrasound has long been used to initiate nucleation in supercooled aqueous solutions (Chalmers, 1964), the exact mechanism that explains this effect is not yet well known. Acoustic cavitation (the sudden formation and collapse of gas bubbles in liquids by means of ultrasound) appears to cause the nucleation of ice. There is a distinction between stable cavitation when a bubble pulsates about an equilibrium radius over many acoustic cycles and transient cavitation when the bubble grows extensively and finally collapses (Knapp et al., 1970; Neppiras, 1980).

According to the theoretical study by Hickling (1965), very high positive pressures occurring during the final stage of the collapse of a bubble in inertial cavitation increase the equilibrium temperature of water and ice (VI or VII, denser than liquid water), thus enhancing nucleation of a specific ice solid phase. The weak point of this scenario is the uncertainty about a subsequent transformation of the nucleated high-pressure phase nucleated into low-pressure regular ice Ih. According to another model (Hunt and Jackson, 1966), nucleation is caused by negative pressures that follow the collapse of the cavitation bubble. This effect will produce low-pressure ice Ih, but this idea was questioned by the experiments of Ohsaka and Trinh (1998) who retained Hickling's hypothesis.

According to some other experimental results (Chow et al., 2005), the moderate oscillation of a bubble in stable cavitation may also induce ice nucleation. These authors suggest micro-streamings as a factor promoting nucleation. The other possible nucleation mechanism is the concentration and agglomeration of ice clusters near the bubble

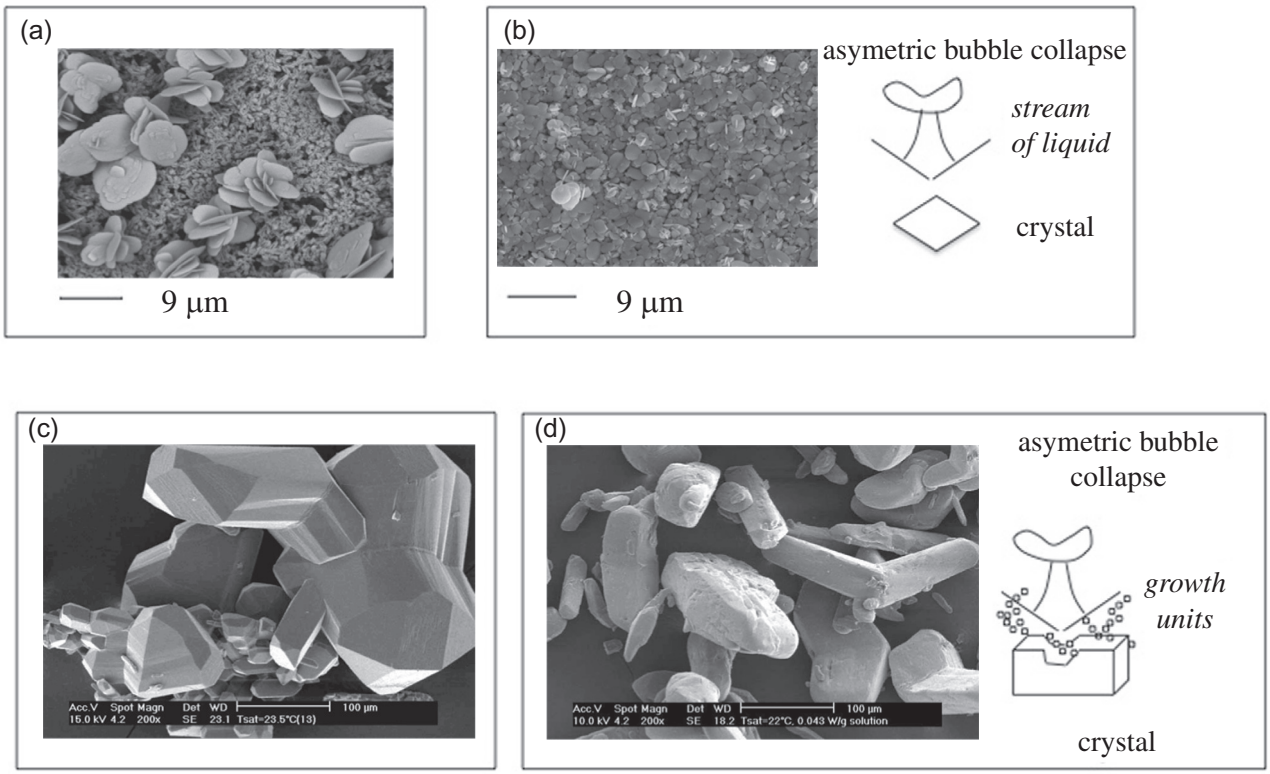


FIGURE 32.9 Action mechanisms of ultrasound on growth rate. (a) Barium sulfate crystallized without ultrasound. (b) Barium sulfate crystallized with ultrasound. (c) Potassium sulfate crystallized without ultrasound. (d) Potassium sulfate crystallized with ultrasound. *SEM photos from Gatumel et al. (1998) and Lyczko et al. (2002).*

due to pressure diffusion (transfer mechanism driving the densest species towards high-pressure zones). On the basis of theoretical considerations, Grossier et al. (2007) and Louisnard et al. (2007) argued that the very high-pressure gradients that are needed for pressure diffusion to be effective are attainable only for collapsing bubbles. They thus indirectly refuted stable cavitation as a nucleation initiator.

A quite novel idea about the nucleation mechanism has arisen very recently (Montes et al., 2012). The physics of inertial cavitation states that the bubble interior heats up due to a quasi-adiabatic compression just before the collapse but then cools down due to a quasi-adiabatic expansion of the bubble just after the collapse. According to simulations, the temperature of the gas mixture inside the bubble falls to between −30°C and −60°C after the collapse, depending on operating conditions. According to the water state diagram, this means that all the water vapor is in a highly metastable undercooled state and could easily transform into ice Ih. This raises two issues, however: is the metastable water period long enough to induce ice nucleation? and how might the ice nuclei invade the surrounding liquid, breaking the bubble? The estimated time left for the nucleation to occur was 200 ns, which corresponds to non-stationary nucleation.

32.7.2 A focus on the positive pressure effect

We chose to work on the positive pressure effect (Hickling's theory) and set up a comprehensive theoretical model starting from the bubble wall motion induced by inertial cavitation and finishing with the number of nuclei generated by the collapse of a single bubble. The exact description of the bubble dynamics during acoustic inertial cavitation can be achieved only by numerical solution of the full set of mass, momentum (Navier–Stokes equations), and energy conservation PDEs on both the gas and liquid sides (Hauke et al., 2007; Szeri et al., 2003). Nevertheless, it had been proven that simplified approaches give satisfactorily precise results (Fuster et al., 2011; Storey and Szeri, 2001). The most straightforward simplification leading to a set of ordinary differential equations (ODEs) is the boundary layer approximation, where the temperature, pressure, and species profiles inside the bubble are supposed to be uniform, with the exception of a thin boundary layer near the bubble wall.

The combination of Navier–Stokes equations in the liquid domain, of a mechanical equilibrium equation at the moving gas–liquid interface, of a gas state equation, and of a compressible liquid state equation allows the bubble wall dynamics to be calculated (Miksis and Keller,

1980; Plesset and Prosperetti, 1977). Starting from the same set of equations, and by adopting an additional hypothesis on the velocity of liquid pressure perturbation propagation (Kirkwood-Bethe hypothesis), it is possible to calculate the pressure and velocity profile in the liquid near the bubble (Gilmore, 1952; Holzfuss et al., 1998; Knapp et al., 1970).

Toegel et al. (2000) aimed at determining the amount of water vapor trapped in the bubble during the collapse and its effect on sonoluminescence. They used the boundary layer approach and considered a model consisting of three ODEs. The bubble wall radius was evaluated by the Keller-Miksis equation, which takes into account water compressibility, whereas the amount of water vapor inside the bubble was derived from a Fickian diffusion flux at the wall. The gas temperature was obtained from an energy balance, which takes into account the heat conduction flux at the bubble wall. The mass and heat fluxes were calculated using a boundary layer thickness evaluated as a diffusion length at a characteristic time scale of the bubble motion. The gas pressure was derived from the van der Waals equation of state. The temperature at the bubble wall was assumed to be constant and equal to that of the far liquid one.

The basic concept of the cavitating bubble model used for simulations presented below is based on Toegel's model, but substantial modifications have been made (Cogné et al., 2016a). First, a more realistic representation of the heat transfer at the bubble wall was introduced through an energy balance involving the interfacial phase change heat source and a conductive heat flux on the liquid side. Second, a rigorous thermal and mechanical description was applied to the liquid, with the solution of the heat conduction–advection equation by the Plesset-Zwick integration method (Plesset and Zwick, 1952; Szeri et al., 2003).

The next step was to relate the pressure and temperature profiles to the nucleation kinetics on the basis of the positive pressure effect, as demonstrated by Virone et al. (2006) in the case of solute crystallization. However, with regard to the prediction of the ice nucleation rate driven by an acoustic field, there are no results published in the literature, and the methodology presented below is quite new. It was first reported by us in a journal paper: Cogné et al. (2016b). Regarding the nucleation rate estimation, the classical equation for primary stationary homogeneous nucleation was applied (Kashchiev, 2000) as a first approximation, but the parameters of this equation had to be made pressure dependent. The most important parameter varying with pressure was the equilibrium solid–liquid temperature, which determined the supercooling level, but some other parameters may also have had an influence: the interfacial solid–liquid energy, the heat of solidification, and the ice density. The great difficulty was that in the literature, thermophysical data are scarce for the very-high-pressure range (up to 10 GPa). The solution was to extrapolate from data in the low-pressure range.

The pressure peaks arising near the bubble occur on very short timescales, so super-cooling is a fast-varying and short-lasting parameter (typically several tenths of a nanosecond). The approximation of stationary nucleation might, therefore, be reconsidered. Avoiding the stationary hypothesis yields an intricate mathematical problem, so that a first approach would consist of comparing the respective timescales of the collapse and of the cluster attachment process involved in the nucleation process. The answer is not unique and strongly depends both on the bubble characteristics and the supercooling level.

The number of nuclei generated by a single bubble was finally calculated by integrating the pressure-dependent nucleation rate over a liquid volume surrounding the bubble and over time. According to our final results (Figure 32.10), the nucleation could be triggered starting from an undercooling as low as 5 K for bubbles of initial radius of 5 μm (or as low as 4 K for 8 μm bubbles, see Figure 32.11) if an acoustic pressure amplitude of around 220 kPa is applied. For moderate acoustic pressures up to 220 kPa, the number of generated nuclei was found to increase with the undercooling level and with the acoustic pressure, which was in good qualitative agreement with already published experimental results (Chow et al., 2005; Inada et al., 2001; Zhang et al., 2003). However, for acoustic pressures above 220 kPa and for a given liquid supercooling level, the number of nuclei was found not to vary anymore with pressure. There is thus a range of acoustic pressure where

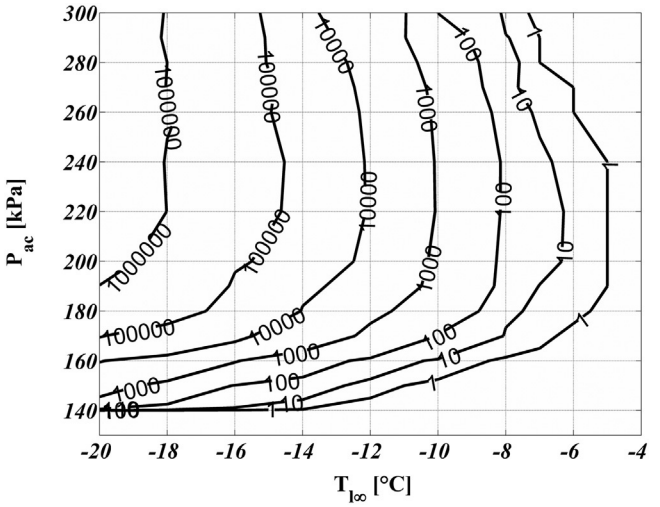


FIGURE 32.10 Number of nuclei generated by a single bubble in inertial cavitation vs the acoustic pressure (P_{ac}) and liquid temperature far from the bubble ($T_{l\infty}$). Calculated for an initial bubble radius of 5 μm and an acoustic frequency of 29 kHz (Cogné et al., 2016b).

the ultrasound is the most efficient and increasing the pressures beyond is not useful.

The difficulty in quantitative comparison comes from different methods of measuring acoustic power (often likened to electrical power delivered to the transducer) and different output parameters (nucleation probability or nucleation temperature) used to evaluate the nucleation rate (see Section 32.2). For instance, for the same operating conditions, the nucleation probability of 100% (according to Inada et al. (2001)) corresponds to a nuclei number of 10 (according to our results). Moreover, if it is supposed that the greater the number of nuclei, the smaller the crystal size, then the trends predicted by the theoretical model described above corresponded quite well, qualitatively speaking, to those given by an empirical model based on an experimental design proposed previously by Saclier et al. (2010) (see Section 32.4). A quantitative validation of the theoretical model was not possible, however, because the responses of the experimental design and of the simulations were not directly comparable. The former provided a number of ice nuclei in the initial liquid and the latter the size of ice crystals in the final frozen product. The continuation of this work will be the further reconciliation of experimental and model-predicted data.

In actual applications, there is a distribution of bubble sizes in a sonicated liquid volume and the initial bubble radius has an important impact on ice nucleation threshold. The contour curves (in the acoustic pressure vs initial radius plane) corresponding to several initial liquid temperatures and representing the conditions for generation of at least one nucleus are plotted in Figure 32.11, along with the line color corresponding to inertial cavitation threshold. The latter was obtained by using the dynamic equation of bubble wall motion (Cogné et al., 2016a) and the cavitation criterion of bubble radius expanding at least twice its initial value. Each contour curve has an upper and lower branch and the zones of possible nucleation lie within these branches. This figure shows even more clearly the existence of an optimal pressure range centered on 225 kPa, especially for low supercooling. There is also an optimal bubble size range centered on 8.5 µm. Nucleation can be already achieved at −5°C over a large size domain (radius from 3 to 13 µm) providing the appropriate acoustic pressure. The influence of the initial radius on nucleation threshold reflects the non-linear evolution of the bubble dynamics with the initial radius. Even if it is not as critical as the applied acoustic pressure, the control of initial bubble size may be helpful for achieving nucleation at a desired temperature.

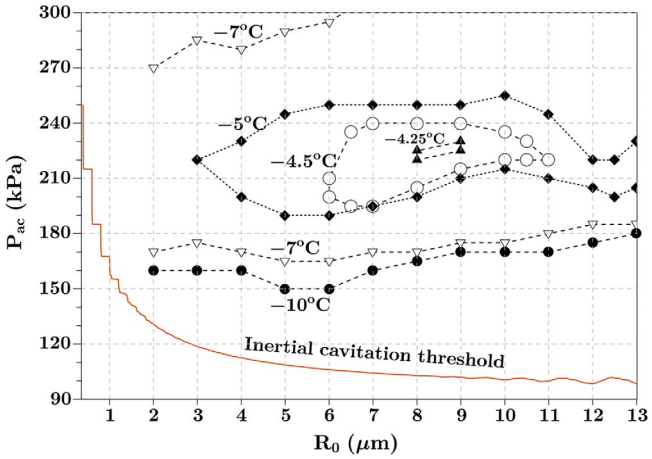


FIGURE 32.11 Isotherms of nucleation threshold (temperature at which one nucleus appears at least) as function of initial bubble radius (R_0) and acoustic pressure (P_{ac}) for an acoustic frequency of 29 kHz (Cogné et al., 2016b).

32.8 Future trends

During a crystallization operation, it is important to control the purity, the yield, the crystalline structure, and the size distribution of crystals, as well as the crystal morphology. Depending on the type of solid and its applications (chemical, pharmaceutical, food, minerals etc.), some of these objectives may be critical (Mersmann, 2001). Ultrasound is an interesting tool that allows us to reduce the metastable zone width, to increase the number of crystals formed, to trigger the nucleation at the chosen supersaturation, to select the crystalline structure, but no application rules (geometry of the transducer, frequency, dissipated power, application volume, duration) have been established to date in a systematic way. We can cite one recent study of Vancleef et al. (2021). In their work, they highlighted the possibility of controlling the secondary nucleation in continuous tubular crystallizers by ultrasonic power. Furthermore, by keeping the ultrasonic power/volume ratio constant, and increasing the tube diameter to keep the residence time constant, they have highlighted a good basis for a scale-up of the process, which can help manufacturers in the transition towards continuous crystallization.

However, in the literature, there are numerous studies on crystallization assisted by ultrasound (by cooling, evaporation, reaction, or by addition of anti-solvent). Research on the unit operation of crystallization assisted by ultrasound has focused mainly on experiments on a specific product. These studies concern solids with a broad range of applications. Different transducers are used with different frequencies, dissipated powers, different pulsations … in different volumes (a few microliters to a cubic meter). Experiments are based on a trial-and-error approach. The wear of the transducer is a problem that is not mentioned in the literature but which needs to be known. Few studies propose a mechanism of ultrasound impact on crystallization (nucleation, growth, or attrition).

A deeper understanding of basic physical mechanisms of ultrasound action is always needed in order to establish a

reliable theory of sono-crystallization and further develop predictive models. In this line, a promising approach is the experimental study of a single cavitating bubble impact on the surrounding liquid. Such studies have already started by isolating a single bubble in a levitation cell filled with a small volume of liquid and forcing it to cavitate (Montes et al., 2012). By means of acoustic and optical detectors, this kind of experiments will provide the information about the exact conditions in which a single bubble in inertial cavitation will produce crystal's nuclei and the precise amount of generated nuclei.

Another, practical way to the engineering of sono-crystallization is to empirically correlate the operating conditions and the process rate.

The knowledge of crystallization kinetics (nucleation, growth, and agglomeration) with ultrasound will permit analysis, evaluation, and prediction of crystallizer performance at different levels of operation, ranging from bench scale to industrial production. Different operating conditions will have to be taken into account like the transducer, frequency, dissipated power, and pulsation of ultrasound. For instance, in a case of cooling crystallization, a compromise needs to be found between the dissipated power and the temperature of the medium.

For the future development of this technology, more fundamental research is still needed in order to identify factors that determine the ability of power ultrasound to perform the desired functions. Considerable research effort is also required with regard to the development of adequate industrial equipment. Some systems are proposed in the literature (Ruecroft, et al., 2005a,b) to try a transposition to the industrial scale, but without real scientific validation.

Kiss et al. (2018) propose an article on the advances of ultrasound technologies that could lead in the near future to significant improvements in commercial activities. They specify in particular that for the pharmaceutical industry, using ultrasound to improve crystallization represents an interesting challenge in terms of speed of development and ease of scaling up, rather than energy consumption. The fine chemicals and food industry may be more sensitive to the argument of reduced energy consumption. The use of pulsed sonication during crystallization processes is therefore recommended, as it can reduce energy consumption by up to 90%, for the same result: large increases in the nucleation rate in crystallization. This makes the use of ultrasound feasible for industrial applications (example of the ultrasound-induced nucleation of paracetamol under pulsed sonication at 30 kHz, with a minimum duty cycle of about 10%, (Gielen et al., 2017). Ultrasonic nucleation in crystallization processes represents an interesting option for processes where seeding cannot be done by the conventional approach (e.g. sterile production).

In terms of conclusion and perspective, Jordens et al. (2019) insist that pulsed ultrasound seems to be a promising method to reduce energy consumption while achieving the positive effects of ultrasound. Scaling up ultrasound-assisted crystallization is one of the biggest challenges for its application in industry (Wang et al., 2018). A serious opportunity for the application of sono-crystallization on an industrial scale is the pharmaceutical industry's interest in continuous manufacturing provides.

Nalesso et al. (2019a) indicate that recent tests (Nalesso et al., 2019b) show that the application of US, during anti-solvent crystallization, over a very short time can be sufficient to induce an effect on crystallization. This considerably reduces the energy cost and makes the application of US on an industrial scale quite feasible.

References

Acton, E., Morris, G.J., 1992. Method and Apparatus for the Control of Solidification in Liquids. pp. 1–49. W.O. 99/20420, USA Patent application, USA.

Al Nasser, W.N., Pitt, K., Hounslow, M.J., Salman, A.D., 2013. Monitoring of aggregation and scaling of calcium carbonate in the presence of ultrasound irradiation using focused beam reflectance measurement. Powder Technol. 238, 151–160.

Aldahri, T., Behin, J., Kazemian, H., Rohani, S., 2016. Synthesis of zeolite Na-P from coal fly ash by thermo-sonochemical treatment. Fuel 182, 494–501. https://doi.org/10.1016/j.fuel.2016.06.019.

Amara, N., Ratsimba, B., Wilhelm, A., Delmas, H., 2001. Crystallization of potash alum: effect of power ultrasound. Ultrason. Sonochem. 8, 265–270.

Belviso, C., Cavalcante, F., Lettino, A., Fiore, S., 2011. Effects of ultrasonic treatment on zeolite synthesized from coal fly ash. Ultrason. Sonochem. 18 (2), 661–668.

Belviso, C., Cavalcante, F., Fiore, S., 2013. Ultrasonics Sonochemistry ultrasonic waves induce rapid zeolite synthesis in a seawater solution. Ultrason. Sonochem. 20 (1), 32–36.

Boels, L., Wagterveld, R.M., Mayer, M.J., Witkamp, G.J., 2010. Seeded calcite sonocrystallization. J. Cryst. Growth 312 (7), 961–966.

Boels, L., Wagterveld, R.M., Witkamp, G.J., 2011. Ultrasonic reactivation of phosphonate poisoned calcite during crystal growth. Ultrason. Sonochem. 18 (5), 1225–1231.

Castro, F., Kuhn, S., Jensen, K., Ferreira, A., Rocha, F., Vicente, A., Teixeira, J.A., 2013. Continuous-flow precipitation of hydroxyapatite in ultrasonic microsystems. Chem. Eng. J. 215-216, 979–987.

Chalmers, B., 1964. Principles of Solidification. J. Wiley.

Cheng, J., Ma, R., Shi, D., Liu, F., Zhang, X., 2011. Rapid growth of magnetite nanoplates by ultrasonic irradiation at low temperature. Ultrason. Sonochem. 18, 1038–1042.

Chow, R., Blindt, R., Chivers, R., Povey, M., 2003. The sonocrystallisation of ice in sucrose solutions: primary and secondary nucleation. Ultrasonics 41 (8), 595–604.

Chow, R., Blindt, R., Chivers, R., Povey, M., 2005. A study on the primary and secondary nucleation of ice by power ultrasound. Ultrasonics 43 (4), 227–230.

Cogné, C., Labouret, S., Peczalski, R., Louisnard, O., Baillon, F., Espitalier, F., 2016a. Theoretical model of ice nucleation induced by acoustic cavitation. Part 1: pressure and temperature profiles around a single

bubble. Ultrason. Sonochem. 29, 447–454. https://doi.org/10.1016/j.ultsonch.2015.05.038.

Cogné, C., Labouret, S., Peczalski, R., Louisnard, O., Baillon, F., Espitalier, F., 2016b. Theoretical model of ice nucleation induced by acoustic cavitation. Part 2: number of ice nuclei generated by a single bubble. Ultrason. Sonochem. 28, 185–191. https://doi.org/10.1016/j.ultsonch.2015.07.019.

Dalvi, S.V., Dave, R.N., 2010. Analysis of nucleation kinetics of poorly water-soluble drugs in presence of ultrasound and hydroxypropyl methyl cellulose during antisolvent precipitation. Int. J. Pharm. 387 (1–2), 172–179.

Devos, C., Van Gerven, T., Kuhn, S., 2021. Nucleation kinetics for primary, secondary and ultrasound-induced paracetamol crystallization. CrystEngComm 23 (30), 5164–5175. https://doi.org/10.1039/d1ce00676b.

Dodds, J., Espitalier, F., Louisnard, O., Grossier, R., David, R., Hassoun, M., Baillon, F., Gatumel, C., Lyczko, N., 2007. The effect of ultrasound on crystallisation-precipitation processes: some examples and a new segregation model. Part. Part. Syst. Charact. 24 (1), 18–28.

Fuster, D., Dopazo, C., Hauke, G., 2011. Liquid compressibility effects during the collapse of a single cavitating bubble. J. Acoust. Soc. Am. 129 (1), 122–131.

Gatumel, C., Espitalier, F., Schwartzentruber, J., Biscans, B., Wilhelm, A., 1998. Nucleation control in precipitation processes by ultrasound. Kona 16, 160–169.

Ghows, N., Entezari, M., 2010. Ultrasound with low intensity assisted the synthesis of nanocrystalline TiO2 without calcination. Ultrason. Sonochem. 17 (5), 878–883.

Gielen, B., Kusters, P., Jordens, J., Thomassen, L.C.J., Van Gerven, T., Braeken, L., 2017. Energy efficient crystallization of paracetamol using pulsed ultrasound. Chem. Eng. Process. Process Intensif. 114, 55–66. https://doi.org/10.1016/j.cep.2017.01.001.

Gilmore, F.R., 1952. The Growth or Collapse of a Spherical Bubble in a Viscous Compressible Liquid. California Institute of Technology, Pasadena, CA. Technical Report, Unpublished.

Grossier, R., Louisnard, O., Vargas, Y., 2007. Mixture segregation by an inertial cavitation bubble. Ultrason. Sonochem. 14 (4), 431–437.

Guo, Z., Jones, A.G., Li, N., 2006a. Interpretation of the ultrasonic effect on induction time during BaSO4 homogeneous nucleation by a cluster coagulation model. J. Colloid Interface Sci. 297, 190–198.

Guo, Z., Jones, A.G., Li, N., 2006b. The effect of ultrasound on the homogeneous nucleation of BaSO4 during reactive crystallization. Chem. Eng. Sci. 61, 1617–1626.

Guo, Z., Jones, A.G., Li, N., Germana, S., 2007. High-speed observation of the effects of ultrasound on liquid mixing and agglomerated crystal breakage processes. Powder Technol. 171, 146–153.

Gürbüz, H., Tokay, B., Erdem-Şenatalar, A., 2012. Effects of ultrasound on the synthesis of silicalite-1 nanocrystals. Ultrason. Sonochem. 19, 1108–1113.

Harzali, H., Baillon, F., Louisnard, O., Espitalier, F., Mgaidi, A., 2011. Experimental study of sono-crystallisation of ZnSO4·7H2O, and interpretation by the segregation theory. Ultrason. Sonochem. 18 (5), 1097–1106.

Harzali, H., Baillon, F., Louisnard, O., Espitalier, F., Mgaidi, A., 2012. Sono-crystallization of ZnSO4·7H2O with variation of solution heights. Chem. Eng. J. 195-196, 332–338.

Hatakka, H., Alatalo, H., Louhi-Kultanen, M., Lassila, I., Haeggström, E., 2010. Closed-loop control of reactive crystallization PART II: polymorphism control of L-glutamic acid by Sonocrystallization and seeding. Chem. Eng. Technol. 33 (5), 751–756.

Hauke, G., Fuster, D., Dopazo, C., 2007. Dynamics of a single cavitating and reacting bubble. Phys. Rev. E 75 (6), 066310.

Hickling, R., 1965. High-pressure solidification associated with cavitation in water. Nature 206, 915–917.

Holzfuss, J., Rüggeberg, M., Billo, A., 1998. Shock wave emissions of a sonoluminescing bubble. Phys. Rev. Lett. 81 (23), 1–4.

Hottot, A., Nakagawa, K., Andrieu, J., 2008. Effect of ultrasound-controlled nucleation on structural and morphological properties of freeze-dried mannitol solutions. Chem. Eng. Res. Des. 86 (2), 193–200.

Hozumi, T., Saito, A., Okawa, S., Matsui, T., 2002. Freezing phenomena of supercooled water under impacts of ultrasonic waves. Int. J. Refrig. 25, 948–953.

Hunt, J.D., Jackson, K.A., 1966. Nucleation of solid in an undercooled liquid by cavitation. J. Appl. Phys. 37 (1), 254–257.

Inada, T., Zhang, X., Yabe, A., Kozawa, Y., 2001. Active control of phase change from supercooled water to ice by ultrasonic vibration 1. Control of freezing temperature. Int. J. Heat Mass Transf. 44, 4523–4531.

Jabbari-Hichri, A., Peczalski, R., Laurent, P., 2014. Ultrasonically triggered freezing of aqueous solutions: Influence of initial oxygen content on ice crystals′ size distribution. J. Cryst. Growth 402, 78–82. https://doi.org/10.1016/j.jcrysgro.2014.05.010.

Jordens, J., Gielen, B., Xiouras, C., Hussain, M.N., Stefanidis, G.D., Thomassen, L.C.J., Braeken, L., Van Gerven, T., 2019. Sonocrystallisation: observations, theories and guidelines. Chem. Eng. Process. Process Intensif. 139, 130–154. https://doi.org/10.1016/j.cep.2019.03.017.

Kashchiev, D., 2000. Nucleation : Basic Theory with Applications. Butterworth, Elsevier, Oxford.

Kashchiev, D., van Rosmalen, G.M., 2003. Review: nucleation in solutions revisited. Cryst. Res. Technol. 38 (78), 555–574.

Kashchiev, D., Verdoes, D., van Rosmalen, G.M., 1991. Induction time and metastability limit in new phase formation. J. Cryst. Growth 110, 373–380.

Kaur Bhangu, S., Ashokkumar, M., Lee, J., 2016. Ultrasound assisted crystallization of paracetamol: crystal size distribution and polymorph control. Cryst. Growth Des. 16, 1934–1941. https://doi.org/10.1021/acs.cgd.5b01470.

Kiani, H., Sun, D.-W., 2011. Water crystallization and its importance to freezing of foods: a review. Trends Food Sci. Technol. 22 (8), 407–426.

Kiani, H., Zhang, Z., Delgado, A., Sun, D., 2011. Ultrasound assisted nucleation of some liquid and solid model foods during freezing. Food Res. Int. 44 (9), 2915–2921.

Kiani, H., Sun, D.-W., Delgado, A., Zhang, Z., 2012. Investigation of the effect of power ultrasound on the nucleation of water during freezing of agar gel samples in tubing vials. Ultrason. Sonochem. 19 (3), 576–581.

Kim, W., Choi, D., Kim, S., 2010. Sonochemical synthesis of zeolite a from Metakaolinite in NaOH solution. Mater. Trans. 51 (9), 1694–1698.

Kiss, A.A., Geertman, R., Wierschem, M., Skiborowski, M., Gielen, B., Jordens, J., John, J.J., Van Gerven, T., 2018. Ultrasound-assisted emerging technologies for chemical processes: ultrasound-assisted emerging technologies for chemical processes. J. Chem. Technol. Biotechnol. 93, 1219–1227. https://doi.org/10.1002/jctb.5555.

Knapp, R.T., Daily, J.W., Hammitt, F.G., 1970. Cavitation. McGraw-Hill.

Kojima, Y., Yamaguchi, K., Nishimiya, N., 2010. Effect of amplitude and frequency of ultrasonic irradiation on morphological characteristics control of calcium carbonate. Ultrason. Sonochem. 17 (3), 617–620.

Kordylla, A., Koch, S., Tumakaka, F., Schembecker, G., 2008. Towards an optimized crystallization with ultrasound: effect of solvent properties and ultrasonic process parameters. J. Cryst. Growth 310, 4177–4184.

Kordylla, A., Krawczyk, T., Tumakaka, F., Schembecker, G., 2009. Modeling ultrasound-induced nucleation during cooling crystallization. Chem. Eng. Sci. 64, 1635–1642.

Larson, M.A., Garside, J., 1986. Solute clustering in supersaturated solutions. Chem. Eng. Sci. 41 (5), 1285–1289.

Li, H., Wang, J., Bao, Y., Guo, Z., Zhang, M., 2003. Rapid sonocrystallization in the salting-out process. J. Cryst. Growth 247, 192–198.

Li, H., Li, H., Guo, Z., Liu, Y., 2006. The application of power ultrasound to reaction crystallization. Ultrason. Sonochem. 13 (4), 359–363.

Louhi-kultanen, M., Karjalainen, M., Rantanen, J., Huhtanena, M., Kallas, J., 2006. Crystallization of glycine with ultrasound. Int. J. Pharm. 320, 23–29.

Louisnard, O., 2008. Analytical expressions for primary Bjerknes force on inertial cavitation bubbles. Phys. Rev. E 78 (3), 036322.

Louisnard, O., Espitalier, F., 2007. Sono-crystallization: form experimental results to microscopical interpretations. In: 19th International Congress on Acoustic Congress on Acoustics, pp. 2–7.

Louisnard, O., Gomez, F.J., Grossier, R., 2007. Segregation of a liquid mixture by a radially oscillating bubble. J. Fluid Mech. 577, 385–415.

Lyczko, N., Espitalier, F., Louisnard, O., Schwartzentruber, J., 2002. Effect of ultrasound on the induction time and the metastable zone widths of potassium sulphate. Chem. Eng. J. 86 (3), 233–241.

Majal, B.L., Ručigaja, A., Tesličb, D., Krajnca, M., 2019. The use of ultrasound in the crystallization process of an active pharmaceutical ingredient. Ultrason. Sonochem. 58, 2–10. https://doi.org/10.1016/j.ultsonch.2019.104642.

Mersmann, A., 2001. In: Dekker, M. (Ed.), Crystallization Technology Handbook, second ed. Elsevier B.V.

Miksis, M., Keller, J.B., 1980. Bubble oscillations of large amplitude. J. Acoust. Soc. Am. 68 (2), 628–633.

Montes, W., Baillon, F., Louisnard, O., Boyer, B., Espitalier, F., 2012. Acoustic detection of foreign bodies near a single bubble in a levitation cell. In: ESS-13 - 13th Meeting of the European Society of Sonochemistry, At Lviv – Ukraine. (July).

Mullin, J.W., 2001. Crystallization, fourth ed. Butterworth-Heinemann, Elsevier.

Myerson, S.A., Lo, P.Y., 1990. Diffusion and cluster formation in supersaturated solutions. J. Cryst. Growth 99, 1048–1052.

Nakagawa, K., Hottot, A., Vessot, S., Andrieu, J., 2006. Influence of controlled nucleation by ultrasounds on ice morphology of frozen formulations for pharmaceutical proteins freeze-drying. Chem. Eng. Process. Process Intensif. 45 (9), 783–791.

Nalesso, S., Bussemaker, M.J., Sear, R.P., Hodnett, M., Lee, J., 2019a. A review on possible mechanisms of sonocrystallisation in solution. Ultrason. Sonochem. 57, 125–138. https://doi.org/10.1016/j.ultsonch.2019.04.020.

Nalesso, S., Bussemaker, M.J., Sear, R.P., Hodnett, M., Lee, J., 2019b. Development of sodium chloride crystal size during Antisolvent crystallization under different sonication modes. Cryst. Growth Des. 19, 141–149. https://doi.org/10.1021/acs.cgd.8b01172.

Neppiras, E.a., 1980. Acoustic cavitation. Phys. Rep. 61 (3), 159–251.

Nikolaev, A.L., Gopin, A.V., Severin, A.V., Rudin, V.N., Mironov, M.A., Dezhkunov, N.V., 2018. Ultrasonic synthesis of hydroxyapatite in non-cavitation and cavitation modes. Ultrason. Sonochem. 44, 390–397. https://doi.org/10.1016/j.ultsonch.2018.02.047.

Ohsaka, K., Trinh, E.H., 1998. Dynamic nucleation of ice induced by a single stable cavitation bubble. Appl. Phys. Lett. 73 (1), 129–131.

Parimaladevi, P., Supriya, S., Srinivasan, K., 2018. The role of ultrasound in controlling the liquid-liquid phase separation and nucleation of vanillin polymorphs I and II. J. Cryst. Growth 484, 21–30. https://doi.org/10.1016/j.jcrysgro.2017.12.023.

Pawar, N., Agrawal, S., Methekar, R., 2018. Modeling, simulation, and influence of operational parameters on crystal size and morphology in Semibatch Antisolvent crystallization of α-lactose monohydrate. Cryst. Growth Des. 18, 4511–4521.

Plesset, M.S., Prosperetti, A., 1977. Bubble dynamics and cavitation. Annu. Rev. Fluid Mech. 9, 145–185.

Plesset, M., Zwick, S., 1952. A nonsteady heat diffusion problem with spherical symmetry. J. Appl. Phys. 23 (1), 95–98.

Ramirez Mendoza, H., Jordens, J., Valdez Lancinha Pereira, M., Lutz, C., Van Gerven, T., 2020. Effects of ultrasonic irradiation on crystallization kinetics, morphological and structural properties of zeolite FAU. Ultrason. Sonochem. 64, 105010. https://doi.org/10.1016/j.ultsonch.2020.105010.

Ruecroft, G., Hipkiss, D., Fennell, M., 2005a. Improving the bayer process by power ultrasound induced crystallization (sonocrystallization) of key impurities. In: Proceedings of the Technical Sessions Presented by the TMS Aluminum Committee at the 134th TMS Annual Meeting, San Francisco, California, February 13-17th, 2005, Light Metals, pp. 163–166.

Ruecroft, G., Hipkiss, D., Ly, T., Maxted, N., Cains, P.W., 2005b. Sonocrystallization: the use of ultrasound for improved industrial crystallization. Org. Process Res. Dev. 9, 923–932.

Saclier, M., Peczalski, R., Andrieu, J., 2010. Effect of ultrasonically induced nucleation on ice crystals' size and shape during freezing in vials. Chem. Eng. Sci. 65 (10), 3064–3071.

Sánchez-García, Y.I., García-Vega, K.S., Leal-Ramos, M.Y., Ivan, S., Gutiérrez-Méndez, N., 2018. Ultrasound-assisted crystallization of lactose in the presence of whey proteins and κ-carrageenan. Ultrason. Sonochem. 42, 714–722. https://doi.org/10.1016/j.ultsonch.2017.12.020.

Sayan, P., Sargut, S.T., Kiran, B., 2011. Effect of ultrasonic irradiation on crystallization kinetics of potassium dihydrogen phosphate. Ultrason. Sonochem. 18 (3), 795–800.

Söhnel, O., Garside, J., 1992. Precipitation: Basic Principles and Industrial Applications. Butterwort, Oxford.

Storey, B.D., Szeri, A.J., 2001. A reduced model of cavitation physics for use in sonochemistry. Proc. R. Soc. A: Math. Phys. Eng. Sci. 457, 1685–1700.

Suslick, K., 1989. The chemical effects of ultrasound. Sci. Am. 260 (2), 80–86.

Suslick, K.S., Zieger, B.W., 2011. Sonofragmentation of molecular crystals. J. Am. Chem. Soc. 133 (37), 14530–14533.

Suslick, K.S., Doktycz, S.J., Flint, E.B., 1990. On the origin of sonoluminescence and sonochemistry. Ultrasonics 28 (5), 280–290.

Szeri, A.J., Storey, B.D., Pearson, A., Blake, J.R., 2003. Heat and mass transfer during the violent collapse of nonspherical bubbles. Phys. Fluids 15, 2576.

Toegel, R., Gompf, B., Pecha, R., Lohse, D., 2000. Does water vapor prevent upscaling sonoluminescence ? Phys. Rev. Lett. 85 (15), 3165–3168.

Vancleef, A., Van Gerven, T., Thomassen, L.C.J., Braeken, L., 2021. Ultrasound in continuous tubular crystallizers: parameters affecting the nucleation rate. Crystals 11, 1054. https://doi.org/10.3390/cryst11091054.

Virone, C., Kramer, H.J.M., van Rosmalen, G.M., Stoop, A.H., Bakker, T.W., 2006. Primary nucleation induced by ultrasonic cavitation. J. Cryst. Growth 294 (1), 9–15.

Wang, J., Li, F., Lakerveld, R., 2018. Process intensification for pharmaceutical crystallization. Chem. Eng. Process. Process Intensif. 127, 111–126. https://doi.org/10.1016/j.cep.2018.03.018.

Wohlgemuth, K., Kordylla, A., Ruether, F., Schembecker, G., 2009. Experimental study of the effect of bubbles on nucleation during batch cooling crystallization. Chem. Eng. Sci. 64 (19), 4155–4163.

Zhang, X., Inada, T., Yabe, A., Lu, S., Kozawa, Y., 2001. Active control of phase change from supercooled water to ice by ultrasonic vibration 2. Generation of ice slurries and effect of bubble nuclei. Int. J. Heat Mass Transf. 44, 4533–4539.

Zhang, X., Inada, T., Tezuka, A., 2003. Ultrasonic-induced nucleation of ice in water containing air bubbles. Ultrason. Sonochem. 10 (2), 71–76.

Zheng, L., Sun, D.-W., 2006. Innovative applications of power ultrasound during food freezing processes—a review. Trends Food Sci. Technol. 17 (1), 16–23.

Zou, Z., Lin, K., Chen, L., Chang, J., 2012. Ultrafast synthesis and characterization of carbonated hydroxyapatite nanopowders via sonochemistry-assisted microwave process. Ultrason. Sonochem. 19 (6), 1174–1179.

Chapter 33

Ultrasonic drying for food preservation

J.V. García-Pérez[a], J.A. Carcel[a], A. Mulet[a], E. Riera[b,c], R.R. Andrés[c], and J.A. Gallego-Juárez[c]

[a]*Universitat Politècnica de València, Valencia, Spain,* [b]*Consejo Superior de Investigaciones Científicas (CSIC), Madrid, Spain,* [c]*Pusonics S.L., Pico Muihacén, Arganda del Rey, Madrid, Spain*

33.1 Introduction

Dehydration could be defined literally as the act of water removal from an object. It is one of the oldest food preservation methods available since prehistoric times. Dehydration entails the reduction of water activity, which avoids or delays food spoilage induced by microbial or enzymatic reactions, as well as other degradative reactions, such as lipid oxidation, non-enzymatic browning, and hydrolysis.

On the one hand, water removal may be accomplished by mechanical and chemical forces, a method normally known as dewatering that includes the pressing, centrifugation, and osmotic dehydration using hypertonic solutions of salts or sugars (Garcia-Noguera et al., 2010). Dewatering involves removing water from the product without any phase change (Vega-Mercado et al., 2001). On the other hand, where liquid is removed from a solid, semi-solid, or even a liquid and a phase change occurs (Lewicki and Michaluk, 2004), a wide group of dehydration methods including air (or convective) drying or freeze drying (lyophilization) (Ratti, 2001; Plaza et al., 2003) are involved.

Although the primary objective of drying is preservation, other aspects are considered more and more (Mayor and Sereno, 2004; Lewicki, 2006; Vega-Gálvez et al., 2012). Convective drying, using hot air, is the most common dehydration technique in the food industry due to its simplicity and relatively low cost. Despite the fact that energy consumption in food drying is lower than in the paper or ceramic industries, there is great emphasis on minimizing it in order to reduce the economical and environmental impact. Current trends in the search for high nutritional and sensory product traits also have significant implications in the drying process (Bonazzi et al., 1996) and on quality attributes (Ratti, 2001) such as browning, shrinkage, loss of rehydration capacity, and degradation of thermo-labile compounds, among others. Keeping the product temperature low during dehydration is a key issue when trying to obtain better-quality products. This led to the development of freeze drying (or lyophilization), the process where water is removed from any kind of product by sublimation in a vacuum chamber and the material kept frozen. Freeze drying enables the production of high-quality foods with minimum shrinkage, color changes, and loss of thermo-sensitive compounds (Pisano et al., 2011). Nevertheless, the use of low temperatures directly involves a low drying rate. Thus, freeze drying is considered a very costly technique, not only in terms of the initial investment but also during processing, so restricting its application to high-quality foods, and is mostly used in the pharmaceutical and biotechnological industries (Fissore et al., 2011).

The impact associated with energy consumption, processing costs, or quality loss during drying may be tempered by combining new technologies with traditional dehydration techniques (Cohen and Yang, 1995; Chou and Chua, 2001; Benali and Kudra (2010)). In this context, the use of power ultrasound emerges as a relevant alternative. Compared to other emerging technologies applied in the drying process such as infrared radiation, microwave, and refractance window, ultrasound has a weak thermal effect. This characteristic facilitates its implementation in drying heat-sensitive materials, where precise process control is required to avoid overheating and also in the so-called low-temperature drying processes. Nevertheless, published research on ultrasound air drying is not very abundant compared to ultrasonic applications in liquid media, i.e., for improving dewatering during osmotic dehydration of fruits (Garcia-Noguera et al., 2010; Cárcel et al., 2007b) and meat salting (Cárcel et al., 2007c).

This book chapter aims to show the recent developments carried out by the "Power Ultrasonics Group, PUG" (ITEFI-CSIC, Spain), Pusonics S.L. and "Group of Analysis and Simulation of Agro-Food Products, ASPA" (Food Technology Department, UPV, Spain) in the development, implementation, and application of power ultrasound devices in the drying process. First of all, the phenomena associated with power ultrasound applications, which are responsible for the effects on the drying process, will be set out. Afterward, the ultrasonic devices developed to assist the convective drying process will be introduced, and

Power Ultrasonics. https://doi.org/10.1016/B978-0-12-820254-8.00027-0
Copyright © 2023 Elsevier Ltd. All rights reserved.

finally, the power ultrasound-assisted drying of food materials will be analyzed. Therefore, this chapter is devoted to the applications of power ultrasound to improve air drying of mainly solid foods, since attempts of improving spray drying of liquid dispersions will not be analyzed (Rodriguez et al., 1999), as well as novel applications in supercritical CO_2 (Morbiato et al., 2019) and in liquid media to improve osmotic dehydration (Cárcel et al., 2007b) and salting (Ozuna et al., 2013).

33.2 Ultrasonic mechanisms involved in transport phenomena

Ultrasound like any acoustic wave can be transmitted through any substance with elastic properties, such as solids, liquids, semi-solids, or gases. The sound source creates a vibration of the particles, which is transmitted to the adjoining ones. In this way, particles suffer periodically repeated cycles (frequency > 20 kHz) of compression and expansion, this being a cyclic mechanical stress causing a series of phenomena, which are largely dependent on the nature of the system, as well as the energy available.

Ultrasonic vibration in a liquid may induce inertial cavitation, this being the most popular phenomena associated with power ultrasound applications in liquid media (Ozuna et al., 2013). As it is well known, inertial cavitation basically consists of an unstable growth of gas bubbles inside the liquid, which culminates in the bubble collapse or implosion. The inception of cavitation needs high pressure levels during ultrasonic air drying, and although cavitation could also be manifested in the liquid phase of food materials, it makes it very difficult to reach the threshold level of acoustic energy using current ultrasonic devices (Gallego-Juárez, 1998). In this way, cavitation during ultrasonic air drying could be almost neglected, making the heating effect much milder than in liquid media application.

In this work, the mechanical effects produced by ultrasound have been classified considering its influence on external (convective) or internal (diffusion) mass transport during ultrasonic air drying, as well as the phenomena linked to heat transport. It should be emphasized that during drying, there is an opposite coupled heat and mass transfer (Aversa et al., 2007). Water moves from the particle to the air, while heat flux is opposite, going from air to particle. Indeed, the effects produced by ultrasonic waves should jointly affect both transport phenomena (García-Pérez et al., 2013). Thus, improved heat transfer may directly involve a faster water removal rate. It remains complicated, in most instances, to determine how ultrasound individually affects both transport phenomena. Therefore, in this section, the effects of ultrasound will be jointly considered and analyzed assuming that they all contribute to the improvement of external and internal water transport, as well as affecting heat transfer.

33.2.1 Convective transport

Water convective transport occurs between the product (solid or semi-solids, such as pastes or purees) surface and air bulk, the active transport being localized in the air boundary layer surrounding the particle. Water transport resistance is mostly controlled by the boundary-layer thickness. Thus, convective water transport may be defined from Eq. (33.1) (Krokida et al., 2001; Bird et al., 2007):

$$J = k(X_{as} - X_a) \tag{33.1}$$

where

J is the water (abbreviated as w) flux density (kg w m^{-2} s^{-1}),
k is the external mass transfer coefficient (kg w m^{-2} s^{-1}),
X_{as} is the water concentration in the air in intimate contact with the product surface (kg w kg dry air^{-1}) and
X_a is the water concentration in bulk air (kg w kg dry air^{-1}).

Convective transport involves water evaporation at the solid surface; thus, water in a liquid state moves to the air in gas phase from the surface. In some cases, the phase change occurs inside the solid and convective transport does not involve a phase change at the solid surface, such as in the case of freeze drying, where water already in gas state moves into the solid toward the surface.

During drying, while the product surface remains saturated, convective transport is the only significant water transport mechanism controlling the drying rate. The importance of convective transport depends on the air turbulence due to its influence on the boundary-layer thickness. Thus, the only way to increase turbulence, and so improve convective transport, lies in the air flow. In most cases, the higher the air flow and thinner the boundary layer, the faster the convective transport. But actually, this has a limit, and it has been established that air velocities around 3–4 m/s constitute a threshold over which any increase in air velocity does not lead to faster drying. Then, drying is controlled by internal diffusion. This fact has been reported multiple times in literature (Blasco et al., 2006; Mulet, 1994). However, ultrasound may interfere in the air flow, since the acoustic waves create an "oscillating velocity" in the interface, further reducing the boundary layer. The effects responsible for this phenomenon are explained as follows.

High-intensity ultrasound can generate a so-called sound wind (or acoustic streaming) in the solid/gas interface, affecting the external resistance to mass transfer by increasing the bulk transport within the fluid (Mulet et al., 2003). The high-intensity mechanical compressions and expansions produced at the gas/solid interfaces create microstreamings, which are formed in the immediate vicinity of the solid surface (Borisov and Gynkina, 1973; Arkhangel'skii and Stanikov, 1973) even inside external pores and exert an important influence reducing the thickness of the boundary layer, increasing mass transfer,

and accelerating diffusion. High-intensity airborne ultrasound also introduces pressure variations at gas/liquid interfaces, enhancing the evaporation rate of moisture. In forced-air drying systems, the ultrasonic wave produces an oscillating velocity effect, which can increase the drying rate at stable air velocity. On the other hand, ultrasonic vibrations produce a kind of microsponge effect inside the material to be dried that favors the quick migration and release of the moisture (Gallego-Juárez, 1998; Gallego-Juárez et al., 2007).

33.2.2 Diffusion transport

In air-drying processes, it is generally assumed that diffusion is the governing water transport phenomena occurring in the solid matrix at the molecular level, being mostly quantified by the first Fick's law (Bird et al., 2007), which is shown in Eq. (33.2) for one-directional flow

$$J = -D\frac{\partial C}{\partial x} \tag{33.2}$$

where

J is the water flux density ($kg\,w\,m^2\,s^{-1}$),
C is the volumetric water concentration ($kg\,w\,m^{-3}$),
x is the mass transport direction, and
D is the diffusion coefficient ($m^2\,s^{-1}$).

In the drying process, instead of the term diffusion coefficient, which is mostly reserved for pure diffusion mechanisms, the term "effective moisture diffusivity" (D_e) is used, which includes not only pure diffusion but also other mechanisms (capillarity, etc.). The effective diffusion coefficient considers water transport as a whole inside the solid.

How may ultrasound improve diffusion transport in the particle? As before mentioned, in solid materials, ultrasonic waves produce a series of rapid and cyclic compressions and expansions of the material that can be compared to a sponge squeezed and released repeatedly (Floros and Liang, 1994; Liang, 1993). This mechanical stress, known as the "sponge effect," helps the liquid to flow out of the samples through natural channels or other channels created by wave propagation (Gallego-Juárez et al., 1999, 2007). In fact, through very intense compressions and expansions, ultrasound may create microchannels, which are better pathways, improving the water removal rate (Muralidhara et al., 1985; Vallespir et al., 2019). These microchannels may be considered a structural effect induced by ultrasound, which facilitates the internal diffusion, and will be addressed in the Section 33.6. In addition, it is reported that if the acoustic energy levels needed to induce cavitation could be reached, it would contribute to the removal of the most strongly attached moisture from the solid (Gallego-Juárez et al., 1999). This issue could be highly relevant for the pharmaceutical, chemical, and oil companies to remove traces of solvent.

As already mentioned, the ultrasound effects seem to be conditioned largely by the available ultrasound energy in the medium. But considering the same energy levels, will the effects produced by ultrasound in water diffusion be the same regardless of the structure of the product being dried? Therefore, the energy issue seems to be a paradigm, especially for airborne applications, as will be illustrated in the following sections.

33.2.3 Heat transport

The aforementioned ultrasonic effects in Sections 33.2.1 and 33.2.2 also have relevant implications on both internal and external heat flows. García-Pérez et al. (2013) reported a mild temperature rise on the air flow for airborne ultrasound application, which could compensate the temperature drop caused by water evaporation, making closer the air temperature to the target one compared to conventional hot air drying. By jointly fitting a coupled heat mass transport model to the drying kinetics and air temperature evolution, García-Pérez et al. (2013) reflected a significant ultrasonic effect on the external individual heat transfer coefficient but considering constant the internal thermal diffusivity. Later, Contreras et al. (2018) have analyzed the heating of dry-cured ham and manifested that ultrasound has the ability of increasing the molecular heat diffusion. The mechanical stress caused by ultrasound in the material, such as the sponge effect, is not only responsible for the enhancement of heat conduction mechanisms reported by Contreras et al. (2018) but also may induce a temperature rise. First, it has to be necessarily mentioned that the thermal effect caused by the structural stress in airborne ultrasonic applications is much weaker compared to the one linked to other technologies, such as microwave. Second, considering its magnitude, the thermal effect has been barely analyzed by the literature (Kowalski, 2015; Colucci et al., 2018). Thus, Kowalski et al. (2017) reported an almost negligible thermal effect of power ultrasound compared to the phenomena linked to microvibrations. However, other studies have shown a relevant thermal effect (Colucci et al., 2017). Differences on the literature about the importance of the thermal effect on airborne ultrasonic application in drying may be linked to the process conditions used (Kowalski, 2015). The relevance of the thermal effect could be larger in drying process conducted at low (Colucci et al., 2017) than at high temperature (Kowalski et al., 2017). On the other hand, thermal effect could differ considering the product being dried, which may control the ultrasonic energy transfer from the air to the product. In airborne ultrasonic applications, the ultrasonic energy entering into the particle is modulated by the transmission coefficient on the interface (Ozuna et al., 2014a), which depends on the

impedance matching between the air and the product. In addition, product properties also condition the internal attenuation, which results in a high thermal effect. The impact of product properties on the performance of airborne ultrasonic application on drying is going to be analyzed in Section 33.5 of this chapter.

33.3 Transducers with stepped plate, flat plate with reflectors, and cylindrical radiators

Despite the potential of ultrasound, the development of industrial applications is very slow and complicated. The main issue again is related to energy aspects since current commercial transducers have low efficiency and power capacity, and of course, this drawback is magnified when processes are scaled up.

One of the main problems for industrial extension is focused in generation devices (Gallego-Juárez et al., 2010). The majority of transducers are still based on the classic piezoelectric transducer developed by Langevin in 1918. This kind of transducer is limited in size, in order to avoid perturbations between their axial and radial vibration. As a result, the cross-sectional diameter has to be smaller than ¼ of the wavelength of the extensional operating vibration mode. Thus, multielement arrangements are necessary to achieve high power capacities. These arrangements have limitations for tuning the operation frequency and therefore in matching production quality standards. Another drawback in power ultrasonic transducers is the appearance of nonlinear effects at high voltages, such as frequency shifts and modal interactions (Gallego-Juárez et al., 2010). Current investigations are seeking strategies to reduce or remove the nonlinear phenomena (Cardoni and Lucas, 2002; Cardoni et al., 2012) and increase the available energy in the medium. The particularities of specific media where ultrasound is applied may increase the associated problems—this is what happens in airborne applications such as convective drying.

The airborne application of high-intensity ultrasound in air-drying processes has been investigated for more than five decades (Borisov and Gynkina, 1973; Arkhangel'skii and Stanikov, 1973). The low density of air involves high energy absorption and low acoustic impedance, which make difficult to achieve high energy levels in the medium. There is a loss of energy due to the high impedance mismatch between the ultrasonic radiators and air, which enormously reduces the acoustic energy transferred into the air. In addition, a high portion of the acoustic energy transferred is lost by air attenuation, which still decreases the energy reaching the air/solid interface. These drawbacks make the acoustic energy transfer during drying more complicated than in liquid media, which is well demonstrated by the reduced number of publications on ultrasound-assisted air drying compared with ultrasonic applications in liquid media, such as the extraction of natural products (Riera et al., 2004; Ahmad-Qasem et al., 2013), osmotic dehydration (Cárcel et al., 2007b) and meat (Cárcel et al., 2007c) and cheese brining (Sánchez et al., 1999), and pretreatments (Soria and Villamiel, 2010).

However, the interest for air drying has remained to this day, and several devices and modes of ultrasound application have been reported in the literature. Therefore, commercial transducers designed for other applications have been tested for air drying. In this sense, Schössler et al. (2012a) equipped a ring sonotrode, originally designed for ultrasonic sieving, with a screen where samples were placed. This device has been used for drying of different vegetables (Schössler et al., 2012a,b). Başlar et al. (2014) designed a vacuum drier where the vacuum vessel with the samples placed in the bottom was introduced in an ultrasonic bath and its performance has been tested for different products, such as nectarine (Souza da Silva et al., 2019) and green beans (Tekin et al., 2017).

However, none of these systems have faced the problems of efficient ultrasonic generation in air. Many of these problems have been in a great part solved in the last few years through the development of specific ultrasonic transducers with high power capacities, good impedance matching to the air, large vibration amplitude and radiating area, and optimal control of the radiation pattern. These developments have been carried out by the Power Ultrasonics Group (PUG) of the Spanish National Research Council (CSIC), and the new airborne ultrasonic systems (AUS) developed are presently manufactured and commercialized by the company PUSONICS S.L.

The basic structure of the new family of transducers is shown in Figure 33.1 (Gallego-Juárez et al., 2010; Riera et al., 2011). It mainly consists of a piezoelectrically activated vibrator, which drives an extensive radiator.

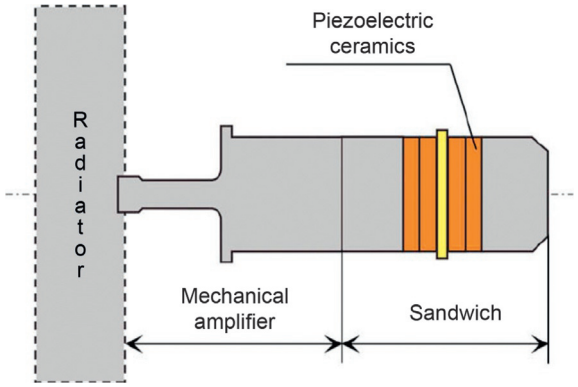


FIGURE 33.1 Basic structure of an ultrasonic transducer employed in drying/dewatering processes. *(Reprinted from Gallego-Juárez et al., 2010, with kind permission of Elsevier Ltd.)*

The vibrator includes a piezoelectric element that generates the vibration, which is amplified by a mechanical element. The radiator has an extensive surface area that increases the radiation resistance to vibration. Therefore, the acoustic impedance improves the coupling with the air and consequently the energy transferred into the air. There are different types of radiators specifically designed for particular applications, differing in power capacities, size, material employed, and mainly shape. In the present section, the transducers with four types of radiators, used for applications in drying process, are presented and referred: the stepped-plate radiator (SPR), the stepped-grooved-plate radiator (SGPR), the cylindrical radiator (CR), and the rectangular flat-plate radiator with reflectors (RFPR).

Circular and rectangular stepped-plate (SPR) and stepped-grooved-plate (SGPR) transducers with an extensive surface area have been used for drying intensification. These devices are shown in Figures 33.2 and 33.3. The radiation pattern is controlled by the stepped profile, so customized patterns can be achieved for specific applications (Gallego-Juárez et al., 2002, 2010). Also, the flat-plate transducer with reflectors at ultrasonic frequencies (RFPR) (Figure 33.4) offers a new tool to be applied in drying processes (Andrés et al., 2021).

In summary, highly directional and focused radiators have been designed to reach high energy levels in airborne drying. Different prototypes of transducers have been developed with aluminum or titanium alloys, rectangular or circular radiators, electro-acoustic efficiencies of 65%–80%, power capacities up to 1 kW, high directivity (3 dB bandwidth <2 degrees), or focusing radiation (2 cm^2 at a distance of about 40 cm) and frequencies in the range 20 to 26 kHz. These properties allow high acoustic intensities (up to 172 dB) to be reached in air. An extensive and detailed information about these transducers is presented in Chapter 7 of this book.

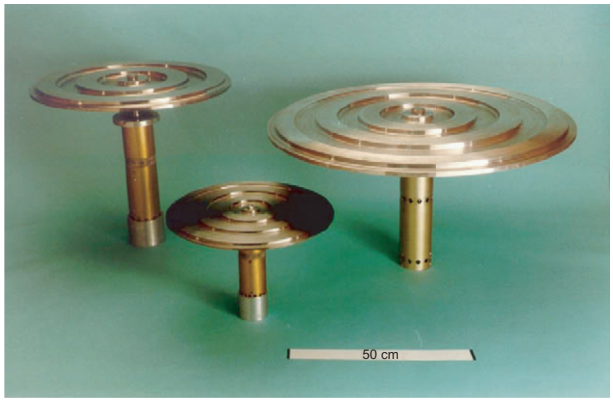


FIGURE 33.2 Circular stepped-plate radiators (SPR) driven by piezoelectric transducers. *(Reprinted from Gallego-Juárez et al. (2010), with kind permission of Elsevier Ltd.)*

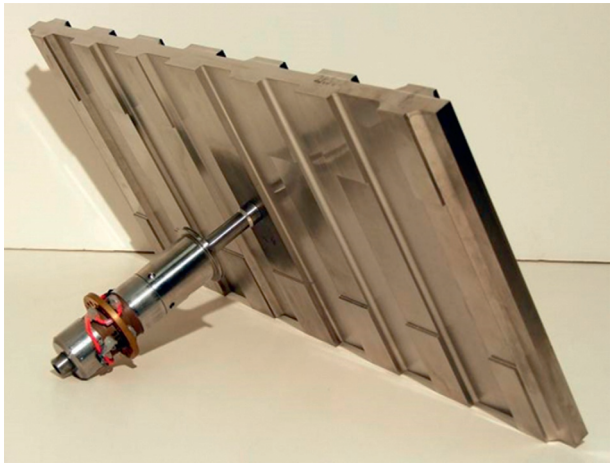


FIGURE 33.3 Rectangular stepped-plate radiator (SPR) driven by piezoelectric transducers. *(Reprinted from Gallego-Juárez et al. (2010), with kind permission of Elsevier Ltd.)*



FIGURE 33.4 Front view of the rectangular flat-plate radiator with the reflector system. *(Reprinted from Andrés et al. (2019) with permission from Elsevier.)*

In Figure 33.5, the scheme of an ultrasonic-assisted convective drier for laboratory purposes is shown, equipped with a rectangular SPR. The system was presented and described by Gallego-Juárez et al. (2007). Its main feature lies in the treatment chamber where samples are placed between the rectangular radiator and a porous material, acting as sample holder, and suction is applied to help the hot air to remove the extracted water. Controlling the position of the sample holder allows the device to carry out airborne or direct-contact application. In the first case, there is a certain distance between the radiator and the sample, while in the direct-contact application, the sample is in intimate contact with the radiator surface. In addition, the prototype allows static pressure to be applied between the samples and transducer.

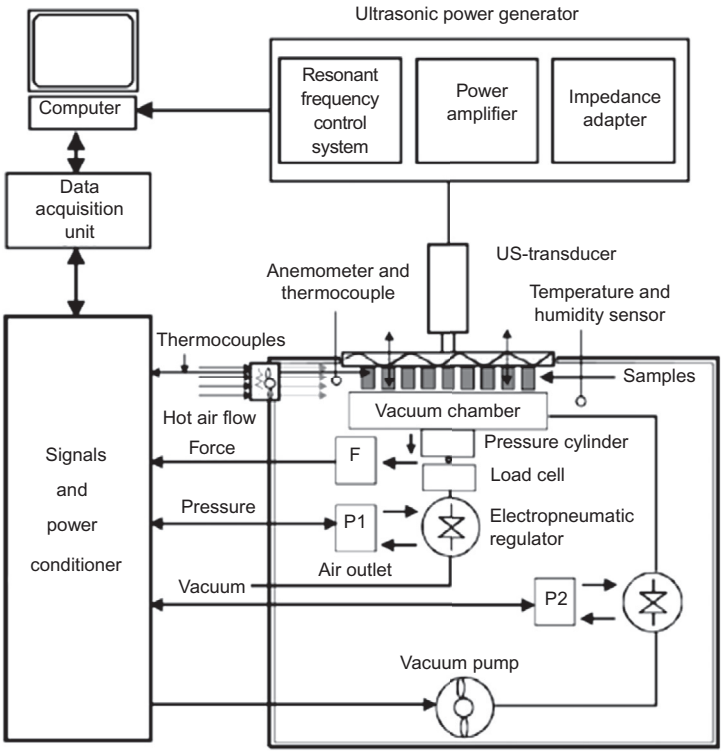


FIGURE 33.5 Ultrasonic-assisted drier equipped with a rectangular stepped-plate radiator (SPR) driven by piezoelectric transducer for airborne and direct-contact ultrasonic applications. *(Reprinted from De la Fuente et al. (2006), with kind permission of Elsevier Ltd.)*

The direct contact allows better vibration transmission avoiding both the high impedance mismatch between radiator and air and energy absorption in the air. Notwithstanding this, a much greater heating effect is expected in the direct-contact applications and its installation in most current drying units would not be feasible.

For applications in specific volumes, like a drying chamber, duct, or pipe, cylindrical radiators (CR) have also been developed (Figure 33.6). The basic feature consists of using the walls of the cylindrical chamber as the radiating element; thus, no additional element is necessary to apply ultrasound. In this way, the drying air is forced to go through the ultrasonically activated drying chamber where the samples are placed. Riera et al. (2011) described how these cylindrical radiators driven by the piezoelectrically activated vibrator were originally designed and further improved by using finite element modeling (Figure 33.7). The CR transducers developed presented the following electro-acoustic features: resonance frequency of 22 kHz, electrical impedance of 365 Ω, bandwidth of 17 Hz, and power capacity of around 90 W.

Figure 33.8 shows the local sound pressure distribution inside the air volume in the cylindrical chamber when 90 W is supplied to the ultrasonic transducer, showing an average sound pressure level of 154.1 dB in stagnant air conditions.

CR transducers were originally designed for fluidized bed drying where samples are freely moving in the drying

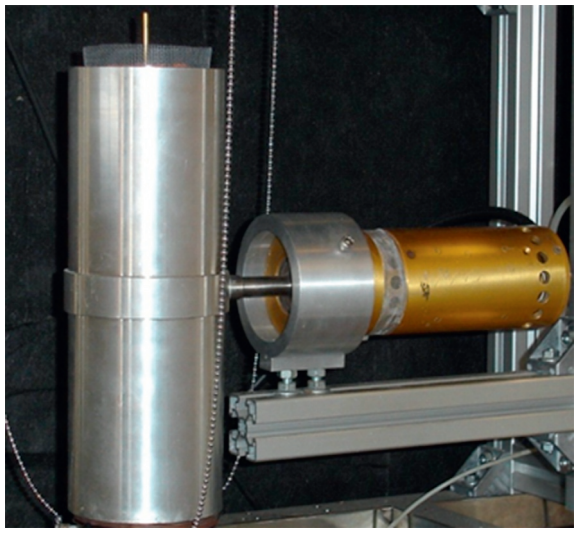


FIGURE 33.6 Cylindrical radiator (CR) driven by a piezoelectric transducer for airborne ultrasonic application in drying.

chamber due to the high air velocities applied. The use of sample holders also allows experiments to be carried out in fixed beds by placing samples in trays along the longitudinal axis of the cylinder or distributed randomly. The CR transducers have been assembled in convective driers of the ASPA Group; this research group has actively collaborated with the PUG to thoroughly analyze how ultrasound affects

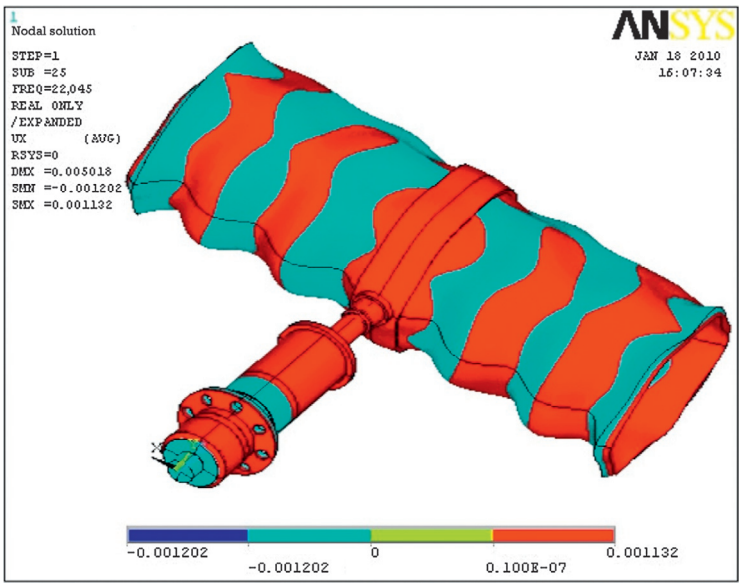


FIGURE 33.7 Design of the cylindrical radiator (CR) by finite element modeling. *(Reprinted from Riera et al. (2011), with kind permission of John Wiley & Sons, Ltd. and Institute of Food Technologists.)*

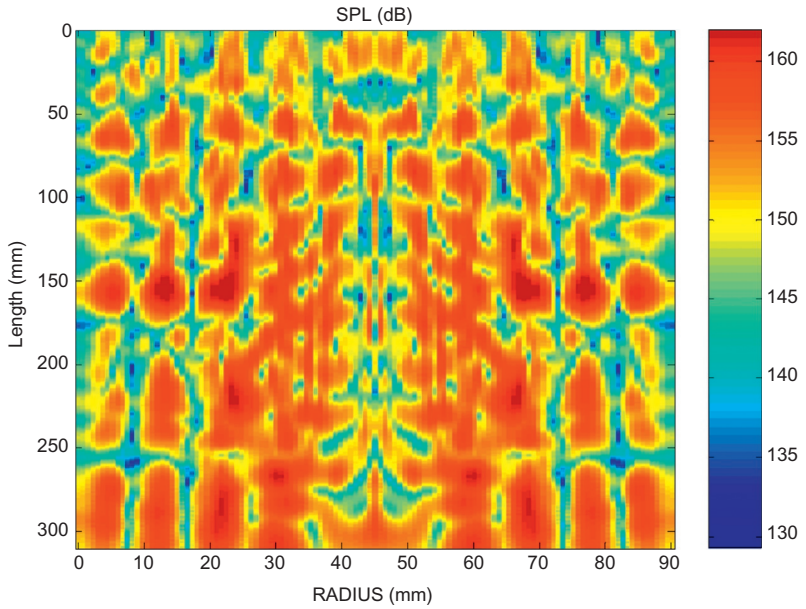


FIGURE 33.8 2D-Sound pressure-level distribution pattern (in dB) inside the cylindrical radiator (CR, electric power supplied 90 W and air velocity 0 m/s). *(Reprinted from Riera et al. (2011), with kind permission of John Wiley & Sons, Ltd. and Institute of Food Technologists.)*

the drying process. Figures 33.9 and 33.10 show the layout of two laboratory-type prototypes of ultrasonically assisted driers equipped with CR transducers acting as drying chambers. Both driers differ mainly in the range of temperatures used: one of them (Figure 33.9) uses hot air and works at temperatures above room temperature, being the working range between 30°C and 100°C (Garcia-Perez, 2007; Riera et al., 2011); however, the other equipment (Figure 33.10) is able to work at temperatures below room temperature, allowing the drying processes to be performed in the range from −15°C to 20°C.

A new convective drier has been designed and constructed by ASPA group in Valencia (Spain) to study the effect of airborne power ultrasound on the freeze-drying processes at atmospheric pressure (Figure 33.11). It consists of a semi-industrial freezing cabinet divided into two sections: a pretreatment chamber and the drying chamber. In the first chamber, the temperature and the relative humidity

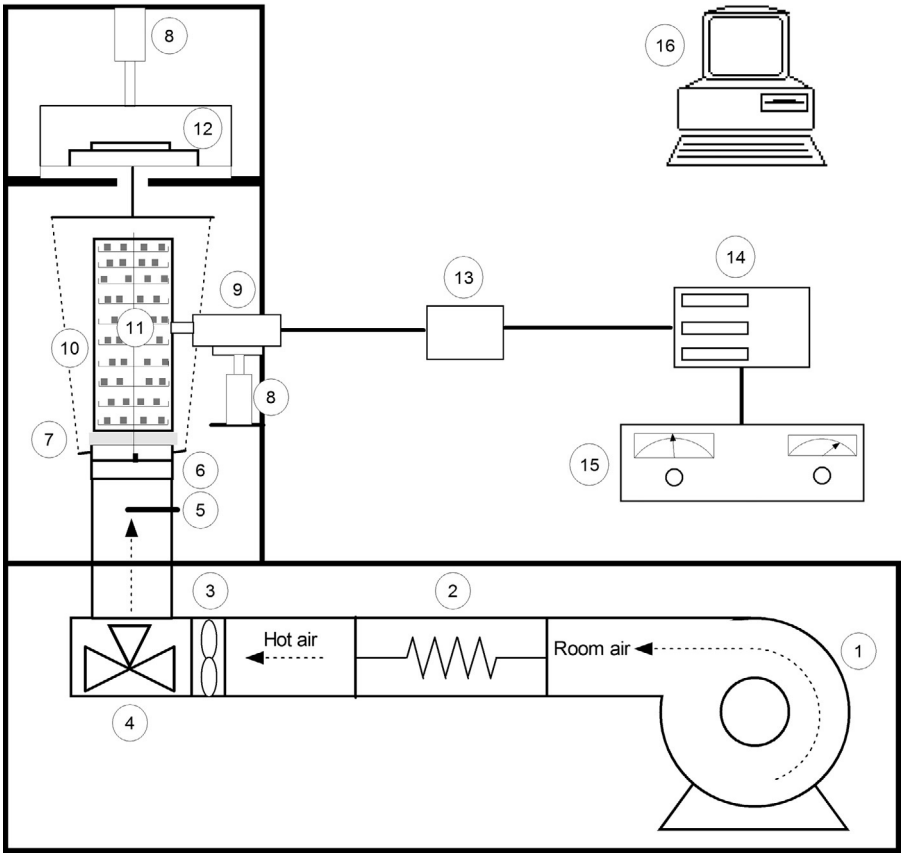


FIGURE 33.9 Hot air drier with a cylindrical radiator (CR) for airborne ultrasonic applications. 1. Fan, 2. Heating unit, 3. Anemometer, 4. 3-Way valve, 5. Thermocouple, 6. Sample loading chamber, 7. Coupling material, 8. Pneumatic moving arms, 9. Ultrasonic transducer, 10. CR, 11. Trays, 12. Balance, 13. Impedance matching unit, 14. Wattmeter, 15. High-power ultrasonic generator, 16. PC. *(Reprinted from Carcel et al. (2010), with kind permission of Taylor & Francis, Ltd.)*

parameters are controlled and kept at constant values. This constant relative humidity is obtained by recirculating the air from the drying chamber through a bed of desiccant material. The drying temperature is maintained at the desired level, by combining the evaporation system of the freezing chamber and an electrical resistance. Temperature and relative humidity sensors allowed monitoring both parameters. A fan provides a flat airflow that is directly focused toward the sample holder. All parameters of the process (temperature humidity and air velocity) are supervised by a Labview application.

The transducer used in this installation incorporate a stepped-grooved-circular radiator (SGPR) (radius of 20 cm). It is mounted inside the dehydration chamber, 19 cm above the sample holder (Figure 33.12). As a result, the volume covered by the transducer, in terms of acoustic efficiency, was 0.0239 m^3 and 0.126 m^2 of the surface. The experimental acoustic characterization indicates that for an electric supply of 50 W to the transducer, the sound pressure level (SPL) achieved in the volume of interest is 147 dB (547 W/m^2). More specifically, the SPL obtained in the area where the food samples were placed was 148 dB (582 W/m^2). The acoustic energy concentrates at the axis of the transducer, obtaining an SPL of 152 dB (1421 W/m^2) in this area (Andrés et al., 2019).

33.4 Testing the effectiveness of ultrasonic drying

This section analyzes how ultrasound affects the drying process of different foodstuffs. Early works about ultrasonic drying carried out by PUG and ASPA teams were published in the late 1990s. Since then, publications have addressed direct-contact applications, but mainly airborne. At the beginning, the applications focused on hot air drying but from 2012, the use of airborne ultrasound has been extended in the field of low temperature below and above the product's freezing temperature. Table 33.1 summarizes some of the works carried out in this field by both research groups and incorporates technical aspects, such as the transducer used, the product being dried, and the process variables analyzed.

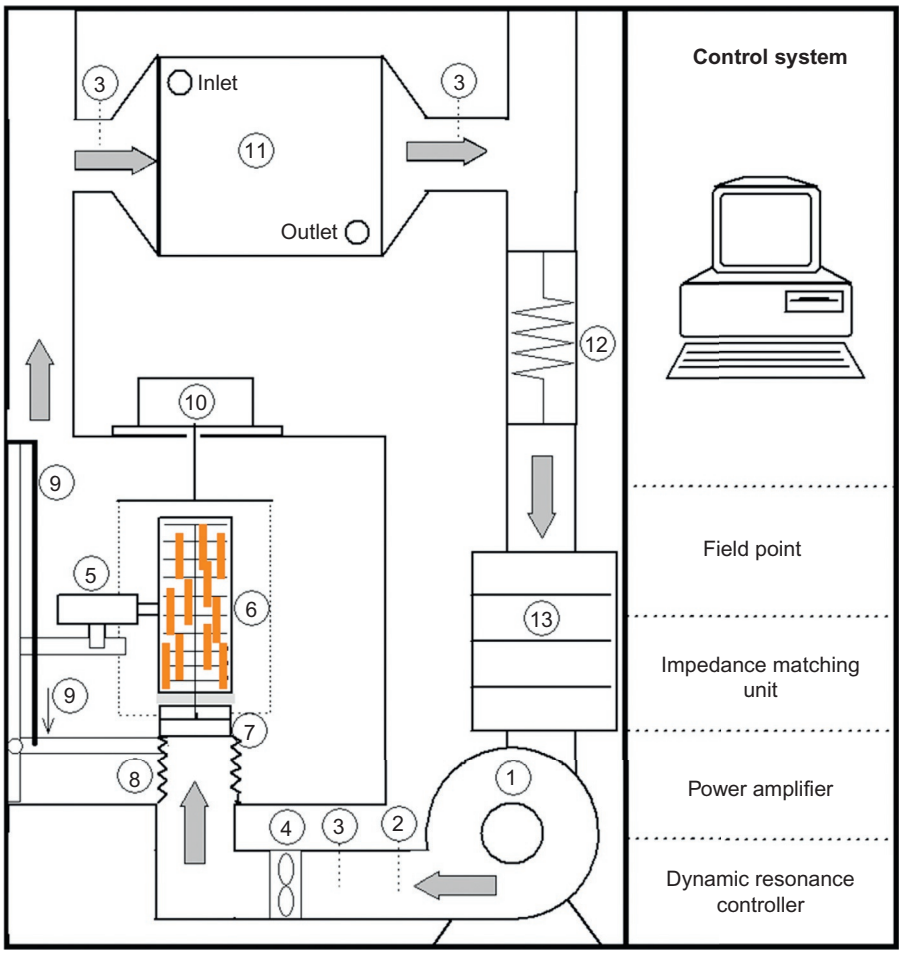


FIGURE 33.10 Low-temperature drier with cylindrical radiator (CR) for airborne ultrasonic applications. 1. Fan, 2. Pt-100, 3. Temperature and relative humidity sensor, 4. Anemometer, 5. Ultrasonic transducer, 6. CR, 7. Sample load device, 8. Retreating pipe, 9. Slide actuator, 10. Weighing module, 11. Heat exchanger, 12. Heating elements, 13. Desiccant tray chamber. *(Reprinted from Garcia-Perez et al. (2012b), with kind permission of Taylor & Francis, Ltd.)*

Drying tests have been carried out to evaluate the efficiency of the ultrasonic devices, and assess the influence of the most important operational parameters being:

- air velocity (from 0.5 to 10 m/s)
- temperature (from −15°C to 70°C),
- mass load (up to 108 kg/m^3)
- ultrasonic power applied (up to 37 kW/m^3).

Modeling tools were used to describe the water transport mechanisms during drying, and quantify the influence of power ultrasound on the kinetic parameters. Moreover, materials with very different internal structures have been used and characterized by macroscopic and microscopic analyses (Ozuna et al., 2011b; Puig et al., 2012) such as density and porosity measurements and SEM and cryo-SEM observations. However, the interaction of product-ultrasound will be addressed in Section 33.5 since material properties have not strictly been considered as operational parameters, while Section 33.7 highlights the influence of ultrasonic-assisted drying on quality properties of the dried products.

33.4.1 Direct-contact applications

The direct contact between the ultrasonic radiator and the sample largely improves the energy transfer, by-passing the air and avoiding acoustic impedance mismatch linked to the gas medium. Consequently, ultrasonic vibration travels directly from the radiator to the sample penetrating deeply into the sample and greatly increasing the phenomena associated with ultrasound (see Section 33.2). The direct-contact application favors cavitation, which can help to remove the most strongly attached moisture from the solid (Gallego-Juárez et al., 2007) and achieve a lower final moisture content than from hot air drying. This last aspect, although not very relevant in the food industry, could be highly interesting in the chemical and pharmaceutical industries for removing traces of organic solvents.

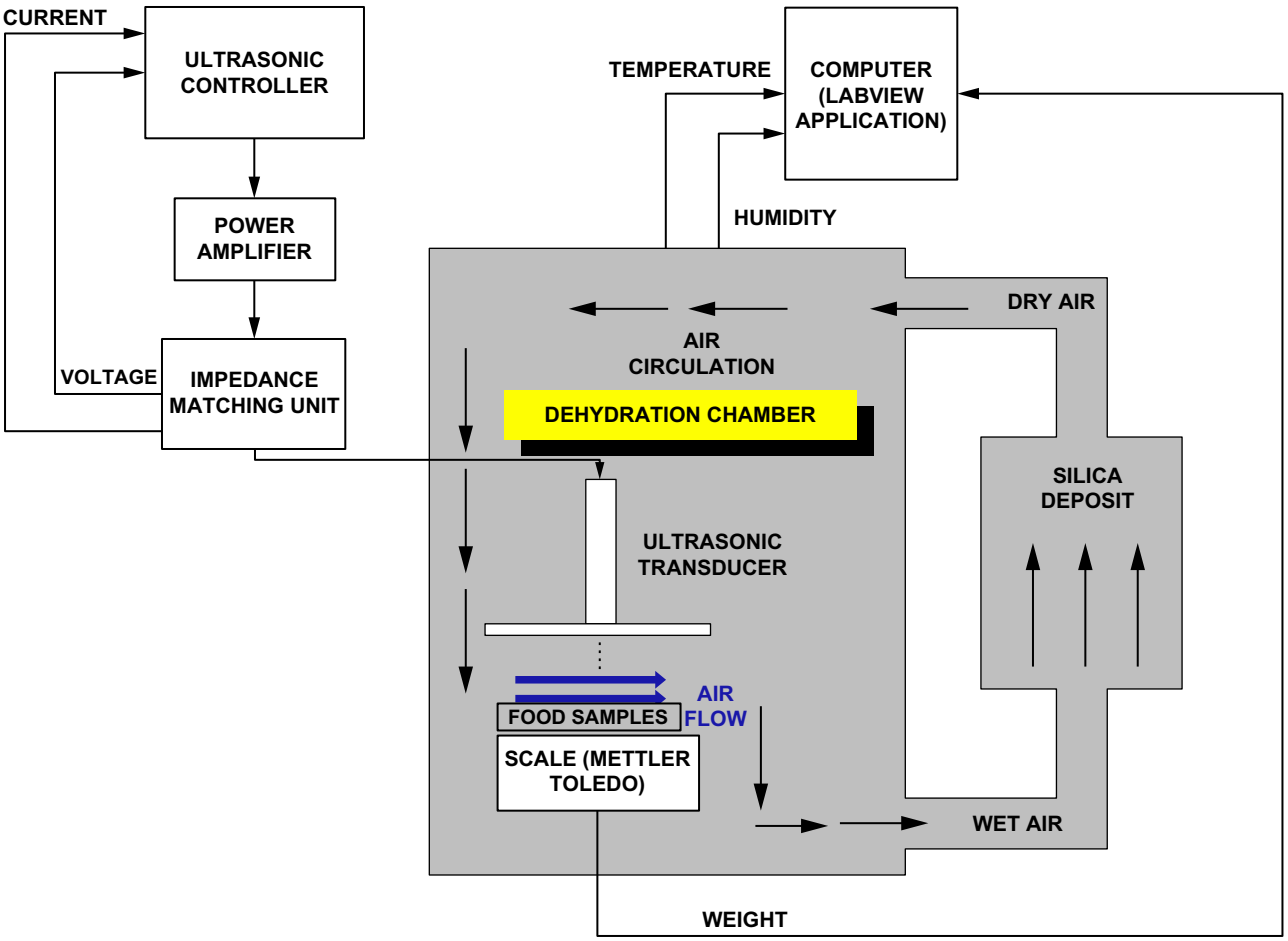


FIGURE 33.11 Experimental setup of the ultrasonically assisted low-temperature drying system with a stepped circular-plate transducer.

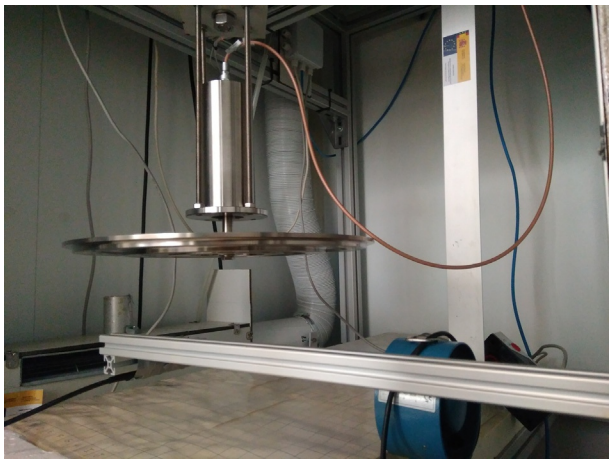


FIGURE 33.12 Stepped-grooved-circular-plate transducer assembled in a low-temperature drier. *(Reprinted from Andrés et al. (2019) with permission from Taylor and Francis.)*

The effectiveness of direct-contact ultrasonic applications is shown in Figure 33.13 where drying kinetics of carrot slices at room conditions (22°C) with and without ultrasound application are compared (Gallego-Juárez et al., 2007). The effect of ultrasound over drying time is paramount, so 4-mm-thick samples are dried in less than 30 min when ultrasound is applied (100 W). However, the same samples present very high moisture content (6 kg w/kg dm) at 50 min in experiments without ultrasound application. Gallego-Juárez et al. (2007) reported an improvement in the effective moisture diffusivity of more than one order of magnitude in the drying of carrot and potato when direct-contact ultrasound is applied.

As mentioned in Section 33.2, exerting a certain static pressure between the samples and the radiator leads to better contact, which directly improves the acoustic vibration transfer and so enhances the available energy in the particle. The improved acoustic transmission may exert large mechanical forces into the particle, creating an intense pumping of the liquid water to the surface. To help remove excess surface water by hot air, a vacuum-suction device was installed in the experimental prototypes (Figure 33.5) and the process could be cataloged as a combined drying-dewatering technique (De la Fuente et al., 2006). Drying experiments at 31°C with apple slices of 1 m/s, applying

TABLE 33.1 Compendium of previous works carried out by GPU and ASPA groups addressing the application of power ultrasound on convective drying

Reference	[a]Process variable under study	[b]HT-LT	Material being tested	[c]Device
Gallego-Juárez et al. (1999)	T, UP	HT	Carrot	SPR
Mulet et al. (2003)	UP	HT	Carrot	SPR
Garcia-Perez et al. (2006a)	V	HT	Carrot	CR
Garcia-Perez et al. (2006b)	V, ML, UP	HT	Carrot	CR
Gallego-Juárez et al. (2007)	T, V, UP	HT	Carrot and apple	SPR
Garcia-Perez et al. (2007)	V	HT	Lemon peel, persimmon and carrot	CR
Carcel et al. (2007)	V	HT	Persimmon,	CR
Garcia-Perez et al. (2009)	UP	HT	Lemon peel and carrot	CR
Carcel et al. (2010)	ML	HT	Carrot	CR
Garcia-Perez et al. (2011)	UP	HT	Eggplant	CR
Ozuna et al. (2011a)	UP	HT	Potato	CR
Garcia-Perez et al. (2012a)	UP	HT	Orange peel	CR
Puig et al. (2012)	UP	HT	Eggplant	CR
Garcia-Perez et al. (2012b)	V	LT	Eggplant, carrot, apple	CR
García-Pérez et al. (2013)	T, UP	HT	Grape stalk	CR
Gamboa-Santos et al. (2014a)	T, UP	HT	Strawberry	CR
Gamboa-Santos et al. (2014b)	T, UP	HT	Strawberry	CR
Rodríguez et al. (2014)	T, UP	HT	Apple	CR
Ozuna et al. (2014b)	T	LT	Cod fish	CR
Ozuna et al. (2014a)	UP	HT	Cassava, apple	CR
Santacatalina et al. (2014)	T	LT	Apple	CR
Fernandes et al. (2015)	T, V	HT	Apple	CR
Santacatalina et al. (2015a)	T, V, UP	LT	Apple	CR
Santacatalina et al. (2015b)	T	LT-HT	Apple	CR
Santacatalina et al. (2016a)	T, V	LT	Eggplant	CR
Santacatalina et al. (2016b)	UP	LT	Apple	CR
Fernandes et al. (2016)	T, V	HT	Tomato	CR
Santacatalina et al. (2016c)	T	LT	Cod fish	CR
Cruz et al. (2016)	T	HT	Grape skin	CR
do Nascimento et al. (2016)	T	HT	Passion fruit	CR
Magalhães et al. (2017)	T, V	HT	Apple	CR
Rodrigues et al. (2017)	T, V	HT	Apple	CR
Colucci et al. (2017)	T, UP	LT	Eggplant	CR
Corrêa et al. (2017)	UP	HT	Pineapple	CR
Moreno et al. (2017)	UP	LT	Apple	CR
Carrión et al. (2018)	UP	LT	Mushroom	CR
Colucci et al. (2018)	T, UP	LT	Eggplant	CR

Continued

TABLE 33.1 Compendium of previous works carried out by GPU and ASPA groups addressing the application of power ultrasound on convective drying—cont'd

Reference	Process variable under study	HT-LT	Material being tested	Device
Rodrigues et al. (2018)	T	LT-HT	Apple	CR
Vallespir et al. (2018)	UP	LT	Beetroot	CR
Vallespir et al. (2019)	T	LT	Kiwi	CR
Andrés et al. (2021)	UP	LT	Apple	SGPR
Martins et al. (2019)	T	LT-HT	Apple peel	CR
Cárcel et al. (2019)	T	HT	Pepper	CR
Mello et al. (2020)	T	LT-HT	Orange peel	CR

[a]T, *air temperature;* V, *air velocity; UP, ultrasonic power;* ML, *mass load.* [b]HT, *high temperature;* LT, *low temperature.* [c]CR, *cylindrical radiators;* SPR, *stepped-plate radiators;* SPGR, *stepped-grooved-plate radiators.*

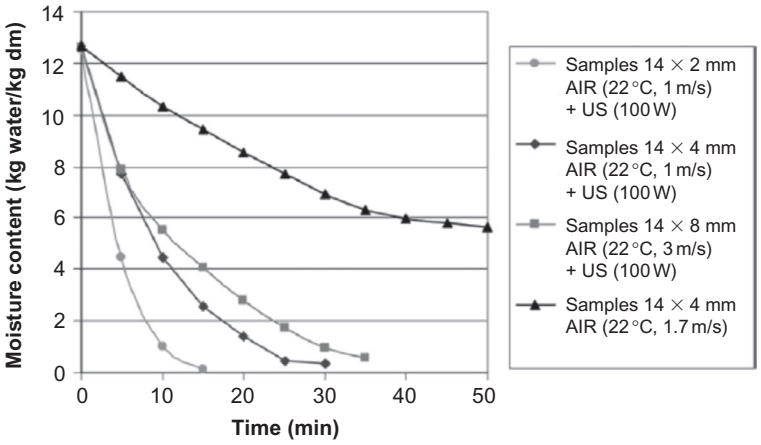


FIGURE 33.13 Drying kinetics of carrot slices (14 mm in diameter and several thickness) at 22°C with (SPR, +US) and without (AIR) direct-contact ultrasound application. *(Reprinted from Gallego-Juárez et al. (2007), with kind permission of Taylor & Francis, Ltd.)*

two different ultrasonic powers (25 and 50 W), and a static pressure of 0.0155 kg/cm^2 are shown and compared with conventional drying (Figure 33.14). Even the ultrasonic powers are lower than those used in the experiments shown in Figure 33.13; ultrasound application only shortened the drying time to 20 min when 50 W was applied. The effect of the ultrasonic power applied is observed when drying kinetics at 25 and 50 W are compared in Figure 33.14: the higher the power, the faster the drying. The same fact has also been observed when drying carrot (Figure 33.15) in a wide range of experimental conditions (De la Fuente et al., 2006). This fact suggests that the available acoustic energy into the medium seems to be a limitation in the extension of the phenomena associated with ultrasound application. Therefore, more effort is required in designing ultrasonic transducers with higher power capacities.

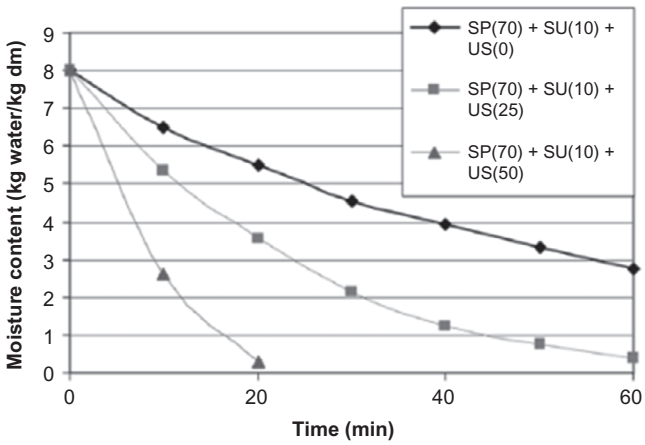


FIGURE 33.14 Drying kinetics of apple slices (24 mm in diameter and 4 mm in thickness) at 70°C and 1 m/s and static pressure, SP(70), with direct-contact ultrasound application (SPR) at two different ultrasonic powers: 25, US(25), and 50 W, US(50), and conventional drying experiments, US(0). *(Reprinted from Gallego-Juárez et al. (2007), with kind permission of Taylor & Francis, Ltd.)*

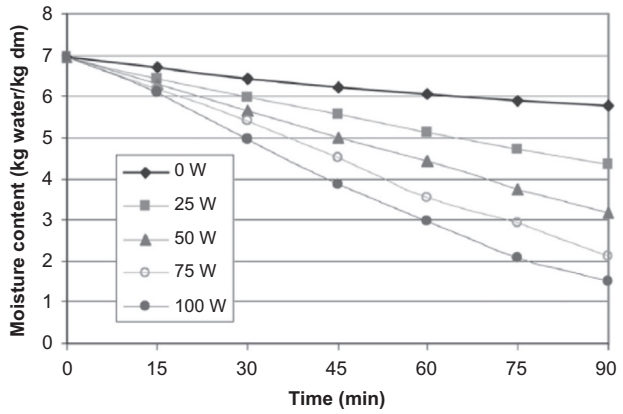


FIGURE 33.15 Drying kinetics of carrot cylinders at 25°C, 2 m/s and with static pressure applying different ultrasonic powers (W). Direct-contact application (SPR). *(Reprinted from Gallego-Juárez et al. (2007), with kind permission of Taylor & Francis, Ltd.)*

The use of commercial ultrasonic devices originally designed for other applications has been addressed in the drying process. Thus, Schössler et al. (2012a) equipped a ring sonotrode originally designed for ultrasonic sieving with a screen, where samples were placed. The vibration amplitude, measured via laser interferometry in the screen surface, reached values between 6 and 13 μm, with the original amplitude of the ring being 4 μm. The system was tested with continuous and intermittent sonication drying red bell pepper and apple at 70°C. Experimental results showed that ultrasound significantly accelerated the drying process, but the effect observed was less noticeable than those found using SPR transducers.

Sabarez et al. (2012) developed a combined direct-contact/air borne ultrasonic system using a SPR transducer. The radiator was placed at a certain distance from the sample but a series of solid contacts (metal bars) connected the radiator and the metallic sample tray. In this way, the sample tray was ultrasonically vibrated and certain amount of the ultrasonic energy by-passed the air and directly reached the sample. Using the combined ultrasonic application system, the authors tested its effect on the drying of apple at different levels of ultrasonic power (up to 90 W) and 40°C and 60°C. Experimental results showed that the drying time reduction caused by ultrasonic application was also dependent on the ultrasonic power reaching figures up to 57%.

33.4.2 Airborne applications

Simply considering the energy issue, direct-contact applications are more suitable than airborne ones due to the limitations associated with ultrasonic propagation in air. So why were airborne ultrasonic applications explored? The main reason lies in the fact that adapting ultrasonic transducers and radiators working in direct-contact mode in current industrial driers is complicated. Consequently, the idea of creating high-energy-level pressure in the air chamber emerged and airborne ultrasound has been addressed by the PUG and ASPA research teams and the company Pusonics S.L. The first works addressing airborne ultrasound were carried out using hot air as a medium for water removal. Based on these results, the use of ultrasound to improve low-temperature drying has recently been explored. In this section, the use of ultrasound in both cases will be analyzed.

As already shown in direct-contact applications, the extension of ultrasonic effects is largely dependent on energy issues. In order to address this issue, the simplest analysis consists in varying the power supplied to the ultrasonic transducer up to the maximum power capacity of the ultrasonic device, as depicted in Figure 33.15 for direct-contact application. Figure 33.16 shows this kind of experiment for drying eggplant (Garcia-Perez et al., 2011) although it has also been performed for several other fruits, vegetables, meat, or fish (Table 33.1).

First of all, it should be noted that the units of ultrasonic power reported in Figures 33.15 and 33.16 are different. In Figure 33.15, it is expressed as the electric power supplied to the ultrasonic transducer, while in Figure 33.16, the electric power is divided by the inner volume of the cylindrical radiator, and thus, it refers to the ultrasonic power density. In this regard, it would be more accurate to record the average sound pressure level (SPL) in the medium for each experiment, but practical difficulties make this a very time-consuming and costly measurement.

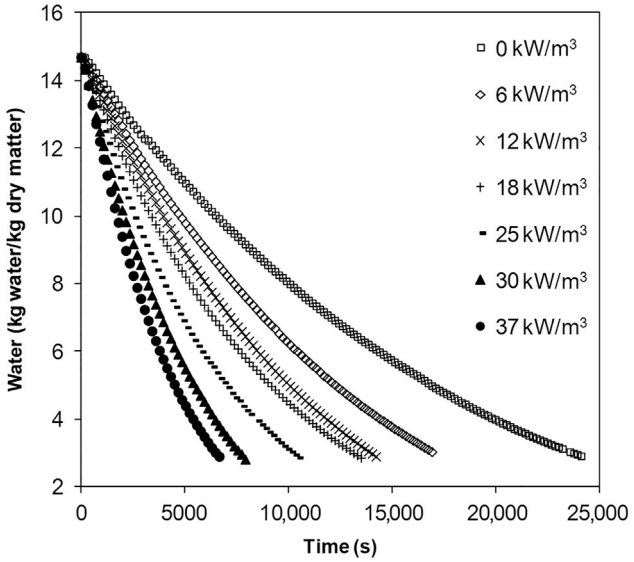


FIGURE 33.16 Drying kinetics of eggplant of eggplant cylinders (height 2 cm and diameter 2.4 cm) carried out at 40°C, 1 m/s and applying different ultrasonic powers (kW/m^3). Airborne application (CR). *(Reprinted from Garcia-Perez et al. (2011), with kind permission of Taylor & Francis, Ltd.)*

As observed in Figure 33.16, the airborne ultrasonic application in the hot air drying of eggplant was very effective, although the effect seems to be less than for direct-contact applications (Figures 33.14 and 33.15). In addition, it was found that an increase in ultrasonic power results in faster drying, as the drying rate is proportional to the ultrasonic power. Thus, the average drying time was shortened by approximately 70% when the maximum power capacity of the transducer (37 kW/m^3) was applied. It should be noted that the effect of ultrasound is not saturated, so even greater improvements should be possible if higher ultrasonic powers are applied.

The kinetic improvement was also accompanied by an energy saving (Table 33.2), which was calculated measuring the power consumption of the ultrasonic transducer, heating elements and fan and considering the drying time needed in each experiment (Riera et al., 2011). Energy consumption varied from 1.15 (without ultrasound) to 0.49 kWh (highest ultrasonic power applied) representing an energy saving of more than 50%. Although this result should be validated on a larger scale, it is worth mentioning when considering further industrial applications. The low energy consumption does not only provide a cost saving but also a positive environmental impact. In this sense, Merone et al. (2020) analyzed the energy consumption and the environmental impact by life cycle assessment (LCA) in an ultrasonically assisted drier working at temperatures below the product freezing point. When ultrasound was applied, the energy consumption of the drying process was reduced up to 70%. However, the LCA analysis evidenced reductions of between 58% and 82% for every impact category. Merone et al. (2020) concluded that both the energy saving and LCA impact category are highly dependent on the product being dried.

TABLE 33.2 Drying time and total energy consumption for drying experiments of eggplant cylinders carried out at different ultrasonic powers and 40°C and 1 m/s. (mass load 70.5 ± 5.8 g)

Power (kW/m^3)	Time (h)	Time saving (%)	Total energy (kWh)	Energy saving (%)
0	6.39		1.15	
6	4.70	26.4	0.92	0.20
12	3.89	39.1	0.82	0.29
18	3.70	42.1	0.83	0.28
25	2.84	55.6	0.68	0.41
30	2.10	67.1	0.54	0.53
37	1.80	71.8	0.49	0.58

Time and energy savings were calculated regarding the experiments without ultrasound application (0 kW/m^3).

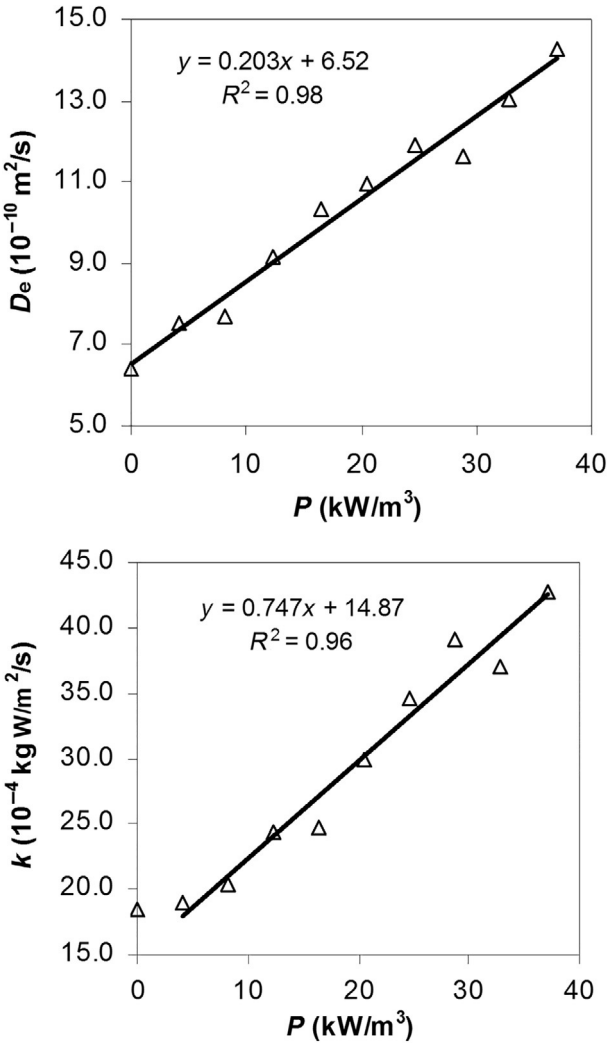


FIGURE 33.17 Influence of the ultrasonic power (P, kW/m^3) on the average effective moisture diffusivity (D_e) and the mass transfer coefficient (k) for lemon peel drying at 40°C and 1 m/s. Airborne application (CR).

From modeling tools and simultaneously considering a mass transport process controlled by convection and diffusion, it has been confirmed that the improvement in water removal is linked to the enhancement of both external and internal transport (Garcia-Perez et al., 2011) (Figure 33.17). Mechanical phenomena associated with ultrasonic wave propagation as mentioned in Section 33.2 could be responsible for increasing both effective moisture diffusivity and the external mass transport coefficient, with the effect being proportional to the ultrasonic power applied. As observed in Figure 33.17 with the maximum power applied, the ultrasound application doubled both kinetic parameters resulting in an increase of around 100%. As repeatedly mentioned, considering the behavior and trends observed in Figure 33.17, even larger increases

should be expected if higher ultrasonic powers were applied. In this regard, it should be mentioned again that in direct-contact applications, effective diffusivity was increased by up to one order of magnitude when drying carrot and apple (Gallego-Juárez et al., 2007).

Another aspect to be considered is the effect on the application of operational parameters not linked to ultrasound application. Analysis has been carried out into the effect of the mass load density (Carcel et al., 2010), air velocity (Garcia-Perez et al., 2006a, 2007; Cárcel et al., 2007a), and temperature (Garcia-Perez et al., 2012b) on airborne ultrasonic-assisted drying. The influence of mass loaded in the drying chamber lies in the available energy per unit of mass. In addition, high mass load densities may disrupt the air flow pattern in the drying chamber. Therefore, in order to analyze how this variable affects the airborne ultrasonic application, drying experiments of carrot cubes were carried out at 30 kW/m^3, 40°C and 1 m/s in a wide range of mass load (from 12 to 120 kg/m^3) (Carcel et al., 2010). A sample holder consisting of 10 trays was placed in a cylindrical radiator. Statistical analysis revealed that even considering the large experimental variability, the application of airborne ultrasound increased the average effective moisture diffusivity in all the ranges tested (Figure 33.18). However, for the external mass transport coefficient, it was found that at high mass load densities, the differences between experiments with and without ultrasound application were not significant ($P < .05$). This fact suggests that applying 30 kW/m^3, the saturation point should be close to 120 kg/m^3, beyond which the available acoustic energy per unit of mass could be ignored.

As reported in Section 33.1, air velocity affects the convective mass transport, so in conventional drying, there is an upper threshold beyond which it should not influence the drying rate since water removal is controlled totally by internal diffusion. This behavior is reported in Figure 33.19 where the effective moisture diffusivity identified in persimmon and carrot drying is plotted for experiments carried out at different air velocities (Garcia-Perez et al., 2007). The increase in effective diffusivity with air velocity should not be misunderstood since the model did not consider the convective transport, so the effective moisture diffusivity includes not only diffusion but also convective phenomena, which affect the drying rate. It is observed that the ultrasonic effect was only significant at low air velocities; thus from approximately 4 m/s, the influence of ultrasound was negligible.

This fact could be explained by considering that ultrasound is only able to affect convective transport. But, as already reported in this work, the ability of ultrasound to improve diffusion has been stated (Figures 33.17 and 33.18). Otherwise, could air velocity affect the airborne ultrasound application? In order to check this hypothesis, the average sound pressure level in the cylindrical radiator

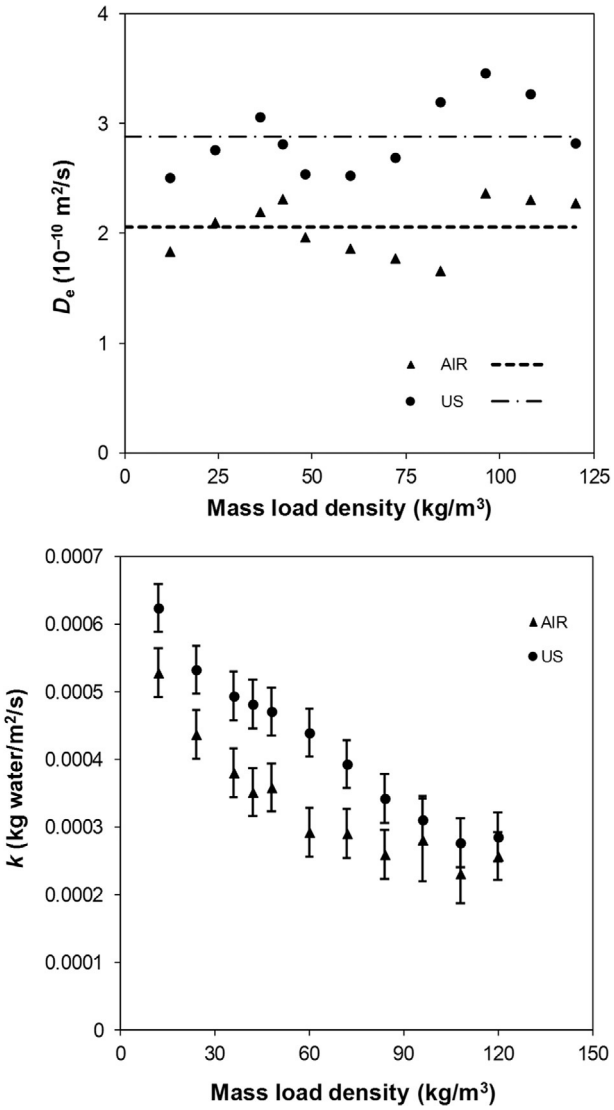


FIGURE 33.18 Influence of the mass load density on the average effective moisture diffusivity (D_e) and the mass transfer coefficient (k) for carrot cubes drying at 40°C and 1 m/s with (CR, US) and without airborne ultrasound application (AIR). *(Reprinted from Carcel et al. (2010), with kind permission of Taylor & Francis Ltd.)*

was measured blowing air through it at different velocities. Figures 33.20 and 33.21 show how the air velocity affects the average and local sound pressure level, respectively. The increase in air flow reduces the average sound pressure level, from figures close to 157 dB to a stationary value around 154 dB for air velocities higher than 8 m/s. Besides, the high air flow introduces a high level of noise at other frequencies, so it seems that the wind (air) blurred the ultrasonic field (Figure 33.21).

The effect of turbulence on acoustic field disruption has also been addressed in a liquid media; thus, the acoustic energy produced by an ultrasonic bath (20 kHz) decreased when a mechanical stirrer is used, compared to those

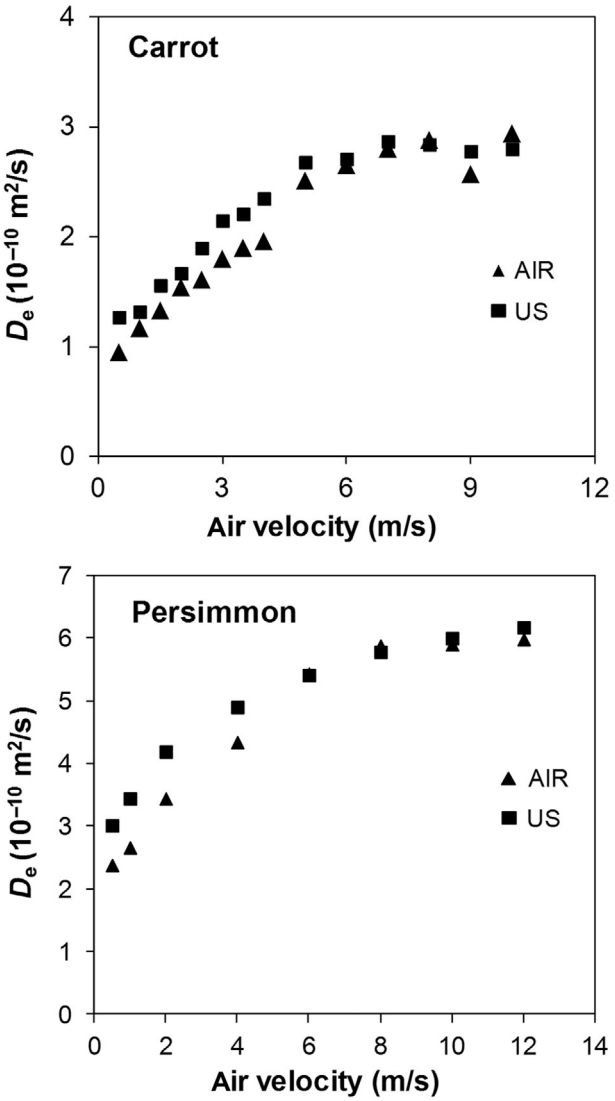


FIGURE 33.19 Influence of the air velocity on the effective moisture diffusivity (D_e) for persimmon cylinder and carrot cubes drying at 40°C, different air velocities and with (CR, US) and without airborne ultrasound application (AIR). *(Adapted from Garcia-Perez et al. (2007), with kind permission of Elsevier Ltd.)*

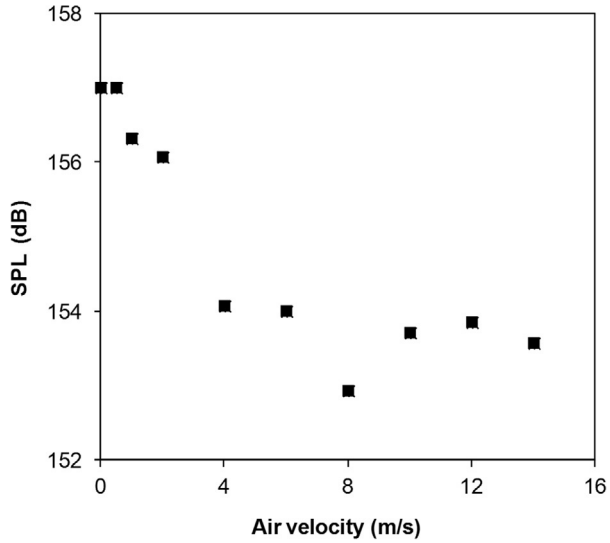


FIGURE 33.20 Influence of the air velocity on the average sound pressure level (SPL) generated by the cylindrical radiator (CR) at different air velocities applying an ultrasonic power of 31 kW/m^3. *(Adapted from Riera et al. (2011), with kind permission of John Wiley & Sons, Ltd. and Institute of Food Technologists.)*

without agitation (Mulet et al., 2003). The influence of air velocity was also observed in airborne ultrasound applications using the stepped-plate radiator, so the effect of ultrasound on carrot drying at 3 m/s was almost negligible (Gallego-Juárez et al., 1999, 2007). The effect of air velocity over airborne ultrasound drying largely restricted its application to fluidized bed drying of solid pieces (Garcia-Perez, 2007) where high air velocities are needed. However, it should be remarked that most industrial convective driers use low air velocities (around 1–2 m/s) due to their large capacities (volumes). Therefore, the introduction of ultrasound energy seems really promising at least for these experimental conditions.

The driving force for convective transport during convective drying lies in the enthalpy of the air mass, which is mainly dependent on air temperature. Thus, water evaporation involves a temperature drop in the air. When ultrasound is applied, both thermal energy and mechanical energy are available in the medium to improve drying. But could temperature affect the ultrasonic effects?

It is widely known that ultrasonic propagation is sensitive to temperature; thus, ultrasonic velocity and acoustic impedance are temperature dependent. This last has been widely addressed in ultrasonic applications for nondestructive testing (Povey and McClements, 1992), but the study of its effect on high power applications is lacking. Figure 33.22 shows drying kinetics of carrot slices carried out at 1.3 m/s and different air temperatures using a SPR transducer (Gallego-Juárez et al., 2007). From experimental results, it is observed that the effect of ultrasound on drying kinetics was significant at 60°C and 90°C, but it was undetected at 115°C. In similar experiments using the CR, it was observed that the effects of ultrasound on the effective moisture diffusivity and mass transport coefficient were reduced at temperatures above 60°C (Figure 33.23) (Garcia-Perez et al., 2006a). Thus, it seems that the effectiveness of airborne ultrasonic application is greatly reduced at high temperatures. This fact could be linked to the proportion of mechanical energy in the medium: the higher the temperature, the lower the acoustic/thermal energy ratio. Thus, there is an upper temperature limit beyond which acoustic energy is almost negligible compared to the total energy available in the medium. Therefore, drying at high temperature is a handicap for ultrasonic intensification.

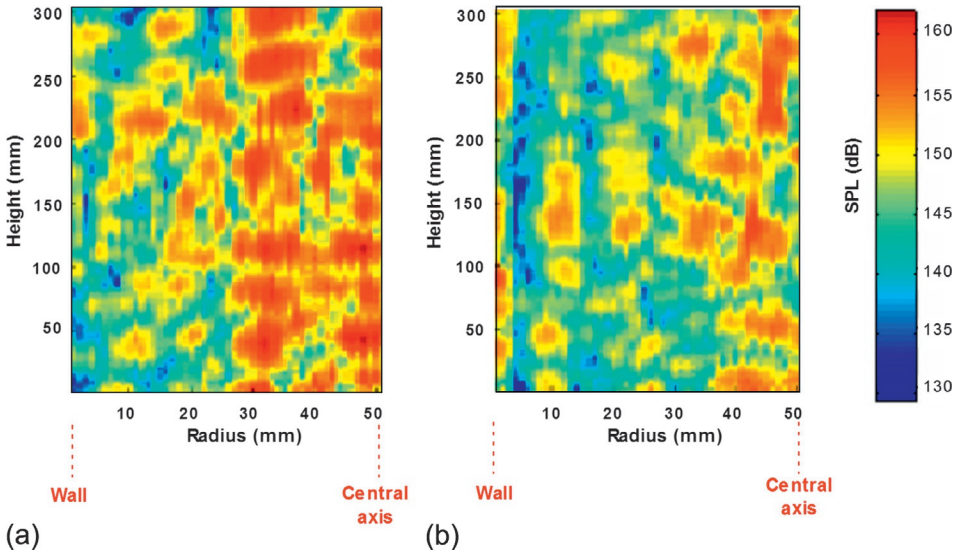


FIGURE 33.21 Influence of the air velocity on the local sound pressure level (SPL) generated by the cylindrical radiator (CR) at 0 (a) and 14 m/s (b) applying an ultrasonic power of 31 kW/m^3. *(Reprinted from Riera et al. (2011), with kind permission of John Wiley & Sons, Ltd. and Institute of Food Technologists.)*

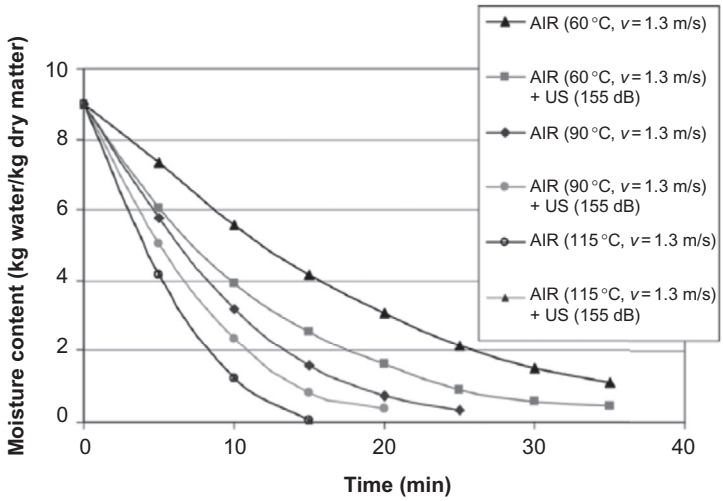


FIGURE 33.22 Drying kinetics of carrot slices at 1.3 m/s and different temperatures with (SPR, AIR + US) and without (AIR) airborne ultrasound application. *(Reprinted from Gallego-Juárez et al. (2007), with kind permission of Taylor & Francis, Ltd.)*

However, this feature opens a new window in the drying field, in which the use of ultrasound seems even more interesting, that is, low-temperature drying.

An important and innovative area in airborne ultrasound applications is low-temperature drying (LTD). LTD may be defined as the dehydration process carried out at temperatures below standard room conditions, e.g., below 20°C or 25°C. Thus, low-temperature drying involves temperatures below and above a product's freezing point. Vacuum freeze drying or lyophilization is the main example of low-temperature drying; this technique provides high-quality dried products, preserving the nutritional properties of fresh food (Ratti, 2001). On freeze drying, the reduction of total and vapor pressure involves an increase in the water removal rate and keeps the temperature of the wet product low, but makes the water removal process very costly. For that reason, freeze drying is only used for high-quality foodstuffs, being more popular in the chemical, pharmaceutical, and biotechnological industries. Otherwise, drying at low temperature can be also performed at atmospheric pressure (Heldman and Hohner, 1974), which simply consists of blowing air at low temperature through the drying chamber where the sample is placed. Thereby, if air temperature is below the product's freezing point, dehydration entails the atmospheric freeze drying (AFD); on the contrary, above the product's freezing point, water state in the particle

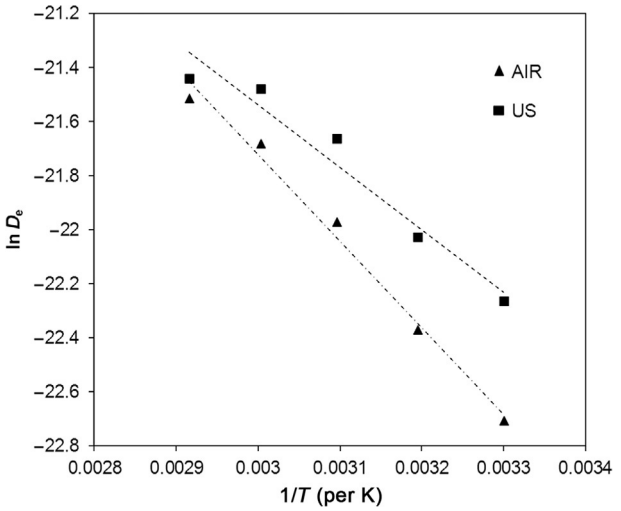


FIGURE 33.23 Influence of the air temperature on the average effective moisture diffusivity (D_e) for carrot cubes drying at 1 m/s with (CR, US) and without airborne ultrasound application (AIR).

is liquid. Drying at low temperature also enables high-quality products to be obtained and makes continuous processing feasible (Stawczyk et al., 2007) so reducing the processing costs compared to vacuum freeze drying (Wolff and Gilbert, 1990a,b). However, at atmospheric pressure, drying at low temperature is quite slow. Coupling new technologies to convective drying at low temperature is an alternative and feasible means of intensification. Due to the temperature needing to be low, the use of novel technologies with high thermal effects, such as infrared radiation or radiofrequency, is complicated since accurate control of the application is required to avoid overheated spots. This drawback is much less significant in the application of ultrasound, which is mainly based on mechanical effects.

Earlier attempts at using acoustic waves to improve drying were addressed by Moy and DiMarco (1970, 1972) who tested the ultrasonic application in both vacuum and non-vacuum freeze drying. In vacuum conditions (Moy and DiMarco, 1972) and using a direct-contact ultrasonic application, they reported an increase in the drying rate of up to 6% for beef samples. However, in atmospheric freeze drying, Moy and DiMarco (1970) reached increases in the drying rate of between 10% and 100% for distilled water, coffee, and tea extracts, which used a steam-jet whistle working within the human hearing range (10.8 and 12.2 kHz). This strategy partially avoids the high acoustic energy attenuation in air systems; however, it may involve an intense noise that could represent a barrier to its use in industrial applications. Recently, other research groups (Bantle and Eikevik, 2011; Schössler et al., 2012b) have also developed low-temperature drying processes assisted by power ultrasound, both direct-contact and airborne, using commercial devices. The results obtained in these works regarding ultrasonic efficiency have been similar to those demonstrated by Moy and DiMarco (1970, 1972) and have also been constrained by the poor transmission of acoustic energy, and low energy available in the medium.

PUG, PUSONICS S.L., and ASPA teams developed a new technique for low-temperature drying assisted by ultrasound (PCT/ES2012/070652, Carcel et al., 2011), which can be applied to liquid, solid, and semi-solid materials to remove not only water, but also other solvents impregnated into them. Even though in the early stages of the technology development, the effect of ultrasound to improve the drying rate of several fruits and vegetables has been shown (Figure 33.24), and drying time reductions of around 70% have been achieved for all products. From modeling, it was determined that the improvement by the application of ultrasound on effective moisture diffusivity (up to 428%) was much larger than for the external mass transport coefficient (up to 170%). This behavior was explained (Garcia-Perez et al., 2012b) by jointly considering both the particular water transport at −14°C and the peculiar structure of the dried material; these aspects will be clarified in the following section where the interaction of the product structure is analyzed. Recent publications have confirmed that the effect of process variables in the ultrasonically assisted low-temperature drying was very similar (Santacatalina et al., 2014, 2015a,b, 2016a,b,c) to the already analyzed for hot air drying applications. The only fact that should be highlighted is the prevalence of the internal resistance to mass transport over the external one due to the low temperature applied, which keeps in low figures the effective moisture diffusivity. Thereby, the influence of the air velocity on the drying kinetics is milder (Santacatalina et al., 2016b) than in the case of hot air drying and experimentally involves that for values higher than 2 m/s, the control of the drying rate is entirely ascribed to the internal moisture diffusion.

The capacity of airborne ultrasound to intensify the removal of organic solvents (Figure 33.25) at very low (−14°C) temperatures has already been explored (Garcia-Perez et al., 2012b), showing a similar kinetic improvement to the one found for drying of foods (around 70% reduction in the removal time). Moreover, the effect of airborne ultrasound for jointly removing moisture and organic solvents at mild temperatures (50°C) has also been tested (Rojas et al., 2020) in raw apple pretreated in ethanol. The removal of organic solvents represents a relevant application of the airborne ultrasonic drying technique for chemical and pharmaceutical sectors in which the use of these solvents is common as underlined in the patent PCT/ES2012/070652 (Carcel et al., 2011).

By using the new convective drier of ASPA (Figure 33.11), an experimental study has been developed to determine the AFD effect assisted by the ultrasonic radiation generated by an airborne SGPR transducer (Figure 33.12). Experimental tests have been conducted at constant air flow velocity

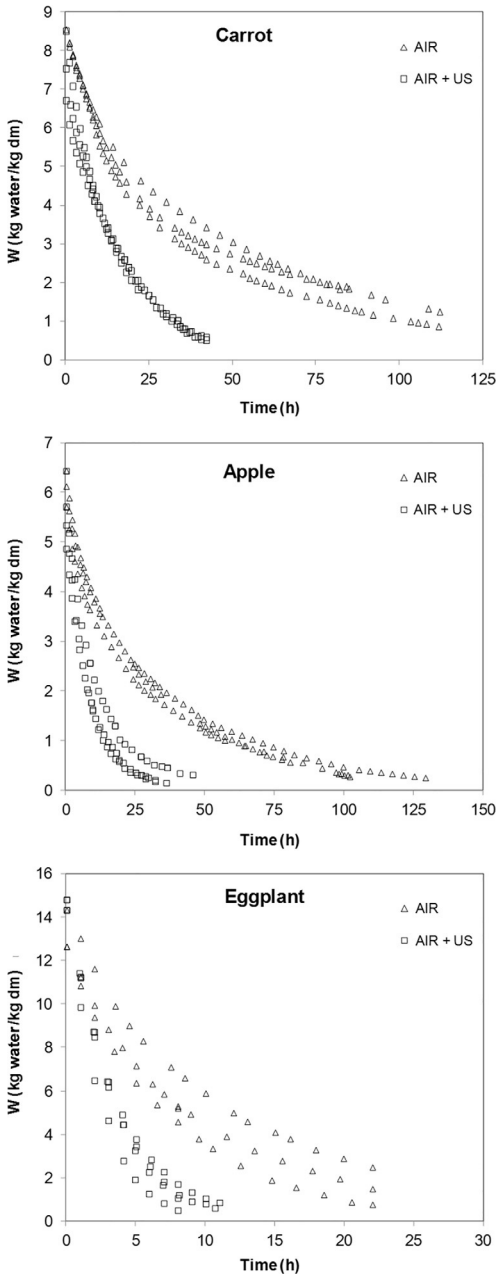


FIGURE 33.24 Drying kinetics of carrot, apple, and eggplant cubes at (−14°C, 2 m/s) with (CR, AIR + US) and without (AIR) airborne ultrasound application. *(Reprinted from Garcia-Perez et al. (2012b), with kind permission of Taylor & Francis, Ltd.)*

(1 m/s), constant temperature (−12°C), and relative humidity below 7% applying three levels of acoustic power (50, 100, and 200 W). Apple slices of 3 mm thickness frozen at −35°C for 1 h with mass loads from 80 up to 100 g have been used for the atmospheric freeze-drying tests. The results confirm that ultrasound application increased both the effective diffusivity and the mass transfer coefficient in about 30% with 50 W and 66% with 200 W supplied (Figure 33.26) (Andrés et al., 2021). Therefore, it has been evidenced that

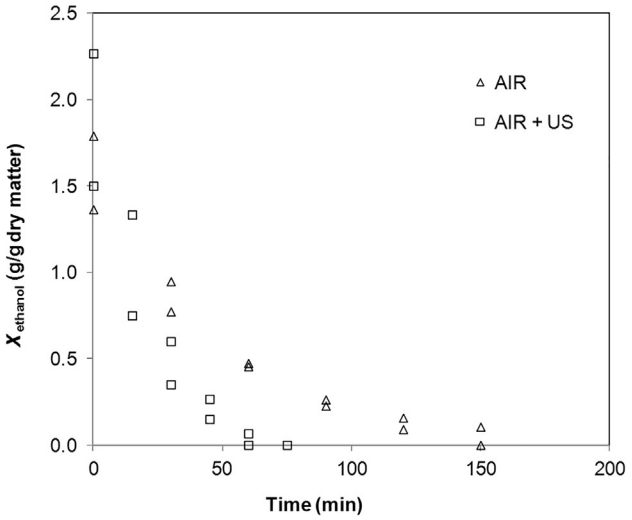


FIGURE 33.25 Kinetics of ethanol removal from dried apple at (−14°C, 2 m/s) with (CR, AIR + US) and without (AIR) airborne ultrasound application. *(Reprinted from Garcia-Perez et al. (2012b), with kind permission of Taylor & Francis, Ltd.)*

the scaling-up of the airborne ultrasonic drying is feasible, which brings to light about the potential industrial implementation of this technology.

33.5 Product properties affecting the effectiveness of ultrasonic drying

The influence of the product structure on ultrasonically assisted drying may be analyzed from two different points of view. On the one hand, it is necessary to determine if the structure affects the extension of the ultrasonic effects, since it is well known that the propagation of ultrasonic waves is largely dependent on the material through which the mechanical waves travel. On the other hand, it also has to be considered whether the mechanical phenomena produced by the ultrasonic waves cause some modifications to the product structure.

In Section 33.4, it was shown how an increase in the ultrasonic power results in faster drying due to the improvement of diffusion and convective kinetic parameters. This fact is also observed in Figure 33.27 for carrot drying, although, if it is compared with Figure 33.17, some differences arise (Garcia-Perez et al., 2012a). First of all, it is found that the improvement in the kinetic parameters for carrot drying did not appear until the acoustic power exceeded a minimum value. However, the influence of ultrasonic application in lemon peel drying was even noticeable when the acoustic energy in the chamber was low (Figure 33.17). Consequently, reaching a minimum acoustic energy level in the drying chamber was necessary to affect the transport phenomena in carrot drying (Figure 33.27). This threshold was between about 8 and 12 kW/m^3. Once the threshold

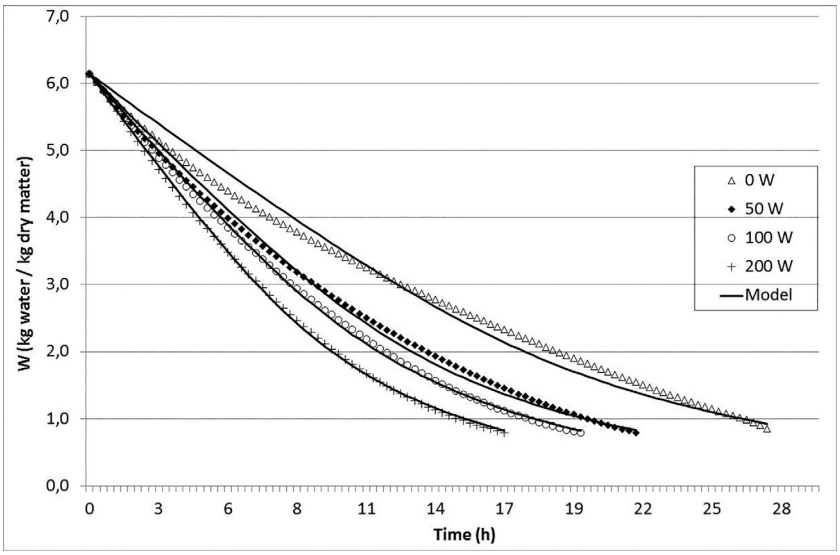


FIGURE 33.26 Drying kinetics at −12°C, 1 m/s, without (0 W) and with ultrasound (50, 100, 200 W) application using the steeped-grooved-plate radiator. *(Reprinted from Andrés et al. (2021) with permission from Elsevier.)*

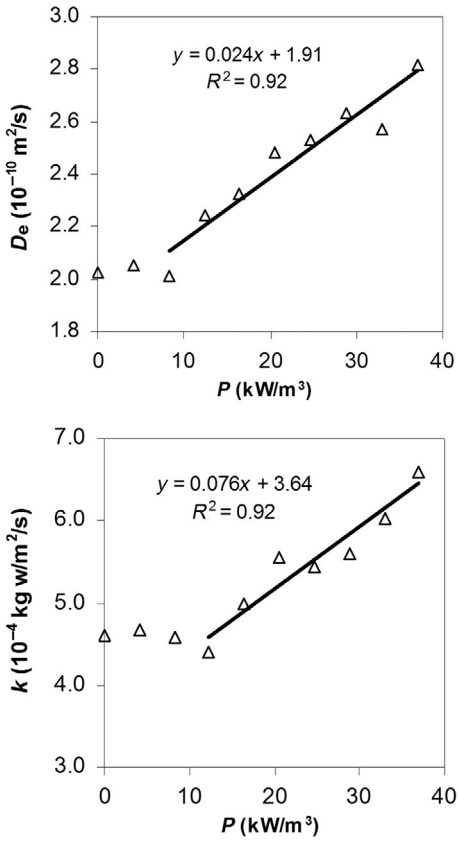


FIGURE 33.27 Influence of the ultrasonic power (P) in the effective moisture diffusivity (D_e) and the external mass transport coefficient (k) identified in the drying of carrot cubes. Airborne ultrasound application (CR).

exceeded, the expected linear increase in the kinetic parameters with the ultrasonic power also becomes apparent for carrot drying. However, the slopes of the linear relationships found for carrot drying are almost one order of magnitude lower than the ones found in lemon peel drying (Figure 33.17), which suggests a greater influence of the application of power ultrasound on mass transfer in lemon peel than in carrot drying. Ozuna et al. (2014a) defined the aforementioned slopes as SDUP, **S**lope of **D**iffusivity versus **U**ltrasonic **P**ower, which quantifies the performance or effectiveness of the ultrasonic application on the convective drying of a particular food material.

The fact that lemon peel and carrots behave so differently due to acoustic energy could be linked to their structure, lemon peel being more porous than carrot (Boukouvalas et al., 2006; Ozuna et al., 2011b). A more exhaustive analysis was carried out by Ozuna et al. (2014a) who analyzed the effect of ultrasonic power in the mass transport for the ultrasonically assisted drying of several products. A significant linear relationship was observed between the SDUP and structural (porosity) and textural (hardness) parameters (Figure 33.28A). In addition, Ozuna et al. (2014a) measured the acoustic impedance of different materials (apple, carrot, potato, eggplant, and cassava) and concluded that the SDUP is strongly linked to this variable (Figure 33.28B). For instance, on the one hand, the high air content and low elastic modulus in the eggplant result in a low density (550 kg/m^3) and acoustic velocity (250 m/s) and so, in a low acoustic impedance. On the other hand, the higher density (1100 kg/m^3) and velocity (600 m/s) in potato tissue cause an increase in the acoustic impedance, which controls the amount of energy entering into the particle. Thus, the closer

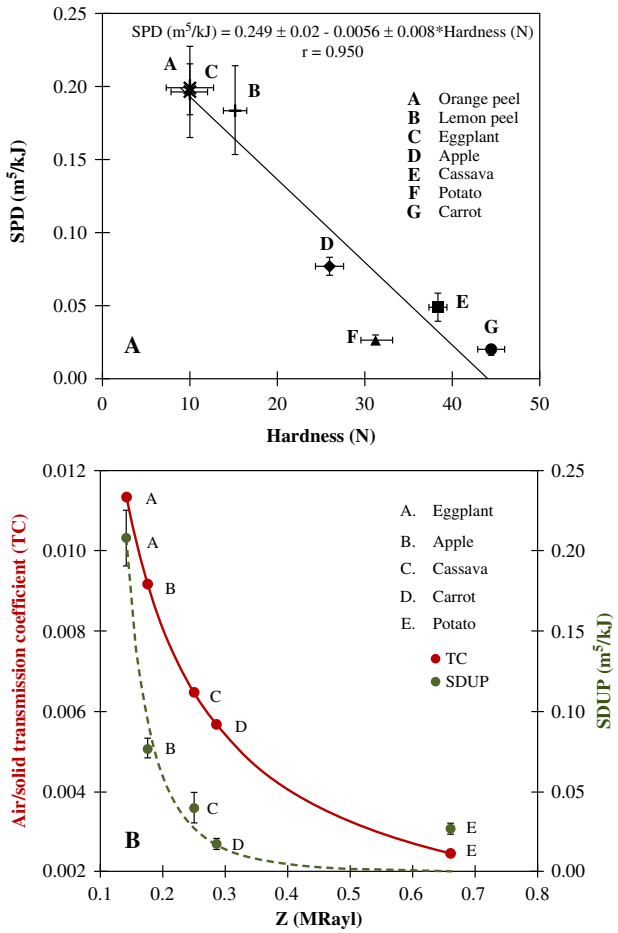


FIGURE 33.28 Influence of the material's hardness on the ultrasonic effectiveness (SDUP) (A) and relationship between the SDUP and the TC with the acoustic impedance (Z) of different vegetable materials. *(Reprinted from Ozuna et al. (2014a) with permission from Elsevier.)*

the product's impedance to the air, the larger the transmission coefficient and as consequence, the larger the amount of energy propagated into the material, which will be available for improving internal mass and heat transport. Eqs. (33.3) and (33.4) show that a similar mathematical pattern exists between the theoretical relationship of the acoustic impedances with the transmission coefficient (33.3) and the empirical one identified by Ozuna et al. (2014a) with the SDUP (33.4), respectively.

$$\mathrm{TC} = \frac{4Z_1Z_2}{(Z_1 + Z_2)^2} \tag{33.3}$$

$$\mathrm{SDUP} = \frac{1.910^{15}Z_1Z_2}{(Z_1 + Z_2)^{4.6}} \tag{33.4}$$

where TC is the air/solid transmission coefficient (dimensionless), SDUP the ultrasonic effectiveness (m^5/kJ), and Z_1 and Z_2 the acoustic impedance (MRayl) of the air and the product, respectively.

The analysis of Ozuna et al. (2014a) should be improved by considering the internal propagation of the acoustic waves in the material. Thus, considering the same acoustic energy level entering the particle, the large intercellular spaces characteristic of high porosity and soft products make it more prone to the compression and expansion of ultrasonic cycles and facilitate water transfer through the solid. The small intercellular spaces and hard structure, characteristic of low-porosity products, involve higher resistance to mechanical stress. As a consequence, high acoustic energy levels are required in dense products to achieve the same mechanical stress in the particle. Besides, greater acoustic energy absorption by attenuation is also expected in highly porous products due to a larger gas volume producing an increase in the internal energy available in the particles. Moreover, the acoustic effects on the boundary layer of intercellular spaces could be more intense in high-porosity products due to a larger porous net. Indeed, these phenomena may also contribute to reduce internal resistance to mass transfer.

The influence of material structure has also been observed in other cases. For example, Garcia-Perez et al. (2007) found a significant influence of airborne ultrasound application in the hot air drying of lemon peel at high air velocities (Figure 33.29). Despite a reduction in the acoustic energy produced by the high air flow, as explained in Section 33.4, the energy still available in the drying chamber was enough to improve the water removal of a soft and porous product, like lemon peel with low acoustic impedance. However, as already mentioned, the effect of airborne ultrasound application on carrot and persimmon hot air drying was negligible at these conditions (Figure 33.19).

The application of airborne ultrasound application in low-temperature drying (Garcia-Perez et al., 2012b; Carcel et al., 2011) showed relevant differences not found previously in

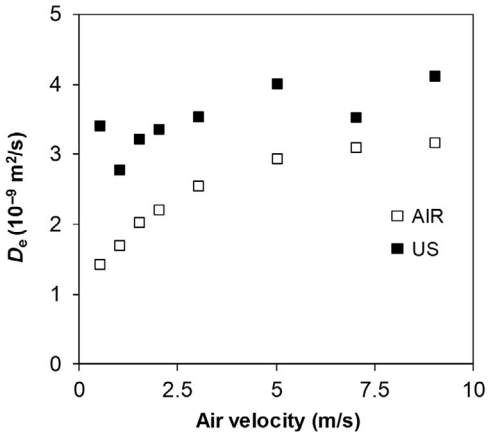


FIGURE 33.29 Influence of the air velocity on the effective moisture diffusivity (D_e) for lemon peel drying at 40°C, different air velocities and with (CR, US) and without airborne ultrasound application (AIR). *(Adapted from Garcia-Perez et al. (2007), with permission of Elsevier Ltd.)*

hot air drying regarding the interaction with the material being dried. First of all, it was observed that the extent of ultrasound effects was very similar (Figure 33.24) for three products with very different original structures, namely, apple, eggplant, and carrot. Why would materials with different structures behave in a similar way at low temperature? Garcia-Perez et al. (2012b) suggested that during hot air drying, shrinkage is a significant phenomenon, which keeps the product porosity almost constant since the mass loss is partly buffered by volume reduction. Nevertheless, in atmospheric freeze drying (−14°C), all the products are being converted into high-porosity matrixes with low acoustic impedance because the product loses weight (water) but the volume remains constant (shrinkage is almost negligible). At these conditions, and considering the most commonly adopted mechanistic theory of the "**URIF-U**niformly **R**etreating **I**ce **F**ront" (Santacatalina et al., 2015a), vapor diffusion happens in the dry outer layer, which gets thicker as drying progresses and the ice core remains in the inner part. Thereby, the ultrasonic phenomena occur in the outer porous layer in all cases, and this is the reason why the ultrasound effect was similar for such different initial matrixes, like eggplant and carrot. Therefore, the influence of original structure on the acoustic effectiveness is largely mitigated when drying below the product's freezing point.

As mentioned in Section 33.4, modeling results from low-temperature drying kinetics showed that the effect of ultrasound was more intense in the effective moisture diffusivity than in external mass transport coefficient (Garcia-Perez et al., 2012b), a fact not previously observed in hot air drying. At low-temperature drying, sublimation occurs at the ice core, so the water vapor diffuses through the porous net to the surface, while for hot air drying, internal water diffusion is mainly in the liquid state. Therefore, it could be expected that the mechanical expansions and contractions produced by ultrasound affect the vapor more than liquid water diffusion.

33.6 Structural changes caused by ultrasound drying

The mechanical stress caused by the airborne ultrasonic application during convective drying not only may improve mass transport but also could induce modifications in the structure of the product being dried, which usually are not visible at macroscopic level but at microscopic one. The use of ultrasound in liquid medium as a pretreatment and effective method to cause structural alterations has also gained the attention of the scientific community for the last years (Llavata et al., 2020), but this will not be addressed in this chapter devoted only to airborne ultrasonic applications.

Figure 33.30 shows cryo-SEM micrographs of the internal flesh (endocarpic tissue) of eggplant dried under

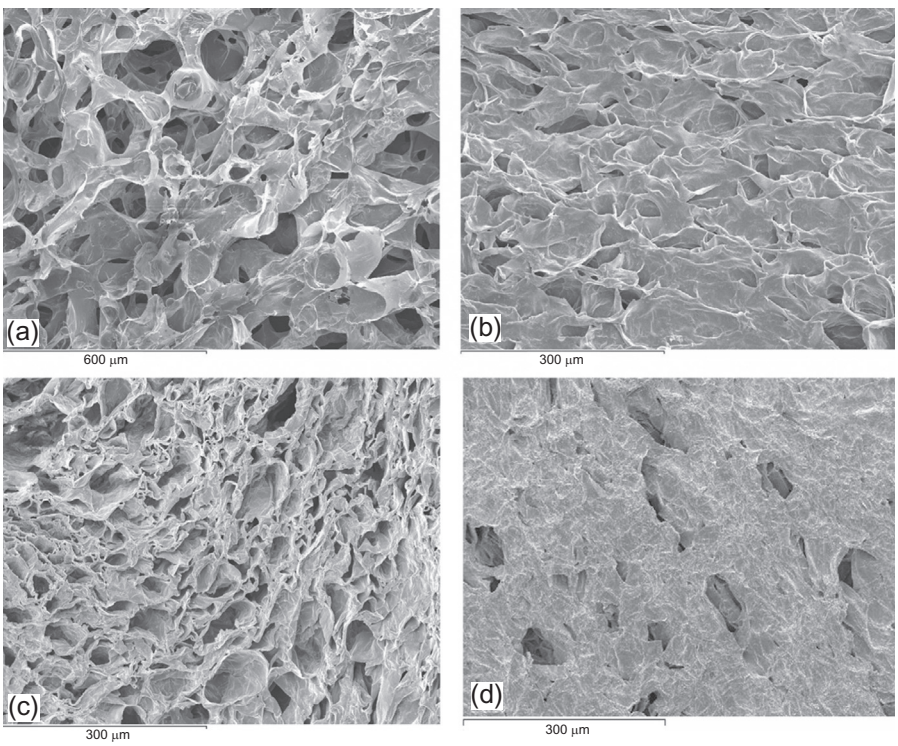


FIGURE 33.30 Cryo-SEM micrographs of the endocarpic tissue in raw eggplant (a) and in dried eggplant samples without (b) and with airborne ultrasound application (CR) at two different ultrasonic power applied 18 (c) and 37 kW/m^3 (d). *(Reprinted from Puig et al. (2012), with kind permission of Elsevier Ltd.)*

different ultrasonic powers (Puig et al., 2012). The cells of the endocarp for samples dried using a mild ultrasonic power (18 kW/m^3, Figure 33.30C) still maintained their individuality and even intact cell walls were found, showing a better structure than those dried without ultrasound application (Figure 33.30B). The better structure was linked both to shortening the drying time (almost 40%) and to the mild mechanical compression and expansion produced by ultrasound. However, when a high ultrasonic power was applied (37 kW/m^3, Figure 33.30D), a highly compacted tissue appeared, even when the drying time was very short (70% less than in experiments without ultrasound application). The significant compaction at high acoustic levels is ascribed to the intense compression and expansion produced by ultrasound in the weak structure of eggplant; the same effect has also been observed in orange peel (Garcia-Perez et al., 2012a) and apple drying (Sabarez et al., 2012; Rodríguez et al., 2014). Rodríguez et al. (2014) manifested that the structural effects caused by the ultrasonically assisted drying were dependent on the temperature used; thus, at moderate temperature (50°C), the structure of dried apple was better preserved than drying at lower (30°C) or higher (70°C) temperatures. The internal structural effects can also be observed in materials with lower porosity, such as potato (Schössler et al., 2012c), beetroot (Vallespir et al., 2018), and meat and fish. Thus, for example, Ozuna et al. (2014b) reported ruptures in fibers, wider spaces between myofibrils, or a more intense salt redistribution in ultrasonically dried salted cod. Section 33.7 will address the question whether structural damage is accompanied by a loss of nutritional components, as has been observed in other ultrasound applications (Soria and Villamiel, 2010).

Structural alterations in the product surface have also been linked to the mechanical effects produced by ultrasound in the interfaces. In airborne ultrasonic drying of orange peel, Garcia-Perez et al. (2012a) observed a disruption in the waxy compounds of the flavedo cuticle. Air drying provoked the loss of the characteristic distribution of the waxy components, which were spread on the cuticle surface and obstructed some pores (Figure 33.31C). Despite the spread of the waxy component in the air-dried samples (Figure 33.31C), the waxy ring shape around the pores is still well defined. However, when ultrasound is applied at a higher power (37 kW/m^3), the ring shape appeared blurred (Figure 33.31D) and all the pores are completely obstructed by the waxy components. The intense spread of waxy compounds observed on the cuticle confirms the effects of ultrasound application on the interfaces. The mechanical effects

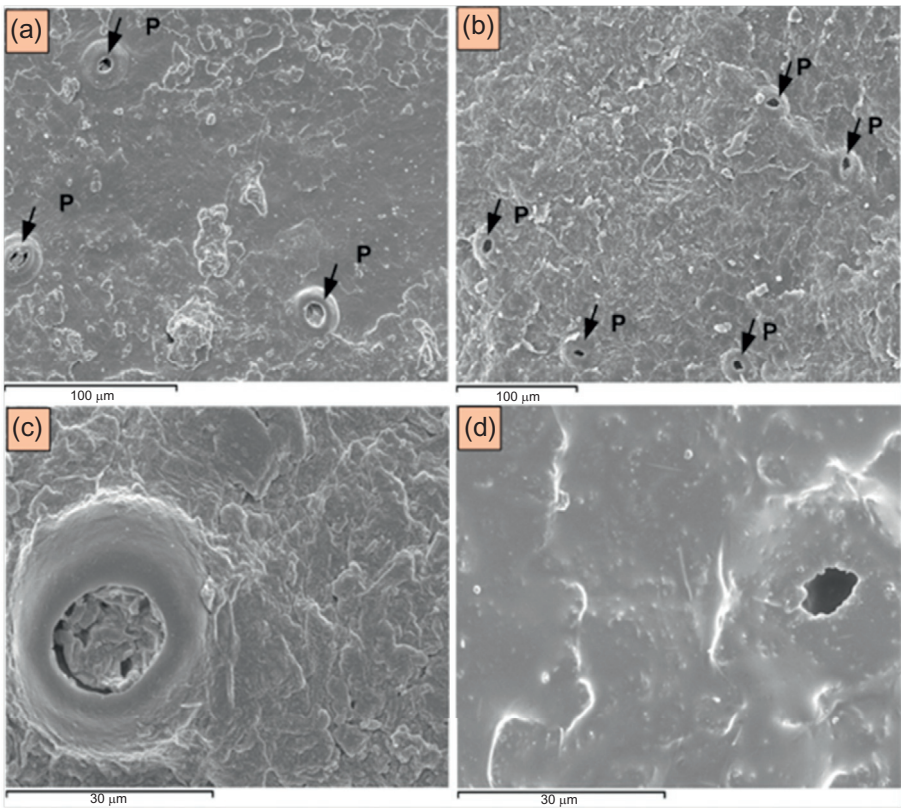


FIGURE 33.31 Cryo-SEM micrographs of cuticle surface: (a) fresh orange peel; (b) hot air dried; (c) detail of pore in air dried and (d) detail of pore in ultrasound-assisted dried samples (37 kW/m^3). (*P*, pores). Airborne ultrasound application (CR). *(Reprinted from Garcia-Perez et al. (2012a), with kind permission of Elsevier Ltd.)*

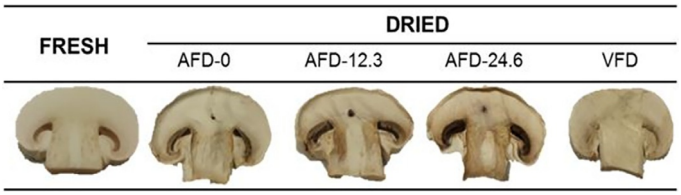


FIGURE 33.32 Fresh mushroom slices, dried by atmospheric freeze drying without (AFD-0) and with ultrasound application, at 12.3 (AFD-12.3) and 24.6 kW/m^3 (AFD-24.6), and dried by vacuum freeze drying. *(Reprinted from Carrión et al. (2018), with kind permission of Taylor and Francis.)*

(alternating compressions and pressure variations) produced by ultrasound waves on the interfaces should bring about not only a greater spread of waxy components on the cuticle but also an improvement in the convective water transport. Modifications of the epidermic surface of eggplant were also illustrated by Puig et al. (2012).

Structural modifications caused by ultrasonically assisted drying may also affect the reconstitution capacity of the dried samples, as well as their textural properties. Thus, Ozuna et al. (2014b) reported an increase in the final water content during rehydration of ultrasonically assisted dried salted cod compared to the conventionally dried ones, and Soria and Villamiel (2010) observed a greater rehydration ability of carrots. On the contrary, noticeable differences have not been found in the rehydration of more porous dried materials with or without ultrasound application, such as eggplant (Santacatalina et al., 2016a) or mushroom (Carrión et al., 2018). The creation of microfissures and microchannels by ultrasound application during drying may increase the paths for water diffusion in low-porosity material, such as cod or carrot, facilitating the water uptake and contributing to a higher rehydration ratio. On the contrary, this fact could be considered almost negligible in materials of larger porosity, such as eggplant or mushrooms.

The influence of ultrasound application in the inner structure can also affect the hardness of dried samples and make them softer than the conventionally dried ones. Thus, Ozuna et al. (2014b) reported that after rehydration, ultrasonically assisted dried (−10°C, 0°C, 10°C, 20°C) salted cod samples were softer than samples dried without ultrasound application. Carrión et al. (2018) observed a similar effect in ultrasonically assisted atmospheric freeze-dried mushrooms (−10°C). In this case, the greater the ultrasonic power applied, the softer the final product. Silva Júnior et al. (2018) also found a softer texture in ultrasonically assisted dried papayas (60°C).

33.7 Impact of ultrasonic-assisted drying on product quality

In recent years, the impact of ultrasonic-assisted drying on several quality attributes that do not link strictly to the food structure has been investigated. Color is one of the most relevant aspects in dried products because it may define the overall acceptability by the consumers. In this sense, ultrasound application during drying can affect the product color in two different ways. On the one hand, the partial collapse of the structure produced by ultrasound can contribute to the release of some components and the development of browning reactions. In this sense, Carrión et al. (2018) found a slight decrease in luminosity when compared atmospheric freeze-dried (−10°C) mushrooms with and without ultrasound application (Figure 33.32). On the other hand, ultrasound shortens drying times, limiting degrading reactions. Thus, compared with conventionally dried samples at the same temperature, Ozuna et al. (2014b) reported higher luminosity in salted cod dried (−10°C and 0°C) with ultrasound application, and Szadzinska et al. (2017) observed lower values of ΔE in ultrasonically assisted dried green pepper (52°C). In the same sense, Kroehnke et al. (2018) found lower ΔE value in carrot dried (45°C) with the application of ultrasound. On the contrary, Schössler et al. (2012b) did not found color differences between freeze-dried red bell pepper (−30°C) dried with or without ultrasound application. Therefore, the influence of ultrasound should be determined for each individual case due to the difference in magnitude of ultrasonic effects produced in each specific product and drying conditions considered.

The effect of ultrasound application during drying in antioxidant properties of products is linked to its interaction with the process variables, such as drying temperature, power applied, and product characteristics. Thus, Rodríguez et al. (2014) found a better retention of antioxidant activity (FRAP and ABTS) of apple dried with ultrasound application at 30°C, while a larger degradation was found at 70°C. Similar results were found by do Nascimento et al. (2016) in the case of passion fruit peel drying, and Cárcel et al. (2019) for red pepper drying. Both studies reported a significant greater antioxidant activity (FRAP) in acoustically dried samples compared to conventionally dried ones at moderate temperatures (40°C and 50°C) but lower at higher ones (60°C and 70°C). Kroehnke et al. (2018) also found greater antioxidant activity (ABTS) in ultrasonically assisted dried carrots at 45°C than in conventionally dried samples. At mild temperature, the effect of ultrasound shortening on the drying process can be positive in the preservation of antioxidant activity. However, at high-temperature drying, degradation kinetics are fast and can be slightly sped up by some cellular disruption produced by ultrasound application.

Recent publications manifested that in low-temperature drying, the application of ultrasound induces a more

noticeable degradation of antioxidant properties than in air drying at high and mild temperature. Thus, Santacatalina et al. (2014) reported a larger degradation of antioxidant activity (FRAP, ABTS, CUPRAC, and DPPH) of apple when ultrasound was applied at drying temperatures from −10°C to 10°C. Colucci et al. (2018) reported a similar result (FRAP) in the case of drying of eggplant at −5, −7.5, and −10°C. The cell disruption is due to the acoustic stress and the long drying time at these temperatures, which largely increases the aeration, and as consequence, the probability of oxidation can be the main reason of these results. In addition, the reduction of antioxidant capacity was similar regardless of the level of ultrasonic power applied (from 10.3 to 30.8 kW/m^3) (Santacatalina et al., 2014; Colucci et al., 2018).

Other important aspect to be taken into account is the size of the dried samples. The influence of ultrasound in the reduction of antioxidant activity could be less in large than in small particles as reported by Moreno et al. (2017) during atmospheric freeze drying of apple or by Colucci et al. (2018) in the case of eggplant. In both studies, the degradation of the antioxidant properties in small samples was more noticeable when ultrasound was applied. This points to the fact that the degradation of antioxidant activity produced by ultrasound could be more intense at the product surface and probably linked not only to a structural effect but also to an enhancement of superficial oxidation reactions. Thus, the high surface/volume ratio of grape skin can explain the large decrease in antioxidant activity when ultrasound was applied during drying found by Cruz et al. (2016). In addition, it could be hypothesized that the lower the product's surface, the lower the specific acoustic impedance, which increases the impedance mismatch with the air, and as consequence, it increases the ultrasonic energy reflected in the interface and diminishes the energy penetrating into the particle.

Drying process and ultrasound application can jointly affect components with bioactivity that can be found in the raw products such as phenolic compounds, vitamins, enzymes, or fiber. In the case of phenolic compounds, the influence of ultrasonic-assisted drying is quite similar to that the analyzed in the previous section for antioxidant activity due to the inherent relationship between both aspects. Thus, the ultrasonically assisted drying at mild temperatures (30–50°C) preserves better the phenolic compounds than the conventional drying. On the contrary, high or low temperatures induce a significant reduction in these components (Cárcel et al., 2019; Colucci et al., 2018; Martins et al., 2019; do Nascimento et al., 2016; Moreno et al., 2017; Rodríguez et al., 2014; Santacatalina et al., 2014; Souza da Silva et al., 2019). In this sense, the content of some vitamins also follows a similar behavior. Although the reported results (Cárcel et al., 2019; Colucci et al., 2018; do Nascimento et al., 2016; Gamboa-Santos et al., 2014a; Fernandes et al., 2016; Martins et al., 2019; Moreno et al., 2017; Vallespir et al., 2019) differ for different products and vitamins, it can be established as a general behavior that the application of ultrasound during drying at moderate and low temperature (5–50°C) can better preserve the vitamin content than the conventional drying process. Furthermore, ultrasound application can improve the bioavailability of some vitamins in some cases. Thus, Fernandes et al. (2015) reported a slight increase in vitamin B6 content of apple dried with ultrasound application. Dried products are frequently used as functional ingredients for different food formula. In these cases, properties related to the fiber content such as swelling capacity and water and fat retention have to be preserved after drying. In this sense, Vallespir et al. (2019) reported a significant increase in fat retention capacity of dried mushroom at low temperature (5°C, 10°C, and 15°C). Similar behavior was found by Mello et al. (2020) during the atmospheric freeze drying (−10°C) of orange peel. On the contrary, Mello et al. (2020) did not observe significant differences when drying at mild temperature (50°C). No influence of ultrasound application during drying has been observed for swelling capacity and water retention (Mello et al., 2020; Vallespir et al., 2019).

33.8 Conclusions and future trends

The use of power ultrasound on drying/dewatering has shown to be highly relevant for foodstuff preservation aiming to pursue a feasible non-thermal processing. The difficult penetration of airborne ultrasonic waves in the solid medium to be dried, due to the impedance mismatch between air and solid, limits the available energy for drying. This is an unquestionably constrain that can be solved by applying the ultrasound in direct contact with the product, but this procedure is not always possible for practical limitations linked to the product and/or the process itself.

The design of efficient, robust, and highly adaptable ultrasonic transducers is fundamental to achieve a competitive position regarding conventional drying technologies. At the same time, the tuning of drying operational parameters plays a key role in reaching an efficient ultrasonic application. Moreover, the interaction between ultrasound and the product has to be conveniently managed not only because it affects the ultrasonic efficiency but also because ultrasound may induce some physical and chemical changes in the food materials, such as affecting texture, antioxidant properties, vitamin content, or appearance of the Maillard reaction. However, these possible changes are in general of little importance if drying takes place at moderate temperatures—that is the way in which the application of ultrasound is more effective to accelerate the drying process.

The good results obtained in the application of ultrasound in low-temperature drying processes, such as atmospheric freeze drying (AFD), is a relevant advance to be

underlined. The low influence of the air velocity on the drying rate and the porous structure that are developed in dried products made that the assistance of ultrasound significantly increases the drying rate. This is a very important factor in these processes due to the long time they require.

Current initiatives for the scaling-up of ultrasonic devices must be necessarily strengthened in the immediate future, bringing this technology closer to industrial drying operations not only in the food sector but also for chemical and pharmaceutical products. In particular, the use of ultrasound to accelerate AFD processes is a very promising line, which clearly requires the study of the best combination of process variables for each product as well as the industrial development of airborne transducers specifically adapted to it.

References

Ahmad-Qasem, M.H., Canovas, J., Barrajón-Catalán, E., Micol, V., Carcel, J.A., García-Pérez, J.V., 2013. Kinetic and compositional study of phenolic extraction from olive leaves (var. Serrana) by using power ultrasound. Innov. Food Sci. Emerg. Technol. 17, 120–129.

Andrés, R.R., Pinto, A., Martínez, I., Riera, E., 2019. Acoustic field generated by an innovative airborne power ultrasonic system with reflectors for coherent radiation. Ultrasonics, 105963.

Andrés, R.R., Riera, E., Gallego-Juárez, J.A., Mulet, A., García-Pérez, J.V., Cárcel, J.A., 2021. Airborne power ultrasound for drying process intensification at low temperatures: use of a stepped-grooved plate transducer. Dry. Technol. 39 (2), 245–258. https://doi.org/10.1080/07373937.2019.1677704.

Arkhangel'skii, M.E., Stanikov, Y.G., 1973. Diffusion in heterogeneous systems. In: Rozenberg, L.D. (Ed.), Physical Principles of Ultrasonic Technology. Plenum Press, New York, NY.

Aversa, M., Curcio, S., Calabrò, V., Lorio, G., 2007. An analysis of the transport phenomena occurring during food drying process. J. Food Eng. 78, 922–932.

Bantle, M., Eikevik, T.M., 2011. Parametric study of high-intensity ultrasound in the atmospheric freeze drying of peas. Dry. Technol 29 (10), 1230–1239. https://doi.org/10.1080/07373937.2011.584256.

Başlar, M., Kiliçli, M., Toker, O.S., Sadiç, O., Arici, M., 2014. Ultrasonic vacuum drying technique as a novel process for shortening the drying period for beef and chicken meats. Innov. Food Sci. Emerg. Technol. 26, 182–190.

Benali, M., Kudra, T., 2010. Process intensification for drying and dewatering. Dry. Technol 28 (10), 1127–1135. https://doi.org/10.1080/07373937.2010.502604.

Bird, R.B., Stewart, W.E., Lightfoot, E.N., 2007. Transport Phenomena, Revised second Ed. Wiley.

Blasco, M., Garcia-Perez, J.V., Bon, J., Carreres, J.E., Mulet, A., 2006. Effect of blanching and air flow rate on turmeric drying. Food Sci. Technol. Int. 12, 315–323.

Bonazzi, C., Dumoulin, E., Raoult-Wack, A.-L., Berk, Z., Bimbenet, J.J., Courtois, F., Trystram, G., Vasseur, J., 1996. Food drying and dewatering. Dry. Technol. 14, 2135–2170.

Borisov, Y.Y., Gynkina, N.M., 1973. Acoustic drying. In: Rozenberg, L.D. (Ed.), Physical Principles of Ultrasonic Technology. Plenum Press, New York, NY.

Boukouvalas, C.J., Krokida, M.K., Maroulis, Z.B., Marinos-Kouris, D., 2006. Density and porosity: literature data compilation for foodstuffs. Int. J. Food Prop. 9, 715–746.

Cárcel, J.A., Garcia-Perez, J.V., Riera, E., Mulet, A., 2007a. Influence of high intensity ultrasound on drying kinetics of persimmon. Dry. Technol. 25, 185–193.

Cárcel, J., Benedito, J., Rosselló, C., Mulet, A., 2007b. Influence of ultrasound intensity on mass transfer in apple immersed in a sucrose solution. J. Food Eng. 78, 472–479.

Cárcel, J., Benedito, J., Bon, J., Mulet, A., 2007c. High intensity ultrasound effects on meat brining. Meat Sci. 76, 611–619.

Carcel, J.A., Garcia-Perez, J.V., Riera, E., Mulet, A., 2010. Improvement of convective drying of carrot by applying power ultrasound. Influence of mass load density. Dry. Technol. 29, 174–182.

Carcel, J.A., Garcia-Perez, J.V., Peña, R., Mulet, A., Riera, E., Acosta, V. M., Gallego-Juarez, J.A., 2011. Method and Device to Improve Mass Transfer in Low Temperature Processing by Using High Power Ultrasound. Patent nº PCT/ES2012/070652.

Cárcel, J.A., Castillo, D., Simal, S., Mulet, A., 2019. Influence of temperature and ultrasound on drying kinetics and antioxidant properties of red pepper. Dry. Technol. 37 (4), 486–493.

Cardoni, A., Lucas, M., 2002. Enhanced vibration performance of ultrasonic block horns. Ultrasonics 40, 203–207.

Cardoni, A., Riera, E., Blanco, A., Acosta, V., Gallego-Juárez, J.A., 2012. Modal interactions in ultrasonic plate transducers for industrial applications. Proc. Inst. Mech. Eng. C J. Mech. Eng. Sci. 226, 2044–2052.

Carrión, C., Mulet, A., García-Pérez, J.V., Cárcel, J.A., 2018. Ultrasonically assisted atmospheric freeze-drying of button mushroom. Drying kinetics and product quality. Dry. Technol. 36 (15), 1814–1823.

Chou, S.K., Chua, K.J., 2001. New hybrid drying technologies for heat sensitive foodstuffs. Trends Food Sci. Technol. 12, 359–369.

Cohen, J.S., Yang, T.C.S., 1995. Progress in food dehydration. Trends Food Sci. Technol. 6, 20–25.

Colucci, D., Fissore, D., Mulet, A., Cárcel, J.A., 2017. On the investigation into the kinetics of the ultrasound-assisted atmospheric freeze drying of eggplant. Dry. Technol. 35, 1818–1831.

Colucci, D., Fissore, D., Rossello, C., Carcel, J.A., 2018. On the effect of ultrasound-assisted atmospheric freeze-drying on the antioxidant properties of eggplant. Food Res. Int. 106, 580–588.

Contreras, M., Benedito, J., Bon, J., Garcia-Perez, J.V., 2018. Accelerated mild heating of dry-cured ham by applying power ultrasound in a liquid medium. Innov. Food Sci. Emerg. Technol. 50, 94–101.

Corrêa, J.L.G., Rasia, M.C., Mulet, A., Cárcel, J.A., 2017. Influence of ultrasound application on both the osmotic pretreatment and subsequent convective drying of pineapple (Ananas comosus). Innov. Food Sci. Emerg. Technol. 41, 284–291. https://doi.org/10.1016/j.ifset.2017.04.002.

Cruz, L., Clemente, G., Mulet, A., Ahmad-Qasem, M.H., Barrajón-Catalán, E., García-Pérez, J.V., 2016. Air-borne ultrasonic application in the drying of grape skin: kinetic and quality considerations. J. Food Eng. 168, 251–258.

De la Fuente, S., Riera, E., Acosta, V.M., Blanco, A., Gallego-Juárez, J.A., 2006. Food drying process by power ultrasound. Ultrasonics 44, e523–e527.

do Nascimento, E.M.G.C., Mulet, A., Ascheri, J.L.R., de Carvalho, C.W.P., Cárcel, J.A., 2016. Effects of high-intensity ultrasound on drying kinetics and antioxidant properties of passion fruit peel. J. Food Eng. 170, 108–118.

Fernandes, F.A.N., Rodrigues, S., Cárcel, J.A., García-Pérez, J.V., 2015. Ultrasound-assisted air-drying of apple (*Malus domestica* L.) and its effects on the vitamin of the dried product. Food Bioprocess Technol. 8 (7), 1503–1511.

Fernandes, F.A.N., Rodrigues, S., García-Pérez, J.V., Cárcel, J.A., 2016. Effects of ultrasound-assisted air-drying on vitamins and carotenoids of cherry tomatoes. Dry. Technol. 34 (8), 986–996.

Fissore, D., Pisano, R., Barresi, A.A., 2011. Monitoring of the secondary drying in freeze-drying of pharmaceuticals. J. Pharm. Sci. 100, 732–742.

Floros, J.D., Liang, H., 1994. Acoustically assisted diffusion through membranes and biomaterials. Food Technol. 48, 79–84.

Gallego-Juárez, J.A., 1998. Some applications of air-borne power ultrasound to food processing. In: Povey, M.J.W., Mason, T.J. (Eds.), Ultrasound in Food Processing. Chapman & Hall.

Gallego-Juárez, J.A., Rodríguez-Corral, G., Gálvez-Moraleda, J.C., Yang, T.S., 1999. A new high intensity ultrasonic technology for food dehydration. Dry. Technol. 17, 597–608.

Gallego-Juárez, J.A., Rodriguez, G., Riera, E., Vazquez, F., Campos, C., Acosta, V.M., 2002. Recent development in vibrating-plate macrosonic transducers. Ultrasonics 40, 889–893.

Gallego-Juárez, J.A., Riera, E., de la Fuente Blanco, S., Rodriguez-Corral, G., Acosta-Aparicio, V.M., Blanco, A., 2007. Application of high-power ultrasound for dehydration of vegetables: processes and devices. Dry. Technol. 25, 1893–1901.

Gallego-Juárez, J.A., Rodriguez-Corral, G., Acosta, V.M., Riera, E., 2010. Power ultrasonic transducers with extensive radiators for industrial processing. Ultrason. Sonochem. 17, 953–964.

Gamboa-Santos, J., Montilla, A., Soria, A.C., Cárcel, J.A., García-Pérez, J. V., Villamiel, M., 2014a. Impact of power ultrasound on chemical and physicochemical quality indicators of strawberries dried by convection. Food Chem. 161, 40–46.

Gamboa-Santos, J., Montilla, A., Cárcel, J.A., Villamiel, M., Garcia-Perez, J.V., 2014b. Air-borne ultrasound application in the convective drying of strawberry. J. Food Eng. 128, 132–139.

Garcia-Noguera, J., Oliveira, F.I.P., Gallão, M.I., Weller, C.L., Rodrigues, S., Fernandes, F.A.N., 2010. Ultrasound-assisted osmotic dehydration of strawberries: effect of pretreatment time and ultrasonic frequency. Dry. Technol. 28, 294–303.

Garcia-Perez, J.V., 2007. Contribución al Estudio de la Aplicación de Ultrasonidos de Potencia en el Secado Convectivo de Alimentos (PhD Thesis). Universitat Politècnica de València.

Garcia-Perez, J.V., Carcel, J.A., De la Fuente, S., Riera, E., 2006a. Ultrasonic drying of foodstuff in a fluidized bed. Parametric study. Ultrasonics 44, e539–e543.

Garcia-Perez, J.V., Rossello, C., Carcel, J.A., De la Fuente, S., Mulet, A., 2006b. Effect of air temperature on convective drying assisted by high power ultrasound. Defect Diffus. Forum 258–260, 563–574.

Garcia-Perez, J.V., Carcel, J.A., Benedito, J., Mulet, A., 2007. Power ultrasound mass transfer enhancement in food drying. Food Bioprod. Process. 85, 247–254.

Garcia-Perez, J.V., Carcel, J.A., Riera, E., Mulet, A., 2009. Influence of the applied acoustic energy on the drying of carrots and lemon peel. Dry. Technol. 27, 281–287.

Garcia-Perez, J.V., Ozuna, C., Ortuño, C., Carcel, J.A., Mulet, A., 2011. Modeling ultrasonically assisted convective drying of eggplant. Dry. Technol. 29, 1499–1509.

Garcia-Perez, J.V., Ortuño, C., Puig, A., Carcel, J.A., Perez-Munuera, I., 2012a. Enhancement of water transport and microstructural changes induced by high intensity ultrasound application on orange peel drying. Food Bioprocess Technol. 5 (6), 2256–2265.

Garcia-Perez, J.V., Carcel, J.A., Riera, E., Rossello, C., Mulet, A., 2012b. Intensification of low-temperature drying by using ultrasound. Dry. Technol. 30, 1199–1208.

García-Pérez, J.V., Carcel, J.A., Simal, S., Garcia-Alvarado, M.A., Mulet, A., 2013. Ultrasonic intensification of grape stalk convective drying: kinetic and energy efficiency. Dry. Technol. 31, 942–950.

Heldman, D.R., Hohner, G.A., 1974. An analysis of atmospheric freeze drying. J. Food Sci. 39, 147–155.

Kowalski, S.J., 2015. Ultrasound in wet materials subjected to drying: a modeling study. Int. J. Heat Mass Transf. 84, 998–1007.

Kowalski, S.J., Mierzwa, D., Stasiak, M., 2017. Ultrasound-assisted convective drying of apples at different process conditions. Dry. Technol. 35, 939–947.

Kroehnke, J., Szadzińska, J., Stasiak, M., Radziejewska-Kubzdela, E., Biegańska-Marecik, R., Musielak, G., 2018. Ultrasound- and microwave-assisted convective drying of carrots—process kinetics and product's quality analysis. Ultrason. Sonochem. 48, 249–258.

Krokida, M.K., Zogzas, N.P., Maroulis, Z.B., 2001. Mass transfer coefficient in food processing: compilation of literature data. Int. J. Food Prop. 4, 373–382.

Lewicki, P.P., 2006. Design of hot air drying for better foods. Trends Food Sci. Technol. 17, 153–163.

Lewicki, P.P., Michaluk, E., 2004. Drying of tomato pretreated with calcium. Dry. Technol. 22, 1813–1827.

Liang, H., 1993. Modelling of Ultrasound Assisted and Osmotically Induced Diffusion in Plant Tissue (PhD Dissertation). Purdue University, Indiana, US.

Llavata, B., Garcia-Perez, J.V., Simal, S., Carcel, J.A., 2020. Innovative pre-treatments to enhance food drying: a current review. Curr. Opin. Food Sci. 35, 20–26.

Magalhães, M.L., Cartaxo, S.J.M., Gallão, M.I., García-Pérez, J.V., Cárcel, J.A., Rodrigues, S., Fernandes, F.A.N., 2017. Drying intensification combining ultrasound pre-treatment and ultrasound-assisted air drying. J. Food Eng. 215, 72–77.

Martins, M.P., Cortés, E.J., Eim, V., Mulet, A., Cárcel, J.A., 2019. Stabilization of apple peel by drying. Influence of temperature and ultrasound application on drying kinetics and product quality. Dry. Technol. 37, 559–568.

Mayor, L., Sereno, A.M., 2004. Modeling shrinkage during convective drying of food materials: a review. J. Food Eng. 61, 373–386.

Mello, R.E., Fontana, A., Mulet, A., Correa, J.L.G., Cárcel, J.A., 2020. Ultrasound-assisted drying of orange peel in atmospheric freeze-dryer and convective dryer operated at moderate temperature. Dry. Technol. 38, 259–267.

Merone, D., Colucci, D., Fissore, D., Sanjuan, N., Carcel, J.A., 2020. Energy and environmental analysis of ultrasound-assisted atmospheric freeze-drying of food. J. Food Eng. 283, 110031.

Morbiato, G., Zambon, A., Toffoletto, M., Poloniato, G., Dall'Acqua, S., de Bernard, M., Spilimbergo, S., 2019. Supercritical carbon dioxide combined with high power ultrasound as innovate drying process for chicken breast. J. Supercrit. Fluids 147, 24–32. https://doi.org/10.1016/j.supflu.2019.02.004.

Moreno, C., Brines, C., Mulet, A., Rosselló, C., Cárcel, J.A., 2017. Antioxidant potential of atmospheric freeze-dried apples as affected by ultrasound application and sample surface. Dry. Technol. 35, 957–968.

Moy, J.H., DiMarco, G.R., 1970. Exploring airborne sound in a nonvacuum freeze drying process. J. Food Sci. 35, 811–817.

Moy, J.H., DiMarco, G.R., 1972. Freeze-drying with ultrasound. Trans. ASAE, 373–376.

Mulet, A., 1994. Drying modelling and water diffusivity in carrots and potatoes. J. Food Eng. 22, 329–348.

Mulet, A., Cárcel, J.A., Sanjuán, N., Bon, J., 2003. New food drying technologies-use of ultrasound. Food Sci. Technol. Int. 9, 215–221.

Muralidhara, H.S., Ensminger, D., Putnam, A., 1985. Acoustic dewatering and drying (low and high frequency): state of the art review. Dry. Technol. 3, 529–566.

Ozuna, C., Cárcel, J.A., Garcia-Perez, J.V., Mulet, A., 2011a. Improvement of water transport mechanisms during potato drying by ultrasonic application. J. Sci. Food Agric. 91, 2511–2517.

Ozuna, C., Cárcel, J.A., Santacatalina, J.V., Mulet, A., Garcia-Perez, J.V., 2011b. Improvement of water transport mechanisms during potato drying by ultrasonic application. In: Proceedings of 11th International Congress of Food Engineering (ICEF 2011), Athens, Greece, pp. 1997–1998.

Ozuna, C., Puig, A., García-Pérez, J.V., Mulet, A., Cárcel, J.A., 2013. Influence of high intensity ultrasound application on mass transport, microstructure and textural properties of pork meat (*Longissimus dorsi*) brined at different NaCl concentrations. J. Food Eng. 119, 84–93.

Ozuna, C., Álvarez-Arenas, T.G., Riera, E., Cárcel, J.A., Garcia-Perez, J. V., 2014a. Influence of material structure on air-borne ultrasonic application in drying. Ultrason. Sonochem. 21 (3), 1235–1243.

Ozuna, C., Cárcel, J.A., Walde, P.M., Garcia-Perez, J.V., 2014b. Low-temperature drying of salted cod (*Gadus morhua*) assisted by high power ultrasound: kinetics and physical properties. Innov. Food Sci. Emerg. Technol. 23, 146–155.

Pisano, R., Barresi, A.A., Fissore, D., 2011. Innovation in monitoring food freeze drying. Dry. Technol. 29, 1920–1931.

Plaza, L., de Ancos, B., Cano, M.P., 2003. Nutritional and health-related compounds in sprouts and seeds of soybean (*Glycine max*), wheat (*Triticum aestivum* L.) and alfalfa (*Medicago sativa*) treated by a new drying method. Eur. Food Res. Technol. 216, 138–144.

Povey, M.J.W., McClements, D.J., 1992. Developments in Acoustics and Ultrasonics. IOP, Bristol, UK.

Puig, A., Perez-Munuera, I., Carcel, J.A., Hernando, I., Garcia-Perez, J.V., 2012. Moisture loss kinetics and microstructural changes in eggplant (*Solanum melongena* L.) during conventional and ultrasonically assisted convective drying. Food Bioprod. Process. 90, 624–632.

Ratti, C., 2001. Hot air and freeze-drying of high-value foods: a review. J. Food Eng. 49, 311–319.

Riera, E., Golas, Y., Blanco, A., Gallego, J.A., Blasco, M., Mulet, A., 2004. Mass transfer enhancement in supercritical fluids extraction by means of power ultrasound. Ultrason. Sonochem. 11, 241–244.

Riera, E., Garcia-Perez, J.V., Acosta, V.M., Carcel, J.A., Gallego-Juarez, J. A., 2011. A computational study of ultrasound-assisted drying of food materials. In: Knoerzer, K., Juliano, P., Roupas, P., Versteeg, C. (Eds.), Multiphysics Simulation of Emerging Food Processing Technologies. IFT Press, Chicago, US.

Rodrigues, S., Fernandes, F.A.N., García-Pérez, J.V., Cárcel, J.A., 2017. Influence of ultrasound-assisted air-drying and conventional air-drying on the activity of apple enzymes. J. Food Process. Preserv. 41 (2), e12832.

Rodrigues, S., Silva, L., Mulet, A., Cárcel, J.A., Fernandes, F.A.N., 2018. Development of dried probiotic apple cubes incorporated with *Lactobacillus casei* NRRL B-442. J. Funct. Foods 41, 48–54.

Rodriguez, L., Passerini, N., Cavallari, C., Cini, M., Sancin, P., Fini, A., 1999. Description and preliminary evaluation of a new ultrasonic atomizer for spray-congealing processes. Int. J. Pharm. 183, 133–143.

Rodríguez, Ó., Santacatalina, J.V., Simal, S., Garcia-Perez, J.V., Femenia, A., Rosselló, C., 2014. Influence of power ultrasound application on drying kinetics of apple and its antioxidant and microstructural properties. J. Food Eng. 129, 21–29.

Rojas, M.L., Augusto, P.E.D., Cárcel, J.A., 2020. Ethanol pre-treatment to ultrasound-assisted convective drying of apple. Innov. Food Sci. Emerg. Technol. 61, 102328.

Sabarez, H.T., Gallego-Juarez, J.A., Riera, E., 2012. Ultrasonic-assisted convective drying of apple slices. Dry. Technol. 30, 989–997.

Sánchez, E.S., Simal, S., Femenia, A., Benedito, J., Rosselló, C., 1999. Influence of ultrasound on mass transport during cheese brining. Eur. Food Res. Technol. 209, 215–219.

Santacatalina, J.V., Rodríguez, O., Simal, S., Cárcel, J.A., Mulet, A., García-Pérez, J.V., 2014. Ultrasonically enhanced low-temperature drying of apple: influence on drying kinetics and antioxidant potential. J. Food Eng. 138, 35–44.

Santacatalina, J.V., Fissore, D., Cárcel, J.A., Mulet, A., García-Pérez, J.V., 2015a. Model-based investigation into atmospheric freeze drying assisted by power ultrasound. J. Food Eng. 151, 7–15.

Santacatalina, J.V., Ahmad-Qasem, M.H., Barrajón-Catalán, E., Micol, V., García-Pérez, J.V., Cárcel, J.A., 2015b. Use of novel drying technologies to improve the retention of infused olive leaf polyphenols. Dry. Technol. 33 (9), 1051–1060.

Santacatalina, J.V., Soriano, J.R., Cárcel, J.A., Garcia-Perez, J.V., 2016a. Influence of air velocity and temperature on ultrasonically assisted low temperature drying of eggplant. Food Bioprod. Process. 100, 282–291.

Santacatalina, J.V., Contreras, M., Simal, S., Cárcel, J.A., Garcia-Perez, J. V., 2016b. Impact of applied ultrasonic power on the low temperature drying of apple. Ultrason. Sonochem. 28, 100–109.

Santacatalina, J.V., Guerrero, M.E., Garcia-Perez, J.V., Mulet, A., Cárcel, J.A., 2016c. Ultrasonically assisted low-temperature drying of desalted codfish. LWT Food Sci. Technol. 65, 444–450.

Schössler, K., Jäger, H., Knorr, D., 2012a. Novel contact ultrasound system for the accelerated freeze-drying of vegetables. Innov. Food Sci. Emerg. Technol. 16, 113–120.

Schössler, K., Jäger, H., Knorr, D., 2012b. Effect of continuous and intermittent ultrasound on drying time and effective diffusivity during convective drying of apple and red bell pepper. J. Food Eng. 108, 103–110.

Schössler, K., Thomas, T., Knorr, D., 2012c. Modification of cell structure and mass transfer in potato tissue by contact ultrasound. Food Res. Int. 49, 425–431.

Silva Júnior, E.V., Melo, L.L., Medeiros, R.A.B., Barros, Z.M.P., Azoubel, P.M., 2018. Influence of ultrasound and vacuum assisted drying on papaya quality parameters. LWT-Food Sci. Technol. 97, 317–322.

Soria, A.C., Villamiel, M., 2010. Effect of ultrasound on the technological properties and bioactivity of food: a review. Trends Food Sci. Technol. 21, 323–331.

Souza da Silva, E., Brandão, S.C.R., Lopes da Silva, A., Fernandes da Silva, J.H., Coêlho, A.C.D., Azoubel, P.M., 2019. Ultrasound-assisted vacuum drying of nectarine. J. Food Eng. 246, 119–124.

Stawczyk, J., Li, S., Witrowa-Rajchert, D., Fabisiak, A., 2007. Kinetics of atmospheric freeze-drying of apple. Transp. Porous Media 66, 159–172.

Szadzinska, J., Łechtanska, J., Kowalski, S.J., Stasiak, M., 2017. The effect of high power airborne ultrasound and microwaves on convective drying effectiveness and quality of green pepper. Ultrason. Sonochem. 34, 531–539.

Tekin, Z.H., Başlar, M., Karasu, S., Kilicli, M., 2017. Dehydration of green beans using ultrasound-assisted vacuum drying as a novel technique: drying kinetics and quality parameters. J. Food Process. Preserv. 41 (6). https://doi.org/10.1111/jfpp.13227. art. no. e13227.

Vallespir, F., Cárcel, J.A., Marra, F., Eim, V.S., Simal, S., 2018. Improvement of mass transfer by freezing pre-treatment and ultrasound application on the convective drying of beetroot (*Beta vulgaris* L.). Food Bioprocess Technol. 11, 72–83.

Vallespir, F., Crescenzo, L., Rodríguez, O., Marra, F., Simal, S., 2019. Intensification of low-temperature drying of mushroom by means of power ultrasound: effects on drying kinetics and quality parameters. Food Bioprocess Technol. 12, 839–851. https://doi.org/10.1007/s11947-019-02263-5.

Vega-Gálvez, A., Ah Hen, K., Chacana, M., Vergara, J., Martínez-Monzó, J., García-Segovia, P., Lemus-Mondaca, R., Di Scala, K., 2012. Effect of temperature and air velocity on drying kinetics, antioxidant capacity, total phenolic content, colour, texture and microstructure of apple (var. Granny Smith) slices. Food Chem. 132, 51–59.

Vega-Mercado, H., Gongora-Nieto, M.M., Barbosa-Canovas, G.V., 2001. Advances in dehydration of foods. J. Food Eng. 49, 271–289.

Wolff, E., Gilbert, H., 1990a. Atmospheric freeze drying. Part 1: design, experimental investigations and energy-saving advantages. Dry. Technol. 8, 385–404.

Wolff, E., Gilbert, H., 1990b. Atmospheric freeze drying. Part 2: modelling drying kinetics using adsorption isotherms. Dry. Technol. 8, 405–428.

Chapter 34

Use of ultrasonic atomization for encapsulation and other processes in food and pharmaceutical manufacturing

P.R. Gogate and R.A. Khaire
Institute of Chemical Technology, Mumbai, India

34.1 Introduction

Liquid atomization is the process in which a liquid film coming out on a solid surface is subjected to a sufficient surface disturbance in the normal direction, such that the liquid gets separated from the surface and essentially splits into small droplets like a fog or mist in the gas phase. Atomization of liquids is important in many industrial processes, including spray drying, spray cooling, film coating, preparation of fine (usually nanosize) powders, incineration, and combustion of liquid fuel and wastes, synthesis of emulsions (sometimes nano-emulsions), etc. In most of these applications, droplets should have a required size distribution and a specific mean size. This is especially important for applications or products where the specific activity is or product characteristics are strongly dependent on the size distribution obtained in the process.

Various types of atomization processes have been practiced in the past, and these processes can be classified based on the mode of energy transfer used to disturb the surface of the liquid film so that the liquid droplets break apart. Mechanical atomization processes such as pressure atomization, two-fluid atomization, and spinning disk atomization use mechanical energy to pressurize the liquid film or increase its kinetic energy for possible disintegration in the form of droplets. Though this is the most popular and convenient approach, mechanical atomization processes require more energy (compared to the theoretical energy requirement for additional surface generation) and have no control on the final droplet size or the velocity at which the droplet is ejected from the surface. Thus, it is imperative to develop new processes for atomization that yield the desired droplet size distribution and desired mean size in an energy-efficient manner. One of the approaches available for obtaining specific droplet size distribution, and at the same time avoiding coalescence of the droplets so that the mean size is lower, is based on the use of ultrasonic irradiation as a medium of energy transfer for inducing atomization. Unlike conventional atomization, ultrasonic atomization can be more energy efficient (based on proper design and operation), requiring only transmission of electrical energy to a piezoelectrically vibrating disk. There are no moving parts in the design of the atomizer (although a separate pump will be required for circulation of fluid through the atomizer), and only mechanical vibrations generated by the supplied electrical energy to the vibrating disk are used for the generation of droplets.

Ultrasonic atomization can be simply achieved by vibrating a liquid layer with a piezoelectric crystal at high frequency (usually in the 50 kHz to 3 MHz range). A thin film of liquid can be formed on the surface using circulation of liquid through the atomizer at the desired flow rate. During the process of atomization, capillary waves will form on the surface of the liquid with a wavelength dependent on the irradiation frequency, power dissipation, and liquid physicochemical properties, most importantly the liquid density and surface tension at the liquid-air boundary. If the liquid is forced to oscillate with sufficient intensity, the tips of capillary waves will begin to pinch off into droplets and atomization is achieved. The size of the generated droplets is independent of the forcing amplitude and hence the mist density. This feature can be useful in designing a system where mist properties should be adjusted independently.

Use of ultrasonic atomization can overcome some of the common disadvantages associated with the conventional atomizers. Rotary, pressure, or two-fluid atomizers use only a fraction of the supplied energy (centrifugal, pressure, or kinetic energy, respectively) to shatter the liquid for forming the droplets, while most of the supplied energy finally appears as the kinetic energy of the particles. As a consequence, problems like partial separation of the components in the mixture, the presence of defects on the particle

Power Ultrasonics. https://doi.org/10.1016/B978-0-12-820254-8.00028-2
Copyright © 2023 Elsevier Ltd. All rights reserved.

surface, improper coating characteristics, wide distribution of droplet sizes, etc., can occur, depending on the specific application. Also, the dimensions of the equipment as well as the associated cost will increase when the speed of the atomized particles/droplets increases. Unlike the conventional atomizing nozzles that rely on mechanical energy to shear a fluid into small drops, ultrasonic atomizers use only low vibrational energy for the generation of drops. Moreover, the association of ultrasound-based atomization with spray drying is a powerful tool that can be harnessed for important applications, especially in food and pharmaceutical industries. Spray drying is in principle a continuous process, giving a good reproducibility and having a good potential for scale-up. If spray drying is based on the use of a pneumatic nozzle, it has disadvantages, such as lack of control over the mean droplet size, broad droplet distributions, and the risk of clogging in the case of suspensions. These common disadvantages can be overcome by employing ultrasonic energy to obtain droplets with a relatively uniform size distribution. Another important process based on a similar controlling mechanism would be spray congealing, where the use of ultrasound can give spherical microparticles or nanoparticles with good encapsulation efficiency and size distribution. Overall, it can be said that ultrasonic atomization is a robust and an innovative single-step procedure with scale-up potential for a variety of applications.

34.2 Fundamentals of ultrasonic atomization

Ultrasonic atomization is the process of the ejection of droplets from a liquid film formed on a surface, with vibrations induced by the passage of ultrasonic energy. Figure 34.1 gives the schematic of the process of ultrasonic atomization. Droplet ejection from the vibrating surface can generally be explained by either of the two major hypotheses: capillary wave hypothesis and cavitation hypothesis.

The occurrence of atomization based on the capillary wave hypothesis, which is based on Taylor instability criteria (Taylor, 1950), can be confirmed by visual observation. This hypothesis considers the formation of capillary waves composed of crests and troughs on the vibrating surface. Atomization occurs when unstable oscillations split the peaks of capillary waves at the surface away from the bulk liquid. In this case, the drop formation is at the crest and the size of drop will be proportional to the wavelength. Capillary wavelength typically decreases with an increase in the frequency of irradiation; hence, fine droplets are formed at higher frequencies. Photographic measurements of the surface disturbances performed by Lang (1962) confirmed that the disturbances are nothing but a pattern of crossed capillary standing waves, and that the observed wavelengths for these patterns are strongly dependent on the frequency of irradiation, clearly supporting the capillary wave hypothesis.

On the other hand, the cavitation hypothesis states that droplet formation is governed by the occurrence of cavitation events in the liquid film at the surface. Cavitation is basically the formation of a cavity in the liquid film on the vibrating surface of an atomizer due to the passage of ultrasonic energy. Collapse of these cavities, especially near the surface, results in direct ejection of liquid droplets; hence, velocity of ejection increases due to the kinetic energy dissipation by cavitational events. The phenomenon can be considered propagation of a shock wave arising from the collapse of cavities and the transfer of momentum to ejecting liquid droplets. The dominance of atomization by cavitation hypothesis is generally applied to high-frequency (16 kHz–2 MHz) and high-energy-intensity (W/m^2) systems. Credence to the cavitation hypothesis is based on the dependence of atomization on the vapor pressure, static pressure, and gas content of the liquid, and also the existence of luminescence in the zone of atomization. Occurrence of cavitation during the atomization process can also be confirmed using simple dosimetry studies, such as potassium iodide decomposition (Gogate et al., 2001) or salicylic acid degradation (Chakinala et al., 2007). Avvaru et al. (2006) investigated the presence of cavitation phenomena by measuring the decomposition of an aqueous potassium iodide solution during atomization and

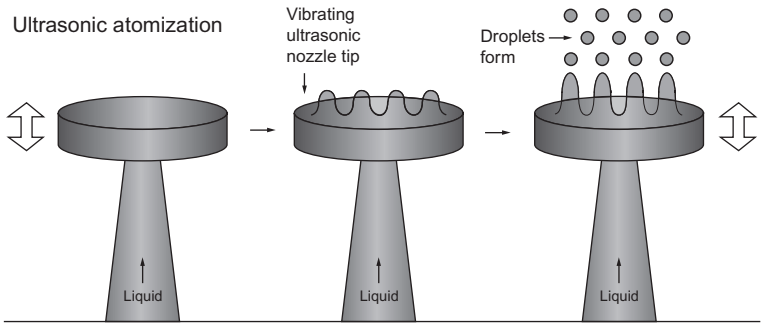


FIGURE 34.1 Schematic representation of ultrasonic atomization.

concluded that cavitational activity indeed has a role in the process of ultrasonic atomization. It is important to note here that cavitating conditions (the number of cavitational events and the intensity of cavity collapse generating the shock waves) are dependent on operating parameters such as the vibrational intensity, liquid flow rate, and physicochemical properties of the liquid to be atomized. Depending on the type of liquid, the contribution of cavitation effect to atomization characteristics will be different. The dosimetry studies, however, clearly establish that it is important to consider the combined effect of capillary wave formation and cavitation while selecting the configuration for the desired application.

Bouguslavskii and Eknadiosyants (1969) coupled these two theories of generation of capillary waves as well as occurrence of cavitation events in the liquid film and proposed a new "conjunction theory." In this case, the periodic hydraulic shocks arising from cavitation disturbance are considered to interact with the finite-amplitude capillary waves and excite them to form droplets. Capillary waves in the conventional atomization process are more random than capillary waves modulated by ultrasonic vibration, which are more regular in nature; hence, more uniform droplet size distribution can be observed with ultrasound-induced atomization.

Apart from understanding of the mechanism, the studies related to atomization on vibrating surfaces have mostly concentrated on measurements of the droplet size, followed by attempts to develop generalized corrections for the prediction of droplet size as a function of different geometric parameters and liquid-phase physicochemical properties. Efforts to understand the concepts of ultrasonic atomization date back to 1830s when Faraday (1831) established that the period of vibrational waves formed on a liquid layer on a vibrating surface is twice the period of the driving vibration. Subsequently, Rayleigh (1883) developed a correlation relating the surface tension of the liquid, vibrational frequency, and capillary wavelength and showed that the surface tension of a liquid can be successfully determined from the measurements of the capillary wavelength observed on the surface of the vibrating liquid. However, Faraday's study concentrated on surface tension measurements. The first work on development of correlation for the droplet diameter was reported by Lang (1962), who performed measurements of droplet diameter generated from the crests of capillary waves for different working fluids, including water, oil, and molten waxes, at vibration frequencies of 10–800 kHz. The relationship between the average diameter of the ejected droplets (d_p) and the liquid properties of density (ρ) and surface tension (σ) is given by the following equation:

$$d_p = 0.34\left(\frac{8\pi\sigma}{\rho f^2}\right)^{0.333}. \tag{34.1}$$

Following the work of Lang (1962), Peskin and Raco (1963) modified the correlation for droplet diameter by considering the amplitude of forced vibration and the thickness of the liquid layer present on the vibrating surface (which in turn depends on liquid flow rate and physicochemical properties). This new correlation is given as:

$$\frac{d_p}{\pi A_m} = \left[\left(\frac{2\sigma}{\rho\omega_0^2 A_m^3}\right) 2\tan h\left(\frac{\pi A_m}{d_p}\right)\left(\frac{t}{A_m}\right)\right]^{\frac{1}{s}} \tag{34.2}$$

where A_m is the amplitude and ω_0 is the oscillation frequency of atomizer tip.

Studies of contributing factors to droplet size distribution by Sindayihebura et al. (1997) and Dobre and Bolle (1999) established that the breakup and formation of the droplet is dependent on different forces, such as buoyancy force, drag force, gravity force, internal/external viscous force, and interfacial force, acting on the liquid sheet formed at the surface. Considering the effect of these forces on the process of drop breakup, Rajan and Pandit (2001) proposed a unified correlation involving dimensionless numbers such as the Weber number (N_{We}) (the ratio of aerodynamic forces to surface tension forces) and the Ohnesorge number (N_{Oh}) (the ratio of the internal liquid viscosity to surface force) and also the vibrational amplitude. The aim was also to explain the effect of different physicochemical properties such as the surface tension, viscosity, and density of the liquid on final droplet size. It is also important to consider the effect of ultrasound operating parameters. Hence, both the dimensionless numbers were modified to consider the frequency of irradiation, and an additional dimensionless number in the form of an intensity number (N_{In}) was proposed to consider the effect of ultrasonic intensity. The resultant equation for droplet size is given as follows:

$$d_p = \left(\frac{\pi\sigma}{\rho f^2}\right)^{\frac{1}{3}}\left[1 + A(N_{We})^{0.22}(N_{Oh})^{0.166}(N_{In})^{-0.0277}\right] \tag{34.3}$$

The dimensionless numbers used in the equation can be given as follows:

$$N_{We} = \frac{fQA}{\sigma} \tag{34.4}$$

$$N_{Oh} = \frac{\eta}{fA_m^2\rho} \tag{34.5}$$

$$N_{In} = \frac{f^2A_m^4}{cQ} \tag{34.6}$$

where c is the velocity of sound in the liquid medium and Q is the liquid flow rate.

A careful analysis of earlier works related to understanding the mechanism and development of correlations

for droplet size indicates that most studies have used a single-frequency operation, and the effect of frequency on the atomization process has not been well established. Ramisetty et al. (2013) studied the atomization process using three different atomizers, operating at frequencies of 20, 40, and 130 kHz, respectively, with an objective of understanding the effect of frequency on droplet size distribution. The work was also directed towards understanding the controlling mechanism governing the atomization process as a function of the operating parameters. The progress of ultrasonic atomization was captured by imaging the droplet formation, using photographic analysis. It has been established that according to capillary wave hypothesis, controlled atomization is only observed at very low liquid flow rates and low ultrasonic power dissipation levels, whereas cavitation is the controlling mechanism at higher frequencies and higher power dissipation levels. The occurrence of cavitation phenomena at higher frequencies and intensities was also confirmed with measurements of the velocity of ejected droplets from the surface of the atomizer, which were significantly higher as compared to the velocity observed at lower power dissipation. An empirical correlation for the prediction of droplet size as a function of different operating parameters such as ultrasonic power, frequency, liquid-phase physicochemical properties, and liquid flow rate has been developed, given in the following equation:

$$d_p = 0.00154\left(\frac{\pi\sigma}{\rho f^2}\right)^{0.33}\left(\begin{array}{c}1+\left(\frac{\pi\sigma}{\rho f^2}\right)^{-0.2}N_{\mathrm{Oh}}{}^{-0.111}\\ N_{\mathrm{We}}{}^{0.154}N_{\mathrm{In}}{}^{-0.033}\end{array}\right) \quad (34.7)$$

Recently, Briceño-Gutierrez et al. (2015) also reported the use of high-speed digital camera to understand the atomization process and established the dependence of atomization threshold on the frequency of operation. It was reported that the theoretical predictions of the atomization threshold based on the theory of Bouguslavskii and Eknadiosyants (1969) match well with the experimental predictions till frequency of 22 kHz beyond which deviations are seen. The work has clearly directed the requirement of future work to include the role of frequency in the theory of ultrasonic atomization.

The mechanistic details presented here confirm that proper selection of operating parameters and geometric parameters will decide the controlling mechanism for atomization (capillary wave, cavitation, or combined effects) and that the actual droplet size will be a strong function of the equipment operating parameters (flow rate, frequency, and power dissipation) and the liquid physicochemical properties (type of the liquid, surface tension, and viscosity).

34.3 Ultrasonic atomizer design

In this section, we will present a description of the typical configuration of an ultrasonic atomizer, with some explanation of the various techniques that can be used for the analysis of droplets. We will also explain how droplet size is dependent on differing operating parameters (both liquid phase and the ultrasound specifications).

A typical ultrasonic atomizer as shown in Figure 34.2 would consist of a vibrating plate with a concentric hole through which the introduced liquid spreads on the surface. A peristaltic or centrifugal pump is required to introduce the liquid into the atomizer depending on the type of application (required flow rate). The plate is connected to the transducer that is driven by an electric generator, where a provision can be made to vary the power delivered to the atomizer tip. Additionally, different frequency generators can be used to control the operating frequency. Other geometric parameters that can be varied depending on the application are the diameter of the concentric hole and of the entire disk, but these cannot be varied significantly, as the surface should be wetted completely by the introduced

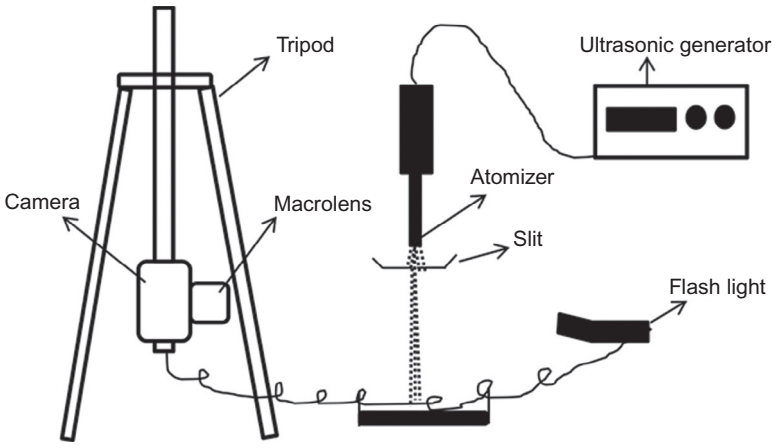


FIGURE 34.2 Schematic representation of the ultrasonic atomizer and setup for capturing the images of the droplets. *(Ramisetty et al. (2013) with permission from Elsevier.)*

liquid. In addition to the geometric and ultrasound parameters, the liquid physicochemical properties such as surface tension, viscosity, type of liquid, and operating temperature are important and can be varied, as per specific requirements.

It is important to note here that the geometry of the atomizer plays an important role in determining the maximum liquid flow rates that can be processed through the atomizer. Droplet size is not affected directly by the flow rate, but there is usually a maximum flow rate above which disintegration is no longer achieved and the introduced liquid leaves the surface without forming any droplets. This can be attributed to the fact that ultrasonic atomization relies on wave growth followed by crest breakup, and when the liquid film depth increases, damping becomes more and more important in preventing wave growth and limiting resonance amplitude. If the upper limit flow rate needs to be enhanced to increase the throughput capacities of the atomizer at actual application level, geometric modifications of the prototype can be an excellent option. Dobre and Bolle (2002) investigated several atomizer geometries (Figure 34.3) with an objective of varying the forcing wave parameters so that the atomizer active surface area is maximized and processing liquid flow rates are higher. The discussed modifications include increase in the resonant surface area by modifying the atomizer tip shape, size change of the entire atomizer, and increase in the wave amplitude by increasing the number of piezoelectric elements. It is important to remember that changing the size of the entire atomizer means that both the resonant surface and the feeding hole size increase. However, if the same effect is to be achieved in a small atomizer (for cost or miniaturization reasons), the novel option of feeding the resonant surface through multiple holes can easily be considered.

An important application of ultrasonic atomization, especially in the case of the food and pharmaceutical industries, is in the area of encapsulation, where handling of multiple fluids is required to get the desired composites (Dalmoro et al., 2012). There are also designs of ultrasonic nozzles that can handle multiple fluids (mainly liquid/liquid). For microencapsulation applications, core and wall material flow in separate channels, and there are no mixing issues until materials reach the delivery tip of the nozzle. Use of nozzles where the two fluids are moving independently can eliminate the need for emulsion formation prior to drying (Legako and Dunford, 2010). A coaxial ultrasonic atomizer (Figure 34.4) can be employed to produce a smooth coaxial jet, comprising an annular shell of liquid flowing in the outer nozzle and core material flowing in the inner nozzle. At the delivery tip of the atomizer, acoustic excitation can be initiated, resulting in the formation of uniform core-shell droplets (Berkland et al., 2004). Due to the vibrations created by the ultrasonic frequency range, both liquids form a double-layer film on the surface of the atomizer tip and are simultaneously fragmented into a large number of drops usually with lower and uniform size. Comparison of fish oil encapsulation using conventional pressure atomizers (pressure nozzles with one and two liquid channels) and an ultrasonic atomizer with two liquid channels revealed that microcapsules produced by the two-channel ultrasonic nozzle are more uniform in size and shape than microcapsules produced with pressure nozzles (Legako and Dunford, 2010). Also, the use of the ultrasonic nozzle resulted in a significantly narrower particle size distribution (Figure 34.5).

Park and Yeo (2003) reported a design for a coaxial ultrasonic atomizer based on interfacial solvent exchange. In this case, poly(D,L-lactide-*co*-glycolide) (PLG) solution in ethyl acetate (acting as external phase) and an aqueous solution containing optional solutes (core phase) were separately fed into an ultrasonic coaxial atomizer, and microcapsules were collected in a water bath containing PVA as a stabilizer. Collection of the microparticles in the water bath requires efficient distribution in the bath; otherwise,

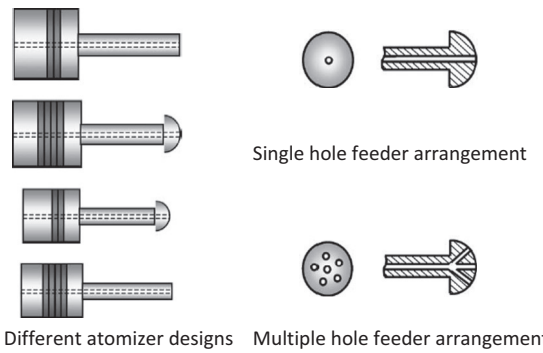


FIGURE 34.3 Different geometries for ultrasonic atomizer including the feeder arrangements.

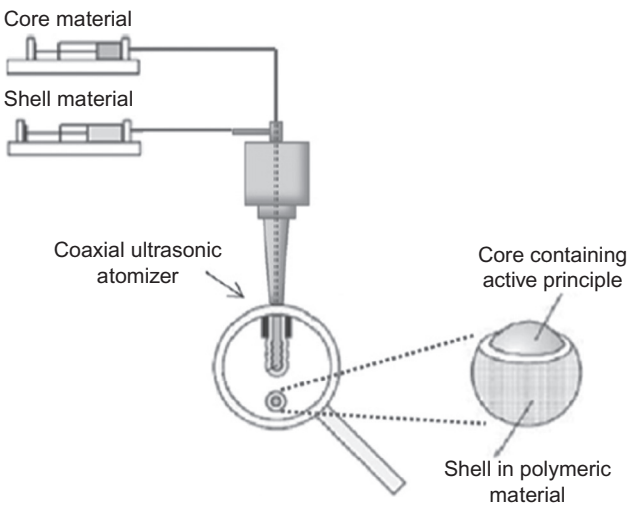


FIGURE 34.4 Schematic representation of principle of coaxial ultrasonic atomization.

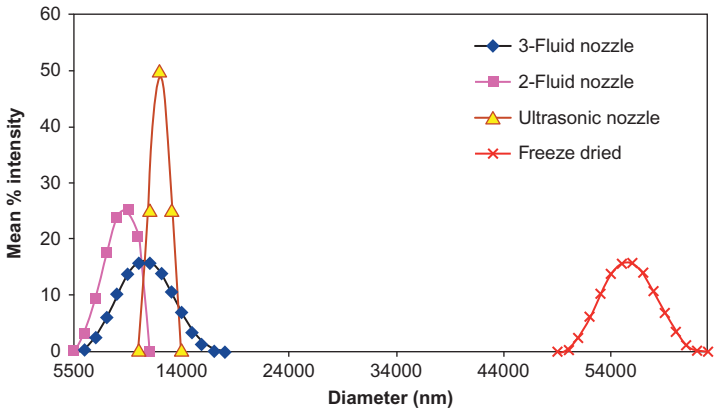


FIGURE 34.5 Comparison of size distribution obtained using ultrasonic and pressure nozzles. *(Legako and Dunford (2010) © 2010 Institute of Food Technologists ® with permission from John Wiley and Sons.)*

there may be preferential accumulation at the surface, hindering subsequent formation of the microparticles. It has been reported that magnetic stirring easily breaks the stability of the water surface, but if this affects the stability of the microparticles, simple vibrations for the bath may be provided by an ultrasonic bath or by sonication probes. Another approach is the removal of polymer solvent by evaporation, combining the solvent exchange method with spray drying. A stream of warm gas introduced to evaporate solvent can be used simultaneously to solidify the microcapsules. Separation of particles and gas can be performed in a cyclone attached to the drying chamber.

The logic of using coaxial flows can be very well extended to multiple concentric nozzles when more than two-fluid phases are used in atomization or the synthesis of composites. Berkland et al. (2004) reported ultrasonic atomization using multiple concentric nozzles for the synthesis of uniform double-walled microspheres comprising PCPH (poly[(1,6-bis-carboxyphenoxy)hexane]) cores and PLG shells designated as PLG(PCPH), as well as microspheres consisting of PLG cores and PCPH shells designated as PCPH(PLG). A dual polymer jet was used in the atomization process, pumping the two different polymer solutions (PLG and PCPH in methylene chloride) in coaxial nozzles. In addition, a coaxial nozzle was used to supply the carrier stream containing a surfactant to surround the emerging dual polymer jet. The carrier stream with surfactant was used to help breakup of the jet and prevent the tendency of the drops to recombine. This is very important to avoid the formation of the agglomerates in the system and give uniform particle size distribution in the final product. The important parameters such as core diameter, shell thickness, and overall particle size can easily be controlled by varying the flow rates of the streams and the formulation parameters. Overall, it was established that the combination of coaxial nozzles with an ultrasonic system allowed the production of microspheres having a shell thickness from less than 2 μm to a few microns, keeping complete core encapsulation.

Recently, Al-Jumaily and Meshkinzar (2017) provided brief overview of the different focused ultrasonic transducers applied for fluid atomization and vaporizers. Specifically, the flat-plate transducers and shell configurations were compared in terms of relative merits and demerits of the configuration. It was reported that vibrating plate atomizers appear to the best configuration as these are low-power-consuming devices capable of giving lower droplets at lower ejection flow rates.

Overall, it can be said that, depending on the application, the use of ultrasonic atomization can be modified in terms of the stage of application in the overall process. Ultrasonic atomization can also aid in replacing some of the required unit operations and results in uniform sizes.

34.4 Measuring droplet size and distribution

Before arriving at an efficient design for an industrial-scale atomizer, it is important to perform laboratory-scale experiments for the specific application under question and arrive at correct scale-up strategies. For the analysis at a laboratory scale, the approach for characterization of droplets (size as well as ejection velocity) is important. A simple technique for the measurement of droplet size is to capture the droplets on a good filter paper (a colored liquid will have to be used so that the droplets are clearly visible) and then analyze them under a microscope (Avvaru et al., 2006; Rajan and Pandit, 2001). The filter paper images can also be captured using a high-resolution camera and digitized using software, such that the area of each droplet can be quantified using an image analysis system.

A more sophisticated technique for measuring droplet size, which can also give the velocity of ultrasonically

atomized liquids, is to photograph directly the release of the droplets from the atomizer tip using a high-resolution camera with very high shutter speed (typically 1/4000 s), freezing the droplets as they are ejected. The typical setup is illustrated in Figure 34.2. Frame freezing using a higher shutter speed can be done for all droplets, irrespective of the governing mechanisms of capillary phenomena and the cavitation phenomena. For such an analysis, it is important to avoid interference of air with the motion of droplets. To achieve this, entire assembly can be enclosed in a wooden box, which can be covered internally with black cloth as a background for proper photography. The typical pattern of atomization is in the form of a cone, as shown in Figure 34.6. The analysis and measurement approach needs to be optimized for accurate results. For example, some droplets may overlap, and droplets in front, closer to the lens, are in focus, whereas droplets at the back appear blurred and unsuitable for photographic analysis. Passing the outlet from the atomizer surface through a slit eliminates the focus problem. The ejection velocity of atomized droplets may be simultaneously measured using a photographic approach that captures the droplets as traveling streaks using a lower shutter speed (1/250 s). Figure 34.7 shows a typical captured image. Velocity of the droplets can be calculated by dividing the streak length (m) by the shutter speed time (s). The captured data can be analyzed using various software, such as ImageJ or Fiji. Macro programs can be written to facilitate the measurement process and also allow export of the processed data to an Excel sheet that includes the area of the droplets, the ratio of minor axis to major axis, and the diameter of the droplets. Spherical droplets should be filtered using circularity between 0.8 and 1 so as to minimize error in the droplet size measurement. Droplet size can be measured using the two-dimensional circular area of each droplet, and the Sauter mean diameter can be obtained to represent the droplet size distribution.



FIGURE 34.6 A representative image of the conical pattern of the atomized droplets. *(Ramisetty et al. (2013) with permission from Elsevier.)*

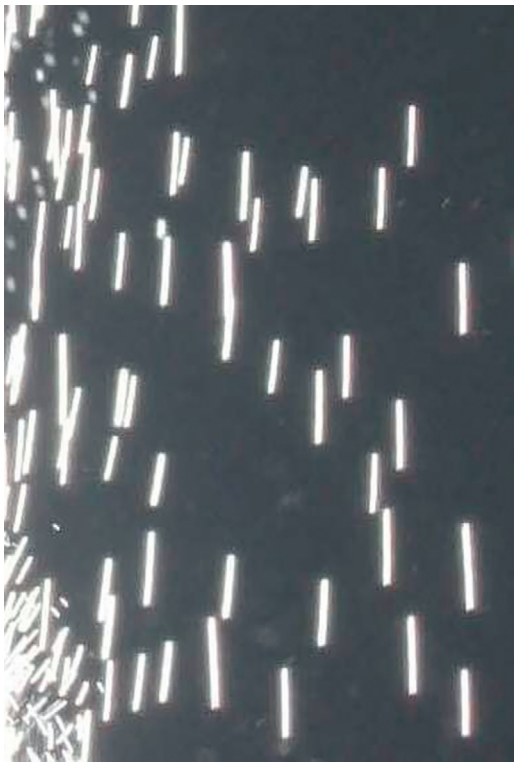


FIGURE 34.7 A typical representation of droplets captured as traveling streaks for velocity measurements.

34.5 The effect of different operating parameters on droplet size

When using the ultrasonic atomizer, droplet size and distribution are strongly dependent on the rheological nature of the atomizing fluid, the viscosity of the liquid, and the ultrasonic operating parameters as power dissipation and frequency of irradiation. Thus, it is imperative to select these operating parameters carefully to obtain the specific required characteristics for the application. Considering this, we thought it imperative to provide some discussion about the effect of different parameters on droplet size.

Under the same operating conditions, droplet size is observed to be smaller for pseudoplastic liquid than for Newtonian liquid with similar viscosity attributed to the zero shear-rate viscosity of the pseudoplastic liquid. Also, droplet size for high-viscous liquid is generally observed to be larger than comparatively low-viscous liquid, a useful observation for ultrasonic atomization (Rajan and Pandit, 2001). It is important to note here that the effect of viscosity is complex and dictated by many interlinking parameters. For example, for highly viscous liquids, it is difficult to spread the liquid laterally on the entire atomizing surface; thus, the liquid is atomized from a smaller area, with requirement of relatively high operating intensity. Due to the pseudocontrol effect of ultrasonic intensity, the droplet size observed is smaller, contrary to what would be expected

for direct proportionality. Also, highly viscous liquids have a tendency to attach to the surface, resulting in a longer period under cavitating conditions, in turn leading to an increase in temperature. Higher temperature lowers viscosity, and smaller size droplets will be formed. It is important to understand that highly viscous liquids are most difficult to atomize, as the shock wave produced on collapse of the cavity quickly gets dampened by higher viscous energy dissipation. The net effect is that the hydraulic shock is unable to tear the liquid capillary wave crest and atomization is not possible for highly viscous liquids.

The second important liquid phase parameter affecting droplet size is the surface tension. Typically, a decrease in surface tension leads to a decrease in the surface capillary wavelength and an increase in the number of capillary waves per surface area unit, resulting in immediate ejection of the droplet from crests. Thus, the number of droplets ejected from liquid film increases, with a corresponding decrease in droplet size under otherwise similar operating conditions. The decreased droplet size is also associated with increased kinetic energy of the liquid droplets. Also, as the liquid film occupies a very thin layer on the vibrating surface, nearly sticking to the surface, decrease in the surface tension is likely to increase the growth of a vaporous cavitational bubble, and this also leads to the formation of smaller droplets, ejected at a higher velocity.

The ultrasound operating parameters such as power dissipation and frequency of irradiation also affect the mean droplet size and distribution. Generally speaking, as the power dissipation increases, the droplet size also increases, which can be explained on the basis of energy being transferred to the atomizing liquid. With an increase in the power dissipation, the tip vibrational amplitude of the atomizer increases, enhancing the net energy transfer to the atomizing liquid. The shape of liquid flow changes from radially outward (trying to spread on the surface after coming out the central hole) to conically downward with a tendency to eject out from the surface rather than spreading on the surface. At lower power dissipation levels, the liquid is capable of spreading over the entire surface of the atomizer, and hence, all the power delivered to the tip can be utilized by the atomizing liquid, leading to a decrease in droplet size. On the other hand, at higher power dissipation, the liquid delivered on the surface atomizes quickly, without allowing it to spread radially on the surface. Ramisetty et al. (2013) have confirmed this observation of cone-like outflow at higher power dissipation levels as illustrated in Figure 34.8. The effect of power dissipation on the size as well as the number of droplets atomized was also studied by Kudo et al. (2017). It was reported that the peak diameter was a weak function of the power dissipation compared to the number of droplets generated. Also, the way in which the power intensity is changed that is by changing either the power or the surface area is also important. The change in surface dimensions was found to be a dominant parameter, and with proper selection, nanosize droplets were reported. It can be thus said that the atomizer surface is wetted by the incoming liquid, which is an important factor that is dependent on the power dissipation. Another important point is that due to the enhanced energy transfer to the atomizing liquid, the velocity of the ejected droplets is also expected to increase with an increase in ultrasound power. This needs to be carefully evaluated, depending on the desired application. Overall, a proper selection of the operating power dissipation using laboratory scale studies is recommended to achieve a balance between the size and velocity of ejection.

Frequency of irradiation is another factor that affects droplet size but is usually not a real variable, as it is difficult to have equipment that operates at variable frequencies. Usually, the best efficiency of the ultrasonic atomizer is observed at the resonating frequency. Still, the effect of frequency needs to be considered in the design of the atomizers so that the desired size distribution and the desired ultrasonic atomization efficiency are obtained satisfactorily at the specific design frequency to be selected in device. Usually droplet size decreases with an increase in the frequency of irradiation, which can be attributed to the fact that increased frequency results in a decrease in the wavelength compressing the dampening node and antinode points. At higher frequencies, the atomizing liquid is exposed to a larger number of compression phases in a given acoustic cycle, reducing the rate of the crest growth and decreasing droplet size. Sindayihebura et al. (1997) reported that the capillary wavelength decreases with an increase in atomizer frequency, and the net result is a decrease in droplet size and an increase in droplet ejection rate (number of droplets per unit of time) from the surface. Kudo et al. (2017) also reported that the peak diameter obtained in the case of mist generated using ultrasound reduced with an increase in the frequency. It was also reported that the number concentration of mist increased in small range but this is an important observation having an impact on specific applications. It is also important to note that as the frequency increases, there is also a decrease in the atomizing surface area available for the formation of droplets, and the threshold liquid flow rate required for covering the entire surface increases. A proper selection of operating flow rate is required so that the complete available surface for atomization is utilized. It is also important to note that the upper limit flow rate, where dripping is observed, will be lower for the high-frequency atomizer than for the case of low-frequency atomizer. Thus, the range of operational flow rates will be limited in the case of high-frequency atomizers. Also, the power requirement for atomization of liquids is expected to be higher in the case of high-frequency operation, similar to the requirement for higher power to generate the cavitating conditions in the case of conventional

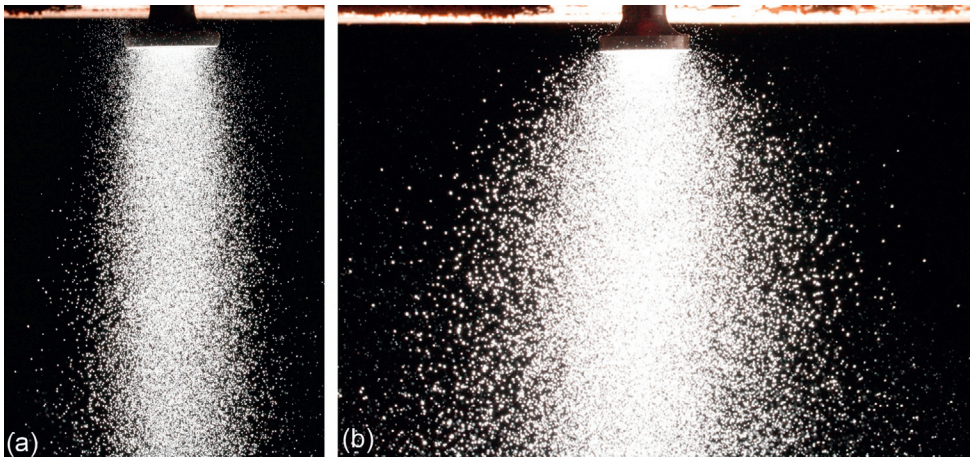


FIGURE 34.8 Changing pattern of flow of atomization with varying power of atomization: (a) low-power of 3 W and (b) high-power dissipation of 9 W. *(Ramisetty et al. (2013) with permission from Elsevier.)*

sonochemical reactors applied for physical processing applications. Based on this discussion, it appears that low-frequency atomizers are still a good option for easy operation, and appropriate droplet size can be obtained by adjusting the other operating parameters.

34.6 Applications of ultrasonic atomization in the food industry: Spray drying and encapsulation

Applications of atomizing devices in the food industry are generally for spray drying (Ashokkumar et al., 2010), as the use of these devices provides a high surface-to-mass ratio during the spray-drying process, enabling rapid heat transfer and high evaporation rates. The two most common atomizing devices used in food industry applications, especially for dairy-based products, are centrifugal (rotary) and pressure (nozzle) atomizers, although ultrasonic atomizers offer a viable alternative (Luz et al., 2007), especially due to better control of droplet size distribution and smaller mean size. It is very important to distinguish between ultrasonic nozzles that produce an aerosol by passing a liquid feed through a vibrating horn and ultrasonic nebulizers that operate at much higher ultrasonic frequencies and generate a fountain-like structure in a thin liquid film. Both these modes have a specific application. Droplet sizes produced by an ultrasonic nebulizer are typically an order of magnitude smaller than those obtained with an ultrasonic nozzle (Niven et al., 1995). It is worthwhile to mention that ultrasonic spray dryers containing nozzles are available for large-scale operations, but ultrasonic nebulizers have been used mostly at an exploratory level and have not yet been developed for large-scale industrial use. However, both devices have advantages over classical spray-drying atomizers in that they produce a controlled spray at a desired velocity, resulting in a relatively smaller spray chamber required for drying. We now present some of the applications reported in the literature to give an idea about the kind of components that have been tried and the distinct benefits obtained using ultrasound-based approach.

Bittner and Kissel (1999) investigated the synthesis of bovine serum albumin (BSA) microspheres using an ultrasonic atomizer fitted to a spray dryer. The purpose of using an atomizer with an air stream carrier was to prevent possible clogging. During the operation, an emulsion of an aqueous BSA solution in an organic polymer solution (PLG in dichloromethane) was slowly fed to the atomizer using a peristaltic pump, yielding the microspheres, which were then lyophilized and stored under desiccation. It was reported that spherical particles with a more or less smooth surface structure were obtained and the mean particle diameter was about 10 μm. A main feature of the ultrasonic system was that the polymer molecular weight (as analyzed by gel permeation chromatography) was not influenced by ultrasonic oscillations. In addition, the BSA solution was not denatured due to the cavitational effect, a fact that needs to be stressed for food industry applications. The main advantages of the microencapsulation in the presence of ultrasound were excellent particle yields and encapsulation efficiencies, without any clogging or broad droplet size distribution (typical problems with conventional pneumatic nozzles). Also, a relatively lower initial protein burst release was seen in the microparticles produced by ultrasonic atomization, and the obtained microspheres had a smooth surface structure, even in the case of the organic polymer solution with the highest viscosity. In summary, it was established that ultrasonic atomization represents a versatile and reliable technique for the production of protein-loaded biodegradable microspheres, retaining the stability of the

polymer matrix, and also that the particle characteristics can be modified by adjusting the formulation parameters and atomization operating conditions in a simple manner.

Freitas et al. (2004) reported a similar approach to spray-drying technique associated with an ultrasonic atomizer, based on the use of reduced pressure rather than hot air drying. Use of an ultrasonic nozzle was reported to enable shorter drying chamber dimensions due to lower velocities of the ejected microdroplets when compared to pressurized nozzles. Also, the use of reduced pressure as a driving force for solvent evaporation from microdroplets was reported to eliminate the requirement for large quantities of sterile hot air. The atomizer used was operated at a 100-kHz frequency, and a protein/polymer emulsion was fed to the chamber using a syringe pump. It was reported that the product yield decreased when the relative atomization power was increased from 30% to 90%, which can be explained by a smaller extent of spreading of fluid on the atomization area due to increased oscillation amplitude. The obtained yield using ultrasound-based atomization was around 80% under optimum conditions, which is much better than that obtained using conventional spray-drying equipment. The obtained particle size was mostly independent of atomization power, and the reproducibility of particle size distribution for repeated production was highly satisfactory, which is another major advantage of an ultrasound-based approach. The particle size was directly dependent on the concentration of polymer solutions for both conventional and ultrasonic spray drying, which can be attributed to the increased viscosity of the more concentrated solution.

Luz et al. (2007) investigated the application of an ultrasonic atomization-based approach for preparation of dextrin microspheres on a laboratory scale. The ultrasonic atomizer was operated at a 1.66-MHz frequency and used for dextrin loading at 20 mg/mL. A detailed characterization of the produced microspheres was presented using SEM/TEM analysis as well as DTA measurements to check the thermal stability of the dextrin powder. The developed ultrasound spray-drying system was reported to give good collection efficiency, as 60% of the atomized feed was collected over the membrane in a dried powder form. SEM images revealed that the prepared particles were spherically shaped, with a diameter range of 0.2 to 2.6 μm. The mean average diameter determined by laser light scattering was 1.7 μm. It was concluded that the simple combination of an ultrasonic atomizer with spray drying can be used successfully for microsphere synthesis, and the application can be extended to several other products.

Klaypradit and Huang (2008) reported another case study of encapsulation technique using an ultrasonic atomizer and the three processing steps of emulsification, ultrasonic atomization, and freeze drying. The different materials for encapsulation of tuna oil powder used included chitosan (CS), maltodextrin (MD), and whey protein isolate (WPI). The size and stability of the emulsion droplet and the properties of the encapsulated powders after freeze drying were characterized. The EPA and DHA contents (240 mg/g) of the encapsulated powder were slightly higher than commercial specification (100 mg/g), and they had low moisture content and water activity and an acceptable appearance and encapsulation efficiency. It was reported that the use of ultrasound was significantly beneficial and that the technology can be applied in the food industry to improve the stability of tuna and other oils.

Legako and Dunford (2010) reported an application of ultrasonic atomization and microencapsulation for the synthesis of fish oil-whey protein microcapsules. Microencapsulation provides an effective means to convert liquid fish oil into a more stable and easy to use dry powder. Also, different ingredients can be used to enhance the applicability. In the reported study, fish oil was encapsulated in WPI because of its reported human health benefits as an ideal protein supplement for the growth of muscle while at the same time helping to reduce fat. Generally, production of microcapsules is done by spray drying an emulsion, as this is a relatively simple and inexpensive process when compared to some of the other available approaches, such as freeze drying. However, the conventional approaches have the limitation of lack of control over droplet size, producing a wide distribution of droplet sizes and clogging. The use of ultrasound-based multiple fluid atomization was indeed reported to result in more uniform size distribution and more uniform shape of the final product. However, the microcapsules obtained using the ultrasonic nozzle showed lower oil encapsulating efficiency when compared to the microcapsules obtained with pressure nozzles and freeze drying, possibly due to nozzle clogging during the microencapsulation process. Modifications in the design of ultrasonic nozzles or the operating parameters (such as ultrasonic power dissipation and stream flow rates) can be effectively used to solve the problems of nozzle clogging.

Food products are frequently modified using certain food supplements to improve the nutritional value. Such study was demonstrated by Taksima et al. (2015) for the fortification of yogurts with astaxanthin. Yogurts are consumed all over the world owing to their content of probiotic microorganisms, which are essential for healthy body functioning. Despite several health benefits, the antioxidant activity in yogurt is low, which could be enhanced by blending with certain food supplements such as astaxanthin. The study reported the use of ultrasonic atomization (40 kHz) for the encapsulation of natural astaxanthin obtained from shrimp waste with alginate-chitosan beads to protect the bioactive properties against adverse process conditions for application in yogurt preparation. Uniform-sized beads with a size of 4.23 mm were accomplished using ultrasonic atomizer with the highest encapsulation

efficiency of 91.34%. The yogurts with astaxanthin beads were tested for sensory properties, and overall acceptable response was obtained for color, texture, aroma, mouthfeel, etc. It is important to note that production of much smaller-sized beads is possible as compared to reported value of 4.23 mm through optimizing the parameters involved in the synthesis such as shell and core components ratio, feed rate, ultrasonic parameters of power dissipation and frequency, etc., which could further improve the taste of yogurts with encapsulated astaxanthin inducing much better sensory properties.

Turan et al. (2015) investigated the use of ultrasonic atomization in microencapsulation of blueberry juice and blueberry's extracted bioactive compounds, i.e., anthocyanins and proanthocyanidins. Such bioactive compounds have wide applications in food industry considering the various health benefits associated. However, these compounds are susceptible to degradation under unfavorable circumstances such as high temperature, pressure, etc., thereby driving attention toward the stability of these food components. Microencapsulation can be used as a tool for the protection of these compounds with the use of proper shell material to achieve highly stable compound with enhanced bioavailability. The study involved the use of ultrasonic nozzle operating at 60 kHz frequency for the spray drying of blueberry juice with maltodextrin and blueberry juice extract with a combination of gum arabic and maltodextrin for encapsulation. The method was also compared with freeze drying and conventional spray drying. The obtained microspheres were evaluated for their phenolic content and antioxidant activity values, which were found to be almost similar for all three cases. Importantly, the microspheres generated using ultrasonic atomization were more uniform in size with narrow size distribution, which contributes to better stability of microspheres. The obtained encapsulated microspheres were also tested for efficacy through their application in cake and ice cream preparation. Minimal color change was observed with ultrasonic and conventional spray-dried samples as compared to freeze-dried microspheres, while the textural changes were not that significant in all samples. The anthocyanin retention in baked product was found to be highest as 80% for the case of ultrasonically atomized microspheres, indicating the efficiency of ultrasonic atomization in microencapsulation for the protection of bioactive compounds from adverse process conditions.

The bakery and dairy processes involves the use of binding agents to enhance the properties and texture of bakery and dairy products. Isleroglu et al. (2018) studied the powder preparation of partially purified microbial transglutaminase, a binding agent used in the preparation of dairy and bakery products. The powder was prepared through microencapsulation using ultrasonic spray freeze drying, where the ultrasonic atomization was performed followed by rapid freezing using liquid nitrogen to protect the biological activity of transglutaminase for long-term storage. The effect of frequency in the range of 48–120 kHz and flowrate in the range of 2–8 mL/min on enzyme activity and particle size was also studied. The obtained results were also compared with results of conventional freeze-drying method. It was clearly reported that ultrasonic atomization substantially improved the enzyme activity of final product with uniform and small size of particles as compared to conventional method, insinuating the role of ultrasonic atomization in producing thermally stable transglutaminase particles with high enzyme activity. It was also demonstrated that most of the enzyme activity loss was during the drying period, and thus, the drying process needs to be revised for developing suitable approach so as to prevent the loss of enzyme activity. As an extension to the aforementioned study, Isleroglu and Turker (2019) also studied the microencapsulation of transglutaminase with a blend of inulin and gum arabic as a coating material using ultrasonic spray freeze-drying process for better thermal stability. An ultrasonic nozzle with 48 kHz frequency was used for the encapsulation process followed by freeze drying. The obtained results were compared with samples obtained through conventional spray drying and freeze drying. Ultrasonic spray freeze drying was demonstrated to be a better approach for obtaining higher thermally stable microencapsulated transglutaminase particles, which was evident through the evaluation of activation energy and free energy values using the thermal kinetics study.

34.7 Other food industry applications of ultrasonic atomization

34.7.1 Extraction

Conventional techniques such as solvent extraction, distillation, cold pressing, and sublimation are widely used methods for the extraction of spice flavor compounds, which are generally in the form of essential oils or oleoresins. Despite their convenient use in extraction processes, there are several drawbacks including low extraction rates, use of toxic solvents, and decomposition of volatile components. Ultrasound-assisted extraction method can come up as a greener and useful alternative approach. Ultrasonic atomizer has been identified as an advanced technique for the extraction, where the extraction time, and therefore the energy consumption, is lesser compared to the conventional methods, also making it more suitable for the volatile compounds.

Wang et al. (2009) used ultrasonic nebulization, which has the similar function as an atomizer, coupled with gas chromatography for the extraction and subsequent determination of trans-anethole in fruits of *Illicium verum* Hook and

Foeniculum vulgare Mill. A simple setup was configured for the process consisting of a customized three-port glass flask as shown in Figure 34.9, with bottom port having same size as the piezoelectric crystal. Ultrasonic humidifier was applied as an ultrasonic source for nebulization (35 W power and 1.7 MHz frequency). The extraction flask with sample and extracting solvent was subjected to ultrasound through the nebulizer, generating aerosol. Figure 34.9 also depicts the different valve positions in the sampling loop for injection and sampling for GC analysis during the online process. The ultrasonic nebulization resulted in the phase transfer of volatile components present in the solid sample to liquid solvent, which further transferred to the gas phase through the gas-liquid mass transfer. The ultrasonic fountain helped in the emission of spice powder and solvent from the bottom to the aerosol, which assisted in the higher collision of extracting solvent and sample for enhanced extraction process compared to the conventional methods. Additionally, the formation of aerosols facilitated the transfer of liquid extract to the gaseous phase due to larger surface area.

As a step further to the ultrasonic atomization-assisted extraction, a combination of ultrasonic atomization with thermal treatment was applied to further enhance the extraction rates. Zhang et al. (2011) included the application of heating tape for intensified extraction of volatile and semi-volatile components from seeds of *Cuminum cyminum* L. The process was also monitored using a heating sensor to avoid undesirable condensation on the extractor caused by semi-volatile flavor compounds. The results were compared with hydrodistillation, which concluded higher extraction for the process of ultrasonic atomization coupled with thermal treatment. However, it is important to note that the temperature needs to be maintained to evade any possible degradation, and this can be achieved using proper cooling mechanism for temperature monitoring.

Recently, Meng and Zhengquan (2019) studied the ultrasonic nebulization extraction for the aroma of green tea. The extraction of volatile compounds from Lu'an Guapian tea was studied using ultrasonic nebulization extraction for different matrices and temperatures to observe the effect on the sensory properties. The ultrasonic nebulization was reported to be very efficient in extracting the aroma even at temperatures as low as 20°C. The aroma extracted using ultrasonic treatment was found to be around 48% higher as compared to the samples without ultrasonic nebulization. The research indeed suggested the possible use of ultrasonic atomization-induced extraction as a convenient and unique way for the intensified extraction of aroma resulting in much better sensory characteristics of beverages.

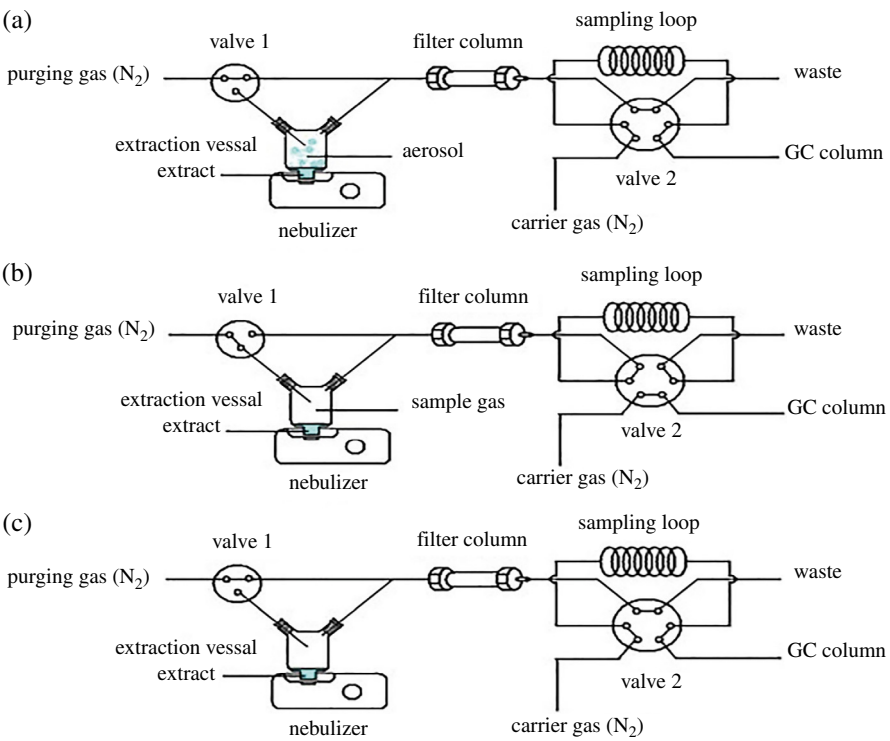


FIGURE 34.9 Schematic diagram of online ultrasonic atomization extraction system. (a: extraction, b: sampling, c: injection). *(Wang et al. (2009) with permission from Elsevier.)*

34.7.2 Nanofibers

One more noteworthy application of ultrasonic atomization is for the fabrication of nanofibers. Food-based nanofibers are especially drawing attention of researchers due to their biodegradability and biocompatibility. Methods such as wet spinning and electrospinning are generally used for the fabrication of nanofibers but shortcomings like high cost or poor orientation are associated with these methods. On the other hand, methods like hand spinning and solution blowing are much effective but employ toxic chemicals and thus, are not recommended for food applications.

Wang and Wakisaka (2015) reported a novel and greener approach, which involved the use of ultrasonic atomization and freezing for chitosan nanofiber fabrication, as shown in Figure 34.10. Chitosan, being a polysaccharide polymer, provides additional benefits such as antimicrobial activity, which is the primary requirement for food packaging and food preservation (Barikani et al., 2014). Chitosan solution was sprayed using ultrasonic atomization on a pre-freeze silicon wafer to obtain chitosan fibers using liquid nitrogen as a freezing medium. The obtained fibers were in the lowest nanorange of 91.58 ± 17.36 nm with uniform orientation and size distribution as well, compared to nanofibers obtained using household spray, airbrush, or freeze drying without ultrasonic spray, indicating the importance of ultrasonic atomization technique in deciding the fiber orientation and size. It was speculated that the ultrasonic atomizer provides high initial velocity mist, which is essential for thin and oriented spread of the solution on the wafer and thus ultimately resulted in lesser diameters and better orientation. A synergistic effect was observed for the combination of ultrasonic atomization with freeze drying, opening up the prospects for the exploration of other combinations such as ultrasonic atomization with vacuum drying for nanofiber fabrications.

34.7.3 Microbial inactivation

Ultrasound treatment can be effectively applied for reducing the microbial load in food products, and the efficacy is generally dictated by the cavitational effects. Microbial inactivation in food is necessary to achieve maximum shelf life and to maintain the quality of the material. Ultrasound treatment along with heat treatment has been proven more lethal in achieving the microbial inactivation for grape juice and whey (Donnell et al., 2010; Prabhuzantye et al., 2019). Spray drying is widely used for the preservation of foods and as an alternative to the conventional method of spray drying with an objective to avoid the high processing times required for enhanced microbial reduction, ultrasonic atomization could be an effective approach. Similar beneficial results were indeed reported by Khmelev et al. (2016) for the study of ultrasonic spray drying of sour milk products applied for maintaining the vitality of microorganisms, where the use of intense cavitating conditions was reported to yield inactivation of microorganisms in highly efficient manner. In another study, ultrasonic spray drying was found to be 10 times

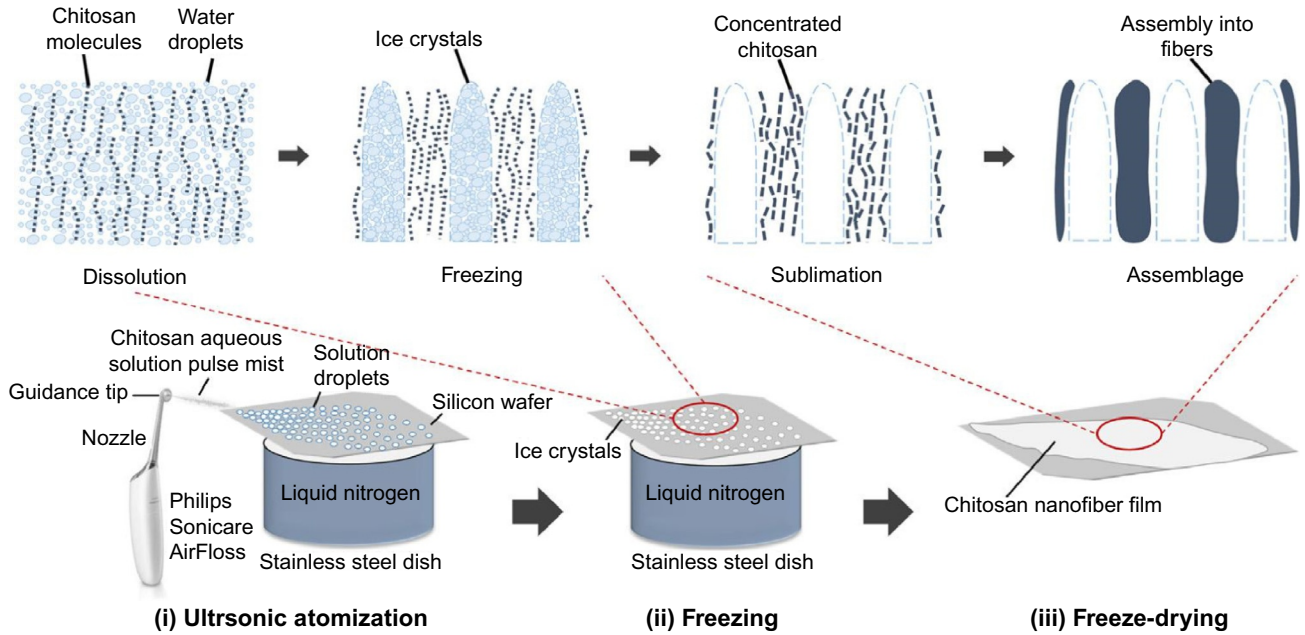


FIGURE 34.10 Schematic illustration of the ultrasonic atomization-freeze casting of chitosan nanofibers. *(Wang and Wakisaka (2015) with permission from Elsevier.)*

more effective in reducing the microbial load as compared to the conventional spray drying. Antonio-Gutiérrez et al. (2017) suggested another novel approach of the combination of ultrasonic atomization with UV treatment for intensified reduction in microbial load of grapefruit and tangerine juice. The exposure of UV along with ultrasonic atomization increases the contact between juice and UV light due to increased surface area owing to the generation of uniform and small-sized droplets. It was demonstrated that the combined effect resulted in substantially higher inactivation of microorganisms as compared to the individual operations. The process was also found to be much more effective in maintaining the product quality over long storage periods.

34.7.4 Analysis in food processing

Apart from a significant use in the generation of microspheres and encapsulated particles, ultrasonic atomization can also be used in analytical facilities that have significant importance in the food industry. This is dictated by the fact that the analysis of trace elements as well as contaminants on a microscale level is especially important given that food products are direct human consumables.

Ultrasonic atomization is principally used to help in more accurate plasma mass spectrometry analysis of very low concentration samples. Ultrasonic atomization (nebulization) is used to achieve a uniform distribution of constituents in the introduced samples. In one of the very early study, Uchida et al. (1993) investigated the detection of ultratrace cadmium, cobalt, copper, nickel, and lead in biological standard samples using inductively coupled plasma atomic emission spectrometry with ultrasonic nebulization. A detailed study of the operating conditions of the ultrasonic system revealed that the ultrasonic system increased transport efficiencies and provided better results than those obtained with the conventional cross-flow nebulizer. In another study, Cubadda et al. (2003) also reported the use of ultrasonic nebulization with an objective of achieving a reduction in solvent-related spectral interferences, while increasing signal intensities and hence improving detection limits. Solvent-related interferences are expected to be reduced due to the use of ultrasound, as the solvent can be removed by the desolvation process. It has been reported that with the use of ultrasonic nebulization, the net signal intensities increased by a factor of 60 for ^{52}Cr and 40 for ^{53}Cr. Also, it was established that accurate and precise Cr determination down to 0.1 μg/L and below is performed with the desired degree of accuracy. Continuing the work on metal detection in food processing, Cubadda and Raggi (2005) investigated the improved detection of five elements, namely, Cd, Pb, Fe, Ni, and Cr, in different samples of commercial importance such as durum wheat grain and derived products, wheat-based reference materials, and drinking water, used both as an food ingredient and for technological purposes in the different industrial processes. The benefits of ultrasonic nebulization in reducing the effects of problematic spectral interferences led to the development of a robust and high-throughput analytical method. Vassileva and Hoenig (2001) also reported similar beneficial results with the use of ultrasonic nebulization for arsenic detection in plant samples.

34.8 Applications of ultrasonic atomization in the pharmaceutical industry: Aerosols for drug delivery

The applications of ultrasonic atomization in pharmaceutical processing have been mainly for drug encapsulation or modifying the distribution profile of drug, with an objective of developing novel drug delivery systems. We now provide an overview of some of the recent applications in this area, highlighting the benefits achieved with the use of ultrasonic irradiation.

Pulmonary delivery has been a subject of interest for the application of an ultrasonic atomization process, as this is capable of producing much smaller particles than the conventional processes. Even though there is an optimal physical size of particles for nasal delivery, smaller particles, which can be more easily obtained by ultrasonic atomization, are more efficient in transporting drugs through the nasal mucosa. Particle size distribution measurements are critical during the development of nasal drug delivery systems; a suitable particle size is most likely less than 20 μm. Small particles suitable for nasal delivery have been created via a number of routes, such as spray-drying, oil-in-water emulsion, water-in-oil-in-water emulsion, solvent extraction/evaporation, solution-enhanced dispersion method, hot melt processing, etc., but it has been reported that the alternative of ultrasonic atomization is superior as it requires neither elevated temperatures nor phase separation-inducing agents. Therefore, it is an easily scalable and commercially viable particle production method, giving micron and submicron monodispersed particles (Forde et al., 2006). As the size of the final particles is crucial to application efficiency, it is important to properly select the different operating parameters, such as solid loading, feed flow rate, and ratio of active ingredients to the support, as well as the ultrasound parameters as power dissipation and frequency of irradiation.

Wiedmann and Ravichandran (2001) reported the use of an ultrasonic spray system for the production of aerosols for ultimate use in the delivery of respiratory drugs. The experimental configuration consisted of a Sono-Tek ultrasonic spray system mounted on top of a baffle, to entrain aerosol particles within the carrier gas. The entrapped solvent was

removed from the aerosol cloud by passing the droplets through drying columns composed of either charcoal or silica. The efficiency of removing ethanol and water was also established by measuring the outflow concentrations in addition to the study of aerosol characteristics. The effect of important operating parameters (such as the liquid flow rate and the drug concentration entering the atomizer) on the output was determined by the filter capture method, whereas the effect on particle size distribution was obtained using a cascade impactor. It was established that the output rate expressed as the mass of aerosol collected in unit time increased nearly proportionately with the liquid flow rate (0.18–0.7 mL/min) and the concentration of drug (0.19–12 mg/mL) entering the nebulizer. The mean particle size increased with solute concentration, but was unaffected by liquid flow rate. It was concluded that the system has the potential of providing a wide range of dose levels for testing of drug delivery, with a controlled and relatively narrow particle size distribution obtained due to the use of ultrasonic irradiation.

Alvarez et al. (2008) reported the design of a surface acoustic wave (SAW) atomizer and investigated its application in the generation of monodisperse aerosols and particles for drug delivery applications. This method was able to generate protein-loaded liquid aerosols in the optimal range for effective pulmonary absorption. In addition, 50- to 100-nm-diameter protein particles for transdermal or buccal delivery were reported to be produced by altering the operating parameters. An analysis of the different applied methods confirmed that the ultrasound-based approach is more flexible and reliable, allowing the rapid generation of aerosols and drug powders without mechanical moving parts, which increases the durability of the equipment. An added advantage is a controlled and narrow size distribution, which ensures excellent efficacy in the end application.

Another study related to the synthesis of materials suitable for nasal delivery was reported by Ho et al. (2008). Biodegradable PLG microspheres containing polyethylenimine (PEI)-condensed plasmid DNA (pDNA) were prepared using a 40-kHz ultrasonic atomization system. The production method was easily scalable for the production of large quantities of microspheres. Also, microencapsulation of pDNA via ultrasonic atomization resulted in microspheres with the majority of pDNA entrapped suitably within the core. A main disadvantage of the most commonly used multiple emulsion method, the occurrence of surface-localized pDNA, was avoided with the ultrasonic atomization approach. Using conventional methods, lower encapsulation efficiencies are obtained due to the diffusion loss of the encapsulated compounds (De Rosa et al., 2002), which is avoided in the case of ultrasonic atomization approach. The higher encapsulation efficiencies can be explained on the basis of the higher atomization rate of ultrasonic atomization, which essentially reduces the probability of loss for encapsulated compounds during the process when compared to the conventional methods.

Gao et al. (2013) developed a novel and continuous method based on ultrasonic atomization followed by deposition through electrostatic adsorption for nanosized drug crystal preparation using amitriptyline hydrochloride as a model drug. The setup consisted of ultrasonic spray of the drug solution in a container, where the aerosol formation takes place. Aerosol was subsequently carried through an inert carrier gas into the oven evaporating the liquid and crystallizing the drug into nanoparticles. The flow was passed through an electrostatic adsorption precipitator containing two electrodes for generating an electrostatic field, which attenuated the agglomeration of nanoparticles. Nanosized crystals of spherical and rectangular shape in the size range of 20 to 400 nm were reported to be effectively prepared at different heating temperatures. Effective results were demonstrated through ultrasonic atomization in producing drug nanocrystals, and the development of continuous process for the generation of nanocrystals of poorly water-soluble drugs was suggested as path forward for commercial exploration.

Dimer et al. (2015) studied the preparation of dry powder inhaler form of resveratrol for pulmonary administration for arterial hypertension treatment using a nanospray dryer B-90 involving ultrasonic atomization. The use of ultrasonic vibrations in producing the drug microparticles resulted in around 50% fine particle formation with approximately 80% yields and less than 2% moisture content. The attributes of the final product increased the flowability of the drug and decreased the density, resulting in aerodynamic properties necessary for enhanced drug delivery and deposition of drug on the bronchial and alveolar regions of lungs.

The application of ultrasonic spray freeze drying was studied by Ye et al. (2017) for obtaining liposomal dry powder with lyoprotectants for pulmonary administration. The ultrasonic spray freeze drying was reported to offer an advantage of narrow size distribution of particles along with the generation of porous structure through water removal by lyophilization. The lyoprotectants used in the study were 5% sucrose and 15% mannitol, and their interaction with drug was investigated using differential scanning calorimetry. Although sugars generally increase the moisture content owing to their hygroscopic nature, the use of the above lyoprotectants was found to be very successful in producing stable microparticles of liposomal powder yielding storage period of up to 3 months at 25°C and 60% relative humidity. The ultrasonic spray freeze drying was given credit for the generation of stable microparticles, which allowed the entrapment of drug with higher efficiency of 80% with uniform drug content and high aerosol efficiency, again confirming the possibility of

ultrasonic spray freeze drying as an effective drug delivery method.

Another novel method for the preparation of aerosol for pulmonary administration was reported by Saboti et al. (2017) using a microfluidic reactor coupled with ultrasonic spray freeze drying for budesonide (BDS), an active pharmaceutical ingredient for asthma treatment. In contrast to conventional method, the process was reported to evade the requisite of homogenization or stabilizer. Suspension of drug in alcohol-water system was produced using the reactor, which was then fed to the ultrasonic atomizer followed by freezing using liquid nitrogen. Further, the obtained BDS particles were blended with lactose for aerosol delivery. The morphology and aerosol performance of drug particles and the blend were studied using scanning electron microscopy and in vitro aerosol performance testing, respectively. The particle size of BDS was reported to be in the range of 5.85 to 8.83 μm with good aerosol performance at 100 L min^{-1} using an Aerolizer with blended fine particle fraction of around 47.6% to 55%. The study proved that the microfluidic reactor and ultrasonic spray freeze drying system could be successfully applied as a single-stage method for the production of dry powder suitable for effective pulmonary administration without using homogenizer or stabilizer.

34.9 Applications of ultrasonic atomization in the pharmaceutical industry: Encapsulation for drug delivery

Encapsulation has been one of the important processes continuously subjected to innovation with an aim of guaranteeing the success of pharmacological therapies. The different steps involved in the process of encapsulation are schematically depicted in Figure 34.11. For applications related to drug delivery, it has been necessary to produce particles at microsize, if not smaller, and the process is referred to as microencapsulation. Microencapsulation can be defined as a process by which solids, liquids, and even gases are entrapped in microscopic particles through the formation of a thin coating around an active substance. The droplet formation step is the controlling step in determining the size and size distribution of the resulting microspheres. The general approaches for droplet formation are stirring, static mixing, extrusion (single pathway system, multichannel system, or membranes), and dripping (single droplet formation or jet excitation), but recently ultrasonic irradiation has also been used with significantly better results (Dalmoro et al., 2012). Some case studies are now presented, with an emphasis on drug delivery.

Burke et al. (2004) investigated the application of ultrasonic atomization for encapsulation of darbepoetin alfa, a synthetic form of glycoprotein hormone that controls red blood cell production. The synthesis process was based on two stages: spray freeze-drying and spray-drying processes, performed on a pilot scale. The first step involved atomizing a suspension of solid protein particles in polymer solution to form nascent microspheres, which were subsequently either frozen in liquid nitrogen (spray freeze drying), followed by the extraction of the polymer solvent in cold ethanol for a period of hours to days, or removed by evaporation based on spray drying followed by carbon dioxide gas treatment. It was reported that the ultrasonic nozzles were capable of producing droplets of comparable median diameter, about 60 μm or less, depending on the polymer type, atomization power, and feed flow rate. The observed encapsulation efficiencies were very high, near 100%, and the robustness of the ultrasound-assisted process was demonstrated by the excellent reproducibility of the physical and chemical characteristics of the synthesized microspheres as well as the in vivo release kinetics.

Qiu and Xia (2008) investigated the application of a novel ultrasonic atomization precipitation method for the synthesis of nano-hydroxyapatite at room temperature and normal atmospheric pressure. It was reported that the obtained powders were homogenous, with a size range of 30–40 nm. Comparison of HAP powders obtained using the ultrasonic method and using the traditional chemical precipitation method under the same conditions revealed that the ultrasound-based approach shortened the reaction time required to make HAP nanopowders and enhanced the synthetic efficiency and crystallinity of HAP

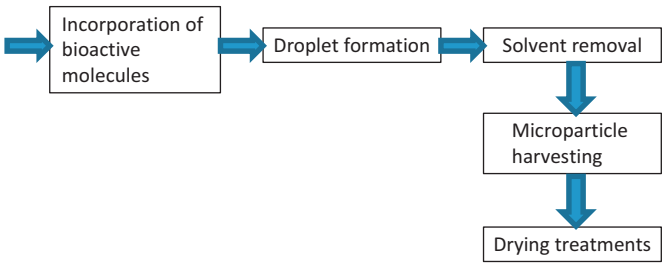


FIGURE 34.11 Steps in microencapsulation process for pharmaceutical applications.

nanopowders. A significant advantage was that the obtained nanoparticles were more homogenous and had a uniform size distribution.

Ho et al. (2008) also investigated the microencapsulation of pDNA using ultrasonic atomization. The study is important as biodegradable microspheres offer the facilitation of DNA vaccine delivery to antigen-presenting cells. Microspheres offer distinct advantage over other delivery techniques for DNA vaccine, as the DNA vaccine is released in its bioactive form in a controlled fashion. The work of Ho et al. (2008) dealt with synthesis of biodegradable PLG microspheres containing PEI condensed pDNA using a 40-kHz ultrasonic atomization system. The process synthesis parameters important to the effective synthesis of microspheres suitable for nasal delivery (with a size of less than 20 μm) were established to be feed flow rate, polymer concentration, volumetric ratio of polymer and pDNA-PEI (pDNA-PEI) complexes, and the nitrogen to phosphorous (N/P) ratio. The ultrasonic synthesis method had excellent reproducibility, with the pDNA encapsulation efficiencies in the range 82%–96% and mean particle sizes between 6 and 15 μm. It was also conclusively established that ultrasonic atomization efficiently overcomes the key obstacles in scaling-up the manufacture of encapsulated vaccine for clinical trials and, ultimately, commercial applications.

Graves et al. (2008) investigated the encapsulation of indomethacin into PLG using coaxial ultrasonic atomization. The effect of drug loading and a change in relative concentration of polymer in the inner and outer layers of co-flowing spray liquids on the physicochemical characteristics of the particles was investigated. It was observed that the micro-/nanocapsules prepared using a drug-free PLG solution outer layer gave higher encapsulation efficiency. Thermal analysis of the formulations confirmed that indomethacin was uniformly dissolved within the PLG matrix. The use of the ultrasound-based approach resulted in the synthesis of smooth and spherical particles. A cross-sectional view of the particles confirmed the clear presence of three different internal morphologies. It has been claimed that this was the first study revealing the cross-sectional view of particles prepared with coaxial ultrasonic atomization technique.

Barba et al. (2009) reported the use of an ultrasonic atomization method for the production of small droplets of biopolymer (alginate) intended for the preparation of encapsulated drug/nutraceutical delivery systems. During the synthesis process, alginate solution was passed through the ultrasonic atomizer, followed by spraying the droplets for small time intervals (4–5 s) into a beaker containing stirred copper sulfate solution. The typical power level for the ultrasonic atomizer was within the range of 4–11 W. The effect of different process parameters, such as alginate concentration, volumetric flow rate, and power delivered, on resulting particle diameters was investigated. The particle diameter increased with an increase in flow rate and alginate concentration, whereas power dissipation had a marginal effect. The obtained data did not fit into the general correlations found in the literature, so a new correlation valid for the specific system and range of parameters was developed, based on parameter regression and careful statistical data analysis. Energy requirement analysis was also performed and the required energy was compared with other atomization techniques. It was established that, compared to two-fluid technology (atomization of a liquid assisted by a compressed gas) and the centrifugal atomizer (in which droplets are obtained because of the fast rotation of the feed), the ultrasonic atomization had a low volumetric energy requirement.

Gao et al. (2011) investigated the application of ultrasonic spray freeze-drying technique for the synthesis of lipid-polymer composite microspheres (LP-MS), which have a great potential for colon-specific drug delivery. The morphological and physicochemical properties of the microspheres, consisting of the pH-sensitive polymer, Eudragit S100 and the nonpolar lipid, Compritol 888 ATO, were characterized. It was established that the synthesized LP-MS had a spherical lipid porous matrix with a smooth pH-sensitive polymer film formed on both the internal and external surfaces. It was also observed that the insoluble drug 10-hydroxycamptothecin was uniformly dispersed in an amorphous state in the carrier. The effect of pH on the morphological changes of the microparticles was studied using confocal laser scanning microscopy, and it was established that the lipid matrix in LP-MS restricted the swelling property of the polymer at pH 6.8. The drug-release studies confirmed that less than 15% of the drug was released below pH 6.8, and more than 30% was released with a sustained-release model at pH 7.4. The study confirmed the efficient use of an ultrasonic atomization-assisted approach for the synthesis of microspheres.

In a recent study, Cascone et al. (2012) reported a method of producing biopolymeric (alginate) microparticles loaded with a small active molecule (theophylline) using ultrasonic-assisted atomization and subsequent separation using centrifugation or filtration followed by drying. Fine-loaded alginate droplets were cross-linked with divalent ions to produce microparticles. It was established that the transport processes play a crucial role in deciding encapsulation efficiency and that the ultrasound-based synthesis approach is effective. Drug loading in the final product was reported to be higher, with a shorter separation time, and a better network structure was achieved using ultrasonic atomization. In another recent work, Barba et al. (2012) confirmed the various advantages of ultrasonic atomization, such as a lower level of mechanical stress on materials, reduced energy requirement, reduced equipment size, etc., as compared to the conventional techniques. In the

reported work, fine drug-loaded particles were produced by ionic reticulation of droplets obtained by ultrasonic atomization of biopolymer solutions, with subsequent characterization in terms of morphology and drug-release kinetics. Polymeric network mesh size (PNMS) investigations with an aim of clarifying its role in controlled drug release confirmed that the calculated PNMS was consistent with a fast release of drugs of small molecular size.

Dalmoro et al. (2014) studied the encapsulation of α-tocopherol (TOC), a major form of vitamin E, with alginate as a shell material using a novel method consisting of coaxial ultrasonic nozzle atomizer (25 kHz) followed by microwave drying at bench scale for the production of stable microparticles. The process flow diagram for the bench-scale apparatus can be seen in detail in Figure 34.12, which was developed for a semi-continuous operation using a single-pot process chamber. The objective was to overcome the challenges generally faced in the commonly applied processes for manufacturing of pharmaceuticals such as batch process where the disadvantages are numerous processing steps resulting in a time-consuming and high-energy process. The developed process resulted in a 100% encapsulation yield with excellent drug release properties insinuating the efficacy of ultrasonic atomizer with microwave drying as an efficient process in achieving the desired process intensification in terms of better energy transfer rates, reduction in chamber volume, and enhanced quality of the product.

Dalmoro et al. (2015) studied the encapsulation of indomethacin, a non-steroidal, anti-inflammatory gastrolesive drug using ultrasonic atomization in combination with two-stage polyelectrolyte complexation. Indomethacin is useful in the treatment of arthritis and to some extent in reducing the colon cancer risk with an oral dosage requirement of 2–3 times a day for adults, which make it difficult for treatment due to very short biological life of the drug. Further, the drug also has some side effects mainly in the gastrointestinal area. Thus, in this study, ultrasonic atomization was used for the encapsulation of indomethacin to develop an energy-efficient process for stable drug formation. The anionic biopolymer, alginate solubilized in water with drug, was sprayed for fine particle formation, and further complexed in two stages using cationic acrylate and anionic copolymer, for high drug encapsulation and better gastro-resistance application. The ultrasound assisted process was found to be better in drug encapsulation efficiency (around 75%) and in enteric properties when compared with the conventional alginate cross-linking process.

Choi et al. (2018) studied the preparation of biodegradable poly(lactic-*co*-glycolic acid) (PLGA) microcapsules loaded with potassium fluoride that can be applied for the suppression of bacterial growth during orthodontic

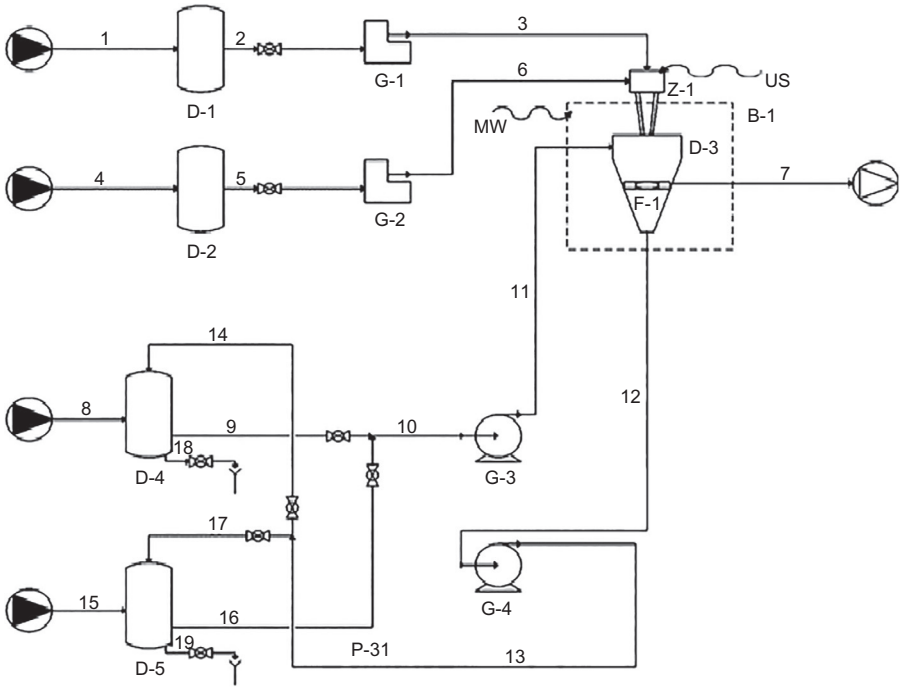


FIGURE 34.12 Single-pot semi-continuous bench-scale process for microencapsulation (Z-1, ultrasonic double-channel atomizer; D-3, wet collector; B-1, microwave oven cavity; G-1/G-2, peristaltic pumps-core and shell feeding channels; G-3/G-4, centrifugal pumps-reticulation solution feeding and suspension recirculation; D-1/D-2, core-and-shell feeding tanks; D-4/D-5, reticulation solution tank, rinsewater tank; and F-1, filter; box with *dashed line*: MW cavity). *(Dalmoro et al. (2014) with permission from ACS through Rightslink.)*

treatment using coaxial ultrasonic atomizer. Further, the microcapsules were loaded on the orthodontic disk using LED light curing. The fluoride content in the microcapsules was found to be stable with 85% fluoride content remaining after 45 days of storage. The obtained microcapsules had a uniform size of about 17.3 μm with an encapsulation efficiency of around 48.5%. Disk containing microcapsules showed a reduction in bacterial growth as compared to the control samples. It was also observed that the ultrasonic atomizer was efficient in delivering fluoride microcapsules with uniform shape and size, reducing the interfacial gap, maintaining the shear bonding strength, and also resulting in an antibacterial agent with good activity, and preserving the mechanical properties of orthodontic resins after incorporation.

Luzardo-Álvarez et al. (2019) studied the coaxial ultrasonic atomization using 60-kHz frequency transducer to preserve the antioxidant activity and to reduce the degradation of resveratrol through microencapsulation using poly-(ε-caprolactone). A mathematical model was developed using an experimental design to optimize the nozzle power, and polymer concentration for desired particle size, and encapsulation efficiency. The nozzle power was varied in the range of 3.58 to 6.41 W and polymer concentration in the range 0.08% to 2.91% considering the nozzle clogging and threshold levels of power and polymer concentration required for particle generation. Ultrasonic atomization was reported to generate uniform-sized spherical microparticles with narrow size distribution. The results confirmed the potential reproducibility and scalability of the technology for possible industrial-scale continuous manufacturing.

Joshi et al. (2020) studied the ultrasonic atomization for the development of doxorubicin (DOX)-chitosan nanoparticles for cancer therapy. Considering the need for controlled release of drug for site-specific conditions in the case of cancer for targeting the cancer cells or tissues, the synthesis and further application of DOX-chitosan nanoparticles have been studied. Chitosan is beneficial in terms of biodegradability and bioactivity, and provides electrostatic bonding with DOX for encapsulation, which was further cross-linked with poly(sodium 4-styrene sulfonate) and sodium tripolyphosphate (PSS and TPP) using ultrasonic atomizer for enhancing the morphological characteristics. An average size of nanoparticles cross-linked with PSS was obtained as 80 ± 30 nm, while using TPP, it was 120 ± 50 nm with encapsulation efficiencies of around 32% and 44%, respectively. The lower encapsulation efficiencies of DOX in chitosan nanoparticles were attributed to their same molecular charge. However, for the in vitro release of drug, the nanoparticles showed controlled release with pH dependency for continuous 168 h with better cellular viability in the case of TPP cross-linking, indicating the successful synthesis of chitosan nanoparticles using ultrasonic atomizer.

A short overview of the different microparticle syntheses based on the use of ultrasonic atomization enables the establishment of the distinct advantages offered by the coupling of ultrasonic irradiations with other unit operations. The process results in uniform particle size distributions with higher encapsulation efficiencies, confirming the utility of ultrasonic atomization in the pharmaceutical field.

34.10 Future trends

Ultrasonic atomization can be exploited for industrial-scale applications, especially for spray drying (food products and pharmaceuticals) and continuous flow atomization. The expected advantages include improved drying efficiency in spraying with better quality product. Further work that can be done in this area, with objectives of making the application more feasible and cost-effective, is as follows:

(1) Developing new atomizer designs that are capable of giving better-quality products with proven tested efficacy at laboratory scales of operation.
(2) Obtaining better understanding of the mechanistic aspects of drop formation and developing unified correlations for the prediction of mean droplet sizes valid for a range of system and operating parameters.
(3) Developing new protocols for optimized synthesis of encapsulated product without losing any of the active materials. Development of novel single-pot ultrasonic-assisted processes to produce microparticles under controlled conditions is of crucial importance for commercial applications.
(4) Development of combined processes based on the use of ultrasound and ultraviolet/infrared irradiation would help obtain better product, especially in the case of pharmaceutical applications.
(5) Developing new protocols for accurate analysis using an ultrasound-based-approach can perform even trace analysis in food processing.

34.11 Conclusions

Ultrasonic atomization offers considerable promise for the generation of droplets with uniform particle size and distribution. The product characteristics can be effectively controlled based on the operating parameters, both equipment parameters and liquid physicochemical properties. Depending on the operating conditions, either the capillary or the cavitation mechanism can be controlling, with a significant effect on the final characteristics.

The geometric design can be tailor-made based on the specific application under question. The equipment operating parameters can be suitably selected, again based on the desired characteristics such as ejection velocities, mean size, and size distribution. The guidelines provided in this

chapter will help design engineers suitably select the design and operational parameters for the desired application.

An overview of specific applications in the food and pharmaceutical industries establishes the effectiveness in terms of higher efficiencies, controlled size distribution, better product specifications, and lower energy requirements, as compared to conventional designs. Also, the use of ultrasonic irradiation-based approaches may enable combining certain unit operations, leading to faster processing.

Overall, it can be said that ultrasonic atomization offers a viable alternative to the more traditionally used pressure atomizers, especially in the pharmaceutical and nutraceutical fields, where product activity specifically depends on size distribution.

References

Al-Jumaily, A.M., Meshkinzar, A., 2017. On the development of focused ultrasound liquid atomizers. Adv. Acoust. Vib. 2017, 7861726. https://doi.org/10.1155/2017/7861726.

Alvarez, M., Friend, J., Yeo, L.Y., 2008. Rapid generation of protein aerosols and nanoparticles via surface acoustic wave atomization. Nanotechnology 19, 455103. https://doi.org/10.3109/1061186X.2013.805335.

Antonio-Gutiérrez, O., López-Malo, A., Ramírez-Corona, N., Palou, E., 2017. Enhancement of UVC-light treatment of tangerine and grapefruit juices through ultrasonic atomization. Innov. Food Sci. Emerg. Technol. 39, 7–12. https://doi.org/10.1016/j.ifset.2016.10.019.

Ashokkumar, M., Bhaskaracharya, R., Kentish, S., Lee, J., Palmer, M., Zisu, B., 2010. The ultrasonic processing of dairy products—an overview. Dairy Sci. Technol. 90, 147–168. https://doi.org/10.1051/dst/2009044.

Avvaru, B., Gogate, P.R., Patil, M.N., Pandit, A.B., 2006. Ultrasonic atomization: effect of liquid phase properties. Ultrasonics 44 (2), 146–158. https://doi.org/10.1016/j.ultras.2005.09.003.

Barba, A.A., D'Amore, M., Cascone, S., Lamberti, G., Titomanlio, G., 2009. Intensification of biopolymeric microparticles production by ultrasonic assisted atomization. Chem. Eng. Process. 48, 1475–1481. https://doi.org/10.1016/j.cep.2009.08.004.

Barba, A.A., Dalmoro, A., D'Amore, M., Lamberti, G., 2012. Controlled release of drugs from microparticles produced by ultrasonic assisted atomization based on biocompatible polymers. Chem. Biochem. Eng. Q. 26 (4), 345–353.

Barikani, M., Oliaei, E., Seddiqi, H., Honarkar, H., 2014. Preparation and application of chitin and its derivatives: a review. Iran. Polym. J. 23 (4), 307–326. https://doi.org/10.1007/s13726-014-0225-z.

Berkland, C., Pollauf, E., Pack, D., Kim, K., 2004. Uniform double-walled polymer microspheres of controllable shell thickness. J. Control. Release 96, 101–111. https://doi.org/10.1016/j.jconrel.2004.01.018.

Bittner, B., Kissel, T., 1999. Ultrasonic atomization for spray drying: a versatile technique for the preparation of protein loaded biodegradable microspheres. J. Microencapsul. 16 (3), 325–341. https://doi.org/10.1080/026520499289059.

Bouguslavskii, Y.Y., Eknadiosyants, O.K., 1969. Physical mechanism of the acoustic atomization of a liquid. Sov. Phys. Acoust. 15, 14–21.

Briceño-Gutierrez, D., Salinas-Barrera, V., Vargas-Hernández, Y., Gaete-Garretón, L., Zanelli-Iglesias, C., 2015. On the ultrasonic atomization of liquids. Phys. Procedia 63, 37–41.

Burke, P., Klumb, L., Herberger, J., Nguyen, X., Harrell, R., Zordich, M., 2004. Poly (lactide-co-glycolide) microsphere formulations of darbepoetin alfa: spray drying is an alternative to encapsulation by spray-freeze drying. Pharm. Res. 21, 500–506. https://doi.org/10.1023/B:PHAM.0000019305.79599.

Cascone, S., Lamberti, G., Titomanlio, G., Barba, A.A., D'Amore, M., 2012. Microencapsulation effectiveness of small active molecules in biopolymer by ultrasonic atomization technique. Drug Dev. Ind. Pharm. 38 (12), 1486–1493. https://doi.org/10.3109/03639045.2011.653814.

Chakinala, A.G., Gogate, P.R., Burgess, A.E., Bremner, D.H., 2007. Intensification of hydroxyl radical production in sonochemical reactors. Ultrason. Sonochem. 14, 509–514. https://doi.org/10.1016/j.ultsonch.2006.09.001.

Choi, H., Um, S., Rhee, S., 2018. Preparation of fluoride-loaded microcapsules for anticariogenic bacterial growth using a coaxial ultrasonic atomizer. J. Biomed. Mater. Res. 106 (B), 31–39. https://doi.org/10.1002/jbm.b.33810.

Cubadda, F., Raggi, A., 2005. Determination of cadmium, lead, iron, nickel and chromium in selected food matrices by plasma spectrometric techniques. Microchem. J. 79 (1–2), 91–96. https://doi.org/10.1016/j.microc.2004.10.007.

Cubadda, F., Giovannangeli, S., Iosi, F., Raggi, A., Stacchini, P., 2003. Chromium determination in foods by quadrupole inductively coupled plasma-mass spectrometry with ultrasonic nebulization. Food Chem. 81 (3), 463–468. https://doi.org/10.1016/S0308-8146(03)00002-5.

Dalmoro, A., Barba, A.A., Lamberti, G., d'Amore, M., 2012. Intensifying the microencapsulation process: ultrasonic atomization as an innovative approach. Eur. J. Pharm. Biopharm. 80, 471–477. https://doi.org/10.1016/j.ejpb.2012.01.006.

Dalmoro, A., Barba, A.A., D'Amore, M., Lamberti, G., 2014. Single-pot semicontinuous bench scale apparatus to produce microparticles. Ind. Eng. Chem. Res. 53, 2771–2780. https://doi.org/10.1021/ie403308q.

Dalmoro, A., Sitenkov, A.Y., Lamberti, G., Barba, A.A., Moustafine, R.I., 2015. Ultrasonic atomization and polyelectrolyte complexation to produce gastroresistant shell–core microparticles. J. Appl. Polym. Sci. 42976, 1–9. https://doi.org/10.1002/app.42976.

De Rosa, G., Quaglia, F., La Rotonda, M., Appel, M., Alphandary, H., Fattal, E., 2002. Poly (lactide-co-glycolide) microspheres for the controlled release of oligonucleotide/polyethylenimine complexes. J. Pharm. Sci. 91, 790–799. https://doi.org/10.1002/jps.10063.

Dimer, F.A., Ortiz, M., Pohlmann, A.R., Guterres, S.S., 2015. Journal of drug delivery science and technology inhalable resveratrol microparticles produced by vibrational atomization spray drying for treating pulmonary arterial hypertension. J. Drug Deliv. Sci. Technol. 29, 152–158. https://doi.org/10.1016/j.jddst.2015.07.008.

Dobre, M., Bolle, L., 1999. Visualization and analysis of liquid film surface patterns formed on ultrasonic atomizers. In: Presentation at ILASS-Europe'99, Toulouse, France.

Dobre, M., Bolle, L., 2002. Practical design of ultrasonic spray devices: experimental testing of several atomizer geometries. Exp. Thermal Fluid Sci. 26, 205–211. https://doi.org/10.1016/S0894-1777(02)00128-0.

Donnell, C.P.O., Tiwari, B.K., Bourke, P., Cullen, P.J., 2010. Effect of ultrasonic processing on food enzymes of industrial importance. Trends Food Sci. Technol. 21 (7), 358–367. https://doi.org/10.1016/j.tifs.2010.04.007.

Faraday, M., 1831. On the forms and states assumed by fluids in contact with vibrating elastic surfaces. Philos. Trans. R. Soc. Lond. 121, 319–340. https://doi.org/10.1098/rstl.1831.0018.

Forde, G., Coomes, A., Giliam, F., Han, Y., Horsfall, M., 2006. Creation of protein loaded biodegradable microparticles via ultrasonic atomization suitable for nasal delivery. Chem. Eng. Res. Des. 84, 178–184. https://doi.org/10.1205/cherd.05142.

Freitas, S., Merkle, H., Gander, B., 2004. Ultrasonic atomisation into reduced pressure atmosphere-envisaging aseptic spray-drying for microencapsulation. J. Control. Release 95, 185–195. https://doi.org/10.1016/j.jconrel.2003.11.005.

Gao, B., Wang, J., Wang, D., Zhu, Z., Qiao, Z., Yang, G., Nie, F., 2013. A novel preparation method for drug nanocrystals and characterization by ultrasonic spray-assisted electrostatic adsorption. Int. J. Nanomedicine 8, 3927–3936. https://doi.org/10.2147/IJN.S48597.

Gao, Y., Zhu, C.-L., Zhang, X.-X., Gan, L., Gan, Y., 2011. Lipid-polymer composite microspheres for colon-specific drug delivery prepared using an ultrasonic spray freeze-drying technique. J. Microencapsul. 28 (6), 549–556. https://doi.org/10.3109/02652048.2011.599442.

Gogate, P.R., Shirgaonkar, I.Z., Sivakumar, M., Senthilkumar, P., Vichare, N.P., Pandit, A.B., 2001. Cavitation reactors: efficiency assessment using a model reaction. AICHE J. 47 (11), 2526–2538. https://doi.org/10.1002/aic.690471115.

Graves, R.A., Poole, D., Moiseyev, R., Bostanian, L.A., Mandal, T.K., 2008. Encapsulation of indomethacin using coaxial ultrasonic atomization followed by solvent evaporation. Drug Dev. Ind. Pharm. 34 (4), 419–426. https://doi.org/10.1080/03639040701662636.

Ho, J., Wang, H., Forde, G., 2008. Process considerations related to the microencapsulation of plasmid DNA via ultrasonic atomization. Biotechnol. Bioeng. 101, 172–181. https://doi.org/10.1002/bit.21876.

Isleroglu, H., Turker, I., 2019. Thermal inactivation kinetics of microencapsulated microbial transglutaminase by ultrasonic spray-freeze drying. LWT-Food Sci. Technol. 101, 653–662. https://doi.org/10.1016/j.lwt.2018.11.091.

Isleroglu, H., Turker, I., Tokatli, M., Koc, B., 2018. Ultrasonic spray-freeze drying of partially purified microbial transglutaminase. Food Bioprod. Process. 111, 153–164. https://doi.org/10.1016/j.fbp.2018.08.003.

Joshi, B., Kaur, J., Khan, E., Kumar, A., Joshi, A., 2020. Journal of drug delivery science and technology ultrasonic atomizer driven development of doxorubicin-chitosan nanoparticles as anticancer therapeutics: evaluation of anionic cross-linkers. J. Drug Deliv. Sci. Technol. 57, 101618. https://doi.org/10.1016/j.jddst.2020.101618.

Khmelev, V.N., Shalunov, A.V., Golykh, R.N., Dorovskikh, R.S., Nesterov, V.A., Shavyrkina, N.A., 2016. Studies of spray drying process of sour milk products with the application of ultrasonic vibrations. In: Int. Conf. Young Spec. Micro/Nanotechnologies Electron Devices, EDM 2016–August, pp. 246–250, https://doi.org/10.1109/EDM.2016.7538734.

Klaypradit, W., Huang, Y.-W., 2008. Fish oil encapsulation with chitosan using ultrasonic atomizer. LWT-Food Sci. Technol. 41 (6), 1133–1139. https://doi.org/10.1016/j.lwt.2007.06.014.

Kudo, T., Sekiguchi, K., Sankoda, K., Namiki, N., Nii, S., 2017. Effect of ultrasonic frequency on size distributions of nanosized mist generated by ultrasonic atomization. Ultrason. Sonochem. 37, 16–22.

Lang, R.J., 1962. Ultrasonic atomization of liquids. J. Acoust. Soc. Am. 34, 6–8. https://doi.org/10.1121/1.1909020.

Legako, J., Dunford, N., 2010. Effect of spray nozzle design on fish oil-whey protein microcapsule properties. J. Food Sci. 75, E394–E400. https://doi.org/10.1111/j.1750-3841.2010.01708.

Luz, P.P., Pires, A.M., Serra, O.A., 2007. A low cost ultrasonic spray dryer to produce spherical microparticles from polymeric matrices. Quim Nova 30, 1744–1746. https://doi.org/10.1590/S0100-40422007000700041.

Luzardo-Álvarez, A., Lamela-Gómez, I., Otero-espinar, F., 2019. Development, characterization, and in vitro evaluation of resveratrol-loaded poly-(ε-caprolactone) microcapsules prepared by ultrasonic atomization for intra-articular administration. Pharmaceutics 11 (249), 1–24. https://doi.org/10.3390/pharmaceutics11060249.

Meng, T., Zhengquan, L., 2019. Influence of ultrasonic nebulization extraction, infusion temperatures, and matrices on aroma release and perception of green tea. LWT 115, 108216.

Niven, R.W., Ip, A.Y., Mittelman, S., Prestrelski, S.J., Arakawa, T., 1995. Some factors associated with the ultrasonic nebulization of proteins. Pharm. Res. 12, 53–59. https://doi.org/10.1023/A:1016282502954.

Park, K., Yeo, Y., 2003. Microencapsulation Using Ultrasonic Atomizers. US6767637.

Peskin, R.L., Raco, R.J., 1963. Ultrasonic atomization of liquids. J. Acoust. Soc. Am. 35, 1378–1381. https://doi.org/10.1121/1.1918700.

Prabhuzantye, T., Khaire, R.A., Gogate, P.R., 2019. Enhancing the recovery of whey proteins based on application of ultrasound in ultrafiltration and spray drying. Ultrason. Sonochem. 55, 125–134. https://doi.org/10.1016/j.ultsonch.2019.03.008.

Qiu, Y., Xia, H.-P., 2008. Preparation of nano-hydroxyapatite by novel ultrasonic atomization precipitation method. J. Mater. Eng. 10, 324–327.

Rajan, R., Pandit, A.B., 2001. Correlations to predict droplet size in ultrasonic atomization. Ultrasonics 39, 235–255. https://doi.org/10.1016/S0041-624X(01)00054-3.

Ramisetty, K.A., Pandit, A.B., Gogate, P.R., 2013. Investigations into ultrasound induced atomization. Ultrason. Sonochem. 20 (1), 254–264. https://doi.org/10.1016/j.ultsonch.2012.05.001.

Rayleigh, L., 1883. On the crispation of fluid resting upon a vibrating support. Philos. Mag. 15, 50–58. https://doi.org/10.1080/14786448308627392.

Saboti, D., Maver, U., Chan, H., Planinšek, O., 2017. Novel budesonide particles for dry powder inhalation (DPI) prepared using a microfluidic reactor coupled with ultrasonic spray freeze drying. J. Pharm. Sci. 106 (7), 1881–1888. https://doi.org/10.1016/j.xphs.2017.02.035.

Sindayihebura, D., Dobre, M., Bolle, L., 1997. Experimental study of thin liquid film ultrasonic atomization. In: Proc ExHFT-97, Bruselles, Belgium, pp. 1249–1256.

Taksima, T., Limpawattana, M., Klaypradit, W., 2015. Astaxanthin encapsulated in beads using ultrasonic atomizer and application in yogurt as evaluated by consumer sensory profile. LWT-Food Sci. Technol. 62 (1), 431–437. https://doi.org/10.1016/j.lwt.2015.01.011.

Taylor, G.I., 1950. The instability of liquid surfaces when accelerated in a direction perpendicular to their planes. Proc. R. Soc. Lond. A 201, 192–196. https://doi.org/10.1098/rspa.1950.0052.

Turan, F.T., Cengiz, A., Kahyaoglu, T., 2015. Evaluation of ultrasonic nozzle with spray drying as a novel method for the microencapsulation of blueberry's bioactive compounds. Innov. Food Sci. Emerg. Technol. 32, 136–145. https://doi.org/10.1016/j.ifset.2015.09.011.

Uchida, T., Isoyama, H., Oda, H., Wada, H., Uenoyama, H., 1993. Determination of ultratrace metals in biological standards by inductively coupled plasma atomic emission spectrometry with ultrasonic nebulisation. Anal. Chim. Acta 283 (2), 881–886. https://doi.org/10.1016/0003-2670(93)85301-Y.

Vassileva, E., Hoenig, M., 2001. Determination of arsenic in plant samples by inductively coupled plasma atomic emission spectrometry with

ultrasonic nebulization: a complex problem. Spectrochim. Acta B At. Spectrosc. 56 (2), 223–232. https://doi.org/10.1016/S0584-8547(01)00156-2.

Wang, Y., Wakisaka, M., 2015. Chitosan nanofibers fabricated by combined ultrasonic atomization and freeze casting. Carbohydr. Polym. 122, 18–25. https://doi.org/10.1016/j.carbpol.2014.12.080.

Wang, L., Liang, Y., Wang, Z., Qu, C., Li, D., Shi, Y., Zhang, H., 2009. Ultrasonic nebulization extraction coupled with on-line gas chromatography for determination of trans-anethole in spices. Talanta 80, 864–869. https://doi.org/10.1016/j.talanta.2009.08.006.

Wiedmann, T.S., Ravichandran, A., 2001. Ultrasonic nebulization system for respiratory drug delivery. Pharm. Dev. Technol. 6 (1), 83–89. https://doi.org/10.1081/PDT-100000016.

Ye, T., Yu, J., Luo, Q., Wang, S., Chan, H.K., 2017. Inhalable clarithromycin liposomal dry powders using ultrasonic spray freeze drying. Powder Technol. 305, 63–70. https://doi.org/10.1016/j.powtec.2016.09.053.

Zhang, H., Shi, Y., Wei, S., Wang, Y., Zhang, H., 2011. Ultrasonic nebulization extraction coupled with headspace single-drop microextraction of volatile and semivolatile compounds from the seed of *Cuminum cyminum* L. Talanta 85, 1081–1087.

Chapter 35

The use of power ultrasound for water treatment

C. Pétrier[a,b] and Z. Wei[c]

[a]*Université Joseph Fourier, Grenoble, France,* [b]*King Abdulaziz University, Jeddah, Saudi Arabia,* [c]*Centre for Water Technology (WATEC) & Department of Biological and Chemical Engineering, Aarhus University, Aarhus, Denmark*

35.1 Introduction

Since 1962, it has been recognized that the propagation of an ultrasonic wave (20 kHz–1 MHz) can be used to eliminate organic pollutants from water (Colarusso and Serpone, 1996; Lur'e et al., 1962; Mason and Pétrier, 2004). This chapter provides an overview of the principles of sonochemistry that are involved in this process and connects ultrasound action with advanced oxidation processes (AOPs).

The literature on the subject is abundant; thus, this chapter does not exhaustively cover the topic. Instead, the discussion includes comprehensive and practical knowledge and information on the potential of the technique, and highlights selected articles that are considered important in the development of the field.

Sections 35.2 and 35.3 provide a basic description and a calibration of the device.

Section 35.4 depicts the chemical processes induced by the propagation of an ultrasonic wave in water. The discussion centers on the phenomenon of ultrasonic cavitation, which leads to the elimination of organic pollutants through thermal and oxidative reactions.

Section 35.5 is devoted to the determination of the kinetic constants and the sonochemical yields that are important for evaluating the potential of the technique.

The important parameters that affect the sonochemical action include the frequency, temperature, pH, and presence of water matrices (inorganic salts and natural organic matters). These parameters are discussed in Section 35.6.

Due to the current importance of the field, the combination of ultrasonic action with other AOPs, i.e., hybrid processes, receives distinctive treatment in Section 35.7.

35.2 Ultrasonic cavitation and advanced oxidative processes (AOPs)

Human activity generates and disperses different classes of chemical compounds into the environment. These compounds can have an ecological impact that can alter water resources. Many biological, chemical, and physical processes have been developed for the treatment of domestic, industrial, and agricultural wastewater and for the treatment of drinking water.

The classical treatment used in wastewater and drinking water plants does not always result in water that meets current and future regulation requirements. To address this need, since the beginning of the 1970s, processes called AOPs have been under development to improve the efficiency of water treatment (Glaze et al., 1987).

35.2.1 Hydroxyl radical and AOPs

AOPs are based on the production and use of the hydroxyl radical (•OH). Most of the times, this powerful chemical entity reacts with organic and mineral compounds at a rate limited only by diffusion (Buxton et al., 1988). This radical's use in organic matter mineralization was evidenced earlier by Fenton's reaction (Reaction 35.1; Walling, 1975).

$$H_2O_2 + Fe^{2+} \rightarrow {}^{\bullet}OH + OH^- + Fe^{3+} \qquad (35.1)$$

The radical can be also produced in different ways: (1) UV irradiation of water, (2) electrochemical reaction, (3) ozone with hydrogen peroxide (H_2O_2), (4) ozone with photodecomposition, and (5) photocatalysis at a semiconductor surface (Parsons and Williams, 2004).

35.2.2 Sonochemistry of water: Cavitation and hydroxyl radical

As early as 1929, it was known that the propagation of an ultrasonic wave in an aqueous medium can result in an oxidation process (Schmitt et al., 1929). Furthermore, as researchers postulated the involvement of the •OH, the technique was evaluated for its use in eliminating organic pollutants in water (Lur'e et al., 1962; Spurlock and Reifsneider, 1971; Srivastava, 1958; Witekowa, 1972).

Power Ultrasonics. https://doi.org/10.1016/B978-0-12-820254-8.00024-5
Copyright © 2023 Elsevier Ltd. All rights reserved.

In the ultrasonic process, the generation of $^{\bullet}OH$ does not arise from a direct interaction between the acoustic wave and the matter, such as that occurs in photochemistry. They are produced upon the pulsation and collapse of cavitation bubbles that are created from the pressure change resulting from the propagation of the wave in the liquid (Henglein, 1987).

Cavitation bubbles grow from small bubbles containing dissolved gas and vaporized water that are expelled from crevices on the surface of suspended solid particles (such solid heterogeneities are always present in a liquid). They also form on the reactor walls during a drop in hydrostatic pressure. Following a periodical change in the pressure, the tiny bubbles pulsate, with their diameter increasing at the depression stage and decreasing when the pressure increases during the compression stage. Equilibration of the vapor pressure inside the bubble leads to the entry of dissolved gas and vaporization of water at the lowest pressure period (i.e., depression step). Conversely, gas from the bubble dissolves in the medium and vaporous water liquefies during the compression step.

The value of the exchange is related to the surface of the bubble. As the surface of the sphere is greater during the depression phase, matter entering the bubble is the dominant transfer process. As a consequence, the size of the bubble increases. The growth is not limitless, as the bubbles may collide with a resulting volume that is conducive to the release of the larger bubbles, or the bubbles can reach a critical size and collapse at the beginning of the compression phase. The duration of the event is very short—less than one quarter of a cycle. For ultrasound generally used in water treatment (20 kHz–1 MHz), the duration of the collapse is in the microsecond range (1–50 ms). In such conditions, compression occurs adiabatically and the gas and vapor are compressed at a very high temperature. Calculations and experiments based upon spectroscopic data converge in their description of the final step of the collapse. The collapse drives the inside of the residual bubble into a plasma state, achieving temperatures above 4000 °C and pressures of 300 atm in water (Lepoint and Lepoint-Mullie, 1998; Rae et al., 2005; Walton and Reynolds, 1984).

For air-saturated water, in extreme conditions, water and oxygen molecules can be driven into an excited state and may dissociate into $^{\bullet}OH$, hydrogen (H), and oxygen (O) radicals. Evidence for H and $^{\bullet}OH$ is obtained through the analysis of the luminescence spectrum that accompanies the final step of collapse of the cavity (Henglein, 1987; Seghal et al., 1980).

$$H_2O \rightarrow {}^{\bullet}OH + H \tag{35.2}$$

$$O_2 \rightarrow 2O \tag{35.3}$$

It is postulated that, similar to the case of a plasma and high temperature chemistry, these radicals can react and combine in different ways in the final condensed phase of the collapse (hot spot chemistry) (Fitzgerald et al., 1956; Riesz et al., 1985).

The main reactions involve combinations of radicals and reactions with vaporized molecules.

$$H + H \rightarrow H_2 \tag{35.4}$$

$$H + {}^{\bullet}OH \rightarrow H_2O \tag{35.5}$$

$$O + H_2O \rightarrow 2{}^{\bullet}OH \tag{35.6}$$

$$H + O_2 \rightarrow {}^{\bullet}OH + O \tag{35.7}$$

$$^{\bullet}OH + {}^{\bullet}OH \rightarrow O + H_2O \tag{35.8}$$

The description of this phenomenon is more complex and involves many more reactions related to plasma and high temperature chemistry.

The fast release of $^{\bullet}OH$ and H radicals in the bulk of water has been demonstrated using ESR spin trapping experiments and specific reactions (Kondo and Riesz, 1991; Riesz et al., 1985; Wei et al., 2017).

Involvement of the $^{\bullet}OH$ in oxidative chemical reactions induced by ultrasonic waves has received considerable attention and is well established; the most prominent example is oxidation of the iodide ion (Hart and Henglein, 1985).

$$3I^- + 2{}^{\bullet}OH \rightarrow I_3^- + 2OH^- \tag{35.9}$$

If ultrasonic treatment is conducted for water that is simply saturated with a rare gas (Ar, Kr, Xe) or oxygen, the medium then accumulates H_2O_2 (Parke and Taylor, 1956; Weissler, 1959).

This H_2O_2 could originate from reactions between the $^{\bullet}OOH$ and $^{\bullet}OH$ in "hot spot" conditions, but considering the thermodynamic characteristics of the reactions and the stability of H_2O_2, most generation occurs in the bulk at the cooler interface of the bubble (Hart and Henglein, 1987; Mark et al., 1998).

$$H + O_2 \rightarrow {}^{\bullet}OOH \tag{35.10}$$

$$^{\bullet}OH + {}^{\bullet}OH \rightarrow H_2O_2 \tag{35.11}$$

$$^{\bullet}OOH + {}^{\bullet}OOH \rightarrow H_2O_2 + O_2 \tag{35.12}$$

The produced H_2O_2 as well as $^{\bullet}OH$ are involved in AOPs and account for the relationship between ultrasonic action and AOPs.

35.3 Sonochemical devices and experimentation

35.3.1 Sonochemical devices

In most cases, the core of the sonochemical equipment is an ultrasonic transducer that converts the electrical signal into mechanical displacements of a flat surface in contact with

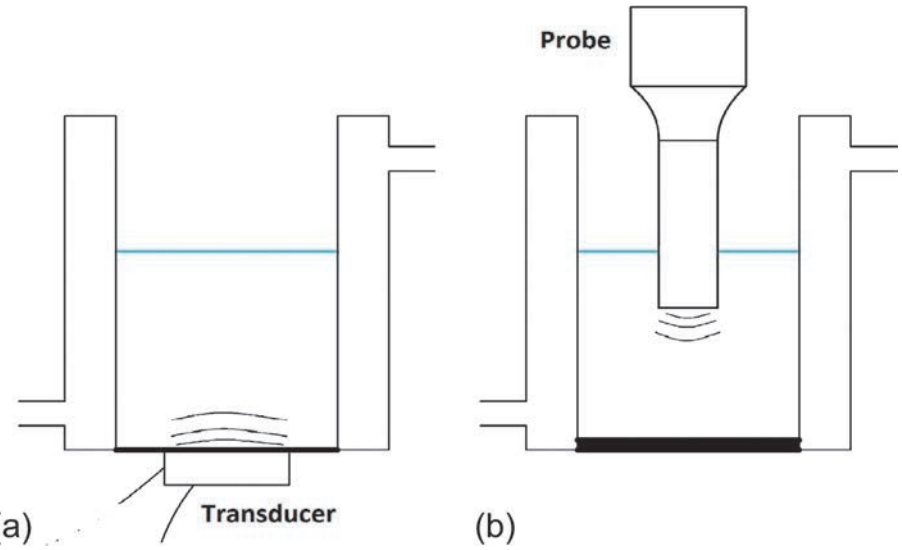


FIGURE 35.1 Scheme of bath (a) and probe (b) ultrasonic reactors.

the liquid to be processed. This emitting component (generally, a disc surface) can be the bottom or a portion of the bottom of the reactor (Bath reactor, Figure 35.1A). Alternatively, the emission can be produced at the tip of a probe immersed in the liquid. The displacement is more important in this latter case than it is with the bath, but the available frequency is restricted to the lower frequency range of 15–80 kHz (Probe system, Figure 35.1B) (Berlan and Mason, 1992).

Given the emerging status of sonochemical AOPs, many novel ultrasonic devices have been developed for improved sonochemical performance and scaled up processes. To overcome the dense cavitation and limited mass transfer of $^{\bullet}$OH, a redesign of typical horn configuration appears to be an attractive solution. For instance, a multiple-step horn configuration has successfully increased energy-emitting surfaces, reactive areas, and cavitation volumes during the sonochemical process (Wei et al., 2015; Abramov et al., 2020). These designs, when mounted in series, enable a large-scale treatment of polluted water. Some pilot applications in flow-type tubular reactors have also been demonstrated for activated sludge disintegration and oil/contaminant extraction from soils (Mason, 2007; Abramov et al., 2009).

35.3.2 Reactor calibration

The calibration of the ultrasonic devices is a rather difficult task but is necessary to insure the reproducibility of the experiments and to compare the results from different sources.

The intensity of the cavitation is defined by the following conditions: the nature of the liquid, the temperature, the pressure, and the dissolved gas linked to the pressure amplitude (P_a) of the wave generated in the liquid by the vibrating surface. The pressure is linked to the amount of energy or acoustic power (P_w) delivered in the medium each second by unit of volume [$P_a = (2\rho P_w)^{1/2}$] (ρ = density of the liquid) (Boucher, 1970).

Due to the size and shape of the reactor and transducer used to conduct the experiments and multiple reflections at the surfaces, P_a and P_w cannot have the same value at each point of volume subjected to ultrasonic action (Mandroyan et al., 2010). To overcome this problem and to globally determine the available power, recourse to the calorimetric method is commonly employed. In this approach, it is assumed that the absorbed ultrasonic power is completely converted into heat. Then, $P_{th} = mC_p(dT/dt)$ {P_{th} = calorimetric power in watts; m = mass of the liquid; C_p = heat capacity of the liquid; T = temperature of the liquid; t = time} (Margulis and Margulis, 2003; Rotoarinoro et al., 1995).

A more complete description of the energy conversion requires the measurement of the input electric power needed to set the transducer in motion. This can be done using a classical watt meter (P_e) and will provide an indication of the efficiency of the energy transfer. For a tuned and designed transducer, the efficiency in the system (P_{th}/P_e) is 45%–70% for bath sonicators (Löning et al., 2002) and <20% for horn type devices (Wei et al., 2015).

35.3.3 Ultrasonic effectiveness for water treatment

In addition to the available energy, it is also important to determine the "ultrasonic effectiveness" in relationship with the target; this is the reaction involving the ultrasonic action. The reactor, the shape of the probe, the medium, and the frequency used all strongly influence the ultrasonic effectiveness. A design that provides high performance

toward achieving one specific goal—mixing, organic reaction, extraction, etc.—could have poor efficiency when contributing to a different purpose, such as crystallization, metal activation, or polymerization (Berlan and Mason, 1992; Gogate et al., 2011; Pugin, 1987).

Several methods can be used in relationship with AOPs to determine the efficiency of H_2O_2 and $^{\bullet}OH$ production for a specific design and to permit constructive comparisons.

These methods, generally known from radiation chemistry, involve H_2O_2 determination or $^{\bullet}OH$ trapping with different organic or mineral reagents (Iida et al., 2005).

A determination of H_2O_2 issuing from Reactions (35.13) and (35.14) can be made using a classical ex situ spectrophotometric analysis involving iodide or titanate oxidation (Eisenberg, 1943; Kormann et al., 1988).

$$I^-/\text{Ammonium molybdate}/H_2O_2 \rightarrow I_3^- \qquad (35.13)$$

I_3^- absorbance at 350 nm; $\varepsilon = 26{,}303\,dm^3/mol/cm$.

$$Ti(IV)/H_2O_2 \rightarrow Ti(O_2)OH \qquad (35.14)$$

$Ti(O_2)OH$ absorbance at 410 nm; $\varepsilon = 750\,dm^3/mol/cm$.

Chemical in-situ $^{\bullet}OH$ determination primarily involves three analytical methods commonly used in radiolysis dosimetry:

- Iodide dosimeter (Hart and Henglein, 1985; Koda et al., 2003) (Reaction 35.15)
- Fricke dosimeter (Koda et al., 2003; Mark et al., 1998) (Reaction 35.17)
- Terephthalate dosimeter (Fang et al., 1996), Figure 35.2.

$$2I^- + 2^{\bullet}OH \rightarrow I_2 + 2OH^- \qquad (35.15)$$

$$I_2 + I^- \rightarrow I_3^- \left(I_3^- \text{ absorbance at 350 nm; } \varepsilon = 26{,}303 dm^3/mol/cm\right) \qquad (35.16)$$

$$Fe^{2+} + {}^{\bullet}OH \rightarrow Fe^{3+} + OH^- \left(Fe^{3+} \text{ absorbance at 304 nm; } \varepsilon = 2197 dm^3/mol/cm\right) \qquad (35.17)$$

A discussion concerning the advantages and drawbacks of each dosimeter is not included here. These methods provide reliable and reproducible measurements that can be used to directly or indirectly evaluate $^{\bullet}OH$ availability (Figure 35.2B) for various reactor configurations in connection with AOPs.

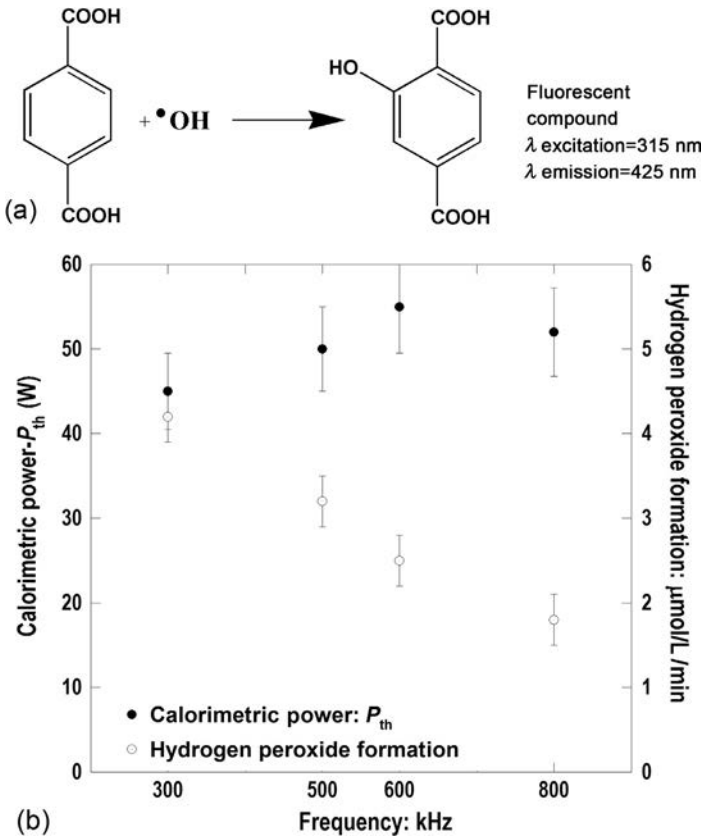


FIGURE 35.2 (a) Chemical reaction involves in the terephthalate dosimeter. (b) Example of calorimetric measurement and hydrogen peroxide formation at 300, 500, 600, 800 kHz determined for a batch cylindrical reactor: 300 mL, electrical input, $P_e = 70$ W.

35.3.4 Ultrasonic power and efficiency

The efficiency of the oxidation reactions occurring in ultrasonic conditions is associated with the phenomenology of "chemically active cavitation" (Ciaravino and Miller, 1983; Lindström, 1955).

A known reactor design under well-defined experimental conditions (the nature of the liquid, pressure, temperature, gas saturation, and input power expressed as P_e or P_{th}) will exhibit lower and upper limit values for an optimized oxidation yield. The lower value corresponds to the threshold amplitude (P_a) of the wave inducing the cavitation onset (Neppiras and Noltingk, 1951). Indeed, no oxidation occurs under this threshold. Above the threshold, the rate of the oxidation reactions increases linearly with the ultrasound power until it reaches a maximum. Above the maximum, any further increase causes a decrease in the oxidation rate (Jiang et al., 2002a; Sivakumar and Pandit, 2001; Weissler, 1953).

35.4 Characteristics of sonochemical elimination

35.4.1 Oxidation of water soluble pollutants

Most of the micropollutants present in water possess an aromatic structure, including dyes, drugs, pesticides, and industrial raw organic chemicals. For this reason, a great deal of the literature is concerned with the elimination of these types of compounds using ultrasound. For example, the case of phenol illustrates the main pathway that leads to the sonochemical elimination of an organic water soluble pollutant (Berlan et al., 1994; Lur'e et al., 1962; Pétrier et al., 1994).

Phenol concentrations found in natural or industrial wastewater ($c < 10\,\text{mM}$) decrease rapidly upon ultrasonic action. An analysis of the products first shows the evolution of hydroquinone and catechol resulting from the $^{\bullet}OH$ reaction. In the second step, more oxidized compounds appear: maleic acid, oxalic acid, and formic acid. Finally, at a later time, the medium releases some carbon dioxide (Figure 35.3A and B).

This characteristic behavior evidencing $^{\bullet}OH$ involvement has been established for many organic structures having a low value of the Henry's law (HL) constant (Table 35.1).

The scheme published by Seghal and Wang (1981) has been used to approximate the reaction location (Figure 35.3C). Radicals generated in the gaseous phase in the bubble react in a condensed layer at the liquid interface. The nature of this interface is under discussion (Hua et al., 1995; Tauber et al., 1999), but it is well established that it accumulates organic molecules depending on their hydrophobic characters (Alegria et al., 1989; Gutierrez and Henglein, 1988; Henglein and Kormann, 1985). The more hydrophobic the structure, the greater the accumulation in the interfacial film, the more it reacts with $^{\bullet}OH$ coming from the inside, and the more rapidly degradation occurs (Nanzai et al., 2008; Park et al., 2011; Sivasankar and Moholkar, 2009). Hydrophilics remain in the bulk phase.

35.4.2 Oxidation of volatile organic molecules

Scheme in Figure 35.3C establishes a good model for many organic pollutants but it cannot be used for a molecule with a high value of the Henry's law constant ($HL > 10^{-5}\,\text{atm}\,\text{m}^3/\text{mol}$) (Table 35.2). In this case, molecules migrated and vaporized in the bubble during the increase of the sphere volume are mostly incinerated at high temperature when the bubble collapses (Riesz et al., 1990). This scheme is supported by the release of carbon dioxide as soon as the pollutant disappears, and for high concentrations of the solute only, traces of products resulting from the reaction with the $^{\bullet}OH$ can be found (Gutierrez et al., 1986; Kim et al., 2012; Pétrier et al., 1998). It should be noted that the efficiency of the degradation yield of volatile molecules is higher than that of nonvolatile molecules (Nanzai et al., 2008; Pétrier et al., 1998).

35.4.3 Eliminating volatile and nonvolatile molecules from a mixture

The bubble of cavitation can be considered as a microreactor that incinerates volatile molecules and oxidizes structures with a low fugacity characteristic in water.

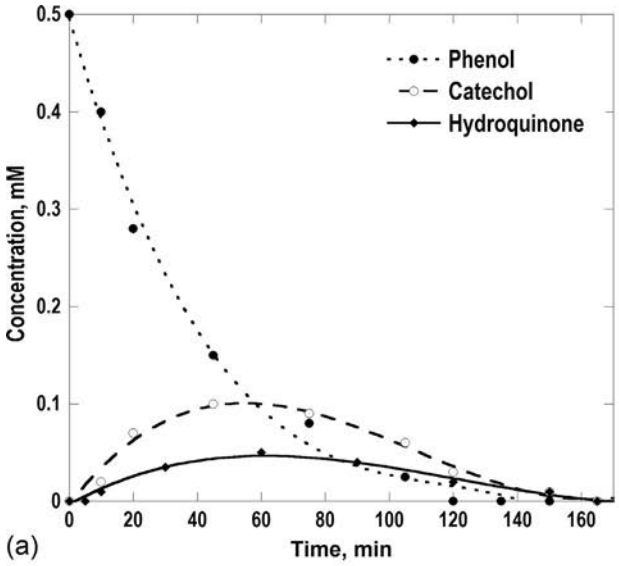
When the two kinds of molecules are present together in aerated water or in water saturated with a rare gas (Pétrier et al., 1998), only the most volatile molecule is eliminated initially. The oxidation of the less volatile molecule occurs only during a second stage after the most volatile molecule has been eliminated.

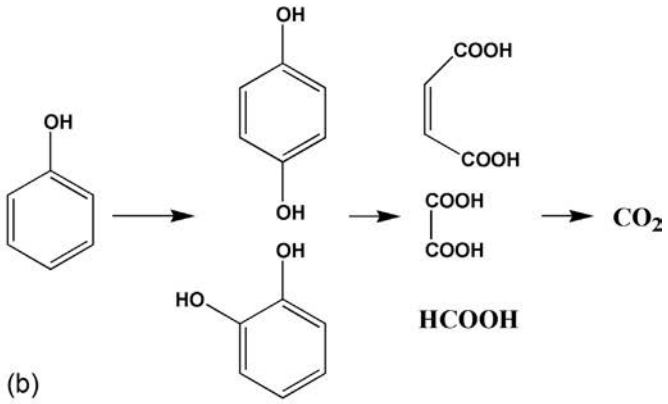
However, simultaneous elimination of the two can be observed in two cases: when carbon tetrachloride is the most volatile compound, or when oxygen is used as the saturating gas.

In the former case, incineration of carbon tetrachloride into the bubble leads to an ejection in the medium of chlorine atoms (Reaction 35.18).

$$CCl_4 \rightarrow CCl_3^{\bullet} + Cl^{\bullet} \qquad (35.18)$$

Chloride atoms can add to the hydrophilic molecules present at the interface or in the bulk of the solution (Kandzas and Mokina, 1962; Mahamuni and Pandit, 2006). Then, in the case of a medium containing both phenol and carbon tetrachloride, the two structures disappear simultaneously at the rate of carbon tetrachloride elimination. However, the products of the phenol reaction include 2-chlorophenol, 4-chlorophenol, and polychlorophenols but do not include hydroxylated compounds. These primary





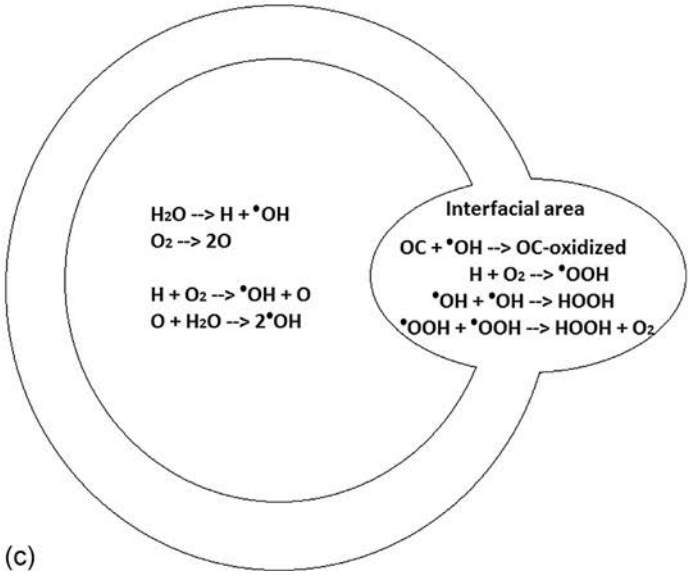


FIGURE 35.3 (a) Concentration of phenol, catechol, hydroquinone as a function of ultrasonic treatment time for aerated water. Frequency = 300 kHz; volume = 300 mL; P_{th} = 40 W. (b) Products detected during degradation of phenol in aerated solution. (c) Scheme of the main reactions occurring in and at the interface of the bubble that account for the hydrophilic organic compound (OC) oxidation.

TABLE 35.1 Nonexhaustive list of hydrophilic organic pollutants eliminated by ultrasonic cavitation

Organic compounds	WS	HL	References
Phenol	8.28×10^4	3.33×10^{-7}	Lur'e et al. (1962), Berlan et al. (1994)
4-Chlorophenol	2.4×10^4	6.27×10^{-7}	Pétrier et al. (1998), Jiang et al. (2006)
4-Nitrophenol	1.16×10^4	4.15×10^{-1}	Tauber et al. (2000), Sivakumar et al. (2002)
3-Chloroaniline	5.4×10^3	1.7×10^{-6}	David et al. (1998)
2,4,-Dichlorophenol	4.5×10^3	3.16×10^{-6}	Sivasankar and Moholkar (2009)
Pentachlorophenol	1.95×10^3	2.45×10^{-8}	Pétrier et al. (1992a), Weavers et al. (2000)
2,4-Dichlorophenoxyacetic acid	6.77×10^2	1.02×10^{-8}	Peller et al. (2001)
Atrazine	2.8×10	4.47×10^{-9}	Koskinen et al. (1994), Pétrier et al. (1996)

TABLE 35.1 Nonexhaustive list of hydrophilic organic pollutants eliminated by ultrasonic cavitation—cont'd

Organic compounds	WS	HL	References
Alachlor	2.4×10^{2}	8.32×10^{-9}	Wayment and Casadonte (2002), Torres et al. (2009)
Parathion	6.54×10	5.65×10^{-7}	Kotronarou et al. (1992)
Bisphenol A	1.20×10^{2}	1.00×10^{-11}	Torres et al. (2008b), Son et al. (2012)
Ethinyl estradiol	1.16×10^{2}	7.94×10^{-12}	Fu et al. (2007)
Ibuprofen	2.44×10^{3}	1.5×10^{-7}	Mendez-Arriaga et al. (2008)
Malachite green	4.00×10^{4}	1.93×10^{-14}	Moumeni et al. (2012)
Rhodamine B	1.20×10^{4}	N.A.	Inoue et al. (2006)
Methylene blue	4.36×10^{4}	1.25×10^{-12}	Kobayashi et al. (2012)
Orange G	8×10^{4}	NA	Madhavan et al. (2010)
Laurylpyridinium chloride	3.52×10^{3}	3.39×10^{9}	Singla et al. (2011)
Perfluorooctane sulfonate	3.1×10^{3}	NA	Vecitis et al. (2010a)
Sodium dodecylbenzene sulfonate	8.0×10^{5}	NA	Manousaki et al. (2004)
Octanol	5.4×10^{2}	2.45×10^{-5}	Théron et al. (2001)
EDTA	1.00×10^{3}	1.17×10^{-23}	Chitra et al. (2004)

WS = Water solubility (mg/L); HL = Henry's law constant (atm m^3/mol).
Source: Howard and Meylan (1997).

TABLE 35.2 Nonexhaustive list of volatile organic pollutants eliminated by ultrasonic cavitation

Organic compounds	WS	HL	References
Carbon tetrachloride	7.93×10^{2}	2.76×10^{-2}	Hua and Hoffmann (1996), Francony and Pétrier (1996)
Methylene chloride	1.30×10^{4}	3.25×10^{-3}	Cheung et al. (1991)
Tetrachloroethene	2.00×10^{2}	1.77×10^{-2}	Inazu et al. (1993)
Trichloroethene	1.10×10^{3}	9.85×10^{-3}	Inazu et al. (1993), Drijvers et al. (1996)
Fluorotrichloromethane	1.10×10^{3}	9.7×10^{-2}	Cheung and Kurup (1994)
Trifluorotrichloroethane	2.09×10	3.08×10^{-2}	Hirai et al. (1996)
Benzene	1.79×10^{3}	5.55×10^{-3}	Thoma and Gleason (1998), Wu et al. (2004)
Chlorobenzene	4.98×10^{2}	3.77×10^{-3}	Pétrier et al. (1998)
n-Butylamine	1.00×10^{6}	1.74×10^{-5}	Fayter and Spurlock (1974)
Methylterbutylether	5.10×10^{4}	5.87×10^{-4}	Kang et al. (1999), Kim et al. (2012)
Cyclohexene	2.13×10^{2}	4.55×10^{-2}	Wu et al. (2004)
Di-n-butylsulfide	3.94×10	4.30×10^{-3}	Spurlock and Reifsneider (1971)
Nitrobenzene	2.09×10^{3}	2.40×10^{-5}	Sivasankar and Moholkar (2009), Nanzai et al. (2008)
Tetranitromethane	8.50×10^{4}	2.56×10^{-5}	Gutierrez and Henglein (1988)
4-Nitrophenyl acetate	1.16×10^{3}	1.86×10^{-3}	Tauber et al. (1999)
Methanol	1.00×10^{2}	4.55×10^{-6}	Gutierrez and Henglein (1988)

WS = Water solubility (mg/L); HL = Henry's law constant (atm m^3/mol).
Source: Howard and Meylan (1997).

chlorinated products constitute a noxious material, but because of their higher HL values, they are rapidly eliminated upon ultrasonic action (Bapat et al., 2008).

For a medium saturated with oxygen in the case of a mixture of chlorobenzene/4-chlorophenol, a simultaneous elimination of the two structures is observed, whereas a sequential disappearance is observed in an argon or aerated medium (Pétrier et al., 2007). The hypothesis that was put forward is related to the fact that, at high temperature inside the cavitation bubble, the pyrolysis of chlorobenzene can produce hydrogen atoms among the various intermediate products (P) (Reaction 35.19).

$$C_6H_5Cl \rightarrow P + H \qquad (35.19)$$

The key reaction in hydrocarbon combustion involves the production of the $^{\bullet}OH$ by a reaction of the hydrogen atom with molecular oxygen (Reaction 35.7). The availability, at the interface of the bubble, of the $^{\bullet}OH$ resulting from chlorobenzene combustion induces the concurrent 4-chlorophenol degradation.

The ability to produce conditions for the simultaneous elimination of two organic compounds in a mixture constitutes a particular occurrence in the field of AOPs. In general, the degradation rate for a mixture of organic compounds is connected to competition kinetics for $^{\bullet}OH$ availability. This feature should be of great importance in the development of the ultrasonic process.

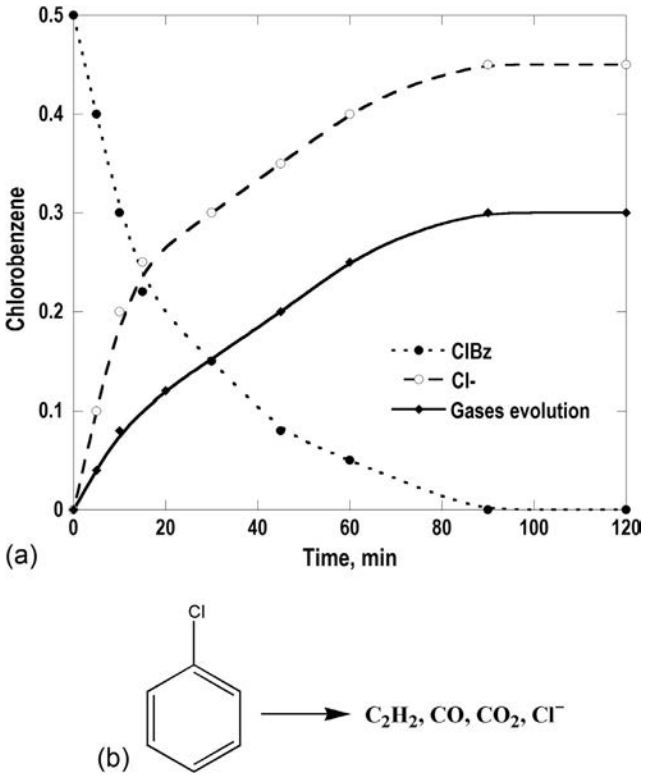


FIGURE 35.4 (a) Concentrations of chlorobenzene and chloride ion release and gas evolution, as a function of ultrasonic treatment time for aerated water. Frequency = 300 kHz; volume = 300 mL; P_{th} = 40 W. (b) Products detected during sonochemical degradation of chlorobenzene in aerated solution.

35.5 Kinetics and sonochemical yields

35.5.1 Kinetic constant of the sonochemical reaction

The kinetic description of pollutant elimination usually follows a pseudo-first-order law because the elimination curve decreases exponentially (Figures 35.3A and 35.4A) and leads to the determination of a rate constant k_d {$r = k_d(C_s)$; with r = degradation rate, C_s = substrate concentration} that is an observed value and declines with an increase in the substrate concentration.

Figure 35.5 reports the evolution of the degradation rates in the case of three pollutants with different HL values.

First, the degradation rate for phenol (HL = 3.33×10^{-7} atm m^3/mol), a hydrophilic compound with low volatility, exhibits an initial degradation rate that increases with an increase in concentration up to a maximum constant rate. This maximum rate remains unchanged at the highest value range.

Next, a characteristic of bisphenol A (BPA; HL = 1.00×10^{-11} atm m^3/mol) and anisole (HL = 4.35×10^{-3} atm m^3/mol) is that the degradation rate increases with the initial concentration but does not exhibit a plateau at the tested concentration range because of the low solubility of these pollutants in the bulk phase.

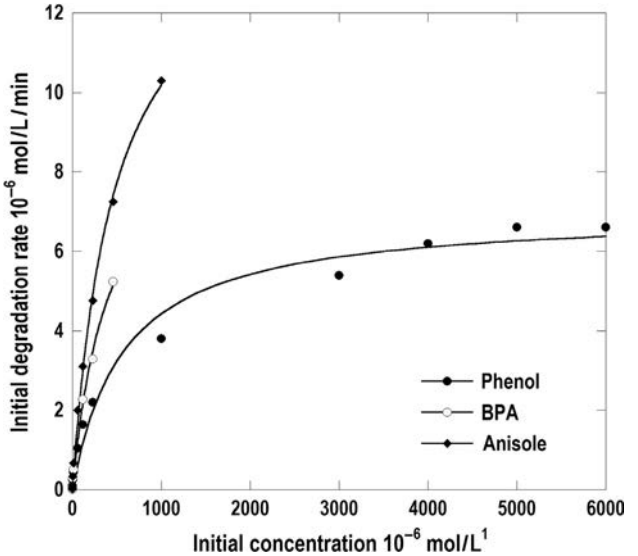


FIGURE 35.5 Initial degradation rates for volatile anisole (HL = 4.35×10^{-3} atm m^3/mol) and nonvolatile phenol (HL = 3.33×10^{-7} atm m^3/mol) and BPA (HL = 1.00×10^{-11} atm m^3/mol) in water aerated solution. Volume treated = 300 mL; Temperature = 20°C; P_{th} = 50 W.

If anisole degradation occurs thermally inside the bubble due to its high HL value (Combet et al., 2003), then the sonochemical degradation of BPA and phenol (the two compounds with a lower HL constant) proceeds through reactions in the interfacial area of the bubble and in the bulk phase. BPA degrades faster than phenol because of its lower solubility, and it accumulates at a higher concentration at the interface.

This difference in degradation kinetics provides evidence of the problems occurring in the modeling of the kinetics based only on a pseudo-first-order constant determined at one concentration.

In the case of nonvolatile organic compounds, the most appropriate kinetic model, developed first by Serpone et al. (1994), is described by two regimes: (1) a regime at the lower concentration in which the reaction occurs in the bulk, and (2) a regime at high concentration in which the sonochemical reactivity occurs at the bubble–liquid interface and connects the sonochemical kinetic to a Langmuir-type mechanism. The overall degradation rate of a solute is the sum of the rates in the bulk and in the interfacial layer.

Then,

$$r = K_b + (kKC_S)/(1 + KC_S)$$

In this equation, r is the degradation rate (mol/L/min), and C_s (mol/L) is the organic compound concentration. K_b (mol/min) is a constant representing the rate of degradation in the bulk liquid, k is the rate constant of the reaction (mol/L/min), and K is the equilibrium constant.

Later, Okitsu et al. (2005) developed another model based on the fact that organic molecules adsorb and desorb from the liquid interface layer surrounding the cavitation bubble, reaching a pseudo-steady state.

$$r = (kKC_S)/(1 + KC_S)$$

In this equation, the degradation rate r (mol/L/min) and the organic compound concentration C_s (M) lead to the determination of the kinetic parameters: k is the rate constant of the reaction (mol/L/min) and K is the equilibrium constant.

Depending on the water solubility and the HL constant, each of these models seems appropriate for describing the sonochemical degradation kinetic of nonvolatile compounds (Chiha et al., 2010).

A model of the kinetic description of a volatile molecule has been developed that accounts for the main reactions occurring at a high temperature in the bubble, along with simultaneous pyrolysis of the volatile pollutant and the pyrolytic intermediates (De Visscher, 2003; De Visscher et al., 1996).

$$k = k_o \, exp\,(-aC_S)$$

In this kinetic model, k is the sonochemical reaction rate constant (1/min), k_o is the sonochemical reaction rate constant at infinite dilution (1/min), and a is a kinetic parameter describing the inhibiting effect of an organic compound on its sonolysis.

35.5.2 Sonochemical yield and energy consumption

Energy consumption evaluation is a difficult task because it needs to account for the starting concentration and the goal. What is the target? The goal is to decrease the concentration under the value determined by regulation. Does this mean a decrease of one or several orders of magnitude of the pollutant concentration? In some cases, a decrease in concentration of the starting material that exhibits some toxic character could be sufficient; however, it would be invaluable if the degradation product exhibits a more toxic nature. In this case, the energy consumption required to mineralize the starting material uses more energy than a simple elimination of the starting structure.

Following the work by Bolton et al. (2001), IUPAC established a formula that has been widely adapted for the determination of energy consumption in AOPs and enables a comparison between different processes (Bolton et al., 2001; Shu et al., 2013; Torres et al., 2007).

The electric energy consumption (E_{EM}) in kilowatt-hours (kWh) is determined as the electrical energy required to degrade 1 kg of a contaminant (C) in the polluted medium.

$$E_{EM} = (P \cdot t \cdot 1000)/V \cdot M \cdot (C_i - C_f)$$

where P (kW) is the rate power consumed in the system, V (L) is the volume of water treated, t is the duration of the treatment in hours (h), M is the molar mass (g/mol) of the compound C, and the factor 1000 converts gram to kilogram. This formula enables the evaluation of the electrical energy consumed while lowering the pollutant concentration between C_i (initial concentration) and C_f (final concentration in mol/L).

35.6 Sonochemical treatment parameters

Although sonochemical treatment can eliminate various organic water pollutants, the yields can exhibit great unevenness depending on the equipment and operational conditions. The most important parameters affecting sonochemical degradation are discussed in the following subsections.

35.6.1 The frequency effect

As presented in Section 35.2, sonochemical treatment can be conducted using two main equipment designs that depend on the transducer operating at a fixed frequency.

A factor that is often neglected is that the energy level with respect to the frequency is not homogeneously dispersed in front of the vibrating surface. The diffusion of the ultrasonic wave depends on the ratio λ/D, where λ is the wavelength and D is the diameter of the emitting area. For a flat disc, most of the energy is located in a conical volume with an angle $\sin \alpha = 1.22\ (\lambda/D)$ (Boucher, 1970). As has been evidenced by different methods, most of the energy, and subsequently the cavitation, occurs in a small volume close to the surface of a low-frequency emitter (20–40 kHz). Then, the use of a 20-kHz probe requires frequent stirring to ensure homogeneity of the whole reactor. This energy is more dispersed in the volume of the reactor with a high frequency transducer (200 kHz–1.2 MHz). Then a high-frequency system works like a well-stirred reactor that exhibits standing waves (Gondrexon et al., 1998; Price et al., 2010).

Starting with the work of Busnel and Picard (1952), there has been an accumulation of evidence supporting the dependence of the yield of H_2O_2 production upon the frequency of the applied ultrasonic wave. Several articles have corroborated this observation in connection with the yield of $^{\bullet}OH$ production and organic pollutants degradation (Beckett and Hua, 2001; Hua and Hoffmann, 1997; Pétrier et al., 1994).

It is now well established that the use of ultrasonic waves in the frequency range above 200 kHz leads to an increased degradation rate of organic pollutants than can be achieved with a lower frequency range.

The optimum appears to occur between 200 and 400 kHz for nonvolatile molecules, while the yield increases for volatile molecules as the frequency increases (Kobayashi et al., 2012; Pétrier and Francony, 1997).

An explanation can be found considering that the size of the collapsing bubbles and the duration of the collapse decrease with the frequency (Pétrier et al., 1994). These effects favor a lower recombination of the radicals $^{\bullet}OH$ and H in the bubble (Reaction 35.5) and improved availability of free radicals at the interface of the bubble. On the other hand, a standing wave setting up at a high frequency results in improved availability of the cavitation energy (Son et al., 2012).

35.6.2 The influence of temperature

The influence of temperature on the sonochemical yields is mainly attributed to its effect on the content of the cavitation bubble and hence the intensity of the collapse (Suslick, 1988).

An increase in the temperature increases the water vapor in the bubble and decreases the dissolved gases in the medium. Consequently, the collapse of the vaporous bubble is less effective due to a reduced hot spot temperature. In addition, an increase in temperature that increases the number of cavitation bubbles also increases the possibility of coalescence among the bubbles, resulting in some of the bubbles losing their activity.

Investigations into the temperature effects in the sonochemistry of water have clearly supported a frequency effect (Entezari and Kruus, 1996). The temperature effect is mostly important in the low frequency range ($f < 80$ kHz). Reaction rates markedly lessen with an increase in the temperature (Sivakumar et al., 2002). Only a few investigations have examined the higher frequency range, and the results indicate that the yields are only weakly affected by temperatures between 10°C and 40°C (Jiang et al., 2006).

35.6.3 The influence of pH of the medium

By itself, the pH has little influence on the phenomenon of cavitation, but it could affect the reactions of the transient species escaping from the bubble.

Two main species escaping from the bubble are the $^{\bullet}OH$ and $^{\bullet}OOH$ that react at the interface through Reactions (35.8), (35.10), and (35.11). If the structure of $^{\bullet}OH$ is unaffected in the usual pH range, $2 < pH < 10$, the perhydroxyl radical appears mainly in the deprotonated form above pH 4.8.

$$^{\bullet}OOH \longleftrightarrow OO^{\bullet -} + H^{+} (pK_a = 4.8) \qquad (35.20)$$

Such modifications do not markedly affect the degradation yields of an organic compound that does not bear an exchangeable proton.

Compounds with modifications of the ionic form will be affected by pH changes because their molecular or ionic form will not present the same hydrophobicity.

Depending on the pH, the ionic form will degrade less rapidly than the molecular form, as it is more soluble than the uncharged structure and therefore has lower accumulation in the interface area (Ince and Tezcanli-Güyer, 2004; Moumeni et al., 2012; Tauber et al., 2000).

For example, 4-nitrophenol with a $pK_a = 7.08$ degrades three times faster at an acidic pH (molecular form) than at a pH value above 8 (ionic form). This differs from aniline ($pK_a = 4.6$), which degrades faster ($\times 3$) at a pH value above pK_a (molecular form) than at pH 3 (ionic form) (Jiang et al., 2002b). In addition to volatility and hydrophobicity of the target compound, Coulombic interactions between compound and cavitation bubble, and radical quantity and reactivity are also considered to explain the pH effects on sonochemical degradation (Wei et al., 2016). But for organic pollutants without ionizable groups (e.g., PAHs and carbamazepine), the oxidation potential and quantity yield of $^{\bullet}OH$ at different pH values were proposed to account for the degradation kinetics of organic pollutants during sonication.

35.6.4 The effect of dissolved gases

It is well established that cavitation onset requires the presence of dissolved gases in the medium and that increasing the gas concentration enhances the number of bubbles (Seghal and Wang, 1981). Additionally, the polythropic ratio (C_P/C_v), conductivity, and solubility of the gas have strong impacts on sonochemical activity, with low conductivity leading to higher energy release at the end of the bubble collapse as well as high temperature and high pressure (Mead et al., 1975; Prudhomme and Grabar, 1949; Suslick et al., 1990).

The presence of nitrogen, helium, carbon dioxide, and hydrogen lowers the H_2O_2 production and results in a lower efficiency of the ultrasonic action for organic degradation in water.

The effects of two gases, argon and oxygen, as well as saturation with atmospheric air require some attention. There is a discrepancy among the published reports, because the gas influence is governed by the frequency (Hua and Hoffmann, 1997; Pétrier et al., 1992b); however, a comparison of the yields of these three gases is rather low. The best yields for oxidation processes are obtained in experiments involving argon with a low percentage of oxygen. The subject has been investigated by Hart and Henglein (1985), who provide evidence that oxygen levels of 10% in argon result in high oxidation yields.

When the nature of the dissolved gas is linked to the relevance of large scale processes, it becomes difficult to use a rare gas to amplify the ultrasonic action (Kim et al., 2012). On the other hand, it should be emphasized that in the absence of oxygen in the medium, the cavitation bubble mainly releases $^{\bullet}OH$ and H radicals that react with organic molecules. This leads to an organic radical R that rearranges or reacts with the radicals present in the medium. The process leads to the elimination of the initial organic target that is polymerized but not to the mineralization of organic matter (Hart et al., 1990; Kim et al., 2012).

Oxygen is required in the medium to enable carbon mineralization towards carbon dioxide, because it reacts rapidly with the radicals resulting from $^{\bullet}OH$ attack (Kunai et al., 1986; von Sonntag and Schuchmann, 1991). After several reaction steps, these oxygenated radicals lead to carbon dioxide evolution (Kitajima et al., 2006; Torres et al., 2007).

35.6.5 Formation of HNO_2 and HNO_3 in an aerated medium

For aerated water, the degradation rates are close to those observed for oxygenated media. However, it has been observed that over time, there is a buildup in nitrite (NO_2^-) and nitrate (NO_3^-) ions (Inoue et al., 2006; Pétrier and Casadonte, 2001; Torres et al., 2007).

NO_3^- and NO_2^- are generally considered to be undesirable byproducts resulting from nitrogen oxidation under hot spot conditions that occur during the collapse of the cavitation bubble (Supeno and Kruus, 2000; Virtanen and Ellfolk, 1950, 1952).

The reaction requires N_2 and O_2 to be dissolved in the aqueous phase (Mead et al., 1976). In the initial stages, molecular oxygen dissociates (Reaction 35.3) and reacts with molecular nitrogen to generate nitric oxide.

$$N_2 + O \rightarrow NO + N \tag{35.21}$$

HNO_2 and HNO_3 would result from the following sequence of reactions occurring at the liquid–bubble interface (Mark et al., 2000).

$$N + O_2 \rightarrow NO + O \tag{35.22}$$

$$NO + O_2 \rightarrow ONOO \tag{35.23}$$

$$ONOO + NO \rightarrow 2NO_2 \tag{35.24}$$

$$2NO_2 + H_2O \rightarrow HNO_3 + HNO_2 \tag{35.25}$$

$$NO + {}^{\bullet}OH \rightarrow HNO_2 \tag{35.26}$$

$$NO_2 + {}^{\bullet}OH \rightarrow HNO_3 \tag{35.27}$$

Because nitrogen fixation occurs inside the bubble, the formation yield for nitrite and nitrate ions is only slightly affected by the presence of hydrophilic molecules; however, it decreases markedly for a medium that contains volatile molecules (Pétrier and Casadonte, 2001).

35.6.6 Enhancers and inhibitors in ultrasonic treatment of natural water

Natural water contains many mineral and organic chemicals that are considered to be inhibitors for most AOPs, because these chemicals are known as scavengers of free radicals. At concentrations found in the natural environment, sulfate, nitrate, chloride, bromide, and carbonate exhibit only small inhibitor effects (Cost et al., 1993; Krüger et al., 1999; Torres et al., 2009). Reduced actions are also seen with the fulvic and humic acids that are the main constituents of natural organic matter (NOM). These limited effects can result from the accumulation of organic targets inside (if volatile) or at the surface of the bubble. Such properties of bubble heterogeneity by nature lessen the inhibitor effect of inorganic and organic chemicals with higher water solubility than the pollutant (Gültekin and Ince, 2008; Tezcanli-Güyer et al., 2003).

Conversely, it should be noted that for a low aromatic pollutant concentration (10 μM), the presence of bicarbonate of natural water (250–500 mg/L) enhances the degradation yield.

This can result from the carbonate and bicarbonate oxidation into the carbonate radical $CO_3^{\bullet-}$. This radical exhibits

lower reactivity than $^{\bullet}OH$, but it has higher diffusion in the bulk of the solution and can efficiently oxidize aromatic structures (Merouani et al., 2010; Minero et al., 2008; Pétrier et al., 2010).

$$HCO_3^- + {}^{\bullet}OH \rightarrow CO_3^{\bullet -} + H_2O \quad (35.28)$$

$$CO_3^{2-} + {}^{\bullet}OH \rightarrow CO_3^{\bullet -} + OH^- \quad (35.29)$$

35.7 Ultrasound in hybrid processes

If ultrasonic cavitation leads to the rapid elimination of volatile organic compounds, then there is reduced elimination of compounds with the lowest value of the Henry's law constant compared to other AOPs (Mahamuni and Adewuyi, 2010). To overcome this problem, the ultrasonic technique can be combined with other methods associated with AOPs.

In most of these cases, the combination is used because H_2O_2 builds up as the treatment progresses over time (Figure 35.6) (Pétrier et al., 1994; Torres et al., 2007).

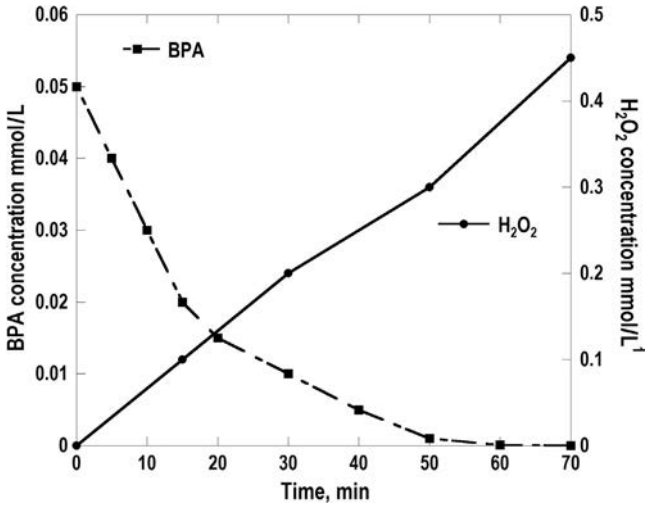


FIGURE 35.6 Hydrogen peroxide evolution during the course of BPA (0.05 mmol/L) elimination upon ultrasonic treatment of aerated water. Ultrasonic frequency: 300 kHz, P_{th}: 47 W, volume: 300 mL: natural pH, temperature: 20°C.

35.7.1 Hydrogen peroxide as a driving force of the hybrid processes

Over the course of an ultrasonic treatment in water, H_2O_2 can be produced in the following three ways:

- Recombination involving $^{\bullet}OH$ that have not encountered the target molecule at the interface of the bubble (Reaction 35.11)
- Perhydroxyl radicals combined with lower reaction rates than $^{\bullet}OH$ toward organic structures at the interface of the bubble (Reaction 35.12) (Neta et al., 1990)
- A combination of perhydroxyl radicals generated during the organic compound degradation in an aerated medium (Figure 35.7) (von Sonntag and Schuchmann, 1991)

This H_2O_2 production leads to several hybrid processes, including ultrasound/UV irradiation, ultrasound/Fenton reaction, ultrasound/photo-Fenton reaction, and ultrasound/ozone.

It should be emphasized that the sole addition of H_2O_2 as an activator of sonochemical reactions, at concentrations usually used in Fenton's reaction for water treatment ($c < 10^{-2}$ mol/L), has only a very limited activating effect, mainly because H_2O_2 cannot accumulate at the interface as any organic molecule does (Ben Abderrazik et al., 2005; Minero et al., 2005).

35.7.2 Ultrasound and UV irradiation processes

The AOP based on H_2O_2 decomposition upon ultraviolet (UV) light irradiation is often applied to water purification (Tuhkanen, 2004).

In the UV-AOP, 254-nm photons emitted generally from a low pressure mercury lamp dissociate H_2O_2 molecules into $^{\bullet}OH$.

$$H_2O_2 + h\nu(254\text{nm}) \rightarrow 2{}^{\bullet}OH \quad (35.30)$$

H_2O_2 exhibits a depleted molar absorption coefficient at 254 nm ($\varepsilon = 18.6$ L/mol/cm) but with a high quantum yield ($\phi = 0.98$) (Legrini et al., 1993).

In addition to the direct photodegradation of molecules that are absorbing at this wavelength, the simultaneous application of ultrasound and UV light enables organic compound elimination in two ways: with ultrasonic cavitation and through a reaction with $^{\bullet}OH$ issued from H_2O_2 photolysis.

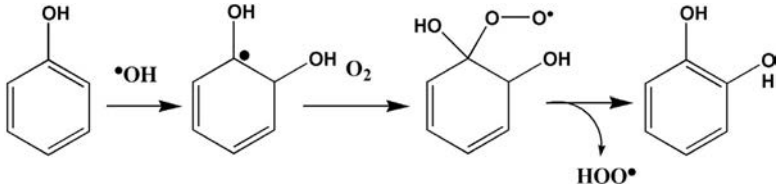


FIGURE 35.7 Formation of hydroperoxyl radical from oxidation of aromatic compound.

Investigations focused on this hybrid process have provided evidence of a limited synergistic effect, which may have occurred because the experiments were conducted using low-frequency equipment that has low efficiency for H_2O_2 generation (Shirgaonkar and Pandit, 1998).

Particularly, efficient oxidation and mineralization of organic structures have been evidenced with the combination of UV (254 nm) and high-frequency ultrasound (300–500 kHz), which has produced H_2O_2 at an elevated rate. In this case, complete oxidation and mineralization that cannot be obtained with UV or ultrasound alone are completed in the combined process.

In contrast to the ultrasonic degradation that is limited to the shell of liquid surrounding the cavitation bubble, the H_2O_2 dissociation occurs mainly in the bulk of the solution, causing mineralization of the product regardless of its hydrophobicity (Naffrechoux et al., 2000; Torres et al., 2007).

35.7.3 Ultrasound action enhancement in Fenton and photo-Fenton processes

The addition of ferrous or ferric ions to enhance ultrasonic action in water treatment has been the subject of numerous studies. Upon Fe(II) or Fe(III) addition, H_2O_2 does not accumulate over time as the sonochemical reaction progresses.

The H_2O_2 consumption in each case results mainly from two reactions:

- Fenton's reaction involving Fe(II) induces the conversion of H_2O_2 to $^{\bullet}OH$ (Reaction 35.1),
- A Fenton-like process from Fe(III) regenerates Fe(II) (Reactions 35.31–35.33).

$$Fe^{3+} + H_2O_2 \rightarrow Fe - OOH^{2+} + H^+ \quad (35.31)$$

$$Fe - OOH^{2+} \rightarrow Fe^{2+} + {}^{\bullet}OOH \quad (35.32)$$

$$Fe^{3+} + {}^{\bullet}OOH \rightarrow Fe^{2+} + O_2 + H^+ \quad (35.33)$$

The regeneration of Fe(II) is of great importance in obtaining a high rate in the $^{\bullet}OH$ generation, because if Fenton's reaction (Reaction 35.1) proceeds at high rate, the reaction turning Fe(III) into Fe(II) constitutes a limiting step in the catalytic cycle (Safarzadeh-Amiri et al., 1996).

In general, the single ultrasonic action alone on nonvolatile molecules is not able to completely oxidize (decrease the chemical oxygen demand, COD) and mineralize (decrease the dissolved organic carbon, DOC) the organic contaminants in water. The addition of Fe(II) or Fe(III) results in only a small increase in the concentration of the organic compound degradation rate but notably improves the COD and DOC removal (Beckett and Hua, 2003; Joseph et al., 2000; Minero et al., 2005; Vassilakis et al., 2004). The process with the same progress can be modified using the elemental iron (Hung et al., 2000; Zhang et al., 2005).

The effectiveness of the process can be improved by artificial or solar irradiation in a photo-assisted Fenton reaction, or "photo-Fenton" (Katsumata et al., 2011; Mendez-Arriaga et al., 2009; Torres et al., 2008a). This enhancement results from H_2O_2 photodecomposition as indicated above, as well as across the photolysis of Fe(III) hydroxide [$Fe(OH)^{2+}$] and complexes [Fe(III)-organic ligand] that produces additional $^{\bullet}OH$ and regenerates Fe(II). The organic ligand can be an organic acid as a product of the pollutant degradation (Jeong and Yoon, 2005; Oliveros et al., 1997).

$$Fe^{3+} + OH^- \rightarrow Fe(OH)^{2+} \quad (35.34)$$

$$Fe(OH)^{2+} + h\nu \rightarrow Fe^{2+} + {}^{\bullet}OH \quad (35.35)$$

$$Fe^{3+}/RO^- + h\nu \rightarrow Fe^{2+} + RO^{\bullet} \quad (35.36)$$

This additional Fe(II) restoration in the Fenton reaction ensures an additional source of $^{\bullet}OH$ and a fast consumption of H_2O_2 resulting from the ultrasonic action.

The electrical energy cost has been compared in the case of Bisphenol A mineralization over the three hybrid processes: ultrasound/UV, ultrasound/Fenton, and ultrasound/photo(UV)-Fenton. The results of this cost comparison support the great advantage of the process combining ultrasound/photo-Fenton for bisphenol A elimination (Table 35.3).

TABLE 35.3 Electric energy cost estimation for bisphenol A degradation in different hybrid AOPs

Process	Power (W)	Time (min)	TOC (% removed)	Energy cost (KWh/m^3)
UV (254 nm)	25	600	Less than 60%	
Ultrasound (300 kHz)	80	600	Less than 60%	
Ultrasound/UV	105	300	66	6010
Ultrasound/Fe(II)	80	600	64	3735
Ultrasound/Fe(II)/UV	105	120	79	1033

BPA concentration: 118 μmol/L; volume treated: 300 mL.

35.7.4 Ultrasound and ozone

Since the end of the nineteenth century, it has been recognized that ozone can be used to disinfect and eliminate organic contaminants in polluted waters.

Ozone may eliminate various organic compounds in two ways: by reacting directly in its molecular form, O_3, in an acidic medium, or in an alkaline medium by reacting indirectly with the radical species generated when it decomposes in water.

$$2O_3 + OH^- \rightarrow {}^{\bullet}OH + OO^{\bullet -} + 2O_2 \qquad (35.37)$$

Because the reaction rates of ozone in its molecular form are low with most organic pollutants and as its activation in an alkaline medium occurs at a low rate, the ozone must be activated to generate $^{\bullet}OH$ in AOPs. Improvement is generally achieved through H_2O_2 or UV activation (Bablon et al., 1991).

The coupling of ozone with ultrasound affords interesting AOPs that take advantage of the $^{\bullet}OH$ generation provided by the two techniques, thereby leading to the development of an efficient hybrid technology (Dahi, 1976; Lesko et al., 2006; Weavers et al., 1998).

Three phenomena occurring from ultrasonic action may be involved in ozone activation:

The bubble of cavitation and sonolysis of ozone generate the $^{\bullet}OH$ available in the interfacial area of the bubble (Reactions 35.37 and 35.6) (Hart and Henglein, 1986).

$$O_3 + \text{ultrasound} \rightarrow O + O_2 \qquad (35.38)$$

In the bulk of the solution, ozone activation by H_2O_2 arises from the combination of the $^{\bullet}OH$ and $^{\bullet}OOH$ in the interfacial area of the bubble (Reactions 35.11 and 35.12).

There is an increase in ozone mass transfer upon acoustic streaming (Gondrexon et al., 1998).

This hybrid process is particularly attractive for the mineralization of organic matter that cannot be removed by ultrasound or ozone alone (Olson and Barbier, 1994; Vecitis et al., 2010b).

In connection with the frequency effect that promotes improved availability of H_2O_2 and $^{\bullet}OH$, the combination results in greater yields in the higher frequency range (Barbier and Pétrier, 1996; Park et al., 2012).

35.7.5 Ultrasound and photocatalysis

TiO_2 photocatalysis at a semiconductor surface is an AOP currently receiving a great deal of attention as a means for water remediation (Bahnemann et al., 1994).

In the process, irradiation with light ($\lambda < 400\,\text{nm}$) transfers an electron from the TiO_2 valence band to the conduction band with the generation of an electron-hole pair.

$$TiO_2 + h\nu \rightarrow TiO_2(h^+ + e^-) \qquad (35.39)$$

Photogenerated electrons can be scavenged by dissolved molecular oxygen or, if available, H_2O_2, limiting the electron/hole recombination.

$$TiO_2(e^-) + O_2 \rightarrow TiO_2 + O_2^{\bullet -} \qquad (35.40)$$

$$TiO_2(e^-) + HOOH \rightarrow TiO_2 + {}^{\bullet}OH + OH^- \qquad (35.41)$$

Organic compounds (M) oxidation may occur directly from charge transfer at the hole. In addition, adsorbed water molecules and surface-bound hydroxide species may be oxidized to form the $^{\bullet}OH$.

$$TiO_2(h^+) + M \rightarrow M^+ + TiO_2 \qquad (35.42)$$

$$TiO_2(h^+) + OH^- \rightarrow {}^{\bullet}OH + TiO_2 \qquad (35.43)$$

The combination of ultrasonic action with photocatalysis, resulting in sonocatalysis, is now well documented. The simultaneous use of the two techniques is found to be highly efficient at treating water polluted with numerous organic compounds having various hydrophobic properties (Johston and Hocking, 1993; Théron et al., 1999).

Ultrasound could ensure a fast initial decrease in the target pollutant concentration. Photocatalytic action is more adapted to achieving the mineralization of hydroxylated byproducts, especially for removing intermediately formed carboxylic acids (Berberidou et al., 2007; He et al., 2011).

The synergistic effect (S) can be defined as the ratio of the rates observed in the combined process (ultrasound and photocatalysis) to the sum of the rates of ultrasound alone and photocatalysis alone, $\left\{S = \frac{R(\text{ultrasound + photocatalysis})}{R(\text{ultrasound}) + R(\text{photocatalysis})}\right\}$. S has been found to be high for ultrasonic action in the high frequency range (300 kHz), mainly because of its high yield production of H_2O_2. In this setup, there is evidence that TiO_2 loading is a crucial parameter for improvement. Excess photocatalyst seems to inhibit cavitational activity (Torres et al., 2008a; Wu and Yu, 2009).

Ultrasound produces mechanical effects on this combined process. First, ultrasonic cavitation should enhance the photocatalytic system performance through high-speed displacement and the collision of particles that increase deaggregation and mass transfer at the catalyst surface. Second, as evidenced in the case of the 20-kHz treatment, collisions also lead to the structural modification of the surface, creating oxygen defects that would render the surface more active (Osorio-Vargas et al., 2012).

An increase in gain for the catalytic activity occurs with Fe(II) addition. In this case, Fe(II), as in Fenton's reaction, dissociates the H_2O_2 coming from ultrasonic cavitation, generating Fe(III).

At the surface of the catalyst, Fe(III) behaves as an electron scavenger for the electrons photochemically promoted in the conduction band, then regenerating Fe(II).

$$Fe^{3+} + TiO_2(e^-) \rightarrow Fe^{2+} + TiO_2 \qquad (35.44)$$

In addition, the trapping results in a photogenerated hole which is available for a reaction with water molecules and hydroxide to form •OH (Torres-Palma et al., 2010).

35.8 Conclusion

Since early research in the field, the use of ultrasonic cavitation for water cleaning has been a subject of growing attention. This is a simple technique, requiring only electrical energy and easy to handle. However, good practice requires knowledge of the basic principles and parameters governing the target application. Distinct attention must be given to the ultrasonic frequency that governs the availability of •OH in the medium.

If the sole application of ultrasound for treating polluted water is too time-consuming and expensive, then the combined process can be chosen for economic viability with regard to other AOPs under development.

References

Abramov, O.V., Abramov, V.O., Myasnikov, S.K., Mullakaev, M.S., 2009. Extraction of bitumen, crude oil and its products from tar sand and contaminated sandy soil under effect of ultrasound. Ultrason. Sonochem. 16, 408–416.

Abramov, V.O., Abramova, A.V., Bayazitov, V.M., Nikonov, R.V., Voitov, Y.I., Fedulov, I.S., 2020. The pecularities of ultrasonic equipment design for stabilization of dispersedstructures of alumosilicic reagents for wastewater treatment. Ultrason. Sonochem. 64, 105041.

Alegria, A.E., Lion, Y., Kondo, T., Riesz, P., 1989. Sonolysis of aqueous surfactant solutions. Probing the interfacial region of cavitation bubbles by spin trapping. J. Phys. Chem. 93, 4908–4913.

Bablon, G., Bellamy, W.D., Bourbigot, M.-M., Daniel, F.B., Doré, M., Erb, F., Gordon, G., Langlais, B., Laplanche, A., Legube, B., Martin, G., Masschelin, W.J., Pacey, G., Reckhow, D.A., Ventresque, C., 1991. Fundamental aspects. In: Langlais, B., Reckhow, D.A., Brink, D.R. (Eds.), Ozone in Water Treatment: Application and Engineering. Lewis, Boca Raton, pp. 11–132.

Bahnemann, B., Cunningham, J., Fox, M.A., Pelizzetti, E., Pichat, P., Serpone, N., 1994. Photocatalytic treatment of water. In: Helz, G.R., Zepp, R.G., Grosby, D.G. (Eds.), Aquatic and Surface Photochemistry. Lewis, Boca Raton, pp. 261–316.

Bapat, P.S., Gogate, P.R., Pandit, A.B., 2008. Theoretical analysis of sonochemical degradation of phenol and its chloro-derivatives. Ultrason. Sonochem. 15, 564–570.

Barbier, P.F., Pétrier, C., 1996. Study at 20kHz and 500kHz of the ultrasound-ozone advanced oxidation system: 4-nitrophenol degradation. J. Adv. Oxid. Technol. 1, 154–159.

Beckett, M., Hua, I., 2001. Impact of ultrasonic frequency on sonoluminescence and sonochemistry. J. Phys. Chem. A 105, 3796–3802.

Beckett, M.A., Hua, I., 2003. Enhanced sonochemical decomposition of 1,4-dioxane by ferrous iron. Water Res. 37, 2372–2376.

Ben Abderrazik, N., Azmani, A., R'kiek, C., Song, W., O'Shea, K.E., 2005. Iron (II)-catalyzed enhancement of ultrasonic-induced degradation of diethylstilbestrol (DES). Catal. Today 101, 369–373.

Berberidou, C., Poulios, I., Xekoukoulotatis, N.P., Mantzavinos, D., 2007. Sonolytic, photocatalytic and sonophotocatalytic degradation of malachite green in aqueous solutions. Appl. Catal. Environ. 74, 63–72.

Berlan, J., Mason, T.J., 1992. Sonochemistry: from research laboratories to industrial plants. Ultrasonics 30, 203–212.

Berlan, J., Trabelsi, F., Delmas, H., Wilhelm, A.-M., Petrignani, J.F., 1994. Oxidative degradation of phenol in aqueous media using ultrasound. Ultrason. Sonochem. 1, S97–S102.

Bolton, J.R., Bircher, K.G., Tumas, W., Tolman, C.A., 2001. Figures-of-merit for the technical development and application of advanced oxidation technologies for both electric- and solar-driven systems. Pure Appl. Chem. 73, 627–637.

Boucher, R.M.G., 1970. Sonochemistry at low and high frequencies. Br. Chem. Eng. 15, 363–367.

Busnel, R.-G., Picard, D., 1952. Rapports entre la longueur d'onde et l'oxydation de l'iodure de potassium par les ultrasons. Comptes Rendus 234, 1217–1220.

Buxton, G.V., Greenstock, C.L., Helman, W.P., Ross, A.B., 1988. Critical review of rate constants for reaction of hydrated electrons, hydrogen atoms and hydroxyl radicals (OH/O) in aqueous solution. J. Phys. Chem. Ref. Data Monogr. 17, 513–886.

Cheung, H.M., Kurup, S., 1994. Sonochemical destruction of CFC 11 and CFC113 in dilute aqueous solution. Environ. Sci. Technol. 28, 1618–1622.

Cheung, H.M., Bhatnagar, A., Jansen, G., 1991. Sonochemical destruction of chlorinated hydrocarbons in dilute aqueous solution. Environ. Sci. Technol. 25, 1510–1512.

Chiha, M., Merouani, S., Hamdaoui, O., Baup, S., Gondrexon, N., Pétrier, C., 2010. Modeling of ultrasonic degradation of non-volatile organic compounds by Langmuir-type kinetics. Ultrason. Sonochem. 17, 773–782.

Chitra, S., Paramasivan, K., Sinha, P.K., Lal, K.B., 2004. Ultrasonic treatment of liquid waste containing EDTA. J. Clean. Prod. 12, 429–435.

Ciaravino, V., Miller, M.W., 1983. A comparison of two techniques for measured iodine release as an indicator of acoustic cavitation. J. Acoust. Soc. Am. 74, 1813–1816.

Colarusso, P., Serpone, N., 1996. Sonochemistry II—effects of ultrasounds on homogeneous chemical reactions and in environmental detoxification. Res. Chem. Intermed. 22, 61–89.

Combet, E., Pétrier, C., Devos, O., Barbe, M., Ravanat, J.-L., Lepoint, T., 2003. Sonochemical Elimination of Methoxylated Aromatic Pollutants. WCU 2003, Paris September 7–10, pp. 1037–1040.

Cost, M., Mills, G., Glisson, P., Lakin, J., 1993. Sonochemical degradation of p-nitrophenol in the presence of chemical components of natural waters. Chemosphere 27, 1737–1743.

Dahi, E., 1976. Physicochemical aspects of disinfection of water by means of ultrasound and ozone. Water Res. 10, 677–684.

David, B., Lhote, M., Faure, V., Boule, P., 1998. Ultrasonic and photochemical degradation of chlorpropham and 3-chloroaniline in aqueous solution. Water Res. 32, 2451–2461.

De Visscher, A., 2003. Kinetic model for the sonochemical degradation of monocyclic aromatic compounds in aqueous solution: new insights. Ultrason. Sonochem. 10, 157–165.

De Visscher, A., Van Eenoo, P., Drijvers, D., Van Langenhove, H., 1996. Kinetic model for the sonochemical degradation of monocyclic aromatic compounds in aqueous solution. J. Phys. Chem. 100, 11635–11642.

Drijvers, D., De Baets, R., De Visscher, A., Van Langenhove, H., 1996. Sonolysis of trichloroethylene in aqueous solution: volatile organic intermediates. Ultrason. Sonochem. 3, S83–S90.

Eisenberg, G.M., 1943. Colorimetric determination of hydrogen peroxide. Ind. Eng. Chem. 15, 327–328.

Entezari, M.H., Kruus, P., 1996. Effect of frequency on the sonochemical reactions. II: temperature and intensity effects. Ultrason. Sonochem. 3, 19–24.

Fang, X., Mark, G., Von Sonntag, C., 1996. OH radical formation by ultrasound in aqueous solutions. Part I: the chemistry underlying the terephthalate dosimeter. Ultrason. Sonochem. 3, 57–63.

Fayter, R.G., Spurlock, L.A., 1974. Chemistry of ultrasound. III: the irradiative behavior of simple aliphatic amines. J. Acoust. Soc. Am. 56, 1461–1468.

Fitzgerald, M.A., Griffing, V., Sullivan, J., 1956. Chemical effects of ultrasonics—"Hot spot Chemistry". J. Chem. Phys. 23, 926–933.

Francony, A., Pétrier, C., 1996. Sonochemical degradation of carbon tetrachloride in aqueous solution at two frequencies: 20KHz and 500KHz. Ultrasonics 3, S77–S682.

Fu, H., Suri, R.P.S., Chimchirian, R.F., Helmig, E., Constable, R., 2007. Ultrasound- induced destruction of low levels of estrogen hormones in aqueous solutions. Environ. Sci. Technol. 41, 5869–5874.

Glaze, W., Kang, J.-W., Chapin, D.H., 1987. The chemistry of water treatment processes involving ozone, hydrogen peroxide and ultraviolet radiation. Ozone Sci. Eng. 9, 335–352.

Gogate, P.R., Sutkar, V.S., Pandit, A.B., 2011. Sonochemical reactors: important design and scale up considerations with a special emphasis on heterogeneous systems. Chem. Eng. J. 166, 1066–1082.

Gondrexon, N., Renaudin, V., Pétrier, C., Clément, M., Boldo, P., Gonthier, Y., Bernis, A., 1998. Experimental study of the hydrodynamic behaviour of a high frequency ultrasonic reactor. Ultrason. Sonochem. 5, 1–6.

Gültekin, I., Ince, N.H., 2008. Ultrasonic destruction of bisphenol-A: the operating parameters. Ultrason. Sonochem. 15, 524–529.

Gutierrez, M., Henglein, A., 1988. Sonolytic decomposition of poly(vinylpyrrolidone), ethanol, and tetranitromethane in aqueous solution. J. Phys. Chem. 92, 2978–2981.

Gutierrez, M., Henglein, A., Fischer, C.H., 1986. Hot spot kinetics of the sonolysis of aqueous acetate solutions. Int. J. Radiat. Biol. 50, 313–321.

Hart, E.J., Henglein, A., 1985. Free radical and free atom reactions in the sonolysis of aqueous iodide and formate solutions. J. Phys. Chem. 89, 4342–4347.

Hart, E.J., Henglein, A., 1986. Sonolysis of ozone in aqueous solution. J. Phys. Chem. 90, 3061–3062.

Hart, E.J., Henglein, A., 1987. Sonochemistry of aqueous solutions: H2-O_2 combustion in cavitation bubbles. J. Phys. Chem. 91, 3654–3656.

Hart, E.J., Fischer, C.-H., Henglein, A., 1990. Pyrolysis of acetylene in sonolytic cavitation bubbles in aqueous solution. J. Phys. Chem. 94, 284–290.

He, Y., Grieser, F., Ashokkumar, M., 2011. The mechanism of sonophotocatalytic degradation of methyl orange and its products in aqueous solutions. Ultrason. Sonochem. 18, 974–980.

Henglein, A., 1987. Sonochemistry: historical developments and modern aspects. Ultrasonics 25, 7–16.

Henglein, A., Kormann, C., 1985. Scavenging of OH radicals produced in the sonolysis of water. Int. J. Radiat. Biol. 48, 251–258.

Hirai, K., Nagata, Y., Maeda, Y., 1996. Decomposition of chlorofluorocarbons and hydrofluorocarbons in water by ultrasonic irradiation. Ultrason. Sonochem. 3, S205–S207.

Howard, P., Meylan, W., 1997. Handbook of Physical Properties of Organic Chemicals. CRC Press, Boca Raton.

Hua, I., Hoffmann, M.R., 1996. Kinetics and mechanism of the sonolytic degradation of CCl_4: intermediates and byproducts. Environ. Sci. Technol. 30, 864–871.

Hua, I., Hoffmann, M.R., 1997. Optimization of ultrasonic irradiation as an advanced oxidation technology. Environ. Sci. Technol. 31, 2237–2243.

Hua, I., Hochemer, R.H., Hoffmann, M.R., 1995. Sonolytic hydrolysis of p-nitrophenyl acetate: the role of supercritical water. J. Phys. Chem. 99, 2335–2342.

Hung, H.-M., Ling, F.H., Hoffmann, M.R., 2000. Kinetics and mechanism of the enhanced reductive degradation of nitrobenzene by elemental iron in the presence of ultrasound. Environ. Sci. Technol. 34, 1758–1763.

Iida, Y., Yasui, K., Tuziuti, T., Sivakumar, M., 2005. Sonochemistry and its dosimetry. Microchem. J. 80, 159–164.

Inazu, K., Nagata, Y., Maeda, Y., 1993. Decomposition of chlorinated hydrocarbons in aqueous solutions by ultrasonic irradiation. Chem. Lett., 57–60.

Ince, N.H., Tezcanli-Güyer, G., 2004. Impacts of pH and molecular structure on ultrasonic degradation of azo dyes. Ultrasonics 42, 591–596.

Inoue, M., Okada, F., Sakurai, A., Sakakibara, M., 2006. A new development of dyestuffs degradation system using ultrasound. Ultrason. Sonochem. 13, 313–320.

Jeong, J., Yoon, J., 2005. pH effect on OH radical production in photo/ferrioxalate system. Water Res. 39, 2893–2900.

Jiang, Y., Pétrier, C., Waite, D.T., 2002a. Kinetics and mechanisms of ultrasonic degradation of volatile chlorinated aromatics in aqueous solutions. Ultrason. Sonochem. 9, 317–323.

Jiang, Y., Pétrier, C., Waite, D.T., 2002b. Effect of pH on the ultrasonic degradation of ionic aromatic compounds in aqueous solution. Ultrason. Sonochem. 9, 163–168.

Jiang, Y., Pétrier, C., Waite, T.D., 2006. Sonolysis of 4-chlorophenol in aqueous solution: effects of substrate concentration, aqueous temperature and ultrasonic frequency. Ultrason. Sonochem. 13, 415–422.

Johston, A.J., Hocking, P., 1993. Ultrasonically accelerated photocatalytic waste treatment. Am. Chem. Soc. Symp. Ser. 518, 106–118.

Joseph, J.M., Destaillats, H., Hung, H.-M., Hoffmann, M.R.J., 2000. The sonochemical degradation of azobenzene and related azodyes: rate enhancements via Fenton's reactions. J. Phys. Chem. A 104, 301–307.

Kandzas, P.F., Mokina, A.A., 1962. Oxidation of phenol in an ultrasonic field in the presence of carbon tetrachloride. Russ. J. Phys. Chem. 36, 545–546.

Kang, J.-W., Hung, H.-M., Lin, A., Hoffmann, M.R., 1999. Sonolytic destruction of methyl tert-butyl ether by ultrasonic irradiation: the role of O_3, H_2O_2, frequency and power density. Environ. Sci. Technol. 33, 3199–3205.

Katsumata, H., Kobayashi, T., Kaneco, S., Susuki, T., Ohta, K., 2011. Degradation of linuron by ultrasound with photoFenton treatment. Chem. Eng. J. 166, 468–473.

Kim, D.K., O'Shea, K.E., Cooper, W.J., 2012. Mechanistic considerations for the degradation of methyl tert-butyl ether (MTBE) by sonolysis: effect of argon vs. oxygen saturated solutions. Ultrason. Sonochem. 19, 959–968.

Kitajima, M., Hatanaka, S.-I., Hayashi, S., 2006. Mechanism of O_2-accelarated sonolysis of bisphenol a. Ultrasonics 44, e371–e373.

Kobayashi, D., Honma, C., Suzuki, A., Takahashi, T., Matsumoto, H., Kuroda, C., Otake, K., Shono, A., 2012. Comparison of ultrasonic

degradation rates constants of methylene blue at 22.8KHz, 127KHz, and 490KHz. Ultrason. Sonochem. 19, 745–749.

Koda, S., Kimura, T., Kondo, T., Mitome, H., 2003. A standard method to calibrate sonochemical efficiency of an individual reaction system. Ultrason. Sonochem. 10, 149–156.

Kondo, T., Riesz, P., 1991. Effect of ultrasound and ionizing radiation on a sterically hindered cyclic secondary amine: an ESR study. Radiat. Res. 127, 11–18.

Kormann, C., Bahnemann, D.W., Hoffmann, M.R., 1988. Photocatalytic production of H_2O_2 and organic peroxides in aqueous suspension of TiO_2, ZnO, and desert sand. Environ. Sci. Technol. 22, 798–806.

Koskinen, W.C., Sellung, K.E., Baker, J.M., Barber, B.L., Dowdy, R.H., 1994. Ultrasonic decomposition of atrazine and alachlor in water. J. Environ. Sci. Health B29, 581–590.

Kotronarou, A., Mills, G., Hoffmann, M.R., 1992. Decomposition of parathion in aqueous solution by ultrasonic irradiation. Environ. Sci. Technol. 26, 1460–1462.

Krüger, O., Schulze, T.-L., Peters, D., 1999. Sonochemical treatment of natural ground water at different high frequencies: preliminary results. Ultrason. Sonochem. 6, 123–128.

Kunai, A., Hata, S., Ito, S., Sasaki, K., 1986. The role of oxygen in the hydroxylation reaction of benzene with Fenton's reagent. ^{18}O tracer study. J. Am. Chem. Soc. 108, 6012–6016.

Legrini, O., Oliveros, E., Braun, A.M., 1993. Photochemical processes for water treatment. Chem. Rev. 93, 671–698.

Lepoint, T., Lepoint-Mullie, F., 1998. Theoretical bases. In: Luche, J.-L. (Ed.), Synthetic Organic Sonochemistry. Spinger Verlag GmbH, Berlin, pp. 3–51.

Lesko, T., Colussi, A.I., Hoffmann, M.R., 2006. Sonochemical decomposition of phenol: evidence for a synergistic effect of ozone and ultrasound for the elimination of total organic carbon from water. Environ. Sci. Technol. 40, 6818–6823.

Lindström, O., 1955. Physico-chemical aspects of chemically active ultrasonic cavitation in aqueous solutions. J. Acoust. Soc. Am. 27, 654–671.

Löning, J.-M., Horst, C., Hoffmann, U., 2002. Investigations on the energy conversion in sonochemical processes. Ultrason. Sonochem. 9, 169–179.

Lur'e, Y.Y., Kandzas, P.F., Mokina, A.A., 1962. Oxidation of phenol in an ultrasonic field. Russ. J. Phys. Chem. 36, 1422–1425.

Madhavan, J., Grieser, F., Ashokkumar, M., 2010. Degradation of orange-G by advanced oxidation processes. Ultrason. Sonochem. 17, 338–343.

Mahamuni, N.N., Adewuyi, Y.G., 2010. Advanced oxidation processes (AOPs) involving ultrasound for waste water treatment: a review with emphasis on cost estimation. Ultrason. Sonochem. 17, 990–1003.

Mahamuni, N.N., Pandit, A.B., 2006. Effect of additives on ultrasonic degradation of phenol. Ultrason. Sonochem. 13, 165–174.

Mandroyan, A., Hihn, J.-Y., Doche, M.-L., Pothier, J.M., 2010. A predictive model obtained by identification for the ultrasonic «equivalent» flow velocity at surface vicinity. Ultrason. Sonochem. 17, 965–977.

Manousaki, E., Psillakis, E., Kalogerakis, N., Mantzavinos, D., 2004. Degradation of sodium dodecylbenzene sulfonate in water by ultrasonic irradiation. Water Res. 38, 3751–3759.

Margulis, M.A., Margulis, I.M., 2003. Calorimetric method for measurement of acoustic power in a volume of liquid. Ultrason. Sonochem. 10, 343–345.

Mark, G., Tauber, A., Laupert, R., Schuchmann, H.-P., Schulz, D., Mues, A., Von Sonntag, C., 1998. OH-radical formation by ultrasound in aqueous solution. Part II: terephthalate and Fricke dosimetry and the influence of various conditions on the sonolytic yield. Ultrason. Sonochem. 5, 41–52.

Mark, G., Schuchmann, H.-P., Von Sonntag, C., 2000. Formation of peroxonitrite by sonication of aerated water. J. Am. Chem. Soc. 122, 3781–3782.

Mason, T.J., 2007. Sonochemistry and the environment - Providing a "green" link between chemistry, physics and engineering. Ultrason. Sonochem. 14, 476–483.

Mason, T., Pétrier, C., 2004. Ultrasound processes. In: Parsons, S. (Ed.), Advanced Oxidation Processes for Water and Wastewater Treatment. IWA Publishing, London, pp. 185–208.

Mead, E.L., Sutherland, R.G., Verrall, R.E., 1975. The ultrasonic degradation of thymine. Can. J. Chem. 53, 2394–2399.

Mead, E.L., Sutherland, R.G., Verrall, R.E., 1976. The effects of ultrasound on water in the presence of dissolved gases. Can. J. Chem. 54, 1114–1120.

Mendez-Arriaga, F., Torres-Palma, R.A., Pétrier, C., Esplugas, S., 2008. Ultrasonic treatment of water contaminated with ibuprofen. Water Res. 42, 4243–4248.

Mendez-Arriaga, F., Torres-Palma, R.A., Pétrier, C., Esplugas, S., Gimenez, J., Pulgarin, C., 2009. Mineralization enhancement of a recalcitrant pharmaceutical pollutant in water by advanced oxidation hybrid processes. Water Res. 43, 3984–3991.

Merouani, S., Hamdaoui, O., Saoudi, F., Chiha, M., Pétrier, C., 2010. Influence of bicarbonate and carbonate ions on sonochemical degradation of rhodamine B in aqueous phase. J. Hazard. Mater. 170, 593–599.

Minero, C., Lucchiari, M., Vione, D., Maurino, V., 2005. Fe (III)-enhanced sonochemical degradation of methylene blue in aqueous solution. Environ. Sci. Technol. 39, 8936–8942.

Minero, C., Pellizzari, P., Maurino, V., Pelizzetti, E., Vione, D., 2008. Enhancement of dye sonochemical degradation by some inorganic anions present in natural waters. Appl. Catal. Environ. 77, 308–316.

Moumeni, O., Hamdaoui, O., Pétrier, C., 2012. Sonochemical degradation of malachite green in water. Chem. Eng. Process. 62, 47–53.

Naffrechoux, E., Chanoux, S., Pétrier, C., Suptil, J., 2000. Sonochemical and photochemical oxidation of organic matter. Ultrason. Sonochem. 7, 255–259.

Nanzai, B., Okitsu, K., Takenaka, N., Bandow, H., Maeda, Y., 2008. Sonochemical degradation of various monocyclic aromatic compounds: relation between hydrophobicities of organic compounds and the decomposition rate. Ultrason. Sonochem. 15, 478–483.

Neppiras, E.A., Noltingk, B.E., 1951. Cavitation produced by ultrasonics: theoretical conditions for the onset of cavitation. Proc. Phys. Soc. B 64, 1032–1038.

Neta, P., Huie, R.E., Ross, A.B., 1990. Rate constants for reactions of peroxyl radicals in fluid solution. J. Phys. Chem. 19, 413–513.

Okitsu, K., Iwasaki, K., Yobiko, Y., Bandow, H., Nishimura, R., Maeda, Y., 2005. Sonochemical degradation of azo dyes in aqueous solution: a new heterogeneous kinetics model taking into account the local concentration OH radical and azo dyes. Ultrason. Sonochem. 12, 255–262.

Oliveros, E., Legrini, O., Hohl, M., Müller, T., Braun, A.M., 1997. Industrial waste water treatment: large scale development of a light-enhanced Fenton reaction. Chem. Eng. Process. 36, 397–405.

Olson, T.M., Barbier, P.F., 1994. Oxidation kinetics of natural organic matter by sonolysis and ozone. Water Res. 28, 1383–1391.

Osorio-Vargas, P., Pulgarin, C., Sienkiewicz, A., Pizzio, L.R., Blanco, M. N., Torres- Palma, R., Pétrier, C., Rengifo-Herrera, J.A., 2012. Low-frequency ultrasound induces oxygen vacancies formation and visible light absorption in TiO_2 P-25 nanoparticles. Ultrason. Sonochem. 19, 383–386.

Park, J.-S., Her, N., Yoon, Y., 2011. Ultrasonic degradation of bisphenol A, 17b-estradiol, 17a-ethynylestradiol. Desalin. Water Treat. 30, 1–3.

Park, B., Shin, D., Cho, E., Khim, J., 2012. Effect of ultrasonic frequency and power density for degradation of dichloroacetonitrile by sonolytic ozonation. Jpn. J. Appl. Phys. 51, 07GD07-1–07GD07-4.

Parke, A.V.M., Taylor, D., 1956. The chemical action of ultrasonic waves. J. Chem. Soc., 4442–4450.

Parsons, S.A., Williams, M., 2004. Introduction. In: Parsons, S. (Ed.), Advanced Oxidation Processes for Water and Wastewater Treatment. IWA Publishing, London, pp. 1–6.

Peller, J., Wiest, O., Kamat, V.J., 2001. Sonolysis of 2,4-dichlorophenoxyacetic acid in aqueous solutions. Evidence for OH-radical-mediated degradation. J. Phys. Chem. 105, 3176–3181.

Pétrier, C., Casadonte, D., 2001. The sonochemical degradation of aromatic and chloroaromatic contaminants. In: Mason, T.J., Tiehm, A. (Eds.), Advances in Sonochemistry. Ultrasound and Environmental Protection, vol. 6. Elsevier, London, pp. 91–109.

Pétrier, C., Francony, A., 1997. Incidence of wave-frequency on the reaction rates during ultrasonic wastewater treatment. Water Sci. Technol. 35, 175–180.

Pétrier, C., Micolle, M., Merlin, G., Luche, J.-L., Reverdy, G., 1992a. Characteristics of pentachlorophenate degradation of aqueous solution by means of ultrasound. Environ. Sci. Technol. 28, 1639–1642.

Pétrier, C., Jeunet, A., Luche, J.-L., Reverdy, G., 1992b. Unexpected effects on the rate of oxidative processes induced by ultrasound. J. Am. Chem. Soc. 114, 3148–3150.

Pétrier, C., Lamy, M.-F., Francony, A., Benhacene, A., David, B., Renaudin, V., Gondrexon, N., 1994. Sonochemical degradation of phenol in dilute aqueous solutions: comparison of the reaction rates at 20 and 487kHz. J. Phys. Chem. 98, 1514–1520.

Pétrier, C., David, B., Laguian, S., 1996. Ultrasonic degradation at 20KHz and 500KHz of atrazine and pentachlorophenol in aqueous solution: preliminary results. Chemosphere 32, 1709–1718.

Pétrier, C., Jiang, Y., Lamy, M.-F., 1998. Ultrasound and environment: sonochemical destruction of chloroaromatic derivatives. Environ. Sci. Technol. 32, 1316–1318.

Pétrier, C., Combet, E., Mason, T., 2007. Oxygen-induced concurrent ultrasonic degradation of volatile and non-volatile aromatic compounds. Ultrason. Sonochem. 14, 117–121.

Pétrier, C., Torres-Palma, R., Combet, E., Sarantakos, G., Baup, S., Pulgarin, C., 2010. Enhanced sonochemical degradation of bisphenol-A by bicarbonate ions. Ultrason. Sonochem. 17, 111–115.

Price, G.J., Harris, N.K., Stewart, A.J., 2010. Direct observation of cavitation fields at 23 and 515kHz. Ultrason. Sonochem. 17, 30–33.

Prudhomme, R.O., Grabar, P., 1949. De l'action chimique des ultrasons sur certaines solutions aqueuses. J. Chim. Phys. 46, 323–331.

Pugin, B., 1987. Qualitative characterization of ultrasound reactors for heterogeneous sonochemistry. Ultrasonics 25, 49–55.

Rae, J., Ashokkumar, M., Eulaerts, O., Von Sonntag, C., Reisse, J., Grieser, F., 2005. Estimation of ultrasound induced cavitation bubble temperatures in aqueous solutions. Ultrason. Sonochem. 12, 325–329.

Riesz, P., Berdhal, D., Christman, C.L., 1985. Free radical generation by ultrasound in aqueous and non aqueous solutions. Environ. Health Perspect. 64, 233–252.

Riesz, P., Kondo, T., Murali Krishna, C., 1990. Sonochemistry of volatile and non-volatile solutes in aqueous solutions: e.p.r. and spin trapping studies. Ultrasonics 28, 295–303.

Rotoarinoro, C., Contamine, F., Wilhelm, A.-M., Berlan, J., Delmas, A., 1995. Power measurement in sonochemistry. Ultrason. Sonochem. 2, S43–S47.

Safarzadeh-Amiri, A., Bolton, J.R., Cater, S.R., 1996. The use of iron in advanced oxidation processes. J. Adv. Oxid. Technol. 1, 18–26.

Schmitt, F.O., Johnson, C.H., Olson, A.R., 1929. Oxidation promoted by ultrasonic radiation. J. Am. Chem. Soc. 51, 370–375.

Seghal, C.M., Wang, S.Y., 1981. Threshold intensities and kinetics of the sonoreaction of thymine in aqueous solutions at low ultrasonic intensities. J. Am. Chem. Soc. 103, 6606–6611.

Seghal, C., Sutherland, R.G., Verrall, R.E., 1980. Optical spectra of sonoluminescence from transient and stable cavitation in water saturated with various gases. J. Phys. Chem. 84, 388–395.

Serpone, N., Terzian, R., Hidaka, H., Pelizzetti, E., 1994. Ultrasonic induced dehalogenation and oxidation of 2-, 3-, and 4-chlorophenol in air-equilibrated aqueous media; similarities with irradiated semiconductor particulates. J. Phys. Chem. 98, 2634–2640.

Shirgaonkar, I.Z., Pandit, A.B., 1998. Sonophotochemical destruction of aqueous solution of 2,4,6-trichlorophenol. Ultrason. Sonochem. 5, 53–61.

Shu, Z., Bolton, J.R., Belosevic, M., Gamal El Din, M., 2013. Photodegradation of emerging micropollutants using the medium-pressure UV/H_2O_2 advanced oxidation processes. Water Res. 47, 2881–2889.

Singla, R., Grieser, F., Ashokkumar, M., 2011. The mechanism of sonochemical degradation of a cationic surfactant in aqueous solution. Ultrason. Sonochem. 18, 484–488.

Sivakumar, M., Pandit, A.B., 2001. Ultrasound enhanced degradation of Rhodamine B: optimization with power density. Ultrason. Sonochem. 8, 233–240.

Sivakumar, M., Tatake, P.A., Pandit, A.B., 2002. Kinetics of p-nitrophenol degradation: effect of reaction conditions and cavitational parameters for a multiple frequency system. Chem. Eng. J. 85, 327–338.

Sivasankar, T., Moholkar, V.S., 2009. Physical insights into the sonochemical degradation of recalcitrant organic pollutants with cavitation bubble dynamics. Ultrason. Sonochem. 16, 769–781.

Son, Y., Lim, M., Khim, J., Kim, L.-H., Ashokkumar, M., 2012. Comparison of calorimetric energy and cavitation energy for the removal of bisphenol-A: the effects of frequency and liquid height. Chem. Eng. J. 183, 39–45.

Spurlock, L.A., Reifsneider, S.B., 1971. The ultrasonic irradiation of some simple organic molecules. Chem. Eng. Prog. Symp. Ser. 67, 27–34.

Srivastava, S.C., 1958. Chemical reactions initiated by ultrasonic waves. Nature 182, 47.

Supeno, Kruus, P., 2000. Sonochemical formation of nitrate and nitrite in water. Ultrason. Sonochem. 7, 109–113.

Suslick, K., 1988. Homogeneous sonochemistry. In: Suslick, K.S. (Ed.), Ultrasound: Its Chemical, Physical and Biological Effects. VCH publishers, New York, pp. 123–163.

Suslick, K.S., Doktycz, S.J., Flint, E.B., 1990. The origin of sonoluminescence and sonochemistry. Ultrasonics 28, 280–290.

Tauber, A., Schuchmann, H.-P., Von Sonntag, C., 1999. Sonolysis of aqueous 4-nitrophenyl acetate. No evidence for hydrolysis induced by transient supercriticality. Chem. A Eur. J. 5, 2198–2202.

Tauber, A., Schuchmann, H.-P., Von Sonntag, C., 2000. Sonolysis of -nitrophenol at low and high pH. Ultrason. Sonochem. 7, 45–52.

Tezcanli-Güyer, G., Ince, N.H., Alaton, I., 2003. Sonochemical destruction of textile dyestuff in washed dyebaths. Color. Technol. 119, 292–296.

Théron, P., Pichat, P., Guillard, C., Pétrier, C., Chopin, T., 1999. Degradation of phenyltrifluoromethyl ketone in water by separated or simultaneous use of TiO_2 photocatalyst and 30 or 515kHz ultrasound. Phys. Chem. Chem. Phys. 1, 4663–4668.

Théron, P., Pichat, P., Pétrier, C., Guillard, C., 2001. Water treatment by TiO_2 photocatalysis and/or ultrasound: degradation of phenyltrifluoromethylketone, a trifluoroacetic- acid-forming pollutant, and octan-1-ol, a very hydrophobic pollutant. Water Sci. Technol. 44, 263–270.

Thoma, G., Gleason, M., 1998. Sonochemical treatment of benzene/toluene contaminated wastewater. Environ. Prog. 17, 154–160.

Torres, R.A., Pétrier, C., Combet, E., Moulet, F., Pulgarin, C., 2007. Bisphenol a mineralization by integrated ultrasound-UV-Iron (II) treatment. Environ. Sci. Technol. 41, 297–302.

Torres, R.A., Nieto, J.I., Combet, E., Pétrier, C., Pulgarin, C., 2008a. Influence of TiO_2 concentration on the synergistic effect between photocatalysis and high-frequency ultrasound for organic pollutant mineralization in water. Appl. Catal. Environ. 80, 168–175.

Torres, R.A., Pétrier, C., Combet, E., Carrier, M., Pulgarin, C., 2008b. Ultrasonic cavitation applied to the treatment of bisphenol A. Effect of sonochemical parameters and analysis of BPA by-products. Ultrason. Sonochem. 15, 605–611.

Torres, R.A., Mosteo, R., Pétrier, C., Pulgarin, C., 2009. Experimental design approach to the optimization of ultrasonic degradation of alachlor and enhancement of treated water biodegradability. Ultrason. Sonochem. 16, 425–430.

Torres-Palma, R.A., Nieto, J.I., Combet, E., Pétrier, C., Pulgarin, C., 2010. An innovative ultrasound, Fe^{2+} and TiO_2 photoassisted process for bisphenol-A mineralization. Water Res. 44, 2245–2252.

Tuhkanen, T.A., 2004. UV/H_2O_2 processes. In: Parsons, S. (Ed.), Advanced Oxidation Processes for Water and Waste Water Treatment. IWA Publishing, London, pp. 86–110.

Vassilakis, C.A., Pantidou, A., Psillakis, E., Kalogerakis, N., Mantzavinos, D., 2004. Sonolysis of natural phenolic compounds in aqueous solutions: degradation pathways and biodegradability. Water Res. 38, 3110–3118.

Vecitis, C.D., Wang, Y.J., Cheng, J., Park, H., Mader, B.T., Hoffmann, M. R., 2010a. Sonochemical degradation of perfluorooctanesulfonate in aqueous film-forming foams. Environ. Sci. Technol. 44, 432–438.

Vecitis, C.D., Lesko, T., Colussi, A.J., Hoffmann, M.R., 2010b. Sonolytic decomposition of aqueous bioxalate in presence of ozone. J. Phys. Chem. A 114, 4968–4980.

Virtanen, A.I., Ellfolk, N., 1950. Nitrogen fixation in an ultrasonic field. J. Am. Chem. Soc. 72, 1046–1048.

Virtanen, A.I., Ellfolk, N., 1952. Inhibition of oxidative nitrogen fixation in ultrasonic field by volatile substances. Acta Chem. Scand. 6, 660–666.

Von Sonntag, C., Schuchmann, H.-P., 1991. The elucidation of peroxyl radical reactions in aqueous solution with the help of radiation chemical methods. Angew. Chem. Int. Ed. Engl. 30, 1229–1253.

Walling, C., 1975. Fenton's reagent revisited. Acc. Chem. Res. 8, 129–131.

Walton, A.J., Reynolds, G.T., 1984. Sonoluminescence. Adv. Phys. 33, 595–660.

Wayment, D.G., Casadonte, D.J., 2002. Frequency effect on the sonochemical remediation of alachlor. Ultrason. Sonochem. 9, 251–257.

Weavers, L.K., Ling, F.H., Hoffmann, M.R., 1998. Aromatic degradation in water using a combination of sonolysis and ozonolysis. Environ. Sci. Technol. 32, 2727–2733.

Weavers, L.K., Malmstadt, N., Hoffmann, M.R., 2000. Kinetics and mechanism of pentachlorophenol degradation by sonication, ozonation, and sonolytic ozonation. Environ. Sci. Technol. 34, 1280–1285.

Wei, Z., Kosterman, J.A., Xiao, R., Pee, G.Y., Cai, M., Weavers, L.K., 2015. Designing and characterizing a multi-stepped ultrasonic horn for enhanced sonochemical performance. Ultrason. Sonochem. 27, 325–333.

Wei, Z., Spinney, R., Ke, R., Yang, Z., Xiao, R., 2016. Effect of pH on the sonochemical degradation of organic pollutants. Environ. Chem. Let. 14, 163–182.

Wei, Z., Villamena, F.A., Weavers, L.K., 2017. Kinetics and mechanism of ultrasonic activation of persulfate: An in situ EPR spin trapping study. Environ. Sci. Technol. 51, 3410–3417.

Weissler, A., 1953. Sonochemistry: the production of chemical changes with sound waves. J. Acoust. Soc. Am. 25, 651–657.

Weissler, A., 1959. Formation of hydrogen peroxide by ultrasonic waves: free radicals. J. Am. Chem. Soc. 81, 1077–1081.

Witekowa, S., 1972. Chemical effects of ultrasonic waves. XIII: investigations of some chemical oxidation and reduction reactions. Soc. Sci. Lodz. Acta Chim. 17, 97–104.

Wu, C.-H., Yu, C.-H., 2009. Effect of TiO_2 dosage, pH and temperature on decolorization of C.I. reactive red 2 in a UV/US/TiO_2 system. J. Hazard. Mater. 169, 1179–1183.

Wu, Z., Lifka, J., Ondruschka, B., 2004. Aquasonolysis of selected cyclic C_6H_x hydrocarbons. Ultrason. Sonochem. 3 (4), 187–190.

Zhang, H., Duan, L., Zhang, Y., Wu, F., 2005. The use of ultrasound to enhance the decolorization of the C.I. Acid orange 7 by zero-valent iron. Dyes Pigments 65, 39–43.

Chapter 36

The use of power ultrasound for wastewater and biomass treatment

U. Neis[a] and R. Cleary[b,*]
[a]Ultrawaves GmbH, Hamburg, Germany, [b]James Watt School of Engineering, University of Glasgow, Glasgow, United Kingdom

36.1 Introduction

Research on ultrasound technology in environmental engineering started in about the middle of the 1990s and was mainly driven by work in Germany. It was recognized early that the innovative technology had a large potential for improving the traditional anaerobic stabilization of organic sludge produced during the biological wastewater treatment process. This traditional process had been in practice for more than half a century with no major improvement and no serious attempt to overcome its technical limitations. The idea was to overcome the rate-limiting hydrolysis step of the anaerobic sludge stabilization by ultrasound, which disintegrates sludge cells and subsequently intensifies the anaerobic degradation process, eventually resulting in more biogas and less residual sludge. The first full-scale ultrasound installations appeared in Germany after the turn of the millennium. Today, about 80 plants equipped with this new technology can be found in various European countries, including France, Spain, Ireland, Switzerland, Denmark, Poland, Italy, and Austria.

Operators of biological wastewater treatment plants (WWTPs) are first responsible for the required good quality of the effluent before it is discharged to the environment. Today, the attention is being shifted more and more to optimizing the operation of treatment plants, not only in order to reduce energy consumption and other costs in an economic sense but also with regard to ecological aspects, such as reduction of greenhouse gas emissions. The challenge is to improve the well-established biological treatment processes targeting these goals without reducing the quality of the effluents.

Research is still being carried out to better understand how ultrasound manifestations can also impact aerobic biomass. This chapter reports on fundamental research as well as full-scale experience for the following applications on WWTP:

- Improving anaerobic sludge/biomass digestion
- Improving nitrogen removal
- Reducing excess sludge
- Combating filamentous microorganisms

The options we have for applying high power ultrasound with WWTP are shown in Figure 36.1.

36.2 Impact of ultrasound on biological suspensions

Ultrasound can be generated at a broad range of sound frequencies (between 20 kHz and 10 MHz) and acoustic intensities. Biological suspensions in water technology contain particulate biomass, i.e., microorganisms. The biological activated sludge reactor of a WWTP is populated by a great number of different bacterial species, most of which are still unidentified. We may also find protozoa and algae. In other words, the complexity of these biological systems is great, and therefore, we do not expect easy understanding of the reactions ultrasound may impose on the diverse organisms. The following phenomena may impact microorganisms when ultrasound is propagated in aqueous media:

1. alternating pressure waves
2. always present no matter which ultrasound frequency or intensity is applied
3. acoustically induced cavitation, causing
   - high mechanical shear stress
   - radical reactions
   - predominantly at mid-range frequencies, between about 100 and 800 kHz, and ultrasound intensities above the cavitation threshold.
     a. creation of H and OH radicals
     b. chemical transformation of (organic) substances
     c. thermal breakdown of volatile hydrophobic substances
     d. sonochemical reactions

36.2.1 Examining bacterial biomass disintegration

Wastewater-activated sludge consists of bacterial cells held together by extracellular polymeric substances in a

*Updated author for the second edition.

Power Ultrasonics. https://doi.org/10.1016/B978-0-12-820254-8.00026-9
Copyright © 2023 Elsevier Ltd. All rights reserved.

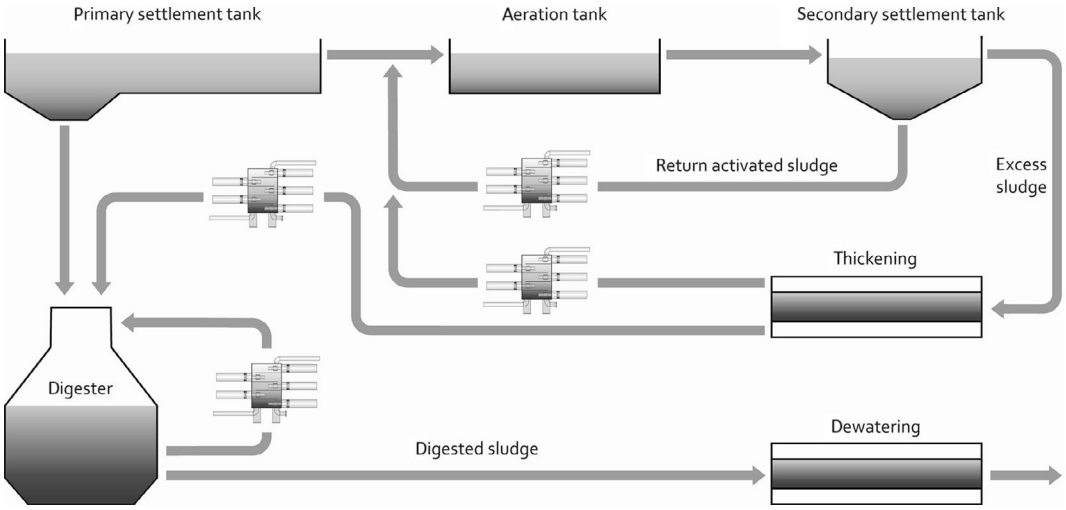


FIGURE 36.1 Possible application points for power ultrasound on WWTP.

flocculent structure. If this sludge is exposed to low ultrasonic energy, the first effect is a de-agglomeration of the sludge flocs. The flocs are separated and dispersed without disrupting cell walls. At higher ultrasonic energies, the microorganism cell walls are perforated or broken, and the intracellular material is released into the liquid phase. Consequently, the amount of dissolved organic material is significantly increased (Tiehm et al., 2001). This two-phase model of the ultrasonic disintegration process is illustrated in Figure 36.2.

The separation of the sludge flocs causes a decrease of the average particle size. Assessment of this de-agglomeration process can be done by particle size distribution analysis (Friedrich et al., 1999). A typical result of a sonication test on the particle size distribution of a sludge sample is shown in Figure 36.3.

King and Forster (1990) tested the effects of sonication on activated sludge floc de-agglomeration using a 20-kHz sonotrode. They also found a larger number of small particles when the higher power dose was applied. A clear relationship between the mean particle size and the sonic power was established and was used to characterize the floc strength of different activated and anaerobically stabilized sludges (Morgan and Forster, 1992).

The extent of cell break-up can be described by chemical or biological parameters. Cell disintegration leads to the release of intracellular organic compounds into the sludge water phase. Therefore, the extent of cell disintegration is determined by the increase of the chemical oxygen demand (COD) in the sludge supernatant. A term often used is the ratio of soluble COD to total sludge COD (SCOD/TCOD) (Chiu et al., 1997). The soluble COD fraction is obtained by high-speed centrifugation (30 min at 40,000 rcf) followed by filtration through 0.45-μm pore size membrane filters. The release of dissolved organic matter (SCOD) typically follows a linear function over a wide range of ultrasound energy dose as is shown in Figure 36.4. High degrees of cell disintegration can be obtained by increasing the energy dose.

Different sludges contain various types of microorganisms with different cell wall strength. A factor DD_{COD} "degree of disintegration" is defined as the ratio of COD increase in the supernatant by sonication (or other disintegration techniques) related to the COD increase by a standardized chemical hydrolyzation method, which is assumed to be able to solubilize 100% of the biomass (Eq. 36.1).

$$DD_{COD} = (COD_{Ultrasound} - COD_{un}/COD_{NaOH} - COD_{un}) \times 100\ [\%] \tag{36.1}$$

where $COD_{Ultrasound}$ is the chemical oxygen demand of the disintegrated sample (here by sonication), [mg/L], COD_{un} is the chemical oxygen demand of the untreated sample [mg/L], COD_{NaOH} is the chemical oxygen demand of a reference sample hydrolyzed chemically in a 0.5 M NaOH solution at 20°C for 22 h [mg/L].

The impact of bacterial cell inactivation can also be assessed by oxygen utilization tests. Because "activated" sludge contains a considerable amount of aerobic bacteria, the oxygen utilization rate (OUR) can be used to characterize the microbial activity. If all bacteria of the sonicated sample are inactivated, the OUR becomes zero and the degree of disintegration ($DD_{OUR)}$ reaches 100% (Lehne and Müller, 1999). The OUR is measured after the addition of acetate as readily available substrate and aeration of the sludge samples. The oxygen utilization rate of a disintegrated sludge sample $OUR_{Ultrasound}$ in relation to the oxygen utilization rate of the untreated sludge OUR_{un} defines DD_{OUR}:

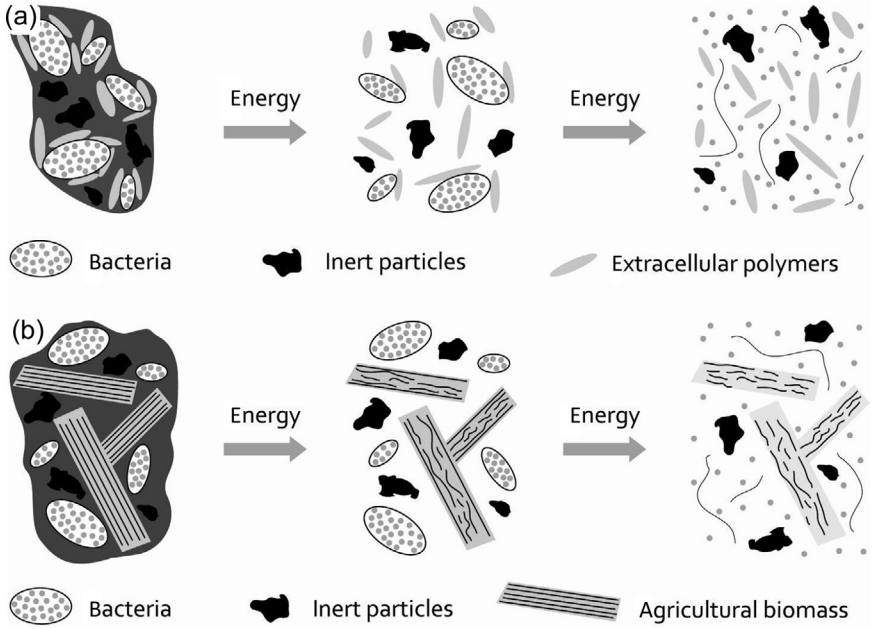


FIGURE 36.2 Effect of ultrasound on (a) the disintegration of biomass at WWTP and (b) the disintegration of biomass at agricultural biogas plants.

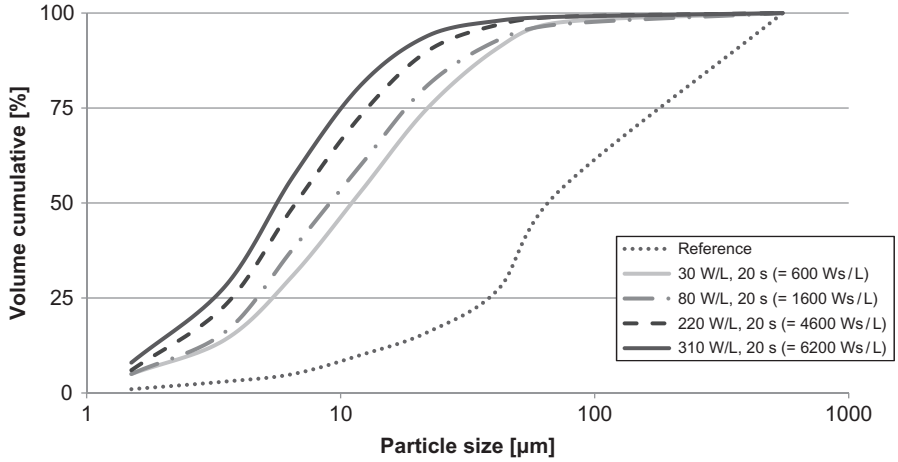


FIGURE 36.3 Impact of sonication on particle size distribution (PSD) of a wastewater treatment effluent. Sonication time was 20 s with various energy densities. PSD shifts clearly to the left with increasing energy input.

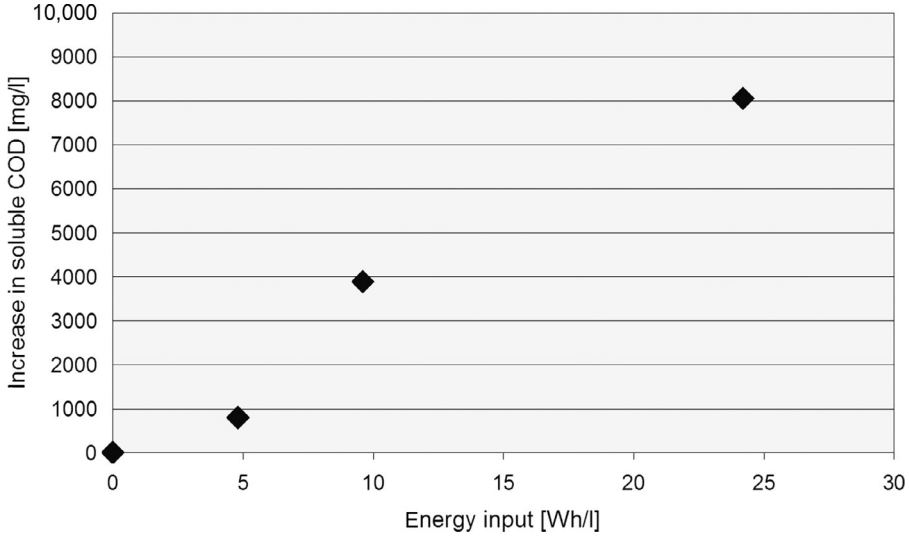


FIGURE 36.4 Impact of sonication on dissolved organic phase (SCOD) of an activated sludge sample, TS = 6.5%, VS = 74.1%.

$$DD_{OUR} = [1 - (OUR_{Ultrasound}/OUR_{un})] \times 100 \quad [\%] \tag{36.2}$$

In earlier studies, we applied ultrasound on waste activated sludge (WAS) in a lab batch reactor with varying frequencies from 41 kHz to 3217 kHz and observed its impact on the DD_{COD}. As can be seen in Figure 36.5, the degree of WAS disintegration decreases with increasing ultrasound frequency. The highest degree of disintegration was 80%, obtained at the lowest frequency, 41 kHz. The resonant cavitation bubble radius increases with decreasing ultrasonic frequency. Upon bubble collapse, hard shock waves are induced by jet streams responsible for the mechanical breakup of the microbiological cell walls. The energy released by a jet stream is a function of the bubble size at the moment of collapse (Neis et al., 2001). The recommendation is to apply low ultrasound frequencies (less than ~40 kHz) for efficient sludge disintegration. Consequently, ultrasound reactors manufactured today preferentially use the 20-kHz frequency for sludge disintegration.

Determination of SCOD or DD_{COD} is a first step in assessing the impact of ultrasound on biomass. More insight into sonicated bacterial biomass is needed to better understand what benefits can be gained by the clever choice of optimal settings for the ultrasound. To that end, a number of investigations were made of the impact of low energy ultrasound on activated sludge and bacterial pure cultures under controlled conditions in the lab (Neis et al., 2012). Activated sludge samples were taken from Seevetal WWTP. The sludge age was 22 days at the time of sampling. Light microscopic analysis showed a normal floc structure of the activated sludge, with an average floc size of 100–500 µm. Many ciliates were also seen. Filamentous species were identified as *Microthrix parvicella* and *Nostocoida limicola* II, Eikelboom Typ 0961.

Bacterial pure cultures studied were *M. parvicella* and *Pseudomonas aeruginosa*. *M. parvicella* is a Gram-positive filamentous organism, which quite often forms clumps. *M. parvicella* often prevails in bulking sludge episodes (Wagner and Amann, 1996). *P. aeruginosa* is a Gram-negative rod-like bacteria with a length of 1–2 µm. It is ubiquitous in soil and water bodies. *Pseudomonas* type species have already been identified as denitrifying bacteria in activated sludge (Seviour and Nielsen, 2009).

36.2.2 Sonication of bacterial biomass

Ultrasound treatment of each biomass sample was performed with an energy input of 2, 5, 10, and 20 Wh/L, respectively, in a 1-L beaker. A Branson 450 sonifier (100 W) was used with a frequency of 20 kHz. The tip of the oscillating horn during sonication dipped from the top into the biomass suspension; furthermore, the sample was thoroughly mixed by a magnetic stirrer. The temperature (20°C) of the sample was held constant by circulating cooling water through the outer ring of the beaker. The increase in soluble organic carbon (DOC) and total nitrogen (TN) was taken as an indicator to assess the impact of ultrasound on the biomass.

Different microscopic techniques were applied to study the effects of sonication on the biomass: light microscopy, scanning electron microscopy (SEM), and transmission electron microscopy (TEM) (Banduch, 2011).

36.2.3 Activated sludge biomass

The SEM analysis of an activated sludge sample from Seevetal WWTP (TS = 4.2 g/L) showed irregular flocs with plenty of filamentous organisms, which lie within as well as peeking out of the flocs (Figure 36.6). Only at a magnification of 20,000 did we discover rod-like and coccoid bacteria, which were embedded strongly in the matrix of extracellular polymeric substances (EPS). The impact caused by ultrasound also increased as the energy input rose: at 10 Wh/L, the floc structure was more or less dissolved and only short fragments of the filaments remained (Figure 36.7). At 20 Wh/L, the floc structure appeared

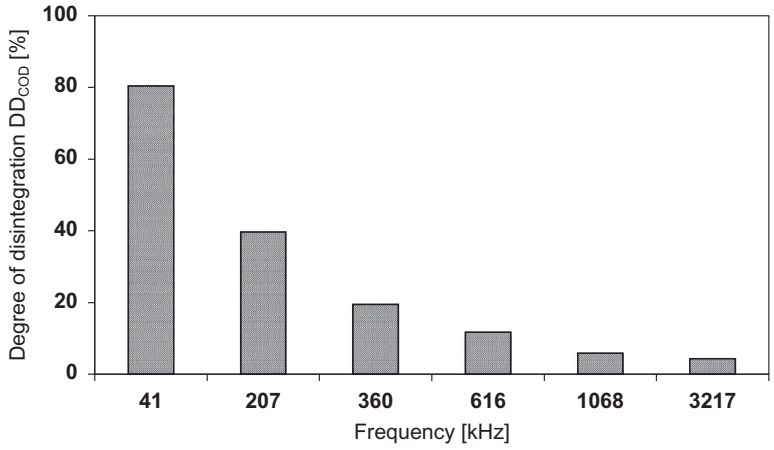


FIGURE 36.5 Effect of ultrasound frequency on the degree of cell disintegration (TS = 20 g/L, ultrasound intensity 1.8 W/cm^2, sonication time 4 h). *(Taken from Tiehm et al. (2001).)*

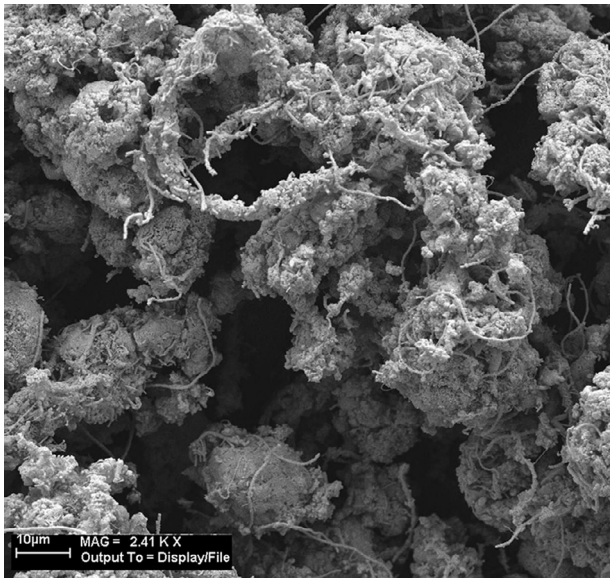


FIGURE 36.6 SEM image of the activated sludge from Seevetal WWTP (untreated). Magnification is 2410.

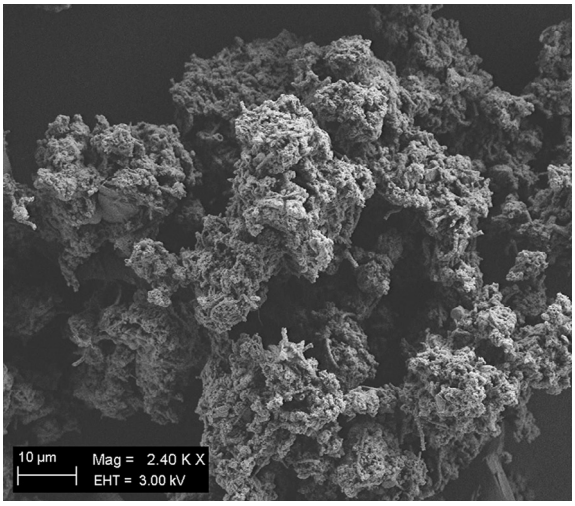


FIGURE 36.7 SEM image of the same activated sludge (sonicated with 10 Wh/L). Magnification is 2400.

completely destroyed, and we could see single bacterial cells, as in Figure 36.8. Here no filaments exist anymore.

Figure 36.9 depicts the release of DOC and TN into solution as a function of the ultrasound energy. The graph demonstrates that already at rather low energy input, soluble carbon and nitrogen are generated from disintegrated cells, meaning substances from within the cell like protein (enzymes, structural protein) transport proteins bound to membranes, as well as EPS, which basically are composed by proteins.

36.2.4 Pure bacterial cultures: M. parvicella and *P. aeruginosa*

The light microscope does not allow one to distinguish in detail morphological elements of *M. parvicella* cells. SEM analysis does provide this information. *M. parvicella* filaments do not possess a sheath (glycocalyx). They are composed of firm compartments having a diameter of 0.5–0.7 µm. We can clearly see the septum (Figure 36.10). Two Wh/L of ultrasound energy applied to *M. parvicella* suspensions do not harm the cell walls; however, there is an impact because the cells appear compressed. At 5 Wh/L, the cell wall is being stressed and appears ragged; furthermore, the cells are deformed and show bumps. Filaments are now disintegrated into short fragments. TEM analysis shows that the cell membranes are often breaking near the septum.

SEM photos show *P. aeruginosa* cells as 1- to 2-µm-long rods, partly equipped with flagella and fimbriae. At a higher magnitude, the typical structure of a Gram-negative outer cell membrane clearly can be seen (Figure 36.11). At 5 Wh/L energy input, there are a number of cells with round damaged dots on the outer membrane, and some cell membranes appear pierced. Here again increasing the ultrasound energy causes an increase in the number and magnitude of damaged cells. Unlike with *M. parvicella,* TEM does not allow one to conclude whether *P. aeruginosa* cytoplasma is being attacked without having destroyed the cell wall. Figure 36.12 is a crosscut (a, b) and a longitudinal cut

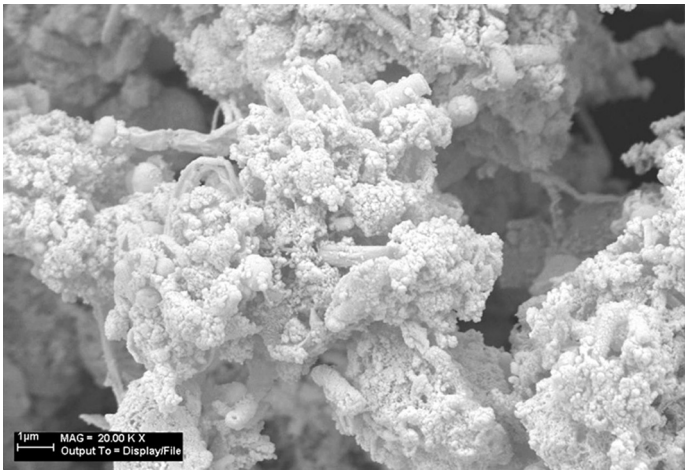


FIGURE 36.8 SEM image of the activated sludge from Seevetal WWTP (sonicated with 20 Wh/L). Magnification is 20,000.

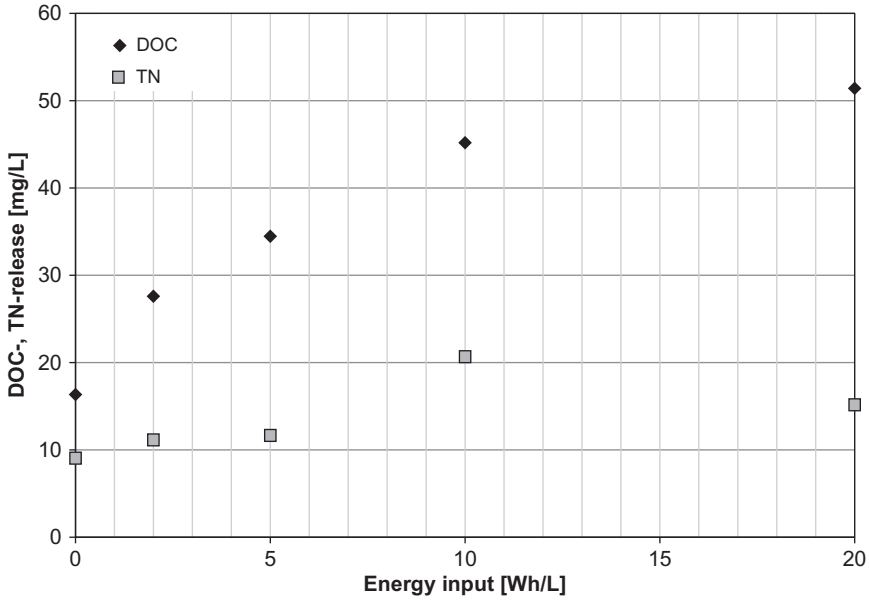


FIGURE 36.9 DOC-, TN-release of the activated sludge due to ultrasonic treatment.

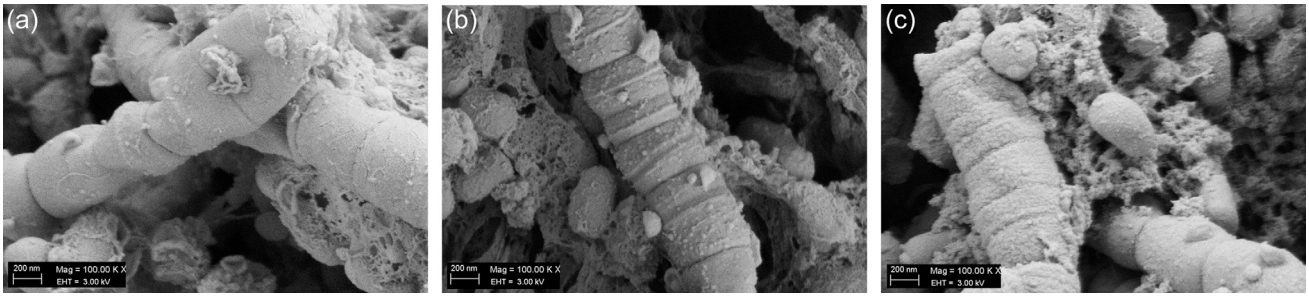


FIGURE 36.10 SEM image of *M. parvicella* (a) untreated, (b) sonicated with 2 Wh/L and (c) sonicated with 5 Wh/L.

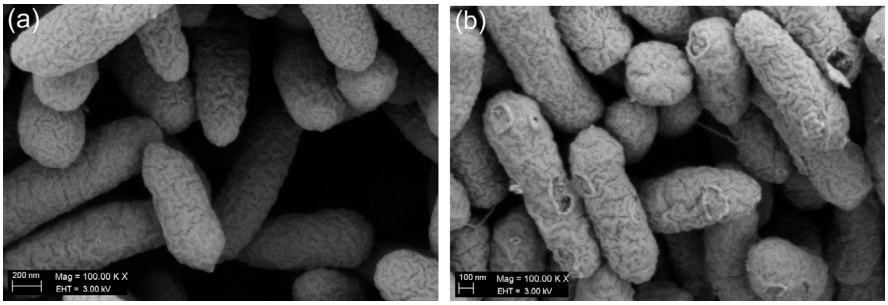


FIGURE 36.11 SEM image of *P. aeruginosa* (a) untreated and (b) sonicated with 5 Wh/L.

(c, d) of a *P. aeruginosa* cell before and after sonication with 20 and 5 Wh/L, respectively. One may conclude that, as a result of sonication, the nucleoid is precipitated. The cell wall remains whole (Banduch and Neis, 2012).

Treating activated sludge biomass with low ultrasound energy causes de-aggregation of the sludge flocs, creating favorable morphological conditions for substrate and oxygen diffusion. This leads to increased bacterial activity. However, some bacterial species, for example, *M. parvicella*, may suffer already at a low energy dose (2 Wh/L) and cell cytoplasm can be released without obviously damaging the cell walls.

At this point, we cannot attribute the effects to hard cavitation (implosion of bubbles creating highly powerful shear forces in the liquid), because the applied ultrasound energy is rather low, meaning a short sonication time and few cavitation events in relation to the very high number of bacterial cells in the suspension. But there is constant stress on the

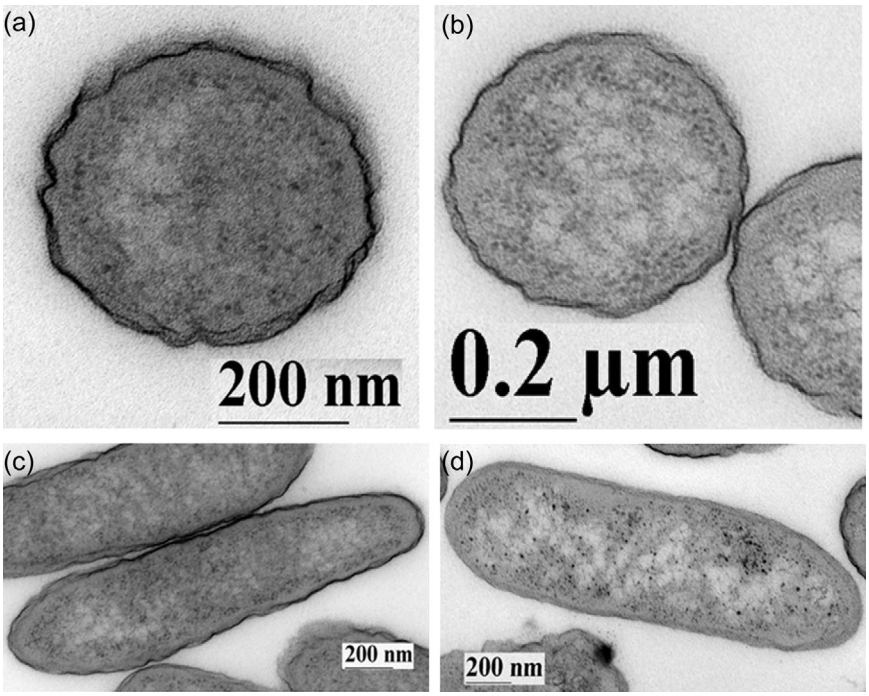


FIGURE 36.12 TEM image of *P. aeruginosa*. (a) Untreated, (b) sonicated with 20 Wh/L, (c) untreated, (d) sonicated with 5 Wh/L.

bacterial biomass by the oscillating high-power ultrasound, causing pressure variation between ±6.6 bar (in this particular case). We have to keep in mind that this pressure change happens 20,000 times per second for minutes. The cell wall structure does not seem to have much influence here, which is surprising if we consider that a Gram-positive cell wall is reported to be able to bear up to 30-bar pressure and a Gram-negative cell wall up to 7 bar.

36.3 Anaerobic digestion processes: Full-scale application

The treatment of wastewater is based on physical, chemical, and biological reactions and transformations. The rate of these reactions determines the necessary volume of the reactors, and the nature and extent of the reactions determine the degree of treatment or, in other words, the removal efficiency. As shown above, ultrasound may impact aqueous biological suspensions in many ways that are a focus of wastewater treatment. Since the early 1990s, it has been recognized that ultrasound has the potential to intensify the processes involved in the treatment of wastewater. Not surprisingly, work started with the anaerobic sludge stabilization process, which due to the enzymatic hydrolysis of the particulate and the colloidal character of the substrate is a very slow and complex process.

Shimizu et al. (1993) compared the decomposition rate of lysed intracellular organic substance with the digestion rate of untreated WAS. The results showed that in the anaerobic process, the fermentation rate of the WAS as well as the decomposition rate of the released organic components resembled a first-order reaction type. The calculated rate constant was 0.16 day^{-1} for the untreated WAS and 1.2 day^{-1} for the released organic substances. Usually, we assume anaerobic sludge hydrolysis reaction rates fall between 0.2 and 0.3 day^{-1}. The authors observed a maximum anaerobic decomposition efficiency of 65% and 90%, respectively, for the untreated WAS and the released dissolved cell components. Thus, the effect of ultrasonic sludge cell disintegration resulted in both improvement of the decomposition reaction rate as well as decomposition efficiency (Table 36.1).

TABLE 36.1 Hydrolysis of WAS, solubilized WAS, and most important biopolymers

Substrate	Hydrolysis rate constant (per day)	Maximum percent of hydrolysis (%)
WAS	0.16	65
Solubilized WAS	1.2	90
Protein	1.3	95
Nucleic acid	1.8	95
Lipid	0.76	88
Carbohydrate	1.2	90

Source: Adapted from Shimizu et al. (1993).

Nickel and Neis (2007) report increase in the first-order reaction rate by a factor of two (from 0.26 to 0.52 day^{-1}) after full sonication (31 kHz) of conventional WAS. Many later publications confirmed the positive effect of sonication on fermentation of biomass (Braguglia et al., 2012; Jiang et al., 2008; Liu et al., 2009). One major concern is finding a functional relation between a parameter defining the ultrasound impact on the substrate (degree of disintegration, for example) and a parameter defining the end product of the subsequent anaerobic process (for example, biogas production). Although this task can be achieved in a lab under controlled conditions, it is impossible in full scale, because in reality, we never encounter stable equilibrium conditions in terms of quantity and quality of sludge fed to the digesters.

Figure 36.13 presents a summary of results of a lab-scale study performed at the author's former institute. The graph also includes a value from a pilot-scale digestion experiment with sonicated WAS and an identical sludge digestion time of 8 days (Tiehm et al., 2001). The graph shows that the volatile solids (VS) decomposition in the digester is intensified with an increasing degree of cell disintegration DD_{COD}. A regression analysis of the data confirms the linear function over a wide range. The slope of the linear function is 1.9. By increasing the degree of disintegration by 10%, the anaerobic VS degradation can be improved by 19%. What may seem surprising at a first glance is the section of the ordinate at 10.4% VS degradation increase. As explained, earlier short sonication times mean low energy input, causing floc de-agglomeration but no cell destruction. The positive effect of floc de-agglomeration on the digestion process can be explained by a better diffusion of substrates and nutrients to single (active) bacteria as compared to bacteria that are embedded and protected in sludge floc agglomerates. Another important point is the release of extracellular polymeric substances (EPS) from cell surfaces as demonstrated by the microscopic analyses described earlier. The EPS have enzymatic character and support the hydrolyzing active bacteria.

To summarize, low-frequency power ultrasound generates the cavitation necessary to produce the mechanical shear forces associated with sludge disintegration. Combined with high-intensity ultrasound generating strong pressure fluctuations, cell aggregates are declumped, single cells are perforated or destroyed, and enzymatic extra- and intracellular material is released into the medium, resulting in a higher degree of substrate bioavailability for the remaining living microorganisms. In effect, the enzymatic-biological hydrolysis, which is the initial and rate-limiting step of the anaerobic food chain, is substituted and catalyzed by this disintegration of the sludge. Results indicate that it is possible to increase the operating performance of the anaerobic digestion process and greatly improve the decomposition rate using sludge with sonicated cells. Therefore, the greatest benefit of the ultrasonic pretreatment is obtained if the organic fraction of the sludge is predominantly composed of biological cells or, in other words, sonicate the WAS fraction and not the raw sludge, which is composed largely of particulate organic matter but not cells. The hydraulic retention time (HRT) in the digester can be shortened without losses in the degradation efficiency. Consequently, digester volumes could be reduced.

36.3.1 Enhancing anaerobic digestion: The Bamberg wastewater treatment plant (WWTP)

The Bamberg WWTP was designed for 220,000 PE. However, as a result of an improvement and extension of the sewerage system, the load on the plant in 2002 increased up to about 330,000 PE. The plant is equipped with three mesophilic anaerobic digesters to treat a mixture of primary and secondary sludge (WAS). As a consequence of the increased load, more sludge was produced and the HRT in the digesters dropped to just 18 days. The initial plan was to construct a new, fourth digester with a volume of 3000 m^3. However, the management of the plant decided

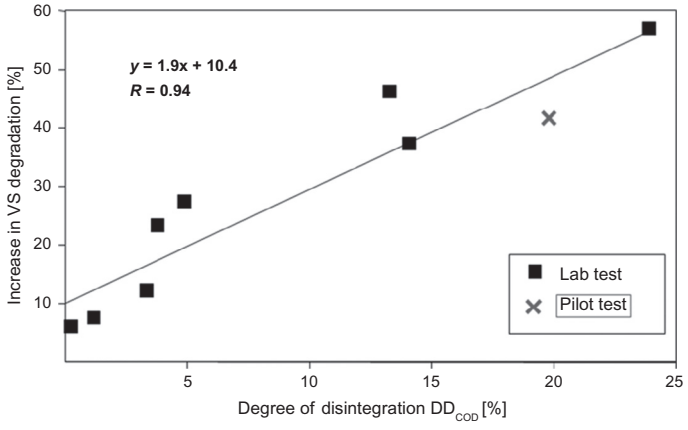


FIGURE 36.13 Enhanced volatile solids (VS) degradation of waste activated sludge (WAS) as a function of the degree of sludge disintegration. The sludge retention time in fermenters was 8 days.

to test the new ultrasound technology developed by ultrawaves during a full-scale trial period of 4 months. After feeding the digesters with ultrasonically treated WAS, the gas production showed a marked increase of almost 30%. The methane content also increased slightly, making the biogas a more attractive and energy rich product. The residual VS content in the digested sludge was reduced from 60% to 54%. The desired goal to reach a minimum of 40% VS degradation was not only met but surpassed.

After the successful trial period in 2002, the Bamberg WWTP management decided to purchase two ultrasound (US) reactors (2×5 kW) instead of building a new digester, thus avoiding the costly undertaking of such a construction. The high-power ultrasound units were installed in August 2004 with the same objective of enhancing VS degradation to a minimum of 40%. In order to achieve this, the system was designed to sonicate at least 30% of the thickened waste-activated sludge (TWAS) flow before being fed to the digesters.

Figure 36.14a is a picture of the two high-power ultrasound reactors that were installed in Bamberg. Figure 36.14b shows the uncovered ultrasound unit. As is clear in both photos, the small footprint of the equipment and the simple way that it can be connected to existing piping and installations make it a very attractive piece of technology. The annual required maintenance is the exchange of the sonotrode tip.

More about the development and the design of that reactor are presented in Section 36.5. The ultrawaves ultrasound equipment has already been implemented in full scale on more than 50 WWTPs worldwide.

Calculating organic matter mass balances at full-scale WWTPs is a challenging task. Steady-state conditions are never reached. Hence, the assessment of the impact of ultrasonic TWAS disintegration on the anaerobic digestion process at Bamberg is based on routinely collected data sets. No additional information can be collected. As a result, comparison can only be made between the period before (1/2003–12/2004) and after the start of ultrasound application, followed by long-term recording of data in order to assess the reliability of the new technology. Figure 36.15 presents the recorded data regarding digester performance from the beginning of 2003 to the end of 2011.

While the VS degradation remained constant at a level of about 34% during the years 2003–2005, it subsequently increased to about 50%, from 2007 onward. The increase of VS degradation followed the increased amount of sonicated waste-activated sludge: While during 2005, roughly

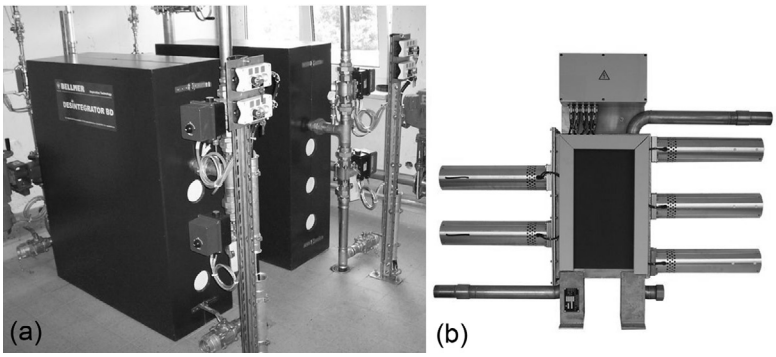


FIGURE 36.14 (a) Two high-power ultrasound reactors of Ultrawaves Co. at Bamberg WWTP for the disintegration of WAS. The two units are equipped with sound protection covers. (b) The sound protection cover is removed from one 5 kW ultrasound unit; inflow lower left, outflow upper right. Five perforated aluminum tubes accommodate mechanical aerators for proper removal of heat from the piezo-ceramic transducers.

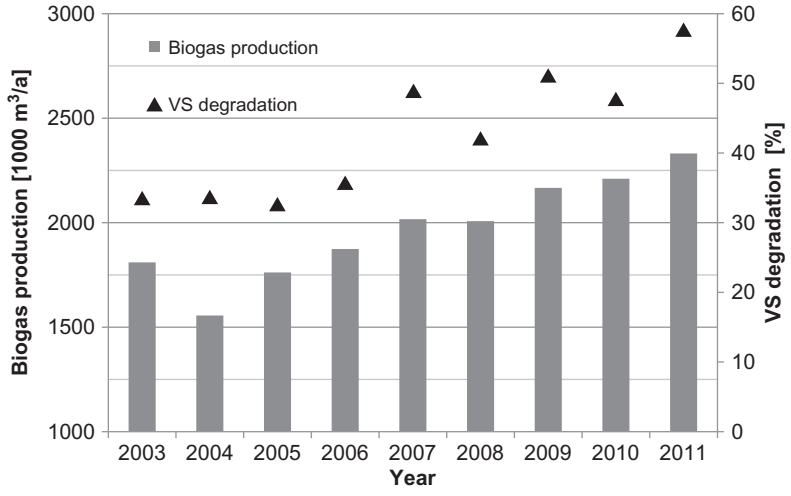


FIGURE 36.15 Biogas production and volatile solids degradation on Bamberg WWTP. Two ultrasound units are in operation since August 2004. Test phase was 2003.

30% of the TWAS flow was treated in the two ultrasound reactors, the share of sonicated TWAS was enhanced stepwise to a constant level of about 80% from the year 2007 onward. The increase in the VS degradation implies that more of the organic matter in the sludge was metabolized in the digestion process. This coincides with the increase in gas production. The average sonicated TWAS flow is 88 m^3/day. This represents an ideal volumetric flow for the two installed ultrasound reactors. The ultrasound units are in operation 24 h per day all year round. The resulting sonication time is 57 s. The annual energy consumed is 70,800 kWh/a, representing only 1.5% of the total energy consumption at the Bamberg WWTP. Based on these data, the calculated average specific energy consumption of the ultrasound units is 2.4 kWh/m^3 TWAS (0.041 kWh/kg DS or 148 kJ/kg DS), a value which is far below frequently published data collected from nonfull-scale, nonreal-life situations.

Renewable sources met 46.3% of Germany's power consumption in 2020 outperforming the government's goal set 10 years previously to meet at least a 35%. The total energy generation from solar, wind, biomass, geothermal, hydroelectric, and waste plants amounted to 251.7 TWh, up from 241.6 TWh a year earlier (www.bdew.de). Biogas production by fermentation of sludge and other organic substrates is now a prominent element of energy production in Germany. In 2011, renewable energies already had a share of 20%, of which 6% (= 36.7 billion kWh) came from biomass conversion. As of 2020, biomass contributed almost 50 billion kWh, 9% of the total power produced. Operators of WWTP are becoming energy rather than waste managers. Bamberg is an example (Figure 36.16) that demonstrates how the implementation of ultrasound together with other operational improvements (especially the integration of a new CHP station in October 2010) has contributed to the intensification of energy production at the plant.

36.3.2 Power ultrasound systems for biogas plants

Power ultrasound systems today are implemented on a number of agricultural biogas plants (ABP) in Germany to intensify anaerobic biological degradation of all kinds of biomass, such as maize, green waste, slurry, manure, etc. Ultrasound either enables an increase in biogas production with unchanged substrate supply or savings in the biomass feed without losses in biogas production. Hence, biogas is produced from renewable resources as a metabolic end product whose main component and actual energy carrier is methane (green energy).

The biological anaerobic degradation process of plant biomass is even slower than the digestion of sludge on a WWTP, because the solid plant biomass contains structured matter that is difficult for bacteria to break down. Therefore, HRTs on biogas plant digesters up to 100 days are quite common. The ultrasound oscillations not only affect the

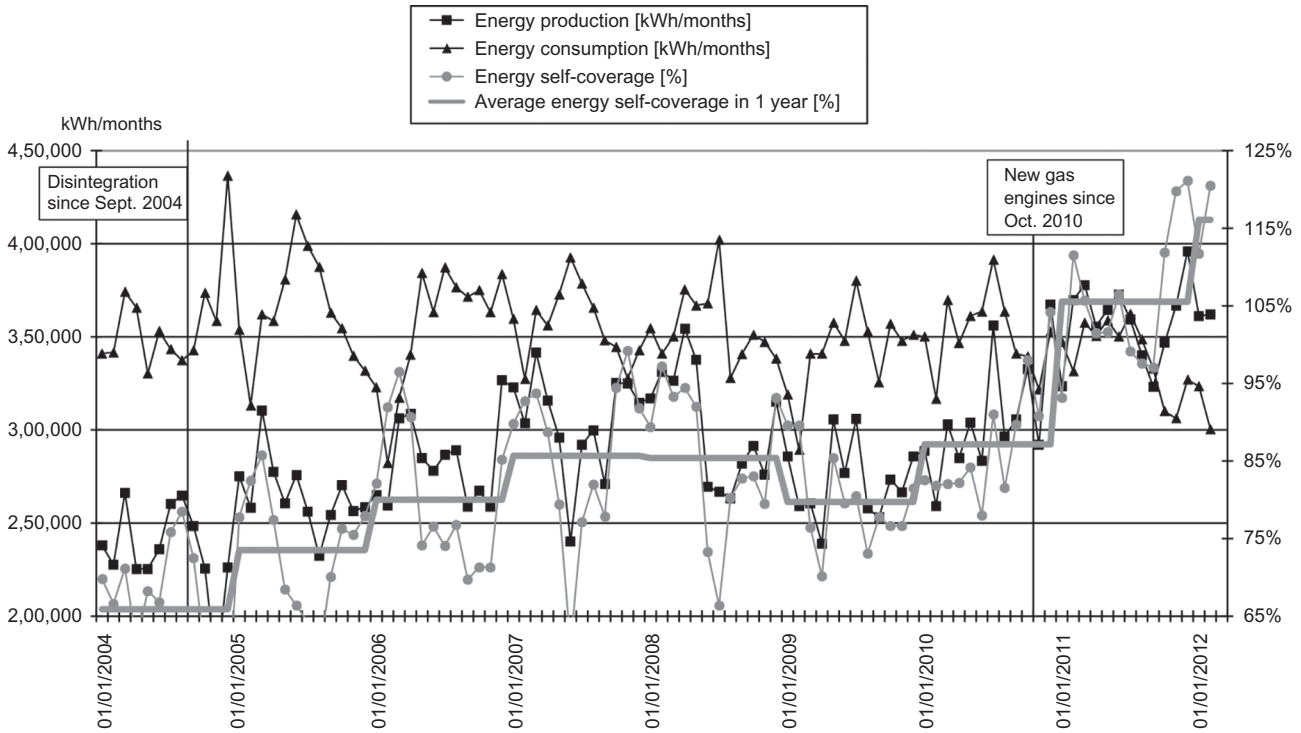


FIGURE 36.16 Time-variation curves of energy production, energy consumption, and energy self-coverage at Bamberg WWTP since the year 2004.

structure of the substrates (breakup of the plant cells) but also of the active microorganisms (stimulation through fluctuating sound pressure and cavitation, prevention of agglomerate formation, release of enzymes). Biological hydrolysis is therefore supported or entirely substituted with the use of ultrasound, so that accelerated and enhanced degradation takes place.

Due to the difficult to degrade agricultural biomass, the methane fraction produced by conventional biogas plants is usually not more than 50%. We normally observe a slight increase of its methane concentration (2%–3%) when sonication takes place, indicating the capacity of ultrasound action to stimulate the complex anaerobic decomposition of substrates.

How ultrasound technology can be integrated in biogas plants is shown schematically in Figure 36.17.

Due to the difficult structure of the raw biomass, we prefer to sonicate a partial flow of the fermented biomass from the main or secondary fermenter. The sonicated sludge is then returned in a loop to the main fermenter. This volumetric flow usually equals 30%–50% of the substrate quantity added daily. The standard ultrawaves ultrasound reactor (5 kW) is adequate for a 500-kW biogas plant, which normally takes a daily biomass load (e.g., maize silage) of between 25 and 30 tons.

In summary, the advantages are as follows:

- Intensification of fermentation
- Increase in biogas production
- Increase in methane content
- Substrate savings
- Viscosity reduction
- Lower power consumption for agitators and pumps

36.3.2.1 The Bordesholmerland biogas plant

Bordesholmerland biogas plant, a maize mono-fermentation plant, is presented here as a practical example and reference. Two parallel lines are operated, one of which (line 2) has been equipped with our standard ultrasound reactor. An aerial view of the biogas plant is presented in Figure 36.18. The test started in May 2011 with the objective of using less substrate while maintaining the same biogas production (6150 m^3 per day per line). A total of 36 m^3 per day of the secondary fermenter content are sonicated in line 2 and are returned to the fermenter. Since the ultrasound system has been in operation, the daily substrate supply has decreased by 4 t/day (17%) compared to line 1, while biogas production remained unchanged. At the same time, the methane content of the biogas has increased by 2%–53%. The acoustic irradiation has also caused a reduction of the viscosity of the fermenter content, which has reduced the power consumption of the agitators and pumps. In total, the net economic benefit of the line equipped with the ultrawaves ultrasound system has increased significantly. More information is available at www.ultrawaves.de.

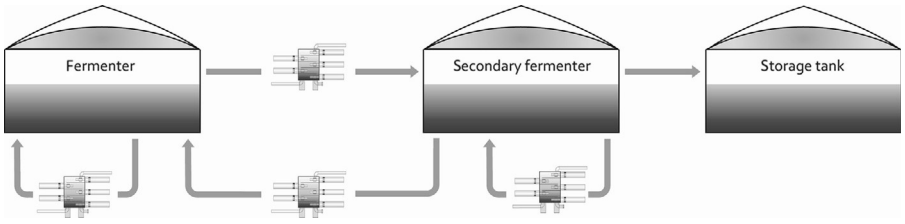


FIGURE 36.17 Integration of ultrasound technology into agricultural biogas plants (ABP).



FIGURE 36.18 An aerial view of the Bordesholmerland biogas plant in North Germany.

36.4 Aerobic biological processes: Full-scale application

36.4.1 Nitrogen removal

Upon ultrasound impact, the microorganisms in the activated sludge get stressed and the colonies break apart. In addition, it is believed that the biological processes in the sludge are stimulated by the release of intercellular material from the damaged cells. Specifically, released enzymes are thought to play a significant role in stimulating various biological processes. The destroyed cellular material itself serves as a nonforeign carbon source for the remaining viable microorganisms in the sludge. In this way, we are able to reach an intensified denitrification. We are promoting this innovative approach by sonicating a fraction of the WAS before returning it to the anoxic sludge tank (Kemalides, 2007), which entails providing an internal carbon source to the denitrifying bacteria. The mechanisms governing the reaction are exhibited through the ultrasonic treatment suppressing nitrite-oxidizing bacteria which enhances the activity of ammonia-oxidizing bacteria (Zheng et al., 2019). Many researchers have published their research on achieving stable mainstream autotropic nitrogen removal by partial nitration and anammox. Ultrasonication is now well-established for enhancing sewage sludge disintegration and subsequent anaerobic digestions (Pilli et al., 2011) with at least 20 full-scale and 17 pilot-scale installations, the majority being in Germany (Zhen et al., 2017).

36.4.1.1 The Bünde WWTP

One ultrawaves ultrasound reactor (5 kW) has been in operation at the Bünde WWTP (actual load 54,000 PE) since September 2006. The nitrogen elimination at the plant occurs via intermittent denitrification. The reason for implementing the ultrasound technology was that denitrification efficiency was suffering as a result of insufficient carbon source. Using sonicated TWAS as an internal carbon source to improve denitrification was seen as a viable option. In total, 30% of the daily TWAS stream was sonicated and conveyed back to the activated sludge tank, providing the process with the carbon source needed.

After sonication ceased in July 2006, the concentrations again climbed to the preultrasound levels observed in 2005. Sonicating a partial stream of the TWAS before it goes back to the activated sludge tank provided the carbon source necessary to facilitate the denitrification. Figure 36.19 shows the design of the Bünde WWTP system.

Utilizing sonicated TWAS as an internal carbon source for the purpose of improving denitrification yielded several positive effects. First, a significant reduction of nitrogen in circulation was achieved; denitrification had been improved. In addition, there were secondary effects that contributed to a higher efficiency of plant operations. Excess sludge was reduced by 25% and foaming and bulking sludge in the activated sludge tank was virtually eliminated.

It is apparent that several positive advantages were reached through the usage of ultrasonically treated sludge. Economically, reimbursement of the investment was immediate, as a result of reduced sewage fees associated with sludge disposal and nitrogen concentrations. Hence, the advantages are clear from an economic perspective as well as at the operational level. As an additional economic advantage, the plant avoided the need to purchase an external carbon source. The plant was ultimately able to conserve resources, optimize the existing process, and acquire a higher degree of operational stability through the incorporation of this ultrasound technology.

36.4.2 Combating filamentous bacteria and bulking sludge: The Seevetal WWTP

Seevetal WWTP lies about 25 km southwest of Hamburg. It has a capacity of 1,65,000 PE and biologically treats municipal sewage (activated sludge including nitrogen removal). Normal turnaround for the sludge is around 25 days. In winter the formation of bulking sludge on the activated sludge tanks is quite common. Additional efforts by the operating staff are required to remove the sludge layers from the surface of the tanks.

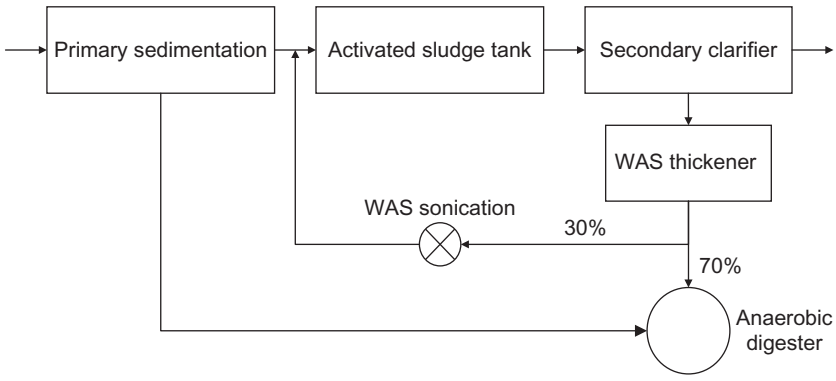


FIGURE 36.19 Schematic diagram of wastewater and sludge flows on Bünde WWTP.

In 2008, intensive tests were conducted with a standard 5-kW ultrasound unit in order to demonstrate its potential to combat bulking sludge. A detailed presentation of the design and results of this work is given by Neis (2007). At Seevetal WWTP, there are a number of activated sludge tanks that are operated in parallel. This was a perfect setting to demonstrate the effect of ultrasound on bulking sludge. One tank was supplied with sonicated return activated sludge (RAS), and the parallel one received the normal return sludge. The idea was to apply ultrasound with rather low energy on a small fraction (approximately 1%) of the return sludge flow, which, of course, was populated by filamentous organisms. By this method, a loop was set up, and sonicated (and therefore stressed) biomass was fed permanently to the activated sludge tank. The results showed that the high-power ultrasound unit (25–50 W/cm^2) could selectively eliminate the filamentous bacteria without hampering the treatment efficiency. The bulking sludge disappeared rapidly on the "sonicated" tank, as is shown in Figure 36.20.

36.5 Development and design of a full-scale ultrasound reactor

Although research with mathematical modeling of sound fields in ultrasonic reactors has been performed in the past, the creation and distribution of cavitation bubble fields still cannot be described adequately by theoretical considerations. Some available data are valid for a single-phase system like water (Keil, 1999). However, sewage sludge is a complex three-phase system consisting of microbial cells (solids) which are suspended in the sludge water phase. The water phase itself is composed of any number of inorganic and organic soluble substances. Due to microbial activities, dissolved and suspended gases are also always present in the sludge suspension. For ultrasonic disintegration of biological sludge cells, the development of a full-scale reactor today has to be based on empirical know-how.

Usually, huge volumes of biosolids suspensions (i.e., 150 m^3/day at 5% solids concentration for a typical sewage treatment plant of 1,00,000 PE) are produced at WWTPs. Sonication of biomass must ensure a sufficient degree of cell disintegration even in the case of varying sludge properties, like solids concentration or viscosity. Table 36.2 highlights some requirements for full-scale operation of ultrasound reactors at WWTPs.

Because it is known that mechanical shear forces (transient cavitation) are mainly responsible for microbial cell disintegration, the recommendation is to apply low frequency, high intensity ultrasound. Consequently, we prefer a sonotrode system ("horn" type) as compared to flat or push–pull transducers. Transient cavitation can only be produced in a high energy microenvironment in the field near the oscillating body. Therefore, our ultrasound reactor design is based on the determination of the cavitation field geometry.

Our first full-scale ultrasound reactor system is shown schematically in Figure 36.21. The full view is already shown in Figure 36.14a and b. The compact reactor has a volume of 29 L and is equipped with five 20-kHz sonotrodes. Each sonotrode is supplied by a 2-kW generator. The intensity can be adjusted in a range from 25 to 50 W/cm^2. The sludge is pumped up through the reactor channels, preventing accumulation of produced gas bubbles by degassing of the sludge water phase.

Hydraulic residence time distribution (tracer) tests were performed in order to optimize the flow through behavior of

TABLE 36.2 Requirements for full-scale ultrasound reactor operation on WWTP

▪ Capacity for treating large volumetric sludge flows
▪ Capacity to accept varying sludge properties (solids concentration, viscosity)
▪ Removal of coarse and shaggy impurities prior to sonication to avoid reactor blocking
▪ Automatic control of operation

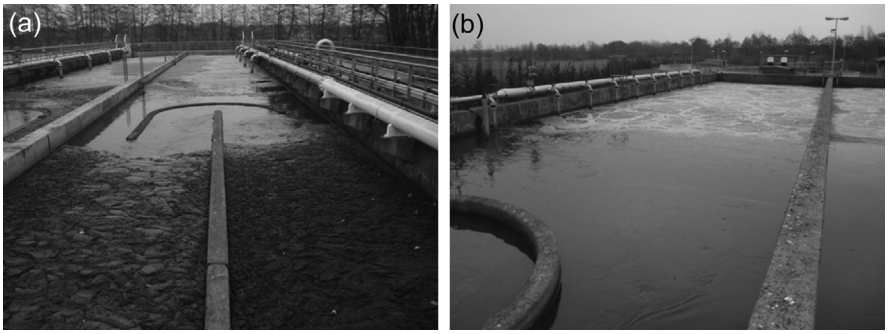


FIGURE 36.20 Activated sludge tanks of Seevetal WWTP during (a) conventional operation and (b) return activated sludge (RAS)-sonication.

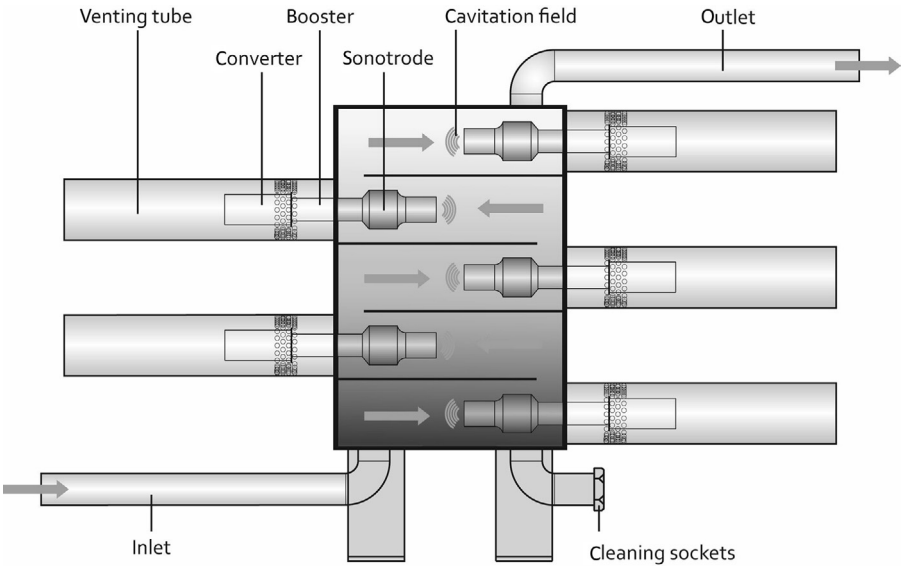


FIGURE 36.21 Schematic diagram of the full-scale ultrasound reactor (Ultrawaves Water and Environmental Technologies, Hamburg, Germany).

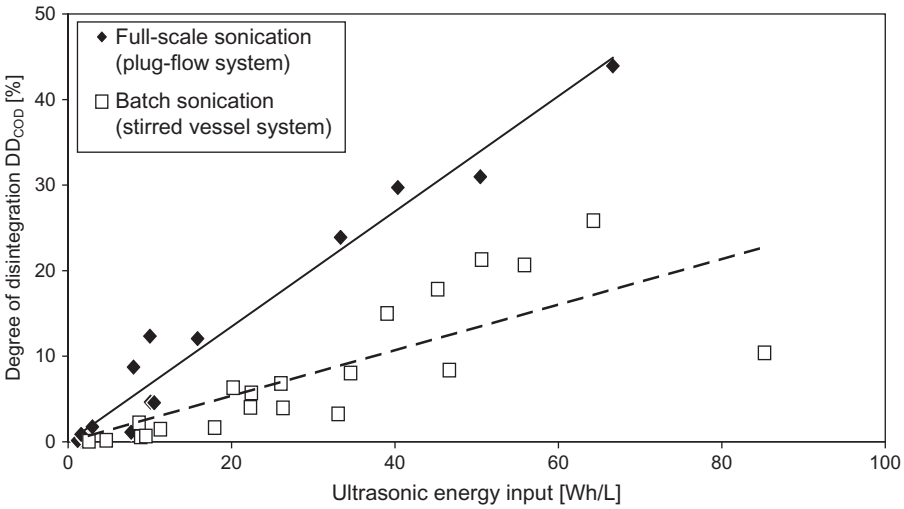


FIGURE 36.22 Sludge cell disintegration in full-scale continuous plug-flow-type ultrasonic reactor as compared to batch-type sonication using the same sonotrode system.

the reactor. It is known from other investigations that ultrasonic breakup of microbial cell walls follows first-order reaction kinetics (Tiehm et al., 2001). Consequently, we tried to realize hydraulic plug-flow behavior in the ultrasound tank. The flow was toward the transducers and therefore against the propagation of the cavitation field. Experiments showed that in this way, the degree of cell disintegration was higher when compared to the parallel flow. In the presence of a cavitation bubble field, the hydraulic characteristics of the reactor did not change significantly. The hydraulic residence time distribution shifted even more toward a plug-flow type. Once cavitation energy dissipation was high enough to destroy bacterial cell walls, the disintegration reaction was fast. However, there was a minimum hydraulic residence time necessary, mainly determined by the maximum flow rate through the reactor, which still allowed maintenance of a constant and homogenous distribution of the cavitation bubble field, without "carrying away" the bubbles. Under this assumption, a minimum hydraulic sludge residence time of about 30 s should be adopted (Nickel and Neis, 2007).

It is interesting to note that the continuously operated plug-flow reactor shows significantly better cell disintegration when compared to batch-type sonication tests with the same type of sonotrode immersed into a fully mixed vessel (Figure 36.22).

36.6 An emerging technology: Ballast water treatment

Ballast water (BW) represented the most significant source of transport of nonindigenous organisms into the marine ecosystem. As a serious threat to the environment and human health, recognition of this problem by governmental and nongovernmental bodies, industries, and the global scientific community prompted changes in regulations managing BW. To combat this, the International Maritime Organization (IMO) adopted the International Convention for the Control and Management of Ship's Ballast Water and Sediments in 2017. The aim of the Convention is to prevent, minimize, and ultimately eliminate the transfer of harmful aquatic organisms and pathogens through the control and management of ship's BW and sediments. Ultrasound technology is widely being considered as part of a hybrid treatment system, preceded by filtration, where cavitation can kill harmful microorganisms in ballast water (Osman et al., 2016). Despite disadvantages such as large energy consumption, multiple products have been recognized in the research and development of ballast water management system including the BSKY management system which involves cyclonic separation plus ultrasonic and ultraviolet treatments and the Qingdao Hadeway Ocean Guard management system which uses filtering and ultrasonic cavitation to produce hydroxyl to kill microorganisms.

36.7 Sources of further information and advice

Foladori, P., Andreottola, G., Ziglio, G., 2010. Sludge Reduction Technologies in Wastewater Treatment Plants. IWA Publishing, UK.

Hood, E.E., Nelson, P., Powell, R., 2011. Plant Biomass Conversion. John Wiley & Sons, USA.

Seviour, R.J., Nielsen, P.H., 2009b. Microbial ecology of activated sludge. IWA Publishing, UK.

Tchobanoglous, G., Burton, F.L., Stensel, H.D., 2003. Wastewater Treatment and Reuse. McGraw-Hill Profes sional, USA.

References

Banduch, I., 2011. Die Wirkung von Ultraschall auf die mikrobiologische Diversität und Abbauleistung eines biologischen Reaktors zur Abwasserreinigung (Ph.D. thesis). TU Hamburg-Harburg, Hamburger Berichte zur Siedlungswasserwirtschaft, p. 78.

Banduch, I., Neis, U., 2012. Die Wirkung von Ultraschall auf Belebtschlamm-Biomasse. gwf-Wasser/Abwasser 6, 706–713.

Braguglia, C.M., Gianico, A., Mininni, G., 2012. Comparison between ozone and ultrasound disintegration on sludge anaerobic digestion. J. Environ. Manag. 95 (Suppl), 139–143.

Chiu, Y.-C., Chang, C.-N., Lin, J.-G., Huang, S.-J., 1997. Alkaline and ultrasonic pretreatment of sludge before anaerobic digestion. Water Sci. Technol. 36 (11), 155–162.

Friedrich, H., Potthoff, A., Friedrich, E., Hielscher, H., 1999. Ultrasound in environmental engineering. In: Tiehm, A., Neis, U. (Eds.), TU Hamburg-Harburg Reports on Sanitary Engineering. vol. 25. GFEU at Technische Universität Hamburg-Harburg, Hamburg, Germany, pp. 245–255 (ISSN 0724-0783).

Jiang, J.G., Zhang, Y., Zhang, Q.F., Chen, M.Z., Du, X.J., 2008. Improvement of disintegration and anaerobic digestion for sewage sludge with ultrasonic generator. Huan Jing Ke Xue 29 (10), 2815–2819.

Keil, F.J., 1999. Modelling of sound fields. In: Ultrasound in Environmental Engineering (Ed.), TU Hamburg-Harburg Reports on Sanitary Engineering, Vol. 25. GFEU at Technische Universität Hamburg-Harburg, Hamburg, Germany, pp. 63–76 (ISSN 0724-0783).

Kemalides, E., 2007. Biologische Abwasserreinigung—Erfahrungen auf der KA Bünde. In: Erfahrungen mit der Desintegration von Belebt- und Überschussschlamm, Workshop Abfall/Klärschlamm, Osnabrück, Tagungsband, pp. 31–46.

King, R.O., Forster, C.F., 1990. Effects of sonication on activated sludge. Enzym. Microb. Technol. 12 (2), 109–115.

Lehne, G., Müller, J., 1999. Ultrasound in environmental engineering. In: Tiehm, A., Neis, U. (Eds.), TU Hamburg-Harburg Reports on Sanitary Engineering. vol. 25. GFEU at Technische Universität Hamburg-Harburg, Hamburg, Germany, pp. 205–215 (ISSN 0724-0783.).

Liu, C., Xiao, B., Dauta, A., Peng, G., Liu, S., Hu, Z., 2009. Effect of low power ultrasonic radiation on anaerobic biodegradability of sewage sludge. Bioresour. Technol. 100 (24), 6217–6222.

Morgan, J.W., Forster, C.F., 1992. A comparative study of the sonication of anaerobic and activated sludges. J. Chem. Technol. Biotechnol. 55 (1), 53–58.

Neis, U., 2007. Bekämpfung von Bläh- und Schwimmschlamm mit Ultraschall, Bericht der DWA Landesgruppe Nord zum Norddeutschen Symposium Microthrix II—Neueste Erkenntnisse zum Betrieb von Belebungsanlagen unter erschwerten Bedingungen— Schaum. Schwimm- und Blähschlamm.

Neis, U., Nickel, K., Tiehm, A., 2001. Ultrasonic disintegration of sewage sludge for enhanced anaerobic biodegradation. In: Mason, T., Tiehm, A. (Eds.), Advances in Sonochemistry. Ultrasound in Environmental Protection, vol. 6. JAI Press, Inc., USA, pp. 59–90.

Neis, U., Banduch, I., Nickel, K., 2012. Stimulation of Aerobic and Anaerobic Processes by Ultrasound. E-WAter, Electronic Publications of the European Water Association, Bonn, Germany.

Nickel, K., Neis, U., 2007. Ultrasonic disintegration of biosolids for improved biodegradation. Ultrason. Sonochem. 14 (4), 450–455.

Osman, H., Lim, F., Lucas, M., Balasubramaniam, P., 2016. Development of an ultrasonic resonator for ballast water disinfection. Phys. Procedia 87, 99–104.

Pilli, S., Bhunia, P., Yan, S., LeBlanc, R.J., Tyagi, R.D., Surampalli, R.Y., 2011. Ultrasonic pretreatment of sludge: a review. Ultrason. Sonochem. 18 (1), 1–18.

Seviour, R.J., Nielsen, P.H., 2009. Microbial Ecology of Activated Sludge. IWA Publishing, London, UK.

Shimizu, T., Kudo, K., Nasu, Y., 1993. Anaerobic waste activated sludge digestion—a bioconversion mechanism and kinetic model. Biotechnol. Bioeng. 41 (11), 1082–1091.

Tiehm, A., Nickel, K., Zellhorn, M., Neis, U., 2001. Ultrasonic waste activated sludge disintegration for improving anaerobic stabilization. Water Res. 35 (8), 2003–2009.

Wagner, M., Amann, R., 1996. Die Anwendung von in-situ-Hybridisierungssonden zur Aufklärung von Struktur und Dynamik der mikrobiellen Biozonosen in der Abwasserreinigung. In: Lemmer, H., Griebe, T., Flemming, H.-C. (Eds.), Oekologie der Abwasserorganismen. Springer Verlag, Berlin, pp. 93–110.

Zhen, G., Lu, X., Kato, H., Zhao, Y., Li, Y.Y., 2017. Overview of pretreatment strategies for enhancing sewage sludge disintegration and subsequent anaerobic digestion: current advances, full-scale application and future perspectives. Renew. Sustain. Energy Rev. 69, 559–577.

Zheng, M., Duan, H., Dong, Q., Ni, B.-J., Hu, S., Liu, Y., Huang, X., 2019. Effects of ultrasonic treatment on the ammonia-oxidizing bacterial (AOB) growth kinetics. Sci. Total Environ. 690, 629–635.

Further reading

BDEW Home, 2021. Available from: http://www.bdew.de/. (Accessed 24 September 2021).

Bräutigam, P., Franke, M., Stolle, A., Schneider, R.J., Ondruschka, B., 2012. Degradation of the antiepileptic drug Carbamazepin in water by hydrodynamic-acoustic-cavitation (HAC). In: Proceedings of the 13th Conference of the European Society of Sonochemistry, Lviv, Ukraine.

Elliott, M., 2003. Biological pollutants and biological pollution—an increasing cause for concern. Mar. Pollut. Bull. 46 (3), 275–280.

GloBallast Home, 2014-2017. Available from: http://globallast.imo.org/. (Accessed 24 September 2021).

King, K., 2005. The Cell Wall Structure of Gram-Positive and Gram-Negative Bacteria, Food Microbiological United Internship. University of Hohenheim.

Ruiz, G.M., Rawlings, T.K., Dobbs, F.C., Drake, L.A., Mullady, T., Huq, A., Colwell, R.R., 2000. Global spread of microorganisms by ships. Nature 408 (6808), 49–50.

Zheng, M., Wu, S., Dong, Q., Huang, X., Yuan, Z., Liu, Y., 2019. Achieving mainstream nitrogen removal via the nitrite pathway from real municipal wastewater using intermittent ultrasonic treatment. Ultrason. Sonochem. 51, 406–411.

Chapter 37

The use of power ultrasound for green organic synthesis: Sonochemical organic reactions in aqueous media

G. Cravotto and Z. Wu

Department of Drug Science and Technology, University of Turin, Turin, Italy

37.1 Introduction

Many chemicals in the traditional synthesis of fine chemicals and drugs, including reactants, solvents, and catalysts, are hazardous, toxic, unsafe, or expensive. Chemical production requires huge energy consumption and generates substantial waste (Draye et al., 2020). According to the 12 principles of green chemistry that emerged in 1998, solvent-free, water-mediated or aqueous media, catalyst-free, 1-pot multicomponent reactions (MCRs), mild or ambient conditions, room temperature (RT), and alternative energy inputs, such as microwaves (MW), ultrasound (US), etc., are important keywords in the field of organic synthesis. The aims here are to obtain excellent yields and selectivity with simple operations and workup in short reaction times while reducing or avoiding the use and generation of hazardous materials via environmentally benign strategies (Gawande et al., 2013; Hasaninejed et al., 2013; Anastas and Eghbali, 2010; Patel et al., 2021; Kidwai, 2006). Recently, the preparation and application of ionic liquids (ILs), organocatalysts, and metal nanocatalysts that are immobilized on biodegradable β-cyclodextrin, cellulose, chitosan, and recyclable magnetic ferrites have been particularly remarkable in green chemistry as they allow catalysts to be reused or biologically degraded to minimize the formation of waste (Varma, 2016; Chate et al., 2016; Akolkar et al., 2020; Hernández and Juaristi, 2012; Devi et al., 2020; Mondal et al., 2020). All the above green approaches should be combined to attain the best chemical and environmental efficiency, but ideal reactions should be simply accomplished in water or solvent-free at RT, either with eco-friendly catalysts or without catalysts and other boosters (Gawande et al., 2013; Sapkal and Kamble, 2020; Banerjee, 2020; Mosallanezhad and Kiyani, 2019; Ranu and Banerjee, 2007).

Water-mediated organic synthesis (WMOS) has long been highlighted since water is abundant, inexpensive, non-toxic, non-flammable, safe and environmentally benign, effective, readily available, separable, and recyclable (Sapkal and Kamble, 2020; Ranu and Banerjee, 2007; Barange et al., 2011; Sharafian et al., 2021). As early as 1931, Diels and Alder reported the cycloaddition of furan and maleic anhydride in water (Diels and Alder, 1931). Compared to conventional solvents, the unique physicochemical properties of water, such as hydrogen bonding, high dielectric constant and polarity, heat capacity, low viscosity, etc., initiate and excite the reactivity of organics (Ranu and Banerjee, 2007; Sahiba et al., 2021). For example, the formation ofthe H-bonds between water and the carbonyl moiety, as well as the N-atom of amines, has been proposed to enhance the electrophilicity of the β-carbon of unsaturated compounds and the nucleophilicity of amines, thus accelerating the aza-Michael reaction in water (Bandyopadhyay et al., 2012). WMOS is divided into two categories: reactions "in water" and reactions "on water." "In-water" reactions are those with fully soluble reactants in water (homogenous reactions), whereas "on-water" reactions involve soluble and insoluble reactants in water (multi-phases, emulsified, or heterogeneous reactions) (Sahiba et al., 2021; Chandrakar et al., 2020; Li et al., 2016; Hooshmand et al., 2019; Chanda and Fokin, 2009). Water can frequently be combined with other green solvents, such as ethyl lactate, to form co-solvent or aqueous media for organic synthesis (Li et al., 2016; Dolzhenko, 2020). In the 1980s, Rideout et al. explored the acceleration of Diels-Alder reactions in suspensions and aqueous solutions, and the effects of hydrophobicity on reaction rates (Breslow et al., 1983; Rideout and Breslow, 1980). Water and aqueous media have been employed as green strategies, to reduce or avoid the adverse impact of organic synthesis on our environment, in a variety of organic syntheses for

Power Ultrasonics. https://doi.org/10.1016/B978-0-12-820254-8.00033-6
Copyright © 2023 Elsevier Ltd. All rights reserved.

the formation of C—C, C—O, or C—N bonds via coupling reactions or condensations, such as cycloadditions, Michael reactions, Aldol reactions, Suzuki reactions, MCRs, etc. (Sahiba et al., 2021; Kidwai et al., 2007).The objectives of green organic chemistry with water media have been achieved in terms of atom economy, yields, selectivity, reaction rates, etc. (Sahiba et al., 2021; Chandrakar et al., 2020; Kerru et al., 2019).

In many cases, however, the poor solubility of reactants in water limits organic synthesis under ambient conditions, since the mass transfer is relatively poor in heterogeneous reactions "on water" (Campos and Berteina-Raboin, 2020). Sonication has long been used as an intensification approach for organic syntheses, including the Knoevenagel condensation, Michael addition, selective hydrogenation, etc. (Wu et al., 2017, 2019; Pelliccia et al., 2018; Li et al., 2005). Sonochemical effects have been attributed to the growth and violent collapse of numerous cavitational bubbles, resulting in extremely high local temperatures and pressures, powerful shockwaves, microjets, and the formation of free radicals, etc., which then enhance the solubility, diffusivity, mass transfer, and the cleaning of the catalyst surface (Bandyopadhyay et al., 2012; Cravotto et al., 2015; Pharande et al., 2017; Lupacchini et al., 2017; Suslick, 1990; Mason, 1997). Sonochemical synthesis and US-assisted synthesis are therefore conducted for shorter reaction times under ambient conditions, and result in simple workup (separation and purification), higher yield and selectivity, lower by-product and waste formation, and thereby significantly contribute to the synthesis of bioactive and pharmaceutical compounds in green chemistry (Barange et al., 2011; Sharafian et al., 2021; Bandyopadhyay et al., 2012; Li et al., 2016; Lupacchini et al., 2017; Joshi et al., 2010).

US (15–1000 kHz) can not only be used directly for organic synthesi but also to prepare catalysts for organic synthesis (Ziarati et al., 2013; Wu et al., 2014, 2015; Chate et al., 2011). In particular, sonication exerts notable effects in one-pot MCRs with/without a solid catalyst (Ramazani et al., 2016; Shabalala et al., 2015; Esmaeilpour et al., 2015). Although the use of non-toxic, less toxic, or recoverable catalysts, such as ILs and magnetic nanocatalysts, is undoubtedly a crucial requirement in green organic synthesis (Wu et al., 2018; Elhamifar et al., 2018), catalyst-free organic synthesis is even more favorable for our environment. Therefore, sonication has long been investigated as a means to partly or fully replace catalysts and accelerate organic reactions (Banerjee, 2017a; Xie et al., 2017).

Although the US-assisted synthesis without solvents is more favorable for our environment, the effects of green solvents, such as water, ILs, ethylene glycol (EG) and its oligomers, glycerol, and other bio-based solvents, on the yield, selectivity, and reaction times of US-assisted organic synthesis have been widely investigated (Campos and Berteina-Raboin, 2020; Cravotto et al., 2015; Lupacchini et al., 2017; Azizi et al., 2014), On the other hand, reaction conditions can alter solvent properties. For example, water becomes a superior solvent for organic reactions at high temperatures and pressures (Campos and Berteina-Raboin, 2020). The solubility of hydrophobic organics is low in viscous glycerol, which is often mixed with other solvents for use as a co-solvent (Shaikh et al., 2020). Fortunately, sonication and its combination with MW can reduce or eliminate the limitations of glycerol as a solvent in the temperature range of 70–100°C (Shaikh et al., 2020; Cravotto et al., 2011).

A large number of investigations into the US-assisted WMOS have been performed, and the combination of sonication and water media holds the key to the development of environmentally friendly organic synthesis (Barange et al., 2011; Cravotto et al., 2015; Banerjee, 2017b). The advantages of the US-assisted WMOS, such as good-to-excellent yields, improved selectivity, being environmentally friendly, simple operation and workup, as well as shorter reaction times in green solvents at mild reaction conditions, have always been highlighted. In particular, the one-pot MCRs have been extensively promoted using sonication in water or aqueous media with organocatalysts (Joshi et al., 2010; Palmisano et al., 2011; Kasar and Thopate, 2019; Jin et al., 2004, 2006; Datta and Pasha, 2012; Gracious et al., 2020; Dandia et al., 2011; Anna et al., 2009), ILs catalysts (Nikoofar and Shahriyari, 2021), recyclable heterogeneous catalysts (Edrisi and Azizi, 2020; Mahdavinia et al., 2009; Arya et al., 2012), nanocatalysts (Rostamizadeh et al., 2010; Maleki et al., 2018), or without catalyst (Sharafian et al., 2021; Xie et al., 2017; Banitaba et al., 2013; Jaiswal et al., 2017; Maury et al., 2021; Rostamnia and Lamei, 2011; Chauhan et al., 2020; Zou et al., 2011; Safari et al., 2012; Jin et al., 2005). Some US-assisted one-pot MCRs contain several name reactions, including Knoevenagel condensation, Michael addition, and cyclization sequences (Li et al., 2020a,b). Organic name reactions are powerful and fundamental pathways for the formation of C—C, C—N, C—O, and C—S bonds, and cyclization (Andrade and Martins, 2020). Sonication also promoted many water-mediated organic name reactions, including aza-Michael reactions (Bandyopadhyay et al., 2012), Ugi-azide reactions (Pharande et al., 2017), Suzuki coupling reactions (Bai and Wang, 2005), Heck coupling reactions (El-bendary et al., 2021), Aldol reactions (Cravotto et al., 2003), Hantzsch condensations (Aute et al., 2020), etc. This work covers several key organic name reactions that involve the formation of C—C and C—N bonds, as well as cyclization so that the efficiency and advantages of the US-assisted WMOS in green chemistry can be exhibited.

37.2 Suzuki coupling reactions

The Suzuki reaction is a Pd-catalyzed cross-coupling of arylboronic acids and organohalides under basic conditions to form a C—C bond. It is also named the Suzuki-Miyaura reaction or Suzuki coupling. Similar C—C cross-coupling reactions include the Sonogashira coupling and Heck coupling reactions (Andrade and Martins, 2020). The Suzuki coupling is an efficient and versatile reaction for preparing unsymmetrical biaryls and the intermediates of fine chemicals and pharmaceuticals, such as substituted biphenyls, polyolefins, and styrenes (Miyaura and Suzuki, 1995). However, this reaction was once restricted by expensive Pd catalysts and boronic acid. The constant effort has therefore been made to improve catalysts, reactants, media, and reaction techniques, making the Suzuki coupling efficient and eco-friendly for use in industrial processes (Bai and Wang, 2005; Li, 2002; Organ et al., 2000; Bauer et al., 2001). Poláčková et al. (2005) reported the enhanced effect of sonication on the Pd-catalyzed Suzuki coupling of arylboronic acid with halobenzenes (Scheme 37.1).

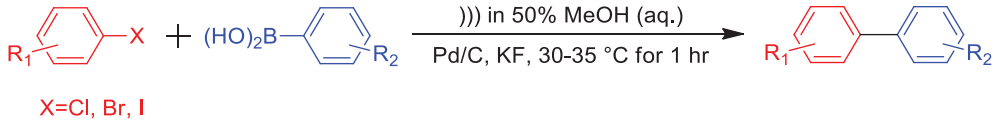
A yield comparison using different catalysts, bases, and solutions led to the US-assisted Suzuki coupling being performed with a Pd/C catalyst and KF as the base in a 50% MeOH (methanol) aqueous solution. For the Suzuki coupling of iodobenzene (1 mmol) with 4-methoxyphenylboronic acids (1.1 mmol), a 66% isolated yield of 4-methoxybifenyl was achieved using sonication with 10 mol% Pd/C and 6 mmol of KF in an ultrasonic cleaning bath (37–42 kHz, 150 W), while only 22% yield was obtained with stirring, all other conditions being equal. Under refluxing conditions, an 87% yield was achieved after 4 h. By contrast, a 95% yield was achieved at 30–35°C after 1 h sonication with 15 mol% Pd/C and 9 mmol of KF in a 50% MeOH aqueous solution. Under the above sonication conditions, most of the Suzuki couplings of substituted iodobenzene with phenylboronic acid or 4-methoxyphenylboronic acid took place successfully with yields of 67% and 62%–95%, respectively (Poláčková et al., 2005). However, only 21% and 23% yields were obtained in the reactions of phenylboronic acid with 4-nitro-iodobenzene, or 4-trifluoromethyl-phenylboronic acid (with strong electron-acceptor) with 4-methyl-iodobenzene (Poláčková et al., 2005).

When bromobenzene replaced iodobenzene, the isolated yield of the Suzuki coupling of 4-methoxyboronic acid (0.5 mmol) with bromobenzene (0.5 mmol), catalyzed with $PdCl_2$ (5 mol%), K_2CO_3 (1.5 mmol), and tetrabutylammonium bromide (TEBA, 1 mol%), decreased to 68% under the optimal conditions: sonication at 30–35°C for 1 h in 50% toluene/water biphasic media. In contrast, a 50% yield can be achieved even in water under sonication. However, only a 6% yield was obtained in 50% toluene/water biphasic media with stirring. Moreover, the yield decreased to 43% without TEBA (triethylbenzylammonium chloride) even when using sonication, indicating that both sonication and phase-transfer catalyst (PTC) play a vital role in the heterogeneous Suzuki coupling thanks to their enhanced effect on mass transfer (Poláčková et al., 2005).

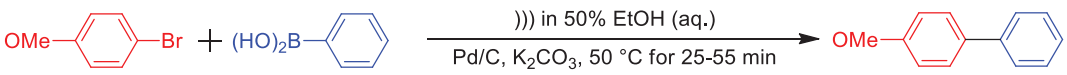
The coupling of substituted bromobenzenes (0.5 mmol) with 4-methoxyphenylboronic acid (0.5 mmol) catalyzed with $PdCl_2$ (5 mol%), K_2CO_3 (1.5 mmol), and TEBA (1 mol%) occurred, only para-substituted, with —CHO and $—COCH_3$, bromobenzenes reached comparable yields (67% and 53%) as unsubstituted bromobenzene in 50% toluene/water biphasic media at 30–35°C after 1 h sonication. Other bromobenzenes that were substituted with $—CH_3$, $—N(CH_3)$, $—CH(OCH_2)_2$, and $—CF_3$ exhibited lower yields (22%–38%). Besides, the coupling of chlorobenzene and 4-methoxyphenylboronic acid under the above conditions did not show any promising results (Poláčková et al., 2005).

Sancheti and Gogate (2018) studied the US-assisted Suzuki-Miyaura coupling of 4-bromoanisole and phenylboronic acid, catalyzed with Pd/C without any PTC in aqueous EtOH (ethanol) solutions (Scheme 37.2).

The effects of reaction conditions, such as ultrasonic device and power, temperature, catalyst loading, solvent composition, various bases, and the molar ratio of reactants, on the Suzuki coupling, were studied (Sancheti and Gogate, 2018). In terms of the conversion efficiency of



SCHEME 37.1 Pd-catalyzed Suzuki coupling of arylboronic acid with halobenzenes in aqueous methanol solutions under sonication (Poláčková et al., 2005).



SCHEME 37.2 Ultrasound-assisted Suzuki-Miyaura coupling of 4-bromoanisole and phenylboronic acid, catalyzed with Pd/C in aqueous ethanol solutions (Sancheti and Gogate, 2018).

4-bromoanisole (1.0 mmol) to 4-methoxybiphenyl with phenylboronic acid, the optimal conditions were found using single-factor tests and an ultrasonic bath (22 kHz): US power of 40 W, reaction temperature of 50°C, Pd/C loading of 1.5 mol%, the ratio of 4-bromoanisole to phenylboronic acid of 1:1.5, and K_2CO_3 (2.0 mmol) in 10 mL of 50% EtOH. Under such optimal conditions, 98% of the conversion was achieved in less than 35 min (Sancheti and Gogate, 2018). The reaction time needed to reach 98% conversion and the energy efficiency (cavitational yield) of the conventional stirring and various sonication processes were compared under optimum conditions, and the results are listed in Table 37.1.

As shown in Table 37.1, the reaction times needed to reach 98% conversion using sonication with the ultrasonic horn, ultrasonic bath with stirring, and sole ultrasonic bath were 25, 35, and 55 min, which are much shorter than using the conventional stirring process (70 min). Moreover, the energy efficiencies of sonication are higher than those of the stirring process. Furthermore, the change in morphology and particle size of the catalyst after sonication and scale-up potential has been discussed in this work, and positive and promising results were gained.

El-bendary et al. (2021) reported a US-assisted Heck coupling reaction in water that was catalyzed by the $[Pd(paOH)_2]\cdot 2Cl$ complex, which was prepared via self-assembly with $PdCl_2$ and pyridine-2-carbaldehyde-oxime (paOH). The Pd(0)-colloidal catalyst, produced in situ by sonication from the $[Pd(paOH)_2]\cdot 2Cl$ complex, was well dispersed and active, leading to the reactions being accelerated and having an increased yield. It is worth noting that Suzuki and Heck cross-coupling reactions can also be accomplished in short time (5–20 min) in water or aqueous media at RT with superior Pd catalysts, which are recyclable and reusable, such as Pd nanoparticles that are immobilized on magnetic chitosan (Hajipour et al., 2018), Pd-loaded magnetic magnesium ferrite nanoparticles (Dasari et al., 2020), and nanometallic Pd-Ni@2-mercaptoethanol (Said et al., 2020).

TABLE 37.1 Effect of type of ultrasonic irradiation on cross-coupling of 4-bromoanisole with phenylboronic acid and comparison with the conventional approach

No.	Process	Time[a] (min)	Cavitational yield (μg/kJ)
1	Conventional stirring (without ultrasound)	70	959.63
2	Direct sonication (ultrasonic horn without stirring)	25	2821.3
3	Indirect sonication (ultrasonic bath with stirring)	35	983.0
4	Indirect sonication (ultrasonic bath without stirring)	55	1282.4

[a]*Time required for maximum (98%) conversion.*

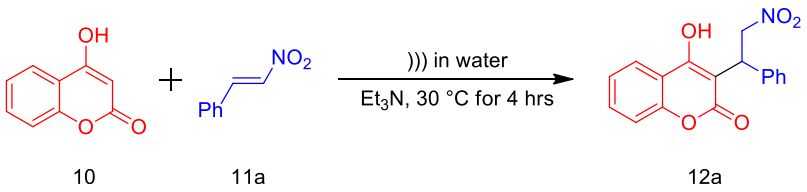
Reprinted from Sancheti and Gogate (2018). Copyright (2018), with permission from Elsevier.

37.3 Michael addition

The Michael addition or reaction is the conjugate addition of a carbanion or another nucleophile (reaction donor, e.g., malonates and nitroalkanes) to an α,β-unsaturated carbonyl compound (reaction acceptor, e.g., activated olefins) that contains an electron-withdrawing group. The Michael addition is a versatile method for forming C—C bonds and is catalyzed by bases (Okino et al., 2003, 2005; Hayashi et al., 2005). However, diverse factors, such as substituents' steric hindrance, temperature, catalysts, solvents, etc., control the reaction rate and the regio- and stereoselectivity of the products. To obtain enantiomerically pure Michael adducts with pharmacological or biological activity, however, harsh reaction conditions, e.g., hazardous solvents (DCM (CH_2Cl_2), PhMe (toluene)), and complex or expensive catalysts (chiral catalyst, Jørgensen-Hayashi catalyst, chiral PTC, helical peptide foldamers, $Yb(OTf)_3$, $Pd(OAc)_2$), have to be used. Even so, a lot of Michael additions require long reaction times (dozens of hours to 5 days) (Okino et al., 2005; Dhakshinamoorthy, 2005; Chi and Gellman, 2005; Wu et al., 2006; Ye et al., 2011; Willis et al., 2005; Palomo et al., 2006; Ooi et al., 2005; Guo et al., 2015; Ding et al., 2006). Sonication has therefore been used to enhance Michael additions and improve the selectivity of products. Meanwhile, environmentally benign water, aqueous media, and solvent-free conditions, as well as catalysts (ILs and organocatalysts), have been used to reduce the negative impact on the environment (Barange et al., 2011; Chi and Gellman, 2005; Ranu and Banerjee, 2005; Das et al., 2012; Bensa et al., 2004; Gomtsyan, 2000; Sarkar et al., 2011; Hara et al., 2006; Ebitani et al., 2006; Smith et al., 2009).

Barange et al. (2011) investigated the US-assisted Michael addition of cyclic 1,3-dicarbonyl compounds to β-nitrostyrenes to synthesize C_3-nitroalkylated-4-hydroxycoumarin and hydroxyiminodihydrofuroquinolinone derivatives. Initially, the addition of 4-hydroxycoumarin **10** (1 mmol) and nitrostyrene **11a** (1.2 mmol) was attempted with catalysis by the base Et_3N (5 mol%) and either stirring or sonication in MeOH and H_2O, respectively (Scheme 37.3).

As a result, no reaction occurred at 30°C for 12 h of stirring in both MeOH and H_2O, but the yield of the Michael adduct **12a** reached 40% at 80°C after 12 h of stirring. Surprisingly, a 95% yield was achieved at 30°C in water after 4



SCHEME 37.3 The Michael addition of 4-hydroxycoumarin and nitrostyrene (Barange et al., 2011)

h sonication (Barange et al., 2011). To extend the scope of US-assisted Michael additions, the reactions of 4-hydroxycoumarin **10** with various nitroalkenes **11a–n** were carried out at 30°C in water using sonication, and yields vs reaction times are shown in Figure 37.1 (Barange et al., 2011).

In terms of yield levels, the Michael adducts are divided into two groups: excellent yields and good yields. In the excellent-yield group, 90%–96% of the isolated yields were achieved in 6–11 h. Based on the required reaction time, the substituted aryl groups are ordered as follows: *p*-methoxylphenyl- **12e** > *o*-nitrophenyl- **12k** = *p*-methylphenyl- **12b** > *p*-nitrophenyl- **12j** = *p*-fluorophenyl- **12h** > *p*-chlorophenyl- **12i** > phenyl- **12a**. Thus, the US-assisted Michael additions of 4-hydroxycoumarin **10** with the above substituted nitroalkenes **11a–n** are efficient. Also, it seems that increasing reaction times favor increasing yields. In the good-yield group, 83%–88% of yields were achieved in 9–16 h. Based on the required reaction time, the substituted aryl groups are ordered as follows: naphthyl- **12n** > 2-furanyl- **12m** = 2-thienyl- **12l** = *o*-methoxylphenyl- **12c** > *m*-methoxylphenyl- **12d** > *o*-trifluoromethyl- **12f** > *o*-fluorophenyl- **12g**. Compared to the excellent yields, the aryls that contain a strong electron-withdrawing group, such as



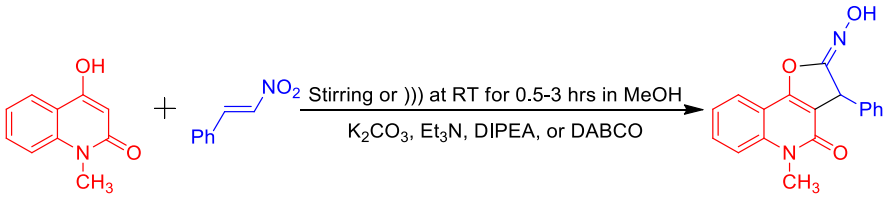
FIGURE 37.1 The yields of 3-substituted 4-hydroxycoumarin derivatives obtained by the US-assisted Michael addition of 4-hydroxycoumarin **10** (1.0 mmol) with various nitroalkenes **11a–n** (1.2 mmol) for different reaction times at 30°C in water. Substituents in product **12a–n**: phenyl- **12a**, *p*-methylphenyl- **12b**, *o*-methoxylphenyl- **12c**, *m*-methoxylphenyl- **12d**, *p*-methoxylphenyl- **12e**, *o*-trifluoromethyl- **12f**, *o*-fluorophenyl- **12g**, *p*-fluorophenyl- **12h**, *p*-chlorophenyl- **12i**, *p*-nitrophenyl- **12j**, *o*-nitrophenyl- **12k**, 2-thienyl- **12l**, 2-furanyl- **12m**, and naphthyl- **12n** (Barange et al., 2011).

—Cl, —F, and —NO_2, in para-substituted nitroalkenes can enhance the Michael addition reaction and reduce the reaction time. By contrast, increased reaction times were required when the substituent is one of the electron-donating groups, such as methyl- and methoxyl-, or electron-withdrawing group located at the *o*- or *m*-position. When naphthyl-, 2-furanyl-, or 2-thienyl- exist in nitroalkene, particularly, longer times were required to accomplish the Michael additions and afford good yields, despite the steric hindrance of (E)-2-(2-nitrovinyl) naphthalene and the weaker potentials for withdrawing electrons (Barange et al., 2011).

When 4-hydroxycoumarin was replaced by an *N*-methyl-4-hydroxyquinolinone moiety **13** (1.0 mmol), a 30% yield of the Z/E isomer (1/1) of hydroxyiminodihydrofuroquinolinone **15a** (1.2 mmol) was obtained in the US-assisted Michael addition with nitrostyrene **11a**, followed by cyclization at 30°C for 12 h without a catalyst in water (Scheme 37.4). All other things being equal, the yield reached only 10% at 80°C without sonication (Barange et al., 2011).

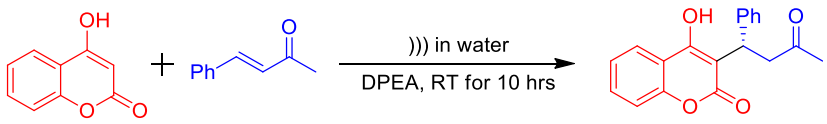
When the water reaction media was replaced by MeOH, 78% and 80% yields were achieved under the catalysis by either K_2CO_3 (20 mol%) or Et_3N (20 mol%) at 30°C with only stirring in 2 h and 1 h, respectively, and the ratio of Z/E isomers was 1/9. The yield remained 80% in 1 h when the reaction was catalyzed by DABCO (1,4-diazobicyclo [2.2.2]octane), but the ratio of Z/E isomers became 1/4. In particular, the yield and the ratio of Z/E isomers increased dramatically to 92% and 1/40 in 1 h under the catalysis by *N*,*N*-diisopropylethylamine (DIPEA, Hunig's base). Likewise, good-to-excellent yields (82%–92%) of hydroxyiminodihydrofuroquinolinone **15** were achieved in reactions of 4-hydroxy-*N*-methylquinolinone (1 mmol) with substituted nitroalkenes (1.2 mmol), including phenyl-, *p*-methylphenyl, *p*-methoxylphenyl-, 3,4-dimethoxylphenyl-, 1,5-dichlorophenyl-, *o*-methoxylphenyl- and naphthyl-, which were catalyzed by 10 mol% DIPEA at RT in MeOH with 0.5 to 3 h stirring. All other things being equal, however, the yield with silica gel catalysis was only 5%, and the TFA (trifluoroacetic acid), PTSA (*p*-toluenesulfonic acid), and NH_2SO_3H acidic catalysts for the reaction were ineffective (Barange et al., 2011).

Warfarin is an efficient anticoagulant that is used clinically, but (*S*)-warfarin exhibits higher activity than its mirror image. Chiral warfarin and analogs are usually synthesized using the Michael addition with chiral catalysts.



13 11a 15a

SCHEME 37.4 US-assisted Michael addition of *N*-methyl-4-hydroxyquinolinone and nitrostyrene **11a** followed by cyclization (Barange et al., 2011).



1 2a-m 3a-m

SCHEME 37.5 Synthesis of chiral warfarin via US-assisted Michael addition on water (Rogozińska-Szymczak and Mlynarski, 2014)

However, the yield, enantioselectivity, and reaction rate depend on the use of catalysts, and the reaction media could play a fundamental role (Halland et al., 2003; Kristensen et al., 2009; Xie et al., 2007; Dong et al., 2009; Kelleher et al., 2010; Kim et al., 2006). Rogozińska-Szymczak and Mlynarski (2014) attempted to use sonication to enhance the Michael addition of 4-hydroxycoumarin **1** to benzylideneacetone **2a** or other α,β-unsaturated ketones **2b–m** to produce chiral warfarin and analogs **3a–m** with higher yields and enantioselectivity, in shorter times on water (Scheme 37.5).

Initially, (*S*,*S*)-diphenylethylenediamine (DPEA) was picked from among various primary amine organocatalysts, and the yield and *ee* (enantiomeric excess) of the above Michael addition of **1** and **2a** reached 98% and 55% (S) in 1 mL of THF (tetrahydrofuran)/H_2O (9/1) at RT for 20 h with DPEA (10 mol%), respectively. The yield and *ee* were the same at 60°C for 12 h, but the *ee* reached 62% at 40°C for 20 h. The yield decreased to 94%, while the *ee* increased to 62% when THF/H_2O (1,1) was used. In particular, the yield reached only 8%, but the *ee* was the same (62%) when only H_2O was used as the media (Rogozińska-Szymczak and Mlynarski, 2014).

Subsequently, the sonochemical method was applied to enhance the "on-water" Michael addition, since reactants **1** and **2a** do not dissolve in water and sonication can promote reactant dispersion in water. Surprisingly, the isolated yield of warfarin reached 92% in 1 mL of H_2O at RT after 10 h sonication with DPEA (10 mol%) in a US bath, while the corresponding *ee* was 60% (Rogozińska-Szymczak and Mlynarski, 2014).

Acid additives can improve enantioselectivity. The *ee* increased to 68% with PhCOOH (10 mol%) and DPEA (5 mol%), but only an 87% yield was achieved at RT in 1 mL of water after 10 h sonication. When using PhCOOH (4 mol%) and DPEA (2 mol%), the yield and *ee* reached 78% and 70%, respectively. By contrast, the yield and *ee* reached 98% and 68%, respectively, with AcOH (20 mol%) and DPEA (10 mol%) at RT in 1 mL of water after 10 h sonication. When the Michael reaction was conducted on a 10 mL scale, the yields were in the range of 52%–61%, and the *ee* (after crystallization) exceeded 99% with AcOH (4 or 20 mol%) and DPEA (2 or 10 mol%) at RT in 10 mL of water after 10 h sonication. When using PhCOOH (4–10 mol%) and DPEA (2–5 mol%), similar results were obtained. However, the yield and *ee* reached 88% and 67% with PhCOOH (20 mol%) and DPEA (10 mol%) at RT in 10 mL of water after 10 h sonication. In addition, DPEA can be recycled and reused three times to ensure the similar efficiency to the original catalyst (Rogozińska-Szymczak and Mlynarski, 2014). To extend the scope of the Michael addition, various α,β-unsaturated ketones **2a–m** (0.60 mmol) were reacted with 4-hydroxycoumarin **1** (0.50 mmol), with PhCOOH (20 mol%) and DPEA (10 mol%) at RT in 1 mL of water after 10 h sonication (Rogozińska-Szymczak and Mlynarski, 2014). The results are listed in Table 37.2.

As listed in Table 37.2, yields of over 90% were achieved, except with substituents 4-ClC_6H_4—, —C_4H_9, and —iPr, and over 66% enantioselectivities were obtained, except for the substituent 4-$NO_2C_6H_4$—, indicating that the US-assisted Michael addition can be widely used for the synthesis of warfarin and analogs "on water" (Rogozińska-Szymczak and Mlynarski, 2014).

Moreover, the Michael addition is also involved in US-assisted MCRs at RT in water, providing a simple, highly efficient, and environmentally benign approach to furnishing bioactive chemicals or pharmaceuticals, such as N-substituted 1, 8-dioxo-decahydroacridines (Chate et al., 2016), rhodanine-furan bis-heterocyclic scaffolds (Hooshmand et al., 2019), pyranopyrazoles (Khandare et al., 2017), and pseudopeptides containing rhodanine scaffolds (Shaabani and Hooshmand, 2018).

TABLE 37.2 Yields and ee of warfarin and analogs by the US-assisted synthesis "on water"[a]

Entry	R	Yield (%)[b]	ee (%)[c]
1	—Ph **3a**	98	72
2	2-ClC_6H_4— **3b**	90	68
3	3-ClC_6H_4— **3c**	93	67
4	4-ClC_6H_4— **3d**	89	72
5	2-$MeOC_6H_4$— **3e**	93	76
6	4-$MeOC_6H_4$ **3f**	94	71
7	2-$NO_2C_6H_4$— **3g**	93	66
8	4-$NO_2C_6H_4$— **3h**	93	60
9	2-$CH_3C_6H_4$— **3i**	91	76
10	3-$CH_3C_6H_4$— **3j**	92	73
11	2-Naftyl— **3k**	97	70
12	—C_4H_9 **3l**	81	74
13	—*i*Pr **3m**	73	72

[a]*The reaction was performed using* ***1*** *(0.50 mmol),* ***2a–m*** *(0.60 mmol), catalyst (0.05 mmol, 10 mol%), PhCOOH (0.10 mmol, 20 mol%), and water (1 mL) at RT for 10 h in an ultrasound bath.* [b]*Isolated yield after silica gel chromatography.* [c]*ee values were determined by HPLC analysis on a chiral phase.*

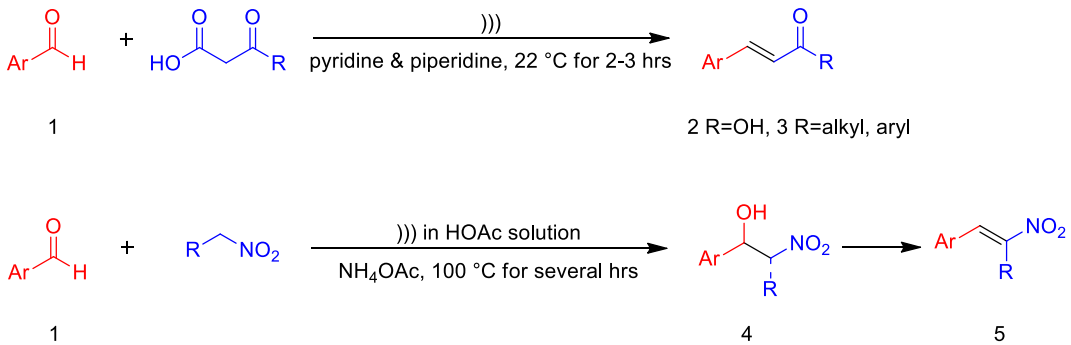
Reprinted from Rogozińska-Szymczak and Mlynarski (2014). Copyright (2014), with permission from Elsevier.

37.4 Knoevenagel condensation

The Knoevenagel condensation is a classic nucleophilic addition of active methylene (e.g., malonic acid or β-ketoacid derivatives) to a carbonyl-containing compound (e.g., aromatic aldehydes **1**) to form a C=C bond for the preparation of an α,β-unsaturated ketone (e.g., cinnamic acid derivatives **2** or cinnamyl ketones **3**) and versatile valuable intermediates of drugs and fine chemicals (Scheme 37.6) (Knoevenagel, 1898; McNulty et al., 1998).

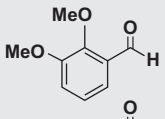
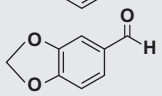
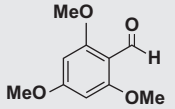
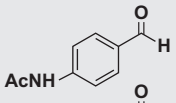
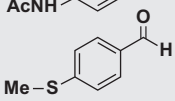
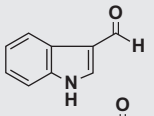
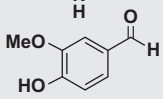
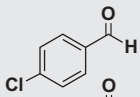
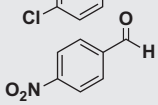
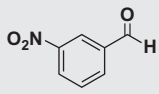
The traditional Knoevenagel condensation generally requires a long reaction time even when promoted by catalysts, such as acids, bases, or ammonium salts. Physical technologies, such as MW, US, and grinding, have therefore been employed to promote the Knoevenagel condensation in water, so that the yield, operation, and application scope can be improved significantly (Yang et al., 2010; Narsaiah et al., 2004; Han et al., 2008). For the Henry reaction (a variant of the Knoevenagel condensation), the condensation of nitroalkanes with aromatic aldehydes was conducted under the catalysis by NH_4OAc in a HOAc solution at 100°C for several hours and low-to-excellent (30%–95%) yields were achieved. An electron-rich aromatic aldehyde (e.g., 2,3-dimethoxybenzaldehyde) provided a lower yield (35%). In addition, this reaction did not occur at RT. McNulty et al. (1998) attempted to use sonication to promote the reaction of 2,3-dimethoxybenzaldehyde and nitromethane with NH_4OAc/HOAc at RT. The condensation was completed in 3 h using sonication, and the yield of nitroalkene **5a** reached 99% (Table 37.3). However, the US-assisted Henry reaction did not occur without the catalysis of NH_4OAc or HOAc. The yields from other substituted aromatic aldehydes are also listed in Table 37.3.

As listed in Table 37.3, good-excellent yields (85%–99%) were achieved from electron-rich aromatic aldehydes, while the steric hindrance of the substituents (2,4,6-trimethoxy derivative) diminished the yield of the corresponding nitroalkene (85%). Sonication can also promote the Henry reaction of electron-deficient aromatic aldehydes, such as 4-chlorobenzaldehyde **1h**, 4-nitrobenzaldehyde **1i**, and 3-nitrobenzaldehyde **1j**, but poor yields were achieved under the above conditions. The yields increased to 51%–70% when the basic catalyst diisopropylethylamine was used (McNulty et al., 1998). To extend the scope of the US-assisted Knoevenagel condensation, cinnamic acid derivatives were synthesized from aromatic aldehyde and malonic acid under the catalysis by pyridine and piperidine. The isolated yield of cinnamic acid derivative **2b** reached only 52% using reflux at 100°C for 3 h, while the corresponding yield reached 91% after 2 to 3 h



SCHEME 37.6 Sonochemical preparation of an α,β-unsaturated ketone and nitroalkene via Knoevenagel condensation and Henry reaction (McNulty et al., 1998).

TABLE 37.3 US-assisted Henry reaction (a modified Knoevenagel condensation)

Entry		Method[10]	Product	Yield
	1a	A	5a	99
	1b	A	5b	99
	1c	A	5c	85
	1d	A	5d	95
	1e	A	5e	96
	1f	A	5f	93
	1g	A	5g	89
	1h	B	4h	70
	1i	B	4i	61
	1j	B	4j	51

Note: Branson 5510 ultrasound bath (40 kHz, 130 W) or a Crest Tru-Sweep ultrasonic cleaner was used with little difference.
Method A: a mixture of aldehyde (20.0 mmol), nitromethane (13.0 mL), glacial acetic acid (3.3 mL), and ammonium acetate (3.324 g), sonicated at 22°C for 3 h.
Method B: a solution of aldehyde (1.0 mmol), nitromethane (1.0 mL), ammonium acetate (2.5 mmol), and diisopropylethylamine (0.1 mmol) was sonicated at 22°C for 3–6 h.
Reprinted from McNulty et al., (1998). Copyright (1998), with permission from Elsevier.

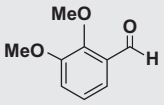
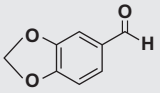
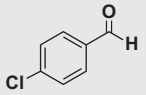
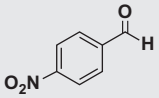
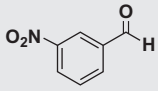
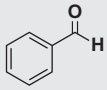
sonication at RT (Table 37.4). The yields from other aromatic aldehydes are also listed in Table 37.4.

As listed in Table 37.4, good-to-excellent yields (87%–99%) of cinnamic acid derivatives were achieved from electron-deficient aromatic aldehydes, such as 4-chlorobenzaldehyde **1h** and 4-nitrobenzaldehyde **1i**. However, the yield from 3-nitrobenzaldehyde **1j** was lower (61%) due to the steric hindrance of the substituent.

Moreover, the US-assisted Knoevenagel condensation was used to prepare bioactive chemicals and pharmaceutical intermediates, such as ethyl α-cyanocinnamates (Li et al., 1999; Wang et al., 2002) and 4-oxo-2-thioxohexahydropyrimidines (Li et al., 2004). Good-to-excellent yields were achieved with catalysts in shorter times. In 2010, Bardajee et al. (2010) reported the sonochemical synthesis of 3-carboxycoumarins via the Knoevenagel condensation of substituted benzaldehydes with Meldrum's acid, catalyzed by zirconium oxide chloride ($ZrOCl_2 \cdot 8H_2O$, ZOC) in water (Scheme 37.7).

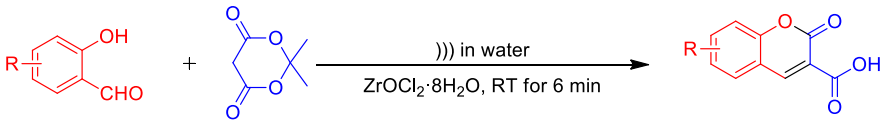
The conversion generally required 10 h in water with reflux without catalyst, and the yield reached 93% (Maggi et al., 2001). With sonication at 20 kHz and 200 W, 1 mmol

TABLE 37.4 Yields of cinnamic acid derivatives via US-assisted Knoevenagel condensation

Entry		Method[10]	Product	Yield
	1a	C	2a	75
	1b	C	2b	91
	1h	C	2h	99
	1i	C	2i	87
	1j	C	2j	61
	1k	C	2k	99

Note: Method C: a solution of aldehyde (1.00 mmol), malonic acid (2.18 mmol) in pyridine (5.7 mmol), and piperidine (0.20 mmol) was sonicated at 22°C for 3 h.

Reprinted from McNulty et al. (1998). Copyright (1998), with permission from Elsevier.



SCHEME 37.7 Sonochemical synthesis of 3-carboxycoumarins in water (Bardajee et al., 2010).

of salicylaldehyde and 1 mmol of Meldrum's acid with ZOC (20 mol%) reacted at RT in 5 mL of water. As a result, an excellent yield (96%) of 3-carboxycoumarin was achieved in 6 min (pulse mode: 2 s on/2 s off) (Bardajee et al., 2010). By contrast, the only good yield was obtained under the catalysis with ZOC without sonication and required a long reaction time even at high temperatures. On the other hand, the conversion of reactants was completed under sonication in 1 h in the absence of a catalyst, and 90% of the yield was achieved at RT (Bardajee et al., 2010). The synergistic effect between ZOC and sonication promoted the formation of 3-carboxycoumarin. Interestingly, the highest yield was achieved in a shorter time in water than with other solvents, such as MeCN (acetonitrile), DMF (*N*,*N*-dimethylformamide), DCM (dichloromethane), EtOH, DEE (diethyl ether), and HEX (*n*-hexane). To extend the scope of the sonochemical synthesis of 3-carboxycoumarins via the Knoevenagel condensation followed by intramolecular cyclization in water, various substituted benzaldehydes were studied. As a result, good-to-excellent isolated yields (84%–96%) of 3-carboxycoumarins were achieved using various substituted benzaldehydes: 96% from 2-hydroxybenzaldehyde **1a**, 92% from 2-hydroxy-5-methoxybenzaldehyde **1b**, 91% from 4-(diethylamino)-2-hydroxybenzaldehyde **1d**, 88% from 2-hydroxy-4-methoxybenzaldehyde **1c**, 87% from 2,4-dihydroxybenzaldehyde **1e**, 86% from 5-chloro-2-hydroxybenzaldehyde **1g**, and 84% from 2,6-dihydroxybenzaldehyde **1f**. It indicated

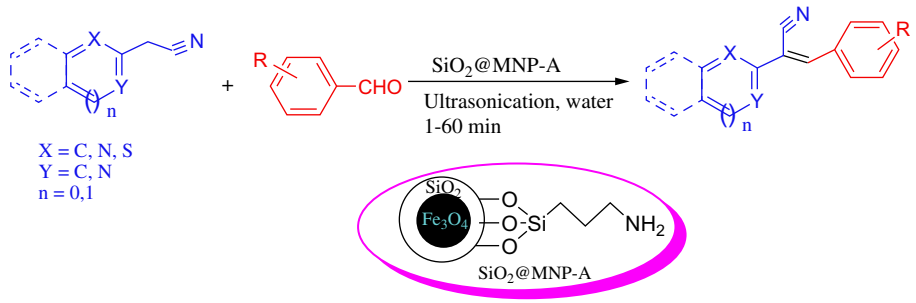
the wide applicability of the sonochemical synthesis of 3-carboxycoumarins via the Knoevenagel condensation followed by intramolecular cyclization. In addition, the yield of 90% for 2-oxo-2H-chromene-3-carboxylic acid **3a** was still achieved after the catalyst was reused three times (Bardajee et al., 2010).

To readily separate the catalyst from the reaction mixture and reuse it, Ying et al. (2015) designed amine-functionalized, silica-coated Fe_3O_4 nanoparticles (SiO_2@MNP-A), with high catalytic activity and low cost, that were used to promote the US-assisted Knoevenagel condensation in water. More interestingly, the active methylene compounds showed lower nucleophilicity due to the steric hin drance of the substituent aryl group (Ying et al., 2015; Fringuelli et al., 1994) (Scheme 37.8).

For the US-assisted Knoevenagel condensation of 10 mmol of benzaldehyde and 10 mmol of benzothiazole-2-acetonitrile, catalyzed by SiO_2@MNP-A at RT in 20 mL of solvent, the highest isolated yield (94%) was initially achieved after 10 min sonication (22 kHz, 250 W) in water, while a comparable yield (90%) was obtained in MeOH. However, lower yields were achieved after longer reaction times in PhMe (63% in 18 min), DCM (72% in 20 min), TCM (trichloromethane, 74% in 25 min), and EtOH (86% in 20 min). By comparison, only a 35% yield was obtained after 2 h stirring without sonication in water. Water is a superior green media, and sonication is an enabling tool for this Knoevenagel condensation. In addition, the reaction time was reduced and the yield increased with increasing US power, while the yield was maintained at the similar level (93%–94%) when US power was in the range of 200–300 W. Moreover, the yield increased with the amount of catalyst used, as follows: 58% (1.0 g in 10 min) < 81% (1.5 g in 10 min) < 93% (2.0 g in 5 min) < 94% (2.5 g in 10 min) (Ying et al., 2015).

It can be seen that the catalyst is a key factor in the US-assisted Knoevenagel condensation in water. Only a trace yield was observed after 30 min of reaction without catalyst. By contrast, 15%, 63%, and 82% yields were obtained in 20 min under the catalysis by SiO_2@MNP (0.4 g), SiO_2@A (silica-supported amine, 3.0 g), and propylamine, respectively. To extend the scope of the US-assisted Knoevenagel condensation in water and evaluate the role of sonication, benzothiazole-2-acetonitrile was chosen to react with various substituted aromatic aldehydes under the catalysis by SiO_2@MNP-A (2.0 mol%) under various conditions, such as stirring at RT, stirring at 60°C (heat), and sonication (US). The results are listed in Table 37.5.

As listed in Table 37.5, the yield reached 83%–92% from the reaction of the selected substituted aromatic aldehydes and benzothiazole-2-acetonitrile in 1–10 min using



SCHEME 37.8 US-assisted Knoevenagel condensation catalyzed by SiO_2@MNP-A in water. *(Reproduced from Ying et al. (2015). Copyright © 2015 Académie des sciences with permission from Elsevier Masson SAS.)*

TABLE 37.5 Comparison of the yields and reaction times of the SiO_2@MNP-A-catalyzed Knoevenagel condensation of various substituted aromatic aldehydes and benzothiazole-2-acetonitrile in water under stirring, heating, and US

Entry	Methylene compound	Aldehyde	Time (min)			Yield (%)[a]		
			RT	Heat	US	RT	Heat	US
1	Benzothiazole-2-acetonitrile	4-CF_3—C_6H_4—	30	20	1	63	76	90
2	Benzothiazole-2-acetonitrile	2-Cl—C_6H_4—	40	15	2	75	72	83
3	Benzothiazole-2-acetonitrile	4-Cl—C_6H_4—	40	20	2	72	70	87
4	Benzothiazole-2-acetonitrile	4-MeO—C_6H_4—	50	30	8	53	68	92
5	Benzothiazole-2-acetonitrile	2-MeO—C_6H_4—	60	35	10	64	73	91

TABLE 37.5 Comparison of the yields and reaction times of the SiO_2@MNP-A-catalyzed Knoevenagel condensation of various substituted aromatic aldehydes and benzothiazole-2-acetonitrile in water under stirring, heating, and US—cont'd

Entry	Methylene compound	Aldehyde	Time (min)			Yield (%)		
			RT	Heat	US	RT	Heat	US
6	Benzimidazolyl acetonitrile	4-MeO—C_6H_4—	40	25	10	72	69	94
7	Benzimidazolyl acetonitrile	3-MeO—C_6H_4—	60	30	8	48	66	85
8	Benzimidazolyl acetonitrile	3-Cl—C_6H_4—	50	30	6	53	58	85
9	2-Indoleacetonitrile	C_6H_5—	120	60	20	36	61	95
10	2-Indoleacetonitrile	4-Me—C_6H_4—	100	60	20	42	59	93
11	Phenylacetonitrile	C_6H_5—	180	80	30	59	66	95
12	Phenylacetonitrile	4-HO—C_6H_4—	180	80	30	63	61	88
13	Phenylacetonitrile	3-MeO—C_6H_4—	150	60	40	63	71	86
14	Phenylacetonitrile	2-MeO—C_6H_4—	280	90	50	65	68	90
15	Phenylacetonitrile	4-MeO—C_6H_4—	180	80	40	63	73	92
16	Phenylacetonitrile	2-Furyl	180	60	35	58	78	92
17	Phenylacetonitrile	1-Naphthyl	180	50	35	69	81	95
18	3-Chloro-phenylacetonitrile	4-MeO—C_6H_4—	240	100	60	61	67	85
19	3-Chloro-phenylacetonitrile	C_6H_4—	240	100	60	66	65	88

[a]*Isolated yield based on aldehyde.*
SiO_2@MNP-A: amine-functionalized silica coated Fe_3O_4 nanoparticles; US, *ultrasonic irradiation;* rt., *room temperature stirring.*
Reproduced from Ying et al. (2015). Copyright © 2015 Académie des sciences with permission from Elsevier Masson SAS.

sonication (22 kHz, 200 W), while lower yields, 68%–76%, were achieved under stirring at 60°C in 15–35 min, and 53%–64% in 30–60 min under stirring at RT. In addition, the reactions of the electron-deficient aromatic aldehydes bearing —CF_3 or —Cl were faster than those of the electron-rich ones that bear —OMe. Similarly, sonication also enhanced the Knoevenagel condensation of phenylacetonitrile and various substituted aromatic aldehydes, and 86%–95% yields were achieved after 30 to 50 min sonication (Ying et al., 2015).

In addition, the sonochemical condensations of benzimidazolylacetonitrile and substituted aromatic aldehydes with the moieties 2-Cl—C_6H_4—, 3-MeO—C_6H_4—, and 4-MeO—C_6H_4— are also efficient. The yields of the corresponding products reached 85%–94% in 6–10 min. The condensations of 2-indoleacetonitrile and substituted aromatic aldehydes with the moieties 4-methyl—C_6H_4— and C_6H_5— were completed after 20 min sonication, and the yields reached 93% and 95%, respectively. Furthermore, the yields of 3-chloro-phenylacetonitrile and substituted aromatic aldehydes with the moieties 4-MeO—C_6H_4— and C_6H_5— reached 85% and 88%, respectively, after 60 min sonication. Furthermore, the US-assisted condensation of a non-cyano-substituted ketone, e.g., acetylacetone, and benzaldehyde gave a 79% yield under the catalysis by SiO_2@MNP-A in water at RT in 35 min. Likewise, the yield from the reaction of 4-methyl-3-oxo-*N*-phenylpentanamide and benzaldehyde reached 87% after 25 min sonication at RT in water (Ying et al., 2015). In summary, sonication significantly enhanced the Knoevenagel condensation under the catalysis by SiO_2@MNP-A at RT in water, reducing the reaction time and increasing the yield from the reaction between the various substituted aromatic aldehydes and active methylene compounds in comparison with the use of stirring at RT and 60°C. However, the subsequent Michael adduct was not formed due to steric hindrance.

Moreover, the enhanced effects of sonication on the Knoevenagel condensation to afford various α,β-unsaturated compounds were demonstrated with the recyclable amino-functionalized FDU-12 catalyst that was used in EtOH aqueous media (Dong et al., 2019). The Knoevenagel condensation of aromatic aldehydes and active methylene compounds, e.g., ethyl 2-cyanoacetate, was also promoted by sonication in the reusable protic IL-catalyst system (HMTA-AcOH-H_2O) (Zhao et al., 2013), and potassium fluoride-clinoptilolite smoothly and cleanly (Keipour et al., 2015). A simple, clean, and efficient US-assisted Knoevenagel condensation was also used to furnish 3-phenyl-4-

pyrazolylmethylene-isoxazol-(5H)-ones under the catalysis with sodium benzoate in aqueous media (Konkala and Dubey, 2017). High yields were achieved in short s, and the catalysts were reused up to six times with the similar catalytic activity.

The Aldol condensation is a modified Knoevenagel condensation. We have promoted the Aldol reaction using sonication in water. The Aldol reaction of acetophenone with non-enolizable aldehydes did not occur for several hours under stirring or reflux, but the reaction was accomplished to produce various polyols under sonication in 15–30 min (Cravotto et al., 2003). Good-to-excellent yields of β-hydroxyl ketones were also achieved via the US-promoted Aldol reactions of active aldehydes with substituted acetophenone in MeOH aqueous media under the catalysis with trisodium phosphate (Ji-Tai et al., 2004).

Moreover, tandem Knoevenagel-Michael reactions in aqueous media are regarded as an efficient strategy to furnish bioactive compounds such as bis-dimedone derivatives (Al-Majid et al., 2017), 3,3′-pyrrolidonyl spirooxindole derivatives (Yu et al., 2013), and highly enantioselective spiro [4H-pyran-3,3′-oxindoles] (Chen et al., 2010). The Knoevenagel condensation has therefore also been used in US-promoted MCRs in water or aqueous media for the synthesis of bioactive or pharmaceutical chemicals, such as 3-(Het)arylmethyl-4-hydroxycoumarins with Hantzsch 1,4-dihydropyridine (Palmisano et al., 2011), 2-amino-4H-benzo[*g*]chromenes catalyzed by NH_4OAc (Gracious et al., 2020), 2-amino-4,6-diphenylnicotinonitriles, 2-amino-7-hydroxy-4H-chromene derivatives and tetrasubstituted pyrrole derivatives without catalyst (Safari et al., 2012, 2017; Pagadala and Anugu, 2018), 6-naphthyridine derivatives catalyzed by solid acid (Li et al., 2020a), 1,6-naphthyridine-2,5-diones catalyzed by HOAc (Li et al., 2020b), dihydropyrano[3,2-*c*]chromenes and amino-benzochromenes catalyzed by sodium malonate (Kiyani and Tazari, 2017), pyrazolo[1,2-*a*]pyridazine catalyzed by triethanolamine (Khoraamabadi-Zad et al., 2014), a 7-amino-2, 4-dioxo-5-phenyl-2, 3, 4, 5-tetrahydro-1H-pyrano [2,3-d] pyrimidine-6-carbonitrile derivative catalyzed by reusable IL choline chloride $ZnCl_2$ (Yadav and Quraishi, 2014), a Knorr pyrazole with a deep eutectic solvent and water (Kamble and Shankarling, 2018), and pyran derivatives catalyzed by a magnetically recyclable nano-organocatalyst (Dam et al., 2015). All of the above approaches provide good-to-excellent yields in short reaction times, with simple workup and recyclable catalysts, which are beneficial for our environment.

37.5 Diels-Alder cycloaddition

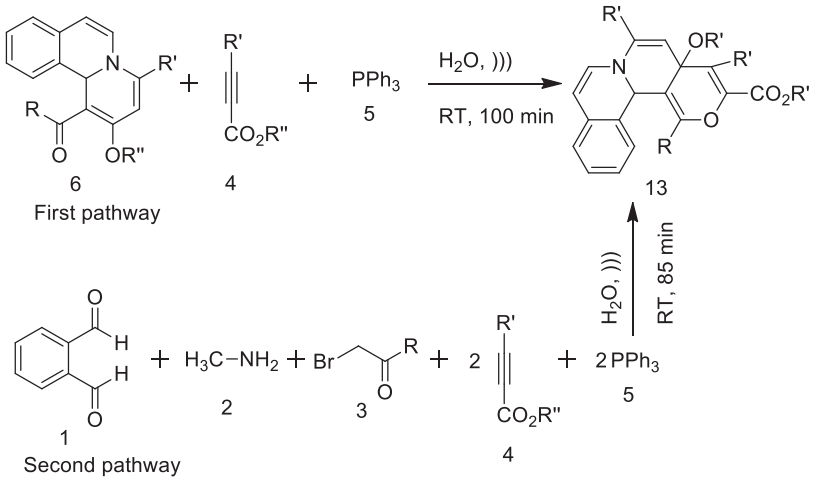
Diels-Alder cycloaddition is an important method to furnish substituted unsaturated six-membered rings with good regio- and stereochemical selectivity via the [4 + 2] cycloaddition of conjugated dienes and substituted alkenes. In particular, the variant reaction, the hetero-Diels-Alder reaction, has been widely applied to prepare corresponding heterocycles with bioactivity, e.g., vitamin B6 (Kloetzel, 1948; Teo and Loh, 2005; Huang and Rawal, 2000; Nicolaou et al., 2002). However, the reaction rate, and the regio- and stereoselectivity of products in Diels-Alder cycloaddition are dominated by several factors, such as substituent steric hindrance, temperature, catalysis, solvents, etc. Harsh reaction conditions, e.g., low or high temperatures (−78°C to 160°C), hazardous solvents (DCM, PhMe, $CDCl_3$), and complex catalysts (chiral oxazaborolidine-aluminum bromide complexes, Brønsted acid-activated chiral oxazaborolidine, DIANANE-Cr(III)-salen complexes), have to be used to obtain the target products (Liu et al., 2007; Payette and Yamamoto, 2007; Gotoh and Hayashi, 2007; Berkessel and Vogl, 2006; Dai et al., 2007; Yang et al., 2017; Esquivias et al., 2007; Ross et al., 2013). Even so, most Diels-Alder cycloadditions require very long reaction times (several hours to days). Enabling techniques, e.g., MW and US, have therefore been investigated as means to accelerate Diels-Alder cycloaddition and improve product selectivity. Meanwhile, environmentally benign water and aqueous media have been used as catalysts to reduce the negative impact on the environment (Fuentes et al., 2005; Hayashi et al., 2008).

Isoquinolines can be used to furnish dyes, paints, insecticides, antifungals, and drugs, e.g., anesthetics, antihypertension agents, vasodilators, etc. Sharafian et al. (2021) have very recently reported two strategies to furnish isoquinoline derivatives using Diels-Alder reactions (Scheme 37.9).

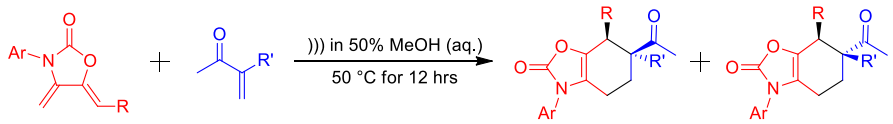
In the first pathway, pyrido[2,1-*a*]isoquinoline derivatives **6**, which were prepared and purified in advance, reacted with acetylenic compounds **4** that were activated with triphenylphosphine (PPh3) **5** in water at RT under sonication. The second pathway is an MCR; compounds **6**, generated by the reactions of phthalaldehyde **1** with methylamine **2** and alkyl bromide **3**, reacted directly (without separation steps) with compounds **4** and **5** in water at RT under sonication. The yields in the second pathway reached 87%–95%, which are significantly higher than those (68%–78%) obtained in the first pathway. It was speculated that MCR reduces the product loss that is caused by the separation. In addition, the shorter reaction times of Diels-Alder reactions (85–100 min) can be achieved using green media, water (Sharafian et al., 2021).

By contrast, the advantages of using sonication, such as increased yields and improved selectivity, were not exhibited in the following example. Fortunately, sonication can reduce the reaction time. Fuentes et al. (2005) explored the effects of solvents, MW, and US on the one-step synthesis of (*Z*)-*N*-substituted 4-methylene-5-propylidene-2-oxazolidinone dienes via Diels-Alder cycloaddition (Schemes 37.10 and 37.11).

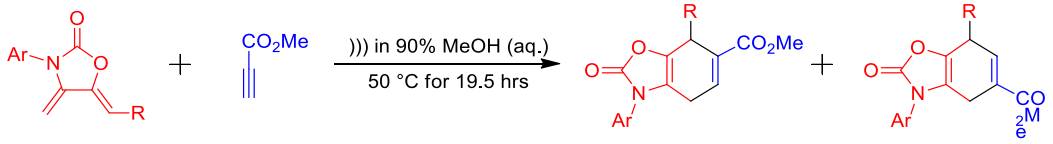
When diene was 3-(4-chlorophenyl)-4-methylene-5-propylideneoxazolidin-2-one with Ar (C_6H_4m-Cl) and R



SCHEME 37.9 Two strategies to furnish isoquinoline derivatives using Diels-Alder reactions in water at room temperature under sonication (Sahiba et al., 2021).



SCHEME 37.10 Ultrasound-assisted Diels-Alder cycloaddition of diene and olefin in aqueous methanol solutions (Fuentes et al., 2005).



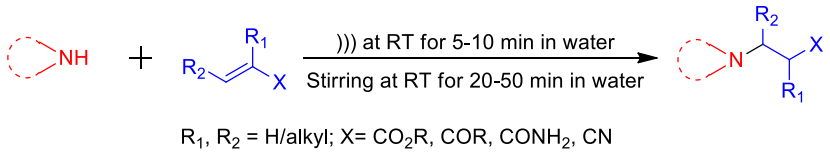
SCHEME 37.11 Ultrasound-assisted Diels-Alder cycloaddition of diene and alkyne in aqueous methanol solutions (Fuentes et al., 2005).

(Et) and olefin was but-3-en-2-one, the reaction occurred at 25°C for 12–72 h in a highly polar co-solvent (MeOH/H_2O), while it took place at 120°C for 1.5 h in *m*-xylene. In addition, higher yields (92%–97%) and *endo*-stereoselectivity (91%–94%) were achieved in MeOH/H_2O than in *m*-xylene (72% yield and 72% endo-selectivity). 50% MeOH was demonstrated to be the optimal solvent in terms of reaction time, endo-selectivity, and yield. In comparison, the reaction time in MeOH/H_2O was reduced to 2 h at 35°C with MW heating, but the yield (86%) and endo-selectivity (92%) cannot increase significantly. As for sonication with an ultrasonic cleaner, a lower yield (80%) was obtained at 50°C after 12 h, but the endo-selectivity remained at a good level (92%). When diene was 3-(4-chlorophenyl)-4-methylene-5-propylideneoxazolidin-2-one with Ar (C_6H_4m-Cl) and R (Et) and olefin was methyl propiolate in MeOH/H_2O (9:1), likewise, the yields reached 96% at 25°C after 408 h under silent conditions and 77% at 50°C after 19.5 h under sonication. Meanwhile, the ortho regioselectivity was 98% under silent conditions and 88% under sonication. Sonication reduced the reaction time, but did not increase the yield and selectivity of the target products in the above cases (Fuentes et al., 2005).

37.6 Aza-Michael reaction

The aza-Michael reaction is a powerful tool for C—N bond formation, i.e., the addition of a nucleophilic amine to electron-deficient α,β-unsaturated ketones, esters, and nitriles to produce β-amino carbonyl derivatives (Scheme 37.12), which are important intermediates for furnishing *N*-containing molecules, such as β-amino alcohols, antibiotics, chiral auxiliaries, and natural products (Ranu and Banerjee, 2007; Bandyopadhyay et al., 2012).

The traditional aza-Michael reaction was generally carried out using Lewis acids or bases, such as transition metals (CuCl, cellulose-supported Cu(0), $Cu(acac)_2$/ionic liquid), ceric ammonium nitrate, lanthanide halides, solid salts, boric acid, etc. (Reddy and Kumar, 2006; Kim et al., 2016; Adapa et al., 2006). In order to extend the reaction scope, avoid or reduce the use of heavy metal salts and hazardous organic solvents, shorten reaction times, and



SCHEME 37.12 Ultrasound-enhanced synthesis of β-amino carbonyl derivatives by aza-Michael reaction in water at room temperature (Ranu and Banerjee, 2007; Bandyopadhyay et al., 2012).

increase yields, a constant effort has been made to develop eco-friendly catalysts, such as quaternary ammonium salts/ionic liquids, β-cyclodextrin, and silica gel, as well as catalyst-free and solvent-free processes for aza-Michael addition (Ranu and Banerjee, 2007; Ying et al., 2014; Azizi et al., 2010). Water is being more gradually used in aza-Michael addition. Ranu and Banerjee (2007) summarized the additions of various primary and secondary amines to α,β-unsaturated carboxylic esters, ketones, nitriles, and amides in water at RT (Table 37.6).

As shown in Table 37.6, 85%–95% yields were achieved at RT in less than 50 min for all of the reactions in water. In particular, the addition of pyrrolidine to CH_2=CH—CO_2Me was accomplished with an excellent yield (95%) in a very short time (20 min). It was speculated that the H-bond formation between water and the carbonyl oxygen atom enhanced the electrophilicity at β-carbon, promoting the connection with the nucleophilic amine. Moreover, H-bond formation between the O-atom of water and the H-atom of amine increases the nucleophilicity of amine. Therefore, water promotes both amine and conjugated alkene to favor the aza-Michael reaction without a catalyst or co-solvent. In addition, only mono-addition products were formed with primary amines, so that the separation procedure for the mono- and bis-addition products can be avoided (Ranu and Banerjee, 2007).

However, no reaction occurred with aromatic amines or tertiary amines in water. Also, α,β-unsaturated aldehydes did not react with any amines in water. Interestingly, the aza-Michael reaction proceeds very slowly in organic solvents, e.g., THF or DCM, and only partially completes even in 10–15 h (Table 37.7).

Bandyopadhyay et al. (2012) evaluated the US-assisted aza-Michael reaction of piperidine (1 mmol) and methyl acrylate (1 mmol) in 1 mL of water at RT in the absence of catalysts. The sonication was carried out in an ultrasonic cleaner (42 kHz, 135 W). As a result, the aza-Michael reaction was accomplished at RT in 5 min under sonication and the isolated yield reached 98%, which is higher than that (96%) obtained in water under stirring alone at RT in 30 min. Moreover, it is higher than that (92%) obtained in the previous study (Table 37.6, in water with stirring alone at RT in 30 min). Therefore, sonication can not only significantly accelerate the aza-Michael reaction but also increase the yield. However, moderate yields were achieved under 1h sonication in organic solvents. The isolated yields reached

TABLE 37.6 Yields for the aza-Michael reaction of selected amines and α,β-unsaturated compounds at RT in various reaction times in water (yields: %) (Ranu and Banerjee, 2007)

α,β-Unsaturated compound		CH_2=CH—CO_2Me			CH_2=CH—CN			CH_2=CH—$CONH_2$	CH_2=C(CH_3)—CO_2Me		CH_3CH=CH—CO_2Et	Cyclohex-2-enone
Reaction time (min)		20	30	35	25	30	35	50	30	35	35	30
Amines	*n*-$BuNH_2$	–	90	–	–	92	–	–	–	–	–	–
	$PhCH_2NH_2$	–	–	–	–	85	–	85	–	–	–	–
	c-$HexNH_2$	–	–	85	–		–	–	–	–	–	–
	$(Et)_2NH$	–	86	–	–	88	–	85	–	–	–	–
	$(i\text{-}Pr)_2NH$	–	–	85	–	–	–	–	–	–	–	–
	Pyrrolidine	95	–	–	90	–	–	–	–	85	86	–
	Piperidine	–	92	–	90	–	–	–	–	–	–	–
	Morpholine	–	–	–	–	90	–	–	86	–	–	86
	1-Phenylpiperazine	–	–	–	–	–	85	–	–	–	–	–

TABLE 37.7 Comparison of yields of selected aza-Michael reactions in water, THF, and DCM (Ranu and Banerjee, 2007)

α,β-Unsaturated compound	CH_2=CH—CO_2Me		CH_2=CH—CN		CH_2=CH—$CONH_2$		
Reaction media	H_2O	THF	H_2O	DCM	H_2O	DCM	THF
Reaction time (h)	0.5	10	0.5	10	0.8	15	15
n-$BuNH_2$	90%	40%	92%	70%	–	–	–
$PhCH_2NH_2$	–	–	–	–	85%	50%	30%
$(Et)_2NH$	–	–	–	–	85%	60%	30%

45%, 48%, 55%, 57%, 62%, and 71% in THF, DEE, DCM, MeOH, EtOH, and MeCN, respectively. It appears that conversion is dominated by the polarity of the solvents; high solvent polarity favors the aza-Michael reaction, except for DCM. More interestingly, sonication reduced the reaction time from 10–15 h to 1 h and gave similar yields as obtained using stirring alone in organic solvents in the previous study (Table 37.8). In addition, a 93% yield was achieved at RT in 15 min under sonication without solvents, which is much slower than the reaction in water (Bandyopadhyay et al., 2012). To extend the scope of US-assisted aza-Michael reactions, several diverse amines with various Michael acceptors were sonicated at RT in water for 5–10 min. The results are listed in Table 37.8.

Under catalyst-free conditions, all the US-assisted aza-Michael reactions were accomplished in 5–10 min, and excellent yields (86%–99%) were achieved without producing side products. In the previous study, no reactions with aromatic amines or tertiary amines were observed under stirring alone in water. Surprisingly, aniline, 4-methoxy-aniline, and phenylmethanamine were also added to Michael acceptors in excellent yields (92%–95%) under 5min sonication at RT in water. The reaction times of all of the reactions were reduced to 5–10 min under sonication, compared with those (30–50 min) driven by stirring alone (Bandyopadhyay et al., 2012). In summary, aza-Michael reaction is an accessible and versatile addition achieved under mild conditions (Genest et al., 2017). The use of sonication enhanced aza-Michael reaction in water and organic solvents reduced the reaction time and increased the yield. In addition, metallic, enzymatic, or corrosive catalysts and hazardous solvents are not necessary.

TABLE 37.8 US-assisted aza-Michael reaction for extended scope (Bandyopadhyay et al., 2012)

α,β-Unsaturated compound		CH_2= CH—CO_2Me	CH_2= CH—CN	CH_2=C (CH_3) —CO_2Me	CH_2= CH—CO_2Et	Cyclohex-2-enone	(E)-chalcone
Reaction time (min)		5	5	5	5	10	10
Amines	*n*-$BuNH_2$	99%	95%	–	–	–	–
	$(Et)_2NH$	97%	–	–	–	–	–
	Pyrrolidine	95%	91%	95%	–	–	–
	Piperidine	98%	96%	–	–	92%	–
	Morpholine	93%	90%	–	–	93%	–
	Aniline	–	–	–	92%	–	–
	4-Methoxy-aniline	–	–	–	95%	–	–
	Phenylmethanamine	–	93%	–	–	–	–
	Piperazine	–	–	–	–	–	87%
	1,3-Di(piperidin-4-yl)propane	–	–	–	–	–	86%

37.7 Hantzsch condensation or cyclization

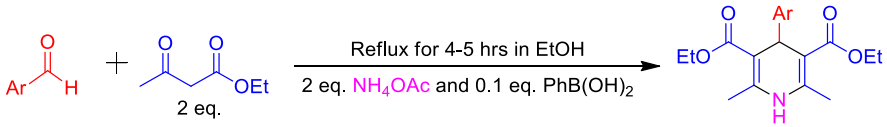
The Hantzsch condensation or cyclization is also named the Hantzsch dihydropyridine (pyridine) synthesis. It provides the condensation of an aldehyde, two equivalents of β-ketoester and ammonia (Scheme 37.13).

Both the Knoevenagel condensation product and the ester enamine produced by the condensation of aldehyde or ammonia and β-ketoester are intermediates. They are then further condensed to produce the 1,4-dihydropyridine (1,4-DHP) derivative. Subsequently, oxidation (or dehydrogenation) produces pyridine-3,5-dicarboxylates, which are further decarboxylated to generate pyridines. As they have diverse bioactivities, 1,4-DHP derivatives have been used to produce diverse drugs, e.g., vasodilator, bronchodilator, antitumor, etc. The traditional synthesis of 1,4-DHP is a one-pot condensation with NH_4OAc or via reflux in alcohol (Debache et al., 2008; Kumar and Maurya, 2008; Wang et al., 2005). In some cases, harsh reaction conditions, e.g., hazardous or highly flammable solvents (TCM, HEX), complex catalysts (covalently anchored sulfonic acid on silica gel, bifunctional Pd/C/K-10, phenylboronic acid, $Yb(OTf)_3$), are necessary (Kumar and Maurya, 2008; Wang et al., 2005; Tang and Wang, 2017; Paul et al., 2007; De Paolis et al., 2008). Even so, many Hantzsch condensations require several hours to days. Therefore, MW and US have been used to reduce the time of Hantzsch condensations and increase yields in water or aqueous media (Kumar and Maurya, 2008; De Paolis et al., 2008). Kumar and Mauya (Kumar and Maurya, 2008) compared the yields of Hantzsch 1,4-dihydropyridine via the condensation of benzaldehyde (1 mmol), and ethyl acetoacetate (2 mmol), with NH_4OAc (1 mmol) and a PTSA catalyst (10 mol%) under stirring and sonication in aqueous SDS (sodium dodecyl sulfate) micelles (Scheme 37.14).

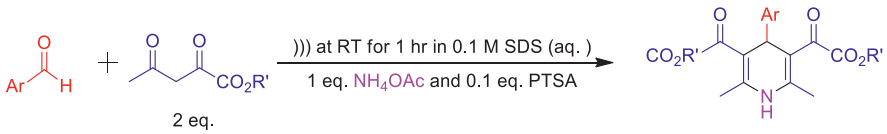
Under stirring at RT for 4 h in the presence of the PTSA catalyst, the yield of 1,4-DHP reached 65%, which is much higher than that (35%) obtained without PTSA. With other catalysts (methane sulfonic acid, and camphor-10-sulfonic acid), similar yields (63% and 62%) were achieved. However, increasing the reaction temperature (using refluxing) did not significantly increase the yields. Moreover, very low yields, i.e., a 16% yield without catalyst and a 28% yield with PTSA, were achieved in water without SDS. As expected, the yield of 1,4-DHP using 1h sonication in the presence of the PTSA catalyst reached moderate-to-excellent levels in various solvents, i.e., a 62% yield in THF, a 74% yield in MeOH, a 78% yield in EtOH, and a 96% yield in aqueous SDS micelles. Sonication enhanced the Hantzsch condensation, reduced the reaction time, and increased the yield. Thus, excellent yields (90%–97%) were achieved in the syntheses of a library of 1,4-DHP derivatives under 1 h sonication with PTAS catalysis in aqueous SDS micelles, in which electron-rich and electron-deficient substituents, aromatic aldehydes, heterocyclic aldehydes, formaldehyde, and acetaldehyde were used to explore the synthesis of 1,4-DHP (Kumar and Maurya, 2008).

In a variant of Hantzsch dihydropyridine synthesis, polyhydroquinoline derivatives have also been furnished via unsymmetrical Hantzsch condensations of aldehydes (1 mmol), acetoacetic ester/acetyl acetone (1 mmol), and cyclic b-diketone (1 mmol) with NH_4OAc (1 mmol), in which the 1 eq. of ester in the traditional Hantzsch condensation was replaced by cyclic 1,3-diketone. The 4-component Hantzsch condensation was catalyzed by PTSA (10 mol%) for 1.5–3 h under sonication in aqueous micelles (Scheme 37.15).

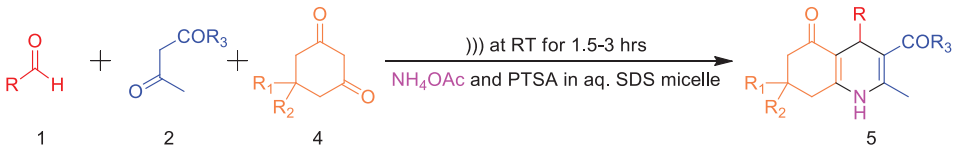
Under the above reaction conditions, moderate-to-excellent yields (72%–92%) of 17 examples of polyhydroquinoline derivatives were achieved with various functional groups, e.g., hydroxy, chloro, nitro, methoxy, and unsaturation. However, when acetylacetone replaced acetoacetic ester as a reactant, a longer time (3 h) was required to accomplish the Hantzsch reaction, giving lower yields (72%–75%). As a result, 4-component symmetrical and unsymmetrical Hantzsch reactions can be achieved with the PTSA catalyst at RT in 1–3 h under sonication in aqueous SDS micelles (Kumar and Maurya, 2008).



SCHEME 37.13 Hantzsch condensation of an aldehyde, two equivalents of β-ketoester and ammonia in ethanol Debache et al., (2008).

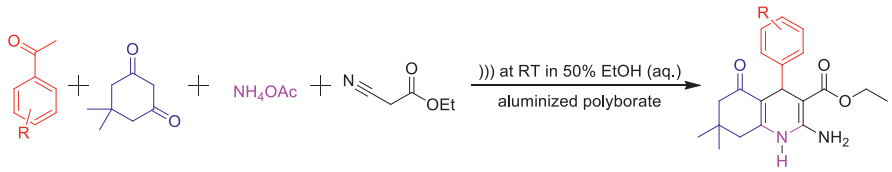


SCHEME 37.14 Ultrasound-assisted Hantzsch condensation of benzaldehyde and ethyl acetoacetate with NH_4OAc and PTSA in aqueous SDS micelles (Kumar and Maurya, 2008).

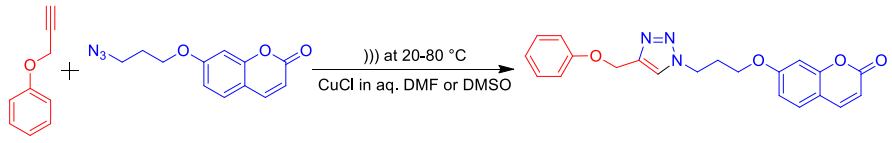


1 2 4 5

SCHEME 37.15 4-Component Hantzsch condensation catalyzed by PTSA in aqueous SDS micelles under sonication (Kumar and Maurya, 2008).



SCHEME 37.16 US-assisted Hantzsch condensation of aromatic aldehydes, dimedone, ethyl cyanoacetate, and NH_4OAc in aqueous ethanol solutions (Aute et al., 2020).



5 4 6

SCHEME 37.17 CuCl-catalyzed Huisgen cycloaddition in aqueous DMF or DMSO solutions under sonication (Li et al., 2016).

Very recently, Aute et al. (2020) reported the US-assisted one-pot 4-component synthesis of hexahydroquinoline derivatives under the catalysis by aluminized polyborate, with the Hantzsch condensation of aromatic aldehydes, dimedone, ethyl cyanoacetate, and NH_4OAc, which was performed in 50% EtOH aqueous media at RT (Scheme 37.16). As a result, excellent yields were achieved with the recyclable aluminized polyborate catalyst in short reaction times. The reaction procedure and workup were simple, clean, and environmentally benign.

37.8 Huisgen cycloaddition

Triazoles are five-membered heterocyclic compounds that contain three nitrogen atoms in the stable heterocyclic core. Triazoles exhibit diverse pharmacological activities, meaning that they are widely used in antifungal, antimalarial, antimicrobial, antitumor, antiviral, and antioxidant agents as well as in fungicides. Generally, 1,2,3-triazoles are prepared via the Huisgen cycloaddition of azides and alkynes under mild conditions (Kashyap and Silakari, 2018; Khandelwal et al., 2020). However, the Huisgen cycloaddition usually results in two regioisomers. A Cu(I) catalyst was thus used to improve the conversion and regioselectivity of the cycloaddition. To prepare coumarin derivatives with diverse bioactivities (Lei et al., 2015), Li et al. (2016) explored the CuCl-catalyzed 1,3-dipolar Huisgen cycloaddition "on water" at RT under sonication. Typically, 7-(3-azidopropoxy)coumarin **4**, prepared in advance, reacted with propargyl phenyl ether **5** under sonication (40 kHz, 150 W) in an ultrasonic cleaner to form 7-hydroxycoumarin derivatives that contain triazole **6** (Scheme 37.17).

Additional bases or ligands, e.g., triethylamine, are usually required in the Huisgen cycloaddition catalyzed by Cu(I) salts to produce stable complexes with the Cu(I) ion. Higher yields (over 90%) were achieved under sonication in water than those (ca. 25%–50%) obtained in water-containing co-solvents (DMF/H_2O and DMSO/H_2O). Furthermore, in water, the yields increased sharply with sonication power (60–150 W), temperature (20–80°C), and CuCl loading (2–10 mol%) (Li et al., 2016). More significantly, the yields were higher under sonication without triethylamine than when the reaction was promoted with triethylamine under silent conditions, indicating that sonication can replace triethylamine, which is difficult to handle, to complete the Cu(I)-catalyzed Huisgen cycloaddition.

With different alkynes and azides under the optimal sonication conditions (150 W at RT in water with 10 mol% CuCl), the reactions of liquid reactants can be completed in 20 min, while the reactions of solid alkynes with poor water solubility were completed in 2 h, but good yields (89%–95%) were achieved in many cases. As a result, a series of coumarin derivatives with a variety of substituted alkynes and 7-(3-azidopropoxy)coumarin 4 were furnished with good yields (86%–95%) (Li et al., 2016).

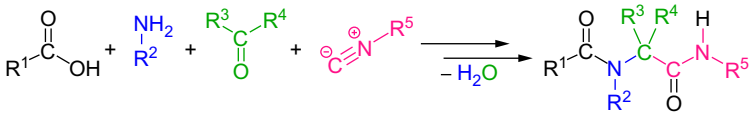
37.9 Ugi-azide reaction and Groebke-Blackburn-Bienaymé reaction

A 4-component reaction including carboxylic acids, amines, ketones or aldehydes, and isocyanides to generate a bis-amide was named the Ugi reaction (Scheme 37.18). The Ugi reaction works well in polar solvents, such as DMF, MeOH, EtOH, and H_2O. High atom economy and yields were achieved without catalysts (Ugi et al., 1959, 2003; Dömling and Ugi, 2000; Tripolitsiotis et al., 2020).

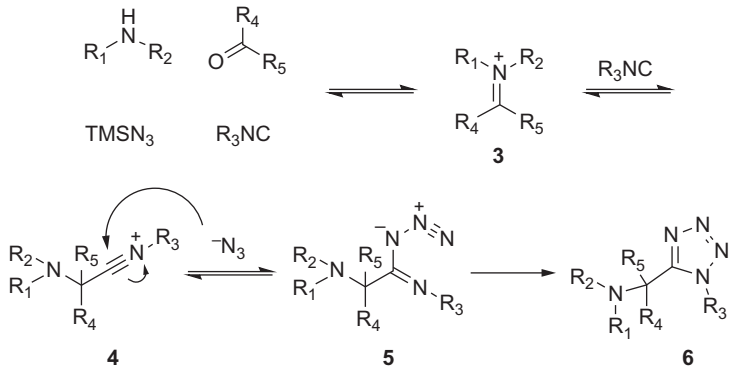
In a variant of the Ugi reaction, carboxylic acid was replaced by trimethylsilyl azide (TMS N_3) to furnish an interesting tetrazole moiety (Scheme 37.19, Ugi-azide reaction). The other three components were kept the same and the nucleophile azide caught the nitrilium intermediates 4, producing 1,5-disubstituted tetrazole (1,5-DS-T's) 6 via [3+2] intramolecular cyclization.

1,5-DS-Ts are a class of heterocycles that are important precursors for the manufacture of antifungal agents, bidentate ligands, metal-organic frameworks, bioimaging agents, photoimaging agents, and high energy materials. However, longer reaction times, higher temperatures (100–150°C), and toxic catalysts are usually required to prepare 1,5-DS-Ts. To accelerate the reaction, Unnamatla et al. (2016) studied the multicomponent one-pot synthesis of 3-tetrazolyl and 3-imidazo [1,2-a] pyridin tetrazolo [1,5-a] quinolines without catalysis at RT in MeOH using sonication and microwave heating, separately. Subsequently, Pharande et al. (2017), from the same group, reported an endogenous water-triggered protocol for the synthesis of 1,5-DS-Ts via the Ugi-azide reaction without catalysts under sonication (Scheme 37.20).

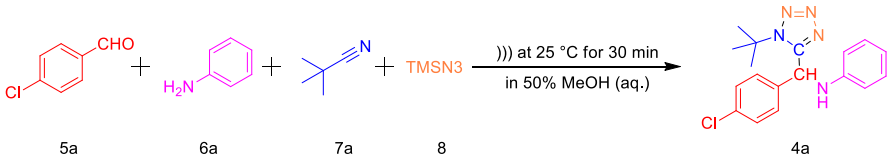
However, the Ugi-azide reaction of 4-chlorobenzaldehyde **5a**, aniline **6a**, *t*-butyl isocyanide **7a,** and $TMSN_3$ **8** cannot via stirring in water at 25°C for 24 h and 80°C for 12 h, but a trace yield was obtained in water at 25°C for 2 h under sonication (42 kHz). Surprisingly, the isolated yield reached 78% after 30 min sonication at 25°C in MeOH, which was higher than that (63%) obtained by stirring at 25°C for 12 h. The optimal yield (81%) was achieved under sonication at 25°C for 30 min in 50% aqueous MeOH solution. In comparison, the highest yield (97%, quantitative yield) was obtained at 25°C for 30 min under sonication in solvent-free conditions, which are



SCHEME 37.18 Synthesis of bis-amide via the Ugi reaction, a 4-component reaction, including carboxylic acids, amines, ketones or aldehydes, and isocyanides (Ugi et al., 1959).



SCHEME 37.19 Pathway of producing 1,5-DS-T 6 via Ugi-azide reaction (Gunawan et al., 2012)



SCHEME 37.20 Synthesis of 1,5-DS-Ts via the Ugi-azide reaction in aqueous methanol solutions at room temperature under sonication (Pharande et al., 2017).

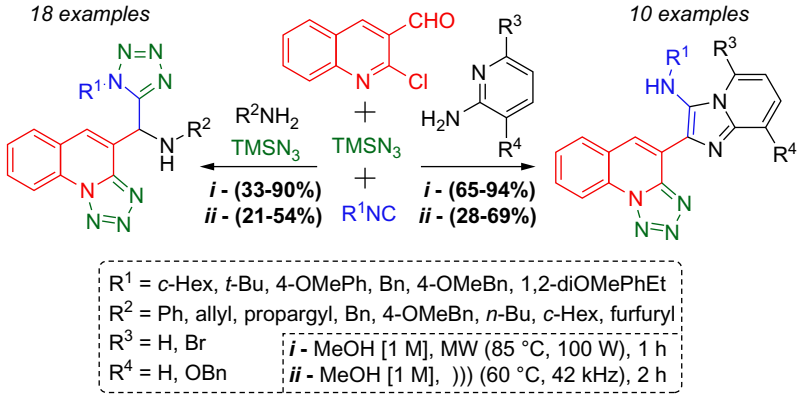
regarded as an environmentally friendly method in organic synthesis. It was speculated that $TMSN_3$ was transferred quickly into hexamethyldisiloxane and hydrazoic acid (HN_3) by water, which is generated in situ by condensation. In contrast, only a 75% yield was achieved for the solvent-free reaction at 25°C for 2 h with stirring. As a result, sonication reduced the reaction time and increased the yield of the Ugi-azide reaction (Pharande et al., 2017).

The Groebke-Blackburn-Bienaymé reaction (GBBR) is a variant of the Ugi-azide reaction that involves the one-pot reaction of heterocyclic amidines with aldehydes and isocyanides. It is an important isocyanide-based MCR for the preparation of fused imidazo heterocycles (Claudio-Catalán et al., 2018; Naseer, 2020). Unnamatla et al. (2016) compared the yields of MW heating and sonication for Ugi-azide- and GBBR-SNAr/ring-chain azido-tautomerization processes (Scheme 37.21).

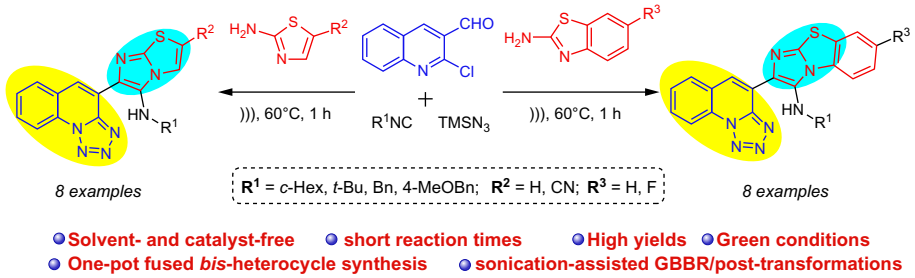
As shown in Scheme 37.21, the yields of the Ugi-azide reaction reached 33%–90% in the synthesis of 3-tetrazolyl-tetrazolo[1,5-*a*]quinolines at 85°C for 1 h with MW heating in 1 M MeOH solution. In contrast, the yields only reached 21%–54% in the same synthesis at 60°C for 2 h under sonication in 1 M MeOH. Likewise, the yields of GBBR reached 65%–94% in the synthesis of 3-imidazo[1,2-*a*] pyridin-tetrazolo[1,5-*a*]quinolines at 85°C for 1 h with MW heating in a 1 M MeOH solution. However, the yields of GBBR only reached 28%–69% in the same syntheses at 60°C for 2 h under sonication in 1 M MeOH. The enhanced efficiency of using MW heating on the Ugi-azide reaction and GBBR is higher than that of using sonication (Unnamatla et al., 2016).

Bis-heterocycles can be applied for the preparation of chelating agents, metal ligands, complexes and metal-organic frameworks, and bioactive molecules, e.g., antidiabetic and antifungal drugs. GBBR is an efficient method for the preparation of bis-heterocycles; however, the reaction is usually performed with expensive catalysts in hazardous solvent (toluene) or at high temperature (160°C). In order to improve US-assisted GBBR/post-transformations at 80°C for 12 h without catalysts, Claudio-Catalán et al. (2018) studied the one-pot syntheses of bound-type fused bis-heterocycle imidazo or benzo[*d*]imidazo[2,1-b] thiazoles and 1,5-DS-Ts that contain the quinoline moiety, which were endogenous water-triggered under environmentally benign conditions (Scheme 37.22 and Table 37.9).

As shown in Table 37.9, the unsymmetrical bound-type bis-heterocycles **12a** were expected to be furnished in water at 25°C after 24 h, and at 80°C after 12 h under traditional conditions, but no reaction occurred. Moreover, no reaction was observed at 25°C after 5 h using sonication, but a trace

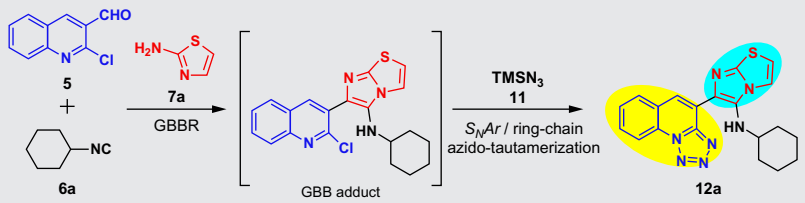


SCHEME 37.21 Sonochemical and microwave processes for Ugi-azide- and GBBR-SNAr/ring-chain azido-tautomerization in aqueous methanol solutions. *(Reprinted from Unnamatla et al. (2016). Copyright (2016), with permission from American Chemical Society.)*



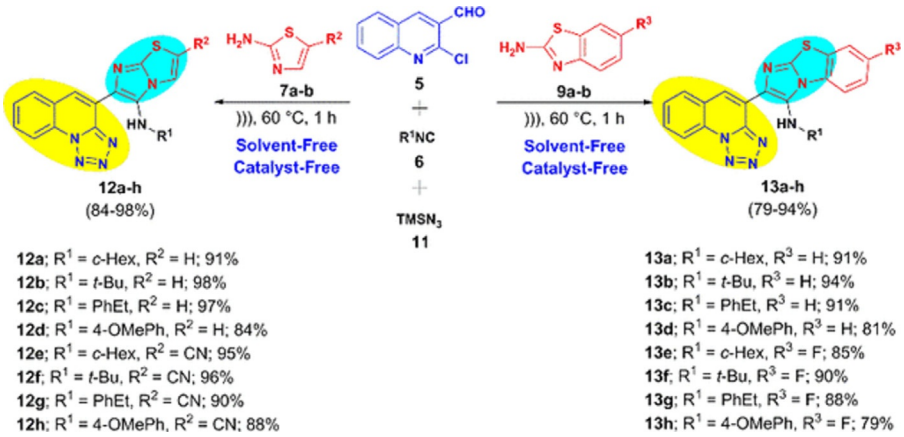
SCHEME 37.22 One-pot syntheses of Imidazo[2,1-*b*]thiazoles and Benzo[*d*]imidazo[2,1-*b*]thiazoles under sonication (Claudio-Catalán et al., 2018). *(Reprinted from Claudio-Catalán et al., (2018). Copyright (2018), with permission from the American Chemical Society.)*

TABLE 37.9 Optimization of the reaction conditions[a] (Claudio-Catalán et al., 2018)



Entry	Conditions	Temp (°C)	Time (h)	Yield[b] (%)
1	H_2O	25	24	NR
2	H_2O	80	12	NR
3	EtOH	25	24	Trace
4	EtOH	80	12	27
5	Neat	80	12	43
6	H_2O/US	25	5	NR
7	H_2O/US	60	2	Trace
8	EtOH/US	60	2	15
9	Neat/US	25	5	Trace
10	Neat/US	60	1	91

[a]*Reaction conditions: equimolar amounts of 5, 6a, 7a, and 11.* [b]*Yield of isolated product. USI (42 kHz).* NR, *no reaction.*
(Reprinted from Claudio-Catalán et al. (2018). Copyright (2018), with permission from the American Chemical Society.)



SCHEME 37.23 Substrate scope (Claudio-Catalán et al., 2018). The reaction was carried out using equimolar quantities of 5, 6, 11, and 7 or 9. *(Reprinted from Claudio-Catalán et al., (2018). Copyright (2018), with permission from the American Chemical Society.)*

yield was achieved at 60°C after 2 h under sonication. When water was replaced by EtOH as the reaction media, trace and 27% yields were achieved at 25°C after 24 h, and at 80°C after 12 h with reflux, respectively, while a 15% yield was obtained at 60°C after 2 h under sonication. Under solvent-free conditions, the yield reached 43% at 80°C after 12 h under silent conditions, and 91% at 60°C after 1 h using sonication (Claudio-Catalán et al., 2018). In summary, sonication can slightly increase the yield in water or EtOH media, but can significantly promote GBBR in the absence of a solvent.

Based on the above investigation, 2-aminoazines and isocyanides were varied to explore the scope of US-assisted GBBR/post-transformations (SNAr/ring-chain azido-tautomerization) without catalysts and solvents (Scheme 37.23). As shown in Scheme 37.23, 84%–98% yields for imidazo

[2,1-*b*]thiazoles **12a–h** were achieved under sonication at 60°C after 1 h, while the yields of benzo[*d*]imidazo[2,1-*b*] thiazoles **13a–h** also reached the range of 79%–94% (Claudio-Catalán et al., 2018).

Moreover, the Ugi reactions are also involved in US-assisted MCRs in water, in particular, the synthesis of pharmacologically significant compounds such as pseudopeptides that contain rhodanine scaffolds (Shaabani and Hooshmand, 2018). The mixture of various primary amines, carbon disulfide, maleic anhydride or itaconic anhydride, aromatic aldehydes, anilines, and isocyanides was sonicated in one pot to perform the tandem Michael/domino cycloaddition/Ugi reaction sequence at RT. As a result, good yields were achieved in this simple and environmentally benign approach.

37.10 Conclusions and future trends

Organic reactions in water or aqueous media remain a challenging task as well as the search of optimal conditions to improve conversion and yield of target products, meanwhile, to minimize the environmental impact. Nevertheless, several organic reactants are slightly soluble or insoluble in water. Aiming to improve the mass transfer under heterogeneous conditions, power ultrasound has been extensively exploited to promote organic reactions in aqueous media. Relevant sonochemical investigations have been herein reviewed, including Suzuki coupling reactions, Michael additions, Knoevenagel condensation, Diels-Alder cycloaddition, aza-Michael reaction, Hantzsch condensation or cyclization, Huisgen cycloaddition, Ugi-azide reaction, and Groebke-Blackburn-Bienaymé reaction. All these sonochemical reactions could be carried out under mild conditions, generally in good or excellent yields in short sonication times, while the use and generation of hazardous materials were dramatically reduced.

In view of greener synthetic procedures, further investigation and scaling-up studies of sonochemical organic reactions in water or aqueous media are expected. A valid ally in cavitation processes is hydrodynamic cavitation, which could be combined with sonication to intensify the organic reactions facilitating the scaling up.

References

Adapa, S., Varala, R., Sreelatha, N., 2006. Ceric ammonium nitrate catalyzed aza-Michael addition of aliphatic amines to α,β-unsaturated carbonyl compounds and nitriles in water. Synlett 2006, 1549–1553. https://doi.org/10.1055/s-2006-941588.

Akolkar, S.V., Kharat, N.D., Nagargoje, A.A., Subhedar, D.D., Shingate, B. B., 2020. Ultrasound-assisted β-cyclodextrin catalyzed one-pot cascade synthesis of pyrazolopyranopyrimidines in water. Catal. Lett. 150, 450–460. https://doi.org/10.1007/s10562-019-02968-4.

Al-Majid, A.M., Islam, M.S., Barakat, A., Al-Qahtani, N.J., Yousuf, S., Choudhary, M.I., 2017. Tandem Knoevenagel–Michael reactions in aqueous diethylamine medium: a greener and efficient approach toward bis-dimedone derivatives. Arab. J. Chem. 10, 185–193. https://doi.org/10.1016/j.arabjc.2014.04.008.

Anastas, P., Eghbali, N., 2010. Green chemistry: principles and practice. Chem. Soc. Rev. 39, 301–312. https://doi.org/10.1039/b918763b.

Andrade, M.A., Martins, L.M.D.R.S., 2020. New trends in c–c cross-coupling reactions: the use of unconventional conditions. Molecules 25, 120–129. https://doi.org/10.3390/molecules25235506.

Anna, G.d.S.S.'., Machado, P., Sauzem, P.D., Rosa, F.A., Rubin, M.A., Ferreira, J., Bonacorso, H.G., Zanatta, N., Martins, M.A.P., 2009. Ultrasound promoted synthesis of 2-imidazolines in water: a greener approach toward monoamine oxidase inhibitors. Bioorg. Med. Chem. Lett. 19, 546–549. https://doi.org/10.1016/j.bmcl.2008.03.001.

Arya, K., Rawat, D.S., Sasai, H., 2012. Zeolite supported Bronsted-acid ionic liquids: an eco approach for synthesis of spiro[indole-pyrido [3,2-e]thiazine] in water under ultrasonication. Green Chem. 14, 1956–1963. https://doi.org/10.1039/c2gc35168d.

Aute, D., Kshirsagar, A., Uphade, B., Gadhave, A., 2020. Ultrasound assisted and aluminized polyborate prompted green and efficient one pot protocol for the synthesis of hexahydroquinolines. Polycycl. Aromat. Compd. 31, 1313–1317. https://doi.org/10.1080/10406638.2020.1781206.

Azizi, N., Baghi, R., Ghafuri, H., Bolourtchian, M., Hashemi, M., 2010. Silicon tetrachloride catalyzed aza-Michael addition of amines to conjugated alkenes under solvent-free conditions. Synlett 2010, 379–382. https://doi.org/10.1055/s-0029-1219195.

Azizi, N., Rahimzadeh-Oskooee, A., Yadollahy, Z., Ourimi, A.G., 2014. Ultrasound-assisted rapid sustainable synthesis of substituted thiourea. Monatsh. Chem. 145, 1675–1680. https://doi.org/10.1007/s00706-014-1238-1.

Bai, L., Wang, J.-X., 2005. Environmentally friendly Suzuki aryl-aryl cross-coupling reaction. Curr. Org. Chem. 9, 535–553. https://doi.org/10.2174/1385272053544407.

Bandyopadhyay, D., Mukherjee, S., Turrubiartes, L.C., Banik, B.K., 2012. Ultrasound-assisted aza-Michael reaction in water: a green procedure. Ultrason. Sonochem. 19, 969–973. https://doi.org/10.1016/j.ultsonch.2011.11.009.

Banerjee, B., 2017a. Recent developments on ultrasound assisted catalyst-free organic synthesis. Ultrason. Sonochem. 35, 1–14. https://doi.org/10.1016/j.ultsonch.2016.09.023.

Banerjee, B., 2017b. Recent developments on ultrasound-assisted organic synthesis in aqueous medium. J. Serb. Chem. Soc. 82, 755–790. https://doi.org/10.2298/JSC170217057B.

Banerjee, B., 2020. Water-mediated catalyst-free organic transformations. Nanotechnol. Life Sci. 494, 63–95. https://doi.org/10.1007/978-3-030-44176-0_4.

Banitaba, S.H., Safari, J., Khalili, S.D., 2013. Ultrasound promoted one-pot synthesis of 2-amino-4,8-dihydropyrano[3,2-b] pyran-3-carbonitrile scaffolds in aqueous media: a complementary 'green chemistry' tool to organic synthesis. Ultrason. Sonochem. 20, 401–407. https://doi.org/10.1016/j.ultsonch.2012.07.007.

Barange, D.K., Kavala, V., Kuo, C.-W., Lei, P.-M., Yao, C.-F., 2011. Synthesis of C3-nitroalkylated-4-hydroxycoumarin and hydroxyiminodihydrofuroquinolinone derivatives via the Michael addition of cyclic 1,3-dicarbonyl compounds to β-nitrostyrenes. Tetrahedron 67, 2870–2877. https://doi.org/10.1016/j.tet.2011.02.062.

Bardajee, G.R., Jafarpour, F., Afsari, H.S., 2010. $ZrOCl_2{\cdot}8H_2O$: an efficient catalyst for rapid one-pot synthesis of 3-carboxycoumarins under ultrasound irradiation in water. Cent. Eur. J. Chem. 8, 370–374. https://doi.org/10.2478/s11532-009-0141-9.

Bauer, A., Miller, M.W., Vice, S.F., McCombie, S.W., 2001. Suzuki arylation of 1,1-dibromo-1-alkenes: synthesis of tetra-substituted alkenes. Synlett 2001, 254–256. https://doi.org/10.1055/s-2001-10776.

Bensa, D., Constantieux, T., Rodriguez, J., 2004. P-BEMP: a new efficient and commercially available user-friendly and recyclable heterogeneous organocatalyst for the Michael addition of 1,3-dicarbonyl compounds. Synthesis 35, 923–927. https://doi.org/10.1002/chin.200437080.

Berkessel, A., Vogl, N., 2006. DIANANE-CrIII-salen complexes as highly enantioselective catalysts for hetero-Diels–Alder reactions of aldehydes with dienes. Eur. J. Org. Chem., 5029–5035. https://doi.org/10.1002/ejoc.200600359.

Breslow, R., Maitra, U., Rideout, D., 1983. Selective Diels-Alder reactions in aqueous solutions and suspensions. Tetrahedron Lett. 24, 1901–1904. https://doi.org/10.1016/s0040-4039(00)81801-8.

Campos, J.F., Berteina-Raboin, S., 2020. Greener synthesis of nitrogen-containing heterocycles in water, peg, and bio-based solvents. Catalysts 10, 429. https://doi.org/10.3390/catal10040429.

Chanda, A., Fokin, V.V., 2009. Organic synthesis "on water". Chem. Rev. 109, 725–748. https://doi.org/10.1021/cr800448q.

Chandrakar, K., Patel, J.L., Mahapatra, S.P., Penta, S., 2020. Recent advances in on-water multicomponent synthesis of coumarin derivatives. Curr. Org. Chem. 24, 2601–2611. https://doi.org/10.2174/1385272824999201013164825.

Chate, A.V., Joshi, R.S., Badadhe, P.V., Dabhade, S.K., Gill, C.H., 2011. Efficient ultrasound enhance novel series of 2-((E)-2,3-dihydro-2-(4-(phenylthio)phenyl)benzo[b][1,4]thiazepin-4-yl)phenol as an antimicrobial agent. Bull. Korean Chem. Soc. 32, 3887–3892. https://doi.org/10.5012/bkcs.2011.32.11.3887.

Chate, A.V., Rathod, U.B., Kshirsagar, J.S., Gaikwad, P.A., Mane, K.D., Mahajan, P.S., Nikam, M.D., Gill, C.H., 2016. Ultrasound assisted multicomponent reactions: a green method for the synthesis of N-substituted 1, 8-dioxo-decahydroacridines using β-cyclodextrin as a supramolecular reusable catalyst in water. Chin. J. Catal. 37, 146–152. https://doi.org/10.1016/S1872-2067(15)61005-1.

Chauhan, S., Verma, P., Mishra, A., Srivastava, V., 2020. An expeditious ultrasound-initiated green synthesis of 1,2,4-thiadiazoles in water. Chem. Heterocycl. Compd. 56, 123–126. https://doi.org/10.1007/s10593-020-02632-5.

Chen, W.-B., Wu, Z.-J., Pei, Q.-L., Cun, L.-F., Zhang, X.-M., Yuan, W.-C., 2010. Highly enantioselective construction of spiro[4h-pyran-3,3′-oxindoles] through a domino Knoevenagel/Michael/Cyclization sequence catalyzed by cupreine. Org. Lett. 12, 3132–3135. https://doi.org/10.1021/ol1009224.

Chi, Y., Gellman, S.H., 2005. Diphenylprolinol methyl ether: a highly enantioselective catalyst for Michael addition of aldehydes to simple enones. Org. Lett. 7, 4253–4256. https://doi.org/10.1021/ol0517729.

Claudio-Catalán, M.Á., Pharande, S.G., Quezada-Soto, A., Kishore, K.G., Rentería-Gómez, A., Padilla-Vaca, F., Gámez-Montaño, R., 2018. Solvent- and catalyst-free one-pot green bound-type fused bis-heterocycles synthesis via Groebke-Blackburn-Bienaymé reaction/SNAr/Ring-Chain azido-tautomerization strategy. ACS Omega 3, 5177–5186. https://doi.org/10.1021/acsomega.8b00170.

Cravotto, G., Demetri, A., Nano, G.M., Palmisano, G., Penoni, A., Tagliapietra, S., 2003. The Aldol reaction under high-intensity ultrasound: a novel approach to an old reaction. Eur. J. Org. Chem. 19, 4438–4444. https://doi.org/10.1002/ejoc.200300369.

Cravotto, G., Orio, L., Gaudino, E.C., Martina, K., Tavor, D., Wolfson, A., 2011. Efficient synthetic protocols in glycerol under heterogeneous catalysis. ChemSusChem 4, 1130–1134. https://doi.org/10.1002/cssc.201100106.

Cravotto, G., Borretto, E., Oliverio, M., Procopio, A., Penoni, A., 2015. Organic reactions in water or biphasic aqueous systems under sonochemical conditions. A review on catalytic effects. Catal. Commun. 63, 2–9. https://doi.org/10.1016/j.catcom.2014.12.014.

Dai, M., Sarlah, D., Yu, M., Danishefsky, S.J., Jones, G.O., Houk, K.N., 2007. Highly selective Diels-Alder reactions of directly connected enyne dienophiles. J. Am. Chem. Soc. 129, 645–657. https://doi.org/10.1021/ja065762u.

Dam, B., Saha, M., Pal, A.K., 2015. Magnetically recyclable nano-FDP: a novel, efficient nano-organocatalyst for the one-pot multi-component synthesis of pyran derivatives in water under ultrasound irradiation. Catal. Lett. 145, 1808–1816. https://doi.org/10.1007/s10562-015-1586-4.

Dandia, A., Singh, R., Bhaskaran, S., Samant, S.D., 2011. Versatile three component procedure for combinatorial synthesis of biologically relevant scaffold spiro[indole-thiazolidinones] under aqueous conditions. Green Chem. 13, 1852–1859. https://doi.org/10.1039/c0gc00863j.

Das, P., Sharma, D., Shil, A., Singh, B., 2012. Consecutive Michael-Claisen process for cyclohexane-1,3-dione derivative (cdd) synthesis from unsubstituted and substituted acetone. Synlett 23, 1199–1204. https://doi.org/10.1055/s-0031-1290900.

Dasari, G.K., Sunkara, S., Gadupudi, P.C.R., 2020. One-step synthesis of magnetically recyclable palladium loaded magnesium ferrite nanoparticles: application in synthesis of anticancer drug PCI-32765. Inorg. Nano Met. Chem. 50, 753–763. https://doi.org/10.1080/24701556.2020.1724147.

Datta, B., Pasha, M.A., 2012. Glycine catalyzed convenient synthesis of 2-amino-4H-chromenes in aqueous medium under sonic condition. Ultrason. Sonochem. 19, 725–728. https://doi.org/10.1016/j.ultsonch.2012.01.006.

De Paolis, O., Baffoe, J., Landge, S.M., Török, B., 2008. Multicomponent domino cyclization-oxidative aromatization on a bifunctional Pd/C/K-10 catalyst: an environmentally benign approach toward the synthesis of pyridines. Synthesis 2008, 3423–3428. https://doi.org/10.1055/s-0028-1083177.

Debache, A., Boulcina, R., Belfaitah, A., Rhouati, S., Carboni, B., 2008. One-pot synthesis of 1, 4-dihydropyridines via a phenylboronic acid catalyzed Hantzsch three-component reaction. Synlett 2008, 509–512. https://doi.org/10.1055/s-2008-1032093.

Devi, V., Singh, G., Monga, V., 2020. Recent advances in the synthetic chemistry of 1,5-benzothiazepines: a minireview. J. Heterocyclic Chem. 57, 3255–3270. https://doi.org/10.1002/jhet.4062.

Dhakshinamoorthy, A., 2005. Cerium(IV) ammonium nitrate: a versatile oxidant in synthetic organic chemistry. Synlett 118, 3014–3015. https://doi.org/10.1055/s-2005-921893.

Diels, O., Alder, K., 1931. Synthesen in der hydroaromatischen Reihe. XII. Mitteilung. ("Dien-Synthesen" sauerstoffhaltiger Heteroringe. 2. Dien-Synthesen des Furans.). Justus Liebigs Ann. Chem. 490, 243–257. https://doi.org/10.1002/jlac.19314900110.

Ding, R., Katebzadeh, K., Roman, L., Bergquist, K.-E., Lindström, U.M., 2006. Expanding the scope of Lewis acid catalysis in water: remarkable ligand acceleration of aqueous ytterbium triflate catalyzed Michael addition reactions. J. Organomet. Chem. 71, 352–355. https://doi.org/10.1021/jo051540n.

Dolzhenko, A.V., 2020. Ethyl lactate and its aqueous solutions as sustainable media for organic synthesis. Sustain. Chem. Pharm. 18, 22855–22872. https://doi.org/10.1016/j.scp.2020.100322.

Dömling, A., Ugi, I., 2000. Multicomponent reactions with isocyanides. Angew. Chem. 39, 3168–3210. https://doi.org/10.1002/1521-3773(20000915)39:18<3168::aid-anie3168>3.0.co;2-u.

Dong, Z., Wang, L., Chen, X., Liu, X., Lin, L., Feng, X., 2009. Organocatalytic enantioselective Michael addition of 4-hydroxycoumarin to α,β-unsaturated ketones: a simple synthesis of warfarin. Eur. J. Org. Chem., 5192–5197. https://doi.org/10.1002/ejoc.200900831.

Dong, H., Yang, H., Du, Q., Zhang, T., Liu, Q., 2019. Ultrasonication-assisted synthesis of α, β-unsaturated compounds catalyzed by amino-functionalized FDU-12 catalyst. ChemistrySelect 4, 1463–1469. https://doi.org/10.1002/slct.201803899.

Draye, M., Chatel, G., Duwald, R., 2020. Ultrasound for drug synthesis: a green approach. Pharmaceuticals 13, 279–288. https://doi.org/10.3390/ph13020023.

Ebitani, K., Motokura, K., Mori, K., Mizugaki, T., Kaneda, K., 2006. Reconstructed hydrotalcite as a highly active heterogeneous base catalyst for carbon–carbon bond formations in the presence of water. J. Organomet. Chem. 71, 5440–5447. https://doi.org/10.1021/jo060345l.

Edrisi, M., Azizi, N., 2020. Sulfonic acid-functionalized graphitic carbon nitride composite: a novel and reusable catalyst for the one-pot synthesis of polysubstituted pyridine in water under sonication. J. Iran. Chem. Soc. 17, 901–910. https://doi.org/10.1007/s13738-019-01820-1.

El-bendary, M.M., Saleh, T.S., Al-Bogami, A.S., 2021. Synthesis and structural characterization of a palladium complex as an anticancer agent, and a highly efficient and reusable catalyst for the Heck coupling reaction under ultrasound irradiation: a convenient sustainable green protocol. Polyhedron 194, 1875–1881. https://doi.org/10.1016/j.poly.2020.114924.

Elhamifar, D., Ramazani, Z., Norouzi, M., Mirbagheri, R., 2018. Magnetic iron oxide/phenylsulfonic acid: a novel, efficient and recoverable nanocatalyst for green synthesis of tetrahydrobenzo[b]pyrans under ultrasonic conditions. J. Colloid Interface Sci. 511, 392–401. https://doi.org/10.1016/j.jcis.2017.10.013.

Esmaeilpour, M., Javidi, J., Dehghani, F., Nowroozi Dodeji, F., 2015. A green one-pot three-component synthesis of tetrahydrobenzo[b]pyran and 3,4-dihydropyrano[c]chromene derivatives using a Fe3O4@SiO2-imid-PMAn magnetic nanocatalyst under ultrasonic irradiation or reflux conditions. RSC Adv. 5, 26625–26633. https://doi.org/10.1039/c5ra01021g.

Esquivias, J., Arrayás, R.G., Carretero, J.C., 2007. Catalytic asymmetric inverse-electron-demand Diels–Alder reaction of N-sulfonyl-1-aza-1,3-dienes. J. Am. Chem. Soc. 129, 1480–1481. https://doi.org/10.1021/ja0658766.

Fringuelli, F., Pani, G., Piermatti, O., Pizzo, F., 1994. Condensation reactions in water of active methylene compounds with arylaldehydes. One-pot synthesis of flavonols. Tetrahedron 50, 11499–11508. https://doi.org/10.1016/s0040-4020(01)89287-5.

Fuentes, A., Martínez-Palou, R., Jiménez-Vázquez, H.A., Delgado, F., Reyes, A., Tamariz, J., 2005. Diels-Alder reactions of 2-oxazolidinone dienes in polar solvents using catalysis or non-conventional energy sources. Monatsh. Chem. 136, 177–192. https://doi.org/10.1007/s00706-004-0244-0.

Gawande, M.B., Bonifácio, V.D.B., Luque, R., Branco, P.S., Varma, R.S., 2013. Benign by design: catalyst-free in-water, on-water green chemical methodologies in organic synthesis. Chem. Soc. Rev. 42, 5522–5551. https://doi.org/10.1039/c3cs60025d.

Genest, A., Portinha, D., Fleury, E., Ganachaud, F., 2017. The aza-Michael reaction as an alternative strategy to generate advanced silicon-based (macro)molecules and materials. Prog. Polym. Sci. 72, 61–110. https://doi.org/10.1016/j.progpolymsci.2017.02.002.

Gomtsyan, A., 2000. Direct synthesis of β-aminoketones from amides via novel sequential nucleophilic substitution/Michael reaction. Org. Lett. 2, 11–13. https://doi.org/10.1021/ol9911122.

Gotoh, H., Hayashi, Y., 2007. Diarylprolinol silyl ether as catalyst of anexo-selective, enantioselective Diels–Alder reaction. Org. Lett. 9, 2859–2862. https://doi.org/10.1021/ol071009+.

Gracious, S.N., Kerru, N., Maddila, S., van Zyl, W.E., Jonnalagadda, S.B., 2020. Facile one-pot green synthesis of 2-amino-4H-benzo[g]chromenes in aqueous ethanol under ultrasound irradiation. Synth. Commun. 50, 1960–1971. https://doi.org/10.1080/00397911.2020.1761393.

Gunawan, S., Ayaz, M., Moliner, F.D., Frett, B., Kaiser, C., Patrick, N., Xu, Z., Hulme, C., 2012. Synthesis of tetrazolo-fused benzodiazepines and benzodiazepinones by a two-step protocol using an Ugi-azide reaction for initial diversity generation. Tetrahedron 68, 5606–5611. https://doi.org/10.1016/j.tet.2012.04.068.

Guo, X.-T., Shen, J., Sha, F., Wu, X.-Y., 2015. Highly enantioselective Michael addition of nitroalkanes to enones and its application in syntheses of (R)-baclofen and (R)-phenibut. Synthesis 47, 2063–2072. https://doi.org/10.1055/s-0034-1380203.

Hajipour, A.R., Sadeghi, A.R., Khorsandi, Z., 2018. Pd nanoparticles immobilized on magnetic chitosan as a novel reusable catalyst for green Heck and Suzuki cross-coupling reaction: in water at room temperature. Appl. Organomet. Chem. 32, e4112. https://doi.org/10.1002/aoc.4112.

Halland, N., Hansen, T., Jørgensen, K.A., 2003. Organocatalytic asymmetric Michael reaction of cyclic 1,3-dicarbonyl compounds and α,β-unsaturated ketones—a highly atom-economic catalytic one-step formation of optically active warfarin anticoagulant. Angew. Chem. Int. Ed. Engl. 42, 4955–4957. https://doi.org/10.1002/anie.200352136.

Han, J., Xu, Y., Su, Y., She, X., Pan, X., 2008. Guanidine-catalyzed Henry reaction and Knoevenagel condensation. Catal. Commun. 9, 2077–2079. https://doi.org/10.1016/j.catcom.2008.04.006.

Hara, T., Kanai, S., Mori, K., Mizugaki, T., Ebitani, K., Jitsukawa, K., Kaneda, K., 2006. Highly efficient C–C bond-forming reactions in aqueous media catalyzed by monomeric vanadate species in an apatite framework. J. Organomet. Chem. 71, 7455–7462. https://doi.org/10.1021/jo0614745.

Hasaninejed, A., Kazerooni, M.R., Zare, A., 2013. Room-temperature, catalyst-free, one-pot pseudo-five-component synthesis of 4,4-(arylmethylene)bis(3-methyl-1-phenyl-1H-pyrazol-5-ol)s under ultrasonic irradiation. ACS Sustain. Chem. Eng. 1, 679–684. https://doi.org/10.1021/sc400081c.

Hayashi, Y., Gotoh, H., Hayashi, T., Shoji, M., 2005. Diphenylprolinol silyl ethers as efficient organocatalysts for the asymmetric Michael reaction of aldehydes and nitroalkenes. Angew. Chem. Int. Ed. Engl. 44, 4212–4215. https://doi.org/10.1002/anie.200500599.

Hayashi, Y., Samanta, S., Gotoh, H., Ishikawa, H., 2008. Asymmetric Diels-Alder reactions of α,β-unsaturated aldehydes catalyzed by a diarylprolinol silyl ether salt in the presence of water. Angew. Chem. Int. Ed. Engl. 47, 6634–6637. https://doi.org/10.1002/anie.200801408.

Hernández, J.G., Juaristi, E., 2012. Recent efforts directed to the development of more sustainable asymmetric organocatalysis. Chem. Commun. 48, 5396–5409. https://doi.org/10.1039/c2cc30951c.

Hooshmand, S.E., Ghadari, R., Mohammadian, R., Shaabani, A., Khavasi, H.R., 2019. Rhodanine-furan bis-heterocyclic frameworks synthesis via green one-pot sequential six-component reactions: a synthetic and computational study. ChemistrySelect 4, 11893–11898. https://doi.org/10.1002/slct.201903361.

Huang, Y., Rawal, V.H., 2000. Hetero Diels–Alder reactions of 1-amino-3-siloxy-1,3-butadienes under strictly thermal conditions. Org. Lett. 2, 3321–3323. https://doi.org/10.1021/ol006404d.

Jaiswal, P.K., Sharma, V., Prikhodko, J., Mashevskaya, I.V., Chaudhary, S., 2017. "On water" ultrasound-assisted one pot efficient synthesis of functionalized 2-oxo-benzo[1,4]oxazines: first application to the synthesis of anticancer indole alkaloid, Cephalandole A. Tetrahedron Lett. 58, 2077–2083. https://doi.org/10.1016/j.tetlet.2017.03.048.

Jin, T.-S., Xiao, J.-C., Wang, S.-J., Li, T.-S., 2004. Ultrasound-assisted synthesis of 2-amino-2-chromenes with cetyltrimethylammonium bromide in aqueous media. Ultrason. Sonochem. 11, 393–397. https://doi.org/10.1016/j.ultsonch.2003.10.002.

Jin, T.-S., Liu, L.-B., Zhao, Y., Li, T.-S., 2005. A clean one-pot synthesis of 7-amino-5-aryl-6-cyano-1,5-dihydro-2H- pyrano[2,3-d] pyrimidine-2,4(3H)-diones in aqueous media under ultrasonic irradiation. J. Chem. Res. 50, 162–163. https://doi.org/10.3184/0308234054213672.

Jin, T.-S., Zhang, J.-S., Wang, A.-Q., Li, T.-S., 2006. Ultrasound-assisted synthesis of 1,8-dioxo-octahydroxanthene derivatives catalyzed by p-dodecylbenzenesulfonic acid in aqueous media. Ultrason. Sonochem. 13, 220–224. https://doi.org/10.1016/j.ultsonch.2005.04.002.

Ji-Tai, L.P., Xu, W.-Z., Chao, X., Li, T.-S., 2004. An efficient and practical synthesis of β-hydroxyl ketones catalysed by trisodium phosphate under ultrasound. J. Chem. Res. 28, 838–839. https://doi.org/10.1016/j.cclet.2017.01.015.

Joshi, R.S., Mandhane, P.G., Diwakar, S.D., Gill, C.H., 2010. Ultrasound assisted green synthesis of bis(indol-3-yl)methanes catalyzed by 1-hexenesulphonic acid sodium salt. Ultrason. Sonochem. 17, 298–300. https://doi.org/10.1016/j.ultsonch.2009.08.015.

Kamble, S.S., Shankarling, G.S., 2018. A unique blend of water, DES and ultrasound for one-pot Knorr pyrazole synthesis and Knoevenagel-Michael addition reaction. ChemistrySelect 3, 2032–2036. https://doi.org/10.1002/slct.201702898.

Kasar, S.B., Thopate, S.R., 2019. Ultrasonically assisted efficient and green protocol for the synthesis of 4h-isoxazol-5-ones using itaconic acid as a homogeneous and reusable organocatalyst. Curr. Organocatal. 6, 231–237. https://doi.org/10.2174/2213337206666190411115402.

Kashyap, A., Silakari, O., 2018. Triazoles: multidimensional 5-membered nucleus for designing multitargeting agents. In: Silakari, O. (Ed.), Key Heterocycle Cores Designing Multitargeting Molecules. Elsevier, pp. 323–342, https://doi.org/10.1016/B978-0-08-102083-8.00009-1 (Chapter 9).

Keipour, H., Hosseini, A., Khalilzadeh, M.A., Ollevier, T., 2015. Ultrasound-promoted knoevenagel condensation catalyzed by KF-clinoptilolite. Lett. Org. Chem. 12, 645–650.

Kelleher, F., Kelly, S., Watts, J., McKee, V., 2010. Structure–reactivity relationships of l-proline derived spirolactams and α-methyl prolinamide organocatalysts in the asymmetric Michael addition reaction of aldehydes to nitroolefins. Tetrahedron 66, 3525–3536. https://doi.org/10.1016/j.tet.2010.03.002.

Kerru, N., Maddila, S., Jonnalagadda, S.B., 2019. Design of carbon-carbon and carbon-heteroatom bond formation reactions under green conditions. Curr. Org. Chem. 23, 3154–3190. https://doi.org/10.2174/1385272823666191202105820.

Khandare, P.M., Ingale, R.D., Taware, A.S., Shisodia, S.U., Pawar, S.S., Kotai, L., Pawar, R.P., 2017. One pot synthesis and biological evaluation of pyranopyrazole in aqueous medium. Eur. Chem. Bull. 6, 410–414. https://doi.org/10.17628/ecb.2017.6.410-414.

Khandelwal, S., Tailor, Y.K., Rushell, E., Kumar, M., 2020. Use of sustainable organic transformations in the construction of heterocyclic scaffolds. In: Banik, B.K. (Ed.), Green Approaches Medicinal Chemistry Sustainable Drug Design. Elsevier, pp. 245–352, https://doi.org/10.1016/B978-0-12-817592-7.00009-5 (Chapter 9).

Khoraamabadi-Zad, A., Azadmanesh, M., Karamian, R., Asadbegy, M., Akbari, M., 2014. Triethanolamine as an inexpensive and efficient catalyst for the green synthesis of novel 1H-pyrazolo[1,2-a]pyridazine-5,8-diones under ultrasound irradiation in water and their antibacterial activity. RSC Adv. 4, 47721–47725. https://doi.org/10.1039/c4ra07096h.

Kidwai, M., 2006. Green chemistry trends toward sustainability. Pure Appl. Chem. 78, 1983–1992. https://doi.org/10.1351/pac200678111983.

Kidwai, M., Bansal, V., Mothsra, P., Saxena, S., Somvanshi, R.K., Dey, S., Singh, T.P., 2007. Molecular iodine: a versatile catalyst for the synthesis of bis(4-hydroxycoumarin) methanes in water. J. Mol. Catal. A Chem. 268, 76–81. https://doi.org/10.1016/j.molcata.2006.11.054.

Kim, H., Yen, C., Preston, P., Chin, J., 2006. Substrate-directed stereoselectivity in vicinal diamine-catalyzed synthesis of warfarin. J. Chin Org. Lett. 8, 5239–5242. https://doi.org/10.1021/ol062000v.

Kim, S., Kang, S., Kim, G., Lee, Y., 2016. Copper-catalyzed aza-Michael addition of aromatic amines or aromatic aza-heterocycles to α,β-unsaturated olefins. J. Organomet. Chem. 81, 4048–4057. https://doi.org/10.1021/acs.joc.6b00341.

Kiyani, H., Tazari, M., 2017. Aqua one-pot, three-component synthesis of dihydropyrano[3,2-c]chromenes and amino-benzochromenes catalyzed by sodium malonate. Res. Chem. Intermed. 43, 6639–6650. https://doi.org/10.1007/s11164-017-3011-7.

Kloetzel, M.C., 1948. The Diels-Alder reactions with maleic anhydride. Org. React. 4, 1–59. https://doi.org/10.1002/0471264180.or004.01.

Knoevenagel, E., 1898. Ueber den Chemismus der condensirenden Wirkung des Ammoniaks und organischer Amine bei Reactionen zwischen Aldehyden und Acetessigester. Ber. Dtsch. Chem. Ges. 31, 738–748. https://doi.org/10.1002/cber.189803101153.

Konkala, V.S., Dubey, P.K., 2017. One-pot synthesis of 3-phenyl-4-pyrazolylmethylene-isoxazol-(5h)-ones catalyzed by sodium benzoate in aqueous media under the influence of ultrasound waves: a green chemistry approach. J. Heterocyclic Chem. 54, 2483–2492. https://doi.org/10.1002/jhet.2848.

Kristensen, T.E., Vestli, K., Hansen, F.K., Hansen, T., 2009. New phenylglycine-derived primary amine organocatalysts for the preparation of optically active warfarin. Eur. J. Org. Chem., 5185–5191. https://doi.org/10.1002/ejoc.200900664.

Kumar, A., Maurya, R.A., 2008. Efficient synthesis of Hantzsch esters and polyhydroquinoline derivatives in aqueous micelles. Synlett 2008, 883–885.

Lei, L., Xue, Y., Liu, Z., Peng, S., He, Y., Zhang, Y., Fang, R., Wang, J., Luo, Z., Yao, G., Zhang, J., Zhang, G., Song, H., Zhang, Y., 2015. Coumarin derivatives from Ainsliaea fragrans and their anticoagulant activity. Sci. Rep. 5, 13544. https://doi.org/10.1038/srep13544.

Li, G.Y., 2002. Highly active, air-stable palladium catalysts for the C–C and C–C bond-forming reactions of vinyl and aryl chlorides: use of commercially available $[(t\text{-Bu})_2P(OH)]_2PdCl_2$, $[(t\text{-Bu})_2P(OH)PdCl_2]_2$, and $[[(t\text{-Bu})_2PO\cdots H\cdots OP(t\text{-Bu})_2]PdCl]_2$ as catalysts. J. Organomet. Chem. 67, 3643–3650. https://doi.org/10.1021/jo010983y.

Li, J.-T., Li, T.-S., Li, L.-J., Cheng, X., 1999. Synthesis of ethyl α-cyanocinnamates under ultrasound irradiation. Ultrason. Sonochem. 6, 199–201. https://doi.org/10.1016/s1350-4177(99)00014-0.

Li, J.-T., Lin, Z.-P., Han, J.-F., Li, T.-S., 2004. One-pot synthesis of 4-oxo-2-thioxohexahydropyrimidines catalyzed by potassium carbonate under ultrasound. Synth. Commun. 35. https://doi.org/10.1002/chin.200450121.

Li, J.-T., Wang, S.-X., Chen, G.-F., Li, T.-S., 2005. Some applications of ultrasound irradiation in organic synthesis. Curr. Org. Synth. 2, 415–436. https://doi.org/10.2174/1570179054368509.

Li, X., Chen, X., Jiang, Y., Chen, S., Qu, L., Qu, Z., Yuan, J., Shi, H., 2016. Highly efficient ultrasonic-assisted cucl-catalyzed 1,3-dipolar cycloaddition reactions in water: synthesis of coumarin derivatives linked with 1,2,3-triazole moiety. J. Heterocyclic Chem. 53, 1402–1411. https://doi.org/10.1002/jhet.2175.

Li, C., Qi, C., Zhang, F., 2020a. Ultrasonic promoted synthesis of 1,6-naphthyridine derivatives catalyzed by solid acid in water. Tetrahedron Lett. 61, 82–91. https://doi.org/10.1016/j.tetlet.2020.152144.

Li, C., Qi, C., Zhang, F., 2020b. An efficient strategy for the synthesis of 1,6-naphthyridine-2,5-dione derivatives under ultrasound irradiation. Synlett 31, 1313–1317. https://doi.org/10.1055/s-0040-1707469.

Liu, D., Canales, E., Corey, E.J., 2007. Chiral oxazaborolidine–aluminum bromide complexes are unusually powerful and effective catalysts for enantioselective Diels–Alder reactions. J. Am. Chem. Soc. 129, 1498–1499. https://doi.org/10.1021/ja068637r.

Lupacchini, M., Mascitti, A., Giachi, G., Tonucci, L., d'Alessandro, N., Martinez, J., Colacino, E., 2017. Sonochemistry in non-conventional, green solvents or solvent-free reactions. Tetrahedron 73, 609–653. https://doi.org/10.1016/j.tet.2016.12.014.

Maggi, R., Bigi, F., Carloni, S., Mazzacani, A., Sartori, G., 2001. Uncatalysed reactions in water: part 2. Preparation of 3-carboxycoumarins. Green Chem. 3, 173–174. https://doi.org/10.1039/b101822c.

Mahdavinia, G.H., Rostamizadeh, S., Amani, A.M., Emdadi, Z., 2009. Ultrasound-promoted greener synthesis of aryl-14-H-dibenzo[a,j]xanthenes catalyzed by NH4H2PO4/SiO2 in water. Ultrason. Sonochem. 16, 7–10. https://doi.org/10.1016/j.ultsonch.2008.05.010.

Maleki, A., Rahimi, J., Demchuk, O.M., Wilczewska, A.Z., Jasiński, R., 2018. Green in water sonochemical synthesis of tetrazolopyrimidine derivatives by a novel core-shell magnetic nanostructure catalyst. Ultrason. Sonochem. 43, 262–271. https://doi.org/10.1016/j.ultsonch.2017.12.047.

Mason, T.J., 1997. Ultrasound in synthetic organic chemistry. Chem. Soc. Rev. 26, 443. https://doi.org/10.1039/cs9972600443.

Maury, S.K., Kumar, D., Kamal, A., Singh, H.K., Kumari, S., Singh, S., 2021. A facile and efficient multicomponent ultrasound-assisted "on water" synthesis of benzodiazepine ring. Mol. Divers. 25, 131–142. https://doi.org/10.1007/s11030-019-10031-y.

McNulty, J., Steere, J.A., Wolf, S., 1998. The ultrasound promoted Knoevenagel condensation of aromatic aldehydes. Tetrahedron Lett. 39, 8013–8016. https://doi.org/10.1016/s0040-4039(98)01789-4.

Miyaura, N., Suzuki, A., 1995. Palladium-catalyzed cross-coupling reactions of organoboron compounds. Chem. Rev. 95, 2457–2483. https://doi.org/10.1021/cr00039a007.

Mondal, D., Kalar, P.L., Kori, S., Gayen, S., Das, K., 2020. Recent developments on synthesis of indole derivatives through green approaches and their pharmaceutical applications. Curr. Org. Chem. 24, 2665–2693. https://doi.org/10.2174/1385272824999201111203812.

Mosallanezhad, A., Kiyani, H., 2019. Green synthesis of 3-substituted-4-arylmethylideneisoxazol-5(4h)-one derivatives catalyzed by salicylic acid. Curr. Organocatal. 6, 28–35. https://doi.org/10.2174/2213337206666190214161332.

Narsaiah, A.V., Basak, A.K., Visali, B., Nagaiah, K., 2004. An eco-friendly synthesis of electrophilic alkenes catalyzed by dimethylaminopyridine under solvent-free conditions. Synth. Commun. 34, 2893–2901. https://doi.org/10.1081/scc-200026625.

Naseer, M.M., 2020. Three heterocyclic rings fused (5-5-6). In: Reference Module Chemistry, Molecular Sciences Chemical Engineering. Elsevier, https://doi.org/10.1016/B978-0-12-409547-2.14827-9.

Nicolaou, K.C., Snyder, S.A., Montagnon, T., Vassilikogiannakis, G., 2002. The Diels-Alder reaction in total synthesis. Angew. Chem. Int. Ed. 41, 1668–1698. https://doi.org/10.1002/1521-3773(20020517)41:10<1668::aid-anie1668>3.0.co;2-z.

Nikoofar, K., Shahriyari, F., 2021. Ultrasound-assisted aqua-mediated synthesis of multi-substituted tetrahydropyridine-3-carboxylates using N-carboxymethyl-3-pyridinium hydrogensulfate ($[N\text{-}CH_2CO_2H\text{-}3\text{-}pic]^+HSO_4^-$) as a new efficient ionic liquid catalyst. SN Appl. Sci. 3, 6639–6650. https://doi.org/10.1007/s42452-021-04671-9.

Okino, T., Hoashi, Y., Takemoto, Y., 2003. Enantioselective Michael reaction of malonates to nitroolefins catalyzed by bifunctional organocatalysts. J. Am. Chem. Soc. 125, 12672–12673. https://doi.org/10.1021/ja036972z.

Okino, T., Hoashi, Y., Furukawa, T., Xu, X., Takemoto, Y., 2005. Enantio- and diastereoselective Michael reaction of 1,3-dicarbonyl compounds to nitroolefins catalyzed by a bifunctional thiourea. J. Am. Chem. Soc. 127, 119–125. https://doi.org/10.1021/ja044370p.

Ooi, T., Ohara, D., Fukumoto, K., Maruoka, K., 2005. Importance of chiral phase-transfer catalysts with dual functions in obtaining high enantioselectivity in the Michael reaction of malonates and chalcone derivatives. Org. Lett. 7, 3195–3197. https://doi.org/10.1021/ol050902a.

Organ, M.G., Cooper, J.T., Rogers, L.R., Soleymanzadeh, F., Paul, T., 2000. Synthesis of stereodefined polysubstituted olefins. 1. Sequential intermolecular reactions involving selective, stepwise insertion of Pd(0) into allylic and vinylic halide bonds. The stereoselective synthesis of disubstituted olefins 1. J. Organomet. Chem. 65, 7959–7970. https://doi.org/10.1021/jo001045l.

Pagadala, R., Anugu, S., 2018. Synthesis of polyfunctionalized pyrroles via green chemical methods. J. Heterocyclic Chem. 55, 181–186. https://doi.org/10.1002/jhet.3022.

Palmisano, G., Tibiletti, F., Penoni, A., Colombo, F., Tollari, S., Garella, D., Tagliapietra, S., Cravotto, G., 2011. Ultrasound-enhanced one-pot synthesis of 3-(Het)arylmethyl-4-hydroxycoumarins in water. Ultrason. Sonochem. 18, 652–660. https://doi.org/10.1016/j.ultsonch.2010.08.009.

Palomo, C., Vera, S., Mielgo, A., Gómez-Bengoa, E., 2006. Highly efficient asymmetric Michael addition of aldehydes to nitroalkenes catalyzed by a simpletrans-4-hydroxyprolylamide. Angew. Chem. Int. Ed. Engl. 45, 5984–5987. https://doi.org/10.1002/anie.200602207.

Patel, A.J., Dholakia, A.B., Patel, V.C., 2021. A green perspective: synthesis of 2-chloro-3-formylquinolines and its derivatives. Synth. Commun. 51, 163–190. https://doi.org/10.1080/00397911.2020.1824277.

Paul, S., Gupta, R., Gupta, R., Loupy, A., 2007. Covalently anchored sulfonic acid on silica gel as an efficient and reusable heterogeneous catalyst for the one-pot synthesis of Hantzsch 1,4-dihydropyridines under

solvent-free conditions. Synthesis 2007, 2835–2838. https://doi.org/10.1055/s-2007-983839.

Payette, J.N., Yamamoto, H., 2007. Regioselective and asymmetric Diels–Alder reaction of 1- and 2-substituted cyclopentadienes catalyzed by a Brønsted acid activated chiral oxazaborolidine. J. Am. Chem. Soc. 129, 9536–9537. https://doi.org/10.1021/ja0735958.

Pelliccia, S., Abbate, V., Meneghetti, F., Frascione, N., Hider, R.C., Novellino, E., Tron, G.C., Giustiniano, M., 2018. On-water pyrrolidine-mediated domino synthesis of 2-iminoisatins. Green Chem. 20, 3912–3915. https://doi.org/10.1039/c8gc01090k.

Pharande, S.G., Corrales Escobosa, A.R., Gámez-Montaño, R., 2017. Endogenous water-triggered and ultrasound accelerated synthesis of 1,5-disubstituted tetrazoles: via a solvent and catalyst-free Ugi-azide reaction. Green Chem. 19, 1259–1262. https://doi.org/10.1039/c6gc03324e.

Poláčková, V., Hut'ka, M., Toma, Š., 2005. Ultrasound effect on Suzuki reactions. 1. Synthesis of unsymmetrical biaryls. Ultrason. Sonochem. 12, 99–102. https://doi.org/10.1016/j.ultsonch.2004.05.011.

Ramazani, A., Rouhani, M., Joo, S.W., 2016. Catalyst-free sonosynthesis of highly substituted propanamide derivatives in water. Ultrason. Sonochem. 28, 393–399. https://doi.org/10.1016/j.ultsonch.2015.08.019.

Ranu, B.C., Banerjee, S., 2005. Ionic liquid as catalyst and reaction medium. The dramatic influence of a task-specific ionic liquid, [bmim]OH, in Michael addition of active methylene compounds to conjugated ketones, carboxylic esters, and nitriles. Org. Lett. 7, 3049–3052. https://doi.org/10.1021/ol051004h.

Ranu, B.C., Banerjee, S., 2007. Significant rate acceleration of the aza-Michael reaction in water. Tetrahedron Lett. 48, 141–143. https://doi.org/10.1016/j.tetlet.2006.10.142.

Reddy, K., Kumar, N., 2006. Cellulose-supported copper(0) catalyst for aza-Michael addition. Synlett 2006, 2246–2250. https://doi.org/10.1055/s-2006-949623.

Rideout, D.C., Breslow, R., 1980. Hydrophobic acceleration of Diels-Alder reactions. J. Am. Chem. Soc. 102, 7816–7817. https://doi.org/10.1021/ja00546a048.

Rogozińska-Szymczak, M., Mlynarski, J., 2014. Asymmetric synthesis of warfarin and its analogues on water. Tetrahedron Asymmetry 25, 813–820. https://doi.org/10.1016/j.tetasy.2014.04.008.

Ross, A.G., Townsend, S.D., Danishefsky, S.J., 2013. Halocycloalkenones as Diels–Alder dienophiles. applications to generating useful structural patterns. J. Organomet. Chem. 78, 204–210. https://doi.org/10.1021/jo302230m.

Rostamizadeh, S., Amani, A.M., Mahdavinia, G.H., Amiri, G., Sepehrian, H., 2010. Ultrasound promoted rapid and green synthesis of 1,8-dioxo-octahydroxanthenes derivatives using nanosized MCM-41-SO_3H as a nanoreactor, nanocatalyst in aqueous media. Ultrason. Sonochem. 17, 306–309. https://doi.org/10.1016/j.ultsonch.2009.10.004.

Rostamnia, S., Lamei, K., 2011. A rapid, catalyst-free, three-component synthesis of rhodanines in water using ultrasound. Synthesis 28, 3080–3082. https://doi.org/10.1055/s-0030-1260158.

Safari, J., Banitaba, S.H., Khalili, S.D., 2012. Ultrasound-promoted an efficient method for one-pot synthesis of 2-amino-4,6-diphenylnicotinonitriles in water: a rapid procedure without catalyst. Ultrason. Sonochem. 19, 1061–1069. https://doi.org/10.1016/j.ultsonch.2012.01.005.

Safari, J., Heydarian, M., Zarnegar, Z., 2017. Synthesis of 2-amino-7-hydroxy-4H-chromene derivatives under ultrasound irradiation: a rapid procedure without catalyst. Arab. J. Chem. 10, S2994–S3000. https://doi.org/10.1016/j.arabjc.2013.11.038.

Sahiba, N., Teli, P., Agarwal, S., 2021. "On water" and "in water" strategies for heterocyclic transformations. In: Advances in Organic Synthesis. Bentham Science Publishers, pp. 1–71, https://doi.org/10.2174/9789811803741121140003 (Chapter 1).

Said, K., Mesni, A., Salem, R.B., 2020. Antioxidant properties of synthesis nanometallic Pd-Ni@2-mercaptoethanol as effective catalyst for suzuki-miyaura reactions. Lett. Org. Chem. 17, 36–45. https://doi.org/10.2174/1570178616666190319160151.

Sancheti, S.V., Gogate, P.R., 2018. Intensification of heterogeneously catalyzed Suzuki-Miyaura cross-coupling reaction using ultrasound: understanding effect of operating parameters. Ultrason. Sonochem. 40, 30–39. https://doi.org/10.1016/j.ultsonch.2017.01.037.

Sapkal, A., Kamble, S., 2020. Sodium toluene-4-sulfonate as a reusable and ecofriendly catalyst for greener synthesis of 5-aminopyrazole-4-carbonitrile in aqueous medium. J. Heterocyclic Chem. 57, 3597–3604. https://doi.org/10.1002/jhet.4077.

Sarkar, D., Bhattarai, R., Headley, A.D., Ni, B., 2011. A novel recyclable organocatalytic system for the highly asymmetric Michael addition of aldehydes to nitroolefins in water. Synthesis 42, 1993–1997. https://doi.org/10.1002/chin.201145047.

Shaabani, A., Hooshmand, S.E., 2018. Diversity-oriented catalyst-free synthesis of pseudopeptides containing rhodanine scaffolds via a one-pot sequential isocyanide-based six-component reactions in water using ultrasound irradiation. Ultrason. Sonochem. 40, 84–90. https://doi.org/10.1016/j.ultsonch.2017.06.030.

Shabalala, N.G., Pagadala, R., Jonnalagadda, S.B., 2015. Ultrasonic-accelerated rapid protocol for the improved synthesis of pyrazoles. Ultrason. Sonochem. 27, 423–429. https://doi.org/10.1016/j.ultsonch.2015.06.005.

Shaikh, M., Wagare, D., Sonone, A., Durrani, A., 2020. Highly efficient ultrasound promoted synthesis of 2-phenylquinoxaline in glycerol-water. Curr. Org. Synth. 17, 483–487. https://doi.org/10.2174/1570179417666200529121602.

Sharafian, S., Hossaini, Z., Rostami-Charati, F., Khalilzadeh, M.A., 2021. Ultrasound-promoted green synthesis of pyrido[2,1-a]isoquinoline derivatives and studies on their antioxidant activity. Comb. Chem. High Throughput Screen. 24, 119–128. https://doi.org/10.2174/1386207323666200606212501.

Smith, A., Atasoylu, O., Beshore, D., 2009. Construction of 5,6-ring-fused 2-pyridones: an effective annulation tactic achieved in water. Synlett 2009, 2643–2646. https://doi.org/10.1055/s-0029-1217749.

Suslick, K.S., 1990. Sonochemistry. Science 247, 1439–1445. https://doi.org/10.1126/science.247.4949.1439.

Tang, M., Wang, H., 2017. Aluminum chloride promoted Hantzsch reaction of N-tosylhydrazones. Synthesis 49, 4893–4898. https://doi.org/10.1055/s-0036-1588496.

Teo, Y.-C., Loh, T.-P., 2005. Catalytic enantioselective Diels-Alder reaction via a chiral Indium (III) complex. Org. Lett. 7, 2539–2541. https://doi.org/10.1021/ol050518d.

Tripolitsiotis, N.P., Thomaidi, M., Neochoritis, C.G., 2020. The Ugi three-component reaction; A valuable tool in modern organic synthesis. Eur. J. Org. Chem., 6525–6554. https://doi.org/10.1002/ejoc.202001157.

Ugi, I., Meyr, R., Fetzer, U., 1959. Versuche mit Isonitrilen. Angew. Chem. 71, 386.

Ugi, I., Werner, B., Dömling, A., 2003. The chemistry of isocyanides, their multicomponent reactions and their libraries. Molecules 8, 53–66. https://doi.org/10.3390/80100053.

Unnamatla, M.V.B., Islas-Jácome, A., Quezada-Soto, A., Ramírez-López, S.C., Flores-Álamo, M., Gámez-Montaño, R., 2016. Multicomponent one-pot synthesis of 3-tetrazolyl and 3-imidazo[1,2-a]pyridin

tetrazolo[1,5-a]quinolines. J. Organomet. Chem. 81, 10576–10583. https://doi.org/10.1021/acs.joc.6b01576.

Varma, R.S., 2016. Greener and sustainable trends in synthesis of organics and nanomaterials. ACS Sustain. Chem. Eng. 4, 5866–5878. https://doi.org/10.1021/acssuschemeng.6b01623.

Wang, S.-X., Li, J.-T., Yang, W.-Z., Li, T.-S., 2002. Synthesis of ethyl α-cyanocinnamates catalyzed by KF–Al2O3 under ultrasound irradiation. Ultrason. Sonochem. 9, 159–161. https://doi.org/10.1016/s1350-4177(01)00115-8.

Wang, L.-M., Sheng, J., Zhang, L., Han, J.-W., Fan, Z.-Y., Tian, H., Qian, C.-T., 2005. Facile Yb (OTf) 3 promoted one-pot synthesis of polyhydroquinoline derivatives through Hantzsch reaction. Tetrahedron 61, 1539–1543. https://doi.org/10.1016/j.tet.2004.11.079.

Willis, M.C., Chauhan, J., Whittingham, W.G., 2005. A new reactivity pattern for vinyl bromides: cine-substitution via palladium catalysed C–N coupling/Michael addition reactions. Org. Biomol. Chem. 3, 3094. https://doi.org/10.1039/b508464d.

Wu, F., Li, H., Hong, R., Deng, L., 2006. Construction of quaternary stereocenters by efficient and practical conjugate additions to α,β-unsaturated ketones with a chiral organic catalyst. Angew. Chem. Int. Ed. Engl. 45, 947–950. https://doi.org/10.1002/anie.200502658.

Wu, Z., Borretto, E., Medlock, J., Bonrath, W., Cravotto, G., 2014. Effects of ultrasound and microwaves on selective reduction: catalyst preparation and reactions. ChemCatChem 6, 2762–2783. https://doi.org/10.1002/cctc.201402221.

Wu, Z., Cherkasov, N., Cravotto, G., Borretto, E., Ibhadon, A.O., Medlock, J., Bonrath, W., 2015. Ultrasound- and microwave-assisted preparation of lead-free palladium catalysts: effects on the kinetics of diphenylacetylene semi-hydrogenation. ChemCatChem 7, 952–959. https://doi.org/10.1002/cctc.201402999.

Wu, Z., Cravotto, G., Gaudino, E.C., Giacomino, A., Medlock, J., Bonrath, W., 2017. Ultrasonically improved semi-hydrogenation of alkynes to (Z-) alkenes over novel lead-free Pd/Boehmite catalysts. Ultrason. Sonochem. 35, 664–672. https://doi.org/10.1016/j.ultsonch.2016.05.019.

Wu, C., Lu, L.-H., Peng, A.-Z., Jia, G.-K., Peng, C., Cao, Z., Tang, Z., He, W.-M., Xu, X., 2018. Ultrasound-promoted Brønsted acid ionic liquid-catalyzed hydrothiocyanation of activated alkynes under minimal solvent conditions. Green Chem. 20, 3683–3688. https://doi.org/10.1039/c8gc00491a.

Wu, Z., Tagliapietra, S., Giraudo, A., Martina, K., Cravotto, G., 2019. Harnessing cavitational effects for green process intensification. Ultrason. Sonochem. 52, 530–546. https://doi.org/10.1016/j.ultsonch.2018.12.032.

Xie, J.-W., Yue, L., Chen, W., Du, W., Zhu, J., Deng, J.-G., Chen, Y.-C., 2007. Highly enantioselective Michael addition of cyclic 1,3-dicarbonyl compounds to α,β-unsaturated ketones. Org. Lett. 9, 413–415. https://doi.org/10.1021/ol062718a.

Xie, L.-Y., Li, Y.-J., Qu, J., Duan, Y., Hu, J., Liu, K.-J., Cao, Z., He, W.-M., 2017. A base-free, ultrasound accelerated one-pot synthesis of 2-sulfonylquinolines in water. Green Chem. 19, 5642–5646. https://doi.org/10.1039/c7gc02304a.

Yadav, D.K., Quraishi, M., 2014. Choline chloride. ZnCl2: green, effective and reusable ionic liquid for synthesis of 7-amino-2, 4-dioxo-5-phenyl-2, 3, 4, 5-tetrahydro-1H-pyrano [2, 3-d] pyrimidine-6-carbonitrile derivative. J. Mater. Environ. Sci. 5, 1075–1078.

Yang, K., Wang, Z., Fu, J., Tan, Y., 2010. Knoevenagel reaction assisted with physical technologies. Prog. Chem. 22, 2126–2133. https://doi.org/10.1002/ptr.6715.

Yang, K., Dang, Q., Cai, P.-J., Gao, Y., Yu, Z.-X., Bai, X., 2017. Reaction of aldehydes/ketones with electron-deficient 1,3,5-triazines leading to functionalized pyrimidines as Diels–Alder/Retro-Diels–Alder reaction products: reaction development and mechanistic studies. J. Organomet. Chem. 82, 2336–2344. https://doi.org/10.1021/acs.joc.6b02570.

Ye, J., Li, W., Wu, W., Yang, J., Liang, X., 2011. Asymmetric direct Michael addition of acetophenone to α,β-unsaturated aldehydes. Synthesis 2011, 1085–1091. https://doi.org/10.1055/s-0030-1258459.

Ying, A., Li, Z., Yang, J., Liu, S., Xu, S., Yan, H., Wu, C., 2014. Dabco-based ionic liquids: recyclable catalysts for aza-Michael addition of α,β-unsaturated amides under solvent-free conditions. J. Organomet. Chem. 79, 6510–6516. https://doi.org/10.1021/jo500937a.

Ying, A., Wang, L., Qiu, F., Hu, H., Yang, J., 2015. Magnetic nanoparticle supported amine: an efficient and environmental benign catalyst for versatile Knoevenagel condensation under ultrasound irradiation. C. R. Chim. 18, 223–232. https://doi.org/10.1016/j.crci.2014.05.012.

Yu, C., Lyu, H., Cai, Y., Miao, X., Miao, Z., 2013. An environmentally benign approach for the synthesis of 3,3′-pyrrolidonyl spirooxindole derivatives via a cascade Knoevenagel-Michael-cyclization multicomponent reaction. RSC Adv. 3, 18857–18862. https://doi.org/10.1039/c3ra44119a.

Zhao, S., Wang, X., Zhang, L., 2013. Rapid and efficient Knoevenagel condensation catalyzed by a novel protic ionic liquid under ultrasonic irradiation. RSC Adv. 3, 11691–11696. https://doi.org/10.1039/C3RA40809D.

Ziarati, A., Safaei-Ghomi, J., Rohani, S., 2013. Sonochemically synthesis of pyrazolones using reusable catalyst CuI nanoparticles that was prepared by sonication. Ultrason. Sonochem. 20, 1069–1075. https://doi.org/10.1016/j.ultsonch.2013.01.005.

Zou, Y., Wu, H., Hu, Y., Liu, H., Zhao, X., Ji, H., Shi, D., 2011. A novel and environment-friendly method for preparing dihydropyrano[2,3-c] pyrazoles in water under ultrasound irradiation. Ultrason. Sonochem. 18, 708–712. https://doi.org/10.1016/j.ultsonch.2010.11.012.

Chapter 38

Ultrasonic agglomeration and preconditioning of aerosol particles for environmental and other applications

E. Riera[a,b], I. González-Gómez[a], G. Rodríguez[b], and J.A. Gallego-Juárez[b]
[a]*Consejo Superior de Investigaciones Científicas (CSIC), Madrid, Spain,* [b]*Pusonics S.L., Pico Muihacén, Arganda del Rey, Madrid, Spain*

38.1 Introduction

The application of a high-intensity acoustic field to an aerosol may originate a coagulation process of the suspended particles that is known as acoustic agglomeration or ultrasonic agglomeration if, as often occurs especially with very fine particles, the process takes place in this frequency range. This process was first experimentally investigated by Patterson and Cawood (1931) and has been extensively studied over many years to understand its basic mechanisms. Brandt and Hiedemann (1936b), Mednikov (1965), Shirokova (1973), and Timoshenko et al. (1976), among others, have greatly contributed to this objective.

A variety of mechanisms have been suggested for the process. At present, it is generally accepted that orthokinetic and hydrodynamic interactions are the predominant mechanisms, while other effects, such as radiation force, acoustic streaming, and turbulence, can play an important role in promoting these interactions.

Orthokinetic interaction (Brandt and Hiedemann, 1936a, b; Brandt et al., 1937) occurs between two or more suspended particles of different sizes when they are located within a distance approximately equal to the displacement amplitude of the sound field in the suspending medium and their relative motion is substantially parallel to the direction of vibration. Because of the differential fluid and inertial forces, the particles vibrate with different amplitudes and phases and such differential motion greatly increases the probability of collision and, therefore, of agglomeration.

Another principal cause of the acoustic agglomeration of particles in suspensions is the action of hydrodynamic forces on the particles (Buranov and Eknadiosyants, 1961; Hoffmann and Koopmann, 1997; Shaw and Tu, 1979; Shirokova and Eknadiosyants, 1966; Temkin, 1994; Tiwary and Reethof, 1986; Zheng and Apfel, 1994). Intense acoustic fields generate hydrodynamic forces that induce the particles to approach from separation distances much larger than their respective acoustic displacements. In particular, these forces govern particle interactions in monodisperse suspensions, where the orthokinetic mechanism vanishes because the particles are similarly entrained by the acoustic field, without probability of direct collision.

Among the several effects induced by hydrodynamic forces, one that plays a significant role is the asymmetry of the slip-flow velocity field in the Oseen regime, known as the acoustic wake effect (AWE). This mechanism was first described by Pshenai-Severin (1959) for two equal spheres aligned with the acoustic field vector. The particle interaction was studied analytically, and an expression was derived for the relative particle drift velocity during an acoustic half-cycle.

Subsequently, other authors described this effect for two different size particles aligned along the acoustic field vector (Dianov et al., 1968; Timoshenko, 1971) during one acoustic cycle. These studies, carried out under one-dimensional conditions, showed discrepancies and contradictory results, evidencing the necessity of further clarification. In addition, the applicability of these studies was restricted by a number of limiting approximations required for their derivation. More recently, an analytical solution has been derived to describe acoustic wake particle interactions in a two-dimensional plane, revealing attraction patterns around the particles (González et al., 2000a,b).

This chapter deals with the historical evolution, theoretical foundations, and experimental and practical development of this process.

38.2 The development of practical applications of aerosol agglomeration

Practical uses of aerosol agglomeration process have been mainly focused on environmental applications. Removal

Power Ultrasonics. https://doi.org/10.1016/B978-0-12-820254-8.00029-4
Copyright © 2023 Elsevier Ltd. All rights reserved.

of particles from gas emissions is one of the most important problems in air pollution abatement. Focus is on very fine particles (less than about 2.5 μm) that are difficult to remove by conventional separation technology and constitute a major health hazard. In fact, these tiny particles cause physiological damage by their ability to penetrate deeply into the respiratory system. In addition, they are generally toxic due to their origin (condensation of chemically active elements produced during combustion processes) and to their ability to act as a vehicle for noxious agents (e.g., viruses, bacteria, dioxins, etc.). Fine particles make up a significant percentage of the particulate emission in oil- and coal-burning processes, such as in power plants, the steel-melting industry, and the cement industry. At present, the particle retention of conventional filters such as electrostatic precipitators drops off steeply for particles under 2 or 3 μm, at which point an improved technology is required. Ultrasonic agglomeration of micron and submicron particles, forming larger particles, might have an important role in cutting down the airborne concentration of fine particles by preconditioning them to be subsequently removed by conventional filtration systems.

Practical applications of the aerosol agglomeration process started in the late 1940s, with the development of powerful air-jet sound generators (sirens). Danser and Neumann (1949) from the Ultrasonic Corporation discussed the design of full-scale acoustic agglomerators using the new sirens driven by compressed air. They briefly described two industrial agglomerators installed in New York City at the time and mentioned exposure time, sound frequency, and sound intensity as the key design variables. Stokes (1950) described research using the same model of siren as Danser and Neumann. In the same period, St. Clair (1949, 1952) investigated the physical causes of acoustic agglomeration and performed small-scale experiments. He discovered that wetting the particles with a fine water or oil spray caused the aggregates to be strongly held together by surface tension. *St*. Clair also noted that increasing sound field intensity leads to more rapid agglomeration.

During World War II, attempts were made in the US to disperse fog on airport runways by using acoustic sirens based on the idea of Amy (1934). Although the tests gave positive results in calm weather, the technique was ineffective under moderate and high wind conditions and the project was abandoned (Sinclair, 1950). Most of the research carried out at the time focused on the coagulation of industrial smokes, fogs, and dust such as ammonium chloride, carbon black, sulfuric acid, calcined soda, molybdenum disulfide, fly ash, open-hearth gas dust, and cement. While the achieved agglomeration efficiencies in these studies were generally satisfactory or at least acceptable, the problems with the aerodynamic acoustic sources employed for the generation of high-intensity waves discouraged industrial interest on the process. In fact, aerodynamic sources of various kinds, such as whistles and sirens, in which the acoustic energy is provided by gas jet, show very low efficiencies, have a poor directivity, emit complex sounds, and have some difficulty reaching ultrasonic frequencies (Greguss, 1964). Therefore, for the efficient generation and transmission of acoustic energy in gases, new powerful and efficient sources were required.

Experimental and theoretical studies were also carried out in other countries such as the Soviet Union and Japan through the 1950s and the 1960s. An excellent report covering all the theoretical, experimental, and applied work developed up to the early 1960s was published by Mednikov (1965) in the Soviet Union, including more than 300 references. Another review work was published by Shirokova (1973).

After a certain period of inactivity, interest in the agglomeration process revived in US and Canada in the 1970s, when stricter air pollution legislation for particle removal was established. A number of groups started agglomeration studies, generally at laboratory scale. Worthy of mention are the work of Scott (1975) in Canada as well as the investigations of Shaw and his colleagues (Cheng et al., 1983; Rajendran et al., 1979; Shaw, 1978; Shaw and Rajendran, 1979; Shaw and Tu, 1979), Reethof, Koopmann, and their colleagues in the US between 1978 and 2000 (Hoffmann, 1993; Hoffmann and Koopmann, 1993, 1996; Reethof, 1988; Song, 1990; Song et al., 1994; Tiwary and Reethof, 1986).

In Europe, the experimental and theoretical studies on acoustic agglomeration were conducted by two main groups: Gallego-Juárez and his colleagues in Spain from 1973 to 2006 and Magill and his colleagues in Germany from 1989 to 1995 (Caperán et al., 1995; Gallego-Juárez et al., 1979, 1996, 1999, 2000; González et al., 2000a,b, 2001, 2002, 2003; Hoffmann, 2000; Hoffmann and Koopmann, 1997; Magill, 1993; Magill et al., 1989a,b, 1990, 1991, 1992; Riera and Gallego-Juárez, 1986; Riera et al., 2000a,b, 2003, 2006). Both groups worked closely during the period from 1989 to 1993. Their joint studies were conducted under static and dynamic conditions with micron and submicron aerosols (Magill et al., 1989a,b, 1991), applying as the sound source a new type of airborne high-efficiency and high-directional power piezoelectric transducer, the stepped-plate transducer, developed for the Gallego-Juárez group (Gallego-Juárez et al., 1978, 1994). Both groups jointly studied at laboratory stage the combination of an acoustic agglomerator as the particle preconditioner for an electrostatic filter to increase its particle removal efficiency in the submicron particle range (Magill et al., 1992). Such a system was developed and tested at the semi-industrial stage in a pilot plant for coal combustion smoke precipitation (Gallego-Juárez et al., 1999). In the 1990s, T. Hoffmann, a former member of the Koopmann group, joined Gallego-Juárez's group to

work on hydrodynamic mechanisms involved in the acoustic agglomeration of monodisperse and polydisperse aerosols. As a result of such collaboration, important advances in the knowledge of the AWE mechanism were reached (González et al., 2000a, 2001, 2002).

The process of acoustic agglomeration of aerosols is recently of renewed interest in connection with the increase in research on energy and environmental problems. One of the most important causes of air pollution is the presence of micron and submicron aerosols in the air. Particles larger than 50 μm settle out of the air quite easily because of gravity. However, the smallest particles (with diameters of less than 2 or 3 μm) tend to remain suspended for long periods of time. In addition, these tiny particles, which are the most difficult to remove from a gas stream, cause most of the physiological damage due to their ability to penetrate and adhere to respiratory tissues. Such very fine particles make up a large part of industrial particle emissions (25% in coal-burning processes such as coal-fired electricity generation, 35% in the steel-smelting industry, and 21% in the cement industry). Besides industrial emissions, large amounts of hazardous material in the form of micron and submicron aerosols can be released into the atmosphere following an industrial or nuclear accident or even a fire, as in Bhopal (chemical plant accident, 1984), Chernobyl (nuclear power plant accident, 1986), the Gulf War (oil wells fire, 1991), and Fukushima (nuclear power plant accident, 2011). Therefore, a process such as the acoustic agglomeration capable of solving the problem by changing the particle size distribution in favor of larger particles that are easily precipitated (by gravity or by any conventional type of separator) appears very attractive.

It is noteworthy that Gallego-Juárez's group, which has been actively involved in this research over the last decades, has developed innovative agglomeration systems based on a new family of sonic and ultrasonic power piezoelectric transducers for airborne ultrasound. Such systems have been shown to be effective at the semi-industrial stage for the removal of micron and submicron particles (Riera et al., 2006). Finally, the recent increasing interest of several R&D groups in China for this process should be noted (Guo et al., 2012; Liu et al., 2009, 2011; Wang et al., 2011).

38.3 Linear acoustic effects that determine the agglomeration process

The acoustic or ultrasonic agglomeration of aerosols via macrosonic fields is governed by several complex mechanisms of interaction that usually are triggered in a combined fashion (Fuchs, 1989; Mednikov, 1965; Shaw, 1978; Shirokova, 1973; Temkin, 1981, 1994). When a particle is suspended in an intense acoustic field, a number of forces will act upon the particle, making it move away from its initial position. Sound-particle interactions can be classified in terms of linear and nonlinear effects, as well as in single and multiple particle interaction processes.

Linear interaction processes include particle entrainment by the primary acoustic wave, and/or by the scattered wave induced by the presence of a nearby obstacle (first-order scattering interaction). In the nonlinear acoustic domain, the primary wave and the scattered sound wave exert a steady force on the obstacles, referred to as the radiation pressure (RP) force. The hydrodynamic mechanism known as the AWE, due to the asymmetry of the flow fields around two adjacent particles under Oseen flow conditions, falls into this category. Moreover, at high acoustic excitation levels, the acoustic streaming, a steady fluid motion related to the acoustic absorption, has to be taken into consideration. Nonlinear effects are discussed in the following section.

The linear mechanisms involved in the agglomeration process have been extensively studied (Andrade, 1936; Brandt and Hiedemann, 1936a, b; Mednikov, 1965; Shaw, 1978; Shirokova, 1973; Temkin, 1994). The basic effect of producing particle collisions is due to the different acoustic entrainments that the vibration induces in particles of different size and weight. More specifically, the motion of particles in a viscous acoustic field is determined by their inertia; larger and heavier particles are less entrained than smaller and lighter ones that tend to move with the fluid motion. This concept is valid for standing as well as for traveling waves.

The resulting relative motion between the particles can lead to particle collision and agglomeration. The larger particles act as collectors of the smaller particles. Larger particles sweep a certain volume in each acoustic cycle. Collision occurs if smaller particles get into the "agglomeration volume" of the larger particle, consisting of a cylinder with a radius equal to the sum of the radii of the two particles and a length equal to twice the difference between the amplitudes of the displacements that the particles undergo during vibration (Mednikov, 1965).

38.4 Nonlinear acoustic effects

38.4.1 Radiation pressure and mutual radiation pressure

The nonlinear acoustic mechanisms involved in the agglomeration process have been the object of numerous theoretical and experimental studies during the last two decades (Gallego-Juárez et al., 1999; González, 1998; González et al., 2000a, 2001, 2002, 2003; Hoffmann, 1993; Hoffmann et al., 1993; Hofmann and Koopmann, 1996; Liu et al., 2011; Riera and Gallego-Juárez, 1986; Wang et al., 2011). The RP is the first nonlinear effect to consider. It expresses the transfer of momentum from the acoustic

wave onto an obstacle, i.e., a particle. The change of momentum in the wave gives rise to a continuous force acting on the particle, the so-called RP force. In the case of a standing wave, the direction of the force is determined by the density ratio of the fluid and the particles. Denser particles suspended in lighter fluids are driven toward the acoustic velocity antinodes, while lighter particles in heavy fluids are conducted toward the velocity nodes.

The standing wave field pattern produced by a high-intensity ultrasonic field at 20 kHz applied to a carbon black aerosol is shown in Figure 38.1. This image was obtained experimentally inside a rectangular section agglomeration chamber by Gallego-Juárez's group.

In general, a single particle suspended in an acoustic field is exposed to the RP force of the primary acoustic wave together with the RP forces induced by the nonlinear interaction of the primary wave with the scattered waves from other nearby particles. This is the so-called mutual radiation pressure (MRP). Two theoretical and experimental studies carried out by Song (1990) and González et al. (2003) have shown that the production of attractions-repulsions between particles depends on the angle that the sound wave propagation forms with the centerline of the particles. Both studies also confirmed that the MRP mechanism has a short-range influence.

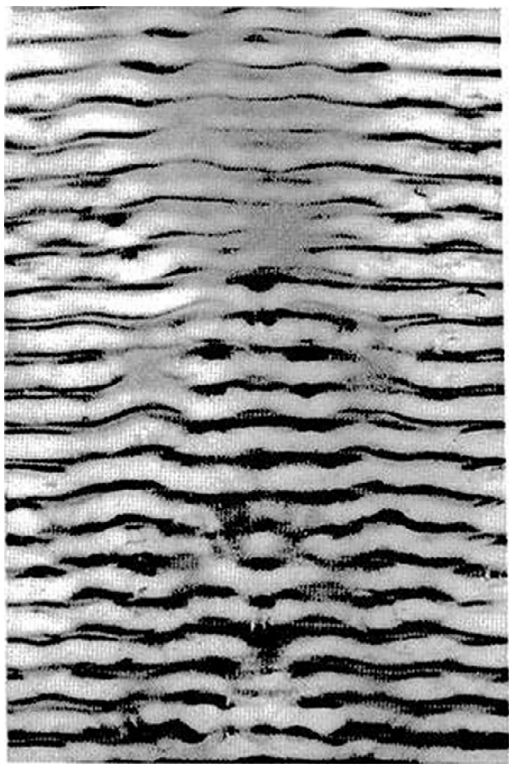


FIGURE 38.1 Standing wave field pattern of carbon black particles of an ultrasonic agglomeration chamber at 20 kHz.

38.4.2 Acoustic wake (AW)

As before mentioned, the orthokinetic particle interaction is the basic agglomeration mechanism for aerosols of different sizes, but when particles are of the same size, the differential relative motion between them vanished and the orthokinetic mechanism no longer takes place. For monodisperse aerosols, hydrodynamic interactions are generally considered to be the dominant acoustic agglomeration mechanisms. The AW is a hydrodynamic mechanism based on the fact that the flow around a particle becomes non-symmetric at moderate or high Reynolds numbers through the time of the acoustic actuation. Let's suppose two particles closely aligned along the acoustic axis, the flow field of the leading particle will disturb the field of the trailing particle. In the wake of the leading particle, the trailing one will experience a drag reduction, and therefore, it moves relatively faster. In an acoustic oscillating field, the two particles will alternatively switch their role as leader and follower. As a result, during each period, the trailing particle will move a little closer toward the leading particle and therefore experiences the wake effect even more strongly (see Figure 38.2). From this motion, an attractive effect between particles results, and they converge after a number of acoustic cycles.

38.4.3 Acoustic streaming and turbulence

The acoustic streaming is a nonlinear acoustic effect in which steady fluid flows are induced by high-intensity acoustic waves. Such steady flows are produced both in the free acoustic beam and near obstacles. The acoustic streaming seems to be mainly induced by radiation forces set up by the absorption of acoustic waves into the medium. Other mechanisms such as diffraction and nonlinearities of the acoustic field may also contribute to this effect. Because

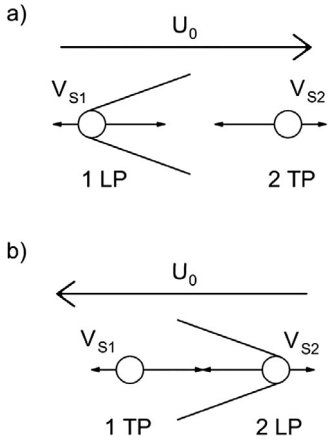


FIGURE 38.2 Convergence due to the acoustic wake effect (AWE) for a pair of particles aligned along the acoustic axis; LP and TP are referred to leading and trailing particles defined with respect to the slip velocity ($u_{slip} = u_0 - u_p$). Fluid velocity: (a) in positive x-direction and (b) in negative x-direction.

these fluid flows are generally not spatially homogeneous, they provoke a number of different effects, such as entrainment, mixing, dispersion, and collision of the suspended particles.

Acoustically induced turbulence is believed to occur at sound pressure levels (SPL) over 160 dB. If the aerosol is in a turbulent state at high acoustic intensities, particle agglomeration may be enhanced depending on specific conditions (Lee et al., 1981). However, Tiwary et al. (1984) demonstrated that acoustic turbulence was not a significant contributor to acoustic agglomeration.

38.4.4 Motion of aerosol particles in an acoustic field: Vibration

Solid or liquid particles suspended in a gas under the action of an acoustic field execute a number of motions that are governed by the different acoustic effects previously mentioned. Thus, particles take some part in the vibrations of the fluid and follow translational motions mainly due to the RP force, the hydrodynamic forces induced by the asymmetry in the motion of particles in the gas medium, or the acoustic streaming.

Let us consider a rigid spherical particle suspended in a gas medium through which a plane wave is propagating. As a result of the interaction of the particle with the acoustic wave, the particle attempts to oscillate with the gas medium. To describe and determine the entrainment ratio of the particle in the fluid motion caused by a sound field, we make use of the Basset-Boussinesq-Oseen (BBO) equation. The total force F_p exerted onto a small and unsteadily translating particle in a viscous flow is given by the following expression (González, 1998):

$$\begin{aligned} F_p &= m_p \frac{du_p}{dt} \\ &= 6\pi\eta a\left(u_g - u_p\right) + V_p\rho_p \frac{du_g}{dt} + \frac{1}{2}\delta m_p \frac{d\left(u_g - u_p\right)}{dt} \\ &\quad + 6a^2\sqrt{\pi\eta\rho_f}\int_{-\infty}^{t} \frac{d\left(u_g - u_p\right)}{d\mu}\frac{d\mu}{\sqrt{\mu - t}} \end{aligned} \tag{38.1}$$

where u_g is the velocity of the fluid in the absence of the particle and u_p is the particle velocity, m_p is the particle mass, a is the particle radius, η is the dynamic viscosity of the gas, and $V_p = \frac{4}{3}\pi a^3$ is the particle volume. The ratio of the gas to particle densities is expressed by $\delta = \frac{\rho_o}{\rho_p}$. The physical meaning of the terms on the right-hand side of Eq. (38.1) is as follows. The first term is the Stokes viscous resistance force; the second gives the force due to the pressure gradient in the fluid in the absence of the particle; the third describes the additional force that originates from the acceleration of the fluid in the vicinity of the particle; and the fourth term gives the so-called time history effect, which limits the influence of the viscous effects at any time t before application of the acoustic field. Equation BBO is the generalized Stokes equation.

Assuming a monochromatic wave, the acoustic velocity can be expressed as:

$$u_g(t) = U_o\, sin\,(\omega t) \tag{38.2}$$

where U_o is the amplitude of the velocity and $\omega = 2\pi f$ is the angular frequency, with f being the frequency in Hz and t time. It is very useful to have the approximate solution of the BBO equation as given by Brandt, Freund, and Hiedemann (BFH) (Brandt et al., 1937). In this case, the equation of motion of the particle is limited to the viscous force as given by Stokeś equation:

$$F_p = \frac{du_p}{dt} = 6\pi\eta a\left(u_g - u_p\right) \tag{38.3}$$

By using Eq. (38.2) and the expression of the relaxation time of the particle τ_p (the time needed for the particle to react to an external excitation) given by

$$\tau_p = \frac{2\rho_p a^2}{9\eta} \tag{38.4}$$

the expression for the entrainment factor q_p of the particle in the vibration of the fluid is given by (Mednikov, 1965):

$$q_p = |H| = \frac{U_p}{U_o} = \frac{A_p}{A_o} = \frac{1}{\sqrt{1 + \left(\omega\tau_p\right)^2}} = \frac{1}{\sqrt{1 + \left(\frac{2\rho_p a^2}{9\eta}\right)^2}} \tag{38.5}$$

H is a complex number known as the entrainment function; A_p and A_o are the respective amplitudes of the displacement and the sound pressure. The relative motion between the particle and the oscillating gas media can be expressed as:

$$\begin{gathered} u_{gp} = u_g - u_p = U_o\sqrt{1 - |H|^2}\, cos\,(\omega t - \varphi) \\ tan\,\varphi = \omega\tau_p \end{gathered} \tag{38.6}$$

where φ is the phase shift between gas and particle velocities.

Figure 38.3 shows the acoustic entrainment coefficient as a function of the relaxation number $\omega\tau_p$ obtained both experimentally and theoretically by using the BFH equation (González et al., 2000a,b; Gucker and Doyle, 1956; Hoffmann and Koopmann, 1997). BFH theoretical predictions agree well with experimental values. As can be seen, smaller and lighter particles are preferentially entrained by oscillating flow as compared to larger and heavier particles. The entrainment coefficient takes values from the unity (particles fully entrained by the wave) to zero (inertial particles that cannot follow the acoustic field). However, fully complete entrainment of particles by the

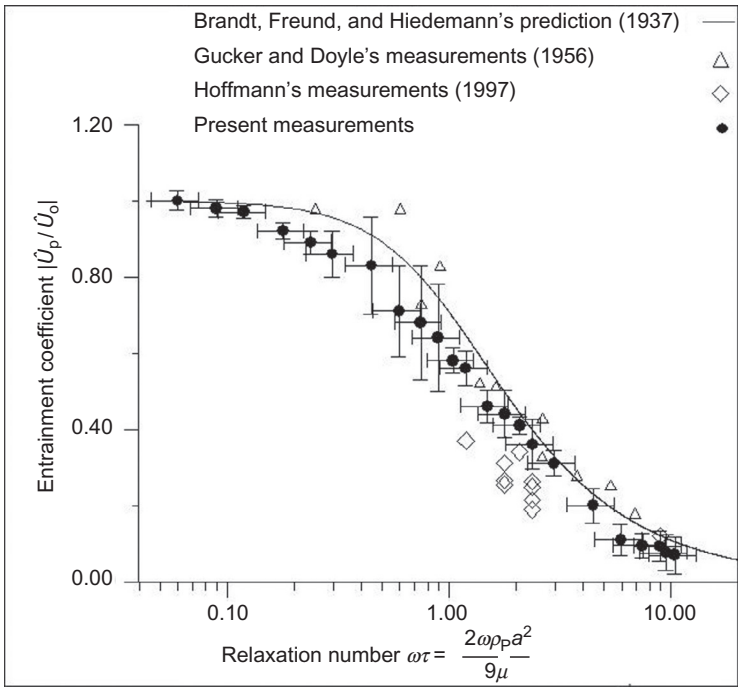


FIGURE 38.3 Comparison of theoretical predictions and experimental measurements of the entrainment coefficient $|H| = |\frac{U_p}{U_0}|$ vs relaxation number $\omega\tau$.

wave is not possible because the particles are carried along as a result of viscous forces which act when a motion with respect to the medium is produced. Larger values of $\omega\tau_p$ refer to more inertial particles less acoustically entrained.

38.5 Translational motion of aerosol particles

There are several effects of the high-intensity acoustic field that may induce translational motions to the particles. The most relevant is the RP exerted by the acoustic wave on the particle, although other effects such as the distortion of the wave, the asymmetry in the vibration of the medium in a standing acoustic wave field, and the periodic changes of viscosity can also play a certain role (Czyz, 1987; Dukhin, 1960; Mednikov, 1965; Shirokova, 1973). We will discuss here briefly the motion induced by the RP force and some other factors.

38.5.1 Translational motion due to radiation force

The RP force exerted on a stationary spherical particle of arbitrary density, of which the radius a is much less than the wavelength, $ka \ll 1$, where k is the wave number, was evaluated by King (1934) for a traveling wave:

$$F_R = \frac{11\pi}{9}\left(\frac{\omega}{c_o}\right)^4 a^6\left(1 - H^2\right)E \tag{38.7a}$$

and for a standing wave

$$F_R = \frac{8\pi}{3}\left(\frac{\omega}{c_o}\right)a^3\left(1 - H^2\right)E\,sin\,(2kx_o) \tag{38.7b}$$

where c_o is the velocity of sound in the gas medium, $E = I/c_o$ is the sound energy density, and I is the intensity of the sound. The radiation force is in the direction of wave propagation for the traveling wave. In a standing wave, x_o is the distance from the particle position to the nearest vibration node, and the radiation force is directed toward the velocity antinodes or nodes, depending on the density of the particles. According to Shirokova (1973), RP plays an important role during the later stages of the agglomeration process when particles have increased in size. In fact, this force produces a spatial rearrangement of particles depending on their density.

38.5.2 Translational motion due to other effects

Translational motion could be also due to the asymmetry of the acoustic field in a standing wave. A distinctive feature of standing acoustic waves is that the displacement and velocity of the particles in the medium, as well as the acoustic pressure, are functions of both time and space.

The mathematical expression for the translational force caused by the asymmetric motion of the particles, averaged over a period of the vibrations, is given by (Czyz, 1987):

$$F_{ASYM} = -\frac{\pi}{3}\left(\frac{\omega}{c_o}\right)a^3 H\left[\frac{9}{2}\left(b^2+b\right)\sqrt{\left(1-H^2\right)} + \left(3+\frac{9b}{2}\right)H\right]E\sin\left(2kx_o\right) \quad (38.8)$$

where $b = \frac{1}{a}\sqrt{\frac{\nu}{\pi f}} = \frac{\delta}{a}$, ν is the kinematic viscosity, and δ is the thickness of the viscous boundary layer around the particle.

A translational motion due to temperature dependence of the viscosity was discussed by Westervelt (1950). His result, adapted to standing wave conditions, may be written as follows:

$$F_{VIS} = 3\pi(\gamma-3)\,\frac{\eta a}{\rho_g c_o}H^2 E\sin 2kx_o \quad (39.9)$$

Here, γ is the adiabatic constant of the gas medium. For the distortion of the acoustic wave, Westervelt (1951) also predicted a translational force, described by the amplitude and phase of the second harmonic arising in a monochromatic wave propagating in a fluid. He obtained an analytical solution for a progressive wave but not for a standing wave condition.

38.6 Interactions between aerosol particles: Orthokinetic effect (OE)

As we have already discussed, particles of different sizes (or densities) are entrained into the oscillatory motion of the acoustic field at different rates of motion. Due to their inertia, larger particles are less mobile, whereas smaller, lighter particles follow the oscillatory motion of the field. In this way, the resulting particle motion gives rise to collisions and agglomerations. This is known as the orthokinetic effect (OE). The relative oscillatory motion creates a region around each larger particle called the agglomeration volume (Figure 38.4).

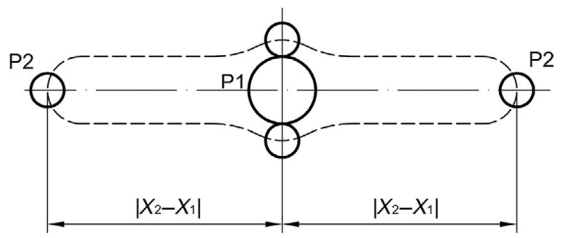


FIGURE 38.4 Acoustic agglomeration volume defined by Mednikov (1965).

According to Mednikov (1965), if there are small particles within the volume, they will collide with the larger particle in one acoustic cycle. After this cycle, there will be no more small particles in the volume and no agglomeration occurs. Thus, the orthokinetic interaction could not predict by itself a continuous agglomeration mechanism. In fact, the OE can explain neither agglomeration of monodisperse aerosols nor the way in which the agglomeration volume is refilled once it is emptied after one cycle. Possibilities for a refill mechanism include other effects previously mentioned, such as scattering, RP, the asymmetry of the flow field around the particles, and acoustic streaming. In addition, gravity settling and Brownian motion may play certain roles.

Nevertheless, on the basis of this agglomeration volume, Mednikov derived an agglomeration rate expression that has been used in subsequent models developed by Shaw and Tu (1979), Song (1990), Volk (1977), and Tiwary (1985). If the velocity of the particles in the medium follows the law given by Eq. (38.2), and assuming for simplicity that the aerosol is a system constituted by two spherical particles of different radii, $a_1 \gg a_2$, the difference between the velocities of the two particles will be

$$u_{21} = u_2 - u_1 = |H_2|U_o\sin(\omega t-\varphi_2) - |H_1|U_o\sin(\omega t-\varphi_1) \quad (38.10a)$$

$$U_{21} = U_2 - U_1 = |H_{21}|U_o = U_o\frac{\omega(\tau_1-\tau_2)}{\sqrt{\left(1+(\omega\tau_1)^2\right)\left(1+(\omega\tau_2)^2\right)}} \quad (38.10b)$$

Here, U_{21} is the amplitude of the relative vibrational velocity between two particles, $|H_{21}|$ is the relative entrainment function between them or the degree of relative motion of the particles, τ_1 and τ_2 are the particle relaxation times for the particles, and φ_1 and φ_2 are the phase angles of the vibration of the particles.

From the degree of relative motion of the particles $\frac{U_2-U_1}{U_0}$, one can deduce the optimum frequency at which it takes its maximum value, given by the equation (Mednikov, 1965):

$$f_{opt} = \frac{9}{4\pi}\,\frac{\eta}{\rho_p a^2} \quad (38.11)$$

This method can be extended to the interaction of multiple particles. Hoffmann (1997) calculated a relative agglomeration volume V_{21} such that all the small particles (size 2) within this volume will collide with the larger particle (size 1) along one acoustic half-cycle, as follows:

$$V_{21} = \pi(a_2+a_1)^2\cdot 2|x_2-x_1| = S_{21}\cdot L_{21} \quad (38.12)$$

where S_{21} is the cross-sectional area of the agglomeration volume, and $L_{21}=2|x_2-x_1|$ is its total length based on

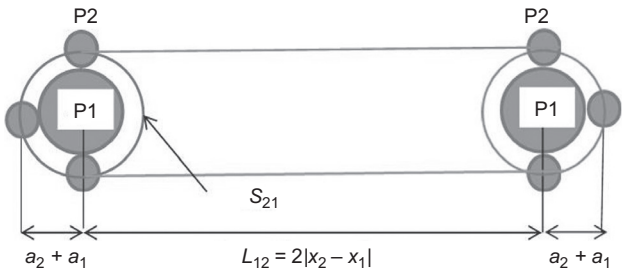


FIGURE 38.5 Relative agglomeration volume of length L_{21} and cross-sectional area S_{21} defined by Hoffman (1997).

the maximum particle separation distance; x_1 and x_2 are the respective displacements of the particles. In Figure 38.5, the relative orthokinetic agglomeration volume with a cylindrical shape is shown.

A refill mechanism of the agglomeration volume was proposed by Song (1990) and Hoffmann (1993), taking into account the mutual scattering interaction between two closely spaced particles. When the particles are inside a distance of several particle diameters, the wave scattering becomes strong and its effect on the relative motion between both particles has to be taken into account (Figure 38.6). Bearing in mind this effect, the expression for the amplitude of the relative vibrational velocity between two particles was obtained by Song (1990).

$$U_{21\ \mathrm{SONG}}^{\mathrm{ORTHO}} = U_o|H_{21} + G_{21}| = U_o q_{s12} \tag{38.13}$$

where G_{21} is the scattering interaction function, which depends on the longitudinal wave number $k = \omega/c_o$ and the viscous wave number $K = (1+i)\sqrt{\omega\rho_o/2\eta}$, with c_o the sound speed of the fluid, ρ_o its density, and q_{s12} a modified relative entrainment factor for spherical particles. All the above expressions are derived assuming that the amplitude of the acoustic velocity in the fluid U_o is much smaller than the sound speed.

38.7 Hydrodynamic mechanisms of particle interaction

Several experimental investigations (Buranov and Eknadiosyants, 1961; Shirokova and Eknadiosyants, 1966; Shaw and Tu, 1979; Hoffmann and Koopmann, 1996; González et al., 2002) have demonstrated the existence of processes of acoustic agglomeration between equal particles in monodisperse suspensions, where the orthokinetic mechanism is inhibited. Therefore, the influence of the hydrodynamic mechanisms as cause of the agglomeration in aerosols has been evidenced.

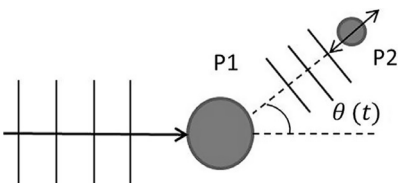


FIGURE 38.6 Acoustic entrainment by the scattered wave.

An important mechanism is the mutual perturbation induced between two nearby particles due to their respective scattering waves. A nonlinear interaction between the incident wave and the wave scattered by each particle gives rise to a resulting wave that disturbs other particle located close to it, leading to an irreversible deviation of its trajectory, and vice versa. It is known as the mutual radiation pressure effect (MRPE).

Other significant hydrodynamic effect, before mentioned, is the acoustic wake effect (AWE) due to the acoustic asymmetries of viscous origin around the particles. As previously explained, the flow field around the particles that are oscillating with the acoustic wave, gives rise to nonreversible alterations in the dynamics of other nearby particles, producing small deviations on their trajectories leading to mutual approaching processes.

Both mechanisms (MRP and AWE) act simultaneously on aerosol particles under an acoustic field. However, they must be separately analyzed to balance their influence on the acoustic agglomeration process.

38.8 Mutual radiation pressure effect (MRPE)

As before explained, radiation pressure (RP) is called to a pressure gradient produced by an acoustic wave relatively intense between the front and rear part of an obstacle, in this case a particle, giving rise to a radiation steady force that causes a displacement of the particle. The mutual radiation pressure effect (MRPE) is a nonlinear interaction between incident and scattering waves acting on particles close to each other, giving rise to the attraction or repulsion processes. Based on the hydrodynamic principle of Bernoulli, this mechanism was studied by König (1891a, b). He derived an expression for the force induced between two immobile spherical particles in an oscillating fluid. Almost a century later, Mironov (1976) extended the model of König to viscous fluids. The inclusion of viscosity generates an increase of the attraction forces up to two orders of magnitude with respect to the ideal fluids. Danilov and Mironov (1984) developed a theory to describe the Bernoulli forces for ideal and viscous fluids and derived expressions for the radiation pressure force on a particle due to the scattering wave from another close particle. They incorporated the concept of time average momentum flux associated with the wave, introduced by Gor'kov (1962), to derive some expressions for the radial and angular components of the radiation force as a function of the dipolar forces associated to the particles oscillating with the acoustic wave.

Song (1990) completed this study, developing complex expressions for the interaction forces generated between two nearby particles as second-order radiation forces established between both particles due to their mutual RP. This theory was based on the assumption that each particle oscillating in an acoustic field behaves as a radiating dipole at large distances. According to the theory, he derived an expression for one force acting on an *i*th particle due to the presence of a nearby particle *k*-th:

$$F_{ik} = \frac{-\rho_0}{4}\int_{V_i}\Big(U_{sk}\left(\nabla^2\Phi_{si} + k^2\Phi_{si}\right) + U^*_{sk}\left(\nabla^2\,\Phi_{si} + k^2\,\Phi_{si}\right)\Big)\mathrm{d}V_i \tag{38.14}$$

Assuming a punctual acoustic dipole for particle *i*:

$$F_{ik} = \frac{i}{4\omega}\left\{\left(D_i^*\nabla\right)U_{sk}\right\}_{r=0} + \left[\frac{i}{4\omega}\left\{\left(D_i^*\nabla\right)U_{sk}\right\}_{r=0}\right]^* \tag{38.15}$$

where D_i is the dipolar force given by

$$D_i = i12\pi\frac{\rho_0\omega}{k^2}A_1 \tag{38.16}$$

associated with the scattering wave of the oscillating particle *i*. In these expressions, the coefficient A_1 was defined as:

$$A_1 = -(1-H)\frac{a_1U_o\left(k\cdot a_p\right)^2}{3}\frac{\left[\left(K\cdot a_p\right)^2 + 3iK\cdot a_p - 3\right]\cdot e^{-iK\cdot a_p}}{\left(K\cdot a_p\right)^2\left[\left(k\cdot a_p\right)^2 + 2ik\cdot a_p - \left(k\cdot a_p\right)^2\left[1 - iK\cdot a_p\right]\right]} \tag{38.17}$$

with $k = \frac{\omega}{c_0}$ and $K = (1+i)\sqrt{\frac{\omega}{2v}}$, being *v* the kinematic viscosity and a_p the particle radius.

The radial and angular components of the scattering velocity amplitude can be expressed as a function of the dipolar and vortex forces, which are proportional to the particle entrainment coefficient through (*1-H*) in the Oseen regime (detailed equations are described in Song (1990). So, the higher the inertial particle behavior, the more intense is the scattering force generated. In the limit case, the scattering becomes null for particles fully entrained by the acoustic field, and vice versa, maximal scattering forces are generated by immobile particles ($H=0$).

It must be remarked that the radiation pressure generates particle displacements but it is not directly involved in processes of particle attraction or repulsion. However, the mutual radiation pressure based on the interactions produced between the waves scattered by nearby particles leads to these interactions.

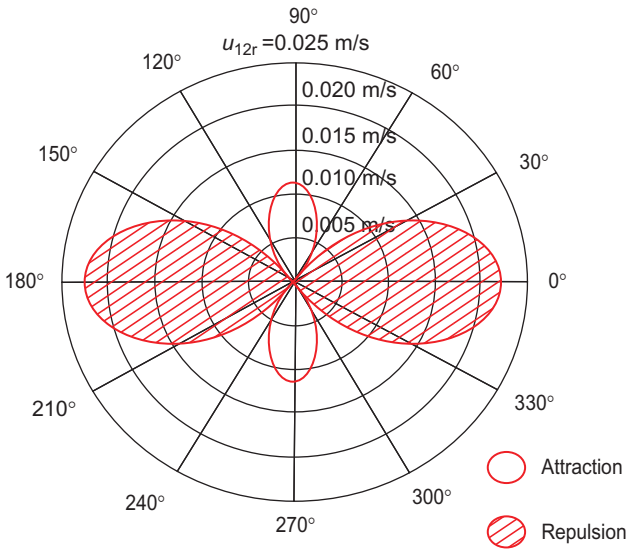


FIGURE 38.7 Radial component of the relative velocity generated by the MRPE between two glass particles in air from $r_0 = 100$ μm with radii $a_1 = 4$ μm and $a_2 = 6$ μm. $U_0 = 1$ m/s at $f = 3$ kHz.

A spatial pattern of the attraction-repulsion velocity derived from the Song's theory due to the MRPE is shown in Figure 38.7 between two equal-sized particles separated at a distance approximately 10 times their diameter in a plane standing wave. According to it, pairs of particles aligned with the acoustic axis repel each other, and on the contrary, particles with their centerline perpendicular to it experience a maximal attraction with velocity amplitude approximately twice weaker.

The attraction-repulsion forces strongly depend on the distance between the particles. Song proposed a range of validity for these interactions that can be applied up to distances to $10(a_i + a_k)$. This force is also dependent on the particle radii, increasing with their size rise.

38.9 Acoustic wake effect (AWE)

The acoustic wake effect was first experimentally verified by Hoffmann and Koopmann (1996), who found particle attraction processes between equal particles in monodisperse aerosols aligned along the acoustic axis. By these experimental observations, the influence of the acoustic wake effect on the particle agglomeration processes was confirmed as the only mechanism able to produce attractions between particles along the acoustic field direction, where the MRPE produces repulsion as before stated.

A theoretical study of the spatial distribution of the AWE was reported for the first time in the literature by González et al. (2000a, 2000b, 2001). The analytical and numerical spatial patterns resulting from those studies were experimentally confirmed, evidencing this 2D-theory (González et al., 2002).The acoustic wake effect is based

on the generation of viscous asymmetries in the flow field around the particles, which oscillate following partially the acoustic field. They are produced under certain flow conditions that favor the generation of asymmetries of the viscous origin around the particles. Such flow conditions exist at Reynolds numbers smaller but not much smaller than unity, so that the convective term of the Navier–Stokes equation has to be accounted for. These flow conditions are termed the Oseen flow regime in which the unsteady term du/dt with respect to the viscous term $v\nabla^2 u$ is neglected, i.e.,

$$\sqrt{\frac{2\upsilon}{\omega}}\left|\frac{\mathrm{d}u}{\mathrm{d}t}\right| \ll |v\nabla^2 u| \tag{38.18}$$

where $\boldsymbol{u}$ is the fluid velocity and v the kinematic viscosity factor. The radial and angular components of the perturbation velocity (υ_{kr} and $\upsilon_{k\theta}$, respectively) generated by a single particle k around were derived by Gonzalez et al. in 2000 (González et al., 2000b) fixed system as:

$$\upsilon_{kr} = \frac{A_{ok}}{r^2} - \frac{A_{ok}}{r^2} e^{\frac{-r}{2\upsilon}(|V_k| - V_k \cos\theta)}\left[1 + \frac{r}{2\upsilon}(|V_k| + V_k \cos\theta)\right] \tag{38.19a}$$

$$\upsilon_{k\theta} = -\frac{A_{ok} V_k}{2r\upsilon} \sin\theta e^{\frac{-r}{2\upsilon}(|V_k| - V_k \cos\theta)} \tag{38.19b}$$

with $A_{ok} = \frac{3\upsilon a_k}{2}\left(1 + \frac{3a_k|V_k|}{8\upsilon}\right)$. In the equation, the distance from the particle center to the point of interest and the angle formed between this line and the acoustic axis are r and θ, respectively, and V_k the "slip-flow velocity" the difference between the fluid velocity at the location of the k-th particle, u_{gk}, and the velocity acquired by particle u_k. The oscillating characteristic of both radial and angular velocity components appears in the changing sign of the slip-flow velocity with the acoustic wave (Figure 38.8).

The derivation of υ_{kr} and $\upsilon_{k\theta}$ requires distances r much shorter than the acoustic wavelength, λ, to satisfy the Oseen flow field equations. Two closely particles perturb mutually their respective motions by means of their respective periodically varying acoustic wakes. The head particle during the first half-cycle experiences the wake of the trailing particle during the second half-cycle, and vice versa. This mutual permutation of the flow fields leads to irreversible deviations from the original particle trajectories. In this way, both particles are mutually affected in a non-symmetrical manner. The dynamics of two nearby rigid and spherical particles in a sound field under Oseen flow conditions can be described by introducing Eqs. (38.19a) and (38.19b) in the system of equations described by Dianov et al. (1968):

$$m_i \frac{\mathrm{d}u_i}{\mathrm{d}t} = 6\pi\eta V_i a_i \left(1 + \frac{3a_i|V_i|}{8\upsilon}\right) \quad i = 1,2 \tag{38.20}$$

where m_i is the mass of the particle i of radius a_i, and η is the dynamic viscosity coefficient of the fluid. The particle motion given by Eq. (38.20) is also described as:

$$\frac{\mathrm{d}u_i}{\mathrm{d}t} + \frac{1}{\tau_i}u_i = \frac{1}{\tau_i}u_{\text{fluid}} + \frac{3a_i V_i|V_i|}{8\upsilon\tau_i} \quad i = 1,2 \tag{38.21}$$

with the particle relaxation time $\tau_i = \frac{2\rho_i a_i^2}{9\eta}$ and ρ_i as the density of the particle. The fluid velocity at the site of i-particle includes the velocity of the acoustic wake generated by another particle k close to it, added to the incident wave velocity:

$$u_{\text{fluid}} = U_o \sin\omega t + \upsilon_{ik} \tag{38.22}$$

In particular, the term υ_{ik} accounts for the change in the fluid vibrational velocity at the i-th particle location due to the presence of the close k-th particle, due to slip-flow velocity generated around it. Expressions of (38.19a) and (38.19b) are introduced into Eq. (38.21) and through Eq. (38.22) to define the two particles dynamics in a 2D model. The resulting system of differential equations cannot be solved analytically without further simplification due to their algebraic complexity. To address it, these complex expressions were replaced by other simpler functions in different angular ranges between 0° and 180° within the Oseen regime, giving rise to three systems of differential equations defined in the three different angular intervals—each of them could be analytically solved (González et al., 2000b). A spatial pattern was derived from that study showing interactions generated along the acoustic axis that turn out to be attractive within an angular range of ±30° around the acoustic axis and the most intense particle attractions along it. This result agrees with earlier experimental observations of Temkin (1994), Hoffmann and Koopmann (1996), and González et al. (1997). These findings revealed the strongest particle attraction processes generated along the acoustic axis ($\theta = 0°$) that became weaker with the angle increase up to $\theta = 45°$. Figure 38.9 shows the spatial pattern of the particle interactions provided by our 2D AWE model. None of particle interaction (neither attraction nor repulsion) is theoretically expected for particles at θ=90°.

The results of this study also agree with the 1D model previously developed by Dianov et al. (1968), for particles aligned along the wave direction. They derived an expression for the relative particle velocity during their approach process linearly dependent on the slip-flow velocities associated with the particles given by:

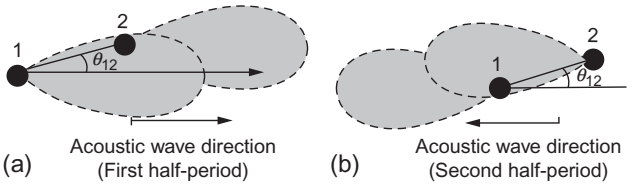


FIGURE 38.8 (a) Particle 2 in the viscous wake generated by the leading Particle 1 during the first semi-acoustic cycle. (b) Particle 1 in the viscous wake generated by Particle 2 during the second semi-acoustic cycle.

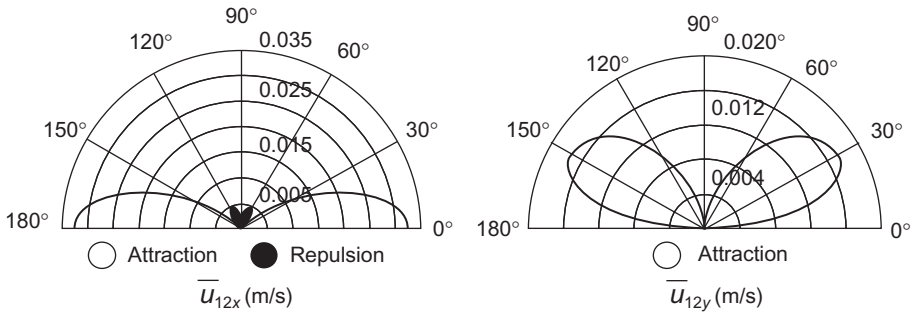


FIGURE 38.9 Analytically calculated spatial distribution of the *x*- and *y*-components of the convergence velocity, u_{12x} and u_{12y} computed for the same-sized particles ($a_1 = a_2 = 4$ μm) in a sound field with a velocity amplitude $U_0 = 1$ m/s at a frequency of 3 kHz as a function of the center-line orientation angle.

$$\overline{u}_{12} = \frac{3}{2}\frac{U_o}{\pi r}(a_1 l_1 + a_2 l_2) \tag{38.23}$$

for a distance between the particles fulfilling the condition $r \gg \upsilon/|V_i|$. In Eq. (38.23), $l_1$and l_2 are the relative slip coefficients in the Oseen regime for particles *1* and *2*, respectively.

The equations of motion of the particles due to the acoustic wake effect were numerically solved by using a 4th-order Runge–Kutta method, suitable for this type of combined differential equations (González et al., 2001). Based on this numerical approach, calculations were performed to compute the relative velocity between pairs of particles interacting under the acoustic wake effect, and their trajectories were derived for diverse approach processes, providing results in good agreement with the analytical study. These results were experimentally verified in a later study (González et al., 2002). Some geometrical parameters were analyzed, such as the distance between the particles and the angle of orientation of their center line with respect to the acoustic axis, as well as the acoustic frequency and pressure amplitude of the incident wave.

Diverse experimental studies have been developed since the eighties with monodisperse aerosols of rigid micron-sized particles, whose results evidenced repeatedly the formation of attraction processes along the acoustic axis (Tiwary and Reethof, 1986; Temkin, 1994; Hoffmann and Koopmann, 1996; González et al., 2000a, b), demonstrating the influence of the acoustic wake effect as a mechanism of interaction between particles of low acoustic entrainment coefficient. Several processes of interaction between particles not aligned along the acoustic axis were experimentally found in the experiments carried out by the Gallego-Juárez's group in CSIC in the early 2000 (González et al., 2002). Their results confirmed the spatial attraction/repulsion patterns theoretically predicted previously and included studies of the influence of parameters, such as the frequency, on these processes (González et al., 2003).

Figure 38.10 shows a complete filmed attraction process developed between two identical glass microspheres

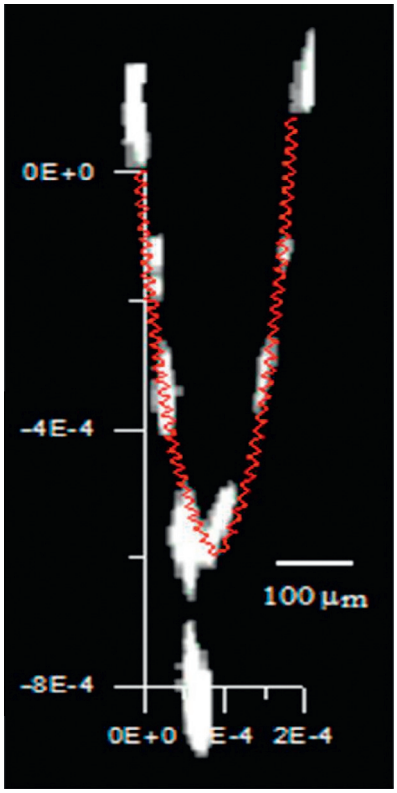


FIGURE 38.10 Particle trajectories numerically simulated (*red lines*) and experimentally described (filmed during their approach process) from initial conditions of $r_0 = 205 \pm 5.9$ μm $\theta_0 = 24° \pm 3.4°$ with respect to the acoustic axis.

($a_1 = a_2 = 4\mu m$) exposed to a horizontal plane acoustic wave during their settling down process due to gravity. Their approach process was filmed a distance $r_0 = 205 \pm 5.9\mu m$ and $\theta_0 = 24° \pm 3.4°$ off the horizontal acoustic axis. In a red line, their trajectories were numerically predicted starting from the same initial conditions. Both theoretical and experimental trajectories are superimposed in the figure, showing a good agreement. The image shows a different progression of the *x*- and *y*-positions of both particles over time during their approaching process until their collision. The highest

particle accelerates its settling down process to reach a position closer to the lower particle, decreasing their angle of orientation with respect to the acoustic axis. Once reached a certain position, they intensify their mutual attraction process, mainly along the x-axis until their collision. In parallel, the particle trajectories numerically predicted show the same evolution behavior.

38.10 Modeling of acoustic agglomeration of aerosol particles

38.10.1 Aerosol dynamics equation

Assuming binary collisions between particles and that all collisions lead to agglomeration, the evolution of the particle number as a function of time may be described by the Smoluchowski equation in the form (Ezekoye and Wibowo, 1999; Hoffmann, 1997; Sheng and Shen, 2006):

$$\frac{dn_k}{dt} = \frac{1}{2}\sum_{\substack{i=j \\ j=k-i}}^{k} \beta_{ij} n_i n_j - n_k \sum_{i=1}^{\infty} \beta_{ik}\, n_i \tag{38.24}$$

Here, the first term on the right hand is the particle gain in size group k by combining particles of the smaller than k size groups i and j, being the factor 1/2 needed to offset the counting of equal size particle pairs twice. The second term refers to the conversion of particles of size k into larger sizes as a result of collision and agglomeration. Mass conservation is satisfied throughout this equation. If the kernels β_{ij} for a given agglomeration mechanism are known in the whole particle size range of interest, the dynamics of the aerosol system can be simulated by the implementation of Eq. (38.24) in a numerical forward iteration scheme. In this way, we can obtain the time history of particle size distribution under the influence of acoustic agglomeration mechanisms.

38.10.2 Acoustic agglomeration kernels and numerical models

The collision kernel of particles, also called the agglomeration kernel or the kernel function, represents the effect of acoustic waves on the particle agglomeration process. In the derivation of the kernel function, a number of simplifying approximations were generally used. It was assumed that particles oscillate along straight lines inside the cylindrical agglomeration volume (see Figure 38.4). This may be true only for fine and isolated particles, but not for particles moving in close vicinity to one another. The models assume particles to be spherical before and after agglomeration. In addition, it is also understood that the density of the particles and the agglomerates is the same. In the derivation of the equations, it was also assumed that the agglomeration volumes are automatically refilled after each cycle so that the number density of the small particles stays constant within these volumes all the time. With these assumptions, the kernel of the orthokinetic agglomeration was initially expressed for the collision of pairs of particles $a_1 \gg a_2$ as follows (Mednikov, 1965):

$$\beta^{\text{ORTHO}}_{\text{Mednikov}} = 2(a_1 + a_2)^2 U_o |H_{12}| \tag{38.25a}$$

Later, Song (1990) proposed to add the effect of scattering interaction previously mentioned, and the kernel turned out to be

$$\beta^{\text{ORTHO}}_{\text{Song}} = 2(a_1 + a_2)^2 U_o |H_{12} + G_{12}| = 2(a_1 + a_2)^2 U_o q_{s12} \tag{38.25b}$$

Here, G_{ik} is the scattering interaction function. Eq. (38.25b) reduces to the Mednikov expression (Eq. 38.25a) when the effects of wave scattering are absent.

Song also derived an expression for the hydrodynamic agglomeration kernel starting from a previous kernel developed by Konig. It is given by Song et al. (1994):

$$\beta^{\text{HYDRO}}_{\text{Song}} = \left(\frac{g_{12}}{4\pi^2}\right)\beta^{\text{HYDRO}}_{\text{Konig}} \quad \text{where } g_{12} = \frac{a_1 g_{12r} + a_2 g_{21r}}{a_1 + a_2} \tag{38.26a}$$

$$\beta^{\text{HYDRO}}_{\text{Konig}} = \frac{2\sqrt{3}}{9}\,\frac{\pi \rho_0 U_o^2}{\mu}\,\frac{(a_1 a_2)^2}{(a_1 + a_2)} \tag{38.26b}$$

where the functions g_{12r} and g_{21r} are complicated expressions, which contain the effects of entrainment and vortex component of the scattering waves.

Then, a combination of both kernels was proposed by Song as a better and more complete approach to the full mechanism of agglomeration:

$$\beta_{\text{Song}} = b_1 \beta^{\text{ORTHO}}_{\text{Song}} + b_2 \beta^{\text{HYDRO}}_{\text{Song}} \tag{38.27}$$

In Eq. (38.27), b_1 and b_2 are two weight factors experimentally determined by Song as $b_1 + b_2 = 1$. The model developed by Song to simulate the agglomeration process and the numerical results obtained showed a good agreement with the experimental results reported by Hoffmann et al. (1993).

Ezekoye and Wibowo (1999) developed a new numerical model also based on the orthokinetic and MRP hydrodynamic mechanisms using a sectional algorithm. For the orthokinetic mechanism, they used the agglomeration kernel derived by Mednikov, whereas for the hydrodynamic kernel, they proposed the expression (38.26a) obtained by Song. These authors also studied contributions to the acoustic kernel from turbulent, Brownian, and gravitational sedimentation effects, which turned out to be very small. The results obtained with their computational model

were compared with several existing experimental data, concluding that the individual basic mechanism proposed for acoustic agglomeration may appear to work for some limited ranges of experimental investigations, but it is still quite far from experimentally validated. Thus, for moderate and high frequencies (above 9 kHz), the ability of this computational model to predict the experimental results is poor.

Sheng and Shen (2006) applied the direct simulation Monte Carlo method (DSMC) to simulate the acoustic agglomeration in traveling sound waves. They claimed that the predictions obtained by applying simple additive combinations of Song's orthokinetic model (Eq. 38.25b) and Song's hydrodynamic model (Eq. 38.26a) with the König equation were validated by some experimental data taken from the literature. Nevertheless, they also found limitations in covering a wide range of experimental conditions. They used a simple additive method to describe the combined contributions of the orthokinetic and MRP mechanisms involved in the process, including the Brownian kernel, which seems to play a not negligible role for very fine particles (Caperán et al., 1993; Funcke and Frohn, 1995). Then, the full kernel proposed by Sheng and Shen is:

$$\beta_{\text{Sheng-Shen}}^{\text{AGGLOMERATION}} = \beta_{\text{Song}}^{\text{ORTHO}} + \beta_{\text{Song}}^{\text{HYDRO}} + \beta^{\text{BROWNIAN}} \tag{38.28a}$$

$$\beta_{1,2}^{\text{BROWNIAN}} = \frac{2kT}{3\mu}\left(\sqrt[3]{v_1} + \sqrt[3]{v_2}\right)\left(C_1\sqrt[3]{v_1} + C_2\sqrt[3]{v_2}\right) \tag{38.28b}$$

where k is the Boltzmann constant, T is the temperature, μ is the viscosity of the medium, v_1 and v_2 are the volumes of particles 1 and 2, and C_1 and C_2 are the Cunningham slip factors for particles 1 and 2, respectively (Allen and Raabe, 1985). Sheng and Shen claim that the introduction of Brownian kernel makes their model more accurate, by comparing its simulation results of agglomeration with experimental data and other simulations. However, neither the kernel of Song nor that of Sheng and Shen can be applied over a broad range of conditions. Therefore, they conclude that further effort is still needed to improve modeling and simulation of the agglomeration process.

An extension of the above DSMC model was published 1 year later by the same authors (Sheng and Shen, 2007). In this new work, they modified the Song orthokinetic kernel as well as the König hydrodynamic kernel, considering the fractal-like morphology of the agglomerates in modeling processes of fly ash and TiO_2 particles. They simulated two different particle size distributions: lognormal and bimodal. They claimed that the agglomeration processes can be described quite accurately for a fractal dimension of about 1.8 and 2.2 for the fly ash and TiO_2 particles, respectively. Both values are in the range of the fractal dimension of solid particle agglomerates reported in the literature.

Recently, Aleixandre et al. (2016a, 2016b) developed a numerical method to study the acoustic agglomeration in a high-intensity standing wave field, based on the combination of the orthokinetic (Temkin 1994), and MRP (Song et al., 1994) mechanisms involved in the process together with scattering (Song et al., 1994) phenomena. The model developed has several assumptions indicated below. The particles are spherical and remain spherical for all the process. The particles are binned by size, and in each bin, the particles are assumed to have the same size. The agglomerates do not break up, and the particles are homogeneously distributed in the agglomeration chamber. The gas was modeled as air at atmospheric pressure and room temperature. The ultrasonic field was modeled as a standing wave. The numerical model proposes that the full mechanism of agglomeration kernel is a linear combination of the Song's orthokinetic kernel (Eq. 38.25b) and Song's mutual radiation pressure kernel (Eq. 38.26a). Thus, the full kernel is given by:

$$\beta_{Aleixandre\ et\ al.}^{AGGLOMERATION} = \beta_{Song}^{ORTHO} + \beta_{Song}^{HYDRO-MRP} \tag{38.29}$$

Figure 38.11 shows the final kernel when all effects are taken into account. The numerical model has been validated experimentally within the range of particle sizes and

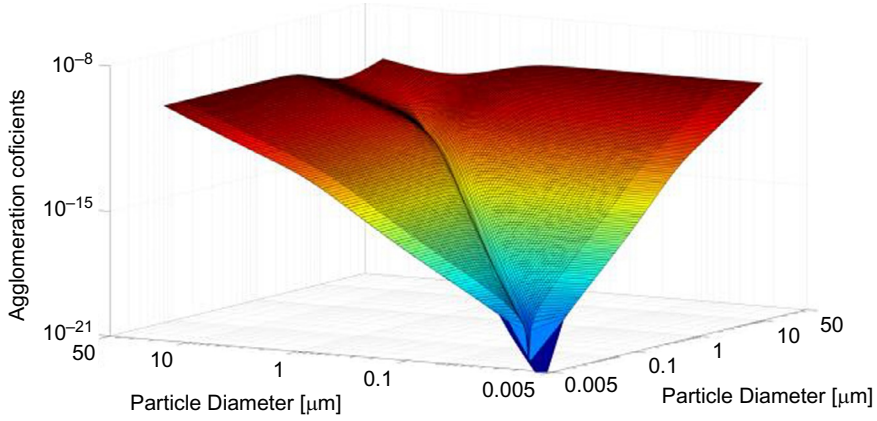


FIGURE 38.11 Full kernel as calculated by Aleixandre et al. (2016b).

concentrations studied for source term mitigation in nuclear accidents (Riera et al., 2016; Del Corno et al., 2017). However, it has been seen that the model has certain limitations because underestimates the results for very low aerosol concentrations or big particle sizes.

38.11 Experimental systems for acoustic agglomeration of aerosol particles

38.11.1 System for the removal of fine aerosol particles

For many years, the most common and almost exclusive airborne power acoustic generators were aerodynamic systems of various kinds, such as whistles and sirens, in which the acoustic energy was provided by a gas jet. Although these devices are able to generate large acoustic powers, their efficiencies are low (less than 10%), the sounds emitted are complex, and, in addition to their poor directivity, they have difficulties for reaching ultrasonic frequencies.

In the 1970s, a new type of piezoelectric air-borne ultrasonic transducer was designed at the Spanish National Research Council, CSIC (Gallego-Juárez et al., 1978). It showed to have a very high efficiency (up to 80%) and directivity, being able to be built for a wide range of ultrasonic frequencies. The structure of the transducer basically consists of a vibrating circular plate with a stepped profile driven at its center by a piezoelectrically activated vibrator. This novel type of transducer has been developed for different frequencies and power capacities to achieve good performances. The design, construction, characteristics, and performances of the different models of these transducers are described in detail in Chapter 7 of this book. A specific electronic system was also developed to drive the transducers with a precise control of the resonance frequency and power applied (Ramos et al., 1985).

The new family of airborne ultrasonic power generators has been the basis for the re-launching of ultrasonic agglomeration technologies essentially focused on micron and submicron particles.

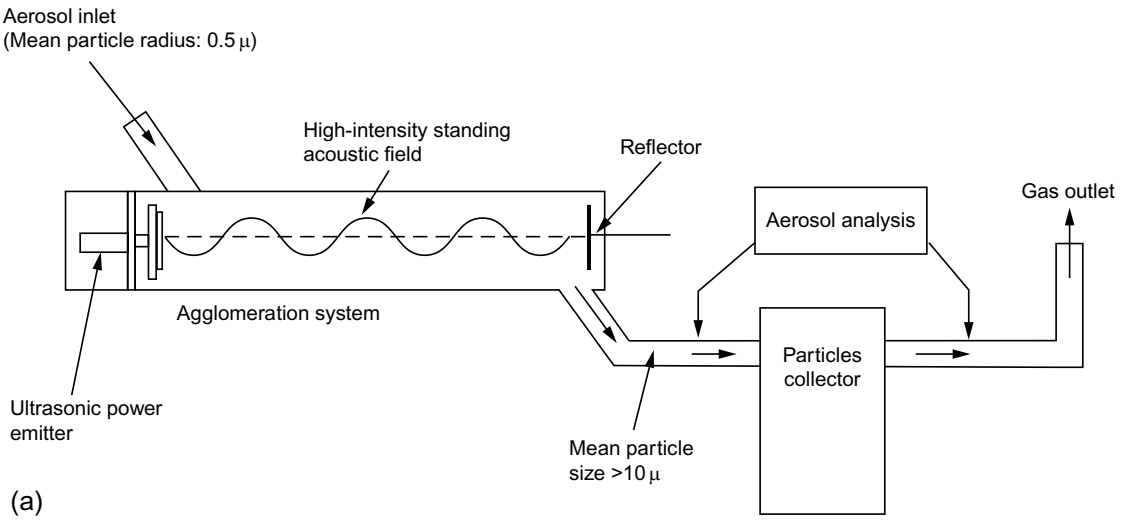
The first experimental acoustic agglomeration system designed consisted of a stepped-plate transducer (with a power capacity of 150 W) operating at 20 kHz, coupled to a cylindrical chamber (220 mm inside diameter and approximately 2 m length) in which a standing wave is generated by placing a reflector opposite the emitter (Gallego-Juárez et al., 1979). Figure 38.12 shows (a) the basic scheme and (b) a picture of the agglomeration system.

The system was initially tested as a precipitator. The average sound pressure level (SPL) inside the chamber was 160 dB. Precipitation tests on polydisperse carbon black smoke (mean diameter 1 μm, standard deviation 2.2) with flow rates around 60 m^3/h and mass loading from 4 to 14 g/m^3 showed mass deposition efficiencies inside the chamber of about 93%, with an energy consumption of approximately 3 kWh/1000 m^3.

The same ultrasonic chamber was also studied as particle preconditioner to be placed upstream of a conventional collector system (cyclone, electrostatic filter, scrubber, etc.). Dynamic tests with an aerosol flow rate of about 100 m^3/h were carried out. An increase of one order of magnitude in the particle mean diameter at the chamber exit was obtained with a residence time of 2.5 s (initial particle mean diameter of 0.6 μm, final particle mean diameter of 9.6 μm) with an energy consumption of approximately 1.5 kWh/1000 m^3 (Figure 38.13). Therefore, these experimental results confirmed the feasibility of the system as an acoustic preconditioner of very fine particles to facilitate their removal by conventional separators.

The system was scaled up for industrial application, by using new transducers of higher power capacity (400 W) operating at 21 kHz. Parallel-piped chambers of 5 and 15 m^3, activated by one and three transducers, respectively, were tested as precipitators. SPL ranging from 160 dB along the axis of the transducer to 140 dB far from the sources were measured. Three types of aerosols were tested with a mass loading of about 1 g/m^3 and particle diameters of around 0.8 μm: dense black soot aerosol (solid), artificial fog aerosol (liquid), and a mixture of both aerosols. The deviation to larger sizes of the distribution curve, along the treatment time, as well as the whole deposition of the aerosol particles after acoustic treatment, provided evidence of the mechanisms and efficiency of the acoustic agglomeration process (Gallego-Juárez et al., 1991).

A new step, for dynamic tests still at laboratory scale, was the installation of an acoustic agglomeration chamber together with an electrostatic filter (EF) to analyze the role of ultrasound as a preconditioner of submicron particles to enhance the removal performance of the EF for very fine particles. The aerosol used in this study was generated by heating glycerol at high temperature and rapidly mixing the hot vapor with cold air. The resulting dense white condensation aerosol has a lognormal particle size distribution, with a geometrical mean diameter of 0.8 μm (standard deviation of 1.4). Standing wave fields at 21 kHz were generated in a rectangular cross-sectional chamber. The aerosol flow rate varied from 150 to 1500 m^3/h, with resulting flow velocities of 0.17–1.7 m/s inside the acoustic chamber and 0.33–3.3 m/s in the EF. The total particle number concentration was $2 \times 10^6\,cm^{-3}$, and mass loading was about 1.35 g^{-3}. The separation efficiency of the EF for 0.8 μm particles increased from 87% to 92% when the ultrasonic energy is applied with a 21-kHz transducer operating at 400 W. In addition, the combined electro-acoustic filter reduces the cumulative rest mass below 5 μm, from



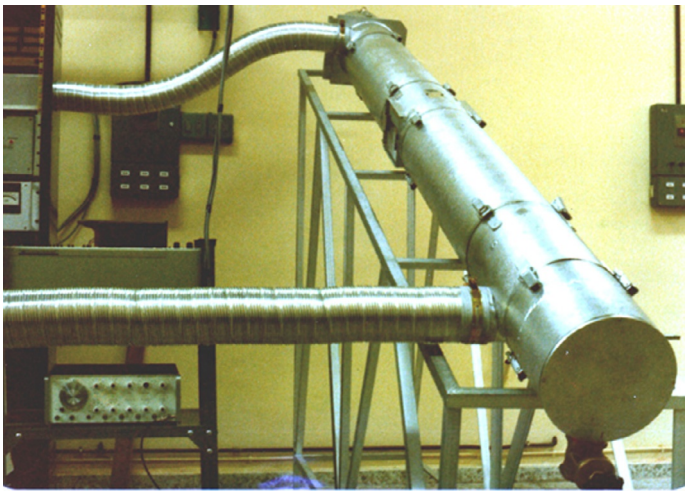


FIGURE 38.12 (a) Basic scheme of the agglomeration system, (b) View of the ultrasonic agglomeration chamber.

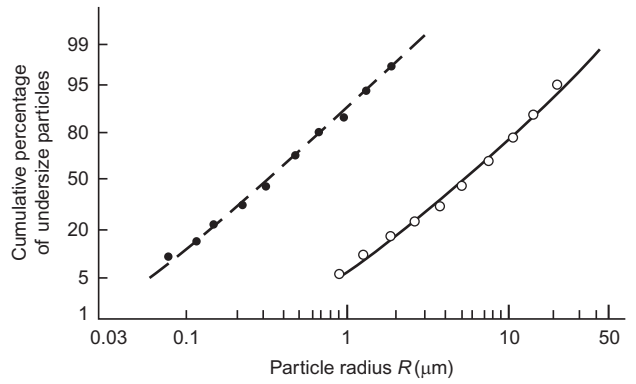


FIGURE 38.13 Particle size distribution before and after ultrasonic treatment at 20 kHz in dynamic tests (flow rate 100 m^3/h).

103 to 74 mg/m^3 (Figure 38.14). These results confirm the benefit of using ultrasonic energy to increase the efficiency of conventional separators in the submicron range (Magill et al., 1992).

38.11.2 Pilot-scale acoustic preconditioning systems for coal combustion fumes

On the long way to industrial application of the novel technology, a multi-frequency acoustic (MFA) chamber was developed to be operated together with an electrostatic filter (EF) in a pilot plant for the treatment of exhaust fumes produced from a 0.5-MWt fluidized bed coal combustor (Figures 38.15a and b). The objective was to quantify the removal effect of the EF on micron- and submicron-sized particles with the acoustic preconditioning by applying two frequencies (20 kHz in first section of the MFA chamber and 10 kHz in the second). The idea behind is to optimize the acoustic effect by applying a lower frequency in the second section of the chamber (10 kHz) once the original very tiny particles have been grown a little in the first section. To be noted that there is a relationship between size and applied frequency (the smaller the particles the higher the required frequency, and vice versa). The acoustic chamber was 3.6 m long with a rectangular cross-section of 0.7×0.5 m. The

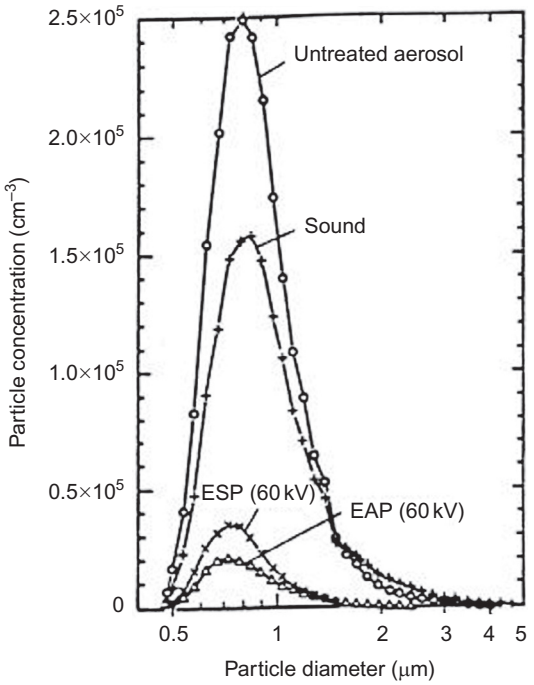


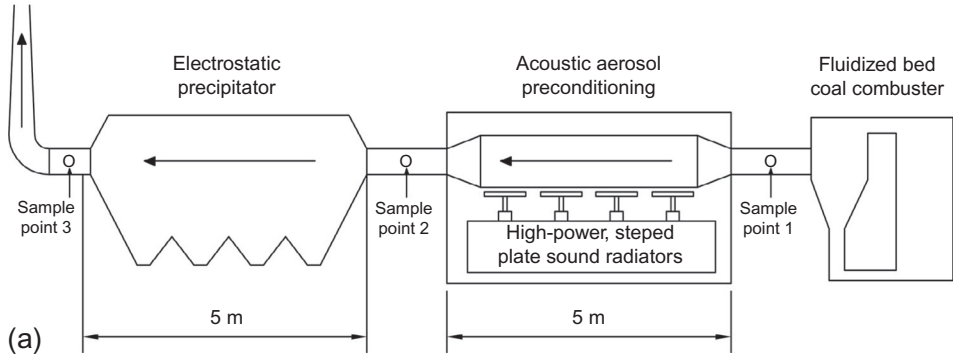
FIGURE 38.14 Characteristics of the electro-acoustic precipitator for a volume flow rate of $560\,m^3/h$, total concentration $2 \times 10^6\,cm^{-3}$, and mass loading of $1.35\,g/m^3$.

residence time of the aerosol in the acoustic chamber was about 2 s. Four stepped-plate transducers of 10 and 20 kHz were used to achieve average SPLs of about 151 dB and peak values of 165 dB in the entire volume of the chamber with an electrical power applied of 400 W to any transducer. In the experiments, the aerosol entered the chamber at 250°C, with a flow rate of $1600\,m^3/h$, mass loading of $5\,g/m^3$, and particle number concentration of $5 \times 10^5\,cm^{-3}$. When the MFA is operating, reductions of 42% and 39% in micron-sized and submicron-sized particles, respectively, are reached compared to emissions when the EF is operating alone (Gallego-Juárez et al., 1999).

Such results support the scaling up of the system for the removal of very fine particles in any industrial process. The preconditioning procedure is equally useful in combination with other filtering or removal systems such as cyclone or ceramic filters. It can also be used in high-pressure and high-temperature environments, opening up a wide range of applications in medium- to large-scale acoustic agglomeration and precipitation processes.

Table 38.1 summarizes the most relevant experimental data on acoustic agglomeration from Gallego-Juárez's group.

In addition, Table 38.2 summarizes the experimental work available from the literature. It contains relevant



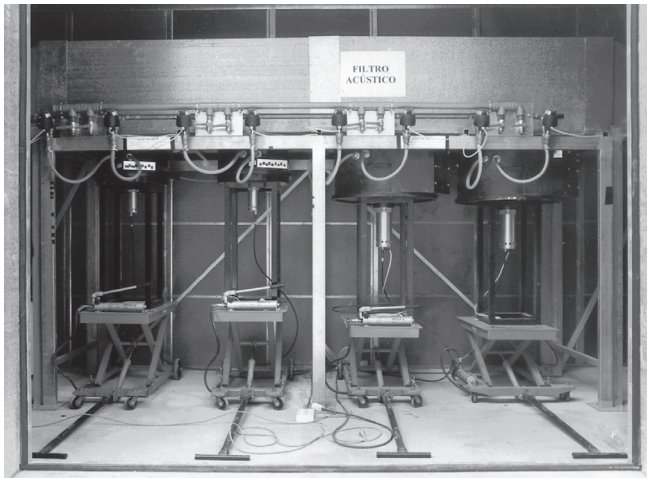


FIGURE 38.15 (a) Scheme of the pilot installation for particle removal from coal combustion fumes. (b) Front view of the acoustic aerosol preconditioner with four plate transducers two at 20 kHz and two at 10 kHz.

TABLE 38.1 Experimental results carried out by Gallego-Juárez's group at laboratory- and pilot-scale plants for industrial and environmental applications

Project	Years	Aerosols tested	Flow conditions	Ultrasonic system	Conditions tested					Measured efficiency
					Mass loading (g/m^3)	Treatment time (s)	Particle diameter (μm)	Frequency (kHz)	Intensity (dB)	
Static mass loading precipitation	1974–1976	Carbon black smoke	Static	Stepped-plate radiator 2NC 3NC	7	900 (– US) 100 (+ US)	0.2 $d_p = 0.5$	22	150	Precipitation 90%
Dynamic mass loading precipitation	1977–1980	Carbon black smoke	Dynamic	Stepped-plate radiator 3NC	4–14	4–5 ($50\,m^3/h$)	0.3 $d_p = 0.5$	20.4	161	Precipitation 90%–93%
Static and dynamic growth of particle size	1979–1980	Carbon black smoke	Static Dynamic	Stepped-plate radiator 3NC	7	5 2.5 ($100\,m^3/h$)	0.8 0.6 0.6	20.4	157 159.5 159.5	Particle growth 33 times 16 times
Dynamic growth of particle size	1982–1984	Carbon black smoke	Dynamic	Stepped-plate radiator 3NC	3–12	2	0.2 0.2 0.8 0.8	20.4	156.4 163.3 156.4 163.3	Particle growth 11–25 times
Static mass load precipitation	1988–1989	Smoke from burning rubber	Static ($4.5\,m^3$ chamber)	Stepped-plate radiator 5NC	0.4 1.0 1.0		< 0.1 0.1	20 21	133,137 142 149 143	Precipitation 11–25 times
Static mass load precipitation Increasing collection efficiency	1989–1993	Black soot glycol fog Mixture glycol fog	Static ($15\,m^3$ chamber) Dynamic	Stepped-plate radiator 5NC EAP	1.0 1.0 1.0	560– $1500\,m^3/h$	0.8 0.8 0.8 0.8 0.8	21 21	140–160 155	Particle number reduction from 10^6 to $10^3\,cm^{-3}$ Particle collection without US 87% with US 92%
Experimental research	1993–1996	Coal combustion fumes (150–300 °C)	Dynamic ($1.5\,m^3$ chamber)	Acoustic preconditioning system	6.0	2–4 s $1600\,m^3/h$	Bimodal 0.07 and 0.9	10 20	145–165	Particle collection 34% submicron 76% micron

Continued

TABLE 38.1 Experimental results carried out by Gallego-Juárez's group at laboratory- and pilot-scale plants for industrial and environmental applications—cont'd

Project	Years	Aerosols tested	Flow conditions	Ultrasonic system	Conditions tested					Measured efficiency
					Mass loading (g/m^3)	Treatment time (s)	Particle diameter (μm)	Frequency (kHz)	Intensity (dB)	
Influence of humidity	1996–1999	Diesel exhaust aerosols (180 °C)	Dynamic (1.5 m^3 chamber)	Acoustic preconditioning system	0.01	2–3 900 m^3/h	0.02–0.8 $d_p = 0.08$	10 20	145–165	Particle collection 25% (+ US) 56% (+ US +6% RH)
Experimental research on AAA	1998–2001	Diesel exhaust aerosols (250 °C)	Dynamic (6 m^3 Chamber)	Acoustic preconditioning system	1.8	1200 m^3/h	0.04–0.6 (SMPS) 0.2–6.0 (PALAS)	7 21	150	Particle collection 57%–78%
Theoretical and experimental research on AWE	2001	Theoretical and experimental research AWE diesel exhausts (250 °C)	Dynamic (1.5 m^3 chamber)	Acoustic preconditioning system	0.01	2–3 900 m^3/h	0.02–0.8 $\overline{d}_p = 0.08$	20	145–165	Good fitting between experimental measurements and theoretical results
Theoretical research on AAA	1993–1996	Coal combustion fumes (170 °C)	Dynamic	Acoustic preconditioning system	6	2–4 s 1600 m^3/h	Bimodal 0.07 and 0.9	10 20	145–165	Particle collection 34% submicron 76% micron
Modeling	1993–1995	Basic and theoretical research AWE/ MRPE	Dynamic	Acoustic preconditioning system	Very low	1–2 s	4 and 8 glass microspheres	20 Hz– 4 kHz	135–145	Visualization of particle entrainment

The particle separation efficiency function is defined by $\eta = 1 - \frac{N_{OUT}(D)}{N_{IN}(D)}$, where $N_{IN}(D)$ and $N_{OUT}(D)$ are the concentrations of particles of diameter D entering and leaving the AAA.

TABLE 38.2 Experimental data sets available in the literature

Experiment	Airborne particle	Frequency	I (dB; W/cm)
Brandt and Hiedemann (1936a)	Paraffin oil	10 kHz	138; 148; 151 dB
Dianov et al. (1962)	Zinc oxide	200–21,000 Hz	0–164 dB
Hinds et al. (1977)	Sodium aerosol	600–1200 Hz	125 dB
Shaw and Tu (1979)	Dioctyl phthalate; Polystyrene latex	1–3 kHz	145 dB
Rajendran et al. (1979)	NH_4Cl	640–1700 Hz	125–160 dB
Tiwary and Reethof (1987)	Coal fly ash	1.42–2.5 kHz	144 and 160 dB
Magill et al. (1989a,b, 1991)	Soot; black soot glycerine Glycol fog aerosol	20 kHz 21 kHz	133,137,142, 149 dB 140–160 dB
Song (1990)	Coal fly ash	1.42–2.5 kHz	144 and 160 dB
Hoffmann et al. (1993)	Fly ash calcined limestone	44 Hz	160 dB
Caperán et al. (1995)	glycol fog aerosol; Soot; TiO_2	10 and 20 kHz	
Hofmann and Koopmann (1996)	glass spheres; quartz particles	400–900 Hz	

information on the aerosol type, size distribution, and characteristics of the acoustic field.

38.11.3 Further experimental studies on the effect of liquid droplets and other additives to improve acoustic agglomeration

In the experiments with liquid fog aerosol, referred in the previous Section 38.12.1, it was seen that liquid particles agglomerate more quickly than soot particles (Gallego-Juárez et al., 1991). Therefore, it appears promising study regarding the use of liquid droplets as an additive to improve the removal of tiny particles.

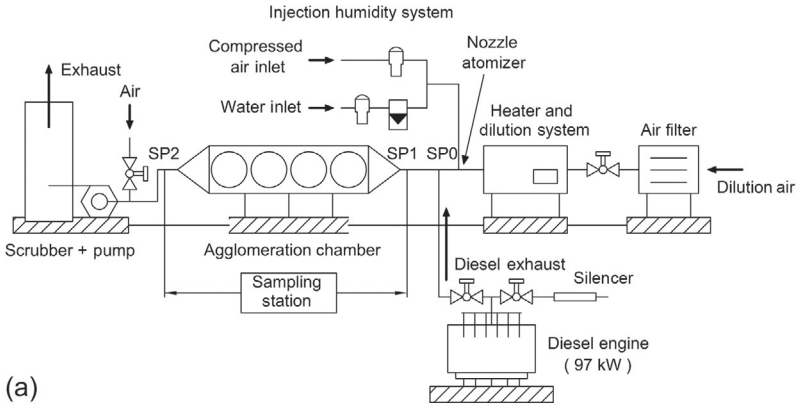
Such experimental study was carried out with an aerosol of 0.2 μm average diameter generated by a 97-kW diesel engine. The acoustic chamber used for these tests was the same MFA above explained but modified by introducing into the agglomeration chamber a dilution system and a nozzle atomizer (Figure 38.16). In addition, the ultrasonic radiation applied was of a sole frequency of 20 kHz. The effect of the ultrasonic treatment, with flow rates of 900 Nm^3/h, was a reduction in the number concentration of particles at the outlet of the acoustic chamber on the order of 25%. This agglomeration rate increased up to 56% by injection of water droplets in order to get a degree of humidity in the fume of about 6% (0.06 kg_{water}/kg_{gas}) (Riera et al., 2003).

Recently, Khmelev et al. (2016) have published some results of applying ultrasound in a Venturi scrubber to improve the removal of fine particles. As well known, the particle removal of Venturi scrubbers is based on trapping the particles with liquid droplets. The particle collection of the Venturi scrubber for particles less than 5 μm size does not exceed 75%. By applying ultrasound (22 kHz, 150 dB) to improve the interaction of ash and water particles, the authors claim that a collection of 2 μm particles increases up to 99%. For that research, the authors employ the ultrasonic circular stepped-plate transducer previously developed and patented by Gallego-Juárez et al. (Gallego-Juárez, 1973; Gallego-Juárez et al., 1978, 2001, 2010, 2015) without referencing it.

Other ways to improve agglomeration of fine particles propose the addition of seed particles (larger than 20 μm), steam, and also liquid droplets. Steam and water are easy to get at low cost in most industrial processes, making these methods attractive and feasible for further industrial applications. However, if the fine particles are hydrophobic, they have difficulty adhering to the surface of water droplets, giving a low efficiency of fine particle removal. On the contrary, if the surface tension of the seed droplets is reduced, and the wetting performance of fine particle is improved, the capture of fine particles can be increased more efficiently (Zhang et al., 2017).

Experimental studies about the influence of steam on the acoustic agglomeration of fine coal-fired ash particles (0.3 μm diameter) show that removal efficiencies of 53%–70% are achieved (Yan et al., 2016a, 2016b, 2017).

Besides water, other additives such as sodium dodecyl sulfonic salt (SDS), fluorinate surfactant (FS-310), primary alcohol ethoxylate (JFC), and modified polysilanol surfactant (Silanol w22) have been investigated to improve fine particle collection. From the results, the authors claim that removal efficiency can be improved by the addition of wetting agents, due to the fact that particles may easily penetrate into the droplet, making the coagulation process irreversible (Yan et al., 2016b, 2017).



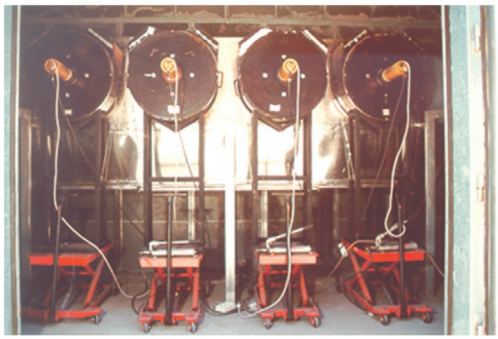


FIGURE 38.16 Scheme (a) and picture (b) of the pilot plant-scale ultrasonic installation at 20 kHz for fine particle agglomeration with diesel exhausts.

38.11.4 Ultrasonic agglomerator system for term mitigation in severe accidents in a nuclear power plant

Practical uses of aerosol agglomeration processes have been mainly focused on environmental applications. Very fine particles (PM2.5) are difficult to remove by conventional separation technology, constituting a major health hazard. Besides industrial emissions, large amount of hazardous material in the form of micron and submicron aerosols can be released into the atmosphere following industrial or nuclear accidents or even in the event of a fire, as it happened in Bhopal (chemical plant accident 1984), Chernobyl (nuclear power plant accident 1986), the Gulf War (oil wells fire 1991), and Fukushima (nuclear power plant 2011) (Riera et al., 2015). After the Fukushima accident, one of the main objectives of the nuclear industry has been the improvement of source term mitigation systems and the search for innovative mitigation procedures such as the acoustic agglomeration.

In the frame of the European project (PASSAM 323217 – Euratom FP7), two Spanish institutions CSIC and CIEMAT have been involved in the investigation of applicability of an innovative acoustic system for source term mitigation in the case of severe accident conditions that could occur in a nuclear power plant (NPP) (Albiol et al., 2013, 2017). The main goal of this applied research has been to investigate the performance of an acoustic agglomerator system at lab scale under conditions, as close as possible, similar to those prevailing under filtered containment venting systems (FCVS) (Herranz et al., 2014). Due to the lack of information, about the experimental behavior of acoustic agglomerators in scenarios as those postulated within a severe accident, the above-mentioned groups have collaborated to integrate and characterize a mitigative system acoustic agglomerator (MSAA), designed and developed by CSIC, within the PECA (Plant for Experimental Characterization of Aerosols) vessel at CIEMAT (Figure 38.17).

The MSAA system consists of a rectangular section chamber in steel to operate in vertical position inside the PECA vessel containing the acoustic field and circulated by the aerosol. Placed inside, there are two stepped-plate power ultrasonic transducers (21 kHz, 300 W) of the same type of that used in previous experiments. The average sound pressure level (SPL) inside the chamber is of 155 dB. This system (Figure 38.18) was placed inside the PECA vessel (Figure 38.19), a configurable installation to generate the circulating aerosol and to control and monitoring flow rate, temperature, humidity, and pressure. PECA also generates the aerosol using a brush system PALAS RGB 100-ph able to achieve a maximum aerosol concentration inside the MSAA chamber of 200 mg/m^3.

The aerosol characteristics were adapted, as much as allowed by the generation system, to those of the expected aerosols in the nuclear event. Experimental tests were carried out with different values of the parameters (flow rate, particle size distribution, mass concentration, treatment time) in order to extract information about the agglomeration

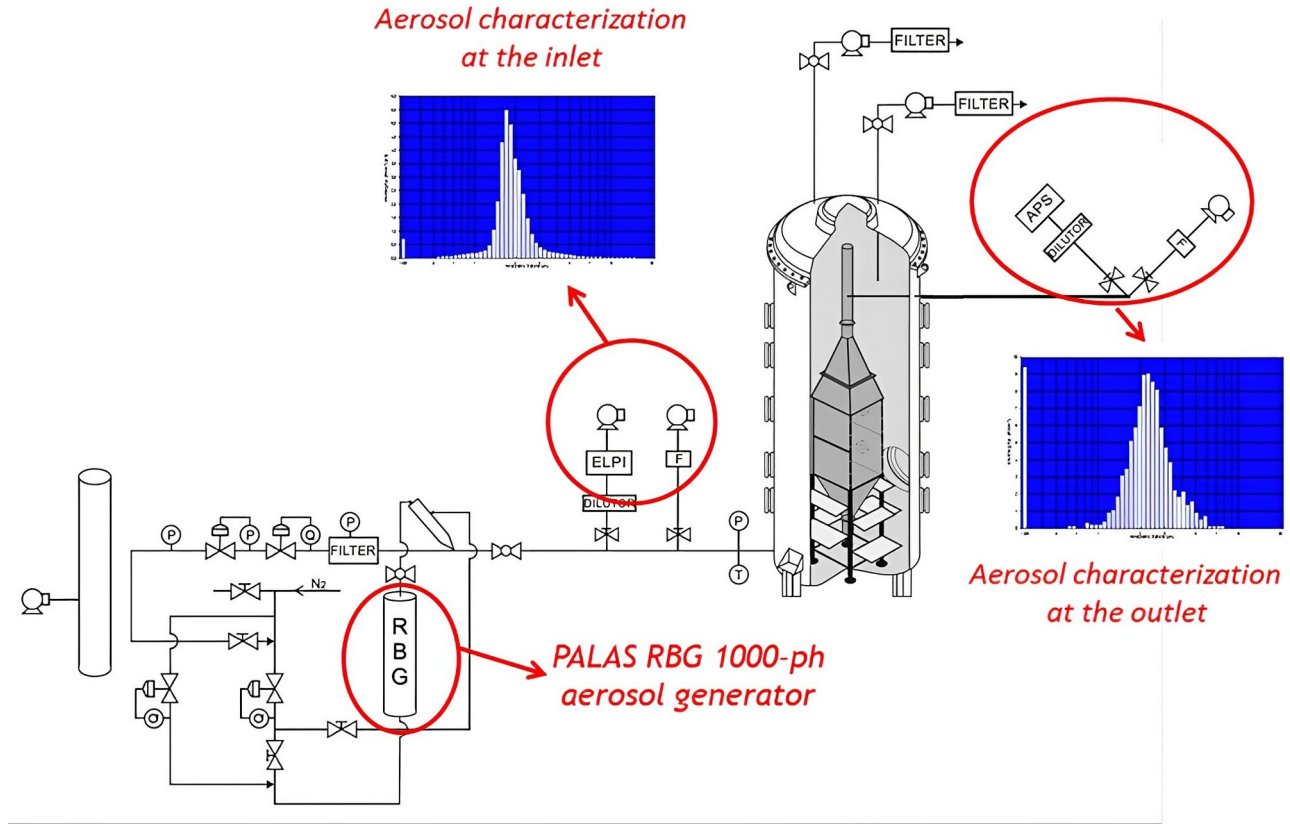


FIGURE 38.17 Lay-out of the PECA-MSAA experimental facility.



FIGURE 38.18 View of the MSAA system with two ultrasonic transducers. Overall height 3444 m.



FIGURE 38.19 Outside view of the MSAA within the PECA vessel.

process. Three different sizes of SiO_2 particles (0.3, 1, and 2.5 μm) were used separately and mixed in weight in different proportions. Also, polydisperse particles of TiO_2 with sizes between 0.01 and 0.05 μm were used (Riera et al., 2016).

The effect of the ultrasound field is illustrated in Figure 38.20 showing the changes in the particle size distribution induced by ultrasonic agglomeration on the aerosol. In the graphic, the peaks correspond to the times in which the ultrasound was not acting and the valleys to those where the ultrasound field was applied to the aerosol. The effect of the ultrasound field in the aerosol particle distribution was measured by two different ways: mass and number concentration reduction and changes on the aerodynamic mass particle distributions (Aleixandre et al., 2015).

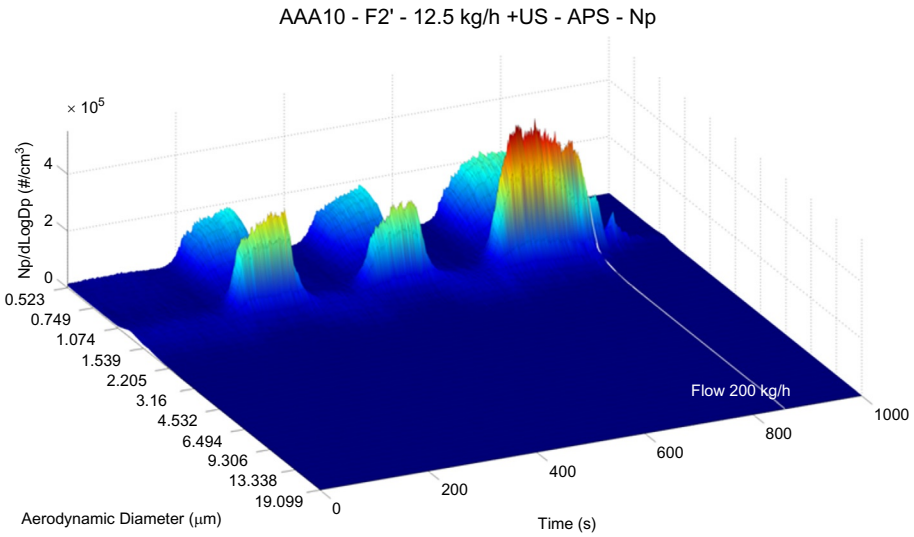


FIGURE 38.20 Particle number concentration with and without ultrasound measured.

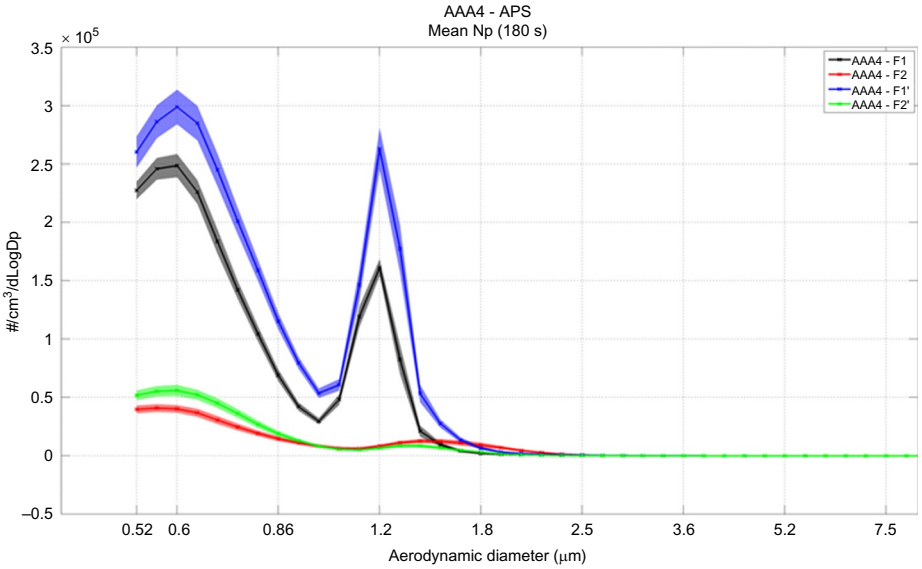


FIGURE 38.21 Particle number concentration of test AAA4 measured in two consecutive runs with two different phases: (I) First run, F1 and F2 without and with ultrasound application, respectively. (II) Second round (repetition), F1´ and F2′ without and with ultrasound application, respectively.

As an example, Figure 38.21 shows four mean distributions (F1 black, F2 red, F1′ blue, F2´ green) for one of the tests, with areas representing the standard deviation of the mean values.

The effect of ultrasound on the particle number was quantified by using the following equation (Eq. 38.30), where Np_b is the particle number concentration with and without applying ultrasound and RC_{Np} is the number reduction coefficient given by.

$$RC_{Np} = \left(1 - \frac{mean\ (N_{Pb\ WITH\ US}}{mean(N_{Pb\ WITHOUT\ US})}\right) * 100\% \quad (38.30)$$

For treatment times of about 80 s and particle number concentrations in the range 10^4–$10^5\,cm^{-3}$ the smaller particles (0.3 μm) experiment, a reduction of over 91% with an acoustic intensity of about 155 dB. Under these conditions, the increase in particle size due to ultrasound application was mainly observed for 1-μm particles, which increases of up to 37% (Del Corno et al., 2017).

The model allows estimating the ultrasonic energy necessary to achieve the removal of 90% of the smallest particles.

38.12 Conclusions and future trends

Sonic agglomeration of aerosols is a process that involves the response of particles suspended in gaseous media to forces arising from an intense sound field. Several different

basic effects have been studied as being responsible for particle collision and agglomeration, mainly orthokinetic and hydrodynamic forces. Such basic effects have been analyzed since the first half of the last century, and consequently, increasing knowledge about them has been achieved. Now it seems clear that orthokinetic collisions and hydrodynamic mechanisms, in particular the AWE, may be considered the dominant effects. The orthokinetic collision is the best known and more largely studied effect, and as previously seen, the main parameters, such as the optimum frequency and the SPL, can be well determined. This is the main mechanism for the agglomeration of polydisperse aerosols. The AWE, which has been deeply studied during recent years by some of the authors of this chapter, is effective for collisions of similar-sized particles. Effects, as well as the mutual RP, have already been modeled, but the complete process model is still far from being achieved due to the changing dynamic of the process and the difficulty of balancing the different effects.

The main practical application field for sonic agglomeration is specifically removal of micron and submicron particles. In fact, this technique has been shown as a form of filtration especially suitable for very tiny particles, by increasing their sizes to be readily collected by electrical or inertial methods. However, the industrial introduction of the systems already tested at small or/and medium scale requires to overcome some practical and technological problems. First, the treatment of great volumes from industrial or power plant exhausts will need a significant number of high-power airborne sonic/ultrasonic generators, involving high costs inherent in the novel sophisticated technologies. On the other hand, the ultrasonic systems have to be flexible to be adapted to different installations by applying different frequencies depending on particle size that even changes during the process. In spite of these issues, the current expectations of this technology are very positive since it is almost unique for the treatment of submicron particles, and presently, the society has definitely assumed the urgent need of their removal.

References

Albiol, T., Herranz, L., Riera, E., Guieu, S., Lind, T., Manzini, G., Auvinen, A., Losch, N., 2013. New Studies on Passive and Active Systems Towards Enhanced Severe Accident Source Term Mitigation—The PASSAM Project, Eurosave Forum—November 5-6, 2012, Bruxelles (Belgium).

Albiol, T., Herranz, L., Riera, E., Dalibart, C., Lind, T., Del Corno, A., Kärkelä, T., Losch, N., Azambre, B., Mun, C., Cantrel, L., 2017. PASSAM Final Synthesis Report. PASSAM-DKS-T28 [D5.5].

Aleixandre, M., Riera, E., Degado, R., Herranz, L., Acosta, V.M., Pinto, A., Martínez, I., Gallego-Juárez, J.A., 2015. Characterization of the Changes of the Particle Size Distribution of Different Aerosols During an Acoustic Agglomeration Process. 2015 Publicación Oficial del Congreso Tecniacústica, pp. 1545–1552.

Aleixandre, M., Riera, E., Gallego-Juárez, J.A., Delgado-Tardáguila, R., Herranz, L.E., 2016a. Characterization of aerosol particle size distribution measurements by fitting lognormal functions during an aerosol acoustic agglomeration process. In: EuroRegio2016, June 13–15 Porto Portugal.

Aleixandre, M., Riera, E., Delgado-Tardáguila, R., Herranz, L.E., Gallego-Juárez, J.A., 2016b. Study about the application of acoustic agglomeration of aerosols for source term mitigation in nuclear accidents. In: Proceedings of the 22nd International Congress on Acoustics (ICA2016), Buenos Aires, 5-9 September, 2016.

Allen, M.D., Raabe, O.G., 1985. Slip correction measurements of spherical solid particles in an improved Millikan apparatus. Aerosol Sci. Technol. 4, 269–286.

Amy, E.V., 1934. Dispersing Particles Suspended in Air. USA Patent N1980171.

Andrade, E.N.d.C., 1936. The coagulation of smoke by supersonic vibration. Trans. Faraday Soc. 134, 1111–1115.

Brandt, O., Hiedemann, E., 1936a. The aggregation of suspended particles in gases by sonic and ultrasonic waves. Trans. Faraday Soc. 24, 1101–1110.

Brandt, O., Hiedemann, E., 1936b. Zur theorie der akustischen koagulation. Kolloid Z. 77, 103–115.

Brandt, O., Freund, H., Hiedemann, E., 1937. Schwebstoffe im Schallfeld. Z. Phys. 104, 511–533.

Buranov, L., Eknadiosyants, O., 1961. On the behaviour of aerosol particles in an acoustic field. Sov. Phys. Acoust. 7, 398–399.

Caperán, P., Somers, J., Richter, K., Fourcaudot, S., 1993. Acoustic agglomeration of sub- micron particles. J. Aerosol Sci. 24, S593–S594.

Caperán, P., Somers, J., Richter, K., Fourcaudot, S., 1995. Acoustic agglomeration of a glycol fog aerosol: influence of particle concentration and intensity of the sound field at two frequencies. J. Aerosol Sci. 26, 595–612.

Cheng, M.T., Lee, P.S., Berner, A., Shaw, D.T., 1983. Orthokinetic agglomeration in an intense acoustic field. J. Colloid Interface Sci. 91, 176–187.

Czyz, H., 1987. The aerosol particle drift in a standing wave field. Arch. Acoust. 12, 199–214.

Danilov, S., Mironov, M., 1984. Radiation pressure force on a small particle in a sound field. Sov. Phys. Acoust. 30, 280–283.

Danser, H.W., Neumann, E.P., 1949. Industrial sonic agglomeration and collection system. Ind. Eng. Chem. 41, 2439–2442.

Del Corno, A., Parozzi, F., Lind, T., Herranz, L., Bosland, L., Dalibart, C., Losch, N., Miklautsch, M., Riera, E., Karkela, T., Gouello, M., Azambre, B., Cantrel, L., 2017. PASSAM Report on Analysis of Experimental Results and Development of Simplified Models and Correlations. PASSAM-THEOR-T26 [D2.3].

Dianov, D.V., Merkulov, L.G., Nikitenko, V.I., 1962. Precipitation of zinc oxide aerosol in an acoustic field. Sov. Phys. Acoust. 8, 44–48.

Dianov, D.B., Podolskii, A.A., Turubarov, V.I., 1968. Calculation of the hydrodynamic interaction of aerosol particles in a sound field under Oseen flow conditions. Sov. Phys. Acoust. 13, 314–319.

Dukhin, S.S., 1960. Theory of aerosol particle drift in a standing sound wave. Kolloid Z. 22, 128–130.

Ezekoye, O.A., Wibowo, Y.W., 1999. Simulation of acoustic agglomeration processes using a sectional algorithm. J. Aerosol Sci. 30 (9), 1117–1138.

Fuchs, N.A., 1989. The Mechanics of Aerosols. Dover Publications Inc, New York.

Funcke, G., Frohn, A., 1995. Investigation of the influence of different parameters on the acoustic agglomeration process using numerical simulation. J. Aerosol Sci. 26, S147–S148.

Gallego-Juárez, J.A., 1973. Axisymetric vibrations of circular plates with stepped thickness. J. Sound Vib. 26, 411–416.

Gallego-Juárez, J.A., Rodriguez, G., Gaete, L., 1978. An ultrasonic transducer for high-power applications in gases. Ultrasonics 16, 267–271.

Gallego-Juárez, J.A., Riera, E., Rodríguez, G., 1979. Evaluation of an ultrasonic agglomerator as a preconditioner for the removal of aerosol particles. In: Ultrasonics International'79 Conference Proceedings, Guildford, Surrey. IPC Science Technology Press, Guildford, Surrey, England, pp. 227–232.

Gallego-Juárez, J.A., Riera-Francode Sarabia, E., Rodriguez-Corral, G., Magill, J., Richter, K., Fourcaudot, S., Barraux, P., 1991. An acoustic system for particulate precipitation. Environ. Pollut. 1, 220–227.

Gallego-Juárez, J.A., Rodriguez, G., San Emeterio, J.L., Montoya, F., 1994. Electroacoustic Unit for Generating High Sonic and Ultrasonic Intensities in Gases and Interphases. USA Patent No. 5299175.

Gallego-Juárez, J.A., Riera, E., Rodríguez, G., Gálvez, J.C., Hoffmann, T. L., Vázquez, F., Rodríguez, J.J., Gómez, F.J., Martin, M., Acha, M., Montoya, F., 1996. Pilot scale acoustic preconditioning of coal combustion fumes to enhance electrostatic precipitator performance. In: Schmidt, E., Gäng, P., Pilz, T., Dittler, A. (Eds.), High Temperature Gas Cleaning. Inst. Mech. Verfahrenstechnik und Mechanok, Karlsruhe, pp. 60–68.

Gallego-Juárez, J.A., Riera, E., Rodríguez, G., Hoffmann, T.L., Gálvez, J. C., Rodríguez, J.J., Gómez, F.J., Bahillo, A., Martin, M., 1999. Application of acoustic agglomeration to reduce fine particle emissions from coal combustion plants. Environ. Sci. Technol. 33, 3843–3849.

Gallego-Juárez, J.A., Rodríguez, G., Riera, E., Campos, C., Vázquez, F., Acosta, V.M., 2000. A macrosonic system for industrial processing. Ultrasonics 38, 331–336.

Gallego-Juárez, J.A., Rodriguez-Corral, G., Riera, E., Vazquez-Martinez, F., Acosta-Aparicio, V.M., 2001. Development of industrial models of high-power stepped-plate sonic and ultrasonic transducers for use in fluids. IEEE.

Gallego-Juárez, J.A., Rodriguez, G., Acosta, V.M., Riera, E., 2010. Power ultrasonics transducers with extensive radiators for industrial processing. Ultrason. Sonochem. 17, 953–964.

Gallego-Juárez, J.A., Rodríguez, G., Acosta-Aparicio, V.M., Riera, E., Cardoni, A., 2015. Power ultrasonic transducers with vibrating plate radiators. In: Gallego-Juárez, J.A., Graff, K.F. (Eds.), Power Ultrasonics. Woodhead Publishing, Cambridge, UK, pp. 159–195, https://doi.org/10.1016/B978-1-78242-028-6.00034-X (Chapter 7).

González, I., 1998. Estudio de las interacciones hidrodinámicas de origen viscoso en la aglomeración acústica de partículas (Ph.D. dissertation). Universidad Complutense de Madrid.

González, I., Hoffmann, T.L., Gallego-Juárez, J.A., 1997. Visualization of interactions between particles subjected to intense acoustic fields. In: Proceedings of World Congress on Ultrasonics (WCU 97), 24–27 August, Yokohama, Japan, pp. 422–423.

González, I., Hoffmann, T.L., Gallego-Juárez, J.A., 2000a. Theory and calculation of sound induced particle interactions of viscous origin. Acta Acust. Acust. 86, 784–797.

González, I., Hoffmann, T.L., Gallego-Juárez, J.A., 2000b. Precise measurements of particle entrainment in a standing-wave acoustic field between 20 and 3500 Hz. J. Aerosol Sci. 31 (12), 1461–1468.

González, I., Elvira, L., Hofmann, T.L., Gallego-Juárez, J.A., 2001. Numerical study of the hydrodynamic interaction between aerosol particles due to the acoustic wake effect. Acta Acust. Acust. 87, 454–460.

González, I., Hofmann, T.L., Gallego-Juárez, J.A., 2002. Visualization of hydrodynamic particle interaction: validation of a numerical model. Acta Acust. Acust. 88, 19–26.

González, I., Gallego-Juárez, J.A., Riera, E., 2003. The influence of entrainment on acoustically induced interactions between aerosol particles—an experimental study. J. Aerosol Sci. 34, 1611–1631.

Gor'kov, L., 1962. On the forces acting on a small particle in an acoustic field in an ideal fluid. Sov. Phys. Acoust. 6, 773–775.

Greguss, P., 1964. The application of air-borne and liquid-borne sounds to industrial technology. Ultrasonics, 5–10.

Gucker, F., Doyle, G., 1956. The amplitude of vibration of aerosol droplets in a sonic field. J. Phys. Chem. 60 (7), 989–996.

Guo, Q., Yang, Z., Zhang, J., 2012. Influence of a combined external field on the agglomeration of inhalable particles from coal combustion plant. Powder Technol. 227, 67–73.

Herranz, L., Lind, T., Dieschbourg, K., Riera, E., Morandi, S., Rantanen, Chebbi M., and Losch, N., 2014. In: Proceedings of NUTHOS-10, Okinawa, Japan, December 14–18.

Hinds, W., Mallovve, E.F., First, M.W., 1977. Acoustic and Turbulent Agglomeration of Sodium Aerosols. Technical report COO-2801-6. Harvard University, Cambridge, MA, pp. 1–21, https://doi.org/10.2172/7257410.

Hoffmann, T.L., 1993. Visualization of Particle Interaction and Agglomeration in an Acoustic Field (Ph.D. dissertation). The Pennsylvania State University.

Hoffmann, T.L., 1997. An extended kernel for acoustic agglomeration simulation based on the acoustic wake effect. J. Aerosol Sci. 26 (6), 919–936.

Hoffmann, T.L., 2000. Environmental implications of acoustic aerosol agglomeration. Ultrasonics 38, 353–357.

Hoffmann, T.L., Koopmann, G.H., 1993. Experimental and numerical analysis of particle agglomeration in an acoustic field. In: Hoback, H. (Ed.), Proceedings 13th ISNA, Bergen, pp. 615–620.

Hoffmann, T.L., Koopmann, G., 1996. Visualization of acoustic particle interaction and agglomeration: theory and experiments. J. Acoust. Soc. Am. 99, 2130–2141.

Hoffmann, T.L., Koopmann, G., 1997. Visualization of acoustic particle interaction and agglomeration: theory evaluation. J. Acoust. Soc. Am. 101, 3421–3429.

Hoffmann, T.L., Chen, W., Koopmann, G., Song, L., Scaroni, A.W., 1993. Experimental and numerical analysis of bimodal acoustic agglomeration. J. Vib. Acoust. 115, 232–240.

Khmelev, V.N., Shalunov, A.V., Golykh, R.N., Dorovskikh, R.S., Nesterov, V.A., Khmelev, S.S., Shalunova, K.V., 2016. Efficiency increase of wet gas cleaning from dispersed admixtures by the application of ultrasonic fields. Arch. Acoust. 41 (4), 757–771.

King, L.V., 1934. On the acoustic radiation pressure on spheres. Proc. R. Soc. Lond. A 147 (861), 212–240.

König, W., 1891. Hydrodynamisch-akustische Untersuchungen: I. Über das Mitschwingen einer Kugel in einer schwingenden Flüssigkeit. Ann. Phys. Chem. 2, 352–370.

König, W., 1891. Hydrodynamisch-akustische Untersuchungen: II. Über das die Kzwwischenzwei Kugelnin einerschwingenden Flüssigkeit und über die Entsebung der Kundt'schenStaubfiguren. Ann. Phys. Chem. 2, 549–563.

Lee, P.S., Cheng, M.T., Shaw, D.T., 1981. The influence of hydrodynamic turbulence on acoustic turbulent agglomeration. Aerosol Sci. Technol. 1 (1), 47–58.

Liu, J., Zhang, G., Zhou, J., Wang, J., Zhao, W., Cen, K., 2009. Experimental study of acoustic agglomeration of coal fired fly ash particles at low frequencies. Powder Technol. 193, 20–25.

Liu, J., Wang, J., Zhang, G., Zhou, J., Cen, K., 2011. Frequency comparative study of coal- fired fly ash acoustic agglomeration. J. Environ. Sci. 23, 1845–1851.

Magill, J., 1993. The effect of fluid forces on acoustic aerosol agglomeration. In: Hoback, H. (Ed.), Proceedings 13th ISNA, Bergen, pp. 621–626.

Magill, J., Pickering, S., Fourcaudot, S., Gallego-Juárez, J.A., Riera, E., Rodriguez, G., 1989a. Acoustic aerosol scavenging. J. Nucl. Mater. 166, 208–213.

Magill, J., Pickering, S., Fourcaudot, S., Gallego-Juárez, J.A., Riera, E., Rodriguez, G., 1989b. Ultrasonic aerosol agglomeration. In: Ultrasonic International 89 Conference Proceedings, pp. 244–249.

Magill, J., Richter, K., Fourcaudot, S., Barraux, P., Gallego-Juárez, J.A., Riera, E., Rodriguez, G., 1990. Agglomeration of aerosol and aerosol mixtures in a sound field. In: Hamilton, M.F., Blackstock, D.T. (Eds.), Frontiers of Nonlinear Acoustics. Proceedings of 12th ISNA. Elsevier Science Publishers Ltd, London, pp. 615–620.

Magill, J., Caperan, P., Somers, J., Richter, K., Rodriguez, G., Riera, E., Gallego-Juárez, J.A., 1991. Frequency dependence of acoustic agglomeration rate of a glycol fog. J. Aerosol Sci. 22 (Suppl. 1), S27–S30.

Magill, J., Caperan, P., Somers, J., Richter, K., Fourcaudot, S., Barraux, P., Lajarge, P., Gallego-Juárez, J.A., Riera, E., Rodriguez, G., 1992. Characteristics of an electro- acoustic precipitator (EAP). J. Aerosol Sci. 23 (Suppl. 1), S803–S806.

Mednikov, E.P., 1965. Acoustic Coagulation and Precipitation of Aerosols. Consultants Bureau, New York.

Mironov, M., 1976. Bjerkness forces in a viscous medium and the acoustic coagulation of aerosols. Sov. Phys. Acoust. 14, 487–492.

Patterson, H.S., Cawood, W., 1931. Phenomena in sounding tube. Nature 127 (3209), 667.

Pshenai-Severin, S.V., 1959. Aggregation of aerosol particles in a sound field under the influence of the Oseen hydrodynamic forces. Dokl. Akad. Nauk SSSR 125, 775–778.

Rajendran, N., Wegrzyn, J., Cheng, M.T., Shaw, D.T., 1979. Acoustic precipitation of aerosols under standing wave condition. J. Aerosol Sci. 10, 329–338.

Ramos, A., Montoya, F., Gallego-Juárez, J.A., 1985. Automatic system for dynamic control of resonance in high power and high Q ultrasonic transducers. Ultrasonics 23 (4), 151–156.

Reethof, G., 1988. Acoustic agglomeration of power plant fly-ash for environmental and hot gas cleaning-up. J. Vib. Acoust. Stress. Reliab. Des. 100, 552–555.

Riera, E., Gallego-Juárez, J.A., 1986. Ultrasonic agglomeration of micron aerosols under standing wave conditions. J. Sound Vib. 110 (1986), 413–427.

Riera, E., Gallego-Juárez, J.A., Rodríguez, G., Elvira, L., González, I., 2000a. Application of high-power ultrasound to enhance fluid/solid particle separation process. Ultrasonics 38 (1–8), 642–646.

Riera, E., Gallego-Juárez, J.A., Rodríguez, G., Acosta, V.M., Rodriguez, J. J., Donrronsoro, J.L., Sanz, D., Gómez, F.J., Martín, M., 2000b. Acoustic agglomeration of submicron particles in diesel exhausts: first results of the influence of humidity at two different frequencies. J. Aerosol Sci. 31 (Suppl. 1), S827–S828.

Riera, E., Elvira, L., González, I., Rodríguez, J.J., Muñoz, R., Dorronsoro, J.L., 2003. Investigation of the influence of humidity on the ultrasonic agglomeration of submicron particles in diesel exhausts. Ultrasonics 41, 277–281.

Riera, E., Gallego-Juárez, J.A., Mason, T.J., 2006. Airborne ultrasound for the precipitation of smokes and powders and the destruction of foams. Ultrason. Sonochem. 13, 107–116.

Riera, E., González, I., Rodríguez, G., Gallego-Juárez, J.A., 2015. Ultrasonic agglomeration and preconditioning of aerosol particles for environmental and other applications. In: Gallego-Juárez, J.A., Graff, K.F. (Eds.), Power Ultrasonics. Woodhead Publishing, Cambridge, UK, pp. 1023–1061. https://doi.org/10.1016/B978-1-78242-028-6.00034-X. (Chapter 34).

Riera, E., Aleixandre, M., Gallego-Juárez, J.A., Herranz, L., Delgado-Tardáguila, R., 2016. Experimental Report for Acoustic Agglomeration System Tests. PASSAM-INNOV-T14 [D4.1].

Scott, D.S., 1975. A new approach to the acoustic conditioning of industrial aerosol emissions. J. Sound Vib. 43, 607–619.

Shaw, D.T., 1978. Acoustic agglomeration of aerosols. In: Shaw, D.T. (Ed.), Recent Developments in Aerosol Science. John Wiley and Sons, New York, pp. 279–319.

Shaw, D.T., Rajendran, N., 1979. Application of acoustic agglomerators for emergency use in liquid-metal fast breeder reactor plants. Nucl. Sci. Eng. 70, 127–134.

Shaw, D.T., Tu, K.W., 1979. Acoustic particle agglomeration due to hydrodynamic interaction between monodisperse aerosols. J. Aerosol Sci. 10, 317–328.

Sheng, C., Shen, X., 2006. Modelling of acoustic agglomeration processes using the direct simulation Monte Carlo method. J. Aerosol Sci. 37, 16–36.

Sheng, C., Shen, X., 2007. Simulation of acoustic agglomeration processes of poly-disperse solid particles. Aerosol Sci. Technol. 41, 1–13.

Shirokova, N.L., 1973. Aerosol coagulation. In: Rozenberg, L.D. (Ed.), Physical Principles of Ultrasonic Technology. vol. 2. Plenum Press, New York, pp. 475–539.

Shirokova, L., Eknadiosyants, O., 1966. Interaction of aerosol particles in an acoustic field. Sov. Phys. Acoust. 11, 346–348.

Sinclair, D., 1950. Handbook of Aerosols. U.S. Atomic Energy Commission, Washington, DC.

Song, L., 1990. Modelling of Acoustic Agglomeration of Aerosol Particles (Ph.D. Dissertation). The Pennsylvania State University.

Song, L., Koopmann, G., Hoffmann, T.I., 1994. An improved theoretical model of acoustic agglomeration. Trans. ASME 116, 208–214.

St. Clair, H.W., 1949. Agglomeration of smoke, fogs, or dust particles by sonic waves. Ind. Eng. Chem. 41, 2434–2438.

St. Clair, H.W., 1952. Theory and basic principles of the sonic smoke flocculators. In: Proceedings US Technical Conference on Air Pollution, pp. 382–387.

Stokes, C.A., 1950. Sonic agglomeration of carbon black aerosols. Chem. Eng. Prog. 6, 423–432.

Temkin, S., 1981. Elements of Acoustics. John Wiley & Sons, New York.

Temkin, S., 1994. Gas dynamic agglomeration of aerosols. I. Acoustic waves. Phys. Fluids 6, 2294–2303.

Timoshenko, V.I., 1971. Calculation of the relative hydrodynamic drift velocity of aerosol particles in a high-intensity sound field. Sov. Phys. Acoust. 17, 106–109.

Timoshenko, V.I., Belenkii, V., Fedoruk, T.Y., 1976. Kinetics of sonic coagulation and precipitation of high disperse aerosols. Ultrasonics 14, 218–222.

Tiwary, R., 1985. Acoustic Agglomeration of Micron and Submicron Fly-Ash Aerosols (Ph.D. dissertation). The Pennsylvania State University.

Tiwary, R., Reethof, G., 1986. Hydrodynamic interaction of spherical aerosol particles in a high intensity acoustic field. J. Sound Vib. 108, 33–49.

Tiwary, R., Reethof, G., 1987. Numerical simulation of acoustic agglomeration and experimental verification. J. Vib. Acoust. Stress. Reliab. Des. 109, 185–191.

Tiwary, R., Reethof, G., McDaniel, O.H., 1984. Acoustically generated turbulence and its effect on acoustic agglomeration. J. Acoust. Soc. Am. 76, 841–849.

Volk, M., 1977. Sonic Agglomeration of Aerosol Particles (Ph.D. dissertation). The Pennsylvania State University.

Wang, J., Liu, J., Zhang, G., Zhou, J., Cen, K., 2011. Orthogonal design process optimization and single factor analysis for bimodal acoustic agglomeration. Powder Technol. 210, 315–322.

Westervelt, J.P., 1950. The mean pressure and velocity in a plane acoustic wave in a gas. J. Acoust. Soc. Am. 22, 319–327.

Westervelt, P.J., 1951. Acoustic radiation pressure. J. Acoust. Soc. Am. 29, 26–29.

Yan, J., Chen, L., Yang, L., 2016a. Combined effect of acoustic agglomeration and vapor condensation on fine particle removal. Chem. Eng. J. 290, 319–327.

Yan, J., Chen, L., Yang, L., 2016b. Removal of fine particles from coal combustion in the combined effect of acoustic agglomeration and seed droplets with wetting agent. Fuel 165, 316–323.

Yan, J., Chen, L., Lin, Q., 2017. Removal 0f fine particles in WFGD system using the simultaneous acoustic agglomeration and the supersatured vapor condensation. Powder Technol. 315, 106–113.

Zhang, G., Zhang, L., Wang, J., Hu, E., 2017. Improving acoustic agglomeration efficiency by addition of sprayed liquid droplets. Powder Technol. 317, 181–188.

Zheng, X., Apfel, R.E., 1994. Acoustic interaction forces between two fluid spheres in an acoustic field. J. Acoust. Soc. Am. 97, 2218–2226.

Chapter 39

The use of power ultrasound in biofuel production, bioremediation, and other applications

J. Virkutyte[a] and R. Cleary[b,*]

[a]Hammontree & Associates Ltd, North Canton, OH, United States, [b]James Watt School of Engineering, University of Glasgow, Glasgow, United Kingdom

39.1 Introduction

Contrary to what the name suggests, biotechnology is not a single technology. It is a group of technologies that share two (common) characteristics: working with living cells and their molecules and having a wide range of practical uses that can improve our lives. Biotechnology is one of the most rapidly developing fields, with wide-ranging impacts in fields such as medicine (enabling the detection and in some cases treatment of diseases such as sickle cell anemia, Tay-Sachs disease, diabetes, and cystic fibrosis), chemistry (development of biocatalysts, such as enzymes, to synthesize chemicals), and agriculture (genetic engineering and the production of more nutritious and better tasting foods, higher crop yields and plants that are naturally protected from disease and insects). It has also provided new opportunities for sustainable production of various products and services.

Biotechnology can be divided into industrial and environmental biotechnology. Industrial biotechnology uses the techniques of molecular biology to improve the efficiency and reduce the environmental impacts of industrial processes like textile, paper and pulp, and chemical manufacturing, whereas environmental biotechnology refers to waste treatment and pollution prevention, and can more effectively clean up several wastes than conventional methods and greatly reduce the dependence on methods for land-based disposal.

Ultrasound is energy generated by sound waves of 20,000 or more vibrations per second, which can be utilized in a vast variety of purposes in numerous areas, including physics, chemistry, biotechnology, and medicine. Ultrasound can be classified into two major groups according to the frequency level (Mason, 2007), (1) high-frequency and low-power (2–10 MHz range) ultrasound, which is usually utilized in medical imaging and chemical analyses, and (2) low-frequency and high-power (20–100 kHz) ultrasound that is used for cleaning, dispersing, and also for sonochemistry.

Recently, the application of ultrasound has received wide attention from the scientific community as a green technology owing to its high effectiveness, low technology requirements, and considerably reduced process time compared with other conventional techniques, and to its economically viable performance (Chen and Sharma, 2011). This chapter focuses on recent advances in ultrasound-induced or ultrasound-assisted bioprocesses and shows the valuable contribution of ultrasound in altering enzyme characteristics, reaction rates, and duration as well as mass transfer in numerous applications, e.g., biofuel production, biocatalysis, enzyme biosensors, and biosludge processing.

39.2 The chemical effects of ultrasound

Chemical effects of ultrasound occur from the cavitation phenomenon. Cavitation is a process in which mechanical activation destroys the attractive forces of molecules in the liquid phase. Applying ultrasound, compression of the liquid is followed by rarefaction (expansion), in which a sudden pressure drop forms small, oscillating bubbles of gaseous substances. These bubbles expand with each cycle of the applied ultrasonic energy until they reach an unstable size; they can then collide and/or violently collapse. Cavitation can be classified into four types based on the mode of generation (Gogate and Kabadi, 2009; Rokhina et al., 2009): acoustic, hydrodynamic, optic, and particle. Only acoustic and hydrodynamic cavitations are able to generate the intensities that can induce physicochemical changes in a system and be used for various chemical reactions. Ultrasound generates acoustic cavitation with intense local heating ($\sim$ 5000 K), high pressures ($\sim$ 1000 atm), and

*Updated author for the second edition.

Power Ultrasonics. https://doi.org/10.1016/B978-0-12-820254-8.00031-2
Copyright © 2023 Elsevier Ltd. All rights reserved.

enormous heating and cooling rates (> 109 K/s) and liquid jet streams (~ 400 km/h) (Suslick, 1998). Furthermore, during acoustic cavitation, free radicals can be formed due to the dissociation of vapors that are trapped in cavities. These radicals can be used to accelerate chemical reactions at near room temperatures that otherwise would require more harsh conditions (Jyoti and Pandit, 2004).

According to Suslick et al. (1999), formed cavitation bubbles are actually vacuum bubbles. The vacuum is created by a fast-moving surface on one side and an inert liquid on the other. Cavitation can be produced in different ways, such as with Venturi nozzles, high-pressure nozzles, high-velocity rotation, or ultrasonic transducers. In all those systems, the input energy is transformed into friction, turbulences, waves, and cavitation. Another important factor that influences the effective transformation of energy into cavitation is the intensity of acceleration. Higher acceleration creates higher pressure differences. This in turn increases the probability of the creation of vacuum bubbles instead of the creation of waves propagating through the liquid. Thus, the higher the acceleration, the higher is the fraction of energy that is transformed into cavitation. In case of an ultrasonic transducer, the intensity of acceleration is described by the amplitude of oscillation. Higher amplitudes result in a more effective creation of cavitation. In addition to the intensity, the liquid should be accelerated in a way to create minimal losses in terms of turbulences, friction, and wave generation. For this, the optimal way is a unilateral direction of movement.

Sonochemistry, the chemistry associated with ultrasound, is governed by parameters that include amplitude and frequency of an applied sound field, temperature, surface tension, vapor pressure, gas content, and nuclei density of the solution as well as vessel and probe geometry (Mason and Lorimer, 2002). Furthermore, parameters determine any potentially damaging effects on biological molecules, which might occur from possible cell disintegration due to the bulk heating and chemical action of the free radicals, which are formed during ultrasound irradiation and which are able to attack cellular material (Mann and Krull, 2004). Several reaction parameters of various ultrasound-assisted bioprocesses are shown in Table 39.1.

Therefore, ultrasound can be used in the preparation of activated metals by the reduction of metal salts; generation of activated metals by sonication; sonochemical synthesis of particles by precipitation of metal (Fe, Cr, Mn, Co) oxides for them to be used as catalysts; impregnation of metals or metal halides on supports; preparation of activated metal solutions; reactions involving metals via in situ generated organo-element species; reactions involving nonmetallic solids; crystallization and precipitation of metals, alloys, zeolites, and other solids; modification of surface morphology and particle size by high-velocity interparticle collisions; formation of amorphous nanostructured materials, including high surface area transition metals, alloys, carbides, oxides, and colloids; agglomeration of crystals; smoothing and removal of passivating oxide coating; micromanipulation (fractionation) of small particles; dispersion of solids; preparation of colloids (Ag, Au, Q-sized CdS); intercalation of guest molecules into host inorganic layered solids; degradation and modification of polymers; synthesis of polymers and sonolysis of organic pollutants in water. For many years, ultrasound has been used in biotechnology, for instance, to disrupt cells and release intracellular enzymes as well as organelles that could be applied in industry or medicine (Chisti, 2003; Sinistera, 1992).

Other applications in bioprocessing include cholesterol oxidation to cholestenone by resting cells of *Rhodococcus erythropolis* ATCC25544 at a frequency of 20 kHz (Bar, 1988), intensification of the bioprocessing of cotton textiles by combined enzyme/ultrasound treatment (Yachmenev et al., 2002; Condon et al., 2009, 2012), and application of bioleaching of nickel from lean grade ores with ultrasound (Swamy Xiao et al., 2005; Vyas and Ting, 2018). Furthermore, ultrasound can be used in enzyme activation and inactivation (Mawson et al., 2011; Islam et al., 2014), in the food industry to analyze food structure and composition at low ultrasonic intensities and high frequencies and to modify ingredients at high ultrasonic intensities and low frequencies (frequencies of 0.1 MHz and ultrasonic intensities of 10–100 $W\,cm^{-2}$; Weiss et al., 2011) and in leather processing facilitating the formation of tannins, providing significant improvement in yield and tannin content useful in bioavailability as well as bioconversion (Sivakumar et al., 2010, 2018). Ultrasound has also influenced reaction kinetics and reduced reaction time for esterification of bile acid (Grönroos et al., 2004), isopropyl ester synthesis from palm fatty acid distillate, and medium-chain triglyceride synthesis from fatty acids and glycerol (Deshmane et al., 2008, 2009), as well as the time for esterification of sodium salicylate to synthesize butyl salicylate by third-liquid phase-transfer catalysis (Yang and Peng, 2010), and the production of fatty acid ethyl ester from oleic acid with short-chain alcohols (ethanol, propanol, and butanol) (Hanh et al., 2009).

Closely consideration of ultrasound irradiation has proven to significantly improve fermentation processes, stimulating lactose metabolism and ethanol production (Chisti, 2003; Sulaiman et al., 2011). Ultrasonic irradiation also boasts the ability to alter filamentous fungi growth morphology and metabolite production (Kwiatkowska et al., 2011; Zhang et al., 2014) and accelerating the transfer of nutrient and metabolites inducing emulsification and cross-linking of proteins into enzyme microspheres in solutions, which are able to sustain enzymatic activity of lysozyme, amylase, and α-chymotrypsin.

TABLE 39.1 Several ultrasound-assisted bioprocesses and parameters used in these processes

Process	Parameters	Time (min)	References
Transesterification of triglycerides and free fatty acids for biofuel production	Freq. 20–48 kHz, power 120–1200 W	10, 60, 140	Georgogianni et al. (2008), Hanh et al. (2008), Siatis et al. (2006), Hanh et al. (2009), Kelkar et al. (2008), Stavarache et al. (2007)
Emulsification of vegetable oil and methanol for biofuel production	40 kHz, 700–1200 W	120	Hanh et al. (2009), Kelkar et al. (2008)
Extraction of virgin olive oil	35 kHz, 150 W	2–10	Clodoveo et al. (2013)
Laccase-catalyzed decolorization of textile effluents	150–850 kHz, 42–120 W	60–540	Basto et al. (2007), Rehorek et al. (2004), Tauber et al. (2008)
Enzymatic processing of leather	58, 132, 192, and 58 +192 kHz, up to 400 W	360–900	Sivakumar et al. (2010)
Emulsification method for oils and fats: leather processing	20 kHz, 60–100 W, 50–60°C	NA	Sivakumar et al. (2012)
Enzymatic un-hairing of leather	20 kHz at 32°C, 2.2 W cm^{-2}	600	Jian et al. (2010)
Enzymatic hydrolysis of leather	40 kHz, 0.64 W cm^{-2}	30–120	Jian et al. (2008)
Dye extraction from different plant materials	20 kHz, 80 W, 30–50°C	180	Sivakumar et al. (2011)
Protease-catalyzed oxidation of un-tanned leather waste	40 kHz	120	Jian et al. (2008)
Grape mash treatment in juice processing	35 kHz, 360 W, 2 W cm^{-2}, 74°C	13	Lieu and Le (2010)
Horseradish peroxidase-catalyzed degradation of phenol	423 kHz, 5.5 W	20–60	Entezari and Pétrier (2004)
Degradation of sericin (degumming) with enzymes	70 W	0–90	Mahmoodi et al. (2010)
Cellulase-catalyzed degradation of distillery wastewater	22.5 kHz, 120 W	30–120	Sangave and Pandit (2006)
Bacillus subtilis var. *niger* detection with immunosensor in USSW system	2–4 MHz	3	Hawkes et al. (2004) and Zourob et al. (2005)
Tyrosinase-laccase immobilization on sonogel-carbon transducer	40 kHz, 600 W	NA	ElKaoutit et al. (2007), Zejli et al. (2008a, 2008b)
Increase in dehydrogenate activity of waste-activated sludge	35 kHz, 80 W	10	Xie et al. (2009)
Scouring of raw wool	36 kHz	30	Bahtiyari and Duran (2013)
Anaerobic digestion of waste-activated sludge	10–20 kHz, energy density 20–60 kJ L^{-1}	NA	Dewil et al. (2006), Yoon et al. (2004)
Enzymatically catalyzed palm oil hydrolysis	23 kHz, 80 W, 55°C for 24 h	720	Awadallak et al. (2013)
Dewatering of waste-activated sludge	100–600 W and energy density > 2000 kJ L^{-1}	NA	Feng et al. (2009)
Anaerobic biodegradability of sewage sludge	Intensity of 0.35 W cm^{-2} and power density of 0.25 W/mL	15	Xiao et al. (2005)
Saccharification and fermentation of corn slurry during pretreatment	20 kHz	90 s	Montalbo-Lomboy et al. (2011)

Adapted from Rokhina et al. (2009).

39.3 The molecular effects of ultrasound

Molecular effects of ultrasound are the potential biological consequences due to the interaction between the ultrasound wave and the tissues, organisms, or cells. The biological effects of ultrasound depend on the total energy applied to a target area. Thus, varying duration of exposure to wave emission, intensity and frequency of the ultrasound, pulsed or continuous emission modality, and acoustic power may lead to significant molecular effects, commonly divided into physical (thermal and nonthermal), chemical (cavitation induced), and stress-induced changes.

39.3.1 Physical changes

The physical effects of ultrasound are related primarily to the production of heat. Heat is generated whenever ultrasound energy is absorbed, and the amount of heat produced depends on the intensity of the ultrasound, the time of exposure, and the specific absorption characteristics of the cell. As much as 70% of the total temperature increase associated with ultrasound occurs within the first minute of exposure, but the temperature continues to rise as exposure time is extended. Thermal effects typically do not cause significant cell damage; however, the extent of actual damage depends on absorption energy, the maximum temperature, and exposure time. Potential cell damage can include partial and full lysis.

Cellular effects of ultrasound generally acknowledged to be essentially nonthermal include changes associated with standing or shock waves, acoustic streaming, micro-streaming, and cavitation (Suslick, 1990). These effects have been demonstrated in vitro and may, in many instances, also occur in vivo. While some stimulate cell activity and can be exploited in ultrasonic therapy, others are potentially hazardous and must be avoided.

Thus, shock waves occur after the collapse of the bubbles and have sufficient force to distribute molecules from around the bubbles to other areas in the solution (Mason, 2007). On the other hand, micro-streaming may occur around a small bubble in a sound field and is able to create flow patterns within the solution dependent on the amplitude of the pressure wave and the viscosity of the solution (Bussemaker and Zhang, 2013). Furthermore, micro-streaming creates hydrodynamic shear stresses and can induce change, damaging cells, contributing to polymer degradation, and enhancing mass transfer. Acoustic streaming is usually due to the attenuation of the pressure wave as this wave travels through the solution (Suslick, 1998). Such attenuation creates a pressure difference in the solution that causes a flow in the direction of the sound field (Bussemaker and Zhang, 2013). At higher frequencies, the momentum of the wave is subject to higher absorption, which makes the acoustic streaming more pronounced.

In the presence of ultrasound, there is an increase in the permeability of the cell membrane; therefore, many molecules travel into the cell, which may cause secondary effects: (i) increase in skin and cell membrane permeability, which in turn changes the ultrastructures within cells and alters enzyme stability; (ii) increase in intracellular calcium, which is known as second messenger for cell function, including protein synthesis; (iii) cellular effects caused by altered growth properties, which could lead to cell lysis; (iv) nucleus rupture and release of DNA; (v) increase in mast cell degranulation; (vi) increase in histamine and chemotactic factor release by granules from mast cells and circulating platelets, which influences circulation and protein synthesis; and (vii) breakage of extracellular polymer substances.

39.3.2 Chemical changes

Radiation force affects gas bubbles in cells. Under the pressure wave (compression and rarefaction), these bubbles expand and contract, which adds further stress to cell boundaries. When bubbles expand and contract without growing to critical size, the activity is called stable cavitation, which is defined as a nonthermal effect of ultrasound. Cavitation sets up currents in the fluid surrounding the vibrating bubbles, and these currents in turn exert a twisting and rotational motion on nearby cells. In the vicinity of vibrating gas bubbles, intracellular organelles are also subjected to rotational forces and stresses. This microscopic fluid movement is called micro-streaming (Figure 39.1). Furthermore, bubble activity enhances the mechanical effect of a pressure wave. The scale of cavitation depends on the ultrasound parameters, and the bubble growth is limited by low-intensity, high-frequency, and pulsed ultrasound. Higher frequency means shorter cycle duration; therefore, the time for bubble growth is restricted. However, this way, higher amounts of bubbles are produced, subsequently allowing them to form more free radicals. On the other hand, lower frequency (under 100 kHz) allows bubbles to grow slower; however, cavitational collapses are much more violent than with higher-frequency irradiation.

Pulsed ultrasound restricts the number of successive growth (excessive energy accumulation) and allows the bubble to regain its initial size during the off period. Cavitation may induce the formation of free radicals, e.g., release of compounds such as nitric acid, nitrous acid, and hydrogen peroxide due to the interaction of formed radicals with the cell. Also, free radicals may decrease the cellular stability.

According to Bussemaker and colleagues, water undergoing sonochemistry initially cleaves the hydrogen–oxygen (H—O) bond in the molecule to produce hydroxyl radicals and hydrogen, which then continue reacting to produce hydrogen peroxide, hydrogen gas, and oxygen gas or recombine to produce water (Bussemaker and

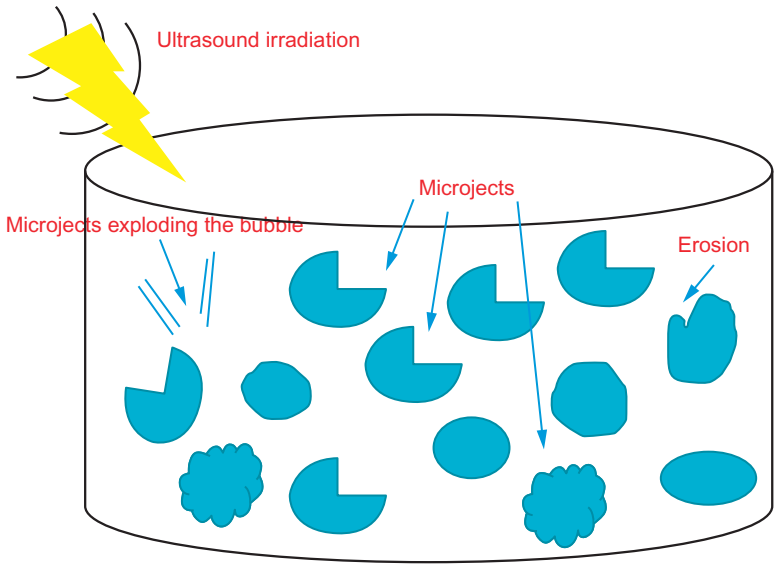


FIGURE 39.1 The formation of microjets and breaking of the bubbles. These formed microjets can break the cell walls and increase the surface area required for heterogeneous catalysis.

Zhang, 2013). Further radical reactions occur in the gas or aqueous phase, producing more radicals or oxidizing species:

$$H_2O \rightarrow H^* + {}^*OH \quad (39.1)$$

$${}^*OH + {}^*OH \rightarrow O + H_2O \quad (39.2)$$

$${}^*OH + H_2O \rightarrow H_2O_2 + O \quad (39.3)$$

$$H^* + {}^*OH \rightarrow H_2O \quad (39.4)$$

$$H^* + H^* \rightarrow H_2 \quad (39.5)$$

$$2O \rightarrow O_2 \quad (39.6)$$

$${}^*OH + {}^*OH(aq) \rightarrow H_2 + O_2 \quad (39.7)$$

$${}^*OH(aq) + {}^*OH(aq) \rightarrow H_2O_2(aq) \quad (39.8)$$

$$HO_2^* + H^* \rightarrow H_2O_2 \quad (39.9)$$

$$HO_2^* + HO_2^* \rightarrow H_2O_2 + O_2 \quad (39.10)$$

$$H^* + O_2 \rightarrow HO_2^* \quad (39.11)$$

$$O_2 \rightarrow 2O \quad (39.12)$$

$$O_2 + O \rightarrow O_3 \quad (39.13)$$

Species present in the solution is more than likely going to react with the generated radicals and hydrogen peroxide. Furthermore, when the solution is saturated with gas, the composition of the gas affects the sonochemical degradation products (Bussemaker and Zhang, 2013):

$$H^* + O_2 \rightarrow {}^*OH + O \quad (39.14)$$

$${}^*OH + N_2 \rightarrow N_2O \rightarrow NO_2^-, O_3^- \quad (39.15)$$

$$O + N_2 \rightarrow N_2O, NO, N \rightarrow NO_2^-, NO_3^- \quad (39.16)$$

39.3.3 Stress-induced changes

The compression phase of an ultrasound wave deforms tissue molecules (cell membrane). This deformation is called radiation force. Acoustic streaming is the physical force of the sound waves that provide a driving force capable of displacing ions and small molecules.

At the cellular level, organelles and molecules of different molecular weight exist. While many of these structures are stationary, many are free floating and may be driven to move around more stationary structures. This mechanical pressure applied by the wave produces unidirectional movement of fluid along and around cell membranes. Therefore, acoustic streaming (nonthermal) may enhance mass transport inside and outside the cell due to altered or disrupted membrane permeability. It may also alter the cell surface charge and even rupture cell membranes.

39.4 Sonochemical reactors

Ultrasound irradiation has been employed as a standalone pretreatment technique or combined with another technology; generally, this is either a chemical (acid, alkali, ionic liquid, ozone) or physical technique (microwave irradiation, thermal, supercritical carbon dioxide) (Bundoo and Mohee, 2018). It is widely accepted that with the use of high-intensity ultrasound, it is possible to intensify numerous technological processes, such as impregnating of composite materials, dissolution, extraction, emulsification, and washing. Thus, to improve these processes, the special apparatus called an ultrasonic reactor should

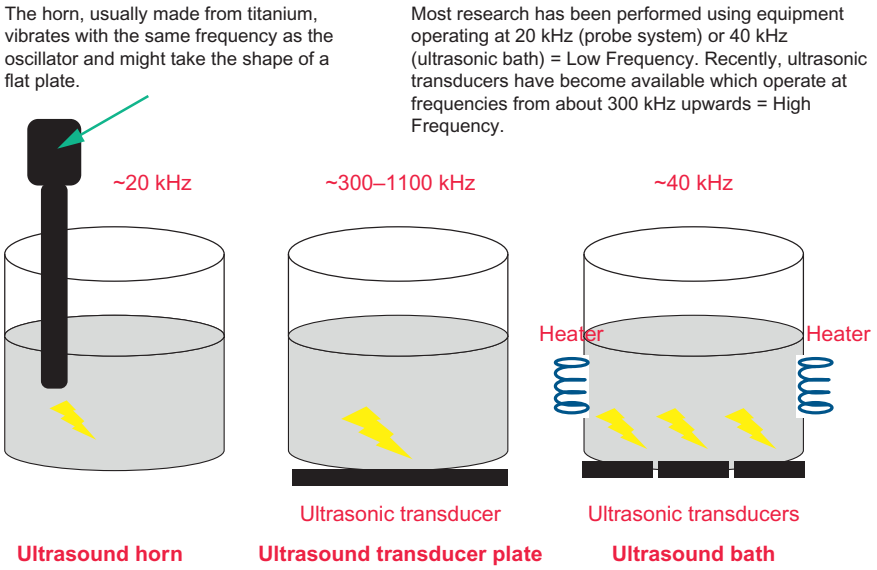


FIGURE 39.2 Ultrasonic devices.

be used. An ultrasonic reactor is comprised of an ultrasonic frequency generator, a transducer, and the reactor itself.

The ultrasonic frequency is generated from the electric current by a sine wave generator whose signal is amplified by a power amplifier. This signal is then turned into a pressure wave via an ultrasonic transducer and delivered into the reactor space filled with a solution to be sonicated (Bussemaker and Zhang, 2013). The pressure wave is delivered to the solution through either an ultrasonic bath, a transducer plate system, or a horn (Mason and Lorimer, 2002). There are three types of devices: ultrasonic baths, ultrasonic horn-type devices, and ultrasonic transducers (Figure 39.2).

The ultrasonic bath and transducer are widely used for cleaning and dispersing at low frequencies and are able to produce low-intensity cavitation in the solution. A horn-type device operates differently. The horn is immersed directly into the solution, a few centimeters from the top, and produces high-intensity ultrasound near the tip of the horn, on the order of several hundred W cm^{-2}. The power can be varied according to research needs, but the frequency is usually fixed at around 20–40 kHz. Cavitation induced by the horn occurs at the tip of the horn, and this can cause erosion of the horn tip. The transducer plate can be singular or in an array and produces ultrasound throughout the solution (Rehorek et al., 2004). According to the information given by the Hielscher Corporation (http://www.hielscher.com/ultrasonics/biodiesel_ultrasonic_mixing_reactors.htm), ultrasonic mixing reactors are developed for the production of biodiesel at any scale. The company recommends the use of these reactors for production capacities of 0.25 ton (80 gal) per hour or more. They also offer ultrasonic reactor combinations that can handle capacities of up to 80 ton/h (25,600 gal/h).

39.5 Biofuel production

Demand for energy is significantly increasing and the world will have to meet this demand with alternative energy sources because fossil fuel reserves are limited and are one of the main causes of pollution and global warming. Therefore, continuous depletion of oil reserves resulted in governmental incentives to establish greater energy independence by promoting research on more environmentally friendly and sustainable biofuels. Manufacturing of biofuel from vegetable oils (e.g., soy, canola, jatropha, sunflower seed, or algae) as well as animal fats usually involves the base-catalyzed transesterification of fatty acids with methanol or ethanol to produce methyl esters or ethyl esters. Furthermore, glycerol is an inevitable byproduct of this reaction. Vegetable oils and animal fats are triglycerides (glycerol) composed of three chains of fatty acids bound by a glycerin molecule. Esters are acids, like fatty acids, combined with an alcohol. In the conversion process, triglyceride esters are turned into alkyl esters (biodiesel, FAME) using a catalyst (lye) and an alcohol reagent, e.g., methanol, which yields methyl esters biofuel. However, as oils and methanol or ethanol are not completely miscible, the mixing efficiency is one of the most important factors that determines biofuel yield (Rokhina et al., 2009). When the process is over, the glycerine (the heavier phase) will sink to the bottom, whereas biofuel (the lighter phase) will float on the top and will be separated by decanters or centrifuges. This conversion process is called transesterification. Unfortunately, the conventional esterification reaction in batch processing is very slow, and phase separation of the glycerine is time-consuming, often taking several hours or more. Main advantages of biofuel over petroleum-based fuels are that it is renewable, biodegradable, and nontoxic and its contribution to greenhouse

gases is minimal as any emitted carbon dioxide is equal to that absorbed by the biomass (Siatis et al., 2006). Unfortunately, if vegetable oils were used directly as a fuel, they might cause severe engine problems such as injector fouling due to the incomplete combustion and incorrect vaporization as well as particle agglomeration due to their high viscosity, which is 10–20 times higher than that of petroleum fuel (Meher et al., 2006).

Ultrasound can be used to enhance and aid in the production of biofuels. Ultrasonic processing of biofuel involves the following steps.

1. Vegetable oil or animal fat is mixed with the methanol (which makes methyl esters) or ethanol (for ethyl esters) and sodium or potassium methoxide or hydroxide;
2. The mixture is subsequently heated to temperatures between 45°C and 65°C;
3. The heated mixture is then sonicated for about 5–15 s;
4. Glycerol drops out or is separated using centrifuges; and
5. The converted biodiesel is washed with water.

Ultrasound has demonstrated a positive impact on biofuel production while significantly increasing the efficiency of removing lignin from biomass in the mixture. Lignin is the chemical compound that binds cellulose and hemicellulose together in plant cell walls. Usually, enzymes or chemicals are used to remove it from biomass and allow the sugars to be dissolved for further processing into biofuel. However, the pretreatment with ultrasound effectively removes lignin so that sugar dissolution occurs near instantly, in comparison with several hours when using traditional mixing systems. Furthermore, hydrolysis of cornstarch could be accelerated using ultrasound irradiation (Chand et al., 2010). According to Chand and his colleagues, in a conventional ethanol plant, ground corn is steamed with jet cookers at boiling point temperatures. This breaks down the corn, leaving a starch mash that is then cooled and treated with enzymes in a process known as hydrolysis to release glucose for fermentation. The initial steaming was replaced with ultrasound, sonically smashing the corn into tiny particles in the same way physicians use ultrasound to shatter kidney stones. The smaller corn fragments provided more surface area for enzymatic action and therefore resulted in fermentation yields comparable to jet cooking. This method might provide numerous economic benefits and could have a payback period of less than 1 year (Chand et al., 2010).

Thus, ultrasound helps to optimize the conversion of triglycerides to biofuel. Effective conversion of triglycerides (Georgogianni et al., 2008; Hanh et al., 2008; Santos et al., 2009; Siatis et al., 2006; Stavarache et al., 2005; Baskar and Aiswarya, 2016), fatty acids (Hanh et al., 2009; Thanh et al., 2012; Malani et al., 2019), and fatty acid odor cut (C_8–C_{10}) (Kelkar et al., 2008) to biofuel was achieved in the presence of alcohols and various catalysts such as sodium hydroxide (NaOH) (Georgogianni et al., 2008; Stavarache et al., 2007; Baskar and Aiswarya, 2016), potassium hydroxide (KOH) (Hanh et al., 2008, 2009), and sulfuric acid (H_2SO_4) (Kelkar et al., 2008; Baskar and Aiswarya, 2016). Biofuel production utilizing ultrasound can be achieved continuously with yields in excess of 99% (Georgogianni et al., 2008; Hanh et al., 2008, 2009; Siatis et al., 2006; Stavarache et al., 2005). Also, ultrasound irradiation may reduce the processing time from the conventional several hours to as fast as 30 s (Georgogianni et al., 2008; Kelkar et al., 2008; Siatis et al., 2006; Stavarache et al., 2005, 2007). Importantly, sonication may reduce the separation time from 5 to 10 h using conventional mixing to less than 60 min. Sonication also helps to reduce the required amount of methanol and the catalyst up to 50% (Hanh et al., 2008, 2009; Santos et al., 2009; Stavarache et al., 2005, 2006) due to the increased chemical activity in the presence of cavitation.

Ultrasound can also be used to monitor biofuel production. Nowadays, gas chromatography, high-performance liquid chromatography, and ^{1}H nuclear magnetic resonance spectroscopy are the main techniques used to assess the quality of biofuel. Unfortunately, all these techniques have numerous drawbacks, including high operational costs, continuous sampling requirements, and time-consuming analyses. If implemented successfully, ultrasound irradiation could be an effective alternative for monitoring and controlling various bioprocesses by providing noninvasive, robust, and fast automated measurements at a relatively low cost (Resa et al., 2004). For instance, ultrasound-based monitoring could be utilized to determine the completion of the transesterification reaction and settling rates of glycerol (Koc and Vatandas, 2006; Koc, 2009). The capability of ultrasonic monitoring of soybean transesterification with methanol, catalyzed by KOH, has been investigated in detail by Baesso et al., proving promising for providing real-time reaction characteristics, which could minimize waste reagents and energy (Baesso et al., 2018, 2019).

Ultrasound irradiation continues to gain increasing interest to assist in the biological conversion of lignocellulosic biomass and water materials to biofuels. Increased bio-methane, bio-hydrogen and bio-ethanol yields have been reported following anaerobic digestion and fermentation processes. However, most of the studies using sonication as a pretreatment reported negative energy efficiencies, implying that the enhanced production does not compensate for the energy input due to ultrasound irradiation (Bundoo and Mohee, 2018). The energy efficiency, scalability, and relevant economics should be optimized through future studies.

39.6 Ultrasound-assisted bioremediation

39.6.1 Enzymes

Over the past years, enzymes have become one of the most important components in a wide range of processes, such as biocatalysis and bioremediation, due to the reduced energy and raw material consumption as well as the reduced amounts of waste and toxic byproduct formation. Therefore, enhanced metabolic productivity of microbial, plant, and animal cells in bioreactors can greatly improve the economics of biotechnology processes.

Enzymes are biological catalysts that facilitate the conversion of substrates into products by providing favorable conditions that lower the activation energy of the reaction. An enzyme may be a protein or a glycoprotein and consists of at least one polypeptide moiety. According to Karigar and Rao (2011), the regions of the enzyme that are directly involved in the catalytic process are called the active sites. An enzyme may have one or more groups that are essential for catalytic activity associated with the active sites through either covalent or noncovalent bonds; the protein or glycoprotein moiety in such an enzyme is called the apoenzyme, and the nonprotein moiety is called the prosthetic group. The combination of the apoenzyme with the prosthetic group yields the holoenzyme.

The degradation of the majority of toxic organic compounds by various microorganisms and fungi is mediated with oxidoreductases through oxidative coupling (Gianfreda et al., 1999). Microorganisms extract energy via energy-yielding biochemical reactions mediated by these enzymes to cleave chemical bonds and to assist the transfer of electrons from a reduced organic substrate (donor) to another chemical compound (acceptor). During such oxidation-reduction reactions, the contaminants are finally oxidized to harmless compounds (Karigar and Rao, 2011). Thus, one type of oxidoreductases is oxygenases that participate in oxidation of reduced substrates by transferring oxygen from molecular oxygen (O_2) utilizing FAD/NADH/NADPH as a cosubstrate. Oxygenases can be grouped into two categories: the mono-oxygenases and di-oxygenases, on the basis of the number of oxygen atoms used for oxygenation. They play a key role in the metabolism of organic compounds by increasing their reactivity or water solubility or bringing about cleavage of the aromatic ring. The mechanism includes the introduction of O_2 atoms into the organic molecule by oxygenase, which results in cleavage of the aromatic rings (Arora et al., 2010).

Microbial laccases (*p*-diphenol: dioxygen oxidoreductase) are a family of multi-copper oxidases produced by certain plants, fungi, insects, and bacteria that catalyze the oxidation of a wide range of phenolic and aromatic contaminants with simultaneous reduction of molecular oxygen to water (Gianfreda et al., 1999; Mai et al., 2000). Laccases generally occur in multiple isoenzyme forms, each of which is encoded by a separate gene. In some cases, the genes have been expressed differently, depending upon the nature of the inducer (Karigar and Rao, 2011). Furthermore, microbial peroxidases (donor: hydrogen peroxide oxidoreductases) such as lignin, manganese, and versatile peroxidases are ubiquitous enzymes that catalyze the oxidation of lignin and other phenolic compounds at the expense of hydrogen peroxide (H_2O_2) in the presence of a mediator. These peroxidases can be hem and nonhem proteins (Karigar and Rao, 2011). In mammals, they are involved in biological processes such as immune system processes or hormone regulation. In plants, they are involved in auxin metabolism, lignin and suberin formation, cross-linking of cell wall components, defense against pathogens, and cell elongation (Koua et al., 2009).

Hydrolytic enzymes such as amylases, proteases, lipases, DNases, pullulanases, and xylanases, as well as hemicellulase, cellulase, and glycosidase, disrupt major chemical bonds in the toxic molecules, resulting in reduction of their toxicity. This mechanism is effective for the biodegradation of oil spill and organophosphate and carbamate insecticides (Karigar and Rao, 2011). Therefore, lipases are ubiquitous enzymes that are able to catalyze the hydrolysis of triacylglycerols to glycerol and free fatty acids. Lipolytic reactions occur at the lipid-water interface, where lipolytic substrates usually form equilibrium between monomeric, micellar, and emulsified states. Cellulases are able to convert waste cellulosic material into foods to meet increasing population demands and are also capable of degrading crystalline cellulose to glucose. Microbial proteases are able to hydrolyze the breakdown of proteinaceous substances that enter the atmosphere due to shedding and molting of appendages, death of animals, and also as byproduct of some industries, such as the poultry, fishery, and leather industries. Proteases belong to group of enzymes that hydrolyze peptide bonds in an aqueous environment and synthesize them in a nonaqueous environment (Karigar and Rao, 2011). Proteases have a wide range of applications in the food, leather, detergent, and pharmaceutical industries (Beena and Geevarghese, 2010).

Ultrasound is one method of intensifying the performance of live biocatalysts. An ultrasound wave can control the enzyme characteristics by changing its structure in response to a dynamic perturbation (Hoshino et al., 2006). Despite the fact that ultrasonication is mainly associated with damage to cells, evidence is emerging of beneficial effects of controlled sonication on conversions catalyzed by live cells (Chisti, 2003). According to Hoshino et al. (2006), ultrasound irradiation would be able to perturb loop and domain regions of an enzyme and thus affect its activity. Such perturbation allows control of enzyme characteristics and alteration of structures. The tolerance of enzymes to

ultrasound highly depends on the physiological location of the enzyme in the cell and its molecular weight (Rokhina et al., 2009).

39.6.2 Effect of ultrasound on enzymes

The effects of ultrasound on enzymes is a contentious research topic with numerous contradictory results claiming the inactivation and activation of enzymes in the presence of ultrasound (Chisti, 2003). Despite this, for many years, it has been employed to accelerate enzymatic reactions and continues to show great potential for further industrial applications (Wang et al., 2018). The application of low-power ultrasound increases growth in microbial cell cultures, but high power causes cell disruption and hence can be considered as microbicidal (Kwiatkowska et al., 2011). Ultrasound has also been used to extract and release intracellular enzymes, and their subsequent activity can be further enhanced by the application of ultrasound irradiation. Furthermore, it has been recently reported that ultrasound irradiation does not destroy the active sites of an enzyme, as demonstrated for α-amylase, horseradish peroxidase, laccase, and alkaline phosphatase (Avivi and Gedanken, 2007; Basto et al., 2007; Ozbek and Ülgen, 2000; Rehorek et al., 2004; Tauber et al., 2008). On the contrary, there are reports showing that alkaline protease, glucose-6-phosphate dehydrogenase, and trypsin can be deactivated in the presence of high-power ultrasound irradiation (500 W) (Basto et al., 2007). Also, earlier, Dunn and Macleod performed an extensive study examining the effects of noncavitating ultrasound on solutions of alpha-chymotrypsin, trypsin, aldolase, lactate dehydrogenase, and ribonuclease (Dunn and Silva, 1968). These irradiations were carried out at different pH levels and temperatures using 1-MHz ultrasound at a power of 75 W/mL, with 10-min continuous exposure, and 11-MHz ultrasound at a power of 1000 W/mL, 0.1 s pulses for 200 s. Subsequently, these enzymes were irradiated with ultrasound intensities of 0.5–39 W/cm^2 at frequencies of 1, 9, and 27 MHz with temperature and pH being constant. Results indicated that cavitation inactivated all the tested enzymes at these particular reaction conditions.

Most likely, this deactivation of enzymes can be attributed to the formation of free radicals due to high ultrasound irradiation power, which subsequently reacts with the protein backbone (Basto et al., 2007). The reaction may lead to enzyme aggregation, which may block the active sites and at the same time decrease protein stability. Another reason for enzyme deactivation, especially when high-power ultrasound irradiation is used, could be associated with the shear forces that occur in the solution during the irradiation process (Ozbek and Ülgen, 2000).

The overall effect of ultrasound on enzymes highly depends on the process parameters, such as frequency, energy intensity, and irradiation time (Basto et al., 2007; Xiao et al., 2005; Nadar and Rathod, 2017a, b), alongside enzyme-related factors such as the concentration, temperature, and pH (Tauber et al., 2008; Ozbek and Ülgen, 2000). Therefore, in order to effectively use target enzymes for various purposes, it is vitally important to optimize all these parameters to avoid deactivation and extend the lifetime of enzymes.

39.6.3 Enzymes as biocatalysts in bioremediation

Bioremediation allows natural processes to clean up harmful chemicals in the environment. Microorganisms live in soil and groundwater, or they, like enzymes, like to eat certain harmful chemicals, such as those found in gasoline and oil spills. When microbes completely digest these chemicals, they change them into water and harmless gases such as carbon dioxide. However, the use of microorganisms for bioremediation is not limited to detoxification of the aforementioned organic compounds. In many cases, selected microorganisms or their enzymes can also reduce the toxic cations of heavy metals (such as selenium) to the much less toxic and much less soluble elemental form. As bioremediation can be effective only where environmental conditions permit microbial growth and activity, its application often involves the manipulation of environmental parameters to allow microbial growth and degradation to proceed at a faster rate (Karigar and Rao, 2011).

Figure 39.3 shows the bioremediation (enzyme-catalyzed destruction) of contaminants.

The enzyme-catalyzed reactions have advantages that conventional treatment methods do not because they are applicable to a variety of contaminants, such as polycyclic aromatic hydrocarbons, polynitrated and polychlorinated aromatic compounds, pesticides (Alcalde et al., 2006; Covino et al., 2010; Demarche et al., 2012; Isaac et al., 2013; Librando and Pappalardo, 2013; Pozdnyakova et al., 2006; Zhang et al., 2006; Uqab et al., 2016), bleach-plant effluents, synthetic dyes (Boucherit et al., 2013; Cristóvão et al., 2008, 2009; Koyani et al., 2013; Mohan et al., 2005; Schückel et al., 2011; Ulson de Souza et al., 2007; Dwivedi and Tomar, 2018), polymers, and wood preservatives, e.g., creosote and pentachlorophenol (Kim et al., 2007; Li et al., 2011; Singh et al., 2008a; Zhang et al., 2006, 2007). Also, these processes can work in the presence of high or low concentrations of contaminants and over a wide range of conditions with regard to pH, temperature, and salinity. The absence of shock loading effects, which are mostly associated with the acclimatization of biomass, is another significant advantage, along with the reduced volume of waste sludge (actually, no biomass is generated) and the ease and simplicity of the process control (Rokhina et al., 2009).

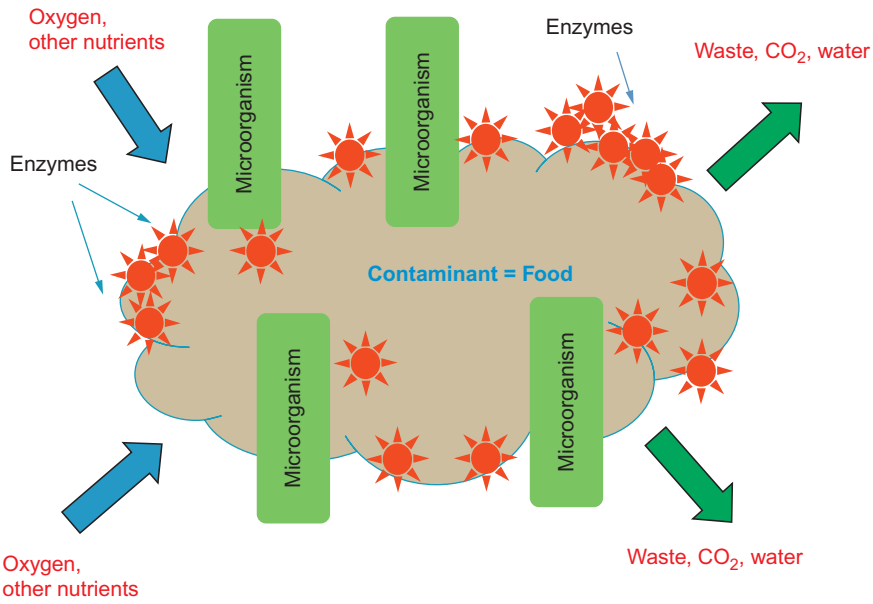


FIGURE 39.3 Bioremediation of contaminants.

Unfortunately, the process is usually slow. Furthermore, many microbial strains are known to be effective as bioremediation agents but only under laboratory conditions. The limitation of bacterial growth is due to changes in pH, temperature, oxygen, soil structure, moisture, and the amount of nutrients as well as poor bioavailability of contaminants, and the presence of other toxic compounds. Although microorganisms can exist in extreme environments, most of them prefer optimal conditions, a situation that is difficult to achieve outside the laboratory (Dua et al., 2002; Vidali, 2001). Also, most bioremediation systems operate under aerobic conditions, but anaerobic environments may also permit microbial degradation of recalcitrant molecules. Both bacteria and fungi rely on the participation of different intracellular and extracellular enzymes, respectively, for the remediation of recalcitrant and lignin and organo-pollutants (Karigar and Rao, 2011).

Enzyme-catalyzed treatment of waste in the presence of ultrasound has also been investigated academically and also in industry. For instance, laboratory-scale, ultrasound-assisted biodegradation (irradiation at 1.12 W cm^{-2} and 423 kHz for about 20–60 min) was able to completely eliminate phenols and chlorophenols with horseradish peroxidase and hydrogen peroxide present in synthetic wastewater (Entezari and Pétrier, 2004). Unfortunately, the scaling-up of these processes is not very effective and is generally influenced by the relatively short biocatalyst lifetime, which is due to the formed hydroxyl radicals that inactivate the enzymes and the still high production costs of relevant enzymes (Entezari and Pétrier, 2004).

On the contrary, ultrasound-assisted enzymatic (e.g., laccase from *Trametes villosa*) decolorization of various textile dyes was successfully implemented on the laboratory and pilot scale. For instance, the application of 60- to 120-W ultrasound irradiation at 850 kHz resulted in complete mineralization of azo dyes within 1–9 h (Rehorek et al., 2004; Tauber et al., 2008). Unfortunately, an increase in ultrasound power from 90 to 120 W resulted in partial deactivation of the enzyme and a significant loss in demineralization efficiency. Indigo carmine has been partially removed (65%–77% removal efficiency) in 1 h from the solution with 47–72 W and 150-kHz ultrasound irradiation (Basto et al., 2007). In order to avoid deactivation of the enzyme, polyvinyl alcohol has been used to create a protective hydrophobic layer around the enzyme in the solution.

Ultrasound-aided biodegradation of solid un-tanned leather waste has been demonstrated with an alkaline protease from *Bacillus licheniformis* at 0.64 W cm^{-2} min and 40-kHz ultrasound irradiation frequency for 2 h (Jian et al., 2008). It was found that 0.64 W cm^{-2} min ultrasound irradiation accelerated the enzymatic hydrolysis and improved the final conversion ratio to 84.1% by increasing the transport of the enzyme through the pores of the leather, affecting the integrity of collagen, the main constituent of the un-tanned leather. Furthermore, two proteases (one was neutral protease (A. S 1398) from *Bacillus subtilis* with an activity of 51,000 μ/g and optimum pH range of 7A. S 1398) from the enzymatic hydrolysis and *B. licheniformis* with an activity of 60,000 μ/g and optimum pH range of 9A.1 and one amylase (the amylase was from *B. subtilis* with an activity of 4000 μ/g and optimum pH range of 5–9) were utilized to un-hair natural leather (Jian et al., 2010). The laboratory-scale reactor was a 1.5-L glass container equipped with 20- to 40-kHz ultrasound irradiation power. The probe-type transducer was immersed 5 cm under the surface of enzyme bath. The effect of frequency indicated the superior performance of 20 kHz over 40 kHz.

It was also proven that ultrasound irradiation had little effect on enzyme activities, and also had little influence on the physical and mechanical properties of leather. It was concluded that ultrasound can enhance the diffusion of enzyme through skins, thus improving the un-hairing capacities of enzymes. Furthermore, it was determined that amylase was able to interact with proteoglycans by attacking saccharide side chains, thus having some un-hairing capacity. Also, ultrasound was able to improve the un-hairing capacity of amylase more effectively. Furthermore, amylase did no harm to the collagen fibrous structure and therefore could be utilized safely without the need for a high degree of control. In addition, the ultrasound-assisted emulsification method for oils and fats (tallow) showed that an optimum (81% fat emulsion obtained) emulsification could be achieved when the tallow/water ratio was 1–10, with 80-W ultrasound irradiation and 2% anionic surfactant present in the reaction system (Sivakumar et al., 2010). Thus, results indicated that tallow fat emulsion could be prepared successfully using ultrasound, with better conversion ratios, even dispensing with external heating as compared to the control process (50–60°C external heating required), and with minimum use of surfactant.

Furthermore, cellulase was the main biocatalyst during the ultrasound-assisted pretreatment of molasses spent wash (MSW) from distillery wastewater (Sangave and Pandit, 2006). Ultrasonic pretreatment resulted in a more than fourfold increase in MSW oxidation rates when compared with a more conventional aerobic oxidation process.

Recent studies produced promising results in enzymatic alcoholysis of monoglyceryl phenolic acids under ultrasound irradiation. The alcoholysis reaction rate proved to enhance the reaction rate threefold over mechanical stirring without damaging essential lipase activity (Xu et al., 2018). More details can be found in recently published reviews (Lofrano et al., 2013; Soares et al., 2011; Dwivedi and Tomar, 2018).

Most of the aforementioned studies provided scientific evidence on the effectiveness of an enzyme and ultrasound irradiation combination for bioremediation in terms of reduced reaction time and accelerated oxidation rates. However, the majority of studies have been performed on the laboratory scale; thus, scaling-up of the process to completely evaluate its effectiveness and industrial competitiveness must be achieved. Furthermore, maintaining catalytic activity and protecting the enzyme from radical attack are anticipated to be one of the priorities of research in this area for it to be successfully implemented on the industrial scale.

39.7 Biosensors

A biosensor is an analytical device that can be used for the detection of an analyte. It combines a biological component with a physicochemical detector component. Usually, it consists of three parts: (1) the "sensitive biological element" (biological materials such as tissues, microorganisms, organelles, cell receptors, enzymes, antibodies, and nucleic acids), a biologically derived material, or a biomimic; the sensitive elements can be created by biological engineering; (2) the "transducer" or the "detector element" (which works in a physicochemical way: optical, piezoelectric, electrochemical, etc.) that transforms the signal resulting from the interaction of the analyte with the biological element into another signal (i.e., transducers) that can be more easily measured and quantified; and (3) associated electronics or signal processors that are primarily responsible for the display of the results in a user-friendly way. According to the receptor type, biosensors can be classified as enzymatic biosensors, geno-sensors, immunosensors, etc. Biosensors can be also divided into several categories based on the transduction process, such as electrochemical, optical, piezoelectric, or thermal/calorimetric. Among these various kinds of biosensors, electrochemical biosensors are a class of the most widespread, numerous, and successfully commercialized devices of biomolecular electronics (Dzyadevych et al., 2008). One of the most common examples of a commercially available biosensor is the blood glucose biosensor, which uses the enzyme glucose oxidase to break down blood glucose (Kuznetsova and Coakley, 2007). The main factors that affect the biosensor response are the mass-transport kinetics of analytes and products and loading of the sensing molecule (Rokhina et al., 2009).

In order to improve the sensitivity and overall efficiency of biosensors, various approaches and techniques are used, including the use of nanocomposites (Ma et al., 2006), half-antibody fragments (Sharma and Mutharasan, 2013), and adjunct probes (Yang and Zhang, 2010). Also, ultrasound irradiation can be used to aggregate (Kuznetsova et al., 2007) and direct (Hawkes et al., 2004; Zourob et al., 2005) microorganisms toward coated sensors using ultrasound standing waves (USSWs). Furthermore, ultrasound can be used to aid immobilization of the target enzyme on sonogel-carbon transducer electrodes, which can detect xenobiotics and organophosphorus pesticides in wastewater (ElKaoutit et al., 2007; Zejli et al., 2008a, b).

Particle aggregation can be achieved in the solution within several minutes with 1.5-MHz USSWs (Kuznetsova et al., 2007). USSWs can be used to control the size of these aggregates, leading to shorter analysis time and preventing sedimentation, which could be detrimental to the ultrasonic transducer and also alter the radiation characteristics of the system (Mason and Lorimer, 2002). USSWs can also be utilized for the deposition of target microorganisms onto the sensors, such as bacteria-detecting immunosensors and optical leaky waveguide sensors. For instance, USSWs increased the deposition of *B. subtilis* spores onto the immunosensor by 70-fold using a pressure amplitude of 460 kPa at a frequency of 2.82 MHz and an

initial spore concentration of 2×10^4 particles mL^{-1} (Martin et al., 2005) and by nearly 200-fold using frequencies from 2 to 4 MHz and a spore concentration of 6.6×10^6 particles mL^{-1} (Hawkes et al., 2004). Furthermore, USSWs can significantly improve the performance of an optical leaky waveguide sensor and shorten analysis time from 20 to 3 min at the detection limit of *B. subtilis* var. *niger* of 10^3 spores mL^{-1} (Zourob et al., 2005).

Immobilization of enzymes onto the transducer surface is a necessary and critical step in the design of biosensors. It may affect biosensor performance in terms of sensitivity, selectivity, and stability, by influencing enzyme orientation, loading, mobility, stability, structure, and biological activity (Sassolas et al., 2012). Biosensors with immobilized enzymes may offer several advantages over the conventional biosensors. For instance, high selectivity, which is determined by the type of enzyme, could be tailored for a specific application and faster response due to the short diffusion path as cell walls are absent (Lei et al., 2006). The choice of immobilization method depends on many factors, such as the nature of the biological element, the type of transducer used, the physicochemical properties of the analyte, and the operating conditions in which the biosensor is to function. Overriding all these considerations, it is necessary for the biological element to exhibit maximum activity in its immobilized microenvironment (Singh et al., 2008b). According to Zhao et al., there are four main methods for enzyme immobilization (Zhao and Jiang, 2010).

1. *Adsorption*: It is the simplest and fastest way to prepare immobilized enzymes. Adsorption can roughly be divided into two classes: physical adsorption and chemical adsorption. Physical adsorption is weak and occurs mainly via Van der Waals forces. Chemical adsorption is stronger and involves the formation of covalent bonds. Many substances adsorb enzymes on their surfaces, e.g., alumina, charcoal, clay, cellulose, kaolin, silica gel, glass, and collagen.
2. *Entrapment*: This refers to mixture of the biomaterial with monomer solution and then polymerization to a gel, trapping the biomaterial. However, this method can give rise to barriers to the diffusion of substrate, leading to reaction delay. In addition, loss of bioactivity may occur through pores in the gel. The gels commonly used include polyacrylamide, starch gels, nylon, silastic gels, and conducting polymers.
3. *Covalent bonding*: In this method, the bond occurs between a functional group in the biomaterial and the support matrix. Some functional groups that are not essential for the catalytic activity of an enzyme can be covalently bonded to the support matrix. It requires mild conditions under which reactions are performed, such as low temperature, low ionic strength, and a pH in the physiological range.
4. *Cross-linking*: For this method, usually, biomaterial is chemically bonded to solid supports or to another supporting material such as cross-linking agent to significantly increase the attachment. It is a useful method for stabilizing adsorbed biomaterials. Glutaraldehyde is the most commonly used bifunctional agent. The agents can also interfere with the enzyme activity, especially at higher concentrations.

Therefore, obviously, the most important step in effective development of biosensors is the immobilization of the sensing enzyme onto an appropriate electrode (transducer), because insufficient immobilization may lead to a lower efficiency of the sensor caused by the partial enzyme destabilization that may occur during the process (Rokhina et al., 2009). Sonogel-carbon transducers, which are usually prepared in the presence of ultrasound irradiation, have a potential to stabilize enzymes due to a very high degree of biocompatibility with enzymes (ElKaoutit et al., 2007). For instance, ultrasound-assisted immobilization of laccase, tyrosinase, and acetylcholine esterase onto the sonogel-carbon (spectroscopic grade graphite) transducer proved to be effective in preventing material shrinkage and preserving the integrity and the shape of the enzyme, as well as achieving the desired response to the analyte (ElKaoutit et al., 2007). According to the authors, immobilized laccase and tyrosinase maintained over 80% of its initial activity for a minimum of 3 weeks. Also, immobilized tyrosinase exhibited nearly 80% of its initial activity after 100 phenol measurements with a detection limit of 3×10^{-7} M (Zejli et al., 2008a).

Acoustic biosensors for ultrasound imaging of enzyme activity remains a keen area of interest in the field for researchers looking to visualize protease activity noninvasively (Lakshmanan et al., 2020). The basis of this initial study is around the buckling mechanics of gas vesicles on the reinforcing protein, which could prove advantageous across a range of future applications.

39.8 Biosludge processing

Activated sludge processes for the treatment of various wastewaters are one of the most used. The activated sludge process uses microorganisms to feed on organic contaminants in wastewater, producing a high-quality effluent. The basic principle behind all activated sludge processes is that as microorganisms grow, they form particles that clump together. These particles (floc) are allowed to settle to the bottom of the tank, leaving a relatively clear liquid free of organic material and suspended solids. Unfortunately, these processes produce vast amounts of sludge that requires additional treatment and disposal (Mason, 2007). Anaerobic digestion is a complex biochemical reaction carried out in a number of steps by several types of

microorganisms that require little or no oxygen to live. During this process, a gas that is mainly composed of methane and carbon dioxide, also referred to as biogas, is produced. The amount of gas produced varies with the amount of organic waste fed to the digester, and temperature influences the rate of decomposition and gas production. Anaerobic digestion is the standard approach to treating waste-activated sludge, which may lead to a reduced content of organic matter and biogas production.

Unfortunately, anaerobic digestion has several disadvantages, including high capital and operational costs, the need for an integrated system, necessity for post-treatment, and the inability of the process to treat sewage to levels suitable for direct discharge and/or landfilling (Xie et al., 2009). Thus, methods and techniques that may enhance the biological activity of the anaerobic sludge and improve anaerobic digestion are required. Currently, numerous pretreatment methods exist, including heating, enzyme addition, ozonation, alkaline treatment, and mechanical disintegration. Unfortunately, none of these methods has proved to be the best in completely preventing the formation of excessive amounts of sludge (Yoon et al., 2004). There are numerous scientific attempts in literature that report successful use of ultrasound irradiation to increase the biological activity of anaerobic sludge, to increase the production of biogas, to disintegrate sludge, and to aid dewatering to some extent (Bougrier et al., 2005; Dewil et al., 2006; Laurent et al., 2009; Wang et al., 2006; Xie et al., 2009; Zhao et al., 2020).

Ultrasound irradiation is one of several technologies that promote hydrolysis, the rate-limiting stage during sludge treatment. The basic principle of ultrasound is based on the destruction of both bacterial cells and difficult-to-degrade organics. In sludge, various substances and agents collect in the form of aggregates and flakes, including bacteria, viruses, cellulose, and starch (Huan et al., 2009). The energy produced during ultrasound treatment causes these aggregates to be mechanically broken down, altering the constituent structure of the sludge and allowing the water to be separated more easily. Because ultrasound attacks the bacterial cell walls, the bacterial cells release exoenzyme that biocatalyzes hydrolytic reactions. This results in accelerated breakdown of organic material into smaller readily biodegradable fractions. The subsequent increase in biodegradable material improves bacterial kinetics, resulting in lower sludge quantities and, in the case of anaerobic digestion, increased biogas production. Therefore, its use is most suited to streams containing large quantities of refractory material and/or cellular matter such as waste-activated sludge streams(Bartholomew, 2002).

Importantly, if the ultrasound irradiation is intensified, materials, e.g., exocellular enzymes, are shaken off the surface of sludge particles. This material is able to catalyze biological hydrolysis reactions and improves biokinetic reaction rates. Consequently, ultrasound technology improves volatile solids destruction, which increases biogas production, lowers solids output during anaerobic digestion, and reduces solids production during activated sludge treatment. Furthermore, at the highest possible level of ultrasound irradiation, sludge particles are completely destroyed and their contents released for consumption by other species. Refractory material is also broken up into smaller biodegradable fractions. This process improves both biogas production during anaerobic digestion and biological nutrient removal during activated sludge treatment.

The effectiveness of sludge dewatering is critical to the efficiency of subsequent processes. The costs of haulage and spreading when cake is recycled are directly related to the effectiveness of dewatering. This is also true of the cost of thermal drying or incineration because dewatering affects the amount of water that has to be evaporated. The better the dewatering, the better the cake will stack, the easier it is to compost or to sanitize with lime, and the smaller the energy requirement for drying. Thus, it is vital to remove water from sludge to reduce operating costs by up to 40% (Wang et al., 2006). Conventional methods such as centrifugation, vacuum and belt pressure filtration, as well as chemical and thermal conditioning methods, can reduce the amount of water in sludge to as low as 55%, which is not enough to significantly reduce operational costs (Feng et al., 2009; Yin et al., 2004).

Ultrasound exhibits properties that could aid the dewatering of sludge. When an ultrasonic field is applied to a liquid medium, tiny bubbles form during the cavitation process (Mason, 2007). These cavitation bubbles implode under extreme forces of temperature and pressure. The force of the bubble implosions breaks up sludge particles when applied in sewage sludge treatment. The effects vary according to the intensity of the ultrasonic field. Thus, stresses that arise in sludge are able to facilitate the migration of moisture through either naturally occurring channels or channels that are formed by wave propagation. Also, air bubbles that are trapped in micropores can grow by rectified diffusion and lead to a displacement of liquid out of these micropores. And finally, cavitation can help to separate the moisture that is colloidal or chemically attached to the solid phase. Unfortunately, with time and with changes in ultrasound intensity, a decrease in dewaterability has been reported, which may be attributed to the water-retaining effect of extracellular polymeric substances (EPS) (Wang et al., 2006).

Ultrasound may be generated by two different methods: magnetostrictive and piezoelectric. The former uses electric energy, passing through a magnetic coil attached to the vibrating piece to produce the mechanical energy, or vibration. The latter uses electrical energy, converted to high-frequency electric energy, which is applied to piezoelectric crystals that vibrate at the same frequency. The

crystals are attached to the vibrating piece (known as the sonotrode, probe, or horn), causing the vibration to be transferred to the liquid. Magnetostrictive systems typically have a longer life but lower energy efficiency, as the electrical energy applied is converted to magnetic energy prior to being converted to mechanical energy. For wastewater applications, it appears that the economics favor the use of piezoelectric systems due to the high energy intensity required to lyse the cellular material in the sludge (Roxburgh et al., 2006).

There are few research attempts that demonstrate the beneficial effect of ultrasound on the dewaterability of waste-activated sludge. For instance, Wolski and colleagues demonstrated the dewaterability of sludge coming from a communal waste treatment plant (Wolski and Zawieja, 2012). The sludge was exposed to 1500-W ultrasound power with a frequency of 20 kHz and an amplitude of 39.42 μm (which corresponded to an amplitude of 100%) for up to 10 days. The sludge subjected to the effect of an ultrasound field exhibited elevated levels of capillary suction time. However, the sonication time had a positive effect on the increase in degree of thickening for each of the amplitudes studied. Also, the process of stabilization positively affected final thickening and dewatering of the sludge. Furthermore, Feng et al. determined that 800 kJ kg^{-1} total solids (TS), which generated sludge with an optimal EPS concentration of 400–500 mg L^{-1}, and particle size distribution with diameters in the range of 80–90 μm were the maximal dewaterability characteristics in the presence of ultrasound irradiation (Feng et al., 2009). Also, 100–600 W and energy densities higher than 2000 kJ L^{-1} induced dewatering of waste-activated sludge nearly fivefold, thereby decreasing the CTS. In a recent study, Meng et al. treated drinking water treatment sludge by ultrasonication under a number of different conditions of sonoreactor type, frequency, and energy density. The study concluded that optimal conditions were low energy density, of 0.03 and 1.0 W/mL, a duration of within 10 min. Also, higher frequencies reduced the dewatering property regardless of energy density or time. Further work concluded that ultrasonic technology is enhanced by the addition of polymer, oxidants (Meng et al., 2018).

In addition, the effect of low-power ultrasonic radiation on anaerobic biodegradability of sewage sludge was investigated (Liu et al., 2009). It was determined that hydromechanical shear forces and the heating effect of low-frequency ultrasound played a major role in the sludge pretreatment process. Also, the increase of soluble substance partly resulted from the destruction of microbial cells by excess ultrasonic pretreatment, which inhibited the anaerobic process. Optimal parameters were an exposure time of 15 min, ultrasonic intensity of 0.35 W cm^{-2}, and ultrasonic power density of 0.25 W mL^{-1}. Under the optimal condition, anaerobic biodegradability of sewage sludge (R (vss ss^{-1})%) was increased by 67.6%.

Also, ultrasound irradiation can be used to improve the hydrolysis step and the overall efficiency of anaerobic digestion. Laboratory- and pilot-scale studies proved that low-frequency (10–20 kHz) and low-density (1000–3000 kJ kg^{-1} TS equal to 20–60 kJ L^{-1} of sludge) ultrasound 20% increased and 4.5% decreased the production of biogas and DS, respectively (Bougrier et al., 2005; Dewil et al., 2006; Yoon et al., 2004). Ultrasound irradiation also significantly promoted the biological activity of the anaerobic sludge. Furthermore, a 35-kHz frequency at 0.2 W cm^{-2} for 10 min increased the dehydrogenate activity almost twofold and reduced the effluent chemical oxygen demand by 30% in comparison with no-ultrasound-irradiation conditions (Xie et al., 2009).

There are numerous ultrasound manufacturers in North America and Europe. However, the number of manufacturers with equipment designed for wastewater treatment applications and with experience in this complicated field is rather limited. The two main suppliers are Ultrawaves, represented in North America by Dorr Oliver Eimco's Sonolyzer equipment, and Sonico with the Sonix system. These two companies have the largest number of installations in wastewater applications, with over 150 installations around the world. According to Roxburgh et al., the largest installation is the Sonico installation for WAS pretreatment for enhanced digestion at the 400-MLD (106-mgd) Mangere WWTP in New Zealand (Roxburgh et al., 2006).

39.9 Conclusions and future trends

The use of ultrasound irradiation has proved to be an environmentally sound, time- and cost-effective approach for various bioprocesses such as the enhancement of emulsification and transesterification of fatty acids for biofuel production and the improvement as well as acceleration of bioprocess monitoring and dewatering of sludge. Other uses include the improvement of biosensors through immobilization of enzymes and disintegration of waste-activated sludge with concomitant biogas production. The economic success of ultrasound use for industrial bioprocesses highly depends on legislation, associated operation costs, governmental incentives for renewable energy, costs of enzymes and other biological entities, dewatering costs, and the type of currently available wastewater treatment.

The areas of biotechnology that have already benefited from the use of power ultrasound continue to grow, and subsequent improvements can be achieved by determining the optimum reaction conditions and parameters of the overall process. It is very likely that ultrasound irradiation will continue to contribute to renewable energy production, biocatalysis, and analytical chemistry in the future. Overcoming the current drawbacks and bottlenecks will increase the number of industrial applications.

References

Alcalde, M., et al., 2006. Environmental biocatalysis: from remediation with enzymes to novel green processes. Trends Biotechnol. 24 (6), 281–287.

Arora, P.K., Srivastava, A., Singh, V.P., 2010. Application of monooxygenases in dehalogenation, desulphurization, denitrification and hydroxylation of aromatic compounds. J. Biorem. Biodegrad. 1, 1–8.

Avivi, S., Gedanken, A., 2007. Are sonochemically prepared α-amylase protein microspheres biologically active? Ultrason. Sonochem. 14 (1), 1–5.

Awadallak, J.A., et al., 2013. Enzymatic catalyzed palm oil hydrolysis under ultrasound irradiation: diacylglycerol synthesis. Ultrason. Sonochem. 20 (4), 1002–1007.

Baesso, R.M., Oliveira, P.A., Morais, G.C., Alvarenga, A.V., Costa-Felix, R.P., 2018. Using ultrasonic velocity for monitoring and analysing biodiesel production. Fuel 226, 389–399.

Baesso, R.M., Costa-Felix, R.P., Miloro, P., Zeqiri, B., 2019. Ultrasonic parameter measurement as a means of assessing the quality of biodiesel production. Fuel 241, 155–163.

Bahtiyari, M.I.Ç., Duran, K., 2013. A study on the usability of ultrasound in scouring of raw wool. J. Clean. Prod. 41, 283–290.

Bar, R., 1988. Ultrasound enhanced bioprocesses: cholesterol oxidation by *Rhodococcus erythropolis*. Biotechnol. Bioeng. 32 (5), 655–663.

Bartholomew, R., 2002. Ultrasound Disintegration of Sewage Sludge: An Innovative Wastewater Treatment Technology. PA Department of Environmental Protection, Bureau of Water Supply and Wastewater Management, Division of Municipal Financial Assistance, Innovative Technology Section. Available at http://www.dep.state.pa.us/DEP/DEPutate/Watermgt/WSM/WSM_TAO/InnovTech/ProjReviewes/Ultrasound-Disintegr.htm.

Baskar, G., Aiswarya, R., 2016. Trends in catalytic production of biodiesel from various feedstocks. Renew. Sust. Energ. Rev. 57, 496–504.

Basto, C., et al., 2007. Stability and decolourization ability of *Trametes villosa* laccase in liquid ultrasonic fields. Ultrason. Sonochem. 14 (3), 355–362.

Beena, A.K., Geevarghese, P.I., 2010. A solvent tolerant thermostable protease from a psychrotrophic isolate obtained from pasteurized milk. Dev. Microbiol. Mol. Biol. 1, 113–119.

Boucherit, N., Abouseoud, M., Adour, L., 2013. Degradation of direct azo dye by *Cucurbita pepo* free and immobilized peroxidase. J. Environ. Sci. 25 (6), 1235–1244.

Bougrier, C., Carrère, H., Delgenès, J.P., 2005. Solubilisation of waste-activated sludge by ultrasonic treatment. Chem. Eng. J. 106 (2), 163–169.

Bundoo, Z.M.A., Mohee, R., 2018. Ultrasound-assisted biological conversion of biomass and waste materials to biofuels: a review. Ultrason. Sonochem. 40, 298–313.

Bussemaker, M.J., Zhang, D., 2013. Effect of ultrasound on lignocellulosic biomass as a pretreatment for biorefinery and biofuel applications. Ind. Eng. Chem. Res. 52 (10), 3563–3580.

Chand, P., et al., 2010. Enhancing biodiesel production from soybean oil using ultrasonics. Energy Fuel 24 (3), 2010–2015.

Chen, D., Sharma, S.K., 2011. Handbook on Applications of Ultrasound: Sonochemistry for Sustainability. CRC Press, Boca Raton.

Chisti, Y., 2003. Sonobioreactors: using ultrasound for enhanced microbial productivity. Trends Biotechnol. 21 (2), 89–93.

Clodoveo, M.L., Durante, V., La Notte, D., 2013. Working towards the development of innovative ultrasound equipment for the extraction of virgin olive oil. Ultrason. Sonochem. 20 (5), 1261–1270.

Condon, B., Easson, M., Yachmenev, V., Lambert, A., Delhom, C.S., Smith, J., 2009. Application of a low-level, uniform ultrasound field for the acceleration of enzymatic bio-processing of cotton. Cellul. Chem. Technol. 43 (9), 443–453.

Condon, B., Easson, M., Yachmenev, V., Lambert, A., Smith, J., 2012. Low-level, uniform ultrasound field effects on enzymatic bioprocessing of greige cotton using three fabric weights. AATCC Rev. 12 (6), 45.

Covino, S., et al., 2010. *In vivo* and *in vitro* polycyclic aromatic hydrocarbons degradation by Lentinus (Panus) tigrinus CBS 577.79. Bioresour. Technol. 101 (9), 3004–3012.

Cristóvão, R.O., et al., 2008. Kinetic modelling and simulation of laccase catalyzed degradation of reactive textile dyes. Bioresour. Technol. 99 (11), 4768–4774.

Cristóvão, R.O., et al., 2009. Modeling the discoloration of a mixture of reactive textile dyes by commercial laccase. Bioresour. Technol. 100 (3), 1094–1099.

Demarche, P., et al., 2012. Harnessing the power of enzymes for environmental stewardship. Biotechnol. Adv. 30 (5), 933–953.

Deshmane, V.G., Gogate, P.R., Pandit, A.B., 2008. Process intensification of synthesis process for medium chain glycerides using cavitation. Chem. Eng. J. 145 (2), 351–354.

Deshmane, V.G., Gogate, P.R., Pandit, A.B., 2009. Ultrasound assisted synthesis of isopropyl esters from palm fatty acid distillate. Ultrason. Sonochem. 16 (3), 345–350.

Dewil, R., Baeyens, J., Goutvrind, R., 2006. Ultrasonic treatment of waste activated sludge. Environ. Prog. 25 (2), 121–128.

Dua, M., et al., 2002. Biotechnology and bioremediation: successes and limitations. Appl. Microbiol. Biotechnol. 59, 143–152.

Dunn, F., Silva, M.R.M., 1968. Effects of intense noncavitating ultrasound on selected enzymes. J. Acoust. Soc. Am. 44, 932–940.

Dwivedi, P., Tomar, R.S., 2018. Bioremediation of textile effluent for degradation and decolourization of synthetic dyes: a review. Int. J. Curr. Res. Life Sci. 7 (4), 1948–1951.

Dzyadevych, S.V., et al., 2008. Amperometric enzyme biosensors: past, present and future. IRBM 29, 171–180.

ElKaoutit, M., et al., 2007. Dual laccase–tyrosinase based sonogel–carbon biosensor for monitoring polyphenols in beers. J. Agric. Food Chem. 55 (20), 8011–8018.

Entezari, M.H., Pétrier, C., 2004. A combination of ultrasound and oxidative enzyme: sono- biodegradation of phenol. Appl. Catal. B Environ. 53 (4), 257–263.

Feng, X., et al., 2009. Dewaterability of waste activated sludge with ultrasound conditioning. Bioresour. Technol. 100 (3), 1074–1081.

Georgogianni, K.G., et al., 2008. Conventional and in situ transesterification of sunflower seed oil for the production of biodiesel. Fuel Process. Technol. 89 (5), 503–509.

Gianfreda, L., Xu, F., Bollag, J.M., 1999. Laccases: a useful group of oxidoreductive enzymes. Biorem. J. 3, 1–25.

Gogate, P.R., Kabadi, A.M., 2009. A review of applications of cavitation in biochemical engineering/biotechnology. Biochem. Eng. J. 44 (1), 60–72.

Grönroos, A., Aittokallio, N., Kolehmainen, E., 2004. Ultrasound accelerated esterification of bile acids. Ultrason. Sonochem. 11 (3–4), 161–165.

Hanh, H.D., et al., 2008. Methanolysis of triolein by low frequency ultrasonic irradiation. Energy Convers. Manag. 49 (2), 276–280.

Hanh, H.D., et al., 2009. Biodiesel production by esterification of oleic acid with short- chain alcohols under ultrasonic irradiation condition. Renew. Energy 34 (3), 780–783.

Hawkes, J.J., et al., 2004. Ultrasonic deposition of cells on a surface. Biosens. Bioelectron. 19 (9), 1021–1028.

Hoshino, Y., Kawasaki, T., Okahata, Y., 2006. Effect of ultrasound on DNA polymerase reactions: monitoring on a 27-MHz quartz crystal microbalance. Biomacromolecules 7 (3), 682–685.

Huan, L., et al., 2009. Effects of ultrasonic disintegration on sludge microbial activity and dewaterability. J. Hazard. Mater. 161 (2–3), 1421–1426.

Isaac, P., et al., 2013. Indigenous PAH-degrading bacteria from oil-polluted sediments in Caleta Cordova, Patagonia Argentina. Int. Biodeterior. Biodegradation 82, 207–214.

Islam, M.N., Zhang, M., Adhikari, B., 2014. The inactivation of enzymes by ultrasound—a review of potential mechanisms. Food Rev. Int. 30 (1), 1–21.

Jian, S., Wenyi, T., Wuyong, C., 2008. Ultrasound-accelerated enzymatic hydrolysis of solid leather waste. J. Clean. Prod. 16 (5), 591–597.

Jian, S., Wenyi, T., Wuyong, C., 2010. Studies on the application of ultrasound in leather enzymatic unhairing. Ultrason. Sonochem. 17 (2), 376–382.

Jyoti, K.K., Pandit, A.B., 2004. Ozone and cavitation for water disinfection. Biochem. Eng. J. 18 (1), 9–19.

Karigar, C.S., Rao, S.S., 2011. Role of microbial enzymes in the bioremediation of pollutants: a review. Enzyme Res. 2011, 11. 805187 https://doi.org/10.4061/2011/805187.11.

Kelkar, M.A., Gogate, P.R., Pandit, A.B., 2008. Intensification of esterification of acids for synthesis of biodiesel using acoustic and hydrodynamic cavitation. Ultrason. Sonochem. 15 (3), 188–194.

Kim, E.Y., Chae, H.J., Chu, K.H., 2007. Enzymatic oxidation of aqueous pentachlorophenol. J. Environ. Sci. 19 (9), 1032–1036.

Koc, A.B., 2009. Ultrasonic monitoring of glycerol settling during transesterification of soybean oil. Bioresour. Technol. 100 (1), 9–24.

Koc, A.B., Vatandas, M., 2006. Ultrasonic velocity measurements on some liquids under thermal cycle: ultrasonic velocity hysteresis. Food Res. Int. 39 (10), 1076–1083.

Koua, D., Cerutti, L., Falquet, L., 2009. PeroxiBase: a database with new tools for peroxidase family classification. Nucleic Acids Res. 37, D261–D266.

Koyani, R.D., et al., 2013. Contribution of lignin degrading enzymes in decolourisation and degradation of reactive textile dyes. Int. Biodeterior. Biodegradation 77, 1–9.

Kuznetsova, L.A., Coakley, W.T., 2007. Applications of ultrasound streaming and radiation force in biosensors. Biosens. Bioelectron. 22 (8), 1567–1577.

Kuznetsova, L.A., Bazou, D., Coakley, W.T., 2007. Stability of 2-D colloidal particle aggregates held against flow stress in an ultrasound trap. Langmuir 23 (6), 3009–3016.

Kwiatkowska, B., et al., 2011. Stimulation of bioprocesses by ultrasound. Biotechnol. Adv. 29 (6), 768–780.

Lakshmanan, A., Jin, Z., Nety, S.P., Sawyer, D.P., Lee-Gosselin, A., Malounda, D., Swift, M.B., Maresca, D., Shapiro, M.G., 2020. Acoustic biosensors for ultrasound imaging of enzyme activity. Nat. Chem. Biol. 16, 988–996.

Laurent, J., Casellas, M., Dagot, C., 2009. Heavy metals uptake by sonicated activated sludge: relation with floc surface properties. J. Hazard. Mater. 162 (2–3), 652–660.

Lei, Y., Chen, W., Mulchandani, A., 2006. Microbial biosensors. Anal. Chim. Acta 568 (1–2), 200–210.

Li, H., et al., 2011. Degradation of pentachlorophenol by a novel peroxidase-catalyzed process in the presence of reduced nicotinamide adenine dinucleotide. Chemosphere 83 (2), 124–130.

Librando, V., Pappalardo, M., 2013. In silico bioremediation of polycyclic aromatic hydrocarbon: a frontier in environmental chemistry. J. Mol. Graph. Model. 44, 1–8.

Lieu, L.N., Le, V.V.M., 2010. Application of ultrasound in grape mash treatment in juice processing. Ultrason. Sonochem. 17 (1), 273–279.

Liu, C., et al., 2009. Effect of low power ultrasonic radiation on anaerobic biodegradability of sewage sludge. Bioresour. Technol. 100 (24), 6217–6222.

Lofrano, G., et al., 2013. Chemical and biological treatment technologies for leather tannery chemicals and wastewaters: a review. Sci. Total Environ. 461–462, 265–281.

Ma, Y., et al., 2006. Enhanced sensitivity for biosensors: multiple functions of DNA- wrapped single-walled carbon nanotubes in self-doped polyaniline nanocomposites. J. Phys. Chem. B 110 (33), 16359–16365.

Mahmoodi, N.M., et al., 2010. Degradation of sericin (degumming) of Persian silk by ultrasound and enzymes as a cleaner and environmentally friendly process. J. Clean. Prod. 18 (2), 146–151.

Mai, C., et al., 2000. Enhanced stability of laccase in the presence of phenolic compounds. Appl. Microbiol. Biotechnol. 54, 510–514.

Malani, R.S., Shinde, V., Ayachit, S., Goyal, A., Moholkar, V.S., 2019. Ultrasound–assisted biodiesel production using heterogeneous base catalyst and mixed non–edible oils. Ultrason. Sonochem. 52, 232–243.

Mann, T.L., Krull, U.J., 2004. The application of ultrasound as a rapid method to provide DNA fragments suitable for detection by DNA biosensors. Biosens. Bioelectron. 20 (5), 945–955.

Martin, S.P., et al., 2005. Spore and micro-particle capture on an immunosensor surface in an ultrasound standing wave system. Biosens. Bioelectron. 21 (5), 758–767.

Mason, T.J., 2007. Developments in ultrasound-non-medical. Prog. Biophys. Mol. Biol. 93, 166–175.

Mason, T.J., Lorimer, J.P., 2002. Applied Sonochemistry: Uses of Power Ultrasound in Chemistry and Processing. Wiley-VCH, Weinheim.

Mawson, R., et al., 2011. Ultrasound in enzyme activation and inactivation. In: Feng, H., Barbosa-Canovas, G., Weiss, J. (Eds.), Ultrasound Technologies for Food and Bioprocessing. Springer, New York, pp. 369–404.

Meher, L.C., Vidya Sagar, D., Naik, S.N., 2006. Technical aspects of biodiesel production by transesterification—a review. Renew. Sust. Energ. Rev. 10 (3), 248–268.

Meng, Z., Zhou, Z., Zheng, D., Liu, L., Dong, J., Yang, Y., Li, X., Zhang, T., 2018. Optimizing dewaterability of drinking water treatment sludge by ultrasound treatment: correlations to sludge physicochemical properties. Ultrason. Sonochem. 45, 95–105.

Mohan, S.V., et al., 2005. Acid azo dye degradation by free and immobilized horseradish peroxidase (HRP) catalyzed process. Chemosphere 58 (8), 1097–1105.

Montalbo-Lomboy, M., et al., 2011. Simultaneous saccharification and fermentation and economic evaluation of ultrasonic and jet cooking pretreatment of corn slurry. Biotechnol. Prog. 27 (6), 1561–1569.

Nadar, S.S., Rathod, V.K., 2017a. Sonochemical effect on activity and conformation of commercial lipases. Appl. Biochem. Biotechnol. 181 (4), 1435–1453.

Nadar, S.S., Rathod, V.K., 2017b. Ultrasound assisted intensification of enzyme activity and its properties: a mini-review. World J. Microbiol. Biotechnol. 33 (9), 1–12.

Ozbek, B., Ülgen, K.O., 2000. The stability of enzymes after sonication. Process Biochem. 35 (9), 1037–1043.

Pozdnyakova, N.N., et al., 2006. Oxidative degradation of polyaromatic hydrocarbons catalyzed by blue laccase from Pleurotus ostreatus D1 in the presence of synthetic mediators. Enzym. Microb. Technol. 39 (6), 1242–1249.

Rehorek, A., Tauber, M., Gübitz, G., 2004. Application of power ultrasound for azo dye degradation. Ultrason. Sonochem. 11 (3–4), 177–182.

Resa, P., Elvira, L., Montero de Espinosa, F., 2004. Concentration control in alcoholic fermentation processes from ultrasonic velocity measurements. Food Res. Int. 37 (6), 587–594.

Rokhina, E.V., Lens, P., Virkutyte, J., 2009. Low-frequency ultrasound in biotechnology: state of the art. Trends Biotechnol. 27 (5), 298–306.

Roxburgh, R., et al., 2006. Sludge minimization technologies—doing more to get less. In: Proceedings of the Water Environment Federation. WEFTEC, Dallas, TX, pp. 506–525 (20).

Sangave, P.C., Pandit, A.B., 2006. Ultrasound and enzyme assisted biodegradation of distillery wastewater. J. Environ. Manag. 80 (1), 36–46.

Santos, F.F.P., Rodrigues, S., Fernandes, F.A.N., 2009. Optimization of the production of biodiesel from soybean oil by ultrasound assisted methanolysis. Fuel Process. Technol. 90 (2), 312–316.

Sassolas, A., Blum, L.J., Leca-Bouvier, B.D., 2012. Immobilization strategies to develop enzymatic biosensors. Biotechnol. Adv. 30 (3), 489–511.

Schückel, J., Matura, A., van Pée, K.-H., 2011. One-copper laccase-related enzyme from Marasmius sp.: purification, characterization and bleaching of textile dyes. Enzym. Microb. Technol. 48 (3), 278–284.

Sharma, H., Mutharasan, R., 2013. Half antibody fragments improve biosensor sensitivity without loss of selectivity. Anal. Chem. 85 (4), 2472–2477.

Siatis, N.G., et al., 2006. Improvement of biodiesel production based on the application of ultrasound: monitoring of the procedure by FTIR spectroscopy. J. Am. Oil Chem. Soc. 83 (1), 53–57.

Singh, S., et al., 2008a. Bioremediation: environmental clean-up through pathway engineering. Curr. Opin. Biotechnol. 19 (5), 437–444.

Singh, M., et al., 2008b. Urea biosensors. Sens. Actuators B Chem. 134, 345–351.

Sinistera, J.V., 1992. Application of ultrasound to biotechnology: an overview. Ultrasonics 30, 180–185.

Sivakumar, V., et al., 2010. Use of ultrasound in leather processing industry: effect of sonication on substrate and substances—new insights. Ultrason. Sonochem. 17 (6), 1054–1059.

Sivakumar, V., Vijaeeswarri, J., Anna, J.L., 2011. Effective natural dye extraction from different plant materials using ultrasound. Ind. Crop. Prod. 33 (1), 116–122.

Sivakumar, V., et al., 2012. Ultrasound assisted cleaner alternate emulsification method for oils and fats: tallow emulsion—fatliquor preparation for leather application. J. Clean. Prod. 37, 1–7.

Sivakumar, V., Princess, A., Veena, C., Devi, R., 2018. Ultrasound assisted vegetable tannin extraction from myrobalan (Terminalia chebula) nuts for leather application. J. Am. Leather Chem. Assoc. 113 (02), 53–58.

Soares, J.C., et al., 2011. Application of immobilized enzyme technologies for the textile industry: a review. Biocatal. Biotransfor. 29 (6), 223–237.

Stavarache, C., et al., 2005. Fatty acids methyl esters from vegetable oil by means of ultrasonic energy. Ultrason. Sonochem. 12 (5), 367–372.

Stavarache, C., Vinatoru, M., Maeda, Y., 2006. Ultrasonic versus silent methylation of vegetable oils. Ultrason. Sonochem. 13 (5), 401–407.

Stavarache, C., Vinatoru, M., Maeda, Y., 2007. Aspects of ultrasonically assisted transesterification of various vegetable oils with methanol. Ultrason. Sonochem. 14 (3), 380–386.

Sulaiman, A.Z., Ajit, A., Yunus, R.M., Chisti, Y., 2011. Ultrasound-assisted fermentation enhances bioethanol productivity. Biochem. Eng. J. 54 (3), 141–150.

Suslick, K.S., 1990. Sonochemistry. Science 247, 1439–1445.

Suslick, K.S., 1998. Kirk-Othmer Encyclopedia of Chemical Technology. Wiley and Sons, New York, pp. 517–541.

Suslick, K.S., et al., 1999. Acoustic cavitation and its chemical consequences. Philos. Trans. R. Soc. A 357, 335–353.

Tauber, M.M., Gübitz, G.M., Rehorek, A., 2008. Degradation of azo dyes by oxidative processes—laccase and ultrasound treatment. Bioresour. Technol. 99 (10), 4213–4220.

Thanh, L.T., Okitsu, K., Van Boi, L., Maeda, Y., 2012. Catalytic technologies for biodiesel fuel production and utilization of glycerol: a review. Catalysts 2 (1), 191–222.

Ulson de Souza, S.M.A.G., Forgiarini, E., Ulson de Souza, A.A., 2007. Toxicity of textile dyes and their degradation by the enzyme horseradish peroxidase (HRP). J. Hazard. Mater. 147 (3), 1073–1078.

Uqab, B., Mudasir, S., Nazir, R., 2016. Review on bioremediation of pesticides. J. Bioremed. Biodegr. 7 (3), 1000343.

Vidali, M., 2001. Bioremediation: an overview. Pure Appl. Chem. Mater. 73, 1163–1172.

Vyas, S., Ting, Y.P., 2018. A review of the application of ultrasound in bioleaching and insights from sonication in (bio)chemical processes. Resources 7 (1), 3.

Wang, F., Ji, M., Lu, S., 2006. Influence of ultrasonic disintegration on the dewaterability of waste activated sludge. Environ. Prog. 25 (3), 257–260.

Wang, D., Yan, L., Ma, X., Wang, W., Zou, M., Zhong, J., Ding, T., Ye, X., Liu, D., 2018. Ultrasound promotes enzymatic reactions by acting on different targets: enzymes, substrates and enzymatic reaction systems. Int. J. Biol. Macromol. 119, 453–461.

Weiss, J., Kristbergsson, K., Kjartansson, G., 2011. Engineering food ingredients with high-intensity ultrasound. In: Feng, H., Barbosa-Canovas, G., Weiss, J. (Eds.), Ultrasound Technologies for Food and Bioprocessing. Springer, New York, pp. 239–285.

Wolski, P., Zawieja, I., 2012. Effect of ultrasound field on dewatering of sewage sludge. Arch. Environ. Protect. 25. https://doi.org/10.2478/v10265-012-0015-7.

Xie, B., Liu, H., Yan, Y., 2009. Improvement of the activity of anaerobic sludge by low- intensity ultrasound. J. Environ. Manag. 90 (1), 260–264.

Xu, C., Zhang, H., Shi, J., Zheng, M., Xiang, X., Huang, F., Xiao, J., 2018. Ultrasound irradiation promoted enzymatic alcoholysis for synthesis of monoglyceryl phenolic acids in a solvent-free system. Ultrason. Sonochem. 41, 120–126.

Yachmenev, V.G., Bertoniere, N.R., Blanchard, E.J., 2002. Intensification of the bio-processing of cotton textiles by combined enzyme/ultrasound treatment. J. Chem. Technol. Biotechnol. 77 (5), 559–567.

Yang, K., Zhang, C.-y., 2010. Improved sensitivity for the electrochemical biosensor with an adjunct probe. Anal. Chem. 82 (22), 9500–9505.

Yang, H.-M., Peng, G.-Y., 2010. Ultrasound-assisted third-liquid phase-transfer catalyzed esterification of sodium salicylate in a continuous two-phase-flow reactor. Ultrason. Sonochem. 17 (1), 239–245.

Yin, X., et al., 2004. A review on the dewaterability of bio-sludge and ultrasound pretreatment. Ultrason. Sonochem. 11 (6), 337–348.

Yoon, S.-H., Kim, H.-S., Lee, S., 2004. Incorporation of ultrasonic cell disintegration into a membrane bioreactor for zero sludge production. Process Biochem. 39 (12), 1923–1929.

Zejli, H., et al., 2008a. Alumina sol–gel/sonogel-carbon electrode based on acetylcholinesterase for detection of organophosphorus pesticides. Talanta 77 (1), 217–221.

Zejli, H., et al., 2008b. Phenol biosensor based on sonogel-carbon transducer with tyrosinase alumina sol–gel immobilization. Anal. Chim. Acta 612 (2), 198–203.

Zhang, X.-X., et al., 2006. Microbial PAH-degradation in soil: degradation pathways and contributing factors. Pedosphere 16 (5), 555–565.

Zhang, J., et al., 2007. Removal of pentachlorophenol by immobilized horseradish peroxidase. Int. Biodeterior. Biodegradation 59 (4), 307–314.

Zhang, H., Ma, H., Liu, W., Pei, J., Wang, Z., Zhou, H., Yan, J., 2014. Ultrasound enhanced production and antioxidant activity of polysaccharides from mycelial fermentation of Phellinus igniarius. Carbohydr. Polym. 113, 380–387.

Zhao, Z., Jiang, H., 2010. Enzyme-based electrochemical biosensors. In: Serra, A. (Ed.), Biosensors. INTECH, Croatia.

Zhao, Q., Li, M., Zhang, K., Wang, N., Wang, K., Wang, H., Meng, S., Mu, R., 2020. Effect of ultrasound irradiation combined with ozone pretreatment on the anaerobic digestion for the biosludge exposed to trace-level levofloxacin: degradation, microbial community and ARGs analysis. J. Environ. Manag. 262, 110356.

Zourob, M., et al., 2005. Optical leaky waveguide sensor for detection of bacteria with ultrasound attractor force. Anal. Chem. 77 (19), 6163–6168.

Xiao, Y.-M., et al., 2005. Ultrasound-accelerated enzymatic synthesis of sugar esters in nonaqueous solvents. Carbohydr. Res. 340 (13), 2097–2103.

Further reading

Bougrier, C., Albasi, C., Delgenès, J.P., Carrère, H., 2006. Effect of ultrasonic, thermal and ozone pre-treatments on waste activated sludge solubilisation and anaerobic biodegradability. Chem. Eng. Process.: Process Intesif. 45 (8), 711–718.

Okitsu, K., Sadanaga, Y., Takenaka, N., Maeda, Y., Bandow, H., 2010. Ultrasound-assisted production of biodiesel fuel from vegetable oils in a small scale circulation process. Bioresour. Technol. 101 (2), 639–645.

Swamy, K.M., Narayana, K.L., Misra, V.N., 2005. Bioleaching with ultrasound. Ultrason. Sonochem. 12 (4), 301–306.

Wang, B., Meng, T., Ma, H., Zhang, Y., Li, Y., Jin, J., Ye, X., 2016. Mechanism study of dual-frequency ultrasound assisted enzymolysis on rapeseed protein by immobilized Alcalase. Ultrason. Sonochem. 32, 307–313.

Index

Note: Page numbers followed by *f* indicate figures, *t* indicate tables, and *s* indicate schemes.

A

ABAQUS, 97
Ablatherm and Sonablate ultrasound-guided transrectal prostate treatment, 587–588
Absorption, 18–19
Acid additives, 838, 839*t*
Acoustic agglomeration of aerosols
  acoustic wake effect (AWE), 869–872, 870–871*f*
  coagulation process, 861
  coal combustion fumes, 875–879, 876*f*, 877–879*t*
  development of practical applications, 861–863
  fine aerosol particle removal, 874–875, 875*f*
  hydrodynamic mechanisms of particle interaction, 868
  linear acoustic effects, 863
  liquid droplet effect, 879, 880*f*
  mutual radiation pressure effect (MRPE), 868–869, 869*f*
  nonlinear acoustic effects, 863–866
  orthokinetic effect (OE), 867–868, 867–868*f*
  particles modeling, 872–874
  pilot-scale preconditioning systems, 875–879, 876*f*, 877–879*t*
  term mitigation in severe accidents in nuclear power plant, 880–882, 881–882*f*
  translational motion of aerosol particles, 866–867
Acoustic biosensors, for ultrasound imaging of enzyme activity, 898
Acoustic cavitation, 134–140, 456, 731
  acoustic methods, 135–138
  chemical methods, 138–139
  container imperfection, 134
  experimental configuration, 141–142, 141*f*
  inertial cavitation, 134
  mechanical methods, 139–140, 140–141*t*
  noninertial cavitation, 134
  optical methods, 139
Acoustic cavitation noise
  bubble splitting, 44–45, 45*f*
  period doubling, 43, 44*f*
  subharmonics, 43, 44*f*
  synchronization, 44, 44–45*f*
  threshold, 24–25, 25*f*
Acoustic dampers, 155–156
Acoustic emissions, 136, 137*t*, 182, 183*f*, 510
  spectra, 642
Acoustic field, 125–129, 126–127*f*
  particle surface cleaning effect, 521
Acoustic impedance
  and attenuation factor, 491
  under cavitation, 490, 491*f*
Acoustic intensity, bubble oscillations, 580
Acoustic isolator, 277–279
Acoustic load, 83
Acoustic longitudinal radiation, 528
Acoustic methods
  acoustic cavitation sensor, 136, 137*t*
  acoustic emission, 135
  broadband methods, 135–138, 138*f*
  hydrophone spectrum, 135, 136*f*
  peak-negative acoustic pressure, 136, 137*f*
Acoustic microstreaming, 560–561, 560*f*, 562–563*f*
Acoustic mode, 8
  finite-aperture sources, 13–14
  high-intensity ultrasound fields, 14–15
  nonlinear distortion and shock formation, 11–12
  quadratic approximation, 11
  shock structure, 12–13
  simple waves, 9–11
Acoustic power, 133
Acoustic pressure, 133–134, 142–143, 143*f*
  and power, 548
Acoustic radiation, 7
  force, 17–18, 525, 548
  streaming, 548
Acoustic softening, 243
Acoustic streaming, 16, 18, 691, 864–865
  and radiation force, 16–18
  and turbulence, 864–865
Acoustic stress, 249
Acoustic wake (AW), 864, 864*f*
Acoustic wake effect (AWE), 869–872, 870–871*f*
Acoustic wake particle interactions, 861
Acoustic wave propagation
  boundary conditions, 152–153
  far-field radiation, 153–157
  finite element method (FEM) formulation, 153
  radiation, 147–148, 157
Acoustic waves, 7–8, 16–20
  absorption, 18–19
  nonlinear, 9–12
  oscillating component, 16
  in shock wave therapy
    ballistic source, 601, 601*f*
    cavitation, 602
    coupling, 601
    direct stress, 602
    electrohydraulic source, 600, 600*f*
    electromagnetic source, 600–601
    piezoelectric source, 601
Acoustoplastic effect (APE), 239, 252–255
Activated sludge biomass, 820–821, 821–822*f*
Active cavitation volume, 141–142
Actuators, 69, 221
Additive manufacturing (AM), 227, 630–631
  build setup, 227–228
  computer-aided design (CAD) 3D model creation, 227
  manufacture of component, 228
  postprocessing of components, 228–229
  process categories, 229, 230*f*
  .stl file conversion, 227
Adjustment factor, 280
Adsorption, 898
Advanced oxidative processes (AOPs), 797–798
  radical hydroxyl and, 797
  sonochemistry of water, cavitation and hydroxyl radical, 797–798
Aerobic biological processes
  filamentous bacteria and bulking sludge, 828–829
  nitrogen removal, 828
Aeroprojects, 261–262, 277–279, 279*f*, 343, 345*f*, 347*f*
Aerosols
  for drug delivery, 786–788
  fine particle removal, 874–875, 875*f*
  production, 571–572
Agglomeration, 2–3, 728
Agricultural biogas plants (ABP), 819*f*, 826, 827*f*
Airborne transducers, 129
Airborne ultrasonic drying technique, 760, 761*f*
Airborne ultrasound, 760, 761*f*
  apple drying, 764–765
  carrot cubes drying, 757, 757*f*
  ethanol removal, dried apple, 760, 761*f*
  persimmon drying, 757, 758*f*
Air-liquid interface, 24
Air pollution control, 861–863
Aldol condensation, 844
Alkaline niobates, 76–77
Aluminum, 178, 190
  alloys, 118
  cable, 181, 182*f*

Aluminum foil erosion phenomena, 642–643
Aluminum foil test, 457
Al 6111 weld sections, 173, 177*f*
American National Standards Institute (ANSI), 70
American Society for Testing and Materials (ASTM), 229
Amplitude control, 96, 97*f*
Amplitude-dependent reduction, 292
Amplitude ratio, 671
Anaerobic digestion, 824–826, 825*f*, 893
  disadvantages, 899
  enhanced volatile solids (VS) degradation, 824, 824*f*
  full-scale application, 823–827, 823*t*
  low-frequency power ultrasound, 824
Anatase–rutile ratio, 435
ANSYS, 97, 99
Antimicrobial drug delivery, 568–569, 570*f*
Antiresonance, 95
Anvil, 233
  temperature, 235
APE. *See* Acoustoplastic effect (APE)
Apoptosis, focused ultrasound for medical therapy, 579
Apple drying, 764–765
Approximate analytical solutions, 54–57
Arc processes/ultrasonics, 194–197, 194–195*f*
Aspiration, 545–546
Aspiration devices, open surgery
  bone cutting, 549
  Cavitron ultrasonic surgical aspirator (CUSA) and derivative devices, 549
  contact debridement, 549
  phacoemulsification devices, 549, 550*f*
Atomic force microscope (AFM), 268–270
Atomization, 2–3
Auger type grinding machine, 514, 515*f*
Aurivillius-type structure ceramics, 76
Automatic sedimentation system, 526, 527*f*
Automation, 222
Aza-Michael reaction, 845–847, 846*s*, 846–847*t*
AZ31 Mg alloy, 198

B

Bacterial biomass
  disintegration, 817–820, 819*f*
  sonication of, 820
Bacterial cell inactivation, 818–820
Bacterial cultures
  hard cavitation, 822–823
  M. parvicella, 821–823
  P. aeruginosa, 821–823, 822–823*f*
Bacterial disinfection, 567–568
Bacterial growth, 896
Bakery and dairy processes, 783
Balamuth and Catuna's dental device, 617–618
Balamuth ultrasonic grinding wheel, 342–343, 343*f*
Ballast water treatment, 831
Ball milling technique, 438–439
Balsa layer, 104, 106*f*
Bamberg wastewater treatment plant (WWTP), 824–826, 825*f*
Barium-calcium zirconate-titanates, 77
Barium titanate (BaTi), 92
Bar-shaped rotary motors, 416, 416*f*
Basset-Boussiness-Oseen (BBO) equation, 865
Battery, 183
Beam frequency, 56
Bending, 298–300, 300–301*f*
  experimental ultrasonic bending, 299, 301*f*
  2024-T351 aluminum alloy, 299–300, 302*f*
  tube draw bending method, 299, 301*f*
  ultrasonic peening, 299, 302*f*
Bent waveguide, 283
Benzimidazolylacetonitrile, 843
$BiFeO_3$ (BFO), 65
Big data techniques, 512
Bilateral sagittal split osteotomy (BSSO) procedure, 629, 629*f*
Bimetal nanocatalysts, 434
$Bi_{0.5}Na_{0.5}TiO_3$ (BNT), 76
Binder jetting (BJT), 229
Biodegradation, 894
Biofilm removal, 561–563, 564*f*
Biofuels, 3
  production, 892–893
Biogas plants, 826–827, 827*f*
Biogas production, 824, 825*f*
Biological suspensions
  wastewater treatment plants (WWTPs)
    activated sludge biomass, 820–821, 821–822*f*
    bacterial biomass disintegration, 817–820, 819*f*
    pure bacterial cultures, 821–823
    sonication of bacterial biomass, 820
Bioremediation, 3
  of contaminants, 895, 896*f*
Biosensors, 897–898
Biosludge processing, 898–900
Biotechnology, 887
  environmental, 887
  industrial, 887
Bis-heterocycles, 851, 851*s*, 852*t*
Bismuth-layered structure ferroelectrics (BLSF), 76
Bismuth-sodium titanates, 77
Blade-tissue interaction, 621
Blaha effect, 243, 253
Blood-brain barrier (BBB) permeability
  ultrasound-mediated, 581, 581*f*
Body contouring, 540
Bolt-clamped Langevin sandwich construction, 107
Bolt-clamped transducer, 103
Bolted Langevin transducer (BLT), 542, 542*f*
Bone cutting, 549
BoneScapel device, 622
Booster, 165, 169–171, 221, 233
Bordesholmerland biogas plant, 827, 827*f*
Boundary conditions, 99–100, 148, 152–153
Boundary element method (BEM), 154–155
Bovine serum albumin (BSA) microspheres, 781–782
Braided wire connections, 182–183
Brandt, Freund, and Hiedemann (BFH) equation, 865
Brining process, 715–716
Broadband cavitation, 141–142, 142*f*
Bromobenzene replaced iodobenzene, 835
Brushing, 459
Bubble clusters, 38–43, 39*f*
Bubble cones, 41, 41*f*
Bubble double layers, 40–41, 40–41*f*
Bubble dynamics analysis, 640
  equation solutions, 640
Bubble ensemble dynamics
  clusters, 38–43, 39*f*
  cones, 41, 41*f*
  double layers, 40–41, 40–41*f*
  filaments, 38–43, 39–40*f*
  N-bubble model, 41–43, 42–43*f*
Bubble filaments, 38–43, 39–40*f*
Bubble models, 25, 26*f*, 28*f*, 33*f*
  habitat, 33–34
  single and multibubble dynamics, 23
  splitting and merging, 34–36
  ultrasonic cleaning, 23
Bubble splitting, 34–36, 44–45, 45*f*
Buffer plate, 183
Bulk deformation, 277
Bünde wastewater treatment plant (WWTP), 828, 828*f*
Burgers equation, 12
Buss bar terminations, 182–183

C

CADCAM software, 234
Calcific tendinitis, 609, 611*t*
Calculi (kidney and ureteric stones), shock waves, 540
Capillary wave hypothesis, 774
Carbide drill, 366, 367*f*
Carbonated hydroxyapatite (CHAp) nanopowders, 438
Cardiac pacemakers, 572
Carrot cubes drying, 757–758*f*, 760*f*
Casting, metals
  composite materials and immiscible alloys, 504–505, 505*f*
  structure refinement, 496–504, 503–504*f*
  ultrasonic cavitation processing, 490–496
  ultrasonic cavitation science and applications, 489–490
  ultrasonic melt processing
    composite materials and immiscible alloys, 504–505
    deagglomeration and dispersion, 501
    emulsification (immiscible alloys), 501–502
    mechanisms, 496–502
Cataract surgery, 539
Catheter-based phased arrays, 585–586
Cavimeter, 141–142
Cavitating systems, 141–143
Cavitation, 133–134, 139, 458–459, 458–459*f*
  acoustic cavitation, 665–666
  and acoustic microstreaming, 560–561, 560*f*, 562–563*f*

acoustic streaming, 666–667
and advanced oxidative processes (AOPs), 797–798
bubbles, 23, 25, 798
chemical effects of ultrasound, 887–889
degassing nuclei, 475–477
energy requirements, 639
erosion or "burning", 468
focused ultrasound for medical therapy
enhancement of drug treatments, 581
mechanism, 580
tissue disintegration and fragmentation, 580–581
mechanism, 701, 702*f*
nuclei and rectified diffusion, 546, 547*f*
operating parameters, 639
sensors, 136, 137*t*, 140, 140*f*
sonochemical reactors
primary effects, 641
secondary effects, 641–642
theoretical techniques, 642–644
stable, 547, 639
transient, 546–547, 639
voids, 460
zone, 491, 494
Cavitation hypothesis, 774–775
Cavitation-induced nucleation, 496
Cavitation nuclei, 25
Cavitation oscillation, 558, 560, 565–566
Cavitation threshold
acoustic, 24–25, 25*f*
static tension threshold, 23–24
Cavitron ultrasonic surgical aspirator (CUSA)
and competitive neurosurgical products, 539
and derivative devices, 549
Cell disintegration, 820, 820*f*
Cell membrane permeability, 890
Cellulase, 897
Central processor units (CPUs), 72
Ceramic blades, 386, 387*f*
Ceramic compliance, 99, 99*t*
Ceramic ring test, 457
Ceramics, 93
characterization methods, 69–72
iterative automatic method, 72–76
lead zirconate titanate piezoceramics, 83
poled barium titanate, 83
Chalcogenide nanoparticles synthesis, 440–441
Chaotic oscillations, 30
Chemical additives, 462
Chemical and biological phenomena, 2
Chemical antifoaming agents, 689, 695–697
Chemical effect, 731, 733–734
Chemical in situ OH determination, 800
Chemical methods, 138–139
Chemical oxygen demand (COD), 674, 674–675*f*
Chinese Chang'e 3 probe, 531
Cholesterol oxidation, 888
to cholestenone, 888
Chongqing Haifu Technology, 582
Chronic foot ulcers, 606–609, 608*t*
Chronic refractory angina pectoris, 609, 610*t*
Cincinnati Machine Tool Company, 249–250
Circular stepped-grooved-plate transducer, 123, 124*f*
Circular stepped-plate transducer, 120, 120*f*
acoustic field, 120, 121*f*
directivity pattern, 120, 121*f*
Civil mining engineering, 510
Coal combustion fumes, preconditioning systems, 875–879, 876*f*, 877–879*t*
Coal combustion smoke precipitation, 862–863
Coalescence, 478–479
Coaxial ultrasonic atomizer, 777
Coefficient of acoustic nonlinearity, 11
Coefficient of thermal expansion (CTE), 240
Coexisting oscillations, 29–30
Cold-rolled sheet steel, 290–291
Committee for Electrotechnical Standardization (CENELEC), 71
Compaction
early developments, 322–324, 322–323*f*
recent developments, 324–325, 324–326*f*
Compared conventional contact-AFM (C-AFM), 268–270
Composite electrode materials, 434
Composite materials, 489
and immiscible alloys, 504–505, 505*f*
manufacturing, 501
Computational fluid dynamics (CFD), 199, 200*f*
Computer-aided design (CAD) model, 111, 228*f*, 234
AM machines, 227–228
creation, 227
postprocessing of components, 228–229
.stl file conversion, 227
Computer-based design iterations, 221
Computer numerical control (CNC), 227
milling, 236
COMSOL Multiphysics 4.2a, 97, 112
Concentric ring array, focal depth control in hyperthermia, 584, 584*f*
Conductance, 127, 129*f*
Confocal microscopy, 448–449, 449*f*
Conjunction theory, 775
Consensus, 131, 139
Constitutive equations, 53–54
Contact assemblies, 182–183
Contact debridement, 549
Contact stresses, 175, 178*f*
Contaminants, 190–191
Continuous flow novel tube ultrasonic reactor, 646, 657*f*
Continuous ultrasonic welding, 217, 218*f*
Continuous ultrasound extraction reactor, 708, 709*f*
Continuous wave (CW), 14–15
Contoured ultrasonic tooling, 343
Convective drying, 743
Convective nonlinearity, 10
Convective transport, 744–745
during convective drying, driving force, 758
Conventional drawing (CCD), 295
Conventional drilling system, 343
Conventional equal channel angular extrusion (CECAE) process, 309–310
Coolants, 352–354, 356*f*
Copper, 178–179, 190, 285
Coulomb's friction law, 264
Coumarins, 849
Coupling, 92
moment, 163–164
Coupling of substituted bromobenzenes, 835
Covalent bonding, 898
COVID-19 pandemic, aerosol production, 572
Cox maze procedure, 586
Cross-contamination, 716–717
Crushing, 512
Crystallinity, 223–224
Crystallization process, 2, 438
growth, 724–725
and breakage mechanisms, 731*f*, 733*f*, 734
on ice crystallization (freezing), 728–730
ice nucleation mechanisms, 734–737
induction time, 725
liquidus curve, 722, 722*f*
metastable zone width, 725
nucleation, 723–724
saturation, 721–722, 722*f*
solute nucleation mechanisms, 730–734
on solute, ultrasound
agglomeration, 728
induction time, 725–726, 726*f*
morphology and size distribution, 727
nucleation and growth rates, 728
polymorphism and crystallinity, 726–727
supersaturation, 722–723
C-scans, 180–181
Curie temperature, 68
Cutting/coagulation devices, harmonic scalpel and derivative devices, 550
CW. *See* Continuous wave (CW)
Cyclic voltammetry, 432
Cylindrical radiator, 746–750, 748–751*f*
Cymbals, 63
transducer, 631–632

D

Dairy systems, 715–716
Damped oscillator, 84–86, 84*f*
Data storage, 125–126
Deagglomeration, 669–670
of nucleating particles, 501
Deep drawing
1960s and 1970s, 287–290, 288–290*f*
1980s onward, 290–295, 290–295*f*
Defoaming methods, 2–3, 687–688, 711. *See also* Ultrasonic defoaming system (UDS)
chemical antifoaming agents, 689, 695–697
mechanical foam breakers, 689
setup in reactors and canning line, 711, 712*f*
thermal and electrical methods, 687–688
Deformation, 58–59, 58*f*, 249–250
Degassing, 2–3, 463
of liquids, ultrasonic
advantages, 473
alloy composition, 480–481
cavitation, 475–477
energy, 477

Degassing *(Continued)*
industrial implementation, 481–486, 482*t*, 482–483*f*
insoluble inclusions, 480
kinetics of hydrogen removal, 473–474, 474*f*
materials production, 473
mechanisms, 474–475
in melts, 477–479, 484*f*
temperature, 480, 480*t*
nuclei, 475–477
quasiequilibrium concentration, 475
scheme with flat sonotrode, 483, 485*f*
treatment time and volume, 481
ultrasonic energy, 479–480
vapor-gas bubbles, 476
Weissler reaction, 473–474
De-gating, 218–219, 219*f*
"Degree of disintegration", 818
Dehydration, 743
Demarcation, 2
Density–based crystal plasticity model, 260
Dental implants, 558, 568
Dental plaque, 558, 568
Dental scaler, 618–619
Dentistry
antimicrobial drug delivery, 568–569, 570*f*
biofilm removal, 561–563, 564*f*
cavitation and acoustic microstreaming, 560–561, 560*f*, 562–563*f*
clinical evaluation of ultrasonic scalers, 564–565
drilling of teeth, 557
endosonics, 565–568
engineering principles, 557
historical overview, 557–558
mechanical action of the ultrasonic scaler, 558–560, 559*f*
surgical applications
aerosol production, 571–572
cardiac pacemakers, 572
COVID-19 pandemic, aerosol production, 572
damage to teeth, 571
hearing, 572
titanium implant surface cleaning, 568, 569*f*
Denver cell
acoustic field, 521
carbon particles, 525
cavitation environment, 524–525
flotation kinetic, 523, 524*f*
ultrasonic assisted flotation, 522–525
ultrasonic capability, 522–525
Deep drawing
acoustic challenges, 290
finite element analysis (FEA) modeling, 292, 293*f*
friction test, 293–294, 296*f*
radial vibration, 290
response surface method, 292–293, 295*f*
1960s and 1970s, 287–290, 288–290*f*
tool set and servo press, 293, 294*f*
ultrasonic-forming test, 292
ultrasonic vibrations, 288
Deterministic chaos, 43
Dewatering, 743
Dextrin microspheres, on laboratory scale, 782
Die-drum spacing, 280
Dielectric permittivity, 68, 68*f*
Diels-Alder cycloaddition, 844–845, 845*s*
Diffusion, 212–214
coefficient, effect on, 732
transport, 745
Diffusive effect, 731
Digital camera, 142–143
Digital image correlation (DIC), 246, 246*f*
(S,S)-Diphenylethylenediamine (DPEA), 838
Direct-chill (DC) casting, 483, 485*t*, 502
Directed energy deposition (DED), 229, 230*f*
Direct simulation Monte Carlo method (DSMC), 873
Dirichlet-to-Neumann (DtN) method, 155
Dislocation mechanism, 249
Dispersion, nucleating particles, 501
Disruption process
abrasion and breakage, 671, 671*f*
alumina suspension, 670
and breakage, 670–672, 671*f*
Kapur function, 671
time, order of magnitude, 672, 672*t*
Dissimilar materials, 190
Dissolution
alumina and silica, particle size reduction, 673
cellulose-improved dissolution, 673
high-power US dissolution, 672
mass transfer coefficient, 673
Sherwood number correlation, 673
tetraethoxysilane hydrolysis, 675
whey protein solubility, 674–675
Dissolution-rectified diffusion boundary, 33
Doi-Edwards mode, 213
Domains, 67–68, 67–68*f*
Doppler shift, 132
Double-cup extrusion tests (DCET), 305
Double layers of bubbles, 40–41, 40–41*f*
Double-sided incremental forming (DSIF), 295
Drilling, 2
of teeth, 557
Driver circuits
driving circuits for ultrasonic motors, 427–428, 427–428*f*
equivalent circuit modeling, 425–426, 425–426*f*
motor performance, 426–427, 426–427*f*
Driving force, convective transport during convective drying, 758
Drug delivery
aerosols, 786–788
encapsulation, 788–791, 788*f*, 790*f*
Dry foams, 688
Drying, 701
Dual frequency flow cell, 645–646, 646*f*
Dual wedge-reed system, 173, 176*f*
Duffing-like system, 624, 624*f*
DYNAFORM, 291–292
Dynamic recrystallization, 180

E

Eckart's quartz wind (Eckart streaming), 468–469*f*, 469
Edison Welding Institute (EWI), 231–232
Eggplant drying, 763–764
Elastic modulus, 209–210
Elastic-plastic cube model, 265–266
Elastic tensors, 54–55
Elastic wave propagation, 148–152
Electrical connections, 182–183, 184*f*
Electrical measurement, 132
Electrical safety, 93
Electric vehicles (EVs), 183–185, 185–186*f*
Electrochemical impedance spectroscopy (EIS), 432
Electrochemistry, 140
Electromechanical coupling, 70–72
Electromechanical transducers, 644
Electronic power generator, 125
Electronic steering, 584–585
Electrostatic filter (EF), 874
Elliptical vibration cutting, 357, 358*f*
Emulsification, 3, 501–502, 502*f*, 708–710, 709*f*
and dispersion, 2
drawbacks, 678
energy density, 679
features of, 679–681
phase-separated system, 677
pressure effect, 678–679, 678*f*
surfactants, 678
three-component model system, 679–681
two-step mechanism, 678
water-in-oil/oil-in-water, 677
Encapsulation
applications, food industry, 781–783
for drug delivery, 788–791, 788*f*, 790*f*
Enclosure case, 93
End effectors
bends and shapes, 545
hollow end effectors, 545
solid end effectors, 545
wires, 545
Endocavity devices, therapeutic ultrasound, 585
Endocavity ultrasound applicators, 585
Endodontics, 565, 566*f*
Endosonics, 565–568
Energy absorption, focused ultrasound for medical therapy, 578, 578*f*
Energy density, 347
Enhanced volatile solids (VS) degradation, 824, 824*f*
Entrapment, 898
Entropy, 7–9
modes, 15–20
Environmental application, 3
Environmental biotechnology, 887
Enzymatic extraction (EE), 708
Enzyme-catalyzed reactions, 895
Enzyme-catalyzed treatment of waste, 896
Enzyme immobilization, transducer surface, 898
adsorption, 898

biosensors, 898
covalent bonding, 898
cross-linking, 898
entrapment, 898
Epicor Medical Ablation System, 586
Equal channel angular extrusion (ECAE), 311, 311–312*f*
Equation of motion, 53–54
Equivalent circuit, 86–87, 91, 94–95
Erosion-based approach, 140
European standard methods, 70–71
ExAblate device, breast cancer, 589
Exit burrs, 366
Experimental modal analysis (EMA), 625
Exploration, power ultrasonics
in granular materials, 532–534
piezoelectric vibration techniques on Mars, 531–532
research for space, 532–534
in ultrasonically assisted drilling, 532–534
ultrasonic motors on Moon, 531
ultrasonic-percussive technique, 532–534
External devices, therapeutic ultrasound, 582–585, 583*f*
Externally applied devices, 551
Extracellular polymeric substances (EPS), 820–821
Extracorporeal pyrotherapy, 582

F

Fabrisonic LLC, 231–232
Fabrisonic SonicLayer 4000, 232, 232*f*
Face cutting mode, 348, 349*f*
Facile method, 437
Far-field radiation
approximate boundary conditions, 155–157
nonlocal boundary conditions, 153–155
Far-field ultrasonic welding, 214–215
Fat separation, 714–715, 714*f*
FEA. *See* Finite element analysis (FEA)
Fenton's reaction, 797
Fermentation processes, 888
Ferroelectric hysteresis, 67–68, 67–68*f*
Ferroelectrics, 65
hysteresis and domains, 67–68, 67–68*f*
single crystal to the ceramic, 65–67, 66*f*
Ferroicity, 65
Ferro-piezoelectric ceramics, 69
ferroelectric hysteresis and domains, 67–68, 67–68*f*
ferroelectric single crystal to the ceramic, 65–67, 66*f*
multifunctional, 69
Fiber-filled thermoplastics, 223
Fick's first law of diffusion, 745
Filamentous species, 820
Filler metals, 191
Finite-aperture sources, 13–14
Finite element analysis (FEA), 75–76, 75*f*, 104, 253, 268, 373, 374*f*, 620
Finite element method (FEM)
problem types, 150
space discretization, 149–150
variational formulation, 148–149, 153
Finite element (FE) modeling, 97–98, 110–112, 111*f*, 121–122
Finite media resonance, 53
Fixture, 221–222
Flat-plate transducers, 123–125, 124–125*f*
Fleischhauer and Kroger grinding machine for suspensions, 512–514, 514*f*
Flextensional transducers, 631–632, 631–632*f*
Flexural-wave linear motor, 413
Flocculation process, 2, 528
Flotation kinetic, ultrasonic-assisted flotation 8-L Denver cell, 523, 524*f*
Flotation process
acoustic field, 519–525
carbon particles, 525
flotation kinetic, 523, 524*f*
ultrasonic assisted flotation, 519–525
ultrasonic capabilities, 522
Flow systems, 645–646, 645–646*f*, 651*f*
Fluid dynamics, 15–16
Fluid-structure coupling, 147, 152–153
Foam
adverse effects, 687–688
aeration and agitation of liquids, 687
characteristics, 688
chemical/biochemical reaction, 689
classification, 688
control, conventional methods for, 689
definition, 687
effects of, 688
electrical methods, 687–688
fermentation industry, 687
foaminess, 687
formation, 711
high-intensity ultrasonic waves, 688
liquid, 687
mechanical methods, 687–689
physical methods, 687–689
stability factors, 687
structure, 688, 688*f*
thermal methods, 687–688
Focused ultrasound (FUS), 577
devices, high-intensity, 551
Food drying, 743
Food hygiene, 786
Food industry
encapsulation, 781–783
extraction, 783–784, 784*f*
food hygiene, 786
microbial inactivation, 785–786
nanofibers, 785, 785*f*
Food preservation by freezing using ultrasound, 712
Food processing
applications
brining, 715–716
marinating, 715–716
pasteurization, 715–716
sterilization, 715–716
cavitation
and acoustic streaming, 665–667
mechanism, 701, 702*f*
defoaming, 711
dispersion or deagglomeration, 669–670
disruption and breakage, 670–672, 671*f*
emulsification, 677–681, 708–710, 709*f*
extraction of plant components, 706, 707–708*t*, 708*f*
fat separation, 714–715, 714*f*
hazard analysis critical control point (HACCP), 716–717
high-power ultrasound, 701
homogenization, 675–677, 677*t*
low-power ultrasound, 701
macromixing, 667
micromixing, 667–668, 668–669*f*
particle and aggregate dispersion and disruption, 668–672
physical operations, 665
solid and liquid dissolution, 672–675
sonocrystallization, 711–714
standing wave patterns, 715, 715*f*
ultrasonically assisted extraction (UAE), 702–708
viscosity modification, 710–711, 711*f*
Food products, food supplements, nutritional value, 782–783
Food technology and pharmaceutical application, 3
Forced vibrations
of an undamped oscillator, 85, 85*f*
damped oscillator, 85–86
rod, 89, 89*f*
Formative-type manufacturing, 227, 228*f*
Formic acid oxidation reaction (FAOR), 432
Fragmentation of primary intermetallics, 498–501, 500*f*
Free vibration
damped oscillator, 84–85, 84*f*
undamped oscillator, 84
Freeze-drying, 743, 749–750
Freezing, 728–730
food and pharmaceutical products, 728–729
mannitol solution sono-freezing, 729
phase change, 729
Frequency applications
high-frequency, 1
low-frequency, 1
Frequency control, 95–96, 96*f*
Frequency mixing, 53, 59–61
Frequency response, 95
Frequency sweeping and mixing signals, 656
Fretting fatigue (FF), 318
Fricke dosimetry, 139, 641, 800
Friction stir spot welding (FSSW), 198
Friction stir welding (FSW), 197–200, 198–200*f*
Friction vector, 261–262
Fuel cell, 183

G

Gain-bandwidth method, 71
Gangue, 519
Gas bubble, 34, 35*f*
Gas-driven transducers, 644
Gases, 191
Gas-metal arc welding (GMAW), 194–196
Gas-tungsten arc welding (GTAW), 194, 194–195*f*

Generators, 457
Giant magnetostrictive materials (GMUT), 106, 106*f*
Giant response, 30
Gibbs-Thompson coefficient, 497
Gilmore model, 27, 28*f*
Glycerol, 888
Gongs, 63
Grain boundary migration, 244
Grain distribution map, 197, 198*f*
Grain microstructure, 199, 200*f*
Grain refinement, 490, 500
Graphene oxide (GO) synthesis, 442–444, 443*f*
Graphene synthesis, 442–444, 443*f*
Green organic synthesis
  Aza-Michael reaction, 845–847, 846*s*, 846–847*t*
  benzimidazolylacetonitrile, 843
  Diels-Alder cycloaddition, 844–845, 845*s*
  Groebke- Blackburn-Bienayme reaction, 850–853, 850–851*s*
  Hantzsch condensation or cyclization, 848–849, 848–849*s*
  Huisgen cycloaddition, 849, 849*s*
  Knoevenagel condensation, 839–844, 839*s*, 840–843*t*, 842*s*
  Michael additions, 836–838
    of 4-hydroxycoumarin and nitrostyrene, 836–838, 837*s*
  substituted aromatic aldehydes, 843
  Suzuki coupling reactions, 835–836, 835*s*
  Ugi-azide reaction, 850–853, 850–851*s*
Grinding process
  chips, 395–397, 396–398*f*
  forces, 388–389, 389–392*f*
  hybrid processes, 397–398, 398–399*f*
  surface roughness, 389–395, 392–396*f*
  temperatures, 388–389, 389–392*f*
  vibration, 388–389, 389–392*f*
  wear, 388–389, 389–392*f*
Gripping/holding, 93
Groebke-Blackburn-Bienayme reaction, 850–853, 850–851*s*
Grooved-plate transducers, 121–122
Growth, crystallization, 724–725
  and breakage mechanisms, 731*f*, 733*f*, 734
Gun drilling, 346–347

H

Haifu JC device, breast cancer, 589
Half-λ criterion, 584, 584*f*
"Hammering" effect, 212
Hantzsch condensation or cyclization, 848–849, 848–849*s*
Hantzsch dihydropyridine synthesis, 848, 849*s*
Hard cavitation, 822–823
Harmonic analysis, 101–102, 102*f*, 151–152
Harmonic balance method, 59, 61
Harmonic generation, 53
Harmonic oscillations, 27–28
Harmonic scalpel, and derivative devices, 550
Harmonic wave, 17
Hartman whistle, 689–690
Hazard analysis critical control point (HACCP), 716–717
Hazards aerosols hearing, 571–572
Hearing, 572
Heat-affected zone (HAZ), 173
Heating, 93
  Heat release, 19–20
  of tissue, 2
  Heat transfer, 208
  Heat transport, 745–746
Helmholtz's integral, 153–154
Hemispherical phased-array transducer, 582, 583*f*
Henan Polytechnic University, 382
Henry's law constant, 801, 802–803*t*
Heterogeneities, 23–24
Heterogeneous nucleation, 734
Hickling's theory, 735
High-intensity focused ultrasound (HIFU) for medical therapy, 551
  bone, 590–591
  brain, 591
  breast, 589
  cavitational interaction
    enhancement of drug treatments, 581
    mechanism, 580
    tissue disintegration and fragmentation, 580–581
  endocavity devices, 585
  external devices, 582–585
  imaging modalities, 587
  interstitial and intraoperative devices, 585–586
  liver, 588–589
  magnetic resonance imaging, 587, 588*f*
  prostate, 587–588
  radiation force, 581–582
  stroke, 591
  thermal interaction
    apoptosis, 579
    energy absorption, 578, 578*f*
    hyperthermia, 579–580
    thermal ablation, 578–579
  thyroid, 590
  ultrasound, 586–587, 586*f*
  uterine fibroids, 589–590
High-intensity ultrasonic tubular reactor (HUTR), 646, 658*f*
High-intensity ultrasonic waves, 2, 14–15
  nonlinear acoustics, 7
  ultrasound propagation effects, 7
High-intensity ultrasound fields, 14–15
High-performance relaxor piezocrystals, 629
High-power hybrid transducer linear motors, 419–422, 420–422*f*
High-power ultrasonic system, 132
High-pressure grinding roll (HPGR), 515–516
High-pressure ultrasonic roller mill (HPURM), 515–516, 516*f*
  efficiency, 516, 517*f*
  material wear testing, 517, 517*f*
  passive and active rolls, 515
  rate of breakage tests, 517–518, 517–519*f*
  "specific rate of breakage", 516–517, 517*f*
Histosonics, benign prostatic hyperplasia and liver tumors, treatment, 581
Holocinematography, 34
Homogenization, 3
  efficiency, 676
  high-pressure homogenizer, 675–676
  milk fat globules, 676
Honing, 399–402, 401*f*
Hot spot theory, 45–46
HP-4194A Impedance Analyzer, 127
Huisgen cycloaddition, 849, 849*s*
Hwacheon vertical machining center, 376, 378
Hybrid manufacturing, 227, 229
Hybrid processes
  in Fenton and photo-Fenton processes, 809, 809*t*
  hydrogen peroxide, driving force, 808, 808*f*
  ozone, 810
  photocatalysis, 810–811
  UV irradiation processes, 808–809
Hybrid transducer linear motors, 417–419, 417–420*f*
Hybrid transducer rotary motors, 422–425, 422–424*f*
Hybrid transducer ultrasonic motors, 417–425
  high-power, 419–422, 420–422*f*
  hybrid rotary motors, 422–425, 422–424*f*
  linear motors, 417–419, 417–420*f*
Hydraulic pressure system, 510, 515
Hydraulic residence time distribution (tracer) tests, 829–830
Hydrodynamic cavitation, 24
Hydrodynamic interaction, 868
Hydrodynamic mechanism, 863
Hydrolytic enzymes, 894
Hydrophones, 131, 135–136, 465, 641
  measurements, 142–143
  spectrum, 136–138, 136*f*
4-Hydroxycoumarin, 837, 838*s*
Hyperthermia, focused ultrasound for medical therapy, 579–580
Hysteresis, 29–30
  cycle, 67–68

I

IC chip connections, 188–189, 188–189*f*
Ice crystallization (freezing), 728–730
Ice nucleation, 712, 713*f*, 734–737
  general survey, 734–735
  mannitol solutions, 729, 730*f*
  micro-streamings, 734–735
  positive pressure effect, 735–737
  sucrose solutions, 729, 729*f*
Image intensifiers, 139
Immiscible alloys, 501–502, 502*f*, 504–505, 505*f*
Immobilization method, 898
Impedance, 86–87, 94–95, 94*f*
  matching, 95, 96*f*
Inclusions, 243–244
Incremental sheet forming (ISF), 295
Industrial biotechnology, 887
Inertial cavitation, 134, 136–138, 138*f*, 580
Infrared (IR) signature, 182, 183*f*
Inhomogeneities, 243–244

Inserting, 219
InSightec's ExAblate 2100 prostate system, 588
Institute of Electrical and Electronic Engineers (IEEE), 70–72
Institute of Radio Engineers (IRE), 70
Intense acoustics, 13–14
Intense ultrasound, 7, 12, 14, 20
Intensity
  high-intensity, 1–2
  low-intensity, 1
Intensity number (NIn), 775
Intermetallics, fragmentation of, 498–501, 500*f*
Intermolecular diffusion, 205, 212–213
Internal combustion engine vehicles (ICEVs), 183–185
International Electrotechnical Commission (IEC), 144
International Symposia on Nonlinear Acoustics (ISNA), 20
Interparticle collisions, 670
Interstitial and intraoperative devices, therapeutic ultrasound, 585–586
Interstitial applicators, 585–586
Intracapsular cataract extraction (ICCE) technique, 618
Iodide dosimeter, 800
Irrigation, 545–546
Isotropic solids
  applications, 58–59
  wavenumber modulation, 57–59
The Iterative automatic method, 72
  ceramics characterization, 72–76

J

Jackhammer effect, 547
Jet formation, 36–38, 36–37*f*
Johnson-Cook constitutive material model, 259
Joint thickness, 191
Joint types, 201
Jordan's cell, for continuous flotation process, 521–522, 521*f*
Jump phenomenon, 624, 624*f*

K

Kapur function, 671
Keller-Miksis equation, 736
Kelman-Cavitron phacoemulsification unit, 619
The Khokhlov-Zabolotskaya-Kuznetsov (KZK) equation, 14–15
Kidney stones, 602, 603*t*
Kinetic effect, 732–733
  diffusion coefficient, effect on, 732
  segregation effect, 730*f*, 732–733
Kinetics of degassing and regassing, 477–478, 478*f*
Knoevenagel condensation, 839–844, 839*s*, 840–843*t*, 842*s*
Knoevenagel-Michael reactions in aqueous media, 844
Kocks-Mecking (KM) model, 260–261
Kristoffy report, 347

L

LabVIEW code, 125–126
Langevin sandwich, 103
Langevin-type transducer, 157, 623
Langmuir-type mechanism, 805
Laparoscopic surgery, 619–620
Lap joints, 191
Lapping, 398
Laser Doppler vibrometry (LDV), 181–182
Laser engineered net shaping (LENS), 229
Laser-produced shock, 24
Laser vibrometry, 132
Lateral drive welding systems, 163
Lateral epicondylitis, 609, 612*t*
Lateral ultrasonically assisted extraction (L-UAE), 309–310, 310*f*
Lattice rotation, 259–260, 260*f*
Lead-free piezoceramics, 68, 76–77
  alkaline niobates, 76–77
  Aurivillius-type structure ceramics, 76
  barium-calcium zirconate-titanates, 77
  bismuth-sodium titanates, 77
Lead titanate zirconate (PZT), 71, 76
Lead zirconate titanate (PZT), 92, 106
Lemon peel drying, 756*f*, 761–762, 763*f*
Length expander transducer, 150–151
Levitation, 2
Lignin, 893
Limiting draw ratio (LDR), 288–289
Linear acoustic effects, 863
Linear viscoelastic bar, 210–211
Linear viscoelastic materials, 209
Lipase catalyzed transesterification, 652–653
Liposuction devices, 540, 551
Liposuction techniques, 619
Liquid atomization, 773
  types, 773
Liquid dissolution, 672–675
Liquid-driven transducers, 644
Liquid droplet effect, 879, 880*f*
Liquid foam, 687
Liquid movement "agitation", 464
Liquidus curve, 722, 722*f*
Lithium-ion battery, 183
Lithium niobate transducer, 106, 107*f*
Long bar resonator, length poled, 74–75
Longitudinal vibrations, 91
  equivalent circuit, 91
  forced vibrations, 89, 89*f*
  governing theory, natural frequencies, 88–89, 88*f*
  three-dimensional effects, 90–91, 90*f*
  ultrasonic horns, 91, 91*f*
Low-amplitude sonications with microbubbles, 591
Low-angle grain boundaries (LAGB), 244–245
Low driving, 29–30, 29–30*f*
Low energy requirements, 191
Low-temperature drying (LTD), 743, 759–760, 763–764, 767–768
Luminol (3-aminophthalhydrazide), 642
Luminol-assisted sonoluminescence, 142–143
Lyophilization, 743

M

Macromixing, 667
Macroscopic behavior of metals
  acoustoplasticity, 253
  AZ31, 255, 257*f*
  early developments, 248–251, 248*f*, 251–252*f*
  finite element analysis (FEA) modeling, 253
  force drops, 253–254
  forming tests, 253–254, 256*f*
  lubrication effects, 254
  1970s through 1990s, 251–253
  tensile test, 253, 254*f*
  ultrasonically assisted material deformation, 258–261
  ultrasonically induced flow stress reduction, 256–258, 258*f*
  ultrasonic plastic deformation, 255
  ultrasonic test setup and tooling, 253, 255*f*
  vibration amplitude effects, 253
Magnesium oxide NPs, 438
Magnetic fluorescent nanospheres (MFNs), 437
Magnetite nanoparticles, 437
Magnetite-nanostructured amylose (AMY) microspheres, 447
Magnetostrictive apparatus, 249
Magnetostrictive effect, 2
Magnetostrictive transducers, 347, 644
Marinating process, 715–716
Mars, piezoelectric vibration techniques, 531–532
Mass optimized Langevin transducer (MOLT), 103, 104*f*
Mass transfer, 140, 834
  under heterogeneous conditions, 853
  Suzuki coupling, 835
Mass transport phenomena, ultrasonic drying
  convective transport, 744–745
  diffusion transport, 745
  heat transport, 745–746
Material extrusion (MEX), 229
Material hardness, 191
Material jetting (MJT), 229
Material nonlinearity, 10
Material-part deformation, 191
Materials inputs, 98–99
Material weldability
  amorphous *vs.* semi-crystalline polymers, 223
  compatibility, 223, 224*f*
  microstructure, 223–224
  mineral fillers, 223
  rheovibron, 223
  thermoplastic composites, 222–223
  weld interface, 223
MCP. *See* Multiphase coexisting point (MCP)
MD. *See* Molecular dynamics (MD)
Measurement methods, 140, 140–141*t*
Mechanical agitation (MA), 709–710, 709*f*
Mechanical atomization, 773
Mechanical damping, 70
Mechanical foam breakers, 689
Mechanical fracture, 498

Mechanical oscillator
displacement/velocity forcing, parallel equivalent circuit, 87, 87*f*
equivalent circuit, impedance, 86–87, 86*f*
vibration results
forced vibration, 85–86
free vibration, 84–85
transient response, 86
Mechanical resonance, 468
Mechanical shear forces (transient cavitation), 829
Medical device regulations
general requirements, 552
International Electrotechnical Commission (IEC) standards, ultrasonic surgical devices, 552
Medical echography, 56
Medium heating, 18–19
Megasonic technology, 468–470, 468–469*f*
configurations, 470
Metal emulsion, 434
Metal foil, 239–240
Metal forming, 243
macroscopic behavior, 248–261
microstructure effects, 243–247
physical effects of vibrations, 243
Metal halide nanoparticles
water-insoluble, 441–442
water-soluble, 442
Metallic nanoparticle synthesis, 432–435
Metallization, 175
Metal oxide nanoparticle synthesis, 435–440, 436*f*
Metal-to-metal adhesion, 171
Metal-to-metal contact, 163
Metal working processes, 261–263
Metastable zone width, 725
Mg alloy AZ31B, 198–199
Mg alloy AZ31B-H24, 199
MgAZ31B, 194
Michael addition, 836–838
of 4-hydroxycoumarin and nitrostyrene, 836–838, 837*s*
Michael adducts, 837
excellent yields, 837
good yields, 837
Micro-and nanosphere synthesis, 446–449, 449*f*
Microbial laccases (*p*-diphenol: dioxygen oxidoreductase), 894
Microbial peroxidases, 894
Microbonding, 185–186
Microelectronics, 185–190
Microencapsulation
of blueberry juice, 783
fish oil-whey protein microcapsule synthesis, 782
of pDNA, 789
of transglutaminase, 783
Microfluidics, 16
Microforming
deep-drawn cups, 328–329, 328*f*
equipment diagram, 327
extrusion press, 327–328, 327*f*
flowchart, 329, 330*f*
microblanking, 329, 329*f*
micro-deep drawing, 328–329, 328*f*
microextrusion tool, 327–328, 327*f*
optical micrograph, 327
porous sonotrode, 327–328, 327*f*
scope, 327
shearing surfaces, 329, 329*f*
tube expansion, 330, 331*f*
ultrasonically drawn cups, 328–329, 328*f*
ultrasonics, 325, 326*f*
Micromixing, 667–668, 668–669*f*
Microprocessor-controlled ultrasonic welders, 222
Microscale, 268–270
Microscopy, 132–133
Microspheres synthesis, 440
Microstreaming, 580, 890
Microstructure, 223–224
absorption loss mechanisms, 243–244
AZ31 magnesium alloy, 246–247
copper and aluminum, 243–244, 244*f*
EBSD orientation map, 244–245, 245*f*
high-temperature processes, 244
low-angle grain boundaries, 246
low-carbon steel, 246, 247*f*
St52 steel, 246
ultrasonic effects, 244–245
ultrasonic vibrations, 243–245, 245*f*
vibrations and waves, 244
Microthrix parvicella, 821–823
Mie scattering, 133
Milling system, 514–515
elastic energy, 516
rollers, 516
Mineral milling system, 514–515
elastic energy, 516
rollers, 516
Miniature bar-shaped rotary motors, 416*f*
Miniaturization of ultrasonic devices, 551
Mining industry, 509–510
in particle size reduction, 512–518
rock mass stress state, 510–512
measurements, transducers, 510–512, 510–511*f*
ultrasonic-assisted flotation process, valuable mineral concentration, 519–525
ultrasonic-assisted sedimentation rate, water-solid separation efficiency, 525–528
Mode nephogram of TRUM-30, 531, 532*f*
Molecular dynamics (MD), 46
Molybdenum, 173–175, 279–280
Monomeric friction coefficient, 213–214
Moonie transducer, 631, 631*f*
Moon, ultrasonic motors on, 531, 532*f*
Morphotropic phase boundary (MPB), 67
Motional resonance, 95
Motion of aerosol particles, in acoustic field, vibration, 865–866, 866*f*
Motor-generator, 96
MPB. *See* Morphotropic phase boundary (MPB)
MR-guided ablation of uterine fibroids, 589
MR-guided focused ultrasound (FUS) ablation, 589–590, 590*f*
Multibubble model, 23
Multibubble sonoluminescence (MBSL), 139
Multicomponent reactions (MCR), 833–834, 838, 844
Multiferroics, 69
Multifrequency reference cavitation, 142, 142*f*
Multifunctional ferro-piezoelectric ceramics, 69
Multifunction ultrasonic transmitter model UGD, 525
Multiphase coexisting point (MCP), 77
Multiphase media, 109, 129
Multiphonic sound, 63
Multiple-element transducer arrays, 591
Multitransducer, 142
Multivalued waveform paradox, 11
Mutual radiation pressure (MRP), 863–864
Mutual radiation pressure effect (MRPE), 868–869, 869*f*

N

$NaKC_4H_4O_6.E4H_2O$, 65
Nanjing University of Aeronautics and Astronautics (NUAA), 531, 532*f*
Nanobubbles, 24
Nanomaterials, 3
Nanometer-sized bubbles, 24
Nano/microelectromechanical systems (N-/MEMS), 268–270
Nanoparticle deagglomeration
interparticle collision, 670
sonication method, 669
specific energy (Ev), 670, 670*t*
vapor–gas nucleus, 669–670, 670*f*
Nanoparticle dispersion
interparticle collision, 670
sonication method, 669
specific energy (Ev), 670, 670*t*
vapor–gas nucleus, 669–670, 670*f*
Nanoparticles deposition on substrates, 444–446, 445*f*
Nanoscale, 268–270
Nanospheres, 446–449
Natural frequencies, 88–89, 88*f*
Navier-Stokes equation, 8
N-bubble model, 41–42
simulation, 42–43, 42–43*f*
Near-field ultrasonic welding, 214
Nebulization, 548–549
Nickel-manganese, 279–280
Nitrogen removal, 828
Noise, 191
Noise-like processes, 30
Nondestructive testing (NDT), 510
Non-inertial cavitation, 134
Non-isothermal healing model, 213
Nonlinear acoustics, 1–2, 7, 9, 9*f*
acoustic streaming and turbulence, 864–865
acoustic wake (AW), 864, 864*f*
arbitrary flow field, 9
entropy equation, 7–9
linear approximation, 7–8
motion of aerosol particles in acoustic field, vibration, 865–866, 866*f*
radiation pressure and mutual radiation pressure, 863–864, 864*f*

theoretical methods, 13, 16
vorticity modes, 7–9
Nonlinear algebraic equations, 59
Nonlinear coupling, 62–63
Nonlinear differential equation
applications, 56–57
constitutive equations and equation of motion, 53–54
Kronecker symbol, 54
Nonlinear dynamics, 53
Nonlinearity, 7, 10, 13–14
coefficient of acoustic, 11
convective, 10
material, 10
Nonlinear propagation, 12, 17
Nonlinear vibration, 112–118
modal interactions, 114–118
piezoelectric responses, 113–114, 113–115*f*
Nonlinear wave, 18
Nonlinear waveform distortion, 11–12, 13*f*
Nonlinear wave modulation, 57, 59
Nonlocal boundary conditions
boundary element method (BEM), 154–155
Dirichlet-to-Neumann (DtN) method, 155
exact conditions, 153–154
Nonmetallic inclusion activation, 496–498
Nonunion/delayed union of bone healing, 604–606, 606–607*t*, 607*f*
NPL Cavitation Sensor, 136–138, 141–142
N-substituted imidazole synthesis, 838
Nuclear power plant, in severe accidents, 880–882, 881–882*f*
Nucleate-rich bubble-containing fluid, 134
Nucleation
and growth rates, 728
heterogeneous, 734
heterogeneous primary, 723
primary nucleation, 724
secondary, 724
ultrasound effect on, 731
Numerical methods, 147–148
alternative, 71–72

O

Ohnesorge number (NOh), 775
"On-water" Michael addition, 838
On-water reactions, 833–834
Optical beam, 132–133
Optical methods, 139
Optical scattering, 132–133
O-rings, 221
Orthokinetic effect (OE), 867–868, 867–868*f*
Orthokinetic interaction, 861
hydrodynamic interactions, 861
Oscillations, 30
amplitude, 30
bubble, 27–28, 30, 32–33
coexisting, 29–30
single-bubble, 42
subharmonic, 27–28
Oscillatory localized harmonic motion, 586, 586*f*
Osteotomies, 540
Oxides, 190–191
Oxygenases, 894
Oxygen utilization rate (OUR), 818–820
Ozone, 810

P

Packaging applications, 183
Palm oil fat crystals, 712–714
Paraelectric phase, 68
Parallel plate reactors, 646
Parallel resonance, 95
Parameter space diagrams, 30–33, 31–32*f*
Parametric excitation, 115
Particle agglomeration, 2
Particle aggregation, 897–898
Particle image velocimetry (PIV), 642
Particle size distribution (PSD), 817–820, 819*f*
Particle size reduction
extraction process, 509
high-pressure ultrasonic roller mill (HPURM)
efficiency, 516, 517*f*
material wear testing, 517, 517*f*
rate of breakage tests, 517–518, 517–519*f*
mineral crushing and grinding, 509
ultrasonic-assisted high-pressure grinding roll, 515–516
Particles modeling, 872–874
acoustic agglomeration kernels and numerical models, 872–874
aerosol dynamics equation, 872
Particle surface cleaning effect, cavitation, 521
Passive ultrasonic irrigation of the root canal, 565–566, 567*f*
Pasteurization, 715–716
$PbTiO_3$ (PT), 65
Peak-to-peak amplitude, 211
PEEK graphite APC-2 composites, 214–215
Peer-reviewed literature, 131
Percutaneous nephrolithotomy (PCNL), 602
Perfectly matched layers (PMLs), 147, 156–157
Period-doubling, 43, 44*f*
sequences, 30, 43
Periodic shock, 135
waves, 143–144
Periodontology, 564
Perovskite lattice, 77
Perovskite-type structure, 67, 76–77
Persimmon drying, 757, 758*f*
Persistent slip bands (PSBs), 118
Perturbations, 8–9, 15–17, 54, 59, 62–63
Perturbative method, 56, 58
Phacoemulsification, 539
devices, 549, 550*f*
and ultrasonic aspiration, 621
Phacoemulsifier tool, 619
Pharmaceutical industry
aerosols for drug delivery, 786–788
encapsulation for drug delivery, 788–791, 788*f*, 790*f*
Phased-array schematic, 582–584, 584*f*
Phase diagrams, 30–31
Phase-matching, 59–61
Phase shift, 211
Phosphoric acid (PA75), 37–38
Photomultipliers, 139
Physical equations, 148, 152–153
Physics-based model, 178–179
Piezoceramic rings PZT-802, 113–114
Piezoceramics, 65, 69–71, 75–77, 113
Piezoelectric ceramics, 83
Piezoelectric element, 63, 64*f*
Piezoelectricity, 83, 147–148, 455–456
ferroelectric crystals, 65
resonances, 69–72
single crystals, 65
Piezoelectric Langevin-type transducer, 157
Piezoelectric materials, 2, 92–93, 92*f*, 98, 168
Piezoelectric matrix, 99, 100*t*
Piezoelectric transducers, 95, 109–110, 125, 644
Piezoelectric vibration techniques, Mars, 531–532, 534*f*
Piezoelectric vibrator, 118
Piezosurgery device
base insert (BI), 625, 625*f*
experimental modal analysis (EMA), 625
harmonic characterization, 625, 625*f*
OT7 insert, 625–626*f*, 626
Pilot scale plants, 877–878*t*
Pilot-scale preconditioning systems, coal combustion fumes, 875–879, 876*f*, 877–879*t*
PIN-PMN-PT (lead indium niobate-lead magnesium niobate-lead titanate), 629–630
Plantar fasciitis, 602–604, 604–605*t*, 605*f*
Plant components, extraction of, 706, 707–708*t*, 708*f*
Plasma arc welding (PAW) process, 195, 195*f*
Plasma-mass spectrometry analysis, 786
Plastic welding
methods, 208
process stages, 205
Plate transducers, 110, 110*f*, 112, 115, 119–125
stepped-plate, 119–121
Platinum (II) concentrations, 433–434, 434*f*
Platinum (IV) concentrations, 433–434, 434*f*
Plesset-Zwick integration method, 736
Plunge-style ultrasonic process, 205
Plunge welding, 216–217, 217*f*
Pneumatic cylinder, 163–164
Pneumatic welder, 205–206
Pohlmann whistle, 701
Poisson effect, 280
Poisson expansion, 265–266
Poisson ratio, 111
Polarization, 68–69, 113
Poled ceramic, 92
Poling process, 68
Polycrystalline diamond tool, 352
Polycrystalline materials, 65–66
Polydisperse cluster, 44
Polyethylene, 223, 224*f*
Polyhydroquinoline derivatives, 438
Polymers
amorphous *vs.* semi-crystalline, 223
chain, 213
semi-crystalline, 223
wave propagation, 210–212, 211–213*f*
weldability, 207–208, 208*t*

Polymorphism, and crystallinity, 726–727
Polytec MSA-100-3D, 132
Polyvinylidene fluoride (PVDF), 72
Positive pressure effect, 735–737
Potassium iodide (KI) oxidation method, 641
Pouch-type BP, 185
Powder bed fusion (PBF), 229, 230*f*
Power, 96–97, 97*f*
  characterization procedure, 126–127, 128*f*
  dissipation levels, 660–661
  draining, 56
  energy, and time, 168, 168*f*
  levels, 1–2
  operation, 125–129
  transducer, modeling, 97–102
Power spectrum, 126–127
Power supply system, 165, 232
  and controller, 220
Power transducers, 109, 125, 128*f*
Power ultrasonics, 132–144, 244, 248
  applications, 3
  biofuel production, 3
  constant amplitude, 132
  electrically, 132
  field of, 1–2
  magnetostrictive-based transducer, 83
  optically, 132–133
  piezo-electric ceramic-based, 83
  transducer, 83, 93–94
Power Ultrasonics Group (PUG), 746
Power ultrasonic transducers
  for biogas plants, 826–827, 827*f*
  finite element simulation, 511, 511*f*
  installation inside mine, 511–512, 512–513*f*
  phase change record, 512, 514*f*
  radiation impedance, 512
  sound velocity propagation
    felsic rock sample vs applied stress, 510–511, 511*f*
    in rock samples under stress, 510–511, 510*f*
Precipitation tests, on polydisperse carbon black smoke, 874
Preconditioning systems, 875–879, 876*f*, 877–879*t*
Pressure effect, 731–732
  negative, 734
  positive, 735–737
Pre-triggering, 217
Primary intermetallics, fragmentation of, 498–501, 500*f*
Primary nucleation, 724
Probe systems, 644
Process controls and systems, 200–201
Process variables, 222
Profound Medical's transurethral prostate ablation device, 588
Progressive waves, 59, 62
Protein microspheres formation, 447
Pseudomonas aeruginosa, 821–823, 822–823*f*
Pulsed acoustic waves, for medical therapy, 599
  ballistic source, 601, 601*f*
  calcific tendinitis, 609, 611*t*
  cavitation, 602
  chronic foot ulcers, 606–609, 608*t*
  chronic refractory angina pectoris, 609, 610*t*
  coupling, 601
  direct stress, 602
  electrohydraulic source, 600, 600*f*
  electromagnetic source, 600–601
  healing of nonunion/delayed union of bones, 604–606, 606–607*t*, 607*f*
  kidney stones, 602, 603*t*
  lateral epicondylitis, 609, 612*t*
  piezoelectric source, 601
  plantar fasciitis, 602–604, 604–605*t*, 605*f*
  transduction mechanisms, 599
Pulsed sonoelectrochemical technique, 432
Pulsed ultrasound, 890
Pulse-echo devices, 57
Push-pull sonotrode design, 231–232, 231*f*
Push–pull system, 200
Push–pull transducers, 456
PVDF. *See* Polyvinylidene fluoride (PVDF)
Pyrazole derivatives, 844
Pyrex glass, 24
Pyrotech, 588–589

Q

Quadratic approximation, 11
Quartz plates, 2
Quasi longitudinal, 54
Quasi-plane-wave approximation, 17
Quasi transversal, 54
Quinolines preparation, 850

R

Radial oscillations, 280
Radial vibrations, 292
Radiation force, 16–18, 890
  focused ultrasound, medical therapy, 581–582
Radiation pressure (RP) and mutual radiation pressure, 863–864, 864*f*
Radio frequency (RF), 236–237
Radius response curves, 29
Random sparse array, 584, 584*f*
Rankine–Hugoniot relation, 19
Rayleigh collapse, 26
Rayleigh–Plesset model, 26–27, 29, 43, 640
Rayleigh–Ritz method, 110–111
Reactive templated grain growth (RTGG), 77
Reaming, 343, 399, 400*f*
Rebound jet, 37–38, 37*f*
Recrystallization, 173
Rectangular-plate configurations, 120–121
Rectangular radiators, 121
Rectangular-voltage waveform, 427
Rectified diffusion, 474, 546, 547*f*, 580, 580*f*
Red copper, 249
Reflected light optical microscopy, 729
Re-gassing, 473–474
Remote disruptive devices, 550–551
Remote signal, 205
Resistance spot welding/ultrasonics
  heat distribution, 172–173
  hybrid welding, 192–193, 192*f*
  plastic welding, 193
  ultrasonic welding operation, 192
  vertical ultrasonic welder, 193, 193*f*
Resonance, 95, 220–221
  four modes, 73, 74*t*
  frequencies, 103, 103*f*, 111–112
  geometries, 73, 74*f*
  piezoelectric, 69–72
Resonator
  cubical, 40–41, 42*f*
  cylindrical, 38, 39–40*f*
  rectangular, 40, 40*f*
Response curve, 61
  high driving, 30
  low driving, 29–30
Reynolds stress tensor, 16–17
Rheovibron, 223
Riemann invariants, 10
RMS values, 126
Rock mass exploration, 511–512
Rock mass stress state at mine facility, 510–512
Rock stress measurement, 509–510
Rosetta type motion, 63
Rotating disk approach, 265
Rotating disk electrode, 432
RPCam, 229–231

S

Salicylic acid, 139
  dosimetry, 641
Satellite resonances, 75–76
Saturation, 721–722, 722*f*
SAWs. *See* Surface acoustic waves (SAWs)
Scrupulous cleanliness, 24
Sedimentation, 525–526
  rate, 526
Seevetal wastewater treatment plant (WWTP), 820, 821*f*, 828–829, 829*f*
Segregation effect, 730*f*, 731–733
Semiautogenous ball mill (SAG), 512
Semi-crystalline
  polymers, 223
  thermoplastics, 205
Sensors, 69
  termination, 182–183
Sequential ultrasonic welding, 217
Series resonance, 95
Serum albumin microspheres, 447
Servo-actuated press, 292
Servo-controlled press, 293
Servo-controlled electric motor, 163–164
Servowelder, 205–206
Shape stability, 34–36
Shear forces, 181, 182*f*
Shearing and blanking, 312–313, 312–314*f*
Shear plate resonator, thickness poled, 74
Shear stress, 214
  gene expression and metabolism, 580
Shear wave imaging, 586–587
Sheet forming processes, 277
Sheet lamination (SHL), 229
Sheffield Company, 342–343
Shock
  formation, 11–12, 13*f*
  structure, 12–13
  waves, 11–12, 14–15, 19–20
  weak, 19

Shock wave emission, 34
Shock wave lithotripsy (SWL), 14
Shock wave therapy (SWT), 599
  ballistic, 599
  electrohydraulic, 599
  electromagnetic, 599
  piezoelectric, 599
  pressure waveform, 599, 600*f*
  transduction mechanisms, 599
Signal processing, 125–126
Simple wave equation, 9–11
  counterpropagating waves, 10
  ideal fluid, 9
  intense standing waves, 10
  Riemann invariants, 10
Single-bubble dynamics
  bubble habitat, 33–38
  bubble models, 26–27
  modeling during cavitation, 640
  parameter space diagrams, 30–33
  response curves, 27–30
Single-bubble sonoluminescence (SBSL), 139
Single bubble system, 712
Single-element, spherically curved transducer, 582, 583*f*
Single-phase ZnO nanoparticles, 435
Skimming, 522
Skraup method, 833–834
Sliding friction, 265, 267*f*
Slowness curves, 60*f*
Sludge cell disintegration, in full-scale continuous plug-flow-type ultrasonic reactor, 829–830, 830*f*
Sludge dewatering, 899
Sludge treatment, ultrasonic, 674
Smits method, 71–72
Softer alloy metals, 168
Soft magnetic materials (SMCs), 325
Soft tissue
  blade-tissue interaction, 621
  debris removal, 621
  dissection, 618–620
  mechanisms, 620–621
Solid dissolution, 672–675
Solid-fluid coupled system, 153
Solidica formation machine, 229–231, 231*f*
Solidification, metals, 502–505
  composite materials and immiscible alloys, 504–505, 505*f*
  ultrasonic cavitation processing, 490–496
  ultrasonic cavitation science and applications, 489–490
  ultrasonic melt processing
    composite materials and immiscible alloys, 504–505
    deagglomeration and dispersion, 501
    emulsification (immiscible alloys), 501–502
Solid-liquid mass transfer coefficient, 642
Solid media, 53
Solid-state single-crystal growth (SSSC) method, 78
Solid-state welding process, 190
Solute nucleation mechanisms
  chemical effect, 733–734
  heterogeneous nucleation, 734
  kinetic effect, 732–733
    diffusion coefficient, effect on, 732
    segregation effect, 730*f*, 732–733
  thermodynamic (temperature and pressure) effect, 731–732
Sonalleve device, breast cancer, 589
Sonar or medical ultrasound systems, 133
Sonar-type hydrophone, 136
Sonication, 701, 710–711
  of bacterial biomass, 820
  on particle size distribution (PSD), 817–820, 819*f*
Sonication on dissolved organic phase (SCOD), 818, 819*f*
SonicLayer 4000, 232
SonicLayer R200, 232
Sonitube, 646, 655*f*
Sonobond dual head wedge-reed welder, 169, 170*f*
Sonochemical deposition methods, 444
Sonochemical devices and experimentation, 798–801
  reactor calibration, 799
  sonochemical devices, 798–799, 799*f*
  ultrasonic effectiveness for water treatment, 799–800
  ultrasonic power and efficiency, 801
Sonochemical elimination, characteristics of, 801–804
  eliminating volatile and nonvolatile molecules from a mixture, 801–804
  oxidation of water soluble pollutants, 801, 802–803*t*, 802*f*
  volatile organic molecules, 801, 803*t*
Sonochemical method, 838
Sonochemical microspherization process, 448
Sonochemical organic reactions in aqueous media
  Aza-Michael reaction, 845–847, 846*s*, 846–847*t*
  benzimidazolylacetonitrile, 843
  Diels-Alder cycloaddition, 844–845, 845*s*
  Hantzsch condensation or cyclization, 848–849, 848–849*s*
  Huisgen cycloaddition, 849, 849*s*
  Knoevenagel condensation, 839–844, 839*s*, 840–843*t*, 842*s*
  Michael additions, 836–838
    of 4-hydroxycoumarin and nitrostyrene, 836–838, 837*s*
  substituted aromatic aldehydes, 843
  Suzuki coupling reactions, 835–836, 835*s*
  Ugi-azide reaction and Groebke-Blackburn-Bienayme reaction, 850–853, 850–851*s*
Sonochemical reactors, 891–892, 892*f*
  for food processing
    bi-modal signals, 653–655
    cavitational activity distribution, 640–644
    cavitational yield, 646, 652*t*
    cavity dynamics, 639
    continuous flow multiprobe ultrasonic cylindrical reactor with horns, 646, 658*f*
    continuous flow novel tube ultrasonic reactor, 646, 657*f*
    cylindrical ultrasonic reactor, 646, 654*f*
    developments in reactor design, 646, 647–650*t*
    experimental apparatus, 646, 656*f*
    flatbed reactor with transducer configurations, 646, 658*f*
    geometrical design, 659–660
    high-intensity ultrasonic tubular reactor (HUTR), 646, 658*f*
    irradiation frequency, 651–652
    liquid phase physicochemical properties, 658–659
    liquids with higher surface tension, 659
    lower liquid vapor pressure, 658–659
    mapping of cavitational activity, 646, 656*f*
    mass transfer limitations and mixing times, 661
    modeling of cavitational reactors, 640
    optimum power dissipation levels, 652–653
    physicochemical properties, 660
    power dissipation levels, 652–653, 660–661
    pulsed mode, 653–655
    scale-up and optimization, 660
    signal type or duty cycle, 653–656
    sonitube, 646, 655*f*
    soundwave reflection and focusing, 646, 653*f*
    with stages, 646, 655*f*
    sweeping mode, 653–655
    temperature selection, 656–657
    types of, 644–646
    ultrasound-assisted air loop reactor, 646, 655*f*
    ultrasound bath with cavitation, 646, 654*f*
  of nanometals, 434
Sonochemical treatment parameters, 805–808
  dissolved gases, effect of, 807
  enhancers and inhibitors, 807–808
  frequency effect, 805–806
  HNO_2 and HNO_3 formation, aerated medium, 807
  pH influence, medium, 806
  temperature influence, 806
Sonochemiluminescence (SCL), 561, 642
Sonochemistry, 23, 25, 41, 48, 134–135, 138–139, 271, 888
  advantages of, 432
  erbium oxide NPs, 437–438
  multicomponent oxides, 438–439
Sonochemistry-based synthesis method, 438
Sono-crystallization, 711–714, 738
Sonoelectrochemistry, 432
  synthesis of Fe–Cr alloy, 432
Sonoluminescence, 45–47, 47–48*f*, 139, 142–144
  luminol-assisted, 142–143
Sonopet ultrasonic aspirator, 623
Sonoporation, ultrasound-mediated, 581
Sono-Tek ultrasonic spray system, 786–787

Sonotrode, 141–142, 164–165, 169, 179, 179*f*, 187, 233
  oscillation amplitude, 235
  topology, 235–236, 235*f*
Sound-assisted chemistry, 138–139
Sound-entropy, 9
Sound-field pressure nodes, 27
Sound-sound, 9
Sound velocity propagation, 510–511, 511*f*
Sound-vorticity, 9
Sound waves, 7, 24
  reflection and focusing, 646, 653*f*
Space, ongoing research, 532–534
Spanish National Research Council (CSIC), 746
Spatial discretization, 149, 153–154
Spectrophotometric analytical procedure, 447
Spherical bubbles, 23, 27, 28*f*, 31, 33–34, 39*f*
Sponge effect, 745
Spot welding, 217–218, 219*f*
Spray-drying technique, 773, 782
Spray system, 459
SSSC method. *See* Solid-state single-crystal growth (SSSC) method
Stable cavitation, 547, 580, 639
Stable cavitation effect, 525
Stainless steel, 285
Staking, 217, 218*f*
Standing wave-field pattern, 864, 864*f*
Standing-wave resonance, 541
Static force, 167
Static pressure, 24
Static tension threshold, 23–24
Stationary nucleation, 724
Stationary waves
  amplitude, 61
  applications, 63
  elastic perturbations, 61
  Fourier series, 62
  harmonic waves, 62
  linear equation, 62
  nonlinearity terms, 61
  nonlinear terms, 61
  perturbation, 62–63
  subharmonic oscillation, 63
  subharmonic waves, 62
  transient solutions, 61
Statistical process control (SPC), 222
Steamjet acoustic generators, 690
Stepped-grooved plate transducers, 123, 124*f*
Stepped-plate airborne transducer, 157, 157–158*f*
Stepped plate radiators, 746–750
Stepped-plate transducers, 112
  directivity diagrams, 119, 119*f*
  phase coherent effect, 119, 119*f*
  radiator, 119–120, 120*f*
  surface elements, 119
Stepped-plate ultrasonic defoamers
  acoustic field distribution, 695, 696*f*
  defoaming rate, 695
  rotary ultrasonic defoaming system, 695, 697*f*
  static system, 695, 696*f*
Stereotaxic therapeutic ultrasound system, 578–579
Sterilization, 715–716
Stiffness matrix, 99, 99*t*
Strain, 210
Streamers, 39
  filamentary, 42, 42*f*
Stress, 210
  analysis, 118–119, 119*f*
Stress-induced changes, 891
Stress-strain curve, 258, 261
Stress superposition hypothesis, 250
Stress superposition model, 252
Subharmonics, 43, 44*f*
  oscillations, 27–28, 63
  waves, 62
Submarine sonar, 1
Substituted aromatic aldehydes, 843
Supercritical fluid extraction (SFE), 706–708
Superposition, 252–253
Supersaturation, 722–723
Supersonic (ultrasonic) frequencies, 521
Supersonic waves, 83
Surface acoustic waves (SAWs), 1, 60
  atomizer, 787
  motor, 414–415, 415*f*
Surface friction
  contour plots, 267, 270*f*
  Coulomb's friction law, 264
  friction reduction, 262–263, 263*f*
  pin-on-disc experimental setup, 266–267, 269*f*
  static and kinetic friction, 266
  strip drawing, 263
  ultrasonic deformation processes, 261–262
  ultrasonic forming processes, 264
  ultrasonic friction reduction studies, 263, 265*f*
  ultrasonic vibration, 261, 262*f*, 266–267
Surface grinding, 341–343, 342–343*f*
Surface tension, 26
Surfactant, 433
Surgery piezosurgery, 558–559, 570–571
Surgical devices and procedures
  aspiration devices, open surgery, 549
  body contouring, 540
  bone drilling and shaping, 540
  compound motions, 544
  coupler/horn, 542
  cutting/coagulation, harmonic scalpel and derivative devices, 550
  dentistry, 539
  device types, 549–551
  end effectors, 543, 543*f*
    bends and shapes, 545
    hollow end effectors, 545
    solid end effectors, 545
    wires, 545
  externally applied devices, 551
  generator, 542
  high-intensity focused ultrasound, 551
  history, 539–540
  International Electrotechnical Commission (IEC) standards, 552
  irrigation and aspiration, 545–546
  lateral and ellipsoidal mode, 544
  longitudinal vibrational mode, 543–544
  mechanisms of action
    acoustic energy, 548
    acoustic radiation force, 548
    acoustic streaming, 548
    cavitation, 546–547
    direct impact, 547
    nebulization, 548–549
    thermal energy, 547–548
  medical device regulations, 551–552
  miniaturization, 551
  minimally invasive laparoscopic surgeries, 539–540
  nonmedical applications, 539
  physician interaction, 546
  probe/wire, 542–543
  remote disruptive devices, 550–551
  resonance, 541
  surgical requirements, 541
  target tissues
    hard tissues, 540–541
    soft tissues, 540
  tissue cutting and coagulation, 539–540, 545, 550
  tissue-preserving devices, 551
  torsional vibrational mode, 544, 544*f*
  transducer, 542
  transmission element, 542–543
  unwanted modes, 544
  wire/rigid cannula approaches, 540
  wire transverse, 544
Suzuki coupling reactions, 835–836, 835*s*
Suzuki-Miyaura coupling, of 4-bromoanisole and phenylboronic acid, 835, 835*s*, 836*t*
Swaging, 217, 218*f*
Swamping, 135–136
Switching process, 65–66
SWL. *See* Shock wave lithotripsy (SWL)
Synchronization, 44, 44–45*f*
System power, 200

T

Tapping, 402–404, 402–403*f*
Targeted drug delivery, 581
Taylor instability criteria, 774
Tech-Sonic closed-loop, 169, 170*f*
Teeth damage, 571
Tektronix oscilloscope, 127–129
Temperature effect, 731–732
Tensile tests, 250, 253, 254*f*
Tension value, 23
Terephthalate dosimeter, 800, 800*f*
Terfenol-D-based magnetostrictive transducer, 254, 325–326
Test validity, ultrasonic cleaning, 464–465
Textile washing process, 470–471
Textured piezoceramics, 630
Theory of acoustic degassing, 474
Therapeutic ultrasound
  bone, 590–591
  brain, 591
  breast, 589
  cavitational interaction
    enhancement of drug treatments, 581
    mechanism, 580

tissue disintegration and fragmentation, 580–581
endocavity devices, 585
external devices, 582–585
imaging modalities, 587
interstitial and intraoperative devices, 585–586
liver, 588–589
magnetic resonance imaging, 587, 588*f*
prostate, 587–588
radiation force, 581–582
stroke, 591
thermal interaction
apoptosis, 579
energy absorption, 578, 578*f*
hyperthermia, 579–580
thermal ablation, 578–579
thyroid, 590
ultrasound, 586–587, 586*f*
uterine fibroids, 589–590
Thermal ablation, focused ultrasound for medical therapy, 578–579
Thermal energy, 547–548
Thermal interaction, focused ultrasound for medical therapy
apoptosis, 579
energy absorption, 578, 578*f*
hyperthermia, 579–580
thermal ablation, 578–579
Thermal mechanically affected zone (TMAZ), 199
Thermal methods for pasteurization and sterilization, 715–716
Thermodynamic analysis of reaction, 477
Thermodynamic (temperature and pressure) effect, 731–732
Thermoplastics, 205
elastomers, 222–223
Thermosonication, 676–677
Thickened waste-activated sludge (TWAS) flow, 825
Thin-disk resonator, thickness poled, 73
Thin-thick combinations, 190
Thread root rolling (TRR), 316, 321*f*
3D manufacturing format (3MF), 227
Three-stage continuous flow sonochemical reactors, 646, 655*f*
Thrust force, 357
Time discretization, 150
Time-domain analysis, 126
Time spectrum evolution, 126–127
Tissue fragmentation, 621
Tissue harmonic imaging, 56
Tissue-preserving devices, 551
Titanium, 118, 285
drilling, 344
implant surface cleaning, 568, 569*f*
Tooling, 169
Torque/thrust, 413
Torsional vibrations, 252
Torsion-assisted milling, 379, 380*f*
Traditional Langevin transducer (TLT), 103, 104*f*
Transcranial focused ultrasound (FUS) surgery, 591
Transducers, 1–2, 93, 165, 232–233, 456–457, 457*f*, 542, 888
airborne stepped-plate, 157
analysis example, 101–102, 101*t*, 101*f*
analysis type, 100–101
analytical model, 104, 105*f*
characterization and control, 94–97
circular stepped-plate radiators (SPR), 747, 747*f*
configurations, 94, 94*f*
convective drier, 749–750, 752*f*
converter, 220–221
cylindrical radiator, 747, 748–751*f*
deformed shape, 104, 105*f*
design, 374, 630
electrical energy, 147
fatigue limitations, 118–119
finite element method (FEM) (*see* Finite element method (FEM))
geometry, 97–98, 98*f*, 101
limits, 103
impedance, 94–95, 94*f*
length expander, 150–151, 151–152*f*
modeling, 97–102
power, energy, and time, 168, 168*f*
power operation, 125–129
practical design, 93–94
rectangular flat-plate radiator, 747, 747–748*f*
rectangular stepped-plate radiator (SPR), 747, 747*f*
resonance frequencies, 103, 103*f*
sound pressure-level distribution pattern, 748, 749*f*
stepped-grooved-circular-plate transducer, 750, 752*f*
with stepped plate, flat plate with reflectors, and cylindrical radiators, 746–750
structure, 109–110, 746–747, 746*f*
vibration amplitude, 165
Transduction, 147–152
materials, 629–630
Transesterification process, 892–893
Transformers, 76
Transient cavitation, 546–547, 639
effect, 525
Transient response, 86
Translational motion
RP force, 866
standing acoustic waves, 866
viscosity temperature dependence, 867
Translational motion of aerosol particles
due to other effect, 866–867
due to radiation force, 866
Translucent media, 132–133
Transmission, 1–2
Transmission electron microscopy (TEM) images, graphene, 442
Transurethral prostate ablation device, 585, 588
Transverse cutting mode, 348
Transverse force, 357, 359*f*
Traveling microscope, 132
Traveling wave linear motors
principle of, 413–414, 414*f*
variations, 414–415, 414–415*f*
Traveling wave rotary motor
bar-shaped configuration, 416, 416*f*
ring or disk shape, 415–416
Traveling-wave ultrasonic motors
bar-shaped configuration, 416, 416*f*
linear, variations, 414–415, 414–415*f*
principle of, 413–414, 414*f*
rotary, ring or disk shape, 415–416
Triglyceride esters, 892–893
Triple frequency hexagonal flow cell, 645–646, 646*f*
TRUM-30A ultrasonic motor, 531, 532*f*
Tube drawing, 277–279, 279*f*
Al 1100 tubing, 283
antifriction, 285, 286*f*
die-drum spacing, 280, 281*f*
drawing stress variation, 285, 287*f*
forming processes, 277, 278*f*
magnetostrictive transducers, 280
process arrangements, 282–283, 284*f*
radially vibrated ultrasonic tube, 283, 285*f*
1970s and 1980s, 280–282, 282–283*f*
skew-type vibration system, 285–287
step-by-step design procedures, 285–287
stress antinode, 279–280
stress contour, 285, 287*f*
theoretical analysis, 283, 286*f*
tube drawing, 280, 281*f*
vibrations, 280
damping block, 277–279
wiredrawing work, 279, 279*f*
Tungsten, 173–175
Tungsten inert gas (TIG), 197
Turbulence, 173, 864–865
on acoustic field disruption, 757–758
Twist drilling, 344, 347*f*, 368–369
Two-point incremental forming (TPIF), 295

U

Ugi-azide reaction, 850–853, 850–851*s*
Ultraharmonic resonances, 29
Ultrasonic additive manufacturing (UAM), 173, 241, 241*f*
complicated geometry, 236–237, 237*f*
dissimilar material bonding, 237–239, 238*f*
hybrid additive/subtractive manufacturing technology, 229
object embedment, 239–241, 239–240*f*
process, 229, 230*f*
process operation, 234–236, 234*f*
system components, 232–233, 233*f*
ultrasonic oscillation, 229
Ultrasonically-assisted drilling (UAD), 532–534
amplitude, 373–379
force measurements, 373–379
recent developments from 2014, 368–373, 369–373*f*
Ultrasonically assisted extraction (UAE), 309–310, 702–708
antioxidants, 705–706, 706*t*
aromas, 704, 705*t*

Ultrasonically assisted extraction (UAE) *(Continued)*
bioactive compounds and industrial applications, 706, 707*t*
lipids, 704–705
natural flavoring compounds, 704, 708*t*, 715–716
oils, 704, 705*t*
power ultrasound to intensify extractions, 706–708
probe treatment, 702–703, 703*f*
process intensification, 702–703
proteins, 703–704
Ultrasonically assisted incremental forming, 295–298, 298*f*
Ultrasonically assisted material deformation, 258–261, 259–262*f*
Ultrasonically assisted turning (UAT)
composites, 364
control, 365–366
cutting forces and temperatures, 358–360, 360–361*f*
data
chip morphology, 352
coolants, 352–354, 356*f*
cutting forces, 354–357, 356–357*f*
DOC and feed rate, 352
elliptical vibration cutting, 357, 358–359*f*
surface quality, 352, 353*f*
tool wear, 352, 354*f*
turning speeds and machining practice, 352, 352*t*
mechanism of, 348–350, 349–351*f*
microstructure, 363, 363*f*
modeling—vibrations, tool stress, 365, 366*f*
process modeling, 364, 365*f*
surface roughness, 360–363, 362*f*
systems hardware, 350–351, 351*f*
tool wear, 363–364
ultrasonic cutting modes, 348, 349*f*
Ultrasonic aspirators, 619
Ultrasonic-assisted convective drier, 747–748
Ultrasonic-assisted Denver cell, 522, 523*f*
Ultrasonic-assisted flotation process
valuable mineral concentration, 519–525
developments in, 522–525, 522–523*f*
flotation process, 519–520, 520*f*
power ultrasound in flotation, 520–522, 521*f*
Ultrasonic-assisted gas metal arc (U-GMAW) process, 196–197
Ultrasonic-assisted liposuction (UAL) system, 540, 551
Ultrasonic assisted (UA) material tests, 255–256
Ultrasonic-assisted milling (UAM)
chip thickness, 383
forces, 382–383, 383*f*
modeling, 384–385, 385*f*
surface roughness, 383, 384*f*
tool wear, 383–384, 384*f*
Ultrasonic-assisted sedimentation rate
for water-solid separation efficiency, 525–526
developments in, 526–528, 526–528*f*
power ultrasound in sedimentation, 526
Ultrasonic atomization
capillary wave hypothesis, 774
disadvantages, 773–774
droplet size and distribution, 778–779, 779*f*
food applications of
extraction, 783–784, 784*f*
microbial inactivation, 785–786
nanofibers, 785, 785*f*
in food industry
encapsulation, 781–783
food hygiene, 786
frequency of irradiation, 780–781
fundamentals, 774–776
low ultrasonic power dissipation levels, 775–776
operating parameters on droplet size, effect of, 779–781
in pharmaceutical industry
aerosols for drug delivery, 786–788
encapsulation for drug delivery, 788–791, 788*f*, 790*f*
single-frequency operation, 775–776
surface tension, 780, 781*f*
measurements, 775
types, 773
ultrasonic atomizer design, 776–778
using multiple concentric nozzles, uniform double-walled microspheres, 778
Ultrasonic atomizer design, 776–778, 776–777*f*
Ultrasonic baths, 644–645
Ultrasonic beam, 56, 57*f*
Ultrasonic bonding, 173
Ultrasonic cavitation processing, 490–496
acoustic impedance
and attenuation factor, 491
under cavitation, 490, 491*f*
acoustic pressure, variation, 492, 493*f*
cavitation strength, 492
first cycle of oscillations, 493–494
gas cavitation bubble evolution in ethanol, 493–494, 495*f*
intensity or transmitted power, 490
power densities, 490
rule of thumb, 494–495
shape instability, 493–494
shielding and scattering effects, 491–492
sonotrodes, 490
steel horns, 490
tensile stress-induced disruptions in liquids, 492
Ultrasonic cavitation science
applications, 489–490
atomization, 489
history, 489–490
metallurgical application, 489
Ultrasonic cleaning, 23, 38–39, 47–48, 48*f*
and testing techniques, 531
Ultrasonic cleaning chemistry, 462–463
temperature, 462–463
Ultrasonic cleaning hardware, 456–457
factors driving development, 457
generators, 457
transducers, 456–457, 457*f*
Ultrasonic cleaning technology
advancements in, 465–468
applications, 455, 470–471
benefits of, 459
cavitation, 458–459, 458–459*f*
erosion or "burning", 468
chemistry, 462–463
temperature, 462–463
cleaning, 455, 459
cost, 470
damage mechanisms, 468
frequency application, 467–468, 468*t*
higher frequency, 470
history, 455–456
mechanical resonance, 468
mechanism of, 457–459
megasonics, 468–470, 468–469*f*
optimum ultrasonic performance, 463–464
passivation, 455
performance evaluation, 464
performance measures, 464–465
new technology, 465
process variables
dissolved gas and the diffusion rate of dissolved gas, 460–461
size and number of cavitation voids, 460
surface tension, 460
temperature and chemistry on liquid properties, 460
ultrasonic frequency, 462
ultrasonic power, 461, 462*f*
vapor pressure, 461, 461*f*
viscosity, 460
ultrasonic cleaning hardware, 456–457
ultrasonic generators, 465–468, 466–467*f*
ultrasonic transducers, 465
Ultrasonic cold forging technology (UCFT), 307, 307*f*
Ultrasonic consolidation (UC), 229–231
Ultrasonic cutting
additive manufacturing (AM), 630–631
for bone cutting, 620
clinical procedure, 629, 630*f*
curve-fitted FRF data, 626, 626*f*
factors affecting device performance
Duffing-like behavior and autoparametric vibrations, 624
multiple-mode devices, 623–624, 623*f*
nonlinear and undesirable behavior, 624–625, 624*f*
flextensional transducers, 631–632, 631–632*f*
harmonic characterization, 626–628, 627–628*f*
maxillofacial procedures, 629, 630*f*
of mineralized tissue, 621–623, 623*f*
modal analysis, 625–626
modes, 348, 349*f*
origins of, 617–618
orthodontic procedures, 629, 630*f*
orthopedic procedures, 629, 630*f*
selective cutting, 628
soft tissue
blade-tissue interaction, 621
debris removal, 621

dissection, 618–620
mechanisms, 620–621
transducer design, 630
transduction materials, 629–630
Ultrasonic debubbling, 689–690
acoustic pressure, 692
acoustic streaming, 691
airborne power ultrasonic generators, 693–694
airborne ultrasonic vibration, 690
bottling and canning lines, 695
in coating layers, 695–697
defoamers, 692–695
drawbacks, 688
experimental setup, 692, 693*f*
foam control methods, 689
Hartman whistle, 689–690, 694*f*
high-frequency rotary siren, 689
mechanisms of, 691–692
radiation pressure, 691
"squeezing" mode waves, 691
Ultrasonic deep drawing, 288–290, 290–291*f*, 292, 294*f*
Ultrasonic defect intensity, 254–255
Ultrasonic defoamers, 692–695, 693–694*f*
Ultrasonic defoaming system (UDS), 689–690
acoustic pressure, 692
acoustic streaming, 691
airborne power ultrasonic generators, 693–694
airborne ultrasonic vibration, 690
bottling and canning lines, 695
in coating layers, 695–697
defoamers, 692–695
drawbacks, 688
experimental setup, 692, 693*f*
foam control methods, 689
Hartman whistle, 689–690, 694*f*
high-frequency rotary siren, 689
mechanisms of, 691–692
radiation pressure, 691
"squeezing" mode waves, 691
Ultrasonic deformation, 249–251, 254, 257*f*
Ultrasonic degassing of liquids
advantages, 473
alloy composition, 480–481
cavitation, 475–477
degassing nuclei, 475–477
energy, 477
industrial implementation, 481–486, 482*t*, 482–483*f*
insoluble inclusions, 480
kinetics of hydrogen removal, 473–474, 474*f*
materials production, 473
mechanisms, 474–475
in melts, 477–479, 484*f*
melt temperature, 480, 480*t*
quasiequilibrium concentration, 475
scheme with flat sonotrode, 483, 485*f*
treatment time and volume, 481
ultrasonic energy, 479–480
vapor-gas bubbles, 476
Weissler reaction, 473–474
Ultrasonic de-gating, 218–219
Ultrasonic drying for food preservation
airborne applications, 753–754*t*, 755–761, 755–759*f*, 756*t*
direct-contact applications, 751–755, 754–755*f*
dried samples, size, 767
enzymes, 767
fiber, 767
inner structure, 766
lemon peel drying, 762–763, 763*f*
material structure, 763
mechanical stress, 764
phenolic compounds, 767
product properties, 761–764, 762–763*f*
on product quality, 766–767, 766*f*
product surface, structural alterations, 765–766, 765*f*
structural changes, 764–766, 764*f*
in transport phenomena
convective transport, 744–745
diffusion transport, 745
heat transport, 745–746
vitamins, 767
Ultrasonic extrusion
distribution of PEEQ, 310, 310*f*
experimental system, 308–309, 309*f*
vibration extrusion system, 309, 309*f*
Ultrasonic fatigue, 252
Ultrasonic force microscopy (UFM), 268–270, 270*f*
Ultrasonic forging and extrusion, 308–311
developments—2000 onward, 305–308, 305–306*f*, 308*f*
early developments, 303–305, 303–304*f*
Ultrasonic-forming test, 292
Ultrasonic frequency, 167, 462
Ultrasonic friction lubrication, 265–266
Ultrasonic friction reduction, 264, 266*f*
Ultrasonic generators, 465–468, 466–467*f*
Ultrasonic granule medium forming (UGMF), 293, 296*f*
Ultrasonic grinding, 385–398, 386–388*f*
chips, 395–397, 396–398*f*
forces, 388–389, 389–392*f*
hybrid processes, 397–398, 398–399*f*
surface roughness, 389–395, 392–396*f*
temperatures, 388–389, 389–392*f*
vibration, 388–389, 389–392*f*
wear, 388–389, 389–392*f*
Ultrasonic horns, 91, 91*f*, 211, 215, 258–259
Ultrasonic joint design, 215–216
Ultrasonic machining
drilling, 344–347, 346*f*, 366–379, 367–369*f*
grinding, 385–398, 386–388*f*
honing, 399–402, 401*f*
lapping, 398
machining/forming, 347
milling, 343–344, 346*f*, 379–385, 379–382*f*
power ultrasonic vibrations, 341, 342*f*
reaming, 343, 399, 400*f*
surface grinding, 341–343, 342–343*f*
tapping, 402–404, 402–403*f*
turning, 343, 344–345*f*, 347–366
Ultrasonic melt processing
of aluminum alloys, 490
deagglomeration and dispersion, of nucleating particles, 501
emulsification (immiscible alloys), 501–502, 502*f*
in solidification and casting, 502–505
structure refinement, 496–501
Ultrasonic metal forming, 277, 278*f*
compaction, 322–325
deep drawing and bending, 287–300
forging and extrusion, 300–311
macroscopic behavior, 248–261
microforming, 325–330
microstructure effects, 243–247
other forming processes, 330–332
physical effects of vibrations, 243
shearing and blanking, 312–313
surface treatment, surface rolling, 315–322
ultrasonic rolling, 314–315
wire and tube drawing, 277–287
Ultrasonic metal welding, 165–166, 166*f*
advantages and disadvantages, 190–192
equipment, 169–171, 170–171*f*
longitudinal vibration wavelength, 176–178
materials, 168
mechanics and metallurgy, 171–180
metallography, 172, 172*f*
monitoring and control, 180–182
monometal, 173–175
part geometry, 169
power, energy, and time, 168, 168*f*
static force, 167
tooling, 169
ultrasonic frequency, 167
ultrasonic vibrations, 163
vibration amplitude, 167
welding heat generation, 172–173
Ultrasonic microbonding, 186, 186*f*
Ultrasonic microforging technology (UMFT), 308, 308*f*
Ultrasonic motors, 76, 151–152
actuators, 413
angular vibration velocity, 425
dynamic preload, 423–424
four-phase driver circuit, 427, 428*f*
high torque/thrust, 413
hybrid transducer ultrasonic motors, 417–425
on Moon, 531, 532*f*
performance of ultrasonic motors and driver circuits, 425–428
position holding, 413
static preload, 421–424
traveling-wave ultrasonic motors, 413–416
two-phase driver circuit, 427, 427*f*
Ultrasonic nondestructive analysis, 180–181, 181*f*
Ultrasonic-percussive technique, 532–534
Ultrasonic plastic deformation, 255
Ultrasonic plastic welding
energy director, 205–206, 211, 214–215
far-field ultrasonic welding, 214–215, 214*f*
general design considerations, 215
joint and part design, 215–216
near-field ultrasonic welding, 214–215, 214*f*

Ultrasonic power, 461, 462–463*f*, 463–464
Ultrasonic probe, 206
Ultrasonic-range finders, 1
Ultrasonic rolling, 251
Ultrasonics, 271
  cleaning, 3
  energy, 2
  imaging, 1
  metal welding, 3
  nondestructive testing, 1
Ultrasonic scalers
  clinical evaluation, 564–565
  clinical trials, 564
  mechanical action, 558–560, 559*f*
  randomized clinical trials, 564
Ultrasonic seam
  welder, 169, 170*f*
  welding, 163
Ultrasonic stack, 220–221, 220–221*f*
Ultrasonic surface rolling (USR), 316–322, 319–322*f*
Ultrasonic surface rolling process (USRP), 316
Ultrasonic thermoplastic weldability, 222–224
Ultrasonic torsion welder, 169–171, 171*f*
Ultrasonic transducers, 69, 83, 89, 91, 113, 163–164, 164*f*, 330–332, 332*f*, 465
  cup-shaped, 104, 105*f*
  power, 109, 112–113, 118, 129
  sandwich construction, 83
  system, 95–96
Ultrasonic vibrations, 83–87, 163, 176, 205, 210, 217, 222, 243–244, 250, 341, 342*f*, 373, 377*f*
  longitudinal vibrations, 87–91
  mechanical oscillator, 84–87
  velocity, 262–263
  wavelengths, 169
Ultrasonic wedge bonding, 187–188, 188*f*
Ultrasonic welding (USW), 201, 229. *See also* Ultrasonic metal welding; Ultrasonic plastic welding
  amorphous and semi-crystalline thermoplastics, 205
  applications, 182–190
  diffusion, 212–214
  equipments, 219–222
  shear joints, 216
  viscoelastic heating of polymers, 208–210, 209*f*
  wave propagation in polymers, 210–212, 211–213*f*
Ultrasonic weld metallography, 172, 172*f*
  contact surfaces, 171, 172*f*
  temperatures, 171, 173, 174*f*
Ultrasonic wire, 277–279, 279*f*
  Al 1100 tubing, 283
  antifriction, 285, 286*f*
  die-drum spacing, 280, 281*f*
  drawing stress variation, 285, 287*f*
  forming processes, 277, 278*f*
  magnetostrictive transducers, 280
  process arrangements, 282–283, 284*f*
  radially vibrated ultrasonic tube, 283, 285*f*
  1970s and 1980s, 280–282, 282–283*f*
  skew-type vibration system, 285–287
  step-by-step design procedures, 285–287
  stress antinode, 279–280
  stress contour, 285, 287*f*
  theoretical analysis, 283, 286*f*
  tube drawing, 280, 281*f*
  vibration damping block, 277–280
  wiredrawing, 279, 279*f*
Ultrasonic wirebonder, 186–187, 187*f*
Ultrasound
  acoustic power, 133
  acoustic pressure, 133–134
  applications, 132
  applicators, 577
  chemical effects of, 887–889
  conditioning (UC), 523
  conditioning and flotation (FCU), 523
  flotation (UF), 523
  intensities, 133–134
  irradiation, 900
  molecular effects of, 890–891
    chemical changes, 890–891
    physical changes, 890
    stress-induced changes, 891
  reaction parameters, 888, 889*t*
  requirements, 131
Ultrasound-aided biodegradation, solid untanned leather waste, 896
Ultrasound-assisted air loop reactor, 646, 655*f*
Ultrasound-assisted bioremediation
  as biocatalysts in, 895–897
  effect of ultrasound, 895
Ultrasound bath with cavitation, 646, 654*f*
Ultrasound cutting/coagulating systems, 540
Ultrasound flotation testing, 523, 528
Ultrasound-generated shear stress, 580
Ultrasound-mediated blood–brain barrier (BBB) permeability, 581
Ultrasound standing waves (USSWs), 897
Ultrasound wave propagation, 577, 578*f*
Ultrasubharmonic resonances, 29
Ultra Turrax emulsification, 679–681
Ultrawaves ultrasound equipment, 825
Unbounded media
  boundary element method (BEM), 154–155
  Dirichlet-to-Neumann (DtN) method, 155
  exact conditions, 153–154
  stepped-plate airborne transducer, 157, 157–158*f*
Undamped oscillator, 84–85, 85*f*
Underground mining
  characteristics, 511
  extraction process, 509
  rock stress tensors, 509–510
Underpinning science, 131, 134
U-PAW process, 195, 195*f*
Ureteroscopy (URS), 602
US-assisted Heck coupling reaction in water, 836
U.S. Bureau of Naval Weapons, 249
U.S. Navy-sponsored research, 249, 277
Uterine arterial embolization (UAE), 589–590
Uterine fibroid ablation with focused ultrasound (FUS), 590

V

Vapor pressure, 461, 461*f*
Vat photopolymerization (VPP), 229
Vertical machining center (VMC), 376, 378
Vertical ultrasonically assisted extraction (V-UAE), 309–310, 310*f*
Very high-power ultrasonic additive manufacturing (VHP-UAM), 232
Vibrating glass rod, 617
Vibration
  acoustic radiation, 157
  amplitudes, 150–151
Vibrational resonance, 219–220
Vibration amplitude, 93, 165, 167, 210, 215
  on cutting forces, 350
Vibration assisted machining, 350
Vibration-assisted tapping system, 402, 402*f*
Vibration behavior, 165
Vibration velocity, 116, 116–118*f*
Vibrometry, 132–133
Viscoelastic attenuation, 211
Viscoelastic heating, 208
  of polymers, 208–210, 209*f*
Viscosity, 26, 61, 460
Viscosity modification, 710–711, 711*f*
Visible and near-infrared imaging spectrometer (VNIS), 531, 532*f*
Voigt-Kelvin model, 209, 214–215
Volatile solids (VS) degradation, 824, 824*f*
Volkov's device, 618
von Misis stresses, 350, 350*f*
Vorticity modes, 7–9, 9*f*, 16–17

W

Waste-activated sludge (WAS), 825–826
  dewaterability of, 900
  in lab batch reactor, 820
Wastewater treatment plants (WWTPs)
  aerobic biological processes, 828–829
  anaerobic digestion processes
    enhanced volatile solids (VS) degradation, 824, 824*f*
    full-scale application, 823–827, 823*t*
    low-frequency power ultrasound, 824
  application, 817, 818*f*
  bacterial cell inactivation, 818–820
  Ballast water treatment, 831
  on biological suspensions
    activated sludge biomass, 820–821, 821–822*f*
    bacterial biomass disintegration, 817–820, 819*f*
    pure bacterial cultures, 821–823
    sonication of bacterial biomass, 820
  cell break-up, 818
  cell disintegration, 820, 820*f*
  development and design, full-scale ultrasound reactor, 829–830, 829*t*
  mechanical shear forces (transient cavitation), 829
  sonication on dissolved organic phase (SCOD), 818, 819*f*
  sonication on particle size distribution (PSD), 817–820, 819*f*

Water convective transport, 744
Water-insoluble metal halides synthesis, 441–442
Water-mediated organic synthesis (WMOS), 833–834
Water-soluble metal halides synthesis, 442
Water treatment
  in hybrid processes, 808–811
  kinetic constant of sonochemical reaction, 804–805, 804*f*
  sonochemical devices and experimentation, 798–801
  sonochemical elimination, characteristics of, 801–804
  sonochemical treatment parameters, 805–808
  sonochemical yield and energy consumption, 805
  ultrasonic cavitation
    and advanced oxidative processes (AOPs), 797–798
Wave amplitude, 56
Wave-guiding system, 481
Wavenumber modulation, 53, 57–59
Wave propagation, 148–152
  in polymers, 210–212, 211–213*f*
Wave velocity, 58–59
Weber number (NWe), 105–106, 775
Wedge-reed ultrasonic welder, 165, 166*f*
Wedge-reed welding systems, 163, 167, 172, 187
Weighted residual method, 153
Welding force, 235
Welding processes, 191–192
Welding speed, 234
Weld power, 168, 168*f*
Weld-to-weld cycle, 191
Weld zone, 166*f*, 167–168, 171, 172*f*, 173, 176–178, 190
The Westervelt equation, 13–14, 17
Wet foams, 688
Wire and tube drawing
  early developments, 277–280, 278–279*f*, 281*f*
  1970s and 1980s, 280–282, 282–283*f*
  1990s onward, 282–287, 284–287*f*
Wire-based ultrasound devices, 542–543
Wirebonding in microelectronics, 186
Wire bonds, 187–190, 189*f*
Wire circle, 287
Wire drawing, 249–250, 254–255, 261–262, 283–285
Working Group 3 of IEC Technical Committee 87, 144

X

Xenon-doped phosphoric acid, 139

Y

Young's modulus, 215

Z

Zero nonlinear terms, 15–16